PHYSICAL REVIEW LETTERS

VOLUME 33 NUMBER 1

1 JULY 1974

THE AMERICAN PHYSICAL SOCIETY

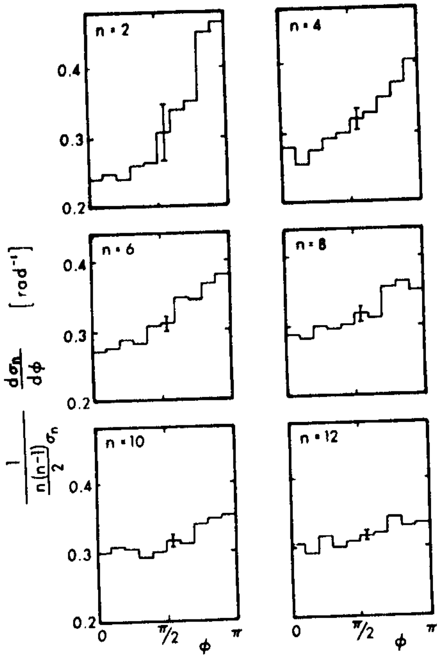

FIG. 1. Semi-inclusive azimuthal distributions for all charged-particle combinations.

dence of the azimuthal distributions on the particle's charge, transverse momentum, and rapidity is also studied.

The results are based on an unbiased inclusive data sample of ~3500 completely measured events obtained from an exposure of the 30-in. FNAL hydrogen bubble chamber to a 205-GeV/c proton beam. Further details of this experiment are given elsewhere.[3] For the analysis of two-particle distributions we make the following choice of kinematic variables: the magnitude of the transverse momentum of particle i, P_{iT}; its center-of-mass rapidity, y_i; and the azimuthal angle between the transverse momenta of particles i and j,[4]

$$\varphi_{ij}=\cos^{-1}\frac{\vec{P}_{iT}\cdot\vec{P}_{jT}}{P_{iT}P_{jT}}.$$

In this paper we analyze the azimuthal distributions

$$\frac{d\sigma_n}{d\varphi}=\sum_{i=1}^{n}\sum_{j<i}\frac{d\sigma_n}{d\varphi_{ij}}$$

and

$$d\sigma/d\varphi=\sum_n d\sigma_n/d\varphi,$$

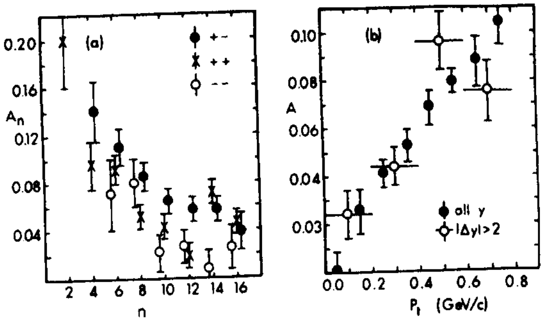

FIG. 2. (a) Asymmetry parameter A_n as defined in Eq. (1) as a function of charged-particle multiplicity n for different charge combinations. (b) Asymmetry A, integrated over all n, as a function of p_T for all y and for $|y_i - y_j| > 2$.

where n is the charged-particle multiplicity.

In Fig. 1 we show the semi-inclusive azimuthal distributions for all charged-particle combinations. It is observed that (a) the distributions are asymmetric and peak near 180° and (b) the asymmetry becomes less pronounced as the charged multiplicity increases. As will be discussed later, these trends may be understood in part as a consequence of transverse-momentum conservation. To parametrize the distributions, we define, for fixed n, the asymmetry parameter A_n:

$$A_n=\left(\int_{\pi/2}^{\pi}\frac{d\sigma_n}{d\varphi}d\varphi-\int_0^{\pi/2}\frac{d\sigma_n}{d\varphi}d\varphi\right)\left(\int_0^{\pi}\frac{d\sigma_n}{d\varphi}d\varphi\right)^{-1}. \quad (1)$$

Table I and Fig. 2(a) present A_n as a function of n for the different charge combinations. In general, for each n, the asymmetry for the (+ −) combination is larger than that for either the (− −) or (+ +) combination. This holds as well for the inclusive values listed in Table I.

There exist simple model calculations which predict a definite relation between the asymmetry A and the total number (n_T) of particles produced in the final state. For example, a statistical model[5] which incorporates only transverse-momentum conservation and a Gaussian distribution in transverse momentum predicts $A = 1/(n_T - 1)$. Applying this model to our measured asymmetry parameters for all charged particles,[6] A_n^{cc}, we give in Table I estimates of n_T for a given number of charged particles, n. We also list in Tabl I the values of n_T calculated using the experimentally observed average number of π^0, K^0, and Λ

PHYSICAL REVIEW LETTERS

Information for Contributors

(Revised January 1973)

Send manuscripts *in triplicate* to the Editors, Physical Review Letters, Brookhaven National Laboratory, Upton, New York 11973. For general format and style consult recent issues of this Journal and the American Institute of Physics *Style Manual*, 2nd ed. revised November 1970 (Pub. R-128.5, price $2.50). The total length of the paper may not exceed 3½ journal pages; see *Editorial* of 6 November 1972.

The manuscript, comprising all material which is to be set in type, must be in English, typewritten (except for mathematical expressions and Greek letters), double spaced (not more than three lines per inch) on good quality white, 8½ × 11 in. paper, using one side of the sheet only and leaving margins of at least 1 in. on all four sides. In lieu of an original typed copy, a clean, sharp, non-erasable, black on white reproduction on hard surfaced paper is acceptable. The manuscript should be carefully proofread by the author to eliminate grammatical errors, misspellings, and omission of symbols; proofs will *not* be sent. Every page, including title page if separate, must be numbered. The author should specify the index category or categories applicable to the paper.

The title should be concise but informative enough to facilitate information retrieval. Every paper must have an abstract of not more than 75 words which should be self-contained for reprinting in abstracting journals; it should indicate clearly to the prospective reader the nature of the information to be obtained from the Letter.

Mathematical expressions should be typed or neatly written in ink. The prime requisite is that the copy shall be clear to the reproduction typist, who is neither a physicist nor a mathematician. Unusual or ambiguous symbols should be identified by marginal notes the first time they appear and subsequently when confusion might arise. Identify unusual nonalphabetic symbols by their number in the listing on pages 23-25 of the *Style Manual*. If a symbol is not to be on the line of type and its position is not unmistakable, it should be marked with a caret above it for a subscript or with an inverted caret below it for a superscript. Note that boldface is *not available*. Three-vectors are set with an arrow above (mark the symbol with the arrow or with the standard black pencil wiggly underline); dyadics may be denoted with double-headed arrows above. More general quantities such as matrices, operators, etc., should not be distinguished from scalars typographically unless absolutely essential to avoid confusion; in such cases a typed straight underline can be used, indicated in manuscript by a straight *blue-penciled* underline (for capital Latin letters, sans serif type is also available).

Avoid complicated superscripts and subscripts. Avoid frequent repetition of a complicated mathematical expression by representing it by some convenient symbol. Use fractional exponents instead of the radical sign, *always* except for the square root of a single-symbol quantity. Use the solidus (/) or negative exponents *always in running text* and in displayed equations whenever clarity is not thereby reduced.

Equations should be punctuated and aligned to bring out their structure. When displayed equations are numbered, the numbers should be enclosed in parentheses and placed at the *right-hand* margin.

Editorial marking by authors (except for the resolution of ambiguities as discussed above) is rarely of sufficient value to warrant the effort. In any case it must be recognized that *Physical Review Letters* has a standard code used for all the Institute's journals and described on pages 11 and 15 of the *Style Manual*. *Departures from this code on the part of authors usually lead to confusion and possibly to* [illegible]

Separate tables, numbered in the order in which they are referred to in text, should be used for all but the simplest tabular material. Each table must have a caption, which should make the table intelligible without reference to the text. The structure of the table should be clear and simple. The column headings should give all units, and should be kept as simple as possible — in some cases by the use of symbols which are explained in the caption. It is preferable to type tables on sheets separate from the running text. Tables which may reasonably be expected to take up more than one-quarter of a journal page (exclusive of caption and footnotes) must be submitted in a form suitable for direct photographic reproduction.

Footnotes, including both references and comments, must be numbered consecutively in order of first citation, and should be given in a double-spaced list at the end of the text. Footnotes to a table must be designated by lower-case roman superscripts, and must be given at the end of the table; if a footnote to a table refers to a footnote referred to in the text before mention of the table, it should be given in the form "See Ref. 8." The asterisk, dagger, etc., are used only for footnotes to the title and by-line. For the proper form of references, see page 6 of the *Style Manual* or recent issues of this Journal.

Figures should be planned for the 3-in. column width of the journal; in some cases, where the figures contain a great deal of detail, 1½ or 2 columns may be used. Figures should be planned for reduction accordingly. In particular, the lettering and plotted points should be large and clear enough to be legible after reduction (the final size of letters should be no less than 2 mm). Also the weight of the line should be suitable for the character size. Plan figures to use space efficiently; avoid waste space, especially at top or bottom.

Every figure *must* be referred to in the text, and the figures are to be numbered in the order in which they are mentioned. Every figure *must* have a caption; the list of captions must be typed (double spaced) and included with the manuscript — not as part of the figure. All but the simplest explanatory material should be made part of the caption, and information given in the caption should not be repeated in the figure. A group of figures that is closely related may share a common caption and be labeled and referred to as "Fig. 1(a)," "Fig. 1(b)," etc.; such a group must be submitted as a single piece. Footnotes referred to in a figure caption are to be cited either as a parenthetic insertion, "(see Ref. 8)," or in the form "Smith, Doe, and Jones, Ref. 8."

The figure itself should have properly labeled axes with correctly abbreviated units (see *Style Manual*, pages 8-10). Use the form "R (10^{-6} Ω)" or "$10^6 R$ (Ω)," not "$R \times 10^6$ Ω." In any case where confusion is possible, identify the top edge of the figure.

The reproduction of figures is a two-stage, black-and-white photographic process, and maximum black-and-white contrast and optimum definition in the copies supplied is essential. Original india ink drawings or good photoprints (preferably glossy) are required. Since the intermediate stage is 25% oversize, it is preferable that the copy be at least that size, but grossly oversize originals should be photographically reduced before submittal. Photographs of equipment and intricately shaded drawings should be avoided, as they will generally convey less information than a well-planned schematic diagram. For more detailed information, consult the *Style Manual*, pages 26-30.

Identify each drawing or photograph on the back with the names of the authors (or the first author plus "et al."), the journal, and the figure number.

PHYSICAL REVIEW
LETTERS

Contents

VOLUME 33, NUMBER 1 1 JULY 1974

Atoms, Molecules, and Related Topics

End-Point Energy Variations in the Noncharacteristic Radiation Produced by S, Cl, Ar, K, Ca, and Ti Bombardment of Si . . . . G. Bissinger and L. C. Feldman 1
New Method for Lamb-Shift Measurements . . . . A. van Wijngaarden, G. W. F. Drake, and P. S. Farago 4
Efficient Positronium Formation by Slow Positrons Incident on Solid Targets . . . . K. F. Canter, A. P. Mills, Jr., and S. Berko 7

Atoms, Nuclei, and Particles in Matter

Raman Scattering from Coherent Spin States in n-Type CdS . . . . R. Romestain, S. Geschwind, G. E. Devlin, and P. A. Wolff 10

Plasmas, Fluids, Thermodynamics, and Related Topics

Molecular Theory of Orientational Fluctuations and Optical Kerr Effect in the Isotropic Phase of a Liquid Crystal . . . . C. Flytzanis and Y. R. Shen 14
Longitudinal Spin Relaxation in ^{3}He Gas at 4.2 K . . . . R. Chapman and M. G. Richards 18
New Universal Quantity for the He^4 Superfluid Transition . . . . M. Ferer 21
$1/f$ Noise from Thermal Fluctuations in Metal Films . . . . John Clarke and Richard F. Voss 24

Solids

Electron-Magnon Bound States . . . . Mukesh Eswaran and J. C. Kimball 27

Nuclei

Failure of the Allowed Assumption in the ϵ/β^+ Decays of ^{145g}Gd and ^{143g}Sm—Experimental Evidence for Interference Effects in Nuclear β Decay . . . . R. B. Firestone, R. A. Warner, Wm. C. McHarris, and W. H. Kelly 30

Elementary Particles and Fields

Measurement of the Positron-Electron Ratio in the Primary Cosmic Rays from 5 to 50 GeV . . . . A. Buffington, C. D. Orth, and G. F. Smoot 34
Solving Equations of the Gell-Mann–Low and Callan-Symanzik Type . . . . B. F. L. Ward 37

(continued on page ii)

PHYSICAL REVIEW LETTERS

Contents

VOLUME 33, NUMBER 1 1 JULY 1974

Atoms, Molecules, and Related Topics

End-Point Energy Variations in the Noncharacteristic Radiation Produced by S, Cl, Ar, K, Ca, and Ti Bombardment of Si . . . G. Bissinger and L. C. Feldman 1
New Method for Lamb-Shift Measurements . . . A. van Wijngaarden, G. W. F. Drake, and P. S. Farago 4
Efficient Positronium Formation by Slow Positrons Incident on Solid Targets . . . K. F. Canter, A. P. Mills, Jr., and S. Berko 7

Atoms, Nuclei, and Particles in Matter

Raman Scattering from Coherent Spin States in n-Type CdS . . . R. Romestain, S. Geschwind, G. E. Devlin, and P. A. Wolff 10

Plasmas, Fluids, Thermodynamics, and Related Topics

Molecular Theory of Orientational Fluctuations and Optical Kerr Effect in the Isotropic Phase of a Liquid Crystal . . . C. Flytzanis and Y. R. Shen 14
Longitudinal Spin Relaxation in ^{3}He Gas at 4.2 K . . . R. Chapman and M. G. Richards 18
New Universal Quantity for the He^4 Superfluid Transition . . . M. Ferer 21
$1/f$ Noise from Thermal Fluctuations in Metal Films . . . John Clarke and Richard F. Voss 24

Solids

Electron-Magnon Bound States . . . Mukesh Eswaran and J. C. Kimball 27

Nuclei

Failure of the Allowed Assumption in the ϵ/β^+ Decays of ^{145g}Gd and ^{143g}Sm—Experimental Evidence for Interference Effects in Nuclear β Decay . . . R. B. Firestone, R. A. Warner, Wm. C. McHarris, and W. H. Kelly 30

Elementary Particles and Fields

Measurement of the Positron-Electron Ratio in the Primary Cosmic Rays from 5 to 50 GeV . . . A. Buffington, C. D. Orth, and G. F. Smoot 34
Solving Equations of the Gell-Mann–Low and Callan-Symanzik Type . . . B. F. L. Ward 37

(continued on page ii)

PHYSICAL REVIEW LETTERS

(continued)

New Experimental Limit on T Invariance in Polarized-Neutron β Decay . . . . R. I. Steinberg, P. Liaud, B. Vignon, and V. W. Hughes 41
Hadron-Neutron Forward Elastic Scattering Amplitude and Hadron-Deuteron Collisions . . . . Victor Franco and Girish K. Varma 44
A Picture of Multiple-Meson Production . . . . Alfred S. Goldhaber 47

Errata

Photoelastic Tensor of Silicon and the Volume Dependence of the Average Gap. . . . . David K. Biegelsen 51

PHYSICAL REVIEW
LETTERS

Contents

VOLUME 33, NUMBER 2 8 JULY 1974

Atoms, Molecules, and Related Topics

Determination of the Singlet-Triplet Separation of H_2 by a "Level-Anticrossing" Technique . . . . R. Jost and M. Lombardi 53
Two-Center Thomas-Fermi Model for Adiabatic Ion-Atom Collisions . . . . J. Eichler and U. Wille 56
Mechanisms for Electron Production in 30-MeV $O^{n+}+O_2$ Collisions . . . . N. Stolterfoht, D. Schneider, D. Burch, H. Wieman, and J. S. Risley 59
Collision-Induced Optical Double Resonance . . . . Richard G. Brewer, R. L. Shoemaker, and S. Stenholm 63

Plasmas, Fluids, Thermodynamics, and Related Topics

Light Scattering from Orientational Fluctuations in a Cholesteric Liquid Crystal. Angular and Field Dependences of the Light-Beating Spectrum . . . . Donald B. DuPré and Russell W. Duke 67
Experimental, Very High-Temperature, Liquid-Uranium Equation of State . . . . G. R. Gathers, J. W. Shaner, and D. A. Young 70
Probability Distribution for Fourier Components of the Electric Field in Weak Plasma Turbulence . . . . T. M. O'Neil 73
Spatially Resolved Measurement of Impurities and the Effective Charge Z in a Tokamak Plasma . . . . D. E. Evans and M. L. Yeoman 76
Ion Heating at Twice the Ion-Cyclotron Frequency in Reactor-Oriented Machines . . . . R. R. Weynants 78

Solids

Absence of Surface States in Cu . . . . R. V. Kasowski 83
Strong $4f$ Resonance Effects in Rare-Earth Appearance-Potential Spectra . . . . W. E. Harte, P. S. Szczepanek, and A. J. Leyendecker 86
New Interpretation of Photoemission Measurements of Trigonal Se and Te . . . . M. Schlüter, J. D. Joannopoulos, and Marvin L. Cohen 89
Localized Enhancement Effects in Pd-Ag Alloys . . . . A. P. Murani 91
Electronic Structure of the Tetracyanoquinodimethane (TCNQ) Molecule . . . . . Frank Herman and I. P. Batra 94
Time-Reversed Antiferromagnetic States in Dysprosium Aluminum Garnet . . . . J. F. Dillon, Jr., E. Yi Chen, N. Giordano, and W. P. Wolf 98

Nuclei

Systematic Pseudomagnetic Measurements of the Spin-Dependent Scattering Length of Slow Neutrons with Atomic Nuclei . . . . P. Roubeau, A. Abragam, G. L. Bacchella, H. Glättli, A. Malinovski, P. Meriel, J. Piesvaux, and M. Pinot 102

(continued on page ii)

PHYSICAL REVIEW
LETTERS

Contents (continued)

Negative-Parity Band in ^{48}V . . . . B. Haas and P. Taras 105

Elementary Particles and Fields

$\Delta I = \frac{1}{2}$ Rule for Nonleptonic Decays in Asymptotically Free Field Theories . . . . M. K. Gaillard and Benjamin W. Lee 108
Observation of Large-Transverse-Momentum Muons Directly Produced by 300-GeV Protons . . . . J. P. Boymond, R. Mermod, P. A. Piroué, R. L. Sumner, J. W. Cronin, H. J. Frisch, and M. J. Shochet 112
Anomalous Muon and Hadron Charge Ratios in Secondary Cosmic Rays. . . . . Robert K. Adair 115
Energy Dependence of the Double-Charge-Exchange Reactions $\pi^- p \rightarrow K^+\Sigma^-$, $K^- p \rightarrow \pi^+\Sigma^-$, and $K^- p \rightarrow K^+\Xi^-$ . . . . C. W. Akerlof, P. K. Caldwell, J. Koschik, P. Kotthaus, D. I. Meyer, and B. Springett 119

Errata

New Measurement of the Σ^- Magnetic Moment . . . . B. L. Roberts, C. R. Cox, M. Eckhause, J. R. Kane, R. E. Welsh, D. A. Jenkins, W. C. Lam, P. D. Barnes, R. A. Eisenstein, J. Miller, R. B. Sutton, A. R. Kunselman, R. J. Powers, and J. D. Fox 122

PHYSICAL REVIEW
LETTERS

Contents

VOLUME 33, NUMBER 3 15 JULY 1974

Atoms, Molecules, and Related Topics

Quantum-Defect Theory of Excited $^1\Pi_u^-$ Levels of H_2 . . . . O. Atabek, Dan Dill, and Ch. Jungen 123
Intensity Variations of K^--Mesonic X Rays . . . . G. T. Condo 126
Resonant Enhancement of Two-Photon Absorption in Sodium Vapor . . . . J. E. Bjorkholm and P. F. Liao 128
Advantages of a Nonharmonic-Oscillator Analysis of Molecular Vibrations . . . . Gary Simons and J. Michael Finlan 131
Electron Impact near the $a\,^3\Pi$ State of CO: Dipole-Dominated Resonances . . . . . . S. F. Wong and G. J. Schulz 134
Variational Bounds on the $1s$-Charge-Exchange Amplitude in Proton-Hydrogen-Atom Scattering . . . . David Storm and Donald Rapp 137

Plasmas, Fluids, Thermodynamics, and Related Topics

Homogeneous Nucleation in a Critical Binary Fluid Mixture . . . . . John S. Huang, S. Vernon, and N. C. Wong 140
Velocity of Fourth Sound . . . . M. Revzen, B. Shapiro, C. G. Kuper, and J. Rudnick 143
Experiments on Dynamic Parallel Magnetism in Superfluid ^{3}He . . . . R. A. Webb, R. L. Kleinberg, and J. C. Wheatley 145
Coupled Nonlinear Electron-Plasma and Ion-Acoustic Waves . . . . Kyoji Nishikawa, H. Hojo, K. Mima, and H. Ikezi 148

Solids

Presence of an Incipient Wigner Electron Lattice in Solid-State Electron Gases . . . . P. M. Platzman and P. Eisenberger 152
Dislocation-Dragging Effects in Quenched and Electron-Irradiated Copper . . . . H. M. Simpson and S. J. Kerkhoff 155
Effect of Structure in the Electronic Density of States on the Temperature Dependence of the Electrical Resistivity . . . . F. Y. Fradin 158
Spectroscopically Observed Valence Mixing in SmS and Related Compounds . . . . J. L. Freeouf, D. E. Eastman, W. D. Grobman, F. Holtzberg, and J. B. Torrance 161
Valence Mixing and Semiconductor-Metal Transition in the Sm Monochalcogenides . . . . M. Campagna, E. Bucher, G. K. Wertheim, and L. D. Longinotti 165

(continued on page ii)

PHYSICAL REVIEW LETTERS

Contents (continued)

Atomic Ordering and Superconductivity in High-T_c A-15 Compounds . . . . A. R. Sweedler, D. G. Schweitzer, and G. W. Webb 168
Magnetic Interference Function of Amorphous Cobalt-Phosphorus Alloys . . . . J. Bletry and J. F. Sadoc 172

Elementary Particles and Fields

$|g_A/g_V|$ in the Decay $\Sigma^- \rightarrow n e^- \bar{\nu}$ . . . . W. Tanenbaum, V. Hungerbuehler, R. Majka, J. Marx, P. Némethy, J. Sandweiss, W. Willis, M. Atac, S. Ecklund, P. J. Gollon, J. Lach, J. MacLachlan, A. Roberts, R. Stefanski, D. Theriot, and C. L. Wang 175
Neutral-Current Limit and Future Prospect at a Fission Reactor . . . . H. S. Gurr, F. Reines, and H. W. Sobel 179

Errata

New Developments in the Application of Hyperspherical Coordinates to Atomic Wave Functions . . . . Dwayne L. Knirk 182

PHYSICAL REVIEW
LETTERS

Contents

OLUME 33, NUMBER 4 22 JULY 1974

nnouncement

omments on Letters 183

toms, Molecules, and Related Topics

easurements of Fine Structures in Excited States of ^{4}He$^+$ by Fast-Beam Radio-Frequency Resonance .... S. Churassy, M. L. Gaillard, and J. D. Silver 185

lastic and Inelastic Electron Scattering at 20 and 60 eV from Atomic Cu .... W. Williams and S. Trajmar 187

bservation of Stimulated Anti-Stokes Raman Scattering in Inverted Atomic Iodine .... R. L. Carman and W. H. Lowdermilk 190

alcium Double K-Shell Ionization Produced from 24.0- to 48.0-MeV Oxygen Bombardment .... David K. Olsen and C. Fred Moore 194

toms, Nuclei, and Particles in Matter

opulation of Excited Electronic Levels by Beta Decay, and Its Influence on Mössbauer Source Spectra .... L. L. Hirst, J. Stöhr, G. K. Shenoy, and G. M. Kalvius 198

asmas, Fluids, Thermodynamics, and Related Topics

apped-Particle Stabilization of Localized Interchange Modes in Axisymmetric Toroidal Plasmas .... J. W. Connor and R. J. Hastie 202

lation Stability of Laser-Driven Implosions .... D. B. Henderson, R. L. McCrory, and R. L. Morse 205

lf-Modulation and Self-Focusing of Electromagnetic Waves in Plasmas .... Claire Ellen Max, Jonathan Arons, and A. Bruce Langdon 209

lids

asiparticle Lifetimes and Microwave Response in Nonequilibrium Superconductors .... A. Rothwarf, G. A. Sai-Halasz, and D. N. Langenberg 212

fects of Dynamic External Pair Breaking in Superconducting Films .... G. A. Sai-Halasz, C. C. Chi, A. Denenstein, and D. N. Langenberg 215

quid-Gas Phase Diagram of an Electron-Hole Fluid .... Gordon A. Thomas, T. M. Rice, and J. C. Hensel 219

R Observation of Close Frenkel Pairs in Irradiated ZnSe .... G. D. Watkins 223

clei

dy of the Reaction ^{54}Fe$(p,n)^{54}$Co to the Antianalog State .... H. W. Fielding, L. D. Rickertsen, P. D. Kunz, D. A. Lind, and C. D. Zafiratos 226

(continued on page ii)

PHYSICAL REVIEW
LETTERS

Contents (continued)

Isospin-Forbidden Proton Partial Width in ^{41}Sc and Similar $A=4n+1$ Nuclei . . . . T. A. Trainor, T. B. Clegg, and W. J. Thompson 229
Discovery of the Missing Two-Particle, Two-Hole 0^+ States in ^{40}Ca . . . . Kamal K. Seth, A. Saha, W. Benenson, W. A. Lanford, H. Nann, and B. H. Wildenthal 233

Elementary Particles and Fields

Measurement of the Polarization Parameter for the Reaction $\pi^- p \rightarrow \pi^0 n$ between 1.03 and 1.79 GeV/c . . . . S. R. Shannon, L. Anderson, A. Bridgewater, R. Chaffee, O. Chamberlain, O. Dahl, R. Fuzesy, W. Gorn, J. Jaros, R. Johnson, R. Kenney, J. Nelson, G. O'Keefe, W. Oliver, D. Pollard, M. Pripstein, P. Robrish, G. Shapiro, H. Steiner, and M. Wahlig 237
Measurement of the Branching Ratio $\Gamma(K_L{}^0 \rightarrow \pi^\pm \mu^\mp \nu)/\Gamma(K_L{}^0 \rightarrow \pi^\pm e^\mp \nu)$ . . . . H. H. Williams, R. C. Larsen, L. B. Leipuner, W. W. Sapp, A. L. Sessoms, L. W. Smith, R. K. Adair, and R. Turner 240
Asymptotic Behavior of Non-Abelian Gauge Theories to Two-Loop Order. . . . . William E. Caswell 244
Is the Cross Section for $e^+e^- \rightarrow$ Hadrons Time Dependent in Colliding Beam Machines? . . . . T. Goldman and Patrizio Vinciarelli 246

Errata

New Parameters for Δ^{++} Resonances from 2170 to 3490 MeV in $\pi^+ p$ Backward Elastic Scattering. . . . . C. A. Rey, A. J. Lennox, J. Poirier, and K. P. Pretzl 250
Solving Equations of the Gell-Mann–Low and Callan-Symanzik Type . . . . B. F. L. Ward 251
Hadron-Neutron Forward Elastic Scattering Amplitude and Hadron-Deuteron Collisions . . . . Victor Franco and Girish K. Varma 251

PHYSICAL REVIEW LETTERS

Contents

VOLUME 33, NUMBER 5 29 JULY 1974

Atoms, Molecules, and Related Topics

Measurement of the Initial Population and Decay Rate of the $(\mu^4\mathrm{He})_{2s}^+$ System in a Helium Target at 50 atm . . . . A. Bertin, G. Carboni, G. Gorini, O. Pitzurra, E. Polacco, G. Torelli, A. Vitale, and E. Zavattini 253
New Rotational Transition in the Hydrogen Molecule . . . . P. W. Gibbs, C. G. Gray, J. L. Hunt, S. Paddi Reddy, R. H. Tipping, and K. S. Chang 256
Multiphoton Ionization of Highly Excited Hydrogen Atoms . . . . J. E. Bayfield and P. M. Koch 258
Inelastic Resonance Emission of X Rays: Anomalous Scattering Associated with Anomalous Dispersion . . . . Cullie J. Sparks, Jr. 262
α Continuous Spectra Following *K* and *L* Autoionization During α Decay of ^{210}Po . . . . J. P. Briand, P. Chevallier, A. Johnson, J. P. Rozet, M. Tavernier, and A. Touati 266
Isotopically Selective Photochemistry of Bromine . . . . Stephen R. Leone and C. Bradley Moore 269

Atoms, Nuclei, and Particles in Matter

Effects of Degeneracy on Self-Induced Transparency . . . . . . G. J. Salamo, H. M. Gibbs, and G. G. Churchill 273

Plasmas, Fluids, Thermodynamics, and Related Topics

Long-Time Behavior of the Velocity Autocorrelation Function for a Fluid of Soft Repulsive Particles . . . . D. Levesque and W. T. Ashurst 277
Photographs of Quantized Vortex Lines in Rotating He II . . . . Gary A. Williams and Richard E. Packard 280
Mass-Fluctuation Waves in Solid ^{3}He-^{4}He Mixtures . . . . Whittak Huang, H. A. Goldberg, M. T. Takemori, and R. A. Guyer 283
Beam-Plasma Instability in a Nonuniform Plasma . . . . George Schmidt 287

Solids

Possibility of a Pressure-Induced Transformation in Cubic (*A*15) V$_3$Si . . . . R. D. Blaugher, A. Taylor, and M. Ashkin 292
Magnetic Breakdown and Dingle Temperature in Zinc Alloys . . . . P. L. Li, J. O. Strõm-Olsen, F. A. Buot, and R. Harris 295
New Interpretation of the Soft-X-Ray Absorption Spectra of Several Alkali Halides . . . . Sokrates T. Pantelides and Frederick C. Brown 299

(continued on page ii)

PHYSICAL REVIEW
LETTERS

Contents (continued)

Bound Electron States in the Wake of Swift Ions in Solids . . . V. N. Neelavathi, R. H. Ritchie, and Werner Brandt 302
Fluctuation Resistivity in One-Dimensional Metals . . . H. Fukuyama, T. M. Rice, and C. M. Varma 305

Nuclei

Diffraction, Refraction, and Interference Phenomena in Heavy-Ion Transfer Reactions . . . W. A. Friedman, K. W. McVoy, and G. W. T. Shuy 308
Search for a Δ-Δ Component in the Deuteron Wave Function Using $\bar{p}d$ Interactions at 5.55 GeV/*c* . . . H. Braun, D. Brick, A. Fridman, J.-P. Gerber, P. Juillot, G. Maurer, A. Michalon, M.-E. Michalon-Mentzer, R. Strub, and C. Voltolini 312
Measurement of Pion Photoproduction at Threshold on ^{6}Li . . . J. Deutsch, D. Favart, R. Prieels, B. Van Ostaeyen, G. Audit, N. de Botton, J.-L. Faure, Cl. Schuhl, G. Tamas, and C. Tzara 316
Fermi Beta Decay, $A>40$: The Masses of ^{42}Sc, ^{46}V, ^{50}Mn, and ^{54}Co. . . . J. C. Hardy, G. C. Ball, J. S. Geiger, R. L. Graham, J. A. Macdonald, and H. Schmeing 320

Elementary Particles and Fields

High-Density Phase Transitions in Gauge Theories . . . Barry J. Harrington and Asim Yildiz 324
Inclusive π^0 Production in *pp* Collisions at 50–400 GeV/*c* . . . D. C. Carey, J. R. Johnson, R. Kammerud, M. Peters, D. J. Ritchie, A. Roberts, J. R. Sauer, R. Shafer, D. Theriot, J. K. Walker, and F. E. Taylor 327
Unified Description of Single-Particle Production in *pp* Collisions . . . D. C. Carey, J. R. Johnson, R. Kammerud, M. Peters, D. J. Ritchie, A. Roberts, J. R. Sauer, R. Shafer, D. Theriot, J. K. Walker, and F. E. Taylor 330
Minimal Three-Body Scattering Theory . . . R. D. Amado 333

Errata

Nuclear Collisions and Factorization. . . . Victor Franco 337
New Interpretation of Photoemission Measurements of Trigonal Se and Te. . . . M. Schlüter, J. D. Joannopoulos, and Marvin L. Cohen 337

PHYSICAL REVIEW
LETTERS

Contents

VOLUME 33, NUMBER 6 5 AUGUST 1974

Atoms, Molecules, and Related Topics

Measurement of the Hyperfine Structure of the $6^2S_{1/2}$ State of ^{23}Na by Two-Step Excitation Using Two cw Dye Lasers . . . . . . H. T. Duong, S. Liberman, J. Pinard, and J.-L. Vialle 339
Direct Observation of Exchange Scattering by Spin Flip of Polarized Electrons in Excitation of Mercury . . . . . . G. F. Hanne and J. Kessler 341

Plasmas, Fluids, Thermodynamics, and Related Topics

Delayed Emission of Cyclotron Harmonics Triggered by a High-Power Microwave Pulse . . . . . . N. Ohyabu, S. Sasaki, and N. Kawashima 344
Heating of a Fully Ionized Plasma Column by a Relativistic Electron Beam . . . . . . C. Ekdahl, M. Greenspan, R. E. Kribel, J. Sethian, and C. B. Wharton 346
Contribution to Sideband Instability Theory . . . . . . M. N. Bussac, I. Mendonça, R. Pellat, and A. Roux 349
Observation of the Coupled Mode of a Collisional Drift Wave and an Alfvén Wave . . . . . . Yasushi Nishida and Kazushige Ishii 352
Magnetic Compression of Intense Ion Rings . . . . . . R. N. Sudan and Edward Ott 355

Solids

Observation of Large Electron-Hole Drops in Germanium . . . . . . Bernard J. Feldman 359
Model for Electroluminescence in GaN . . . . . . J. I. Pankove and M. A. Lampert 361
Measurement of Selected Phonons in Rubidium as a Function of Temperature and Volume . . . . . . J. R. D. Copley, C. A. Rotter, H. G. Smith, and W. A. Kamitakahara 365
Exciton Contributions to the Nonlinear Optical Susceptibility . . . . . . B. F. Levine 368
New Bond-Charge Model for the Lattice Dynamics of Diamond-Type Semiconductors . . . . . . W. Weber 371
Observation of Covalency Effects in K_2CuF_4 by Critical Scattering of Neutrons . . . . K. Hirakawa and H. Ikeda 374
Phase Separation in the Two-Dimensional Ising Ferromagnet . . . . . . D. B. Abraham and P. Reed 377

Nuclei

Search for Evidence of a $\Delta(1236)$-$\Delta(1236)$ Component of the Deuteron . . . . . . C. P. Horne, S. Hagopian, V. Hagopian, N. D. Pewitt, P. K. Williams, B. Wing, J. R. Bensinger, F. C. Porter, G. P. Yost, H. H. Bingham, W. B. Fretter, W. R. Graves, R. Harris, H. J. Lubatti, K. Moriyasu, W. J. Podolsky, A. Firestone, G. Goldhaber, and M. Goldhaber 380

(continued on page ii)

PHYSICAL REVIEW
LETTERS

Contents (continued)

Nuclear–Coulomb Interference in Inelastic Scattering of α Particles from ^{166}Er, ^{184}W, and ^{186}W . . . .
. . . . I. Y. Lee, J. X. Saladin, C. Baktash, J. E. Holden, and J. O'Brien 383

Elementary Particles and Fields

Remarks on Dirac's New Theory . . . . J. L. Pietenpol, R. Incoul, and D. Speiser 387
Evidence for a New Scaling Hypothesis in High-Energy Collisions . . . .
. . . . . . F. T. Dao, R. Hanft, J. Lach, E. Malamud, F. Nezrick, V. Davidson, A. Firestone, D. Lam,
F. Nagy, C. Peck, A. Sheng, R. Poster, P. Schlein, W. Slater, and A. Dzierba 389
Upper Bounds on Massive-Lepton-Pair Production, $pN \to l^+l^-X$, in the Quark-Parton Model . . . .
. . . . Robert Savit and Martin B. Einhorn 392

Cumulative Author Index. iii

Cumulative Author Index

The authors of all papers published in preceding issues of this volume are listed alphabetically with the page number following the dash. Page numbers with (E) refer to Errata.

Abragam, A.—102
Adair, Robert K.—115, 240
Akerlof, C. W.—119
Amado, R. D.—333
Anderson, L.—237
Arons, Jonathan—209
Ashkin, M.—292
Ashurst, W. T.—277
Atabek, O.—123
Atac, M.—175
Audit, G.—316

Bacchella, G. L.—102
Ball, G. C.—320
Barnes, P. D.—122(E)
Batra, I. P.—94
Bayfield, J. E.—258
Benenson, W.—233
Berko, S.—7
Bertin, A.—253
Biegelsen, David K.—51(E)
Bissinger, G.—1
Bjorkholm, J. E.—128
Blaugher, R. D.—292
Bletry, J.—172
Boymond, J. P.—112
Brandt, Werner—302
Braun, H.—312
Brewer, Richard G.—63
Briand, J. P.—266
Brick, D.—312
Bridgewater, A.—237
Brown, Frederick C.—299
Bucher, E.—165
Buffington, A.—34
Buot, F. A.—295
Burch, D.—59

Caldwell, P. K.—119
Campagna, M.—165
Canter, K. F.—7
Carboni, G.—253
Carey, D. C.—327, 330
Carman, R. L.—190
Caswell, William E.—244
Chaffee, R.—237
Chamberlain, O.—237
Chang, K. S.—256
Chapman, R.—18
Chen, E. Yi—98
Chevallier, P.—266
Chi, C. C.—215
Churassy, S.—185
Churchill, G. G.—273
Clarke, John—24
Clegg, T. B.—229
Cohen, Marvin L.—89, 337(E)
Condo, G. T.—126
Connor, J. W.—202
Cox, C. R.—122(E)
Cronin, J. W.—112

Dahl, O.—237
De Botton, N.—316
Denenstein, A.—215
Deutsch, J.—316
Devlin, G. E.—10
Dill, Dan—123
Dillon, J. F., Jr.—98
Drake, G. W. F.—4
Duke, Russell W.—67
DuPré, Donald B.—67

Eastman, D. E.—161
Eckhause, M.—122(E)
Ecklund, S.—175
Eichler, J.—56
Eisenberger, P.—152
Eisenstein, R. A.—122(E)
Eswaran, Mukesh—27
Evans, D. E.—76

Farago, P. S.—4
Faure, J.-L.—316
Favart, D.—316
Feldman, L. C.—1
Ferer, M.—21
Fielding, H. W.—226
Finland, J. Michael—131
Firestone, R. B.—30
Flytzanis, C.—14
Fox, J. D.—122(E)
Fradin, F. Y.—158
Franco, Victor—44, 251(E), 337(E)
Freeouf, J. L.—161
Fridman, A.—312
Friedman, W. A.—312
Frisch, H. J.—112
Fukuyama, H.—305
Fuzesy, R.—237

Gaillard, M. K.—108
Gaillard, M. L.—185
Gathers, G. R.—70
Geiger, J. S.—320
Gerber, J.-P.—312
Geschwind, S.—10
Gibbs, H. M.—273
Gibbs, P. W.—256
Giordano, N.—98
Glättli, H.—102
Goldberg, H. A.—283
Goldhaber, Alfred S.—47
Goldman, T.—246
Gollon, P. J.—175
Gorini, G.—253
Gorn, W.—237
Graham, R. L.—320
Gray, C. G.—256
Grobman, W. D.—161
Gurr, H. S.—179
Guyer, R. A.—283

Haas, B.—105
Hardy, J. C.—320
Harrington, Barry J.—324
Harris, R.—295
Harte, W. E.—86
Hastie, R. J.—202
Henderson, D. B.—205
Hensel, J. C.—219
Herman, Frank—94
Hirst, L. L.—198
Hojo, H.—148
Holzberg, F.—161
Huang, John S.—140
Huang, Whittak—283
Hughes, V. W.—41
Hungerbuehler, V.—175
Hunt, J. L.—256

Ikezi, H.—148

Jaros, J.–237
Jenkins, D. A.–122(E)
Joannopoulos, J. D.–89, 337(E)
Johnson, A.–266
Johnson, J. R.–327, 330
Johnson, R.–237
Jost, R.–53
Juillot, P.–312
Jungen, Ch.–123

Kalvius, G. M.–198
Kammerud, R.–327, 330
Kane, J. R.–122(E)
Kasowski, R. V.–83
Kelly, W. H.–30
Kenney, R.–237
Kerkhoff, S. J.–155
Kimball, J. C.–27
Kleinberg, R. L.–145
Knirk, Dwayne L.–182(E)
Koch, P. M.–258
Koschik, J.–119
Kunselman, A. R.–122(E)
Kunz, P. D.–226
Kuper, C. G.–143

Lach, J.–175
Lam, W. C.–122(E)
Lanford, W. A.–233
Langdon, A. Bruce–209
Langenberg, D. N.–212, 215
Larsen, R. C.–240
Lee, Benjamin W.–108
Leipuner, L. B.–240
Lennox, A. J.–250(E)
Leone, Stephen R.–269
Lèvesque, D.–277
Leyendecker, A. J.–86
Li, P. L.–295
Liao, P. F.–128
Liaud, P.–41
Lind, D. A.–226
Lombardi, M.–53
Longinotti, L. D.–165
Lowdermilk, W. H.–190

Macdonald, J. A.–320
MacLachlan, J.–175
Majka, R.–175
Malinovski, A.–102
Marx, J.–175
Maurer, G.–312
Max, Claire Ellen–209
McCrory, R. L.–205
McHarris, Wm. C.–30
McVoy, K. W.–308
[illegible], P.–102
[illegible], R.–112

Meyer, D. I.–119
Michalon, A.–312
Michalon-Mentzer, M.-E.–312
Miller, J.–122(E)
Mills, A. P., Jr.–7
Mima, K.–148
Moore, C. Bradley–269
Moore, C. Fred–194
Morse, R. L.–205
Murani, A. P.–91

Nann, H.–233
Neelavathi, V. N.–302
Nelson, J.–237
Némethy, P.–175
Nishikawa, Kyoji–148

O'Keefe, G.–237
Oliver, W.–237
Olsen, David K.–194
O'Neil, T. M.–73
Orth, C. D.–34

Packard, Richard E.–280
Pantelides, Sokrates T.–299
Peters, M.–327, 330
Piesvaux, J.–102
Pinot, M.–102
Piroué, P. A.–112
Pitzurra, O.–253
Platzman, P. M.–152
Poirier, J.–250(E)
Polacco, E.–253
Pollard, D.–237
Powers, R. J.–122(E)
Pretzl, K. P.–250(E)
Prieels, R.–316
Pripstein, M.–237

Rapp, Donald–137
Reddy, S. Paddi–256
Reines, F.–179
Revzen, M.–143
Rey, C. A.–250(E)
Rice, T. M.–219, 305
Richards, M. G.–18
Rickertsen, L. D.–226
Risley, J. S.–59
Ritchie, D. J.–327, 330
Ritchie, R. H.–302
Roberts, A.–175, 327, 330
Roberts, B. L.–122(E)
Robrish, P.–237
Romestain, R.–10
Rothwarf, A.–212
Roubeau, P.–102
Rozet, J. P.–266
Rudnick, J.–143

Sadoc, J. F.–172
Saha, A.–233
Sai-Halasz, G. A.–212, 215
Salamo, G. J.–273
Sandweiss, J.–175
Sapp, W. W.–240
Sauer, J. R.–327, 330
Schlüter, M.–89, 337(E)
Schmeing, H.–320
Schmidt, George–287
Schneider, D.–59
Schuhl, Cl.–316
Schulz, G. J.–134
Schweitzer, D. G.–168
Sessoms, A. L.–240
Seth, Kamal K.–233
Shafer, R.–327, 330
Shaner, J. W.–70
Shannon, S. R.–237
Shapiro, B.–143
Shapiro, G.–237
Shen, Y. R.–14
Shenoy, G. K.–198
Shochet, M. J.–112
Shoemaker, R. L.–63
Shuy, G. W. T.–308
Silver, J. D.–185
Simons, Gary–131
Simpson, H. M.–155
Smith, L. W.–240
Smoot, G. F.–34
Sobel, H. W.–179
Sparks, Cullie J., Jr.–262
Springett, B.–119
Stefanski, R.–175
Steinberg, R. I.–41
Steiner, H.–237
Stenholm, S.–63
Stolterfoht, N.–59
Stöhr, J.–198
Storm, David–137
Ström-Olsen, J. O.–295
Strub, R.–312
Sumner, R. I.–112
Sutton, R. B.–122(E)
Swedler, A. R.–168
Szczepanek, P. S.–86

Takemori, M. T.–283
Tamas, G.–316
Tanenbaum, W.–175
Taras, P.–105
Tavernier, M.–266
Taylor, A.–292
Taylor, F. E.–327, 330
Theriot, D.–175, 327, 330
Thomas, Gordon A.–219
Thompson, W. J.–229
Tipping, R. H.–256
Torelli, G.–253

Torrance, J. B. – 161
Touati, A. – 266
Trainor, T. A. – 229
Trajmar, S. – 187
Turner, R. – 240
Tsara, C. – 316

Van Ostaeyen, B. – 316
van Wijngaarden, A. – 4
Varma, C. M. – 305
Varma, Garish K. – 44, 251(E)
Vernon, S. – 140
Vignon, B. – 41
Vinciarelli, Patrizio – 246
Vitale, A. – 253
Voltolini, C. – 312
Voss, Richard F. – 24

Wahlig, M. – 237
Walker, J. K. – 327, 330
Wang, C. L. – 175
Ward, B. F. L. – 37, 251(E)
Warner, R. A. – 30
Watkins, G. D. – 223
Webb, G. W. – 168
Webb, R. A. – 145
Welsh, R. E. – 122(E)
Wertheim, G. K. – 165
Weynants, R. R. – 78
Wheatley, J. C. – 145
Wieman, H. – 59
Wildenthal, B. H. – 233
Wille, U. – 56
Williams, Gary A. – 280
Williams, H. H. – 240
Williams, W. – 187
Willis, W. – 175
Wolf, W. P. – 98
Wolff, P. A. – 10
Wong, N. C. – 140
Wong, S. F. – 134

Yeoman, M. L. – 76
Yildiz, Asim – 324
Young, D. A. – 70

Zafiratos, C. D. – 226
Zavattini, E. – 253

PHYSICAL REVIEW
LETTERS

Contents

OLUME 33, NUMBER 7 12 AUGUST 1974

toms, Molecules, and Related Topics

lkali-Metal Hyperfine Shift in the Van der Waals Molecule KAr . . . . . . Richard R. Freeman, Edward M. Mattison, David E. Pritchard, and Daniel Kleppner 397

lasmas, Fluids, Thermodynamics, and Related Topics

ynamics of Freedericksz Deformation near a Nematic–Smectic-*A* Transition. . . . . . Cheng-Cher Huang, Ronald S. Pindak, Philip J. Flanders, and John T. Ho 400
heory and Experiments on Configurations with Cylindrical Symmetry in Liquid-Crystal Droplets. . . . . . M. J. Press and A. S. Arrott 403

olids

Tensors and Tensor Interactions—Their Effect on Conduction-Electron Spin Resonance. . . . . M. B. Walker 406
ngular Forces in Tetrahedral Solids . . . . . . Walter A. Harrison and J. Christopher Phillips 410
eutron Inelastic Scattering by Coupled Defect-Phonon Modes in KCl-CN. . . . . . D. Walton, H. A. Mook, and R. M. Nicklow 412
xciton-Enhanced Photoemission from Doped Solid Rare Gases . . . . . . Zohar Ophir, Baruch Raz, and Joshua Jortner 415
emperature Dependence of Conductivity of Tetrathiafulvalene-Tetracyanoquinodimethane (TTF-TCNQ) Single Crystals . . . . . . R. P. Groff, A. Suna, and R. E. Merrifield 418
yperfine Studies of Site Occupation in Ternary Systems . . . . . . T. J. Burch, T. Litrenta, and J. I. Budnick 421
nomalous Small-Angle Magnetic Scattering from Amorphous TbFe$_2$ and YFe$_2$. . . . . . S. J. Pickart, J. J. Rhyne, and H. A. Alperin 424
olycritical Points and Floplike Displacive Transitions in Perovskites . . . . . . Amnon Aharony and Alastair D. Bruce 427

uclei

ystematics of Nuclear Single-Particle States. . . . . . M. A. K. Lodhi and B. T. Waak 431
ultinucleon Removal in the Absorption of π^- at Rest and at 60 MeV. . . . . . H. Ullrich, E. T. Boschitz, H. D. Engelhardt, and C. W. Lewis 433

(continued on page ii)

PHYSICAL REVIEW LETTERS

Contents (continued)

Size of Barely Bound Many-Body Systems . . . . F. Calogero and Yu. A. Simonov 436

Elementary Particles and Fields

Remark on the Existence of φ_4^4 . . . . James Glimm and Arthur Jaffe 440
Death of White Holes in the Early Universe . . . . Douglas M. Eardley 442
Integral Formalism for Gauge Fields . . . . C. N. Yang 445
Observation of Single-Pion Production by a Weak Neutral Current . . . .
. . . . S. J. Barish, Y. Cho, M. Derrick, L. G. Hyman, J. Rest, P. Schreiner, R. Singer,
R. P. Smith, H. Yuta, D. Koetke, V. E. Barnes, D. D. Carmony,
and A. F. Garfinkel 448
Hierarchy of Interactions in Unified Gauge Theories . . . . H. Georgi, H. R. Quinn, and S. Weinberg 451
Gaussian Distributions in Electroproduction and Inclusive e^+e^- Annihilation . . . .
. . . . S. J. Orfanidis and V. Rittenberg 455

PHYSICAL REVIEW
LETTERS

Contents

VOLUME 33, NUMBER 8 19 AUGUST 1974

Atoms, Molecules, and Related Topics

(e, $2e$) Reaction as a Probe for Details of the Helium Wave Function . . . . I. E. McCarthy, A. Ugbabe, E. Weigold, and P. J. O. Teubner 459
Determination of the Avogadro Constant. . . . . R. B. Deslattes, A. Henins, H. A. Bowman, R. M. Schoonover, C. L. Carroll, I. L. Barnes, L. A. Machlan, L. J. Moore, and W. R. Shields 463

Atoms, Nuclei, and Particles in Matter

Linear Polarizability Contribution to the Nonadditive Three-Molecule Potential . . . . E. Bergmann 467
Theory of Induced Molecular-Orbital K X Rays in Heavy-Ion Collisions. . . Berndt Müller and Walter Greiner 469
Evidence for Quasimolecular K X-Ray Emission in Heavy-Ion Collisions from the Observation of the X-Ray Directional Anisotropy . . . . J. S. Greenberg, C. K. Davis, and P. Vincent 473
Anisotropic Emission of Noncharacteristic X Rays from Low-Energy I-Au Collisions . . . . G. Kraft, P. H. Mokler, and H. J. Stein 476

Plasmas, Fluids, Thermodynamics, and Related Topics

Determination of the s-Electron Contact-Density Ratio for the Fe Configurations $3d^6 4s^2$ and $3d^7 4s$ from Matrix-Isolation Mössbauer Spectroscopy . . . . H. Micklitz and F. J. Litterst 480

Solids

Light Scattering by ^{3}He-^{4}He Mixtures near the Tricritical Point. . . P. Leiderer, D. R. Watts, and W. W. Webb 483
Existence of Two Types of Insulating States in the Hubbard Model . . . . Tadashi Arai 486
Observation of Recombination-Enhanced Defect Reactions in Semiconductors . . . . D. V. Lang and L. C. Kimerling 489
Brillouin-Scattering Evidence for a New Phase Transition in Perovskite Crystals: PrAlO$_3$ . . . . P. A. Fleury, P. D. Lazay, and L. G. Van Uitert 492
New Transport Phenomenon in a Semiconductor "Superlattice". . . . . L. Esaki and L. L. Chang 495

Nuclei

Polarization in Heavy-Ion Inelastic Scattering in the Coulomb-Nuclear Interference Region . . . . S. G. Steadman, T. A. Belote, R. Goldstein, L. Grodzins, D. Cline, M. J. A. de Voigt, and F. Videbæk 499

(continued on page ii)

PHYSICAL REVIEW LETTERS

Contents (continued)

Mass-Yield Distributions in the Reaction of ^{84}Kr Ions with ^{238}U. . . . . .J. V. Kratz, A. E. Norris, and G. T. Seaborg 502

Elementary Particles and Fields

Interference between ρ and ω Production in $\pi^{\pm}N \rightarrow \pi^{+}\pi^{-}N$ at 3, 4, and 6 GeV/c . . . . S. L. Kramer, D. S. Ayres, R. Diebold, A. F. Greene, A. J. Pawlicki, and A. B. Wicklund 505
Influence of Meson Charge Exchange on $\bar{p}$-Absorption Evidence for Neutron Halos. . . . . .William J. Gerace, Morton M. Sternheim, and James F. Walker 508

PHYSICAL REVIEW LETTERS

Contents

VOLUME 33, NUMBER 9 26 AUGUST 1974

Atoms, Molecules, and Related Topics

Polyatomic Molecular Relaxation in the Absence of Collisions . . . . S. L. Shapiro, R. C. Hyer, and A. J. Campillo 513
Electron Bremsstrahlung from Neutral Atoms . . . . H. K. Tseng and R. H. Pratt 516

Atoms, Nuclei, and Particles in Matter

Lattice Location and Hyperfine Fields of Rare-Earth Ions Implanted into Iron . . . . R. L. Cohen, G. Beyer, and B. Deutch 518

Solids

Thermoreflectance of Tetrathiafulvalinium-Tetracyanoquinodimethanide (TTF-TCNQ) . . . . P. I. Perov and J. E. Fischer 521
Effect of Spatial Dispersion upon Physisorption Energies: He on Metals . . . . George G. Kleiman and Uzi Landman 525
Raman Detection of One-Phonon-Two-Phonon Interactions in CuCl . . . . M. Krauzman, R. M. Pick, H. Poulet, G. Hamel, and B. Prevot 528
Distinction between Lattice and Cluster Models of the Jahn-Teller Effect in an Orbital Doublet . . . . M. Abou-Ghantous, P. C. Jaussaud, C. A. Bates, J. R. Fletcher, and W. S. Moore 530
High-Resolution Measurements of the Nitrogen *K-LL* Auger Transitions of Chemisorbed Ammonia on a Molybdenum Surface . . . . Tomoji Kawai, Kimio Kunimori, Tamotsu Kondow, Takaharu Onishi, and Kenzi Tamaru 533
Phosphorescence Microwave Double Resonance Spectroscopy in Ionic Solids and Its Application to Coherent Jahn-Teller States in *F* Centers of CaO . . . . C. B. Harris, M. Glasbeek, and E. B. Hensley 537
Approximate Renormalization Group Based on the Wegner-Houghton Differential Generator . . . . J. F. Nicoll, T. S. Chang, and H. E. Stanley 540

Nuclei

Superheavy Elements and the Strutinsky Prescription . . . . R. R. Chasman 544

Elementary Particles and Fields

Physical Significance of the Topology of the Bondi-Metzner-Sachs Group . . . . Michael Crampin and Patrick J. McCarthy 547

(continued on page ii)

PHYSICAL REVIEW
LETTERS

Contents (continued)

Muon-Deuteron Deep Inelastic Scattering . . . . I. J. Kim, A. Entenberg, H. Jöstlein, K. Königsmann, I. Kostoulas, A. C. Melissinos, E. Aslanides, L. Lederman, P. Limon, M. May, P. Rapp, H. Gittleson, T. Kirk, M. Murtagh, M. J. Tannenbaum, J. Sculli, T. White, and T. Yamanouchi 551

Observation of the Decay $K_L{}^0 \to \pi^+\pi^-\gamma$ . . . . G. Donaldson, D. Hitlin, R. Kennelly, J. Kirkby, J. Liu, A. Rothenberg, and S. Wojcicki 554

Charge and Particle Conservation in Black-Hole Decay . . . . B. Carter 558

Extraction of $R=\sigma_L/\sigma_T$ from Deep Inelastic e-p and e-d Cross Sections . . . . E. M. Riordan, A. Bodek, M. Breidenbach, D. L. Dubin, J. E. Elias, J. I. Friedman, H. W. Kendall, J. S. Poucher, M. R. Sogard, and D. H. Coward 561

PHYSICAL REVIEW LETTERS

Contents

VOLUME 33, NUMBER 10 2 SEPTEMBER 1974

Atoms, Molecules, and Related Topics

Coherence in He I and II Excited States Produced by an Asymmetric Collision . . . . D. A. Church, W. Kolbe, M. C. Michel, and T. Hadeishi 565
Muonium Formation in Noble Gases and Noble-Gas Mixtures . . . . R. D. Stambaugh, D. E. Casperson, T. W. Crane, V. W. Hughes, H. F. Kaspar, P. Souder, P. A. Thompson, H. Orth, G. zu Putlitz, and A. B. Denison 568
Behavior of Positive Muons in Liquid Helium . . . . T. W. Crane, D. E. Casperson, H. Chang, V. W. Hughes, H. F. Kaspar, B. Lovett, A. Schiz, P. Souder, R. D. Stambaugh, G. zu Putlitz, and J. R. Kane 572

Plasmas, Fluids, Thermodynamics, and Related Topics

Injection and Control of Intense Relativistic Electron Beams in a Torus . . . . J. Benford, B. Ecker, and V. Bailey 574
Strong Phonon Conversion at the Helium-Solid Interface . . . . H. Kinder and W. Dietsche 578

Solids

Dielectric Response in the Wannier Representation: Application to the Optical Spectrum of Diamond . . . . W. Hanke and L. J. Sham 582
Direct Transform-Deconvolution Method for Surface-Structure Determination . . . . D. L. Adams and Uzi Landman 585
Backward Scattering in the One-Dimensional Electron Gas . . . . A. Luther and V. J. Emery 589

Nuclei

Angular-Momentum Effects on Continuum Gamma Rays Following Heavy-Ion Reactions . . . . P. O. Tjøm, F. S. Stephens, R. M. Diamond, J. de Boer, and W. E. Meyerhof 593
Average Multiplicity of Unresolved Photon Cascades in the De-excitation of Highly Excited Compound Nuclei . . . . E. der Mateosian, O. C. Kistner, and A. W. Sunyar 596
Nucleus-Nucleus Optical Potential Using a Density-Dependent Two-Body Interaction . . . . Bikash Sinha 600

Elementary Particles and Fields

Observation of a Dip Due to $I=0$ t-Channel Exchange in the Reaction $\pi N \to A_2 N$ at 4.5 and 6 GeV/c . . . . H. A. Gordon, M. Habibi, I. Stumer, and Kwan-Wu Lai 603

(continued on page ii)

PHYSICAL REVIEW
LETTERS

Contents (continued)

Exotic Interactions of Charged Leptons . . . . M. A. B. Bég and G. Feinberg 606

A_3-A_1 Interference Phase . . . . G. Ascoli, L. M. Jones, R. Klanner, U. E. Kruse, and H. W. Wyld 611

Comments

Weinberg Angle as a Test of SU(n)-Type Unified Gauges . . . . S. P. Rosen 614

Cumulative Author Index iii

Cumulative Author Index

The authors of all papers published in preceding issues of this volume are listed alphabetically with the page number following the dash. Page numbers with (E) refer to Errata.

Abou-Ghantous, M. – 530
Abragam, A. – 102
Abraham, D. B. – 377
Adair, Robert K. – 115, 240
Aharony, Amnon – 427
Akerlof, C. W. – 119
Alperin, H. A. – 424
Amado, R. D. – 333
Anderson, L. – 237
Arai, Tadashi – 486
Arons, Jonathan – 209
Arrot, A. S. – 403
Ashkin, M. – 292
Ashurst, W. T. – 277
Aslanides, F. – 551
Atabek, O. – 123
Atac, M. – 175
Audit, G. – 316
Ayres, D. S. – 505

Bacchella, G. L. – 102
Baktash, C. – 383
Ball, G. C. – 320
Barish, S. J. – 448
Barnes, I. L. – 463
Barnes, P. D. – 122(E)
Barnes, V. E. – 448
Bates, C. A. – 530
Batra, I. P. – 94
Bayfield, J. E. – 258
Belote, T. A. – 499
Benenson, W. – 233
Bensinger, J. R. – 380
Bergmann, F. – 467
Berko, S. – 7
Bertin, A. – 253
Beyer, G. – 518
Biegelsen, David K. – 51(E)
Bingham, H. H. – 380
Bissinger, G. – 1
Bjorkholm, J. E. – 128
Blaugher, R. D. – 292
Bletry, J. – 172
Bodek, A. – 561
Boschitz, E. T. – 433
Bowman, H. A. – 463
Boymond, J. P. – 112
Brandt, Werner – 302
Braun, H. – 312
Breidenbach, M. – 561
Brewer, Richard G. – 63
Briand, J. P. – 266
Brick, D. – 312
Bridgewater, A. – 237
Brown, Frederick C. – 299
Bruce, Alastair D. – 427
Bucher, E. – 165
Budnick, J. I. – 421
Buffington, A. – 34
Buot, F. A. – 295
Burch, D. – 59
Burch, T. J. – 421
Bussac, M. N. – 349

Caldwell, P. K. – 119
Calogero, F. – 436
Campagna, M. – 165
Campillo, A. J. – 513
Canter, K. F. – 7
Carboni, G. – 253
Carey, D. C. – 327, 330
Carman, R. L. – 190
Carmony, D. D. – 448
Carroll, C. L. – 463
Carter, B. – 558
Caswell, William E. – 244
Chaffee, R. – 237
Chamberlain, O. – 237
Chang, K. S. – 256
Chang, L. L. – 495
Chang, T. S. – 540
Chapman, R. – 18
Chasman, R. R. – 544
Chen, E. Yi – 98
Chevallier, P. – 266
Chi, C. C. – 215
Cho, Y. – 448
Churassy, S. – 185
Churchill, G. G. – 273
Clarke, John – 24
Clegg, T. B. – 229
Cline, D. – 499
Cohen, Marvin L. – 89, 337(E)
Cohen, R. L. – 518
Condo, G. T. – 126
Connor, J. W. – 202
Copley, J. R. D. – 365
Coward, D. H. – 561
Cox, C. R. – 122(E)
Crampin, Michael – 547
Cronin, J. W. – 112

Dahl, O. – 237
Dao, F. T. – 389
Davidson, V. – 389
Davis, C. K. – 473
De Botton, N. – 316
Denenstein, A. – 215
Derrick, M. – 448
Deslattes, R. B. – 463
Deutch, B. – 518
Deutsch, J. – 316
Devlin, G. E. – 10
de Voigt, M. J. A. – 499
Diebold, R. – 505
Dill, Dan – 123
Dillon, J. F., Jr. – 98
Donaldson, G. – 554
Drake, G. W. F. – 4
Dubin, D. L. – 561
Duke, Russell W. – 67
Duong, H. T. – 339
DuPré, Donald B. – 67
Dzierba, A. – 389

Eardley, Douglas M. – 442
Eastman, D. E. – 161
Eckhause, M. – 122(E)
Ecklund, S. – 175
Eichler, J. – 56
Einhorn, Martin B. – 392
Eisenberger, P. – 152
Eisenstein, R. A. – 122(E)
Ekdahl, C. – 346
Elias, J. E. – 561
Engelhardt, H. D. – 433
Entenberg, A. – 551
Esaki, L. – 495
Eswaran, Mukesh – 27
Evans, D. E. – 76

Farago, P. S. – 4
Faure, J.-L. – 316
Favart, D. – 316
Feldman, Bernard J. – 359
Feldman, L. C. – 1
Ferer, M. – 21
Fielding, H. W. – 226

Finland, J. Michael – 131
Firestone, A. – 380, 389
Firestone, R. B. – 30
Fischer, J. E. – 521
Flanders, Philip J. – 400
Fletcher, J. R. – 530
Fleury, P. A. – 492
Flytzanis, C. – 14
Fox, J. D. – 122(E)
Fradin, F. Y. – 158
Franco, Victor – 44, 251(E), 337(E)
Freeman, Richard R. – 397
Freeouf, J. L. – 161
Fretter, W. B. – 380
Fridman, A. – 312
Friedman, J. I. – 561
Friedman, W. A. – 312
Frisch, H. J. – 112
Fukuyama, H. – 305
Fuzesy, R. – 237

Gaillard, M. K. – 108
Gaillard, M. L. – 185
Garfinkel, A. F. – 448
Gathers, G. R. – 70
Geiger, J. S. – 320
Georgi, H. – 451
Gerace, William J. – 508
Gerber, J.-P. – 312
Geschwind, S. – 10
Gibbs, H. M. – 273
Gibbs, P. W. – 256
Giordano, N. – 98
Gittleson, H. – 551
Glasbeek, M. – 537
Glättli, H. – 102
Glimm, James – 440
Goldberg, H. A. – 283
Goldhaber, Alfred S. – 47
Goldhaber, G. – 380
Goldhaber, M. – 380
Goldman, T. – 246
Goldstein, R. – 499
Gollon, P. J. – 175
Gorini, G. – 253
Gorn, W. – 237
Graham, R. L. – 320
Graves, W. R. – 380
Gray, C. G. – 256
Greenberg, J. S. – 473
Greene, A. F. – 505
Greenspan, M. – 346
Greiner, Walter – 469
Grobman, W. D. – 161
Grodzins, L. – 499
Groff, R. P. – 418
Gurr, H. S. – 179
Guyer, R. A. – 283

Haas, B. – 105
Hagopian, S. – 380
Hagopian, V. – 380
Hamel, G. – 528
Hanft, R. – 389
Hanne, G. F. – 341
Hardy, J. C. – 320
Harrington, Barry J. – 324
Harris, C. B. – 537
Harris, R. – 295
Harris, R. – 380
Harrison, Walter A. – 410
Harte, W. E. – 36
Hastie, R. J. – 202
Henderson, D. B. – 205
Henins, A. – 463
Hensel, J. C. – 219
Hensley, E. B. – 537
Herman, Frank – 94
Hirakawa, K. – 374
Hirst, L. L. – 198
Hitlin, D. – 554
Ho, John T. – 400
Hojo, H. – 148
Holden, J. E. – 383
Holzberg, F. – 161
Horne, C. P. – 380
Huang, Cheng-Cher – 400
Huang, John S. – 140
Huang, Whittak – 283
Hughes, V. W. – 41
Hungerbuehler, V. – 175
Hunt, J. I. – 256
Hyer, R. C. – 513
Hyman, L. G. – 448

Ikeda, H. – 374
Ikezi, H. – 148
Incoul, R. – 387
Ishii, Kazushige – 352

Jaffe, Arthur – 440
Jaros, J. – 237
Jaussaud, P. C. – 530
Jenkins, D. A. – 122(E)
Joannopoulos, J. D. – 89, 337(E)
Johnson, A. – 266
Johnson, J. R. – 327, 330
Johnson, R. – 237
Jortner, Joshua – 415
Jost, R. – 53
Jöstlein, H. – 551
Juillot, P. – 312
Jungen, Ch. – 123

Kalvius, G. M. – 198
Kamitakahara, W. A. – 365
Kammerud, R. – 327, 330
Kane, J. R. – 122(E)
Kasowski, R. V. – 83
Kawai, Tomoji – 533
Kawashima, N. – 344
Kelly, W. H. – 30
Kendall, H. W. – 561
Kennelly, R. – 554
Kenney, R. – 237
Kerkhoff, S. J. – 155
Kessler, J. – 341
Kim, I. J. – 551
Kimball, J. C. – 27
Kimerling, L. C. – 489
Kirk, T. – 551
Kirkby, J. – 554
Kleiman, George G. – 525
Kleinberg, R. L. – 145
Kleppner, Daniel – 397
Knirk, Dwayne L. – 182(E)
Koch, P. M. – 258
Koetke, D. – 448
Kondow, Tamotsu – 533
Königsmann, K. – 551
Koschik, J. – 119
Kostoulas, I. – 551
Kraft, G. – 476
Kramer, S. L. – 505
Kratz, J. V. – 502
Krauzman, M. – 528
Kribel, R. E. – 346
Kunimori, Kimio – 533
Kunselman, A. R. – 122(E)
Kunz, P. D. – 226
Kuper, C. G. – 143

Lach, J. – 175, 389
Lam, D. – 389
Lam, W. C. – 122(E)
Lampert, M. A. – 361
Landman, Uzi – 525
Lanford, W. A. – 233
Lang, D. V. – 489
Langdon, A. Bruce – 209
Langenberg, D. N. – 212, 215
Larsen, R. C. – 240
Lazay, P. D. – 492
Lederman, L. – 551
Lee, Benjamin W. – 108
Lee, I. Y. – 383
Leiderer, P. – 483
Leipuner, L. B. – 240
Lennox, A. J. – 250(E)
Leone, Stephen R. – 269
Levesque, D. – 277
Levine, B. F. – 368
Lewis, C. W. – 433
Leyendecker, A. J. – 86
Li, P. L. – 295
Liao, P. F. – 128
Liaud, P. – 41

iberman, S. – 339
imon, P. – 551
ind, D. A. – 226
itrenta, T. – 421
itterst, F. J. – 480
iu, J. – 554
odhi, M. A. K. – 431
ombardi, M. – 53
onginotti, L. D. – 165
owdermilk, W. H. – 190
ubatti, H. J. – 380

acdonald, J. A. – 320
achlan, L. A. – 463
acLachlan, J. – 175
ajka, R. – 175
alamud, E. – 389
alinovski, A. – 102
arx, J. – 175
attison, Edward M. – 397
aurer, G. – 312
ax, Claire Ellen – 209
ay, M. – 551
McCarthy, L. E. – 459
McCarthy, Patrick J. – 547
McCrory, R. L. – 205
cHarris, Wm. C. – 30
McVoy, K. W. – 308
Melissinos, A. C. – 551
Mendonça, I. – 349
eriel, P. – 102
ermod, R. – 112
errifield, R. E. – 418
Meyer, D. I. – 119
Michalon, A. – 312
Michalon-Mentzer, M.-E. – 312
Micklitz, H. – 480
Miller, J. – 122(E)
Mills, A. P., Jr. – 7
Mima, K. – 148
Mokler, P. H. – 479
Mook, H. A. – 412
Moore, C. Bradley – 269
Moore, C. Fred – 194
Moore, L. J. – 463
Moore, W. S. – 530
Moriyasu, K. – 380
Morse, R. L. – 205
Müller, Berndt – 469
Murani, A. P. – 91
Murtagh, M. – 551

Nagy, F. – 389
Nann, H. – 233
Neelavathi, V. N. – 302
Nelson, J. – 237
Némethy, P. – 175
Nezrick, F. – 389
Nicklow, R. M. – 412
Nicoll, J. F. – 540
Nishida, Yasushi – 352
Nishikawa, Kyoji – 148
Norris, A. E. – 502

O'Brien, J. – 383
Ohyabu, N. – 344
O'Keefe, G. – 237
Oliver, W. – 237
Olsen, David K. – 194
O'Neil, T. M. – 73
Onishi, Takaharu – 533
Ophir, Zohar – 415
Orfanidis, S. J. – 455
Orth, C. D. – 34
Ott, Edward – 355

Packard, Richard E. – 280
Pankove, J. I. – 361
Pantelides, Sokrates T. – 299
Pawlicki, A. J. – 505
Peck, C. – 389
Pellat, R. – 349
Perov, P. I. – 521
Peters, M. – 327, 330
Pewitt, N. D. – 380
Phillips, J. Christopher – 410
Pick, R. M. – 528
Pickart, S. J. – 424
Piesvaux, J. – 102
Pietenpol, J. L. – 387
Pinard, J. – 339
Pindak, Ronald S. – 400
Pinot, M. – 102
Piroué, P. A. – 112
Pitzurra, O. – 253
Platzman, P. M. – 152
Podolsky, W. J. – 380
Poirier, J. – 250(E)
Polacco, E. – 253
Pollard, D. – 237
Porter, F. C. – 380
Poster, R. – 389
Poucher, J. S. – 561
Poulet, H. – 528
Powers, R. J. – 122(E)
Pratt, R. H. – 516
Press, M. J. – 403
Pretzl, K. P. – 250(E)
Prevot, B. – 528
Prieels, R. – 316
Pripstein, M. – 237
Pritchard, David E. – 397

Quinn, H. R. – 451

Rapp, Donald – 137
Rapp, P. – 551
Raz, Baruch – 415
Reddy, S. Paddi – 256
Reed, P. – 377
Reines, F. – 179
Rest, J. – 448
Revzen, M. – 143
Rey, C. A. – 250(E)
Rhyne, J. J. – 424
Rice, T. M. – 219, 305
Richards, M. G. – 18
Rickertsen, L. D. – 226
Riordan, E. M. – 561
Risley, J. S. – 59
Ritchie, D. J. – 327, 330
Ritchie, R. H. – 302
Rittenberg, V. – 455
Roberts, A. – 175, 327, 330
Roberts, B. L. – 122(E)
Robrish, P. – 237
Romestain, R. – 10
Rothenberg, A. – 554
Rothwarf, A. – 212
Rotter, C. A. – 365
Roubeau, P. – 102
Roux, A. – 349
Rozet, J. P. – 266
Rudnick, J. – 143

Sadoc, J. F. – 172
Saha, A. – 233
Sai-Halasz, G. A. – 212, 215
Saladin, J. X. – 383
Salamo, G. J. – 273
Sandweiss, J. – 175
Sapp, W. W. – 240
Sasaki, S. – 344
Sauer, J. R. – 327, 330
Savit, Robert – 392
Schlein, P. – 389
Schlüter, M. – 89, 337(E)
Schmeing, H. – 320
Schmidt, George – 287
Schneider, D. – 59
Schoonover, R. M. – 463
Schreiner, P. – 448
Schuhl, Cl. – 316
Schulz, G. J. – 134
Schweitzer, D. G. – 168
Sculli, J. – 551
Seaborg, G. T. – 502
Sessoms, A. L. – 240
Seth, Kamal K. – 233
Sethian, J. – 346
Shafer, R. – 327, 330
Shaner, J. W. – 70
Shannon, S. R. – 237
Shapiro, B. – 143
Shapiro, G. – 237
Shapiro, S. L. – 513

Shen, Y. R. – 14
Sheng, A. – 389
Shenoy, G. K. – 198
Shields, W. R. – 463
Shochet, M. J. – 112
Shoemaker, R. L. – 63
Shuy, G. W. T. – 308
Silver, J. D. – 185
Simonov, Yu. A. – 436
Simons, Gary – 131
Simpson, H. M. – 155
Singer, R. – 448
Slater, W. – 389
Smith, H. G. – 365
Smith, L. W. – 240
Smith, R. P. – 448
Smoot, G. F. – 34
Sobel, H. W. – 179
Sogard, M. R. – 561
Sparks, Cullie J., Jr. – 262
Speiser, D. – 387
Springett, B. – 119
Stanley, H. E. – 540
Steadman, S. G. – 499
Stefanski, R. – 175
Stein, H. J. – 479
Steinberg, R. L – 41
Steiner, H. – 237
Stenholm, S. – 63
Sternheim, Morton M. – 508
Stolterfoht, N. – 59
Stöhr, J. – 198
Storm, David – 137
Ström-Olsen, J. O. – 295
Strub, R. – 312
Sudan, R. N. – 355
Sumner, R. I. – 112
Suna, A. – 418
Sutton, R. B. – 122(E)
Swedler, A. R. – 168
Szczepanek, P. S. – 86

Takemori, M. T. – 283
Tamaru, Kenzi – 533
Tamas, G. – 316
Tanenbaum, W. – 175
Tannenbaum, M. J. – 551
Taras, P. – 105
Tavernier, M. – 266
Taylor, A. – 292
Taylor, F. E. – 327, 330
Teubner, P. J. O. – 459
Theriot, D. – 175, 327, 330
Thomas, Gordon A. – 219
Thompson, W. J. – 229
Tipping, R. H. – 256
Torelli, G. – 253
Torrance, J. B. – 161
Touati, A. – 266
Trainor, T. A. – 229
Trajmar, S. – 187
Tseng, H. K. – 516
Turner, R. – 240
Tzara, C. – 316

Ugbabe, A. – 459
Ullrich, H. – 433

Van Ostaeyen, B. – 316
Van Uitert, L. G. – 492
van Wijngaarden, A. – 4
Varma, C. M. – 305
Varma, Garish K. – 44, 251(E)
Vernon, S. – 140
Vialle, J.-L. – 339
Videbæk, F. – 499
Vignon, B. – 41
Vincent, P. – 473
Vinciarelli, Patrizio – 246
Vitale, A. – 253
Voltolini, C. – 312
Voss, Richard, F. – 24

Waak, B. T. – 431
Wahlig, M. – 237
Walker, J. K. – 327, 330
Walker, James F. – 508
Walker, M. B. – 406
Walton, D. – 412
Wang, C. L. – 175
Ward, B. F. L. – 37, 251(E)
Warner, R. A. – 30
Watkins, G. D. – 223
Watts, D. R. – 483
Webb, G. W. – 168
Webb, R. A. – 145
Webb, W. W. – 483
Weber, W. – 371
Weinberg, S. – 451
Welsh, R. E. – 122(E)
Wertheim, G. K. – 165
Weynants, R. R. – 78
Wharton, C. B. – 346
Wheatley, J. C. – 145
White, T. – 551
Wicklund, A. B. – 505
Wiegold, E. – 459
Wieman, H. – 59
Wildenthal, B. H. – 233
Wille, U. – 56
Williams, Gary A. – 280
Williams, H. H. – 240
Williams, P. K. – 380
Williams, W. – 187
Willis, W. – 175
Wing, B. – 380
Wojcicki, S. – 554
Wolf, W. P. – 98
Wolff, P. A. – 10
Wong, N. C. – 140
Wong, S. F. – 134

Yamanouchi, T. – 551
Yang, C. N. – 445
Yeoman, M. L. – 76
Yildiz, Asim – 324
Yost, G. P. – 380
Young, D. A. – 70
Yuta, H. – 448

Zafiratos, C. D. – 226
Zavattini, E. – 253

PHYSICAL REVIEW LETTERS

Contents

OLUME 33, NUMBER 11 9 SEPTEMBER 1974

toms, Molecules, and Related Topics

bservation of Protoplasmic Streaming by Laser-Light Scattering . . . . R. V. Mustacich and B. R. Ware 617

asmas, Fluids, Thermodynamics, and Related Topics

uclear Spin-Lattice Relaxation in Liquid Crystals by Fluctuations in the Nematic Director . . . . J. W. Doane, C. E. Tarr, and M. A. Nickerson 620

nisotropy in the *B* Phase of He^3 . . . . W. F. Brinkman, H. Smith, D. D. Osheroff, and E. I. Blount 624

hase Diagram of Liquid ^{3}He between 0.7 and 2.5 mK . . . . A. I. Ahonen, M. T. Haikala, M. Krusius, and O. V. Lounasmaa 628

uperfluid Mass of Liquid Helium Three . . . . A. W. Yanof and J. D. Reppy 631

ime-Resolved Laser-Plasma Backscatter Studies . . . . B. H. Ripin, J. M. McMahon, E. A. McLean, W. M. Manheimer, and J. A. Stamper 634

olids

luctuation Conductivity in the Incommensurate Peirels System. . . . . Bruce R. Patton and L. J. Sham 638

bservation of Thermal Fluctuations in Superconducting Microbridges . . . . F. J. Rachford, C. Y. Huang, M. Nisenoff, and S. Wolf 641

emperature-Modulated Reflectance of Gold from 6 to 35 eV. . . C. G. Olson, M. Piacentini, and D. W. Lynch 644

tability of Electron-Hole Drops in Germanium under Uniaxial Stress. . . . . T. Ohyama, T. Sanada, and E. Otsuka 647

esonant Scattering of Electrons in Mercury Telluride. . . . . W. Walukiewicz 650

lectron Energy-Loss Spectroscopy of GaAs and Ge Surfaces . . . . R. Ludeke and L. Esaki 653

uclei

iant-Dipole-Resonance Region of ^{15}N Observed via ^{14}C$(p,p)^{14}$C Cross Section and Polarization Measurements . . . . H. R. Weller, N. R. Roberson, D. Rickel, and D. R. Tilley 657

lementary Particles and Fields

bservation of Nuclear Transparency in Proton-Nucleus Collisions at 200 GeV . . . . P. L. Jain, M. Kazuno, Gerald Thomas, and B. Girard 660

(continued on page ii)

PHYSICAL REVIEW LETTERS

Contents (continued)

Observation of the Reactions $e^+e^- \to e^+e^-$, $e^+e^- \to \gamma\gamma$, and $e^+e^- \to \mu^+\mu^-$ at a Center-of-Mass Energy of 5.2 GeV . . . . B. L. Beron, J. F. Crawford, R. L. Ford, R. Hofstadter, E. B. Hughes, R. Kose, P. LeCoultre, T. W. Martin, L. H. O'Neill, R. E. Rand, L. Resvanis, R. F. Schilling, and J. W. Simpson 6

e^+e^- Annihilation into Hadrons in Quantum Field Theory . . . . Hung Cheng and Jeffrey Mandula 6

Errata

Bound Electron States in the Wake of Swift Ions in Solids . . . . V. N. Neelavathi, R. H. Ritchie, and Werner Brandt 6

PHYSICAL REVIEW
LETTERS

Contents

VOLUME 33, NUMBER 12 16 SEPTEMBER 1974

Atoms, Molecules, and Related Topics

Photoionization Cross Sections of the Outer s-Subshell Electrons in the Rare Gases. . . . . James A. R. Samson and J. L. Gardner 671
Nonlinear Optical Processes by Van der Waals Interaction during Collision . . . . S. E. Harris and D. B. Lidow 674
Radiative Decay of the 2^3S_1 and 2^3P_2 States of Heliumlike Vanadium ($Z = 23$) and Iron ($Z = 26$) . . . . Harvey Gould, Richard Marrus, and Peter J. Mohr 676

lasmas, Fluids, Thermodynamics, and Related Topics

Reverse Temperature Gradient in the Kinetic Theory of Evaporation. . . . . J. R. Thomas, Jr., T. S. Chang, and C. E. Siewert 680
New Factors Affecting the Measured Lifetime of Electrons Trapped on Vortex Lines in He II . . . . Keith DeConde, Gary A. Williams, and Richard E. Packard 683
Nuclear Magnetic Resonance of Superfluid He^3 near T_c in High Magnetic Fields. . . . . D. D. Osheroff and P. W. Anderson 686
on Heating by an Intense Relativistic Electron Beam . . . . J. P. VanDevender, J. D. Kilkenny, and A. E. Dangor 689
Dissipative Trapped-Electron Instability in Cylindrical Geometry. . . . . S. C. Prager, A. K. Sen, and T. C. Marshall 692

Solids

Polarized-Neutron Diffraction from Spin-Polarized Protons: A Tool in Structure Determination? . . . . J. B. Hayter, G. T. Jenkin, and J. W. White 696
Evidence of Optical Transitions in X-Ray Inelastic Scattering Spectra: Li Metal. . . . . N. G. Alexandropoulos, G. G. Cohen, and M. Kuriyama 699
Band Structure of PbPo and Trends in the Pb Chalcogenides . . . . S. Rabii and R. H. Lasseter 703
Critical Scattering Parameters for General Fields and Temperatures . . . . M. Combescot, M. Droz, and J. M. Kosterlitz 705

Nuclei

Coulomb Energy of He^3 and Charge Symmetry of Nuclear Forces . . . . S. S. Mehdi and V. K. Gupta 709
Deeply Bound Hole States as a Giant-Resonance-Like Phenomenon . . . . S. Y. van der Werf, B. R. Kooistra, W. H. A. Hesselink, F. Iachello, L. W. Put, and R. H. Siemssen 712

(continued on page ii)

PHYSICAL REVIEW LETTERS

Contents (continued)

Resolving Ambiguities in Heavy-Ion Potentials . . . . D. A. Goldberg and S. M. Smith 71

Elementary Particles and Fields

Hadron Production at Large Transverse Momentum . . . . J. A. Appel, M. H. Bourquin, I. Gaines, D. C. Hom, L. M. Lederman, H. P. Parr, J.-P. Repellin, D. H. Saxon, H. D. Snyder, J. M. Weiss, J. K. Yoh, B. C. Brown, J.-M. Gaillard, and T. Yamonouchi 71
Observation of Direct Production of Leptons in p-Be Collisions at 300 GeV . . . . J. A. Appel, M. H. Bourquin, I. Gaines, D. C. Hom, L. M. Lederman, H. P. Paar, J.-P. Repellin, D. H. Saxon, H. D. Snyder, J. M. Weiss, J. K. Yoh, B. C. Brown, J.-M. Gaillard, and T. Yamanouchi 72
Neutron-Proton Total Cross Sections from 30 to 280 GeV/c . . . . Michael J. Longo, Cyril A. Ayre, H. Richard Gustafson, Lawrence W. Jones, P. V. Ramana Murthy, Patrick Skubic, and Bruce Cork 72
Pion-Nucleon Form Factor in the Chew-Low Theory . . . . C. B. Dover, D. J. Ernst, R. A. Friedenberg, and R. M. Thaler 72

PHYSICAL REVIEW
LETTERS

Contents

ME 33, NUMBER 13 — 23 SEPTEMBER 1974

s, Molecules, and Related Topics

acterization of Charge States of Energetic Ions in Solids from Associated *K* X-Ray Production .... Sheldon Datz, B. R. Appleton, J. R. Mowat, Roman Laubert, R. S. Peterson, R. S. Thoe, and I. A. Sellin 733

ing-Trap Technique for Studying Electron-Atom Collisions at Low Energy .... Michael D. McGuire and E. Norval Fortson 737

s, Fluids, Thermodynamics, and Related Topics

inear Skin Effect of High-Power Microwaves Incident on a Collisionless Magnetized Plasma .... K. Minami, K. P. Singh, M. Masuda, and K. Ishii 740

ay Emission from Laser-Produced Plasmas .... D. J. Nagel, P. G. Burkhalter, C. M. Dozier, J. F. Holzrichter, B. M. Klein, J. M. McMahon, J. A. Stamper, and R. R. Whitlock 743

surements of Energetic X Rays from Laser-Produced Plasmas .... F. C. Young 747

tons and Resonant Absorption .... E. J. Valeo and W. L. Kruer 750

Ion Beam Instability in a Cylindrical Geometry .... Noah Hershkowitz, Thomas Romesser, Georg Knorr, and Christoph K. Goertz 754

tron Cyclotron Emission from a Tokamak Plasma: Experiment and Theory .... A. E. Costley, R. J. Hastie, J. W. M. Paul, and J. Chamberlain 758

leigh-Taylor Instability and Laser-Pellet Fusion .... Stephen E. Bodner 761

Heating by the Current-Driven Electrostatic Ion-Cyclotron Instability .... N. Rynn, D. R. Dakin, D. L. Correll, and Gregory Benford 765

ls

ational Polarization of Molecular Groups in Solids .... S. Emid, R. A. Wind, and S. Clough 769

ermination of the Optical Properties and Absolute Concentrations of Electron-Hole Drops in Germanium .... J. M. Worlock, T. C. Damen, K. L. Shaklee, and J. P. Gordon 771

stal Fields in Dilute Rare-Earth Metals Obtained from Magnetization Measurements on Dilute Rare-Earth Alloys .... P. Touborg and J. Høg 775

(continued on page ii)

PHYSICAL REVIEW LETTERS

Contents (continued)

Magnetic Properties of Ho–Co and Ho–Fe Amorphous Films . . . . Neil Heiman and Kenneth Lee

Nuclei

Resonances in $^{12}C + ^{13}C$ . . . . D. J. Crozier and J. C. Legg

Three-Body Breakup Reaction $^{40}Ca(^{16}O, ^{12}C\alpha)$. . . . . D. C. Slater, J. R. Hall, J. R. Calarco, B. A. Watson, and J. A. Becker

New Interpretation of the Coriolis Kinking Effect in Odd-Even Nuclei . . . . B. Giraud and A. Jaffrin

Electroexcitation of the Giant Resonance in ^{16}O . . . . A. Hotta, K. Itoh, and T. Saito

Elementary Particles and Fields

New Negative Result for Gravitational Wave Detection, and Comparison with Reported Detection. . . . . James L. Levine and Richard L. Garwin

Azimuthal Correlations in *pp* Interactions at 205 GeV/*c* . . . . M. Pratap, R. Engelmann, T. Kafka, Y. Cho, T. H. Fields, L. G. Hyman, R. Singer, L. Voyvodic, R. Walker, and J. Whitmore

PHYSICAL REVIEW LETTERS

VOLUME 33 1 JULY 1974 NUMBER 1

End-Point Energy Variations in the Noncharacteristic Radiation Produced by S, Cl, Ar, K, Ca, and Ti Bombardment of Si

G. Bissinger*†
Rutgers University, New Brunswick, New Jersey 08903

and

L. C. Feldman
Bell Laboratories, Murray Hill, New Jersey 07974

(Received 1 May 1974)

The noncharacteristic radiation observed in heavy-ion bombardment of Si was investigated with 200-keV ^{32}S, ^{35,37}Cl, ^{40}Ar, ^{39,41}K, ^{40}Ca, and ^{48}Ti projectiles ($16 \leq Z \leq 22$) on Si. The high-energy tail of the noncharacteristic radiation is observed to shift to higher energies as projectile Z is increased. The observed end-point energy shifts are in agreement with the interpretation that the radiation arises from the radiative decay of a projectile $2p$ vacancy in the quasimolecule formed by the projectile and the target atom during the collision.

The noncharacteristic radiation (NCR) extend- g to ≈ 1 keV observed in Ar bombardment of gh-purity C, Al, Si, and Fe targets, first re- rted by Saris, van der Weg, Tawara, and Lau- rt,[1] has been the subject of intense investiga- on.[2-4] Using the Fano-Lichten description[5] of avy-ion collisions, the authors of Ref. 1 inter- eted the radiation as arising from the radiative cay of a projectile $2p$ vacancy in the quasimol- ule formed during the collision by the projec- le and an atom (either implanted Ar[1] or the tar- t itself[4]). The energy of the emitted radiation en depends on the internuclear separation at e time the vacancy is filled, and on the partic- ar combination of projectile and target atom. he maximum energy (end-point energy) occurs hen the vacancy decays at the distance of clos- t approach, ρ_{min}; for zero internuclear sepa- tion, the energy is just that of the united-atom x ray, in the absence of additional velocity- oadening effects. Experimental reports have w confirmed[2,3] the original observation of the NCR, demonstrated that the NCR is a broad photon energy distribution whose low-energy cutoff (as observed in previous experiments) was due to detector-window transmission effects,[4] and studied the projectile-energy dependence of the NCR in the Ar + Si system[1] and in a similar process in the C + C system.[6]

Since the radiation is expected to be a continuum, the end-point energy is a distinctive characteristic of the proposed model. However, for a variety of reasons (e.g., collision broadening and experimental determination of end-point energies), the absolute value of the end-point energy is rather poorly defined. In this Letter we report the first systematic investigation of the end-point energy dependence on Z_1, the atomic number of the projectile. As a result of using a set of projectiles with closely spaced atomic numbers, we can make use of the end-point energy differences, thus reducing much of the ambiguity in the direct comparison of experimental and theoretical end-point energies. This sensitive and

© 1974

explicit test of the explanation of the source of the NCR confirms the general model given in Ref. 1.

The experiment utilized mass-analyzed 200-keV beams of $^{32}S^+$, $^{35,37}Cl^+$, $^{40}Ar^+$, $^{39,41}K^+$, $^{40}Ca^+$, and $^{48}Ti^+$. The target chamber and associated equipment have been described elsewhere.[4] Dose-related effects were kept to a minimum by keeping all doses below 10^{16} atoms/cm^2 where projectile-implanted-projectile collision contributions to the NCR first become noticeable,[4] and also by changing the target position frequently. A Si(Li) detector with a 12.7-μm Be window was used to detect the x radiation; count rates were kept below 300 counts/sec to reduce pileup and gain shifts.

Thick Si targets were bombarded with the various projectiles; the spectra collected for ^{32}S and ^{48}Ti projectiles are shown in Fig. 1(a) and clearly demonstrate the upward shift on the high-energy side of the NCR for the higher-Z projectile. Intermediate shifts are observed for the other projectiles, depending only on Z_1. To demonstrate that the projectile mass does not affect the end-point energy, the spectra obtained for two isotopes of Cl are shown in Fig. 1(b). No variation in the end-point energy was observed for the two K isotopes either (not shown).

Following the procedure in Ref. 6, we defined an end-point energy as the intersection of the line drawn tangent to the high-energy side at the half-maximum and the abscissa on a linear scale. Since all the NCR spectra had similar shapes on the high-energy side, this approach does not have as large a systematic error as the determination of end-point energies for varying projectile *energy* does,[1,6,7] because of the variation in peak shape observed in the latter. However, the variation in the detector-window transmission is stil important in this energy region, ranging from about 25 to 45% for 1 to 1.5 keV. This transmission variation has the effect of increasing the en point energy determined as described above, an is most important for the lowest-Z projectiles. It also reduces the end-point energy differences between spectra for adjacent Z_1, particularly fo lower Z. The experimental end-point energies are shown in Fig. 2(a), and demonstrate the mon tonic increase in end-point energy as projectile Z increases. The errors shown in Fig. 2(a) represent an estimate of random errors only and do not include systematic errors due to the following: (i) detector resolution (approximately constant over our energy range), (ii) Si K tail (whic is small and makes approximately the same contribution for all projectiles since for the lower-Z projectiles the Si K is more intense but relatively far from the half-maximum of the NCR), and (iii) NCR shape variations on the high-energy side and detector-window (and detector Si dead-layer) transmission effects. The latter error is expected to be the dominant one for the lower-Z projectiles (if one disregards the systematic error inherent in our method of determining end-point energies).

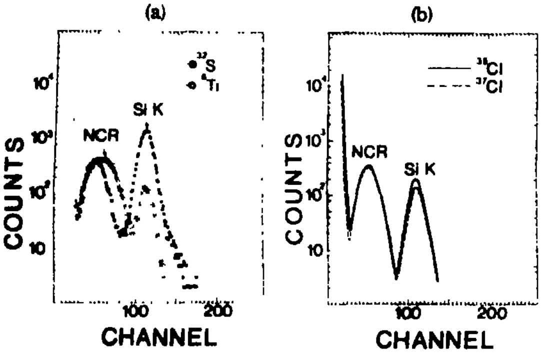

FIG. 1. (a) 200-keV ^{32}S and ^{48}Ti on thick Si. Spectra are shifted vertically to overlap noncharacteristic radiation near 1 keV. (b) 200-keV ^{35}Cl and ^{37}Cl on thick Si. Spectra have been normalized to collected charge.

As a means of removing some of the systematic errors, experimental end-point energy differences were extracted and normalized to the maximum possible differences associated with the 2p binding energy in the united atom. First, we define

$$C_i(\rho_{\min}) \equiv E_i/E_i(2p),$$

where E_i is the binding energy of the 2$p\pi$ level

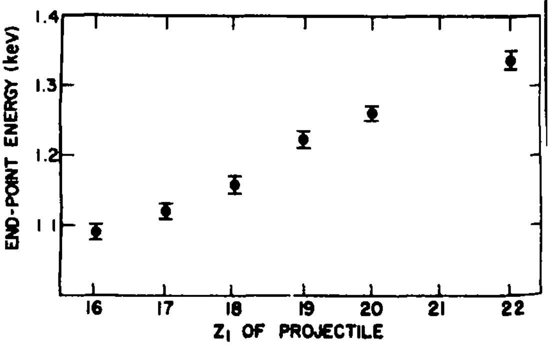

FIG. 2. End-point energies for S, Cl, Ar, K, Ca, and Ti on thick Si.

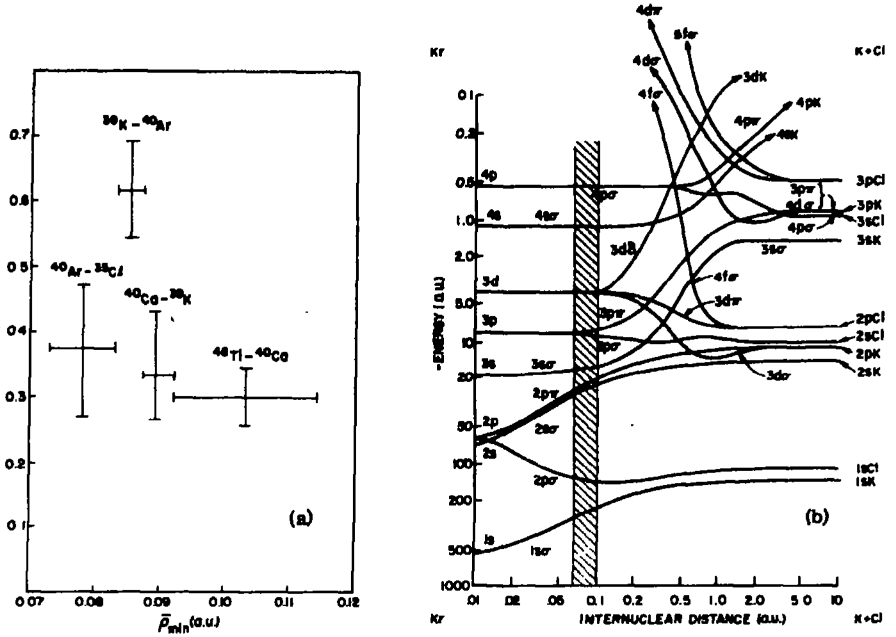

FIG. 3. (a) $\bar{C}_i(\rho_{min})$ as a function of ρ_{min}. The horizontal flag on a datum point is derived from the two distances of closest approach associated with the two projectiles. (b) the K + Cl correlation diagram (from Ref. 8) indicating the region of internuclear separation measured.

at ρ_{min} for the projectile $Z = i$ and $Z = 14$ system, and $E_i(2p)$ is the $2p$ binding energy of the united atom formed by $Z = i$ and $Z = 14$, i.e., at $\rho_{min} = 0$. Furthermore we assume

$$C_i \cong C_{i+1} \equiv \bar{C}_i ;$$

that is, we assume that the *shape* of the molecular orbital (MO) diagrams does not vary greatly over the small differences in ρ_{min} and Z associated with two neighboring projectiles. We then calculate

$$\frac{E_{i+1}(\exp) - E_i(\exp)}{E_{i+1}(2p) - E_i(2p)} = \bar{C}_i(\rho_{min}),$$

where $\bar{C}_i$ is a measure of the binding energy of the united-atom $2p$ level at $\bar{\rho}_{min}$, and $E_i(\exp)$ is the experimentally determined cutoff energy. The large advantage in this formulation is the use of the difference of two experimental cutoffs, thus canceling many uncertainties in the end-point energy definition. Figure 3(a) shows the results of this analysis and indicates that $\bar{C}_i \cong 0.4$ with an indication of a trend to higher $\bar{C}_i$ with smaller ρ_{min} (the S-Cl difference has been omitted because of the uncertainty in the window correction). The horizontal flag on a datum point is determined by the two distances of closest approach associated with the two projectiles, while the vertical error bar is estimated from the reproducibility of the cutoff energy. The Ar-Cl point may be low because of the large effect of the Be window on the Cl + Si distribution. The formula for $\bar{C}_i(\rho_{min})$ and the assumptions in its derivation have been extended and applied to obtain the Ca-Ti point where the atomic number varies by 2.

Figure 3(b) shows the MO diagram for the K + Cl system $(Z_1 + Z_2 = 36)^8$ corresponding to a united atom which is the same as the Ti + Si system described here. We also note that the order of the tightly bound levels is the same for the two systems. Indicated in the diagram is the region of internuclear separation explored in this study; in particular, for an internuclear distance of 0.1 a.u. the diagram yields $C_i = 0.33$, while the experimental result derived from the ^{48}Ti-^{40}Ca measurements is 0.30. If the present experiments were systematically carried to higher energy, the minimum internuclear separation would decrease and the experimental end-point energy differences would presumably lead to C_i approaching 1. This seems to be a way of experimentally mapping out the MO diagram. It would, of course, be useful to have more exact calculations for the particular systems studied here, as well as extending these experiments to a broader range of p.

The yield of Si K x rays present in the spectra of Fig. 1 will be discussed in detail elsewhere.[9] Additional experiments have shown that at the energy used in the present study, they do not primarily arise from a $2p$ vacancy transfer to the Si K level but from recoil Si-Si collisions as has been shown for Ar-Al.[10] At sufficiently higher energies, however, the minimum internuclear separation is small enough to make vacancy transfer to the $1s$ level of Si the dominant mechanism for Si K x-ray production.

The present results strongly support the original interpretation of the NCR. The systematic shift with Z_1 is in accord with expectation and the quantitative magnitude of the shift is quite consistent with the range of minimum internuclear separations produced in 200-keV collisions.

We would like to acknowledge useful discussions with J. S. Briggs, W. L. Brown, and J. R. Macdonald and the technical aid of J. W. Rodgers.

---

*Work supported in part by the National Science Foundation.

†Present address: Physics Department, East Carolina University, Greenville, N. C. 27834.

[1] F. W. Saris, W. F. van der Weg, H. Tawara, and R. Laubert, Phys. Rev. Lett. 28, 717 (1972).

[2] J. Macek, J. A. Cairns, and J. S. Briggs, Phys. Rev. Lett. 28, 1298 (1972).

[3] J. R. Macdonald and M. D. Brown, Phys. Rev. Lett. 29, 4 (1972).

[4] G. Bissinger and L. C. Feldman, Phys. Rev. A 8, 1624 (1973).

[5] U. Fano and W. Lichten, Phys. Rev. Lett. 14, 627 (1965); W. Lichten, Phys. Rev. 164, 131 (1967).

[6] J. R. Macdonald, M. D. Brown, and T. Chiao, Phys. Rev. Lett. 30, 471 (1973).

[7] F. W. Saris *et al.*, in *Proceedings of the International Conference on Inner-Shell Ionization Phenomena and Future Applications, Atlanta, Georgia, 1972,* edited by R. W. Fink, J. T. Manson, I. M. Palms, and R. V. Rao, CONF-720404 (U.S. Atomic Energy Commission, Oak Ridge, Tenn., 1973).

[8] M. Barat and W. Lichten, Phys. Rev. A 6, 211 (1973).

[9] L. C. Feldman, G. Bissinger, and J. S. Briggs, to be published.

[10] K. Taulbjerg, B. Fastrup, and E. Laegsgaard, Phys. Rev. A 8, 1814 (1973).

New Method for Lamb-Shift Measurements*

A. van Wijngaarden, G. W. F. Drake,† and P. S. Farago‡
Department of Physics, University of Windsor, Windsor, Ontario, N9B 3P4, Canada

(Received 7 May 1974)

The anisotropy in the quenching radiation of H atoms in the metastable $2s$ state has been studied with the aim of developing a new method for Lamb-shift measurements in hydrogenic ions. The extrapolated value of the anisotropy at zero field strength is 0.1392 ± 0.0015, in good agreement with the theoretical prediction 0.139 04 based on the accepted value of the Lamb shift and a consideration of hyperfine coupling effects. Our anisotropy corresponds to a Lamb shift of 1059 ± 13 MHz.

The comparison of Lamb-shift measurements in hydrogen and the hydrogenic ions with theoretical calculations remains one of the important tests of quantum electrodynamics.[1] The Lamb shifts in H,[2] D,[3] He$^+$,[4] and Li^{2+} [5] are now accurately known from experiments using microwave resonance techniques, but no technique of comparable accuracy is available for the heavier ions. A much less accurate method based on a measurement of the quenching rate of the metastable $2s_{1/2}$ state in an electric field has been applied to Li^{2+},[6] C^{5+},[7] and O^{7+},[8,9] but the results are far from matching the accuracy of the calculations of Erickson.[10] We report in this Letter some preliminary results for hydrogen which indicate that a method recently suggested by Drake and Grimley[11] is capable of an accuracy at least as good as obtained by the quenching-rate technique. In addition, the results resolve a possible discrepancy between theory and experiment found by Ott, Kauppila, and Fite[12] in their measurement of the polarization of the quenching radiation.

Fite, Kauppila, and Ott[12] and Casalese and Gerjuoy[13] first pointed out that the quenching radiation is polarized, but it was not appreciated until recently that in addition the radiation summed over both polarizations is anisotropic.[11] Since the anisotropy is approximately proportional to the Lamb shift, a measurement of the total numers of Lyman-α photons emitted in the directions parallel and perpendicular to the quenching ield is sufficient to determine the Lamb shift. (A detailed account of the theory is given in Ref. 11.) The anisotropy is defined by

$$R=(I_{\parallel}-I_{\perp})/(I_{\parallel}+I_{\perp}), \qquad (1)$$

where $I_{\parallel}$ and $I_{\perp}$ are the *total* intensities emitted in the parallel and perpendicular directions. Since R is independent of field strength in the limit of weak fields, a short extrapolation to zero field strength eliminates all systematic errors which are proportional to powers of the field strength. No field strength calibration or accurate spatial resolution is necessary, thereby eliminating some of the sources of error in the quenching-rate measurements. Difficulties arising from ion-beam deflection in the quenching field and background noise are minimized because measurements need be done at only a single point near the region of optimum photon counting statistics.

A schematic diagram of the apparatus used by us is shown in Fig. 1. A monoenergetic (10 keV) beam of protons traverses a heated chamber containing Cs vapor. The emerging beam contains metastable H atoms in the $2s$ state produced in the near-resonant reaction $H^{+}+Cs\rightarrow H(2s)+Cs^{+}$. Protons are deflected out of this beam by a weak electric field (~10 V/cm) between the prequenching plates. A collimated beam of neutrals then enters the observation region where the metastables are quenched by a dc electric field between two parallel plates. The resulting Ly-α radiation passes through a slit system, through an O_2 cell which has a transmission "window" at the Ly-α wavelength, and then into an ultraviolet detector which is connected to standard counting equipment. The pair of quenching plates equipped with a fine mesh screen 1 and a similar screen 2 can be rotated together by 90° about the neutral beam axis leaving the slit and detector system in a fixed position. Mesh 1 is employed to maintain a uniform field in the quenching region, and mesh 2 is introduced for the sake of optical symmetry. Thus the photons can be observed through identical optical systems when emitted either parallel or perpendicular to the applied field. The photon counts $N_{\parallel}$ and $N_{\perp}$ obtainable in the two positions of the quenching plates are automatically normalized to a constant neutral-beam intensity by monitoring the neutral-beam current with the aid of a current-to-frequency converter to define the length of the counting period for each measurement. Since the dependence of the total intensity I on the angle between the field and the direction of observation θ is of the form $I=U\cos^2\theta+V\times\sin^2\theta$,[11] where U and V are functions of the field strength, I is very insensitive to small errors in angular settings in the neighborhood of $\theta=0°$ and 90°, making it easy to correct for the effect of a finite solid angle of observation.

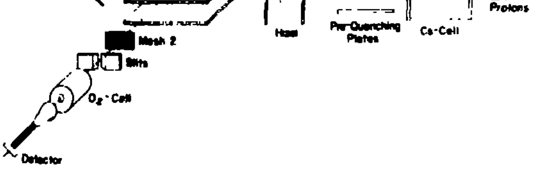

FIG. 1. Schematic diagram of apparatus.

There are several factors which can introduce an instrumental asymmetry. (i) Changes in acceptance angle with the rotation of the quenching plates. This does not occur because the slit system is kept fixed. (ii) Different transparencies of the screens 1 and 2. A calibration run with a beam-foil source of $2p$-$1s$ Ly-α radiation indicated that they are equal to an accuracy of 3 parts in 10^4. (iii) The presence of stray magnetic fields $\vec{B}$ giving rise to a motional electric field $\vec{E}=\vec{v}\times\vec{B}$. With weak quenching fields this effect could be detected by reversing the direction of the quenching field. By defining the measured radiation intensity as the mean of two values obtained with field directions reversed this effect is eliminated to a high degree of accuracy. (iv) Reflections from surfaces. This was reduced as much as possible by careful design and the blackening of all surfaces.

The observed photon counts $N_{\parallel}$ and $N_{\perp}$ were corrected for background noise by applying a high (1500 V/cm) field to the prequenching plates and determining the isotropic component of the radition still observed. The noise thus defined amounted to 1–2% of the signal obtained in the absence of the prequenching field. The normalized photon counts $N_{\parallel}$ and $N_{\perp}$ corrected for background noise and the finite solid angle of observation are identified as the intensities $I_{\parallel}$ and $I_{\perp}$, respectively. The radiation anisotropy R is then defined by Eq. (1).

The anisotropy was measured at a sequence of

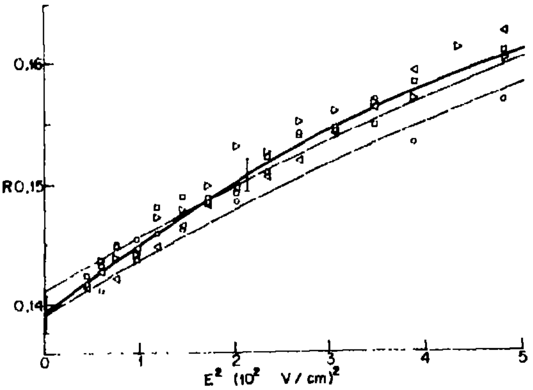

FIG. 2. Variation of anisotropy with field strength. Solid curve, a least-squares fit to four independent runs; upper dashed curve, theory without hyperfine structure; lower dashed curve, theory with hyperfine structure.

different quenching field strengths E, and a curve

$$R=\sum_{k=0}^{n}a_kE^{2k}$$

was fitted to the experimental results. In performing the least-squares fitting to single runs the approximation to a degree $n=2$ was always found to be statistically significant. While curves thus obtained for individual runs were slightly different in detail, they always led to extrapolated values $R(E\to 0)$ which agreed with one another within their error margins.

The experimental results obtained from four independent runs are plotted in Fig. 2. The various symbols represent individual experimental results corrected for noise and the finite solid angle of observation. The statistical error is the same in each case and is indicated by one error bar. The solid curve is a quadratic least-squares fit to the *combined* data of the four runs and the error bar at the left is the computed uncertainty in the extrapolated value of R at zero field strength. The lower and upper dashed curves are the results of theoretical calculations[14] based on the accepted value of the Lamb shift (1057.9 MHz) with and without hyperfine-structure coupling effects, respectively. The theory contains a summation of the infinite time-dependent perturbation series for finite field strengths and includes the progressive nuclear spin uncoupling with increasing field strength and interaction time.

The extrapolated zero-field value of R, 0.1392 ± 0.0015, agrees with the theoretical value 0.139 04 including hyperfine-structure effects, but lies below the value 0.141 12 obtained by neglecting hyperfine structure. The apparent disagreement between theory and experiment at high field strengths is undoubtedly a field-dependent instrumental effect which is largely eliminated by the extrapolation to zero field strength. The percentage error in the Lamb shift derived from R is nearly equal to the percentage error in R. Our value corresponds to a Lamb shift of 1059 ± 13 MHz.

It can easily be shown from Eqs. (7) and (10) of Ref. 11 that R is related to the polarization P of the quench radiation by

$$P=2R/(R-1). \qquad (2)$$

This result remains valid at all field strengths. Our zero-field value of R therefore corresponds to $P=-0.3235\pm 0.0040$ in agreement with the theoretical value -0.3230 including hyperfine structure. It seems likely that the smaller value -0.30 ± 0.02 measured directly by Ott, Kauppila, and Fite[13] is due to an instrumental effect rather than a genuine disagreement with theory.

The results reported here were obtained from a very simple "hand-controlled" experiment without the use of sophisticated data collection techniques. The accuracy can be improved by at least an order of magnitude with improved controls and photon counting statistics. The introduction of a double counter system to monitor both $I_{\parallel}$ and $I_{\perp}$ simultaneously would be particularly advantageous. The apparatus is currently undergoing modification to incorporate these refinements and extend the measurements to the hydrogenic ions. Similar results have been obtained by replacing the rotating plates with a symmetric quadrupole field which can be switched electronically. This geometry avoids possible changes in the background when the field direction is rotated.

---

[*] Research supported by the National Research Council of Canada.

[†] Alfred P. Sloan Research Fellow.

[‡] On leave of absence from the Department of Physics, University of Edinburgh, Edinburgh, Scotland.

[1] B. E. Lautrup, A. Peterman, and E. de Rafael, Phys. Rep. 3C, 196 (1972).

[2] S. Triebwasser, E. S. Dayhoff, and W. E. Lamb, Jr., Phys. Rev. 89, 98 (1953); R. Robiscoe and T. Shyn, Phys. Rev. Lett. 24, 559 (1970).

[3] B. Casens, Phys. Rev. 173, 49 (1968).

[4] M. Narashimham, thesis, University of Colorado, 1969 (unpublished).

[5] M. Leventhal and P. E. Havey, Phys. Rev. Lett. 32, 808 (1974).

[6] C. Fan, M. Garcia-Munoz, and I. Sellin, Phys. Rev. 161, 6 (1967).

[7] H. W. Kugel, M. Leventhal, and D. E. Murnick, Phys. Rev. A 6, 1306 (1972).

[8] M. Leventhal, D. E. Murnick, and H. W. Kugel, Phys. Rev. Lett. 28, 1609 (1972).

[9] F. P. Lawrence, C. Y. Fan, and S. Bashkin, Phys. Rev. Lett. 28, 1612 (1972).

[10] G. W. Erickson, Phys. Rev. Lett. 27, 780 (1971).

[11] G. W. F. Drake and R. B. Grimley, Phys. Rev. A 8, 157 (1973). Equation (9) of this reference is incorrect. It should read

$$\sum_{\theta_2} |Q(\omega_1,\omega_2)|^2 = \tfrac{1}{3}(|A|^2 + |A'|^2)\sin^2\theta + \tfrac{2}{3}|A'|^2\cos^2\theta.$$

[12] W. L. Fite, W. E. Kauppila, and W. R. Ott, Phys. Rev. Lett. 20, 409 (1968); W. R. Ott, W. E. Kauppila, and W. L. Fite, Phys. Rev. A 1, 1089 (1970).

[13] J. S. Casalese and E. Gerjuoy, Phys. Rev. 180, 327 (1969).

[14] G. W. F. Drake, to be published.

Efficient Positronium Formation by Slow Positrons Incident on Solid Targets*

K. F. Canter, A. P. Mills, Jr., and S. Berko
Department of Physics, Brandeis University, Waltham, Massachusetts 02154

(Received 1 April 1974)

A beam of slow positrons in the few-eV region is directed at bakable solid targets in a vacuum of $(2-4)\times10^{-8}$ Torr. Measurements of the $2\gamma/3\gamma$ annihilation-yield ratio indicate the conversion of the incident positrons into positronium. The conversion efficiency depends on the target material and incident positron energy, varying from less than 25% at 300 K to 40–85% at 900 K.

In this Letter we report the observation that an external slow-positron (e^+) beam (a few eV) forms positronium (Ps) with high efficiency when colliding with solid targets. The experiment is the first designed explicitly to study the collisions of slow positrons with solid targets, and has been made possible by recent developments in the production of high-flux e^+ beams.[1-4] The large e^+-to-Ps conversion efficiency reported here, besides its intrinsic interest, is particularly relevant to the interpretations of recent observations of slow-e^+ emission from metal surfaces,[4,5] Ps emission from oxide powders,[6,7] and the intermediate-lifetime component in metal powders.[8] These phenomena have been observed with fast (≈0.5 MeV end-point energy) e^+ that have slowed down internally in the solid, as contrasted to the external-beam technique reported here.

The experimental setup consists of a slow-e^+ beam and a target stage. Slow e^+ are produced in a converter similar to that originally used for e^+-helium scattering-cross-section measurements.[3] The converter consists of MgO-coated gold foils, 0.15 mm thick, arranged in a venetian-blind geometry on a 1-cm-diam ring, behind which is placed a ^{58}Co fast-e^+ source. In order to have the target far from the source, the e^+ are magnetically transported through a 1.5-m-long beam tube with a 30° bend in the middle. The tube is baffled internally against fast e^+ and wound externally with a solenoid; with a field of 75 G, only the slow e^+ are able to reach the target. Approximately one in 3×10^4 of the ^{58}Co e^+ emerge as slow e^+. The e^+ beam has a measured longitudinal energy distribution of less than 2-eV width, with an intrinsic average energy of 1 to 2 eV with respect to a grounded tungsten grid in front of the converter. The converter can be biased with an accelerating voltage V_A.

Figure 1 shows the details of the target chamber at the end of the beam tube. Pressures at the target range from (2 to 4)$\times10^{-8}$ Torr, with a pump-oil-vapor background of less than 10^{-15} Torr. The target cage and target stage can be biased with respect to ground by a voltage V_T. Suitably changing V_A and keeping $V_A - V_T$ fixed, we can keep the incident e^+ energy constant with V_T positive or negative. When tests of target polarity are not being made, the target cage and the grid in front of the cage are removed from the target chamber. Annihilation spectra of the incident e^+ are obtained with a NaI(Tl) detector.

Figure 2 shows the NaI(Tl) pulse-height spectra for 10-eV e^+ incident on a Ti target at 300 and 770 K. The dashed curve labeled "pure 2γ" was obtained by accelerating the e^+ into the Ti target at 300 K with $V_A - V_T = 360$ V. The same spectral shape is obtained by placing a ^{22}Na source surrounded by copper at the location of the target stage.. When the Ti target is heated from 300 to

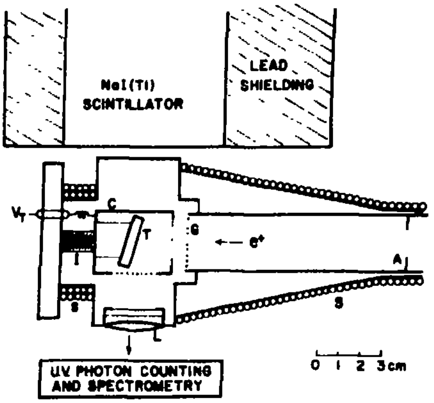

FIG. 1. Target chamber. *A*, aperture; *S*, solenoids; *G*, grounded grid; *C*, target cage; *T*, target stage; *I*, insulator; *L*, quartz window and lens. *C* and *T* are at the same bias V_T. The 3 in.×3 in. NaI(Tl) scintillator is coupled to an RCA 8575 photomultiplier. A heater in the target stage allows target specimens to be heated to 900 K.

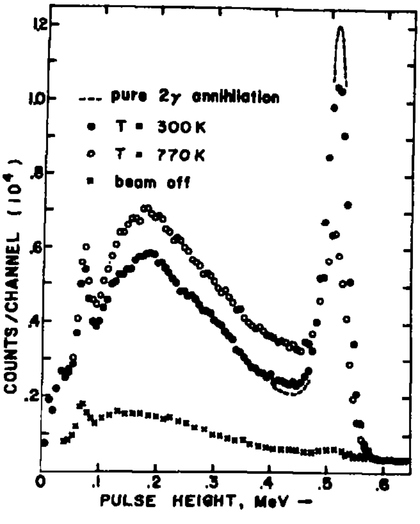

FIG. 2. NaI(Tl) pulse-height spectra of 10-eV e^+ annihilation γ's from Ti. Run time per spectrum is 80 min, using a 6-mCi ^{58}Co fast-e^+ source. The pure-2γ spectrum corresponds to no Ps formation.

770 K, a reduction in the 511-keV photopeak accompanied by an increase in the counting rate below 511 keV is observed. We attribute this change to an increase in 3γ annihilation, indicating an increase in freely annihilating Ps formation. At 770 K the photopeak is reduced by 50% compared to the pure-2γ spectrum, after subtraction of the "beam-off" background. Taking into account the 2γ annihilations from $\frac{1}{4}$ of the Ps formed in the spin-singlet state, and correcting for the probability that two photons from the 3γ annihilations of spin-triplet Ps can enter the scintillator simultaneously and contribute counts under the 511-keV photopeak, the observed 50% photopeak reduction is estimated to correspond to a free Ps formation efficiency ϵ of $(80 \pm 10)\%$. The same analysis yields $\epsilon = (25 \pm 10)\%$ at a 300-K target temperature.

The loss of 2γ annihilations was also measured using two NaI detectors 180° apart. The coincidence rate as a function of target temperature is shown in Fig. 3. Starting with point *A* (e^+ energy 360 eV, $\epsilon \lesssim 5\%$) and multiplying the observed fractional loss in coincidences by $\frac{4}{3}$ yields ϵ (23% and 80% for target temperatures of 300 and 750 K, respectively). Estimating the fraction of 3γ annihilations detected in coincidence yields corrected values of ϵ equal to $(25 \pm 5)\%$ and $(85 \pm 5)\%$.

Let us consider the validity of the Ps-formation interpretation of the observed effect of temperature on the single-NaI-detector spectra. The only other way in which the peak counting rate *P* at 511 keV might decrease with a simultaneous increase in the valley (between the photopeak and

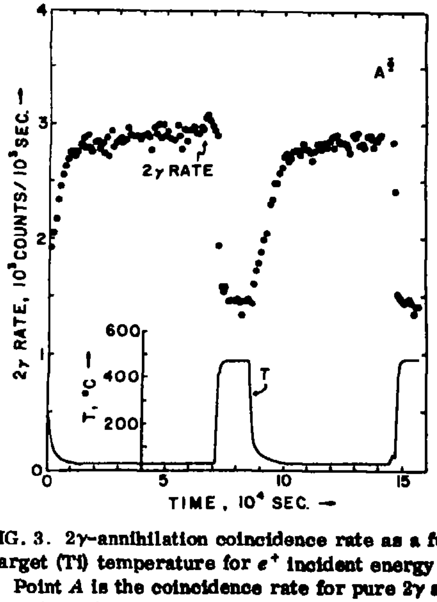

FIG. 3. 2γ-annihilation coincidence rate as a function of target (Ti) temperature for e^+ incident energy of 10 eV. Point *A* is the coincidence rate for pure 2γ annihilations (no Ps). Note that when the target is cooled, the 2γ rate responds by increasing with a characteristic time of 10^4 sec.

the 340-keV Compton edge) count rate V is for some of the 2γ annihilations to originate from locations out of direct sight of the scintillator, and to undergo Compton scattering into the detector. However, we have found experimentally that the magnetic guiding field constrains the e^+ to annihilate only at the target stage or far back into the beam tube. Further, a pure 2γ source was moved to various positions inside the target chamber in an attempt to simulate a geometry-related reduction in P/V. The largest reduction of P/V achieved was 30%, but at a cost of a 40% reduction in total count rate. In sharp contrast, baking a Ti target, for example, yields a 60% decrease in P/V, accompanied by a 15% *increase* in total count rate. An increase is to be expected as a result of the higher detection probability for 3γ annihilation.

In lieu of an arrangement of three shielded scintillation detectors (not permitted by the spatial limitations imposed by the pumping system at the target chamber), a second detector with a 2 cm × 8 cm Pb slit geometry was placed at 90° and 30 cm away from the target. Upon our baking an etched Au target (which shows the same P/V change as does Ti), the coincidence rate between the two counters increased above the 300-K coincidence rate by 0.50 ± 0.01 sec^{-1} with a slow-e^+ beam of 6000 e^+ sec^{-1}. This agrees with an estimate of the increase in 3γ annihilations which result in two of the three γ's being detected, using the values of ϵ given above.

Measurement of the P/V changes with and without the target cage, and a search for 2γ coincidences away from the target, have also been carried out to differentiate between the possibilities of freely annihilating Ps being very weakly bound to the target surface and its actually escaping from the target. Although the results presently indicate that the Ps escapes, the escape velocity cannot be determined until the reflection coefficient of Ps colliding with the interior walls of the target chamber is known. Measurements of the effect of changing the polarity of V_T [while keeping the e^+ incident energy $E_i \approx e(V_A - V_T)$ constant] show that (1) P/V is independent of target polarity, and (2) the fraction of incident e^+ which are reemitted by the target as slow e^+ is less than 10% for $E_i > 10$ eV.

The measured values of ϵ (to the nearest 5%) for 10-eV e^+ incident on the targets at 800 K are as follows: Au, etched, 85%; Au, unetched, 60%; Ti, 85%; Cu, oxygen-free high-conductivity, 60%; graphite, pyrolytic single crystal, 70%; fused quartz (Suprasil), 65%; MgO, single crystal, 75%; Al, 75%; ZnO, powder, 80%; quartz, single crystal, 50%. None of the samples investigated exhibit appreciable changes in ϵ when the target temperature is varied from 750 to 900 K. For all targets at room temperature, ϵ is less than 25% for $E_i > 10$ eV. At intermediate temperatures ϵ exhibits a complex dependence on the target's bakeout history. In addition to the thermal effects, ϵ varies with E_i. For example, for Ti at 800 K, ϵ decreases from 85% for $E_i = 10$ eV to 40% for $E_i = 350$ eV. At room temperature ϵ decreases from 25% to less than 5% over the same range of E_i. The variation of ϵ with E_i is smaller for Au targets.

We interpret the effect of temperature on the increase in Ps formation to be the result of desorbing the many physisorbed layers of water as well as other possible contaminants typically present on surfaces in nonultrahigh vacuum. However, the baking does not necessarily remove the oxide or activated oxide-hydrocarbon compound layers; thus Ps formation might be due to such nonmetal surface layers, since oxide powders are known to be efficient converters of internally thermalized e^+ into Ps.[6,7]

A preliminary measurement of ϵ for 10-eV e^+ incident on a special tungsten filament target yields $\epsilon = (80 \pm 5)\%$ at 1800 K. This result perhaps comes closest to indicating Ps formation at a pure metal surface, although at this temperature an oxide layer can still persist on W. Even though Ps formation in bulk metals is forbidden,[9] formation at metal surfaces might still be possible by virtue of the electron cloud extending beyond the positive-ion background of the metal.[10]

To date, slow-e^+ emission has only been observed to be relatively efficient from surfaces having several adsorbed layers of contaminants. Recent measurements show that e^+ emission from metals is reduced significantly upon baking the surfaces at 500 K in a vacuum of 10^{-7} Torr.[11] Other experiments show a reduction in the slow-e^+ yield as a function of the length of time that the surfaces have been kept in vacuum.[3] Moreover, our results indicate that Ps formation is the dominant low-energy e^+ surface process when most of the adsorbed contaminants are removed by baking. Such effects are consistent with an earlier suggestion that slow-e^+ emission from "metals" at room temperature is a result of dissociated Ps.[2] However, there may be some fundamental difference in the surface effects between e^+ diffusing to the surface as a result of thermalization inside the bulk solid and e^+ being introduced externally at low energies. In any case, the interpretation of these effects in terms of pure metal surfaces is premature, and ultrahigh-vacuum experiments are needed.

The photon counting system referred to in Fig. 1 is being employed in a search for 2430-Å photons resulting from the Lyman-α transition of the Ps if any is formed in the $n=2$ excited state.[12] If at least 0.1% of the Ps were formed in the $n=2$ state, we would observe a significant signal (95% confidence level) after a 24-h run with our present sensitivity. As of this writing, we have observed no Lyman-α photons for any target material investigated.

The authors wish to acknowledge valuable discussions regarding surface conditions with Dr. E. W. Plummer, University of Pennsylvania, and Dr. J. C. Tracy, General Motors Technical Center.

Note added.—The positronium formation has now also been confirmed by a direct 3γ coincidence measurement. Using an extended target chamber we obtain a triple coincidence rate between three 3×3-in. NaI(Tl) detectors, 10 cm from a Ti target, of $0.362 \pm 0.027 \text{ sec}^{-1}$ at 525°C versus $0.064 \pm 0.013 \text{ sec}^{-1}$ at 30°C with a background rate $\approx 0.017 \text{ sec}^{-1}$.

---

*Work supported by the National Science Foundation and the U. S. Army Research Office, Durham, N. C.

[1] P. G. Coleman, T. C. Griffith, and G. R. Heyland, Proc. Roy. Soc., Ser. A 331, 561 (1973).

[2] K. F. Canter, P. G. Coleman, T. C. Griffith, and G. R. Heyland, J. Phys. B: Proc. Phys. Soc., London 5, L167 (1972).

[3] W. C. Keever, B. Jaduszliwer, and D. A. L. Paul, in *Atomic Physics 3*, edited by S. J. Smith and G. K. Walters (Plenum, New York, 1973), p. 561.

[4] S. Pendyala, P. W. Zitzewitz, J. W. McGowan, and P. H. R. Orth, Phys. Lett. 43A, 298 (1973).

[5] D. G. Costello, D. E. Groce, D. F. Herring, and J. W. McGowan, Phys. Rev. B 5, 1433 (1972).

[6] R. Paulin and G. Ambrosino, J. Phys. (Paris) 29, 263 (1968).

[7] S. M. Curry and A. L. Schwalow, Phys. Lett. 37A, 5 (1971).

[8] R. Paulin, R. Ripon, and W. Brandt, Phys. Rev. Lett. 31, 1214 (1973).

[9] H. Kanagawa, Y. H. Ohtsuki, and S. Yanagawa, Phys. Rev. 138, A1115 (1965), and references therein.

[10] N. D. Lang and W. Kohn, Phys. Rev. B 3, 1215 (1971).

[11] S. Pendyala, D. M. Bartell, and J. W. McGowan, Bull. Amer. Phys. Soc. 18, 1505 (1973).

[12] L. W. Fagg, Nucl. Instrum. Methods 85, 53 (1970), and references therein. Recently two groups [S. L. Varghese, E. S. Ensberg, V. W. Hughes, and I. Lindgren, Bull. Amer. Phys. Soc. 18, 1503 (1972); S. L. McCall, Bull. Amer. Phys. Soc. 18, 1512 (1973)] have reported experiments to excite ground-state Ps to the $n=2$ state.

Raman Scattering from Coherent Spin States in *n*-Type Cds

R. Romestain,* S. Geschwind, and G. E. Devlin
Bell Laboratories, Murray Hill, New Jersey 07974

and

P. A. Wolff†
Department of Physics, Massachusetts Institute of Technology, Cambridge, Massachusetts 02139

(Received 8 May 1974)

When the donor spins in *n*-CdS are simultaneously irradiated with laser light at frequency ω_L and microwaves at frequency ω_0 near the spin resonance, intense sidebands at $\omega_L \pm \omega_0$ are observed for forward scattering which are more than 3 orders of magnitude greater than those for spontaneous spin-flip Raman scattering. This phenomenon is explained as Raman scattering from coherent states.

We have observed intense sideband radiation at frequencies $\omega_L \pm \omega_0$, when the electron spins in *n*-CdS are simultaneously irradiated with laser light at frequency ω_L and microwaves at frequency ω_0, close to the donor-spin resonance frequency. These huge sidebands are observed in the forward direction and are at least *3 orders of magnitude stronger than those due to spontaneous spin-flip Raman scattering* (SFRS). This effect has been seen in crystals ranging in concentration from $(1 \text{ to } 5) \times 10^{17}$ (excess donors)/cm^3. It may be described as coherent SFRS from coherent spin states or, alternatively, as parametric conversion of light via the macroscopic magnetic dipole precessing at frequency ω_0. In optimal cases a conversion efficiency of 6% has been seen.

The experiment described below is a new type of optically detected EPR, which may prove advantageous in studying semiconductors in the Mott-transition regime, covered by our sample concentrations,[1] where EPR and relaxation measurements have been difficult.

The apparatus used to observe SFRS and simultaneously irradiate the sample with microwaves is similar to that previously used to study the microwave-phonon bottleneck with Brillouin scattering.[2] It was simply modified for observation of forward light scattering (as compared to 90° scattering) by use of a mirror as shown in Fig. 1(a). The laser beam—a single-mode Ar$^+$ at 4880 Å—propagates at a small angle θ relative to the c axis of the crystal. It should be emphasized, however, that the scattered light is viewed along the direction of the laser beam, as the coherent SFRS is collinear with the incident beam as will be discussed below.

Figure 1(a) shows the SFRS spectrum as analyzed by a piezoelectrically scanned Fabry-Perot interferometer in a sample with 2×10^{17} excess donors. The observed ratio of Stokes to anti-Stokes emission is in rough accord with the expected Boltzmann factor for a temperature of 2°K and a field of 9600 G. These measurements parallel earlier work on spontaneous SFRS in n-CdS.[3,4] Here, however, lower field and higher resolution are used.

Figure 1(b) illustrates the more than 3 orders of magnitude increase in forward sideband scattering that occurs when a resonant microwave field H_1 is applied to the sample. The observed difference in intensity between Stokes and anti-Stokes emission in Fig. 1(b), and its reversal when the polarization of the incident laser beam is rotated by 90°, as illustrated in Fig. 1(c), is due to phase-matching conditions detailed below. The larger peaks in Figs. 1(b) and 1(c) correspond to an intensity which is approximately 5% of the laser beam. The variation in intensity of the scattered light as the magnetic field is swept through its resonant value $H_0=\hbar\omega_0/g\mu_B$ reflects the EPR signal as discussed below. However, its frequency shift is always equal to the driving frequency ω_0.

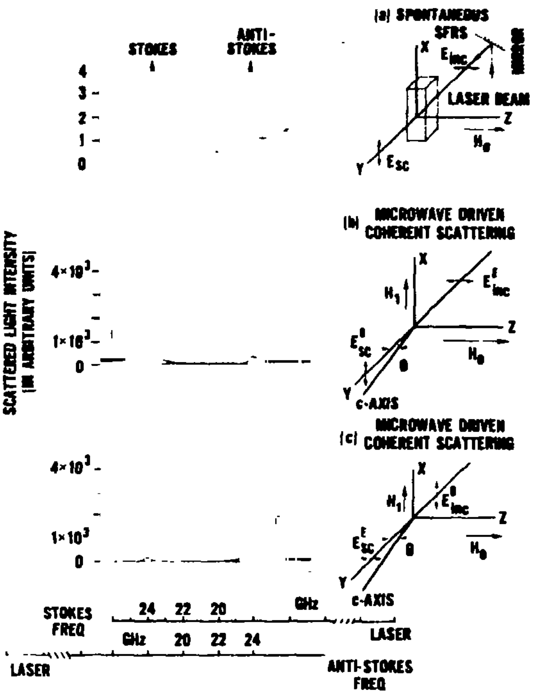

FIG. 1. Forward SFRS spectra at 2°K and associated geometries: (a) without resonant 23.96-GHz microwave excitation of the spins; (b) and (c) with microwave excitation (spectrum a is shown for comparison). The c axis is in the y-z plane. Depending upon whether E_L is in this plane (b) or perpendicular to it (c), phase matching favors Stokes or anti-Stokes emission, respectively. The other weak component is also seen as a result of depolarization of incident light.

The coherent effect described above may be calculated by following a semiclassical treatment. Raman scattering between two general states $|a\rangle$ and $|b\rangle$ may be viewed as radiation from a Raman dipole resulting from the admixture of excited states $|n\rangle$ into $|a\rangle$ and $|b\rangle$ via coupling to the electric field $\vec{E}_L\cos(\omega t)$ of the incident light beam. To lowest order in E_L, the modified ground states $|\psi_a\rangle$ and $|\psi_b\rangle$, with energies $\hbar\omega_a$ and $\hbar\omega_b$, respectively, may be written as[6]

$$|\psi_a\rangle=\exp(-i\omega_a t-i\varphi)\{|a\rangle-\tfrac{1}{2}\textstyle\sum_n|n\rangle[\langle n|\vec{E}_L\cdot e\vec{r}|a\rangle/(E_n-E_a-\hbar\omega_L)]\exp(-i\omega_L t)\}. \qquad (1)$$

For simplicity we have dropped the nonresonant term in $|\psi_a\rangle$ as the frequency of the laser light is close to an intermediate-state resonance. $|\psi_b\rangle$ is given by an equation similar to (1) with b replacing a, but without the factor $e^{-i\varphi}$, which describes the relative phase between the states and is random for spontaneous scattering.

It is convenient to introduce an effective Raman dipole operator $\vec{D}^{(2)}$ which operates in the two-dimensional manifold of the unperturbed states $|a(t)\rangle = |a\rangle \exp(-i\omega_a t - i\varphi)$ and $|b(t)\rangle = |b\rangle \exp(-i\omega_b t)$ such that

$$\langle \psi_b(t)| e\vec{r}| \psi_a(t)\rangle = \langle b(t)| \vec{D}^{(2)}| a(t)\rangle. \tag{2}$$

In most general fashion any such operator may be expressed in terms of a fictitious spin $S = \frac{1}{2}$ formalism.[6] Thus

$$D_k^{(2)} = \sum_{ij} \alpha_{ijk} E_{Li} \sigma_j \exp(-i\omega_L t) + \beta_{ik} E_{Li} \tilde{I} \exp(-i\omega_L t) + \text{c.c.}, \tag{3}$$

where the σ_j's are the Pauli matrices and where we have taken $E_n - E_a \simeq E_n - E_b$. For the case where $|a\rangle$ and $|b\rangle$ are time-reversed states split by a magnetic field along z and for cubic symmetry,[7] it follows easily that

$$\vec{D}^{(2)} = \vec{\sigma} \times \vec{E}_L[\alpha \exp(-i\omega_L t) + \text{c.c.}] + [\beta \vec{E}_L \tilde{I} \exp(-i\omega_L t) + \text{c.c.}], \tag{4}$$

where[8]

$$\alpha = \sum_n \tfrac{1}{2} i \langle a|ex|n\rangle\langle n|ez|b\rangle / (E_n - E_a - \hbar\omega_L). \tag{5}$$

In Eq. (4), β corresponds to the usual polarizability which gives rise to the Rayleigh scattering. Interaction of $\vec{D}^{(2)}$ with the Raman-scattered light $\vec{E}_R$ immediately yields the effective spin-flip Hamiltonian,

$$\mathcal{H}_{sf}^{(2)} = \tfrac{1}{2} \alpha \vec{\sigma} \cdot (\vec{E}_L \times \vec{E}_R) \exp[-i(\omega_L - \omega_R)t] + \text{c.c.}, \tag{6}$$

previously used to describe spontaneous SFRS in semiconductors[9] and the parametric generation in the far infrared by the mixing of two laser beams.[10]

Spontaneous Raman scattering between $|a\rangle$ and $|b\rangle$ is associated with the Raman electric dipole,

$$\langle b(t)| \vec{D}^{(2)}| a(t)\rangle = \exp(+i\omega_{ba} t - i\varphi)[\alpha \exp(-i\omega_L t) + \text{c.c.}]\langle b|\vec{\sigma}| a\rangle \times \vec{E}_L. \tag{7}$$

The appropriate dipole to use in the classical radiation formula is $\langle b(t)|\vec{D}^{(2)}|a(t)\rangle + \text{c.c.}$, where for Stokes emission one omits the energy nonconserving term $\exp[+i(\omega_L + \omega_{ba})t]$. Similarly, for anti-Stokes emission one omits the $\exp[+i(\omega_L - \omega_{ba})t]$ term. Radiation in the transverse plane of this dipole can be expressed in terms of a spontaneous differential Raman cross section per center, given by

$$(d\sigma/d\Omega)_{\text{sp}} = 4|\alpha|^2(\omega_L \pm \omega_{ba})^4/c^4. \tag{8}$$

The important point to be emphasized is the random-phase factor φ in Eq. (7) which results in the incoherent spontaneous Raman scattering from the centers. By contrast, we now consider the case where the system is prepared as a coherent superposition of states $|a\rangle$ and $|b\rangle$ as is done in our experiment by application of a coherent microwave field of frequency ω_0 near resonance with ω_{ba}, i.e.,[11]

$$c(t) = \lambda| a\rangle + \mu \exp(i\omega_0 t)| b\rangle. \tag{9}$$

λ and μ are related to the components of $\langle\vec{\sigma}\rangle$ which are in turn given by solutions to the Bloch equations,[12] neglecting the feedback of the Raman light. The magnitude of the transverse component of precessing magnetization is $\sigma_T = \frac{1}{2}|\lambda\mu|$. By the use of (4) and (9), it is seen that the state $|c(t)\rangle$ displays an oscillating Raman dipole,

$$\vec{D}_{cc}^{(2)} = \langle c(t)| \vec{D}^{(2)}|c(t)\rangle = [\lambda\mu^*\langle a|\vec{\sigma}|b\rangle \times \vec{E}_L \exp(-i\omega_0 t) + \text{c.c.}][\alpha \exp(-i\omega_L t) + \text{c.c.}]. \tag{10}$$

All dipoles in Eq. (10) have their phase unambiguously defined in contrast to spontaneous scattering [Eq. (7)]. These coherent electric dipoles constitute a superradiant source in the Dicke sense[13] which will emit cooperatively in the forward direction at frequencies $\omega_L \pm \omega_0 = \omega_S$ provided that a phase-matching condition $\Delta k = k_L - k_S - k_0 = 0$ is fulfilled, or $k_L - k_S \simeq 0$ since the microwave frequency corresponds to $k_0 \simeq 0$. It should be noted that emission depends on σ_T and will therefore persist for the phase memory time T_2 of σ_T even after the microwaves are removed.

Using $\eta \vec{D}_{cc}^{(2)}$ as a source term in Maxwell's equations, one has for the geometry shown in Fig. 1

$$2ik_s\left(\frac{\partial E_s}{\partial y}+\frac{\gamma}{2}E_s\right)\propto-\frac{4\pi\omega^2}{c^2}D_{cc}^{(2)}\eta e^{i\Delta ky}. \qquad (11)$$

Here E_s is the sideband field amplitude, k_s the sideband wave vector, γ the absorption coefficient, and η the concentration. Note that $D_{cc}^{(2)}$ has the factor $e^{-\gamma y/2}$ via E_L. Equation (11) can be integrated to estimate P_s/P_0, the ratio of intensities of Raman to laser light exiting from the crystal. The factor α appearing in $D_{cc}^{(2)}$ can be expressed in terms of $(d\sigma/d\Omega)_{\rm sp}$ via Eq. (8), giving

$$\frac{P_s}{P_0}=\frac{1}{2}\left(\frac{d\sigma}{d\Omega}\right)_{\rm sp}\frac{\lambda_s^2\eta^2\sigma_T^2}{\epsilon}\frac{1-\cos(\Delta kL)}{\Delta k^2}, \qquad (12)$$

where λ_s is the free-space optical wavelength, ϵ the optical dielectric constant, and L the interaction length ($L=1$ mm). From the measured values of T_1 and T_2 given below, we estimate $\sigma_T^2\simeq 3\times10^{-6}$. $d\sigma/d\Omega\simeq10^{-19}$ cm^2 for 4880 Å light in moderately doped n-CdS[3,4] with $\eta=2\times10^{17}$. Thus, $P_s/P_0\simeq0.08$ for our sample, in reasonable agreement with experiment, considering the large uncertainties in several of the quantities appearing in the numerical calculations.

As ω_L is very close to the band gap, one cannot neglect the dispersion $d=\pm(\partial k/\partial\omega)\omega_0$, in attempting to satisfy $\Delta k=0$, even though ω_0 is only as small as 0.8 cm^{-1}. However, since according to the selection rules of Eq. (11) $\vec{E}_L\perp\vec{E}_s$, this dispersion may be compensated for by the birefringence $b(\theta)$ of the uniaxial CdS crystal, which for propagation at angle θ close to the c axis may be expressed as $b(\theta)\simeq(n_0-n_E)\theta^2$. The birefringence cancels the dispersion when $\theta=[d/(k_0-k_E)]^{1/2}$, *provided the higher-frequency wave propagates as an extraordinary wave.* Using $d=5\times10^{-4}$[14] and our measured value of $n_0-n_E=0.22$, one finds $\theta\simeq3°$ in agreement with observation within experimental error. At this angle, the Stokes generation is phase matched if $\vec{E}_L$ is in the extraordinary polarization [Fig. 1(b)]. If $\vec{E}_L$ is changed to ordinary, the intensities should reverse [Fig. 1(c)].

When the dc magnetic field is swept through resonance, the intensity of the coherent SFRS sidebands reflects a nonconventional EPR signal. In most EPR experiments, one observes a signal proportional to either of the transverse components of spin in the rotating frame, $S_{x'}$ or $S_{y'}$, which are, respectively, in phase or out of phase with the rotating microwave field. In contrast, the signal we observe is proportional to $\sigma_T^2=S_{x'}^2+S_{y'}^2$. This distinction becomes quite marked in the saturation of the EPR line when $\lambda_e H_1(T_1T_2)^{1/2}>1$, at which point a double peak appears in σ_T^2 as seen in Fig. 2(a).

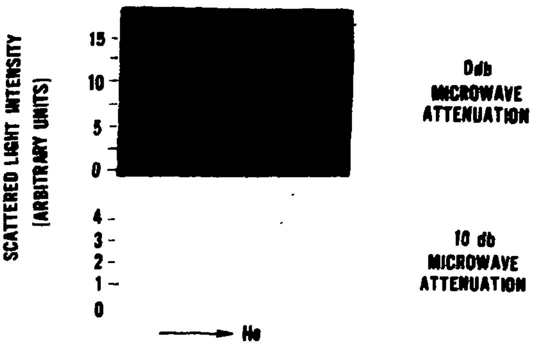

FIG. 2. Magnetic-field dependence of the intensity of the coherent Raman scattering. The resonance field corresponds to $g_\perp=1.77$. The broadening and dip at full power (a) indicates that the unsaturated EPR line, (b) is homogeneous with $T_2=4\times10^{-9}$ sec.

Transient microwave studies, to be reported later, on these signals have yielded a value of $T_1=5\times10^{-6}$ sec for a sample with $\eta=2\times10^{17}$ donors. A detailed analysis of the saturation behavior of σ_T^2, as displayed in Fig. 2(a), shows that the line is indeed homogeneous with $T_2=4\times10^{-9}$ sec. This short value of T_2 may be caused by loss of phase memory from exchange flipping between donors, or electron hopping at the onset of the Mott transition. Such unequal values of T_1 and T_2 in a hopping regime are contrary to the often-made assumption of $T_1=T_2$ in this regime.

We wish to thank P. A. Fleury, J. A. Giordmaine, P. Hu, S. L. McCall, L. R. Walker, and Y. Yafet for many helpful discussions and S. Bortas for polishing of the CdS samples.

---

*On leave from Centre National de la Recherche Scientifique, France.

†Research sponsored by the U. S. Air Force Office of Scientific Research, Air Force Systems Command, under Contract/Grant No. AFOSR 71-2010.

[1] S. Toyotomi and K. Morigaki, J. Phys. Soc. Jpn. 25, 807 (1968).

[2] W. J. Brya, S. Geschwind, and G. E. Devlin, Phys. Rev. B 6, 1924 (1972).

[3] D. G. Thomas and J. J. Hopfield, Phys. Rev. 175, 1021 (1968).

[4] J. F. Scott, T. C. Damen, and P. A. Fleury, Phys.

Rev. B 6, 3856 (1972).

[5] A. S. Davydov, *Quantum Mechanics* (Pergamon, New York, 1965), p. 316.

[6] See for example Sect. II of the paper by M. Blume, S. Geschwind, and Y. Yafet, Phys. Rev. 181, 478 (1969).

[7] While the noncubicity of CdS modifies the selection rules given by Eq. (4) (see Ref. 3), it has a small effect on our subsequent computation of the sideband power.

[8] Spin-orbit interaction is implicit in the wave functions $|n\rangle$. See Ref. 3 and Y. Yafet, Phys. Rev. 152, 855 (1956).

[9] Yafet, Ref. 8.

[10] T. L. Brown and P. A. Wolff, Phys. Rev. Lett. 29, 362 (1972); V. T. Nguyen and T. J. Bridges, Phys. Rev. Lett. 29, 359 (1972).

[11] Raman scattering from coherent states prepared by different techniques where the coherence was at the natural frequency of the system rather than a driving frequency, as in our case, has been described by J. A. Giordmaine and W. Kaiser, Phys. Rev. 144, 676 (1966); R. G. Brewer and E. L. Hahn, Phys. Rev. A 8, 464 (1973).

[12] A. Abragam, *Principles of Nuclear Magnetism* (Oxford Univ. Press, Oxford, England, 1961), pp. 44 ff.

[13] R. H. Dicke, Phys. Rev. 93, 99 (1954).

[14] K. F. Rodgers, Jr., unpublished.

Molecular Theory of Orientational Fluctuations and Optical Kerr Effect in the Isotropic Phase of a Liquid Crystal

C. Flytzanis and Y. R. Shen*
Laboratoire d'Optique Quantique, Centre National de la Recherche Scientifique, 91405 Orsay, France

(Received 28 February 1974)

By use of Kubo's statistical formalism, we show that the orientational fluctuations of interacting molecules are responsible for both the narrow central component and the broad Rayleigh-wing component in the light-scattering spectrum of a liquid crystalline material. The same formalism also describes the optical Kerr effect. We also point out the difference between the microscopic and the macroscopic order parameters.

The spectrum of light scattering from an isotropic nematic substance has a narrow central component presumably arising from fluctuations of the order parameter.[1] The order parameter here describes the orientational order of the long molecules in the medium.[2] On the other hand, a much broader central component was also observed in the spectrum.[3] Such a component always exists in ordinary liquids and is often called the Rayleigh-wing component.[4] It is well known that the Rayleigh-wing component comes from orientational fluctuations of molecules.[4] Thus, from the microscopic point of view, both components appear to be due to orientational fluctuations of molecules. It is then interesting to see how the orientational fluctuations can give rise to two very different components in the spectrum and how they are related. In this paper, we show from microscopic derivations that interaction between molecules is responsible for the observed results, and, in particular, the narrow central component appears because of the large mean-field modification on the orientational motion near a phase transition.

The orientational fluctuations are also directly related to the optical Kerr effect as a result of molecular reorientation.[5] From Kubo's fluctuation-dissipation theory,[6] we can express the birefringence induced by a linearly polarized optical field of sinusoidally varying intensity, $|E_0|^2(t)=|\mathcal{E}_0|_\Omega^2\exp(-i\Omega t)$, in the isotropic phase as

$$\begin{aligned}&\delta n(\Omega)=(2\pi/n)F(\Omega)|\mathcal{E}_0|_\Omega^2,\\&F(\Omega)=\delta\chi(\Omega)/|\mathcal{E}_0|_\Omega^2=\beta\langle\delta\chi(0)\delta\chi(0)\rangle+i\Omega\beta\int_0^\infty\langle\delta\chi(0)\delta\chi(t)\rangle e^{-i\Omega t}\,dt,\end{aligned}\tag{1}$$

where $\beta\equiv 1/kT$, $\delta\chi(t)$ is the anisotropy in the susceptibility induced by the field, and the angular brackets indicate the ensemble average. On the other hand, the average induced anisotropy of the polarizability for each molecule is

$$\begin{aligned}&\delta\alpha(\Omega)=f(\Omega)|\mathcal{E}_0|_\Omega^2,\quad f(\Omega)=(\Delta\alpha)Q(\Omega)/|\mathcal{E}_0|_\Omega^2,\\&Q(\Omega)=\left[\beta\langle S(0)S(0)\rangle+i\Omega\beta\int_0^\infty\langle S(0)S(t)\rangle e^{-i\Omega t}\,dt\right](2\Delta\alpha/3N)|\mathcal{E}_{1oc}|_\Omega^2\equiv\gamma(\Omega)|\mathcal{E}_{1oc}|_\Omega^2,\end{aligned}\tag{2}$$

where $\Delta\alpha = \alpha_\parallel - \alpha_\perp$ is the anisotropy of the molecular polarizability;

$$S = \sum_{i=1}^{N} s_i, \quad s_i = \tfrac{1}{2}(3\cos^2\theta_i - 1),$$

such that $Q = \langle S\rangle/N$ is the usual order parameter; N is the number of molecules per unit volume; and θ_i is the angle between $\vec{\mathrm{E}}_0$ and the long axis of the ith molecule. $|\mathcal{E}_{\mathrm{loc}}|^2$ is the local field which is related to $|\mathcal{E}_0|^2$ by

$$\tfrac{2}{3}\Delta\alpha|\mathcal{E}_{\mathrm{loc}}|_\Omega^2 = V_0 Q(\Omega) + \tfrac{2}{3}\Delta\alpha|\mathcal{E}_0|_\Omega^2, \tag{3}$$

where $V_0 Q(\Omega)$ is the local-field correction due to intermolecular interaction in the mean-field approximation.[2] We then obtain from Eq. (2)

$$f(\Omega) = (\Delta\alpha)\gamma(\Omega)[1 - \gamma(\Omega)V_0/\tfrac{2}{3}\Delta\alpha]^{-1}. \tag{4}$$

The relation between $F(\Omega)$ and $f(\Omega)$ is, from the Claussius-Mosotti equation,

$$F(\Omega) = Nf(\Omega)/(1 - \tfrac{4}{3}\pi N\alpha), \tag{5}$$

where α is the average polarizability.

Now that the spectrum of scattered radiation is given by

$$I(\Omega) = \mathrm{Re}\big[A\int_0^\infty \langle\delta\chi(0)\delta\chi(t)\rangle e^{-i\Omega t}\,dt\big], \tag{6}$$

where A is a proportional constant, we see immediately from Eq. (1) that

$$I(\Omega) = \mathrm{Re}\{[F(\Omega) - F(0)]A/i\omega\beta\}. \tag{7}$$

Then, in order to find $I(\Omega)$, we need only to find $\gamma(\Omega)$. We have calculated $\gamma(\Omega)$ after Zwanzig's approach.[7] We shall only sketch, in the following, the important steps of the calculations.

To find $\gamma(\Omega)$, we must first calculate the integral

$$(1/N)\int_0^\infty dt\, e^{-i\Omega t}\langle S(0)S(t)\rangle = (1/N)\int_0^\infty dt\, e^{-i\Omega t}\int d\mathfrak{A}_0\, d\mathfrak{A}\, \rho(\mathfrak{A}_0)g(\mathfrak{A}_0, \mathfrak{A}, t)\sum_{i,j} s_i(0)s_j(t), \tag{8}$$

where $\mathfrak{A}_0$ and $\mathfrak{A}$ are the abbreviations indicating the orientations of the set of molecules initially and at time t, respectively, $\rho(\mathfrak{A}_0)$ is the initial equilibrium distribution, and $g(\mathfrak{A}_0, \mathfrak{A}, t)$ is the probability of finding a specific set of orientations $\mathfrak{A}$ at t when the initial set of orientations is $\mathfrak{A}_0$. Thus, we have

$$\rho(\mathfrak{A}_0) = e^{-\beta V}/\int d\mathfrak{A}_0\, e^{-\beta V}, \tag{9}$$

where V is the intermolecular interaction potential. We shall use the simple form proposed by Maier and Saupe[2,8] for V:

$$V = \sum_i V_i = \sum_{i,j} C_{ij}s_i s_j, \quad i \neq j. \tag{10}$$

The function $g(\mathfrak{A}_0, \mathfrak{A}, t)$ obeys the rotational diffusion equation

$$\partial g/\partial t = \mathfrak{D}g, \tag{11}$$

where

$$\mathfrak{D}g = (1/\beta\zeta)\textstyle\sum_n \vec{\Omega}_n\cdot[\vec{\Omega}_n g + \beta g\vec{\Omega}_n V], \quad \vec{\Omega}_n = \vec{\mathrm{r}}_n \times \nabla_n,$$

and ζ is the frictional coefficient. The above equation, with the initial condition $g(t=0) = \delta(\mathfrak{A}_0 - \mathfrak{A}_0)$, gives

$$\int_0^\infty dt\, g(t)e^{i\Omega t} = -\delta(\mathfrak{A} - \mathfrak{A}_0)/(i\Omega + \mathfrak{D}). \tag{12}$$

Consequently, we can obtain from Eqs. (2) and (8)

$$\gamma(\Omega) = \gamma(0) + i\Omega\beta\frac{2\Delta\alpha}{3N}\int d\mathfrak{A}\,\Big(\sum_j s_j\Big)\frac{-1}{i\Omega + \mathfrak{D}}\rho(\mathfrak{A})\sum_i s_i, \quad \gamma(0) = \beta\frac{2\Delta\alpha}{3N}\int d\mathfrak{A}\,\rho(\mathfrak{A})\sum_{i,j} s_i s_j. \tag{13}$$

The evaluation of the above integrals is then carried out by perturbation expansion by assuming the intermolecular interaction potential V to be small compared with kT. This assumption is justified since, in the isotropic phase, we expect $\langle s_i s_j \rangle \ll 1$ and hence $\beta V_i \ll \beta \sum_j C_{ij} \approx 1$. The detailed calculations and the results are very similar to those in Zwanzig's case.[7] We find, to the second order,[9] that

$$\gamma(\Omega) \simeq \tfrac{2}{15}\beta(\Delta\alpha)\left[\frac{1+18.4R}{1-4.4R-i\Omega\tau} + \frac{10R}{1-i\Omega\tau/2} + \frac{-4.2R}{1-i3\Omega\tau/13}\right], \tag{14}$$

where $\tau = \zeta/6kT$ and $R = (2/35)^2\beta^2 \sum_{l,k} C_{lk} C_{kl}$. Then, from Eqs. (4) and (5), we obtain the expression

$$F(\Omega) = B\sum_k C_k/(1-i\Omega\tau_k) \tag{15}$$

where

$$\begin{aligned}
&B = [N/(1-\tfrac{4}{3}\pi N\alpha)]\tfrac{2}{75}(\Delta\alpha)^2;\\
&\tau_1 = \tau/[1-(T_c/T)+\theta(\beta^2C^2)], \quad \tau_2 = (\tau/2)[1+\theta(\beta^2C^2)], \quad \tau_3 = (3\tau/13)[1+\theta(\beta^2C^2)],\\
&C_1 = [1-(T_c/T)]^{-1}[1+28.6R/(1-T_c/T)][1+\theta(\beta^2C^2)],\\
&C_2 = 10[1+(T_c/T)]^{-2}R+\theta(\beta^3C^3), \quad C_3 = -4.2[1+(T_c/T)]^{-2}R+\theta(\beta^3C^3), \quad T_c = V_0/5k;
\end{aligned} \tag{16}$$

$\theta(\beta^n C^n)$ is a term of the order of $\beta^n C^n$.

The spectrum of light scattering by orientational fluctuations can now be obtained by inserting Eq. (15) into Eq. (7). We see immediately that the spectrum is composed of several Lorentzian components with the intensity ratio given by $C_1{:}C_2{:}C_3$. The strongest component is C_1 and has a half-width $1/\tau_1$. We notice in Eq. (16) that if we neglect terms of $\theta(\beta^n C^n)$ with $n \geq 2$, then we can write

$$C_1 = T/(T-T_c), \quad \tau_1 = \zeta/6k(T-T_c), \tag{17}$$

which have the same forms as those derived for order-parameter fluctuations from the Landau-de Gennes theory.[10] T_c here is in fact identical to the second-order phase transition temperature derived from the mean-field theory by Maier and Saupe.[2] Consequently, we can say that the C_1 component is the same component known to be due to order-parameter fluctuations,[1,10] or, in our present language, it is due to orientational fluctuations of molecules under the influence of the mean field created by intermolecular interaction. Both the intensity and the inverse width of this component show the critical behavior which has been demonstrated experimentally in liquid crystalline materials.[1] In ordinary liquids, T_c is below the liquid-solid transition temperature and cannot be reached.

The other components in the spectrum arise from the correlated effect of intermolecular interaction. The fluctuating molecule modifies the dynamics of the orientational motion of neighboring molecules which, in turn, modify the dynamics of the orientational fluctuations of the original molecule. This case is analogous to the case of coupled damped harmonic oscillators. In both cases, new modes are created through coupling. Since $V_0 = \sum_k C_{ik}$ and hence $R \approx 4T_c/49T$, we find from Eq. (16) that C_2 and C_3 are about 10^4 times smaller than C_1. The corresponding half-widths $1/\tau_2$ and $1/\tau_3$ are characteristics of orientational fluctuations of a few molecules. Both components should not show critical behavior as $T \to T_c$.

The experimental results of Rayleigh-wing scattering in N-[p-methoxybenzylidine]-p-butylaniline (MBBA) indeed showed two broad Lorentzian components with no critical behavior.[3] Their integrated intensities were about 10^4 times smaller than that of the component due to order-parameter fluctuations studied by Stinson and Litster.[1] The variation of $1/\tau_2$ and $1/\tau_3$ with temperature is shown in Fig. 1 in comparison with theoretical predictions. For the theoretical curve, we have used $\xi = \alpha\eta(T)$, where α is an adjustable constant different for different components[1] and $\eta(T)$ is

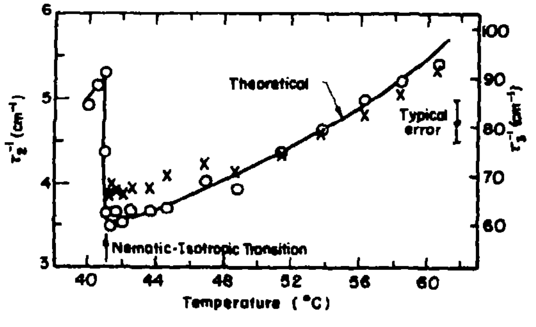

FIG. 1. Comparison of theoretical Rayleigh-wing linewidths in MBBA as a function of temperature with experimental data (circles for τ_2^{-1} and crosses for τ_3^{-1}) obtained by Amer, Lin, and Shen in Ref. 3.

the shear viscosity determined by Martinoty, Candau, and Debeauvais.[11] The agreement between theory and experiment is fairly good. We should, however, emphasize here that our theory is only meant to explain qualitatively the characteristic difference between the various components of light scattering due to molecular orientational fluctuations. Like other microscopic theories for liquids, because of the simplifying assumption on molecular interaction, it would not explain experimental results quantitatively. For example, we have not taken into account molecular collision which is believed to have strong influence on Rayleigh-wing scattering.[4]

From Eqs. (1) and (15), we can also find the time variation of the field-induced refractive index induced by a time-dependent field[6] $|\mathcal{E}_0|^2(t)$:

$$\delta n(t) = (2\pi/n)B\textstyle\sum_k(C_k/\tau_k)\int_{-\infty}^{t}|\mathcal{E}_0|^2(t')\exp[-(t-t')/\tau_k]dt'. \tag{18}$$

Again, the C_1 component dominates here. This equation applies to the optical Kerr effect. Such an effect in an isotropic nematic substance has recently been measured.[12]

Finally, we can obtain the equation of motion for $\delta n(t)$, or $\delta\chi(t) = n\delta n(t)/2\pi$, from Eq. (18):

$$(\partial/\partial t)\delta\chi(t) + A\textstyle\sum_k(C_k/\tau_k^2)\int_{-\infty}^{t}|\mathcal{E}_0|^2(t')\exp[-(t-t')/\tau_k]dt' = A\sum_k(C_k/\tau_k)|\mathcal{E}_0|^2(t). \tag{19}$$

If we retain only the C_1 terms in Eq. (19), we then find

$$(\partial/\partial t + \tau_1^{-1})\delta\chi(t) = A(C_1/\tau_1)|\mathcal{E}_0|^2. \tag{20}$$

de Gennes[10] has pointed out that $\delta\chi$ can be taken as the macroscopic order parameter. We recognize that Eq. (20) is in exactly the same form as the equation of motion for the macroscopic order parameter derived by de Gennes from thermodynamic consideration.[10] As seen from the above derivation, the macroscopic order parameter is different from the microscopic order parameter $Q = \langle\sum_i(3\cos^2\theta_i - 1)/2\rangle/N$. The two are related through the local field correction.

In conclusion, we have shown that the orientational fluctuations of molecules are responsible for both the narrow central component (known to be due to order parameter fluctuations) and the broad Rayleigh-wing component in the light-scattering spectrum of an isotropic liquid crystalline substance. The broad wing is due to coupling between fluctuating molecules through intermolecular interaction. We have also derived expressions for the optical Kerr response due to molecular reorientation and the equation of motion for the macroscopic order parameter. The theory is general. In particular, it also applies to solids such as the plastic crystals. Observations of light scattering by orientational fluctuations and the corresponding optical Kerr effect in a plastic crystal have recently been reported.[13,14]

One of us (Y.R.S.) thanks Dr. N. M. Amer for helpful discussions in formulating the problem. He also acknowledges the partial research support from the U. S. Atomic Energy Commission and the Guggenheim Memorial Foundation, and the hospitality of Professor J. Ducuing at the Laboratoire d'Optique Quantique.

---

[*] Present address: Department of Physics, University of California, Berkeley, Calif. 94720.

[1] T. W. Stinson and J. D. Litster, Phys. Rev. Lett. 25, 503 (1970).

[2] W. Maier and A. Saupe, Z. Naturforsch. 13a, 564 (1958), and 14a, 882 (1959), and 15a, 287 (1960).

[3] N. M. Amer, Y. S. Lin, and Y. R. Shen, in Proceedings of the Fourth International Liquid Crystal Conference, Kent, Ohio, August 1972 (to be published).

[4] See, for example, I. L. Fabelinskii, *Molecular Scattering of Light* (Plenum, New York, 1968), Chaps. II and VIII.

[5] R. W. Hellwarth, J. Chem. Phys. 52, 2128 (1970).

[6] R. Kubo, J. Phys. Soc. Jpn. 12, 570 (1957).

[7] R. Zwanzig, J. Chem. Phys. 38, 2766 (1963).

[8] K. K. Kobayashi, J. Phys. Soc. Jpn. 29, 101 (1970), and Mol. Cryst. Liquid Cryst. 13, 137 (1971).

[9] There are terms proportional to $\beta\sum_j C_{ij}$ in $\gamma(\Omega)$. They contribute to the mean local-field correction which has already been taken into account through Eq. (3). See R. Rosenberg and M. Lax, J. Chem. Phys. 21, 424 (1953).

[10] P. G. de Gennes, Mol. Cryst. Liquid Cryst. 12, 193 (1971).

[11] P. Martinoty, S. Candau, and F. Debeauvais, Phys. Rev. Lett. 27, 1123 (1971).

[12] G. K. L. Wong and Y. R. Shen, Phys. Rev. Lett. 30, 895 (1973).

[13] L. Boyer, R. Vacher, L. Cecchi, M. Adam, and P. Bergé, Phys. Rev. Lett. 26, 1435 (1971).

[14] T. Bischofberger and E. Courtens, Phys. Rev. Lett. 32, 163 (1974).

Longitudinal Spin Relaxation in ^{3}He Gas at 4.2 K†

R. Chapman and M. G. Richards*
Department of Physics, University of British Columbia, Vancouver, Canada
(Received 29 January 1974)

The first measurements of longitudinal spin relaxation due to binary atomic collisions in bulk ^{3}He gas are reported. At 4.2 K the data are fitted by the expression $\rho T_1 = 61 \pm 2$ sec g cm^{-3} for densities ρ such that $0.01 < \rho < 0.05$ g cm^{-3}. At lower densities wall relaxation predominates and at higher densities a binary collision theory is inadequate. A model of wall relaxation is given which identifies the role of the absorbed phase of ^{3}He on the wall.

Longitudinal nuclear-spin relaxation in ^{3}He has been studied thoroughly[1] in the liquid and solid phases, but there are no published data for pure bulk ^{3}He gas. Recent theoretical calculations[2,3] have shown how measurements of the spin longitudinal relaxation time T_1 are sensitive to the form of the spin-independent interparticle potential. We report here the first measurements of T_1 in bulk ^{3}He gas.

From the point of view of NMR, ^{3}He gas has long been recognized as an unusually simple system in which the interatomic dipole-dipole coupling is not overwhelmed by strong intramolecular interactions present in molecular gases like H_2 and CH_4,[4] but emerges as the dominant relaxation mechanism. Bloembergen[5] suggested that dilute ^{3}He gas would relax via the collisional modulation of the dipole-dipole interaction between pairs of atoms. In the framework of this model, a ^{3}He spin experiences a changing magnetic field for a period of time of the order of the duration of a collision, but is unaffected between collisions. The local field seen by a spin is a series of spikes of width equal to the time $\tau \sim d/v$ for which a collision lasts, where d is the distance of closest approach and v the thermal velocity. This time ($\sim 10^{-12}$ sec) is sufficiently short that $\tau \ll \omega_0^{-1}$, the inverse angular Larmor frequency, for fields attainable with laboratory electromagnets. In this limit $T_1 = T_2$, and to estimate T_2 we consider the effects of binary collisions which occur incoherently at an average frequency ν_{coll}.[6] If in each collision the transverse spin magnetism dephases by $\Delta\varphi \ll 1$, then

$$1/T_2 \sim \langle \Delta\varphi^2 \rangle \nu_{\text{coll}}. \tag{1}$$

$$\langle \Delta\varphi^2 \rangle \sim (\hbar^2\gamma^4/d^6)(d/v)^2, \quad \nu_{\text{coll}} \sim n\pi d^2 v,$$

and so

$$1/T_1 = 1/T_2 \sim n(m/kT)^{1/2}\hbar^2\gamma^4/d^2 \propto P/T^{3/2}, \tag{2}$$

where n is the number density of atoms (mass m) in the gas.

This is a crude treatment ignoring the precise nature of the interparticle potential which will affect the length of time of a collision and make it energy (and therefore temperature) dependent.[2] There will also be a contribution from the transient spin-rotation interaction associated with effects of electric polarization during a collision.[7]

Evaluation of expression (2) at 1 atm pressure shows T_1 to be about 10^7 sec at room temperature and about 10^4 sec at 4 K. Previously reported measurements[8-12] of T_1 on ^{3}He gas are all much shorter than these values, undoubtedly because of the presence of paramagnetic impurities or of wall relaxation. Oxygen molecules will make a significant contribution to $1/T_1$ when their fractional concentration reaches $[\gamma(^3\text{He})/\gamma(O_2)]^2 \sim 10^{-6}$. When making measurements at or above 77 K concentrations of at least this magnitude are difficult to avoid, but at 4.2 K where the present data were recorded all impurities except ^{4}He will be condensed out on the walls. Wall effects are more difficult to estimate. Masnou-Seeuws and Bouchiat[13] have distinguished two regimes depending on the nature of the surface. For sufficiently dirty surfaces T_1 is determined by the time needed for an atom to reach the walls, because in a much shorter subsequent time it will make enough collisions with the wall to flip its spin. In this regime

$$(T_1)_{\text{wall}} = R^2/\pi^2 D \propto n \tag{3}$$

for a spherical sample of radius R. T_1 is independent of α, the spin-flip probability per wall collision, provided α is large enough to keep the system in this regime.

In the other (clean surface) regime, an average particle diffuses to the wall and then makes too few collisions with the wall to relax its spin before returning to the bulk gas. The average wall collision frequency in a sphere is $3v/4R$ and the relaxation time is

$$(T_1)_{\text{wall}} = 4R/3\alpha v. \tag{4}$$

The gas density does not affect T_1 in this regime except perhaps indirectly through α.

Since the relaxation rates add,

$$(1/T_1)_{\text{obs}} = (1/T_1)_{\text{wall}} + (1/T_1)_{\text{bulk}}, \tag{5}$$

and we may hope to identify $(T_1)_{\text{bulk}}$ by the different density dependence of Eq. (2) and Eq. (3) or (4).

The measurements reported here were all made at 4.2 K. The sample chamber consists of an approximately spherical bulb of volume about 1 cm^3 blown at the end of $\frac{1}{2}$-mm-i.d. Pyrex thick-walled capillary tubing. The cleaning procedure used was similar to that described by Horvitz.[14] Molecules adsorbed on the glass wall are driven off by exciting a discharge in low-pressure helium gas in the sample chamber and flushing out the resulting impurities. The sample of ^{3}He gas is cleaned and stored in a misch-metal oxygen getter.[15]

A simple twin-*T* bridge spectrometer[16] operating at 3.5 MHz is employed to monitor the NMR adiabatic fast-passage signal. The very long relaxation times are measured by sweeping the field through resonance once to a resting field off resonance in order to invert the magnetization, and at later times sampling the magnetization nondestructively by cycling the field to resonance and then returning to the resting field. The magnetization, therefore, continues on its original relaxation curve and the measurement can be made in a period of about $3T_1$. As long as the adiabatic conditions are satisfied, there is negligible loss of magnetization each time the signal is monitored.

Measurements of T_1 were made over a density range varying from the dilute-gas limit in which $\lambda \gg d$ to a dense-gas regime in which $\lambda \sim d$. Two series of measurements were taken, with the initial and final runs of each series here reported. Between runs in each series there was intensive cleaning of the sample chamber. Values of T_1 plotted versus the density ρ in Fig. 1 fall into three regimes. At densities around 7×10^{-2} g cm^{-3}, T_1 varies approximately as ρ^{-2}. This dependence is expected[17] in a regime where many-body collisions are important and $T_1 \propto D/n \propto n^{-2}$. We note that the density at which this regime begins is close to the liquid density (7×10^{-2} g cm^{-3} on the saturated-vapor pressure curve at 2.6 K[18]), and that $d/\lambda \approx \pi n d^2 \approx 0.7$ at this density. At moderate densities the results approach a common envelope given by $T_1\rho = 61$ sec g cm^{-3}. At low pressure $T_1 \propto \rho$, with T_1/ρ increasing as the cleaning process is carried out more carefully. The middle region has the correct density dependence for bulk relaxation and we attribute the data here to refer to an intrinsic process of the kind developed in Eq. (2).

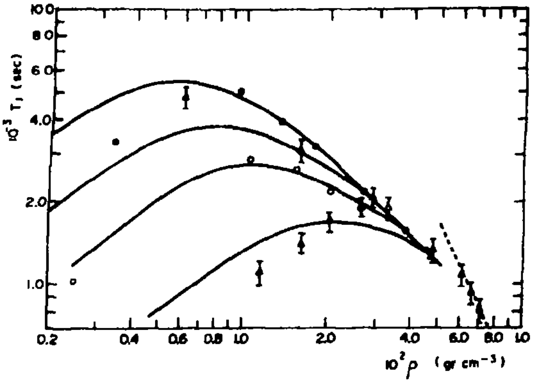

FIG. 1. Measurements of T_1 in ^{3}He gas versus density ρ at 4.2 K and a frequency of 3.5 MHz. Open triangles, series *A*, 1st run; filled triangles, series *A*, final run (after cleanings); open circles, series *B*, 1st run; filled circles, series *B*, final run (after cleanings). The solid lines are best fits with Eq. (6) and the dashed line is a slope corresponding to $T_1 \propto \rho^{-2}$.

Since, in practice, it is found that

$$(1/T_1)_{\text{obs}} = c_1\rho + c_2/\rho, \tag{6}$$

where the first term on the right is characteristic of bulk relaxation, ρ/T_1 can be plotted versus ρ^2 to find the slope c_1. Values so found for the four runs of Fig. 1 are given in Table I together with a recent theoretical expression[8] obtained using the best interatomic potentials currently available. The agreement suggests that while an alternative relaxation process may be present as a contributory factor, the nuclear dipole-dipole coupling seems to be the major source of longitudinal spin relaxation.

The low-density region does not seem consistent with Bouchiat's treatment of wall relaxation since if a $T_1 \propto \rho$ region is observed it should (a) be independent of cleaning and (b) have $T_1/\rho = R^2/\pi^2 D\rho \approx 10^3$ cm^3 sec g^{-1},[8] instead of the range 10^5–10^6 observed. However, it is possible that what is observed here is the clean-surface result $(T_1)_{\text{wall}} = 4R/3\alpha v$ with α dependent on pressure. At these pressures and temperatures, there will be[19] be-

TABLE I. Parameters used to fit T_1 data with $1/T_1 = c_1\rho + c_2/\rho$.

	c_1 ($\mathrm{cm^3\ sec^{-1}\ g^{-1}}$)	$c_1^{-1} = \rho(T_1)_{\mathrm{bulk}}$
Series *A*: Initial run	1.50×10^{-2}	67 ± 6
Final run	1.64×10^{-2}	61 ± 6
Series *B*: Initial run	1.66×10^{-2}	60 ± 1
Final run	1.65×10^{-2}	61 ± 1
Theory (Ref. 3)	...	76

tween one and two layers of adsorbed atoms of ^{3}He on the walls, and collisions will only be specially effective for relaxation if they result in adsorption since then T_1 is greatly shortened, partly by the presence of paramagnetic impurities and partly by the much slower motion in the adsorbed phase. In this situation $\alpha = \alpha_{\mathrm{ad}}\tau_{\mathrm{ad}}/(T_1)_{\mathrm{ad}}$, where α_{ad}, τ_{ad}, and $(T_1)_{\mathrm{ad}}$ are, respectively, the probability that a collision will result in a particle entering the adsorbed phase, the average time spent in the adsorbed phase, and T_1 in the adsorbed phase (assumed to be $\gg \tau_{\mathrm{ad}}$). τ_{ad} is given by (surface density of adsorbed atoms)/(flux of particles leaving the adsorbed phase). In equilibrium the outward flux will equal the inward flux and the latter is given by $\alpha_{\mathrm{ad}} n\bar{v}/4$. Hence

$$\tau_{\mathrm{ad}} = 4/n\bar{v}\alpha_{\mathrm{ad}}\sigma,$$

where σ is the surface area per atom adsorbed. Equation (4) now gives

$$(T_1)_{\mathrm{wall}} = R\sigma n (T_1)_{\mathrm{ad}}/3.$$

Using $m = 5\times 10^{-24}$ g, $\sigma \approx 15 \times 10^{-16}$ cm^2, and $R = 0.5$ cm we have

$$(T_1)_{\mathrm{wall}} = 0.5\times 10^{8}\rho (T_1)_{\mathrm{ad}}.$$

Typical values[20] for $(T_1)_{\mathrm{ad}}$ in ^{3}He are in the range 10^{-3} to 10^{-1} sec depending on temperature, frequency, substrate, paramagnetic impurity, and amount of adsorbed material. Hence $10^7\rho > (T_1)_{\mathrm{wall}} > 10^5\rho$ which is consistent with the data in the low-density regime. The effect of cleaning the sample chamber and sample gas is to lengthen $(T_1)_{\mathrm{ad}}$, but this has an upper limit of $\sim 10^{-1}$ sec due to the intrinsic process and hence it would be impossible to measure T_1 for bulk ^{3}He gas at 4 K in the present sample chamber for densities below 10^{-3} g cm^{-3}. Increasing R and/or working at higher fields where $(T_1)_{\mathrm{ad}}$, and therefore $(T_1)_{\mathrm{wall}}$, are increased would be necessary.

Future work will involve extending the work to low densities and temperatures to look for the effects of long-lived collisions when pseudomolecules of $^3\mathrm{He}_2$ may be formed.[3]

Stimulating conversations with M. Bloom, A. L. Thomson, and B. Shizgal, and assistance with glass blowing by J. Lees, are gratefully acknowledged.

---

†Work supported by The National Research Council of Canada.

*Permanent address: School of Mathematical and Physical Sciences, University of Sussex, Brighton, BN1 9QH, England.

[1] M. G. Richards, Advan. Magn. Resonance 5, 305 (1971).

[2] B. Shizgal, J. Chem. Phys. 58, 3424 (1973).

[3] B. Shizgal, Chem. Phys. Lett. 20, 265 (1973).

[4] M. Bloom, in *MTP International Review of Science, Series One*, edited by H. J. Emeleus *et al.* (University Park Press, Baltimore, Md., 1972), Vol. 4, Chap. 7.

[5] N. Bloembergen, *Nuclear Magnetic Relaxation* (Benjamin, New York, 1961).

[6] D. Pines and C. P. Slichter, Phys. Rev. 100, 1014 (1955).

[7] H. C. Torrey, Phys. Rev. 130, 2306 (1963); I. Oppenheim, M. Bloom, and H. C. Torrey, Can. J. Phys. 42, 70 (1964).

[8] K. Luszczynski, R. E. Norberg, and J. E. Opfer, Phys. Rev. 128, 186 (1962).

[9] W. A. Fitzsimmons, L. L. Tankersley, and G. K. Walters, Phys. Rev. 179, 156 (1969).

[10] R. S. Timsit, J. M. Daniels, and A. D. May, Can. J. Phys. 49 560 (1971).

[11] P. Cornaz, Helv. Phys. Acta 38, 841 (1965).

[12] J. G. Ganiere, Helv. Phys. Acta 46, 147 (1973).

[13] F. Masnou-Seeuws and M. Bouchiat, J. Phys. (Paris) 28, 406 (1967).

[14] E. P. Horvitz, Phys. Rev. A 1, 1708 (1970).

[15] H. S. Sandhu, J. Lees, and M. Bloom, Can. J. Chem. 38, 493 (1960).

[16] H. L. Anderson, Phys. Rev. 76, 1460 (1949).

[17] J. F. Harmon and B. H. Muller, Phys. Rev. 182, 400 (1969).

[18] E. C. Kerr, Phys. Rev. 96, 551 (1954).

[19] A. J. Symonds, D. Phil. thesis, University of Sussex, 1966 (unpublished).

[20] D. F. Brewer, D. Creswell, Y. Goto, M. G. Richards, J. Rolt, and A. L. Thomson, *Monolayer and Submonolayer Helium Films*, edited by J. G. Daunt and E. Lerner (Plenum, New York, 1973), p. 101.

New Universal Quantity for the He^4 Superfluid Transition*

M. Ferer
Department of Physics, West Virginia University, Morgantown, West Virginia 26506
(Received 25 March 1974)

Two-scale-factor universality is used to show that a simple combination of measurable critical amplitudes is universal. Good experimental agreement is observed.

One of the most striking aspects of critical behavior is the universality of the critical indices and the scaling functions, i.e., their independence of nonsymmetry-changing details in the Hamiltonian.[1] Because the order parameter associated with the superfluid transition in He^4 is unphysical, there are only two accessible critical indices; α from the specific heat and ν from the superfluid density.[2-4] The universality of these indices has been experimentally verified[5-7]; but little work has investigated the universality of the scaling functions for this system because, heretofore, its only observable consequence has been the universality of the ratio of the high- and low-temperature values of a critical amplitude.[5] Using results determined originally by Josephson from hydrodynamic arguments,[2,3] we will show that the universality of

$$X_{\mathrm{He}} = t^2 C_{p,\,\mathrm{sing}} (T_\lambda/\rho_s)^3 \big|_{T=T_\lambda}, \quad t = |1 - T_\lambda/T| \tag{1}$$

is a further consequence of two-scale-factor universality, which is an explicit formulation of the universality of the scaling functions.[8-11] In the above expression, ρ_s is the superfluid density and $C_{p,\,\mathrm{sing}}$ is the singular part of the constant-pressure specific-heat density.

Comparing X_{He} with X defined in Refs. 8 and 9, it is clear that the universality of X_{He} follows from the universality of X provided that T/ρ_s scales like the correlation length, i.e., provided that T/ρ_s depends on the reduced temperature t and nonuniversal quantities in the same way as the correlation length. It has been verified that they have the same t dependence[2,3]; using similar arguments, we will show that they have the same dependence on nonuniversal quantities.

In addition to demonstrating the consistency of the universality of X_{He} with two-scale-factor universality, we test their validity by determining X_{He} for various values of pressure using data given in Refs. 5–7 which investigated the pressure dependence of the specific heat and the superfluid density, respectively. As predicted, these values of X_{He}, presented in Table I, are indeed universal, i.e., independent of pressure.

To ascertain that the universality of X_{He} is a consequence of two-scale-factor universality, we must find expressions for ρ_s and $C_{p,\,\mathrm{sing}}$ in terms of universal parameters and the two, independent, nonuniversal scale factors. Such expressions have been determined for the generalized susceptibility and the standard thermodynamic quantities such as the specific-heat density but *not for the* superfluid density.[8-10] However, using hydrodynamic arguments, Josephson determined relations between ρ_s and the quantities for which scaling expressions are known.[2,3] Therefore, we can use his relations to determine a scaling expression for ρ_s.

Josephson postulated the following expression

TABLE I. Values of ${}^1X_{\mathrm{He}}$ and ${}^2X_{\mathrm{He}}$ determined using Eq. (10) and the data of Refs. 5–7.

P (bar)	$10^{-4}\,{}^1X_{\mathrm{He}}$	$10^{-3}\,{}^2X_{\mathrm{He}}$ $\left[\frac{R}{\mathrm{cm}^3}\left(\frac{\mathrm{K\ cm}^3}{\mathrm{mole}}\right)^3\right]$
0.05	2.06	3.11
1.65	2.02	3.07
7.33	1.99	3.01
15.03	2.02	3.10
18.18	1.99	3.10
22.53	1.96	3.12
25.87	2.19	3.47

for the free-energy density F, which is valid in the hydrodynamic limit[2,3]:

$$F=(1/V)\int d^3r\left[f(|\Psi_{\vec r}|^2)+\tfrac{1}{2}A_\perp|(\nabla_{\vec r}\Psi_{\vec r})_\perp|^2+\tfrac{1}{2}A_\parallel|(\nabla_{\vec r}\Psi_{\vec r})_\parallel|^2-h_{\vec r}(\Psi_{\vec r})_\perp\right]. \tag{2}$$

In this expression, $\Psi_{\vec r}$, the order parameter, is $\langle\psi_{\vec r}\rangle$ where $\psi_{\vec r}$ is the annihilation operator for He^4 atoms; $\parallel$ and $\perp$ denote the real and imaginary components respectively; and $h_{\vec r}$ is a fictitious field coupled to the order parameter through a term, $\int h_{\vec r}i(\psi_{\vec r}^\dagger-\psi_{\vec r})d^3r$ in the Hamiltonian. The function $f(x)$ and the constants $A_\parallel$ and $A_\perp$ depend on temperature and field. From this hydrodynamic expression for the free energy, Josephson showed that

$$\rho_s=A_\perp(m/\hbar)^2|\Psi|^2, \tag{3}$$

where m is the mass of a He^4 atom, and that

$$A_\perp/kT=2\lim_{q\to0}[q^2\chi_\perp(q)]^{-1}, \tag{4}$$

where $\chi_\perp(q)$ gives the response of the order parameter to the uniform, fictitious field.[2,3]

In uniform field, scaling and two-scale-factor universality predict the following expressions: the singular part of the free energy density,

$$\frac{F_{h_{\vec r}=h}}{kT}=\frac{(gt)^{2-\alpha}}{n}\mathfrak{F}\left(\frac{nh}{(qt)^{\Delta}}\right); \tag{5a}$$

the singular part of the order parameter,

$$\Psi=\Psi_{\vec r}|_{h_{\vec r}=h}=(gt)^{\beta}d(nh/(gt)^{\Delta}); \tag{5b}$$

the singular part of the zero-field specific-heat density,

$$t^2C_{h,\,\mathrm{sing}}=-(2-\alpha)(1-\alpha)(gt)^{2-\alpha}n^{-1}\mathfrak{F}(0); \tag{5c}$$

and the singular part of the perpendicular susceptibility,

$$\chi_\perp(q)=n(gt)^{-2\nu+\eta\nu}G(ql/(gt)^{\nu},nh/(gt)^{\Delta}). \tag{5d}$$

In these expressions, $\mathfrak{F}(y)$, $d(y)$, and $G(z,y)$ are undetermined but universal functions; α, Δ, β, ν, and η are the conventionally defined critical indices; and n, l, and g are the system-dependent scale factors with n and l being related through the universality of n/l^3.[4,8-10] Thus all nonuniversal system dependence is explicitly contained in the scale factors.

To determine the scaling form of ρ_s, via Eq. (3), we need the scaling form of Ψ given in Eq. (5b) and the scaling form of $A_\perp$. This latter quantity can be determined in two ways. The first uses Eq. (5d) in Eq. (4) and yields

$$A_\perp/T=B(gt)^{-\eta\nu}/l,\quad B=2k\frac{l^3}{n}\lim_{x\to0}[x^2G(X,0)]. \tag{6}$$

Note that B is a universal constant. The second way requires that the second term in Eq. (2) have the correct scaling form, i.e.,

$$\tfrac{1}{2}A_\perp|(\nabla_{\vec r}\Psi_{\vec r})|_{h_{\vec r}=0}{}^2/kT=(gt)^{2-\alpha}n^{-1}\mathfrak{F}_2(0). \tag{7}$$

Writing all but $A_\perp/T$ in terms of scaled variables,

$$\frac{1}{2}\frac{A_\perp}{kT}\left(\frac{(qt)^{\nu}}{l}\right)^2(gt)^{2\beta}\left|\left(\nabla_{(gt)^{\nu}\vec r/l}\frac{\Psi_{\vec r}}{(gt)^{\beta}}\right)_\perp\right|^2\Bigg|_{h_{\vec r}=0}=\frac{(gt)^{2-\alpha}}{n}\mathfrak{F}_2(0) \tag{8}$$

predicts the same scaling form for $A_\perp/T$ as in Eq. (6) since $2(1-\beta-\nu)-\alpha=-\eta\nu$,[4] but it does not provide a readily accessible expression for the universal constant B. Now using this result, Eq. (6), and Eq. (5b) in Eq. (3) yields the following scaling form for T/ρ_s

$$T/\rho_s=B'l(gt)^{-\nu},\quad B'=(\hbar/m)^2/B|d(0)|^2, \tag{9}$$

since $2\beta-\eta\nu=\nu$.[4] Thus, since B' is a universal constant, T/ρ_s scales like the correlation length (see Ref. 8), and the universality of X_{He} follows from the universality of X defined in Refs. 8 and 9.

Having verified that the universality of X_{He} is a consequence of two-scale-factor universality, let us use our result for a further test of the validity of two-scale-factor universality. Using the data in Refs. 5-7 which investigated the pressure dependence of the specific heat and the superfluid density, we can determine values of X_{He} for several different values of pressure, which is expected to be an irrelevant variable. If, consistent with our earlier arguments, we assume that $3\nu=2-\alpha$, we can rewrite Eq. (1) using the amplitudes defined in Refs. 5-7:

$$X_{\mathrm{He}}=\frac{A_0'(P)}{V_\lambda(P)}\left(\frac{T_\lambda(P)V_\lambda(P)}{k(P)}\right)^3. \tag{10}$$

In this equation, $A_0'(P)$ denotes the critical amplitude of the molar specific heat at constant pressure in units of the universal gas constant R; $T_\lambda(P)$ and $V_\lambda(P)$, the values of which are given in Table I of Ref. 5, denote, respectively, the temperature and the molar volume on the λ line; and $k(P)$ denotes the critical amplitude of the normalized superfluid density, ρ_sV_λ, with the units of ρ_s being moles per unit volume.

In using the values given for $A_0'(P)$ and $k(P)$, we must realize that the values of these amplitudes depend on the values of the indices used in their determination. We, therefore, have a choice between several alternative values of the same amplitude depending upon the particular value used for the related index. Given the experimental uncertainty in the indices, we should choose those values of the indices which not only seem to be the most correct, $0.00 > \alpha > -0.03$ and $0.666 < \nu < 0.674$,[5-7] but which also are in closest agreement with scaling and universality predictions because the amplitudes should not be expected to obey scaling and universality if the indices do not.[8] Unfortunately, the values used in the literature do not allow us to satisfy both these conditions. For this reason, we present two separate determinations of X_{He} in Table I. The first determination, ${}^1X_{\mathrm{He}}$, best satisfies the first condition, while the second, ${}^2X_{\mathrm{He}}$, best satisfies the second condition. In determining the values for ${}^1X_{\mathrm{He}}$, we used Eq. (10), the values of $A_0'(P)$ from Table XI of Ref. 5 consistent with $\alpha = -0.02$, and the values of $k(P)$ from Eq. (13) of Ref. 7 consistent with $\nu = 0.669$. These values of the indices are close to what seem to be the most correct values; but they represent a small violation of the scaling law $2 - \alpha - 3\nu = 0$. We should note that if $2 - \alpha - 3\nu \neq 0$, Eq. (1) is trivially universal and not identical to Eq. (10). We also expect that using amplitudes consistent with a violation of this scaling law will introduce nonuniversal trends in ${}^1X_{\mathrm{He}}$.[8] However, the numerical smallness of this discrepancy would imply small, if not negligible, nonuniversal trends in ${}^1X_{\mathrm{He}}$. In determining ${}^2X_{\mathrm{He}}$, we used Eq. (10), the values of $A_0'(P)$ from Table X of Ref. 5 consistent with $\alpha = 0.00$, and the values of $k(P)$ from Eq. (11) of Ref. 6 consistent with $\nu = \frac{2}{3}$. Quite probably these values are slightly incorrect, but they obey the scaling law $3\nu = 2 - \alpha$ exactly. Excepting the values for 25.87 bar, both ${}^1X_{\mathrm{He}}$ and ${}^2X_{\mathrm{He}}$ are universal, i.e., independent of pressure, to within 2 or 3% which seems a plausible estimate of the experimental uncertainty. The deviation of the values for the largest pressure is not understood.

Additional investigations of the universality of X_{He}, involving not only the dependence on pressure in pure systems but also the dependence on other irrelevant variables such as the fraction of He^3 in He^3-He^4 mixtures, would be of interest as further tests of the universality of the scaling functions.

The author wishes to acknowledge helpful discussions with M. E. Fisher as well as the hospitality of Professor G. V. Chester and Professor M. E. Fisher and of Cornell University where part of this work was completed.

---

*Part of this work done at Cornell University under National Science Foundation Grant No. GH 36457.

[1] L. P. Kadanoff, in *Critical Phenomena, Proceedings of the International School of Physics "Enrico Fermi," Course 51*, edited by M. S. Green (Academic, New York, 1971).

[2] B. D. Josephson, Phys. Lett. 21, 608 (1966).

[3] M. E. Fisher, M. N. Barber, and D. Jasnow, Phys. Rev. A 8, 1111 (1973).

[4] L. P. Kadanoff *et al.*, Rev. Mod. Phys. 39, 395 (1967).

[5] G. Ahlers, Phys. Rev. A 8, 530 (1973).

[6] D. S. Greywall and G. Ahlers, Phys. Rev. Lett. 28, 1251 (1972).

[7] D. S. Greywall and G. Ahlers, Phys. Rev. A 7, 2145 (1973).

[8] D. Stauffer, M. Ferer, and M. Wortis, Phys. Rev. Lett. 29, 345 (1972).

[9] M. Ferer, D. Stauffer, and M. Wortis, in *Magnetism and Magnetic Materials—1972*, AIP Conference Proceedings No. 10, edited by C. D. Graham, Jr., and J. J. Rhyne (American Institute of Physics, New York, 1973), p. 836.

[10] M. Ferer, and M. Wortis, Phys. Rev. B. 6, 3426 (1972).

[11] A. Aharony, Phys. Rev. B 9, 2107 (1974).

VOLUME 33, NUMBER 1 PHYSICAL REVIEW LETTERS 1 JULY 1974

$1/f$ Noise from Thermal Fluctuations in Metal Films[*]

John Clarke[†] and Richard F. Voss[‡]
Department of Physics, University of California, Berkeley, California 94720,
and Inorganic Materials Research Division, Lawrence Berkeley Laboratory, Berkeley, California 94720

(Received 26 December 1973)

The observed dependence of the $1/f$ noise in metal films on the temperature coefficient of resistance and on sample volume, and the observation of frequency-dependent spatial correlations of the noise, suggest the noise is due to a thermal-diffusion mechanism. The assumption of a spectrum for the intrinsic temperature fluctuations with an explicit $1/f$ region, and the condition $\langle(\Delta T)^2\rangle = kT^2/C_V$, yield quantitative predictions of the noise power in excellent agreement with experiment.

Several authors[1,2] have studied diffusion of heat or particles as a possible mechanism for $1/f$ noise. The spectra calculated for simple uniform systems, although "$1/f$-like," do not exhibit a convincing $1/f$ behavior over many decades of frequency. As a consequence, diffusion has not been accepted as a source of $1/f$ noise.[2] In this Letter, we present experimental evidence that strongly supports a thermal-diffusion mechanism as the source of $1/f$ noise in thin metal films.

As an example of a thermal-diffusion system, consider an infinite uniform medium with thermal diffusivity D. If $\theta(\vec{x}, t)$ is the temperature at $\vec{x}$ at time t, θ obeys the diffusion equation $D\nabla^2\theta = \partial\theta/\partial t$. The average temperature of a bar-shaped volume Ω of length l_1 and rectangular cross section $l_2 l_3$ $(l_1 \gg l_2 \gg l_3)$, $T(t) = \Omega^{-1}\int_\Omega \theta(\vec{x}, t)\, d^3x$, is a fluctuating quantity.[3] In equilibrium at temperature T, $\langle(\Delta T)^2\rangle = k_B T^2/C_V$, and is independent of D, where C_V is the heat capacity of the bar. The spectrum of the fluctuations, $S_T(\omega) \equiv \langle T^*(\omega)T(\omega)\rangle$, does, however, depend on D, and on the manner in which a given fluctuation decays in space and time. The characteristic dimensions of the bar, $l_3 \ll l_2 \ll l_1$, define characteristic frequencies, $\omega_3 \gg \omega_2 \gg \omega_1$, through the relation $\omega_i = D/l_i^2$. The spectrum[1,4] is approximated by $S(\omega) \propto$ const $(\omega \ll \omega_1)$, $S(\omega) \propto \ln(1/\omega)$ $(\omega_1 \ll \omega \ll \omega_2)$, $S(\omega) \propto \omega^{-1/2}$ $(\omega_2 \ll \omega \ll \omega_3)$, and $S(\omega) \propto \omega^{-3/2}$ $(\omega \gg \omega_3)$. For two dimensions, $S(\omega) \propto \ln(1/\omega)$ $(\omega \ll \omega_1)$, $S(\omega) \propto \omega^{-1/2}$ $(\omega_1 \ll \omega \ll \omega_2)$, and $S(\omega) \propto \omega^{-3/2}$ $(\omega \gg \omega_2)$. For one dimension, $S(\omega) \propto \omega^{-1/2}$ $(\omega \ll \omega_1)$, and $S(\omega) \propto \omega^{-3/2}$ $(\omega \gg \omega_1)$. Normalization is achieved by $\int_0^\infty S_T(\omega)\, d\omega = \langle(\Delta T)^2\rangle$.

The spectra are best understood in terms of the frequency-dependent correlation length, $\lambda(\omega) \equiv (2D/\omega)^{1/2}$. The quantity $c(\vec{r}, \omega) \equiv \langle\theta^*(\vec{x}, \omega)\theta(\vec{x} + \vec{r}, \omega)\rangle$ is a measure of how fluctuations at $\vec{x}$ are related to those $\vec{r}$ away at frequency ω. In one dimension

$$c_1(\vec{r}, \omega) \propto \exp(-|\vec{r}|/\lambda)\cos(\pi/4 + |\vec{r}|/\lambda);$$

in three dimensions

$$c_3(\vec{r}, \omega) \propto |\vec{r}|^{-1}\exp(-|\vec{r}|/\lambda)\cos(|\vec{r}|/\lambda).$$

λ is thus a measure of the average spatial extent of a fluctuation at ω. Low-ω fluctuations on the average take place over larger volumes and have greater amplitudes than those at high ω. Changes in the spectrum occur when $\lambda \approx l_i$.

Although the heat flow is uniform throughout the system, we assume that electrical conduction is confined to the bar, of resistance R and temperature coefficient of resistance $\beta \equiv (1/R) \times \partial R/dT$. A constant current in the bar produces an average voltage V and a voltage noise spectrum $S_V(\omega) = V^2\beta^2 S_T(\omega)$. The spectrum is $1/f$-like, increasing as f is lowered, but there is no substantial $1/f$ region.

Hooge and Hoppenbrouwers[5] have studied $1/f$ noise in gold films, and found that the voltage spectrum $S_V(f)$ could be described by

$$S_V(f)/V^2 \approx 2.4 \times 10^{-3}/N_C f, \qquad (1)$$

where N_C is the number of carriers in the sample. Although both the numerical coefficient and the exact $1/f$ law represent a rather approximate fit for a large number of samples, Eq. (1) is a useful basis for comparison. We have repeated these experiments using films typically 150 μm $\times$ 10 μm $\times$ 400 to 2000 Å evaporated or sputtered onto glass substrates. A constant current was passed along each sample, and the voltage spectrum from 0.1 to 25 Hz was measured using tuned circuits modeled in a PDP-11 computer. The amplifier background spectrum ($V = 0$), which was 1–4 orders of magnitude smaller, was measured and subtracted out for each sample. The samples were usually placed in a closed metal box during the measurements. We also measured several samples under vacuum, and found no detectable change in the noise, indicating that atmospheric turbulence did not contribute to the noise. The observed spectra varied as $1/f^{\alpha}$ where $1.0<\alpha<1.4$. We also found $S_V(f)\propto V^2$, and by varying sample dimensions, that $S_V(f)$ was approximately inversely proportional to sample volume. Samples of identical geometry showed variations of up to a factor of 3 in noise power. The measured average values of $S_V(f)/V^2$ at 10 Hz for seven different materials are summarized in Table I, together with the measured temperature coefficients of resistance for the same films. The negative β for the bismuth was probably due to the somewhat amorphous nature of the evaporated films. The resistivities of all the materials, including bismuth, were close to the bulk values.

Table I contains important evidence for the diffusion mechanism. The measured β for the Manganin films was $<10^{-4}$ K^{-1}, more than an order of magnitude below that of the other materials. There was no detectable $1/f$ noise in the Manganin films. This result strongly suggests that the noise in the other metal films arises from temperature modulation of the resistance.

As a second test of the diffusion mechanism, we measured the frequency-dependent spatial correlation. A bismuth film of thickness 1000 Å was cut into two strips each of length l and width 12 μm [Fig. 1(a)]. Separate batteries and large resistors R_0 were used to supply a constant current to each strip. The two noise voltages $V_1(t)$ and $V_2(t)$ were separately amplified and the spectrum of their sum or difference measured with the PDP-11. If $S_+(f)$ and $S_-(f)$ are the spectra of $[V_1(t)+V_2(t)]$ and $[V_1(t)-V_2(t)]$, the fractional correlation between the strips is

$$C(f)=[S_+(f)-S_-(f)]/[S_+(f)+S_-(f)]. \qquad (2)$$

When $V_1(t)$ and $V_2(t)$ are independent, $S_+(f)=S_-(f)$ and $C(f)=0$. When the two strips are completely correlated $V_1(t)=V_2(t)$, $S_-(f)=0$, and $C(f)=1$. For temperature fluctuations at high f, $\lambda\ll l$ and $C(f)\rightarrow 0$, while at low f, $\lambda\gg l$ and $C(f)\rightarrow$ const. We expect the change from correlated to uncorrelated noise to occur when $\lambda\approx l$. Results for two different l are shown in Fig. 1(b). The condition $\lambda=l$ corresponds to frequencies of 0.13 and 1.2 Hz for $l=7.5$ and $l=2.5$ mm (with $D=0.2$ cm^2 sec^{-1}). The measured $C(f)$ is in good agreement with our expectations. As l is increased,

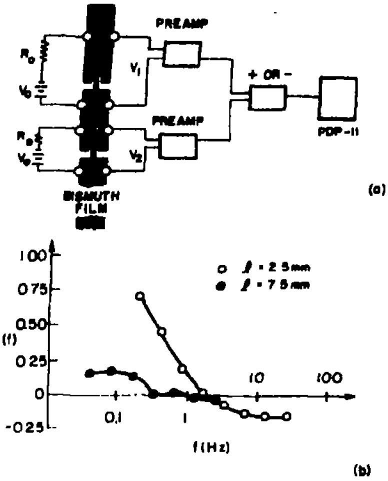

FIG. 1. (a) Experimental configuration for correlation measurement. (b) Fractional correlation for two samples.

TABLE I. The measured and calculated noise power at 10 Hz and the measured temperature coefficient of resistance for seven materials.

Material	$S_V(f)/V^2$ measured at 10 Hz (10^{-16} Hz^{-1})	$S_V(f)/V^2$ calculated at 10 Hz (10^{-16} Hz^{-1})	Measured β (K^{-1})
Cu	10	16	0.0038
Ag	10	2	0.0035
Au	1	0.76	-0.0012
Sn	12	7.7	0.0036
Bi	20	9.3	-0.0029
Manganin	$<10^{-2}$	$<3.5\times10^{-3}$	$\lvert\beta\rvert<10^{-4}$
InSb	3×10^{4}	20	-0.0054

the low-f limit of $C(f)$ decreases because (in two or three dimensions) a fluctuation in one strip has an increasing probability of decaying without influencing the other strip [cf. $c_3(\vec{r}, \omega)$]. For $l > 7.5$ mm, scatter in the data obscured any possible correlations.

Although the scaling of the noise as V^2/Ω, the absence of the noise in Manganin, and the frequency-dependent correlation all indicate a thermal-diffusion mechanism, the observed spectrum of a thin film differs from that calculated for the uniform system. There are several possible reasons for the discrepancy. The sample is not in thermal equilibrium. The power dissipated in the sample raises its temperature above ambient temperature. Moreover, a temperature fluctuation, by changing the resistivity, changes the power dissipated in its neighborhood resulting in a feedback effect. We expect this effect to change the dependence of the noise power on V^2 as well as to produce vastly different spectra for positive and negative feedback. The observed close dependence on V^2 and the similarity of the spectra for metals ($\beta > 0$) and bismuth ($\beta < 0$), however, lead us to believe that feedback is not generally a dominant mechanism. Only to lowest order is the sample resistance proportional to the average temperature. It is possible to have a temperature distribution which does not change the average temperature yet which does change the current paths and hence the resistance. We expect this effect to be negligible for λ greater than the strip width, and to be independent of β.

The major reason for the discrepancy, however, is probably the thermal inhomogeneity of the system. Although neither the very different diffusivities of ilm and substrate, nor the presence of boundary resistance can affect $\langle(\Delta T)^2\rangle$, both can seriously modify $S_T(f)$, which depends on the decay of the temperature fluctuations. In an attempt to investigate the importance of the thermal environment of the film, we coated several samples with an electrically insulating layer of photoresist: No change in the noise was observed. However, a layer of copper about 5000 Å thick evaporated over the photoresist decreased the noise by roughly a factor of 2 below about 1 Hz, but did not affect the noise at higher frequencies. The spectrum, then, depends in a detailed way on the thermal environment of the film. At high frequency, we expect fluctuations to decay predominantly along the film (two-dimensional decay) because of the high thermal conductivity of the metal. Only at lower frequencies, where λ is comparable with the sample length, does the substrate become important and the decay more three dimensional.

We therefore expect $S_T(f)$ to be constant for $f \ll f_1$, and to be proportional to $f^{-3/2}$ for $f \gg f_2$, where f_1 and f_2 are the characteristic frequencies for the length l_1 and the width l_2 of the strip. We postulate that the thermally inhomogeneous system has a $1/f$ spectrum in the intermediate frequency region. We model the spectrum by $S_T(f) = A/f_1$ $(f < f_1)$, $S_T(f) = A/f$ $(f_1 < f < f_2)$, and $S_T(f) = A f_2^{1/2}/f^{3/2}$ $(f > f_2)$. Using the normalization condition, we find for the $1/f$ region

$$S_V(f) = V^2 \beta^2 k_B T^2 / C_V [3 + \ln(f_2/f_1)] f. \tag{3}$$

At room temperature $C_V \approx 3N_A k_B$, where N_A is the number of atoms in the sample, and

$$S_V(f)/V^2 \approx \beta^2 T^2 / 3N_A [3 + 2\ln(l_1/l_2)] f. \tag{4}$$

The last column of Table I contains the calculated values of $S_V(f)/V^2$ for the films at 10 Hz. Both metals ($N_C \approx N_A$) and bismuth ($N_A \approx 10^5 N_C$) show good agreement with Eq. (4). For the samples of Hooge and Hoppenbrouwers[5] (800×10 μm), using our measured β for gold, we find $S_V(f)/V^2 \approx 3.6 \times 10^{-3}/N_A f$ in remarkable agreement with Eq. (2), provided we set $N_C = N_A$.

We believe Eq. (3) should apply to any system. However, diffusion may not be the only or dominant source of $1/f$ noise. As an example, consider our results for evaporated InSb semiconducting films shown in Table I. The noise intensity was 3 orders of magnitude above that predicted by Eq. (3). In addition, we observed no spatial correlation of the noise. We conclude that the thermal-diffusion mechanism was *not* the dominant source of $1/f$ noise in these samples.

The frequency-dependent spatial correlation, the lack of $1/f$ noise in Manganin films, and the scaling of the noise as $V^2\beta^2/N_A$ constitute strong experimental evidence that the $1/f$ noise in metal films arises from the modulation of the resistance by intrinsic thermal fluctuations. We feel, therefore, that a diffusion mechanism can produce $1/f$ noise, and that the inability of theory to predict the observed $1/f$ spectrum is due to the approximation of the experimental system by a uniform diffusive medium. The assumption of an explicit $1/f$ region in $S_T(f)$, together with $\langle(\Delta T)^2\rangle = k_B T^2/C_V$, yields quantitative predictions in good agreement with experiment.

We are grateful to Professor G. I. Rochlin and Dr. D. McBride for the use of their interfaced PDP-11 computer. We thank Professor L. M.

Falicov, Professor A. B. Pippard, Professor K. M. van Vliet, and Dr. J. R. Waldram for their critical comments. Finally, it is a pleasure to thank Professor C. Kittel for his advice and encouragement throughout the course of this work.

---

*Work supported by the U.S. Atomic Energy Commission.

†Alfred P. Sloan Foundation Fellow.

‡National Science Foundation and IBM Graduate Fellow.

[1] G. G. Macfarlane, Proc. Phys. Soc., Sect. B 63, 807 (1950); J. M. Richardson, Bell Syst. Tech. J. 29, 117 (1950); R. L. Petritz, Phys. Rev. 87, 535 (1952); K. M. van Vliet and E. R. Chenette, Physica (Utrecht) 31, 985 (1965); M. Lax, Rev. Mod. Phys. 32, 25 (1960); M. Lax and P. Mengert, Phys. Chem. Solids 14, 248 (1960); I. Lundström, D. McQueen, and D. Klason, Solid State Commun. 13, 1941 (1973). A general review and extensive references are given by K. M. van Vliet and J. R. Fassett, in *Fluctuation Phenomena in Solids*, edited by R. E. Burgess (Academic, New York, 1965), pp. 267–354.

[2] K. M. van Vliet and A. van der Ziel, Physica (Utrecht) 24, 415 (1958).

[3] In the usual treatment of a system in thermal equilibrium with a reservoir, the temperature is defined by the reservoir and the internal energy E of the system fluctuates. Here, by temperature fluctuations, we mean $\Delta T = \Delta E / C_V$.

[4] An alternative derivation of these results is to be published.

[5] F. N. Hooge and A. M. H. Hoppenbrouwers, Physica (Utrecht) 45, 386 (1969).

Electron-Magnon Bound States

Mukesh Eswaran and J. C. Kimball
Department of Physics and Astronomy, Louisiana State University, Baton Rouge, Louisiana 70803

(Received 25 February 1974)

Interactions between strongly correlated electrons (or holes) and spin waves are investigated with the aid of a simple physical model. The model is the large-interaction limit of the Hubbard model with an additional ferromagnetic Heisenberg interaction between nearest-neighbor singly occupied sites. We find that even though there is no obvious electron-magnon attraction in the model, electron-magnon bound states exist for some crystal structures.

We have found electron-magnon bound states in a simple model of a ferromagnetic semiconductor or insulator. The bound states are characterized by a large mass (about one hundred times the electron mass), a binding energy considerably less than the electron bandwidth, complicated symmetries, and relatively large size. These bound states are peculiar in the sense that they can exist even though there is no *ad hoc* electron-magnon interaction in this model. An effective binding appears because for some crystal structures the kinetic energy of strongly correlated electrons or holes is decreased by the presence of a spin wave. We feel that spin waves can quite generally influence electronic kinetic energies in both ferromagnets and antiferromagnets to produce electron-magnon bound states. For simplicity, the following discussion will be primarily restricted to an exactly solvable, ferromagnetic model.

Qualitatively, we envision the electrons to be hopping from site to site, but because of the Coulomb interaction two electrons cannot simultaneously occupy the same site. In addition, we assume that there is an effective exchange interaction between neighboring electron-spin moments. Since we are interested in particle-spin-wave bound states, only the case in which there is one "hole" and one "spin flip" will be considered. We are thus treating the case of hole-magnon bound states. The corresponding case of electron-magnon bound states is identical to the above problem with the sign of the hopping matrix element reversed.

For the ferromagnetic model with only nearest-neighbor hopping, we find that the existence of hole-magnon (or electron-magnon) bound states depends crucially on the lattice structure. Electron kinetic energies can be lowered by spin waves only in those lattices where "self-returning paths" can have an odd number of hops. These lattices include the face-centered cubic, hexagonal close packed, and triangular structures. Results presented here are primarily for the fcc lattice.

The model Hamiltonian H is the sum of the infinite-interaction Hubbard Hamiltonian[1] which describes the hopping of a single hole, and a Heisenberg Hamiltonian which produces the ferromagnetism. The lowest order correction to this model for a large but finite intra-atomic interaction U is an effective antiferromagnetic exchange between nearest-neighbor singly occupied sites. Realistically, the exchange in our model should be interpreted as having been normalized by $-2t^2/U$, where t is the Hubbard hopping matrix element. Although higher order terms in $1/U$ are complicated, we believe that the qualitative features of electron-magnon bound states described here remain valid as long as one is securely in the strong-coupling regime and the effective exchange is ferromagnetic.

For infinite U, we may restrict ourselves to a subspace of state space which excludes doubly occupied sites. Denoting the projection onto this subspace as P, the projected Hamiltonian is

$$H = -P\{\sum_{i,\Delta} t(a_{i\uparrow}{}^\dagger a_{i+\Delta\uparrow} + a_{i\downarrow}{}^\dagger a_{i+\Delta\downarrow}) + J(\vec{S}_i \cdot \vec{S}_{i+\Delta} - \tfrac{1}{4})\}P, \tag{1}$$

where $a_{i\sigma}{}^\dagger$ is the creation operator for an electron with spin σ at site i, site $i+\Delta$ is a nearest neighbor of site i, and the spin operators can be written in terms of the Pauli matrices as

$$\vec{S}_i = \sum_{\alpha\beta} a_{i\alpha}{}^\dagger \vec{\sigma}_{\alpha\beta} a_{i\beta}. \tag{2}$$

The only states we are concerned with are linear combinations of states produced by the operation of a single hole operator $(a_{i\uparrow})$ and a single spin-flip operator $(a_{j\downarrow}{}^\dagger a_{j\uparrow})$ on the completely ferromagnetic state $|\varphi\rangle$. Eigenstates of H of this type with translational periodicity given by a wave vector $\vec{q}$ can be written as a linear combination of basis functions $|\mu\rangle$ with amplitudes b_μ:

$$|\psi_q\rangle = \sum_\mu b_\mu |\mu\rangle, \tag{3}$$

where

$$|\mu\rangle = \frac{1}{\sqrt{N}} \sum_\nu \exp(i\vec{q} \cdot \vec{R}_\nu) a_{\nu-\mu\uparrow} a_{\nu\downarrow}{}^\dagger a_{\nu\uparrow} |\varphi\rangle. \tag{4}$$

Physically, $|\mu\rangle$ describes a hole-spin-flip pair separated by a distance R_μ propagating with a wave vector $\vec{q}$.

The matrix elements of H between states $|\mu\rangle$ and $|\gamma\rangle$ ($H_{\mu\gamma}$ for $\mu,\gamma \neq 0$) are

$$H_{\mu\gamma} = t\sum_\Delta(\delta_{\mu,\gamma+\Delta} + \delta_{\mu,\Delta}\delta_{\gamma,-\Delta}e^{-i\vec{q}\cdot\vec{\Delta}}) - J\sum_\Delta[e^{-i\vec{q}\cdot\vec{\Delta}}\delta_{\mu,\gamma+\Delta} + \tfrac{1}{2}\delta_{\mu,\gamma}(\delta_{\mu,\Delta} - 3)]. \tag{5}$$

The state $|\mu = 0\rangle$ is undefined but the Hamiltonian matrix can be expanded by defining

$$H_{\mu,0} = H_{0,\gamma} = 0. \tag{6}$$

This adds an additional eigenvalue of zero to the spectrum of H but does not otherwise alter the results. The eigenvalues of H can be found by Fourier transform,

$$H_{pk} = \frac{1}{N}\sum_{\mu,\gamma} \exp[-i(\vec{p}\cdot\vec{R}_\mu - \vec{k}\cdot\vec{R}_\gamma)]H_{\mu\gamma} = \delta_{p,k}\{th(\vec{k}) - J[h(\vec{k}+\vec{q}) - \tfrac{1}{2}Z]\} + V_{pk}/N, \tag{7}$$

where Z is the lattice coordination number,

$$V_{p,k} = -t[h(\vec{k}) + h(\vec{p}) + h(\vec{q}+\vec{k}+\vec{p})] + J[h(\vec{k}+\vec{q}) + h(\vec{p}+\vec{q}) - \tfrac{1}{2}h(\vec{k}-\vec{p})], \tag{8}$$

and

$$h(\vec{k}) = \sum_\Delta e^{i\vec{k}\cdot\vec{\Delta}}. \tag{9}$$

The bound state energies of this system are obtained as poles in the t matrix of H_{pk}. Because $_{p,k}$ is separable, i.e.,

$$V_{p,k} = \sum_{l=1}^{m} f_l(p)g_l(k), \tag{10}$$

he t matrix may be found *exactly*. The diagonal -matrix elements are

$$t_{kk} = \mathrm{Tr}\{\varphi(k)[1 - \theta(\omega)]^{-1}\}, \tag{11}$$

where

$$\varphi_{i,j}(k) = f_i(k)g_j(k), \tag{12}$$

$$\theta_{ij}(\omega) = \sum_p \varphi_{ij}(p)G_{pp}{}^0(\omega), \tag{13}$$

and $G_{pk}{}^0(\omega)$ is the Green's function for the matrix $(H - V/N)_{p,k}$.

Poles in t_{kk} appear as zeros of the determinant of $[I - \theta(\omega)]$. At a general point in the Brillouin zone for q, the t matrix is of a large dimension. However, at various symmetry points and along the symmetry axes, the use of group theory drastically reduces the dimensionality of this matrix. For the fcc lattice, at the Γ point ($q = 0$) the t matrix is one-dimensional, and the bound-state energy is given by that value of ω which satisfies the equation

$$1 + 2(t + \tfrac{1}{2}J)/\pi^3 \int_0^\pi \int_0^\pi \int_0^\pi \frac{[\cos(k_x) - \cos(k_y)]^2 \sin^2(k_z)}{\omega - 12J - (t - J)h(k)} \, dk_x \, dk_y \, dk_z = 0, \tag{14}$$

where for this lattice

$$h(k) = 4[\cos(k_x)\cos(k_y) + \cos(k_x)\cos(k_z) + \cos(k_y)\cos(k_z)]. \tag{15}$$

This bound state belongs to the Γ_{25} representation and is triply degenerate. Along the various symmetry axes of the Brillouin zone, this degeneracy is either partially or completely lifted.

The band structure of the hole-spin-wave bound state for $J \ll t$ is shown in Fig. 1. The band minimum occurs at the point X of the Brillouin zone of the fcc lattice. The ratio of the maximum binding energy to the bandwidth is $\simeq 0.02$. The effective mass of the bound system around the point X is approximately 100 times that of the electron. The size of the bound states is 10 lattice spacings or more.

We feel that electron-magnon or hole-magnon states may be observable. Further approximate calculations indicate that electrons or holes bind to only one magnon, so for small J, the electron-magnon bound states are the lowest-energy single-particle-type excitations of the model. If the model is valid, these states should lie below the absorption edge for the creation of simple electron-hole pairs in magnetic semiconductors.

The band structure along the Δ axis for the same lattice when $J = 0.1t$ is shown in Fig. 2(a). The energy level belonging to the representation Δ_5 now lies deeper than that belonging to Δ_2. For $J > 0.02t$ the bound state at X is absorbed into the continuum,[3] and so the bound states are found only near Γ.

The binding energy of the triply degenerate bound state at Γ is an increasing function of J as long as $0 < J < t$ [see Fig. 2(b)], and rapidly decreases for $J > t$. There is no bound state for $J \gtrsim 1.12t$. This is consistent with the requirement that for a purely Heisenberg interaction ($J \gg t$), there can be no such bound system.[3]

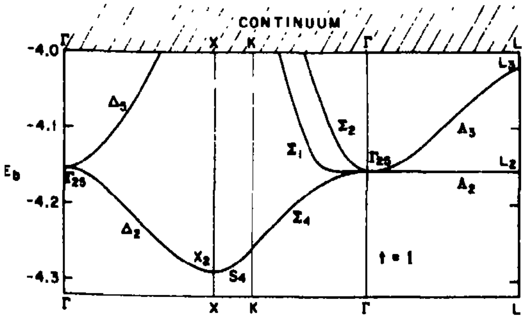

FIG. 1. The band structure of the hole-magnon bound state in a fcc lattice for $J \ll t$.

There are, unfortunately, few insulating ferromagnets. Although these ferromagnets may be adequately described by this model, many more insulating antiferromagnets exist (e.g., some transition-metal chalcogenides) which might be well described by this model if it could be solved for $J < 0$. We believe that electron-magnon or hole-magnon bound states can also exist for antiferromagnets. Nagaoka[4] has shown that for many infinite-interaction Hubbard lattices the antiferromagnetic state with one hole does not have the lowest energy. This suggests that a spin wave in an antiferromagnet could lower the energy of the hopping electron or hole and produce an electron-antiferromagnetic-magnon bound state. Although some evidence for the existence of electron-magnon binding effects comes from a moment expansion of the density of states for electrons in Néel antiferromagnets, we can offer no rigorous proof

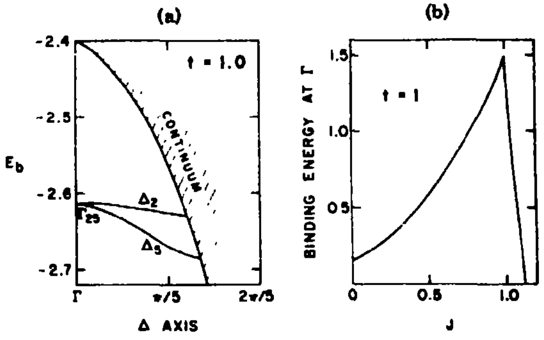

FIG. 2. (a) The band structure of the hole-magnon bound state along the Δ axis for $J = 0.1$. Note that the bound states disappear into the continuum as the center-of-mass momentum increases. (b) The binding energy of the Γ_{25} bound state as a function of the Heisenberg exchange coupling, J.

lattice.

The model Hamiltonian H is the sum of the infinite-interaction Hubbard Hamiltonian[1] which describes the hopping of a single hole, and a Heisenberg Hamiltonian which produces the ferromagnetism. The lowest order correction to this model for a large but finite intra-atomic interaction U is an effective antiferromagnetic exchange between nearest-neighbor singly occupied sites. Realistically, the exchange in our model should be interpreted as having been normalized by $-2t^2/U$, where t is the Hubbard hopping matrix element. Although higher order terms in $1/U$ are complicated, we believe that the qualitative features of electron-magnon bound states described here remain valid as long as one is securely in the strong-coupling regime and the effective exchange is ferromagnetic.

For infinite U, we may restrict ourselves to a subspace of state space which excludes doubly occupied sites. Denoting the projection onto this subspace as P, the projected Hamiltonian is

$$H = -P[\sum_{i,\Delta} t(a_{i\uparrow}^\dagger a_{i+\Delta\uparrow} + a_{i\downarrow}^\dagger a_{i+\Delta\downarrow}) + J(\vec{S}_i \cdot \vec{S}_{i+\Delta} - \tfrac{1}{4})]P, \tag{1}$$

where $a_{i\sigma}^\dagger$ is the creation operator for an electron with spin σ at site i, site $i+\Delta$ is a nearest neighbor of site i, and the spin operators can be written in terms of the Pauli matrices as

$$\vec{S}_i = \sum_{\alpha\beta} a_{i\alpha}^\dagger \vec{\sigma}_{\alpha\beta} a_{i\beta}. \tag{2}$$

The only states we are concerned with are linear combinations of states produced by the operation of a single hole operator $(a_{i\uparrow})$ and a single spin-flip operator $(a_{j\downarrow}^\dagger a_{j\uparrow})$ on the completely ferromagnetic state $|\varphi\rangle$. Eigenstates of H of this type with translational periodicity given by a wave vector $\vec{q}$ can be written as a linear combination of basis functions $|\mu\rangle$ with amplitudes b_μ:

$$|\psi_q\rangle = \sum_\mu b_\mu |\mu\rangle, \tag{3}$$

where

$$|\mu\rangle = \frac{1}{\sqrt{N}} \sum_\nu \exp(i\vec{q}\cdot\vec{R}_\nu) a_{\nu-\mu\uparrow} a_{\nu\downarrow}^\dagger a_{\nu\uparrow} |\varphi\rangle. \tag{4}$$

Physically, $|\mu\rangle$ describes a hole-spin-flip pair separated by a distance R_μ propagating with a wave vector $\vec{q}$.

The matrix elements of H between states $|\mu\rangle$ and $|\gamma\rangle$ ($H_{\mu\gamma}$ for $\mu, \gamma \neq 0$) are

$$H_{\mu\gamma} = t\sum_\Delta(\delta_{\mu,\gamma+\Delta} + \delta_{\mu,\Delta}\delta_{\gamma,-\Delta}e^{-i\vec{q}\cdot\vec{\Delta}}) - J\sum_\Delta[e^{-i\vec{q}\cdot\vec{\Delta}}\delta_{\mu,\gamma+\Delta} + \tfrac{1}{2}\delta_{\mu,\gamma}(\delta_{\mu,\Delta} - 3)]. \tag{5}$$

The state $|\mu = 0\rangle$ is undefined but the Hamiltonian matrix can be expanded by defining

$$H_{\mu,0} = H_{0,\gamma} = 0. \tag{6}$$

This adds an additional eigenvalue of zero to the spectrum of H but does not otherwise alter the results. The eigenvalues of H can be found by Fourier transform,

$$H_{pk} = \frac{1}{N}\sum_{\mu,\gamma} \exp[-i(\vec{p}\cdot\vec{R}_\mu - \vec{k}\cdot\vec{R}_\gamma)]H_{\mu\gamma} = \delta_{p,k}\{th(\vec{k}) - J[h(\vec{k}+\vec{q}) - \tfrac{3}{2}Z]\} + V_{pk}/N, \tag{7}$$

where Z is the lattice coordination number,

$$V_{p,k} = -t[h(\vec{k}) + h(\vec{p}) + h(\vec{q}+\vec{k}+\vec{p})] + J[h(\vec{k}+\vec{q}) + h(\vec{p}+\vec{q}) - \tfrac{1}{2}h(\vec{k}-\vec{p})], \tag{8}$$

and

$$h(\vec{k}) = \sum_\Delta e^{i\vec{k}\cdot\vec{\Delta}}. \tag{9}$$

The bound state energies of this system are obtained as poles in the t matrix of H_{pk}. Because V_{pk} is separable, i.e.,

$$V_{pk} = \sum_{l=1}^{\infty} f_l(p)g_l(k), \tag{10}$$

the t matrix may be found *exactly*. The diagonal t-matrix elements are

$$t_{kk} = \mathrm{Tr}\{\varphi(k)[1 - \theta(\omega)]^{-1}\}, \tag{11}$$

where

$$\varphi_{i,j}(k) = f_i(k)g_j(k), \tag{12}$$

$$\theta_{ij}(\omega) = \sum_p \varphi_{ij}(p)G_{pp}^0(\omega), \tag{13}$$

and $G_{pk}^0(\omega)$ is the Green's function for the matrix $(H - V/N)_{p,k}$.

Poles in t_{kk} appear as zeros of the determinant of $[I - \theta(\omega)]$. At a general point in the Brillouin zone for q, the t matrix is of a large dimension. However, at various symmetry points and along he symmetry axes, the use of group theory drastically reduces the dimensionality of this matrix. For the fcc lattice, at the Γ point ($q = 0$) the t matrix is one-dimensional, and the bound-state energy s given by that value of ω which satisfies the equation

$$1 + 2(t + \tfrac{1}{2}J)/\pi^3 \int_0^\pi \int_0^\pi \int_0^\pi \frac{[\cos(k_x) - \cos(k_y)]^2 \sin^2(k_z)}{\omega - 12J - (t - J)h(k)} \, dk_x \, dk_y \, dk_z = 0, \tag{14}$$

/here for this lattice

$$h(k) = 4[\cos(k_x)\cos(k_y) + \cos(k_x)\cos(k_z) + \cos(k_y)\cos(k_z)]. \tag{15}$$

'his bound state belongs to the Γ_{25} representation nd is triply degenerate. Along the various symmetry axes of the Brillouin zone, this degeneracy s either partially or completely lifted.

The band structure of the hole-spin-wave bound ate for $J \ll t$ is shown in Fig. 1. The band minium occurs at the point X of the Brillouin zone the fcc lattice. The ratio of the maximum binding energy to the bandwidth is $\simeq 0.02$. The effecve mass of the bound system around the point X approximately 100 times that of the electron. ie size of the bound states is 10 lattice spacgs or more.

We feel that electron-magnon or hole-magnon states may be observable. Further approximate calculations indicate that electrons or holes bind to only one magnon, so for small J, the electron-magnon bound states are the lowest-energy single-particle-type excitations of the model. If the nodel is valid, these states should lie below the bsorption edge for the creation of simple electron-hole pairs in magnetic semiconductors.

The band structure along the Δ axis for the ame lattice when $J = 0.1t$ is shown in Fig. 2(a). The energy level belonging to the representation Δ_5 now lies deeper than that belonging to Δ_2. For $J > 0.02t$ the bound state at X is absorbed into the ontinuum,[2] and so the bound states are found only near Γ.

The binding energy of the triply degenerate bound state at Γ is an increasing function of J as long as $0 \leqslant J \leqslant t$ [see Fig. 2(b)], and rapidly decreases for $J > t$. There is no bound state for $J \gtrsim 1.12t$. This is consistent with the requirement that for a purely Heisenberg interaction ($J \gg t$), there can be no such bound system.[3]

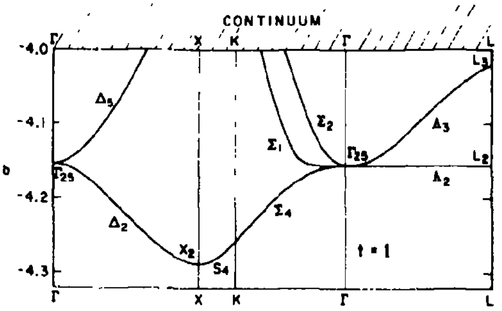

FIG. 1. The band structure of the hole-magnon bound state in a fcc lattice for $J \ll t$.

There are, unfortunately, few insulating ferromagnets. Although these ferromagnets may be adequately described by this model, many more insulating antiferromagnets exist (e.g., some transition-metal chalcogenides) which might be well described by this model if it could be solved for $J < 0$. We believe that electron-magnon or hole-magnon bound states can also exist for antiferromagnets. Nagaoka[4] has shown that for many infinite-interaction Hubbard lattices the antiferromagnetic state with one hole does not have the lowest energy. This suggests that a spin wave in an antiferromagnet could lower the energy of the hopping electron or hole and produce an electron-antiferromagnetic-magnon bound state. Although some evidence for the existence of electron-magnon binding effects comes from a moment expansion of the density of states for electrons in Néel antiferromagnets, we can offer no rigorous proof

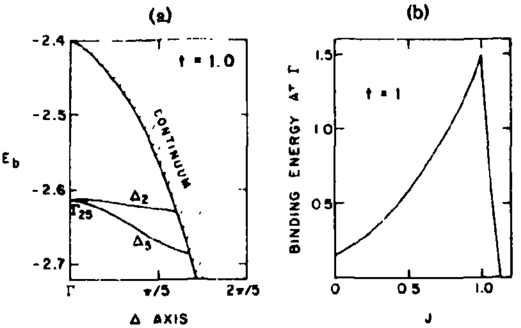

FIG. 2. (a) The band structure of the hole-magnon bound state along the Δ axis for $J = 0.1$. Note that the bound states disappear into the continuum as the center-of-mass momentum increases. (b) The binding energy of the Γ_{25} bound state as a function of the Heisenberg exchange coupling, J.

of their existence.

We wish to acknowledge helpful discussions with Professor J. Callaway.

---

[1] J. Hubbard, Proc. Roy. Soc., Ser. A 276, 238 (1963), and 281, 401 (1964).

[2] A similar phenomenon is observed in two-magnon bound states. See M. Wortis, Phys. Rev. 132, 85 (1963); R. G. Boyd and J. Callaway, Phys. Rev. 138, A1621 (1965).

[3] D. Hone, in *Localized Excitations in Solids*, edited by R. F. Wallis (Plenum, New York, 1968), p. 335.

[4] Y. Nagaoka, Phys. Rev. 147, 392 (1966).

Failure of the Allowed Assumption in the ϵ/β^+ Decays of ^{145g}Gd and ^{143g}Sm—Experimental Evidence for Interference Effects in Nuclear β Decay

*R. B. Firestone, R. A. Warner, and Wm. C. McHarris**
Department of Chemistry,† Cyclotron Laboratory,‡ and Department of Physics,
Michigan State University, East Lansing, Michigan 48823

and

W. H. Kelly
Cyclotron Laboratory‡ and Department of Physics, Michigan State University, East Lansing, Michigan 48824

(Received 8 April 1974)

Anomalous ϵ/β^+ decay branching ratios for "hindered allowed" transitions (measured by $\gamma^{\pm}$-γ and x-γ coincidence techniques) have been found in ^{145g}Gd → ^{145}Eu(808.5-keV state) and ^{143g}Sm → ^{143}Pm(1173.2-keV state). These ratios exceed theoretical predictions by factors of 24 and 5, respectively. Thirteen additional ratios from these nuclei and ^{143}Eu agree with the predictions. This is the first conclusive evidence of the failure of the allowed assumption in nuclear β decay and of the presence of interference effects.

Numerous past measurements of ϵ/β^+ (electron-capture to positron) decay branching ratios[1-4] tend to support modern β-decay and weak-interaction theory. These measurements generally involved simple, fast allowed transitions and were quite difficult to perform inasmuch as only very small deviations from the theoretically predicted ratios were involved and are difficult to detect. With the discovery of parity nonconservation and the success of the universal $V-A$ interaction, most of the interest in measuring these ratios disappeared, and in recent years only a few additional values have been measured. Studies on ^{145g}Gd decay in this laboratory[5] indicated an anomalous branching ratio involving a highly hindered allowed transition. In this work we study this transition more thoroughly and report a similar anomaly in ^{143g}Sm decay. We then discuss some of the ramifications of our findings.

All activities discussed here were prepared with beams from the Michigan State University sector-focused cyclotron. ^{145g}Gd ($t_{1/2} = 22.9$ min) was prepared by the reaction ^{144}Sm(^{3}He, $2n$) using a 20-MeV ^{3}He beam on a target enriched to 95.10% in ^{144}Sm. ^{143}Eu ($t_{1/2} = 2.6$ min) was produced by ^{144}Sm(p, $2n$) using a 28-MeV p beam on similar targets, and its daughter ^{143g}Sm ($t_{1/2} = 8.83$ min) was studied along with it.

The relative β^+ feedings were measured by the $\gamma^{\pm}$-γ triple coincidence method described by Kelly and co-workers.[6] Briefly, the two halves of an 8×8-in. NaI(Tl) split annulus were gated on the 511-keV $\gamma^{\pm}$ radiation indicative of a β^+ event and a third γ-ray coincidence was sought in a large Ge(Li) detector inside the annulus tunnel. A resolving time of 50 nsec and the triple-coincidence requirement made chance events very rate. The relative β^+ feedings to each level were inferred from the coincident γ-ray spectrum after correcting for γ-ray feeding from higher-lying levels. The high efficiency of the annulus (60% at 511 keV) caused significant chance summing of annihilation quanta with γ rays in coincidence with those detected in the Ge(Li) detector, so only levels de-exciting primarily through a single direct ground-state transition could be studied. Fortunately, the nuclei discussed here decay predominantly to levels de-exciting directly to the ground states.

Relative ϵ feedings were measured by an x-γ coincidence experiment. A 5-mm-thick planar Ge(Li) detector with 550-eV resolution at 122 keV was gated on the K x-ray region to indicate an ϵ event, and a large Ge(Li) detector was gated on γ rays tagging the ϵ-fed level. (The γ transitions in the nuclei studied here all have high enough energies to make x rays resulting from internal conversion negligible.) The data were listed, three addresses per event (E_x, E_γ, and time), and were sorted off-line with subtraction of the continuum from both the x-ray and time axes. The resultant coincident γ-ray spectra were analyzed to obtain the relative ϵ feedings. Final ϵ feedings were corrected for L capture.[7]

The two sets of intensities were normalized to each other for ^{145m}Gd decay by assuming the theoretical ratio for decay to the 1757.8-keV level, which was chosen because it is fast ($\log ft = 5.8$) and the statistics are excellent. These relative eedings are presented in Table I. (If the theoretical predictions were correct, the choice of transition for normalization should not be significant; however, had we chosen the transition to the 808.5-keV level for normalization, the total β^+ feeding would far exceed 100%.) The measured ϵ/β^+ branching ratios are compared in Table I with the values tabulated by Gove and Martin[8] for $Q_\epsilon = 5.3$ MeV.[9] The data can perhaps be best compared with theory by defining a "skew ratio" $R = (\epsilon/\beta^+)_{\text{expt}}/(\epsilon/\beta^+)_{\text{theor}}$. It is thus a measure of how much the ϵ branch is enhanced or the β^+ branch is suppressed. Agreement is generally good except for the transition to the 808.5-keV level, where R has a value of 24. A 20% excess is also seen in the transition to the 1041.9-keV level.

The ^{143m}Sm and ^{143}Eu decays are more difficult to study because of the short half-lives involved. Only total feedings and relative β^+ feedings were measured, so ϵ feedings were inferred from these. The measured ratios in Table I are normalized to theory for the transitions to the 1056.6-keV level of ^{143}Pm and to the 1107.2-keV level of ^{143}Sm. Q_ϵ was assumed to be 3.32 meV for ^{143m}Sm decay[10] and 5.5 MeV for ^{143}Eu decay.[11] Again, agreement is good except for the transition to the 1173.2-keV level of ^{143}Pm, where the experimental ϵ/β^+ exceeds the theoretical one by a factor of 5.

The excellent agreement of most of the data with theory makes the exceptions stand out quite strongly. They are not easy to explain away. For

TABLE I. ϵ/β^+ branching ratios for ^{145m}Gd, ^{143m}Sm, and ^{143}Eu decays.

	Energy[a] (keV)	Q_ϵ (MeV)	ϵ(tot)/β^+ experimental	ϵ(tot)/β^+[b] theoretical	Skew ratio R (expt/theor)
^{145m}Gd	808.5	4.5	10.7 ± 2.0	0.45	24
	1041.9	4.3	0.72 ± 0.05	0.60	1.2
	1757.8	3.5	≡ 1.17 ± 0.05[c]	1.17	1.0
	1880.6	3.4	1.34 ± 0.05	1.37	0.98
	2494.8	2.8	3.07 ± 0.5	3.39	0.91
	2642.2	2.7	4.70 ± 0.5	4.41	1.07
^{143m}Sm	1056.6	2.26	≡ 9.7 ± 0.7[c]	9.7	1.0
	1173.1	2.15	63 ± 10	13	4.9
	1403.1	1.92	35 ± 5	29	1.2
	1515.0	1.80	30 ± 7	49	0.61[d]
^{143}Eu	1107.2	4.4[e]	≡ 0.51 ± 0.06[f]	0.46	1.11
	1536.7	4.0	0.62 ± 0.06	0.69	0.90
	1565.9	3.9	0.69 ± 0.15	0.72	0.96
	1715.1	3.8	0.75 ± 0.17	0.83	0.90
	1912.6	3.6	1.07 ± 0.11	1.02	1.05

[a] Only the ratios for the most significantly fed levels are included in this table.

[b] Values from Ref. 8.

[c] ϵ/β^+ ratios are normalized to this transition.

[d] An error of only 100 keV in the reported decay energy would bring this value in line with theory without significantly affecting the fit of the rest of the data.

[e] The total available decay energy for ^{143}Eu was chosen as 5.5 MeV to obtain the best comparison with the theoretical values.

[f] The ^{143}Eu experimental ratio normalization was adjusted slightly to give the best and most consistent agreement with theory.

example, extreme care was taken to insure that the β^+'s were completely annihilated within the source package in the annulus tunnel, so effects such as incomplete annihilation cannot be the explanation. The γ transitions associated with the levels that receive the anomalous β decay are all well understood from previous studies[5,12,13] and should not be delayed, so this cannot be the explanation either. This was also seen in the time-to-amplitude converter spectra for ^{145g}Gd, where all the transitions were prompt. Errors in the decay schemes must be small, as virtually 99% of the γ-ray intensity is firmly placed in each. Corrections for L capture are straightforward and affect the relative feedings only slightly.

The implications of these anomalous ϵ/β^+ branching ratios may be quite significant. Close observation of the ^{145g}Gd and ^{143g}Sm anomalies indicates that they are not random cases but instead particularly hindered allowed transitions of a similar nature. (The "fast" transitions in the decays of these nuclei have been shown[5,10] to lead to three-quasiparticle states.)

Actually, our arguments do not hinge on the detailed nature of these transitions—for the purposes of what follows they might just as well be considered "fast" transitions between states of unknown structure. It was also shown by Biryukov and Shimanskaya[15] that the transition to the ground state of ^{143}Pm gives the predicted ratio. On the other hand, the anomalous transitions of ^{145g}Gd to the 808.5-keV state in ^{145}Eu and of ^{143g}Sm to the 1173.1-keV state in ^{143}Pm both proceed through the $\pi s_{1/2}$ states of the daughters. These *hindered transitions are of the (over-simplified)* form

$$(\pi d_{5/2})^2(\nu s_{1/2})^{-1} \rightarrow (\pi s_{1/2})(\nu s_{1/2})^{\text{full}}, \quad \log ft = 7.1,$$

for ^{145g}Gd decay and

$$(\pi d_{5/2})^2(\nu d_{3/2})^{-1} \rightarrow (\pi s_{1/2})(\nu d_{3/2})^{\text{full}}, \quad \log ft = 6.4,$$

for ^{143g}Sm decay. As written, these are complex multiparticle decays and rearrangements and may very well proceed through small components of the wave functions. The important fact, however, is that the anomalous ϵ/β^+ branching ratios occur in these *hindered allowed* transitions. (It should be emphasized that the basic characters of all of these shell-model states are well known from a combination of decay-scheme, atomic-beams,[16] and single-particle-transfer[17-19] studies; *these are* indeed allowed transitions.) The transitions to the $\pi d_{3/2}$ states at 1041.9 keV ($\log ft = 6.7$) in ^{145}Eu and 1403.1 keV ($\log ft = 6.3$) in ^{143}Pm are also complex but to a lesser extent. They display smaller anomalies ($\approx 15\%$) in the ϵ/β^+ branching ratios.

The transition amplitude squared for β decay can be written[20]

$$h_{fi} = \xi(1 \pm b\langle W\rangle^{-1})$$

for e^+ decay, where

$$\xi = [|C_S|^2 + |C_V|^2](\textstyle\int 1)^2 + [|C_A|^2 + |C_T|^2](\int \sigma)^2 + [|C_A|^2 + |C_P|^2](\int \gamma_5)^2 + [|C_S|^2 + |C_T|^2](\int \alpha)^2$$

and

$$b\xi = 2[C_S C_V(\textstyle\int 1)^2 + C_A C_T(\int \sigma)^2 + C_A C_P(\int \gamma_5)^2 + C_S C_T(\int \alpha)^2].$$

Here C_S, C_V, C_A, C_T, and C_P are the coupling constants for the scalar, vector, axial-vector, tensor, and pseudoscalar interactions, respectively (with terms for odd and even couplings implicit), and the matrix elements have their customary definitions. The ϵ/β^+ branching ratios give evidence of interference terms because of the opposite signs of b in the expression for h_{fi}. This can be seen in the equation for the electron-capture to positron transition-probability ratio,

$$\lambda_K/\lambda_+ \approx \tfrac{1}{2}\pi(W_0 + 1)^2 g_K{}^2(1 + b)/(1 - b\langle W^{-1}\rangle).$$

In the allowed assumption $\int \gamma_5$ and $\int \alpha$ are considered to be much smaller than $\int 1$ and $\int \sigma$ because they are proportional to v/c (≈ 0.1)—thus, they are ignored.

The fact that the anomalous ϵ/β^+ branching ratios occur for hindered transitions brings into question the allowed assumption. If the allowed matrix elements $\int 1$ and $\int \sigma$ are small, this does not necessarily mean that the higher order corrections are also reduced. It is conceivable that in some cases the "correction" terms could be considerably larger than the allowed terms. In such cases the higher order terms will lead to VA interference, which will give considerably larger ϵ/β^+ ratios than those predicted for allowed transitions. This is borne out in measurements of ϵ/β^+ ratios in second-forbidden unique transitions where the ratios are as much as 6 times the corresponding allowed values.[21] Unfornately, as many as six matrix elements can conribute to our anomalous transitions, so the net ffect cannot be predicted. Calculations are curently underway in this laboratory to estimate etter the relative contributions of higher order atrix elements.

As long as higher order matrix elements are ossibly important, the C_AC_P interference term ust also be considered. The pseudoscalar couling has never been adequately eliminated for decay, and this may be a good way to test it. he *AP* interference will also lead to larger ϵ/β^+ ranching ratios than predicted for allowed decay, d it is more importantly a critical test of two-omponent neutrino theory and exclusively left-anded particles. Measurements of β helicity d possibly spectrum shapes on hindered tranitions should provide a sensitive test for such terference.

In conclusion, we have found solid experimenl evidence for ϵ/β^+ branching ratios for hindred allowed transitions that are much larger an theory would predict. Thus, allowed β-deay theory is inadequate to explain these transions, and large interference effects are indiated. Other hindered transitions should prove be good places to search for such effects, and elicity and shape measurements should provide ore insight into the exact nature of the interfernce.

---

[*] Alfred P. Sloan Fellow, 1972–1974.

[†] Work supported in part by the U. S. Atomic Energy ommission.

[‡] Work supported in part by the U. S. National Science oundation.

[1] B. L. Robinson and R. W. Fink, Rev. Mod. Phys. 32, 7 (1960).

[2] D. Berenyi, Rev. Mod. Phys. 40, 390 (1968).

[3] M. L. Fitzpatrick, K. W. D. Ledingham, J. Y. Goury, and J. G. Lynch, in *Proceedings of the Internation Conference on Inner Shell Ionization Phenomena and ture Applications, Atlanta, Georgia, 1972,* edited R. W. Fink, J. T. Manson, I. M. Palms, and R. V. Rao, CONF-720404 (U. S. Atomic Energy Commission, Oak Ridge, Tenn., 1973), p. 2013.

[4] D. Berenyi, Nucl. Phys. 48, 121 (1963).

[5] R. E. Eppley, Wm. C. McHarris, and W. H. Kelly, Phys. Rev. C 3, 282 (1971). The decay of ^{145g}Gd has been thoroughly restudied and differs from the published results in a few minor points, nothing essential to this Letter: R. B. Firestone, R. A. Warner, Wm. C. McHarris, and W. H. Kelly, to be published.

[6] W. H. Kelly and Wm. C. McHarris, in *Proceedings of the International Conference on Radioactivity in Nuclear Spectroscopy, Vanderbilt University, Nashville, Tennessee, 1969* (Gordon and Breach, New York, 1972), p. 1077; R. L. Auble, D. B. Beery, G. Berzins, L. M. Beyer, R. C. Etherton, W. H. Kelly, and Wm. C. McHarris, Nucl. Instrum. Methods 51, 61 (1967).

[7] C. M. Lederer, J. M. Hollander, and I. Perlman, *Table of Isotopes* (Wiley, New York, 1968), 6th ed., p. 576.

[8] N. B. Gove and M. J. Martin, Nucl. Data, Sect. A 10, 205 (1971).

[9] L. Chiao and M. J. Martin, Nucl. Data, Sect. B 2, 81 (1967).

[10] J. H. E. Mattauch, W. Thiele, and A. H. Wapstra, Nucl. Phys. 67, 1 (1965).

[11] K. Kotajima, K. W. Brockman, Jr., and G. Wolzak, Nucl. Phys. 65, 109 (1965); these authors report $Q_\epsilon = 5.0 \pm 0.2$ MeV, but 5.5 MeV appears to fit the data much better—even choosing 5.0 MeV gives an acceptable fit of the measured ϵ/β^+ ratios with theory.

[12] R. B. Firestone, R. A. Warner, Wm. C. McHarris, and W. H. Kelly, "The Decay of ^{143}Eu" (to be published).

[13] R. B. Firestone, R. A. Warner, Wm. C. McHarris, and W. H. Kelly, "The Decay of ^{143}Sm" (to be published).

[14] Wm. C. McHarris, D. B. Beery, and W. H. Kelly, Phys. Rev. Lett. 22, 1191 (1969).

[15] E. I. Biryukov and N. S. Shimanskaya, Yad. Fiz. 11, 246 (1970) [Sov. J. Nucl. Phys. 11, 138 (1970)].

[16] C. Ekström, S. Ingleman, M. Olsmats, and B. Wannberg, Phys. Scr. 6, 181 (1972).

[17] O. Hansen, O. Nathan, L. Vistisen, and R. Chapman, Nucl. Phys. A113, 75 (1968).

[18] E. Newman, K. S. Toth, R. L. Auble, R. M. Gaedke, M. F. Roche, and B. H. Wildenthal, Phys. Rev. C 3, 1118 (1970).

[19] B. H. Wildenthal, E. Newman, and R. L. Auble, Phys. Lett. 27B, 628 (1968).

[20] E.g., E. J. Konopinski, *The Theory of Beta Radioactivity* (Clarendon Press, Oxford, 1966).

[21] M. L. Perlman, J. P. Welker, and M. Wolfsberg, Phys. Rev. 110, 381 (1958).

Measurement of the Positron-Electron Ratio in the Primary Cosmic Rays from 5 to 50 GeV*

A. Buffington, C. D. Orth, and G. F. Smoot
Space Sciences Laboratory and Lawrence Berkeley Laboratory, University of California, Berkeley, California 94720

(Received 9 May 1974)

We report the first measurement of primary-cosmic-ray positrons above 5 GeV. Both e^+ and e^- fluxes were measured, using a balloon-borne magnetic spectrometer. Background was suppressed using a new technique which combines both selective trigger and identification of bremsstrahlung photons created by $e^\pm$ upon entering the instrument. If no positrons originate at cosmic-ray sources, our observed ratio $e^+/(e^+ + e^-) = 0.08 \pm 0.02$ requires source protons to traverse 3.5 ± 1.5 g/cm^2 of interstellar material.

Primary cosmic rays generate secondary cosmic rays through interactions with the interstellar gas. The fluxes of secondaries are a measure of the material traversed by their parents. While secondary nuclei (e.g., Li, Be, B) arise from low-momentum-transfer fragmentation of heavier nuclei, positrons are the decay products of pions produced in highly inelastic proton interactions. As a result, secondary nuclei have the same energy per nucleon as their parents, while positrons have energies typically 5 to 30 times smaller than their parents.

Cosmic-ray nuclei traverse a mean column density which diminishes from about 4 g/cm^2 at a few GeV/nucleon to about 2 g/cm^2 by 50 GeV/nucleon.[1-5] A measurement of the positron flux above a few GeV provides the means to see if this diminishing trend continues, since these positrons are produced by protons with energies above 50 GeV.

In this Letter we present the first separated e^+ and e^- flux measurements in the energy range from 5 to 50 GeV. We used a new technique which combines a radiator to produce bremsstrahlung photons, a superconducting magnetic spectrometer to deflect the incident $e^\pm$, and a multigap lead-plate spark chamber to identify the resulting photon and $e^\pm$ showers. The shower from the bremsstrahlung photons appears in the lead-plate chamber near the extrapolated tangent of the incident $e^\pm$ trajectory, while the shower from the $e^\pm$ appears at the end of its deflected trajectory. Figure 1 is a schematic of the apparatus: more complete details appear elsewhere.[6,7] A good $e^\pm$ event presents a unique topology: a single particle passing through the optically viewed spectrometer spark chambers, and two showers properly located in the lead-plate spark chamber. When combined with an initial background rejection accomplished by triggering with a high threshold on a scintillator located below the lead chamber, this topology requirement reduces the proton and other background to a negligible level. This was verified for 4.5-GeV/c protons from the Lawrence Berkeley Laboratory Bevatron, where calibration of the apparatus gave a rejection of better than 10^{-4}.

The instrument was flown to an altitude of 35.3 km on a balloon from Palestine, Texas, on the night of 2 November 1972. The events from the flight were scanned to impose the proper $e^\pm$ topology. Events thus selected were measured by hand and analyzed to reconstruct the particle trajectory, determine its energy, and predict the proper shower locations in the lead-plate chamber.[8] The final rejection of background was made by a comparison of the predicted bremsstrahlung-conversion locations with the observed locations. Figure 2 shows a scatter plot of the results. A dense region of correct predictions lies in the middle of the plot, and a small scatter of events

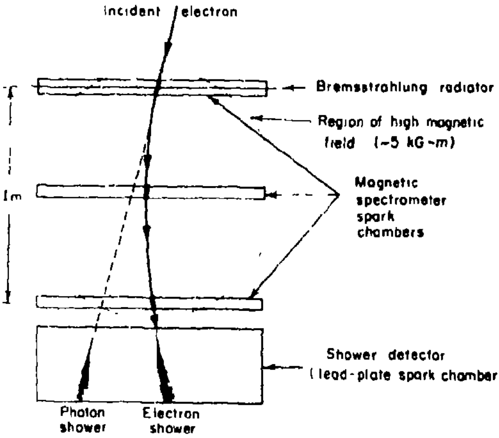
Incident electron
Bremsstrahlung radiator
Region of high magnetic field (~5 kG-m)
~1m
Magnetic spectrometer spark chambers
Shower detector (lead-plate spark chamber)
Photon shower
Electron shower

FIG. 1. Schematic diagram for the apparatus.

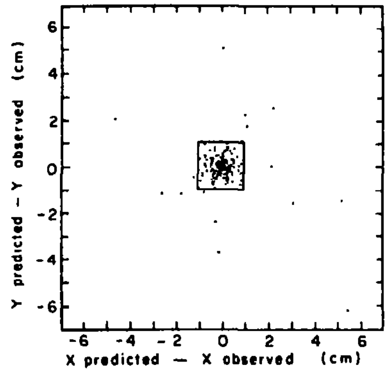

FIG. 2. Comparison of bremsstrahlung-photon real-space location as predicted by the spectrometer measurement, and as actually observed for a portion of our data. We have included only events above 2 GeV in the spectrometer, since multiple Coulomb scattering broadens the distribution below this energy. Events outside of the 2-cm box are rejected as "background."

with wrong predictions lies away from the center. About two thirds of the events outside the selection box shown are positively charged, presumably proton background. Assuming that such background puts these "bremsstrahlung photon showers" inside the selection box with about the same density as just outside the box, we conclude that no more than one or two of the events inside the box which we call positrons could actually have been protons simulating all criteria for true e^+. Similarly, from a study of the distribution of true $e^\pm$, we see that no more than 5% of real $e^\pm$ could have been lost by imposing the bremsstrahlung-box criterion. In any case, the details of the selection box are not relevant for the ratio $e^+/(e^+ + e^-)$ reported here because the proton background is so low and the $e^\pm$ analysis is charge symmetric.

To determine the overall efficiency of the technique for $e^\pm$ detection, we made a preflight test at the Stanford Linear Accelerator Center. There we found the efficiency to be 55% for detecting e^- at 5 and 15 GeV. The efficiency was expected to drop slowly to about 25% at 50 GeV, where the two showers in the lead-plate chamber begin to merge and cannot be separately discerned. Efficiency in flight was expected to be slightly reduced by the added gondola material above the spectrometer.

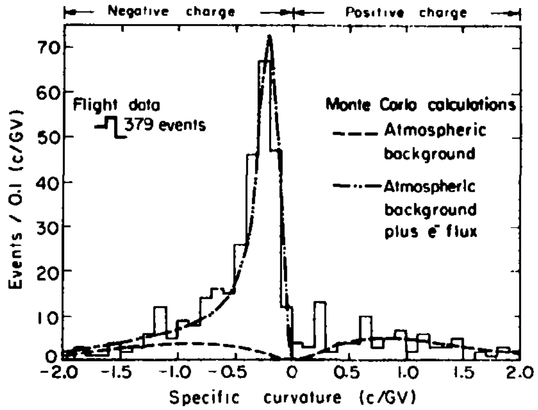

FIG. 3. Specific curvature (inverse momentum per unit charge) distribution for events selected as $e^\pm$. Resolution = 0.02 c/GV.

As a cross check of the expected efficiency in flight, we selected as good e^- in a portion of our data all negatively charged events which showered in the lead-plate chamber. The result was 108 good e^- events with properly identified bremsstrahlung showers and 57 good e^- events not meeting the bremsstrahlung-scan criteria. Using a Monte Carlo program simulating the apparatus geometry and the bremsstrahlung radiation process, we predict that these two event categories and the category of e^- events failing the other selection criteria should be in the respective fractions 0.51, 0.32, and 0.17. These figures compare favorably with the scanning results, and therefore verify the efficiency of our technique. Including trigger efficiency, our overall efficiency was 0.47.

After analyzing 77% of our data, representing about 27 min of live time with a geometry factor of 840 ± 30 cm^2 sr, we found 379 $e^\pm$ events. The distribution of these events as a function of specific curvature (the inverse of momentum per unit charge) is shown in Fig. 3. To convert specific curvature to primary energy, one must invert and then scale up by the bremsstrahlung-degradation factor. This factor is energy and spectrum dependent, but is about 1.4 for our data. Scaling is required because the observed energy of an $e^\pm$ is not its primary energy, but its energy as degraded by bremsstrahlung in 0.54 radiation length of material above the spectrometer (0.39 from the gondola, 0.15 from the atmosphere). The degradation for an e^+ is of course the same as the degradation for an e^-.

To obtain primary $e^\pm$ fluxes, we must subtract the atmospherically generated flux of $e^\pm$ from the distribution in Fig. 3. This was done using a Monte Carlo program, a proton flux of $dN/dE = 1.9\times10^{4}E^{-2.75}/\mathrm{m}^2$ sr sec GeV,[9,10] hadron interaction properties, and an experiment exposure factor. The resulting absolute e^+ background expected from proton interactions in the 5.6 g/cm^2 of atmosphere above the apparatus is shown in Fig. 3 (dashed curve). The falloff in background above ±1 c/GV is due to apparatus trigger threshold. Reentrant albedo is expected to be a small effect, and indeed we see no enhancement of low-energy events.

A subtraction of atmospheric background leaves 267 e^+ events. Taking the efficiency into account, we estimate an absolute $e^+ + e^-$ flux of 4.2 ± 0.6 particles/m^2 sr sec above an assumed average geomagnetic cutoff of 4 GV/c. In a future publication, we will analyze the importance of this flux measurement, as well as our study of the spectral indices of the e^+ and e^- fluxes. In this Letter, we concentrate on the ratio $e^+/(e^+ + e^-)$.

Proper treatment of the atmospheric background is essential to extract a meaningful ratio $e^+/(e^+ + e^-)$ from our data. Note that the background near zero specific curvature in Fig. 3 is very small. There are two reasons for this. First, because the cosmic-ray spectrum of proton parents is a power law, the atmospheric background vanishes at zero specific curvature (infinite momentum). Second, the time-dilation-inhibited decay of high-energy muons in the atmosphere reduces the background near zero specific curvature even further.

The dot-dashed curve in Fig. 3 is the total expected spectrum derived by adding the atmospheric background and a Monte Carlo prediction for the bremsstrahlung-degraded flux of primary e^-. For the primary e^- spectrum, we used $dN/dE \propto E^{-2.83}$ (the 2.83 was obtained by drawing a line through a recent compilation of e^+ data[11]), and normalized to our observed e^- flux. The fit for the total e^- curve is good, but there is an excess above background near zero specific curvature for positive charge. These events we interpret as the true observed e^+ signal originating outside of the atmosphere. We emphasize that this e^+ signal could not have resulted from "spillover" from the large e^- peak because the position of the bremsstrahlung shower uniquely determines the charge for each event and our resolution is much less than our bin size. Our rejection of protons is sufficiently strong that proton contamination in the e^+ sample could not be more than 10%. An improper assessment of atmospheric background could not possibly account for all of the e^+ signal, even though our atmospheric calculation might be in error by as much as 40% at high energies.

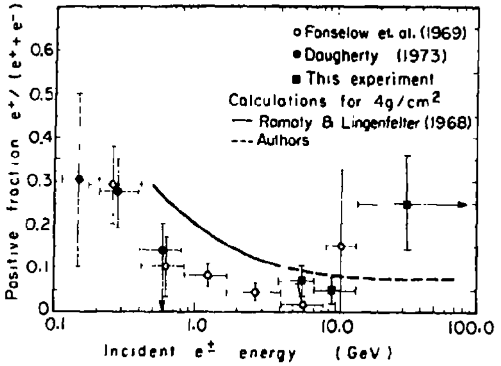

FIG. 4. Ratio $e^+/(e^+ + e^-)$ as a function of incident energy, corrected to top of atmosphere. Smooth curves indicate the expected ratio of e^+ production from interactions of cosmic-ray protons and nuclei with the interstellar gas, divided by the total measured $e^+ + e^-$ primary flux.

Figure 4 shows the ratio $e^+/(e^+ + e^-)$ obtained from Fig. 3 and scaled to energy at the top of the atmosphere. Also shown are the previous lower-energy measurements.[12,13] Ratios at higher energies have been inferred from east-west asymmetry measurements,[14,15] but the results are only qualitative.

To determine the mean interstellar column density associated with our results in Fig. 4, we have plotted the expected ratio for 4 g/cm^2 based on Ramaty and Lingenfelter's calculation of e^+ secondaries,[16] our measured total $e^{\pm}$ flux, our assumed $e^{\pm}$ spectral index, and a smooth connection to low-energy data.[12,13] We have also included our own estimate for 4 g/cm^2 at higher energies. This calculation could be in error by as much as 40%, partly from uncertainty in the flux of parent protons, and partly from uncertainties in proton interaction dynamics.

We find that our average ratio $e^+/(e^+ + e^-) = 0.08\pm0.02$ can be explained by protons of 50 to 1000 GeV having traversed approximately 3.5 ± 1.5 g/cm^2 of interstellar material, if no positrons originate at the source of cosmic rays. Considering the uncertainties, we feel that this result is consistent with the $\lesssim 2$ g/cm^2 traversed by nuclear cosmic rays, and thus protons and nuclear cosmic rays have probably had the same history. We also feel that there is no significant evidence for positrons in our energy range coming directly from the sources.

---

*Work supported by Grant No. NAS 9-7801 from the National Aeronautics and Space Administration and by the Lawrence Berkeley Laboratory.

[1] G. F. Smoot, L. H. Smith, A. Buffington, L. W. Alvarez, and M. A. Wahlig, "Primary Cosmic Ray Nuclear Rigidity Spectra," in Proceedings of the Joint Meeting of the American Physical Society and the American Astronomical Society, San Juan, Puerto Rico, December 1971 (unpublished), and in Information zur Kernforschung und Kerntechnik Zentralstelle Für Atomkernenergie Documentation No. 3 (1972).

[2] E. Juliusson, P. Meyer, and D. Müller, Phys. Rev. Lett. 29, 445 (1972).

[3] J. F. Ormes and V. K. Balasubrahmanyan, Nature (London), Phys. Sci. 241, 95 (1973).

[4] W. R. Webber, J. A. Lezniak, J. C. Kish, and S. V. Damle, Nature (London), Phys. Sci. 241, 96 (1973).

[5] L. H. Smith, A. Buffington, G. F. Smoot, L. W. Alvarez, and M. A. Wahlig, Astrophys. J. 180, 987 (1973).

[6] A. Buffington, G. F. Smoot, L. H. Smith, and C. D. Orth, in *Proceedings of the Thirteenth International Conference on Cosmic Rays, Denver, Colorado, 1973* (University of Colorado, Denver, Colo., 1973), Vol. 1, p. 318.

[7] A. Buffington, C. D. Orth, and G. F. Smoot, "A Bremsstrahlung Identification Technique for Cosmic Ray Electrons and Positrons" (to be published).

[8] A complete description of our data analysis techniques is presented in Ref. 5.

[9] M. J. Ryan, J. F. Ormes, and V. K. Balasubrahmanyan, Phys. Rev. Lett. 28, 985 (1972).

[10] K. Pinkau, U. Pollvogt, W. K. H. Schmidt, and R. W. Huggett, in *Proceedings of the Eleventh International Conference on Cosmic Rays, Budapest, 1969*, edited by T. Gémesy *et al.* (Akademiai Kiado, Budapest, 1970), Vol. 1, p. 291.

[11] D. Müller and P. Meyer, Astrophys. J. 186, 841 (1973).

[12] J. L. Fanselow, R. C. Hartman, R. H. Hildebrand, and P. Meyer, Astrophys. J. 158, 771 (1969).

[13] J. K. Daugherty, Goddard Space Flight Center Report No. X-660-74-16, 1974 (to be published).

[14] B. Agrinier *et al.*, in *Proceedings of the Ninth International Conference on Cosmic Rays, London, 1965*, edited by A. C. Stickland (Institute of Physics and The Physical Society, London, 1966), Vol. 1, p. 331.

[15] K. C. Anand, R. R. Daniel, and S. A. Stephens, in *Proceedings of the Eleventh International Conference on Cosmic Rays, Budapest, 1969*, edited by T. Gémesy *et al.* (Akademiai Kiado, Budapest, 1970), Vol. 1, p. 235.

[16] R. Ramaty and R. E. Lingenfelter, Phys. Rev. Lett. 20, 120 (1968).

Solving Equations of the Gell-Mann–Low and Callan-Symanzik Type

B. F. L. Ward
Stanford University, Stanford, California 94305
(Received 7 January 1974)

An examination is made of the dimensional analysis usually employed to solve the renormalization group equations for the asymptotic region. It is argued that if this analysis is done systematically, one must in general add new inhomogeneous terms to the asymptotic equations even after invoking Weinberg's theorem to discard the (generalized) mass insertion term. These new inhomogeneities are entirely determined by the physical thresholds of the theory. They are shown to provide a natural explanation of Bjorken scaling in interacting field theories.

Recently, some of the most exciting work[1] in the context of renormalizable quantum field theory has been done by employing the Gell-Mann–Low[2] and Callan-Symanzik[3] equations in the deep Euclidean region. These equations relate the responses of the one-particle irreducible (1PI) Green's functions of a renormalizable field theory to changes in the parameters of the theory. For example, in a theory with one field we have

$$[\mu\partial/\partial\mu+\beta(g)\partial/\partial g-n\gamma(g)]\Gamma_{\text{asy}}^{(n)}=0, \tag{1}$$

where $\Gamma_{\text{asy}}^{(n)}$ is the ultraviolet asymptotic part of the 1PI renormalized n-particle Green's function, β and γ are finite functions of the renormalized coupling constant g, and μ is the mass parameter of the theory, being either the renormalized mass or, for massless theories, the Euclidean renormalization point. Of course, in writing (1) for theories with masses, we are using Weinberg's theorem.[4]

Equation (1) provides, among other things, a convenient starting point for the discussion of Bjorken scaling in the context of renormalizable quantum field theory. And, indeed, it has recently been shown[1] that in non-Abelian gauge theories, the origin $\bar{g}=0$ of the effective coupling constant $\bar{g}$ defined by

$$(d/dt)\bar{g}(t,g)=\beta(\bar{g}),\quad \bar{g}(0,g)=g, \tag{2}$$

is ultravioletly attractive in the sense of Wilson.[5] Thus, when g is in the corresponding region of attraction, these theories are viewed[1] as being asymptotically free and exhibiting Bjorken scaling, within calculable logarithmic corrections, with the following form for the solution of (1):

$$\Gamma_{\mathrm{asy}}{}^{(n)}(\lambda p_1,\ldots,\lambda p_n;g;\mu)\xrightarrow[\lambda\to\infty]{} I_n\Gamma_{\mathrm{asy}}{}^{(n)}(p_1,\ldots,p_n;0;\mu)\lambda^{4-n}(\ln\lambda)^{-n\gamma_1/b_0}, \tag{3}$$

where I_n is an unknown constant and $a=\gamma_1/b_0$ with γ_1 and b_0 defined by

$$\gamma=\gamma_1 g^2+O(g^4);\quad \bar{g}^2(t,g)=b_0{}^{-1}t^{-1}+O(t^{-2}\ln t),\quad t\to\infty. \tag{4}$$

As is apparent from (1) and (3), this formulation of the solutions of (1) has relied quite crucially on dimensional analysis. In this note we should like to question the way in which this analysis has been effected.

To be specific, we recall the strict Callan-Symanzik equation corresponding to (1):

$$[\mu\partial/\partial\mu+\beta(g)\partial/\partial g-n\gamma(g)]\Gamma^{(n)}=i\Gamma_{\Delta}{}^{(n)}, \tag{5}$$

where $\Gamma^{(n)}$ is the renormalized 1PI n-particle Green's function, and $\Gamma_{\Delta}{}^{(n)}$ is the renormalized 1PI n-particle Green's function with one (generalized) mass insertion[3] at zero momentum transfer. In passing to the deep Euclidean region we shall ultimately again use Weinberg's theorem when necessary to discard $\Gamma_{\Delta}{}^{(n)}$ in (5). However, in solving the resulting equation we should like to note that $\Gamma^{(n)}$ will in general possess step functions and other singularities associated with the physical thresholds of the theory. As a result, when we write (in a theory with only a massless boson field, for example)

$$\Gamma^{(n)}(\lambda p_j;g,\mu)=\mu^{4-n}\varphi, \tag{6}$$

as is customarily done in solving (1), the function φ, because of these generalized thresholds, may not satisfy

$$(\mu\partial/\partial\mu+\lambda\partial/\partial\lambda)\varphi=0. \tag{7}$$

For example, if

$$\varphi=\rho(\lambda p_j/\mu)\theta(\lambda^2(\textstyle\sum_j p_j)^2-m^2), \tag{8}$$

where ρ satisfies (7), then φ clearly does not, in general.[6] We therefore let $I\varphi$ denote the terms in φ which violate (7). We may rewrite (5) in the form

$$\{-\lambda\partial/\partial\lambda+\beta(g)\partial/\partial g+4-n[1+\gamma(g)]\}\Gamma^{(n)}=i\Gamma_{\Delta}{}^{(n)}-\mu^{4-n}(\mu\partial/\partial\mu+\lambda\partial/\partial\lambda)I\varphi. \tag{9}$$

Thus, on using Weinberg's theorem we obtain for the deep Euclidean region

$$\{-\lambda\partial/\partial\lambda+\beta(g)\partial/\partial g+4-n[1+\gamma(g)]\}\Gamma_{\mathrm{asy}}{}^{(n)}=R\Gamma^{(n)}, \tag{10}$$

where we have defined

$$R\Gamma^{(n)}=-\mu^{4-n}(\mu\partial/\partial\mu+\lambda\partial/\partial\lambda)I\varphi. \tag{11}$$

For massless non-Abelian gauge theories, the solutions of (10) with $R\Gamma^{(n)}$ set equal to zero (the homogeneous solutions) are precisely the results of Ref. 1 as illustrated by (3) above. The complete solution of (10) for any $\Gamma_{\mathrm{asy}}{}^{(n)}$ is of course just a constant multiple of the respective homogeneous solution *plus* a particular solution of (10). In particular, in the event that the homogeneous solutions are absent because of boundary conditions, $\Gamma_{\mathrm{asy}}{}^{(n)}$ is essentially determined by $R\Gamma^{(n)}$.

The form of $R\Gamma^{(n)}$ is under investigation. In the absence of precise knowledge about its structure, let us construct an example of the form it may take in order to illustrate its possible effect on $\Gamma_{\mathrm{asy}}{}^{(n)}$. We take a theory described by a bare Lagrangian with one massive particle (a fermion, say) and a massless boson and let μ^2 denote the boson renormalization point. We take the relevant physical thresholds to generate only step-function discontinuities and δ functions in ${}^b\Gamma^{(n)}$ (the n-boson 1PI

Green's function) and, hence, to make the following contribution to ${}^b\Gamma^{(n)}(\lambda p_j;\mu;g)$ (the dependences on the fermion mass will be suppressed where possible):

$$I\varphi=\mu^{4-n}\left[\sum_\alpha \rho_\alpha{}^1(\lambda^2(\sum p_{j_\beta})^2/\mu^2)\theta(\lambda^2(\sum_{i_\alpha} p_{i_\alpha})^2-m_\alpha{}^2)+\sum_\nu \rho_\nu{}^2(\lambda^2(\sum p_{j_\delta})^2/\mu^2)\mu^2\delta(\lambda^2(\sum p_{i_\nu})^2-m_\nu{}^2)\right], \qquad (12)$$

where the ρ^i are presumed to satisfy the analog[7] of (7). In general, the physical thresholds may generate more general terms in $\Gamma^{(n)}$, but, for the purpose of illustration, we shall just consider (12). The form of $R\Gamma^{(n)}$ following from (12) is

$$R\Gamma^{(n)}=-2\mu^{4-n}\sum_{\alpha'}\tilde{\rho}_{\alpha'}\left(\frac{m_{\alpha'}{}^2(\sum p_{j_\beta})^2}{\mu^2(\sum p_{i_{\alpha'}})^2}\right)m_{\alpha'}{}^2\delta(\lambda^2(\sum_{i_{\alpha'}} p_{i_{\alpha'}})^2-m_{\alpha'}{}^2), \qquad (13)$$

where $\tilde{\rho}$ is clearly determined by $\{\rho_\alpha{}^1\}$ and $\{\rho_\nu{}^2\}$. Equation (10) now reads

$$[-\lambda\partial/\partial\lambda+\beta\partial/\partial g+4-n(1+\gamma)]{}^b\Gamma_{\text{asy}}{}^{(n)}=-2\mu^{4-n}\sum_\alpha\tilde{\rho}_\alpha m_\alpha{}^2\delta(\lambda^2(\sum p_{i_\alpha})^2-m_\alpha{}^2). \qquad (14)$$

Let

$$g'=2\int_{g_0}^{g}dx/\beta(x). \qquad (15)$$

We introduce $\bar{\rho}_\alpha$ and σ_α by

$$-\mu^{4-n}m_\alpha{}^2\tilde{\rho}_\alpha\left(\frac{m_\alpha{}^2(\sum p_{j_\beta})^2}{\mu^2(\sum p_{i_\alpha})^2}\right)=\int dl\,\bar{\rho}_\alpha e^{ilg'},\quad -m_\alpha{}^2/(\sum p_{i_\alpha})^2=\int dr\,\sigma_\alpha(r)e^{irg'}. \qquad (16)$$

We are assuming we can invert (15). Defining $t=\ln\lambda^2$, we have, from (14) and (16),

$$\sum_\alpha\int\frac{dk\,dl}{2\pi}\sum_{j_1,j_2}\int\frac{dr_1\cdots dr_{j_2}}{(\sum p_{i_\alpha})^2}\bar{\rho}_\alpha\frac{\sigma(r_1)\cdots\sigma(r_{j_2})(ik)^{j_1+j_2}}{j_1!\,j_2!}\exp[j_1t+i(\sum_i r_i+l)g']$$
$$=\left[-\frac{\partial}{\partial t}+\frac{\partial}{\partial g'}+2-\frac{n}{2}(1+\gamma)\right]{}^b\Gamma_{\text{asy}}{}^{(n)}. \qquad (17)$$

This last equation has the general solution (see Symanzik[3])

$${}^b\Gamma_{\text{asy}}{}^{(n)}=\frac{1}{2\pi}\int_t^{[t+g'+h(t+g')]/2}dt'\sum_\alpha\int dk\,dl\sum_{j_1,j_2}\int\frac{dr_1\cdots dr_{j_2}}{(\sum p_{i_\alpha})^2}\bar{\rho}_\alpha\frac{\sigma_\alpha(r_1)\cdots\sigma_\alpha(r_{j_2})(ik)^{j_1+j_2}}{j_1!\,j_2!}$$
$$\times\exp\left(j_1t'+i(\sum r_i+l)(g'+t-t')+\int_{g'+t-t'}^{g'}dx\{\tfrac{1}{2}n[1+\gamma(g(x))]-2\}\right)+B_n{}^b\Gamma^{(n)}_{\text{asy,hom}}, \qquad (18)$$

where h is arbitrary, B_n is a constant, and ${}^b\Gamma^{(n)}_{\text{asy,hom}}$ is a homogeneous solution of (10). Note that in general h may not be set equal to ∞ in (18). We write

$$h(g'+t)=g'+t+2h_0(g'+t), \qquad (19)$$

where h_0 is a function which we may constrain by the requirement that the first term on the right-hand side of (18), which we denote by ${}^b\Gamma_{\text{asy},p}{}^{(n)}$, agrees with the following formal particular integral of (14):

$${}^b\Gamma_{\text{asy},p}{}^{(n)}=\int\frac{dk\,dl}{2\pi}\sum_{\alpha,j_1,j_2}\int\frac{dr_1\cdots dr_{j_2}}{(\sum p_{i_\alpha})^2}\bar{\rho}_\alpha\frac{\sigma(r_1)\cdots\sigma(r_{j_2})(ik)^{j_1+j_2}\exp[j_1t+i(\sum r_i+l)g']}{j_1!\,j_2![-j_1+i(l+\sum r_i)+2-n/2]}$$
$$+\frac{n}{2}\int dk\,dl\sum_j\frac{\langle\gamma\Gamma_{\text{asy},p}{}^{(n)}\rangle(ik)^je^{jt+ilg'}}{j!(-j+il+2-n/2)}, \qquad (20)$$

where $\langle\gamma\Gamma_{\text{asy},p}{}^{(n)}\rangle$ is defined by

$$\gamma^b\Gamma_{\text{asy},p}{}^{(n)}=\int dk\,dl\,\langle\gamma\Gamma_{\text{asy},p}{}^{(n)}\rangle e^{i(lg'+\lambda^2k)}. \qquad (21)$$

Making a change of variable $t'-t=s$ in (18), we see that as $\lambda\to\infty$,

$${}^b\Gamma_{\text{asy}}{}^{(n)}\to\frac{1}{2\pi\lambda^2}\int dk\,dl\sum_{\alpha,j_1}\frac{\bar{\rho}_\alpha(ik)^{j_1}e^{ilg'}}{(\sum p_{i_\alpha})^2j_1!}\lim_{t\to\infty}\int_0^{g'+h_0}ds\exp[(j_1+\tfrac{1}{2}n-2-il)s+\tfrac{1}{2}n\int_{g'-s}^{g'}dx\,\gamma(g(s))]$$
$$+O(\lambda^{-4})+B_n{}^b\Gamma^{(n)}_{\text{asy,hom}}, \qquad (22)$$

where we have used (20). Of course, here we are assuming that the interchanges in the orders of limits and integrations which we have made are legitimate. Clearly, if the boundary conditions which determine B_n are such that $B_n=0$, then it is possible that ${}^s\Gamma^{(n)}(\lambda p_j)$ behaves like $1/\lambda^2$ in the deep Euclidean region, for $n \geq 4$.

One of the most pleasing features of this development is the possibility of a natural explanation of Bjorken scaling. Indeed, consider the familiar Wilson[8] expansion for the product of two electromagnetic or weak currents at lightlike distances:

$$J(y/2)J(-y/2) \approx \sum C_n(y^2;g)O_{\mu_1\cdots\mu_n}{}^{(n)}(0)y^{\mu_1}\cdots y^{\mu_n}, \tag{23}$$

where we suppress all tensor and quantum-number labels. The Fourier transforms of the functions C_n satisfy an equation analogous to (10) in the deep Euclidean region:

$$(-\lambda\partial/\partial\lambda+\beta\partial/\partial g-2-\gamma_n)C_{n,\mathrm{asy}}(\lambda^2q^2,\mu;g)=RC_n, \tag{24}$$

where γ_n is the anomalous dimension of O_n, and RC_n represents the physical thresholds. Assuming step-function discontinuities and δ functions in C_n due to thresholds $\{m_\alpha{}^2\}$, we have

$$RC_n=-2\mu^{-2}\sum_\alpha\xi_\alpha{}^{(n)}(m_\alpha{}^2/\mu^2)m_\alpha{}^2\delta(\lambda^2q^2-m_\alpha{}^2), \tag{25}$$

where we take $\xi_\alpha{}^{(n)}$ to satisfy the analog of (7). From (22) it is clear that, for $q^2<0$,

$$C_{n,\mathrm{asy}}(\lambda^2q^2)\xrightarrow[\lambda\to\infty]{}\mathrm{const}^{(n)}(g',\mu)/\lambda^2q^2+E_nC_{n,\mathrm{asy,hom}}+O(\lambda^{-4}), \tag{26}$$

where

$$\mathrm{const}^{(n)}(g',\mu)=\frac{1}{2\pi}\int dk\,dl\sum_{\alpha,j}\frac{\bar{\xi}_\alpha{}^{(n)}(ik)^je^{ilg'}}{j!}\lim_{t\to\infty}\int_0^{g'+k_0}ds\exp[(j_1+1-il)s+\tfrac{1}{2}\textstyle\int_{g'-s}^{g'}dx\,\gamma_n(g(x))], \tag{27}$$

with $\xi_\alpha{}^{(n)}$ defined by

$$-\mu^{-2}m_\alpha{}^2\xi_\alpha{}^{(n)}=\int dl\,\bar{\xi}_\alpha{}^{(n)}(l)e^{ilg'}. \tag{28}$$

In (26), E_n is a constant and $C_{n,\mathrm{asy,hom}}$ is a homogeneous solution of (24). The homogeneous solutions $C_{n,\mathrm{asy,hom}}$ have been discussed[9] in Ref. 1, for example, and are known to give at least logarithmic deviations from Bjorken scaling in the absence of RC_n. Thus, in view of the deep inelastic data we take such solutions to be absent from (27). Then, as $\lambda\to\infty$,

$$C_{n,\mathrm{asy}}(\lambda^2q^2)-\mathrm{const}^{(n)}(g',\mu)/\lambda^2q^2=O(\lambda^{-4}), \tag{29}$$

which is clearly the desired naive free-field-theory scaling result (Bjorken scaling). We emphasize that $\mathrm{const}^{(n)}$ is essentially determined by the physical thresholds. Note that our argument need not depend on the sign of $\beta(g)$!

We should also mention that in the asymptotic timelike q^2 region, the contribution of $RC^{(n)}$ will also be given by (29). However, in this region, for theories with a massive Lagrangian, one may not in general neglect the mass-insertion inhomogeneous term in (5) above. This insertion may in general generate deviations from the scale-invariant result (29). We conjecture that this is the reason for the fast onset of scaling in the deep-inelastic scattering region compared with the annihilation region. Of course, this is well known.

To conclude, we have argued that, contrary to the approach of Ref. 1, it is possible that it is the physical thresholds, serving as sources, that generate naive Bjorken scaling in interacting field theories, the boundary conditions being such as to disallow scale-violating homogeneous solutions to contribute to the appropriate asymptotic physical solutions of the Callan-Symanzik equations in the deep Euclidean region. Specifically, the step-function discontinuities and δ functions which are familiar characteristics of these thresholds can naturally generate Bjorken scaling behavior in the deep-inelastic scattering region. This latter statement is independent of the sign of $\beta(g)$ in the renormalization-group equation.

---

*Work supported by the U. S. Atomic Energy Commission.

[1] D. J. Gross and F. Wilczek, *Phys. Rev. Lett.* 30, 1343 (1973), and *Phys. Rev. D* 8, 3633 (1973); H. D. Politzer,

Phys. Rev. Lett. 30, 1346 (1973).

[2] M. Gell-Mann and F. E. Low, Phys. Rev. 95, 1300 (1954); E. C. G. Stueckelberg and A. Petermann, Helv. Phys. Acta 24, 153 (1951).

[3] C. G. Callan, Jr., Phys. Rev. D 2, 1541 (1970); K. Symanzik, Commun. Math. Phys. 18, 227 (1970), and in *Springer Tracts in Modern Physics*, edited by G. Höhler (Springer, Berlin, 1971), Vol. 57, p. 222.

[4] S. Weinberg, Phys. Rev. 118, 838 (1960).

[5] K. G. Wilson, Phys. Rev. D 3, 1818 (1971).

[6] Violations of dimensional analyses are easy to find in renormalized perturbation theory. For example, in quantum electrodynamics, for the Pauli form factor $F_2(t)$ to order α^3, we have

$$(m\partial/\partial m+\lambda\partial/\partial\lambda)\,\mathrm{Im}F_2(\lambda^2t)=\tfrac{1}{3}m^2\pi^3(\alpha/\pi)^2\delta(\lambda^2t-4m^2).$$

See R. Barbieri, J. A. Mignaco, and E. Remiddi, Nuovo Cimento 11A, 824, 865 (1972).

[7] By "analog of (7)" we mean the obvious:

$$\left(\sum_i m_i\partial/\partial m_i+\sum_j\mu_j\partial/\partial\mu_j+\lambda\partial/\partial\lambda\right)\varphi=0,$$

where m_i are the fundamental masses of the theory and the μ_j represent the possible (Euclidean) renormalization points.

[8] K. G. Wilson, Phys. Rev. 179, 1499 (1969).

[9] For further references to the discussion of C_n in this connection, see the references in Ref. 1.

New Experimental Limit on T Invariance in Polarized-Neutron β Decay*

R. I. Steinberg†
Yale University, New Haven, Connecticut 06520, and Institut des Sciences Nucléaires, 38044 Grenoble, France

and

P. Liaud and B. Vignon
Institut des Sciences Nucléaires, 38044 Grenoble, France

and

V. W. Hughes
Yale University, New Haven, Connecticut 06520

[illegible] number
22.5437
[illegible] 31-12-94

(Received 9 May 1974)

We report an improved experimental upper limit for D, the triple-correlation coefficient in polarized-neutron decay. A nonzero value for this coefficient implies a breakdown of T invariance. We find that $D=-(1.1\pm1.7)\times10^{-3}$, consistent with T invariance.

We are reporting a new measurement of D, the iple-correlation coefficient[1] in the β decay of e polarized free neutron. This coefficient is reponsible for a term in the decay rate equal to

$$D\vec{P}\cdot(\vec{p}_e\times\vec{p}_{\bar{\nu}})/E_eE_{\bar{\nu}}, \qquad (1)$$

here $\vec{P}$ is the neutron polarization and $\vec{p}_e$, $\vec{p}_{\bar{\nu}}$, E_e, nd $E_{\bar{\nu}}$ are the lepton momenta and energy, reectively. Since this quantity is odd under time eversal, a measurement of its coefficient D proides a test of T invariance, provided final-state iteractions and momentum-transfer-dependent ffects can be neglected. In neutron β decay the nly significant final-state interaction is the Coumb interaction, and the contribution to D from is interaction vanishes in a pure $V-A$ theory.[2] With present measured limits on possible scalar and tensor terms[3] in the effective weak Hamiltonian, this contribution is at most 10^{-5}. The principal momentum-transfer-dependent contribution to D is due to weak magnetism and has been calculated[4] using the conserved-vector-current hypothesis to be 2×10^{-5}. A measurement of D therefore provides a test of time-reversal invariance valid at least to the level of 10^{-5}.

The precision of the best previous measurement[5] of D was severely limited by counting statistics. A polarized-neutron beam intensity of 3×10^7 neutrons/sec yielded a counting rate of only 1/min, which allowed observation of 10^5 decay events. The resulting value of D was -0.01 ± 0.01.

In the present experiment, a beam intensity of 10^9 neutrons/sec was achieved. Furthermore, since the beam consisted of cold neutrons (mean velocity ≈1100 m/sec) rather than the previously used thermal neutrons (2200 m/sec), a further twofold increase in the effective source strength was obtained. In addition, we have improved the detection geometry, so that a counting rate of 1.5 decays/sec was observed. Based upon observation of more than 5×10^6 events, we report the value

$$D = -(1.1 \pm 1.7) \times 10^{-3},$$

where the error quoted is 1 standard deviation and is dominated by counting statistics. This value is consistent with T invariance and corresponds to a phase angle ψ between the coupling constants g_A and g_V given by

$$\psi = 180.14 \pm 0.22^\circ.$$

The experiment was performed at the high flux reactor (central flux = 1.5×10^{15} neutrons/cm^2 sec) of the Institut Laue-Langevin in Grenoble. Figure 1 shows the arrangement of the experiment. The beam was obtained from H14 (A in the figure), one of the five curved guide tubes viewing the liquid-deuterium cold-neutron moderator. The curvature of this guide tube ($\lambda_{\text{cutoff}} = 2.8$ Å) allowed high transmission of cold neutrons but effectively removed nearly all fast neutrons and γ rays originating in the reactor core, which would otherwise have constituted an intense source of background. The flux of the cold-neutron beam leaving H14 was 3×10^9 neutrons/cm^2 sec. The beam was then polarized by a magnetized curved guide tube (B). This instrument has been described previously.[6] The mean polarization of the beam was measured to be (70 ± 7)% using a second magnetized guide tube as analyzer. The polarization measurement was performed both before and after the experiment as well as at approximately 2-week intervals during the $2\frac{1}{2}$-month period of data collection. No variations in the polarization were observed.

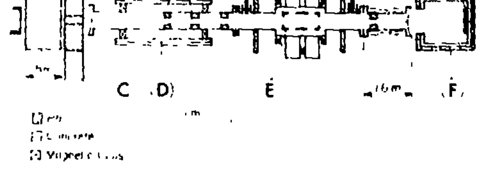

FIG. 1. Vertical section of the experimental setup: A, curved neutron-guide tube H14; B, polarizing guide tube; C, shielding; D, spin flipper; E, detection chamber; F, beam catcher; 1, Al entrance window to vacuum chamber; 2, beam collimators (Li^6F and Pb); 3, gate valves; 4, detectors; 5, LiF; 6, Li^6F.

Upon leaving the polarizer, the beam had an intensity of 10^9 neutrons/sec and was roughly 5 cm high and 6 mm wide. The polarization direction, initially vertical, was adiabatically turned into the beam direction by means of the two coils of the spin flipper (D). For simple spin transmission, these two coils generated parallel magnetic fields, while spin flip was accomplished by reversing the current in the first coil, as suggested by Drabkin *et al.* and Hughes and Burgy.[7] With the two coils thus producing opposing magnetic fields, a region in which the combined magnetic field rapidly reversed direction was generated approximately midway between the coils. The neutron beam passed this region nonadiabatically and thereby underwent a spin flip. Depolarization of the beam in this low-field region was prevented by surrounding the entire two-coil spin flipper with a three-layer magnetic shield to exclude stray fields. The spin-flipping efficiency of this apparatus was 97%. During the experiment, the neutron polarization was reversed every second. The 3-G guide field in the decay region (E) was, of course, constant both in direction and magnitude to minimize gain shifts of the photomultiplier tubes. This guide field was maintained parallel to the beam direction within an error of 1°. After the decay region, the beam passed through a drift tube into the beam catcher (F).

A cross section of one section of the decay chamber is shown in Fig. 2. The beam direction was perpendicular to the plane of the paper. The decay chamber consisted of two such sections in series, for a total of eight detectors. Since the momentum of the neutron may be neglected, conservation of linear momentum allows the term (1) to be written

$$D\vec{P} \cdot (\vec{p}_p \times \vec{p}_e)/E_e E_{\bar{\nu}},$$

where $\vec{p}_p$ is the momentum of the recoil proton. The experimental geometry maximized the triple product by arranging the three vectors to be mutually perpendicular. At the same time the symmetrical arrangement greatly reduced systematic errors, as will be made clear below. Decay electrons originating from the beam (1) were detected by means of conventional plastic scintillation de-

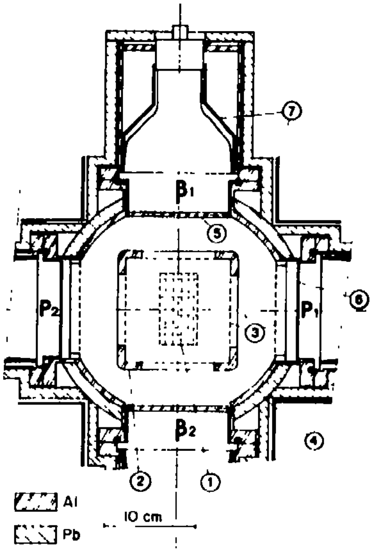

FIG. 2. Cross section of one section of decay chamber: 1, polarized neutron beam; 2, high-voltage box (20 kV); 3, proton-acceleration gap; 4, vacuum-chamber wall; 5, plastic scintillation β detector; 6, vacuum-evaporated 4000-Å layer of NaI(Tl) for proton detection; 7, magnetic shielding for photomultiplier tubes.

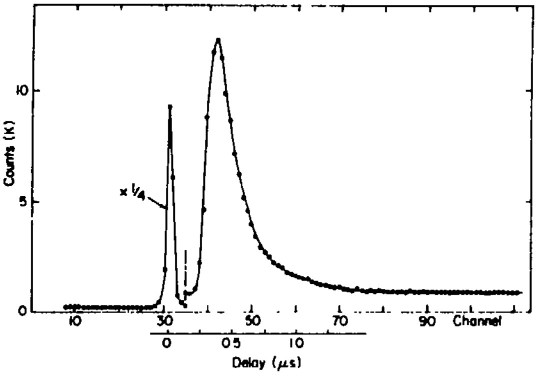

FIG. 3. Time-delay spectrum for coincidence pair $\beta 2 p 1$ for one of the two spin states. These data represent about two weeks of running time.

tectors (5) biased to accept electron energies between 100 and 500 keV. The recoil protons, after drifting through the field-free region inside the high-voltage box (2), were accelerated to 20 keV n the gap (3) and were counted by scintillation detectors (6) consisting of a vacuum-evaporated 4000-Å layer of NaI(Tl). The extreme thinness of hese detectors allowed reduction of background while maintaining sensitivity to the protons. Special handling of the detectors was necessary because of the extremely hygroscopic character of NaI.

The electronics was based upon a single, multiplexed time-to-pulse-height converter which was started by pulses from the β detectors and stopped by pulses from the proton detectors. The sixteen resulting time spectra (four coincidence pairs for each sign of the neutron spin and for each of the two detector sections) were routed nto separate regions of the memory of a 4096-hannel analyzer. Figure 3 shows a time-delay pectrum for the coincidence pair $\beta 2 p 1$. The eak at channel 31 corresponding to $t = 0$ is caused y background radiation being scattered from one detector into another. The broad peak at 0.4 μsec is due to the recoil protons, while the flat background is caused by accidental coincidences. The 0.4-μsec decay corresponds quite well with calculation of the transit time of the recoil protons from the decay volume through the field-free region and into the proton detector. The number of true coincidences was determined by simple subtraction of the flat background from the integrated recoil-proton peak.

The data are analyzed as follows. Let $\overrightarrow{N}_{\beta_i p_j}$ and $\overleftarrow{N}_{\beta_i p_j}$ be the numbers of true coincidences between β detector i and proton detector j for the two directions of the polarization vector. Thus

$$\overleftarrow{N}_{\beta_1 p_1} = c\Omega_{\beta_1}\Omega_{p_1}\overleftarrow{e}_{\beta_1}\overleftarrow{e}_{p_1}(1+KPD),$$

$$\overrightarrow{N}_{\beta_1 p_1} = c\Omega_{\beta_1}\Omega_{p_1}\overrightarrow{e}_{\beta_1}\overrightarrow{e}_{p_1}(1-KPD),$$

etc., where c is a constant proportional to the beam intensity, the Ω's are the solid angles subtended by counters $\beta 1$ and $p1$, and the e's are the detection efficiencies, where the possibility of shifts in these efficiencies as a function of the polarization direction has been allowed for. K is an instrumental coefficient, which for our apparatus has been calculated to be 0.45 ± 0.05.

Forming the combination

$$R = \frac{\overleftarrow{N}_{\beta_1 p_1}}{\overrightarrow{N}_{\beta_1 p_1}} \frac{\overrightarrow{N}_{\beta_1 p_2}}{\overleftarrow{N}_{\beta_1 p_2}} \frac{\overrightarrow{N}_{\beta_2 p_1}}{\overleftarrow{N}_{\beta_2 p_1}} \frac{\overleftarrow{N}_{\beta_2 p_2}}{\overrightarrow{N}_{\beta_2 p_2}} = \frac{(1+KPD)^4}{(1-KPD)^4},$$

it will be seen that variations in counter efficiencies, solid angles, and beam intensity are canceled. The symmetrical detector arrangement can also be shown to remove the effect of small misalignments of the polarization axis relative to the beam direction. The value of D is then determined from

$$D=\frac{1}{KP}\frac{R^{1/4}-1}{R^{1/4}+1}.$$

The authors wish to thank the Institut Laue-Langevin for allowing use of its excellent facilities, as well as Professor J. P. Longequeue and Professor J. Yoccoz for their interest in our work. The excellent technical assistance of Mr. C. Barnoux, Mr. J. Pouxe, and others is gratefully acknowledged as well as the help of Dr. V. Sailor and Dr. H. F. Foote, Jr., during the early stages of the experiment. One of us (R.I.S.) would also like to thank the National Science Foundation for a one-year postdoctoral fellowship and the Rutherford High Energy Laboratory for a research associateship.

---

*Work supported in part by the U.S. Atomic Energy Commission under Contract No. AT(11-1)-3075, in part by the Research Corporation, and in part by the Institut National de Physique Nucléaire et de Physique des Particules.

†Present address: Department of Physics and Astronomy, University of Maryland, College Park, Md. 2074

[1] J. D. Jackson, S. B. Treiman, and H. W. Wyld, Jr., Phys. Rev. 106, 517 (1957).

[2] J. D. Jackson, S. B. Treiman, and H. W. Wyld, Jr., Nucl. Phys. 4, 206 (1957).

[3] H. F. Schopper, *Weak Interactions and Nuclear Beta Decay* (North Holland, Amsterdam, 1966).

[4] C. G. Callan, Jr., and S. B. Treiman, Phys. Rev. 162, 1494 (1967).

[5] B. G. Erozolimsky, L. N. Bondarenko, Yu. A. Mostovoy, B. A. Obinyakov, V. P. Zakharova, and V. A. Titov, Yad. Fiz. 11, 1049 (1970) [Sov. J. Nucl. Phys. 11, 583 (1970)].

[6] K. Berndorfer, Z. Phys. 243, 188 (1971).

[7] G. M. Drabkin, E. I. Zabidarov, Ya. A. Kasman, and A. I. Okorokov, Zh. Eksp. Teor. Fiz. 56, 478 (1969) [Sov. Phys. JETP 29, 261 (1969)]; see also D. J. Hughes and M. T. Burgy, Phys. Rev. 81, 498 (1951).

Hadron-Neutron Forward Elastic Scattering Amplitude and Hadron-Deuteron Collisions*

Victor Franco and Girish K. Varma
Physics Department, Brooklyn College of the City University of New York, Brooklyn, New York 11210

(Received 23 May 1974)

Coulomb-nuclear interference in high-energy charged-hadron–deuteron collisions is treated exactly within the framework of Glauber theory. Charge-distribution effects are included. Applications are made to pd measurements below 70 GeV to extract ρ_n, the ratio of real to imaginary parts of the proton-neutron forward elastic scattering amplitude. An alternative and earlier analysis is shown to yield comparable values for ρ_n. Both results for ρ_n differ significantly from an earlier analysis.

Among the important quantities in particle physics are the ratios of the real to imaginary parts of hadron-hadron forward elastic scattering amplitudes. At high energies this ratio ρ_n for proton-neutron collisions is generally obtained indirectly from proton-proton and proton-deuteron measurements. Extensive pd elastic-scattering measurements have recently been made between 10 and 70 GeV at the Serpukhov accelerator[1] and between 50 and 400 GeV at the National Accelerator Laboratory.[2] The analysis of pd measurements can be done by means of the Glauber approximation. Within the framework of this approximation, additional simplifications have previously been made, such as approximating the Coulomb phase-shift functions appearing in the general expression by constants and treating the incident hadron as a point charge,[3] or treating the Coulomb phase-shift functions exactly but considering both the incident hadron and the bound proton as point charges.[4]

We present here an exact solution for xd elastic scattering in the Glauber approximation, with both the incident charged hadron x and the bound proton having extended charge distributions. We then use the results to analyze recent pd measurements[1] in order to extract ρ_n. The values obtained are compared with those from a previous analysis of the pd data[5] and with values obtained from an analysis using a result derived in Ref. 3. The latter analysis involves a rather simple expression and gives values which are comparable to those obtained using the full theoretical expression.

Hadron-deuteron (xd) cross sections may be obtained from the scattering amplitude operator[5,6]

$$F(\vec{q},\vec{s}) = (ik/2\pi)\int e^{i\vec{q}\cdot\vec{b}}\Gamma(\vec{b},\vec{s})d^2b, \qquad (1)$$

where $\hbar\vec{k}$ is the incident momentum, $\hbar\vec{q}$ is the momentum transfer, $\vec{b}$ is the impact parameter, and $\vec{s}$ is the projection of the internal coordinate of he deuteron onto the plane perpendicular to $\vec{k}$. The operator Γ is given by

$$\Gamma(\vec{b},\vec{s}) = 1 - \exp[i\chi_n(\vec{b}-\tfrac{1}{2}\vec{s}) + i\chi_p(\vec{b}+\tfrac{1}{2}\vec{s})], \qquad (2)$$

where χ_n and χ_p represent the phase-shift functions for xn and xp scattering. χ_p is written as a sum of strong-interaction and Coulomb phase-shift functions,

$$\chi_p = \chi_{ps} + \chi_C, \qquad (3)$$

and the Coulomb phase-shift function χ_C is written as the sum of a point-charge phase-shift function χ_{pt} plus a remainder due to the extended charge distribution,

$$\chi_C = \chi_{pt} + \chi_E. \qquad (4)$$

If we write

$$\Gamma_j(\vec{b}) = 1 - \exp[i\chi_j(\vec{b})], \quad j = n, ps, \mathrm{pt}, E, \qquad (5)$$

Eq. (2) becomes

$$\begin{aligned}\Gamma(\vec{b},\vec{s}) = {} & \Gamma_{pt}(\vec{b}+\tfrac{1}{2}\vec{s}) + \exp[i\chi_{pt}(\vec{b}+\tfrac{1}{2}\vec{s})] \\ & \times\{\Gamma_E(\vec{b}+\tfrac{1}{2}\vec{s}) + \exp[i\chi_E(\vec{b}+\tfrac{1}{2}\vec{s})][\Gamma_{ps}(\vec{b}+\tfrac{1}{2}\vec{s}) + \Gamma_n(\vec{b}-\tfrac{1}{2}\vec{s}) - \Gamma_{ps}(\vec{b}+\tfrac{1}{2}\vec{s})\Gamma_n(\vec{b}-\tfrac{1}{2}\vec{s})]\}. \qquad (6)\end{aligned}$$

When this is inserted into Eq. (1), we obtain for $F(\vec{q},\vec{s})$ (apart from an unimportant constant phase factor) the result

$$\begin{aligned}F(\vec{q},\vec{s}) = e^{-i\vec{q}\cdot\vec{s}/2}k^{2in}\Big\{ & f_{pt}(q)k^{-2in} + ik\int_0^\infty J_0(qb)b^{2in+1}\Gamma_E(b)\,db \\ & + (1/4\pi^2)\int e^{i(\vec{q}-\vec{q}\,')\cdot\vec{b}}b^{2in}e^{i\chi_E(\vec{b})}[f_p(\vec{q}\,') + f_n(\vec{q}\,')e^{i\vec{q}\,'\cdot\vec{s}}]d^2q'\,d^2b \\ & + (i/8\pi^3k)\int e^{i(\vec{q}-\vec{q}\,'-\vec{q}\,'')\cdot\vec{b}}e^{i\vec{q}\,''\cdot\vec{s}}b^{2in}e^{i\chi_E(\vec{b})}f_p(\vec{q}\,')f_n(\vec{q}\,'')d^2q'\,d^2q''\,d^2b\Big\}, \qquad (7)\end{aligned}$$

where $n = Ze^2/\hbar v$ and

$$f_{pt}(q) = -2nkq^{-2}\exp\{-2i[n\ln(q/2k) - \arg\Gamma(1+in)]\}. \qquad (8)$$

here Ze is the charge of the incident hadron and f_n and f_p are the xn and xp strong-interaction elastic scattering amplitudes. The xd elastic scattering amplitude $F_{el}(q)$ is obtained by taking the matrix element of $F(\vec{q},\vec{s})$ in the deuteron ground state.

If the basic hadron-nucleon elastic scattering amplitudes are taken to be of the form

$$f_j(q) = c_j\exp(-\tfrac{1}{2}a_jq^2), \qquad (9)$$

$$c_j = k\sigma_j(i+\rho_j)/4\pi, \quad j = n, p, \qquad (10)$$

d if the deuteron ground-state form factor $S(q)$ is a Gaussian,

$$S(q) = \exp(-\beta q^2), \qquad (11)$$

en F_{el} can be reduced to single integrals, and becomes

$$\begin{aligned}F_{el}(q) = e^{-\beta q^2/4}\Big\{ & f_{pt}(q) + k^{2in}\Big[ik\int_0^\infty J_0(qb)b^{2in+1}\Gamma_E(b)\,db \\ & + (c_p/a_p)\int_0^\infty J_0(qb)b^{2in+1}\exp[i\chi_E(b)]\exp(-b^2/2a_p)\,db \\ & + (c_n/A)\exp(\beta^2q^22A)\int_0^\infty J_0(Gqb/A)b^{2in+1}\exp[i\chi_E(b)]\exp(-b^2/2A)\,db \\ & + (ic_nc_p/kAa_p)\exp(\beta^2q^2/2A)\int_0^\infty J_0(Gqb/A)b^{2in+1}\exp[i\chi_E(b)]\exp(-Hb^2/2Aa_p)\,db\Big]\Big\}, \qquad (12)\end{aligned}$$

here $G = a_n + \beta$, $A = G + \beta$, and $H = A + a_p$.

For $\chi_E(b)$ we assume that the projectile and the bound proton have charge form factors given by p$(-\tfrac{1}{4}c^2q^2)$ and $\exp(-\tfrac{1}{4}d^2q^2)$, respectively, and obtain[7]

$$\chi_E(b) = nE_1[b^2/(c^2+d^2)], \qquad (13)$$

here $E_1(z)$ is the exponential integral. The xd elastic scattering intensity $(d\sigma/d\Omega)_{el}$ may be computed om Eqs. (12) and (13).

normally only one quark in the projectile intercepts one quark in the target. This is required by the success of the additive quark model for total cross sections.[2] When the two quarks collide, they provide a source for a mesonic "spark," just as an electrical discharge acts as a source of light. Let us suppose for simplicity that the associated meson field is scalar, and self-interacting. If we look in any Lorentz frame in which the projectile is moving rapidly to the right, while the target moves rapidly to the left ("rapidly" means with high rapidity, i.e., speed imperceptibly infraluminal), then the colliding quarks will have negligible thickness in their direction of motion, and the mesonic source will be effectively a noncircular disk: a delta function in time and in the longitudinal direction, but spread by a typical quark-quark interaction radius in the transverse direction. If the quarks are small and totally black, then that radius is about $\frac{1}{3}$ fm for nonstrange quarks, less for strange.

Clearly, from case to case, the source strength will vary, but I suppose that the self-interaction of the meson field will make the number of produced mesons insensitive to the exact value of this strength, once it surpasses a certain threshold. Consequently, the inclusive rapidity distribution will be flat in the central region of rapidity, with a multiplicity per unit rapidity interval, or rapidity density, independent of the nature of projectile and target. This is because in each Lorentz frame in the central region, the meson source will flash, fast hadronic matter will depart rapidly to right and left, and slow mesons will materialize in a time of about 1 fm/c, knowing nothing about the precise nature of their source.

Diffraction can certainly be incorporated in the standard Good-Walker[3] way; it is simply a quantum-wave "leftover" of the dynamic interaction which produces sparks.

The main formal distinctions between this scheme and one with multiperipheral pion exchange are that the exchange line which radiates pions (or clusters of pions) carries a large mass, of the order of 1 GeV (to account for the small quark-quark interaction range), and that many exchange lines cross independently from projectile to target, each producing a single forward meson line. This contrasts with the multiperipheral case, where a single exchange line shakes off many mesons. Also, the associated diagram would be a "screened" graph, since the radiated mesons interact strongly with their near-rapidity neighbors. The result is a form similar to the "inside-outside" graph discussed by Bjorken, and Casher, Kogut, and Susskind.[4,5]

The main conclusions from the mesonic-spark picture of production processes are the same as from many other models,[6] and so we turn to the differences. If this picture is right, then occasionally (perhaps 1% of the time) in a proton-proton collision, two distinct quark collisions will occur, separated in impact parameter by a sufficient distance to produce distinct sparks. (If the collisions were very close together, they would simply provide a single effective source for the meson spark, of twice the usual strength. Because of the assumed insensitivity of the spark to source strength, the resulting spark would be indistinguishable from that of a single quark-quark collision.) For these events the mean multiplicity would be roughly twice that in the typical event. Such an effect might be detected as a correlation between multiplicities in the left and the right hemispheres for very high multiplicities in either hemisphere.

Now let us apply the same assumptions to the collision of a proton with a nucleus. Using the known p-p inelastic cross section, we may deduce ν, the expected number of collisions with different nucleons of a proton passing through a given target nucleus on a straight-line trajectory (neglecting any effect of a particular collision on the probability of further collisions). The multiplicity of slow mesons in the target rest frame will be ν times as great as that for a hydrogen target. This is simply because ν different target nucleons are independently fragmented, and is a result which follows in many different pictures. There is one qualification—secondary interactions of the fragments may somewhat increase their number while degrading their energy, but these should not be drastic effects. A 1-GeV π^+ (rapidity 2.7) incident on a proton yields only one charged relativistic particle, more than 90% of the time. Furthermore, as I have argued before, a produced particle with rapidity greater than this is not likely to develop its full power of interaction with a target nucleon before leaving the nucleus.

The spark picture provides a natural cutoff to the rapidity interval for which mean multiplicity is multiplied by ν. Let L be the mean length in the lab frame between successive sparks produced by a very high-rapidity projectile. These sparks are then separated by the lightlike interval

$$\Delta t = L, \quad \Delta z = L. \tag{1}$$

In a frame that moves in the projectile direction with a lab rapidity y, we have

$$\Delta t' = e^{-y}L, \quad \Delta z' = e^{-y}L. \tag{2}$$

We have already discussed the assumption that two simultaneous sparks can develop independently only if their sources are separated by a criti- al distance, call it d. The existence of a d reater than the quark-quark interaction range $\frac{1}{3}$ fm) is necessary if the picture is to be com- atible with experiment. Otherwise the two ends f a single spark could both generate mesons hroughout the rapidity plateau, leading to strong, ong-range rapidity correlations in the two-parti- le inclusive distribution. Clearly, d cannot be much greater than 1 fm, the maximum range of nown strong interactions. For definiteness, I dopt the value $d = \frac{2}{3}$ fm. We shall see later the onsequences of changing this value.

What if two sources act at the same point, but ifferent times? Since the spark from the first source cannot fly out faster than c, two indepen- ent sparks could not be generated unless the ime interval were greater than d/c. It is possi- le that an even longer interval might be needed, ut for simplicity we take the same criterion in ime as in space.

Combining the two cases, we arrive at a cri- erion that two sources separated by the Lorentz nterval $(\Delta T, \Delta X)$ in a given inertial frame will ndependently generate slow mesons in that frame:

$$(\Delta T)^2 + (\Delta X)^2 > d^2. \tag{3}$$

Substituting $\Delta t'$, $\Delta z'$ from Eq. (2), and taking $L \approx 3$ fm[8] we get a cutoff rapidity $Y_c \approx 2$. Below Y_c, he rapidity density is amplified by a factor ν. How sharp is the cutoff at Y_c? Two factors enter ere. First, collisions can occur with a larger eparation in the lab. This could give one more nit in rapidity. Secondly, the essence of our echnique is to estimate the production of slow articles in a particular Lorentz frame. "Slow" means with rapidity of order 1 in that frame. Hence, the cutoff should become completely ef- ective at $y \approx 4$, and so this will be the applica- tion in what follows:

The rapidity density is multiplied by ν for

$$y \lesssim Y_c = 4. \tag{4}$$

Above Y_c, only those collisions in which independent sparks are separated transversely by a distance greater than d will exhibit a doubled rapidity density. This should be roughly 10% of all collisions, estimated as follows. The proton has a radius of about $\frac{2}{3}$ fm. If two sparks are to be separated by $\frac{2}{3}$ fm, then each must be in the outer half of the proton cross section [probability $\approx (\frac{1}{2})^2$], and they must be more or less on opposite hemidisks (probability $\approx \frac{1}{2}$). This gives a probability of sufficient separation

$$P \approx \tfrac{2}{3} \times \tfrac{1}{2} \times \tfrac{1}{2} \times \tfrac{1}{2} \approx 0.1, \tag{5}$$

where the first factor is the probability that two distinct projectile quarks interact in the successive collisions. Clearly, the order of magnitude is not changed if there are 3 or 4 collisions. Also, the estimate is not better than an order of magnitude. The main point is that upward fluctuations of rapidity density in the entire plateau would be an order of magnitude more likely with a nuclear target than with a nucleon target.

While the cutoff Y_c in Eq. (4) is only weakly sensitive to the value of d, the probability P in Eq. (5) is very sensitive: For $d = \frac{4}{3}$, P vanishes. Thus, the prediction of enhanced multiplicity at low laboratory rapidity is much less sensitive to detailed assumptions than is the prediction of a 10% excess at higher rapidity.

At present, there are not data of sufficient quality at sufficiently high energy to detect the proposed 10% increase in mean multiplicity in the plateau region. Gottfried[1] has proposed a different model which leads to a 70% increase in multiplicity in emulsion, independent of energy, and associated entirely with the lower third of the rapidity plot. His result is in excellent agreement with data from 70 to 10 000 GeV, or an interval from 5 to 10 in projectile rapidity.[9] There are two observations to be made on Gottfried's model. The first is aesthetic. An observer watching a very high-rapidity hadron collide with a very high-rapidity nucleus could tell whether the nucleus-to-hadron rapidity ratio in his frame was greater or less than $\frac{1}{2}$, simply by counting the number of slow produced particles he sees. This violates a "generalized Lorentz invariance principle", that only absolute differences of rapidity should have measurable consequences, and not fixed ratios of rapidities which become arbitrarily large. The second comment is practical. The lower part of the energy range studied is clearly preasymptotic, while Gottfried's is an asymptotic formula. If only the 1- and 10-TeV data are taken as asymptotic, it becomes very hard to distinguish between the multiplicity formula of Gottfried,

$$n(\text{emulsion}) \approx n(\text{hydrogen})(1+\tfrac{2}{3}), \qquad (6)$$

and that suggested here,

$$n(\text{emulsion}) \approx 1.1n(\text{hydrogen}) + (\approx 3)(\nu - 1), \quad \nu \approx 3. \qquad (7)$$

Unfortunately, the small samples of cosmic-ray data at these higher energies do not permit a sufficiently detailed study of rapidity distributions to help make the distinction. Even with more data, one is hamstrung by the fact that the lower third of the rapidity plot is contained within Y_c, even at 10 TeV.

What about nucleus-nucleus collisions? At energies like 1 TeV per nucleon, our picture implies

$$n(\text{nuc-nuc}) \sim \zeta n(p\text{-}p), \qquad (8)$$

where ζ is the mean number of independent columns of projectile nucleons which pass through columns of target nucleons. This is distinct from the multipheripheral-model guess of Gribov.[10] He takes a very different approach in which only surface nucleons can act as anchors of a multiperipheral chain, implying that, for fantastic energies, nucleus-nucleus cross sections go like $A^{1/3}$ (where A is mass number), but the $(A\text{-}A)/(p\text{-}p)$ multiplicity ratio goes to 1.

It seems likely that multiperipheral-*cum*-parton models would agree with the expectation of excess particles with finite rapidity in the laboratory following collision with a nuclear target of a high-rapidity hadron. However, these models could hardly generate the asymptotic Gottfried rapidity distribution, nor the ≈ 10% uniform excess predicted here. A 500-GeV exposure of a variety of nuclear targets might at least settle this point, and could bury the spark picture.

The essential feature of this, as well as many other schemes, is that no large transfers of momentum or energy occur in short times.[11] This immediately implies a great similarity of multiparticle production processes for collisions of particles with widely different baryon numbers. In particular, our strongest single prediction is an asymptotically flat rapidity density in the central region of rapidity. The magnitude of that density is less certain, but in our picture would be about 10% higher for hadron-nucleus than for hadron-hadron collisions, and much higher for nucleus-nucleus collisions. As usual, at either end of the rapidity plot will be fragmentation regions, with nuclear fragmentation having a substantially higher multiplicity than hadron fragmentation.

Despite the difficulty of distinguishing experimentally between this and other models, even the present nuclear data enforce the view that high-energy strong processes are really rather slow and not so strong.

I thank J. D. Bjorken, K. Gottfried, J. Kogut, C. Quigg, L. Susskind, and L. Van Hove for helpful comments.

---

*Research supported in part by the National Science Foundation under Grant No. GP-32998X.

[1] The relevant phenomenology of multiple production with nuclear targets is reviewed by K. Gottfried, in Proceedings of the Fifth International Conference on Nuclear Structure, Uppsala, Sweden, 18–22 June 1973 (to be published), and Phys. Rev. Lett. 32, 957 (1974). In the latter paper Gottfried proposes a model for production different from that discussed here.

[2] E. M. Levin and L. L. Frankfurt, Zh. Eksp. Teor. Fiz., Pis'ma Red. 2, 105 (1965) [JETP Lett. 2, 65 (1965)]; H. J. Lipkin and F. Scheck, Phys. Rev. Lett. 16, 71 (1966).

[3] M. L. Good and W. D. Walker, Phys. Rev. 120, 1857 (1960).

[4] J. D. Bjorken, unpublished; A. Casher, J. Kogut, and L. Susskind, Cornell University Report No. CLNS 251 (to be published).

[5] If the exchange lines are identified as the well-know vector mesons, one obtains a qualitative explanation the smaller cross section of strange quarks; it comes from the shorter range and weaker coupling to quarks of the φ (coupled to strange q) compared to the ω (coupled to nonstrange q). One could not demand a quantitative result, since the relative source strengths for meson production of overlapping ω fields, of overlapping ω and φ fields, or of overlapping φ fields are not known. Although this qualitative correlation of quark cross sections with vector-meson masses is quite striking, it does not appear prominently in the literature.

[6] This is not quite true. The assumption of a fixed number of quarks, together with the natural use of longitudinal phase space, leads to a total cross sectio rising asymptotically as $[\ln(\ln s)]^2$, but even the highes foreseeable energies would scarcely serve to distinguish this from $[\ln s]^2$, since $\ln s$ would not be very large.

[7] A. S. Goldhaber, Phys. Rev. 7, 765 (1973).

[8] L is set equal to the mean free path of the incident hadron between inelastic collisions in the nucleus, treated as a dilute gas of nucleons. Gottfried (Ref. 1) uses a smaller value of L, obtained from a uniform nucleus with a sharp edge. Note that the dependence of Y_c deduced below on L and d is weak, $Y_c \approx 2.5 + \ln(L/d)$

[9] A recent analysis demonstrates that most, if not all, cess particles come at low rapidities ($\lesssim 4$) in 67 and 00 GeV emulsion exposures. R. Hołyński, S. Krzywd-ński, and K. Zalewski, University of Cracow Report No. INP 856/PH (to be published).

[10] V. N. Gribov, Yad. Fiz. **9**, 640 (1969) [Sov. J. Nucl. Phys. **9**, 369 (1969)].

[11] A point at the heart of Ref. 7.

ERRATUM

PHOTOELASTIC TENSOR OF SILICON AND THE VOLUME DEPENDENCE OF THE AVERAGE GAP. David K. Biegelsen [Phys. Rev. Lett. **32**, 1196 (1974)].

It should be noted that Cardona, Paul, and Brooks (Ref. 11) also measured the pressure dependence of the radio frequency dielectric constant of silicon. They obtained $d\ln\epsilon/dP = (-4\pm1)\times10^{-7}\ \mathrm{kg}^{-1}\ \mathrm{cm}^2$. This implies a value of $\bar{p} = -0.098\pm0.025$, in somewhat better agreement with our measurement of $\bar{p} = -0.059\pm0.003$ than their optical measurements. It is assumed that in their samples impurity and free-carrier effects on the rf dielectric constant were negligible.

PHYSICAL REVIEW
LETTERS

VOLUME 33 8 JULY 1974 NUMBER 2

Determination of the Singlet-Triplet Separation of H_2 by a "Level-Anticrossing" Technique*

R. Jost and M. Lombardi
*Laboratoire de Spectrométrie Physique,† Université Scientifique et Médicale de Grenoble,
38041 Grenoble Cedex, France*

(Received 13 May 1974)

We show that the singlet-triplet separation of H_2 must be lowered by 157.7 ± 0.2 cm^{-1} compared to the hitherto accepted value of Dieke. We have used a new kind of "level anticrossing" method in which the anticrossing is due to the coupling of a singlet and a triplet state by spin-orbit or hyperfine Fermi contact interaction.

Hydrogen, H_2, is the simplest of the neutral molecules, and is therefore a good test for fundamental molecular calculations. Very refined calculations have been made by Kolos and Wolniewicz[1]: They achieved an accuracy of a few inverse centimeters in the calculation of the location and properties of singlet energy levels. When applied to triplet levels, these calculations, confirming older and less precise ones of Rothenberg and Davidson,[2] have raised a problem[3]: The accepted experimental value of the separation of singlet and triplet levels is apparently some 150 cm^{-1} too great. However, the experimental situation is not clear: Separation within singlet and riplet levels is determined with the usual accuracy by optical spectroscopy but, since H_2 has a very good Russell-Saunders spin coupling scheme, no transition between singlet and triplet levels has been identified and so the relative position of hese two groups of levels is uncertain. The experimental separation of singlet and triplet levels in H_2 is based on an uncertain determination of ionization potentials by extrapolation of the Rydberg series. There have been variations in his assignment: The now generally accepted results of Dieke,[4] which we shall use as a basis in his Letter, are 141 cm^{-1} higher than the older ones of Beutler and Jünger.[5] Recently, Herzberg and Jungen[6] have obtained by absorption in the uv the ionization potential of singlet states of H_2 with better precision.

To see if the anticrossing experiment was possible we had to find pairs of singlet-triplet levels whose separation did not exceed 10 cm^{-1} (because of magnetic-field limitation). Assuming, as is the feeling of most of the specialists we know, that the theoretical results are more reliable than Dieke's experimental ones we have looked for another experimental determination of this separation. The method is based upon comparison of $3d$ and $4d$ levels in H_2 and in He (there is a singlet-triplet line in He) since He is the united-atom limit of H_2, and since in both cases there is a large hydrogenoid outer $3d$ and $4d$ orbit around a small core.

The separation of $3d\,^1D$ and $3d\,^3D$ levels of He is 3.32 cm^{-1} and the separation of $4d\,^1D$ and $4d\,^3D$ is 1.88 cm^{-1}. In H_2 we have selected $3d\,\Pi^-$, $4d\,\Pi^-$, $3d\,\Delta^-$ levels; $3d$ and $4d$ Σ, Π^+, and Δ^+ levels are perturbed differently and the singlet-triplet separation of a pair of levels with the same N and v is somewhat erratic. Within Π^- or Δ^- levels, on the contrary, there is great regularity and a weak and smooth dependence on v. The singlet-triplet separation in Dieke's basis, extrapolated to rotational zero and $v = -\frac{1}{2}$, is re-

Copyright © 1974 by
The American Physical Society

spectively -149, -153, -145, and $-153\ \mathrm{cm}^{-1}$ (uncertain) for $3d\,\Pi^-$, $4d\,\Pi^-$, $3d\,\Delta^-$, and $4d\,\Delta^-$. This raises immediately the following question: Why are all these separations of the order of $-150\ \mathrm{cm}^{-1}$ instead of plus a few inverse centimeters as in He? If we suppose that the ratio of singlet-triplet separations between $n=3$ and $n=4$ is the same in H_2 and He, it follows that triplets must be lowered by $158\ \mathrm{cm}^{-1}$ for Π^- and $162\ \mathrm{cm}^{-1}$ (uncertain) for Δ^- levels. We then assume provisionally a lowering of $158\ \mathrm{cm}^{-1}$ of the triplet levels. In this hypothesis, therefore, we choose for our study three pairs of levels, $3d\ ^{1-3}\Sigma$, $v=0$, $N=2$ and 3, and the $3d\ ^{1-3}\Delta$, $v=1$, $N=3$ levels, which are less than $5\ \mathrm{cm}^{-1}$ apart.

The general form of "anticrossing" experiments has been described by Wieder and Eck.[7] In the "pure anticrossing" case, two radiating levels are populated differently by various excitation mechanisms, and the mechanism of detection can discriminate, at least partially, between light emitted by the two levels. These levels would cross for a particular value of an external (usually magnetic) field, unless a coupling between these two levels by some repulsive interaction V occurs. Roughly speaking, at the anticrossing point, the population of one level oscillates back and forth between the two levels, producing an even distribution. The resultant resonancelike signal is centered on the anticrossing point. Its amplitude is proportional both to the population difference of the two levels and to the difference of detection efficiency of the same levels. It has a width given by the field needed to separate the two levels by an amount of the order of V (or the mean value of their inverse lifetime if V is smaller than this quantity). In earlier experiments V is due either to an electric field[7-9] or to the hyperfine interaction within a fine or hyperfine multiplet.[7] In our experiment

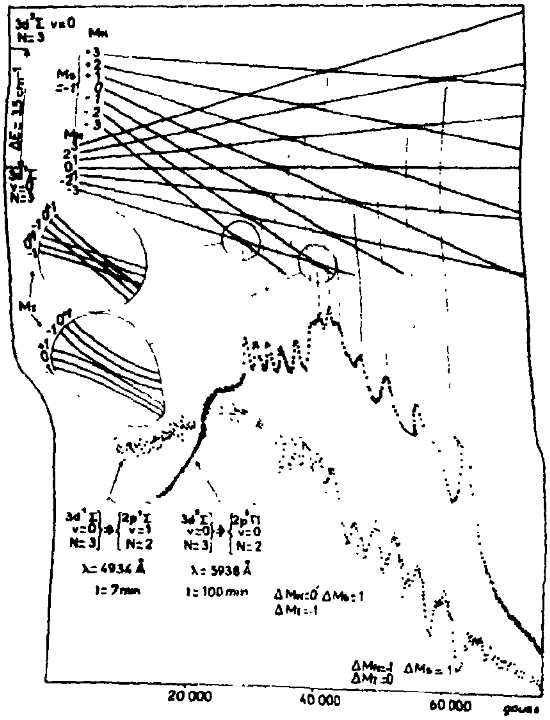

FIG. 1. Anticrossing signal both on the 4934-Å $R2$ singlet and on the 5938-Å $R2$ triplet ortho lines, and the corresponding Zeeman energy level diagram. The hyperfine sublevels are sketched very roughly only in the circles because fine and hyperfine structures are not known. The signal amplitude is a few percent.

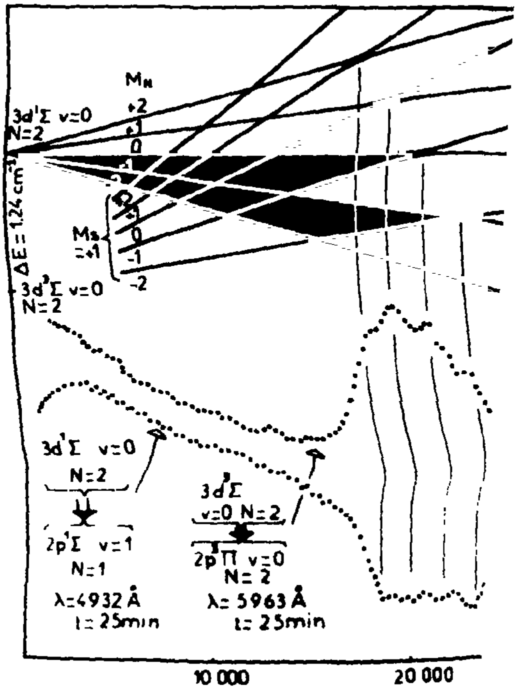

FIG. 2. Anticrossing signal both on the 5963- triplet and on the 4932-Å $R1$ singlet para lines corresponding Zeeman energy level diagram. Z field fine structure of triplet is not known. The tion of intensities of the various anticrossings i lines is different because they are respectively $R1$ lines.

TABLE I. Zero-field separations of levels.

Levels	Triplet minus singlet separation measured (cm^{-1})	Triplet levels must be lowered by (cm^{-1})
$3d\,^{1-3}\Sigma$ $v=0$, $N=2$	-1.24 ± 0.1	157.69
$3d\,^{1-3}\Sigma$ $v=0$ $N=3$	$+3.5\ \pm0.2$	157.75
$3d\,^{1-3}\Delta$ $v=1$, $N=3$	$+1.16\pm0.1$	157.64

the coupling is due either to spin-orbit interaction (which, as is well known, couples singlet and triplet levels, causing transition from *LS* to *jj* coupling) or to hyperfine Fermi contact interaction (the coupling of the analogous $3d$-$4d$ singlet and triplet levels of He by this Hamiltonian has been calculated for other purposes by Bessis, Lefebvre-Brion, and Moser[10]).

We used a 150-kG Bitter coil. H_2 was excited t a pressure of 10^{-1} Torr within a small Pyrex ell by a capacitive discharge (with electric field arallel to the magnetic field) induced by a 30-W, 50-MHz AMECO high-frequency generator. The ntensity of the light emitted parallel to the mag- etic field was detected by a EMI 9558 photomulti- lier and stored on a DIDAC 800 multichannel nalyzer. Between four and fifty scans of 100 ec were used. Lines were separated by a Jobin- von H.R.S. monochromator whose slit width was lways great enough not to separate the Zeeman omponents. Figures 1 and 2 show the most char- cteristic results.

The position of the anticrossing gives first the ro-field separations described in Table I. results are in good agreement and we con- that triplet levels must by lowered by 157.7 cm^{-1} as compared to Dieke's data.[4] Second- ie splitting of the various M_N anticrossings the difference between orbital singlet and t Landé g factors. Using the singlet Landé ors measured by Dieke, Cunningham, and ,[11] we found the following preliminary re-

$$_{J}(3d\,^3\Sigma,\ v=0,\ N=2)=0.70\pm0.02,$$

$$_{J}(3d\,^3\Sigma,\ v=0,\ N=3)=0.55\pm0.02.$$

ally, the width of the curve can give a mea- of the fine- and hyperfine-structure con- . The complete analysis of these results a more detailed calculation and further experiments are in progress which will be reported in the future. We notice that the ultimate accuracy of our method is limited by the width of the curves which is given by the fine- or hyperfine-structure constants. This is better than the Doppler-limited accuracy with which the separations within the singlet and the triplet group of levels are known. Natural-lifetime accuracy could be achieved with an existing Momrie[9] apparatus, at least for the $3d\,^{1-3}\Delta$, $v=1$, $N=3$ levels for which the anticrossings are at about 12 kG: One cannot induce resonance between pure singlet and triplet levels except in the vicinity of an anticrossing point where the two levels are mixed.

We thank the Service National des Champs Intenses of the Centre National de la Recherche Scientifique at Grenoble which made available to us the 150-kG Bitter coils. We thank also the Max Planck Institute of Grenoble for the loan of optical apparatus.

---

*Work performed at the Service National des Champs Intenses at Grenoble (Centre National de la Recherche Scientifique).

†Laboratoire associé au Centre National de la Recherche Scientifique.

[1] W. Kolos and L. Wolniewicz, J. Chem. Phys. 41, 3663 (1964), and 43, 2429 (1965), and 45, 509 (1966), and 48, 3672 (1968).

[2] S. Rothenberg and E. R. Davidson, J. Chem. Phys. 45, 2560 (1966).

[3] W. Kolos, Chem. Phys. Lett. 1, 19 (1967).

[4] G. H. Dieke, J. Mol. Spectrosc. 2, 494 (1968), and in *The Hydrogen Molecule Wavelength Tables of Gerhard Heinrich Dieke*, edited by H. M. Crosswhite (Wiley-Interscience, New York, 1972).

[5] H. Beutler and H. O. Jünger, Z. Phys. 101, 285 (1936).

[6] G. Herzberg and Ch. Jungen, J. Mo. Spectrosc. 41, 425 (1972).

[7] H. Wieder and T. G. Eck, Phys. Rev. 153, 103 (1967);

T. G. Eck, L. L. Foldy, and H. Wieder, Phys. Rev. Lett. 10, 239 (1963).

[8] D. H. Levy, J. Chem. Phys. 56, 5493 (1972).

[9] R. S. Freund and T. A. Miller, to be published.

[10] N. Bessis, H. Lefebvre-Brion, and C. M. Moser, Phys. Rev. 135, A957 (1964).

[11] G. H. Dieke, S. P. Cunningham, and F. T. Byrne, Phys. Rev. 92, 81 (1953).

[12] M. Lombardi, J. Chem. Phys. 58, 797 (1973), and references quoted there.

Two-Center Thomas-Fermi Model for Adiabatic Ion-Atom Collisions

J. Eichler and U. Wille
Hahn-Meitner-Institut für Kernforschung Berlin GmbH, Bereich Kern- und Strahlenphysik, Berlin, West Germany, and Freie Universität Berlin, Fachbereich Physik, Berlin, West Germany

(Received 14 May 1974)

We propose a two-center model for the description of ion-atom collisions proceeding via a quasimolecular (adiabatic) mechanism. The electronic potential of the model is given by a superposition of modified *atomic* Thomas-Fermi potentials, each centered about one of the colliding nuclei. Molecular correlation diagrams calculated for the Ne-Ne system show good agreement with results from molecular-orbital Hartree-Fock calculations.

In the past few years the electron-promotion model[1] has proven to be quite successful[2] in describing the excitation of inner-shell electrons in adiabatic ion-atom collisions. Based on the Born-Oppenheimer approximation, the model assumes the formation of a transient quasimolecule whose electronic energy spectrum as a function of the internuclear distance ("correlation diagram") is the starting point for any dynamical treatment of the process. While for a few cases quantitative adiabatic correlation diagrams have been calculated by the Hartree-Fock method,[3,4] the evaluation of most of the experimental results has been based on rather qualitative "diabatic" diagrams. They are obtained from the known electronic spectra in both the united-atom and the separated-atom limits using the correlation diagrams for unscreened Coulomb centers as a guide to connect the limiting cases.[1,5]

It is quite clear that for a more quantitative discussion of experiments and a detailed dynamical theory a method is needed which yields accurate adiabatic correlation diagrams like the Hartree-Fock method and yet is flexible and simple enough to be easily applicable to any given combination of collision partners.

In the present note we propose a model which we believe to meet these requirements. We start from the observation that *atomic* energy levels may, to a good accuracy, be derived from a statistical Thomas-Fermi (TF) model with a universal spherical single-electron potential $V^{\mathrm{TF}}(r)$ (including corrections for self-interaction and exchange effects). Latter[6] has calculated energy levels for a large number of atomic states using potentials of the form (atomic units are used throughout)

$$V^{\mathrm{TF}}(r)=\begin{cases}\left\{-\dfrac{Z}{r}\Phi(x)+\dfrac{3\sqrt{2}}{4\pi}\left[\dfrac{r}{Z}\Phi(x)\right]^{1/2}\right\}, & \text{if } |V^{\mathrm{TF}}(r)|>\dfrac{1}{r};\\ -r^{-1}, & \text{otherwise.}\end{cases}\qquad(1)$$

Here, $x=r/\mu$ with $\mu=0.8853Z^{-1/3}$, and the screening function $\Phi(x)$ is given by the analytic expression

$$\Phi(x)=(1+0.02747x^{1/2}+1.243x-0.1486x^{3/2}+0.2302x^{2}+0.007298x^{5/2}+0.006944x^{3})^{-1}.\qquad(2)$$

The corrections for electronic self-interaction and exchange included in the potential (1) have been discussed in detail by Coulson and Sharma.[7] Although the TF approximation cannot compete in accuracy with elaborate atomic Hartree-Fock calculations available today,[8] it should be sufficiently reliable for the treatment of inner-shell electrons relevant to atomic collision processes.

We here assume that the TF method not only gives a resonable description of the potential felt by a single electron in the united-atom and seprated-atom limits, but is also able to account or the mutual screening and polarization of the toms at finite internuclear distances $2R$. The otential V acting on a single electron at the distance r_1 from the screened nucleus 1 and at the istance r_2 from the screened nucleus 2 might be btained by solving the TF equation with the appropriate boundary conditions.[9] While it has been hown by Teller[10] that the TF model cannot give rise to molecular binding it still should provide a reasonable approximation for inner-shell electrons whose binding energy by far exceeds molecular dissociation energies.

Instead of attempting a complete numerical solution of the TF equation, we adopt an idea put orward by Hund[11] as early as 1932 which leads o a simple and transparent approximate form of he electronic potential. According to Hund[11] the molecular potential V for a given internuclear distance $2R$ is represented by a sum of two effective (R-dependent) *atomic* TF potentials $V_i^{\mathrm{eff}}(r_i)$ plus a correction term $W(r_1, r_2)$. Subsequently, the functions $V_i^{\mathrm{eff}}(r_i)$ are chosen separately for each value of R in such a way that $W(r_1, r_2)$ is minimized. In the cases considered explicitly by Hund the quantity W has been shown to be negligibly small[11] and thus

$$V = V_1^{\mathrm{eff}}(r_1) + V_2^{\mathrm{eff}}(r_2). \tag{3}$$

We assume this representation of the molecular potential to be approximately valid for any combination of atomic collision partners and all internuclear separations.

Generalizing Hund's *Ansatz* to allow for nonsymmetric systems ($Z_1 \neq Z_2$) and for the inclusion of exchange terms we may write

$$V_i^{\mathrm{eff}}(r_i) = \begin{cases} -\dfrac{Z_i}{r_i}\left\{\Phi(x_i(R)) + \dfrac{3\sqrt{2}}{4\pi}\left[r_i f_i(R)\Phi(x_i(R))\right]^{1/2}\right\}, & \text{if } |V_i^{\mathrm{eff}}(r_i)| > \dfrac{Z_i}{r_i} f_i(R); \\ -\dfrac{Z_i}{r_i} f_i(R), & \text{otherwise,} \end{cases} \tag{4}$$

vhere Φ is the screening function defined in Eq. (2). With the abbreviations $\rho_i = r_i/R$, $y_i = (Z_1 + Z_2)/Z_i$ ve have

$$x_i(R) = \frac{r_i Z_i^{1/3}}{0.8853}\,\frac{\lambda^2 + y_i^{1/3}\rho_i^2}{\lambda^2 + \rho_i^2} \tag{5}$$

nd

$$f_i(R) = \frac{1}{Z_i}\,\frac{\lambda^2 + \rho_i^2}{\lambda^2 + y_i\rho_i^2}. \tag{6}$$

he functions (5) and (6) interpolate between the limiting cases and guarantee that the total potential V pproaches the correct values for $r_i \to = 0, \infty$ (R fixed) and $R \to 0, \infty$ (r_i fixed). The "smoothing parameter" λ^2 has been determined by Hund to be $\lambda^2 = 3$ for the ground states of the N_2 and F_2 molecules. In neral, one may expect a dependence of λ^2 on the atomic numbers Z_1 and Z_2.

Having established the potentials (4) acting on the electron, the Hamiltonian of our two-center TF odel is expressed by

$$H = -\tfrac{1}{2}\nabla^2 + V_1^{\mathrm{eff}}(r_1) + V_2^{\mathrm{eff}}(r_2). \tag{7}$$

ie eigenenergies are obtained by diagonalizing the Hamiltonian (7) in a basis set which has originally en introduced by Hylleraas[12] and recently been used[13] for treating the unscreened relativistic twonter, one-electron problem. It is given by

$$\Psi_{nl}^{m}(\xi, \eta) = (\xi^2 - 1)^{m/2}\exp\left(-\frac{\xi - 1}{2a}\right) L_n^{m}\left(\frac{\xi - 1}{a}\right) P_l^{m}(\eta), \tag{8}$$

ere $\xi = (r_1 + r_2)/2R$ and $\eta = (r_1 - r_2)/2R$ are proe spheroidal coordinates and L_n^m and P_l^m are associated Laguerre polynomials and Legene functions, respectively. The quantum numr m is the (positive) projection of the electronangular momentum on the internuclear axis, d $n = 0, 1, \ldots, n_{\max}$; $l = m, m+1, \ldots, l_{\max}$ label the matrix elements in our truncated representation. The scaling factor a is connected with the asymptotic behavior of the wave functions and may be adjusted for a given basis set so as to give optimal convergence. It should be mentioned that the set (8) is nonorthogonal with respect to the labels n and l. For obtaining the eigenvalues one has therefore, to prediagonalize the overlap matrix. In a second step the Hamiltonian (7) is diagonalized in the resulting orthogonal representation. It is clear that for large internuclear separations the basis (8) ceases to be suitable. Then one may use, for example, the combined space of two spherical representations associated with the two nuclei.

As a test on our computer program we have recalculated the well-known energy spectrum of the H_2^+ molecule[11] and achieved an accuracy generally better than 10^{-3} for a wide range of internuclear distances and energies ($2R \leq 20$, principal quantum number $n \leq 5$ with $n_{max} = 6$, $l_{max} = m + 7$, $a = 1/R$).

By way of example we have calculated the adiabatic correlation diagram for the Ne-Ne system (Ne on Ne) shown in Fig. 1. We have chosen this case in order to compare with the Hartree-Fock calculations of Larkins.[3] In fact, it turns out that we are able to reproduce the results of those detailed calculations with a remarkable degree of accuracy. An avoided crossing $3\sigma_g$-$4\sigma_g$ is found at $2R = 0.31$, $E = -0.40$ with a closest separation of $\Delta E = 0.01$.

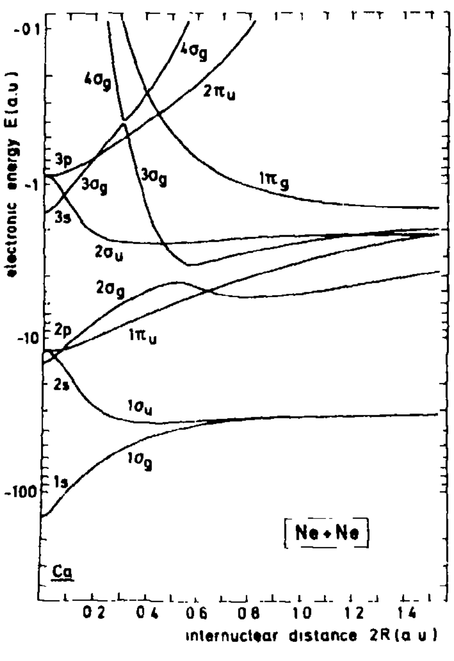

FIG. 1. Correlation diagram for the Ne-Ne system, calculated from the Hamiltonian (7). The calculation has been restricted to σ ($m = 0$) and π ($m = 1$) states; the levels are labelled according to their "gerade" (g) or "ungerade" (u) character. The parameter values used in the calculation are $\lambda^2 = 3$, $a = 1/10R$, $n_{max} = 6$, $l_{max} = m + 7$. At $R = 0$, the electronic energies have been determined directly by solving the radial Schrödinger equation with the united-atom TF potential.

It should be pointed out that in the absence of a screening potential the *avoided* crossings would turn into *real* crossings due to the existence of an additional symmetry for the two-center Coulomb problem.[15] The resulting correlation diagrams are usually called *diabatic* diagrams. Since the closest separation of electronic energy levels near avoided crossings is a direct measure of the deviation from a two-center Coulomb potential (screening), possible experimental information on such separations may, conversely, be used to test and correct the theoretically assumed screening.

In conclusion we wish to summarize what we believe are the main advantages of the proposed two-center TF model: (i) The model gives a conceptually very simple picture which might serve as a basis for the discussion of adiabatic ion-atom collisions. (ii) Comparisons with existing Hartree-Fock calculations indicate that the model gives quantitatively reliable results. (iii) While for heavier systems complete two-center Hartree-Fock calculations are hardly feasible, the numerical effort required by our model is independent of the number of electrons in the system. We may therefore calculate adiabatic correlation diagrams for systems which hitherto have been inaccessible. (iv) Because of the simplicity of obtaining energy levels and one-electron wave functions (which possibly may *not* have the same quality as the energies) our model may serve as a suitable starting point for calculations on the collision dynamics. As a first extension we intend to investigate, in the framework of a modified TF approximation, the effect on correlation diagrams caused by outer-shell ionization and by inner-shell vacancies.

We wish to express our appreciation to Dr. J. S. Briggs and Dr. J. Macek for helpful comments on the manuscript and furthermore to Dr. Q. K. K. Liu for separate calculation of electronic energies in the united-atom limit. Thanks are due to Mrs. B. Bohne for her help in computer programming.

---

[1] U. Fano and W. Lichten, Phys. Rev. Lett. 14, 627 (1965); W. Lichten, Phys. Rev. 164, 131 (1967).

[2] Q. C. Kessel and B. Fastrup, Case Stud. At. Phys. 3, 137 (1973); J. D. Garcia, R. J. Fortner, and T. M. Kavanagh, Rev. Mod. Phys. 45, 111 (1973).

[3] F. P. Larkins, J. Phys. B: Proc. Phys. Soc., London 5, 571 (1972).

[4] E. W. Thulstrup and H. Johansen, Phys. Rev. A 6, 206 (1972); J. S. Briggs and M. R. Hayns, J. Phys. B: Proc. Phys. Soc., London 6, 514 (1972).

[5] M. Barat and W. Lichten, Phys. Rev. A 6, 211 (1972).

[6] R. Latter, Phys. Rev. 99, 510 (1955).

[7] C. A. Coulson and C. S. Sharma, Proc. Phys. Soc., London 79, 920 (1962).

[8] J. P. Desclaux, Nucl. Data, Sect. A 12, 311 (1973).

[9] J. R. Townsend and G. S. Handler, J. Chem. Phys. 36, 3325 (1962).

[10] E. Teller, Rev. Mod. Phys. 34, 627 (1962).

[11] F. Hund, Z. Phys. 77, 12 (1932).

[12] E. Hylleraas, Z. Phys. 71, 739 (1931).

[13] B. Müller, thesis, University of Frankfurt, 1973 (unpublished); B. Müller, J. Rafelski, and W. Greiner, Phys. Lett. 47B, 5 (1973).

[14] D. R. Bates and R. H. G. Reid, Advan. At. Mol. Phys. 4, 13 (1968).

[15] H. A. Erikson and E. L. Hill, Phys. Rev. 75, 29 (1949); S. P. Alliluyev and A. V. Matveyenko, Zh. Eksp. Teor. Fiz. 51, 1873 (1966) [Sov. Phys. JETP 24, 1260 (1967)]; C. A. Coulson and A. Joseph, Int. J. Quantum Chem. 1, 337 (1967).

Mechanisms for Electron Production in 30-MeV $O^{n+} + O_2$ Collisions*

N. Stolterfoht and D. Schneider
Hahn-Meitner-Institut für Kernforschung Berlin GmbH, Berlin-West 39, Germany

and

D. Burch, H. Wieman, and J. S. Risley
Department of Physics, University of Washington, Seattle, Washington 98195

(Received 29 April 1974)

Absolute cross sections for electron emission in the complete energy and angular ranges were measured for 30-MeV $O^{n+} + O_2$ collisions at incident charge states of $n = 4$ to 8. Rises in inner- and outer-shell ionization of the target are studied for increasing n. Electrons ejected from the outer shell of the projectile are found to be very intense at forward emission angles θ. Auger electrons from the projectile are observed at $\theta < 42°$ for n as large as 6.

Most previous measurements of electron production in ion-atom collisions have been made with projectile energies lower than a few MeV; for recent progress in this field see current reviews.[1,2] Only recently, Burch and co-workers[3-5] and Matthews and co-workers[6] using ions from tandem Van de Graaff accelerators reported on electron production in experiments with projectiles having energies an order of magnitude higher than previously used. In these experiments, however, electrons have been measured only at fixed backward angles with respect to the incident beam, and only certain fractions of the electron spectra (target Auger peak[3,5,6] and projectile "electron-loss" peak[4]) have been detected. Our purpose in this work is to study the overall angular and energy distributions of secondary electrons produced by energetic heavy ions with a variety of incident charge states. This is the first such comprehensive investigation for high-energy collisions and it is made to obtain a general picture of ionization mechanisms with ions supplied from high-energy accelerators.

We report absolute cross sections for electrons ejected in 30-MeV $O^{n+} + O_2$ collisions with projectile charge states of n from 4 to 8. Measurements were made at forward observation angles of 25 to 90°; the data do not substantially change in the range of backward angles. The measured electron spectra indicate pronounced structures, each of which can be attributed to certain excitation and de-excitation processes in the target or the projectile atom. It is found that most of the spectral structures are strong only at forward electron-ejection angles. In particular, at small angles outer-shell electrons emitted from the projectile are found to dominate the electron spectra. Furthermore, Auger electrons ejected from the 30-MeV projectile can be observed only at angles smaller than 42°. At 25°, projectile Auger electrons are found for projectile charge states as high as 6, indicating the presence of collision processes such as simultaneous vacancy creation in the inner shell and transfer of two electrons to

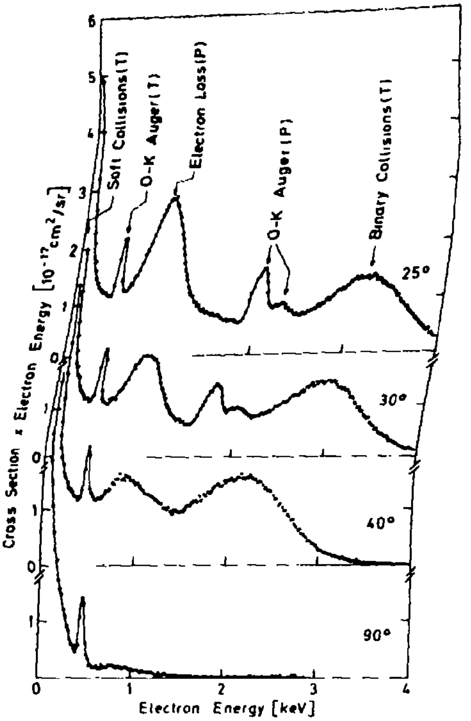

FIG. 1. Cross section times electron energy for electron production in 30-MeV $O^{5+} + O_2$ collisions at different electron observation angles.

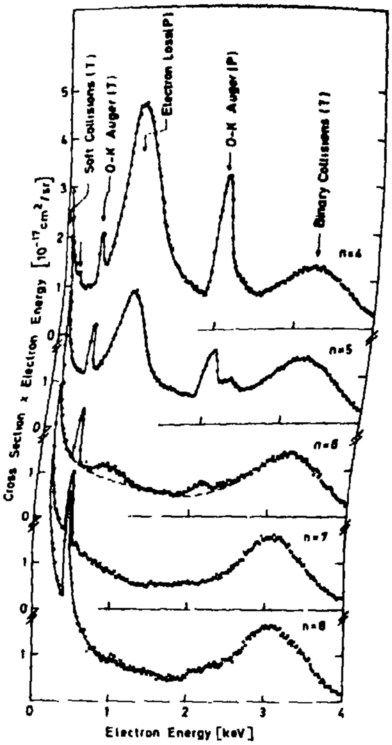

FIG. 2. Cross section times electron energy for electron production in 30-MeV $O^{n+} + O_2$ collisions at an electron observation angle of 25° for different projectile charge states *n*.

outer shells of the projectile.

The measurements were made using the crossed-beam apparatus of the Hahn-Meitner-Institut Berlin which was temporarily transported to the FN tandem accelerator laboratory of the University of Washington. The apparatus has been described in detail previously.[7] Electrons produced in ion-atom collisions were analyzed by a parallel-plate electrostatic spectrometer with an energy resolution of 2.6% full width at half-maximum. The spectrometer efficiency and its energy dependence were known in the studied electron-energy range,[7] so that absolute cross sections for electron production could be determined. Low pressures were maintained in the system to provide single-collision conditions. Between the charge-state analyzing magnet and the gas target (of ~3 mm thickness) the ion beam traversed a 10-m beam tube and a 30-cm section of the scattering chamber. The pressures in the beam tube, the chamber, and the target were 5×10^{-7}, 5×10^{-6}, and $\sim3\times10^{-4}$ Torr, respectively. Assuming an upper-limit value[8] of 10^{-16} cm^2 for the charge-exchange cross section, it was calculated that less than 1% of the incident particles underwent charge-exchange collisions.

In Figs. 1 and 2 experimental results are given for different observation angles and for several charge states of the incident ion, respectively. The electron spectra show several peaks which are discussed individually below. In Table I are given cross sections obtained by integration of the Auger peaks. Total cross sections for Auger

TABLE I. Total cross section per atom (in units of 10^{-18} cm^2) for Auger-electron ejection from the target T and the projectile P in 30-MeV $O^{n+} + O_2$ collisions as a function of the projectile charge state *n*.

	4	5	6	7	8
T	6.4 ±1.5	7.4 ±1.8	8.8 ±2.3	11.4 ±2.6	17.5 ±3.
P	6.3 ±1.5	2.7 ±0.6	0.72 ±0.18	•••	•••

ectron ejection from the projectile and the tar- t were calculated assuming isotropic electron nission in the rest frame of the corresponding rticles.

Soft and binary collision peaks.—The peaks la- led "Soft Collisions (T)" and "Binary Collisions)" are due to electrons produced by Coulomb teraction of the incident (screened) nucleus th, primarily, outer-shell electrons of the tar- t. Similar peaks have previously been studied low-energy collisions with light-ion impact; e for instance the spectra[7,9] obtained by H$^+$ in- ient on He. In the theoretical description based the Born approximation, "soft" and "binary" collisions correspond, respectively, to the minimum and maximum momentum transfer from projectile to the target atom. The soft-collision peak is nearly isotropic in intensity and position, whereas the binary-collision peak is strongly shifted to lower energies with increasing observation angle and vanishes at angles larger than 90°. Figure 2 shows the projectile-charge dependence of the peak intensities. It is found that for charge states of 4 to 8 the soft-collision peak (at 40 eV) and the binary-collision peak (at its maximum) increase by factors of 5.2 and 1.25, respectively. These numbers show that in the case of soft collisions the screening effect of the projectile electrons on the incident nucleus is considerably larger than in the case of hard or binary collisions.

Electron loss peak.—The peak labeled "Elec- ron Loss (P)" represents electrons ejected from he projectile by elastic scattering from the screened Coulomb field of the target. Such elec- rons have recently been observed by Wilson and Toburen[10] and Burch, Wieman, and Ingalls[4] who have also given a binary-encounter description of the electron-loss process. The centroid ener- y of the peak corresponds to an electron velocity qual to the projectile velocity. Using the formu- as in Ref. 4 it can be shown that the base width of the electron-loss peak is given in first order y $4(E_BE_i)^{1/2}$, where E_B is the binding energy of he "lost" electron and E_i is its mean ejection nergy. In high-energy (30-MeV) collisions the lectron-loss peak was previously observed[4] only t 90° where its intensity is relatively small (Fig.). The present results, however, indicate that e electron-loss peak is very intense in the spec- a measured at forward angles.

From the base-width formula given above, it ollows that the observed electron-loss peak is roduced only by outer-shell electrons of the projectile. (Electrons originating from the projectile *K* shell are hardly seen as they are too much spread out over the spectrum.) Indeed, integration of the present electron spectra shows that the studied peak for O^{4+} impact is twice as large as the peak for O^{5+}. However, for O^{6+} impact the intensity of the electron-loss peak is still considerable, i.e., 0.12 of that for O^{5+}. This intensity is probably too large to be due to an O^{5+} contamination in the O^{6+} beam. It is possible that a contamination of O^{6+} ions excited to metastable states partly produces the observed intensity.

Target Auger peak.—The peak labeled "O-*K* Auger (T)" is produced by Auger electrons following vacancy creation in the *K* shell of the target by the incident (screened) nucleus. Recently, Burch *et al.*[5] have shown for high-energy collisions that Auger-electron measurements are appropriate to study the incident charge-state dependence of inner-shell vacancy production.

The numbers in Table I show that the Auger-electron production cross section for the target increases by a factor of 2.8 as the projectile charge state increases from 4 to 8. It should be noted that the projectile velocity is slightly larger than the velocity of the oxygen *K*-shell electron; hence, the inner-shell ionization of the target is expected to take place primarily via a direct Coulomb excitation process. The factor-2.8 rise of the Auger-electron production cross section is intermediate between the factor-1.28 and -5.2 rise in the intensities of the binary-collision and soft-collision peaks, respectively. It appears reasonable, as in the case of outer-shell ionization, to explain the variation of the target *K*-shell ionization primarily by screening effects of the projectile nuclear charge.[5]

Projectile Auger peak.—The peak labeled by "O-*K* Auger (P)" is produced by Auger electrons ejected from the moving projectile after the collision. Previously, projectile Auger electrons have been measured in gas-target experiments only at relatively small ion energies, below about 1 MeV; see Refs. 1 and 2. For 30-MeV oxygen large shifts of the projectile Auger peak appear as a result of kinematic (Doppler) effects. Projectile Auger electrons are visible only at angles smaller than 42° (Fig. 1). In this angular range the peak appears twice in the spectrum, i.e., at 180 and 2050 eV for 25° (note also the unlabeled arrow above the O^{4+} spectrum in Fig. 2). The appearance of two projectile Auger peaks in the spectrum is well understood in terms of different velocity vector diagrams. Furthermore, at the high-energy side, the Auger peak shows a shoulder which might be attributed to double K-shell ionization or electron excitation to upper bound states.

For O^{4+} the centroid energy of the Auger electrons in the projectile rest frame was calculated to be 420 eV which is considerably smaller than the centroid energy (470 eV) of the target Auger electrons. Auger peaks are shifted to lower energies as an increasing number of outer-shell electrons are missing.[1,2] This shows that the precollision difference in the charge states of the two collision partners is partly preserved in the K-shell ionization collision. Despite this charge-state difference, the Auger-electron production cross sections are found to be equal for projectile and target in $O^{4+}+O_2$ collisions (Table I).

For O^{5+} impact the production of projectile Auger electrons needs the simultaneous vacancy creation in the inner shell and the transfer of an electron to an outer shell of the projectile. (Auger transitions require at least two electrons in outer shells.) This transfer can take place by K- to L-shell electron excitation in the projectile or by capture of an electron from the target. The relatively strong Auger-electron intensity for O^{5+} indicates a rather large probability for this process. In the case of O^{6+} impact two electrons must be transferred to the projectile outer shells in addition to the inner-shell vacancy production. It is seen that this process is still present, as the intensity of the projectile Auger peak for O^{6+} is larger than expected from a possible O^{5+} contamination of the O^{6+} beam. The intensity ratio of the projectile Auger peaks for O^{6+} and O^{5+} is 0.27 (see Table I), whereas the same ratio for the electron-loss peaks is 0.12 which gives an upper limit for possible beam contamination.

In summary we have shown by using electron spectroscopy, primarily at forward observation angles, that a variety of identifiable mechanisms contribute to the ionization process in energetic heavy-ion–atom collisions. Strong features were observed in the electron spectra and attempts were made to explain the spectral structures qualitatively in terms of simple ionization models.

---

*Work supported in part by the U. S. Atomic Energy Commission, the National Science Foundation, and the Army Research Office (Durham).

[1] G. N. Ogurtsov, Rev. Mod. Phys. 44, 1 (1972).

[2] M. E. Rudd and J. H. Macek, Case Stud. At. Phys. 3, 47 (1972).

[3] D. Burch, W. B. Ingalls, J. S. Risley, and R. Heffner, Phys. Rev. Lett. 29, 1719 (1972).

[4] D. Burch, H. Wieman, and W. B. Ingalls, Phys. Rev. Lett. 30, 823 (1973).

[5] D. Burch, N. Stolterfoht, D. Schneider, H. Wieman, and J. S. Risley, Phys. Rev. Lett. 32, 1151 (1974).

[6] D. L. Matthews, B. M. Johnson, J. J. Mackey, and C. F. Moore, Phys. Rev. Lett. 31, 1331 (1973); B. M. Johnson, D. L. Matthews, L. E. Smith, and C. F. Moore, J. Phys. B: Proc. Phys. Soc., London 6, L444 (1973).

[7] N. Stolterfoht, Z. Phys. 248, 81 (1971); N. Stolterfoht, D. Schneider, and P. Ziem, Phys. Rev. A (to be published).

[8] For example, charge-exchange cross sections for 30-MeV $O^{n+}+N_2$ collisions do not exceed the value of 5×10^{-17} cm^2 as measured by J. R. Macdonald and F. W. Martin, Phys. Rev. A 4, 1965 (1971).

[9] M. E. Rudd, C. A. Sauter, and C. L. Bailey, Phys. Rev. 151, 20 (1966).

[10] W. E. Wilson and L. H. Toburen, Phys. Rev. A 7, 1535 (1973).

Collision-Induced Optical Double Resonance*

Richard G. Brewer, R. L. Shoemaker,† and S. Stenholm‡
IBM Research Laboratory, San Jose, California 95193

(Received 9 May 1974)

The double-resonance concept is extended to the situation of two coherently driven optical transitions that do not share a common level but are coupled by molecular collisions that tip the angular momentum vector while preserving the molecular velocity and the rotational energy. This collision-induced double resonance is observed as sharp resonances, free of Doppler broadening, and can be explained in the same order of perturbation theory as the ordinary double-resonance experiment. They appear as satellite lines accompanying the usual double resonance or Lamb-dip spectra.

In the double-resonance effect, which is well own at both radio and optical frequencies,[1-3] a olecule interacts simultaneously with two radiaion fields, causing a transition from an initial to final state through an intermediate level [Fig. (a)]. This Letter reports observations and theoy for a double-resonance phenomenon that inolves a single molecular velocity group undergong two optical transitions that do not share a ommon level [Fig. 1(b)]. The two transitions, xcited by monochromatic laser radiation of frequencies Ω_1 and Ω_2, are coupled by molecular colisions that change the magnetic quantum state ut tend to preserve molecular velocity. Recent uantitative measurements[4] have revealed this ersistence in velocity for a molecular gas such s CH_3F where the average velocity jump for a inary collision is only 200 cm/sec. It has not een realized until now, however, that even if he velocity remains essentially unchanged by a ollision, the molecular angular momentum vecor for a symmetric top may be readily tipped, ausing a transition from an initial M state to a eighboring one. This circumstance causes an nusual double-resonance effect, characterized y a sharp resonant tuning behavior, free of Doppler broadening, and with an intensity comparable to the traditional double-resonance signal. Indeed, the new and the older double-resonance effects appear, as we shall show, in the same order of perturbation theory. The effect thus provides a new and simple way of studying molecular collisions that reorient the angular momentum vector.

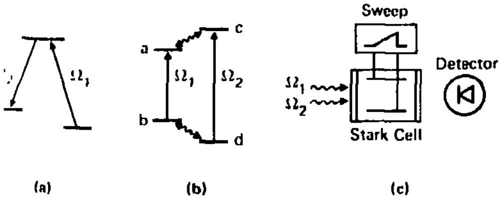

FIG. 1. (a) Traditional double-resonance level conuration. (b) Collision-induced double-resonance vel configuration; wavy lines indicate collision-inced transition. (c) Experimental arrangement for onitoring optical double-resonance signals.

Collision-induced double resonance clearly is not restricted to angular momentum tipping alone but can involve other degrees of freedom as well. Velocity preserving collisions involving molecular inversion[5] or angular momentum transfer[6] have been reported also in other double-resonance experiments.[7]

Collision-induced double resonance can be understood easily in terms of the level structure of Fig. 1(b) and the optical geometry of Fig. 1(c). Consider first the coherent optical field $E_1\exp[i\times(\Omega_1 t - k_1 z)]$ (z is the direction of the optical beam) which is in resonance with the transition a-b for a narrow velocity group v_z, where saturation takes place. The second transition c-d involving the resonant field $E_2\exp[i(\Omega_2 t - k_2 z)]$ will communicate effectively with the first transition only (1) if it is tuned to the same velocity group and (2) if velocity-preserving collisions cause transitions of the type $c\rightarrow a$ and $b\rightarrow d$, which in the present case represent $\Delta M\neq 0$ transitions. In this way, population changes induced by the first field can be monitored by the second. The two laser fields select resonant velocity groups according to $\Omega_1=\omega_{ab}-kv$ and $\Omega_2=\omega_{cd}-kv'$, and the two transitions communicate when the velocities coincide giving the double-resonance condition

$$\Omega_2-\Omega_1=\omega_{cd}-\omega_{ab}, \qquad (1)$$

where ω_{ij} is the transition frequency.

This tuning behavior, as well as other features, is contained in a more rigorous calculation,[8] derived from the coupled Maxwell-Scrödinger equations. The change in intensity of both optical fields arising from collision-induced double resonance is thus of the form (after time and Doppler averaging)

$$\frac{c}{8\pi}(\Delta E^2)=16\sqrt{\pi}(\hbar\Omega)\frac{NL\alpha_1^2\alpha_2^2(\Delta\rho_{dc}^{\,0}+\Delta\rho_{ba}^{\,0}(\gamma'/\gamma)\exp[-\Delta_1^2/(ku)^2]}{[(\Delta_2-\Delta_1)^2+4\gamma^2]ku}, \tag{2}$$

where we do not distinguish between Ω_1 and Ω_2 in the prefactor $\hbar\Omega$. Equation (1) is now evident in the resonance denominator where $\Delta_2=\Omega_2-\omega_{cd}$ and $\Delta_1=\Omega_1-\omega_{ab}$ and the linewidth of 2γ is just twice the width predicted for the ordinary double resonance. Like the ordinary double resonance,[9] this new effect is proportional to the product of the two intensities $\alpha_1^2\alpha_2^2$ where $\alpha_1=\mu_{ab}E_1/2\hbar$ and $\alpha_2=\mu_{cd}E_2/2\hbar$. Here, ku is the Doppler width, L is the optical path length, and $\Delta\rho_{ij}$ is the zeroth-order difference in occupation probability of levels i and j. It will be noticed that Eq. (2) is virtually the same as that for the usual double-resonance effect except that it is reduced by the factor (γ'/γ), where γ' is the linewidth contribution for the specific collision channel which couples the two transitions and γ represents the total linewidth arising from all sources. Since γ is composed of a pressure-independent contribution (molecular time of flight across the laser beam) and a pressure-dependent part, the new double-resonance signal will vary as the molecular density N at elevated pressure and as N^2 at low pressure.

Other mechanisms, based on purely optical interactions, could also give double-resonance behavior for Fig. 1(b). However, calculations show these effects to be too weak and with a line shape contradicting the experiments.[8]

Collision-induced double resonance has been observed in our laboratory in two different types of experiments. Consider again the experimental arrangement of Fig. 1(c). The two radiation fields are derived from two fixed frequency, continuous-wave CO_2 lasers and propagate together through a $^{13}CH_3F$ gas sample that can be tuned by sweeping a dc Stark field.[10] In Fig. 2, a double-resonance spectrum is shown for the $^{13}CH_3F$ ν_3-band line $(J, K)=(4,3)\rightarrow(5,3)$ at 1035.474 cm^{-1}. One laser is frequency locked to the other with $\Omega_1-\Omega_2=30.008$ MHz by a servo loop that compares their beat frequency with an rf reference. After being expanded to 1 cm diam, the two beams have power densities of ~1.2 and 0.4 W/cm^2; they are polarized perpendicularly to the Stark field, imposing $\Delta M=\pm1$ selection rules.

All of the lines of Fig. 2 satisfy the relation $\Omega_1-\Omega_2=(m\Delta_l-n\Delta_u)\epsilon$, where ϵ is the Stark field, m and n are integers, and Δ_u and Δ_l are the first-order Stark tuning rates of the upper and lower vibration-rotation states.[11] Thus, in Fig. 2 we find that $(\Omega_1-\Omega_2)/\epsilon$ equals $4\Delta_l-2\Delta_u$ (line a), $3\Delta_l-\Delta_u$ (b), $2\Delta_l$ (c), $\Delta_l+\Delta_u$ (d), $2\Delta_u$ (e), and $3\Delta_u-\Delta_l$ (f) to an accuracy of one part in 1000 or better. The strong lines c and e are the ordinary double resonances [Fig. 1(a)] and correspond to $\Delta M=2$ intervals in the lower and upper vibrational states. The other lines are the collision-induced reso-

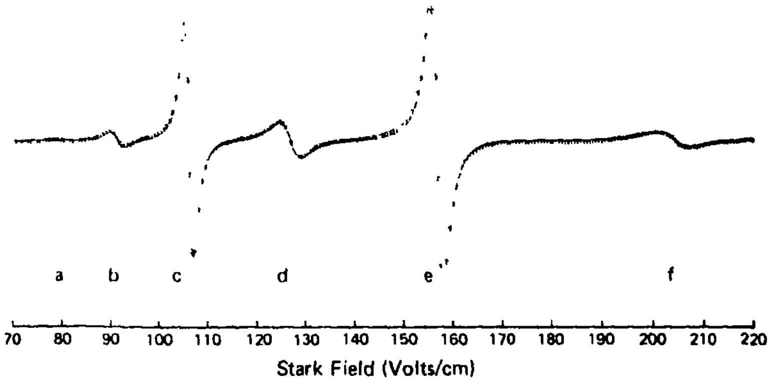

FIG. 2. Optical double-resonance spectrum for $^{13}CH_3F$ at ~3 mTorr pressure and $\Omega_1-\Omega_2=30.008$ MHz. Lines c and e correspond to the level configuration of Fig. 1(a) and the others to Fig. 1(b). The Stark sweep is computer driven in steps and the output signal is digitized (squares) and least-squares fitted to Lorentzian line shapes (solid line). The Stark gap spacing is 0.602 56 cm and the sample path length is 10 cm.

nances; they all have the level configuration of Fig. 1(b) where the two transitions do not share a common level; they display linewidths (~800 kHz) about twice as large as that of c and e, in agreement with Eq. (2), but considerably narrower than a 60 MHz Doppler width. If the plane of polarization of one or both beams is rotated by $\frac{1}{2}\pi$, to allow $\Delta M = 0$ transitions, the spectrum is drastically altered but the fundamental behavior remains unchanged. From Fig. 2, both types of double-resonance signals are seen to be of the same order of magnitude and, furthermore, depend on the product of the two field intensities, as predicted by Eq. (2). As expected, the collision-induced signals vary linearly with pressure at high pressure and appear to approach a quadratic dependence at very low pressure.

We have also observed analogous collision-induced resonances in Lamb-dip spectra for the same transition of $^{13}CH_3F$. For example, when the selection rule is $\Delta M = 0$, Lamp dips are monitored for the $M = 3 \rightarrow 3$ and $4 \rightarrow 4$ transitions, but an additional line occurs midway between them due to the collision-induced resonance. Clearly it cannot be an ordinary double resonance ("crossover" resonance) since there is no level common to both transitions. In this case, a double resonance occurs when the resonance conditions $\Omega_1 - k_1 v_z = \omega_{ab}$ and $\Omega_1 + k_1 v_z' = \omega_{cd}$ are simultaneously satisfied for the same velocity group, $v_z = v_z'$. Consequently, the double-resonance condition becomes $\Omega_1 = (\omega_{ab} + \omega_{cd})/2$. Here, the two oppositely propagating waves play the same role as the two unidirectional waves of different frequency in the above discussion, and the two transitions are similarly coupled by collisions.

The mechanism which tips the angular momentum vectors of two colliding CH_3F molecules is the long-range anisotropic interaction of their permanent electric dipoles. For this process, collision partners will retain their initial rotational energy but will exchange a small orientational or Stark energy for translational energy, which is not detected in the linewidth. The collisional transition $(J, K, M) \rightarrow (J, K, M \pm 1)$ occurs for this interaction because symmetric tops like CH_3F have a nonvanishing dipole matrix element.[12] To first order, the corresponding transition rate for one of the collision partners will be proportional to the matrix element squared $K^2(J \pm M \pm 1)(J \mp M)/[J^2(J+1)^2]$. Hence, molecules with high rotational quantum number J or small K are not tipped easily in agreement with the classical gyroscope description. It is for this reason that collision-induced double resonance has been seen here in the $^{13}CH_3F$ transition $(J, K) = (4, 3) \rightarrow (5, 3)$ but not in our earlier studies[10] of the $^{12}CH_3F$ $(J, K) = (12, 2) \rightarrow (12, 2)$ transition. From the intensity ratio of lines d to c or d to e, we obtain $(\gamma'/\gamma) = 0.15$, and a cross section of ~100 Å^2 for $\Delta M = \pm 1$ reorienting collisions of the $(J, K) = (4, 3)$ or $(5, 3)$ state. Hence, for this case about 15% of the collisions change the M state while J remains fixed and the remaining 85% presumably involve changes in J and M. Microwave experiments[13] in OCS, on the other hand, failed to show any evidence for $\Delta M = \pm 1$ collisions, because the symmetry of a linear molecule prevents electric dipole transitions between magnetic sublevels of a given J.

In future experiments, the collisional selection rules might be tested. Multiple quantum jumps in M could occur either in a single step or sequentially and might depend critically on the choice of a foreign buffer gas and its specific interaction with CH_3F.

We acknowledge with pleasure discussions with A. Luntz, J. Levy, and E. L. Hahn.

---

*Work sponsored in part by the U. S. Office of Naval Research under Contract No. N00014-72-C-0153.

†Present address: Optical Sciences Center, University of Arizona, Tucson, Ariz. 85721.

‡On leave from the Research Institute for Theoretical Physics, University of Helsinki, 00170 Helsinki 17, Finland.

[1] V. W. Hughes and L. Grabner, Phys. Rev. 79, 314 (1950); P. Kusch and V. W. Hughes, in *Encyclopedia of Physics*, edited by S. Flügge (Springer, Berlin, 1959), Vol. 37, Sect. 30.

[2] J. Brossel, P. Sagalyn, and F. Bitter, Phys. Rev. 79, 225 (1950); J. Brossel and F. Bitter, Phys. Rev. 86, 308 (1952).

[3] K. Shimoda, in "Topics in Applied Physics," edited by H. Walther (Springer, Berlin, to be published), Vol. II.

[4] J. Schmidt, P. R. Berman, and R. G. Brewer, Phys. Rev. Lett. 31, 1103 (1973).

[5] S. M. Freund, J. W. C. Johns, A. R. McKellar, and T. Oka, J. Chem. Phys. 59, 3445 (1973).

[6] T. W. Meyer and C. K. Rhodes, Phys. Rev. Lett. 32, 637 (1974).

[7] T. Oka, in *Advances in Atomic and Molecular Physics*, edited by D. R. Bates (Academic, New York, 1973), Vol. 9, p. 127, reviews both optical and microwave studies.

[8] R. L. Shoemaker, S. Stenholm, and R. G. Brewer, to be published.

[9] M. S. Feld and A. Javan, Phys. Rev. 177, 540 (1969).

[10] R. G. Brewer, Phys. Rev. Lett. 25, 1639 (1970); see also R. G. Brewer, Science 178, 247 (1972).

[11] The first-order Stark shift is given by $\Delta W_1 = \mu\epsilon MK/[J(J+1)]$ and the rate $\Delta = \Delta W_1/\epsilon$. From lines c and e of Fig. 2, we obtain the dipole moment μ for the lower and upper vibration-rotation states, 1.8578(6) and 1.9038(6) D, respectively. Spectra taken for different $(\Omega_1 - \Omega_2)$ show that the Stark effect is highly linear and, hence, molecular or optical perturbations which might significantly mix the M levels of a particular vibration-rotation state are small.

[12] P. W. Anderson, Phys. Rev. 76, 647 (1949), see Part II.

[13] A. P. Cox, G. W. Flynn, and E. B. Wilson, Jr., J. Chem. Phys. 42, 3094 (1965); M. L. Unland and W. H. Flygare, J. Chem. Phys. 45, 2421 (1966).

Light Scattering from Orientation Fluctuations in a Cholesteric Liquid Crystal. Angular and Field Dependences of the Light-Beating Spectrum

Donald B. DuPré and Russell W. Duke
Department of Chemistry, University of Louisville, Louisville, Kentucky 40208
(Received 26 February 1974)

Examination of the Rayleigh line of a lyotropic cholesteric polypeptide liquid crystal by the techniques of quasielastic-light-scattering spectroscopy reveals the presence of two new purely dissipative, low-frequency light-scattering modes of comparable intensity. Angular and electric field dependences of the deconvoluted spectra are consistent with the identification of the mechanism as due to twist and viscous-splay normal modes recently predicted theoretically. Analysis of the twist mode on this basis yields a value of γ_1, the twist viscosity coefficient of the medium.

Recent theoretical considerations[1] of orientational fluctuations in an incompressible cholesteric liquid crystal demonstrate that there are two dominant, slowly relaxing hydrodynamic modes that should be observable by light scattering. One mode corresponds to a twisting and untwisting of the supramolecular spiral arrangement, whereas the other is a combination of viscous-splay motion about the molecular director. Both modes are overdamped and would lead therefore to a broadening, but no overall displacement, in the frequency of scattered laser radiation. Theory suggests several possible means of identifying and separating the modes, which in principle should be easier to accomplish than in the case of nematic liquid crystals which also have been shown, both theoretically[2] and experimentally,[3] to exhibit two interesting, purely dissipative light-scattering modes. To our knowledge there has been no reported experimental observation of these modes in a cholesteric liquid crystal. This may be due to prohibitive experimental complications in the more common thermotropic cholesterics. We present here the results of our study on a lyotropic cholesteric liquid crystal of polypeptide origin. The Rayleigh line was examined by the techniques of laser light-beating spectroscopy and found to be resolvable into two Lorentzian components of comparable intensities, one broad and one sharp. The line shapes and angular dependences of the spectral half-widths of the two components are in accordance with the identification of one as a cholesteric twist normal mode and the other as a viscous-splay normal mode. Analysis of the sharp mode which we associate with twist deformations leads to a value of κ_{22}/γ_1, the ratio of the twist elastic constant to the twist viscosity coefficient of the medium. An independent measurement[4] of κ_{22} allows the determination of γ_1 for this liquid crystal. Experimental results and discussion will follow a brief resume of the theoretical predictions of Fan, Kramer, and Stephen.[1]

The twist normal mode involves a twisting oscillation about the spiral axis of neighboring molecular planes with a restoring force given by the twist elastic constant κ_{22}, and a resistance in proportion to the dissipative coefficient γ_1. The mode is overdamped and would result, therefore, in a broadening in the frequency of scattered laser radiation, with a contribution to the half-width of the Rayleigh line theoretically given by

$$\Gamma_t = (\kappa_{22}/\gamma_1)q^2, \tag{1}$$

where q is the magnitude of the scattering vector. The predicted line shape is Lorentzian and is most intense at momentum transfers corresponding to those required for Bragg scattering, i.e., $\vec{q} = \pm 2\vec{q}_0$, where π/q_0 is the pitch of the cholesteric helix. In the presence of an applied electric or magnetic field, Eq. (1) is modified, at least for small q, by a multiplicative function which depresses the half-width for all scattering angles and predicts a band gap in the dispersion curve for the damping constant at $\vec{q} = \vec{q}_0$.

The hydrodynamic equations also yield a set of independent relations which are identified with fluctuations about the molecular director in viscous splay.[2] These modes are also overdamped and one is dominant in the light scattering with a damping constant given by

$$\Gamma_S = \beta(\kappa_{33}q_0^{\,2} + \kappa_{11}q^2), \tag{2}$$

where κ_{11} and κ_{33} are the splay and bend elastic moduli, respectively, and $\beta = (\alpha_2 + \alpha_4 + \alpha_5)/[\gamma_1(\alpha_4 + \alpha_5) - \gamma_2\alpha_2]$ is a collection of viscosity coefficients (the Leslie coefficients). The predicted line shape of this normal mode is also Lorentzian, but in this case is sharpest at half the Bragg condition: $\vec{q} = \pm\vec{q}_0$. The effect of a weak magnetic field on this spectral half-width was also considered. A band gap in the mode spectrum also occurs, but in the approximation the damping constant, Eq. (2), is unchanged.

The theory was restricted to orientational fluctuations that propagate solely along the cholesteric spiral axis, z. In the general case, which was not developed, where the direction of propagation is at an angle to this axis the hydrodynamics of the director field fluctuations becomes more complicated and the above relations for the spectral half-widths would be presumably modified.

The influence of the two modes on the light-scattering spectrum could conceivably be separated in one of two ways: (a) One mode is shown to scatter light most strongly for momentum transfers exactly equal to the Bragg condition, whereas the other does so at intermediate angles. (b) The angular dependence of the half-widths of the two contributions though both quadratic in q are very different. Eq. (1) for the twist-mode half-width goes to zero at zero scattering angle, whereas Eq. (2) has a finite intercept.

There are complications in either procedure. In case (a) one must examine the light-scattering spectrum at exceedingly small angles if the periodicity of the cholesteric structure is large (small q_0). For more manageable scattering angles (q_0 large), the periodicity of the structure would have to be the order of the wavelength of the light. This is, of course, the condition for strong light scattering and the unique iridescent appearance of cholesteric liquid crystals in white light. Problems with multiple scattering may prevent spectral analysis in this case. On the other hand, if both modes contribute significantly to the light-scattering spectrum, a detailed angular-dependent study of the half-widths [case (b)] may be hampered by the unavailability of a number of viscoelastic constants that appear in equations for the spectral half-widths and intensities. In our study only procedure (b) was practical.

Liquid crystal solutions of poly-γ-benzyl-l-glutamate of molecular weight 310 000 were prepared (0.2 g/ml) in Millipore-filtered chloroform which had been distilled from NaOH solution to remove traces of water that could result in electrolytic hydrolysis of the polypeptide. The polymer is known to form a lyotropic liquid crystal of the cholesteric structure in this solvent at this concentration.[5] After maturation, samples were observed to be of high optical clarity with a zero-field pitch corresponding to $q_0 = 7.48\times10^3$ cm^{-1}. We could not, however, prepare uniformly oriented homogeneous or homeotropic samples of this liquid crystal, the state of the art of such surface orientation in polypeptide liquid crystals being much less advanced than in the more extensively researched thermotropics. In these experiments we do not, therefore, meet the condition of the theoretical paper that $\vec{q}$ lie strictly along the cholesteric z axis. Using the techniques of laser light beating, or quasielastic spectroscopy, the Rayleigh line of scattered laser radiation was examined as a function of scattering angle and applied electric field. Our apparatus is essentially that described elsewhere[6,7] with a 3-mW He-Ne laser as a light source and a signal-averaging capability provided by a programmable calculator interfaced to the spectrum analyzer. Spectra were recorded at scattering angles ranging from 20 to 90° in 5° increments with the sample under the influence of an electric field of 0 to 300 V/cm. Fields were applied perpendicular to the scattering plane and were well below the critical value for the electrotropic cholesteric-to-nematic phase transition as previously determined.[8] Light-scattering spectra much below 20° were found to be unsuitable for analysis as they contained both homodyne and heterodyne components. Resultant spectra could not be described by a simple Lorentzian line-shape function. Broad wings of measurable intensity extending in some cases out to 5000 Hz were evident. In all cases, however, spectra could be separated by a deconvolution process into two overlapping Lorentzian components, one broad and one sharp. The half-width of the broader component is quadratic in q and has a nonzero intercept when extrapolated to zero scattering angle (Fig. 1). The half-width of this mode is depressed with increasing field strength but the intercept is common to all fields. The angular dependence of the narrow component is also quadratic in q, but has a zero intercept. Application of an electric field also depresses the spectral half-width. Although the existence of randomly oriented microdomains within the scattering volume precludes a definitive identification of the origin of the two light-scattering modes observed, the angular and field dependences of our results are suggestive that the scattering mechanism giving rise to the braod mode is the cholesteric viscous-splay mode and that of the sharp mode is the twist deformation. Given this, the analysis of the angular depen-

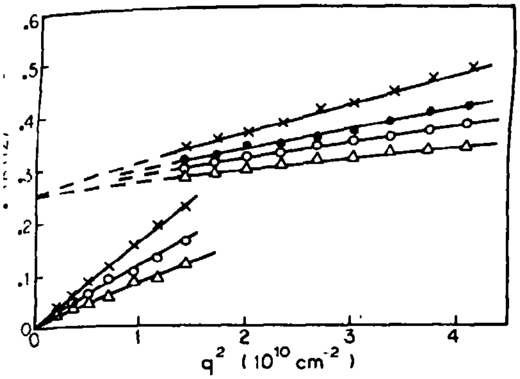

FIG. 1. Spectral half-widths Γ of the deconvoluted ectra versus the scattering vector q^2 for a cholesterpolypeptide liquid crystal. Crosses, scattering with e electric field $E = 0$; solid circles, $E = 100$ V/cm; en circles, $E = 200$ V/cm; triangles, $E = 300$ V/cm. e broader component with a nonzero intercept when trapolated to zero scattering angle may be identified th the theoretically predicted viscous-splay normal ode. The narrow component is in accordance with e angle dependence of the line shape for the choles ric twist normal mode.

ence of the sharp component yields a value of $_2/\gamma_1 = 7.7\times10^{-8}$ cgs. Taking $\kappa_{22} = 12.1\times10^{-7}$ emu s from a previous experiment[4] we find that γ_1 16.2 P. This value is 2 orders of magnitude reater than γ_1 reported for a smectic liquid stal[9] and 3 orders of magnitude above that for natic systems.[10] The trend is understandable erms of the greater response times to exter- disturbances noted for polypeptide liquid stals (~10–20 min) as compared to thermopics (~milliseconds).

lthough the value of γ_1 derived from the data the low-frequency (sharp) mode is in line with t reported on other systems, viscoelastic connts obtained from the broad mode associated h viscous-splay deformations are anomalous. nsidering Eq. (2), we see that

$$\frac{q_0^2\,d\Gamma_s/d(q^2)}{\Gamma_s(q=0)} = \frac{\kappa_{11}}{\kappa_{33}}. \tag{3}$$

m the slope and intercept of the zero-field a of Fig. 1, we obtain a ratio of $\kappa_{11}/\kappa_{33} \sim 10^{-5}$. In most liquid crystals all the κ_{ii} are of the same order of magnitude. This anomaly does not necessarily constitute reason to reject the association of the broad mode with splay deformations. κ_{33}, for example, has been shown to diverge near the nematic-smectic-*A* phase transition in a thermotropic liquid crystal.[11] Although this is certainly not the case here, recent work in our laboratory[12] and that elsewhere[13] have shown a wide variability of measured values of κ_{22} for the polypeptide liquid crystal of this study. κ_{22}'s that are orders of magnitude greater than those of thermotropics have been observed and are extremely sensitive to variation in solvent and polymer molecular weight. Although direct data on κ_{11} and κ_{33} are not yet available, it may be these moduli are also anomalous in this liquid crystal.

A search for the predicted band gaps of Ref. 1 proved impractical in our system. The large pitch of this liquid crystal, which is fundamentally responsible for its optical clarity, would require a scattering angle of less than 0.5°.

We acknowledge support of this research from the donors of the Petroleum Research Fund, administered by the American Chemical Society, and from Research Corporation.

---

[1] C. Fan, L. Kramer, and M. J. Stephen, Phys. Rev. A 2, 2482 (1970).

[2] Groupe d'Etude des Cristaux Liquides (Orsay), J. Chem. Phys. 51, 816 (1969).

[3] Orsay Liquid Crystal Group, Phys. Rev. Lett. 22, 1361 (1969).

[4] R. W. Duke and D. B. DuPré, J. Chem. Phys. 60, 2759 (1974).

[5] C. Robinson, Tetrahedron 13, 219 (1961).

[6] D. Berge and M. Dubois, C. R. Acad. Sci., Ser. B 269, 842 (1969).

[7] S. B. Dubin, J. H. Lunacek, and G. B. Benedek, Proc. Nat. Acad. Sci. 57, 1164 (1967).

[8] R. W. Duke and D. B. DuPré, to be published.

[9] Y. Galerne, J. L. Martinand, G. Durand, and M. Veyssie, Phys. Rev. Lett. 29, 562 (1972).

[10] J. Prost and H. Gasparoux, Phys. Lett. 36A, 245 (1971).

[11] L. Cheung, R. B. Meyer, and H. Gruler, Phys. Rev. Lett. 31, 349 (1973).

[12] D. B. DuPré and R. W. Duke, to be published.

[13] C. Guha-Sridhar, W. A. Hines, and E. T. Samulski, to be published.

Experimental, Very High-Temperature, Liquid-Uranium Equation of State*

G. R. Gathers, J. W. Shaner, and D. A. Young
Lawrence Livermore Laboratory, University of California, Livermore, California 94550
(Received 20 May 1974)

U wire samples under very high confining gas pressures are heated Ohmically into the liquid phase. The sample diameter is measured after achievement of thermodynamic equilibrium. Enthalpy-volume isobars and resistivity-enthalpy curves are obtained. The data are fitted with a soft-sphere theory of liquids, and the critical point of U is estimated.

One of the main problems in high-temperature physics is the containment of a hot solid or liquid sample so that thermodynamic equilibrium is obtained and contamination by container material is avoided.[1] For this reason, good experimental data above 3000 K are rare. In the present Letter we describe equation-of-state and resistivity data obtained by a new method, for uranium in thermodynamic equilibrium up to 9000 K.

The apparatus consists of a pressure cell capable of holding He gas to 0.4 GPa (4 kbar) and a critically damped 45-kJ capacitor bank for resistively heating the 1-mm-diam by 25-mm-long sample. A large ballast resistor is in series with the sample so that the current pulse is independent of the sample resistivity. The energy deposited is controlled by timing the firing of a spark gap which short-circuits the sample, so that only a fraction of the capacitor charge passes through the sample. The current pulse is long enough (15-30 μsec) so that the skin effect is negligible and the sample is very near equilibrium at all times during the pulse. Further details of this part of the apparatus have been described elsewhere.[2] Refinements to the apparatus described in Ref. 2 include (1) a new sample and voltage-probe assembly which reduces the magnitude of the inductive contribution to the voltage measurement, (2) the addition of sapphire windows which allow us to replace the flash x-ray shadowgraph picture of the sample with an optical shadowgraph, and (3) the addition of a streaking camera to record the complete diameter-versus-time history of the expanding sample.

The equation-of-state data are the pressure, volume, and enthalpy of the hot liquid uranium. The pressure of the He gas surrounding the sample is constant during the expansion since the cell volume is much greater than the sample volume. This pressure is controlled and measured to within 1%. The enthalpy is controlled by varying the length of the current pulse and is computed as the time integral of the product of the current through the sample times the voltage drop across a carefully measured length of the sample. The inductive voltage is estimated and subtracted from the total voltage, although the overall correction to the enthalpy from this procedure is negligible. The sample volume is measured by streaking a slit image of the rod diameter. The sample is illuminated from behind with the 514.5-nm line from an argon-ion laser, while a narrow-band filter in front of the camera discriminates against the blackbody radiation. An actual streak record is shown in Fig. 1. Since the expansion is constrained to be only in the radial direction, the volume is proportional to the square of the diameter. Uniformity of the sample expansion along the axis has been demonstrated

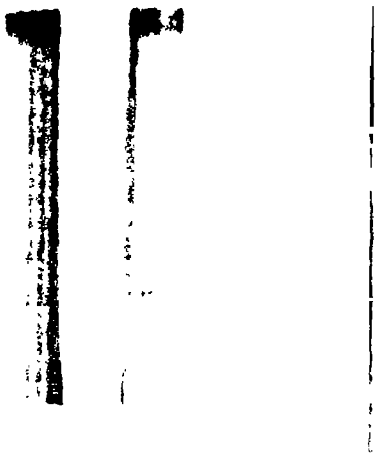

FIG. 1. A streak record of the expansion of the sample diameter. The initial diameter (bottom of record) is 1.0 mm while the final diameter (middle of record) is 1.16 mm. The pressure is 0.1 GPa (1 kbar); the final enthalpy is 0.59 MJ/kg; the streak duration is 200 μsec.

with both flash x-ray shadowgraphs[2] and optical snapshots using a pulsed ruby laser. Based on the accuracy of the diameter measurement in the streak record and the diameter uniformity in the snapshot, the estimated error in the volume measurement is ±2%.

The long duration of constant expanded volume in Fig. 1 indicates that thermodynamic equilibrium has been achieved within a few microseconds of the end of the current pulse, and that the hydrodynamic instabilities characteristic of a long liquid column do not set in for at least several hundred microseconds. The final volume measurement is made during this time interval. The highest enthalpy shots for both 0.1- and 0.2-GPa isobars showed short stagnations (10–20 μsec) followed by rapid expansion. This could be due to the entry of all or part of the sample into the liquid-vapor two-phase region. Work is underway to investigate the cause of this late-time expansion.

The enthalpy-versus-volume isobars along with static ($P = 1$ bar) experimental data[3] and theoretical curves are shown in Fig. 2. The hard-sphere Van der Waals theory[4] (which has no adjustable parameters) shows poor agreement with the experimental data. This is probably due to the unrealistic coefficient of thermal expansion predicted by the hard-sphere model. We use instead a "soft-sphere" theory based on Monte Carlo calculations with smooth inverse-power interparticle potentials.[5] This theory is used as an empirical fit to the data, since we do not have a reliable theory of liquid uranium at expanded volumes. The soft-sphere pressure and energy are given by

$$\frac{pV}{NkT} = 1 + \tfrac{1}{3} n C_n \rho^{n/3}\left(\frac{\epsilon}{kT}\right) + \tfrac{1}{18} n(n+4)\rho^{n/9}\left(\frac{\epsilon}{kT}\right)^{1/3} - m\rho^{m}\left(\frac{\epsilon}{kT}\right), \qquad (1)$$

$$\frac{E}{NkT} = \tfrac{3}{2} + C_n \rho^{n/3}\left(\frac{\epsilon}{kT}\right) + \tfrac{1}{6}(n+4)\rho^{n/9}\left(\frac{\epsilon}{kT}\right)^{1/3} - \rho^{m}\left(\frac{\epsilon}{kT}\right) + \frac{E_0}{NkT}, \qquad (2)$$

$$\rho = N\sigma^3/\sqrt{2}\,V. \qquad (3)$$

Here N is the number of atoms, k is Boltzmann's constant, C_n is the lattice constant[6] corresponding to n, and E_0 is the cohesive energy. There are four adjustable parameters: n, m, ϵ, and σ. The parameters ϵ and σ are determined from the properties of uranium at the melting point. The parameters n and m are then adjusted to fit the experimental data. There are a number of (n, m) sets that fit the data, so an additional condition is required to narrow the choices further. We choose this condition to be reasonable agreement with the critical temperature and pressure as predicted by the hard-sphere Van der Waals theory. We have some confidence in these numbers, based on correlation of theory and experiment for the alkali metals and mercury.[4]

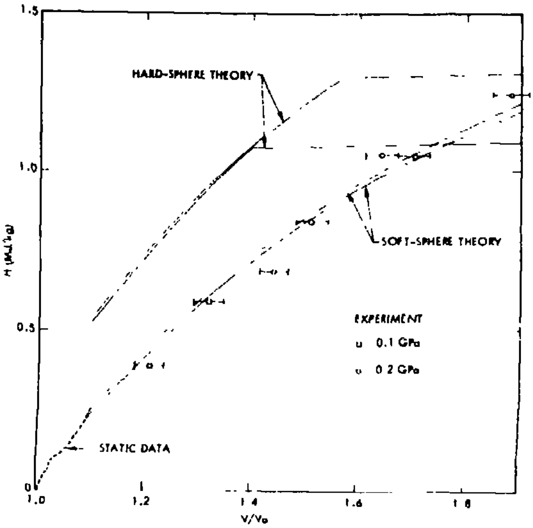

FIG. 2. Experimental enthalpy–relative-volume isobars compared with static data and theory. The breaks in the hard-sphere curves represent entry into the liquid-vapor region. The soft-sphere theory has been fitted to the experimental data. In both pairs of theoretical curves the upper and lower curves correspond to 0.2 and 0.1 GPa, respectively. The static data are available up to the melting point of uranium and the curve shows a change of curvature due to solid-solid phase transformations. In this plot the enthalpy at room temperature and normal volume (V_0) is taken to be zero. The corrections to the experimental enthalpy points due to the initial compression are negligible.

The best soft-sphere theory fit is obtained for $n = 6$ and $m = 0.75$. This fit predicts the temperatures for the highest experimental enthalpy points to be 6730 K (0.1 GPa) and 9260 K (0.2 GPa). The entry into the liquid-vapor region is predicted to take place at $V/V_0 = 1.95$ (0.1 GPa) and $V/V_0 = 2.30$ (0.2 GPa). The predicted critical constants are $T_c = 12\,434$ K, $V_c = 0.2662$ m^3/Mg, and $p_c = 0.4950$ GPa. The critical temperature is in close agreement with Grosse's estimate[7] of 12 500 K.

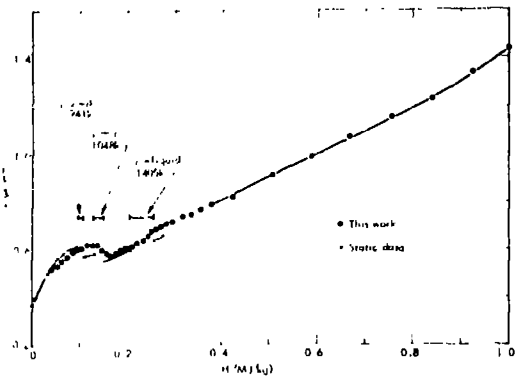

FIG. 3. Resistivity of uranium compared with static data. The solid-solid and solid-liquid transitions are indicated by the horizontal bars, along with the transition temperatures.

Since the sample diameter, the current, and the voltage are all measured as a function of time, the resistivity of the sample can be measured during the expansion. These data are presented in Fig. 3, with a comparison with the moderate-temperature static data of Busch, Guntherodt, and Künzi.[8] The quantitative agreement between the dynamic and static data is another indication that the sample is close to thermodynamic equilibrium at all times during the heating pulse. We have not attempted to make a theroetical calculation of the resistivity. The resistivity-versus-volume curve is, however, similar to that reported for expanded copper by Ben-Yosef and Rubin.[9]

By overcoming the containment problem and achieving thermodynamic equilibrium we have been able to extend equation-of-state and resistivity measurements to much higher temperatures than were before possible. Also, by using an inert gas as the confining medium, we can subject the sample to accurately measured pressures comparable to the sample critical pressure, thus covering a large portion of the liquid range. Experiments are now being continued with carbon, and will later be extended to other materials. The experiment will be improved by extension of the pressure range and by direct measurement of the temperature.

We thank W. G. Hoover for the use of his unpublished soft-sphere theory.

---

*Work performed under the auspices of the U. S. Atomic Energy Commission.

[1] L. S. Nelson, Advan. High Temp. Chem. 4, 171 (1971).

[2] K. W. Henry, D. R. Stephens, D. J. Steinberg, and E. B. Royce, Rev. Sci. Instrum. 43, 1777 (1972).

[3] *Thermophysical Properties of High Temperature Solid Materials*, edited by Y. S. Touloukian (Macmillan, New York, 1967), Vol. 1, p. 1058.

[4] D. A. Young and B. J. Alder, Phys. Rev. A 3, 364 (1971). The critical constants for uranium in this paper are based on an inaccurate value of the normal volume V_0. In the present calculation we use $V_0 = 0.0524$ m^3/Mg.

[5] W. G. Hoover, M. Ross, K. W. Johnson, D. Henderson, J. A. Barker, and B. C. Brown, J. Chem. Phys. 52, 4931 (1970); and W. G. Hoover, private communication.

[6] J. O. Hirschfelder, C. F. Curtiss, and R. B. Bird, *Molecular Theory of Gases and Liquids* (Wiley, New York, 1964), p. 1040. The number C_n used in the present paper is one half the tabulated value C_s for the face-centered cubic lattice.

[7] A. V. Grosse, J. Inorg. Nucl. Chem. 22, 23 (1961).

[8] G. Busch, H. J. Güntherodt, and H. U. Künzi, Phys. Lett. 32A, 376 (1970).

[9] N. Ben-Yosef and A. G. Rubin, Phys. Rev. Lett. 23, 289 (1969).

Probability Distribution for Fourier Components of the Electric Field in Weak Plasma Turbulence*

T. M. O'Neil
Department of Physics, University of California, San Diego, La Jolla, California 92037
(Received 2 May 1974)

Probability distributions for Fourier components of the electric field, including joint distributions for different Fourier components and multiple-time distributions for the same component, are determined using two assumptions within the spirit of weak-turbulence theory. This statistical framework is then applied to the special case where the turbulence is dominated by the wave-particle interaction (i.e., the quasilinear case).

Weak-turbulence theory[1] determines the ensemble-average spectral density of the electric field [i.e., $\langle |E_k(t)|^2\rangle$], for turbulence arising from certain weak plasma instabilities. To have a complete theory one needs in addition probability distributions for the Fourier components of the electric field, including joint distributions for different components and multiple-time distributions for the same component. In this Letter, I show that all these distributions are approximately Gaussian. The basic reason for this is that the Fourier integral defining each component typically extends over a range much larger than the spatial autocorrelation length for the turbulence. Consequently, each component is the sum of many statistically independent terms, and the central-limit theorem of probability theory[2] implies that such a quantity has an approximately Gaussian distribution. This result would be known to electrical engineers as the statement that the output of a narrow-band filter is approximately Gaussian, for any stationary random input signal of sufficiently short autocorrelation time. Here I merely transcribe the previous demonstrations[2,3] of this fact into a language appropriate to weak-turbulence theory.

As an application of this statistical framework, I consider the special case where the turbulence is dominated by the wave-particle interaction. For this case quantities appearing in the distributions as parameters, such as the standard deviation, are determined by quasilinear theory[4] and Dupree's[5] recent theory of phase-space granulation,[6] or "clumps."

First we establish the Gaussian nature of the distributions. Consider a one-dimensional plasma of length L with periodic boundary conditions at each end.[7] The Fourier components of the electric field are defined as

$$E_k(t) = (1/L)\int_0^L dx\, E(x,t)\exp(-ikx),$$

where $k = 2\pi n/L$. It is convenient to introduce the real and imaginary part of each component [i.e., $E_k(t) = E_k^{(R)}(t) + iE_k^{(I)}(t)$]. We will need the following two assumptions: (1) The statistical properties of $E(x,t)$ are spatially homogeneous [i.e., $E(x,t)$ is stationary in x]; for example, $\langle E(x,t)\rangle$ and $\langle E(x,t)E(x+\xi,t)\rangle$ are independent of x. (2) $E(x,t)$ and $E(x+\xi,t)$ are statistically independent for $\xi \gtrsim l$, where $l \ll L$. The first assumption is simply a statement that there is nothing in the problem to single out a particular value of x. The end points do not do this, because we have assumed periodic boundary conditions. The second assumption certainly is true if L is much larger than the product of the largest velocity in the problem and the duration of the experiment. This is similar to the weak-turbulence (or quasilinear) assumption that the spectrum is dense, that is, that $2\pi/L \ll \gamma/v$ or $L \gg v(2\pi/\gamma)$, where v is the velocity of a resonant particle and γ is the growth rate.

As a first step in the derivation, we summarize the implications of assumption (1). The x independence of $\langle E(x,t)\rangle$ implies that $\langle E_k^{(R)}(t)\rangle = \langle E_k^{(I)}(t)\rangle = 0$ for $k \neq 0$. Likewise the x independence of $\langle E(x,t) \times E(x+\xi,t)\rangle$ implies that

$$\langle E_{k_1}^{(R)}(t)E_{k_2}^{(R)}(t)\rangle = \langle E_{k_1}^{(I)}(t)E_{k_2}^{(R)}(t)\rangle = \langle E_{k_1}^{(I)}(t)E_{k_2}^{(I)}(t)\rangle = 0, \tag{1}$$

for $k_1 \neq k_2$. Since a change in the origin of the x axis by $\Delta x = \pi/2k$ changes $E_k^{(R)}(t)$ to $E_k^{(I)}(t)$ and $E_k^{(I)}(t)$ to $-E_k^{(R)}(t)$, spatial homogeneity also implies that

$$\begin{aligned} \langle E_k^{(R)}(t)E_k^{(R)}(t+\tau)\rangle &= \langle E_k^{(I)}(t)E_k^{(I)}(t+\tau)\rangle = \tfrac{1}{2}\mathrm{Re}\langle E_k(t)E_k^*(t+\tau)\rangle, \\ \langle E_k^{(R)}(t)E_k^{(I)}(t+\tau)\rangle &= -\langle E_k^{(I)}(t)E_k^{(R)}(t+\tau)\rangle = -\tfrac{1}{2}\mathrm{Im}\langle E_k(t)E_k^*(t+\tau)\rangle. \end{aligned} \tag{2}$$

Next we use assumption (2) to express $E_k(t)$ as the sum of many statistically independent terms. Choose a length s such that $L \gg s \gg l$ and rewrite $E_k(t)$ as

$$E_k(t) = \frac{1}{L} \sum_{j=1}^{N} \int_{(j-1)s}^{js} dx\, e^{-ikx} E(x,t), \tag{3}$$

where $N = L/s$. The terms in this sum are statistically independent, since $s \gg l$ and $E(x+\xi, t)$ and $E(x, t)$ are statistically independent for $\xi \geqslant l$.

The central-limit theorem of probability theory[2] states that if a vector $\vec{X}$ is the sum of many statistically independent vectors $\vec{x}_j$ (i.e., $\vec{X} = \sum_j \vec{x}_j$), then the components of $\vec{X}$ are distributed according to the Gaussian

$$P[X_1, X_2, \dots, X_M] = \exp(-\tfrac{1}{2}\vec{X}^\dagger \cdot \mu^{-1} \cdot \vec{X}) / [(2\pi)^M |\overleftrightarrow{\mu}|]^{1/2}, \tag{4}$$

where $\mu_{ij} = \langle X_i X_j \rangle$, $\overleftrightarrow{\mu}^{-1}$ is the inverse of $\overleftrightarrow{\mu}$, $|\overleftrightarrow{\mu}|$ is the determinant of $\overleftrightarrow{\mu}$, and $\vec{X}^\dagger$ is the transpose of $\vec{X}$. Also, Eq. (4) has been written in a form that assumes $\langle \vec{X} \rangle = 0$. This condition will be satisfied for all our applications since we will choose the components of $\vec{X}$ to be various Fourier components of the field, and assumption (1) implies that these components have zero mean (i.e., $\langle E_k \rangle = 0$).

As a first application, we let $\vec{X} = [E_k^{(R)}(t), E_k^{(I)}(t)]$. By setting $\tau = 0$ in Eq. (2), one can see that $\mu_{11} = \mu_{22} = \frac{1}{2}\langle |E_k(t)|^2 \rangle$ and $\mu_{12} = 0$. Consequently, the distribution for $X_1 = E_k^{(R)}(t)$ and $X_2 = E_k^{(I)}(t)$ takes the simple form

$$P[X_1, X_2] = [\pi \langle |E_k(t)|^2 \rangle]^{-1} \exp[-(X_1^2 + X_2^2)/\langle |E_k(t)|^2 \rangle]. \tag{5}$$

To determine the joint distribution for many different Fourier components, we let $\vec{X} = [E_{k_1}^{(R)}, E_{k_1}^{(I)}, E_{k_2}^{(R)}, E_{k_2}^{(I)}, \dots]$. From Eq. (1) one can see that the elements of $\overleftrightarrow{\mu}$ connecting different Fourier components all vanish (i.e., $\mu_{13} = \langle E_{k_1}^{(R)} E_{k_2}^{(R)} \rangle = 0$, etc.). Consequently, the joint distribution for many Fourier components reduces to a product of distributions for the individual components [i.e., Eq. (5)]. This implies that triple and higher-order correlations of different components all vanish. Note that spatial homogeneity alone does not force these correlations to vanish, provided the various wave numbers sum to zero. The correlations are simply higher order in the small parameter l/L [e.g., $\langle E_{k_1} \times E_{k_2} E_{k_3} \rangle / \langle |E_{k_1}|^2 \rangle^{3/2} \simeq O((l/L)^2)/O((l/L)^{3/2})$]. By retaining corrections to the central-limit theorem, we would have found nonzero higher-order correlations. It is interesting to note that although the phases are random to lowest order in l/L, the corrections arise in such an order that the present theory cannot be used to justify the random phase approximation (RPA). The RPA assumes that the sum $\sum_p \langle E_{k-q} \times E_q E_{p-k} E_{-p} \rangle$ can be replaced by $2\langle |E_{k-q}|^2 \rangle \langle |E_q|^2 \rangle$. The neglected terms are all of order $(l/L)^3$ [i.e., $\langle E_{k_1} E_{k_2} E_{k_3} E_{k_4} \rangle \sim O((l/L)^3)$ for $k_1 \neq k_2 \neq k_3 \neq k_4$], whereas the two terms retained are of order $(l/L)^2$. However, the sum over p introduces a factor L/l in the neglected terms, so the RPA cannot be justified by the present argument.

By setting $\vec{X} = [E_k^{(R)}(t), E_k^{(I)}(t), E_k^{(R)}(t+\tau), E_k^{(I)}(t+\tau)]$ we can determine the two-time distribution for a single Fourier component, $P[X_1, X_2, X_3, X_4]$. However, more interesting than the two-time distribution itself is the conditional two-time distribution $P[X_3, X_4 | X_1, X_2] = P[X_1, X_2, X_3, X_4]/P[X_1, X_2]$, which gives the probability that E_k will have the value $X_3 + iX_4$ at time $t+\tau$ given that it had the value $X_1 + iX_2$ at time t. Using Eqs. (2), (4), and (5), we can write this distribution as

$$P[X_3, X_4 | X_1, X_2] = (\pi\Theta)^{-1} \exp[-\Theta^{-1} |(X_3 + iX_4) - (X_1 + iX_2)\langle E_k^*(t) E_k(t+\tau) \rangle / \langle |E_k(t)|^2 \rangle|^2], \tag{6}$$

where

$$\Theta = \langle |E_k(t+\tau)|^2 \rangle - |\langle E_k^*(t) E_k(t+\tau) \rangle|^2 / \langle |E_k(t)|^2 \rangle.$$

Thus far we have developed a rather general statistical framework that must be satisfied by any turbulent field satisfying assumptions (1) and (2). We now apply this statistical framework to the special case where the turbulence is dominated by the wave-particle interaction (i.e., the quasilinear case). We choose this case because it is central to weak-turbulence theory and because it is particularly susceptible of confusion in the present context. One of the conclusions of quasilinear theory is that

$$E_k(t+\tau) = E_k(t) \exp[-i\omega_k \tau + \int_t^{t+\tau} \gamma_k(t')\,dt'], \tag{7}$$

where ω_k is the frequency and $\gamma_k(t)$ the instantaneous growth rate. From this expression one can see that Θ is identically zero, so that the conditional distribution reduces to a delta function, (X_3+iX_4) [i.e., $E_k(t+\tau)$] being predicted exactly by (X_1+iX_2) [i.e., $E_k(t)$]. If this were in fact true, the present statistical theory would be rather superfluous. However, recent computer simulations[8] designed to verify quasilinear theory show that $E_k(t+\tau)$ does not evolve according to Eq. (7), but rather follows a curve that varies stochastically about the τ dependence predicted by Eq. (7). The point is that $E_k(t+\tau)$ is not predictable from knowledge of $E_k(t)$ alone; $E_k(t+\tau)$ depends as well on $E_{k'}(t)$, for example. Quasilinear theory neglects this dependence, at least the phase dependence, by averaging over the complicated nonlinear structure of the particle distribution in the resonant region.

Dupree[5] has calculated corrections due to this structure in his recent theory of phase-space granulation or "clumps." The "clumps" are produced by the turbulence and then free-stream like ballistic perturbations. As they stream they emit by Cherenkov radiation new waves uncorrelated with the original ones. In this way, randomness is introduced during the evolution, and Θ takes a nonzero value.[9] A calculation[10] of this effect for the case of electron-wave turbulence yields the results

$$\begin{aligned}
&\Theta=\langle|E_k(t+\tau)|^2\rangle\left(1-\exp\left\{-\int_t^{t+\tau}[12\gamma_k^2(t')/\omega_p]\,dt'\right\}\right),\\
&\langle|E_k(t+\tau)|^2\rangle=\langle|E_k(t)|^2\rangle\exp\left\{\int_t^{t+\tau}[2\gamma_k(t')+12\gamma_k^2(t')/\omega_p]\,dt'\right\},\\
&\langle E_k^*(t)E_k(t+\tau)\rangle/\langle|E_k(t)|^2\rangle=\exp\left[-i\omega_k\tau+\int_t^{t+\tau}\gamma_k(t')\,dt'\right],
\end{aligned}\tag{8}$$

where we have assumed that τ is larger than the autocorrelation time for the field as seen by a resonant electron. One can think of this calculation as carrying quasilinear theory to second order in the small parameter $(\gamma/\omega_p)^2$, the relative importance of the Cherenkov-radiated waves being determined by the integral $\int_t^{t+\tau}[12\gamma_k^2(t')/\omega_p]dt'$. When this integral is small, Θ is much smaller than $\langle|E_k(t+\tau)|^2\rangle$, and the conditional distribution [i.e., Eq. (6)] is strongly peaked about the quasilinear value $X_3+iX_4=(X_1+iX_2)\exp[-i\omega_k\tau+\int_t^{t+\tau}\gamma_k(t')dt']$. When the integral is large, $\Theta=\langle|E_k(t+\tau)|^2\rangle$ and $\langle|E_k(t+\tau)|^2\rangle\to\langle|E_k(t)|^2\rangle\exp[2\int_t^{t+\tau}\gamma_k(t')dt']$, so the conditional distribution [i.e., Eq. (6)] reduces to the unconditional distribution [i.e., Eq. (5)] evaluated at time $t+\tau$.

The author has enjoyed useful discussions with S. Bodner, C. Driscoll, J. Malmberg, S. Rice, W. Thompson, and C. Van Atta.

---

*Work supported by the National Science Foundation under Grant No. GP-40765X and by the Alfred P. Sloan Foundation.

[1] R. Z. Sagdeev and A. A. Galeev, *Nonlinear Plasma Theory* (Benjamin, New York, 1969).

[2] *Selected Papers on Noise and Stochastic Processes*, edited by N. Wax (Dover, New York, 1954), pp. 182, 255.

[3] M. Rosenblatt, Quart. Appl. Math. 18, 387 (1961).

[4] W. E. Drummond and D. Pines, Nucl. Fusion, Suppl. Part 3, 1049 (1962); A. A. Vedenov, E. P. Velikhov, and R. Z. Sagdeev, Nucl. Fusion, Suppl. Part 2, 465 (1962).

[5] T. H. Dupree, Phys. Fluids 15, 334 (1972).

[6] B. B. Kadomtsev and O. P. Pogutse, Phys. Fluids 14, 2470 (1971), also have discussed phase-space granulation. However, their theory applies to a beam which is initially cold, whereas we are interested in the warm-beam case (i.e., quasilinear case) discussed by Dupree.

[7] The results can be extended easily to three dimensions.

[8] D. Biskamp and H. Welters, Nucl. Fusion 12, 89 (1972); J. Byers, Bull. Amer. Phys. Soc. 15, 1420 (1970).

[9] Note that also mode-coupling can produce a nonzero value of Θ, and this may even dominate in the later stages of the evolution. The spirit of the present calculation is to focus on the randomness associated with the wave-particle interaction alone.

[10] Details of the calculation will be presented in a later paper.

Spatially Resolved Measurement of Impurities and the Effective Charge $\bar{Z}$ in a Tokamak Plasma

D. E. Evans
United Kingdom Atomic Energy Authority Research Group, Culham Laboratory, Abingdon, Berkshire, United Kingdom

and

M. L. Yeoman
Royal Holloway College (University of London), Egham, Surrey, United Kingdom

(Received 1 April 1974)

Laser-radiation scattering is proposed as a method for measuring impurities in tokamak or toroidal pinch plasmas. A direct measurement of the effective charge for momentum transfer, $\bar{Z}$, appears feasible by this technique.

The importance of plasma impurities to the outcome and interpretation of experiments on magnetically confined plasmas of the tokamak or toroidal pinch types is widely recognized. A large fraction of the energy input can be lost through radiation by impurity ions, while the increase in the plasma effective charge $\bar{Z}$ incurred by the addition of high-Z ions results in enhanced resistivity, and the impurity concentration affects the particle containment time.[1,2] Moreover, the possibility that heavy impurities will tend to diffuse inwards and collect on the axis of the discharge[3] has a critical effect upon the steady-state reactor concept, and emphasized the exceptional significance of a detailed study of impurity behavior. In this Letter we draw attention to the feasibility of performing a sensitive, spatially resolved measurement of impurity concentration which relies upon the influence of a small fraction of heavy, $Z > 1$ material on the frequency spectrum of laser radiation scattered by a plasma.[4]

Tokamak plasmas acquire heavy-ion impurities by evaporating limiter and wall material, giving rise to populations of, for example, molybdenum ($M = 96$, $Z = 42$) or tungsten ($M = 184$, $Z = 74$). These appear in the plasma as highly charged or even, at temperatures of several keV, as fully stripped ions.

The expression for the frequency distributions of collective fluctuations in a contaminated plasma, given in Ref. 4, has been evaluated for cases where the principal ion is deuterium and the impurity is fully stripped molybdenum or tungsten. Results of this calculation are shown in Fig. 1, where the abscissa x is the frequency shift $\Delta\omega$ normalized to the thermal spectrum width of the deuterium, kv_{deut}, and the parameter α is the usual ratio of scattering scale length to plasma Debye length. The heavy ions manifest themselves at the center of the ion feature as a narrow peak which remains detectable at levels of contamination as low as ten heavy ions per million deuterons.

It appears to be impossible to identify different species from their simultaneous contributions to a composite fluctuation spectrum. However, it turns out that the very important effective charge of the plasma for momentum transfer $\bar{Z}$, where

$$\bar{Z} = \sum Z_j^2 N_j / \sum Z_i N_i,$$

is susceptible to direct measurement in a scattering experiment. An examination of Eq. (3) of

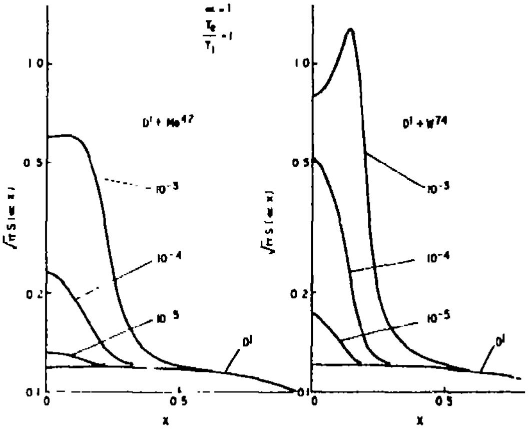

FIG. 1. Computed frequency distribution of collective electron fluctuations in deuterium plasmas containing fully stripped molybdenum or tungsten at concentrations 10^{-3}, 10^{-4}, and 10^{-5} times the deuterium particle density. Curves labeled D^1 refer to pure deuterium. $x = \Delta\omega / kv_{\mathrm{deut}}$.

Ref. 4 modified to take account of electron drift and magnetic field reveals that, provided all ions have the same temperature T_i, the analytic expression for the scattering form factor of a plasma composed of a mixture of ionic species contains the effective charge $\bar{Z}$ explicitly when evaluated at the spectrum center ($x=0$):

$$\sqrt{\pi}\,S(\alpha,0)=\left[a_e\left(\frac{g}{\cos\theta}\right)\left(\frac{1}{\alpha^2}+\frac{T_e}{T_i}\bar{Z}\right)^2+\Gamma\right]\times\left[1+\frac{1}{\alpha^2}+\frac{T_e}{T_i}\bar{Z}\right]^{-2},$$

where a_e is the ratio of thermal speeds of ions of the most abundant kind and the electrons,

$$g=\exp[-(\omega_{pe}/\omega_{ce})^2|\sin^2\theta/\alpha^2,$$

θ is the angle between the scattering vector $\vec{k}$ and the magnetic field $\vec{B}$, T_e is the electron temperature, and Γ is independent of α. Two scattering experiments performed at different values of α, i.e., at different scattering angles in the same plasma, eliminate Γ and allow the solution of the above equation for $\bar{Z}$ in terms of α_1, α_2, $S(\alpha_1,0)$, and $S(\alpha_2,0)$. Figure 2 shows spectra calculated for the contaminants reported for the hydrogen plasma of the Princeton University ST tokamak[5] at scattering angles corresponding to $\alpha_1=1.0$ and $\alpha_2=10$. The field factor $g/\cos\theta$ was set equal to unity. The effective charge is calculated from these distributions to be $\bar{Z}=3.30$, in good agreement with the Princeton value.

The possibility that electron drift current may obscure the influence of impurity ions on the frequency spectrum has been investigated, as far as is possible within the linear theory of plasma density fluctuations, by introducing multiple ion species into the equation given by Boyd, Evans, and Gardner[6] for the dynamic form factor incorporating electron drift and magnetized electrons. Because the electron drift velocity v_D in a tokamak is not expected to exceed the ion thermal velocity v_i, and because the electron gyro frequency ω_{ce} is comparable with the plasma frequency ω_{pe}, the distortion of the spectrum by drift can be approximated, to first order in v_D/v_e (the drift velocity normalized to the electron thermal speed), by the expression

$$\frac{S(y)}{S(y=0)}\cong 1+\frac{2\sqrt{\pi}D(v_D/v_e)}{(\cos\theta/g)[(A+1)^2+D^2+D^2]+2\sqrt{\pi}a_eDx},$$

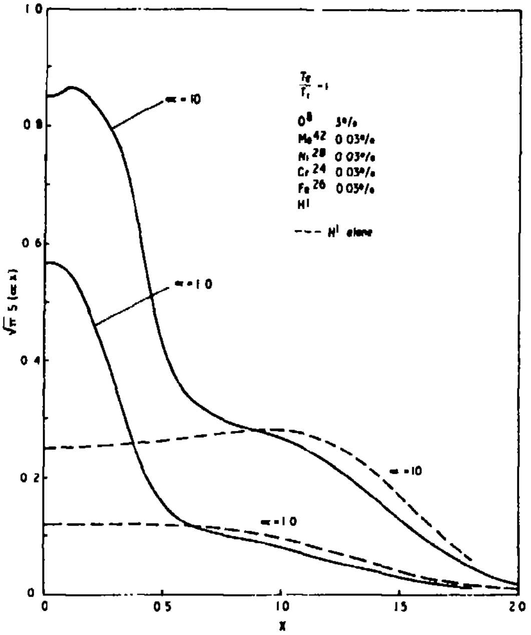

FIG. 2. Computed frequency distributions of collective electron fluctuations in hydrogen plasma with contaminants found in the Princeton University ST tokamak (Ref. 5). Concentrations given as fraction of hydrogen number density. Ions are assumed fully stripped. $\bar{Z}=3.30$. Here $x=\Delta\omega/kv_{\text{hydro}}$.

where

$$A=\frac{1}{\alpha^2}+\frac{\sum_j Z_j^2N_j}{\sum Z_iN_i}\frac{T_e}{T_j}R(a_jx),$$

$$D=\frac{\sum_j Z_j^2N_j}{\sum Z_iN_i}\frac{T_e}{T_j}I(a_jx),$$

$$a_j=[(M_j/M_1)(T_1/T_j)]^{1/2},\quad x=\omega/kv_i,$$

and eZ_j, M_j, N_j, and T_j are charge, mass, number density, and temperature of ions of the jth kind, respectively. $R(a_jx)$ and $I(a_jx)$ are real and imaginary parts of the plasma dispersion function.

This shows that, at least to first order in v_D/v_e, electron drift produces no distortion at the spectrum center ($x=0$) since $D(\arg=0)=0$, and also that drift distortion is asymmetric with respect to the center in contrast to the symmetric enhancement expected for impurity ions. Decreasing the magnetic field, or making the angle between the scattering vector $\vec{k}$ and magnetic field $\vec{B}$ depart from perpendicular, increases the field factor $\cos\theta/g$ and diminishes the enhancement produced by a fixed drift. Numerical examples demonstrate that the comparatively weak drift current expected in a tokamak has almost no effect unless $\vec{k}$ and $\vec{B}$ are nearly perpendicular. Thus with $v_D = v_i$ and $\theta = 0$, $S(y)/S(y=0) - 1 = 10^{-4}$ near the maximum ($x = 0.18$) of the spectrum of the deuterium plasma containing 10^{-3} Mo^{42} ions per deuteron shown in Fig. 1. Enhancement as large as 1% is achieved only when θ reaches 89.7°. Similarly, the drift perturbation of the ST tokamak spectrum illustrated in Fig. 2 was computed at $x = 0.2$ to be less than 2% if θ was less than 60°. So, provided $\vec{k}$ and $\vec{B}$ are far enough from perpendicular, the influence of electron drift on the ion feature expected for a tokamak plasma appears to be negligible compared with impurity effects.

Since the Debye length in a tokamak plasma is 75 to 100 μm, the laser needed to reach the required α values at scattering angles large enough to retain the spatial resolution inherent in scattered-light experiments might be either HCN, operating at 337 μm for which a pulsed power of 1 kW has been reported,[7] or CO_2-pumped methyl fluoride at 496 μm at a pulsed power of 30 kW.[8] In either case, heterodyne detection[9] would be obligatory.

We conclude that contamination of a hydrogen plasma by heavy, high-Z ions can be measured by collective scattering of laser radiation down to about 10 ppm. In contrast to conventional spectroscopy, fully stripped ions are detectable. Moreover, a correctly designed scattering experiment could measure the effective charge $\bar{Z}$ of the plasma directly. Within the approximations of the linear theory of fluctuations, electron drift of the strength expected in a tokamak has negligible effect on these conclusions, provided that the angle between the magnetic field and the scattering vector is sufficiently far from perpendicular. Spatial resolution, without recourse to Abel inversion, is a feature inherent in the scattering technique.

We are indebted to Dr. J. Sheffield for drawing our attention to this problem, and to Dr. A. Wootton for valuable comment.

---

[1] D. L. Dimock, H. P. Eubank, E. Hinnov, L. C. Johnson, and E. B. Meservey, Princeton Plasma Physics Laboratory, Report No. MATT-906, July, 1972 (unpublished).

[2] L. A. Artsimovich, Nucl. Fusion 12, 215 (1972).

[3] J. B. Taylor, Phys. Fluids 4, 1142 (1961).

[4] D. E. Evans, Plasma Phys. 12, 573 (1970).

[5] W. Stodiek, in *Proceedings of the Fifth European Conference on Controlled Fusion and Plasma Physics, Grenoble, France, 1971* (Service d'Ionique Générale, Association EURATOM—Commissariat à l'Energie Atomique, Centre d'Etudes Nucléaires de Grenoble, Grenoble, France, 1972).

[6] T. J. M. Boyd, D. E. Evans, and G. A. Gardner, in *Proceedings of the Tenth International Conference on Phenomena in Ionized Gases, Oxford, England, 1971* (Donald Parsons, Oxford, England, 1971), p. 412.

[7] L. E. Sharpe and A. T. Wetherall, Appl. Opt. 11, 1737 (1972).

[8] F. Brown, S. R. Horman, and A. Palevsky, Opt. Commun. 9, 28 (1973).

[9] E. R. Wooding, M. L. Yeoman, and D. E. Evans, in Proceedings of the Eleventh International Conference on Phenomena in Ionized Gases, Prague, 1973 (to be published), Paper S.3.2.

Ion Heating at Twice the Ion-Cyclotron Frequency in Reactor-Oriented Machines

R. R. Weynants*

Laboratorium voor Plasmafysica, Associatie "EURATOM–Belgische Staat,"

Koninklijke Militaire School, 1040 Brussels, Belgium

(Received 18 March 1974)

A systematic study is made of the efficiency of first-harmonic ion-cyclotron heating in hot, dense, large plasmas. Promising heating times are derived when the imposed axial wavelength satisfies the rather restrictive high-temperature, high-density limitation $k_z \lesssim \omega_{pi}^2 V_i \omega_{ci}^{-1} c^{-2}$.

Heating at the first harmonic of the ion-cyclotron frequency ($\omega = 2\omega_{ci}$) is considered to be one of the more attractive supplementary heating schemes for reaching ignition in large tori. As is well known,[1-3] this heating method depends upon the excitation of the fast hydromagnetic wave, whose electric field at $\omega = 2\omega_{ci}$ has an appreciable left-hand polarized component, i.e., in the sense of the ion rotation. Efficient excitation of the fast wave is, however, only possible above a threshold density, corresponding to the lowest radial magnetoacoustic resonance (see, e.g., Messiaen and Vandenplas[4]). This limit proves to be quite severe for most small-scale machines and little experimental evidence for heating is available until now. Dollinger *et al.*[5] reported wave damping and plasma heating in the beach of a linear device. Hosea and Hooke studied the fast-wave propagation in toroidal geometry[6] and reported ion heating.[7]

In the present Letter, we summarize a systematic study of the optimization of harmonic ion-cyclotron heating of large, dense, hot plasmas. The wave-particle interaction leading to such heating can be formulated by means of the collisionless dielectric tensor[8] expanded in powers of $\lambda_\alpha = k_\perp^2 KT_\alpha m_\alpha^{-1}\omega_{c\alpha}^{-2}$, where $k_\perp$ is the component of the wave vector perpendicular to the magnetic field, α denotes the species, T_α is the temperature (assumed to be isotropic), m_α the mass, and $\omega_{c\alpha}$ the cyclotron frequency. As usual,[2,3] the expansion parameter is then assumed to be such that terms of order higher than 1 need not be retained. A bounded-geometry description was first sketched by Vasileev *et al.*,[1] and a more thorough one given by Cato[9] with application to a particular experimental cold-plasma setup. The present treatment differs from the latter in its scope and in various amendments which will be systematically pointed out, but particularly through the boundary conditions which here apply to a magnetically confined plasma. First, we consider a homogeneous cylindrical plasma in a constant magnetic field, toroidal effects being discussed afterwards.

The infinite plasma column of radius a is surrounded by vacuum and excited from outside by a rf field periodic along the z axis, which can be expanded in a sum of transverse electric (TE) and transverse magnetic (TM) cylindrical waves, defined by their axial magnetic (H_{za}) and electric (E_{za}) field components[4]:

$$\begin{bmatrix} H_{za} \\ E_{za} \end{bmatrix} = \sum_{n=-\infty}^{\infty} \begin{bmatrix} F_n \\ G_n \end{bmatrix} J_n[(k_0^2 - k_{zn}^2)^{1/2} r] \times \exp[i(n\theta + k_{zn} z - \omega t)], \qquad (1)$$

where r, θ, and z are the cylindrical coordinates, k_{zn} is the axial wave number corresponding to the nth azimuthal component, $k_0 = \omega c^{-1}$ is the vacuum wave number, and J_n is the Bessel function of order n. The applied field induces a rf field inside the plasma, given below, and a scattered field

$$\begin{bmatrix} H_{zsc} \\ E_{zsc} \end{bmatrix} = \sum_{n=-\infty}^{\infty} \begin{bmatrix} D_n \\ L_n \end{bmatrix} H_n^{(1)}[(k_0^2 - k_{zn}^2)^{1/2} r] \times \exp[i(n\theta + k_{zn} z - \omega t)], \qquad (2)$$

where $H_n^{(1)}$ is a Hankel function. After imposing the boundary conditions, one can calculate the absorbed power P by applying Poynting's theorem over a surface S surrounding the plasma. The dielectric tensor elements K_{ij}, as given in Ref. 8, Eq. (9.9), are introduced in

$$c^2 \vec{k} \times (\vec{k} \times \vec{E}) + \omega^2 \overleftrightarrow{K} \cdot \vec{E} = 0, \qquad (3)$$

giving a dispersion relation of third order in $k_\perp^2$. By the inverse transformation from $k_\perp^2$ to $-\Delta_\perp^2$, a factorable sixth-order differential equation describing the perturbations inside the plasma is then found, the solution of which has the form

$$H_z = \sum_{j=1}^{3} A_{jn} J_n(k_{\perp j} r) \exp[i(n\theta + k_{zn} z - \omega t)], \qquad (4)$$

where the $k_{\perp j}^2$ are the three roots of the dispersion relation. All other field components can then be expressed in terms of the same constants A_{jn}. For a given n, there must be five boundary conditions to determine the five unknowns: the A_{jn}, D_n, and L_n. Via the relationship between kinetic λ ordering and moment expansion of the Boltzmann equation (see also Ref. 10), we obtain the following constraints at the plasma (p)-vacuum (v) interface[11]:

$$\begin{aligned} &B_z^p - B_z^v B_0^v / B_0^p = -\mu_0 p_{rr} / B_0^p, \\ &E_z^p = E_z^v, \quad B_\theta^p = B_\theta^v, \quad p_{r\theta} = 0, \qquad (5) \\ &B_r^p B_0^v / B_0^p - B_r^v = -\mu_0 p_{rz} / B_0^p. \end{aligned}$$

Aside from the familiar continuity of E_z and B_θ, these equations express the fact that like the equilibrium plasma pressure, the perturbed plasma-pressure components p_{rr}, $p_{r\theta}$, and p_{rz} must be balanced by a jump in magnetic field.

The numerical evaluation was carried out for typical thermonuclear parameters. The applied field is purely TE ($G_n = 0$) and is characterized by a B_{za}^v of $10^{-4} B_0^v$ at the plasma boundary. We note the following:

(i) A typical dependence of the absorbed power per unit axial length P' on density (N) is shown in Fig. 1 for fixed k_z and $\omega = 2\omega_{ci}$. The absorption, which is low below the infinite-plasma cutoff $\omega_{pi}^2 k_z^{-2} c^{-2} = \frac{3}{4}$, is very much enhanced by the first magnetoacoustic resonances which are superposed on a background curve that increases roughly proportionally to density. At higher densities, it levels off or even drops. The overall behavior can be understood qualitatively on the basis of the infinite-plasma formula

$$p_i' = \pi^{3/2}a^2\epsilon_0\omega_{pi}^{\ 2}V_ik_\perp^{\ 2}\exp\left[-\left(\frac{\omega-2\omega_{ci}}{k_zV_i}\right)^2\right]|iE_r-E_\theta|^2(8k_z\omega_{ci}^{\ 2})^{-1}, \tag{6}$$

where ω_{pi} is the ion plasma frequency, ϵ_0 the vacuum permittivity, and $V_i=(2KT_im_i^{\ -1})^{1/2}$ the ion thermal velocity. It can be shown that

$$\alpha_n=\left|\frac{iE_r-E_\theta}{iE_r+E_\theta}\right| \doteq \left|\frac{(iR+1)J_{n+1}(k_\perp r)}{(iR-1)J_{n-1}(k_\perp r)}\right|,$$

where $k_\perp$ is that of the fast wave. When $\omega_{pi}^{\ 2} > k_z^{\ 2}c^2$, R can be approximated by $R \doteq -i(\frac{4}{3}-S)/(-\frac{2}{3}+S)$, with

$$S=\tfrac{1}{4}(\omega V_i\omega_{pi}^{\ 2}/c^2k_z\omega_{ci}^{\ 2})Z,$$

where Z is the plasma dispersion function of argument $(\omega-2\omega_{ci})k_z^{\ -1}V_i^{\ -1}$. For $n=0$ and cold plasmas, the left-hand component equals $\frac{1}{3}$ of the right-hand one. However, α_0 drops significantly when $\omega_{pi}^{\ 2}V_i \gg k_z\omega_{ci}c^2$. For instance, for the case $T_i=10^8$ of Fig. 1, α_0 decreases from 0.39 at $N=10^{12}$ cm^{-3} to 0.05 at $N=10^{14}$ cm^{-3}. Physically, this very important hot dense plasma effect results from wave confluence (see Fig. 2) of the fast wave with an ion Bernstein wave. The third wave present is of lesser importance. Over the range where the fast wave is ion Bernstein like, its heating properties are very much reduced.

In Fig. 1, not only the relative importance of the left-hand component decreases with density, but also the magnitude of the average field inside the plasma. At fixed $B_{zz}^{\ v}$, this can be due to two effects: a change of the surface impedance $(-E_\theta H_z^{\ -1})$ or a change of the field distribution inside the plasma which is characterized by an e-folding length proportional to $\mathrm{Re}k_\perp/\mathrm{Im}k_\perp$. As these are mainly bounded-plasma effects, general considerations are difficult to formulate.

(ii) A typical dependence of P' on k_z for fixed N (10^{14} cm^{-3}) and $\omega=2\omega_{ci}$ is shown in Fig. 3, where the k_z absorption band is strikingly clear. However, k_z values higher than 10 m^{-1} are entirely unsatisfactory for the large plasmas under consideration due to the exponentiallike $I_n(k_zr)$ falloff of the exciting field ($k_z>k_0$). As a result, the k_z bandwidth is even more reduced.

(iii) The absorption around $\omega=2\omega_{ci}$ is often very asymmetric. On the one hand, there is the influence of the ion Bernstein wave which can propagate for $\omega<2\omega_{ci}$ (see Fig. 2). On the other hand, the magnetoacoustic resonances which are excluded from the immediate vicinity of $2\omega_{ci}$ when $\omega_{pi}^{\ 2}V_i>k_z\omega_{ci}c^2$ can be superposed anywhere on the $(\omega-2\omega_{ci})^2$ Gaussian of Eq. (6) when the inequality is reversed.

We now briefly turn to the implications for toroidal field geometry. Because of the magnetic inhomogeneity, absorption only occurs in a reso-

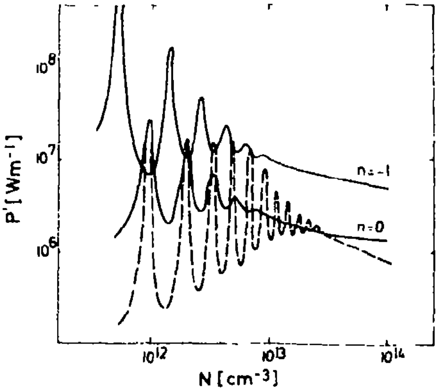

FIG. 1. P' versus density for a cylindrical plasma with parameters: deuterium, $a=1.3$ m, $B_0^{\ v}=5$ T, $k_z = 1$ m^{-1}, $T_e = 10^8$ K. The solid lines apply to an ion temperature $T_i = 10^8$ K and azimuthal mode numbers $n=0$ and -1. For the dashed curve, $T_i=10^6$ K and $n=0$. The influence of n is seen to be quite significant.

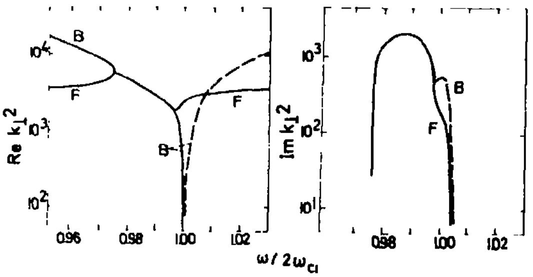

FIG. 2. Real and imaginary parts of the square of the perpendicular wave numbers of the first (F) and ion Bernstein (B) waves around $2\omega_{ci}$. The plasma parameters are those of Fig. 1, with $T_i=10^8$ °K and $N=10^{14}$ cm^{-3}. The solid lines represent positive values, the dashed lines negative ones. The waves are complex conjugate from the confluence up to close to $2\omega_{ci}$.

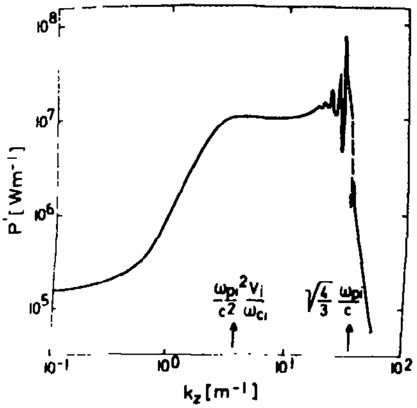

FIG. 3. P' versus axial wave number k_z for a cylindrical plasma whose parameters are those of Fig. 1, with $T_i = 10^8$ °K and $N = 10^{14}$ cm^{-3}. The arrows mark the position of the infinite-plasma cutoff $(\frac{4}{3})^{1/2}\omega_{pi}c^{-1}$ and the hot-plasma limit $\omega_{pi}^2 V_i \omega_{ci}^{-1} c^{-2}$.

nance zone of approximate width $\Delta = k_z V_i R\omega_{ci}^{-1}$ where R is the major radius. In Fig. 2, it can be seen that, when $\omega_{pi}^2 V_i \geq k_z \omega_{ci} c^2$, a fast wave approaching from the high-field side will encounter a zone of mode conversion before getting to this resonance zone. However, this is in no way restrictive, since the easiest way to launch waves experimentally is from the outside or low-field area of the torus. As regards the absorbed power, one can assume[3] that the energy is distributed over the whole plasma by means of the rotational transform, in which case the values found in the cylindrical approximation have to be multiplied by $\beta = (2/\pi)\Delta a^{-1}$. This leads to an important reduction when Δ, i.e., k_z is small. However, the values thus found are too pessimistic. Indeed, in our cylindrical approximation resonance exists everywhere and a wave entering the plasma will gradually damp as it proceeds. The equivalent field in Eq. (6) is then averaged over the whole plasma. In toroidal geometry, the wave remains undamped until it hits the resonance zone. While it will then damp with about the same e-folding length as before, the average field will now be higher.

On this basis, we attempt a final assessment of the heating efficiency for a deuterium plasma with $a = 1.3$ m, $N = 10^{14}$ cm^{-3}, $T_e = 10^8$ K, and $B_0^{\nu} = 5$ T and $R/a = 5$ under axisymmetric excitation. The normalization is now based on the assumption that for technological reasons the electric field E_θ at the plasma boundary must be limited to 3000 V/m. Table I shows typical optimal heating times τ for various T_i and k_z combinations. τ_1 is defined as $NKT_i\pi a^2/\beta P'$, while τ_2 is the average corrected value based on the computed e-folding lengths. As regards the $k_z = 10$-m^{-1} values, one should bear in mind that in order for a structure located at $r = 1.5$ m to create the assumed field, the E_θ value at that radius would have to be some 2×10^4 V/m. As τ scales as E_θ^{-2}, very promising heating times could be achieved when higher fields are permitted.

TABLE I. Typical optimized heating times without (τ_1) and with (τ_2) field correction.

	$k_z = 1$ m^{-1}		$k_z = 10$ m^{-1}	
T_i (°K)	τ_1 (sec)	τ_2 (sec)	τ_1 (sec)	τ_2 (sec)
10^8	15.5	5.5	1.5	0.4
10^7	5.5	0.6	0.5	0.2
10^6	1.4	0.15	0.18	0.18

The author acknowledges with pleasure discussions with A. M. Messiaen and P. E. Vandenplas.

---

*Aangesteld Navorser bij het Belgisch Nationaal Fonds voor Wetenschappelijk Onderzoek. Present address: Max-Planck-Institut für Plasmaphysik, 8046 Garching, West Germany.

[1] M. P. Vasileev, L. I. Grigoreva, V. V. Dolgopolov, B. I. Smerdov, K. N. Stepanov, and V. V. Chechkin, Zh. Tekh. Fiz. 34, 974 (1964) [Sov. Phys. Tech. Phys. 9, 755 (1964)].

[2] J. E. Cato, M. Kristiansen, and M. O. Hagler, Bull. Amer. Phys. Soc. 14, 1020 (1969).

[3] J. Adam, in *Proceedings of the International School of Plasma Physics—Plasma Heating and Injection, Varenna, 1972* (Editrici Compositori, Bologna, Italy, 1973), p. 83.

[4] A. M. Messiaen and P. E. Vandenplas, Plasma Phys. 15, 505 (1973).

[5] R. Dollinger, M. Kristiansen, M. O. Hagler, and J. Bergström, in *Proceedings of the Sixth European Conference on Controlled Fusion and Plasma Physics* (U.S.S.R. Academy of Sciences, Moscow, 1973), Vol. 1, p. 583.

[6] J. C. Hosea and W. M. Hooke, Phys. Rev. Lett. 31, 150 (1973).

[7] W. M. Hooke and J. C. Hosea, in *Proceedings of the Fifth European Conference on Controlled Fusion and Plasma Physics* (Service d'Ionique Générale, Association EURATOM—Commissariat à l'Energie Atomique, Centre d'Etudes Nucléaires de Grenoble, France, 1972), Vol. I, p. 107.

[8] T. H. Stix, *The Theory of Plasma Waves* (McGraw-Hill, New York, 1962), Chap. 9.

[9] J. E. Cato, Ph.D. dissertation, Texas Technical University, 1971 (unpublished).

[10] In Ref. 9, a sixth-order equation is obtained in a different manner. Our procedure is equivalent with the first-order temperature description derived from the moment equations, as demonstrated by T. W. Johnston, J. Plasma Phys. 4, 283 (1970). See also J.-L. Montfort and P. E. Vandenplas, Transp. Theor. and Statist. Phys. 2, 1 (1972).

[11] R. J. Hosking and G. L. Karla, J. Plasma Phys. 7, 545 (1972); F. N. Arumi and M. E. Oakes, Phys. Fluids 15, 837 (1972).

Absence of Surface States in Cu

R. V. Kasowski
Experimental Station, Central Research Department, E. I. du Pont de Nemours and Company, Wilmington, Delaware 19898

(Received 12 March 1974)

The linear combination of muffin-tin orbitals technique has been used to calculate the electronic energy levels of a five-layer Cu (001) film. We do not find any surface states in the *s-d* gap as had been predicted and calculated in other theoretical studies. Instead we find the energy levels to be nearly indistinguishable from those of the bulk crystal, which agrees with ion-neutralization-spectroscopy data on Cu crystals and with photoemission data from thin overlayers of Cu on Ag substrates.

The linear combination of muffin-tin orbitals (LCMTO) method[1] has been used to calculate the electronic states of a five-layer-thick Cu (001) film. We find that the energy levels correspond closely to those of bulk Cu and that there are no surface states even though the surface-charge regions are included. The absence of surface states for Cu is in agreement with the experimental photoemission data of Eastman and Cashion[2] and with the ion-neutralization-spectroscopy (INS) data of Hagstrum.[3] More recently, Eastman and Grobman[4] have found that photoemission from thin overlayers of Cu on Ag substrates is characteristic of the bulk for overlayer thicknesses greater than four layers. Therefore, our results for a five-layer thin film should be representative of thick films and crystal surfaces.

Absence of surface states in the *s-d* gap is contrary to previous theoretical predictions[5] and calculations.[6] We are able to find states in the *s-d* gap when we mix bulk and thin-film states. However, we will show that these states are an artifact resulting from the interface between the thin film and bulk and that these gap states would have been mistaken for surface states if we had limited the film thickness to one or two layers.

Application of the LCMTO method to thin films proceeds exactly as in solids except that the layer structure constants of Kambe[7] are used in place of the bulk structure constants of Ham and Segall.[8]

The Cu (001) thin-film model consists of a total of seven layers. The inner five layers contain Cu atoms with the outermost two layers being empty of Cu atoms. Potentials for the seven layers were constructed by overlapping Herman-Skillman[9] atomic charge densities. The potential in the outer two layers will be referred to as surface charge because it results from the charge-density tails of the five inner layers. Potentials for the outer two occupied layers will be called surface potentials while the potentials for the innermost three layers (which were nearly identical) will be called bulk potentials. Nonspherical corrections to the potential were included since the site symmetry is C_{3v}.

The basis set for layers one to five consisted of thirteen muffin-tin orbitals (MTO) centered on each Cu site and all orthogonalized to the $1s2s2p$ core states. Four MTO's represent the $3s, 3p$ core states and nine MTO's represent the valence bands. Four MTO's were used for each surface-charge region. At a general k point, our matrix size is 73×73.

The reliability and adequacy of the basis set described above was tested by using this basis set along with the Cu Chodorow potential[10] to calculate the bulk energy bands with our crystal LCMTO energy-band procedure. We find differences of at most 0.005 Ry with the Burdick augmented-plane-wave[11] (APW) values at the Γ, X, and L symmetry points.

The accuracy of our method of constructing potentials was verified by recalculating the bulk energy bands at Γ, X, and L, using the potentials of the innermost three layers. We find, at most, 0.01-Ry differences with the Burdick APW results, thus indicating we have constructed a good potential and basis set.

In Fig. 1(a) the energy states for the seven-layer film at the Γ point of the two-dimensional Brillouin zone are arranged at $\frac{1}{5}$ intervals to emphasize their similarity with the bulk energy bands in Fig. 1(b). Investigation of the thin-film wave functions reveals approximate Bloch symmetry in that the sign of the coefficients of the MTO's alternate as $e^{i\vec{k}\cdot\vec{R}_n}$ from layer to layer although the magnitudes of the coefficients from layer to layer are not equal as required for Bloch symmetry. This approximate Bloch symmetry serves

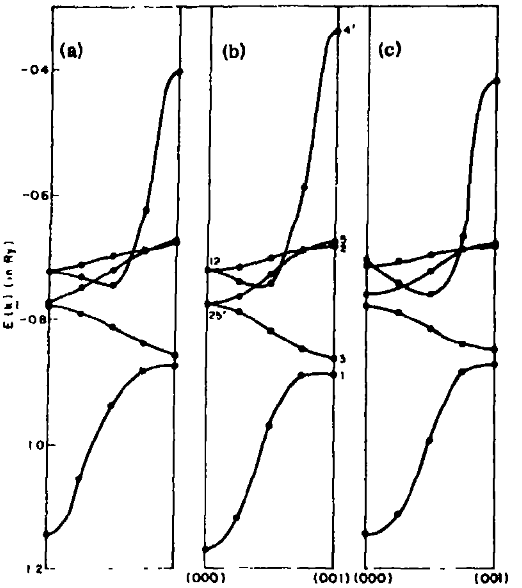

FIG. 1. Comparison of the eigenstates of (a) 5-layer Cu thin film with the eigenstates of (b) 100 layers and (c) 5-layer thick films, respectively, where the wave functions are constrained to Bloch form in (b) and (c).

as further justification for arranging the thin-film energy states to correspond to bulk energy states. Furthermore, the wave functions are found to extend over the full five layers so that none of the states can be interpreted as a surface state.

If the thin-film calculation is repeated without surface charge (the potential is discontinuous at surface), the top of the s-d band which corresponds to $X_{4'}$ is raised from -0.403 to -0.310 Ry, and the state corresponding to X_1 is bent downwards by 0.003 Ry. Surface charge makes quantitative not qualitative differences. Furthermore, the similarity between bulk and thin-film states holds for the Chodorow potential also.

In Figs. 1(b) and 1(c), we graph the results of calculations on 100-layer and five-layer films, respectively, where the wave functions are constrained to Bloch form in the z direction and the surface-charge regions are excluded.

In Table I, we tabulate the band extrema of Fig. 1 and compare to bulk. The 100-layer Bloch-function results are within about 0.02 Ry of the results of a bulk calculation. Thus, we can consider Fig. 1(b) to be representative of the bulk. It is also clear from Fig. 1 and Table I that the energy states of the thin film in Fig. 1(a) more closely resemble the bulk states than do the five-layer Bloch-function results of Fig. 1(c). For example, the $\Gamma_{25'}$ states are nondegenerate by 0.018 Ry (0.762–0.780) in Fig. 1(c) whereas the nondegeneracy is only 0.005 Ry (0.772–0.777) in Fig. 1(a). Thus, relaxation of the Bloch condition allows the states to assume energy eigenvalues which more closely resemble the bulk values.

TABLE I. Comparison of thin-film and band states at the Γ point of the two-dimensional Brillouin zone.

Symmetry	Note a	Note b	Note c	Note d
$\Gamma_{25'}\ xz, yz$	−0.772	−0.776	−0.762	−0.778
$\Gamma_{25'}\ xy$	−0.777	−0.777	−0.780	−0.778
$\Gamma_{12}\ x^2y^2$	−0.721	−0.724	−0.716	−0.720
$\Gamma_{12}\ s, z^2$	−0.725	−0.725	−0.731	−0.720
$\Gamma_1\ s, z^2$	−1.140	−1.168	−1.146	−1.177
X_5	−0.676	−0.673	−0.678	−0.670
X_3	−0.857	−0.864	−0.850	−0.868
X_2	−0.679	−0.686	−0.685	−0.683
$X_{4'}$	−0.403	−0.339	−0.417	−0.365
X_1	−0.866	−0.889	−0.874	−0.893

[a] Thin-film results of Fig. 1(a).
[b] 100-layer results of Fig. 1(b).
[c] 5-layer results of Fig. 1(c).
[d] Bulk calculation using potential of innermost layers.

In Table II we give the extrema of the thin-film bands as a function of layer thickness in order to show how rapidly the bandwidths approach the bulk values. The table leads one to expect closer correspondence with the bulk if we were to increase the number of layers. For example, the nondegeneracy of the $\Gamma_{25'}$-like states is 0.02 Ry (0.779–0.759) for three layers, 0.012 Ry (0.766–0.778) for four layers, and only 0.005 Ry (0.772–0.777) for five layers.

Comparison of thin-film states and bulk states have also been performed for the X (100) and M ($\frac{1}{2}\frac{1}{2}0$) symmetry points. No surface states appear and the difference between bulk and five-layer thin films is a little larger than at the Γ point but always less than 0.04 Ry.

Previously, surface states had been predicted and calculated in the s-d gap[5,6] between -0.75 and -0.88 Ry. These methods depend upon continuing the bulk wave functions into the surface regions with the matching plane between bulk and surface being one layer or so below the surface.

We now show how states can be introduced into the s-d gap which, however, are not true surface states. The Cu crystal is divided into a 100-lay-

TABLE II. Band extrema at the Γ point of the two-dimensional Brillouin zone as a function of number of layers.

	Number of layers				
Symmetry	1	2	3	4	5
xz,yz	−0.701	−0.686	−0.680	−0.678	−0.676
		−0.742	−0.759	−0.766	−0.772
xy	−0.793	−0.782	−0.779	−0.778	−0.777
		−0.832	−0.847	−0.853	−0.857
x^2-y^2	−0.682	−0.679	−0.679	−0.679	−0.679
		−0.708	−0.716	−0.719	−0.721
s,z^2	−0.709	−0.571	−0.482	−0.433	−0.403
		−0.734	−0.722	−0.727	−0.725
s,z^2	−0.851	−0.853	−0.866	−0.806	−0.866
		−1.033	−1.098	−1.126	−1.140

er-thick region and a thin-film region of thicknesses between one and five layers. The film is represented by the usual MTO's while the bulk region is represented by the five 100-layer Bloch functions of Fig. 1(b) with $\vec{k}$ vectors (0, 0, 0), (0, 0, 0.2), (0, 0, 0.4), (0, 0, 0.8), and (0, 0, 1). Regardless of film thickness, one state always results in the s-d gap with energy depending on layer thickness but varying between −0.79 and −0.81 Ry. The remaining energy states correspond to those of the bulk states exactly as in the thin-film results of Fig. 1(a). The charge density of the gap state is almost exclusively localized at the layer dividing the thin film from the bulk 100 layers. This gap state can easily be mistaken to be a surface state when a thin-film thickness of one or two layers is used. However, if the thin-film thickness is increased to five layers, this state resides totally within the crystal at the interface region and appears to separate two crystals of Cu. We would expect this gap state to disappear if we include all the Bloch functions of the 100-layer film.

In conclusion, we find no evidence of surface states in Cu. More generally, our results indicate that the relaxation of the Bloch condition on the wave functions may exist deeper into the crystal than the one or two layers now assumed in matching techniques. Relaxation of the Bloch condition near the surface is essential to maintaining close correspondence with bulk states.

We wish to thank Dr. K. Kambe for helpful comments concerning the structure constants.

---

[1] O. K. Andersen and R. V. Kasowski, Phys. Rev. B 4, 1063 (1971); R. V. Kasowski and O. K. Andersen, Solid State Commun. 11, 799 (1972).

[2] D. E. Eastman and J. K. Cashion, Phys. Rev. Lett. 24, 310 (1970); D. E. Eastman, Phys. Rev. B 3, 1769 (1970).

[3] H. D. Hagstrum, Phys. Rev. 150, 495 (1966).

[4] D. E. Eastman and W. D. Grobman, Phys. Rev. Lett. 30, 177 (1973).

[5] F. Forstmann and V. Heine, Phys. Rev. Lett. 24, 1419 (1970); F. Forstmann and J. B. Pendry, Z. Phys. 235, 75 (1970).

[6] S. J. Gurman and J. B. Pendry, Phys. Rev. Lett. 31, 637 (1973).

[7] K. Kambe, Z. Naturforsch. (a) 22, 322 (1967).

[8] F. S. Ham and B. Segall, Phys. Rev. 124, 1786 (1961).

[9] F. Herman and S. Skillman, *Atomic Structure Calculations* (Prentice-Hall, Englewood Cliffs, N.J., 1963).

[10] M. Chodorow, Phys. Rev. 55, 675 (1939).

[11] C. A. Burdick, Phys. Rev. 129, 138 (1963).

Strong 4f Resonance Effects in Rare-Earth Appearance-Potential Spectra

W. E. Harte, P. S. Szczepanek, and A. J. Leyendecker
Laboratory for Physical Sciences, College Park, Maryland 20742
(Received 6 May 1974)

Soft-x-ray appearance-potential spectra of rare-earth elements are interpreted in terms of strong resonance interactions between the incident electrons and atomic 4f states. These interactions account for both the large intensity and the threshold shifts of the measured signal. This resonance persists in La, Ce, Pr, and Nd when present as only a few atomic percent in a NiCr alloy reflecting the local character of the interaction.

Recently, attempts have been made to exploit the technique of soft-x-ray appearance-potential spectroscopy (SXAPS) to investigate the electronic structure and composition of solid surfaces. The spectral line shapes are thought to be determined by a self-convolution of the density of empty conduction-band states[1] while the positions of the excitation thresholds provide a measure of the core-level binding energies and serve to identify the surface constituents. Our investigation of a NiCr alloy containing small amounts of the rare earths La, Ce, Pr, and Nd and a comparison with a pure La sample show that the presence of localized f states disrupts the expected appearance-potential spectra. The unusually large intensities, the line shapes, and the positions of the rare-earth spectra are determined by a strong resonance involving an interaction of the incident electron with localized 4f states. The occurrence of this resonant behavior has been recorded by Liefeld, Burr, and Chamberlain (LBC)[2] and Chamberlain, Burr, and Liefeld (CBL)[3] using a series of continuous emission spectra to follow the resonance emission. In a recent paper evidence of the effect of the emission resonance on the SXAPS line shape of Sm has been reported near the M_5 and N_5 threshold energies only.[4] Our investigation demonstrates the resonance effect on SXAPS whenever there exist allowed transitions between a core state and localized states near the Fermi energy. For elements in the beginning of the lanthanide series these effects occur near the threshold energies of the M_5 and M_4 transitions. Resonance phenomena may also affect the SXAPS of elements in both the transition and the actinide series.

The spectrometer used in these experiments is basically the same as those reported on by other SXAPS experimenters. The NiCr alloy contained 70% nickel with the rare earths determined to constitute less than 1 at.%. The La sample was prepared in an argon atmosphere to prevent oxidation. Both the La surface and the alloy surface were further processed by electron heating until evidence of surface contaminants could no longer be detected in the SXAPS spectra.

There are three anomalous features which are evident in the SXAPS spectra of the NiCr alloy. The spectrum is reproduced in Fig. 1. First, the features which are associated with the M_5 core level of La and the M_5 and M_4 core levels of Ce, Pr, and Nd do not have the line shape characteristic of the L_3, L_2 core level transitions of Ni. Therefore, the line shapes either of the rare-earth or of the Ni core level transitions (or both) cannot represent the self-convolution of the empty density of states of the alloy. Second, the measured threshold energies, defined as the point of inflection of the leading edge of each spectral line,[5] deviate from the binding energies of the corresponding core levels as given by Bearden and Burr (BB).[6] The measured threshold energy for La is larger than published by BB; for the other rare-earth elements the measured

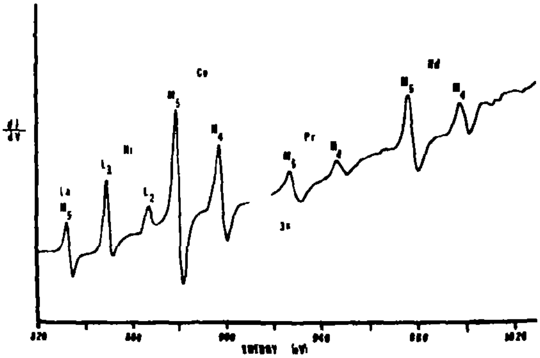

FIG. 1. The SXAPS spectrum from a NiCr alloy containing small amounts of the rare-earth elements La, Ce, Pr, and Nd. The displayed region encompasses the M_5, M_4 excitation lines of the rare-earth elements and the L_3, L_2 lines of Ni.

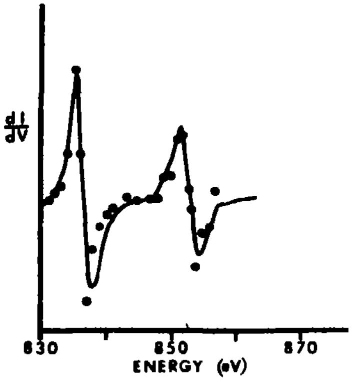

FIG. 2. The SXAPS spectrum of La in the vicinity of the M_5, M_4 excitation energies. A comparison is made between the measured solid curve and the points calculated on the basis of emission spectra recorded by LBC.

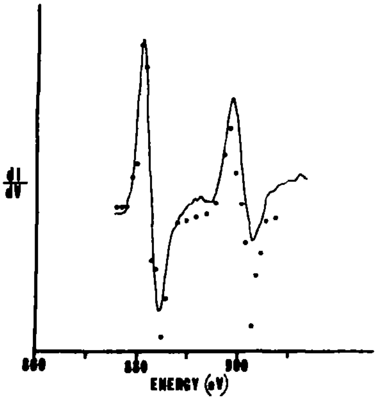

FIG. 3. A comparison between the SXAPS alloy spectrum (solid curve) in the vicinity of the M_5, M_4 threshold of the Ce solute and computed values (dashed curve) of the energy derivative of the Ce resonance emission isolated by CBL.

threshold is less than the BB results. Third, the SXAPS of rare-earth elements, when adjustment is made for the relative densities of the alloy constituents, is nearly 2 orders of magnitude larger than the Ni spectra.

The SXAPS of pure La for energies from 800 to 875 eV is shown in Fig. 2. Both the position and the shape of the structure near the M_5 threshold are essentially identical to the La emission measured from the alloy. Therefore, other parameters unaffected by alloying must determine the SXAPS of La. The experiments on La show further that not all core level transitions are associated with large intensities in the SXAPS spectra. The M_5, M_4 and N_5, N_4 levels exhibit large peaks while the spectra of other levels such as the M_3, M_2, M_1 and N_3, N_2, and N_1 are more than an order of magnitude smaller[7] and indicate the absence of an associated resonance phenomenon.

The details of the measured SXAPS line shapes are accounted for by the resonance emission as measured in La and Ce by CBL. The changes in the total x-ray emission per unit change in incident electron energy computed from the series of spectra measured on La by LBC have been plotted in Fig. 2 along with the La SXAPS spectrum. The SXAPS spectrum represents the derivative of the total x-ray yield and is nearly identical to the derivative of the x-ray emission identified by LBC as arising primarily from the resonance phenomena. Cerium, for which CBL have isolated the resonance contribution, shows more clearly the dominance of the resonance emission in determining SXAPS spectra. The energy derivative calculated on the basis of the isolated resonance emission as determined by CBL is compared to the SXAPS line shape of Ce in Fig. 3. The two spectra agree in both position and shape when plotted as a function of incident electron energy. The slight offset between the resonance contribution and the measured SXAPS may consist of emission attributable to band effects predicted in the Park and Houston theory.[1]

Intense structure occurs in the rare-earth spectra only for those core levels having proper symmetry consistent with dipole transitions to final *f* states. The thresholds of these intense lines are also consistent with transitions involving the 4*f* states of the rare-earth elements. In Fig. 4(a) the discrepancies between the measured threshold energies and published binding energies for the M_5 (or M_4) lines are plotted together with the energies of the $N_{6,7}$ levels for the four rare-earth elements present in the alloy.[2,6] It is apparent that the measured threshold energies reflect the separations between the $M_{5,4}$ and $N_{6,7}$ levels rather than the binding energies of the 3*d* electrons. In La, in which the energy of the 4*f* state is greater than the Fermi energy, the resonance does not begin until the incident electron has an additional energy beyond the binding energy to interact with the empty 4*f* level. For the other rare-earth elements the interaction begins below the M_5 (or M_4) binding energy by an amount cor-

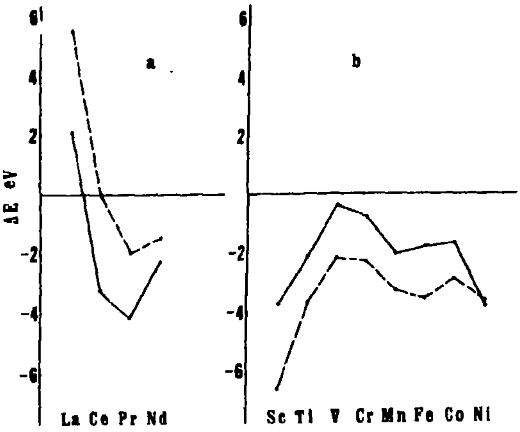

FIG. 4. (a) The binding energies of the 4f levels for La, Ce, Pr, and Nd (dashed curve) are compared with the difference (solid curve) between the BB values of the binding energies of the M_5 (or M_4) levels and the SXAPS threshold energies. (b) A similar comparison of the binding energies of the 3d levels of the transitions elements (dashed curve) and differences (solid curve) between the SXAPS threshold energies as measured by Park and Houston and the binding energies of the L_3, L_2 core levels.

responding to the $N_{6,7}$ energy. In Fig. 4(b), we have made a similar comparison for the transition elements using the SXAPS thresholds of the L_3 and L_2 lines as measured by Park and Houston.[1] The deviations between the BB binding energies and the $L_{3,2}$ thresholds track the reported $M_{4,5}$ values in a manner similar to that of the rare earths and suggest a similar threshold resonance phenomenon in the transition elements. In support of this conclusion, Hanzely and Liefeld[8] have reported a moving peak below the electron-beam bombarding energy in the L_3 soft-x-ray emission spectrum of iron. This energy peak is found only on the high-energy side of the La line and decreases in intensity upon moving away from threshold.

The existence of similar SXAPS line shapes for La in both its pure form and as a dilute solution in the NiCr alloy reflects the nature of the f states in the rare-earth elements. These states are localized, have little overlap with adjacent atoms, and are not significantly affected by alloying. By recognizing the importance of the resonance interaction between the incident electron and the f states present in rare-earth atoms we have been able to explain the puzzling properties of their SXAPS spectra. Their intense response is the consequence of an increase of over 2 orders of magnitude in x-ray emission due to the resonance. The existence of the resonance line shapes for dilute amounts of rare earths in the NiCr alloy has shown that the localized f states are still present in the alloy and that SXAPS samples their local atomic environment. The enhancement by resonance of the SXAPS spectra also makes this technique a very sensitive means of detecting rare-earth elements. The ability to measure the behavior of the localized f states and to characterize their transition line shapes and positions relative to a sharp core level should make the SXAPS technique extremely important in providing data for theoretical calculations.

---

[1] R. L. Park and J. E. Houston, Phys. Rev. B 6, 1073 (1972).

[2] R. J. Liefeld, A. F. Burr, and M. B. Chamberlain, Phys. Rev. A 9, 316 (1974).

[3] M. B. Chamberlain, A. F. Burr, and R. J. Liefeld, Phys. Rev. A 9, 663 (1974).

[4] M. B. Chamberlain and W. L. Baun, J. Vac. Sci. Technol. 11, 441 (1974).

[5] The inflection point corresponds to a peak in the second-derivative SXAPS spectrum which has been previously used in reporting values in the literature. Other conventions would result only in energy values differing from the present values by a relatively constant energy.

[6] J. A. Bearden and A. F. Burr, Rev. Mod. Phys. 39, 125 (1967).

[7] W. E. Harte and P. S. Szczepanek, to be published.

[8] S. Hanzely and R. J. Liefeld, in *Electronic Density of States, Proceedings of the Third International Materials Research Symposium, Gaithersburg, Maryland, 1969*, edited by L. H. Bennett, National Bureau of Standards Special Publication No. 323 (U.S. GPO, Washington, D.C., 1971), p. 319.

New Interpretation of the Soft-X-Ray Absorption Spectra of Several Alkali Halides*

M. Schlüter,† J. D. Joannopoulos, and Marvin L. Cohen
Department of Physics, University of California, Berkeley, California 94720,
and Inorganic Materials Research Division, Lawrence Berkeley Laboratory, Berkeley, California 94720
(Received 22 April 1974)

New pseudopotential calculations of the densities of states of trigonal Se and Te (in excellent agreement with recent photoemission measurements) are used to show that two easily resolved peaks in the photoemission data are directly related to interchain and intrachain bonding. This identification is accomplished by calculating electronic charge densities as a function of energy for different energy regions. Finally we introduce a new method for determining bonding charges by extracting short-wavelength components of the electronic charge density.

The electronic structure of trigonal Se and Te has been the subject of many experimental and theoretical studies.[1] Recently the advent of new ultraviolet (UPS)[2] and x-ray (XPS)[2,3] photoemission measurements has provided important information about all the valence bands and has revealed some inadequacies of present theoretical calculations.[4-8] In one of these calculations[4] a complete merging of s- and p-like bands was proposed which disagrees qualitatively with the recent photoemission data. Other calculations[5,6] show a separation of s- and p-like bands which is in qualitative agreement with these experiments; however, bandwidths and important structure in the p-like bonding states are not obtained correctly. The experimentally observed characteristic two-peak structure in the p-like bonding states is, as we shall show, *intimately related to two distinct types of bonding states* so that precise calculations are necessary before a detailed understanding of the electronic structure and bonding nature of Se and Te can be obtained. Finally the information gained by a careful examination of the crystalline forms of Se and Te is a considerable aid in understanding the amorphous phases[3,7] of Se and Te as well.

In this Letter we thus present new calculations of the electronic densities of states of trigonal Se and Te [using the empirical pseudopotential method (EPM)[8]] which for the first time agree quantitatively with all the observed structure in the experimental photoemission spectra. A detailed discussion of the calculations and the parameters used will be given elsewhere.[3] In Fig. 1 we show the results of our EPM calculations for the density of states along with the recent photoemission results of Shevchik *et al.*[2] for Se and Joannopoulos *et al.*[3] for Te. The calculated spectra were convoluted with an energy-dependent broadening function in order to facilitate comparisons with experiment. The experiments on Se were obtained by using UPS and XPS measurements on sputtered and subsequently annealed films, while those on Te were obtained using XPS on a single crystal. All observed structures in the experimental spectra are reproduced to within 0.3 eV. As in earlier EPM calculations,[5,6,9] the lowest band represents essentially

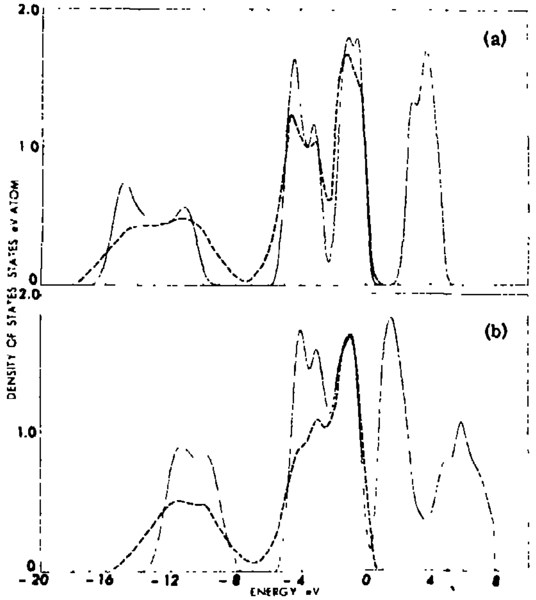

FIG. 1. Calculated densities of states (solid lines) for trigonal Se (a) and Te (b), which have been broadened by 1.2 eV for the s-like states and by 0.7 eV for the remaining states. Superimposed are the experimental photoemission spectra (dashed lines). The scales for the XPS and UPS curves are arbitrary.

the atomic s-like states of Se and Te. The next band contains p-like bonding states which lie between − 6.0 and − 2.2 eV for Se and for Te. Finally the topmost valence states are predominately nonbonding p-like in nature. These identifications are reconfirmed on our present calculations; moreover the widths, positions, and number of peaks in the densities of states are now in good quantitative agreement with experiment.

In order to understand the origin of the characteristic two-peak structure found in the p-like bonding states of both Se and Te we have calculated the electronic charge distributions of states in each peak following standard procedures.[10] This entails summing over states whose energies (in eV) fall within $[-6.0, -3.6]$ and $[-3.6, -2.25]$ for Se and $[-6.0, -3.5]$ and $[-3.5, -2.2]$ for Te. Once we have calculated the total charge density of each energy interval, we can go one step further and isolate the short-wavelength Fourier components from the long-wavelength Fourier components. This introduces a new method of defining bonding charges and a way to separate out the effects of metallicity. The cutoff or boundary wavelength λ_0 between short- and long-wavelength components was found to lie naturally at $\lambda_0 \approx d$, where d is the nearest-neighbor separation in Se and Te. The results obtained for Se by retaining only Fourier components with $\lambda \lesssim \lambda_0$ are shown in Figs. 2(a) and 2(b) for the energy intervals $[-6.0, -3.6]$ and $[-3.6, -2.25]$, respectively. This charge distribution reproduces just the localized parts of the total charge density in this energy range. The results for Te are similar and will not be presented here.[7] We notice immediately that the lower energy peak in the p-like bonding states represents states involved in *intrachain bonding*. The charge is well localized in the bonds between atoms belonging to the same chain. In the upper or higher energy peak of the p-like bonding states we find states which arise in part from hybridization and which contribute to the *interchain bonding* in the crystal. Now the charge is displaced out of the bonds and is concentrated in the region between neighboring chains [right half of Fig. 2(b)]. The charge found within the chains [left half of Fig. 2(b)] is a residual charge of the lower bonding p states. In fact both Figs. 2(a) and 2(b) show some residual charge, indicating that an absolute separation on the energy scale of the two types of states is impossible. The intrachain bonding states lie lower in energy than the interchain bonding states since the potential is strongest between neighboring atoms within a chain.

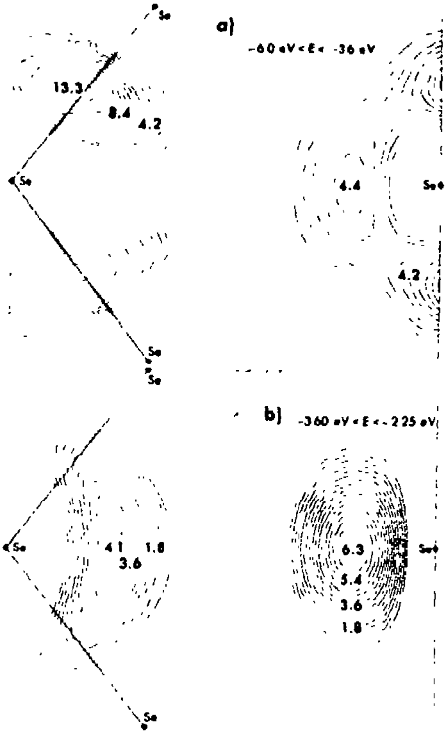

FIG. 2. Bonding charge of trigonal Se for the (a) lower and (b) upper p-like bonding states, calculated as described in the text. Only positive contours are shown, with values in units of e/Ω. The contour separation is 0.84 units in (a) and 0.36 units in (b).

Some measure of intrachain versus interchain bonding strengths is given by the magnitude of the respective bonding charges. For Se we have found $0.07e$ for the intrachain bond and $0.04e$ for the interchain bond. It is instructive to compare these values with $0.05e$ and $0.04e$ for the intrachain and interchain bonds of Te, respectively. The ratio ξ of intrachain to interchain bonding charge decreases from 1.75 for Se to 1.25 for Te and thus reflects the more three-dimensional or more isotropic character of Te. Furthermore, we believe that the smaller amount of total bonding charge in Te is indicative of its more metallic character.

Finally we should emphasize that the accuracy of the bonding charges we have obtained should be considered mostly in a relative sense rather than individually.

Part of this work was done under the auspices of the U.S. Atomic Energy Commission.

---

*Work supported in part by the National Science Foundation, Grant No. GH 35688.

†Swiss National Science Foundation postdoctoral fellow.

[1] J. Stuke, in *The Physics of Se and Te*, edited by W. C. Cooper (Pergamon, New York, 1969), p. 3.

[2] N. J. Shevchik, J. Tejeda, M. Cardona, and D. W. Langer, Solid State Commun. 12, 1285 (1973).

[3] M. Schlüter, J. D. Joannopoulos, M. L. Cohen, L. Ley, S. Kowalczyk, R. A. Pollak, and D. A. Shirley, to be published.

[4] S. Tutihasi and I. Chen, Phys. Rev. 158, 623 (1967); I. Chen, Phys. Rev. B 7, 3672 (1973).

[5] R. Sandrock, Phys. Rev. 169, 642 (1968).

[6] B. Kramer, K. Maschke, and L. D. Lande, Phys. Rev. B 8, 5781 (1973).

[7] J. D. Joannopoulos, M. Schlüter, and M. L. Cohen, to be published.

[8] M. L. Cohen and V. Heine, in *Solid State Physics*, edited by H. Ehrenreich, F. Seitz, and D. Turnbull (Academic, New York, 1970), Vol. 24, p. 37.

[9] M. Schlüter, Int. J. Quantum Chem. 7, 527 (1973).

[10] J. P. Walter and M. L. Cohen, Phys. Rev. B 4, 1877 (1971).

Localized Enhancement Effects in Pd-Ag Alloys

A. P. Murani
Physics Department, Imperial College, London SW7 2BZ, England

(Received 1 April 1974)

Low-temperature electrical resistivities of Pd-Ag alloys show a positive T^2 temperature dependence in the concentration range above 60 at.% Ag. This behavior supplements the well-known resistivity minima observed in alloys with lower concentrations of Ag, and strongly favors the model of scattering from localized exchange-enhanced Pd *d* states, as against $s \to d$ scattering in the rigid-, or collective-, band description of the alloys.

Two conflicting models for the electronic structure of Pd-Ag alloys are currently being advanced as possible explanations of the electrical resistivity behavior of these alloys. The resistivity minima observed by Edwards, Chen, and Legvold[1] in Pd-Ag alloys in the concentration range between 25 and 55 at.% Ag have been explained by the authors in terms of scattering of conduction electrons from exchange-enhanced pockets of holes associated with statistical clusters of Pd atoms—a distinction being made between the localized density of *d* states and the itinerant *d* band, also associated with Pd atoms. However, Rowlands and Greig[2] who observed similar minima in the Pd-Rh system found the calculated value of the coefficient A of the T^2 term in the resistivity of an alloy containing 4% Rh (obtained by using the rigid-band model[3] approximation as applied to the Pd-Ag system by Coles and Taylor[4]) to be very close to the experimental value, and therefore they argued in favor of the rigid-, or collective-, band description of the alloys. This assertion is further supported, it is now claimed, by some recent resistivity measurements on the Pd-Ag system by Ahmad and Greig,[5] who have observed two resistance minima in a Pd$_{0.60}$Ag$_{0.40}$ alloy, as also found in the Cu-Ni system.[6] These authors have put forward a qualitatively plausible explanation of the anomaly as due to a combination of two terms in the resistivity—a term $\rho_0(1-AT^2)$ due to the reduction of $s \to d$ scattering cross section resulting from the broadening of the Fermi level within the d-band states,[4,7] and an ideal resistivity term $\rho_{\text{ideal}} \sim BT^2 + CT^4$ at low temperatures which changes to a term linear in T at higher temperatures, giving rise to the maximum in the resistivity which follows the first minimum at lower temperatures. The second minimum results since the low-temperature $1-AT^2$ dependence is gradually modified and flattens off at high temperatures, as it must, leaving the linear term in the resistivity dominant. On the basis of this, the authors argue, the observed anomalies in the Pd-Ag and Cu-Ni systems may be regarded as caused by $s \to d$ scattering of conduction electrons into the d-band states.[4,7]

As suggested by Edwards, Chen, and Legvold,[1] of course, the $1-AT^2$ term in the resistivity discussed above could equally well be obtained from the process of scattering of conduction electrons from exchange-enhanced localized pockets of holes. Hence at first sight and on a qualitative basis it appears difficult to make a distinction between the two models. It is, however, useful to remember that direct evidence of a separate "band" associated with Pd in Ag-rich Ag-Pd alloys has been found in the optical absorption studies of the alloys by Myers, Wallden, and Karlsson.[8] Similar evidence is also seen in the photoemission experiments of Norris and Nilsson[9] and Norris and Myers.[10] The results have been explained by these authors in terms of a Friedel-Anderson virtual bound state[11] for Pd atoms in the Ag matrix, situated above the Ag *d* band and about 2 eV below the Fermi level. Formation of statistical near-neighbor clusters results in further broadening of the *d* states, but they remain localized on the Pd atoms, the authors suggest, until the concentration of Pd reaches 40 at.%. Also, Kjollerström[12] has shown that the dielectric-constant, the residual-resistivity, and the specific-heat data of dilute Ag-Pd alloys can be satisfactorily accounted for by the Anderson model using a half-width of 0.6 eV for the impurity state, which lies 2.2 eV below the Fermi level.

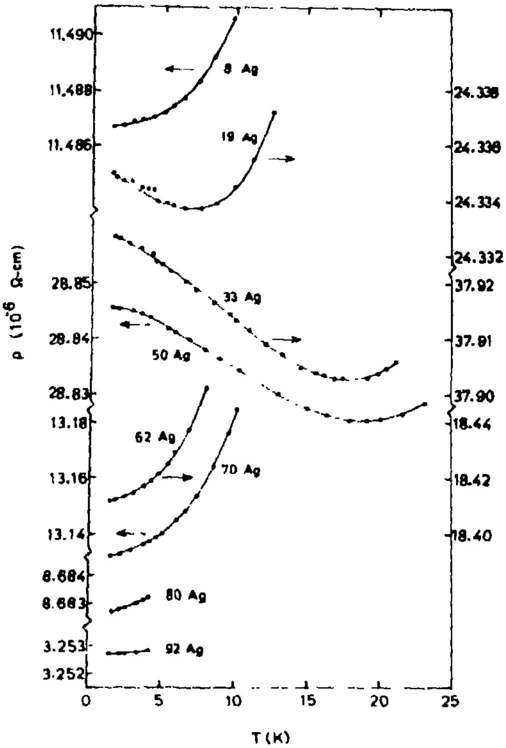

FIG. 1. Electrical resistivity of Pd-Ag alloys as a function of temperature. The concentration of Ag in the binary matrix is indicated on the respective curves. Note the changes of vertical scale, particularly between the alloys at the two ends and those in the middle of the series.

I wish to report here some preliminary measurements of the electrical resistivity of several Pd-Ag alloys which, I believe, lend strong support to the model of localized *d*-state formation in the alloy system. The low-temperature resistivity behavior in the concentration range above 60 at.% has, apparently, remained unmeasured so far despite an active interest in this alloy system for a long time.

The results are shown in Fig. 1 where the electrical resistivity is plotted as a function of temperature for a series of Pd-Ag alloys covering the whole concentration range. In the Pd-rich region with up to 50 at.% Ag, resistance minima are observed in good qualitative agreement with the results obtained by Edwards, Chen, and Legvold.[1] However, in the next concentration alloy with about 62% Ag the resistivity behavior changes dramatically and shows the positive T^2 temperature dependence (see Fig. 2). Further in-

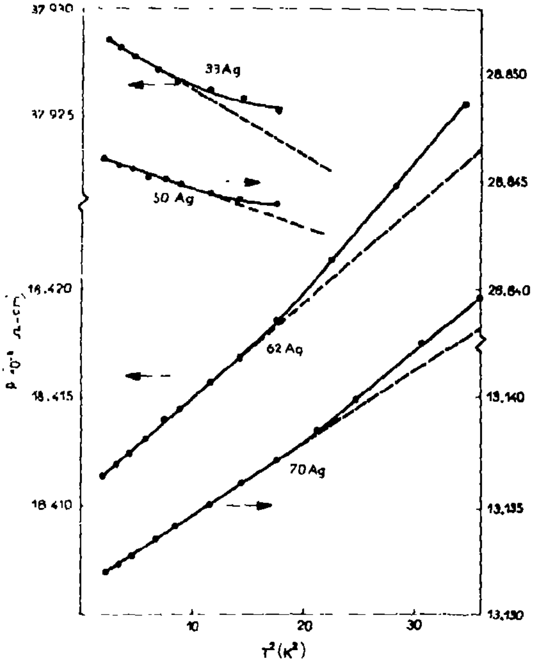

FIG. 2. Electrical resistivity plotted against T^2 for four Pd-Ag alloys containing Ag concentrations as indicated.

crease in the Ag concentration results in a decrease in the strength of the T^2 dependence, but it is possible that a maximum is reached at some concentration between 62 and 70 at.% Ag before this happens.

I argue that the localized-d-states model can account for the observed behavior in a quite natural way. As mentioned earlier, there is ample evidence that in Ag-rich alloys the localized states associated with statistical clusters of Pd atoms are situated below the Fermi level. Hence, at $T=0$ their contribution to the scattering of conduction electrons should be small. Any additional scattering from localized enhancement effects, or spin fluctuations, therefore gives an increasing contribution to the resistivity in a straightforward manner.[13,14] The appearance of holes in the d states when the concentration reaches above 40 at.% is accompanied by a change of slope in the residual resistivity versus concentration curve, which has been ascribed to the appearance of $s\rightarrow d$ scattering channel.[4] The situation is similar in some ways to that of *Pd*U where above a concentration of 8 at.% U, a large increase in the residual resistivity per atomic percent of U is observed as the "Fermi level becomes pinned to the U virtual f level."[15] If the $s\rightarrow d$ scattering in the present system gives rise to large phase shifts at $T=0$, then additional scattering due to spin fluctuations will result in a T^2-like decrease in the resistivity[14,16] as observed. In *Pd*U a change of sign of the T^2 dependence in the resistivity with concentration is also observed, but this is in opposite sense to the present one if the reduced diagram of the electronic specific-heat coefficient γ versus the electron/atom ratio is considered.[17] However, the mechanism for the anomaly is essentially the same for both systems. In *Pd*U the observed behavior is due to f levels in relatively dilute alloys, whereas in Pd-Ag alloys it is the localized d states on Pd atoms in alloys containing substantial Ag concentrations which are thought to give rise to the observed anomalies. I should mention, however, that the idea of localized pockets of holes existing in Pd-rich alloys is at variance with the claim by Norris and Myers[10] that Pd d states become itinerant above the concentration of 40 at.% Pd. It is nevertheless possible that d states on certain configurations of statistical clusters of Pd atoms remain localized (in some spatial sense) while others form "fully" itinerant band states.

The strong positive temperature dependence in the resistivity of Ag-rich alloys is more difficult to justify on band-model arguments than perhaps is the negative one (i.e., resistance minima). It should be noted, however, that the results of Edwards, Chen, and Legvold[1] indicate that the coefficient A of the T^2 term, which should roughly follow the depth of the minimum (even after due allowance for B), goes through a maximum value at around 40 at.% Ag in the binary matrix and becomes negligibly small in alloys with Pd concentrations above 80 at.%. This behavior would be impossible to obtain from the rigid-band formula of Coles and Taylor[4] taken together with the well-known specific-heat behavior of the Pd-Ag system.[18] (For instance, the value of A for the Pd-19-at.%-Ag alloy, Fig. 1, is an order of magnitude smaller than that expected from the formula of Coles and Taylor.) It also does not seem possible that an appropriately shaped d band or a two-band structure as considered by Dugdale and Guenault[19] for the Pd-Ag system and earlier by Coles[20] for the Cu-Ni system could simultaneously account for both the resistivity and the specific heat of the alloys. For the positive T^2 dependence the situation is even more clearcut, for band arguments require the Fermi level to be situated close to a minimum in the density of states.[7] It is difficult to imagine that any band model would indicate that it will remain fixed to a minimum over such a large concentration range of about 30–40 at.%.

I conclude by saying that the observed positive temperature dependence in the resistivity enables us, for the first time, to make an unambiguous choice of the model to describe the electronic structure of Pd-Ag alloys, regarding which considerable controversy exists in the literature. Although rigid-, or collective-, band arguments seem qualitatively appealing in the case of the negative temperature dependence, they fail completely when details such as the variation of the coefficient A of the T^2 term with concentration are considered. Even more important is the fact that the model is in direct conflict with the positive T^2 temperature dependence observed over a wide concentration range in silver-rich alloys. Scattering of conduction electrons from localized exchange-enhanced states associated with Pd atoms, on the other hand, can satisfactorily account for the T^2 resistivity behavior including the change in sign of the coefficient A. Hence this model seems to be the most appropriate description of this and similar alloy systems.

The author acknowledges discussions with Professor B. R. Coles concerning his collective-band arguments for Pd-Ag. Financial support received from the Science Research Council during a part of this work is also gratefully acknowledged.

[1] L. R. Edwards, C. W. Chen, and S. Legvold, Solid State Commun. 8, 1403 (1970).

[2] J. A. Rowlands and D. Greig, J. Phys. F: Metal Phys. 1, L29 (1971).

[3] N. F. Mott, Proc. Phys. Soc., London 47, 571 (1935).

[4] B. R. Coles and J. C. Taylor, Proc. Roy. Soc., Ser. A 267, 139 (1962).

[5] H. M. Ahmad and D. Greig, Phys. Rev. Lett. 32, 833 (1974).

[6] R. W. Houghton, M. P. Sarachick, and J. S. Kouvel, Phys. Rev. Lett. 25, 238 (1970).

[7] H. Jones, in *Handbuch der Physik*, edited by S. Flügge (Springer, Berlin, 1956), Vol. 19, p. 267.

[8] H. P. Myers, L. Wallden, and Å. Karlsson, Phil. Mag. 18, 725 (1968).

[9] C. Norris and P. O. Nilsson, Solid State Commun. 7, 649 (1968).

[10] C. Norris and H. P. Myers, J. Phys. F: Metal Phys. 1, 62 (1971).

[11] P. W. Anderson, Phys. Rev. 124, 41 (1961).

[12] B. Kjollerström, Solid State Commun. 7, 705 (1969).

[13] P. Lederer and D. Mills, Phys. Rev. Lett. 20, 1036 (1968).

[14] A. B. Kaiser and S. Doniach, Int. J. Magn. 1, 11 (1970).

[15] S. Doniach, in "Actinides," edited by J. Darby and A. J. Freeman (Academic, New York, to be published).

[16] N. Rivier and V. Zlatić, J. Phys. F: Metal Phys. 2, L87 (1972).

[17] W. J. Nellis and M. B. Brodsky, Phys. Rev. B 2, 4590 (1970).

[18] H. Montgomery, G. P. Pells, and E. M. Wray, Proc. Roy. Soc., Ser. A 301, 261 (1967).

[19] J. S. Dugdale and A. M. Guenault, Phil. Mag. 13, 503 (1966).

[20] B. R. Coles, Proc. Phys. Soc., London, Sec. B 65, 221 (1952).

Electronic Structure of the Tetracyanoquinodimethane (TCNQ) Molecule

Frank Herman* and I. P. Batra
IBM Research Laboratory, San Jose, California 95193

(Received 21 January 1974; revised manuscript received 23 May 1974)

The electronic structure of an isolated TCNQ molecule has been calculated by the self-consistent statistical-exchange multiple-scattering method. By using overlapping atomic spheres in place of nonoverlapping atomic spheres, a significant increase in physical realism has been achieved. The theoretical model provides a satisfactory account of the photoemission spectra of TCNQ vapor and solid TCNQ. The singlet-triplet splitting for the lowest optical transition is found to be 0.84 eV.

During the past few years, interest in the physics of organic solids has grown rapidly. Of particular interest are highly conducting charge-transfer salts[1-3] such as tetrathiofulvalinium-tetracyanoquinodimethanide (TTF-TCNQ).[4,5] Most current discussions of the physical properties of these organic solids are based on idealized one-dimensional models.[1-5] However, there are indications[6] that realistic three-dimensional models are required for a thorough understanding of these properties. Also, conclusive theoretical interpretations of the photoemission spectra of TCNQ vapor and solid TCNQ have not yet appeared.

In this paper we describe a simple theoretical model which can be used to generate realistic energy-level structures for large planar organic molecules such as TCNQ. Our calculations for the TCNQ molecule were carried out within the general framework of the self-consistent statistical-exchange ($X\alpha$) multiple-scattering method.[7,8] In an initial effort,[9] the calculations were carried out on the basis of the standard muffin-tin model[7,8] by which we mean nonoverlapping atomic spheres embedded in an intersphere region, all surrounded by a bounding outer sphere (cf. Fig. 1). This type of model had been used previously to study other large planar organic molecules.[10] It was clear from the preliminary study of the TCNQ molecule[9,11] that the standard muffin-tin model was not sufficiently accurate for our purposes, and that a significant improvement in physical realism was necessary if we hoped to deal successfully with the TCNQ molecule.

It is possible to improve upon the standard muffin-tin model by introducing nonspherical terms

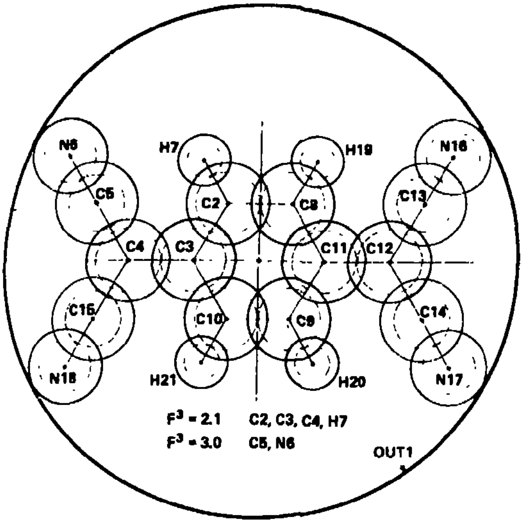

FIG. 1. Nonoverlapping atomic-sphere model (dashed circles) and overlapping atomic-sphere model (solid circles) for the TCNQ molecule. The outer sphere (OUT1) for the former is not shown in the interest of clarity. The outer sphere is assigned serial number 1 and the atomic spheres serial numbers 2 through 21. The ratio of the volumes of the overlapping and corresponding nonoverlapping atomic spheres is denoted by F^3.

in the atomic spheres as well as nonconstancy terms in the uniform intersphere region.[12-14] However, these improvements require extensive modification of existing scattered-wave computer programs.[15,16] Fortunately, one can take a major step[9,13,17,18] in the direction of improved realism without making any significant changes in existing computer programs. One simply replaces nonoverlapping atomic spheres by overlapping atomic spheres (cf. Fig. 1), and retains the following two simplifying assumptions: (a) Inside each atomic sphere, and outside the bounding sphere, potentials and charge distributions are spherically averaged. (b) In the intersphere region, these quantities are volume averaged. A theoretical justification for this overlapping atomic-sphere model is presented elsewhere,[13] ogether with additional information concerning TCNQ calculations based on overlapping atomic-phere models.

From a practical point of view, the overlapping tomic-sphere model is incomplete until all the tomic-sphere radii (and the outer-sphere radius) re specified. At the present time, the choice of radii must be dealt with pragmatically. After examining a number of possibilities it was found that substantially the same electronic energy-level structure was predicted by various choices of atomic- and outer-sphere radii, provided these radii were chosen with the following two guidelines in mind: (a) The calculated value of the virial coefficient should be equal to -2, thereby insuring an optimum balance of potential and kinetic energy within the framework of the present approximational scheme.[19] (b) The calculated value of the first ionization energy should agree with the experimental value. The second guideline is necessary for establishing an accurate absolute energy scale. If one wishes to avoid any appeal to experimental energy-level information, one must greatly refine the existing model and related computer programs. For our purposes, it is more expedient to adjust the radii so that the first ionization energy agrees with experiment.

We will illustrate our results for the isolated TCNQ molecule by considering an overlapping atomic-sphere model having the following attributes: (a) The statistical-exchange parameter α is set equal to 0.75 for all regions of space. (b) The TCNQ molecule is assumed to be planar and to have D_{2h} symmetry. Internuclear distances were obtained by averaging x-ray crystallographic data for the TCNQ crystal[20] in accordance with these assumptions, both of which are justifiable in the present context. (c) The choice of nonoverlapping atomic spheres was dictated by the requirements that they touch wherever possible and that (in the case of C5 and N6) they have chemically reasonable proportions.[21] (d) The outermost sphere was drawn externally tangent to the outermost atomic spheres. (e) The ratio of the volumes of the overlapping and corresponding nonoverlapping atomic spheres for C2, C3, C4, and H7 was 2.1, and for C5 and N6, 3.0. These ratios were chosen so that our two guidelines would be satisfied.

The energy-level structure calculated for this model is shown in Fig. 2 by the long lines. These levels were obtained by the transition-state method[7,8] so that relaxation effects are taken into account. For purposes of comparison, the results of a recent *ab initio* minimal-basis-set molecular-orbital self-consistent field (MO-SCF) calculation[24] are shown by the short lines. In the latter, the energy levels were obtained by taking the differences between the total energies of the ground and ionic states, thereby allowing for relaxation effects. The symmetry notation for the

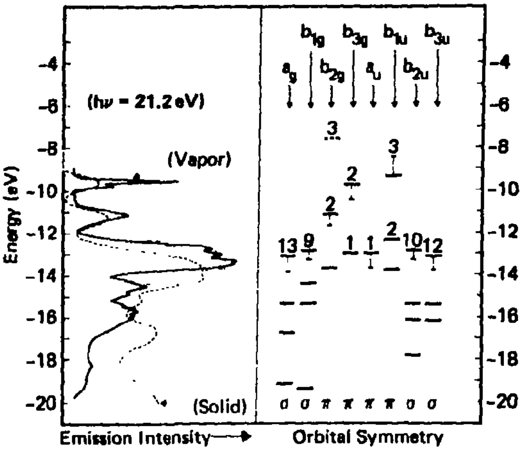

FIG. 2. Comparison of theoretical energy-level structure and experimental photoemission spectra of TCNQ vapor (Ref. 22) and solid TCNQ (Ref. 23). Results of present calculations are shown by the long lines. Results of *ab initio* SCF MO calculation (Ref. 24) are indicated by the short lines. Corresponding energy levels are connected by vertical lines. Occupied levels are denoted by solid lines, unoccupied levels by dashed lines. The symbols σ and π at the bottom right refer to reflection with respect to the plane of the molecule. For each symmetry species, the levels are labeled by serial numbers in order of increasing energy. Only a few of these serial numbers are actually shown.

D_{2h} point group is that of Cotton.[25]

For all the overlapping atomic-sphere models for TCNQ that have been investigated so far, the two highest occupied levels are invariably $3b_{1u}$ and $2b_{3g}$. These two levels usually lie very close together in energy. Accordingly, the present theoretical model was so chosen that the center of gravity of these two levels would be equal to the experimental value of the first ionization energy, which is given by photoemission measurements for TCNQ vapor as 9.6 eV.[22] This spectrum, as well as the photoemission spectrum for solid TCNQ,[23] are reproduced in Fig. 2.

Let us first consider the vapor spectrum for TCNQ since this corresponds more closely to the energy-level spectrum of an isolated molecule. By design, the highest experimental peak at − 9.6 eV is attributed to transitions from the two highest occupied levels, $3b_{1u}$ and $2b_{3g}$. The next peak at − 11.2 eV is due to transitions from $2b_{3g}$. The small structure on the leading (upper) edge of the large peak at − 12.6 eV is due to $2b_{1u}$. The main structure between − 12.8 and − 14.0 eV is due to transitions from six levels: $13a_g$, $9b_{1g}$, $1b_{3g}$, $1a_u$, $10b_{2u}$, $12b_{3u}$. The peak at − 14.5 eV is probably due to three levels: $8b_{1g}$, $1b_{2g}$, $1b_{1u}$. The peak at − 15.8 eV is due to six levels: $12a_g$, $7b_{1g}$, $8b_{2u}$, $9b_{2u}$, $10b_{3u}$, $11b_{3u}$. Contour maps of the electronic charge distributions for representative molecular orbitals of TCNQ are reported elsewhere.[13,26]

The experimental spectrum for solid TCNQ has been superimposed on the vapor spectrum so that their highest peaks coincide. This was done to illustrate the fact that the two spectra are qualitatively similar, but not everywhere coincident. This lack of coincidence must arise from solid-state effects, i.e., shifts of various levels by slightly different amounts because of interaction with neighboring molecules. If we superimpose the two spectra so that the main peaks are in registry, the vapor peaks at − 9.6 and − 11.2 eV lie about 0.5 eV below their solid counterparts, and the vapor peak at − 15.8 eV lies about 0.5 eV above its solid counterpart. Making allowance for these solid-state shifts, one can interpret the photoemission spectrum for solid TCNQ in the same manner that we interpreted the vapor spectrum above. The magnitude of the solid-state shifts appears to depend on the method of sample preparation, since a comparison of the TCNQ-vapor spectrum with another solid-TCNQ spectrum[27] reveals smaller solid-state shifts.

Turning to the excited states we find that the lowest unoccupied level is $3b_{2g}$. The next higher unoccupied levels lie about 2 eV above $3b_{2g}$. In TCNQ$^-$ and TCNQ^{-2}, the $3b_{2g}$ level is singly and doubly occupied. The lowest-energy orbitally allowed optical transition is from $3b_{1u}$ to $3b_{2g}$. A spin-restricted calculation for the present model leads to an excitation energy of 1.9 eV for this transition. A spin-unrestricted calculation leads to a singlet-triplet splitting of 0.84 eV. To obtain a reasonable estimate of the singlet-singlet and singlet-triplet transition energies, we set the center of gravity at 1.9 eV, and weigh the $3b_{2g}$ triplet state three times as heavily as the $3b_{2g}$ singlet state. This leads to an excitation energy of 1.7 eV for the forbidden singlet-triplet transition and 2.5 eV for the allowed singlet-singlet transition. The latter is undoubtedly responsible for the 3.1-eV optical peak observed for TCNQ in solution.[28]

The present study of the TCNQ molecule thus provides a basis for interpreting optical and photoemission spectra of TCNQ vapor, TCNQ molecules in solution, and solid TCNQ. The physical realism achieved by adopting the overlapping atomic-sphere model is quite striking. Our work has demonstrated the feasibility of carrying out similar calculations for other large planar organic molecules, and for arrays of such molecules. A companion study of the TTF molecule will be reported elsewhere.[29]

The authors are pleased to acknowledge fruitful discussions with A. J. Epstein, W. D. Grobman, K. H. Johnson, D. A. Liberman, and W. E. Rudge. The authors are grateful to J. N. A. Ridyard for permission to reproduce his photoemission spectrum for TCNQ vapor. F. H. particularly wishes to thank M. Balkanski for his hospitality at the Université de Paris VI, where some of the research reported here was conducted. The authors are grateful to Professor K. H. Johnson for sending them a copy of the original Massachusetts Institute of Technology scattered-wave computer program. A modified version of this program was used in the present study.

---

*Exchange Professor, Université de Paris VI, September 1973.

[1] R. Foster, *Organic Charge-Transfer Complexes* (Academic, London, 1969).

[2] I. F. Shchegolev, Phys. Status Solidi (a) 12, 9 (1972).

[3] H. R. Zeller, in *Festkörperprobleme*, edited by H. J. Queisser (Pergamon, New York, 1973), Vol. XIII, p. 31.

[4] A. J. Epstein, S. Etemad, A. F. Garito, and A. J. Heeger, Phys. Rev. B 5, 952 (1972); L. B. Coleman, J. J. Cohen, D. J. Sandman, F. G. Yamagishi, A. F. Garito, and A. J. Heeger, Solid State Commun. 12, 1125 (1973).

[5] J. Ferraris, D. O. Cowan, V. Walatka, Jr., and J. H. Perlstein, J. Amer. Chem. Soc. 95, 948 (1973).

[6] M. H. Cohen, J. A. Hertz, P. M. Horn, and V. K. S. Shante, to be published.

[7] K. H. Johnson, J. Chem. Phys. 45, 3085 (1966); J. C. Slater and K. H. Johnson, Phys. Rev. B 5, 844 (1972); J. C. Slater, Advan. Quantum Chem. 6, 1 (1972); K. H. Johnson, Advan. Quantum Chem. 7, 143 (1973).

[8] K. H. Johnson, J. G. Norman, Jr., and J. W. D. Connolly, in *Computational Methods for Large Molecules and Localized States in Solids*, edited by F. Herman, A. D. McLean, and R. K. Nesbet (Plenum, New York, 1973), p. 161.

[9] F. Herman and I. P. Batra, in Proceedings of the Colloquium on Many-Electron Effects in Solids, Taormina, Sicily, Italy, September, 1973 (to be published).

[10] D. A. Liberman and I. P. Batra, J. Chem. Phys. 59, 3723 (1973).

[11] The nonoverlapping atomic-sphere model for TCNQ yielded a virial coefficient of -1.858 (rather than the theoretical value of -2), a first ionization energy of 16.4 eV (experimental value: 9.6 eV), and a set of high-lying occupied energy levels that were much closer together than would be suggested by experimental photoemission spectra.

[12] See for example A. R. Williams and J. van W. Morgan, J. Phys. C: Proc. Phys. Soc., London 7, 37 (1974).

[13] F. Herman, A. R. Williams, and K. H. Johnson, to be published.

[14] J. C. Slater, to be published.

[15] K. H. Johnson and F. C. Smith, Jr., Massachusetts Institute of Technology Scattered-Wave Computer Program, July, 1972.

[16] D. A. Liberman and I. P. Batra, IBM Research Report No. RJ 1224, 1973 (unpublished). This report documents a modified version of Ref. 15. Still another version of Ref. 15 is documented: J. W. D. Connolly, University of Florida, Gainesville, Report No. 282, 1972 (unpublished).

[17] D. A. Liberman, private communication.

[18] N. Rösch, W. G. Klemperer, and K. H. Johnson, Chem. Phys. Lett. 23, 149 (1973); N. Rösch and K. H. Johnson, Chem. Phys. Lett. 24, 179 (1974).

[19] It is assumed that the TCNQ molecule is in equilibrium for the assigned nuclear coordinates. For a discussion of the virial theorem and the virial coefficient within the context of the statistical exchange approximation, see J. C. Slater, J. Chem. Phys. 57, 2389 (1972).

[20] R. E. Long, R. A. Sparks, and K. N. Trueblood, Acta Crystallog. 18, 932 (1965) (TCNQ crystal). The C-H bond distance was taken as 1.09 Å.

[21] J. B. Hendrickson, D. J. Cram, and G. S. Hammond, *Organic Chemistry* (McGraw-Hill, New York, 1970), 3rd ed., p. 58.

[22] J. N. A. Ridyard, private communication. The TCNQ-vapor spectrum was obtained with a Perkin-Elmer Model PS 18 spectrometer.

[23] W. D. Grobman, R. A. Pollak, D. E. Eastman, E. T. Maas, Jr., and B. A. Scott, Phys. Rev. Lett. 32, 534 (1974).

[24] H. T. Jonkman, G. A. van der Velde, and W. C. Nieuwpoort, Chem. Phys. Lett. 25, 62 (1974). Dr. Jonkman has advised the authors in a private communication that his calculation yields a value of 3.68 eV for the first singlet excited state and a value of 3.43 eV for the singlet-triplet splitting. Our singlet-triplet splitting of 0.84 eV appears to be more realistic.

[25] F. A. Cotton, *Group Theory with Chemical Applications* (Wiley-Interscience, New York, 1971), 2nd ed.

[26] F. Herman, W. E. Rudge, and I. P. Batra, to be published.

[27] P. Nielsen, A. J. Epstein, and D. J. Sandman, to be published.

[28] H. T. Jonkman and J. Kommandeur, Chem. Phys. Lett. 15, 496 (1972).

[29] B. I. Bennett and F. Herman, to be published.

Time-Reversed Antiferromagnetic States in Dysprosium Aluminum Garnet

J. F. Dillon, Jr., and E. Yi Chen
Bell Laboratories, Murray Hill, New Jersey 07974

and

N. Giordano and W. P. Wolf
*Becton Center, Yale University, New Haven, Connecticut 06520**

(Received 15 April 1974)

The field dependences of the magneto-optical rotation of the two time-reversed states of antiferromagnetic dysprosium aluminum garnet show significant differences. These are interpreted in terms of the spatial variation in the signs of the spin-spin interactions demanded by the crystal symmetry. The coexistence of the two time-reversed states has been studied by microscopy made possible by the rotation difference and also by a striking "decoration" of the domain walls by paramagnetic nuclei.

Largely because it appeared to approximate closely a simple two-sublattice Ising system, the antiferromagnet dysprosium aluminum garnet (DyAlG), with fields along [111], has been much studied over the past decade.[1] Recently in the course of magneto-optical studies of this crystal, we encountered a number of new and puzzling phenomena. These included (a) an unexpected dependence of the magnetization on past history[2] and (b) related microscope observations of magnetically active domains with curious properties seemingly unrelated to the accepted magnetic phase diagram. These phenomena can now be understood in the light of a recent discussion by Blume *et al.*[3] in which they pointed out that an applied field may induce significant antiferromagnetic order in DyAlG, so that the two time-reversed (TR) antiferromagnetic states become distinguishable in a field. In this paper we shall present magneto-optical observations of the TR states in DyAlG and a detailed interpretation in terms of the specific mechanism described in a separate publication.[4]

Following Blume *et al.*,[3] we show in Fig. 1(a) the revised phase diagram for DyAlG in a field H_i along [111]. Both positive and negative fields are included to emphasize the zero-field phase boundary separating the two TR antiferromagnetic states for $T < T_N$. The two TR states, A^+ and A^-, are characterized by different values of the order parameter $\vec{L}$, which is here the staggered magnetization $\vec{M}_b - \vec{M}_a$, where a and b are the two inequivalent types of sites discussed previously.[3,4] The variation of $\vec{L}$ with H_i for the two TR states at a temperature $T < T_c$ is shown schematically in Fig. 1(b). In zero field time-reversal symmetry demands that $\vec{L}(A^+) = -\vec{L}(A^-)$, but in a nonzero field TR symmetry only requires $\vec{L}(A^+, H) = -\vec{L}(A^-, -H)$. For a given field we can thus have $\vec{L}(A^+, H) \neq -\vec{L}(A^-, H)$. Correspondingly, the total magnetization $\vec{M} = \vec{M}_a + \vec{M}_b$ will show TR symmetry $\vec{M}(A^+, H) = -\vec{M}(A^-, -H)$, but for a given field we can have $\vec{M}(A^+, H) \neq \vec{M}(A^-, H)$ [Fig. 1(c)]. In the presence of a field only one of the two states will be stable but, in common with other first-order transitions, we may expect the possibility of a metastable state as the phase boundary is crossed. The essential feature, first recognized by Blume

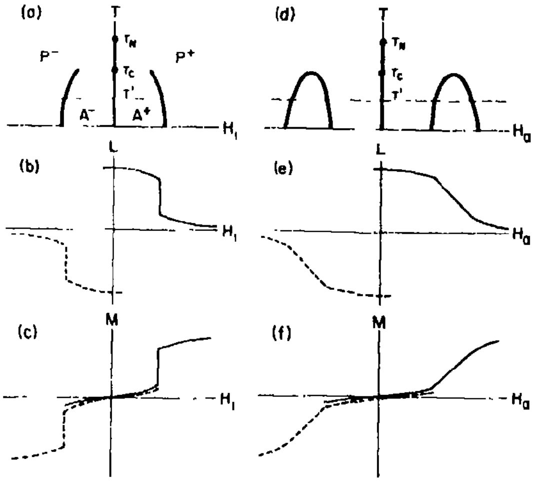

FIG. 1. (a) Revised phase diagram (schematic) for DyAlG (after Ref. 2). For low positive H_i the stable phase is A^+, and A^- is metastable. (b) Variation of the order parameter $\vec{L} = \vec{M}_b - \vec{M}_a$ for $T < T_c$. (c) Corresponding variation of the magnetization $\vec{M} = \vec{M}_a + \vec{M}_b$. (d)–(f) Similar plots in terms of the externally applied field $H_a = H_i + NM$.

et al.,[3] is that DyAlG is unusual in that a field along [111] (and indeed in almost all other directions[5]) will couple to the order parameter, removing the degeneracy and hence the ambiguity between the two states, thus making it possible to follow a given state from one side of the zero-field phase boundary to the other.

DyAlG is not unique in this respect, but in the other systems which have been studied,[6] the field was always effective through an allowed weak ferromagnetic moment, with the result that the two TR states became distinct in both L and M, even in zero field.

Under actual experimental conditions, the situation is complicated by demagnetizing effects and in Figs. 1(d)–1(f) we show the corresponding behavior as a function of the applied field $H_a = H_i + NM$, where N is the demagnetizing factor. The only essential difference is the fact that the two phase boundaries in nonzero H are spread over a region of H_a, within which the antiferromagnetic and paramagnetic phases coexist in varying proportions.[1] This coexistence makes it possible to nucleate a small and controllable amount of one phase in the other and we have utilized this fact in our microscope observations.

In the first experiments measurements were made of the magneto-optical rotation, which is proportional to M under the conditions of our experiments.[2] The data were taken by an automatic technique described earlier.[2] The sample was 690 μm thick and roughly elliptical in shape with major and minor diameters of 16 and 7 mm. The effective demagnetizing factor was close to 4π and all field measurements were recorded as the corresponding internal fields. The results are shown in Fig. 2 as solid lines.

It can be seen that there are two distinct curves at each temperature, depending on the previous field history of the sample. The upper curve in each case was obtained by first exposing the sample to a large positive field, and, provided the field was never allowed to go negative, it was completely reversible. In terms of our Fig. 1 we interpret this as the magnetization of the state A^+. The lower set of curves were obtained by irst exposing the sample to a large negative field nd then making measurements in positive fields which were not allowed to exceed the critical ield for the phase transition to the paramagnetic state. We interpret these curves as the behavior of the A^- state, which is metastable in low positive fields.

The difference in the response of the two TR states to an applied field may be understood quantitatively in terms of two different mechanisms, both involving a crystallographic inequivalence between two types of sites for the Dy^{3+} spins. The mechanism proposed by Blume *et al.*[3] involves a difference in the effective magnetic moments and this may be estimated from previously determined g values and Van Vleck susceptibilities. An estimate of the effect of these differences on the behavior of the two TR states shows[7] that it should be very small, suggesting that some other mechanism is in fact dominant under most conditions. Such a mechanism was proposed recently by Giordano *et al.*,[4] and it involves a difference in the geometrical arrangement of the

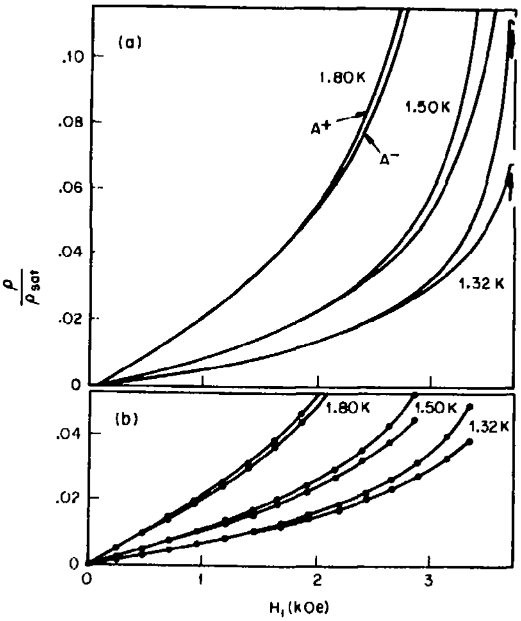

FIG. 2. (a) Automatic data plots of reduced magneto-optical rotation (ρ/ρ_{sat}) of two antiferromagnetic states of DyAlG versus internal field H_i at several temperatures. The upper curves (A^+) were obtained with a sample previously exposed to large positive H_i while the lower curves (A^-) were obtained following exposure to large negative H_i. The breaks in the 1.32-K curves indicated by arrows correspond to entry into the mixed phase; their nature must be discussed elsewhere. For negative fields the curves were entirely similar and consistent with the time-reversal requirement $\vec{M}(A^+, H) = -\vec{M}(A^-, -H)$. (b) Corresponding theoretical curves for a range of low magnetizations calculated according to the microscopic mechanism proposed in Ref. 4. Published interaction parameters were used.

spin-spin interactions. Values of the individual spin-spin interactions have been estimated from various thermodynamic measurements on DyAlG[8] and we can use these results directly in a low-field, low-temperature series expansion to predict M for both A^+ and A^-.

The calculation was made by including first-, second-, and third-nearest neighbors explicitly and the effect of all other neighbors in terms of a mean field, using the published values for the nondipolar interaction parameters and dipole sums calculated from the structure. Details of the calculation will be given elsewhere,[4,9] and we will note here only that it was necessary to include terms involving the simultaneous excitations of three nearest-neighbor spins before there was any difference between A^+ and A^-.

The results of the calculations are shown as the broken lines in Fig. 2. It can be seen that the agreement is quite satisfactory, especially at the lower temperatures where the approximation should be the best. It should also be noted that the calculated behavior is here based on a Hamiltonian which only includes Ising terms and that the difference between the two sublattices is an intrinsic property of this type of Ising model.

The substantial difference between the magneto-optical rotations of A^+ and A^- at elevated fields makes it possible to observe mixed antiferromagnetic states microscopically. As in Ref. 2, the apparatus consisted of a polarizing microscope whose optical axis lay along the axis of an electromagnet. The sample was immersed in superfluid helium in a Dewar with flat glass windows. Linearly polarized monochromatic light impinged on the sample. The analyzer was set to give the most revealing contrast.

In Figs. 3(a)–3(c) we show a sample which had been prepared in A^-, subjected to various field changes indicated schematically on the right. The temperature throughout was maintained constant at 1.32 K, as indicated by the hatched shading.

In Fig. 3(a) the field has taken the sample just into the mixed phase region and bright P^+ nuclei can be seen against the dark A^- background. If the field is now reduced back into the region where only A^+ is stable, the P^+ regions will transform into A^+ and in Fig. 3(b) we see the A^+ regions in A^-, as expected. The rotation contrast is here not as great as that between A^- and P^+ because of the much smaller difference in the magnetizations, but the coexisting domains are clearly visible. If the field is once again raised into the mixed phase region, P^+ is again nucleated and we can observe all three phases simultaneously [Fig. 3(c)]. It is interesting to note that P^+ is nucleated at the A^+-A^- boundary so that the antiferromagnetic domain walls have been effectively "decorated." That such nucleation would occur was noted by Jacobs and Lawrence,[10] and has recently been discussed by Mitsek and Gaidanskii.[1]

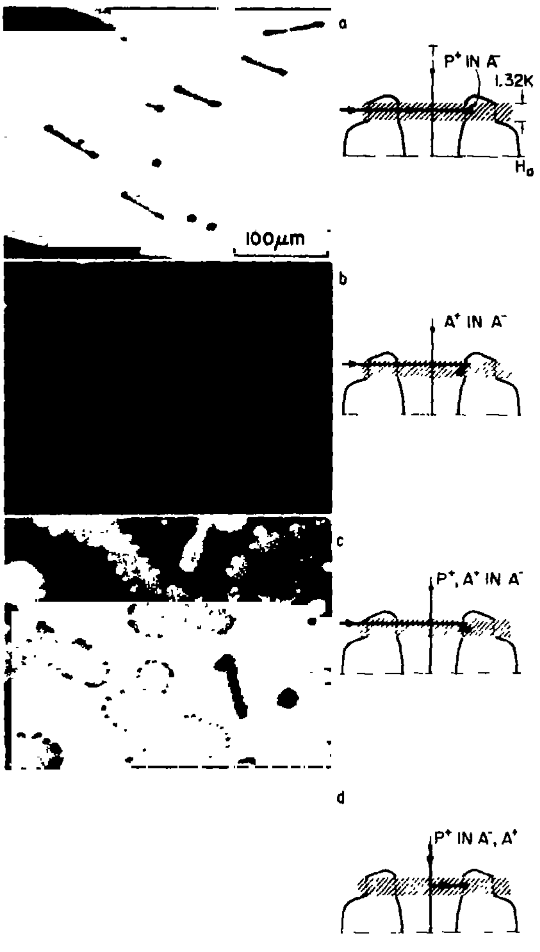

FIG. 3. Micrographs of the A^+, A^-, and P^+ magnetic phases obtained by various field and temperature treatments. All were taken at 1.32 K. For (a), (b), and (c) the sample was 690 μm thick; for (d), 190 μm. The field and temperature treatments used to obtain the four cases are indicated schematically on the right and are discussed in the text.

Neither this situation nor that of Fig. 3(a) is stable. In the course of minutes the P^+ slowly converts to a larger volume of A^+, corresponding to the lowest free-energy state. At higher temperatures the conversion is still more rapid, as one might expect.

Figure 3(d) shows the result of an experiment in which we cooled from above T_N in zero field ($<10^{-3}$ Oe) and at 1.32 K gently entered the mixed-phase region. The result of this procedure is a dense array of small needles of the paramagnetic phase. From experiments such as (c) above, we know that in the presence of an A^+-A^- mixture P^+ will nucleate on the domain walls, and we therefore interpret the present result as indicating an extremely finely divided mixture of A^+ and A^- in the initially cooled system. Cooling in larger fields produces various more complicated situations and we shall discuss these elsewhere.

These experiments have shown that it is possible to prepare a DyAlG sample either predominantly A^+ or predominantly A^- or else as various mixtures of the two. The distinctive rotation-versus-field curves of the two antiferromagnetic states has enabled us to study their properties directly. We have seen that two microscope techniques are effective for visualizing the TR domains. The first relies on the rotation difference at moderate fields, which provides a direct contrast when the sample is viewed between suitably set polarizers. This is applicable to all antiferromagnets in which the field couples to the antiferromagnetic order parameter.[6] The second technique makes use of the fact that the paramagnetic phase with its large rotation nucleates along A^+-A^- walls. We can thus "decorate" the antiferromagnetic walls with readily visible paramagnetic nuclei, an effect of still wider applicability. Further experiments are now in progress and will be reported elsewhere.

We would like to thank R. Alben, M. Blume, L. M. Corliss, and J. M. Hastings for a number of stimulating discussions.

---

[*] Work at Yale University supported in part by the U. S. Army Research Office, Durham, North Carolina.

[1] D. P. Landau, B. E. Keen, B. Schneider, and W. P. Wolf, Phys. Rev. B 3, 2310 (1971). This paper also gives extensive references to earlier work.

[2] J. F. Dillon, Jr., E. Y. Chen, and W. P. Wolf, in Proceedings of the International Conference on Magnetism, Moscow, U.S.S.R., 22–28 August 1973 (to be published).

[3] M. Blume, L. M. Corliss, J. M. Hastings, and E. Schiller, Phys. Rev. Lett. 32, 544 (1974).

[4] N. Giordano, W. P. Wolf, J. F. Dillon, Jr., and E. Yi Chen, to be published.

[5] R. Alben (private communication) has pointed out that the presently assumed magnetic symmetry of DyAlG, *Ia3d*, predicts similar effects provided $H_x H_y H_z \neq 0$.

[6] A good review of previous work has been given by A. S. Borovik-Romanov, in *Elements of Theoretical Magnetism*, edited by S. Krupicka and J. Sternberk, translated by W. S. Bardo (CRC Press, Cleveland, Ohio, 1968), p. 193.

[7] R. Alben and N. Giordano, private communication.

[8] B. Schneider, D. P. Landau, B. E. Keen, and W. P. Wolf, Phys. Lett. 23, 210 (1966), and to be published; R. Bidaux, P. Carrara, and B. Vivet, J. Phys. (Paris) 28, 187 (1967).

[9] N. Giordano, thesis, Yale University (to be published).

[10] I. S. Jacobs and P. E. Lawrence, Phys. Rev. 164, 866 (1967).

[11] A. I. Mitsek and P. F. Gaidanskii, Zh. Eksp. Teor. Fiz. 62, 2252 (1972) [Sov. Phys. JETP 35, 1178 (1972)]; A. I. Mitsek, Phys. Status Solidi (b) 59, 309 (1973).

Systematic Pseudomagnetic Measurements of the Spin-Dependent Scattering Length of Slow Neutrons with Atomic Nuclei

P. Roubeau, A. Abragam, G. L. Bacchella, H. Glättli, A. Malinovski,* P. Meriel,
J. Piesvaux, and M. Pinot
Service de Physique du Solide et de Résonance Magnétique, Centre d'Etudes Nucléaires de Saclay,
91190 Gif-sur-Yvette, France
(Received 21 May 1974)

The magnitude and the sign of spin-dependent scattering lengths of slow neutrons by nuclei of Li^7, Al^{27}, Sc^{45}, Zr^{91}, Nb^{93}, La^{139}, and Ta^{181} have been determined by measuring the dependence of the precession angle of the neutron spins on the nuclear polarization of the scattering target.

The scattering of slow neutrons by a fixed nucleus can be described by the scattering length

$$\mathfrak{a}_N = a_0 + a_N \vec{I}_N \cdot \vec{s},$$

where $\vec{I}_N$ and $\vec{s}$ are the spins of the nucleus and the neutron, respectively. The parameter $a_N = (a_+ - a_-)/(I_N + \frac{1}{2})$ (a_+ *and* a_- *being the nuclear* scattering lengths of the nucleus for the two spin channels $I_N + \frac{1}{2}$ and $I_N - \frac{1}{2}$) is unknown for most nuclei. The growing use of polarized neutron beams, and targets with sizable polarizations obtained either in static fields at very low temperatures or by dynamic nuclear polarization, makes the knowledge of a_N of greater interest. In this Letter, we report values of a_N for a few nuclei.

In analogy to neutron magnetic scattering, a new formalism has been introduced previously, and its physical validity experimentally demonstrated.[1-3] It defines, inside a nuclear target, a pseudomagnetic field H^* produced by the pseudomagnetic moments μ^* of the target nuclei such that

$$H^* = 4\pi M^* = 4\pi N \mu^* P,$$

where N is the number of nuclei per unit volume, P is their polarization, and μ^* is given by

$$\mu^*/\mu_B = -a_N I_N / g_n r_0 = 1.855 \times 10^{12} I_N a_N$$
$$1.855 \times 10^{12} [I_N/(I_N + \tfrac{1}{2})](a_+ - a_-),$$

with μ_B the Bohr magneton, r_0 e^2/mc^2 the classical radius of the electron, and g_n $\mu_n/\mu_N = -1.913$ the neutron magnetic moment expressed in nuclear magnetons. In a static field H_0, the neutron magnetic moment will precess with the Larmor frequency $\omega_L = -\gamma_n H_0$, where $\gamma_n = 2\mu_n/\hbar = -2\pi \times 2917\ \mathrm{sec}^{-1}\ \mathrm{G}^{-1}$ is the gyromagnetic factor of the neutron. The effect of the pseudomagnetic field H^* is to change the Larmor precession frequency ω_L of the neutrons inside the target by an amount $\Delta\omega_L = -\gamma_n H^*$, as first shown theoretically by Barytchevski and Podgoretzki.[4] A very sensitive method to measure small changes in precession frequency is through the change in the precession angle of the neutron polarization. Such a method has been described in a previous Letter.[5] The extra precession angle due to the *pseudomagnetic field is* $\alpha = -\gamma_n H^* t = -\gamma_n H^* l/v$, l being the sample length and v the neutron velocity. This extra precession angle is measured from the ratio $R = I^+/I^-$ by the relation

$$\cos\alpha = (1 - R)/Dp^2(1 - eR),$$

where I^+ and I^- are the counting rates of the analyzer for opposite incoming-neutron polarizations (corrected for background), p^2 is the product of the polarizing and analyzing efficiencies, and e is the efficiency of the flipping coil used to reverse the incoming-neutron polarization. In our setup, $p^2 = 0.990$ and $p^2 e = 0.981$. The coefficient D takes into account any dephasing process resulting in a decrease of the measured polarization. It has been measured separately for each sample.

The large pseudomagnetic moments of H^1 and V^{51} give measurable precession angles even at 1 K.[5] But for many nuclei, μ^* is much smaller and, consequently, much higher polarizations are needed. Two somewhat complementary methods can be used to achieve sizable nuclear polarizations. The first consists in lowering the temperature of the sample down to the millikelvin region. The second uses microwave techniques to polarize the nuclei dynamically.

In the first method, the main problem is to achieve equilibrium through thermal contact between sample and coolant, and, inside the sample, between the lattice and the nuclear spins. The former is generally good down to, at least, 80 mK, while the latter is satisfactory for metals down to very low temperatures (the spin-lattice relaxation time $\tau \sim 1/T$) and almost nonexistent at these temperatures for most insulators ($\tau \sim e^{a/T}$).

The second method is able to cool the nuclei far below the lattice temperature. Therefore, it calls for substances with weak spin-lattice coupling, i.e., insulators. It has the advantage that it may be possible to polarize selectively and thus to sort out the contribution of different isotopes in samples with several nuclear-spin species. A disadvantage is the difficulty of measuring the polarization accurately.

Whatever the polarization method, a plot of α against nuclear polarization P is a straight line, whose slope gives μ^*. For static nuclear polarization, P is generally small, and

$$\alpha \cong \xi\left(\frac{I+1}{3I}\right)\left(\frac{\mu^*}{\mu_B}\right)\left(\frac{\mu}{\mu_N}\right)\frac{Idc}{A}\frac{1}{T}, \tag{1}$$

where μ is the magnetic moment of the nucleus, μ_B and μ_N are the electronic and the nuclear Bohr magneton, respectively, d is the density and A the atomic weight of the element, and c is the abundance of the isotope with spin I. ξ is defined by

$$\xi = -\frac{H}{v}\,4\pi\gamma_n\frac{(\mu_B N_0)^2}{R}\left(\frac{\mu_N}{\mu_B}\right),$$

where N_0 is Avogadro's number and $R = N_0 k_B$ is the gas constant per mole. $\xi = (H/v)\times 47.06 = 3.185$ cm^3 K in our case ($H = 25$ kG, $v = 3.694\times 10^5$ cm/sec).

We now state briefly some improvements made to the equipment described in Ref. 5.

To obtain a good stability of amplitude and phase of the rf fields, capacitive dividers pick up the rf field close to each coil. The amplitudes of the pickup control voltages are used to drive the respective automatic gain control states which hold the amplitude constant to better than 0.1%. At the same time, the phase difference between the two signals is measured and used to stabilize the relative phase between the two rf coils to better than 0.1 deg.

The dc magnetic field H_0 is stabilized through the NMR of a proton sample placed outside the cryostat. A long-term stability of the order of 50 mG is achieved, corresponding to a phase shift of the order of 1 deg.

The dynamic polarizations have been obtained in a conventional He^4 cryostat using a 70-GHz microwave source (the static field is about 25 kG). For static polarizations, a dilution refrigerator was used. It has been specially designed for simple operation, easy positioning and interchange of samples, well-defined temperature of the samples, and a minimum amount of He^3 in the path of the neutron beam. A detailed description of this cryostat will be given elsewhere.[6] The lowest temperature reached inside the dilution chamber was of the order of 20 mK. However, for most samples, a higher limit was set by the very long cool-down times. This is due to the conjunction of the Kapitza boundary resistance and nuclear heat capacity which leads to a very steep temperature dependence of the cooling times. The temperature was measured by a carbon resistor calibrated as follows: The value of $(2.10\pm 0.02)\mu_B$ for $\mu^*(\mathrm{V}^{51})$ was obtained between 1 and 4.2 K using the He^4 vapor pressure as a temperature scale (a value in excellent agreement with the known spin-incoherent scattering cross-section value[7]). Then a measurement of the precession in V^{51} down to 40 mK provided, through formula (1), a value of the temperature against which the resistor was calibrated.

As an example, a plot of α against $1/T$ for Al^{27} is given in Fig. 1. At temperatures below 50 mK, where the arrows indicate the time sequence of the measurements, there is clear evidence that the sample does not follow the temperature changes in the dilution chamber.

Results obtained for seven nuclei are given in Table I. Two values of μ^* have also been obtained by dynamic polarization: for Li^7 in a LiF single crystal, and for Al^{27} in a ruby single crystal. All other results have been obtained with static polarizations in the dilution refrigerator. The room-temperature densities used to calcu-

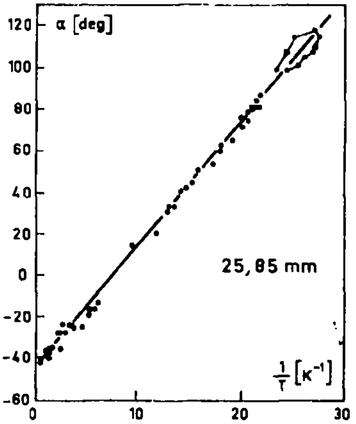

FIG. 1. Observed variation of the extra precession angle α with $1/T$ for Al^{27}.

TABLE I. Experimental values of μ^* and of $a_+ - a_-$ for seven nuclei. For comparison, values for $a_+ - a_-$ obtained from cross-section measurements are also given.

Isotope	Spin	d (g cm^{-3})	$\alpha T/l$ (deg cm^{-1} K)	μ^*/μ_B	$a_+ - a_-$ (10^{-12} cm)	$\lvert a_+ - a_-\rvert_\sigma$ (10^{-12} cm)	$T_{\min}$[b] (K)
Li^7	3/2	0.540	15.8	-0.62 ± 0.03	-0.45 ± 0.02	0.52	0.100
				-0.65 ± 0.03[a]	-0.47 ± 0.02		
Al^{27}	5/2	2.70	2.39	$+0.077 \pm 0.004$	$+0.050 \pm 0.003$	•••	0.037
				$+0.088 \pm 0.010$[a]	$+0.057 \pm 0.006$		
Sc^{45}	7/2	2.99	48.2	$+1.95 \pm 0.04$	$+1.20 \pm 0.03$	1.45	0.083
Zr^{91}	5/2	6.51	0.66	$+0.74 \pm 0.10$	$+0.48 \pm 0.07$	•••	0.024
Nb^{93}	9/2	8.57	2.0	-0.046 ± 0.004	-0.028 ± 0.002	0.44	0.083
La^{139}	7/2	6.14	11.4	$+1.19 \pm 0.04$	$+0.73 \pm 0.03$	0.44	0.067
Ta^{181}	7/2	16.6	1.6	-0.096 ± 0.010	-0.059 ± 0.006	•••	0.071

[a] Measurements with dynamical nuclear polarization.

[b] Lowest temperature obtained in the experiment.

late μ^* from the slope $\alpha T/l$ and values of $a_+ - a_-$ derived from μ^* are included in Table I. For comparison, $|a_+ - a_-|$ obtained from the cross-section data, whenever possible, are also shown. No correction has been made for the change of density with temperature or for the contribution of the nuclear magnetization proper to the precession angle, since both corrections are in all cases below the error limits of our measurements.

It now appears that all neutron spin-dependent nuclear scattering lengths, with the possible exception of nuclei with very large absorption cross sections, are accessible to this method and that the main obstacles would be lack of time, lack of money (for the rare isotopes), and/or lack of motivation. Some possible applications of nuclear pseudomagnetism to the study of bulk matter have been discussed elsewhere.[3]

The authors (who are not nuclear physicists) would be grateful for suggestions of nuclei of particular interest. Is O^{17} of sufficient special interest to be investigated in spite of its very small isotopic abundance? Is an *accurate* measurement of μ^* for the deuteron of interest to specialists of the three-body problem? What about magic nuclei plus or minus a nucleon? For many isotopes differing by two neutrons, spins are identical and magnetic moments very near. Is the ratio of their pseudomagnetic moments worth investigating, etc.? We welcome suggestions.

It is a pleasure to acknowledge our indebtness to Professor R. V. Pound for pointing to one of us the manifold advantages of using in our experiments phase-shift measurements rather than frequency shifts.

---

*Permanent address: Institute of Physics, Bulgarian Academy of Sciences, Sofia, Bulgaria.

[1] A. Abragam, G. L. Bacchella, H. Glättli, P. Meriel, J. Piesvaux, and M. Pinot, C.R. Acad. Sci., Ser. B 274, 423 (1972).

[2] A. Abragam, G. L. Bacchella, H. Glättli, P. Meriel, J. Piesvaux, M. Pinot, and P. Roubeau, in *Proceedings of the Seventeenth Congress Ampère, Turku, Finland, 1972*, edited by V. Hovi (North Holland, Amsterdam, 1973), p. 1.

[3] A. Abragam, in *Trends in Physics* (European Physical Society, Geneva, 1973), p. 177.

[4] V. Barytchevshi and M. Podgoretzki, Zh. Eksp. Teor. Fiz. 47, 1050 (1964) [Sov. Phys. JETP 20, 704 (1965)].

[5] A. Abragam, G. L. Bacchella, H. Glättli, P. Meriel, M. Pinot, and J. Piesvaux, Phys. Rev. Lett. 31, 776 (1973).

[6] P. Roubeau, to be published.

[7] C. G. Shull and R. P. Ferrier, Phys. Rev. Lett. 10, 295 (1963).

Negative-Parity Band in ^{48}V

B. Haas* and P. Taras
Laboratoire de Physique Nucléaire, Université de Montréal, Montréal, Canada
(Received 7 May 1974)

The electromagnetic decays of levels in ^{48}V have been studied via the reaction ^{34}S(^{16}O, *pn*)^{48}V at incident ion energies of 30–36 MeV. Spins, parities, and branching and mixing ratios were obtained from angular distribution, excitation function, γ-γ, and n-γ coincidence measurements. Six, and possibly seven, members of a very pure rotational negative-parity band were identified. This band is based on a 1^- low-lying core excited state with probable configuration $(\pi d_{3/2})^{-1}(\pi f_{7/2})^4(\nu f_{7/2})^5$.

A systematic study of nuclei in the $1f_{7/2}$ shell populated in heavy-ion-induced reactions is currently underway in this laboratory. The odd-odd cross-conjugate nucleus ^{48}V was the first to be studied since a knowledge of its properties is quite important for a proper understanding of the forces coming into play in this shell. In this Letter we report evidence for a negative-parity band built on a low-lying core excited state. This band has amazing regularity indicating the presence of a rigid structure with a rather large deformation.

The levels in ^{48}V were populated via the reaction ^{34}S(^{16}O,*pn*)^{48}V. The ^{16}O beam from the Université de Montréal EN tandem Van de Graaff accelerator was typically 150 nA in the 5^+ charge state. Targets enriched to 85.6% in ^{34}S were made by evaporation of ~500 μg/cm^2 of CdS onto thick nickel backings. The beam energy was varied between 30 and 36 MeV in steps of 2 MeV. Several exit channels were open at these bombarding energies, the most important being *pn*, *2pn*, *2p*, *αp*, *αn*, and *2n* in roughly decreasing order of importance. The γ rays emitted in the decay of ^{48}V were identified through high-resolution γ-γ and n-γ coincidence measurements using two Ge(Li) and one NE213 detectors. The angular distributions of the decay γ rays were measured at seven angles in the horizontal plane.

TABLE I. Experimental results for the negative-parity band in ^{48}V.

E_x(keV)	E_γ(keV)	J_i^π	J_f^π	Branching ratios(%)	δ^d	a_2/a_0	a_4/a_0	W(0)/W(90)
518.6	98.0 ± 0.2	1^-	1^+	29 ± 2	0.0 ± 0.02	.04 ± .01	-	
	210.4 ± 0.2	1^-	2^+	71 ± 2	$-0.09 \le \delta \le 0.02$	-.09 ± .02	-	
744.9	226.3 ± 0.2	2^-	1^-	93 ± 2	0.02 ± 0.04	-.29 ± .01	-	
	324.2 ± 0.5	2^-	1^+	3 ± 1	a	a		
	436.7 ± 0.5	2^-	2^+	5 ± 2	a	a		
1055.7	310.8 ± 0.2	3^-	2^-	91 ± 3	$-0.02 \le \delta \le 0.07$	-.32 ± .02	-	
	537.2 ± 1.0	3^-	1^-	9 ± 3	$-0.03 \le \delta \le 0.15$	.45 ± .06	-.38 ± .08	
1557.6	501.9 ± 0.2	4^-	3^-	71 ± 7	0.12 ± 0.04	-.51 ± .04	.07 ± .04	
	812.7 ± 1.0	4^-	2^-	29 ± 7	b	b		1.42 ± 0.25
2062.5	504.9 ± 0.2	5^-	4^-	70 ± 7	-0.07 ± 0.07	-.17 ± .04	-	
	1006.3 ± 1.0	5^-	3^-	30 ± 7	b	b		1.34 ± 0.21
2779.4	716.9 ± 1.0	6^-	5^-	69 ± 10	c	c		0.46 ± 0.18
	1221.8 ± 1.5	6^-	4^-	31 ± 10	b	b		1.39 ± 0.18
3586.0	806.6 ± 1.0	(7^-)	6^-	68 ± 15	c	c		0.42 ± 0.23
	1523.5 ± 1.6	(7^-)	5^-	32 ± 15	e	e		

[a] Intensity of γ rays too weak to yield meaningful data.

[b] Difficult to analyze because of interference of other γ rays and Doppler shift effect; however, the ratio $W(0)/W(90)$ is consistent with stretched quadrupole transitions.

[c] Same as b, but with stretched dipole transitions.

[d] Mixing ratio defined as in Rose and Brink (Ref. 1).

[e] Masked by ^{42}Ca $2^+ \rightarrow 0^+$ 1524.2-keV transition. Branching ratios obtained from γ-γ total projection spectrum.

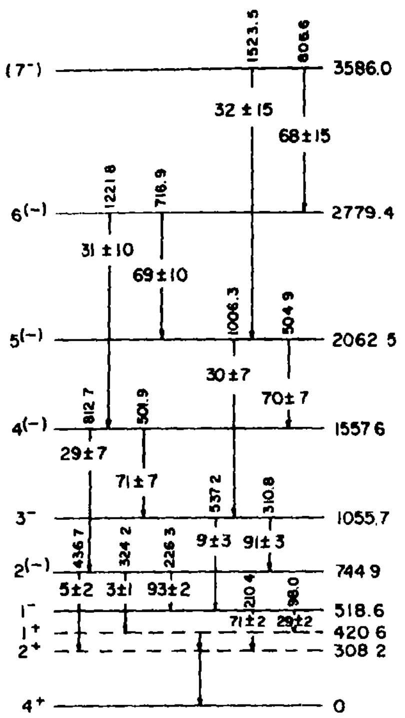

FIG. 1. Partial level scheme of ^{48}V showing the negative-parity band and its modes of decay.

The energies of the coincident γ rays and their time distribution were recorded event by event on magnetic tape by means of an on-line computer. The results of the analysis are summarized in Table I and Fig. 1. The levels at 2062.5, 2779.4, and 3586.0 keV have not been reported previously.

The members of the negative-parity band have been definitely established up to $J=6$ on the basis of the following arguments:

(i) Each one of the γ rays proposed to be a member of the γ-ray cascade is in coincidence with all the other members. Figure 2 shows, as an example, the resulting coincidence spectrum with the gate set on the (308.2 + 310.8)-keV transitions. Further evidence for the weaker 717- and 807-keV γ-ray transitions is given in the inset of Fig. 2 which shows part of the total γ-γ projection spectrum. These γ rays are also quite prominent in the n-γ spectrum.

(ii) The relative intensities of the γ-ray transitions in the singles spectra show a gradual decrease with increasing spin. This feature is consistent with a statistical picture of the de-excitation process of the compound nucleus.[2]

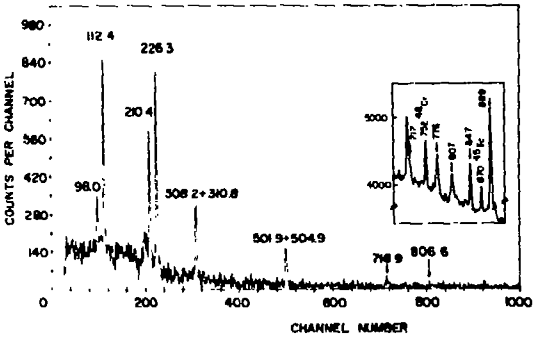

FIG. 2. γ-γ coincidence spectrum resulting from a gate placed on the (308.2 + 310.8)-keV transitions. In the inset we display part of the total γ-γ projection spectrum showing the weak transitions between the upper members of the band.

(iii) In the coincidence spectra, the relative intensities of all the transitions following a gate transition are equal within statistics, while those of the transitions preceding the gate transition are in the same proportion as in the singles spectra.

(iv) In addition, excitation functions have been measured for bombarding energies ranging from 30 to 36 MeV. The results display the systematic variation with spin expected from a statistical de-excitation mechanism,[2] e.g., over the above energy range the intensity of the 505-keV $5^- \rightarrow 4^-$ transition increases by a factor of ~2.5 while that of the 226-keV $2^- \rightarrow 1^-$ transition increases by only 15%.

Prior to the beginning of our work only the ground and first two excited states had definite spin and parity assignments. The allowed values of J and δ presented in Table I are based on a χ^2 analysis of the measured γ-ray angular distributions. All spin combinations yielding up to octupole-hexadecapole γ-ray admixtures and consistent with the excitation-function results have been considered. Further details[3] on this type of analysis will be given in the general context of spin assignments following heavy-ion-induced reactions. It was difficult to obtain a complete angular distribution for the weaker dipole and quadrupole transitions because of interference from other γ rays and Doppler-shift effect. However, the ratio of their intensities at 0° and 90° with respect to the beam axis was consistent with stretched ($J \rightarrow J-1$) dipole and ($J \rightarrow J-2$) quadupole transitions, respectively (see Table I). 'he results for the first four states are in agreenent with recent work by Samuelson *et al.*[4] who ised the reaction ^{48}Ti(p,n)^{48}V and analyzed their lata with the statistical compound-nuclear comuter code MANDY.

The 518.6-keV state was assigned $J^\pi=1^-$ acording to the following arguments. Our results or this state rule out $J=0$ and $J\geq 3$, and in conunction with the mean lifetime[5] of the level (τ 3.92 ± 0.09 nsec) $J^\pi=2^-$ could also be rejected ,ince it would lead to unacceptable $M2$ strengths >190 Weisskopf units (W.u.)]. Dorenbusch *et al.*[6] iave populated this level in the reaction ^{47}Ti(^{3}He, ')^{48}V. Their deuteron angular distribution was itted with a pure $l_p=3$ component ($J^\pi=5^+$ or 6^+). Iowever, their distribution could have also coneivably been fitted with $l_p=2$ ($0^-\leq J^\pi\leq 5^-$). Thus he 518-keV state could be assigned $J^\pi=1^-$. Furher support for this assignment comes from reent work on the reaction ^{46}Ti(^{3}He,p)^{48}V by Smith 't al.[7] These authors found a large number of 1^+ ind 2^+ states but failed to observe the 518-keV evel. In addition, if this low-lying state were to iave positive parity one would expect it to have)article configurations similar to the ground and irst two excited states thus giving rise to rapid $M1$ decay. On the other hand, a negative parity vith a particle configuration of $(\pi d_{3/2})^{-1}(\pi f_{7/2})^4$ $\times(\nu f_{7/2})^5$ would yield j-forbidden $E1$ decays in greement with the observed long lifetime of the evel. The observed $E1$ strengths are (5.28 ± 0.12) $\times 10^{5}$ W.u. and (1.45 ± 0.05)$\times 10^{-6}$ W.u. for the 98- ind 210-keV γ-rays, respectively. The correiponding values for $M1$ transitions would have ieen (2.46 ± 0.23)$\times 10^{-3}$ W.u. and (0.61 ± 0.03)$\times 10^{-3}$ V.u., respectively.

The parity of the higher states shown in Fig. 1 vas inferred from the fact that the band follows xtremely well the $J(J+1)$ rule expected of a rigd rotor (Fig. 3). This behavior gives strong supiort to the interpretation of the band as being a 'otational band built on a core excited state. The iarity of these states should eventually be meaured, for example, by a γ-ray linear polarizaion measurement. However, the complex γ-ray ingles spectrum necessitates the use of an exiensive Ge(Li) polarimeter which is not at presnt available in our laboratory. The lifetime neasurements of the higher lying states of this 'and are currently in progress in our laboratory. 'reliminary results on the 744.9-keV state (τ 25 psec) and on the 1055.7-keV state ($\tau\approx 5$ psec) ndicate that the $E2$ transition strengths of the decay γ rays of these levels could be as high as 18 and 24 W.u., respectively. Unfortunately, the values of δ are close to zero and the errors, even though small, then lead to a rather large range of $E2$ strengths. It is interesting to note that the 537-keV $3^-\to 1^-$ transition strength is of the order of 30 W.u. if $E2$ and 1337 W.u. if $M2$, clearly indicating that the 1055- and 518-keV states have the same parity.

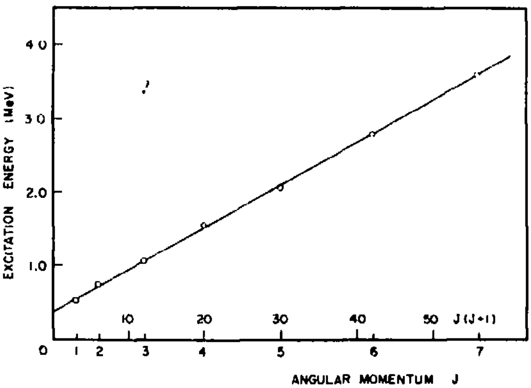

FIG. 3. Excitation energies of the members of the negative-parity band versus $J(J+1)$.

It should also be pointed out that all the γ-ray transitions occurred within the negative-parity band; none was observed to a number of other neighboring states whose parity is believed to be positive. This is not surprising since the positive-parity states appear to be fairly well accounted for on the assumption of a pure $f_{7/2}$ nucleon configuration.[8] In addition, transitions from the members of the negative-parity band based on a $(\pi d_{3/2})^{-1}$ configuration to the positive-parity states whose configurations are expected to be mainly $(\pi f_{7/2})^3(\nu f_{7/2})^{-3}$ would entail $M2$ transitions which are expected to be retarded.

The variation of the excitation energy E_x of the members of the negative-parity band as a function of $J(J+1)$ is very well reproduced by the relation $E_x=E_0+(\hbar^2/2\vartheta)J(J+1)$ with $E_0=405$ keV and $\hbar^2/2\vartheta=56.7$ keV, the largest deviation being $\simeq 2\%$ for the 5^- state. This is rather surprising since one might have expected some band mixing. The purity of the band seems to indicate that the nucleus in its 518-keV state must have a rather rigid structure corresponding to a rather large deformation. Taking $\delta=0.06$ for the 226-keV $2^-\to 1^-$ transition, we obtain for the intrinsic quadrupole moment $Q_0=0.79$ b, for the deformation $\beta = 0.24$, and a rather large value of 0.78 for the quantity $(g_K - g_R)$.

No theoretical predictions on the negative-parity states of ^{48}V have yet been published. It might be interesting to undertake SU(3) calculations to try to understand the appearance of core excited states at such low excitation energies (also known[9] to exist in other nuclei of the $1f_{7/2}$ shell) and in particular to try to find out why they appear to be so pure, as in ^{48}V.

The authors would like to thank Professor Jean LeTourneux for enlightening discussions. Financial support for this project was provided by the National Research Council of Canada.

---

*Present address: Laboratoire de Physique Nucléaire et Physique des Particules, Strasbourg, France.

[1] H. J. Rose and D. M. Brink, Rev. Mod. Phys. 39, 306 (1967).

[2] I. Halpern, B. J. Shepherd, and C. F. Williamson, Phys. Rev. 169, 805 (1968).

[3] P. Taras and B. Haas, to be published.

[4] L. E. Samuelson *et al.*, in *Proceedings of the International Conference on Nuclear Physics, Munich, 1973*, edited by J. de Boer and H. J. Mang (North-Holland, Amsterdam, 1973), Vol. 1.

[5] L. E. Samuelson, C. B. Morgan, T. L. Khoo, and W. H. Kelly, Bull. Amer. Phys. Soc. 18, 767 (1973).

[6] W. E. Dorenbusch, T. A. Belote, J. Rapaport, and K. G. Nair, Nucl. Phys. A112, 385 (1968).

[7] J. W. Smith, L. Meyer-Schützmeister, G. Hardie, and P. P. Singh, Phys. Rev. C 8, 2232 (1973).

[8] R. D. Lawson, Nucl. Phys. A173, 17 (1971).

[9] *Nuclear Level Schemes, A = 45 through A = 257, from Nuclear Data Sheets*, edited by Nuclear Data Group, Oak Ridge National Laboratory (Academic, New York, 1973).

$\Delta I = \frac{1}{2}$ Rule for Nonleptonic Decays in Asymptotically Free Field Theories

M. K. Gaillard* and Benjamin W. Lee†
National Accelerator Laboratory, Batavia, Illinois 60510

(Received 10 April 1974)

The effective nonleptonic weak interaction is examined assuming the Weinberg-Salam theory of weak interactions and an exactly-conserved-color gauge symmetry for strong interactions. It is shown that the octet part of the nonleptonic weak interaction is more singular at short distances than the $\underline{27}$ part. The resulting enhancement of the octet term in the effective local weak Lagrangian, together with suggested mechanisms for the suppression of matrix elements of the $\underline{27}$ operator, may be sufficient to account for the observed $|\Delta I| = \frac{1}{2}$ rule.

The purpose of this paper is to discuss the effectively local form of nonleptonic weak interactions in models in which weak interactions are described by a Weinberg-Salam-type gauge theory[1] and strong interactions by an exactly-conserved-color gauge-symmetry group,[2] and to comment on the origin of the $\Delta I = \frac{1}{2}$ (or octet) rule observed in strangeness-changing decays.

Our discussion is based on the operator-product expansion of the product of two weak currents. In an asymptotically free field theory,[3] it is possible to compute the short-distance behavior of coefficient functions in the operator-product expansion; we find that the $\Delta I = \frac{1}{2}$ part of the interaction is more singular at short distances. This is much as anticipated by Wilson.[4] (See also Mathur and Yen[5]; however, our conclusions differ substantially from theirs.)

In the following, we shall use the 't Hooft-Feynman gauge to describe both the weak bosons and the color gluons. In the 't Hooft-Feynman gauge, effects of (unphysical) Higgs scalar fields may be neglected, since they are of order $(m/m_W)^2$ compared to the W exchange, where m is a characteristic mass scale of hadrons and m_W the mass of the charged vector meson W.

It is useful to consider first the case of free quarks. The effective nonleptonic weak interaction is of the form

$$-f^2 \int d^4x\, D_F(x; m_W^2)\, T[j_{\mu N}^{\dagger}(x) j_S^{\mu}(0)], \tag{1}$$

where $j_{\mu N}$ and $j_{\mu S}$ are strangeness-conserving and -changing charged currents:

$$j_{\mu N} = (\bar{\mathcal{P}} \cos\theta - \bar{\mathcal{P}}' \sin\theta)\gamma_\mu(1-\gamma_5)\mathfrak{N} + \dots \tag{2}$$

and

$$j_{\mu S} = (\bar{\mathcal{P}} \sin\theta + \bar{\mathcal{P}}' \cos\theta)\gamma_\mu(1-\gamma_5)\lambda + \dots . \tag{3}$$

In Eq. (2), $\mathcal{P}'$ denotes the fourth quark field associated with the proposal of Glashow, Iliopoulos, and Maiani,[6] and θ is the Cabibbo angle. The time-ordered product of two currents in (1) may be expanded in the form

$$T[j_{\mu N}{}^\dagger(x)j_S{}^\mu(0)]=\sum_{i,m}\mathfrak{F}_m{}^{(i)}(x^2)\mathcal{O}_m{}^{(i)}, \tag{4}$$

where the $\mathfrak{F}$ are c-number functions of the separation distance and the $\mathcal{O}^{(i)}$ are operators of $(2i)$ quark fields.

Let us consider the operators bilinear in quark fields (one-body operators). The operators $\bar{\mathfrak{N}}\lambda$ and $\mathfrak{N}\gamma\cdot\partial\lambda$ will have coefficient functions which scale as x^{-2} at short distances. Such terms will have divergent coefficients in Eq. (1), but contribute only to mass and wave-function renormalizations of the quark fields. Operators of dimension six or higher, such as $\bar{\mathfrak{N}}\gamma\cdot\partial\partial^2\lambda$, can in principle contribute to Eq. (1) to order $m_W{}^{-2}$, but these operators automatically give $\Delta I=\frac{1}{2}$, and are expected to have coefficients proportional to $(m_{\mathcal{P}'}{}^2-m_{\mathcal{P}}{}^2)/m_W{}^2$ because the contractions of $\mathcal{P}$ and $\mathcal{P}'$ quarks contribute to them with the opposite sign.

Next we consider the operators quartic in quark fields. There are two of them:

$$\mathcal{O}_1{}^{(2)}=:\bar{\mathfrak{N}}\gamma_\mu(1-\gamma_5)\mathcal{P}\bar{\mathcal{P}}\gamma^\mu(1-\gamma_5)\lambda:$$

and

$$\mathcal{O}_2{}^{(2)}=:\bar{\mathfrak{N}}\gamma_\mu(1-\gamma_5)\mathcal{P}'\bar{\mathcal{P}}'\gamma^\mu(1-\gamma_5)\lambda:.$$

The second is automatically $\Delta I=\frac{1}{2}$ and the first a mixture of $\Delta I=\frac{1}{2}$ and $\frac{3}{2}$. The associated c-number functions $\mathfrak{F}_1{}^{(2)}$ and $\mathfrak{F}_2{}^{(2)}$ are constants, so that the operators $\mathcal{O}_1{}^{(2)}$ and $\mathcal{O}_2{}^{(2)}$ contribute to Eq. (1) with the coefficient

$$\sim -f^2\int d^4xD_F(x^2;\, m_W{}^2)=f^2/M_W{}^2=G_F/\sqrt{2}.$$

The quartic operators (or two-body operators) of higher dimensions such as $:\{\partial^2[\bar{\mathfrak{N}}\gamma^\mu(1-\gamma_5)\mathcal{P}]\}\bar{\mathcal{P}}\gamma_\mu\times(1-\gamma_5)\lambda:$ will have coefficients of order $G_Fm_W{}^{-2}$ and may be neglected in Eq. (1). Thus the effective local form of the interaction (1) to leading order in $m_W{}^{-2}$ is

$$[\mathfrak{L}_W]_{eff}=(G_F/\sqrt{2}):j_{\mu N}{}^\dagger(0)j_S{}^\mu(0):+\text{H.c.} \tag{5}$$

We shall now extend similar considerations to models in which strong interactions are mediated by unbroken-color gluons. For definiteness we consider the model of color SU(3). We write the color quark fields as column matrices. Strong interactions are described by the Lagrangian

$$\mathfrak{L}_S=\sum_{i=\mathcal{P},\mathfrak{N},\lambda,\mathcal{P}'}\bar{q}_i i\gamma_\mu(\partial^\mu-\tfrac{1}{2}g\underline{\lambda}\cdot\underline{G}^\mu)q_i+\text{mass terms} \tag{6}$$

where $\underline{G}^\mu$ are the octet of color gluon fields. The comments made for the free-quark model on the one-body operators $\mathcal{O}_m{}^{(1)}$ that appear on the right-hand side of Eq. (4) also apply to the color (or singlet) vector gluon scheme; in particular, as shown by Weinberg,[7] the terms containing the operators $\bar{\mathfrak{N}}\lambda$ and $\bar{\mathfrak{N}}\gamma\cdot\partial\lambda$ in Eq. (1) are "transformed away" by the mass and amplitude renormalizations of quark fields: The remaining operators are $\Delta I=\frac{1}{2}$, but their coefficients are in general of order $G_F(m_{\mathcal{P}'}{}^2-m_{\mathcal{P}}{}^2)/m_W{}^2$.

We need only consider two-body operators of lowest dimensions which conserve charm and which are antisymmetric in $\mathcal{P}$ and $\mathcal{P}'$. There are two operators we must deal with:

$$\mathcal{O}_\mp{}^{(2)}=\tfrac{1}{2}N[(\bar{\mathfrak{N}}\mathcal{P})(\bar{\mathcal{P}}\lambda)\mp(\bar{\mathfrak{N}}\lambda)(\bar{\mathcal{P}}\mathcal{P})-(\bar{\mathfrak{N}}\mathcal{P}')(\bar{\mathcal{P}}'\lambda)\pm(\bar{\mathfrak{N}}\lambda)(\bar{\mathcal{P}}'\mathcal{P}')], \tag{7}$$

where we have dropped the reference to the spinor structure; thus, $(\bar{A}B)(\bar{C}D)=\bar{A}\gamma_\mu(1-\gamma_5)B\bar{C}\gamma^\mu(1-\gamma_5)D$. The symbol N stands for Zimmermann's normal ordering,[8] except that the subtraction point should be chosen in the Euclidean region of the external momenta to avoid infrared difficulties. The combinations (7) are chosen so that each one transforms like the U_z component of a U-spin triplet.[9] That the two combinations form a complete set of operators is a consequence of the Fierz identity. Note further that the first operator in (7) is pure $\Delta I=\frac{1}{2}$, while the second is a mixture of $\Delta I=\frac{1}{2}$ and $\frac{3}{2}$. The first operator $\mathcal{O}_-{}^{(2)}$ is antisymmetric with respect to color indices of $\bar{\mathfrak{N}}_i$ and $\bar{\mathcal{P}}_j$ (or $\mathcal{P}_i$ and λ_j) while the second is symmetric. To lowest order in g^2, the two operators in Eq. (7) are renormalized multiplicatively.

The associated functions $\mathfrak{F}_{\underline{8},\underline{8}',\underline{27}}{}^{(2)}$ may be evaluated for small x^2, $m^2x^2\ll1$, by the method of Christ, Hasslacher, and Mueller,[10] using the Gell-Mann, Low,[11] Callan, Symanzik[12] equation. We consider the irreducible vertex

$$\langle T[j_{\mu N}{}^\dagger(x)j_S{}^\mu(0)q(p_1)q(p_2)\bar{q}(p_3)\bar{q}(p_4)]\rangle^{\text{irr}}$$

in the limit of vanishing quark mass, and choose $p_1{}^2=p_2{}^2=p_3{}^2=p_4{}^2=-\mu^2$, $s=t=u=-4\mu^2/3$ as the subtraction point. The renormalized matrix element

$$\langle T[\mathcal{O}_m{}^{(2)}q_1q_2\bar{q}_3\bar{q}_4]\rangle^{\text{irr}}$$

has the form, as far as the dependence on μ is concerned,

$$\{1+\gamma_m[\ln\mu+\dots]\},$$

where γ_m is a number which can be computed from one-gluon-exchange diagrams in perturbation theory. As discussed explicitly by Politzer and Georgi,[13] the functions $\mathcal{F}_m^{(2)}$ satisfy the Callan-Symanzik equations

$$\left[\mu\frac{\partial}{\partial\mu}+\beta(g)\frac{\partial}{\partial g}-4\gamma+\gamma_m\right]\mathcal{F}_m^{(2)}(\mu^2x^2,g)=0 \tag{8}$$

with the usual meanings for β and γ.[12]

In asymptotically free theories, the asymptotic form of $\mathcal{F}_m^{(2)}$ can be reliably estimated. Writing

$$\beta(g)=-(g^3/16\pi^2)[b+O(g^2)],\quad \gamma_m=(g^2/16\pi^2)[d_m+O(g^2)], \tag{9}$$

and recalling that $\gamma=(g^2/16\pi^2)(4/c)^2$ we find that

$$\mathcal{F}_m^{(2)}(\mu^2x^2,g)\xrightarrow[x^2<0]{\mu^2x^2\ll 1}\mathcal{F}_m^{(2)}(1,0)[1-(g^2/8\pi^2)b\ln(\mu\sqrt{-x^2})]^{d_m/2b}, \tag{10}$$

where

$$(\cos\theta\sin\theta)^{-1}\mathcal{F}_m^{(2)}(1,0)=(1/\sqrt{2},1/\sqrt{10},2/\sqrt{10}),$$

for $m=\underline{8}$, $\underline{8}'$, and $\underline{27}$, respectively. In the three-color quartet scheme,

$$b=25/3 \tag{11}$$

(Ref. 2), and

$$d_m=8 \text{ for } \underline{8},\quad d_m=-4 \text{ for } \underline{8}' \text{ and } \underline{27}. \tag{12}$$

[If the color gauge group is SU(N), we have $b=(11N-8)/3$, $d_{\underline{8}}=6(N+1)/N$, $d_{\underline{8}',\underline{27}}=-6(N-1)/N$.] Thus, we see that the short-distance behavior associated with $\mathcal{O}_{\underline{8}}^{(2)}$ is more singular than those associated with $\mathcal{O}_{\underline{8}',\underline{27}}$: The former is of the form $(\ln|x|)^{0.48}$, the latter $(\ln|x|)^{-0.24}$.

This difference in the short-distance behavior is reflected in the coefficients of the operators $\mathcal{O}_m^{(2)}$ in the effective local Lagrangian for nonleptonic weak interactions. Substituting Eqs. (4) and (10) in Eq. (1), and performing the integration over x after the Wick contour rotation, we obtain

$$\mathcal{H}_W=\frac{G_F}{\sqrt{2}}\cos\theta\sin\theta\,\{c_1\mathcal{O}_{\underline{8}}^{(2)}+c_2\mathcal{O}_{\underline{8}'}^{(2)}+c_3\mathcal{O}_{\underline{27}}^{(2)}+\text{H.c.}\}, \tag{13}$$

where

$$\mathcal{O}_{\underline{8}}^{(2)}=N[(\bar{\mathcal{N}}\mathcal{P})(\bar{\mathcal{P}}\lambda)-(\bar{\mathcal{N}}\lambda)(\bar{\mathcal{P}}\mathcal{P})]/\sqrt{2},$$

$$\mathcal{O}_{\underline{8}'}^{(2)}=N[(\bar{\mathcal{N}}\mathcal{P})(\bar{\mathcal{P}}\lambda)+(\bar{\mathcal{N}}\lambda)(\bar{\mathcal{P}}\mathcal{P})+2(\bar{\mathcal{N}}\lambda)(\bar{\mathcal{N}}\mathcal{N})+2(\bar{\mathcal{N}}\lambda)(\bar{\lambda}\lambda)]/\sqrt{10},$$

$$\mathcal{O}_{\underline{27}}^{(2)}=N[2(\bar{\mathcal{N}}\mathcal{P})(\bar{\mathcal{P}}\lambda)+2(\bar{\mathcal{N}}\lambda)(\bar{\mathcal{P}}\mathcal{P})-(\bar{\mathcal{N}}\lambda)(\bar{\mathcal{N}}\mathcal{N})-(\bar{\mathcal{N}}\lambda)(\bar{\lambda}\lambda)]/\sqrt{10},$$

and

$$\begin{aligned} c_1&\simeq\frac{1}{\sqrt{2}}\left[1+\left(\frac{g^2}{4\pi}\right)\frac{b}{2\pi}\ln\frac{m_W}{\mu}\right]^{0.48},\\ \sqrt{10}c_2&=\sqrt{5/2}c_3\simeq\left[1+\left(\frac{g^2}{4\pi}\right)\frac{b}{2\pi}\ln\frac{m_W}{\mu}\right]^{-0.24}. \end{aligned} \tag{14}$$

To get some idea of the magnitude of these constants, we choose μ to be the onset of scaling of the form (10), which we assume optimistically to be $\simeq 1$ GeV.[14] The gluon-quark coupling at that subtraction point is assumed to be $(g^2/4\pi)\simeq 1$.

Taking $m_W\simeq 100$ GeV, we have

$$1+(g^2/4\pi)(b/2\pi)\ln(M_W/\mu)\simeq 7, \tag{15}$$

so that $c_1/c_3\simeq 5$.

The relative enhancement of an octet piece in Eq. (13) is not by itself sufficient to account for the observed small violation of the $\Delta I=\frac{1}{2}$ rule of about 5% (in amplitude) in nonleptonic decays of hyperons and K mesons. (For a review of this and related subjects, see for instance Ref. 8.)

It has often been remarked that the effective strength of $|\Delta S| = 1$ nonleptonic transitions is of order G_F, rather than $G_F \sin\theta$, and that some enhancement of the $\Delta I = \frac{1}{2}$ part by a dynamical mechanism is necessary.[15] Since we expect $c_1 \sin\theta \simeq 1$ n Eq. (13) we do have such a mechanism for enhancing the $\Delta I = \frac{1}{2}$ part. However, if the typical hadronic matrix element of $\mathcal{O}_{27}^{(2)}$ is comparable o that of $\mathcal{O}_8^{(2)}$, one expects only a 20% validity for the $\Delta I = \frac{1}{2}$ rule, which is not sufficient to explain the data. Thus to explain the observed $\Delta I = \frac{1}{2}$ rule, it is further necessary that the matrix elements of $\mathcal{O}_{27}^{(2)}$ are suppressed by a factor of 4 relative to those of $\mathcal{O}_8^{(2)}$. Such a suppression may come about in a number of ways; for example, the duality considerations of Nussinov and Rosner[16] indicate the suppression of the 27 operator. Pati and Woo[17] have shown in the context of free color quarks that the baryon-to-baryon matrix elements of the 27 operator vanish. This result, which is a consequence of the color symmetry of $\mathcal{O}_{27}$ in Eq. (7), remains true for quarks oupled to color gauge gluons, provided the SU(6) ground-state wave function is assumed. It then ollows from the usual lore of current algebra hat the $\Delta I = \frac{3}{2}$ amplitudes vanish in the soft-pion imit for both baryon and K decays. (Of course, he continuation in pion momenta is problematic is always!) Consequences of our results for $\Delta S = 0$ transitions, the decays of charmed particles, and Ω^- decay, and a detailed account of the results discussed in this Letter will be presented elsewhere.

We have benefited from discussions with D. J. Gross, H. Georgi, H. D. Politzer, S. B. Treiman, and S. Weinberg, and participants of the Weinberg seminar at Harvard University.

---

[*] On leave of absence from Laboratoire de Physique Theorique et Particules Elementaires, Orsay (Laboratoire associe au Centre National de la Recherche Scientifique).

[†] On leave of absence from the Institute of Theoretical Physics, State University of New York, Stony Brook, N.Y. 11790.

[1] S. Weinberg, Phys. Rev. Lett. 19, 1264 (1967), and 27, 1688 (1971); A. Salam, in *Proceedings of the Eighth Nobel Symposium on Elementary Particle Theory, Relativistic Groups, and Analyticity, Stockholm, Sweden, 1968*, edited by N. Svartholm (Almquist and Wiksel, Stockholm, 1968).

[2] D. Gross and Wilczek, Phys. Rev. D 8, 3633 (1973); S. Weinberg, Phys. Rev. Lett. 31, 494 (1973); H. Fritsch, M. Gell-Mann, and H. Leutwyler, California Institute of Technology Report No. CALT-68-409, 1973 (to be published).

[3] H. D. Politzer, Phys. Rev. Lett. 30, 1346 (1973); D. Gross and F. Wilszek, Phys. Rev. Lett. 30, 1343 (1973).

[4] K. Wilson, Phys. Rev. 179, 1499 (1969), especially Sect. E, and references cited therein. See also V. S. Mathur and P. Olesen, Phys. Rev. Lett. 20, 1527 (1968).

[5] V. S. Mathur and H. C. Yen, Phys. Rev. D 8, 3569 (1973).

[6] S. L. Glashow, J. Iliopoulos, and L. Maiani, Phys. Rev. D 2, 1285 (1970).

[7] S. Weinberg, Phys. Rev. D 8, 4482 (1973).

[8] W. Zimmermann, in *Lectures on Elementary Particles and Quantum Field Theory*, edited by S. Deser *et al.* (Massachusetts Institute of Technology Press, Cambridge, Mass., 1970), Vol. I, p. 397.

[9] M. K. Gaillard, in "Text Book on Elementary Particle Physics," edited by M. Nikolic (to be published).

[10] N. Christ, B. Hasslacher, and A. H. Mueller, Phys. Rev. D 6, 3543 (1972).

[11] M. Gell-Mann and F. E. Low, Phys. Rev. 95, 1300 (1954).

[12] C. B. Callan, Phys. Rev. D 2, 1541 (1970); K. Symanzik, Commun. Math. Phys. 18, 227 (1970).

[13] H. D. Politzer and H. Georgi, Phys. Rev. D 9, 416 (1974).

[14] Although the products $c_i\mathcal{O}_8^{(2)}$, are invariant under the renormalization group, the c's and $\mathcal{O}$'s in Eq. (13) are not separately invariant. The point is that the operators $\mathcal{O}^{(2)}$ contain the Zimmermann N ordering, so that they depend on the subtraction point; near the subtraction point high-momentum gluon exchange becomes negligible. Since we are interested in matrix elements of $\mathcal{O}^{(2)}$ between hadron states, the subtraction point should not be too far from the mean momentum squared of the confined quarks.

[15] R. F. Dashen, S. C. Frautschi, M. Gell-Mann, and Y. Hara, in *Proceedings of the Twelfth International Conference on High Energy Physics, Dubna, U.S.S.R., 1964* (Atomizdat., Moscow, U.S.S.R., 1966).

[16] S. Nussinov and J. Rosner, Phys. Rev. Lett. 23, 1264 (1969).

[17] J. C. Pati and C. H. Woo, Phys. Rev. D 3, 2920 (1971).

Observation of Large-Transverse-Momentum Muons Directly Produced by 300-GeV Protons*

J. P. Boymond, R. Mermod,† P. A. Piroué, and R. L. Sumner
Department of Physics, Joseph Henry Laboratories, Princeton University, Princeton, New Jersey 08540
and
J. W. Cronin, H. J. Frisch, and M. J. Shochet
The Enrico Fermi Institute, University of Chicago, Chicago, Illinois 60637
(Received 8 May 1974)

We have observed muons produced directly in Cu and W targets by 300-GeV incident protons. We find a yield of muons which is approximately a constant fraction (0.8×10^{-4}) of the pion yield for both positive and negative charges and for transverse momenta between 1.5 and 5.4 GeV/c.

In this Letter we report on the observation of muons produced directly in nuclear targets by 300-GeV incident protons. Study of muon production at high transverse momentum was originally motivated by the search for the intermediate vector boson. Early experiments were carried out at the Argonne zero-gradient synchrotron[1] and the Brookhaven alternating-gradient synchrotron[2] with negative results. More recently, several experiments have shown evidence for the direct production either of single muons[3,4] or of muon pairs[5] in nucleon-nucleon collisions. Extensive theoretical work[6,7] suggests that collisions of pointlike constituents of the nucleon would result in the direct production of muons.

In this experiment, performed at the National Accelerator Laboratory (NAL), we have used an apparatus described in a previous publication.[8] It consists of a single-arm focusing spectrometer equipped with two Cherenkov counters and a calorimeter to identify hadrons, and a 15-ft-long steel filter sampled each 2.5 ft with dE/dx counters to identify muons. The spectrometer viewed secondaries produced in a heavy target at an angle of 77 mrad relative to the incident 300-GeV proton beam. This angle corresponds to ~90° in the nucleon-nucleon c.m. system. Direct muons from the target were separated from muons coming from π and K decays in flight with the aid of two absorbers which could be inserted into the spectrometer close to the target. The first absorber was a 23-in.-long W block with its upstream face 9.5 in. from the center of the target. The second absorber was a 42-in.-long Fe block with its upstream face 42 in. from the target. We used a 2-in.-long W target, primarily in runs with negative muons, and a 3-in.-long Cu target primarily in runs with positive muons.

Data were taken under three conditions: (1) no absorber, (2) W absorber inserted only, and (3) Fe absorber inserted only. Runs were made at 10-GeV/c intervals between 20 and 70 GeV/c corresponding to transverse momenta ($P_\perp$) from 1.5 to 5.4 GeV/c. At 20 and 30 GeV/c, data were also taken with both absorbers in the beam as a consistency check. To verify that the muons were associated with the target, we also took data with the target removed for the three principal conditions at 20, 30, and 40 GeV/c.

For each absorber condition we measured the ratio of muons detected at the end of our apparatus to pions of the same charge detected by the apparatus when the absorber was absent. Two counter telescopes which looked at the target at 90° laboratory angle permitted normalization of different runs. The yield of pions with no absorber was corrected for nuclear absorption in the remainder of the apparatus and for decay in flight.

The hadrons were attenuated by factors of ~200 and ~270 with the W and Fe absorbers, respectively. These rather small attenuations resulted in a significant hadron penetration. These hadrons were identified by the combination of the Cherenkov counters and the hadron calorimeter. Those decaying appeared as muons. Thus the observed muons with absorber in place consisted of three components: (1) muons produced directly in the target, (2) muons produced by hadrons decaying upstream of the absorber, and (3) decay muons from hadrons which penetrated the absorber.

For process (3) the ratio of muons to pions[9] was directly measured at each momentum and polarity in runs without the absorbers; the corresponding muon yield in the absorber runs is calculated from the observed penetrating pions. The remaining muon yield coming from process-

TABLE I. Reduction of raw data to direct muon yield at the target. Processes (1), (2), and (3) are referred to in the text. "Tungsten" and "Iron" refer to the particular absorber used.

	Tungsten	Iron
Observed muons	795 ± 28	623 ± 25
Observed pions	13 580	4985
Ratio μ/π without absorber	$(2.03 \pm 0.10) \times 10^{-2}$	
Muons from hadron	276 ± 13	
penetration of absorber, process (3)	276 ± 13	101 ± 5
Muons from processes (1) and (2)	519 ± 31	522 ± 26
Absorber loss factor	0.71 ± 0.04	0.40 ± 0.02
Corrected muons from processes (1) and (2)	731 ± 60	1305 ± 92
Pions at target	4.60×10^6	4.62×10^6
Muons/pions at target	$(1.59 \pm 0.13) \times 10^{-4}$	$(2.83 \pm 0.20) \times 10^{-4}$
Effective distance to target (m)	0.35	1.25
Extrapolated μ/π at target	$(1.10 \pm 0.15) \times 10^{-4}$	

s (1) and (2) is then corrected for the loss due to the absorber insertion (e.g., multiple scattering). Finally, the direct muon yield is obtained by linear extrapolation to zero decay path.

In Table I we present the reduction of the raw data from a typical run at 40 GeV/c. The absorber loss factors, calculated by Monte Carlo techniques, are presented in Table II. These factors account for the multiple-scattering loss, as well as the increased yield due to acceptance of smaller $P_\perp$ when the absorber is in place. The dependence of yield on $P_\perp$ was taken from our previous measurements of hadron production.[8] We thus assume that the direct muon component has a similar dependence on $P_\perp$, an assumption that can be checked *a posteriori*. Figure 1 shows the corrected results of a typical run along with the *predicted* slope. The points are plotted at a distance $d+\lambda$, where d is the distance between the target and the upstream end of the absorber and λ is the measured interaction length in the absorber.

The predicted slope can be obtained from the rate of hadron decay between the target and the absorber. It was calculated by numerical integration as a function of momentum. The yield of decay muons between the target and absorber depends on both K and π decays. Kaons are twice

TABLE II. Calculated absorber loss factors.

Momentum (GeV/c)	Tungsten	Iron
20	0.42 ± 0.03	0.182 ± 0.015
30	0.56 ± 0.03	0.300 ± 0.015
40	0.71 ± 0.04	0.40 ± 0.02
50	0.81 ± 0.05	0.47 ± 0.02
60	0.87 ± 0.04	0.54 ± 0.02
70	1.02 ± 0.04	0.62 ± 0.03

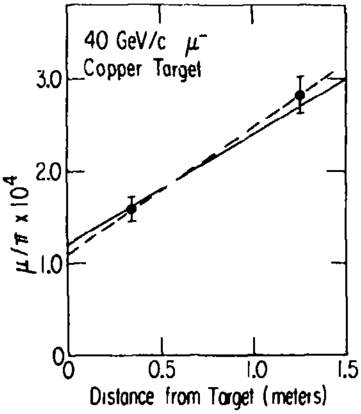

FIG. 1. Plot of data reduced in Table I. Dashed curve, linear extrapolation to the target; solid line, calculated slope.

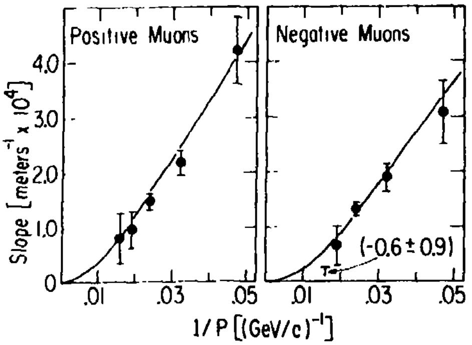

FIG. 2. Plot of observed slope and calculated slope versus reciprocal of the muon momentum. Points, experimentally measured slopes; solid line, calculated slope. The slope as a function of $1/P$ is expected to be a parabola. The decrease in the K/π ratio towards low momentum distorts the parabolic shape.

as effective as pions in producing detected muons. Thus the slope is sensitive to the K/π ratio at the target. Figure 2 shows for both charges the predicted and observed slopes plotted against the inverse of the muon momentum.

The agreement between calculated and observed slopes is a significant verification of the corrections which are quite different in nature for the two absorbers. The W absorber is more sensitive to the broadening of the acceptance because of its proximity to the target, but is less sensitive to multiple scattering for the same reason. The inverse is true for the Fe absorber.

Table III gives the ratio of direct muons to pions at the target for all conditions. The most striking aspect of these results is the constancy of the ratio μ/π. The constancy for different target materials is particularly interesting. In a separate experiment, to be reported in a subsequent publication, we have found the yield of pions per interacting proton at 3-GeV/c $P_\perp$ to be 3.5 times larger from a W target than a Be target. This effect is believed to be due to secondary scattering in the nucleus. Since the direct muons follow the same pattern, a strongly interacting, short-lifetime source is suggested for the muons.

One such source can be the known vector mesons. For example, if ρ and φ were each produced with the same cross section as π, we would expect a ratio $(\mu/\pi)\times 10^4$ of 0.68, 0.46, and 0.33 at $P_\perp$ of 1.5, 3.0, and 4.5 GeV/c, respectively.

TABLE III. Ratio of directly produced muons to pions in the proton-nucleus collision. The number of observed pions emerging from the 0.4-interaction-length target is multiplied by a factor 1.25 to account for absorption in the target itself.

$P_\perp$ (GeV/c)	$10^4\times\mu/\pi$ (target) Positive	Negative
1.62	0.66±0.25 (Cu)	0.86±0.20 (W)
2.38	0.72±0.11 (Cu)	0.67±0.12 (W)
3.15	0.88±0.18 (Be)	...
3.15	0.94±0.16 (Cu)	0.88±0.12 (Cu)
3.15	0.60±0.15 (W)	0.74±0.16 (W)
3.91	0.98±0.23 (Cu)	0.88±0.26 (W)
4.67	0.87±0.30 (Cu)	1.02±0.34 (W)
5.44	0.94±0.47 (Cu)	1.20±0.46 (W)

In Figure 3 we plot the invariant cross section per nucleon for inclusive muon production. Also plotted is the inclusive pion cross section multiplied by 10^{-4} and the inclusive muon cross section expected from a model based on parton-antiparton annihilation.[10] It is clear that the yield of muons is everywhere in excess of the parton-model prediction.[11]

We wish to thank the staff of the Proton Section

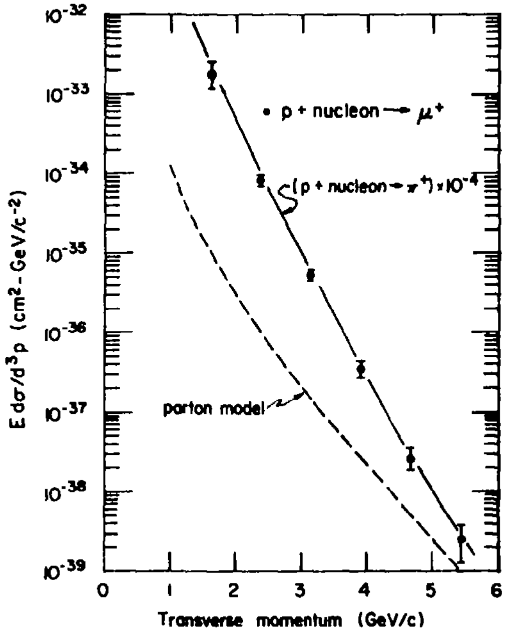

FIG. 3. Plot of the invariant cross section for direct muon production versus P. Also shown is the pion cross section multiplied by 10^{-4} and the cross section predicted by a parton model.

of NAL for their magnificent support of this experiment. We also wish to thank V. L. Fitch, S. B. Treiman, E. A. Paschos, and G. R. Farrar for valuable discussions. Finally, one of us (R.M.) wishes to thank NAL for its hospitality and support.

---

*Work supported by the National Science Foundation and the U. S. Atomic Energy Commission.

†On leave at NAL from the University of Geneva, Geneva, Switzerland.

[1] R. C. Lamb *et al.*, Phys. Rev. Lett. 15, 800 (1965).

[2] R. Burns *et al.*, Phys. Rev. Lett. 15, 830 (1965).

[3] P. J. Wanderer *et al.*, Phys. Rev. Lett. 23, 729 (1969).

[4] G. B. Bondarenko *et al.*, as cited by V. Lebedev in *Proceedings of the Sixteenth International Conference on High Energy Physics, The University of Chicago and National Accelerator Laboratory, 1972*, edited by J. D. Jackson and A. Roberts (National Accelerator Laboratory, Batavia, Ill., 1973), Vol. 2, p. 329.

[5] J. Christenson *et al.*, Phys. Rev. Lett. 25, 1523 1523 (1970).

[6] S. D. Drell and T. M. Yan, Phys. Rev. Lett. 25, 316 (1970).

[7] J. D. Bjorken, J. Phys. (Paris), Colloq. 34, C1-385 (1973).

[8] J. W. Cronin *et al.*, Phys. Rev. Lett. 31, 1426 (1973).

[9] For convenience we normalize to pions; the pions serve as a measure of all hadrons.

[10] G. R. Farrar, to be published.

[11] The yield of muons from the parton-antiparton annihilation process depends critically on the assumed antiparton distributions in the nucleon. The constraints on these distributions from inelastic electron and neutrino scattering make it unlikely that a parton model can account for the large observed muon yields.

Anomalous Muon and Hadron Charge Ratios in Secondary Cosmic Rays

Robert K. Adair
Yale University, New Haven, Connecticut 06520

(Received 18 March 1974)

Secondary cosmic-ray muon and hadron fluxes are calculated for particle energies above 200 GeV using accelerator data on inclusive hadron cross sections and the known primary flux. The gross differences between the calculated and measured muon and hadron charge ratios require radical reexamination of conventional views on hadron interactions or the neutron-proton ratio in the primary flux.

It is clearly possible to derive the characterisics of secondary cosmic-ray fluxes knowing the omposition of the primary flux and the details of adron-hadron interactions. In the energy region f 1000 GeV per nucleon, the primary flux inteniity can be described by the relation[1,2]

$$dN/dE = A(\gamma - 1)E^{-\gamma}, \tag{1}$$

vhere $A = 1.5 \pm 0.25$ cm^{-2} sec^{-1} sr^{-1}, $\gamma = 2.72$ .0.05, and E, the energy per nucleon, is meaured in GeV. Measurements of the charge specrum[2] of the primaries at energy extending up to 00 GeV per nucleon indicate that about 89% of he nucleon flux are protons and 11% neutrons asuming that charge-1 particles are protons and harge-2 particles are α particles. Only hadronadron inclusive cross sections are necessary or an understanding of inclusive secondary fluxs; and proton-proton inclusive cross sections ave been measured[3] up to laboratory energies of 500 GeV at the CERN intersecting storage ring SR) facility, and meson interactions have been studied in accelerator experiments at lower energies. From this knowledge of the primary flux and the hadron interaction inclusive cross sections and the use of conventional assumptions concerning charge independence and factorization in the hadron-hadron fragmentation region, one can calculate secondary cosmic-ray fluxes precisely, in principle, if one neglects correlation effects or coherent effects in the projectile or target. Since these effects are not likely to be large, plausible estimates of these nuclear effects allow reliable calculations of the secondary fluxes. Although there is a long history of such calculations,[4] and the results presented here differ from many, but not all, of the previous conclusions, only now do we have sufficiently extensive and reliable data on the basic hadron interactions so that complete calculations can be made which are sufficiently accurate so that differences between the results of the calculations and measurements can confidently be ascribed to inadequacies in the conventional assumptions used in the calculations.

Since the mean transverse momentum of secondary particles is small, it is possible to assume that all secondary particles travel in the same direction as the primary particles. We can then adequately describe the hadron-hadron interactions in terms of the invariant inclusive cross sections $E_s\,d\sigma_s/dp_L$, where E_s is the energy and p_L is the longitudinal component of the momentum of the secondary particle s. In accord with the measurements, we assume that these invariant cross sections are approximately independent of the interaction energy or scale[5] but we use the scaling assumption only as a convenient way to interpolate and extrapolate the basic input cross sections taken from ISR data[6] and the results are neither sensitive to, nor do they test, scaling.

Any parametrization of the accelerator data is constrained by conservation laws: The conservation of energy requires

$$(1/\sigma_t)\textstyle\sum_s \int_0^1 E_s(d\sigma_s/dx)\,dx = E_i, \tag{2}$$

where E_i and E_s are the primary and secondary particle energies, the summation is over all particle states s emitted in the forward direction in inelastic processes, σ_t is the total nonelastic cross section, and the integration is taken over x in the forward direction in the center-of-mass system, where $x = p_L/p_i$ and p_i is the center-of-mass momentum of an incident particle. We neglect processes in the backwards direction inasmuch as their contribution to the secondary fluxes is negligible.

The conservation of charge imposes the constraint

$$(1/\sigma_t)\textstyle\sum_s q_s \int_0^1 (d\sigma_s/dx)\,dx = q_i, \tag{3}$$

where q_s is the charge of the secondary particle s and q_i is the charge of the beam particle. Here we assume that charge exchange is not important when the incident particle and the target particle have different charges—this follows from factorization, a more general assumption that particle distributions in the forward direction depend only on the identity of the beam particle and the backwards distribution depends only on the target particle.

The conservation of baryon number can be expressed as

$$(1/\sigma_t)\textstyle\sum_s B_s \int_0^1 (d\sigma_s/dx)\,dx = B_i, \tag{4}$$

where B_i and B_s are the baryon numbers of the incident and secondary particles.

Another useful constraint derives from the precise measurements of the multiplicity M_c of charged particles produced in the interaction. We then require

$$(2/\sigma_t)\textstyle\sum_s |q_s| \int_0^1 (d\sigma_s/dx)\,dx = M_c, \tag{5}$$

where M_c is the charged-particle multiplicity.

The experimental measurements of inclusive cross sections are made at specific angles and momenta and it is necessary to determine $E_s\,d\sigma_s/dp_L$ by integrating over the transverse momenta. For this purpose we assume that the cross sections take one of the following forms:

$$\begin{aligned} &\text{(i)}\;\; E\,d^3\sigma/dp^3 = E\,d\sigma/dp_L(c^2/\pi)\exp(-c^2 p_t^2),\\ &\text{(ii)}\;\; E\,d^3\sigma/dp^3 = E\,d\sigma/dp_L(b^2/2\pi)\exp(-b p_t); \end{aligned} \tag{6}$$

and we calculate $E\,d\sigma/dp_L$ from the measured values of $E\,d^3\sigma/dp^3$ as a function of x for $p_t = 400$ MeV/c. With the cross section known at this transverse momentum, the value of $E_s\,d\sigma_s/dp_L$ is determined almost independent of the choice of distribution or the value of a or b.

Since we are interested in the best values of $d\sigma/dp_L$ rather than fits to the differential cross sections $E\,d^3\sigma/dp^3$, standard least-squares techniques were inadequate and I established a "best fit" to the data subjectively. The cross sections so defined for production of various secondaries are shown graphically in Fig. 1 together with measurements of differential cross sections measured at $p_t = 400$ MeV multiplied by an appropriate factor as suggested above. The uncertainties in the integrations over the transverse momenta are approximately equal to the measurement errors shown on the figure. While estimates of antiproton and antineutron cross sections are included[3] and the choice of values for pion and K-meson cross sections reflect the results of the production and decay of strange baryons, the effect on the secondary fluxes of these production modes is not important.

Although the calculations reported here were made using Monte Carlo techniques where each particle and its tree of descendants were followed through their history, the numerical calculations were made in parallel with analytic calculations which depended upon appropriate weighted averages W_s of the inclusive cross sections for the production of the particles s:

$$W_s = (1/\sigma_t)\int_0^1 x^{\gamma-1}(d\sigma_s/dx)\,dx.$$

The flux of secondaries produced by the first interaction of the primary protons with protons

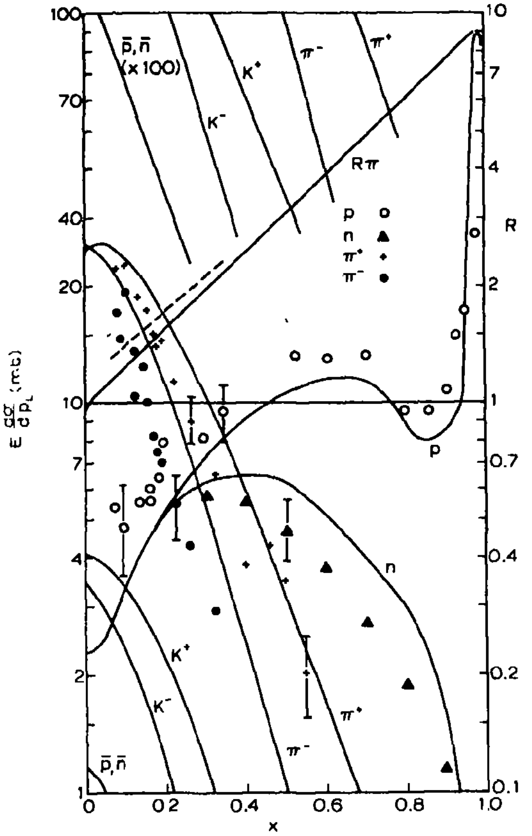

FIG. 1. The solid curves present the invariant proton-proton inclusive cross sections $E\,d\sigma/dp_L$ used in the analysis while the points represent values of $E\,d^3\sigma/dp^3$ measured at $p_t = 0.4$ GeV/c multiplied by 1.80 GeV^2. A solid line shows the π^+/π^- ratio from the curves while the dashed line gives the ratio from the data at $p_t = 0.4$ GeV/c.

would have the form

$$dN_s/dE_s = W_s\, dN/dE = W_s A(\gamma - 1)E_s^{\gamma}.$$

Values of W_s corresponding to the cross sections of Fig. 1 are given in Table I together with values of the total cross section for the production of the particles and the ratio of the mean momentum given to the secondary particle to the momentum of the primary in the center-of-mass system. Inasmuch as invariant cross sections scale, the production of secondaries near $x = 0$, and then the multiplicity and total cross sections for the production of secondary particles, increase logarithmically with energy. The total cross sections are then listed for a specific energy, 200 GeV.

TABLE I. Quantities which derive from the invariant cross sections used in the calculations. The cross sections are taken at 200 GeV lab energy.

Particle	σ_t (mb)	E_s/E_t	W_s
p	23.53	0.323	0.2426
n	14.43	0.120	0.0662
π^+	60.07	0.193	0.0624
π^0	55.18	0.160	0.0483
π^-	50.28	0.130	0.0347
K^+	8.55	0.035	0.0077
K^-	5.91	0.014	0.0036
K_L^0	7.23	0.020	0.0056
$\bar{p}$	1.96	0.005	0.0012
$\bar{n}$	1.96	0.005	0.0012

Neutron cross sections are taken as the same as proton cross sections modified by charge symmetry, that is with n and p and π^+ and π^- reversed in Fig. 1, and with K^+ and K^- cross sections held equal to each other and to the mean of the K-meson cross sections from proton interactions. The production weights for pions produced by positive (or negative) mesons are taken to be the same as for protons (or neutrons) except that a value of 0.07 is added to the weight W_s corresponding to the incident particle to account for the leading particle effect connected with diffraction dissociation. The production of K mesons and nuclear pairs by mesons is neglected.

Since the incident primary nucleons interact with light atmospheric nuclei, not free nucleons, one must consider the complications imposed by nuclear effects. From the steepness of the primary spectrum and the large proportion of nucleons near the "edge" of light nuclei, we can be confident that single nucleon-nucleon interactions will be most important but multiple interactions cannot be disregarded. Almost independent of specific models, we can expect that multiple interactions will produce secondary particles with lower mean momenta and less charge asymmetry than single interactions. Since an incoherent model of multiple interactions, though implausible physically, has these properties and is easily treated in calculations, I chose to consider the nuclear effects by using a one-dimensional incoherent-interaction model of the nucleus where we treat the nucleus as a slab of nucleon gas with a thickness of h mean free paths for nucleons and $2h/3$ paths for mesons and follow the particles and their collision products through the slab. The mean free path for nucleon interactions producing mesons in the atmosphere was taken[6] as 92 g/cm^2 at 200 GeV, decreasing slowly (as the nucleon cross section increases) to 80 g/cm^2 at 2000 GeV. A best value of $h = 1.0$ was found to give a hadron attenuation length equal to the measured length of 120 g/cm^2 and a meson mean free path at 200 GeV of 119 g/cm^2. In this model, 58% of the interactions are single nucleon-nucleon interactions which contribute about 81% of the secondary flux.

With this description of the nucleus, the hadron-hadron interactions, and the primary flux, the vertical flux of protons, neutrons, charged mesons, and $K_L{}^0$ mesons was calculated as a function of atmospheric depth, and the sea-level muon intensity and charge ratio was calculated for intrgral fluxes over 200 GeV. No approximations of any significance were required in the course of the numerical calculations. The energy range was chosen so that the spectra could be calculated using cross sections measured at the ISR with a minimal burden of extrapolation; the increases in total nucleon-nucleon cross sections which have been noted were not too important as they might be at higher energies, and nuclear effects and n-p charge exchange effects would not be expected to be important as they might be at lower energies.

While the hadron intensities and attenuation lengths and the muon intensities which are calculated are found to be in agreement with observations within experimental error, the calculated muon charge ratio of 1.53 is far larger than the measured value[7] of 1.30 ± 0.03. The calculated value is determined primarily by the ratio of the charged-pion weight functions of Table I where $W(\pi^+)/W(\pi^-) = 1.80$, as K-meson decays contribute only about 11% of the muon flux. We note from Fig. 1 that the pion charge ratio used in the calculations from the fitted data is appreciably smaller than the ratios derived from the unfitted data and we then regard our calculated value of the muon charge ratio of 1.53 as a conservative minimum; using the unfitted pion data, we get a muon charge ratio of about 1.64.

The calculated neutron-proton ratio at atmospheric depths from 600 to 800 g/cm^2 is 0.41. The measured neutral-to-charged hadron ratio in this range of energy and altitude[1] is about 0.70 ± 0.05 where there should be little contribution to the neutral flux besides neutrons but mesons should contribute substantially to the charged flux. The measured ratio is then a minimum while the calculated ratio is taken, conservatively, from fitted neutron cross sections which tend to be larger than the reported measurements as shown in Fig. 1.

It then seems impossible to reconcile the measured and calculated charge ratios for either the muon flux or the hadron flux; in each case there are more positive particles predicted than are measured. The experiments are straightforward and seem unimpeachable and the calculated results derive from the input data and well-defined, conservative, assumptions in a straight-forward way. I then conclude that the origin of the differences must be found in a breakdown of the basic assumptions used in the calculation. I list what seem to me to be the least unattractive possibilities: (a) The cosmic-ray neutron-proton ratio at energies near 1000 GeV per nucleon must be near 25:75 rather than 11:89 and hence a large fraction, about 20%, of the charge one flux must be deuterons. (b) At energies near 1000 GeV, there is very extensive charge exchange in p-n interactions so that the average total charge in the forward hemisphere in the center-of-mass system is much less than 1 and this effect extends into the fragmentation region. (c) Effects such as described in (b) might follow from coherent three-body effects (nuclear effects) which we cannot now anticipate.

---

[1] S. Hayakawa, *Cosmic Ray Physics* (Interscience, New York, 1969).

[2] M. J. Ryan, J. F. Ormes, and V. K. Balasubrahmanyan, Phys. Rev. Lett. 28, 985 (1972).

[3] Valuable reviews are presented by J. C. Sens and by D. R. O. Morrison, in *Proceedings of the Fourth International Conference on High Energy Collisions, Oxford, England, 1972* (Rutherford High Energy Laboratory, Chilton, Didcot, Berkshire, England, 1972). Also see M. G. Albrow *et al.*, Nucl. Phys. B54, 6 (1973); A. Bertin *et al.*, Phys. Lett. 38B, 260 (1972); L. G. Ratner *et al.*, Phys. Rev. Lett. 27, 68 (1971); W. Bartel, W. Flauger, and H. Schopper, paper presented to the Second Aix en Provence International Conference on Elementary Particles, 1973 (unpublished).

[4] Typical calculations were presented by Y. Pal and B. Peters, Kgl. Dan. Vidensk. Selsk., Mat.-Fys. Medd 33, No. 15 (1964); L. Volkova and G. T. Zatsepin, in *Proceedings of the Ninth International Conference on Cosmic Rays*, edited by A. C. Stickland (Institute of Physics and Physical Society, London, England, 1966) R. K. Adair, Phys. Rev. 172, 1370 (1968); W. R. Frazer, C. H. Poon, D. Silverman, and H. J. Yesian, Ph Rev. D 5, 1653 (1972); Z. Garrafo, A. Pignotti, and G. Zgrablich, Nucl. Phys. B53, 419 (1973).

[5] R. P. Feynman, Phys. Rev. Lett. 23, 1415 (1969);

J. Benecke *et al.*, Phys. Rev. 188, 2159 (1969).

[6] G. Bellettini *et al.*, Nucl. Phys. 79, 609 (1966).

[7] T. H. Burnett *et al.*, Phys. Rev. Lett. 30, 937 (1973); C. A. Ayre *et al.*, in *Proceedings of the Thirteenth International Cosmic Ray Conference, Denver, 1973* (University of Colorado, Denver, Colo., 1973); L. Leipuner *et al.*, in *Proceedings of the Thirteenth International Cosmic Ray Conference, Denver, 1973* (University of Colorado, Denver, Colo., 1973), and private communication.

Energy Dependence of the Double-Charge-Exchange Reactions $\pi^-p\to K^+\Sigma^-$, $K^-p\to\pi^+\Sigma^-$, and $K^-p\to K^+\Xi^-$†

C. W. Akerlof, P. K. Caldwell,* J. Koschik, R. Kotthaus,‡ D. I. Meyer, and B. Springett§
Physics Department, The University of Michigan, Ann Arbor, Michigan 48104

(Received 25 March 1974)

In an experiment at the Argonne National Laboratory zero-gradient synchrotron we have determined the forward differential cross sections for the double-charge-exchange reactions $\pi^-p\to K^+\Sigma^-$, $K^-p\to\pi^+\Sigma^-$, and $K^-p\to K^+\Xi^-$ for incident beam momenta up to 5 GeV/*c*. The production angle and momentum of the forward-going positive particle (π^+ or K^+) were measured with a high-resolution focusing wire-spark-chamber spectrometer and the two-body final states were selected by the missing-mass technique.

Our current understanding of high-energy hadron collisions is based on the idea that particle exchange provides the dominant force for interactions above a few GeV/*c* incident momentum. In time, the theoretical or phenomenological models which have embodied this primitive notion have grown steadily more ornate to allow greater freedom in fitting the expanding experimental data. Consequently, these models have become less testable by direct experiment and there have been no new guides to lead our physical intuition.

As a partial solution to this problem we have continued an earlier study[1] of the double-charge-exchange (DCX) reactions $\pi^-p\to K^+\Sigma^-$, $K^-p\to\pi^+\Sigma^-$, and $K^-p\to K^+\Xi^-$. The significance of these three reactions is that none of them can take place by the single exchange of any singly charged particle. Thus in the absence of normally large exchange forces we have a sensitive test for the existence of any of the three possible competing processes: (1) double particle exchange, (2) exotic single particle exchange, (3) intermediate *s*-channel resonance formation. In addition, by examining the energy behavior of the DCX cross sections we can hope to identify the dominant contribution in the asymptotically high-energy regime. This has been expected to be the double-particle-exchange diagrams which would yield differential cross sections with an $s^{-2.5}$ to s^{-3} behavior.[2]

The three reactions listed above also have some common properties which should set further limits on viable theoretical descriptions. For example, $\pi^-p\to K^+\Sigma^-$ and $K^-p\to\pi^+\Sigma^-$ are related by line crossing, so that these cross sections should be identical if induced by single exotic exchange and at least similar if induced by double particle exchange. $K^-p\to\pi^+\Sigma^-$ and $K^-p\to K^+\Xi^-$ have the same quantum numbers in the *s* channel, so that energy-dependent structure due to Y^* resonances should be expected in both reactions for the same incident momenta.

From our previous work we had experience with the experimental difficulties which beset measurements of the DCX reactions. Since the cross sections are all very small, an intense beam of incident particles is required on the hydrogen target. With available π/K ratios of the order of 200, the largest number of events could be obtained for the reaction $\pi^-p\to K^+\Sigma^-$, so that the experimental design concentrated on the detection of this particular channel. This required that a final-state K^+ be identified against an overwhelming background of pions and protons. At 5 GeV/*c*, for every K^+ from the reaction $\pi^-p\to K^+\Sigma^-$ there were 1000 π^+ and 200 protons within the missing-mass resolution of the experimental apparatus. To obtain sufficient rejection ratios against competing particle species, four Cherenkov counters were constructed to identify the positive particle in the final state. An unavoidable consequence was that the mass of the Cherenkov radiator to count kaons also produced substantial Coulomb scattering of the detected particle. Finally, since the cross section for the reaction $\pi^-p\to K^+\Lambda^0\pi^-$ rises steeply at the $\Lambda^0\pi^-$ threshold, high resolution was required to separate the Σ^- missing-mass peak from the onset of the $\Lambda^0\pi^-$ continuum which is 58 MeV higher.

A high-intensity negative beam was created in an internal target inside the vacuum chamber of the Argonne zero-gradient synchrotron. This beam was momentum dispersed through a 20° bend, focused onto a momentum-defining hodoscope of ten scintillation counters, and then transported through a second stage to a final focus on a 24-in.-long hydrogen target. The mass of the beam particle was tagged with four Cherenkov counters: one to count kaons and three to count pions. Two hodoscopes of five counters each tagged the horizontal and vertical divergence of the beam 5 m upstream from the hydrogen target.

The positive particles emitted in the forward direction were detected in a focusing quadrupole spectrometer consisting of five magnetic elements. The first of these following the hydrogen target was a 36-in.-long bending magnet to steer the positive particles created in the target away from the negative beam. Three quadrupoles were arranged to bring the particles from within a 2.5-msr solid angle into an approximately parallel bundle at the final quadrupole exit. This allowed a 2-m-long drift space on each side of a 72-in.-long momentum-analyzing magnet without further reduction of the subtended solid angle.

Four sets of wire spark chambers determined the bend angle through the analyzing magnet; the drift region between chambers was kept low in mass to reduce multiple Coulomb scattering. In particular this dictated the placement of the spectrometer Cherenkov counters upstream of the first wire spark chamber. The electronic trigger was arranged to fire on either a π^- in the incident beam yielding a K^+ or a K^-, or a $\bar{p}$ yielding any positive particle in the spectrometer. After every five beam spills the trigger was altered under computer control to include incident π^- yielding final-state protons. This permitted the simultaneous acquisition of π^-p backward-scattering data which continuously monitored the experimental apparatus.

Data were taken for eleven different values of incident momentum from 1.90 to 5.00 GeV/c. At each momentum the π^-p backward elastic missing-mass peak checked the spectrometer dispersion and resolution. Analysis for every reaction channel was performed identically. First, the three beam hodoscopes were checked for uniqueness. If more than one counter in any of the three arrays fired the event was ignored. Data from the wire spark chambers were used to construct a trajectory through the analyzing magnet and to determine the particle momentum. This trajectory was then traced back through the three quadrupoles and steering magnet to find the original momentum three-vector. With the tagged Cherenkov-counter data to identify the beam and spectrometer particle masses, the missing mass was computed. Even at the highest momentum of 5 GeV/c the Σ^- peak was clearly resolved from the $\Lambda^0\pi^-$ threshold. The inelastic background behaved like a step function at threshold with the observed shape dominated by the experimental missing-mass resolution. The number of events within the Σ^- peak was determined by fitting the shape of the missing-mass distribution with the sum of a Gaussian signal and a background function consisting of a constant plus an error-function integral centered at the $\Lambda^0\pi^-$ threshold. All of the nonlinear parameters for these distributions were independently determined from the π^- mass peak from π^-p backward elastic scattering so that the fits to the DCX data required a minimal number of free parameters. With this procedure the fitted number of events in the Σ^- peak was quite stable under a variety of modifications of the background function.

The differential cross sections were corrected for beam muon contamination, hodoscope losses, wire-spark-chamber inefficiencies, and particle absorption and decay. The results are plotted in Figs. 1 and 2. Because the systematic errors vary slowly, the uncertainty in the energy dependence should be dominated by statistical errors only. Furthermore, the data for different momenta were interlaced in time so that no long-term experimental drifts could seriously affect the energy behavior.

For reasons indicated earlier, the best statistics were obtained for the $\pi^-p \to K^+\Sigma^-$ channel. From Fig. 1(a) it is apparent that the energy dependence of this differential cross section changes markedly for incident momenta above 3 GeV/c. Below this point the cross section drops very rapidly with a power-law behavior of $s^{-9.6}$. In the region above 3 GeV/c the magnitude of the slope sharply decreases so that between 4 and 5 GeV/c the cross section behaves like $s^{-1.1}$ with a statistical error of ±0.8 in the exponent. This remarkable change in energy dependence is inconsistent with the Regge-cut descriptions which asymptotically expect a more rapid decrease, like s^{-3}, at high energy.[8] Equally significant is the magni-

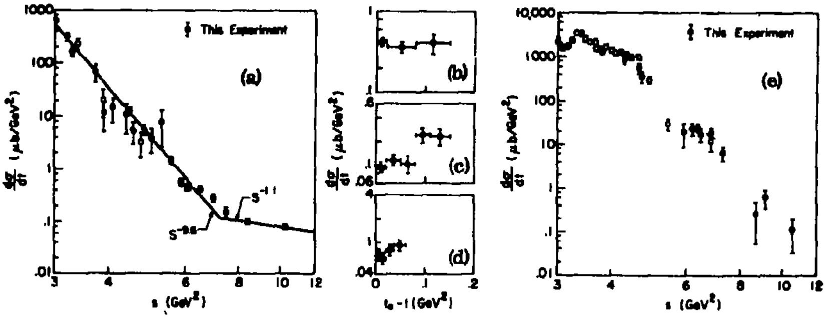

FIG. 1. (a) Energy dependence of the $\pi^-p \to K^+\Sigma^-$ differential cross section at zero degrees averaged over the angular acceptance of the spectrometer. This corresponds to an average t' value of 0.02 (GeV/c)^2 at 5.0 GeV/c and proportionally smaller at lower momenta. Other data from Ref. 3. (b)–(d) Angular distributions for $\pi^-p \to K^+\Sigma^-$ at 3.0, 4.0, and 5.0 GeV/c, respectively. (e) Energy dependence of the $K^-p \to \pi^+\Sigma^-$ differential cross section at zero degrees. Other data from Ref. 4.

tude of the DCX cross section which is some 5000 times smaller than the comparable single-exchange reaction $\pi^+p \to K^+\Sigma^+$ at 5 GeV/c. Regge-cut models which require large cut amplitudes to fit the single-exchange processes find difficulty in reconciling these small DCX results.

Some information about the angular distribution of the $\pi^-p \to K^+\Sigma^-$ channel was obtained at 3 and 4 GeV/c by increasing the current in the spectrometer steering magnet. Geometry restricted the maximum momentum transfer to 0.15 (GeV/c)^2; the differential cross sections are plotted in Figs.)–1(d) for 3, 4, and 5 GeV/c, respectively. here is a forward dip structure at 4 GeV/c which probably also present at 5 GeV/c. Unfortunate- , we do not cover large enough momentum ansfers to make any definitive comparisons th the cut models.

The precipitous decrease of the $\pi^-p \to K^+\Sigma^-$ oss section from 1.5 to 3.0 GeV/c is matched similar behavior in the line-crossed reaction $p \to \pi^+\Sigma^-$ [see Fig. 1(e)]. This s^{-10} characteristic dependence has been noted previously for otic exchange reactions such as $K^-p \to pK^-$ [6] and $\to \bar{p}p$,[7] as well as for the lower-energy data for actions such as $\pi^-p \to \varphi n$.[8] The prevalence of is effect in so many different channels suggests at the low-energy cross sections are dominated s-channel resonances which decouple above a w GeV/c. This is corroborated by the comparin of the $K^-p \to \pi^+\Sigma^-$ and $\pi^-p \to K^+\Sigma^-$ reactions 3 GeV/c, where the $K^-p \to \pi^+\Sigma^-$ cross section 43 times larger, which is difficult to reconcile th any single- or double-exchange mechanism. e evidence of structure in the K^--induced reaction at 3 GeV/c also confirms the idea that this channel maintains resonant forces to somewhat higher energies than the π^-p system.

After a suggestion of Frautschi,[9] we have examined the possibility of fitting the energy behavior of the DCX data with the statistical model. This model is consistent with the rapid decrease of the cross sections at low energy but cannot account for the large difference in magnitude between $\pi^-p \to K^+\Sigma^-$ and $K^-p \to \pi^+\Sigma^-$. Moreover, the apparent onset of exchange forces above 3 GeV/c restricts the testability of this theory to a narrow range in energy.

Cross sections for $K^-p \to K^+\Xi^-$ are shown in Fig. 2. Although the data are much poorer statistically, they show that the cross sections for $K^-p \to K^+\Xi^-$ and $\pi^-p \to K^+\Sigma^-$ are similar in magnitude

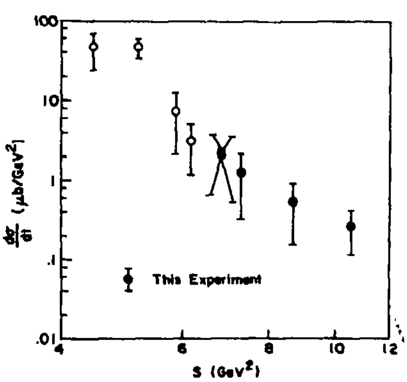

FIG. 2. Energy dependence of the $K^-p \to K^+\Xi^-$ differential cross section at zero degrees. Other data from Ref. 5.

out to 4 GeV/c or so. Note also that at around 5 GeV/c the $\pi^-p\to K^+\Sigma^-$ and $K^-p\to\pi^+\Sigma^-$ cross sections are approximately equal, suggesting that exchange forces dominate at this energy. If the $s^{-1.1}$ behavior of the $\pi^-p\to K^+\Sigma^-$ channel remains true above 5 GeV/c, we may be required to consider the exchange of four or more quarks as a force not intrinsically different from the exchange of a ρ or K^*, only considerably weaker in amplitude.

We acknowledge with gratitude the support of the zero-gradient synchrotron staff of the Argonne National Laboratory. In addition we also thank Lawrence Barak, Aaron Benisch, Hadi Bozorgmanesh, Jay Chapman, David Nitz, and Gary Raffel for their help in setting up the experimental equipment and taking data.

---

†Work supported by the U.S. Atomic Energy Commission.

*University of California, San Diego, La Jolla, Calif. 92037.

‡Max Planck Institute for Physics and Astrophysics, Munich, Germany.

§Oakland University, Rochester, Mich. 48063.

[1] C. W. Akerlof *et al.*, Phys. Rev. Lett. 27, 539 (1971).

[2] R. J. N. Phillips, Phys. Lett. 24B, 342 (1967); N. W. Dean, Nucl. Phys. B7, 311 (1968); C. Michael, Phys. Lett. 29B, 230 (1969); M. Ross, F. S. Henyey, and G. L. Kane, Nucl. Phys. B23, 269 (1970); C. Quigg, Nucl. Phys. B34, 77 (1971).

[3] $\pi^-p\to K^+\Sigma^-$ data references: O. I. Dahl *et al.*, Phys. Rev. 163, 1430 (1967); M. L. Good and R. R. Kofler, Phys. Rev. 183, 1142 (1969); O. Goussu *et al.*, Nuovo Cimento 42A, 606 (1966).

[4] $K^-p\to\pi^+\Sigma$ data references: Amsterdam-Nijmegen Collaboration, in Proceedings of the Second Aix en Provence International Conference on Elementary Particles, Aix en Provence, France, September, 1973 (unpublished), Contributed Paper No. 225; J. Badier *et al.*, Commissariat à l'Energie Atomique, Saclay, Report No. CEA-R3037, 1966 (unpublished); A. Berthon *et al.*, Nucl. Phys. B24, 417 (1970); P. M. Dauber *et al.*, Phys. Lett. 23, 154 (1966); D. F. Kane, Jr., Phys. Rev. D 5, 1583 (1972); G. W. London *et al.*, Phys. Rev. 143, 1034 (1966).

[5] $K^-p\to K^+\Xi^-$ data references: Badier *et al.*, Ref. 4; P. M. Dauber *et al.*, Phys. Rev. 179, 1262 (1969).

[6] A. S. Carroll *et al.*, Phys. Rev. Lett. 23, 887 (1969); C. A. Smith, thesis, University of Rochester (unpublished); V. Chabaud *et al.*, Phys. Lett. 38B, 445 (1972), and CERN NP Internal Report No. 72-12 (unpublished); A. Eide *et al.*, Nucl. Phys. B60, 173 (1973).

[7] W. W. M. Allison *et al.*, Nucl. Phys. B56, 1 (1973); V. Chabaud *et al.*, Phys. Lett. 38B, 449 (1972), and CERN NP Internal Report No. 72-12 (unpublished); W. A. Cooper *et al.*, Nucl. Phys. B16, 155 (1970); Eide *et al.*, Ref. 6; W. M. Katz *et al.*, Phys. Rev. Lett. 19, 265 (1967); G. R. Lynch *et al.*, Phys. Rev. 131, 1276 (1963); J. Lys, Phys. Rev. Lett. 21, 1116 (1968); D. L. Parker *et al.*, Nucl. Phys. B32, 29 (1971); J. K. Yoh *et al.*, Phys. Rev. Lett. 23, 506 (1966).

[8] D. Bollini *et al.*, Nuovo Cimento 60A, 543 (1969); J. H. Boyd *et al.*, Phys. Rev. 166, 1458 (1968); O. I. Dahl *et al.*, Phys. Rev. 163, 1377 (1967); R. Diebold, private communication; B. D. Hyams *et al.*, Nucl. Phys. B22, 189 (1970); H. H. Williams, Ph.D. thesis, Stanford University, 1972 (unpublished).

[9] S. Frautschi, Nuovo Cimento 12A, 134 (1972), and private communication.

ERRATUM

NEW MEASUREMENT OF THE Σ^- MAGNETIC MOMENT. B. L. Roberts, C. R. Cox, M. Eckhause, J. R. Kane, R. E. Welsh, D. A. Jenkins, W. C. Lam, P. D. Barnes, R. A. Eisenstein, J. Miller, R. B. Sutton, A. R. Kunselman, R. J. Powers, and J. D. Fox [Phys. Rev. Lett. 32, 1265 (1974)].

The last named author was inadvertently left off. The byline should include J. D. Fox, Brookhaven National Laboratory, Upton, New York 11973 (Present address: Centre d'Etudes Nucléaires de Saclay, Gif-sur-Yvette, Paris, France).

PHYSICAL REVIEW
LETTERS

VOLUME 33 15 JULY 1974 NUMBER 3

Quantum-Defect Theory of Excited $^1\Pi_u^-$ Levels of H_2

O. Atabek
Laboratoire de Photophysique Moléculaire, Université Paris-Sud, 91405 Orsay, France

and

Dan Dill
Department of Chemistry, Boston University, Boston, Massachusetts 02215

and

Ch. Jungen*
Centre de Mécanique Ondulatoire Appliquée, Paris 19e, France

(Received 18 April 1974)

Quantum-defect methods are used to calculate, by a single unified procedure, the full spectrum of $J=1$ $^1\Pi_u^-$ Rydberg levels of H_2, extending from the lowest levels of the $2p\pi^-$ $C^1\Pi_u^-$ state to the high members of the $np\pi^-$ series between the $H_2^+(v=0)$ and $H_2^+(v=1)$ ionization thresholds. Results for the C state are substantially improved over previous calculations based on direct integration of the vibrational Schrödinger equation, while results at higher energies reproduce with high accuracy the recently observed spectrum, including local perturbations.

We have carried out, by a single unified procedure, a calculation of the full spectrum of $J=1$ Rydberg levels in H_2 of $^1\Pi_u^-$ symmetry, correponding to an excited $np\pi^-$ electron, from the owest levels of the $2p\pi^-$ $C^1\Pi_u^-$ state to the higher members of the $np\pi^-$ series between the $H_2^+(v=0)$ and $H_2^+(v=1)$ ionization thresholds. The calculation is the first application of the channel-interaction methods of quantum-defect theory[1] to electron-vibration interactions.[2,3]

The calculation is based on an R-dependent quantum defect $\mu_{p\pi}(R)$ (R is the internuclear disance) derived from the accurate *ab initio* (fixed-nuclei) potential-energy curve for the C state.[4] This single function $\mu_{p\pi}(R)$, together with the vibrational wave functions of the $H_2^+(v)$ $1s\sigma$ $X^2\Sigma_g^+$ state, serves to characterize completely the vibration-electron interaction throughout the full spectrum of Rydberg levels: The deviation from experiment of the calculated levels of the C state is reduced by as much as 2 orders of magnitude compared to values obtained by direct integration of the vibrational Schrödinger equation with the C-state potential[5]; at the same time the predicted positions of the higher members of the $np\pi^-$ series ($J=1$) correspond closely to the spectrum of $Q(1)$ lines of the $np\pi$ $^1\Pi_u^- - X^1\Sigma_g^+$ bands, based on accurate measurements which have just recently become available.[2,6]

Most previous work on vibration-electron coupling was based on the Born-Oppenheimer approximation. Effects of the breakdown of this approximation were accounted for at best by successively introducing diagonal correction terms (adiabatic approximation) and nondiagonal interaction between electronic states (nonadiabatic effects). The power of the quantum-defect method is that it builds the interaction between electron-

Copyright © 1974 by
The American Physical Society

ic and molecular rotational and vibrational motions into the theory from the start by referring to the two extreme situations (A and B)[1] of completely coupled nuclear and electronic motion and completely independent nuclear and electronic motion. Situation A prevails when the electron is a short distance from the molecular core; the difference $\Delta\epsilon$ between electronic levels ($\epsilon = -\mathcal{R}/n^{*2}$ for discrete states, where $\mathcal{R}$ is the Rydberg constant and n^* the effective quantum number) by far exceeds the vibrational spacings, $|\Delta\epsilon| \gg \omega$ (n^* small), and the electronic motion is fast compared to that of the nuclei. Situation B pertains to large electron-molecular-core separation; $\Delta\epsilon$ is then small compared to the vibrational spacings, $|\Delta\epsilon| \ll \omega$ (n^* large), and the electronic motion can no longer effectively follow that of the nuclei.

Thus, in situation A the Born-Oppenheimer approximation is valid. Here one can average over the fast electronic motion at each internuclear distance R, and use a quantum-defect expression of the total electronic energy, i.e., a sum of core and Rydberg electron energies,[2,3,7]

$$U^{np\pi}(R) = U^+(R) - \mathcal{R}/[n - \mu_{p\pi}(R)]^2, \qquad (1)$$

as the potential for the vibrational motion. The fixed-nuclei potential-energy curve $U^+(R)$ of the core consists of the energies of the core electron plus nuclear repulsion. The contribution of the Rydberg electron to the bonding of the molecule determines the quantum-defect function $\mu_{p\pi}(R)$. A key feature is that $\mu_{p\pi}(R)$ is independent of the degree of electronic excitation.

In situation B the slow motion of the electron relative to the nuclear motion means, on the other hand, that the positions of the Rydberg levels are now characterized by the vibrational quantum number v of the core. Thus these levels are obtained by averaging $\mu_{p\pi}(R)$ over the vibrational motion of the core,[2] i.e.,

$$T(v)(J=1) = T^+(v)(N=1) - \mathcal{R}/[n - \mu_{p\pi}(v)]^2, \qquad (2)$$

where

$$\pi\mu_{p\pi}(v) = \arctan M_{vv}, \qquad (3)$$

and

$$M_{vv'} = \int \chi_v^+(R) \tan[\pi\mu_{p\pi}(R)]\chi_{v'}^+(R)\, dR. \qquad (4)$$

The $T^+(v)(N=1)$ are the (exact) vibrational levels of the ion with rotational quantum number $N = 1$ and the $\chi_v^+(R)$ are the corresponding vibrational wave functions. Note that Eq. (2) describes the situation opposite to that implied by the Born-Oppenheimer approximation.

As n increases along the Rydberg series, the Rydberg electron roams farther and farther from the molecular core and a transition from situation A to situation B occurs. This transition corresponds to an uncoupling of the electronic motion from the vibrations of the core, and is the vibrational analog of the rotational l uncoupling well known to spectroscopists. Thus adiabatic and nonadiabatic effects in electronic states of low excitation are early stages of the uncoupling towards situation B. At the other extreme, local perturbations between high members of series converging to different limits $T^+(v)(N=1)$ are precursors of the departure toward situation A. The quantum-defect theory unifies these alternative extremes by means of the unitary transformation connecting the eigenfunctions of electronic motion in situation A, characterized by the (fixed) internuclear distance R, and the eigenfunctions of electronic motion in situation B, characterized by the vibrational quantum number v of the residual ion. The matrix elements of this unitary transformation are $(R|v)$, i.e., just the vibrational wave functions $\chi_v^+(R)$.[3,8]

This analysis[3] expresses the level positions

$$T = T^+(v)(N=1) - \mathcal{R}/[n^*(v)]^2 \qquad (5)$$

in terms of an eigenvalue problem of a type introduced by Seaton,[9] i.e.,

$$\det|\tan[\pi n^*(v')]\delta_{vv'} + M_{vv'}| = 0. \qquad (6)$$

The solution of Eq. (6) has been carried out in two steps. First, the quantum-defect function $\mu_{p\pi}(R)$ was calculated using Eq. (1) with $n = 2$ and the (fixed-nuclei) curves $U^+(R)$ of Wind[10] and $U^{2p\pi}(R)$ of Kołos and Wolniewicz.[4] This function was then used to calculate the matrix elements $M_{vv'}$ for $0 \leq (v, v') \leq 6$. In a second step Eq. (6) was solved using the following additional theoretical input data: (i) the H_2^+ vibrational levels $T^+(v)(N=1) - T^+(0)(N=0)$ obtained by Beckel, Hansen, and Peek,[11] and (ii) the ionization potential $T^+(0)(N=0) = 124\,417.3\ \mathrm{cm}^{-1}$ of Hunter and Pritchard (see Ref. 2).

Some of the results obtained in this way are listed in Tables I and II. Table I concerns a case close to situation B, namely the energy region between the $v=0$ and $v=1$ ($N=1$) ionization limits. Theoretical and experimental levels agree within less than 1 cm^{-1} for almost all cases. Figure 1 shows a quantum-defect plot of the same data. For each level n the quantum defect $n - n^*$ with respect to the $v = 1$, $N = 1$ limit is plotted against

TABLE I. Experimental and theoretical energies of $-p\pi^-$, $J=1$ levels of H_2 between the $v=0$ and $v=1$ ($N=1$) onization limits (in units of cm^{-1}).

Approximate description[a]	Observed[b,c]	Theoretical[c]
$6p\pi^-$ $v=1$ $J=1$	126 240.1	126 239.9
$5p\pi^-$ $v=1$ $J=1$	126 182.6	126 181.8
$4p\pi^-$ $v=1$ $J=1$	126 111.2	126 111.0
$3p\pi^-$ $v=1$ $J=1$	126 023.5	126 023.3
$2p\pi^-$ $v=1$ $J=1$	125 913.2	125 913.0
$1p\pi^-$ $v=1$ $J=1$	125 774.9	125 775.3
$6p\pi^-$ $v=2$ $J=1$	125 763.1	125 764.3
$0p\pi^-$ $v=1$ $J=1$	125 585.6	125 585.4
$9p\pi^-$ $v=1$ $J=1$	125 335.1	125 335.3
$8p\pi^-$ $v=1$ $J=1$	124 985.8	124 986.7
$5p\pi^-$ $v=2$ $J=1$	124 501.5	124 503.8
$7p\pi^-$ $v=1$ $J=1$	124 471.4	124 473.0

[a] Assuming situation B.

[b] From Herzberg and Jungen, Ref. 2.

[c] Above $v=0$, $J=0$ of $X^1\Sigma_g^+$.

TABLE II. Experimental and theoretical energies of $J=1$ levels of the $C\,^1\Pi_u^-$ state in H_2 (in units of cm^{-1}).

Approximate description[a]	Observed[b,c]	Theoretical[c] This work	Theoretical[c] Ref. 5[d]
$2p\pi^-$ $v=3$ $J=1$	105 667.64	105 671.4	105 609.1
$2p\pi^-$ $v=2$ $J=1$	103 627.74	103 630.0	103 567.1
$2p\pi^-$ $v=1$ $J=1$	101 456.33	101 457.7	101 394.2
$2p\pi^-$ $v=0$ $J=1$	99 150.72	99 151.2	99 086.7

[a] Assuming situation A.

[b] From Dabrowski and Herzberg, Ref. 6.

[c] Above $v=0$, $J=0$ of $X^1\Sigma_g^+$.

[d] Kołos and Wolniewicz, Ref. 5. These values have been obtained by subtracting from the theoretical $n=2$ dissociation limit in the Born–Oppenheimer approximation ($\approx 118\,302.3$ cm^{-1} above the theoretical $v=0$, $J=0$ level of $X^1\Sigma_g^+$, corrected for adiabatic and nonadiabatic effects) the values in the column "$J=1$, $\Lambda=0$" of Ref. 5.

he energy measured from this limit. The theoetical values (circles) lie on the curve repreenting $n-n^*(1)$ as a function of $T-T^+(1)$ accordng to Eq. (6). Obviously all levels except $n=7$ nd 11 are close to situation B, having a constant uantum defect $n-n^*(1)\approx\mu_{p\pi}(v=1)=(1/\pi)\arctan M_{11}$ -0.087. The levels $n=7$ and 11 are perturbed y the members of $n=5$ and 6, respectively, of he series converging to the next higher limit, $T^+(v=2)(N=1)$. These perturbations had been oberved by Herzberg and Jungen,[2] who interpreted hem as due to vibration-electron coupling and etermined the element M_{12} by perturbation theoy. The present *ab initio* calculation predicts orrectly both the unperturbed levels and the perurbations. (Note that, e.g., the perturbation at $=11$ corresponds to an energy-level displacement of 3.5 cm^{-1}.)

Table II refers to a case close to situation A, amely to the $C\,^1\Pi_u^-$ state which is the lowest ember of the $np\pi^-$ series. The first column ists the values observed by Dabrowski and Herzerg for $J=1$[6]; the second and third columns give he results of our calculations and of the Born-Oppenheimer calculation of Kołos and Wolnieicz,[5] respectively. Both theoretical calculations re based on the *same* potential-energy curve, ut the agreement between theory and experiment s greatly improved in our calculation. Kołos and Volniewicz[5] assumed situation A to hold strictly nd determined the level positions by solving the vibrational Schrödinger equation for the potential (1). Since the difference between their results and the observed energies must correspond to the sum of adiabatic and nonadiabatic corrections, we can say that they are built into the quantum-defect treatment.

The calculations reported here are limited to a small range of low v values. Similar calculations involving higher v quantum numbers, or the vibrational continuum (predissociation), would require two improvements of the theory. First, at intermediate R values ($\approx 2R_e$) strong configuration mixing occurs,[7] necessitating the inclusion of states with an excited H_2^+ core. Second, at still larger R values, the quantum number $l=1$ of the Rydberg electron ceases to be well defined, and mixing with $l=3, 5, \ldots$ states becomes possible.

A detailed account of this work will be given

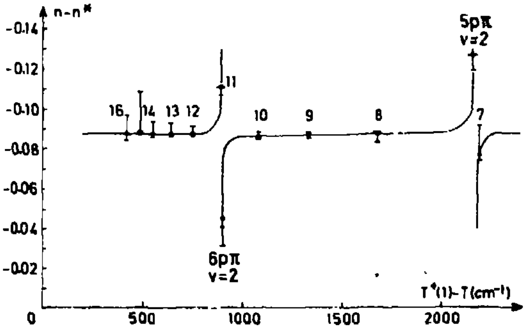

FIG. 1. Quantum-defect plot of the $np\pi^-$, $v=1$, $J=1$ Rydberg series of H_2.

elsewhere.[12] A similar study of the $np\,{}^1\Sigma_u^-$ excited states of H_2 is in progress, as well as an extension to the effect of predissociation and preionization on the profile of lines lying above the dissociation and ionization limits.

We are greatly indebted to Dr. G. Herzberg and Miss I. Dabrowski for communicating their unpublished experimental results and we thank Professor U. Fano for his critical reading of the manuscript. One of us (O.A.) thanks Professor R. Lefebvre for stimulating discussions, and another of us (D.D.) is grateful to Dr. J. B. Tellinghuisen for advice on some of the calculations.

---

*Mailing address: Laboratoire de Photophysique Moléculaire, Université Paris-Sud, 91405 Orsay, France.

[1] U. Fano, Phys. Rev. A 2, 353 (1970).
[2] G. Herzberg and Ch. Jungen, J. Mol. Spectrosc. 41, 425 (1972).
[3] D. Dill, E. S. Chang, and U. Fano, in *Abstracts of Papers, Proceedings of the Eighth International Conference on the Physics of Electronic and Atomic Collisions, Belgrade, 1973*, edited by B. C. Dobić and M. V. Kurepa (Institute of Physics, Belgrade, 1973), p. 536.
[4] W. Kołos and L. Wolniewicz, J. Chem. Phys. 43, 2429 (1965).
[5] W. Kołos and L. Wolniewicz, J. Chem. Phys. 48, 3672 (1968).
[6] I. Dabrowski and G. Herzberg, to be published.
[7] R. S. Mulliken, J. Amer. Chem. Soc. 88, 1849 (1966).
[8] E. S. Chang and U. Fano, Phys. Rev. A 6, 173 (1972).
[9] M. J. Seaton, Proc. Phys. Soc., London 88, 801 (1966).
[10] H. Wind, J. Chem. Phys. 42, 2371 (1965).
[11] Ch. Beckel, B. Hansen, and H. Peek, J. Chem. Phys. 53, 3681 (1970).
[12] O. Atabek, D. Dill, and Ch. Jungen, to be published.

Intensity Variations of K^--Mesonic X Rays*

G. T. Condo
Department of Physics and Astronomy, University of Tennessee, Knoxville, Tennessee 37916
(Received 29 April 1974)

We show that there exists a strong correlation between the atomic diameter of target metals and their K^- mesonic x-ray intensity. The smaller x-ray intensities observed from smaller atoms suggests that the initial capture into large angular momentum states is inhibited in smaller atoms which could be understood if the meson is not localized about a single atom until its kinetic energy is somewhat less than has been presumed. This tendency for mesons to avoid higher angular momentum states when captured by small atoms also explains some previous muonic-atom results.

Recently Wiegand and Godfrey[1] have performed an encyclopedic experiment where the intensities of 346 K^--mesonic x-ray lines were measured for a variety of targets spanning the periodic table. These authors observed unexpected variations in intensities of many of the lines not expected to be influenced by nuclear absorption, even in nearby elements. For example, the intensity of the $n=11$ to $n=10$ transition in Au^{179} was found to be 0.16 ± 0.05 x rays per K^- stop, whereas this same transition in Bi^{209} had an intensity of 0.36 ± 0.07. Similar sharp variations in x-ray intensities for muonic atoms have been reported by Kessler *et al.*[2] and by Quitmann *et al.*[3] On the basis of available theoretical models, such intensity variations must be considered anomalous. Leon and Seki,[4] who have recently calculated the expected K^- x-ray intensities from a semiclassical model, suggest that these fluctuations derive from variations in atomic structure. While we cannot exclude this possibility, we wish to point out, that, for the metallic targets used by Wiegand and Godfrey,[1] there is a close correlation between the observed intensities and the internuclear spacing (atomic diameter) of the target material. I only consider metallic targets to avoid any effects on the kaons' cascade due to electron depletion in the mesonic atom.

In Fig. 1, I plot the observed x-ray intensities versus Z of the target element for the Group IV, V, VI metals studied by Wiegand and Godfrey.[1] For the Group IV metals the transition intensities plotted are an average of the $n=7-6$ and $n=6-5$ intensities, while for the Group V metals, I plot an average of the $n=8-7$ and $n=7-6$ intensities, and for Group VI, I use an average of the $n=11-10$ and $n=10-9$ transitions. The use of average values should tend to smooth out any individ-

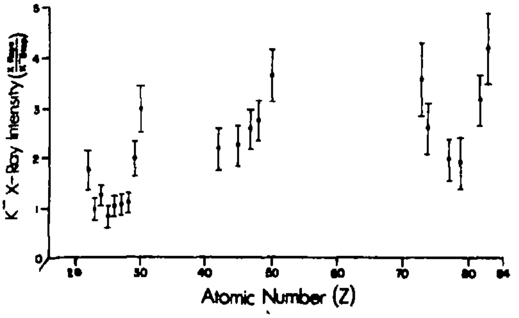

FIG. 1. Average circular orbit K^- mesonic x-ray intensities versus atomic number for metallic substances.

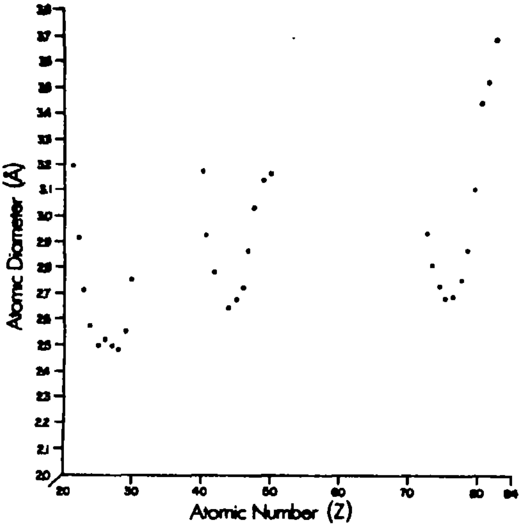

FIG. 2. Atomic diameter versus atomic number for Group IV–VI metals.

ual fluctuations in the data. I have excluded potassium from the plot since only the $n = 5 \rightarrow 4$ intensity was measured and this line could be affected by nuclear absorption. I have also omitted the data from the various metallic oxides obtained in Ref. 1 as these could be affected by electron depletion as well as from differing percentages of oxygen captures in the various compounds. In Fig. 2, for comparison, I plot the atomic diameters (internuclear spacing) listed in American Institute of Physics Handbook.[5] It is clear that there is a strong correlation between the magnitudes of the x-ray intensities and the atomic diameters. The correlation is especially sharp for the metals with $Z = 22 - 30$ and $Z = 73 - 83$. Aside from a possible deviation at $Z = 42$ (Mo), the Group V metals follow a similar trend.

The general equations for Auger and radiative de-excitation of mesonic atoms[6,7] imply that the vast majority of the $n \rightarrow n-1$ x rays derive from circular orbit transitions, $(n, l = n-1) \rightarrow (n-1, l = n-2)$. Thus, the $n \rightarrow n-1$ transitions measured by Wiegand and Godfrey[1] can, to high accuracy, be considered to reflect the population of the circular orbit states $(n, l = n-1)$. Previous calculations[4,6-8] suggest that this circular orbit population should be a fairly smooth function of Z (increasing as Z increases), whereas the K^- data exhibit sharp fluctuations. The correlation noted above then suggest that the circular orbits (maximum l states) are populated more heavily as the size of the target atom increases.

It is conventional to consider the distribution in angular momentum states at $n = (M_K/M_e)^{1/2}$ (the region of the electronic K shell) or at $n \approx 15$ as the starting points of cascade calculations to predict the various x-ray intensities. Rook[8] and Leon and Seki[4] both show that the kaons, angular momentum distribution at the electronic K shell has the same shape as it does at the initial capture. Thus the data of Wiegand and Godfrey[1] imply that a truncation of the angular momentum distribution occurs at large l for elements of small internuclear spacing. For example, the initial l distribution for kaons captured in Bi ($R = 1.82$ Å) must have a far greater population of high-l states than that for Au ($R = 1.44$ Å).

These considerations can also explain some previously peregrine phenomena in muonic atom spectra. Thus, in an early muonic atom experiment, Quitmann *et al.*[3] measured the K series x-ray intensities for a variety of elements with $Z < 30$. It was observed that the higher K x rays $(K_\beta, K_{\gamma,\delta,\ldots})$ suffered a sharp decline in intensity at potassium, and that these higher x-ray intensities increased monotonically through Ca and Ti and remained more or less constant for $Z = 24$ to $Z = 29$. This is precisely the behavior expected if the higher l states are preferentially populated upon capture by larger atoms.

Another arcane aspect of muonic atom spectra occurred in the high-statistics experiment of Kessler *et al.*[3] using Ti and Mn targets. These authors found that their data for titanium required a statistical $(2l+1)$ distribution in l at the $n = 14$ level for Ti, while for Mn, an l distribution of the form $(2l+1)e^{-l/10}$ was necessary. No reason for this behavior was proffered and, subsequently, Ponomarev[9] has suggested that such a violent change in the initial l distribution, for nearby elements, seems unnatural. From the point of view of atomic dimensions, however, this is precisely the expectation, since the atomic diameters of Ti and Mn are 2.93 and 2.5 Å, respectively. Thus, we would expect a truncation in l for the initial angular distribution in Mn which would be reflected later in the cascade by a diminished circular orbit population for Mn as compared to Ti.

It may be possible to understand the reluctance of mesons to be captured into large angular momentum states in metals with small internuclear spacings on purely classical grounds. For a kaon to be captured into a state of $l=100\hbar$ by an atom of radius 1 Å requires the kaon to have a minimum kinetic energy of ~50 eV. Thus, if the kaon succeeds in escaping localization upon a single atom until it has a lower energy than this, capture into large-l states would be quite unlikely. It should be pointed out that, even though there are many uncertainties in the calculations, several studies of the capture of slow negative mesons[8,10] have found that capture by a single atom occurs at energies somewhat in excess of this value.

It would certainly be beneficial to extend mesonic atom x-ray intensity measurements to other targets and other incident projectiles ($\bar{p}, \Sigma^-$, etc.). However, on the basis of the observations presented here, a study of the low-lying mesonic x-ray intensities in manganese or zinc in several of their crystalline forms should prove most interesting.

It is a pleasure to thank Professor Wiegand for a copy of his work before publication.

---

*Research supported, in part, by the U. S. Atomic Energy Commission, under Contract No. AT-(10-1)-3956.

[1] C. E. Wiegand and G. L. Godfrey, University of California, Lawrence Berkeley Laboratory Report No. LBL-1074, 1973 (to be published).

[2] D. Kessler, H. L. Anderson, M. S. Dixit, H. J. Evans, R. J. McKee, C. K. Hargrove, R. D. Barton, E. P. Hincks, and J. D. McAndrew, Phys. Rev. Lett. 18, 1179 (1967).

[3] D. Quitmann, R. Engfer, U. Hegel, P. Brix, G. Backenstoss, K. Goebel, and B. Stadler, Nucl. Phys. 51, 609 (1964).

[4] M. Leon and R. Seki, Phys. Rev. Lett. 32, 132 (1974).

[5] *American Institute of Physics Handbook*, edited by D. E. Gray (McGraw-Hill, New York, 1972), 3rd ed.

[6] A. D. Martin, Nuovo Cimento 27, 1359 (1963).

[7] Y. Eisenberg and D. Kessler, Phys. Rev. 130, 2352 (1963).

[8] J. R. Rook, Nucl. Phys. B20, 14 (1970).

[9] L. I. Ponomarev, Annu. Rev. Nucl. Sci. 23, 395 (1973).

[10] M. Y. Au-Yang and M. L. Cohen, Phys. Rev. 174, 468 (1963).

Resonant Enhancement of Two-Photon Absorption in Sodium Vapor

J. E. Bjorkholm and P. F. Liao
Bell Telephone Laboratories, Holmdel, New Jersey 07733

(Received 23 May 1974)

Resonant enhancement of over 7 orders of magnitude of the two-photon absorption cross section is observed in sodium vapor. Two cw dye-laser beams of different frequencies and propagating in opposite directions are utilized to generate high-resolution spectra which allow the enhancement as well as destructive-interference effects of nearly resonant intermediate states to be clearly demonstrated.

Recently there have appeared a number of papers demonstrating high-resolution two-photon spectroscopy in atomic vapors.[1,2] Especially interesting are the techniques which eliminate Doppler broadening by causing the atoms to absorb one photon from each of two beams of equal frequency propagating in opposite directions.[2] We have utilized a generalization of the opposing-beam technique to demonstrate resonant enhancement of the two-photon absorption cross section in sodium vapor. Our experiments were carried out using two single-mode, cw dye lasers operating at different frequencies. Large enhancements of more than 7 orders of magnitude and destructive-interference effects due to nearly resonant intermediate states are clearly demonstrated.

The basic theory of two-photon absorption was given by Göppert-Mayer in 1931,[3] and since that time there has been considerable work on the theory of two-photon absorption in both solids and gases.[4] In the latter case calculations of two-photon photoionization[5] predicted strong enhancement of the photoionization cross section whenever a single photon energy approaches that of an allowed atomic transition. Destructive interference between the contributions from different intermediate states was also predicted. From second-order perturbation theory one can calculate the absorption cross section of an atom for light at frequency ν_1 induced by light at ν_2. The atomic transitions correspond to the atom absorbing one photon from each of the radiation fields. For linearly polarized light this induced-absorption cross section for transitions from the ground state g to the excited state f is given by

$$\sigma(\nu_1)=1.15\times10^{-34}\left|\sum_n\langle f|z|n\rangle\langle n|z|g\rangle\left[(E_n-h\nu_1)^{-1}+(E_n-h\nu_2)^{-1}\right]\right|^2\nu_1\rho(\nu_1+\nu_2)I_2\ \mathrm{cm}^2, \tag{1}$$

where I_2 is the intensity in W/cm^2 of the radiation field at ν_2, $\rho(\nu_1+\nu_2)$ is the normalized line-shape function for the transition, the matrix elements are expressed in Bohr radii, and the summation is carried out over all intermediate states of energy E_n, expressed in rydbergs. In our experiments we observe the $3S$-$4D$ transitions in sodium and the dominant intermediate states are the $3P$ levels. The induced cross section for this transition is approximately $(5\times10^{-14})I_2$ cm^2 when $E_{3P}-h\nu_2=0.1$ cm^{-1}. This can easily be made comparable to the single-photon absorption cross section per atom $(\lambda^2/4\pi)$ of the strongly allowed $3S$-$3P$ resonance transition which is about 3×10^{-10} cm^2. Consequently it is not surprising that fluorescence caused by two-photon absorption was brightly visible in our experiments.

The basic experimental setup was straightforward. The light from two single-axial-mode, cw dye lasers propagated in opposite directions through a Pyrex cell containing sodium vapor. The beams were focused to a minimum beam radius in the vapor of about 40 μm and typical laser powers were 50 mW, so that maximum light intensities were about 10^3 W/cm^2. The vapor pressure was on the order of 10^{-5} Torr. Two-photon transitions to the $4D$ levels were monitored by using a 1P28 photomultiplier to detect the 330-nm fluorescence ($4P$-$3S$ transition) resulting from the decay from the $4D$ levels.

In making an experimental run, one laser was operated at a fixed frequency ν_2 while the other laser was operated at the frequency ν_1 which was electronically tuned across the two-photon transition. Because the frequencies of the two absorbed photons are not exactly equal, Doppler effects are not totally eliminated and the absorption linewidths contain residual Doppler broadening. Nonetheless, for the conditions of our experiments the observed linewidths (~60 MHz) are much smaller than the Doppler width (~3.4 GHz) and high-resolution spectra such as that shown in Fig. 1 were obtained. Calculations show[6] that the linewidth predicted for the conditions of Fig. 1 is 30 MHz; the experimentally observed linewidth (full width at half-maximum, FWHM) is 60 MHz. The increased linewidth is due to frequency jitter of the two lasers. The stability of the fixed-frequency laser was ± 35 MHz and that of the scanned laser[7] was about ± 10 MHz. (Note that for purposes of spectroscopy the 60-MHz linewidth of our experiment corresponds to a 30-MHz linewidth in the previous experiments[1,2] in which both photons were of the same frequency.) Averaging over seventeen curves like that of Fig. 1 we have measured the fine-structure splitting of the $4D$ state to be 1027 ± 16 MHz. This is in good agreement with previous measurements.[1]

The residual Doppler effects make it impossible to be resonant simultaneously with all velocity groups of the Maxwellian thermal distribution. Consequently the use of two photons of unequal frequencies results in a decrease of excitation efficiency. For the peaks of the lines, it

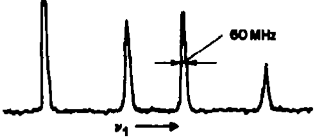

FIG. 1. The excitation spectrum for two-photon excitation of the $4D$ level with $\lambda_2=5835$ Å. Proceeding in the direction of higher frequency, the peaks correspond to the following transitions: $3S(F=2)\to4D_{5/2}$, $3S(F=2)\to4D_{3/2}$, $3S(F=1)\to4D_{5/2}$, $3S(F=1)\to4D_{3/2}$. The splittings 1.772 and 1.027 GHz correspond to the ground-state hyperfine splitting and our measurement of the $4D$ fine-structure splitting, respectively.

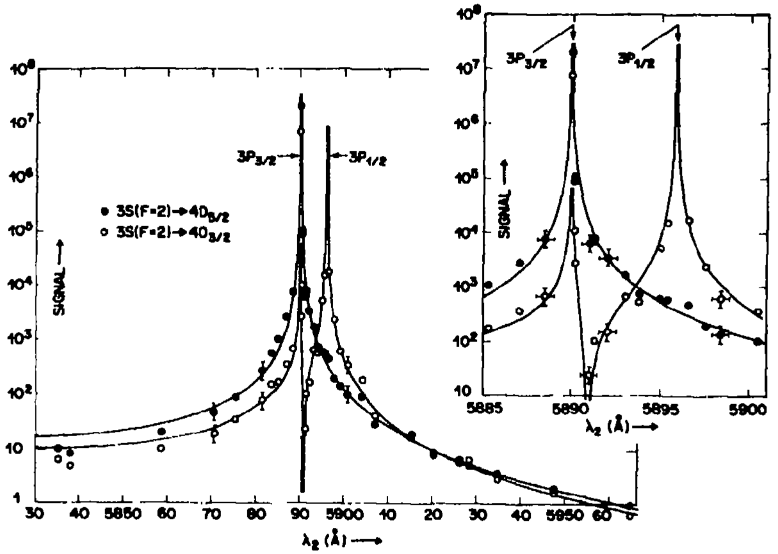

FIG. 2. Normalized two-photon transition rates for the $3S(F=2)\to 4D_{5/2}$ and $3S(F=2)\to 4D_{3/2}$ transitions as a function of the wavelength of the fixed-frequency laser, λ_2. (Note that $\nu_1=\nu_2$ for $\lambda_2=5787$ Å.) The points are experimental and the curves are theoretical. The inset shows the behavior in the region from 5885 to 5900 Å with an expanded horizontal axis.

can be shown that the fraction η of atoms which can make two-photon transitions is given by[6]

$$\eta = ye^{y^2}\operatorname{erfc}(y). \qquad (2)$$

In the above, $y=(\ln 2)^{1/2}\nu_0/[\pi\tau\Delta\nu_D(\nu_1-\nu_2)]$, where $h\nu_0$ is the energy of the $3S$-$4D$ transition ($\nu_0=1.036\times 10^{15}$ Hz), τ is the natural lifetime of the excited state (52 nsec),[7] and $\Delta\nu_D$ is the Doppler width of the two-photon transition (~3.4 GHz). Over the tuning range used in our work η varied from 0.38 to 0.08. (The calculated linewidth varied from 30 to 100 MHz.)

To demonstrate resonant enhancement, a series of runs giving curves like that of Fig. 1 were carried out, each with a different λ_2, the wavelength of the fixed-frequency laser. In Fig. 2 we plot the normalized strengths of the $3S(F=2)\to 4D_{5/2}$ and $3S(F=2)\to 4D_{3/2}$ transitions as a function of λ_2. These normalized strengths were obtained by dividing the peak line strengths of each transition by the product of the incident laser powers. [The strengths of the transitions from the $3S(F=1)$ level to the two $4D$ levels are related to the respective transitions from the $3S(F=2)$ level by 0.6 and display the same behavior.] Recall that these lines are separated by much less than the Doppler width and that they could not be resolved without the use of the opposed-beam technique. For the point at the $3P_{3/2}$ resonance care was taken to attenuate the laser powers so that saturation effects such as line broadening were not present. Attenuation of about 10^3 was required. Saturation effects were not observed at all other points. Both transitions show strong dispersion as the laser frequency ν_2 approaches the frequency of the relevant $3P$ intermediate states. For the $3S(F=2)\to 4D_{5/2}$ transition only the $3P_{3/2}$ state can act as an intermediate state since the $3P_{1/2}\to 4D_{5/2}$ single-photon transition is forbidden, while for the $3S(F=2)\to 4D_{3/2}$ transition both the $3P_{3/2}$ and $3P_{1/2}$ levels are intermediate states. The wavelength dependence of the two-photon absorption cross section of the latter transition contains a sharp feature due to destructive interference between the contributions of the two intermediate levels for wavelengths lying between them. The cross section drops rapidly on the long-wavelength side of the $3P_{3/2}$ level and has a minimum only 1.00 Å from its maximum at the $3P_{3/2}$ level. The curves in Fig. 2 are theoretical curves calculated using Eqs. (1) and (2) where the sum in Eq. (1) has been restricted to the $3P$ levels. Except for an overall normalization factor, there are no adjustable parameters in this calculation. The relative amplitudes of all matrix elements were determined using angular momentum relations. The fit between experiment and theory is very satisfying. The slight discrepancy for the shortest wavelengths is due to the frequency jitter of the lasers. In this wavelength range the calculated absorption linewidth is comparable to or smaller than the total jitter.

In addition to the sharp two-photon signals, another feature was observed when the fixed-frequency laser was tuned close to one of the intermediate states. As the laser frequency ν_1 was scanned, this feature appeared at the frequency corresponding to $3P-4D$ transitions and was a broad resonance line with a width of about 1.9 GHz, the Doppler width for such transitions. Because the sum of the laser photon energies, $h\nu_1+h\nu_2$, is not equal to the $3S-4D$ energy separation, we believe this signal is due to a two-step absorption process in which the first step involves direct excitation of $3S-3P$ transitions. This excitation requires a phase-interrupting collision simultaneous with the absorption of a photon, $h\nu_2$, to satisfy energy conservation. The second step consists of $3P-4D$ transitions. We are investigating this feature in more detail.

The large enhancements we have demonstrated clearly have important implications for potential applications of two-photon transitions. Such applications include selective two-photon excitation for isotope separation and the generation of sum and difference frequencies via three-wave mixing.[9]

We are pleased to acknowledge helpful discussions with M. D. Levenson of Harvard University and with A. Kiel, K. R. German, and J. P. Gordon of Bell Laboratories.

---

[1] D. Pritchard, J. Apt, and T. W. Ducas, Phys. Rev. Lett. 32, 641 (1974).

[2] F. Biraben, B. Cagnac, and G. Grynberg, Phys. Rev. Lett. 32, 643 (1974); M. D. Levenson and N. Bloembergen, Phys. Rev. Lett. 32, 645 (1974); N. Bloembergen, M. D. Levenson, and M. M. Salour, Phys. Rev. Lett. 32, 867 (1974); T. W. Hänsch, K. C. Harvey, G. Meisel, and A. L. Schawlow, to be published.

[3] M. Göppert-Mayer, Ann. Phys. (Leipzig) 9, 273 (1931).

[4] For a recent review see J. M. Worlock, *Laser Handbook*, edited by F. T. Arecchi and E. O. Schulz-DuBois (North-Holland, Amsterdam, 1972), p. 1323. For the theory of two-photon absorption without Doppler effects see L. S. Vasilenko, V. P. Chebotaev, and A. V. Shishaev, Pis'ma Zh. Eksp. Teor. Fiz. 12, 161 (1970) [JETP Lett. 12, 113 (1970)].

[5] W. Zernik, Phys. Rev. 135, A51 (1964); H. B. Bebb, Phys. Rev. 149, 25 (1966); J. L. Hall, IEEE J. Quantum Electron. 2, 361 (1966).

[6] J. E. Bjorkholm and P. F. Liao, to be published.

[7] Spectra-Physics System 580 dye laser.

[8] F. Karstensen and J. Schramm, Z. Phys. 195, 370 (1966).

[9] R. T. Hodgson, P. P. Sorokin, and J. J. Wynne, Phys. Rev. Lett. 32, 343 (1974); S. E. Harris and D. M. Bloom, Appl. Phys. Lett. 24, 229 (1974); D. M. Bloom, J. T. Yardley, J. F. Young, and S. E. Harris, Appl. Phys. Lett. 24, 427 (1974).

Advantages of a Nonharmonic-Oscillator Analysis of Molecular Vibrations*

Gary Simons
Department of Chemistry, Wichita State University, Wichita, Kansas 67208

and

J. Michael Finlan†
Department of Chemistry, The Johns Hopkins University, Baltimore, Maryland 21218

(Received 20 May 1974)

It is suggested that the theory of molecular vibrations, currently based on the harmonic oscillator potential, should be reformulated in terms of the potential $V=K[(x-x_e)/x]^2$. The proposed potential is shown to possess numerous advantages, including an improved physical form, superior eigenfunctions and eigenvalues, the ability to include rotation analytically, and a set of continuum wave functions. The standard classical vibrational analyses are retained.

The harmonic-oscillator potential,

$$V_{\mathrm{HO}}=(K/2)[(x-x_e)/x_e]^2, \qquad (1)$$

where x is a generalized coordinate with an equilibrium value of x_e, is widely used in the study of vibrations; indeed, this potential is so firmly entrenched that alternative analyses are rarely employed. Thus we find that the theory of molecular vibrations of diatomic and polyatomic molecules is based upon V_{HO}, even though this function is known to be inaccurate. In the following we demonstrate that V_{HO} could be profitably replaced as the standard simple description of most molecular vibrations by the function

$$V = (K/2)[(x - x_e)/x]^2. \qquad (2)$$

As described by Nielsen,[1] the theory of internal molecular motions is based upon the solution of an appropriate nuclear Schrödinger equation. Since this eigenvalue equation cannot be solved exactly, both the kinetic term and the Born-Oppenheimer potential are expanded in a series, and the problem is treated via perturbation theory. Conventionally, the potential is expanded as a power series in normal coordinates and the zeroth-order problem reduces to a combination of rigid rotors and harmonic oscillators. The zeroth-order wave functions and energies obtained in this manner may be sufficient for some purposes; however, higher-order corrections can be calculated and are often important.[1,2] The value of this perturbation treatment is, of course, largely determined by the accuracy of the zeroth-order Hamiltonian H^0. The closer H^0 is to the actual Hamiltonian H the more useful the results of the perturbation development should be. Unfortunately, the harmonic-oscillator potential is usually accurate only for values of x near x_e. Away from equilibrium V_{HO} behaves "unphysically" and is a poor approximation to the actual Born-Oppenheimer potential. As previously noted,[3-5] for example, V_{HO} does not possess the asymmetry expected for bond-stretch modes and becomes infinite as $x \to \infty$. Consequently, the eigenfunctions obtained using V_{HO} are not accurate for large values of x, the eigenvalues of high vibrational levels are inaccurate, and it is not surprising that one must often employ high orders of perturbation theory. As an alternative, based on results given previously[3-6] and the following discussion, we suggest that an improved H^0 and a correspondingly better description of vibrations can be achieved by employing the potential of Eq. (2) for those vibrational modes which do not require a symmetric potential.

One reason for the widespread use of V_{HO} is that in a power-series expansion of the potential in terms of $(x - x_e)/x_e$ no linear term appears because of the nature of the equilibrium, and terms cubic and higher are small for x near x_e. These same properties are possessed by an expansion in powers of $(x - x_e)/x$. In addition, V [Eq. (2)] qualitatively describes the asymmetry of bond stretches and the dissociation process,[3-5] and may be decomposed by a virial-theorem analysis which attributes the x^{-1} term to potential energy and the x^{-2} term to kinetic energy.[7] Thus Eq. (2) possesses at least as much physical content as Eq. (1).

A second reason for the application of the harmonic-oscillator approximation is that it is susceptible to classical analysis. The classical solution is sinusoidal and leads to the well-known and highly successful normal-coordinate and FG matrix methods.[8] These techniques are formulated in the limit of infinitesimal vibrations, however, and since

$$\frac{K}{2}\left(\frac{x - x_e}{x}\right)^2 = \frac{K}{2}\left(\frac{x - x_e}{x_e}\right)^2 - K\left(\frac{x - x_e}{x_e}\right)^3 + \dots, \qquad (3)$$

for infinitesimal vibrations the harmonic-oscillator potential and the suggested alternative potential are equivalent. Therefore one can retain the same classical concepts and methods for Eq. (2) that have proved so useful for Eq. (1).

The third major reason for the adoption of the harmonic-oscillator potential is that it possesses closed-form quantum-mechanical solutions. In the one-dimensional case its eigenvalues are given by

$$E_v = (\hbar/x_e)(K/\mu)^{1/2}(v + \tfrac{1}{2}), \quad v = 0, 1, 2, \dots, \qquad (4)$$

and its eigenfunctions are

$$\psi_v = N_v \exp[-\alpha(x - x_e)^2/2] H_v[\alpha^{1/2}(x - x_e)], \qquad (5)$$

where N_v is a normalization constant, $\alpha = (K\mu)^{1/2}/\hbar x_e^2$, μ is the mass, and H_v is the appropriate Hermite polynomial. Equation (4) is attractive in that it displays the even vibrational spacing actually observed for the lower levels, while the simple form of Eq. (5) allows a straightforward evaluation of the integrals necessary in investigations of various vibrational properties or in perturbation treatments of higher-order potential terms. The Schrödinger equation for V [Eq. (2)] plus a rotational term may be solved just as simply; its eigenvalues are

$$E_{v,J} = K/2 - (K/2)\gamma(v + \tfrac{1}{2} + \beta)^{-2}, \qquad (6)$$

and its eigenfunctions are

$$\psi_{v,J} = N_{v,J}^{1} x^{\beta + 1/2} \exp(-\xi x/2x_e) L_v^{2\beta}(\xi x/x_e), \qquad (7)$$

where $N_{v,J}^{1}$ is a normalization constant, $\gamma = K\mu x_e^2/\hbar^2$, $\beta = [\gamma + \tfrac{1}{4} + J(J+1)]^{1/2}$, $\xi = \gamma/2(v + \tfrac{1}{2} + \beta)$, and $L_v^{2\beta}$ is the appropriate generalized Laguerre polynomial.[9] *In contrast to the harmonic oscillator,* *the inclusion of rotation in Eq. (2) by the addition of a potential term* $\hbar^2 J(J+1)/2\mu x^2$ *still permits an exact analytical solution of the Schrödinger equation, thus avoiding the rigid-rotor approximation!* Equation (6) may be expanded for small values of the vibrational quantum number v, and one obtains the same formula as for the harmonic oscillator. But for larger values of v, Eq. (6) correctly predicts that the spacing should decrease and the excited vibrational levels will be closer together. The eigenfunctions of Eq. (7) provide a sound basis for further computations, as one can exploit the properties of the Laguerre polynomials to evaluate the necessary integrals. These wave functions lack the rigid parity displayed by the harmonic-oscillator eigenfunctions, and should, therefore, yield more realistic values for vibrational transition probabilities. There are also a well-defined set of continuum wave functions for this potential, so that bound-state–continuum transitions can be described. Moreover, we note that the Laguerre polynomials are normalized over the physically realistic range $0 \leqslant x \leqslant \infty$, while Hermite polynomials are normalized for $-\infty \leqslant x \leqslant +\infty$, which includes negative bond lengths!

We emphasize that the determination of the eigenfunctions and eigenvalues of Eqs. (6) and (7) does not require sophisticated mathematics; this analysis is no more complicated than the traditional harmonic-oscillator–rigid-rotor treatment. Although potentials of the form $C_1/x + C_2/x^2$ have been previously studied,[10-12] the considerable pedagogical, conceptual, and computational advantages of this alternative analysis seem to have been largely unappreciated. For diatomic molecules, at least, these appear to be compelling reasons for discarding the harmonic-oscillator approach in favor of the one proposed here.

Current results[3-6] suggest that many of the quantum-mechanical aspects of the theory of molecular vibrations, e.g., the work of Nielsen,[1] could be profitably reformulated in terms of Eq. (2). This could be done at the zeroth-order level, where one would have a simple analytic solution which includes some of the effects of vibrational anharmonicity and vibration-rotation interaction, or it could be done at a higher level of perturbation theory, where we anticipate that the use of Eqs. (2), (6), and (7), along with perturbations in powers of $(x-x_e)/x$, as opposed to $(x-x_e)/x_e$, will improve the convergence properties of the perturbation method. Investigations of various aspects of this problem are now underway.

We are grateful to Professor R. G. Parr and Professor M. E. Zandler for helpful discussions.

---

*Acknowledgment is made of partial support of this research by the Petroleum Research Fund, administered by the American Chemical Society. The National Institutes of Health also provided support.

†Current address: Department of Chemistry, University of Ottawa, Ottawa, Ontario, Canada K1N 6N5.

[1] H. H. Nielsen, Rev. Mod. Phys. 23, 90 (1951).

[2] M. Goldsmith, G. Amat, and H. H. Nielsen, J. Chem. Phys. 23, 1178 (1956); G. Amat, M. Goldsmith, and H. H. Nielsen, *ibid.* 27, 838 (1951); G. Amat and H. H. Nielsen, *ibid.* 27, 485 (1957), and 29, 655 (1958), and 36, 1859 (1962); J. Overend, Annu. Rev. Phys. Chem. 21, 265 (1970).

[3] G. Simons, R. G. Parr, and J. M. Finlan, J. Chem. Phys. 59, 3229 (1973).

[4] J. M. Finlan and G. Simons, to be published.

[5] G. Simons, to be published.

[6] R. W. Bickes, Jr., and R. B. Bernstein, to be published.

[7] R. F. Borkman and R. G. Parr, J. Chem. Phys. 48, 1116 (1968); R. F. Borkman, G. Simons, and R. G. Parr, *ibid.* 50, 58 (1969).

[8] E. B. Wilson, Jr., J. C. Decius, and P. C. Cross, *Molecular Vibrations* (McGraw-Hill, New York, 1955).

[9] *Handbook of Mathematical Functions*, edited by M. Abramowitz and I. A. Stegun, National Bureau of Standards Applied Mathematics Series No. 55 (U. S. GPO, Washington, D. C., 1964).

[10] A. E. Ruark and H. C. Urey, *Atoms, Molecules and Quanta* (McGraw-Hill, New York, 1930), pp. 666–671.

[11] E. Fues, Ann. Phys. (Leipzig) 80, 367 (1926).

[12] L. D. Landau and E. M. Lifschitz, *Quantum Mechanics* (Addison-Wesley, Reading, Mass., 1958); G. Simons, J. Chem. Phys. 55, 756 (1971).

Electron Impact near the $a^3\Pi$ State of CO: Dipole-Dominated Resonances*

S. F. Wong and G. J. Schulz
Department of Engineering and Applied Science, Mason Laboratory, Yale University, New Haven, Connecticut 06520

(Received 8 May 1974)

Sharp structures have been observed in the elastic and vibrational ($v = 1$ and $v = 2$) cross sections of the ground electronic state of CO at energies coincident with the $v = 0$, 1, and 2 levels of the $a^3\Pi$ state of CO. The large electric dipole moment of the $a^3\Pi$ state of CO (1.38 D) appears to be sufficient to bind temporarily the incoming electron at or near the top of the potential well. The potential energy curve for this "dipole-dominated resonance" coincides with that of the $a^3\Pi$ state.

The behavior of elastic and inelastic cross sections by electron impact near the threshold of an electronic state is still poorly understood, for either atoms or molecules.[1] In our search for relevant experiments which could shed light on this problem, we have studied effects near the thresholds of several states in molecules and we report here our results for the elastic and the vibrational cross sections in the vicinity of the $a^3\Pi$ state[2] in CO (6.01 eV) and its isoelectronic counterpart, the $B^3\Pi_g$ state[3] in N_2 (7.35 eV). Both these states are valence states and the transition involved in the inealstic process is $\sigma \to \pi$ ($n = 2$). However the $a^3\Pi$ state of CO has a large electric dipole moment[4] of 1.38 D, whereas the equivalent state in N_2 ($B^3\Pi_g$) has *no* permanent dipole moment. *Thus we shall be able to attribute the major differences between the* $^3\Pi$ *states in CO and* N_2*, which we observe experimentally, to the difference in dipole moments.*

We should also note that the lowest $^3\Pi$ states of CO and N_2, being valence states, have no resonances associated with them which are bound by an appreciable amount (~200–500 meV) to these states. Various attempts to find such "Feshbach" resonances at energies below these valence states led to negative results and it is now believed that only Rydberg states of molecules exhibit resonances which lie below their parent states.[1]

The experimental arrangement consists of a hemispherical electrostatic monochromator, a collision region in which a molecular beam crosses the path of the electron beam, and a hemispherical energy analyzer. The instrument has been described in detail previously[5,6] and for the present study we use a resolution of about 35 meV for vibrational excitation and 55 meV for elastic scattering. The energy scale for each gas is established with respect to its own lowest Feshbach resonance,[1] namely, the 10.04-eV resonance in CO and 11.48-eV resonance in N_2. The accuracy of the energy scale is estimated to be within 30 meV.

Figure 1 shows the cross section for elastic scattering and for vibrational excitation to the $v = 2$ levels of the $X^1\Sigma^+$ ground state of CO. The energy scale spans the region of the first few vibrational levels of the $a^3\Pi$ state and these levels are indicated by vertical arrows in Fig. 1. Of interest is the sharp structure existing in all the cross sections at energies coincident with the low vibrational levels ($v = 0, 1, 2$) of the $a^3\Pi$ state. The data shown for vibrational excitation are tak-

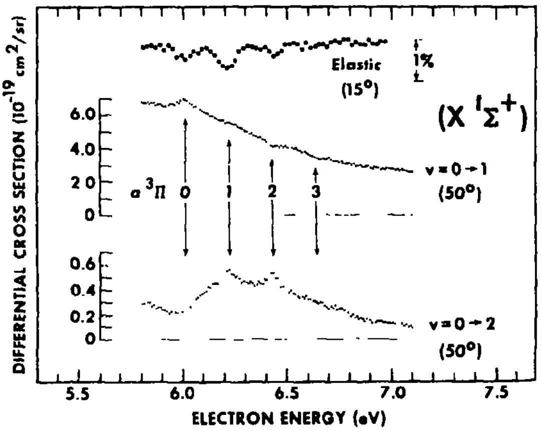

FIG. 1. Energy dependence of the differential elastic and vibrational excitation cross sections in CO. Sharp structures in each of the curves coincide in energy with the vibrational levels ($v = 0,1,2$) of the first-excited electronic valence state, $a^3\Pi$. Experimental errors in the *absolute magnitude* of the vibrational cross sections are about 30%. The 1% mark represents the change in the elastic cross section and is used to show the relative size of the elastic structure only.

en at an angle of observation of 50 deg; *at 90 deg, the sharp structures retain the same absolute values* and the smooth "background" cross section at 90 deg is comparable to the cross section at 50 deg.

Structures in the elastic cross section which are coincident in energy with the levels of an excited state are often interpreted by invoking Wigner cusps. In the present case, such a Wigner cusp[7,8] would arise from the opening of the $a\,^3\Pi$ channel ($5\sigma \rightarrow 2\pi$ transition) and thus it would exist in the p wave, both for elastic scattering and for vibrational excitation. We would therefore expect that the structures associated with such a cusp would decrease strongly at 90 deg. Since we do not observe this expected decrease, we must reject an interpretation based solely on Wigner cusps. Rather, we attribute the structures visible in the elastic cross section and in the vibrational cross sections to a resonance dominated by the dipole moment of the $a\,^3\Pi$ state.

When we study elastic or vibrational excitation in the energy range of the $B\,^3\Pi_g$ state of N_2, we observe none of the sharp features of Fig. 1. The $B\,^3\Pi_g$ state in N_2 is analogous to the $a\,^3\Pi$ state in CO, but it does not have a permanent dipole moment. Figure 2 shows the present results on the vibrational excitation for $v=1$ and $v=2$ in N_2 at 50 deg. At 90 deg, the shape of the curves is similar.

We postulate that the resonant structures shown n Fig. 1 can best be explained in terms of a CO^- tate whose potential energy curve is coincident r nearly coincident with the potential energy urve for the $a\,^3\Pi$ state of the neutral molecule. wo tests can be made to substantiate the above postulate:

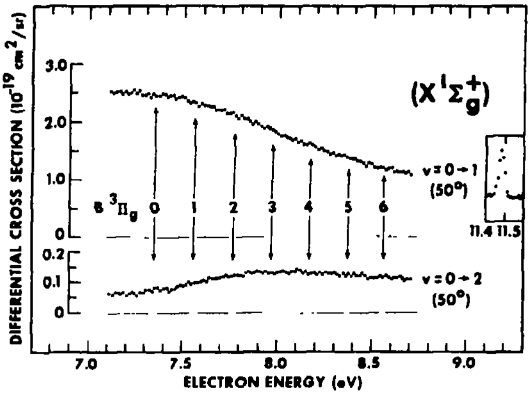

FIG. 2. Energy dependence of the differential vibrational cross sections in N_2. While the trend of the excitation curves is similar to the corresponding curves in CO, no structures are evident at the positions of the vibrational levels of the $B\,^3\Pi_g$ state. Experimental errors in the *absolute magnitude* of the cross sections are about 30%. The inset shows the 11.48-eV Feshbach resonance, as observed in the $v=0\rightarrow 1$ vibrational excitation, at a scattering angle of 50 deg.

(i) The resonant structure must be coincident in energy with the levels of the $a\,^3\Pi$ state. As shown in connection with Fig. 1, this is the case.

(ii) The excursion in the resonant structure must be consistent with the Franck-Condon factors for the $a\,^3\Pi$ state. To establish this, consider a single resonance at an energy E_r with autoionization decay width Γ. In the neighborhood of E_r, the vibrational cross section from the initial state $|v_i\rangle$ to the final state $|v_f\rangle$ is given as

$$\sigma(E)=|A+\langle v_f|v_r\rangle\langle v_r|v_i\rangle B/[(E-E_r)+\tfrac{1}{2}i\Gamma]|^2, \tag{1}$$

here A and $2B/\Gamma$ are, respectively, the background and the resonant amplitudes; $\langle v_f|v_r\rangle$ and $\langle v_r|v_i\rangle$ re the Franck-Condon overlap integrals involving an intermediate $|v_r\rangle$ state. If we now assume that $A|^2 \gg |2B/\Gamma|^2$, which seems to conform to the experimental results of Fig. 1, we obtain

$$\sigma(E)\simeq|A|^2+2\langle v_f|v_r\rangle\langle v_r|v_i\rangle\mathrm{Re}\{AB/[(E-E_n)+\tfrac{1}{2}i\Gamma]\}. \tag{2}$$

ence, the resonant excursion should be linearly roportional to the Franck-Condon overlap integral $\langle v_f|v_r\rangle\langle v_r|v_i\rangle$. Figure 3 shows, by vertical ars, calculated Franck-Condon overlap integrals, starting from the ground vibrational state f CO ($X\,^1\Sigma^+$), via the CO ($a\,^3\Pi$) state and termiating on the $v_f=0$, 1, and 2 levels of CO ($X\,^1\Sigma^+$). he absolute magnitudes of the Franck-Condon integrals were obtained from the compilation of Krupenie[2] and the sign was obtained by inspection of the potential energy curves. Also shown in Fig. 3 are the experimentally measured excursions from a smooth background, obtained from Fig. 1. The agreement between experiment and the calculation lends support to our model.

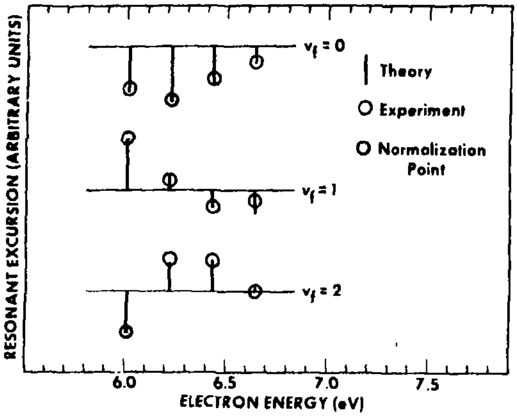

FIG. 3. Comparison of measured and calculated resonant excursions in the energy range of the $a\,^3\Pi$ state of CO. The vertical bars indicate the magnitude and the sign of the calculated Franck-Condon overlap integrals using the $a\,^3\Pi$ state as an intermediate state. The open circles show the measured resonant excursions which were obtained from Fig. 1 by taking the difference between the measured curve and a smooth background. The size of the circles brackets the experimental error. The theory and experiment have been normalized at the largest excursion for each final vibrational channel, v_f.

Resonant structures which are coincident or nearly coincident in energy with an electronic state have cropped up in *atomic* systems before: in the case of the alkali atoms[9,10] near the ^2P states); in the case of atomic hydrogen[1] (near the $n=2$ states); and in the case of the 2^1S state of helium.[11] Until now these have been viewed as accidental occurrences, but the multiplicity of cases makes it probable that we are dealing with a more general phenomenon. It appears that these types of states in molecules can be supported by a large enough dipole moment and, in the case of atoms, the polarizability of the target atom probably plays a large role. When the energy of an observed peak coincides exactly with the energy of the parent excited state, we may designate such objects as "virtual states." Although from an experimental viewpoint such virtual states are not easily distinguishable from Feshbach resonances, the theoretical nature of these two objects differ in principle.

Finally, we wish to point out that structure which is coincident in energy with the $a\,^3\Pi$ state of CO has been previously observed in a transmission experiment,[12] which measures the total scattering cross sections. However, this structure has been attributed[12] to the sharpness of the inelastic cross section near threshold. As a result of the present work we would say that the dipole-dominated resonance plays a key role in the total cross section in the energy range 6–7 eV, by causing structure in the elastic and vibrational cross sections and by enhancing the cross section to the $a\,^3\Pi$ state near threshold.

We acknowledge many illuminating conversations with A. Herzenberg, J. Comer, and P. D. Burrow.

---

*Work supported by the National Science Foundation.

[1] For a review, see G. J. Schulz, Rev. Mod. Phys. 45, 378, 423 (1973).

[2] P. H. Krupenie, *The Band Spectrum of Carbon Monoxide*, National Standard Reference Data Series NSRDS-NBS-5 (U. S. GPO, Washington, D. C., 1966).

[3] W. Benesch, J. T. Vanderslice, S. G. Tilford, and P. G. Wilkinson, Astrophys. J. 142, 1227 (1965).

[4] R. S. Freund and W. Klemperer, J. Chem. Phys. 43, 2422 (1965).

[5] M. J. W. Boness and G. J. Schulz, Phys. Rev. A 9, 1969 (1974).

[6] S. F. Wong and G. J. Schulz, Phys. Rev. Lett. 32, 1089 (1974).

[7] E. P. Wigner, Phys. Rev. 73, 1002 (1948).

[8] A. I. Baz', Zh. Eksp. Teor. Fiz. 33, 923 (1957) [Sov. Phys. JETP 6, 709 (1958)].

[9] D. Andrick, M. Eyb, and M. Hofmann, J. Phys. B: Proc. Phys. Soc., London 5, L15 (1972).

[10] T. A. Patterson, H. Hotop, A. Kasan, D. W. Norcross, and W. C. Lineberger, Phys. Rev. Lett. 32, 189 (1974).

[11] H. Ehrhardt, L. Langhans, and F. Linder, Z. Phys. 214, 179 (1968).

[12] L. Sanche and G. J. Schulz, Phys. Rev. Lett. 26, 943 (1971).

Variational Bounds on the 1*s*—Charge-Exchange Amplitude in Proton-Hydrogen-Atom Scattering*

David Storm and Donald Rapp
The University of Texas at Dallas, Richardson, Texas 75230

(Received 3 April 1974)

With a relatively simple trial wave function, nontrivial variational bounds are obtained on some transition amplitudes for the 1*s*-charge-exchange reaction in the impact-parameter model for H$^+$-H scattering. Preliminary results imply that the two-state traveling molecular expansion is superior to the two-state traveling atomic expansion below 25 keV, that the Euler-Lagrange variational method is not necessarily superior to the static method, and that neither is the "best variational method."

Proton-hydrogen-atom scattering in the keV energy range is customarily described by the impact-parameter model for ion-atom collisions.[1] Within the framework of the impact-parameter model, it has been possible to derive upper and lower variational bounds which bracket the exact transition amplitudes for the excitation and charge-exchange processes,[2-4] and therefore it is possible, in principle, to calculate exact amplitudes in a variational calculation. In addition, it has been proposed that the error function

$$\Delta_1(\chi_n)=\int_{-\infty}^{\infty}\|D(\chi_n)\|dt \qquad (1)$$

be used as a measure of the error in the calculation in which χ_n is the approximate or trial wave function corresponding to the initial state n.[3-4] The quantity $\|D(\chi_n)\|$ is the norm of the deviation vector in the Schrödinger equation:

$$D(\chi_n)=(H-i\partial/\partial t)(\chi_n-\psi_n)=(H-i\partial/\partial t)\chi_n, \qquad (2)$$

where ψ_n is the exact solution, and H is the Hamiltonian for the impact-parameter-model system.[1] The quantity $\chi_n-\psi_n=\delta\psi_n$ is the variation about the exact solution ψ_n represented by the approximate wave function χ_n; therefore $\|D(\chi_n)\|$ is the error (per unit time) in the Schrödinger equation, and so Δ_1 is a natural measure of the error in the calculation.[3-4] Variational bounds on the exact 1*s*-charge-exchange amplitude A_{1s} can be written as follows[3-4]:

$$|C_{1s}|-\Delta_k\le|A_{1s}|\le|C_{1s}|+\Delta_k, \qquad (3)$$

where C_{1s} is a second-order accurate approximation to the exact amplitude A_{1s} obtained with the trial wave function χ_{1s},[3] and Δ_k is either the first-order bound Δ_1 (the error function defined above), or the second-order bound,

$$\Delta_2=\tfrac{1}{2}\Delta_1^2, \qquad (4)$$

on the second-order error term in the variational principle previously given.[3-4] As previously discussed,[3] trial wave functions are customarily generated by expressing the approximate wave function as a time-dependent linear combination of a suitable finite set of basis functions, and the linear expansion coefficients, which are ultimately interpreted as approximate transition amplitudes, are determined by solving the usual set of coupled equations. In this preliminary study of the 1*s*-charge-exchange reaction, we have been concerned with three questions: (1) What are the magnitudes of the bounds Δ_1 and Δ_2 for some common trial functions, and does it appear to be practical to use the variational bounds in Eq. (3) to calculate exact amplitudes? (2) In what energy range is the traveling-molecular-type expansion superior to the traveling-atomic-type expansion? Aspects of this question have been discussed by Ferguson,[5] McCarroll, Piacentini, and Salin,[6] and McCarroll and Piacentini.[7] (3) Is the Euler-Lagrange dynamic variational method used by Cheshire[8] and by McCarroll, Piacentini, and Salin[6] superior to the static variational method in which the variable parameters in the basis functions are determined by minimizing the well-known energy functional? A simple "two-state" trial wave function was used in all of our calculations. The orbitals in the basis functions were atomiclike functions with variable parameters. The most sophisticated orbital utilized was a 1*s*-hydrogen-like orbital containing a variable nuclear-charge parameter, plus a polarization parameter multiplying a $2p_0$-hydrogen-like orbital containing another variable nuclear-charge parameter.

In our first series of calculations we were only concerned with the effect of a variable nuclear charge in the 1*s* orbital, and so the orbitals were simply 1*s*-hydrogen-like functions with variable nuclear-charge parameters. Some of the values obtained for the error function Δ_1 in these calculations are shown in Fig. 1. The charge-exchange

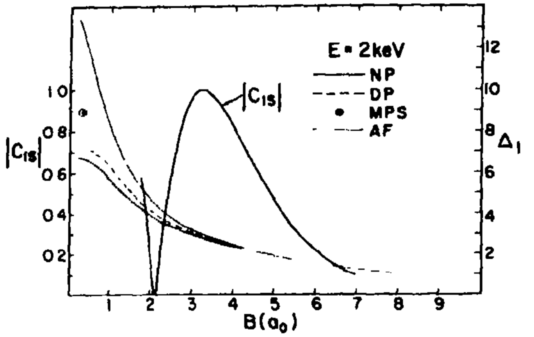

FIG. 1. Absolute value of charge-exchange amplitude $|C_{1s}|$ (corresponding to no-parameter case) and error function Δ_1 for various two-state trial wave functions (see text) versus impact parameter B.

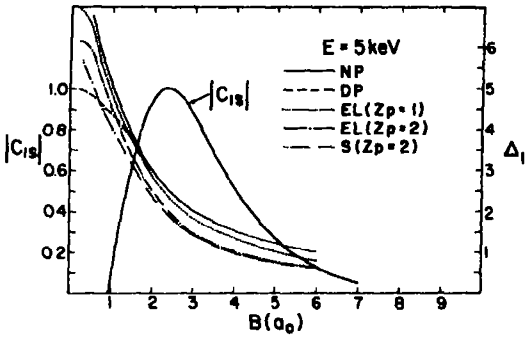

FIG. 2. Absolute value of charge-exchange amplitude $|C_{1s}|$ (corresponding to no-parameter case) and error function Δ_1 for various two-state trial wave functions (see text) versus impact parameter B.

amplitude $|C_{1s}|$ (corresponding to the no-parameter case, see below) is shown in Figs. 1-3 for orientation. The charge-exchange cross section is largely determined by the outer oscillation in the amplitude curve, and so it is these amplitudes that we wish to calculate most accurately. The Δ_1 curve marked NP (no parameters) corresponds to an atomic-type expansion, a two-state traveling hydrogenic expansion. The Δ_1 curve marked DP (Dalgarno and Poots) corresponds to a molecular-type expansion, a two-state traveling molecular expansion where the approximate molecular orbitals are linear combinations of atomiclike functions with nuclear-charge parameters determined by minimizing the energy functional.[9] The point marked MPS corresponds to a calculation in which the variable charge parameters previously given by McCarroll, Piacentini, and Salin[6] were used, and the fact that this point is above the DP curve indicates that within the framework of the two-state approximation the static variational method is superior to the dynamic Euler-Lagrange procedure for this parameter at an energy of 2 keV. The Δ_1 curve marked AF (arbitrary functions) corresponds to a calculation in which arbitrary functions were used for the variable nuclear-charge parameters, and the fact that this curve lies below the DP curve and the MPS point indicates that neither the static nor the dynamic variational methods is best for this problem.

In the second series of calculations we were only concerned with the effect of a polarization parameter; in this case, the orbitals were 1s-hydrogen-like functions plus a polarization parameter multiplying a $2p_0$-hydrogen-like function. The nuclear scale factors were taken as constants. Some of the results of this calculation are shown in Fig. 2. The Δ_1 curves marked NP and DP again correspond to the same atomic and molecular expansions discussed above. The Δ_1 curve marked S (static) also corresponds to a molecular-type calculation: In this case the approximate molecular orbitals contained only polarization parameters. The Δ_1 curve marked EL (Euler-Lagrange) corresponds to an atomic-type expansion with a dynamically determined polarization parameter. The molecular-type expansions again appear superior to the atomic-type expansions, and the static variational meth-

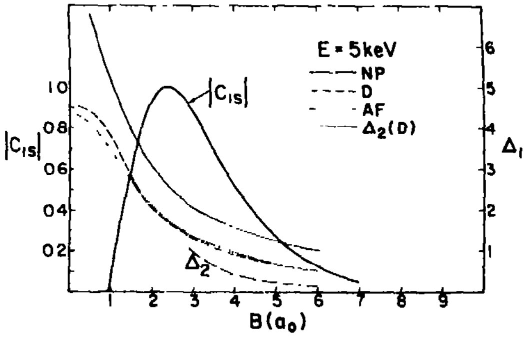

FIG. 3. Absolute value of charge-exchange amplitude $|C_{1s}|$ (corresponding to no-parameter case) and error function Δ_1 for various two-state trial wave functions (see text) versus impact parameter B. Values of the second-order bound Δ_2 are also shown on the same right-hand vertical scale as Δ_1.

od again appears superior to the dynamic Euler-Lagrange procedure.

The most sophisticated orbitals were used in the last series of calculations: The orbitals were 1s-hydrogen-like functions with a variable nuclear-charge parameter plus a polarization parameter multiplying $2p_0$-hydrogen-like functions with a variable nuclear-charge parameter. The parameters in the orbitals were determined by minimizing the energy functional,[10] and we believe these orbitals are adequate representations of the $1s\sigma_g$ and $2p\sigma_u$ molecular states. Values of the error function Δ_1 obtained in these calculations are shown in Fig. 3. The Δ_1 curve marked NP again corresponds to the atomic-type expansion discussed above; the Δ_1 curve marked D corresponds to the molecular-type expansion in which the $1s\sigma_g$ and $2p\sigma_u$ orbitals[10] were used; and the Δ_1 curve marked AF again corresponds to a calculation in which an arbitrary set of parameters were used. The fact that the D curve is lower than the NP curve is good evidence that the two-state traveling molecular trial wave function is superior to the two-state traveling atomic trial wave function. We also show values of the second-order bound Δ_2. It is interesting to note that the second-order bound is slightly smaller than the amplitudes in the range of impact parameters 3.5-5. We are extremely encouraged by this result, considering the simplicity of the trial wave function.

In conclusion, our results tend to indicate that the traveling-molecular-type expansion is superior to the traveling-atomic-type expansion in the energy range 0.1-25 keV, and that the dynamic Euler-Lagrange variational method is not necessarily superior to the static method in this energy range. Finally, it is encouraging that a bound Δ_2 which is the same order of magnitude as a transition amplitude can be calculated with such a simple trial wave function. It is well known that the simple two-state approximation is inadequate even for the lower energies.[11-12] With the addition of more states, there is a likelihood that Δ_2 can be reduced to the point where nontrivial bounds on the 1s-charge-exchange amplitude can be obtained.

---

*Work partially supported by the Robert A. Welch Foundation under Grant No. AT-464.

[1] D. Storm, Phys. Rev. A 8, 1765 (1973).

[2] L. Spruch, *Lectures in Theoretical Physics*, edited by S. Geltman, K. T. Mahanthappa, and W. E. Brittin (Gordon and Breach, New York, 1968), Vol. XIC, pp. 77-87.

[3] D. Storm, Phys. Rev. A 8, 1789 (1973).

[4] D. Storm, "Variational Bounds on Transition Amplitudes" (to be published).

[5] A. F. Ferguson, Proc. Roy. Soc., Ser. A 264, 540 (1961).

[6] R. McCarroll, R. D. Piacentini, and A. Salin, J. Phys. B: Proc. Phys. Soc., London 3, 137 (1970).

[7] R. McCarroll and R. D. Piacentini, J. Phys. B: Proc. Phys. Soc., London 3, 1336 (1970).

[8] I. M. Cheshire, J. Phys. B: Proc. Phys. Soc., London 1, 428 (1968).

[9] A. Dalgarno and G. Poots, Proc. Phys. Soc., London, Sect. A 67, 343 (1954).

[10] D. Dinwiddie, private communication.

[11] D. R. Bates and D. A. Williams, Proc. Phys. Soc., London 83, 425 (1964).

[12] S. B. Schneiderman and A. Russek, Phys. Rev. 181, 311 (1969).

Homogeneous Nucleation in a Critical Binary Fluid Mixture

John S. Huang
Department of Physics, University of Pittsburgh, Pittsburgh, Pennsylvania 15260

and

S. Vernon and N. C. Wong
Department of Physics, Rutgers University, New Brunswick, New Jersey 08903

(Received 22 April 1974)

We have studied homogeneous nucleation in a binary fluid mixture near the critical point for a temperature range $2\times10^{-5}<\epsilon<2\times10^{-2}$, where $\epsilon=(T_c-T)/T_c$. We find that the measured degree of critical supercooling is in good agreement with the predictions of a nucleation theory with a nonclassical free energy proposed by Sarkies and Frankel. A slight difference between the temperature dependence of the nucleation curve and that of the coexistence curve is also observed.

The degree of critical supercooling of a binary mixture of methylcyclohexane and perfluoromethylcyclohexane observed by Sundquist and Oriani[1,2] and more recently by Heady and Cahn[3] was shown to have grossly exceeded the limit predicted by classical theories[4-6] of homogeneous nucleation. These results are quite surprising, for the observed maximum degree of supercooling (critical supercooling δT_c) is expected to deviate from the theories only by falling short of the predicted values, since ionic impurities, dust, vibrations, etc. are likely to induce nucleation before the theoretical limit can be reached.

On the other hand, one may expect that the classical theories, featuring the formation of a critical nucleus as the principal mechanism for phase separation, could work better as the critical point is approached. The reason is that the radius of the critical droplet increases as the correlation length is increased, so that the droplet is large enough for the bulk properties to be properly assigned to it. However, the classical theories fail to take into account the fact that the classical equations of state are no longer very good approximations in the critical region. Sarkies and Frankel (SF)[7,8] made an effort to modify the classical nucleation theory of Cahn and Hilliard[6] by incorporating a generalized form of the equation of state similar to that proposed by Fisk and Widom.[9] An expression for the work of formation of a critical nucleus was derived by SF, and from it one can calculate the critical supercooling δT_c (δT_c is defined as the maximum supercooling measured below the normal phase-separation temperature in units of degrees centigrade).

In this work we report an observation of cloud points (temperatures at which homogeneous nucleation begins) in a binary mixture of cyclohexane-methanol near the critical point. Two samples of critical composition were separately prepared; special care was taken to avoid excessive dust contamination. The preparation steps included filtration, distillation through a 6-ft column, and several slow vacuum distillations before sealing in glass cells containing magnetic stirrers. The critical temperature of the two cells agreed within 3 mK (the reported value for T_c is 45.14°C). Critical supercooling values δT_c were measured with the samples immersed in a water bath which was temperature controlled to within 1 mK over several hours. At the start of the run, the samples were allowed to come to equilibrium at about $\Delta T=T_c-T\approx5$ mK below T_c when each sample separated into two, clear, coexisting phases. Then the temperature was dropped slowly, at a rate of 1 mK/min, until the cloud point of the upper phase was reached. At this temperature a uniform cloudiness suddenly set in, and the temperature difference $\delta T_c(\Delta T)$ was noted. A typical run took from several minutes to one and a half hours depending on ΔT. Then the systems were both allowed to come to equilibrium again at a temperature slightly lowe than the last cloud point before the next run took place. The equilibration time in the two-phase region was typically 1 to 2 days. However, it should be noted that even the time for the system to separate out into two, clear, coexisting phase under the influence of gravity was on the order o 1 day, but the time constant for the temperature of the system to follow a change in the water-bat temperature was on the order of 1 min. We trie to lower the temperature in steps of a few millidegrees, and waited a few minutes before lowering the temperature by another step. This procedure could change the time to reach the cloud point, but it evidently had no effect on the cloud-point temperature. We also monitored the laser scattering intensity and the linewidth at several scattering angles during the supercooling stages. As a rule, the scattered intensity increased slightly (~10%) as the temperature was lowered near the cloud point, and exhibited an angular distribution similar to that of the equilibrium states. There was no indication of the formation of invisible droplets before the cloud point.[10] The linewidth of the scattered light, on the other hand, narrowed slightly (~10%) and always showed a Lorentzian line shape. Both the intensity and the linewidth of the scattered light measured in the supercooled states were found to be quite stable for several hours if the bath temperature was allowed to stablize before the cloud point was reached. This is indicative of the fact that concentration flux through the interface during a 1-h run was negligibly small, and the two phases of each cell were effectively acting independently. So what we had was essentially two continuous variable-concentration samples; by choosing different temperatures at which the system could be brought to equilibrium in the two-phase region, we were able to study the degree of supercooling from any point on the coexistence curve. However, at $\Delta T \sim 6$°C, it was difficult to produce a homogeneous nucleation in our system, so no asurement is reported below this temperature.

)ur results are shown in Fig. 1, where the ree of critical supercooling δT_c is plotted ainst $T_c - T$ on a log-log scale. The straight-e fit to the data has a slope very close to 1.0,

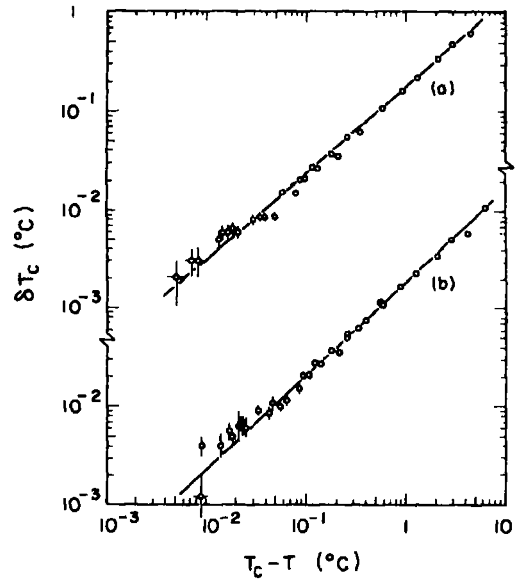

FIG. 1. A log-log plot of the degree of critical supercooling δT_c versus $\Delta T = T_c - T$, where T is the equilibrium temperature of the system from which δT_c is measured. The two curves a and b represent measurements from two critical samples.

indicating that the temperature dependence of the nucleation curve (which is the locus of the cloud points on the temperature-concentration plane) is very similar to that of the coexistence curve. The ratio $\delta T_c / \Delta T \approx 0.2$ for both samples.

Sarkies and Frankel extended the theory of Cahn and Hilliard[6] by incorporating a generalized equation of state similar to that proposed by Fisk and Widom[9]:

$$\mu(\rho) - \mu(\rho_c) = (\rho - \rho_c)[T - \tau(\rho)](T_c - T)^{\gamma-1} j([T_c - \tau(\rho)]/(T_c - T)), \tag{1}$$

ere μ is the chemical potential, ρ_c is the critical concentration, $T = \tau(\rho)$ represents the coexistence rve, as chosen by SF, and

$$j(\omega) = j(1)(1 - \omega^{4\beta})/4\beta(1 - \omega). \tag{2}$$

the above expression, they have used the scaling relation $\gamma = (\delta - 1)\beta$, and have taken $\delta = 5$. Then y proceeded to calculate the difference W between the total free energy of a homogeneous system d an inhomogeneous one containing a critical nucleus. The parameter W, called the work of forman for a critical nucleus, is given by

$$W = 4\pi \int_0^\infty \int_{\rho_0}^{\rho} [\mu \, d\rho - \tfrac{1}{2}(\rho - \rho_0)(\mu + \mu_0)] r^2 \, dr, \tag{3}$$

h ρ and μ depending on the position r in the sample. Substituting Eqs. (1) and (2) into (3) they obned

$$W = W' I_c (T_c - T)^{\mu - 2\nu}, \tag{4}$$

where

$$W' = (4\sqrt{2}\,\pi K^{3/2}/a^2\beta)G^{1/2}, \tag{5}$$

and

$$(\partial^2 f/\partial\rho^2)_T = G(T_c - T)^\gamma$$

is the compressibility, with $a = [T_c - \tau(\rho)]/(\rho - \rho_c)^{1/\beta}$ and β the critical exponent for the coexistence curve. The parameter K is a measure of the surface energy of the system, and is expected to depend only weakly on temperature[11];

$$I_c = \int_0^\infty \{2\int_{z_0}^{z} z(z^4-1)dz - (z - z_0)[z(z^4-1) - z_0(z_0^4-1)]\} r_0^2\, dr_0. \tag{6}$$

The new variable $z(r_0)$ is a reduced density which must satisfy the Euler equation (from the minimization of the total free energy) for the shape of the critical droplet profile with

$$z = [a/(T_c - T)]^\beta(\rho - \rho_c), \tag{7}$$

$$\frac{\partial^2 r}{\partial r_0^2} + \frac{2}{r_0}\frac{\partial z}{\partial r_0} = z(z^4 - 1) - z_0(z_0^4 - 1), \tag{8}$$

and the reduced background density

$$z_0 = \lim_{r\to\infty} z(r).$$

The pertinent parameters for this binary mixture can be obtained as follows. From the turbidity measurement of Huang,[12] and the index-of-refraction measurement of Gilmer *et al.*,[13] we can determine the value $(\partial^2 f/\partial\rho^2)_T = 9.07\times10^5$ ergs/cm^3 at $\Delta T = 1°\mathrm{C}$ from the following relation[14]:

$$\tau = \frac{4}{3}\frac{2\pi^3}{\lambda_0^4}\left(\frac{\partial n^2}{\partial c}\right)^2_{pT}\frac{k_B T}{(\partial^2 f/\partial\rho^2)_T}, \tag{9}$$

where τ is the turbidity, λ_0 the wavelength of light, and n the index of refraction. From the light-scattering measurements of Wong and Huang[15] as well as from Ref. 11, we have $\gamma = 1.22$ for $T < T_c$. Also from Ref. 12 we have $a^\beta = 6.89$ $(°\mathrm{C})^\beta$. From the interface-thickness measurement of Huang and Webb,[16] we can determine $K = 3.89\times10^{-7}$ erg/cm, so that from Eq. (5) we get $W' = 1.31\times10^{-13}$ erg. The cloud point was determined by[6] $W = 60k_BT$. Combining this with Eq. (4), we get $I_c = 19.95$. Substituting this value into Eq. (6), we get $z_0^{1/\beta} = [T_c - \tau(\rho)]/(T_c - T) = 0.82$ which in turn gives us $\delta T_c/\Delta T = [\tau(\rho) - T]/[T_c - \tau(\rho)] = 0.22$. This value agrees extremely well with the measured value of $\delta T_c/\Delta T \cong 0.20$ at $\Delta T = 1°\mathrm{C}$. It might be added that the homogeneous nucleation in the metastable region studied in this work is caused by intense concentration fluctuations of size exceeding the critical radius and subsequent growth of these critical nuclei. However, the system is stable against infinitesimal fluctuations extended over long distances. A second mechanism for phase separation, spinodal decomposition,[17,18] is expected to occur if the system is quenched along the critical-concentration line into the "spinodal region" where the system is unstable instead of metastable. The process of spinodal decomposition has been studied by Huang, Goldburg, and Bjerkaas.[19]

Finally, we plot $\delta T_c/\Delta T$ versus ϵ where $\epsilon = (T_c - T)/T_c$, as shown in Fig. 2, and we fit a function $a/(1 + b\ln\epsilon)^{1/2}$ to the ratio $\delta T_c/\epsilon$, as suggested by Langer and Turski.[20] We find $a \simeq 48$ and $b \simeq 6.1\times10^{-2}$ over a temperature range $10^{-5} < \epsilon < 10^{-2}$. We note that the value of a is very close to the values evaluated for CO$_2$ by all the nucleation theories,[4,20] but the value of b represents a much better agreement with the prediction of Langer and Turski than with the Becker-Doring theory.[4]

One of us (J.S.H.) wishes to thank Professor Walter I. Goldburg, Professor David Jasnow, and Professor J. S. Langer for helpful discus-

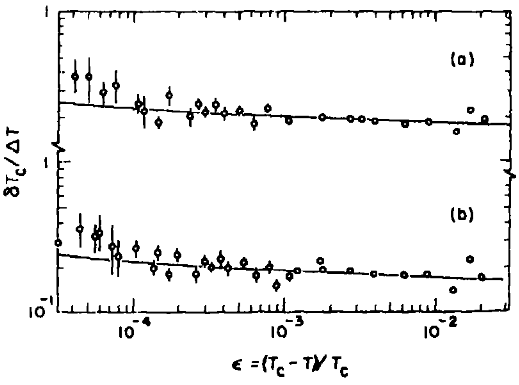

FIG. 2. A log-log plot of $\delta T_c/\Delta T$ versus $\epsilon = (T_c - T)/T_c$. The solid lines represent a two-parameter fit of the function $a/(1 + b\ln\epsilon)^{1/2}$ for $\epsilon > 10^{-4}$. Curves a and b represent measurements from two critical samples.

sions.

---

[1] B. E. Sundquist and R. A. Oriani, J. Chem. Phys. 36, 2604 (1962).

[2] B. E. Sundquist and R. A. Oriani, Trans. Faraday Soc. 63, 561 (1967).

[3] R. B. Heady and J. W. Cahn, J. Chem. Phys. 58, 896 (1973).

[4] R. Becker and W. Döring, Ann. Phys. (Leipzig) 24, 719 (1935).

[5] D. Turnbull and J. C. Fisher, J. Chem. Phys. 17, 71 (1949).

[6] J. W. Cahn and J. E. Hilliard, J. Chem. Phys. 31, 688 (1959).

[7] K. W. Sarkies and N. E. Frankel, J. Chem. Phys. 54, 433 (1971).

[8] K. W. Sarkies and N. E. Frankel, to be published.

[9] S. Fisk and B. Widom, J. Chem. Phys. 50, 3219 (1969).

[10] For temperatures $\epsilon > 5\times10^{-3}$, a few isolated droplets were observed before the cloud point was reached.

[11] O. K. Rice, J. Chem. Phys. 64, 976 (1960).

[12] J. S. Huang, Ph.D. thesis, Cornell University, 1969 (unpublished).

[13] G. H. Gilmer, W. Gilmore, J. Huang, and W. W. Webb, Phys. Rev. Lett. 14, 491 (1965).

[14] P. Calmettes, I. Lagues, and C. Laj, Phys. Rev. Lett. 28, 478 (1972).

[15] N. C. Wong and J. S. Huang, unpublished.

[16] J. S. Huang and W. W. Webb, J. Chem. Phys. 50, 3677 (1969).

[17] J. W. Cahn, J. Chem. Phys. 42, 93 (1965).

[18] J. W. Cahn, Trans. AIME 242, 166 (1968).

[19] J. S. Huang, W. I. Goldburg, and A. W. Bjerkaas, Phys. Rev. Lett. 32, 921 (1974).

[20] J. S. Langer and L. A. Turski, Phys. Rev. A 8, 3230 (1973).

Velocity of Fourth Sound

M. Revzen, B. Shapiro, C. G. Kuper, and J. Rudnick
Department of Physics, Technion-Israel Institute of Technology, Haifa, Israel

(Received 4 February 1974)

We reconsider the flow of a superfluid through the interstices of a porous medium, taking account of the finite volume of the grains and the resulting hydrodynamic drag. A correction factor to the velocity of fourth sound is found, which reconciles a long-standing discrepancy between theory and experiment.

Fourth sound has proved useful as a probe[1,2] for studying the properties of superfluid ^{4}He, and is currently being sought[3] as a confirmation of the possible superfluidity of the low-temperature phases of ^{3}He. However, the measured velocity[2] differs systematically from Atkins's[4] prediction. In Atkins's theory, the finite volume of the powder grains is neglected; their only role is to lock the normal component: $v_n = 0$. But when an ideal fluid accelerates around obstacles of finite volume, the obstacles exert a drag force,[5] which we denote F_d (per unit mass). This drag has been measured by Kojima *et al.*[1]

We reformulate the Euler-like equation of Landau's two-fluid hydrodynamics[6] to include the drag. We call the drag correction a "dynamic" one, since F_d is proportional to the relative acceleration of the superfluid to the grains. We shall also include a "static" correction for the finite volume of the powder. This static correction can be interpreted[7] as arising from the fact that Landau's driving force is not the pressure p but rather the chemical potential μ.

These two corrections appear in the form of a factor modifying the density ρ in the Landau equation, and hence modifying the velocity c_4 of fourth sound. Using Atkins's[4] value c_4^0 as a reference standard, we define an "index of refraction" n:

$$n = c_4^0/c_4. \tag{1}$$

We are interested in the long-wavelength limit (long compared to grain size; cf. the way in which dielectric polarization determines the low-frequency refractive index for electromagnetic waves). However, in a typical porous medium the size of the grains is comparable with that of the interstices, and the direct calculation of flow patterns is intractable. We bypass the difficulty by using experimental values[1] of the drag.

For simplicity we neglect the temperature fluctuations in a fourth-sound wave.[8] Atkins's expression for the fourth-sound velocity then reduces to

$$c_4^0 = (\rho_s/\rho)^{1/2} c_1, \tag{2}$$

where ρ_s/ρ is the superfluid fraction and c_1 is the velocity of first sound.

In the Kojima *et al.* drag experiments[1] the porous medium is contained in an annular region, and rotated at an angular velocity ω_n (typically ~1 Hz; c.f. typical fourth-sound frequencies ω^{IV} ~10 kHz). The observed superfluid current is found to be proportional to the angular velocity ω_n of the powder (and hence of the normal fluid). We believe that the rotational aspects of the motion are irrelevant, and write an empirical relation for the average linear velocity of the superfluid

$$v_s = \lambda v_n. \tag{3}$$

The coefficient λ $(0 \leqslant \lambda \leqslant 1)$ depends mainly on the "porosity"[10] $\mathcal{P}$, which is defined to be the ratio of fluid volume Ω_f to total volume Ω. The measured value for $\mathcal{P} = 0.65$, $T = 1.35$ K, and grain size ~200 Å is $\lambda = 0.46$.

We assume that the equality (3) is attained very rapidly (on the time scale of $1/\omega^{\mathrm{IV}}$), so that we can write

$$\dot{v}_s = \lambda \dot{v}_n. \tag{3'}$$

Hence the drag force per unit mass is $F_d = \lambda \dot{v}_n$. We wish to express F_d in terms of the relative acceleration[10] $\dot{v}_r = \dot{v}_s - \dot{v}_n$. Subtracting $\dot{v}_n$ from both sides of Eq. (3′), we obtain $\dot{v}_n$ in terms of $\dot{v}_r$, so that

$$F_d = -\dot{v}_r \lambda/(1-\lambda). \tag{4}$$

If F_{ext} is the external force[7]

$$F_{\mathrm{ext}} = -\Omega \nabla p, \tag{5}$$

the equation of motion of the fluid is

$$F_{\mathrm{ext}} + \rho\Omega_f F_d = \rho\Omega_f \dot{v}_s.$$

In fourth-sound experiments $\dot{v}_n = v_n = 0$ (hence $\dot{v}_r$ $\dot{v}_s$), and hence

$$-\nabla p = \rho \dot{v}_s \mathcal{P}/(1-\lambda), \tag{6}$$

where $\dot{v}$ means the "hydrodynamic" derivative $\partial v/\partial t + v \cdot \nabla v$. For acoustic propagation we neglect the $v \cdot \nabla v$ terms as usual. Since $v_n = 0$, the equation of continuity takes the form

$$\dot{\rho} + \rho_s \nabla \cdot v_s. \tag{7}$$

Equations (6) and (7) give the fourth-sound velocity; the only new feature is the factor $\mathcal{P}/(1-\lambda)$ in (6), and hence, by Atkin's analysis,[4]

$$c_4 = c_4/n(\lambda, \mathcal{P}), \tag{8}$$

where

$$n^2 = \mathcal{P}/(1-\lambda). \tag{9}$$

In Eq. (10) the factors $\mathcal{P}$ and $1/(1-\lambda)$ are, respectively, the "static" and "dynamic" corrections. For the measured[1] λ, we predict $n^2 = 1.2$; the observed value[2] is $n^2 \simeq 1.3$.

Over a wide range of porosities, Rudnick and co-workers find[2]

$$n^2 = 2 - \mathcal{P}. \tag{11}$$

Substituting (11) in (10), we predict

$$\lambda = 2(1 - n^{-2}), \tag{12}$$

which agrees well with preliminary measurements.[11]

To summarize we have shown that the velocity of fourth sound is modified by the finite size of the powder grains—both directly through the "static" porosity factor and indirectly via the drag. Our correction reconciles a long-standing discrepancy between theory and experiment.

---

[1] H. Kojima, W. Veith, S. J. Putterman, E. Guyon, and I. Rudnick, Phys. Rev. Lett. 27, 714 (1971).

[2] K. A. Shapiro and I. Rudnick, Phys. Rev. 137, A1383 (1965); M. Kriss and I. Rudnick, J. Low Temp. Phys. 3, 339 (1970).

[3] We are aware of work along these lines by J. C. Wheatley and co-workers, and by Y. Eckstein and J. Landau at our own institute.

[4] K. R. Atkins, Phys. Rev. 113, 962 (1959); I. M. Khalatnikov, *Introduction to the Theory of Superfluidity* (Benjamin, New York, 1965).

[5] See, e.g., H. Lamb, *Hydrodynamics* (Cambridge Univ. Press, Cambridge, England, 1932) 6th ed., Sect. 92; L. D. Landau and E. M. Lifshitz, *Fluid Mechanics* (Pergamon, New York, 1959), p. 31.

[6] L. D. Landau and E. M. Lifshitz, *Fluid Mechanics* (Pergamon, New York, 1959), p. 516.

[7] For a deeper understanding of the factor $\mathcal{P}$ in Eq. (6) we may derive this "static" correction from the Gibbs-Duhem relation $n_f d\mu_f + n_g d\mu_g = dp$. Here n_f and n_g are the mass densities and μ_f and μ_g the chemical potentials of the fluid and the powder grains, respectively. If M_f is the mass of the fluid, $n_f = M_f/\Omega = (M_f/\Omega_f)(\Omega_f/\Omega$ $= \mathcal{P}\rho$. When we assume that the change in the chemical potential of the powder is negligible, we have $\nabla p = \mathcal{P}\rho\nabla$ We owe this observation to S. G. Eckstein and Y. Eckstein. Both this derivation and the one in the text implicitly assume homogeneity and isotropy on the average.

[8] This approximation is good for all temperatures because $c_1 \rho_s{}^{1/2}$ is large compared with $c_2(\rho - \rho_s)^{1/2}$ when c_1 and c_2 are the speeds of first and second sound.

[9] The drag coefficient λ should not be sensitive to temperature or to grain size, except close to the transition

temperature. Near T_λ, the healing length becomes large, and the apparent porosity will be reduced. For ^{4}He in 200-Å powders below 1.6 K, the effect is negligible. But in ^{3}He the correlation length is believed to be at least 10^3 Å and possibly even 10^4 Å. With grain sizes ~30 μm, this can lead to a correction of from 1 to 10%.

[10] Although we have derived Eq. (4) from Eq. (3), it is obvious that (4) is really the more general relation —it expresses the proportionality of F_d to $\dot{v}_r$ and in particular the obvious requirement that there shall be no drag if $\dot{v}_r = 0$ (even if $\dot{v}_n \approx \dot{v}_s \neq 0$).

[11] We wish to thank Professor I. Rudnick for providing us with preliminary data for a range of porosities in the region $\mathcal{P} \sim 0.7$. These results strongly suggest a form close to Eq. (12).

Experiments on Dynamic Parallel Magnetism in Superfluid ^{3}He†

R. A. Webb, R. L. Kleinberg, and J. C. Wheatley
Department of Physics, University of California, San Diego, La Jolla, California 92037

(Received 28 May 1974)

Observations are reported of the ringing of parallel magnetization in superfluid ^{3}He when an incremental magnetic field parallel to a steady field is suddenly turned off.

We report novel experiments on the dynamic response of the nuclear magnetization of superfluid ^{3}He *A* and ^{3}He *B parallel* to the axis of a magnetic field which is suddenly changed by an incremental amount parallel to itself. These experiments, motivated by the theoretical work of Leggett[1] and the experimental static magnetization measurements of Paulson, Johnson, and Wheatley,[2] both illuminate the theoretical concepts and provide new insights into the nature of the superfluid state. The present experiments, performed over wide ranges of temperature, pressure, and magnetic field, reflect and support the remarkable parallel-resonance experiments on liquid ^{3}He at melting pressure of Osheroff and Brinkman[3] and of Bozler *et al.*[4] which were reported while our measurements were in progress. Our experiments also allow important nonlinear phenomena to be studied. Moreover, they may be interpreted, at least in the case of ^{3}He *A* and following both Leggett[1] and Maki and Tsuneto,[5] as a manifestation of an internal Josephson effect in the spin-triplet superfluid.

The ^{3}He measured was contained in a 3-mm-i.d. tower above a main cell nearly filled with powdered cerium magnesium nitrate (CMN). A steady field H_0 parallel to the axis of the cylinder was trapped in a 6.5-mm-i.d. Nb tube. An incremental field ΔH parallel to H_0 was provided by a single-layer Nb solenoid of 3.25-mm i.d. The ^{3}He magnetization was sensed by a 4-mm-i.d. by 4-mm-long Nb pickup coil with one end 3.5 mm from the end of the solenoid. The pickup coil was connected with Nb leads to an rf-biased superconducting quantum interference device operated as a nonoverloading, wide-band flux sensor of low dynamic range. Temperatures were sensed both in CMN in a second magnetically shielded tower above the cell and in the main CMN, although the latter could not be used while small fields in the magnetizing solenoid were controlling the temperature. Liquid ^{3}He provided thermal contact between all parts of the cell. Provisional Kelvin temperatures based on noise thermometry and the attenuation of zero sound were assigned to magnetic temperatures by comparison with the line of second-order transitions (P, T_c) as in our earlier work.[6]

Concepts regarding the nature of superfluid ^{3}He which we used to design our experiments are illustrated in Fig. 1. The superfluid is assumed to be characterized by a vector order parameter $\vec{d}$ in spin space which is a function of orbital variables described by the direction $\vec{n}$ of BCS-like triplet pairs.[8,1] To be specific, consider the case of ^{3}He *A* where, following Anderson and Brinkman[7] and in the absence of boundary or other orienting effects, the vector $\vec{d}$ is thought to lie in a plane perpendicular to H_0, as in Fig. 1(a). For a fixed orbital configuration the temperature-dependent average nuclear dipolar interaction energy E_D varies periodically with angle θ as shown in Fig. 1(b) leading to a torque R_D on the nuclear spins [Fig. 1(c)] which is also periodic in θ. At equilibrium, in this example, θ is either 0 or π. In our experiment a steady field $(H_0+\Delta H)\hat{z}$ is applied for a sufficiently long time, and then at time t_0 it is suddenly reduced to $H_0\hat{z}$ as in Fig. 1(d). Following Leggett[1] and neglecting relaxation, the equation for the change of the z compo-

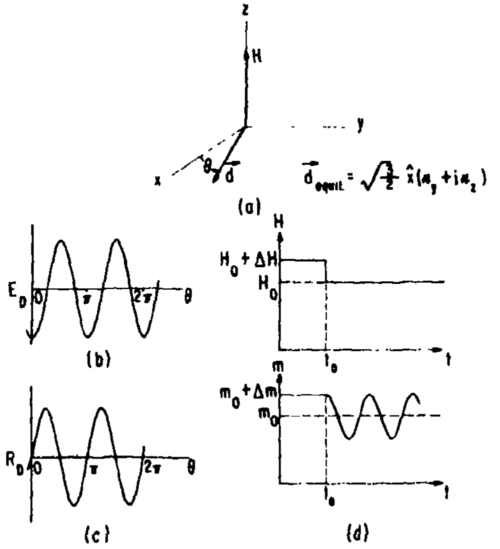

FIG. 1. (a) Configuration of field H_0 and order parameter $\vec{d}$ for the nonequilibrium ABM state (Ref. 7). (b) Dipolar energy versus θ for fixed orbital variables. (c) Dipolar torque versus θ for fixed orbital variables. (d) Schematic dependence of magnetic field $\vec{H}$ and parallel magnetization $\vec{m}$ on time for the conditions of our experiment. The ringing frequency of $\vec{m}$ depends on temperature.

nent of spin angular momentum per unit volume is

$$d\,\Delta S_z/dt = R_D \simeq \lambda\theta, \qquad (1)$$

where in approximating R_D we assume that θ is small. Leggett showed that $\vec{d}$ precesses in the field $\vec{H} - \gamma\vec{S}/\chi$, where γ is the gyromagnetic ratio and χ is the susceptibility, so in the present case we have

$$\dot{\theta} = \gamma(\Delta H - \gamma\Delta S_z/\chi). \qquad (2)$$

It is assumed that the orbital variables do not change during this precession. Combining the above two equations, we find that

$$d^2\Delta S_z/dt^2 + \gamma^2\lambda\,\Delta S_z/\chi = \gamma\lambda\Delta H. \qquad (3)$$

The magnetization γS_z thus rings at the temperature-dependent frequency $(\gamma/2\pi)(\lambda/\chi)^{1/2}$ with amplitude $\chi\Delta H$ as shown in Fig. 1(d). A similar result has recently been derived for ^{3}He A by Maki and Tsuneto[5] who observe that the angle 2θ is the phase difference between the order parameters $d_{\uparrow\uparrow}$ and $d_{\downarrow\downarrow}$ of the two equal-spin-pairing states which are coupled by the phase-dependent coupling energy E_D of Fig. 1(b) in an internal Josephson effect.

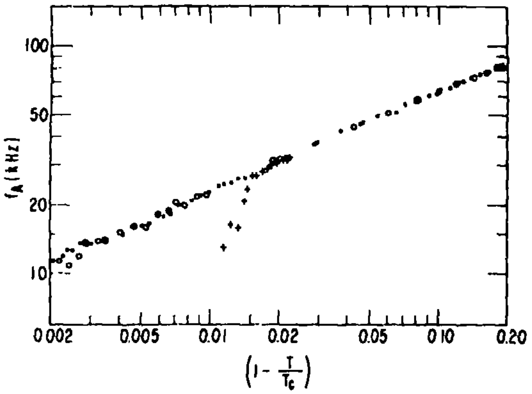

FIG. 2. Ringing frequency in ^{3}He A versus reduced temperature difference for 29.4 bar and $H_0 = 50$ and 310 G (closed and open circles, respectively). The plus symbols denote response to a nonlinear effect; see text.

The ringing phenomenon has been observed in ^{3}He A over a pressure range from 8.5 to 33 bar and an H_0 range from 1 to 310 G, consistent with the effect of field on the phase diagram.[9] Typical ringing-frequency results as a function of $1 - T/T_c$ are shown in Fig. 2 for two values of H_0 at a pressure of 29.4 bar. The ringing frequency f_A is field independent. However, f_A can depend on ΔH, as shown in Fig. 2 by the plus symbols, for which $\gamma\Delta H/2\pi = 25$ kHz. If ΔH is too large the angle θ can become too large and the response is nonlinear. We will discuss this interesting effect elsewhere; for the present results we maintained $\gamma\Delta H/2\pi \gtrsim \frac{2}{5}f_A(T)$, where $f_A(T)$ is the ΔH-independent ringing frequency. A plot of $f_A^2(T)$ versus T was linear near T_c although the extrapolation to zero did not give perfect agreement either with the center of the second-order specific-heat transition[6] in the main cell or with the center of the $A-N$ magnetic feature.[10] The data in Fig. 2 use T_c from the specific-heat transition. The ringing frequency at $1 - T/T_c = 0.01$ varied from about 24.5 kHz at 33 bar to about 19 kHz at 21 bar. At 33 bar our values of f_A agreed within 1 or 2% over the full range of comparison possible with the resonance frequencies and shifts given by Osheroff and Brinkman[3] at melting pressure, but were lower by 5 to 10% than those of Bozler *et al.*[4] At very low values of H_0 the signal was degraded: For $H_0 = 0$, degradation was observed for $1 - T/T_c < 0.01$ with the region of degradation progressively narrowing for 0.3 and 1 G. In all

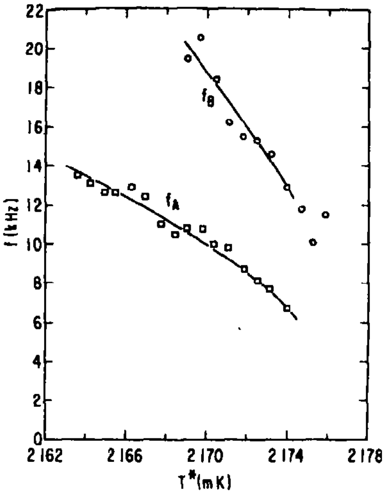

FIG. 3. Comparison of ringing frequencies f_B and f_A ı ^{3}He B and ^{3}He A at 21.2 bar and 30 G. The slope of e line through the f_B data points is 1.9 times the slope the line through the f_A points. Note that f_B can be ob- rved at higher temperature than f_A. T^* is a magnetic mperature scale.

elds decay of signals in ^{3}He A was not reproduc- le and was characterized more by a "beating" henomenon than by exponential decay. Good uality ringing was observed typically for 0.5 – 1 sec.

Ringing has been observed in ^{3}He B in the pres- ure range from 8.5 to 21.5 bar in H_0 from 0 to 10 G, consistent with the phase diagram and the bservation that for $H_0 > 1$ to 5 G *no* persistently ood quality ringing is observed unless $1 - T/T_c$ less than 0.1 to 0.2%. Within this temperature ange and for fields from 5 to 310 G we observed equencies like those shown in Fig. 3 for 21.2 ar and 30 G. The A-phase frequencies f_A were bserved as functions of magnetic temperature * on cooling below T_c, while the B-phase fre- uencies f_B were observed on warming. The rtunate temperature overlap is a consequence supercooling-superheating effects. Except be- w ca. 10 G, we found $f_B(T)/f_A(T) \simeq 1.9 \pm 0.1$, in- ependent of magnetic field to 310 G. The region good B-phase signals did increase somewhat s H_0 increased up to about 30 G, but observa- ons at 100 and 300 G showed no further change. this region the signal had acceptable quality r 0.3–0.5 msec.

At fields of 0, 0.3, and 1 G we observed an en- rely different behavior in ^{3}He B. Very near T_c some typical B-phase ringing might be observed. Then for $1 - T/T_c \gtrsim 0.01$ we observed a ringing phenomenon in which the frequency depended only weakly, if at all, on temperature and pressure. (Signal quality did decrease at lower temperatures, but this may have reflected only the decreasing susceptibility.) Rather the frequency depended both on ΔH and time. For $\Delta H = 2$ G the frequency damping was not perceptible, but for $\Delta H = 10$ G the frequency could be observed to drop to $1/e$ of its initial value in about 2 msec. The initial ringing frequency f depended approximately linearly on ΔH, for ΔH in the range 2 to 10 G, with $2\pi f \simeq \alpha(\gamma \Delta H)$. The coefficient α is about $\frac{1}{2}$ at $H_0 = 0$ and somewhat larger at $H_0 = 1$ G.

Owing to the presence of a significant magnetic background it was not possible to study the nonoscillatory decay of the ^{3}He magnetization to its new equilibrium value following an incremental field change.

The existence of ringing in ^{3}He B suggests that it, like ^{3}He A, may be a spin-triplet superfluid.[1] Observation of ringing would also agree with the parallel absorption reported by Osheroff and Brinkman.[3] The ratio of 1.9 ± 0.1 for f_B/f_A is greater than the $(\frac{5}{2})^{1/2}$ expected near T_c and the polycritical point from Leggett's calculations[1] if ^{3}He A were the Anderson-Brinkman-Morel (ABM) state[7] and ^{3}He B the Balian-Werthamer (BW) state.[8,1] However, Maki[11] has suggested a variety of nearly degenerate BW-like states, each giving a different possible f_B/f_A ratio. Osheroff and Brinkman[3] and Brinkman *et al.*[12] have interpreted perpendicular NMR in ^{3}He B at melting pressure and for $T/T_c \lesssim 0.8$ in a 6-mm-diam container as being profoundly affected by boundaries in the entire field range of our experiments. Our parallel-ringing measurements, carried out at lower pressures, in a 3-mm-diam tube and at temperatures down to about $0.8T_c$, show low- and high-field regions with a transition between them in the range 1 to 5 G for both ^{3}He A and ^{3}He B. We presently suspect that all these different measurements represent truth and that ^{3}He B is more complex than currently believed. Experiments have been performed under sufficiently different conditions as to make intercomparison questionable, particularly regarding magnetic properties. We cite in this connection Ahonen, Haikala, and Krusius[13] who find in ^{3}He B mixed with platinum powder a profoundly altered magnetic state but little change in thermal properties such as T_c and T_{AB}.

We suspect that the easily observed ringing in

^{3}He *A* and the rather sudden appearance of good quality ringing in ^{3}He *B* only very near to T_c reflect the known flow properties of the two phases.[14] The chemical potential differences in space produced by ΔH in our rather inhomogeneous geometry are comparable to those due to ΔT in heat-flow experiments which drive ^{3}He *A* supercritical over a wide temperature range in ^{3}He *A*, and ^{3}He *B* supercritical only very near T_c. The tendency to "stir" the system by the flow of magnetization supercurrents[15,5] is thus inhibited in ^{3}He *A* but not inhibited in ^{3}He *B* except very near T_c. Experiments to test this possibility are now being considered.

We wish to acknowledge discussions with Dr. D. R. Fredkin, Dr. Bruce Patton, Dr. John Bardeen, and Dr. K. Maki, and helpful correspondence with Dr. A. J. Leggett and Dr. W. F. Brinkman. We are also grateful for conversations with Dr. D. M. Lee and Dr. D. D. Osheroff regarding their experiments.

---

†Work supported by the U. S. Atomic Energy Commission under Contract No. AT(04-3)-34.

[1] A. J. Leggett, Phys. Rev. Lett. 31, 352 (1973), and J. Phys. C: Proc. Phys. Soc., London 6, 3187 (1973), and to be published.

[2] D. N. Paulson, R. T. Johnson, and J. C. Wheatley, Phys. Rev. Lett. 31, 746 (1973).

[3] D. D. Osheroff and W. F. Brinkman, Phys. Rev. Lett. 32, 584 (1974).

[4] H. M. Bozler, M. E. R. Bernier, W. J. Gully, R. C. Richardson, and D. M. Lee, Phys. Rev. Lett. 32, 875 (1974).

[5] K. Maki and T. Tsuneto, to be published.

[6] J. C. Wheatley, Physica (Utrecht) 69, 218 (1973), Appendix A.

[7] P. W. Anderson and W. F. Brinkman, Phys. Rev. Lett. 30, 1108 (1973).

[8] R. Balian and N. R. Werthamer, Phys. Rev. 131, 1553 (1963).

[9] D. N. Paulson, H. Kojima, and J. C. Wheatley, Phy Rev. Lett. 32, 1098 (1974).

[10] D. N. Paulson. H. Kojima, and J. C. Wheatley, to b published.

[11] K. Maki, private communication.

[12] W. F. Brinkman, H. Smith, D. D. Osheroff, and E. Blount, to be published.

[13] A. I. Ahonen, M. T. Haikala, and M. Krusius, Phy Lett. 47A, 215 (1974).

[14] T. J. Greytak, R. T. Johnson, D. N. Paulson, and J. C. Wheatley, Phys. Rev. Lett. 31, 452 (1973).

[15] M. Vuorio, J. Phys. C: Proc. Phys. Soc., London 65 (1974).

Coupled Nonlinear Electron-Plasma and Ion-Acoustic Waves

Kyoji Nishikawa, H. Hojo, and K. Mima
Faculty of Science, Hiroshima University, Hiroshima, Japan

and

H. Ikezi
Institute of Plasma Physics, Nagoya University, Nagoya, Japan

(Received 11 February 1974)

We obtain solutions describing stationary one-dimensional propagation of a coupled nonlinear electron-plasma wave and a nonlinear ion-acoustic wave. These waves have amplitudes linearly proportional to one another, and propagate with approximately the ion-acoustic velocity in the form of periodic wave trains, including solitary waves as a special case.

Nonlinear stationary propagation of plasma waves has been investigated extensively in recent years.[1-4] One-dimensional propagation of small- but finite-amplitude ion-acoustic waves in a collisionless cold-ion plasma is described by a Korteweg-deVries equation,[5] and the theoretical prediction of steepening and soliton formation has been confirmed by experiments.[6] A long-wavelength electron-plasma wave obeys a nonlinear Schrödinger equation.[7] Its stationary solutions in the one-dimensional case include en lope soliton, periodic wave train, and finite- plitude plane wave. The latter is subject to modulational instability under certain condit

In this paper, we present some special sol tions which describe coupled, stationary, or dimensional propagation of a nonlinear elect wave and a nonlinear ion wave. The basic e tions are the Schrödinger equation for the el tron wave, with a potential proportional to t ion-density perturbation, and the cold-ion fluid equations for the ion wave, supplemented by the lectron-pressure-balance equation. Our soluons have the form of periodic wave trains, inluding solitary waves as a special case, and ave the following properties: (i) Both electron id ion waves move with a group velocity very lose to the ion-acoustic velocity C_s, and (ii) the nplitudes of the two waves are proportional to ich other.

Our solution appears to be of particular imortance in the nonlinear stage of parametric inabilities due to an electron-plasma wave acting the pump. The basic physical mechanism inolved is the same as for the oscillating twoream and modulational instabilities.[7] Namely, e ponderomotive force associated with the elecon wave induces an ion-density perturbation hich in turn traps the electron wave. The difrence lies in the consideration of the dynamical d resonantly enhanced ion response to the nderomotive force. In the usual linear stability eories, the ion response is assumed to be stac and hence is very small, being of second der in the pump amplitude. In our case, the n perturbation moves with the ion-acoustic eed while trapping the electron wave, and ereby the ion response to the ponderomotive rce is resonantly enhanced, becoming of first der in the pump amplitude and hence nonlinear. he importance of such a resonance effect in the odulational instability has been pointed out by asegawa[8] and our solution can be regarded as escribing a final nonlinear stage of his stimulat- modulational instability.

The following equation gives an adequate deription of one-dimensional propagation of a nall- but finite-amplitude, long-wavelength ectron-plasma wave[10]:

$$\frac{\partial^2 u_e}{\partial t^2} - 3v_e{}^2\frac{\partial^2 u_e}{\partial x^2} + \omega_{pe}{}^2\left(1+\frac{\delta n_e}{n_0}\right)u_e = 0, \qquad (1)$$

here u_e, v_e, ω_{pe}, n_0, and δn_e are, respectively, e fluid velocity, thermal velocity, plasma freency, average density, and low-frequency denty perturbation of the electron. We write

$$u_e(x,t) = \tilde{u}_e(x,t)e^{-i\omega_0 t} + \tilde{u}_e{}^*(x,t)e^{i\omega_0 t},$$

d assume that $\omega_0 \simeq \omega_{pe}$ and $\tilde{u}_e$ is slowly varying time. We then neglect $\partial^2\tilde{u}_e/\partial t^2$ and approxiate $\omega_0{}^2 - \omega_{pe}{}^2$ by $2\omega_{pe}\Delta$, where $\Delta = \omega_0 - \omega_{pe}$. rom now on, we use $\omega_{pe}{}^{-1}$ and $\lambda_D = v_e/\omega_{pe}$ as its of time and length and denote the dimensions variables $\tilde{u}_e/v_e$, Δ/ω_{pe}, and $\delta n_e/n_0$ simply by $\tilde{u}_e$, Δ, and δn_e. Equation (1) then becomes

$$i\,\partial\tilde{u}_e/\partial t + \tfrac{3}{2}\,\partial^2\tilde{u}_e/\partial x^2 + (\Delta - \tfrac{1}{2}\,\delta n_e)\tilde{u}_e = 0. \qquad (2)$$

As will be shown later, δn_e depends only on the amplitude of $\tilde{u}_e$ and not on its phase. Then, if $\tilde{u}_e = w(x,t)$ is a solution of (2), any function produced by the following transformation is also a solution:

$$w(x - x_0 - Vt, t)\exp(\tfrac{1}{3}iVx - \tfrac{1}{6}iV^2t + i\theta), \qquad (3)$$

where V, x_0, and θ are arbitrary parameters. Keeping this in mind, we look for a stationary solution, $w(\xi)$, which satisfies

$$\tfrac{3}{2}\partial^2 w(\xi)/\partial\xi^2 + [\Delta - \tfrac{1}{2}v(\xi)]w(\xi) = 0, \qquad (4)$$

where $\xi = x - x_0 - Vt$ and we put $\delta n_e = v(\xi)$ which is also assumed to be stationary.

For a low-frequency perturbation, we can neglect the electron inertia, obtaining from the electron equation of motion

$$\partial|\tilde{u}_e|^2/\partial x = (\partial/\partial x)[\varphi - \ln(1+\delta n_e)], \qquad (5)$$

where φ is the low-frequency potential measured in units of T/e, T being the electron temperature and $-e$ the electron charge. The left-hand side describes the ponderomotive force. We combine this equation with the ion equations of continuity and motion,

$$\epsilon^{-1}\partial\,\delta n_i/\partial t + (\partial/\partial x)[(1+\delta n_i)u_i] = 0, \qquad (6)$$

$$\epsilon^{-1}\partial u_i/\partial t + u_i\,\partial u_i/\partial x + \partial\varphi/\partial x = 0, \qquad (7)$$

and the Poisson equation,

$$\partial^2\varphi/\partial x^2 = (\delta n_e - \delta n_i), \qquad (8)$$

where ϵ^2 is the electron-to-ion mass ratio, δn_i the ion-density perturbation normalized by n_0, and u_i the ion fluid velocity normalized by $C_s = \epsilon v_e$. The ion temperature is neglected in (7). Since we are interested in the stationary solution moving with velocity V, we can replace $\partial/\partial t$ by $-V\partial/\partial\xi$ and $\partial/\partial x$ by $\partial/\partial\xi$.

If we make the linear approximation, we obtain from (6) and (7),

$$\delta n_i = \epsilon u_i/V = \epsilon^2\varphi/V^2. \qquad (9)$$

If in addition we assume local charge neutrality, $\delta n_e = \delta n_i$, we get from (5) and (9)

$$\delta n_e = |\tilde{u}_e|^2(V^2/\epsilon^2 - 1)^{-1}. \qquad (10)$$

Substitution of (10) into (2) yields the usual nonlinear Schrödinger equation for the long-wavelength electron wave. It is modulationally unstable when the group velocity is subsonic (i.e., The linear approximation breaks down if V is very close to ϵ. In order to derive an appropriate nonlinear equation, we differentiate (8) with respect to ξ and add the result to the sum of (7) and ϵ/V times (6). Using (5) and keeping the terms up to second order in δn_e, one obtains

$$(\partial/\partial\xi)\{(\epsilon/V)[(1-V^2/\epsilon^2)u_i+\delta n_i u_i]+\tfrac{1}{2}u_i^2+|\tilde{u}_e|^2-\tfrac{1}{2}(\delta n_e)^2+\partial^2\varphi/\partial\xi^2\}=0. \tag{11}$$

This equation contains only small terms, either nonlinear or linear with higher derivative or small coefficient $1-V^2/\epsilon^2$. One can therefore use the linear relations (9) as well as the local charge neutrality, $\delta n_e=\delta n_i=v(\xi)$. Also, V/ϵ may be replaced by unity except for the term $V-\epsilon$. Equation (11) can then be reduced to the form

$$\frac{\partial^2 v}{\partial\xi^2}-2\lambda v+v^2+|w|^2+W=0, \tag{12}$$

where we replaced $|\tilde{u}_e|^2$ by $|w|^2$, λ is the excess Mach number, $\lambda=(V-\epsilon)/\epsilon$, and W is the integration constant. Equations (4) and (12) are our basic equations.

We expect a solution for which $|w|$ and $|v|$ are of comparable order. It is then natural to assume the form

$$|w|^2=a+bv+cv^2. \tag{13}$$

Equations (12) with (13) have a general solution expressible in terms of Jacobi's elliptic function $\mathrm{cn}(\alpha\xi;k)$[11]:

$$v=v_0+A\,\mathrm{cn}^2(\alpha\xi;k), \tag{14}$$

where v_0 is determined by the condition that the spatial average of v should vanish,

$$v_0=-[A/2\alpha K(k)]\int_0^{2K}dx\,\mathrm{cn}^2(x;k), \tag{15}$$

with $K(k)$ being the complete elliptic integral of the first kind. The other constants are to be determined such that the coefficient of each power of $\mathrm{cn}^2(\alpha\xi;k)$ vanishes in (12). There are three such relations.

Our next procedure is to separate w into amplitude and phase by writing $w=R^{1/2}e^{i\Psi}$; since v, as a solution of (13), is a function of R only, one can easily find two integrals of (4) as

$$R\,d\Psi/d\xi=M=\mathrm{const}, \tag{16}$$

$$R^{-1}[(dR/d\xi)^2+\tfrac{8}{3}(\Delta+b/4c)R^2-(R/9c^2)(b+2cv)^3+4M^2]=E=\mathrm{const}. \tag{17}$$

Substituting (14) into (13) and then into (17) gives an algebraic equation for $\mathrm{cn}^2(\alpha\xi;k)$ in fifth power. Setting the coefficient of each power equal to zero, we get six relations, of which only five are found to be independent. For a given value of Δ, there are twelve independent parameters: a, b, c, A, α, k, λ, W, M, E, x_0, and θ or $\Psi(\xi=0)$. Of these, we can determine only eight parameters, four being left free to be chosen.

Particularly simple solutions are obtained in the case $M=0$, i.e., $d\Psi/d\xi=0$. In this case, we find a solution in the form

$$w=B\,\mathrm{cn}(\alpha\xi;k)\mathrm{sn}(\alpha\xi;k) \tag{18}$$

with

$$A=-18k^2\alpha^2,\quad B=(432)^{1/2}k^2\alpha^2,\quad \alpha^2=\tfrac{2}{3}(5k^2-4)^{-1}(\tfrac{1}{2}v_0-\Delta),$$

$$k^2-1=[(v_0-2\lambda)v_0+W]/2A\alpha^2,\quad -\lambda+v_0=2\alpha^2(1+4k^2).$$

Clearly, $|A|$ and $|B|$ are of the same order, so are $|w|$ and $|v|$. The general form of (14) and (18) describes a periodic wave train with three parameters, W, x_0, and θ, being left free to be chosen. In t special case in which $k^2=1$, the period of the wave train becomes infinite and the solution is reduced to a solitary wave. In this case, $K\to\infty$ and hence $v_0\to 0$, so that W must be zero. The explicit form o the solution is

$$v(\xi)=12\Delta\,\mathrm{sech}^2[(-2\Delta/3)^{1/2}\xi], \tag{19}$$

$$w(\xi)=(192)^{1/2}\Delta\,\mathrm{sech}[(-2\Delta/3)^{1/2}\xi]\tanh[(-2\Delta/3)^{1/2}\xi]. \tag{20}$$

Since Δ has to be negative, this solution can exist only in the overdense region ($\omega_0<\omega_{pe}$). The density perturbation $v(\xi)$ is negative, implying a density depletion, but is of the same order as $|w(\xi)|$. Since $|v(0)|$ is 12 times as large as $|\Delta|$, the plasma is locally underdense and the electron wave is trapped in that region. The excess Mach number λ is negative, i.e., subsonic, and is given by $20\Delta/3$. Whereas the ion-density perturbation is symmetric around $\xi=0$, the electron wave is antisymmetric and shows a phase jump at $\xi=0$. For given Δ, the only free parameters are the initial position x_0 and the initial phase θ, all the other parameters being uniquely determined by Δ.

Let us finally discuss the effect of Landau damping. First, the ion Landau damping due to a finite ion temperature prevents a sharp resonance at $V=C_s/v_e=\epsilon$, $|\lambda|$ $(=|V-\epsilon|)$ becoming at least of order ν_i/ω_s, where ν_i and ω_s are the damping rate and the frequency of the ion-acoustic wave. On the other hand, a large ion-density perturbation (of order $|v|\sim|w|$) predicted by the present theory assumes $|\lambda|$ to be of order $|w|$ or less; otherwise, $|v|$ becomes much smaller, being of order $|w|^2$. This implies that in the case when $|w|$ acts as a pump the ion Landau damping brings in a threshold ($|w|>\nu_i/\omega_s$) for the occurrence of a large ion-density perturbation. Secondly, the Landau damping of the electron wave will cut down the large-wave-number components and thereby will tend to smooth the perturbation. Finally, a large ion-density perturbation will benefit the ion heating as compared with the usual parametric instabilities where only electrons are selectively heated.[12] However, this ion heating will eventually destroy the present solution by increasing the threshold.

---

[1] See, for instance, R. C. Davidson, *Methods in Nonlinear Plasma Theory* (Academic, New York, 1972), Chaps. 1–4.

[2] A. Jeffrey and T. Kakutani, SIAM Rev. 14, 582 (1972).

[3] N. Asano, T. Taniuti, and N. Yajima, J. Math. Phys. (N.Y.) 10, 2020 (1969).

[4] B. B. Kadomtsev and V. I. Karpman, Usp. Fiz. Nauk 103, 193 (1971) [Sov. Phys. Usp. 14, 40 (1971)].

[5] H. Washimi and T. Taniuti, Phys. Rev. Lett. 17, 996 (1966).

[6] H. Ikezi, R. J. Taylor, and D. R. Baker, Phys. Rev. Lett. 25, 11 (1970); H. Ikezi, Phys. Fluids 16, 1668 (1973).

[7] A. Y. Wong and G. Schmidt, University of California, Los Angeles, Plasma Physics Group Report No. PPG-151, 1973 (unpublished).

[8] A. Hasegawa, Phys. Rev. A 1, 1746 (1970).

[9] V. N. Oraevskii and R. Z. Sagdeev, Zh. Tek. Fiz. 32, 1291 (1962) [Sov. Phys. Tech. Phys. 7, 955 (1963)].

[10] See, for instance, V. E. Zakharov, Zh. Eksp. Teor. Fiz. 62, 1745 (1972) [Sov. Phys. JETP 35, 908 (1972)].

[11] H. T. Davis, *Introduction to Nonlinear Differential and Integral Equations* (Dover, New York, 1962), Chap. 7.

[12] W. L. Kruer, P. K. Kaw, J. M. Dawson, and C. Oberman, Phys. Rev. Lett. 24, 987 (1970); J. J. Thomson, R. J. Faehl, and W. L. Kruer, Phys. Rev. Lett. 31, 918 (1973).

Presence of an Incipient Wigner Electron Lattice in Solid-State Electron Gases

P. M. Platzman and P. Eisenberger
Bell Telephone Laboratories, Murray Hill, New Jersey 07974

(Received 23 April 1974)

In x-ray studies of the dynamic structure factor $S(k,\omega)$ in Be, graphite, and Al a new type of excitation spectrum is observed for momentum transfers k between k_F and $2k_F$. The similarity of the observed spectra in these systems, when scaled according to electron-gas parameters, strongly indicates that the new excitation is a property of a solid-state electron gas and not a one-electron band-structure effect.

In previous inelastic x-ray[1,2] and electron[3] scatring experiments it has been observed that the asmon dispersion in solid-state systems deates from mean-field theoretical predictions in hat the dispersion is much less than predicted or momentum transfers k in the region of the Fermi momentum k_F. Various unsuccessful theoretical attempts have been made to explain these observations by modifying existing mean-field theories for the electron gas by including lifetime effects for the excited electron-hole pair[4] or by ncluding band-structure effects.[5,6]

In this work we extend, for the first time, the region of experimental investigation to the momentum transfer region between k_F and $2k_F$. We discover in Be, graphite, and Al that the observed spectrum deviates qualitatively from mean-field-theory predictions. More precisely we find that, contrary to theoretical predictions, a plasmonlike excitation exists in this region. It is primarily the presence of this excitation which is responsible for the deviation of the observed pectra from mean-field theoretical predictions. To distinguish this rather broad excitation from he well-defined long-wavelength plasmon it will henceforth be refered to as a plasmon band.

The similarity of the observed spectra, when caled to electron-gas parameters, in the disarate systems Be, graphite, and Al strongly suggests that the observed plasmon band is a general property of the solid-state electron gas and not a property of the one-electron band structure. We will propose that the plasmon band is a manifestation of the spatial inhomogeneity in olid-state electron gases which in turn is a reult of the combined effect of the electrons' interaction with other electrons and with the positive background. Such a model can qualitatively be viewed as a soft Wigner electron lattice.[7] In fact, such properties (as we shall see) of the electron attice as negative dispersion of the elementary excitations are indeed observable in our experimental results.

The measured scattered intensity $I(k,\omega)$ for weak scattering of nonrelativistic x rays is quite generally related to the inverse dielectric function $[\epsilon(k,\omega)]^{-1}$, i.e.,

$$I(k,\omega)=(d\sigma/d\Omega)_0 S(k,\omega) \tag{1}$$

with

$$S(k,\omega)=(k^2/4\pi e^2)\,\mathrm{Im}[1/\epsilon(k,\omega)]. \tag{2}$$

Here k, ω are the momentum and energy transfers involved in the scattering process, and $(d\sigma/d\Omega)_0$ is the Thomson cross section.

The experimental apparatus and procedure is as described previously[2] except that in this study the samples were in a vacuum at nitrogen temperatures and Ge(111), rather than Ge(220), reflections were used in the double-crystal dispersive spectrometer. The low temperature was used to reduce quasielastic scattering [or thermal diffuse scattering (TDS)] and the Ge(111) spectrometer gave 25% worse resolution but three times the scattered intensity. The experiments are performed by fixing k and analyzing the energy distribution of the scattered x rays. In Fig. 1(a) are displayed the spectra obtained in studying Be in the region $1\leq k/k_F\leq 2$. Each spectrum is taken at a fixed momentum transfer. In Fig. 1(b) we show a series of theoretical curves at corresponding k/k_F values calculated using the conventional random-phase approximation (RPA), i.e., Lindhard dielectric function with no band-structure effects included. The theoretical results have been smeared by the experimental resolution function, a Lorentzian with a full width at half-maximum of 5.0 eV. The experimental data are uncorrected for finite-resolution effects.

Calculations within a mean-field picture have shown that the characteristic loss function (energy transfers of the order of 50 eV) of a metal such as Be is only weakly effected by band-structure effects.[6] The essential validity of this as-

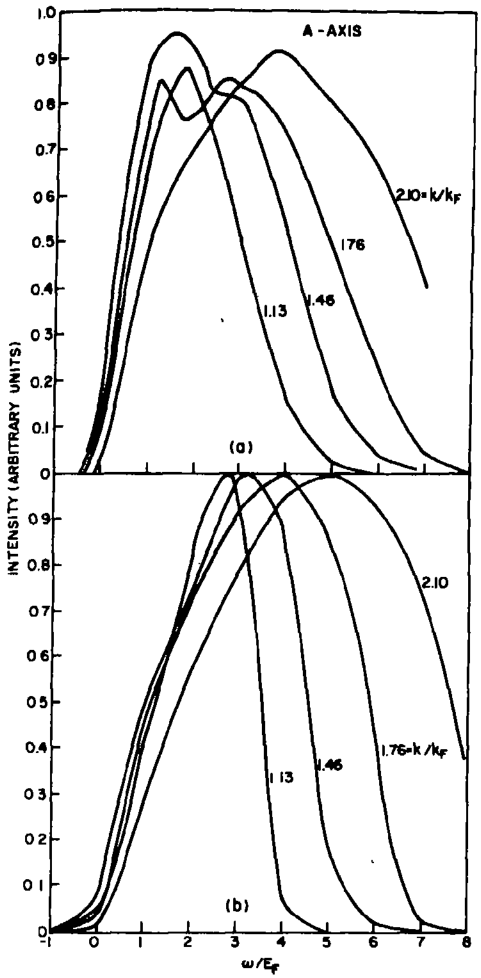

FIG. 1. Plots of $S(k,\omega)$ for fixed k. (a) Experimental results in Be. (b) Theoretical results obtained in RPA.

sumption is strongly supported by the results presented in Fig. 2. Here representative results for Al and graphite as well as Be are displayed. The similarity of the three spectra in these disparate systems is a strong experimental indication that the observed spectra are *not* a result of simple one-electron properties of those systems, since the one-electron band structure of these materials is so different. For other orientations and for other momentum transfers the basic similarity of the spectra is maintained. Indeed in studies of Li, Mg, and Si similar observations have also been made. The results for all systems will be more completely described in a subsequent work. The major thrust of this work is that the observed phenomenon is a general property of solid-state electron gases.

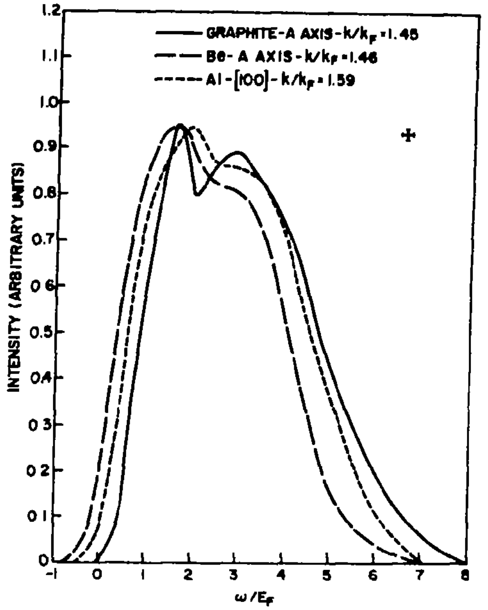

FIG. 2. Plot of $S(k,\omega)$ ($k \approx 1.5k_F$) for Al, Be, and graphite.

A comparison of Figs. 1(a) and 1(b) for $k/k_F = 1.13$ together with the plasmon-dispersion studies in Be in the region $0 \leqslant k/k_F = 1$ would lead to the conclusion made by ourselves[8] and others[1] that the experimentally observed dispersion is simply smaller than theoretically predicted. In Ref. 8 we attempted to explain this lagging behind by use of the so-called f-sum rule to relate the position of the peak $[\omega(k)]$ in the spectrum to the Fourier transform of the pair correlation function $[S(k)]$, i.e.,

$$\omega(k) = \frac{k^2/2m}{S(k)}. \qquad (3)$$

The slowing down of the dispersion was attributed to the enhancement of $S(k)$ at values of k corresponding to periodicities arising from the short-range order present in the electron liquid. This kind of argument works well in liquid He where the collective phonon-roton peak does indeed dominate the spectrum.[9] In this case, however, the sequence of spectra taken at higher momentum transfers tells us that the situation is somewhat more complicated. The data [see Fig. 1(a)] at $k/k_F = 1.4$, 1.76, and 2.10 lead to the conclusion that the spectra are more accurately described as being comprised of two portions, one broad RPA-like component and another sharper, relatively local excitation, the plasmon band superimposed upon it. As k increases the relative intensity in the plasmon band decreases until it is swallowed by the broad single-particle-like piece at $(k/k_F) \approx 2$.

The presence of negative dispersion for the plasmon-band peak in the region $\omega/E_F = 1.5$ is also observable from Fig. 1(a). That figure together with Fig. 2 of a previous work[2] give a rather complete picture of the "plasmon" dispersion in Be. Starting at $k = 0$ with a sharp plasmon peak at $\omega/E_F = 1.3$, the plasmon originally has a positive nearly k^2 dispersion. In the region $0.5 \leq k/k_F \leq 1$, the plasmon is broad; the dispersion has slowed but is still positive with peak reaching a value $\omega/E_F = 1.7$. In the region $1 \leq k/k_F \leq 2$ the plasmon-band central frequency decreases with increasing k possibly reaching a value as low as $\omega/E_F = 1.2$ before it becomes very weak in intensity and poorly defined.

It seems clear to us that qualitatively the behavior of the spectrum in this intermediate-momentum-transfer regime is roughly characteristic of an ordered electron (Wigner) solid.[7] Of course this ordering is only incipient, i.e., present on a very short time scale, and probably arises from a combination of electron-electron correlations and the coupling of the electron to the periodically distributed ion cores.

To see qualitatively how such a spectrum arises we must think of an electron as localized and the scattering (for these momentum transfers) as roughly coming from one electron at a time. The electron doing the scattering finds itself in a potential well created self-consistently by the other electrons and ion cores. The scattering from a single electron in such a well roughly consists of two parts, so-called Raman and Compton scattering.

(1) Raman scattering is discrete. It consists of the excitation of the electron to the next excited state in the well. It is, we believe, the analog of the plasmon band. In this simple picture, of course, this feature of the spectrum has no dispersion, i.e., it is strictly a local excitation. Dispersion arises from coupling between wells; in fact, it is well known that the dispersion of such a longitudinal mode in a real Wigner crystal is negative. As k increases the mode decreases in energy.

(2) Compton scattering consists of excitation of the electron to the continuum. The spectrum in this case is a broad smear whose exact shape and width is characterized by the Doppler shift associated with the motion of the electron in its ground state. This type of spectrum is roughly characteristic of the broad RPA-like portion of the spectrum.

The relative intensities in these two types of scattering qualitatively behave in the observed manner. As the momentum transfer increases it becomes more probable to excite transitions to the continuum. The Compton part, as in the experiment, soaks up the intensity. The characteristic crossover occurs when the recoil energy $k^2/2m$ exceeds the local-mode frequency ω_p. As in Fig. 1(a), this is roughly what is observed.

While this picture gives us a rather physically reasonable and qualitatively accurate picture of the experimental results, no real quantitative theory exists. The importance of these experimental results lies in the fact that they graphically point up the inadequacies of an RPA type of calculation. They clearly focus on features of the electron liquid which we knew must be present but which had not been probed before.

We would like to thank W. A. Marra for technical assistance and H. Fukuyama and W. A. Brinkman for informative discussions.

---

[1] D. M. Miliotis, Phys. Rev. B 3, 701 (1971), N. G. Alexandropoulos, J. Phys. Soc. Jpn. 31, 1790 (1971).

[2] P. Eisenberger, P. M. Platzman, and K. C. Pandey, Phys. Rev. Lett. 31, 311 (1973).

[3] H. Raether, in *Springer Tracts in Modern Physics, Ergebnisse der exakten Naturwissenschaften*, edited by G. Höhler (Springer, Berlin, 1965), Vol. 38, p. 85; P. Zacharias, to be published.

[4] K. L. Kliewer and H. Raether, Phys. Rev. Lett. 30, 971 (1973).

[5] M. S. Haque and K. L. Kliewer, Phys. Rev. B 7, 2416 (1972).

[6] K. C. Pandey, P. M. Platzman and P. Eisenberger, to be published.

[7] See the discussion and references in C. Herring, in *Magnetism*, edited by G. T. Rado and H. Suhl (Academic, New York, 1966), Vol. IV.

[8] P. M. Platzman and P. Eisenberger, Solid State Commun. 14, 1 (1973).

[9] A. Miller, and D. Pines, Phys. Rev. 127 1452 (1962).

Dislocation-Dragging Effects in Quenched and Electron-Irradiated Copper*†

H. M. Simpson and S. J. Kerkhoff
Department of Physics, Wright State University, Dayton, Ohio 45431

(Received 18 March 1974)

Damping and modulus measurements were made on high-purity copper subjected to both quenching and 1.0-MeV electron irradiation. During isothermal annealing at room temperature, following quenching from 700°C, we observe a monotonic decrease in the logarithmic decrement with a concurrent increase in the modulus. However, both slow cooling and quenching of the sample followed by 1.0-MeV electron irradiation give rise to a substantial increase in the decrement; i.e., the Simpson-Sosin "peaking effect" is clearly evident.

One of the remaining problems in the field of radiation damage is the identification of the point defect or defects that cause dislocation pinning in copper near room temperature. There are three distinct and viable possibilities: (1) The normal "fast" interstitial that is observed in the stage-I (60°K) recovery region of irradiated copper with a migration energy $E_{\mathrm{I}} \approx 0.12$ eV; (2) the single vacancy with migration energy $E_v' \approx 1.0$ eV; and (3) the thermally converted stage-I interstitial with $E_{\mathrm{II}} \approx 0.64$ eV, sometimes called the "slow interstitial." For an excellent review of the status of the various defect models see the recent article by Schilling and Sonnenberg.[1]

In an attempt to determine the nature of the defects causing pinning (or dragging) at room temperature, we have performed a series of both quenching and electron-irradiation experiments on high-purity polycrystalline copper. The internal friction and modulus defect were used as monitors of the state of the dislocation pinning.

Most dislocation-pinning studies have involved the use of radiation-produced Frenkel pairs, which results in the creation of equal numbers of interstitials and vacancies in the lattice. This obviously complicates pinning experiments since it is never absolutely clear which defect one is detecting at the dislocation. This is particularly true at high temperatures where the vacancy becomes mobile. Recent work by Thompson and co-workers has indicated the presence of the slow interstitial for irradiations performed between 333 and 393°K.[2-5] Simpson and co-workers were also able to account for their observations following electron irradiation in terms of the slow interstitial.[6,7] However earlier work by Keefer and co-workers on quenched copper and gold has shown that vacancies migrate to and pin dislocations at about 300°K.[8-10] Similar observations have also been made by Roswell and Nowick on quenched gold.[11]

Simpson and Sosin[12-14] have shown that the usual interpretation of dislocation-pinning experiments in terms of the Koehler-Granato-Lücke[15-17] theory is questionable in the subkilohertz frequency range. Instead of dislocation pinning, Simpson and Sosin propose that dislocation drag of point defects is a more likely mechanism at low frequencies. The model predicts, and experiments confirm, the striking result that the logarithmic decrement can increase as a result of the addition of point defects to the dislocation line. For continuous irradiation experiments this gives rise to a peak in the decrement as a function of irradiation time. Such a phenomenon will be referred to as a dislocation "peaking effect." It seems reasonable that the drag (or pinning) of vacancies should be considerably different from the drag of interstitials. If this is so, then the presence or absence of a peaking effect could serve as a monitor of the existence of vacancies or interstitials on the dislocation.

All of our internal-friction experiments were performed on the same high-purity (99.999%) copper sample. The sample material was obtained from the American Smelting and Refining Company and machined into the form of a cantilevered beam, which could be driven electrostatically, with a flexural resonant frequency of 600 Hz. The specimen was then mounted in a special sample chamber which allowed both electron irradiation and quenching experiments to be performed. Quenches could be made from 700°C to about 15°C, with an initial quench rate of approximately 200°C/sec. For the irradiation runs, 1.0-MeV electrons were used with a flux of $6.5 \times 10^{10}\ e^-/\mathrm{cm}^2$ sec resulting in a Frenkel-pair production rate of 2.7×10^{10} defects/cm^3 sec (close pair and correlated recovery are excluded). Young's modulus and the logarithmic decrement

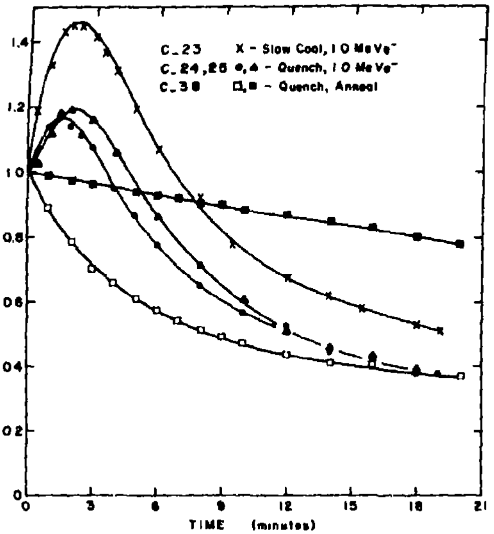

FIG. 1. The decrement normalized with respect to its initial value and plotted as a function of time. The time scale for the *open*-squares quench data is in units of 10 min.

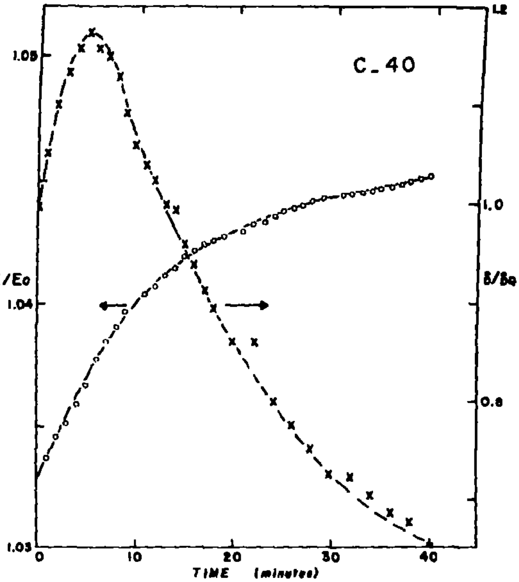

FIG. 2. The modulus normalized to its value immediately following a quench plotted as a function of irradiation time, and the decrement normalized to its value at the beginning of the irradiation and plotted as a function of time. The sample was quenched and annealed for 40 days prior to irradiation. The temperature was 26°C.

were monitored continuously. All decrement measurements were made at constant strain in the amplitude-independent region. A complete describtion of the automatic data logging system and the method of quenching will be presented elsewhere.

Experimental results for the logarithmic decrement, as affected by quenching only, quenching followed by irradiation, and slow cooling, are presented in Fig. 1. Note the large peaking effect for the slow-cool data. This is typical of results obtained for samples with this treatment. For the quench and irradiation data, the sample was quenched from 700 to 37°C and irradiation began immediately. A substantial peaking effect exists although it is somewhat subdued in comparison to the slow-cool data. Finally, a quench from 700 to 41°C with isothermal annealing at 41°C is presented. Both the early-time (solid squares) and extended-time (open squares) data give no evidence for a peaking effect, even though the possibility for such exists, since peaking occurred for the quench-irradiation run. Of course the pinning proceeds slowly for the isothermal-quench data since the lattice is being continually depleted of vacancies. These data show in a most convincing manner that the defects arriving at dislocations following quenching are entirely different from those caused by the irradiation.

A long-time (40 days) isothermal anneal was performed at room temperature following a quench from 700°C. After this extended anneal the decrement was reduced by about a factor of 4 and the modulus increased by about 3%. The sample was then subjected to the standard irradiation treatment. Results for the room-temperature irradiation are presented in Fig. 2. Even though the decrement was reduced by a factor of 4 by the post-quench annealing, the addition of radiation defects causes the peaking effect to occur. At the same time the modulus continues to increase. This indicates most convincingly that the peaking effect is not due to depinning or the modulus would decrease. It seems clear that the effect of radiation-induced defects is strikingly different from that of the quench-produced defects.

In Fig. 3 we present the results of a quench followed by an isothermal anneal at 41°C for 80 min whereupon the standard irradiation was commenced. Again, even though the isothermal annealing leads to a reduction in the decrement by

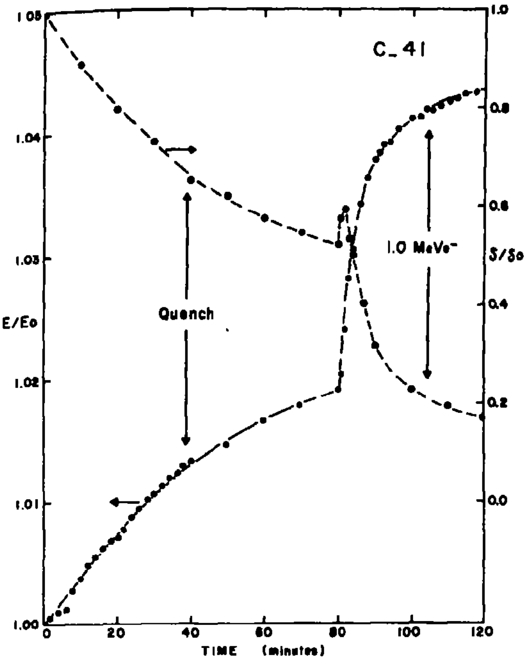

FIG. 3. The modulus and decrement normalized to their post-quench, pre-irradiation values and plotted as a function of annealing time for 80 min. Irradiation began at 80 min. The temperature was 41°C.

a factor of 2, at the onset of irradiation the peaking effect occurs. At the same time the modulus continues to increase, which rules out depinning of dislocation lines.

Additional data are presented in Table I. The subscript zero refers to the values measured at the stated temperature immediately (20–30 sec) following a quench.

The quench and irradiation data indicate most convincingly that two different defects are responsible for the dislocation-dragging (or pinning) effects in the two cases. The simplest possible nterpretation of the data would be as follows. uring the irradiation, the highly mobile interstitials are collected on dislocations and the reulting dragging effects give rise to the peaking ffects. Following a quench, vacancies and diacancies diffuse rather slowly to the dislocation here they act more like pinning points than dragging points; i.e., the drag of a vacancy is suffiiently limited so that the peaking effect can not ccur. Although the results presented here point irmly to the conclusion that interstitials arrive at dislocation lines during irradiation near room temperature, they do not distinguish directly between the fast and slow interstitials.

TABLE I. Data for quench and irradiation runs.

Run	Condition	δ_0 (10^{-5})	$(\Delta E/E)_0$ (%)	Temp. (°C)
C-23	Slow cool	5.78	3.90	37
C-24	Quench + irr.	10.4	4.16	37
C-26	Quench + irr.	11.1	4.40	37
C-38	Quench	14.7	4.47	40
C-40	Quench + irr.	14.7	4.73	26
C-41	Quench + irr.	14.9	4.55	41

A somewhat speculative explanation of the differences in dislocation-pinning experiments at room temperature using electron and γ irradiation would be as follows. During the high defect-production-rate (2.7×10^{10} defects/sec cm^3) electron-irradiation experiments presented here and elsewhere by Simpson and co-workers,[6,7] the fast interstitial is detected on the dislocation line and since it is highly mobile gives rise to the peaking effect. In the γ-irradiation (0.25×10^7 defects/sec cm^3) experiments of Thompson and co-workers the long periods of time involved allow the fast interstitial to disappear to sinks.[2-5] Thus Thompson and co-workers measure the effects of vacancies on the dislocation.

The authors are very grateful for the help received from the radiation damage group at the Aerospace Research Laboratory with special thanks to Dr. Jon Meese.

---

*Work supported in part by the Research Corporation.

†Electron irradiations were performed at the Aerospace Research Laboratory located at Wright Patterson Air Force Base, Ohio.

[1] W. Schilling and K. Sonnenberg, J. Phys. F: Metal Phys. 3, 322 (1973).

[2] D. O. Thompson, O. Buck, R. S. Barnes, and H. B. Huntington, J. Appl. Phys. 38, 3051 (1967).

[3] D. O. Thompson, O. Buck, H. B. Huntington, and R. S. Barnes, J. Appl. Phys. 38, 3057 (1967).

[4] D. O. Thompson and O. Buck, J. Appl. Phys. 38, 3068 (1967).

[5] L. V. Meisel and D. O. Thompson, J. Appl. Phys. 39, 3447 (1968).

[6] H. M. Simpson, A. Sosin, and D. F. Johnson, J. Appl. Phys. 44, 1435 (1973).

[7] H. M. Simpson, A. Sosin, and S. L. Seiffert, J. Appl. Phys. 42, 3977 (1971).

[8] D. Keefer, J. C. Robinson, and A. Sosin, Acta Met.

135 (1967).
Keefer, J. C. Robinson, and A. Sosin, Acta Met. .409 (1966).
Sosin and D. W. Keefer, in *Microplasticity*, edited . J. McMahon (Wiley, New York, 1968).
. E. Roswell and A. S. Nowick, Acta Met. 5, 228 7).
. M. Simpson, A. Sosin, G. R. Edwards, and S. L. fert, Phys. Rev. Lett. 26, 897 (1971).
i. M. Simpson and A. Sosin, Phys. Rev. B 5, 1382 (1972).
[14] H. M. Simpson, A. Sosin, and D. F. Johnson, Phys. Rev. B 5, 1393 (1972).
[15] J. S. Koehler, in *Imperfections in Nearly Perfect Crystals*, edited by W. Shockley *et al.* (Wiley, New York, 1952), p. 197.
[16] A. V. Granato and K. Lücke, J. Appl. Phys. 27, 583 (1956).
[17] A. V. Granato and K. Lücke, J. Appl. Phys. 27, 789 (1956).

Effect of Structure in the Electronic Density of States on the Temperature Dependence of the Electrical Resistivity*

F. Y. Fradin
Argonne National Laboratory, Argonne, Illinois 60439
(Received 16 May 1974)

I discuss the effect of sharp structure in the electronic density of states on the temperature dependence of the interband-*s*-*d*-phonon-scattering resistivity. The *a priori* density of states of Pd is used to calculate the resistivity, which is found to be in excellent agreement with experimental high-temperature results.

The temperature dependence of the electrical resistivities of the pure transition metals[1] palladium and platinum, as well as the actinide metals[2] uranium, neptunium, and plutonium, exhibits high-temperature behavior that departs drastically from the classical linear T dependence. The low-temperature behavior has been found to obey a T^2 law that has led to descriptions in terms of spin fluctuations. Similarly many intermetallic compounds, especially those exhibiting finite superconducting transition temperatures,[3,4] exhibit high-temperature resistivities that tend to bend away from linear T behavior toward the temperature axis. These compounds are usually found to obey a T^3 law indicative of s-d phonon scattering at low temperature.

The present paper involves a generalization of the model[5,6] of interband s-d (or s-f) phonon scattering for cases in which there is sharp structure in the electronic density of states $N(\epsilon)$ in the vicinity of the Fermi level E_F. It is suggested that this interband-phonon-scattering mechanism is responsible for the high-temperature resistivity behavior. Because the model does not involve the exchange-enhanced spin susceptibility as does the spin-fluctuation model of the resistivity, simple model densities of states can be used to understand the temperature dependence of both the resistivity ρ and the spin susceptibility χ.

The density of states $N(\epsilon)$ of palladium is well known from relativistic augmented-plane-wave calculations,[7,8] and I will demonstrate the resistivity calculation using the *a priori* calculation of $N(\epsilon)$. The valence electrons in the transition metals are normally divided into two groups. The first forms an s band with a spherical Fermi surface; the second, a d band with a complex Fermi surface, but with a Fermi velocity much less than that in the s band. The lattice resistivity is then divided into three parts. The first, ρ_{s-s}, describes scattering of electrons within the s band; the second, ρ_{s-d}, is due to scattering of s electrons into the d band; and the third is due to d-d scattering. Since most of the current is carried by the s electrons, only the first two processes will contribute to the resistivity due to electron-phonon scattering. The contribution ρ_{s-s} can be estimated from the resistivity of Ag, which is well behaved. We use an indirect model for the calculation of ρ_{s-d}. That is, we assume the momentum selection rule is always satisfied such that there are always phonons of sufficient size to cause interband scattering. This assumption will be invalid at very low temperatures where no phonons exist that can cause interband transitions. A Debye model for the phonon spectrum is then employed, and the resistivity is calculated following Ziman[6] except that the integral over $N(\epsilon)$ is treated generally; i.e., $N(\epsilon)$ is not assumed to be a slowly varying function of energy.

The resistivity due to phonon absorption is given by

$$\rho_{s\text{-}d}=\frac{\rho_0}{k_BT}\int_0^{\Theta_D}\frac{\omega^2d\omega}{\frac{1}{3}\Theta_D^3}n(\omega)\int_0^{\infty}d\epsilon\frac{N_d(\epsilon+\omega)}{N(0)}f(\epsilon)[1-f(\epsilon+\omega)], \tag{1}$$

where ρ_0 is a constant, k_B is Boltzmann's constant, T is the absolute temperature, Θ_D is the Debye temperature, $n(\omega)$ is the Bose function, $N_d(\epsilon)$ is the d (or f) fraction of the total density of states, and $f(\epsilon)$ is the Fermi function. Prange and Kadanoff[9] have demonstrated that the unrenormalized density of states enters the resistivity expression. To calculate the resistivity due to phonon emission, $n(\omega)$ is replaced by $n(\omega)+1$ and $\epsilon+\omega$ goes over to $\epsilon-\omega$ in the integral. The Fermi function depends on the value of the chemical potential μ, which is iteratively calculated at each temperature to hold the number of occupied states constant to within 5 parts in 10^7:

$$\int_0^{\infty}f(\epsilon,\mu,T)N(\epsilon)d\epsilon=\text{const.} \tag{2}$$

Equation (1) reduces to the functional form given by Wilson[5] either when $N_d(\epsilon)$ is a constant equal to $N_d(0)$, the density of d states at the Fermi level, or at sufficiently low temperatures, i.e., when $\rho_{s\text{-}d}$ is proportional to T^3 as $T\rightarrow 0$. For sufficiently high temperatures and a sufficiently narrow peak in $N_d(\epsilon)$, $\rho_{s\text{-}d}$ approaches a constant value.

In contrast to recent calculations[10] of the spin-fluctuation contribution to the resistivity, the only adjustable parameter in the present calculation is the coefficient ρ_0. Figure 1 illustrates the calculation of $\rho_{s\text{-}d}$ for palladium. $N_d(\epsilon)$ is taken as $N(\epsilon)$ of Mueller *et al.*,[7] $\Theta_D=275°\text{K}$,[11] and ρ_0 is set equal to 3.1 μΩ cm in order to fit the data[1] at 298°K. We assume the s density of states is a small free-electron-like contribution to $N(\epsilon)$. The contribution due to scattering within the s band, $\rho_{s\text{-}s}$, is estimated to be equal to the resistivity of Ag. Thus, comparison between theory and experiment is made between $\rho_{s\text{-}d}$ and $\rho_{\text{Pd}}-\rho_{\text{Ag}}$ in Fig. 1. The temperature dependence of $\rho_{s\text{-}d}$ is insensitive to the features of the phonon spectrum above about 100°K, i.e., once the resistivity is above the low-temperature T^3 regime. However, varying Θ_D does alter the magnitude of $\rho_{s\text{-}d}$ at high temperatures. The resolution, 1 mRy, in the palladium $N(\epsilon)$ calculation limits the accuracy of the calculated quantities below about 20°K. However, a remarkable fit to the resistivity data is obtained.

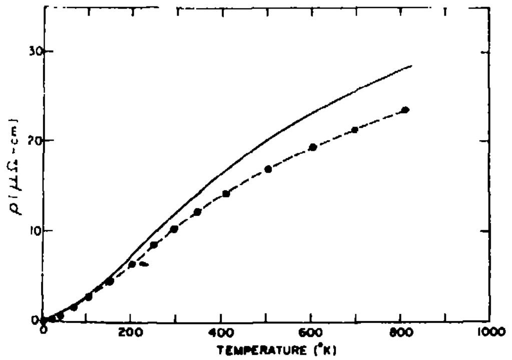

FIG. 1. Electrical resistivity of Pd. Solid line, experimental results (Ref. 1) for ρ_{Pd}; dashed line, $\rho_{\text{Pd}}-\rho_{\text{Ag}}$; circles, calculated values of $\rho_{s\text{-}d}$ normalized to $\rho_{\text{Pd}}-\rho_{\text{Ag}}$ at 298°K.

The coefficient ρ_0 due to normal processes can be estimated from[12]

$$\rho_{0\text{N}}\approx 3m_s\lambda\omega_D/e^2\pi^2k_D^2(6\pi^2n_s)^{1/3}, \tag{3}$$

where m_s and n_s are the mass and number per unit volume of the current carriers, ω_D and k_D are the Debye frequency and wave vector, and λ is the mass enhancement. The contribution due to umklapp processes, $\rho_{0\text{U}}$, is usually considered to be about a factor of 10 larger than $\rho_{0\text{N}}$.[6] An order-of-magnitude estimate of $\rho_0=\rho_{0\text{N}}+\rho_{0\text{U}}$ based on a mass enhancement λ of 0.5 and 0.5 s electrons per palladium yields ρ_0 of order 1 μΩ cm. Thus, we find that the simple calculation of the resistivity due to s-d interband scattering gives a good accounting of the temperature dependence of the resistivity of Pd at high temperatures. The resistivity at very low temperatures, which follows a T^2 law,[1] is undoubtedly due to spin-fluctuation scattering. However, any treatment of the high-temperature resistivity must take full account of the effect of structure in $N(\epsilon)$ on the phonon-induced interband scattering.

Although $\rho_{s\text{-}d}$ is not sensitive to shifts in the Fermi level $E_F\equiv\mu(T=0)$ of a few millirydbergs, the temperature dependence of the susceptibility is quite sensitive. The susceptibility is calculated from the indirect model ignoring matrix elements,

$$\chi_0(T)=(2\mu_B^2/k_BT)\int_0^{\infty}N(\epsilon)f(\epsilon)[1-f(\epsilon)]d\epsilon. \tag{4}$$

The value $\mu(T=0)=0.518$ Ry is used in both the $\rho_{s\text{-}d}$ and $\chi_0(T)$ calculations. Comparison is made

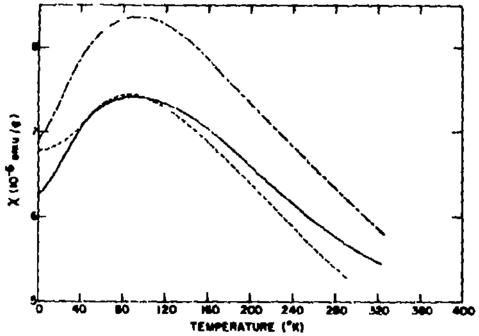

FIG. 2. Magnetic susceptibility of Pd. Dashed line, experimental results (Ref. 13); solid line, calculated values of χ with $S = 7.6$; dot-dashed line, calculated values of χ with $S = 8.4$.

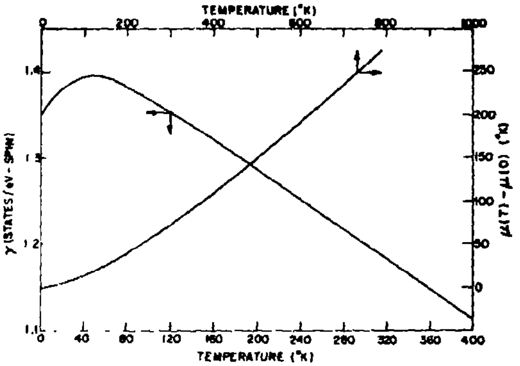

FIG. 3. Calculated temperature dependence of the electronic specific-heat coefficient γ and the shift in the chemical potential $\mu(T) - \mu(0)$ for Pd.

with the experimental[13] results in Fig. 2. The molecular-field approximation, which assumes a temperature-independent exchange interaction I, is used; i.e., $\chi(T) = \chi_0(T)/[1 - I\chi_0(T)]$. Enhancement factors $S \equiv \chi(T=0)/\chi_0(T=0)$ of 7.6 and 8.4 are used in the calculated curves in Fig. 2. The departure of the experimental from the theoretical susceptibility below 40°K is due in part to the inaccuracies of the present calculation and to the assumptions made in subtracting the impurity contribution from the experimental data.[13]

The temperature dependence of the bare electronic specific-heat coefficient γ and the chemical potential are shown in Fig. 3. γ is calculated from

$$\gamma = (1/T)(\partial/\partial T)\int_0^\infty \epsilon N(\epsilon) f(\epsilon)\,d\epsilon. \tag{5}$$

It is interesting to note that the electronic specific-heat coefficient γ changes by about 17% between 0 and 400°K. This is a considerably larger change than the unenhanced spin susceptibility χ_0 suffers. Also, the chemical potential increases by over 100°K for a temperature increase from 0 to 400°K. The breakdown of the lowest-order T^2 correction to γ and χ_0 is evident by 40°K.

The *a priori* band calculations for Pd have a number of inaccuracies of importance for the present calculation. Detailed comparisons between theoretical and experimental Fermi surfaces indicate that the relative position of the s and d bands is only known to within 1000°K.[8] However, near E_F nearly 90% of $N(\epsilon)$ is contributed by the purely d-like fifth band. The energies within this band are accurate to order 10°K. Thermal expansion[14] can give rise to a temperature-dependent $N(\epsilon)$ and possibly a temperature-dependent exchange interaction, which are not accounted for in the present calculation. Our calculated results use a Fermi level 2 mRy lower in energy than that of the *a priori* calculation of Mueller *et al.*[7] A similar calculation of $\chi_0(T)$ by van Dam and Anderson[15] based on the band structure calculation by Anderson[8] requires a shift of ~ 0.03 electrons or about 1 mRy to lower energy.

In conclusion, we find that interband s-d phonon scattering can explain the high-temperature electrical resistivity of Pd. This scattering mechanism is also capable of explaining the anomalous resistivity of other metals and intermetallic compounds that show curvature of the high-temperature resistivity toward the temperature axis, yet have weakly temperature-dependent susceptibilities with small enhancement factors. Examples are uranium, neptunium, and plutonium[2] and many intermetallic compounds.[4]

---

*Work performed under the auspices of the U. S. Atomic Energy Commission.

[1] A. I. Schindler, R. J. Smith, and E. I. Salkovitz, Phys. Chem. Solids 1, 39 (1956); T. Ricker and E. Pfluger, Z. Metallk. 57, 39 (1966).

[2] A. J. Arko, M. B. Brodsky, and W. J. Nellis, Phys. Rev. B 5, 4564 (1972).

[3] R. W. Cohen, G. D. Cody, and J. H. Halloran, Phys. Rev. Lett. 19, 840 (1967).

[4] Z. Fisk and A. C. Lawson, Solid State Commun. 13, 277 (1973).

[5] A. H. Wilson, Proc. Roy. Soc, Ser. A 167, 580 (1938).

[6] J. M. Ziman, *Electrons and Phonons* (Oxford Univ. Press, Oxford, England, 1960).

[7] F. M. Mueller, A. J. Freeman, J. O. Dimmock, and A. M. Furdyna, Phys. Rev. B 1, 4617 (1970).

[8] O. K. Andersen, Phys. Rev. B 2, 883 (1970).

[9] R. E. Prange and L. P. Kadanoff, Phys. Rev. 134, A566 (1964).

[10] S. Doniach, in *Magnetism and Magnetic Materials —1971*, AIP Conference Proceedings No. 5, edited by C. D. Graham, Jr., and J. J. Rhyne (American Institute of Physics, New York, 1972), p. 549; J. Jullien, M. T. Beal-Monod, and B. Coqblin, Phys. Rev. B 9, 1441 (1974).

[11] G. S. Knapp and R. W. Jones, Phys. Rev. B 6, 1761 (1972).

[12] G. Gladstone, M. A. Jensen, and J. R. Schrieffer, in *Superconductivity*, edited by R. D. Parks (Marcel Dekker, New York, 1969), Vol. 2, p. 665.

[13] A. J. Manuel and J. M. P. St. Quinton, Proc. Roy. Soc., Ser. A 273, 412 (1963).

[14] S. G. Das, D. D. Koelling, and F. M. Mueller, Solid State Commun. 12, 89 (1973).

[15] J. E. van Dam and O. K. Andersen, Solid State Commun. 14, 645 (1974).

Spectroscopically Observed Valence Mixing in SmS and Related Compounds*

J. L. Freeouf, D. E. Eastman, W. D. Grobman, F. Holtzberg, and J. B. Torrance
IBM Watson Research Center, Yorktown Heights, New York 10598

(Received 18 March 1974)

Photoemission spectra for semiconducting SmS and metallic $\mathrm{Sm}_{0.5}\mathrm{Y}_{0.5}\mathrm{S}$ give evidence of strong configuration interaction of localized states near the Fermi level involved in semiconductor-to-metal phase transitions and in unusual trasport and magnetic properties. An analysis of the observed multiplet structure in photoemission spectra for semiconducting SmS shows a localized state of a mixed f^6+f^5d character.

Recently the samarium monochalcogenides have been widely studied because of their intriguing optical,[1-3] electrical,[4] and magnetic[5] properties. For example, SmS undergoes a pressure-induced semiconductor-to-metal phase transition at the remarkably low pressure of 6.5 kbar,[4] while certain mixed $\mathrm{Sm}_{1-x}\mathrm{Gd}_x\mathrm{S}$ crystals undergo an explosive transition upon cooling at atmospheric pressure.[6] Also, certain $\mathrm{Sm}_{1-x}\mathrm{Y}_x\mathrm{S}$ and $\mathrm{Sm}_{1-x}\mathrm{La}_x\mathrm{S}$ crystals show an expansion upon cooling.[7] The unusual properties of these materials are associated with the presence of a highly correlated atomiclike six-electron configuration as the highest occupied electronic state.[1,4,5,8] The metal-to-semiconductor transition occurs when it becomes energetically favorable to delocalize one of these electrons[1,4,6] (i.e., the "valence" of the Sm ion changes).

We report photoemission energy-level measurements for semiconducting SmS and SmSe as well as for metallic $\mathrm{Sm}_{0.5}\mathrm{Y}_{0.5}\mathrm{S}$ (actual composition $\mathrm{Sm}_{0.54}\mathrm{Y}_{0.46}\mathrm{S}$). Both semiconducting SmS and SmSe show a valence-orbital binding-energy edge of ~0.3 eV below the Fermi energy E_F, while $\mathrm{Sm}_{0.5}\mathrm{Y}_{0.5}\mathrm{S}$ is metallic. An analysis of the photoemission binding energies and spectral shapes of the emission from these localized states demonstrates that both semiconducting SmS and metallic $\mathrm{Sm}_{0.5}\mathrm{Y}_{0.5}\mathrm{S}$ are in a "mixed-valence" state even at atmospheric pressure.

Photoemission energy distributions were taken with a previously described system[9] using synchrotron radiation from the 2.5-GeV storage ring at the Cambridge Electron Accelerator. Oriented (100) single-crystal specimens of 2 mm × 2 mm cross section were cleaved and measured *in situ* at about 2×10^{-10} Torr.

In a previous paper[8] we studied the valence electronic states of *s*, *p*, *d*, and *f* character as seen in photoelectron-energy-distribution curves. We identified the uppermost energy levels (for semiconducting SmS) at binding energies ~0.3 to 2.7 eV below E_F as being of primarily $4f$ character. These levels lie in the gap between the sulfur $3p$-derived valence bands (extending from ~3.4 to 7.5 eV below E_F) and the empty conduction bands.[8]

In this paper we concentrate upon the emission features associated with these localized states. The observed spectral shape of the emission from these localized electrons near E_F is complicated by the existence of final-state multiplet structures. As we shall describe, these structures can be used to identify the electronic configuration of the ground state. We need first to understand the expected spectral shape (i.e., final-state multiplet structure) for the limit of pure divalent Sm (six "*f*" electrons in the $^7F_0$ conguration). A fractional-parentage method for eating these atomiclike localized excitations inolving f-electron configurations has been develped by Racah.[10] Applying this technique to the $f^6(^7F_0)$ configuration, we expand the six-elecron wave function in terms of products of five-lectron and one-electron wave functions.[10] Using tabulated coefficients of fractional parentage,[11] one may prove that only six five-electron wave functions are contained in this expansion. These states are $^6H_{5/2}$, $^6H_{7/2}$, $^6F_{5/2}$, $^6F_{7/2}$, $^6P_{5/2}$, and $^6P_{7/2}$.

For photoionization and optical excitations, we are interested in dipole matrix elements. The dipole operator is a one-electron operator, so the remaining five electrons are constrained to the above-mentioned six states. As these six states have different energies,[12] and energy is conserved, the kinetic energy of the excited electron (in photoemission) will reflect these differences. The dipole matrix element may readily be calculated in terms of this fractional-parentage expansion[10] if we know the final excited single-electron state. We have treated this state as a free electron in our calculations of photoemission line shape for the $^7F_0$ state, which is summarized in Fig. 1(a). The vertical lines in Fig. 1 have heights proportional to the square of the dipole matrix element, are separated by the energy spacings reported for atomic Sm^{3+},[12] and are placed to line up with the observed peaks.

As shown in Fig. 1(a), four multiplet lines contribute to the photoemission-spectroscopy structure within ~2 eV of E_F, while two other lines (not shown) are ~3 eV below E_F and hence are obscured by valence-band emission. We compare the four uppermost multiplet lines (Gaussian broadened) with experimental results at $h\nu = 30$ eV for SmSe, SmS, and $Sm_{0.5}Y_{0.5}S$. We note good agreement in spectral shape for SmSe (and for SmTe, not shown but similar to SmSe), and conclude that, in these materials, Sm is essentially divalent.

However, the spectrum for SmS is ~0.3 eV broader than that of SmSe and contains an extra shoulder on its leading edge [Fig. 1(b)]. For photon energies in the range $10 \leq h\nu \leq 40$ eV, as well as at 1500 eV,[13] the strength of this shoulder relative to the rest of the "localized emission" decreases as the photon energy increases, implying a lower-angular-momentum character and/or less localization (in fact, at $h\nu \sim 1500$ eV we find that this shoulder is imperceptible, a result which has recently been reported by Campagna, Wertheim, and Bucher[13]). We interpret this extra shoulder near E_F as indicating a significant admixture of a localized $f_\ell^5 d$ character[14] in the ground state of Sm in semiconducting SmS, as is shown schematically in Fig. 1(b). Furthermore, as shown in Fig. 1(c), upon substituting Y for Sm (effectively removing "f" electrons and adding "d" electrons) a metallic phase is formed,[7] the shoulder increases in strength, and the entire localized emission shifts toward E_F. Note that there is still significant emission due to f^6 levels and the energy difference E_R between the "f^6" peak and the "f^5d" peak is, within experimental error, the same as for SmS. Relaxation processes reflecting the different screening of "f^6" and "$f_\ell^5 d$" are responsible for E_R. The shoulder on the leading edge of our photoemission data occurs

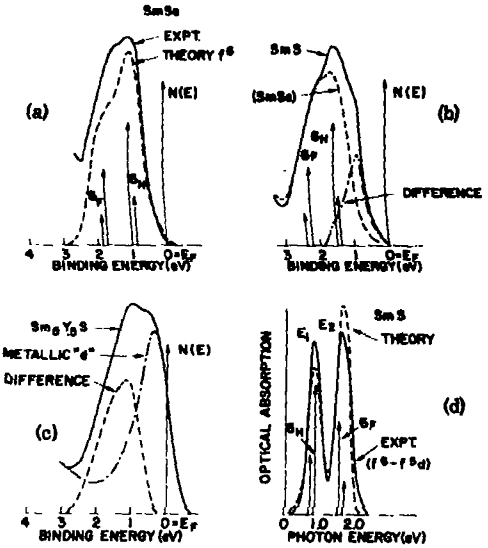

FIG. 1. (a) Photoemission energy distribution (PED) for SmSe (solid curve) and Gaussian-broadened theoretical $f^6 \rightarrow f^5$ multiplet intensity spectrum (dashed curve). Photon energies are $h\nu = 30$ eV and experimental resolutions are 0.35, 0.4, and 0.4 eV for (a), (b), and (c), respectively. (b) PED for SmS (solid curve). The total spectrum has been decomposed into an f^6 spectrum (dashed curve is that of SmSe) and an f^5d spectrum (dash-dotted curve is difference curve between solid and dashed curves. (c) PED of $Sm_{0.5}Y_{0.5}S$ (solid curve). Dash-dotted curve is estimated d-band contribution (shape that was observed in YS) to total emission. Dashed curve is difference curve between total emission and d-band curves. (d) Solid curve is measured optical absorption of SmS (Ref. 3). Dashed curve is Gaussian-broadened calculated $\omega\epsilon_2$ (see text).

because the f_d^5 final state is more relaxed (by E_R) than are any f_f^5 final states.[14]

The ratio of the integrated intensity of this "d-derived" structure relative to that of the sulfur-derived valence "p" bands (ratio ~0.07 at $h\nu = 30$ eV) is about 30% that of corresponding "d"/"p" ratios for NdS (0.21), GdS (0.18), DyS (0.17), and ErS (0.22) at $h\nu = 30$ eV, all of which are metallic with one "d-like" conduction electron.[8] This comparison implies that there might be as much as 30% d admixture in the ground state of semiconducting SmS. This value is an upper limit since we believe the d-electron wave function in SmS to be more localized than for metallic trivalent rare-earth sulfides, which would enhance its emission intensity at this photon energy. Based on (1) the above comparison, (2) lattice-constant measurements,[7] and (3) x-ray photoemission spectroscopy measurements,[13] we estimate ~(15 ± 5)% d admixture in SmS.[15]

This "f_d^5d" admixture implies that the ground state of semiconducting SmS has a "mixed valence". We attribute the origin of this mixed valence to a ground-state Coulombic configuration interaction V between the two six-electron wave functions $f^6(^7F_0)$ and "f_d^55d". Since the Coulomb interaction commutes with space inversion,[16] it cannot mix f and d electrons from the same site and therefore it is intrinsically a nearest-neighbor-samarium effect and strongly dependent upon lattice constant.

Additional information on these localized states is given by an analysis of their optical-absorption spectrum (again using a fractional-parentage method). In low-energy optical absorption, the excited electron state is t_{2g}.[3] The relevant parameter for comparison with experiment is the oscillator strength, which is proportional to the square of the dipole matrix element times $h\nu$ (the energy associated with this transition).

In Fig. 1(d) we show a Gaussian-broadened curve of our calculated optical spectrum and a previously reported[3] experimental absorption curve for $f^6 - f^5t_{2g}$ excitations for SmS. The agreement in spectral shape (spacing) is excellent. The relative magnitudes of the two peaks agree to ~±10%, quite satisfactory since the theoretical curve assumes a constant index of refraction n and neglects the band character of the t_{2g} final state. It is interesting to note that the admixture of f^5d character is not observed in low-energy optical absorption, i.e., the spectra for SmS, SmSe, and SmTe are similar. This occurs because the lowest conduction band is the d-derived t_{2g}, and d-to-d transitions are forbidden.

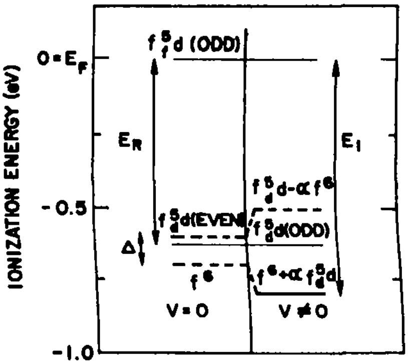

FIG. 2. Schematic diagram of our proposed energy-level scheme for SmS. All energy levels are peak positions of six-electron eigenstates.

Combining the results of photoemission and optical-absorption measurements, we present a schematic diagram of our proposed energy-level model for SmS in Fig. 2. The lines on the right-hand side of the figure represent the ionization energies of the existing six-electron states of the system (peak positions). The 0.8-eV gap follows from the optical data,[3] and the position of the Fermi level is derived from our photoemission data. To the left we reconstruct states that would exist without the interatomic Coulomb interaction V; the second lowest state is the f_d^5d, which lies $E_R \sim 0.65$ eV (the relaxation energy observed in our photoemission spectra) below the optical final state f_f^5d. Note that this state must have odd parity to be the final state of an optical transition. However, the parity operator commutes with the Hamiltonian at only a few points of the Brillouin zone (e.g., Γ, X), and therefore there are even components of this state at similar energies (slightly higher if the optical transition is at X [3]). Perturbation theory then implies that $0.85 - 0.65 = 0.2$ eV $\cong \Delta + V$, where Δ is the energy difference between the unperturbed f_d^5d (even) and f^6, and V is the interatomic configuration interaction between these two levels. The amount of admixture (~15%) implies that $\Delta \sim 0.14$ eV and $V \sim 0.07$ eV, a reasonable magnitude for this interaction.[17]

From photoemission and optical data alone, one may not distinguish between a mixed-configuration ground state and a pure $f^6(^7F_0)$ ground state (i.e., negligible configuration interaction V) with a thermally populated f_d^55d excited state. However for the latter model, the amount of admixed d character (at room temperature) would imply that the $f_d^5 5d$ is within ~40 meV of the ground state. It appears unreasonable to assume a configuration interaction V such that $V \ll 40$ meV, as would be necessary to get a pure configuration with only thermal population. To test this conclusion, we have measured the dependence of the lattice constant of semiconducting SmS for $85 < T < 300$°K. Our results indicate that the lattice constant continuously decreases upon cooling from 300 to 85°K by ~0.013 Å. This change is much smaller than and of opposite sign to the ~0.05-Å increase expected from a thermal-population model, thus supporting our mixed-configuration model.

To summarize, we have established that semiconducting SmS is a "mixed-valence" material. This implies that the semiconductor-to-metal phase transition of SmS is between two states of nonintegral valence. We have also noted (Fig. 1) that the metallic mixed crystal $Sm_{0.5}Y_{0.5}S$, in which the lattice constant and resistivity ascribe a primarily trivalent character to the samarium ions, is also a "mixed-valence" material with appreciable admixed f^6 character. Finally, we have proposed an electron-energy model for SmS with an interaction of sufficient magnitude to explain this effect.

We gratefully acknowledge the contributions of M. Erbudak, M. Freiser, W. Paul, and the entire staff of the Cambridge Electron Accelerator.

---

*Work supported in part by U. S. Air Force Office of Scientific Research Grant No. F44620-70-C-0089, National Science Foundation Grant No. GH-35823, and U. S. Atomic Energy Commission Grant No. AT(11-1) 3063.

[1] E. Kaldis and P. Wachter, Solid State Commun. 11, 907 (1972).

[2] R. Suryanarayanan and C. Paparoditis, J. Appl. Phys. 43, 4105 (1972).

[3] F. Holtzberg and J. B. Torrance, in *Magnetism and Magnetic Materials—1971*, AIP Conference Proceedings No. 5, edited by C. D. Graham, Jr., and J. J. Rhyne (American Institute of Physics, New York, 1971), pp. 860–865.

[4] A. Jayaraman, V. Narayanamurti, E. Bucher, and R. G. Maines, Phys. Rev. Lett. 25, 1430 (1970).

[5] M. B. Maple and D. Wohlleben, Phys. Rev. Lett. 27, 511 (1971).

[6] A. Jayaraman, E. Bucher, P. D. Dernier, and L. D. Longinotti, Phys. Rev. Lett. 31, 700 (1973).

[7] F. Holtzberg, in *Magnetism and Magnetic Materials—1973*, AIP Conference Proceedings No. 18, edited by C. D. Graham, Jr., and J. J. Rhyne (American Institute of Physics, New York, 1974).

[8] D. E. Eastman *et al.*, in *Magnetism and Magnetic Materials—1973*, AIP Conference Proceedings No. 18, edited by C. D. Graham, Jr., and J. J. Rhyne (American Institute of Physics, New York, 1974).

[9] D. E. Eastman, J. Freeouf, and M. Erbudak, J. Phys. (Paris) 34, 6 (1973).

[10] G. Racah, Phys. Rev. 76, 1352 (1949).

[11] C. W. Nielson and George F. Koster, *Spectroscopic Coefficients for the p^n, d^n, and f^n Configurations* (MIT Press, Cambridge, Mass., 1963); P. A. Cox, Y. Baer, and C. K. Jorgensen, Chem. Phys. Lett. 22, 433 (1973).

[12] G. H. Dieke and H. M. Crosswhite, Appl. Opt. 2, 675 (1963).

[13] M. Campagna, G. K. Wertheim, and E. Bucher, Bull. Amer. Phys. Soc. 19, 234 (1974).

[14] "f_d^5" refers to the five-f-electron wave function in the presence of a sixth, "d" electron, whereas "f_f^5" refers to the five-f-electron wave function in the presence of a sixth "f" electron.

[15] The presence of Sm^{3+} implies additional emission features due to f_d^4 final states lying from 7.5 to 11 eV below E_F. These weak lines are not unambiguously seen in our spectra because they are obscured by valence-band and secondary-electron emission.

[16] R. Jullien and B. Coqblin, Phys. Rev. B 8, 5263 (1973).

[17] T. Kasuya, IBM J. Res. Develop. 14, 214 (1970).

Valence Mixing and Semiconductor-Metal Transition in the Sm Monochalcogenides

M. Campagna, E. Bucher, G. K. Wertheim, and L. D. Longinotti
Bell Laboratories, Murray Hill, New Jersey 07974

(Received 18 April 1974)

Sm ions in "chemically collapsed" phases of SmS, e.g., $Sm_{0.85}Th_{0.15}S$ and $Sm_{0.82}Gd_{0.18}S$, are found to be in the state of interconfiguration fluctuations. In contrast, valence fluctuations in pure SmS are shown to be not larger than 3%. Conduction-electron screening does not drastically affect either the location or the effective intra-atomic Coulomb interaction U_{eff} of $4f$ levels in photoemission spectra.

In this Letter we present x-ray photoemission spectra (XPS) of the Sm monochalcogenides, which all exhibit semiconductor-to-metal transitions under pressure, of SmSb, and of "collapsed" phases of SmS. From these data we conclude that the degree of configuration mixing in pure SmS at atmospheric pressure and room temperature is less than 3%. In contrast, $Sm_{0.85}Th_{0.15}S$ and $Sm_{0.82}Gd_{0.18}S$ show unambiguously the coexistence of divalent and trivalent Sm ions, as is demonstrated both by the observed $4f$-multiplet structures and chemical shifts of core levels. The data give strong evidence for the existence of a unique mechanism underlying the semiconductor-metal transition in the Sm monochalcogenides and exclude the possibility of a valence-conduction band-gap closing as origin for the transition in SmSe and SmTe.[1]

Electronic semiconductor-to-metal phase transitions without any structural changes have been reported for divalent rare earth (RE) compounds.[2] The transition is thought to involve the delocalization of a $4f$ electron to the $5d, 6s$ conduction-band states with the consequent valence change of the RE ion. The peculiar magnetic properties of the collapsed phase of SmS (magnetic susceptibility intermediate between those of $4f^6$ and $4f^5$ configurations and absence of magnetic ordering down to 1°K) lead Maple and Wohlleben[3] to the conclusion that SmS above 6 kbar, like SmB_6 at atmospheric pressure, could be described by a system of ions showing the phenomenon of interconfiguration fluctuations (ICF) first described by Hirst.[4] The characteristic feature of a system in the state of ICF is that it contains ions fluctuating between divalent and trivalent states, with $4f$ shells emitting and absorbing "conduction electrons."[3,5,6]

Single crystals of semiconducting SmS, SmSe, SmTe, and metallic SmSb, $Sm_{0.85}Th_{0.15}S$, and $Sm_{0.82}Gd_{0.18}S$ with ~20-mm^2 area were prepared for this XPS study as described in Ref. 6. A Hewlett-Packard 5950-A spectrometer was used.

In Fig. 1 we show the valence-band and $4f$-multiplet structure of semiconducting divalent Sm monochalcogenides and of metallic trivalent SmSb in the binding energy range 0–9 eV. A smooth background has been subtracted from the data for SmSe, SmTe, and SmSb. In each case the structure corresponds to the final-state multiplets of the photoionized $4f^n$ shell; thus the $^7F_0$ initial state of Sm^{2+} $4f^6$ produces the ^6H, ^6F, and ^6P states of $4f^5$ whose separations are known from the optical spectroscopy of Sm^{3+}.[7,8] The location of this sextet structure relative to E_F was adjusted for optimum fit to the data. The expected intensities of the $4f$-multiplet structure have been discussed recently by Cox, Baer, and Jørgensen[9] within the approximation of a Russell-Saunders coupling scheme. In the case of SmSb we have plotted the term separation labeled by a and b, increased by about 10%, in order to take into account the fact that the final state produced by photoexcitation of Sm^{3+} has an ionic charge larger by 1 than the corresponding isoelectronic Pm^{3+} ion. We conclude from Fig. 1 that the overall agreement between theory and experiment is quite good and that for SmSb and SmTe the initial configurations of the Sm ions are strictly $4f^5$ and $4f^6$, respectively. We assign the structure observed in the region 0–5 eV in SmSb and between 3 and 6 eV in SmTe to the largely anion-derived valence bands and the bump near 8 eV, present in each case of chalcogenides, to an energy loss.[10]

We now examine the data for SmSe and SmS in Fig. 1, especially in order to establish an upper bound for the ratio of configuration mixing $r = f^6/f^5d^1$. The absence of the strong ^5I peak expected at a binding energy ~6 eV is the first evidence against a relevant admixture of the f^5d^1 configuration in the ground state of SmS. From the data in Fig. 1 we estimate r to be less than 3%, i.e., much smaller than has been proposed.[11] This ences cited therein.

[3] M. B. Maple and D. K. Wohlleben, Phys. Rev. Lett. 27, 511 (1971).

[4] L. L. Hirst, Phys. Kondens. Mater. 11, 255 (1970), and to be published.

[5] X-ray absorption studies by E. E. Vainshtein, S. M. Blokhin, and Yu. B. Paderno, Fiz. Tverd. Tela 6, 2909 (1964) [Sov. Phys. Solid State 6, 2318 (1965)], showed the coexistence of divalent and trivalent Sm ions in SmB_6. In analogy to the conclusion reached by W. Klemm and H. Bommer, Z. Anorg. Allg. Chem. 231, 138 (1937), in their magnetochemical investigation on Sm metal, Vainshtein, Blokhin, and Paderno interpret the x-ray absorption data as evidence for a static spatial distribution of ambivalent Sm ions in SmB_6.

[6] M. Campagna, E. Bucher, G. K. Wertheim, D. N. E. Buchanan, and L. D. Longinotti, Phys. Rev. Lett. 32, 885 (1974).

[7] G. H. Dieke and H. M. Crosswhite, Appl. Opt. 2, 675 (1963).

[8] W. T. Carnall, P. R. Fields, and K. Rajnak, J. Chem. Phys. 49, 4412 (1968).

[9] P. A. Cox, Y. Baer, and C. K. Jørgensen, Chem. Phys. Lett. 22, 433 (1973).

[10] The relation between these parts of the spectra and band-structure calculations for cubic RE compounds, form, and binding energies of core levels, will be discussed in a more extended publication.

[11] J. L. Freeouf, D. E. Eastman, W. D. Grobman, F. Holzberg, and J. B. Torrance, Bull. Amer. Phys. Soc. 19, 233 (1974), and private communication, and Phys. Rev. Lett. 33, 161 (1974) (this issue).

[12] J. F. Herbst, D. N. Lowy, and R. E. Watson, Phys. Rev. B 6, 1913 (1973).

Atomic Ordering and Superconductivity in High-T_c A-15 Compounds*

A. R. Sweedler and D. G. Schweitzer
Brookhaven National Laboratory, Upton, New York 11973

and

G. W. Webb†
David Sarnoff Research Center, RCA, Princeton, New Jersey 08540

(Received 15 April 1974)

Large, reversible changes in the superconducting transition temperature T_c of the Nb-based A-15 compounds Nb_3Al, Nb_3Sn, Nb_3Ga, $Nb_3(Al, Ge)$, and Nb_3Ge are observed when irradiated with high-energy ($E > 1$ MeV) neutrons at 60°C. The transition widths of the irradiated samples are of the same order as the unirradiated samples and the original T_c's are recovered by annealing. The results are discussed in terms of atomic ordering in the A-15 structure.

The effect of high-energy ($E > 1$ MeV) neutron irradiations on the superconducting transition temperature T_c of several A-15 (β-W) compounds was first reported by Swartz, Hart, and Fleischer[1] who observed small depressions, 0.10–0.22°K, for several A-15 compounds when irradiated to a fluence of 1.5×10^{18} neutrons/cm^2. Cooper[2] also observed a slight reduction, 0.16–0.20°K, in T_c for Nb_3Sn for a fluence of 2.7×10^{18} neutrons/cm^2. Recently, Bett[3] has observed large depressions, 1–13°K, of T_c for commercially prepared Nb_3Sn tapes for fluences up to 5×10^{19} neutrons/cm^2. We report here the effect of high-energy ($E > 1$ MeV) neutrons on T_c for the Nb-based A-15 compounds Nb_3Al, Nb_3Sn, Nb_3Ga, Nb_3Ge, and $Nb_3(Al, Ge)$. We observe large depressions, up to 17°K, of T_c for a fluence of 5.0×10^{19} neutrons/cm^2. The transition widths of the irradiated samples are of the same order as the unirradiated samples, and the effect is reversible in that T_c is restored to its unirradiated value by annealing. To the best of our knowledge, these are the largest depressions of T_c reported for the high-T_c A-15 compounds. The results are discussed in terms of atomic ordering in the A-15 structure and a model is developed which relates T_c to the long-range order parameter S.

The samples were prepared in a variety of ways. The preparation of Nb_3Ga,[4] Nb_3Sn,[5,6] and $Nb_3(Al, Ge)$[6] have previously been described. The compositions of the A-15 phase of Nb_3Sn, Nb_3Ga, Nb_3Al, and Nb_3Ge were 75.0, 75.0, 75.5, and 81 at.% Nb, respectively, as deduced from their measured lattice parameters.[4,5,7-9] Details of sample preparation will be presented in a later publication. The irradiations were carried out in the Brookhaven National Laboratory high flux beam reactor (HFBR) where the samples

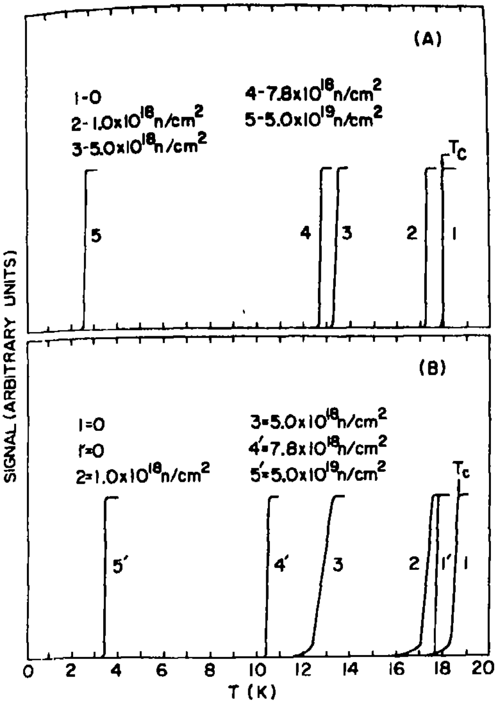

FIG. 1. Superconducting transition curves of (a) Nb_3Sn and (b) Nb_3Al for different fluence values. 90% of the measured transitions are shown. Primed numbers refer to unannealed sample.

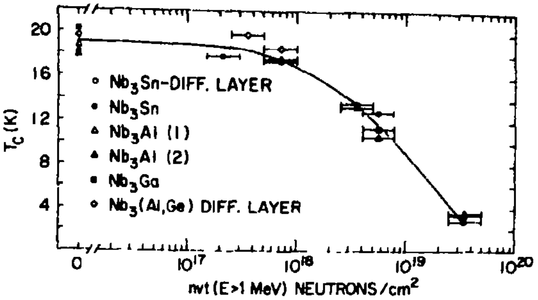

FIG. 2. Superconducting transition temperature T_c against fluence, nvt ($E > 1$ MeV). Curve is drawn as a visual aide. Fluence values quoted in text and Fig. 1 are the highest values shown in the above figure.

were exposed to the whole spectrum of the reactor.[10] In the following only the fast flux ($E > 1$ MeV) will be considered. The calculated temperature of the samples during irradiation was 60 ±5°C. Superconductivity was detected by a standard mutual-inductance technique operating at 37 Hz, the temperature being determined by a calibrated carbon or Ge thermometer.

The results for Nb_3Sn and Nb_3Al are presented in Fig. 1 where the transitions for different fluence values are shown. It is seen that as T_c is progressively depressed, the transition widths remain constant. In Fig. 2, we have plotted T_c against fluence for all the systems studied. The T_c's are the highest value measured for the particular sample and the error bars for the fluence represent the uncertainty in the flux. It is seen that below a fluence of 1.0×10^{18} neutrons/cm^2, the depression of T_c is quite small, 3.9, 4.9, and 5.8% of the unirradiated value for Nb_3Sn, Nb_3Al, and $Nb_3(Al,Ge)$, respectively. Above 1.0×10^{18} neutrons/cm^2, T_c is rapidly depressed and for a fluence of 5.0×10^{19} neutrons/cm^2, the highest used in these experiments, T_c is reduced by 84.5, 80.8, and 83.3% for Nb_3Sn, Nb_3Al, and Nb_3Ga, respectively. This apparent threshold at $\sim 1.0 \times 10^{18}$ neutrons/cm^2 is explained below. The T_c of arc cast Nb_3Ge was reduced from 6.5 to 4.9°K for a fluence of 7.8×10^{18} neutrons/cm^2, a 24.6% reduction. No evidence of saturation in the depression of T_c is observed, to the highest fluence used, 5.0×10^{19} neutrons/cm^2.

The width of the superconducting transition, ΔT_c, defined as the temperature range over which 90%[11] of the sample is superconducting, was the same for the irradiated and unirradiated samples, ~0.2–2°K. This strongly suggests that neutrons uniformly disorder the samples throughout their entire volume. We have been able to recover the unirradiated value of T_c for Nb_3Sn, Nb_3Ga, and Nb_3Ge by annealing at 750°C. Thus, after a 0.5-h anneal, Nb_3Sn that had been irradiated to 5.0×10^{19} neutrons/cm^2 increased its T_c from 2.8 to 14.3°K. A 5-h anneal yielded a T_c of 18.0°K and a 20.5-h anneal restored T_c to 18.1°K. For Nb_3Ga, irradiated to the same fluence, a 5-min anneal increased T_c from 3.4 to 11.4°K and after 20 min T_c was 19.5°K.[12] Nb_3Ge, irradiated to 7.8×10^{18} neutrons/cm^2, increased its T_c from 4.9 to 6.5°K after a 2-h anneal at 750°C The upper critical field, $H_{c2}(T)$, was also measured for samples irradiated to 5.0×10^{19} neutrons/cm^2 in a manner previously described.[13] $H_{c2}(T)$ was 200 ± 100 G at 2.3°K, 4700 ± 50 G at 1.64°K, and 7700 ± 50 G at 1.49°K for Nb_3Sn, Nb_3Al and Nb_3Ga, respectively. For purposes of comparison H_{c2} at 4.2°K for unirradiated Nb_3Sn, Nb_3Al, and Nb_3Ga is 235, 295, and 340 kG, respectively.[14,15]

There are at least three effects of neutron irradiation: (1) interchange of atoms between sites, (2) creation of interstitial-vacancy pairs, and (3) creation of new elements.[16] The creation of new elements is not important here, as T_c is recovered by annealing and the levels of any new elements would be in the ppm range. As the temperature for migration of interstitials is considerably less than the temperature of the irradiation, 60°C, there should be no free interstitials. The remaining vacancies are estimated to be $<1\%$ of the atom replaced.[17] Moreover, the effect of neutron irradiation on the T_c of those superconducting elements and compounds that are not sensitive to atomic order is small.[18]

Thus, in this case, the principal result of neutron irradiation is the exchange of atoms between sites. We can describe the positions of the atoms in the unit cell by the Bragg-Williams long-range-order parameter $S = (P-r)/(1-r)$, where $0 \leqslant S \leqslant 1$, P is the probability of an A site being occupied by an A atom, and r is the fraction of A atoms in the binary alloy. Aronin[19] derived a relationship between S and the fluence n, which he has successfully used to describe results of neutron-induced order-disorder transformations in Ni_3Mn and Cu_3Au. His expression is $S = S_0 e^{-kn}$, where S_0 is the value of S before irradiation, n the fluence, and k is a proportionality constant. Aronin assumed k to be the same for both A and B atoms, a procedure criticized by Damask,[20] but we feel that is justified in the case of Nb_3Sn as the elastic cross section for neutrons, σ, for Nb and Sn at 1 MeV are equal and the masses are not too dissimilar. If a value of k could be obtained, it would be possible to relate S to T_c via the fluence n.

Aronin also noted that the number of atoms exchanged dQ per primary knock-on dc in a fast flux dn is given by k/σ. We have used the model of Kinchin and Pease[16,21] to calculate dQ/dc, and hence k, for the case of Nb_3Sn. The model neglects all irradiation effects except replacement collisions and, as the masses of Nb and Sn are relatively heavy, we assume both atoms lose energy to the lattice by atomic collisions and neglect any energy loss due to ionization effects. Assuming a monoenergetic beam of 1-MeV neutrons we obtain a value of 1501 ± 450 atoms replaced per primary knock-on, the error, indi ing the accuracy of the calculation, being abou 30%.[22] The value of σ for Nb and Sn is 6.1×10^{-24} cm^2,[23] yielding a value of $k = (0.9 \pm 0.3) \times 10^{-20}$ cm^2/neutron. We can now compare T_c directly with S through the fluence n. The results are shown in Fig. 3 where we have plotted the reduced transition temperature, T_c/T_{c0}, against the reduced order parameter, S/S_0. We find that T_c depends exponentially on S and is given by $T_c = T_{c0} \exp[-\alpha \times (1 - S/S_0)]$, where $\alpha = 5.0 \pm 1.5$, $T_{c0} = 18.1$°K, and we have used $S_0 = 1$, complete order, at $T_c = T_{c0}$. The exponential dependence of T_c on S, and of S on the fluence n, explains the apparent threshold in the depression of T_c at $n \sim 1.0 \times 10^{18}$ neutrons/cm^2. At this fluence S has changed by only 1% and T_c by 5.5%. However, by a fluence of 5×10^{18} S has changed by 4.5% and T_c by 20%, and for $n = 5 \times 10^{19}$, S has changed by 37% and T_c by 85%, in good agreement with the observed T_c's.

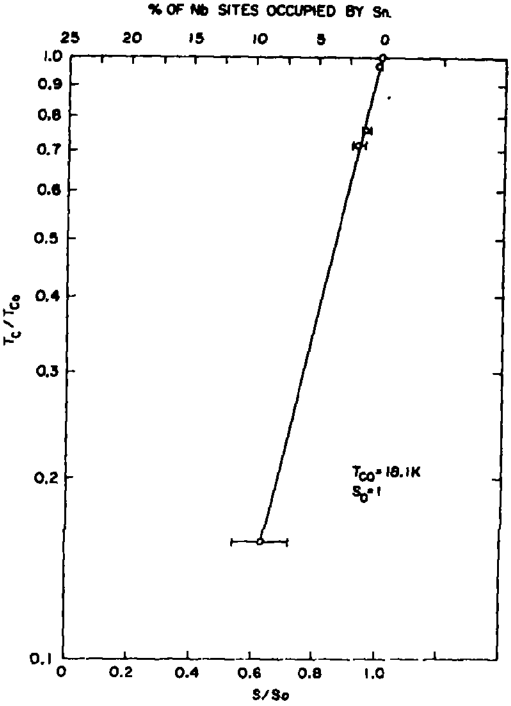

FIG. 3. Reduced transition temperature, T_c/T_{c0}, against reduced long-range-order parameter, S/S_0, for neutron irradiated Nb_3Sn. Also shown is the percentage of Nb sites occupied by Sn.

Depressions of T_c for sintered and chemically-vapor-deposited Nb_3Sn have previously been observed.[24-27] These authors could not unambiguously ascribe the changes in T_c as due to disorde since the composition of the samples had to be varied in order to vary T_c. In our experiment, however, the depression of T_c is clearly due to disorder as the composition of the alloy is unaffected by irradiation and T_c is recovered by annealing. Splat-cooled Nb_3Sn displays a broad superconducting transition from 16.7 to 4°K indicating an inhomogenous disordering process due to the nonuniform cooling rate.[28] The measured average long-range-order parameter of 0.2 ± 0.15 in that case and our deduced values are not in good agreement, a fact which we hope to resolve by measuring the order parameters for our samples.

It is not possible to determine whether A- or B-site disorder is more important in the depression of T_c from an experiment of the type described here. However, available models[29-31] used to describe the properties of A-15 compounds have invoked the concept of "A chain integrity," i.e., A sites occupied by A atoms, as being important in determining the properties of these materials. Assuming this to be the case we can relate the depression of T_c to the replacement of Nb (A) atoms by Sn (B) atoms in Nb_3Sn. In Fig. 3 the percentage of Nb sites occupied by Sn for stoichiometric Nb_3Sn is also shown. At $T_c = T_{c0}$ a replacement of 1% Nb by Sn results in a T_c depression of 3.3°K and, when 9% of the Nb has been replaced by Sn, T_c has fallen to 2.8°K.

The results reported here indicate that high-energy neutron irradiation of superconductors can be a useful technique in the study of order-disorder effects, especially in the case where homogeneous disorder is difficult or impossible to induce by conventional means. Experiments are underway to measure S directly by x-ray and neutron diffraction techniques in the irradiated samples and to see the effect of disorder on the martensitic phase transition.

The authors would like to thank R. Jones for expert experimental assistance. We also wish to thank D. Parkin, G. Dienes, D. Welsch, and L. J. Vieland for helpful and informative discussions.

---

*Work performed under the auspices of the U. S. Atomic Energy Commission.

†Work supported in part by the U. S. Air Force Office of Scientific Research, Contract No. F44620-72-C-0042.

[1] P. S. Swartz, H. R. Hart, and R. L. Fleischer, Appl. Phys. Lett. 4, 71 (1964).

[2] J. L. Cooper, RCA Rev. 25, 405 (1964).

[3] R. Bett, unpublished.

[4] G. W. Webb, L. J. Vieland, R. E. Miller, and A. Wicklund, Solid State Commun. 9, 1769 (1971).

[5] J. J. Hanak, K. Strater, and G. W. Culler, RCA Rev. 25, 342 (1964).

[6] H. Bauer, Ph.D. thesis, University of Geissen, West Germany, 1972 (unpublished).

[7] C. E. Lundin and A. S. Yamamoto, Trans. AIME 236, 863 (1966).

[8] A. Muller, Z. Naturforsch. 25a, 1659 (1970).

[9] J. H. Carpenter, J. Phys. Chem. 67, 2141 (1963).

[10] Brookhaven National Laboratory Report No. 7661, 1964 (unpublished).

[11] For Nb_3Ga, 50% of the transition widths were used since the unirradiated sample had a tail extending to 15.9°K.

[12] This recovery is a necessary though not sufficient condition for the high-T_c stoichiometric composition Nb_3Ga to be a stable phase in the equilibrium phase diagram [G. W. Webb, *Superconductivity in d- and f-Band Metals*, AIP Conference Proceedings No. 4, edited by D. H. Douglass (American Institute of Physics, New York, 1972), p. 139].

[13] D. G. Schweitzer, M. Garber, and B. Bertman, Phys. Rev. 159, 296 (1967).

[14] S. Foner, E. J. McNiff, Jr., B. T. Matthias, T. H. Geballe, R. H. Willens, and E. Corenzwit, Phys. Lett. 31A, 349 (1970).

[15] S. Foner, E. J. McNiff, Jr., G. W. Webb, L. J. Vieland, R. E. Miller, and A. W. Wicklund, Phys. Lett. 38A, 323 (1972).

[16] G. J. Dienes and G. H. Vineyard, *Radiation Effects in Solids* (Interscience, New York, 1957), Chap. 2.

[17] A. C. Damask and G. J. Dienes, *Point Defects in Metals* (Gordon and Breach, New York, 1963), p. 215.

[18] D. G. Schweitzer and D. M. Parkin, to be published; H. Bauer, E. J. Sauer, and D. G. Schweitzer, in Proceedings of Fifth International Cryogenic Engineering Conference, Kyoto, Japan, 1974 (to be published).

[19] L. R. Aronin, J. Appl. Phys. 25, 344 (1954).

[20] A. C. Damask, in *Studies in Radiation Effects on Solids*, edited by G. J. Dienes (Gordon and Breach, New York, 1967), Vol. 2.

[21] G. H. Kinchin and R. S. Pease, J. Nucl. Energy 1, 200 (1955).

[22] A more recent calculation by G. Duesing and G. Leibfried [Phys. Status Solidi 9, 463 (1965)] on ⟨110⟩ focusing collision chains in fcc crystals indicates that the number of atoms replaced per primary knock-on may be about 20% lower than the calculation used here. Thus the error may be as high as 50%, but the functional relation between T_c and S will not be affected.

[23] Brookhaven National Laboratory Report No. 325, 1966 (unpublished), 2nd ed., 2nd Suppl.

[24] L. J. Vieland, RCA Rev. 25, 366 (1964).

[25] T. B. Reed, H. C. Gatos, W. J. La Fleur, and J. T. Roddy, *Metallurgy of Advanced Materials*, edited by G. Brock (Interscience, New York, 1962), p. 41.

[26] T. H. Courtney, G. W. Pearsall, and J. Wulff, Trans. Met. Soc. AIME 233, 212 (1965).

[27] F. Bachner and H. Gatos, Trans. Met. Soc. AIME 236, 1261 (1966).

[28] B. T. Matthias, T. H. Geballe, R. H. Willens, E. Corenzwit, and G. W. Hull, Jr., Phys. Rev. 139,

A1501 (1965).

[29]M. Weger, Rev. Mod. Phys. 36, 175 (1964).

[30]J. Labbé and J. Friedel, J. Phys. (Paris) 27, 1115 (1966).

[31]R. W. Cohen, G. D. Cody, and J. J. Halloran, Phys. Rev. Lett. 19, 840 (1967).

Magnetic Interference Function of Amorphous Cobalt-Phosphorus Alloys

J. Bletry
Institut Laue-Langevin, 38042 Grenoble Cedex, France

and

J. F. Sadoc
Laboratoire de Physique des Solides, Faculté des Sciences d'Orsay, 91400 Orsay, France

(Received 20 March 1974)

A magnetic interference function has been observed for an amorphous ferromagnetic cobalt-phosphorus alloy by unpolarized-neutron diffraction. The distribution of the magnetic moments of cobalt is analyzed in terms of a partial pair-correlation function. Comparison with x-ray results gives good agreement.

The measurements of Rhyne, Pickart, and Alperin[1] on Tb-Fe alloys showed that the magnetic structure of amorphous alloys can be elucidated in the same way as magnetic structures of crystallized substances by unpolarized-neutron experiments. In such a study one has to make two essential choices: the nature of the alloy and the experimental method. We chose the cobalt-phosphorus system because in this alloy there is only one kind of magnetic atom, namely cobalt. Therefore, one can give an interpretation of the measurements in terms of a single pair-correlation function $G_{\text{Co-Co}}$. As pointed out by Rhyne, Pickart, and Alperin[1] such an interpretation is impossible if both constituents carry moments, as in Tb-Fe alloys, since in that case three pair-correlation functions have to be introduced.

In order to separate the magnetic scattering, one of two experimental methods can be used. Rhyne, Pickart, and Alperin obtained the magnetic contribution by subtracting two scattering patterns, one taken at a temperature above and one below the Curie temperature T_c of the sample. In Co-P alloys, however, complete crystallization has been reported to take place in the sample when heated to about 100°C[2] above T_c, the necessary temperature to obtain a perfectly disordered paramagnetic state. Therefore we chose to extract the magnetic signal by making difference measurements with a magnetic field applied successively parallel and perpendicular to the scattering vector and keeping the sample well below T_c (at room temperature).

Amorphous platelets of Co-P of five different concentrations around the eutectic composition (19 at.%) were prepared by electrodeposition from baths analogous to those described by Brenner, Couch, and Williams.[3] The platelets were 50 mm × 10 mm large and about 0.5 mm thick. Their amorphous structure was carefully checked by x ray.

Neutron experiments were performed on the D2 diffractometer at the Institut Laue-Langevin. The neutron flux on the sample was 3×10^7 neutrons/cm^2 sec with horizontal collimations of 60′ in the pile, 60′ between the monochromator and the sample, and 20′ in front of the counter. The instrumental resolution over the whole κ range, $\Delta\kappa/\kappa$, was better than 5%[4] and no resolution corrections were necessary.

Two wavelengths λ were used: 0.94 Å reflected from a copper monochromator ($\lambda/2$ contamination less than 0.5%), and 1.92 Å reflected from a germanium monochromator ($\lambda/3$ contamination less than 0.8%). This permitted the recording of diffraction patterns between $\kappa_1 = 1$ Å^{-1} and $\kappa_2 = 7$ Å^{-1}, where $\kappa = (4\pi/\lambda)\sin\theta$. Measurements below κ_1 have to be performed on a small-angle-scattering apparatus. Beyond κ_2, measurements are practically impossible since the magnetic signal is roughly proportional to the square of the form factor of crystalline cobalt, which drops down to 1% of its initial value near $\kappa = 7.5$ Å^{-1}.[5]

A magnetic field of 15000 G was used to magnetize the sample up to saturation. During the experiments the sample platelet was oriented so that its normal was always perpendicular to the scattering vector (Fig. 1).

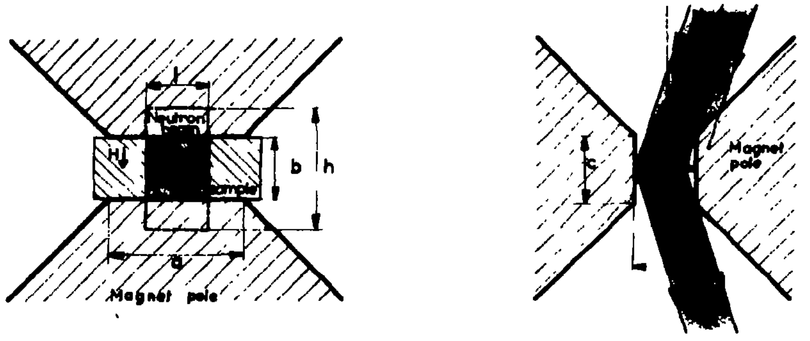

ⓐ Front view. H ⊥ ϰ. ⓑ Top view. H // ϰ.

FIG. 1. Setup of the experiment with the magnetic field $\vec{H}$ (a) perpendicular, (b) parallel to the scattering vector $\vec{\kappa}$.

The observed experimental intensity I_{exp} must be corrected for background, scattering geometry, and absorption before the cross section can be derived. The background intensity I_B measured without the sample was subtracted from the experimental intensity after reduction by the absorption factor. The geometry correction factor arising from the variation of the volume of scattering material in the beam is, in the case of $\vec{H}$ perpendicular to $\vec{\kappa}$,

$$G^{\perp} = 1/\cos\theta,$$

and in the case of $\vec{H}$ parallel to $\vec{\kappa}$,

$$G^{\parallel} = (h/l)[1 - (c/2b)\tan\theta],$$

with h, l, c, and b as defined in Fig. 1. The absorption correction factor in the simple $(\theta, 2\theta)$ arrangement is, for a platelet,

$$A = T^{1/\cos\theta},$$

where T is the transmission factor of the sample. So, finally, the corrected intensity, which in turn is proportional to the cross section, is

$$I^i = (I_{\text{exp}}{}^i - I_B{}^i A)/AG^i, \qquad (1)$$

where the index i stands for parallel or perpendicular (see Fig. 2).

We checked these three corrections with an annealed Co-P platelet geometrically and chemically analogous to our samples. The ratio of the two incoherently scattered intensities $I^{\perp}/I^{\parallel}$ was constant within 2% precision, confirming Eq. (1).

The total cross section is the sum of two contributions, namely, nuclear and magnetic. The nuclear contribution is independent of the magnetization direction. Hence, neglecting inelastic gnetic effects, the difference $I^{\perp} - I^{\parallel}$ is proportional to the elastic magnetic cross section.

If we assume that all the magnetic moments are centered on cobalt atoms, with a spin S, a gyromagnetic ratio g, and a normalized form factor $F(\kappa)$, the coherent magnetic cross section per atom is, in the static approximation,

$$(d\sigma/d\Omega)_{\text{mag}}{}^{\text{coh}} = (r_0\gamma)^2\langle\tfrac{1}{2}gS_z F(\kappa)\rangle^2 \sin^2\alpha\, \mathcal{J}_{\text{Co-Co}}, \qquad (2)$$

where $r_0 = 2.8\times10^{-13}$ cm is the classical electron radius, $\gamma = -1.91$ is the neutron gyromagnetic ratio, $\langle\tfrac{1}{2}gS_z F(\kappa)\rangle$ is the mean value of $\tfrac{1}{2}gS_z F(\kappa)$, and α is the angle between the magnetization direction z and the scattering vector. The partial interference function for cobalt atoms can be ex-

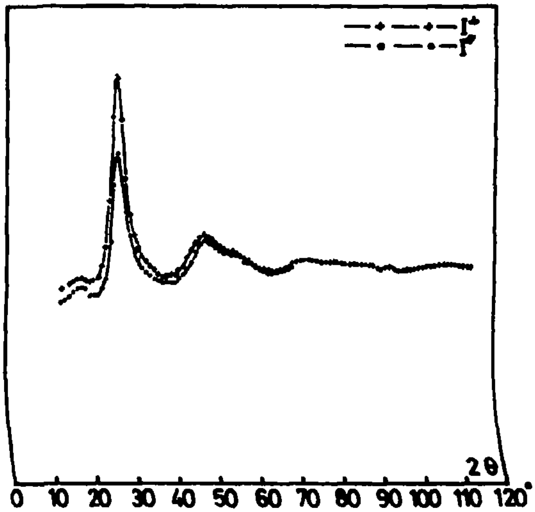

FIG. 2. Corrected intensities $I^{\perp}$ and $I^{\parallel}$ versus 2θ.

pressed as

$$\mathcal{J}_{\text{Co-Co}}(\kappa)=C_{\text{Co}}+C_{\text{Co}}^{2}(4\pi/v)\kappa^{-1}\int_0^\infty r[P_{\text{Co-Co}}(r)-1]\sin(\kappa r)\,dr, \tag{3}$$

where C_{Co} is the cobalt atomic concentration. v is the mean atomic volume in the alloy, and $P_{\text{Co-Co}}(r)$ is the probability per unit volume of finding a cobalt atom at a distance r from another cobalt atom, normalized in such a way that $P_{\text{Co-Co}}(r)$ goes to unity for large r.[6]

Local variations in the cobalt neighborhood would give rise to magnetic-moment fluctuations. The magnetic moment may fluctuate in "magnitude" or in "direction" and it is impossible to separate these two kinds of fluctuations by unpolarized-neutron measurements. However, polarized-neutron experiments[7] have shown that fluctuations of the magnetic-moment direction are negligible. The remaining fluctuations in magnitude are very analogous to critical magnetic fluctuations in a ferromagnetic crystal. The difference is that magnetic fluctuations in an amorphous ferromagnet well below its Curie temperature should appear almost static to the incident neutrons since they are mainly due to static fluctuations in the cobalt neighborhood and not to thermal fluctuations as in critical phenomena. Thus, these fluctuations can be fairly well treated in a quasistatic or quasielastic approximation.[8] Within this approximation the incoherent magnetic cross section per atom for $\kappa=0$ is directly proportional to the mean square fluctuation of the magnetic moment:

$$(d\sigma/d\Omega)_{\text{mag}}^{\text{inc}}(\kappa=0)=(r_0\gamma)^2\sin^2\alpha\, C_{\text{Co}}^{2}\langle(\tfrac{1}{2}gS_z-\langle\tfrac{1}{2}gS_z\rangle)^2\rangle=A\sin^2\alpha, \tag{4}$$

and with increasing κ it decreases roughly like

$$(d\sigma/d\Omega)_{\text{mag}}^{\text{inc}}(\kappa)=A\sin^2\alpha\,\langle F(\kappa)\rangle^2\chi(\kappa)/\chi_0, \tag{5}$$

where χ_0 is the static susceptibility and $\chi(\kappa)$ is the wave-vector-dependent susceptibility which describes the response of the amorphous ferromagnet to an external magnetic field with a spatial dependence $\cos(\kappa z)$.

Neglecting this incoherent magnetic scattering we obtain, in arbitrary units,

$$I_{\text{mag}}=I^{\perp}-I^{\parallel}=\langle F(\kappa)\rangle^2\mathcal{J}_{\text{Co-Co}}(\kappa). \tag{6}$$

For $\langle F(\kappa)\rangle$ we used the cobalt spherical form factor as measured by Moon[5] which is well fitted by the analytical formula of Lisher and Forsyth.[9] This is questionable since in Co-P alloys the phosphorus valence electrons filling the half d band of cobalt reduce its magnetic moment[10] and may modify the shape of the d-electron cloud. Nevertheless, the interference function $\mathcal{J}_{\text{Co-Co}}(\kappa)$ obtained from this assumption is very similar to the x-ray interference function $\mathcal{J}(\kappa)$ which is dominated by a Co-Co pair contribution.[11,12] Discrepancies lie within experimental accuracy (Fig. 3).

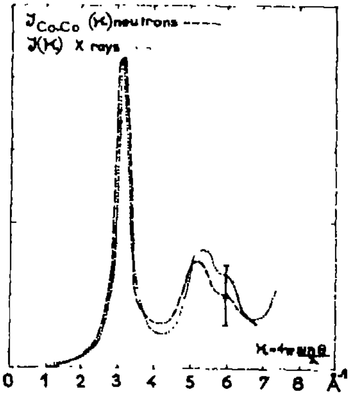

FIG. 3. Neutron magnetic and x-ray interference functions versus $\vec{k}$.

These results prove, as assumed earlier, that the cobalt magnetic moments and the cobalt nuclei have the same distribution. Furthermore, if there were large magnetic fluctuations, an incoherent background of the order of A would be added to the coherent interference function. Since we do not observe such a phenomenon, the magnetic fluctuations must be weak. All these results may be related to the fact that the magnetic moments in these alloys are large (of the order of 1 μ_B/atom). Indeed, if fluctuations in the neighborhood of a cobalt atom produced local antiferromagnetism by changing the sign of the exchange integral, the magnetic moment would be strongly reduced, the interference function distorted and a strong incoherent magnetic scattering added.

To summarize, the magnetic structure of a highly absorbing Co-P alloy has been studied with satisfactory precision using a high-flux neutron beam. An interpretation in terms of a partial interference function has been proposed which allows comparison with x-ray results. The agreement is good.

We are indebted to Dr. P. Burlet and Mr. Convert for helpful cooperation in performing the

easurements.

---

[1] J. J. Rhyne, S. J. Pickart, and H. A. Alperin, Phys. ev. Lett. **29**, 23, 1562 (1972).

[2] D. Pan and D. Turnbull, J. Appl. Phys. **45**, 3, 1406 (1974).

[3] A. Brenner, D. E. Couch, and E. K. Williams, J. Res. Nat. Bur. Stand. **44**, 109 (1950).

[4] P. Burlet, R. Chagnon, and P. Convert, Institut Laue-Langevin Instrument Description Report No. ID 2/73, 1973 (unpublished).

[5] R. M. Moon, Int. J. Mag. **1**, 219 (1971).

[6] T. E. Faber and J. M. Ziman, Phil. Mag. **11**, 153 (1965).

[7] To be published.

[8] W. Marshall and S. W. Lovesey, *Theory of Thermal Neutron Scattering* (Oxford Univ. Press, Oxford, England, 1971), p. 467.

[9] E. J. Lisher and J. B. Forsyth, Acta Crystallogr., Sect. A **27**, 545 (1971).

[10] A. W. Simpson and D. R. Brambley, Phys. Status Solidi (b) **43**, 291 (1971).

[11] J. F. Sadoc, J. Dixmier, and A. Guinier, J. Non-Cryst. Solids **12**, 46 (1973).

[12] C. S. Cargill, III, and R. W. Cochrane, in *Amorphous Magnetism*, edited by H. O. Hooper and A. M. de Graaf (Plenum, New York, 1973) p. 313.

$|g_A/g_V|$ in the Decay $\Sigma^- \to ne^-\bar{\nu}$

W. Tanenbaum, V. Hungerbuehler,[*] R. Majka, J. Marx, P. Nemethy, J. Sandweiss, and W. Willis[†]
Yale University, New Haven, Connecticut 06520[‡]

and

M. Atac, S. Ecklund, P. J. Gollon, J. Lach, J. MacLachlan, A. Roberts, R. Stefanski, and D. Theriot
National Accelerator Laboratory, Batavia, Illinois 60510[§]

and

C. L. Wang
Brookhaven National Laboratory, Upton, New York 11973[∥]

(Received 11 March 1974)

The decay $\Sigma^- \to ne^-\bar{\nu}$ was studied using a hyperon beam at the Brookhaven alternating-gradient synchrotron. The Σ^- and e^- momenta were measured by magnetic spectrometers with magnetostrictive wire spark chambers. A threshold Cherenkov counter and a total-absorption calorimeter identified the electron and neutron, respectively. From a sample of 3507 reconstructed events we have found $|g_A/g_V| = 0.435 \pm 0.035$.

We report a measurement of the magnitude of the ratio of the axial vector to vector form factors, $|g_A/g_V|$, from the observation of 3507 decays of the type $\Sigma^- \to ne^-\bar{\nu}$. These events were produced using the Yale University–National Accelerator Laboratory–Brookhaven National Laboratory high-energy negative hyperon beam at the Brookhaven National Laboratory alternating-gradient synchrotron.[1] The hyperon beam delivers a flux of approximately 200 Σ^- per machine pulse, produced in the forward direction, at a central momentum of 23 GeV/c at the exit of the magnetic channel. Figure 1 depicts the beam and the associated electronic detection apparatus which are described in more detail elsewhere.[1] Beam particles of mass less than that of a proton are vetoed by a threshold Cherenkov counter (C_B) which forms part of the beam channel, and are also vetoed by a scintillation counter located at the downstream end of the apparatus. A cluster of high-pressure, high-resolution magnetostrictive spark chambers[2] determine the momentum of the emerging hyperons to 1%. A set of small counters on either side of these chambers (B) and a hole veto counter (V_H) define the beam and discriminate against upstream hyperon decays.

Located downstream of the 115-in. decay region is a magnetic spectrometer with conventional magnetostrictive wire spark chambers which determines the momentum of the electron from the decay $\Sigma^- \to ne^-\bar{\nu}$ to about 5%. Situated after the spectrometer is a Cherenkov counter (C) filled with hydrogen at atmospheric pressure. This counter, which has a large phase-space acceptance, identifies electrons from the desired leptonic decay among the more copious pions produced in the major decay mode, $\Sigma^- \to n\pi^-$. This counter suppresses the trigger rate for the major

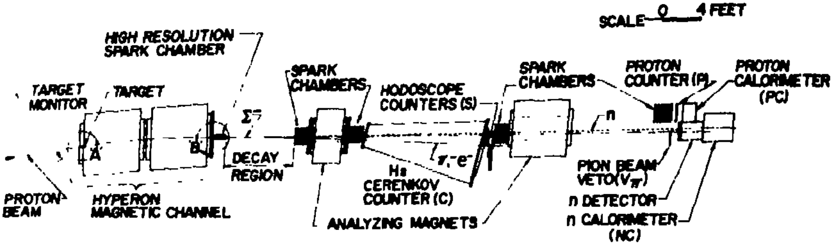

FIG. 1. Schematic diagram of the high-energy hyperon beam.

decay mode by a factor of approximately 80. Following the Cherenkov counter is a hodoscope of scintillation counters (*S*), each of which shadows one of the five optical cells of the electron Cherenkov counter. In addition, the counter nearest to the beam line is backed by a lead and scintillator shower counter to give extra discrimination against nonleptonic backgrounds.

A multiplate, proportional-chamber, scintillator neutron detector[3] is situated downstream of the second spectrometer magnet and provides a measure of the decay-neutron direction to 1 mrad. The hadron calorimeter (*NC*) is used to discriminate against background muons by requiring a minimum pulse height in the trigger. The crude information on the neutron energy (± 25%) is not used in the reconstruction.

The decay $\Sigma^- \rightarrow ne^-\bar{\nu}$ was signified by the trigger

$$\bar{C}_B B \bar{V}_H C S(NC) \bar{V}_\pi .$$

Two-body decays, $\Sigma^- \rightarrow n\pi^-$, and beam pions were also recorded at a scaled-down rate to provide a flux normalization and to monitor the efficiency and resolution of the chambers and neutron detector. The total trigger rate was a few per machine pulse. For each trigger we recorded the configuration of scintillation-counter hits, the pulse heights from the electron Cherenkov counter, shower counter, and hadron calorimeter, and the time difference between signals from the electron Cherenkov counter and the S counter hodoscope, as well as the spark-chamber and multiwire-proportional-chamber information. The major source of background in the leptonic trigger came from the decay $\Sigma^- \rightarrow n\pi^-$ in coincidence with a background muon which triggered the electron Cherenkov counter. A major task of the analysis was to remove this background (which is thrice overconstrained) from the signal of leptonic decays.

Figure 2(a) shows the beam mass spectrum of events with a decay angle of greater than 9 mrad when reconstructed under the hypothesis $\Sigma^- \rightarrow n\pi^-$. The broad distribution contains the leptonic events and the sharp peak at the Σ^- mass contains the two-body background. A reduction of the nonlep-

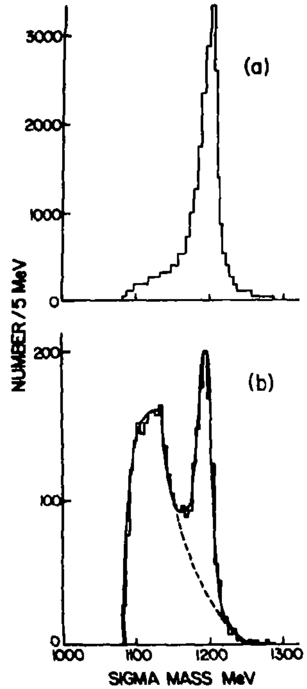

FIG. 2. (a) Mass spectrum of beam particles for leptonic decays at an early stage of the analysis when reconstructed under the hypothesis $\Sigma^- \rightarrow n\pi^-$. The leptonic events being sought are in the broad tail; the two-body background events are in the sharp peak. (b) The same spectrum at the last stage in the analysis. The smooth curves indicate the shapes predicted by the Monte Carlo calculation: dashed, $\Sigma^- \rightarrow ne\nu$ only; solid, $\Sigma^- \rightarrow ne\nu$ plus $\Sigma^- \rightarrow n\pi^-$. A final mass cut of 1165 MeV was made and events below that mass were considered to be leptonic decays.

TABLE I. Results for $|g_A/g_V|$ and the maximum value of likelihood fits from neutron spectrum in the c.m. system.

Spectrometer field integral	$\|g_A/g_V\|$	ln£(data)	ln£(Monte Carlo)	Probability £(Monte Carlo) < £(data)
6 kG m	0.420 ±0.045	−51.68	−53.28 ±3.26	69%
13 kG m	0.455 ±0.055	−52.11	−49.62 ±3.18	22%

tonic background was made by requiring a large pulse height in the shower counter when relevant, a proper time difference between the electron Cherenkov counter and appropriate *S* counter, and that the reconstructed negative track point to the proper cell of the Cherenkov counter and the proper *S* counter. These consistency requirements serve to define decay electrons and eliminate events having a background muon triggering the electron Cherenkov counter, reducing the nonleptonic backgrounds to the level depicted in Fig. 2(b). The smooth curve in Fig. 2(b) indicates the excellent agreement between the data and the spectrum as generated by a Monte Carlo calculation. The final sample of 3507 $\Sigma^- \to ne^-\bar{\nu}$ decays results from a cut requiring the reconstructed Σ^- mass, assuming the hypothesis $\Sigma^- \to n\pi^-$, to be less than 1165 MeV.

Since for this leptonic decay there is a square-root ambiguity resulting from the zero-constraint fit, we cannot assign an event a unique position on a Dalitz plot. In order to obtain the maximum information in a bias-free manner, both solutions were kept and each event plotted on a three-dimensional Dalitz plot. The electron energy and two neutron energies define the coordinates. The form-factor ratios were obtained from the final event sample by a maximum-likelihood fit to projections of the three-dimensional "Dalitz plot" weighted by a Monte Carlo calculation of the acceptance of the detection apparatus. Our c.m. neutron and electron energy resolution (about 5 MeV) corresponds to five neutron energy bins for each solution and twenty electron energy bins.

Data were taken for two values of the magnetic field in the spectrometer magnet. The two results for the absolute value of the form-factor ratio as computed from a likelihood-function (£) fit to the neutron spectrum only are presented in Table I. In obtaining these results, it was assumed that second-class currents are negligible and that the effect of weak magnetism is that predicted by the conserved-vector-current hypothesis. The result is quite insensitive to the amount of weak magnetizm present. The full two-dimensional neutron spectrum was used in the actual maximum-likelihood fit. We can also construct a one-dimensional spectrum by giving both solutions equal weight. Figure 3 shows the resulting neutron spectrum for the 6-kG-m data compared with expected spectra for $|g_A/g_V| = 0.3$ and $|g_A/g_V| = 0.5$. We present this comparison to give a visual indication of the sensitivity of the measurement.

The quality of the likelihood fit described above was evaluated with standard Monte Carlo techniques, and the results of this evaluation are presented in Table I. The detection efficiency calculated for leptonic decays was 11%. Most of the loss was due to Σ^- decaying upstream of the fiducial region or to decay electrons hitting the

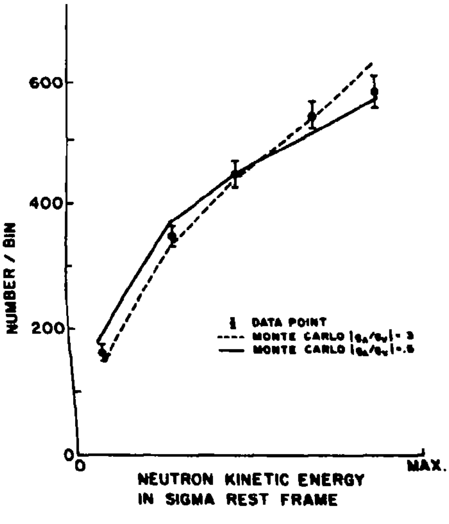

FIG. 3. A comparison of the experimentally determined neutron c.m. energy spectrum and those expected for two values of $|g_A/g_V|$. Both solutions for the energy are used with equal weight.

TABLE II. Summary of $\Sigma^- \to ne^-\bar{\nu}$ form-factor experiments.

Experiment	Year	No. of Events	$\lvert g_A/g_V\rvert$
Maryland[a]	1969	49	0.23 ± 0.16
Heidelberg[b]	1969	33	0.37 [illegible]
Columbia-Stony Brook[c]	1972	36	0.29 [illegible]
This experiment	1973	3507	0.435 ± 0.035

[a] Ref. 5 [b] Ref. 6. [c] Ref. 7.

spectrometer magnet. The probability of a decay electron hitting the spectrometer magnet was extremely weakly correlated with the neutron c.m. energy. The size of the neutron detector was chosen to intercept 100% of the neutrons. The efficiency of neutron detection was independent of angle and only weakly dependent on laboratory momentum (less than 5% variation). The detection efficiency was thus almost entirely independent of the neutron c.m. energy.

The errors assigned to $\lvert g_A/g_V\rvert$ are purely statistical. However, none of the small systematic corrections considered contributes significant uncertainties. The $\Sigma^- \to n\pi^-$ background contamination after the mass cut was 1.5% of the leptonic sample for the 6-kG-m data. This was determined by looking at the mass spectrum of real $\Sigma^- \to n\pi^-$ events. This background was included in the Monte Carlo simulation. The result for $\lvert g_A/g_V\rvert$ was found to be insensitive to such background of up to 10%. The final result for the absolute value of the form-factor ratio is obtained by averaging the results from the two data samples to yield

$$\lvert g_A/g_V\rvert = 0.435 \pm 0.035.$$

It is interesting to note that the Cabibbo theory[4] predicts $g_A/g_V = 0.33 \pm 0.04$. Table II contains a comparison of this experiment with the results of previous experiments.

We wish to thank our engineering staff, Andy Disco, Satish Dhawan, Cordon Kerns, Stan Ladsinski, Blaise Lombardi, and Irving Winters, and our technicians Alan Wandersee, Jon Blomquist, and Ed Steigmeyer for their help in the design and setup of the apparatus. We also thank the alternating-gradient synchrotron staff, in particular David Berley, Eugene Halek, and Gerry Tanguay, for providing the technical support needed for the success of this experiment.

---

*Present address: Université de Genève, Genève, Switzerland.

†Present address: CERN, Geneva, Switzerland.

‡Research supported by the U. S. Atomic Energy Commission under Contract No. AT(11-1).

§Operated by Universities Research Association Inc. under contract with the U. S. Atomic Energy Commission.

‖Research supported in part by the U. S. Atomic Energy Commission.

[1] V. Hungerbuehler *et al.*, Nucl. Instrum. Methods 115, 221 (1974).

[2] W. J. Willis *et al.*, Nucl. Instrum. Methods 91, 33 (1971).

[3] M. Atac *et al.*, Nucl. Instrum. Methods 106, 263 (1973).

[4] H. Ebenhoh *et al.*, Z. Phys. 241, 473 (1971).

[5] A. P. Colleraine *et al.*, Phys. Rev. Lett. 23, 198 (1969).

[6] F. Eisele *et al.*, Z. Phys. 223, 487 (1969).

[7] C. Baltay *et al.*, Phys. Rev. D 5, 1569 (1972).

Neutral-Current Limit and Future Prospect at a Fission Reactor*

H. S. Gurr, F. Reines, and H. W. Sobel
Department of Physics, University of California at Irvine, Irvine, California 92664
(Received 22 April 1974)

Data are presented which yield a new upper limit for the weak neutral- current reaction $\bar{\nu}_e + d \to n + p + \bar{\nu}_e$ in the MeV range of 6 times theoretical expectation at a 3-standard-deviation level. These data also demonstrate the feasibility of a test which is an order of magnitude more sensitive.

The possible existence of neutral currents in the weak interaction has aroused intense interest recently with the reported observations at CERN[1] and the National Accelerator Laboratory.[2] Measurements at our Savannah River Plant fission-reactor neutrino facility have resulted in an improved upper limit for a neutral-current $\bar{\nu}_e$ reaction and also indicate the feasibility of a neutral-current test at the level of theoretical expectation in the well-shielded environment which we have constructed in connection with our $\bar{\nu}_e$-e^- scattering search.[3] The reaction under discussion,

$$\bar{\nu}_e + d \to n + p + \bar{\nu}_e, \qquad (1)$$

was studied in an energy range (2.2 to ~5 MeV) which differs greatly from that explored at high-energy accelerators (>1 GeV), and $\bar{\nu}_e$ is involved instead of ν_μ ($\bar{\nu}_\mu$). Further, according to the Weinberg theory, the rate of (1) is independent of the Weinberg angle since at these low energies only the axial vector (Gamow-Teller) contributes to this reaction,[4] leaving no arbitrary parameters. These widely differing conditions motivate the study of (1).

In an earlier attempt[5] the deuteron target was contained in a deuterated scintillator to which gadolinium was added. The object there was to identify the reaction by the distinctive delayed-coincidence signal provided by the product proton and the γ rays associated with neutron capture in gadolinium. The experimental sensitivity was limited, primarily because of the small (~2%) probability of the proton receiving enough energy to appear above random background. Clearly the detection efficiency would be greatly enhanced if the product neutron alone provided a sufficiently distinctive signature. The experiment under discussion is based on the fact that we have succeeded in drastically reducing the neutron background.

The measurements were made with H_2O or pure D_2O and a large BF_3 neutron counter as indicated in Fig. 1. Not shown in the schematic is the massive Pb, water, and concrete shield in which the liquid scintillation anticoincidence detector is enclosed. Table I summarizes the results obtained for a variety of target and shielding configurations in the inner region with the reactor on and off. A Pu-Be neutron source was used for energy calibration, for system stability checks, and in the determination of neutron detection efficiency. The dead-time–corrected (~40%) BF_3 rates tabulated refer to the main α-particle peak (~81% of the neutron-capture spectrum). The time referred to in the "Liquid scintillator" column is the duration of the system block following the penetration of the scintillator by a cosmic-ray muon.[6] We use these data and neutron detection efficiencies together with reaction cross sections for fis-

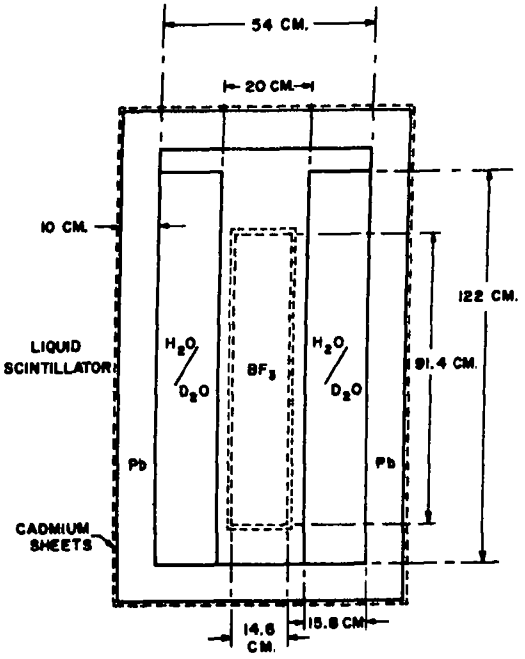

FIG. 1. Schematic diagram of the detector.

sion $\bar{\nu}_e$ for the processes

$$\bar{\nu}_e + p \to n + e^+ \ (1.0\times10^{-43}\ \mathrm{cm}^2/\bar{\nu}_e,\ \text{experimental}),$$

$$\bar{\nu}_e + d \to n + n + e^+ \ [(2.4\pm0.4)\times10^{-45}\ \mathrm{cm}^2/\bar{\nu}_e,\ \text{theoretical}^7],$$

and

$$\bar{\nu}_e + d \to n + p + \bar{\nu}_e \ (4.4\times10^{-45}\ \mathrm{cm}^2/\bar{\nu}_e,\ \text{theoretical}^4),$$

and together with the $\bar{\nu}_e$ flux at our detector, $2.4\times10^{13}\ \bar{\nu}_e/\mathrm{cm}^2\ \mathrm{sec}$, *to set a new upper limit on* (1).

To test our system we filled it with H_2O and measured the reactor-associated neutron rate (runs I and II). *The resultant difference*, 52 ± 24 day^{-1}, compared with the predicted rate, ~39 day^{-1}, indicates that we were probably observing Reaction (2) via the product neutron[8] without benefit of the delayed coincidence between e^+ and n pulses previously required.[9] According to runs III and IV, reactor-associated neutrons originating external to the detector contribute a small part (< 15 day^{-1}, at 1 standard deviation) of the observed signal[10] and increase the statistical uncertainty from ± 24 day^{-1} to ± 35 day^{-1}.

The D_2O *data are used to set an upper limit on* the neutral-current reaction (1). Runs III and IV yield a reactor-associated neutron rate of 1.4 ± 7.2 day^{-1}. To obtain a more restrictive limit we subtract the calculated[11] charged-current contribution of Reaction (3),

$$(0.30\ \mathrm{kg}^{-1}\ \mathrm{day}^{-1})\times(178\ \mathrm{kg})\times0.082 = 4.3\ \mathrm{day}^{-1},$$

and obtain -2.9 ± 7.2 day^{-1}. This number is to be compared with that predicted for the neutral-current reaction, 4.0×0.81. From these numbers we obtain a 3-standard-deviation upper limit on the ratio,

$$\frac{\sigma_{\mathrm{expt}}}{\sigma_{\mathrm{neutral\ theory}}} < \frac{-2.9+3(7.2)}{4.0\times0.81} < 6.$$

This limit is a factor >100 lower than the previous attempt.[5]

TABLE I. BF_3 counting rate for various experimental configurations.

Run	Reactor condition	H_2O/D_2O	Liquid scintillator[a] anti condition	BF_3 rate (day^{-1})
I	Down	H_2O	700-μsec block	63.4 ± 7.2
II	Up	H_2O	700	116 ± 23
III	Down	D_2O	3000-μsec block and 1000 μsec	54.7 ± 5.8
IV	Up	D_2O	3000 and 1000 μsec	56.2 ± 4.3

[a] Ref. 6.

The neutron counter envisaged in an improv experiment would be filled with ^{3}He to a press of 3.7 atm. As shown in Fig. 2 it would surrou a 130-liter D_2O target. The anticipated overa neutron *detection efficiency of the system* is ~75%.

The $\bar{\nu}_e$ signals anticipated are as follows: neu*tral-current reaction*, ≅ 60 day^{-1}; *charged-cur-rent reaction*, ≅ 16 day^{-1} (single detected neutro ≅ 24 day^{-1} (two detected neutrons).[12]

The reactor-independent background arises *from a variety of causes:* α activity in the count er, external neutrons, and photoneutrons. Scaling the background as seen in the BF_3 experimen we predict[13] a value of ~900/day. The reactor-dependent background arises from two sources: neutrons which penetrate the liquid anticoincidence shield and photoneutrons. Scaling the data from the present experiment (Table I) yields a prediction -40 ± 100 day^{-1} in the absence of a neu

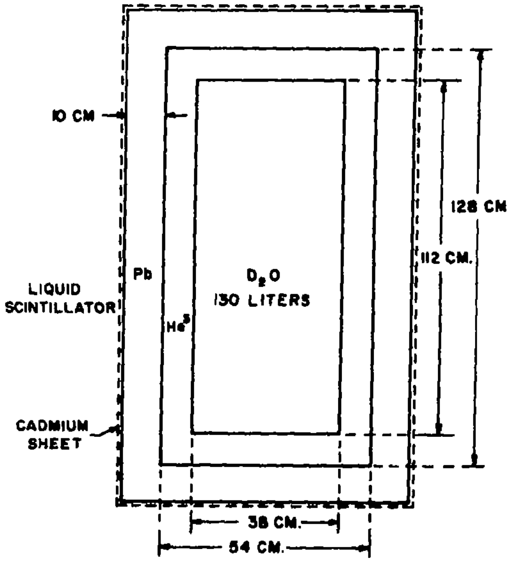

FIG. 2. Schematic diagram of the proposed experimental configuration.

tral-current signal or -100 ± 100 day^{-1} if a neutral current exists. The photoneutron component calculated from a measurement of the γ-ray spectrum *in situ* yields an acceptable upper limit of a few counts per day.

If a signal is observed it can be tested by use of neutron differential shielding techniques and by observation of the effect of a neutron source. The sensitivity of the system to neutrinos can also be tested by observation of the two neutrons from the charged-current reaction (2), and by use of an H_2O filling and observation of Reaction (3).

We now estimate the statistical precision expected from a modest run sequence with the reactor on for 30 days and off for 10 days. The reactor-dependent neutron background is taken to be negligible since on the basis of present neutron limits there appears to be no obstacle to achieving this condition. Then

$$\frac{\Delta S}{S} = \pm\frac{1}{S}\left(\frac{S+B}{t_{\rm on}}+\frac{B}{t_{\rm off}}\right)^{1/2}, \qquad (4)$$

where $S = 76$ day^{-1} is the total $\bar{\nu}_e$ signal, $B = 900$ day^{-1} is the background, and $\Delta S/S = \pm 0.15$. If we allow for the statistical accuracy of the charged-current portion of the signal, S_c, in this period of time, $\Delta S_c/S_c = \pm 0.04$, and the neutral current would be determined in terms of the theoretical prediction S_n to an accuracy of $\Delta S_n/S_n = \pm 0.19$.

We wish to thank H. H. Chen and J. Lathrop for helpful discussions, and A. A. Hruschka for help in the design and installation of the equipment. We would also like to thank the Harshaw Chemical Company for the loan of the BF_3 counter and associated electronics and in particular B. M. Shoffner for his advice in setting up this apparatus. The continuing hospitality and assistance of the E. I. Dupont de Nemours Company which operates the Savannah River Plant for the U.S. Atomic Energy Commission is gratefully acknowledged.

---

[*] Work supported by the U. S. Atomic Energy Commission.

[1] F. J. Hasert *et al.*, Phys. Lett. 46B, 138 (1973).

[2] A. Benvenuti *et al.*, Phys. Rev. Lett. 32, 800 (1974).

[3] H. S. Gurr, F. Reines, and H. W. Sobel, Phys. Rev. Lett. 28, 1406 (1972).

[4] T. W. Donnelly, D. Hitlin, M. Schwartz, J. D. Walecka, and S. J. Wiesner, Phys. Lett. 49B, 5 (1974); T. W. Donnelly, private communication; Yu. V. Gaponov and I. V. Tyutin, Zh. Eksp. Teor. Fiz. 47, 1526 (1964) [Sov. Phys. JEPT 20, 1231 (1965)]. This reaction and its detection has been considered in a series of publications related to neutral currents by T. Ahrens, R. W. King, and collaborators: T. Ahrens and T. P. Lang, Phys. Rev. C 3, 979 (1971). The question of nucleon energy correlations in this reaction was discussed by C. P. Frahm, Phys. Rev. D 3, 663 (1971).

[5] J. H. Munsee and F. Reines, Phys. Rev. 177, 2002 (1969); V. K. Bogatyrev, Yad. Fiz. 12, 753 (1970) [Sov. J. Nucl. Phys. 12, 407 (1971)].

[6] In the D_2O runs an extra (1000 μsec, low threshold) anticoincidence condition was imposed to identify and reduce the background due to knock-on protons from neutron collision. This reduced the measured BF_3 rate by about a factor of 2. The cosmic-ray muon anticoincidence time for the D_2O runs was increased from 700 to 3000 μsec to take into account the increased neutron diffusion time in this medium.

[7] This reaction has been detected, but in view of the large experimental uncertainty [$(3.0 \pm 1.5) \times 10^{-44}$ cm^2], we use the theoretically predicted value. T. L. Jenkins, F. E. Kinard, and F. Reines, Phys. Rev. 185, 1599 (1969).

[8] The neutron detection efficiency in this case is estimated to be about 15%.

[9] F. Reines and C. L. Cowan, Jr., Phys. Rev. 113, 273 (1959); F. A. Nezrick and F. Reines, Phys. Rev. 142, 852 (1966).

[10] This limit on the reactor-associated neutron background is derived from the rate -2.9 ± 7.2 day^{-1} (see following paragraph) by applying the ratio of the neutron detection efficiences for H_2O and D_2O (0.15/0.043).

[11] The overall neutron detection efficiency (η_n) with a D_2O target has been conservatively estimated as 0.043. The contributing factors are neutron absorption in D_2O, 0.87; solid-angle considerations, 0.29; BF_3 efficiency (counter filled to a pressure of 20 cm Hg), 0.19; Fe-wall attenuation factor, 0.9. The efficiency, 0.082, that enters in this calculation is the probability of seeing at least one neutron, $\sim 2\eta_n(1-\eta_n)$.

[12] The background for such a distinctive signal—two neutron pulses in delayed coincidence with a time interval of ~1 msec—is negligible under the conditions envisaged.

[13] Further neutron shielding and pulse-shape discrimination against α contamination in the counter walls can be expected to reduce this background.

ERRATUM

NEW DEVELOPMENTS IN THE APPLICATION OF HYPERSPHERICAL COORDINATES TO ATOMIC WAVE FUNCTIONS. Dwayne L. Knirk [Phys. Rev. Lett. 32, 651 (1974)].

In Eq. (15), the expansion coefficients for the linear term in r should be $2\pi^{3/2}[(\lambda_\nu-1)(\lambda_\nu+5)]^{-1}\times W(\nu/\nu_0)$, where ν_0 labels the lowest generalized angular momentum eigenfunction, $s(\nu_0|\Omega)=\pi^{-3/2}$. In the definition of Q_2, the expression in brackets should read

$$\left[\frac{1}{(1-\sin 2\eta\cos\theta)^{1/2}}+\frac{(1-\sin 2\eta\cos\theta)^{1/2}}{\sin 2\eta}\right]$$

to accord with the result in Ref. 6.[1]

Professor U. Fano has brought to my attention Macek's analysis[2] of the convergence of the hyperspherical expansion for He.

---

[1] D. L. Knirk, Proc. Nat. Acad. Sci. U.S.A. 71, 1291 (1974).

[2] J. H. Macek, Phys. Rev. 160, 170 (1967).

ANNOUNCEMENT

Comments on Letters

For some time now, each of the *Physical Reviews* has contained a section of "Comments." As originally envisioned, these sections were to include papers reporting relatively minor modifications or additions to papers already published in the *Physical Reviews* as well as in *Physical Review Letters.*

There has been, almost from the outset, quite a bit of discussion as to whether this arrangement was entirely satisfactory. One problem arises from the fact that the *Physical Reviews* are divided by subject matter, while *Physical Review Letters* covers all areas of physics. Even within a subject area, the readerships of the *Physical Reviews* and *Physical Review Letters* are not identical. Thus, a comment on a Letter could be missed by an interested reader. The situation has become even more complicated now that the Division of Biophysics of the American Physical Society has recommended that Letters in that field should be accepted by *Physical Review Letters*, but that detailed articles in this area do not belong in the *Physical Reviews.*

In view of these considerations, we have decided to inaugurate a "Comments" section in *Physical Review Letters*, beginning with the issue of 2 September. In this section we will publish short notes that present small additions to Letters previously published in this journal, without demanding that they themselves have the quality of timeliness expected of regular Letters. We will insist, however, that Comments make genuine contributions of their own. We are not interested in providing a forum for disputes over priority, or over the most elegant way to obtain a result. What we will look for is better exemplified by a notice that a particular paper has implications—or limitations!—not brought out in the original presentation.

We believe that this change will increase the usefulness of our journal. As always, we welcome expressions of opinion from our readers.

S. A. Goudsmit
George L. Trigg

PHYSICAL REVIEW
LETTERS

VOLUME 33 22 JULY 1974 NUMBER 4

Measurements of Fine Structures in Excited States of ^{4}He$^+$ by Fast-Beam Radio-Frequency Resonance

S. Churassy and M. L. Gaillard
Laboratoire de Spectrometrie Ionique et Moleculaire, 69621 Villeurbanne, France

and

J. D. Silver
Clarendon Laboratory, Department of Physics, University of Oxford, Oxford OX1 3PU, England

(Received 3 June 1974)

We report measurements of s-p, f-g, and g-h transitions in electronically excited states of ^{4}He$^+$ observed via electric dipole resonances on a fast helium ion beam.

Measurements of fine structures in hydrogenic atoms are interesting in that the results obtained may be used to test predictions of quantum electrodynamic theory.[1] We have extended the "fast-beam radio-frequency" technique of Fabjan and Pipkin[2] to some excited electronic levels of ^{4}He$^+$, and we present here a preliminary report of our experiments.

The principle of the method is to observe, at a fixed time t after excitation, light arising from the decay of levels having several values of orbital angular momentum l, belonging to the same principal quantum number n; investigation of the variation of this light intensity when the ions are subject to an oscillating electric field in the time interval between excitation and t can lead to an evaluation of certain of the fine structure separations for that n. If the rf oscillation frequency corresponds to a fine-structure separation for which $\Delta l = 1$, the atom can undergo an electric dipole transition; the lifetimes of states of different l are different, so that a change in light intensity observed at time t is to be expected. In practice, the beam of He$^+$ was excited by passage through a thin carbon foil; it then passed through a region where it was subjected to rf whose amplitude and frequency could be varied, and a monochromator (or interference filter) -photomultiplier combination was arranged to observe light emitted by ions emerging from the region of rf irradiation. We shall give a brief description of the apparatus, followed by the results we have obtained so far.

Our ^{4}He$^+$ beam source was a 2-MeV Van de Graaff accelerator which furnishes a beam of low divergence; this was mass analyzed and velocity stabilized with a bending magnet, and we took measurements at 300, 400, and 500 keV, corresponding to beam velocities of (3.7, 4.3, and 4.8)$\times 10^8$ cm/sec, respectively. Beam currents used were typically 2 μA, and self-supporting carbon foils of between 5 and 10 μg/cm^2 were used to excite the beam, whose cross section was 2 mm$\times$6 mm to allow the use of a convenient configuration for the parallel-plate transmission line used to set up the rf field. The direction of travel of the rf wave could be chosen to be either parallel or antiparallel to the beam direction. The chamber was continuously pumped, and maintained at a pressure less than 2×10^{-6} mm hg.

The rf region was a parallel-plate transmission line constructed to have a characteristic impedance of 50 Ω. It was fed from a Rhode & Schwartz power rf generator via a HP 778D dual directional coupler, whose forward and backward pickoffs could be used to monitor the frequency and the reflected rf power, respectively. The frequency was measured with a Hewlett-Packard 5245L digital frequency meter with appropriate plug-in heterodyne converters. The parallel-plate line was terminated with a Hewlett-Packard 423A detector diode, which was also used as rf power monitor for leveling. The rf generator was on-off modulated at 1 kHz to facilitate digital phase-sensitive detection of the signal.

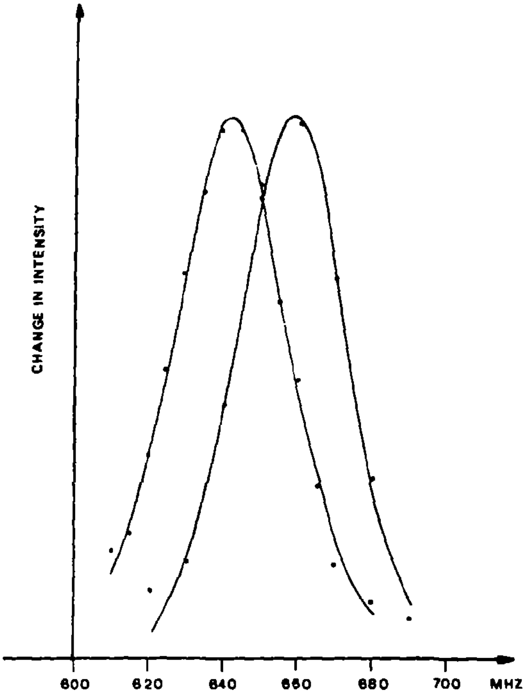

FIG. 1. Change in intensity (arbitrary units) as a function of applied radio frequency (MHz) for the 6560-Å transition of ^{4}He$^+$. Each curve is an unresolved blend of the nearly coincident $6f_{7/2}$-$6g_{9/2}$ and $6g_{7/2}$-$6h_{9/2}$ resonances. The curve displaced to higher frequency was obtained with the beam and rf wave traveling in the same direction, the other curve with the beam and wave traveling in opposite directions; the displacements arise from the first-order Doppler effect.

Light intensity emitted from the beam, from the region following the rf plates, in selected lines, was measured by photon counting, using a cooled EMI 6256S photomultiplier tube for all lines except 6560 Å, for which a cooled EMI 9658 tube was used. The photomultiplier tube was followed by pulse amplifiers and a discriminator; shaped pulses were fed to a digital phase-sensitive detection system. This consisted of two scalers, and the 1-kHz rf modulating signal was used to control the counters so that one (A) counted with rf on, and the other (B) with rf off. In this way, the difference in light intensity emitted from the beam with or without rf applied could be measured as a function of frequency. In the later experiments, the two-scaler system was replaced by an SSR digital synchronous computer. In order to observe a resonance, the rf generator would be set to a number of frequencies in turn so as to cover the range of interest; for each frequency, the rf power was leveled manually, and the SSR computer set to count for a preset number of modulation periods, generally 10^5 (100 sec). The difference between counters A and B, normalized to a constant count in A, was noted. This constituted the raw experimental signal. A recording showing the $J=\frac{7}{2}-J=\frac{9}{2}$ transition for $n=6$ is shown in Fig. 1. The two curves show the first-order Doppler effect in the measurements, with the resonance displaced to higher frequency corresponding to measurements

TABLE I. Lamb shifts $ns_{1/2}$-$np_{1/2}$ in ^{4}He$^+$.

Principal quantum number, n	Wavelength of optical transition observed (Å)	Measured frequency (MHz)	Previous observations (MHz)	Theory[c] (MHz)
4	4686 (3–4)	1755 ± 44	1768 ± 5[a]	1769.4
5	3203 (3–5)	902 ± 15	909 ± 7[b]	906.3
6	2733 (3–6)	524 ± 13	⋯	524.5
6	6560 (4–6)	530 ± 10	⋯	524.5
7	2511 (3–7)	333 ± 8	⋯	330.0

[a] Ref. 3. [b] Ref. 4. [c] Ref. 5.

made with the rf wave traveling in the same direction as the beam. For the data shown in the figure, the solid curve represents a computer least-squares fit of the experimental points by a Lorentzian curve of variable amplitude, width, baseline, and position. The results given in Tables I and II were, however, obtained from a graphical analysis of the resonance curves.

The errors quoted are larger than the statistical errors in finding the peak centers; they arise from errors in rf power leveling (especially serious for $n=4$), uncertainties in profile shapes, corrections due to motional Stark effect from an uncanceled Earth's field, and with the exception of results for 6560 Å, errors in the Doppler shifts arising from small uncertainties in beam velocity. For 6560 Å, however, this source of error was avoided by taking measurements for both directions of rf wave.

We have shown that the method of Fabjan and Pipkin may be readily extended to measurements of fine structures in electronically excited states f ^{4}He$^+$, and presented the first rf measurements f such structures in $n=6$ and 7. Although the recision of the results we have so far obtained s not high enough to constitute a test of quantum lectrodynamic calculations for the Lamb shifts measured, there seems no fundamental reason why the measurements of Jacobs, Lea, and Lamb[3] or $n=4$ and of Baumann and Eibofner[4] for $n=5$ annot be improved upon by the present technique; he possibility of using double quantum transiions, as suggested recently by Kramer *et al.*[6] ould even eventually lead to an improved value for the fine-structure constant. Nonetheless, for the higher values of n studied, the presence of many closely spaced components makes precise measurements of the fine-structure separations rather difficult.

TABLE II. Fine structures for $n=6$ of ^{4}He$^+$ measured in the 6560-Å transition.

Transition	Measured frequency (MHz)	Theory[a] (MHz)
$g_{9/2}-h_{11/2}$	437 ±10	432.3
$f_{7/2}-g_{9/2}$	648.5 ± 5	648.5
$g_{7/2}-h_{9/2}$		649.0

[a] Ref. 5.

---

[1] For an up-to-date survey, see V. W. Hughes, in *Proceedings of the Third International Conference on Atomic Physics, Colorado, 1972*, edited by S. J. Smith (Plenum, New York, 1973); N. M. Kroll, *ibid.*

[2] C. W. Fabjan and F. M. Pipkin, Phys. Rev. A 6, 556 (1972).

[3] R. Jacobs, K. Lea, and W. Lamb, Jr., Phys. Rev. A 3, 884 (1971).

[4] M. Baumann and A. Eibofner, Phys. Lett. 43A, 105 (1973).

[5] The values given in the tabulation of J. Garcia and J. Mack, J. Opt. Soc. Amer. 55, 654 (1965), are sufficiently accurate for our purposes.

[6] P. Kramer, S. Lundeen, B. Clark, and F. Pipkin, Phys. Rev. Lett. 32, 635 (1974).

Elastic and Inelastic Electron Scattering at 20 and 60 eV from Atomic Cu†

W. Williams and S. Trajmar
Jet Propulsion Laboratory, California Institute of Technology, Pasadena, California 91103
(Received 2 May 1974)

Normalized differential and integral electron-impact cross sections for elastic scattering and for the excitation of the $^2D_{5/2}$, $^2D_{3/2}$, and $^2P_{3/2,1/2}$ levels of atomic copper have been determined at 20 and 60 eV. An unexpectedly large cross section was found for the excitation of the $^2P_{3/2,1/2}$ levels, which at certain angular and energy ranges surpasses the cross section for elastic scattering. The integral cross sections in units of 10^{-16} cm^2 are elastic, 91.0 and 59.0; $^2D_{5/2}$, 1.85 and 0.36; $^2D_{3/2}$, 1.26 and 0.26; $^2P_{3/2,1/2}$, 77.2 and 36.5, at 20 and 60 eV, respectively.

esides a general interest in Cu in atomic phys, a need for electron-impact scattering cross tions has developed recently in connection with Cu vapor lasers.[1-8] We are not aware of any experimental measurements on electron scattering by atomic Cu. Here, we present normal-

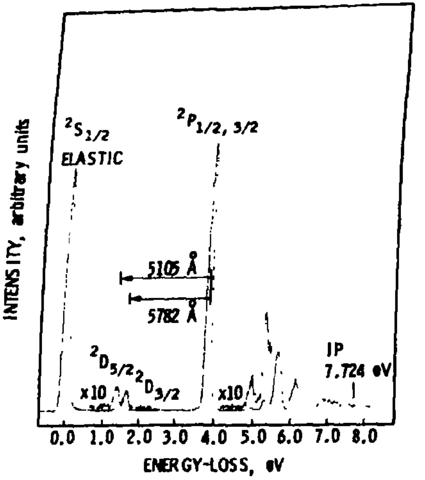

FIG. 1. Energy-loss spectrum of Cu at 20 eV impact energy and 18° scattering angle.

ized differential and integral cross sections at 20- and 60-eV impact energies for elastic scattering and for the excitation of the ^2P and ^2D states (upper and lower laser levels, respectively, for the 5106-Å and 5782-Å lasers).

The angular distribution for elastic scattering shows oscillations similar to those observed for other heavy elements. It has been found that at certain energy and angular ranges the cross section for the unresolved $^2P_{3/2}$ and $^2P_{1/2}$ excitations is larger than that for elastic scattering (see Figs. 1–3). An inelastic cross section of this magnitude, particularly when considered relative to the elastic cross section, is quite unexpected and may be an important factor from the point of view of laser applications. The cross sections for the $^2D_{5/2}$ and $^2D_{3/2}$ excitations are very similar. They are both strongly forward peaked and about an order of magnitude smaller than those for the combined ^2P excitation. Previous estimations of the ^2P and ^2D excitations based on semiclassical[1] calculations differ significantly from these results.

The measurements were carried out in a crossed-beam configuration and with utilization of an electron-impact spectrometer similar to the one described earlier.[6] An atomic Cu beam was generated by the heating of a tantalum crucible containing Cu by electron bombardment to approximately 1250°C. The Cu vapor diffused through a 0.1-cm diam, 0.5-cm-long channel to form the target beam. An energy-selected electron beam (full width at half-maximum around 80 meV) crossed the Cu beam at right angles at about 0.2 cm above the tip of the crucible. The electron beam was monitored and trapped by a Faraday cup.

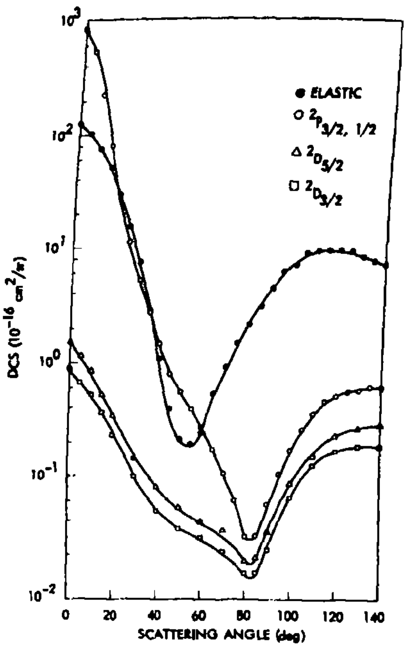

FIG. 2. Differential cross sections for elastic scattering, and for the excitation of the $(^2P_{3/2}+{}^2P_{1/2})$, $^2D_{5/2}$, and $^2D_{3/2}$ states at 20 eV. The elastic scattering points below 10° are obtained by extrapolation.

The scattering intensities at fixed impact energy (E_0) and scattering angle (θ) were determined as a function of energy loss (ΔE) by the use of pulse counting by multichannel-scaling techniques. Energy-loss spectra were obtained by our superimposing several energy-loss scans with the aid of the 1024-channel scaler. The impact-energy scale is believed to be accurate to ± 0.5 eV. The angular resolution can be estimated as described earlier[7] to be between 1.7 to 3.2°. A typical spectrum is shown in Fig. 1. The two components of the ^2P transition are separated only by 0.031 eV and are not resolved in the present measurements. Double-scattering features similar to th one observed by Hertel and Ross for potassium[7] ($^2P+{}^2P$) were not observed and therefore their effects can be neglected compared with other errors involved in the measurements.

Ratios of the inelastic-scattering intensities to the elastic-scattering intensity were determined

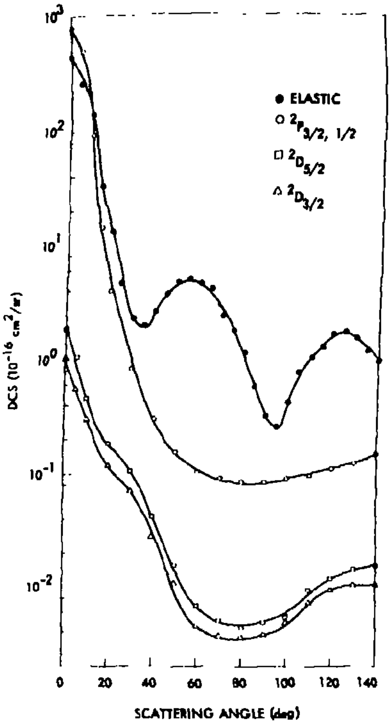

FIG. 3. Differential cross sections for elastic scat-ring, and for the excitation of the $(^2P_{3/2}+^2P_{1/2})$, $D_{5/2}$, and $^2D_{3/2}$ states at 60 eV. The elastic scattering ints below 10° are obtained by extrapolation.

r each spectrum in the range 10 to 140°. The astic-scattering angular dependence in the same gular range was measured in a time short comred to the instrumental drift. The measureents were repeated several times until a relile elastic-scattering distribution was obtained. ta below 10° were not taken because of directm contribution. The elastic-scattering intenties were converted to differential cross secns in arbitrary units with an effective scattering-path-length correction. The accurate determination or calibration of the effective path-length correction is not feasible in the present apparatus, but one determined in another apparatus with similar scattering geometry was used. The low-angle behavior of the inelastic cross sections were determined down to 0° (no direct-beam contribution). The actual 0° scattering angle was determined by finding the point of symmetry in the ^2P angular scattering distribution around 0°.

The elastic differential cross sections were extrapolated to 0° and to 180° and integrated to obtain integral cross sections. These integral elastic cross sections were normalized to the integral elastic cross-section values calculated by Winter and Cartwright.[9] The intensity ratios combined with the normalized elastic cross sections yielded normalized inelastic cross sections. The details of this calculation and the justification for the normalization procedure will be discussed elsewhere.[9] Based on comparison of integral elastic cross sections obtained by this calculational method to experimental data, in case of potassium, we believe that the absolute value of the normalized cross sections is accurate to within ± 50 and ± 75% for 60 and 20 eV, respectively. When more accurate calculations or experimental procedures become available, the cross sections can be easily renormalized. The relative values of the cross sections are estimated to be accurate to within ± 20% on the basis of a procedure described previously.[7] A normalization to the optical f value was employed by Hertel and Ross[8] for potassium. We found that this procedure for the ^2P excitation was not more reliable than the one which we followed above even though our measurements extend to lower momentum-transfer values than those of Hertel and Ross. The normalized ^2P cross section when plotted as a function of momentum transfer can, however, be extrapolated reasonably well to the optical f value of 0.711 as given by Corliss.[10]

TABLE I. Summary of integral cross sections (in units of 10^{-16} cm^2).

	Present Results					Leonard	
E_0 (eV)	Elastic	Momentum transfer	$^2P_{3/2,1/2}$	$^2D_{5/2}$	$^2D_{3/2}$	$^2D_{5/2}$	$^2P_{3/2}$
20	91.0	84.7	77.2	1.85	1.26	0.2	6.2
60	59.0	17.5	36.5	0.86	0.26	0.014	4.0

Figures 2 and 3 show the results for 20- and 60-eV impact energies, respectively.

The integral cross sections are summarized in Table I. A more detailed description of the results as well as cross sections at other impact energies and for other electronic transitions will be published later.

---

†This paper presents the results of one phase of research carried out at the Jet Propulsion Laboratory, California Institute of Technology, under Contract No. NAS7-100, sponsored by the National Aeronautics and Space Administration.

[1] D. A. Leonard, IEEE J. Quantum Electron. 3, 380 (1967).

[2] W. T. Walter, IEEE J. Quantum Electron. 4, 355 (1968).

[3] A. A. Isaev, M. A. Kazaryan, and G. G. Petrash, Pis'ma Zh. Eksp. Teor. Fiz. 16, 40 (1972) [JETP Lett. 16, 27 (1972)].

[4] G. G. Petrash, Usp. Fiz. Nauk 105, 645 (1971) [Sov. Phys. Usp. 14, 747 (1972)].

[5] C. J. Chen, N. M. Nerheim, and G. Russel, Appl. Phys. Lett. 23, 514 (1973).

[6] A. Chutjian, D. C. Cartwright, and S. Trajmar, Phys. Rev. Lett. 30, 195 (1973).

[7] S. Trajmar, Phys. Rev. A 8, 191 (1973).

[8] I. V. Hertel and K. J. Ross, J. Phys. B: Proc. Phys. Soc., London 2, 285 (1969).

[9] N. Winter and D. C. Cartwright, private communication, and to be published. We are grateful to Dr. Winter and Dr. Cartwright for supplying us with their results prior to publication.

[10] C. H. Corliss, J. Res. Nat. Bur. Stand., Sect. A 74, 781 (1970).

Observation of Stimulated Anti-Stokes Raman Scattering in Inverted Atomic Iodine*

R. L. Carman† and W. H. Lowdermilk
Lawrence Livermore Laboratory, University of California, Livermore, California 94550

(Received 23 May 1974)

Nonresonant stimulated anti-Stokes Raman scattering from an inverted population in atomic iodine has been observed. The population inversion was achieved by flash photolysis of trifluoromethyliodide. A gain of e^7 was measured for a laser probe pulse at the anti-Stokes wavelength passing through the inverted iodine coincident with a laser pump pulse. This result is in good agreement with theoretical predictions.

In the presence of intense electromagnetic radiation of optical frequency ω_1, atoms in an excited metastable state of energy $\hbar\omega_0$ can decay through enhanced two-photon emission[1] and anti-Stokes Raman scattering.[2] In the first process, two photons are emitted with frequencies ω_1 and $\omega_2 = \omega_0 - \omega_1$. In the second process, the incident photon is absorbed and simultaneously a photon of energy $\omega_2 = \omega_0 + \omega_1$ is emitted. If the intensity at frequency ω_2 becomes sufficiently large, these emission processes will be stimulated. Resonant stimulated anti-Stokes Raman scattering has been observed by Sorokin *et al.*[3] in potassium vapor in which a population inversion between the two 4^2P excited states was produced through absorption of laser light by atoms in the $4^2S_{1/2}$ ground state. In this Letter we report the first observation of nonresonant stimulated anti-Stokes Raman scattering (ASRS) in a medium in which a population inversion was produced by an incoherent pumping source. An inversion between the $5^2P_{3/2}$ ground state and the metastable $5^2P_{1/2}$ excited state of atomic iodine was achieved by flash photolysis of trifluoromethyliodide (CF_3I). The ASRS was then observed by measuring the gain at the anti-Stokes wavelength experienced by a laser probe pulse as it passed through the inverted iodine coincident with a 1.06-μm laser pump pulse. Since the iodine metastable energy $\hbar\omega_0 = 7604\ \mathrm{cm}^{-1}$ was less than the incident photon energy $\hbar\omega_1 = 9391\ \mathrm{cm}^{-1}$, only the anti-Stokes Raman decay process could occur. The possible use of ASRS in iodine to produce frequency up-conversion of high-power lasers was recently suggested by Vinogradov and Yukov.[4]

The experimental arrangement used is shown in Fig. 1. The neodymium-doped yttrium aluminum garnet oscillator[5] was electro-optically Q switched permitting reliable time synchronization between the laser pulse and the flashlamp discharge used to invert the iodine. The oscillator produced a train of pulses each of 0.75-nsec duration with a transform-limited bandwidth of 0.020 cm^{-1}. The pulse duration was as short as possible, consistent with the limit imposed by steady-state Raman scattering theory,

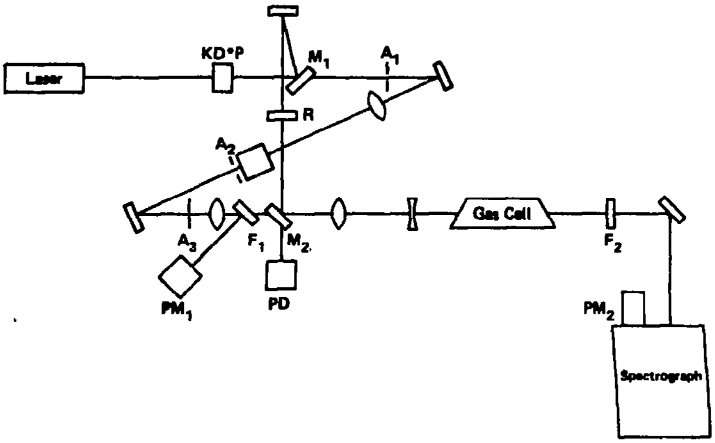

FIG. 1. Experimental arrangement used to measure anti-Stokes Raman gain in inverted iodine. *A*, aperture; *F*, filter; *M*, mirror; *PD*, photodiode; *PM*, photomultiplier; and *R*, half-wave rotator.

to minimize difficulties with optical breakdown and saturation of the Raman gain by depletion of the excited-state population. A single pulse from the train was selected, passed through a spatial filter, and then amplified by Nd:glass amplifiers to an energy of 0.25 J. After amplification, the beam intensity was 10^9 W/cm^2, and the divergence angle was 250 μrad.

This pulse passed through a deuterated potassium dihydrogen phosphate crystal in which approximately 10% of the energy was converted to the second-harmonic wavelength of 5324 Å. Mirror M_1 reflected the pulse at the fundamental wavelength and transmitted the second harmonic. The second-harmonic pulse was then used to pump a traveling-wave rhodamine *B* dye laser which provided the ASRS probe pulse. The dye laser consisted of a 1-cm quartz cell containing a $10^{-4}M$ solution of the dye in water. Its emission occurred in a 100-cm^{-1} bandwidth with the peak at 5850 Å. The dye cell windows were tilted to Brewster's angle with respect to the laser pulse direction so interference effects were avoided and a smooth spectral intensity distribution was produced. The apertures A_1, A_2, and A_3 were used to restrict the diameter and angular divergence of the dye laser probe pulse to equal, as nearly as possible, the diameter and divergence of the pump pulse. This restriction was necessary since only the portion of the probe pulse which overlapped with the pump pulse in the iodine could experience gain and any additional probe light reaching the detection apparatus would have reduced the signal-to-noise ratio. To avoid saturation of the Raman gain, the power of the probe pulse was reduced to about 100 W by filter F_1. The probe-pulse energy E_1 was measured by the photomultiplier PM_1. A half-wave plate was used to make the polarization of the pump pulse parallel to that of the probe pulse. The photodiode *PD* measured the pump-pulse intensity and the time at which the photodiode signal occurred was compared with the flashlamp discharge current to verify proper time synchronization. The probe and pump pulses were recombined at mirror M_2. Considerable attention was given to maintaining exact spatial and temporal overlap of the two beams over the length of the iodine cell. An inverted Gallilean telescope reduced the beam diameters to 2 mm. Entering the iodine cell, the pump-pulse intensity was approximately 10^{10} W/cm^2. The maximum laser pump intensity in the collimated beam was limited by the damage threshold of the quartz cell window. A collimated-beam, rather than a focused-beam, geometry was chosen again to avoid optical breakdown and gain saturation, and also to minimize the effects of line broadening due to the optical Stark effect. As the two pulses passed through the inverted iodine, the portion of the dye emission spectrum at the anti-Stokes Raman wavelength was amplified as indicated in Fig. 2. After passing through the iodine cell, the pump pulse was blocked by the filter F_2, and the probe pulse entered the 1-m Spex spectrograph which was set to transmit a bandwidth of 0.3 cm^{-1} at the anti-

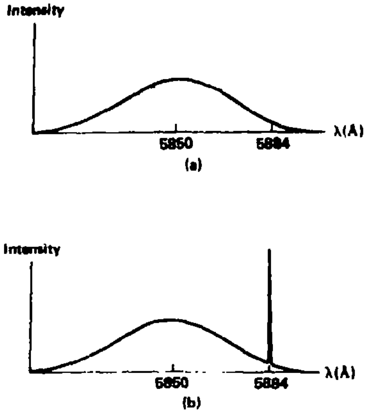

FIG. 2. Schematic representation of the laser probe pulse spectrum (a) before and (b) after passing through the inverted iodine coincident with the laser pump pulse.

Stokes wavelength. The amplitude of the signal from the photomultiplier PM_2 was proportional to the transmitted probe pulse energy E_2. The ASRS gain was obtained from the ratio E_2/E_1 which was measured to be 7.4 ± 0.5. No gain was observed when the iodine was not inverted, when the laser intensity was reduced by a factor of 3, or when the spectrograph was tuned 0.5 cm^{-1} away from the anti-Stokes wavelength.

Atomic iodine was chosen for these investigations for several reasons. A number density of inverted atoms sufficient to produce a measurable electronic Raman gain could be generated by flash photolysis of CF_3I under reasonable flashlamp pumping conditions. Since the transition ${}^2P_{1/2}-{}^2P_{3/2}$ is the 1.315-μm atomic iodine laser transition, the ways in which to produce efficiently and measure quantitatively the population inversion had been well studied,[6] and information concerning the relevant kinetics was available.[7] At the laser intensities used in this experiment, stimulated vibrational Raman scattering did not occur in CF_3I or the dissociation products.

An iodine laser head designed to assure uniform pumping of the CF_3I was used for these experiments. The CF_3I was contained at a pressure of 100 Torr in a tube 60 cm long with 12 mm diam. Pumping was accomplished by four linear flashlamps with 7-mm bore and 50-cm arc length. The flashlamp discharge lasted 20 μsec with equal 10-μsec rise and decay. With the addition of an external mirror to provide feedback at 1.315 μm, laser action in the iodine cell occurred. The iodine transition is magnetic-dipole allowed with a single-photon emission cross section $\sigma = 2\times10^{16}$ cm^2 for 100 Torr CF_3I. Measurements of the output energy at laser threshold allowed an estimate of the peak inversion density of $N = (2-5)\times10^{16}$ atoms/cm^3. Significantly higher inversion densities were not possible because of the superfluorescence decay of the excited state. Since for CF_3I pressure of 100 Torr, the excited-state lifetime of ~ 50 μsec is long compared to the flashlamp discharge, the peak inversion occurred at the end of the discharge. It was a major concern that shock waves would be generated in the CF_3I by flashlamp heating before a significant inversion existed and the resulting light scattering would prevent the observation of gain. To study this effect, a He-Ne laser beam of various diameters was passed through the iodine cell followed by a lens-aperture spatial filter. The transmitted intensity, measured by a photomultiplier, decreased abruptly 25 μsec after initiation of the flashlamp discharge. Thus, the laser pulses had to pass through the iodine cell within 5 μsec of the end of the discharge. Since the excited-state lifetime is sensitive to small concentrations of impurity molecules, notably I_2 and O_2,[8] the gas cell was pumped and refilled after each shot.

According to the theory of stimulated Raman scattering,[9] exponential amplification $I_2 = I_1 \times \exp(gI_LL)$ occurs if the amplified ASRS intensity I_2 is small compared to the laser intensity I_L. I_1 is the incident ASRS intensity, L is the interaction length, and the steady-state gain coefficient g is given by[10]

$$g = \frac{2\lambda_{AS}{}^2 N(\partial\sigma/\partial\Omega)}{\hbar\omega_L}\,\frac{\Gamma}{\Gamma^2+\Delta\omega^2}\,. \tag{1}$$

Here $\partial\sigma/\partial\Omega$ and Γ are the spontaneous Raman scattering differential cross section and linewidth (half width at half-maximum), respectively; λ_{AS} is the anti-Stokes wavelength; ω_L is the laser frequency; and $\Delta\omega = \omega_L - \omega_{AS} - \omega_0$ is the frequency offset from exact resonance. The Raman scattering cross section for atomic iodine can be estimated from general formulas.[11] Since the energy levels of interest are far from all other atomic levels and from the ionization continuum, a summation over virtual states can be carried out approximately by the use of sum rules. Such an estimate gives the value of $\partial\sigma/\partial\Omega \simeq 10^{-28}$ cm^2/sr for a pump wavelength of 1.06 μm. The collisionally broadened Raman linewidth is $\Gamma \simeq 0.05$ cm^{-1}.[12] The optical Stark shift of the iodine levels under the influence of a laser intensity of 10^{10} W/cm^2 is approximately 0.03 cm^{-1}. From Eq. (1) the expected ASRS gain was estimated to be approximately e^7. Since the pump pulse duration t_p satisfies the relationship $t_p > gI_L L\Gamma^{-1}$, the gain may be calculated by use of the steady-state theory.[13]

The experimentally measured quantity is the energy ratio E_2/E_1 where E_1 and E_2 are, respectively, the incident and amplified pulse energies in the 0.3-cm^{-1} (full width at half-maximum) bandwidth transmitted by the spectrograph. Thus, to compare with the experiment, the ASRS intensity gain must be expressed in terms of this ratio. The pulse energies are obtained from the intensities by integration over time t, radius r, and frequency offset $\Delta\omega$:

$$E_{1,2} = \int I_{1,2}(r,t,\Delta\omega)2\pi r\,dr\,dt\,d\Delta\omega. \tag{2}$$

The incident probe and pump pulses are taken to be Gaussian with the same radius and duration:

$$I_{1,L} = I_{10,L0}\exp\{-[(r/r_0)^2 + (t/t_0)^2]\}. \tag{3}$$

In addition, we assume the pump pulse to be monochromatic, and the probe intensity to be constant as a function of frequency over the bandwidth of interest.

We introduce the parameters $R = r/r_0$, $T = t/t_0$, $\omega = \Delta\omega/\Gamma$, and $\gamma = g(0)I_{L0}L$ which is the gain coefficient on resonance at the maximum laser intensity. The integration to obtain E_1 can be done exactly. However, only the radial part of the E_2 integral can be done, so an approximation must be made. For $R^2, T^2, \omega^2 \ll 1$ and $\gamma \gg 1$, I_2 may be approximated by

$$I_2 \simeq I_{10}\exp[\gamma(1 - R^2 - T^2 - \omega^2)]. \tag{4}$$

The effects of "gain narrowing" are immediately apparent as the half-width in R, T, or ω of the amplified pulse is proportional to $(\ln 2/\gamma)^{1/2}$. Thus for sufficiently large values of γ, the amplified pulse energy E_2 is obtained to a high degree of accuracy by integration over the volume in the (R, T, ω) parameter space which does not violate the initial assumption of the approximation given by Eq. (4) to I_2. The calculated value of the energy ratio is then $E_2/E_1 = 0.3(e^\gamma/\gamma^2)$. From the experimental value of the ratio $E_2/E_1 = 7.4 \pm 0.5$, the peak ASRS gain e^γ occurring under the conditions of this experiment is found to be $e^{7.1\pm0.2}$. Using this value for the peak gain, the error in the approximation to E_2 was estimated by numerical integration and found to be less than 15%. In view of the uncertainties in experimental parameters, the observed gain is in good agreement with theoretical predictions.

The authors gratefully acknowledge many interesting discussions with Dr. C. K. Rhodes, Dr. D. W. Gregg, and Dr. A. J. Glass and the expert technical assistance of Mr. T. C. Kuklo.

---

*Work performed under the auspices of the U. S. Atomic Energy Commission.

†Present address: Los Alamos Scientific Laboratory, University of California, Los Alamos, N. Mex. 87544.

[1] S. Yatsiv, M. Rokni, and S. Barak, Phys. Rev. Lett. 20, 1282 (1968).

[2] J. Ducuing, G. Hauchecorne, A. Mysyrowicz, and F. Pradere, Phys. Lett. 28A, 746 (1969).

[3] P. P. Sorokin, N. S. Shiren, J. R. Lankard, E. C. Hammond, and T. G. Kazyaka, Appl. Phys. Lett. 10, 44 (1967).

[4] A. V. Vinogradov and E. A. Yukov, Pis'ma Zh. Eksp. Teor. Fiz. 16, 631 (1972) [JETP Lett. 16, 447 (1972)].

[5] B. C. Johnson, L. L. Steinmetz, R. L. Carman, and W. H. Lowdermilk, in *Proceedings of the IEEE–Optical Society of America Conference on Laser Engineering and Applications, Washington, D. C., 1973* (Institute of Electrical and Electronic Engineers, New York, 1973).

[6] D. E. O'Brien and J. R. Bowen, J. Appl. Phys. 42, 1010 (1971).

[7] D. E. O'Brien and J. R. Bowen, J. Appl. Phys. 40, 4767 (1969).

[8] R. J. Donovan and D. Husain, Trans. Faraday Soc. 68, 2023 (1966).

[9] N. Bloembergen, Amer. J. Phys. 35, 784 (1967).

[10] M. Maier, W. Kaiser, and J. A. Giordmaine, Phys. Rev. 177, 580 (1969).

[11] W. Heitler, *The Quantum Theory of Radiation* (Oxford Univ. Press, Oxford, England, 1954).

[12] K. Hohla, dissertation, Universität München, 1971 (unpublished). For discussion of the iodine hyperfine structure, see also V. S. Zuev, V. A. Katulin, V. Yu. Nosach, and O. Yu. Nosach, Zh. Eksp. Teor. Fiz. 62, 1673 (1972) [Sov. Phys. JETP 35, 870 (1972)].

[13] N. M. Kroll, J. Appl. Phys. 36, 34 (1965); see also C. S. Wang, Phys. Rev. 182, 482 (1969).

Calcium Double K-Shell Ionization Produced from 24.0- to 48.0-MeV Oxygen Bombardment*

David K. Olsen and C. Fred Moore
Center for Nuclear Studies, University of Texas, Austin, Texas 78712
(Received 28 May 1974)

We have measured relative x-ray-production cross sections for Ca $K\alpha$ satellite and hypersatellite transitions produced from 24.0- to 48.0-MeV oxygen bombardment of thick targets. All cross-section ratios as functions of projectile energy for initial defect configurations K^kL^l, where $k = 1, 2$ and $l = 0, 1, 2, 3, 4$, are in qualitative agreement with configuration-space binary-encounter-approximation predictions.

Inner-shell ionization by fast heavy-ion impact has received much attention in recent years.[1] Coulomb ionization by protons and α particles is reasonably well understood; however, as the projectile charge increases many new phenomena occur and many small effects become large.[1] In particular, the number of electron vacancies produced increases which greatly complicates a description of the collision. It has been proposed that such a collision can be described with classical and semiclassical impact-parameter formalisms.[2-4]

In this Letter we report the measurement for the first time of both satellite and hypersatellite relative x-ray-production cross sections over a range of beam energies. Relative Ca x-ray-production cross sections were measured for all initial defect configurations K^kL^l, where $k = 1, 2$

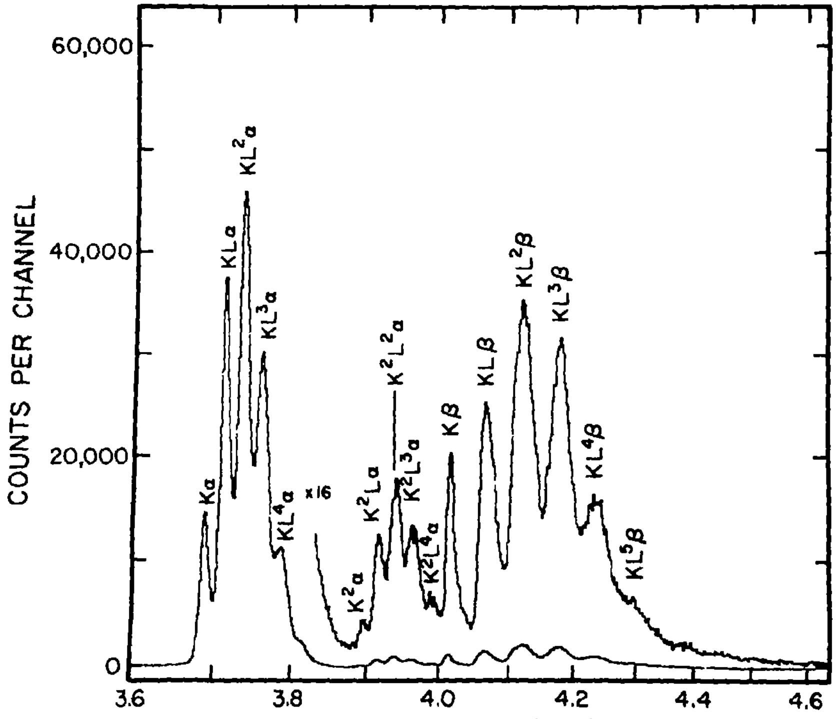

FIG. 1. Calcium $K\alpha$ and $K\beta$ x-ray spectrum produced with 48.0-MeV O^{7+} bombardment. A total charge of 2.0 μC was collected for each channel which had a constant wavelength width of 0.000 76 Å. Each line is labeled by the electron vacancies in the initial state where the transition energies are given in Table I. Note the similar relative intensities distributions for the satellite (K^1L^l) and hypersatellite (K^2L^l) groups.

and $l = 0, 1, 2, 3, 4$, from 24.0- to 48.0-MeV oxygen bombardment in 3.0-MeV steps. Previously, thick-target hypersatellite yield ratios have been measured only at a single energy,[5] whereas satellite cross-section ratios have been measured as functions of beam energy[6,7] and projectile and target charge.[8] The additional cross-section ratios given by the hypersatellite lines provide a much more stringent test of the impact-parameter formalism and ionization mechanisms.

The measurements were made with O^{6+} to O^{7+} beams from the University of Texas EN tandem Van de Graaff accelerator which were focused onto thick calcium targets mounted at 45°. The resulting x-ray spectra were measured at 90° with an Applied Research Laboratory curved-crystal spectrometer employing a LiF crystal ($2d = 4.027$ Å). Figure 1 shows a spectrum produced with 48-MeV oxygen bombardment. At this high energy the total double-K-vacancy $K\alpha$ yield is 2.0% of the total single-K-vacancy $K\alpha$ yield. Table I compares the experimental transition energies with Hartree-Fock-Slater[9] (HFS) and Hartree-Fock[10] (HF) calculations normalized by adding a constant energy to each transition in order to give the experimental $K\alpha$ diagram energy. The HF calculations reproduce within a few eV the experimental hypersatellite energies, whereas the HFS energies are off by about 40 eV. Evidently the Slater approximation for the exchange integral is not adequate for double K-shell vacancies. This HF agreement with the transition energies, coupled with the one-to-one correspondence in the relative intensities between the satellite and hypersatellite yields for each value of l, gives us confidence that we have identified the number of L-shell vacancies for the hypersatellite lines correctly.

TABLE I. Calculated and experimental satellite and hypersatellite x-ray transition energies in eV.

X-ray	HFS	HF	Exp.
$K\alpha$	3690	3690	3690
$KL\alpha$	3710	3708	3714
$KL^2\alpha$	3732	3729	3737
$KL^3\alpha$	3754	3750	3761
$KL^4\alpha$	3779	3773	3785
$K^2\alpha$	3848	3891	3890
$K^2L\alpha$	3869	3911	3913
$K^2L^2\alpha$	3892	3932	3936
$K^2L^3\alpha$	3916	3955	3959
$K^2L^4\alpha$	3941	3979	3985
$K\beta$	4012	4014	4013

Thick-target spectra were taken from 48.0 MeV down to 24.0 Mev in 3.0-MeV steps. Most spectra were repeated more than once to insure the consistency of the data. The total single-K-vacancy $K\alpha$ yield decreased by about a factor of 23 over this energy range, whereas the total double-K-vacancy $K\alpha$ yield decreased by a factor of about 150. Below 24.0 MeV the hypersatellite lines could not be observed clearly above the background. For each spectrum, the number of counts in each peak was unfolded by fitting the spectral region from the $K\alpha_{1,2}$ line up to and including the $K\alpha_{1,3}$ line with the sum of a linear background and twelve symmetric Gaussians. From these yields, relative thick-target yield ratios as a function of beam energy were found, and relative cross-section ratios as a function of beam energy were calculated based on Eq. (5.2) of Merzbacher and Lewis.[11] Stopping powers from Northcliffe and Schilling,[12] absorption coefficients from Dewey, Maples, and Reynolds,[13] and low-resolution x-ray cross sections for oxygen on calcium from Burch[14] and Gray *et al.*[15] were employed. Because we are only interested in cross-section ratios, much of the error in extracting cross sections from thick-target yields canceled out.

Figure 2 shows the ratio of the total double K-shell x-ray cross section σ_{2K}, summed over all

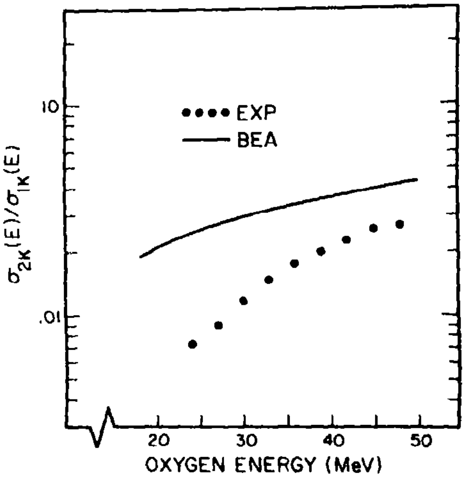

FIG. 2. Experimental ratio of the total double K-shell ionization cross section to the single K-shell ionization cross section summing over all possible L-shell vacancies. The smooth curve is a configuration-space BEA prediction for this ratio from Eq. (2).

L-shell vacancies, to the total single *K*-shell x-ray cross section σ_{1K}. As shown in Fig. 2, at 24 MeV σ_{2K} is 0.0072 times σ_{1K}, whereas at 48.0 MeV this ratio is 0.027. In addition to this cross-section ratio, both the satellite cross-section fractions and the hypersatellite cross-section fractions were extracted from the experimental yields, but are not shown.

These data can be understood using an impact-parameter formalism with a direct Coulomb mechanism. Assuming uncorrelated electrons and shells, and assuming no difference between 2*s* and 2*p* subshells, we can write the cross sections for ejecting *k* *K*-shell electrons and *l* *L*-shell electrons as[2]

$$\sigma_{kK,lL}=\int_0^\infty \binom{2}{k}P_K{}^k(b)[1-P_K(b)]^{2-k}\binom{8}{l}P_L{}^l(b)[1-P_L(b)]^{8-l}2\pi b\,db, \tag{1}$$

where $P_k(b)$ and $P_L(b)$ are the probabilities per electron at impact parameter *b* for removing *K*- and *L*-shell electrons, respectively, and of course depend on the incident projectile energy *E*. After summation over *l*, the ratio of the double *K*-shell cross section to the single *K*-shell cross section is given by

$$\sigma_{2K}/\sigma_{1K}=\int_0^\infty P_K{}^2(b)2\pi b\,db\Big/\int_0^\infty 2P_K(b)[1-P_K(b)]2\pi b\,db. \tag{2}$$

For *K*-shell ionization, $P_L(b)$ in Eq. (1) is confined to only those values of *b* for which $P_K(b)\neq 0$. In this case it is a good approximation to set $P_L(b)=P_L(0)$ which implies that the ionization satellite fractions and hypersatellite fractions are given by the same binomial distribution. That is,

$$\frac{\sigma_{1K,lL}}{\sigma_{1K}}=\frac{\sigma_{2K,lL}}{\sigma_{2K}}=\binom{8}{l}P_L{}^l(0)[1-P_L(0)]^{8-l}. \tag{3}$$

If our assumptions and the impact-parameter formalism are valid, then the satellite fractions and the hypersatellite fractions must be the same; that is, both sets of intensity distributions are generated from the same $P_L(0)$. This can be observed in Fig. 1 for thick-target x-ray yields. For a given number of *L*-shell vacancies, the relative intensity of a satellite line is roughly equal to the relative intensity of the corresponding hypersatellite line. This correspondence is shown more quantitatively in Fig. 3 which shows the $P_L(0)$ extracted from both the satellite and hypersatellite ionization fractions by the use of Eq. (3) for a one-parameter fit at each energy. The x-ray fractions were converted to ionization fractions with fluorescence yields by the use of the statistical model of Larkins,[16] and by the assumption that 2*s* vacancies are transferred to the 2*p* shell by fast Coster-Kronig transitions. The problems associated with this assumption are discussed in Ref. 6. The fits to the fractions are not shown, but were good. The $P_L(0)$ from the two distributions are nearly equal; at 24.0 MeV the $P_L(0)$ from the hypersatellite lines is 20% higher than that from the satellite lines, whereas at 48.0 MeV it is only 10% higher. Part of this difference could be caused by the uncertainty in the exact background level under the hypersatellite lines and deviations of the fluorescence yields from the statistical model. In any case the impact-parameter formalism appears to be valid. The smooth curve is a configuration-space binary-encounter-approximation[3] (BEA) prediction of $P_L(0)$ for direct Coulomb ionization

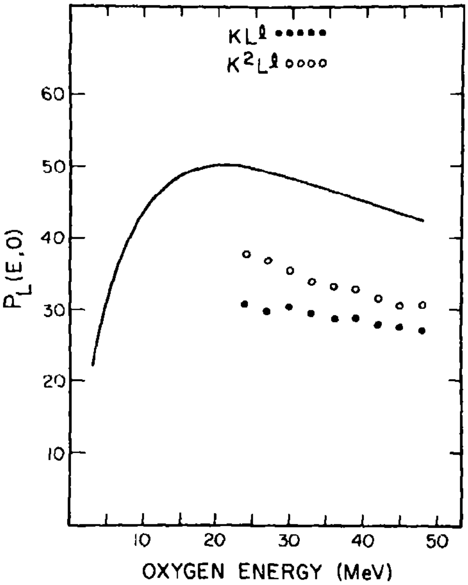

FIG. 3. Experimental $P_L(E,0)$ extracted at each energy from the measured satellite and hypersatellite x-ray fractions using the binomial distribution of Eq. (3) for a one-parameter fit. Statistical-model fluorescence yields were used. The smooth curve is a configuration-space BEA prediction of $P_L(E,0)$.

assuming a point charge of seven for the oxygen projectile and averaging the $2s$ and $2p$ subshells. Although it has the correct shape, this calculated curve is roughly 50% higher than the experimental data. If on the other hand, Eq. (1) were integrated directly with the use of calculated $P_L(b)$, the comparison between experiment and theory would not be transparent because the satellite and hypersatellite fractions depend on $P_L(b)$ raised to high powers.

Similarly the smooth curve in Fig. 2 is a prediction of σ_{2K}/σ_{1K} obtained by integrating Eq. (2) using configuration-space BEA[3] $P_K(b)$ with a projectile charge of seven. Both the experimental ratio and the calculated ratio increase with increasing bombarding energy; however, the theory predicts this ratio to be a factor of 3 too large at 24.0 MeV and 50% too large at 48.0 MeV. The ratio of σ_{2K}/σ_{1K} is sensitive to both the shape and magnitude of $P_K(b)$ because σ_{2K} depends on the square of this probability.

In summary, for the first time both satellite and hypersatellite x-ray-production cross sections have been measured. In particular, it has been measured that the satellite and hypersatellite fractions are very similar, and that multiple L-shell ionization is decreasing whereas multiple K-shell ionization is increasing over the projectile energy range which is considered. The general trend of all the experimental cross section-ratios are given by BEA configuration-space calculations[3]; however, for both the K and L shells the BEA gives more multiple inner-shell ionization than is experimentally measured. Most of the deviations between experiment and theory are thought to arise from the inability to account accurately for binding-energy changes and distortion effects during the collisions. For example, it can be argued that Eq. (2) should be recast to account for the increase in binding of one K-shell electron due to the prior removal of the other. This would lower σ_{2K} and improve the agreement with experiment; however, since the collision time is very short such procedures are subject to interpretation.

The authors thank J. McWherter for assistance with the data taking and W. Hodge for assistance with the HF calculations. Constructive conversations concerning this work with James H. McGuire are gratefully acknowledged.

---

*Work supported in part by the U. S. Atomic Energy Commission under Contract No. AT-(40-1)-2972.

[1] J. D. Garcia, R. J. Fortner, and T. M. Kavanagh, Rev. Mod. Phys. 45, 111 (1973).

[2] J. M. Hansteen and O. P. Mosebekk, Phys. Rev. Lett. 29, 1361 (1972).

[3] J. S. Hansen, Phys. Rev. A 8, 822 (1973).

[4] J. H. McGuire and P. Richard, Phys. Rev. A 8, 1374 (1973).

[5] P. Richard, W. Hodge, and C. F. Moore, Phys. Rev. Lett. 29, 393 (1972).

[6] A. R. Knudson, D. J. Nagel, and P. G. Burkhalter, Phys. Lett. 42A, 69 (1972).

[7] A. R. Knudson, P. G. Burkhalter, and D. J. Nagel, in *Proceedings of the International Conference on Inner Shell Ionization Phenomena and Future Applications, Atlanta, Georgia, 1972*, edited by R. W. Fink *et al.*, CONF-720404 (U. S. Atomic Energy Commission, Oak Ridge, Tenn., 1973); D. K. Olsen, C. F. Moore, and R. L. Kauffman, Phys. Lett. 44A, 109 (1973); P. Richard, R. L. Kauffman, J. H. McGuire, C. F. Moore, and D. K. Olsen, Phys. Rev. A 8, 1369 (1973).

[8] R. L. Kauffman, P. Richard, J. H. McGuire, and C. F. Moore, Phys. Rev. A 8, 1233 (1973); F. Hopkins, D. O. Elliott, C. P. Bhalla, and P. Richard, Phys. Rev. A 8, 2952.

[9] F. Herman and S. Skillman, *Atomic Structure Calculations* (Prentice-Hall, Englewood Cliffs, N. J., 1963).

[10] C. Froese Fischer, Comput. Phys. Commun. 1, 151 (1969).

[11] E. Merzbacher and H. W. Lewis, in *Encyclopedia of Physics*, edited by S. Flügge (Springer, Berlin, 1958), Vol. 34, p. 166.

[12] L. C. Northcliffe and R. F. Schilling, Nucl. Data, Sect. A 7, 233 (1970).

[13] R. D. Dewey, R. S. Maples, and T. W. Reynolds, *Progress in Nuclear Energy* (Pergamon, New York, 1969), Vol. 9, Ser. 9.

[14] D. F. Burch, Ph.D. thesis, University of Texas, 1971 (unpublished).

[15] T. J. Gray, R. P. Chaturvedi, J. L. Duggan, C. C. Sachtleben, and J. Lin, private communication.

[16] F. P. Larkins, J. Phys. B: Proc. Phys. Soc., London 4, L29 (1971).

Population of Excited Electronic Levels by Beta Decay, and Its Influence on Mössbauer Source Spectra

L. L. Hirst,* J. Stöhr, G. K. Shenoy,† and G. M. Kalvius
Physik Department, Technische Universität München, 8046 Garching, German Federal Republic

(Received 13 May 1974)

In a Mössbauer source experiment the β decay produces a large initial population of the excited electronic levels of the Mössbauer source atom. It is shown that this causes such excited levels to contribute more prominently in the source experiment than in the corresponding absorber experiment. These contributions can provide a particularly sensitive method for studying relaxation rates among the excited electronic levels. A detailed discussion and model calculations are given for dilute paramagnetic $4f$ impurities in a metal.

In Mössbauer (MB) source experiments there is initially a large population of high-lying electronic levels of the MB atom following the β decay. The relaxation of these populations toward their thermal-equilibrium values is referred to as rearrangement. In the past, rearrangement has been considered mainly in the special sense of the transfer of electrons to or from the source atom, i.e., *configurational* rearrangement.[1] Here we point out that the time for *intraconfigurational* rearrangement [e.g., the thermalization of initial populations of excited crystal-field (CEF) levels] can be appreciable even when the time needed for the configurational rearrangement is negligibly small. In such a case, the MB spectrum in a source experiment contains appreciable contributions from the intraconfigurational excited states which would be absent from the corresponding absorber spectrum. We shall indicate how these intraconfigurational rearrangement effects can be dealt with theoretically, and show that in favorable cases the MB source experiments provide a particularly powerful technique for investigating relaxation processes involving intraconfigurational excited levels.

Such intraconfigurational rearrangement effects can affect the MB source spectra of various substances, including insulators and intermetallic compounds.[2] For brevity, however, we restrict the present discussion to the MB spectra of dilute $4f$ impurities in metals.[3-5] To achieve sufficient intensity at high dilution, such impurities have always been studied as sources. Although absorber experiments appear impractical, it is still of interest to compare theoretical spectra for the source and absorber cases.

Experiments of the type considered here are performed using as a source a metal foil containing neutron-activated $4f$ impurities which are the radioactive parent of the MB atom. The β decay of such an impurity prepares the emission of the MB γ quantum, and also starts a rearrangement of the electronic shell of the impurity in response to the change in nuclear charge. The rearrangement proceeds as a multistep cascade from higher to lower levels, with different times characteristic of the various decay steps. Any decay step can be regarded as quasi-instantaneous as far as the MB effect is concerned when its characteristic time is short compared to $(\omega_{\mathrm{hf}})^{-1} \approx 10^{-10}$ sec, where $\hbar\omega_{\mathrm{hf}}$ is the total hyperfine splitting.[6]

Since the β decay increases the nuclear charge by one, the first rearrangement step to consider in the electronic shell is the configurational rearrangement $4f^{n-1} \rightarrow 4f^{n}$. The decay of the unstable configuration occurs by absorption of a conduction electron into the $4f$ shell via the Anderson mixing interaction. The rate is approximately $\Delta/\hbar \approx 2\times10^{13}$ sec^{-1}, where we have assumed a value of 0.01 eV for the virtual bound-state width Δ. The configurational rearrangement is therefore quasi-instantaneous.

The $4f^{n}$ ground configuration of the MB atom is split into various $[SL]$-J manifolds. The ground manifold is subject to an overall CEF splitting of ~0.01 eV, and the excited manifolds lie 0.1 eV or more above it. The configurational rearrangement will leave the electronic shell in a highly excited state within the ground configuration, so an intraconfigurational rearrangement is necessary to reach thermal equilibrium. This is provided by the k-f coupling in the sense of a generalized Schrieffer-Wolff effective interaction.[7,8] When written in its most general form, this interaction provides transitions among all pairs of states belonging to the ground configuration. In second-order perturbation theory the transition rate may be written[8,9]

$$w_{i\to f} = 2\pi |I\rho(\epsilon_F)|^2 \zeta(E_f - E_i, kT). \quad (1)$$

Here $\rho(\epsilon_F)$ is the density of conduction-electron states, I is a coupling constant characterizing the generalized k-f interaction, and $\zeta(E,kT) \equiv E[\exp(E/kT) - 1]^{-1}$. We have omitted from Eq. (1) a sum over matrix elements which depends upon the specific transition but is of the order of unity. For the initial steps of the intraconfigurational rearrangement we are interested in decays from high-energy states, for which $E_i - E_f \gg kT$. Then $\zeta \approx E_i - E_f$, so that the decay rate is temperature independent and proportional to the energy difference. Taking $I\rho(\epsilon_F) = 10^{-2}$ from electron paramagnetic resonance (EPR) studies,[10] we find that such a high-energy decay is quasi-instantaneous ($w_{i\to f} \gg w_{\mathrm{hf}}$) when $E_i - E_f \gg 0.01$ eV. The rearrangement among $[SL]$-J manifolds can thus be regarded as quasi-instantaneous. The rearrangement among the lowest CEF levels, however, will in general be slow enough to influence the MB spectrum.

Solutions for MB spectra in the presence of electronic relaxation can be obtained by solving an appropriate equation of motion.[3,11] The intraconfigurational rearrangement results from the same electronic relaxation processes and hence is implicit in the equation of motion; all that is necessary is to make the proper choice of the initial population distribution appearing in the theory. For a MB *absorber*, the appropriate initial population is a thermal Boltzman weighting of the nucleonic eigenstates with the nucleus in its ground state. In the case of a $4f$ impurity as the MB *source*, the cascade of quasi-instantaneous decays through the higher electronic levels following the β decay will produce an essentially random initial population of the CEF levels within the $[SL]$-J ground manifold. The initial nuclear-spin orientation is also random. Hence, the proper initial population distribution is the one in which the occupation probability is equal for all nucleonic eigenstates containing the nucleus in its excited state and the electronic shell in its $[SL]$-J ground manifold.

The numerical evaluation of the above solution does pose practical problems, since, in general, it is necessary to include all CEF levels in the treatment. If the methods of Ref. 3 are applied straightforwardly, one obtains matrix equations with a dimensionality of several hundred in typical cases. This dimensionality can be reduced considerably by the application of symmetry considerations,[3] but the computational problem remains a major one. We shall therefore illustrate our discussion with model calculations for Yb^{3+} in a cubic CEF where only three levels exist. Such calculations are shown in Fig. 1. The solid curves show source spectra at various temperatures. For comparison the corresponding absorber spectra are shown as dashed curves. The CEF parameters were chosen to produce a Γ_7 doublet ground level, and Γ_8 and Γ_6 excited levels at 17.5 and 18.2 K, respectively. The relaxation arises from a generalized Schrieffer-Wolff[7,8] interaction with $I\rho(\epsilon_F) = 0.01$. The two main peaks of the low-temperature spectra result from the Γ_7 ground level.[5] The low-temperature source spectra show additional contributions from the

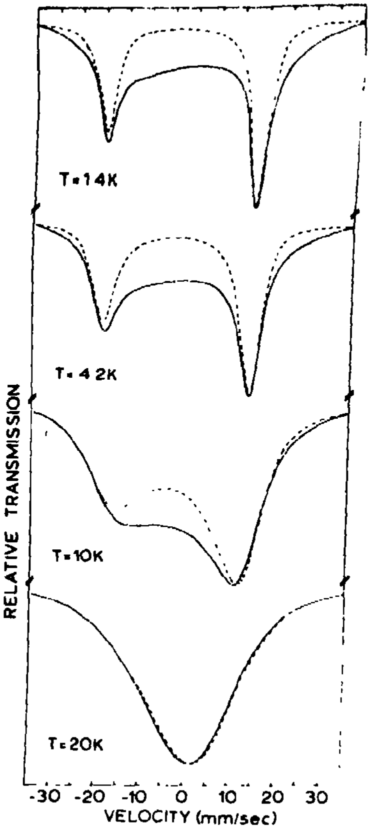

FIG. 1. Model calculations for the $2^+ \to 0^+$ Mössbauer spectrum of ^{170}Yb^{3+} impurities in a metal, where the relaxation is produced by a generalized Schrieffer-Wolff coupling with $I\rho(\epsilon_F) = 0.01$. Source and absorber spectra are indicated by solid and dashed curves, respectively.

CEF excited levels, which are absent from the corresponding absorber spectra. As indicated by Eq. (1), the rate of relaxation from a higher to a lower CEF level approaches a finite limit for temperatures small compared to the CEF energy difference. *Since the initial populations are also temperature independent in a source experiment, the contributions from the excited CEF levels approach a finite limiting form at temperatures small compared to the CEF splittings. This is in contrast to the absorber case, where contributions from excited CEF levels vanish in the low-temperature limit.*

The CEF parameters of our Yb^{3+} model calculation have deliberately been chosen so as to produce Yb^{3+} CEF levels resembling the three lowest CEF levels believed[5,10] to occur in *Au*:Er. Actual calculations for Er^{3+} are not yet available because of its larger number of electronic levels; they can, however, be expected to yield spectra qualitatively similar to Fig. 1. In fact, our earlier measurements of the ^{166}Er resonance of dilute *Au*:^{166}Ho sources[5] yielded spectra with a central structure resembling that seen in Fig. 1. This structure was originally assumed to result from Ho clusters in the *Au*:Ho sources, since it could not be accounted for by a theory assuming a Boltzman initial population of the excited CEF levels.[5] However, much evidence (autoradiographs, good reproducibility of the results) points to an absence of clusters in this alloy, as opposed to other alloys such as *Ag*:Ho where clustering does occur.[12] We now believe the central structure observed in Ref. 5 to be the result of intraconfigurational rearrangement.

If the parameters are changed so as to decrease $w_{e\to g}$, the rate of decay from an excited CEF level to the ground level, then the excited-level contributions become more prominent and finally take the form of well-resolved peaks. If $w_{e\to g}$ is increased, the excited level contributions become less prominent and disappear in the limit $w_{e\to g} \gg \omega_{\rm hf}$. In this case, the excited CEF levels may still influence the spectrum insofar as they provide an additional channel for relaxation.[2,9,10]

In Fig. 2 we present a further model calculation for Yb^{3+} with the same CEF parameters as before, but with a *k*-*f* coupling of the "exchange" form $-2J_{\rm cx}'\vec{J}\cdot\vec{s}$, which has traditionally been assumed in discussing the EPR of 4*f* impurities in metals.[9,10] Whereas the generalized Schrieffer-Wolff coupling[7,8] produces comparable transition rates between any pair of CEF levels (aside from the energy dependences), the selection rules on the vector operator $\vec{J}$ do not allow a direct transition from the Γ_8 excited CEF level to the Γ_7 ground level. The large initial population of the Γ_8 excited level in a MB source experiment can only decay slowly via the Γ_6 level and thus contributes a well-resolved hf structure to the spectrum. The differences between Figs. 1 and 2 demonstrate that MB source experiments provide an unusually sensitive test for the form of the *k*-*f* coupling.

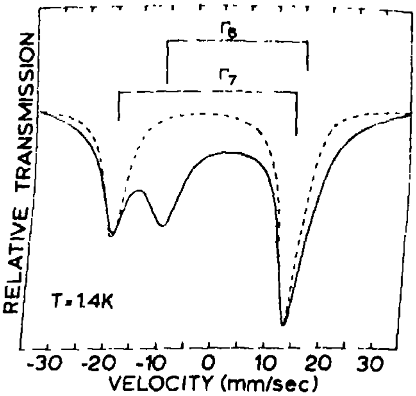

FIG. 2. Model calculations as in Fig. 1, except that the relaxation is produced by an "exchange" coupling $-2J_{\rm cx}'\vec{J}\cdot\vec{s}$. We take $2J_{\rm cx}'\rho(\epsilon_F)=0.0031$, which produces the same relaxation rate within the CEF ground doublet as the coupling used in Fig. 1. The source spectrum (solid curve) is a superposition of two narrow-line contributions from the Γ_7 CEF ground level and two from the Γ_8 excited level; in the absorber spectrum (dashed curve) the excited-level contributions are negligible.

Finally, we remark that intraconfigurational rearrangement effects similar to those discussed here need also to be taken into account in the analysis of perturbed angular correlation experiments.

---

*Present address: Institut für Theoretische Physik, Universität Frankfurt am Main, Frankfurt am Main, German Federal Republic.

†Permanent address: Laboratoire de Chimie Nucléaire, 67037 Strasbourg, Cedex, France.

[1] H. H. Wickman and G. K. Wertheim, in *Chemical Applications of Mössbauer Spectroscopy*, edited by V. I. Goldanskii and R. H. Herber (Academic, New York, 1968).

[2] L. L. Hirst, to be published.

[3] L. L. Hirst, J. Phys. Chem. Solids 31, 655 (1969).

[4] F. Gonzalez-Jimenez, P. Imbert, and F. Hartmann-Boutron, Phys. Rev. B 9, 95 (1974).

---

[5] G. K. Shenoy, J. Stöhr, and G. M. Kalvius, Solid State Commun. 13, 909 (1973).

[6] Our estimate applies to the usually encountered case $(\omega_{hf})^{-1} < \tau$, where τ is the lifetime of the nuclear excited state. If one had $\tau < (\omega_{hf})^{-1}$ then the comparison would be to τ instead of $(\omega_{hf})^{-1}$.

[7] B. Coqblin and J. R. Schrieffer, Phys. Rev. 185, 847 (1969).

[8] L. L. Hirst, Z. Phys. 244, 230 (1971).

[9] L. L. Hirst, Phys. Rev. 181, 597 (1969).

[10] D. Davidov, C. Rettori, A. Dixon, K. Baberschke, E. P. Chock, and R. Orbach, Phys. Rev. B 8, 3563 (1973).

[11] The treatment of Ref. 3 included only the CEF ground level, but the extension to many CEF levels is immediate.

[12] J. Stöhr and G. K. Shenoy, Solid State Commun. 14, 583 (1974).

Trapped-Particle Stabilization of Localized Interchange Modes in Axisymmetric Toroidal Plasmas

J. W. Connor and R. J. Hastie
United Kingdom Atomic Energy Authority Culham Laboratory, Abingdon, Berkshire, United Kingdom

(Received 6 June 1974)

A stability criterion for localized modes in an axisymmetric toroidal plasma is derived from the kinetic energy principle, taking account of trapped particles. This criterion predicts greater stability than the Mercier criterion.

Tokamaks will, in the near future, operate in the "banana" regime of collision frequencies: $\nu_{\mathrm{eff}}\tau_b \ll 1$, where $\nu_{\mathrm{eff}} = \nu/\epsilon$ is the effective collision frequency and $\tau_b = Rq/\epsilon^{1/2}v_{\mathrm{th}}$ is the bounce time of a trapped particle. Here $\epsilon = a/R$ is the inverse aspect ratio of the torus with a the minor and R the major radius, ν is the 90° collision frequency, v_{th} is a thermal velocity, and q is the safety factor. The stability properties of tokamaks with regard to gross kink modes and localized interchange modes have been established almost exclusively from investigations of the magnetohydrodynamic (MHD) equations and especially the MHD energy principle.[1] These are only valid when $\nu\tau_{\mathrm{MHD}} \gg 1$, where $\tau_{\mathrm{MHD}} \sim (Ra)^{1/2}/v_{\mathrm{th}}$ is a typical MHD time scale. In the banana regime this inequality is in fact reversed and justification for the use of MHD equations relies on the inequality $\delta W_K \geq \delta W_{\mathrm{MHD}}$ relating the kinetic energy principle[2,3] to the MHD one. This inequality implies that stability predictions based on magnetohydrodynamics will err on the pessimistic side, so that the criteria obtained, though sufficient, may not be necessary for the stability of the types of modes considered. In this paper we derive a less pessimistic energy principle from the kinetic one, and apply it to a detailed study of the localized interchange instability in an axially symmetric toroidal equilibrium.

The equilibrium configuration we shall be concerned with is that of an isotropic-pressure plasma in an axially symmetric toroidal magnetic field. Following Bernstein *et al.*[1] we employ the Ψ, φ, χ coordinate system in which Ψ is the poloidal magnetic flux function, φ is the angle about the axis of symmetry, and surfaces of constant χ are orthogonal to those of φ and Ψ. Thus the plasma pressure $p = p(\Psi)$, the poloidal magnetic field is B_χ, and the toroidal magnetic field $B_\varphi = I(\Psi)/R$, where R is the distance to the axis of symmetry; the Jacobian of the transformation is denoted by J.

We now consider the MHD and kinetic energy principles, listing a number of relevant properties. In terms of the infinitesimal plasma displacement $\vec{\xi}$, the MHD energy integral δW_{MHD} for a plasma bounded by perfectly conducting rigid walls may be written in the form

$$\delta W_{\mathrm{MHD}}(\vec{\xi}) = \delta W_0(\vec{\xi}_\perp) + \delta W_1(\vec{\xi}_\perp, \xi_\parallel), \tag{1}$$

where

$$\delta W_0 = \int d^3x [\vec{Q}^2 - \vec{j}\cdot\vec{Q}\times\vec{\xi} + (\vec{\xi}\cdot\nabla p)(\nabla\cdot\vec{\xi})], \tag{2}$$

$$\delta W_1 = \int d^3x\, \gamma p (\nabla\cdot\vec{\xi})^2, \tag{3}$$

and

$$\vec{Q} = \nabla\times(\vec{\xi}\times\vec{B}). \tag{4}$$

As anticipated by the notation it can be shown that δW_0 is stationary with respect to variations of $\xi_\parallel = \vec{\xi}\cdot\vec{B}/B$. The minimization of δW_1 with respect to $\xi_\parallel$ can be performed without difficulty, but the result obtained for equilibria with closed field lines differs from that obtained when field lines cover a magnetic surface ergodically. In the former case the result is

$$\min \delta W_1(\xi_\parallel) = \int d^3x\, \gamma p \langle\nabla\cdot\vec{\xi}_\perp\rangle^2, \tag{5}$$

where

$$\langle A\rangle = \frac{\oint A\, dl/B}{\oint dl/B}$$

and the loop integral is around a closed field line. In the latter case

$$\min \delta W_1(\xi_\parallel) = 0. \tag{6}$$

For the particular case of an axisymmetric toroidal equilibrium, Eq. (6) appears in Mercier's[4] investigation of localized modes as a minimization of δW_1 with respect to $Z \equiv \xi_\chi/B_\chi$, provided $m\oint \nu\, d\chi \neq 2k\pi$ (k any integer), where m is the toroidal mode number and $\nu = IJ/R^2$.

The kinetic energy principle in its one-fluid form[2,3] can be written (for isotropic particle dis tributions)

$$\delta W_K = \delta W_0(\vec{\xi}_\perp) + \delta W_2(\vec{\xi}_\perp), \tag{7}$$

$$\delta W_2 = \int d^3x\, m \int d^3v\, (\partial F/\partial\epsilon)\langle v_\parallel^2 \vec{n}\vec{n}:\nabla\vec{\xi} + \mu B(\nabla\cdot\vec{\xi} - \vec{n}\vec{n}:\nabla\vec{\xi})\rangle^2, \tag{8}$$

where $\vec{n} = \vec{B}/|\vec{B}|$, $v_\parallel^2 = 2(\epsilon - \mu B)$, and ϵ, μ, and F are the particle energy per unit mass, magnetic moment per unit mass, and equilibrium distribution function, respectively. The average is defined by

$$\langle A\rangle = \frac{\oint A\, dl/|v_\parallel|}{\oint dl/|v_\parallel|},$$

with the loop integral over one cycle of the periodic particle trajectory. For trapped particles, or passing particles on closed field lines, this period is well defined, but its meaning is not precise for passing particles when field lines generate magnetic surfaces. To investigate this case in detail we consider an axisymmetric toroidal equilibrium and, following Rosenbluth and Rostoker,[2] we solve the linearized Vlasov equation for the perturbed distribution function δf. Using the conventional m/e expansion and the same ordering of frequency and wavelength as in Ref. 2, we obtain for the guiding center (i.e., gyrophase averaged) part of δf the equation

$$(v_\parallel \vec{n}\cdot\nabla + i\omega)(\delta f + \vec{\xi}\cdot\nabla F) = i\omega(\partial F/\partial\epsilon)[v_\parallel^2 \vec{n}\vec{n}:\nabla\vec{\xi} + \mu B(\nabla\cdot\vec{\xi} - \vec{n}\vec{n}:\nabla\vec{\xi})], \tag{9}$$

where the time dependence of δf and $\vec{\xi}$ has been taken as $\sim e^{i\omega t}$. Now, with the Fourier analysis of δf and $\vec{\xi} \sim e^{im\varphi}$, consideration of one Fourier mode, and introduction of the variables X, U, Z, where $X = RB_\chi \xi_\Psi$ and $U = \xi_\theta/R - IZ/R^2$, the general solution of Eq. (9) may be derived for either trapped or passing particles by using the periodicity of δf in the variable χ. In the low-frequency limit, $\omega\tau \ll 1$ where τ is the bounce time, and with $\omega \to 0$ these results reduce to

$$\begin{aligned} &\delta f + X\partial F/\partial\epsilon = 0, \quad \text{passing particles (provided } m\oint \nu\, d\chi \neq 2k\pi), \\ &\delta f + X\partial F/\partial\epsilon = (\partial F/\partial\epsilon)\langle A \exp(im\int_{\chi_1}^{\chi'} \nu\, d\chi)\rangle, \quad \text{trapped particles,} \end{aligned} \tag{10}$$

where $A = [v_\parallel^2 \vec{n}\vec{n}:\nabla\vec{\xi} + \mu B(\nabla\cdot\vec{\xi} - \vec{n}\vec{n}:\nabla\vec{\xi})]$ and the average is between turning points in χ.

We are not surprised to find that the kinetic analog (δW_2) of the $\gamma p(\nabla\cdot\vec{\xi})^2$ term of the MHD energy integral now takes different form for closed-line and magnetic-surface configurations.

Returning to the Rosenbluth-Rostoker[2] derivation of Eq. (8) we conclude that when the field lines generate magnetic surfaces the velocity-space integration in δW_2 should be over the trapped particles only. With this modification the variational principle established in Ref. 2 in the limit $\omega \to 0$ remains valid, and we proceed by deriving a lower bound for δW_K which has the advantage of being a "fluid energy integral", i.e., one which contains no velocity-space information. Using a Schwartz inequality we obtain the result

$$\delta W_K \geq \delta W_0 + \delta W_3, \tag{11}$$

$$\delta W_3 = \iint d\Psi\, d\varphi\, \gamma p \{\oint J\, d\chi[(\nabla\cdot\vec{\xi})(1-t)^{3/2} + \tfrac{3}{2}t(1-t)^{1/2}(\nabla\cdot\vec{\xi} - \vec{n}\vec{n}:\nabla\vec{\xi})]\}^2 [\oint J\, d\chi (1-t)^{1/2}]^{-1}, \tag{12}$$

where $t = B/B_m$, B_m is the maximum value of B on a field line, and $\gamma = \frac{5}{3}$. The expression for δW_3 can readily be shown to be stationary with respect to variations of $Z \equiv \xi_\chi/B_\chi$, and consequently we may show that

$$\delta W_3 = \min \delta W_4(Z), \tag{13}$$

$$\delta W_4 = \int d^3x\, \gamma p[(\nabla\cdot\vec{\xi})(1-t)^{3/2} + \tfrac{3}{2}t(1-t)^{1/2}(\nabla\cdot\vec{\xi} - \vec{n}\vec{n}:\nabla\vec{\xi})]^2. \tag{14}$$

With the derivation of expression (12) [or equivalently (14)] we have obtained a useful lower bound for the kinetic energy principle, which will nevertheless predict greater stability than the MHD energy principle.

We use the form $\delta W_0 + \delta W_4$ to investigate the stability of the localized interchange perturbations studied by Mercier.[4] All the minimizations performed by Mercier can be repeated in this more complicated calculation, producing the stability criterion

$$p'\frac{\partial}{\partial\Psi}\oint J\, d\chi - (p')^2\oint \frac{J\, d\chi}{B_\chi^2} + \frac{(\frac{1}{2}\oint \nu'\, d\chi - p'\oint \nu\, d\chi/B_\chi^2)^2}{\oint B^2 J\, d\chi/R^2 B_\chi^2} + \gamma p T^2 > 0, \tag{15}$$

where T is a complicated function depending on the number of trapped particles, i.e., on $(1-t)^{1/2}$, and the prime now denotes differentiation with respect to Ψ. The first three terms in expression (15) constitute the Mercier stability criterion. The additional stabilization apparent in the last term arises because of the nonvanishing contribution of the trapped particles to δW_2 [the analog of $\gamma p(\nabla\cdot\vec{\xi})^2$ in the MHD energy integral]. On any magnetic surface which is also a surface of constant B (no trapping), $t\to 1$ and this term would vanish.

This rather complicated stability criterion can be applied to the particular case of a large-aspect-ratio tokamak, where $a/R \ll 1$, $\beta = 2p/B^2 \sim a^2/R^2$, and magnetic surfaces are displaced circles.[5-7] The result is

$$\frac{1}{4}\left(\frac{q'}{q}\right)^2+\frac{2p'}{rB_\varphi^{\,2}}(1-q^2)+\gamma p\left(\frac{2r}{R}\right)^{1/2}\frac{1}{R^2B_\theta^{\,2}}>0, \tag{16}$$

where $q=\oint\nu\,d\chi$ is the safety factor and B_θ is the poloidal field. Without the γp term, inequality (16) reduces to the criterion of Shafranov and Yurchenko[8] and Soloviev[9] (valid for any value of r/a). The additional stabilizing contribution, although formally $(a/R)^{1/2}$ smaller than the magnetic-well term, is nevertheless the dominant term near the magnetic axis. Localized modes are therefore *stable* on the axis of such an equilibrium *whatever the value of q*. The apparent singularity of the γp term as $r\to 0$ is caused by the use of the displacement variable $X=RB_\theta\xi_r$: In fact the stabilizing energy on axis is proportional to $\gamma p(r/R)^{1/2}$, the trapped-particle pressure. This result indicates that unless there are ew trapped particles (i.e., $1-B/B_{\max}\to 0$ faster than r^4 as $r\to 0$), then toroidal-pinch equilibria will also be stable to localized modes on axis.

A more sophisticated multispecies version of the kinetic energy principle has been developed by Kulsrud[10] and Grad,[11] but it is possible to demonstrate[11] that the multispecies energy integral always predicts greater stability than the single-species version. We conclude that the criteria derived above are indeed sufficient for the stability of the type of perturbation considered, even on the basis of the most sophisticated guiding-center variational principle.

Strictly speaking the perturbations considered in deriving the criteria (15) and (16) are of the trapped-particle variety[12] rather than the flute variety, i.e., they satisfy the condition

$$\omega\tau \ll \left(m\oint\nu\,d\chi-2k\pi\right) \text{ or } \omega\tau \ll mq'\delta\Psi, \tag{17}$$

where $\delta\Psi$ is the spread in Ψ of a localized mode, rather than the reverse inequalities. It is apparent that, since the variational principle[2] is derived in the limit of $\omega\to 0$, Eq. (17) is the correct approximation provided the modes are not highly localized. However for localized modes of the Mercier type the analysis reveals that $m\delta\Psi$ may be made arbitrarily small without modifying the final result. This party is because the guiding-center theory has already rejected finite-Larmor-radius information which n practice would determine the localization. Thus within the guiding-center model it is acceptable to reverse the limits $\omega\to 0$ and $m\delta\Psi\to 0$, so that

$$\omega\tau \gg mq'\delta\Psi, \tag{18}$$

which we shall call the "flute limit" of the localized interchange. In this limit the trajectory integral n the expression for δf (passing) reappears, so that the velocity-space integration in Eq. (8) is over all velocity space. A Schwartz inequality again leads to the result (11), but now with $t\equiv 0$. The minimization of this new form of δW for localized interchange perturbations leads to a modified version of criterion (15), and on application to the large-aspect-ratio tokamak equilibrium the stability criterion becomes

$$\frac{1}{4}\left(\frac{q'}{q}\right)^2+\frac{2p'}{rB_\varphi^{\,2}}(1-q^2)+\frac{\gamma p}{B_\theta^{\,2}}\left[\frac{1}{2}\left(\frac{q'}{q}\right)+\frac{2B_\theta^{\,2}}{B_\varphi^{\,2}}\frac{(1-q^2)}{r}\right]^2>0, \tag{19}$$

where some negligible terms have been dropped. The shear terms in the above expression do not vanish on axis unless the current profile is pathologically flat there. In particular, for parabolic presure and current profiles inequality (19) predicts stability.

We conclude that for tokamaks in the "banana regime" of collision frequencies the kinetic or guiding-enter energy principle provides a more accurate picture of the stability properties than do the MHD quations and that for the localized interchange mode the appropriate criteria are given by (16) and

(19), for the trapped-particle and flute limits of the perturbation, respectively.

[1] I. B. Bernstein, E. A. Frieman, M. D. Kruskal, and R. M. Kulsrud, Proc. Roy. Soc., Ser. A **244**, 17 (1958).
[2] M. N. Rosenbluth and N. Rostoker, Phys. Fluids **2**, 23 (1959).
[3] M. D. Kruskal and C. R. Oberman, Phys. Fluids **1**, 275 (1958).
[4] C. Mercier, Nucl. Fusion **1**, 47 (1960).
[5] V. D. Shafranov, in *Reviews of Plasma Physics*, edited by M. A. Leontovich (Consultants Bureau, New York, 965), Vol. 2, p. 103.
[6] A. A. Ware and F. A. Haas, Phys. Fluids **9**, 956 (1966).
[7] J. M. Greene, J. L. Johnson, and K. E. Weimer, Phys. Fluids **14**, 671 (1971).
[8] V. D. Shafranov and E. I. Yurchenko, Zh. Eksp. Teor. Fiz. **53**, 1167 (1967) [Sov. Phys. JETP **26**, 682 (1968)].
[9] L. S. Solov'ev, Zh. Eksp. Teor. Fiz. **53**, 626 (1968) [Sov. Phys. JETP **26**, 400 (1968)].
[10] R. M. Kulsrud, Phys. Fluids **5**, 192 (1962).
[11] H. Grad, Phys. Fluids **9**, 225 (1966).
[12] M. N. Rosenbluth, Phys. Fluids **11**, 869 (1968).

Ablation Stability of Laser-Driven Implosions*

D. B. Henderson, R. L. McCrory, and R. L. Morse
University of California, Los Alamos Scientific Laboratory, Los Alamos, New Mexico 87544

(Received 29 April 1974)

Perturbation analysis of the stability of ablative, laser-driven implosions of homogeneous spherical pellets shows stability of the ablation surface, a necessary condition for achieving the high densities required for laser fusion. This conclusion is supported by physical arguments.

Recent interest in laser-driven implosion of spherical pellets of thermonuclear fuel to high densities has raised questions about the possibility of maintaining sufficient symmetry in such implosions to achieve the desired high densities. The problem has two complementary parts which are similar in their role and relationship to one another as are the equilibrium and stability of magnetic confinement of plasma. First, the flow of heat to the ablation surface of an implosion system must have sufficient spherical symmetry that the implosion can be approximately spherical; i.e., that asymmetries are not forced to occur by asymmetry of the external-laser-energy deposition and flow. Second, the ablation surface itself must be stable, a subject about which there is disagreement. Instability of this surface would almost certainly preclude success of laser fusion. In fact some positive stability may be required to compensate for small heat-input asymmetries. That these two problems are different and distinct becomes especially clear when one considers implosion systems in which the thermally conducting plasma cloud outside of the ablation surface is highly asymmetrical.

It has been observed by Henderson and Morse[1] that small departures from spherical symmetry of the coupled hydrodynamic and heat-flow processes involved can be analyzed by a linear perturbation expansion in scalar spherical harmonics $Y_l^m(\Omega)$, and that the analysis is greatly simplified by a decoupling of equations for different l's and a degeneracy with respect to the m's. This technique has been applied to the symmetry problem, by the use of stationary zero-order densities and temperatures, and criteria for acceptable symmetry of laser illumination have been developed.[2] Here we present calculations done with a combined zero- and first-order computer code developed specifically for the purpose of studying the stability problem with self-consistent, time-dependent zero-order densities and temperatures. This code is entirely distinct from that used in Ref. 2. These calculations show positive stability of the ablation surface during the implosion of homogeneous, spherical DT pellets. Physical arguments are presented which support our conclusion. Shiau, Goldman, and Weng,[3] using the same perturbation-expansion technique but not the identical numerical method, have reached the opposite conclusion.

The zero-order spherical-implosion case cho-

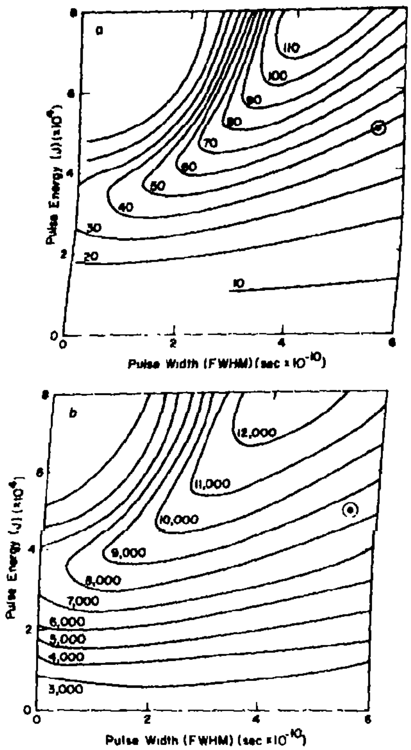

FIG. 1. Contours of (a) maximum center density in g/cm^3 and (b) temperature in eV at time of maximum density as a function of pulse energy, E, and full width at half-maximum, τ. Circled points indicate the example case.

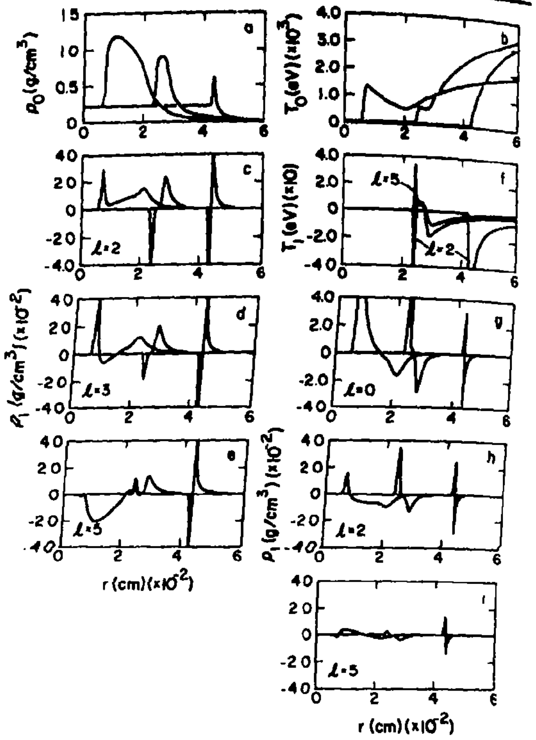

FIG. 2. Zero- and first-order quantities as a function of r at times $t=-0.21\times10^{-9}$, $+0.24\times10^{-9}$, and $+0.53\times10^{-9}$ sec with respect to the peak of the Gaussian pulse.

sen here as our example was taken from a study of implosions of 500-μm-radius frozen DT spheres isotropically irradiated by Gaussian laser pulses with a wavelength of 1.06 μm. The zero-order computations were done by a single-temperature Lagrangian hydrodynamics code with electron thermal conduction. Figure 1(a) is a contour plot of the maximum central densities achieved as a function of the total pulse energy, E, and the full width of the pulse at half-maximum, τ. Figure 1(b) is a plot of the corresponding center temperatures at the times of maximum density. The circled points indicate the case chosen, $E=50$ kJ, $t=5.5\times10^{-10}$ sec. This case, which is on the long-pulse side of that value of τ which gives the maximum density for the chosen value of E, produces a shock clearly separated from the ablation surface and a shocked region in between that is much cooler than the blowoff plasma during most of the implosion. In Figs. 2(a) and 2(b) the zero-order density and temperature, ρ_0 and T_0, are plotted at three different times ($t=-0.21\times10^{-9}$, $+0.24\times10^{-9}$, and $+0.53\times10^{-9}$ sec) with respect to the peak time of the Gaussian pulse, on the same axes. As we go out from $r=0$, the shock is where ρ_0 and T_0 rise sharply; the ablation front is when ρ_0 subsequently falls sharply just outside its maximum and T_0 begins to rise again. This class of implosion is quite similar to those produced by highly optimized pulses up to a time just before peak compression (see Refs. 2 and 3 for further references). Values of τ near the maximum density value or on the short-pulse side give implosions in which the ablation and shock surfaces are not so clearly separated, the region just behind the shock is not very much cooler than the blowoff plasma, and the resulting higher themal conductivity in this region further increases the stability of the flow. It is not asserted that this case is the least-stable possible case but rather that this case is representative of those relevant to laser fusion. *We do not know of a relevant* class of homogeneous-pellet cases which we expect would be significantly less stable.

Angle-dependent first-order perturbations of all zero-order dependent variables are represented by time- and radius-dependent coefficients of spherical harmonics of various l values, and are calculated by integration along the unperturbed characteristics of the zero-order Lagrangian flow, according to the method described in Ref. 2. Ablation stability is isolated from effects of illumination asymmetry by the assumptions of symmetric irradiation and an initial perturbation of the pellet of the incompressible form

$$\xi_r = \xi_0 (r/a)^{l-1},$$
$$(\nabla\cdot\vec{\xi})_{\bar{\Omega}} = -(l+1)(\xi_0/a)(r/a)^{l-2},$$

which gives the pellet a bumpy surface. The unperturbed radius of the pellet is a, which is 500 μm for the case shown here. The scale of all first-order quantities is set by our taking $\xi_0 = 1$ μm, and thus giving the bumpy surface this amplitude. We prefer this form of regular initial perturbation over the random-noise approach of Shiau, Goldman, and Weng[3] for estimating the effect of initial pellet irregularities and any instability on implosion symmetry. Figures 2(c)-2(e) show the perturbed density coefficients ρ_1 for $l = 2$, 3, and 5, respectively, at the same three times at which ρ_0 and T_0 are plotted. At $t = -0.21 \times 10^{9}$ sec for all l's, the inside negative spike of ρ_1, which is well resolved by our grid, comes mostly from the convective contribution given by the product of the large $\partial\rho_0/\partial r$ at the shock and $-\xi_r$ there. The negative sign of the spike reflects the fact that at the angular phase $\cos\theta = 1$, where first-order quantities are defined, and, in general, wherever $Y_l^m(\bar{\Omega}) > 1$, the perturbed surace is initially raised, i.e., displaced outward, and the inward progress of the shock is retarded at early times relative to the zero-order flow by having to pass through additional material. The outward displacement of the critical surface, in he vicinity of where the light is absorbed, also ontributes to shock retardation at this angular phase. Artificial viscosity distributes the shock ump, which is in principle discontinuous, over nough zones to permit accurate calculation of ρ_1 nd other first-order quantities. The area under his spike is a measure of the perturbed radial hock displacement. The rest of ρ_1 behind the hock can be taken at face value. The positive feature of ρ_1 at $t = -0.21 \times 10^{-9}$ sec for all l's is lso primarily convective, reflecting the initial outward displacement and the negative $\partial\rho_0/\partial r$ of the ablation front.

Subsequently, the following sequence of events occurs for all $l > 1$. Angular thermal conductivit increases the total heat flow into the regions of $\bar{\Omega}$ in which the surface of the pellet is initially raised, causing material to be ablated from these regions with greater energy, i.e., with greater specific impulse. The greater ablation pressure in the initial raised regions of $\bar{\Omega}$ causes the shock to be stronger there and hence to produce a higher shocked pressure behind and to move inward faster. The shock in the initially depressed regions of $\bar{\Omega}$ is correspondingly weaker and slower than the zero-order shock. The shock in the raised regions, which starts out retarded, in fact catches up with and moves ahead of the zero-order shock. This is first seen for $l = 5$ in Fig. 2(e) at $t = 0.24 \times 10^{-9}$ sec from the sign reversal of the spike in ρ_1 at the shock front from negative at the earlier time to positive. The same transition is seen to occur between $t = 0.24 \times 10^{-9}$ and 0.53×10^{-9} sec for $l = 2$ and 3. This motion of the shock front from one side of its zero-order position to the other might be expected to exhibit overstability, but this has not been observed. Thus, the observed behavior is positively stable. The reversal of shock retardation occurs sooner at higher l numbers because the angular wavelength is shorter and the angular thermal conduction is larger, as discussed in detail in Ref. 2.

The angular variation of perturbed pressure behind the shock front also causes a perturbed angular fluid flow which decreases the density in the initially raised regions of $\bar{\Omega}$. This density decrease is seen in a fully developed state at $t = 0.53 \times 10^{-9}$ sec for $l = 5$ and it is beginning to occur for $l = 3$. The above behavior corresponds to a tendency for the implosion to converge to separate points located on those radii on which there occurred initial minima of the pellet surface radius, i.e., minima of $Y_l^m(\bar{\Omega})$, as opposed to converging uniformly to the spherical center. This tendency to form local density maxima in the imploding shell of compressed material can be seen from the fact that Fig. 2(e) at $t = 0.53 \times 10^{-9}$ sec exhibits a negative maximum of ρ_1 at the same radius as the maximum of ρ_0 [Fig. 2(a)]. (If, on the other hand, the maximum of ρ_1 occurred in either of the regions of large $\pm\,\partial\rho_0/\partial r$ and if the zeros of ρ_1 and $\partial\rho_0/\partial r$ coincided, it would instead indicate only a waviness of the surface of maximum density with no isolated points of maximum density on this surface.) Figure 2(f) helps in visualizing the ablation stabilization process described above. On the same scales are plotted T_1 for $l = 2$ at $t = 0.21 \times 10^{-9}$ sec and T_1 for $l = 2$ and 5 at $t = 0.24 \times 10^{-9}$ sec. The major contribution to $T_1(l = 2, t = -0.21 \times 10^{-9})$ is from retardation of the nonlinear thermal wave form of T_0 [Fig. 2(b)] at this time. [T_1 for $l = 3$ and 5 at this time is almost identical to $T_1(l = 2)$]. However, between $t = -0.21 \times 10^{-9}$ and $+0.24 \times 10^{-9}$ sec the angular conduction damping of T_1 in the vicinity of the ablation front is significantly greater for higher l's. Thus, at $t = 0.24 \times 10^{-9}$ sec in this vicinity the negative magnitude of $T_1(l = 5)$ is noticeably smaller than that of $T_1(l = 2)$. However, in the shocked layer, where T_1 for $l = 2$ and 5 is positive and almost flat, the magnitude of $T_1(l = 5)$ is the greater, indicating stronger shocking as described above. The spikelike features nearest the origin are indicators of the perturbed shock displacement, just as are the corresponding ρ_1 features, and have opposite signs at this time because the $l = 5$ shock has crossed over and $l = 2$ has not. $T_1(l = 3, t = 0.24 \times 10^{-9})$ lies everywhere between $T_1(l = 2)$ and $T_1(l = 5)$. Inspection of $(\nabla \cdot \vec{\xi})_{\bar{\Omega}}$ shows that the additional curvature of the surface introduced by the surface perturbation also contributes to strengthening the shock and speeding the implosion in the initially raised regions of $\bar{\Omega}$ by making the implosion at early times converge more rapidly than in zero order, as if converging to points out from the origin on radii passing through initial maxima of $Y_l^m(\bar{\Omega})$. This purely hydrodynamic effect may make an important contribution to increasing the symmetry of imploding shells of fuel.

Regular initial perturbations of internal density give results very similar to those obtained from regular surface perturbations.

In order to learn the relative contributions of initial surface perturbations and of perturbations of illumination uniformity to implosion asymmetry, we have calculated the perturbed response of our same zero-order case to angular radiation variations scaled here to a relative modulation of 10^{-2}. Figures 2(g)–2(i) show the results for $l = 0$, 2, and 5 at the same times as above. Comparison of such $l = 0$ calculations with appropriately defined differences between two zero-order runs with only slightly different input power provides an extremely valuable verification of the numerical method. The $l = 2$ and 5 results show the smoothing effect of higher l's pointed out in Ref. 2 although without the distinction made there between early- and late-time irradiation asymmetry. Comparison shows that for $l = 2$ the magnitude of the late-time effect of an initial 1-μm surface-radius perturbation amplitude on this 500-μm-radius pellet (0.2%) is approximately the the same as that caused by a 1% variation of illumination intensity.

Similar calculations of the effects of these kinds of perturbation (incompressible bumpiness, perturbed density, and asymmetric illumination) have been done with 50-μm pellets with qualitatively very similar results.

It is pointed out in Refs. 1 and 2 that several physical effects that are neglected here, including thermoelectrically generated magnetic fields, spoil the m degeneracy and l decoupling of our perturbation treatment.

In fact Tidman and Shanny have pointed out[4] that spontaneously generated magnetic fields, which would reduce thermal conductivity, may grow unstably. However, at present such fields are being neglected not just for simplicity but also because experimental evidence indicates anomalous collision frequencies of such a large magnitude that the magnetic fields would be almost entirely suppressed. The understanding of laser-driven implosion stability will, however, not be satisfactory until this point is cleared up.

---

[*] This work performed under the auspices of the U. S. Atomic Energy Commision.

[1] D. B. Henderson and R. L. Morse, Bull. Amer. Phys. Soc. 18, 684 (1973).

[2] R. L. Morse, Bull. Amer. Phys. Soc. 18, 1359(T) (1973); D. B. Henderson and R. L. Morse, Phys. Rev. Lett. 32, 355 (1973).

[3] J. N. Shiau and E. B. Goldman, Bull. Amer. Phys. Soc. 18, 1358 (1973); J. N. Shiau, E. B. Goldman, and C. I. Weng. Phys. Rev. Lett. 32, 352 (1973).

[4] D. A. Tidman and R. A. Shanny, "Field Generating Thermal Instability In Laser Heated Plasma" (to be published).

Self-Modulation and Self-Focusing of Electromagnetic Waves in Plasmas

Claire Ellen Max* and Jonathan Arons†
University of California, Berkeley, California 94720

and

A. Bruce Langdon
Lawrence Livermore Laboratory, Livermore, California 94550

(Received 22 April 1974)

The nonlinear frequency shift of a strong electromagnetic wave in a plasma, due to weak relativistic effects and the $\vec{v}\times\vec{B}$ force, can cause modulation and self-focusing instabilities. These processes are explored, and their relation to self-focusing driven by the ponderomotive force is described.

We describe a new mechanism producing self-modulation and self-focusing of strong electromagnetic (EM) waves in plasmas. These effects occur because relativistic plasma dynamics produces a nonlinear index of refraction for the plasma. Even *weak* v^2/c^2 relativistic corrections can produce interesting self-modulation and -focusing, for parameters of high-power lasers presently existing or under construction.

Previous mechanisms for self-modulation and self-focusing of EM waves in collisionless plasmas[1-6] have used the ponderomotive force.[7] Joule heating can produce self-focusing in collisional plasmas.[5,8] The *temporal* evolution of these two processes relies on ion motion, and thus occurs with characteristic frequencies $|\omega^2| \lesssim \omega_{pi}^2 = 4\pi Ne^2/M_i$. The relativistic mechanism explored here requires motion only of the plasma electrons. Hence modulations of an incident wave can grow quickly compared to ion time scales, for incident light of sufficiently high intensity. Litvak[5] and Kidder[9] used nondynamical, geometrical optics considerations to estimate self-focusing lengths. Forslund, Kindel, and Lindman[10] described nonrelativistic modulational instability in a magnetic field. To our knowledge, the present analysis is the first treatment of EM modulational instability with $B_0 = 0$.

To derive the simplest features of relativistic self-modulation and self-focusing, we model the plasma as a cold uniform electron fluid with fixed ion density N, irradiated by a linearly polarized EM wave $\vec{E} = \hat{x}E_0\cos\chi_0$, $\chi_0 = \omega_0 t - k_0 z$. The usual relation between k_0 and ω_0 is modified, for two reasons.[11-13] First, because of their motion in the incident EM wave, electrons acquire a relativistic Lorentz factor $\gamma_0 \cong 1 + \frac{1}{2}(\nu_0 \sin\chi_0)^2$, where $\nu_0 \equiv eE_0/m_e c\omega_0 \ll 1$. This gives the electrons an amplitude-dependent mass in the plasma response, and results in an "inertial" current because of the difference between $\vec{p}$ and $\vec{v}$. Second, the $\vec{v}_0\times\vec{B}_0$ force on the electrons produces a density perturbation ΔN_0 having frequency $2\omega_0$: $\Delta N_0 = -N\nu_0^2(\cos 2\chi_0)(\omega_0^2 - \omega_p^2)/(4\omega_0^2 - \omega_p^2)$. The resulting nonlinear current $\Delta N_0 \vec{v}_0$ has a component at the pump frequency ω_0, and acts as a source for $\vec{E}_0$ and $\vec{B}_0$. The index of refraction due to these two nonlinear effects is[11]

$$n^2 = \frac{k_0^2 c^2}{\omega_0^2} = 1 - \frac{\omega_p^2}{\omega_0^2} + \frac{\nu_0^2\omega_p^2}{2\omega_0^2}\left(\frac{3}{4} - \frac{\omega_0^2 - \omega_p^2}{4\omega_0^2 - \omega_p^2}\right), \qquad (1)$$

where $\omega_p^2 \equiv 4\pi Ne^2/m_e$.[14]

To study the *dynamics* of self-modulation and self-focusing, we use a linear instability analysis. Our equilibrium is the EM wave described above, together with its second-harmonic density perturbation, ΔN_0, and the nonlinear $\omega_0(k_0)$ given by (1). Linearized quantities vary in the y-z plane. The perturbed vector potential $\delta\alpha_x \equiv e\delta A_x/m_e c^2$ (Coulomb gauge) obeys the linearized wave equation

$$\left(c^2\nabla^2 - \frac{\partial^2}{\partial t^2}\right)\delta\alpha_x = \omega_p^2\left[\frac{\delta v_x}{c}\left(\frac{1+\Delta N_0}{N}\right) + \frac{\delta n}{N}\frac{v_{0x}}{c}\right], \qquad (2)$$

where δn is the first-order electron density perturbation, and $v_{0x}/c = -\nu_0 \sin\chi_0 + O(\nu_0^3)$.

To find a self-consistent solution, we must know the values of δv_x and δn. In terms of the dimensionless momentum $u_x = p_x/m_e c$, δv_x is given by

$$\delta v_x/c = (\delta u_x/\gamma_0) - \delta\gamma(u_{x0}/\gamma_0^2) = (\delta u_x/\gamma_0^3). \qquad (3)$$

Conservation of x canonical momentum relates δu_x with the vector potential: $\delta u_x = \delta\alpha_x \equiv e\delta A_x/$

$m_e c^2$. Hence Eq. (3) becomes[15]

$$\delta v_x/c = \delta\alpha_x[1 - \tfrac{3}{2}\nu_0^2 \sin^2\chi_0] + O(\nu_0^3). \qquad (4)$$

The next task is to find the electron density perturbation δn. It is sufficient to have the wave equation correct to order $\nu_0^2 \sim |v_{0x}^2|/c^2$. Since δn appears in Eq. (2) multiplied by v_{0x}, we need only find δn correct to order ν_0. The continuity equation and Lorentz-force equation are

$$\partial^2\delta n/\partial t^2 + N\nabla\cdot(\partial\delta\vec{v}/\partial t) = 0 + O(\nu_0^2), \qquad (5)$$

$$\partial\delta\vec{v}/\partial t = e\nabla\delta\varphi/m_e - \hat{z}k_0c^2\nu_0\cos\chi_0\delta\alpha_x + c^2\nu_0\sin\chi_0\nabla\delta\alpha_x + O(\nu_0^2), \qquad (6)$$

where $\delta\varphi$ is the electrostatic potential perturbation.

We now put the pieces together and derive a dispersion relation. Take the Fourier transform of Eqs. (2) and (4)–(6) in y, z, and t. Write (2) as two equations for the two quantities $\delta\alpha_x^{\pm} \equiv \delta\alpha_x(\vec{k}\pm\vec{k}_0, \omega\pm\omega_0)$. Substitute the appropriate Fourier amplitudes of δn and δv_x, determined from (4)–(6), into the right-hand side of these two equations for $\delta\alpha_x^{\pm}$. The equations for $\delta\alpha_x^{\pm}$ involve Fourier components of the electron density at $\delta n^{\pm 2}$ and at δn^0. For ponderomotive force mechanisms of self-modulation and self-focusing, it is the δn^0 component which dominates. In contrast, for the present relativistic process the $\delta n^{\pm 2}$ terms are more important in the ratio $\omega_p^2/k^2c^2 \gg 1$. For the instabilities we discuss here, the two scattered EM waves $\delta\alpha_x^{\pm}$, and their accompanying density perturbations $\delta n^{\pm 2}$, closely resemble the *driving* wave $E_0\cos\chi_0$ and its second-harmonic density perturbation ΔN_0. The components $\delta\alpha_x^{\pm 3}$ contribute terms smaller than $O(\nu_0^2)$, and hence will be neglected.

The above procedures result in two homogeneous equations for the Fourier amplitudes $\delta\alpha_x^{\pm}$. The dispersion relation is the requirement that the determinant of the coefficients vanish. We assume $|\omega| \ll (\omega_p^2/\omega_0)$ and $k^2 \ll k_0^2$ [ω and $\vec{k}$ correspond to the low-frequency density perturbation $\delta n^0 \equiv \delta n(\omega, \vec{k})$], and obtain

$$(\omega^2 - k^2c^2)^2 - 4(\omega\omega_0 - \vec{k}\cdot\vec{k}_0c^2)^2 + \nu_0^2\omega_p^2 q(\omega^2 - k^2c^2) = 0, \qquad (7)$$

$$q \equiv \tfrac{3}{4} - (\omega_0^2 - \omega_p^2)/(4\omega_0^2 - \omega_p^2). \qquad (8)$$

To solve Eq. (7) for self-modulation, we take $\vec{k} \parallel \vec{k}_0$ and set $\omega = k(c^2k_0/\omega_0) + \Delta\omega \equiv kV_g^0 + \Delta\omega$. With the ordering $\Delta\omega \sim \nu_0^2\omega_0$, $k \sim \nu_0(\omega_0/c)$, we retain terms through $O(\nu_0^4)$ in (7) and find

$$\Delta\omega \cong (kc/2)(\omega_p/\omega_0)^2[(kc/\omega_0)^2 - \nu_0^2 q]^{1/2}. \qquad (9)$$

The first term in the square brackets represents the mismatch between the sidebands and the pump. For simplicity of presentation we have also taken $\omega_0^2 \gg \omega_p^2$. There is instability for $k < (\omega_0/c)\nu_0 q^{1/2}$. The maximum growth rate occurs for $k = (\omega_0/c)\nu_0(q/2)^{1/2}$, and is given by

$$\gamma_{\max} = (\omega_p^2/4\omega_0)\nu_0^2 q. \qquad (9a)$$

The maximum spatial growth rate is $\kappa_{\max} = \gamma_{\max}/V_g^0$. During the instability, the driving wave acquires two growing EM sidebands, at frequencies $\omega_0 \pm \vec{k}\cdot\vec{V}_g^0$ and wave numbers $(k_0 \pm k)\hat{z}$. The presence of these sidebands is equivalent to modulation of the driving wave, because the *total* EM response is of the form

$$\sin\chi_0 + \epsilon[\sin(\chi_0+\varphi) + \sin(\chi_0-\varphi)] \cong \sin(\chi_0 + 2\epsilon\sin\varphi), \quad \epsilon \ll 1.$$

A simple argument leads to possible modulational instability for *any* weakly nonlinear wave with dispersion relation $\omega(k,\nu) = \omega_0(k) - A\nu^2$, with ν the wave amplitude.[16] From the phase function $\theta(z,t)$ we define $k \equiv \partial\theta/\partial z$, $\omega \equiv -\partial\theta/\partial t$. Then the relation $\partial k/\partial t = -\partial\omega/\partial z$ requires

$$(\partial/\partial t + V_g^0\partial/\partial z)k = A\partial\nu^2/\partial z. \qquad (10)$$

Consider a sinusoidal perturbation $\Delta\nu$ to the original wave amplitude ν_0 (Fig. 1). In a frame moving with the group velocity $V_g^0 \equiv (\partial\omega_0/\partial k)_{k=k_0}$, Eq. (10) says that the wave number $\Delta k = k - k_0$ changes in time at the rate $2\nu_0 A\partial\Delta\nu/\partial z_0$. Here z_0 is a Lagrangian coordinate specifying position on the wave envelope, and A is positive. In region *a* of

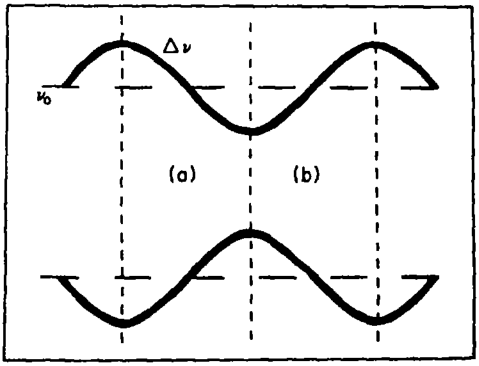

FIG. 1. The original wave envelope ν_0, and the modulated envelope $\nu_0 + \Delta\nu$, during self-modulation.

Fig. 1, where $\partial\Delta\nu/\partial x_0 < 0$, Δk decreases with time. When $\partial V_g{}^0/\partial k$ is positive, the decrease of Δk implies that V_g decreases with time. Thus in region *a*, energy slowly moves backward in the frame moving with the average group velocity $V_g{}^0$. Analogous arguments imply that energy slowly propagates forward in region *b*. Thus energy accumulates at the local maxima of $\Delta\nu$, causing a purely growing instability in the frame moving with $V_g{}^0$. The ponderomotive force is not a major effect in the dynamics of the instability.

For the contrasting case of self-focusing we take $\hat{\mathrm{k}}\cdot\hat{\mathrm{k}}_0 = 0$, and assume $\omega \sim \nu_0{}^2\omega_0$, $k \sim \nu_0(\omega_0/c)$. We retain terms through $O(\nu_0{}^4)$ in (7) to obtain

$$\omega \cong \pm \tfrac{1}{2} ikc[(kc/\omega_0)^2 - \nu_0{}^2 q(\omega_p/\omega_0)^2]^{1/2}. \qquad (11)$$

The first term in square brackets represents diffraction, and is stabilizing. The maximum wave number for instability is given by $k < (\omega_p/c)\nu_0 q^{1/2}$, smaller by the factor ω_p/ω_0 than the analogous k for self-modulation. The maximum growth rate is the *same* as for self-modulation, but occurs at a k smaller by the factor ω_p/ω_0. Computer simulations[17] support the growth rates predicted by Eqs. (9) and (11). Steady-state self-focusing can be understood by arguments from geometrical optics. By Eq. (1), if the light intensity $\nu_0{}^2$ is locally enhanced at a point, the phase velocity is decreased there relative to its value on either side. The wave front curves, further enhancing the intensity by focusing the light "downstream" in the $\hat{k}_0$ direction.

For simplicity we have neglected ion motion, and hence have suppressed ponderomotive-force-
iven instabilities which compete with the pro-
sses considered here. We emphasize that, for
ʒh laser intensities, the relativistic instabil-
es derived here can grow so quickly in time
ıt ion inertia prevents the ions from following
ɔng. For self-focusing we estimate the inten-
ies when this can occur, by comparing the
owth rate due to ponderomotive force, γ_{pond}
$\nu_0\omega_{pi}/2^{1/2}$, with the maximum relativistic growth
te (9a). The relativistic process is more im-
rtant than the ponderomotive force, for the
nporal development of self-focusing, if ν_0
$\omega_0\omega_{pi}/\omega_{pe}{}^2)(2^{1/2}/q)$. A more detailed study of
ese two mechanisms for self-focusing verifies
s simple estimate.[17] Neglect of ion motion in
modulational instability of Eq. (9) is justified
en $|\omega| = kV_g{}^0 > \omega_{pi}$. For the k of maximum
owth, this condition is $\nu_0 > (\omega_{pi}/ck_0)(2/q)^{1/2}$.
The assumptions $|\omega| \ll \omega_p{}^2/\omega_0$, $k^2 \ll k_0{}^2$, and k^2
$\omega_p{}^2/c^2$ necessary for the above results to hold are summarized by two inequalities. For an underdense plasma we must have $\nu_0 \ll (\omega_p/\omega_0)^2$. Near critical density, on the other hand, the condition $k_0 c \gg \nu_0\omega_0$ must be satisfied.

The temporal growth rates represented by Eqs. (9) and (11) are interesting for high-power lasers. For example, consider a Nd-glass laser ($c/\omega_0 = 1.06$ μm), $I = 5\times10^{16}$ W/cm^2, incident on a plasma with $\omega_0 = 1.7\omega_{pe}$. Then the fastest growth time is 6×10^{-13} sec for both modulational and self-focusing instabilities. The exponentiation length for these processes is 140 μm. For self-modulation the modulating wavelength is 14 μm, and the modulating frequency a tenth of the laser frequency. For self-focusing, the filament width for fastest growth is 23 μm. Intensities of $\sim10^{16}$ W/cm^2 are probably higher than those contemplated for laser fusion applications. However, such lasers are presently coming into use in target experiments.[18] The above numbers indicate that modulations and filaments may exponentiate significantly if the strong laser pulse lasts longer than a few picoseconds, or if the blow-off plasma becomes larger than a few hundred microns. Modulations could represent a mechanism to *broaden the frequency spectrum* of the incident laser. This effect may be important because resonant instabilities (e.g., stimulated Brillouin scattering or the parametric decay instability) can be inhibited if the driving wave is not monochromatic.

A major unanswered question about relativistic self-modulation and focusing concerns competition between these processes and other laser-plasma instabilities.[1,4,10] The Raman process has a far larger growth rate, and if it occurs it should be dominant for $\omega_0 > 2\omega_{pe}$. Even for $\omega_0 < 2\omega_{pe}$, strong-coupling Brillouin scattering has a larger growth rate than the relativistic instabilities considered here. However, density gradients and frequency broadening can stabilize Raman and Brillouin scattering. At present we see no mechanism for density-gradient stabilization of relativistic self-modulation and focusing, and we argue that self-modulation may itself cause frequency broadening. The presence or absence of these processes may ultimately depend on "nonideal" effects, such as spatial nonuniformity and frequency spread of the incident laser beam.

C.E.M. would like to thank W. Kruer for the hospitality of Lawrence Livermore Laboratory.

---

*Physics Department. Work supported in part by U. S.

Air Force Office of Scientific Research Contract No. 44620-C-70-0028.

†Astronomy Department.

‡Work supported by the U. S. Atomic Energy Commission.

[1] J. Drake, P. K. Kaw, Y. C. Lee, G. Schmidt, C. S. Liu, and M. N. Rosenbluth, Phys. Fluids 17 (1974).

[2] J. W. Shearer and J. L. Eddleman, Phys. Fluids 16, 1753 (1973).

[3] P. K. Kaw, G. Schmidt, and T. Wilcox, Phys. Fluids 16, 1522 (1973).

[4] W. Manheimer and E. Ott, to be published.

[5] A. G. Litvak, Zh. Eksp. Theo. Fiz. 57, 629 (1968) [Sov. Phys. JETP 30, 344 (1970)].

[6] C. E. Max and A. B. Langdon, Bull. Amer. Phys. Soc. 18, 1359 (1973).

[7] G. Schmidt, *Physics of High Temperature Plasmas* (Academic, New York, 1966), p. 47.

[8] F. W. Perkins, E. J. Valeo, and G. D. Thome, to be published.

[9] R. Kidder, in *Physics of High Energy Density, Proceedings of the International School of Physics "Enrico Fermi," Course 48*, edited by P. Caldirola (Academic, New York, 1971), p. 306.

[10] D. W. Forslund, J. M. Kindel, and E. L. Lindman, Phys. Rev. Lett. 29, 249 (1972).

[11] F. W. Sluijter and D. Montgomery, Phys. Fluids 8, 551 (1965).

[12] D. Montgomery and D. A. Tidman, Phys. Fluids 7, 242 (1964).

[13] J. Arons and C. E. Max, to be published.

[14] N. Tzoar and J. I. Gersten [Phys. Rev. B 4, 3540 (1971), and Phys. Rev. Lett. 26, 1634 (1971)] show that in degenerate semiconductors, a nonparabolic energy-momentum relation produces nonlinearities analogous to the relativistic dependence of $\vec{p}$ on $\vec{v}$. They study the resulting self-focusing in the steady state.

[15] S. E. Bodner and J. L. Eddleman, Phys. Rev. A 5, 355 (1972).

[16] B. B. Kadomtsev and V. I. Karpman, Usp. Fiz. Nauk 103, 193 (1971) [Sov. Phys. Usp. 14, 40 (1971)].

[17] A. B. Langdon and B. F. Lasinski, to be published.

[18] D. V. Giovanielli, R. P. Godwin, and G. H. McCall, Bull. Amer. Phys. Soc. 18, 1255 (1973); L. M. Goldman, J. Soures, and M. J. Lubin, Phys. Rev. Lett. 31, 1184 (1973).

Quasiparticle Lifetimes and Microwave Response in Nonequilibrium Superconductors*

A. Rothwarf,† G. A. Sai-Halasz, and D. N. Langenberg
Department of Physics and Laboratory for Research on the Structure of Matter, University of Pennsylvania, Philadelphia, Pennsylvania 19174

(Received 21 March 1974)

A theoretical treatment is presented of the quasiparticle-recombination dynamics of a nonequilibrium superconductor. The microwave reflectivity of a superconducting film in the presence of external pair breaking is calculated. It is shown how microwave experiments may permit the separation of the effective recombination time into its intrinsic and recombination-phonon components.

Testardi[1] has shown experimentally that when a thin superconducting film is driven normal by intense pulsed optical radiation, the transition displays characteristics which cannot be accounted for by simple lattice heating. He suggested that excess quasiparticles created by photon-induced pair breaking were responsible. Motivated by this observation, Owen and Scalapino[2] investigated a modified BCS model of a superconductor in which the quasiparticle density is maintained at a level above the thermal-equilibrium value by an external source of dynamic pair breaking. Among the predictions of this model are a dependence of the energy gap on the excess quasiparticle density, and a first-order transition to the normal state at a critical excess quasiparticle density. Some of the model's predictions have been experimentally confirmed by Parker and Williams[3] using tunnel junctions irradiated with laser light.

Some time ago, Rothwarf and Taylor[4] pointed out the crucial importance of recombination phonons in the coupled quasiparticle-pair-phonon system in a nonequilibrium superconductor. The interpretation of nonequilibrium experiments using tunnel junctions depends on assumptions about the behavior of these phonons in the relatively complex junction structure. It would obviously be desirable to test the Owen-Scalapino model in a simple thin film, in which the phonons can be accounted for with greater certainty. The use of microwave-frequency reflection, absorption, or transmission measurements as a probe of the quasiparticle density makes this possible. The quasiparticle density can be monitored in the superconducting state in contrast to the quasi-dc experiment of Testardi, in which only the transition to the normal state could be studied. Furthermore, experiments of this type offer the possibility of direct time-resolved studies of quasiparticle dynamics if the relevant times are sufficiently long. Such experiments are reported in the following Letter.[5] In this Letter we present the theoretical framework required for interpretation of the experiments.

We first require a connection between the quasiparticle density and an observable microwave parameter. In the Owen-Scalapino model, it is assumed that the quasiparticles and phonons are in thermal quasiequilibrium at temperature T, but that the quasiparticles are not in chemical equilibrium with the pairs. The distribution function of the quasiparticles is

$$f(E,T,n)=\{\exp((kT)^{-1}[E-\mu^*(T,n)])+1\}^{-1}, \qquad (1)$$

where E is the quasiparticle energy, μ^* is the quasiparticle chemical potential, and n is the quasiparticle density excess over the thermal-equilibrium value at temperature T, measured in units of $4N(0)\Delta_0$. $N(0)$ is the single-spin density of states at the Fermi level, and Δ_0 is the BCS gap parameter at zero temperature and in equilibrium ($n=0$), with the pair chemical potential $\mu=0$. Both E and μ^* depend on the gap parameter, which in turn depends on T and n. We have used the formulas given by Mattis and Bardeen,[6] modified by inserting the distribution function Eq. (1) and the Owen-Scalapino results for $\Delta(T,n)$ and $\mu^*(T,n)$, to calculate the real and imaginary parts of the normalized conductivity, $\sigma_1(T,n)/\sigma_N$ and $\sigma_2(T,n)/\sigma_N$. Using these, we have calculated the normal-incidence microwave reflectivity of a film-substrate combination. An example of the results is shown in Fig. 1.

Next we need a connection between n and the intensity of the external pair-breaking source, e.g., incident light intensity. This link is provided by recombination dynamics. Rothwarf and Taylor[4] in their work assumed that the phonon pair-breaking probability $\beta/2$ and the quasiparticle recombination coefficient R are independent of the number of excess quasiparticles. However, these parameters depend on the gap parameter, and hence, in general, on n. We assume that each depends on n only through its explicit dependence on Δ. With this assumption and from the rate equations[4,7] for the equilibrium case, we find the ratio $\beta/R=N_T^2(T,\Delta(T,n))/N_{\omega T}(T,\Delta(T,n))$, where N_T is the thermal-equilibrium quasiparticle density and $N_{\omega T}$ is the thermal-equilibrium density of phonons with energy greater than 2Δ, each for given T and $\Delta(T,n)$. If, as assumed by Owen and Scalapino, the quasiparticle and phonon distributions can be characterized by the same temperature T, then for $kT/\Delta \ll 1$, β/R is simply proportional to $\Delta^{-1}(T,n)$, and is otherwise temperature independent.

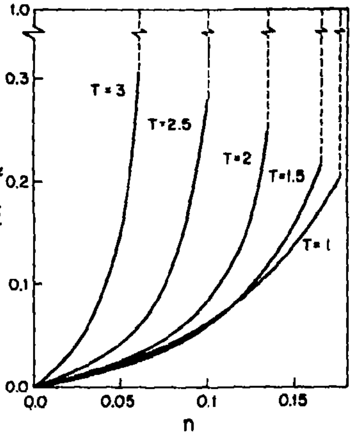

FIG. 1. Normalized change in microwave reflectivity (70 GHz) of a 500-Å-thick Sn film as a function of normalized excess quasiparticle density, with temperature as a parameter in Kelvin degrees. R_N is the normal-state reflectivity, $R(0)$ is the superconducting-state reflectivity, and $R(n)$ is the reflectivity of the state with n excess quasiparticle density. The vertical line at the right-hand end of each curve marks the first-order transition to the normal state predicted by the Owen-Scalapino model (Ref. 2).

With this change, from the rate equations[4,7] for the steady state or quasiequilibrium, we get

$$N^2=N_T^2(T,n)+I_0\left(\frac{1}{R}+\frac{N_T^2(T,n)}{2N_{\omega T}(T,n)}\,\tau_\gamma\right), \qquad (2)$$

where $N=N_T(T,n)+\Delta N$ is the total quasiparticle density, $\Delta N=n[4N(0)\Delta_0]$, I_0 is the quasiparticle injection rate, and τ_γ^{-1} is the net transition probability for loss of phonons from the energy range $>2\Delta$ through processes other than pair breaking.

We now suppose that the external pair-breaking source is light and that the film absorbs energy flux P. We assume that in quasiequilibrium a fraction F of this energy is converted to quasiparticles. Then $I_0=FP/dE_{qp}$, where d is the film thickness and E_{qp} is the average quasiparticle energy. The factor F can be estimated with the assumption that the high-energy quasiparticles created by an incident photon decay by the emission of phonons. The phonons emitted will be predominantly those corresponding to peaks in the phonon density of states. These phonons in turn can create quasiparticles by breaking pairs. These quasiparticles will tend to fall to the gap edge by the emission of phonons because of the large density of states at the gap. If the emitted phonon can further break pairs, the process continues until the emitted phonons have an energy less than 2Δ. The conversion efficiency can thus be obtained from the ratio of the energies at peaks in the phonon density of states to the energy gap. In Pb we find conversion efficiencies of ~0.6, 0.7, and 0.8 for the two transverse phonon peaks and the longitudinal peak, respectively. Since we expect the transverse peaks to be more effective as a result of the predominance of the umklapp scattering in Pb, a value of $F \approx \frac{2}{3}$ is reasonable for Pb. For Sn, taking into consideration all peaks in the phonon spectrum, we get $F \approx \frac{3}{4}$.

Other loss mechanisms such as the emission *of phonons with energy less than 2Δ, during the* high-energy quasiparticle bremsstrahlung, or the creation of low-energy phonons from high-energy ones by inelastic processes, account for a negligible portion of the energy.

The rate at which the high-energy phonons will create quasiparticles can be estimated from the fact that the 2Δ phonon lifetime against pair breaking is at least a factor 10 smaller than the quasiparticle lifetime, even when the latter is sharply reduced at large excess quasiparticle densities. Consequently almost all the energy resides in the quasiparticle component of the system. This conclusion is also supported by direct calculations of the total excess quasiparticle energy, $\Delta N\bar{E}_{qp}$, and the total excess phonon energy, $\Delta N_\omega \bar{E}_\omega$, based on Rothwarf and Taylor's equations. For any reasonable set of parameter values, $\bar{E}_{qp}$ is very nearly Δ, $\bar{E}_\omega$ is very nearly 2Δ, and $\Delta N_\omega \ll \Delta N$. F depends on n through $\Delta(n)$ in general, but is nearly always close to unity. Hence we can write

$$I_0 = FP/d\Delta(T,n). \tag{3}$$

Equations (2) and (3) together give the required connection between absorbed light power P and the excess quasiparticle density n. The microwave reflectivity as a function of P will therefore give information about recombination dynamics.

An effective quasiparticle lifetime τ_{eff} can be defined in quasiequilibrium by $\Delta N = I_0 \tau_{eff}$.[7] From Eq. (2),

$$\tau_{eff} = \left(\frac{1}{R} + \frac{N_T^2(T,n)}{2N_{\omega T}(T,n)}\tau_\gamma\right)(\Delta N + 2N_T)^{-1}. \tag{4}$$

The coefficient of τ_γ varies as $1/\Delta(n)$ for $kT \ll \Delta$, making the role of the recombination phonons even more important than in Rothwarf and Taylor's original work. In the strong-injection regime, $\Delta N \gg N_T$, and τ_{eff} can become very short, making time-resolved experiments very difficult.

An experimentally useful form of Eq. (2) is

$$(\Delta N^2 + 2\Delta N N_T)\delta/I_0 = \delta/R + \alpha\tau_\gamma, \tag{5}$$

where $\delta(T,n) \equiv \Delta(T,n)/\Delta(T,0)$. This factor has been added so that $\alpha = \delta N_T^2/2N_{\omega T}$ becomes independent of T and n for low T. The left-hand side of Eq. (5) can be determined from experimentally measured quantities. Hence, the right-hand side can be determined and the contributions of the two terms can perhaps be separated.

If the δR^{-1} term can be experimentally separated, the n dependence of Δ makes possible the determination of the dependence of R on Δ, information which is otherwise quite difficult to obtain. Theoretical calculations[8,9] yield $R \propto \Delta^m$, with m depending on whether the recombination process involves normal or umklapp phonon emission. For the normal process with the recombining particles at the gap edge, $m = 2$. For the umklapp process there appears to be theoretical disagreement: Rothwarf and Cohen[8] find $m = 1$, while Gray[9] finds $m = 3$. The relative importance of the normal and umklapp processes is also not generally well established experimentally. Theoretically, the umklapp process is found to be about 100 times faster than the normal process in Pb,[8] while in Al they appear to go at comparable rates.[9] Experiments of the type discussed here may be able to resolve some of these questions.

If the $\alpha\tau_\gamma$ term is dominant, the study of R becomes more difficult. In estimating τ_γ, it is important to realize that in a film with two effectively infinite dimensions, phonon random-walk diffusion is important even for $\lambda \gg d$, where λ is the phonon mean free path against pair breaking. This is a typical experimental situation: In Sn, λ is probably ~2000–2500 Å, while a typical film thickness is 500 Å. Assuming that the phonons scatter diffusely at the film surfaces and can leave the film only at the film-substrate interface, we obtain, to a good approximation,

$$\tau_\gamma = \frac{d}{\eta c_s}\left(\frac{\xi(3 + 2\ln\xi)}{2\xi - 1}\right), \quad \xi = \frac{\lambda}{d} > 1. \tag{6}$$

η is the average phonon transmission probability at the film-substrate interface and c_s is the sound velocity. For specular reflection at the film surfaces, and for $\eta \approx 4\xi^{-1}$ (a condition usually met in practice), we estimate $\tau_\gamma \approx 4d/\eta c_s$. These two estimates of τ_γ are in essential agreement for typical experimental parameters.

From the above, we see that if $\alpha\tau_\gamma$ is not too large compared with δR^{-1}, it should be possible to separate the two terms using the dependence of τ_γ on film thickness d. The right-hand side of Eq. (5) may display a gap dependence ranging from Δ^{-2} to Δ^0, depending on the relative dominance of various terms and the correct gap dependence of R for umklapp processes. When the τ_γ term dominates, the excess quasiparticle density becomes almost independent of film thickness for a given incident light power. The separation of the various terms of interest, while possible in principle, in practice may place stringent requirements on experimental accuracy.

We would like to thank C. S. Owen and D. J. Scalapino for providing us with a copy of their detailed numerical results and C. Allyn for numerical calculations.

---

*Work supported by the National Science Foundation and the U.S. Army Research Office (Durham).

†Present address: Institute of Energy Conversion, University of Delaware, Newark, Del. 19711.

[1] L. R. Testardi, Phys. Rev. B 4, 2189 (1971).

[2] C. S. Owen and D. J. Scalapino, Phys. Rev. Lett. 28, 1559 (1972).

[3] W. H. Parker and W. D. Williams, Phys. Rev. Lett. 29, 925 (1972).

[4] A. Rothwarf and B. N. Taylor, Phys. Rev. Lett. 19, 27 (1967).

[5] G. A. Sai-Halasz, C. C. Chi, A. Denenstein, and D. N. Langenberg, following Letter [Phys. Rev. Lett. 33, 215 (1974)].

[6] D. C. Mattis and J. Bardeen, Phys. Rev. 111, 412 (1958).

[7] In general, one can picture both a quasiparticle injection current, I_0, and a flux of phonons with energy greater than 2Δ, J_0. Under these conditions, the rate equations are

$$dN/dt = I_0 - RN^2 + \beta N_\omega,$$

$$dN/dt = J_0 + \tfrac{1}{2}RN^2 - \tfrac{1}{2}\beta N_\omega - (1/\tau_\gamma)(N_\omega - N_{\omega T}).$$

We can define, in steady state, τ_{eff} by

$$\Delta N = I_{\text{eff}}\tau_{\text{eff}},$$

where

$$I_{\text{eff}} = I_0 + J_0[2N_T^2R\tau_\gamma/(2N_{\omega T} + N_T^2R\tau_\gamma)].$$

One finds

$$N^2 = N_T^2 + I_0[(1/R) + (N_T^2/2N_{\omega T})\tau_\gamma] + J_0[(N_T^2/N_{\omega T})\tau_\gamma]$$

and

$$\tau_{\text{eff}} = [(1/R) + (N_T^2/2N_{\omega T})\tau_\gamma](\Delta N + 2N_T)^{-1}.$$

Thus, the formal expression for τ_{eff} remains unchanged, but in the analysis of data I_{eff} should be used.

[8] A. Rothwarf and M. Cohen, Phys. Rev. 130, 1401 (1963).

[9] K. E. Gray, Phil. Mag. 20, 267 (1969).

Effects of Dynamic External Pair Breaking in Superconducting Films*

G. A. Sai-Halasz, C. C. Chi, A. Denenstein, and D. N. Langenberg
Department of Physics and Laboratory for Research on the Structure of Matter,
University of Pennsylvania, Philadelphia, Pennsylvania 19174

(Received 21 March 1974)

Effects of dynamic external pair breaking in superconducting films are studied using microwave reflectivity to probe excess quasiparticle densities. For weak pair breaking, agreement with theory is good, permitting determination of effective quasiparticle recombination times. For strong pair breaking, an expected first-order transition to the normal state is not observed. Instead, a partially dc-resistive state is found in a broad injection region.

We have experimentally investigated nonequilibrium effects in superconducting Sn films under the influence of external pair breaking, using microwave reflectivity as a probe of the quasiparticle density. The results reported here are interpreted using the theory discussed in the previous Letter.[1] They give new insight into the problem of measuring the intrinsic recombination time of quasiparticles. In addition, they provide a test of the Owen-Scalapino[2] model of a nonequilibrium superconductor under weak and strong pair breaking.

Pair breaking was accomplished with a pulsed GaAs laser (λ = 904 nm) generating a maximum peak power of 15 W. cw 70-GHz microwaves reflected from the film were detected and amplified, then averaged in a boxcar integrator and recorded against time. Because of ac coupling, the signal is zero in equilibrium and proportional to $R(0)-R(n)$ (notation follows Ref. 1) in the nonequilibrium situation. Typically, 60–90-nsec pulses were used at a 100-sec^{-1} rate. The absorbed light energy per pulse was less than 5 ergs at maximum intensity, assuming 62% reflection from the films. This amount of energy was insignificant in raising the substrate temperature; heating effects in general have been discussed earlier.[3,4] On the other hand, the pulses were of sufficient duration to establish quasiequilibrium in the superconductor. The low repetition rate assured the restoration of equilibrium between pulses. The light intensity was variable by a factor more than 10^4. The minimum detectable change in the microwave reflectivity was $2\times10^{-4}[R(0)-R_N]$ with an overall system rise time (10–90%) of 25 nsec. The films, ranging in thickness from 150 to 1100 Å, were evaporated on optically flat quartz substrates. Measurements were made in a vacuum can as a precaution against deposition of ice on the film during transfer of helium.

Care was taken to assure uniformity of light intensity over the region of the film probed by the microwaves. The inside of a brass cylinder was fumed with MgO, forming a "white box," the light pipe entered in the side of the cylinder close to the bottom, and the film formed the top side of the cylinder. The probed area was ~25% of the total irradiated portion, placed in the center of it. Over this area the diffusely scattered light was of uniform intensity within our ability to measure it, ~2%.

A typical light pulse (measured by a *p-i-n* diode photodetector) and a signal are shown in Fig. 1. The top of the signal is flat, indicating that quasiequilibrium is established. The rise and fall times are those of the electronics, implying that the effective quasiparticle recombination time is less than 25 nsec and cannot be measured in this direct way. It can, however, be found indirectly through a measurement of the pulse height (signal amplitude) versus light intensity, as shown in the previous paper. Such data were obtained for all films at several temperatures. The qualitative features of these data were the same in all cases; data points for one case are shown in Fig. 2, together with a theoretical curve derived from Ref. 1. It is apparent that experi-

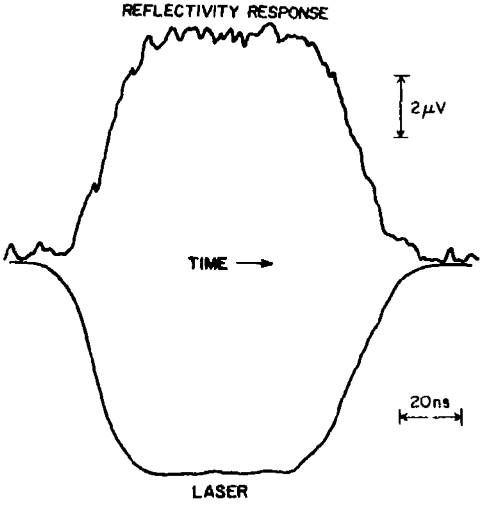

FIG. 1. Typical microwave reflectivity signal and laser pulse. The signal amplitude is proportional to $R(0)-R(n)$, and the voltage scale refers to the microwave detector output. The light is detected by a *p-i-n* diode, and the scale is arbitrary.

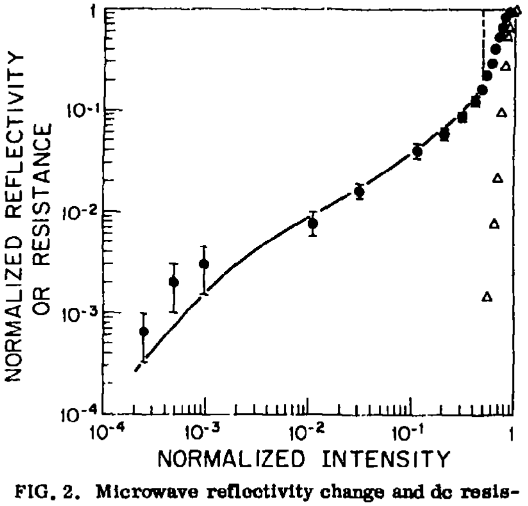

FIG. 2. Microwave reflectivity change and dc resistance as a function of relative pair-breaking intensity for Sn at 1.2 K. Closed circles: reflectivity change $R(0)-R(I)$ normalized with respect to the full change $R(0)-R_N$ between the equilibrium superconducting and normal states for a 400-Å-thick film; intensity at 1 is 8 W cm^{-2}. Solid line: theoretical curve of Ref. 1. Dashed line: where the predicted first-order transition should have occurred. Triangles: resistance $r(I)$ normalized to the normal-state value r_N for a 500-Å strip; for this curve, absolute light power at 1 is 7.6 W cm^{-2}.

ment and theory are in good agreement over 3 orders of magnitude in light intensity and signal. (The figure shows the least satisfactory fit of all the cases studied.) However, the sharp transition to the normal state at high light intensities predicted by the Owen-Scalapino modes does not occur! We shall return to this feature below, after considering the implications of the region where theory and experiment do agree.

In all cases the theoretical curve was fitted to the data by adjusting only the light-intensity scale, using the relation $CI_0 = \Delta N^2 + 2N_T\Delta N$. The scaling constant C contains the physically interesting parameters. The importance of τ_γ, the time required for recombination phonons to leave the film, can now be determined. In this event, $C = 1/R + N_T^2\tau_\gamma/2N_{\omega T}$ should display a dependence on film thickness. The data plotted in Fig. 3 show that this is indeed the case. In comparing values of τ_γ obtained from these data with the theoretical estimates of Ref. 1, it should be borne in mind that, in addition to other limitations of the latter estimates, the wavelength of the recombination phonons is more than 100 Å, approaching the thickness of the films used. This undoubtedly further limits the reliability of the theoretical estimates. However, the experimental values of τ_γ are of the right magnitude. For our 900-Å film (where the nonzero wavelength of the recombination phonons should have the least effect), assuming specular reflection of phonons from the film surfaces (the diffuse reflection case is not very different), we find the phonon escape probability $\eta \simeq 7\times10^{-2}$, taking the conversion efficiency of the light power $F = \frac{1}{4}$. This is in reasonable agreement with values estimated by combining experimental Kapitza resistance measurements[5] and theory.[6]

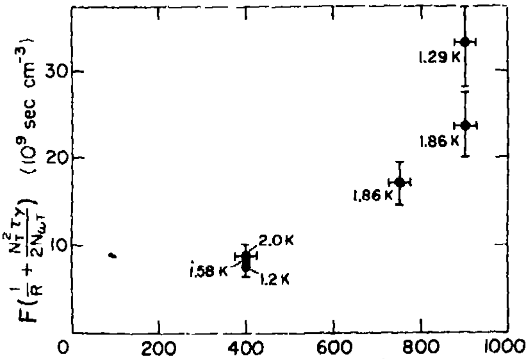

FIG. 3. Fitting parameter as a function of film thickness. This parameter is obtained from reflectivity data, as in Fig. 2. Error bars represent relative errors; an overall 30% uncertainty exists due to the uncertainty in absolute light power.

In principle, one may attempt to obtain the intrinsic[7] recombination time $\tau_R = (2N_TR)^{-1}$ either from extrapolation of data like that in Fig. 3 to zero film thickness, or directly from measurements on very thin films. In one attempt on a 150-Å film, we have established the existence of effective quasiparticle lifetimes much shorter than in the thicker films, and we are currently pursuing this possibility. The extrapolation procedure imposes severe requirements on experimental accuracy; it is apparent that the data of Fig. 3 permit only the establishment of an upper limit on τ_R. Assuming that τ_R is not much larger than the uncertainty (~25%) in $\tau_{\rm eff}(\Delta N = 0)$ for the 400-Å film (where the τ_γ term still clearly dominates), we find $\tau_R \leq 3\times10^{-11}F^{-1}t^{-1/2}\exp[\Delta(T)/kT]$. To our knowledge, this is the first time that the overwhelming contribution of τ_γ in the quasiparticle recombination process has been established, and a limit given for the intrinsic recombination time.

Returning now to the absence of the expected first-order transition to the normal state, we note (cf. Fig. 2) that, although the slope of the signal-amplitude versus light-intensity curve does increase at high light intensity, the reflectivity approaches its normal value over about a factor of 2 in light intensity, converging to it with essentially zero slope. Limiting the film sizes to the area of microwave incidence had no effect, indicating that quasiparticle diffusion out of the probed area was of no importance.

To gain more insight into the state of the superconductor in the region near the transition, we correlated dc measurements with the microwave measurements. We used strip films, typically 1.5 mm wide and 2 cm long. The microwaves and light were incident on the middle on a spot of ~0.5 cm diam. Outside the illuminated area, leads for a four-terminal resistivity measurement were connected. Measuring currents were typically 1–5 mA. The electronic processing of the dc voltage signals was the same as for the microwave signals. Signals stemming from an Ohmic resistance (inductive effects are insignificant) appear, with zero slope, close to the point where the transition should have occurred, and gradually increase with pair-breaking intensity. The shapes of the dc-signal pulses are exact replicas of the microwave signal pulses. The maximum dc signal corresponded exactly to the normal resistance of the film strip, as measured the standard way at 4.2 K, and in light intensity corresponded to the point where the microwave reflectivity indicated the normal state. For a given light intensity the dc signals displayed a perfectly Ohmic character. The dc current had no effect on the microwave signals and vice versa. Typical dc data points are shown in Fig. 2.

It appears from both the microwave and dc measurements that, rather than undergoing a sharp transition to the normal state, the films undergo a transition to what may be a new type of superconducting state, a sort of photon-induced dynamic intermediate state. Following is a highly speculative discussion which, in our view, represents a possible picture of this state. It is known that the recombination phonons play a central role in the recombination dynamics. Suppose that a critical excess quasiparticle density is reached and the film turns normal discontinuously. In the normal state, there is no bottleneck for the incoming energy flux in the form of quasiparticles of energy $\sim\Delta$ and phonons of energy $\sim 2\Delta$, that are the most effective in impeding pairing. The film goes back to the superconducting state, starting the process over. The larger the pair-breaking intensity, the shorter the time the film spends in the superconducting state. Beyond the temporal fluctuations, spatial breakup is probably inevitable, but of secondary importance, due, for example, to slight inhomogeneities in film thickness. If the temporal scale is $\lesssim 10$ nsec, both the microwave and dc signals would indicate an average of the measured parameter, behaving as if a well-defined fraction of the film is normal at all times.

We have been able to put an upper limit on the time scale of these processes. The dc signals at sufficiently high intensities are large enough to be observed directly on a sampling oscilloscope. The measured fall time was 1 nsec. However, this might have resulted from the fall time of the light intensity and must be regarded as an upper limit.

A proper theoretical understanding of this dynamic intermediate state will obviously require consideration of a possible superconducting-normal interface energy, and of the bremsstrahlung phonons created in the cooling of the primary high-energy particles.

Another feature of our data should be mentioned: The change in the microwave reflectivity of the films is delayed measurably after arrival of the light. This "initial delay" was proportional to thickness (approximately 1 nsec per 100 Å), but independent of the light intensity. The latter indicates that the initial delay is not connected with the recombination process. In most of our experiments, the light was incident on the side of the film opposite to that which the microwaves sampled, and the possibility arises that it takes this delay time for the effect to cross the film. This in turn could be an indication of a nonuniformity across the film, making our results questionable. However, both quasiparticles and phonons cross the films in less than 10^{-10} sec, making it virtually impossible for nonuniformity to exist on the 10^{-8}-sec time scale of our work. To check this point, in one case we irradiated a film from the front side. No differences were noted in any respect; in particular, the initial delay was unchanged. This leads us to believe that the initial delay is the result of the cascade process through which each photon distributes its energy among quasiparticles and phonons. It is known[8,9] that high-energy electrons are dumped overwhelmingly by phonon emission, rather than by pair breaking. Accordingly, the cascade process involves several phonon emission and adsorption steps, the total time of which can be of the order of a few nanoseconds. However, we measured the initial delay also in a Pb film where, according to the same theory, the emission and adsorption processes are at least an order of magnitude faster, and found approximately the same initial delay as in similar thickness Sn films. This leaves us with no firm explanation of the phenomenon, or its thickness dependence.

Shortly before submitting this Letter it came to our attention[10] that photoinduced effects in superconductors have also been investigated independently by other groups.

The authors are greatly indebted to A. Rothwarf for illuminating discussions.

---

*Research supported in part by the National Science Foundation and by the U.S. Army Research Office (Durham).

[1] A. Rothwarf, G. A. Sai-Halasz, and D. N. Langenberg, preceding Letter [Phys. Rev. Lett. 32, 212 (1974).

[2] C. S. Owen and D. J. Scalapino, Phys. Rev. Lett. 28, 1559 (1972).

[3] L. R. Testardi, Phys. Rev. B 4, 2189 (1971).

[4] W. H. Parker and W. D. Williams, Phys. Rev. Lett. 29, 925 (1972).

[5] M. K. Maul, M. W. P. Strandberg, and R. L. Kyhl, Phys. Rev. 182, 522 (1969).
[6] W. A. Little, Can. J. Phys. 37, 334 (1959).
[7] A. Rothwarf and B. N. Taylor, Phys. Rev. Lett. 19, 27 (1967).
[8] L. Tewordt, Phys. Rev. 128, 12 (1962).
[9] V. L. Prokrovskii, Zh. Eksp. Teor. Fiz. 40, 143 (1961) [Sov. Phys. JETP 13, 100 (1961)].
[10] L. Morelli, J. N. Lechevet, L. Leopold, and W. D. Gregory, Bull. Amer. Phys. Soc. 19, 276 (1974); J. Shah, R. F. Leheny, and A. H. Dayem, Bull. Amer. Phys. Soc. 19, 277 (1974); P. Hu, R. C. Dynes, and V. Narayanamurti, Bull. Amer. Phys. Soc. 19, 277 (1974).

Liquid-Gas Phase Diagram of an Electron-Hole Fluid

Gordon A. Thomas, T. M. Rice,* and J. C. Hensel
Bell Laboratories, Murray Hill, New Jersey 07974
(Received 21 May 1974)

Measurements and theoretical estimates are presented of the liquid-gas phase diagram of an electron-hole fluid in pure germanium. The critical point is found to occur in a region where the fluid is an electron-hole plasma at $T_c = 6.5 \pm 0.1$ K and $n_c = (8 \pm 2) \times 10^{16}$ cm^{-3}.

We present here a study of the phase diagram f the electron-hole condensate in germanium, ased upon information obtained from the lumiescence spectrum under constant optical pumpig. The luminescence from the condensed phase, hich has been observed in Si[1] and Ge,[2] indicates rom the low-temperature line shape[2-4] and its emperature dependence[4]) that the condensate is n electron-hole liquid. While it is well establshed that excitons exist at low carrier densities the gas phase,[5] we shall present evidence that e gas is an electron-hole plasma at high denses near the critical point. We shall discuss ony briefly the transformation between excitons nd plasma, since it is not as yet understood.

The liquid-gas phase diagram for electrons nd holes in germanium has been measured using wo different aspects of the recombination lumiescence. First, the line shape of the luminesence from the liquid has been used to obtain its bsolute density as a function of temperature. his procedure has been discussed previously[4] r temperatures below 4.25 K and is here extendd to higher T. Second, onsets of liquid luminesence as a function of T at constant pumping powr have been used to determine the relative denity in the gas at the boundary of the two-phase egion. Onsets analogous to these have been easured in luminescence,[2,6] in cyclotron resoance,[7] and in noise pulses,[8] in the temperature egion below 4.2 K.

At high densities the electron-hole liquid is etallic and there is good agreement between the irst-principles calculations,[9-11] based on the ranom-phase approximation (RPA) at $T = 0$ and modifications thereof, and experiment. As temperature is raised the density n of the liquid is reduced through thermal expansion.[4] Within the RPA one may write the free energy per particle as

$$F(n,T) = F_0(n,T) + F_{xc}(n,T), \tag{1}$$

where F_0 is the free energy of a noninteracting set of electrons and holes and F_{xc} represents the exchange and correlation corrections due to the interactions. In the metallic regime one can, to a good approximation, ignore the explicit T dependence of F_{xc} and write $F_{xc}(n,T) \equiv F_{xc}(n)$. The validity of this approximation, which we have checked by direct calculation, can be understood since, within the RPA, the excitation spectrum is strongly perturbed by the interactions only at energies of order of the plasma frequency ω_p. Since, in Ge, $\omega_p \approx 14\tilde{n}^{1/2}$ meV, where $\tilde{n} = n \times (10^{-17}$ cm$^3)$, the condition $k_BT \ll \hbar\omega_p$ is satisfied. The main effect of the interactions is to lower rigidly the bottom of the band with only a negligible change in effective mass.[12] This effect diminishes rapidly as the density drops. It can be estimated theoretically by computing the exchange and correlation contributions to the chemical potential, $\mu_{xc}(n) \equiv F_{xc} + n\partial F_{xc}/\partial n$. Finally, on theoretical grounds, one might expect that at a sufficiently low density $n = n_{MI}$ the fluid ceases to be metallic, where

$$n_{MI} = (1/8\pi)(k_BT/E_x)a_x^{-3}. \tag{2}$$

This is the Mott criterion for nondegenerate carriers (based on the Debye screening length) where E_x and a_x are the exciton Rydberg and Bohr ra-

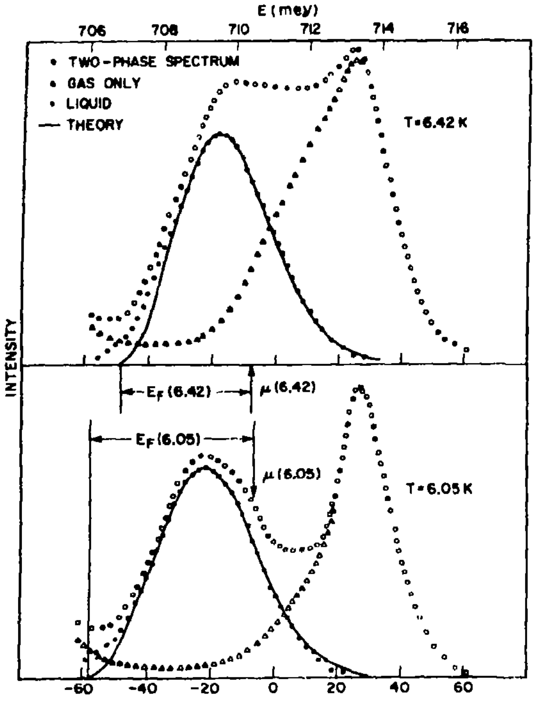

FIG. 1. Energy spectra of luminescence from the electron-hole liquid (lower energy lines) and the electron-hole gas (higher energy lines) in Ge at two temperatures approaching the critical point. At each T, a complete spectrum is obtained in the two-phase region (open circles) and then a second spectrum with only gas present (triangles) is recorded. We find that the effective gas line shape for the subtraction procedure is best measured for each power level at a T just above the two-phase region. The theoretical fits to the data (solid lines) indicate that the liquid density [calculated from $E_F(T)$] is decreasing rapidly between 6.05 and 6.42 K (see Fig. 2).

dius, respectively.

The experiments were carried out under the same conditions discussed previously,[4] but with the samples in a glass chamber filled with a variable pressure of He^4 exchange gas surrounded by superfluid He^4. The density in the droplets was measured from the line shape assuming that the recombination luminescence intensity can be described simply as a joint density of states of electrons and holes. The fit to the data then determines the sum of the electron and hole Fermi energies $E_F(T)$ relative to the bottom of the band which, in turn, determines the densities using the band effective masses.

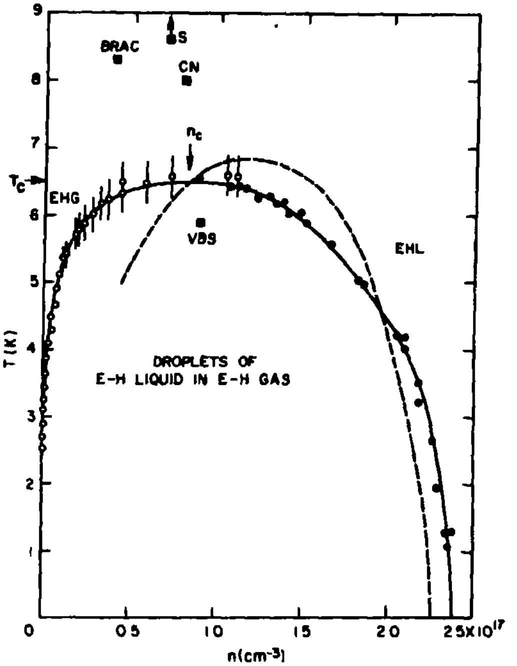

FIG. 2. Phase diagram in temperature and density of electrons and holes in pure Ge. The solid points on the liquid side of the coexistence curve are obtained as illustrated in Fig. 1. The open circles were determined from onsets of the two-phase region (as a function of T at constant power). The solid curve corresponds to the theoretical behavior for low T in the liquid (see Ref. 4) and to the shape of the scaled phase diagram for simple fluids near T_c. The dashed curve is an empirical estimate using the data of Fig. 3.

As T increases toward T_c, the liquid and gas lines gradually merge, as shown in Fig. 1. Above ~ 5 K the liquid line shape is deconvolved by subtraction. Our measurements of the spatial profile of the luminescence in the sample indicate that the region of gas is not uniform in density and varies as a function of pumping power; however, the liquid density measurement should be reliable as the density within the drops should be nearly uniform and only a function of T.

As seen from the liquid-line shapes in Fig. 1, the main effect of T on the liquid is to shift upward the bottom of the band (the lowest energy of the fitted luminescence spectrum) as n decreases. On the other hand, the chemical potential $\mu(T)$ shifts downward only slightly following the T^2 dependence reported at lower temperatures.[4] The density measurements of the liquid are summarized by the solid dots in Fig. 2. We fit the data with the solid curve which corresponds to a T^2 dependence up to about 4 K smoothly joined to the scaled phase diagram of simple fluids[13] near T_c. Because of uncertainties in determining absolute densities on the gas coexistence curve, we have extrapolated to the critical point from a fit to the liquid side of the phase diagram. This procedure, using the data for $\tilde{n}>1.0$, gives the agreement shown in Fig. 2 and a critical point at $T_c = 6.5 \pm 0.1$ K and $\tilde{n} = 0.8 \pm 0.2$.

The gas boundary of the phase diagram shown in Fig. 2 has been estimated from onset measurements of the liquid luminescence. These onsets (open circles) were obtained by decreasing the temperature at constant pumping power while nonitoring the integrated intensity from 708.5 o 709.5 meV, and also by recording an array of omplete spectra covering all accessible regions f T and pumping power. The absolute gas denities in Figs. 2 and 3 were fixed (at $T = 6$ K) by ssuming that the gas coexistence curve is aproximated by the scaled phase diagram in the icinity of T_c. Alternatively a rough estimate of he absolute value of the gas density can be obained from the position of the lower energy edge f the gas line relative to $\mu(T)$ assuming that the as is an electron-hole plasma. A third, less eliable, method uses the measured pumping powrs but requires assumptions as to the effective liffusion lengths and carrier lifetimes. All three nethods give roughly consistent results; hower, further studies will be necessary to renove the rather large uncertainty in the nature f the gas phase and its average density.

In Fig. 3 we plot the bottom of the band as a unction of density. Note that these measurenents are not at constant temperature but along he coexistence curve. In the high-density reime, where the data are best, the values are iot expected to vary much with temperature. The heoretical estimate for $\mu_{xc}(n)$ of Brinkman *et al.*[9] BRAC) is plotted as the solid line with $\mu(0)$ chosn at 63 K below the unperturbed band gap. These alues were determined by fitting a quadratic orm to the correlation energy points calculated it density values of $\tilde{n} = 3.4$, 0.43, and 0.05. The greement between theory and experiment is ood.

Combescot has shown[14] that a critical point vithin the metallic regime can be obtained using he free energy, Eq. (1). She used a low-temperture expansion for $F_0(n,T)$ and the Combescotozières results for $F_{xc}(n)$ to obtain $\tilde{n}_c = 0.7$ and $_c = 8.2$ K. Earlier, Silver[15] obtained $\tilde{n}_c = 0.7$, $T_c = 15.8$ K based on Hartree-Fock theory, while Vashishta[11] reports a value $\tilde{n}_c = 0.9$ and $T_c = 5.9$ K. We have calculated the critical point using the exact temperature dependence of F_0 and the BRAC form discussed above for $F_{xc}(n)$ and obtain the values $\tilde{n}_c = 0.4$, $T_c = 8.3$ K. This wide range of theoretical values shows the extreme sensitivity of the estimates to the detailed form of $F_{xc}(n)$. This sensitivity is not too surprising since the condition for a critical point involves the third derivative $\partial^3 F/\partial n^3$.

In order to test the basic approximation that F_{xc} is independent of T we made an empirical fit to the bottom-of-the-band energies (Fig. 3) and then used this form in Eq. (1) to determine a phase diagram. The results are shown as the dashed curves in Figs. 2 and 3. The values obtained are $T_c = 6.8$ K and $\tilde{n}_c = 1.2$ and the overall

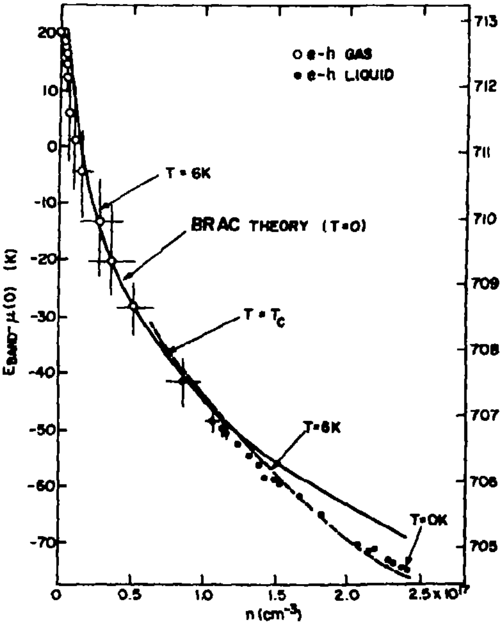

FIG. 3. Variation of the absolute position of the bottom of the electron-hole fluid band as a function of its equilibrium density with temperature as an implicit variable. The open circles (gas-phase points) begin near the exciton energy position and, with increasing temperature, move toward the critical point where the fluid enters the liquid phase (solid circles); the points then correspond to decreasing temperature. The dashed line is a rough empirical line through the data which is used to obtain the dashed approximate phase diagram shown in Fig. 2. The solid line is the BRAC theoretical estimate.

agreement with the phase diagram is good. The largest deviation occurs at the lower densities. It is clear that strong exciton or electron-hole correlations will significantly alter the entropy and therefore cause F_{xc} to vary with T at lower densities. A criterion for the complete breakdown of the metallic nature of the fluid is $|\mu_{xc}| = E_B$, where E_B is the exciton binding energy. From the BRAC theory[9] in Fig. 3 we estimate a value $\tilde{n}_{MI} \approx 4\times10^{-3}$. This value is roughly comparable to that obtained from the Mott criterion, Eq. (2), which, in Ge at 5 K is $\tilde{n}_{MI} = 6\times10^{-3}$. At present our data are insufficient to determine n_{MI} experimentally. Indeed we cannot rule out the interesting possibility that the metal-insulator transition occurs as a separate first-order phase change. Such a possibility was suggested many years ago for liquid metals by Landau and Zel'dovich.[16] We can, however, conclude that the two transitions are well separated and $n_{MI} \ll n_c$.

We would like to thank R. E. Miller and F. C. Unterwald for experimental assistance, and B. I. Halperin, P. W. Anderson, E. O. Kane, T. G. Phillips, and W. F. Brinkman for useful comments and discussions. We also thank P. Vashishta for permission to quote his results prior to publications.

---

*Present address: Department of Physics, Simon Fraser University, Burnaby 2, B. C., Canada.

[1] J. R. Haynes, Phys. Rev. Lett. 17, 860 (1966).

[2] Ya. E. Pokrovskii, Phys. Status Solidi (a) 11, 385 (1972). A discussion of previous work is presented here and in a review by J. Bille, in *Festkörperprobleme XIII*, edited by H. J. Queisser (Pergamon, New York, 1973), p. 111.

[3] C. Benoît à la Guillaume and M. Voos, Phys. Rev. B 7, 1723 (1973).

[4] G. A. Thomas, T. G. Phillips, T. M. Rice, and J. C. Hensel, Phys. Rev. Lett. 31, 386 (1973). The temperature dependence of the liquid density reported here has been reproduced by T. K. Lo, to be published.

[5] See, for example, G. G. McFarlane, T. P. McLean, J. E. Quarrington, and V. Roberts. Phys. Rev. 108, 1377 (1957); K. J. Button, L. M. Roth, W. H. Kleiner, S. Zwerdling, and B. Lax, Phys. Rev. Lett. 2, 161 (1959).

[6] T. K. Lo, B. J. Feldman, and C. D. Jeffries, Phys. Rev. Lett. 31, 224 (1973).

[7] J. C. Hensel, T. G. Phillips, and T. M. Rice, Phys. Rev. Lett. 30, 227 (1973).

[8] J. C. McGroddy, M. Voos, and O. Christensen, Solid State Commun. 13, 1801 (1973).

[9] W. F. Brinkman, T. M. Rice, P. W. Anderson, and S. T. Chui, Phys. Rev. Lett. 28, 961 (1972). See also W. F. Brinkman and T. M. Rice, Phys. Rev. B 7, 1508 (1973).

[10] M. Combescot and P. Nozières, J. Phys. C: Proc. Phys. Soc., London 5, 2369 (1972).

[11] P. Vashishta, P. Bhattacharyya, and K. S. Singwi, Phys. Rev. Lett. 30, 1248 (1973). The critical-point values are from P. Vashishta, private communication.

[12] Apparently any contribution from the zero-sound modes within RPA is not important. T. M. Rice, to be published.

[13] A summary of the simple-fluid results is given by P. Heller, Rep. Progr. Phys. 30, 731 (1967), and by E. A. Guggenheim, J. Chem. Phys. 13, 253 (1945). A comparison of various scaled phase diagrams and some experimental estimates in Ge is discussed by Z. A. Insepov and G. E. Norman, Zh. Eksp. Teor. Fiz. 62, 2290 (1972) [Sov. Phys. JETP 35, 1198 (1972)].

[14] M. Combescot, Phys. Rev. Lett. 32, 15 (1974).

[15] R. N. Silver, Phys. Rev. B 8, 2403 (1973).

[16] L. Landau and G. Zel'dovich, in *Collected Works of L. D. Landau*, edited by D. ter Haar (Gordon and Breach–Pergamon, New York, 1965), p. 380.

EPR Observation of Close Frenkel Pairs in Irradiated ZnSe†

G. D. Watkins
General Electric Corporate Research and Development, Schenectady, New York 12301

(Received 6 May 1974)

Four distinct EPR spectra observed in ZnSe irradiated by 1.5-MeV electrons at 20.4°K are identified as simple zinc-vacancy, zinc-interstitial close pairs of different microscopic configuration. Correlation of defect alignment with incident-electron-beam direction confirms the identification. Isolated zinc vacancies are also produced but with zero initial production rate, suggesting that their production is a two-step process, the first being the formation of close pairs.

In this Letter I report the EPR observation of everal discrete zinc-vacancy, zinc-interstitial ose pairs in ZnSe. Although such Frenkel pairs ave often been called upon to explain radiation- amage behavior in solids, I believe this is the rst direct unambiguous observation of these mple fundamental defects in a solid.[1]

Irradiation of ZnSe with 1.5-MeV electrons at 0.4°K produces two prominent well-resolved isotropic EPR spectra, with $S=\frac{1}{2}$. One, la- led V, has been previously identified as arising om the isolated zinc lattice vacancy.[2,3] Its spec- um is axially symmetric along a ⟨111⟩ axis of e crystal with $g_\parallel=1.9548$, $g_\perp=2.2085$. This, oupled with the analysis of resolved Se^{77} hyper- ne interactions, has revealed that the spectrum rises from a hole primarily located in the $4p$ ell of a single selenium neighbor to a zinc va- ancy. The defects align under externally ap- led stress at cryogenic temperatures (i.e., the le can "hop" between the four equivalent selen- m neighbors of the vacancy and seeks out the west-energy one under stress). This establish- that the reduced local symmetry of the vacan- results from a trigonal ⟨111⟩ Jahn-Teller dis- rtion and that otherwise the vacancy has the ll tetrahedral symmetry (T_d) of the zinc lattice te, with no defect close enough nearby to pro- ce a strain field comparable to that which can applied externally.

The second spectrum, V^{I}, also has ⟨111⟩ axial ymmetry: Its g tensor and Se^{77} hyperfine inter- ctions differ only slightly from those for V, in- icating that it also results from a zinc vacancy. niaxial stress does not produce measurable lignment,[3] however, suggesting that here the acancy is in the strain field of a nearby defect cated in a ⟨111⟩ direction from the vacancy.

Figure 1 shows the results of annealing. There re several discrete stages between 60 and 180°K which other well-resolved EPR centers, V^{II}, V^{III}, V^{IV}, grow and disappear. These additional centers show small departures from axial symmetry but are otherwise very similar to V and V^{I}, indicating that they too are perturbed zinc vacancies. For V^{II} and V^{III}, uniaxial stress produces partial alignment revealing a restricted type of reorientational motion available to each. For V^{II}, the hole can hop between three of the four selenium neighbors which suggests the presence of a nearby defect in the ⟨111⟩ direction of the fourth selenium neighbor. For V^{III}, the hole motion is between two of the selenium neighbors indicating a defect in a ⟨100⟩ direction from the vacancy. The intensity of V^{IV} is too weak to make reliable stress measurements on it.

This Letter establishes that the defects V^{I}, V^{II}, V^{III}, and V^{IV} are zinc lattice vacancies which are perturbed by the presence of the nearby interstitial produced in the damage event. As such, they are simple zinc-vacancy, zinc-interstitial

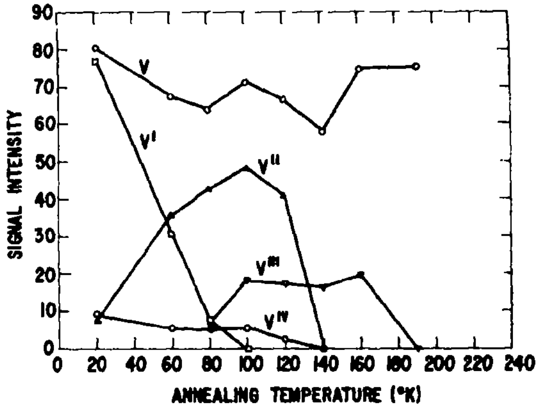

FIG. 1. Intensities of EPR spectra observed at 20.4°K in irradiated ZnSe after 15-min isochronal anneals. The sample was irradiated at 20.4°K with 1.5-MeV electrons to a fluence of 4×10^{17} electrons/cm^2.

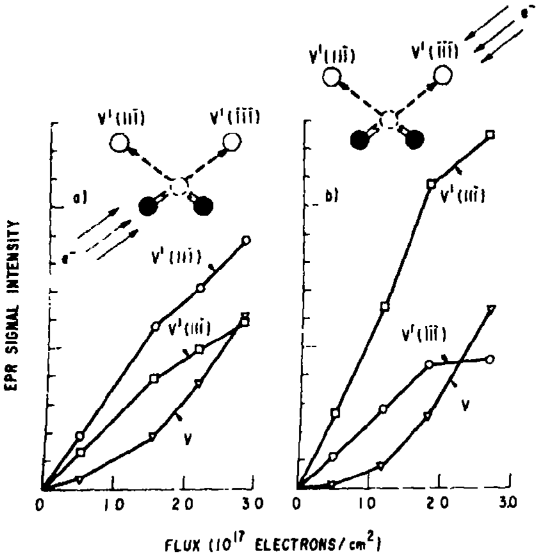

FIG. 2. Production of V and oriented V^{I} centers versus 1.5-MeV-electron fluence at 20.4°K for two different beam directions: (a) $e^- \parallel [\bar1\bar1\bar1]$; (b) $e^- \parallel [111]$.

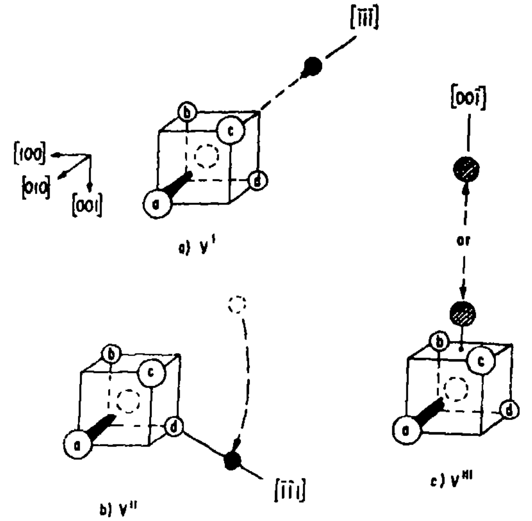

FIG. 3. *Models for the Frenkel close pairs. The open circles represent selenium ions, the cross-hatched ones, the interstitial zinc. For each, the hole is on atom a, as indicated by the black orbital.*

close pairs of different microscopic configurations. In this model V^{I} is formed as a primary damage event when the zinc atom is knocked out of its lattice site into a nearby interstitial site by the incoming electron. The other spectra result from different microscopic arrangements for the pair. Some of these may also be produced directly as a primary event (Fig. 1) but for the most part they appear to arise from annealing.

A direct test of this identification is possible as follows: In the primary damage event the incoming electron transmits the maximum recoil energy to a zinc atom when it recoils in the direction of the bombarding electron. There should, therefore, be a strong correlation between the orientation of interstitial-vacancy close pairs and the bombarding beam direction.

Figures 2(a) and 2(b) show the results for electron irradiation along the $[\bar1\bar1\bar1]$ and $[111]$ directions, respectively. For the $[\bar1\bar1\bar1]$ irradiation, Fig. 2(a), the production rate for V^{I} defects aligned along the beam direction, $V^{\mathrm{I}}[\bar1\bar1\bar1]$, is 50% greater than that for those oriented along the other $\langle 111\rangle$ directions, as monitored by $V^{\mathrm{I}}[1\bar11]$. Radiation along the $[111]$ direction, Fig. 2(b), reverses the effect, the $V^{\mathrm{I}}[\bar1\bar1\bar1]$ production rate now being less than half that for $V^{\mathrm{I}}[11\bar1]$. For these studies the sample thickness along the beam direction was ~0.017 in which leads to a mean square scattering angle of the beam of ~55° upon emerging from the other side of the crystal.[4] The electron beam in the sample is, therefore, described by a diffuse cone along the beam direction and the true anisotropy must be considerably larger than that observed in Fig. 2.

I interpret this anisotropy, representing unambiguous memory of the damage event, as convincing evidence of the close-pair identification for V^{I}. At the same time, the *sense* of the anisotropy confirms that the defect is being produced on the zinc lattice, the $[\bar1\bar1\bar1]$ recoil direction [see insets in Figs. 2(a) and 2(b)] being into an accessible interstitial space for the zinc atom. From the $\langle 111\rangle$ axial symmetry of the V^{I} center I tentatively identify V^{I} as a zinc-vacancy, zinc-interstitial close pair with the interstitial in the nearest available site in the $[\bar1\bar1\bar1]$ direction ($\frac{1}{2}\sqrt{3}a$ distant from the vacancy, with $a = 5.65$ Å), as shown in Fig. 3(a). Here the hole is Coulombically repelled from the positively charged interstitial zinc ion and locates on the selenium ion opposite the vacancy, as shown.

Starting with the preferential alignment of $V^{\mathrm{I}}[\bar1\bar1\bar1]$ after $[\bar1\bar1\bar1]$ irradiation of ~1.5:1, Fig. 2(a), one finds after annealing that V^{II}, V^{III}, and V^{IV} also display substantial correlated alignment. The V^{II} alignment, as measured by the $\langle 111\rangle$ axis around which stress alignment reorientation is tected, is of opposite sense and smaller in agnitude than that for V^{I}, the $[\bar{1}\bar{1}\bar{1}]/[11\bar{1}]$ ratio eing ~1.0:1.2. This suggests the model of Fig. (b). Here in the $V^{\mathrm{I}} \rightarrow V^{\mathrm{II}}$ conversion the intertitial moves to a position equidistant from the acancy but behind selenium atom *d* (or *b* or *c*, hich are equivalent). These three equivalent hoices reduce the net alignment by a factor of and result in a net *depletion* of the $[\bar{1}\bar{1}\bar{1}]$ alignent, as observed. In this model, Coulomb reulsion again forces the hole to the other side of e vacancy. In this case there are three equivaent atoms for the hole [*a*, *b*, or *c*, for the coniguration of Fig. 3(b)] and a Jahn-Teller distorion localizes it on one (*a* as shown in the figure). n physical grounds V^{II} might be expected to ave a lower energy than V^{I} because of the added inding energy resulting from the polarizable e^{--} ion between the defects.

The alignment observed for V^{III} is best decribed in terms of the model in Fig. 3(c). The nterstitial is located in a $\langle 100 \rangle$ direction from he vacancy and the preferred direction is equally istributed between $[\bar{1}00]$, $[0\bar{1}0]$, and $[00\bar{1}]$. The bserved alignment ratio $[00\bar{1}]/[001]$ is $\gtrsim 2.0$. (The zinc site is not a site of inversion symmetry and the $[00\bar{1}]$ and $[001]$ spectra are distinct.) The three preferred positions, $[\bar{1}00]$, $[0\bar{1}0]$, and $[00\bar{1}]$, lie on the surfaces enclosing the $[\bar{1}\bar{1}\bar{1}]$ octant and reflect the strong correlation of these defects with the initial $[\bar{1}\bar{1}\bar{1}]$ irradiation direction. The large alignment observed reveals that these cannot be derived solely from the annealing of V^{I}. (As for V^{II}, the three choices would reduce the net alignment to ~1.2.) They must, therefore, derive primarily from other more distant pairs, not being initially resolved, which have higher anisotropy of damage production. As shown in the figure, the interstitial could be in the nearest position, $\frac{1}{2}a$ away from the vacancy, or in the next position, $\frac{3}{2}a$ away. The hole is localized on one of the two equivalent selenium atoms on the opposite side of the vacancy, again associated with a Jahn-Teller distortion.

V^{IV} also displays a strong alignment correlated with the $[\bar{1}\bar{1}\bar{1}]$ beam direction of $\gtrsim 2.0$. A detailed model is not possible but the symmetry of the spectrum indicates an interstitial in a low-symmetry direction in the $[\bar{1}\bar{1}\bar{1}]$ octant.

Figure 2 reveals another interesting result. We note that the "isolated" vacancy, V, is not produced linearly versus dose (φ). The initial production rate is zero, the centers growing in as $\sim\varphi^n$, where n appears to be between 2 and 3. This reveals that the vacancy production is at least a two-step process and suggests that the first step is the close-pair production.

In summary, several discrete zinc-vacancy, zinc-interstitial close pairs have been identified by EPR in irradiated ZnSe. Correlation with initial electron-beam direction and stress alignment studies have allowed detailed models to be proposed for the defects. At 20.4°K, with 1.5-MeV irradiation, the primary damage process on the zinc lattice appears to be the production of Frenkel close pairs. Isolated zinc vacancies are also produced but involve at least one other step in the process.

Frenkel close pairs might be expected to be good luminescent centers, the nearby positively charged, interstitial zinc-atom "donor" serving to activate the vacancy double acceptor in a manner similar to that performed by chemical donors for the self-activated luminescent center in II-VI materials.[5] The possibility that the close pairs observed here are responsible for the luminescence reported by Detweiler and Kulp[6] in low-temperature irradiated ZnSe is currently being investigated.

---

†Research supported in part by the U. S. Air Force Aerospace Research Laboratory under Contract No. F33615-72-C-1505.

[1] Hayes and co-workers [W. Hayes and R. F. Lambourn, J. Phys. C: Proc. Phys. Soc., London 6, 11 (1973); W. Hayes, R. F. Lambourn, G. Rangarajan, and I. M. Ritchie, J. Phys. C: Proc. Phys. Soc., London 6, 27 (1973); W. Hayes and R. F. Lambourn, Phys. Status Solidi (b) 57, 693 (1973)] have recently presented optical, EPR, and electron-nuclear double-resonance evidence of *F* centers perturbed by nearby interstitial halogen ions in alkaline earth halides. These centers, produced by x irradiation at low temperatures, therefore involve Frenkel pairs, but the possible additional involvement of an impurity as well has not been ruled out [P. J. Call, W. Hayes, J. P. Stott, and A. E. Hughes, to be published].

[2] G. D. Watkins, Bull. Amer. Phys. Soc. 14, 312 (1969).

[3] G. D. Watkins, in *Radiation Effects in Semiconductors*, edited by J. W. Corbett and G. D. Watkins (Gordon and Breach, London, 1971), p. 301.

[4] J. W. Corbett, *Electron Radiation Damage in Semiconductors and Metals* (Academic, New York, 1966), p. 30 ff.

[5] See, for instance, D. Curie and J. S. Prener, in *Physics and Chemistry of II-VI Compounds*, edited by M. Aven and J. S. Prener (North-Holland, Amsterdam, 1967), p. 445 ff.

[6] R. M. Detweiler and B. A. Kulp, Phys. Rev. 146, 513 (1966).

Volume 33, Number 4 PHYSICAL REVIEW LETTERS 22 July 1974

Study of the Reaction ^{56}Fe(p,n)^{56}Co to the Antianalog State*

H. W. Fielding
Department of Physics, University of Wyoming, Laramie, Wyoming 82070

and

L. D. Rickertsen, P. D. Kunz, D. A. Lind, and C. D. Zafiratos
Nuclear Physics Laboratory, Department of Physics and Astrophysics, University of Colorado, Boulder, Colorado 80302

(Received 14 January 1974)

The reaction ^{56}Fe(p,n)^{56}Co was studied at $E_p = 22.8$ MeV for both the isobaric-analog-state (IAS) and antianolog-state (AAS) transitions. The difference in the observed angular distributions for these two $L=0$ transitions is not as striking as in (^{3}He,t) measurements. The strong cancelation expected for the AAS case was observed. The shapes of the angular distributions for both the IAS and AAS were improved by inclusion of a coherent two-step (p,d)(d,n) process.

Nuclear reactions such as (p,n), (^{3}He, t), and (π^+, π^0) can proceed through a simple charge-exchange mechanism. This mechanism explains the strong population of the isobaric analog state (IAS) which is observed for (p,n) and (^{3}He, t) reactions on target nuclei with more neutrons than protons. The IAS has the same spin and space wave function as the target ground state, differing only in the z projection of the nuclear isospin. In the case that the excess neutrons occupy several neutron orbitals their contribution to the IAS cross section is coherent and constructive for a charge-exchange reaction.

When the excess neutrons occupy more than one shell in the lowest-order shell model, one can construct states in the residual nucleus with the same J and π as for the IAS but with isospin one unit smaller.[1] These states are called antianalog states (AAS). In the event that the charge-exchange transition amplitudes associated with various neutron orbitals are similar, strong cancelation should occur so that charge-exchange reaction cross sections to the AAS should be weak relative to those for the IAS.[1] Because of the strong cancelation, the AAS cross section should be quite sensitive to details of the target-nucleon configuration. It is of more than usual interest, then, to study charge-exchange reactions leading to AAS.

Identification of AAS of even-even targets has generally been made by finding a single 0^+ level below the IAS. A variety of reactions have been used to make such assignments including the low-energy ^{40}Ar(p,n)^{40}K study by Twin, Olsen, and Wong.[2] In that study, however, the reaction was completely dominated by the compound-nucleus mechanism rather than a charge-exchange mechanism. When AAS were studied by the (^{3}He, t) reaction by Hinrichs *et al.*[3] it was found that the observed angular distributions were roughly out of phase with those of the IAS and could not be explained by a one-step charge-exchange mechanism.

A suggestion was made by Schaeffer and Bertsch[4] that an out-of-phase shape could be obtained by contributions from the (^{3}He, α)(α, t) reaction. Their suggestion led to a detailed calculation by Coker, Udagawa, and Wolter[5] who showed that the cancelation of the coherent one- and two-step amplitudes gave an out-of-phase angular distribution.

It remained to be seen whether the (p,n) reaction at a higher energy where the compound-nucleus effects are smaller would exhibit AAS angular distributions which were markedly different from those of the IAS, and whether a similar two-step process could successfully describe (p,n) AAS data. In this Letter we report the first reasonably complete angular-distribution data for a (p,n) reaction to an AAS with a bombarding energy clearly in the direct-reaction regime. These data were acquired with a unique new experimental facility which allows the use of heavily shielded long-flight-path detectors while still retaining the ability to take angular distributions over a wide range of angles.

We have chosen to study the (p,n) reaction to AAS for two reasons. First, the nucleon-nucleus optical potential is well founded in comparison to that for complex projectiles, making analysis more straightforward. Second, the (p,n) reaction is more sensitive to interior portions of the nuclear wave function while the (^{3}He, t) reaction is mainly influenced by the nuclear surface because of strong absorption of complex projectiles, thus making the predicted one-step cancelation for AAS with (p, n) reactions more striking than in the (^{3}He, t) reaction. The (p, n) reaction study is, of course, experimentally more difficult; however, these difficulties are partially offset by larger cross sections and by the use of thicker targets than those that can be used in (^{3}He, t) studies.

We chose the reaction ^{56}Fe(p, n)^{56}Co for our first study. The measurements were made with the University of Colorado rotating-beam neutron time-of-flight spectrometer[6] at a proton energy of 22.8 MeV. This new system employs neutron detectors at fixed, well-shielded positions and varies the angle of incidence of the beam upon the target to obtain an angular distribution. Initial data were obtained at 9 m flight path where Gaussian unfolding procedures were necessary to extract the area of the AAS peak at 1.45 MeV from that of the neighboring 1.72-MeV level. These data were verified and extended by subsequent measurements at a flight path of 29 m. Two 2.54-cm × 20-cm NE-224 liquid scintillation deectors were placed side by side in an earthen-shielded bunker for these longer-flight-path measurements. The 9-m measurements utilized hree similar detectors in concrete shields arranged so that data for three angles were obained simultaneously. Neutron-γ discrimination was employed to reduce background. A time-of-flight spectrum is shown in Fig. 1 with shorter flight times and hence higher neutron energies to the right and a time per channel of 0.3 nsec. The known doublet character[7] of the IAS in ^{56}Co was evidenced by the increased width seen for this peak compared to adjacent peaks.

The incident proton beam was varied in angle to obtain data between 10 and 120° lab angles. The target was 6-mg/cm^2 natural iron. The ^{54}Fe component of natural iron cannot produce neutrons with energies above those of the IAS group in Fig. 1. The ^{57}Fe and ^{58}Fe components can. Spectra taken with an ^{57}Fe target indicated no sharp levels near the ^{56}Co AAS. The 0.33% ^{58}Fe component cannot produce a detectable neutron group except possibly for its IAS transition which would lie beside the ^{56}Fe IAS group.

The angular distributions for the ^{56}Fe IAS and AAS transitions are shown in Fig. 2. The strong cancelation predicted for an AAS is quite evident in the data. The clear-cut difference in phase of the angular distributions seen in (^{3}He, t) measurements is not nearly so evident in the (p, n) data although there are substantial differences in the two $L = 0$ transitions of Fig. 2.

The solid curves in Fig. 2 are distorted-wave Born approximation (DWBA) calculations for a one-step charge-exchange process with a 1-fm-range Yukawa interaction between the projectile and target nucleons. The dashed curves are the calculations for the (p, d)(d, n) process[8] from a

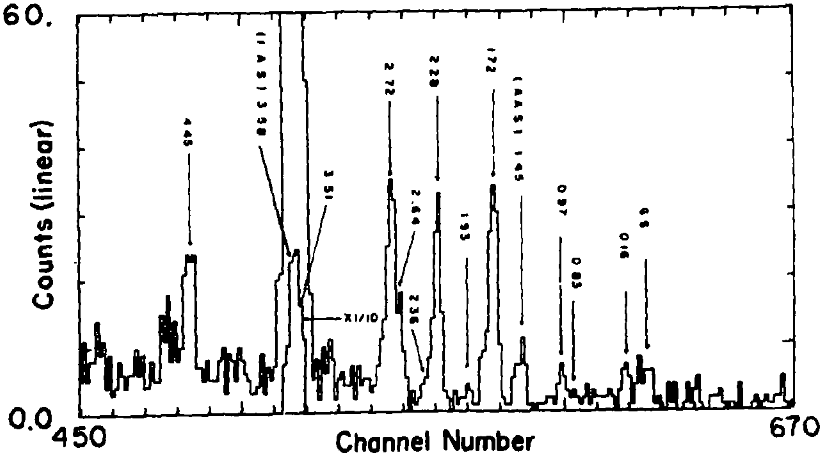

FIG. 1. Time-of-flight spectrum for ^{56}Fe(p, n)^{56}Co taken with one 1-in. × 8-in. detector at the 29-m station at an angle of 10°. Time per channel is 0.3 nsec. The AAS level is at 1.45 MeV excitation.

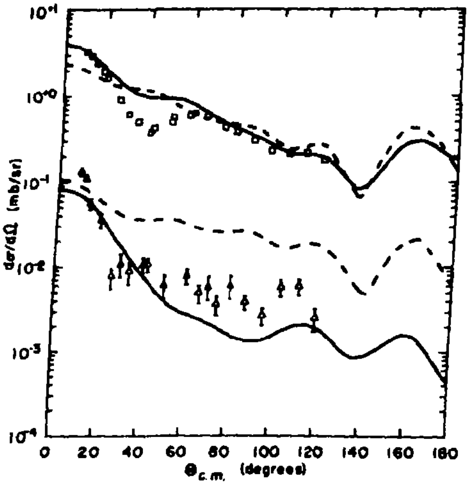

FIG. 2. IAS (squares) and AAS (triangles) angular distributions obtained for ^{56}Fe(p,n) at $E_p = 22.8$ MeV. Solid curves result from DWBA (charge-exchange only) calculations normalized to IAS. Dashed curves are absolute $(p,d)(d,n)$ two-step calculations using experimental (p,d) spectroscopic factors.

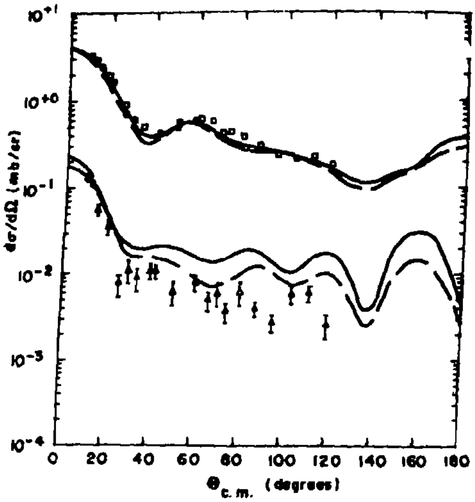

FIG. 3. Second-order DWBA calculations for IAS (squares) and AAS (triangles) angular distributions. Calculations include $(p,d)(d,n)$ two-step process and charge exchange. Solid curves give results due to experimental spectroscopic factors for the (p,d) reaction, and dashed curves result from arbitrarily modified spectroscopic factors and show the relative sensitivity of the AAS prediction to details of the ^{56}Fe wave function. Charge-exchange strength, 33 MeV.

differential-equation solution for the second-order DWBA term. The intermediate states in the deuteron channel include the first six states of ^{55}Fe.

The charge-exchange calculation is normalized to the IAS cross section with the one free parameter, $V_\tau = 22$ MeV. Optical-model potentials for the projectiles are given in Table I. No reasonable variation in the range of the interaction, optical potentials, or nuclear wave function was found which could substantially improve the shape of the calculated angular distributions. The $(p, d)(d, n)$ calculation uses the experimental spectroscopic amplitudes and hence has no free parameters.

The coherent addition of the charge exchange and $(p, d)(d, n)$ amplitudes gives the angular distributions in Fig. 3. The charge-exchange strength must be increased to $V_\tau = 33$ MeV because of the destructive interference between the one- and two-step amplitudes for the IAS state. This strength is the same as found previously in analysis[8] of (p, n) reactions in neighboring nuclei. The resulting shape of the angular distributions is improved for both the IAS and the AAS. Variations of the Yukawa range in the one-step component between $0.7 < \mu < 1.2$ did not greatly alter the AAS/IAS ratio but did slightly worsen the IAS fit.

The calculations for the solid curves in Fig. 3 have been made with published values[9] of the spectroscopic factors:

$$S_{5/2} = 0.87, \quad S_{3/2} = 1.00, \quad S_{1/2} = 0.42.$$

TABLE I. Optical-model potentials.

	V_R (MeV)	r_R (fm)	a_I (fm)	W_V (MeV)	W_D (MeV)	R_I (fm)	a_I (fm)	V_{SO} (MeV)	r_{SO} (fm)	a_{SO} (fm)
$p + {}^{56}$Fe	51.1	1.17	0.75	2.34	6.93	1.32	0.56	6.0	1.01	0.75
$n + {}^{56}$Co	$53.1 - 0.3E_n$	1.17	0.75	$0.22E_n - 2.7$	$11.4 - 0.25E_n$	1.32	0.56	6.0	1.01	0.75
$d + {}^{55}$Fe	$110.7 - 0.32E_d$	1.17	0.779	0	$24.5 - 0.25E_d$	1.32	0.593	12.0	1.01	0.75

An indication of the sensitivity to the details of the nuclear wave functions is given in a second set of calculations made with

$$S_{5/2}=0.47, \quad S_{3/2}=1.40, \quad S_{1/2}=0.42.$$

The IAS prediction is virtually unchanged. The AAS prediction was changed, however, with the results shown in the lower dashed curve of Fig. 3. Thus, even though two-step processes may significantly affect the (p,n) reactions as well as $(^3He, t)$ reactions, the expected sensitivities to nuclear wave-function details for the AAS transitions remain in the (p,n) calculations. It should be further noted that the two-step processes in (p,n) reactions appear to be less important than in $(^3He, t)$ reactions where the two-step process alone can fully account for the IAS and AAS cross sections.[5]

The present calculations are fairly crude. For example, we have not explicitly included the knock-on exchange[10] but have accounted for it implicitly in renormalization of the charge-exchange strength; thus we have assumed it has the same effect for the AAS transition as for the IAS. Furthermore, the charge-exchange interaction was taken to be of Yukawa form which may be somewhat too simple to provide a satisfactory monopole form factor.[11] Finally, we have not included ther possibly important two-step processes. We ave calculated multistep contributions through nelastic channels and found them to be of negligible importance for both the IAS and AAS transitions. We cannot, however, rule out the possible importance of other $(p, X)(X, n)$ processes where X is a cluster more complicated than dinucleons.

---

*Work supported in part by the U. S. Atomic Energy Commission.

[1] J. B. French and M. H. Macfarlane, Phys. Lett. 2, 255 (1962).

[2] P. J. Twin, W. C. Olsen, and E. Wong, Phys. Lett. 29B, 570 (1969).

[3] R. A. Hinrichs, R. Sherr, G. M. Crawley, and I. Proctor, Phys. Rev. Lett. 25, 829 (1970).

[4] R. Schaeffer and G. F. Bertsch, Phys. Lett. 38B, 159 (1972).

[5] W. R. Coker, T. Udagawa, and H. H. Wolter, Phys. Lett. 41B, 237 (1972).

[6] University of Colorado Nuclear Physics Laboratory Technical Progress Report No. COO-535-693, 1973 (unpublished).

[7] T. G. Dzubay, R. Sherr, F. D. Becchetti, Jr., and D. Dehnhard, Nucl. Phys. A142, 488 (1970).

[8] L. D. Rickertsen and P. D. Kunz, Phys. Lett. 47B, 11 (1973).

[9] R. L. Auble and J. Rapaport, Nucl. Data, Sect. B 3, Nos. 3-4, 1 (1970); J. C. Legg and E. Rost, Phys. Rev. 134, B752 (1964).

[10] F. Petrovich, H. McManus, V. A. Madsen, and J. Atkinson, Phys. Rev. Lett. 22, 895 (1969).

[11] M. B. Johnson, L. W. Owen, and G. R. Satchler, Phys. Rev. 142, 748 (1966); W. G. Love and G. R. Satchler, Nucl. Phys. A159, 1 (1970).

Isospin-Forbidden Proton Partial Width in ^{41}Sc and Similar $A = 4n + 1$ Nuclei*

T. A. Trainor,† T. B. Clegg, and W. J. Thompson
University of North Carolina, Chapel Hill, North Carolina 27514, and Triangle Universities Nuclear Laboratory, Durham, North Carolina 27706

(Received 2 November 1973; revised manuscript received 3 June 1974)

The lowest $T=\frac{3}{2}$ level in ^{41}Sc is observed as an isospin-forbidden resonance in $^{40}Ca(p, p_0)^{40}Ca$ at $E_{p,\text{lab}}=4.978$ MeV with proton partial width $\Gamma_p=55\pm5$ eV, which is about 50 times smaller than that previously assigned and 6 times smaller than theoretical width estimates. The trend of the proton reduced widths for $T=\frac{3}{2}$ isospin-forbidden resonances obtained from Γ_p values for target nuclei with $4 \leq Z \leq 20$ is shown to be consistent with a Z^2 dependence.

Nuclear levels can be characterized by the isopin quantum number T which would be unique r each level if electromagnetic (predominantly oulomb) and charge-dependent nucleon-nucleon teractions were absent.[1] However, there is amle experimental evidence for isospin mixing[2-5] by which small admixtures of other T values arise. Isospin mixing is generally believed to increase rapidly with nuclear charge Z for $Z \leq 20$, perhaps as $Z^{8/3}$ for $T=0$ ground states,[6] and then to decrease steadily with Z for heavier nuclei.[3,4,6] One effect of the mixing is the small but nonzero proton partial width Γ_p for exciting nominally isospin-forbidden $T = \frac{3}{2}$ compound-nucleus resonances in $Z = N + 1$ nuclei by proton ($T = \frac{1}{2}$) elastic scattering from $Z = N$ (nominally $T = 0$) nuclei.[5] The nonzero width Γ_p can arise in two possible ways: from a small $T = 1$ admixture in the $T = 0$ ground state of the target nucleus, and from a $T = \frac{1}{2}$ admixture in the $T = \frac{3}{2}$ resonant compound-nuclear state.

This Letter reports the most precise measurement to date of Γ_p for an isospin-forbidden resonance. The measurement was made using the heaviest stable $Z = N$ target, ^{40}Ca, to produce the compound nucleus ^{41}Sc. We find that for the lowest $T = \frac{3}{2}$ level in ^{41}Sc, Γ_p is a factor of 50 smaller than suggested by previous measurements,[5,7] and a factor of 6 smaller than the lowest theoretical estimate.[8] Reduced widths γ_p^2 for $T = \frac{3}{2}$ levels observed by proton scattering from $4n$ target nuclei having $Z \leq 20$ are extracted from the present and previous measurements of Γ_p. These reduced widths increase at least as fast as Z^2, consistent with estimates of the Z dependence of isospin mixing based on the results of Ref. 6 for $Z = N$ target nuclei.

A polarized proton beam was used to determine spins and parities of resonance levels near the energy expected for the lowest $T = \frac{3}{2}$ state in ^{41}Sc. A beam from the Triangle Universities Nuclear Laboratory (TUNL) Lamb-shift polarized source[9] and tandem accelerator with an energy resolution of about 2 keV was incident on a 1-keV-thick natural Ca target (97% ^{40}Ca). Analyzing power and differential-cross-section excitation functions for $^{40}\text{Ca}(p, p_0)^{40}\text{Ca}$ were measured at two scattering angles. The energy range chosen included the expected resonance energy $E_{p,\text{lab}} = 4.972$ MeV for the $T = \frac{3}{2}$ level as obtained from recent β-delayed proton ($\beta^+\bar{p}$) measurements.[10] Our analyzing-power measurements reported earlier[11] showed that the level at $E_{p,\text{lab}} = 4.899$ MeV previously assigned[5,7] as the lowest $T = \frac{3}{2}$ state in ^{41}Sc has spin and parity $J^\pi = \frac{5}{2}^+$ in disagreement with $\frac{3}{2}^+$ for the parent isobaric analog state, the ^{41}K ground state. The polarized-beam, low-resolution data are shown in Figs. 1(a) and 1(b). The theoretical fits shown in Fig. 1 use a single-level resonance plus a nonresonant, optical-model background. The optical-model parameters were obtained by analysis of nearby off-resonance angular distributions.[12] A Gaussian distribution of incident energy with full width at half-maximum $\Delta = 2$ keV was folded with the theoretical curves to obtain fits to the data. A $\frac{3}{2}^+$ assignment gives a much better fit than $\frac{5}{2}^+$ and the lab resonance energy $E_{p,\text{lab}} = 4.978 \pm 0.005$ MeV is in excellent agreement with 4.972 ± 0.006 MeV predicted fro the recent $\beta^+\bar{p}$ result.[10]

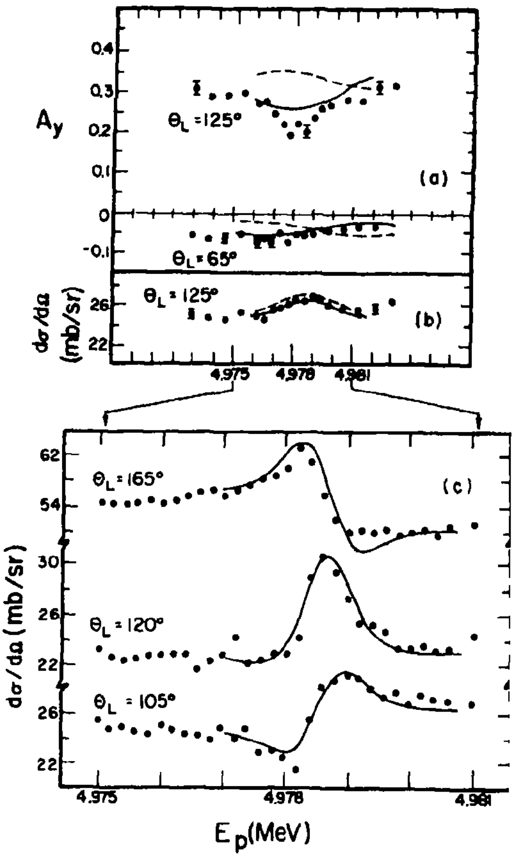

FIG. 1. (a) Vector analyzing power A_y in the Basel convention for $^{40}\text{Ca}(p, p_0)^{40}\text{Ca}$ at lab scattering angle $\theta_L = 65$ and 125° for the proton lab bombarding energy range $4.973 \leq E_p \leq 4.983$ MeV with incident energy res lution of 2 keV. Typical statistical error bars are shown. Solid (dashed) curves are theoretical fits for resonance $J^\pi = \frac{3}{2}^+$ ($\frac{5}{2}^+$) as discussed in the text. (b) Di ferential cross section and fits at $\theta_L = 125°$ obtained from the same experiment as in (a). (c) Differential cross section at $\theta_L = 105$, 120, and 165° for $4.975 \leq E$ ≤ 4.981 MeV with incident energy resolution of 800 e Error bars are smaller than the points. Solid curves are theoretical fits for $J^\pi = \frac{3}{2}^+$ as discussed in the tex

Precise determination of the $T = \frac{3}{2}$ resonance width was made by measuring differential-cros section excitation functions with an incident bea having good energy resolution obtained by using the TUNL beam-energy-homogenizer system.[13]

Calcium targets used for these data were about 100 eV thick, and the overall incident energy resolution determined from analysis of the resonance data was about 800 eV. The accelerator energy was calibrated against the nearby threshold energies for the reactions ^{19}F(p, n)^{19}Ne and ^{27}Al(p, n)^{27}Si.[14] Parts of extensive high-resolution excitation functions, which include the $T=\frac{3}{2}$ level, are shown in Fig. 1(c) for three scattering angles. The complete excitation functions show no other resonance anomalies within 30 keV of this region. The resonance parameters used in Fig. 1 are total width $\Gamma = 55$ eV and $\Gamma_p/\Gamma = 1$. The branching ratio for decay of this level to the ground state of ^{40}Ca is now estimated[15] in the $\beta^+\tilde{p}$ experiment to be about 1, rather than ≥ 0.86 as originally estimated.[10] The previously assigned $T=\frac{3}{2}$ level[6,7] has $\Gamma_p = 2.6$ keV; thus Γ_p, and consequently the isospin mixing in ^{41}Sc, are about 50 times smaller than previously determined.

The exact nature of the isospin mixing from which this proton width arises is difficult to determine, both experimentally and theoretically. The strong dependence of Γ_p on the penetrability P of the Coulomb-plus-centripetal barrier, which affects the formation and decay of the compound nucleus, may obscure systematic variation of isospin-mixing effects with Z. Therefore we have extracted the proton reduced widths $\gamma_p^2 = \Gamma_p/2P$ from measured Γ_p values for lowest-lying $T=\frac{3}{2}$ resonances in $Z=N+1$ nuclei. Experimental Γ_p values[3,16-20] for ^{9}B, ^{13}N, ^{17}F, ^{21}Na, ^{25}Al, ^{29}P, ^{33}Cl, and ^{37}K were obtained from Refs. 16, 3, 3, 17, 18, 18, 19, and 20, respectively. Extracted γ_p^2 values for P evaluated at a proton-nucleus separation $R = 1.4A^{1/3}$ fm are plotted in Fig. 2. It is seen that the reduced widths increase at least as fast as Z^2 with noticeably regular fluctuations about the Z^2 curve.

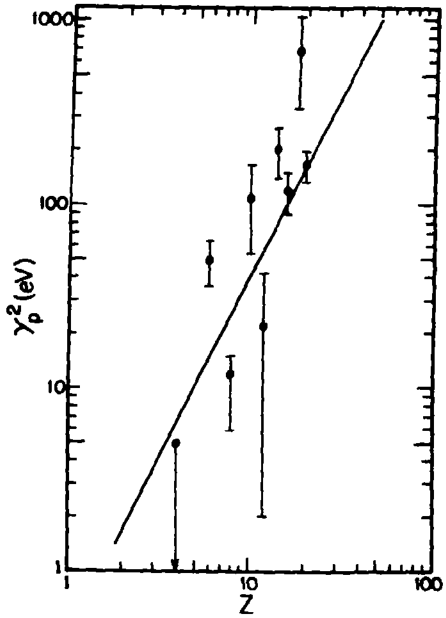

FIG. 2. Proton elastic-scattering reduced widths γ_p^2 for $T=\frac{3}{2}$ compound-nucleus resonances observed in proton interactions with $Z=N$ target nuclei. The error bars reflect uncertainties in proton-elastic-scattering partial widths Γ_p. The line represents a Z^2 dependence of the reduced widths γ_p^2, arbitrarily chosen to pass through the experimental value for ^{40}Ca(p, p_0)^{40}Ca.

The observed $T=\frac{3}{2}$ states can undergo isospin-allowed decay through collective $T=1$ admixtures in the nominally $T=0$ target ground states. A calculation using a hydrodynamic model[6] predicts that this $T=1$ isospin mixing probability $\alpha^2 = 5.55 \times 10^{-7} Z^{8/3}$. Of this Z dependence, a factor Z^2 comes from the Coulomb matrix element and $Z^{2/3}$ comes from a $Z^{-2/3}$ dependence of an energy denominator through systematics of the $T=1$ monopole-mode excitation energy. Hartree-Fock calculations[21] of $T=1$ mixing for the same states indicate similar Z dependence but magnitudes 2.5 times larger. If these $T=\frac{3}{2}$ levels decay predominantly through $T=1$ admixtures in $T=0$ target ground states, then it is expected that γ_p^2 has a Z dependence determined by $\alpha^2\gamma^2$. Here γ^2, the reduced width for isospin-allowed decay to the $T=1$ impurity, is assumed to have the same Z dependence as the Wigner limit[22] ($\propto Z^{-2/3}$ for $A=2Z$ nuclei). This, with the $Z^{8/3}$ dependence of α^2, gives a Z^2 dependence for γ_p^2.

If, on the other hand, decay of the $T=\frac{3}{2}$ levels proceeds mainly through admixtures of neighboring $T=\frac{1}{2}$ compound-nucleus levels, there are several alternative forms for the Z dependence of γ_p^2. In each case a factor Z^2 comes from the Coulomb matrix element in the isospin-mixing amplitude, and a factor $Z^{-2/3}$ from the Wigner-limit-type dependence of the isospin-allowed decay width of the $T=\frac{1}{2}$ admixture, contributing together a factor $Z^{4/3}$ to γ_p^2. In addition there are several possibilities for the Z dependence of the energy denominator in the mixing amplitude depending on which $T=\frac{1}{2}$ compound-nucleus states are responsible for the isospin mixing: (1) A calculation of Γ_p for the lowest $T=\frac{3}{2}$ state in ^{41}Sc and three other $4n+1$ nuclei, assuming that the only significant mixing is with the $T=\frac{1}{2}$ antianalog state, was made by Auerbach and Lev.[8] Their results exceed the new experimental width by a factor of 6 for ^{41}Sc and the experimental widths for other nuclei by factors ranging between ~1.3 and ~3.8. If the principal admixed state is the antianalog-configuration state of Auerbach and Lev, the energy denominator of the mixing amplitude should vary approximately as $1/Z$ (Ref. 2) giving a $Z^{10/3}$ dependence for γ_p^2. (2) Although less likely for these light nuclei, the isovector monopole state[23] may form an appreciable contribution to the reduced width. The energy denominator of the amplitude then varies as $Z^{-1/3}$, again giving a Z^2 dependence for γ_p^2, just as in the case of the target monopole contribution. (3) A third contribution to γ_p^2 can come from nearby $T=\frac{1}{2}$ levels, other than the antianalog or isovector monopole state, but having the same spin and parity as the $T=\frac{3}{2}$ state. Because the densities of levels with the appropriate spin and parity are not large near the excitation energies of the lowest $T=\frac{3}{2}$ states in these light nuclei,[7] the energy denominators in the mixing amplitudes vary widely and the contribution of these nearby levels to γ_p^2 should not be strongly correlated with Z. Thus if this third contribution dominates, γ_p^2 should show considerable variation about a general $Z^{4/3}$ trend.

In the absence of more detailed information, one must allow the possibility that all of these sources of isospin mixing contribute in a coherent way to the proton reduced widths. If the Z^2 trend in γ_p^2 suggested in Fig. 2 is appropriate, a closer investigation of the $T=1$ monopole admixtures is warranted. However, a trend as rapid as Z^3 is not inconsistent with the data, so other mixing mechanisms may be important.

Currently, several of the $T=\frac{3}{2}$ levels are being measured at TUNL.

---

*Work supported in part by the U.S. Atomic Energy Commission.

†Present address: Department of Physics, University of Washington, Seattle, Washington 98195.

[1] For the concept and applications of isospin see *Isospin in Nuclear Physics*, edited by D. H. Wilkinson (North-Holland, Amsterdam, 1969).

[2] Isospin mixing is reviewed by G. F. Bertsch and A. Mekjian, Annu. Rev. Nucl. Sci. 22, 25 (1972).

[3] E. G. Adelberger, A. B. McDonald, C. L. Cooke, C. N. Davids, A. P. Shukla, H. B. Mak, and D. Ashery, Phys. Rev. C 7, 889 (1973).

[4] J. M. Soper, Ref. 1, p. 229.

[5] G. M. Temmer, Ref. 1, p. 693.

[6] A. Bohr, J. Damgaard, and B. R. Mottelson, in *Nuclear Structure*, edited by A. Hossain *et al.* (North-Holland, Amsterdam, 1968).

[7] P. M. Endt and C. Van der Leun, Nucl. Phys. A214, 1 (1973), and references therein.

[8] N. Auerbach and A. Lev, Phys. Lett. 34B, 13 (1971).

[9] T. B. Clegg, G. A. Bissinger, W. Haeberli, and P. A. Quin, in *Polarization Phenomena in Nuclear Reactions*, edited by H. H. Barschall and W. Haeberli (Univ. of Wisconsin Press, Madison, Wis., 1970), p. 835.

[10] R. A. Gough, R. G. Sextro, and J. Cerny, Phys. Lett. 43B, 33 (1973).

[11] T. A. Trainor, T. B. Clegg, and W. J. Thompson, Bull. Amer. Phys. Soc. 18, 602 (1973).

[12] T. A. Trainor, Ph.D. thesis, University of North Carolina, 1973 (University Microfilms, Ann Arbor, Mich., 1973).

[13] T. G. Dzubay, E. G. Bilpuch, F. O. Purser, J. C. Moses, and H. W. Newson, Nucl. Instrum. Methods 101, (1972).

[14] J. C. Davis and F. T. Noda, Nucl. Phys. A134, 361 (1969).

[15] R. G. Sextro, Ph.D. thesis, University of California, Berkeley, 1973 (unpublished).

[16] J. C. Adloff, W. K. Lin, K. H. Souw, and P. Chevallier, Phys. Rev. C 5, 664 (1972).

[17] A. B. McDonald, J. R. Patterson, and H. Winkler, Nucl. Phys. A137, 545 (1969).

[18] B. Teitelman and G. M. Temmer, Phys. Rev. 117, 1656 (1969).

[19] U. Abbondanno, R. Giacomich, L. Granata, M. Lagonegro, and G. Poiani, Nuovo Cimento 70A, 391 (1970).

[20] D. R. Goosman and R. W. Kavanagh, Phys. Rev. 161, 1156 (1967).

[21] H. C. Lee and R. Y. Cusson, Ann. Phys. (New York) 72, 353 (1972).

[22] A. M. Lane and R. G. Thomas, Rev. Mod. Phys. 30, 257 (1958).

[23] A. Lev and N. Auerbach, Nucl. Phys. A206, 536 (1973).

Discovery of the Missing Two-Particle, Two-Hole 0^+ States in ^{40}Ca

Kamal K. Seth and A. Saha
Northwestern University, Evanston, Illinois 60201

and

W. Benenson, W. A. Lanford,* H. Nann,† and B. H. Wildenthal
Michigan State University,‡ East Lansing, Michigan 48823

(Received 25 March 1974)

A good-resolution study of the reaction ^{42}Ca$(p,t)^{40}$Ca has revealed the existence of three new 0^+ states in ^{40}Ca at 7698, 8284, and 8438 keV excitation. Arguments are presented to show that these states are indeed the long sought-after 0^+, $T=0$ states with predominantly two-particle, two-hole configurations.

Ever since Gerace and Green[1] identified the 0_2^+ state at 3353 keV in ^{40}Ca as being predominantly four-particle, four-hole (4p-4h) in nature, the most intriguing and challenging question in the spectroscopy of ^{40}Ca has been that relating to the crucially important 0^+ states of the 2p-2h, $T=0$ configuration which have been predicted to lie between 7- and 9-MeV excitation,[1-3] but which have eluded experimental identification so far.[4] In the earlier studies of the reaction ^{42}Ca$(p,t)^{40}$Ca,[4-8] $L=0$ transitions could only be identified to the ground state (g.s.) 0_1^+, the 3353-keV 0_2^+ state, and the 0^+ states with $T=1$ and $T=2$ at about 9.4 and 12.0 MeV, respectively. Further, while the 2p-2h 0^+ states in the 7–9-MeV excitation region were not found, it was noted that the so-called 4p-4h 0_2^+ state at 3353 keV is populated about an order of magnitude more strongly than expected. These observations have led[6-8] to the speculation that perhaps the main part of the 2p-2h, 0^+

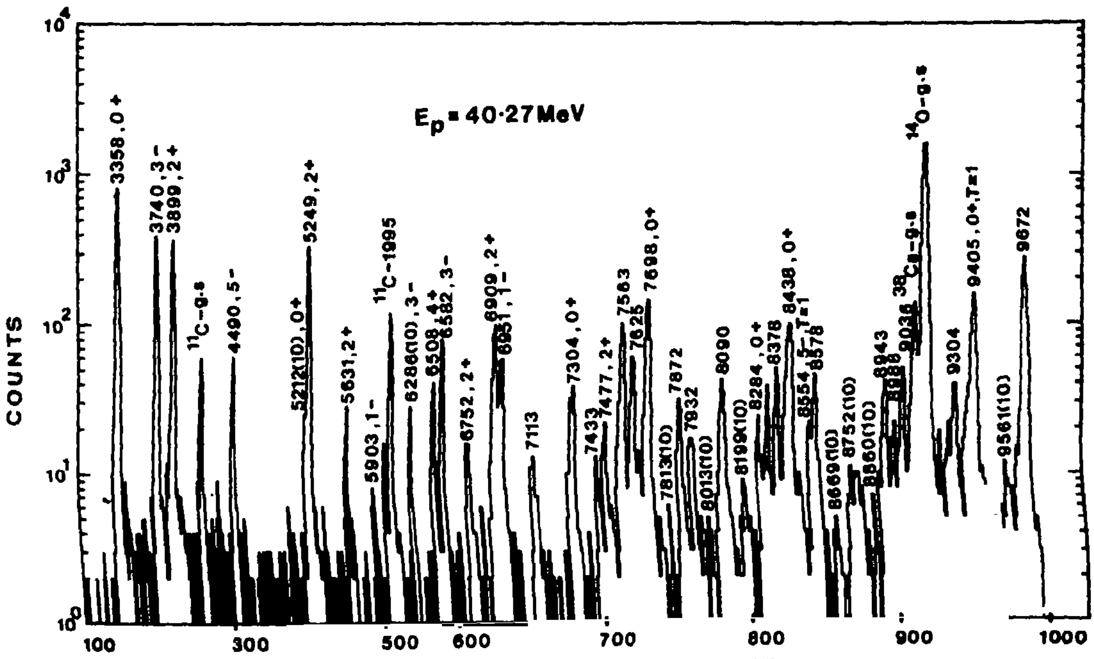

FIG. 1. Spectrum at θ(lab) = 6° for the reaction ^{42}Ca$(p,t)^{40}$Ca. The g.s. transition is not displayed. Excitation energies (in keV) are from the present experiment. Errors are ±5 keV unless otherwise specified. The abscissa has been expanded by a factor of 2 beyond channel number 600.

strength does indeed lie in the 3353-keV state, in contradiction to the theoretical calculations. Before accepting such drastic conclusions, it is necessary to reexamine the situation critically. The unexpectedly strong excitation of the 3353-keV state poses a serious problem, but the problem of the missing 0^+ states in the 7–9-MeV excitation region is even more serious. Several rather dissimilar calculations[1,2] predict two or three 0^+, $T=0$ states in this energy region. It does not appear very likely that extending the configuration space used in these calculations or modifying the interaction will drastically alter the predictions about their existence. It is therefore of crucial importance to make a concerted effort to find the missing 0^+ states. In this Letter we report on just such an experiment, and on our success in finding three "new" 0^+ states at 7698(5), 8284(10), and 8438(5) keV in ^{40}Ca.

The reaction ^{42}Ca$(p,t)^{40}$Ca was studied using the 40.27-MeV proton beam from the Michigan State University cyclotron and an Enge split-pole spectrograph equipped with a single-wire proportional counter in its focal plane. An overall energy resolution of about 22 keV (full width at half-maximum) was achieved. Figure 1 shows a typical spectrum. Most of the known states in ^{40}Ca up to 9.5 MeV were excited. Energy calibration, expected to be accurate to ± 5 keV, was based on the accurately known energies[4,9] of several strong states in ^{40}Ca up to 8.5-MeV excitation and the accurately known Q value for the ^{16}O$(p,t)^{14}$O(g.s.) transition. One significant result of the accurate energy calibration is that for the reaction ^{40}Ca$(p,t)^{38}$Ca we find $Q_0 = -20\,452(5)$ keV. The 1971 mass tables give $Q_0 = -20\,484(16)$ keV.

Absolute cross-section normalization, expected to be accurate to within ± 10%, was based on the known thickness and isotopic analysis of a self-supporting rolled target. Our cross sections are in excellent agreement with those reported by Bayman and Hintz[5] and Schapira *et al.*[6] at $E_p = 40$ MeV. The absolute cross sections recently reported by Debevec[7,8] at $E_p = 41.7$ MeV are about 30% smaller than ours.

In Fig. 2 we show angular distributions for all $L=0$ transitions. The 3353-keV transition shows a first minimum which is displaced by about 2° from that for the g.s. This feature was observed earlier[10] and was attributed to a predominantly d^2 pickup as opposed to the mainly f^2 pickup for the ground state.

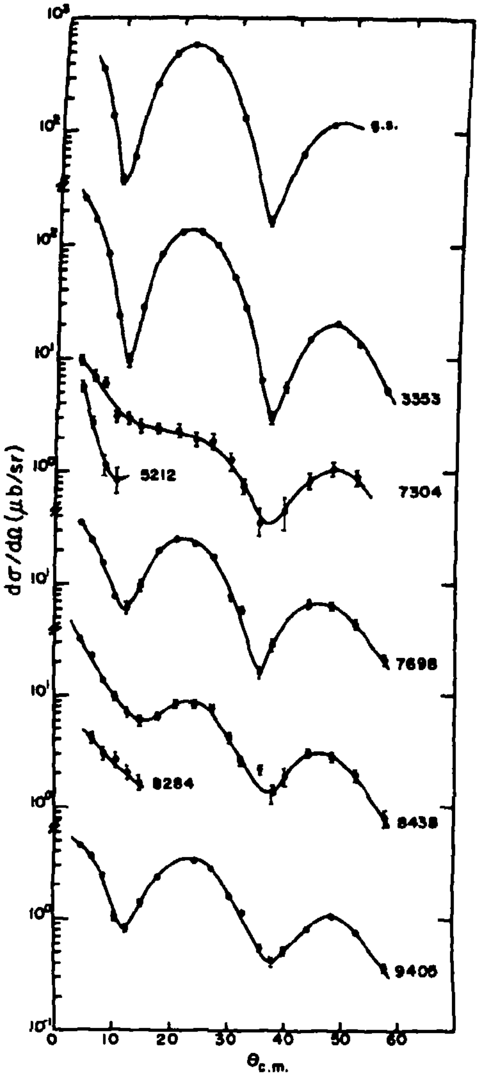

FIG. 2. Measured differential cross sections for all $L=0$ transitions observed in the present experiment. The curves through the points have been drawn only to guide the eye; they have no theoretical significance.

In previous (p,t) experiments no clear evidence for excitation of the known 0^+ states at 5.2 and 7.3 MeV could be obtained. In the present experiment the weakly excited state at 5212(10) keV could be successfully resolved from the strong 2^+ state at 5249(5) keV at the most forward angles. The expected $L=0$ nature of the transition is confirmed and it is estimated that the strength of this state is ~ 0.5% that of the ground state. The state at 7304(5) keV is found to be weak though clearly identifiable at all angles. The unambiguous $L=0$ transitions to states 7698(5) and 8438(5) keV have not been identified previously. The 7698-keV state was actually observed in earlier (p,t) experiments,[6-8] but since the data were limited to $\theta \geq 12°$, it was misidentified as the 3^- state seen at 7695 keV in (^{3}He,d) experiments.[11] Nolen[9] has verified that indeed there is a 7-keV doublet at this energy.

In a recent ^{36}Ar(^{6}Li,d)^{40}Ca experiment strong excitation of a 0^+ state at 8280(20) keV has been reported.[12] In our experiment the transition to the state at 8284(10) keV is very weak but can be identified clearly at the most forward angles where it displays $L=0$ behavior. We estimate that this state is populated with a strength about 0.3% of the g.s. A strongly excited 0^+ state has been reported at 8.28 ± 0.1 MeV in a recent ^{38}Ar(^{3}He,n) experiment[13] with 0.4-MeV energy resolution. It most likely corresponds to our weakly excited state at 8284(10) keV but may also include contributions from the 0^+ states at 7698(5) and 8438(5) keV.

In Table I we summarize our results for all the $L=0$ transitions observed. Since the 9405(5)-keV state is the known $T=1$ analog of the lowest 0^+ state in ^{40}K, all the other states are expected to be $T=0$.

We now refer to the two kinds of theoretical calculations which are available. In the "coexistence model" calculations, the states of ^{40}Ca are described as arising from a mixing of the spherical shell-model states and the deformed states constructed by promoting pairs of particles from the filled $d_{3/2}$ shell to the unfilled f-p shells.[1] It has been shown that[7,8,3] these calculations lead to predictions of a completely washed out angular distribution and to an *underestimate* of the cross section to the 0_2^+, 3353-keV state by almost an order of magnitude and an equally

TABLE I. Summary of results.

EXPERIMENT			THEORETICAL CALCULATIONS							
			NEW FP CALCULATIONS[b]						COEXISTENCE CALCULATIONS[a,c]	
J,T	E^*(±keV)	σ(rel)	E^*	σ(rel)	Overlaps $f^2 \pm d^2$	% Components 0p-0h	2p-2h	4p-4h	E^*	σ(rel)
0_1^+,0	0	100.	0	100.	0.973-0.371	$\underline{56.6}$	33.7	9.7	0	100
0_2^+	3358(5)	24.0	3525	3.4	0.105+0.405	22.6	11.0	$\underline{66.4}$	3500	2.7(6.6)
0_3^+	5212(10)	0.5	5457	2.5	0.031-0.246	11.8	20.2	$\underline{68.0}$	5100	(6.2)
0_4^+	7304(5)	0.6	8160	1.4	0.135+0.036	0.1	$\underline{75.6}$	24.3	7200	5.1
0_5^+	7698(5)	5.3	8610	1.32	0.109-0.032	3.3	17.6	79.1	7800	
0_6^+	8284(10)	0.3	9637	0.54	0.059-0.046	0.8	26.0	73.2		
0_7^+	8438(5)	2.6	10173	0.08	0.035+0.066	0.5	4.4	95.1		
			10311	0.08	0.037+0.033	0.3	42.3	57.4		
0_8^+,1	9405(5)	7.9	6835	29.	0.167-0.887		69.2	30.8		99
0_9^+,2	11970[a]	12.[a]	11440	58.	0.390-1.133		52.1	47.9		50
0_1^+	0(^{38}Ca)	101.								
0_1^+	0(^{42}Ca)					54.5	44.9	0.6		
						2p-0h	4p-2h	6p-4h		

[a] From Debevec (Ref. 7) and Adelberger *et al.* (Ref. 8).

[b] These results are from the new calculations using the interaction of Federman and Pittel (Ref. 2) (see text). For the calculation of σ(rel) optical-model parameters used by Schapira *et al.* (Ref. 6) were employed.

[c] These numbers are due to Debevec (Ref. 7) and Adelberger *et al.* (Ref. 8) and for $T=0$ states are based on wave functions of Gerace and Green (Ref. 1). The numbers in parentheses are due to Erikson, Horsfjord, and Nilsson (Ref. 3), obtained by introducing triaxial deformations.

large *overestimate* of the cross section to the 0_3^+, 5212-keV state. Recently Erikson, Horsfjord, and Nilsson[3] have tried to improve on this situation by introducing triaxially deformed components which contain admixtures of the $s_{1/2}$ hole state, but have achieved only nominal success.

The first of the "shell-model" type of calculations was done by Federman and Pittel[2] (FP) in the $f_{7/2}d_{3/2}$ basis. To clear up some ambiguities and to remove some unnecessary approximations we have repeated their calculations with the Oak Ridge National Laboratory–Rochester University code using the FP interaction and considering configurations up to 4p-4h in ^{40}Ca and up to 6p-4h in ^{42}Ca. The results in Table I are from these "new" FP calculations. As can be seen, in these "shell-model" calculations also the problems with the 0_2^+ and 0_3^+ states persist, and almost equally serious problems surface for other excited states. We have tried several other interactions which have been used in this mass region but with no improvement in the situation. Within the limited $f_{7/2}d_{3/2}$ basis we have been able to search an interaction for the $A = 38-42$ nuclei which leads to predictions of strong excitation of the 3353-keV 0_2^+ state (26.1% g.s. with well-structured angular distribution) and weak excitation of the 5212- and 7304-keV states (3.3 and 1.2%, respectively). However, such an interaction makes the 0_2^+ state mostly (70%) 2p-2h and the 0_3^+ and 0_4^+ states mostly (72 and 97%, respectively) 4p-4h. It also predicts strong excitation of the 0_2^+ state in the (^{3}He, n) experiment which is contrary to the experiment,[13] and has several other unpalatable consequences for other nuclei in the $A = 38-42$ region. If we consider the 4p-4h nature of the 0_2^+ state as being experimentally established by its very strong population (70% of g.s.) in the reaction ^{36}Ar(^{6}Li, d), we have to conclude that the problems with the (p,t) results reflect either the basic inadequacies of the reaction theory which takes no account of correlations between the two picked-up particles or the basic inadequacy of the $f_{7/2}d_{3/2}$ space.

A clue to the nature of the configuration space required to explain the data is provided by a comparison of the results of our (p,t) pickup experiment and the two stripping experiments. Strong pickup takes place *from* filled orbits and strong stripping takes place *to* empty orbits. The 3353-keV state is populated with appreciable strength (24% of g.s.) by the (p,t) reaction, but only weakly (~5% of g.s.) by the (^{3}He, n) reaction. This suggests that this state has an appreciable component of the f^2s^{-2} type. Similarly the very weak population of the 8284-keV state (~0.3% of g.s.) in our (p,t) experiment and its strong population (~40% of g.s.) in the two stripping experiments would suggest that this state contains appreciable amount of p^2 particles in it. These considerations would suggest that a comprehensive attempt to explain these data requires a configuration space which includes at least $s_{1/2}d_{3/2}f_{7/2}p_{3/2}$ shells. This is much too large a space for the extended shell-model calculations possible at present.

---

[*] Now at Yale University, New Haven, Conn. 06520.

[†] On leave of absence from Institut für Kernphysik der J. W. Goethe Universität, Frankfurt am Main, Germany.

[‡] The Michigan State University Cyclotron Laboratory is supported by the National Science Foundation.

[1] W. J. Gerace and A. M. Green, Nucl. Phys. A93, 110 (1967), and A123, 241 (1968).

[2] P. Federman and S. Pittel, Phys. Rev. 186, 1106 (1969), also private communication.

[3] T. Erikson, V. Horsfjord, and B. Nilsson, Phys. Lett. 46B, 173 (1973).

[4] P. M. Endt and C. Van der Leun, Nucl. Phys. A214, 1 (1973).

[5] B. F. Bayman and N. M. Hintz, Phys. Rev. 172, 1113 (1968).

[6] J. P. Schapira, M. Chabre, Y. Dupont, and P. Martin, Phys. Rev. C 5, 1593 (197).

[7] P. T. Debevec, Ph.D. dissertation, Princeton University, 1972 (unpublished).

[8] E. G. Adelberger, P. T. Debevec, G. T. Garvey, and R. Ohanian, Phys. Rev. Lett. 29, 883 (1972).

[9] J. A. Nolen, Jr., to be published.

[10] K. K. Seth, H. Ohnuma, T. Suehiro, S. Yamada, and S. Takeda, Phys. Rev. Lett. 30, 132, 250(E) (1973).

[11] K. K. Seth, J. A. Biggerstaff, P. D. Miller, and G. R. Satchler, Phys. Rev. 164, 1450 (1967).

[12] H. T. Fortune, R. R. Betts, J. N. Bishop, M. N. I. Al-Jadir, and R. Middelton, Bull. Amer. Phys. Soc. 18, 1399 (1973), also private communication.

[13] W. P. Alford, R. A. Lindgren, D. Elmore, and R. N. Boyd, Phys. Lett. 46B, 356 (1973).

Measurement of the Polarization Parameter for the Reaction $\pi^- p \rightarrow \pi^0 n$ between 1.03 and 1.79 GeV/c*

S. R. Shannon, L. Anderson, A. Bridgewater,† R. Chaffee,‡ O. Chamberlain, O. Dahl, R. Fuzesy,
W. Gorn,§ J. Jaros, R. Johnson, R. Kenney, J. Nelson, G. O'Keefe, W. Oliver,‖ D. Pollard,
M. Pripstein, P. Robrish, G. Shapiro, H. Steiner, and M. Wahlig
Lawrence Berkeley Laboratory, University of California, Berkeley, California 94720

(Received 1 April 1974)

The polarization parameter for the reaction $\pi^- p \rightarrow \pi^0 n$ has been measured at five incident beam momenta between 1.03 and 1.79 GeV/c. The results are compared with predictions of recent phase-shift analyses.

We report here the results of an experiment at he Lawrence Berkeley Laboratory (LBL) Beva- ron in which we measured the polarization pa- ameter $P(\theta)$ for the reaction $\pi^- p \rightarrow \pi^0 n$ ($\pi^0 \rightarrow \gamma\gamma$) : the five incident beam momenta 1030, 1245, 440, 1590, and 1790 MeV/c. Charge-exchange olarization measurements have been made pre- ously at higher energies,[1] primarily to test igh-energy interaction mechanisms, but except or one very rough measurement by Hill *et al.*,[2] : 310 MeV, this marks the first time that mea- rements of $P(\theta)$ have been made in a region here phase-shift analyses are available (< 2 eV/c). These measurements of $P(\theta)$, together ith recent results on the differential cross sec- on for the charge-exchange reaction,[3] should rovide a strong constraint on the solutions to e various phase-shift analyses. Preliminary esults from this experiment have been reported lsewhere.[4]

The experimental layout is shown schematically Fig. 1 (and detailed by Shannon).[5] The π^- beam ith a typical momentum bite of ± 1.5% was fo- sed onto a polarized-proton target (primarily ropylene glycol), with length along the beam di- ection of 7.5 cm and a cross-sectional area 2.5 2.5 cm. The polarization of the target averaged etween 50 and 55% (at 1°K). The target polariza- on was reversed every 2–3 h to reduce possible ystematic errors. The free protons constituted ly about 14% of the protons in the target, the est being protons bound in the carbon and oxy- n nuclei of the propylene glycol and in the heav- r nuclei of the cavity. To measure the nonhy- rogen background, we also collected data from "dummy" target at each momentum. This dum- y (essentially graphite) contained no free pro- ns but otherwise simulated the target as closely s possible.

Neutrons produced in the final state were de- cted in twenty 20-cm-thick scintillation counters. These neutron counters, each subtending a lab angle of ~2.5°, at a distance of ~5 m from the target, typically spanned the angular range ~0.78 $< \cos\theta_{\text{c.m.}} < 0.87$ in the center-of-mass system; further, they provided neutron time-of-flight measurements accurate to ± 0.6 nsec. The photons from the π^0 decay were detected in two lead-plate optical spark chambers. The chamber plates were made thin (~0.14 radiation lengths) to ensure a low energy γ-ray detection threshold of about 10 MeV.[3,6] The downstream chamber (1.52 × 1.52 m) was 9 radiation lengths thick, and the side chamber (1.22 × 1.22 m) was 8 radiation lengths thick.

Surrounding the target was a system of scintillation counters that allowed identification of those $\pi^- p$ interactions having neutral final states. Those veto counters not in the incident beam were also used to veto events that had γ rays emitted in directions other than toward the spark chambers.

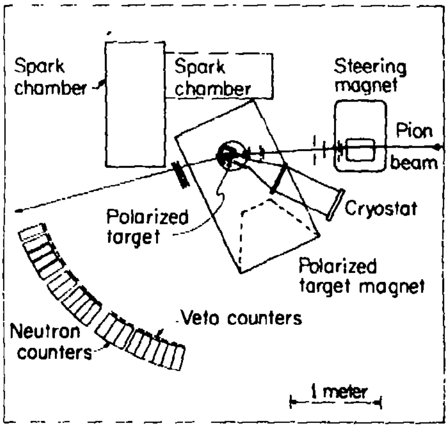

FIG. 1. Experimental layout (the distances of the neutron counters from the target are not to scale). Scintillation counters are indicated (but not labeled) along the beam line.

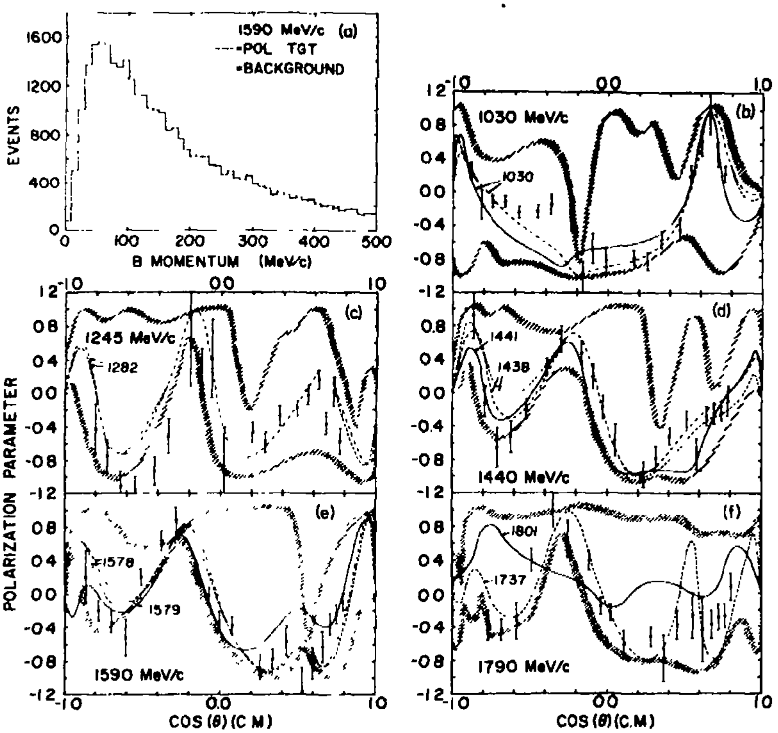

FIG. 2. (a) Fitted momentum distribution for recoil B in the reaction $\pi^- C \to \pi^0 n B$ for both the polarized-target events and (normalized) dummy-target events summed over all neutron counters at 1590 MeV/c. (b)–(f) The $\pi^- \to \pi^0 n$ polarization parameter results. The smooth curves are the predictions of Almehed and Lovelace (Ref. 11) (solid), of Ayed *et al.* (Ref. 13) (dash-dotted), and of Bareyre and Ayed (Ref. 12) (dashed) evaluated at the indicated momenta closest to our beam momenta. Isospin bounds given in Ref. 12 are indicated with slashed lines. Only Ayed *et al.* predictions were available at 1737 MeV/c; the predictions of both Refs. 12 and 13 at the lower momenta are nearly the same over much of the angular range.

These counters had scintillator and γ converter (1–2 radiation lengths of either Pb, W, or Pt) in a sandwich construction.

An event was recorded whenever the following criteria were satisfied: (1) A charged pion went into the target and no veto counter had a pulse, and (2) a neutral particle went into one of the neutron counters and was detected there. Those events which satisfied our conditions for candidates for $\pi^- p \to \pi^0 n$ (a neutron count within a wide timing window, and two showers in the spark chambers as determined by a scan of the film) were then measured and digitized using the semiautomatic scanner system[7] at LBL.

With the program SQUAW,[8] least-squares kinematic fits were made to the hypotheses $\pi^- p \to \pi^0 n$ and $\pi^- C \to \pi^0 n B$, using the measured directions of the two γ rays and the time-of-flight and direction of the neutron. Here C represented ^{12}C, and the mass of the recoil boron (B) was chosen to be one proton mass less than that of C.[9] B was assumed to have zero measured momentum, but with a large uncertainty of ± 300 MeV/c in each component.

We used the following method to determine the background contribution. Those events which satisfied the hypothesis $\pi^- C \to \pi^0 n B$ but fit the hypothesis $\pi^- p \to \pi^0 n$ with a confidence level $< 0.1\%$ were predominantly nonhydrogen events. Similar failing events from the dummy target, normalized to those from the polarized target, have a fitted momentum (p_B) distribution for B which agrees very well in shape with the corresponding distribution of failing events from the polarized target. (The normalization ratio is consistent with the ratio of beam fluxes incident on the dummy and polarized

TABLE I. Polarization parameter $P(\theta)$ in $\pi^- p \rightarrow \pi^0 n$ scattering. The error $\Delta P(\theta)$ is statistical only; the estimated systematic errors are ±0.06 for each momentum except 1245 MeV/c, for which the error is ±0.09.

1030 MeV/c			1245 MeV/c			1440 MeV/c			1590 MeV/c			1790 MeV/c		
osθ_{cm}	$P(\theta)$ ±	$\Delta P(\theta)$	cosθ_{cm}	$P(\theta)$ ±	$\Delta P(\theta)$	cosθ_{cm}	$P(\theta)$ ±	$\Delta P(\theta)$	cosθ_{cm}	$P(\theta)$ ±	$\Delta P(\theta)$	cosθ_{cm}	$P(\theta)$ ±	$\Delta P(\theta)$
0.755	0.24	0.10	0.770	-0.57	0.16	0.783	-0.09	0.19	0.792	-0.10	0.10	0.803	0.08	0.17
0.705	0.46	0.15	0.723	0.02	0.18	0.738	-0.24	0.08	0.749	-0.24	0.11	0.761	-0.27	0.14
0.655	0.94	0.23	0.676	-0.36	0.13	0.693	-0.24	0.13	0.705	-0.36	0.13	0.719	-0.28	0.16
0.604	0.61	0.15	0.627	0.17	0.11	0.645	-0.27	0.12	0.659	-0.63	0.18	0.675	-0.38	0.17
0.535	0.20	0.13	0.561	-0.02	0.12	0.582	-0.72	0.19	0.598	-0.82	0.18	0.616	-0.44	0.38
0.464	-0.44	0.12	0.492	-0.18	0.10	0.516	-0.30	0.10	0.533	-1.16	0.29	0.554	-0.26	0.27
0.347	-0.56	0.09	0.379	-0.27	0.12	0.406	-0.52	0.10	0.425	-0.56	0.18	0.449	-0.38	0.17
0.256	-0.82	0.11	0.290	-0.58	0.13	0.319	-0.78	0.15	0.340	-0.77	0.11	0.366	-0.79	0.27
0.168	-0.77	0.09	0.203	-0.47	0.12	0.234	0.97	0.15	0.256	-0.87	0.15	0.283	-0.52	0.11
0.014	-0.82	0.15	0.022	-0.88	0.47	0.054	-0.57	0.19	0.077	-0.37	0.10	0.107	-0.61	0.16
0.099	-0.67	0.18	-0.063	0.41	0.47	-0.031	-0.17	0.14	-0.008	-0.33	0.13	0.022	-0.23	0.10
0.164	-1.48	0.65	-0.128	0.26	0.27	-0.097	0.20	0.14	-0.074	-0.02	0.10	-0.044	-0.15	0.10
0.235	-0.26	0.21	-0.200	0.92	0.84	-0.170	0.48	0.14	-0.146	0.24	0.12	-0.117	0.39	0.12
0.365	-0.14	0.12	-0.332	-0.51	0.21	-0.304	0.65	0.15	-0.283	0.88	0.15	-0.255	0.65	0.21
0.450	-0.22	0.08	-0.420	-0.93	0.17	-0.394	0.31	0.11	-0.374	0.64	0.12	-0.348	1.06	0.29
0.572	-0.24	0.07	-0.547	-1.16	0.17	-0.524	-0.19	0.12	-0.507	0.21	0.10	-0.485	0.40	0.13
0.660	-0.11	0.07	-0.639	-1.11	0.18	-0.620	-0.53	0.19	-0.605	-0.51	0.22	-0.586	-0.33	0.22
0.741	-0.11	0.08	-0.724	-0.75	0.19	-0.708	-0.65	0.23	-0.697	-0.33	0.12	-0.681	-0.43	0.13
0.815	-0.15	0.17	-0.802	-0.42	0.30	-0.791	-0.10	0.19	-0.781	-0.19	0.12	0.770	-0.38	0.18
0.882	0.26	0.09				-0.866	0.92	0.28	-0.860	0.20	0.32			

targets.) The normalization ratio was then applied to all the $\pi^0 n$B events from the dummy data to give the total background distribution, indicated in Fig. 2(a) along with the total events (for both signs of target polarization) from the polarized target. For each counter, the polarization parameter was evaluated for a series of cuts in p_B, and was relatively independent of the value of p_B used. The value of the polarization parameter quoted is the one having minimum error (typically for $p_B < 120$ MeV/c). A complete description of the data-analysis procedures, including an independent check[10] on the evaluation of $P(\theta)$, is given in Ref. 5.

The results are tabulated in Table I and are also compared in Figs. 2(b)–2(f) with current phase-shift predictions[11-13] and with isospin bounds calculated from the Bareyre-Ayed phase shifts.[13] Qualitatively, the Bareyre-Ayed phase-shift predictions reproduce reasonably well the general features of the data at all momenta, except for the backward region at 1030 MeV/c. This is also true of the Almehed-Lovelace predictions[11] except at 1790 MeV/c where the disagreement is quite severe. This disagreement is also manifest in the comparison of the charge-exchange differential cross-section measurements of Ref. 3 with the predictions given in Ref. 11 for momenta $\gtrsim 1790$ MeV/c. A quantitative test of the effect of these results on the phase-shift solutions must await further analyses with these data included as input (along with other recent data).

We thank the Bevatron staff for their assistance. We also thank Dr. R. Kelly for helpful discussions, and M. Long and T. Daly for excellent technical support. We are grateful to E. Epstein and D. Stevenson and the group of scanners for their contribution.

---

*Work done under the auspices of the U.S. Atomic Energy Commission.

† Present address: National Science Foundation, Washington, D.C. 20550.

‡ Present address: Stanford Linear Accelerator Center, Stanford, Calif. 94305.

§ Present address: University of California at Riverside, Riverside, Calif. 92502.

‖ Present address: University of Washington, Seattle, Wash. 98105.

[1] P. Bonamy *et al.*, Nucl. Phys. B16, 335 (1970) (5.1 and 11.2 GeV/c); P. Bonamy *et al.*, Nucl. Phys. B52, 392 (1973) (5 and 8 GeV/c); D. Drobnis *et al.*, Phys. Rev. Lett. 20, 274 (1968) (3.47 and 5.0 GeV/c); D. Hill *et al.*, Phys. Rev. Lett. 30, 239 (1973) (3.5 and 5.0 GeV/c).

[2] R. E. Hill *et al.*, Phys. Rev. D 2, 1199 (1970) (one point at $T = 310$ MeV).

[3] J. E. Nelson *et al.*, Phys. Lett. B47, 281 (1973).

[4] S. R. Shannon *et al.*, Lawrence Berkeley Laboratory Report No. LBL-2114 (unpublished).

[5] S. R. Shannon (Ph.D. thesis), Lawrence Berkeley Laboratory Report No. LBL-2607, 1974 (unpublished).

[6] J. E. Nelson (Ph.D. thesis), Lawrence Berkeley Laboratory Report No. LBL-1019, 1972 (unpublished).

[7] A. R. Clark and L. T. Kerth, in *Proceedings of the International Conference on Instrumentation for High Energy Physics, Stanford, California, 1966* (International Union of Pure and Applied Physics and U.S. Atomic Energy Commission, Washington, D.C., 1966), p. 355.

[8] O. I. Dahl, T. B. Day, F. T. Solmitz, and N. L. Gould, LBL Group A programming note P-126 (unpublished).

[9] This method is also valid for the other heavy nuclei in the target (e.g., ^{16}O); the significant fact is that the mass difference $m_C - m_B$ equals the proton mass.

[10] This method used the entire event sample (i.e., regardless of γ-ray multiplicities) and completely ignored information on the γ rays. $P(0)$ was evaluated from the neutron time-of-flight distribution for each counter. The neutron time-of-flight distributions for the dummy target were used to determine the background. The results from both analyses were in excellent agreement.

[11] S. Almehed and C. Lovelace, Nucl. Phys. B40, 157 (1972).

[12] P. Bareyre and R. Ayed, private communication; R. Ayed *et al.*, presented at the Second International Conference on Elementary Particles, Aix-en-Provence, France, 1973 (unpublished), Paper No. 311.

[13] R. Ayed *et al.*, in *Proceedings of the Sixteenth International Conference on High Energy Physics, The University of Chicago and National Accelerator Laboratory, 1972*, edited by J. D. Jackson and A. Roberts (National Accelerator Laboratory, Batavia, Ill., 1973), Paper No. 990, and "Zero Strangeness Baryon States below 2.5 GeV Mass" (to be published).

Measurement of the Branching Ratio $\Gamma(K_L{}^0 \to \pi^\pm \mu^\mp \nu)/\Gamma(K_L{}^0 \to \pi^\pm e^\mp \nu)$†

H. H. Williams, R. C. Larsen, L. B. Leipuner, W. W. Sapp,* A. L. Sessoms,‡ and L. W. Smith
Brookhaven National Laboratory, Upton, New York 11973

and

R. K. Adair and R. Turner§
Yale University, New Haven, Connecticut 06520

(Received 28 March 1974)

We present the results of a measurement of the $K_{\mu 3}{}^0/K_{e3}{}^0$ branching ratio, obtained from a study of $K_L{}^0$ decays using a multiwire-proportional-chamber spectrometer. The $K_{\mu 3}{}^0$ and $K_{e3}{}^0$ events were separated by muon range counters, and $K_{\pi 3}{}^0$ events were separated from the $K_{e3}{}^0$ sample kinematically. From a sample of approximately 10 000 $K_{\mu 3}{}^0$ and $K_{e3}{}^0$ events, we obtain a value of the branching ratio $\Gamma(K_{\mu 3}{}^0)/\Gamma(K_{e3}{}^0) = 0.662 \pm 0.037$.

The decays $K_L{}^0 \to \pi^\pm \mu^\mp \nu$ and $K_L{}^0 \to \pi^\pm e^\mp \nu$ have been the subject of intense theoretical interest and experimental investigation for almost a decade.[1] With the assumption of the $V - A$ theory of weak interactions, the amplitude for $K_L{}^0 \to \pi \mu \nu$ may be written in terms of two form factors $f_+(q^2)$ and $f_-(q^2)$ $[q^2 = (p_K - p_\pi)^2]$, and much of the interest in these decays has stemmed from the possibility of comparing the measured form factors with a variety of theoretical predictions. In particular, a determination of the form factors provides an important test of the hypotheses of partial conservation of axial-vector currents and chiral SU(3) ⊗ SU(3) algebra of weak currents. Proceeding directly from these hypotheses, Callan and Treiman predicted that the scalar form factor

$$f(q^2) = f_+(q^2) + q^2 f_-(q^2)/(M_K{}^2 - m_\pi{}^2)$$

should assume the values f_K/f_π at the unphysical point $q^2 = M_K{}^2$.[2]

Although a detailed determination of the form factors as a function of q^2 requires a study of the decay rate or muon polarization as a function of the position of the Dalitz plot, a measurement of the $K_{\mu3}^0/K_{e3}^0$ branching ratio provides an important constraint on the form factors. In particular, if the q^2 variation of the form factors is assumed to be linear, a measurement of the branching ratio allows a determination of λ_0, the slope of $f(q^2)$, which is quite insensitive to the slope λ_+ assumed for $f_+(q^2)$.

The apparatus used in this experiment consisted of an evacuated decay region followed by a multiwire-proportional-chamber spectrometer, which has been described in detail elsewhere.[3] Two chambers placed upstream of a wide-gap magnet and five planes of chambers downstream of the magnet measured the angles and momenta of the two charged particles. Following the last chamber, there was a scintillation-counter hodoscope which provided a trigger when two charged particles passed through the apparatus. Finally, downstream of this hodoscope, there were two iron blocks, each 60 cm thick, symmetrically placed on either side of the beam and immediately followed by scintillation counters. These scintillation counters, hereafter referred to as the "muon counters," were used to identify as muons those particles that penetrated the iron blocks.

The technique used for event identification was to label as $\pi\mu\nu$ those events in which a particles penetrated the iron to produce a count in one of the muon counters, while all those events that did not produce a count were K_{e3}^0 candidates. This latter category consists almost entirely of K_{e3}^0 and $K_{\pi3}^0$ decays, which can be readily separated kinematically.

For each event it was required that the trajectories of both particles intersect the iron blocks and furthermore that the particles not be allowed to enter the same block. In addition, it was required that each particle have a momentum greater than 900 MeV/c to ensure that a muon would penetrate the iron.

The distribution of $P_0'^2$, a commonly used parameter for separating K_{l3} and $K_{\pi3}$ events, is shown in Fig. 1 for the $K_{\mu3}$ and K_{e3} candidates, along with Monte Carlo calculations of the same distributions for pure $K_{\mu3}^0$ and K_{e3}^0 event samples.[4] It is seen that the Monte Carlo calculation for $K_{\mu3}^0$ events agrees quite well with the data, except for a small excess of events at $P_0'^2 \approx 0.005$ (GeV/c)^2. This excess is produced by $K_{\pi3}^0$ decays where one of the charged pions succeeds in firing the muon counters, either by the decay $\pi\to\mu\nu$ or by penetrating the steel directly.

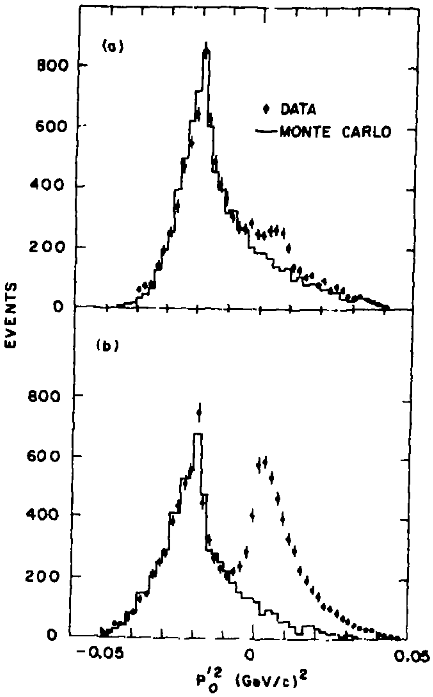

FIG. 1. $P_0'^2$ distributions for (a) the $K_{\mu3}^0$ and (b) the K_{e3}^0 candidates.

The $P_0'^2$ distribution for the K_{e3}^0 candidates exhibits two peaks, centered approximately at -0.02 (GeV/c)^2 and at 0.005 (GeV/c)^2, which correspond respectively to K_{e3}^0 and $K_{\pi3}^0$ events. It is apparent that there is a rather clean separation between the two classes of events. In the absence of resolution effects, the distribution for $K_{\pi3}^0$ events extends only over positive values and peaks at $P_0'^2 = 0$ (GeV/c)^2. To eliminate the $K_{\pi3}^0$ events, in both the $K_{\mu3}^0$ and K_{e3}^0 samples, we have applied the cut $P_0'^2 < -0.01$ (GeV/c)^2. Since the shapes of the distributions for $K_{\mu3}^0$ and K_{e3}^0 events are quite similar, the ratio of events retained is quite insensitive to the location of this cut. By subtracting the Monte Carlo calculation for K_{e3}^0 events from the observed data, and by studying the calculated $P_0'^2$ distribution for $K_{\pi3}^0$ events, including resolution, we have estimated that the background of $K_{\pi3}^0$ events in the selected K_{e3}^0 sample is less than 1%.

In selecting the sample of events used in determining the branching ratio, the only additional cuts imposed were that the decay vertex originate within the evacuated region, and within the fiducial volume of the beam, and that the momentum of each particle transverse to the beam be less than the kinematical maximum. The number of events which failed this last requirement, or which had a decay vertex outside the cross section of the beam, was only 1.5%, indicating that the data sample is quite free from backgrounds due to either accidentals or nondecay processes. The total number of $K_{\mu 3}{}^0$ and $K_{e3}{}^0$ events remaining in the selected sample was approximately 10 000.

There are several corrections that must be made to the raw ratio of $K_{\mu 3}{}^0$ and $K_{e3}{}^0$ candidates. The most significant correction is that for $K_{e3}{}^0$ events that are registered as $K_{\mu 3}{}^0$ because the pion triggers the muon counters. We are able to measure this pion "feedthrough" directly, by observing the number of events, subject to the same cuts as above, in which both muon counters fired. These events must be $\pi\mu\nu$ events in which the pion counted as well as the muon. In this way, we determine that the probability that a pion counts in the muon counters is $(12\pm 1)\%$. Although this value has been determined for $\pi\mu\nu$ events, the kinematic distributions of the pion in the laboratory system are sufficiently similar for $K_{\mu 3}{}^0$ and $K_{e3}{}^0$ events that the probability that a pion decays or penetrates the steel may be expected to be the same for both classes of events.

A background subtraction of $(1.5\pm 1)\%$ has been made from the $K_{\mu 3}{}^0$ sample to allow for contributions of $(1\pm 1)\%$ from $K_{\pi 3}{}^0$ events, and approximately 0.5% from $K_L{}^0 \to 2\pi$ decays. No correction has been made for accidentals or for nondecay events since backgrounds of this kind have been estimated to be less than 1% and, to the extent that they exist, are equal for both classes of events. The $K_{\mu 3}{}^0$ sample has been corrected for losses of $(4.8\pm 2)\%$ and $(2.3\pm 1)\%$ due to measured differences in the chamber efficiency and trigger efficiency for $K_{\mu 3}{}^0$ events versus $K_{e3}{}^0$ events.

The contributions of higher-order radiative processes to the measured number of $K_{\mu 3}{}^0$ and $K_{e3}{}^0$ events include modification of the $K_{\mu 3}{}^0$ and $K_{e3}{}^0$ decay rates due to virtual radiative diagrams and the existence of $K_{l3\gamma}{}^0$ background since the photon escapes unobserved. These contributions have been evaluated by Ginsberg, and we have calculated the corrections appropriate to this experiment in the following manner[5]: Since the detection efficiency for $K_{l3\gamma}{}^0$ events becomes identical to that for $K_{l3}{}^0$ decays as the γ-ν invariant mass $x\to 0$, the bremsstrahlung contribution with $x<10$ MeV (this includes the infrared divergence) has been combined with the virtual contribution and the total correction calculated assuming three-body kinematics. For $x>10$ MeV, $K_{l3\gamma}{}^0$ events have been generated as a function of x, over the entire four-body phase space, with each event weighted by the appropriate detection efficiency. The resulting corrections are $K_{\mu 3}{}^{\rm OBS} = (1.018\pm 0.002)K_{\mu 3}{}^{\rm NR}$ and $K_{e3}{}^{\rm OBS} = (0.996\pm 0.005)\times K_{e3}{}^{\rm NR}$, where $K_{l3}{}^{\rm OBS}$ is the observed decay rate, and $K_{l3}{}^{\rm NR}$ represents the decay rate in the absence of radiative effects. It is the ratio $K_{\mu 3}{}^{\rm NR}/K_{e3}{}^{\rm NR}$ which we quote as the branching ratio and use to determine the form factors.

Having applied the above corrections to the data, the ratio of $\pi\mu\nu$ to $\pi e\nu$ events is found to be 1.106 ± 0.058. The error quoted includes the statistical error and uncertainties in the corrections made.

The branching ratio is then determined by dividing this corrected ratio by the relative detection efficiency for the two types of events. Although in principle it is necessary to know the form factors describing the $\pi\mu\nu$ and $\pi e\nu$ decays in order to calculate the detection efficiency, information regarding the form factors may be determined directly in the following manner. It is assumed that the form factors are linear in the region of physical interest, $f_\pm(q^2)=f_\pm(0)[1+\lambda_\pm q^2/m_\pi{}^2]$, an assumption that is plausible on theoretical grounds and for which there is considerable evidence experimentally. The distribution of events across the Dalitz plot may then be parametrized in terms of λ_+, λ_-, and $\xi(0)=f_-(0)/f_+(0)$, and one obtains by Monte Carlo calculations an expression for the *detected* ratio of $K_{\mu 3}{}^0$ and $K_{e3}{}^0$ events, $R_{\rm DET}$, in terms of these three parameters. For the case $\lambda_-=0$,

$$R_{\rm DET}=\frac{2.28+12.9\lambda_+ +21.7\lambda_+{}^2+0.44\xi(0)+1.57\xi(0)\lambda_+ +0.070\xi^2(0)}{1.26+5.69\lambda_+ +8.73\lambda_+{}^2}\times 0.6172.$$

[The results obtained below are rather insensitive to the value of λ_- assumed, but the explicit effect may be included by adding the following terms to the numerator: $0.582\xi^2(0)\lambda_-$, $1.34\xi^2(0)\times\lambda_-{}^2$, $6.48\xi(0)\times\lambda_+\lambda_-$, $1.57\xi(0)\lambda_-$.]

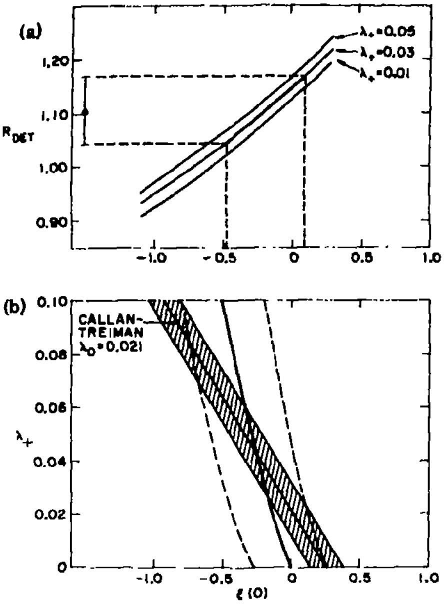

FIG. 2. (a) A plot of the calculated ratio of $K_{\mu 3}^0$ events detected to K_{e3}^0 events detected, as a function of $\xi(0)$, for different values of λ_+. The dashed lines indicate the value of $\xi(0)$ corresponding to the measured ratio, for $\lambda_+ = 0.03$. (b) The value of $\xi(0)$ deduced as a function of λ_+. Also shown is the correlation between $\xi(0)$ and λ_+ which obtains if the Callan-Treiman relation is valid. The shaded area indicates the approximate theoretical uncertainty.

It is apparent that any error in the Monte Carlo calculation affects directly the values obtained for the form factors. However, it is only the *ratio* of the detection efficiencies that is important and since the kinematic distributions of $\pi\mu\nu$ and $\pi e\nu$ events in the laboratory are very similar, we may expect that this ratio is not very sensitive to the details of the geometry. To verify this, we have made substantial variations in several parameters in the Monte Carlo calculation and have studied the resulting changes in the ratio of the detection efficiencies; these changes were always less than 2%.

The above expression for the detected ratio of $K_{\mu 3}^0$ and K_{e3}^0 events is plotted in Fig. 2(a), as a function of $\xi(0)$, for several values of λ_+. One may readily determine from this plot that the observed $K_{\mu 3}^0/K_{e3}^0$ ratio of 1.106 ± 0.058 corresponds to the value $\xi(0) = -0.20 \pm 0.29$ for $\lambda_+ = 0.03$. For purposes of illustration in the figure, the 2% uncertainty in the Monte Carlo calculation of R_{DET} has been folded into the error of the observed ratio of events. Similarly, one may determine the value of $\xi(0)$ for any other value of λ_+. The results are presented in Fig. 2(b), along with the correlation between λ_+ and $\xi(0)$ that obtains if the Callan-Treiman relation is valid. For values of λ_+ between 0.0 and 0.08, the value of $\xi(0)$ obtained is consistent within the errors with the Callan-Treiman prediction.

The quantity that is perhaps of more direct theoretical interest than $\xi(0)$ is λ_0, the slope of the form factor $f(q^2)$. Assuming that $f(q^2)$ is also linear, and again assuming that $\lambda_- = 0$, it follows that $\lambda_0 = \lambda_+ + \xi(0) m_\pi^2/(M_K^2 - m_\pi^2)$. The value of $\xi(0)$ deduced above, for $\lambda_+ = 0.03$, then corresponds to the value $\lambda_0 = 0.013 \pm 0.025$ as compared with the Callan-Treiman prediction of 0.021.

Finally, the branching ratio is determined from the detected $K_{\mu 3}^0/K_{e3}^0$ ratio by dividing by the relative detection efficiency. Although it depends in principle on the assumed values of λ_+ and $\xi(0)$, in practice, for our apparatus, the relative detection efficiency for $K_{\mu 3}^0$ and K_{e3}^0 decays is independent of $\xi(0)$ over the range -1.0 to 0.0, and varies by less than 2% for values of λ_+ between 0.01 and 0.05. We find, assuming a nominal value of $\lambda_+ = 0.03$, that $\Gamma(K_{\mu 3}^0)/\Gamma(K_{e3}^0) = 0.662 \pm 0.037$. This value is in reasonable agreement with other recent measurements.[6]

---

†Work performed under the auspices of the U. S. Atomic Energy Commission.

*Now at Schweizerisches Institute für Nuklearforschung, Switzerland.

‡Now at CERN, Geneva, Switzerland.

§Now at University of Miami Medical School, Miami, Fla.

[1] For a recent review of K_L^0 decays, see B. Stech, J. Phys. (Paris), Colloq. 34, C1-71 (1973); V. Soergel, *ibid.* 83 (1973); D. R. Nygren, in *Particles and Fields —1973*, AIP Conference Proceedings No. 14, edited by H. H. Bingham, M. Davier, and G. R. Lynch (American Institute of Physics, New York, 1973), p. 20.

[2] C. G. Callan and S. B. Treiman, Phys. Rev. Lett. 16, 153 (1966).

[3] H. H. Williams *et al.*, Phys. Rev. Lett. 31, 1521 (1973).

[4] The variable $P_0'^2$ represents the square of the momentum of the incident K_L^0 in that frame in which the total longitudinal momentum of the two charged particles is zero with the event interpreted as a $K_{\pi 3}^0$ decay.

[5] E. S. Ginsberg, Phys. Rev. D 1, 229 (1970). See also the comments by Soergel, Ref. 1.

[6] G. W. Brandenburg *et al.*, Phys. Rev. D 8, 1978 (1973), and the references contained therein.

Asymptotic Behavior of Non-Abelian Gauge Theories to Two-Loop Order*

William E. Caswell
Joseph Henry Laboratories, Princeton University, Princeton, New Jersey 08540
(Received 2 May 1974)

We have calculated the value of the Callan-Symanzik β function to order g^5 for non-Abelian gauge theories with fermions. We discuss internal consistency of the calculation, and consider the approach to the aymptotic energy range in such theories.

There has recently been much interest in non-Abelian gauge theories of the strong interactions. Renormalization-group parameters have been calculated to lowest order,[1] and a subclass of these theories has been found to asymptotically free.[2] The value of β in g^5 order is interesting for study of the approach to the asymptotic energy range. It also provides some control over the "effective coupling constant," leading to field theories with short- and long-distance behavior calculable in perturbation theory. We present below the result of a calculation of β.

The bare Lagrangian for a theory of interacting fermions and gauge mesons is

$$\mathcal{L} = -\tfrac{1}{2}\operatorname{Tr}\{\partial_\mu B_\nu - \partial_\nu B_\mu + ig[B_\mu, B_\nu]\}^2 - \alpha^{-1}\operatorname{Tr}\{(\partial^\mu B_\mu)^2\}$$
$$+2\operatorname{Tr}\{\partial_\mu\varphi^*\partial^\mu\varphi + ig\partial_\mu\varphi^*[B_\mu,\varphi]\} + \bar\psi(i\not\partial - g\not B^a\sigma_a - M)\psi. \qquad (1)$$

The gauge field is $B_\mu = \sum_a B_\mu{}^a\tau_a$; the τ_a are the matrices of the adjoint representation of G, a compact Lie group. The ghost field is $\varphi = \sum_a \varphi^a\tau_a$, the fermion field is $\psi = \sum_a \psi^a\sigma_a$, and the σ_a are the matrices of R, the representation of G under which the fermions transform. The term α^{-1} fixes the gauge. The group invariants which enter into the result are $C_2(G)$ and $C_2(R)$, the quadratic Casimir operators of the adjoint and fermion representations, and the trace $T(R)$ of the fermion representation, defined by $T(R)\delta_{ab} = \operatorname{Tr}\{\sigma_a\sigma_b\}$.

β was calculated using the dimensional-regularization technique of 't Hooft and Veltman.[3] The scaling equations in this renormalization framework were derived by 't Hooft.[4] The Green's functions of the theory with l fermions, m gauge bosons, and n ghosts satisfy the "new" renormalization-group equations[4-6]

$$\left[\mu\frac{\partial}{\partial\mu} + B(g)\frac{\partial}{\partial g} + \delta(g,\alpha)\frac{\partial}{\partial\alpha} + \hat\gamma_F(g)M\frac{\partial}{\partial M} + m\gamma_B(g,\alpha) + 2n\gamma_G(g,\alpha) + 2l\gamma_F(g,\alpha)\right]G^{(l,m,n)} = 0. \qquad (2)$$

The renormalized coupling constant is g, the gauge parameter is α, the renormalization scale parameter is μ, and the fermion mass matrix is M. Within this renormalization framework, β is independent of α.[7] For simplicity, β was evaluated in Feynman gauge ($\alpha = 1$).

The renormalization counterterms were fixed by requiring that they be of the form

$$Z = 1 + z/\epsilon + \text{higher order terms in } 1/\epsilon, \qquad (3)$$

where n is the dimension of space-time and $\epsilon = 4 - n$. Z and z are power series in g^2 and the gauge parameter α. The counterterms calculated include those for the ghost propagator ($\tilde Z_3$), the ghost gauge boson vertex ($\tilde Z_1$), the gauge boson propagator (Z_3), and the triple boson vertex (Z_1). These are related by a Ward-Takahashi identity,[8] $Z_1/Z_3 = \tilde Z_1/\tilde Z_3$. To check the calculation, all four were computed independently. The connection between β and the counterterms is given by[4,5]

$$\beta(g) = g^3(\partial/\partial g^2)(\tilde Z_1 - \tilde Z_3 - \tfrac{1}{2}Z_3) = g^3(\partial/\partial g^2)(Z_1 - \tfrac{3}{2}Z_3). \qquad (4)$$

There are similar formulas for anomalous dimensions of the fields. The technique used to calculate the pole terms will be explained in detail in a future publication.

There are several internal checks on the calculation. No terms of the form $\ln q^2$ or (equivalently, in this theory) γ_E (Euler's constant) should appear. The double-pole ($1/\epsilon^2$) terms may be independently calculated using the scaling equations of 't Hooft. Only the check using the Ward identities is nontrivial. Because of the complexity of the algebra, this check was considered necessary.

We find that

$$\beta(g) = -b_0 \frac{g^3}{16\pi^2} + b_1 \frac{g^5}{(16\pi^2)^2} + O(g^7), \quad b_0 = \tfrac{11}{3} C_2(G) - \tfrac{4}{3} T(R),$$
$$b_1 = -\tfrac{34}{3} C_2^2(G) + \tfrac{20}{3} C_2(G) T(R) + 4 C_2(R) T(R). \tag{5}$$

In the following examples we will specialize to SU(N), and choose for R the vector representation. We assume m fermion multiplets. The relevant group invariants are then $C_2(G) = N$, $T(R) = \frac{1}{2}m$, and $C_2(R) = (N^2 - 1)/2N$.[1]

For SU(3), $\beta(g)/g$ near the origin is presented in Fig. 1. The effective perturbation-expansion parameter is $g^2 C_2(\mathrm{SU}(N))/16\pi^2$. We may choose the number of fermion multiplets to obtain the theory with the smallest value of the first nontrivial zero of β. With sixteen fermion multiplets we obtain a theory with calculable short-distance ($g \to 0$) and long-distance ($g \to g_1$) behavior, for g initially between 0 and g_1. g_1 is β's first zero past the origin, $g_1^2/16\pi^2 = 1/302$ + higher-order corrections. The fractional correction due to the three-loop contribution is expected to be roughly $(g_1^2/16\pi^2)T(R) \sim \frac{1}{40}$, and is probably negligible. If the coefficient of the three-loop term is surprisingly large, we may consider SU(N) for N larger than 3. Choosing m to minimize the first (b_0) term, we may ensure the existence of a zero of $\beta(g)$ valid in perturbation theory, even for abnormally large g^7 contributions.[9] g_1 is a simple zero of $\beta(g)$. As $g \to g_1$, the theory approaches a dilatation- and conformal-invariant Gell-Mann–Low limit theory.[10] Solving the renormalization group equations, with λ scaling all momenta of the Green's functions ($t = \ln\lambda$), we find deviations from the limit theory smaller by powers of λ rather than by logarithms (which characterize the $g \to 0$ end):

$$g_1^2 - \bar{g}^2(t,g) \underset{\lambda \to 0}{\simeq} \lambda^{2b_1(g_1^2/16\pi^2)^2} = \lambda^{1/453}, \tag{6}$$

for SU(3) with sixteen fermion multiplets.

For pure gauge theories the g^5 term is negative, and the approach to the asymptotic region is enhanced. We might expect the domain of attraction of the origin to be large (which would be appealing in a theory of the strong interactions). The effective coupling constant $\bar{g}(t,g)$ satisfies

$$d\bar{g}/dt = \beta(\bar{g}), \quad \bar{g}(0,g) = g. \tag{7}$$

As $\lambda \to \infty$ ($t \to \infty$), $\bar{g}$ approaches zero as

$$\frac{\bar{g}^2(t,g)}{16\pi^2} \underset{t\to\infty}{\approx} \frac{1}{2b_0 t} + \frac{b_1}{4b_0^3}\frac{\ln t}{t^2} + O\left(\frac{1}{t^2}\right). \tag{8}$$

For SU(3) with three fermion triplets, which may be relevant for theories of the strong interactions,

$$\frac{\bar{g}^2(t,g)}{16\pi^2} \underset{t\to\infty}{\approx} \frac{1}{18t} - \frac{16}{729}\frac{\ln t}{t^2} + O\left(\frac{1}{t^2}\right). \tag{9}$$

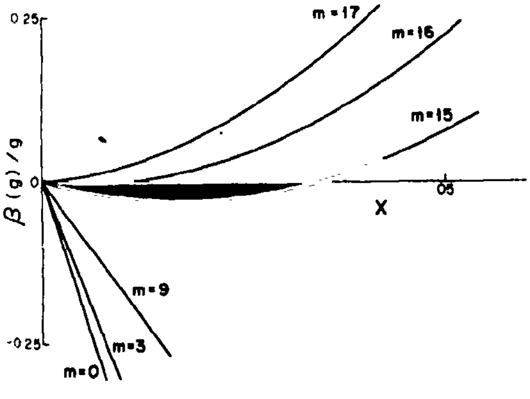

FIG. 1. Shape of $\beta(g)/g$ near the origin, for SU(3) with m fermion multiplets. x = effective expansion parameter $= (g^2/16\pi^2)C_2(\mathrm{SU}(3))$.

The second-order term slightly enhances the approach to zero. For $m=16$,

$$\frac{\bar{g}^2(t,g)}{16\pi^2} \underset{t\to\infty}{\approx} \frac{3}{2t}+\frac{1359}{2}\frac{\ln t}{t^2}+O\left(\frac{1}{t^2}\right), \tag{10}$$

and, as we expect for $\beta(g)$ small, $\bar{g}$ approaches its asymptotic values ($\bar{g}=0$ and $\bar{g}=g_1$) only slowly.

We do not expect to find a gauge theory of the above type where β starts out positive and goes negative near enough to the origin for the zero to be valid in perturbation theory. If the lowest-order term is fixed to be zero, then

$$\beta(b_0=0)=g^5(16\pi^2)^{-2}[7C_2^2(G)+11C_2(G)C_2(R)]>0, \tag{11}$$

for an arbitrary gauge group G. This is approximately the case for SU(3) with $m=17$ ($b_0=-\frac{1}{3}$).

I am grateful to C. Callan for his advice and support throughout this project. I wish to thank T. Regge, E. Speer, and particularly F. Wilczek for helpful conversations.

---

*Research supported in part by the National Science Foundation under Grant No. GP-30738X.

[1] D. J. Gross and F. Wilczek, Phys. Rev. Lett. 26, 1342 (1973); H. Politzer, Phys. Rev. Lett. 26, 1346 (1973); G. 't Hooft, unpublished.

[2] S. Coleman and D. Gross, Phys. Rev. Lett. 31, 851 (1973).

[3] G. 't Hooft and M. Veltman, Nucl. Phys. B44, 189 (1972), and CERN Report No. 73-9 (unpublished); E. Speer, J. Math. Phys. (N.Y.) 15, 1 (1974).

[4] G. 't Hooft, Nucl. Phys. B61, 455 (1973).

[5] They may be derived using 't Hooft's results and the chain rule for partial derivatives. Other techniques for showing this connection have appeared in J. C. Collins and A. J. MacFarlane, to be published; S. Y. Lee, to be published.

[6] S. Weinberg, Phys. Rev. D 8, 3497 (1973); C. Callan, unpublished.

[7] W. E. Caswell and F. Wilczek, Phys. Lett. B49, 291 (1974).

[8] G. 't Hooft, Nucl. Phys. B33, 173 (1971); G. 't Hooft and M. Veltman, Nucl. Phys. B50, 318 (1972); B. W. Lee, Phys. Rev. D 5, 3121 (1972).

[9] In theories as the above for which g_1 is calculable in perturbation theory, the effective coupling constant is constrained to remain small for all momenta. We expect a range of theories, for differing group structures, which have a finite zero of β. The possibility of dynamical quark confinement, arising from an infinite effective coupling constant in the infrared region, is not realized in this class of theories. Whether a group structure exists such that β is negative definite, providing a possible mechanism for achieving "infrared slavery," is a nonperturbative question.

[10] G. Mack, *Strong Interaction Physics* (Springer-Verlag, New York, 1973), and references therein.

Is the Cross Section for $e^+e^-\to$ Hadrons Time Dependent in Colliding Beam Machines?*

T. Goldman† and Patrizio Vinciarelli‡
Stanford Linear Accelerator Center, Stanford University, Stanford, California 94305

(Received 1 April 1974)

If $e^++e^-\to\Phi\to$ hadrons, where Φ is a scalar, radiative beam polarization in storage rings will induce an apparent time dependence of the cross section during an experimental run. This should provide a critical test for models which rely on such a scalar mechanism to enhance the cross section in the present energy range. A model of this kind is presented which identifies Φ with a composite Higgs field in gauge theories. We check for consistency with other processes and note that there may be an important relation to the shoulder in the dimuon mass distribution in $pp\to\mu^+\mu^-X$.

Synchrotron radiation in an e^+e^- storage ring leads to transversely polarized beams where the electrons (positrons) are polarized antiparallel (parallel) to the guide magnetic field.[1] The magnitude of the polarization builds up toward a limiting value from the time of injection of the beams into the ring, with a characteristic time constant dependent upon the energy and other machine parameters.[2] This effect may provide a useful constraint to model builders[3] as it has some interesting implications if the e^+e^- annihilation cross section is not completely dominated by the one-photon mechanism as has conventionally been assumed.[4] In particular, the polarization dependence of other mechanisms will induce an apparent time dependence of the annihilation cross section corresponding to the polarization buildup. As an interesting example, we present here a particular "no-photon" model,[5] which assumes that $\sigma(e^+e^-\to\text{hadrons})$ at the highest Cambridge Electron Accelerator (CEA) and SPEAR energies is dominated by a heavy hadronic scalar (intermediate state) resonance which couples directly to neutral (scalar) leptonic currents. The origin of such a mechanism may find theoretical justification in a composite[6] Higgs scalar within the framework of gauge models of the strong and weak interactions.[7,8]

It is simple enough to see how the difference in polarization dependence of the cross section between one-photon and one-scalar intermediate states occurs. We represent an electron (positron) with four-momentum p_-^{μ} (p_+^{μ}) and spin vector s_-^{μ} (s_+^{μ}) by the spinor $u(p_-,s_-)$ $[v(p_+,s_+)]$. Then the leptonic factors in the (noninterfering) squared amplitudes for annihilation into a scalar or into a photon (summed over photon polarizations ϵ_λ^{μ}) are given by

$$|\bar v(p_+,s_+)u(p_-,s_-)|^2=(p_+\cdot p_- -m^2)(1-s_+\cdot s_-)+(p_+\cdot s_-)(p_-\cdot s_+) \qquad (1)$$

and

$$\textstyle\sum_\lambda|\bar v(p_+,s_+)\not\epsilon_\lambda u(p_-,s_-)|^2 =2p_+\cdot p_- +4m^2-2m^2s_+\cdot s_-\simeq 2p_+\cdot p_-, \qquad (2)$$

respectively, where the approximate form of Eq. (2) is valid in the high energy limit $(p_+\cdot p_-\gg m^2)$. t is obvious from Eq. (2) that the photonic case s completely independent of the fermion beam olarizations (in the high energy limit). However, f the fermions are completely polarized in the 'natural" direction for colliding beam machines, .e.,

$$s_+^{\mu}=(0,0,0,+1) \qquad (3)$$

nd

$$s_-^{\mu}=(0,0,0,-1), \qquad (4)$$

here the z direction is that of the magnetic uide field of the beams, then explicit evaluation of Eq. (1) gives the result

$$|\bar v(p_+,s_+)u(p_-,s_-)|^2=0. \qquad (5)$$

That is, the contribution of the scalar vanishes when the polarization is complete. (The opposite effect occurs for a pseudoscalar; i.e., its contribution doubles for this polarization.) Denoting the the one-photon and one-scalar contributions for the unpolarized case by σ_γ and σ_Φ, respectively, we conclude that the polarization dependence of the total cross section for $e^+e^-\to\text{hadrons}$ in colliding beam machines is

$$\sigma_{\text{tot}}^{e^+e^-\to h}(P)=\sigma_\gamma+(1-|P|^2)\sigma_\Phi, \qquad (6)$$

where P is the (common) polarization coefficient of the beams. Thus, for a time-dependent polarization as described in Ref. 2,

$$|P|=\frac{8\sqrt3}{15}[1-\exp(-\tau/\tau_0)][\tau_{\text{dep}}/(\tau_{\text{pol}}+\tau_{\text{dep}})], \qquad (7)$$

where τ = time from injection, τ_{pol} and τ_{dep} are machine-dependent time parameters and $\tau_0=(1/\tau_{\text{pol}}+1/\tau_{\text{dep}})^{-1}$, Eq. (6) predicts an apparently time-dependent cross section that may change by up to a limiting factor of $1-{\sim}0.85[\tau_{\text{dep}}/(\tau_{\text{pol}}+\tau_{\text{dep}})]^2$ during an experimental run. We would like to stress that this effect is characteristic of a scalar contribution to the total annihilation cross section and would provide a clear signal for the presence of such a contribution.

We shall now describe, at the phenomenological level, a model which adopts such a scalar mechanism to enhance the $e^+e^-\to\text{hadrons}$ cross section in the present energy range. We shall show that the model yields nontrivial predictions for some processes other than e^+e^- annihilation, and that it easily survives all present experimental tests.

We postulate the existence of a hadronic scalar field Φ of mass m_Φ, with the quantum numbers of the vacuum[9] and with a Yukawa coupling to leptons l and quarks q as described by the interaction Lagrangian density

$$L_I=h\bar l l\Phi+g\bar q q\Phi, \qquad (8)$$

where $h\sim e^2$ and $g\sim 1$. The reader will recall that similar scalar fields are present in various gauge-theory models of the weak and strong interactions.[7] These are the by now well-known Higgs fields,[10] which are conventionally introduced as elementary fields on the Langrangian level. The effect of such fields other than the provision of the origin of symmetry breaking are usually minimized in those models by requiring that they be sufficiently massive. Our attitude is

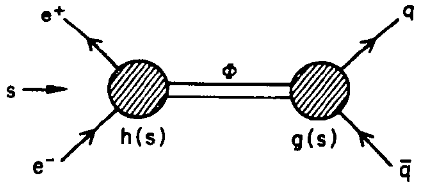

FIG. 1. Contribution of Φ to the amplitude for $e^+e^- \to$ hadrons.

that they need not be so experimentally inaccessible and that they may indeed be responsible for the surprising results from CEA and SPEAR. We also feel that, purely within the context of gauge theories, there are notable advantages if such scalars are bound states.[6] Equation (8) should therefore be regarded as describing an effective interaction accurate only in the neighborhood of the mass shells of the particles involved. Outside of this neighborhood, say for Φ significantly off shell ($k^2 \neq m_\Phi^2$), h and g should be regarded as functions of k^2: $h(k^2)$ and $g(k^2)$.

A simple-minded calculation[11] of the contribution of Φ to the unpolarized cross section for e^+e^- annihilation into hadrons (see Fig. 1) yields

$$\sigma_\Phi{}^U = \tfrac{1}{4}\sigma_\Phi{}^P = \frac{g^2(s)h^2(s)}{4\pi} s[(s - m_\Phi{}^2)^2 + m_\Phi{}^2\Gamma^2]^{-1}, \quad (9)$$

where Γ is the width of Φ, and $g(k^2 = s)$ and $h(s)$ are presumably slowly varying functions for s in the neighborhood of $m_\Phi{}^2$. Using Eq. (9) together with the usual one-photon (colored) quark-model contribution, it is easy to fit the CEA and preliminary SPEAR data[12] which are consistent with an approximately constant cross section of ~ 23 nb for $9\ \mathrm{GeV}^2 \lesssim s \lesssim 25\ \mathrm{GeV}^2$. However, given the magnitude of the reported error bars,[12] and the number of parameters that are at our disposal in Eq. (9), as well as the quark-model parameter in the one-photon contribution, it is pointless to write down any particular fit at this time.[13,14] In any case, this is not our intent here, as such a fit can be obtained from many different models and our model is no more compelling than any other (except, perhaps, to gauge theorists already accustomed to the use of Higgs scalars). Rather, we want to point out that models of the kind presented here, although not inconsistent with the present data, are subject to critical polarization tests.

Of course, like any other, this model must meet the tests of many well-established experiments, and we discuss a few here briefly. Typically, when one fiddles with leptonic couplings one must maintain the good agreement of quantu electrodynamics (QED) with such experiments a Bhabha scattering, $e^+e^- \to \mu^+\mu^-$, the value of $g - 2$ for the muon, and the Lamb shift in muonic atoms. The first two are clearly not affected, as the amplitudes calculated in QED in the one-photon Born approximation are of order e^2 and the analogous one-Φ contribution is of order $h^2 \sim e^4$. The one-virtual-Φ vertex correction to the muon $g - 2$ is immediately seen to be of order $h^2(m_\mu{}^2/m_\Phi{}^2)\ln(m_\mu{}^2/m_\Phi{}^2) \sim 10^{-4}e^4$, and higher order corrections are manifestly smaller. As present experiments are not yet sufficiently sensitive to test severely the order-e^6 QED calculations (including estimates of hadronic corrections to the photon propagator), the effect of the Φ is obviously too small to be seen. The additional vertex correction contribution to the Lamb shift is negligible as it is of the same size. Besides this loop contribution, there is also a contribution from the effective potential due to a virtual Φ in the t channel (replacing the photon). The ratio of this effect to that of the highest-order Lamb-shift calculation is $\sim e^{-4}g(0)h(0)(m_\mu/m_\Phi)^2 \sim 10^{-4}/e^2$ for muonic atoms even if we neglect the k^2 dependences of $g(k^2)$ and $h(k^2)$. Thus such an effect is also not experimentally detectable.[15]

One of the main difficulties in the construction of sensible models is the need to reconcile the apparent lack of scaling[12] in the annihilation channel with the early onset of scaling in the scattering channel,[16] i.e., deep inelastic electroproduction as observed at Stanford Linear Accelerator Laboratory (SLAC). The contribution of Φ to the electroproduction structure functions $W_i(q^2, \nu)$ may be estimated by replacing photons by Φ's in a quark-model calculation: The ratio of the Φ effect to the photon contribution is then of order $\alpha^{-2}h^2(q^2)g^2(q^2)(1 + m_\Phi{}^2/|q^2|)^{-2}$. Thus, in the relatively low-q^2 region ($q^2 \sim 2$–$5\ \mathrm{GeV}^2$) the Φ contribution is suppressed by the propagator factor to the few percent level. However, at the highest q^2 values at SLAC ($q^2 \sim 25\ \mathrm{GeV}^2$) this factor rises to ~ $\frac{1}{4}$ and one may need to invoke the extra suppression due to the q^2 dependence of the vertex functions $h(q^2)$ and $g(q^2)$, which reflect the composite nature of Φ. The need for the latter suppression mechanism may be even stronger to accommodate the μ-p scaling experiments at the National Accelerator Laboratory (NAL).

There are many qualitative predictions implicit in the scalar-Φ model. We have not sufficient-y detailed the $\Phi\to$ multihadrons vertex to make pecific statements about the hadronic final states. For instance, we cannot explain the large ratio (~ 1) of neutral to charged particles that has been observed at SPEAR, although the fact that Φ has opposite C parity might be a clue, as t can decay into $\pi^0\pi^0$, but *not* $\pi^+\pi^-$, unlike the C-odd (heavy) photon, which can go into $\pi^+\pi^-$ in a wo-body decay. [That is, there are in general additional C-even multi-π^0 final states which can be produced via the Φ, which may be preferred Φ-)decay modes over multi-charged-pion final states and which enhance the neutral-to-charged particle ratio.] Nonetheless, one would naturaly expect a typically hadronic falloff in the transverse momentum distribution which is indeed observed.[13] Also, because Φ is a scalar and because it provides a growing contribution to the annihilation cross section as $\sqrt{s}$ approaches the Φ mass and as τ (time from beam injection) decreases, the one-particle inclusive distribution is a function of θ (the angle between the detected particle and the beams) should behave like $1+a(s,\tau)\cos^2\theta$ with $a(s,\tau)$ decreasing toward a small value ($\ll 1$) in that limit.

The Φ will be difficult to see in purely hadronic scattering experiments as we expect it to be very broad and to decay preferentially into multibody (~ 4–8) final states not amenable to Dalitz-plot analysis. Experiments where the effect of Φ might be visible include $e^-e^-\to e^-e^-+X$ (as at DORIS) and $pp\to\mu+X$ (as at CERN intersecting storage rings or NAL). A more interesting and straightforward case is a double-arm experiment such as $pp\to\mu^+\mu^-+X$ as was carried out at Brookhaven National Laboratory.[17] Our mechanism,

$$\begin{array}{l} pp\to\Phi+X \\ \qquad \llcorner\!\!\to \mu^+\mu^- , \end{array} \tag{10}$$

can easily account for the observed shoulder in the mass distribution of dimuon pairs[18] if $m_\Phi \simeq 4$ GeV and $\Gamma\sim 1$ GeV. One may also turn the argument around and use it to predict that if the error bars on the SPEAR data can be reduced, *a peak in the annihilation cross section at $s\simeq 16$ GeV^2 will be revealed.*[19]

In conclusion, we have presented a model which appears to be consistent with present experiments. It leads us to a sharp relation between the unexpected results from CEA and SPEAR and the anomalous results in $pp\to\mu^+\mu^-+X$. We wish to reemphasize that models such as this which are sensitive to the naturally occurring polarization in colliding rings may be more easily and critically tested in such experiments than in any other way. Definite experimental results on the polarization dependence of the cross section, now in progress at SPEAR, would therefore be of great help to model builders.

We have enjoyed and benefited from conversations with I. Bigi, J. D. Bjorken, S. Brodsky, Min-Shih Chen, S. Drell, E. Eichten, M. Einhorn, F. Gilman, Ling-Fong Li, and B. Ward.

---

*Work supported in part by the U. S. Atomic Energy Commission.

†National Research Council of Canada Post-doctoral Fellow.

‡Address after 1 June 1974: Theory Division, CERN, Geneva, Switzerland.

[1] V. N. Baier, in *Physics of Intersecting Storage Rings*, *Proceedings of the International School of Physics "Enrico Fermi," Course XLVI*, edited by B. Touschek (Academic, New York, 1971), p. 1; A. A. Sokolov and I. M. Ternov, Dokl. Akad. Nauk. SSSR 153, 1052 (1963) [Sov. Phys. Dokl. 8, 1203 (1964)].

[2] R. F. Schwitters, SLAC Report No. SLAC-PUB-1348 (I, A), 1973 (to be published).

[3] Model builders could use some help as there is little to chose among a rapidly proliferating set of models.

[4] R. P. Feynman, *Photon-Hadron Interactions* (Benjamin, New York, 1972), pp. 163–166.

[5] Here we follow a classification scheme for e^+e^- models: "no-photon," "one-photon," "two-photon," ..., described to us by J. D. Bjorken, who, with I. Bigi, has systematically analyzed the implications of a direct four-Fermi coupling of leptons to quarks. The first public suggestion of a "no-photon" mechanism that we know of was made by B. Richter, invited talk in Proceedings of the Conference on Lepton Induced Reactions, Irvine, California, 1973 (to be published). The question of polarization-dependent effects from such mechanisms has been independently considered from an experimental point of view by B. Richter and R. Schwitters (private communication).

[6] T. Goldman and P. Vinciarelli, SLAC Report No. SLAC-PUB-1357 (T), 1973 (to be published).

[7] See, for example, S. Weinberg, Phys. Rev. Lett. 31, 494 (1973); H. Georgi and S. L. Glashow, Phys. Rev. Lett. 32, 438 (1974).

[8] We thank I. Bars for pointing out the usefulness of a scalar similar to the one introduced here in resolving the π-η degeneracy problem.

[9] This may not be necessary, but it is the easiest case to analyze.

[10] See the review by E. S. Abers and B. W. Lee, Phys. Rep. 9C, 1 (1974).

[11] We adopt the usual parton model assumption that the quark-antiquark rescattering into final states of ordinary hadrons does not significantly affect the form of

the result.

[12] A. Litke *et al.*, Phys. Rev. Lett. **30**, 1189 (1973); G. Tarnopolsky *et al.*, Phys. Rev. Lett. **32**, 432 (1974); Richter, Ref. 5.

[13] For example, if we assume $\Gamma/m_\Phi \sim \frac{1}{2}$, then m_Φ may lie anywhere in the range 4 to 10 GeV for reasonable values of g^2 (1 to 10). See below for a better estimate from $pp \to \mu^+\mu^- + X$.

[14] Note that the contribution of Eq. (9) may be reasonably expected to die off faster than s^{-1} as $s \to \infty$ because of the assumed composite nature of Φ.

[15] Although the QED calculation has been done to next higher order for ordinary atoms, the additional suppression of $(m_e/m_\mu)^2$ more than compensates.

[16] M. Breidenbach *et al.*, Phys. Rev. Lett. **23**, 935 (1969).

[17] J. H. Christenson *et al.*, Phys. Rev. D **8**, 2016 (1973).

[18] T. Goldman and P. Vinciarelli, SLAC Report No. SLAC-PUB-1414 (to be published). The shoulder should also appear in muon-trident production and similar experiments: $\nu p \to \mu\Phi X \to \mu\mu\mu X$, $\mu p \to \mu\Phi X \to \mu\mu\mu X$, $ep \to e\Phi X \to e\mu\mu X$, etc.

[19] Note, however, that this relation, abstracted here from the scalar Φ model, can be expected to hold for any s-channel resonance model.

ERRATA

NEW PARAMETERS FOR Δ^{++} RESONANCES FROM 2170 to 3490 MeV IN π^+p BACKWARD ELASTIC SCATTERING. C. A. Rey, A. J. Lennox, J. Poirier, and K. P. Pretzl [Phys. Rev. Lett. 32, 908 (1974)].

Because of an error in the Regge amplitude parametrization, the entries in Table II for cases which included the Regge contribution are in error. The corrected values are given herewith. Cases which did not include the Regge amplitude remain unchanged. The averages previously quoted in Table I, part C are essentially unchanged but should be considered only as the results of a pure resonance-model fit.

Lastly, a factor $\hbar c$ was erroneously typed in the denominator of Eq. (1). For consistency this factor should not appear in Eq. (1) but instead a factor $(\hbar c)^2$ should appear as a multiplier of the right-hand side of the fifth equation.

We wish to thank Dr. Gordon Shaw and Dr. Ernest Ma for helpful discussions related to their model.

TABLE II. Best fit values for parameters describing the Δ (2200), Δ (2420), Δ (2850), and Δ (3230) using a model which includes both resonance and Regge amplitudes. The four fits correspond to whether or not the 1* resonances were included and two choices of an exponential resonance damping factor d. The χ^2 for each fit was ~ 15 for 26 degrees of freedom.

	1* Resonance	Regge	d	Δ(2200)	Δ(2420)	Δ(2850)	Δ(3230)
Mass (MeV/c^2)	No	Yes	.01	2243	2473	2949	3444
	Yes	Yes	.01	2220	2475	2951	3457
	No	Yes	.10	2282	2543	2959	3392^a
	Yes	Yes	.10	2246	2535	2974	3366^a
	Average			2248	2506	2958	3450
	Mean Statistical Error			$^{+19}_{-17}$	$^{+17}_{-87}$	$^{+45}_{-42}$	$^{+140}_{-68}$
Width (MeV/c^2)	No	Yes	.01	234	461	288	637
	Yes	Yes	.01	273	459	266	684
	No	Yes	.10	144	348	367	347^a
	Yes	Yes	.10	240	354	287	272^a
	Average			223	406	302	660
	Mean Statistical Error			$^{+126}_{-58}$	$^{+150}_{-77}$	$^{+233}_{-174}$	$^{+2730}_{-220}$
X(J + 1/2)	No	Yes	.01	.51	.59	.15	.25
	Yes	Yes	.01	.75	.61	.14	.19
	No	Yes	.10	.34	.38	.16	$.10^a$
	Yes	Yes	.10	.46	.32	.13	$.06^a$
	Average			.52	.47	.14	.22
	Mean Statistical Error			$^{+.23}_{-.10}$	$^{+.25}_{-.11}$	$^{+.04}_{-.08}$	$^{+.05}_{-.06}$

[a] This entry is not statistically significant and was excluded from the average and the mean statistical error.

SOLVING EQUATIONS OF THE GELL-MANN–LOW AND CALLAN-SYMANZIK TYPE. B. F. L. Ward [Phys. Rev. Lett. 33, 37 (1974)].

Equation (29) should read

$$C_{n,\mathrm{asy}}(\lambda^2q^2) \to \mathrm{const}^{(n)}(g',\mu)/\lambda^2q^2 + O(\lambda^{-4}).$$

HADRON-NEUTRON FORWARD ELASTIC SCATTERING AMPLITUDE AND HADRON-DEUTERON COLLISIONS. Victor Franco and Girish K. Varma [Phys. Rev. Lett. 33, 44 (1974)].

The following corrections of typographical errors should be made. In the third line of Eq. (12), β^2q^22A should read $\beta^2q^2/2A$. In the eighth row of Table I, -0.02 should read 0.02; in the ninth row, -0.13 should read 0.13.

In Eq. (16), r^2 should read c^2+d^2.

PHYSICAL REVIEW
LETTERS

VOLUME 33 29 JULY 1974 NUMBER 5

Measurement of the Initial Population and Decay Rate of the $(\mu^4\,\mathrm{He})_{2S}{}^+$ System in a Helium Target at 50 atm

A. Bertin, G. Carboni, G. Gorini, O. Pitzurra, E. Polacco, G. Torelli, A. Vitale, and E. Zavattini
CERN, Geneva, Switzerland, and Istituto di Fisica dell'Università di Pisa and Istituto Nazionale di Fisica Nucleare, Sezione di Pisa, Italy, and Istituto di Fisica dell'Università di Bologna and Istituto Nazionale di Fisica Nucleare, Sezione di Bologna, Italy

(Received 3 June 1974)

We have measured the fraction and lifetime of the $(\mu^4\mathrm{He})_{2S}{}^+$ systems formed by stopping negative muons in gaseous helium at 50 atm. An estimate of the external Auger effect, which contributes to depopulate the $(\mu\mathrm{He})_{2S}{}^+$ level, is given. First experimental evidence of the two-photon decay of such a level is presented.

When negative muons are stopped in a helium target, they first get captured forming a highly excited $(\mu\mathrm{He})^*$ atom, which then decays to a stable or metastable state. This occurs in a time of the order of 10^{-10} sec through an electromagnetic cascade which eventually results in leaving a $(\mu\mathrm{He})^+$ ion in the $1S$ ground state or in the $2S$ metastable state. For any experimental study which is based on the existence of the $(\mu\mathrm{He})_{2S}{}^+$ systems, therefore, the two following points are of major interest: (a) to establish which fraction ϵ_{2S} of the stopped muons lands on the $2S$ level; and (b) since the $2S$ level can depopulate through the different channels summarized in Table I,[1-4] to know how much the lifetime τ_{2S} of the $(\mu\mathrm{He})_{2S}{}^+$ systems—formed in a given physical condition—differs from the zero-density value

$$\tau_{2S}(0\text{ atm}) = [\lambda_{2S,\mathrm{tot}}(0\text{ atm})]^{-1} = 1.78\ \mu\text{sec}. \tag{1}$$

These questions were partially answered by the experimental investigation by Placci *et al.*,[2] who stopped negative muons in a target of pure helium at 7 atm, and observed the time distribution of the delayed x rays coming from the two-photon deexcitation of the $(\mu\mathrm{He})_{2S}{}^+$ level. These authors obtained

$$\epsilon_{2S}(7\text{ atm}) = (3.4 \pm 0.7)\times 10^{-2}, \tag{2}$$

$$\tau_{2S}(7\text{ atm}) = (1.8 \pm 0.4)\ \mu\text{sec}, \tag{3}$$

$$\lambda_{St}(7\text{ atm}) \leqslant 2\times 10^{-2}\lambda_{2\gamma}. \tag{4}$$

Later results by Carboni *et al.*[5] gave some evidence for a small Auger effect on the $(\mu\mathrm{He})_{2S}{}^+$ systems formed at helium pressures between 30 and 40 atm.

When higher-density conditions are taken into consideration, the two above points (a) and (b) need a more definitive investigation. Since we are presently interested in working with $(\mu\mathrm{He})_{2S}{}^+$ metastable ions at pressures around 50 atm,[6] we have performed a measurement of ϵ_{2S} and τ_{2S} for negative muons stopped in a target of pure helium at 50 atm and 293°K. The purpose of this Letter is to report on this measurement.

The experiment was carried out using part of an apparatus already described[6] (see Fig. 1), which has recently been used at CERN to determine the energy difference between the $2S_{1/2}$ and $2P_{3/2}$ levels of the $(\mu\mathrm{He})^+$ ion.[7] The method followed here essentially coincides with the one used by Placci *et al.*[2] The only relevant differ-

Copyright © 1974 by
The American Physical Society

TABLE I. Disappearance channels for the $(\mu^4\mathrm{He})_{2S}{}^+$ system and corresponding rates.

Process, rate symbol	Rate (sec^{-1})
Muon decay, λ_0	4.54×10^5
Muon capture, λ_c	45 ± 5[a]
Stark-mixing collision, $\lambda_{St}(P)$[b,c]	$<3\times10^2$[d]
External Auger effect, $\lambda_A(P)$[c]	$(2.7\pm1.6)\times10^3$[e]
Spontaneous M_1 transition, λ_{M_1}[b]	0.53[f]
Two-photon decay, $\lambda_{2\gamma}$[g]	1.06×10^5[h]
Total disappearance rate $\lambda_{2S,\mathrm{tot}}$:	
at zero density, $\lambda_{2S,\mathrm{tot}}(0\ \mathrm{atm})\simeq\lambda_0+\lambda_{2\gamma}$	5.6×10^5
at pressure P. $\lambda_{2S,\mathrm{tot}}(P)$	$\lambda_{2S,\mathrm{tot}}(0\ \mathrm{atm})$ $+\lambda_{St}(P)+\lambda_A(P)$

[a] Experimental value (see Ref. 1) corrected for the case that the nuclear capture proceeds from the 2S state of the μHe atom.

[b] These processes yield the emission of an 8.2-keV x ray.

[c] P is the pressure of the helium target; the rates given here are then to be considered in units of $\mathrm{sec}^{-1}/\mathrm{atm}$.

[d] See Ref. 2.

[e] Result obtained in the present work.

[f] See Ref. 3.

[g] This process occurs through the emission of two x rays; the sum of their energies is 8.2 keV.

[h] See Ref. 4.

ence lies in the fact that, in the present case, the delayed x rays were detected by eight NaI(Tl) counters (A_1–A_8 in Fig. 1), which subtended a solid angle larger than 80%, whereas in the former work[2] a proportional counter was used. To reduce the accidentals, the A_i counters were also requested to detect the muon decay electron in delayed coincidence.

The muons stopped within the useful volume in of gaseous helium (see Fig. 1) were defined by a coincidence-anticoincidence signal MUSTOP $=[1,3,4,-(2+5+\sum A_i)]$; here (–) means "not." An x-ray signal was defined by a coincidence between the MUSTOP signal and a pulse coming from any of the A_i detectors within a gate, 4 μsec long, opened by the MUSTOP pulse. A delayed muon-decay electron was recognized by a large-amplitude signal in one of the A_i counters and accepted after the x-ray signal during a gate 2 μsec long. The x-ray coincidence started the recording of the following main information for each event: (i) the digitized amplitudes of the signals from the A_i detectors (one or more within 200 nsec) which had been triggering; (ii) the delay of the x-ray signal with respect to the MUSTOP time; (iii) the delay of the muon decay electron—if this was present—with respect to the MUSTOP time.

An effective calibration of the energy response of the A_i counters was obtained on-line, by recording continuously the K-line x rays coming from the deexcitation of the $(\mu\mathrm{He})^+$ system, of which 62%[2] are due to the $K\alpha$ line (8.2 keV).

The measurements were carried out for a total amount of about 10^8 MUSTOP pulses in the target filled with pure helium. These runs were alternated with measurements performed keeping the target under vacuum, which supplied information on the time and energy spectrum of the accidentals. The rate λ_n of accidental counts was found to be $\lambda_n=5\times10^4\ \mathrm{sec}^{-1}$.

For the measurements under pressure conditions, the decay rate $\lambda_{\mathrm{expt,tot}}$ of the differential time distribution for the detected x rays can be

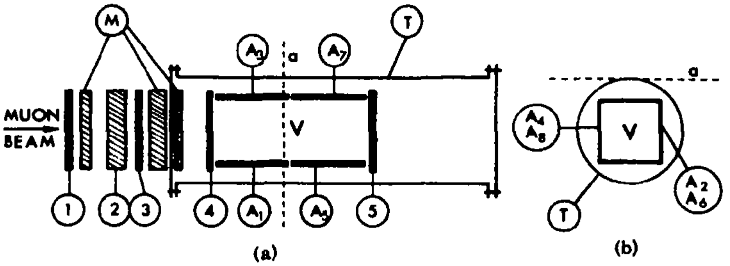

(a) (b)

FIG. 1. Simplified scheme of the apparatus. (a) Side view; T = stainless steel tank; V = useful volume of helium for stopping muons ($40\times40\times140\ \mathrm{mm}^3$); M = CH_2 moderators; 1, 3, 4, 5 = plastic scintillators; 2 = Plexiglas Cherenkov counter, used to anticoincide the electron contamination in the muon beam; A_1–A_8 = NaI(Tl) detectors. (b) Front view of the target.

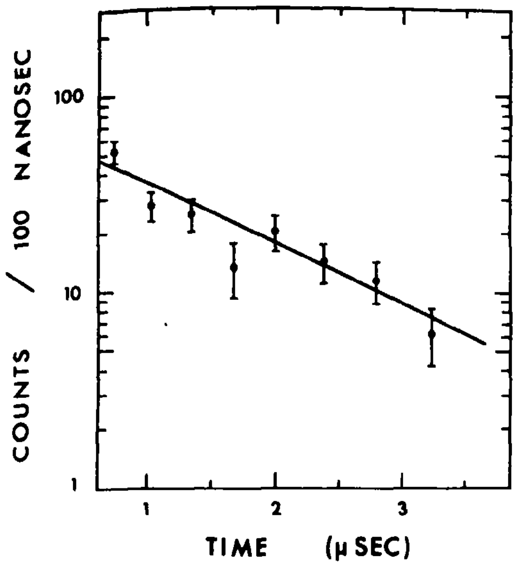

FIG. 2. Experimental time distribution ($dn_{X,e}/dt$) of the delayed x rays observed in the present measurement after negative muons had been stopped in pure helium at 50 atm. The events are those for which the muon-decay electron had also been detected. The full line is a best fit ($\chi^2=9$) corresponding to a lifetime $\tau_{\mathrm{expt,tot}}=(1.34\pm0.13)$ μsec $=1/\lambda_{\mathrm{expt,tot}}$.

written as (see Table I)

$$\lambda_{\mathrm{expt,tot}}=\lambda_{2S,\mathrm{tot}}+\lambda_{\mu}. \tag{5}$$

The experimental time distribution $dn_{X,e}/dt$ of the delayed x rays for which also the muon decay electrons had been observed is given in Fig. 2, after subtracting out the accidentals and with a low-energy cut at 3.2 keV. From these data,

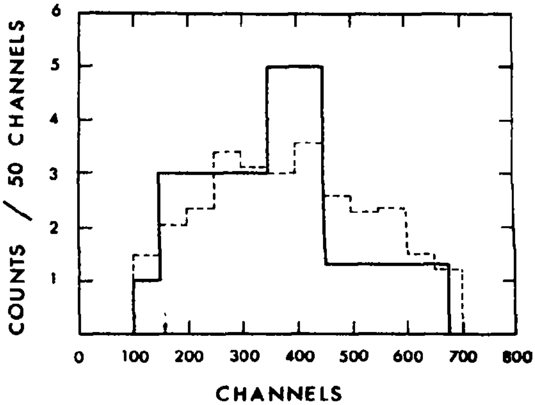

FIG. 3. The full line represents the energy spectrum of the summed amplitudes for each of the 29 "two-photon" events observed in the present measurement. (Abscissa: 1 keV ≈ 50 channels.) The muon-decay electron had also been observed for the presented events. The arrow on the abscissa indicates the 3.2-keV low-energy cut which was operated for the analysis of the single-photon events. The dashed line represents the experimental energy spectrum—normalized to an equal area—of the prompt K-line x rays coming from the deexcitation of the $(\mu\mathrm{He})^+$ system.

keeping in account Eq. (5), one gets

$$\lambda_{2S,\mathrm{tot}}(50\text{ atm})=(7\pm0.75)\times10^{5}\text{ sec}^{-1}, \tag{6}$$

i.e.,

$$\tau_{2S}(50\text{ atm})=(1.43\pm0.15)\ \mu\text{sec}. \tag{7}$$

Remembering the definition of $\lambda_{2S,\mathrm{tot}}(P)$ given in Table I, one may derive from Eq. (6)

$$(\lambda_{\mathrm{St}}+\lambda_{A})_{50\text{ atm}}=(1.4\pm0.75)\times10^{5}\text{ sec}^{-1}. \tag{8}$$

If we now assume (see Table I) $\lambda_{\mathrm{St}}(50\text{ atm})\leq1.5\times10^{4}\text{ sec}^{-1}$, one may extract from Eq. (8)

$$(1.25\pm0.75)\times10^{5}\text{ sec}^{-1}\leq\lambda_{A}(50\text{ atm})\leq(1.4\pm0.75)\times10^{5}\text{ sec}^{-1}. \tag{9}$$

If N is the total number of events of Fig. 2, ϵ_{2S} can be estimated from the expression

$$N=\epsilon_{2S}F\lambda_{2\gamma}\Omega_{2\gamma}[1+(\Omega_{8\,\mathrm{keV}}/\Omega_{2\gamma})(\lambda_{\mathrm{St}}/\lambda_{2\gamma})], \tag{10}$$

where $F=0.3$ is a constant defined by the time acceptance of the apparatus for the x rays and the muon decay electrons, $\Omega_{2\gamma}$ ($\simeq0.37$) is the efficiency for detecting one of the x rays from the two-photon decay, and $\Omega_{8\,\mathrm{keV}}$ ($\simeq0.61$) is the efficiency for the 8-keV x rays emitted following a Stark-mixing collision of the $(\mu\mathrm{He})_{2S}^{+}$ ion. $\Omega_{2\gamma}$ and $\Omega_{8\,\mathrm{keV}}$ were evaluated by a Monte Carlo calculation. From these numbers, and setting in Eq. (10) the two limits $\lambda_{\mathrm{St}}(50\text{ atm})=0$ or 1.5×10^{4} sec^{-1}, one gets for ϵ_{2S} the two extreme values

$$\epsilon_{2S}(50\text{ atm})_{\text{no Stark effect}}=(4.3\pm0.6)\times10^{-2}, \tag{11}$$

$$\epsilon_{2S}(50\text{ atm})_{\text{max Stark effect}}=(3.5\pm0.5)\times10^{-2}. \tag{12}$$

The quoted errors include the uncertainties on N, F, and the calculated parameters of Eq. (10).

During the measurements, 29 events were observed in which both the x rays coming from the two-photon decay of the $(\mu\mathrm{He})_{2S}^{+}$ level had been detected by two separate A_i counters, and the delayed muon-decay electron had been observed. The number of these events is the number expected from the value of N and from the results of the Monte Carlo calculation. The energy spectrum of the summed amplitudes of the two-photons for each of these "double" events is given in Fig. 3. To our knowledge, this is the first direct experimental evidence of the two-photon decay of the $(\mu\mathrm{He})_{2S}^{+}$ system.

The following conclusions can now be drawn:

(i) The fraction ϵ_{2S} of $(\mu\mathrm{He})_{2S}^{+}$ systems formed by stopping negative muons in a target of pure helium does not vary in a sensitive way with the helium pressure going from 7 to 50 atm [see Eqs. (2), (11), and (12)].

(ii) The observed value of $\tau_{2S}(50\text{ atm})$ [see Eq. (7)] is large enough to make the $(\mu\mathrm{He})_{2S}^{+}$ systems available for observation for a time interval of the order of 1 μsec at least.

(iii) Pressure-dependent effects contribu depopulate the $(\mu\mathrm{He})_{2S}^{+}$ state to an extent o [see Eqs. (6) and (8)]. The allowed range o ation for $\lambda_4(50\text{ atm})$ is given by Eq. (9), wh in agreement with the findings by Carboni e

The authors wish to acknowledge the colla tion of Dr. J. Duclos, Dr. U. Gastaldi, Dr. , Picard, and Dr. A. Placci.

---

[1] R. Bizzarri *et al.*, Nuovo Cimento 33, 1497 (19 M. M. Block *et al.*, Nuovo Cimento 55, 501 (1968)

[2] A. Placci *et al.*, Nuovo Cimento 1A, 445 (1971).

[3] R. W. Schmieder and R. Marrus, Phys. Rev. Le 25, 1692 (1970).

[4] J. Shapiro and G. Breit, Phys. Rev. 113, 179 (1

[5] G. Carboni *et al* ., Lett. Nuovo Cimento 6, 233(

[6] A Bertin *et al.*, to be published.

[7] The data are at present under analysis.

New Rotational Transition in the Hydrogen Molecule*

P. W. Gibbs, C. G. Gray, and J. L. Hunt
Department of Physics, University of Guelph, Guelph, Ontario, Canada

and

S. Paddi Reddy, R. H. Tipping, and K. S. Chang
Department of Physics, Memorial University of Newfoundland, St. John's, Newfoundland, Canada

(Received 22 April 1974)

Pressure-induced rotational-vibrational U transitions ($\Delta J=4$) of hydrogen gas have been observed for the first time at 195 K for densities in the range 180–300 amagat. The spectrum is interpreted in terms of a hexadecapolar induction mechanism, and from the experimental integrated absorption coefficient of the $U(1)$ line, rough values are obtained for the hydrogen-molecule hexadecapolar moment and its derivative.

We report here the first spectroscopic observations of molecular $U(J)$ rotational transitions in H_2 corresponding to the selection rule $\Delta J=4$. The $U(1)$ line ($J=1-5$) has been observed in the fundamental rotational-vibrational (near-infrared) band and the integrated absorption coefficient has been obtained. An analysis is given below in terms of hexadecapolar induction.

In Fig. 1 is shown the near-infrared spectrum in the region 5550–5900 cm^{-1} taken at a temperature of 195 K and a density of 300 amagat, together with the computed S-branch ($\Delta J=2$) and Q-branch ($\Delta J=0$) contributions following MacTaggart and Welsh.[1] The peak of the observed feature is shifted by about 50 cm^{-1} towards higher frequencies from the calculated position of the $U(1)$ line for the free molecule. From spectra such as that of Fig. 1 recorded over the density range 180–300 amagat, we have obtained the integrated absorption coefficient $\tilde{\alpha}=\int\tilde{A}(\nu)d\nu$ (as defined by Van Kranendonk[2]) as a function of the density ρ. In Fig. 2 where we have plotted the experimental $\tilde{\alpha}/\rho$ against ρ, it is apparent that a good fit is obtained for a straight line passing through the origin confirming that the line arises from a binary-collision mechanism.

The theory of the integrated absorption coefficient $\tilde{\alpha}$ has been developed in general by Van Kranendonk[2] and in detail for higher-multipolar induction by Gray.[3] For the hexadecapolar-induced $U(J)$ lines we find that the binary absorption coefficient $\tilde{\alpha}_1$, defined by the density expansion $\tilde{\alpha} = \tilde{\alpha}_1\rho^2 + \tilde{\alpha}_2\rho^3 + \ldots$, is given by

$$\tilde{\alpha}_1(U(J)) = 10\kappa\sigma^{-9}I_{12}(T)\rho_J(T)C(J\ 4\ J+4;\ 0\ 0\ 0)^2[(\Phi'l\alpha)^2 + (\Phi l\alpha')^2], \tag{1}$$

where $\kappa = (4\pi^3/3h)$, $l = \langle 1|R - R_e|0\rangle = (h/8\pi^2 m\nu_0)^{1/2}$ is the $v = 0 \to 1$ vibrational matrix element with ν_0 the vibrational frequency, $C(J\ 4\ J+4;\ 0\ 0\ 0)$ a Clebsch-Gordan coefficient, σ the Lennard-Jones diameter, α the mean molecular polarizability, and α' its derivative with respect to internuclear separation R. The quantity

$$\rho_J(T) = Z^{-1}g_J(2J+1)\exp(-\epsilon_J/kT) \tag{2}$$

is the normalized Boltzmann factor for the level J, and Φ' is the derivative of the molecular hexadecapole moment Φ, defined by

$$\Phi = \int \rho(\vec{r})r^4P_4(\cos\theta)d^3r, \tag{3}$$

where $\rho(\vec{r})$ is the total charge density of the molecule. The quantity $I_{12}(T)$ is a dimensionless integral[4]

$$I_{12}(T) = 4\pi\int g_0(x)x^{-12}x^2\,dx, \tag{4}$$

where $x = R/\sigma$, and $g_0(x)$ is the low-density limit of the pair correlation function. The term involving $(\Phi'l\alpha)$ in (1) corresponds to single transitions in which one molecule of the colliding pair makes both the vibrational and rotational jump, while the term involving $(\Phi l\alpha')$ corresponds to double transitions in which one molecule makes a vibrational and the other a rotational jump. The triangles in Fig. 1 indicate the expected positions of these transitions.

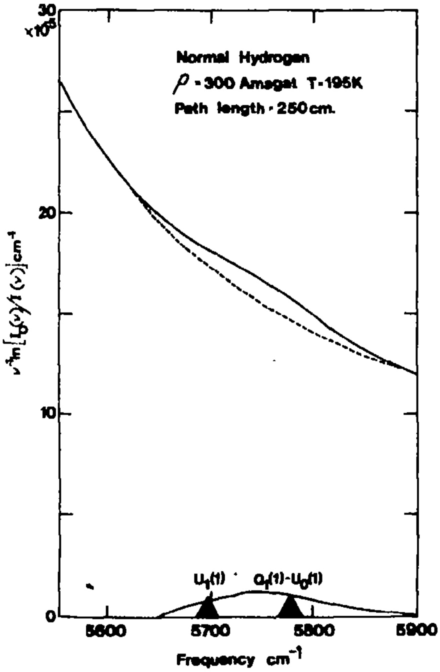

FIG. 1. High-frequency wing of the spectrum of pure normal hydrogen. The dashed curve shows the sum of all $\Delta J = 0, 1$ transitions. The difference of the two curves is shown at the bottom. The triangles indicate the frequencies of the $U_1(1)$ and $Q_1(1) + U_0(1)$ transitions calculated from the molecular constants of the free molecule.

From Fig. 2 we obtain the experimental value $\tilde{\alpha}_1(U(1)) = (0.78 \times 10^{-10} \pm 20\%)$ cm^{-1} amagat^{-2}. Since Eq. (1) depends on both Φ and Φ', one of these must be known before the other can be obtained from the single experiment.

Previously, Gush and Van Kranendonk[5] invoked the intermolecular quadrupole-hexadecapolar interaction in solid hydrogen with a value $\Phi = 1.2ea_0^4$, to explain the observed fine structure of the $S_1(0)$ line. A rough theoretical estimate, based on a point-charge model constructed to give the known quadrupole moment $Q = 0.46ea_0^2$, leads to $\Phi = 0.34ea_0^4$. A recent theoretical calculation[6] using the Heitler-London-Wang wave function to obtain $\rho(\vec{r})$ in (3), gives $\Phi = 0.1ea_0^4$ and $\Phi' = 0.2ea_0^3$. Assuming the hexadecapolar-induction mechanism dominates and using Eq. (1), we obtain from the experimental spectrum upper limits for Φ and Φ' of $|\Phi| = 0.59ea_0^4$ and $|\Phi'| = 0.47ea_0^3$. From the

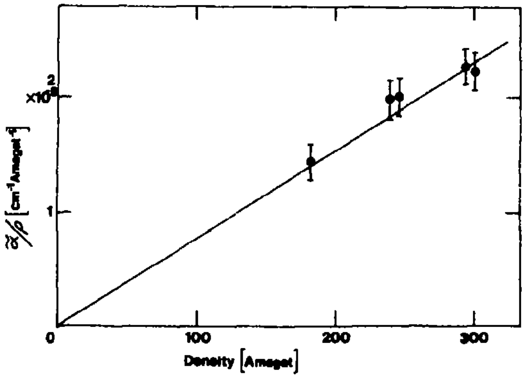

FIG. 2. Variation of transitions probability per unit density with density for pure normal hydrogen at 195 K.

fact that the peak of the experimental spectrum (Fig. 1) falls midway between the single- and double-transition frequencies, and from previous results on the quadrupole-induced lines,[7] we expect the single and double transitions to contribute roughly equal amounts to the spectrum of Fig. 1. Assuming exactly equal contributions would give $|\Phi| = 0.42ea_0^4$ and $|\Phi'| = 0.33ea_0^3$.

Finally, we mention other possible induction mechanisms, in addition to the hexadecapolar mechanism. The quadrupole-induced double transitions $S_0(1)+S_1(3)$, $S_1(1)+S_0(3)$, and $S_0(2)+S_1(2)$, which fall within the linewidth of Fig. 1, can be ruled out. To do this the group of double-S transitions near 5300 cm^{-1} (outside Fig. 1) were observed[8] and their intensity compared with the expected intensity of the double-S transitions in question; the latter is expected to be about 5% of the intensity of the lines near 5300 cm^{-1}. Since the observed peak of Fig. 1 is about 50% of the intensity of the 5300 cm^{-1} lines, we see that the double-S transition mechanism fails, by an order of magnitude, to explain the observed peak. Rough estimates of the dispersion and overlap mechanisms indicate that they too are small. The "level-mixing" mechanism of Herman[9] is estimated to be of importance here only if Φ is of order $0.1ea_0^4$ or less.

Work is now in progress to obtain accurate absorption coefficient for the pure rotational lines of H_2, and the lines of H_2-rare-gas mixtures. An analysis of all these experiments together should yield more accurate values for both $|\Phi|$ and $|\Phi'|$.

The authors are grateful to Professor G. Karl, Professor E. Obryk, Professor J. Poll, and professor R. Herman for discussions.

---

*Work supported by the National Research Council of Canada.

[1] J. W. MacTaggart and H. L. Welsh, Can. J. Phys. 51, 158 (1973).

[2] J. Van Kranendonk, Physica (Utrecht) 23, 825 (1957).

[3] C. G. Gray, J. Phys. B: Proc. Phys. Soc., London 4, 1661 (1971).

[4] A. D. Buckingham and J. A. Pople, Trans. Faraday Soc. 51, 1173 (1955).

[5] H. P. Gush and J. Van Kranendonk, Can. J. Phys. 40, 1461 (1962).

[6] G. Karl, E. Obryk, and J. D. Poll, Can. J. Phys. 51, 2216 (1974).

[7] A. Watanabe and H. L. Welsh, Can. J. Phys. 45, 2859 (1967).

[8] P. W. Gibbs, M. Sc. thesis, University of Guelph, 1973 (unpublished).

[9] R. M. Herman, J. Chem. Phys. 52, 2040 (1970).

Multiphoton Ionization of Highly Excited Hydrogen Atoms*

J. E. Bayfield and P. M. Koch
J. W. Gibbs Laboratory, Yale University, New Haven, Connecticut 06520

(Received 29 April 1974)

A new method for the experimental study of multiphoton processes uses production of highly excited atoms in keV electron-transfer collisions. Such atoms can be ionized over a wide range of frequencies of an external electromagnetic field, permitting studies of multiphoton-ionization processes for regimes not yet achieved in laser experiments. Results for microwave ionization of hydrogen atoms with principal quantum numbers in the band $63 \leq n \leq 69$ are discussed in terms of the available theory.

The multiphoton ionization of atoms by intense oscillating electromagnetic fields is not well understood at present. Theoretical interpretation of laser-ionization experiments has treated the electric field $F\cos(\omega t)$ as a perturbing influence on the electronic motion within the atom, under conditions where the field oscillates rapidly with a period T short compared to the time of flight τ of the electron to a distance r_0 where the external field F would dominate over the attractive force F_0 of the atomic nucleus. However, when pulsed lasers of greater power become available for experiments on ground-state atoms, new regimes will be reached where either or both of the conditions $F \ll F_0$ and $T \ll \tau$ becomes inapplicable. It is the purpose of this paper to demonstrate that experiments within these new regimes can be done now by lowering the frequency into the microwave region to give larger T while reducing the field strengths required by using highly excited atomic electronic states with smaller F_0. For a simple one-electron system, the hydrogen atom, we present ionization data for $T \ll \tau$, $T \sim \tau$, and $T \gg \tau$. Our experiments constitute the first observations of the microwave ionization of highly excited atoms.

For a fixed frequency ω several possible breakdowns of perturbation theory (PT) can occur as F is increased. One theoretically considered situation occurs when the decrease of r_0 with increasing F makes $T \gtrsim \tau$, while $F \ll F_0$ still holds.[1] The ionization is then viewed analogously to the static-field case as a quantum mechanical tunneling of the electron through a time-varying barrier produced by the superposition of the external and Coulomb forces on the electron. Since the ionization rate should be a maximum when the field is near its peak value F, T can be taken as the ratio r_1/v of the minimum barrier width for an electronic state of binding energy $I = \frac{1}{2}\kappa^2$ to the electronic velocity v. Using atomic units[2] and considering only a hydrogen atom, for which the electron momentum $\kappa = n^{-1}$, we have for $F \ll \frac{1}{16}n^{-4}$ (the approximate classical ionization-threshold field), approximately, $v = \kappa$, $r_1 = \kappa^2 2F$, and hence $\tau = \kappa/2F$. In the PT limit the transition rate is given by a sum of energetically allowed terms involving increasing numbers of photons in a power series in a quantity proportional to field intensity. The breakdown of PT occurs when one such quantity useful for excited states, $1/4\gamma^2$, increases to order unity, where $\gamma = 2\omega\tau = \omega/nF$ is called the adiabatic tunneling parameter[1,3] (see Ref. 3, Eq. 22). An untested theory for the adiabatic region $\gamma \ll 1$ has been developed, and the connections to the PT limit $\gamma \gg 1$ and the static limit γ 0 indicated.[3,4] The region $\gamma \approx 1$ remains intracable in practice. This is also true for the situaion $F \approx F_0$ where the energy levels of the atom ndergo huge Stark shifts and Stark broadening, nd the atom loses its low-field identity through trong mixing of the various bound and continuum tates.

Past experimental studies of the multiphoton onization of atoms and molecules have all conentrated on laser interactions. For the peak laer powers used the γ's have been in the range 2 p to 10^3.[5] As the laser studies are extended both higher powers and to shorter pulse lengths, wer values of γ will become involved.

In the present paper we present results on the ultiphoton ionization of a fast beam of highly exited hydrogen atoms with principal quantum umber n near 66, using radio-frequency and microwave electric fields. To our knowledge this is the largest value of n studied in a laboratory experiment.

The highly excited hydrogen atoms H(high n) were usually produced by H^+-Xe electron-transfer collisions at an incident H^+ energy near 11 keV. Other inert gases have also been used, with the observed H(high n) ionization signals scaling with gas type according to the known cross sections for the production of states within the range $7 \le n \le 28$.[6,7] Our measurements are consistent with the Jackson-Schiff n^{-3} scaling rule for the n dependence of the H(high n) production cross section all the way up to $n = 80$.

Our identification of beam atoms in a narrow band of n values is based on the observation by Il'in[8] that the experimentally measured values of the static electric field strength F needed to produce a given ionization probability for each value of n satisfy the expression $F = \text{const} \times n^{-s}$, where the constant depends somewhat upon the geometrical factors for a given experiment and $s \sim 4$. This rule has been verified within the range $9 \le n \le 28$ in four different experiments, giving the expressions $F = 8.67 \times 10^8 n^{-4.07}$ V/cm,[8] $F = 1.66 \times 10^9 n^{-4.33}$ V/cm,[9] $F = 4.31 \times 10^8 n^{-3.85}$ V/cm,[10] and $F = 5.96 \times 10^8 n^{-4.00}$ V/cm.[11] This behavior is also supported by numerical calculations for $7 \le n \le 25$,[6,12] and is the classical answer to the question, "What state is at the top of the barrier for a given field?"[13] On the basis of extrapolating all the above-mentioned field-ionization data to $n \sim 65$, we feel that our values of n are known to within ± 5 units. In the present experiments a band of n's about five units wide was defined by switching a prequenching static electric field between two different field strengths and observing the resultant difference in field-ionization signals.[9]

The dependence on γ of the H(high n) multiphoton-ionization probability was measured with the apparatus shown schematically in Fig. 1. The fast beam leaving the Xe gas target cell (A) was charge analyzed by a very weak transverse electric field (B) and the pure neutral-atom component then passed through a transverse, static, n-band–defining electric field (C) followed by one of several highly-excited-atom field-ionization regions (D, E, F, G). The protons so produced were detected by the use of a carefully biased and secondary-electron–suppressed Faraday cup (H) on the beam axis. The n-band–defining field was gated at 44 Hz between field values of 28.5 and 41.0 V/cm corresponding to nominal values

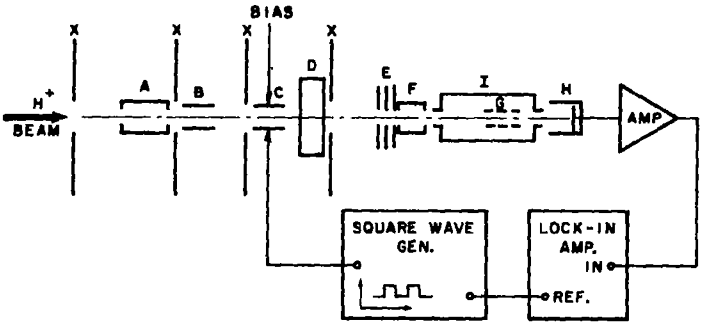

FIG. 1. Apparatus for the multiphoton-ionization experiments. A, electron-transfer gas cell; B, ion-removal plates; C, n-band–defining static field; D, broad-band rf structure; E, G, Einzel-lens axial static field structures; F, X-band microwave cavity; H, Faraday cup; I, liquid-helium cryopump; X, differential pumping apertures.

of n of 69 and 63, respectively. The resultant ac Faraday-cup current was amplified by a field-effect-transistor preamplifier and detected with a phase-sensitive lock-in amplifier.

We have used three different multiphoton electric field structures. The first (D) was a broadband parallel-plate rf structure which permitted the study of both transverse static fields and transverse rf fields with frequencies in the region 0.9–1.8 GHz. The second structure (F) was an X-band axial microwave field from one of several available TM_{01n} modes of a high-Q cylindrical cavity with its axis along the beam direction. The third structure was an electrostatic Einzel lens (G) which, because of the beam velocities used, applied a one-cycle wave to the highly excited atoms with a principal Fourier frequency component of about 30 MHz. For these experiments, theory predicts the behavior at this last frequency and our field strengths (i.e., small γ) to be similar to that for a completely static field.[1]

The results for several of the direct-ionization experiments are shown in Fig. 2, where the field-ionization signal S for the n band $63 \leq n \leq 69$ is plotted versus γ for the various multiphoton-transition structures, using the central value of n of 66 and peak values F of the applied electric field strength. The data when plotted as a function of peak electric field qualitatively confirm one prediction of the adiabatic theory,[3] namely, that for γ's near the adiabatic limit ($\gamma \ll 1$) and for the same peak field strength F, higher-frequency waves are more effective for ionization than lower-frequency waves. We emphasize, however,

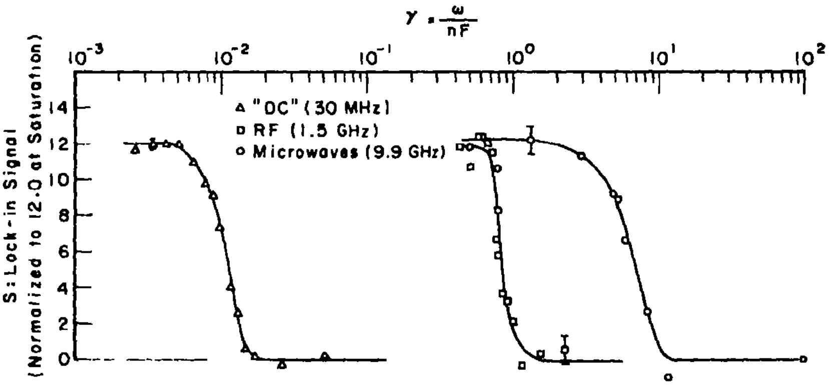

FIG. 2. The ionization of hydrogen atoms with principal quantum numbers in the band $63 \leq n \leq 69$, as a function of the tunneling parameter γ. Shown are curves for (1) an essentially static axial applied electric field, (2) a transverse 1.50-GHz rf field, and (3) an axial 9.9-GHz microwave field. Smooth curves have been drawn through the data points to aid the eye. Each curve exhibits experimental saturation at lower values of γ (higher values of field strength F).

that most of the 1.5-GHz data points of Fig. 2 are in the region $\gamma \approx 1$ where no theoretical predictions are available.

In the absence of saturated resonant intermediate states[1,14] or an ionization potential lowered by the intense field,[3,15] the number k (multiplicity) of photons required for ionization would be equal to $[I/\hbar\omega + 1]$, where $[x]$ refers to the integer value of x. For the 1.5-GHz ($\gamma \sim 1$) data and the 9.9-GHz ($2 \lesssim \gamma \lesssim 9$) data k is 502 and 76, respectively. The actual or effective multiplicity is defined by the slope of a log-log plot of S versus F^2. These values are about 2.0 and 1.5, respectively. We are not aware of any multiplicity-reduction theory directly applicable to our data, but in some limits the theory of Ref. 3 predicts that k is decreased by a number of order n, a large effect for $n = 66$ and $k = 76$.

As these experiments studied extremely delicate atoms, many different auxiliary tests of the apparatus were made. Among the principal results was a determination that the dominant effect (> 90%) of the applied field was indeed ionization rather than bound-bound transitions either to states of lower principal quantum number n or to states of somewhat higher n. In addition, another type of experiment was performed to check directly that the ions produced were caused by the applied electric fields and not by spurious effects such as collisions with the background gas. In the experiment the ionization of an atom in a static axial electric field region "labeled" with a positive electric potential resulted in an acceleration of the ion as it left the region. The corresponding increase in velocity labeled the kinetic energy of only those protons produced in this spatial region, which were then isolated for detection using kinetic-energy analysis. We varied the pressure of the background gas in such a region located inside a liquid-helium cryopump from our normal 10^{-8}-Torr operating range to a measured pressure of less than 10^{-11} Torr with no observable (< 4%) change in results.

Let us, in conclusion,. indicate some further possibilities for the study of multiphoton processes using highly excited atomic beams. An important improvement for some atomic species will be a narrowed high-n band produced by laser pumping specific, more-populated, lower-energy states present in the beam. In addition, microwave powers orders of magnitude larger than presently used would permit studies at lower values of n and γ. It also appears possible to use lasers to extend our field-ionization measurements to optical frequencies. Different systems (alkali atoms, for example) could be used with the goal being the study of possible inner-shell core effects on the multiphoton processes. Finally, one should be able to do experiments oriented towards searching for the transparency of atoms to superstrength ($F \gg F_0$) electromagnetic fields.[16,17]

---

*Research supported in part by the U. S. Air Force Office of Scientific Research (AFSC) under contract No. AFOSR F44620-71-C-0042.

[1] L. V. Keldysh, Zh. Eksp. Teor. Fiz. 47, 1945 (1964) [Sov. Phys. JETP 20, 1307 (1965)].

[2] H. Bethe and E. E. Salpeter, *Quantum Mechanics of One- and Two-Electron Atoms* (Academic, New York, 1957). Here $m_e = \hbar = e = 1$.

[3] A. M. Perelomov, V. S. Popov, and V. P. Kuznetsov, Zh. Eksp. Teor. Fiz. 54, 841 (1968) [Sov. Phys. JETP 27, 451 (1968)], and earlier papers quoted therein.

[4] A. I. Nikishov and V. I. Ritus, Zh. Eksp. Teor. Fiz. 52, 223 (1967) [Sov. Phys. JETP 25, 145 (1967)], and earlier papers quoted therein.

[5] C. Lecompte, C. Mainfray, C. Manus, and F. Sanchez, Phys. Rev. Lett. 32, 265 (1974), and papers quoted therein.

[6] J. E. Bayfield, G. A. Khayrallah, and P. M. Koch, Phys. Rev. A 9, 209 (1974).

[7] A. C. Riviere, United Kingdom Atomic Energy Establishment Report No. AERE-R4818, 1964 (unpublished), p. 124.

[8] R. N. Il'in, in *Atomic Physics 3*, edited by S. J. Smith and G. K. Walters (Plenum, New York, 1973), pp. 309–326.

[9] A. C. Riviere and D. R. Sweetman, in *Atomic Collision Processes*, edited by M. R. C. McDowell (North-Holland, Amsterdam, 1964), pp. 734–742.

[10] A. C. Riviere and D. R. Sweetman, in *Proceedings of the Sixth International Conference on Ionization Phenomena in Gases, Paris, 1963*, edited by P. Hubert (S.E.R.M.A., Paris, 1964), Vol. 1, p. 105.

[11] R. N. Il'in, B. I. Kikiani, V. A. Oparin, E. S. Solov'ev, and N. V. Federenko, Zh. Eksp. Teor. Fiz. 47, 1234 (1964) [Sov. Phys. JETP 20, 835 (1965)].

[12] D. S. Bailey, J. R. Hiskes, and A. C. Riviere, Nucl. Fusion 5, 41 (1965).

[13] L. B. Mendelsohn, Phys. Rev. 176, 90 (1968). The author speaks only of the ground state, but a simple insertion of the expression for the Bohr energies, $E_n = -\frac{1}{2}n^{-2}$, generalizes the problem for arbitrary n. Although these are the field-free energies, his physical picture is clear.

[14] B. Held, G. Mainfray, C. Manus, J. Morellec, and F. Sanchez, Phys. Rev. Lett. 30, 423 (1973).

[15] C. K. Choi, W. C. Henneberger, and F. C. Sanders, Phys. Rev. A 9, 1895 (1974).

[16] S. Geltman and M. R. Teague, J. Phys. B: Proc. Phys. Soc., London 7, L22 (1974).

[17] M. H. Mittleman, Phys. Lett. 47A, 55 (1974).

Inelastic Resonance Emission of X Rays: Anomalous Scattering Associated with Anomalous Dispersion*

Cullie J. Sparks, Jr.
Metals and Ceramics Division, Oak Ridge National Laboratory, Oak Ridge, Tennessee 37830

(Received 13 May 1974)

An inelastic resonance scattering of monochromatic Cu *K*α x rays incident on various targets is observed when an absorption edge of the target is just above the energy of the incident x rays. This frequency-dependent and angular-independent inelastic scattering is interpreted with the x-ray scattering theory of anomalous dispersion. Conservation-of-intensity arguments allow a comparison of the observed inelastic intensity with the real part of the anomalous dispersion corrections to the coherent atomic scattering factors for x rays.

I have observed a kind of inelastic x-ray scattering process that differs from the previously reported Compton and more recently described Compton-Raman[1,2] inelastic scattering. The inelastically scattered radiation was found when a Si(Li) detector was used for energy analysis of the x rays scattered from targets on which monochromatic Cu *K*α or Mo *K*α x rays impinged. As the incident radiation approaches an absorption edge of the target element, the inelastic scattering increases rapidly in intensity. The cross section for the observed scattering is shown to be predicted by the $\vec{P}\cdot\vec{A}$ term in second-order perturbation theory, a term previously neglected in inelastic x-ray scattering calculations.

An experiment similar to our diffuse-x-ray experiments[3] was constructed to measure the radiation given off by elements irradiated by a source of Cu *K*α or Mo *K*α x rays monochromatized by diffraction from the basal planes of highly oriented graphite.[4] This arrangement is shown in Fig. 1(a). The angle of the incident (exciting) radiation was equal to the angle of the detected radiation with respect to the specimen surface, so that the absorption path length is independent of scattering angle φ for thick samples. An ORTEC Si(Li) detector, with 190-eV resolution at 5.9 keV, associated electronics, and a multichannel analyzer were used to record the energy spec-

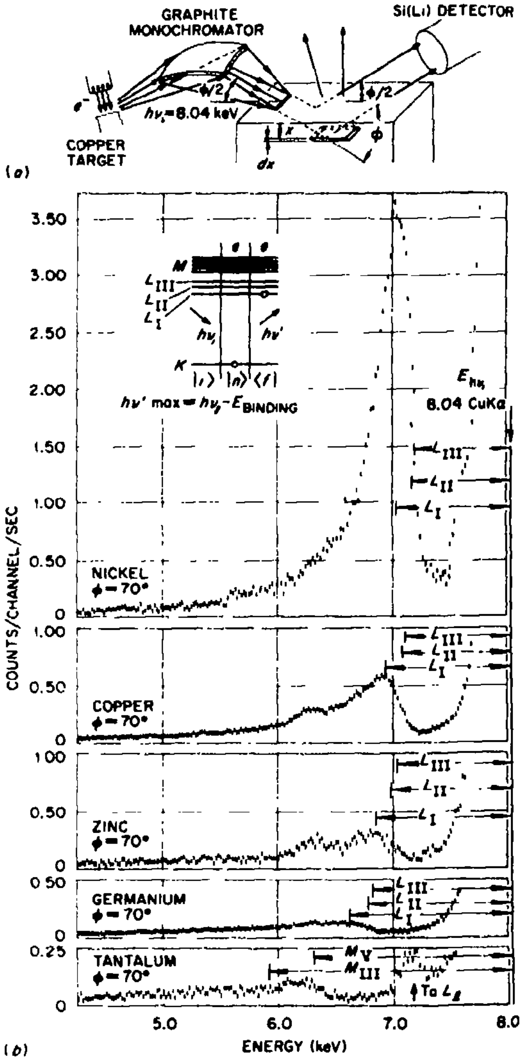

FIG. 1. (a) The experimental arrangement for the monochromatization of the incident x rays and detection of the scattered radiation. (b) Energy distribution of anomalous scattered x rays from elements irradiated with Cu *K*α x rays. Upper left inset shows the proposed quantum mechanism for the anomalous scattering; the electron hole may be in any of the three *L*-shell sublevels. The transitions may occur between any inner and outer shell.

trum of the radiation from various elements and their combinations. Figure 1(b) gives the results for a few elements. The main intensity maximum at 8.04 keV is due to the incident Cu $K\alpha$ x rays scattered from the specimen by Bragg scattering, thermal motion, and Compton scattering. The Compton shift is not large enough to be resolved by this detector. Lower-energy photons peaked in intensity at an energy E_s equal to that of the incident photon minus the binding energy of the most tightly bound electron shell from which electrons could be ejected by the 8.04-keV x rays. Although the spectra plotted were measured at $\varphi = 70°$, the intensity is isotropic, being independent of angle for the angles $10 < \varphi < 140°$ permitted by the experimental arrangement. Measurements were also made with monochromatic Mo $K\alpha$ x rays incident on various elements with similar results. A small part of the incident beam (subharmonics passed by the monochromator) accounts for the Ta L_1 fluorescent radiation in Fig. 1(b). Diagrammed at the upper left of Fig. 1(b) are the transitions from the initial ground state of the atom, $|i\rangle$, to the intermediate virtual state $|n\rangle$, and then to the final state $\langle f|$ where the atom is left with a hole in the L shell, and an x ray of energy $h\nu'$ has been emitted.

To facilitate the comparison of this observed inelastic radiation with theoretical predictions, I converted the measured intensity into absolute units following the procedure given in Ref. 3. A standard unit is the scattering by a free classical electron, as calculated by Thomson.[3] I have assumed that the inelastic scattering is unpolarized since the intensity is angular independent in its spatial distribution.

Data such as in Fig. 1(b) were corrected for background, for the small Si escape peak generated in the Si(Li) solid-state detector, and for absorption in the sample. The corrected intensity was then integrated from 4.8 keV (background on the low-energy side) to the minimum just at the high-energy side of the inelastic spectrum. These results in electron units per atom are given in Table I with the theoretical values of the Compton-scattered intensity for comparison.

X-ray satellites on the high-energy side of primary (characteristic) x-ray spectral lines have been observed since the early days of x rays and are accounted for by multiple ionization of inner shells. More recently, satellites on the low-energy side of characteristic lines have been reported and attributed to a semi-Auger effect.[6] Lower-energy lines such as the early observations by Das Gupta[1] and more recently by Suzuki *et al.*[2] have been attributed to a Compton-Raman type of scatter in which a bound electron recoils with just enough energy to be ejected, leaving the photon reduced in energy by the binding energy of this ejected K electron. The latter observation on low-Z materials reports the intensity to be angular dependent.

Perturbation theory[7] is normally used to describe electron-photon interactions in problems

TABLE I. Cross sections in electron units per atom for the observed anomalous spectrum excited with Cu $K\alpha$ radiation. Compton scattering cross sections and theoretical predictions are given for comparison.

Element	φ (deg)	Compton[a] (e.u./atom)	Anomalous scattering Obs. (e.u./atom)	Anomalous scattering Calc. (e.u./atom)
Ni	30	4.88	7.0 ± 0.2	6.74
	90	12.14		
Cu	30	4.47	2.5 ± 0.4	3.4
	90	12.06		
Zn	30	4.61	1.3 ± 0.5	2.3
	90	12.21		
Ge	30	5.23	1.1 ± 0.4	1.6
	90	12.64		
Ta	30	8.18	7.0 ± 1.5	5.3
	90	21.43		

[a] D. T. Cromer, J. Chem. Phys. 50, 4857 (1969); D. T. Cromer and J. B. Mann, *ibid.* 47, 1892 (1967).

of this kind. The perturbation is the interaction Hamiltonian

$$\Delta V = e^2A^2/2mc^2 - e\vec{P}\cdot\vec{A}/mc, \tag{1}$$

where $\vec{P}$ is the electron momentum, and $\vec{A}$ is the vector potential for the electromagnetic field. The Compton-Raman[1,2] observation was reportedly explained[6] by the two-photon process which arises from applying first-order perturbation theory to the A^2 term in ΔV and which predicts a frequency-independent cross section for the nominal 10-keV x rays used.

To explain my observations, I chose to look at the $\vec{P}\cdot\vec{A}$ term in second-order perturbation theory[7] for the following reasons: This term gives the observed angular independence for the intensity, and the energy denominators are small when the incident frequency approaches an absorption edge, giving the observed frequency dependence. This term has been used in the theory of anomalous dispersion, giving the factors $\Delta f'$ (real) and $\Delta f''$ (imaginary) which are the frequency-dependent but angular-independent corrections to the coherent atomic scattering factors.[8] The term $\Delta f'$ is often referred to as the Hönl correction. With these corrections for dispersion, the coherent x-ray atomic scattering factor is written as

$$f' = f_0 + \Delta f' + i\Delta f'', \tag{2}$$

where f_0 is the usual coherent atomic scattering factor uncorrected for frequency dependence (dispersion). Coherent scattering (no change in incident x-ray frequency) occurs when the final state of the atom, $\langle f|$, is the same as the initial state $\langle i|$.[6,7] If $\Delta f'$ is negative, some of the coherent scattering events, represented by the atomic scattering amplitude f_0 calculated from the A^2 term in first-order perturbation theory, do not take place. To conserve energy or intensity, we need to account for those photons associated with the negative amplitude $\Delta f'$. These inelastic events are contained in the solution to the $\vec{P}\cdot\vec{A}$ term in second order for $\langle f| \neq \langle i|$.

There is a similar analogy to this argument for the coherent and Compton (incoherent) scattering cross sections calculated from the A^2 term. The coherent scattering amplitude f_0 is calculated from the A^2 term with $\langle f| = \langle i|$, but the Compton scattering is calculated from the A^2 term with $\langle f| \neq \langle i|$. For forward scattering, f_0 equals Z, the number of electrons in the atom. As the scattering angle increases, f_0 decreases, but the Compton cross section increases in such a manner that intensity tends to be conserved for eac electron when all final states of the atom are c sidered for the A^2 term. This result, discusse by James,[8] is assumed to hold for the $\vec{P}\cdot\vec{A}$ ter in second order, as this calculation for the condition $\langle f| \neq \langle i|$ has not been made for x-ray scattering. However, we may test the possibility that the amplitude of the inelastically scattered x rays observed in my experiment may be due t those lost from the coherent process with amplitude $\Delta f'$ by using the results obtained from the wave-mechanical treatment for oscillators as reviewed by James.[8]

As the observed intensity is incoherent, we may sum the scattering from each electron. Negative values contributed to $\Delta f'$ by the individual electrons will be taken as contributions to the incoherent scattering process. As $\Delta f''$ always makes a positive contribution to the coherent scattering, it cannot contribute to the inelastic anomalous scattering.

To calculate the intensity, we define an anomalous scattering amplitude factor per k electron, f_k^A, as

$$f_k^A = \Delta f'/n_k, \tag{3}$$

where the subscript k denotes the electron shell or subshell and n_k the number of electrons in it. The division by n_k to obtain f_k^A is required as listings of $\Delta f_k'$ include all the electrons in the kth level. The intensity in electron units per atom is obtained by squaring the amplitude for each electron and then summing the intensity from each electron in the atom according to the following formula:

$$I/N = \sum_k |f_k^A|^2 = \sum_k |\Delta f_k'/n_k|^2, \tag{4}$$

where the anomalous scattering amplitude $\Delta f_k'$ for the kth shell is in units of the Thomson scattering, and the sum is over those electrons in the energy levels that are in near resonance with the incident energy.

The real part of the anomalous scattering amplitude is given by James[8] (Eq. 4.30a, p. 145) as

$$\Delta f' = \sum_k \int_{\nu_k}^{\infty} \frac{\nu^2 (dg/d\nu)_k}{\nu_i^2 - \nu^2}\, d\nu, \tag{5}$$

where ν is the variable of integration, ν_k and ν_i the frequencies of the absorption edge and the incident radiation, respectively, and $(dg/d\nu)_k$ the oscillator density at ν. Following the earlier work of Wheeler and Bearden,[10] Cromer[11] applied the concept of the sum rule to calculate the oscillator strengths without making the extrapolation ver the continuum of the hydrogenlike atom. Cromer's oscillator strengths were used with the calculations given by Parratt and Hempstead[12] for the frequency-dependent part of the integral of Eq. (5) to determine the contribution of the kth-shell electrons to $\Delta f_k'$. The contributions from the K shell dominated my results except for the case of Ta where the L shell makes the major contribution when the incident radiation is Cu $K\alpha$. These values of $\Delta f_k'$ were then used to compute the incoherent intensity from Eq. (4). Results from these calculations are listed in Table for comparison with the observed incoherent intensity, listed with an estimate of the error based on the counting statistics.

I was unable to observe the anomalous scatter shifted by the binding energy of the M shell for elements of Z around 30 since the detector could not resolve the approximately 100-eV energy shift from the incident energy. As my measurements did not include this inelastic scatter or energies below 4.8 keV, the observed values are expected to be less than those predicted by my calculation.

The virtual transition of the electron to a higher-energy state in an attempt to scatter coherently may result in the ejection of an electron from the atom. The kinetic energy with which the electron leaves the atom accounts for the energy distribution on the low-energy side of the anomalous spectrum. Electron spectroscopy[13,14] supports this view with observations that electrons leave the atom with little or no kinetic energy, often referred to as "electron shakeoff."

An experiment reported by Åberg and Utriainen[6] showed a broad x-ray spectrum on the low-energy side of the $K\alpha$ line with a long, low-energy tail as observed here. It is difficult to say if their weak spectrum, excited by raw Cr target x rays, arise from the initial K-electron vacancy being filled by a radiative Auger effect as they have interpreted it, or whether it arises from the large amount of fluorescent $K\alpha$ radiation produced in their sample which is in near resonance with its own K absorption edge. This latter explanation based on the work reported here fits their gross observations well.

The author would like to thank J. S. Faulkner for help in the quantum mechanical theory and encouragement in this study, J. Korringa for interpreting my understanding of the quantum analog, H. C. Schweinler for sharing his helpful insights concerning oscillator strengths, and B. S. Borie and H. L. Yakel for corrections and comments on the manuscript.

---

*Research sponsored by the U. S. Atomic Energy Commission under contract with the Union Carbide Corporation.

[1] K. Das Gupta, Phys. Rev. Lett. 3, 38 (1959).

[2] T. Suzuki, T. Kishimoto, T. Kaji, and S. Suzuki, J. Phys. Soc. Jpn. 29, 730 (1970).

[3] C. J. Sparks and B. Borie, *Local Atomic Arrangements Studied by X-Ray Diffraction* (Gordon and Breach, New York, 1966), Chap. I.

[4] R. W. Gould, S. R. Bates, and C. J. Sparks, Appl. Spectrosc. 22, 549 (1968).

[5] R. W. James, *The Optical Principles of the Diffraction of X-Rays* (G. Bell and Sons, Ltd., London, 1965).

[6] T. Åberg and J. Utriainen, Phys. Rev. Lett. 22, 1346 (1969).

[7] W. Heitler, *The Quantum Theory of Radiation* (Oxford Univ. Press, Oxford, England, 1944).

[8] Y. Mizuno and Y. Ohmura, J. Phys. Soc. Jpn. 22, 445 (1967).

[9] D. T. Cromer and D. Liberman, J. Chem. Phys. 53, 1891 (1970).

[10] J. A. Wheeler and J. A. Bearden, Phys. Rev. 46, 755 (1934).

[11] D. T. Cromer, Acta Crystallogr. 18, 17 (1965).

[12] L. G. Parratt and C. F. Hempstead, Phys. Rev. 94, 1593 (1954).

[13] M. O. Krause, T. A. Carlson, and R. D. Dismukes, Phys. Rev. 170, 37 (1968).

[14] T. A. Carlson and M. O. Krause, Phys. Rev. 140, A1057 (1965).

α Continuous Spectra Following *K* and *L* Autoionization During α Decay of ^{210}Po

J. P. Briand, P. Chevallier, A. Johnson, J. P. Rozet, M. Tavernier, and A. Touati
Laboratoire Curie de l'Institut du Radium (Laboratoire associé au Centre National de la Recherche Scientifique), 75231 Paris Cedex 05, France, and Université Paris VI, Paris, France

(Received 8 May 1974)

The α spectra emitted during *K* and *L* ionization following α decay of ^{210}Po are investigated in a coincidence experiment with x rays. We present the first observation of α continuous spectra emitted by radioactive samples. The probabilities of this phenomenon and the shape of the α spectra are discussed in the scope of an α collision with zero impact parameter.

What happens during the change of the atomic cloud accompanying nuclear decay is a problem which has been investigated by nuclear physicists for a very long time. During the rearrangement of the atomic cloud, internal ionization processes may occur. This phenomenon, the probability of which is very small, has been extensively studied, especially in the case of β decay.[1] Concerning α autoionization the x-ray emission following α decay was first discovered by Curie and Joliot in 1931,[2] but the first theory of this process was not given until 1941 by Migdal[3] and refined later by Levinger[4,5] and Rubinson.[6]

The rate of change of the nuclear charge, i.e., the velocity of the outgoing nuclear particle, is a very important point in the theory of this process. When the outgoing particle is moving slowly in comparison to the velocity of the atomic electrons, as in the case of α decay, the process may be considered as adiabatic and can be treated in the adiabatic limit of time-dependent perturbation theory. In the case of a fast outgoing particle, as in β decay, for example, the change of the nuclear charge is sudden and the probability of an ionization during the decay is then approximately given by the imperfect overlap of the wave functions of initial and final states, i.e., in the sudden-approximation limit of time-dependent perturbation. In the case of α decay of ^{210}Po, the velocity of the α particle is low relative to those of inner-shell electrons, but fast for the outer-shell electrons. Therefore, the probability of α autoionization for the *K* and *L* shells is exceedingly small as might be expected in the adiabatic approximation. However, there has been a very large discrepancy between experimental values of the probabilities and the theoretical predictions. This problem has only been resolved at the beginning of this year,[7] as discussed below.

Let us now consider the energetics of this autoionization process. The energy of the electron ejected during α autoionization may be derived, in a simple way, from the original theory of Migdal. The electron spectrum is expected to be continuous and to decrease in probability very rapidly, following an $E^{-9/2}$ rule. The mean energy of this continuous spectrum is lower than the binding energy of the ejected electron in the atom. It is then very low in energy and too near the electron background to be observed experimentally. The energy of the α particle is then modified and becomes $E_\alpha = E_\alpha{}^n - B_K - E_e$, in the case of *K* ionization, where $E_\alpha{}^n$ is the energy of the α particle when the final state is neutral, B_K the binding energy of the *K* electron, and E_e the kinetic energy of the ejected electron. Thus we can expect to observe a continuous α spectrum with a maximum energy of $E_\alpha{}^n - B_K$ which is symmetric in shape with the electron spectrum (Fig. 1). This situation is quite similar to that of the electron shake-off spectra but with a faster decrease of the energy spectrum. (In the case of shake-off spectra the decrease in energy is assumed to follow an $E^{-7/2}$ rule.) We present in this paper the first observation of these continuous α spectra in the case of *K* ionization as well as in the case of *L* ionization.

The principle of our experiment is to observe the α spectra emitted in coincidence with the *K* or *L* rays which follow the rearrangement of the autoionized atom. The α spectra were studied with a Si surface-barrier detector of 14-keV resolution at 5 MeV, and the x-ray spectra, with a Ge(Li) or Si(Li) detector [Ge(Li) in the case of *K* rays, the energy of which is of the order of 70 keV, and Si(Li) for the study of *L* rays]. We used a 1-μCi sample of ^{210}Po prepared by autodeposition on a silver foil of 6 μm thickness, set between the two detectors, in a vacuum chamber closed by a beryllium window.

We present in Fig. 2 the experimental spectrum observed in coincidence with *K* x rays. This

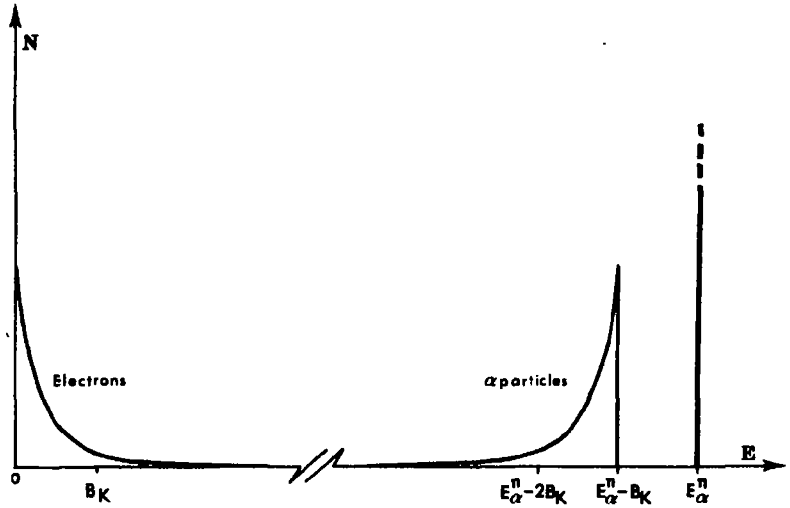

FIG. 1. Theoretical shapes of a continuous α spectrum following K autoionization.

spectrum was obtained in a two-month exposure. One observes in this figure an α continuous spectrum, the maximum energy of which is $E_\alpha^n - B_K$ and which decreases rapidly with decreasing α energy. The probability of K autoionization deduced from this experiment is $(2 \pm 0.5) \times 10^{-6}$. In Fig. 3 one can observe the spectrum in coincidence with all L x-rays emitted. The probability deduced from this experiment, corrected by the

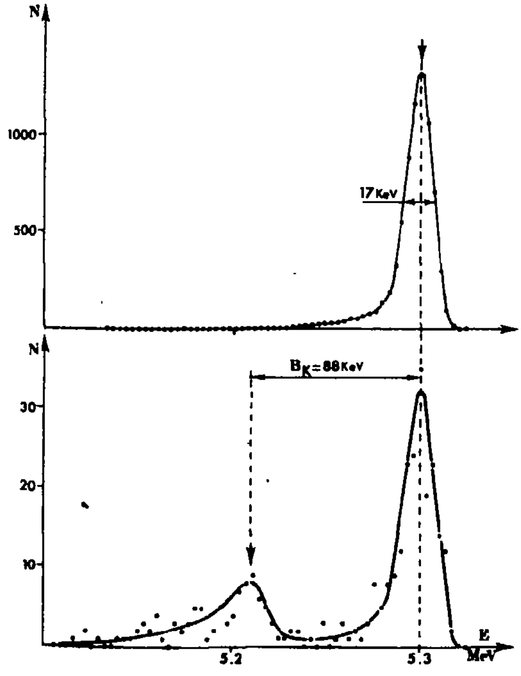

FIG. 2. Experimental α spectrum in coincidence with K x rays of Pb. Upper curve, direct α spectrum; lower curve, coincidence α spectrum. The peak at 5.3 MeV is a chance coincidence peak (for Pb, B_K = 88 keV).

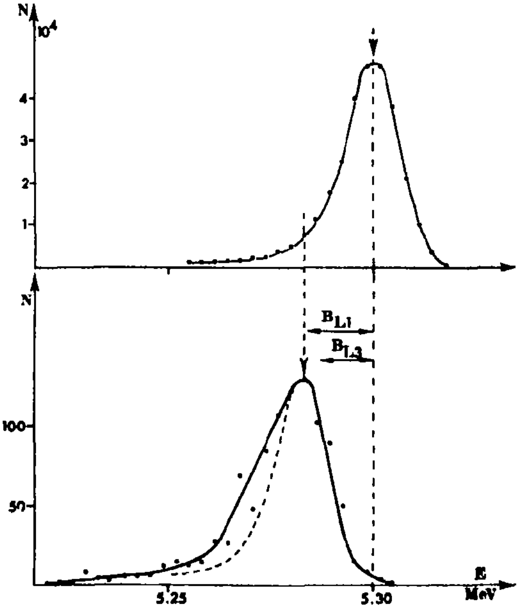

FIG. 3. Experimental α spectrum in coincidence with L x rays of Pb. Upper curve, direct α spectrum; lower curve, coincidence α spectrum.

values of fluorescence yield, Coster-Kronig probabilities, and intensity ratios of the L lines, is $(3.2 \pm 0.8) \times 10^{-4}$. The duration of this experiment was only one week.

The probabilities we obtained are in good accordance with the previous measurements for both K and L autoionization (for the K shell, the previous measurements gave 1.5×10^{-6}, 2×10^{-6}, 1.6×10^{-6}, and 1.5×10^{-6},[8-11] and for the L shell, 2.2×10^{-4}, 2.93×10^{-4}, and 4×10^{-4}[10,11,1]).

Our values, as well as the previous ones, are in large disagreement with the calculations of Migdal, Levinger, and Rubinson, which lead to an order of magnitude of 2×10^{-7} for the internal-ionization probability for the K shell, and with that of Ciochetti[12] ($P_K = 8.7 \times 10^{-7}$). We therefore had tentatively computed the probability in the scope of collision theory.

In fact, α autoionization may be considered as a collision process due to the Coulombic interaction between the moving α particle and an atomic cloud which is still nearly that of Po. The autoionization process during α decay is, in fact, the only case of collision with purely zero impact parameter which can be studied experimentally. Therefore, there are two important differences between autoionization and an ordinary collision of an α particle with a Pb atom. Firstly, the collision originates in the center-of-mass reference frame and the recoil energy is lower (~100 keV); secondly, the α particle travels exclusively from the center of the atom to infinity. Following the calculation of Hansteen and Mosebekk[13] in the semiclassical approximation to the theory of collisions and interpolating their results, one deduces at zero impact parameter a value of the probability of 4×10^{-7} for the K shell, which is of the same order of magnitude as in the previous calculations based on time-dependent perturbation of Migdal, Levinger, and Rubinson.

Very recently, and during the writing of the present paper, Hansen[7] reported the first calculation which agrees well with experimental results, perhaps resolving a problem which has existed for 30 years. Hansen, using the new binary-encounter approximation of collision theory,[14] has taken into account two refinements with respect to the previous theories: relativistic effects and the variation of the kinetic energy of the α particle in the vicinity of the nucleus, i.e., in the region where the probability of collision is largest. He found for the K shell a probability of 1.96×10^{-6}, which agrees very well with all previous experimental values and with our own measurement. Also for L-shell ionization his calculation, after all corrections for fluorescence yields etc. have been made, fits with the experimental values (Hansen predicts 2.3×10^{-4}).

The shape of the α continuous spectrum is not given in Hansen's paper. In view of the importance of the effects taken into account in his calculation, it is not too meaningful to compare the shape of our experimental spectrum for K-shell ejection with the previous prediction given by Migdal's theory. It may be noticed, however, that the predicted $E^{-9/2}$ shape of the electron spectrum is not very far from the shape we observe.

---

[1] See M. S. Freedman, "Atomic Structure Effects in Nuclear Events" (to be published), for a review of most experimental data.

[2] I. Curie and F. Joliot, J. Phys. Radium 2, 20 (1931).

[3] A. Migdal, J. Phys. (U.S.S.R.) 4, 449 (1941).

[4] J. S. Levinger, Phys. Rev. 90, 11 (1953).

[5] J. S. Levinger, thesis (unpublished).

[6] W. Rubinson, Phys. Rev. 130, 2011 (1963).

[7] J. S. Hansen, Phys. Rev. A 9, 40 (1974).

[8] M. A. Grace, R. H. Allen, D. West, and H. Halban, Proc. Phys. Soc., Sect. A 64, 493 (1951).

[9] W. C. Barber and R. H. Helm, Phys. Rev. 86, 275 (1952).

[10] M. Riou, J. Phys. Radium 13, 487 (1952).

[11] W. Rubinson and W. Rubinstein, Phys. Rev. 86, 545 (1952).

[12] G. Ciochetti and A. Molinari, Nuovo Cimiento 40B, 69 (1965).

[13] J. M. Hansteen and O. P. Mosebekk, in *Proceedings of the International Conference on Inner-shell Ionization Phenomena and Future Applications, Atlanta, Georgia, 1972*, edited by R. W. Fink, J. T. Manson, I. M. Palms, and R. V. Rao, CONF-720404 (U.S. Atomic Energy Commission, Oak Ridge, Tenn., 1973).

[14] J. S. Hansen, Phys. Rev. A 8, 822 (1973).

Isotopically Selective Photochemistry of Bromine*

Stephen R. Leone and C. Bradley Moore
Department of Chemistry, University of California, Berkeley, California 94720

(Received 3 June 1974)

A tunable narrow-frequency laser is used to produce an isotopically selected reaction product of bromine. Natural Br_2 ($^{79}Br/^{81}Br = 1$) is photopredissociated by selective excitation into the $^3\Pi_{0^+u}$ state. Bromine atoms enriched in one isotope react with HI before scrambling occurs to produce 80–85% $H^{81}Br$. The method should yield an efficient technique for isotope separation. Spectroscopic requirements and the optimum reaction conditions are discussed. The relative amount of nonselective product from excitation of the Br_2 continuum is determined.

The development of tunable lasers has stimulated a resurgence of interest in selective photochemical reactions for isotope separation. Recent papers review the requirements and suggested methods for laser isotope separation.[1,2] We describe here an isotopically selective photochemical reaction sequence for bromine (natural abundance 50.5% ^{79}Br, 49.5% ^{81}Br). Although a number of recent reports of laser isotope separation require two-step photoionization or dissociation,[3-5] here we use a single photon absorption followed by molecular predissociation.[6] Tuning of the laser to desired isotopic absorption lines is facilitated by visual observation of fluorescence in cells containing $^{79}Br_2$, $^{81}Br_2$, and natural $^nBr_2$. We choose here to detect the product isotopic enrichment from the vibrational chemiluminescence of the $H^{79}Br$ and $H^{81}Br$ produced in the reaction $Br + HI \rightarrow HBr(v = 0, 1, 2) + I$.[7] The advantage of this technique over the usual mass spectral determinations is that the isotopically selective photochemical steps are confirmed independently of subsequent slower chemistry. Practical separation devices may then be devised with better success.

The 558- and 532-nm lines of a Chromatix frequency-doubled neodymium-doped yttrium-aluminum-garnet (YAlG) laser (1 mJ, 10^{-7}-sec pulses, 80 pulses/sec) are used for excitation of Br_2. The ~1-cm^{-1} gain bandwidth of the YAlG laser is narrowed by an internal etalon with a finesse of 7. The resulting spectral output is 1.2 GHz wide as observed with a spectrum analyzer, and is smoothly tunable over the YAlG gain by angular adjustment. A 50-mm-diam quartz cell is used for the reaction studies. The HI flows into the cell from 25-mm tubing. The Br_2 is injected into the HI stream by a series of five 0.4-mm pinholes at the cell entrance. The Br_2 jets point in the direction of the flow. 50 cm of 14-mm-diam tubing connect the cell to liquid-nitrogen traps for pumping. An all-Monel MKS Baratron capacitance manometer is used to measure the pressures of HI and Br_2. Br_2, the minor constituent, is added after the HI flow is established.

Infrared fluorescence is observed with a Ge:Cu photoconductive detector (~15°K). The detector, cell, lens geometry, and signal averaging system have been described previously.[8] A narrow-band filter transmits primarily the HBr 1 → 0 *R* branch. About 30% of the total signal is from the shorter-radiative-lifetime 2→1 fluorescence produced in the Br + HI reaction. Quartz filter cells of $H^{79}Br$ and $H^{81}Br$ containing 30 Torr in a 5-cm path length completely block the $H^{79}Br(v = 1)$ and $H^{81}Br(v = 1)$ emissions, respectively. In a separate experiment the ratio of transmissions of the desired $HBr(v = 1)$ isotope signals was accurately measured. Isotopic gases are prepared from $Na^{79}Br$ (99.75%) and $Na^{81}Br$ (97.8%) obtained from Oak Ridge National Laboratory.

The primary photochemical step is excitation of Br_2 into the bound levels of the $^3\Pi_{0^+u}$ state (Fig. 1) followed by predissociation and collision-induced dissociation. It has been proposed that this type of excitation could lead to isotopically selective chemistry.[9] The laser is tuned to absorption lines by visual observation of fluorescence from cells each containing 1 Torr of $^{79}Br_2$, $^{81}Br_2$, and $^nBr_2$. With experience, reasonable estimates of the relative magnitudes of absorption lines can be made. The strongest lines are easily picked out. Lines can be observed which appear to discriminate in favor of $^{81}Br_2$ over $^{79}Br_2$ (and vice versa) by as much as 2 orders of magnitude. Continuum absorption exists throughout the 558- and 532-nm regions. The laser can be tuned to wavelengths for which no line fluorescence is observed and only the nonselective continuum absorbs.

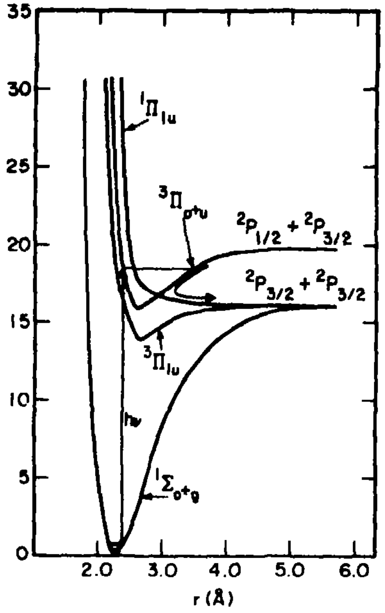

FIG. 1. Approximate potential diagram for Br_2 [D. B. Gibbs and E. A. Ogryzlo, Can. J. Chem. 43, 1905 (1965)] showing excitation step and collisionally induced dissociation at 558 nm.

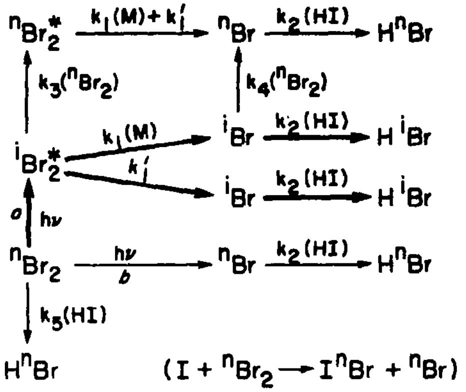

FIG. 2. Isotopically selective reaction sequence for bromine. Here, *a* is the line absorption and *b* is the continuum absorption; *n* denotes nonselected and *i* isotopically selected bromine. k_1 is the rate constant for collisionally induced dissociation and k_1' the predissociation rate. k_2 is the rate constant for the reaction Br + HI, k_3 for electronic energy transfer, k_4 for Br atom exchange, and k_5 for the bimolecular reaction Br_2 + HI. The heavy arrows are the desired separation path. *M* is either Br_2 or HI.

The relative absorptions of lines versus continuum were measured at 558 and 532 nm. The product-HBr vibrational emission intensity is observed as the laser is tuned on and off the fluorescence line. The strongest line of a single isotope at 532 nm has a line-to-continuum ratio (a:b) of 1:4. At 558 nm, however, several lines of single isotopes have line-to-continuum ratios of 3:2. This is not unexpected, since the continuum absorption is rapidly decreasing toward longer wavelengths.[10] At room temperature the Doppler width of Br_2 is 500 MHz, much less than our 1.2-GHz laser. A laser with a 200-MHz linewidth at 558 nm could provide a line-to-continuum ratio a:b of greater than 4:1, or an abundance of the selected isotope in the excitation step of $(2a+b)/2(a+b)=90\%$. With our laser the maximum abundance is presently limited to about 80%. It may be possible to increase the ratio a:b by tuning to longer wavelengths where the continuum approaches zero or by exciting just below the dissociation threshold. However, the line absorptions would be weaker. The ratio a:b may also vary with temperature.

Predissociation, k_1', and collisionally induced dissociation, $k_1(M)$, in Fig. 2 are discussed in more detail in a recent review.[11] With 558 nm, predominantly ground-state Br atoms are produced. At 532 nm, a large fraction of electronically excited atoms is detected by electronic-to-vibrational transfer processes.[12] The only lifetime and quenching studies[13] on Br_2 to determine k_1 and k_1' are in doubt.[10] However, if Br_2 is similar to I_2, the collisionally induced dissociation cross sections may be gas kinetic. The first attempt to separate the isotopes of Br_2 used a ruby laser to excite the $^3\Pi_{1u}$ state.[14] The rapid collisional dissociation produced atoms which on collision with $^n\mathrm{Br}_2$ became isotopically scrambled.

A rapid chemical scavenging method is necessary to trap the isotopically selected atoms. The choice of HI (Fig. 2) is a favorable one. An estimate of the rate constant k_2 measured in our system with the infrared fluorescence method[7] is $(1.1\pm0.4)\times10^{-11}$ cm^3/molecule sec. Rate measurements for Br + HI and Br* + HI are in progress.[15]

In order for the desired reaction sequence to reflect the selectivity of the excitation step, the scrambling processes k_3, k_4, and k_5 must be suppressed. The necessary conditions are that $k_1(M)+k_1'\gg k_3(\mathrm{Br}_2)$, that $k_2(\mathrm{HI})\gg k_4(\mathrm{Br}_2)$, and that the

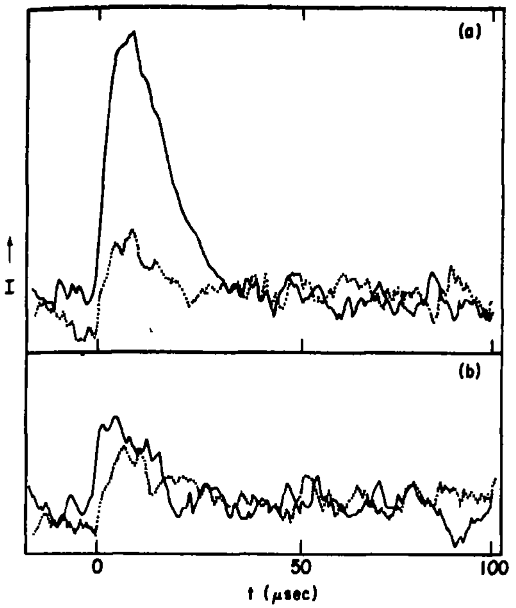

FIG. 3. (a) $H^{81}Br$ ($v = 1$) emission intensity plus 2 → 1 leakage. (b) $H^{79}Br$ ($v = 1$) intensity plus 2 → 1 leakage. The solid curves are with excitation of $^{81}Br_2$ at 558 nm. The dotted curves are for excitation of the continuum only. The rise time after the laser pulse is the reaction rate k_2 and the decay is $V \rightarrow V$ of HBr ($v = 1$) to HI ($v = 1$) [H.-L. Chen, J. Chem. Phys. 55, 5557 (1971)].

time in the flow is much shorter than the prereaction rate $k_5(Br_2)(HI)$. Some enrichment is observed with flow ratios HI:Br_2 of 20:1, although the best obtained was with 50:1. Thus, the first two of these conditions may be fulfilled. If the collisionally induced dissociation is quite fast, then the electronic energy transfer k_3 is a minor source of scrambling. The atom exchange k_4 ($^iBr + Br_2 \rightarrow {}^iBrBr + Br$) is the major cause of scrambling the isotopically selected atoms.

Figure 3 shows a typical set of $H^{79}Br(v = 1)$ and $H^{81}Br(v = 1)$ intensities demonstrating the isotopic selectivity of the product HBr after excitation of $^{81}Br_2$ with the 558-nm line. From the previously measured line-to-continuum ratio of 3:2, the maximum product abundance is 80% $H^{81}Br$ and 20% $H^{79}Br$. From the observed signals an estimate of the vibrationally excited product isotope distribution may be calculated. All filter transmission factors (interference and gaseous) are included in the calculation, as well as the leakage of 2→1 fluorescence and the different radiative lifetimes of the 2→1 and 1→0 emissions. The product vibrational distribution is taken to be $(v = 2)/(v = 1) = 1.0$.[16] The product abundance for the ~50:1 flow ratio is 80–85% $H^{81}Br$.

Prereaction, k_5, is a severe practical problem for an isotope separation system. To minimize prereaction, these measurements were carried out in a darkened room with flow rates which exchanged the gases in the cell every 10 msec. These fluorescence results are relatively insensitive to prereaction. However, if as much as 10% prereaction occurs in this experiment, the $H^{79}Br$ and $H^{81}Br$ signals would approach each other by $V \rightarrow V$ transfer[8] before the decays are over. A second chemical problem for practical isotope separation with this sequence is the subsequent reaction of I with Br_2. Iodine atoms react with $^nBr_2$ to produce IBr + ^nBr with a rate constant of 8.8×10^{-14} cm^3/molecule sec.[17] A regenerative chain scrambling may occur which cannot be prevented by the iodine recombination rate at the low I-atom pressures produced. These difficulties necessitate rapid removal of either the Br_2 or I atoms (or both) at the walls of the reaction chamber.

We have obtained conclusive evidence for an isotopically selective photochemical process in bromine. The single-visible-photon excitation and high enrichment possible make the process attractive for practical isotope separation. The visible and infrared observation techniques used here have wide applicability to other isotopically selective systems. These types of experiment will allow the resolution and assignment of overlapping discrete and continuous spectra, the study of predissociation rates and mechanisms, the measurement of rates of electronic energy transfer, atom exchange, and chemical reaction, and the observation of product energy-state distributions.

---

*This work was partially supported by the National Science Foundation and the U.S. Army Research Office (Durham).

[1] V. S. Letokhov, Science 180, 451 (1973).

[2] C. B. Moore, Accounts Chem. Res. 6, 323 (1973).

[3] R. V. Ambartzumian, V. S. Letokhov, G. M. Makarov, and A. A. Puretskii, Appl. Opt. 11, 354 (1972), and Pis'ma Zh. Eksp. Teor. Fiz. 17, 91 (1973) [JETP Lett. 17, 63 (1973)].

[4] R. H. Levy and G. S. Janes, U.S. Patent No. 3 772 519 (1973).

[5] U. Brinkmann, W. Hartig, H. Telle, and H. Walther,

Verh. Deut. Phys. Ges. 7, 455 (1974).

[6] E. S. Yeung and C. B. Moore, Appl. Phys. Lett. 21, 109 (1972).

[7] F. J. Wodarczk and C. B. Moore, to be published.

[8] S. R. Leone and C. B. Moore, Chem. Phys. Lett. 19, 340 (1973).

[9] S. H. Dworetsky and R. S. Hozack, J. Chem. Phys. 59, 3856 (1973).

[10] J. A. Coxon, in *The Chemical Society Specialist Periodical Report on Molecular Spectroscopy*, edited by R. F. Barrow (The Chemical Society, London, 1973), Vol. 1, p. 177.

[11] M. S. Child and R. B. Bernstein, J. Chem. Phys. 59, 5916 (1973).

[12] S. R. Leone and F. J. Wodardzyk, J. Chem. Phys. 60, 314 (1974).

[13] G. Capelle, K. Sukarai, and H. P. Broida, J. Chem. Phys. 54, 1728 (1971).

[14] W. B. Tiffany, J. Chem. Phys. 48, 3019 (1968).

[15] K. Bergmann and C. B. Moore, to be published.

[16] D. H. Maylotte, J. C. Polanyi, and K. B. Woodall, J. Chem. Phys. 57, 1547 (1972).

[17] M. A. A. Clyne and H. W. Cruse, J. Chem. Soc., Faraday Transactions II 68, 1377 (1972).

Effects of Degeneracy on Self-Induced Transparency

G. J. Salamo
Physics Department, Brooklyn College of the City University of New York, Brooklyn, New York 11210

and

H. M. Gibbs and G. G. Churchill
Bell Laboratories, Murray Hill, New Jersey 07974

(Received 29 April 1974)

The effects of degeneracy on self-induced transparency (SIT) have been studied using optical pulses gated from a cw dye laser and four different degenerate systems in Na. Delays, nonlinear transmission, peaking, and breakup were altered only slightly by degeneracy. This unexpected insensitivity to degeneracy of SIT features is in agreement with the McCall-Hahn pulse-area, pulse-energy description, computer simulations, and a simple physical explanation of general applicability.

Degeneracy has been assumed to prevent the observation of such characteristic features of self-induced transparency (SIT) as peak amplification and breakup of an optical pulse.[1-3] We report an experiment which clearly demonstrates that degenerate transitions do not prevent the observation of all of the characteristic features of SIT.

SIT was first demonstrated in ruby[4] and immediately afterwards in SF_6.[5] The complicated energy-level structure of SF_6 led to interest in the effects of degeneracy, but it was assumed that degeneracy prevented peaking and pulse breakup.[1-3] The effects of degeneracy on SIT phenomena are clarified here in sodium vapor using a dye laser. There are three advantages of this system over the CO_2 laser-SF_6 system. First, sodium (Na) is a simpler system with clearly defined degenerate transitions with known dipole moments. Second, for weak magnetic fields here are at least two sets of clearly defined combinations of moments which can be studied ndependently. Third, in high magnetic fields he Na system becomes nondegenerate. Thereore, the same system can be used to study both nondegenerate and degenerate SIT.

The basic apparatus consisted of a cw dye laser[6] and Na absorption cell. The spectral profile of the dye laser was reduced from about 0.5 Å to 0 MHz in a single longitudinal mode by the use of three etalons. The output of the dye laser was hen gated through a Glan prism by a Pockels cell at the rate of 100 pulses per second.[7] This resulted in 5-nsec pulses which were focused by a 38-cm lens into a 2-mm sodium cell. The sodium cell was housed in an oven and placed in a magnetic field which could be varied from 0 to 8 kG. A 15-cm lens was used to image the excited region in the cell onto a 100-μm aperture in order to select only the uniform-plane-wave region for observation.[7] The output from the aperture was then focused by a third lens onto a fast detector and then displayed on a 7904 Tektronix oscilloscope.[7]

A quantitative study of peak amplification and breakup was carried out by Gibbs and Slusher, using a Hg laser and Rb atoms.[7] Because they found such good agreement between theory and experiment, it is desirable to start with a similar nondegenerate system and then observe what happens when degeneracy is added. In large magnetic fields Na transitions of different M_J are well resolved, but several M_I transitions are excited as a result of a large Doppler width. However, the system is effectively nondegenerate since the moments are all equal. As shown in Fig. 1, the dye-laser–Na data taken in a large magnetic field are in good agreement with computer simulations of the experiment using Bloch's and Maxwell's equations for a nondegenerate transition.[8] Figure 1 illustrates the potential use of SIT phenomena to measure relative, or even absolute, transition dipole strengths. The output pulse shape depends on the area of the input pulse, $A=(2p/\hbar)\int\mathcal{E}(t)\,dt$, which is proportional to the time integral of the slowly varying electric field envelope $\mathcal{E}(t)$ and the dipole moment p.

The near-ideal Na–dye-laser system was then used to study the degeneracies that occur in weak magnetic fields. The good quantum numbers are then F and M_F, and several different transitions can be excited simultaneously. For example, for the D_1 ($^2S_{1/2}-{}^2P_{1/2}$) transition in fields of 0 to 60 G, dye laser pulses tuned to the $F=2$ to $F'=1,2,$

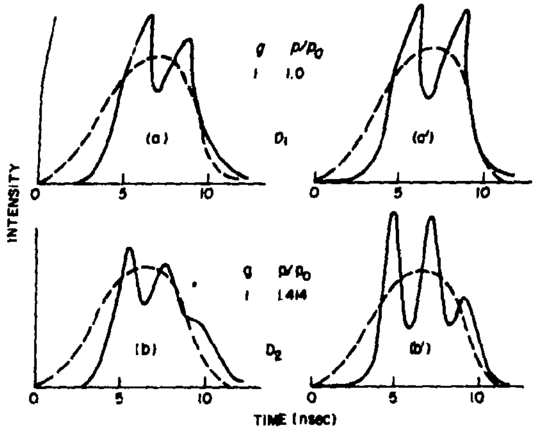

FIG. 1. Experimental output pulse shapes for linearly polarized ($\Delta M_J = 0$) nondegenerate transitions: (a) D_1 and (b) D_2. The corresponding computer simulations are (a′) D_1, $A = 16$, $T_1 = 24$, $T_2 = 32$, and (b′) D_2, $A = 15$, $T_1 = 19.2$, $T_2 = 32$. Note the different output shapes for the same input, demonstrating the use of SIT to measure relative dipole strengths. The dipole moments are theoretically in the ratio $1:\sqrt{2}$; the g's are statistical weights. Moment-dependent output pulse shapes were also seen for circularly polarized transitions where the relative moments are $\sqrt{2}:1:\sqrt{3}$.

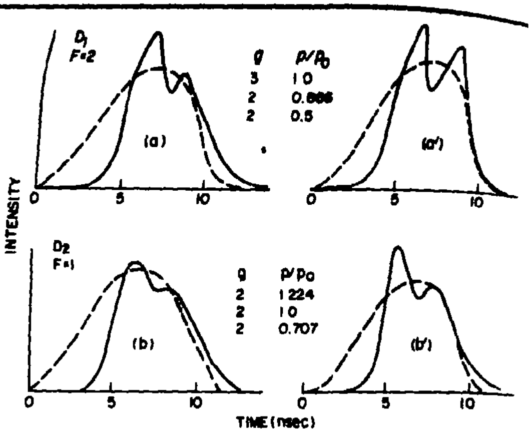

FIG. 2. Experimental output pulse shapes for the degenerate cases: (a) $D_1(F=2)$ and (b) $D_2(F=1)$. (a′), (b′) The corresponding computer simulations with input areas A_0 of 16 and 15, respectively, and $T_1 = 24$, $T_2 = 32$.

$\Delta M_F = 0$, transitions excited moments with ratios 1.0:0.87:0.5. Figure 2(a) shows that the characteristic features of peaking and breakup were clearly present in this case. The computer simulation in Fig. 2(a) is in good agreement with experimental results. Nonlinear transmission and delays did not differ much from the nondegenerate case. Similar results were found for $D_1(F=1)$ transitions. Surprisingly, all of the characteristics of SIT were similar to those in the nondegenerate case.

For the D_2 ($^2S_{1/2} - {}^2P_{3/2}$) transitions from $F = 1$ in fields of 60 to 120 G, several moments were excited with ratios 1.2:1.0:0.707; see Fig. 2(b). Peaking and pulse breakup were diminished while the nonlinear transmission and delays remained relatively unchanged. In Fig. 2(b′) the computer simulation is shown to be in good agreement with experiment. Similar results were found for $D_2(F=2)$ transitions.

These experimental results can be understood in a qualitative way with a pulse-area, pulse-energy analysis.[9] The advantage of this approach is its simplicity and low cost as compared to computer solutions of the Bloch and Maxwell equations.[10] The area theorem describes the evolution and predicts the stable values of the pulse area: $dA_0/dz = -\alpha S/2$, where $S/A_0 = [\sum g_i p_i \times \sin(A_0 p_i)]/A_0 \sum g_i p_i^2$ is the nonlinear correction to the small-area peak absorption coefficient $\alpha/2$, g_i is the statistical weight of the ith dipole moment whose value is p_i relative to the high-field $\Delta M_J = 0$ D_1 moment $p_0 = 2.6 \times 10^{-18}$ esu cm, and $A_0 = (2p_0/\hbar)\int \mathcal{E}(z,t)\,dt$ is the area for a moment of value p_0. The pulse energy per unit area τ varies as $d\tau/dz = -\alpha\tau F(A_0)$, where $\tau = (c/4\pi) \times \int [\mathcal{E}(z,t)]^2\,dt$. A good approximation[9] to F for smooth pulse shapes is related to the energy $W(A_0)$ of N atoms at exact resonance after the passage of a pulse of area A_0:

$$W(A_0) + \frac{N\hbar\omega}{2} = \frac{N\hbar\omega}{2}\,\frac{\sum g_i[1-\cos(p_i A_0)]}{\sum g_i} = A_0^2 F(A_0)\,\frac{\sum g_i p_i^2}{\sum g_i}.$$

The high-area oscillations are more apparent on a plot of W than F.

S and W curves are shown in Fig. 3. The positively sloped zero in the D_1 $S(A_0)$ curve (a) at about 4.2π predicts a stable area for which the atoms are returned as efficiently as possible to the ground state. The D_1 W curve (a) indicates that the modulation in the energy stored in the atoms is not very different from the nondegenerate case (c). Thus, breakup and peaking are predicted to be similar to the nondegenerate case in agreement with experimental results. The dipoles 1.00 and 0.87 are nearly equal and there-

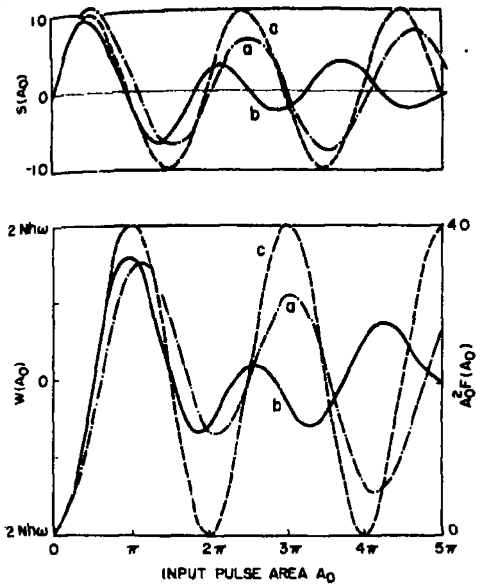

FIG. 3. S and W for (curves a) degenerate $D_1(F=2)$ nsitions, (curves b) degenerate $D_2(F=1)$ transitions, d (curves c) nondegenerate transition. The modula- n of the output pulse for the same number of atoms ould be ideal, good, and poor in the nondegenerate, enerate D_1, and degenerate D_2 cases, respectively. perimental results agree with these predictions.

re act together and effectively modulate the lse. The 0.5 dipole has little effect on pulse odulation and peaking because its oscillations e slower and absorption much weaker.

The D_2 S curve (b) indicates that a stable area ists at 3.3π. The W curve (b) indicates that the odulation of energy stored in the atoms is re- ced from the D_1 case and therefore, in agree- ent with experimental results, peaking and eakup are expected to be diminished. The dif- rence between two of the transition dipole mo- ents (1.22 and 1.00) prevents them from absorb- g and reradiating energy simultaneously. More ergy is lost than in the D_1 case since a 4π-area lse for one dipole will be about 3π in area for e second dipole and therefore leave atoms ex- ted as the pulse propagates through the medium. wever, it is important to note that propagation sses and delay times are affected similarly by eneracy and relaxation losses and that in prac- e relaxation effects often dominate.[3]

Previously the effects of degeneracy on nonlin- r transmission, delays, and low-loss propagation rather than on reshaping have been stressed.[1,3] It was expected, as a rule, that degeneracy would prevent breakup and peaking. The remarkable point of this Letter is that pulse breakup and peaking are seen in degenerate systems and are found to be more sensitive indicators of degeneracy effects. Degeneracy prevents breakup only when there are several moments of comparable absorption that differ by enough to compete but not enough that one oscillates much more slowly than the other. If all transitions have the same weight, moments less than one-half the maximum value will have too little absorption to have much effect. Therefore, it is the exception rather than the rule that degeneracy prevents breakup.

It is interesting that D_2 SIT was observed to be near ideal again in zero field. The spectral width of the 5-nsec pulse is greater than the hyperfine splitting of the $^2P_{3/2}$ excited state so that each ground state is excited into a linear combination of two excited states. Each excited transition now has the same transition dipole moment predicting that nondegenerate SIT should be observed.[11] Experimental results were in excellent agreement with this prediction. This observation emphasizes that the effect of degeneracy on SIT depends not solely on the atom but also on the spectral width of the exciting laser.

In summary, the Na-dye system is ideal for testing the effects of degeneracy on SIT. The experiment demonstrated the usefulness of dye lasers in studying coherent optical effects[12] and measuring the relative magnitudes of transition dipole moments. It was clearly demonstrated that degeneracy does not necessarily prevent the observation of peaking and pulse breakup. A pulse-area, pulse-energy analysis is a good, qualitative, inexpensive indicator of the relative peaking and modulation to be expected. A general rule for good 4π breakup may be followed. If several of the degenerate moments are nearly equal and dominate the absorption, good breakup will be observed. On the other hand, if the difference between the moments dominating the absorption prevents them from absorbing and reradiating cooperatively, breakup will be diminished. For example, for P or R linearly polarized transitions in molecules, the moments cluster close to their largest value. Therefore, breakup and peaking are predicted in SF_6 as reported.[3]

The authors thank S. L. McCall for helpful suggestions. One of us (G.J.S.) would like to acknowledge partial support from the National Science

Foundation.

---

[1] C. K. Rhodes, A. Szoke, and A. Javan, Phys. Rev. Lett. 21, 1151 (1968); C. K. Rhodes and A. Szoke, Phys. Rev. 184, 25 (1969).

[2] A. Zembrod and Th. Gruhl, Phys. Rev. Lett. 27, 287 (1971).

[3] F. A. Hopf and C. K. Rhodes, Opt. Commun. 8, 88 (1973); F. A. Hopf, C. K. Rhodes, and A. Szoke, Phys. Rev. B 1, 2833 (1970).

[4] S. L. McCall and E. L. Hahn, Phys. Rev. Lett. 18, 908 (1967), and Phys. Rev. 183, 457 (1969).

[5] C. K. N. Patel and R. E. Slusher, Phys. Rev. Lett. 19, 1019 (1967).

[6] A. Dienes, E. P. Ippen, and C. V. Shank, IEEE J. Quantum Electron. 8, 388 (1972).

[7] H. M. Gibbs and R. E. Slusher, Phys. Rev. Lett. 24, 638 (1970); R. E. Slusher and H. M. Gibbs, Phys. Rev. A 5, 1634, and 6, 1255 (1972).

[8] Degeneracy was added to the program of Ref.
the degenerate transitions the approximate values
$=24$ nsec and $T_2=32$ nsec were used. Because of
short input pulse, output shapes depend only weakly
the relaxation times. Relaxation was assumed not
couple the degenerate transitions; experimentally,
was not always the case. A careful study of relaxat
details would have to include coupling.

[9] S. L. McCall and E. L. Hahn, in *The Physics of Quantum Electronics*, edited by S. F. Jacobs and J. B. Mandelbaum (Optical Sciences Center, The University of Arizona, Tucson, Ariz., 1968), pp. 65–99; Rhodes, Szoke, and Javan, Ref. 1; S. L. McCall and E. L. Hahn, Phys. Rev. A 2, 861 (1970).

[10] The $S(A)$ and $W(A)$ curves were run on a PDP-8 computer and could be done on many calculators.

[11] See p. 864 of McCall and Hahn, third citation of Ref. 9.

[12] For example, we have observed large Faraday rotations of SIT pulses on the D_2 transition in sodium.

Long-Time Behavior of the Velocity Autocorrelation Function for a Fluid of Soft Repulsive Particles

D. Levesque
Laboratoire de Physique Théorique et Hautes Energies, Université de Paris-Sud, 91405 Orsay, France*

and

W. T. Ashurst
Sandia Laboratories, Livermore, California 94550

(Received 5 June 1974)

By a molecular-dynamics simulation of a three-dimensional system of 4000 particles, we show that the long-time tail of the velocity autocorrelation function has the form $\alpha_0 t^{-3/2}$, where t is the time and α_0 a coefficient depending on the kinematic viscosity and on the diffusion coefficient.

Alder and Wainwright[1] have shown through moecular-dynamics computations on systems of ard disks and hard spheres that the velocity utocorrelation function (vaf) decreases like $_0 t^{-d/2}$ when the time t is large compared to the ollision time (d is the dimensionality of the sysem, α_0 is a coefficient dependent upon the denity ρ). This behavior has been justified in the mit of small densities by kinetic theory[2] and as been shown to be plausible for a fluid system all densities on the basis of hydrodynamical rguments.[3] Thus, for three dimensions at large me, the vaf $\langle\vec{V}(0)\cdot\vec{V}(t)\rangle$ should be given by

$$\langle\vec{V}(0)\cdot\vec{V}(t)\rangle = \frac{2k_BT}{\rho m}\frac{1}{[4\pi(D+\nu)t]^{3/2}},$$

here k_B is Boltzmann's constant, T the temperure, m the mass of the particles, D the self-ffusion coefficient, and ν the kinematic viscosy.

However, in molecular-dynamics calculations, the asymptotic behavior $\alpha_0 t^{-3/2}$ can be observed only for times t such that the boundary conditions have no influence on the vaf. More precisely, the time t has to be smaller than some characteristic time $t_0 \sim l/c$, where l is the length of the edge of the cubic box containing the system and c is the sound velocity. Thus, when the number of particles is too small, at any density, l is too small for the asymptotic regime to be reached for $t < t_0$. In the work of Alder and Wainwright[1] on hard spheres, the number of particles is 500 and t_0 is nearly equal to the time when the asymptotic regime starts. The aim of the present study is to calculate the velocity autocorrelation of a fluid system with a number of particles sufficiently large for the asymptotic regime to be reached at a time $t < t_0$. This allows an accurate test of the validity of the above expression for α_0 at high density.

We have computed the vaf for a system of 4000 particles interacting through a potential

$$V(r) = 4\epsilon[(\sigma/r)^{12} - (\sigma/r)^6] + \epsilon \quad \text{for} \quad r \leq 2^{1/6}\sigma,$$
$$= 0 \quad \text{for} \quad r > 2^{1/6}\sigma.$$

The density is $\rho = 0.45$ particles/σ^3 and the temperature $T = 2.17\epsilon/k_B$. At this density and temperature the thermodynamic properties are

$$P/\rho k_BT = 2.72, \quad U_i/Nk_BT = 0.347,$$
$$C_v/k_B = 1.89, \quad (k_BT)^{-1}(\partial P/\partial T) = 5.70,$$
$$(k_B\rho)^{-1}(\partial P/\partial T)_\rho = 2.34,$$

where P is the pressure, U_i the internal energy, and C_v the specific heat at constant volume. These thermodynamical properties are computed either in the molecular-dynamics calculation, or by the perturbation theory[4] which is accurate to within a few percent. The sound velocity is $c = 0.621\sigma/\tau_0$, where τ_0 is the chosen time unit

$$\tau_0 = (m\sigma^2/48\epsilon)^{1/2}.$$

At the density considered, the system is enclosed in a cube whose edge is

$$l = 20.714\sigma,$$

so that $t_0 \sim 33\tau_0$. The movement of the particles is calculated by the algorithm

$$\vec{x}_i(t+h) = \vec{x}_i(t-h) - 2\vec{x}_i(t) + h^2\vec{F}_i(t),$$
$$\vec{v}_i(t+h) = \vec{v}_i(t-h) + 2h\vec{F}_i(t),$$

where $\vec{x}_i(t)$ and $\vec{v}_i(t)$ are the position and velocity of particle i at time t; h is the integration step, $h = 0.032\tau_0$.

The vaf $f(t)$ is obtained at time $t = kh$, where k

TABLE I. Normalized vaf of the two molecular dynamics computations and the weighted average. The time t is divided by the step of the integration h.

t/h			
0	1.0	1.0	1.0
20	0.69170	0.69166	0.69169
40	0.41428	0.41378	0.41410
60	0.25893	0.25834	0.25872
80	0.17202	0.17135	0.17178
100	0.12202	0.12118	0.12172
120	0.09166	0.09070	0.09131
140	0.07162	0.07091	0.07136
160	0.05735	0.05711	0.05726
180	0.04655	0.04663	0.04658
200	0.03845	0.03870	0.03854
220	0.03217	0.03243	0.03226
240	0.02723	0.02711	0.02719
260	0.02305	0.02272	0.02293
280	0.01986	0.01905	0.01957
300	0.01716	0.01654	0.01694
320	0.01504	0.01485	0.01497
340	0.01343	0.01334	0.01340
360	0.01224	0.01227	0.01225
380	0.01102	0.01109	0.01105
400	0.00989	0.00960	0.00979
420	0.00903	0.00829	0.00876
440	0.00815	0.00724	0.00782
460	0.00735	0.00654	0.00706
480	0.00658	0.00605	0.00639
500	0.00599	0.00555	0.00583
520	0.00551	0.00527	0.00542
540	0.00513	0.00494	0.00506
560	0.00469	0.00492	0.00477
580	0.00440	0.00485	0.00656
600	0.00431	0.00454	0.00439
620	0.00421	0.00441	0.00428
640	0.00396	0.00409	0.00401
660	0.00380	0.00399	0.00387
680	0.00382	0.00375	0.00379
700	0.00359	0.00350	0.00356
720	0.00323	0.00356	0.00335
740	0.00312	0.00356	0.00328
760	0.00324	0.00339	0.00329
780	0.00320	0.00340	0.00327

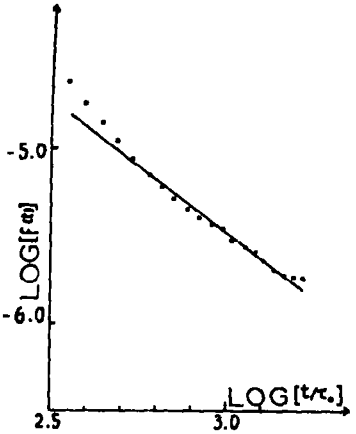

FIG. 1. The log-log plot of the function $f(t)$ for $t > 400h$ (dots). The full line is a straight line with a slope $-\frac{3}{2}$.

is an integer, by the formula

$$f(kh)=\frac{\sum_{l=k_0,k_0+n,\ldots}^{p}\left\{\sum_{i=1}^{N}\vec{v}_i(lh)\cdot\vec{v}_i[(l-k)h]\right\}}{\sum_{l=k_0,k_0+n,\ldots}^{m}\left\{\sum_{i=1}^{N}\vec{v}_i(lh)\cdot\vec{v}_i(lh)\right\}},$$

where p is the total number of integration steps carried out from given initial conditions. For practical reasons, the sum over l is not computed over all integration steps but only for $l=k_0$, $l=k_0+n$, $l=k_0+2n$, $l=k_0+3n, \ldots$ with $n=20$ and $k_0=800$. The maximum value of k is $k_m=780$. The values of p for two calculations done at the same temperature but starting from different initial conditions were $p=18\,600$ and $p=24\,000$.

Last, to avoid any rounding-off error in the calculation, all computations were made using the integer arithmetic of the computer. Each calculation takes about 30 h on a UNIVAC 1110 computer.

The results of the two calculations are given in Table I, together with the weighted average according to the number of integration steps. Figure 1 shows, on a log-log scale, the average vaf. Figure 2 shows the ratio $R(t)$ of the vaf $f(t)$ to a function $\gamma t^{-3/2}$, where γ is chosen so that for $t=620h$ this ratio is 1.

From the numbers of Table I, one can estimate the statistical error on the vaf: The difference between the two calculations is maximum for $k=740$, where it amounts to 14% of the average value of $f(t)$. Between $t=0$ and $t=200h$, this difference is smaller than 1%, between $t=220h$ and

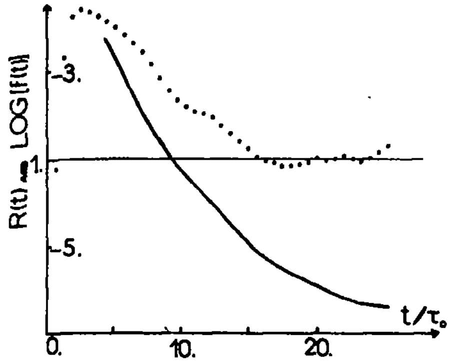

FIG. 2. The ratio $f(t)t^{3/2}/\gamma$ (dots) and the function $\log f(t)$ (full curve) versus t.

$400h$ it is of the order of 2% but sometimes reaches 4%; finally between $400h$ and $780h$ it is roughly 5 or 6%, with the already mentioned exception at $740h$. The average error on $f(t)$, for $t > 400h$, can therefore be estimated to be 7 or 8%. The maximum time for which $f(t)$ is calculated is $t_m \simeq 25\tau_0$. This time is sufficiently smaller than $t_0 \sim 33\tau_0$ for the effect of the boundary conditions to be negligible.

Figure 1 shows the log-log plot of $f(t)$: For $t > 460h$ the plot is nearly linear. This result is confirmed in Fig. 2, where the ratio $R(t) = f(t)/\gamma t^{-3/2}$ fluctuates around 1 for $t > 460h$. The amplitude of the oscillation of $R(t)$ around 1 is never greater than 7%, which is within the error on $f(t)$.

If one assumes that for $t > 460h$, $f(t)$ is of the form $f(t) \sim \alpha t^{-3/2}$ with $\alpha = \alpha_0 m/3k_B T$ one finds for α the value

$$\alpha = (0.377 \pm 0.01)\tau_0^{3/2}$$

[the uncertainty takes into account the statistical uncertainty in $f(t)$]. This value can be compared with the value predicted by Eq. (1).

If one integrates the vaf from $t = 0$ to $t \sim 460h$ (the time at which the asymptotic $t^{-3/2}$ behavior is reached) one gets a diffusion coefficient $D = 0.0764$. If one then calculates the contribution due to the long-time tail of the vaf, with the value of α given above, one obtains 0.0088, yielding a total D of 0.0852. The contribution of the long-time tail between $t = 460h$ and $t = 780h$ is 0.0020.

The calculation of the kinematic viscosity has been made by one of us by simulation of a Couette flow[5] through molecular dynamics; the result is $\nu = 0.143 \pm 0.03$. The corresponding value for α is $(0.31 \pm 0.07)\tau_0^{3/2}$. The uncertainty comes mainly from the uncertainty in ν; the uncertainty in D is less than 1%. One sees, therefore, that the transport coefficients obtained by molecular dynamics are compatible with Eq. (1). At this degree of accuracy, there is no need to introduce "bare" transport coefficients.[6]

Our calculation shows that the asymptotic regime is reached after a relatively short time. Since the interparticle potential is purely repulsive and of finite range, one can define a collision time using the equivalent hard-sphere radius of perturbation theory.[4] At the density and temperature considered, this collision time is $\tau_{\text{col}} = 0.797\tau_0 = 25.53h$. The asymptotic regime is therefore reached after approximately 18 collisions.

Note that the accuracy of our calculation does not enable us to test the predictions concerning the corrections[7] to the main term $\alpha t^{-3/2}$. The coefficient in front of the $t^{-7/4}$ term is indeed a hundred times smaller than α when it is computed using the equivalent hard-sphere radius and the Enskog formulas for the transport coefficients.

For times smaller than $400h$, when the asymptotic regime is not yet reached, the present results are identical to those already obtained[8] at similar density and temperature. In this temperature range, there are two relaxation regimes for the vaf, one quasi-Gaussian, at small times $(0 < t < 200h)$, the other quasi-exponential at times $200h < t < 440h$. This can be seen in Fig. 2. This behavior can be represented in terms of memory function as in Ref. 8.

A last remark concerns the possibility of experimentally observing the asymptotic regime, for example, in argon. The only possibility seems to be to use neutron diffraction measurements of the incoherent dynamic structure factor $S_s(k, \omega)$. One knows that

$$\tilde{f}(\omega) = \lim_{k \to 0} \frac{m\omega^2 S_s(k, \omega)}{k_B T k^2},$$

where $\tilde{f}(\omega)$ is the Fourier transform of $f(t)$ and $\vec{k}$ is the wave vector, and one expects that

$$\tilde{f}(\omega) \sim b - a\alpha\sqrt{\omega} + \dots,$$

where a, b are some constants. In our calculation, such a behavior is reached for $\omega < 0.02\tau_0^{-1}$. On the other hand, the analysis made in Ref. 8 shows that the amplitude $c_s(k, t)$ of the current autocorrelation function, whose Fourier transform is $\omega^2 S_s(k, \omega)$, decreases very rapidly for large times $(t > 200h)$ when k increases; it is therefore difficult to make the $k=0$ extrapolation in Eq. (2) when $\omega \to 0$.

This molecular-dynamics calculation shows that the vaf of a dense gas at a near-critical temperature behaves asymptotically like $\alpha t^{-3/2}$; the value of the coefficient α can be deduced from the transport coefficients ν and D. These results confirm those obtained by Alder and Wainwright[1] and by Wood[9] for systems of 500 and 4000 hard spheres.

The authors are particularly grateful to L. Verlet and J. J. Weis for their help in realizing this work.

---

*Laboratoire associé au Centre National de la Recherche Scientifique.

[1] B. J. Alder and T. E. Wainwright, Phys. Rev. A 1, 18 (1970).

[2] J. R. Dorfman and E. G. D. Cohen, Phys. Rev. A 6, 776 (1972).

[3] Y. Pomeau, Phys. Rev. A 5, 2569 (1972); M. H. Ernst, E. H. Hauge, and J. M. J. van Leeuwen, Phys. Rev. A 4, 2055 (1971).

[4] H. C. Andersen, J. D. Weeks, and D. Chandler, Phys. Rev. A 4, 1597 (1971).

[5] W. T. Ashurst and W. G. Hoover, Bull. Amer. Phys. Soc. 17, 1196 (1972), and Phys. Rev. Lett. 31, 206 (1973).

[6] R. Zwanzig, in *Proceedings of the Sixth IUPAP Conference on Statistical Mechanics*, edited by S. A. Rice, K. F. Freed, and J. C. Light (University of Chicago Press, Chicago, Ill., 1972); R. Kapral and M. Weinberg, Phys. Rev. A 8, 1008 (1973).

[7] Y. Pomeau, Phys. Rev. A 7, 1134 (1973).

[8] D. Levesque and L. Verlet, Phys. Rev. A 2, 2514 (1970).

[9] W. Wood, private communication.

Photographs of Quantized Vortex Lines in Rotating He II*

Gary A. Williams and Richard E. Packard
University of California, Berkeley, California 94720

(Received 28 May 1974)

The spatial positions of discrete quantized vortex lines in rotating superfluid helium have been directly visualized by a photographic technique. The positions of the lines in the apparatus do not form a regular array.

The unique properties of He II have been associated with the existence of a macroscopic wave function which determines the behavior of the superfluid component. From this idea Onsager[1] and Feynman[2] predicted that He II should exhibit vorticity with circulation quantized in units of h/m, where h is Planck's constant and m is the mass of the helium atom. For almost two decades physicists have been exploring theoretically and experimentally the phenomena associated with these vortices.[3] A wealth of convincing information is available which supports the existence of vortices, the most direct experiments being those which proved that circulation in He II is quantized[4,5] and that He II comes into rotation in a series of quantum steps.[6] There has still been one experiment which has enticed workers for some time: actually to make directly visible the discrete vortex lines in the rotating He II. (An analogous experiment has been done to visualize fluxoids in a superconductor.[7]) This Letter describes the first successful experiment which records the positions of the vortex lines in helium. We point out that according to current ideas the vortex core is a node in the macroscopic wave function. This is one of the only measurements we know which directly measure the positions of the nodes of a wave function.

The method we employ is conceptually simple.[8] Vortex lines should appear in a container of He II rotating at angular velocity ω, with a predicted density[2] of $2\omega m/h$ lines/cm^2. Electrons formed near a radioactive source are injected into the rotating He II. The electrons form bubbles (radius ~ 16 Å) which become trapped on vortex lines in a Bernoulli trapping potential.[9] The lines are charged for about 10 sec, after which an axial electric field is applied which pulls the ions through the liquid meniscus. Once free of the liquid, the electrons are accelerated and impinge on a phosphor screen where they produce a flash of light, thus marking the position of the line where it meets the free surface.

There are numerous complications which conspire to defeat the simplicity of this method. First of all, the experiment must be done at temperatures below 0.6 K so that the helium vapor pressure is low enough to allow the use of elecon optics. Second is the empirical fact that ectrodes in the space above the liquid will sup-ort a potential difference of only about 500 V ithout an electric discharge occurring. This mits the electron accelerating energy and con-quently the light output. A more fundamental oblem is the question of stability of the vortex nes. Although calculations show that in equilib-ium the vortices should form a triangular lat-ce,[10,11] at rest in the rotating frame, it is not nown how large a disturbance would be neces-ary to destroy the regularity of the array. Sev-ral authors have presented the opinion that the ortices would not exhibit a rigid lattice in a real ituation.[10,12]

The basic experimental configuration is shown Fig. 1. Electrons, formed near a 13-mCi tri-um source, are manipulated by applied poten-als so that they become trapped on the vortex nes. When the maximum charge is stored, the urce is switched off and the charge is extracted d accelerated into a ZnO:Zn phosphor. An ax-l magnetic field of 3 kG prevents defocusing of e electrons. The phosphor is deposited onto a ber optics disc which is covered with a transpar-t conductive coating.[13] The disc butts against a 3.2-mm-diam image conduit which conveys the light to room temperature.[14] The light signal is quite weak (of the order of 100 photons per vortex line at the room-temperature end) and is amplified with a three-stage image intensifier.[15] The intensifier output is imaged 1:1 onto high-speed recording film[16] through optics with an effective aperture of $f/0.9$. The overall system, including the electron optics, has a resolution of approximately 10 lines/mm at 30% modulation and a sensitivity sufficient to record an image due to several hundred electrons hitting the phosphor at one point within a 30-msec period.

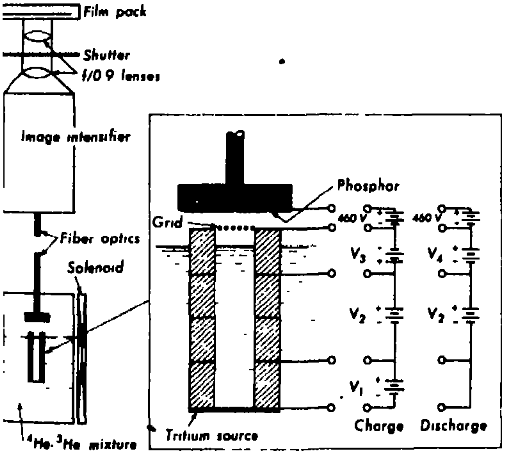

FIG. 1. Cross-sectional sketch of the electron op-s used to photograph vortex lines. The chamber ntaining the cell is cooled by a dilution refrigerator. e inset shows the electrodes used to charge and dis-arge the vortex lines. In the 0.8% mixture the bias tentials used were $V_1=45$, $V_2=90$, $V_3=8$, and V_4 5 V. The "bucket" is 3 cm long and consists of a 8-mm-diam hole drilled in four carbon resistors ef. 6). The voltage gradient along the resistive walls oduces the required electric fields.

This system was initially part of a ^{3}He refrigerator which allowed the cell to be cooled to 0.3 K.[17] The entire apparatus, including the camera system and refrigerator, is smoothly rotated on an air bearing. Extensive resolution tests showed that this apparatus possessed the sensitivity and resolution to photograph individual vortices. However, the actual photographs using rotating He II showed no discernible detail; i.e., the image of the light, produced by the electrons emitted by the vortices, was a complete blur. We conclude that at temperatures near 0.3 K the vortex array in ^{4}He is not stable on the time scale of the exposure time (~30 msec). This is not surprising because at low temperatures there is a negligible amount of normal fluid to damp any nonequilibrium motion of the lines. The instability of the vortex array can also be seen in measurements of trapped-electron lifetimes.[18]

In order to stabilize the vortices we decied to add ^{3}He to the superfluid. At low temperatures the ^{3}He acts as a fixed amount of normal fluid and thus provides a damping mechanism for nonequilibrium motion of the vortices. Since the addition of ^{3}He raises the vapor pressure of the fluid[19] it was necessary to perform the experiment at temperatures lower than 0.3 K. Thus we assembled a rotating dilution refrigerator[20] which provides temperatures below 0.1 K. The inset in Fig. 1 shows the cell used for the mixtures.

The addition of ^{3}He does indeed act to stabilize the vortices and we finally see, for the first time, the image of the vortex-line positions. Figure 2 shows three typical photographs taken with a ^{3}He concentration of 0.8%. The concentrated white spots mark the location of the vortex lines. Based on approximately 50 such pictures, several comments can be made.

(1) A stable triangular lattice is not apparent in the photographs.

(2) Even with 0.8% ^{3}He there is still some mo-

FIG. 2. Photographs of discrete quantized vortex lines in He II rotating at (a) $\omega = 0.25$ sec^{-1}, (b) $\omega = 0.5$ sec^{-1}, (c) $\omega = 1.0$ sec^{-1}. The temperature was approximately 75 mK, exposure time 60 msec. The distinct bright spots mark the positions of the lines where they meet the free surface. Because of a slight misalignment of the fiber optics the field of view in these pictures is only about one half of the bucket. The center of the picture does not coincide with the center of the bucket.

tion of the vortices, as deduced from the fact that consecutive photographs, taken less than 1 min apart, show no similarity in the distribution of vortex lines. Whether the random motion of the vortices is intrinsic to the rotating He II or is caused by mechanical disturbances in the apparatus is difficult to determine. The rotating refrigerator is supported on an air bearing and we have taken precautions to eliminate most sources of vibration. Nevertheless, only future tests will shed light on this question

(3) Well above the predicted critical velocity for the first line the pictures show that the number of lines increases linearly with angular velocity but there are less than $2\omega m/h$ lines per unit area (20 lines/mm^2 for $\omega = 1$ sec^{-1}). Our method records only those vortices which have not migrated to the walls during the 10-sec charging period. In addition the line must terminate at the free surface rather than the bucket's wall. We as yet do not have enough data to make any quantitative statements on the fraction of lines which might not be displayed in the pictures. In the pictures taken in the 0.8% mixture there seem to be about one half the number of lines predicted from theory.

(4) When many lines are visible the nearest-neighbor spacing is approximately $(h/2\omega m)^{1/2}$ as expected from Feynman's argument.

(5) We have thus far taken pictures at ^{3}He concentrations of 0.1, 0.4, and 0.8%. It seems that the lines become more stable at the higher concentrations. Future observations will explore this phenomenon.

An obvious question to ask is what is the evidence that the dots in the photographs do indeed mark the positions of the vortex lines? We have performed several tests to check this point.

(i) Using a tunnel-cathode emitter and a pinhole grid to simulate the low-energy electrons leaving the vortex lines, we found that with the magnetic focusing field on, the charge was accurately imaged onto the phosphor. With the field off, a uniform blur was obtained. In the actual helium experiment if the focusing field is turned off the dots in the picture disappear, producing a uniform blur.

(ii) If the electric field in front of the radioactive source is turned off, the photographs show no signal with a typical exposure time (60 msec). A longer exposure (500 msec) shows a uniform background, presumably caused by the ultraviolet light produced in the liquid helium near the radioactive source.

Now that we have demonstrated the feasibility of this vortex-line imaging system there are numerous interesting questions whose answers can be sought. The most useful extension of this technique would be the addition of a TV system to provide a real-time image of the lines. Then one could hope to observe the detailed motion of the lines in the vessel and thereby determine if classical hydrodynamics accurately determines the line motion. In addition one could see where the lines are created.

Our immediate plans are to learn about the stability conditions of the vortex array by photographing the vortices in various geometries and state preparations, and different ^{3}He concentraions.

In summary, we have produced direct visual vidence that individual, discrete vortex lines xist as predicted by Feynman and Onsager. It pears that under our experimental conditions o stable vortex array is observed; rather the otating He II exists in a dynamic state involving mplex motion of vortex lines.

We are grateful to T. M. Sanders who suggested e electron trapping technique and provided any stimulating discussions. We also thank . DeConde and F. Reif who gave frequent help- l comments.

---

*Work supported by the National Science Foundation.

[1] L. Onsager, Nuovo Cimento 6, Suppl. No. 2, 249 1949).

[2] R. P. Feynman, in *Progress in Low Temperature hysics*, edited by C. J. Gorter (North-Holland, Amsterdam, 1955), Vol. 1.

[3] For example, see J. Wilks, *The Properties of Liq- id and Solid Helium* (Clarendon Press, Oxford, Eng- nd, 1967), Chaps. 12 and 13; R. J. Donnelly, *Experi- ental Superfluidity* (The University of Chicago Press, hicago, 1967), Chap. 2.

[4] W. F. Vinen, Proc. Roy. Soc., Ser. A 260, 218 1961); S. C. Whitmore and W. Zimmermann, Jr., hys. Rev. 166, 181 (1968).

[5] G. W. Rayfield and F. Reif, Phys. Rev. 136, A1194 1964).

[6] R. E. Packard and T. M. Sanders, Jr., Phys. Rev. A , 799 (1972).

[7] H. Trauble and U. Essman, J. Appl. Phys. 39, 4052 (1968).

[8] For another approach see J. Maynard, thesis, Princeton University, 1973 (unpublished).

[9] P. E. Parks and R. J. Donnelly, Phys. Rev. Lett. 16, 45 (1966).

[10] D. Stauffer and A. L. Fetter, Phys. Rev. 168, 156 (1967).

[11] V. K. Tkachenko, Zh. Eksp. Teor. Fiz. 50, 1573 (1966) [Sov. Phys. JETP 23, 1049 (1966)].

[12] P. G. DeGennes, in *Proceedings of the Ninth International Conference on Low Temperature Physics, Columbus, Ohio, 1964*, edited by J. G. Daunt *et al.* (Plenum, New York, 1966), p. 25.

[13] R. Gomer, Rev. Sci. Instrum. 24, 993 (1953).

[14] The details of the cryogenic seals to the fiber optics can be seen in G. A. Williams and R. E. Packard, to be published.

[15] Model No. 8586, Varo Corp., Garland, Texas.

[16] Film No. 2485, Eastman Kodak, Rochester, New York. Developed at ASA 6400.

[17] G. A. Williams and R. E. Packard, in *Proceedings of the Thirteenth International Conference on Low Temperature Physics, Boulder, Colorado, 1972*, edited by W. J. O'Sullivan, K. D. Timmerhaus, and E. F. Hammel (Plenum, New York, 1973).

[18] K. DeConde, G. A. Williams, and R. E. Packard, to be published.

[19] R. Radebaugh, *Thermodynamic Properties of He^3–He^4 Solutions with Applications to the He^3–He^4 Dilution Refrigerator*, U. S. National Bureau of Standards Technical Note No. 362 (U. S. GPO, Washington, D. C., 1967).

[20] The details of the rotating vacuum seals for the rotating dilution refrigerator are in G. A. Williams and R. E. Packard, to be published.

Mass-Fluctuation Waves in Solid ^{3}He-^{4}He Mixtures*

Whittak Huang, H. A. Goldberg, M. T. Takemori, and R. A. Guyer
Department of Physics and Astronomy, University of Massachusetts, Amherst, Massachusetts 01002

(Received 22 January 1974)

We give an explanation of the data of Richards, Pope, and Widom in terms of the incoherent tunneling of strongly interacting particles.

The concept of "impuritons" or "mass-fluctua- on waves" was invented independently by An- reev and Lifshitz[1] and Guyer and Zane.[2] The arly survey experiments by Myoshi, Cotts, reenberg, and Richardson[3] suggested that dilute olid mixtures of ^{3}He in ^{4}He are a suitable sys- m in which to seek evidence for these excita- ons.[4] Subsequently Greenberg, Thomlinson, nd Richardson[5,6] reported T_1 and T_2 measure- ents that showed compelling evidence for ^{3}He tunneling in ^{4}He. Richards, Pope, and Widom (RPW)[7,8] have undertaken an extensive set of measurements on dilute ^{3}He in ^{4}He mixtures designed to find evidence for the coherent motion of the impurity, i.e., for the existence of ^{3}He "impuritons." These measurements include diffusion data in addition to T_1 and T_2 data. RPW have argued that a diffusion measurement gives a clear signature for coherent motion. Recently Grigor'ev and co-workers[9] have verified the diffusion measurements of RPW.

Many aspects of the data of RPW are consistent with the qualitative features expected using the "impuriton" description of the ^{3}He motion.[7,8] But there are two serious difficulties in the quantification of such a description: (1) The rate of ^{3}He-^{4}He tunneling must be taken to be about 2 orders of magnitude below what is regarded as a plausible theoretical value,[10] and (2) the interaction between ^{3}He impurities must be taken to be about 3 orders of magnitude below what is regarded as a plausible theoretical value.[4] This paper provides an explanation of the measurements of RPW and of Grigor'ev and co-workers in terms of ^{3}He tunneling in the presence of a strong ^{3}He-^{3}He interaction.

The theory of ^{3}He motion through solid ^{4}He that we discuss depends in a crucial way on the ^{3}He-^{3}He interaction. To learn about this interaction we reformulate the mixture problem for general concentration in order to derive the ^{3}He-^{3}He interaction in a framework that permits us to determine its magnitude from first principles and to determine its relationship to the phase-separation problem. We take a mixture of ^{3}He in ^{4}He at concentration $x_3 = N_3/(N_3+N_4)$ to be described by $\mathcal{H} = \bar{\mathcal{H}} + \mathcal{H}'$, where

$$\bar{\mathcal{H}} = \sum_R \tfrac{1}{2} p_R^2 \langle m^{-1} \rangle + V, \tag{1}$$

$$\mathcal{H}' = \sum_R \tfrac{1}{2} p_R^2 (m_R^{-1} - \langle m^{-1} \rangle) = \sum_R \Delta \bar{K}(R), \tag{2}$$

with $\langle m^{-1} \rangle = x_3 m_3^{-1} + (1-x_3) m_4^{-1}$ and V the pairwise atom-atom interaction between atoms localized on lattice sites R. We solve the ground-state problem for the average crystal described by $\bar{\mathcal{H}}$ at various concentrations, employing a typical quantum-crystal procedure,[10] and find a set of low-lying single-particle states and the corresponding t-matrix elements required to second quantize $\mathcal{H}$. Using the states and matrix elements appropriate to concentrations x_3, we obtain the Hamiltonian in the form

$$\mathcal{H}(x_3) = E_0(x_3) + \mathcal{H}_p + \mathcal{H}_I, \tag{3}$$

where $E_0(x_3)$ is the ground-state energy of the average crystal, $\mathcal{H}_p$ is the phonon Hamiltonian, and

$$\mathcal{H}_I = -\sum_{RR'} \Delta \bar{K}(R)_{02} \mathfrak{D}(RR') \Delta \bar{K}(R')_{02}. \tag{4}$$

Here

$$\Delta \bar{K}(R)_{02} = -\tfrac{1}{2}\hbar^2 (\nabla^2)_{02} (m_R^{-1} - \langle m^{-1} \rangle)$$

and

$$\mathfrak{D}(RR') = \sum_{SS'} t(R,S)_{02,01} (\Delta\epsilon_{20})^{-1} D(SS') (\Delta\epsilon_{20})^{-1} t(S'R')_{01,02}. \tag{5}$$

We have used three low-lying single-particle states: the ground state 0, the displacement state 1, and the width-fluctuation state 2.[11] The t-matrix element $t(R,S)_{02,01}$ is the coupling of a width fluctuation at R [due to the deviation of $m^{-1}(R)$ from $\langle m^{-1} \rangle$] to a displacement fluctuation at S; it is proportional to the cubic anharmonicity. $\Delta\epsilon_{20} = \epsilon_2 - \epsilon_0$; $D(SS')$ is the inverse of the dynamical matrix. We evaluate $D(SS')$ using elastic continuum theory[12] and determine $\Delta \bar{K}(R)_{02} (\Delta\epsilon_{20})^{-1} t(RR')_{02,01}$ by comparison of the theoretical near-neighbor displacement $u_{R'} = x_{01} (\Delta\epsilon_{10})^{-1} t(R'R) (\Delta\epsilon_{20})^{-1} \Delta K(R)_{02}$ with the numerical results of Mullin[13] and Glyde.[14] Altogether we obtain

$$\mathcal{H}_I = -V_0 \sum_{RR'} (\Delta / |\vec{R} - \vec{R}'|)^3 [n_3(R) - x_3][n_3(R') - x_3], \tag{6}$$

with $V_0/k_B \approx 10^{-3}$ K at 21.0 cm^3/mole and Δ the interparticle spacing. Phase separation is determined entirely by $E_0(x_3)$ and involves basic energies quite different in source and magnitude from the energies associated with $\mathcal{H}_I$.

Our primary concern is to determine the effect of $\mathcal{H}_I$ on the propagation of a ^{3}He impurity through ^{4}He. It is important to note that the rate of ^{3}He-^{4}He tunneling, $J_{34}/\hbar$, is expected to be at most comparable with[4] $|J_{33}|/\hbar \approx 5 \times 10^{-5}$ K so that we have $|J_{34}|/V_0 < 10^{-2}$. We take $x_3 < 10^{-2}$ as defining the low-concentration region which we further divide into a *dilute region*, $\bar{x} < x_3 < 10^{-2}$, and an *"impuriton" region*, $0 < x_3 < \bar{x}$.

The primary effect of the interaction in $\mathcal{H}_I$ is to hinder the tunneling of a ^{3}He-^{4}He pair. In the initial configuration, ^{3}He at R and ^{4}He at R', the potential energy of the pair is

$$V(RR') = -V_0 \sum_{S \neq (RR')} \left[\left(\frac{\Delta}{|\vec{R} - \vec{S}|} \right)^3 (1 - x_3) - \left(\frac{\Delta}{|\vec{R}' - \vec{S}|} \right)^3 x_3 \right] [n_3(S) - x_3], \tag{7}$$

whereas after the tunneling process we have

$$V(R'R)=+V_0\sum_{S\neq(RR')}\left[\left(\frac{\Delta}{|\mathbf{R}-\mathbf{S}|}\right)^3 x_3-\left(\frac{\Delta}{|\mathbf{R}'-\mathbf{S}|}\right)^3(1-x_3)\right][n_3(S)-x_3], \tag{8}$$

or a net change in potential energy of

$$\Delta V(RR')=-V_0\sum_{S\neq(RR')}\left[\left(\frac{\Delta}{|\mathbf{R}'-\mathbf{S}|}\right)^3-\left(\frac{\Delta}{|\mathbf{R}-\mathbf{S}|}\right)^3\right][n_3(S)-x_3)]. \tag{9}$$

If $\Delta V(RR')$, proportional to the gradient of $\mathcal{H}_I$, is small compared to J_{34}, the tunneling process occurs easily; if $\Delta V(RR')$ is larger than J_{34}, the tunneling process is hindered. In this latter circumstance energy can be conserved in the transition only if the tunneling is accompanied by the absorption or emission of a phonon. But a sequence of phonon-assisted steps is incoherent. Thus we expect that a ^{3}He impurity will propagate as an impuriton in regions of space where the gradient of $\mathcal{H}_I$ is small. At the very lowest concentrations a ^{3}He impurity propagates coherently as an impuriton until it approaches within $\bar{r}$ of a second impurity, where $\bar{r}$ is defined by $J_{34}=\Delta|\nabla\mathcal{H}_I(\bar{r})|$. Thus $\pi\bar{r}^2\approx\pi\Delta^2(3V_0/J_{34})^{1/2}$ is the cross section for impuriton-impuriton scattering and the corresponding mean free path is

$$\lambda=(\Delta/\pi x_3)(J_{34}/3V_0)^{1/2}. \tag{10}$$

So in the "impuriton" region the diffusion constant is

$$D_I\approx\pi^{-1}\Delta^2 J_{34}(J_{34}/3V_0)^{1/2}(1/x_3). \tag{11}$$

As the concentration is increased through the value $\bar{x}$ to concentrations at which a typical ^{3}He atom is continually in interaction with its neighbors, the calculation of D proceeds differently than above. At $x_3>\bar{x}$ the Kubo formula[15] for D can be manipulated to yield

$$D_D=z(\pi/6)\Delta^2 J_{34}P(0), \tag{12}$$

where $P(0)$ is the probability that $\Delta V(RR')$ is of order $2|J_{34}|$. This equation describes diffusion over steps of length Δ at the rate $J_{34}P(0)$. This rate involves two factors: J_{34}, an attempt frequency (for the transition $RR'\rightarrow R'R$), and $P(0)$, the probability that the transition can go (that the energy difference between the two arrangements if of order J_{34} and the transition $RR'-R'R$ is energy conserving). We have made a Monte Carlo study of the spectrum of $\Delta V(RR')$, Eq. (9), and of $P(0)$ as a function of concentration for various values of the ratio $|J_{34}|/V_0$. For the choice $J_{34}=0.5|J_{33}|=2.5\times10^{-5}$ K and $V_0=10^{-2}$ K we find the results for D shown in Fig. 1. The spectrum of $\Delta V(RR')$ is strongly peaked near zero at low concentrations, $P(0)$ approaches 1 as x_3 gets small, and $P(0)$ is greater than $\frac{1}{2}$ at $x_3=10^{-2}$ (see Fig. 2). The behavior we find for D_D is similar to that described by Landesman and Winter.[16] At $x_3<10^{-2}\approx\bar{x}$ a ^{3}He has a better than 50% probability of being in a low-gradient region. Thus we expect impuriton behavior at $x_3\ll\bar{x}$. The results of a generalization of this procedure to include multistep processes are also shown in Figs. 1 and 2.

Can this discussion of the D data also lead to a satisfactory explanation of the T_1 and T_2 data? We begin by exhibiting an expression for T_2 as $\omega_0\rightarrow0$:

$$\frac{1}{T_2}=M_2(1)x_3\left[\sum_{R'\neq(R)}\left(\frac{\Delta}{|\mathbf{R}-\mathbf{R}'|}\right)^6\int_0^{+\infty}dt\,\langle\langle n_3(R,0)n_3(R',0)n_3(R,t)n_3(R',t)\rangle\rangle\Big/\sum_{R'\neq(R)}\left(\frac{\Delta}{|\mathbf{R}-\mathbf{R}'|}\right)^6\right]. \tag{13}$$

This formula exhibits the most important feature of T_1 and T_2 data. Because the dipolar field falls off so rapidly, r^{-6}, the pairs of particles that make important contributions to T_1 and T_2 are always well within the interaction range $\bar{r}$ where the particle motions are incoherent. Thus it is *impossible* to see impuriton behavior in T_1 and T_2 data. To carry out a calculation of T_2 we approximate the correlation function in Eq. (13) by assuming that the particles at R and R' move separately; i.e.,

$$\langle\langle n(r,0)n(R',0)n(R,t)n(R',t)\rangle\rangle\approx\langle\langle(R,0)n(R,t)\rangle\rangle_R\langle\langle n(R',0)n(R',t)\rangle\rangle_R;$$

here the subscript on $\langle\langle n(R,0)n(R,t)\rangle\rangle_{R'}$ means that we calculate the correlation function for a particle at R given that there is a ^{3}He spectator particle fixed at R'. Following an argument similar to that

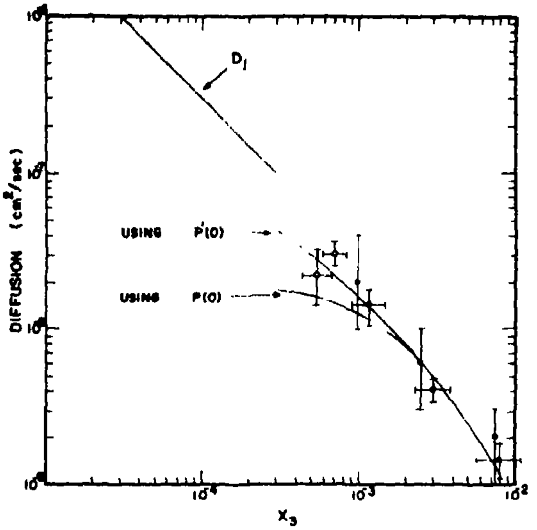

FIG. 1. Diffusion constant as a function of concentration. In the range $6\times10^{-4}<x_3<2\times10^{-2}$ the value of D given by Eq. (12) with $V_0=10^{-2}$ and $J_{34}=2.5\times10^{-5}$ is shown as the lower solid line. The data of Richards, Pope, and Widom and Grigor'ev and co-workers are indicated as open and closed circles, respectively. At low concentration we show the value of D in the "impuriton" region calculated from Eq. (11) using V_0 and J_{34} as above. We also show the results of an improvement in the theory which includes the possibility of particle motion over more than one step, the curve labeled $P'(0)$. These multistep processes are important at lower concentrations, $x_3\lesssim10^{-3}$.

leading to Eq. (12) for the diffusion constant, we obtain

$$\frac{1}{T_2(0)}=M_2(1)x_3\,\frac{1}{\pi J_{34}\bar{P}(0)}$$
$$\equiv M_2(1)x_3\,\frac{1}{W_2(x_3)_{RR'}},\qquad(14)$$

where $\bar{P}(0)$ is the weighted average of $P_{R''}(0)$, the probability that $\Delta V(RR')$ is of order J_{34} given that there is a spectator ^{3}He at R''. The weighting factor is $|R-R''|^{-6}$. We have made Monte Carlo studies of $\bar{P}(0)$ and $W_2(x_3)_{RR'}$ for the choice $J_{34}/V_0=2.5\times10^{-3}$ for various concentrations. For $x_3<10^{-2}$ we find $W_2(x_3)_{RR'}$ to be essentially independent of x_3 and of order 4×10^4 rad/sec (see Fig. 2). Thus in both the dilute and impuriton regions we have $T_2^{-1}\propto x_3$. We state this result for T_2 in terms of the ratio of D to T_2. We find from Eqs. (12) and (14) that

$$D/T_2=M_2(1)\Delta^2x_3[2P(0)/\bar{P}(0)].\qquad(15)$$

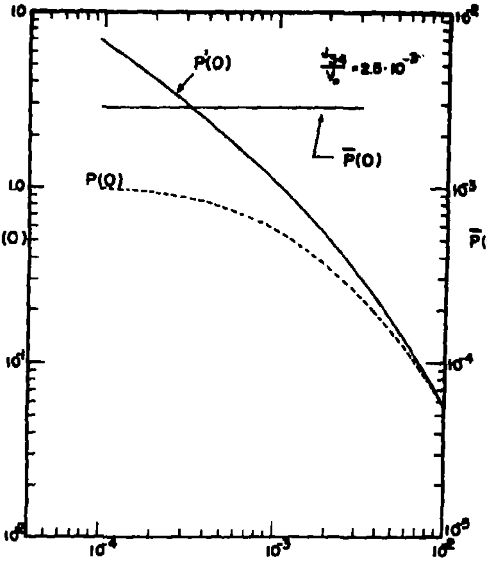

FIG. 2. $P(0)$ and $\bar{P}(0)$ as a function of concentration. $P(0)$ is read from the left-hand scale and $\bar{P}(0)$ is read from the right-hand scale. Monte Carlo studies of Eq. (4) permit the calculation of $P(0)$ and $\bar{P}(0)$ as a function of concentration. The probability $P(0)$ approaches 1 at $x_3\ll10^{-3}$; it has value $\frac{1}{2}$ at $x_3\approx10^{-3}$. Thus we take 10^{-3} as the lower edge of the dilute region. The probability $\bar{P}(0)$ is essentially concentration independent for $x_3<10^{-2}$. We also show $P'(0)$, a generalization of $P(0)$ to processes of more than one step.

Using the results from our Monte Carlo studies of $P(0)$ and $\bar{P}(0)$ shown in Fig. 2 [$P'(0)\approx10^{-3}x_3^{-1}$, $\bar{P}(0)\approx3\times10^{-3}$], we find

$$D/T_2\approx0.7M_2(1)\Delta^2.\qquad(16)$$

This result is in reasonable agreement with the observations of RPW who find that this ratio (for their experiments) is the same as for gaseous ^{3}He.

We find that an interaction model, applied in the dilute-concentration region, can satisfactorily explain both the D and T_2 data of Richards, Pope, and Widom. Further this model makes use of plausible values of the parameters required to describe the system. For $V_0\approx10^{-2}$ K we require $J_{34}\approx\frac{1}{3}|J_{33}|$. We believe that a more satisfactory explanation of the behavior of ^{3}He impurities in the dilute-concentration region $F<x_3<10^{-2}$ is given by this model than by the "impuriton" model. We set an upper limit on the concentration at which impuriton behavior occurs, $x_s \ll \bar{x} = 10^{-8}$. The interaction model yields a simple explanation of the strong volume dependence of the basic rate observed by Greenberg, Thominson, and Richardson and by Grigor'ev and coworkers.

We would like to thank Professor H. Wagner for offering the hospitality of Institute für Festkörperforschung der Kernforschungsanlage where this work was begun.

---

*Work supported in part by the National Science Foundation and the Alexander von Humboldt Foundation.

[1] A. F. Andreev and I. M. Lifshitz, Zh. Eksp. Teor. Fiz. 56, 2057 (1969) [Sov. Phys. JETP 29, 1107 (1969)].

[2] R. A. Guyer and L. I. Zane, Phys. Rev. Lett. 24, 660 (1970).

[3] D. S. Miyoshi, R. N. Cotts, A. S. Greenberg, and R. C. Richardson, Phys. Rev. A 2, 870 (1970).

[4] R. A. Guyer, R. C. Richardson, and L. I. Zane, Rev. Mod. Phys. 43, 532 (1961).

[5] A. S. Greenberg, W. G. Thomlinson, and R. C. Richardson, Phys. Rev. Lett. 27, 179 (1971).

[6] A. S. Greenberg, W. C. Thomlinson, and R. C. Richardson, J. Low Temp. Phys. 8, 3 (1972).

[7] M. G. Richards, J. Pope, and A. Widom, Phys. Rev. Lett. 29, 708 (1972).

[8] M. G. Richards, J. Pope, and A. Widom, in *Proceedings of the Thirteenth International Conference on Low Temperature Physics, Boulder, Colorado, 1972*, edited by W. J. O'Sullivan, K. D. Timmerhaus, and E. F. Hammel (Plenum, New York, 1973).

[9] V. N. Grigor'ev, B. N. Esel'son, V. A. Mikheev, V. A. Slusarev, M. S. Strzhemechny, and Yu. E. Shul'man, J. Low Temp. Phys. 13, 65 (1973); V. N. Grigor'ev, B. N. Esel'son, V. A. Mikheev, and Yu. E. Shul'man, Pis'ma Zh. Eksp. Teor. Fiz. 17, 25 (1973) [JETP Lett. 17, 16 (1973)]; V. N. Grigor'ev, B. N. Esel'son, and V. A. Mikheev, Pis'ma Zh. Eksp. Teor. Fiz. 18, 289 (1973) [JETP Lett. 18, 16 (1973)].

[10] R. A. Guyer and L. I. Zane, Phys. Rev. 188, 445 (1969); see also Ref. 4.

[11] R. A. Guyer, Phys. Lett. 27A, 452 (1968).

[12] P. H. Dederich and G. Liebfried, Phys. Rev. 188, 1175 (1969).

[13] W. J. Mullin, Phys. Rev. Lett. 20, 254 (1968).

[14] H. R. Glyde, Phys. Rev. 177, 202 (1969).

[15] R. Kubo, Can. J. Phys. 34, 1279 (1956).

[16] A. Landesman and J. M. Winter, in *Proceedings of the Thirteenth International Conference on Low Temperature Physics, Boulder, Colorado, 1972*, edited by W. J. O'Sullivan, K. D. Timmerhaus, and E. F. Hammel (Plenum, New York, 1973).

Beam-Plasma Instability in a Nonuniform Plasma

George Schmidt
Stevens Institute of Technology, Hoboken, New Jersey 07030

(Received 24 April 1974)

The behavior of the beam-plasma instability in a nonuniform plasma depends only on the dimensionless quantity $\lambda \sim k_i^{-2}\partial k/\partial x$, where k_i is the spatial growth rate in the homogeneous plasma. If $|\lambda| \gg 1$ the instability is quenched.

The beam-plasma instability for a weak beam in a uniform plasma is the result of resonant coupling between the beam and an eigenmode of the plasma. If the plasma is nonuniform, because of density or magnetic field gradients, the plasma eigenmode characteristics are spatially dependent and one may expect a detuning of the beam plasma resonance along the gradient. Indeed, this process is similar to that of parametric instabilities in nonuniform media where density gradients result in increased thresholds and reduced growths of the instabilities.[1] Gradients are inevitable in experimental arrangements, and therefore it is important to understand their consequences for instabilities. Indeed, there is some experimental evidence of localization and thresholds of the beam-plasma instability due to density gradients along the direction of beam propagation.[2,3]

The problem of quasilinear relaxation of an ultrarelativistic beam with a large velocity spread in an inhomogeneous plasma has been treated by Breizman and Ryutov[4] and the behavior of a wave packet in a cold nonuniform plasma with a cold beam by Vianna and Bers.[5] In the following we investigate the electrostatic instability of a cold electron beam propagating along a weak gradient in the plasma. The gradient can be one of density, temperature, magnetic field, etc.

The linearized equations of motion for an electron beam are

$$-i\omega n + d(Nv + Vn)/dx = 0, \tag{1}$$

$$-i\omega v + V dv/dx + eE/m = 0, \tag{2}$$

where the time dependences have been Fourier decomposed ($e^{-i\omega t}$ dependence), V and N are the equilibrium beam velocity and density, and v and n are the linear deviations from equilibrium. For a relativistic beam the electron mass m is to be replaced by the longitudinal mass $m = m_0\gamma^3$.

Eliminating v between (1) and (2) gives

$$\left(1 + i\frac{V}{\omega}\frac{d}{dx}\right)^2 n + \frac{eN}{m\omega^2}\frac{dE}{dx} = 0. \tag{3}$$

From Poisson's equation

$$dE/dx = -(e/\epsilon_0)(n + n_p), \tag{4}$$

where n_p is the (linearized) electron density in the plasma, $n_p = -i\omega^{-1} dJ_p/dx$, with J_p the electron current density in the plasma. Applying the operator $[1 + i(V/\omega)d/dx]^2$ on (4) and using (3) results, after integration, in

$$\left(1 + \frac{iV}{\omega}\frac{d}{dx}\right)^2 \left[E - \frac{ie}{\epsilon_0\omega} J_p\right] = \frac{\omega_b^2}{\omega^2} E, \tag{5}$$

where ω_b is the plasma frequency associated with the beam. (For the relativistic beam case again $m = \gamma^3 m_0$.) Introducing the plasma conductivity $\sigma(\omega, k)$ and dielectric function $\epsilon(\omega, k)$, one finds

$$E - \frac{ie}{\epsilon_0\omega} J_p = F^{-1}\left[E(k) - \frac{ie}{\epsilon_0\omega}\sigma(\omega, k, x)E(k)\right] = F^{-1}\epsilon(\omega, k, x)E(k), \tag{6}$$

where F^{-1} is the inverse Fourier operator, and σ and ϵ are slowly varying functions of x on the wavelength scale.

Expanding ϵ around $k = k_0$, $x = 0$, where $\epsilon(\omega, k_0, 0) = 0$,

$$F^{-1}\epsilon(\omega, k, x)E(k) = \left(\frac{\partial\epsilon}{\partial k}\right)_{k_0}\left[-i\frac{dE}{dx} - k_0 E\right] + \left(\frac{\partial\epsilon}{\partial x}\right)_0 xE + \dots, \tag{7}$$

one obtains from (5)

$$\left(1 + \frac{iV}{\omega}\frac{d}{dx}\right)^2 \left[\alpha i\frac{d}{dx} + \alpha k_0 - \beta x\right] E = \frac{\omega_b^2}{\omega^2} E, \tag{8}$$

where $\alpha = -(\partial\epsilon/\partial k)_{k_0}$ and $\beta = -(\partial\epsilon/\partial x)_0$. Choosing $k_0 = \omega/V$ (this determines the point $x = 0$), one writes $E(x) = a(x)\exp(ik_0 x)$ to find

$$i\frac{d^3a}{dx^3} - \frac{\beta}{\alpha}x\frac{d^2a}{dx^2} - 2\frac{\beta}{\alpha}\frac{da}{dx} + \frac{\omega_b^2}{V^2\alpha}a = 0. \tag{9}$$

Introducing now the dimensionless length $x(\omega_b^2/V^2\alpha)^{1/3}$ and the parameter $\lambda = (\beta/\alpha)(\omega_b^2/V^2\alpha)^{-2/3}$ leads to the differential equation

$$ia''' - \lambda(xa)'' + a = 0 \tag{10}$$

which depends only on the dimensionless parameter λ.

The solution of (10) may be written as a Fourier transform, using a method developed by Liu, Rosenbluth, and White.[6] Writing $a = \int_C f(k)e^{ikx}dk$, where the path of integration C is to be chosen in such a way that the integrand and appropriate derivatives vanish at the endpoints, one finds

$$k^3 f + i\lambda k^2 df/dk + f = 0, \tag{11}$$

with the solution

$$f = f_0 \exp\left[\frac{1}{i\lambda}\left(\frac{1}{k} - \frac{k^2}{2}\right)\right],$$

yielding

$$a = \left(a_1\int_{C_1} + a_2\int_{C_2} + a_3\int_{C_3}\right)\exp\left\{i\left[kx + \frac{1}{\lambda}\left(\frac{k^2}{2} - \frac{1}{k}\right)\right]\right\}dk. \tag{12}$$

For $\lambda > 0$, when $k \to 0$ the integrand (and derivatives) vanish if k is on the upper half plane, while for $k \to \infty$, k must be in the first or third quadrant. For the three linearly independent solutions of (10) we choose the paths of integration as shown in Fig. 1. imilar considerations for $\lambda < 0$ lead to a diagram that may be obtained by inverting Fig. 1 about the eal axis.

For large values of $|x|$ the integrals may be arried out by the saddle-point method. Defining

$$\varphi(k) = i\left[kx + \frac{1}{\lambda}\left(\frac{k^2}{2} - \frac{1}{k}\right)\right], \tag{13}$$

the positions of the saddle points are defined by he equation

$$k_i^3 + \lambda x k_i^2 + 1 = 0. \tag{14}$$

For $|\lambda x| \gg 1$ the solutions may be approximated by $k_1 \approx \lambda x$, $k_{2,3} \approx \pm i/(\lambda x)^{1/2}$. The corresponding values for $\varphi(k)$ are

$$\varphi(k_1) \approx -i\lambda x^2/2, \quad \varphi(k_2) \approx -2(x/\lambda)^{1/2},$$

$$\varphi(k_3) \approx 2(x/\lambda)^{1/2},$$

and for $\varphi''(k)$,

$$\varphi''(k_1) \approx i/\lambda, \quad \varphi''(k_{2,3}) \approx \pm 2\lambda^{1/2}x^{3/2}.$$

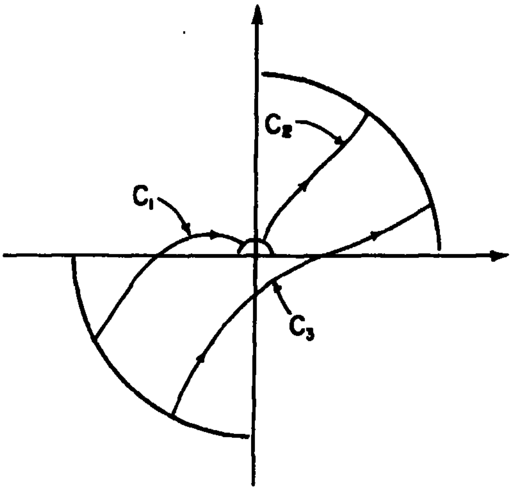

FIG. 1. Contours of integration in the k plane for $\lambda > 0$.

It is easy to see that the first root corresponds to a plasma essentially unaffected by the presence of he beam, while the second and third roots correspond to nonresonant beam modes. The saddle-point integrals are easily carried out yielding, e.g., for $x, \lambda > 0$,

$$a = a_1(2\lambda\pi)^{1/2}\exp i[\tfrac{1}{4}\pi - \tfrac{1}{2}(\lambda x^2)] + a_2\pi^{1/2}\lambda^{-1/4}x^{-3/4}\exp[i\tfrac{1}{2}\pi - 2(x/\lambda)^{1/2}] + a_3\pi^{1/2}\lambda^{-1/4}x^{-3/4}\exp 2(x/\lambda)^{1/2} \tag{15}$$

and for $\lambda > 0$, $x < 0$,

$$a = a_1\pi^{1/2}\lambda^{-1/4}|x|^{-3/4}\exp i[\tfrac{1}{4}\pi + 2(|x|/\lambda)^{1/2}] + a_2\{\pi^{1/2}\lambda^{-1/4}|x|^{-3/4}\exp i[\tfrac{3}{4}\pi - 2(|x|/\lambda)^{1/2}]$$
$$+ (2\lambda\pi)^{1/2}\exp i[\tfrac{1}{4}\pi - \tfrac{1}{2}(\lambda x^2)]\} + a_3(2\lambda\pi)^{1/2}\exp[\tfrac{1}{4}\pi - \tfrac{1}{2}(\lambda x^2)]. \tag{16}$$

It may be seen that for waves propagating in the positive x direction ($V > 0$) the third mode exhibits he largest amplification, the first mode is amplified to a lesser degree, while the second mode is attenuated.

It is instructive to follow the motion of the saddle points as x varies. This is shown in Fig. 2. The astest growing mode corresponds to saddle points located in the fourth quadrant of the k plane. Near $= 0$, exponential growth takes place as in a uniform plasma. The third mode starts out as a plasma node at $x \to -\infty$, turns into a resonant beam plasma mode at $\lambda x = -2^{1/3}\tfrac{3}{2}$, reaches its maximum growth ate at $x = 0$ growing as $\exp(\tfrac{1}{2}\sqrt{3}x)$, and continues to grow at a reduced rate as $x \to \infty$.

It seems as if no inhomogeneous threshold exists for the beam plasma instability. Under experimenal conditions, however, the δ-function approximation holds only if the phase velocity of the wave diffi ers from the beam velocity by more than the beam spread. As a saddle point approaches the origin n the k plane this approximation breaks down and the actual growth rate is quickly reduced. Furthernore as $k \to 0$, the wave phase velocity approaches the beam velocity and the beam gets trapped, leadng to further dispersion of the beam velocity distribution. If sufficient beam spread is attained, the opology of Fig. 2 changes and the unstable beam mode connects with a damped Landau-type mode.[7] o estimate the actual wave growth we investigate the solution around $x = 0$. Expanding the growing olution about this point yields for the saddle point

$$k_0 \approx \frac{1}{2} - \frac{\sqrt{3}}{2}i - \frac{\lambda x}{3}, \quad \varphi(k_0) \approx i\frac{x}{2} + \frac{\sqrt{3}}{2}x - \frac{3}{4}\frac{i}{\lambda} + \left(\frac{3}{4\lambda}\right)^{3/2} - i\frac{\lambda x^2}{3}, \quad \varphi''(k_0) = \frac{3i}{\lambda} + ix + \sqrt{3}x.$$

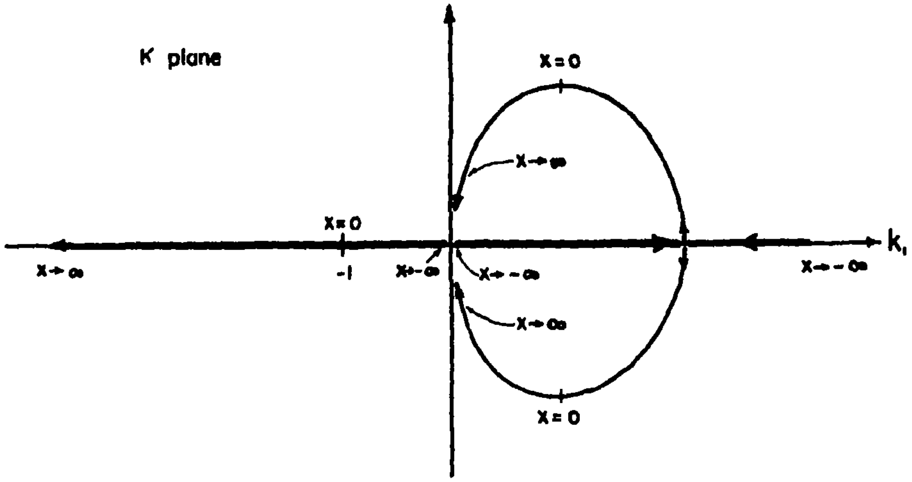

FIG. 2. Motion of saddle points for $\lambda > 0$ as a function of x.

Integration gives for the relevant mode

$$a \approx a_3 \frac{(\pi\lambda)^{1/2}}{3} \exp\left[i\frac{x}{2} - \frac{3i}{4\lambda} + i\frac{\pi}{4} - i\frac{\lambda x^2}{3} + \frac{\sqrt{3}}{2}x + \left(\frac{3}{4\lambda}\right)^{3/2}\right]. \qquad (17)$$

For the δ-function beam approximation to hold, we must have $\lambda x < 1$. The total number of e-foldings are about $5\sqrt{3}/4\lambda$. These considerations lead to an approximate threshold near $\lambda = 1$.

The $\lambda < 0$ case can also be easily calculated. The results are the same as (15) and (16) except for unimportant phase shifts, if one changes the signs of x as well as λ. The threshold is also the same and one finds that the fast growing mode goes over into a plasma eigenmode when $x \to \infty$.

Computer solutions of (10) are in good agreement with these approximate analytic solutions.

In conclusion, the behavior of the beam-plasma instability is characterized by the dimensionless parameter $\lambda = \beta/\alpha(V^2\alpha/\omega_b^2)^{1/3}$. This quantity has a simple physical meaning. If the spatial growth rate in a uniform plasma is k_i, and the wave number of a wave in the nonuniform plasma changes as $\partial k/\partial x$ in the absence of the beam, then aside of a numerical factor λ is $k_i^{-2}\partial k/\partial x$. The threshold condition for substantial wave growth is given by $|\lambda| \ll 1$. If $\lambda > 0$, a plasma wave propagating in the nonuniform plasma couples to the beam in the resonant region producing exponential growth. Past the resonant region the wave phase velocity approaches the beam velocity, the growth is reduced, and the δ-function beam-distribution approximation, as well as linear theory, breaks down, leading to beam spreading followed by transition to a Landau-type mode. These results are consistent with recent experiments on the nonuniform threshold and mode conversion in a nonuniform beam-plasma system.[3] If $\lambda < 0$ a beam mode with a phase velocity close to the beam velocity leads to exponential growth in the resonant region with a decreasing phase velocity, while past resonance the mode becomes decoupled from the beam and goes over into a regular plasma wave in the nonuniform medium for large values of x. If one injects an electron (or ion) beam into a confined plasma with a large density, temperature, or magnetic field gradient at the boundary, beam heating can be expected to take place only in the plasma interior, where the profile is flat.

It should be noted that if the beam is sufficiently spread out in velocity space, so that the bump-on-tail approximation holds, the threshold is independent of $\partial k/\partial x$. This case has been studied by Breizman and Ryutov.[4]

The author wishes to acknowledge useful discussions with Dr. W. Carr and R. Harvey. Thanks are due to Mr. D. Uptegrove for obtaining the numerical solutions of (10), and to Dr. B. Rosen for lending his computer program for the solu-

tion of this equation. This work was supported in part by the U. S. Atomic Energy Commission.

---

[1] M. N. Rosenbluth, Phys. Rev. Lett. 29, 565 (1972).

[2] H. Bohmer, E. A. Jackson, and M. Raether, Phys. Fluids 16, 1064 (1973).

[3] L. D. Bollinger, W. Carr, H. Liu, and M. Seidl, Bull. Amer. Phys. Soc. 18, 1287 (1973); also W. Carr, private communication.

[4] B. N. Breizman and D. D. Ryutov, Zh. Eksp. Teor. Fiz. 57, 1401 (1969), and 60, 408 (1971) [Sov. Phys. JETP 30, 759 (1970), and 33, 220 (1971)].

[5] M. L. Vianna and A. Bers, Bull. Amer. Phys. Soc 18, 1351 (1973).

[6] C. S. Liu, M. N. Rosenbluth, and R. B. White, Phys. Rev. Lett. 31, 697 (1973).

[7] T. M. O'Neil and J. H. Malmberg, Phys. Fluids 11, 1754 (1968).

Possibility of a Pressure-Induced Transformation in Cubic (*A* 15) V_3Si†

R. D. Blaugher, A. Taylor, and M. Ashkin
Westinghouse Research Laboratories, Pittsburgh, Pennsylvania 15235

(Received 22 April 1974)

X-ray measurements of the shift in lattice parameter $\Delta a/a$ versus pressure up to 120 kbar indicate that V_3Si is *not* following a normal cubic dependence for a stable lattice. Hydrostatic pressures in excess of 15 kbar have produced a lattice distortion which may be representative of a cubic to tetragonal transformation.

Considerable interest has recently been directed towards the influence of pressure on the superconducting properties of the *A*15 compounds.[1,2] This class of compounds is especially important in view of its continual production of high-T_c superconductors.[3] The pressure studies to date have generated much controversy with respect to the exact theoretical interpretation for the observed pressure dependence of the superconducting transition temperature. The difficulty in interpretation is due to the multiplicity of competing mechanisms and the observed experimental result which indicates that T_c for different *A*15 compounds may follow either a positive or negative pressure dependence. A review paper by Smith[4] should be referred to for a recent survey of the experimental and theoretical pressure effects on superconducting *A*15 compounds. We would like to report on recent x-ray measurements at room temperature at pressures up to 120 kbar which we feel may have a direct influence on the understanding of superconducting properties of *A*15 compounds under pressure. These measurements are confined to the *A*15 compound V_3Si which has been studied extensively in recent years in both the normal and superconducting states.[5]

The superconducting transition temperature of V_3Si exhibits a positive pressure dependence provided hydrostatic pressure is maintained.[1,2] If a deviatoric (nonhydrostatic) stress is present, as may occur with use of the ice-bomb technique[6] or under actual uniaxial stress,[7] the T_c follows a negative pressure dependence. In view of the known influence of shear stress upon the low-temperature structural transformation in V_3Si, a possibility exists that the presence of deviatoric strain components affects the structural properties and thus influences the observed pressure dependence of the superconducting transition temperature. However, this connection is complicated by the fact that some V_3Si samples do not exhibit this structural transformation; the V_3Si used by Smith,[2] for example, was a nontransforming type. Moreover, the interpretations of the pressure measurements, in particular those argued to be hydrostatic, are based on the assumption that the material remains cubic under the application of pressure.

This latter assumption thus appeared completely untested and a doubt as to its validity initiated the present investigation. It is important to note that the clamp technique employed in most low-temperature pressure studies applies the stress at room temperature.

Carcia, Barsh, and Testardi[8] have found for V_3Si that the first pressure derivative of the shear modulus $C_s = (C_{11} - C_{12})/2$ becomes negative at 77°K. Testardi[9] indicated that this negative coefficient in V_3Si could lead to a pressure-dependent low-temperature structural instability. Larsen and Ruoff[10] extended these experiments to temperatures below 77°K with similar results for the sign of the derivative. They used the first pressure derivatives to predict a pressure-induced structural transformation at various temperatures. Thus the idea of a pressure-induced transformation in V_3Si is not new; however, at room temperature the pressure derivative is positive and the connection with the low-temperature results is not clear.

The present experiments were conducted in a tetrahedral anvil press described in detail by Taylor and Doyle.[11] The experimental arrangement, which is shown in Fig. 1, provides a high degree of pure hydrostatic strain.

The tetrahedral anvil press is discussed in a review article by Banus[12] on x-ray diffraction at high pressures. In this review the tetrahedral anvil press is regarded as one of the better techniques for establishing minimum pressure gradients and low shear components, especially in the range below 100 kbar. A pure hydrostatic environment, however, is less important in this experiment since the elastic properties for V_3Si at room temperature are isotropic or glasslike.[5]

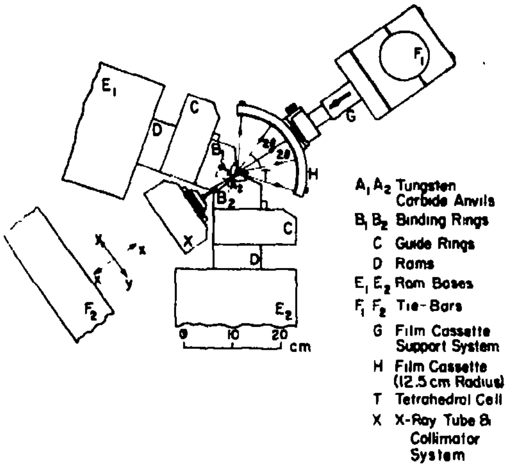
E$_1$
C
D
B$_1$
2θ
2θ
T
H
G
F$_1$
B$_2$
C
D
X
X
x
y
F$_2$
E$_2$
0
10
20
cm
A$_1$ A$_2$ Tungsten Carbide Anvils
B$_1$ B$_2$ Binding Rings
C Guide Rings
D Rams
E$_1$ E$_2$ Ram Bases
F$_1$ F$_2$ Tie-Bars
G Film Cassette Support System
H Film Cassette (12.5 cm Radius)
T Tetrahedral Cell
X X-Ray Tube & Collimator System

FIG. 1. Plane section through x-ray tube, collimator system, film cassette, and two hydraulic rams of tetrahedral anvil.

Finally, the influence of shear on V_3Si usually cited is a low-temperature effect. There has been no evidence of pronounced shear effects in V_3Si at room temperature. The measured pressure derivative of the shear modulus for V_3Si at room temperature is very small.[8,10] Following Taylor and Doyle,[11] a boron-polypropylene tetrahedral cell (shown as T in Fig. 1) was utilized as the pressure transmitting medium. In order to eliminate compositional difficulties a single crystal of V_3Si, which was kindly furnished by L. Testardi of Bell Laboratories, was employed as a master sample. Small pieces of the master sample were reduced to polycrystalline form suitable for x-ray investigation by grinding in an agate mortar and conventional ball milling. Great care was undertaken to eliminate contamination during the ball milling. The resultant powder (~400 mesh) was carefully x rayed prior to insertion in the press by ordinary Debye-Scherrer techniques. A sharp cubic ($A15$) pattern was observed with no evidence of additional lines.

An initial attempt was made to convert cubic V_3Si to the tetragonal form by subjecting a polycrystalline sample of the material at room temperature to pressures of up to 120 kbar in the tetrahedral anvil press. In order to obtain as strong a diffraction pattern as possible, no calibration material (such as NaCl) was mixed with the x-ray sample. X-ray diffraction patterns of the material under pressure were obtained with Ag $K\alpha+\beta$ radiation, the strongest recorded lines being 200, 210, and 211, the strongest being 210 at a Bragg angle $\theta = 7.626°$.

Except for an easily measured shift of the lines toward higher Bragg angles resulting from the reduction in cell dimensions, no splitting of the lines occurred which would be indicative of a change to tetragonal symmetry. However, such a symmetry change could easily be missed if the axial ratio was close to unity.

The low-temperature transformation from cubic to tetragonal for V_3Si produces a change in axial symmetry of $c/a = 1.002$ which is indeed quite close to unity. A similar magnitude of axial change in the present experiment is thus insufficient at 7.6° to produce an observable split of the 210 cubic line into the 210, 102 tetragonal pair. From the observed change in lattice parameter and the published elasticity data for V_3Si by Carcia, Barsch, and Testardi[8] it was possible to estimate the pressure applied to the sample. The maximum linear compression $(\Delta a/a)$ was measured to be 2.25% which would correspond to an applied pressure of 120 ± 5 kbar. These initial results thus could not determine whether a structural transformation had occurred in V_3Si up to pressures of 120 ± 5 kbar.

A detailed consideration of the data on $\Delta a/a$ versus pressure, however, should provide a means for determining the occurrence of a structural transformation. The predicted *cubic* fractional change in lattice parameter $\Delta a/a$ can be calculated from the measured pressure dependence of the bulk modulus. Deviations from the normal behavior are usually indicative of a phase change.

This pressure dependence was recently obtained for V_3Si by Carcia, Barsch, and Testardi from 77 to 300°K.[8] The dashed curve in Fig. 1 has been calculated from

$$-\frac{\Delta a}{a} = \frac{1}{3}\frac{dp}{dB}\ln(1+pb) \text{ with } b = \frac{1}{B_0}\frac{dB}{dp},$$

using $B_0 = 1.76\times10^3$ kbar (Testardi and Bateman[12]) and $dB/dp = 4.3$ (Carcia, Barsch, and Testardi[8]), and represents the normal cubic behavior for a solid stiffening under pressure without undergoing any structural phase changes.

For these measurements the applied pressure was determined by mixing the V_3Si powder with NaCl (55/45) before placement in the boron-polypropylene cell. In addition to its use as a calibrant, NaCl tends to reduce any effects due to

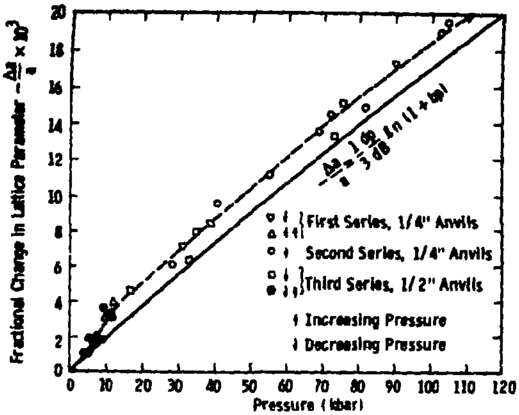

FIG. 2. The fractional change in lattice parameter ($-\Delta a/a$) versus pressure P of V_3Si at room temperature. The dashed line has been extrapolated to higher pressures from the low-pressure derivative of Carcia, Barsch, and Testardi (Ref. 8) and is typical of a nontransforming solid.

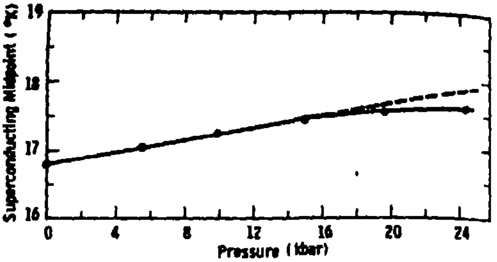

FIG. 3. The midpoint of the superconducting transition temperature of V_3Si as a function of pressure obtained from the results of Smith (Ref. 2). The dashed line is a linear extrapolation of the results on T_c versus pressure up to 15 kbar.

shear. The shear modulus for V_3Si (at room temperature) is quite large with a value of ~0.85 $\times 10^{12}$ dyn/cm^2,[5] which is approximately 5 times that of NaCl. Several runs were performed at pressures up to 120 kbar with $\Delta a/a$ determined for both increasing and decreasing pressure. The addition of the NaCl required fairly long x-ray exposures, of the order of 14 h for each pressure setting. The pressure was maintained during each exposure by a photocell feedback which immediately corrected for any drift in pressure. This technique thus reduced the relative error in pressure determination to less than the relative measurement error in $\Delta a/a$. Larger ($\frac{1}{2}$-in.) anvils were also used to reduce the measurement errors further. The use of these anvils provides more intense diffraction patterns which improves the accuracy in $\Delta a/a$ for pressures below ~30 kbar. These larger anvils, however, are not reliable at higher pressures because of the difficulty in applying the proper corrections for sample movement, etc.[11]

The observed results shown in Fig. 2 definitely indicate that V_3Si is not following a normal cubic dependence. The observed change in $\Delta a/a$ (above ~15 kbar) is much greater than can be explained by the sum of all the possible errors in measurement, i.e., pressure and $\Delta a/a$. These results indicate that V_3Si softens under pressure up to ~15 kbar at which point the structure stiffens and follows a normal cubic dependence. This observed behavior could be produced either by a transformation to a new structure or the material remaining cubic and softening elastically.

In summary, the x-ray results thus suggest that beyond a certain pressure (~15 kbar) V_3Si has undergone a structural phase transition (at room temperature) to an unknown phase with an axial symmetry close to unity, i.e., nearly cubic. This transformation is completely reversible and the material returns to the cubic $A15$ structure upon reducing the pressure to atmospheric. The preceding description is analogous to the known low-temperature tetragonal behavior; hence it is tempting to associate the observed pressure-induced effect with a similar tetragonal behavior. The experimental technique used is considered to apply the smallest fraction of nonhydrostatic stress in the pressure range studied.

The measured variation of T_c with pressure for V_3Si,[1,2,6,7] and quite possibly all $A15$ compounds, may in fact bear little relation to whether the material remains cubic or transforms to a new structure. On the other hand, a demonstration of such a connection between structure and the variation of T_c under pressure may be quite important. It is interesting to note that Smith's[2] observed T_c versus P for samples pressurized at room temperature deviates from linearity at pressures (see Fig. 3) above ~15 kbar. This admittedly small deviation from linearity of T_c versus P occurs in the same region suspected to include a structural transition. It would indeed be interesting to obtain T_c data at even higher pressures to validate this trend. A recent paper by Smith *et al.*[14] on $NbSe_2$ demonstrated that the change in slope observed in their investigation of T_c versus pressure was similarly related to a crystallographic phase change.

We would like to acknowledge the many useful discussions with L. Testardi and his kind loan of the V_3Si sample.

---

†Work supported by the U. S. Army Research Office, Durham.

[1] H. Neubauer, Z. Phys. **226**, 211 (1969).

[2] T. F. Smith, Phys. Rev. Lett. **25**, 1483 (1970).

[3] G. W. Webb, L. J. Vieland, R. E. Miller, and A. Wickland, Solid State Commun. **9**, 1769 (1971); J. R. Gavaler, Appl. Phys. Lett. **23**, 480 (1973).

[4] T. F. Smith, J. Low Temp. Phys. **6**, 171 (1972).

[5] L. R. Testardi, in *Physical Acoustics*, edited by W. P. Mason (Academic, New York, 1973), Vol. 10.

[6] C. B. Muller and E. J. Saner, Rev. Mod. Phys. **36**, 103 (1964).

[7] M. Weger, B. G. Silbernagel, and E. S. Greiner, Phys. Rev. Lett. **13**, 521 (1964).

[8] P. F. Carcia, G. R. Barsch, and L. R. Testardi, Phys. Rev. Lett. **27**, 944 (1971).

[9] L. R. Testardi, Phys. Rev. B **5**, 4342 (1972).

[10] R. E. Larsen and A. L. Ruoff, J. Appl. Phys. **44**, 1021 (1973).

[11] A. Taylor and N. J. Doyle, J. Appl. Crystallogr. **4**, 109 (1971).

[12] M. D. Banus, High Temp.-High Pressures **1**, 483 (1969).

[13] L. R. Testardi and T. B. Bateman, Phys. Rev. **154**, 402 (1967).

[14] T. F. Smith, L. E. Delong, A. R. Moodenbaugh, T. H. Geballe, and R. E. Schwall, J. Phys. C: Proc. Phys. Soc., London **5**, L230 (1972).

Magnetic Breakdown and Dingle Temperature in Zinc Alloys

P. L. Li, J. O. Ström-Olsen, F. A. Buot, and R. Harris
Eaton Electronics Laboratory, McGill University, Montreal, Quebec, Canada

(Received 18 March 1974)

Measurements of magnetic breakdown in dilute alloys of zinc show that the breakdown field between the second-zone monster and the third-zone needles increases linearly with the Dingle temperature with the same scaling factor for all alloys measured. A WKB calculation yields a general expression for breakdown in the presence of scattering which is in good agreement with experimental observations.

A study of the Dingle temperature in the de Haas-van Alphen (dHvA) effect is one of the most effective ways of investigating conduction-electron scattering in metals and alloys. The measured Dingle temperature X for a particular orbit is a direct measure of the average scattering around that orbit.[1] In some metals, however, such as zinc and its alloys, measurement of X is hampered by the occurrence of magnetic breakdown (MB) which permits electrons arriving at a zone boundary to tunnel between different sheets of the Fermi surface. In zinc the two relevant sheets are the second-zone-monster surface and the third-zone needles. This tunneling, characterized by a breakdown field H_0 and a corresponding transition probability $\exp(-H_0/H)$,[2] reduces the dHvA amplitude and, unless corrections are made, yields spurious values for X. On the other hand, in spite of the evident importance of the problem, there has been very little attempt to investigate magnetic breakdown occurring concurrently with strong scattering. Theoretical treatments[3] have only considered the interaction between the magnetic field and the lattice potential, so that the breakdown field is given purely in terms of band parameters. This approach appears to be valid in pure metals, where the scattering is weak and dominated by dislocations, but there is no justification for it in alloys, nor any experimental evidence to support it.[4]

We have therefore made and analyzed measurements of the breakdown field and the Dingle temperature for the needle surface in several alloys of zinc containing up to 210 ppm Mn and 165 ppm Cr. These alloys are so dilute that any large change in H_0 cannot be accounted for by change in the band structure[4] since this is almost the same as for pure zinc. The results show unequivocally that, far from being independent of scattering, magnetic breakdown is very strongly affected by it and that the breakdown field is related to the Dingle temperature in a very simple way.

Both H_0 and X were determined from the *absolute* amplitude of dHvA oscillations by a torque method already used by two of the authors for pure zinc.[5] The use of absolute amplitudes is necessary since, as explained in Ref. 5, relative amplitudes can only be relied on to give a lower bound to H_0. To avoid any change of scattering from the magnetic field, data were analyzed only at 4.2 K in the field range 0 to 9 kG,[6] while the magnetic field was aligned within 15° of the c axis. Only the fundamental oscillation of the torque, $\Gamma_0(H)$, was observed and an expression for this is given by the Lifschitz-Kosevich[7] expression for the free energy of conduction electrons in a magnetic field modified for the presence of MB.

Falicov and Stachowiak[8] allow directly for leakage out of the orbit while preserving the phase coherence of the electron wave function during tunneling and around the orbit. This gives

$$\beta(H,H_0)=\beta_0\exp\left[\frac{-2\pi^2k_Bm^*c}{e\hbar}\frac{X}{H}\right], \tag{1}$$

where $\beta(H,H_0)$ is related to $\Gamma_0(H)$ by

$$\beta(H,H_0)=\Gamma_0(H)\left(\frac{\sinh(2\pi^2k_BTm^*c/e\hbar H)}{TH^{1/2}}\right)\times\{1-\exp(-H_0/H)\}^{-3/2}. \tag{2}$$

β_0, the infinite-field intercept, contains the usual curvature factor for the extremal area (defined exactly for the needles in Ref. 5) and includes both the spin-splitting factor and the volume of the specimen (~0.25 cm^3). Here it is *calculated* from a knowledge of the shape of the needle surface. Even for the most concentrated alloys it has a value within 7% of pure zinc.[5,9] X is the Dingle temperature and the remaining quantities in (2) have their usual meaning. An alternative method was suggested by Condon[4] in which breakdown is regarded simply as a scattering process so that a term

$$\frac{e\hbar H}{2\pi^2k_Bm^*c}\left[\tfrac{1}{2}\exp\left(\frac{-H_0}{H}\right)\right],$$

is added to X. With their more concentrated alloys, Higgins and Marcus[4] were unable to distinguish experimentally between these two approaches but preferred the latter since the data could then be fitted with the same H_0 as for pure zinc. Our data however cannot be described at all by the Condon expression whereas it fits the Falicov and Stachowiak model very well. We therefore conclude that Eq. (1) is correct and use it to determine X and H_0 graphically as illustrated in Fig. 1.

Figure 2 summarizes the results for ZnMn and ZnCr. We see that both X and H_0 increase rapidly and linearly with concentration, though at slightly different rates in the two systems. However, the ratio

$$\alpha=(\partial H_0/\partial x)/(\partial X/\partial x),$$

(where x is the solute concentration) is a constant for all our alloys and has a value of about 0.35 kG/°K. This very striking *empirical* relation would seem to hold for all zinc alloys so far measured, as is shown in Table I, even though the individual concentration dependences of X

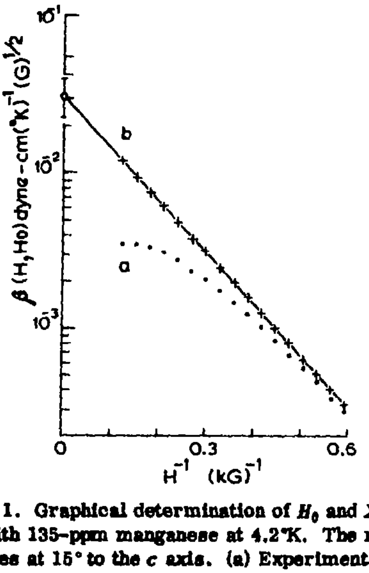

FIG. 1. Graphical determination of H_0 and X for zinc with 135-ppm manganese at 4.2°K. The magnetic field lies at 15° to the c axis. (a) Experimental data uncorrected for breakdown, i.e., $\beta(H,H_0)$ with $H_0=\infty$. (b) H_0 chosen as 4.8 kG which causes the plot to be linear and to take the calculated infinite-field intercept, β_0, shown on the ordinate with error bar. The slope yields X.

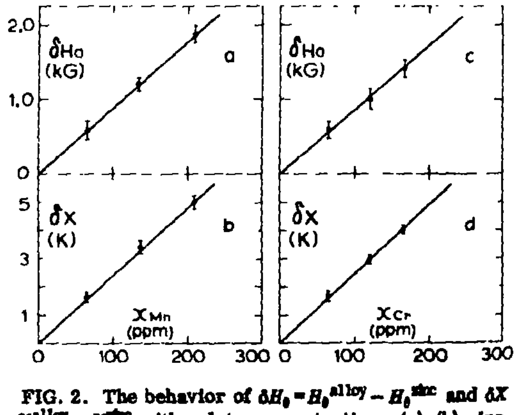

FIG. 2. The behavior of $\delta H_0=H_0^{\text{alloy}}-H_0^{\text{zinc}}$ and $\delta X=X^{\text{alloy}}-X^{\text{zinc}}$ with solute concentration. (a),(b) zinc manganese; (c),(d) zinc chromium. $H_0^{\text{zinc}}=3.5\pm0.3$ kG. X^{zinc} is taken from the value in the alloys extrapolated to zero concentration (see also Ref. 12).

TABLE I. A summary of the breakdown field and Dingle temperature in zinc alloys showing the constancy of α.

Alloy	$\partial H_0/\partial x$ (kG/at.%)	$\partial X/\partial x$ (°K/at.%)	α (kG/°K)
ZnMn	90	248	0.36 ± 0.06
ZnCr	88	240	0.36 ± 0.06
ZnAl[a]	23	45	0.50 ± 0.25[c]
ZnCu[a]	11	22	0.50 ± 0.25
ZnHg[b] ZnCd[b]	2.2	5	0.44 ± 0.20

[a] Ref. 4, interpreted on the basis of Ref. 8.

[b] W. L. Gordon, private communication.

[c] Ref. 11.

and H_0 vary over 2 orders of magnitude.

It is therefore clear that conventional analyses of breakdown are only valid in the limit of weak scattering and that strong scattering inhibits the tunneling process. Qualitatively one can understand this by visualizing the two processes as in direct competition, so that an electron arriving at a zone boundary can either be scattered by the impurities or can tunnel to a neighboring sheet of the Fermi surface. Thus the effective tunneling probability is reduced. We have made a quantitative analysis of this effect by following the usual WKB calculations, starting with a Hamiltonian which includes impurities through a self-energy Σ whose imaginary part gives the scattering. The details of the calculation will be presented elsewhere.[9] Here we give only the result, using a $\vec{k}\cdot\vec{p}$ Hamiltonian whose validity for the needles in zinc is well established.[10]

If we follow the usual procedure of evaluating the tunneling between the points of closest approach[3] of the two surfaces and also assume that he electron scattering is completely isotropic, then the tunneling probability becomes:

$$P=\exp\left\{-\frac{H_{00}+\alpha'\delta X}{H}\right\}, \tag{3}$$

where $H_{00}=(\pi\Delta^2c/4\hbar e v_x v_y)$, the conventional expression for the breakdown field, $\alpha'=(2\pi c k_B/\hbar e v_x v_y)$, and $\delta X=(X^{\text{alloy}}-X^{\text{zinc}})=\mathrm{Im}(\Sigma)/\pi k_B$. Δ is he band gap, while v_x, v_y are the components of he free-electron velocity perpendicular and parallel to the zone face where breakdown occurs. Equation (3) gives a form for the tunneling in greement with the two features of the experimental results; the breakdown field increases inearly with the Dingle temperature with a scaling factor which is a property of the host, *not* the impurity.[11] Substituting the band parameters for zinc we find $\alpha' \approx 0.20$ kG/°K, rather lower than the experimental value. However, agreement may be substantially improved if we adopt a suggestion of Chambers[13] and carry out the tunneling integration over a "free-electron" path between the two surfaces rather than the line of closest approach. Furthermore, preliminary analysis indicated that this approach may also explain the angular dependence of H_0 for zinc alloys.[9] We are at present pursuing this line of investigation and are also extending our experimental investigations to magnesium alloys.

In conclusion, measurements of magnetic breakdown in dilute alloys of zinc have shown that the tunneling probability is sensitive to electron scattering. A WKB calculation has yielded a general expression relating the breakdown field and the Dingle temperature in general agreement with the experimental observations.

We would like to thank F. T. Hedgcock for drawing our attention to this problem and for his critical readings of the manuscript.

---

[1] M. Springford, Advan. Phys. 20, 493 (1971).

[2] See, for example, R. W. Stark and L. M. Falicov, Progr. Low Temp. Phys. 5, 20 (1968).

[3] E. I. Blount, Phys. Rev. 126, 1636 (1962); W. G. Chambers, Phys. Rev. 149, 493 (1966); and many others.

[4] R. J. Higgins and J. A. Marcus, Phys. Rev. 161, 589 (1967). The present experiment was in fact suggested by the authors in that paper.

[5] P. L. Li and J. O. Ström-Olsen, J. Low Temp. Phys. 12, 255 (1973).

[6] Both *Zn*Cr and *Zn*Mn are Kondo alloys, so some field and temperature dependence to the scattering might be expected. However both our dHvA data and our (unpublished) magnetoresistance data indicate that at and above 4 K such dependence is insignificant (< 2%) in the field range 0 to 9 kG.

[7] I. M. Lifschitz and A. M. Kosevich, Zh. Eksp. Teor. Fiz. 29, 730 (1955) [Sov. Phys. JETP 2, 636 (1956)].

[8] L. M. Falicov and H. Stachowiak, Phys. Rev. 147, 505 (1966).

[9] F. A. Buot, P. L. Li, and J. O. Ström-Olsen, to be published.

[10] J. P. Van Dyke, J. W. McClure, and J. F. Doar, Phys. Rev. B 1, 2511 (1970).

[11] We have used the value of H_0^{zinc} from Ref. 5 which is somewhat different from the value in Ref. 4. The large error bar, however, covers this discrepancy.

[12] A direct comparison between H_0 and X cannot be made since X is sensitive to dislocations while H_0 is

not. We have verified this experimentally (Ref. 9) in several samples of pure zinc and it is also consistent with our theoretical analysis. Dislocations increase X through "dephasing" of the electron wave function [A. B. Pippard, Proc. Roy. Soc., Ser. A 287, 165 (1965)] while H_0 only changes with direct scattering. We thus compare H_0 with the *change* in X due to the solute.

[12] R. G. Chambers, Proc. Phys. Soc., London 88, 701 (1966).

New Interpretation of the Soft-X-Ray Absorption Spectra of Several Alkali Halides[*]

Sokrates T. Pantelides
Department of Applied Physics, Stanford University, Stanford, California 94305
and
Frederick C. Brown
Xerox Palo Alto Research Center, Palo Alto, California 94304

(Received 23 April 1974)

Theoretical calculations have thus far been used to interpret the soft-x-ray spectra of several alkali halides in terms of band structures alone, excluding the possibility that core excitons are formed below the band edge. By independently determining the threshold for band transitions from x-ray photoemission spectroscopy and optical-gap data, we conclude that these spectra are in fact almost entirely excitonic in nature.

Absorption spectra are well known to contain valuable information about the excited states of a crystal. X-ray spectra are particularly convenient for this purpose since electrons are excited from core states which are flat and thus introduce no structure. By assuming constant transition matrix elements over the range of interest, one expects the observed structure to correlate directly with structure in the density of states (DOS) of the conduction bands. Because of the difficulty of computing absolute transition energies, a common practice has been to freely move the DOS on the energy axis until a reasonable correspondence between theoretical and experimental peaks and valleys is obtained. This approach has led to the interpretation of the soft-x-ray spectra of various alkali halides[1-3] in terms of band structures alone, dismissing the possibility that excitons are formed below the band edge. More recent theoretical work[4,5] has arrived at similar conclusions by using calculated transition energies instead of freely aligning spectra.

Such an interpretation of soft-x-ray spectra may be tested directly by making use of additional experimental information from x-ray photoemission spectroscopy (XPS) and optical-gap data in order to pin down the position of the conduction-band edge with respect to the core levels.[6] In this Letter we will use this powerful technique to show that several soft-x-ray spectra must be reinterpreted in a way that contradicts most of the previous work on the subject.

We first concentrate on the lithium halides LiF, LiCl, LiBr, and LiI. Haensel, Kunz, and Sonntag[7] first measured their Li^+ K spectra (Fig. 1) and suggested that the prominent peak in each spectrum at about 60–62 eV is probably an exciton while the remaining structure may be transitions to p-like band states. No band edges were identified.

The same spectra were measured and interpreted shortly thereafter by Brown *et al.*[1] These authors, and subsequently Kunz and Lipari,[2] performed Hartree-Fock band calculations for LiCl and LiBr and computed the DOS of the conduction bands. By freely shifting the DOS on the energy axis, they aligned theoretical and experimental peaks and valleys and concluded that the observed spectra are entirely due to transitions to conduction-band states with no excitons being formed. By analogy with LiCl and LiBr, Kunz, Devreese, and Collins[8] assumed that the band threshold for LiF lies at 60.5 eV and proceeded to identify a two-electron excitation (core-to-band plus a valence exciton) at about 70 eV. More recently, band calculations for LiF were reported by Menzel *et al.*[4] who used Slater exchange and by Kunz, Mickish, and Collins[5] who used nonlocal Fock exchange. In both cases, the observed structure was identified with similar structure in the computed interband spectra.[9] Both Refs. 4 and 5 predicted a long weak tail to the left of the main

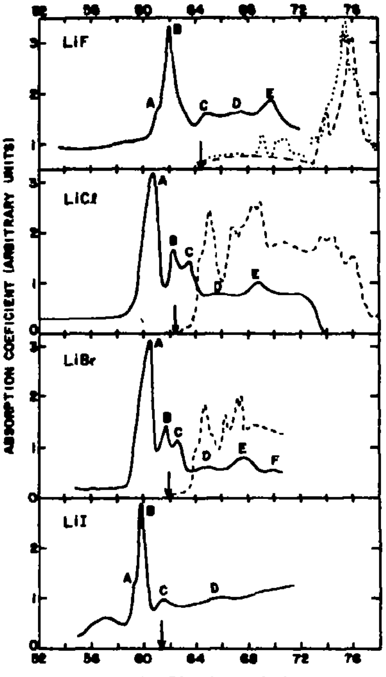

FIG. 1. Li^+ K spectra of the lithium halides. Solid curves are experimental (Ref. 7; low-energy tail of LiF spectrum from Ref. 10). Dotted curve (from Ref. 4) and dashed curves (from Ref. 5 for LiF, Refs. 1 and 2 for LiCl, LiBr) are theoretical interband spectra positioned on the energy axis according to interband thresholds determined here (vertical arrows).

TABLE I. Various energies in the Li halides. E_v is the top of the valence band relative to the Li^+ $1s$ core level. E_{vc} is the optical band gap. $E_c = E_v + E_{vc}$ is the bottom of the conduction band relative to the Li^+ $1s$ level. "Peak" denotes the position of the dominant peak in the observed spectrum and E_B is the energy separation between the peak and E_c (excitonic binding energy). All energies are in eV.

Substance	E_v	E_{vc}	E_c	Peak	E_B
LiF	50.8[a]	13.6[b]	64.4	61.9[c]	2.5
LiCl	52.9[d]	9.4[b]	62.3	60.8[c]	1.5
LiBr	54.2[e]	7.6[b]	61.8	60.4[c]	1.4
LiI	55.5[e]	6.1[b]	61.6	59.8[c]	1.8

[a] Ref. 11.
[b] Ref. 15.
[c] Ref. 7.
[d] Ref. 14.
[e] Ref. 17.

peak, corresponding to the Γ_1 band minimum. Subsequently, Sonntag[10] detected such a weak tail, in apparent support of the band-theoretic predictions. He suggested, nevertheless, that this may not be conclusive evidence for interpreting the spectrum in terms of a one-electron-band model alone.

We now wish to show in a simple way that the prominent peak appearing near the onset of absorption in the lithium halides is purely excitonic and not an interband transition. This is done by combining XPS and optical-gap data. The former measure the binding energies of electrons in the valence bands and in the core levels. The relative difference between a given core level and the top of the valence band is then accurately determined.[11,12] By adding this value to the optical band gap (energy difference between the valence-band top and the conduction-band bottom), the position of the conduction-band edge is unambiguously established.[13] Any structure in the observed spectrum appearing below this threshold can then be conclusively identified as *purely excitonic*.

Accurate XPS data exist for LiF[11] and LiCl.[14] By combining these with optical-gap data, the band thresholds shown in Fig. 1 by vertical arrows are obtained with an accuracy of about 0.5 eV. All the relevant quantities are listed in Table I. The dominant peak is seen to lie 1.5–2.5 eV below the arrow in each case, which clearly demonstrates that it is purely excitonic, contrary to previous band-theoretic interpretations.[1,2,4,5] The binding energy relative to the band edge is not atypical for insulators. However, in view of the fact that the bottom of the conduction band is Γ_1, we must exclude the possibility that the observed exciton derives from that critical point in an effective-mass picture. This is because such an exciton would be s to s and hence dipole forbidden. Clearly, the observed exciton must derive from higher conduction-band states which are p-like in character. In the case of LiF, the computed DOS[4,5] shows that most states lie 10–13 eV above the band edge. This indicates an unusually strong electron-hole interaction which mixes band states over a range of a rydberg. It is in agreement with the strength of electron-hole attraction estimated by Kunz *et al.*[5] (~10 eV) from free-ion calculations. The strength of this interaction in the crystal is not disturbing if we recall that the valence electrons in these ionic crystals are almost entirely on the halogen ions; thus the Coulomb potential of a hole in a core shell of the alkali ion is essentially not screened at all and attracts and binds the electron very strongly. The observation that the $1s^2 - 1s2p$ transition in the free Li^+ ion is at 61.3 eV, extremely close to the prominent peaks in the spectra of all the Li halides, lends support to these arguments.

In Fig. 1 we also show the theoretical interband spectra positioned according to the present determination of band thresholds. We observe that there is little or no correspondence between the theoretical interband spectra and experiment. From the positions of the arrows one may identify the upturn leading to peaks *C* as coinciding with the onset of band transitions. However, such transitions near the band edge are suppressed by symmetry and one must allow for a strong exciton contribution. In short, one may conclude that the observed spectra are almost entirely excitonic in nature.[16] The strong electron-hole interaction simply draws the oscillator strength into an excitonic DOS which accidentally resembles the DOS of Bloch-type conduction-band states.

XPS data for LiBr and LiI are not available. Nevertheless, definite patterns among the binding energies of the Li and Na halides allowed us to estimate by interpolation the corresponding quantities in LiBr and LiI as well.[17] Adding the corresponding band gaps,[15] the band thresholds shown by the arrows in Fig. 1 were obtained. Considerable uncertainties in these numbers do exist, but the similarity of the four spectra and the analogy with the free-Li^+-ion transition suggests that our conclusions for LiF and LiCl apply to LiBr and LiI as well.

We have seen how by independently pinning down the thresholds for band transitions we were led to revise the interpretation of the soft-x-ray spectra of the Li halides. We have done the same for other alkali halides and results will be published elsewhere.[18] Here we give one more illustration to further our conclusions. We consider the Cl^- $L_{2,3}$ spectrum of NaCl reported by Brown *et al.*[15] (Fig. 2, solid line). These authors suggested an interpretation of the first four observed peaks in terms of transitions to critical points in the conduction bands arguing that no significant exciton effects are expected. They also suggested that peaks 5, 6, and 7 might be replicas of 1, 2, and 3, caused by two-electron excitations. Lipari and Kunz[3] subsequently supported this interpretation. They performed a Hartree-Fock band calculation and freely aligned the computed interband spectrum so as to match its first peak with peak 1 of experiment. This is shown in Fig. 2 by the dotted curve. We note that such an interpretation would imply a threshold for band transitions below 198 eV. XPS plus optical-gap data, however, place this threshold more than 5 eV higher, at 203.3 eV.[19] The uncertainty in this number is not more than 0.5 eV, which allows us unambiguously to assign the first experimental peak to an exciton below the band edge, with a binding energy of about 1.5 eV. In view of the very low density of states near the band edge, peak 2 is to be identified as an exciton which is at worst metastable, possibly being degenerate with band states. The higher peaks seem to bear a similarity to the band densities, but no definite identification is possible at present. Overall, the electron-hole interaction appears to be weaker in this case as a result of the fact that the hole is in the halogen core and its Coulomb potential is screened by the valence electrons quite effectively.

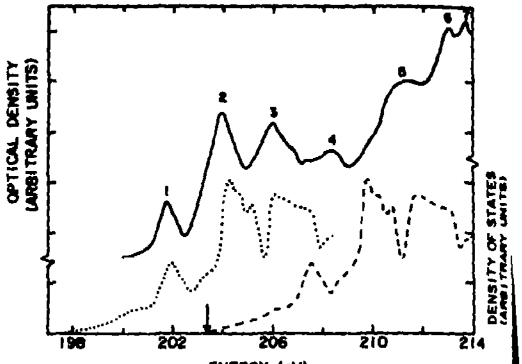

FIG. 2. Cl^- $L_{2,3}$ spectrum of NaCl. Solid curve is experimental (Ref. 15). Dotted curve is theory of Ref. 3. Dashed curve is theoretical interband spectrum of Ref. 3 (same as dotted curve) but positioned on the energy axis according to interband threshold (vertical arrow) determined independently. See text.

We conclude that exciton effects are very pronounced near threshold in the soft-x-ray spectra of alkali halides and that band structure alone cannot be used to interpret the observed structure. This is in agreement with interpretations that have been proposed for other soft-x-ray spectra of alkali halides.[20] We conclude further that any attempt to correlate observed spectra with conduction-band DOS must be accompanied by an accurate determination of the threshold energy for band transitions.

We would like to thank Dr. W. A. Harrison, Dr. A. B. Kunz, Dr. D. J. Mickish, Dr. R. M. Martin,

d Dr. P. N. Sen for valuable discussions.

---

*Work supported in part by the National Science Foundation through Grant No. GH-39811.

[1] F. C. Brown, C. Gähwiller, A. B. Kunz, and N. O. ipari, Phys. Rev. Lett. 25, 927 (1970).

[2] A. B. Kunz, J. Phys. C: Proc. Phys. Soc., London , 1542 (1970), and Phys. Rev. B 2, 5015 (1970); A. B. unz and N. O. Lipari, J. Phys. Chem. Solids 32, 1141 971).

[3] N. O. Lipari and A. B. Kunz, Phys. Rev. B 3, 491 971); A. B. Kunz and N. O. Lipari, Phys. Rev. B 4, 374 (1971).

[4] W. P. Menzel *et al.*, Phys. Rev. Lett. 30, 1313 1973).

[5] A. B. Kunz, D. J. Mickish, and T. C. Collins, Phys. ev. Lett. 31, 756 (1973).

[6] W. Scheifley, thesis, University of Illinois, 1973 (unpublished).

[7] R. Haensel, C. Kunz, and B. Sonntag, Phys. Rev. Lett. 20, 262 (1968).

[8] A. B. Kunz, J. T. Devreese, and T. C. Collins, J. Phys. C: Proc. Phys. Soc., London 5, 3259 (1972).

[9] In Ref. 4, a straight energy-band calculation yielded an interband spectrum with a peak at 64 eV, which was identified with the prominent peak at 62 eV in the observed spectrum. In Ref. 5, the Hartree-Fock band calculation yielded an interband spectrum with a prominent peak at 85 eV. The authors argued that the experimental peak is not due to excitons below the band edge and thus identified it with the 85-eV peak in the theoretical spectrum. They then included effects beyond band theory, including electron-hole interactions. They argued that these effects shift both bands and excitons rigidly and estimated a net shift of 20 eV for the calculated interband spectrum. The agreement with the observed spectrum is then reasonable, but the authors suggest that, because of the nature of the approximations, this agreement must be considered accidental.

[10] B. Sonntag, Phys. Rev. B. 9, 3601 (1974).

[11] S. P. Kowalczyk, F. R. McFeely, L. Ley, R. A. Pollak, and D. A. Shirley, Phys. Rev. B 9, 3573 (1974).

[12] K. Siegbahn *et al.*, Nova Acta Regiae Soc. Sci. Upsal. 20, 72 (1967).

[13] The validity of this approach is based on a general theorem that energy bands beyond the Hartree-Fock approximation (i.e., after all correlation and relaxation corrections are included, except for electron-hole attraction) are still "rigid." Electron-hole interactions may introduce additional localized states (excitons), but do not move the band continua. A proof is given in S. T. Pantelides, D. J. Mickish, and A. B. Kunz, Phys. Rev. B (to be published).

[14] P. H. Citrin and T. D. Thomas, J. Chem. Phys. 57, 4446 (1972); W. Pong and J. A. Smith, Phys. Rev. B 9, 2674 (1974); V. V. Nemoshkalenko, A. I. Senkevich, and V. G. Aleshin, Dokl. Akad. Nauk 206, 593 (1972) [Sov. Phys. Dokl. 17, 936 (1973)].

[15] F. C. Brown *et al.*, Phys. Rev. B 2, 2126 (1970).

[16] The tail observed in Ref. 10 in LiF and similar tails in the other compounds may be attributed to "forbidden" *s* excitons, though other possibilities exist, such as background due to transitions from other shells, etc.

[17] Details will be given elsewhere (S. T. Pantelides, to be published). The values used here are given in Table I.

[18] Pantelides, Ref. 17.

[19] The value of Ref. 12 was corrected by using the more recent optical-gap value of 8.97 eV [D. M. Roessler and W. C. Walker, Phys. Rev. 166, 599 (1968)].

[20] M. Watanabe, J. Phys. Soc. Jpn. 34, 428 (1973); S. Nakai *et al.*, J. Phys. Soc. Jpn. 30, 428 (1971); C. Y. Fong and M. L. Cohen, Phys. Rev. 185, 1168 (1969); T. Åberg and J. L. Dehmer, J. Phys. C: Proc. Phys. Soc., London 6, 1450 (1973).

Bound Electron States in the Wake of Swift Ions in Solids*

V. N. Neelavathi and R. H. Ritchie
Health Physics Division, Oak Ridge National Laboratory, Oak Ridge, Tennessee 37830, and
Department of Physics and Astronomy, University of Tennessee, Knoxville, Tennessee 37916

and

Werner Brandt
Department of Physics, New York University, New York, New York 10003

(Received 2 May 1974)

Fluctuations of valence-electron density are expected to occur in the wake of a fast charged particle moving through condensed matter. Electrons can be trapped into wake-riding states by the potential minima associated with domains of electron-density depletion with binding energies ranging from ~10 eV behind protons to several hundred eV behind highly charged heavy ions. Observable phenomena possibly linked to wake-riding states are discussed.

The energy loss of a fast charged particle moving in condensed matter can be described in terms of the complex dielectric function of the medium.[1] Physically the target response manifests itself as a cylindrically symmetric wake of electron-density fluctuations behind the particle.[2] Its axis defines the particle track. The wake consists of a series of domains, at distinct distances behind the projectile, in which the electron density is alternately enhanced and depleted relative to the mean density n_0 in the medium. Domains of density enhancement create regions of negative electric potential, and domains of depletion regions of positive potential. If sufficiently deep, these potential troughs can trap, respectively, positive or negative particles and sweep them along in wake-riding states trailing the projectile. Experimental verification of wake-riding states would contribute significantly to the understanding of the dynamic many-body response of condensed matter to moving charged particles. Moreover, projectile trailing by particles may contribute to several important phenomena associated with the penetration of charged particles through dense matter.

Consider a homogeneous isotropic medium characterized by the dielectric response function $\epsilon(\vec{k}, \omega)$, where $\vec{k}$ and ω are the wave vector and the frequency of the perturbing field, respectively. In linear-response theory a point particle of charge Ze moving in the medium with velocity v generates a scalar potential $\Phi(\vec{r}, t)$ given by[3]

$$\Phi(\vec{r},t)=\frac{2Ze}{\pi v}\int_0^\infty \kappa J_0(\kappa\rho)\,d\kappa\int_0^\infty \tilde{k}^{-2}\,\mathrm{Re}\{\epsilon^{-1}(\tilde{k},\omega)\exp[i(\omega/v)(z-vt)]\}\,d\omega, \tag{1}$$

where $\kappa^2=\tilde{k}^2-(\omega/v)^2$. The Cartesian coordinates of the projectile at time t are taken to be $(0,0,vt)$. The radial distance from the z axis is denoted by ρ, and J_0 is the zero-order Bessel function of the first kind. Suppose that the medium can sustain well-defined plasmons of energy $\hbar\omega_p=\hbar(4\pi n_0 e^2/m_0)^{1/2}$ in the sense that the plasmon decay rate γ is so small that $\gamma/\omega_p \ll 1$. In a metal, the density of the participating electrons n_0 would correspond to the density of valence electrons. As long as $v < v_F \simeq v_0 = e^2/\hbar$, where v_F is the Fermi velocity of the electron gas, the potential set up by the moving particle is screened out over a distance $v_F/\omega_p \approx 1$ Å in typical metals. However, when $v \gg v_F$, the potential assumes the form

$$\Phi(\vec{r})=Zek[g(\vec{r})-2\sin(kz)K_0(k\rho)\exp(-\gamma kz/2\omega_p)\theta(z)], \tag{2}$$

where $k=\omega_p/v$; K_0 denotes the zero-order modified Bessel function of the second kind, and $\theta(z)$ the unit step function.[3] In Eq. (2) the coordinate system moves with the particle placed at the origin and has the positive z axis in the direction of $-\vec{v}$. The first term in Eq. (2) represents the potential in close proximity to the projectile and need not concern us here in detail. The second term represents a damped periodic potential set up by oscillatory electron density fluctuations in the wake of the projectile. The oscillatory portion of $V=-e\Phi(\vec{r})$ is shown schematically in Fig. 1.

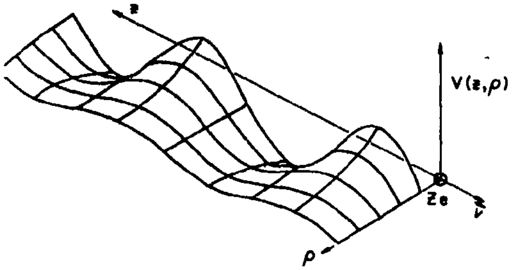

FIG. 1. Schematic representation of the oscillatory rtion of the potential energy of an electron as a func- on of position behind a projectile of charge Ze. The arge is assumed to be moving with velocity v in the rection of the negative z axis of a coordinate system ith origin placed at the projectile.

In condensed matter the potential can persist er many wavelengths behind the projectile. It important to note that in the limit $\gamma\to 0$, the atial integral over the electron density fluctua- on from the origin to the first zero at the dis- nce $z=\pi v/\omega_p$ is just equal to Ze, the charge of e moving ion.

In the approximation of Eqs. (1) and (2), the pth of the first trough increases linearly with , and is approximately $Ze\omega_p/v$. If this quantity sufficiently large, bound quasistationary states particles in the oscillating tail of $\Phi(r)$ may ist. In a medium with given ω_p, the number of und states in a trough depends upon Z/v. Heavy ojectiles may carry a core of tightly bound lectrons extending over a distance comparable or smaller than the Thomas-Fermi radius $_{\rm TF}=0.8853a_0Z^{-1/3}$. Since the extension of ion ores is small compared with the wavelength $2\pi v/$ $_p$, characteristic of their wakes, which in the near-response approximation does not depend on Z, heavy ions can be treated in this context point particles with a velocity-dependent ef- ctive charge number $Z_{\rm eff}(v)\leq Z$.

The nonlocal aspects of the wake phenomenon ake a self-consistent solution of the wave equa- on of a trapped electron intractable except by merical methods. For a first study of the und states we make the *Ansatz* $u_0(\vec{r})=A\exp(\alpha\zeta^2$ $\beta\rho^2)$ for the ground-state wave function of a ake-riding electron. Here α and β are varia- onal parameters, and ζ is the z coordinate mea- red from the center of a given positively charged tential trough. With this *Ansatz* all operations ading to a variational lower bound E_0 for the binding energy of the ground state can be carried out easily for the potential given in Eq. (2). The correlation effects between a trapped electron and the medium will tend to decrease the electron density near the trough and thus increase the binding energy further, perhaps by a fraction $1/Z$. This applies also to a positive particle wake-riding in a negatively charged potential trough, between two positively charged troughs, because here correlation tends to enhance the electron density. We neglect variations of $g(\vec{r})$ and the damping factor $\exp(-\gamma kz/2\omega_p)$ over the extension of a given trough, but evaluate them at the center of each trough. Electron-trapping, positively charged troughs appear behind the projectile at the distances z_m given by the condition $\omega_p z_m/v=\pi(4m+3)/2$, where $m=0,1,2,\ldots$. Negatively charged troughs which, for example, may trap protons, appear when $\omega_p z_m/v=\pi(4m+1)/2$. In the following all energies and frequencies are expressed in units of $\mathcal{R}=e^2/2a_0=\frac{1}{2}$ a.u. $=13.6$ eV and all lengths in units of $a_0=\hbar^2/m_0e^2=1$ a.u. $=0.529$ Å. The energy $E_0^{(m)}$ designates the variational ground-state energy of an electron in the mth trough.

Standard techniques lead to the result

$$E_0^{(m)}=\frac{\omega_p^2}{8v^2}\left\{W_m\left[\ln\left(\frac{W_m}{2\Gamma}\right)\right]-\left[W_m\ln\left(\frac{W_m}{2\Gamma}\right)\right]^{1/2}\right\}, \tag{3}$$

if $W_m\equiv 16Zk^{-1}\exp(-\gamma kz_m/2\omega_p)$ is much larger than unity. This condition on W_m is well satisfied in all cases we consider. Also $\ln\Gamma=0.5772$ is Euler's constant.

Figure 2 displays the variation of the ground-state binding energy $E_0^{(0)}$ for an electron in the first potential trough ($m=0$) behind hydrogen, oxygen, and sulfur ions as a function of their kinetic energy. The ions are assumed to move in a medium like aluminum metal for which $\hbar\omega_p=15.4$ eV and $\gamma/\omega_p=4.6\times10^{-2}$. The curves labeled O^{+8} (bare) and S^{+16} (bare) were computed assuming that the ions remain stripped during their passage through the medium. Such high-charge states may be selected in experiments with channeled ions,[4] where the low probability of small-impact-parameter collisions between a channeled ion and crystal ion cores makes electron capture from the solid unlikely compared to the situation in random media. The curves labeled $O^{+Z_{\rm eff}}$ and $S^{+Z_{\rm eff}}$ were computed assuming a velocity-dependent effective charge number of

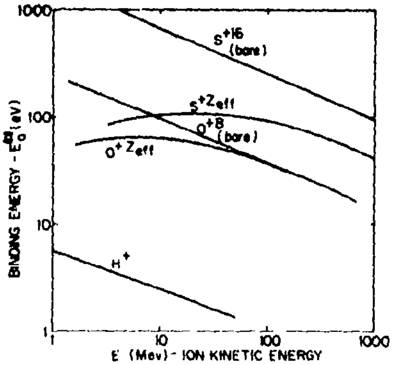

FIG. 2. Ground-state binding energies (in eV) of an electron in the first ($m=0$) trough of the polarization potential created in a medium like aluminum by ions of hydrogen, oxygen, and sulfur as a function of their kinetic energies. The curves labeled $O^{+Z_{eff}}$ and $S^{+Z_{eff}}$ were calculated for effective ion charges $Z_{eff}(v)$ as described in the text.

TABLE I. Variational ground-state binding energies $E_0^{(m)}$ of electrons trapped by the mth potential trough in the wakes at distances Z_m behind 2.5-MeV protons, 40-MeV O^{+8} ions and 80-MeV S^{+16} ions moving in a metal like aluminum.

m	Z_m (Å)	$E_0^{(m)}$ (eV) 2.5-MeV H^+	40-MeV O^{+8}	80-MeV S^{+16}
0	44.03	4.08	56.4	125.8
1	102.74	3.09	43.4	99.0
2	161.46	2.33	33.9	77.8
3	220.16	1.75	26.4	61.0

the form $Z_{eff}(v)=Z[1-\exp(v/Z^{2/3}v_0)]$.[5]

Table I illustrates how the ground-state binding energy varies with the position of the trough along the wakes behind bare O^{+8} and S^{+16} ions at velocity $v=10v_0$ in a medium like aluminum. The binding energies of wake-riding states can range from tens to hundreds of eV in situations of experimental interest. More realistic estimates, taking into account nonlinear effects in Z, should not change these values substantially and are expected to display the same trends with Z, Z_{eff}, ω_p, and v as obtained here.

Auger-type capture into these states should be efficient. Assuming that the binding energy of the states is dissipated through particle-hole pair production in the conduction band of the metal, one estimates, e.g., a mean free path of ~300 Å for capture into a wake-riding state behind a 2-MeV O^{+8} ion in Al metal. It may be possible to detect electron capture into these states by observing the associated Auger electrons, or the soft x rays generated in the capture process. The related radiative capture of electrons into inner shells of stripped swift ions in solids has been discovered recently.[6-8]

When an ion trailed by a wake-riding electron emerges from a metal into vacuum, the potential trough seen by the electron vanishes. Then in first approximation, we expect these electrons to appear outside the metal as a group of electrons with velocities centered about v, and with a spread determined by the momentum transform of the wake-riding-electron wave packet. These electrons should contribute a component to the electron distribution associated with the emergence of positive ions from metals, which so far have been explained only in terms of capture into continuum states on the positive ions *in vacuo*.[9]

We mention other possible consequences of wake-riding states in solids:

(a) The amount of charge separation in solid-state detectors of ionizing radiation may be affected by the existence of spatially coherent electron states of moving particles. Such states would be expected not only to reduce particle-hole recombination in solid-state detectors, but also to diminish the recombination of electrons with geminate ions in insulators such as organic liquids.

(b) Correlated capture and loss into wake-riding states may determine the velocity dependence of the neutral-beam fraction in experiments with charged particles emerging from solid surfaces.[10,11] The binding energy of an electron trailing an energetic proton is ~10 eV ~ 1 Ry in a typical metal. Thus, the interesting picture of a dynamically stabilized solid-state H atom emerges, in which the proton rides ahead, trailed by the wave packet of the electron at a distance ~$3\pi v/2\omega_p$. An antimorph of the entity which might exist by virtue of the wake phenomenon is the *dielectron*. Two electrons might experience strong spatial correlation due to density fluctuations. Energy lost by a dielectron in distant collisions should be altered relative to that by a single electron; its mean free path in condensed matter may be longer than that of either electron separately, enhancing the likelihood that it will produce observable effects.

(c) The experiments of Gaillard, Poizat, and Remillieux[12] on the transmission probability of anneled H_2^+ ions through gold foils show that a gnificant fraction emerges from the foils as olecules. H^+H^+ pairs locked in spatial correla-n may contribute significantly to this transmis-on probability. It would be interesting to ascer-in the importance of wake-riding states of pro-ns behind heavier ions, for example, in trans-ssion experiments with incident fast molecules ch as LiH, CH, OH, or hydrogen halides.

Helpful conversations with B. R. Appleton and Datz are gratefully acknowledged.

Research sponsored by the U. S. Atomic Energy mmission under contract with the Union Carbide rporation.

E. Fermi, Phys. Rev. 56, 1242 (1939), and 57, 485 40).

J. Neufeld and R. H. Ritchie, Phys. Rev. 98, 1632 55), and 99, 1125 (1955); R. H. Ritchie, Ph.D. the-, University of Tennessee, 1959 (unpublished); Pines, Phys. Rev. 92, 626 (1953).

Plasmon dispersion is neglected in obtaining Eq. (2). inclusion gives rise to a spreading-out of the poten-l function corresponding to the formation of a "Che-kov"-type wake because of the intrinsic motion of ctrons making up the plasma (see Ref. 2). We expect that the inclusion of this effect will not change our conclusions appreciably as long as $v \gg v_0$.

[4] S. Datz, F. W. Martin, C. D. Moak, B. R. Appleton, and L. B. Bridwell, Radiat. Eff. 12, 163 (1972).

[5] H. D. Betz, Rev. Mod. Phys. 44, 465 (1972); W. Booth and I. S. Grant, Nucl. Phys. 63, 481 (1965).

[6] H. W. Schnopper, H. D. Betz, J. P. Delvaille, K. Kalata, A. R. Sohval, K. W. Jones, and H. E. Wegner, Phys. Rev. Lett. 29, 898 (1972).

[7] P. Kienle, M. Kleber, B. Povh, R. M. Diamond, F. S. Stephens, E. Grosse, M. R. Maier, and D. Proetel, Phys. Rev. Lett. 31, 1099 (1972).

[8] B. R. Appleton *et al.*, in Proceedings of the Fifth International Conference on Atomic Collisions in Solids, Gatlinburg, Tennessee, 24–28 September 1973 (Plenum, New York, to be published).

[9] K. G. Harrison and M. W. Lucas, Phys. Lett. 33A, 142 (1970); S. Datz, B. R. Appleton, J. R. Biggerstaff, M. G. Menendez, and C. D. Moak, Bull. Amer. Phys. Soc. 18, 662 (1973).

[10] W. Brandt and R. Sizmann, Phys. Lett. 37A, 115 (1971), and in Proceedings of the Fifth International Conference on Atomic Collisions in Solids, Gatlinburg, Tennessee, 24–28 September 1973 (Plenum, New York, to be published).

[11] A. Chateau-Thierry and A. Gladieux, in Proceedings of the Fifth International Conference on Atomic Collisions in Solids, Gatlinburg, Tennessee, 24–28 September 1973 (Plenum, New York, to be published).

Fluctuation Resistivity in One-Dimensional Metals

H. Fukuyama,* T. M. Rice,† and C. M. Varma
Bell Laboratories, Murray Hill, New Jersey 07974

(Received 18 March 1974)

The resistivity of one-dimensional metals is calculated for two models in which impurity scattering is the only mechanism for dissipating momentum. In the first model, impurity scattering is added to the Fröhlich Hamiltonian. In the fluctuation regime above an incommensurate Peierls transition it is found that the resistivity is enhanced. For a general two-body interaction Hamiltonian it is found that charge-density-wave fluctuations predominate over Cooper-pair fluctuations leading to enhanced resistivity.

There has been much speculation recently that enhanced conductivity can be obtained from fluctuation contributions in one-dimensional metals.[1-6] A general feature of one-dimensional metals is their inherent instability towards the formation of a charge-density wave with a period of twice the Fermi wave vector $(2k_F)$.[7-10] In this Letter we examine two models for which impurity scattering is the only dissipative mechanism for momentum and find that the density fluctuations lead to an enhanced resistivity, not conductivity. One is the Peierls instability arising from the electron-phonon coupling. The second problem is that of a one-dimensional metal with a general two-body Hamiltonian. In this case even though attractive interactions cause a divergence in the Cooper-pair response function, the scattering time is dominated by the divergence in the electronic polarizability at $2k_F$, and the fluctuation contribution leads to a divergence in the resistivity.

We consider first the Peierls instability with a

Hamiltonian of the form

$$H = H_0 + H_1 + H_2, \tag{1}$$

$$H_0 = \sum_{k\sigma} \epsilon(k) a_{k,\sigma}{}^\dagger a_{k,\sigma}, \tag{2}$$

$$H_1 = L^{-1/2} \sum_{kk'\sigma j} U \exp[i(k-k')R_j] a_{k',\sigma}{}^\dagger a_{k,\sigma}, \tag{3}$$

$$H_2 = L^{-1/2} \sum_{k\sigma q} g[a_{k+q,\sigma}{}^\dagger a_{k,\sigma}(b_{-q}{}^\dagger + b_q) + \text{H.c.}] + \sum_q \omega_q b_q{}^\dagger b_q. \tag{4}$$

The first term is the kinetic energy of the electrons and $a_{k,\sigma}{}^\dagger$ is an electron creation operator. The third term is the Fröhlich electron-phonon coupling term and $b_q{}^\dagger$ is a phonon creation operator. We have included in the Hamiltonian a term representing the impurity scattering with an impurity potential U.

A calculation of the conductivity is meaningful only in the presence of impurity or umklapp phonon scattering. Ohterwise, as Peierls has pointed out,[7] there is perfect phonon drag and no relaxation of the current. We will consider an incommensurate model with the main relaxation arising from impurity scattering. In a strongly commensurate case, such as a half-filled band, Patton and Sham[11] have shown that the fluctuation contributions enhance the resistivity. In discussing the conductivity in one-dimensional metals it is more convenient to use the momentum-relaxation-rate formulation rather than the current-current response-function formulation. A convenient formulation of the former has been given recently by Mori[12] and by Götze and Wölfle[13] and used by Luther and Peschel[14] in the context of impurity scattering in the Tomonaga model. However, it requires some care to apply this formula to the electron-phonon system where the above-mentioned phonon drag is essential. First we note that within the Born approximation for impurity scattering the relaxation rate τ^{-1} of the total momentum P, defined by

$$P = \sum_{k\sigma} k a_{k\sigma}{}^\dagger a_{k\sigma} + \sum_q q b_q{}^\dagger b_q, \tag{5}$$

can be expanded in powers of c as

$$\tau^{-1} = \frac{c}{\omega} U^2 \sum_{kk'} \left(\frac{\partial\epsilon}{\partial k} - \frac{\partial\epsilon}{\partial k'}\right)^2 \operatorname{Im}N(k-k', \omega), \tag{6}$$

where c is the concentration of impurities. $N(q, \omega)$ is the density-density response function evaluated for $H_0 + H_2$, Eqs. (3) and (4). In the steady state ($\omega = 0$) under a weak static electric field, which is the usual circumstance of measuring conductivity, the relaxation time of the electronic current is the same as that of the total momen P, since within the Hamiltonian (1) phonons cannot dissipate their momentum without the scattering of electrons.

The calculation of τ^{-1} reduces then to the calculation of $\operatorname{Im}N(2k_F, \omega)$. If we assume a finite value for the transition temperature T_P, then an expansion of $\operatorname{Im}N(2k_F, \omega)$ in terms of ϵ $[= (T - T_P)/T_P]$ leads to a consideration of the diagram in Fig. 1(b) as the leading correction to the lowest-order diagram in Fig. 1(a), where the wavy line represents a fluctuation propagator of the form $D^{-1}(q, \omega) = -\omega_0{}^2(\epsilon + c_\parallel v_F{}^2 q_\parallel{}^2/T^2 + c_\perp v_F{}^2 q_\perp{}^2/T^2 - i\pi\omega/8T)$. Here $\tilde{q}$ is the deviation from $2k_F$, v_F is the Fermi velocity, and $c_\parallel$ and $c_\perp$ are numerical constants. We have used a more general form for D^{-1} than that of Ref. 11 in order to include possible phonon dispersion in the directions perpendicular to the chains. If we denote the zone-boundary value of $q_\perp$ by q_m, the condition to be met in the three-dimensional limit is $c_\perp v_F{}^2 q_m{}^2/T^2 > \epsilon$, and in this limit the leading correction to the rate is

$$\tau^{-1} = \tau_0{}^{-1}\left(1 + \frac{\pi \ln^2(E_F/T)}{32 c_\parallel{}^{1/2} c_\perp \epsilon^{1/2} v_F{}^2 q_m{}^2/T^2}\right), \tag{7}$$

where $\tau_0{}^{-1} = 2cU^2 v_F{}^{-1}$ is the normal momentum relaxation rate. In the opposite limit the behavior is one-dimensional and

$$\tau^{-1} = \tau_0{}^{-1}\left(1 + \frac{\pi \ln^2(E_F/T)}{16 c_\parallel{}^{1/2} \epsilon^{3/2}}\right). \tag{8}$$

In these formulas E_F is the electronic energy cutoff. In both cases an enhancement of the momentum relaxation rate is obtained. In the one-dimensional case, the expression is only the leading order in an uncontrolled expansion, e.g., Fig. 1(c) contributes a term $\sim \epsilon^{-5/2}$ to the expansion.

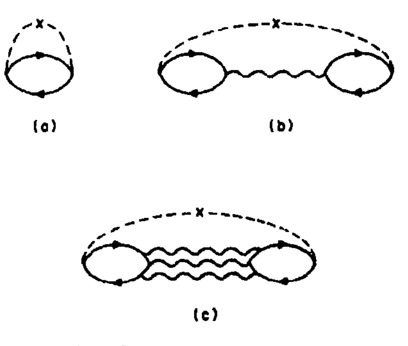

FIG. 1. Leading fluctuation contributions to the momentum relaxation rate according to Eq. (6).

ile the coefficient of $\epsilon^{-3/2}$ in (8) is larger by factor $\ln^2(E_F/T)$ it is clear that there is no oice of parameters for which this expansion is nvergent. This implies that the critical region this problem is of the order of the transition nperature and nonlinear fluctuation effects are portant. However, the main consequence of higher-order fluctuations is to renormalize critical temperature to zero temperature, but y are not expected to change the overall qualtive behavior of N. It is noteworthy that the m shown in Fig. 1(b) is the high-temperature unterpart of the pinning term which was found[8] destroy Fröhlich superconductivity in an orred state. In such a state it is the collectivede scattering with momentum transfer of $2k_F$ the impurity which is responsible for the ping of the charge-density wave and destruction Fröhlich superconductivity. In the fluctuation gime, this process leads to an enhancement of momentum relaxation rate and therefore of resistivity.

n passing from τ^{-1} to the resistivity ρ a factor m^*/ne^2 enters, where n is the electron density m^* is an effective mass. The value of m^* y be obtained by examining the transport equans in the phonon-drag regime in the absence impurities, or the expression for ρ^{-1} obtained the ordered phase.[5] In both cases m^* is ennced by a factor containing the number of phons at $2k_F$ and this factor will give rise to an adional enhancement of the resistivity in the fluction regime.

et us now consider a general two-body interion Hamiltonian of the form $H_0+H_1+H_2$, where

$$H_2=(g_1/L)\sum a_{k_1,\alpha}{}^\dagger a_{k_2-2k_F,\beta}{}^\dagger a_{k_3,\beta}a_{k_4-2k_F,\alpha} + (g_2/L)\sum a_{k_1,\alpha}{}^\dagger a_{k_2-2k_F,\beta}{}^\dagger a_{k_3-2k_F,\beta}a_{k_4,\alpha}. \qquad (9)$$

All the k_i are near $+k_F$. The coupling constants g_1 and g_2 represent scattering with momentum transfer near $2k_F$ and 0, respectively. Again one can relate the momentum relaxation rate τ^{-1} to $\mathrm{Im}N(2k_F,\omega)$ within the Born approximation. The response functions for a momentum transfer near $2k_F$ have been calculated using the renormalization-group method by Sólyom.[10] For an attractive interaction at $2k_F$ ($g_1<0$) the first-order renormalization method leads to a singularity at finite T and the coupling scales to the strong-coupling limit. Second-order renormalization-group methods remove the singularity to zero temperature as must be the case for a one-dimensional system[13] and Sólyom[10] finds the result

$$\mathrm{Re}N(2k_F+q,\omega)\sim[\max(v_F|q|,\omega,T)/E_F]^{-3/2}. \qquad (10)$$

Using the Kramers-Kronig relation one obtains corresponding results for $\mathrm{Im}N(2k_F+q,\omega)$, and one obtains the result, using (10), that

$$\tau^{-1}\sim\tau_0{}^{-1}(T/E_F)^{-3/2}. \qquad (11)$$

Again the fluctuations enhance the momentum relaxation rate and thus lead to an *enhanced resistivity.* In this system the Cooper-pair response function Δ is also diverging and the effect of this divergence can be traced as a high-order set of terms in the perturbation expansion for N, which are opposite in sign to the dominant terms arising from the Peierls instability. Formula (6) is applicable only in the weak-scattering limit ($\tau T>1$). As the scattering rate grows this condition is violated and one must include impurity scattering to higher order, especially in the calculation of N itself.

The Hubbard model represents a special case of the Hamiltonian (9), in which $g_1=g_2=g$. Thus for $g<0$, resistive fluctuations are predicted. An interesting limiting case occurs if we set $g_1=0$. The model is then the Tomonaga model. The form of $N(2k_F+q,\omega)$ within the renormalization method is drastically changed and one finds

$$N(2k_F+q,\omega)\sim[\max(v_F|q|,\omega,T)/E_F]^{-g_2/\pi v_F}. \qquad (12)$$

Thus for attractive interactions ($g_2<0$), $N\to 0$ as $T\to 0$. A similar result holds for the imaginary part and one finds $\tau^{-1}\sim\tau_0{}^{-1}(T/E_F)^{-g_2/\pi v_F}$. Within this model the fluctuations *enhance the conductivity.* These results are in agreement with the exact results of Luther and Peschel[14] and of Mattis[15] for the Tomonaga model. For the more general model with $g_1\neq 0$, the behavior will be governed by g_1 primarily and the conditions to obtain enhanced conductivity, i.e., $N\to 0$ rather than $N\to\infty$, are $g_1>0$, and $2g_2-g_1<0$. In practice these conditions will be hard to realize since a study[17] of the combined electron-phonon and electron-electron Hamiltonian shows a strengthening of the singularity in $N(2k_F,\omega)$ and a diminishing of that in $\Delta(2k_F,\omega)$.

In conclusion, we find that for most circumstances, a one-dimensional metal will have a divergence in the electronic polarizability near $2k_F$ which will lead to enhanced momentum scattering rate from impurities in the fluctuation regime. However the overall behavior of the resistivity as the temperature is decreased will be determined by the combined umklapp phonon scattering rate and the impurity scattering rate. The leading umklapp process will decrease exponentially with temperature and, depending on sample conditions, may be the dominant contribution.

It is a pleasure to thank our colleagues E. I. Blount, B. I. Halperin, and P. A. Lee for illuminating discussions.

---

*Present address: Department of Physics, Tohoku University, Sendau, Japan.

†Present address: Department of Physics, Simon Fraser University, Burnaby 2, B. C., Canada.

[1] L. B. Coleman, M. J. Cohen, D. J. Sandman, F. G. Yamagishi, A. F. Garito, and A. J. Heeger, Solid State Commun. 12, 115 (1973).

[2] J. Bardeen, Solid State Commun. 13, 357 (1973).

[3] D. Allender, J. W. Bray, and J. Bardeen, Phys. Rev. B 9, 119 (1974).

[4] P. W. Anderson, P. A. Lee, and M. Saitoh, Solid State Commun. 13, 595 (1973).

[5] P. A. Lee, T. M. Rice, and P. W. Anderson, Solid State Commun. 14, 703 (1974).

[6] S. Strassler and G. A. Toombs, Phys. Lett. 46A, 321 (1974).

[7] R. Peierls, Ann. Phys. (Leipzig) 4, 121 (1930), and *Quantum Theory of Solids* (Oxford Univ. Press, Oxford, England, 1955).

[8] Yu. A. Bychkov, L. P. Gor'kov, and I. E. Dzyaloshinsky, Zh. Eksp. Teor. Fiz. 50, 738 (1966) [Sov. Phys. JETP 23, 489 (1966)].

[9] N. Menyhard and J. Sólyom, J. Low Temp. Phys. 12, 529 (1973).

[10] J. Sólyom, J. Low Temp. Phys. 12, 546 (1973).

[11] B. R. Patton and L. J. Sham, Phys. Rev. Lett. 31, 631 (1973).

[12] H. Mori, Progr. Theor. Phys. 33, 423 (1965), and 34, 399 (1965).

[13] W. Götze and P. Wölfle, Phys. Rev. B 6, 1226 (1972).

[14] A. Luther and I. Peschel, Phys. Rev. Lett. 32, 992 (1974).

[15] Note that because the invariant coupling still becomes large, for $g_1 < 0$, the results of the second-order renormalization-group methods are only qualitative, at best (see Refs. 9 and 10 and H. Fukuyama, T. M. Rice, C. M. Varma, and B. I. Halperin, to be published).

[16] D. Mattis, Phys. Rev. Lett. 32, 714 (1974).

[17] S. T. Chui, T. M. Rice, and C. M. Varma, to be published.

Diffraction, Refraction, and Interference Phenomena in Heavy-Ion Transfer Reactions

W. A. Friedman, K. W. McVoy, and G. W. T. Shuy
Department of Physics, University of Wisconsin, Madison, Wisconsin 53706

(Received 20 May 1974)

The forward-angle oscillations recently observed in heavy-ion transfer reactions are explained as the Young interference pattern of a refractive two-slit "optical system" in l space, and a new phenomenon is predicted.

The forward-angle oscillations observed[1-3] in heavy-ion transfer reactions undergo a characteristic modification as the bombarding energy is increased into the range where the nuclear force significantly modifies the Coulomb trajectory. We offer here an analysis of distorted-wave Born-approximation (DWBA) calculations which fit these oscillations, to show that their energy dependence can be understood in simple optical terms (diffraction, refraction, and interference), and to predict an interesting new feature of the oscillatory pattern which should appear at bombarding energies somewhat higher than those employed up to now.

An example of these angular distributions is shown in Fig. 1, which displays LOLA[4] calculations of the (one-step) reaction $^{48}\mathrm{Ca}(^{16}\mathrm{O}, {}^{14}\mathrm{C})^{50}\mathrm{Ti}$ to the ground state. The familiar "grazing-angle peak" seen in the 40-MeV curve moves to more forward angles and becomes "inundated" by the oscillatory pattern at 56 MeV. This is further accentuated in the 85-MeV distribution, which also exhibits the qualitatively new feature, a "modulation" of the envelope of the oscillations, giving them exceptionally large peak-to-valley ratios at 0, 35, and 70°, with small peak-to-valley ratios at 15 and 50°.

Several interesting papers[1,3,5-7] have recently provided partial explanations of certain of these features. Our purpose here is to indicate how these discussions can be unified, and extended to explain the amplitude modulation seen in the 85-MeV curve of Fig. 1. The oscillations, as pointed out by Chasman, Kahana, and Schneider,[1] (CKS) are an interference phenomenon, arising basically from the highly peripheral nature of these transfer reactions. This "surface peaking" forces the trajectories which contribute substantially to the reaction to pass through two narrow "l windows," centered at $l = l_0$, on either side of the target nucleus. The narrowness of these windows (they have a full width $\Delta l \approx 4$ to 6 in the cases studied here) causes the passing beams to fan out diffractively into two "grazing-angle peaks" of full width $\Delta\theta \gtrsim 2/\Delta l$, which at low energy are separated by an angular distance $2\theta_0$. This is the equivalent of a two-slit optical system with oppositely slanted prisms behind the slits to separate the two beams; the forward oscillations seen at 40 MeV in Fig. 1 are the Young interference pattern resulting from the overlap of the tails of the grazing-angle peaks centered at $\pm\theta_0$.

To see more clearly how this comes about, we consider first the simplest case of zero l transfer (the conclusions, however, are general) and, for the semiclassical case $l_0 \gg 1$, employ the large-l approximation to $P_l(\cos\theta)$ for $\theta > 1/l$. The partial-wave decomposition of the transfer amplitude, $f(\theta) = \sum f(l - l_0)P_l(\cos\theta)$, then takes the form

$$f(\theta) \approx (\tfrac{1}{2}\pi l_0 \sin\theta)^{1/2}\{\exp(i[(l_0 + \tfrac{1}{2})\theta - \tfrac{1}{4}\pi])\textstyle\sum f(l - l_0)\exp[i(l - l_0)\theta] + \exp(-i[(l_0 + \tfrac{1}{2})\theta - \tfrac{1}{4}\pi])\textstyle\sum f(l - l_0)\exp[-i(l - l_0)\theta]\}, \qquad (1)$$

in which each of the two sums represents a beam passing through one of the l windows. In order for them to interfere destructively to produce deep minima, their amplitudes must be equal at the same θ. To see where this occurs, we define the single-slit amplitude

$$g(\theta) = \textstyle\sum f(l - l_0)\exp[-i(l - l_0)\theta], \qquad (2)$$

which is the Fourier transform of $f(l - l_0)$. The single-slit pattern (or grazing-angle peak) has the shape $|g(\theta)|^2/\sin\theta$, and Fig. 2 displays $|g(\theta)|^2$ and $|g(-\theta)|^2$ for the three cases of Fig. 1. It shows the merging of the two peaks with increasing energy, and in addition makes clear the way in which the amplitude modulations of Fig. 1 arise from the curve crossings of the two peaks of Fig. 2. These modulations are due entirely to

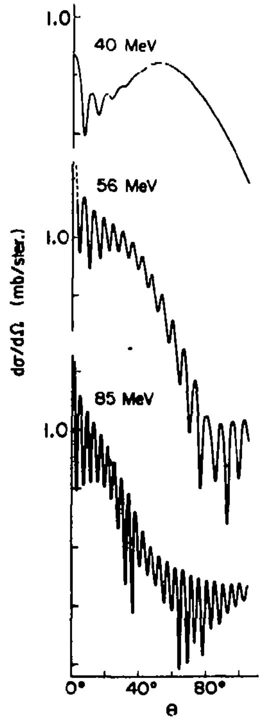

FIG. 1. DWBA calculations (log scale) for ^{42}Ca(^{16}O, ^{14}C)^{44}Ti, with the parameters of Ref. 2. The optical potential has a transparent surface, $R_V - R_W = 0.5$ fm.

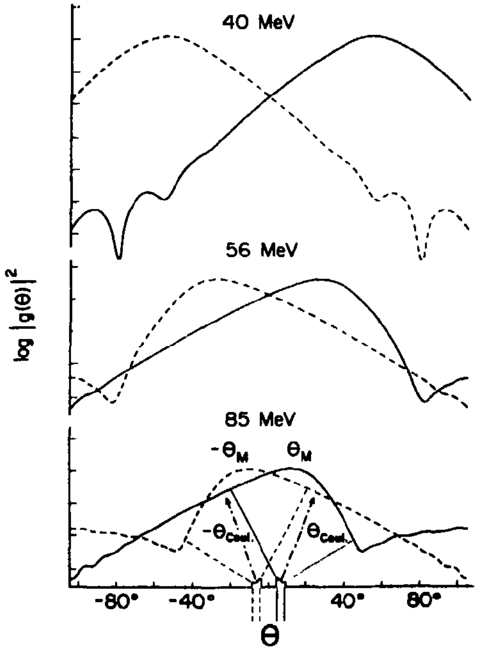

FIG. 2. Single-slit diffraction-refraction patterns from the DWBA calculations of Fig. 1. The refractive two-slit system is suggested at the bottom of the figure.

(a) the *asymmetries* and (b) the *minima* shown by the single-slit peaks. We turn next to a consideration of their origin.

Writing $f(l-l_0)=\rho(l-l_0)\exp[2i\delta(l-l_0)]$, we can associate $\rho(l-l_0)$, the "shape" of the l window, with the *diffractive* spreading of the beam, and $\delta(l-l_0)$ with its *refractive* focusing and deflection, as though lenses were placed behind the windows to produce different "optical paths" for different impact parameters. As an example, CKS assume a phase linear in l, $\delta(l-l_0)=(l-l_0)\theta_0$, which will clearly just shift the Fourier transform of $\rho(l-l_0)$ by the angle θ_0: A linear phase implies prismatic refraction.

In order to study the refractive and diffractive effects of $\delta(l-l_0)$ and $\rho(l-l_0)$, we must examine the single-slit patterns $g(\theta)$ which are the Fourier transforms of the reaction amplitudes $f(l-l_0)$. Insight into their properties may be obtained by converting the l sum to an integral and evaluating the latter by the method of stationary phase, a technique fruitfully exploited for elastic scattering by Ford and Wheeler. For this purpose it is convenient to consider $f(l-l_0)$ in the form $\exp[i\Delta(l-l_0)]$, where $\Delta(l-l_0)=2\delta(l-l_0)+i\ln\rho(l-l_0)$. With $\ln\rho(l-l_0)=0$, one can carry out the conventional stationary-phase treatment of *refraction*, and determine the trajectories for which l and the "classical" reaction angle θ are related by $2d\delta(l-l_0)/dl=\theta(l)$. At the other extreme, i.e., for $\delta(l-l_0)=0$, the stationary-phase evaluation leads to the familiar *diffraction* results. For example, a $\Delta(l-l_0)$ of $i(l-l_0)^2/\Gamma^2$ provides $g(\theta)\sim\exp[-(\Gamma^2\theta^2)/4]$ which comes from a "stationary phase" associated with a complex l, $l=l_0+i\frac{1}{2}\Gamma^2\theta$. Clearly a stationary-phase treatment of a fully complex Δ_l is capable of treating simultaneously both refractive and diffractive effects.

In Fig. 3 we have plotted $\rho(l-l_0)$, and $2\delta(l-l_0)$ obtained from the 85-MeV LOLA calculation. We have also plotted $\theta=2d\delta(l-l_0)/dl$, which is seen to have a minimum as a function of l. Such a minimum is analogous to the minimum scattering angle conventionally referred to as a "rainbow" angle θ_R, in semiclassical terms. This type of refractive dip was seen at each of nine energies ranging from 40 to 120 MeV, and in each case was positioned with striking accuracy at the center of the l window, l_0. For an optical potential whose imaginary part is of shorter range than its real part, this seems to have a simple explanation in the Sopkovich model,[8] in which $2\delta(l-l_0)$ is the sum of the channel phases. The channel Coulomb phases together give $2d\sigma_c/dl\approx2\tan^{-1}\eta_c/l_c=\theta_{\rm Coul}$ which provides the monotonic background from which the dip "hangs." The dip, however, is determined by the behavior of the nuclear phase shift δ^N. For large l, δ_l^N is zero; approaching the window from above, δ_l^N begins to rise as the nuclear force pulls the flux forward from $\theta_{\rm Coul}$, but with the onset of absorption the rise is stalled and a point of inflection is introduced at which $d^2\delta_l^N/dl^2=0$. Note, this inflection point (and consequently the minimum θ) comes at the onset of the absorptive effects and thus always occurs at approximately l_0, or the center of the window. The value of θ_R, on the other hand, is determined by both Coulomb and nuclear forces, the Columb force giving the background, and the nuclear force determining the extent of the dip. This dip, at the center of the l window, guarantees both asymmetry and broadening in the single-slit patterns $|g(\theta)|^2$.

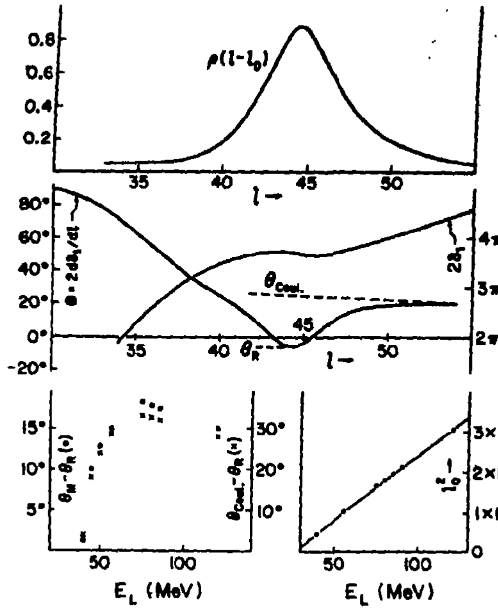

FIG. 3. Top and center: magnitude, phase, and phase derivative for the 85-MeV DWBA amplitudes. Lower figures are explained in text.

To obtain qualitative features arising from the interplay of refractive and diffractive effects we have used stationary-phase techniques to examine $g(\theta)$. A model which can reproduce the general features of the one-slit patterns of Fig. 2 is $f(l-l_0)=\exp[-(l-l_0)^2/\Gamma^2]\exp[2i\delta(l-l_0)]$, with $\delta(l-l_0)=(l-l_0)\theta_R+\frac{1}{3}\beta(l-l_0)^3$; this approximates the "nuclear-rainbow" dip in $\theta(l)$ by a parabola. It is convenient to define a "refraction parameter" Φ, as that area of the dip which is contained within the l window. For the present model $\Phi = \frac{4}{3}\beta\Gamma^3$. In nuclear terms, it is a measure of the amount by which the deflection angle deviates from θ_{Coul}, for trajectories which pass through the l window.

The resulting $|g(\theta)|^2$, which is very similar to those of Fig. 2, is best understood by noting that the curves in Fig. 2 bear a striking resenblance to the Airy function which describes a classical rainbow. The right-hand (solid) curves are oriented with the bright side of the rainbow (steeper falloff from the principal maximum) toward larger angles and the dark side (gentler falloff from the principal maximum) toward smaller angles. The minimum, on the bright side (at 80° at 56 MeV and at 50° at 85 MeV), is to be associated with the first rainbow zero; the rainbow angle θ_R is *on the opposite side of the main peak* (at $-5°$ in the 85-MeV case, as Fig. 3 indicates).

The $g(\theta)$ for the present model has two simple limits for large and small Φ. For $\Phi \to 0$, $|g(\theta)|^2 \to \exp[-\frac{1}{2}\Gamma^2(\theta-\theta_R)^2]$, the symmetric CKS peak, centered at $\theta = \theta_R$. However, if $\Phi = \frac{4}{3}\beta\Gamma^3$ *is* increased by opening the window, the asymmetric refraction due to β is introduced. This shifts the peak at θ_M away from θ_R toward the bright (right-hand) side of the rainbow and simultaneously brings a zero down toward the peak from above, producing the asymmetric principal peak of the Airy function. Note that this is exactly the type of change observed in the curves of Fig. 2 as the energy rises above the Coulomb barrier and the nuclear influence on the trajectory, measured by β, causes an increase in Φ. This interpretation is reinforced by the lower left-hand inset in Fig. 3, which shows the two differences, $\theta_M - \theta_R$, and $\theta_{\mathrm{Coul}} - \theta_R$, as a function of laboratory energy E_L.

In summary, it is our conclusion that the minimum seen in the 56- and 85-MeV curves is primarily a *refractive* or rainbow-type minimum, due principally to the nuclear-force influence on $\delta(l-l_0)$, rather than a diffraction zero arising from $\rho(l-l_0)$. In fact, the Fourier transform of the LOLA $\rho(l-l_0)$ alone is found to exhibit no minima at any of these energies.[9] Thus the amplitude modulation of Fig. 1, which is in part a consequence of this minimum, appears to be extremely sensitive to the tail of the optical potential, and may prove to be a means for determining this tail with great accuracy. In this regard, the lower right-hand inset in Fig. 3 shows that $l_0 = kR$ with $R = 8.7$ fm; for comparison, $R_V = 8.3$ fm and $R_W = 7.8$ fm.

Ascuitto and Glendenning[5] have noted that decreasing R_W by 5% can increase the $\theta = 0$ cross section by a factor of 10. Careful inspection of their curve suggests that this is also best understood as a similar asymmetric-refraction effect: Decreasing R_W increases Φ by opening the l window and increasing $\theta_R - \theta_{\mathrm{Coul}}$. This tips the $|g(\theta)|^2$ so as to increase the cross section at angles below the grazing-angle peak, and decreases it at angles above the peak. An even more interesting phase effect can be seen by comparing one- and two-nucleon transfers. The smaller binding energy and mass transfer of the former increases its form-factor range by 2 relative to that for the two-nucleon transfer, thus opening the right-hand side of the l window substantially. This exposes much more of the slowly-varying Coulomb phase for $l > l_0$ and so builds up a large grazing-angle peak at $\theta = \theta_{\mathrm{Coul}}$ which is missing from the two-nucleon cross section. This is illustrated clearly in the ^{16}O + ^{64}Ni data of Ref. 3, and might even suffice to distinguish sequential transfer of two nucleons from a one-step process.

We are very grateful to W. Henning, D. G. Kovar, B. Zeidman, and J. R. Erskine of the Argonne National Laboratory for making their data available prior to publication and providing the LOLA calculations analyzed here.[10]

---

[1] C. Chasman, S. Kahana, and M. J. Schneider, Phys. Rev. Lett. 31, 1074 (1973).

[2] W. Henning, D. G. Kovar, B. Zeidman, and J. R. Erskine, Phys. Rev. Lett. 32, 1015 (1974).

[3] M.-C. Lemaire, M. C. Mermaz, H. Sztark, and A. Cunsolo, to be published.

[4] R. M. DeVries, Phys. Rev. C 8, 951 (1973). The LOLA parameters used are those of Ref. 2, where the potentials are chosen to fit the 56-MeV data.

[5] R. J. Ascuitto and N. K. Glendenning, Phys. Lett. 48B, 6 (1974); N. K. Glendenning, in *Proceedings of the Symposium on Heavy-Ion Transfer Reactions, Argonne, Illinois, 1973*, CONF 730312 (Argonne National Laboratory, Argonne, Ill., 1973), p. 518.

[6] R. C. Fuller and O. Dragun, Phys. Rev. Lett. 32, 617 (1974).

[7] V. M. Strutinsky, Phys. Lett. 44B, 245 (1973).

[8] See W. E. Frahn and M. A. Sharaf, Nucl. Phys. A133, 593 (1969).

[9] We note in passing that the width of this Fourier transform is only about half that of $g(\theta)$. That is, the fanning out of the beam as it passes through the l window is as much refractive (defocusing) as it is diffrac-

tive.

[19] We thank H. L. Harney, P. Braun-Munzinger, and C. K. Gelbke for a preprint that arrived while this manuscript was in preparation, which similarly emph sizes some of the two-slit features of these cross sections.

Search for a Δ-Δ Component in the Deuteron Wave Function Using $\bar{p}d$ Interactions at 5.55 GeV/c

H. Braun, D. Brick, A. Fridman, J.-P. Gerber, P. Juillot, G. Maurer,
A. Michalon, M.-E. Michalon-Mentzer, R. Strub, and C. Voltolini
Groupe des Chambres à Bulles à Hydrogène, Centre de Reçherches Nucléaires, Strasbourg, France

(Received 4 April 1974)

From a bubble-chamber experiment, we studied the $\bar{p}d \to p_s\bar{p}p\pi^-$, $p_s\bar{p}p\pi^-\pi^0$, $p_s\bar{n}p\pi^-\pi^-$ reactions at 5.55 GeV/c in order to see whether a Δ-Δ component of the deuteron wave function can be observed in our data. This was achieved by searching for spectator $\Delta \to p_s\pi$ systems. We observed significant production of $\Delta \to p_s\pi$, a fraction of which is emitted in the backward laboratory hemisphere. The meaning of this high $\Delta \to p_s\pi$ production rate is discussed.

Recently the possibility that virtual Δ's may be present in the nucleus has been considered.[1,2] It has been suggested that a way to test such a picture is to study inelastic reactions on the deuteron.[3,4] Because of isospin conservation, the deuteron can transform into only two Δ's. Then following the impulse approximation, a fraction of the interactions induced by fast beam particles may occur on a virtual Δ, the other appearing as a Δ spectator (Δ_s). In this approach the observation of Δ_s in inelastic channels may give some information about the Δ-Δ component of the deuteron wave function. Furthermore the presence of Δ in the deuteron may also offer a way to study interactions on virtual Δ targets.

The percentage of the Δ-Δ component in the deuteron wave function has been estimated from theoretical calculations to be a few percent.[1,2] Although this percentage is small, we attempted to see if Δ_s appear among the outgoing particles in $\bar{p}d$ interactions at 5.55 GeV/c by collecting data from the following channels

$$\bar{p}d \to p_s\bar{p}p\pi^- \quad (1348 \text{ events}), \tag{1}$$

$$\to p_s\bar{p}p\pi^-\pi^0 \quad (651 \text{ events}), \tag{2}$$

$$\to p_s\bar{n}p\pi^-\pi^- \quad (221 \text{ events}). \tag{3}$$

The present data which have already been partially *studied*[5] were *obtained from a bubble chamber* experiment. All the considered events contain an outgoing proton (p_s) stopping in the chamber. One has thus a sample in which the p_s presents roughly the behavior of a spectator proton. In order to search for Δ_s in the final state, we will consider the various outgoing $p_s\pi$ systems, and discuss later the biases introduced by taking only events having a proton stopping in the chamber. To decrease complications due to resonance reflection, we studied $p_s\pi$ systems in which the π does not contribute to resonance production with the remaining outgoing particles. In Reaction (1) we thus excluded the $\bar{p}d \to p_s\bar{\Delta}^{--}p$ subsample obtaining 1348 events. For channel (2) we consider all of the $p_s\pi^0$ systems since the π^0 contribute in a negligible amount to resonance production. Within the present statistics this is likewise true for the π^- in channel (3), allowing us to consider the two $p_s\pi^-$ combinations.

Using the $p_s\pi$ systems thus selected, we present in Fig. 1(a) the scatter plot of $\cos\theta$ versus the $p_s\pi$ effective mass ($M_{p_s\pi}$). Here θ is the laboratory emission angle of the $p_s\pi$ system defined with respect to the incoming beam direction. One sees from this plot that the events having their $M_{p_s\pi}$ in the Δ band ($1.15 < M_{p_s\pi} < 1.32$ GeV/c^2) are distributed over all the $\cos\theta$ range. A similar structure observed[3] in the reaction $\pi^+d \to p_sp\pi^+\pi^-\pi^0$ at 15 GeV/c[3] was accounted for by the existence of virtual Δ in the deuteron since the $p_s\pi^+$ systems in the Δ band seem to be emitted isotropically in the laboratory system as predicted by the impulse-approximation approach.[3] Even in this model such a picture is oversimplified because one neglects, among other things, the following effects: the cross-section variation of the studied process for the c.m. energy spread

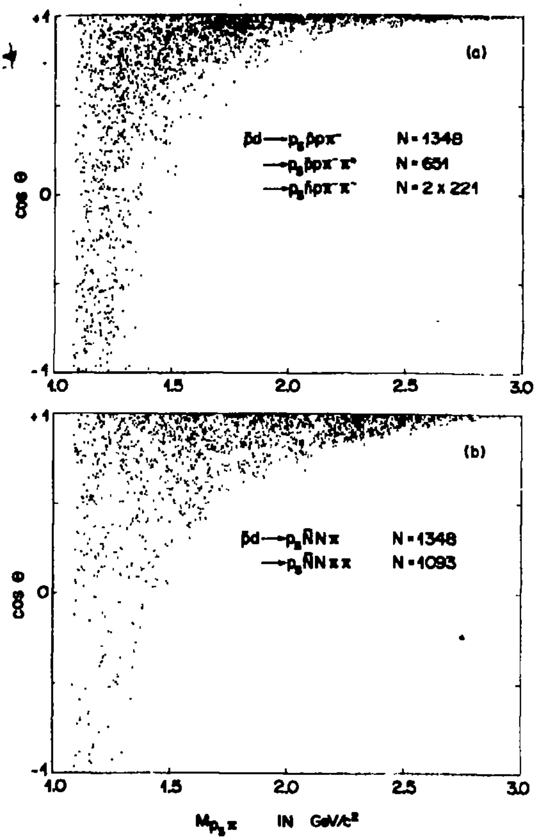

FIG. 1. (a) The $M_{p_s\pi}$, $\cos\theta$ scatter plot; the same plot for Monte Carlo events.

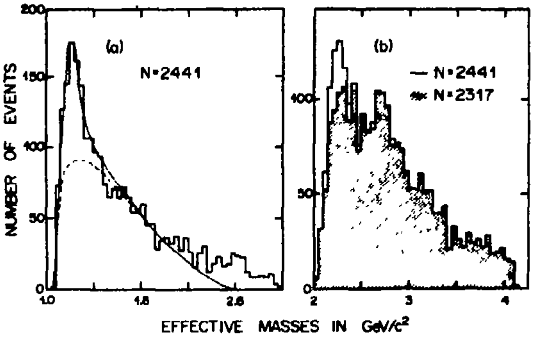

FIG. 2. (a) The $M_{p_s\pi}$ distribution. The solid curve represents the fitted data while the dashed line is the peripheral phase space. (b) The $M_{p_s p\pi^-}$ [channels (1) and (3)] and $M_{p_s p\pi^0}$ [channel (2)] effective mass distribution. The shaded area is obtained by excluding the events in the $\Delta \to p_s\pi$ band and emitted in the $\cos\theta > 0.75$ region.

introduced by the Fermi motion of the Δ target, the variation of the invariant flux factor due to different beam-target momentum configurations, and the influence of the bias introduced by taking only events having an outgoing proton stopping in the bubble chamber. Nevertheless the observation of $\Delta \to p_s\pi$ emitted in the backward hemisphere ($\cos\theta < 0$) may support the idea that this Δ is a spectator system. This is because from kinematical considerations the Δ produced by the interaction of the beam particle with the deuteron or with their bound nucleons cannot be emitted in the $\cos\theta < 0$ region. Our data [Fig. 1(a)] show that we have a rather important number of $p_s\pi$ systems in the Δ mass band which are emitted in the $\cos\theta < 0$ range.

For comparison, we present in Fig. 1(b) a scatter plot obtained from phase-space events. These events were generated by a Monte Carlo method in the same amount as that given by our various channels. For the simulation of channel (1), we excluded the events having an $M_{\bar{p}\pi^-}$ mass value in the $\bar{\Delta}^{--}$ mass band. The calculation was made by assuming that p_s is a spectator proton described by the Hulthén wave function. The concentration of the events in the Δ band is more important for the experimental data than for the phase-space events, as can also be seen from the $M_{p_s\pi}$ distribution [Fig. 2(a)]. We fitted this distribution using an incoherent mixture of a Breit-Wigner function due to the $\Delta \to p_s\pi$ resonance and peripheral phase space obtained by a Monte Carlo calculation similar to that described above. This time each generated event was weighted by a factor $a\exp(b_1t_1)\exp(b_2t_2)$ for describing the peripheral nature of the studied reactions. Here t_1 (t_2) is the four-momentum transfer between the incident $\bar{p}$ (bound n) and the outgoing $\bar{N}$ (N) particle. The slopes b_1 and b_2 were adjusted simultaneously for each channel in such a way that the integrated t_1 and t_2 distributions agree with the experimental data (see Table I). As a result of

TABLE I. Slopes used for calculating the peripheral phase space.

Final state	b_1 [(GeV/c)$^{-2}$]	b_2 [(GeV/c)$^{-2}$]
$p_s\bar{p}p\pi^-$	4.4 ± 0.4	4.0 ± 0.4
$p_s\bar{p}p\pi^-\pi^0$	1.7 ± 0.1	2.2 ± 0.2
$p_s\bar{n}p\pi^-\pi^-$	1.7 ± 0.2	1.1 ± 0.1

this fit we obtain 401 ± 63 events that contribute to the $\Delta \to p_s\pi$ peak. One notices from Fig. 2(a) that the peripheral phase space does not describe the experimental distribution in the $M_{p_s\pi} \gtrsim 2.3$ GeV/c^2 region because of the influence of the resonance reflections. Indeed our data show that high-mass $\bar{p}\pi^-$ resonances (weakly present here) are populating the $M_{p_s\pi} > 2.3$ GeV/c^2 region. Let us also note that we attempted unsuccessfully to use a nonperipheral phase space to fit our data.

The percentage of Δ lost because of our event selection has been estimated by generating $\bar{p}d \to \Delta\bar{N}N$, $\Delta\bar{N}N\pi$ events with a Monte Carlo method and assuming that the Δ's decay isotropically in their rest frame. The generation was done according to our experimental Δ momentum distribution, the shape of which is not strongly affected by our bias as shown by our calculation. We obtain a loss of about 7%.

The important observed $\Delta \to p_s\pi$ production rate partly arises from the so-called d^* phenomenon studied in earlier papers.[6,7] We showed in particular that an important part (~20%) of the events fitting the reaction $\bar{p}d \to p_s\bar{p}n\pi^+\pi^-$ result from $\bar{p}d \to \bar{p}\pi^-d^*$, where the d^* enhancement at 2.18 GeV/c^2 transforms into a $p_sn\pi^+$ system. In this case most (~90%) of the $p_s\pi^+$ and $n\pi^+$ effective masses are in the Δ mass bands as can be seen from a $p_sn\pi^+$ Dalitz plot calculated for the d^* mass.[7] For the channels considered here, a similar d^* enhancement can appear, with $d^* \to pp\pi^-$ [channels (1) and (3)] or $d^* \to pp\pi^0$ [channel (2)]. The Clebsch-Gordan coefficients predict a branching ratio of $(d^* \to pp\pi^0, pp\pi^-)/(d^* \to pn\pi^+) = \frac{1}{2}$. Figure 2(b) displays the distribution of the $p_sp\pi$ effective mass ($M_{p_sp\pi}$) in which a prominent enhancement can be seen at 2.18 GeV/c^2. In order to remove the d^* events without eliminating the numerous events which are in the $M_{p_sp\pi} \sim 2.18$ GeV/c^2 region, we apply a cut on cosθ. Indeed the study of the d^* enhancement in the reaction $\bar{p}d \to p_s\bar{p}n\pi^+\pi^-$ has shown that practically all of the $p_s\pi^+$ systems coming from the $d^* \to pn\pi^+$ enhancement are emitted in the $\cos\theta > 0.75$ range. Excluding from our sample the events which have their $p_s\pi$ system in the Δ mass band and which are emitted in the $\cos\theta > 0.75$ range, we obtain the shaded histogran shown in Fig. 2(b). The d^* bump practically disappears.

Therefore to avoid a misinterpretation of our data we first consider the effective-mass distribution of the $p_s\pi$ system having its $\cos\theta < 0.75$. This $M_{p_s\pi}$ distribution [Fig. 3(a)] was fitted with a Breit-Wigner function and peripheral phase space deformed according to our selection criteria. The presence of a high number of $\Delta \to p_s\pi$ resonances (255 ± 40) clearly indicates that our data cannot be explained completely in terms of interactions having a real spectator proton in the final state. For estimating the number of $\Delta \to p_s\pi$ emitted in the backward hemisphere, it is difficult to fit the $M_{p_s\pi}$ distribution in the $-1 < \cos\theta < 0$ interval since the Δ(1236) Breit-Wigner function has a behavior very similar to the peripheral phase space in this region. Therefore we consider the $M_{p_s\pi}$ distribution in the $0 < \cos\theta < 0.75$ range from which 73 ± 35 events contribute to the $\Delta \to p_s\pi$ peak. This allows us to estimate by substraction that 182 ± 53 $\Delta \to p_s\pi$ are emitted in the $\cos\theta < 0$ region.

Figure 3(b) presents the cosθ distribution for events in the Δ mass band. In this band the Δ

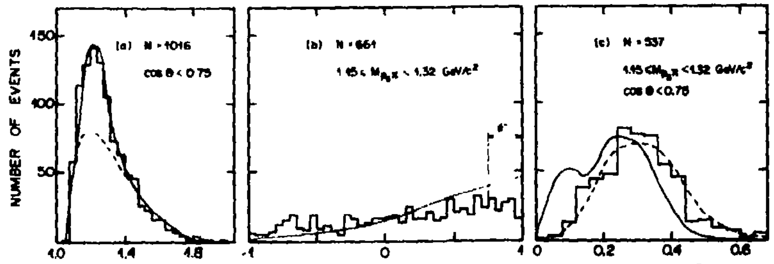

FIG. 3. (a) The $p_s\pi$ mass distribution with the full curve representing the fitted distribution and the dashed line the peripheral phase space. (b) The cosθ for the $p_s\pi$ system with the curve representing the peripheral phase space normalized in $-1 < \cos\theta < 0.75$. (c) The laboratory momentum distribution of the $p_s\pi$ systems. The full curve is the calculation from Ref. 4 deformed by our selection criteria. The dashed curve is peripheral phase space.

over background ratio is about 40%. The curve in Fig. 3(b) represents the peripheral phase space prediction normalized to the data in the $\cos\theta < 0.75$ range where the d^* production is negligible. The experimental distribution presents an isotropic component which cannot be accounted for by only the phase space prediction. For the events in the $\Delta \to p_s\pi$ mass band and with $\cos\theta < 0.75$ we compare the experimental momentum distribution of the $p_s\pi$ system [Fig. 3(c)] with the peripheral phase space (dashed curve) and the distribution (full curve) deduced from the Δ-Δ component of the deuteron wave function calculated in Ref. 4. To this end we calculated the modifications introduced in the theoretical distribution because of our event selection. This was achieved by a Monte Carlo calculation assuming still an isotropic decay of the Δ_s. In contrast to the peripheral phase-space prediction [see Fig. 3(c)], the distribution obtained is not able to describe our data. The same calculation also showed that the expected isotropic distribution of the Δ_s in the laboratory system is not affected by selecting events with a stopping proton.

To summarize, we showed that an important fraction of the studied events have $\Delta \to p_s\pi$ resonances in the final state. Even if we remove the $d^* \to p_s p\pi$ events present in our sample we still have about 255 ± 40 $\Delta \to p_s\pi$ events, 182 ± 53 of which are emitted in the backward hemisphere. The $\Delta \to p_s\pi$ production rate is even higher if one takes into account the losses (~7%) due to our event selection.

In contrast to the laboratory momentum distribution of the $\Delta \to p_s\pi$ events, the laboratory angular distribution of these resonances is not well described by peripheral phase space since there is an excess of $\Delta \to p_s\pi$ events in the $\cos\theta < 0$ region. This last fact as well as the strong $\Delta \to p_s\pi$ production rate may support the idea of events produced with spectator Δ in the final state. If one assumes that all the $\Delta \to p_s\pi$ are spectator systems and that the $\bar{p}n$ and $\bar{p}\Delta$ interactions leading to the observed final states have equal cross sections, one obtains that the Δ-Δ component of the deuteron wave function is about ~16%. This high percentage when compared with theoretical calculations may suggest that other mechanisms contribute to the $\Delta \to p_s\pi$ production. In particular one can also worry about the validity of the impulse approximation for systems having a large binding energy as for the Δ-Δ case. In any case the high $\Delta \to p_s\pi$ production rate clearly establishes that an important part of our events cannot be considered as being produced with real spectator nucleons. Further theoretical and experimental investigations will certainly be necessary in order to relate more closely the Δ observed in the final state with the possible existence of the Δ-Δ component of the deuteron wave function.

---

[1] S. Jena and L. S. Kisslinger, in *Proceedings of the International Conference on Nuclear Physics, Munich, Germany, 1973*, edited by J. de Boer and H. J. Mang (North-Holland, Amsterdam, 1973).

[2] H. Arenhövel, M. Danos, and H. T. Williams, Phys. Lett. 31B, 109 (1970), and Nucl. Phys. A162, 121 (1971).

[3] M. Goldhaber, J. Phys. (Paris), Colloq. 34, C1-209 (1973).

[4] L. K. Kisslinger, Phys. Lett. 48B, 410 (1974).

[5] H. Braun *et al.*, Phys. Rev. D 2, 488 (1970).

[6] H. Braun *et al.*, Phys. Rev. D 2, 1212 (1970); D. Evrard, A. Fridman, and A. C. Hirshfeld, Nucl. Phys. B14, 699 (1969).

[7] H. Braun *et al.*, Phys. Rev. D 3, 2572 (1971).

Measurement of Pion Photoproduction at Threshold on ^{6}Li[†]

J. Deutsch, D. Favart,[*] R. Prieels, and B. Van Ostaeyen[*]
Institut de Physique Corpusculaire, Université Catholique de Louvain, B-1348 Louvain-la-Neuve, Belgium

and

G. Audit, N. de Botton, J.-L. Faure, Cl. Schuhl, G. Tamas, and C. Tzara
Centre d'Etudes Nucléaires de Saclay, 91190 Gif-sur-Yvette, France

(Received 21 May 1974)

As a test of soft-pion theorems in nuclei, we measured near threshold the ratio of positive-pion photoproduction cross sections on ^{6}Li and on protons. If the total cross section of the reaction $\gamma + p \rightarrow \pi^+ + n$ is expressed as $\sigma_p = a_p q/k$, our result for the reaction $\gamma + {}^6\mathrm{Li} \rightarrow \pi^+ + {}^6\mathrm{He}_{\mathrm{g.s.}}$ is

$$\sigma_{\mathrm{Li}} = (0.073 \pm 0.002) a_p \frac{q}{k} \frac{12.5/q}{\exp(12.5/q) - 1},$$

where q is the pion and k the photon c.m. momenta expressed in units of MeV/c. This result is considerably lower than the existing theoretical predictions.

Soft-pion theorems seem to apply remarkably well to elementary particles[1,2]; their validity for nuclei calls for more experimental tests. A possible one is offered by the comparison of radiative pion capture with muon capture and beta decay.[3-9] However, it is only for the pion s-wave amplitude that the theory is directly applicable and we cannot extract this contribution from the existing radiative-capture experiments in a model-independent way.

In order to avoid the contribution of $l \neq 0$ waves which plague radiative pion capture even in the lightest nuclei,[7] one may turn to the inverse process, i.e., photoproduction of pions sufficiently near threshold to make any $l \neq 0$ contribution negligible.[9] We report here a first experiment of this type.

The two main problems of the experiment are the normalization and the detection of low-energy pions ($\lesssim$ 2 MeV). The difficulties of normalization (and of detection-efficiency determination) were overcome by performing a *relative* measurement: The photoproduction yield on ^{6}Li was compared with that on hydrogen[10] at a corresponding excess energy above threshold. The photoproduced pions of interest, having submillimetric range, were stopped in the target and detected through their well-known decay chain pion → muon → positron, i.e., by the observation of high-energy positrons whose time distribution showed the characteristic muon lifetime. The time structure of the beam allowed us to observe the positrons between the beam bursts, i.e., when the noise level was greatly reduced. We shall discuss now some of the salient features of the experiment.

The γ-ray beam was derived from a 0.01-radiation-length Au converter hit by the electrons of the Saclay linear accelerator. The energy of the electrons was changed in steps of about 300 keV in the energy range of interest (around 150 MeV); the momentum resolution was 10^{-3}. The repetition rate of the pulses was 2 kHz and their width was about 3 μsec. Collimators restricted the photon beam to 3.3 mrad around 0°, resulting in a spot of 6 cm diameter at the target location.

The main target was a Li cylinder of 10 cm diameter and 10 cm length, enriched to 94.8% in ^{6}Li and hermetically sealed in a thin-walled container, coaxially placed in the beam. The target could be remotely interchanged with a "hydrogen" one of exactly the same dimensions. This last target consisted of chemically pure polyethylene ($\mathrm{CH_2}$), in granular form, with a density $\rho = 0.321$ g/cm^3. This density was chosen by computation so as to equalize the escape probability of the muon positrons from this target and from the Li one ($\rho = 0.457$ g/cm^3). Since the photoproduction threshold on carbon is about 3 MeV above the proton threshold, the carbon content of the target did not contribute to the pion production.

The detector system consisted of two Lucite Cherenkov counters 4.5 cm and 4.0 cm thick observed in coincidence; the entrance face of the first was placed 9.5 cm off the beam axis and parallel to it. A 2-mm Cu sheet inserted between the two detectors and a suitable pulse-height selection excluded coincidences between the detectors due to ^{12}B activity induced by (n, p) reaction on the carbon content of the detector.

The measurement itself consisted of (1) the determination of the number of muon-decay positrons originating from the pions photoproduced at different values of the beam energy for both targets, and (2) the measurement of the corresponding γ-beam intensity. The total number of positrons was deduced from their time distribution given by a time-to-amplitude converter started by a synchronization pulse and stopped by the detector signal. The synchronization pulse derived from the accelerator control arrived 2 μsec after the end of the burst. The observation of the positrons lasted for 6 μsec. A careful check showed that no primary beam was present any more during this interval. Before fitting the time distribution of the positrons with an exponential having a decay constant characteristic of the muon lifetime, we subtracted from it both the accidental coincidences measured simultaneously and the background as measured between 12 and 36 μsec after the synchronization signal. At the lowest energy above threshold in ^{6}Li the accidental coincidences amounted to at most 15% of the real ones and the background-to-signal ratio, at the beginning of the observation interval, was less than 10%. As these ratios were found to be about inversely proportional to the photoproduction yield, they were negligible for most of our data points. Let us note also that the off-beam character of the measurement and the muon-lifetime signature excluded from the signal any target-associated electrons.

The photon-beam intensity was measured by a Wilson-type quantameter.[11] In order to get a normalization free of the effect of the fluctuating time structure of each beam burst, we integrated the quantameter output, according to the "leaky-capacitor" method,[12] with a time constant characteristic of the muon lifetime. The resulting pulses were sampled at the instant of the synchronization signal. These samplings were digitized and accumulated in a scaler.

The results of the measurement, corrected for the relative amount of ^{6}Li and proton in our targets, are reported in Table I as a function of the energy of the primary electron beam. For our purposes only the accurate knowledge of the energy increments was required. These increments were known to better than 10 keV. The indicated absolute energy scale is deduced from our proton data.

The yield measured at the primary electron beam energy E_e is proportional to the integral

$$\int_{E_0}^{E_e} B(E, E_e)\sigma(E - E_0)\, dE,$$

where E_0 is the photon energy corresponding to the photoproduction threshold, $B(E, E_e)$ is the differential bremsstrahlung, and $\sigma(E - E_0)$ is the total photoproduction cross section. If we wish to proceed further, we have to make assumptions about the functions $B(E, E_e)$ and $\sigma(E - E_0)$.

For $B(E, E_e)$ we took the form given by Jabbur and Pratt.[13] As, however, their derivation is not valid near the end point, we used at this point the accurate value[14] and interpolated in the last 300-keV region between the prescriptions of the two references. One should also note that these expressions assume integration of the photons over all angles. We shall comment later on the implications of these approximations. We took into account also the 10^{-3} momentum spread of the primary beam and the effect of the finite converter thickness.

For the proton, the analytical form of $\sigma_p(E - E_0)$

TABLE I. Photoproduction yield as a function of the energy of the electron beam.

Target	Electron-beam energy (MeV)	Photoproduction yield (arbitrary units)
^{6}Li	145.68	1.38 ± 0.52
	145.93	8.4 ± 1.1
	146.33	26.0 ± 1.6
	146.83	76.3 ± 2.5
	147.33	140.1 ± 3.3
CH$_2$	151.90	215.6 ± 4.8
	152.30	681.4 ± 9.2
	152.70	1335 ± 17
	154.35	6175 ± 49

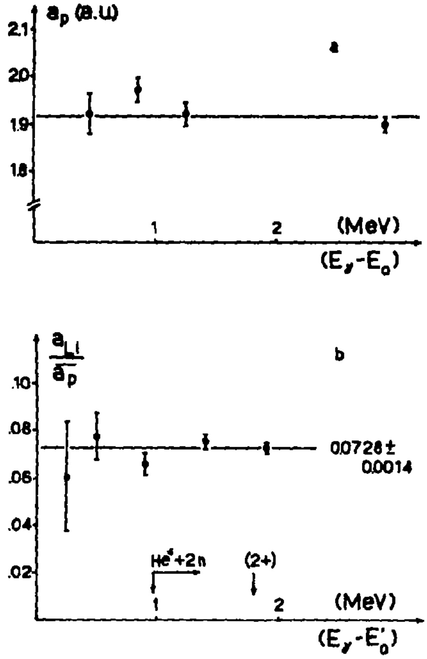

FIG. 1. (a) Coefficient a_p of the photoproduction on proton as a function of the lab photon energy above threshold. The line indicates the best-fit value $\bar{a}_p$. (b) Coefficient a_{Li} of the photoproduction on ^{6}Li normalized to the average a_p as a function of the lab photon energy above threshold. The position of the continuum and the 2^+ level in ^{6}He are also shown.

$=a_p q/k$, where q and k are the c.m. momenta o the pion and the γ ray, is well established both experimentally[10] and theoretically.[3] For the lit ium, the repulsive electrical field between the and the ^{6}He depresses the cross section. It has been shown[9] that even for an extended charge an in the presence of a strong potential its expression near threshold follows the same analytical form as for the point charge:

$$\sigma_{Li}(E-E_0') = a_{Li}\frac{q}{k}\frac{b/q}{\exp(b/q)-1},$$

$$b = 2\pi\alpha Z\bar{m}c \simeq 12.5\ \mathrm{MeV}/c,$$

where $\alpha = 1/137$, $Z = 2$ (He), and $\bar{m}$ is the reduce mass of the final state. The energy dependence of the cross section, computed numerically in Ref. 9, is indeed in excellent agreement with that expression which we have used in our data analysis.

In Fig. 1(a) we show the fit to the proton data obtained with the expressions $B(E,E_p)$ and σ_p discussed above. Figure 1(b) shows the value $a_{Li}/\bar{a}$ that we obtain from our Li data, where the mean value $\bar{a}_p$ of all the proton data is used to normalize the ^{6}Li result obtained at each energy. Combining all the ^{6}Li results we get $a_{Li}/\bar{a}_p = (7.28 \pm 0.14)\times 10^{-2}$. In this result are included all the points up to 1.9 MeV above threshold. At this energy, only 100 keV above the threshold of the 2^+ state, the contribution of that state must still be negligible. As for the excitation of the continuum, we believe it to be negligible too because of

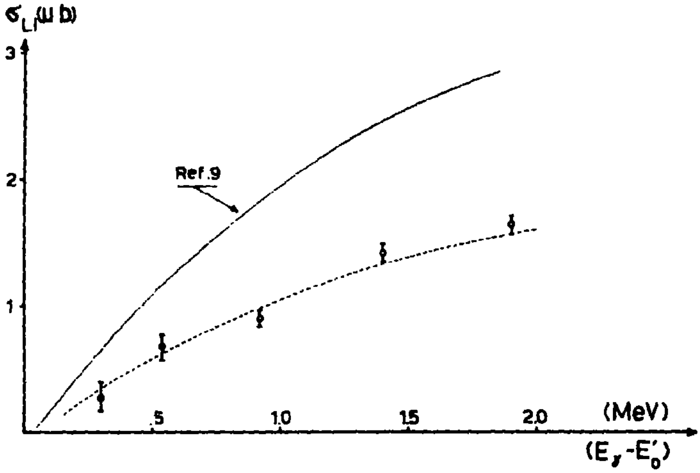

FIG. 2. Total photoproduction cross section for ^{6}Li + γ → ^{6}He$_{g.s.}$ + π^+ found in this experiment compared to the theoretical prediction, Ref. 9. The errors include the inaccuracy of σ_p, Ref. 10. The dashed curve is our best fit; it is 0.54 times the value from Ref. 9.

ase-space arguments. Nevertheless, if one ishes to avoid these assumptions one may use r first three data points only, which lie under e threshold of the continuum. These points ould yield the result $a_{\rm Li}/\bar{a}_p=(6.76\pm0.37)\times10^{-2}$.

Before comparing these results to the theoretical predictions, we should comment on possible errors of a nonstatistical nature. The only one which turned out to be nonnegligible was the possible error introduced by our assumptions on $B(E,E_e)$. We considered deviations from the assumed shape of $B(E,E_e)$ which still yielded a satsfactory fit to our proton data. For all these hapes the result $a_{\rm Li}/\bar{a}_p$ stayed within ± 1% of its nost probable value.

Our final result is $a_{\rm Li}/\bar{a}_p=(7.3\pm0.2)\times10^{-2}$, vhere the error includes both the statistical and he estimated systematic error. Using the measured photoproduction coefficient $a_p=193.5\pm6.7$ b,[10] we obtain the experimental cross section $\sigma_{\rm Li}$ (Fig. 2) which we compare now to the theoretcal predictions.

The two predictions actually available[9,15] were omputed in impulse approximation but with wave unctions tailored so as to match all the observbles of the states involved. The first one[9] is hown in Fig. 2. The second one, obtained with more complete Hamiltonian and a more relible pion wave function, yields a preliminary alue of $a_{\rm Li}/a_p=0.123$. One notes that our result s only about half of the impulse-approximation redictions.[16]

The high skill of the Accélérateur Linéaire de aclay operation group under Dr. F. Netter was nstrumental to the success of this experiment vhich required very unconventional beam condiions. The technical contribution of A. Bloch and . Lopata as well as the help of J. Martin are ratefully acknowledged. The Louvain group wishes to acknowledge also the friendly hospitality enjoyed in Saclay. One of us (J.D.) is indebted to Dr. A. Bernstein for valuable discussions.

---

†Work partially supported by Institut Interuniversitaire des Sciences Nucléaires, Belgium.

*Chercheur Institut Interuniversitaire des Sciences Nucléaires, Belgium.

[1] S. L. Adler and R. F. Dashen, *Current Algebras and Applications to Particle Physics* (Benjamin, New York, 1968).

[2] P. De Baenst, Nucl. Phys. B25, 633 (1970).

[3] M. Ericson and A. Figureau, Nucl. Phys. B3, 609 (1967), and B11, 621 (1969).

[4] J. P. Deutsch *et al.*, Phys. Lett. 26B, 315 (1968).

[5] H. W. Baer *et al.*, Phys. Rev. C 8, 2029 (1973).

[6] O. Zaimidoroga *et al.*, Zh. Eksp. Teor. Fiz. 51, 1646 (1966) [Sov. Phys. JETP 24, 1111 (1967)]; P. Truöl *et al.*, Phys. Rev. Lett. 32, 1238 (1974).

[7] M. Ericson and M. Rho, Phys. Rep. 5C, 59 (1972).

[8] C. Tzara, Nucl. Phys. B18, 246 (1970).

[9] J. H. Koch and T. W. Donnelly, Nucl. Phys. B64, 478 (1973).

[10] M. I. Adamovitch *et al.*, Yad. Fiz. 9, 848 (1969) [Sov. J. Nucl. Phys. 9, 496 (1969)].

[11] R. Wilson, Nucl. Instrum. Methods 1, 101 (1957).

[12] J. L. Black and J. Mahieux, Nucl. Instrum. Methods 58, 93 (1968).

[13] R. J. Jabbur and R. H. Pratt, Phys. Rev. 129, 184 (1963), footnote 18.

[14] R. J. Jabbur and R. H. Pratt, Phys. Rev. 133, B1091 (1964).

[15] J. Delorme, A. Figureau, and M. Krell, private communication.

[16] After submission of this paper, we were informed by Dr. Donnelly and Dr. Koch, authors of Ref. 9, that they find a ratio $a_{\rm Li}/a_p$ in agreement with our result (but in disagreement with other computations, Ref. 15) and that the basic coupling used by them overestimates by the same factor both σ_p of Ref. 10 and $\sigma_{\rm Li}$ reported in this paper.

Fermi Beta Decay, $A > 40$: The Masses of ^{42}Sc, ^{46}V, ^{50}Mn, and ^{54}Co

J. C. Hardy, G. C. Ball, J. S. Geiger, R. L. Graham, J. A. Macdonald, and H. Schmeing
Atomic Energy of Canada Limited, Physics Division, Chalk River Nuclear Laboratories,
Chalk River, Ontario, Canada K0J 1J0

(Received 15 May 1974)

The Q values for (^{3}He,t) reactions on ^{26}Mg, ^{34}S, ^{42}Ca, ^{46}Ti, ^{50}Cr, and ^{54}Fe have been measured relative to that for ^{27}Al(^{3}He,t)^{27}Si. The results lead to significant deviations from previously accepted values for the β-decay end-point energies of ^{42}Sc, ^{46}V, and ^{54}Co. The new ft values for these transitions now agree with other known superallowed transitions ($A < 40$); only the decay of ^{50}Mn remains anomalous. A limit is also set on the $Z^2\alpha^3$ radiative correction term.

There are nine superallowed $0^+ \rightarrow 0^+$ β transitions whose ft values have been determined with an accuracy better than ± 1%. The lightest parent nucleus in this group is ^{14}O; the heaviest is ^{54}Co. Ideally, the ft values for all nine transitions should be identical to the extent that radiative corrections and charge-dependent mixing can be properly accounted for. If such self-consistency were established, then the average ft value would determine the vector coupling constant of nuclear β decay and would contribute to a stringent test of of Cabibbo theory through comparison with corresponding values obtained for decay of the μ and K^+ mesons.

Until now, this picture has been clouded by the fact that, while the five transitions between nuclei with $A < 40$ were consistent with one another, the ft values for the decays of ^{42}Sc, ^{46}V, ^{50}Mn, and ^{54}Co were significantly higher even after the calculated corrections had been applied.[1] This has caused doubt in the accuracy of the corrections and ultimately in the reliability of the vector coupling constant. We have remeasured the transition energies, upon which the statistical rate functions f depend, for six of these transitions, including all four between nuclei with $A > 40$. Our results for ^{42}Sc, ^{46}V, and ^{54}Co indicate a considerable change from the previously accepted decay energies, with the result that the ft values for their decays now agree with those measured for lighter nuclei.

The experiment involved Q-value measurements for (^{3}He,t) reactions on a variety of two-component composite targets bombarded by a magnetically analyzed 33.00-MeV beam from the Chalk River MP tandem accelerator. The targets used (and their enrichments) were ^{26}Mg (99.7%), Cd^{34}S (85.6%), ^{42}Ca (93.7%), ^{46}Ti (81.2%), ^{50}Cr (96.8%), and ^{54}Fe (97.4%), each ~ 100 μg/cm^2 thick and evaporated onto the same thickness of ^{27}Al. In

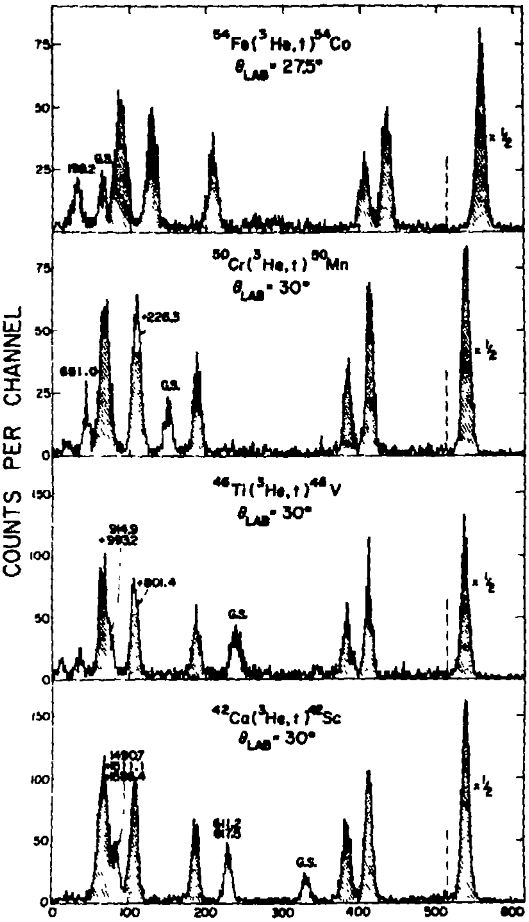

FIG. 1. Sample energy spectra accumulated for a total ^{3}He^{++} charge of ~ 10^4 μC. The shaded peaks are from the reaction ^{27}Al(^{3}He,t)^{27}Si. All others are from the identified reactions; excitation energies are labeled in keV [from Ref. 3 and N. S. P. King *et al.*, Nucl. Phys. A177, 625 (1971)].

ddition, targets of ^{42}Ca + ^{26}Mg and ^{42}Ca + ^{50}Cr ere employed. Reaction products were detected two surface-barrier counter telescopes, each omprising a 1-mm ΔE and a 2-mm E detector. or all target combinations four separate measurements were made in which the telescopes enoted A and B) and target normal (T) were riented with respect to the beam as follows[2]: 1) $A = +30°$, $B = -30°$, $T = 0°$; (2) $A = +30°$, B $-30°$, $T = 180°$; (3) $A = -30°$, $B = +30°$, $T = 180°$; 4) $A = -30°$, $B = +30°$, $T = 0°$. A total of eight pectra were thus accumulated for each target ombination. Several examples appear in Fig. 1 here the energy resolution is about 60 keV or etter.

Each spectrum was analyzed to yield the energy difference between the ground-state Q values for the two targets involved. The reaction ^{27}Al(^{3}He, t)^{27}Si was common to most measurements and provided an energy scale from the well-known[3] excitation energies of states in ^{27}Si, viz., 0.0, 780.3 ± 0.3, 956.8 ± 0.3, 2163.3 ± 0.6, and 2647.0 ± 0.7 keV. In all cases, the energy scale was linear over the region of interest and yielded an acceptable χ^2 when fitted by the five states of ^{27}Si. The eight measured values of the ground-state Q-value differences for each target combination were averaged together. Although individual values showed the effects of energy loss in the target, the specific choice of relative target and telescope angles ensured that the average was independent not only of target thickness but also of beam-direction variations. Nevertheless, the target thickness was confirmed by measuring the energy loss of 5.5-MeV α particles from ^{241}Am, and the beam direction was controlled by tight collimation (less than ± 0.1° at the target), which was optically aligned in advance.

The measured Q-value differences are shown in Table I. The quoted errors include the effects of uncertainties both in the peak-centroid determinations (~ 2 keV) and in the energy of the ^{27}Si states used for calibration (~ 0.5 keV); in addition there is an allowance (~ 0.1 to ~ 1.0 keV from A = 26 to A = 54) for possible uncertainty in the beam energy. Of the eight Q-value differences tabulated, the last two serve as cross checks on the primary ^{27}Al-based measurements; they agree with the primary data to within 2.1 ± 4.8 and 0.7 ± 4.5 keV, respectively. Previously accepted values are also shown in the table. In determining the latter values, the Q value for the reaction ^{27}Al(^{3}He, t)^{27}Si was taken to be − 4828.7 ± 0.9 keV, which is derived from the average of nine[4,5] mutually consistent measurements of the ^{27}Al(p, n)^{27}Si threshold energy. The Q values for the reactions ^{26}Mg(^{3}He, t)^{26}Al and ^{34}S(^{3}He, t)^{34}Cl have also been derived from extensive earlier data,[4,6,7] and for these cases there is excellent agreement with our results.

By contrast, the accepted values[4] for the masses of ^{42}Sc, ^{46}V, ^{50}Mn, and ^{54}Co are based solely upon the (p, n) threshold measurements of one group.[8,9] Their results are consistently lower than ours for masses 42, 46, and 54, which may possibly reflect the existence, as discussed in Ref. 9, of undetected compound-nucleus resonances just above the (p, n) threshold, although the discrepancies seem too large to be accounted for by that effect alone. In any event, in estab-

TABLE I. Q-value differences obtained from composite targets.

Reactions		$Q_X - Q_Y$ (keV)	
X	Y	This work	Previous work
^{26}Mg(^{3}He,t)^{26}Al	^{27}Al(^{3}He,t)^{27}Si	808.2 ± 2.0	805.4 ± 1.1 [a,b]
^{34}S(^{3}He,t)^{34}Cl	^{27}Al(^{3}He,t)^{27}Si	− 678.7 ± 2.3	− 680.3 ± 1.8 [b,c]
^{42}Ca(^{3}He,t)^{42}Sc	^{27}Al(^{3}He,t)^{27}Si	− 1611.7 ± 2.6	− 1621.1 ± 2.5 [a,b]
^{46}Ti(^{3}He,t)^{46}V	^{27}Al(^{3}He,t)^{27}Si	− 2230.8 ± 2.7	− 2244.3 ± 2.4 [a,b]
^{50}Cr(^{3}He,t)^{50}Mn	^{27}Al(^{3}He,t)^{27}Si	− 2820.0 ± 2.8	− 2821.1 ± 2.8 [a,b]
^{54}Fe(^{3}He,t)^{54}Co	^{27}Al(^{3}He,t)^{27}Si	− 3432.5 ± 3.0	− 3439.8 ± 3.9 [a,b]
^{42}Ca(^{3}He,t)^{42}Sc	^{26}Mg(^{3}He,t)^{26}Al	− 2417.8 ± 3.5	− 2426.5 ± 2.4 [a]
^{50}Cr(^{3}He,t)^{50}Mn	^{42}Ca(^{3}He,t)^{42}Sc	− 1207.6 ± 2.3	− 1200.0 ± 3.5 [a]

[a] Ref. 4

[b] The Q value for the reaction ^{27}Al(^{3}He,t)^{27}Si (− 4828.7 ± 0.9 keV) was derived from an average of the results from Refs. 4 and 5.

[c] The Q value for the reaction ^{34}S(^{3}He,t)^{34}Cl (− 5509.0 ± 1.5 keV) was derived from a recent compilation (Ref. 6) for A = 34.

TABLE II. End-point energies and calculated ft values for superallowed decay branches.

Parent nucleus	$E_{\beta\max}$ (keV)	$t_{1/2}$[a] (msec)	ft[b] (sec)	$\mathcal{F}t$ (sec)
^{26m}Al	2982.5 ± 0.5[c]	6347 ± 5	3039 ± 3	3078 ± 3
^{34}Cl	4467.9 ± 1.3[d]	1530 ± 4	3052 ± 9	3084 ± 9
^{42}Sc	5399.9 ± 2.2[e]	683.9 ± 0.9	3051 ± 7	3093 ± 7
^{46}V	6018.8 ± 2.8[e]	425.7 ± 0.7	3045 ± 8	3090 ± 8
^{50}Mn	6607.8 ± 2.1[e]	285.7 ± 0.5	3064 ± 7	3110 ± 7
^{54}Co	7220.5 ± 3.1[e]	193.4 ± 0.6	3049 ± 11	3092 ± 11

[a] All results taken from Ref. 1 except those for ^{34}Cl which are from Ref. 6.

[b] Partial half-lives include a correction [N. B. Gove and M. J. Martin, Nucl. Data Tables 10, 206 (1971)] for electron capture.

[c] Result from this work averaged with previous results summarized in Ref. 1.

[d] Result from this work averaged with those from Ref. 6.

[e] Result from this work.

lishing the "best" Q values from which to determine the β end-point energies, we have chosen simply to use our own results for those cases with $A > 40$, while averaging with previous work[1,6] for masses 26 and 34.

The resultant β-decay energies are listed in Table II. Apart from the data in Table I, they depend only upon the Q value already noted for the reaction ^{27}Al(^{3}He, t)^{27}Si. The best current half-life results[1,6] are also shown, together with calculated ft values for each transition. In terms of the nuclear matrix element and the vector coupling constant, the ft value for a superallowed β decay between $T = 1$, $J^\pi = 0^+$ states is given by[1]

$$ft(1+\delta_R) = K/G_v'^2|M_v|^2,$$

with

$$G_v'^2 = G_v^2(1+\Delta_R), \quad |M_v|^2 = 2(1-\delta_c), \tag{1}$$

where $K = 1.230\,63 \times 10^{-94}$ cgs units. Here t is the partial half-life for the transition, G_v (G_v') is the (effective) vector coupling constant, M_v is the Fermi matrix element, δ_R (Δ_R) is the outer (inner) radiative correction, and δ_c is the correction to the Fermi matrix element that results from charge-dependent forces. The values of f used in Table II were computed from the decay energies according to the procedure described by Towner and Hardy.[1]

Since the correction terms δ_R and δ_c vary from transition to transition the ft values are not necessarily constant. However the quantity $\mathcal{F}t = ft(1+\delta_R)(1-\delta_c)$ should be independent of the transition involved and should yield directly a value for G_v'. The $\mathcal{F}t$ values listed in Table II incorporate δ_c an δ_R terms taken from Ref. 1. In the case of δ_c, both the Coulomb force and an *ad hoc* charge-dependent nuclear force were considered in evaluating the effect. The radiative correction δ_R to first order in α ($\approx\frac{1}{137}$) is independent of Z, but to higher orders may be expressed[10] as a series of terms of $Z^m\alpha^n$ ($n \geq 2$, $m < n$); the correction we have actually applied[1,11] is accurate to all orders in terms of the type $Z^m\alpha^{m+1}$. The term of order $Z^2\alpha^3$ is probably negligible[11] but, having never been explicitly evaluated, it must be considered as the only possibly significant term for which any uncertainty remains.

The $\mathcal{F}t$ values from Table II are presented graphically in Fig. 2 together with the three other accurately known[1,6,12] superallowed transitions, viz., the decays of ^{14}O, ^{34}Ar, and ^{38}K^m. The weighted average of all nine values is $\mathcal{F}t = 3085.0 \pm 1.8$ sec, but the corresponding normalized χ^2 is 2.6, which has a probability <1% of occurring by chance. However, upon removing the ^{50}Mn value the average becomes $\mathcal{F}t = 3083.2 \pm 1.9$ sec with $\chi^2 = 1.0$ (curve c, Fig. 2). If we accept the possibility of a significant $Z^2\alpha^3$ term in the radiative correction, then the magnitude of that term may be determined by fitting the data with an expression of the form $\mathcal{F}t = (\mathcal{F}t)_0(1 + CZ^2\alpha^3)$, where C is a constant. The results, with and without ^{50}Mn (curves a and b), give $C \sim 0.2$ and ~ 0.1 with $\chi^2 = 1.5$ and 0.8, respectively. The corresponding $(\mathcal{F}t)_0$ values are 3078.7 ± 2.7 and 3080.5 ± 2.8 sec.

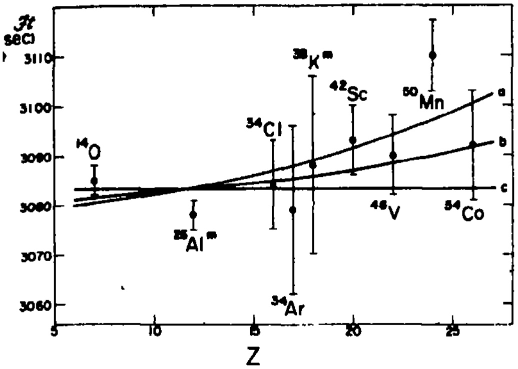

FIG. 2. The corrected experimental $\mathcal{F}t$ values plotted s a function of Z for all cases known to an accuracy etter than ±1%. The points are labeled by the decay arent. The significance of the curves is explained in he text.

Evidently, with the exception of the ^{50}Mn case, all accurately known $\mathcal{F}t$ values are now concordant. Furthermore, in contrast with a similar analysis of previous data,[13] there is now no positive indication of a $Z^2\alpha^3$ radiative correction term (the coefficient $C \lesssim 0.2$). Finally, after incorporating all apparent uncertainties, including those arising from the various fitting procedures, we recommend $\mathcal{F}t = 3082 \pm 3$ sec as the best current value for nuclear $0^+ \rightarrow 0^+$ β decay. It corresponds to $G_v' = (1.4130 \pm 0.0007) \times 10^{-49}$ erg cm^3. These results now lead to the same conclusion for the inner radiative correction and Cabibbo angle as were derived in Ref. 1, although that earlier work was restricted to nuclei with $A < 40$.

As a concluding remark it should be noted that the half-life of ^{50}Mn rests essentially upon a single measurement[8]; before attaching too much significance to the anomalous nature of the ^{50}Mn decay, a re-examination of its half-life is indicated.

We should like to thank both Dr. J. S. Forster for his assistance with the experiment, and particularly Mr. J. L. Gallant for a virtuoso performance of target preparation.

---

[1] I. S. Towner and J. C. Hardy, Nucl. Phys. A205, 33 (1973).

[2] In the case of ^{54}Fe + ^{27}Al, several peaks were unresolved at 30°; consequently 27.5° was chosen to achieve kinematic separation. Four measurements, equivalent to those listed for 30°, were performed.

[3] P. M. Endt and C. Van der Leun, Nucl. Phys. A214, 1 (1973).

[4] A. H. Wapstra and N. B. Gove, Nucl. Data Tables 9, 267 (1971); N. B. Gove and A. H. Wapstra, Nucl. Data Tables 11, 128 (1972).

[5] J. C. Overly, P. D. Parker, and D. A. Bromley, Nucl. Instrum. Methods 68, 61 (1969).

[6] A recent compilation of relevant data for $A = 34$ is given by J. C. Hardy, H. Schmeing, J. S. Geiger, and R. L. Graham, to be published.

[7] P. De Wit and C. Van der Leun, Phys. Lett. 30B, 639 (1969).

[8] J. M. Freeman, G. Murray, and W. E. Burcham, Phys. Lett. 17, 317 (1965).

[9] G. Murray, J. M. Freeman, J. G. Jenkin, and W. E. Burcham, in *Proceedings of the Third International Conference on Atomic Masses, Winnipeg, Manitoba, Canada, 1967*, edited by R. C. Barber (University of Manitoba Press, Winnipeg, Manitoba, Canada, 1967), p. 545.

[10] M. A. B. Bég, J. Bernstein, and A. Sirlin, Phys. Rev. Lett. 23, 270 (1969).

[11] W. Jaus and G. Rasche, Nucl. Phys. A143, 202 (1970); W. Jaus, Phys. Lett. 40B, 616 (1972).

[12] J. S. Ryder, Atomic Energy Research Establishment, Harwell, Report No. AERE-R7379, 1973 (unpublished).

[13] D. H. Wilkinson, Comments Nucl. Part. Phys. 5, 135 (1972).

High-Density Phase Transitions in Gauge Theories

Barry J. Harrington and Asim Yildiz*
Lyman Laboratory of Physics, Harvard University, Cambridge, Massachusetts 02138

(Received 22 April 1974)

By the introduction of a chemical potential for an absolutely conserved fermion quantum number, we determine the onset of a phase transition in a general renormalizable, finite-temperature field theory with spontaneously broken symmetries. We also briefly investigate the possible physical existence of such a phase transition in black holes and in the early universe.

Recent investigations[1,2] on phase-transition phenomena in a renormalizable quantum field theory indicate that finite-temperature effects can restore a symmetry which is broken at zero temperature. This occurs through the generation of a temperature-dependent scalar boson mass (or inverse correlation length) which, for sufficiently high temperatures, may vanish. The question we address is whether the same mechanism is operative for a large chemical potential due to an absolutely conserved fermion quantum number. Alternatively expressed, can a large fermion number density effect a phase transition?

In the framework of a weakly interacting, renormalizable field theory characterized by a coupling constant $e \ll 1$, the effective boson mass can only vanish if powers of the temperature θ or chemical potential μ can compensate for powers of the coupling e. Weinberg has shown[2] that when $\bar{\mu} = \mu/\theta \ll 1$, the leading terms in any graph for e small and θ large are those in which all loops beyond the lowest order are quadratically divergent. The finite part of such a loop contributes a factor proportional to $e^2\theta^2$, so that the critical temperature is attained when $e^2\theta^2$ is of the order of the square of the renormalized mass at zero temperature, $\mathfrak{M}_R^2$, i.e., $\theta_{\mathrm{crit}} \approx \mathfrak{M}_R/e$. In typical gauge theories of the weak and electromagnetic interactions,[3] $\mathfrak{M}_R/e$ is of the order of $G_F^{-1/2}$ so that $\theta_{\mathrm{crit}} \approx 300\ \mathrm{GeV} \approx 10^{16}\ {}^\circ\mathrm{K}$.

We are particularly interested in isolating the leading terms to any graph for e small and μ large, and $\bar{\mu} \gg 1$. Considering a loop expansion[2,4] we have a factor of e^{2L} in a graph with L loops. To determine the powers of μ contributed by each loop, we concentrate on a single loop with superficial degree of divergence D. We rescale by θ all dimensional factors in the single-loop integration so that the whole loop takes the form

$$\theta^D I(p_{\mathrm{ext}}/\theta, \omega_{\mathrm{ext}}/\theta, m_{\mathrm{int}}/\theta, \bar{\mu}), \tag{1}$$

where p_{ext} and ω_{ext} represent the set of external momenta and energies, and m_{int} represents the internal masses. Now the single loop integration will contain[5] a Fermi distribution function in the integrand of the form

$$F\left(\frac{\mathcal{E}}{\theta}, \bar{\mu}\right) = \frac{1}{e^{(\mathcal{E}-\mu)/\theta}+1} + \frac{1}{e^{(\mathcal{E}+\mu)/\theta}+1}, \tag{2}$$

where $\mathcal{E} = (p^2+m^2)^{1/2}$ and m is an eigenvalue of the the fermion mass matrix. Since $\bar{\mu} \gg 1$, the second term in (2) will act as an exponentially damping factor in the loop momentum p, while the first term will begin providing an exponential falloff in p when $\mathcal{E} \gtrsim \mu$, i.e., above the Fermi energy. We are primarily interested in μ large (≈ 300 GeV) and thus much greater than m, so that the integral in (1) is effectively cut off when $p \sim \mu$. Thus

$$\theta^D I(p_{\mathrm{ext}}/\theta, \omega_{\mathrm{ext}}/\theta, m_{\mathrm{int}}/\theta, \bar{\mu}) \sim \theta^D \bar{\mu}^D = \mu^D. \tag{3}$$

Since we are considering renormalizable field theories, the largest value of D that concerns us is $D = 2$. In addition, all quadratic divergences can be eliminated by a renormalization of the boson self-mass (with the assumption that there are no gauge-invariant scalar fields). Thus, the effective boson self-mass will contain a term of the form $e^2\mu^2$, and we anticipate a phase transition when $\mu_{\mathrm{crit}} \approx \mathfrak{M}_R/e$. Again, in typical gauge theories of the weak and electromagnetic interactions[3] this transition would occur for $\mu_{\mathrm{crit}} \approx 300$ GeV. Dimensionally, for $\bar{\mu} \gg 1$, we expect $\mu \sim n^{1/3}$, where n is the fermion number density, so that the critical fermion number density would be of the order $n_{\mathrm{crit}} \sim 10^{[illegible]}/\mathrm{cm}^3$.

These anticipated results can be explicitly verified by calculating the leading (in μ) one-loop contributions to the boson self-mass. We consider a general renormalizable Lagrangian[6] which possesses a gauge invariance with respect to some compact semisimple Lie group G:

$$\mathcal{L} = -\tfrac{1}{4}F_{\alpha\mu\nu}F_{\alpha}{}^{\mu\nu} - \tfrac{1}{2}(D_\mu\varphi)_i(D^\mu\varphi)_i - \overline{\psi}\gamma^\mu D_\mu\psi - \overline{\psi}m_0\psi - P(\varphi) - \overline{\psi}\Gamma_i\psi\varphi, \tag{4}$$

where $F_{\alpha\mu\nu}$ is the gauge-covariant curl of a set of Hermitian gauge fields, $(D_\mu\varphi)_i$ is the gauge-covariant derivative of a multiplet of real, spin-0 fields, $D_\mu\psi$ is the gauge-covariant derivative of a multiplet of spin-$\frac{1}{2}$ fields, m_0 is the Hermitian and gauge-preserving bare fermion mass matrix, $P(\varphi)$ is a real fourth-order gauge-invariant polynomial in φ, and Γ_i is the set of Hermitian and gauge-covariant Yukawa coupling matrices. The gauge invariance of the Lagrangian is broken by allowing the scalar fields φ_i to develop spontaneously a nonvanishing vacuum expectation value.

We consider this Lagrangian at finite temperature and incorporate a fermion chemical potential as a Lagrange multiplier of the number density η given by

$$\eta = \psi^\dagger\psi = \overline{\psi}\gamma_4\psi. \tag{5}$$

Thus, the chemical potential μ will alter the fourth component of the fermion propagator, which, at finite temperature, implies the replacement of the discrete energy $\mathcal{E}_n = (2n+1)\pi\theta$, n an integer, by $\mathcal{E}_n - i\mu$.

As previously mentioned, the leading chemical-potential effects, as well as all quadratic divergences, can be absorbed into a redefinition of the quadratic terms in the potential $P(\varphi)$ by defining an effective potential[2]

$$P_{\text{eff}}(\varphi) = P(\varphi) + \tfrac{1}{2}Q_{ij}(\mu)\varphi_i\varphi_j \tag{6}$$

and by adding a compensating counterterm to the Lagrangian,

$$\delta\mathcal{L} = \tfrac{1}{2}Q_{ij}(\mu)\varphi_i\varphi_j. \tag{7}$$

Here, $Q_{ij}(\mu)$ is some chemical-potential–dependent, quadratically divergent matrix which contributes to the formation of an effective scalar boson mass. After shifting the scalar fields by their zeroth-order vacuum expectation value λ, we note that the contributions to the quadratic divergences in any renormalizable theory come from tadpoles T_i and the boson self-energy Π_{ij}. Furthermore, $Q_{ij}(\mu)$ is determined by requiring that the counterterms provided by (7) cancel these quadratic divergences as well as those terms proportional to $e^2\mu^2$. It is the latter terms that we wish to isolate, since the former terms can be absorbed into a temperature- and chemical-potential-independent renormalized scalar mass $\mathfrak{M}_R$. But the chemical potential enters the calculation only through the fermion propagators. Thus, the graphs of interest are the fermion-loop tadpole (Fig. 1) and the fermion-loop contributions to the boson self-energy (Fig. 2).

The fermion-loop tadpole at finite temperature and chemical potential is given by

$$T_i^\psi = i(2\pi)^4\operatorname{Tr}\{\Gamma_i\gamma_4\Gamma_j\gamma_4\}\lambda_j I_F(\theta,\mu), \tag{8}$$

where

$$I_F(\theta,\mu) = \theta\sum_{n=-\infty}^{+\infty}\int\frac{d^3p}{(2\pi)^3}\,\frac{1}{\mathcal{E}^2 + (\mathcal{E}_n - i\mu)^2} \tag{9}$$

and $\mathcal{E}^2 = p^2 + m^2$. Performing the summation over n and renormalizing at $\theta = \mu = 0$, we find

$$I_F{}^R(\theta,\mu) = -\frac{1}{2}\int\frac{d^3p}{(2\pi)^3}\,\frac{1}{\mathcal{E}}\,F\left(\frac{\mathcal{E}}{\theta},\overline{\mu}\right), \tag{10}$$

where the Fermi function F is defined in (2). In the limiting case of n large and $\overline{\mu} \gg 1$, we have

$$I_F{}^R(\theta,\mu) \approx -\frac{\theta^2}{4\pi^2}\int_0^\infty dx\,x\left(\frac{1}{e^{x+\overline{\mu}}+1} + \frac{1}{e^{x-\overline{\mu}}+1}\right). \tag{11}$$

This integral can be done exactly to yield

$$I_F{}^R(\theta,\mu) \simeq -\tfrac{1}{24}\theta^2[1 + (3/\pi^2)\overline{\mu}^2]. \tag{12}$$

But the counterterm (7) contributes a term

$$\delta T_i^\psi = i(2\pi)^4 Q_{ij}(\mu)\lambda_j, \tag{13}$$

so that we have for the finite part of $Q_{ij}(\mu)$ in the limit $\overline{\mu} \gg 1$

$$Q_{ij}{}^{\text{fin}}(\mu) = (\mu^2/8\pi^2)\operatorname{Tr}\{\Gamma_i\gamma_4\Gamma_j\gamma_4\}. \tag{14}$$

Thus, the effective scalar boson mass matrix is

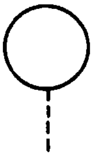

FIG. 1. Fermion-loop tadpole. Dashed line, scalar; solid line, spinor.

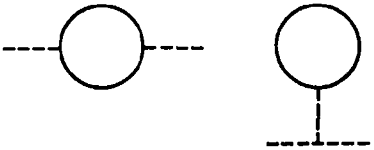

FIG. 2. Fermion-loop contributions to the boson self-energy.

given by

$$[\mathfrak{M}^2(\mu)]_{ij} = [\mathfrak{M}_R{}^2]_{ij} + (\mu^2/8\pi^2)\mathrm{Tr}\{\Gamma_i\gamma_4\Gamma_j\gamma_4\}, \qquad (15)$$

where the chemical potential provides a positive-definite contribution. The vanishing of $\mathfrak{M}^2(\mu)$ determines μ_{crit} in the one-loop approximation. In the case of a spontaneously broken symmetry where $\mathfrak{M}_R{}^2<0$, we have $\mu_{\mathrm{crit}} \sim \mathfrak{M}_R/e$ since the Yukawa coupling matrices are each proportion to e.

This result can be checked by noting that the counterterms provided by (7) also cancel the leading fermion-loop contributions to the scala boson self-energy (see Fig. 2) given by

$$\Pi_{ij}{}^{\phi} = i\theta \sum_{n=-\infty}^{+\infty} \int \frac{d^3p}{(2\pi)^3} \mathrm{Tr}\{\Gamma_i(i\gamma_\alpha p^\alpha + m)^{-1}\Gamma_j(i\gamma_\alpha p^\alpha + m)^{-1}\} + i f_{ijk} M_{kl}{}^{-2} \sum_{n=-\infty}^{+\infty} \int \frac{d^3p}{(2\pi)^3} \mathrm{Tr}\{\Gamma_l(i\gamma_\alpha p^\alpha + m)^{-1}\}, \qquad (1$$

where

$$p^0 = \mathcal{E}_n - i\mu, \quad M_{ij}{}^2 = \frac{\partial^2 P(\varphi)}{\partial\varphi_i\partial\varphi_j}\bigg|_{\varphi=\lambda}, \quad \text{and } f_{ijk} = \frac{\partial^3 P(\varphi)}{\partial\varphi_i\partial\varphi_j\partial\varphi_k}\bigg|_{\varphi=\lambda}.$$

Isolating the quadratically divergent part of (16) and the leading terms in μ, we find

$$\Pi_{ij}{}^{\phi} \simeq -Q_{ij}(\mu) + f_{ijk}M_{kl}{}^{-2}Q_{lm}(\mu)\lambda_m. \qquad (17)$$

The first term is canceled directly by the counterterm in (7), while the second term is canceled by a tadpole produced by the counterterm.

We can equivalently express our result in terms of a critical number density n_{crit}, where n is the number of fermions minus the number of antifermions in a unit volume V:

$$n = (1/V)\int d^3x\,\eta(\vec{x}). \qquad (18)$$

Using (5) and the μ-dependent free-fermion propagator at finite temperature, we have for the renormalized (at $\theta = \mu = 0$) number density

$$n_R(\theta,\mu) \simeq \frac{\theta^3}{\pi^2}\int_0^\infty dx\, x^2\left(\frac{1}{e^{x-\overline{\mu}}+1} - \frac{1}{e^{x+\overline{\mu}}+1}\right), \qquad (19)$$

where the fermion mass is again negligible compared to μ. This integral can be done exactly and we find

$$n_R(\theta,\mu) \simeq (\theta^3/3\pi^2)(\overline{\mu}^3 + \pi^2\overline{\mu}). \qquad (20)$$

Inverting (20) yields approximately

$$\mu \simeq (3\pi^2 n_R)^{1/3}[1 + O(1/\overline{\mu})], \qquad (21)$$

thus confirming our earlier dimensional argument leading to the estimate of the critical fermion number density of $10^{48}/\mathrm{cm}^3$. Densities of this magnitude or greater are considered in the evolution of black holes[7] and of the universe.[8]

A gravitationally collapsing star with mass M and original radius R_0 will theoretically reach a point of infinite density in a finite proper time given by[7]

$$\tau = \pi(R_0{}^3/8M)^{1/2}, \qquad (22)$$

i.e., the time for total collapse as measured by a clock on the surface of the collapsing star depends only on the initial density. Since a typical stellar mass is $\approx 10^{33}$ g (which is of the order of the Chandrasekhar and Oppenheimer-Volkoff limits),[9] there may be up to 10^{57} baryons. Then, the critical density would occur when the radius was $\approx 10^3$ cm and when the proper time was given essentially by (22).

It has been noted[1] that a phase transition which produces massless vector particles may lead to anomalously great repulsive forces between the particles of the system. Whether this force is sufficient to reverse the collapse of the star has yet to be determined.

Similar considerations can be applied to the universe as a whole, extrapolating backwards in time and assuming the standard big-bang model with elementary particles.[10] If we take the present radius of the universe as 10^{10} light years and the density as 10^{-30} g/cm^3, we find a maximum number of baryons of 10^{78}. This would lead to a phase transition when the radius of the universe was approximately 10^{10} cm.

However, from the observed cosmic-radiation temperature and mass density, we know that the dimensionless chemical potential is small today, i.e., $\overline{\mu} \simeq 10^{-8}$–$10^{-9}$.[2,9] In addition, when $\overline{\mu} \ll 1$, $\overline{\mu} \propto 1/\sigma$, where σ is the dimensionless specific entropy per baryon. Now if we presume an adiabatic expansion of the universe, σ is constant, so that $\overline{\mu}$ would never grow large enough to effect a phase transition. The adiabatic assumption, though, leaves unexplained both the origin of the large specific entropy and the origin of the galaxies. An attractive solution[11-13] which could solve these problems simultaneously asserts that the viscous dissipation of anisotropies and possible inhomogeneities would serve to generate ntropy but preserve "small" mass fluctuations f galactic size. Such a solution would necessar-y imply a growth of the specific entropy in time r a corresponding increase of $\bar{\mu}$ extrapolated ack in time, with $\bar{\mu} \gg 1$ allowed in principle.

We thank Steve Weinberg who generously provided his time and an early version of his paper "Gauge and Global Symmetries at High Temperature." We are also grateful for frequent valuable discussions with Jürg Fröhlich.

---

*Work supported in part by the National Science Foundation under Grant No. GP-40397X.

[1] D. A. Kirzhnits and A. D. Linde, Phys. Lett. 42B, 471 (1972); D. A. Kirzhnits, Pis'ma Zh. Eksp. Teor. Fiz. 15, 745 (1972) [JETP Lett. 15, 529 (1972)].

[2] S. Weinberg, "Gauge and Global Symmetries at High Temperature" (to be published).

[3] S. Weinberg, Phys. Rev. Lett. 19, 1264 (1967); A. Salam, in *Elementary Particle Physics*, edited by N. Svartholm (Almquist and Wiksells, Stockholm, Sweden, 1968), p. 367.

[4] S. Coleman and E. Weinberg, Phys. Rev. D 7, 1888 (1973).

[5] A. L. Fetter and J. D. Walecka, *Quantum Theory of Many-Particle Systems* (McGraw-Hill, New York, 1971), Chap. 7.

[6] S. Weinberg, Phys. Rev. D 7, 1887 (1973).

[7] C. W. Misner, K. S. Thorne, and J. A. Wheeler, *Gravitation* (Freeman, San Francisco, 1973).

[8] E. R. Harrison, Annu. Rev. Astron. Astrophys. 2, 155 (1973).

[9] S. Weinberg, *Gravitation and Cosmology: Principles and Applications of the General Theory of Relativity* (Wiley, New York, 1972).

[10] In the composite-particle model [see R. Hagedorn, Nuovo Cimento, Suppl. 3, 147 (1965); S. Fubini and G. Veneziano, Nuovo Cimento 64A, 811 (1969)], the chemical potential grows without bound while there is a maximum temperature, so that the condition $\bar{\mu} \gg 1$ is attained. However, because of the richness of fermion states, the typical thermodynamic quantities (e.g., pressure, density, and number density) grow exponentially with the chemical potential [see K. Huang and S. Weinberg, Phys. Rev. Lett. 25, 895 (1970)], so that the validity of a one-loop approximation would be questionable.

[11] C. W. Misner, Astrophys. J. 151, 431 (1968).

[12] S. Weinberg, Astrophys. J. 168, 175 (1971).

[13] R. Matzner and C. W. Misner, Astrophys. J. 171, 415 (1972).

Inclusive π^0 Production in pp Collisions at 50–400 GeV/c*

D. C. Carey, J. R. Johnson, R. Kammerud, M. Peters,† D. J. Ritchie, A. Roberts,
J. R. Sauer, R. Shafer, D. Theriot, and J. K. Walker
National Accelerator Laboratory, Batavia, Illinois 60510

and

F. E. Taylor
Physics Department, Northern Illinois University, DeKalb, Illinois 60115
(Received 15 May 1974)

We have measured the single-photon cross section in the reaction $p+p\rightarrow\gamma+\text{anything}$ for incident proton momenta from 50 to 400 GeV/c and lab angles of 80, 100, and 120 mrad. It is shown that in the range $p_\perp=0.3$ to 4.3 GeV/c, the derived π^0 invariant cross section can be factorized into a product of two functions, one in $p_\perp$ and the other in a new scaling variable $x_R'=p^*/p_{\max}^*$, where p^* is the total c.m. momentum of the π^0.

The study of the production of pions with large transverse momentum $p_\perp$ in proton-proton collisions is expected to give insight into the short-distance structure of the proton.[1-3] Great interest in this field has been stimulated by the experimental results obtained at the CERN intersecting storage rings[4-6] and at the National Accelerator Laboratory (NAL).[7,8] Büsser *et al.*[4] at the intersecting storage rings were the first to show that near 90° in the pp c.m. system, the large-$p_\perp$ data were consistent with a scaling behavior with respect to the variable $x_\perp=2p_\perp/\sqrt{s}$. On the other hand, it has been known for several years that the small-$p_\perp$ single-pion inclusive data exhibit scaling with respect to the variable $x_\parallel=2p_\parallel^*/\sqrt{s}$ at all c.m. angles. In this experiment, data have been obtained on single-π^0 inclusive spectra from 40 to 110° in the pp c.m. system and for $0.3\le p_\perp \le 4.3$ GeV/c. It has been found that the cross sections scale when the "radial" variable $x_R=p^*/$

$p_{\max}{}^*$ is used. This new radial scaling variable, x_R, may be regarded as a generalization of the previous variables $x_\perp$ and $x_\parallel$. Clearly, in the appropriate limits of small $p_\perp$, x_R tends to $x_\parallel$, while at small $p_\parallel{}^*$, x_R tends to $x_\perp$.

We have measured the photon energy spectrum in the process $p+p\rightarrow\gamma+\text{anything}$ for incident proton energies from 50 to 400 GeV. Data were accumulated at three angles, 80, 100, and 120 mrad, over a range in photon transverse momentum from 0.3 to about 4.3 GeV/c. On the assumption that all the detected photons came from π^0 decay,[4,9] the observed photon energy spectra were then converted into invariant π^0 cross sections using Sternheimer's[10] prescription.

The experiment was performed at the internal target area at NAL, using both a hydrogen gas jet[11] and a rotating carbon-fiber target which intercepted the accelerator's internal proton beam. The detection system[7] consisted of a lead-glass shower counter which was used to measure the γ-ray energy, and scintillation counters which were used to separate incident γ rays from hadrons and muons. Because the γ-ray opening angle in the decay $\pi^0\rightarrow 2\gamma$ was larger than the angular acceptance of the spectrometer, the detector was sensitive to only one of the two π^0-decay photons.

At each angle, the normalization of the γ-ray cross sections, and hence the π^0 invariant cross sections, was determined from a short run using the hydrogen-jet target, where a solid-state detector was used to monitor the rate of recoil protons elastically scattered at small momentum transfer. By using the known[12,13] pp elastic cross section to determine the luminosity, the absolute γ-ray cross section was then obtained. The major portion of the data at each angle was taken while using the rotating carbon-fiber target. To establish that the experiment was not sensitive to complex target effects, γ-ray data were collected for both carbon and hydrogen at 100 mrad for incident energies between 50 and 400 GeV and $p_\perp$ up to 3 GeV/c. There was no observable difference in the shapes of the γ-ray spectra from the two types of targets.[7]

Figure 1 displays the $p_\perp$ dependence of the π^0 invariant cross section for the data obtained at 80 mrad. At a fixed $p_\perp$, the cross section rises with increasing incident momentum; at $p_\perp=2$ GeV/c, there is roughly a factor of 25 between the cross sections at incident momenta of 50 and 250 GeV/c. Furthermore, the slope of the cross section at large $p_\perp$ decreases with increasing incident momentum.

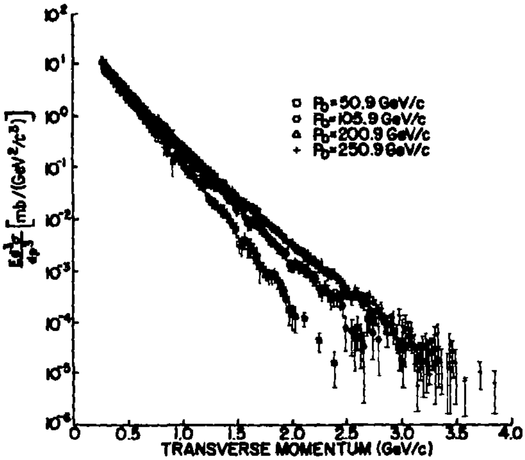

FIG. 1. The invariant π^0 cross sections at $\theta_{\text{lab}}=80$ mrad plotted versus $p_\perp$ for four incident proton momenta, 50.9, 105.9, 200.9, and 250.9 GeV/c.

The π^0 invariant cross section reveals a strikingly simple behavior when it is expressed in terms of certain variables. For the three lab angles 80, 100, and 120 mrad, we find that the invariant π^0 cross section is well represented by the product of two functions, $f(x_R)$ and $g(p_\perp)$; that is,

$$E\,d^3\sigma/dp^3=f(x_R)g(p_\perp).$$

The variable $p_\perp$ is the familiar transverse momentum of the π^0 while the radial scaling variable x_R is the ratio of the π^0 momentum to the maximum momentum,

$$x_R\equiv p^*/p_{\max}{}^*\cong 2p^*/\sqrt{s}.$$

For a particular lab angle, the data from this experiment cover a large range of x_R for fixed $p_\perp$ and thereby allow an accurate determination of the scaling function $f(x_R)$. By an iterative procedure, self-consistent solutions for the functions $f(x_R)$ and $g(p_\perp)$ were obtained from the invariant π^0 cross sections. The resulting functions $f(x_R)$ and $g(p_\perp)$ for 80 mrad are shown in Figs. 2 and 3.[14]

The degree to which the radial scaling function $f(x_R)$ is independent of the transverse momentum $p_\perp$ for a particular lab angle can be seen in Fig. 2. This figure shows that $f(x_R)$ is, to a good approximation, a unique function of x_R, which demonstrates the validity of the factorization of the π^0 invariant cross section. The solid line of Fig.

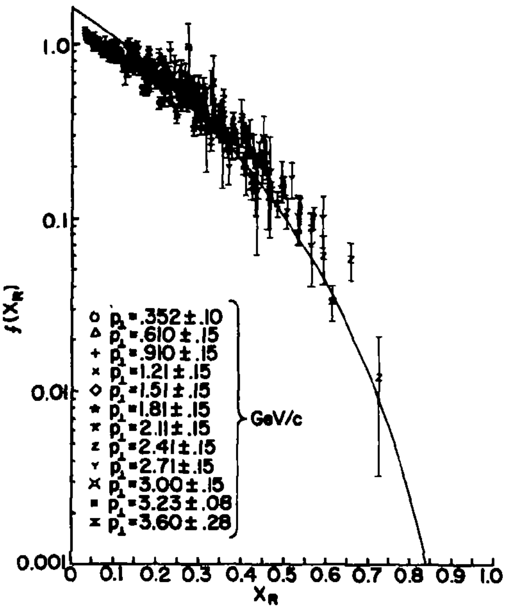

FIG. 2. The functions $f(x_R)$ calculated for twelve fixed $p_\perp$ values for the 80-mrad data are compared with each other and with the functional form $(1-x_R)^4$.

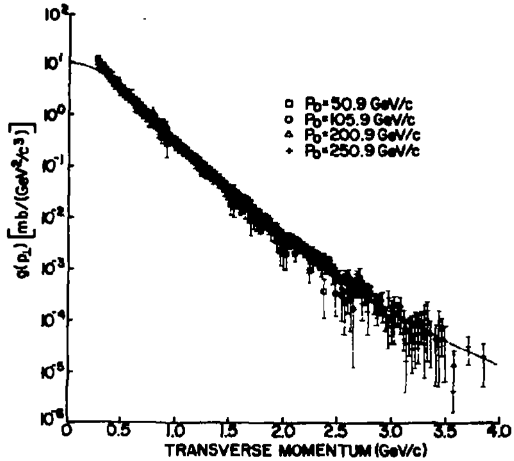

FIG. 3. The functions $g(p_\perp)$ calculated for four incident momenta at 80 mrad are compared with each other and with the functional form $(p_\perp^2+0.86)^{-4.5}$.

2 is a constant times $(1-x_R)^4$ and gives a convenient although rough description of the scaling function $f(x_R)$. The representation of $f(x_R)$ used in subsequent analysis was a minimum-χ^2 fit by a fourth-order polynomial in x_R.

Having determined a unique $f(x_R)$, we compute the transverse momentum function $g(p_\perp)$ for each incident momentum as the invariant cross section at that momentum divided by $f(x_R)$. In Fig. 3, this result has been plotted for four different incident proton momenta from 50 to 250 GeV/c for the same lab angle, 80 mrad. It can be seen that $g(p_\perp)$ appears to be a universal function over six decades in magnitude, even though, as noted previously, the π^0 inclusive cross sections vary widely in shape and magnitude over this same range in $p_\perp$ and incident momentum. This implies that $g(p_\perp)$ has reached its asymptotic limit even at an incident momentum as low as 50 GeV/c. The solid line in Fig. 3 has the functional dependence $(p_\perp^2+0.86)^{-4.5}$ and fits the data well for $p_\perp > 0.5$ GeV/c.

The functions $f(x_R)$ and $g(p_\perp)$ were determined separately at each angle of 80, 100, and 120 mrad. The radial scaling functions $f(x_R)$ agreed to within ±10% for $0.1 \leq x_R \leq 0.7$. Similarly the three intrinsic transverse momentum functions $g(p_\perp)$ were consistent with each other within the errors of the data. A three-parameter minimum-χ^2 fit was made to the 80-mrad $g(p_\perp)$ function for each incident momentum bin from 50 to 300 GeV/c, and an average fit was determined. Comparing this average fit to the 80-, 100-, and 120-mrad $g(p_\perp)$ functions over their respective incident momentum ranges yielded an average χ^2 per degree of freedom of 0.7, 0.4, and 1.6, respectively.

In conclusion, from 40 to 110° in the c.m. system and from 50 to 400 GeV/c incident momenta, we have shown the following: (a) The π^0 inclusive production cross section in pp collisions factorizes into a product of two functions, $f(x_R)$ and $g(p_\perp)$. (b) Both the radial scaling function $f(x_R)$, where x_R is a new scaling variable, and the transverse-momentum function $g(p_\perp)$ are universal functions over these kinematic ranges. (c) Approximate analytic expressions for these functions are

$$f(x_R) \propto (1-x_R)^4$$

and

$$g(p_\perp) \propto (p_\perp^2+0.86)^{-4.5}.$$

We gratefully acknowledge the enthusiastic support of D. Jovanovic and the staff of the internal target area. We are indebted to the State Committee for Utilization of Atomic Energy of the U.S.S.R. for development and construction of the hydrogen-jet target. We would like to thank members of the Joint Institute for Nuclear Research–NAL–University of Rochester–Rockefeller University collaboration for providing solid-state detectors for monitoring *pp* elastic rates. D. Burandt, R. Olsen, and J. Hanks provided valuable technical assistance. Finally, we would like to recognize the encouragement given to us by R. R. Wilson, E. L. Goldwasser, and J. Sanford in the course of this work.

---

*Work supported by the U. S. Atomic Energy Commission.

†Permanent address: Physics Department, University of Hawaii, Honolulu, Haw. 96822.

[1] R. Blankenbecler, S. J. Brodsky, and J. F. Gunion, Phys. Lett. 42B, 461 (1972).

[2] P. V. Landshoff and J. C. Polkinghorne, Phys. Lett. 45B, 361 (1973).

[3] J. D. Bjorken and J. Kogut, Phys. Rev. D 8, 1341 (1973).

[4] F. W. Büsser *et al.*, Phys. Lett. 46B, 471 (1973).

[5] M. Banner *et al.*, Phys. Lett. 41B, 547 (1972).

[6] B. Alper *et al.*, Phys. Lett. 44B, 521, 527 (1973).

[7] D. C. Carey *et al.*, Phys. Rev. Lett. 32, 24 (1974).

[8] J. W. Cronin *et al.*, Phys. Rev. Lett. 31, 1426 (1973).

[9] D. Swanson *et al.*, ANL Report No. ANL/HEP 7357, 1973 (unpublished); G. R. Charlton and G. H. Thomas, Phys. Lett. 40B, 378 (1972); S. N. Ganguli and P. K. Malhotra, Phys. Lett. 39B, 632 (1972).

[10] R. M. Sternheimer, Phys. Rev. 99, 277 (1955).

[11] V. D. Bartenev *et al.*, in *Advances in Cryogenic Engineering*, edited by K. D. Timmerhaus (Plenum, New York, 1973), Vol. 18, p. 460.

[12] U. Amaldi *et al.*, Phys. Lett. 43B, 231 (1973).

[13] V. Bartenev *et al.*, Phys. Rev. Lett. 31, 1367 (1973).

[14] The shape of the radial function $f(x_R)$ is sensitive to errors in the energy dependence of our normalization to the *pp* elastic cross section and in the energy calibration of our lead glass counter, especially near the phase-space boundary $x_R = 1$. The absolute normalization of the data is reflected in the magnitude of the $p_\perp$ function.

Unified Description of Single-Particle Production in *pp* Collisions*

D. C. Carey, J. R. Johnson, R. Kammerud, M. Peters,† D. J. Ritchie, A. Roberts, J. R. Sauer,
R. Shafer, D. Theriot, and J. K. Walker
National Accelerator Laboratory, Batavia, Illinois 60510

and

F. E. Taylor
Physics Department, Northern Illinois University, DeKalb, Illinois 60115

(Received 15 May 1974)

We show that over a very wide range of c.m. angles, energies, and transverse momenta, the invariant cross sections for inclusive production of hadrons in *pp* collisions show a very simple behavior when expressed in terms of a new radial scaling variable $x_R \equiv p^*/p_{\max}^*$, where p^* is the total c.m. momentum of the hadron.

In a separate Letter,[1] we have presented data on inclusive π^0 production from *pp* collisions at the National Accelerator Laboratory (NAL), showing that for c.m. angles from 40 to 110°, transverse momenta from 0.3 to 4.3 GeV/*c*, and incident energies from 50 to 400 GeV, the invariant cross sections factorize very simply into the product of two universal functions:

$$E\,d^3\sigma/dp^3 = f(x_R)g(p_\perp), \tag{1}$$

where x_R is an angle-independent scaling variable,

$$x_R \equiv p^*/p_{\max}^* \approx 2p^*/\sqrt{s}. \tag{2}$$

The observed dependence on x_R can be approximated by

$$f(x_R) \propto (1-x_R)^4, \tag{3}$$

and the intrinsic transverse-momentum dependence by

$$g(p_\perp) \propto (p_\perp^2 + m^2)^{-4.5}, \quad m^2 = 0.86\ \text{GeV}^2. \tag{4}$$

The simplicity of this factorization and the wide kinematic range over which we have found it applicable make it desirable to examine other *pp* inclusive data. Although the available data are limited, we feel it is important to provide an initial overview of an emerging pattern for inclusive measurements in strong interactions.

We have compared our results with other inclusive pion measurements near 90° in the c.m. system by the Chicago-Princeton group at NAL[2] ($\pi^\pm$) and the CERN-Columbia University-Rockefeller University collaboration at the CERN intersecting storage rings (ISR)[3] (π^0). In the region of energy and transverse momentum where the data overlap, the agreement is satisfactory. However, we would like to test the scaling behavior over as wide a range as possible of c.m. angles and energies, beyond the region covered by our experiment. For this, we consider recent data from the CERN-Università di Bologna group[4] at the ISR at smaller c.m. angles (5-20°) and higher energies, and lower-energy data from Allaby *et al.*[5] ($P_{\rm inc}$= 24 GeV/c) and Akerlof *et al.*[6] ($P_{\rm inc}$= 12.4 GeV/c). To minimize diffractive or leading-particle effects, we restrict ourselves to negative produced particles. Figure 1 shows the x_R dependence, for fixed $p_\perp$, of invariant cross sections for $p+p \to \pi^- +$ anything. The open circles represent the ISR data at $p_\perp = 0.8$ GeV/c and show a dependence on x_R in good agreement with that found in our π^0 results, shown as the solid curve (arbitrarily normalized to pass through the points at small x_R). This agreement is rather remarkable considering the different kinematic regions covered by the two sets of data. We have extended the comparison to include the lower-energy data from Allaby *et al.* at $p_\perp = 0.8$ GeV/c and from Akerlof *et al.* at $p_\perp = 1.0$ GeV/c, which cover a wide range of c.m. angles and extend rather close to the kinematic boundary $x_R = 1$ (see inset in Fig. 1). The results of Akerlof *et al.*, when scaled from $p_\perp = 1.0$ GeV/c to $p_\perp = 0.8$ GeV/c by using Eq. (4), agree very well in absolute normalization with the data of Allaby *et al.* at $p_\perp = 0.8$ GeV/c. However, both must be scaled down by about 40% to line up with the ISR points in the region of x_R where there is overlap (this could be due to a slight deviation from scaling over the enormous energy spread involved, or to experimental normalization differences). When this is done, as shown in Fig. 1, it is apparent that the x_R dependence is very similar for all four sets of data. It therefore appears that a single universal scaling expression is consistent with inclusive pion data from pp collisions, independent of c.m. angle from 5 to 110° and for $25 \lesssim s \lesssim 4000$, if the data are expressed in terms of the variable x_R.

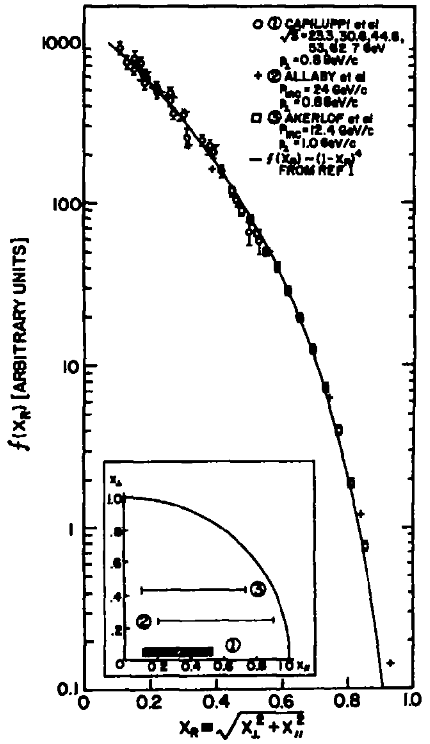

FIG. 1. Invariant cross sections for $p+p \to \pi^- +$ anything plotted versus x_R for fixed $p_\perp$. The solid curve represents the x_R dependence found in our experiment. Arbitrary normalization shifts have been made to illustrate the agreement in the x_R dependence. The inset shows the values of $x_\perp \equiv p_\perp/p_{\rm max}^*$ and $x_\parallel \equiv p_\parallel^*/p_{\rm max}^*$ covered by the three sets of data points.

Thus encouraged, we are led to ask whether a similar universality exists for K^- and $\bar{p}$ data. The Chicago-Princeton[2] results taken at NAL near 90° in the c.m. system can be compared with measurements taken at very-small c.m. angles by the CERN-Bologna group.[4] Since in the NAL data both $p_\perp$ and x_R are varying, we assume that the intrinsic $p_\perp$ dependences $g(p_\perp)$ for π^-, K^-, and $\bar{p}$ are the same for large enough $p_\perp$. We then divide out the $p_\perp$ dependence in the NAL data by comparing particle ratios K^-/π^- and $\bar{p}/\pi^-$ between the two experiments. This comparison is shown in Fig. 2. The upper set of points in Fig. 2(a) shows the K^-/π^- ratios measured by the Chicago-Princeton experiment for $p_\perp > 3$ GeV/c. The ratio K^-/π^- can be seen to fall with increasing x_R. This means, given the assumption of similar forms of $g(p_\perp)$ for K^- and π^-, that the K^- radial scaling function has a more rapid x_R dependence than that for the π^- mesons. The CERN-Bologna data were taken at a fixed $p_\perp$ of 0.8 GeV/c and are shown as the lower set of points in Fig. 2(a). Although the errors on the data are large it appears that the ratio K^-/π^- again decreases with

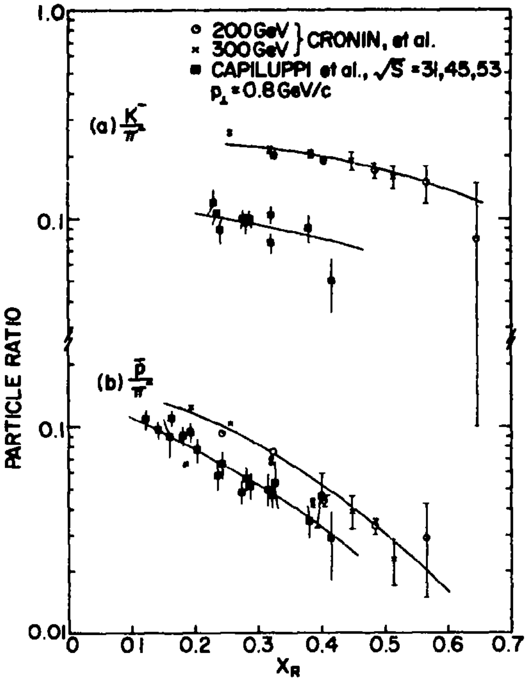

FIG. 2. Particle ratios K^-/π^- and $\bar{p}/\pi^-$ plotted versus x_R for data from Refs. 2 and 4. The curves were generated by Eqs. (5)–(7).

increasing x_R. In fact a comparison of the two sets of data, one taken at 90° and the other at very small angles in the c.m. system, shows that they are consistent with being parallel and therefore with having the same K^- radial scaling function $f_{K^-}(x_R)$. The magnitudes of the ratios K^-/π^- from the two experiments are different, but this difference may arise from the low $p_\perp$ value of the ISR data. A simple mechanism for describing this difference is to assume the form of Eq. (4) with a species-dependent mass term. To illustrate this, curves are shown in Fig. 2(a) which are good fits to the observed K^-/π^- ratios. The functions used to generate the curves are

$$E\frac{d^3\sigma}{dp^3}(\pi^-)=N(p_\perp^2+0.86)^{-4.5}(1-x_R)^4 \qquad (5)$$

and

$$E\frac{d^3\sigma}{dp^3}(K^-)=0.36N(p_\perp^2+1.22)^{-4.5}(1-x_R)^5, \qquad (6)$$

where N is an overall normalization constant. Thus a species dependence in the mass term in $g(p_\perp)$ can significantly affect the magnitude of the particle ratio at small transverse momentum.

Figure 2(b) shows the same comparison for the $\bar{p}/\pi^-$ ratios measured at 90° by the Chicago-Princeton group at NAL and at small angles by the CERN-Bologna group at the ISR. In this case the data from the two experiments allow a more detailed comparison. The ratio $\bar{p}/\pi^-$ at 90° can be seen to fall rapidly with increasing x_R. This means, given the assumption of similar forms of $g(p_\perp)$ for $\bar{p}$ and π^-, that the $\bar{p}$ radial scaling function has a much more rapid x_R dependence than that for π^- mesons. The small-angle ISR $\bar{p}/\pi^-$ data are strikingly parallel to the large-angle NAL data. Thus both sets of data are consistent with having the same $\bar{p}$ radial scaling function $f_{\bar{p}}(x_R)$.

Once again the magnitudes of the ratios $\bar{p}/\pi^-$ from the two experiments are different. As before we ascribe this to a species dependence in the mass term of $g(p_\perp)$ in Eq. (4). The curves shown in Fig. 2(b) were generated from Eq. (5) for the π^- cross section and the following expression for $\bar{p}$ production:

$$E\frac{d^3\sigma}{dp^3}(\bar{p})=0.26N(p_\perp^2+1.04)^{-4.5}(1-x_R)^7. \qquad (7)$$

In conclusion, we have shown that when the invariant cross sections are expressed in terms of a new scaling variable x_R, available data from the Argonne National Laboratory zero-gradient synchrotron, the CERN proton synchrotron, NAL, and the ISR on inclusive π^0, π^-, K^-, and $\bar{p}$ production are consistent with (a) a factorized form:

$$E\,d^3\sigma(\pi)/dp^3=f_\pi(x_R)g_\pi(p_\perp),$$

$$E\,d^3\sigma(K^-)/dp^3=f_{K^-}(x_R)g_{K^-}(p_\perp),$$

$$E\,d^3\sigma(\bar{p})/dp^3=f_{\bar{p}}(x_R)g_{\bar{p}}(p_\perp),$$

where (b) the intrinsic $p_\perp$ dependences $g(p_\perp)$ for $\pi^{0,-}$, K^-, and $\bar{p}$ are the same for large enough $p_\perp$ i.e.

$$g_\pi(p_\perp)\propto g_{K^-}(p_\perp)\propto g_{\bar{p}}(p_\perp), \quad p_\perp \gg m_i,$$

and (c) the radial scaling functions are given approximately by

$$f_\pi(x_R)=(1-x_R)^4,$$

$$f_{K^-}(x_R)=(1-x_R)^5,$$

$$f_{\bar{p}}(x_R)=(1-x_R)^7.$$

We would like to thank Professor T. T. Wu for a careful reading of the manuscript and for constructive suggestions.

---

*Work supported by the U. S. Atomic Energy Commission.

†Permanent address: Physics Department, University of Hawaii, Honolulu, Hawaii 96822.

[1] D. C. Carey *et al.*, preceding Letter [Phys. Rev. Lett. 33, 327 (1974)].

[2] J. W. Cronin *et al.*, Phys. Rev. Lett. 31, 1426 (1973).

[3] F. W. Büsser *et al.*, Phys. Lett. 46B, 471 (1973). Although the data from this experiment agree with our results where the energy ranges overlap, at higher energies their cross sections vary more rapidly with x_R for fixed $p_\perp$. This could be due to an energy-dependent normalization difficulty.

[4] P. Capiluppi *et al.*, "Charged Particle Production in Proton-Proton Inclusive Reactions at Very High Energies" (to be published).

[5] J. V. Allaby *et al.*, in *Proceedings of the Fourth International Conference on High-Energy Collisions, Oxford, England, 1972* (Science Research Council, London, England, 1972), Vol. 2, p. 85.

[6] C. W. Akerlof *et al.*, Phys. Rev. D 3, 645 (1971).

Minimal Three-Body Scattering Theory

R. D. Amado*
Department of Physics, University of Pennsylvania, Philadelphia, Pennsylvania 19174

(Received 10 June 1974)

We show that implementation via unitarity and analyticity of quantum mechanical constraints due to pair final-state interactions in three-body states leads to the simplest form of linear scattering integral equations usually used for the three-body problem. This form of the separable interaction equation is therefore the minimal equation compatible with these general constraints of quantum mechanics.

The general problem of final-state interactions in three-body final states is very poorly understood in spite of a wide variety of remarkably successful three-body calculations in particular systems. In this note we show that the dynamical scheme used in most of these calculations is essentially the minimal embodiment of the general constraints of quantum mechanics required by these final-state interactions. This provides a bridge between the usual formalism, based on linear off-shell scattering integral equations with separable interactions, and the general constraints of quantum mechanics expressed through on-shell unitarity and analyticity. Apparently much of the structure in three-body scattering successfully accounted for in these calculations is little more than the manifestation of the nearly kinematic constraints due to two-body final-state interactions. This may account for the great success of the simple dynamical calculations, as well as stressing again that they give little detailed dynamical insight. The technical difficulty of doing this calculation also shows that implementing final-state unitarity and analyticity in the three-body problem is complicated.

In a recent Letter,[1] referred to hereafter as A-A, we showed that unitarity applied to three-body final states implies singularities in the quasi-two-body amplitudes usually assumed to be slowly varying in the analysis of three-body final states. The strength of these singular parts is linearly related back to these same amplitudes —a manifestation of important coherence in the final state. In this Letter we exploit the fact that unitarity provides the discontinuity across the pair subenergy cut to write a dispersion relation for the amplitude. Because of the linear relation of the discontinuity to the amplitude itself, this dispersion relation yields a linear scattering integral equation which turns out to be the simplest version of the separable interaction three-body equation.

Consider an amplitude $T_{2,3}$ for going from a two-body state to a three-body state. Make the standard isobar, Faddeev, sequential-decay, or multiple-scattering decomposition of $T_{2,3}$ into a sum of terms depending on which pair interacts last:

$$T_{2,3}=\sum_i f_i \tau_i \tag{1}$$

where τ_i is the two-body scattering amplitude of the j-k pair ($i\neq j\neq k$) and f_i is its coefficient in $T_{2,3}$. Usually τ_i is taken to be dominated by a particular partial wave l_i, and then a factor of q^{-l_i} (where q_i is the j-k relative momentum) is explicitly removed from f_i. In A-A we showed that unitarity forces f_i to have a square-root singularity in the i-pair subenergy,[3] and that the discontinuity across that cut (called the absorptive part in A-A) is given by

$$\mathrm{Disc} f_i = q_i \sum_{j \neq i} f_j \tau_j , \tag{2}$$

where the q_i term comes from the density of states. If we assume that f_i has only this singularity in the pair subenergy we can write a dispersion relation for f_i. Since the discontinuity (2) involves f_j, this dispersion relation will yield a linear integral equation for the f_k's.

We now turn to an explicit derivation of the three-body scattering integral equation starting from (2). To keep the algebra simple, we consider a final state of three identical spinless bosons interacting in relative s waves only. The initial state we take as one boson incident on a $J=0$ state of two. It does not matter whether this is a bound state or an elementary particle coupled to two bosons, so long as it is stable. The amplitude f_i can be written in the center-of-mass system as $\langle \vec{k} | f(E) | \vec{p}_i \rangle$, where $\vec{k}$ is the relative momentum in the initial state, $\vec{p}_i$ is the momentum of the ith particle in the final state, and E is the total center-of-mass energy. Energy and momentum conservation require that the subenergy of the ith pair be $\sigma_i = E - \frac{3}{2} p_i^2$. Fleshed out, the unitarity relation (2) becomes, for this case,

$$\mathrm{Disc}\langle \vec{k} | f(E) | \vec{p} \rangle = -\frac{1}{2} \int \frac{d^3p'}{(2\pi)^3} \langle \vec{k} | f(E) | \vec{p}\,' \rangle \tau(E - \tfrac{3}{2} p'^2) \delta(E - 2p^2 - 2p'^2 - 2\vec{p}\cdot\vec{p}\,'), \tag{3}$$

where $\tau(\epsilon)$ is the two-body t matrix for relative energy ϵ normalized to the two-body unitarity relation

$$32\pi^2 \,\mathrm{Im}\,\tau(\epsilon) = -(\epsilon/2)^{1/2} |\tau(\epsilon)|^2 . \tag{4}$$

It is not (3), but its partial-wave projection that has a simple subenergy cut. We define that by

$$\langle \vec{k} | f(E) | \vec{p} \rangle = \sum_{l,m} Y_{l;m}(\hat{k}) \langle k | f_l(E) | p \rangle Y_{l,m}{}^*(\hat{p}) ; \tag{5}$$

then (3) becomes

$$\mathrm{Disc}\langle k | f_l(E) | p \rangle = -\pi \int \frac{p'^2 dp'}{(2\pi)^3} \langle k | f_l(E) | p' \rangle \tau(E - \tfrac{3}{2} p'^2) \int_{-1}^{1} dz\, p_l(z) \,\delta(E - 2p^2 - 2p'^2 - 2pp'z) . \tag{6}$$

The discontinuity is in the subenergy $\sigma = E - \frac{3}{2}p^2$ for $0 < \sigma < \infty$ or, for fixed E, in p^2 for $-\infty < p^2 < \frac{2}{3}E$.[2] If we assume that the only contribution to the discontinuity across the p^2 cut is given by (6), we can use Cauchy's theorem to write the dispersion relation

$$\langle k | f_l(E) | q \rangle = \langle k | R_l(E) | q \rangle - \frac{1}{\pi} \int_{2/3E}^{-\infty} \frac{dp^2}{p^2 - q^2} \mathrm{Disc}\langle k | f_l(E) | p \rangle , \tag{7}$$

where $\langle k | R_l(E) | q \rangle$ is the l-wave projection of the part of f that has no unitarity cut. This is essentially the Born term. Unfortunately there are a number of technical impediments to the direct use of (6) in (7). First, even though the unitarity cut of f_l does run to $-\infty$, the expression (6) for the discontinuity is only valid for $0 < p^2 < \frac{2}{3}E$. To use (6) in (7) we must analytically continue the discontinuity expression. A simple way to do that is to substitute (6) into (7) and interchange the order of the p' and p^2 integrations. For small p', the argument of the δ function will have its zeros for $0 < p^2 < \frac{2}{3}E$. Having done the p^2 integral, the expression may be continued to all p'. Hence we need only consider

$$B_l(q, p') = \int_{2/3E}^{-\infty} \frac{dp^2}{p^2 - q^2} \int_{-1}^{1} dz\, P_l(z) \delta(p^2 + p'^2 + pp'z - \tfrac{1}{2}E) , \tag{8}$$

in terms of which (7) becomes

$$\langle k | f_l(E) | q \rangle = \langle k | R_l(E) | q \rangle + \frac{1}{2} \int \frac{p'^2 dp'}{(2\pi)^3} \langle k | f_l(E) | p' \rangle \tau(E - \tfrac{3}{2} p'^2) B_l(q, p') . \tag{9}$$

The argument of the δ function in (8) has roots at

$$p = \tfrac{1}{2}\{-p_z^{1} \pm [2E - p'^2(4 - z^2)]^{1/2}\} \equiv \tfrac{1}{2}(-p'z \pm \gamma) , \tag{10}$$

but only the root with the positive square root is on the first sheet of the p^2 plane. Using standard rules for the integral of a δ function we obtain

$$B_l(q,p')=-\int_{-1}^{1}P_l(z)(-p'z+\gamma)dz/\gamma[q^2-\tfrac{1}{4}(-p'z+\gamma)^2]\,. \tag{11}$$

We exploit the fact that for even l, $P_l(z)=P_l(-z)$ to symmetrize this integral and find

$$B_l(q,p')=\int_{-1}^{1}P_l(z)\,dz\;/(\tfrac{1}{2}E-p'^2-q^2-p'qz) \tag{12}$$

for even l. This is just the l-wave projection of the usual particle-exchange Born term but for even l only. For odd l we must be more careful. The partial-wave projection defined in (5) will make $\langle k|f_l(E)|q\rangle$ a function of q^2 only for even l but makes it odd in q for odd l. [This is particularly easy to see at threshold where $\langle k|f_l(E)|q\rangle\sim q^l$.] Hence we cannot use (7) for odd l since $\langle k|f_l(E)|q\rangle$ then has an additional kinematic branch cut in q^2 in the interval $0<q^2<\infty$. This difficulty is circumvented by studying $q\langle k|f_l(E)|q\rangle$ for odd l. The extra factor of q removes the kinematical cut. Carrying out the steps (7) to (12) for this function we find that (9) is valid with B_l defined as in (12) for all l. Therefore, implementing the minimal analyticity required by subenergy unitarity (3) leads to the linear integral equation

$$\langle\vec{k}|f(E)|\vec{q}\rangle=\langle\vec{k}|R(E)|\vec{q}\rangle+\int\frac{d^3p'}{(2\pi)^3}\frac{\langle\vec{k}|f(E)|\vec{p}'\rangle\tau(E-\frac{3}{2}p'^2)}{E-2p'^2-2q^2-2\vec{p}'\cdot\vec{q}}\,, \tag{13}$$

for which (9) with (12) is the partial-wave reduction. This equation is the usual separable-interaction integral equation for the three-boson problem with s-wave interaction in the special case of unit vertex functions. The assumption of unit vertex functions was made in (7) where we took the amplitudes to have no subenergy cuts other than those required by subenergy unitarity. Vertex functions would produce additional cuts for negative q^2. It is easy to see that in a simple theory of the 2-3 process (or of a 1 → 3 decay), the Born term has the correct features (and no unitarity cut) to be R so long as the two-body state is stable. Equation (13) with unit vertex function has been analyzed some years ago.[3] It is a Fredholm integral equation if the two-boson state is "elementary," but not if it is a bound state, since in that case the appropriate integrals over the kernel do not converge at their upper limits. The vertex functions provide this convergence in the usual Schrödinger theory, but in the dispersion approach presented here it could equally well be provided by making a subtraction in (7). Since for many applications to scattering problems the detailed form of the vertex is not important, an approach via (13) with subtractions might be attractive. Clearly much work remains to be done to investigate the usefulness of this and related approaches.

It is perhaps surprising that a strict on-shell S-matrix approach, the implementation of analyticity and unitarity, should lead to a linear scattering integral equation of the form (13) which is normally motivated by off-shell considerations. This comes about because we study subenergy analyticity. This subenergy can be varied independently for fixed total energy E, a latitude not normally present in two-body problems. Hence this connection of on-shell and off-shell approaches is a direct consequence of the additional freedom inherent in a multiparticle system.

The derivation presented here is easily extended to cases involving more particle types, spin, interaction in higher waves, etc. It should also be straightforward to do the relativistic case. In fact many of the same unitarity arguments used here including the isobar assumption (1) were previously used to derive the Blankenbecler-Sugar form of the relativistic three-body equations.[4] But in that work the existence of a linear scattering integral equation was assumed. Here we have derived it.

In conclusion, we have shown that implementation of the constraints of two-body unitarity on a three-body final state (in the context of the isobar or quasiparticle formalism) leads directly to the simplest form of the three-body separable interaction linear scattering equation. This sheds new light on the remarkable success of that formalism for a wide range of three-body scattering problems, and shows that in some sense those equations are the minimal set compatible with the general constraints of quantum mechanics.

---

*Work supported in part by the National Science Foundation.

---

[1] R. Aaron and R. D. Amado, Phys. Rev. Lett. 31, 1157 (1973).

[2] See also D. D. Brayshaw, Phys. Rev. 176, 1855 (1968); R. D. Amado, D. R. Freeman, and M. H. Rubin, Phys. Rev. D 4, 1032 (1971); T. J. Brady and I. H. Sloan, Phys. Rev. C 9, 4 (1974); S. K. Adhikari a R. D. Amado, Phys. Rev. D 9, 1467 (1974).

[3] R. D. Amado, Phys. Rev. 132, 485 (1963).

[4] R. Aaron, R. D. Amado, and J. E. Young, Phys. Rev. 174, 2022 (1968).

ERRATA

NUCLEAR COLLISIONS AND FACTORIZATION. Victor Franco [Phys. Rev. Lett. **32**, 911 (1974)].

The points in Fig. 1 are incorrectly plotted and should be lowered by ~0.10 units for $86 < s < 1000$ GeV^2 and by ~0.025 units for $s > 1000$ GeV^2. These results therefore generally fall below the factorization prediction by ~11–17%.

The following is the complete title and byline for the Letter by Schlüter, Joannopoulos, and Cohen of hich the original appeared in Phys. Rev. Lett. **33**, 89 (1974). Through a slip-up in the production proess, the Letter appeared under an erroneous title. This page has been so designed that the material elow can be cut out and pasted over the original version.

New Interpretation of Photoemission Measurements of Trigonal Se and Te[†]

M. Schlüter,[*] J. D. Joannopoulos, and Marvin L. Cohen
Department of Physics, University of California, Berkeley, California 94720, and
Inorganic Materials Research Division, Lawrence Berkeley Laboratory, Berkeley, California 94720

he first two footnotes are then mislabled and should appear as follows:

[†] Work supported in part by the National Science Foundation, Grant No. GH 35688.

[*] Swiss National Science Foundation postdoctoral fellow.

PHYSICAL REVIEW
LETTERS

VOLUME 33 5 AUGUST 1974 NUMBER 6

Measurement of the Hyperfine Structure of the $5^2S_{1/2}$ State of ^{23}Na by Two-Step Excitation Using Two cw Dye Lasers

H. T. Duong, S. Liberman, J. Pinard, and J.-L. Vialle
Laboratoire Aimé Cotton, Centre National de la Recherche Scientifique II, 91405-Orsay, France

(Received 30 April 1974)

We report a direct measurement of the hyperfine splitting of the $5^2S_{1/2}$ state in sodium using a two-step excitation of an atomic beam with two cw tunable dye lasers. The linewidth obtained is 24 MHz and we measure a hyperfine splitting $\Delta\nu(5^2S_{1/2}) = 159 \pm 6$ MHz, in good agreement with the theoretical value.

As noted in a recent paper by Liao, Gupter, nd Happer,[1] the measurements of the hyperfine tructure of sequences of excited states in light alkaline atoms are of particular interest. In that aper, the authors report the first measurement f the $4^2S_{1/2}$ state of sodium using the method of ascade rf spectroscopy and show the difficulties f populating the $4^2S_{1/2}$ level of sodium. In this Letter, we report a direct measurement of the fs of the $5^2S_{1/2}$ level of sodium using a purely ptical method.

The principle of our method is illustrated on he atomic level scheme of Na I (Fig. 1). In order to populate selectively the hyperfine levels f the $5^2S_{1/2}$ state, which cannot be reached from he ground state by a single-step excitation, we se a two-step excitation via the $3^2P_{1/2}$ state. This type of method has been used to measure the lifetime of the *D* levels in Na I,[2] but in that ase pulsed dye lasers with broad spectral bandwidths were used. Our method is a generalization of the method of spectroscopy using a single-tep excitation with detection by fluorescence.[3,4] n that case, as in ours, the spectral width of the exciting laser (a few MHz) must be comparable r less than the natural linewidth of the transition considered. Another new method, first proosed by Vasilenko, Chebotaev, and Shisheaev,[5] to populate a level not connected to the ground state (two-photon spectroscopy using two-photon absorption) and to obtain a result without Doppler broadening has been developed[6] and has recently given the first experimental results[7-9]; we will compare the different results later. In our meth-

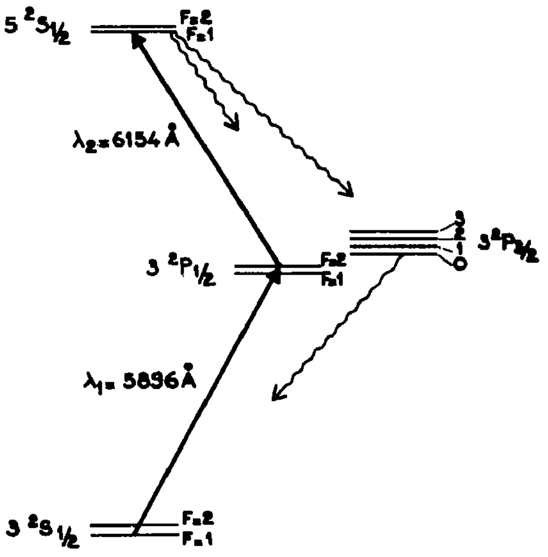

FIG. 1. Level diagram of Na.

Copyright © 1974 by

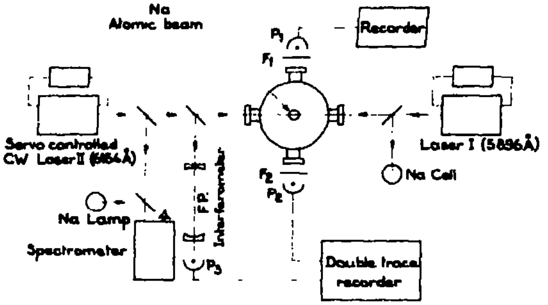

FIG. 2. Double-step-excitation experimental setup. The filters F_1 and F_2 transmitted respectively the lines at 5896 and 6154 Å.

od, the first laser (frequency ν_1) is locked on a hyperfine transition of the D_1 line at 5896 Å and the second laser (frequency ν_2) is scanned continuously over the entire structure of the $3^2P_{1/2}$ — $5^2S_{1/2}$ line at 6154 Å. When the laser frequency ν_2 is tuned to a hyperfine transition from the state with $F=1$ or $F=2$ of the $5^2S_{1/2}$ level, the emitted fluorescent light following the decay to the lower levels is detected and recorded as a function of the frequency ν_2: The signal, which is proportional to the population of the upper hyperfine levels, gives a representation of the level spectrum of $5^2S_{1/2}$.

Figure 2 shows our experimental setup. We use an atomic beam of sodium with a 300/1 collimation ratio.[10] The two cw dye lasers are identical and have been described earlier[11]; they are single mode and the output power is of the order of a few milliwatts. We remark that high power density is not desirable; we have effectively observed a power broadening if the laser light is focused on the atomic beam. A calculation of the laser power required in order to get an appreciable broadening has been done by Feneuille[12] and is in good agreement with our observations. The ability of our lasers to scan continuously over 15 GHz makes the experiments relatively easy. The two laser beams are sent collinearly and in opposite directions on the atomic beam. The fluorescent light is observed perpendicular to the laser beams by two photomultipliers. The signal given by the first one, looking at the fluorescence at 5896 Å from the $3^2P_{1/2}$ level, is used to adjust ν_1 to the absorption frequency of one of the four hyperfine components of the D_1 line of interest. The second photomultiplier looks at the fluorescence from the $5^2S_{1/2}$ level. The intensity of this fluorescent light is recorded as a functio of the frequency ν_2; for this purpose, a portion of the laser beam at 6154 Å is sent into a Fabry Perot interferometer with a free spectral range of 103 MHz, and the recorded fringe signal give the calibration scale.

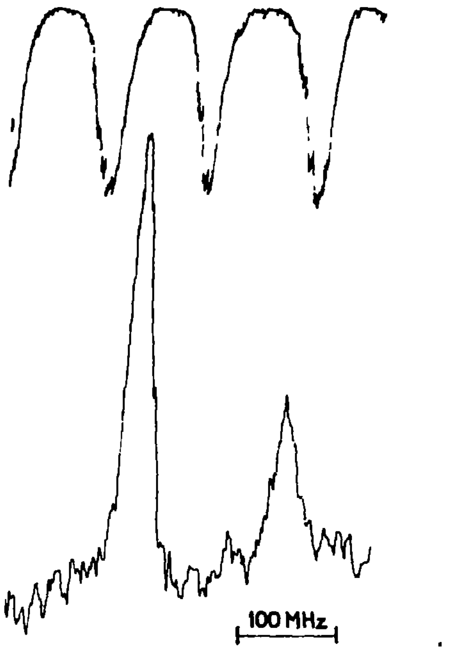

FIG. 3. hfs of the $5^2S_{1/2}$ level [$5^2S_{1/2}$ ($F=1,2$) → $3^2P_{1/}$ ($F=2$)]. The upper trace shows the reference fringes.

A single recording of the $5^2S_{1/2}$ hfs is shown i Fig. 3. The linewidth, 24 MHz, is close to the one expected by taking into account the residual Doppler width and the combined width of the tw cw lasers. Theoretically the intensity of the tw components must be the same; the anomalous i tensity ratio observed is probably due to optica pumping effects related to the use of polarized light and we intend to investigate this effect in the near future. One recording of the hfs structure takes about 1 min; this has to be compare to a recording time of about 3 h by the method cascade rf spectroscopy. The mean value of th measured hyperfine splitting for ten recording is 159 MHz with an uncertainty of ±6 MHz, in perfect agreement with the theoretical value of 157 MHz obtained using the Fermi-Segre form

If we now compare our results to the results tained in Refs. 7–9, we can make some observ ions.

Two-photon absorption spectroscopy requires high-power laser; thus, this method still suffers from some practical limitations. Moreover, the selection rule in two-photon spectroscopy is more restrictive and, for example, the $5^2S_{1/2}$ hfs in sodium cannot be measured directly.

We hope to have shown that this method of very high-resolution spectroscopy of excited states is a very promising one. It is clear that its application is not limited to the relatively narrow frequency range of cw tunable lasers and can be extended from near uv to infrared by using pulsed dye lasers or parametric oscillators operating in a single mode.

We wish to thank M. Baronnet for his continued and skillful technical assistance.

---

[1] K. H. Liao, R. Gupta, and W. Happer, Phys. Rev. A 8, 2811 (1973).

[2] W. Gornik, D. Kaiser, W. Lange, J. Luther, H. H. Radloff, and H. H. Schulz, Appl. Phys. 1, 285 (1973).

[3] W. Hartig and H. Walther, Appl. Phys. 1, 171 (1973).

[4] W. Lange, J. Luther, B. Nottbeck, and H. W. Schröder, Opt. Commun. 2, 157 (1973).

[5] L. S. Vasilenko, V. P. Chebotaev, and A. V. Shishaev, Pis'ma Zh. Eksp. Teor. Fiz. 12, 161 (1970) [JETP Lett. 12, 113 (1970)].

[6] B. Cagnac, G. Grynberg, and F. Biraben, J. Phys. (Paris) 34, 56 (1973).

[7] D. Pritchard, J. Apt, and T. W. Ducas, Phys. Rev. Lett. 32, 641 (1974).

[8] F. Biraben, B. Cagnac, and G. Grynberg, Phys. Rev. Lett. 32, 643 (1974).

[9] M. D. Levenson and N. Bloembergen, Phys. Rev. Lett. 32, 645 (1974).

[10] Since the first-step excitation populates the $3P$ level only with atoms of a given longitudinal velocity range, it should not be necessary to use an atomic beam to reach a resolution beyond the Doppler limit; but in that case some parasitic lines could appear if the intermediate level is not single. We plan to do some experiments with a sodium vapor cell.

[11] S. Liberman and J. Pinard, Appl. Phys. Lett. 24, 3 (1974).

[12] S. Feneuille, to be published.

Direct Observation of Exchange Scattering by Spin Flip of Polarized Electrons in Excitation of Mercury

G. F. Hanne and J. Kessler
Physikalisches Institut der Universität Münster, Münster, Germany

(Received 13 May 1974)

Exchange scattering has been directly observed in the excitation of the 6^3P state of mercury by measuring the spin flip of polarized electrons. Between threshold and 8 eV exchange scattering dominates, resulting in a reversal of the direction of polarization of the scattered electrons. Above 8 eV the influence of exchange decreases rapidly for scattering in the forward direction.

In a conventional electron-atom scattering experiment it is impossible to decide whether the observed electron has suffered a "direct" or an "exchange" collision. Thus the direct and exchange cross sections $|f(\Theta)|^2$ and $|g(\Theta)|^2$ cannot be measured separately. This is different, if the colliding electrons are distinguishable, i.e., if their spins are antiparallel and each electron retains its spin direction during the scattering event. In this case, by determining its spin direction, the observed electron can definitely be stated to have, or to have not, suffered an exchange collision.

This is one of the reasons why scattering experiments with polarized particles are so appealing. Such experiments are feasible today, as the pioneer work of Bederson's group[1] shows. The authors used spin-state-selected alkali atoms as the target and observed the angular distribution and the change of spin state of the recoil atoms. A group at the Joint Institute for Laboratory Astrophysics,[2] which measured cross sections for direct elastic scattering at a few angles, also used state-selected alkali atoms and observed the spins of the scattered electrons. For atoms other than alkalis no such experiments have been made. They can, of course, only be performed with atoms which have unsaturated spins.

Another approach to the separate measurement of direct and exchange scattering can be made by bombarding unpolarized atoms by polarized electrons, but "there has not yet been any scattering experiment in low-energy atomic physics employing polarized electrons."[3] This paper reports an experimental study of electron exchange in the excitation of mercury atoms by slow polarized electrons. Inelastic exchange scattering leading to the 6^3P state of this "two-electron atom" was directly observed by measuring the depolarization of the scattered electrons.

Numerical results for the size of the effects to be expected were not available. We were, however, encouraged by the following considerations to perform the experiment: Theoretical calculations[4] have shown that the cross section for the 6^3P excitation in the range up to about 5 eV above threshold should be dominated by exchange. At higher energies, direct scattering becomes increasingly important. (Direct scattering is caused by the fact that there is a certain $^1P_1$ admixture to the $^3P_1$ state.) If this is correct, the polarization of the scattered electrons should be affected below 10 eV as a result of the spin flips occurring by exchange excitation of the ^3P state, whereas above about 10 eV the scattered electrons should still have the initial polarization.

The ratio of the final and initial polarization should be $P'/P = -\frac{1}{3}$, if exchange scattering were the only way to excite the ^3P state. This is because for electrons with spin $+\frac{1}{2}$ the probability for excitation of the atomic substates $M_S = +1$ (opposite spin directions of observed and incident electron) is twice as large as that for excitation of $M_S = 0$ (equal spin directions of these electrons), as can be shown by a simple calculation. $M_S = -1$ cannot be excited by electrons with spin $+\frac{1}{2}$ if spin conservation is valid. Since there is, however, a certain percentage of direct scattering due to the $^1P_1$ admixture, the probability of non-spin-flip processes is somewhat increased, so that the ratio P'/P is shifted to more positiv values. The exact value of P'/P yields the exte to which direct and exchange processes contribute to the excitation [cf. Eq. (2) at the end].

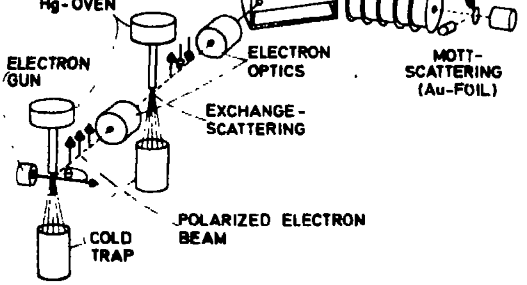

FIG. 1. Schematic diagram of the apparatus.

In the present experiment the depolarization o the electrons scattered in the forward direction has been determined. For these electrons exchange scattering is the only possible spin-flip mechanism; no other spin flips due to spin-orbi coupling occur. This can be concluded from the measurements of spin polarization resulting from elastic and inelastic electron scattering on mercury.[5,6] They showed that the influence of spin-orbit coupling is appreciable only for scattering angles larger than 30°.

Figure 1 gives a schematic diagram of the apparatus. Transversely polarized electrons resulting from elastic scattering by a mercury-vapor beam[7] ($E = 80$ eV, $\Theta = 80°$, $P = 0.22$) are decelerated to 5–20 eV and focused on a second mercury-vapor beam (target density 10^{-2}–10^{-3} Torr). The intensity of the incident polarized electron beam measured after deceleration to 5 eV and selection by the spectrometer was appro imately 5×10^{-11} A. The counting rate of the inelastically scattered electrons finally was 60–200 counts/min.

Figure 2 shows the experimental results. The error bars include the statistical error and the reproducibility of the measured polarizations P and P', as well as the reproducibility of the energy. At energies below 8 eV strong depolariza

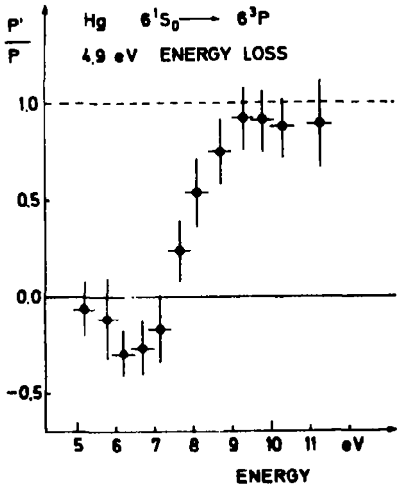

FIG. 2. Measured values of the depolarization ratio versus incident energy.

tion or even reversal of the direction of polarization has been observed. This agrees with the theoretical prediction that exchange scattering dominates at these energies. Above 8 eV, however, the number of spin-flip processes decreases more rapidly than expected from Ref. 4: Above 9 eV significant depolarization could no longer be observed.

We want to point out that the theoretical calculation[4] refers to the total excitation cross section only. Theoretical predictions of exchange cross sections at small angles are controversial and depend strongly on the approximation made.[8,9] The present measurements show that the influence of exchange scattering is very strong even at small angles.

Apart from improving the accuracy we hope to resolve the $^3P_0$, $^3P_1$, and $^3P_2$ transitions in the forthcoming measurements. Making the assumption that the spin-orbit relaxation time is long compared with the excitation time (which is not well-established for Hg), we found for transversely polarized electrons the depolarization ratios P'/P to be

$$-\frac{|g_0|^2}{|g_0|^2+2|g_1|^2}, \quad -\frac{|g_1|^2}{|g_0|^2+2|g_1|^2}, \quad -\frac{3|g_1|^2+2|g_0|^2}{5|g_0|^2+10|g_1|^2}, \tag{1}$$

for $^3P_0$, $^3P_1$, and $^3P_2$, respectively. Here g_0 and g_1 are the amplitudes for inelastic exchange scattering with excitation of the $M_L=0$ and $M_L=\pm 1$ substates of ^3P. If the polarization is parallel to the quantization axis the rotation of the coordinates transforms $|g_1|^2$ and $|g_0|^2$ into $|g_0|^2$ and $2|g_1|^2-|g_0|^2$, respectively. When the admixture of the $^1P_1$ state to the $^3P_1$ state is taken into account, the second of the above expressions is replaced by

$$\frac{P'}{P}=\frac{\beta^2(|f_0^s-g_0^s|^2+2|f_1^s-g_1^s|^2)-\alpha^2|g_1|^2}{\beta^2(|f_0^s-g_0^s|^2+2|f_1^s-g_1^s|^2)+\alpha^2(|g_0|^2+2|g_1|^2)}, \tag{2}$$

where f^s and g^s are the direct and exchange scattering amplitudes for excitation of the ^1P state, and α and β are the coupling coefficients.[4] Since at the 4.9-eV energy loss studied here the transitions to the $^3P_1$ state are dominant, it was mainly expression (2) which was measured in the present experiment. The contribution of the other channels ($^3P_0$ and $^3P_2$) is roughly estimated to be less than 40% (the overall energy resolution was 0.8 eV).

At threshold, according to angular momentum conservation, only the amplitudes with $M_L=0$ can be excited. Thus the limiting value for the $^3P_1$ state should be $P'/P=0$, which is obviously confirmed by the experiment. Resolution of the $^3P_0$ and $^3P_2$ transitions would yield more information about g_1 and g_0.

We gratefully acknowledge support by the Deutsche Forschungsgemeinschaft.

---

[1] B. Bederson, in *Atomic Physics 3*, edited by S. J. Smith and G. K. Walters (Plenum, New York, 1973), Vol. 3, p. 401, and further references quoted therein.

[2] D. Hils, M. V. McCusker, H. Kleinpoppen, and S. J. Smith, Phys. Rev. Lett. 29, 398 (1972).

[3] B. Bederson, Comments At. Mol. Phys. 1, 65 (1969).

[4] J. C. McConnell and B. L. Moiseiwitsch, J. Phys. B: Proc. Phys. Soc., London 1, 406 (1968).

[5] W. Eitel and J. Kessler, Z. Phys. 241, 355 (1971).

[6] J. Kessler, Rev. Mod. Phys. 41, 3 (1969).

[7] K. Jost and J. Kessler, Z. Phys. 195, 1 (1966).

[8] J. C. Steelhammer and S. Lipsky, J. Chem. Phys. 53, 1445 (1970).

[9] R. A. Bonham, J. Chem. Phys. 57, 1604 (1972).

Volume 33, Number 6 PHYSICAL REVIEW LETTERS 5 August 1974

Delayed Emission of Cyclotron Harmonics Triggered by a High-Power Microwave Pulse

N. Ohyabu, S. Sasaki, and N. Kawashima
Institute of Space and Aeronautical Science, University of Tokyo, Komaba, Meguro-ku, Tokyo, Japan
(Received 29 April 1974)

We study the interaction of high-power microwaves with a magnetized plasma. Delayed emissions at cyclotron harmonics are observed after the termination of the pumping wave when the frequency of the pumping wave is equal to one of the harmonics of the cyclotron frequency and is near the plasma frequency.

There has been much interest recently in the interaction of intense electromagnetic waves with plasma concerned with laser-induced fusion and nonlinear plasma wave phenomena in the magnetosphere.[1,2] Such an interaction can produce numerous nonlinear phenomena.[3-10] Here we will present interesting experimental results of the interaction of high-power microwaves with a magnetized plasma in which delayed emissions at cyclotron harmonics are observed after the termination of the pumping wave when the frequency of the pumping wave is equal to one of the harmonics of the cyclotron frequency and is near the plasma frequency.

The experimental layout is shown in Fig. 1. A helium plasma is produced in the steady state by ionization due to electrons which are emitted from an oxide-coated cathode and accelerated by the electric field between anode and cathode. The plasma density is around $10^{12}/\text{cm}^3$ and the neutral-gas pressure P_0 is 1×10^{-4} Torr. The plasma is confined in a magnetic mirror field produced by coils I-IV and the radius of the plasma column is about 1 cm. High-power microwaves at $f_0 = 9.36$ GHz are transmitted transverse to the plasma column from an open-ended wave guide. The maximum power and the duration time of the pumping microwaves are 10 kW and 5–20 μsec, respectively. Microwave emissions from the plasma are measured by a spectrum analyzer (EMA 910) with a frequency range from 1 to 10 GHz.

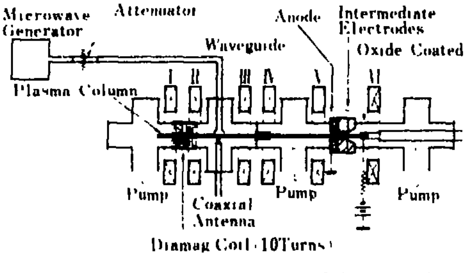

FIG. 1. Schematic layout of the experiment.

An output signal of microwave emissions from the plasma is shown in Fig. 2, in which the pumping frequency is 5 times the electron-cyclotron frequency ($f_0 = 5f_{ce}$) and the measured frequency is tuned to the second harmonic of the electron-cyclotron frequency. A strong microwave emission is observed simultaneously with the microwave pumping (between t_1 and t_2 in Fig. 2). After the termination of the pumping, pulsating microwave emissions appear with a maximum delay time of up to 50 μsec.

Such delayed emissions appear only when the resonance condition $f_0 = nf_{ce}$ ($n = 2, 3, 4, 5, \ldots$) is satisfied; the frequency spectrum of the delayed emission for $n = 4, 5$ is shown in Fig. 3. From Fig. 3, the following rule about the spectrum of the delayed emission is obtained: (i) spectra have peaks at the cyclotron harmonics (mf_{ce}) ($m = 2, 3, \ldots, n-1$); (ii) the emission at the second harmonic is the strongest; (iii) emissions a frequencies f_{ce} (fundamental) and nf_{ce} (i.e., the pumping frequency f_0) are so weak that they are difficult to distinguish from the noise level of th receiver.

The delayed emission is quite different from

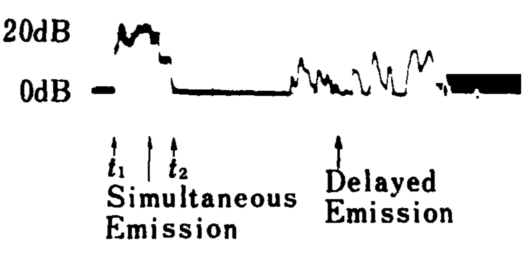

FIG. 2. Signal of the microwave emission at the second cyclotron harmonic from the plasma. The fre quency of the pumping wave is 5 times that of the cyc tron frequency and the pumping wave is applied from the time t_1 to the time t_2; 12.5 μsec/div.

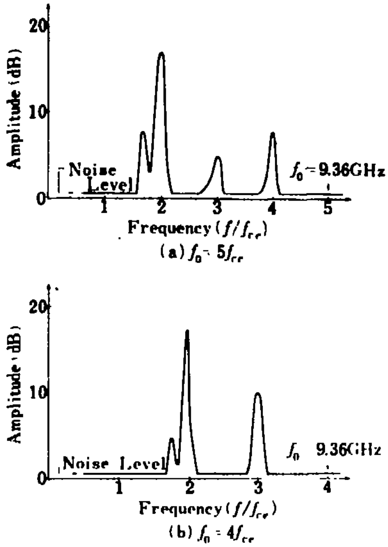

FIG. 3. Frequency spectrum of the delayed emission for (a) $f_0 \approx 5f_{ce}$, and (b) $f_0 = 4f_{ce}$.

he simultaneous emission that is observed durng the pumping time. First, the width of the resonance ($f_0 = nf_{ce}$) for simultaneous emission s very broad (15%), but the delayed emission requires a much more severe resonance condition; he magnetic field strength should be tuned within 3% of the resonant-field strength in order to obtain the delayed emission. Second, the delay emissions appear only when the pumping frequency is near the plasma frequency ($f_0 \simeq f_{pe}$), while the simultaneous emission increases as he plasma density is increased (Fig. 4). Third, he power of the simultaneous emission increases almost linearly with that of the pumping wave in the measurable microwave power region of our receiver, but for the delayed emission there exists a clear threshold level of the pumping wave power (5 kW). When the pumping power is increased above this critical level, the delayed emission appears and increases sharply. Fourth, the simultaneous emission does not change very much even when the mirror ratio of the magnetic field is varied. The delayed emission, however, decreases as the mirror ratio is decreased and does not appear at all in a straight magnetic field. This implies the existence of hot electrons heated by the pumping wave; these should play an important role in the delayed-emission mechanism. Diamagnetic-signal and x-ray observations also support this possibility, although the magnetic field strength at which the diamagnetic signal, the total amount of x-ray emission, and the power of simultaneous emission show their maximum values is slightly, but definitely, different from the magnetic field strength where the delayed emission appears. The electron heating at electron-cyclotron harmonics has been observed in a number of experiments[11,12] and it is reasonable to believe that the pumping microwave power is converted into the energy of hot electrons confined in the magnetic mirror field and by some triggering mechanism, the stored energy is abruptly released accompanying the delayed emission.

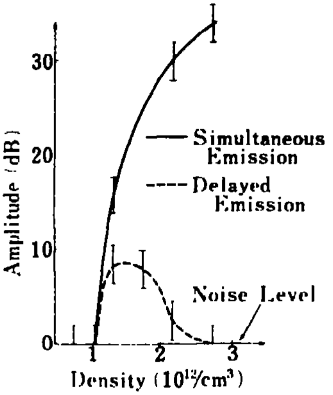

FIG. 4. Dependence of the delayed emission and simultaneous emission on the plasma density; $f_0 = 3f_{ce}$.

Although the relation between the delay time of the delayed emission and the experimental conditions is important in order to clarify its mechanism, no definite correlation has been observed within the present experimental accuracy and reproducibility. The polarization of the incident and emitted wave cannot be specified because our experimental apparatus is a multimode system due to the reflection from the metal wall.

Including the above problems a more detailed mechanism is now under investigation.

---

[1] C. F. Kennell, F. L. Scarf, R. W. Fredricks, J. H. McGehee, and F. V. Coroniti, J. Geophys. Res. 75, 6316 (1970).

[2] H. Oya, J. Geophys. Res. 75, 4279 (1970).

[3] S. Tanaka, R. Sugaya, and K. Mizuno, Phys. Lett. 28A, 650 (1969).

[4] R. A. Stern, Phys. Rev. Lett. 22, 767 (1969).

[5] M. Porkolab and R. P. H. Chang, Phys. Rev. Lett.

22, 826 (1969).

[6] H. Eubank, Phys. Fluids 14, 2551 (1971).

[7] H. Dreicer, C. Ingraham, and D. Henderson, Phys. Rev. Lett. 26, 1616 (1971).

[8] A. Y. Wong and R. J. Taylor, Phys. Rev. Lett. 27, 644 (1971).

[9] R. P. H. Chang, M. Porkolab, and B. Grek, Phys. Rev. Lett. 28, 206 (1972).

[10] M. Porkolab, Nucl. Fusion 12, 329 (1972).

[11] H. Ikegami, S. Aihara, and M. Hosokawa, Phys. Fluids 15, 2054 (1972).

[12] B. Grek and M. Porkolab, Plasma Physics Laboratory, Princeton University Report No. Matt-953, 1973 (unpublished).

Heating of a Fully Ionized Plasma Column by a Relativistic Electron Beam*

C. Ekdahl, M. Greenspan, R. E. Kribel,† J. Sethian, and C. B. Wharton
Laboratory of Plasma Studies, Cornell University, Ithaca, New York 14850

(Received 10 June 1974)

A magnetized plasma column ($n_p \approx 6\times10^{13}$ cm^{-3}) is heated by the injection of an intense relativistic electron beam along the magnetic field. The energy per electron-ion pair transferred to the plasma increases linearly with the beam-to-plasma density ratio n_b/n_p. The electron heating is attributed to the electron-electron beam-plasma interaction while the energetic ions are produced by an electrostatic acceleration. After heating, the plasma column oscillates radially at a frequency proportional to $B/n_p^{1/2}$.

Advances in electron-beam technology have made possible the production of very intense relativistic electron beams with power levels as high as 10^{13} W. With the capability of delivering several megajoules of energy in a time less than 100 nsec, these beams have several applications in fusion research. One of the more promising is in their use for rapid heating of plasma to thermonuclear termperatures. The coupling between relativistic electron beams and plasmas of thermonuclear interest via Coulomb collisions is rather weak, but collective interactions can result in very significant energy transfer. Two collective interactions are expected, the electron-electron two-stream instability[1] involving the high-energy beam electrons streaming through the plasma, and the electron-ion streaming instability driven by the induced return currents flowing within the beam.[2] There have been several experimental studies of plasma heating by relativistic electron beams in which significant heating has been observed,[3-7] but as yet the dominant heating mechanism has not been positively identified. Most of the experiments were complicated by the presence of wall effects, un-ionized gas, or uncertainties in beam or plasma parameters which made comparison with theory difficult.

In the experiments described here, the plasma column is fully ionized and confined in a hard vacuum ($p \leq 2\times10^{-6}$ Torr) away from the vacuum chamber walls. The relativistic electron beam is produced in a diode having a foil anode which isolates the diode from the plasma, thus decoupling the beam parameters from those of the plasma. The latter feature eliminates the ambiguity that existed in earlier experiments using foilless diodes.[6] Recent observations of very weak x-ray production and paramagnetic signals indicate that only a weak beam, if any, was present in the foilless diode experiments and the observed heating was due to plasma currents driven by large axial electric fields within the plasma column.[8]

The experiments have been performed on the Cornell turbulent heating machine (THM) modified by the addition of a relativistic electron-beam accelerator.[6] A plasmoid is injected into a magnetic mirror trap where a plasma column is formed having a length of 1.8 m, a mean diameter of 6–10 cm, and a density that can be varied from 10^{12} to 6×10^{13} cm^{-3} on axis. It is confined by a 2.6-kG magnetic field in a cylindrical vacuum chamber of 40 cm. The device has the capability of heating the plasma column by the axial injection of a relativistic electron beam and by the application of a large axial electric field which produces current-driven turbulent heating.[9] The beam heating experiments are the subject of this paper.

The electron-beam accelerator consists of a Marx generator driving a 5.8-Ω, water-filled, coaxial pulse line which feeds a diode. It is capable of producing an 80-kA pulse of 500-keV elec-

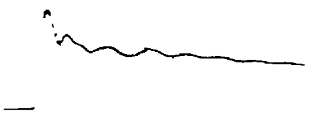

FIG. 1. Typical diamagnetic loop signal. Sweep speed is 200 nsec/(large) div.

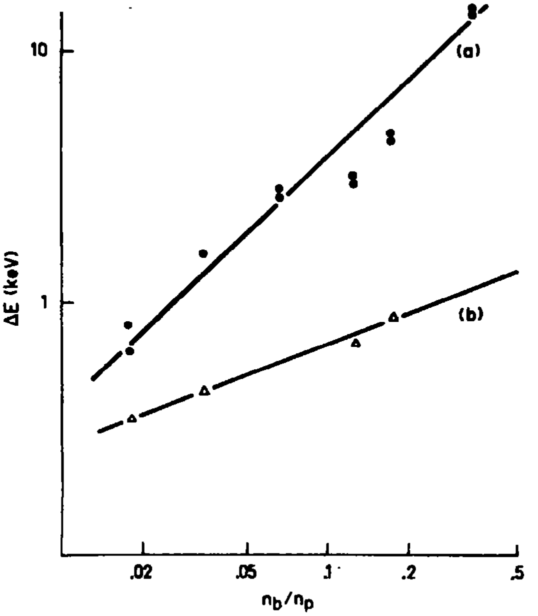

FIG. 2. The increase in net perpendicular energy per electron-ion pair (curve *a*) and perpendicular ion energy (curve *b*) versus the beam-to-plasma density ratio n_b/n_p. These data obtained by varying the plasma density with the beam parameters held fixed.

trons lasting 60 nsec; however, the beam currents in these experiments did not exceed 45 kA. The diode is located at the peak of the downstream magnetic mirror field and consists of a tungsten-coated aluminum cathode and a thin metal anode foil. Several foil thicknesses have been used, ranging from 12.5-μm aluminized Mylar to 50-μm titanium. In most of the experiments the initial beam diameter is 3 cm expanding to about 6 cm in the midplane of the trap. The plasma is monitored with 4- and 8-mm microwave interferometers, fast diamagnetic loops, capacitive wall probes, magnetic probes, charge-exchange neutral-energy analyzers, and x radiation from targets inserted into the plasma. The net plasma heating is determined from the diamagnetic loop output which measures the perpendicular energy transferred to the plasma. A typical oscilloscope trace of the diamagnetic loop output is shown in Fig. 1. The energy increase per electron-ion pair is shown in Fig. 2, curve *a*, as a function of the beam-to-plasma density ratio n_b/n_p. The dependence of the plasma heating on n_b/n_p is in agreement with observations in other heating experiments[4] and with the results of one-dimensional computer simulation of the relativistic electron-electron beam-plasma interaction.[10] In addition, the data in Fig. 3 show that there exists no threshold beam current for heating. Since magnetic probe observations show that the plasma column is at least 95% magnetically neutralized during the beam transit, these data also indicate that there is no threshold return current for heating in contrast to what has been observed in current-driven turbulent heating experiments. There currents in excess of 8 kA were required to produce significant heating.[11] Even when the plasma column was preheated by current-driven turbulent heating, no sharp threshold for beam heating was observed. Furthermore, the rate of plasma heating in the beam heating experiments is at least an order of magnitude greater than that observed in current-driven turbulent heating experiments on the same plasma column at comparable current levels. These observa-

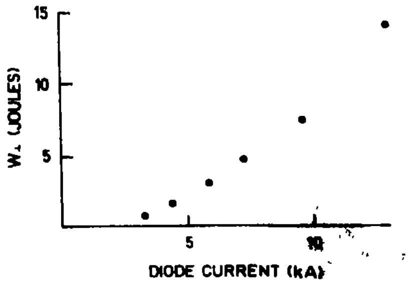

FIG. 3. The net perpendicular energy transferred to the plasma as a function of the diode current.

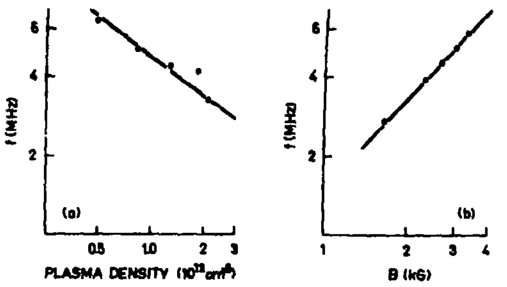

FIG. 4. Frequency of plasma column oscillations versus (a) plasma density and (b) magnetic field. The currents plotted in (a) and (b) are proportional to $n_p^{-1/2}$ and B, respectively.

tions indicate that the electron-electron two-stream interaction dominates the return-current interaction in these experiments. Under these circumstances most of the energy deposited in the plasma should show up in the electron distribution with little heating of ions. However, energy analyses of the charge-exchange neutrals escaping from the plasma column indicate that the ion energies, which are shown in Fig. 2, curve *b*, are comparable to the electron temperatures. It appears that ion heating occurs during a second stage after the electrons have been heated. The preferential electron heating results in the formation of positive plasma potentials of several kilovolts which have been observed with capacitive wall probes. The dominant radial electric field then accelerates the ions outward producing heating as the directed ion energies are randomized.[12]

The initial radial ion momentum leads to the excitation of $m = 0$ oscillations of the plasma column which are clearly evident on the signals from the diamagnetic loops (see Fig. 1). The frequencies observed are generally slightly greater than the ion-cyclotron frequency, i.e., $\Omega_i < \omega < 4\Omega_i$, where ω is the angular oscillation frequency and Ω_i is the ion-cyclotron frequency in the midplane. With the ordering of frequencies ($\Omega_i \ll \omega_{pi} \ll \Omega_e \ll \omega_{pe}$) which exists in the experiment, the angular frequency of radial oscillations for a magnetized plasma column is approximately[12, 13] $\omega \propto V_A$, where the proportionality constant depends on the relative magnitudes of $k_\parallel$ and $k_\perp$. Here Ω_e is the electron-cyclotron frequency in the midplane, ω_{pi} and ω_{pe} are the ion and electron plasma frequencies, respectively, $k_\parallel$ and $k_\perp$ are the components of the wave vector parallel and perpendicular to the magnetic field, V_A is the Alfvén velocity $V_A = B/(4\pi n_p M_i)^{1/2}$, and n_p is the plasma density. The observed oscillation frequencies, plotted in Fig. 4, indeed show the expected dependences on both the magnetic field and the plasma density. The radial oscillations damp out in less than 2 μsec indicating that the radial ion motion is being randomized on that time scale. A time-dependent angular analysis of the charge-exchange neutral flux escaping from the plasma verifies this most clearly at low plasma densities, where energetic ions are observed in the radial direction, i.e., 90° to the magnetic field, immediately after beam heating. However there is a time lag of ~2 μsec before the maximum flux of energetic ions is observed at an angle of 110°. The mechanism responsible for the ion scattering has not been identified.

The authors wish to acknowledge stimulating discussions with H. H. Fleischmann, R. Sudan, and K. R. Chu. The assistance of P. Brown in preparation for these experiments is also appreciated.

---

*Research supported in part by the U. S. Atomic Energy Commission and the Office of Naval Research.

†Permanent address: Department of Physics, Madison College, Harrisonburg, Va. 22801.

[1] L. I. Rudakov, Zh. Eksp. Teor. Fiz. 59, 2091 (1970) [Sov. Phys. JETP 32, 1134 (1971)].

[2] R. V. Lovelace and R. N. Sudan, Phys. Rev. Lett. 27, 1256 (1971).

[3] A. T. Altyntsev *et al.*, Pis'ma Zh. Eksp. Teor. Fiz. 13, 197 (1971) [JETP Lett. 13, 139 (1971)].

[4] C. A. Kapetanakos and D. A. Hammer, Appl. Phys. Lett. 23, 17 (1973).

[5] P. A. Miller and G. W. Kuswa, Phys. Rev. Lett. 30, 958 (1973).

[6] P. Korn, F. Sandel, and C. B. Wharton, Phys. Rev. Lett. 31, 579 (1973).

[7] G. C. Goldenbaum *et al.*, Phys. Rev. Lett. 32, 830 (1974).

[8] C. Ekdahl, M. Greenspan, R. E. Kribel, J. Sethian, and C. B. Wharton, to be published.

[9] T. H. Jensen and F. R. Scott, Phys. Fluids 11, 1809 (1968).

[10] L. E. Thode, Ph.D. thesis, Cornell University, 1973 (unpublished), Fig. 4.21; L. E. Thode and R. N. Sudan, to be published.

[11] S. Robertson *et al.*, IEEE Trans. Plasma Sci. 2, 17 (1963).

[12] K. R. Chu and M. Lampe, Bull. Amer. Phys. Soc. 19, 510 (1974).

[13] T. H. Stix, *The Theory of Plasma Waves* (McGraw-Hill, New York, 1962), p. 89.

Contribution to Sideband Instability Theory

M. N. Bussac, L. Mendonça, R. Pellat, and A. Roux
Centre de Physique Théorique de l'Ecole Polytechnique, 75230 Paris Cedex 05, France

(Received 29 January 1974)

The O'Neil trapping regime is known to take place only after a finite damping of the main wave. As a consequence of that finite damping, one obtains a beam-type distribution function for the detrapped particles. By including in the stability analysis this detailed distribution function, we give a new interpretation of the sideband generation.

The original observations by Wharton, Malmberg, and O'Neil[1] that satellite frequencies of a large-amplitude collisionless electron plasma wave are unstable were interpreted in terms of trapped-electron instability.[2,3] From that time, numerical simulations[4] and laboratory experiments[5-7] have made more precise the features of this instability. This instability is very sensitive to the time behavior of the main wave. It has been shown[8] that several regimes are possible according to the values of $|\gamma_L/\omega_{b_0}|$, where γ_L is the Landau damping rate and ω_{b_0} the initial electron bounce frequency: $\omega_{b_0}=k_0\{|e|\Phi_0/m_e\}^{1/2}$. Firstly, if $|\gamma_L/\omega_{b_0}|>1$, the main wave is Landau damped. Secondly, if $|\gamma_L/\omega_{b_0}|\ll 1$, the main-wave amplitude oscillates around a constant mean value (O'Neil's regime[9]). Lastly, if $0.2 \lesssim |\gamma_L/\omega_{b_0}| \lesssim 0.7$, the potential-wave amplitude decreases first and oscillates after a while, whereas one or three sidebands grow with frequencies approximately given by $\omega - kV_{\Phi_0} \simeq \pm\omega_{b_0}, 2\omega_{b_0}$. Here, V_{Φ_0} is the main-wave phase velocity. Measurements of the sideband growth rate[1,5,6] show that, depending on the initial-wave potential, one obtains $\gamma_s \propto \omega_{b_0}{}^n$ with $1 \leqslant n \leqslant 2.4$. Moreover, after the initial main-wave damping, the electron distribution function exhibits an accumulation of untrapped particles at the edge of the well.[4]

These experimental features suggest the following mechanism to explain the sideband instability. For simplicity, we restrict ourselves to the case $\mu = V_{\Phi_0}\omega_{b_0}/k_0 V_{Te}{}^2 < 1$ (V_{Te} is the electron thermal velocity), which enables us to neglect the nonlinear frequency shift.[10] Let us assume an initially Maxwellian plasma where a monochromatic wave is injected at $t=0$. During the first-half bounce period, trapped electrons with velocities $V < V_{\Phi_0}$ are accelerated by the wave electric field, whereas electrons with $V > V_{\Phi_0}$ are decelerated. If the damping rate is small compared to the bounce time, the net energy exchange between wave and particles tends to be null. Conversely, if these two scales are comparable, many of the accelerated particles are not reflected during the second-half bounce period, and they become a beam of detrapped particles. On the other hand, reflected particles lose kinetic energy to the wave, inducing a new rise of the main-wave amplitude. A lower-amplitude oscillatory regime takes place when the slope of the distribution function of the remaining trapped particles is small enough. Then the main effect of the wave damping is to give rise to a beam of detrapped particles, which we show to be responsible for the sideband instability.

Before proceeding with the stability analysis, we calculate the distribution function at the end of the damping stage. In order to be able to solve the particle equation of motion in the wave frame,

$$\frac{d^2x}{dt^2} = -\frac{|e|}{m_e}k_0\Phi(t)\sin(k_0x), \tag{1}$$

we choose a particular time dependence for $\Phi(t)$:

$$\frac{1}{\Omega^2(t)}\frac{\partial\Omega(t)}{\partial t} = 2\epsilon = \text{const}, \tag{2}$$

with

$$\Omega(t) = k_0[\,|e|\Phi(t)/m_e]^{1/2}.$$

Since in most experiments the oscillatory regime is reached after half a mean bounce period, we use Eq. (2) for $0 < t \leqslant \bar{T}/2$, where $\bar{T}/2$ is defined by $\pi = \int_0^{\bar{T}/2}\Omega(t)\,dt$. For $t > \bar{T}/2$, we assume a constant amplitude, $\Phi_1 = \Phi(\bar{T}/2)$. We have to assume $|\epsilon| < 1$, otherwise the wave will be completely damped before one trapping oscillation could take place. On the other hand, $|\epsilon|$ must not be too small, otherwise the time variation of the potential is adiabatic, and only a negligible number of particles are detrapped. The parameter ϵ will be determined from the energy balance.

First we consider Eq. (1) for $t < \bar{T}/2$. Setting $y = \int_0^t\Omega(t)\,dt$, we have to solve

$$\frac{d^2k_0x}{dy^2} + 2\epsilon\frac{dk_0x}{dy} + \sin k_0x = 0. \tag{3}$$

This is the equation of a pendulum with a negative friction term. It has been solved by Bogolioubov and Mitropolski.[11] Expanding $\sin k_0 x$, one shows that the solution which is obtained when retaining only the linear terms describes the motion of 95% of the initially trapped particles within an accuracy of better than 5%. Thus, in the following we use this approximation. If we set $\kappa^2 = 2|e|\Phi(t)/[W + |e|\Phi(t)]$, where W is the particle energy, we deduce, from Eq. (3), $\kappa_1^2 = \kappa^2(\overline{\tau}/2) = \kappa^2(0)\exp(2\epsilon\pi)$. For a stationary potential, one checks easily that $\kappa^2 < 1$ for untrapped particles and $\kappa^2 > 1$ for trapped particles. Here, because of the finite potential variation, we must distinguish three kinds of trajectories in the phase plane (x, V): (1) Particles with $\kappa_1^2 < e^{2\epsilon\pi}$ are always untrapped. For these particles we neglect the modulation of their velocity v in the wave frame. Thus their distribution function remains Maxwellian. (2) Particles with $\kappa_1^2 > 1$ remain trapped, and $v(\overline{\tau}/2) = -v(t=0)e^{\epsilon\pi}$. (3) Particles with $e^{2\epsilon\pi} < \kappa_1^2 < 1$ are trapped at $t = 0$, and untrapped at $t = \overline{\tau}/2$. Depending on their initial energy, these particles can suffer one or no reflection. For initially trapped particles, those having $e^{2\epsilon\pi} < \kappa_1^2 < e^{\epsilon\pi}$ are not reflected, whereas one reflection occurs for those with $e^{\epsilon\pi} < \kappa_1^2 < 1$. Then $v(\overline{\tau}/2) = -v(t=0)e^{\epsilon\pi}$ if $1 > \kappa_1^2 > e^{\epsilon\pi}$, and $v(\overline{\tau}/2) = v(t=0)e^{\epsilon\pi}$ if $e^{\epsilon\pi} > \kappa_1^2 > e^{2\epsilon\pi}$. Consequently the main wave energy absorption during the first-half bounce period is due to particles with $\kappa_1^2 > e^{\epsilon\pi}$, the distribution function of which exhibits an inverted slope at $t = \overline{\tau}/2$, as shown on Fig. 1(a). From the energy balance equation we evaluate the amplitude characteristic scale of variation, $\epsilon = \gamma_L/4\omega_{b0}$.

The time development of the sideband instability can be studied when the oscillatory regime is established (i.e., for $t \gg \overline{\tau}/2$). We use the same methods as Bud'ko, Karpman, and Shkylar.[3] As in Ref. 3, we find that for $\mu < 1$, the main contribution to the growth rate comes from the ergodic terms of the distribution function. But as a result of the detrapping process we have previously described, we get the ergodic distribution function shown on Fig. 1(b). As for $1 > \kappa^2 > e^{\epsilon\pi}$, the sign of the κ-dependent term is opposite to the one obtained in Ref. 3, and the instability soon occurs even for $\mu \ll 1$. Nevertheless, provided that the contribution of ergodic terms dominates, it is convenient to work in the asymptotic time regime. As long as $\Phi_1/\Phi_0 = \exp(\pi\gamma_L/\omega_{b0})$ is not too small, the energy of detrapped particles is sharply peaked $[(\Phi_1/\Phi_0)^{1/4} < \kappa^2 < 1]$. Then their distribution function may be regarded as identical to that of a beam and the hole from which the beam came,

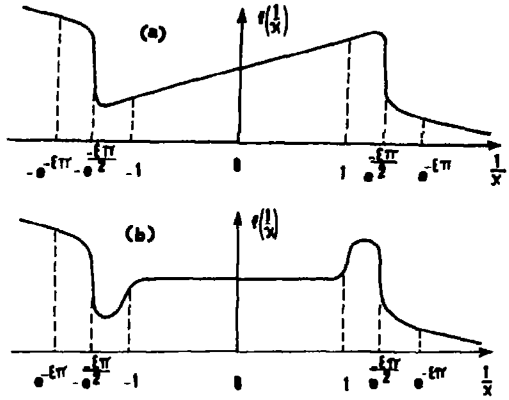

FIG. 1. Electron distribution in the wave frame as a function of κ^{-1} (κ having the sign of v). (a) At $t = \overline{\tau}/2$ the distribution exhibits an inverted slope compared to the initially Maxwellian function. (b) At $t = \infty$, the electrons exhibit a beam-type distribution function.

$$f_D = \pm \frac{\pi n_D \kappa^2 \sqrt{m_e}}{4K(\kappa)[|e|\Phi_1]^{1/2}} \delta(\kappa - \kappa_D), \tag{4}$$

where K is the complete elliptic integral and $2n_D$ is the number of detrapped particles,

$$\frac{n_D}{n_0} = \frac{2\omega_{b1}^2\omega_{b0}}{\omega_p^2\omega_0}\left(\frac{\gamma_L}{\omega_{b0}}\right)^2\left(\frac{\Phi_0}{\Phi_1}\right)^{1/4}. \tag{5}$$

Here $\omega_p^2 = 4\pi n_0 e^2/m_e$, ω_0 is the main wave frequency, and κ_D is given by the balance equation which reads, with our approximation, $|\kappa_D|K(\kappa_D) \simeq \frac{1}{2}\pi e^{\epsilon\pi/2}(-\epsilon\pi)^{-1/2}$.

Because of the spatial periodicity in the wave frame, all the Fourier components of the perturbed electric field $\tilde{E}(k + nk_0)$ are coupled together through the periodic modulation of the susceptibility.[12] In the laboratory frame the equation for $\tilde{E}(k, \omega)$ has the form

$$\sum_s [\mathscr{E}(k + sk_0, \omega + s\omega_0)\delta(l, s) + \chi_{l,s}]\tilde{E}(k + sk_0, \omega + s\omega_0) = 0, \tag{6}$$

where the fluid dispersion relation $\mathscr{E}(k, \omega) = 1 - \omega_p^2/(\omega^2 - 3k^2V_T^2)$ describes the initially untrapped particles, for which we kept only zeroth order terms in Φ_1.[12] The ergodic trapped-particle distribution function is independent of κ to the lowest order in μ. Then the only contribution to the susceptibility $\chi_{l,s}$ comes from detrapped particles. We retain the most important components of the field, $\tilde{E}(k, \omega)$ and $\tilde{E}(k-2k_0, \omega-2\omega_0)$. Limiting ourselves to terms up to second order in $q_D = \exp[-\pi K'(\kappa_D)/K(\kappa_D)]$ the susceptibilities $\chi_{l,s}$ read

$$\chi_{0,0} = -\chi_{-2,-2} = -\frac{\pi^2 E}{2K^3}\frac{\omega_D{}^2 k_0 U}{1-\kappa_D{}^2}(\omega - kV_{\Phi_0})A, \quad A = \frac{1-4q_D{}^2}{[(\omega-kV_{\Phi_0})^2 - k_0{}^2U^2]^2} + \frac{16q_D{}^2}{[(\omega-kV_{\Phi_0})^2 - 4k_0{}^2U^2]^2}, \tag{7}$$

$$\chi_{0,-2} = -\chi_{-2,0} = -\frac{\pi^2 E\omega_D{}^2 k_0 U(\omega - kV_{\Phi_0})}{2K^3(1-\kappa_D{}^2)}\frac{4q_D{}^2}{[(\omega-kV_{\Phi_0})^2 - k_0{}^2U^2]^2}, \tag{8}$$

where ω_D is the beam plasma frequency, $U = \pi\omega_{b1}/|\kappa_D|K(\kappa_D)k_0$ is the averaged velocity of the beam, and K and E are complete elliptic integrals. Setting $\omega = \omega_0 + \delta\omega$ and $k = k_0 + \delta k$, the dispersion equation is solved to the first order in q_D. The maximum growth rate is obtained for $\delta k = \pm k_0 U(V_{\Phi_0}/3V_T{}^2)$. In the laboratory frame

$$\begin{aligned} \gamma_{\Omega_b} &= \frac{\sqrt{3}}{2}\omega_{b0}\left\{\frac{E\pi^2}{8K^3}\frac{e^{3\epsilon\pi}}{1-\kappa_D{}^2}\left(\frac{\gamma_L}{\omega_{b0}}\right)^2\frac{\omega_p{}^2}{\omega_0{}^2}\right\}^{1/3}, \\ \omega - \omega_0 &= \pm\Omega_b = \pm\frac{k_0 U}{1 - V_{\Phi_0}{}^2/3V_T{}^2}\left\{1 - \tfrac{1}{2}\left[\frac{E\kappa_D{}^3 e^{-3\epsilon\pi}\omega_p{}^2}{8\pi(1-\kappa_D{}^2)\omega_0{}^2}\left(\frac{\gamma_L}{\omega_{b0}}\right)^2\right]^{1/3}\right\}. \end{aligned} \tag{9}$$

Retaining now the second-order terms in q_D, we find that sidebands with frequencies $\omega - \omega_0 \simeq \pm 2\Omega_b$ are destabilized. Since $\gamma_{2\Omega_b} = (2q_D{}^2)^{1/3}\gamma_{\Omega_b}$, they will be observed only if κ_D is not too far from unity. Let us now take into account the sideband amplitude coupling terms. Solving the set of equations (6), $\tilde{E}(k, \omega)$ and $\tilde{E}(k-2k_0, \omega-2\omega_0)$ are coupled through the second-order terms in q_D:

$$\tilde{E}(\omega_0 \pm \Omega_b, k) = \{-\chi_{0,-2}/[(\delta\mathcal{E})^2 + \chi_{0,-2}{}^2]^{1/2} \mp \delta\mathcal{E}\}\tilde{E}(k-2k_0, \pm\Omega_b - \omega_0),$$

where

$$\delta\mathcal{E} = [(\delta\omega)^2 - 3(\delta k)^2 V_{Te}{}^2]\omega_p{}^{-2}.$$

Then, in the laboratory frame, the red satellite has larger amplitude than the violet one, if $V_{\Phi_0}{}^2 > 3V_{Te}{}^2$, which is the usual experimental case. The ratio of $\tilde{E}(\omega_0 - \Omega_b, k_0)$ to $\tilde{E}(\omega_0 + \Omega_b, k_0)$ depends on q_D through $\chi_{0,-2}$. For very small values of q_D, $|\chi_{0,-2}| < |\delta\mathcal{E}|$ and $\tilde{E}(\omega_0 + \Omega_b) \ll \tilde{E}(\omega_0 - \Omega_b)$; while for $q_D < 1$, but not too small, $|\chi_{0,-2}| > |\delta\mathcal{E}|$ and $\tilde{E}(\omega_0 - \Omega_b) \sim \tilde{E}(\omega_0 + \Omega_b)$.

Collecting the previous results, three sidebands should appear if γ_L/ω_{b0} is small ($\kappa_D{}^2 \lesssim 1$). Conversely, if γ_L/ω_{b0} is large ($\kappa_D{}^2 \ll 1$), only one sideband should appear. In this case the beam is wider, thus explaining the broadening of the spectra when only one sideband is observed.[5] This regime is rather limited in γ_L/ω_{b0}, at least if we maintain $\mu \ll 1$. If $\mu \sim 1$, nonlocal damping effects and nonlinear frequency shift will occur.[10] Then there should be one enhanced beam with $\kappa_D{}^2 \ll 1$, inducing a large-amplitude unique sideband wave. This regime is the natural extension of the regime $\mu < 1$, $\kappa_D{}^2 < 1$, where only one sideband was found. Furthermore, when $\mu \sim 1$, one can expect that the sideband growth rate will not be proportional to $\Phi_0{}^{1/2}$.[6]

We gratefully acknowledge useful discussions with T. M. O'Neil and J. H. Malmberg.

---

[1] C. B. Wharton, J. M. Malmberg, and T. M. O'Neil, Phys. Fluids 11, 1761 (1968).

[2] W. L. Kruer, J. M. Dawson, and R. N. Sudan, Phys. Rev. Lett. 23, 838 (1969).

[3] N. I. Bud'ko, V. I. Karpman, and D. R. Shklyar, Zh. Eksp. Teor. Fiz. 61, 1463 (1971) [Sov. Phys. JETP 34, 778 (1972)].

[4] W. L. Kruer and J. M. Dawson, Phys. Fluids 13, 2747 (1970).

[5] R. N. Franklin, S. M. Hamberger, H. Ikezi, G. Lampis, and G. J. Smith, Phys. Rev. Lett. 28, 1114 (1972).

[6] G. Jahns and G. Van Hoven, Phys. Rev. Lett. 31, 436 (1973).

[7] C. B. Wharton, J. M. Malmberg, and T. M. O'Neil, private communication.

[8] R. N. Franklin, S. M. Hamberger, and G. J. Smith, Phys. Rev. Lett. 29, 914 (1972).

[9] T. M. O'Neil, Phys. Fluids 8, 2255 (1965).

[10] G. J. Morales and T. M. O'Neil, Phys. Rev. Lett. 28, 417 (1972).

[11] N. Bogolioubov and I. Mitropolski, *Les Méthodes Asymptotiques en Théorie des Oscillations Non Linéaire* (Gauthier-Villars, Paris, 1962).

[12] M. V. Goldman, Phys. Fluids 13, 1281 (1970).

Observation of the Coupled Mode of a Collisional Drift Wave and an Alfvén Wave

Yasushi Nishida
Department of Electrical Engineering, Utsunomiya University, Utsunomiya, Japan

and

Kazushige Ishii
Institute of Plasma Physics, Nagoya University, Nagoya, Japan

(Received 4 April 1974)

We observe a low-frequency instability with $\omega \ll \omega_{ci}$ in a steady high-density plasma $(n_0 \simeq 10^{13-14}\ \mathrm{cm}^{-3})$. This instability has components of magnetic field fluctuations as well as density fluctuations. By introducing the dispersion relation, the instability is interpreted as the coupled mode of the collisional drift wave and the Alfvén wave.

There have been many works on the collisional drift wave in rather low-density, low-β plasmas $(\beta \ll m/M)$, in which only an electrostatic mode is precisely considered.[1] In rather high-density plasmas with $1 \gg \beta \gg m/M$, however, the hydromagnetic mode must be taken into account as the electrostatic approximation breaks down. β is the ratio of the plasma pressure to the magnetic pressure, and m and M are the mass of an electron and an ion, respectively. Kadomtsev[2] has shown in a collisionless plasma the existence of the normal mode of the coupled Aflvén wave and collisionless drift wave, but no experimental verification has been reported. Woods[3] extended a theory on the current-convective instability presented by Kadomtsev[4] to that of the hydromagnetic wave, and has shown that the hydromagnetic mode is unstable if a radial resistivity gradient and/or a steady current along the magnetic field exists. But this mode is different from the drift-wave branch characterized in Refs. 1 or 2.

In the present Letter, we show that a low-frequency oscillation $(\omega \ll \omega_{ci})$ observed in a rather high-density, large-β $(1 \gg \beta \gg m/M)$ plasma without a current along the magnetic field may be interpreted as the coupled mode of the collisional drift wave and the Alfvén wave. The same kinds of experiments have been reported,[5,6] but all of them have not necessarily satisfied the large-β condition mentioned here, and no observation of the collisional drift wave in such a high-density plasma has been reported. But in fusion devices in which high-density high-temperature plasma is produced and in which β is high, the coupled collisional and Alfvén waves may be expected to be unstable, resulting in reduced confinement of the plasma by the magnetic field.

Experiments are performed on the "TPD-1" machine of Nagoya University.[7] A helium plasma, which is produced by an arc discharge of a maximum current of 100 A in a high–neutral-pressure region $(p \simeq 0.5\text{–}1$ Torr) under a strong magnetic field, diffuses into a low-pressure experimental region with weak magnetic field through an anode orifice (diameter 8 mm), and ends on the floating target electrode. So, the fully ionized, current-free plasma exists in the experimental region. The magnetic field B_0 in the experimental regio is varied up to 4.0 kG. The plasma density n_0 measured by a HCN laser[8] ranges from 10^{12} to $2 \times 10^{14}\ \mathrm{cm}^{-3}$ in the column center, with a background neutral pressure of $(6\text{–}7) \times 10^{-4}$ Torr. The plasma diameter is about 15 mm. Langmu probes are used for measuring plasma parameters. The electron temperature T_e is about 6– eV, and the temperature ratio $R = T_i/T_e$ is abou 0.5–1 depending on the discharge conditions, where T_i is an ion temperature.

Plasma profiles of the steady state and of flu tuations are measured by optical probes which are constructed with an optical guide and a phot multiplier. The optical guide has a collimating slit with a hole 2.0 mm and a length 42.3 mm. The optical signal detected is the He II (4686 Å) line. The fluctuating signals are analyzed by a real-time autocorrelator and cross correlator and a spectrum analyzer. The velocity of the plasma rotation around the axis is measured by the Doppler shift of the He II line.[9] Fluctuation of the magnetic field are detected by a water-cooled magnetic probe which, unfortunately, ca not be inserted into the center of the plasma co umn because the probe would melt, although th wave dominated region can be measured.

In the region where the radial density gradie

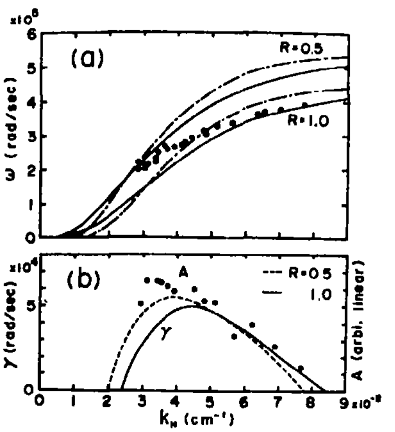

FIG. 1. (a) Dispersion relation of the collisional drift mode coupled with the Alfvén mode. Dot-dashed lines show the results for $D_0 = 0$ (see text). $k_\perp = 2.5$ cm^{-1}, $k_x = 1.5$ cm^{-1}, $k_y = 2.0$ cm^{-1}, $\lambda = 1.2$ cm^{-1}, $B_0 = 1.5$ kG, $n_0 = 3.0 \times 10^{13}$ cm^{-3}, and $T_e = 10$ eV. Closed circles show experimental results. (b) Growth rate γ as a function of parallel wave number for the collisional drift mode obtained from Eq. (1). Parameters are the same as in (a). Closed circles are the instability amplitude $A = n_1/n_0$ obtained experimentally.

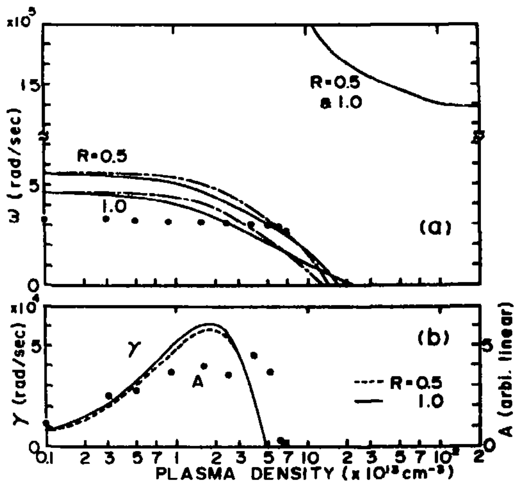

FIG. 2. (a) Frequency ω versus the plasma density. Solid lines are obtained from Eq. (1), and dot-dashed lines from $D_0 = 0$. Upper branch is the Alfvén branch and the lower ones are for the collisional drift mode. The parameters are the same as in Fig. 1 except with $k_\parallel = 0.05$ cm^{-1}. Closed circles are the experimental results. (b) Growth rate γ versus the plasma density calculated from Eq. (1) for lower-branch mode with the same parameters as in (a). Closed circles are the instability amplitude.

is maximum, 4–6 mm from the column center, there exists typically an ~50-kHz oscillation (f_1 mode) at the magnetic field intensity of 1.5 kG, while in the column center there exists an ~10-kHz oscillation (f_2 mode). Here, we are interested in the f_1 mode. The maximum relative density fluctuation of the f_1 mode is 10–15%. The variation of the frequency is measured as a function of the steady magnetic field intensity. The frequency of the instability increases almost linearly with the magnetic field strength till about 3 kG, but it becomes almost constant under stronger field. The amplitude becomes larger until $B_0 \simeq 1.8$ kG, and decreases gradually with increasing magnetic field strength, although the spectrum becomes broader.

The mode number in the azimuthal direction is found to be $m = 1$, from the cross-correlation measurement, and the wave travels in the direction of the electron diamagnetic velocity. A higher mode ($m = 2$) is also observed, but its amplitude is much smaller than the fundamental mode. The instability amplitude is also measured along the plasma column (z direction), and is found to e minimum near the anode and target electrodes, nd maximum near the middle of the column. The phase is constant over the whole of the plasma column length at fixed radial and azimuthal position. Thus, the half wavelength along the plasma column should be determined by the length between the anode and target electrodes. When the column length is made shorter, the frequency increases, while the instability amplitude decreases. An example of the dispersion relation is shown in Fig. 1, which is obtained by changing the plasma column length, after correcting for plasma rotation which will be mentioned later. In this example, the instability disappears at $k_\parallel \simeq 8.0 \times 10^{-2}$ cm^{-1} as seen in Fig. 1(b).

Steady-state plasma rotation has been observed,[9] and it has been found that the rotation angular velocity in the electron diamagnetic direction is constant at about $(4-5) \times 10^5$ cm/sec within 2.5–3 mm from the column axis at $B_0 = 4.0$ kG. Outside of this region where the wave amplitude is maximum, a small obscure rotation of the plasma column is observed [$(1-2) \times 10^5$ cm/sec].

When the discharge current I_d is changed from 10 to 100 A, the plasma density can change from 1×10^{12} to 2×10^{14} cm^{-3} in the column center. The *density is not necessarily proportional to the discharge current.* The present instability onsets at about $n_0 \gtrsim 3\times10^{12}$ cm^{-3} at $B_0=1.5$ kG, and the instability amplitude n_1/n_0 increases until $n_0 \simeq 4\times10^{13}$ cm^{-3}, as shown in Fig. 2(b). After that the amplitude decreases strongly, being extinguished at $n_0 \simeq 7\times10^{13}$ cm^{-3}. The instability frequency decreases monotonically from 53 to 42 kHz as the discharge current increases.

Fluctuations of the magnetic field are measured on the azimuthal B_θ and axial B_z components, as there is the possibility of hydromagnetic instability or of plasma rotation. An example of the results is shown in Fig. 3. We cannot measure the values in the plasma column center, because the water-cooled magnetic probe would melt and, further, it would disturb the plasma strongly. Figure 3 shows that both B_θ and B_r are larger than B_z, although B_θ is a little *larger than B_r. These facts are consistent* with the theoretical results, and indicate the existence of a nonelectrostatic instability.

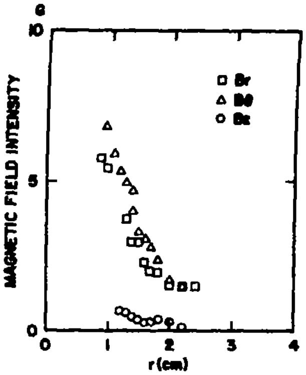

FIG. 3. Magnetic field fluctuations measured by the magnetic probe at $n_0 \simeq 4.5\times10^{13}$ cm^{-3} and $B_0=1.5$ kG.

The interpretation of this instability is based on the coupled mode of the collisional drift mode and the Alfvén mode. By starting with the ion and electron fluid equations with ion viscosities *across and electron collisions with ions along* the magnetic field, and without current, we obtain the dispersion relation[10]

$$D_0(k,\omega)+D_A(k,\omega)=0, \tag{1}$$

where

$$D_0(k,\omega)=i\frac{\Omega}{R}\,\omega^2-\frac{\Omega}{bR}\{\omega_\perp+[R+b(1+R)]\omega_\parallel+i\Omega\omega_*\}\,\omega+\frac{\Omega}{b}(\omega_\parallel-\omega_\perp)\omega_*-i\frac{\Omega}{b}\,\frac{1+R}{R}\,\omega_\parallel\omega_\perp,$$

$$\begin{aligned}D_A(k,\omega)=\omega^3&+\left[(R-1)\omega_*+i\left(\frac{\omega_\perp}{b}-\kappa\frac{1+R}{R}\,b\omega_{ci}\right)\right]\omega^2\\&+\left[-R\omega_*^2+\kappa\frac{1+R}{R}\,\omega_{ci}\omega_\perp+i\left(\frac{R-1}{b}\,\omega_*\omega_\perp+\kappa\frac{1+R}{R}(b+R)\omega_{ci}\omega_*\right)\right]\omega\\&-\kappa\frac{1+R}{R}\,\omega_{ci}\omega_\perp\omega_*-i\left(\frac{R}{b}\,\omega_\perp\omega_*^2+\kappa(1+R)\omega_{ci}\omega_*^2\right),\end{aligned}$$

$\kappa=k_\parallel(k_x-k_y)/k_\perp^2$, and $k_\perp^2=k_x^2+k_y^2$.

Here, we assume that the fluctuating electric field is nonelectrostatic, i.e., $\vec{E}=-\nabla\varphi-(1/c)\times(\partial A_z/\partial t)\cdot\hat{z}$, and $1\gg\beta\gg m/M$ and $\nabla n_0/n_0 \gg \nabla T/T$ are the experimental conditions. Further we assume $k_y, k_x \gg \lambda$, although in the experiments $k_x \not\gg \lambda$. φ is the scalar potential, $\vec{A}$ is the vector potential, $b=\rho_i^2k_\perp^2/2$, $\omega_\parallel=T_ek_\parallel^2/m\nu_{ei}$, $\omega_\perp=b^2\nu_{ii}/4$, $\omega_A=V_Ak_\parallel$, V_A is the Alfvén speed, $\lambda=-(\partial/\partial x)\ln n_0$, $\Omega=\omega_A^2b/\omega_\parallel$, and ω_* is the drift frequency caused by the density gradient. Other notations are standard. From the experimental results the effect of parallel motion of the ions and $\nabla T/T$ can be neglected, but strictly these should be taken into account.[11] If we use the electrostatic approximation, Eq. (1) reduces to the dispersion relation of the collisional drift wave obtained by Hendel *et al.*,[12] i.e., $D_0=0$.

Examples of numerical values of Eq. (1) are shown in Fig. 1 by the solid lines, which are obtained by the use of experimental parameters. In the same figure the results obtained from $D_0=0$ are also shown by the dot-dashed lines.

We further mention that the growth rate of this mode increases with density, to a maximum at about 2×10^{13} cm^{-3}, and decreases rapidly to become negative for $n_0 \geq 5\times10^{13}$ cm^{-3}. The calculated frequency is almost constant for $n_0 \leq 1\times10^{13}$ cm^{-3} and decreases for densities above this value. These characteristics agree with those observed experimentally as also shown in Fig. 2. Little differences between the theory and experiments may depend on the fact that the plasma density in the experiments is taken for the values in the column center. The lower branch of Reω in Fig. 2(a) seems not to be a pure collisional drift mode but a mode coupled with the Alfvén mode, and the upper one is the Alfvén mode modified by the collisional drift mode. The Alfvén mode always damps in the present conditions.

In conclusion, the unstable mode of the collisional drift wave coupled with the Alfvén mode would be observed in a steady high-density plasma with $1 \gg \beta \gg m/M$, although the Alfvén mode is not unstable in under these conditions. In a large-β plasma with an axial current both the Alfvén and the collisional drift modes may be unstable,[3] resulting in reduced confinement of the plasma by the magnetic field. More precise experiments on coexcitation and control of these modes are now in progress.

The authors are grateful to Mr. A. Ogata for his measurement of cross-correlation and autocorrelation of the instability. They are also grateful to Mr. Y. Edano for his kind help in the numerical computations. One of the authors (Y.N.) is indebted to Professor S. Kawamata of Utsunomiya University for his continuous encouragements, and Professor F. F. Chen of the University of California, Los Angeles, for his discussions.

This work was performed under the Collaborating Research Program of the Institute of Plasma Physics, Nagoya University.

---

[1] See, for example, *Methods of Experimental Physics*, edited by H. A. Griem and P. H. Lovberg (Academic, New York, 1970), Vol. 9, Pt. A, p. 345.

[2] B. B. Kadomtsev, *Plasma Turbulence* (Academic, London, 1965), p. 79.

[3] L. C. Woods, Phys. Fluids 6, 729 (1963).

[4] B. B. Kadomtsev, Zh. Tekh. Fiz. 31, 1209 (1961) [Sov. Phys. Tech. Phys. 6, 882 (1962)].

[5] Y. Tanaka, Annual Review of the Institute of Plasma Physics, Nagoya University, 1964–1965 (unpublished).

[6] A. Malein, Nucl. Fusion 5, 352 (1965).

[7] K. Takayama, M. Otsuka, Y. Tanaka, K. Ishii, and Y. Kubota, in *Proceedings of the Eighth International Conference on Phenomena in Ionized Gases, Vienna, 1967* (Springer, Berlin, 1967), p. 551.

[8] A. Nishizawa, private communication; S. Kon, M. Otsuka, M. Yamanaka, and H. Yoshinaga, Jpn. J. Appl. Phys. 7, 433 (1968).

[9] M. Otsuka, private communication.

[10] The dispersion relation has the form $(\omega-\omega_*+i\Omega/R)\times(\omega^3+a\omega^2+b\omega+c)=0$, where a, b, and c are the complex coefficients. The formulation in the second set of parantheses can be rewritten as in Eq. (1).

[11] L. G. Schlitt and H. W. Hendel, Phys. Fluids 15, 1578 (1972).

[12] H. W. Hendel, T. K. Chu, and P. A. Politzer, Phys. Fluids 11, 2426 (1968).

Magnetic Compression of Intense Ion Rings*

R. N. Sudan and Edward Ott
Laboratory of Plasma Studies, Cornell University, Ithaca, New York 14850
(Received 10 June 1974)

It is shown how Lawson criterion for controlled fusion might be achieved by magnetic compression of intense ion rings to field reversal.

It is well known that Astron E layers[1] consisting f relativistic electrons are not practical as a ısion-reactor concept because at the required lectron energy (>100 MeV) and magnetic fields ıe synchrotron radiation is prohibitive. This retriction does not apply to the use of protons or eavier ions as pointed out by Christofilos. Given a sufficiently powerful ion source intense ion ings could be created by exploiting the injection ɜchniques successfully used for electron rings.[2] The possibility of producing intense ion beams by modern high-power electrical pulse technology has been suggested.[3] Indeed Humphries, Lee, and Sudan[4] have recently reported 50-nsec proton pulses of 500 A at 100 kV and 5000 A at 300 kV at current density ~10 A/cm^2 from a triode configuration in which the net electron current was suppressed by a factor of 20–30. With the advent of these powerful ion sources the possibility of creating ion rings intense enough to cause the reversal of magnetic field in the ring and thus provide ideal magnetohydrodynamic stability for a confined thermonuclear plasma deserves serious attention. By increasing the axial magnetic field an ion ring can be compressed in both its major and minor radii, thus increasing the circulating current and ion energy. Furthermore since protons are practically nonrelativistic at energies up to a few hundred MeV the field reversal factor $\alpha \equiv B^s/B$ increases with compression; B is the axial Z component of the external magnetic field and B^s is the magnitude of the self-field at the surface of the ring. This is a significant point because an ion ring which at injection misses field reversal ($\alpha = 1$) by a large factor can by subsequent compression reach field reversal.[5] In what follows we discuss the dynamics of such an adiabatic compression of an ion ring and the subsequent plasma heating by the beam.

Ion beams are observed to emerge electrostatically neutralized[4] from the ion source by dragging along an equivalent number of electrons. We will therefore assume that an ion ring of major and minor radii R and r, respectively,[6] is electrostatically neutral, i.e., $Zn = n_e$ where n and n_e are beam and electron densities and Ze is the ion charge. The external field is pulsed to increase from B_0 to its final value B_1 in a time t_c and it is maintained at this level for a period t_d. For adiabatic compression the azimuthal momentum balance and radial force balance for a nonrelativistic ion ring are given by

$$\dot{u}_\varphi + \ddot{R}_\varphi = -\frac{Ze}{mcR}\frac{d}{dt}(RA_\varphi)$$

$$= -\frac{Ze}{mc2\pi R}\frac{d}{dt}[\pi R^2 B + L(I + I_e)], \qquad (1)$$

$$\frac{-u_\varphi^2}{R} = \frac{Ze}{m}\{E_r + \frac{1}{c}\langle u_\varphi(B + B_z^s)\rangle\}, \qquad (2)$$

where

$$\langle u_\varphi B_z^s\rangle \equiv (\pi r^2)^{-1}\int d^2s\, u_\varphi \frac{d}{\rho d\rho}(\rho A_\varphi)$$

$$\approx u_\varphi L(I + Ie)/2\pi R^2 \qquad (2a)$$

for $r \ll R$; the integral is over the cross section of the ring and u_φ is assumed approximately constant over this cross section, the ring inductance $L = (4\pi/c)R\{\ln(8R/r) - \frac{7}{4}\} \equiv Rl$, $I = ZNeu_\varphi/2\pi R$ is the beam current, N is the total number of beam ions, $I_e = -ZNev_\varphi/2\pi R$ is the electron current, and E_r is the radial polarization field. It is reasonable to assume that $L/\mathfrak{R} \gg t_c$ (compression time) where the ring resistance $\mathfrak{R} = 2R/\sigma r^2$, $\sigma = n_e e^2 \tau_{eb}/m_e$, and τ_{eb} is the momentum exchange time between the electrons and the beam ions. In this case the electron equation is simply $\vec{E} + \langle\vec{v} \times(\vec{B} + \vec{B}^s)\rangle/c = 0$. The electrons drift radially inwards with the beam and the φ and r components of the electron equation furnish

$$E_r + \langle v_\varphi(B + B_z^s)\rangle/c = 0, \qquad (3)$$

$$E_\varphi - \dot{R}(B + B_z^s)/c = 0. \qquad (4)$$

Equation (4) states that the azimuthal electric field in the frame moving radially inwards with the beam vanishes which ensures that the flux linked by the ring [see Eq. (1)] remains constant, i.e.,

$$\pi R^2 B + L(I + I_e) = \Phi_0 \equiv \pi R_0^2 B_0 + L_0 I_0. \qquad (5)$$

The electron current is taken to vanish in the initial state. From Eqs. (1) and (4) we obtain

$$R u_\varphi = R_0 u_0, \qquad (6)$$

$$R^2 I = R_0^2 I_0. \qquad (7)$$

Substituting for E_r in Eq. (2) from (3) and taking the averages in the sense of (2a) we obtain[7]

$$R = -\frac{u_\varphi}{\Omega}\frac{(1 + W/K)}{(1 + I_e/I)} \qquad (8)$$

with $\Omega = ZeB/mc$; $W = (1/2c)L(I + I_e)^2$ and $K = \frac{1}{2}Nmu_\varphi^2$ are the beam self-magnetic and kinetic energies, respectively. Equations (5), (7), and (8) completely define the problem of beam compression. It is possible to show that R/R_0 scales as $(B_0/B)^{1/2}$ for low compression and as $(B_0/B)^{2/5}$ for large compression. Combining Eqs. (6) and (7) we find that the external flux linked by the ring varies as

$$R^2 B = R_0^2 B_0 (1 + W/K)[(1 + W_0/K_0)(1 + I_e/I)]^{-1}. \qquad (9)$$

It can be readily checked by appealing to the principle of adiabatic compression that the minor radius also shrinks such that the aspect ratio scales as

$$(r/R) = (r_0/R_0)(1 + I_e/I)^{-1}. \qquad (10)$$

The field reversal factor $\alpha = 2(I + I_e)/crB$ scales as

$$\alpha/\alpha_0 = (1 + I_e/I)^2 R_0^3 B_0/R^3 B. \qquad (11)$$

Notice also that,

$$W/K = (1 + I_e/I)^2 N Z^2 e^2 l/(2\pi)^2 mRc$$

$$\approx (R_0/R)(W_0/K_0)(1 + I_e/I)^2, \qquad (12)$$

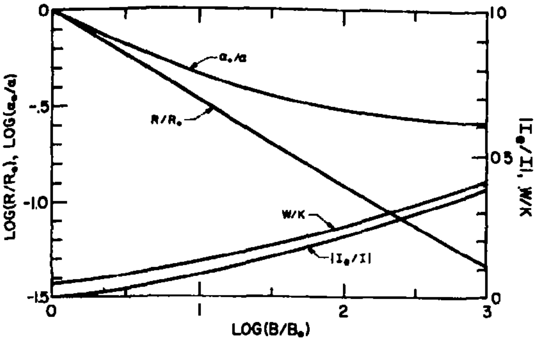

FIG. 1. Variation of R/R_0, $|I_e/I|$, W/K, and α_0/α with B/B_0, for $W_0/K_0=0.05$; note that I_e is actually negative, i.e., it opposes the beam current.

since $l \equiv L/R$ is relatively insensitive to changes in the aspect ratio. Figure 1 shows the variation of R/R_0, I_e/I, W/K, α/α_0 with B/B_0 from a numerical solution of Eqs. (5), (6), and (8).

Towards the end of the compression phase the plasma is created in the ring possibly by the introduction of a pellet which is rapidly ionized. The electron current decays quickly because of the high resistivity of the low-temperature plasma,[8] which results in a shrinkage of the minor radius and an increase in the field-reversal factor. The beam delivers energy to the plasma electrons and, since the beam ion velocity is much greater than the electron thermal speed, the heating time is given by the characteristic slowing down time of the ions,[9] viz., $\tau_s=0.63\times10^{11}(m/m_{pr})W^{3/2}/n_p$ sec, where W is the ion energy in MeV, m_{pr} is the proton mass, and n_p is the density of the plasma electrons in cm^{-3}. The beam ion deflection time $\tau_d\approx(m/m_e)\tau_s$ so that there is no significant scattering of the beam during this heating period. As the plasma heats up to keV temperatures its resistivity drops rapidly and $L/\mathfrak{R}\gg\tau_s$. In this stage the flux linking the ring is again conserved but the canonical azimuthal momentum is not. Introducing the slowng down time τ_s in Eq. (1) yields

$$Ru_\varphi=R_1u_1(1-3t/\tau_{s1})^{1/3}, \tag{13}$$

where the subscript 1 denotes quantities at the beginning of the heating stage. The mechanical momentum of the beam is picked up by the plasma ions since $(d/dt)(Nmu_\varphi+N_im_iu_i)=0$. For $N_i\gg N$ the bulk of the beam energy is transferred o the thermal energy of plasma electrons which eventually equilibrates with the ion thermal energy. As the beam slows down the major radius R does not shrink to zero because the flux will now be sustained by an induced plasma current. The asymptotic limit of this radius obtained from Eqs. (8) and (13) and flux conservation is

$$R_2=R_1|1-W_1/K_1|^{1/2}/(1+W_1/K_1)^{1/2}. \tag{14}$$

The number of beam ions needed for $\alpha=1$, i.e., for creating closed lines of force in the ring is easily computed to be

$$NZ^2e^2/mc^2\approx\pi r/[1-1.4r/R],\ \text{for } r/R\sim\tfrac{1}{3}. \tag{15}$$

To achieve Lawson condition the following additional requirements have to be satisfied:

$$n\tau=10^{14}$$

(Lawson criterion),

$$2nT=(B^*)^2/8\pi$$

(plasma pressure balance),

$$NE>2\pi^2r^2RnT$$

(heating energy requirement),

$$n\tau=2.5\times10^{13}I^2T^{1/2}$$

(pseudoclassical diffusion),[10] where I is in MA, E is the ion energy at the end of the compression stage, and n and T are plasma density and temperature, respectively. Assume that by the injection of a 10^{-7} sec, 150-kA pulse of 5-MeV protons containing $N\sim10^{17}$ ions, a ring with initial parameters $I_0=125$ kA, $r_0=20$ cm, $R_0=60$ cm, $\alpha_0=0.226$ in a field $B_0=5.5$ kG and with $W/K=0.08$ is created. A compression in radius by a factor of 10 results in the following final ring parameters (after decay of the electron current induced in the compression phase): $E\sim500$ MeV, $I\sim10^7$ A, $r=2$ cm, $R=6$ cm, $W/K\sim0.80$, $B\sim0.55$ MG, $\alpha=2.26$. A plasma density $\sim10^{16}$ cm^{-3} at 10 keV can be confined in such a ring, $\tau_s\lesssim10^{-3}$ sec, and the confinement time obtained from the pseudoclassical diffusion formula far exceeds the Lawson time. The stability of such an ion ring to the equivalent of the Kruskal-Shafranov mode looks good because of the stabilization provided by the axial magnetic field B through the finite ion gyroradius effects. The optimization of such a scheme, the stability of the plasma loaded ion ring, and the role of microinstabilities if any will be discussed in a more detailed publication. However, it is noteworthy that since almost all of the beam energy is provided by magnetic compression the efficiency of the ion source is not a serious consideration. One technique available for compression to megagauss fields is to adopt the approach of magnetically imploding a cylindrical metallic liner, the so called LINUS concept.[11] Static, spatially varying, magnetic fields can also be considered for compression.[12]

Finally, we wish to state that the possibility of delivering the compressed ring energy to a DT pellet is available to achieve fusion by pellet compression as in electron-beam or laser fusion.[13] However, the following must be kept in mind: (a) The ring would have to be accelerated axially to impact the pellet in a time of a few nanoseconds (moving the pellet into a stationary ring would probably require unrealistically large pellet velocities). (b) Suitable high-Z, stripped, ring ions with appropriate stopping lengths with respect to the pellet size would be required.[14]

We wish to acknowledge the help of Dr. R. L. Ferch in computing the curves of Fig. 1 and interesting discussions with Dr. R. V. Lovelace, Dr. S. Humphreys, Jr., Dr. H. P. Furth, and Dr. M. N. Rosenbluth.

---

*Work supported by the U. S. Office of Naval Research under Contract No. NOOO-4-67-A-0077-0025 and the U. S. Atomic Energy Commission under Contract No. AT(11-1)3170.

[1] N. Christofilos, in *Proceedings of the Second United Nations International Conference on the Peaceful Uses of Atomic Energy, Geneva, 1958* (United Nations, Geneva, Switzerland, 1958), Vol. 32, p. 279.

[2] M. L. Andrews, H. Davitian, H. H. Fleischmann, R. E. Kribel, B. R. Kusse, J. A. Nation, R. Lee, R. V. Lovelace, and R. N. Sudan, in *Proceedings of the Fourth International Conference on Plasma Physics and Controlled Nuclear Fusion Research, Madison, Wisconsin, 1971* (International Atomic Energy Agency, Vienna, 1972), Vol. 1, p. 169; M. Friedman, Phys. Rev. Lett. 24, 1092 (1970).

[3] R. N. Sudan and R. L. Lovelace, Phys. Rev. Lett. 31, 1482 (1973); F. Winterberg, Phys. Rev. 174, 212 (1968).

[4] S. Humphries, J. J. Lee, and R. N. Sudan, Bull. Amer. Phys. Soc. 19, 510 (1974), and Appl. Phys. Lett. 25, 20 (1974).

[5] This is in sharp contrast to the compression of relativistic electrons in which the field reversal factor remains constant because the electron velocity is practically constant $\sim c$: A. W. Trivelpiece, R. E. Pechacek, and C. A. Kapetanakos, Phys. Rev. Lett. 21, 1436 (1968); A. Sessler, University of California, Berkeley, Report No. UCRL-18013, 1968 (unpublished); G. Schmidt, Phys. Rev. Lett. 26, 952 (1971).

[6] Although Christofilos assumed that a field-reversed "E layer" would be a long annular cylindrical layer it was pointed out by E. Ott and R. N. Sudan [Phys. Fluids 14, 1226 (1971)] that the situation is more likely to resemble a fat doughnut or ring because of the self-fields. This is confirmed in the experiments of Ref. 2.

[7] This expression is similar to G. I. Budker's expression {At. Energ. 1, No. 5, 9 (1956) [Sov. At. Energy 1, 673 (1956)]} and that obtained in Ref. 6 by more elaborate arguments for relativistic electrons; see also J. D. Lawson, "Equilibrium Radius of a Ring Current in an External Magnetic Field Comparison of Published Calculations," Rutherford High Energy Laboratory, Didcot, England, Report No. RHEL/M/A4, 1971 (unpublished).

[8] The decay time of the electron current compared to the heating time $L/\Re\tau_e \approx 5\times10^{-8}(\omega_e r/c)^2(T_e/W)^{3/2}$, where the electron temperature T_e is in eV and W the ion energy is in MeV; ω_e is the plasma frequency.

[9] L. Spitzer, *Physics of Fully Ionized Gases* (Interscience, New York, 1956).

[10] S. Yoshikawa and N. C. Christofilos, in *Proceedings of the Fourth International Conference on Plasma Physics and Controlled Nuclear Fusion Research, Madison, Wisconsin, 1971* (International Atomic Energy Agency, Vienna, 1972), Vol. 2, p. 357.

[11] E. Velikhov, private communication; J. Boris and R. Shanny, in *Proceedings of the Fifth European Conference on Plasma Physics and Controlled Fusion, Grenoble, France, 1971* (Service d'Ionique Générale, Association EURATOM–Commissariat à l'Energie Atomique, Centre d'Etudes Nucléaires de Grenoble, Grenoble, France, 1972), Paper 20; A. E. Robson, "The Flying Cusp: A Compact Pulsed Fusion System," U. S. Naval Research Office, Washington, D. C., Report No. 2692, 1973 (unpublished).

[12] H. P. Furth and M. N. Rosenbluth, "Static Field Acceleration of Electron Rings," University of California, Berkeley, Report No. UCRL-18013, 1968 (unpublished), p. 210.

[13] L. I. Rudakov and A. Samarsky, in *Proceedings of the Sixth European Conference on Plasma Physics and Controlled Fusion Research, Moscow, U.S.S.R., 1973* (U.S.S.R. Academy of Sciences, Moscow, 1973), p. 487; G. Yonas, J. W. Poukey, J. R. Freeman, K. R. Prestwich, A. J. Toepfer, M. J. Clauser, and E. H. Beckner, *ibid.*, p. 483.

[14] This topic will be elaborated upon in a future publication.

Observation of Large Electron-Hole Drops in Germanium*

Bernard J. Feldman
Department of Physics, University of California, Berkeley, California 94720

(Received 25 March 1974)

This Letter reports the first direct observation of electron-hole drops (EHD) in germanium. An intense, focused laser beam creates a single, large EHD, whose shape and size are determined by the spatial distribution of its luminescence. The observed drops are spherical in shape with radii that increase from 0.25 mm to over 1 mm with increasing laser power. These results confirm size measurements of the EHD by recent decay-kinetics and dimensional-resonance studies.

This Letter reports the first direct observation of electron-hole drops (EHD) in germanium. An intense, focused laser beam creates a single, large EHD, whose size and shape are determined by the spatial distribution of its luminescence. The observed drops are spherical in shape with radii that increase from 0.25 mm to over 1 mm with increasing laser power. Previously, the drop size was inferred by Rayleigh scattering,[1,2] charge pulses in p-n junctions,[3,4] far-infrared absorption,[5] and cyclotron resonance[6]; these experiments gave drop radii from 1 to 20 μm. Very recently, decay-kinetics[7] and dimensional-resonance[8] studies suggested the existence of large EHD radii of the order of 0.2 mm; those latest drop-size measurements are confirmed by this work.

The experimental procedure consists of the following[9]: A 2-W Ar-Kr ion laser beam is focused onto the germanium samples by a lens mounted on an x-y micrometer translator. The two samples used are 2.5-cm-diam disks with thicknesses d of 0.5 and 1.0 mm of very high-purity p-type Ge[10] which are optically polished and etched in a CP-4 solution. The crystals are mounted on an aluminum flange with a 0.15-mm-thick vertical slot (see Fig. 1), and then immersed in liquid He in an optical cryostat. The EHD recombination luminescence (709 meV) that passes through the slot is collected and focused onto the entrance slit of a monochromator, and then collected from the monochromator exit slit and focused onto a Ge photodetector, in an arrangement similar to that previously reported.[11]

The theory behind this experiment is very straightforward. The translating lens moves the focused laser beam—and with it the one large EHD—across the vertical slot. If the drop radius is much greater than the slot width, the EHD luminescence through the slot, I, is proportional to the cross-sectional area of the drop subtended by the slot (see Fig. 1). For a spherical drop of radius R and a lens position x, measured from the center of the slot, $I(x) \propto R^2 - x^2$ for $|x| \leq R$, and $I(x) = 0$ for $|x| > R$. The volume of the drop, V, is proportional to $\int_{-\infty}^{\infty} I(x)\,dx$, and the cross-

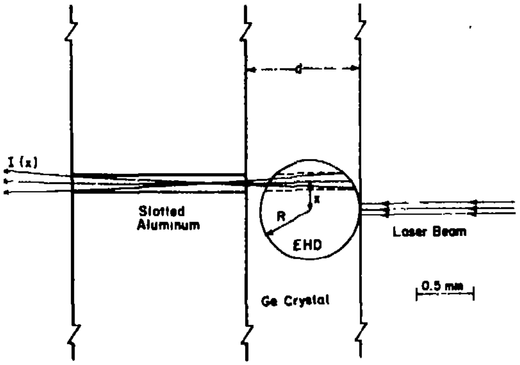

FIG. 1. Schematic diagram of the Ge sample and ample holder showing the optical geometry of the xperiment.

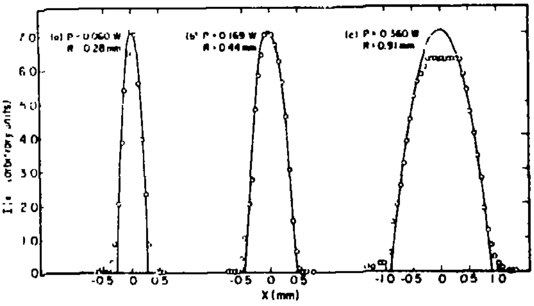

FIG. 2. The luminescence intensity I as a function of the lens position x for three laser powers P. The circles are the experimental points; the solid line is the theory $I(x) \propto R^2 - x^2$. The sample temperature is 2.0°K and the sample thickness is 1 mm.

sectional area of the drop, A, is proportional to $I(x=0)$.

A typical spectrum of $I(x)$ is shown in Fig. 2(a). *The circles are the experimental points, and the solid line is just the function R^2-x^2, with $R=0.28$ mm chosen for the best fit to the data.* Even without a slit function folded into the theory, the agreement between theory and experiment is excellent.

As the laser power P is increased,[12] the drop radius increases as shown in Figs. 2(b) and 2(c). A plot of $R(P)$ for the $d=1$-mm sample is given in Fig. 3, which also includes the experimental values of $V^{1/3}(P)$ and $A^{1/2}(P)$. The fact that $R(P)$, $A^{1/2}(P)$, and $V^{1/3}(P)$ have the same dependence on P, namely $P^{0.4\pm0.1}$, is further evidence that the drop is spherical.

The interesting behavior of $I(x)$, R, and $A^{1/2}$ at high values of P is due to the fact that the drop diameter becomes greater than the sample thickness. Then the EHD growth is limited by the sample surfaces in one direction and expands in the other two dimensions; the drop keeps its density fixed and starts to resemble a pancake. The flattening of the peak of $I(x)$ in Fig. 2(c) is just the flattening of the pancake. The relative decrease in $A^{1/2}$ and increase in R in Fig. 3 correspond to the bounded growth of the drop in one dimension and the increased expansion in the other two. Notice that the divergence in $A^{1/2}(P)$ and $R(P)$ starts approximately at $R=0.5$ mm, one half of the sample thickness. In the $d=0.5$-mm sample, this behavior starts at $R=0.25$ mm.

The free-exciton (FE) luminescence (714 meV) is unobservable at 2.0°K because the FE equilibrium concentration is so low at that temperature.[11] *However, at 4.2°K both the FE and EHD luminescence are observed as shown in Fig. 4.* The spatial distribution of the FE has an exponential behavior characteristic of a diffusion process and is in sharp contrast to that observed for the EHD.

These experimental results are inconsistent with the idea of a gas of small EHD. The spatial distribution of such a gas would follow that of the FE gas, namely exponential in shape and relatively insensitive to P. This model cannot explain the observed spherical distribution, its expansion with increasing P, and its interaction with the back surface of the crystal. All these results strongly suggest the existence of one large, spherical EHD.

There is one primary reason why such large single drops are created in this experiment: An intense laser beam of the order of 0.1 W that is

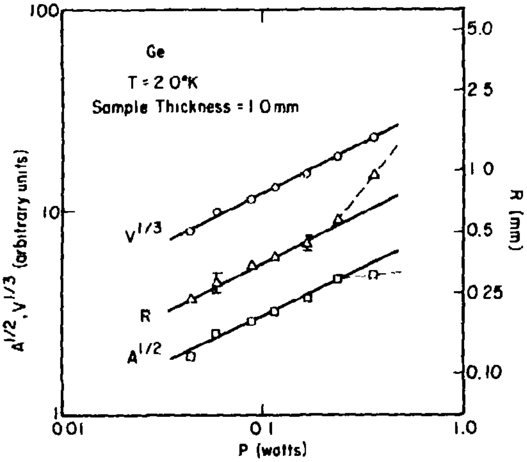

FIG. 3. The experimental values of the EHD radius R, area A, and volume V as a function of the incident laser power P.

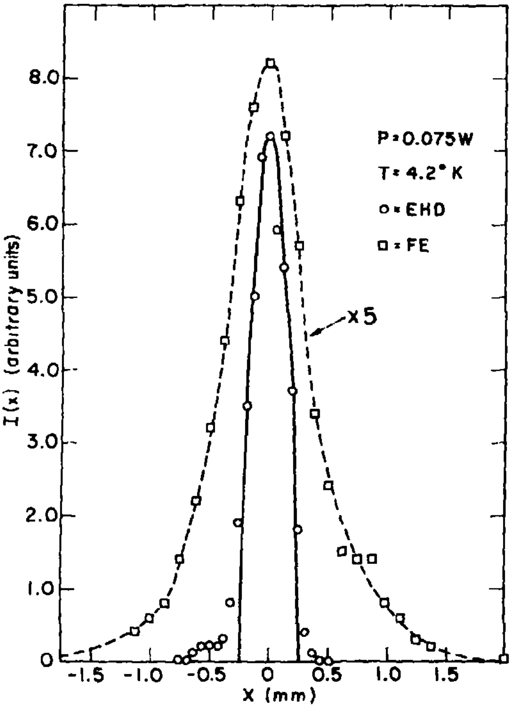

FIG. 4. The FE and EHD luminescence intensity I as a function of the lens position x. The solid line is the EHD line-shape theory with $R=0.25$ mm.

ell focused to a spot size of about 0.1 mm ×0.1
m creates an extremely high and localized con-
entration of free excitons that can condense into
e large drop. Many of the previous experi-
enters[1-6] that measured much smaller drop
izes worked with lower light intensities and
rger spot sizes which could create many small
rops instead of one large drop.

There is one serious problem with this large
HD model: The maximum drop radius calcu-
ted from knowing the incident laser power[13] is
pproximately one half of that measured by fitting
x). There are a number of possible explana-
ons for this disagreement: (1) an underestima-
on of the laser power or its electron-hole con-
rsion efficiency; (2) an overestimation of the
op radius; (3) the existence of voids inside the
HD occupied by free excitons; (4) an enhance-
ent of the EHD lifetime for such large drops;
(5) some combination of the above. This ques-
on is being presently investigated.

I am very grateful to W. L. Hansen and E. E.
aller for providing the Ge samples and to C. D.
ffries, R. S. Markiewicz, and T. K. Lo for both
perimental assistance and stimulating discus-
ons.

---

*Work supported in part by the U. S. Atomic Energy Commission, Report No. UCB-34P20-165.

[1] Y. E. Pokrovskii and K. I. Svistunova, Pis'ma Zh.
ksp. Teor. Fiz. 13, 297 (1971) [JETP Lett. 13, 212
1971)].

[2] J. M. Worlock, D. H. Olson, and K. L. Shaklee, Bull.
mer. Phys. Soc. 18, 301 (1973).

[3] V. M. Asnin, A. A. Rogachev, and N. I. Sablina, Fiz. Tverd. Tela 14, 399 (1972) [Sov. Phys. Solid State 14, 332 (1972)].

[4] C. Benoît à la Guillaume, M. Voos, F. Salvan, J. M. Laurant, and A. Bonnot, C. R. Acad. Sci., Ser. B 272, 236 (1971).

[5] V. S. Vavilov, V. A. Zayats, and V. N. Murzin, Pis'ma Zh. Eksp. Teor. Fiz. 10, 304 (1969) [JETP Lett. 10, 192 (1969)].

[6] J. C. Hensel, T. G. Phillips, and T. M. Rice, Phys. Rev. Lett. 30, 227 (1973).

[7] R. M. Westervelt, T. K. Lo, J. L. Staehli, and C. D. Jeffries, Phys. Rev. Lett. 32, 1051 (1974).

[8] R. S. Markiewicz, J. P. Wolfe, and C. D. Jeffries, Bull. Amer. Phys. Soc. 18, 1606 (1973), and to be published.

[9] A similar experimental technique was employed by Y. E. Pokrovskii and K. I. Svistunova, Fiz. Tverd. Tela 13, 1485 (1971) [Sov. Phys. Solid State 13, 1241 (1971)]; C. Benoît à la Guillaume, M. Voos, and F. Salvan, Phys. Rev. Lett. 27, 1214 (1971); R. W. Martin, Phys. Status Solidi (b) 61, 223 (1974). However, our observations and conclusions are quite different.

[10] The samples used in this work are from the same boule as samples 145A and 145B of T. K. Lo, B. J. Feldman, and C. D. Jeffries, Phys. Rev. Lett. 31, 224 (1973).

[11] Lo, Feldman, and Jeffries, Ref. 10.

[12] The laser power absorbed by the Ge crystal is approximately 36% of P (Figs. 2 and 3), as a result of losses in the optics and reflection from the Ge surface. For $P=0.1$ W, the calculated sample heating is less than 0.1°K.

[13] The maximum radius is calculated by assuming that each absorbed photon creates one electron-hole pair, all of which condense into one drop with a density of 2×10^{17} electrons/cm^3 and a lifetime of 3.5×10^{-6} sec (Ref. 7).

Model for Electroluminescence in GaN

J. I. Pankove and M. A. Lampert
RCA Laboratories, Princeton, New Jersey 08540

(Received 10 April 1974)

A model to explain dc electroluminescence in GaN diodes is presented. The voltage applied to the diode is partially localized at sharp points and ridges at the cathode. Electrons, tunnel-injected into the active material at the points and ridges, gain sufficient kinetic energy in the high field to cause impact excitation of the luminescent center either directly or indirectly (electron-hole-pair impact excitation across the GaN gap with subsequent hole capture by the luminescent center).

Electroluminescence (EL) from GaN diodes
ithout p-n junctions has previously been report-
d,[1] but the mechanisms of charge transport, ex-
itation, and de-excitation were not clearly un-
erstood. More recent work has made possible new insights into the properties of GaN m-i-n (metal-insulator-n-type) diodes.

The GaN EL diodes are made by a technique described earlier[2]: First, undoped n-GaN is grown by chemical vapor deposition[3] onto a sapphire

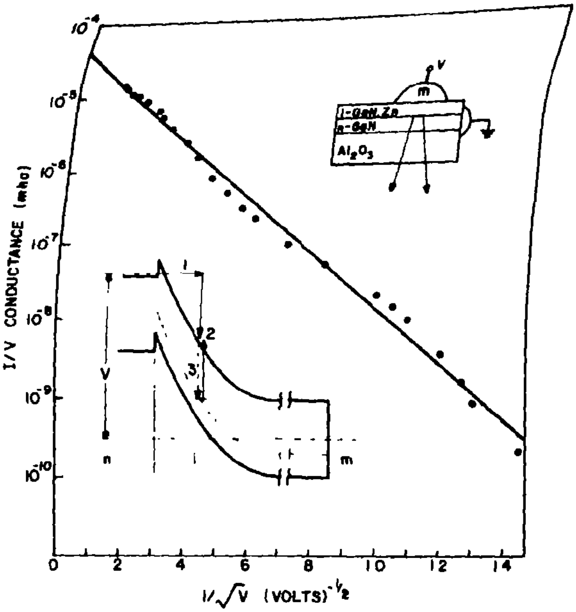

FIG. 1. Fowler-Nordheim-like plot of the I-V characteristic for a typical Zn-doped diode with m biased positively. The diode structure is shown in the upper inset. The band diagram under the m-positive bias condition is shown in the lower inset. The proposed model for the process is (1) tunneling; (2) impact excitation (direct case); (3) radiative recombination.

substrate; then, a Zn-doped compensated insulating layer, which contains the light-emitting region, is grown on the n-GaN; finally, indium electrodes are soldered both to the n region and to the insulating layer to complete the m-i-n structure. Such a diode can, depending on the doping, emit blue, green, yellow, or red light at room temperature.[3] Violet emission has been obtained in GaN diodes where the insulating region was doped with Mg.[4] In the green, external quantum efficiencies of 1.1% and power efficiencies of 0.1% have been obtained with selected crystals.

A typical I-V (current-voltage) characteristic for a Zn-doped diode is shown in Fig. 1, plotted to exhibit its Fowler-Nordheim-like tunneling behavior,[5] namely, with $\ln(I/V)$ versus $1/\sqrt{V}$. The previously reported[1] quadratic dependence, $I \propto V^2$, approximates the data only over a relatively narrow range of biases as compared to the range in Fig. 1. We conclude that tunneling rather than space-charge limitation is the mechanism controlling the current. The high fields required to yield the observed tunneling currents have their origin in partial localization of the applied voltage at numerous sharp points and ridges at the growth interfaces. A typical scanning-electron-microscope photograph of the growth interface is shown in Fig. 2. The topography of the n-i and i-m interfaces are similar. Clearly, the current carriers (electrons) enter the active region of the diode at very high fields. Our model for the observed EL assumes that in these high-field regions the tunnel-injected electrons acquire sufficient kinetic energy to cause impact excitation of the luminescent centers, either directly or possibly indirectly, by initially impact exciting electron-hole pairs across the GaN energy gap. (In the competition between the direct and the indirect processes, relaxation of the crystal-momentum conservation requirement favors the direct process,[6] while the larger number of valence-band states, as compared to Zn centers, favors the indirect process. Further work is necessary to settle this question.) It will be shown below that other conceptually possible mechanisms, not involving hot electrons, are totally unlikely.

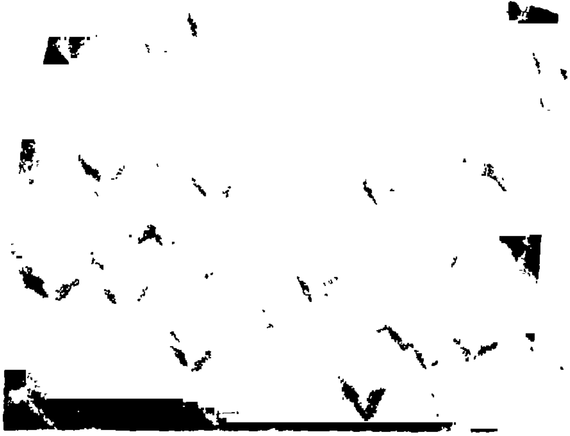

FIG. 2. Scanning-electron-microscope photograph of the m-i interface at the free surface of a typical m-i-n diode. Scale bar indicates 1 μm.

Several experiments have directly determined the critical role of the cathode interface. First, the voltage for the onset of EL does not depend on the thickness of the insulating region, an observation very difficult to understand except on the basis of localization of part of the applied

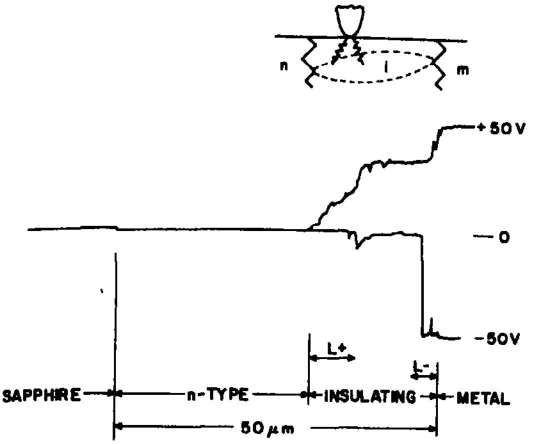

FIG. 3. Potential scans, for both polarities, across a typical *m-i-n* diode. The region of light emission is delineated by the double-headed arrow, *L*+ at positive metal polarity and *L*− at negative metal polarity. The inset figure schematically illustrates the likely role of distributed series resistance in desharpening of the potential step at the points in the *n-i* interface.

voltage. Second, in diodes which have a very thick *i* layer, the depth resolution of a stereoscopic microscope enables one to determine the region of origin of the light: With the In dot negative the light is emitted at the *m-i* interface, and with the polarity reversed the light is emitted at the *i-n* interface; i.e., the light is always generated at the negative electrode (cathode), as indicated in Fig. 3. Third, the experimental potential profile across the diode, Fig. 3, exhibits considerable localization, particularly at the metal electrode. This measurement was made with a tungsten probe moved by a differential micrometer and connected to an electrometer. Resolution on the order of 0.5 μm was obtainable. With positive bias on the metal electrode, a localization of potential gradient is obtained at the *n-i* interface and, correspondingly, a sheet of light is generated in this region. We believe that the potential rise in the region of light emission is considerably more abrupt than revealed by the probe scan, and that its sharpness is obscured by distributed series resistance of the material between the probe and the subsurface local regions of high current density—an effect not encountered at the metal electrode. (This effect is schematically illustrated in the inset in Fig. 3). The precise thickness of the luminous sheet is difficult to determine because of the transparency of the crystal; however, no light is generated in the *n*-substrate material. With the polarity of the bias reversed a large potential drop appears at the *m-i* interface and light is emitted at this interface. Note that localization of the applied potential at the contacts leaves large field-free and low-field regions in the insulating material, with both polarities—a matter we return to below. Finally, the importance of the cathode interface region is brought out by electron-beam experiments on a sectioned *m-i-n* diode, in which it is shown that bombardment-induced conductivity occurs only at the cathode.[7]

An important consequence of the localization of the high-field region is the relatively low quantum efficiency of the EL process—low compared to the efficiencies obtainable with *p-n* junctions in other direct, but lower, band-gap semiconductors. The reason for the reduced efficiency is that the transit time of an injected electron across the high-field region, and hence its dwell time in the vicinity of an empty radiative center, is much shorter than its time for capture by the center (recombination time). Here, "full" or "empty" shall refer to electron occupancy. The emission efficiency can be estimated as follows: First we shall overestimate the transit time by inferring it from that geometry which favors the thickest depletion region for a given voltage drop, namely, the plane-parallel geometry (infinite radius of injecting point). For a 10-V drop and an assumed donor-acceptor pair concentration of 10^{18} cm^{-3}, corresponding to that in working diodes, the depletion region thickness is 10^{-5} cm. A factor-of-10 change in concentration would correspond to a factor-of-3 change in depletion width. Taking a saturated drift velocity for electrons of 10^7 cm/sec,[8] we find that the electron transit time across the depletion region is 10^{-12} sec. A reasonable value for a neutral capture cross section is 10^{-16} cm^2. This value leads to a capture time of $\tau_{h,\mathrm{cap}} = 1/Nv\sigma \simeq 10^{-9}$ sec. These numbers lead to an estimate for the capture, and hence emission, efficiency of 10^{-3}, consistent with measured results. Note that a neutral capture cross section for a *hot* electron cannot be significantly greater than 10^{-16} cm^2, so that our efficiency estimate is a rather good one.

In addition to the proposed hot-electron, impact-excitation mechanism two other conceptual models might be considered candidates to account for the observed dc EL: conventional double injection and direct-field-induced (nonimpact) excitation of the luminescent center. Double injection is highly unlikely on several accounts: (i) It cannot be reconciled with the observation that light is emitted only near the cathode interface. Double injection would necessarily lead to a region of light emission also near the anode interface, as well as diffuse emission throughout the interior of the *i* region. (ii) Double-injection currents would have to be field driven throughout most of the *i* region. Substantial field-free, or very low-field, regions, such as are evident in Fig. 3, are totally incompatible with bulk, field-driven currents. (iii) The low-injection-level hole lifetime, $\tau_{h,\mathrm{low}}$, in the heavily Zn-doped *i* region is readily estimated to be $\sim 10^{-12}$ sec, corresponding to a Zn concentration of 10^{18} cm^{-3} and a hole capture cross section $\sim 10^{-13}$ cm^2 corresponding to a Coulomb-attractive, filled Zn center. On the other hand, the shortest possible hole transit time, $t_{h,\mathrm{min}}$, between anode and cathode is also readily estimated to be $L/v_{h,\mathrm{sat}} \sim 2 \times 10^{-3}/10^7 \sim 2\times 10^{-10}$ sec. This result, $\tau_{h,\mathrm{low}} \ll t_{h,\mathrm{min}}$, makes it impossible for holes to penetrate significantly beyond the anode. (iv) If a significant hole current were indeed possible, it must invert the initially electron-filled Zn-center population. This population inversion must, in turn, produce a large drop in voltage,[9] i.e., a pronounced current-controlled negative resistance. No such negative resistance is seen experimentally.

A model based on direct-field-induced (tunneling) excitation of the Zn center must also be rejected. The electron ground state of the Zn center is at least 2.5 eV below the conduction-band minimum of the GaN host. Concomitantly, the empty (hole-occupied) ground state of the Zn acceptor is less than 1 eV removed from the valence band of the GaN host. Thus, at any specified high field, the lifetime of an electron in the ground state of the Zn acceptor against tunneling into the GaN conduction band is orders-of-magnitude larger than the lifetime of the hole in the ground state of the same center against tunneling into the GaN valence band. Consequently, a negligible fraction of the Zn centers would be empty, whatever the field, and observed luminescence efficiencies would be orders-of-magnitude smaller than observed.

On the positive side, there is very strong evidence for electron-impact excitation of the luminescent center in the dc EL cells involving other host materials, in particular sulfide crystals. For a ZnS host, this mechanism has been established for Tb,[10] Er,[11] and Mn centers.[12] It is possible that the same mechanism is operating in ZnSe *m-i-n* diodes where EL has been observed at the cathodic *i-n* interface.[13] For CaS (band gap ≃ 5 eV) this mechanism has been established for Ce and Er centers.[12] For the rare earths in CaS, the argument we have given above, against a model based on direct, tunneling excitation, is supplemented by an equally strong, related argument—namely, if the ground state could be emptied by tunneling into the conduction band, then the excited state for the bound-to-bound transition yielding the observed light would be emptied by the identical mechanism in a time orders-of-magnitude shorter. Consequently, a negligible fraction of the luminescent centers would have an electron occupying the excited state, and the obtainable emission efficiency would be exceedingly small.

In conclusion we wish to note that although we may be completely confident that the basic excitation mechanism for dc EL in GaN:Zn involves hot electron impact excitation of the Zn center, important details remain to be filled in. We do not know, at this writing, whether the impact excitation is a direct process or an indirect one involving initially electron-hole impact-excitation across the GaN gap, with subsequent capture of the hole by a filled Zn center. Closely related to this uncertainty is another one, namely, whether the luminescent transition is a free-to-bound or a bound-to-bound transition. These problems are under active investigation.

The authors are grateful to E. A. Miller for growing the material, to Mrs. M. Harvey for sample preparation, to J. E. Berkeyheiser for assistance with the measurements, to E. R. Levin for the scanning-electron-microscope topograph, and to I. Ladany, P. D. Southgate, H. Kressel, and A. M. Goodman for valuable discussions.

---

[1] J. I. Pankove, E. A. Miller, and J. E. Berkeyheiser, RCA Rev. 32, 383 (1971), and J. Lumin. 5, 84 (1972).

[2] J. I. Pankove, J. Lumin. 7, 114 (1973).

[3] H. P. Maruska and J. J. Tietjen, Appl. Phys. Lett. 15, 327 (1969).

[4] H. P. Maruska, D. A. Stevenson, and J. I. Pankove, Appl. Phys. Lett. 22, 303 (1973).

[5] R. H. Fowler and L. Nordheim, Proc. Roy. Soc., Ser. A 119, 173 (1928).

[6] P. T. Landsberg and M. J. Adams, J. Lumin. 7, 3 (1973).

[7] J. I. Pankove and E. R. Levin, to be published.

[8] P. D. Southgate attempted a determination of the saturation velocity of electrons in undoped GaN from *I*(*V*) characteristics by using very short pulses. The

material was Ohmic up to 10^4 V/cm where the electron velocity was 7×10^6 cm/sec, setting this value as a lower limit for the saturation velocity. It is conceivable that in Zn-doped GaN this limit could be lower.

[9] M. A. Lampert, Phys. Rev. 125, 126 (1962); A. Waxman and M. A. Lampert, Phys. Rev. B 1, 2735 (1970).

[10] D. C. Krupka, J. Appl. Phys. 43, 476 (1972).

[11] H. Kobayashi, S. Tanaka, and H. Sasakura, Jpn. J. Appl. Phys. 12, 1637 (1973).

[12] P. N. Yocom, private communication.

[13] Y. S. Park, C. R. Gresner, and B. K. Shin, Appl. Phys. Lett. 21, 567 (1972).

Measurement of Selected Phonons in Rubidium as a Function of Temperature and Volume*

J. R. D. Copley†
Solid State Science Division, Argonne National Laboratory, Argonne, Illinois 60439

and

C. A. Rotter‡
Department of Physics, West Virginia University, Morgantown, West Virginia 26506

and

H. G. Smith and W. A. Kamitakahara
Solid State Division, Oak Ridge National Laboratory, Oak Ridge, Tennessee 37830

(Received 20 June 1974)

The first measurements of phonon frequencies in a metal as a function of temperature, at constant values of the atomic volume, are reported. The [ζ00]T, $\zeta=0.2$ mode exhibits considerable temperature dependence at constant volume, whereas modes in the [ζ00]L, [ζζ0]L, and [ζζ0]T1 branches show little such dependence. The mode Grüneisen parameters are also determined.

In this Letter we report the first neutron-scattering measurements of normal modes of vibration in a metal, as a function of temperature from 80 to 295 K, for fixed values of the volume between $(79 \text{ and } 89)\times10^{-24}$ cm^3 atom^{-1}. The temperature dependence of the phonon spectrum at atmospheric pressure has been studied in many materials, including Rb,[1] and the pressure dependence of selected normal modes, at room temperature, has been measured in a few crystals, including RbI,[2] Pb,[3] NaI,[4] and Na.[5] In addition, experiments to determine anharmonic effects at constant volume in Ne[6] and He[7] have been reported. Rubidium was selected for the present study because the harmonic dynamical properties are reasonably well understood, and there exists a volume-dependent effective potential[8] which has been successfully used to compute a number of properties in both the solid[9,10] and liquid[11] states. Furthermore the metal has a large compressibility[12] and thermal expansivity,[13] as well as favorable neutron cross sections.

The sample, a single crystal of Rb 5.2 cm long and 1.6 cm in diameter with a [001] direction close to the cylindrical axis, was grown by a modified Bridgman method.[14] The crystal was contained in a 7075-T6 aluminum pressure vessel with a minimum outer diameter of 6.4 cm, which was designed and lent to us by Professor W. B. Daniels of the University of Delaware. The vessel was housed in a variable-temperature liquid-nitrogen cryostat, and hydrostatic pressure was applied using a two-stage helium-gas-generating system,[15] on loan from Argonne National Laboratory. The measurements were made using the HB-4A triple-axis spectrometer at the high-flux isotope reactor, Oak Ridge National Laboratory. We used a fixed incident energy of 13.6 meV (3.30 THz), produced by Bragg reflection from a pyrolytic graphite (002) monochromator; a pyrolytic graphite filter was employed to remove higher orders, and a zinc (002) crystal was used as analyzer. The measurements were made using the constant-$\vec{Q}$ mode of operation.

Data were obtained at four temperatures. At each temperature T the pressure P was adjusted to obtain selected values of the lattice parameter a (Table I). In each case a was determined by measuring the scattering angles for various Bragg reflections. By extrapolating our 295-K data to 5 kbar, we obtain $a=5.408$ Å giving a ratio of 0.854 for the atomic volumes at 0 and 5

TABLE I. Measured values of the lattice parameter a for various temperatures T and pressures P. The estimated errors for a and P are better than ±0.005 Å and ±0.01 kbar, respectively. The values of a for $P=0$ were obtained by interpolation of the numbers given in Ref. 10.

$T=80$ K		$T=150$ K		$T=230$ K		$T=295$ K	
P (kbar)	a (Å)	P (kbar)	a (Å)	P (kbar)	a (Å)	P (kbar)	a (Å)
0	5.610	0	5.637	0	5.670	0	5.700
1.86	5.502	0.28	5.622	0.71	5.620	0.34	5.675
2.36	5.475	2.26	5.502	2.71	5.502	1.02	5.620
4.23	5.394	4.43	5.402	4.61	5.408	2.07	5.555
						3.02	5.502
						3.75	5.470
						4.75	5.420

kbar, whereas Vaidya, Getting, and Kennedy[12] obtained a value of 0.862 for this quantity. Our data at 80 K are insufficient for us to make a useful comparison with the work of Gutman and Trivisonno.[16]

In Fig. 1 we show some neutron groups for the best-determined mode, $[\zeta 00]$T at $\zeta = 0.2$. Clearly the frequency of this mode changes both with V at constant T and with T at constant V. There is also evidence of an increase in the width of this mode with increasing T. Figure 2 shows a selection of our results for the frequencies of four normal modes. Since the results for $a = 5.41$ Å were in fact obtained for slightly different values of a (see Table I), small corrections (<0.01 THz) were applied to these data, using mode Grüneisen parameters determined from this experiment (see below). Note that our results have not been corrected for instrumental resolution: Only the $[\zeta\zeta 0]$T1 mode would be significantly affected.[1]

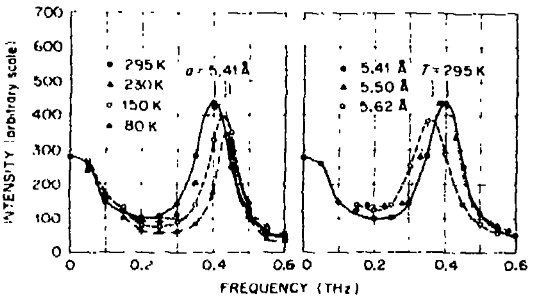

FIG. 1. Neutron groups for the $[\zeta 00]$T, $\zeta = 0.2$ mode, measured at $\vec{Q} = [2, 0.2, 0] \times 2\pi/a$, normalized to the same number of monitor counts. The lines are drawn to guide the eye.

From Fig. 2 it is clear that only one mode, $[\zeta 00]$T at $\zeta = 0.2$, shows a definite change in phonon frequency with temperature, at constant volume. Using our data at the four temperatures we have computed average values for the zero-pressure mode Grüneisen parameters $\gamma_i = -\partial \ln \nu_i / \partial \ln V$, as follows: $[\zeta 00]$L, $\zeta = 0.2$, 2.15 ± 0.23; $[\zeta\zeta 0]$L, $\zeta = 0.2$, 1.65 ± 0.07; $[\zeta 00]$T, $\zeta = 0.2$, 0.99 ± 0.13; and $[\zeta\zeta 0]$T1, $\zeta = 0.3$, 1.31 ± 0.25. Copley[10] computed Grüneisen parameters of 2.1, 1.7, 1.1, and 3.4, respectively. The calculated parameter for

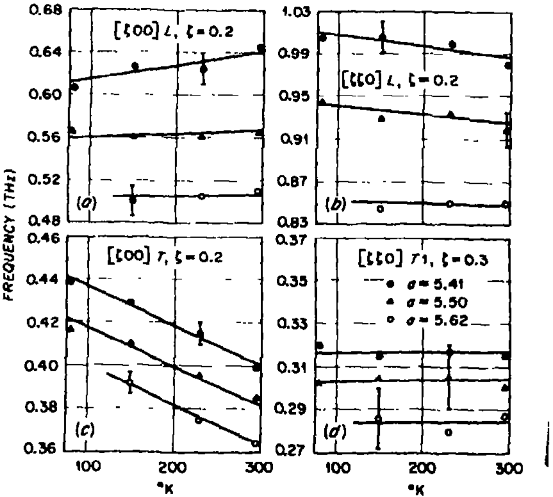

FIG. 2. The temperature dependence of four normal modes, for three values of the lattice parameter. Typical error bars are shown. Note the different ordinate scales. The modes shown in (a), (b), (c), and (d) were measured at $\vec{Q}$'s of {[2.2, 0, 0], [1.2, 1.2, 0], [2, 0.2, 0], and [0.7, 1.3, 0]} × $2\pi/a$, respectively. The lines are drawn to guide the eye.

he $[\zeta\zeta 0]$T1 mode is clearly far too large, but for he other modes the agreement between calculation and experiment is very encouraging.

Since the $[\zeta 00]$T, $\zeta = 0.2$ mode shows definite dependence on T at constant V (Fig. 2), it is clear hat the quasiharmonic approximation is insufficient. It should be remembered that, to first order in anharmonic perturbation theory, *two* contributions to the phonon self-energy must be included. Calculations[10,17] have shown that for most branches the two contributions are of opposite sign and largely cancel. Thus the absence of a detectable shift in a mode's frequency, with T at constant V, does not imply the absence of anharmonicity. Though we cannot explain the fact that only the $[\zeta 00]$T mode shows an appreciable shift, we would offer two comments. First, the constant-volume anharmonic shifts in neon,[6] for the $\zeta 00]$ branches at small ζ, show a similar behavor to that observed in Rb. Second, the present results are consistent with the fact that the calculated[10,17] cubic and quartic shifts in Rb and K, for the $[\zeta 00]$T branch, are of the same sign (negative with increasing T), whereas the corresponding shifts for the $[\zeta 00]$L, $[\zeta\zeta 0]$L, and $[\zeta\zeta 0]$T1 branches are of opposite sign. However, it is not clear why this particular result follows from the anharmonic calculations.

This investigation represents the first attempt at a detailed study of the lattice dynamics of a metal as a function of both temperature and volume. Considerable experimental difficulties exst because of inevitable scattering from the pressure vessel and demands on instrumental resolution. Nevertheless the measurements clearly provide valuable data for comparison with anharmonic calculations. Further measurements are planned for the near future.

We are grateful to Professor W. B. Daniels for he loan of the pressure vessel and for his coninued interest in this work. We thank R. Kleb, R. H. Stefiuk, T. C. Erickson, and G. E. Ostrowski for their assistance at all stages in the preparation of this experiment, and J. L. Sellers for is technical assistance during the measurements. Two of us (J.R.D.C. and C.A.R.) thank the members of the Solid State Division, Oak Ridge National Laboratory, for their hospitality throughout the course of this work.

---

[*] Work supported by the U. S. Atomic Energy Commission.

[†] Present address: Institut Laue-Langevin, BP 156 Centre de tri, 38042 Grenoble Cedex, France.

[‡] Work supported by U. S. Atomic Energy Commission—Oak Ridge Associated Universities Research Participation Contract No. S-1328.

[1] J. R. D. Copley and B. N. Brockhouse, Can. J. Phys. 51, 657 (1973).

[2] D. H. Saunderson, Phys. Rev. Lett. 17, 530 (1966); R. Lechner, private communication.

[3] R. Lechner and G. Quittner, Phys. Rev. Lett. 17, 1259 (1966).

[4] G. Quittner, S. Vukovich, and G. Ernst, in *The Fourth IAEA Symposium on Neutron Inelastic Scattering, Copenhagen, Denmark, 1968* (International Atomic Energy Agency, Vienna, Austria, 1968), Vol. I, p. 367.

[5] G. Ernst, Acta Phys. Austr. 33, 27 (1971).

[6] J. A. Leake, W. B. Daniels, J. Skalyo, Jr., B. C. Frazer, and G. Shirane, Phys. Rev. 181, 1251 (1969); J. Skalyo, Jr., V. J. Minkiewicz, G. Shirane, and W. B Daniels, Phys. Rev. B 6, 4766 (1972).

[7] F. P. Lipschultz, V. J. Minkiewicz, T. A. Kitchens, G. Shirane, and R. Nathans, Phys. Rev. Lett. 19, 1307 (1967).

[8] W. M. Shyu, K. S. Singwi, and M. P. Tosi, Phys. Rev. B 3, 237 (1971).

[9] D. L. Price, K. S. Singwi, and M. P. Tosi, Phys. Rev. B 2, 2983 (1970).

[10] J. R. D. Copley, Can. J. Phys. 51, 2564 (1973).

[11] A. Rahman, Phys. Rev. Lett. 32, 52 (1974), and Phys. Rev. A 9, 1667 (1974); D. L. Price, private communication.

[12] S. N. Vaidya, I. C. Getting, and G. C. Kennedy, J. Phys. Chem. Solids 32, 2542 (1971).

[13] W. B. Pearson, *Handbook of Lattice Spacings and Structures of Metals* (Pergamon, London, 1958); see also Copley, Ref. 10.

[14] W. B. Daniels, Phys. Rev. 119, 1246 (1960).

[15] The high-pressure system will be described in a separate report.

[16] E. J. Gutman and J. Trivisonno, J. Phys. Chem. Solids 28, 805 (1967).

[17] W. J. L. Buyers and R. A. Cowley, Phys. Rev. 180, 755 (1969).

Exciton Contributions to the Nonlinear Optical Susceptibility

B. F. Levine
Bell Laboratories, Murray Hill, New Jersey 07974
(Received 6 May 1974)

By using a simple hydrogenic model, we are able to account for the magnitude, sign, and tensor character of the exciton contribution to the nonlinear optical susceptibility in CuCl and ZnO.

Haueisen and Mahr,[1] and more recently Kramer, Parsons, and Bloembergen,[2] have done a beautiful series of experiments on the excitonic contribution to the nonlinear optical susceptibility. By tuning a dye laser (at frequency ω) so that the generated second harmonic frequency (2ω) swept through the exciton resonances, Haueisen and Mahr[1] were able to experimentally determine the magnitude, the sign, and the dispersion of the exciton contribution to the second-order nonlinear optical susceptibility d_{ijk}^{ex}, in CuCl and ZnO. Kramer, Parsons, and Bloembergen[2] also measured the dispersion of the exciton nonlinearity in CuCl using a different technique, namely resonant third-order mixing. We suggest below an extremely simple and physically transparent model which adequately accounts for the magnitude and sign of the exciton nonlinear polarizability and its close relationship to the exciton linear polarizability.

However, before describing this model it is instructive to examine first the equation of motion of the exciton and the total polarization P_i of the crystal. Following Yablonovitch, Flytzanis, and Bloembergen[3] and Kramer, Parsons, and Bloembergen[2] these are given by

$$M(\ddot{Q}_i+\Gamma\dot{Q}_i+\omega_T^2Q_i)=e_i^*E_i+\tfrac{1}{2}\alpha_{ijk}E_jE_k \tag{1}$$

and

$$P_i=Ne_i^*Q_i+\chi_{ii}E_i+N\alpha_{ijk}E_jQ_k+d_{ijk}E_jE_k, \tag{2}$$

where Q, Γ, ω_T, e^*, M, N, and α_{ijk} are the exciton internal coordinate, damping, transverse resonant frequency, effective charge, reduced mass, number density, and transverse "Raman" coefficient, respectively; χ_{ii} and d_{ijk} are the electronic linear and second-order susceptibilities, respectively. By combining Eqs. (1) and (2) to second order, the total linear $\chi_{ii}^{\mathrm{tot}}(\omega)$ and nonlinear susceptibility $d_{ijk}^{\mathrm{tot}}(\omega)$ can be obtained as[2,3]

$$\chi_{ii}^{\mathrm{tot}}(\omega)=\chi_{ii}+\frac{N(e_i^*)^2/M}{\omega_T^2-\omega^2+i\omega\Gamma}, \tag{3}$$

and

$$d_{ijk}^{\mathrm{tot}}(\omega)=d_{ijk}+\frac{\frac{3}{2}Ne_i^*\alpha_{ijk}/M}{\omega_T^2-\omega^2+i\omega\Gamma}, \tag{4}$$

where the second terms in Eqs. (3) and (4) are the resonant exciton contributions. At high frequencies ($\omega \gg \omega_T$) only the nonresonant electronic contribution remains whereas in the low-frequency limit ($\omega \ll \omega_T$) the exciton contributions to the linear χ_{ii}^{ex} and nonlinear d_{ijk}^{ex} susceptibilities tend toward constant values,

$$\chi_{ii}^{\mathrm{tot}}(0)=\chi_{ii}+N(e_i^*)^2/M\omega_T^2\equiv\chi_{ii}+\chi_{ii}^{\mathrm{ex}}, \tag{5}$$

$$d_{ijk}^{\mathrm{tot}}(0)=d_{ijk}+\frac{3}{2}\,\frac{Ne_i^*\alpha_{ijk}}{M\omega_T^2}\equiv d_{ijk}+d_{ijk}^{\mathrm{ex}}. \tag{6}$$

In the notation of Haueisen and Mahr[1] these low-frequency excitonic contributions are denoted as A and B, i.e.,

$$B\equiv 4\pi\chi_{ii}^{\mathrm{ex}}=4\pi N(e_i^*)^2/M\omega_T^2 \tag{7}$$

and

$$A\equiv d_{ijk}^{\mathrm{ex}}=\tfrac{3}{2}Ne_i^*\alpha_{ijk}/M\omega_T^2. \tag{8}$$

By fitting the expressions for the frequency-dependent susceptibilities $\chi_{ii}^{\mathrm{tot}}(\omega)$ and $d_{ijk}^{\mathrm{tot}}(\omega)$ [i.e., Eqs. (3)–(8)] to their resonant second-harmonic measurements, Haueisen and Mahr[1] determined the excitonic linear and nonlinear polarizabilities B and A.

Because of the complexity of CuCl and ZnO, wave functions of sufficient accuracy are not available (i.e., CuCl has important d-band contributions and the Zn and O atoms have much different covalent radii), and thus a fundamental microscopic quantum mechanical calculation of d_{ijk}^{ex} would be difficult. We are therefore led to attempt a much simpler macroscopic approach.

For the basis of our model we assume that the origin of the exciton nonlinearity, i.e., the origin of the electric field dependence of the exciton polarizability, is associated with the dependence of the core screening on the applied electric field. That is, an applied optical field changes the crystal dielectric constant ϵ (via the electronic nonlinearity d_{ijk}) and hence changes the effective core charge $Z_{\rm eff}=Z/\epsilon$ of a hydrogenic-like exciton (where Z is the unscreened core charge). The hydrogenic problem can of course be solved exactly, and it is trivial to show that the linear polarizability of a hydrogenic system is proportional to $(Z_{\rm eff})^{-4}$, and therefore

$$\chi^{\rm ex}\propto\epsilon^4. \tag{9}$$

Physically the reason that $\chi^{\rm ex}$ increases as ϵ^4 is that the exciton binding energy $E_{\rm ex}$ decreases with ϵ $[E_{\rm ex}\propto(Z_{\rm eff})^2\propto\epsilon^{-2}]$, while the exciton radius $a_{\rm ex}$ increases with ϵ $[a_{\rm ex}\propto Z_{\rm eff}\propto\epsilon]$, both of which increase the exciton polarizability $[\chi^{\rm ex}\propto(a_{\rm ex})^2/E_{\rm ex}\propto\epsilon^4]$. Thus, since ϵ is a function of field (via d_{ijk}) the exciton screening and polarizability are nonlinear. More precisely, an examination of the $d_{ijk}E_jE_k$ term in Eq. (2) shows that the change in the electronic dielectric constant $\Delta\epsilon$ caused by an optical field E_k can be written as

$$\Delta\epsilon_{ij}=8\pi d_{ijk}E_k. \tag{10}$$

As Eq. (9) shows, this change $\Delta\epsilon$ of the electronic polarizability will produce a corresponding change in the exciton polarizability $\Delta\chi^{\rm ex}$ of an amount

$$\Delta\chi_{ij}^{\rm ex}=(4\chi_{ii}^{\rm ex}/\epsilon)(8\pi d_{ijk}E_k). \tag{11}$$

Using the definition of the exciton nonlinearity $d_{ijk}^{\rm cx}$ corresponding to that for the electronic nonlinearity of Eq. (10), namely

$$\Delta(4\pi\chi_{ij}^{\rm ex})=8\pi d_{ijk}^{\rm ex}E_k, \tag{12}$$

yields our final result, namely

$$d_{ijk}^{\rm ex}=4(4\pi\chi_{ii}^{\rm ex}/\epsilon)d_{ijk}. \tag{13}$$

In the notation of Haueisen and Mahr,[1] i.e., Eqs. (7) and (8), and defining $d_{ijk}\equiv d^\infty$, Eq. (13) can be written as

$$(A/d^\infty)=4(B/\epsilon). \tag{14}$$

Our expression for $d_{ijk}^{\rm cx}$ [Eqs. (13) and (14)] redicts a number of remarkably simple results.[4] irst the exciton nonlinearity $d_{ijk}^{\rm ex}$ is proportionl to both the electronic linear χ_{ii} and nonlinear $_{ijk}$ susceptibilities. Thus, the selection rules or the allowed $d_{ijk}^{\rm cx}$ coefficients are deterined by the requirement that both d_{ijk} and χ_{ii} ot vanish. For example, the A exciton in CdS s only strong for E perpendicular to the c axis i.e., $\chi_{11}^{\rm cx}\neq0$, $\chi_{33}^{\rm ex}\simeq0$). Therefore, $d_{333}^{\rm cx}\simeq0$, $_{311}^{\rm ex}\simeq0$, but $d_{113}^{\rm ex}\neq0$ which is, of course, a trong violation of the Kleinman symmetry relation $d_{ijk}^{\rm cx}=d_{kji}^{\rm ex}$. Further, for nonzero $\chi_{ii}^{\rm ex}$, Eq. (13) implies (a) that the absolute signs of the excitonic and electronic nonlinearities are the same, (b) that all the different tensor components of $d_{ijk}^{\rm ex}$ have nearly the same proportionality constant, i.e., the ratio $d_{ijk}^{\rm cx}/d_{ijk}$ is almost independent of the tensor indices *ijk* (since $\chi_{ii}^{\rm cx}$ is quite isotropic for zinc-blende and wurtzite crystals), and (c) that the ratio of the fractional contribution of the exciton nonlinear polarizability [i.e., $d_{ijk}^{\rm ex}/d_{ijk}\equiv A/d^\infty$] to the fractional contribution of the exciton linear polarizability [i.e., $4\pi\chi_{ii}^{\rm ex}/\epsilon\equiv B/\epsilon$] is independent of any crystal parameters and is, in fact, a *pure constant*, i.e., $(d_{ijk}^{\rm ex}/d_{ijk})/(4\pi\chi_{ii}^{\rm cx}/\epsilon)=+4$, as shown by Eqs. (13) and (14).

We can now compare the experimental values of Haueisen and Mahr[1] with our theoretical predictions based on Eqs. (13) and (14), for the various components $d_{ijk}^{\rm ex}$ for both CuCl and ZnO. In this connection it is important to note that the crystal dielectric constant ϵ appearing in Eqs. (13) and (14) (and elsewhere) is that appropriate to the particular exciton of interest for which the linear and nonlinear susceptibilities $\chi_{ii}^{\rm cx}$ and $d_{ijk}^{\rm ex}$ have been determined. The reason for this is that it is well known that the appropriate effective dielectric screening is a function of the exciton radius,[5,6] i.e., $\epsilon=\epsilon(r)$. This is true since for large-orbit excitons the lattice motion can follow the slowly moving exciton and hence the relevant dielectric constant is the static one ϵ_0. However, for small-radius excitons the exciton motion is too rapid for lattice screening to be effective and hence the optical-frequency dielectric constant ϵ_∞ is appropriate. For excitons of intermediate radius, the effective dielectric screening constant varies smoothly between these limits.

Table I shows that the magnitude and sign of the experimental values of $d_{ijk}^{\rm ex}/d_{ijk}$ are in good agreement with the predicted value of $16\pi\chi_{ii}^{\rm ex}/\epsilon$.[11] It is especially noteworthy that the experimental values of $d_{ijk}^{\rm ex}/d_{ijk}$ are the same for both the $d_{333}^{\rm cx}$ and $d_{311}^{\rm ex}$ exciton resonances as predicted by Eqs. (13) and (14), even though the nonlinear coefficients $d_{333}^{\rm ex}$ and $d_{311}^{\rm cx}$ differ not only in magnitude by a factor of 2, but also in sign (i.e., $d_{333}^{\rm ex}/d_{311}^{\rm ex}=-2$). Further, it is worth mentioning that this good agreement is obtained in spite of the complexity of the electronic nonlinearity in CuCl and ZnO. That is, CuCl and ZnO are among the few *negative* nonlinear susceptibilities [i.e., d_{333}(ZnO) < 0, d_{123}(CuCl) < 0] in

TABLE I. The experimental measurements of Haueisen and Mahr (Ref. 1) for the ratio of the excitonic to electronic second-order nonlinear susceptibilities (d_{ijk}^{ex}/d_{ijk}) are compared with our theory [Eqs. (13) and (14)], and are seen to be in good agreement. The experimental absolute signs of d_{ijk} are shown (note especially d_{333} and d_{311} of ZnO) to indicate that the ratio d_{ijk}^{ex}/d_{ijk} is independent of these signs as predicted by Eq. (13).

Crystal	Coefficient (Sign)	Exciton Symmetry	ω_T (eV)	ϵ	$4\pi\chi^{ex}$ (10^{-3})	d_{ijk}^{ex}/d_{ijk} (10^{-3}) Theory	d_{ijk}^{ex}/d_{ijk} (10^{-3}) Experiment
CuCl[a,b]	$d_{123}(-)$	$1f(\Gamma_6\times\Gamma_7)$	3.204	5.4	20	+15	+17
CuCl[a,b]	$d_{123}(-)$	$1d(\Gamma_6\times\Gamma_8)$	3.268	6	50	+33	+24
ZnO[a,c]	$d_{333}(-)$	$C(\Gamma_7\times\Gamma_7)$	3.420	8.6	30	+14	+17
ZnO[a,c]	$d_{311}(+)$	$C(\Gamma_7\times\Gamma_7)$	3.420	8.6	30	+14	+17
GaAs[d]	$d_{123}(+)$	$(\Gamma_1\times\Gamma_5)$	1.515	12.6	1.6	+0.51	
InP[e]	$d_{123}(+)$		1.419	12.1	2.35	+0.78	
ZnS[f]	$d_{123}(+)$	A	3.799	8.1	10.4	+5.1	
ZnSe[f]	$d_{123}(+)$	A	2.799	8.7	5.4	+2.5	
ZnTe[f]	$d_{123}(+)$	A	2.381	9.7	4.4	+1.8	
CdTe[f]	$d_{123}(+)$	A	1.596	9.7	4.8	+2.0	
CdS[f]	$d_{113}(-)$	A	2.554	8.5	12.5	+5.9	
CdS[f]	$\begin{Bmatrix} d_{113}(-) \\ d_{333}(+) \\ d_{311}(-) \end{Bmatrix}$	B	2.563	8.5	8.2	+3.9	

[a] Ref. 1.
[b] Ref. 6.
[c] Ref. 7.
[d] Ref. 8.
[e] Ref. 9.
[f] Ref. 10.

the class of tetrahedral semiconductors; most of the other compounds such as GaAs are simpler and *positive.*[12] This unusual behavior for these two crystals arises from unrelated complications. In CuCl there is a significant d-band contribution from the noble-metal d electrons,[13] whereas in ZnO it is the unequal covalent radii of the Zn and O atoms which produce the negative nonlinearity.[13] Therefore, it would certainly be of great interest to do this type of exciton-resonance experiment on a simpler crystal such as GaAs which has an extremely well characterized[8] and closely hydrogenic exciton, and for which $d_{123} > 0$. To encourage such measurements we have listed our theoretical predictions for GaAs as well as for other common zinc-blende and wurtzite semiconductors in Table I. The predicted large differences between the III-V, II-VI, and I-VII semiconductors provide good opportunities to test this theory.

In conclusion, by the use of an extremely simple physically transparent model [i.e., Eq. (9)] we have been able to adequately account for the magnitude, sign, and tensor character of the exciton contribution d_{ijk}^{ex} to the second-order nonlinear optical susceptibility in CuCl and ZnO. We have also predicted d_{ijk}^{ex} for a variety of common III-V, II-VI, and I-VII zinc-blende and wurtzite semiconductors.

---

[1] D. C. Haueisen and H. Mahr, Phys. Rev. B 8, 734 (1973), and Phys. Rev. Lett. 26, 838 (1971).

[2] S. D. Kramer, F. G. Parsons, and N. Bloembergen, Phys. Rev. B 9, 1853 (1974).

[3] E. Yablonovitch, C. Flytzanis, and N. Bloembergen, Phys. Rev. Lett. 29, 865 (1972).

[4] Of course these simple expressions can only be expected to hold for the ground state ($n = 1$ exciton). The excited states ($n = 2, 3$, etc.) are obviously more complex and a quantum mechanical treatment would be required. For example, the $n = 2$ C exciton in ZnO ($\omega_T = 3.465$ eV) has a nonlinearity (from Ref. 1) of ($d_{ijk}^{ex}/d_{ijk}) \simeq -0.05$, whereas the value calculated from Eq. (13) is $+0.005$. This sign change and order of magni-

tude increase (for the $n=2$ excited state) over the ground state ($n=1$) calculation may be related to the nearly degenerate $2s$ and $2p$ exciton energy levels $E(2s)$ and $E(2p)$. In fact $[E(2p)-E(1s)]/[E(2p)-E(2s)] \simeq -17$ [R. Dinges, D. Fröhlich, B. Staginnus, and W. Staude, Phys. Rev. Lett. 25, 922 (1970).

[5] H. Haken, Fortschr. Phys. 38, 271 (1958).

[6] J. Ringeissen, A. Coret, and S. Nikitine, in *Localized Excitations in Solids*, edited by R. G. Wallis (Plenum, New York, 1968).

[7] Y. S. Park, C. W. Litton, T. C. Collins, and D. C. Reynolds, Phys. Rev. 143, 512 (1966); W. Y. Liang and A. D. Yoffe, Phys. Rev. Lett. 20, 59 (1968).

[8] D. D. Sell, Phys. Rev. B 7, 4568 (1973).

[9] F. Evangelisti, J. U. Fischbach, and A. Frova, Phys. Rev. B 9, 1516 (1974).

[10] B. Segall and D. T. F. Marple, in *Physics and Chemistry of II-VI Compounds*, edited by M. Aven and J. S. Prener (North-Holland, Amsterdam, 1967), Chap. 7.

[11] It might be noted that the CuCl $1d$ (diffuse) exciton is over 2 orders of magnitude more highly damped than the $1f$ (sharp) exciton. Perhaps this affects the results slightly.

[12] R. C. Miller and W. A. Nordland, Phys. Rev. B 2, 4896 (1970); R. C. Miller, S. C. Abrahams, R. L. Barns, J. L. Bernstein, W. A. Nordland, and E. H. Turner, Solid State Commun. 9, 1463 (1971).

[13] B. F. Levine, Phys. Rev. B 7, 2600 (1973).

New Bond-Charge Model for the Lattice Dynamics of Diamond-Type Semiconductors

W. Weber
Max-Planck-Institut für Festkörperforschung, 7 Stuttgart-1, Bundesrepublik Deutschland

(Received 26 February 1974)

A new bond-charge model for phonons in semiconductors of diamond structure is presented. I show that the flattening of the transverse acoustic phonon branches in these materials can be understood by interactions involving the bond charges, when these move adiabatically. The phonon spectrum of Ge is calculated using only four parameters, all of which are physically meaningful, and very good agreement with experimental values is obtained.

The phonon dispersion relations of all semiconductors with diamond or sphalerite structure[1] exhibit one characteristic feature, from which only diamond itself is excepted: The transverse acoustic (TA) phonon branches have very low frequencies and are very flat away from the zone center, although the corresponding shear moduli have rather high values. In the following, I show that this can be understood by interactions involving the bond charges (BC's), if these are allowed to move adiabatically. My model also enables us to elucidate the differences in the nature of the binding forces in the group IV materials.

Based on Phillips's bond-charge model[2] for covalent crystals, Martin[3] has used a dielectric screening model to calculate the phonon spectrum of Si. He assumed that the bare-ion-core potentials are screened in a nearly free-electron-like manner; i.e., by the diagonal elements of the inverse dielectric function $\epsilon^{-1}(\vec{q}+\vec{G},\vec{q}+\vec{G}')$. This metallike binding gives rise to short-range central forces between the ions, which die out rapidly beyond nearest neighbors. The effect of the off-diagonal elements of ϵ^{-1} is described by Coulombic interactions involving the BC's. These forces represent the covalent character of the binding; they lead to effective noncentral forces between the ions, which produce the stability of the diamond structure against shear. The specific assumption was made that the BC's were fixed midway between the ions, even when the latter are displaced. Martin obtained fair agreement with experimental dispersion curves, except that the flattening of the TA phonons could not be reproduced.

In 1959, Cochran[4] pointed out that this flattening of TA branches, which in a Born and von Kármán model requires very long-range force constants,[5] is in fact due to mainly short-range ion-electron and electron-electron interactions. Cochran's shell model (SM), however, has many drawbacks. The noncentral two-body forces, which are crucial for the stability against shear, are not adequately understood.[6] Further, the electrons in a bond are shared by two atoms and it is unphysical to divide them between the two.[7] Finally, it turned out to be impossible to extend the SM to III-V compounds without introducing many new parameters, although the phonon spectra are very similar.[1]

The starting point of my work is the bond-charge model; i.e., I describe the effect of the metallike binding by central forces between nearest-neighbor ions; the covalent binding shows up in interactions involving the BC's. However, I relax the constraint that the BC's are fixed midway between the ions. Instead, I allow that the BC's move adiabatically like the electronic shells in a SM. As a consequence, I have to introduce short-range ion-BC forces in order to stabilize the BC's on their sites. I also take into account interactions between neighboring bonds.

The dynamical matrix in my model is derived in the usual way[8] by treating the BC's as independent lattice particles. In the harmonic and adiabatic approximations, the Fourier-transformed equations of motion for diamond-structure crystals may then be written as

$$m\omega^2\underline{u} = [\underline{R} + (4z^2/\epsilon)\underline{C}_R]\underline{u} + [\underline{T} - (2z^2/\epsilon)\underline{C}_T]\underline{s}, \qquad (1)$$

$$\underline{0} = [\underline{T}^+ - (2z^2/\epsilon)\underline{C}_T{}^+]\underline{u} + [\underline{S} + (z^2/\epsilon)\underline{C}_s]\underline{s}. \qquad (2)$$

Here m, z, and ϵ are the ion mass, the value of the BC, and the dielectric constant, respectively. The hypervectors $\underline{u}$ and $\underline{s}$ denote the displacements of the (two) ions and (four) BC's. $\underline{R}$, $\underline{T}$, and $\underline{S}$ are the respective Fourier-transformed force-constant matrices of the short-range ion-ion, ion-BC, and BC-BC interactions. $\underline{C}_R$, $\underline{C}_T$, and $\underline{C}_S$ denote the corresponding Coulomb matrices. The adiabatic approximation is expressed by having put the mass of the BC's equal to zero on the left-hand side of Eq. (2). Thus, we are able to eliminate the BC degrees of freedom $\underline{s}$ in Eq. (1).

We have limited the short-range ion-BC and BC-BC interactions to nearest neighbors. The corresponding force-constant matrices are of the same form as those between nearest and next-nearest neighbor ions, respectively.[9] Moreover, one can show that they enter the expressions for the elastic constants in the same manner as those ion-ion force constants, although divided by a factor of 2 or 4, respectively. This comes from the fact that, in the long-wavelength limit, the BC's move in phase with the ions, as if they were fixed midway between them, just as in the Phillips-Martin model. At shorter wavelengths, however, the BC's move adiabatically under the influence of net forces acting on them.

This is a crucial point for the understanding of the dispersion of TA phonons. To illustrate this, let us consider a monoatomic linear chain with BC's midway between the ions. We assume a short-range ion-BC force constant f, and for the sake of simplicity we neglect the Coulomb forces. The interactions between two neighboring bonds are described by a potential as first used by Keating:

$$V = (\beta/a^2)(\vec{x}_{0i}\cdot\vec{x}_{0j} + a^2/4)^2. \qquad (3)$$

Here $\vec{x}_{0i} = \vec{r}_{0i} + \vec{u}_0 - \vec{u}_i$ is the distance vector between atom 0 and BC i, with $\vec{r}_{0i}$ being the equilibrium value; further $a^2/4 = -\vec{r}_{0i}\cdot\vec{r}_{0j}$. In the linear case, V yields only a force constant $f' = \beta/2$ between neighboring BC's. Proceeding then along the lines sketched above, one finds the dispersion equation

$$m\omega^2 = 2f\frac{(f+2f')\sin^2(\frac{1}{2}qa)}{f+2f'\sin^2(\frac{1}{2}qa)}. \qquad (4)$$

The Phillips-Martin constraint leads to

$$m\omega^2 = 2f\sin^2(\tfrac{1}{2}qa) + f'\sin^2(qa). \qquad (5)$$

In Fig. 1, various dispersion curves are shown for the two approaches. The elastic constant $\propto f + 2f'$ is kept fixed for all curves, while the ratio f'/f is varied. If $f'/f \gg 1$, Eq. (4) depicts the typical flattening of the dispersion curve away from $q \approx 0$. In this case, the ions are coupled only weakly to the BC's, which form an almost rigid lattice. The ions vibrate like Einstein oscillators in this lattice, and their frequency is given by the weak ion-BC force constant f. Only in the long-wavelength limit, where the BC's move in phase with the atoms, does the strong bond-bond interaction contribute to the dynamics of the atoms, thus producing the high value of the

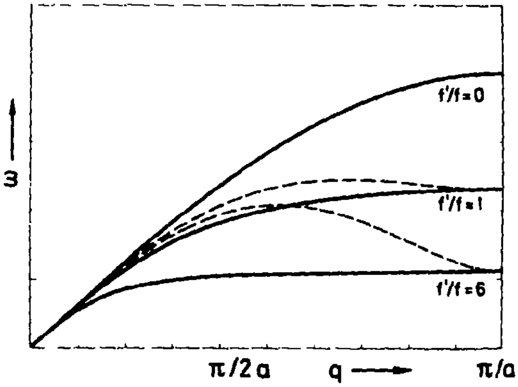

FIG. 1. Dispersion curves for a monoatomic linear chain with bond charges. Solid and dashed lines depict, respectively, the curves according to Eq. (4) (adiabatically moving bond charges) and Eq. (5) (Phillips-Martin constraint). The elastic constant is kept fixed for all curves.

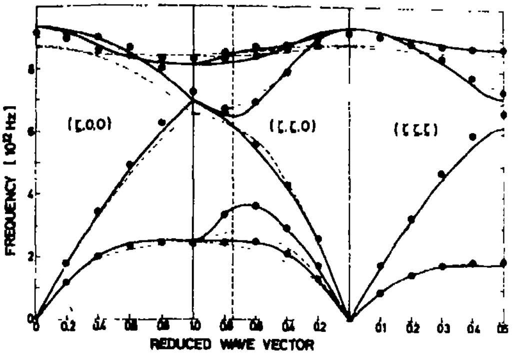

FIG. 2. Phonon dispersion curves for Ge. Solid circles represent the experimental values of Ref. 11. Solid lines show the results of my four-parameter bond-charge model. Dashed lines depict the results from the shell model of Ref. 4. The unpublished curves in the $(\zeta, \zeta, 0)$ direction were kindly provided by W. Kress and K. Kunc.

elastic constant.

In our calculation for Ge we have used four types of interactions: (a) a central potential $\varphi_{i-i}(\tau)$ between nearest-neighbor ions; (b) Coulombic interactions of point charges at the sites of the ions and the bonds; (c) a central potential $\varphi_{i-BC}(\tau)$ between nearest-neighbor ions and BC's; and (d) the interactions between two adjacent bonds described by Keating's potential as given in Eq. (3). The condition of stable equilibrium relates the first derivatives of the short-range potentials with the Madelung energy of the system (see Ref. 3).

The phonon dispersion curves of Ge, as calculated with this model, are shown in Fig. 2. They are compared to Cochran's five-parameter SM,[4] which also has the merit of limiting the short-range force constants within nearest neighbors.[10] In our model four parameters are used; their values have been found by a least-squares fit rom the neutron data of Nilsson and Nelin.[11] Asuming $\varphi_{i-BC}'=0$, we have obtained $\varphi_{i-i}''(\tau_0) = 10.15$, $\varphi_{i-BC}''(\tau_0/2)=8.76$, $\beta=4.3$ (all in units 10^4 dyn/cm); $z^2/\epsilon=0.1616$. The equilibrium condition leads to $\varphi_{i-i}'/\tau_0=-1.13$. The average deviation from experimental values of Ref. 11 is about 2%, while the maximum error at some frequencies is 5%. We may also compare the elastic constants (in units 10^{12} dyn/cm^2): $c_{11}=1.326$ 1.29), $c_{11}-c_{12}=0.825$ (0.81), $c_{44}=0.65$ (0.67); he experimental values as quoted in Ref. 6 are given in parentheses.

The direct ion-ion force constant φ_{i-i}'' dominates in all phonon branches except in the TA modes, which are independent of it. Thus, the TA phonons depend only on the interactions involving the BC's. Just as for the linear chain model, we obtain the peculiar shape of the TA branches if the interactions between neighboring bonds are rather strong as compared to the ion-BC coupling. The latter consists both of the short-range and the Coulomb part, which cancel each other partially, so that the effective ion-BC force constants are small: $\varphi_{\text{eff}}''=0.61$ and $\varphi_{\text{eff}}'/\tau_0=2.03$. The Coulomb interaction between more distant neighbors turns out to be less important; one can show that a short-range model with effective ion-BC force constants, but without a Coulomb term, yields very similar dispersion curves. The contribution of φ_{i-i}' due to the equilibrium condition also turns out to be small and, moreover, destabilizing. Furthermore, in the short-wave TA modes, the BC's approximately move on surfaces where the potentials of Eq. (3) remain constant. Therefore, in these modes, only very small forces are transmitted between the ions. Thus the ions vibrate like Einstein oscillators, and their frequencies are given by the magnitude of the effective ion-bond coupling.

In the long-wavelength limit, the strong bond-bond coupling yields the high values of the shear moduli. As was indicated above, in this limit the interactions involving the BC's can be written as effective interactions between the atoms. Apart from some Coulombic term, we obtain the bond-stretching and bond-bending force constants $\alpha_{i-i}=4.84$ (3.8), $\beta_{i-i}=1.07$ (1.3). These values are quite similar to those of Keating,[6] which are given in parentheses. Moreover, concerning more elaborate valence force field models,[12] the transmission of forces due to the adiabatic motion of the BC's provides a physical understanding of terms which correlate bond lengths and bond angles of adjacent tetrahedra.

Furthermore, the BC has the value of $z\simeq1.6$, which is comparable to $z=2$ used by Phillips and Martin. However, in my model the BC's do contribute to the electronic susceptibility $\chi=(\epsilon-1)/4\pi$. I have obtained $4\pi\chi_{BC}=1.7$. This number, which represents the off-diagonal contribution to ϵ, is small compared to $4\pi\chi_{\text{exp}}=15$ in Ge. Thus, my result confirms the assumption of Phillips and Martin that the dominant part of ϵ comes from the diagonal or metallike screening. This is also corroborated by band-structure calculations.[13]

Detailed calculations for all diamond-type crystals will be presented elsewhere; here we summarize the most important results. When scaled with the ion plasma frequency, Si and α-Sn are very similar to Ge. In diamond, the ion-BC coupling is much stronger than in the other materials; the bond-bond interaction increases to a lesser extent. According to the above discussion, this can be seen from the variation both of the TA zone boundary frequencies and of the shear moduli. Furthermore, the direct ion-ion forces due to the metallike binding show up only in semiconductors; in diamond, however, all forces between the ions act via the bonds. Altogether, we find that, with the increase of the metallike binding, the sublattices of the ions and the BC's tend to decouple from each other.

I have presented a new bond-charge model for the phonons in tetrahedrally coordinated semiconductors. For Ge, I have obtained very good agreement with experimental phonon curves, using a four-parameter theory. The parameters describe the two types of binding in Ge. The metallike binding shows up in central forces between nearest-neighbor ions. These forces influence dominantly the longitudinal acoustic and the optic modes. The covalent binding is represented by interactions involving the BC's, only these forces determine the dispersion of TA phonons; they are essential for the stability of the diamond structure against shear. When the BC's are allowed to move adiabatically, the typical flattening of TA branches away from the zone center is obtained, if the ion-BC coupling is weak compared to the interactions between neighboring bonds. Thus, in the short-wave TA modes, the atoms vibrate like Einstein oscillators; at long waves, however, the strong bond-bond coupling contributes to the dynamics of the atoms, thus producing the high values of the shear moduli.

It is a pleasure to thank H. Bilz, W. Kress, K. Rustagi, and R. Zeyher for many helpful discussions, and also K. Rustagi, R. M. Martin, and B. Szigeti for critically reading the manuscript.

---

[1] A comprehensive review of the phonons in semiconductors including a critical survey of earlier model theories has been given by S. K. Sinha, CRC Crit. Rev. Solid State Sci. 4, 273 (1973).

[2] J. C. Phillips, Phys. Rev. 166, 832 (1968).

[3] R. M. Martin, Phys. Rev. 186, 871 (1969).

[4] W. Cochran, Proc. Roy. Soc., Ser. A 253, 260 (1959).

[5] F. Herman, J. Phys. Chem. Solids 8, 405 (1959).

[6] P. N. Keating, Phys. Rev. 145, 637 (1966).

[7] J. C. Phillips, Phys. Rev. 168, 905 (1968).

[8] A. A. Maradudin, E. W. Montroll, G. H. Weiss, and I. P. Ipatova, *Theory of Lattice Dynamics in the Harmonic Approximation* (Academic, New York, 1971), 2nd ed.

[9] Note, however, that there is no one-to-one correspondence between the BC-BC force constant matrices and the next-nearest-neighbor ion-ion force constant matrices.

[10] This calculation was adjusted to the early neutron data of B. N. Brockhouse and P. K. Iyengar, Phys. Rev. 111, 747 (1958). By readjusting the parameters, one could obtain slightly better agreement. We want to note that, with a "breathing" shell model, W. Kress [Phys. Status Solidi (b) 49, 235 (1972)] has improved the SM results.

[11] G. Nilsson and G. Nelin, Phys. Rev. B 3, 364 (1971).

[12] A. W. Solbrig, J. Phys. Chem. Solids, 32, 1761 (1971).

[13] J. P. Walter and M. L. Cohen, Phys. Rev. B 2, 1821 (1970).

Observation of Covalency Effects in K_2CuF_4 by Critical Scattering of Neutrons

K. Hirakawa and H. Ikeda

The Institute for Solid State Physics, The University of Tokyo, Roppongi, Minato-ku, Tokyo, Japan

(Received 20 May 1974)

Direct evidence of covalency effects on spin densities of the $Cu^{2+}-F^-$ antibonding orbital in ferromagnetic K_2CuF_4 has been observed by means of critical scattering of neutrons. The form factor observed was in good agreement with the one calculated based on linear combination of atomic orbital wave functions using covalency parameters determined by NMR.

According to Hubbard and Marshall,[1] the form factor of a magnetic ion surrounded by ligand ions is modified by the covalency, and such effect should be observed directly by neutron scattering. This effect should produce on the form factor a forward peak at small scattering angles less than

$\sin\theta/\lambda \sim 0.1$, which is attributed to the ligand contribution for most fluorides. It also makes the form factor at higher scattering angles appear flatter than would have been expected for an isolated Cu^{2+} ion for reasons to be discussed later. As is well known, most fluorides become antiferromagnetic and ligand ions lie, in many cases, in between the two magnetic ions, their spins being antiparallel with each other. In such a case, the spin moment on the F$^-$ ion is more or less canceled out because of the nature of the antiparallel spin configuration. Accordingly, the forward peak and the moment value obtained from magnetic reflections would be reduced by a factor dictated by the covalency and the resulting form factor looks much flatter.

In a ferromagnetic fluoride in which no such cancelation occurs, we could directly observe the above-mentioned covalency effect, and in such a case, paramagnetic disorder scattering would be of great use[2] because of the easy access to extremely small scattering angular region contrary to the use of Bragg scattering. We have, however, several disadvantages when such disorder scattering is employed; extremely small scattering cross section, short-range-order effect, simultaneous reflection effect, phonon scattering effect, etc., have to be properly taken into account. In our previous paper,[3] these difficul- es were successfully avoided by making use of e two-dimensional character of ferromagnetic $_2$CuF$_4$ whose $T_c = 6.25$ K.[4] It is well known that two-dimensional ferromagnet would manifest sharp critical scattering in the form of a ridge long one of the reciprocal lines. In K$_2$CuF$_4$, the idge appears along the $[00\zeta]$. However, in the resent case, the system is not of an ideally per- ect two-dimensional character. The scattering ross section scanned along the $[00\zeta]$ line should e expressed as a product of two parts, one pro- ortional to $f^2(\vec{K})$, which is $f^2(\zeta)$ in this case, nd the other depends on $\vec{q}$. The $\vec{q}$ dependence of e latter is symmetrical around each magnetic ragg point giving rise to periodically modified idge in the reciprocal space. Intensity measure- ents were made along the ridge at $T = T_c$ and lso well above T_c. By taking the difference of e two cases, most of the troublesome effects entioned above were removed, and we were left ith a quantity proportional to $f^2(\vec{K})\times${a periodic nction along ζ with a period of $2c^*$}. The de- ired $f(\zeta)$ would then be deduced rather easily. applying the present method, resolution correc- ion has to be carefully assessed. Fortunately, however, when the $\vec{K}$ dependence of the cross section is expressible in a ridgelike shape in reciprocal space, it has been proved[3] that the integrated intensities across the ridge are independent of the change of resolution function, and they can be expressed simply as $f^2(\zeta)\times${a periodic function with the period of $2c^*$}.

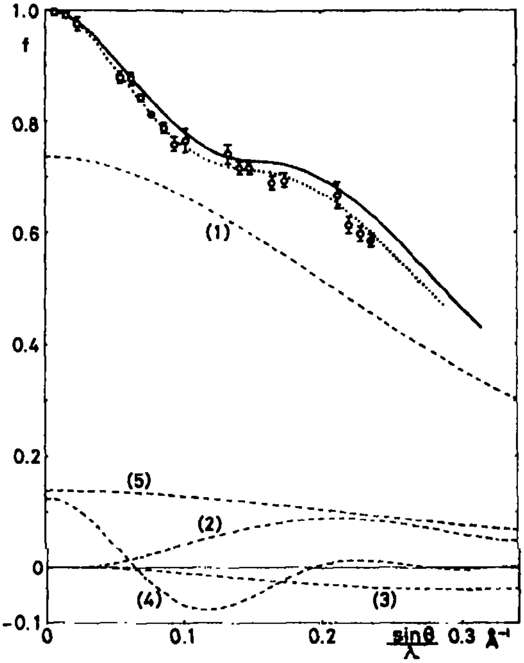

FIG. 1. Open circles, observed form factor by critical scattering; closed circles, observed form factor by Bragg scattering. The full form factor calculation using Eq. (3) is shown by the full line. The numbered broken lines are the contributions from the successive terms in Eq. (4).

In Fig. 1, the form factor thus obtained is shown by the open circles, where it is normalized with respect to the extrapolated (000) value. In the same figure, the form factor observed for (002) and (006) Bragg reflections using the polarized neutrons is also given.[5] For the latter, it is normalized by the bulk magnetization value. The agreement is quite satisfactory. In the following, we shall see how the above form factor can be explained by the theory proposed by Hubard and Marshall.

K$_2$CuF$_4$ has the K$_2$NiF$_4$ structure. In K$_2$CuF$_4$, the Cu^{2+} ion is surrounded by the deformed 6F$^-$ octahedra in the way shown in Fig. 2,[6] where Cu^{2+}–F$^-$ distances are also indicated.[6] The deformation of the octahedra results in the tetragonal local symmetry, and the ground-state d wave function may well be approximated by the form $x^2 - z^2$. The d wave function situated at the nearest-neighbor positions can be obtained by rotating the central local coodinates by $\pi/2$ around the c axis.[7] As the (00ζ) reflections see the Fourier-transformed spin densities projected on the c axis, $Cu^{2+} - 6F^-$ clusters lying in the basal plane would appear equivalent for these reflections. Consequently, we need to discuss the effect of covalency only for one $Cu^{2+} - 6F^-$ cluster. Furthermore, since the p wave function of the F^- ion lying on the b axis is orthogonal to the d wave function of the centered Cu^{2+} we could safely neglect the overlap effect of these orbitals. We thus calculate only for the $Cu^{2+} - 4F^-$ cluster. The fractions of spin densities A_σ^2 and A_s^2 on the $2p_\sigma$ and $2s$ orbitals are already determined by NMR measurements and they are given as[10]

$$(A_s^c)^2 = 0.43\% \text{ and } (A_\sigma^c)^2 = 5.76\% \text{ for } F_c^-, \qquad (A_s^a)^2 = 0.46\% \text{ and } (A_\sigma^a)^2 = 6.52\% \text{ for } F_a^-. \tag{1}$$

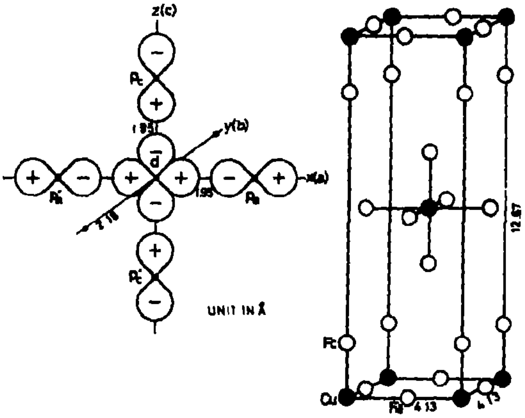

FIG. 2. The crystal structure of K_2CuF_4, in which a cooperative Jahn-Teller distortion can be seen. The crystal is composed of distorted $Cu^{2+} - 6F^-$ octahedron giving rise to a superlattice structure with the cell dimensions $C = 2c$ and $A = 2a$. In the figure, the fundamental cell in which K^+ ions are omitted is shown. Note the slight displacements of F^- ions in the basal plane. On the left, a deformed $Cu^{2+} - 6F^-$ octahedron with the associated orbitals to be calculated is shown.

Since the spin densities on the $2s$ orbitals are very small, we are justified in assuming that the whole unpaired spin density on the F^- ions is of p character. Hereafter we shall use

$$(A_\sigma^c)^2 = 6.19\% \text{ and } (A_\sigma^a)^2 = 6.98\%. \tag{2}$$

The antibonding orbital (linear combination of atomic orbitals) may be written as follows using the atomic wave functions $d(r)$ and $p(r)$:

$$\Psi_{AB} = N_\sigma\{d(r) - A_\sigma^c p_c(r) + A_\sigma^c p_c'(r) + A_\sigma^a p_a(r) - A_\sigma^a p_a'(r)\}, \tag{3}$$

where N_σ is the normalization constant.

Direct calculation of the form factor from the Ψ_{AB}^2 is indeed possible. However the expansion of Ψ_{AB}^2 would give the better physical picture in understanding the resultant modification of the isolated Cu^{2+} ion form factor by the covalency effect, and the spin densities $D(r)$ correct to the second order are given as

$$\begin{aligned} D(r) = \Psi_{AB}^2 \cong{} & d^2(r)[1 - 2(A_\sigma^c)^2 - 2(A_\sigma^a)^2] + 2A_\sigma^c\{2S_\sigma^c d^2(r) - d(r)p_c(r) + d(r)p_c'(r)\} \\ & + 2A_\sigma^a\{2S_\sigma^a d^2(r) - d(r)p_a(r) + d(r)p_a'(r)\} + (A_\sigma^c)^2\{p_c^2(r) + p_c'^2(r)\} + (A_\sigma^a)^2\{p_a^2(r) + p_a'^2(r)\}, \end{aligned} \tag{4}$$

where $S_\sigma^c = \langle d(r) | p_c'(r)\rangle$ and $S_\sigma^a = \langle d(r) | p_a(r)\rangle$.

The Fourier transformations of the successive terms in Eq. (4) have been computer calculated using the unperturbed wave functions of Cu^{2+} including the angular factor given by Watson,[11] and of F^- given by Froese.[12] The results are shown by the broken lines in Fig. 1. The first term in Eq. (4) is simply a form factor of an isolated Cu^{2+} ion reduced by a factor of $2(A_\sigma^c)^2 + 2(A_\sigma^a)^2$. The second and the third terms come from overlap densities and, in particular, the former is responsible for flattening of the form factor. The last two terms originate from the spin moment remnants on the F^- ions; of these the former is responsible for the observed forward peak. Som of these terms are shown by the dotted line in Fig. 1. In view of the approximate nature of Eq. (4), we have made a full calculation using Eq. (3 the result of which is also shown by the full line in Fig. 1. Without any adjustable parameters, w could obtain rather satisfactory agreements between the calculated and the observed values as indicated. Some systematic deviations manifest at higher angles indicate about 10% expansion of the calculated values compared with the observed one. Further, about 4% expansion may be expected[13] from the orbital moment since $g = 2.30$. We believe the above-mentioned expansion of the calculated form factor would be attributed to the approximate nature of the Hartree-Fock atomic wave functions. It should be noted that even in an ionic crystal such as K_2CuF_4, covalency effect on the form factor is quite large and one tends to overlook such an effect with the use of conventional Bragg scattering technique.

We are grateful to Professor Y. Ito, Dr. J. Akimitsu, and Dr. S. Wako for useful discussions. We are also grateful to Dr. G. Shirane for the critical reading of the manuscript.

---

[1] H. Hubbard and W. Marshall, Proc. Phys. Soc., London 86, 561 (1965).

[2] B. C. Tofield and B. E. F. Fender, J. Phys. C: Proc. Phys. Soc., London 4, 1279 (1971).

[3] K. Hirakawa and H. Ikeda, J. Phys. Soc. Jpn. 35, 1608 (1973).

[4] K. Hirakawa and H. Ikeda, J. Phys. Soc. Jpn. 35, 1328 (1973).

[5] J. Akimitsu and Y. Ito, to be published.

[6] It is suggested [D. I. Khomskii and K. I. Kugel, Solid State Commun. 13, 763 (1973)] and shown [K. Tanaka, J. Akimitsu, and N. Saito, to be published] recently that the Knox's structure [K. Knox, J. Chem. Phys. 30, 991 (1959)] hitherto used is wrong. Strictly speaking, the crystal is orthorhombic, but the lattice parameters are well described by tetragonal with $a = 4.13$ Å and $c = 12.67$ Å.

[7] Tanaka, Akimitsu, and Saito, Ref. 6.

[8] Khomskii and Kugel, Ref. 6.

[9] I. Yamada, J. Phys. Soc. Jpn. 33, 979 (1972).

[10] R. E. Watson, Massachusetts Institute of Technology Technical Report No. 12, 1959 (unpublished).

[11] C. Froese, Proc. Cambridge Phil. Soc. 53, 206 (1957).

[12] M. Blume, Phys. Rev. 124, 96 (1961).

Phase Separation in the Two-Dimensional Ising Ferromagnet

D. B. Abraham* and P. Reed

Department of Theoretical Chemistry, Oxford OX1 3TG, England

(Received 1 May 1974)

The interface density profile of the two-dimensional Ising ferromagnet is investigated for all temperatures below the critical point. The width of the interface diverges in the thermodynamic limit.

The phase-separation phenomenon in the Ising model of ferromagnetism with dimensionality $d = 2, 3$ has recently been investigated. It has been shown[1,2] that symmetry-breaking boundary conditions can induce *phase separation* with an associated *surface tension.* Gallavotti[3] then demonstrated that the interface for $d = 2$ is *very diffuse,* unlike the situation for $d = 3$, where the interface was shown by Dobrushin[4] to be localized. These results were obtained for $0 \leq T < T_0(d)$ with $T_0(d) \ll T_c(d)$, where $T_c(d)$ is the critical temperature for dimension d. This shows, contrary to folklore, that the existence of surface tension is not necessarily concomitant with the existence of a sharp interface. Subsequently Weeks, Gilman, nd Leamy[5] investigated the interface profile for he three-dimensional system at higher temperatures $[0 < T < T_c(d)]$ than Dobrushin considered sing a series-expansion procedure. They found e interface to be *well defined* for $0 \leq T < T'$ but *ffuse* for $T' < T \leq T_c(d)$, where $T' \sim T_c(2)$. These results motivated a more detailed investigation of the $d = 2$ separation phenomenon, valid for $0 \leq T < T_c(2)$, the results of which are reported here.

We consider a vertical-right-cylindrical lattice with M columns and $2N+1$ rows. There is a spin $\sigma_i = \pm 1$ at each vertex, labeled $i = (m, n)$ in Cartesian coordinates, where $n = -N, -N+1, \ldots, N$ and $m = 1, \ldots, M$. The energy of a spin configuration is

$$E_\Lambda(\{\sigma_i\}) = -J\sum \sigma_i \sigma_j - \sum h_j \sigma_j, \qquad (1)$$

where the first sum is over nearest-neighbor pairs of spins on Λ and the second sum is over spins in the top and bottom rows; $J > 0$ is a ferromagnetic coupling. The second term represents fields h_j acting on the top and bottom boundary rows of Λ, denoted $\partial\Lambda_+$ and $\partial\Lambda_-$. Two different boundary conditions are considered: On both $\partial\Lambda_+$ and $\partial\Lambda_-$ we have either (1) $h_j = +\infty$ for $j = 1, \ldots, s$ and $h_j = -\infty$ for $j = s+1, \ldots, M$, denoted $+-$, or

(ii) $h_j = +\infty$ for all j, denoted $++$. In the thermodynamic limit, the $++$ boundary conditions should lead to a pure state with magnetization $+m^*$,[6] whereas in the $+-$ case as $s\to\infty$ we should have a macroscopic region with magnetization $+m^*$ lying between regions with magnetization $-m^*$ to the left and right. There will be two interface regions; with each of these we may associate a long contour on the dual lattice separating opposite spins on Λ, in the sense of Ref. 2. The contours, whose ends are pinned, cluster (become independent) as $s\to\infty$.

The canonical partition for a lattice at temperature β^{-1} is denoted $Z_{NM}{}^b(\beta)$ where $b=+-$ or $b=++$. The surface tension τ is defined by[1,2]

$$\tau = \lim_{N\to\infty}\frac{1}{4N}\lim_{s\to\infty}\lim_{M\to\infty}\ln\left(\frac{Z_{NM}{}^{+-}(\beta)}{Z_{NM}{}^{++}(\beta)}\right), \tag{2}$$

and the interface profile is described by the magnetization

$$\langle\sigma_{0p}\rangle = \lim_{s\to\infty}\lim_{M\to\infty}[Z_{NM}{}^{+-}(\beta)]^{-1}\,\mathrm{Tr}[\exp(-\beta E_\Lambda)\sigma_{0p}]. \tag{3}$$

These quantities have been obtained rigorously using the transfer matrix V along the cylinder axis and the matrix element techniques of Abraham.[7] Our results are

$$\tau = \lim_{N\to\infty}\frac{1}{2N}\ln\left(\frac{1}{2\pi i}\oint\frac{dt}{t}g(t)^{2N}f(t)\right), \tag{4}$$

and

$$\langle\sigma_{0p}\rangle_N = -\frac{m^*}{2}\left(\frac{1}{\pi i}\oint\frac{dt}{t}g(t)^{2N}f(t)\right)^{-1}\frac{1}{\pi i}\oint dt\,t^{p-2}g(t)^N\frac{1}{\pi i}\oint\left(\frac{dz}{z-t}z^{3-p}-dz\,z^{2-p}\right)$$
$$\times g(z)^N[U(z)T(t)+U(t)T(z)], \tag{5}$$

with

$$f(t) = -t\,\Phi(t)/[1-t\Phi(t)]^2,$$

$$g(t) = e^{-\gamma(t)},$$

where $\gamma(t)\geqslant 0$ for $|t|=1$,

$$\cosh\gamma(t) = \cosh 2K^*\cosh 2K - (t+t^{-1})/2,$$

and

$$\Phi(t) = -\frac{A^{1/2}}{B}\frac{1}{t}\left(\frac{(t-A^{-1})(t-B)}{(t-A)(t-B^{-1})}\right)^{1/2},$$

with $K=\beta J$, $\exp(-2K^*)=\tanh K$, $A=\exp[2(K+K^*)]$, and $B=\exp[2(K-K^*)]$. Therefore, $A>B>1$ for $T<T_c$.

Finally,

$$T(z) = \frac{\Phi(z)}{1-z\Phi(z)}\left(\frac{z-B^{-1}}{z-A^{-1}}\right)^{1/2},$$

and

$$z^2U(z)T(z) = f(z).$$

All the contours are the positive unit circle, and principal parts are to be taken where appropriate. In (4) and (5) there are corrections due to additional bands in the spectrum of V but these are $O(\exp[-4N\gamma(0)])$ and may be neglected as $N\to\infty$ compared with the given terms.

Asymptotic analysis gives the result

$$\tau = -\gamma(0), \tag{6}$$

in agreement with results based on different definitions.[8] With the scaling $p=\alpha N^\delta$, $\delta\geqslant 0$, (5) gives

$$\lim_{N\to\infty}\langle\sigma_{0p}\rangle_N = 0 \text{ if } \delta<\tfrac{1}{2},$$
$$\lim_{N\to\infty}\langle\sigma_{0p}\rangle_N = m^*\,\mathrm{sgn}\,p \text{ if } \delta>\tfrac{1}{2} \tag{7}$$

for $T_c(2)>T>0$. When $T=0$, we have

$$\langle\sigma_{0p}\rangle_N = m^*\,\mathrm{sgn}\,p \text{ for all } \delta, N. \tag{8}$$

Thus for $d=2$ we obtain a rigid interface only when $T=0$. For $T_c(2)>T>0$ the interface has width $\sim N^{1/2}$ in agreement (in an appropriate domain of T) with the analysis of Gallavotti.[3] One cannot induce a translationally noninvariant equilibrium state for $T>0$ with the type of symmetry breaking boundary conditions considered. Nevertheless, we suspect, but cannot prove, that suppression (in a suitable sense) of the long-wavelength Fourier components of the "long contour" would make the interface sharp, possibly without affecting the surface tension appreciably.[9]

Identical results may be obtained using a rectangular lattice with + (−) boundary in the upper (lower) half.[10]

D. B. Abraham thanks M. E. Fisher, G. Gallavotti, J. L. Lebowitz, O. Penrose, and C. J. Preston very much for helpful comments. He is also most grateful for the hospitality of the Aspen Institute for Physics, the Ecole Polytechnique, and Yeshiva University where parts of this work were carried out. The work of P. Reed was supported by the Science Research Council.

---

*Work partially supported by the U. S. Air Force Office of Scientific Research Grant No. 73-2430.

[1] W. J. Camp and M. E. Fisher, Phys. Rev. B 6, 946 (1972), and Ref. 19 cited therein.

[2] R. A. Minlos and J. G. Sinai, Mat. USSR Sbornik 2, 335 (1967) [Trans. Moscow Math. Soc. 19, 121 (1968)]; G. Gallavotti and A. Martin-Löf, Commun. Math. Phys. 25, 87 (1972); see also excellent reviews by G. Gallavotti, Riv. Nuovo Cimento 2, 133 (1972); G. Gallavotti, A. Martin-Löf, and S. Miracle-Sole, in *Statistical Mechanics and Mathematical Problems*, edited by A. Lenard (Springer, Berlin, 1973), p. 162.

[3] G. Gallavotti, Commun. Math. Phys. 27, 103 (1972).

[4] R. L. Dobrushin, Teor. Veroyat. Ee Primen. 17, 619 (1972).

[5] J. D. Weeks, G. H. Gilman, and H. J. Leamy, Phys. Rev. Lett. 31, 619 (1973).

[6] A. Martin-Löf, Commun. Math. Phys. 24, 253 (1972); J. L. Lebowitz and A. Martin-Löf, Commun. Math. Phys. 25, 276 (1972); D. Ruelle, Ann. Phys. (New York) 69, 364 (1972); G. Bennettin, G. Gallavotti, G. Jona-Lasinio, and A. L. Stella, Commun. Math. Phys. 30, 45 (1973); D. B. Abraham and A. Martin-Löf, Commun. Math. Phys. 32, 245 (1973).

[7] D. B. Abraham, Stud. Appl. Math. 51, 179 (1972).

[8] L. Onsager, Phys. Rev. 65, 117 (1944); A. E. Ferdinand and M. E. Fisher, Phys. Rev. Lett. 19, 169 (1967); M. E. Fisher and W. J. Camp, Phys. Rev. Lett. 26, 565 (1971); D. B. Abraham, G. Gallavotti, and A. Martin-Löf, Physica (Utrecht) 65, 73 (1973). Consult also Ref. 1 above.

[9] F. P. Buff, R. A. Lovett, and F. H. Stillinger, Jr., Phys. Rev. Lett. 30, 601 (1973).

[10] D. B. Abraham, unpublished work, using some of the results of Abraham and Martin-Löf, Ref. 6. The surface-tension calculation reported there contains an error but the result is correct. It is related by duality to the edge-to-edge pair correlation function with free boundaries, given by D. B. Abraham, Stud. Appl. Math. 50, 71 (1971).

Search for Evidence of a Δ(1236)-Δ(1236) Component of the Deuteron*

C. P. Horne, S. Hagopian, V. Hagopian, N. D. Pewitt, P. K. Williams, and B. Wind
Florida State University, Tallahassee, Florida 32306

and

J. R. Bensinger
Brandeis University, Waltham, Massachusetts 02154,† and University of Pennsylvania, Philadelphia, Pennsylvania 19104

and

F. C. Porter, G. P. Yost, H. H. Bingham, W. B. Fretter, and W. R. Graves
University of California, Berkeley, California 94720

and

R. Harris, H. J. Lubatti,‡ K. Moriyasu, and W. J. Podolsky
Visual Techniques Laboratory, University of Washington, Seattle, Washington 98195

and

A. Firestone
California Institute of Technology, Pasadena, California 91109

and

G. Goldhaber
Lawrence Berkeley Laboratory, University of California, Berkeley, California 94720

and

M. Goldhaber
Brookhaven National Laboratory, Upton, New York 11973
(Received 28 May 1974)

Evidence for a bound $\Delta_{33}(1236)$-$\Delta_{33}(1236)$ component of the deuteron is sought by using π^+, π^-, and K^+ mesons as probes of nuclear structure. Events are observed which might contain Δ(1236) "spectators" in the breakup of a deuteron in a ΔΔ state. However, other mechanisms may contribute to the signal, and we cannot unambiguously ascribe our events to a ΔΔ contribution in the deuteron. With certain assumptions we obtain an upper limit of ~ 0.7% for the ΔΔ component of the deuteron.

It has been known for some time that the conventional nuclear theory which assumes nuclei to be composed of weakly bound protons and neutrons has some small but persistent discrepancies with experiments. It has been suggested[1] that these inconsistencies may be explained by the presence of nucleon isobar components in the nuclear wave function. Kerman and Kisslinger[2] have proposed such a model to explain the large backward "pick-up" peak in pd scattering.

We have searched[3] for direct evidence of a ΔΔ component of the deuteron wave function (note: an $N\Delta$ component is forbidden by isospin) by looking for the process diagrammed in Fig. 1(a). In this model, a beam meson (m) scatters "elastically" on a virtual Δ^- from a deuteron in a $\Delta^{++}\Delta^-$ bound state. If the impulse approximation is qualitatively valid, this yields a "spectator" $\Delta^{++}(\Delta_s^{++})$ on breakup. For a discussion of this point see

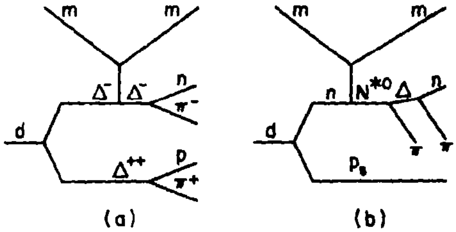

FIG. 1. Diagrams for (a) ΔΔ model, and (b) N^* model.

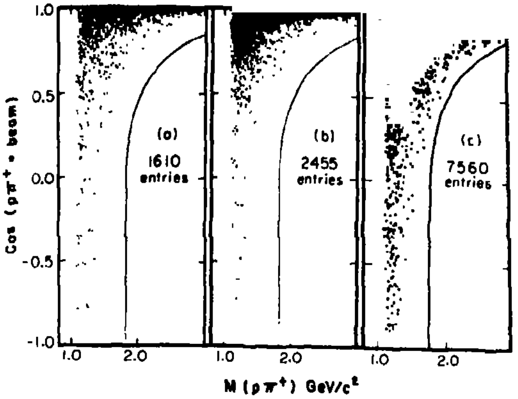

FIG. 2. $M(p\pi^+)$ versus $\cos(p\pi^+,\text{beam})$ in the lab for $d\to m\pi^+\pi^-pn$, where m is (a) π^+, (b) π^-, (c) K^+. urves show kinematic boundaries.

ef. 2. We use the presence of $n\pi^-$ and $p\pi^+$ com- nations simultaneously in the Δ mass region efined here as $M(N\pi) < 1360$ MeV], with the $p\pi^+$ combination backward in the laboratory frame, as the signature of this process. We estimate background from competing processes to be less serious for this case than for other $\Delta\Delta$ states available to this experiment.

The channel $md\to m\pi^+\pi^-pn$ (with visible proton), where m is the beam meson, has been studied in three independent experiments performed with the Stanford Linear Accelerator Center 82-in. deuterium-filled bubble chamber: 15-GeV/c π^+ (350 000 photos analyzed by Florida State University-University of Pennsylvania), 15-GeV/c π^- (500 000 photos, University of California, Berkeley-University of Washington, Seattle), and 12-GeV/c K^+ (500 000 photos, Lawrence Berkeley Laboratory–California Institute of Technology). Channel ambiguities are reduced by cuts on missing mass, confidence level, fits to alternative channels, and ionization-density measurements of positive tracks, as appropriate for each experiment. Proton-π^+ identification ambiguities are small for backward-going π^+p combinations.

Evidence for $\Delta\Delta$ *events.*—Figure 2 shows the cosine of the laboratory angle between the mo- ientum vectors of the π^+p combination and the eam (with no restriction on masses) versus the ^+p mass. We observe events in the backward emisphere ($\cos\theta<0$) in the Δ mass region.

The combined π^-n mass distribution for events ith a backward Δ^{++} candidate is shown in Fig. (a). A peak in the Δ^- mass region suggests that the $n\pi^-$ combination is a Δ resonance a substantial fraction of the time. Table I lists the numbers of events found.

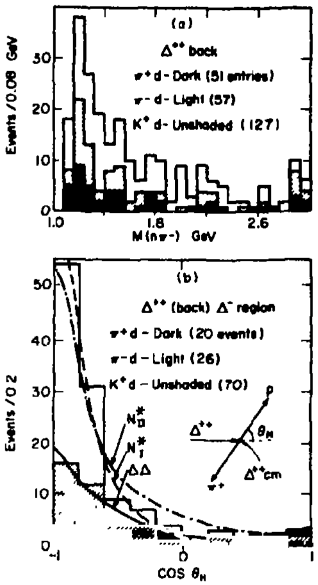

FIG. 3. Sum of the data from the $m\pi^+\pi^-pn$ channel of all three experiments: (a) $M(\pi^-n)$ for events with $p\pi^+$ in backward Δ^{++} region. (b) $\cos\theta_H(p\pi^+)=\hat{p}\cdot\hat{\theta}$, where $\hat{p}$ is the proton direction in the $p\pi^+$ rest frame and $\hat{\theta}$ is the direction of the $p\pi^+$ combination in the lab frame, for events in the Δ^{++}(back)Δ^- region. The N^* model curves (broken) are normalized to $\cos\theta_H<0$; N_I^* uses the pure Hulthén spectrum, N_{II}^* uses the modified spectator proton spectrum. The $\Delta\Delta$ model curve (solid) is normalized to $\cos\theta_H>0$.

Backgrounds.—Nucleon dissociation into $\Delta\pi$ states (here referred to as N^*'s, even though not necessarily resonant), well known in hydrogen and deuterium data,[4] is probably the major background for the Δ^{++}(back)Δ^- signal. We have cal-

TABLE I. Results for the reaction $md\to m\pi^+\pi^-pn$; $m=\pi^+,\pi^-,K^+$.

	π^+d	π^-d	K^+d
Total events	1809	3474	12693
Δ^{++}(back)	56	48	132
Δ^{++}(back)Δ^-	20	26	73
$\sigma(\Delta\Delta_J)$ (mb)	0.04[a]	0.03[a]	0.06[a]
R (%)	0.6[b]	0.5[b]	1.3[b]

[a] Upper limit, statistical error $\lesssim0.01$ mb.

[b] Upper limit, statistical error $\lesssim\pm0.15$ (see Ref. 10).

culated[5] the expected shape using the model of Fig. 1(b) assuming the same mass, width, and momentum-transfer distributions found in hydrogen data at similar energies.[4] Two different "spectator" proton momentum spectra are used in the impulse approximation. One is based entirely on the Hulthén wave function; the other modifies this spectrum above 200 MeV/c to resemble the backward proton spectrum from the $K^+d\to K^0pp$ ($K^0\to\pi^+\pi^-$) reaction of the K^+ experiment, in attempt to include contributions in the high-momentum region from double scattering and possible inadequacies of the Hulthén wave function. In the K^0pp channel contamination from other reactions is quite small, and isobar terms in the deuteron wave function are not expected to contribute significantly to the spectator spectrum.

This model gives a backward $p\pi^+$ mass distribution in good agreement with the data. Further evidence for an N^*-model contribution is the asymmetry of the decay angular distribution of the backward Δ^{++} candidate, Fig. 3(b). The forward component of this angular distribution is in poor agreement with the N^* model using the pure Hulthén spectrum (curve labelled N_I^*) but consistent with the model using the modified spectrum (N_{II}^*).

In the $\Delta\Delta$ model (solid curve) this distribution is expected to show forward-backward symmetry if the Δ^{++} does not decay until leaving the interaction region. The spectator Δ^{++}, generated by using the $d(\Delta\Delta)$ wave functions according to Kisslinger[7] (neglecting double scattering), was given a $1+3\cos^2\theta_B$ decay angular distribution. The result is insensitive to the details of $m\Delta$ elastic scattering. Events with nonstopping protons are lost in the π^+d and K^+d data; simulation of this loss (done for all models) results in the asymmetry of this curve. This effect alone is not adequate to explain the observed asymmetry and N^* contribution is needed.

Within the approximations, we cannot distinguish the contributions of the $\Delta\Delta$ model and the N^* model with the modified Hulthén spectrum. Basing this calculation on the K^0pp data, while probably an improvement over a pure Hulthén spectrum, neglects final-state interactions (other than those in the K^0pp channel) and possible significant variation with channel of double-scattering contributions. In addition, the impulse approximation may not be adequate in the region of large ($\gtrsim 300$ MeV/c) spectator momenta, where the greatest sensitivity to differences between the models may lie.

Probability of $d(\Delta\Delta)$.—If we assume that the cross section for off-mass-shell $m\Delta$ elastic scattering leading to deuteron breakup is equal to the mN elastic cross section[8] (leading to breakup), then the ratio $R=\sigma(md\to\Delta\Delta_s)/\sigma(md\to mpn)$ is a rough estimate of the $\Delta\Delta$ fraction of the deuteron.

The cross sections $\sigma(md\to mpn)$ are not measured but may be estimated by using Glauber theory.[9] We find for $\sigma(\pi^\pm d\to\pi^\pm pn)$ at 15 GeV/c and $\sigma(K^+d\to K^+pn)$ at 12 GeV/c the estimates 6.8 ± 0.6 mb and 4.8 ± 0.5 mb, respectively. We obtain an *upper limit* to $\sigma(md\to m\Delta\Delta_s)$ by counting *all* the Δ^{++}(back)Δ^- candidate events. Correcting this number by factors of (i) 2 for the probability that Δ^- is the spectator, (ii) 3 for the approximate probability that the spectator travels forward,[2] (iii) 2 for the equal probability of $d(\Delta^+\Delta^0)$ and $d(\Delta^{++}\Delta^-)$, and (iv) 1.2 for nonstopping proton events lost in π^+d and K^+d—loss of protons too short to be seen is neglected (based on the $\Delta\Delta$ model)—we obtain the upper limits shown in Table I. A statistically weighted average gives $R<(0.7\pm0.1)\%$.[10]

Neglecting final-state interactions and interference between the N^* and $\Delta\Delta$ models, we obtain a more restrictive upper limit to R by integrating under the (properly symmetrized) $\Delta\Delta$ curve of Fig. 3(b) (which was normalized to $\cos\theta_B>0$). This more model-dependent limit is ~60% of the above limit for R, with the difference possibly due to the N^* contribution. It is probable that the N^* background relative to $\Delta\Delta$ production varies with the bombarding particle. Our results are compatible with theory.[7] The "spectator" method, with further refinements, may prove valuable in other situations where possible isobar effects may be more easily distinguished.

We are grateful to the Stanford Linear Accelerator Center 82-in. bubble-chamber staff and to A. S. Goldhaber and H. A. Gordon for helpful discussion. J. Lannutti, J. Albright, and W. Selove assisted in the π^+d experiment; D. M. Chew, L. A. Dunn, and L. Stutte in π^-d; and D. Lissaue and G. H. Trilling in K^+d. We thank the scannin measuring, and analysis staffs of each laborator

---

*Work supported in part by the U. S. Atomic Energy Commission and the National Science Foundation.

†Present address.

‡A. P. Sloan Foundation Research Fellow.

[1] For a review see H. Arenhövel and H. J. Weber, i *Springer Tracts in Modern Physics*, edited by G. Hö (Springer, Berlin, 1972), Vol. 65, p. 59.

[2] A. Kerman and L. S. Kisslinger, Phys. Rev. 180,

1483 (1969); L. S. Kisslinger, Phys. Lett. 48B, 410 (1974).

[3] Preliminary results on part of these data were presented by M. Goldhaber, J. Phys. (Paris), Colloq. 34, C1-209 (1973). We have recently received a report from H. Braun *et al.* [see Phys. Rev. Lett. 33, 312 (1974)], reporting a ΔΔ component upper limit much la larger than ous. G. Ekspong (private communication) has studied the *pd* case.

[4] For a recent review see: H. J. Lubatti, Acta Phys. Pol. B 3, 721 (1972). We used peaks at ~1410 and 1690 MeV with relative normalization according to our data.

[5] The calculations were done by the Monte Carlo technique.

[6] L. Hulthén and M. Sugawara, in *Encyclopedia of Physics*, edited by Flügge (Springer, Berlin, 1957), Vol. 39.

[7] L. S. Kisslinger, "Baryon Resonances and the Nuclear Ground State" (to be published).

[8] S. B. Gerasimov, Pis'ma Zh. Eksp. Teor. Fiz. 14, 385 (1971) [JETP Lett. 14, 260 (1971)]. We neglected any effects of the different deuteron form factors.

[9] V. Franco and R. J. Glauber, Phys. Rev. 142, 1195 (1966). Meson-proton elastic cross sections from CERN Reports No. CERN-HERA 72-1 and No. CERN-HERA 72-2 (unpublished).

[10] Uncertainties in microbarn equivalents and in $\sigma(\pi d \to \pi p n)$ give systematic errors of ~ ±0.2.

Nuclear-Coulomb Interference in Inelastic Scattering of α Particles from ^{168}Er, ^{184}W, and ^{186}W†

I. Y. Lee, J. X. Saladin, C. Baktash, J. E. Holden, and J. O'Brien
Scaife Nuclear Physics Laboratory, University of Pittsburgh, Pittsburgh, Pennsylvania 15260

(Received 10 June 1974)

Excitation functions for the 0^+, 2^+, and 4^+ states of ^{168}Er, ^{184}W, and ^{186}W were measured at 140° and 173.5° with incident α-particle energies between 12.5 and 19 MeV. Strong destructive nuclear-Coulomb interference effects were observed. A coupled-channels code was developed and the deformation parameters β_2^N and β_4^N of the optical potential were determined and are compared with those of the charge distribution, β_2^c and β_4^c.

In recent years systematic experimental information has been accumulated concerning quadrupole and hexadecapole deformations in the rare-earth region using two different methods, i.e., Coulomb excitation by means of α particles[1-4] and inelastic scattering of α particles well above the Coulomb barrier.[5,6] From Coulomb excitation experiments it is possible, after making some reasonable model assumptions, to extract deformation parameters β_2^c and β_4^c for the *charge* distribution. Experiments far above the barrier, on the other hand, yield the deformation parameters of the optical potential. Early comparisons between the two types of experiments seemed to indicate that the deformation parameters obtained from high-energy (α, α') scattering were substantially smaller than those obtained by electromagnetic methods. This difference may, in principle, be attributed to one or both of two reasons:

(1) There is no *a priori* reason why the electric charge distribution and the optical potential need to have *exactly* the same deformation parameters, though one would certainly expect them not to be too different.

(2) It is well known that the quantities determined by inelastic scattering are not the β_λ's rather something like a deformation length $\beta_\lambda R$,[7] where R is the nuclear radius. The extraction of β_λ's from electromagnetic moments, on the other hand, depends critically (approximately like $R^{-\lambda}$) on the radius parameter chosen for the charge distribution. Thus some care must be exercised in comparing β_λ's obtained by these two different classes of experiments.

The question of the connection between the deformation of the charge distribution and that of the optical potential is an intriguing one. We expected experiments in the interference region between Coulomb and nuclear excitation to be most sensitive to possible differences or equalities in the two types of deformation parameters. Experiments were carried out at laboratory scattering angles of 140° and 173.5° in the energy range from 12 to 19 MeV on the isotopes ^{168}Er, ^{184}W, and ^{186}W. The experimental setup was similar to that used in earlier work of our group.[8] Its salient features are an annular surface-barrier detector at 173.5°, two surface-barrier detectors at ±140°, and another pair of detectors at ±30° which served as monitors. All detectors were cooled to

~ − 20°C and overbiased. Spot targets of 3 mm diam, about 20 $\mu g/cm^2$ thick, on 20-$\mu g/cm^2$ carbon backing were produced by vacuum evaporation of the enriched isotope oxides. The energy resolution for all detectors was ~25 keV full width at half-maximum. The yields of the elastic and inelastic peaks were evaluated by means of an iterative computer program which is based on the assumption that all peaks have the same shape. The overall uncertainty in the 2^+ and 4^+ yields is about 2% and 3–5%, respectively. In the sub-Coulomb region the uncertainties are smaller, about 1% and 3%. The values of the reduced matrix elements $\langle 0^+ \| \mathfrak{M}(E2) \| 2^+ \rangle$ and $\langle 0^+ \| \mathfrak{M}(E4) \| 4^+ \rangle$ were extracted from the low-energy cross-section ratios with the help of the quantum-mechanical coupled-channels code AROSA for Coulomb excitation.[8] From the moments, charge deformation parameters $\beta_\lambda{}^c$ were derived within the framework of the axially symmetric rigid-rotor model, using a deformed Fermi-charge distribution

$$\rho(r,\theta) = \rho_0(1+\exp\{[r-R(\theta)]/a\})^{-1},$$

with

$$R(\theta) = R^c[1+\beta_2{}^c Y_{20}(\theta)+\beta_4{}^c Y_{40}(\theta)].$$

The procedure for choosing the parameters R_0, ρ_0, and a was identical to that used in earlier work of our group.[3] The experimental points in Fig. 1(a) represent the ratios $d\sigma_{\rm exp}/d\sigma_{\rm cx}$ of the experimental elastic cross section to the elastic cross section calculated under the assumption of pure Coulomb excitation. The experimental points in Fig. 1(b) are the double ratios $(d\sigma_{2^+}/d\sigma_{0^+})_{\rm expt}/d\sigma_{2^+}/d\sigma_{0^+})_{\rm cx}$ plotted as a function of energy. Figure 1(c) is an analogous plot for the 4° double ratios. The most conspicuous feature of the data is the sharp increase in destructive interference of the excitation of the 4^+ state between ^{168}Er and the W isotopes. This is in agreement with recent results of Bemis *et al.*[9] on ^{154}Sm, ^{166}Er, and ^{182}W. In order to interpret the data in the interference region we expanded the coupled-channels Coulomb excitation code AROSA to include excitation via a deformed optical potential. We found it necessary to integrate the radial equations out to arguments $\rho = kr = 450$. In the region of nonvanishing optical potential a Numerov integration routine is used. Further out a Taylor expansion is employed which is particularly fast in regions where the interaction is purely electromagnetic.[8] The convergence in the sum of partial amplitudes from different channel spins is considerably improved by using a procedure which is related to the Padé approximation.[8,10] Thus in a typical case only about 45 partial waves need to be cal-

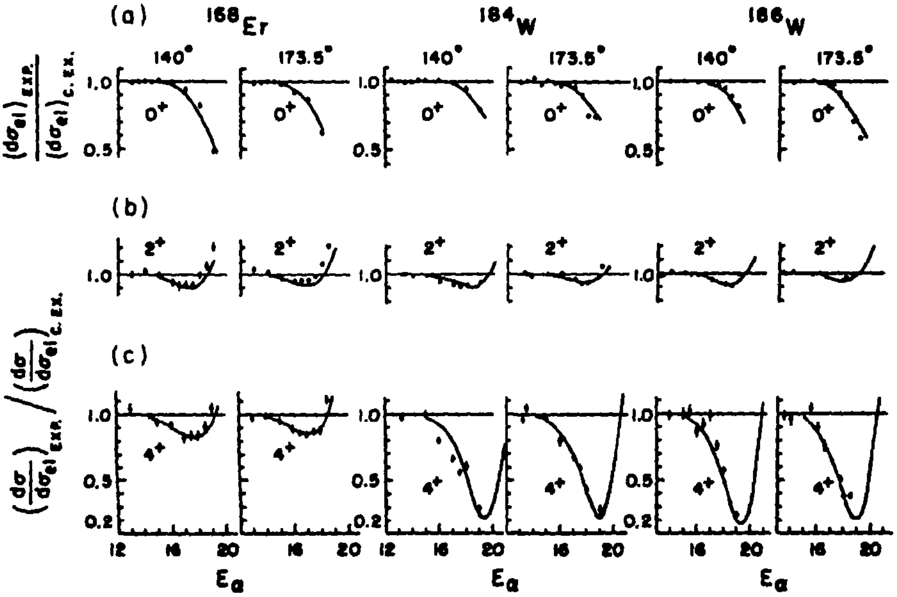

FIG. 1: Coulomb-nuclear interference in the elastic and inelastic scattering of α particles. The solid curves represent the results of coupled-channel calculations. For details, see text.

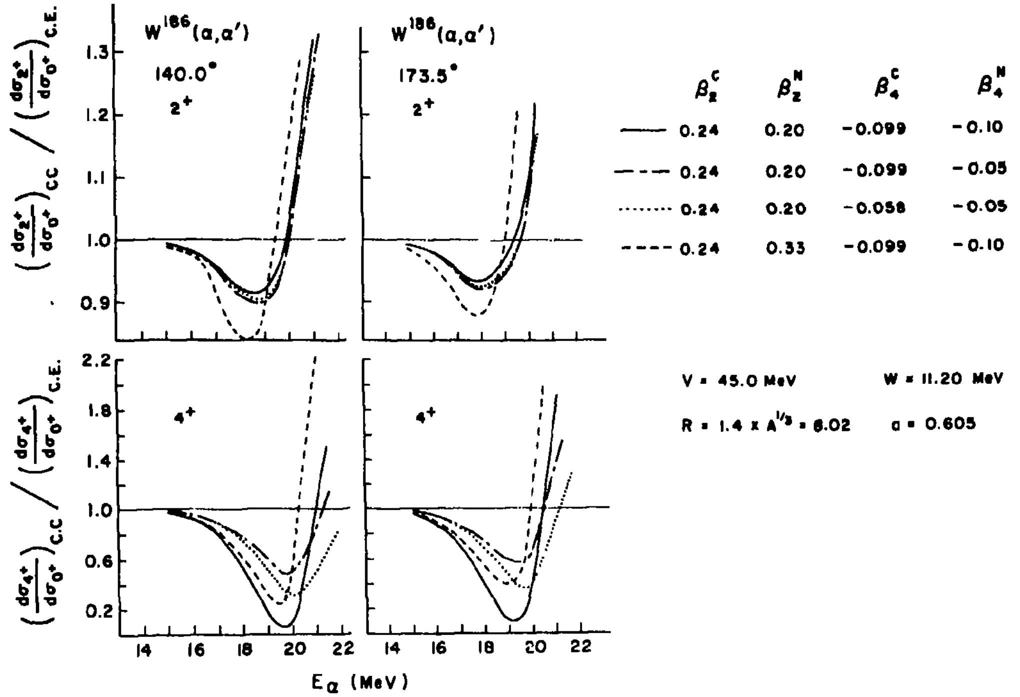

FIG. 2: Sensitivity of coupled-channels calculations to the relative size of charge and optical potential deformation.

culated explicitly where about 300 partial waves would be needed without the use of the Padé approximation.

In fitting the data, the following procedure was adopted. We started out using essentially the same optical potential used by Aponick *et al.* for the interpretation of (α,α') scattering far above the Coulomb barrier.[6] This potential was origi- ally derived from elastic scattering on nuclei st before the onset of permanent deformation. he interaction radius and potential depth V were en slightly adjusted such as to fit the elastic cattering. The final parameters were $V=47$ eV, $W=11.2$ MeV, and $a=0.605$ fm. The other gredients of the calculations are the reduced atrix elements $\langle 0^+\|\mathfrak{M}(E2)\|2^+\rangle$ and $\langle 0^+\|\mathfrak{M}(E4)\|4^+\rangle$ nd the deformation parameters β_2^N and β_4^N of the ptical potential. The Coulomb-excitation contri- ution from the interior of the nucleus was calcu- ted by assuming a uniform charge distribution $=\rho_0$ for $r<R^u(\theta)$ with $R^u(\theta)=R^u(1+\beta_2^u Y_{20}+\beta_4^u Y_{40})$, here R^u and the β_λ^u are adjusted such as to give e correct charge and reduced matrix elements. he position, depth, and shape of the interference minimum for the 4⁺ state is very sensitive to both the nuclear deformation parameter β_4^N and the reduced matrix element $\langle 0^+\|\mathfrak{M}(E4)\|4^+\rangle$. Thus the interference data permit a more precise (though somewhat more model-dependent) determination of the $E4$ moments than do sub-Coulomb measurements alone, particularly in the region of negative β_4 values where the sub-Coulomb cross section is rather insensitive to the $E4$ moment. Figure 1 shows the best fits to the data. The sensitivity of the calculations to the parameters is shown in Fig. 2. The sensitivity of the experiments is ~20% in the β_4^N and the β_4^c deformations. It has been pointed out earlier by Brückner *et al.*[11] and is confirmed by the present investigation that measurements in the interference region permit an unambiguous determination of the sign of the β_4 deformation which is not possible from sub-Coulomb data alone. Table I summarizes the results. The deformation parameters β_λ^c are those derived from the E_λ moments, whereas $\beta_2^{N,\mathrm{int}}$ are the optical potential deformation parameters derived from the interference data. R^N is the radius of the optical potential.

TABLE I. Reduced $E2$ and $E4$ transition moments and charge and optical-potential deformation parameters. For details, see text.

	$\langle 0^+ \Vert \mathfrak{M}(E2) \Vert 2^+ \rangle$ (e b)	β_2^c	$\beta_2^{N'}$	$\beta_2^{N,\mathrm{int}}$	$\langle 0^+ \Vert \mathfrak{M}(E4) \Vert 4^+ \rangle$ (e b^2)	β_4^c	$\beta_4^{N'}$	$\beta_4^{N,\mathrm{int}}$	R^c (Fm)	$R^{N'}$	$R^{N,\mathrm{int}}$
^{168}Er	2.42 (0.03)	0.336	0.260	0.263	0.179 (0.054)	−0.019	−0.025	−0.028	6.07	7.92	7.91
^{184}W	1.94 (0.03)	0.254	0.192	0.192	−0.243 (0.090)	−0.089	−0.075	−0.076	6.257	8.09	8.17
^{186}W	1.83 (0.03)	0.239	0.181	0.182	−0.266 (0.095)	−0.090	−0.075	−0.077	6.28	8.11	8.18

Our β_4 deformation parameters for $W^{184,186}$ are considerably smaller than those obtained by Bemis *et al.*[9] from sub-Coulomb data on W^{182}. However if one includes in the analysis of the Oak Ridge National Laboratory data the interference results, one obtains a β_4^c value of ~ 0.11.

Hendrie[12] has recently proposed a method of scaling between the two types of deformation parameters which takes into account the geometry of the situation. The parameters $\beta_c^{N'}$ and $R^{N'}$ are those calculated from the β_λ^c and R^c using Hendrie's prescription. The agreement between the $\beta_\lambda^{N'}$ and the $\beta_\lambda^{N,\mathrm{int}}$ is extremely good, showing that the two types of deformation parameters are in the sense of Hendrie's model very consistent with each other. It should be pointed out that the expressions of Ref. 12 are derived under the assumption that projectile and target have sharp surfaces. They are therefore not strictly correct but they are probably a pretty good approximation for the geometrical aspects of the situation. A more rigorous approach would involve the use of folded potentials which has been successfully employed by West, Cotanch, and Robson.[13]

---

†Work supported by the National Science Foundation.

[1] F. S. Stephens, R. M. Diamond, N. K. Glendenning, and J. de Boer, Phys. Rev. Lett. 24, 1137 (1970); F. S. Stephens, R. M. Diamond, and J. de Boer, Phys. Rev. Lett. 27, 1151 (1971).

[2] T. K. Saylor, III, J. X. Saladin, I. Y. Lee, and K. A. Erb, Phys. Lett. 42B, 51 (1972); K. A. Erb, J. E. Holden, I. Y. Lee, J. X. Saladin, and T. K. Saylor, Phys. Rev. Lett. 29, 1010 (1972).

[3] A. H. Shaw and J. S. Greenberg, to be published.

[4] R. M. Ronningen, J. H. Hamilton, L. L. Riedinger, A. V. Ramayya, G. Garcia-Bermudez, R. O. Sayer, R. L. Robinson, and P. H. Stelson, Bull. Amer. Phys. Soc. 19, 524 (1974); J. H. Hamilton, L. Varnell, R. M. Ronningen, A. V. Ramayya, J. Lange, L. L. Riedinger, R. L. Robinson, and P. H. Stelson, Bull. Amer. Phys. Soc. 19, 579 (1974).

[5] D. L. Hendrie, N. K. Glendenning, B. G. Harvey, O. N. Jarvis, H. H. Duhm, J. Sandinos, and J. Mahoney, Phys. Lett. 26B, 127 (1968).

[6] A. A. Aponick, Jr., C. M. Chesterfield, D. A. Bromley, and N. K. Glendenning, Nucl. Phys. A159, 367 (1970).

[7] N. Austern and J. S. Blair, Ann. Phys. 33, 15 (1965).

[8] F. Roesel, J. X. Saladin, and K. Alder, to be published.

[9] C. E. Bemis, Jr., P. H. Stelson, F. K. McGowan, W. T. Milner, J. L. C. Ford, Jr., R. L. Robinson, and W. Tuttle, Phys. Rev. C 8, 1934 (1973).

[10] K. Alder and H. K. A. Pauli, Nucl. Phys. A128, 193 (1969).

[11] W. Brückner, J. G. Merchinger, D. Pelte, U. Smilansky, and K. Traxel, Phys. Rev. Lett. 30, 57 (1973).

[12] D. L. Hendrie, Phys. Rev. Lett. 31, 478 (1973).

[13] L. West, S. Cotanch, and D. Robson, in *Proceedings of the International Conference on Nuclear Physics, Munich, Germany, 1973*, edited by J. de Boer and H. J. Mang (North-Holland, Amsterdam, 1973), Vol. 1, p. 383.

Remarks on Dirac's New Theory

J. L. Pietenpol, R. Incoul, and D. Speiser
Institut de Physique Théorique, Université Catholique de Louvain, B-1348 Louvain-la-Neuve, Belgium

(Received 20 May 1974)

We show that Dirac's proposed scalar-tensor theory of gravitation and electromagnetism can be rewritten in such a way that the scalar field decouples from the rest of the world. The symmetry breaking implicit in the formalism is shown to be unobservable.

Recently, Dirac has proposed a foundation for a new theory of gravitation and electromagnetism.[1] The fundamental objects of the theory are a metric tensor $g_{\mu\nu}=g_{\nu\mu}$, a vector field κ_μ (to be identified with the electromagnetic potential), and a scalar field β (assumed to be everywhere positive). The equations of the theory are obtained from an action functional which is required to be invariant under gauge transformations in the sense of Weyl:

$$g_{\mu\nu}'(x)=\lambda^2(x)g_{\mu\nu}(x),$$
$$\kappa_\mu'(x)=\kappa_\mu(x)+\partial_\mu\ln\lambda(x),$$
$$\beta'(x)=\lambda^{-1}(x)\beta(x),$$

where λ is an arbitrary positive function. The metric and the vector field form the basis of Weyl's geometry, while the β field is introduced in order to avoid fourth derivatives of the metric in the field equations.

Our purpose is to point out that the theory can be recast in a form such that the scalar field is ompletely decoupled from the other dynamical ariables.[2] We define a new set of variables as llows:

$$h_{\mu\nu}(x)\equiv\beta^2(x)g_{\mu\nu}(x),$$
$$A_\mu(x)\equiv\kappa_\mu(x)+\partial_\mu\ln\beta(x).$$

hese relations are invertible (because $\beta\neq 0$), so at instead of $g_{\mu\nu}$, κ_μ, and β we can just as well take $h_{\mu\nu}$, A_μ, and β as independent field variables. Under a Weyl gauge transformation, we have

$$h_{\mu\nu}'(x)=h_{\mu\nu}(x),$$
$$A_\mu'(x)=A_\mu(x),$$
$$\beta'(x)=\lambda^{-1}(x)\beta(x).$$

Thus, in terms of the new variables, an action functional I is Weyl gauge invariant if and only if it is independent of β. The field equation $\delta I/\delta\beta(x)=0$ then reduces to the identity $0=0$, while the other field equations are independent of β. The Weyl gauge invariance of the theory thus seems to be devoid of physical content.

In general, there will be additional dynamical variables to describe the source. If these are Weyl gauge invariant, the foregoing argument still holds. If they are "cotensors", say,

$$q'(x)=\lambda^p(x)q(x),$$

we can define new variables

$$Q(x)\equiv\beta^p(x)q(x)$$

and then apply the preceding argument to the set of variables $h_{\mu\nu}$, A_μ, β, and Q. (Even if the transformation law of q should be more complicated then that of a cotensor, it suffices to define Q as the value taken by q in the gauge where $\beta=1$.)

Dirac's action functional for the vacuum (his equation 5.3),

$$I=\int(\tfrac{1}{4}g^{\mu\lambda}g^{\nu\sigma}F_{\mu\nu}F_{\lambda\sigma}-\beta^2R+6g^{\mu\nu}\beta_{,\mu}\beta_{,\nu}+c\beta^4)\sqrt{-g}\,d^4x,\quad F_{\mu\nu}\equiv\kappa_{\mu,\nu}-\kappa_{\nu,\mu},$$

hen re-expressed in terms of the new variables, becomes

$$I=\int(\tfrac{1}{4}h^{\mu\lambda}h^{\nu\sigma}F_{\mu\nu}F_{\lambda\sigma}-R_h+c)\sqrt{-h}\,d^4x,\quad F_{\mu\nu}\equiv A_{\mu,\nu}-A_{\nu,\mu},$$

ere R_h is the scalar curvature associated with , and a divergence has been dropped from the ion density. Apart from numerical coefficints, this is just the usual action for general ativity with cosmological constant and electrognetic field. Likewise, the proposed action a charged particle (Dirac's equations 8.1 and 8.3),

$$I_1+I_2=-m\int\beta\,ds+e\int\kappa_\mu dx^\mu,$$

becomes

$$I_1+I_2=-m\int ds_h+e\int A_\mu dx^\mu,$$

with neglect of a total differential, and again we have the same expression as in the standard theory.[3]

Dirac suggests that an observable violation of charge-conjugation and time-reversal invariance will result if the particle action contains a term of the form (his equation 10.1)

$$I_3 = a\int g^{\mu\nu}(\beta^{-3}\beta_{,\mu}\beta_{,\nu} + 2\beta^{-2}\beta_{,\mu}\kappa_\nu + \beta^{-1}\kappa_\mu\kappa_\nu)\,ds.$$

In terms of the new variables this becomes

$$I_3 = a\int h^{\mu\nu}A_\mu A_\nu\,ds_h$$

and, while such a term does violate ordinary gauge invariance (which is equivalent to Dirac's "transformations of the type 3"), it does not violate invariance under C or T. Dirac's contention that it does rests on the assertion that, while one may always work in the "Einstein gauge" $\beta = 1$, one must first obtain the field equation from the variation of β before putting $\beta = 1$, and "this field equation will still show symmetry breaking."[4] But we have shown that $\delta I/\delta\beta = 0$ is an identity for one set of independent variables, and it is clear that, for *any* choice of variables, this equation cannot be independent of the other dynamical equations. We conclude that the symmetry breaking, while undeniably present in Dirac's *formalism*,[5] is unobservable.

Despite the pessimistic nature of our remarks, it is tempting to try to salvage something from Dirac's theory. In section 2 of his paper, he proposes two special gauges: an "atomic" gauge corresponding to the space-time interval defined by an atomic standard; and an Einstein gauge, in which the Schwarzschild solution is valid *and* in which a test particle follows geodesic motion. In this way it would be possible to accommodate a variable gravitational constant (expressed in atomic units), as suggested by numerical coincidences among certain large dimensionless quantities,[6] without spoiling the prediction of general relativity for the perihelion precession. Unfortunately, the atomic metric is never introduced into the formalism; moreover, to do so would obviously break the Weyl gauge invariance by singling out a particular gauge, which is just what Dirac wishes to avoid.[7]

Nevertheless, it is interesting to try to incorporate the two-metric idea into a theory (without insisting on Weyl gauge invariance), and an attempt in this direction will be published elsewhere.[8] The theory the one is led to gives the same predictions as general relativity for the classic tests, but suffers from at least one serious disease: It seems impossible to incorporate ordinary electromagnetic gauge invariance in a satisfactory way.

---

[1] P. A. M. Dirac, Proc. Roy. Soc., Ser. A 333, 403 (1973).

[2] A similar observation, in the context of the Brans-Dicke theory, has been made by J. L. Anderson, Phys. Rev. D 3, 1689 (1971).

[3] Except that the sign of the mass term seems to be inconsistent with the overall sign of the vacuum action.

[4] Ref. 1, p. 417.

[5] For example, in Dirac's formalism the charge e is a dimensionless number, so that the two signs of charge are formally inequivalent.

[6] P. A. M. Dirac, Proc. Roy. Soc., Ser. A 165, 199 (1938).

[7] Ref. 1, p. 409.

[8] J. L. Pietenpol, "A New Scalar-Tensor Theory of Gravitation" (to be published).

Evidence for a New Scaling Hypothesis in High-Energy Collisions*

F. T. Dao, R. Hanft, J. Lach, E. Malamud, and F. Nezrick
Fermi National Accelerator Laboratory,† *Batavia, Illinois 60510*

and

V. Davidson, A. Firestone, D. Lam, F. Nagy, C. Peck, and A. Sheng
California Institute of Technology, Pasadena, California 91109

and

R. Poster, P. Schlein, and W. Slater
University of California, Los Angeles, California 90024

and

A. Dzierba
Indiana University, Bloomington, Indiana 47401

(Received 3 June 1974)

Single-particle distributions in transverse and longitudinal momenta have been studied in pp interactions at 300 GeV/c. By comparing these distributions for different multiplicities of produced particles and with published low-energy data, we put forth the hypothesis of a new type of scaling: The shape of distributions in p_T and p_L are independent of multiplicity and incident energy.

The scaling behavior of a distribution $f(x_1, x_2)$ ith independent variables x_1 and x_2 can be dened in terms of a homogeneous equation,

$$f(\lambda_1 x_1, \lambda_2 x_2) = \lambda f(x_1, x_2). \tag{1}$$

he distribution f scales if there exist scaling paameters λ_1, λ_2, and λ for which Eq. (1) is satisied. For the special choice $\lambda_1 = 1/\langle x_1\rangle$, $\lambda_2 = 1/\langle x_2\rangle$, nd $\lambda = \langle x_1\rangle\langle x_2\rangle$, we obtain the scaling equation

$$f(x_1, x_2) = \frac{1}{\langle x_1\rangle\langle x_2\rangle} f\left(\frac{x_1}{\langle x_1\rangle}, \frac{x_2}{\langle x_2\rangle}\right). \tag{2}$$

e propose a new hypothesis of scaling for highnergy collisions: Distributions resulting in mulparticle production at high energies satisfy Eq.) when $x_1 = p_T$ and $x_2 = p_L$. In other words, the stributions maintain their shapes if they are otted against the *mean* variable $x_i/\langle x_i\rangle$ and prorly normalized. The energy, initial state, and ultiplicity dependencies lie in the average value $_i\rangle$. It can be shown that Eq. (2) maintains its rm when it is integrated over either one of the riables.

n this Letter we present an analysis of the insive single-particle distributions in the transrse (p_T) and the longitudinal (p_L) momentum iables in the c.m. system. These events were duced by 300-GeV/c protons in the 30-in. hygen bubble chamber at the Fermi National Acrator Laboratory. A sample of 877 events (see Table I) with prong multiplicity as high as 26 prongs were track matched in three views by physicists and scanners on the high-magnification (×72) Fermi-Lab-designed "MOMM" tables using the bubble pattern of the charged track. These events were then measured and processed through the program TVGP. In this study we restricted ourselves to the negatively charged secondary tracks, to which we have assigned the pion mass. Based on our previous determination of the K_s^0 inclusive cross section[2] at this energy, we esti-

TABLE I. Events from 300-GeV/c pp interactions used in this analysis.

Prong multiplicity n_c	Number of events[a]	$\langle p_T\rangle$ (GeV/c)	$\langle p_L\rangle$ (GeV/c)
4	516	0.34 ± 0.02	0.93 ± 0.04
6	246	0.35 ± 0.02	0.72 ± 0.03
8	69	0.36 ± 0.02	0.64 ± 0.05
20	17	0.33 ± 0.02	0.41 ± 0.04
22	17	0.31 ± 0.02	0.43 ± 0.04
24	7	0.28 ± 0.02	0.44 ± 0.04
26	6	0.33 ± 0.03	0.41 ± 0.06

[a] To increase statistics, we have in our subsequent analysis combined these events into two groups, $4 \leq n_c \leq 8$ and $20 \leq n_c$, and properly weighted them according to the topological cross sections (see Ref. 1).

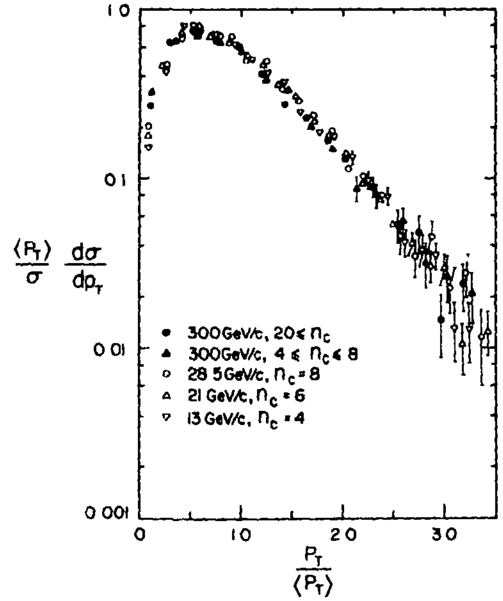

FIG. 1: Plot of $(\langle p_T\rangle/\sigma)d\sigma/dp_T$ versus $p_T/\langle p_T\rangle$ for the reactions $pp\to\pi^-$. Low-energy data at 13, 21, and 28.5 GeV/c are from Ref. 3.

mate our kaon contamination as about 10% of the negatively charged tracks.

According to the hypothesis mentioned above, we should test the following scaling equation:

$$\frac{1}{\sigma}\frac{d^2\sigma}{dp_T\,dp_L}=\frac{1}{\langle p_T\rangle\langle p_L\rangle}\varphi\left(\frac{p_T}{\langle p_T\rangle},\frac{p_L}{\langle p_L\rangle}\right), \tag{3}$$

where φ is a function independent of incident energy, initial states, and prong multiplicity.

In Fig. 1 we examine the π^- spectra in transverse momentum from pp interactions at 13,[3] 21,[3] 28.5,[3] and 300 GeV/c by plotting $(d\sigma/dp_T)\times\langle p_T\rangle/\sigma$ versus $p_T/\langle p_T\rangle$. We observe that the data are remarkably similar and strongly hint at a universal function despite the fact that a wide range of incident momenta and prong multiplicities were selected.

In Fig. 2 we plot $(d\sigma/dp_L)\langle p_L\rangle/\sigma$ versus $p_L/\langle p_L\rangle$ (where the forward and backward hemispheres are folded together) and show again that the data are consistent with a universal function. We note that if these data are plotted in the Feynman variable x $(=2p_L/\sqrt{s}$, where $\sqrt{s}$ is the c.m. energy) instead of the mean variable $p_L/\langle p_L\rangle$, the distributions will not scale for such diverse prong multiplicities as we have presented in Fig. 2. The fact that the shapes of the distributions are similar leads us to speculate that (a) there is one dominant production mechanism in high-energy collisions, and (b) dependences in incident energy, initial state,[4] and prong multiplicity are manifested only in the average values.

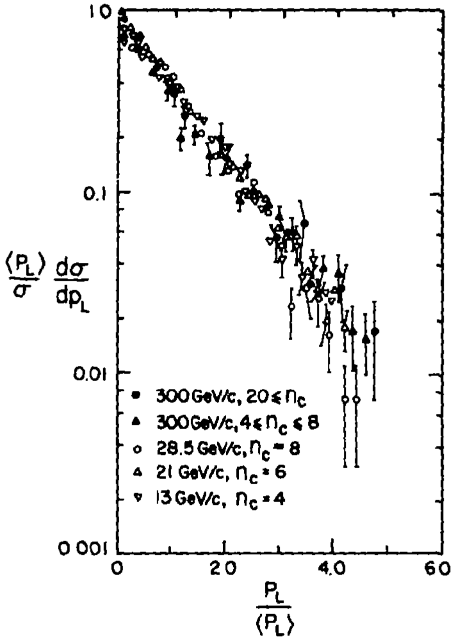

FIG. 2: Plot of $(\langle p_L\rangle/\sigma)d\sigma/dp_L$ versus $p_L/\langle p_L\rangle$ for $pp\to\pi^-$. Low-energy data at 13, 21, and 28.5 GeV/c are from Ref. 3.

To show that the data presented in Figs. 1 and 2 follow a universal distribution, we fitted the data to two functions suggested by the thermodynamic model,[3,5]

$$\varphi_T=a\left(\frac{p_T}{\langle p_T\rangle}\right)^c\exp\left[-b\left(\frac{p_T}{\langle p_T\rangle}\right)\right],$$ (4

$$\varphi_L=d\exp\left[-e\left(\frac{p_L}{\langle p_L\rangle}\right)-f\left(\frac{p_L}{\langle p_L\rangle}\right)^2\right],$$ (

and obtained the following results: $a=6.23\pm0.$ $b=2.37\pm0.04$, $c=1.37\pm0.03$, $d=0.91\pm0.15$, $e=0.83\pm0.04$, and $f=0.03\pm0.01$. The χ^2 per degree of freedom are 104/109 and 134/100, respectively.[6] If the average values are not divi out, the shapes of the distributions are differe To test this point, we fitted the same data wit out dividing them by the average value [namel the distributions $(d\sigma/dp_T)/\sigma$ versus p_T and $(d\sigma$ $dp_L)/\sigma$ versus p_L] and by using the same funct al form given by Eqs. (4) and (5). The result

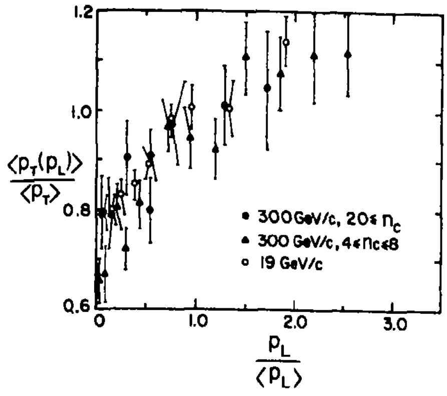

FIG. 3: Plot of $\langle p_T(p_L)\rangle/\langle p_T\rangle$ versus $p_L/\langle p_L\rangle$, where $\langle p_T(p_L)\rangle \equiv \int_0^\infty (d^2\sigma/dp_T\,dp_L)p_T\,dp_T/\int_0^\infty (d^2\sigma/dp_T\,dp_L)dp_T$, for $pp\to\pi^-$. Data at 19 GeV/c are from Ref. 6.

were poor and we obtained χ^2 of 757 and 1509, respectively.

The correlation between p_T and p_L can be studied in terms of the ratios of moments $\langle p_T{}^m p_L{}^n\rangle/\langle p_T\rangle^m\langle p_L\rangle^n$, which are constants according to Eq. (3). We examine the first moment of this correlation. From Eq. (3) one can derive

$$\langle p_T(p_L)\rangle \equiv \frac{\int_0^\infty p_T(d^2\sigma/dp_T dp_L)dp_T}{\int_0^\infty (d^2\sigma/dp_T dp_L)dp_T} = \langle p_T\rangle g(p_L/\langle p_L\rangle). \tag{6}$$

In Fig. 3 we plot 300-GeV/c data and data at 19 GeV/c.[7] The figure shows that within the present statistics Eq. (6) is satisfied. Thus the shape of the well-known "seagull effect" (p_T and p_L correlation) as given by $g(p_L/\langle p_L\rangle)$ is also shown to be independent of energy and prong multiplicity.

Other variables can be used in Eq. (2). For example, if $x_1 = n_c$, the number of charged particles, and $x_2 = n_0$, the number of neutral particles, then we have the familar Koba-Nielsen-Olesen KNO) scaling.[8] It may further be possible to generalize Eq. (2) to more than two variables.

In summary we note the following:

(i) The scaling hypothesis proposed in this Let- er should be regarded as an attempt, without re- orting to specific theoretical models, to summa- ze the bulk of the pion production data presently vailable from high-energy hadron collisions.

(ii) Insofar as these distributions are universal d independent of energy and initial state, we nclude that there is one dominant mechanism r pion production at high energies and the process can be described in terms of a few parameters. One such candidate is the thermodynamic model in which a very important concept (parameter) is the temperature of the hadron system.

(iii) The scaling hypothesis makes no mention of the energy dependence of the average value in the distribution. Consequently, one can study this dependence on energy and initial state as a separate problem (for example, to see whether $\langle p_T\rangle$ increases logarithmically or as a power).

We are grateful to the Fermi Lab Film Analysis Facility staff for their careful and painstaking work in track matching and measuring the high-multiplicity events.

---

*Work supported in part by the U. S. Atomic Energy Commission and the National Science Foundation.

†Operated by Universities Research Association Inc. under contract with the U. S. Atomic Energy Commission.

[1] A. Firestone *et al.*, Phys. Rev. D (to be published).

[2] F. T. Dao *et al.*, Phys. Rev. Lett. 30, 1151 (1973).

[3] D. B. Smith, Ph. D. thesis, Lawrence Berkeley Laboratory Report No. UCRL-20632, 1971 (unpublished). See also D. B. Smith *et al.*, Phys. Rev. Lett. 23, 1064 (1969).

[4] There are no published data on single-particle distributions from high-energy (>100 GeV/c) πp interactions. However we have studied the initial-state dependence of the functions φ_T and φ_L given in Eqs. (4) and (5), using the 25-GeV/c $\pi^- p$ data of J. W. Elbert *et al.* [Phys. Rev. Lett. 20, 124 (1968)] and J. W. Elbert [Ph D. thesis, University of Wisconsin, 1971 (unpublished)]. We found that the π^+ (nonleading particle) spectra in this case have the same functional dependence as the π^- spectra from pp collisions. Since in πp collisions there is an asymmetry in p_L between forward and backward hemispheres, we scale p_L in each hemisphere by $\langle p_L\rangle$, the average value in that hemisphere.

[5] R. Hagedorn, Nuovo Cimento 25, 1017 (1962).

[6] The use of the ratios of moments may be a more sensitive test of this scaling hypothesis and possible systematic deviation from it. For example, the ratio of moments $\langle p_L\rangle/(\langle p_L{}^2\rangle - \langle p_L\rangle^2)^{1/2}$ has the following values: 0.98 ± 0.04 (300-GeV/c pp, $n_c \geq 20$), 1.10 ± 0.02 (300-GeV/c pp, $2 \leq n_c \leq 10$), 1.16 ± 0.01 (13-GeV/c pp, $n_c = 4$), 1.11 ± 0.01 (21-GeV/c pp, $n_c = 6$), and 1.14 ± 0.02 (28-GeV/c pp, $n_c = 8$).

[7] H. Bøggild *et al.*, Nucl. Phys. B57, 77 (1973).

[8] Z. Koba, H. B. Nielsen, and P. Olesen, Nucl. Phys. B40, 317 (1973). For an experimental review of KNO scaling, see P. Slattery, Phys. Rev. D 7, 2073 (1973); F. T. Dao and J. Whitmore, Phys. Lett. 46B, 252 (1973), and references therein. Of course KNO scaling is used here in the general sense where some modified scaling law of the same general type may be more applicable, for example, with Wroblewski's modification $x_1 = n_c - 1$ instead of $x_1 = n_c$.

Upper Bounds on Massive-Lepton-Pair Production, $pN \to l^+l^-X$, in the Quark-Parton Model

Robert Savit and Martin B. Einhorn
National Accelerator Laboratory, Batavia, Illinois 60510
(Received 30 April 1974)

We present rigorous bounds on the process $pN \to l^+l^-X$ derived in the context of quark-parton models. As constraints we use the positivity of the parton probability functions and data on deep inelastic leptoproduction. Generally, our upper bounds fall below the Brookhaven National Laboratory data on muon-pair production. This result forces us to conclude that the Brookhaven data do not represent the scaling limit for this process, and/or that the usual ideas of the (colored) quark-parton model are not all correct.

The intriguing successes of parton models for processes involving large spacelike momentum transfers, especially deep inelastic lepton scattering, have been well demonstrated over the past several years. In stark contrast are the results on e^+e^- annihilation from the Cambridge Electron Accelerator, and more recently from SPEAR. These results are in gross disagreement with parton-model expectations. Another process which has been the subject of much theoretical and experimental study is the production of massive lepton pairs in hadronic collisions. This process, first discussed in the parton model by Drell and Yan,[1] is supposed to occur when a parton from one incident hadron annihilates with an antiparton from the other incident hadron, producing a heavy photon which finally decays into a lepton pair. The cross section for this process in proton-proton collisions is given by

$$Q^4 d\sigma/dQ^2 = \tfrac{4}{3}\pi\alpha^2\tau \int_\tau^1 (dx/x) \textstyle\sum_i e_i^2[q_i(x)\bar{q}_i(\tau/x) + \bar{q}_i(x)q_i(\tau/x)], \tag{1}$$

where $\tau = Q^2/s$, e_i is the charge of parton of type i, and $q_i(x)$ $[\bar{q}_i(x)]$ is the probability of finding a parton (antiparton) of type i with a fraction x of the parent proton's longitudinal momentum.

The rates for this process as measured at Brookhaven National Laboratory (BNL) by Christensen *et al.*[2] have generally been larger than theoretical estimates, but no firm conclusions about whether the parton model could describe these results have been drawn. In this Letter we present some rigorous bounds on this cross section and compare them with the BNL data. The bounds are based on the positivity of the parton probability distributions and the constraints on these distributions imposed first by the Stanford Linear Accelerator Center (SLAC) electroproduction data[3] and, later, by the neutrino experiments at Gargamelle.[4] The probability distributions are regarded as generalized coordinates in a variational problem, and constraints are imposed by using the method of Lagrange multipliers generalized to incorporate inequality constraints.[5] The positivity requirements are

$$q_i(x), \bar{q}_i(x) \geq 0, \tag{2}$$

for all x and i.

In the first problem that we consider, we use only the data from SLAC on νW_2 for protons and neutrons.[3] These data are quite good, and so our bound will provide a very clean test of the parton model. In the parton model these structure functions are given by certain linear combinations of the parton probability distributions. Specifically, if the partons are quarks and carry, in addition, SU(3) color, we have

$$\nu W_2^{\gamma p}(x)/x = \tfrac{4}{9}U(x) + \tfrac{1}{9}D(x) + \tfrac{1}{9}S(x),$$
$$\nu W_2^{\gamma n}(x)/x = \tfrac{4}{9}D(x) + \tfrac{1}{9}U(x) + \tfrac{1}{9}S(x),$$

where

$$U(x) = u_r(x) + \bar{u}_r(x) + u_w(x) + \bar{u}_w(x) + u_b(x) + \bar{u}_b(x),$$

and similarly for $S(x)$ and $D(x)$. The subscripts refer to the color degrees of freedom.

When combined with the inequalities (2), thes
constraints provide rather severe restrictions
the cross section (1). The full derivation of thi
bound is too long to describe here, and will be
presented in detail (along with a number of add
tional results) elsewhere.[6] The result is show
and compared with the BNL data in Fig. 1. Cu
A is the bound computed with the constraints d
scribed for the process $pU \to \mu^+\mu^-X$, since the
target used was uranium. That is, it is a wei
ed average of the upper bounds for $pp \to \mu^+\mu^-X$
and $pn \to \mu^+\mu^-X$. Curve B is the same as curv
corrected to incorporate the detection efficie
of the BNL experiment, and curve C is the 2
GeV/c data from BNL.[7] For $0.2 \lesssim Q^2/s \lesssim 0.5$

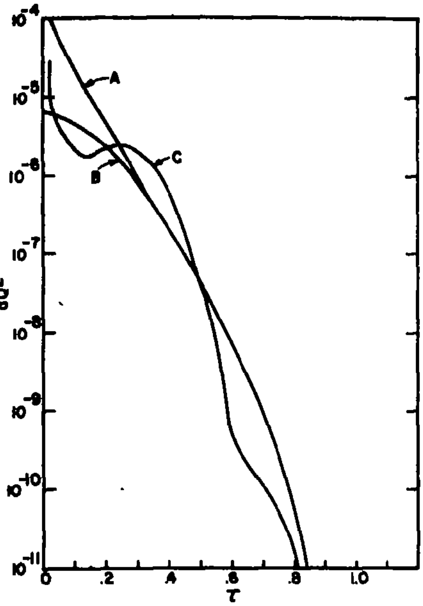

FIG. 1. Curve A, upper bounds for the process $pU \to \mu^+\mu^- X$ calculated as a weighted average of bounds on $pp \to \mu^+\mu^- X$ and $pn \to \mu^+\mu^- X$. Curve B, same bound corrected to include detection efficiency at BNL. Curve C, 29.5-GeV/c data from BNL.

upper bound falls significantly below the data proving that the colored-quark-parton model cannot possibly describe the result.

Corresponding bounds for the quark-parton model without color are obtained by multiplying curves A and B by a factor of 3. Even in this theory, the data come dangerously close to violating the bounds.

In the problem considered above, the q_i and $\bar{q}_i$ distributions enter symmetrically. However, for nonzero x, the usual notions of the parton model suggest that there is a significant difference between the quark and antiquark distributions. To implement this difference in our variational problem, we turn to a consideration of neutrino scattering. Using the preliminary data on neutrino-nucleon scattering from Gargamelle,[4] and the SLAC data on νW_2 for protons and neutrons, one can deduce the four different linear combinations of quark probability distributions shown in Fig. 2(a). In the colored-quark-parton model, the labels of the curves in this figure should be understood as sums over color, e.g., $u(x) = u_r(x) + u_w(x) + u_b(x)$, etc. There are many reasons to be skeptical about the preliminary data from Gargamelle, and their interpretation in terms of parton distributions (for instance, most of the data are not at large enough Q^2 to expect scaling), but at the very least, they are probably indicative of what cleaner data will show. Interpolating these points and modifying slightly the curves at small Q^2 (i.e., x),[5] we take as our "data" the curves of Fig. 2(b). A detailed discussion of the Gargamelle data and further elaboration of Fig. 2(b) may be found in Ref. 6.

We can now use these data, which distinguish between quarks and antiquarks, as constraints in a new variational problem. Again we impose the positivity requirements (2), and maximize the functional. The result of this tedious, but straightforward, calculation[6] is shown in Fig. 3,

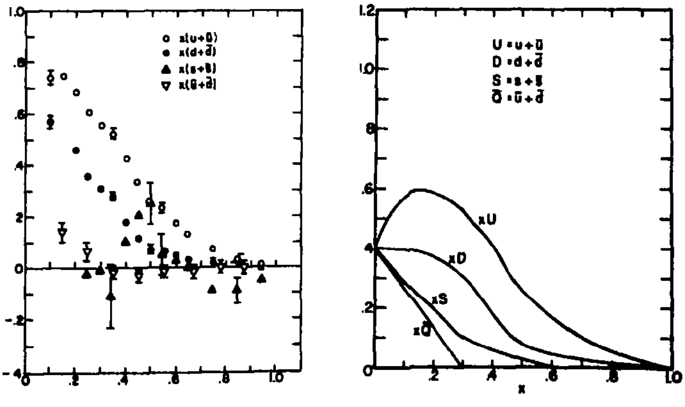

G. 2. (a) Parton distribution functions gleaned from SLAC and Gargamelle data. (b) Modified version of (a) text).

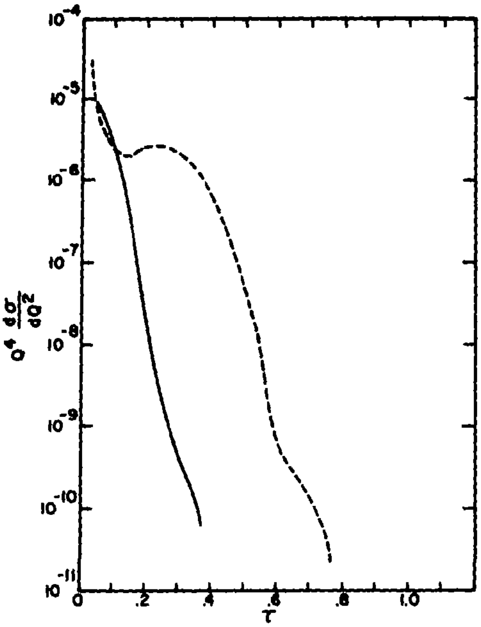

FIG. 3. Upper bound derived using data of Fig. 2 (solid line) compared with BNL data (dashed line).

where it is compared with the BNL data.[9] Again, the upper bound falls far below the data leading to the conclusion that the parton model and the BNL data are incompatible. As before, the same bound derived in the uncolored-quark model is precisely 3 times as large as the bound of Fig. 3.

One might worry that, since the Gargamelle data have such large error bars, and since the process in question is so sensitive to the size of the antiquark distributions at large x, the bound of Fig. 3 could change drastically within the error bars of the data. However, model studies[6] indicate that while the upper bound does change significantly when one changes the data, it is still at least 1 or 2 orders of magnitude smaller than the data for $0.2 \lesssim \tau \lesssim 0.6$. In any event, no matter what the neutrino data eventually turn out to be, the bound can never rise above that of Fig. 1 which depends only on electron scattering and makes no assumptions about the weak interactions. We also want to stress that the method of solution for this problem, which is given in Ref. 6, does not depend on the form of the data in Fig. 2(b) and can easily be applied to other data when they become available.

These bounds, which are perfectly rigorous in the context of the usual parton models, force us to conclude that at least one of the following statements is correct. (i) The BNL data for the experimentally observed cross section per nucleon are not the scaling limit for the process $pN \to \mu^+\mu^- X$. (ii) The Drell-Yan formula for $pp \to \mu^+\mu^- X$ must be modified. (iii) The colored-quark-parton model is wrong.

Let us briefly comment on each possibility:

(i) Nuclear effects which were thought to be well understood may, in fact, significantly alter the observed cross section per nucleon. Inasmuch as experiments on hydrogen will not be available for quite some time, an experiment utilizing different nuclear targets is urgently needed. Another effect which may be important at large τ is the interactions of secondary mesons produced in the target. Since mesons are supposed to have many more antiquarks at large x than baryons, this effect may be important in a thick target such as that at BNL. It must be remarked, however, that model-dependent estimates suggest that this contribution is still at least an order of magnitude below the observed signal.[10] Finally, it is possible that the Brookhaven experiment is not the scaling limit for this reaction. Similar experiments at other energies such as those being planned and carried out at th National Accelerator Laboratory are obviously o great interest.

(ii) Theoretically, the most unsatisfactory aspect of the Drell-Yan formula is its apparent neglect of strong interactions. Such interactions are generally required in deep inelastic phenom ena, especially in a quark-parton model, to dispose of the isolated quark quantum numbers. H ever, these effects may leave the parton-mode results for deep inelastic lepton scattering unchanged, but alter the predicted cross section for processes, such as the one discussed here which involve more than one hadron in both th initial and final states.[11] Our results make th fundamental and unresolved question that muc more salient.

(iii) The colored-quark-parton model may b incorrect in one or both of two ways. On the hand, the correct parton model may have cor stituents other than colored quarks. For suc theories, bounds similar to those presented can be derived. In general, we can anticipat that the greater the mean squared charge, t smaller the bound will be, so the situation w be worse in most such models. On the othe hand, the ideas of the naive parton model m not be applicable in their present form to p cesses involving timelike photons. [This possibility is related to option (ii), discussed above.] Indeed, it is intriguing that in the two large-Q^2 processes involving timelike photons which have been measured—e^+e^- annihilation and massive-muon-pair production—the observed cross sections are larger than the predictions of the parton model.

The ideas of the parton model, which have worked so well in describing processes with large spacelike momentum transfers, seem to fail, in their present form, in the timelike region. We have shown in this paper, by presenting rigorous bounds in the context of parton models, that the most popular versions cannot describe the BNL data on $pN \to \mu^+\mu^- X$. The Cambridge Electron Accelerator and SPEAR results in e^+e^- annihilation, and the present bounds on nassive-lepton-pair production, make it exremely important to carry out further experinents in the deep timelike region, and to focus ur theoretical attention on the exciting paradoxs presented by the parton model.

One of us (M.B.E.) would like to thank Profesor G. C. Fox for conversations and for his hositality during his stay at the California Institute f Technology, where part of this work was done.

---

[1] S. D. Drell and T. M. Yan, Phys. Rev. Lett. 25, 316 1970), and Ann. Phys. (New York) 66, 578 (1971).

[2] J. H. Christensen *et al.*, Phys. Rev. D 8, 2016 (1973).

[3] A. Bodek, Ph.D. thesis, Massachusetts Institute of Technology, MIT Laboratory for Nuclear Studies Report No. COO-3069-116, 1972 (unpublished); E. M. Riordan, Ph.D. thesis Massachusetts Institute of Technology, MIT Laboratory for Nuclear Studies Report No. COO-3-69-176, 1973 (unpublished).

[4] D. H. Perkins, Oxford University Report No. Ref. 67-73 (to be published).

[5] M. B. Einhorn and R. Blankenbecler, Ann. Phys. (New York) 67, 480 (1971).

[6] M. B. Einhorn and R. Savit, NAL Report No. NAL-Pub-74/35-THY (to be published).

[7] In presenting the data, we have drawn a smooth curve through the data points and have not indicated statistical errors, which range between 5 and 25% for $0.02 \leq \tau \leq 0.45$ and are larger for larger τ. However, the dominant errors are systematic, ranging between 25 and 65% for $0.02 \leq \tau \leq 0.61$, and are correlated from point to point. Consideration of these errors does not vitiate our conclusions. We also point out that the difference between calculating the average of the upper bounds on p and π targets and the upper bounds on the average nucleon in uranium is negligible for our purposes. For further details, see Ref. 6.

[8] The modification is desirable for several reasons: for example, to make the probability distributions nonpositive.

[9] Actually, the curve in Fig. 3 is a bound for the process $pp \to \mu^+\mu^- X$, not $pU \to \mu^+\mu^- X$ as in Fig. 1. However, the bounds for proton and neutron targets typically differ by a factor of 2 or so, and for the purpose of Fig. 3 this difference is insignificant. See Ref. 6 for more details.

[10] G. Farrar and G. C. Fox, private communication.

[11] Different points of view on this question are suggested by R. P. Feynman, *Photon-Hadron Interactions* (Benjamin, New York, 1972), p. 152; and P. V. Landshoff and J. C. Polkinghorne, Nucl. Phys. B33, 221 (1971). See also Ref. 6 above.

PHYSICAL REVIEW
LETTERS

VOLUME 33 | 12 AUGUST 1974 | NUMBER 7

Alkali-Metal Hyperfine Shift in the Van der Waals Molecule KAr

Richard R. Freeman, Edward M. Mattison,* David E. Pritchard, and Daniel Kleppner
Research Laboratory of Electronics and Department of Physics, Massachusetts Institute of Technology, Cambridge, Massachusetts 02139

(Received 22 May 1974)

The hyperfine interaction of K in KAr has been measured in several vibrational states of KAr. The results yield a value for the hyperfine shift α as a function of internuclear separation R given by $\alpha = -115(R - R_0)$ kHz, where R is in bohrs and $R_0 = 12.0$ bohr, valid over the range 10.25 bohr $< R <$ 12.0 bohr.

The problem of how the hyperfine interaction in
alkali atom is modified by the proximity of a
re-gas atom has been the subject of lively the-
retical interest ever since the experimental dis-
very that the inert gas used as a buffer in opti-
l-pumping experiments causes a shift in the
kali hyperfine separation.[1] This so-called
pressure shift" arises from two competing in-
ractions; long-range polarization effects that
duce the density of the alkali valence electron
the nucleus, decreasing the hyperfine interac-
n, and short-range overlap effects that tend to
centrate the valence electron near the alkali
leus, increasing the hyperfine interaction.
h light rare gases, such as He and Ne, the
rt-range forces dominate and produce a posi-
pressure shift; for the heavier rare gases,
h as Kr or Xe, the pressure shifts are gener-
negative. This suggests that the competition
een the long- and short-range effects may
a rapid change in the hyperfine coupling
nt with internuclear separation. Unfortu-
, a precise comparison between experiment
eoretical predictions of the dependence of
perfine shift on internuclear separation has
o far, been possible because optical-pump-
easurements necessarily involve a broad
al average over angular momenta and ener-
obscures many of the details of the interaction.

We report here the observation of the hyperfine shift in the bound alkali–rare-gas molecule KAr by molecular-beam magnetic resonance.[2] KAr is a particularly interesting system to study because the polarization and overlap effects are approximately equal, yielding an anomalously small pressure shift.[3] The experimental results (see Fig. 1) have a well-resolved structure which can be identified with the vibrational states of the molecule. The observed strong variation of the hyperfine shift with vibrational level is an indication of a rapid variation of hyperfine interaction with internuclear separation, and offers the possibility of determining the hyperfine interaction strength as a function of the internuclear separation R.

The principle magnetic interactions in an alkali–rare-gas Van der Waals molecule immersed in an external magnetic field H_0 are described by the Hamiltonian

$$\mathcal{H} = h[a + \alpha(R)]\,\vec{I}\cdot\vec{S} + g_s\mu_B\vec{S}\cdot\vec{H}_0 + h\gamma(R)\vec{S}\cdot\vec{N}, \qquad (1)$$

where $\hbar I$, $\hbar S$, and $\hbar N$ are, respectively, the angular momenta of the alkali nuclear spin, the alkali valence electron spin, and the molecular rotation. $g_s\mu_B\vec{S}$ is the magnetic dipole moment of the valence electron; a is the hyperfine coupling constant of the free atom; $\alpha(R)$ is the shift in the

Copyright © 1974 by
The American Physical Society

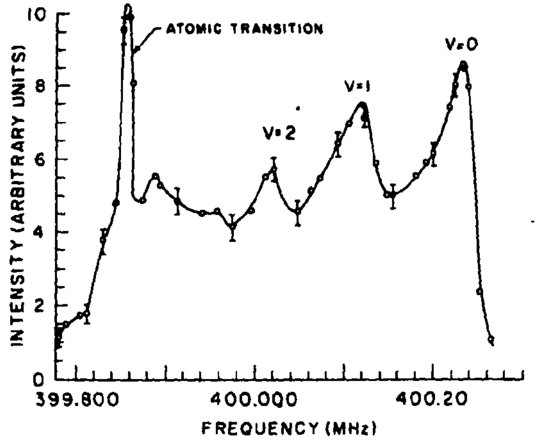

FIG. 1. Magnetic resonance curve for the transition $(F=2, m_F=-1)\rightarrow(F=1, m_F=-1)$ in KAr at a field of 82.5 G, where structure due to the spin-rotation interaction vanishes to first order. If there were no shift in a, the molecular and atomic resonance curves would be identical. The atomic resonance, due to residual atoms in the molecular beam, appears at the left; the peaks identified with the first three vibrational states of the molecule are marked $v=0,1,2$.

alkali hyperfine constant a; R is the internuclear separation, and $\gamma(R)$ is the molecular spin-rotation coupling strength.

The energy levels of Eq. (1) are similar to those of atomic potassium, but have an additional fine structure due to the spin-rotation interaction and the hyperfine shift. In zero magnetic field the hyperfine interactions couples $\vec{I}$ and $\vec{S}$ to form $\vec{F}=\vec{I}+\vec{S}$; in the fields used in this experiment the condition $g_s\mu_B H_0 \gg N\gamma$ holds, so m_F is still an approximately good quantum number, and the molecular states may be labeled (F, m_F, m_N). The spin-rotation interaction splits the observable transitions of KAr by separating states of different m_N, broadening the spectrum, and reducing the signal intensity.[3] In addition, the strong state dependence of the spin-rotation constant $\gamma(R)$ obscures the contribution of $\alpha(R)$, whose measurement is the aim of this experiment. Fortunately, in a magnetic field given by

$$H_0 = ah/2\mu_B \tag{2}$$

the frequency of the hyperfine transition $(F=2, m_F=-1)\rightarrow(F=1, m_F=-1)$ is independent of field, the spin-rotation splitting is eliminated to first order, and the quantum number m_N can be ignored. Under this condition, any displacement or broadening of the KAr spectrum relative to the atomic-potassium spectrum is due to the hyperfine shift $\alpha(R)$.

Figure 1 is the observed spectrum for the transition $(2,-1)\rightarrow(1,-1)$ in a field that satisfies Eq. (2) for potassium, 82.5 G. The peak marked "atomic transition" is due to residual potassium atoms not removed from the beam; its width is characteristic of the apparatus resolution. The peaks marked $v=0$, 1, and 2 are caused by KAr molecules in the lowest three vibrational states, while the smearing on the low-frequency side of each peak is due to the rotational structure of the vibrational level.

To determine the R dependence of α, we have compared the experimental data with a spectrum computed from a simple analytic model for α. Eigenvalues and wave functions were computed using Baylis's potential,[4] and expectation values of R were computed numerically. In an initial attempt we approximated $\alpha(R)$ by a straight line, shown in Fig. 2(a) (solid line). The relative populations of the molecular states were assumed to be described by vibrational and rotational temperatures $T_{vib}=25$ K, $T_{rot}=15$ K, values which are consistent with our most recent data on the spin-rotation interaction. The resulting line spectrum [Fig. 2(b)] agrees well with the observ spectrum in the region of positive shift. This suggests that for 10.25 bohr $< R <$ 12.0 bohr, $\alpha(R$ can be described by

$$\alpha(R) = -M(R-R_0) \quad ($$

where $M=115$ kHz/bohr, and $R_0=12.0$ bohr.

Clearly the linear model for $\alpha(R)$ cannot be valid for all interatomic separations: While th hyperfine interaction is expected to be negativ at large R, eventually it must vanish, implyin a negative shift that decreases to zero for ver large R. The dashed curve in Fig. 2(a) shows expected form for $\alpha(R)$ for large R. The minimum in α has two implications: It sets a low limit on the possible KAr hyperfine seperatio and it produces a bandhead in the spectrum a ing from states with negative shifts. The exp mental spectrum has a cutoff approximately 5 kHz below the atomic value, confirming the e tence of a minimum value of α at least 25 kH deep. Unfortunately, the vibrational levels g rise to the negative shifts are the highest-lyi states, which are weakly populated, so the s drops rapidly near the bandhead. In addition the unwanted atomic line further obscures th structure of the bandhead.

More detailed analysis of our data and exp

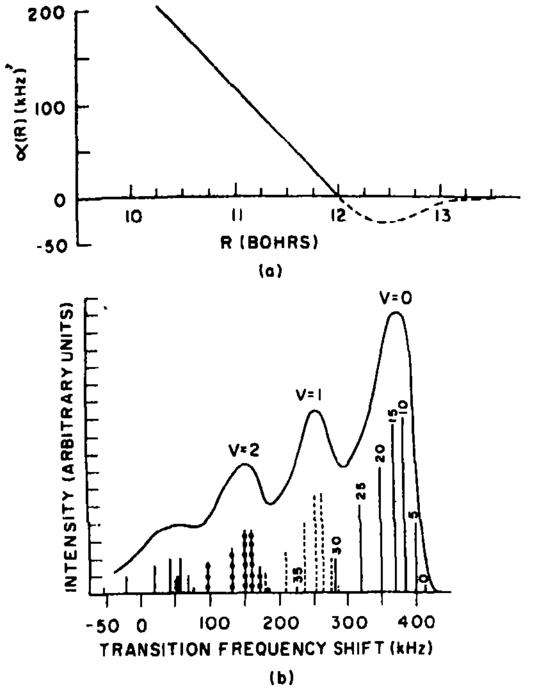

IG. 2. (a) The functional form of $\alpha(R)$ used to cal- ate the spectrum in (b). The solid line corresponds nternuclear separations well resolved in this experi- nt. The dashed line is an indication of the form for) for large R extracted from the cutoff bandhead r zero shift shown in Fig. 1. (b) Calculated line ctrum assuming $\alpha(R)$ given by solid line in (a). The s in each grouping are rotational structure of each rational level. The rotational number N is labeled the $v=0$ state. The solid curve shows the result of grating the line spectrum over the apparatus reso- on (approximately 25 kHz). The populations of the rational and rotational levels are taken to be given $T_{\rm vib}=25$ K, $T_{\rm rot}=15$ K.

ments in progress on the large-R contribution to α should determine $\alpha(R)$ with sufficient accuracy that the size and temperature dependence of the KAr pressure shift can be calculated. At present, the pressure shift in KAr is known only approximately (-0.4 ± 1.4 Hz/Torr),[3] and its temperature dependence has not been determined. We hope that these results will encourage more detailed measurements of the pressure shift in KAr, and more detailed theoretical calculations on the radial dependence of the pressure shift.

We should like to thank the National Science Foundation for supporting this work, and to acknowledge the assistance of Richard S. Goldhor in carrying out the numerical computations.

---

*Present address: Smithsonian Astrophysical Observatory, Cambridge, Mass.

[1] An extensive review of the literature through 1971 is given by W. Happer, Rev. Mod. Phys. **44**, 169 (1972). See also W. D. Davison and Y. C. Liew, J. Phys. B: Proc. Phys. Soc., London **5**, 309 (1972); B. K. Rao, D. Ikenberry, and T. P. Das, Phys. Rev. A **8**, 1673 (1973); C. M. Dutta, N. C. Dutta, and T. P. Das, Phys. Rev. A **7**, 60 (1973); P. J. Fortune and P. R. Certain, J. Phys. B: Proc. Phys. Soc., London **6**, L39 (1973).

[2] E. M. Mattison, D. E. Pritchard, and D. Kleppner, Phys. Rev. Lett. **32**, 507 (1974).

[3] A. L. Bloom and J. B. Carr, Phys. Rev. **119**, 1946 (1960).

[4] W. E. Baylis, Joint Institute for Laboratory Astrophysics Report No. 100, available from Scientific Reports Editor, Joint Institute for Laboratory Astrophysics, University of Colorado, Boulder, Colorado 90302. Some corrections to these potentials have been calculated (W. E. Baylis, private communication).

Dynamics of Freedericksz Deformation near a Nematic–Smectic-A Transition*

Cheng-Cher Huang,† Ronald S. Pindak,† Philip J. Flanders, and John T. Ho†‡
Laboratory for Research on the Structure of Matter, University of Pennsylvania,
Philadelphia, Pennsylvania 19174
(Received 6 May 1974)

We have used the dynamic Freedericksz-deformation method to measure in detail the temperature dependence of the twist viscosity γ_1 in N-p-cyanobenzylidene-p-octyloxyaniline near the nematic-smectic-A transition. We have demonstrated that the intrinsic contribution γ_1^0 can be determined independently by extrapolating data on doped samples. Our analysis shows γ_1 to diverge with a critical exponent $\zeta = 0.37 \pm 0.05$, in agreement with theoretical expectations.

There has been considerable interest in static properties near the nematic-smectic-A transition in liquid crystals. These properties are related to the smectic correlation length ξ which diverges near an apparent transition temperature T_c in the form[1]

$$\xi = \xi_0 (T/T_c - 1)^{-\nu}, \tag{1}$$

where the critical exponent ν is estimated to be 0.67. The bend and twist elastic constants are also expected to diverge with the same exponent ν. Various theoretical considerations have recently been made to extend these discussions to dynamic properties near the transition.[2-4] One result of these theories is the prediction that the twist viscosity γ_1 in the nematic phase should diverge like

$$\gamma_1 = \gamma_1^0 + C(T/T_c - 1)^{-\zeta}, \tag{2}$$

where γ_1^0 is the "intrinsic" twist viscosity in the absence of the smectic-A transition, and the exponent ζ is given by

$$\zeta = \nu/2. \tag{3}$$

We report here a detailed measurement of γ_1 in nematic N-p-cyanobenzylidene-p-octyloxyaniline (CBOOA) near the smectic-A phase using the dynamic Freedericksz-deformation technique, and the comparison of the results with theoretical expectations.

The material CBOOA has been studied widely because of its nearly second-order nematic-smectic-A transition.[5-9] An anomalous increase in γ_1 near the transition has been observed in rotating-field measurements,[10-12] but these results have not led to convincing data analysis. Our experimental setup is similar to that in geometry I of Pieranski, Brochard, and Guyon.[13] A planar sample is formed between two glass slides coated with obliquely deposited SiO thin film,[14] separated by a Teflon spacer of thickness $d = 119$ μm. We obtain a well-aligned sample with an extinction ratio of 500. The sample is situated between crossed polarizers whose transmission axes are oriented at 45° to the molecular alignment axis of the sample. An electromagnet supplies a magnetic field up to 4 kG normal to the sample. A light beam at a wavelength $\lambda = 6328$ Å from a He-Ne laser is incident perpendicular to the sample and parallel to the field, and the transmitted light is detected by a photodiode. The incident light is modulated with a mechanical chopper and the detector signal is analyzed with a lock-in am plifier. The sample temperature is controlled t a stability of 3 mK and measured with a platinu resistance thermometer.

In zero magnetic field the phase difference δ b tween light polarized parallel and perpendicular to the sample axis has the value

$$\delta_0 = 2\pi d \Delta n/\lambda, \qquad ($$

where $\Delta n = n_e - n_o$ is the birefringence of the sa ple. Freedericksz deformation occurs when a field larger than the critical value

$$H_c = (\pi/d)(K_{11}/\Delta\chi)^{1/2}$$

is applied, where K_{11} is the splay elastic cons and $\Delta\chi = \chi_\parallel - \chi_\perp$ is the anisotropy of the diama netic susceptibility. In our experiment, a fiel H_1 slightly larger than H_c is first applied, cau ing a distortion of the molecular alignment of sample and a reduction in δ. After allowing sample to come to equilibrium, the field is q ly reduced to a value H_2 less than H_c. To avo domain formation, the sample is tilted away f its normal orientation while the field is being creased to H_1, and then adjusted to be perpen ular to the light beam before the field is lowe Following the derivation of Ref. 13, in a time after the field is set at H_2, we expect the pha difference δ to relax exponentially toward its undistorted value:

$$\delta(t) = \delta_0 - D(H_1)\exp[-t/\tau(H_2)]. \qquad (6)$$

A maximum (minimum) in the transmitted intensity occurs whenever δ is an odd (even) multiple of π. The time dependence of the maxima and minima in the measured intensity, as displayed with a chart recorder, is fitted with Eq. (6) to yield both δ_0 and $\tau(H_2)$. The former quantity allows us to determine the detailed temperature dependence of Δ*n* in CBOOA using Eq. (4).[15] Typical relaxation times of several seconds are obtained. For a given temperature, the measurement is repeated with different values of the final field H_2. The relaxation time $\tau(H_2)$ depends on H_2 in the form[13]

$$\tau^{-1}(H_2) = \tau^{-1}(0)[1-(H_2/H_c)^2], \qquad (7)$$

ıere

$$\tau^{-1}(0) = 2H_c^2\Delta\chi/\gamma_1. \qquad (8)$$

ıe data are fitted with Eq. (7) to obtain H_c and 0), from which the twist viscosity γ_1 can be lculated using the relation

$$\gamma_1 = 2\tau(0)H_c^2\Delta\chi. \qquad (9)$$

though data on Δχ in CBOOA are available in f. 10, we have used instead the temperature dendence of Δ*n* that we have measured simultanesly. In the temperature range of interest, the nperature dependences of the two quantities ree to within 2%. The actual values of γ_1 are tained by comparing the Δ*n* and Δχ data, and consistent with rotating-field results. The solute calibration is probably good to about 2%. e expressions used in the above analysis are ained by neglecting any backflow effects, which expected to be unimportant in this experimen- geometry and have been found to be small with nethoxybenzylidene-*p*′-*n*-butylaniline (MBBA).[13] our data are fitted by Eqs. (6) and (7) very ll, showing that backflow effects are indeed ligible for CBOOA. This geometry also has advantage that the critical field H_c depends on and is therefore not expected to change drasily with temperature.

e temperature dependence of γ_1 in the nemat- ase of CBOOA is shown in Fig. 1. Our data in fair agreement with those of Hardouin using the rotating-field method,[10] but con- three times their density of points and conably less temperature uncertainty. The lous increase of γ_1 near the smectic-*A* phase at 82.8°C is evident.

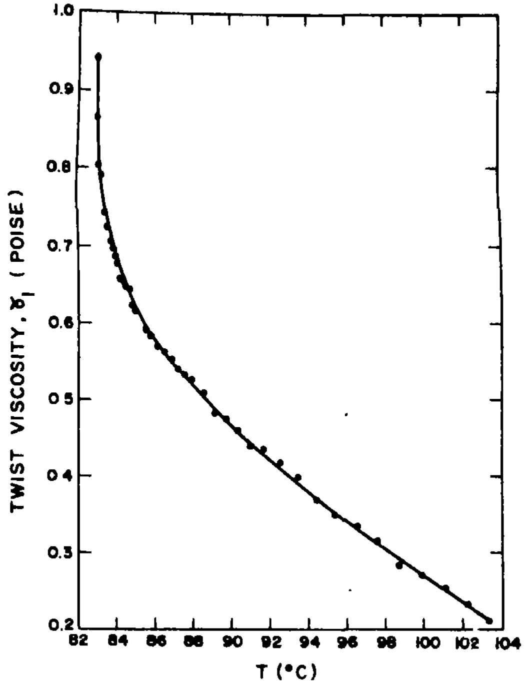

FIG. 1. Temperature dependence of twist viscosity γ_1 of CBOOA.

The major difficulty in attempting to compare the data with Eq. (2) is associated with the large background term γ_1^0. While various proposals have been made for the temperature dependence of the intrinsic twist viscosity of a nematic liquid crystal,[16-18] the evidence from a large amount of experimental data[13,19,20] on nematics that do not possess a smectic phase is that, except in the vicinity of the isotropic phase, γ_1^0 is well described by the activation-energy form

$$\gamma_1^0 = Ae^{B/T}. \qquad (10)$$

Because of the large contribution of γ_1^0, any least-squares fit of the data on CBOOA by expressions such as Eqs. (2) and (10), with five adjustable parameters, would not produce unambiguous results. It is also not possible to obtain the values of *A* and *B* directly from the high-temperature γ_1 data, because of the uncertainty about the contribution, however small, of the pretransitional behavior to these data. Therefore we have attempted to determine γ_1^0 independently by an extrapolation scheme involving data on doped CBOOA, similar to a method that has been used successfully to analyze the pitch divergence near a cholesteric–smectic-*A* transition.[21]

Samples of CBOOA are doped with different concentrations x by weight of MBBA. Both the isotropic-nematic and the nematic-smectic transition temperatures decrease with increasing x. When x exceeds about 0.04, no smectic phase is found. The twist viscosity is measured in four mixtures with x between 0.110 and 0.258. Since these measurements demand less stringent temperature stability, we have used the Tsvetkov rotating-field method[22,12] because of its simplicity of calibration. We find that not only do the doped samples not exhibit a smectic phase, but there is also no tendency toward a smectic transition. This is evident from the fact that while a plot of $\ln\gamma_1$ versus $1/T$ for the undoped sample is nonlinear and shows strong divergence near the smectic phase, the plots for the doped samples are linear up to the solid phase. As these data are free from smectic pretransitional effects, it is hoped that, when extrapolated to $x=0$, they will give a realistic estimate of γ_1^0 in pure CBOOA. The activation energy $B(x)$ is found to be essentially independent of x, with an average value of 5.28×10^3 K. The coefficient $A(x)$, on the other hand, decreases linearly with x, extrapolating to a value of 1.75×10^{-7} P at $x=0$. It is therefore reasonable to expect the intrinsic twist viscosity γ_1^0 in pure CBOOA to follow Eq. (10) with parameters $A=1.75\times10^{-7}$ P and $B=5.28\times10^3$ K. We estimate the uncertainty in the values of γ_1^0 found in this extrapolation scheme to be about 6%.

Using the above determination of γ_1^0, a least-squares fit of the data in Fig. 1 on undoped CBOOA by Eq. (2) yields the optimum parameters $T_c=355.94$ K, $C=2.7\times10^{-2}$ P, and $\zeta=0.37\pm0.05$, as illustrated in Fig. 2. The uncertainty in ζ is due mainly to the estimated errors in the background term γ_1^0. Our result for ζ is in agreement with the prediction of 0.33 by Jähnig and Brochard.[3] The value of C is higher than the theoretical estimate of 5×10^{-4} P,[23] but this estimate is derived from a Ginzburg-Landau formalism and may not be directly applicable here. In accordance with Eq. (3), the value of ζ also appears to be consistent with the values of the exponent ν reported in the elastic-constant measurements on CBOOA by Cheung, Meyer, and Gruler[7] and Delaye, Ribotta, and Durand,[8] and in some of the samples of Cladis.[9] We have mainly demonstrated here the feasibility of accurately measuring γ_1 and self-consistently analyzing the data to obtain ζ. Obvious extensions of this work include a more precise measurement on the doped samples to determine γ_1^0 better and a study of possible effect of sample purity on the divergence of γ_1.

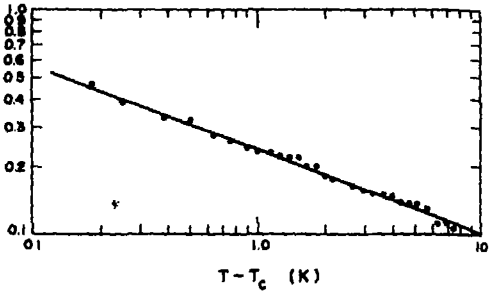

FIG. 2. Log-log plot of $\gamma_1-\gamma_1^0$ versus $T-T_c$. Equation (10) with $A=1.75\times10^{-7}$ P and $B=1.28\times10^3$ K is used for γ_1^0. The straight line has a slope $\zeta=0.37$.

We would like to thank W. J. Romanow for advise on thin-film technique and Professor T. C. Lubensky for helpful discussions.

---

*Work supported in part by the National Science Foundation under Grant No. GH-33633.

†Also Department of Physics.

‡Work supported in part by the Research Corporatio

[1] P. G. de Gennes, Solid State Commun. 10, 753 (1972 and Mol. Cryst. Liquid Cryst. 21, 39 (1973).

[2] F. Brochard, J. Phys. (Paris) 34, 411 (1973).

[3] F. Jähnig and F. Brochard, J. Phys. (Paris) 35, 30 (1974).

[4] W. L. McMillan, Phys. Rev. A 9, 1720 (1974).

[5] W. L. McMillan, Phys. Rev. A 7, 1419 (1973).

[6] B. Cabane and W. G. Clark, Solid State Commun. 1 129 (1973).

[7] L. Cheung, R. B. Meyer, and H. Gruler, Phys. Re Lett. 31, 349 (1973).

[8] M. Delaye, R. Ribotta, and G. Durand, Phys. Rev Lett. 31, 443 (1973).

[9] P. E. Cladis, Phys. Rev. Lett. 31, 1200 (1973), to be published.

[10] F. Hardouin, M. F. Archad, and H. Gasparoux, Solid State Commun. 14, 453 (1974).

[11] S. Meiboom, private communication.

[12] P. J. Flanders, to be published.

[13] P. Pieranski, F. Brochard, and E. Guyon, J. Ph (Paris) 34, 35 (1973).

[14] J. L. Janning, Appl. Phys. Lett. 21, 173 (1972).

[15] C. C. Huang, R. S. Pindak, and J. T. Ho, to be lished.

[16] W. Helfrich, J. Chem. Phys. 56, 3187 (1972).

[17] H. Imura and K. Okano, Jpn. J. Appl. Phys. 11, (1972).

[18] A. F. Martins, to be published.

[19] I. Haller and J. D. Litster, Phys. Rev. Lett. 25

560 (1970).

[20] S. Meiboom and R. C. Hewitt, Phys. Rev. Lett. 30, 61 (1973).

[21] R. S. Pindak, C. C. Huang, and J. T. Ho, Phys. Rev. ett. 32, 43 (1974), and Solid State Commun. 14, 821 .974).

[22] V. N. Tsvetkov, Acta Physicochim. U.R.S.S. 10, 555 (1939).

[23] This estimate of C is obtained by substituting $K_{11} = 10^{-6}$ dyne, $\rho = 1$ g cm^{-3}, and $\xi_0 = 10$ Å into Eqs. (6.6) and (6.7) of Ref. 3. The estimate $C = 10^{-2}$ P in Eq. (6.8) of Ref. 3 appears to be a numerical error.

Theory and Experiments on Configurations with Cylindrical Symmetry in Liquid-Crystal Droplets

M. J. Press and A. S. Arrott
Department of Physics, Simon Fraser University, Burnaby, British Columbia, Canada V5A 1S6

(Received 13 May 1974)

Elasticity theory is applied to nematic liquid crystals with particular boundary conditions. The calculus of variations is used to derive the torque equations, the solutions of which are found by relaxation methods on a digital computer. These solutions are used to draw pictures of the molecular arrangements and with the aid of Maxwell's equations to predict the observed optical patterns, including the case of magnetic fields applied along the symmetry axis.

We have obtained agreement between elastic ontinuum calculations and optical patterns oberved with crossed polarizers in nematic liquidrystal droplets. We started with the simple uestion: What is the minimum-energy configuation of a drop in which the molecules within the rop tend to be parallel to one another, yet are inned at a definite angle to the surface of the rop? It is a simple conclusion that these drops hould show surface singularities of molecular ze in extent, and that a cylindrically symmetric olution would put the singularities (point disinations) at the north and south poles of the ops. To observe the molecular configurations out these poles we floated droplets on the surce of water. This procedure has the three imrtant advantages that the droplets are lens aped resulting in better optics than obtained h spheres, the water provides a very homogeous and reproducible substrate which for many uid crystals gives droplets with cylindrical nmetry in the molecular alignment, and for hoxybenzylidene butylaniline (MBBA, the liqcrystal we use most often) the drops remain he nematic state for many hours despite some dual absorption of water. Figure 1 shows droplets similarly prepared and of similar which when viewed between crossed polarizexhibit three distinct patterns: a right-hand- left-handed, and a normal configuration. ar patterns have been observed for almost tury, with Lehman[1] devoting a lifetime to such studies. The theory of such observations has received little attention despite the possibility that such a macroscopic element with three states might have some technological interest.

The successful analysis of this problem yields the computer graphics of Figs. 2 and 3 for the orientation of the molecules. To obtain the opti-

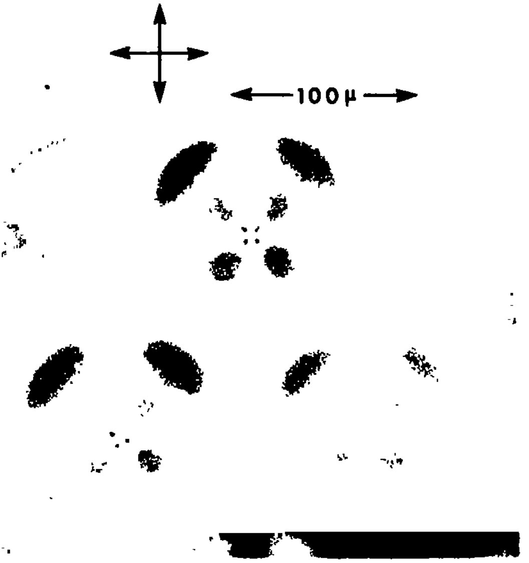

FIG. 1. MBBA droplets on a water substrate observed between crossed polarizers with white light displaying the three different configurations.

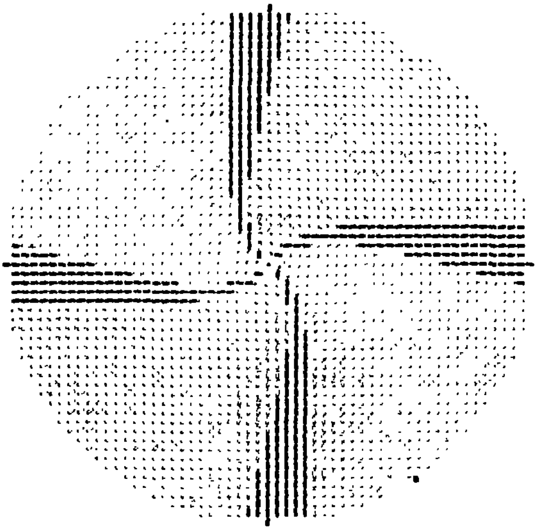

FIG. 2. View of a layer in the ρ-φ plane just below the water surface for the twisted configuration with $S/B=0.8$ and $T/B=0.5$ with $\rho_0/z_0=4$. The inserted crosses indicate those molecules whose projections in the ρ-φ plane lie within 7° of either the polarizer or the analyzer axis.

cal patterns observed with the droplets between crossed polarizers one should solve Maxwell's equations in the medium. This is carried out under the assumption of local translational invariance in the plane perpendicular to the light path.[2] This assumption is not quite adequate at the center of the droplets, but nevertheless is sufficiently valid to yield agreement between theory and experiments for the molecular configurations. Crudely one can see the effect by considering a representative slice parallel to the water substrate near the water interface as in Fig. 2. Where the light is polarized parallel or perpendicular to the projections of the molecules, its polarization is maintained and it is absorbed in the analyzer. The result is the "brush" pattern indicated by the darkened molecules. The brush pattern referred to as the normal configuration corresponds to the molecules confined to the radial-vertical plane.

The principal source of the problem is that the boundary conditions are not compatible with the vanishing of the derivative in the bulk. For the water interface the molecules are pinned to lie in the surface. For the air surface the molecules are pinned to lie in a cone making an angle of 15 deg between the molecular axis and the normal to the surface. Minimization of the energy in the bulk proceeds primarily by a process which is here termed "splay canceling". A radial component of the directrix produces a term in the divergence which offsets the contribution to the divergence from the variation in the directrix from the top surface to the bottom surface.

The elastic continuum theory starts with a directrix $\hat{n}$ which describes the mean orientation of the molecules at each point. The energy in the bulk is given by[3]

$$E=\pi\iint d\rho\,dz\,[S|\nabla\cdot\hat{n}|^2+T|\hat{n}\cdot(\nabla\times\hat{n})|^2+B|\hat{n}\times(\nabla\times\hat{n})|^2]\rho, \tag{1}$$

where cylindrical symmetry has been imposed in correspondence to the direct observation that rotation of the drops between crossed polarizers causes no change in the optical patterns. S, T, and B refer to the splay, twist, and bend elastic constants, respectively.

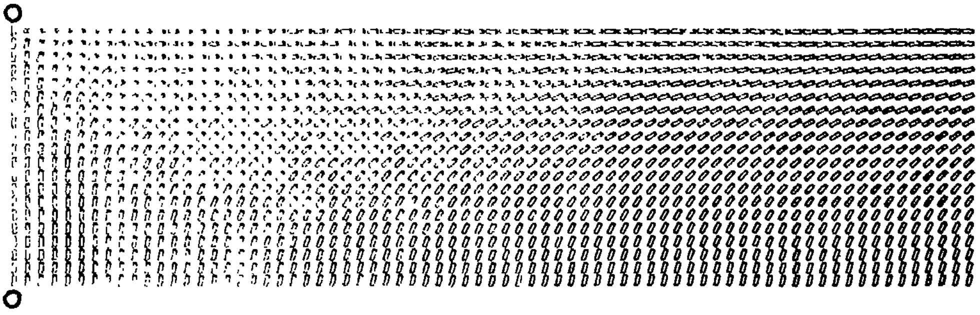

FIG. 3. The molecules in the ρ-z plane of the twisted configuration with $S/B=0.8$ and $T/B=0.5$ with $\rho_0/z_0=4$. OO is the axis of symmetry.

With the directrix expressed in terms of the usual two polar angles θ and φ and using the cylindrical coordinates ρ and z, one finds that the energy expression contains 24 terms, or 25 when we include the effect of a magnetic field along the symmetry axis. A typical set of three terms is

$$\rho \sin^2\theta\, \varphi_\rho^{\,2}(S \sin^2\varphi + T\cos^2\theta \cos^2\varphi + B \sin^2\theta \cos^2\varphi),$$

where φ_ρ is a partial derivative.

Carrying out the calculus of variations produces two torque equations, one with 31 and the other with 27 terms plus boundary conditions. The torque equations are simultaneous nonlinear second-order partial differential equations. The olutions we report here are for the simple case where the upper and lower boundaries are flat, orizontal, and separated by a distance z_0, and he outside boundary is cylindrical, vertical, and t $\rho = \rho_0$. We use hard pinning on the horizontal oundaries. On the upper one we take $\theta = \pi/2$, with φ to be determined from a first-order non-inear partial differential equation with 5 terms, while on the lower one we take $\theta = \pi/12$, again with φ to be determined from this partial differential equation. On the outside surface we use ree boundary conditions, and thus two simulta-eous first-order partial differential equations, ach with 8 terms, must be satisfied here. The hoice of $\theta = \pi/2$ corresponds to the water-liquid-rystal interface with the liquid-crystal mole-ules strongly attracted to the polarizable water. The choice of $\theta = \pi/12$ corresponds roughly to the bserved behavior of MBBA at an air interface.[4] The free boundary conditions at $\rho = \rho_0$ are an ap-roximation that produces a small amount of arti-ce into the behavior near $\rho = \rho_0$. But we are con-erned primarily with the behavior over the cen-ral "flat" portion of the drop, so this is of little onsequence.

Our assumptions of a flat surface, of hard pinning at other than $\theta = 0$, and of cylindrical symmetry are not compatible at the center of the sur-ce. We treat this part of the problem in detail sewhere. Here it is sufficient to say that on e scale of 100 nm to 100 μm in which we treat e present problem it is adequate to ignore the tails of how the infinite energy density of the ngularity is relaxed.

The torque equations with the above boundary nditions have been solved by relaxation meth- using typically a grid of 30 by 39 points, with riable grid spacing, becoming finer near the ndaries and the z axis. The relaxation is ade-te after 1000 to 2000 passes. We have results $\rho_0/z_0 \simeq 2$, 4, and 8 for several values of the ra- B/S and T/S. The behavior of the region ρ becomes independent of ρ_0/z_0 for $\rho_0/z_0 > 4$. At $\rho = 2z_0$ the θ values are within 1% of the values calculated for $\rho \rightarrow \infty$. For $T/S \geqslant 1$ we find the normal configuration which has $\varphi = 0$ everywhere. For $T/S \leqslant 0.9$ we find the three solutions which we are seeking. The degree of rotation of the cross decreases with increasing T/S for $T/S \leqslant 0.9$. The two solutions with handedness, which are mirror images of each other about $\varphi = 0$ with the same energy, differ from the normal solution primarily in the φ values. The θ values are quite close. The energy of the normal solution, while higher, is only slightly higher. Extrapolation to infinite radius suggests that the energy difference is no more than 10^{-9} erg for the whole drop (for $T = 0.4$ μdyn, $S = 0.65$ μdyn, and $B = 0.8$ μdyn which are suitable choices for MBBA[5]).

A much more important saving in energy common to all three cases occurs in the cancelation of two terms in the divergence:

$$\operatorname{div}\hat{n} = [\sin\theta(\cos\varphi)/\rho - \sin\theta\, \theta_z + \dots].$$

This cancelation occurs for $\varphi = 0$, but not for $\varphi = \pi$ (also a solution) in the case where θ_z is positive as it is here. It is this that requires φ to go to zero as the terms in θ_ρ and φ_ρ become negligible at larger radius. It should be recalled that θ_z remains large because of the conflicting boundary conditions. That this cancelation is most effective when $\rho \sim z_0$ results in a minimum in the energy density in this region, and even the total energy per unit area of the drop goes through a minimum with increasing radius. Thus there is a possibility that a large-area layer might achieve lower energy by supporting an array of point disclinations.

We have also studied the effects of vertical magnetic fields both under the microscope and on the computer and have obtained quantitative agreement.

The full equations, the optical calculations, the comparison of theory and experiment, and the details of the phase diagram will be reported elsewhere.

We wish to acknowledge the helpful advice of Dr. R. D. Russell concerning relaxation methods and the encouragement of Professor P. G. de Gennes in the initial stages of this work. This research has been supported by the National Research Council of Canada.

---

[1] O. Lehman, Ann. Phys. (Leipzig) 66, 323 (1921).

[2] The calculation of S. C. Chou, L. Cheung, and R. B. Meyer, Solid State Commun. 11, 997 (1972), has been expanded to allow the molecules complete freedom in their orientations.

[3] F. C. Frank, Discuss. Faraday Soc. 25, 19 (1958).

[4] M. A. Bouchiat and D. Langevin-Cruchon, Phys. Lett. 34A, 331 (1971).

[5] I. Haller, J. Chem. Phys. 57, 1400 (1972).

---

g Tensors and Tensor Interactions—Their Effect on Conduction-Electron Spin Resonance*

M. B. Walker
Department of Physics and Scarborough College, University of Toronto, Toronto M5S 1A7, Ontario, Canada

(Received 1 April 1974)

Conduction-electron *g* tensors depending on electron momentum can (through the cyclotron motion of the electron) cause transitions between spin Zeeman levels which broaden and shift the conduction-electron spin resonance. Tensor quasiparticle interactions are capable of similar effects. The relaxation time and exchange parameter controlling motional and exchange narrowing of the conduction-electron spin resonance are precisely defined.

Lubzens, Shanabarger, and Schultz[1] have recently reported detailed measurements of the frequency dependence, temperature dependence, and dependence on resistivity ratio of the *g* value and linewidth of conduction-electron spin resonance (CESR) in aluminum. The initial report[2] of CESR in aluminum led Dupree and Holland[3] to suggest that *g* anisotropy might be important, and theories of motional and exchange narrowing of *g* anisotropy have been formulated by de Botton[4] and Fredkin and Freedman.[5] The results of Lubzens, Shanabarger, and Schultz[1] fit very well the predictions of these latter theories.[1,5]

In the present work, the tensor nature of the *g* value is explicitly considered (for the first time) and such considerations lead to new processes affecting the linewidth and *g* shift of the CESR. In the light of this development, a reinterpretation of the results of Lubzens, Shanabarger, and Schultz[1] would be useful, as it is believed that these new results may strongly affect the value of the parameter *B* (defined below).

Also, the motional-narrowing relaxation rate is given in terms of a weighted average of the impurity scattering cross section,[6] the weighting factor being different from that determining the resistivity relaxation rate. Similarly, the exchange parameter *B* controlling exchange narrowing is precisely defined.

Finally, we follow up a remark of de Botton[4] that the influence of spin-orbit coupling on the quasiparticle interaction can produce effects qualitatively similar to those produced by *g* anisotropy. A new type of tensor quasiparticle interaction is introduced and is shown to give rise to contributions to the effective *g* tensor. Nothing is presently known about the magnitude of such tensor interactions, but it is known that the magnitude of the *g* anisotropy required to account for the aluminum results is surprisingly large.[1] A first-principles estimate of the magnitude of the tensor interaction would thus be of value.

We shall study in detail an isotropic electronic Fermi liquid. For a Zeeman Hamiltonian of the form $H_Z = -g(\vec{p})\mu_B\vec{s}\cdot\vec{H}$ to be invariant with respect to simultaneous rotations of $\vec{s}$, $\vec{H}$, and $\vec{p}$, we must have $g(\vec{p})$ independent of the direction $\vec{p}$. Anisotropy in *g* can only be introduced by the us of a *g* tensor, and we therefore assume a Zeeman Hamiltonian

$$H_Z = -\mu_B\vec{s}\cdot\overleftrightarrow{g}\cdot\vec{H}, \quad \overleftrightarrow{g} = g_0\overleftrightarrow{1} + \tfrac{1}{2}g_2\overleftrightarrow{T}, \qquad \text{(}$$

$$\overleftrightarrow{T} = 3\vec{p}\vec{p} - \overleftrightarrow{1}. \qquad \text{(}$$

The quantity $\overleftrightarrow{1}$ is the unit dyadic, and $\vec{p}$ denote a unit vector in the direction of the electron m mentum.

The tensor part of the Zeeman interaction c be written in the form $-g_2\mu_B\vec{s}\cdot\vec{H}_{eff}$, where $\vec{H}$ is an effective magnetic field given by $\vec{H}_{eff} = \frac{1}{2}[3\vec{p}(\vec{p}\cdot\vec{H}) - \vec{H}]$. The effective field has a co ponent in the direction of the momentum of th electron, as well as a component along the ex ternal field. Since the electron momentum precesses around the external field at the cyclotron frequency, ω_c, the effective magnetic field has a time-dependent component which can cause transitions between the spin energy levels. As a result of collisions of the electron with impurities or phonons, however, the cyclotron frequency is not sharply defined, and $\vec{H}_{eff}$ possesses a spectrum of frequencies lying in the range $\omega_c - \tau^{-1} < \omega < \omega_c + \tau^{-1}$, τ^{-1} being the collision frequency. So long as the electron spin-resonance frequency lies within this range, $\vec{H}_{eff}$ can mit the lifetime of the spin by causing transions between its energy levels. The precessing omponent of $\vec{H}_{eff}$ also gives rise to a g shift, s will be seen below. Thus the tensor nature of ie g value gives rise to new effects which are ot present in previous theories[4,5] assuming a calar g value.

Following Silin,[7] and making use of the Zeeman iteraction as defined by (1), the spin-dependent art of the quasiparticle interaction is written $\epsilon_{op}(\vec{p},\vec{r},\vec{t}) = \vec{\sigma}_{op}\cdot\vec{\epsilon}_2(\vec{p},\vec{r},\vec{t})$, where the compoents of $\vec{\sigma}_{op}$ are Pauli matrices,

$$\vec{\epsilon}_2(\vec{p},\vec{r},\vec{t}) = -\tfrac{1}{2}\mu_B\vec{g}\cdot\vec{H} + \sum\nolimits_{\vec{p}'}\psi(\vec{p},\vec{p}')\vec{\sigma}(\vec{p}',\vec{r},\vec{t}), \qquad (3)$$

nd $\frac{1}{2}\vec{\sigma}(\vec{p},\vec{r},\vec{t})$ is the spin density in phase space t time t. As a result of the assumed isotropy, depends only on the angle θ between $\vec{p}$ and $\vec{p}'$ nd can be written

$$\rho\psi(\theta) = \sum\nolimits_l (2l+1)B_l P_l(\cos\theta), \qquad (4)$$

here ρ is the density of states.

Now let $\vec{\sigma} = \vec{\sigma}_0 + \delta\vec{\sigma}$, where $\frac{1}{2}\vec{\sigma}_0$ is the spin density duced by the static external field $\vec{H}_0$, and write

$$\delta\vec{\sigma} = -(\partial f_0/\partial\epsilon)\vec{G}(\vec{p},\vec{r},\vec{t}), \qquad (5)$$

ere $f_0 = 2[\exp(\beta\epsilon_p)+1]^{-1}$. We shall look for the mogenous normal modes only (i.e., assume t $\vec{G}$ is independent of $\vec{r}$). The components G_α $=0, \pm 1$) of $\vec{G}$ are defined by $G_0 = G_z$, and $G_{\pm 1}$ $1/\sqrt{2})(G_x \pm iG_y)$; the external field $\vec{H}_0$ is asned along the z axis. $G_\alpha(\vec{p})$ can be expanded spherical harmonics, i.e.,

$$G_\alpha(\vec{p}) = \sum_{lm} G_{\alpha lm} Y_{lm}(\theta,\phi). \qquad (6)$$

equation of motion for $G_{\alpha lm}$ is [from Eq. of Silin]

$$G_{\alpha lm} = (i\alpha\bar{\omega}_0 - im\omega_c - 1/\tau_l)(1+B_l)G_{\alpha lm} + \int d\Omega\, Y_{lm}^*[\vec{\omega}_2\times\vec{G}']_\alpha, \qquad (7)$$

where $\hbar\bar{\omega}_0 = -[g_0\mu_B H_0/(1+B_0)]$ (note $g_0 < 0$ for electrons), $\hbar\vec{\omega}_2 = -\frac{1}{2}[g_2/(1+B_2)]\mu_B\vec{T}\cdot\vec{H}_0$, and $\vec{G}' = \vec{G} + \delta\vec{\epsilon}_2$. Collisions of electrons with impurities are described by the τ_l's in (7) following Wilson and Fredkin,[8] *the* τ_l*'s being defined as in the* electrical-resistivity problem (e.g., see Peierls[9]), i.e.,

$$\tau_l^{-1} = \int[1 - P_l(\cos\theta)]w(\theta)\,d\Omega, \quad l \geq 1. \qquad (8)$$

The resistivity is controlled by τ_1.[9] τ_0^{-1} as defined by (8) is zero, but is assumed to have a small nonzero value arising from spin-orbit coupling.

The tensor g value couples the different components, G_α, of $\vec{G}$ in Eq. (7), and this makes the solution of (7) more complex than in cases previously considered.[4,5,7,8,10] Therefore we introduce a different method motivated by the approach of Wangsness and Bloch, and Redfield[11] to the general motional-narrowing problem. The starting point is a transformation to an interaction representation in which $\tilde{G}_r$ is defined by

$$G_r(t) = \tilde{G}_r(t)\exp(i\omega_r t), \qquad i\omega_r = (i\alpha\bar{\omega}_0 - im\omega_c - \tau_l^{-1})(1+B_l), \qquad (9)$$

where $r = (\alpha, l, m)$. Matrices

$$A_{rr'}(t) = \exp(-i\omega_r t)A_{rr'}(0)\exp(i\omega_{r'}t) \qquad (10)$$

are defined by the equation

$$\exp(-i\omega_r t)\int d\Omega\, Y_{lm}^*[\vec{\omega}_2\times\vec{G}']_\alpha = i\sum\nolimits_{r'}A_{rr'}(t)\tilde{G}_{r'}(t). \qquad (11)$$

Equation (7) now becomes, in this interaction representation,

$$d\tilde{G}_r(t)/dt = i\sum\nolimits_{r'}A_{rr'}(t)\tilde{G}_{r'}(t). \qquad (12)$$

We are interested in the frequency and decay rate of the CESR mode which, in the limit $\vec{\omega}_2 = 0$, is an oscillation of G_{-100}; we call this the $r=0$ mode [i.e., $(\alpha, l, m) = (-1, 0, 0)$ implies $r = 0$]. Therefore, Eq. (12) is solved by iteration to second order in $A_{rr'}$ subject to the initial condition that, at $t=0$, $\tilde{G}_r = \tilde{G}_0(0)\delta_{r,0}$. This yields the expression

$$\omega_R - \frac{i}{T_2} = \omega_0 - i\frac{(1+B_0)}{\tau_0} + \sum_{r\neq 0}\frac{A_{0r}(0)A_{r0}(0)}{\omega_r - \omega_0} \qquad (13)$$

for the frequency, ω_R, and transverse relaxation time, T_2, of the CESR. This solution is valid when $|A_{r0}| \ll |\omega_r - \omega_0|$, where $r \neq 0$; this inequality implies, for example, that our results have no significance in the limit $B_l \to 0$ first, and $\tau_l \to \infty$ later. The result (13) is valid, however, for cases[1] of current interest experimentally. The values of r contributing to (13) are $r=(0,2,1)$ and $r=(-1,2,0)$ and the explicit evaluation of (13) leads to the results

$$\frac{\omega_g-\omega_0}{\omega_0}=\frac{(1+B_2)B\langle\omega_{2z}^2\rangle\tau_2'^2}{1+(B\bar{\omega}_0\tau_2')^2}+\frac{(1+B_2)(\omega_0-\omega_c')\frac{1}{2}[\langle\omega_{2x}^2\rangle+\langle\omega_{2y}^2\rangle]\tau_2'^2}{\bar{\omega}_0[1+(\omega_0-\omega_c')^2\tau_2'^2]}, \tag{14}$$

$$\frac{1}{T_2}=\frac{1}{\tau_0'}+\frac{(1+B_0)(1+B_2)\langle\omega_{2z}^2\rangle\tau_2'}{1+(B\bar{\omega}_0\tau_2')^2}+\frac{(1+B_0)(1+B_2)\frac{1}{2}[\langle\omega_{2x}^2\rangle+\langle\omega_{2y}^2\rangle]\tau_2'}{1+(\omega_0-\omega_c')^2\tau_2'^2}. \tag{15}$$

The notation $\langle\cdots\rangle=(4\pi)^{-1}\int(\cdots)d\Omega$ giving

$$\langle\omega_{2z}^2\rangle=\tfrac{4}{5}\langle\omega_{2x}^2\rangle=\tfrac{4}{5}\langle\omega_{2y}^2\rangle=\tfrac{1}{5}[g_2\mu_B H/(1+B_2)\hbar]^2.$$

Also $\tau_0'=\tau_0/(1+B_0)$, $\tau_2'=\tau_2/(1+B_2)$, $\omega_c'=\omega_c(1+B_2)$, and

$$B=B_0-B_2=(4\pi)^{-1}\rho\int[1-P_2(\cos\theta)]\psi(\theta)\,d\Omega. \qquad (1$$

A Zeeman Hamiltonian of the form

$$H_Z=-g(p)\mu_B\vec{s}\cdot\vec{H}\equiv-[g_0+\tfrac{1}{2}g_2T_{zz}(p)]\mu_B\vec{s}\cdot\vec{H}$$

would give the terms in (14) and (15) linear in $\langle\omega_{2z}^2\rangle$; these are thus formally analogous to results obtained previously.[1,5] The terms linear in $\frac{1}{2}[\langle\omega_{2x}^2\rangle+\langle\omega_{2y}^2\rangle]$ give the contribution of the new lifetime effect. Note that the latter terms can be obtained from the former by replacing B with $[(\omega_0-\omega_c')/\bar{\omega}_0]$, and $\langle\omega_{2z}^2\rangle$ with $\frac{1}{2}[\langle\omega_{2x}^2\rangle+\langle\omega_{2y}^2\rangle]$.

The value of B for Al obtained by Lubzens, Shanabarger, and Schultz[1] is unreliable as they were not aware of the possible influence of a g tensor in producing the lifetime effect described here.

In the case of a nonspherical Fermi surface, there will be a distribution of cyclotron frequencies depending on the external field direction; this will cause the g shift and linewidth to be anisotropic (anisotropy is observed in Cu and Ag[1]).

The experiments of Lubzens, Shanabarger, and Schultz[1] show that the motional-narrowing relaxation rate differs from the resistivity relaxation rate. Both rates are weighted averages of the impurity scattering cross section $w(\theta)$ [see Eq. (8)], but the motional-narrowing rate τ_2^{-1} uses a weight factor $[1-P_2(\cos\theta)]$ which weights most heavily collisions which significantly change the g value, whereas the resistivity rate τ_1^{-1} uses the weight factor $[1-P_1(\cos\theta)]$ which favors backward scattering. These weight factors are compared in Fig. 1. The weight factor $[1-P_2(\cos\theta)]$ also determines the exchange parameter B responsible for exchange narrowing; this is consistent with the fact that exchange between electrons with equal g values is unimportant in the exchange-narrowing process. The recent progress in determining impurity scattering cross sections[6] means that one might soon be able to calculate τ_2 from Eq. (8) for specific impurities, and this would be useful in interpreting CESR experiments.

The preceding discussion assumes an interac tion between quasiparticles with momenta $\vec{p}$ an $\vec{p}'$ of the form $\psi(\vec{p},\vec{p}')\vec{\sigma}\cdot\vec{\sigma}'$ [see Eq. (3)]. For isotropic model, however, interactions betwe quasiparticles of the form

$$\rho^{-1}D\vec{\sigma}\cdot[\overleftrightarrow{T}(\vec{p})+\overleftrightarrow{T}(\vec{p}')]\cdot\vec{\sigma}'$$

are allowed by symmetry (D is a dimensionle parameter which characterizes the strength c this interaction, which se call the tensor inte tion). Following Silin[7] [but including the tens interaction (17)] the energy of a quasiparticle an external field $\vec{H}_0$ is written $\epsilon=\vec{\sigma}\cdot\vec{\epsilon}_{20}$ wher integral equation [Silin's Eq. (6)] is found to termine $\vec{\epsilon}_{20}$. The solution of this equation is

$$\vec{\epsilon}_{20}=-\tfrac{1}{2}\bar{g}_0'\mu_B\vec{H}_0-\tfrac{1}{4}\bar{g}_2'\mu_B\overleftrightarrow{T}\cdot\vec{H}_0,$$

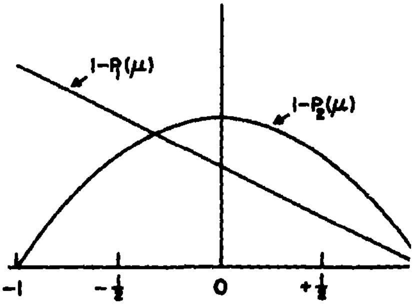

FIG. 1. Comparison of the weight factors [1 and $[1-P_2(\mu)]$ used to define the resistivity an al-narrowing relaxation rates; $\mu=\cos\theta$ and θ i scattering angle.

where

$$\bar{g}_0' = \frac{g_0}{1+B_0}\left[1 - \frac{Dg_2}{g_0(1+B_0)} + \frac{2D^2}{(1+B_0)(1+B_2)}\right],$$

$$\bar{g}_2' = \frac{g_2 - 2D\bar{g}_0'}{1+B_2},$$

orrect to second order in D and g.

Since tensor quasiparticle interactions con-
ibute to $\bar{g}_2'$ in (19), they can be expected to
oduce effects similar to those produced by a
nzero g_2 in Eq. (1). A complete analysis of
ese effects bears out these expectations.

Since the g tensors and tensor interactions
nsidered in this paper limit the lifetime of a
in, a contribution to T_1^{-1} similar to the final
rm in (15) will result. No such contribution
T_1^{-1} will result in the case of the scalar g
nsidered in Refs. 4 and 5. A measurement of
would thus distinguish between models em-
oying a scalar g and those employing a tensor g.

In summary, the above results [Eqs. (14) and
5)] provide a basis for a qualitative interpre-
tion of motionally and exchange narrowed CESR
milar to that observed in Cu, Ag, and Al.[1] To
ke the interpretation quantitatively accurate,
vever, the true Fermi-surface geometry must
considered (because of its effect on the cyclo-
n frequency, for example); this would be of
ticular interest in the cases of Cu and Ag
ch display anisotropic CESR.

inally, we note that the question "which has
dominant effect on CESR, the momentum-
endent g tensor, or tensor quasiparticle in-
tion?" has yet to be answered.

I would like to thank S. Schultz for suggesting to me that a solution to the problem of the correct definition of the motional-narrowing relaxation time, and its difference from the resistivity relaxation time, would be useful; this provided my initial interest in this problem. I would also like to thank Mme. Lewiner (née de Botton) for sending me a copy of her thesis.[4]

---

*Work supported by the National Research Council of Canada.

[1] D. Lubzens, M. R. Shanabarger, and S. Schultz, Phys. Rev. Lett. 29, 1387 (1972).

[2] S. Schultz, G. Dunifer, and C. Latham, Phys. Lett. 23, 192 (1966).

[3] R. Dupree and B. W. Holland, Phys. Status Solidi 24, 275 (1967).

[4] C. de Botton, Memoire présenté à l'Université de Paris, 1968 (unpublished).

[5] D. R. Fredkin and R. Freedman, Phys. Rev. Lett. 29, 1390 (1972).

[6] For an example of recent progress in the calculation of impurity scattering cross sections, see P. T Coleridge, J. Phys. F: Metal Phys. 2, 1016 (1972).

[7] V. P. Silin, Zh. Eksp. Teor. Fiz. 35, 1243 (1958) [Sov. Phys. JETP 8, 870 (1959)].

[8] A. Wilson and D. R. Fredkin, Phys. Rev. B 2, 4656 (1970).

[9] R. E. Peierls, *Quantum Theory of Solids* (Oxford Univ. Press, Oxford, England, 1955).

[10] P. M. Platzman and P. A. Wolff, Phys. Rev. Lett. 18, 280 (1967).

[11] R. K. Wangsness and F. Bloch, Phys. Rev. 89, 728 (1953); A. G. Redfield, IBM J. Res. Develop. 1, 19 (1957); A. Abragam, *Nuclear Magnetism* (Oxford Univ. Press, Oxford, England, 1961); C. P. Slichter, *Principles of Magnetic Resonance* (Harper and Row, New York, 1963).

Angular Forces in Tetrahedral Solids*

Walter A. Harrison and J. Christopher Phillips
Applied Physics Department, Stanford University, Stanford, California 94305
(Received 3 June 1974)

The bond-orbital model is generalized to the treatment of elastic shear constants by assuming a reduction in covalent energy V_2 proportional to the square of the angular misalignment of the two hybrids forming a bond. The result, proportional to $[(1-\alpha_p^2)^{1/2}-S]\times V_2$, gives a good account of the shear constants in all zinc-blende and wurtzite crystals for which they are known, except for the noble-metal halides.

The bond-orbital model[1,2] provides a sufficiently simple description of the electronic structure of tetrahedrally coordinated solids that one can calculate a very wide range of properties in terms of it. By comparison of the calculated and experimental optical properties it has been possible to obtain[2] the three parameters (covalent, polar, and metallic energies) for each material, in terms of which each of these properties is given. Few of the properties which have been considered involved displacements of the atoms from their equilibrium positions and for those that did an understanding was possible in terms of the measured shift in covalent energy with change in bond length. However, tetrahedral structures can be deformed without changing bond lengths and stability itself requires angular forces. Thus an extension of the model is required for a discussion of the elastic shear constants.

In the bond-orbital model each bond orbital is constructed from two sp^3 hybrids extending into that bond. The total energy contains a sum of bond energies,

$$\epsilon_b = V_2 S - (V_2^2 + V_3^2)^{1/2}, \tag{1}$$

where V_2 is the covalent energy, V_3 is the polar energy, and S is the overlap of the two hybrids, taken as 0.5 in Ref. 2 but not included explicitly in Ref. 1. This value of ϵ_b was obtained by minimizing the energy with respect to the linear combination of atomic orbitals making up the bond orbital.

We now seek the change in energy when the lattice is deformed without changing the bond length. If we retain the same tetrahedral angles between hybrids we may expect a decrease in the covalent energy proportional to the square of the angle of misalignment of the two hybrids in each bond. We in fact find that a single proportionality constant, and the assumption that this is the only important contribution to the angular force, yields quantitative agreement with experiment for all of the III-V, II-VI, and elemental semiconductors for which we have data.

The calculation in the zinc-blende structure is most conveniently performed by applying a strain field[3]

$$\begin{aligned} \epsilon_1 &= \epsilon_{xx} = \partial u/\partial x = \epsilon, \\ \epsilon_2 &= \epsilon_{yy} = \partial v/\partial y = -\epsilon. \end{aligned} \tag{2}$$

The symmetry of the distortion around each ion guarantees that there is no tendency for rotation of the rigid tetrahedral hybrids on that ion. Thus the angle of misalignment θ of the [111] hybrid with the corresponding neighbor is obtainable from

$$\cos\theta = \frac{[1,1,1]\cdot[1+\epsilon, 1-\epsilon, 1]}{3^{1/2}(3+2\epsilon^2)^{1/2}}. \qquad (3$$

(Note, in passing, that the change in bond lengt is of order ϵ^2 so the radial interaction energy, of order ϵ^4, is negligible.) Expanding Eq. (3) for small ϵ and small θ, we obtain $\theta^2 = 2\epsilon^2/3$. The same result applies for every bond. Thus the assumption that the covalent energy chang according to

$$\Delta V_2 = -\lambda V_2 \theta^2,$$

and that any change in V_3 is negligible, may b combined with Eq. (1) to give a change in ene per electron of

$$\begin{aligned} \Delta\epsilon_b &= \frac{\partial \epsilon_b}{\partial V_2}\Delta V_2 \\ &= \frac{-2\lambda}{3} V_2 \left(S - \frac{V_2}{(V_2^2+V_3^2)^{1/2}}\right)\epsilon^2. \end{aligned}$$

Noting that there are 32 electrons per unit c of edge a, the same change in energy may b written in terms of the elastic constants:

$$\Delta\epsilon_b = \frac{a^3}{32}(c_{11}-c_{12})\epsilon^2;$$

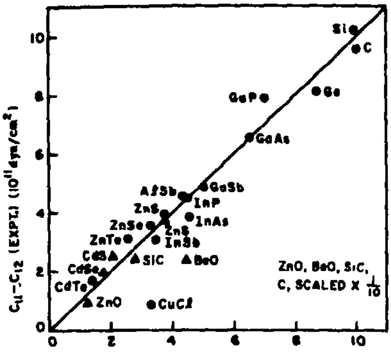

FIG. 1. Experimental shear constant [as compiled
y R. M. Martin, Phys. Rev. B 1, 4005 (1970)] plotted
gainst the bond-orbital model form [Eq. (7) with λ tak-
n as 4.3] for fifteen zinc-blende structures. Note that
ıe experimental and theoretical values for four mate-
ials have been reduced by a factor of 10 for plotting.
Effective cubic constants" were also plotted, as trian-
les, for the wurtzite structure. They were taken from
Martin (Ref. 4). Covalent and polar energies, as well
s S, were taken from Ref. 2.

ombining Eqs. (5) and (6) we have

$$c_{11}-c_{12}=\frac{64\lambda}{3a^3}V_2(\alpha_c-S), \qquad (7)$$

ere the *covalency* α_c is related to the polarity
by[1,2]

$$\alpha_c=(1-\alpha_p^2)^{1/2}=V_2/(V_2^2+V_3^2)^{1/2}. \qquad (8)$$

he parameters V_2 and V_3 were obtained from
ical properties and tabulated in Ref. 2; S was
en as 0.5 in Ref. 2. Thus we may directly
the experimental $c_{11}-c_{12}$ against the coeffi-
nt of λ in Eq. (7) and obtain λ from the slope.
s is done in Fig. 1 leading to the value $\lambda=4.3$.
rms fit to give a best "experimental" value
S leads to 0.47, within experimental error of
so we retain the value 0.5.

e same analysis could be carried out for the
zite structure but it was more convenient to
he "effective" cubic elastic constants for the
zite structures obtained by Martin,[4] which
then directly included in Fig. 1.

e that the model predicts the correct de-
ence upon metallicity, or row of the peri-
able (e.g., see C, Si, Ge) as well as upon
ity (e.g., see Ge, GaAs, ZnSe). These two
s follow from the form of the model and only the single scale parameter λ is required to make the predictions quantitative. Note, however, that CuCl is not well described, presumably because of force contributions from the copper d states. It is interesting that Eq. (7) indicates, and Fig. 1 confirms the trend, that the shear constant would be negative for a covalency less than one half. This result is consistent with the observation that the covalency for all tetrahedral solids is greater than one half.

The above angular forces may be interpreted as a change in energy $\frac{1}{2}C_1(\Delta\theta_{ij})^2$ due to the deviation $\Delta\theta_{ij}$ of each angle between adjacent bonds from the tetrahedral angle.[5] Then

$$C_1=2\lambda[\alpha_c-S]V_2/3. \qquad (9)$$

Similarly a change in energy $\frac{1}{2}C_0(\Delta d/d)^2$ may be associated with the fractional change $\Delta d/d$ of each bond length. There are important contributions to C_0 which have not yet been incorporated in the bond-orbital model. However, C_0 may be obtained from a measurement of the bulk modulus (or guessed since it is near 50 eV for most tetrahedral solids) and all three elastic constants estimated for the zinc-blende structures, or all six for the wurtzite structures. Indeed there have been a variety of calculations of vibrational frequencies and modes based upon such force constants. These may be combined with effective charges,[2] also obtainable in the bond-orbital model, to obtain properties such as the piezoelectric constant. It is also possible, using the bond-orbital model, to add the corrections for long-range forces which arise from electrostates and quadripole interactions. However, it is clear that the principal angular rigidity is due to the covalent bonding.

---

*Work supported in part by National Science Foundation Grant No. PG 25945 and in part by the National Science Foundation through the Center for Materials Research at Stanford University.

[1] W. A. Harrison, Phys. Rev. B 8, 4487 (1973).

[2] W. A. Harrison and S. Ciraci, Phys. Rev. B (to be published).

[3] We use the notation of C. Kittel, *Introduction to Solid State Physics* (Wiley, New York, 1967), 3rd ed., pp. 111ff.

[4] R. M. Martin, Phys. Rev. B 6, 4546 (1972).

[5] We choose to use the parameter C_1 which reflects purely angular forces rather than the more customary β which includes some radial interaction in addition.

Neutron Inelastic Scattering by Coupled Defect-Phonon Modes in KCl-CN

D. Walton*
Department of Physics and Institute for Materials Research, McMaster University, Hamilton, Ontario

and

H. A. Mook and R. M. Nicklow†
Solid State Division, Oak Ridge National Laboratory,‡ Oak Ridge, Tennessee 37830

(Received 28 May 1974)

A clear splitting, present only at low temperatures, is observed where the unperturbed phonon curve crosses the CN$^-$ T_{1u} and T_{2u} levels in a KCl crystal doped with 6×10^{19} CN$^-$ cm^{-3}. Calculated dispersion curves require coupling constants which agree within experimental uncertainty with those determined ultrasonically. The absence of the splitting at high temperatures can be explained because the phonon gain and loss processes in the interaction with the CN$^-$ level cancel almost completely.

It is well known that the resonant scattering of excitations otherwise describable as plane waves leads to coupled modes which can be described as a mixture of the wave functions of the excitation and the scattering system. For light, the phonon-photon coupled modes are referred to as the "polariton," and similar effects occur with magnons, etc. Coupled modes can also arise from a random distribution of defects, even at low concentrations. For sound, or phonons, the coupling to the spin of magnetic defects leads to coupled modes as was first shown by Jacobsen and Stevens.[1] This is still an active subject for theoretical research, but a general result common to all approaches is that close to resonance the normal modes of the crystal cease to be simply excitations in the displacement field but contain a magnetic contribution as well. Furthermore a phonon contribution also appears in what could otherwise be described as the normal modes of the paramagnetic defect.[2]

It is clear that similar behavior can be expected for phonons interacting with any resonant scatterer. Thus it has been shown that similar dispersion relations can be obtained for scattering of phonons by nonmagnetic defects. We wish to present here the first direct experimental evidence for the fact that a low concentration of defects does indeed lead to coupled modes. We will show that it is possible to scatter neutrons from the phonon component of the coupled mode.

The system chosen was KCl-CN because of the large interaction which exists between the phonons and the librational modes of the CN$^-$ ion. The lowest energy levels for CN$^-$ in KCl consist of a ground state, split by tunneling into three states separated by 1.1 and 2.0 cm^{-1} from the ground state.[3] Above these tunneling states there are three librational levels[4] at 13.5, 16.4, and 18.6 cm^{-1}.

Results obtained by Byer and Sack[5] reveal a large change in velocity of sound (~2% in the low-temperature limit for 1.65×10^{19} cm^{-3} CN$^-$) for phonons of E_g symmetry in KCl doped with various concentrations of KCN. The data reveal that the change increases as the temperature is lowered until a temperature of roughly 15°K is reached. As the temperature is lowered still further an additional increase occurs, but it is smaller. This behavior may be understood if it is assumed that the major interaction occurs between the E_g phonon and the librational levels —the change in self-energy of the phonon will tend to saturate when the temperature becomes sufficiently low for $\hbar\omega_l/kT > 1$, where $\hbar\omega_l$ is the energy of the librational level.

Viewed in a similar fashion, Byer and Sack's results indicate that an even stronger interaction exists between phonons of T_{2g} symmetry and the lower tunneling states at 1.1 and 2.0 cm^{-1}; however, these are too low in energy to be accessible with neutron inelastic scattering and will have no effect on these experiments. The experimental task then is not only to obtain the dispersion curves in the crossover region, but also to compare the neutron data with the ultrasonic results. It should be noted that these effects will only appear at low temperatures, that is, at temperatures such that $\hbar\omega_l/kT \gtrsim 1$, where $\hbar\omega_l$ is the energy of the librational levels.

The specimen used in these experiments was grown by G. Schmidt of Cornell University. It

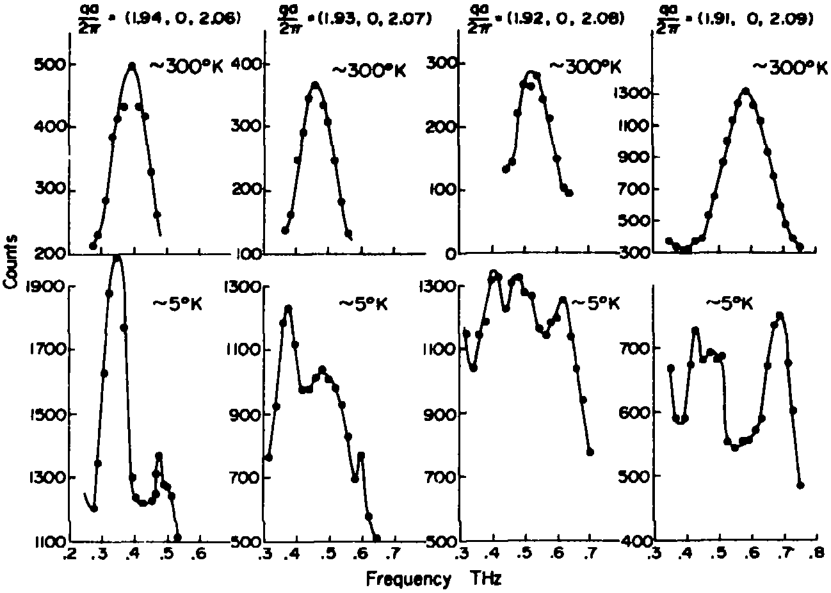

FIG. 1. Phonon peaks at room and liquid-helium temperatures for KCl + 6 × 10^{19} CN cm^{-3}. The data were taken at various monitor counts. The solid lines were not calculated and are included only to guide the eye.

was a single crystal of KCl doped with CN^-. From infrared absorption[6] a concentration of 6.0 × 10^{19} ions/cm^3 (0.4%) was obtained. The approximate dimensions of the sample used were 2 cm × 2 × 5 cm. The experiments were performed on the Oak Ridge high-flux isotope reactor on a triple-axis spectrometer of conventional design. We have studied phonons of E_g symmetry with wave vector in the ⟨110⟩ direction polarized in the ⟨1$\bar{1}$0⟩ direction. The polarization and wave vector are identical to those studied by Byer and Sack.[5]

Results for four phonons in the crossover region are shown in Fig. 1. The dispersion relations at 4°K in the vicinity of the cross over region are shown in Fig. 2.

It is clear from Fig. 1 that the neutron peaks show structure at 5°K which is nonexistent at room temperature. The structure is consistent with the presence of one strong peak and two weaker peaks. Although the resolution is only barely adequate (at best) to resolve the two weaker peaks, their presence is expected when the dispersion relations for the coupled modes are calculated.

It can be shown[7] that the shift in phonon frequency due to the interaction with a resonant scatter-

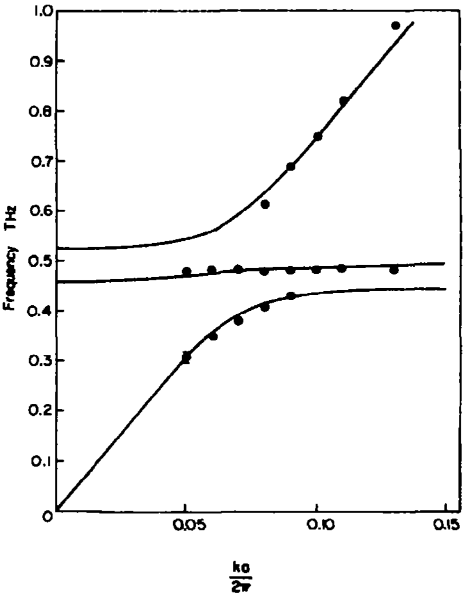

FIG. 2. Experimental (points) and calculated (solid line) dispersion relations for phonons in KCl + 6 × 10^{19} CN cm^{-3} at ~ 5°K.

Neutron Inelastic Scattering by Coupled Defect-Phonon Modes in KCl-CN

D. Walton*
Department of Physics and Institute for Materials Research, McMaster University, Hamilton, Ontario

and

H. A. Mook and R. M. Nicklow†
Solid State Division, Oak Ridge National Laboratory,‡ Oak Ridge, Tennessee 37830

(Received 28 May 1974)

A clear splitting, present only at low temperatures, is observed where the unperturbed phonon curve crosses the CN$^-$ T_{1u} and T_{2u} levels in a KCl crystal doped with 6×10^{19} CN$^-$ cm^{-3}. Calculated dispersion curves require coupling constants which agree within experimental uncertainty with those determined ultrasonically. The absence of the splitting at high temperatures can be explained because the phonon gain and loss processes in the interaction with the CN$^-$ level cancel almost completely.

It is well known that the resonant scattering of excitations otherwise describable as plane waves leads to coupled modes which can be described as a mixture of the wave functions of the excitation and the scattering system. For light, the phonon-photon coupled modes are referred to as the "polariton," and similar effects occur with magnons, etc. Coupled modes can also arise from a random distribution of defects, even at low concentrations. For sound, or phonons, the coupling to the spin of magnetic defects leads to coupled modes as was first shown by Jacobsen and Stevens.[1] This is still an active subject for theoretical research, but a general result common to all approaches is that close to resonance the normal modes of the crystal cease to be simply excitations in the displacement field but contain a magnetic contribution as well. Furthermore a phonon contribution also appears in what could otherwise be described as the normal modes of the paramagnetic defect.[2]

It is clear that similar behavior can be expected for phonons interacting with any resonant scatterer. Thus it has been shown that similar dispersion relations can be obtained for scattering of phonons by nonmagnetic defects. We wish to present here the first direct experimental evidence for the fact that a low concentration of defects does indeed lead to coupled modes. We will show that it is possible to scatter neutrons from the phonon component of the coupled mode.

The system chosen was KCl-CN because of the large interaction which exists between the phonons and the librational modes of the CN$^-$ ion. The lowest energy levels for CN$^-$ in KCl consist of a ground state, split by tunneling into three states separated by 1.1 and 2.0 cm^{-1} from the ground state.[3] Above these tunneling states there are three librational levels[4] at 13.5, 16.4, and 18.6 cm^{-1}.

Results obtained by Byer and Sack[5] reveal a large change in velocity of sound (~2% in the low-temperature limit for 1.65×10^{19} cm^{-3} CN$^-$) for phonons of E_g symmetry in KCl doped with various concentrations of KCN. The data reveal that the change increases as the temperature is lowered until a temperature of roughly 15°K is reached. As the temperature is lowered still further an additional increase occurs, but it is smaller. This behavior may be understood if it is assumed that the major interaction occurs between the E_g phonon and the librational levels —the change in self-energy of the phonon will tend to saturate when the temperature becomes sufficiently low for $\hbar\omega_l/kT>1$, where $\hbar\omega_l$ is the energy of the librational level.

Viewed in a similar fashion, Byer and Sack's results indicate that an even stronger interaction exists between phonons of T_{2g} symmetry and the lower tunneling states at 1.1 and 2.0 cm^{-1}; however, these are too low in energy to be accessible with neutron inelastic scattering and will have no effect on these experiments. The experimental task then is not only to obtain the dispersion curves in the crossover region, but also to compare the neutron data with the ultrasonic results. It should be noted that these effects will only appear at low temperatures, that is, at temperatures such that $\hbar\omega_l/kT\gtrsim1$, where $\hbar\omega_l$ is the energy of the librational levels.

The specimen used in these experiments was grown by G. Schmidt of Cornell University. It

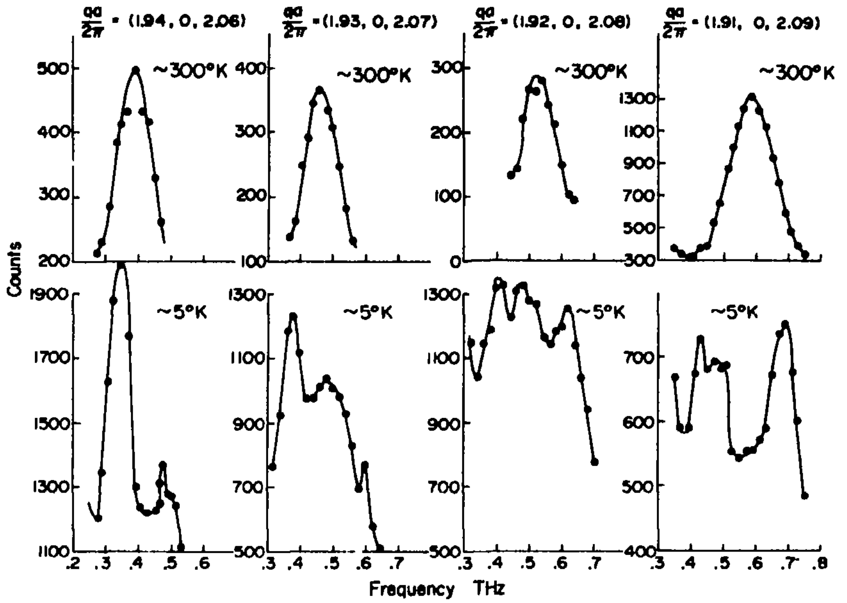

FIG. 1. Phonon peaks at room and liquid-helium temperatures for KCl + 6×10^{19} CN cm^{-3}. The data were taken at various monitor counts. The solid lines were not calculated and are included only to guide the eye.

was a single crystal of KCl doped with CN^-. From infrared absorption[6] a concentration of 6.0 $\times10^{19}$ ions/cm^3 (0.4%) was obtained. The approximate dimensions of the sample used were 2 cm $\times 2\times 5$ cm. The experiments were performed on the Oak Ridge high-flux isotope reactor on a triple-axis spectrometer of conventional design. We have studied phonons of E_g symmetry with wave vector in the ⟨110⟩ direction polarized in the ⟨1$\bar{1}$0⟩ direction. The polarization and wave vector are identical to those studied by Byer and Sack.[5]

Results for four phonons in the crossover region are shown in Fig. 1. The dispersion relations at 4°K in the vicinity of the cross over region are shown in Fig. 2.

It is clear from Fig. 1 that the neutron peaks show structure at 5°K which is nonexistent at room temperature. The structure is consistent with the presence of one strong peak and two weaker peaks. Although the resolution is only barely adequate (at best) to resolve the two weaker peaks, their presence is expected when the dispersion relations for the coupled modes are calculated.

It can be shown[7] that the shift in phonon frequency due to the interaction with a resonant scatter-

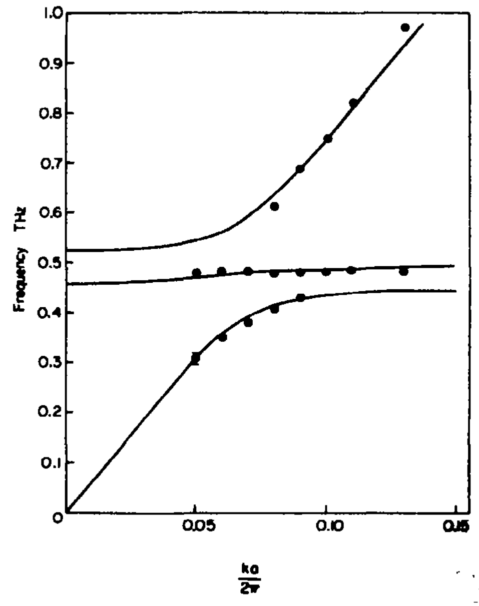

FIG. 2. Experimental (points) and calculated (solid line) dispersion relations for phonons in KCl + 6×10^{19} CN cm^{-3} at ~ 5°K.

er is given by

$$\frac{\Delta\omega}{\omega_k}=\rho_d\sum_i\frac{A_i}{\omega_i}\left(\frac{\omega^2}{\omega_i^2}-1\right)^{-1}\times\frac{1-\exp(-\beta\omega_i)}{1+\sum_i g_i\exp(-\beta\omega_i)},\qquad(1)$$

where ω_i is the frequency of level i, of degener-cy g_i; $\beta=\hbar/k_BT$, A_i is the coupling constant to evel i, ω_k is the unshifted frequency, ω is the hifted frequency, and ρ_d is the number of defects er unit volume. At high temperatures, the fac-or $1-\exp(-\beta\omega_i)$ weakens the dispersion intro-uced by the interaction. The resonant frequen-ies are ~20°K and therefore the effect would be xpected to become unobservable at room tem-erature, and a single phonon peak would be ob-erved.

When all the energy levels of the CN$^-$ ion in Cl are considered, a large number of potential ransitions are revealed. Although symmetry onsiderations can be expected to reduce their umber, it should be recalled that Byer and Sack[5] ave noted that in some respects this system is nomalous. Nevertheless, if group theory is ap-lied in a straightforward manner, we note that n E_g phonon can only induce transitions between ie T_{1u} levels in the tunnel-split multiplet and the $_{1u}$ and T_{2u} librational levels. Therefore if the omplexities peculiar to the CN$^-$ are neglected, e obtain two possible transitions:

$$\hbar\omega_1/c=16.4-1.1=15.3\ \mathrm{cm}^{-1},$$

$$h\omega_2/c=18.6-1.1=17.5\ \mathrm{cm}^{-1}$$

In the low-temperature limit, close to reson-nce, Eq. (1) becomes approximately

$$\Delta\omega/\omega_k=B_1(\omega^2-\omega_1^2)^{-1}+B_2(\omega^2-\omega_2^2)^{-1}.\qquad(2)$$

y using this expression, and leaving B_1 and B_2 s adjustable parameters, the solid lines in Fig. were obtained. The value of B_1/ω_1^2 is 0.008 nd of B_2/ω_2^2 is 0.07, if ω_1 and ω_2 are in terahertz.

From Byer and Sack's ultrasonic results we obtain a value for the sum $B_1/\omega_1^2+B_2/\omega_2^2=0.06$. Considering the difficulty in making an absolute determination of CN$^-$ concentration, we consider the agreement to be satisfactory.

We conclude that the extra peaks which appear at low temperatures are due to neutrons inelastically scattered from the phonon component of levels which would be the CN$^-$ librational levels in the absence of any phonon-defect interaction. At room temperature the phonon virtual gain and loss processes cancel almost completely and the extra peaks disappear. Because of the low concentration of CN in the sample, the CN$^-$ modes themselves are unobservable. Therefore the extra peaks that appear at low temperature must be due to the mixing of phonons into the CN$^-$ librational levels.

The authors wish to express their gratitude to B. N. Brockhouse and R. F. Wood for the many very helpful suggestions they have made.

---

*Research supported by the National Research Council of Canada.

†Research sponsored by the U. S. Atomic Energy Commission under contract with the Union Carbide Corporation.

‡Operated by Union Carbide Corporation under contract with the U. S. Atomic Energy Commission.

[1] E. H. Jacobsen and K. W. H. Stevens, Phys. Rev. 129, 2036 (1963).

[2] R. J. Elliott and J. B. Parkinson, Proc. Phys. Soc., London 92, 1024 (1967).

[3] M. C. Hetzler and D. Walton, Phys. Rev. B 8, 4801 (1973).

[4] V. Narayanamurti and R. O. Pohl, Rev. Mod. Phys. 42, 201 (1970).

[5] N. E. Byer and H. S. Sack, Phys. Status Solidi 30, 569 (1968).

[6] J. P. Harrison, P. P. Peressini, and R. O. Pohl, Phys. Rev. 167, 856 (1968).

[7] D. Walton, Phys. Rev. B 7, 3925 (1973).

VOLUME 33, NUMBER 7 PHYSICAL REVIEW LETTERS 12 AUGUST 1974

Exciton-Enhanced Photoemission from Doped Solid Rare Gases*

Zohar Ophir, Baruch Raz, and Joshua Jortner
Department of Chemistry, Tel-Aviv University, Tel-Aviv, Israel

(Received 9 April 1974)

We report the observation of exciton-induced photoemission resulting from electronic energy transfer from "free" exciton levels to impurity states in solid Xe and Kr. A diffusion length of $l_0 \simeq 75$ Å for Wannier excitons in solid Xe was deduced, corresponding to a diffusion coefficient of $D = 0.5$ cm^2 sec^{-1}. The energy of the bottom of the conduction band is $V_0 = -0.46 \pm 0.1$ eV for Xe and $V_0 = -0.23 \pm 0.1$ eV for Kr.

The physical information available concerning exciton dynamics in simple insulators such as solid rare gases is rather meager. The vacuum-ultraviolet luminescence spectra of pure solid Ar, Kr, and Xe exhibit the emission from rare-gas diatomic molecules, which results from an efficient exciton-trapping process.[1] No emission could be detected from exciton states in these solids.[2,3] Thus, from the exciton radiative lifetime $\tau_r \simeq 10^{-9}$ sec, we infer that exciton trapping occurs within $\tau_0 < \tau_r/100 \simeq 10^{-11}$ sec. Relevant information regarding exciton dynamics can be obtained from experimental studies of photoemission resulting from electronic energy transfer to impurity states in solid rare gases. The impurity energy gap $E_G{}^i$ in these simple solids is $E_G{}^i = I_g{}^i + P_+{}^i + V_0$, where $I_g{}^i$ is the impurity gas-phase ionization potential, $P_+{}^i$ is the medium polarization energy by the impurity positive ion, and V_0 represents the energy of the matrix conduction band (relative to the vacuum level).[4] The photoemission threshold from the impurity is $E_x{}^i = E_G{}^i - V_0$. The lowest Wannier exciton states of the matrix, characterized by the energy levels E_n $(n = 1, 2, \ldots)$, can be located either above or below $E_x{}^i$. In the former case, i.e., $E_n > E_x{}^i$, one will observe direct photoemission from impurity states in the energy range $E_x{}^i \leqslant E \leqslant E_1$. In the latter case, when $E_1 \leqslant E_x{}^i$, one can expect photoemission due to energy transfer from free exciton states, E_n $(n \geqslant 1)$, of the solid to the impurity. This Auger-type impurity ionization process can result only from the "collision" of a free exciton with the impurity. The electronic energy E_M of the trapped diatomic molecule[1-3] is too low, i.e., $E_M \leqslant E_x{}^i$, to induce impurity ionization. We have observed a dramatic enhancement of the photoemission yield of lightly doped solid rare gases (doping level <1%) when excited into the exciton manifold of the host crystal. Exciton-induced photoemission was reported twenty years ago in alkali halides containing F centers.[5] The present experiments on solid rare gases provide information regarding free-exciton dynamics on the time scale $\tau_0 \approx 1$ psec,[6] prior to exciton trapping.

The systems studied were C_6H_6/Xe ($E_G{}^i = 7.75$ ev[7] and $E_1 = 8.40$ eV[8]), and Xe/Kr [$E_G{}^i = 10.4$ eV and $E_1(^3P_1) = 10.17$ eV].[9] Photoemission studies were carried out in the energy range 6–11.5 eV. The vacuum-ultraviolet light source consisted of a high-pressure (2–5 atm), high-intensity, gas pulsed discharge lamp.[10] The light was passed through a 0.3-m Czerny-Turner monochromator employing a spectral resolution of 5 Å (~0.025 eV). The monochromator was separated from the sample chamber by a LiF window. The optical arrangement allowed for a simultaneous measurement of optical absorption and photoemission yield. The emitter electrode consisted of a 3-mm-wide gold strip evaporated on a LiF window. The collector electrode was a gold ring 15 mm in diameter, located 30 mm from the emitter. The signal was amplified in two stages and integrated by a boxcar integrator. A noise level of 5×10^{-15} A was achieved. The samples were prepared by deposition of a gaseous mixture on the emitter electrode mounted on a variable-temperature helium-flow cryostat at 30–40°K. The gaseous mixtures were prepared and handled in an ultrahigh-vacuum system previously pumped down to less than 10^{-9} Torr. The sample chamber was pumped by an ion pump and a cryogenic pump down to less than 10^{-9} Torr.

The curve of photoemission yield,[11] for pure Xe, Fig. 1, agrees with previous work.[12,13] A square-root extrapolation of the yield versus energy (see Fig. 1) results in $E_x = 9.74 \pm 0.05$ eV which together with the spectroscopic value $E_G = 9.28 \pm 0.05$ eV results in $V_0 = -0.46 \pm 0.10$ eV for pure Xe. At energies lower than the threshold a structure is observed (photoemission yield ~1%) at 1380 Å, which coincides with the E_2 exciton states of Xe. Several possible interpretations of this effect are as follows: (1) Impurity ioniza-

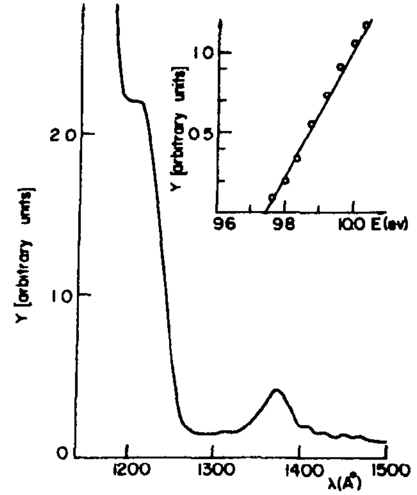

FIG. 1. Photoemission yield from solid Xe at 40°K. Upper inset: square-root extrapolation of the yield versus energy.

tion.[12] On the basis of our data for the C_6H_6/Xe we infer *inter alia* that the (unidentified) impurity concentration should exceed 5 ppm, which is rather high under our experimental conditions. (2) Nonlinear *processes such as exciton-exciton collisions*[14] *or exciton photoionization*,[14] which can be ruled out for the low light intensity employed in these experiments and in view of our observations that Y is independent of the light intensity. (3) Exciton diffusion to the gold substrate followed by electron ejection from the electrode. A preliminary result indicating that the 1380-Å photoemission peak decreases with increasing the sample thickness tends to support this mechanism.

In Fig. 2 we display the photoemission-yield curves for C_6H_6/Xe and for Xe/Kr. The emission onset for C_6H_6/Xe occurs at $E_x{}^i = 8.15 \pm 0.05$ eV which together with the spectroscopic value[7] $E_G{}^i = 7.75$ eV results in $V_0 = -0.4 \pm 0.1$ eV for solid Xe in good agreement with the result for the pure solid. For Xe/Kr the onset $E_x{}^i = 10.68 \pm 0.1$ eV together with $E_G{}^i = 10.40$ eV results in $V_0 \approx -0.28 \pm 0.1$ eV for solid Kr.

The most prominent feature of these results involves the large photoemission yield in the energy range where light absorption occurs predominantly into the host-matrix exciton states below the photoemission threshold for the pure solids. The absolute quantum yields for photoemission from C_6H_6/Xe are estimated[15] to be approximately $Y \approx 20\%$ at 1455 Å and $Y \approx 30\%$ at 1380 Å. The photoemission originates from exciton-induced Auger-type impurity ionization.

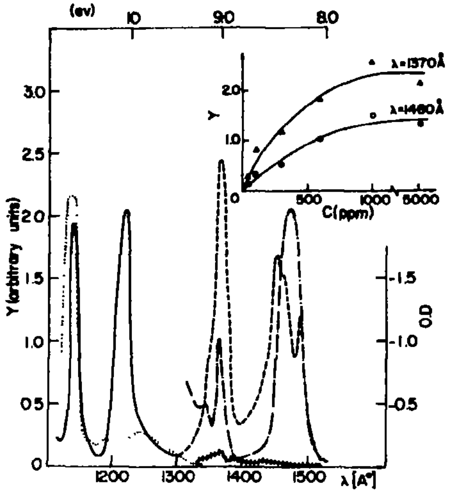

FIG. 2. Photoemission-yield curves from dilute (1%) impurity states in solid Xe and solid Kr measured at 30°K. Dashed curve, photoemission from benzene/Xe; dotted curve, photoemission from Xe/Kr. A photoemission-yield curve (hatched) for pure Xe is presented in the same arbitrary units as that for C_6H_6/Xe. The photoemission-yield curves are compared with the absorption spectra of pure Xe (dot-dashed curve) and of pure Kr (solid curve). Upper inset: the dependence of the photoemission yield on the benzene concentration C in C_6H_6/Xe solid films.

The line shapes of the emission curves are expected to provide pertinent information regarding exciton dynamics. The C_6H_6/Xe system exhibits a minimum in the Y curve at 1480 Å which coincides with the maximum of the $n = 1$ exciton state. The photoemission peaks at 1380 and 1350 Å practically coincide with the exciton energies E_2 (1380 Å) and E_3 (1345 Å). The dip in the photoemission curve at 1480 Å cannot be adequately explained in terms of the "dead-layer" theory,[16] which results in $L \simeq 150$ Å for the electron escape length and in the unphysically large value $h > 70$ Å for the width of the dead layer.

An attractive alternative approach to this problem involves a kinetic picture where competition between exciton trapping and energy transfer from excitons to homogeneously distributed impurities is considered. The number density $n(x, t)$ of "free" excitons at the distance x from the surface is governed by the diffusion equation

$$\frac{\partial n(x,t)}{\partial t}=D\frac{\partial^2 n(x,t)}{\partial x^2}+kI_0\exp(-kx)-\frac{n(x,t)}{\tau_0}-S[X]n(x,t), \qquad (1)$$

where D is the exciton diffusion coefficient, k the absorption coefficient, I_0 the incident light intensity, S the rate constant for impurity ionization, and $[X]$ the impurity concentration. Under steady-state conditions, $n(x,t)=n(x)$, and Eq. (1) is readily solved using the appropriate boundary conditions $n(0)=n(\infty)=0$. The photoemission quantum yield Y can be expressed in the form

$$Y=\frac{S[X]\tau}{1-(kl)^2}\left[\frac{kL}{kL+1}-\frac{kl}{(l/L)+1}\right], \qquad (2)$$

where the effective exciton lifetime is $\tau=(1/\tau_0+S[X])^{-1}$ and $l=[D(1/\tau_0+S[X])^{-1}]^{1/2}$ is the exciton diffusion length in the doped crystal, which is related to the diffusion length $l_0=(D\tau_0)^{1/2}$ in the pure crystal via $l=l_0(1+S\tau_0[X])^{-1/2}$.

In the limit $l=0$, $Y\propto kL(kL+1)^{-1}$ and a monotonic increase of Y with k is exhibited. Thus our observation of the splitting of the Y curve about the $n=1$ exciton state implies that l is finite. Numerical calculations of $Y=Y(k)$ were performed utilizing the experimental absorption spectrum of solid Xe and employing a wide range of parameters $k_{\max}^{(1)}L$ and l/L. These calculations result in the following conclusions: (1) For $k_{\max}^{(1)}L>2$ and $l/L>0.03$ the Y curve around the $n=1$ exciton band exhibits a symmetric splitting revealing a minimum at $E_1^{\max}$. (2) The Y curve around the $n=2$ exciton band peaking at $E_2^{\max}$, which is characterized by a lower absorption coefficient $k_{\max}^{(2)}\simeq 0.25k_{\max}^{(1)}$, is unsplit, its maximum coinciding with $E_2^{\max}$ for $k_{\max}^{(1)}L<8$. (3) The Y value at $E_{\max}^{(2)}$ and the maximum value of Y around $n=1$ are practically identical for the range of parameters mentioned in point (1). Our experimental results are in qualitative agreement with these features. The asymmetric splitting observed around $E_1^{\max}$ results from the energy dependence of L about the threshold, while the ratio Y(1370 Å)/Y(1450 Å) $\simeq 1.5$ which is larger than the expected value of unity may originate from the inefficient electronic relaxation of the $n=2$ state to the $n=1$ state on the time scale of $\tau_0\simeq 10^{-12}$ sec, whereupon the parameters l_0 and L for the two electronic states may be somewhat different.

A semiquantitative fit of the Y line shape, the concentration dependence of Y, and the absolute Y values was accomplished using Eq. (2) with the parameters $k_{\max}^{(1)}L=2.5$, $l_0/L=0.2$, and $S\tau_0=5\times 10^{-19}$ cm^{-3}, all of which are reliable within a numerical factor of 2. The parameters l_0 and $S\tau_0$ for the $n=1$ excitons and for the $n=2$ excitons are identical within this margin of uncertainty. From $k_{\max}^{(1)}=6\times 10^5$ cm^{-1}, we estimate a mean value of $L\simeq 380$ Å, which is reasonable for solid rare gases at sufficiently high energies. The "free" exciton diffusion length is $l_0\simeq 75$ Å.

The diffusion length of excitons in solid Xe is lower than the corresponding values in organic crystals, i.e., $l_0=150$ Å for singlet excitons[17] ($\tau_0=25\times 10^{-9}$ sec) and $l_0=10^5$ Å for triplet excitons[18] ($\tau_0=25\times 10^{-3}$ sec) in crystalline anthracene. However, the exciton diffusion process in the solid rare gas occurs on an extremely short time scale, $\tau_0\simeq 10^{-12}$ sec, which implies that $D\simeq 0.5$ cm^2 sec^{-1} in this system. The rate constant $S\simeq 5\times 10^{-7}$ cm^{-3} sec^{-1} is consistent with this high D value. We now focus our attention on the interesting question of whether the excited motion is coherent or diffusive. Setting $S=\pi R^2\langle V^2\rangle^{1/2}$ and $D=\Lambda\langle V^2\rangle^{1/2}$, where R is the reaction radius, $\langle V^2\rangle^{1/2}$ the rms exciton group velocity, and Λ the exciton mean free path, we get $\Lambda=(D/S)\pi R^2$, which with $R=10$ Å results in $\Lambda\simeq 3$ Å. Thus Λ is of the order of the lattice spacing and the exciton motion is diffusive (at least above ~20°K).

Complementary information concerning dynamics of free excitons is obtained from optical line-shape studies.[19,20] The Wannier exciton results in an $n=1$ exciton optical linewidth $\hbar\Gamma=3.19\times 10^{-4}m^{3/2}E_d^2$ (eV) for weak exciton-phonon coupling.[19] Taking the experimental value $m=0.5$ for the effective mass[8,9] and $E_d=1-3$ eV[20,21] for the deformation potential, we estimate $\hbar\Gamma\simeq 10^{-4}-10^{-3}$ eV which is appreciably lower than the experimental value $\hbar\Gamma=0.075$ eV for the $n=1$ ($^3P_1$) state. Thus the solid-rare-gas exciton states are close to the limit of strong exciton-phonon coupling which together with the low value of Λ provides *a posteriori* justification for the diffusion model adopted herein.

The photoemission yield of Xe/Kr (1% xenon), portrayed in Fig. 2, reveals that light absorption into the low-energy $n=1$ ($^3P_1$) exciton state of solid Kr does not lead to impurity photoemission. The $n=1$ ($^1P_1$) state of solid Kr is active in Auger-type energy transfer to the Xe impurity state. Thus the nonradiative $n=1(^1P_1)-n=1(^3P_1)$ multiphonon relaxation process in solid Kr is slow on the time scale of energy transfer from the mobile "free" excitons to the Xe impurity.

---

*Work supported by the National Council for Research and Development, Israel.

[1] J. Jortner, L. Meyer, S. A. Rice, and E. G. Wilson, J. Chem. Phys. 42, 4250 (1965).

[2] A. Gedanken, B. Raz, and J. Jortner, J. Chem. Phys. 58, 1178 (1973).

[3] O. Cheshnovsky, B. Raz, and J. Jortner, J. Chem. Phys. 59, 3301 (1973).

[4] B. Raz and J. Jortner, Proc. Roy. Soc., Ser. A 317, 113 (1970).

[5] L. Apker and E. Taft, Phys. Rev. 79, 964 (1950), and 81, 698 (1951).

[6] M. Martin, J. Chem. Phys. 54, 3289 (1971).

[7] Gedanken, Raz, and Jortner, Ref. 2.

[8] G. Baldini, Phys. Rev. 128, 1562 (1962).

[9] G. Baldini, Phys. Rev. 137, A508 (1965).

[10] Z. Ophir, U. Even, B. Raz, and J. Jortner, "Pulsed High Pressure Lamp for the Vacuum Ultraviolet" (to be published).

[11] The photon current was normalized to the total photon flux hitting the sample. A small (10%) correction due to reflection of the pure matrix was neglected.

[12] J. F. O'Brien and K. J. Teegarden, Phys. Rev. Lett. 17, 919 (1966).

[13] N. Schwentner, M. Skibowski, and W. Steinmann, to be published.

[14] S. I. Choi and S. A. Rice, J. Chem. Phys. 38, 366 (1963).

[15] This estimate is based upon taking the absolute value $Y = 13\%$ for solid Xe at 10.3 eV, obtained by Schwentner (private communication).

[16] M. Hebb, Phys. Rev. 81, 702 (1951).

[17] O. Simpson, Proc. Roy. Soc., Ser. A 238, 402 (1957).

[18] P. Avakian, V. Ern, R. E. Merrifield, and A. Suna, Phys. Rev. 165, 974 (1968).

[19] Y. Toyozawa, Progr. Theor. Phys. 20, 53 (1958).

[20] A. Gold and R. S. Knox, J. Chem. Phys. 36, 2805 (1962).

[21] S. D. Druger, J. Chem. Phys. 54, 2339 (1971).

Temperature Dependence of Conductivity of Tetrathiafulvalene-Tetracyanoquinodimethane (TTF-TCNQ) Single Crystals

R. P. Groff, A. Suna, and R. E. Merrifield
Central Research Department, E. I. du Pont de Nemours and Company, Wilmington, Delaware 19898

(Received 22 May 1974)

The conductivity of single crystals of tetrathiafulvalene–tetracyanoquinodimethane (TTF-TCNQ) was measured over the temperature range 40–300 K. The maximum low-temperature conductivity parallel to the *b* axis ranged from 12–35 times the corresponding room-temperature value. The temperature dependence of the intrinsic conductivity (after residual resistivities were excluded) was the same for all crystals measured and was fitted by a $T^{-2.33\pm0.14}$ dependence for $60 \leqslant T \leqslant 300$ K.

Extraordinary maxima[1] in the apparent electrical conductivity of single crystals of tetrathiafulvalene-tetracyanoquinodimethane (TTF-TCNQ) have alternately been ascribed to the presence of superconducting fluctuations[1] or experimental artifacts.[2] There is considerable disagreement on the experimental results for the conductivity obtained in different laboratories.[3,4] We have measured the conductivity along the *a* and *b* axes of a number of TTF-TCNQ single crystals. Our measurements show that the temperature dependence of the *b*-axis conductivity of TTF-TCNQ can be described by a single function, even for crystals whose conductivity enhancement differs by a factor of 3.

Solution-grown TTF-TCNQ crystals were prepared under argon, at room temperature, in acetonitrile, by diffusion of $5\times10^{-3}M$ solutions of the two components into an equal volume of pure solvent. Both the TTF and TCNQ had been twice gradient sublimed under argon. Crystal growth was allowed to proceed for five days before harvesting. These crystals grow preferentially along the *b* axis with a laminar structure in which individual laminae are oriented parallel to the *a*-*b* plane. In order best to deal with the problem of nonuniform conductivity between laminae for *b*-axis measurements, crystals were selected with one perfectly developed *a*-*b* face and as free as possible from defects, inclusions, etc., visible in transmission microscopy with collimated incident light. Conventional dc measurement techniques were adopted with four silver-paste (Du Pont No. 7941 thinned with octyl acetate or hexyl acetate) electrodes attached to the best developed *a*-*b* face. This arrangement gave more reproducible results than such alternative electrode configurations as wrapping the

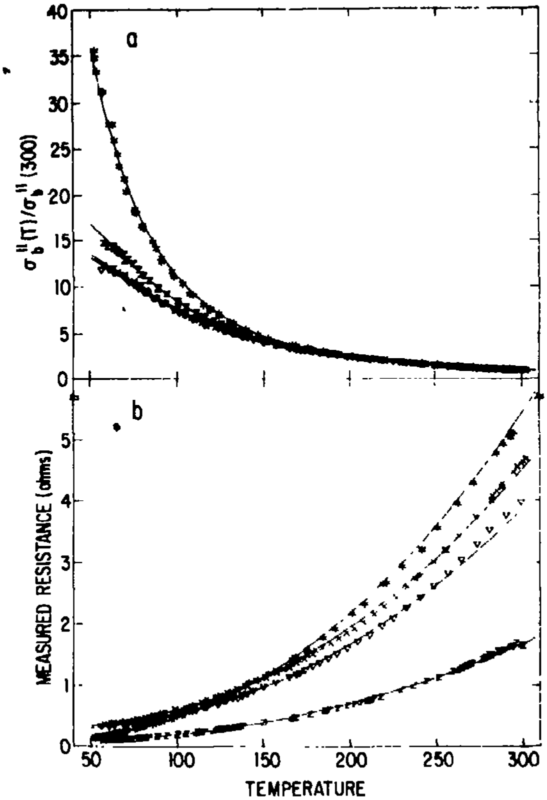

FIG. 1. (a) Normalized conductivity measured parallel to the b axis for four TTF-TCNQ crystals. (b) Measured resistance versus temperature for the same crystals. (Vertical scale expanded 10 × for the crosses). Solid curves in both parts of the figure are fits by $\rho = \rho_0 + AT^{2.33}$.

electrodes around the crystals. Crystals with resistances not reproducing to better than 2% upon warming and cooling the sample were discarded. Room-temperature conductivities[5] along the b axis ($\sigma_b^{\parallel}$) typically ranged from 250–500 $(\Omega\ \mathrm{cm})^{-1}$.

All conductivity measurements along the a axis ($\sigma_a^{\parallel}$) were made on single crystals grown from the vapor which grew preferentially along the a axis. These crystals were prepared in sealed Pyrex ampules under 1–10 Torr He at ca. 400 K. Room-temperature conductivities were typically 1 $(\Omega\ \mathrm{cm})^{-1}$, increasing to ca. 2.2 $(\Omega\ \mathrm{cm})^{-1}$ at the transition.[6]

Figure 1(a) shows a plot of the conductivity $\sigma_b^{\parallel}$ versus temperature for four crystals with low-temperature maxima ranging from 12 to 35 times the corresponding values at 300 K. Although we show only data above the apparent transition, none of the samples shown here exhibited any traces of the "double maximum" reported in Ref. 4. Figure 1(b) shows the same data plotted as resistances.

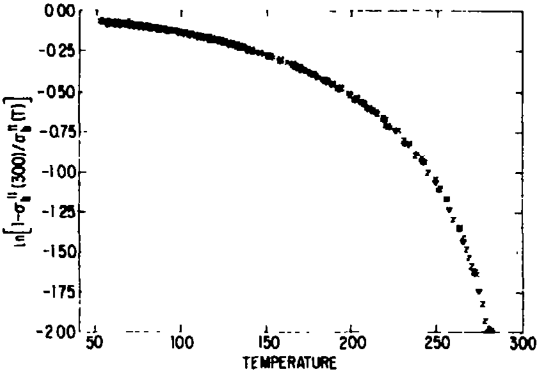

FIG. 2. Plot of $\ln[1-\sigma_b^{\parallel}(300)/\sigma_b^{\parallel}(T)]$ versus temperature for the four crystals in Fig. 1 (see text for explanation).

If we suppose that we can separate the sample resistivity $\rho(T)$ into a sample-dependent residual component ρ_0 and some unknown function $f(T)$ which describes the intrinsic temperature dependence of the material, i.e.,

$$\rho(T) = \rho_0 + f(T), \tag{1}$$

we can write

$$\ln\left(1-\frac{\rho(T)}{\rho(T_1)}\right) = \ln\left(1-\frac{f(T)}{f(T_1)}\right) - \ln\left(1+\frac{\rho_0}{f(T_1)}\right), \tag{2}$$

where T_1 is some conveniently chosen normalization temperature. The important feature here is that properties having to do with a given crystal appear in the second term on the right-hand side while the first term contains only the intrinsic temperature dependence of the material. Hence a plot of $\ln[1-\sigma(T_1)/\sigma(T)]$ versus T should yield a series of identical curves displaced parallel to one another along the vertical direction. (A simple plot of ρ versus T would also have this feature; however, it is not possible to determine absolute values of ρ accurately.[5]) Figure 2 shows such a plot using data shown in Fig. 1 and choosing $T_1 = 300$ K. The curves have been displaced vertically to make comparison easier.[7]

The bottom curve of Fig. 3 shows typical results of conductivity $\sigma_a^{\parallel}(T)$ plotted in a similar fashion. For comparison the points in the middle

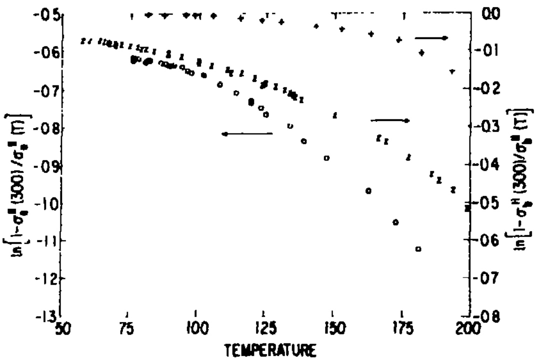

FIG. 3. Comparison of functional forms of (bottom curve) conductivity parallel to the *a* axis, (middle curve) conductivity parallel to the *b* axis, and (top curve) intentionally generated "false" conductivity data of Ref. 2.

curve show a sample from Fig. 1 with a low-temperature conductivity maximum ca. 12 times its room-temperature value. The different functional forms are clearly evident. The top curve shows the intentionally generated "false" conductivity data of Ref. 2 plotted in this fashion.

The method outlined above provides a sensitive test for making quantitative comparisons between theory and experiment. For example, it has been suggested[4,8] that

$$f(T)=AT\exp(B/T). \tag{3}$$

However, a plot such as shown in Figs. 2 and 3 demonstrates dramatically that Eq. (3) does not fit the available data (with $T_1=300$ K), although a limited region can be fitted if T_1 is chosen to be below 200 K (cf. Ref. 4).

We have found that a remarkably good fit (2% standard deviation) to all our data, over the temperature range 60 to 300 K, can be obtained with

$$f(T)/f(T_1)=(T/T_1)^{\lambda} \tag{4}$$

where $\lambda=2.33$. The solid curves of Fig. 1 have been obtained from Eqs. (1) and (4), by least-squares adjustment of ρ_0 and the normalization of $f(T)$. The mean square *relative* deviation[9] has been minimized, so that an equally good fit appears in plots of the conductivity [Fig. 1(a)] and of the resistance [Fig. 1(b)]. Somewhat improved fits can be obtained by optimizing λ for each crystal separately. The resulting values of λ were 2.23, 2.35, 2.36, and 2.40 for the crystals in Fig. 1, with normalized conductivity maxima of 35, 12.5, 12, and 15, respectively. In each case the standard deviation in the value of λ was about 0.14.

The original data of Ferraris *et al.*[3] on less highly purified samples were fitted by a $\lambda=2$ power law for $T\gtrsim 120$ K. This is not inconsistent with $\lambda=2.3$ in view of their experimental uncertainties and lack of reproducibility upon heating and cooling.

A power-law behavior of the conductivity has been calculated by Luther and Peschel[10] in the Tomonaga model of a one-dimensional metal. It is also implied in the second-order renormalization-theory calculations of Sólyom.[11] In a theory similar to that of Luther and Peschel, Mattis[12] finds

$$\sigma(T)=\sigma_0[T/(T+\theta)]^{g}. \tag{5}$$

Our data are fitted by this form only in the limit of infinite θ, although a fit with $\theta\sim E_F/k_B\sim 3000$ K, $g\sim -2.5$ cannot be ruled out. Although Mattis's result was evaluated only for $|g|\ll 1$, no such restriction on the temperature exponent seems to be present in Ref. 10, while Sólyom[11] argues that this exponent should be a universal number, independent of the electron-electron coupling.[13] The power law, Eq. (4), with $\lambda=2.33$, is furthermore consistent with a prediction of Cohen *et al.*[14] that resistivity in a one-dimensional system subject to dynamic disorder should vary as T^2 times a slowly varying function of T.

We also attempted to fit $f(T)$ by the form $(T-T_c)^{\lambda}$, with both T_c and λ variable, but found that only negative values of T_c could improve the fit over the obtained via Eq. (4), and then only slightly. The fact that $f(T)$ thus seems to depend only on T, and not on $T-T_c$, $T_c\sim 58$ K, strongly suggests that the rise in conductivity above the metal-insulator transition near 58 K is not related to this transition but rather is an intrinsic rise which is interrupted by the transition (as, for example, suggested in Ref. 8 and by Lee, Rice, and Anderson[15]).

By setting $\rho_0=0$, we find the maximum expected conductivity enhancement at 58 K: For $\lambda=2.47$, the largest value consistent with our measurements, we have $\sigma(58)/\sigma(300)_{\max}=58$, a result which contradicts greater values reported by workers at the University of Pennsylvania.[1,4]

We wish to thank L. R. Melby and G. J. Sloan for providing the crystals used in this study and P. C. Hoell for use of a computer program.

---

[1] L. B. Coleman, M. J. Cohen, D. J. Sandman, F. G. Yamagishi, A. F. Garito, and A. J. Heeger, Solid State

Commun. 12, 1125 (1973).

[2] D. E. Schafer, F. Wudl, G. A. Thomas, J. P. Ferraris, and D. O. Cowan, Solid State Commun. 14, 347 (1974).

[3] J. P. Farraris, D. O. Cowan, V. Walatka, Jr., and J. H. Perlstein, J. Amer. Chem. Soc. 95, 948 (1973).

[4] M. J. Cohen, L. B. Coleman, A. F. Garito, and A. J. Heeger, Phys. Rev. B (to be published).

[5] Because of uncertainties in where the electrodes actually make contact, these values could be at least a factor of 2 in error. Nevertheless, relative conductivities can be measured with great precision.

[6] Measurements of $\sigma_a{}'$ tended to be exceptionally reproducible. This is quite unlike the case with $\sigma_b{}''$ where many crystals had to be discarded to obtain measurements reproducible to ±2%.

[7] The shape of curves such as those shown in Fig. 2 is extremely sensitive to the values of T_1 and $\sigma(T_1)$; hence, reproducible measurements are essential.

[8] P. W. Anderson, P. A. Lee, and M. Saitoh, Solid State Commun. 13, 595 (1973).

[9] Residual $= |R_{\mathrm{meas}} - R_{\mathrm{calc}}|/R_{\mathrm{calc}}$.

[10] A. Luther and I. Peschel, Phys. Rev. Lett. 32, 992 (1974).

[11] J. Sólyom, J. Low. Temp. Phys. 12, 547 (1973).

[12] D. C. Mattis, Phys. Rev. Lett. 32, 714 (1974).

[13] The relation between Sólyom's results and those of the Tomonaga model, Refs. 10 and 12, is discussed by H. Fukuyama, T. M. Rice, and C. M. Varma, Phys. Rev. Lett. 33, 305 (1974); they contend, however, that the sign of the exponent in Sólyom's theory (where conductivity is not explicitly evaluated) would in most cases be such as to give a decreasing conductivity with decreasing temperature.

[14] M. H. Cohen, J. A. Hertz, P. M. Horn, V. K. S. Shante, to be published.

[15] P. A. Lee, T. M. Rice, P. W. Anderson, Phys. Rev. Lett. 31, 462 (1973).

Hyperfine Studies of Site Occupation in Ternary Systems

T. J. Burch* and T. Litrenta
Fordham University,† Bronx, New York 10458

and

J. I. Budnick‡
University of Connecticut, Storrs, Connecticut 06268

(Received 4 June 1974)

The analysis of spin-echo spectra of V, Mn, Co, Ru, Rh, Os, and Ir in Fe_3Si shows that these impurities unexpectedly enter one of the two available Fe sites in a selective manner. Those impurities to the left of Fe in the periodic table prefer the Fe site with eight first-neighbor Fe atoms. Those beneath and to the right of Fe in the periodic table enter the Fe site with four Fe and four Si first neighbors.

From a pulsed NMR study of dilute transition-metal impurities in Fe_3Si and slightly iron-rich off-stoichiometric Fe_3Si, we report an unexpected selective site occupation. Fe_3Si exhibits long-range crystallographic order with a bcc structure and therefore two inequivalent iron sites. In Fig. 1 an element of the Fe_3Si structure is shown. Table I gives the near-neighbor configurations for both Fe and Si out to the third neighbor. Fe_3Si

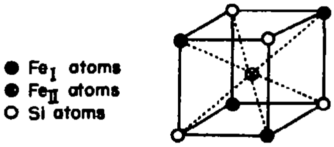

FIG. 1. An element of the Fe_3Si structure showing the Fe_I, Fe_{II}, and Si sites. One Fe site, Fe_I, is on the cube edge and has eight Fe first neighbors; the other Fe site, Fe_{II}, is at the body center and has four Fe and four Si first neighbors; Si is on a cube edge with eight first neighbors.

TABLE I. The first-, second-, and third-nearest-neighbor (nn) configurations for both the Fe and Si sites in Fe_3Si. We specify whether the Fe neighbors are in Fe_I or Fe_{II} sites. If the alloy is slightly Fe-rich, the extra Fe atoms occupy Si sites randomly, producing Fe_{II} sites with not only four but also five, six, and seven Fe first neighbors.

	1 nn	2 nn	3 nn
Fe_{II}	4 Fe_I 4 Si	6 Fe_{II}	12 Fe_{II}
Fe_I	8 Fe_{II}	6 Si	12 Fe_I
Si	8 Fe_{II}	6 Fe_I	12 Si

alloys have been investigated in a number of NMR,[1,2] Mössbauer,[3,4] and neutron-scattering studies.[5,6] Previously, it was believed that dilute concentrations of transition-metal atoms added to an Fe_3Si matrix would enter the two iron sites randomly. The NMR experiments reported in this paper for the *3d* impurities V, Mn, and Co, the *4d* impurities Ru and Rh, and the *5d* impurities Os and Ir and Fe_3Si show for the first time that in each of these cases the impurity atoms enter only one of the two iron sites.

Small amounts of the desired ternary impurity were combined with master ingots of Fe_3Si and iron-rich off-stoichiometric Fe_3Si by arc melting to provide alloys of the desired concentrations. Care was taken to insure that little sample loss occurred during comixing. The resulting ingots were powdered by crushing and subsequently annealed at 600°C for 2 h and then slowly furnace cooled to produce well-ordered Fe_3Si. Homogenization of several Co samples prior to the ordering heat treatment indicated no significant difference in the results compared to samples not homogenized.

The spin-echo spectra were taken with a variable-frequency spectrometer at about 1.4°K. A measurement of the echo amplitude, when suitably corrected,[7] provides a measure of the hyperfine field distribution in the sample.

In Fig. 2, we show two previously published spectra important for the understanding of the new NMR results for the substitutional impurities.[1] Figure 2(a) shows a spectrum of Fe_3Si in which the peaks at 30.05, 31.47, and 46.57 MHz arise from the Fe_{II}, Si, and Fe_I sites, respectively. In Fig. 2(b), a spectrum for $Fe_{0.77}Si_{0.23}$ is presented. We note particularly that the peaks at 29.9, 37.0, and 42.7 MHz have been clearly identified as originating from Fe_{II} sites with four, five, and six Fe first neighbors.[1,2] We also note that a satellite on the Fe_I line at 47.2 MHz corresponds to Fe_I sites with a single Fe second neighbor.[2]

In Fig. 3(a), the spectrum arising from Co in $(Fe_{0.74}+Co_{0.01})Si_{0.25}$ is presented. Only a single sharp line with a center frequency of 195.0 MHz is observed. An intensive search from 10 to 420 MHz indicated that no other Co line was present. The spectra for Fe and Si (not shown) are similar to the spectra shown in Fig. 2(a) and confirmed that the alloys were well ordered and of approximately the desired composition. If Co entered the Fe_I site, the spectrum of the stoichiometric sample would show a clear Co-Co third-neighbor interaction. Furthermore, the spectrum of Co in the iron-rich off-stoichiometric sample would

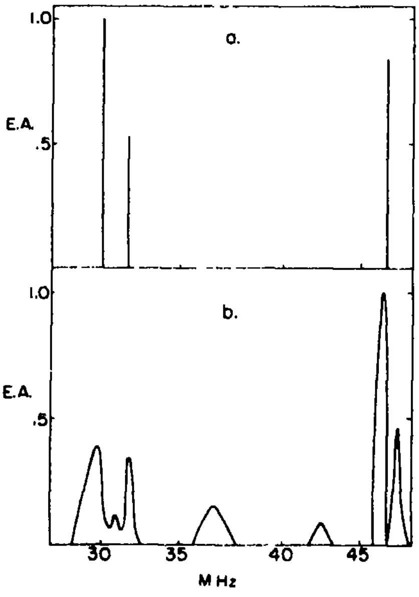

FIG. 2. Plots of the normalized echo amplitude versus frequency: (a) Fe_3Si; (b) $Fe_{0.77}Si_{0.23}$.

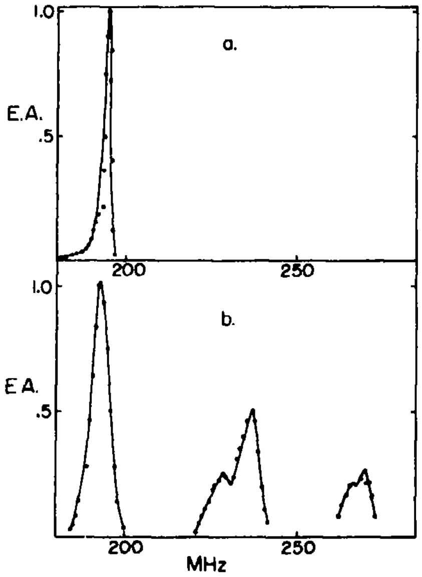

FIG. 3. Plots of the normalized echo amplitude versus frequency: (a) $(Fe_{0.74}+Co_{0.01})Si_{0.25}$; (b) $(Fe_{0.76}+Co_{0.01})Si_{0.23}$.

show a line arising from the Co atoms having as neighbors iron atoms which replace some Si. If Co entered the Fe_{II} site, the spectrum of Co in the stoichiometric sample should contain a single peak. The spectrum of Co in the off-stoichiometric sample should then contain peaks corresponding to first-near-neighbor configurations of four Fe and four Si atoms, five Fe and three Si atoms, and six Fe and two Si atoms. Figure 3(b) shows a spectrum of Co in $(Fe_{0.76}+Co_{0.01})Si_{0.23}$. The Co spectrum is similar in distribution and relative intensity to the spectrum of the Fe_{II} sites in this alloy and in the $Fe_{0.77}Si_{0.23}$ spectrum shown in Fig. 2(b). Thus we identify the lines at 192.5, 237.5, and 270.0 MHz as arising from Co atoms which have entered the Fe_{II} sites and have four, five, and six Fe first neighbors in the off-stoichiometric sample.

Figure 4 shows a spectrum of Mn in $(Fe_{0.745}+Mn_{0.005})Si_{0.25}$. The spectrum shows a series of three almost equally spaced peaks. This spectrum can be explained only if Mn entered the Fe_I sites randomly.

For stoichiometric $(Fe_{3-x}+Mn_x)Si$, an atom on an Fe_I site has eight Fe_{II} first neighbors, six Si second neighbors, and some combination of twelve Fe_I and Mn third neighbors (see Table I). The relative intensity of the lines in this spectrum is that of Mn in sites with zero, one, and two Mn third neighbors. This is also found in spectra of other stoichiometric alloys with different Mn concentrations. In Fig. 4(b), a spectrum of Mn in $(Fe_{0.76}+Mn_{0.01})Si_{0.23}$ is presented. The peaks at 273.2, 267.0, and 260.8 MHz are from Mn atoms with eight Fe_{II} first neighbors, six Si second neighbors, and zero, one, and two Mn third neighbors, respectively. The peak at 276.8 MHz is from Mn atoms with eight Fe_{II} first neighbors, five Si and one Fe second neighbors, and twelve Fe third neighbors. This satellite is similar to that produced by second-neighbor iron atoms at 47.2 MHz in the $Fe_{0.77}Si_{0.23}$ spectrum shown in Fig. 2(b). Peaks corresponding to Mn atoms with eight Fe_{II} first neighbors, five Si and one Fe second neighbors, and eleven Fe and one Mn as well as ten Fe and two Mn third neighbors exist at about 270.6 and 264.4 MHz, respectively. However, these peaks lie underneath the main lines at 273.2 and 267.0 MHz and therefore are not evident.

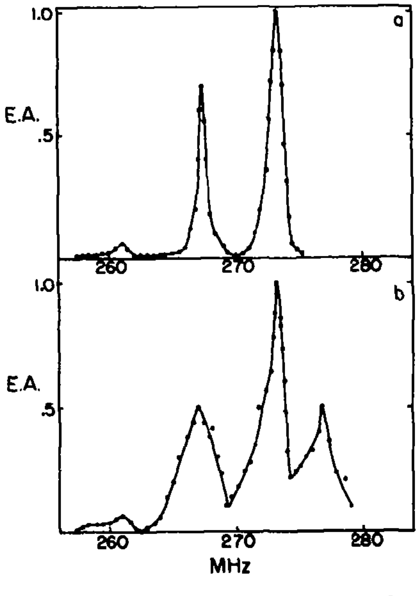

FIG. 4. Plots of the normalized echo amplitude versus frequency: (a) $(Fe_{0.745}+Mn_{0.005})Si_{0.25}$; (b) $(Fe_{0.76}+Mn_{0.01})Si_{0.23}$.

The spectra for V impurities in Fe_3Si alloys behave in the same way as those for Mn. Thus, for the 3*d* impurities we have studied, we conclude that those to the left of Fe in the periodic table enter the Fe_I site and those beneath and to the right enter the Fe_{II} site.

This observation can be confirmed by a neutron-scattering study of the site occupancy in the two magnetically inequivalent Fe sites. A preliminary study carried out in cooperation with Dr. S. Pickart of the U.S. Naval Ordnance Laboratory at the National Bureau of Standards reactor has already verified the selective site occupation deduced from the NMR spectra for the V, Mn, and Co substitutions.[8] Further neutron studies are in progress.

To explore further the possible systematics for the substitutional transition-metal impurities, we have found NMR signals arising from the 4*d* impurities Ru and Rh, and the 5*d* impurities Os and Ir. For both Ru and Rh, the spectra clearly suggest that they enter the Fe_{II} site as does Co. However, from studies of iron-rich off-stoichiometric samples, a strong preference is observed for the Fe_{II} site with four Fe_I first neighbors. We find that both Os and Ir enter the Fe_{II} site.

At present with the experimental results already obtained, we can clearly conclude that for the 3*d*, 4*d*, and 5*d* elements studied, those to the left of Fe on the periodic table enter the Fe_I site exclusively. Those beneath and to the right of

Fe on the periodic table enter the Fe_{II} site exclusively, but different elements show different near-neighbor preferences in iron-rich off-stoichiometric samples. On the basis of these investigations, we conclude that an additional parameter which specifies the selective site occupation in Fe_3Si when transition-metal impurities are added could shed some light on the ternary phase diagrams[9] of these systems.

The regularity of these results suggest a direct relationship to the large class of magnetic Heusler alloys.[10] If one writes Fe_3Si as $(Fe_{II})_2Fe_ISi$ the similarity to the Heusler structure, A_2BC, is clear.[11] In the known Heusler alloys, the transition metals most to the left in the periodic table prefer the B site, while those to the right enter the A site. Our results that V and Mn enter the Fe_I site whereas Co, Ru, Rh, Os, and Ir enter the Fe_{II} site suggest a basis for the systematics of the transition-metal site occupancy of the known Heusler alloys. An interpretation of these results based on size and valency factors is actively being pursued.

During the course of this investigation, a similar conclusion for the $(Fe_{3-x}+Mn_x)Si$ system was reached on the basis of a neutron experiment which concluded that Mn entered the Fe_I site.[12]

We would like to thank Dr. J. H. Wernick for providing the master ingots used in the initial phases of this study, Dr. S. Pickart for his helpful collaboration, and Dr. S. Skalski for his comments.

---

[*] Work supported in part by the National Science Foundation.

[†] Work supported in part by a Fordham Faculty Research Grant.

[‡] Work supported in part by the University of Connecticut Research Foundation.

[1] J. I. Budnick, S. Skalski, T. J. Burch, and J. H. Wernick, J. Appl. Phys. 38, 1137 (1967).

[2] M. B. Stearns, Phys. Rev. B 4, 4069 (1971).

[3] M. B. Stearns, J. Appl. Phys. 35, 1095 (1964).

[4] M. B. Stearns, Phys. Rev. 129, 1136 (1963).

[5] A. Paoletti and L. Passari, Nuovo Cimento 32, 25 (1964).

[6] D. Meinhardt and O. Krisement, Z. Phys. 174, 472 (1963).

[7] J. I. Budnick and S. Skalski, *Hyperfine Interactions*, edited by A. J. Freeman and R. Frankel (Adademic, New York, 1967).

[8] S. Pickart, private communication.

[9] See, for example, S. Setz, H. Nowotny, and F. Benesovsky, Monatsh. Chem. 99, 2014 (1968).

[10] J. H. Westbrook, *Intermetallic Compounds* (Wiley, New York, 1967).

[11] A. J. Bradley and J. W. Rodgers, Proc. Roy. Soc., Ser. A 144, 340 (1934).

[12] J. G. Booth, J. Clark, J. O. Ellis, and P. J. Webster, in Proceedings of the International Conference on Magnetism, Moscow, U.S.S.R., 22–28 August 1973 (to be published).

Anomalous Small-Angle Magnetic Scattering from Amorphous $TbFe_2$ and YFe_2[†]

S. J. Pickart, J. J. Rhyne, and H. A. Alperin
Naval Ordnance Laboratory, Silver Spring, Maryland 20910, and
National Bureau of Standards, Washington, D. C. 20234
(Received 24 June 1974)

Small-angle quasielastic neutron scattering measurements have revealed an intense magnetic component at low temperatures in amorphous $TbFe_2$ and YFe_2, in addition to a weak critical divergence at T_c in $TbFe_2$. These observations are interpreted as evidence that spatial fluctuations remain "frozen in" below the Curie point of $TbFe_2$, and that only short-range order is achieved in YFe_2.

Recent neutron scattering measurements on sputtered, amorphous magnetic alloys have provided information on the atomic and spin correlation functions[1] and excitation spectra[2] of these novel materials. Small-angle quasielastic scattering provides additional information about the longer-range, spatial fluctuations in the magnetization, particularly in the critical region near the transition temperature. We report here the observation by this method of an intense, strongly temperature-dependent small-angle component of magnetic origin in amorphous $TbFe_2$ and YFe_2, accompanied by a weak divergence near T_c in $TbFe_2$. We believe that these phenomena provide insight into the anomalous nature of the phase transition in amorphous magnets.

The measurements were taken at the National Bureau of Standards reactor with a double-axis

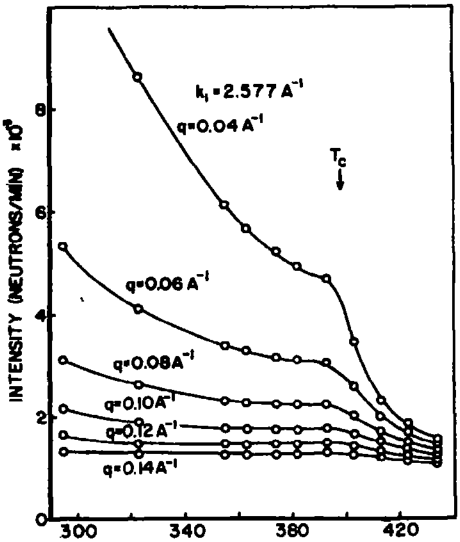

FIG. 1. Small-angle neutron scattering from amorphous $TbFe_2$ in the critical region, corrected for absorption and instrumental background. (Data taken for $q = 0.02\ \text{Å}^{-1}$ would be off scale and are not plotted for convenience, while data at higher q continue to decrease slightly and are essentially flat with T.) The indicated T_c is the average derived from Ref. 3.

spectrometer using a 20′-10′-10′ collimator sequence. This allows observations without excessive background contamination down to a momentum transfer $q \approx 0.02\ \text{Å}^{-1}$, with the incident wave vector of $2.577\ \text{Å}^{-1}$ obtained from a curved graphite monochromator.

Data obtained in the critical region for $TbFe_2$ are presented in Fig. 1. Two interesting features are visible in these data: a weak "critical" anomaly near T_c and a further precipitous rise as T decreases below T_c.

Measurements at closer intervals than indicated in the figure at a fixed q of $0.04\ \text{Å}^{-1}$ demonstrate that the anomaly is not at all sharp, as expected in a normal ferromagnetic second-order phase transition, but rounds off and transforms smoothly into the unexpected small-angle component. If the high-temperature asymptotic level of the scattering is subtracted (a somewhat arbitrary procedure because the highest safe temperature to avoid recrystallization does not reach into the completely paramagnetic regime), the shape of the angular dependence above and immediately below T_c in Fig. 1 is closely Lorentzian. The correlation length obtained by fitting the resolution-corrected intensity increases from ≈ 15 Å at the highest T to ≈ 70 Å just below T_c. This slower than normal divergence, plus the rounded character of the anomaly, suggest that the fluctuations are "frozen in" at T_c and never become long range.

On the other hand, the angular dependence of the small-angle component below T_c is far from Lorentzian. It is strongly temperature dependent, increasing at $q = 0.02\ \text{Å}^{-1}$ by over 2 orders of magnitude as T falls from room temperature to 4 K. It is found to scale very nearly with the square of the spontaneous magnetization,[3] which suggests an interpretation in terms of magnetic inhomogeneities or clusters, i.e., the magnetic analog of particle size broadening effects.[4] Since the forward beam, the (000) reflection, is the only in-phase component in the scattering from an amorphous medium, it is the only region in scattering space that will reflect inhomogeneities on a scale large compared to the interatomic spacing. It is important to note, however, that the intensity far above T_c shows no rapid falloff with q; thus, since the nuclear and magnetic cross sections are comparable, there is no similar small-angle scattering of *nuclear* origin. Hence these magnetic clusters are apparently *not* connected with chemical or structural inhomogeneities.

We have attempted to analyze the small-angle scattering below T_c by the methods[4] of Guinier and Porod; although these theories apply strictly only to noninteracting particles, a sufficiently random distribution may minimize interference effects. For a collection of N identical particles with moment μ and radius R the intensity is

$$I(q) \sim N\mu^2 \exp(-q^2R^2/3),$$

where the factor in the exponent, but not the Gaussian dependence, is modified by resolution corrections. We find on plotting the intensity on a logarithmic scale versus q^2 that the curves have a continuous upward curvature at small q, thus indicating a distribution of radii and effectively preventing determination of an upper limit to R by extrapolation to $q = 0$. We find, however, that for temperatures below room temperature the data exhibit a q^{-n} dependence with $n \approx 2.4$, in remarkable agreement with Porod's limiting formula[4] for a distribution of particle sizes with total surface area S and magnetization density m,

$$I(q) \sim 2\pi m^2 S/q^4,$$

where the q^{-4} dependence is reduced to $q^{-2.8}$ after correction for vertical and horizontal resolution. Using the theoretical magnetization density (rare-earth and iron spins antiparallel) we obtain from the absolute intensity at $q = 0.02$ Å^{-1} a specific surface area of ≈4 Å^2/ atom, almost exactly the same value as a spherical particle with a diameter equal to the correlation length above T_c. The agreement is probably fortuitous, since we have no idea of the shape and distribution of the particles, but does lend credence to the model.

In order to investigate the effect of substituting a nonmagnetic rare earth, we have also measured diffraction patterns and small-angle scattering from sputtered YFe_2, which is nonmagnetic at room temperature. Fourier transforms of the nuclear scattering observed at 300 K are strikingly similar to our previous $TbFe_2$ data,[2] with peaks corresponding to combinations of the ionic radii of Y and Fe pairs and clusters, as expected for a dense random-packing model.[5] Small-angle scattering data exhibited a temperature-dependent component in this material as well (see Fig. 2), but less intense than in $TbFe_2$ and with a Lorentzian angular dependence at all temperatures. The correlation length ranges from ≈6 Å at 175 K to ≈8 Å at the lowest temperatures. These results suggest that YFe_2 is not ordered magnetically on a long-range basis, as confirmed by subsequent magnetization measurements.[3] The broad peak at ~40 K for $q = 0.04$ Å^{-1} corresponds to the appearance of hysteresis in the magnetization, and may result from anisotropy effects.

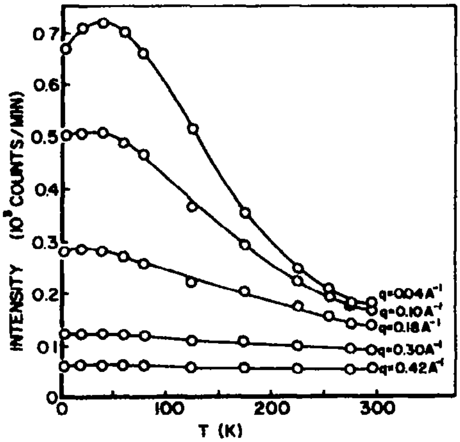

FIG. 2. Small-angle scattering observed in amorphous YFe_2 as a function of temperature.

A question naturally arises as to the inelasticity of this small-angle scattering, as could happen for instance if the counter angle is at all temperatures below the spin-wave cutoff given by $\theta_c = \hbar^2/2mD$, where D is the spin-wave stiffness. Under these conditions, if D renormalizes as $T \rightarrow T_c$, the spin-wave cone opens up and the intensity decreases because of the finite vertical collimation. There are two pieces of evidence against this interpretation. First, our previous[2] elastic and total scattering measurements on $TbFe_2$ indicate that the energy-integrated inelastic scattering decreases with T, and, in fact, is hardly observable at 4 K. Second, with a strongly temperature-dependent D one would expect renormalization effects near T_c to be visible; however, data taken on a triple-axis spectrometer (shown in Fig. 3), although extremely limited in energy range by geometric factors, show no evidence of energy broadening. We therefore conclude that the small-angle scattering is primarily elastic.

As a result of these data, we have arrived at the following tentative model for the qualitative nature of the phase transition in these amorphous magnets. Fluctuations begin to build up as T approaches T_c from above in the normal manner,

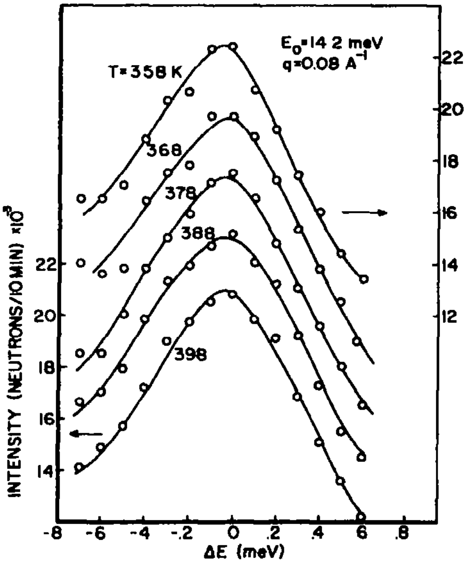

FIG. 3. Energy dependence of the small-angle scattering component in $TbFe_2$ in the critical region. The collimation was greatly relaxed (40′ throughout) from the data in Fig. 1. Since the scans overlap, the scale is shifted up progressively by one ordinate unit.

but are interrupted by the spatial disorder of the lattice and are "frozen in" at the ordering temperature with some finite mean correlation length, thus preventing the wavelength-dependent susceptibility from diverging.[6] These frozen-in fluctuations must in some manner be stabilized by the rare-earth–iron interaction, since in the absence of a magnetic rare earth the fluctuations are of much shorter range and never spontaneously order. We are undertaking experiments on other rare-earth–iron compositions to corroborate this model for the amorphous magnetic transition and determine whether the exchange or crystal field interactions are predominantly responsible for the anomalous behavior.

We are grateful for helpful discussions on these results with Dr. J. Cullen and Dr. A. Clark. The samples were fabricated by Battelle Northwest under ARPA support.

---

†Work supported by the Naval Ordnance Laboratory Independent Research Fund, Office of Naval Research, and Naval Air Systems Command.

[1] J. J. Rhyne, S. J. Pickart, and H. A. Alperin, Phys. Rev. Lett. 29, 1562 (1972).

[2] J. J. Rhyne, S. J. Pickart, and H. A. Alperin, in *Magnetism and Magnetic Materials—1973*, AIP Conference Proceedings No. 18, edited by C. D. Graham, Jr., and J. J. Rhyne (American Institute of Physics, New York, 1974), p. 563; H. A. Alperin, S. J. Pickart, and J. J. Rhyne, in Proceedings of the International Conference on Magnetism, Moscow, U.S.S.R., 22–28 August 1973 (to be published).

[3] J. J. Rhyne, J. Schelleng, and N. Koon, to be published.

[4] See A. Guinier and G. Fournet, *Small Angle Scattering of x-rays* (Wiley, New York, 1955).

[5] D. Polk, J. Non-Cryst. Solids 11, 381 (1973); S. Cargill, in *Magnetism and Magnetic Materials—1973*, AIP Conference Proceedings No. 18, edited by C. D. Graham, Jr., and J. J. Rhyne (American Institute of Physics, New York, 1974), p. 631.

[6] D. Shapero, J. R. Cullen, and E. Callen, Bull. Amer. Phys. Soc. 19, 487 (1974).

Polycritical Points and Floplike Displacive Transitions in Perovskites

Amnon Aharony and Alastair D. Bruce*
Baker Laboratory and Materials Science Center and Laboratory of Atomic and Solid State Physics,
Cornell University, Ithaca, New York 14850

(Received 29 April 1974)

The critical behavior occurring at displacive phase transitions in anisotropically stressed perovskite crystals is examined. It is shown that, under various conditions, the asymptotic critical behavior may be of Ising, *XY*-model, or Heisenberg type. The existence of a "spin-flop"-like transition (at zero stress) between two differently ordered phases is predicted. An explanation of the discrepancy between the measured exponents and those predicted theoretically is proposed, and several new experiments are suggested.

It is well known that stressed crystals undergoing displacive phase transitions exhibit phase diagrams with interesting complexities.[1,2] In this Letter we show that, under different stress conditions, perovskite crystals may display a variety of types of critical behavior, including *tricritical and bicritical points*, *crossover phenomena*, and *floplike transitions* of the type proposed recently for anisotropic antiferromagnets.[3,4] The analysis raises the interesting possibility that the discrepancy between recent theoretical predictions[5-7] and measurements of the critical exponents characterizing the structural transitions in the perovskites $SrTiO_3$ and $LaAlO_3$[8] arises through the existence of systematic residual strains in the crystals studied. We show that these (conjectured) strains precipitate a crossover from the Heisenberg-like (or cubiclike) behavior, previously predicted,[5-7] to an Ising-like behavior. We use scaling theory to study this crossover, and propose several experiments which should elucidate the situation.

Our conclusions are based on an analysis of an effective Hamiltonian that is a natural extension of the Landau-type potential used in previous mean-field investigations of the 105°K phase transition in $SrTiO_3$.[2,9] The Hamiltonian embodies a coupling between the local rotational coordinates of the characteristic perovskite octahedra, $Q_\alpha(\vec{x})$ ($\alpha = 1, 2, 3$), in which the primary ordering occurs, and the elastic strain coordinates $e_i(\vec{x})$ ($i = 1, \ldots, 6$ in the Voigt notation). Allowing for an applied stress T_i ($i = 1, \ldots,$

6), we have[10]

$$\mathcal{K}=\int d^3x\,\{\tfrac{1}{2}[r_0\vec{Q}^2+(\nabla\cdot\vec{Q})^2]+u_0\vec{Q}^4+v_0\sum_{\alpha=1}^{3}Q_\alpha^4+\tfrac{1}{2}C_{11}\sum_{\alpha=1}^{3}e_\alpha^2+C_{12}\sum_{\alpha<\beta}e_\alpha e_\beta+\tfrac{1}{2}C_{44}\sum_{\alpha=4}^{6}e_\alpha^2-\sum_{\alpha=1}^{6}e_\alpha T_\alpha$$
$$-B_1\sum_{\alpha=1}^{3}e_\alpha Q_\alpha^2-B_2[e_1(Q_2^2+Q_3^2)+e_2(Q_1^2+Q_3^2)+e_3(Q_1^2+Q_2^2)]$$
$$-B_3(e_4Q_2Q_3+e_5Q_1Q_3+e_6Q_1Q_2)\},\qquad(1)$$

where r_0 is proportional to $T-T_0$,[10] while the remaining coupling constants are assumed to depend only weakly upon temperature and pressure. The C_{ij} are to be regarded as "bare" elastic constants, appropriate in the absence of any coupling to the fluctuations in the Q_α. The effects of such fluctuations are represented by the term $[\nabla\cdot\vec{Q}(\vec{x})]^2$; terms of the form $[\nabla e_i(\vec{x})]^2$ have not been included in (1), however, since it is believed that they are irrelevant (in the renormalization-group sense),[11] so that the only source of divergent fluctuations in the strains lies in their coupling to the coordinates Q_α. In the absence of such terms the strain coordinates may be integrated out of the partition function defined by the Hamiltonian (1), yielding a reduced Hamiltonian of the form[12]

$$\bar{\mathcal{K}}=\int d^3x\,\{\tfrac{1}{2}[r_0\vec{Q}^2+(\nabla\cdot\vec{Q})^2]+\bar{u}_0\vec{Q}^4+\bar{v}_0\sum_{\alpha=1}^{3}Q_\alpha^4$$
$$-\sum_{\alpha=1}^{3}T_\alpha[(L_1-L_2)Q_\alpha^2+L_2\vec{Q}^2]-L_3(Q_1Q_2T_6+Q_2Q_3T_4+Q_3Q_1T_5)\},\qquad(2)$$

where the new parameters are completely defined in terms of the parameters of the original Hamiltonian.

The primary effect of an *isotropic stress* ($T_i=-p$; $i=1,2,3$) is merely to renormalize the parameter r_0, and hence the transition temperature. In addition, however, although the symmetry of the Hamiltonian (2) remains the same as that of the stress-free crystal, an isotropic stress may lead to a change in the critical behavior, through the pressure dependence of the elastic constants which leads, in turn, to a pressure dependence of $\bar{u}_0$ and $\bar{v}_0$ in (2). A renormalization-group analysis shows that,[6] for $\bar{v}_0$ greater than some critical value v_c,[13] a second-order Heisenberg-like transition is to be expected[14]; for $\bar{v}_0=v_c$ one finds a cubiclike tricritical behavior; while for $\bar{v}_0<v_c$ a divergence of the renormalization-group equations is indicative of a first-order transition.[6] Note that the crossover exponent φ_c from the cubic tricritical behavior to the Heisenberg-like critical behavior is very small[6]; thus, cubic corrections to the Heisenberg scaling behavior may persist very close to the critical point.[15]

The application of an *anisotropic stress* leads, through Eq. (2), to a Hamiltonian with a *different symmetry* from that of the stress-free crystal; the changes in the critical behavior are striking. For *a stress along the* [100] *axis*, $T_i=-p\delta_{i1}$, the Hamiltonian (2) becomes

$$\bar{\mathcal{K}}^{[100]}=\int d^3x\,\{\tfrac{1}{2}[r_1Q_1^2+r_2(Q_2^2+Q_3^2)+(\nabla\cdot\vec{Q})^2]+\bar{u}_0\vec{Q}^4+\bar{v}_0\sum_{\alpha=1}^{3}Q_\alpha^4\},\qquad(3)$$

with $r_1=r_0+2pL_1$ and $r_2=r_0+2pL_2$. Thus, the effects of such a stress are similar to those of an anisotropic exchange in magnetic systems. The latter have recently been extensively investigated, using renormalization-group and series-expansion techniques[16]; we thus use the results of these investigations in what follows.

Certain aspects of the p-T phase diagram for the Hamiltonian (3) depend upon the parameters in (3). We discuss first the case of $SrTiO_3$ (see Fig. 1), where studies of anharmonic properties have shown[17] that L_1 is positive, L_2 is negative, and $\bar{v}_0$ is small and negative (but $\bar{v}_0\gtrsim v_c$, since the transition seems to be of second order[18]). Thus, for $p<0$ we have $r_1<r_2$, so that the asymptotic critical behavior is dominated by the terms in (3) involving only Q_1. The transition is therefore Ising like, into a tetragonal phase with an ordering along [100]. For $p>0$ the critical behavior is XY-like, with an ordering perpendicular to the [100] direction. The ordered state asymptotically close to $T_c(p)$ has rotational invariance in the (100) plane; for finite $T_c(p)-T$, however, cubic corrections to scaling, associated with $\bar{v}_0$, will lead to predominantly [010] or [001] ordering.

The line $p=0$, separating the two ordered phases, locates a first-order phase boundary, at which the pseudospin order parameter $\langle\vec{Q}\rangle$ *flops* from the [100] direction to the (100) plane. This is strongly analogous to the spin-flop tran-

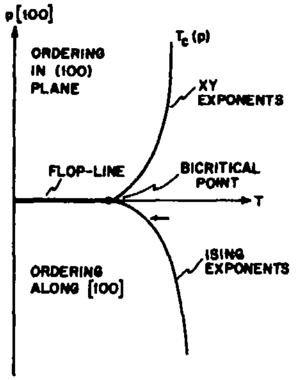

FIG. 1. Schematic phase diagram for a perovskite with a [100] stress, assuming $v_c<\bar{v}_0<0$ (SrTiO$_3$). The arrow locates qualitatively what we conjecture to be the position of the observed transition in monodomain SrTiO$_3$.

sition found in uniaxially anisotropic antiferromagnets.[3] The flop line terminates at $T=T_c(p=0)$, in a *bicritical* point.[3,4]

The crossover (from Heisenberg to Ising or *XY* behavior), expected in the vicinity of the bicritical point, is displayed in the scaling form of the free energy, given by a renormalization-group analysis as[3,16]

$$G(T,p)\approx|t|^{2-\alpha_{\mathrm{H}}}f(\hat{p}/|t|^{\varphi}). \tag{4}$$

Here we have introduced $t\equiv[T-T_c(p=0)]/k_{\mathrm{B}}T$, and $\hat{p}\equiv p/k_{\mathrm{B}}T$, while α_{H} is the Heisenberg specific-heat exponent ($\simeq-0.10$)[19] and φ the crossover exponent ($\simeq1.25$).[16] Following Fisher and Nelson[3] we conclude the following from (4): (a) At the flop line ($p=0$, $t<0$) the thermodynamic conjugate to $T_1=-p$, namely, the elastic strain e_1, exhibits a discontinuity which varies with t as $\Delta e_1\sim|t|^{\tilde{\beta}}$, with $\tilde{\beta}=2-\alpha-\varphi\simeq0.85$. (b) The components of the elastic compliance diverge, for $p=0$, as $|t|^{-\tilde{\gamma}}$, with $\tilde{\gamma}=2\varphi+\alpha-2$ ($\simeq0.4$). (c) At $t=0$, $\hat{p}\sim|e_1|^{\tilde{\delta}}$, where $\tilde{\delta}\equiv\varphi/\tilde{\beta}$ ($\simeq1.47$). (d) The phase boundary lines near the bicritical point vary as $\hat{p}(t)\approx\pm w_{\pm}t^{\varphi}$, where $w_{\pm}$ are constants.

To our knowledge, none of the experiments suggested by (a)–(d) has been performed, although investigations of the ultrasonic properties of SrTiO$_3$ have succeeded in demonstrating the existence of critical anomalies (in addition to the discontinuities expected from mean-field theory[9]) in the elastic constants.[20] Note that, in contrast to the system discussed in Ref. 3, the symmetry of our problem enables us to identify the scaling field causing the crossover as being purely the pressure $\hat{p}$: This should make experimental verification of the above predictions easier.

The nature of the *XY*-like transition ($p>0$), and the resulting ordered state, may change with the value of $\bar{v}_0$: For $\bar{v}_0<v_c$, we expect the transition to be of first order, into a tetragonal phase, with $\vec{Q}$ along [010] or [001]. For $\bar{v}_0>0$, as is appropriate in LaAlO$_3$,[9] the transition remains of second order, and the cubic corrections to scaling lead to an ordering along [011]. In this case, when the ordering tendency of $\bar{v}_0$ and of the applied stress are in competition, a further decrease in temperature may lead to additional phase transitions.

A similar analysis has also been applied for the case of a [111] stress, with similar results. For SrTiO$_3$ ($\bar{v}_0<0$), further first-order transitions may occur, as described above and as observed in Ref. 1. Such situations require further investigation.

We now turn to review the existing experimental results on the critical behavior of SrTiO$_3$. A striking feature of the EPR experiments[8] (regarded as the most accurate measurements of the critical exponents) is that, in the interests of accuracy, they were performed on samples shaped in such a way as to transform into a *monodomain* low-temperature phase.[8] Moreover, subsequent experiments on these samples have clearly demonstrated a strong *anisotropy* in the order-parameter fluctuations above T_c, these fluctuations being preferentially about the ordering axes of the monodomain sample.[21] We interject the remark that this anisotropy, which clearly shows the presence of an "orienting mechanism"[21] that breaks the cubic symmetry, is to be distinguished from the *cubic* anisotropic terms omitted from (1), but discussed elsewhere,[5,7] which give rise to "pancakelike" anisotropy in the correlations: *This* anisotropy should *not* affect the asymptotic critical behavior.[7] Although the existence of an "orienting" mechanism in these samples has been recognized,[21] the implications for the critical behavior have, to our knowledge, not been examined. In the light of the above analysis we conjecture that this mechanism is simply a systematic strain field which breaks the cubic symmetry, as discussed above, and leads to a *crossover* from the purely Heisenberg critical behavior expected for a strain-free sample to an *Ising-like behavior*, as indicated in Fig. 1.[22] We note that the experimental value[8] of $\beta=0.33\pm0.02$ is quite consistent with this suggestion since we must presume that the experiments were performed in the crossover region, in which the effective value of β changes from its Heisenberg value, $\beta_H \simeq 0.37$, to that appropriate for the Ising system, $\beta_I \simeq 0.31$.[19] A partial experimental check of this conjecture would be provided by a measurement of the exponent β in samples subjected to an external stress. Application of the appropriate stress (e.g., a tensile stress along [100] or, equivalently, a biaxial stress along [010] and [001] in $SrTiO_3$) should reveal that the asymptotic exponents are truly of Ising type in this situation. In addition, specific-heat experiments on such stressed samples should reveal a divergence ($\alpha_I \simeq 0.125$[19]) in contrast to the behavior of well annealed crystals (that transform into a polydomain) for which a cusp is to be expected ($\alpha_H \simeq -0.10$).[23] Finally, experiments to test the predictions (a)–(d), discussed above, would also provide a check on the overall picture that we have proposed.

The authors have benefited from stimulating discussions with D. R. Nelson and with Professor M. E. Fisher. Support by the National Science Foundation, in part through the Materials Science Center at Cornell University, a Fulbright-Hays scholarship (A.A.), and a British Science Research Council research fellowship (A.D.B.) are also acknowledged.

---

[*] Permanent address: Physics Department, Edinburgh University, United Kingdom.

[1] K. A. Müller, W. Berlinger, and J. C. Slonczewski, Phys. Rev. Lett. 25, 734 (1970).

[2] J. C. Slonczewski, Phys. Rev. B 2, 4646 (1970).

[3] M. E. Fisher and D. R. Nelson, Phys. Rev. Lett. 32, 1350 (1974).

[4] D. R. Nelson, J. M. Kosterlitz, and M. E. Fisher, to be published.

[5] R. A. Cowley and A. D. Bruce, J. Phys. C: Proc. Phys. Soc., London 6, L191 (1973).

[6] A. Aharony, Phys. Rev. B 8, 4270 (1973).

[7] A. D. Bruce, to be published.

[8] K. A. Müller and W. Berlinger, Phys. Rev. Lett. 26, 13 (1971).

[9] J. C. Slonczewski and H. Thomas, Phys. Rev. B 1, 3599 (1970).

[10] For a discussion of the Hamiltonian (1) see Ref. 5, in which, however, the coupling to elastic strain was ignored.

[11] F. J. Wegner, to be published.

[12] Here we have ignored the effects of the free surfaces of the sample; a similar procedure has been used, for an Ising system, by A. Aharony [Phys. Rev. B 8, 4314 (1973)]. Such effects were found in Ref. 11 to lead ultimately to a first-order transition. However, experiments suggest that the first-order character of such transitions may be quite small (C. W. Garland, private communication).

[13] The critical value v_c may depend on all the parameters in the system Hamiltonian.

[14] Expansions in $\epsilon = 4 - d$ and a Padé analysis indicate (A. Aharony, unpublished) that the n-component Heisenberg-type fixed point is stable against a cubic perturbation for $n < n_c = 4 - 2\epsilon + 2.59\epsilon^2 + O(\epsilon^3) \simeq 3.13$, and hence for $n = 3$.

[15] This results in interesting values of several tricritical exponents: A. Aharony, paper presented at the Conference on Critical Phenomena in Multicomponent Systems, Athens, Georgia, 15–17 April 1974 (unpublished).

[16] E. K. Riedel and F. J. Wegner, Z. Phys. 225, 195 (1969); M. E. Fisher and P. Pfeuty, Phys. Rev. B 6, 1889 (1973); F. J. Wegner, Phys. Rev. B 6, 1891 (1973); P. Pfeuty, M. E. Fisher, and D. Jasnow, in *Magnetism and Magnetic Materials—1972*, AIP Conference Proceedings No. 10, edited by C. D. Graham, Jr., and J. J. Rhyne (American Institute of Physics, New York, 1973), p. 817, and Phys. Rev. B (to be published).

[17] A. D. Bruce and R. A. Cowley, J. Phys. C: Proc. Phys. Soc., London 6, 2422 (1973).

[18] B. Berre, K. Fossheim, and K. A. Müller, Phys. Rev. Lett. 23, 589 (1969).

[19] M. E. Fisher and D. Jasnow, "Theory of Correlations in the Critical Region," edited by C. Domb and M. H. Green (Academic, New York, to be published).

[20] K. Fossheim and B. Berre, Phys. Rev. B 5, 3292 (1972). Note that these experiments were performed using a high biaxial pressure to suppress domain structure. In this situation we expect the elastic compliance to diverge with the weaker singularity $t^{-\alpha_I}$, where α_I is the Ising specific-heat exponent ($\simeq 0.125$). See also Ref. 3.

[21] K. A. Müller, in "Anharmonic Lattices, Structural Transitions and Melting," Proceedings of the NATO Advanced Study Institute, Geilo, Norway, 24 April–1 May 1973 (to be published); E. Courtens, Phys. Rev. Lett. 29, 1380 (1972).

[22] Similarly, we suggest that the transition observed in monodomain $LaAlO_3$ (Ref. 8) is also of Ising type.

[23] Measurements of the specific heat of $SrTiO_3$ [P. R. Garnier, Phys. Lett. 35A, 413 (1971)] resolved only the jump predicted by mean-field theory.

Systematics of Nuclear Single-Particle States

M. A. K. Lodhi and B. T. Waak
Department of Physics, Texas Tech University, Lubbock, Texas 79409

(Received 3 June 1974)

Semiempirical model-independent formulas for single-particle energies of neutrons and protons in bound nuclei have been obtained as functions of nuclear parameters A and Z for given states specified by nlj. These formulas are almost as convenient as the harmonic oscillator energy formulas to use. The single-particle energies computed from these formulas have been compared with the experimental data and found in good agreement for occupied states.

In several recent works, various models have been used to obtain the energy levels of nuclei along the line of β stability and have yielded extensive information on the energies of single-particle states.[1-5] These energies seem to follow some regular patterns from nucleus to nucleus. Recently, Millener and Hodgson[1] have shown that the energies of 2s single-particle states vary in a regular and systematic way from nucleus to nucleus in the range $35 \leq A \leq 65$.[1] One would naturally think as a next step that a simple formula for the single-particle energies would be more convenient to use, for example, as an initial energy guess for an energy-dependent potential. The purpose of this study is to develop model-independent, semiempirical formulas for the single-particle energies of states for the entire range of nuclei.

The semiempirical formulas for these single-particle energies are in terms of the nuclear parameters $(A,Z;n,l,j)$. Various combinations of these parameters have been tested for their correlations with the single-particle energies. After a reasonably complete set of variables has been generated, the problem is to find the coefficients of the significant variables. This is accomplished by using a stepwise multiple linear regression analysis.[6] Only linear combinations of the variables in the given set are used in the analysis. Coefficients for the most significant terms are computed first, followed by the next most significant terms in the descending order of significance. The constants are reevaluated on the addition of each term until there are no more variables left or until the significance of the remaining variables is below some specified value. Single-particle neutron and proton energies for nuclei along the β-stable line have been used as the input data[5] in the regression analysis. The single-particle energy states up to the Fermi level have been used in this analysis including 352 states for neutrons and 250 states for protons. The resulting model-independent, semiempirical energy formulas for neutron and proton states, given by

$$E_n(\mathrm{MeV}) = -94.902 + 70.838l/A^{1/3} + 17.951n + 90.000n/A^{1/3} - 18.038j(j+1)/A^{2/3} - 2.572n^2 + 43.285l(l+1)/A\,, \tag{1}$$

and

$$E_p(\mathrm{MeV}) = -95.020 + 82.382l/A^{1/3} + 24.020n + 76.284n/A^{1/3} - 17.540j(j+1)/A^{2/3} - 2.954n^2, \tag{2}$$

have multiple correlation coefficients 0.9938 and 0.9956, respectively. The first six terms of E_n and E_p are the same, the neutron-proton differences being reflected in the values of the coefficients. The first two variables of Eqs. (1) and (2) involving the terms $l/A^{1/3}$ and n as the predominant terms are about equally significant and they account for the major effects, with their multiple correlation coefficient $\simeq 0.92$.

The constant terms of Eqs. (1) and (2) place the energies at a very negative value. The next three terms ($+l/A^{1/3}$, $+n$, and $+n/A^{1/3}$) can be attributed to harmonic oscillator effects and give the required increase (decrease in magnitude) in energy as n and/or l increases. The term $-j(j+1)/A^{2/3}$ gives the spin-orbit splitting proportional to $2l+1$, exhibiting the proper doublet sequence, and also shows the reduced spin-orbit effect as A increases. The n^2 term illustrates a slight nonlinearity in the principal quantum number. The $l(l+1)/A$ term in Eq. (1) accounts for a residual

TABLE I. Single-particle energies (MeV) of protons. Question marks indicate level assignment is uncertain.

State	Cal.	Exp.
^{16}O		a
$1s_{1/2}$	45.75	44±7
$1p_{3/2}$	21.35	19.1±1.4
$1p_{1/2}$	13.06	12.7±1.4
^{32}S		a
$1s_{1/2}$	51.23	---
$1p_{3/2}$	30.50	(p) 29.7±6.1?
$1p_{1/2}$	25.28	
$1d_{5/2}$	13.26	16.2±1.6
$1d_{3/2}$	4.55	13.3±1.6
$2s_{1/2}$	12.05	9.5±1.4
^{40}Ca		b
$1s_{1/2}$	52.77	49.1±12 77±14
$1p_{3/2}$	33.18	33.3±6.5
$1p_{1/2}$	28.68	32±4^{c}
$1d_{5/2}$	16.59	14.9±2.5 13.8±7.5
$1d_{3/2}$	9.09	8.4±0.5 7.7±2.6^{c}
$2s_{1/2}$	15.31	10.6±1.1^{a} 12.1±5.4
^{58}Ni		b
$1s_{1/2}$	55.12	57.3±7.5?
$1p_{3/2}$	37.35	(p) 37.6±7.9
$1p_{1/2}$	33.84	---
$1d_{5/2}$	21.92	(d) 20.2±9.8
$1d_{3/2}$	16.07	11.72^{e,f}
$2s_{1/2}$	20.26	$12.6^{+9.3}_{-2.7}$ 11.19^{e,f}
$1f_{7/2}$	8.84	10.1±5.6
^{120}Sn		b
$1s_{1/2}$	59.03	54.0±8.1?
$1p_{3/2}$	44.49	(1p) 40.2±7.2?
$1p_{1/2}$	42.33	---
$1d_{5/2}$	31.39	(d) 30.0±6.9
$1d_{2/2}$	27.79	---
$2s_{1/2}$	28.41	29.0±6.8
$2p_{3/2}$	13.87	16±6.3
$2p_{1/2}$	11.70	---
$1f_{7/2}$	19.74	---
$1f_{5/2}$	14.69	(1f+1g) 16±6.8
$1g_{7/2}$	9.52	---
^{208}Pb		g
$1g_{7/2}$	13.33	11.45
$2d_{5/2}$	9.61	9.65
$1h_{11/2}$	9.42	9.30
$2d_{3/2}$	7.11	8.30
$3s_{1/2}$	11.30	7.95 9.0^{b}
$1h_{9/2}$	3.92	3.8
$2f_{7/2}$	+0.80	2.9
$1i_{13/2}$	2.01	2.2
$2f_{5/2}$	+4.29	0.8^{h}
$3p_{3/2}$	+1.11	0.5^{h}

[a] Quoted in Ref. 7.
[b] Ref. 8.
[c] Ref. 9.
[d] Quoted in Ref. 10.
[e] Quoted in Ref. 11.
[f] Ref. 11.
[g] Quoted in Ref. 12.
[h] Quoted in Ref. 13.

TABLE II. Single-particle energies (MeV) of neutrons. The experimental values are taken from Ref. 12.

State	Calc	Expt
	^{16}O	
$1s_{1/2}$	45.94	47.00
$1p_{3/2}$	20.94	22.00
$1p_{1/2}$	12.41	15.70
	^{40}Ca	
$1d_{5/2}$	18.78	21.30
$2s_{1/2}$	17.81	18.20
$1d_{3/2}$	11.07	15.80
	^{208}Pb	
$1h_{9/2}$	11.03	10.70
$2f_{7/2}$	8.64	9.50
$1i_{13/2}$	8.91	8.90
$3p_{3/2}$	8.18	8.20
$2f_{5/2}$	5.04	7.80
$3p_{1/2}$	6.64	7.30
$4s_{1/2}$	3.88	1.91

effect in the orbital angular momentum not taken care of by the $l/A^{1/3}$ term.

The nuclear systematics obtained from Eqs. (1) and (2) show the distinctiveness of the single-particle states, the increase in binding energies as A increases, and the tendency to level off for deeply bound states in heavy nuclei, thus exhibiting the saturation property of nuclear forces. Both the neutron and proton systematics show gaps in the shell structure at all the observed magic numbers. Gaps are also exhibited for all the semimagic numbers in the appropriate region.

Calculated and experimental single-particle energies are listed in Tables I and II. There is generally a reasonable agreement with the experimental data.[7-13] Nevertheless, it seems appropriate to make a few remarks in general on the discrepancies that one may observe between the results of this work and the experimental data compared with them. They are partly due to the errors associated with the experimental data themselves. The calculated levels are generally too low for unoccupied or partially occupied levels. This effect may be attributed to the input data which were used for the occupied state primarily. Nevertheless, the semiempirical formulas for single-particle energies given by Eqs. (1) and (2) give an overall good description of the bound-state spectrum for occupied states in nuclei and these formulas are almost as convenient to use as ones belonging to the harmonic oscillator potential.

---

[1] D. J. Millener and P. E. Hodgson, Phys. Lett. 35B, 495 (1971).

[2] H. Meldner, Ark. Fys. 36, 593 (1967); H. Meldner, Phys. Rev. 178, 1815 (1969); K. T. R. Davies and R. J. McCarthy, Phys. Rev. C 4, 81 (1971).

[3] M. A. K. Lodhi, Phys. Rev. 182, 1061 (1969), and Phys. Rev. C 1, 365, 1895 (1970).

[4] R. Y. Cusson, H. Trivedi, and D. Kolb, Phys. Rev. C 5, 2120 (1970); L. R. Miller and A. E. S. Green, Phys. Rev. 184, 1012 (1969); A. E. S. Green, G. Darewych, and R. Berezdivin, Phys. Rev. 157, 929 (1967).

[5] M. A. K. Lodhi and B. T. Waak, Phys. Rev. Lett. 29, 301 (1972); B. T. Waak, Ph.D. dissertation, Texas Tech University, 1972 (unpublished).

[6]Program No. BMDO2R, Health Sciences Computing Facility, University of California at Los Angeles.

[7]G. Jacob and Th. A. J. Maris, Rev. Mod. Phys. 38, 121 (1966).

[8]A. N. James, P. T. Andrews, P. Kirbly, and B. G. Lowe, Nucl. Phys. A138, 145 (1969).

[9]U. Amaldi Jr., Phys. Lett. 22, 593 (1966).

[10]M. Riou, Rev. Mod. Phys. 37, 375 (1965).

[11]G. Mairle *et al.*, Nucl. Phys. A134, 180 (1969).

[12]A. Bohr and B. R. Mottelson, *Nuclear Structure* (Benjamin, New York, 1969), pp. 325, 328.

[13]E. Rost, Phys. Lett. 28B, 184 (1968).

Multinucleon Removal in the Absorption of π^- at Rest and at 60 MeV*

H. Ullrich,† E. T. Boschitz,† H. D. Engelhardt,† and C. W. Lewis†
Institut für Experimentelle Kernphysik der Universität und des Kernforschungszentrums Karlsruhe, Karlsruhe, Germany

(Received 29 April 1974)

The intensities of γ rays from π^- absorption at rest on O, F, Mg, P, Ca, and Nb have been measured. The results are compared with those at 220 MeV, previously published. The α removal processes which have been reported to dominate at higher energies are not as pronounced in the present work.

Recent studies on the interaction of 220-[1] and 380-MeV[2] negative pions with nuclei have shown unexpectedly large cross sections for integral "α-particle" (i.e., multiples of two neutrons + two protons) removal. This is surprising, either as an intrinsic property of pion interaction, or from the point of view of nuclear structure. The measurements have been made via the observation of de-excitation γ rays in the final nucleus, so that it is not possible to distinguish the course of the preceding sequence of particle emissions, or even their identities (single nucleons or heavier particles). From the design of these experiments there has also been no distinction made between absorption and nonabsorption processes.

The purpose of this Letter is to present results of a similar study with π^- at rest for a range of nuclei and a case of π^- interaction at 60 MeV kinetic energy. In this study the pion interaction is clearly an absorption process for π^- at rest. Because of the experimental conditions, the results for π^- at 60 MeV are also due predominantly to absorption.

The measurements were done with a negative pion beam from the CERN synchrocyclotron. Targets with 5 g/cm^2 nominal thickness of natural H_2O, LiF, Mg, P, Ca, and Nb were used in a standard stopped-pion experimental arrangement as described earlier.[3] γ rays were detected by a 40-cm^3 Ge(Li) detector (at 90° to the beam direction) in coincidence with stopped-pion logic $(1, 2, 3, \bar{4})$ from the beam telescope. The absolute yields per stopped pion were determined by comparison with muonic x rays.[5] In Fig. 1 (upper curve), as an example, the prompt γ-ray spectrum from pions absorbed at rest on ^{31}P is shown with an energy resolution of 3 keV (full width at half-maximum) at 1 MeV. Background lines determined in a separate measurement are indicated by arrows below the spectrum.

For the measurement with pions in flight the same arrangement has been used. Since counter 4 was close behind the target, and both were tilted by 45° with respect to the beam direction, a $(1, 2, 3, +4)$ trigger condition covers all processes where the pion is scattered in the forward direction, and to some extent also pions with larger scattering angles. In a phosphorus target measurement made under this trigger condition, none of the γ-ray lines from residual nuclei present in the upper curve of Fig. 1 were observed. The γ spectrum taken under the complementary condition $(1, 2, 3, \bar{4})$, however, shows a striking similarity to the spectrum obtained with π^- at rest from the same target (Fig. 1). The drastic reduction of the pionic x-ray yield from phosphorus in the lower curve proves that the contribution from pions at rest is negligible in this spectrum. In Table I the ratios of intensities of corresponding lines in the two spectra are listed, and are seen to be similar within about a factor of 2. This indicates that absorption at rest and at 60 MeV are similar processes. Also, since the order of magnitude of the 60-MeV absorption cross sections is 10 mb, considerations[4] which neglect absorption at nonzero pion energies are questionable.

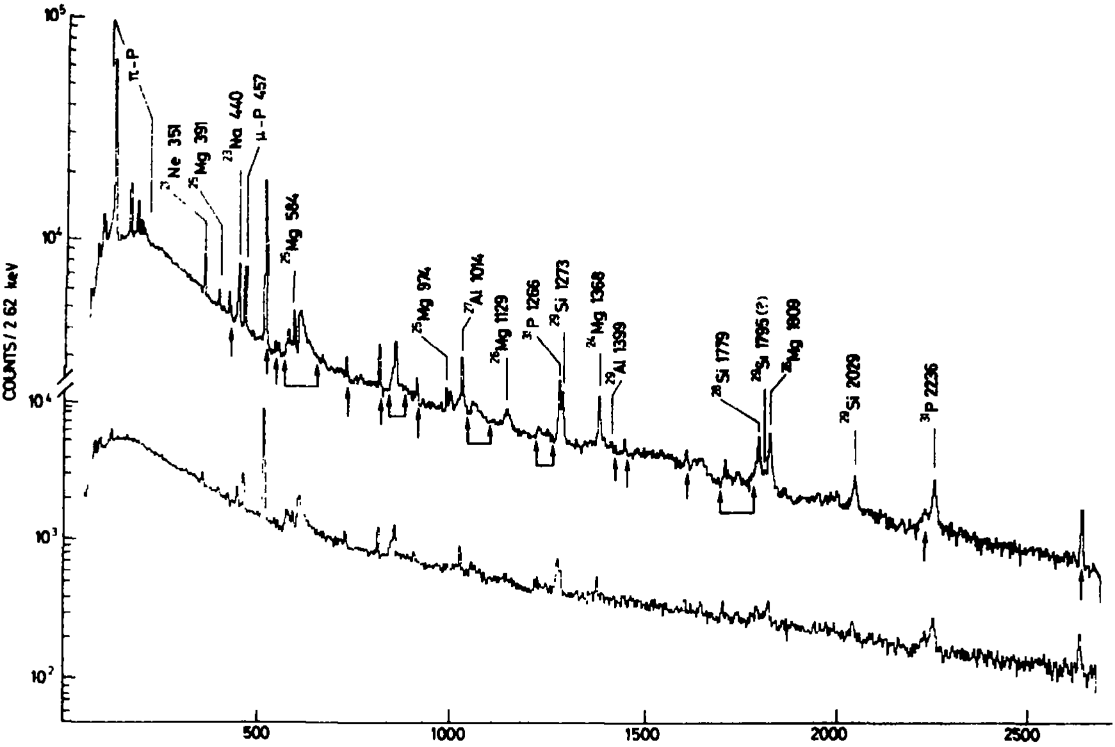

FIG. 1. γ-ray spectra from π^- interaction on ^{31}P with pions at rest (upper curve) and at 60 MeV (lower curve) under trigger condition $(1,2,3,\bar{4})$.

Table I also compares all cross sections given in Ref. 1 for multinucleon removal processes with 220-MeV pions with the respective yields per stopped pion from our measurements for the three targets common to the two studies. Systematic uncertainties in all the yield values may be as large as 30%, but relative errors should be less than 10%. For meaningful comparison the conventions in the two sets of measurements are the same: (a) Only the lowest observed γ-ray transition (usually first to ground) in each residual nucleus is listed, and (b) the yield and cross section for each γ ray listed is without regard to whether it occurs by direct excitation or by γ-ray cascading. The comparison shows no simple proportionality between cross sections and yields for corresponding transitions. We must conclude that pion interaction at 220 MeV is very different from absorption at rest.

It should also be pointed out that Table I is not complete as far as our own results are concerned. This can be seen in Fig. 2, where the observed γ-ray yields from π^- absorption at rest are show for six nuclei. Again, the same conventions as before are used. Lines with ambiguous assignments as well as lines from the target nuclei have been omitted. The complete results of our measurements will be presented elsewhere.

In Fig. 2 it is apparent that π^- absorption at rest leads very frequently to the emission of more than two nucleons. It can also be seen that most of the observed processes are found along the diagonal line, with the number of protons and neutrons being about equal. The processes connected with the removal of one or two α particles are, in fact, observed with relatively high abundance. For the three lighter nuclei they give rise to the strongest transition. For the heavier nuclei, however, they are less important. In the case of niobium, no removal of α particles has been observed.

Multinucleon removal caused by pion absorptio

TABLE I. Comparison of γ-ray production by π^- at rest and in flight. The ratio of γ-ray intensities at 0 and 60 MeV from Fig. 1 is given by R. The absolute value of R has no significance. The 220-MeV cross sections are from Ref. 1.

Observed transition (keV)	Nucleons removed	0 MeV yield (%)	R or σ(mb)
^{31}P Target			R
^{29}Si(1273-0)	1p 1n	3.4	4.9
^{28}Si(1779-0)	1p 2n	5.0	7.3
^{27}Al(1014-0)	2p 2n	2.0	3.8
^{26}Mg(1809-0)	3p 2n	4.0	4.9
^{25}Mg(585-0)	3p 3n	2.0	7.4
^{24}Mg(1369-0)	3p 4n	2.9	4.7
^{23}Na(440-0)	4p 4n	3.0	4.9
^{21}Ne(351-0)	5p 5n	1.1	3.4
^{16}O Target			σ(220 MeV)
^{13}C (3684-0)	2p 1n	1.3	<1.4
^{12}C (4440-0)	2p 2n	4.0	16.8
^{24}Mg Target			σ(220 MeV)
^{21}Ne(2789-351)	2p 1n	0.4	6.3
^{20}Ne(1634-0)	2p 2n	2.5	18.4
^{16}O (6131-0)	4p 4n	2.9	0.5
^{40}Ca Target			σ(220 MeV)
^{37}Ar(1410-0)	2p 1n	0.7	21.7
^{36}Ar(1970-0)	2p 2n	1.5	137.9
^{32}S (2230-0)	4p 4n	0.7[a]	114.8
^{28}Si(1779-0)	6p 6n	<0.1	66.1
^{24}Mg(1369-0)	8p 8n	<0.2	36.2
^{20}Ne(1634-0)	10p10n	<0.1	27.4

[a] Large uncertainty from line shape.

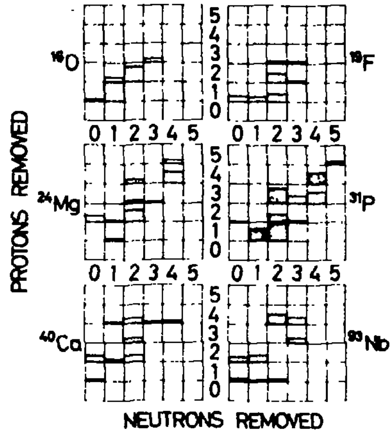

FIG. 2. γ-ray yields in residual nuclei from π^- absorption at rest, plotted versus the corresponding number of missing nucleons. Yields of the lowest observed γ-ray transition only (usually first to ground) are shown. An entire square corresponds to 5% per stopped pion.

may in principle be explained by the following reaction mechanisms:

(i) The initial pion interaction involves more than two nucleons. Indications for such processes have already been reported,[3,5] especially for the case of α-cluster absorption.

(ii) The pion is absorbed by two nucleons with high separation energies, thus producing highly excited two-hole states. These states decay via nuclear Auger effects with the emission of, preferentially, two more nucleons. Since in the first step the removal of a neutron-proton pair seems to be dominant, the subsequential emission of a second neutron-proton pair is likely.

(iii) The initial pion interaction leads to the emission of two loosely bound nucleons with high kinetic energy giving rise to an intranuclear cascade. Numerical calculations based on such a model show narrow Z distributions for residual nuclei of the same mass.[6]

All three mechanisms can finally lead to evaporation processes, where eventually α-particle emission is favored because of low thresholds. From our data, in fact, none of the three principal possibilities can be excluded.

The present results distinguish pion absorption from general interaction in flight for the first time in this class of experiments. The main qualitative result is the small variation between "zero energy" and 60 MeV, and the large change between 60 and 220 MeV. Recent results from a radiochemical study[7] of π^- interaction at 65 and 215-373 MeV on Cu also support the latter observation. Finally, according to our results at low pion energies, cluster removal is comparable to other reaction channels, while at higher energies (Refs. 1 and 2) the removal of α clusters seems to be dominant.

---

*Work supported in part by the Bundesministerium für Forschung und Technologie of the Federal Republic of Germany.

†Visiting Scientists at CERN, Geneva, Switzerland.

[1] V. G. Lind, H. S. Plendl, H. O. Funsten, W. J. Kossler, B. J. Lieb, W. F. Lankford, and A. J. Buffa, Phys. Rev. Lett. 32, 479 (1974).

[2] H. E. Jackson, L. Meyer-Schützmeister, T. P. Wangler, R. P. Redwine, R. E. Segel, J. Tonn, and J. P. Schiffer, Phys. Rev. Lett. 31, 1353 (1973).

[3] C. W. Lewis, H. Ullrich, H. D. Engelhardt, and E. T. Boschitz, Phys. Lett. 47B, 339 (1973).

[4] D. Ashery, M. Zaider, Y. Shamai, S. Cochavi, M. A. Moinester, A. I. Yavin, and J. Alster, Phys. Rev. Lett. 32, 943 (1974).

[5] D. M. Lee, R. C. Minehart, S. E. Sobotka, and K. O. H. Ziock, Nucl. Phys. A197, 106 (1972).

[6] G. D. Harp, K. Chen, G. Friedlander, Z. Fraenkel, and J. M. Miller, Phys. Rev. C 8, 581 (1973), and references quoted therein.

[7] C. K. Garrett and A. L. Turkevich, Phys. Rev. C 8, 594 (1973).

Size of Barely Bound Many-Body Systems

F. Calogero* and Yu. A. Simonov

Institute of Theoretical and Experimental Physics, Moscow, Union of Soviet Socialist Republic

(Received 23 May 1974)

It is pointed out that, in contrast to the case of S-wave two-body bound states, the size of a many-body bound state remains finite (irrespective of its angular momentum) even if its binding energy vanishes. Physical implications for barely bound many-body systems are outlined.

The size of an S-wave two-body bound state diverges as the binding energy of the bound state vanishes.[1] This has an important physical implication, recognized long ago in connection with the first investigations of the deuteron[2]: The size of an S-wave barely bound state is approximately $1/(2\mu|E|)^{1/2}=1/q$, where $\mu=m_1m_2/(m_1+m_2)$ is the reduced mass of the two-body system and E is its binding energy ($\hbar=c=1$). Thus any (reasonable) model of the neutron-proton interaction that fits the deuteron binding energy yields a deuteron wave function having essentially the same extension, $\sim 1/q$ (much larger than the range r_0 of the interaction[3]). Therefore any additional information on the neutron-proton interaction, besides that implied by the value of the binding energy, can result only from measurements of the deuteron size that are sufficiently accurate to display corrections of order qr_0 relative to the dominant term.[2,4]

This phenomenon is peculiar to S-wave two-body bound states. In fact, the wave function of a two-body l-wave bound state is proportional, for $r \gg r_0$ (where r is the interparticle separation, and r_0 is the range of the forces[5]), to the (asymptotically vanishing) free solution of the l-wave Schrödinger equation, $(qr)^{-1/2}K_{l+1/2}(qr)$,[6] and therefore it becomes $c(2l-1)!!(qr)^{-(l+1)}$ for $r_0 \ll r \ll 1/q$ and $c(qr)^{-1}\exp(-qr)$ for $r \gg 1/q$, c being a constant whose value is determined by the behavior of the wave function for $r \lesssim r_0$, and by the normalization condition. It follows that, in the zero-energy case, the wave function is asymptotically proportional to $r^{-(l+1)}$, being therefore, for $l>\frac{1}{2}$, still normalizable, and implying that the expectation value of $r^{|p|}$ is finite for $|p|<p_0=2l-1$. Moreover, simple power counting shows that, for an l-wave two-body barely bound state (i.e., such that $qr_0 \ll 1$), the expectation value of $r^{|p|}$ is of order $r_0^{|p|}$ for $|p|<p_0$, $-r_0^{|p|}\ln(qr_0)$ for $|p|=p_0$, and $r_0^{|p|}(qr_0)^{p_0-|p|}$ for $|p|>p_0$. These estimates refer to the case $l>\frac{1}{2}$, i.e., when the normalization integral remains finite for $q=0$; note that in all cases the result depends on r_0. For $l<\frac{1}{2}$ one finds instead, as a result of the divergence of the normalization integral for $q=0$, that the expectation value of $r^{|p|}$, is of order $q^{-|p|}$, i.e., independent of the value of r_0 (provided $qr_0 \ll 1$).

These results display the exceptional nature of the two-body S-wave case, and imply that even rough measurements on two-body higher-wave barely bound states would yield more information on the forces than that conveyed by the binding-energy value—in contrast to the S-wave case.

This property of higher-wave barely bound states originates from the normalizability of the bound-state wave function in the zero-energy case, or, equivalently, from the finite size of the zero-energy bound state. The purpose of this Letter is to point out that, in analogy to the two-body higher-wave case, and in contrast to the two-body S-wave case, *the size of an N-body ($N > 2$) bound state*[7] *remains finite (irrespective of its angular momentum) when its binding energy vanishes, provided no ($N-n$)-body* ($0 < n < N-1$) *bound state exists*.[8,9] We prove here this result for $N = 3$, and outline the proof for $N > 3$. For simplicity we prove the result for spinless identical particles interacting via two-body potentials, but none of these restrictions is essential for its validity.[10]

The physical implications of this result refer to barely bound many-body bound states, and are analogous to those indicated above in the higher-wave two-body case. They are outlined in the last part of this Letter; we hope to be able in the near future to publish a more complete treatment.

The proof for the three-body case is based on the homogeneous Faddeev equation[11]:

$$\chi(\vec{k}, \vec{p}; E) = -m\int d^3p'[t(\vec{k}, -\tfrac{1}{2}\vec{p}-\vec{p}', E-\tfrac{3}{4}p^2/m)\chi(\vec{p}+\tfrac{1}{2}\vec{p}', \vec{p}', E) + t(\vec{k}, \tfrac{1}{2}\vec{p}+\vec{p}', E-\tfrac{3}{4}p^2/m)\chi(-\vec{p}-\tfrac{1}{2}\vec{p}', \vec{p}', E)]/(p^2+p'^2+\vec{p}\cdot\vec{p}'-mE). \quad (1)$$

Here $\vec{k}$ and $\vec{p}$ are connected to the momenta of the three particles in the usual way, $\vec{k} = \frac{1}{2}(\vec{k}_2 - \vec{k}_3)$, $\vec{p} = \frac{1}{3}(\vec{k}_2 + \vec{k}_3 - 2\vec{k}_1)$, E is the total energy in the c.m. frame, and $\chi(\vec{k}, \vec{p}, E)$ is related to the Fourier-transformed three-body wave function $\Psi(k_1, k_2, k_3)$ by the relation

$$\Psi(\vec{k}_1, \vec{k}_2, \vec{k}_3) = [(1+P_{12}+P_{23})\chi(\vec{k}, \vec{p}, E)]/(\tfrac{3}{4}p^2+k^2-mE), \quad (2)$$

where P_{ij} is the operator that permutes particles i and j, and m is the mass of the particles. Thus the normalization condition for the bound state sets the integral

$$I = \int d^3k\, d^3p |\chi(\vec{k}, \vec{p}, E) + \chi(-\tfrac{1}{2}\vec{k}-\tfrac{3}{4}\vec{p}, -\tfrac{1}{2}\vec{p}+\vec{k}, E) + \chi(-\tfrac{1}{2}\vec{k}+\tfrac{3}{4}\vec{p}, -\tfrac{1}{2}\vec{p}-\vec{k}, E)|^2/(\tfrac{3}{4}p^2+k^2-mE)^2 \quad (3)$$

equal to a constant. The task is to prove that I remains convergent (at $k \simeq 0$, $p \simeq 0$) even for a solution of Eq. (1) with $E = 0$.

The function $t(\vec{k}, \vec{p}, E')$ in Eq. (1) is the two-body *off-shell t matrix*, *and it is certainly finite at* $k=0$, $p=0$. It is moreover nonsingular for $E' < 0$, and finite for $E' = 0$, *provided there are no two-body bound states*. But then Eq. (1) implies that $\chi(\vec{k}, \vec{p}, E)$ is also finite at $k = p = E = 0$, and then simple power counting shows that I remains convergent at $k \approx 0$, $p \approx 0$ even for $E = 0$, Q.E.D.

Using the fact that $\chi(\vec{k}, \vec{p}, 0)$ is finite at $k = p = 0$, one can easily evaluate the asymptotic behavior of the three-body wave function $\Psi(\vec{r}_1, \vec{r}_2, \vec{r}_3)$:

$$\Psi(\vec{r}_1, \vec{r}_2, \vec{r}_3) \sim \mathrm{const}(r_{12}^2 + r_{23}^2 + r_{31}^2)^{-2}, \quad (4)$$

implying again convergence at large r_{ij} of the normalization integral

$$\int d^3r_1\, d^3r_2\, d^3r_3\, \delta(\vec{r}_1 + \vec{r}_2 + \vec{r}_3)|\Psi(\vec{r}_1, \vec{r}_2, \vec{r}_3)|^2. \quad (5)$$

Note that Eq. (4) corresponds simply to the behavior at large r_{ij} of the (asymptotically vanishing) free solution of the zero-energy three-body Schrödinger equation; indeed for negative energy E and in the N-body case, this solution is just the free translation-invariant Green's function[12]

$$G_N(E; \vec{r}_1, \dots, \vec{r}_N) = -2m(2\pi)^{-3(N-1)/2} q^{(3N-5)/2} \rho^{-(3N-5/2)} K_{(3N-5)/2}(q\rho), \quad (6)$$

where m is the mass of the particles, $q^2 = 2m|E|$, and

$$\rho^2 = \sum_{i>j=1}^{N} |\vec{r}_i - \vec{r}_j|^2/N.$$

This remark displays the connection of the many-body case with the higher-wave two-body case discussed above, indicating the similarity of the mechanisms that bring about the convergence of the zero-energy normalization integrals.[13] This same remark indicates that the result must be true for $N > 3$; a formal proof can be based on the Faddeev-Jakubowski equations,[14] the requirement of nonexistence of ($N-n$)-body bound states being related to the occurrence of ($N-n$)-body off-shell t matrices as kernels in these equations.

The Faddeev (and Faddeev-Jakubowski) equations provide the most convenient tool to prove our result, since they neatly display the role played by the requirement that there be no ($N-n$)-body bound states. It is, however, illuminating to also try to understand in more physical, if less rigorous, terms the mechanism whereby the presence of $(N-n)$-body bound states alters the asymptotic behavior of the zero-energy many-body wave function.

Let us refer, for simplicity, to the three-body case, and focus our attention on the physically more interesting case of a barely bound state (i.e., such that $qr_0 \ll 1$, with $q^2 = 2m|E|$). Then if a two-body bound state, with (negative) energy $E_2 > E$, exists, the three-body bound-state wave function contains asymptotically several terms (that give the dominant behaviors in different sectors of configuration space),[15] one of which is proportional to $(q_1\xi)^{-1/2}K_{l+1/2}(q_1\xi)\varphi(\eta)$, with, say, $\vec{\xi} = 6^{-1/2}(\vec{r}_2 + \vec{r}_3 - 2\vec{r}_1)$, $\vec{\eta} = 2^{-1/2}(\vec{r}_2 - \vec{r}_3)$, $q_2^2 = m|E_2|$, and $q_1^2 + 2q_2^2 = q^2$. This term is of course to be interpreted as a quasi-two-body bound state of angular momentum l, composed of particle 1 and the two-body bound state (with wave function φ) made up of particles 2 and 3. The size associated to this term will then be much larger than r_0, if the bound state of particles 2 and 3 has zero angular momentum (in which case it would have a size of order $1/q_2 > 1/q \gg r_0$), or if $l = 0$ (in which case it would have a size of order $1/q_1 > 1/q \gg r_0$), or if both things happen (in which case it would have a size or order $1/q_1$ or $1/q_2$, whichever is larger).[16] It is also clear, on the grounds of physical continuity, that similar estimates of the size of the three-body barely bound state obtained under the hypothesis that, in place of two-body barely-bound states, there exist two-body, very low-energy resonances or virtual states.[17] But if instead no two-body barely bound states, nor virtual states, nor very low-energy resonances exist, then our result implies that the size of a three-body barely bound state is of order $r_0 \ll 1/q$.[18]

As indicated by these considerations, the main phenomenological implication of our remark relates to the size of barely bound N-body systems; it would therefore lead to specific predictions for several observables involving such systems (*form factors, vertex functions, transition probabilities, reactions*). Suffice it here to note that the main parameters affecting such predictions are the expectation values of $r^{|p|}$, and that for these quantities, under the conditions implied by the above discussion, exactly the same results as given above for a two-body l-wave barely bound state hold, except for a redefinition of p_0, that now reads $p_0 = 2K_{\min} + 3N - 7$.[19] Here $K_{\min}$ is a nonnegative integer that is uniquely determined by the angular momentum, parity, etc. of the N-body state, and by the properties of the particles that constitute it (in particular, the kind of statistics they satisfy); it equals the minimal value taken by the sum of the quantum numbers l_j characterizing the angular momenta of the Jacobi coordinates.[20]

Finally we mention that, while in this paper we have focused on bound states, many of the phenomenological considerations also apply to (very low-energy) N-body resonances. A convenient technique to display the analogy is the Hilbert-Schmidt technique, that allows one to associate normalizable wave functions also to resonances, and therefore provides a firm ground for the discussion of properties related to their size.[21]

It is a pleasure to acknowledge useful conversations on the subject of this paper with A. M. Badalyan. One of us (F.C.) would like to thank the Institute of Theoretical and Experimental Physics for the kind hospitality provided during a one-month visit, effected in the framework of the Comitato Nazionale per l'Energia Nucleare–Goskomitet po Islol'zovaniyu Atomnaya Energii scientific exchange agreement.

---

[*] Permanent affiliations: Istituto di Fisica, Università di Roma, 00185 Rome, Italy, and Istituto Nazionale di Fisica Nucleare, Sezione di Roma, Italy.

[1] Throughout this paper, for simplicity of language, we refer to zero-energy two-body S-wave states, even though, as discussed below, the corresponding wave functions are not normalizable (so that, strictly speaking, one should refer to such states as zero-energy resonances).

[2] E. P. Wigner, Z. Phys. 83, 253 (1933), and Phys. Rev. 43, 252 (1933); H. A. Bethe and R. Peierls, Proc. Roy. Soc., Ser. A 149, 176 (1935).

[3] For the deuteron, $1/q = 4.3$ fm; the pion Compton wavelength λ, that sets the scale of the *longer*-range part of the nucleon-nucleon interaction, is less than one third of that ($\lambda \simeq 1.4$ fm).

[4] The Wigner-Bethe-Peierls argument applies only to the S-wave part of the deuteron wave function (see below); indeed any property of the deuteron related to the (small) D-wave part of the wave function does provide additional information on the nucleon-nucleon potential, besides that implicit in the value of the deuteron binding energy.

[5] We are assuming, for simplicity, that the potentials vanish exponentially at infinity; but for the validity of the main result it is sufficient that they be integrable at long range (i.e., in three-dimensional space, that $r^{3+\epsilon}V(r)$ vanish asymptotically for some $\epsilon > 0$). The *exclusion of long-range potentials (for instance, Coulomb)* is of course essential.

[6] Here, and in the following, $K_\nu(Z)$ is the modified Bessel function of the third kind. Also note that, where-

ever we mention the wave function, we understand the full (three-dimensional) wave function, namely, that normalized by $\int d^3r|\Psi|^2=1$.

[7] Here, and always in the following, we exclude the exceptional case of positive-energy bound states.

[8] This result (for $N=3$) is implicitly contained in a report given some years ago by one of us [Yu. A. Simonov, in *Proceedings of the Problem Symposium of Nuclear Physics, Tbilisi, U.S.S.R., 1967,* Vol. I, p.7], and has been explicitly evinced from this reference by V. N. Efimov, who (in an unpublished seminar) metioned this fact as the reason why the Efimov effect {V. N. Efimov, [JETP Lett. 16, 34 (1972)], and Nucl. Phys. A210, 157 (1973)} is not expected to occur for $N>3$. It should be emphasized that the result reported here for zero-energy bound states cannot be obtained by a simple limiting process from the results given in the recent papers dealing with the asymptotic behavior of the three-body wave function, that consider only nonzero-energy states: S. P. Merkuriev, Teor. Mat. Phys. 8, 235 (1971), and Yad. Fiz. 19, 447 (1974) [Sov. J. Nucl. Phys., to be published]; R. G. Newton, Ann. Phys. (New York) 74, 324 (1972).

[9] The condition excluding $(N-n)$-body bound states might appear trivial, as a result of the assumed existence of a zero-energy N-body bound state (see also Ref. 7). But the critical assumption for the validity of the theorem consists in the exclusion of *zero-energy* $(N-n)$-body bound states; and this is not an altogether exceptional eventuality, since it is for instance known that a zero-energy two-body bound state implies the existence of an infinite number of three-body bound states, whose energies accumulate at zero (this is the Efimov effect; see Ref. 8). The importance of this condition relates however mainly to the physically more relevant case of an N-body barely bound state, i.e., a state with nonvanishing, but very small, binding energy (see below). Let us also emphasize that the N-body bound state under consideration need not be the ground state of the N-body system.

[10] We treat for simplicity only the case of ordinary (three-dimensional) space; the structure of the proof implies that the main result remains valid in d-dimensional space, provided $d(N-1)>4$.

[11] L. D. Faddeev, Zh. Eksp. Teor. Fiz. 39, 1459 (1960) [Sov. Phys. JETP 12, 1014 (1961)].

[12] See, for instance, F. Calegero and Yu. A. Simonov, Nuovo Cimento 56B, 71 (1968). We refer here, for simplicity, to the case of spinless bosons. For the more general case, one must introduce the quantum number $K_{\min}$ (see below).

[13] The connection between the many-body bound-state problem and the higher-wave two-body problem has been been already pointed out and exploited in a different, but related, context: F. Calogero and Yu. A. Simonov, Phys. Rev. 169, 789 (1968).

[14] O. A. Jakubowsky, Yad. Fiz. 5, 1312 (1967) [Sov. J. Nucl. Phys. 5, 937 (1967)]; L. D. Faddeev, in *Three-Body Problem in Nuclear and Particle Physics*, edited by J. S. C. McKee and P. M. Rolph (North-Holland, Amsterdam, 1970), p. 154.

[15] See, for instance, Merkuriev, Ref. 8, where, however, the function $z^{-1/2}K_{l+1/2}(z)$ is replaced by its asymptotic part $z^{-1}\exp(-z)$.

[16] An example of the last kind (and with $q_1 \ll q_2$) is hypertritium ($E_{\mathrm{deut}}=-2.23$ MeV, $E_{\mathrm{hyptrit}}\approx-2.3$ MeV).

[17] One such example might be the trineutron, if it exists as a bound state (or resonance; see below).

[18] These arguments indicate that, if selection rules prevent a barely bound state for dissociating into S-state components, then its size would be of order $r_0 \ll 1/q$ even if two-body bound states or resonances exist. A three-body bound state with odd angular momentum and positive orbital parity is one such example.

[19] Of course the coefficient of the term giving the dominant contribution for small q depends on N, and on the precise definition of r.

[20] See, for instance, the report by Yu. A. Simonov, in *The Nuclear Many-Body Problem*, Proceedings of the Symposium on Present Status and Novel Developments in the Nuclear Many-Body Problem, Rome, 1972, edited by F. Calogero and C. Ciofi degli Atti (Editrice Compositori, Bologna, 1974), Vol. 1, p. 527. For instance, for a 1^- system composed of three pions (like the ω meson), $K_{\min}=2$; for a 0^- state of four identical fermions, $K_{\min}=3$; and of course for the two-body case, $K_{\min}=l$.

[21] See, for instance, S. Weinberg, Phys. Rev. 131, 440 (1936), and, for a more detailed discussion of three-body resonances, A. M. Badalyan and Yu. A. Simonov, Yad. Fiz. 17, 441 (1973), and 18, 73 (1973) [Sov. J. Nucl. Phys. 17, 225 (1973), and 18, (1973)].

Remark on the Existence of φ_4^4

James Glimm
Rochefeller University, New York, New York 10021

and

Arthur Jaffe*
Harvard University, Cambridge, Massachusetts 02138

(Received 10 June 1973)

The bound $|S_\epsilon^{(2)}(f\otimes g)| \leq \mathrm{const}\,|f|_{\mathcal{S}}|g|_{\mathcal{S}}$, uniform as the lattice spacing $\epsilon \to 0$, is sufficient to yield construction of a φ^4 field theory. In perturbation theory, this bound holds in space-time dimensions $d \leq 4$. The bounds on the n-point Schwinger functions follow from the given bound by the use of Lebowitz's inequalities. They yield the growth $|S^{(n)}| \leq O(n!)$, consistent with the Osterwalder-Schrader axioms, which allow reconstruction of a real-time theory.

We remark that a uniform bound on the two-point Schwinger function (with a lattice approximation) yields the existence of a $\varphi_4^4 - \mu\varphi$ model without cutoffs, including the case $\mu = 0$. We assume that the two-point functions are labeled by a cutoff parameter ϵ, the lattice spacing, and that for some $\mathcal{S}$ norm, independent of ϵ,

$$|S_\epsilon^{(2)}(f\otimes g)| \leq |f|_{\mathcal{S}}|g|_{\mathcal{S}}. \tag{1}$$

Theorem 1.—With the assumption of (1), there exists a set of Schwinger functions $S^{(n)}(x_1, \ldots, x_n) = \lim_{\epsilon_j} S_{\epsilon_j}^{(n)}(x_1, \ldots, x_n)$ which satisfy the Osterwalder-Schrader axioms,[1] with the possible exception of Euclidean covariance and clustering. Here ϵ_j denotes a subsequence of lattice cutoffs, and $\epsilon_j \to 0$.

Remark.—As Wilson observed,[2] the nontriviality of the φ_4^4 model may be more difficult to establish than its existence. In particular, the hypothesis of Theorem 1 does not require the correct charge or mass renormalization, even in perturbation theory. Thus the limiting theory could describe a free field, and, still worse, the possibility $S^{(n)} \equiv 0$ is not excluded. Correct mass (and field-strength) renormalization prevents the vanishing of $S^{(2)}$.

We obtain uniform bounds on the n-point function in terms of the two-point function, and convergence of the $S_{\epsilon_j}^{(n)}$ by compactness. The uniform bounds depend on correlation inequalities which were proved in statistical mechanics by Lebowitz,[3] and which follow in φ^4 field theory by the spin-$\frac{1}{2}$ approximation of Simon and Griffiths.[4] Our use of these inequalities in field theory was suggested by the work of Feldman[5] and especially the work of Spencer[6] on the elimination of even bound states in the φ^4 model. See also Glimm and Jaffe,[7] where the inequality on the connected four-point function, $S_T^{(4)} \leq 0$, yields bounds on critical exponents by their mean-field values.

Proposition 1.—Under the above hypothesis (1), with $f_i \geq 0$ and $\mu \geq 0$,

$$0 \leq S_\epsilon^{(n)}(f_1 \otimes \cdots \otimes f_n) \leq 2^{n-1}(n-1)!\prod_{i=1}^{n} |f_i|_{\mathcal{S}}, \tag{2}$$

where $|f_i|_{\mathcal{S}}$ is the same norm as in (1).

Proof.—The proof involves an induction hypothesis. We assume $\mu \geq 0$ and use the Lebowitz inequalities[3]

$$\langle qt\rangle - \langle q\rangle\langle t\rangle \leq 0. \tag{3}$$

Here

$$t(x) = \tfrac{1}{2}(\varphi + \tilde{\varphi}), \quad q(x) = \tfrac{1}{2}(\varphi - \tilde{\varphi}),$$

$$t = \Pi_i t(x_i), \quad q = \Pi_i q(x_i),$$

and $\tilde{\varphi}$ denotes a duplicate Euclidean field variable. The restriction $\mu \geq 0$ is no loss of generality, by the $\varphi \to -\varphi$ symmetry. We take

$$t = \prod_{i=1}^{n} t(x_i), \quad q = q(x_{n+1})q(x_{n+2}),$$

and we write (3) as

$$\textstyle\sum_X S(\sim X)[S(X, x_{n+1}, x_{n+2}) - S(X)S(x_{n+1}, x_{n+2}) + S(X)S(x_{n+1})S(x_{n+2})] \leq \sum_X S(X, x_{n+1})S(\sim X, x_{n+2}), \tag{4}$$

where X denotes a subset of $x_1, \ldots, x_n$, and $\sim X$ the complement of X. By the Griffiths-Kelly-Sherman inequalities,[8] each term on the left-hand side of (4) is positive. Thus, in particular,

$$0 \leq S^{(n+2)}(x_1, \ldots, x_{n+2}) \leq S^{(n)}(x_1, \ldots, x_n)S^{(2)}(x_{n+1}, x_{n+2}) + \textstyle\sum_X S(X, x_{n+1})S(\sim X, x_{n+2}), \tag{5}$$

and we have bounded $S^{(n+2)}$ by a sum of products of lower-order Schwinger functions.

The inductive hypothesis we use is (2) for $f_i \geqslant 0$ and $n \geqslant 1$. For $n = 2$, the hypothesis follows from (1), while for $n = 1$, it follows from the Schwarz inequality and from (1):

$$S^{(1)}(f) \leqslant S^{(2)}(f \otimes f)^{1/2} \leqslant |f|_{\mathcal{S}}.$$

Assuming the inductive hypothesis for $S^{(1)}, \ldots, S^{(n+1)}$, we prove it for $S^{(n+2)}$. By (5),

$$S^{(n+2)}(f_1 \otimes \cdots \otimes f_n) \leqslant 2^n\Big[(n-1)! + \sum_X |X|!(n - |X|)!\Big] \prod_{i=1}^{n+2} |f_i|_{\mathcal{S}} \leqslant 2^{n+1}(n+1)! \prod_{i=1}^{n+2} |f_i|_{\mathcal{S}}.$$

Here we use the fact that with $|X| = j$ there are $\binom{n}{j}$ choices for the subset. This completes the proof of the induction hypothesis.

We consider the norms on $\mathcal{S}(R^d)$,

$$|f|_r = \sup_x |(1+x^2)^r f(x)|.$$

Proposition 2.—With the assumption of (1), there exists $r < \infty$ such that

$$|S_\epsilon^{(2)}(f \otimes g)| \leqslant \mathrm{const}\, |f|_r |g|_r,$$

with the constant uniform in ϵ.

Proof.—Because $S^{(2)}$ is positive, and defined on $\mathcal{S} \otimes \mathcal{S}$, it is a positive measure. Let $0 \leqslant \chi_j(x) = \chi(x - j$ be a C_0^∞ partition of unity, with $j \in Z^d$. Then

$$|S^{(2)}(f \otimes g)| \leqslant \sum_{i,j} (\sup_{\mathrm{supp}\,\chi_i \otimes \chi_j} |f \otimes g|) S^{(2)}(\chi_i \otimes \chi_j).$$

Since the χ_i are translates of a particular function, for some $m < \infty$,

$$S^{(2)}(\chi_i \otimes \chi_j) < |\chi_i|_{\mathcal{S}} |\chi_j|_{\mathcal{S}} \leqslant \mathrm{const}(1+i^2)^m(1+j^2)^m,$$

with the constant uniform in ϵ. By choosing $r = m + d$, the proposition follows.

By linearity, we then obtain from Propositions 1 and 2 the following:

Corollary.—With the assumption of (1), there exists $r < \infty$, and $c < \infty$, such that

$$|S_\epsilon^{(n)}(f_1 \otimes \cdots \otimes f_n)| \leqslant c^n n! \prod_{i=1}^{n} |f_i|_r. \qquad (6)$$

Here $f_i \in \mathcal{S}(R^d)$, and the constants are uniform in ϵ.

Proof of Theorem 1.—The existence of a convergent subsequence, as $\epsilon \to 0$, follows from the Corollary to Proposition 2 by compactness, and the same bounds hold in the limit. The symmetry and Osterwalder-Schrader positivity of the lattice Schwinger functions are known for a finite-volume theory[9] and easily extended to the infinite-volume and $\epsilon = 0$ limits. This completes the proof.

Corollary.—With the assumption of (1), the generating function

$$Z\{f\} = \sum_{n=0}^{\infty} S^{(n)}(f \otimes \cdots \otimes f)/n!$$

is an analytic function for f in a neighborhood of the origin in $\mathcal{S}(R^d)$. It is also the characteristic function for a unique measure dq on $\mathcal{S}'(R^d)$, i.e.,

$$Z\{f\} = \int e^{\varphi(f)} dq, \quad S^{(n)}(f_1, \ldots, f_n) = \int \varphi(f_1) \cdots \varphi(f_n)\, dq. \qquad (7)$$

Proof.—The existence and analyticity of Z follow immediately from (6), while the existence and uniqueness of dq follow by Minlos's theorem.

We remark that a number of other known properties of $(\varphi^4 - \mu\varphi)_2$ are also a consequence of hypothesis (1). In two and three dimensions, Theorem 1 may provide an alternative method for proof of existence of the φ^4 theory. In three dimensions, the finite-space-time-volume φ^4 theory exists[10-11] and is a limit as $\epsilon \to 0$ of a lattice theory.[12] It is sufficient to verify hypothesis (1) in the finite-volume, $\epsilon = 0$ theory, since the Lebowitz inequality (3) and the proof of (2) extend

---

to the $\epsilon = 0$ limit. Then the norm $|f|_{\mathcal{S}}$ must be uniform in the volume.

---

[*] Work supported in part by the National Science Foundation under Grant No. NSF GP 40354X.

[1] K. Osterwalder, in *Constructive Quantum Field Theory*, edited by G. Velo and A. Wightman (Springer, Berlin, 1973). See also J. Fröhlich, to be published; K. Osterwalder and R. Schrader, to be published, Axiom (E0″).

[2] K. Wilson and J. Kogut, to be published.

[3] J. Lebowitz, Commun. Math. Phys. 35, 87 (1974).

[4] B. Simon and R. Griffiths, Commun. Math. Phys. 33, 145 (1973).

[5] J. Feldman, "On the Absence of Bound States in the φ^4 Quantum Field Model without Symmetry Breaking" (to be published).

[6] T. Spencer, "The Absence of Even Bound States in φ_2^4" (to be published).

[7] J. Glimm and A. Jaffe, Phys. Rev. D (to be published).

[8] J. Ginibre, Commun. Math. Phys. 16, 310 (1970).

[9] F. Guerra, L. Rosen, and B. Simon, to be published; J. Fröhlich, to be published.

[10] J. Glimm and A. Jaffe, Fortschr. Phys. 21, 327 (1973).

[11] J. Feldman, to be published.

[12] Y. Park, "Lattice Approximation of the $(\varphi^4-\mu\varphi)_3$ Field Theory in a Finite Volume" (to be published).

[13] We have been informed that J. Feldman has independently proved Proposition 1.

Death of White Holes in the Early Universe*

Douglas M. Eardley
California Institute of Technology, Pasadena, California 91109

(Received 10 June 1974)

A white hole (a compact, long-delayed region of the big bang) cannot exist, because it suffers an exponentially growing instability that converts it into a black hole. Such instabilities might have homogenized the early universe.

Little is known about the dissipation of inhomogeneities in the big bang.[1] This Letter reports an analysis of one very simple class of inhomogeneous cosmological models, the "white-hole" or "lagging-core" models due to Novikov and Thorne[2,3] and to Ne'eman.[4] In such a model, a small region of matter emerges from the initially singular state at a much later time than its surroundings do (emerging either all at once or, more generally, gradually). The main conclusion is that a white-hole inhomogeneity is violently unstable and inevitably converts itself into a black hole. Detailed calculations leading to this conclusion will be published elsewhere.[5] The ζ models, mentioned below, suggest the general conjecture that such instabilities would have been a powerful dissipator of severe inhomogeneities in the early universe, while leaving mild inhomogeneities untouched.

During its lifetime, a white hole acts as a compact body of some mass M; M decreases as matter flows out. The white hole attracts and is attracted gravitationally, and it has a finite capture cross section for photons, $\sigma = 27\pi M^2$. (Units are natural, $G=c=1$, so M stands indifferently or mass, radius, or light crossing time. The white hole is taken as nonrotating.) But the fate of accreted matter (ions, photons, neutrinos, ...) is unique: Matter cannot reach the initial singularity within the white hole; it piles up at a particle horizon[6] (one-way surface allowing only outward flow). Now, any physical agent which thus compresses photons must shift them to the blue, by conservation of phase space. In fact, calculations show that photons are strongly compressed at the particle horizon, and blue-shifted[7] according to $h\nu \propto \exp(t/4M)$. Other forms of matter, and also gravitational waves, suffer the same fate. So a white hole is unstable to the formation of an exponentially strengthening "blue sheet" of accreted, highly accelerated mater at the particle horizon. Even the minutest amount of accretion suffices, because of the exponential growth.[8] Two consequences ensue.

Firstly, the blue sheet interacts with and strongly heats any matter that emerges from the singularity and flows out of the white hole. But this heating process cannot go on for long. There is a second, dominant process. Even with the neglect of matter-matter interactions, the gravitational field of the blue sheet becomes dynamically important after a short time interval, $\Delta t \approx 4M \ln(M/\delta M)$ ($\approx$ a few hundred M, at most); here δM is the original mass energy of accreted matter.

The effect of this gravitational field is to focus outgoing null rays so strongly that they reconverge. Therefore the entire white hole becomes sheathed in an event horizon[8,9] outside the blue sheet. From the viewpoint of an external observer, it is converted into a black hole. Matter which emerges from the singularity at still later times immediately recollapses, without being externally observable. (The increasing stress energy of the blue sheet does not change the externally measured mass M, because the blue sheet forms exactly at the surface of unity binding energy.)

The following simple model demonstrates the gravitational effect of the blue sheet. Take maximally extended Schwarzschild space-time in double-null Kruskal coordinates,[10]

$$ds^2 = -(32M^3/r)\exp(-r/2M)du\,dv + r^2(d\theta^2 + \sin^2\theta\, d\varphi^2),$$

where r is related to u and v by $uv = (1 - r/2M) \times \exp(r/2M)$, and where v is constant on ingoing null rays, u on outgoing ones. Cut it into two pieces along the entire ingoing or particle horizon $v = 0$. Paste the pieces back together with a warp,[11] according to $(u, v = 0^-, \theta, \varphi) = (u + a, v = 0^+, \theta, \varphi)$, where a is a positive constant.[12] The horizon $v = 0$ thereby becomes a blue sheet: The Riemann tensor now has a term proportional to $\delta(v)$; this term represents, through the Einstein equations $G_{\mu\nu} = 8\pi T_{\mu\nu}$, precisely the gravitational field of a null stress, $T_{\mu\nu} = a\delta(v)v_{,\mu}v_{,\nu}/[4\pi\exp(1)]$, due to matter streaming ultrarelativistically along the horizon $v = 0$. (This model is a limiting form of the Vaidya solution.[13]) A time translation $t \to t + b$ (here t is Schwarzschild time, $t = 2M \times \ln|v/u|$, and b is a constant) has on this model the effect $a \to a\exp(b/4M)$; the blue sheet strengthens exponentially in time.[14]

Now, a white-hole model[2] consists of a piece of the Schwarzschild solution, interpolated between the surrounding universe and the eventually emergent matter; see Fig. 1(a). The unstable particle horizon is necessarily present, and any accretion whatsoever at sufficiently early times engenders a blue sheet (strictly speaking, not exactly on the particle horizon, but exponentially close). The model above then shows that an event horizon forms; see Fig. 1(b). So the lifetime of a white hole against turning into a black hole via the blue-sheet instability is very short, say $t \lesssim 400M \approx 2\times10^{-3}(M/M_\odot)$ sec; white holes cannot exist in the present universe.

Then, were dying white holes an important source of heat in the early universe? The main difficulty with this idea is that the resulting black holes are implausibly large and numerous. In plausible models, such as the ζ models below, thermal energy imparted to outgoing matter by the blue sheet cannot much exceed the rest-mass energy of the black hole. Cosmologically, thermal energy is lost by adiabatic expansion, while black-hole mass is conserved.[3] It follows that this process is barely adequate to explain the entire present entropy content of the cosmic microwave background only if the process continued until nearly the time of recombination[15] ($t \approx 2\times10^{14}$ sec); since only huge ($M \cong 10^{17}M_\odot$) white holes could live even that long, equally huge black holes must presently be a major form of mean mass density ($\Omega \gtrsim 0.10$), which can be ruled out observationally.[16]

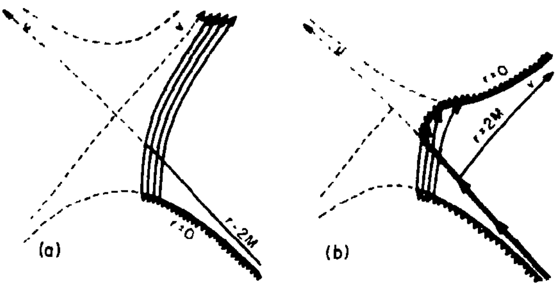

FIG. 1. (a) A white hole. Space-time to the right of the emerging matter (arrows) is part of the Schwarzschild solution. The rest of the Schwarzschild solution is not physically present (dashed lines); it is replaced by some interior solution for the sphere of emerging matter. The singularity ($r = 0$) is a delayed part of the big bang; it is enclosed in a particle horizon ($r = 2M$). The rest of the universe lies far to the right. (b) When a blue sheet (double line) forms at the particle horizon, an event horizon ($r = 2M$) appears, entailing the recollapse of the matter to a future singularity ($r = 0$), and forming a black hole.

A white hole represents a very severe, local inhomogeneity in the big bang; we discover a very violent instability. Can we now place a limit on the inhomogeneity of the early universe by distorting a homogeneous cosmological model toward more and more severe inhomogeneity, and noting the onset of this instability? In particular, consider a white hole of mass M_0 and total delay t_0; choose the single parameter $\zeta \equiv t_0/M_0$ as a dimensionless measure of the severity of inhomogeneity.

Define the one-parameter sequence of cosmological "ζ models"[6]: These are just spherically symmetric,[17,18] marginally bound, similarity solutions[19,20] of the Einstein equations for pressureless matter (dust). The proper mass of each spherical dust shell is dM; $M = \int dM$ is the total proper mass within a given shell, and serves as a radial coordinate. The coordinate t measures proper time for each shell. The space-time metric is

$$ds^2 = -dt^2 + X^2\, dM^2 + Y^2(d\theta^2 + \sin^2\theta\, d\varphi^2),$$

where $X = (t + 3\zeta M)/[6M^2(t + \zeta M)]^{1/3}$, $Y = [9M(t + \zeta$

$\times M)^2/2]^{1/3}$. A shell M emerges from the singular state (marked by $Y = 0$) at time $t = -\zeta M$; hence, during its lifetime, the white hole disgorges matter at the constant rate $dM/dt = -1/\zeta$. For $\zeta = 0$, the ζ model is identical with the homogeneous, spatially flat Friedmann cosmology; for $\zeta \to \infty$, it locally approaches a piece of Schwarzschild space-time.

Consider distortions in causal structure, particularly the appearance of horizons, as one moves along the sequence of ζ models from $\zeta = 0$. For all ζ, there is a region of past-trapped[9] spheres to the past of the hypersurface $t = -(\zeta - 4/3)M$, keeping future-directed timelike curves from approaching the singularity. But for small ζ, there is no well-defined horizon where geodesics pile up. For values $\zeta \gtrsim \zeta_{\text{crit}} = \frac{26}{3} + 5\sqrt{3} \cong 17.327$, there appears just outside the past-trapped region a *similarity horizon* (that is, a null hypersurface, the generators of which are parallel to the "similarity vector,"[20] $t\partial_t + M\partial_M$). This similarity horizon is the hypersurface $t = -z(\zeta)M$, where $z(\zeta_{\text{crit}}) = 7 + 4\sqrt{3}$, and $z(\zeta) = \zeta - \frac{4}{3} - 8/\zeta + O(\zeta^{-2})$ as $\zeta \to \infty$. As $\zeta \to \infty$, the similarity horizon becomes the particle horizon in Schwarzschild space-time. This similarity horizon attracts photons, and shifts them to the blue according to $k^t \propto |t|^{-p(\zeta)}$, where $p(\zeta_{\text{crit}}) = 1$, and $p(\zeta) = \zeta/4 - \frac{7}{3} + O(\zeta^{-1})$ as $\zeta \to \infty$. So it is unstable to the formation of a blue sheet. Therefore, along the sequence of ζ models, a sufficiently mild inhomogeneity ($\zeta \lesssim \zeta_{\text{crit}}$) is stable to blue-sheet formation. The value ζ_{crit} marks the onset of the blue-sheet instability; the instability is weak at onset $[p(\zeta_{\text{crit}}) = 1]$, but becomes increasingly violent as ζ increases further [e.g., $p(100) \cong 22.62$].

The gravitational effect of a blue sheet in a ζ model for $\zeta \gtrsim \zeta_{\text{crit}}$ can be treated exactly, by the method above; if the blue sheet becomes dynamically important at time t, the product is a black hole, $M \cong |t|/\zeta$, with no strong disturbance to dust outside M.

The ζ models motivate the general conjecture that blue-sheet instabilities limited the inhomogeneity of the early universe to finite values, perhaps forming black holes. It will be of great interest to investigate the blue-sheet instability in other inhomogeneous cosmological models, with noncompact particle horizons,[20] where there exists the possibility that no black hole forms, and that all of the strongly heated matter is dispersed into the expanding universe.

I am grateful to W. H. Press, M. Demianski, S. A. Teukolsky, and K. S. Thorne for discussion and comments.

---

*Work supported in part by the National Science Foundation under Grant No. GP-36687X.

[1] C. W. Misner, in *Battelle Rencontres, 1967*, edited by C. M. DeWitt and J. A. Wheeler (Benjamin, New York, 1968), p. 117.

[2] I. D. Novikov, Astron. Zh. 41, 1075 (1964) [Sov. Astron. AJ 8, 857 (1965)].

[3] I. D. Novikov and K. S. Thorne, in *Black Holes, Les Houches 1972*, edited by C. DeWitt and B. DeWitt (Gordon and Breach, New York, 1973), p. 445.

[4] Y. Ne'eman, Astrophys. J. 141, 1303 (1965).

[5] D. M. Eardley, to be published.

[6] W. Rindler, Mon. Notic. Roy. Astron. Soc. 116, 662 (1956).

[7] Such "blue-shifting horizons" occur in other space-times; see C. W. Misner and A. H. Taub, Zh. Eksp. Teor. Fiz. 55, 233 (1968) [Sov. Phys. JETP 28, 122 (1969)].

[8] Accretion was discussed by Ya. B. Zel'dovich and I. D. Novikov, Astron. Zh. 43, 758 (1966) [Sov. Astron. AJ 10, 602 (1967)], but the exponential growth was not discussed. These authors each have very recently discussed quantum particle creation inside white holes.

[9] S. W. Hawking and G. F. R. Ellis, *The Large Scale Structure of Spacetime* (Cambridge Univ. Press, London, 1973).

[10] C. W. Misner, J. A. Wheeler, and K. S. Thorne, *Gravitation* (Freeman, San Francisco, 1973), p. 828.

[11] R. Penrose, in *General Relativity: Papers in Honour of J. L. Synge*, edited by L. O'Raifeartaigh (Clarendon Press, Oxford, England, 1972), p. 101.

[12] A function $a(\theta\varphi)$ describes an arbitrary anisotropic accretion, see Ref. 5.

[13] P. C. Vaidya, Proc. Indian Acad. Sci., Sect. A 33, 264 (1951).

[14] The observational interpretation of this statement is a little involved; see Ref. 5.

[15] Compare M. J. Rees, Phys. Rev. Lett. 28, 1669 (1972).

[16] W. H. Press and J. E. Gunn, Astrophys. J. 185, 397 (1973).

[17] R. C. Tolman, Proc. Nat. Acad. Sci. 20, 169 (1934).

[18] H. Bondi, Mon. Notic. Roy. Astron. Soc. 107, 410 (1947).

[19] M. E. Cahill and A. H. Taub, Commun. Math. Phys. 21, 1 (1971).

[20] D. M. Eardley, California Institute of Technology Report No. OAP-347 (to be published).

Integral Formalism for Gauge Fields

C. N. Yang
Institute of Theoretical Physics, University of Wroclaw, Wroclaw, Poland, and
Institute of Theoretical Physics, State University of New York, Stony Brook, New York 11990
(Received 10 June 1974)

A new integral formalism for gauge fields is described. Further developments are presented, including gravitation equations related to, but not identical with, Einstein's equations.

It was pointed out by Weyl many years ago that the electromagnetic field can be formulated in terms of an Abelian gauge transformation. This idea was extended[1] in 1954 to the concept of gauge fields for non-Abelian groups. That formulation, like the Weyl formulation for electromagnetism, was based on the replacement of ∂_μ by $\partial_\mu - ieB_\mu$. One might call such formulations differential formulations. It is the purpose of the present paper to reformulate the concept of gauge fields in an *integral formalism.* The new formalism is conceptually superior to the differential formalism and allows for natural developments of additional concepts. It further allows a mathematical and physical discussion of the gravitational field *as a gauge field,* resulting in equations related, but not identical, to Einstein's.

The basic point is the fact that *electromagnetism is a nonintegrable phase factor,* a fact discussed many years ago by Dirac, Peierls, and others, and more recently by many authors.[2] This fact is now generalized as follows:

Definition of a gauge field.—Consider a manifold with points on it labeled by x^μ ($\mu = 1, 2, \ldots, n$) and consider a gauge G which is a Lie group with generators X_k ($k = 1, 2, \ldots, m$). [For $G = U(1)$ we have electromagnetism; for G non-Abelian we have non-Abelian gauge fields.] Define a path-dependent (i.e., nonintegrable) phase factor φ_{AB} as an element of the group G associated with path AB between two points A and B on the manifold. The association is to have the group property: $\varphi_{ABC} = \varphi_{AB}\varphi_{BC}$, where the paths AB and BC are segments of ABC. Furthermore for an infinitiesimal path A to $A + dx^\mu$ the phase factor is close to the identity I of G, so that[3]

$$\varphi_{A(A+dx)} = I + b_\mu{}^k(x) X_k \, dx^\mu \,. \tag{1}$$

The function $b_\mu{}^k(x)$ defined on the manifold will be called a *gauge potential;* φ_{AB} will be called a *gauge phase factor.*

With this definition additional concepts and theorems are naturally developed. We summarize some of these below. Details will be published elsewhere.

Gauge field strength.—Consider a path $ABCDA$ forming the border of an infinitesimal parallelogram with sides dx and dx'. φ_{ABCDA} can be computed by multiplying four phase factors like (1) together, resulting in

$$\varphi_{ABCDA} = I + f_{\mu\nu}{}^k X_k \, dx^\mu \, dx^{\nu\prime} \,; \tag{2}$$

where

$$f_{\mu\nu}{}^k = \frac{\partial b_\mu{}^k}{\partial x^\nu} - \frac{\partial b_\nu{}^k}{\partial x^\mu} - b_\mu{}^i b_\nu{}^j C_{ij}{}^k = -f_{\nu\mu}{}^k \tag{3}$$

in which $C_{ij}{}^k$ is the structure constant of G:

$$X_k X_j - X_j X_k = C_{kj}{}^i X_i \,. \tag{4}$$

$f_{\mu\nu}{}^k$ will be called a *gauge field,* or gauge field strength. They are the Faraday-Maxwell fields when $G = U(1)$.

Gauge transformation.—A gauge transformation in the integral formalism is defined by a transformation

$$\varphi_{AB} \to \varphi_{AB}{}' = \xi_A \varphi_{AB} \xi_B{}^{-1} \,, \tag{5}$$

where ξ_A is an element of G which depends on the point A. It is clear that under (5)

$$\varphi_{ABCDA} \to \varphi_{ABCDA}{}' = \xi_A \varphi_{ABCDA} \xi_A{}^{-1} \,. \tag{6}$$

Thus

$$f_{\mu\nu}{}^{k\prime} = \langle k | R_{\mathrm{adj}} | j \rangle f_{\mu\nu}{}^j \,, \tag{7}$$

where R_{adj} is the adjoint representation for the element ξ_A. The simple transformation property (7) is the definition for the concept that $f_{\mu\nu}{}^k$ is *gauge covariant.* Generalization to other representations R of G for a gauge-covariant quantity $\psi_{\alpha\beta\gamma}{}^K$ is immediate[3]:

$$\psi_{\alpha\beta\gamma}{}^{K\prime} = \langle K | R(\xi_A) | J \rangle \psi_{\alpha\beta\gamma}{}^J \,. \tag{8}$$

$b_\mu{}^k$ is not gauge covariant; $f_{\mu\nu}{}^k$ is.

Gauge-covariant differentiation.—To *retain* *gauge covariance* in differentiation we define

$$\psi^K{}_{|\mu} = \frac{\partial \psi^K}{\partial x^\mu} + b_\mu{}^k \langle K|Z_k|J\rangle \psi^J , \tag{9}$$

where Z_k is the matrix representation of X_k. Generalization to other cases is obvious. An interesting theorem is that

$$f_{\mu\nu|\lambda}{}^k + f_{\nu\lambda|\mu}{}^k + f_{\lambda\mu|\nu}{}^k = 0 , \tag{10}$$

which is the gauge-Bianchi identity.

Introduction of a Riemannian metric.—So far we need no metric for the manifold. Now we introduce a metric for it and discuss arbitrary coordinate transformations. We come then naturally to *Riemannian covariant* quantities and *doubly covariant derivatives.* $b_\mu{}^k$ is Riemannian covariant, since φ_{AB} is coordinate-system independent. $f_{\mu\nu}{}^k$ is doubly covariant. We have

$$\begin{aligned} &\psi^K{}_{\|\mu} = \psi^K{}_{|\mu} , \\ &\psi^{K\nu}{}_{\|\mu} = \psi^{K\nu}{}_{|\mu} + \left\{ \begin{matrix} \nu \\ \mu\alpha \end{matrix} \right\} \psi^{K\alpha} , \\ &f_{\mu\nu\|\lambda}{}^k = f_{\mu\nu|\lambda}{}^k - \left\{ \begin{matrix} \alpha \\ \mu\lambda \end{matrix} \right\} f_{\alpha\nu}{}^k - \left\{ \begin{matrix} \alpha \\ \nu\lambda \end{matrix} \right\} f_{\mu\alpha}{}^k , \end{aligned} \tag{11}$$

etc. It is easily shown that

$$f_{\mu\nu\|\lambda}{}^k + f_{\nu\lambda\|\mu}{}^k + f_{\lambda\mu\|\nu}{}^k = 0 \tag{12}$$

which is satisfied by *all* gauge fields on *all* Riemannian manifolds.

Source of gauge fields.— We *define*, in analogy with electromagnetism, a *source* four-vector $J_\mu{}^k$ for a gauge field:

$$J_\mu{}^k = g^{\nu\lambda} f_{\mu\nu\|\lambda}{}^k = f_{\mu\nu}{}^{k\|\nu} . \tag{13}$$

After some computation one derives a theorem:

$$g^{\mu\lambda} J_{\mu\|\lambda}{}^k = 0 \quad \text{(conserved current)} , \tag{14}$$

which in electromagnetism states charge conservation. In Ref. 1 this was Eq. (14). One can also generalize Eqs. (15) and (16) of Ref. 1, leading to the concept of "total charge."

Parallel-displacement gauge field.—For any Riemannian manifold, the important concept of parallel displacement defines, along any path AB, a *linear* relationship between any vector V_A at A and its parallel vector V_B at B. Thus parallel displacement is defined by an $n\times n$ matrix M_{AB} which gives this linear relationship. M_{AB} is a representation of an element of GL(n). Thus we have the following:

Theorem.—Parallel displacement defines a gauge field with G being GL(n). The index k has n^2 values and we write $k=(\alpha\beta)$. The gauge potential and gauge fields are respectively

$$b_\mu{}^{(\alpha\beta)} = \left\{ \begin{matrix} \alpha \\ \beta\mu \end{matrix} \right\}, \quad f^{(\alpha\beta)}{}_{\mu\nu} = -R^\alpha{}_{\beta\mu\nu} . \tag{15}$$

It is important to recognize that in this definition we have chosen a fixed coordinate system. A coordinate transformation would generate a linear transformation in the vector spaces V_A and V_B. In other words $M_{AB} \to N_A M_{AB} N_B{}^{-1}$. Comparison with (5) shows thus that a coordinate transformation generates a simultaneous gauge transformation of the parallel-displacement gauge potential. In fact, the usual nonlinear term in the transformation of $\left\{ \begin{smallmatrix} \alpha \\ \alpha\gamma \end{smallmatrix} \right\}$ is precisely the nonlinear term needed in the gauge transformation of the gauge noncovariant quantity $b_\mu{}^{(\alpha\beta)}$. In this connection we observe that for GL(n),

$$C^{(\alpha\beta)}_{(\lambda\mu)(\eta\zeta)} = \delta_{\mu\eta}\delta_{\alpha\lambda}\delta_{\beta\zeta} - \delta_{\lambda\zeta}\delta_{\alpha\eta}\delta_{\beta\mu} . \tag{16}$$

Thus by definitions (9) and (11)

$$\begin{aligned} \psi^{(\alpha\beta)}{}_{\|\mu} &= \frac{\partial \psi^{(\alpha\beta)}}{\partial x^\mu} + b_\mu{}^{(\lambda\nu)} C^{(\alpha\beta)}_{(\lambda\nu)(\eta\zeta)} \psi^{(\eta\zeta)} \\ &= \psi^\alpha{}_{\beta;\mu} , \end{aligned} \tag{17}$$

where the semicolon represents the usual Riemannian covariant differentiation with α and β treated as usual contravariant and covariant indices. The rule works also in general. E.g.,

$$f^{(\alpha\beta)}{}_{\mu\nu\|\lambda} = -R^\alpha{}_{\beta\mu\nu,\lambda} . \tag{18}$$

Nontrivial sourceless gauge fields.—Gauge fields for which $f_{\mu\nu}{}^k \neq 0$ and $J_\mu{}^k = 0$ are of physical interest. So far only nonanalytic examples are known.[1]

We now can construct two general types of general types of examples.

(a) Consider the natural Riemannian geometry of a semisimple Lie group. Its parallel-displacement gauge field is sourceless and analytic.

(b) Consider the same Riemannian manifold of a group G as above in (a). Define φ_{AB} as that for an infinitesimal path AB, $\varphi_{AB} = (A^{-1}B)^{1/2}$. This gauge phase factor which is itself an element of G gives a gauge field which is analytic and sourceless.

Pure spaces.—A Riemannian manifold for which the parallel-displacement gauge field is sourceless will be called a pure space. A necessary and sufficient condition for a pure space is

$$R_{\mu\alpha;\beta} = R_{\mu\beta;\alpha} \tag{19}$$

A four-dimensional Einstein space, i.e., one for which $R_{\alpha\beta}=0$, is a pure space.

Gravitational field as a gauge field.—The electromagnetic field and the usual gauge fields are special cases of gauge fields, satisfying (12) and (13). A natural question is whether one should identify these *same equations* for the parallel-displacement gauge field as the equations for the gravitational field. There are advantages in this identification and we shall come back to this topic in a later communication. If one adopts this identification then gravitational equations are third-order differential equations[5] for $g_{\mu\nu}$. A pure gravitational field is then described by a pure space as defined above.

Variational principles.—Equation (13) with $J_\mu{}^k=0$ follows from a variational principle $\delta\int\sqrt{-g}\,d^nx=0$, where

$$L=f_{\mu\nu}{}^k f_{\alpha\beta}{}^j g^{\mu\alpha}g^{\nu\beta}C_{ka}{}^bC_{jb}{}^a. \tag{20}$$

In the variation $g_{\mu\nu}$ is kept fixed and $b_\mu{}^k$ is varied, and $f_{\mu\nu}{}^k$ is given by (3); $C_{ka}{}^b$ are not varied. One could also find a variational principle which is satisfied by a pure space (19). Choose $C_{ka}{}^b$ to be the structure constants for GL(n), given by (16). Write the L of (20) as a functional of $b_\mu{}^{(\alpha\beta)}$ and $g^{\lambda\nu}$:

$$L=L(b_\mu{}^{(\alpha\beta)},g^{\lambda\nu}), \tag{21}$$

which of course also contains derivatives of $b_\mu{}^k$ and $g^{\lambda\nu}$. Now form the variation

$$\delta\int\left[L(b_\mu{}^{(\alpha\beta)},g^{\lambda\nu})-L\left(\left\{{\alpha \atop \beta\mu}\right\},g^{\lambda\nu}\right)\right]\times\sqrt{-g}\,d^nx=0, \tag{22}$$

in which $b_\mu{}^{(\alpha\beta)}$ and $g^{\lambda\nu}$ are independently varied. The resultant equations are satisfied by (15) and (19).

It is a great pleasure to acknowledge the warm hospitality extended to me during my visit to the Institute of Theoretical Physics at Wrocław where this paper was written.

---

[1] C. N. Yang and R. L. Mills, Phys. Rev. 96, 191 (1954).

[2] S. Mandelstam, Ann. Phys. (New York) 19 1, 25 (1962); I. Białynicki-Birula, Bull. Acad. Pol. Sci., Ser. Sci. Math. Astron. Phys. 11, 135 (1963).

[3] We use the summation convention for repeated indices. *Greek indices run from 1 to n. Lower case* Latin indices run from 1 to m. m of course is also the dimension of the adjoint representation of G. Upper case Latin indices run from 1 to M, where M is the dimension of a representation of G.

[4] T. T. Wu and C. N. Yang, in *Properties of Matter under Unusual Conditions*, edited by H. Mark and S. Fernbach (Wiley, New York, 1969), p. 349.

[5] R. Utiyama, Phys. Rev. 101, 1957 (1956), had concluded that Einstein's equations are gauge-field equations. We believe that was an unnatural interpretation of gauge fields.

Observation of Single-Pion Production by a Weak Neutral Current*

S. J. Barish, Y. Cho. M. Derrick, L. G. Hyman, J. Rest, P. Schreiner,
R. Singer, R. P. Smith, and H. Yuta
Argonne National Laboratory, Argonne, Illinois 60439

and

D. Koetke
Concordia Teachers College, River Forest, Illinois 60305

and

V. E. Barnes, D. D. Carmony, and A. F. Garfinkel
Purdue University, Lafayette, Indiana 47907
(Received 28 May 1974)

In exposures of the Argonne National Laboratory 12-ft bubble chamber filled with hydrogen and deuterium to a neutrino beam, we have observed events consisting of (1) a single π^+ meson originating in the liquid, and (2) a proton with an e^+e^- pair pointing to it. Only a small fraction of these events can be ascribed to known reactions such as $np \to nn\pi^+$ and $np \to np\pi^0$. The remaining events, which correspond to a signal of about 4.5 standard deviations, we ascribe to the reactions $\nu p \to \nu n\pi^+$ and $\nu p\pi^0$.

In the conventional current-current theory of the weak interaction, only charge-changing lepton bilinear combinations $(\nu_\mu \mu^-)$, etc., are used and, although the theory is not renormalizable, it accounts in a quantitative way for almost all experimental facts. Direct evidence for neutral-current combinations such as (ν, ν) is difficult to obtain, and it is only recently that experiments searching for the existence of the inclusive reactions $\nu N \to \nu +$anything and $\bar{\nu} N \to \bar{\nu} +$anything have reported positive results.[1] In strangeness-changing decays, no evidence has been seen for neutral currents and very stringent limits have been set. Formulations of weak interaction theory that are renormalizable have been proposed[2] and require the existence of neutral currents or heavy leptons. Thus, the question of the existence and properties of the neutral-current interaction is of paramount importance.

Our experiment measures single-pion production through the reactions[3]

$$\nu_\mu p \to \nu_\mu n\pi^+, \tag{1}$$

$$\nu_\mu p \to \nu_\mu p\pi^0. \tag{2}$$

Three separate exposures of the Argonne National Laboratory 12-ft bubble chamber were used: the first with a hydrogen filling and the other two with deuterium fillings. Each exposure consisted of about 300 000 pictures and had about 4×10^{17} protons incident on the primary production target. An analysis of single-pion production in the charged-current reaction

$$\nu p \to \mu^- p\pi^+ \tag{3}$$

and a brief description of the experimental arrangement have been published.[4]

The signal for Reaction (1) is a single π^+ meson originating in the chamber fiducial volume of 11.1 m^3. Ten events were uniquely identified as π^+ mesons because the single positive track stopped in the chamber and decayed via the chain $\pi^+ \to \mu^+ \to e^+$. Four events were identified because the track scattered giving a unique kinematic fit to $\pi^+ p$ elastic scattering. In addition, four leaving π^+ tracks were uniquely identified on the basis of energy loss. If interpreted as protons, they were overstopped by 5 or more standard deviations, and they are inconsistent with incoming π^-.[5]

The signal for Reaction (2) is a proton track originating in the chamber fiducial volume with a converted γ ray (e^+e^- pair) pointing to the origin of the proton track. We find thirteen events of this topology which we refer to as one-prong $+\gamma$. Because our experiment is done near threshold, 99% of the protons from the $\nu p \to \mu^- p\pi^+$ events have the azimuth and dip of the proton track within 60° of the neutrino beam direction, and we apply this selection to the proton track of the one-prong$+\gamma$ events. In addition, 88% of protons from Reaction (3) have momentum <1 GeV/c, so we apply this cut. Eight one-prong$+\gamma$ events satisfy these criteria.

Since the Reactions (1) and (2) are not constrained, we cannot prove that any individual event originates from these reactions and not from such processes as

$$np \to nn\pi^+, \qquad (4)$$

$$np \to np\pi^0. \qquad (5)$$

We measure the neutron background using events of the reaction[6]

$$np \to pp\pi^-, \qquad (6)$$

which are observed as three-prong events and are identified by a one-constraint kinematic fit. Since the final states $nn\pi^+(\pi^0)$ and $pp\pi^-(\pi^0)$ are charge symmetric, the number of events fitting the $pp\pi^-$ hypothesis is a direct measure of the number of π^+ mesons coming from the $nn\pi^+$ final state.[6]

In order to scale our observed number of $np \to pp\pi^-$ events to measure the background from Reactions (4) and (5) within our selection criteria, a number of correction factors are necessary. These corrections were measured in a separate experiment in which the bubble chamber was exposed to a 0- to 3-GeV/c neutron beam. This exposure well simulates the neutron background we observe in the neutrino exposure.

Figure 1 shows the pion momentum spectrum for (a) the single-π^+ meson sample, (b) the $\mu^- p\pi^+$ events, (c) the $pp\pi^-$ events in the ν film, and (d) the $pp\pi^-$ events observed in the auxiliary neutron experiment. As seen in Fig. 1(b), only 12% of the charged-current events have pion momentum $\geqslant 400$ MeV/c; in addition, our detection efficiency for single π^+ is low above this momentum so we select as a neutral-current signal π^+ mesons with momentum below 400 MeV/c. Furthermore, we find that 90% of the background neutrons which give rise to Reaction (6) enter through the top of the chamber (where the shielding is weakest because of the camera ports), and produce a π^- which also goes downwards. Hence, we choose events with the pion traveling upwards in the chamber. These selections give a neutron-induced background from Reaction (4) of 0.55 ± 0.55 events.

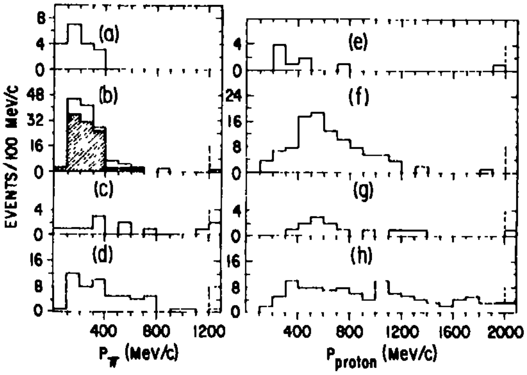

FIG. 1. Pion momentum spectrum for (a) the single-π^+-meson sample, eighteen events; (b) $\nu p \to \mu^- p\pi^+$, 133 events; (c) $np \to pp\pi^-$ in the neutrino film, twelve events; and (d) $np \to pp\pi^-$ in the neutron film, 51 events. The shaded events in (b) represent the $\nu p \to \mu^- p\pi^+$ events after applying our detection efficiency on the single π^+ sample. Proton momentum spectrum for (e) the one-prong $+\gamma$ sample, nine events; (f) $\nu p \to \mu^- p\pi^+$, 102 events; (g) $np \to pp\pi^-$ in the neutrino film, fourteen entries; and (h) $np \to pp\pi^-$ in the neutron film, 102 entries.

In order to measure the background from photoproduced mesons $\gamma p \to n\pi^+$, etc., we use the e^+e^- pairs found in a scan of 55 000 pictures. Almost all of these pairs are close to cosmic-ray tracks as the photon has been produced by bremsstrahlung in the magnet iron above the chamber. By rejecting all events having the vertex within 20 cm of any cosmic ray, we drastically reduce this background.[5] After this selection, the measured photoproduced background to Reaction (1) is 0.33 ± 0.10 events.

For those events where the π^+ leaves the chamber, a possible background is $\bar{\nu}p \to \mu^+ n$. Using our $\bar{\nu}$ beam contamination, we calculate a background of 0.04 ± 0.04 events from this reaction. Finally, $K_L{}^0$-induced background from, for example, $K_L{}^0 \to \Lambda\pi^+$ has been measured and is found to be negligible.

We now discuss the background contributions to the one-prong $+\gamma$ events. Figure 1(e) shows the proton momentum distribution for these after the angle selections discussed previously. Figures 1(f)-1(h) show the proton momentum spectrum from the $\nu p \to \mu^- p\pi^+$ events and the $np \to pp\pi^-$ events from the ν film and the neutron film, respectively. Applying the same selections to the $pp\pi^-$ events as to the one-prong $+\gamma$ events, we are left with five $pp\pi^-$ events. We have measured the empirical ratio of one-prong $+\gamma$ events to $pp\pi^-$ events to be 0.19 ± 0.04 in our neutron experiment, so after some small corrections, the neutron background to Reaction (2) is 0.92 ± 0.40 events.

The photoproduced background $\gamma p \to p\pi^0$ was measured as described above and is only 0.02 ± 0.01 events. The probability of a converted γ

ray accidentally pointing to a one-prong event was determined to be 0.11 ± 0.11 events. The $K_L{}^0$-induced background was again found to be negligible. Finally, for the one-prong $+\gamma$ events, there is a background source consisting of an incoming π^- that undergoes charge exchange with the subsequent conversion of one γ ray from the π^0. We have measured this background by analyzing $\pi^- p \to \pi^- p$ scatters of all π^- that enter the chamber and whose tracks could not be distinguished from a leaving proton. By scaling from the known elastic and charge-exchange cross sections, this background was measured to be 0.52 ± 0.23 events.

Table I gives a summary of the events found. With the selections mentioned, we observe with no other corrections seven single-π^+ events and seven one-prong $+\gamma$ events with a total measured background of 2.49 ± 0.73 events. Folding the Poisson-distributed fluctuations of the background with the uncertainty of 0.73 in the measured background level, the probability of seeing fourteen or more events when 2.49 are expected is 1.2×10^{-5} which corresponds to a 4.3 standard deviation effect. We conclude then that neutral currents exist and are responsible for the exclusive reactions (1) and (2).

In order to compare to the measured cross section for $\nu p \to \mu^- p \pi^+$, we must treat the π^+ and proton tracks in the $\mu^- p \pi^+$ events in the same way as the neutral-current candidates and know the overall detection efficiencies for the $\nu n \pi^+$ and $\nu p \pi^0$ final states. These are 75% and 6%, respectively. The number of $\mu^- p \pi^+$ events on the sample of film is about 100. Applying the corrections, we obtain the ratios[7]

$$R_0 = \frac{\sigma(\nu p \to \nu p \pi^0)}{\sigma(\nu p \to \mu^- p \pi^+)} = 0.51 \pm 0.25, \quad p_p < 1\ \mathrm{GeV}/c,$$

and

$$R_+ = \frac{\sigma(\nu p \to \nu n \pi^+)}{\sigma(\nu p \to \mu^- p \pi^+)} = 0.17 \pm 0.08,$$

$$p_{\pi^+} < 400\ \mathrm{MeV}/c,$$

with $R_0 + R_+ = 0.68 \pm 0.28$. The value of $R_0 + R_+$ is somewhat larger than, but not inconsistent with, the value predicted in the Salam-Weinberg theory,[8] which gives $0.15 < R_0 + R_+ < 0.44$ for our spectrum. Our measured ratio

$$\frac{\nu p \to \nu p \pi^0}{\nu p \to \nu n \pi^+} = 3.1 \pm 2.1$$

suggests isospin-$\frac{3}{2}$ dominance of the final state, which does not support the suggestion of Sakurai[9] that the neutral current may be an isoscalar, but the errors on this ratio are too large to rule this out.

Finally, we note that all other experiments on neutral currents have problems of muon identification and/or neutron background that must be estimated using a Monte Carlo calculation. The events of the present experiment consist of a single positive track and so the absence of a μ^- particle is evident. In addition, we make direct measurements of all background contributions.

We wish to thank the staff of the zero-gradient synchrotron and the bubble chamber operators for fine cooperation in obtaining the pictures. Our scanners, under Hope Chafee, have responded well to a difficult and tedious job. J. Campbell, R. Engelmann, A. Mann, U. Mehtani, and B. Musgrave gave help in the earlier stages of the experiment.

TABLE I. Event and background summary. For the H_2 exposure, all three π^+ modes have been analyzed; for the D_2 exposure, somewhat different fractions of the film have been processed for the three modes.

Events	H_2	D_2	Sum	Cosmic cut	π^+ dip cut
π^+ Events					
Stop	2	8	10	7	6
Scatter	3	1	4	3	1
Leave	3	1	4	3	0
One-prong $+\gamma$ events	3	5	8	7	7
Total			26	20	14

Background	π^+	One-prong $+\gamma$
Neutron	0.55 ± 0.55	0.92 ± 0.40
γ induced	0.33 ± 0.10	0.02 ± 0.01
$\nu p \to \mu^+ n$	0.04 ± 0.04	...
$\pi^- p \to \pi^0 n$	...	0.52 ± 0.23
Accidental γ pointing	...	0.11 ± 0.11
Totals	0.92 ± 0.56	1.57 ± 0.47
Total background	2.49 ± 0.73	

---

*Work supported by the U. S. Atomic Energy Commission.

[1] F. Hasert *et al.*, Phys. Lett. 46B, 138 (1973); A. Benvenuti *et al.*, Phys. Rev. Lett. 32, 800 (1974); B. Aubert *et al.*, Phys. Rev. Lett. 32, 1454 (1974).

[2] A. Salam and J. C. Ward, Phys. Lett. 13, 168 (1964); S. Weinberg, Phys. Rev. Lett. 19, 1264 (1967).

[3] We are really measuring the sum of the cross sections $\nu p\rightarrow\nu n\pi^+ l\pi^0$ and $\nu p\rightarrow\nu p\pi^0 l\pi^0$, $l\geq 0$, but since our neutrino spectrum peaks at 500 MeV/c and is down by an order of magnitude by 1500 MeV/c, we expect the contribution of the final states with additional π^0's to be very small.

[4] J. Campbell *et al.*, Phys. Rev. Lett. 30, 335 (1973).

[5] More details of the experiment are given by S. J. Barish, Argonne National Laboratory Report No. ANL/HEP 7418 (unpublished).

[6] Y. Cho *et al.*, in Proceedings of the Sixteenth International Conference on High Energy Physics, The University of Chicago and National Accelerator Laboratory, 1972 (unpublished), paper 473.

[7] In doing this we are implicitly assuming that the characteristics of our neutral- and charged-current events are the same. This is true on the Salam-Weinberg model but may not be true in general. For the charged-current events, we measure the ratio $N(\nu p\rightarrow\mu^- p\pi^+\pi^0)/N(\nu p\rightarrow\mu^- p\pi^+)=0.1\pm 0.05$ and, therefore, we reduce the observed $\nu N\pi/\mu^- p\pi^+$ ratios by 10%. In addition, for the one-prong $+\gamma$ events, a small contribution from the reaction $\nu d\rightarrow\nu n\pi^0(p_s)$ has been subtracted.

[8] S. Adler, private communication.

[9] J. Sakurai, Phys. Rev. D 9, 250 (1974).

Hierarchy of Interactions in Unified Gauge Theories*

H. Georgi,† H. R. Quinn, and S. Weinberg
Lyman Laboratory of Physics, Harvard University, Cambridge, Massachusetts 02138

(Received 15 May 1974)

We present a general formalism for calculating the renormalization effects which make strong interactions strong in simple gauge theories of strong, electromagnetic, and weak interactions. In an SU(5) model the superheavy gauge bosons arising in the spontaneous breakdown to observed interactions have mass perhaps as large as 10^{17} GeV, almost the Planck mass. Mixing-angle predictions are substantially modified.

The scaling observed in deep inelastic electron scattering suggests that what are usually called the strong interactions are not so strong at high energies. Asymptotically free gauge theories of the strong interactions[1] provide a possible explanation: The gluon coupling constant $g(\mu)$ (defined as the value of a three-gluon or gluon-fermion-fermion vertex with momenta characterized by a mass μ) is small when μ is several GeV or larger, but becomes large when μ is small, through the piling up of the logarithms encountered in perturbation theory. In one recent calculation[2] a fit was found for a gauge coupling [in a color SU(3) model][3] with $g^2(\mu)/4\pi\simeq 0.1$ when $\mu\simeq 2$ GeV.

If $g(\mu)$ is small when μ is large, then perhaps the strong gauge coupling at some large fundamental mass is of the same order as the couplings in gauge theories of the weak and electromagnetic interactions.[4] Georgi and Glashow[5] have recently gone one step farther, and proposed a model based on the *simple* gauge group SU(5), in which there naturally appears only one free gauge coupling. In their model, SU(5) suffers a spontaneous breakdown to the gauge subgroups SU(3) and SU(2)⊗U(1), which are associated respectively with the strong[3] and the weak and electromagnetic[6] interactions. In order to suppress unobserved interactions, Georgi and Glashow made the necessary assumption[7] that some vector bosons are superheavy.

We find the notion of a simple gauge group uniting strong, weak, and electromagnetic interactions extraordinarily attractive. However, as emphasized by Georgi and Glashow, the success of any such scheme hinges on an understanding of the effects which produce the obvious disparity in strength between the strong and the weak and electromagnetic interactions at ordinary energies. We therefore wish to present in this paper a general formalism for the calculation of such effects. This will lead us to an estimate of the mass of the superheavy gauge bosons. Where a specific model of the gauge groups of the observed interactions is needed as an example, we shall assume that the strong and the weak and electromagnetic interactions are described by color SU(3)[3] and by SU(2)⊗U(1), respectively, and where a specific example of a unifying simple gauge group is needed, we shall use SU(5).

If we neglect all renormalization effects, the embedding of the gauge groups G_i of the observed interactions in a larger simple group G imposes a relation among their coupling constants. We normalize the generators T_α of G so that in any representation D of G we have

$$\mathrm{Tr}(T_\alpha T_\beta) = N_D \delta_{\alpha\beta}, \tag{1}$$

where N_D may depend on the representation but not on α and β. We use the same normalization conventions for the gauge groups of the observed interactions. Then invariance under G implies that the coupling constants g_G, g_3, g_2, and g_1 associated with the group G and the subgroups SU(3), SU(2), and U(1), respectively, are equal. The usual SU(2) and U(1) coupling constants[6] may be identified as

$$g = g_2, \quad g' = g_1/C, \tag{2}$$

where C is a constant entering the relation between the charge Q and the SU(2) and U(1) generators $\vec{T}$ and T_0, normalized according to Eq. (1):

$$Q = T_3 - CT_0. \tag{3}$$

The weak mixing angle[6] is then given by

$$\sin^2\theta = e^2/g^2 = g'^2/(g^2 + g'^2) = (1 + C^2)^{-1}. \tag{4}$$

In any representation of G, reducible or irreducible,

$$\mathrm{Tr}(Q^2) = (1 + C^2)\mathrm{Tr}(T_3^2). \tag{5}$$

If we take our representation to consist of the left-handed states of three quartets of colored quarks, three antiquark quartets, and ν_e, ν_μ, e^-, e^+, μ^-, μ^+, then there are eight SU(2) doublets, and so $\mathrm{Tr}(T_3^2) = 4$, while $\mathrm{Tr}(Q^2) = \frac{32}{3}$, so that

$$C^2 = \tfrac{5}{3}, \quad \sin^2\theta = \tfrac{3}{8}. \tag{6}$$

This is the case for the SU(5) model.[5] We shall leave C arbitrary in what follows, and will find that the choice of the simple unifying group G enters the calculation only through the single parameter C.

Now let us see how to take renormalization effects into account. The gauge couplings are functions of the momentum scale μ, and the above relations among gauge couplings really only apply when μ is much larger than the superheavy boson masses, where the breaking of G may be neglected. However, the observed values of the gauge couplings refer to much smaller values of μ, of the order of the W and Z masses, or even smaller. The problem is to bridge the gap between superlarge values of μ, where G imposes relations among the gauge couplings, and ordinary values of μ, where the gauge couplings are observed.

In order to accomplish this, we make use of the theorem[8] that all matrix elements involving only "ordinary" external particles with momenta and masses much less than all superheavy masses may be calculated in an effective renormalizable field theory, which is just the original field theory with all superheavy particles omitted, but with coupling constants that may depend on the superheavy masses. All other effects of the superheavy particles are suppressed by factors of an ordinary mass divided by a superheavy mass.

When μ is large compared with all ordinary masses but small compared with all superheavy masses, the μ dependence of the couplings is governed by a renormalization-group equation,[9]

$$\mu \frac{d}{d\mu} g_i(\mu) = \beta_i(g_i(\mu)), \tag{7}$$

with β_i calculated in the effective field theory based on the "observed" gauge group G_0. If all $g(\mu)$ are small, then β_i depends only on g_i, with[10]

$$\beta_i(g(\mu)) \simeq b_i g_i^3(\mu) \text{ for } |g_i| \ll 1, \tag{8}$$

so that

$$g_i^{-2}(\mu) \simeq \text{const} - 2b_i \ln\mu. \tag{9}$$

The integration constants are determined by the underlying simple group G. Specifically, if we suppose that all superheavy gauge bosons have masses of the order of some typical superheavy mass M, and if we take μ to be of the order of but somewhat smaller than M, then the $g_i(\mu)$ may be calculated perturbatively in the simple gauge theory based on G, and as long as $g_i(M)$ is sufficiently small, each gauge coupling will be essentially given by its group-theoretic value g_G neglecting all renormalizations. Thus Eq. (9) gives

$$g_i^{-2}(\mu) = g_G^{-2}(M) + 2b_i \ln(M/\mu) \tag{10}$$

for $\mu \ll M$.

The gauge coupling constants g_{i_0} observed in present experiments are essentially given by the values of the $g_i(\mu)$ when μ is some "ordinary" mass m, of the order of 10 GeV. Since all these couplings are small and therefore slowly varying in the range of interest, our result is not particularly sensitive to the value of the "ordinary" mass at which we choose to study the couplings.

Let us now specifically assume that the "observed" gauge group is SU(3)⊗SU(2)⊗U(1), but for the moment leave open the choice of the group G. Choosing convenient linear combinations of

(10), we have

$$\frac{C^2}{g_{1o}^2}+\frac{1}{g_{2o}^2}-\frac{(1+C^2)}{g_{3o}^2}=\frac{1}{e^2}-\frac{(1+C^2)}{g_{3o}^2}$$
$$=2\ln\left(\frac{M}{m}\right)[b_1C^2+b_2-b_3(1+C^2)], \qquad (11)$$

$$C^2(g_{1o}^{-2}-g_{2o}^{-2})=e^{-2}[1-(1+C^2)\sin^2\theta]$$
$$=2C^2(b_1-b_2)\ln(M/m). \qquad (12)$$

To calculate the b's, we note that any multiplet of particles forming a representation of G does not contribute at all to the b's if *all* particles are superheavy, while it contributes equally to all b's if *no* particles in the multiplet are superheavy, and therefore in either case has no effect in Eqs. (11) and (12). We shall assume that the only multiplet which contains *both* ordinary and superheavy particles is the gauge multiplet itself, in which case[1]

$$b_2=-\tfrac{22}{3}(4\pi)^{-2}+b_1, \quad b_3=-11(4\pi)^{-2}+b_1; \qquad (13)$$

so (11) and (12) give

$$\ln\left(\frac{M}{m}\right)=\frac{3(4\pi)^2}{22(1+3C^2)}\left(\frac{1}{e^2}-\frac{(1+C^2)}{g_{3o}^2}\right), \qquad (14)$$

$$\sin^2\theta=(1+3C^2)^{-1}(1+2C^2e^2/g_{3o}^2). \qquad (15)$$

For $C^2=\frac{5}{3}$ [the SU(5) value], $m=10$ GeV, and reasonable values of $g_{3o}^2/4\pi$, we obtain the results displayed in the following table:

$g_{3o}^2/4\pi$	M (GeV)	$\sin^2\theta$
0.5	2×10^{17}	0.175
0.2	2×10^{16}	0.187
0.1	5×10^{14}	0.207
0.05	2×10^{11}	0.248

It is intriguing that we are led to contemplate elementary particle masses as high as 2×10^{17} GeV, of about the same order of magnitude as the Planck mass, $G^{-1/2}=1.2206\times10^{19}$ GeV. Perhaps gravitation has something to do with the superstrong spontaneous symmetry breaking, or perhaps the spontaneous breakdown of the simple gauge group has something to do with setting the scale of the gravitational interaction.

Equation (15) predicts lower values for $\sin\theta$ than does Eq. (4). While the available data favor the higher value, they are rather preliminary, and the strong constraints on $\sin^2\theta$ follow only if the *Z mass is assumed to satisfy the relation* $M_W^2=M_Z^2\cos^2\theta_W$, which depends on the Higgs structure of the model.[11] If this relation is abandoned, $\sin^2\theta_W$ must be inferred from the ratio of the ratio of neutral- to charged-current events seen in neutrino scattering to that seen in antineutrino scattering.[11]

In the SU(5) example, it is not necessarily true *that all effects of order m/M are negligible*, because some of the superheavy vector bosons mediate proton decay into lepton plus pions. Since the proton is otherwise stable, such very small effects may be observable. Calculation of the proton lifetime involves details of the strong interactions at small momenta, but we can give an order-of-magnitude estimate on dimensional grounds. The lifetime must be proportional to M^4 and so it must approximately equal M^4/m_p^5. Taking $M=5\times10^{15}$ GeV, for example, gives a proton lifetime of about 6×10^{31} yr. The present experimental lower limit is 10^{30} yr.[12] The observation of proton decay with a lifetime of this order of magnitude would be a startling confirmation of the ideas discussed here.

Before concluding, we emphasize again the approximation which went into the derivation of Eqs. (14) and (15). We have idealized the two transition regions: the region in momentum scale around M where the three coupling constants are merging into one, and the region from m into the timelike domain where we actually measure e^2. The corrections to (14) and (15) due to changes of the coupling constants in these regions can be calculated using perturbation theory in the relevant coupling constants. The corrections for the second region are electromagnetic and therefore small (g_{3o} can in principle be measured directly in the spacelike region through the observation of logarithmic violations of scaling in electroproduction). The corrections from the first region will be small if $g_G(M)$ is small. To calculate $g_G(M)$ we need to know the fermion and scalar-meson content of the theory. For the SU(5) model with $M=5\times10^{15}$ GeV (see the table), $g_G^2(M)/4\pi=(48\pm1)^{-1}$.

We have also assumed that the lowest-order form for β_i, Eq. (8), is valid down to $\mu=m$. Next-order corrections to β have been calculated by Belavin and Migdal.[13] We use their results and find the ratio of the correction to the lowest-order value in the SU(5) theory to be about $0.6g^2/4\pi$. Such corrections are obviously only relevant for $g_3(\mu)$, and even for $g_{3o}^2/4\pi=0.5$, the largest value used in the table, the correction is only 30%.

Finally we want to emphasize what seems to us to be the most disturbing feature of the class of models discussed here, that is, the existence of two stages of spontaneous symmetry breaking characterized by radically different mass scales. In the context of the conventional Higgs mechanism, we can find no natural explanation of the enormous ratio of superheavy mass to ordinary mass. We have nothing quantitative to say about this mystery, but the following speculation seems attractive to us. Suppose that only superstrong breaking takes place via the Higgs mechanism. There is only one mass scale in the theory and it is superheavy. All of the scalar mesons are either superheavy or Goldstone bosons (note that this obviates the difficulties associated with superlarge trilinear couplings among ordinary-mass scalars). Well below the superheavy mass scale the theory is an effective $SU(3)\otimes SU(2)\otimes U(1)$ theory containing only gauge fields and fermions. The next stage of symmetry breaking is dynamical and hence nonperturbative. The mass scale associated with this stage is the mass at which $g_3(\mu)$ gets large enough that nonperturbative effects become important.

We are grateful for discussions with T. Appelquist, S. Coleman, S. L. Glashow, and H. D. Politzer.

---

*Work supported in part by the National Science Foundation under Grant No. GP40397X.

†Junior Fellow, Harvard University Society of Fellows.

[1] H. D. Politzer, Phys. Rev. Lett. 30, 1346 (1973); D. J. Gross and F. Wilczek, Phys. Rev. Lett. 30, 1343 (1973).

[2] H. D. Politzer, to be published. Of course, given the available data, any such estimate is necessarily very crude.

[3] W. Bardeen, H. Fritsch, and M. Gell-Mann, in *Scale and Conformal Invariance in Hadron Physics*, edited by R. Gatto (Wiley, New York, 1973), p. 139. Also see R. H. Dalitz, in *High Energy Physics*, edited by C. De-Witt and M. Jacob (Gordon and Breach, New York, 1966), p. 287.

[4] S. Weinberg, J. Phys. (Paris), Colloq. 34, C1-45 (1973), and to be published.

[5] H. Georgi and S. L. Glashow, Phys. Rev. Lett. 32, 438 (1974).

[6] S. Weinberg, Phys. Rev. Lett. 19, 1264 (1967); A. Salam, in *Elementary Particle Physics*, edited by N. Svartholm (Almquist and Wiksels, Stockholm, 1968), p. 367.

[7] S. Weinberg, Phys. Rev. D 5, 1962 (1972).

[8] T. Appelquist and J. Carrazone, to be published. A different proof of the same result for graphs including only a single superheavy line is given by S. Weinberg, Phys. Rev. D 8, 605, 4482 (1973). This theorem and hence our entire discussion could be invalidated if there were superlarge trilinear couplings among scalar fields. The survival of any light scalars already requires that certain scalar self-couplings in the symmetric theory were made extremely small. It appears that the problem of large trilinear couplings can always be avoided by some device. We will discuss later in this paper a possible point of view which avoids this unattractive situation altogether.

[9] M. Gell-Mann and F. E. Low, Phys. Rev. 95, 1300 (1954); C. G. Callan, Phys. Rev. D 2, 1541 (1970); K. Symanzik, Commun. Math. Phys. 18, 227 (1970).

[10] It was H. D. Politzer who pointed out to us that perturbation theory could be used down to the energy where the strong interactions begin to be much stronger than the weak and electromagnetic interactions, so that it is not necessary here to worry about the region where the strong interactions are really strong.

[11] A. De Rújula, H. Georgi, S. L. Glashow, and H. Quinn, to be published.

[12] F. Reines and M. F. Crouch, Phys. Rev. Lett. 32, 493 (1974).

[13] A. A. Belavin and A. A. Migdal, to be published. We learned recently that the same calculation has been performed by W. E. Caswell [Phys. Rev. Lett. 33, 244 (1974)]. His result differs slightly from that given by Belavin and Migdal, but the difference is insignificant as far as our estimate is concerned.

Gaussian Distributions in Electroproduction and Inclusive e^+e^- Annihilation*

S. J. Orfanidis and V. Rittenberg†
Rockefeller University, New York, New York 10021

(Received 28 May 1974)

In a large class of theories, including asymptotically free theories, and theories with an eigenvalue for the coupling constant, it is shown that under an important uniformity assumption, the electroproduction and inclusive annihilation structure functions should, for large Q^2, be Gaussian in the variable $y = \ln\omega$. The average and width of the distribution are increasing functions of Q^2. This result is compared with preliminary data from SPEAR on the one-particle inclusive distributions.

Much theoretical activity has been devoted to the study of the moments of the electroproduction and inclusive e^+e^- annihilation structure functions, as a means of gaining insight into the properties of the structure functions themselves. The moments lend themselves particularly well to theoretical treatment because renormalization-group techniques in conjuction with light-cone expansions can be applied directly to them, and their asymptotic behavior for large Q^2 can be derived. However, the moments are not very useful from the experimental point of view, and one would prefer to make direct theoretical statements about the behavior of the structure functions.

The purpose of this note is to show that in a large class of models and independently of the details of any particular model, the structure functions in electroproduction and the one-particle inclusive distribution in e^+e^- annihilation should become Gaussian functions of the variable $y = \ln\omega$ when Q^2 becomes large, and to compare this prediction with recent results from SPEAR.

We begin by considering the moments of any positive-definite structure function. For definiteness, we shall work with the structure function $F_2(\omega, Q^2)$ of the proton defined to be equal to νW_2 in electroproduction and $\omega^{-2}\nu\overline{W}_2$ in annihilation and discuss later the changes that occur in considering different types of particles. The moments of F_2 are defined (for $n = 0, 1, 2, \ldots$) by

$$\begin{aligned}\mu_n(Q^2) &= \int_1^\infty d\omega\, \omega^{-n-2} F_2(\omega, Q^2)\\ &= \int_0^\infty dy\, e^{-(n+1)y} F_2(y, Q^2), \quad y = \ln\omega, \qquad (1)\end{aligned}$$

where ω is defined so that in electroproduction $\omega = 2p\cdot q/Q^2$ and in annihilation $\omega = Q^2/2p\cdot q$, where q, p are the four momenta of the photon and proton and $Q = (|q^2|)^{1/2}$.

The class of models that we are considering is such that the asymptotic behavior of the moments $\mu_n(Q^2)$ for large Q^2 and for each fixed n is of the form

$$\mu_n(Q^2) = c_n[\nu(Q^2)]^{-a_n}, \qquad (2)$$

where the c_n's and a_n's are constants and $\nu(Q^2)$ is an increasing function of Q^2 such that $\nu(Q^2) \to \infty$ as $Q^2 \to \infty$. We must point out that in most of the models that we are going to consider Eq. (2), being an asymptotic expression, is not exact, but there are correction terms in the right-hand side, which, for each fixed n, can be neglected as $Q^2 \to \infty$. For our considerations we must make an important assumption of uniformity; namely, that these correction terms can be neglected for each fixed and large value of Q^2 and all n's. Without this uniformity assumption the asymptotic expressions in Eq. (2) lose their usefulness in determining properties of $F_2(\omega, Q^2)$.

The class of models that have moments as in Eq. (2) includes in the electroproduction case asymptotically free theories[1] and theories with an eigenvalue[2] $\beta(g_\infty) = 0$ $(g_\infty \neq 0)$. In the former case $\nu(Q^2) = b\ln(Q^2/m^2)$, where b is a constant and m is an undetermined mass scale, and in the latter case $\nu = Q^2/m^2$. In both cases the c_n's are undetermined and the a_n's are related to the anomalous dimensions of the operators appearing in the Wilson expansion of two currents. Typical examples of the form of a_n are

$$a_n = \text{const}\left(1 - \frac{2}{(n+1)(n+2)} + 4\sum_{j=2}^{n+1}\frac{1}{j}\right)$$

for $g_\infty = 0$ and

$$a_n = \text{const}\left(1 - \frac{2}{(n+1)(n+2)}\right)$$

for $g_\infty \neq 0$. In e^+e^- annihilation Eq. (2) can be shown in φ^4 theory[3] with a fixed point, theories based on conformal invariant bootstrap schemes,[4] and branching-processes models[5] (the latter providing very transparent interpretations for the coefficients c_n and a_n[6]). In all these models $\nu(Q^2)$

$=Q^2/m^2$. In branching-process models the uniformity assumption is trivially satisfied since Eq. (2) is an exact expression.

In this note we are interested in inverting Eq. (2) to obtain $F_2(\omega, Q^2)$ in some appropriate region of ω. As is suggested in Eq. (1) the special limits $n\to\infty$ and $n\to-1$ correspond, for fixed Q^2, to the behavior of $F_2(\omega, Q^2)$ as $y\to 0$ and $y\to\infty$, respectively. The inverse problem has already been dealt with in the context of asymptotically free theories using the same assumption of uniformity.[7] Here, we are interested in yet a third limit which corresponds to considering the behavior of F_2 as both y and Q^2 increase, but their rates of increase are not independent of each other, both increasing together in a specified way.

We now formulate our result. Since it is based on the central limit theorem of probability theory, we rewrite Eq. (2) in a form that suggests the application of this theorem. To this end we define

$$k(Q^2)=\ln\nu(Q^2). \tag{3}$$

It is convenient to normalize our moments μ_n to 1, when $n=0$ (normalization at some other point $n=n_0\geq 0$ is a translation in n and would represent no essential difference in our results). We define

$$\hat{\mu}_n(Q^2)=\frac{\mu_n(Q^2)}{\mu_0(Q^2)};\quad Z_c(n)=\frac{c_n}{c_0};$$
$$Z(n)=\exp(-a_n+a_0); \tag{4}$$

then $\hat{\mu}_0(Q^2)=Z_c(0)=Z(0)=1$ and Eq. (2) becomes

$$\hat{\mu}_n(Q^2)=Z_c(n)[Z(n)]^{k(Q^2)}. \tag{5}$$

In electroproduction the 0th moment $\mu_0(Q^2)$ corresponds to the Callan-Gross integral,[8] and a_0 to the anomalous dimension of the energy-momentum tensor and, as usually argued, we set $a_0=0$. In annihilation, on the other hand, $\mu_0(Q^2)$ is related to the average multiplicity $\bar{n}(Q^2)$ of the type of particle considered by $\mu_0(Q^2)=Q^2\sigma_{\text{tot}}(Q^2)\times\bar{n}(Q^2)$, where $\sigma_{\text{tot}}(Q^2)$ is the total annihilation cross section. We now make the assumption that both the $Z_c(n)$'s and $Z(n)$'s are themselves the moments of some positive functions and hence that they can be represented as

$$Z_c(n)=\int_0^\infty dy\, e^{-ny}H_c(y);$$
$$Z(n)=\int_0^\infty dy\, e^{-ny}H(y), \tag{6}$$

where the normalization conditions $Z_c(0)=Z(0)=1$ mean that $H_c(y)$ and $H(y)$ can be considered as probability densities. That $Z_c(n)$ and $Z(n)$ are representable as in Eq. (6) can be justified as follows: For such a representation to be possible it is necessary and sufficient that $Z_c(n)$'s and $Z(n)$'s satisfy certain positivity conditions,[9] namely

$$\sum_{l=0}^{k}(-1)^{k-l}\binom{k}{l}Z(n+k-l)\geq 0$$

for all $k, n=0, 1, 2, \ldots$. It can be shown that all the models considered so far for a_n satisfy these conditions for the $Z(n)$'s. The $Z_c(n)$ being undetermined do not necessarily satisfy the positivity constraints but this is not essential since if they do not, we may eliminate them from Eq. (5) at two energies and set $\hat{\mu}_n(Q^2)=\hat{\mu}_n(Q'^2)[Z(n)]^{k-k'}$, where $k'=\ln\nu(Q'^2)$, and note that this expression has the same structure as (5) with the replacement $k\to k-k'$ and $Z_c(n)\to\hat{\mu}_n(Q'^2)$. The new $Z_c(n)$'s now satisfy these conditions. Now, from Eq. (5), we obtain that $F_2(y, Q^2)$ is expressible as a multiple convolution product of probability densities: Approximating $k(Q^2)$ by an integer, *for large* Q^2, we have

$$h(y, Q^2)=\int dy_1\cdots dy_k H_c\Big(y-\sum_{i=1}^{k}y_i\Big)$$
$$\times H(y_1)\cdots H(y_k), \tag{7}$$

where we have defined

$$h(y, Q^2)=\frac{1}{\mu_0(Q^2)}\frac{1}{\omega}F_2(\omega, Q^2),\quad y=\ln\omega. \tag{8}$$

The central limit theorem[10] can now be immediately applied to Eq. (7) to give our main result that $h(y, Q^2)$ tends to a Gaussian[11]:

$$h(y, Q^2)\underset{Q^2\to\infty}{\sim}\frac{1}{\sqrt{2\pi}\sigma}\exp\left(-\frac{(y-\langle y\rangle)^2}{2\sigma^2}\right), \tag{9}$$

where

$$\langle y\rangle=\bar{y}_c+\bar{y}k(Q^2),\quad \sigma^2=\bar{\sigma}_c^{\,2}+\bar{\sigma}^2k(Q^2), \tag{10}$$

with

$$\bar{y}_c=\int_0^\infty dy\, yH_c(y),\quad \bar{\sigma}_c^{\,2}=\int_0^\infty dy\,(y-\bar{y}_c)^2H_c(y); \tag{11}$$

and similar definitions for $\bar{y}$ and $\bar{\sigma}^2$ in terms of $H(y)$.

In terms of the experimental quantities we now have for electroproduction on protons and neutrons

$$F_2^{(p)}(\omega, Q^2)=\mu_0^{(p)}\omega h^{(p)}(y, Q^2),$$
$$F_2^{(n)}(\omega, Q^2)=\mu_0^{(n)}\omega h^{(n)}(y, Q^2), \tag{12}$$

where $\mu_0^{(p)}$ and $\mu_0^{(n)}$ are the values of the corresponding Callan-Gross integrals and $h^{(p)}$ and $h^{(n)}$ are Gaussians as in Eq. (9) with different parameters $\bar{y}_c$ and $\bar{\sigma}_c^2$ but with the same $\bar{y}$ and $\bar{\sigma}$. For large $k(Q^2)$, Eq. (10) implies that the proton and neutron structure functions become proportional to each other. For the difference $F_2^{(p)}-F_2^{(n)}$, the moment μ_{-1} [$n=-1$ in Eq. (1)] is finite.[7] If the positivity conditions derived from the corresponding c_n [see Eq. (2)] are satisfied, we have

$$F_2^{(p)}-F_2^{(n)}=\mu_{-1}^{(p-n)}h^{(p-n)}(y,Q^2), \tag{13}$$

where $h^{(p-n)}$ is again a Gaussian.

For the inclusive e^+e^- annihilation cross section we have

$$\frac{1}{\bar{n}(Q^2)}\frac{1}{\sigma_{\text{tot}}}\frac{d\sigma}{dy}=h(y,Q^2). \tag{14}$$

We assumed for simplicity that $\sigma_T=\sigma_L$ in this case. The parameters of the Gaussians in annihilation and electroproduction need not be the same. Equations (12)-(14) state that for any sufficiently large value of Q^2 and as long as y is large enough to be centered around $\langle y\rangle$ the Gaussian approximation is a good one. Furthermore, this region of y is the most important one since $h(y,Q^2)$ peaks there. Experimental verification of such Gaussian behavior could, in principle, distinguish between asymptotically free and $g_\infty\neq 0$ theories by determining how the average and width change with Q^2 ($k\sim\ln\ln Q^2$ and $k\sim\ln Q^2$ in the two cases).

We were not able to check the predictions in Eqs. (12) and (13) in the electroproduction case because there are no experimental data for large ω at large fixed Q^2 but such an experimental check will be possible when the National Accelerator Laboratory data become available.

In inclusive one-pion e^+e^- annihilation, we can compare our prediction with recent data from SPEAR.[12] The function $h(y,Q^2)$ is related to the inclusive spectrum by Eq. (14). We took as a good representation of the data an inclusive spectrum given in Ref. 12,

$$\frac{1}{\sigma_{\text{tot}}}E\frac{d\sigma}{d^3P}=\text{const}\,e^{-5.5E}$$

(E is the c.m. energy of the pion in GeV), and plotted the corresponding function $h(y,Q^2)$ at two energies $Q=3$ and 5 GeV. The results are shown in Fig. 1 where the 3-GeV curve is compared with a Gaussian. The (continuous line) curve to the right represents the 5-GeV data. The shift between the 3- and 5-GeV curves suggests an increase of the average of the Gaussian with Q, in the way suggested by Eq. (10). We consider our predictions in qualitative agreement with experiment, but a more quantitative comparison must await the appearance of detailed results from SPEAR.

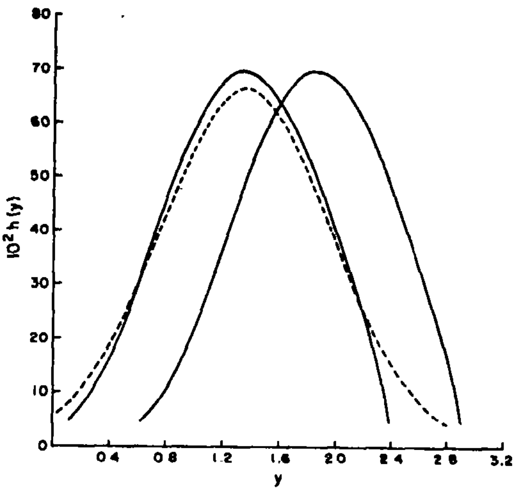

FIG. 1. A Gaussian curve (dashed line) is superimposed on the 3-GeV data (continuous line) of the one-pion inclusive e^+e^- annihilation from Ref. 12. The (continuous-line) curve to the right represents the 5-GeV data.

In view of the above considerations, therefore, we would like to stress the importance of presenting the data at fixed Q^2 in terms of the variable y, both in e^+e^- annihilation and in electroproduction.

It is a pleasure to thank our colleagues at the Rockefeller University for useful discussions.

---

*Work supported in part by the U. S. Atomic Energy Commission under Contract No. AT(11-1)-2232.

†On leave from the Tel-Aviv University, Ramat-Aviv, Israel.

[1] H. Georgi and H. D. Politzer, Phys. Rev. D 9, 416 (1974); D. J. Gross and F. Wilczek, Phys. Rev. D 9, 980 (1974).

[2] N. Christ, B. Hasslacher, and A. H. Mueller, Phys. Rev. D 6, 3543 (1972), and earlier references therein; G. Parisi, Phys. Lett. 43B, 207 (1973).

[3] A. H. Mueller, Phys. Rev. D 9, 963 (1974).

[4] A. M. Polyakov, Zh. Eksp. Teor. Fiz. 59, 542 (1970), and 60, 1572 (1971) [Sov. Phys. JETP 32, 296 (1971), 33, 850 (1971)].

[5] S. J. Orfanidis and V. Rittenberg, Rockefeller Uni-

versity Report No. COO-2232B-54 (unpublished).

[6] In this model $a_n = -a \ln[\mu Z(n)]$, where a and μ are constants; $Z(n)$ is the Laplace transform of a probability distribution.

[7] D. J. Gross and S. B. Treiman, Princeton University Report No. COO-3072-25 (to be published). A. De Rújula, S. L. Glashow, H. D. Politzer, S. B. Treiman, F. Wilczek, and A. Zee, to be published.

[8] C. G. Callan, Jr., and D. J. Gross, Phys. Rev. Lett. 21, 311 (1968).

[9] D. Widder, *The Laplace Transform* (Princeton Univ. Press, Princeton, N. J., 1946).

[10] W. Feller, *An Introduction to Probability Theory and Its Applications* (Wiley, New York, 1966), Vol. II.

[11] For the derivation of this result it is not necessary to require the above positivity conditions even though they are valid in our class of models. It is sufficient to require only that a_n, continued to real values of n, satisfies the condition $\partial^2 a_n / \partial n^2 |_{n=0} < 0$.

[12] B. Richter, (invited talk) in Proceedings of the Conference on Lepton-Induced Reactions, Irvine, California, 1973 (to be published).

PHYSICAL REVIEW
LETTERS

VOLUME 33 19 AUGUST 1974 NUMBER 8

$(e, 2e)$ Reaction as a Probe for Details of the Helium Wave Function

I. E. McCarthy, A. Ugbabe, E. Weigold, and P. J. O. Teubner
School of Physical Sciences, The Flinders University of South Australia, Bedford Park, South Australia, 5042, Australia

(Received 26 June 1974)

The differential-cross-section ratios have been measured for excitation of the $n=2$ and $n=1$ He^+ states in the electron-impact ionization of helium using the coplanar symmetric geometry. This reaction is a crucial test of the reaction model and of the helium wave function. The experiment is sensitive enough to rule out the Hartree-Fock function. Excellent agreement is obtained by using a configuration-interaction wave function.

The $(e, 2e)$ reaction on atomic and molecular systems was first proposed[1] as a method of measuring electron momentum distributions. Recent work[2] has shown that it is possible, with the aid of sufficiently sophisticated reaction theory, to extract this information from angular correlations. The reaction theory is the distorted-wave off-shell impulse approximation using an averaged eikonal approximation for the distorted waves with parameters derived from fitting elastic scattering in the appropriate two-body subsystem with an optical model.[3]

It has also been shown[4] that much more explicit information about atomic and molecular states is available. In particular the angular momenta, parities, and spectroscopic strengths of single-particle states for ion eigenstates have been derived and checked by the appropriate sum rule. For argon, krypton, and xenon marked effects due to correlation are observed in the valence s-hole states. Where there is only one eigenstate of a given angular momentum and parity, we are justified in believing that the Hartree-Fock model should give a good representation of its wave function. In such cases the Hartree-Fock wave function in the distorted-wave off-shell impulse approximation gives the measured angular correlation within experimental error.

In view of the complete success of the technique in describing single-particle momentum distributions and ion spectroscopy, we are led to ask how sensitive is the technique to fine details of wave functions. The simplest nontrivial $(e, 2e)$ reaction is that on helium. It has already been shown[3,5] that the reaction leaving the ion in its ground state is completely understood in terms of the Hartree-Fock wave function. However, it is possible to calculate the amplitude for leaving the ion in a $2s$ (or higher s) state in the Hartree-Fock model because of nonorthogonality of the helium atom and ion wave functions. If a correlated wave function is used for the atom, the amplitude for $2p$ (and higher) states is also nonvanishing.

Since the experimental apparatus, shown in Fig. 1, is described in more detail elsewhere,[5] only a brief description will be given here. Electrons from an electron gun collided with a beam of helium atoms produced by leading high-purity helium gas through a liquid-nitrogen trap and into the vacuum system through a length of stainless-steel tubing of 0.023-cm internal diameter. The stainless-steel tubing terminated 3 mm below an aperture placed 2 mm below the interaction region. The ambient pressure in the vacuum system was maintained at approximately 1×10^{-5}

Copyright © 1974 by
The American Physical Society

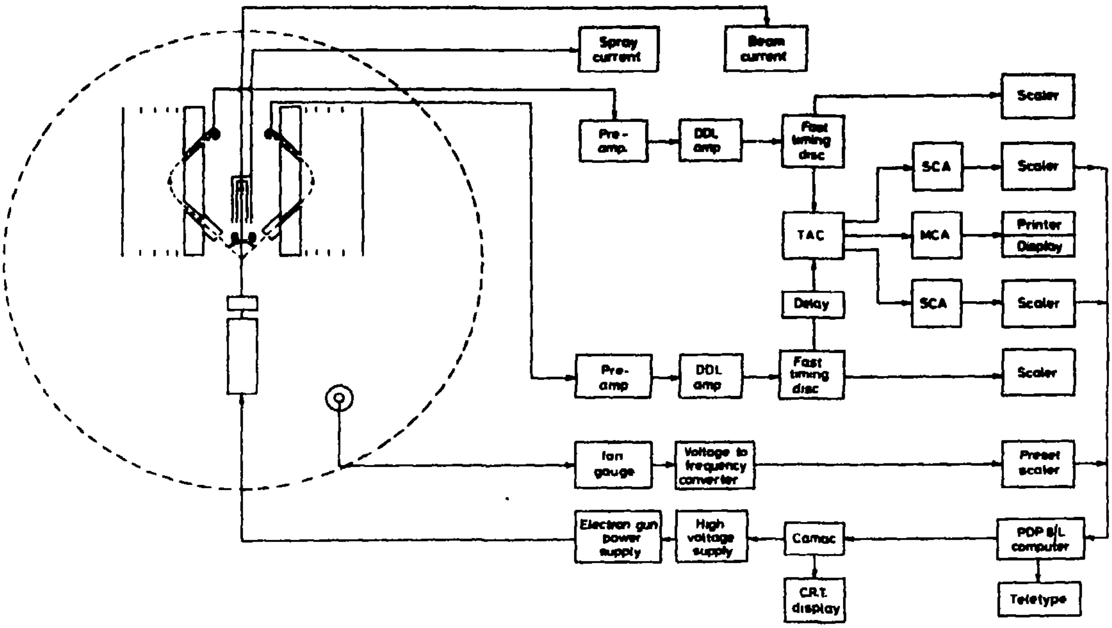

FIG. 1. Schematic diagram of experimental apparatus and associated electronics.

Torr, the base pressure being approximately 4 $\times 10^{-7}$ Torr. The pressure in the interaction region was several orders of magnitude higher than the ambient background pressure. Electron beam currents were in the range 50–120 μA. The effects of magnetic fields were minimized by shielding the vacuum chamber with Mumetal and by use of a set of Helmholtz coils.

Two cylindrical-mirror analyzers, mounted on arms pivoting about the helium beam, were used to select and energy analyze the electrons emerging from the interaction region. In the present work the symmetric coplanar geometry was employed, the two spectrometers subtending equal angles θ relative to the incident direction, and the energies of the two emitted electrons being selected to be equal. The full acceptance angle of the spectrometers was approximately 3°.

The signal-processing electronics, shown schematically in Fig. 1, was similar to that described previously in experiments employing the noncoplanar symmetric situation.[2,4] The output pulses from the time-to-amplitude converter (TAC) were fed to two single-channel analyzers (SCA) and a multichannel analyzer (MCA) used for monitoring and setting up purposes.

Figure 2 shows a typical timing spectrum obtained at an incident energy of 824.5 eV, the two outgoing electrons each having an energy of 400 eV. One of the two single-channel analyzers had its window set over the coincidence peak; the other was used to record accidental coincidences, its window being set wider than the coincidence window by a factor of 12 in order to provide a truer average background count.

Data recording was fully automated using a flexible program written in machine language for the PDP 8/L. The incident electron energy E_0 was varied by means of a programmable power supply, the energies of the outgoing electrons remaining fixed in order to keep the transmission factors of the spectrometers constant. The time pulses for gating the scalers were obtained from a preset scaler monitoring the ambient helium pressure. This was always constant to within a few percent. After being triggered by the preset scaler, the computer recorded the counts in the coincidence and background scalers, subtracted the background counts from the coincidence counts (after taking into account the relative window widths), calculated the statistical error for the point, and restarted the scalers after setting the new incident energy. The progress of the experiment was monitored on a real-time dis-

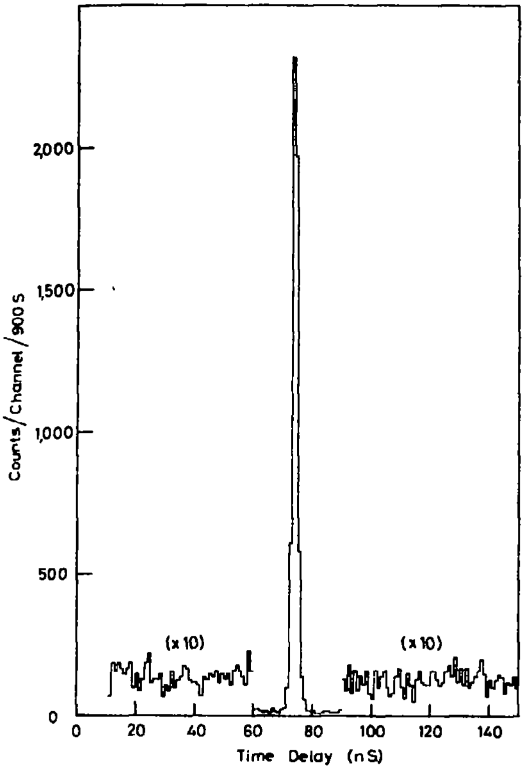

FIG. 2. Multichannel-analyzer spectrum showing ime delay between the start and stop inputs on the ime-to-amplitude converter for the ground-state tran-ition at a total (final) electron energy of 800 eV.

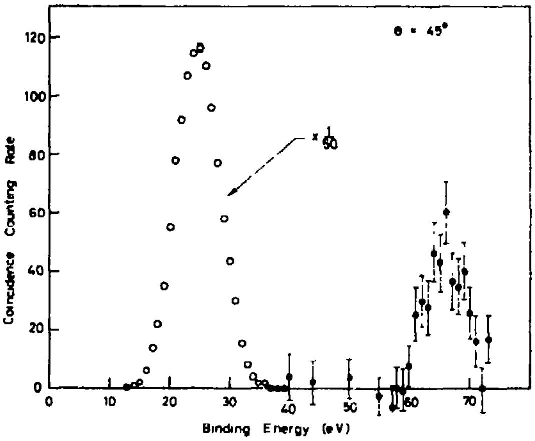

FIG. 3. Binding-energy spectrum for helium at $E = 800$ eV. The binding energy for the $\mathrm{He}(e,2e)\mathrm{He}^+$ ground-state transition is 24.6 eV, whereas that for the first excited state is 65.4 eV.

lay, which on request included the display of he statistical error for a selected point.

The binding-energy spectrum obtained for elium at $\theta = 45°$ is shown in Fig. 3, the total en-rgy E of the outgoing electrons being 800 eV. The binding energy is equal to the difference be-ween the incident and total outgoing energies, ince the energy of the recoiling helium ion is egligible. The dominant feature in the spectrum s the excitation of the ground state of He^+ at $=24.6$ eV. However, the excitation of the $n=2$ tate at $\epsilon = 65.4$ eV can also be clearly seen.

The shape of the angular correlation between he outgoing electrons obtained for both the non-oplanar symmetric geometry[3] and the present eometry[5] for the reaction leaving the ion in its round state is completely described by the Har-ree-Fock wave function of Froese-Fischer.[6] his is true even for incident energies as low as 200 eV. It is therefore interesting to see how well the Hartree-Fock wave function describes the reaction leading to the first excited state of He^+.

The excitation of the $n=2$ states is regarded as a probe for the overlap integral

$$\langle \Psi_{\mathrm{atom}} | \Psi_{\mathrm{ion}} \rangle .$$

This integral is a function of the coordinates of the ejected electron. The integration is performed for the electrons common to the atom and ion. Because of the nonorthogonality of the ion ns wave functions and the wave function for the helium atom with a 1s hole, the Hartree-Fock (independent particle) model predicts an amplitude for the reaction leaving the ion in the 2s state (or higher s states with $\epsilon \geqslant 73$ eV).

For the Hartree-Fock wave function this overlap integral has the same radial shape for both 1s and 2s excitations. The angular correlation, however, is not expected to have the same shape for both, since the off-shell kinematics of the Coulomb t matrix depends on the binding energy.

Since the overlap integral is very small we regard the ratio of the differential cross sections for $n=2$ to $n=1$ excitations as an extremely fine probe for details of the helium-atom wave function (the helium-ion wave function is known exactly). Measurement of such ratios are also independent of any small systematic variation in sensitivity of the apparatus as a function of angle.

Table I lists the experimental ratios of the total differential cross section of the $n=2$ states to that for the $n=1$ state at $\theta=45°$, 49°, and 53°. This is compared with the ratio predicted by the Hartree-Fock wave function of Froese-Fischer. This model is in serious disagreement with experiment. Not only is the magnitude too large, but the ratio decreases with angle instead of increasing. The almost negligible effect of the finite acceptance angles of the spectrometers has been included in the calculated cross-section ratios.

It is evidently necessary to use a correlated wave function for the helium atom. We have used the wave function of Joachain and Vanderpoorten,[7] which has the form

$$\Psi(\vec{r}_1,\vec{r}_2)=\frac{1}{4\pi}\sum\nolimits_l F_l(r_1,r_2)P_l(\cos\theta_{12}),$$

$$F_l(r_1,r_2)=\sum_{m,n} B_{mn}^{(l)} r_>^{l+m} r_<^{l+n}\exp[-\beta(r_>+r_<)/2].$$

The constants are listed in Ref. 7. We have used their best wave function, which predicts 98% of the correlation energy.

This configuration-interaction wave function includes the possibility of excitation of the $2p$ state as well as the $2s$ state. It predicts exactly the same differential cross section for the ground-state transition as the Hartree-Fock wave function, the latter being in agreement with experiment.[2,5] We have compared the cross-section ratios for $2s$ and $2s+2p$ relative to $1s$ with experiment at the various angles in Table I. Once again, the finite acceptance of the spectrometers was allowed for in the calculated cross-section ratios. Excellent agreement is obtained for the $2s+2p$ to $1s$ cross-section ratio.

The configuration-interaction wave function predicts that at $\theta=45°$ the excitation of the $n=3$ states (with $\epsilon=73$ eV) should be almost an order of magnitude smaller than that for the $n=2$ states. This is in agreement with the observations (Fig. 3).

We therefore conclude that both our reaction theory and the wave function of Ref. 7 are extremely accurate. This gives us confidence in applying the reaction theory to other atomic and molecular cases both as a tool for extracting electron momentum distributions and as a probe for details of correlated wave functions. It must also be noted that the experiment is sufficiently accurate to require such fine detail in the wave function.

TABLE I. Differential cross-section ratios for the excitation of $n=2$ and $n=1$ states of He^+, expressed as a percentage.

θ	HF[a]	Correlated wave function[b] $2s$	 $2s+2p$	Expt.
45°	2.75	0.65	0.67	0.72 ± 0.04
49°	2.07	0.77	0.88	0.97 ± 0.10
53°	1.94	1.42	1.74	1.54 ± 0.30

[a] Ref. 6. [b] Ref. 7.

---

[1] G. A. Baker, Jr., I. E. McCarthy, and C. E. Porter, Phys. Rev. 120, 254 (1960); Yu. F. Smirnov and V. G. Neudachin, Zh. Eksp. Teor. Fiz. Pis'ma Red. 3, 298 (1966) [JETP Lett. 3, 192 (1966)]; A. E. Glassgold and G. Ialongo, Phys. Rev. 175, 151 (1968); U. Amaldi, Jr., A. Egidi, R. Marconero, and G. Pizzella, Rev. Sci. Instrum. 40, 1001 (1969).

[2] S. T. Hood, I. E. McCarthy, P. J. O. Teubner, and E. Weigold, Phys. Rev. A 8, 2494 (1973).

[3] J. B. Furness and I. E. McCarthy, J. Phys. B: Proc. Phys. Soc., London 7, 541 (1974).

[4] E. Weigold, S. T. Hood, and P. J. O. Teubner, Phys. Rev. Lett. 30, 475 (1973); S. T. Hood, I. E. McCarthy, P. J. O. Teubner, and E. Weigold, Phys. Rev. A 9, 260 (1974); E. Weigold, S. T. Hood, and I. E. McCarthy, to be published; S. T. Hood, E. Weigold, I. E. McCarthy, and P. J. O. Teubner, Nature (Phys. Sci.) 245, 65 (1973); E. Weigold, S. T. Hood, I. E. McCarthy, and P. J. O. Teubner, Phys. Lett. 44A, 531 (1973).

[5] A. Ugbabe, E. Weigold, and I. E. McCarthy, to be published.

[6] C. Froese-Fischer, At. Data 4, 302 (1972).

[7] C. J. Joachain and R. Vanderpoorten, Physica (Utrecht) 46, 333 (1970).

Determination of the Avogadro Constant

R. D. Deslattes, A. Henins, H. A. Bowman, R. M. Schoonover, and C. L. Carroll
Optical Physics Division, National Bureau of Standards, Washington, D. C. 20234

and

I. L. Barnes, L. A. Machlan, L. J. Moore, and W. R. Shields*
Analytical Chemistry Division, National Bureau of Standards, Washington, D. C. 20234

(Received 17 June 1974)

Measurements are reported on the densities and isotopic-abundance ratios of nearly perfect Si single crystals. These, when combined with optical interferometry of the crystal repeat distance, yield a new value for the Avogadro constant. This result, $N_A = 6.022\,094\,3 \times 10^{23}$ mol^{-1} (1.05 ppm), represents a more than thirty-fold reduction in the uncertainty of previous direct measurements.

We have measured the densities, isotopic abundances, and lattice parameters for some highly perfect Si crystals. Our measurements improve on those previously made in that they are independent of an assumed density for water; they do not employ an x-ray wavelength scale; and they involve "absolute" isotopic-abundance determinations, i.e., abundances were measured against synthetic ratio standards. They yield a new value for the Avogadro constant, as follows from the equation of Bragg,[1] viz., $N_A = nA/\rho a_0^3$, where n atoms of average atomic weight A occupy a unit-cell volume a_0^3 and ρ is the macroscopic density. Here, we report these new results, reconcile them with overtly discordant ones obtained by previous workers, and consider some implications regarding present knowledge of the fundamental constants.[2]

Limitations of density determinations which use water as a standard are suggested by the 6-ppm difference in the only two available "first-principles" measurements.[3] We have, instead, made use of readily available, highly spherical steel artifacts as local and temporary "standards" of density. Their masses were determined in terms of the U. S. national standard (kilogram replica number 20) by well understood procedures.[4] Volumes at temperatures referred to the International Practical Temperature Scale-1968 were inferred from diameters measured by interferometry using a hollow Fabry-Perot etalon[5] illumi-
ed by a He-Ne (633 nm) laser calibrated in
ns of a ^{86}Kr lamp approximately realizing the
sent definition of length.[6]

e compared the densities of these spheres
those of four 200-g Si objects (X_2, X_3, X_4,
in a highly redundant (24 intercomparisons)
rostatic determination in a fluorocarbon immersion medium.[7] Subsequently, three rather perfect specimens, D_1, D_2, D_3, were compared with X_2, X_3, X_4, X_5 in twelve hydrostatic measurement cycles. Each trial using two of the "X" crystals and two of the "D" crystals gave relative volumes for the pairwise combinations. Least-squares values for the densities are given in Table I in the second column.

Observed densities need to be corrected for the presence of C and O in D_1 and D_2. As found by current procedures[8] of the American Society for Testing and Materials, D_3 was clean while the D_1 and D_2 material had oxygen at 6.0×10^{16}/cm^3 and carbon at 3.9×10^{16}/cm^3. The fractional density change due to introduction of an impurity can be written $\Delta\rho/\rho = \Delta A/A - 3\Delta a/a$. For oxygen, there is an expansion, $\Delta a/a$, of $3.8 \times 10^{-24} n_\mathrm{O}$[9] and for carbon a contraction of $6.5 \times 10^{-24} n_\mathrm{C}$,[10] where n_O and n_C are the respective number densities (cm^{-3}). For interstitial O, the net density change is nearly zero while for substitutional C, there is a net increase of 0.31 ppm. This correction was applied to obtain the "corrected" densities for D_1 and D_2 listed in Table I.

Isotopic-abundance measurements for the specimens D_1, D_2, and D_3 were carried out relative to another large homogeneous specimen which was wafered to form a publicly available Standard Reference Material, SRM 990.[11] This comparison was effected by the use of a 15-cm 60° magnetic sector mass spectrometer using the abundance procedure described by Smith, Shields, and Tabor[12] and by Rodden.[13] To obtain absolute values of the abundance ratios the mass spectrometer was calibrated by using known mixtures prepared from chemically pure and nearly isotopically pure separated isotopes. From the absolute isotopic ratios, the atomic weight of the

TABLE I. Densities of Si crystals and estimated components of error. The estimate for σ_T contains contributions from σ_m and the following other sources in ppm: temperature of interferometry (0.23); wavelength calibration (0.08); phase shift on reflection (0.12); photographic nonlinearity (0.01); bath temperature (0.03); mass of steel balls (0.18); mass of Si crystals (0.06); balance calibration (hydrostatic) (0.27). The larger error in the case of D_3 is due to small sample size.

Sample	Obs. density (g/cm^3)	Corr. density (g/cm^3)	σ_m (ppm)	σ_T (ppm)
D_1	2.328 9917	2.328 9910	0.22	0.48
D_2	2.328 9906	2.328 9899	0.44	0.62
D_3	2.329 0003	2.329 0003	0.94	1.04

reference and thus of samples D_1, D_2, and D_3 can be calculated using the nuclidic masses reported by Wapstra and Gove.[14] The complete details of these measurements will be reported elsewhere.[15]

Results of the measurements of the absolute isotopic abundances of SRM 990 are given in Table II along with provisional error estimates. The principal limitations in the precision and accuracy obtained here arise from the difficulty in measurement of the very small amount of the minor isotopes present in the separated isotope preparations because of the very small amount of ^{30}Si available (ca. 100 mg). Table II also gives the results for the crystals D_1, D_2, and D_3. These were obtained from measurements of the differences $A(990) - A(D_3) = 0.68$ ppm, $A(D_1) - A(D_2) = 0.75$ ppm, and $A(D_3) - A(D_2) = 4.54$ ppm. These comparisons do not contribute significant additional uncertainty.

Data in Tables I and II may be combined to give estimates of the formally invariant quantity A/ρ. These are listed in Table III with standard deviations derived from repeated observations and estimates of uncontrolled systematic variability. The results are sufficiently concordant that a weighted average seems appropriate. It appears to be of considerable significance that, while both density and atomic weight values spread over 5 ppm, the A/ρ ratios lie within 0.3 ppm.

The lattice parameter (and hence the volume of a unit cell) was obtained by means of simultaneous x-ray and optical interferometry of a common baseline for a sample of the crystal D_3 only.[16] Measurement accuracy has recently been improved by use of an iodine-stabilized laser[17] and direct measurement of the cavity length to permit evaluation of the Fresnel phase shift.

The Fresnel-phase-shift correction accounts

TABLE II. Abundances and atomic weights for SRM 990 and the samples D_1, D_2, and D_3. Abundances for SRM 990 were obtained from measurement of the ratios ^{28}Si/^{30}Si and ^{29}Si/^{30}Si. Abundances for the D crystals were obtained by difference measurements as indicated in the text. The error contributions in ppm: mixing separated isotopes (0.30); separated isotope ratio (0.30); SRM 990 ratio (0.59)—yielding $\sigma_T = 0.73$ ppm.

		SRM 990 Isotope	
	^{28}Si	^{29}Si	^{30}Si
Atomic %	92.228 948	4.669 981	3.101 071
Nuclidic mass	27.976 9286	28.976 4969	29.973 7722
Weight %	91.872 310	4.818 128	3.309 562
	A(SRM 990) = 28.085 532(21)		
	D_1	D_2	D_3
Atomic weights	28.085 406	28.085 385	28.085 513

TABLE III. Values for the formally invariant quantity A/ρ for each of the "D" crystals at 25°C.

Sample	A/ρ	σ_m (ppm)	σ_T (ppm)
D_1	12.059 0444	0.48	0.88
D_2	12.059 0411	0.62	0.96
D_3	12.059 0422	1.03	1.27
Weighted mean	12.0590427	0.53	0.75

or the fact that the distance traveled in a scan rom cavity length L_1 to L_2 differs from the hange in optical order number by[18] $\cos^{-1}[(1-L_2/$ $)^{1/2}]-\cos^{-1}[(1-L_1/R)^{1/2}]$ for the hemispherical eometry used here, with curved mirror radius . We determined L by measuring the distance L (using x-ray interferometry) between micro- vave sidebands of the visible radiation differing n frequency by a known interval 2ω near 20 GHz,[19] e., $L=c\delta L/2\omega\lambda$. The order numbers obtained a. 1000) were essentially exact. An uncertainty 1 order number would contribute less than 0.01 m to the lattice-constant uncertainty.

Each lattice-parameter–determining run was rrected for Fresnel phase shift and for depar- re of the measurement temperature (deter- ined by well calibrated small thermistors in lose proximity to the crystal) from the refer- nce temperature (25°C) by using $\alpha=2.56\times10^{-6}$ $^{-1}$.[20] From 165 determinations, a standard de- lation of the mean, σ_m, is obtained as 0.03 ppm. rror estimates for this lattice-parameter mea- urement are given in Table IV. The indicated alue $a_0=0.543\,106\,61$ nm (0.25 ppm) corrected to 5°C gives a unit-cell volume, $a_0^3=0.160\,197\,33$ m^3 (0.75 ppm).

The final result is thus at hand: We combine e determination of A/ρ and that of a_0^3 to obtain $_A=6.022\,094\,3\times10^{23}$ mol^{-1} (1.05 ppm). The un- ertainty is taken as the square root of the sum of the squares of that associated with A/ρ and that associated with a_0^3 and is intended to reflect our estimate of 1 standard deviation for a hypothetical replication of our total procedure.

TABLE IV. Lattice-parameter–determination re- ults and error contributions. The estimated error ontributions in ppm: relative optical-x-ray interfer- meter drift (0.20); laser (product of order number d estimated first-derivative lock instability) (0.13); mperature (0.02); Fresnel phase shift (0.01); σ_m tandard deviation of mean) (0.03).

Laser wavelength (pm)	632 990.0742 ± 0.0009
Fringe count ratio	1648.2641 (0.25 ppm)
a_0 (25°C)	543.106 61 (0.25 ppm)

There is no previous result to which the present one may be properly compared since all of these were referred to an x-ray scale, i.e., the measured quantity was $N_A\Lambda^3$ where Λ is the conversion factor from x-ray scale to angstroms. A comparison is nonetheless possible with one outstanding representative of this class of measurement[21] by translating the present result to an x-ray wavelength scale. Also, we can compare our result with an indirect value for N_A obtained from electrical measurements.[2]

In the case of the x-ray measurements (basically a_0/λ determinations) reported in Ref. 21 there is substantial agreement. Densities given in Ref. 21 are referred to that of water which is assigned the value obtained by Tilton and Taylor.[3] These results group about 6 ppm above those reported here. Our peripheral work on water has indicated that the values obtained by Thiessen, Schell, and Disselhorst[3] lie closer to observed values on local water. Hence, the densities reported in Ref. 21 might be reduced by a few parts per million which would lead to better agreement with our results. There is not much impact on N_A here since the results of Ref. 21 require use of Λ and involve unknown isotopic abundances for Si.

The indirect value of $N_A=6.022\,045\times10^{23}$ mol^{-1} from the least-squares adjustment[2] has a 1σ uncertainty of 5.1 ppm. The discrepancy between the indirect value and that reported here is 8.2 ppm or 1.6σ. A more relevant statement is that introducing this new result into the least-squares adjustment of all the constants[2] changes the Birge ratio from 0.83 to 0.89,[22] suggesting that at present further analysis is not needed.

It is possible to make certain speculations about what further improvements are possible in this type of measurement. Use of enriched ^{28}Si, say 99%, and present mass spectroscopic procedures would give the atomic weight to 0.01 ppm. New processing techniques appear capable of reducing the vacancy cluster problem.[23] Transfer from artifact mass and volume to crystal density could be made at the 30-kg level yielding 0.01-ppm densities for an aggregation of material which need not be isotopically enriched or highly perfect. Subsequent ordering of these specimens via a Cartesian diver apparatus[24] or with density columns using certain newly available liquids would permit 0.01-ppm transfers to ca. 100-g specimens of enriched material. Controllable systematic effects in the x-ray/optical interferometer could be reduced to a level below 0.01 ppm (the precision is already at hand). It would thus appear that a value of N_A is obtainable with an uncertainty of the order of 0.01 ppm. Should this be achieved, one might wish to assert that the artifact kilogram is redundant and that masses can be obtained via an algorithm of realization from the atomic mass unit.

---

[*] Present address: Teledyne Isotopes, Timonium, Md. 21093.

[1] W. H. Bragg, Proc. Roy. Soc., Ser. A 88, 428 (1913), and 89, 246, 430 (1914).

[2] E. R. Cohen and B. N. Taylor, J. Phys. Chem. Ref. Data 2, 663 (1973).

[3] M. Thiessen, K. Scheil, and H. Disselhorst, Wiss. Abh. Phys.-Tech. Reichsanst. 3, 1 (1900); P. Chappuis, Trav. Mem. BIPM 13, D1 (1907), and 14, B1, D1 (1910); L. W. Tilton and J. K. Taylor, J. Res. Nat. Bur. Stand. 18, 205 (1937).

[4] P. O. Pontius, *Mass and Mass Values*, U. S. National Bureau of Standards Monograph No. 133 (U. S. GPO, Washington, D. C., 1974).

[5] J. B. Saunders, J. Res. Nat. Bur. Stand., Sect. C 76, 11 (1972).

[6] Proces-Verb. Seances, Com. Int. Poids Mes. 28, 70 (1960).

[7] H. A. Bowman, R. M. Schoonover, and C. L. Carroll, J. Res. Nat. Bur. Stand., Sect. A 78, 13 (1974).

[8] *Annual Book of ASTM Standards* (American Society for Testing and Materials, Philadelphia, Pa., 1973), Part 8, Designations: F120-70T; F121-70T, and F123-70T.

[9] W. L. Bond and W. Kaiser, Phys. Chem. Solids 16, 44 (1960).

[10] J. A. Baker, T. N. Tucker, N. E. Moyer, and R. C. Buschert, J. Appl. Phys. 39, 4365 (1968).

[11] Standard Reference Materials are available through the Office of Standard Reference Materials, Room B306, Building 222, National Bureau of Standards, Washington, D. C. 20234.

[12] R. L. Smith, W. R. Shields, and C. D. Tabor, U. S. Atomic Energy Commission Research and Development Report No. GAT-171/REV. 1, 1956 (unpublished).

[13] C. J. Rodden, *Selected Measurement Methods for Plutonium and Uranium in the Nuclear Fuel Cycle* (U. S. Atomic Energy Commission, Washington, D. C. 1972).

[14] A. H. Wapstra and N. B. Gove, Nucl. Data Tables 9, 267 (1971).

[15] I. L. Barnes, L. J. Moore, L. A. Machlan, and W. R. Shields, to be published.

[16] R. D. Deslattes and A. Henins, Phys. Rev. Lett. 31, 972 (1973).

[17] W. G. Schweitzer, E. G. Kessler, R. D. Deslattes, H. P. Layer, and J. R. Whetstone, Appl. Opt. 12, 2927 (1973).

[18] H. Kogelnik and T. Li, Proc. IEEE 54, 1312 (1966).

[19] Z. Bay, G. G. Luther, and J. A. White, Phys. Rev. Lett. 29, 189 (1972).

[20] We are indebted to R. Kirby for this measurement.

[21] A. Henins and J. A. Bearden, Phys. Rev. 135, A890 (1964).

[22] We are indebted to B. N. Taylor for this result.

[23] A. J. R. deKock, P. J. Roksnoer, and P. G. T. Booron, in *Semiconductor Silicon 1973*, edited by H. R. Huff and R. R. Burgess (The Electrochemical Society, New York, 1973), pp. 83–94.

[24] H. A. Bowman and R. M. Schoonover, J. Res. Nat. Bur. Stand., Sect. C 64, 227 (1965).

Linear Polarizability Contribution to the Nonadditive Three-Molecule Potential

E. Bergmann
Batelle Institute, Advanced Studies Center, CH-1227 Carouge-Geneva, Switzerland

(Received 25 June 1974)

In its diagrammatic form the perturbation expansion for the dispersion interaction can be rearranged to an expansion in the degree of hyperpolarizability considered. The total contribution of the linear dipole polarizabilities is given explicitly.

The appearance of good multiparameter two-body potentials for the noble gases[1,2] has stimulated the analysis of the influence of nonadditive three-body forces on solid[3-6] and fluid properties.[7-10] Most calculations[4,7-10] are based on Axilrod and Teller's result[11] for the triple-dipole interaction. However, Doran and Zucker[5] found that the contribution of the four-dipole three-body force to the binding energy is negligible only for Ne but rises to 40% of the triple-dipole contribution in Xe, in contradiction to previous claims.[12] In this Letter we calculate the total contribution of dipole forces to the three-molecule potential. Since the final result is not much more complex than Axilrod and Teller's, its use in calculations of solid and fluid properties should present no difficulties.

We start from the general sth order contribution of dispersion forces for the three-body potential of spherical molecules. This convenient starting point is justified by the good separability of the other long-range forces[13] and a Heitler-London short-range interaction[14] from the dispersion interaction. We have

$$U^{(s)}(R_A,R_B,R_C)=\sum_{\substack{\alpha_1\ldots\alpha_{s_1}\\ \beta_1\ldots\beta_{s_2}\\ \gamma_1\ldots\gamma_{s_3}}}{}' (1/s!)\sum_{\{n\}}\Big[\prod_m{}' V(m,m+1)\Big]\prod_m{}'[E(m)-3E_0]^{-1}, \qquad (1)$$

$$s_1+s_2+s_3=2s+1,\quad s_i\neq 0.$$

e first sum runs over the quantum states of the molecules. The prime indicates the omission of mplete ground states in each triple. The second sum runs over all ordered triple distributions one n form from the sets $\{0,\alpha_1\ldots\alpha_{s_1},0\}$, etc. by always changing two elements between successive tries. The two products run over all triples of a distribution, the primes indicating the omission of the st and last terms in the second and the last term in the first product. $V(m,m+1)$ is the matrix element of the Coulomb interaction between two molecules, $E(m)$ the energy of the three molecules in e state $m=(\alpha_i,\beta_j,\gamma_k)$. Equation (1) can be represented in the usual way by a set of Goldstone diaams.[15,16] The restriction on the first sum appears then as a restriction to connected diagrams. uation (1) and the corresponding diagrams still contain all the degeneracies of "time ordering." so, whenever a ground state appears among the three quantum numbers of a triple we must, in fact, t the particle line of the molecule concerned in the diagram and close-by hole lines as illustrated Fig. 1. Because of the restriction to spherical molecules, only those cuts are possible which do t lead to particle lines met by an odd number of interaction lines. By a systematic insertion of ound states we replace Eq. (1) by expressions where the first sum does not include the ground state ymore. The factors of the second product can be split in the usual way by introducing frequency egrals.[17] This leads to a reinterpretation of the terms corresponding to the fully cut diagrams. A

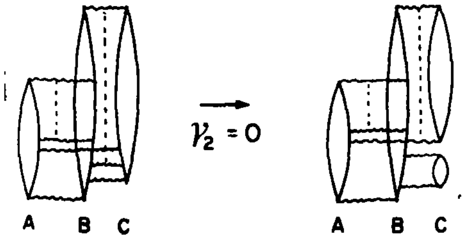

FIG. 1. Cut in a Goldstone diagram caused by the insertion of a ground state for molecule C after two interaction lines.

particle line met by $2l$ interaction lines corresponds to a mutual hyperpolarizability[18,19] of degree $l-1$. The maximal degree of hyperpolarizability appearing in a term is a very good ordering parameter for a perturbation expansion. At each order the minimum degree of hyperpolarizability corresponds to the maximal contribution since the second product in Eq. (1) becomes a maximum.

For the two-molecule potential the Van der Waals interaction is the only linear polarizability contribution. For three molecules, however, the potential consists of all ring diagrams. In each ring, one molecule appears only once while the other two alternate along the ring. We will give only the calculation for a ring with an odd number, the even case being closely analogous.

$$I_{2l+1}(R_A, R_B, R_C) = \frac{\hbar}{12\pi}\int d\omega\, dz_1\, dz_2\, \alpha_A(z_1, z_2, i\omega)\prod_{j=1}^{l} dx_{2j-1}\, dx_{2j}\, dy_{2j-1}\, dy_{2j}\, \alpha_B(x_{2j-1}, x_{2j}, i\omega)$$
$$\times \alpha_C(y_{2j-1}, y_{2j}, i\omega)\,|z_1 - x_1|^{-1}|z_j - y_l|^{-1}\sum_{i=1}^{2l-1}|x_{i+1} - x_i| + \text{permutations } (ABC); \qquad (2)$$

$\alpha_A(r_1, r_2, i\omega)$ denotes the mutual polarizability of atom A at imaginary frequency $i\omega$. We will retain only the dipole terms of the multipole expansion of Coulomb factors. However, the inclusion of the higher multipoles is indeed simple as it leads essentially only to a replacement of the dipole polarizabilities by multiple ones. Then

$$I_{2l+1} = \frac{\hbar}{12\pi}\,\mathrm{Tr}[T(R_1)T(R_2)T(R_3)^{2l-1}]\int_{-\infty}^{+\infty} d\omega\, \alpha_A(i\omega)\alpha_B{}^l(i\omega)\alpha_C{}^l(i\omega) + \text{perm} \qquad (3)$$

with $R_1 = R_A - R_B$, $R_2 = R_A - R_C$, and $R_3 = R_B - R_C$. In the case of multipoles the expression under the trace is replaced by a polynomial of order $2l+1$ in all combinations of multipole tensors. Evaluation of the trace is straightforward and gives

$$\mathrm{Tr}[T(R_1)T(R_2)T(R_1)^{2l-1}] = (R_1R_2)^{-3}R_3{}^{-6l+3}[3(1+\cos\theta_1\cos\theta_2\cos\theta_3) - 2(2^{2l-2}-1)$$
$$\times(1 - 3\cos^2\theta_1 - 3\cos^2\theta_2 - 9\cos\theta_1\cos\theta_2\cos\theta_3)]. \qquad (4)$$

In the evaluation of the frequency integral we use the one frequency model for polarizability which is known to give satisfactory results at least for noble gases,[17]

$$\alpha(i\omega) = \alpha\omega_0{}^2(\omega^2 + \omega_0{}^2)^{-1}, \qquad (5)$$

α being the static polarizability of the molecule. We choose the at present only interesting case of three identical molecules. Then

$$\int_{-\infty}^{+\infty} d\omega\, \alpha^{2l+1}(i\omega) = 2\omega_0\sqrt{\pi}\,\alpha^{2l+1}\frac{(2l+\frac{1}{2})!}{(2l)!(4l+1)}. \qquad (6$$

For the even case we find

$$I_{2l} = -\frac{\hbar\omega_0(2l-\frac{1}{2})!}{12\sqrt{\pi}(2l-1)!(4l-1)}R_1{}^{-6}R_3{}^{-6l+6}[6 + (2^{2l-2}-1)(1+3\cos^2\theta_2)] + \text{perm}. \qquad (7$$

Even and odd terms have to be summed separately and lead finally to

$$U = A_1R_1{}^{-3}\{4a_{32}(6\cos^2\theta_1 - 2 + \lambda)[(1+x_3)^{-1/2} + (1-x_3)^{-1/2} - 2] + 2a_{32}(1 + \lambda - 3\cos^2\theta_1)$$
$$\times[(1+2x_3)^{-1/2} + (1-2x_3)^{-1/2} - 2] + 2a_{31}\}(5 - 3\cos^2\theta_2)[(1+x_3)^{-1/2} - (1-x_3)^{-1/2} + x_3]$$
$$+ a_{31}(1 + 3\cos^2\theta_2)[(1+2x_3)^{-1/2} - (1-2x_3)^{-1/2} + 2x_3)] + \text{perm}, \qquad ($$

where we used the following notation:

$$A_i = \alpha\hbar\omega_0(96R_i{}^3)^{-1}, \quad a_{ij} = (R_iR_j{}^{-1})^3, \quad x_i = \alpha R_i{}^{-3}, \quad \lambda = 1 + 3\cos\theta_1\cos\theta_2\cos\theta_3.$$

Equation (8) represents the total contribution of the linear polarizability to the dispersion interactio of three identical molecules. Since the integral in Eq. (6) can also be evaluated for three different molecules with the same residue method, the extension to this case is immediate. The inclusion of multipoles leads to additional sums for every included multipole polarizability. Their inclusion is important, because it was observed[5,20] that the contribution of the third-order dipole-dipole-quadrupole term to the cohesion energy of noble gases largely cancels the fourth-order pure-dipole contribution. Inclusion of hyperpolarizabilities leads to connected rings. The fact that the result is analytic should allow its use for the calculation of liquid and solid properties.

The author would like to thank Professor L. Jansen for many very helpful discussions.

---

[1] M. V. Bobetic and J. A. Barker, Phys. Rev. B 2, 4169 (1970).

[2] M. V. Bobetic, J. A. Barker, and M. L. Klein, Phys. Rev. B 5, 3185 (1972).

[3] A. Hüller, Z. Phys. 245, 324 (1971).

[4] J. A. Barker, M. L. Klein, and M. V. Bobetic, Phys. Rev. B 2, 4176 (1970).

[5] M. B. Doran and I. J. Zucker, J. Phys. C: Proc. Phys. Soc., London 4, 307 (1971).

[6] K. F. Niebel and J. A. Venables, Proc. Roy. Soc., Ser. A 336, 365 (1974).

[7] N. R. Kestner and D. A. Copeland, J. Chem. Phys. 49, 5214 (1968).

[8] I. R. McDonald and C. V. Woodcock, J. Phys. C: Proc. Phys. Soc., London 3, 722 (1970).

[9] J. S. Rowlinson, R. J. Dulla, and W. R. Smith, Mol. Phys. 21, 299 (1971).

[10] J. A. Barker, R. A. Fischer, and R. O. Watts, Mol. Phys. 21, 657 (1971).

[11] B. M. Axilrod and E. Teller, J. Chem. Phys. 11, 299 (1943).

[12] W. L. Bade, J. Chem. Phys. 28, 282 (1958).

[13] B. Linder and D. A. Rabenold, Advan. Quantum Chem. 6, 203 (1972).

[14] E. Bergmann, to be published.

[15] A detailed discussion of diagram expansions can, e.g., be found in C. Bloch, in *Studies in Statistical Mechanics*, edited by J. De Boer and G. E. Uhlenbeck (North-Holland, Amsterdam, 1965), Vol. 3.

[16] Goldstone diagrams for molecules have been discussed by H. P. Kelly, Advan. Chem. Phys. 14, 129 (1969).

[7] H. Margenau and N. R. Kestner, *Theory of Intermolecular Forces* (Pergamon, New York, 1969), Chap. 2. The tension of Eq. (82) to an arbitrary number of molecules is straightforward through the product theorem for La- ace transforms.

[8] For a complete discussion of hyper- and multipole polarizabilities, see A. D. Buckingham, Advan. Chem. Phys. , 107 (1967).

[9] S. Baer, J. Chem. Phys. 49, 3632 (1968).

[0] J. A. Barker, Ch. J. Johnson, and T. H. Spurling, Aust. J. Chem. 25, 1811 (1972).

Theory of Induced Molecular-Orbital *K* X Rays in Heavy-Ion Collisions*

Berndt Müller and Walter Greiner
Wright Nuclear Structure Lab, Yale University, New Haven, Connecticut 06520

(Received 3 June 1974)

The mechanisms of spontaneous and induced emission of radiation are derived from the Dirac equation in a rotating coordinate system. The molecular-orbital x-ray spectra exhibit a strong asymmetry with respect to the beam axis. The asymmetry peaks for the high-energy transitions, which can be used for spectroscopy of two-center orbitals.

During collisions of heavy ions with heavy tar- ts at moderate energies (below the Coulomb rrier) intermediate molecular electronic states ll be formed. It has been expected that the di- ct proof for this theoretical prediction would nsist in the observation of radiative transitions tween such molecular states.[1] Indeed, reports the detection of molecular x rays have been ven by various experimental groups.[2] However, ckground effects such as electronic and nuclear emsstrahlung occur as competing effects in these measurements. Only recently Greenberg, Davis, and Vincent[3] have carried out experiments with monoisotopic Ni beam and target where nuclear dipole bremsstrahlung is forbidden.

The unique signature of molecular x rays comes from the fact that—contrary to atomic x rays—in addition to the *spontaneous* x rays *induced* radiative transitions also occur, which can be recognized by their asymmetric angular distribution relative to the beam axis. It is the purpose of this note to discuss the x-ray spectrum due to both spontaneous and induced transitions including the most important dynamical effects.

The adiabatic molecular states are given by the two-center Dirac equation given by Müller, Rafelski, and Greiner.[4] Nonadiabatic effects and radiative coupling can be described by writing the generally covariant form of the Dirac equation[5,6] in a rotating, instantaneous, coordinate system whose z axis is along the line connecting the two scattering nuclei[6]:

$$\gamma^k\left(\frac{\partial}{\partial x^k}-\frac{ie}{\hbar c}A_k+\Gamma_k\right)\Psi+\frac{m_ec}{\hbar}\Psi=0. \tag{1}$$

The $\Gamma_k=\frac{1}{4}\gamma^l(\gamma_{l|k}-\{{}^{s}_{lk}\}\gamma_s)-\frac{1}{16}\mathrm{Tr}(\gamma\gamma^l\gamma_{l|k})\gamma$ are the generalized connections for spinor differentiation, and the Dirac matrices γ^k are determined via the metric g^{lk} of the coordinates in the rotating frame.[6] Explicit evaluation for a system with angular velocity $\vec{\omega}_{\mathrm{rot}}(t)$ gives

$$i\hbar\,\partial\psi/\partial t=\{c\vec{\alpha}\cdot[\vec{p}-(e/c)\vec{A}]+V+\beta m_ec^2\}\psi-\vec{\omega}_{\mathrm{rot}}\cdot\{\vec{r}\times[\vec{p}-(e/c)\vec{A}]+\tfrac{1}{2}\hbar\sigma\}\psi-(i\hbar/4c)(\dot{\vec{\omega}}_{\mathrm{rot}}\times\vec{r})\cdot\vec{\alpha}\psi. \tag{2}$$

Two mechanisms for photon emission are a spontaneous one via the operator $H_{\mathrm{rad\,spon}}=e\vec{\alpha}\cdot\vec{A}=-i(e/\hbar)\times[H,\vec{r}]\cdot\vec{A}$ and an induced emission caused by $H_{\mathrm{rad\,ind}}=(e/c)\vec{\omega}_{\mathrm{rot}}\times\vec{r}\cdot\vec{A}$, where the former current is imaginary while the latter is real. Therefore no interference occurs and the cross section for the two processes is given in the approximation of Fermi's Golden Rule by[6,7]

$$\frac{d\sigma_{\mathrm{spon}}}{d\omega\,d\Omega_K\,d\Omega_{\mathrm{ion}}}=\frac{\omega^2}{2\pi\hbar c^3}|d_{fi}|^2\sin^2\theta_{Kd}\left(\frac{d\sigma}{d\Omega_{\mathrm{ion}}}\right)_{\mathrm{Ruth}},\quad\frac{d\sigma_{\mathrm{ind}}}{d\omega\,d\Omega_K\,d\Omega_{\mathrm{ion}}}=\frac{\omega\omega_{\mathrm{rot}}^2}{2\pi\hbar c^3}\left|\frac{\vec{I}}{|I|}\times\vec{d}_{fi}\right|^2\sin^2\theta\left(\frac{d\sigma}{d\Omega_{\mathrm{ion}}}\right)_{\mathrm{Ruth}}. \tag{3}$$

Averaging over all possible orientations of the molecular dipole $\vec{d}_{fi}$ (closed shells!) gives a uniform *distribution for the spontaneous radiation, and for the induced radiation a distribution*

$$d\sigma_{\mathrm{ind}}/d\omega\,d\Omega_K\,d\Omega_{\mathrm{ion}}\propto 1-\tfrac{1}{2}\sin\theta_{KI},$$

where θ_{KI} is the angle between the photon and the rotation axis $\vec{I}/I$, or if we integrate also over the azimuthal ion scattering angle

$$d\sigma_{\mathrm{ind}}/d\omega\,d\Omega_K\sin\theta_{\mathrm{ion}}\,d\theta_{\mathrm{ion}}\propto\tfrac{1}{2}+\tfrac{1}{4}\sin^2\theta_K,$$

where θ_K is the angle between the photon and the beam axis. Only the $2p_{3/2}\sigma$, $2p_{3/2}\pi$, and $2p_{1/2}\sigma$ to $1s_{1/2}\sigma$ transitions are included in our calculations. They are so far assumed to be equally occupied with electrons. Unequal population (alignment) of the $2p_{3/2}\pi$, $2p_{3/2}\sigma$, and $2p_{1/2}\sigma$ molecular orbitals (MO's) with probabilities A^2, B^2, and C^2, respectively, leads to the following asymmetry as a function of photon energy $\hbar\omega$, photon scattering angle θ_K, and ion energy E:

$$\eta(\omega,\theta_K,E)=\frac{d\sigma(\theta_K)}{d\omega\,d\Omega_K}\left(\frac{d\sigma(\theta_K=0)}{d\omega\,d\Omega_K}\right)^{-1}-1=\frac{3}{2}\sin^2\theta_K\frac{A^2-B^2-(A^2-\frac{1}{3}B^2-\gamma C^2)\alpha_3^2}{3A^2+5B^2+6\beta C^2+(3A^2+B^2+3\gamma C^2)\alpha_3^2}, \quad (4$$

where $\beta=D_1^2/D_3^2$ is the ratio of the square of the induced dipole matrix elements of the $2p_{1/2}\sigma$ and $2p_{3/2}\pi,\sigma$ to the $1s_{1/2}\sigma$ states, $\gamma=D_1^2\alpha_1^2/D_3^2\alpha_3^2$, and $\alpha_\nu=v/R_\nu(\omega)\omega=(2ME)^{1/2}/R_\nu(\omega)\omega$. $R(\omega)=R_0[(\omega_c-\omega$ $(\omega-\omega_s)]^{1/2}$ is the (approximate) two-center distance as a function of the photon energy. For the $2p_{1/2}$ MO one has $\hbar\omega_s=0$ and $\hbar\omega_c=31.8$ keV, and for the $2p_{3/2}$ MO, $\hbar\omega_s=7.5$ keV and $\hbar\omega_c=34$ keV. $R_0=2100$ fm. Obviously η is largest perpendicular to the beam axis ($\theta_K=90°$). The comparison of (4) with experiments[3] can serve as a determination of the alignments A^2/B^2 and A^2/C^2.

As a result of the nonadiabatic effects the molecular states obtain a width $\Gamma(t)$ which is composed three different parts[7]:

$$\Gamma_{\mathrm{rad\,spon}}=\mathop{S}_{nk\epsilon}\left|e(2\pi/\hbar\omega)^{1/2}\int_0^t dt'\exp\left[i\int_0^{t'}d\tau\,\omega_{mn}(\tau)+i\omega t'\right]\omega_{mn}\langle n(R)|\vec{r}\cdot\vec{A}|m(R)\rangle\right|^2,$$

$$\Gamma_{\mathrm{rad\,ind}}=\mathop{S}_{nk\epsilon}\left|e(2\pi/\hbar\omega)^{1/2}\int_0^t dt'\exp\left[i\int_0^{t'}d\tau\,\omega_{mn}(\tau)+i\omega t'\right]\vec{\omega}_{\mathrm{rot}}\times\langle n(R)|\vec{r}\cdot\vec{A}|m(R)\rangle\right|^2,$$

$$\Gamma_{\mathrm{non\,rad}}=\sum_{n\neq m}\left|\int_0^t dt'\exp\left[i\int_0^{t'}d\tau\,\omega_{mn}(\tau)\right]\langle n(R)|\dot{R}\,\partial/\partial R+\vec{\omega}_{\mathrm{rot}}\cdot\vec{J}/\hbar|m(R)\rangle\right|^2,$$

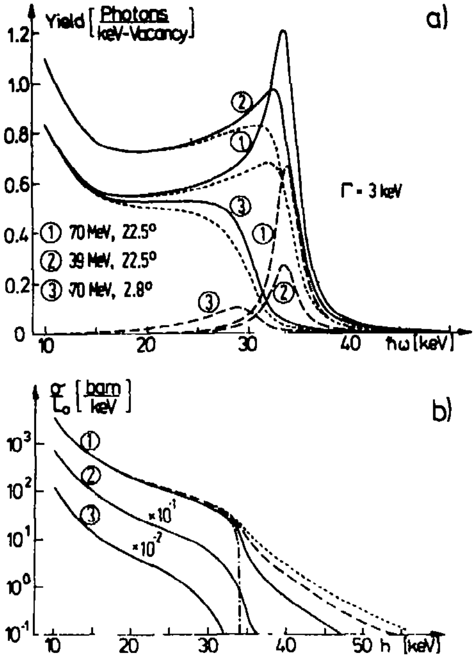

FIG. 1. (a) The MO x-ray yield for coincidence experiments with 70-MeV Ni-Ni at (1) 11.2° and (3) 1.4° scattering angle, and (2) 39-MeV Ni-Ni at 11.2° scattering angle (all quantities in the lab system). The ld lines show the total yield; the dotted and dashed s the spontaneous and induced contributions, rectively. Observe that the peaks are strongly enced by the induced-emission mechanism. (b) MO x-cross sections for the singles experiment Ni-Ni. Yield for 70-MeV collision. The solid line corrends to $\Gamma = 1$ keV, the dashed and dotted lines to 3 5 keV, respectively. The dashed-dotted lines give spectrum without collision broadening which sharputs off at the limiting atom $K\alpha$ energy. (2) Specm for 19-MeV collision, (3) for 5 MeV, both with 1 keV. All quantities in the lab system.

re S represents integration or summation as ropriate. In our present calculations an eftive parameter Γ has been chosen for the sum hese widths,[7] and has been varied between 1 5 keV to establish the dependence of the spec- on the width which is a function of scattering rgy ($\Gamma \sim \sqrt{E}$). It leads to a smooth transition m the molecular x-ray spectrum into the quadole bremsstrahlung background,[8] which can ve for its determination [see Fig. 1(b) above]. reover, we have neglected interference efts of the radiation for high-energy x-ray tranons.[9] The cross sections are calculated here by integrating (3) along the trajectory and, for the singles spectrum, by further integrating over all ion scattering angles. The transition energies and dipole matrix elements are taken from the exact relativistic one-electron states for the Ni-Ni system.[4,10] For the symmetric Ni-Ni collision, the symmetrized Rutherford cross section is used. The results for a coincidence experiment (equal population assumed) at various scattering angles and energies are shown in Fig. 1(a). The spectra at moderate forward angles exhibit a pronounced peak at the high-energy end which is essentially due to the additional induced radiation that is strongly peaked at high photon energies. The induced radiation also grows with increasing scattering energy, whereas the spontaneous yield per K vacancy drops. Of course, the K-vacancy production will increase with rising energy. For low scattering energy (e.g., 5 MeV) the molecule no longer reaches the asymptotic "runway" region[4] and no peak structure occurs. For very forward or more backward angles ($\theta < 10°$, $\theta > 45°$) the contribution from induced radiation decreases with respect to the spontaneous x-ray yield. Especially for very forward angles ($\theta < 3°$) the runway region is forbidden and the peak vanishes altogether [Fig. 1(a)]. The width of the peak at the end of the spectra at forward angles is almost completely determined by the collision broadening $\Gamma(l)$ and not so much by the shape of the level diagram. For the singles experiment the spectra shapes look essentially exponential [Fig. 1(b)]. The calculation assumes that a K vacancy is brought into the collision (two-step process). For a one-step process (ionization and x ray in the same collision) the impact-parameter dependence of K-vacancy production has to be folded into the integration over Rutherford cross section. The end point of the spectrum is a function of scattering energy, because Γ itself increases with scattering energy. For very low scattering energies, e.g., 5 MeV in Fig. 1(b), the experimental end point of the spectrum may even lie before the united-atom limit as the asymptotic region of the level diagram is not reached in the collision. For comparing theory with experiment we note that the backgrounds of the tails of the atomic $K\alpha,\beta$ lines, the electron bremsstrahlung, transitions from higher MO's, and also the contribution of the slower recoil ions to the MO x-ray production[3] are expected to contribute mostly in the low-energy part of the x-ray continuum. This leads to a greater "filling up" of the spectrum shown in

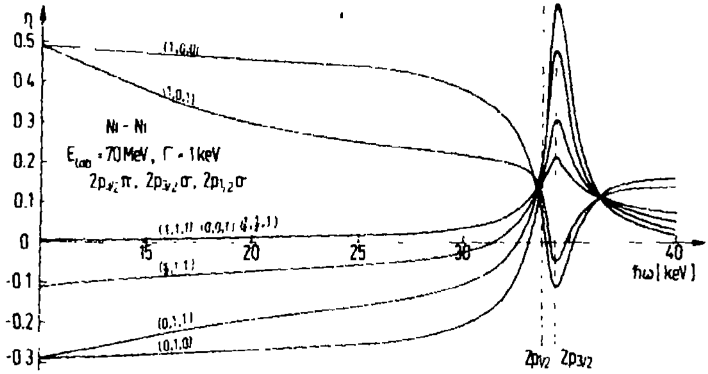

FIG. 2. The asymmetry as a function of photon energy for 70 MeV Ni-Ni collisions. The alignment (A^2, B^2, C^2) is indicated.

Fig. 1(b) at lower energies. It will be discussed in a forthcoming paper. The asymmetries (4) are shown in Fig. 2 for various alignments. For not too small scattering energies they show a practically linear dependence on energy, which is to a large extent compensated by the inverse energy dependence of the width Γ. They exhibit a strong dependence on photon energy $\hbar\omega$, which is entirely due to the induced transitions. The observation of this effect by Greenberg, Davis, and Vincent[3] uniquely proves the existence of molecular x rays and of induced transitions at the same time.

The shape (peaking) of the coincidence spectra gives great hope for future spectroscopy of two-center orbitals. In Ni-Ni collisions, e.g., it should ultimately be possible to determine the center of the peak to within a few hundred eV. This general feature should also hold for much heavier systems because the induced radiation always comes from the "compound-atom" region of the two-center level diagram. Experimentally this opens up the completely new field of x-ray spectroscopy of superheavy molecules which is of fundamental interest for quantum electrodynamics of strong fields. For example, in a system with $Z_1+Z_2 \sim 150$ the contribution of vacuum polarization from the Uehling potential is expected to be of the order of 5 keV for the $2p_{3/2}$-$1s_{1/2}$ transition and exceeds the self-energy contribution. Thus it would be for the first time possible to measure vacuum polarization as the dominant quantum electrodynamical effect.

We acknowledge the encouragement of and stimulating discussions with Professor D. A. Bromley and Professor J. S. Greenberg. We are especially grateful for the warm hospitality Professor Bromley and various members of the Yale Physics Department have extended to us.

---

[*] Work supported by the Deutsche Forshungsgemeinschaft, by Gesellschaft für Schwerionenforschung, and by the U. S. Atomic Energy Commission under Contract No. AT(11-1)3074.

[1] The idea of intermediate molecular states and corresponding x-ray transitions for superheavy systems was first suggested by the authors during Gesellschaft für Schwerionenforschung seminars. It has first been published in J. Rafelski, L. Fulcher, and W. Greiner, Phys. Rev. Lett. 27, 958 (1971).

[2] F. W. Saris *et al.*, Phys. Rev. Lett. 28, 717 (1972); P. H. Mokler *et al.*, Phys. Rev. Lett. 29, 827 (1972); W. E. Meyerhof *et al.*, Phys. Rev. Lett. 30, 1279 (1973); D. Burch *et al.*, private communication; C. K. Davis and J. S. Greenberg, Phys. Rev. Lett. 32, 1215 (1974); K. O. Groeneveld, B. Knaf, and G. Presser, private communication.

[3] J. S. Greenberg, C. K. Davis, and P. Vincent, following Letter [Phys. Rev. Lett. 33, 473 (1974)].

[4] B. Müller, J. Rafelski, and W. Greiner, Phys. Lett. 47B, 5 (1973).

[5] H. Tetrode, Ann. Phys. (Leipzig) 50, 336 (1926).

[6] B. Müller, R. Kent-Smith, and W. Greiner, Phys. Lett. 49B, 219 (1974). See also B. Muller and W. Greiner, "The Two-Center Dirac Equation" (to be published

[7] R. Kent-Smith, B. Müller, and W. Greiner, "Intermediate Molecular Phenomena in Heavy Ion Scattering" (to be published).

[8] J. Reinhardt *et al.*, "Multipole Bremsstrahlung in Heavy Ion Collisions" (unpublished).

[9] Note that the expressions (5) and similar ones for the cross section show "rainbow effects" due to the time dependence of the matrix elements, of $\omega_{mn}(t)$, and of $\Gamma(t)$ itself. These effects shall be separately

investigated in a forthcoming paper. Since these interference effects show up where the phase difference between contributions from approaching and leaving ions along the scattering trajectory are largest, they should occur most pronounced for low-energy transitions and their oscillation frequency should increase with bombarding energy of the ions.

[10] We acknowledge help in the calculations by W. Betz.

Evidence for Quasimolecular K X-Ray Emission in Heavy-Ion Collisions from the Observation of the X-Ray Directional Anisotropy*

J. S. Greenberg, C. K. Davis, and P. Vincent
Wright Nuclear Structure Laboratory, Yale University, New Haven, Connecticut 06520

(Received 3 June 1974)

We have observed an anisotropic angular distribution for the high-energy continuum x rays emitted in high-energy collisions of Ni ions with Ni atoms. The variation of the anisotropy with photon energy is uniquely characteristic of induced radiative transitions in quasimolecules, and hence provides strong evidence for the quasimolecular origin of these radiations.

A search for the formation of intermediate electronic molecules in close collisions of very heavy ions has been motivated recently by the prospect that such united atom phenomena may ultimately provide access to the spectroscopy of superheavy atoms and, therefore, to fundamental processes associated with the quantum electrodynamics of strong fields.[1] Proof for the existence of such quasimolecules has been sought in the emission of K x-ray radiation from transitions between the molecular orbitals that may be formed in the collision.[2-6] In this paper we report on the results of an investigation to detect such transitions in the ^{58}Ni + ^{58}Ni ion-atom system colliding at high energy. We discuss particularly the observation, for the first time, of a directional asymmetry for the high-energy continuum x rays emitted in the collision, which we utilize as a distinctive characteristic for identifying the quasimolecular origin of these radiations.

Studies with light-ion-atom systems have provided some of the more convincing demonstrations of molecular orbital x-ray emission.[2,5] However, the interpretation of experiments involving high-energy collisions of heavy-ion-atom systems,[3,4] which are more relevant to the future investigations noted above, are presently more speculative, relying on an ability to extrapolate detailed identifying features from mechanisms found applicable previously in light sysems. The interpretation of these experiments s particularly complicated by the exponential nergy dependence of the continuous spectra oberved, by uncertainties with regard to the mechanisms dominating K-vacancy production during high-energy heavy-ion collisions, by collision broadening effects, and most important, by the lack of a definitive signature for distinguishing this radiative process from other competing radiations.[4]

Recently, Müller, Smith, and Greiner[7] have noted that the characteristic angular distribution expected for molecular orbital K x-ray emission furnishes such a unique signature. This suggestion centers on the existence of the important, but previously neglected, induced transitions between molecular orbitals which specifically reflect the nonstationary character of the molecular electronic states as they adjust to the rotation of the internuclear axis. Reflecting the nuclear motion, the induced transitions can only be associated with the formation of quasimolecules. They add incoherently to the spontaneous molecular transitions with a relative intensity that grows with increasing photon energy. In the absence of a spatial alignment of the molecular orbitals, the induced radiations are predicted to exhibit an angular emission pattern relative to the ion-beam axis of the form $\frac{1}{2}+\frac{1}{4}\sin^2\theta$, while the spontaneous radiations are expected to be isotropic.[7] Thus the incoherent sum of the two produces a prominent enhancement of the angular distribution asymmetry near the united atom K x-ray energy.[8] As demonstrated in Ref. 8 we note that although an alignment of the molecular orbitals may modify these features quantitatively by changing the angular distributions of both the induced and spontaneous transitions, the observation of an anisotropy which peaks near the united atom K x-ray energy can only imply the existence of induced transitions, and thus of intermediate molecular states. The presence of an alignment of molecular orbitals, as reflected in the angular distribution, in itself speaks for the existence of intermediate molecules.

We have observed an anisotropic angular distribution for the high-energy continuum x rays produced in ^{58}Ni + ^{58}Ni collisions which favors photon emission at 90° over 0°, measured with respect to the ion-beam axis. The anisotropy also exhibits the enhancement, referred to above, for the higher energy x rays. By eliminating the nucleus-nucleus electric dipole bremsstrahlung with the utilization of monoisotopic targets and projectiles, and by accentuating the high-energy portion of the spectra with an Al filter, we were able to extend the investigation of the x-ray continuum over an intensity range of more than 3 orders of magnitude, revealing important features of the high-energy tail. The selection of identical nuclei for target and projectile not only suppressed the nuclear bremsstrahlung background, but equally important, it ensured the absence of radiations from coherent interference of nuclear dipole and quadrupole bremsstrahlung.[9] Unlike the individual multipoles, which produce an excess of radiation at 0° relative to 90°, the anisotropy from their interference has the same sign as the induced transitions.[9]

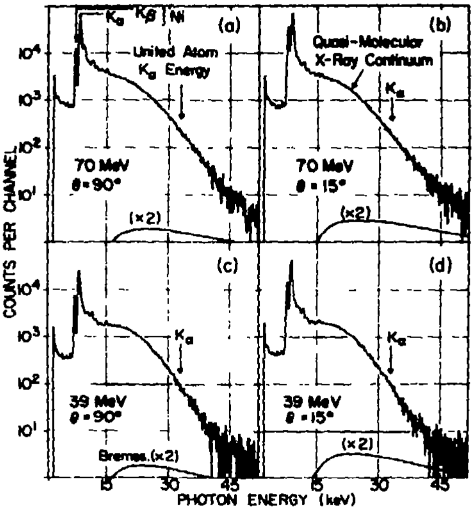

FIG. 1. (a), (b) Unnormalized x-ray spectra taken at bombarding energies 70 MeV and (c), (d) 39 MeV; (a), (c) detector angles are 90° and (b), (d) 15°. Detector resolution is 250 eV at 6.4 keV. The K_α and K_β lines are attenuated by factors of 3.5×10^{-6} and 1.4×10^{-4}, respectively.

Figure 1 illustrates x-ray spectra obtained with a thin target (~200 μg/cm^2) after subtractions of a small (~5 counts/channel) ambient background and still smaller contributions from nuclear Coulomb excitation and nuclear bremsstrahlung. The total calculated bremsstrahlung intensity shown in Fig. 1 includes approximately equal parts of quadrupole radiation from the target and bremsstrahlung from a Be beam stop.[9] It is clear that all these backgrounds produce only a negligible distortion of the spectra. Other processes contributing to the x-ray continuum include (1) electron bremsstrahlung,[10] (2) radiative electron capture,[10,11] and (3) collision broadening of the Ni K_α, K_β lines.[12] Their significant effect on the spectra, however, is confined to photon energies below ~15 keV. The interesting small oscillations in photon intensity, clearly visible in the spectra for energies below 15 keV, probably reflect interference effects from the phase difference between radiation from approaching and outgoing ions along the scattering trajectory[8]; this effect will be discussed in more detail in a forthcoming paper. We have limited the present discussion to photon energies above 15 keV to avoid these complicating features and the competing backgrounds mentioned.

Above 15 keV the spectra shown decrease almost exponentially with increasing energy after they are corrected for distortion by the Al filter and counter efficiency. With a range of 3 orders of magnitude in intensity available before background is encountered, it is clear that the high-energy continuum extends beyond the united atom K_α energy of ~32 keV by a considerable amount, and that the extent of the tail depends on the projectile energy. Müller and Greiner[8] have shown that dynamic broadening[12] with an effective collision width of a few keV can completely account for the extensive tails we observe. A collision width of a few keV is reasonable for the collision times encountered in this experiment. It is important to note, therefore, that with sufficient suppression of background, dynamic broadening of the molecular-orbital spectra shifts the apparent end point to a degree determined by the projectile velocity and counting statistics. This is particularly relevant for high-energy collisions where such broadening can obscure the identification of transition frequencies associat with the united atom limit, thus limiting the va ue of a straightforward utilization of the classical united atom limit for identifying quasimolecular formation.

The angular distribution asymmetries for photon energies above 15 keV were obtained from the measured spectra after they were corrected for absorption, counter efficiency, and Doppler-shift effects. An absolute beam integration was provided by an electron-suppressed Faraday chamber, and the relative normalization was corroborated by another x-ray detector which was fixed in position. We define the asymmetry as the intensity ratio [I(90°)/I(15°) − 1], where the angles are measured relative to the beam axis, and the photon interval summed is 5 keV. The results are summarized in Fig. 2 as a function of photon energy for bombarding energies of 39 and 70 MeV.

The Doppler-shift corrections are particularly important because of the exponential dependence of the photon intensity with energy. We must note that the calculation of the relevant Doppler shift involves assumptions regarding the mechanisms that dominate the molecular-orbital x-ray production. In the event that the *K*-vacancy production and molecular radiative relaxation occur in a single ion-atom encounter, it is clear that the relevant velocity is the velocity of the center of mass. This one-step mechanism, therefore, is associated with the maximum possible Doppler shift. The calculation of the Doppler-shift effect for a two-step process (*K*-vacancy production in one collision followed by the emission of a molecular orbital x ray in a second encounter of either he scattered projectile or the recoiling atom) involves the impact-parameter dependence of *K*-vacancy production in the first step. We have extracted an average effective velocity for the lat- er case, by analyzing the Doppler broadening and shift[13] of the characteristic Ni *K* x rays which reflect the *K*-vacancy production processes. This analysis indicates that the mean scattering angle for *K*-vacancy production is generally small; for example, it is ≲10° for 70-MeV projectiles, which agrees with the trends from other recent studies[14] and with the Massey criterion that the onization centers around impact parameters v/E_K, where E_K is the *K* binding energy. There- ore the participation of the scattered projectile n the two-step process produces a Doppler shift hich is only marginally smaller than the shift or the one-step process, while the contribution om the much slower laterally recoiling atoms duces the average shift particularly for the lower energy photons in the spectrum. Figure 2 shows the asymmetries uncorrected for Doppler shift as well as asymmetries which have been corrected for the maximum Doppler shift. It is evident that even the uncorrected asymmetries are large, and that in both extreme cases the asymmetries exhibit the characteristic peaking near the united atom *K* x-ray energy. Although there is presently some uncertainty as to the exact Doppler-shift correction to be applied at each bombarding energy due to a lack of precise information on the relative importance of one- and two-step processes, it is clear, nevertheless, that the asymmetries lie between the two extreme limits shown in Fig. 2, and that they display the important qualitative features expected for induced quasimolecular transitions.

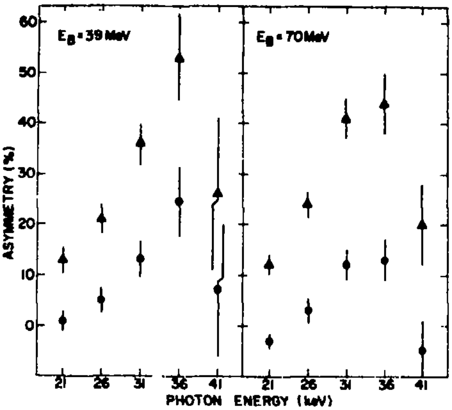

FIG. 2. Asymmetry ≡ [I(90°)/I(15°) − 1]; triangles and circles are for maximum and no Doppler shift corrections, respectively.

In addition to the data presented herein, we have also investigated the production of the x-ray continuum for bombarding energies from 5 to 70 MeV. These studies will be the subject of a forthcoming paper. For the present we note that these data display the expected changes in the structure of the high-energy x-ray tail predicted by relativistic calculations with the two-center potential by Müller and Greiner.[8] All these observations reflect the distinctive features that are associated with formation of intermediate molecules, and in particular, the measured asymmetries provide convincing evidence that the continuous spectra observed in these measurements are indeed quasimolecular in origin.

We are grateful to Professor D. A. Bromley for the constant encouragement and assistance which enabled us to carry out these measurements. The stimulating discussions with Professor W. Greiner and Dr. B. Müller, which guided and motivated our progress throughout the experiment, are especially acknowledged.

---

*Work supported by U. S. Atomic Energy Commission Contract No. AT(11-1)-3074.

[1] B. Müller, H. Peitz, J. Rafelski, and W. Greiner, Phys. Rev. Lett. 28, 1235 (1972), and Z. Phys. 257, 183 (1972).

[2] J. R. Macdonald, M. D. Brown, and T. Chiao, Phys. Rev. Lett. 30, 471 (1973).

[3] W. E. Meyerhof *et al.*, Phys. Rev. Lett. 30, 1279 (1973).

[4] C. K. Davis and J. S. Greenberg, Phys. Rev. Lett. 32, 1215 (1974).

[5] F. W. Saris, C. Foster, A. Langenberg, and J. v. Eck, to be published.

[6] For L and M x-ray investigations see F. W. Saris *et al.*, Phys. Rev. Lett. 28, 717 (1972); P. H. Mokler, H. J. Stein, and P. Armbruster, Phys. Rev. Lett. 29, 827 (1972).

[7] B. Müller, R. K. Smith, and W. Greiner, to be published.

[8] B. Müller and W. Greiner, preceding Letter [Phys. Rev. Lett. 33, 469 (1974)].

[9] J. Reinhardt *et al.*, "Multipole Bremsstrahlung in Heavy Ion Collisions" (to be published). We thank J. Reinhardt and W. Greiner for supplying the calculations prior to publication.

[10] P. Kienle *et al.*, Phys. Rev. Lett. 31, 1099 (1973).

[11] H. Schnopper *et al.*, Phys. Rev. Lett. 29, 898 (1972).

[12] J. H. Macek and J. S. Briggs, to be published; W. Lichten, Phys. Rev. A 9, 1458 (1974).

[13] R. G. Stokstad *et al.*, Nucl. Phys. A156, 145 (1970).

[14] J. H. McGuire, Phys. Rev. A 9, 286 (1974).

Anisotropic Emission of Noncharacteristic X Rays from Low-Energy I-Au Collisions

G. Kraft
Gesellschaft für Schwerionenforschung, Darmstadt, Germany

and

P. H. Mokler
Gesellschaft für Schwerionenforschung, Darmstadt, Germany, and Universität zu Köln, Köln, Germany

and

H. J. Stein
Institut für Kernphysik, Kernforschungsanlage Jülich, Jülich, Germany

(Received 10 June 1974)

The x-ray emission for 6- to 60-MeV iodine bombardment on thin Au targets was measured. Spectra, cross sections, and angular dependence of x-ray emission are reported. Special emphasis is placed on the noncharacteristic radiation formerly interpreted as M radiation of a quasiatom with an effective atomic number of 132. The emission of this radiation is found to be nonisotropic strongly supporting the model of induced emission in the collision molecule.

X-ray spectra from heavy-ion–atom collisions may show both characteristic lines of the separated collision partners, as well as broad noncharacteristic bands. In slow collisions the noncharacteristic x rays have been ascribed to radiative transitions between molecular orbitals (MO's) of transiently formed collision molecules.[1,2] Such noncharacteristic x rays, for instance, were observed at 11-MeV iodine bombardment on thick gold targets.[3,4] In these measurements the noncharacteristic band revealed a broad peak at about 8 keV. This energy corresponds to $4f-3d$ transitions[5] in a united atom. Therefore, the x-ray band has been interpreted as M radiation from a short-lived "superheavy quasiatom" wit an effective atomic number $Z=Z_1+Z_2=132$. A double-collision mechanism is assumed to be r sponsible for these x rays. In a first collision L vacancy is produced in the moving I ion. In second collision this inner-shell vacancy can cay in the I-Au collision molecule. The existe as well as the origin, of these x rays has bee confirmed by measurements at the University Rochester.[6] Nevertheless, this MO x-ray en sion is still not completely understood. Two ical features remain unexplained: first the b yield and second the spectral distribution.

In order to get more information on the emission mechanism we investigated in more detail the I-Au collision system at the Cologne tandem accelerator. Using thin Au targets and a high-resolution Si(Li) detector we determined the spectral distribution more precisely and we measured the x-ray production cross sections. In addition, the angular dependence of the x-ray emission was studied.

The experiments were performed with different setups. For spectral-distribution and cross-section measurements a conventional arrangement was used, see, e.g., Ref. 4 (target angle $\alpha = 45°$, x-ray emission angle $\theta = 90°$, cf. inset in Fig. 1). In order to determine cross sections it is necessary to count the total number of incident ions. For this purpose a special beam monitor was developed.[7] The primary ion intensity is measured via x rays produced in a beam chopper added just in front of the target chamber. For the measurement of the angular dependence of x-ray emission a special target chamber was used. X-ray emission angles θ between 15° and 105° were feasible (target angle $\alpha = -30°$, cf. inset in Fig. 2). The beam intensity was monitored via x rays registered in a fix-positioned proportional counter. The 30-mm² Si(Li) detectors used had resolutions of 170 and 260 eV (full width at half-maximum) at 6.4 keV. In all cases pile-up rejection with at least 1-μsec pulse-pair resolution within the whole energy range was applied. To reduce the rate from lower-energy x rays, Al absorbers could be inserted between target and detector.

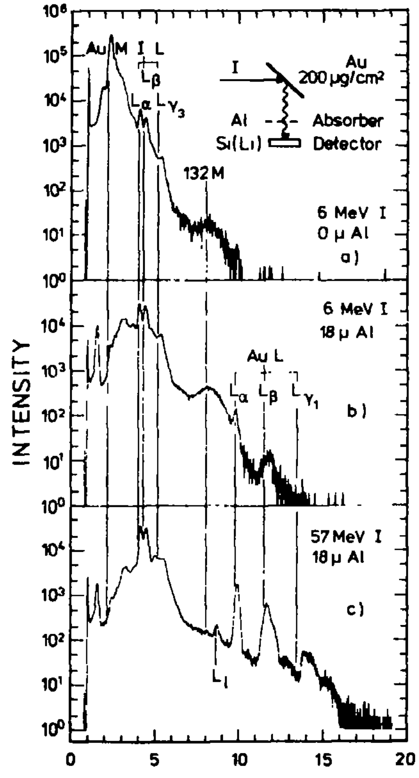

IG. 1. X-ray spectra from I → Au collisions.' (De-
tor resolution 170 eV at 6.4 keV.)

Figure 1 shows good resolved spectra from a 200-μg/cm² Au target. To determine the true spectral shape at low impact energies, spectrum (a) was taken without Al absorber. Absorption due to detector and target-chamber windows (0.3 mil Be, 5 mm air, 6 μm Hostaphan) and target self-absorption is only significant for lower-energy x rays. In the interesting energy range between 7 and 9 keV the total transmission varies by less than 2% per keV. Therefore, spectrum (a) definitively proves the existence of real peak structure. To get better statistics spectrum (b) was recorded with an 18-μm Al absorber. In both cases the count rates were low enough to ensure negligible pile-up contributions. A comparison of both these spectra indicates that at 6-MeV I impact the 8-keV band is composed of a broad peak (at 8.3 keV with a width of 1.5 keV) and a steeply descending continuum. With in-

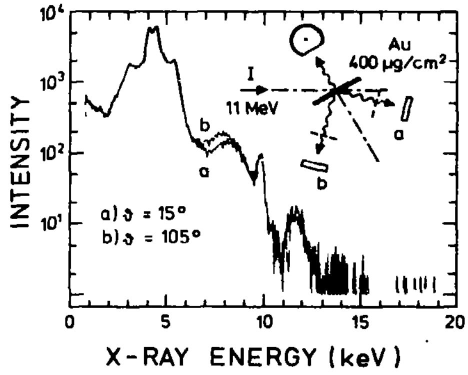

FIG. 2. Two x-ray spectra applying two different x-ray emission angles. (An 18-μm Al absorber is inserted between target and detector, detector resolution 260 eV at 6.4 keV.)

TABLE I. X-ray production cross sections (barns) for I→ Au collisions.

	I energy (MeV) 11	34	57
I *L* (3.6–6.5 keV)	4.0×10^3	2.5×10^4	9.5×10^4
MO (6.5–9.5 keV)	4.5×10^1	1.8×10^2	...
Au *L* (9.5–14.5 keV)	6.5×10^0	2.3×10^1	8.0×10^2

creasing impact energy the peak broadens; at 57 MeV only a flat continuum is present, cf. spectrum (c) in Fig. 1.

In Table I total x-ray cross sections are given for the 8-keV band as well as for the characteristic radiations of the separated collision partners.[7] These cross sections correspond to x-ray emission within the energy ranges indicated in brackets. The typical uncertainty is below 50%; isotropic emission has been assumed.

In order to check the emission characteristic we have measured the angular dependence of the x-ray emission at 11 MeV. Figure 2 displays two spectra taken at a detector position θ of 15° and 105°, respectively. Target angle ($\alpha = -30°$) and emission angles were chosen in such a way that target self-absorption is equal for both detector positions. The spectra are normalized to equal beam intensity. Besides the small Doppler shift of the I *L* radiation a significant difference is only seen for the 8-keV band. In Fig. 3 the angular dependence of the x-ray emission for the 8-keV band is given. Each datum point comprises all x rays in the corresponding spectrum between 7.1 and 9.5 keV. All spectra were corrected point by point on absorption[8] and on the tails of the characteristic lines. Uncertainties due to these corrections and errors in beam monitoring add to the indicated uncertainty of 4%. A $\sin^2$ function is fitted through the data points, yielding a mean anisotropy of 15% for all x rays in the band. However, it should be noted that the anisotropy varies with x-ray energy, cf. Fig. 2, being largest between 7.5 and 8 keV.

Summarizing the experimental facts we point out: (i) At low impact energies the 8-keV band is peaked. (ii) The peak structure broadens and finally vanishes with increasing impact energy. (iii) At 11 MeV the cross section for x-ray production between 6.5 and 9.0 keV is about 50 b. (iv) At 11 MeV the x rays are preferentially emitted perpendicular to beam direction. Regarding these facts, significant contributions from nuclear bremsstrahlung and bremsstrahlung from δ rays can be excluded (cf. the spectral shape and the high cross sections).[6] Contributions from target contaminations and radiative electron capture are also negligible.[3,4] Only MO radiation remains to be responsible for the 8-keV band. However, it is difficult to explain quantitatively the data in the simple model based on a comparison of collision time and *spontaneous decay* time of the vacancy carried into the quasimolecule in a second collision.[3] To overcome this difficulty a *collisionally induced de-excitation* reducing the lifetime of the vacancy in the quasimolecule has been proposed in Ref. 3, cf. also Ref. 7. Recently, from a theoretical point of view, Müller, Kent-Smith, and Greiner have postulated the occurence of such induced transitions in heavy-ion collisions.[9] In their model th rotation of the internuclear axis during collisio is responsible for induced radiative transitions As consequences they find: (a) The ratio betw induced and spontaneous emission increases r idly with decreasing distance of closest appro (as long as small- or medium-angle scatterin prevails). (b) This ratio increases with incre ing collision velocity. (c) The induced x-ray emission is nonisotropic showing—in dipole proximation—an angular dependence given by $I(\theta)\propto\frac{1}{2}+\frac{1}{4}\sin^2\theta$.

This induced-emission mechanism has the propriate features which in principle can ex the experimental results reported here: Fr point (a) the observed peak structure may b duced. From point (b) the dependence of th spectral shape on impact energy may follov large cross sections can be caused by the duced lifetime due to induced transitions.

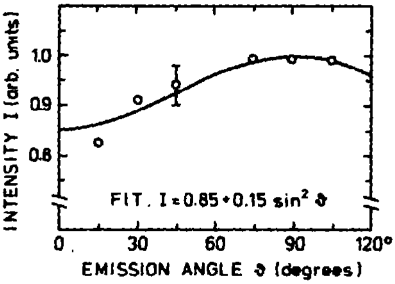

FIG. 3. Anisotropy of the noncharacteristic x rays between 7.1 and 9.5 keV for 11-MeV I impact on a 400-μg/cm^2 thick Au target.

we would like to emphasize the principal agreement between observed anisotropy of the noncharacteristic x rays and the theoretical predictions. This can be regarded as a strong evidence for the existence of stimulated emission in heavy-ion collisions contributing appreciably to quasimolecular x-ray emission.

The authors would like to acknowledge the good cooperation with I. Physikalisches Institut and Institut für Kernphysik der Universität zu Köln. We thank the tandem staff for producing a good I beam. We are grateful for stimulating discussions with P. Armbruster, W. Greiner, B. Müller, and R. Kent-Smith. One of us (H.J.S.) acknowledges fruitful discussions with I. Lovas.

---

[1] F. W. Saris, W. F. von der Weg, H. Tawara, and R. Laubert, Phys. Rev. Lett. 28, 717 (1972).

[2] F. W. Saris, I. V. Mitchell, D. C. Santry, J. A. Davies, and R. Laubert, in *Proceedings of the International Conference on Inner-Shell Ionization Phenomena and Future Applications, Atlanta, Georgia, 1972*, edited by R. W. Fink, J. T. Manson, I. M. Palms, and R. V. Rao, CONF-720 404 (U. S. Atomic Energy Commission, Oak Ridge, Tenn., 1973), Vol. 2, p. 1255.

[3] P. H. Mokler, H. J. Stein, and P. Armbruster, Phys. Rev. Lett. 29, 827 (1972).

[4] P. H. Mokler, H. J. Stein, and P. Armbruster, in *Proceedings of the International Conference on Inner-Shell Ionization Phenomena and Future Applications, Atlanta, Georgia, 1972*, edited by R. W. Fink, J. T. Manson, I. M. Palms, and R. V. Rao, CONF-720 404 (U. S. Atomic Energy Commission, Oak Ridge, Tenn., 1973), Vol. 2, p. 1283.

[5] B. Fricke and G. Soff, Gesellschaft für Schwerionenforschung Report No. GSI-T1-74, 1974 (unpublished).

[6] H. E. Gove, F. C. Jundt, and H. Kubo, Bull. Amer. Phys. Soc. 18, 559 (1973); F. C. Jundt and H. E. Gove, private communication.

[7] H. J. Stein, Gesellschaft für Schwerionenforschung Report No. GSI-73-11, 1973 (unpublished), p. 106.

[8] E. Preuss, Kernforschungsanlage Jülich Report No. Jül-856-TP, 1972 (unpublished).

[9] B. Müller, R. Kent-Smith, and W. Greiner, Phys. Lett. 49B, 219 (1974).

Determination of the *s*-Electron Contact-Density Ratio for the Fe Configurations $3d^64s^2$ and $3d^64s$ from Matrix-Isolation Mössbauer Spectroscopy

H. Micklitz and F. J. Litterst
Physik-Department, Technische Universität München, 8046 Garching, West Germany

(Received 13 June 1974)

^{57}Fe$^+$($3d^64s$) ions have been produced by uv irradiation of a xenon matrix containing 0.65% ^{57}Fe. The stabilization of these ions was accomplished by mixing ~1% of HI into the Xe matrix gas. The Mössbauer isomer shift of the ^{57}Fe$^+$($3d^64s$) resonance is +0.26 ±0.03 mm/sec against iron metal at 300 K. From this we obtain the ratio of the electron densities at the ^{57}Fe nucleus, $[\rho(0)_{3d^64s^2}-\rho(0)_{3d^6}]/[\rho(0)_{3d^64s}-\rho(0)_{3d^6}]=1.80\pm0.15$.

Mössbauer studies of neutral atoms have been performed as absorption experiments using the rare-gas-matrix-isolation (RGMI) technique.[1] Mössbauer source experiments with RGMI ^{57}Co[2] and RGMI ^{119m}Sn[3] extended these studies to charged ions (^{57}Fe$^+$ and ^{119}Sn$^+$). The electronic configuration of these ions, however, depends on the specific recombination mechanism of the highly charged ions created by the Auger cascade following the radioactive decay. These ions are not stable against recombination with free electrons ($\tau_{\text{recomb}}\sim3\times10^{-7}$ sec at 4.2 K).[2] A method for the production of these ions as stable species is of great interest, especially in connection with the problem of isomer-shift (IS) calibration. Stable ions then can be well specified and measured in absorption experiments.

We have generated and stabilized (for more than three weeks) ^{57}Fe$^+$($3d^64s$) ions in a xenon matrix at ~4.5 K. The measured IS of this ion, together with the known IS of ^{57}Fe($3d^64s^2$) and ^{57}Fe^{2+}($3d^6$), gives an experimentally determined value for the ratio $\rho(0)_{4s^2}/\rho(0)_{4s}$ [here $\rho(0)$ is the difference in the relativistic electron density at the iron nucleus between the electron configuration given as the subscript and the Fe^{2+}($3d^6$) configuration]. This ratio is a sensible test for existing self-consistent-field (SCF) calculations of $\rho(0)$.

The generation and stabilization of the ^{57}Fe$^+$ ions was accomplished by uv irradiation (wavelengths ~2500–3100 Å or photon energies ~4–5 eV) of a xenon matrix containing (0.65 ± 0.15)% ^{57}Fe as electron donor and ~1% HI as electron acceptor. This method has already been used by Kasai[4] for EPR studies of RGMI ions. Similar to Kasai we propose the following two-step process taking place during uv irradiation:

(1) Photodissociation of HI. HI shows continuous absorption between 2500 and 3100 Å leading to the $^3\Pi$ and $^1\Pi$ excited states of HI, which spontaneously dissociate into H and I.[5]

(2) Photoexcitation of Fe accompanied by a charge-transfer process between the excited Fe and the I atom: Fe* + I → Fe$^+$ + I$^-$. Fe atoms in a xenon matrix have six strong absorption bands between 2500 and 3100 Å leading to the different configurations of the excited states $3d^64s4p$ and $3d^74p$, respectively.[6] The charge-transfer process probably occurs between the $3d^64s4p$ excited Fe states and the I$^-$ state, since there is an energy resonance between these states [E_{ion}(Fe $3d^64s4p$) ~ E_{ion}(I$^-$)]; such charge-transfer processes due to "energy resonance" between the two electronic levels involved have been reported earlier.[2,7]

The resulting charged species Fe$^+$ and I$^-$ should be separated by an average distance of ~20 Å. Such a separation is considered large enough that the influence of I$^-$ on $\rho(0)$ of Fe$^+$ can be neglected provided both charged species are in their ground state configuration.[4] The electric field gradient (EFG) at the iron nucleus due to the splitting of the Fe$^+$(^6D) state in the axial electric field of the I$^-$, however, is not negligible and will be discussed below.

The ^{57}Fe-doped Xe(HI) matrix was obtained by evaporating an iron foil (~80% enriched ^{57}Fe) ou of an alumina crucible, and mixing the iron ato ic beam with a stream of Xe gas containing ~1 HI. This mixture was condensed on a liquid-he um-cooled beryllium disk (~4.5 K). Depositio rates were determined as described elsewhere In this way a Xe(HI) matrix with an iron atomi concentration of (0.65 ± 0.15)% corresponding t an amount of 65 ± 15 μg/cm^2 ^{57}Fe or ~6×10^{17} atoms/cm^2 was produced. For the uv irradiat of the matrix we used a 450-W high-pressure xenon lamp together with a filter combination sisting of an uv filter (Schott UG5) and a solu filter of NiSO$_4\cdot$6H$_2$O (0.3 g/ml H$_2$O, 5 cm ab tion length); this filter combination is transp

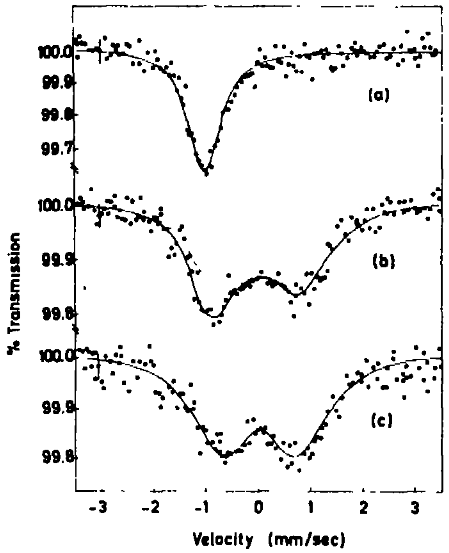

FIG. 1. Mössbauer absorption spectra of a xenon matrix containing (0.65 ±0.15)% ^{57}Fe (65 ±15 μg/cm^2 ^{57}Fe) and 1% HI. Matrix temperature ~4.5 K. Doppler velocities with respect to a ^{57}Co(Cu) source at 300 K. (a) Spectrum before uv irradiation; (b) spectrum taken after ~5 h of uv irradiation; (c) spectrum taken after ~15 h of uv irradiation.

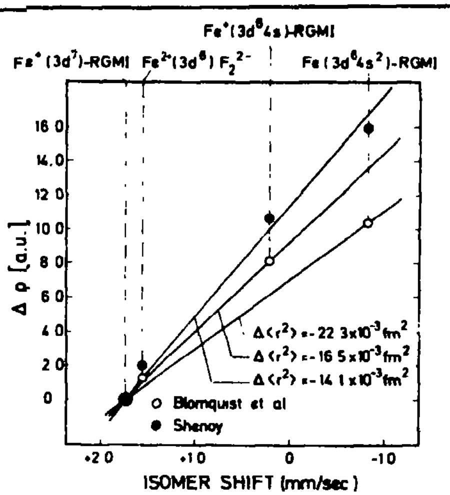

FIG. 2. Correlation between the relativistic electron density $\rho(0)$ at the ^{57}Fe nucleus and the isomer shift for ^{57}Fe. Isomer-shift values are given with respect to iron metal at 300 K. $\rho(0)$ values as calculated by Blomquist, Roos, and Sundbom, Ref. 11, and Shenoy, Ref. 13.

ent for wavelengths from 2500–3100 Å. The uv photon flux was ~5×10^{15} sec^{-1}cm^{-2} at the matrix.

Figure 1(a) shows the Mössbauer absorption pectrum of the ^{57}Fe-doped Xe(HI) matrix before v irradiation. The spectrum shows a single res- nance line (linewidth $\Gamma = 0.70 \pm 0.02$ mm/sec) ith an IS of -0.74 ± 0.02 mm/sec with respect) iron metal at 300 K. This spectrum is identi- al with that found earlier for ^{57}Fe atoms in a Xe ıatrix without HI admixture.[8,9] The Mössbauer bsorption spectra taken after ~5 h (~10^{20} pho- ons/cm^2) and ~15 h (~3×10^{20} photons/cm^2) of uv rradiation are shown in Figs. 1(b) and 1(c), re- pectively. After ~5 h of uv irradiation a small raction of the resonance line due to neutral 'Fe($3d^64s^2$) atoms can still be seen. After ~15 of uv irradiation this resonance line is com- etely replaced by a quadrupole doublet with an of 0.26 ± 0.03 mm/sec against iron metal at 0 K and a splitting of $\Delta E_Q = 1.39 \pm 0.03$ mm/sec. Ve interpret the quadrupole doublet in Figs.) and 1(c) as the resonance of the charged $^+$($3d^64s$) state. The quadrupole interaction is sed by the EFG of the Fe$^+$(^6D) level split in the axial electric field of a neighboring I$^-$. This splitting of the Fe$^+$(^6D) level has been estimated to be ~10 cm^{-1} for an Fe$^+$-I$^-$ distance of ~20 Å.[10] The distribution of the Fe$^+$-I$^-$ distances results in a variation of the Fe$^+$(^6D) level splittings, and therefore in a distribution of the EFG at the iron nuclei. This is reflected in the large linewidth, $\Gamma = 1.42 \pm 0.02$ mm/sec, of the quadrupole doublet.

Figure 2 shows a plot of the observed IS of RGMI ^{57}Fe($3d^64s^2$), RGMI ^{57}Fe$^+$ ($3d^64s$), and RGMI ^{57}Fe$^+$ ($3d^7$) together with the IS of ^{57}Fe in FeF$_2$ versus the charge densities $\rho(0)$ of the corresponding configurations as calculated by Blomquist, Roos, and Sundbom[11] [nonrelativistic Hartree-Fock procedure corrected by a uniform relativistic enhancement factor $S'(Z) = 1.29$[12]] and as calculated by Shenoy[13] (Dirac-Fock-Slater procedure). With the charge densities calculated by Shenoy the three RGMI "calibration" points of Fig. 2 are essentially consistent with a value of $\Delta\langle r^2\rangle = -(14.1 \pm 0.7)\times10^{-3}$ fm^2. This is not the case if we use the values obtained by Blomquist, Roos, and Sundbom. In this case one finds $\Delta\langle r^2\rangle = -(22.3 \pm 0.5)\times10^{-3}$ fm^2 from RGMI Fe$^+$($3d^7$) and RGMI Fe($3d^64s^2$) and $\Delta\langle r^2\rangle = -(16.5 \pm 0.5)\times10^{-3}$ fm^2 from RGMI Fe$^+$($3d^7$) and RGMI Fe$^+$($3d^64s$).

The $\Delta\langle r^2\rangle$ value obtained from the $\rho(0)$ calculations by Shenoy is in agreement with those obtained by Duff[14] [$\Delta\langle r^2\rangle = -(15.5 \pm 1.5)\times 10^{-3}$ fm^2] from a critical re-evaluation of the existing IS calibration attempts and by Kalvius and Shenoy[15] [$\Delta\langle r^2\rangle = -(15 \pm 5)\times 10^{-3}$ fm^2]. It also is in less disagreement with those obtained from measurements of the change in the lifetime of the 14.4-keV state in ^{57}Fe with the chemical environment: $\Delta\langle r^2\rangle = -(8 \pm 1.5)\times 10^{-3}$ fm^2 [16] and $-(6^{+7}_{-2})\times 10^{-3}$ *fm*^{2}.[17]

Effects of the rare-gas matrix on $\rho(0)_{4s^2}$ in the Fe($3d^6 4s^2$) *atom* seem to be ≲5% as estimated from the observed IS differences of Fe atoms isolated in different inert matrices (Ar, Kr, Xe [8,9]; N_2 [18]; CH_4, CO_2 [19]). Matrix effects on the spin density (hf-coupling constant) of RGMI Cu($3d^{10}4s$) as measured by EPR experiments[20] are of the same order of magnitude (≲ +5%). Matrix effects on RGMI *ions* can be estimated from EPR experiments with RGMI ions; the observed effects on the hf-coupling constant in Mn$^+$ ($3d^5 4s$) and Cd$^+$-($4d^{10}5s$) again are ≲−5%.[4] From these experimental facts we conclude that the rare-gas-matrix effects on $\rho(0)$ are ≲ ±5% *for* all Fe configurations.

From the IS data of Fig. 2 we derive the ratio $[\rho(0)_{4s^2}/\rho(0)_{4s}]_{\text{exp}} = 1.80 \pm 0.15$. Taking into account possible influences of the rare-gas matrix, as discussed above, would lower this value by maximal 5%, that is, to $[\rho(0)_{4s^2}/\rho(0)_{4s}]_{\text{exp}} = 1.65 \pm 0.15$. This value is in good agreement with the calculations of Shenoy which give $[\rho(0)_{4s^2}/\rho(0)_{4s}]_{\text{calc}} = 1.6$. It is, however, in serious disagreement with the ratio $[\rho(0)_{4s^2}/\rho(0)_{4s}]_{\text{calc}} = 1.3$ as obtained by Blomquist, Roos, and Sundbom. From optical isotope-shift measurements on $6s$- and $7s$-electron configurations one finds $[\rho(0)_{ns^2}/\rho(0)_{ns}]_{\text{OIS}} = 1.6 \pm 0.1$ for $n = 6$ [21] and $n = 7$ [22] again in excellent agreement with our measured value for $n = 4$.

Therefore we come to the conclusion that the calculated value of Blomquist, Roos, and Sundbom for the Fe($3d^6 4s^2$) configuration is probably ~35% too low, i.e., the s shielding within the $4s$ shell seems to be overestimated in these calculations. This could be caused by the use of a single relativistic enhancement factor $S'(Z)$ for all Fe configurations despite the known fact that relativistic contributions to the shielding ratios can be important.[23]

Our measurement shows that SCF calculations have to be treated with care. The relatively good agreement of our experimental data with the Dirac-Fock-Slater calculations by Shenoy could be just fortuitous. More SCF calculations of ratios of charge densities of different iron configurations are needed. Their comparison with various density ratios from experiments provides a crucial test for the quality of such calculations.

We acknowledge helpful discussions with G. M. Kalvius, K. Luchner, G. K. Shenoy, and F. Wagner.

---

[1] P. H. Barrett and H. Micklitz, in *Perspectives in Mössbauer Spectroscopy*, edited by S. G. Cohen and M. Pasternak (Plenum, New York, 1973), p. 117, and references contained therein.

[2] H. Micklitz and P. H. Barrett, Phys. Rev. Lett. 28, 1547 (1972).

[3] H. Micklitz, P. H. Barrett, J. T. Waber, and H.-S. Kwoh, to be published.

[4] P. H. Kasai, Phys. Rev. Lett. 21, 67 (1968).

[5] R. S. Mulliken, Phys. Rev. 51, 310 (1937).

[6] D. M. Mann and H. P. Broida, J. Chem. Phys. 55, 84 (1971).

[7] G. Gerth, K. Luchner, and H. Micklitz, Phys. Status Solidi (b) 53, 593 (1972).

[8] T. K. McNab and P. H. Barrett, in *Mössbauer Effect Methodology* (Plenum, New York, 1971), Vol. 7, p. 59.

[9] T. K. McNab, H. Micklitz, and P. H. Barrett, Phys. Rev. B 4, 3787 (1971).

[10] H. L. Schlaefer and G. Gliemann, *Einführung in die Ligandenfeldtheorie* (Akademische Verlagsgesellschaft, Frankfurt, Germany, 1967), p. 351 ff.

[11] J. Blomquist, B. Roos, and M. Sundbom, J. Chem. Phys. 55, 141 (1971).

[12] D. A. Shirley, Rev. Mod. Phys. 36, 339 (1964).

[13] G. K. Shenoy, private communication.

[14] K. J. Duff, Phys. Rev. B 9, 66 (1974).

[15] G. M. Kalvius and G. K. Shenoy, to be published.

[16] R. Ruegsegger and W. Kuendig, Phys. Lett. 39B, 62 (1972).

[17] R. N. Verma and G. T. Emery, Phys. Rev. B 9, 3666 (1974).

[18] H. Micklitz and P. H. Barrett, Appl. Phys. Lett. 2 387 (1972).

[19] C. Klee, T. K. McNab, F. J. Litterst, and H. Micklitz, to be published.

[20] P. H. Kasai and D. McLeod, J. Chem. Phys. 55, 1566 (1971).

[21] H. Kopfermann, *Kernmomente* (Akademische Verlagsgesellschaft, Frankfurt, Germany, 1956), p. 16

[22] J. Blaise and A. Steudel, Z. Phys. 209, 311 (1968

[23] M. A. Coulthard, J. Phys. B: Proc. Phys. Soc., London 6, 23 (1973).

Light Scattering by ^{3}He-^{4}He Mixtures near the Tricritical Point

P. Leiderer, D. R. Watts,* and W. W. Webb
School of Applied and Engineering Physics and Laboratory for Atomic and Solid State Physics, Cornell University, Ithaca, New York 14850

(Received 8 July 1974)

Scattering intensity and related measurements have established the tricritical exponents for the divergences of the concentration susceptibility, γ, and of the correlation length for concentration fluctuations, ν, have indicated a probable value for the exponent η, and have established a region of tricritical scaling.

We have measured the intensity of light scattering by liquid isotropic mixtures of ^{3}He and ^{4}He around the tricritical point (T_t, x_t), where the λ line delineating the concentration-dependent temperature $T_\lambda(x)$ of the continuous superfluid transition terminates at the top of a miscibility gap and the mixture begins a first-order separa- on into two phases, one a normal ^{3}He-rich fluid nd the other a ^{4}He-rich superfluid.[1-3] Light- cattering intensities give a direct measure of e concentration susceptibility $(\partial x/\partial\Delta)_{TP}$ near $_t$ in the small-scattering-vector limit $(q \to 0)$ in ontrast with experiments on specific heat[2] and aturated vapor pressure,[4] and the q dependence ives the correlation length ξ for concentration uctuations. Here x is the atomic fraction of He and $\Delta = \mu_3 - \mu_4$ is the difference between the hemical potentials of ^{3}He and ^{4}He.

The scattering power is proportional to the ex- nction length

$$h = A(\lambda)\frac{k_B T}{v^2}\left[\frac{1}{v}\left(\frac{\partial v}{\partial x}\right)_{TP}^2\left(\frac{\partial x}{\partial \Delta}\right)_{TP} + \beta_{Tx}\right], \tag{1}$$

here $A(\lambda) = (2\pi/\lambda)^4[4\pi\alpha N_0)^2/6\pi]$ and $\beta_{Tx} = -(1/$ $)(\partial v/\partial p)_{Tx}$. Here v is the molar volume,[3] αN_0 the molar polarizability of helium, and λ is e light wavelength. The isothermal compress- ility β_{Tx} varies only weakly near the tricritical oint (T_t, x_t),[6] whereas the concentration susceptibility $(\partial x/\partial\Delta)_{TP}$ is expected to diverge. Since e atomic volumes of ^{3}He and ^{4}He differ, con- entration fluctuations dominate the scattering d the critical opalescence is determined by the ivergence of $(\partial x/\partial\Delta)_{TP}$.

In summary, our results are as follows: First, e found a steep increase in scattered intensity cooling just below the λ line and an accom- nying local scattering maximum at $x - x_t > 0.01$. cond, on approaching T_t we found a divergence the scattering intensity indicating $\partial x/\partial\Delta \propto \epsilon^{-\gamma}$, ere $\epsilon = |T_t - T|/T_t$ and $\gamma = 1.0$ with high accu- cy. Third, we found evidence for a strong tricritical divergence in the superfluid phase of the correlation length ξ for concentration fluctuations that is consistent with model calculations of Furman and Blume.[7] The combined experiments provide a satisfactory test and confirmation of recent theoretical discussions on tricritical scaling.[8-12] Finally to cope with substantial concentration gradients near (T_t, x_t) due to the earth's gravitational field, we have measured them interferometrically and have determined the tricritical point and neighboring coexistence curve by using a reflectometric technique that is immune to gravitational perturbations. Our preliminary reports are corrected here.[13-15]

In our experiments, the temperature was (necessarily) controlled to better than ±1μK for a few hours to attain demonstrable equilibrium, and was calibrated to ±0.001 K absolute by vapor-pressure thermometry. Laser power was limited to avoid effects of heating at windows. Temperature differences $T_t - T$ were established to better than ±0.1 mK, as described below. Actual compositions, x_1 to x_5, were known to ±0.0016 absolute and ±0.0007 relative to each other. (Watt's thesis provides some experimental details[15] and more will be published elsewhere.)

Preliminary light-scattering data[12] on four compositions around x_t were obtained with the scattering volume positioned at two fixed heights for measurements in coexisting normal and superfluid phases. They coincide in the phase-separated region only until gravitational effects begin to grow near T_t. A sharp step in scattered intensities occurs in the mixtures with $x < x_t = 0.6750$[3] as they reach the transition from superfluid to normal fluid at their λ temperatures. In the scattering by the mixture $x_1 = 0.6318$ we noted a small, reproducible, nonhysteretic, rounded maximum slightly below $T_\lambda(x_1)$. This maximum is about 5% above the intensity at $T \lesssim T_\lambda$ and about 10 mK wide, and was not observed closer to x_t in the mixture $x_2 = 0.6623$.[16] The origin of the maximum is uncertain; it implies a weak singularity, in either $(\partial x/\partial\Delta)_{TP}$ or β_{Tx}, that vanishes as $x \to x_t$.[16]

Strong gravitational effects on measurements near the tricritical point are expected as a result of vertical gradients in composition induced by the gravitational potential whenever the concentration susceptibility is large.[17,18] There is a predicted concentration change with height of $\delta x(z) \propto z^{1/\delta} \sim z^{1/2}$. We determined $\delta x(z, T)$ to about 0.001 over a range ~4 mm by using a modified Jamin interferometer to measure changes of the index of refraction n, and thus composition changes by using $dn/dx \cong -0.0070$ near (x_t, T_t). From the results we estimated corrections for gravitational effects in the phase diagram reported by Alvesalo *et al.*[2] and confirmed the diagram given by Ahlers and Greywall[3] in clear preference to all others proposed.[1,2]

Because these effects obfuscate determination of the tricritical point, we have also redetermined it. We measured the limiting angle of total reflectivity of the interface in the phase-separated mixture, obtaining values for the discontinuity of the refractive index across the interface and hence the concentration difference $\Delta x = x_n - x_s$ between normal and superfluid coexisting phases. Δx was found to decrease linearly on approaching T_t with exactly the absolute value expected from the corrected phase diagram. Thus we confirm $\Delta x \propto \epsilon^{\beta}$ where the tricritical exponent is precisely $\beta = 1.00$ in the range $8\times10^{-4} \lesssim \epsilon \lesssim 10^{-2}$. The value of the tricritical temperature was determined as $T_t = 0.866 \pm 0.001$ K, in good agreement with only the result of Ahlers and Greywall, 0.867 K.[3] This experiment provides calibration for temperature differences from T_t to better than 0.1 mK, and determines the phase diagram free of gravity perturbations, since only the interface itself is involved in the measurement.

To avoid the gravitational effects on light scattering for measurements very close to T_t in the mixture $x_s = 0.6749$ $(x_t = 0.6750)^3$ the laser beam was focused and scanned vertically across the sample cell. In this was the scattered intensity was monitored $\simeq 0.2$ mm from the interface, thus providing data essentially free of gravity effects when $T_t - T \gtrsim 0.002$ K. The wave-number dependence in x_s was determined by using two wavelengths, $\lambda = 6328$ and 4880 Å, and two scattering angles, $\theta = 90$ and 15°, thus providing data at four wave numbers. Apparent concentration susceptibility data $(\partial x/\partial\Delta)_{TP}$, shown in Fig. 1, were obtained from the scattered intensities by using Eq. (1), i.e., by heuristically assuming isotropi scattering for the $q \to 0$ limit. The results were fitted by the expected power-law divergence of the form $(\partial x/\partial\Delta)_{TP} = G\epsilon^{-\gamma}$.

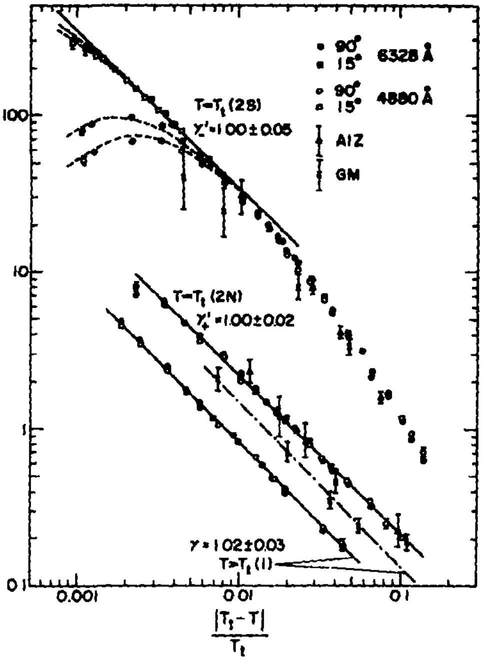

FIG. 1. Log plot of $(\partial x/\partial\Delta)_{TP}$ versus ϵ for the single phase (1), and for the coexisting normal (2N) and superfluid (2S) phases for the mixture $x_s = 0.6749$. For comparison, data of Alvesalo *et al.* (AIZ) and Goellner and Meyer (GM) (Refs. 2 and 4) are shown. The dashed lines show the best fit to our data calculated according to Eq. (2). At $\epsilon \lesssim 10^{-3}$, the remaining small discrepancy is attributable to gravity effects.

For the single-phase critical isochore and th normal coexisting phase, power laws were four to hold in the entire investigated temperature i terval. In contrast, the tricritical region for t superfluid seems to be confined to $T_t - T \lesssim 10$ mK, about the same temperature interval in which the phase diagram is linear. The best-f critical exponents γ and prefactors G (in mole are $\gamma = 1.02 \pm 0.03$, $G = (7.7 \pm 1)\times10^{-3}$, $\gamma_+' = 1.0$ ± 0.02, $G_+' = (2.2 \pm 0.2)\times10^{-2}$, $\gamma_-' = 1.00 \pm 0.05$, $= (3.2 \pm 0.6)\times10^{-1}$, where γ and G apply at $T >$ along the critical isochore, and γ_+' and G_+', γ_-' and G_-' apply at $T < T_t$ in the normal and perfluid coexisting phases, respectively. Va of $(\partial x/\partial\Delta)_{TP}$ obtained from the specific-heat of Alvesalo *et al.*[2] and from the saturated-vapor-pressure data of Goellner and Meyer[4] are included in Fig. 1 for comparison.

The onset of q dependence of the 90° scattering intensities in the coexisting superfluid is clearly evident in Fig. 1 for $\epsilon \lesssim 0.007$. We compared the scattered intensities in the coexisting superfluid phase with the modified Ornstein-Zernicke expression for the correlation function obtained from the Blume-Emery-Griffiths[12] model by Furman and Blume.[7] Their Fourier transform $C(\vec{q}, \epsilon)$ of the two-point correlation function, which is proportional to the scattering intensity, has the form $C(\vec{q}, \epsilon) \approx (aq^2 + b\epsilon)/(aq^2 + c\epsilon^2)$, where a, b, and c are constants given by the model. We find that our data can be well represented by this expression. The fit to our data at four values of q shown in Fig. 1 yields $a/c \approx 1.6\times10^{-16}$ and $aq^2 \ll b\epsilon$ for $\epsilon > 10^{-3}$.

Therefore, for $\epsilon > 10^{-3}$, we have[19]

$$C(\vec{q}, \epsilon) \approx \frac{\text{const}}{q}\left(\frac{q/\epsilon}{1.6\times10^{-16}q^2/\epsilon^2+1}\right). \qquad (2)$$

If we *define* the critical exponents η and ν by writing $C(\vec{q}, \epsilon) = (1/q^{2-\eta})F(q/\epsilon^{\nu})$,[10] we find that our experimental results are consistent with the critical exponents $\nu_-' = 1$ and $\eta_-' = 1$, which together with $\gamma_-' = 1$ fulfill the scaling relationship $\gamma = (2 - \eta)\nu$. Thus the correlation length ξ_-' for concentration fluctuations in the superfluid phase (*not* the superfluid correlation length) is given by $\xi = 1.3\epsilon^{-1}$ Å. The tricritical exponents for ^{3}He-^{4}He mixtures below T_t are thus $\beta = \gamma_{\pm}' = \nu_-' = \eta_-' \approx 1.0$ consistent with tricritical scaling. Note that the Furman-Blume form is consistent with simple scaling only in the region $aq^2 \ll b\epsilon$.

We are pleased to acknowledge many helpful suggestions by R. B. Griffiths, R. C. Richardson, and J. D. Reppy; stimulating discussions with H. Meyer and W. Zimmermann; experimental contributions by L. Jackel and J. Schwartz; theoretical advice by D. Nelson; and a preprint by D. Furman. This research was supported by the National Science Foundation and has benefited from the facilities of the Materials Science Center at Cornell. One of us (P.L.) acknowledges financial support by the Deutsche Forschungsgemeinschaft.

---

*Now at Department of Geology and Geophysics, Yale University, New Haven, Connecticut 06520.

[1] E. H. Graf, D. M. Lee, and J. D. Reppy, Phys. Rev. Lett. 19, 417 (1967).

[2] T. Alvesalo, P. Berglund, S. Islander, G. R. Pickett, and W. Zimmermann, Jr., Phys. Rev. Lett. 22, 1281 (1969), and Phys. Rev. A 4, 2354 (1971).

[3] G. Ahlers and D. S. Greywall, Phys. Rev. Lett. 29, 849 (1972), and in *Proceedings of the Thirteenth International Conference on Low Temperature Physics, Boulder, Colorado, 1972*, edited by W. J. O'Sullivan, K. D. Timmerhaus, and E. F. Hammel (Plenum, New York, 1973).

[4] G. Goellner and H. Meyer, Phys. Rev. Lett. 26, 1534 (1971); G. Goellner, R. Behringer, and H. Meyer, J. Low Temp. Phys. 13, 113 (1973).

[5] E. C. Kerr, Phys. Rev. Lett. 12, 185 (1964), and in *Proceedings of the Fifth International Conference on Low Temperature Physics and Chemistry, Madison, Wisconsin, 1957*, edited by J. R. Dillinger (Univ. Wisconsin Press, Madison, Wis., 1957), p. 158.

[6] R. B. Griffiths and J. C. Wheeler, Phys. Rev. A 2, 1047 (1970).

[7] D. Furman and M. Blume, to be published.

[8] R. B. Griffiths, Phys. Rev. Lett. 24, 715 (1970).

[9] R. B. Griffiths, Phys. Rev. B 7, 545 (1973).

[10] E. K. Riedel, Phys. Rev. Lett. 28, 675 (1972).

[11] E. K. Riedel and F. J. Wegner, Phys. Rev. Lett. 29, 349 (1972).

[12] M. Blume, V. J. Emery, and R. B. Griffiths, Phys. Rev. A 4, 1071 (1971).

[13] D. R. Watts, W. I. Goldburg, L. D. Jackel, and W. W. Webb, J. Phys. (Paris), Colloq. 33, C1-155 (1972).

[14] D. R. Watts and W. W. Webb, in *Proceedings of the Thirteenth International Conference on Low Temperature Physics, Boulder, Colorado, 1972*, edited by W. J. O'Sullivan, K. D. Timmerhaus, and E. F. Hammel (Plenum, New York, 1973).

[15] D. R. Watts, Ph.D. thesis, Cornell University, 1973 (unpublished).

[16] Zimmermann has reported a preliminary indication from fountain-pressure measurements of a pronounced peak in $dx/d\Delta$ at T_λ in a composition $x \sim x_t$. L. D. Dockendorf, C. A. Gearhart, Jr., and W. Zimmermann, Jr., in Proceedings of the Conference on Critical Phenomena in Multicomponent Systems, Athens, Georgia, 15–17 April 1974 (to be published).

[17] A. T. Berestov, A. V. Voronel', and M. Sh. Giterman, Pis'ma Zh. Eksp. Teor. Fiz. 15, 273 (1972) [JETP Lett. 15, 190 (1972)].

[18] P. C. Hohenberg and M. Barmatz, Phys. Rev. A 6, 289 (1972).

[19] To allow for some modification of this expression, which still leads to $C(0,\epsilon) \propto \epsilon^{-1}$, we set $C(\vec{q},\epsilon) \propto \epsilon^{-1}/(mq^n/\epsilon^2+1)$. The best fit was obtained for $m = 1.6\times10^{-16}$ and $n = 2.0$.

or

$$N=\sum_{k\sigma}\int_{-\infty}^{\infty}\frac{d\omega}{2\pi}A_1^{N+1}(k\sigma)f(\omega), \qquad (4')$$

where $f(\omega)=1/\{\exp[(\omega-\mu)/k_BT\}-1\}$. The excitation spectrum of an electron *added to* the lattice is calculated by G_{el} and the ground-state energy is given by $\int_0^N\mu(N)\,dN$. However, the energy spectrum of an electron *removed from* the lattice has to be computed by G_{hole}. Since $A_1^{N-1}(k\sigma)>A_1^{N+1}(k\sigma)$, the right-hand side of Eq. (4′) becomes greater than N if A_1^{N+1} is replaced by A_1^{N-1}. Therefore the hole state k_{max}^{N-1} with the maximum energy ξ_{max}^{N-1} cannot be k_F but $k_{max}^{N-1}<k_F$ and it should be calculated by

$$N=\sum_{k,\sigma}\int_{-\infty}^{\infty}\frac{d\omega}{2\pi}A_1^{N-1}(k\sigma)f(\omega). \qquad (5)$$

This is possible because, after losing an electron, the lattice of $N-1$ electrons is no longer in the ground state but in the excited state with a hole in k_{max}^{N-1}. The energy $-\xi_1^{N-1}(k\sigma)$ of a removed electron calculated by G_{hole} is then higher by the amount $\delta\xi_1^N$ than the corresponding energy $\xi_1^{N+1}(k\sigma)$ obtained by G_{el}, suggesting that an activation energy $\Delta_\epsilon(N)=\delta\xi_1^N$ supplied externally is needed to remove the electron.[7]

In conclusion, the ground state of the Hubbard lattice is a coherent (localized) state with a forbidden band $k_{max}^{N-1}\sim k_F^N$ between the occupied and unoccupied spectra; the activation energy $\Delta_\epsilon(N)$ and the momentum $k_F-k_{max}^{N-1}$ are needed to excite an electron into an unoccupied state, making the lattice an insulator with a small indirect gap $\Delta_\epsilon(N)$. The temperature dependence of the conductivity will be proportional to $\exp(-\Delta_\epsilon/2k_BT)$ of the carrier concentration.

Even if the number of electrons increases, the lattice will remain insulating. When the lower band is nearly half-filled the gap $\Delta_\epsilon(N)$ will attain its maximum value of $(2/3\pi)D$ (which may be ~0.3 eV if the original bandwidth $2D$ is of the order 3 eV) and then decrease gradually. Even if the lower band for electrons is filled with N' electrons, the "hole" band will be terminated at the state $k_{max}^{N'-1}$ and the small gap parameter d for G_{hole} will remain negative and finite. Consequently, the energy required to remove an electron from the lattice is equal to the activation energy $\Delta_\epsilon(N)$ but the lowest energy level into which the electron can be excited is in the upper band with energy $\xi_2^{N'+1}(k_0\sigma)$, thus suddenly increasing the activation energy to a large value $\xi_2^{N'+1}-\xi_1^{N'+1}\approx\Delta_I$. This energy gap is the same as the gap involved in the Hubbard result in magnitude as well as in physical origin. Even if more electrons are added to the lattice, however, the lattice remains a Hubbard insulator. Only after $\Delta N'$ electrons are added and the lower "hole" band is extended to the zone boundary does the lattice return to the small-gap semiconductor. By this time, $\Delta N'$ states in the lower part of the upper band for electrons are filled, yielding a finite negative value for the gap parameter d involved in G_{el}, and the arguments for the small-gap semiconductor developed for the lower band will be applied to this case. Only if the lattice is nearly empty or full does the gap parameter d vanish as $1/N_a$ and the lattice become metallic with the conventional Fermi surface.

As the bandwidth $2D$ increases, the gap parameter d increases, stabilizing the small-gap insulating state. If $2D$ becomes much greater than λI, however, energies in the upper half of the lower band and in the lower half of the upper band become complex, introducing finite widths in the spectra and, at the same time, reducing their spectral weights. Then the above tendency is reversed and eventually the lattice will become a normal metal with a single band, but a more precise calculation is needed to discuss the metal-nonmetal transition.

So far we have neglected explicit consequences of the third solution ω_3' since, in the narrow-band region, its spectral weight is of the order $(d/I)^2$ and smaller than the quantities δA and $\delta\xi$ of the order d/I needed in obtaining the foregoing conclusion. If the bandwidth increases, this is no longer the case. We have calculated the inverse Green's function correctly up to terms linear in ϵ_k by extending the perturbation up to an infinite order and found that the effect of ω_3' can be included properly and that the present conclusions remain correct.

---

*Based on work performed under the auspices of the U. S. Atomic Energy Commission.

[1] J. Hubbard, Proc. Roy. Soc., Ser. A 276, 238 (1963), and 281, 401 (1964).

[2] C. Herring, in *Magnetism*, edited by G. T. Rado and H. Suhl (Academic, New York, 1966).

[3] J. M. Luttinger, Phys. Rev. 119, 1153 (1960).

[4] N. F. Mott, Phil. Mag. 6, 287 (1961).

[5] This mechanism is parallel to the mechanism leading to Anderson's localizability of electrons in random lattices. See P. W. Anderson, Phys. Rev. 109, 1492 (1958); E. N. Economou and M. H. Cohen, Phys. Rev. B 5, 2931 (1972); F. Yonezawa and M. Watabe, Phys. Rev. B 8, 4551 (1973).

[6] T. Arai and M. Tosi, Solid State Commun. 14, 947 (1974).

[7] If $N=1$, the energy of an electron added to the lattice is $\epsilon_k-\Delta$ with $\Delta>0$, because of the attractive interaction between two electrons involved, but the energy of an electron removed from the lattice with $N=1$ is ϵ_k since only a single electron is present. This illustrates that the difference Δ is the activation energy needed to break up the bound pair. This two-electron N-site problem was originally solved exactly by J. C. Slater, H. Statz, and G. F. Koster, Phys. Rev. 91, 1323 (1953). The present result suggests that the same attractive interaction appears between the lattice with $N\to\infty$ and an electron added.

Observation of Recombination-Enhanced Defect Reactions in Semiconductors

D. V. Lang and L. C. Kimerling
Bell Laboratories, Murray Hill, New Jersey 07974

(Received 26 June 1974)

Recombination-enhanced annealing of defects in semiconductors has been observed directly for the first time. The defects were produced in GaAs by 1-MeV electron irradiation and observed by transient-junction-capacitance techniques. The data clearly relate the enhanced defect annealing rate to electron-hole recombination processes at the defect.

We have observed a new mechanism for the enhancement of defect reactions in semiconductors, namely enhancement by electron-hole recombination at the defect. A direct correlation of defect reactions with electron-hole recombination processes at the defect has not previously been observed. The details of such recombination-enhanced processes are crucial to the basic understanding of both defect motion and nonradiative recombination phenomena in semiconductors.

The recombination-enhanced mechanism was observed to produce a significant increase in the annealing rate of 1-MeV-electron irradiation defects in n-GaAs under conditions of minority-carrier injection. The specific identity of these defects is at this time unknown, but it is reasonable to expect that they are isolated vacancies, interstitials, and/or simple complexes. These radiation-induced defects are observed by a new junction-capacitance technique, deep level transient spectroscopy (DLTS).[1] With this technique it is possible to measure for each defect the activation energy for thermal emission of a carrier to the nearest band edge, the concentration, and the capture rates for electrons and holes. These properties are highly specific to a particular defect and allow us to resolve five levels whose acivation energies for electron emission to the onduction band are 0.08, 0.19, 0.45, 0.76, and .96 eV and three levels with activation energies or hole emission to the valence band of 0.32, .44, and 0.76 eV. A typical DLTS spectrum is hown in Fig. 1. The full details of the properties of these defects will be published elsewhere.[2] For the purpose of demonstrating recombination enhancement we will focus on the 0.45-eV electron trap shown in Fig. 1.

Junction-capacitance techniques such as DLTS are ideal for these studies since it is possible to independently vary both the average charge state and the electron-hole (e-h) recombination rate at a particular defect. The charge state can be var-

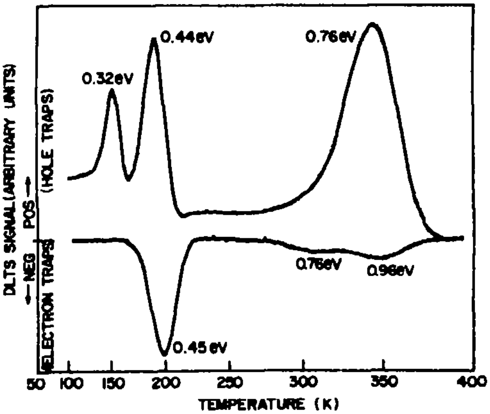

FIG. 1. A typical DLTS spectrum of 1-MeV electron irradiated n-GaAs. The energies shown are the measured activation energies for emission of a carrier to the nearest band edge. The positive signals are due to hole traps (injection pulse scan) while the negative signals are due to electron traps (majority-carrier pulse scan).

ied by placing the observed traps either in the depletion region (reverse bias) or in neutral material (zero bias). The effects of e-h recombination as well as charge-state changes are present in the annealing behavior under forward bias. It is known that a change in the charge state of a defect can have a significant influence on its annealing rate. This has been observed for the vacancy in silicon by EPR,[3,4] for the F center in alkali halides by optical spectroscopy,[5] and for the phosphorus-vacancy pair in silicon by Hall effect[6,7] and by junction-capacitance techniques.[8] Thus it is important to determine whether the enhanced annealing observed in our experiments is due to the dynamics of e-h recombination or to a change in the defect charge state.

The GaAs samples used in this study were asymmetric p^+n junctions grown by liquid-phase epitaxy. The p side of the junction in all cases was doped to 2×10^{18} cm^{-3} with Ge. In various samples the n-GaAs net donor concentration was between 4×10^{15} and 8×10^{16} cm^{-3} with the lower values in undoped samples and higher values in Sn-doped samples. Under these conditions the DLTS spectrum is sensitive to defects in only the n-type material. Our measurements showed that a radiation fluence of 1×10^{15} 1-MeV electrons/cm^2 at room temperature produced a uniform density of 7×10^{14} cm^{-3} of the 0.45-eV electron traps in undoped samples.

As mentioned above, the defect under study was observed by monitoring the electron trap level with a 0.45-eV activation energy shown in Fig. 1. This state was observed to disappear in a single thermal-annealing stage at approximately 200°C. No new states or increases in other states were observed. Measurements between 175 and 225°C give an activation energy $\Delta E_{\text{th}} = 1.4 \pm 0.15$ eV for a first-order annealing process with an exponential prefactor of 10^{11} sec^{-1}.

All observations of recombination-enhanced processes were below 100°C where the thermal annealing rate was negligible both at zero bias and under reverse bias. Thus the charge state of the defect had no effect on the annealing below 100°C. This conclusion follows from the fact that at zero bias the 0.45-eV electron traps which are observed by DLTS are in neutral material below the Fermi level and thus filled with electrons, whereas under reverse bias these same traps are in the depletion region of the junction where they are empty of electrons due to the fact that their charge state here is determined by the respective carrier thermal emission rates (electron emission rate ≫ hole emission rate). The physical basis of the DLTS measurement scheme[1] is, in fact, this same phenomenon: the alternate capture of electrons by the trap at zero bias followed by thermal emission of electrons at reverse bias. Thus the traps observed by DLTS are *by definition* those which undergo charge-state changes as a result of bias changes. A significant amount of annealing was observed, however, when the diode was in forward bias at these temperatures. The dependence of the defect annealing rate on injected current density at 100°C is shown for a sample with net donor concentration of 4×10^{15} cm^{-3} in Fig. 2.[9] This type of saturation versus current behavior is also characteristic of the e-h recombination rate at the defect. The rate is initially linear with current where capture of injected minority carriers is the limiting process and constant at large values of current where majority capture is the limiting process. DLTS measurements between 216 and 272 K show that the steady-state minority carrier (hole) occupation of this level, and hence the recombination rate, saturates at roughly the same forward current density as the annealing rate in Fig. 2. Measurements of the saturated annealing rate as a function of temperature between room temperature and 100°C yield an activation energy of 0.34 ± 0.03 eV. The saturated annealing rate at a fixed temperature in different samples is proportional to the net donor concentration as shown in Fig. 3. The saturated e-h recombination rate is also proportional to the net donor concentration.

We conclude from the above that the rate of the

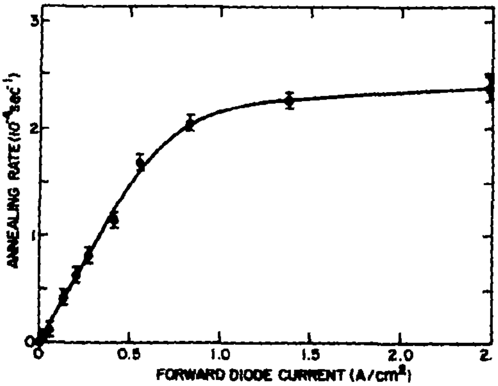

FIG. 2. Annealing rate of the 0.45-eV electron tr versus forward diode current at 100°C in a sample a net donor concentration of 4×10^{15} cm^{-3}.

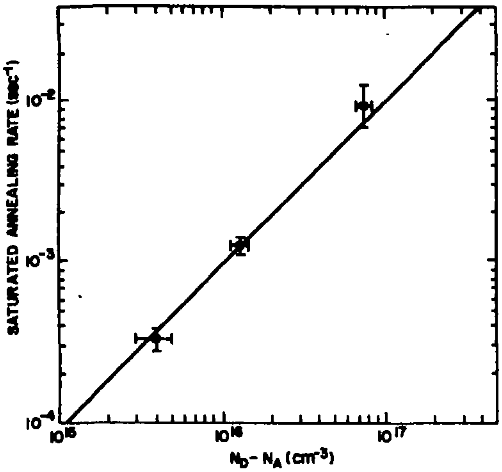

FIG. 3. Saturated annealing rate of the 0.45-eV electron trap versus net donor concentration in three sets of samples at 100°C. The solid line is a linear fit to the data.

enhanced defect annealing process is directly related to the rate of recombination at the defect. In addition, it has been determined that the enhancement under forward bias results from a recombination event at the defect and *not the accompanying change in the average defect charge state which is also described by the saturation versus current in Fig. 2.* This is because, as mentioned above, we saw no change in the signal due to heat treating at 100°C in either charge state.[10] Thus we rule out the possibility that the enhancement is due to a low-energy path characteristic of an alternate charge state.

Oscillatory changes in the charge state were also found to produce no measureable enhancement of the annealing process. By pulsing the reverse bias on and off at a high rate (1.7 MHz) in a 4×10^{15} cm^{-3} doped sample at 100°C we can produce the same total number of charge-state oscillations in 3 h as occur during 11 min of saturated e-h recombination (2×10^{10} oscillations). The bias oscillations produced essentially no change in the defect concentration (i.e., less than the noise level of 0.5%) while the recombination produced a 14% change. Thus the dynamics of e-h recombination and not simply charge-state oscillations are the important factor in enhancing the annealing rate of the defect.

Since we observe no increase in the concentrations of other defects and no new defects during the course of the annealing experiments we conclude that the decrease in the concentration of the 0.45-eV electron trap most probably corresponds to the annihilation of the corresponding lattice defect. Such an annihilation process could be the result of only a few reorientational jumps as in the case of a near-neighbor vacancy-interstitial pair (Frenkel defect) or an antistructure pair (Ga atom on As site and vice versa). It also could result from long-range diffusion of the defect to a suitable sink, e.g., vacancy or interstitial diffusion to a dislocation or a surface. In either case atomic jumps on the scale of a lattice constant are involved. The fact that e-h recombination at a defect can significantly enhance such jumps, which would otherwise require 1.4 eV of thermal energy, indicates strong electron-lattice coupling at the defect.

We believe that these data firmly establish the phenomenon of recombination-enhanced defect reactions in semiconductors. We have ruled out charge-state effects of the type observed for the vacancy in silicon[3,4] and proposed to explain injection annealing experiments in silicon.[11] In addition, a charge-state dependent saddle-point mechanism[12,13] has been eliminated by the null result of the oscillating bias experiments. Thus the enhancement is believed to be a unique result of a recombination event at the defect and related in no simple way to the defect charge state.

The effect may be of importance in a wide variety of systems. In particular it explains the observation that γ irradiated GaAs laser diodes regain their initial efficiency after operating at forward bias.[14] Recombination-enhanced processes of this type may also be active in the observed degradation only under forward bias of a wide variety of injection-mode devices such as GaAs tunnel diodes,[15] GaP light-emitting diodes,[16] and GaAs injection laser diodes.[15,17]

Clearly, a detailed understanding of recombination-enhanced lattice processes is very important for it will greatly increase our understanding not only of defect motion but also of possible mechanisms of nonradiative recombination as well.

The authors wish to thank R. A. Logan for growing the samples used in these experiments and A. J. Williams for fabricating the *p-n* junctions from this material. We especially wish to thank C. H. Henry for providing the initial motivation for this work.

---

[1] D. V. Lang, to be published, and Bull. Amer. Phys.

Soc. 19, 298 (1974).

[2] L. C. Kimerling, D. V. Lang, and R. A. Logan, unpublished.

[3] G. D. Watkins, J. Phys. Soc. Jpn. 18, 22 (1963).

[4] G. D. Watkins, in Symposium on Radiation Effects in Semiconductor Components, Toulouse, France, 1967 (unpublished).

[5] F. Lüty, in *Physics of Color Centers*, edited by W. B. Fowler (Academic, New York, 1968), p. 184.

[6] L. C. Kimerling, H. M. DeAngelis, and C. P. Carnes, Phys. Rev. B 3, 427 (1971).

[7] L. C. Kimerling and C. P. Carnes, J. Appl. Phys. 42, 3548 (1971).

[8] L. C. Kimerling, H. M. DeAngelis, and J. W. Diebold, Bull. Amer. Phys. Soc. 19, 210 (1974).

[9] At current densities above about 10 A/cm^2 the annealing rate begins to rapidly increase due to sample heating; this can be eliminated by pulsed current with low average power dissipation.

[10] A property of the DLTS measurement technique is that under reverse bias the observed defects are empty of electrons while under zero bias the same defects are filled with electrons.

[11] B. L. Gregory, J. Appl. Phys. 36, 3765 (1965).

[12] J. C. Bourgoin and J. W. Corbett, Phys. Lett. 38A, 135 (1972).

[13] G. D. Watkins, R. P. Messmer, C. Weigel, D. Peak, and J. W. Corbett, Phys. Rev. Lett. 27, 1573 (1971).

[14] C. E. Barnes, Phys. Rev. B 1, 4735 (1970).

[15] H. Kressel and N. E. Byer, Proc. IEEE 57, 25 (1969).

[16] R. L. Hartman, B. Schwarz, and M. Kuhn, Appl. Phys. Lett. 18, 304 (1971).

[17] S. A. Steiner and R. L. Anderson, Solid-State Electron. 2, 65 (1968).

Brillouin-Scattering Evidence for a New Phase Transition in Perovskite Crystals: PrAlO$_3$

P. A. Fleury, P. D. Lazay, and L. G. Van Uitert
Bell Laboratories, Murray Hill, New Jersey 07974

(Received 17 June 1974)

Brillouin scattering experiments have revealed a new structural phase transition in PrAlO$_3$ at 118 K, in which strain is the sole order parameter. This fact, together with the second-order nature of the transition, suggests that it belongs to a class of structural transitions first delineated nearly ten years ago by Anderson and Blount.

The cubic perovskite family of solids is well known to be potentially unstable toward structural phase transitions driven by soft phonon modes.[1] Several such purely lattice-dynamical phase transitions have been observed, driven by both Brillouin-zone-center[1] and -zone-boundary soft modes. PrAlO$_3$, for example, undergoes a cubic-rhombohedral transition at 1320 K driven by a soft R-point phonon.[2] In this respect it is similar to LaAlO$_3$ and several other members of the perovskite family.[3] However, because of the interaction between the Pr^{3+} 4f electronic levels and the PrAlO$_3$ lattice phonons, two additional structural phase transitions are known to occur as the temperature is lowered: a first-order rhombohedral-orthorhombic transition at 205 K, and a second-order orthorhombic-monoclinic transition at 151 K.[2,4]

We report here a new structural phase transition, of second order, at 118.5 K, which is driven by a soft transverse acoustic phonon. Despite several previous careful studies by a wide variety of techniques (optical absorption[2,5] and fluorescence,[2] neutron[4,6] and Raman scattering,[2] x-ray,[7] ESR,[8] specific heat,[9] and refractive index[10] measurements) this transition has remained heretofore undetected. This fact, together with the extremely large (~99%) acoustic anomaly observed in our Brillouin scattering experiments, strongly suggests that strain is the sole order parameter for this transition. Since the transition is apparently second order and involves a change of crystal symmetry, we suggest that this transition belongs to a class of structural transitions first delineated nearly a decade ago by Anderson and Blount.[11] Furthermore, it lies entirely outside the framework of present theories[1] of PrAlO$_3$, its properties, and its phase transitions, which have otherwise proven so successfu in imposing order on the multitude of magnetic, structural, and spectroscopic observations in this material.

The sequence of the previously known phase transitions in PrAlO$_3$ can conveniently be viewe in terms of changes in the direction of the axis about which the AlO$_6$ octahedra rotate in adjace cubic unit cells.[2,6] Between 1320 and 210 K thi axis is along ⟨111⟩. Between 210 and 151 K, it ⟨101⟩. Below 151 K it begins to rotate, and cor tinuously approaches ⟨001⟩ as the temperature approaches absolute zero. Both of these transitions arise from strong interactions between the Pr^{3+} electronic states (excitons) and the perovskite lattice modes (phonons), with the result that virtually *all* of the experiments cited in the previous paragraph can couple rather directly to the order parameter. Indeed, the $PrAlO_3$ 151-K transition is probably the most completely studied structural phase transition from the viewpoint of direct order-parameter measurements.[2,4,6,8] It was, in fact, the observed linear coupling between the soft quadrupolar exciton[4] and the ⟨101⟩-directed TA phonon near 151 K which led to our initial Brillouin studies of $PrAlO_3$. The results of our experiments on the 151-K transition will be detailed elsewhere. Here we shall concentrate on the new transition.

The results reported here were obtained by right-angle ($\theta = \frac{1}{2}\pi$) Brillouin scattering, excited by a stabilized single-mode argon ion laser operating at 5145 Å. To avoid heating of the sample, power levels were restricted to between 10 and 20 mW. The spectra were obtained using a pressure-scanned flat Fabry-Perot interferometer. The samples were single crystals a few millimeters on a side and of a medium green color (a room-temperature absorption length for 5145-Å light of ~1 cm), grown from a $PbO \cdot PbF_2 \cdot P_2O_5$ flux. Because of previously reported[4,7,8] sensitivity to mounting strains for domain structure, etc., we employed both (a) cold-finger and (b) flowing-gas variable-temperature Dewars, with temperature stabilities of 0.01 and 0.05 K, respectively. Arrangement (b) permitted strain-free sample mounting, while (a) required bonding of the sample to the copper cold finger. Although deliberate straining did reduce the acoustic anomaly near 118 K, our usual mounting procedure gave identical results in configurations (a) and (b), indicating that any strain effects arose from internal rather than external strains. Further evidence for this came from the observed sample-to-sample variations as high as 5% in the maximum size of the acoustic anomaly near T_c. Detailed results are presented for the most strain-free samples.

Figure 1 exhibits the Stokes-Brillouin spectra for right-angle scattering [$q = (4\pi n/\lambda)\sin\frac{1}{2}\theta = 3.45 \times 10^5\ \mathrm{cm}^{-1}$; $n = 1.99$[10]] near $T_c = 118.5$ K. The two other expected acoustic modes were observed at higher frequencies, but exhibited no unusual temperature dependence. In Fig. 2 the temperature dependence of the observed elastic constant $c_{ij} = \rho V_s^2$ (where $\rho = 6.68\ \mathrm{g/cm^3}$ and $V_s = 2\pi\nu_B/q$) is shown. The following features of these results are noteworthy: (a) A nearly 99% decrease in c_{ij} occurs between 160 and 118 K. (b) Over a wide range, both above and below T_c, the anomalous temperature variation is mean-field-like ($c_{ij} = a|T - T_c|$). (c) The temperature coefficient is much larger above than below T_c ($a_> = 0.80 \times 10^{11}$ dynes/cm^2 K; $a_< = 0.10 \times 10^{11}$ dynes/cm^2 K) which differs greatly from the usual mean field ratio $(a_>/a_<)_{MF} = 2$. (d) Scattering and polarization geometries show that the new soft mode is transverse and propagates in either the ⟨110⟩ or ⟨011⟩ direction, polarized in the ⟨001⟩ or ⟨100⟩ direction. All directions are referred to cubic perovskite axes. The ⟨010⟩ or b direction in the orthorhombic phase is defined as in Ref. 8, and is operationally identified in our samples by observation of the soft mode responsible for the 151-K transition, which has $\hat{q} = \langle 101 \rangle$ and $\hat{e} = \langle \bar{1}01 \rangle$. (e) Variation of the phonon $\hat{q}$ direction by up to ±5° (in-

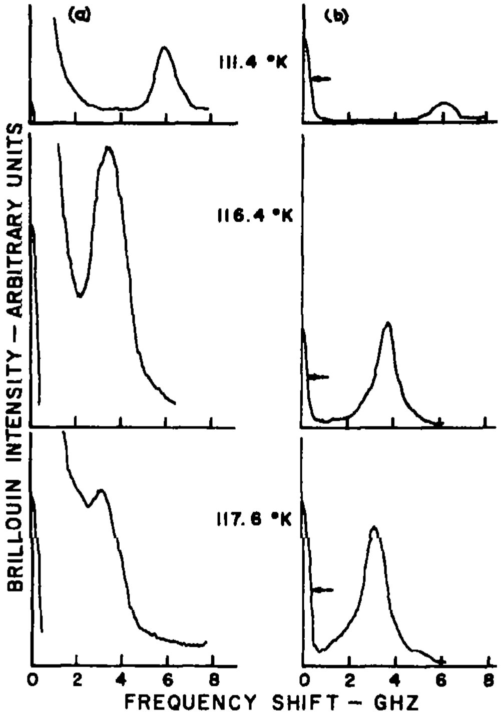

FIG. 1. Stokes-Brillouin spectra near T_c in $PrAlO_3$. (a) Without I_2 filter; elastic intensity reduced 100 ×; (b) with I_2 filter to reduce elastically scattered intensity. Arrows indicate instrumental width. Experimental geometry is $X(ZX)Y$ as discussed in the text.

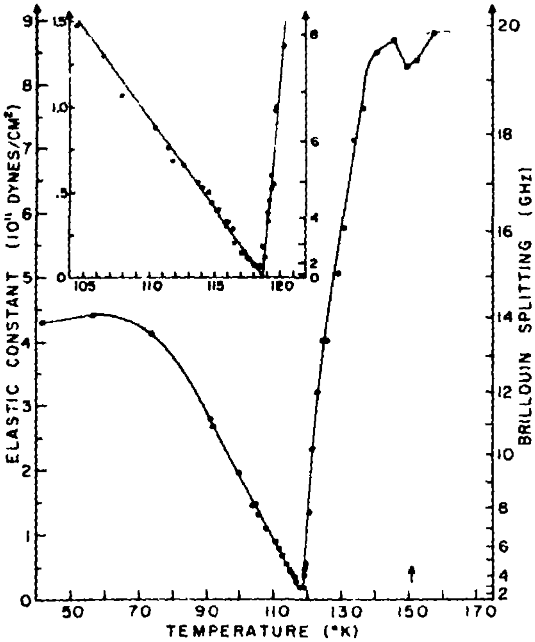

FIG. 2. Temperature dependence of soft-mode splitting ν_B (right-hand axis) and elastic constant (left-hand axis). Inset shows linear behavior of c_{ij} in $|T-T_c|$ on both sides of T_c.

ternal) with respect to the ⟨110⟩-type direction shows that contributions of nonanomalous elastic constants[12] reduce the size of the observed elastic anomaly by less than 1% when q is within ± 2° of ⟨110⟩. (f) Both above and below T_c the Brillouin spectra reveal that ⟨110⟩ and ⟨$\bar{1}$10⟩ are *not* equivalent phonon propagation directions. In particular, for the "wrong" direction no softening of the TA mode is observed. This inequivalence of +45° and −45° directions relative to the b axis is incompatible with the currently accepted monoclinic[4,6] structure below 151 K. (g) An *increase* in crystal symmetry *below* T_c is implied by the observed polarization selection rules. [For the $X(\alpha\beta)Y$ scattering geometry, relative soft-mode scattering intensities of 1.0, 0.81, 0.58, and 0.33 were observed at 121 K for $\alpha\beta$ equal to ZZ, YZ, ZX, and YX, respectively. At 112 K the corresponding relative intensities were 0.03, 0.89, 1.00, and 0.05, respectively.] (h) As $T\to T_c$ and the mode softens, the scattering intensity increases. This increase is, within experimental error (± 5%), in accord with the expected relation $I_B\nu_B^2 = \text{const}$.[13] (i) Very near T_c the frequency decrease saturates so that the soft mode does not actually reach zero. Among other possible reasons for this, discussed below, is the existence of a dynamic central peak arising from the soft mode as T_c is approached. However, a more detailed examination using an I_2 filter[14] to suppress elastic scattering [see Fig. 1(b)] revealed no dynamic quasielastic scattering outside the instrumental resolution (400 MHz, full width at half-maximum).

These observations (a)–(i) imply that $PrAlO_3$ undergoes a symmetry-changing (d), second-order (a) structural transition near 118 K which in some respects (b) is mean-field-like, but in others (c) not. Because of the negligible effect of this transition on quantities sensed by Raman, ESR, fluorescence, and absorption spectroscopy, together with its immense effect on the shear elastic properties, it appears that strain is the sole order parameter for this transition. Symmetry arguments applied to those transitions in which the strain is the only order parameter in the Landau sense permit only three classes of pure strain transition.[11] Two of these, which heretofore exhausted all known real examples, require that the transition be *first order*. The third permits a second-order, pure strain transition provided (a) there is a change in symmetry, and (b) all cubic and trigonal, and most hexagonal, symmetries are not involved. The only possible point of doubt regarding the admissibility of the 118-K transition to this class lies in point (i) above: the failure of the mode frequency to soften completely to zero. There could be five possible causes or contributions to this behavior: (I) The transition ultimately is first-order, albeit with at least 99% second-order character; (II) internal strain fields "round" the transition; (III) the phonon mode observed is not purely the relevant strain[12] (e.g., $\hat{q}$ could be slightly off the required axis); (IV) the emergence of a dynamic central peak may cause a saturation in the decrease of ν_B; (V) "$q\xi$" effects round the critical behavior when the inverse correlation length ξ^- approaches the wave vector of the experiment.[15] For this effect to account for the observed rour ing, assuming mean field behavior ($\xi^2 = \xi_0^2|T_c/(T-T_c)|$), a value of $\xi_0 \sim 50$ Å would be requir While large, this is not unreasonable for structural transitions.[6] Measurements at much sm er $q\xi$ (e.g., ultrasonics) would resolve this aspect of the question.

Except for (I) these effects would not preclu the classification of the 118-K transition as a

Anderson-Blount transition. Based on experiments in a large number of samples, we believe that (II) is the dominant effect and is probably responsible for all the observed ν_B saturation.

Regardless of whether or not this transition strictly belongs to the Anderson-Blount class, it is of particular interest for at least two additional reasons. First, it lies entirely outside the framework of our present understanding of $PrAlO_3$ and therefore possibly of other cooperative Jahn-Teller systems. Additional symmetry complications in $PrAlO_3$ uncovered by this work pose challenges to the proper extension of these theories. Because Brillouin experiments cannot give unambiguous determination of crystal symmetry, careful neutron or x-ray studies near 118 K are needed. Second, and of perhaps wider interest, is the generality of the occurrence in perovskite-like lattices of this type of transition. Certainly it has not yet been observed in any other such material, but could easily have been missed because of the negligible coupling of the order parameter to other than acoustic probes. Although the electronic and optical phonon modes play no direct role in this transition, does it occur because of a particular set of anharmonic circumstances which themselves result from the higher temperature exciton-phonon–driven transitions in $PrAlO_3$? Unless this rather unlikely situation is indeed the case, it is quite reasonable to suppose that there are other pure-strain structural transitions in perovskite-like materials awaiting discovery.

We are grateful to R. J. Birgeneau and E. I. Blount for numerous helpful discussions and to S. Bortas for polishing the samples.

Note added.—Recent neutron diffraction studies (P. G. Woralton and R. A. Byerlein, to be published) of the pressure-induced phase transition[13] in TeO_2 confirm that this transition is also of the Anderson-Blount type.

---

[1] See, for example, *Light Scattering in Solids*, edited by M. Balkanski (Flammarion, Paris, 1971).

[2] R. T. Harley, W. Hayes, A. M. Perry, and S. R. P. Smith, J. Phys. C: Proc. Phys. Soc., London 6, 2382 (1973).

[3] J. F. Scott, Phys. Rev. 183, 823 (1969).

[4] J. K. Kjems, G. Shirane, R. J. Birgeneau, and L. G. Van Uitert, Phys. Rev. Lett. 31, 1300 (1973).

[5] E. Cohen *et al.*, Phys. Rev. 186, 476 (1969).

[6] R. J. Birgeneau, J. K. Kjems, G. Shirane, and L. G. Van Uitert, Phys. Rev. B (to be published).

[7] R. D. Burbank, J. Appl. Crystallogr. 3, 112 (1970).

[8] E. Cohen, M. D. Sturge, R. J. Birgeneau, E. I. Blount, L. G. Van Uitert, and J. K. Kjems, Phys. Rev. Lett. 32, 232 (1974).

[9] F. S. L. Hsu, private communication.

[10] R. C. Miller, private communication.

[11] P. W. Anderson and E. I. Blount, Phys. Rev. Lett. 14, 217 (1965).

[12] A recent example of such effects on the Brillouin spectrum of a solid was presented by P. S. Peercy and I. J. Fritz, Phys. Rev. Lett. 32, 466 (1974).

[13] See, for example. P. A. Fleury, Comments Solid State Phys. 4, 149, 167 (1972).

[14] G. E. Devlin *et al.*, Appl. Phys. Lett. 19, 138 (1971).

New Transport Phenomenon in a Semiconductor "Superlattice"*

L. Esaki and L. L. Chang
IBM Thomas J. Watson Research Center, Yorktown Heights, New York 10598

(Received 1 July 1974)

We report electronic transport properties in a GaAs-AlAs periodic structure known as a "superlattice" prepared by a molecular-beam epitaxy. Its differential conductance in the superlattice direction first gradually decreases, followed by a rapid drop to negative values, then, at high fields, exhibits an oscillatory behavior with respect to applied voltages. This observation is interpreted in terms of the formation and expansion of a high-field domain. The voltage period of the oscillation provides the energy of the first-excited band which is in good agreement with that predicted by the theory.

has been proposed[1,2] that quantum states with irable energies or bandwidths can be created monocrystalline semiconductors, once a well-ined structure with extremely narrow poten- barriers and wells is achieved in a controlled manner: The transport of electrons in the structure is then expected to be largely governed by such quantum states.

In this Letter, we report transport properties in a periodic structure known as a "superlattice."

The current and conductance as a function of applied voltage show nonlinear characteristics and exhibit an oscillatory behavior beyond a certain threshold voltage. The observed period of the oscillation in terms of applied voltage appears to coincide with the energy difference between the quantized states or bands. This result, we believe, not only suggests the formation of a high-field domain but also confirms the creation of the ground and first-excited bands in the superlattice.

The superlattice used in the present experiments typically comprises fifty periods. Each period has a thickness of 85 Å, consisting of 45 Å GaAs and 40 Å AlAs. The latter provides a potential barrier of a height of 0.4–0.5 eV. The structure has been grown on GaAs substrates by the advanced facilities of computer-controlled molecular-beam epitaxy.[3] The conduction-electron density is $\sim 10^{17}$ cm^{-3} in the superlattice region and $\sim 10^{18}$ cm^{-3} in contacting GaAs regions, the substrate on one side and an overlaid layer on the other. The formation of such a superfine structure has been verified by a combined technique of Auger electron spectroscopy and argon-ion sputter etching,[4] and more recently by small- and large-angle x-ray scattering techniques.[5]

The allowed energy bands in a superlattice can be calculated from the following expression, assuming a one-dimensional, periodic square-well potential.[6]

$$-1 \leqslant \cos\frac{a(2mE)^{1/2}}{\hbar}\cosh\frac{b[2m(V-E)]^{1/2}}{\hbar}+\left(\frac{V}{2E}-1\right)\left(\frac{V}{E}-1\right)^{-1/2}\sin\frac{a(2mE)^{1/2}}{\hbar}\sinh\frac{b[2m(V-E)]^{1/2}}{\hbar}-1,$$

where E is the electron energy in the superlattice direction, V the barrier height (0.4 eV), a the well width, b the barrier width, and m the effective mass ($0.1m_0$). The hatched region in Fig. 1 indicates the two energy bands, E_1 and E_2, as a function of well width, with the barrier width constant at 40 Å. In the present case with a well width of 45 Å, the widths of the ground and first-excited bands, E_1 and E_2, are as narrow as 5 and 40 meV, respectively. Such narrow bandwidths are a result of the relatively tight-binding potential in the present structure,[7] as compared with that previously investigated.[8] Thus the location of E_1 and E_2 in this case are essentially the san as those of discrete energy levels in a single square well. Since the scattering time τ is estimated to be of the order of 10^{-13} sec in our epitaxial structure,[8] an inherent broadening ev for these discrete levels is expected to be 6–7 meV. Therefore, in order to test these theor cal curves, we have employed the method of t previously reported resonant tunneling in doul barriers.[9] The energies, E_1 and E_2, for thre different well widths, 40, 50, and 65 Å, wer obtained from a large number of double barr Although there is some understandable spre as shown in Fig. 1, because of thickness flu tion and other imperfections, the measured ues generally fall on the calculated curves, ticularly well for the ground state.

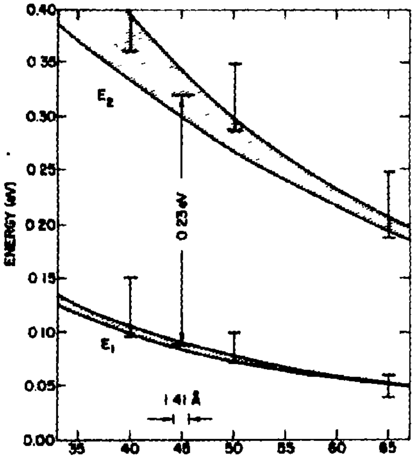

FIG. 1. Two superlattice energy bands, E_1 and E_2, calculated as a function of well width with a barrier width of 40 Å. Each range indicates some spread of experimental values taken from double barriers. Distance of 1.41 Å represents the spacing between (100) atomic planes in GaAs or AlAs.

Transport measurements were made on t present superlattice with two-terminal spe mens of an area of about 10^{-7} cm^2. The cu is found to increase smoothly with applied ages up to a few tenths of a volt. Subseque it starts to saturate or decrease and at hi ages a fine oscillatory behavior is develo Results of 50-nsec pulsed measurements essentially the same. Figure 2 illustrate differential conductance as a function of voltage at four different temperatures: 210, and 300°K. At room temperature, ductance neither becomes negative nor

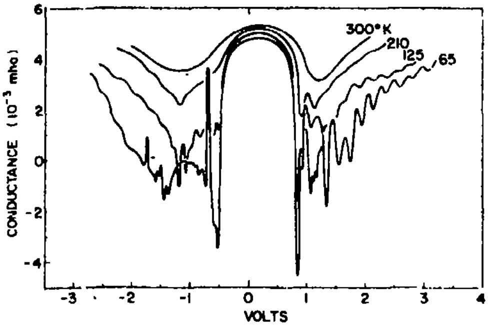

FIG. 2. Differential conductance versus applied voltage in a superlattice at four specified temperatures.

fine structure. The oscillatory behavior is observable at 210°K and becomes increasingly pronounced at lower temperatures. On the other hand, both the conductance near zero bias and a threshold voltage where the conductance begins to drop sharply are relatively insensitive to the temperature variation. Instabilities sometimes exist in the negative-conductance range which give rise to spurious conductance curves. The asymmetric characteristic with respect to polarity, as seen in Fig. 2, is fairly common in many specimens, and is likely due to an asymmetry in the potential profile, although its origin is not clear at this moment. In measuring over 20 specimens, the general features of the conductance, however, are quite reproducible: The onset voltage for the negative differential conductance ranges from 0.4 to 0.8 V and the period of the oscillation falls between 0.21 and 0.24 V.

The observed characteristics are interpreted s schematically illustrated in Fig. 3. At low ap- lied fields, a marginal band-type conduction robably governs the electron transport. The obility deduced from the conductance near zero oltage is of the order of 50 cm^2/V sec in the di- ection of the superlattice. After showing a slow crease as in Fig. 3(a), the conductance starts drop rapidly at a field of ~10^4 V/cm: The vol- ge drop per unit cell (per one period) approach- about 8 meV, if a uniform field distribution is sumed. Beyond this point it seems reasonable assume that the band conduction fails to be tained throughout the entire superlattice re- n and a narrow high-field domain is spontane- ly generated. Although the domain region initially extend only to one barrier [Fig.] or two [Fig. 3(b′)], a substantial fraction of the total voltage will be applied across it. This will leave intact the band conduction in the rest of the superlattice region. It should be pointed out that the high-field domain formation, initiated possibly by a random noise fluctuation or more likely an unavoidable nonuniformity in the superlattice structure, is indeed an inherent feature of the voltage-controlled negative-conductance medium.[10]

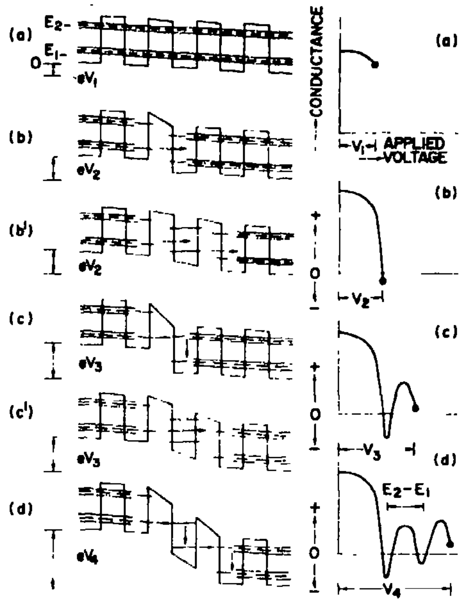

FIG. 3. Schematic energy diagrams (left-hand side) and corresponding conductances (right-hand side): (a) band conduction; (b) and (b′) spontaneous generation of a domain; (c), (c′), and (d) development of domain expansion.

We proceed to analyze tunneling characteristics across the high-field domain, because it will dominate the total conductance characteristic of the superlattice system. As shown in Figs. 3(b) and 3(c) or in Figs. 3(b′) and 3(c′), one may realize that this situation is somewhat analogous to the double-barrier tunneling.[9] In the most simple case, a single barrier is sufficient to provide a current peak or a negative conductance arising from matching or mismatching of energy levels on both sides of the domain, as shown in Fig. 3(c), because all involved electrons here are two dimensional in nature. In this domain tunneling, the current peak or dip is expected to be just as sharp as that in the case of the double-barrier where electrode electrons are three dimensional, if the transverse-momentum conservation of electrons is invoked.[11] The tunneling current across the domain will increase at the matching condition when the applied voltage across it reaches a value corresponding to the difference between E_1 and E_2, as shown in Figs. 3(c) and 3(c′). With further increase in applied voltage, the domain region will be expanded to the adjacent barriers, one by one, and, correspondingly, off- and on-matching conditions will be alternately repeated. Figure 3(d) shows that both barriers in the domain are simultaneously at the matching condition. This discrete nature in the domain expansion will give the oscillatory behavior in the conductance curve, as illustrated sequentially from top to bottom on the right-hand side of Fig. 3. Therefore, the observed voltage period (0.21–0.24 V) will provide the experimental value for $E_2 - E_1$, which is in good agreement with the estimated value (0.23 eV) shown in Fig. 1.

The observed negative conductance is not due to the Gunn effect, because the onset voltage (0.4–0.8 V) for the negative conductance, the electron mobility (50 $\mathrm{cm}^2/\mathrm{V\,sec}$), and the electron mean free path (a few hundred angstroms) in the structure are much too low to activate the electron transfer mechanism.[12] Furthermore, the observation of the oscillatory effect will exclude the possibility of the involvement of hot electrons. The involvement of the optical phonons, $\hbar\omega_0$, is also clearly denied because, in that case, the oscillation peaks are predicted to occur at fields F given by $eFd = \hbar\omega_0/n$, where n is an integer and d is the superlattice period.[13]

In the proposed model, we have used simplified assumptions[14] such as a square-well potential profile, a constant effective mass, ignoring a number of possible effects such as the upper valley in GaAs, band bending, junction problems between the superlattice region and the heavily doped contact regions, etc. These, however, are believed to play rather minor roles and will be required only for further refinement of the theory. The suprisingly good agreement between the calculated and experimental values of the location of the first-excited band seems to support our model and elucidates the most fundamental aspects of the transport characteristics in the superlattice.

We are grateful to R. Tsu, A. Koma, and L. F. Alexander for their cooperation in the project. Technical contributions of L. E. Osterling, C. C. Periu, and M. S. Christie are also acknowledged.

---

*Research sponsored in part by the U. S. Army Research Office (Durham).

[1] L. Esaki and R. Tsu, IBM J. Res. Develop. 14, 61 (1970).

[2] R. Tsu and L. Esaki, Appl. Phys. Lett. 22, 562 (1973).

[3] L. L. Chang, L. Esaki, W. E. Howard, R. Ludeke, and G. Schul, J. Vac. Sci. Technol. 10, 655 (1973); L. Esaki, J. Jpn. Soc. Appl. Phys., Suppl. 43, 452 (1974).

[4] R. Ludeke, L. Esaki, and L. L. Chang, Appl. Phys. Lett. 24, 417 (1974).

[5] A. Segmüller, private communication.

[6] I. I. Gol'dman and V. Krivchenkov, *Problems in Quantum Mechanics* (Addison-Wesley, Reading, Mass., 1961), p. 60.

[7] R. F. Kazarinov and R. A. Suris, Fiz. Tekh. Poluprov. 5, 797 (1971) [Sov. Phys. Semicond. 5, 707 (1971)]

[8] L. Esaki, L. L. Chang, W. E. Howard, and V. L. Rideout, in *Proceedings of the Eleventh International Conference on the Physics of Semiconductors, Warsaw Poland, 1972*, edited by The Polish Academy of Scien (PWN-Polish Scientific Publishers, Warsaw, Poland, 1972), p. 431.

[9] L. L. Chang, L. Esaki, and R. Tsu, Appl. Phys. Lett. 24, 593 (1974).

[10] For instance, see S. M. Sze, *Physics of Semiconductor Devices* (Wiley, New York, 1969), p. 732.

[11] For instance, see L. Esaki, Science 183, 1149 (1 Fig. 12 and its explanation.

[12] For instance, see Ref. 10, p. 743.

[13] M. Saitoh, J. Phys. C: Proc. Phys. Soc., Londo 914 (1972).

[14] The barrier height is taken to be 0.4 eV. The of the value in that neighborhood is not critical for culated results on the location of energy levels. A seen in Ref. 8, about 80% of the band-gap mismat the heterostructure is considered to be accommo in the conduction band, although the actual situat GaAs-AlAs is somewhat complicated because of X band crossing.

Polarization in Heavy-Ion Inelastic Scattering in the Coulomb-Nuclear Interference Region

S. G. Steadman, T. A. Belote, R. Goldstein, and L. Grodzins
Laboratory for Nuclear Science, Massachusetts Institute of Technology, Cambridge, Massachusetts 02139*
and
D. Cline and M. J. A. de Voigt
Nuclear Structure Research Laboratory,† University of Rochester, Rochester, New York 14627
and
F. Videbæk
The Niels Bohr Institute, University of Copenhagen, Copenhagen, Denmark
(Received 10 July 1974)

The polarization in the region of Coulomb-nuclear interference has been determined from the γ-ray correlation following excitation of the 856-keV 2^+ state in ^{56}Fe by 43-MeV ^{16}O ions. Elastic and inelastic scattering cross sections were also measured. Dramatic interference effects are observed in the transition amplitudes which can be reproduced by coupled-channel distorted-wave calculations.

Inelastic scattering data for heavy ions exhibit, in certain cases,[1] a narrow and deep minimum in the inelastic cross section at a scattering angle corresponding to a grazing collision. This dip, attributed to Coulomb-nuclear interference, can be reproduced by distorted-wave calculations using several optical potentials.[1] The analysis of such data yields the heavy-ion–nucleus potential in the surface region which is also important for transfer reactions. To understand better the reaction mechanism and to determine the optical-model parameters for these reactions the elastic cross section for 43-MeV ^{16}O ions scattered by ^{56}Fe has been measured along with the inelastic cross section of the 856-keV, 2^+ excited state. The m-state transition amplitudes, which are nore sensitive for the Coulomb-nuclear interference, have also been determined from a complete -ray angular-correlation measurement as a unction of the particle scattering angle. The later measurement gives a check of the validity of e Coulomb-nuclear interference explanation of e observed behavior. Coupled-channel effects, particular the reorientation effect due to the nzero static electric quadrupole moment of the e 2^+ state,[2] have also been investigated and n to be important.

The elastically and inelastically scattered ions re measured at angles from 15° to 110° by us- a 43-MeV ^{16}O beam from the Rochester MP dem Van de Graaff accelerator. The two most-ndant charge states of ions scattered by a 5- μg/cm² isotopically enriched ^{56}Fe target (on a μg/cm² carbon backing) were detected by two position-sensitive silicon detectors in the focal plane of the Enge split-pole magnetic spectrometer. The charge-state distribution of scattered ^{16}O ions was measured repeatedly during the experiment. Since the two most-abundant charge states contained at least 75% of the total strength, the uncertainty due to the charge-state distribution was negligible. The elastic cross section, plotted as a ratio to the Rutherford cross section, and the inelastic scattering cross section are shown at the top of Fig. 1. The inelastic scattering data has a minimum at the grazing angle $\varphi_{\mathrm{gr}} \simeq 80°$ where the elastic cross section displays a maximum.

The de-excitation γ correlation was measured using a 150 μg/cm² isotopically enriched ^{56}Fe target on a 20 μg/cm² carbon backing. Four silicon surface-barrier particle detectors, masked to subtend 1.8° in the scattering plane, were placed in a hemispherical chamber to detect the scattered ^{16}O ions. Six 3 in. × 3 in. NaI(Tl) γ-ray detectors were placed at 15 cm from the target and at any angle in the upper hemisphere. Data for any one of the six γ detectors in coincidence with any one of the four particle detectors (24 independent measurements) were simultaneously collected. A time resolution of 1.3 nsec (full width at half-maximum) was sufficient to discriminate against contaminant groups mainly from transfer reactions which had different times of flight. The particle and γ energy, time difference, and counter identification were stored event by event on magnetic tape and subsequently analyzed using the Rochester Nuclear Structure Research Labor-

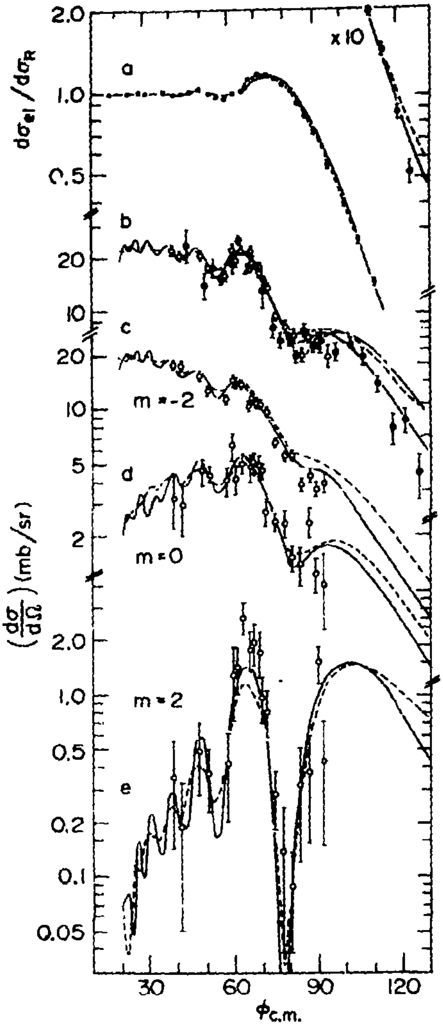

FIG. 1. As a function of the c.m. scattering angle, (a) the ratio of elastic to Rutherford cross sections, (b) the inelastic cross section to the 2^+ state, and (c)–(e) the m-substate populations of the 2^+ state. Dots are data with the magnetic spectrometer; open circles are γ-ray angular-correlation data. The solid lines show the coupled-channel calculation results, the dashed lines show distorted-wave Born-approximation (DWBA) predictions and the dotted line in (b) shows the coupled-channel calculation assuming $Q_{2^+} = 0$. The quantization axis is chosen in the direction $\vec{k}_i \times \vec{k}_f$.

atory PDP-6, PDP-8 data-acquisition system.[3] Measurements were performed at 28 particle detector angles in the range $\varphi_{c.m.} = 38°$ to $131°$ and many γ angles, giving a total of about 550 data points, each with statistics of a few hundred counts.

The de-excitation γ-correlation data are sufficient to determine completely the transition amplitudes for any particle scattering angle. The transition amplitudes are most conveniently expressed in a coordinate system in which the x axis is along the beam direction and the z axis is in the $\vec{k}_i \times \vec{k}_f$ direction. In this system the odd-m amplitudes are zero, and the three magnitudes $|T_{+2}|$, $|T_{-2}|$, and $|T_0|$ and two relative phases $\delta_{+2} - \delta_{-2}$ and $\delta_0 - \delta_{-2}$ of the even amplitudes completely determine the transition.[4] Furthermore, the in-plane γ correlation depends only on the ± 2 transition amplitudes. For a point detector the in-plane angular correlation is given by

$$\omega(\theta_\gamma = 90°, \varphi_\gamma) = A - B\cos[4(\varphi_\gamma - \varphi_0)], \qquad (1)$$

where

$$A = (5/16\pi)(|T_{+2}|^2 + |T_{-2}|^2), \qquad (2)$$

the anisotropy

$$B/A = 2|T_{+2}||T_{-2}|/(|T_{+2}|^2 + |T_{-2}|^2), \qquad (3)$$

and the symmetry angle

$$\varphi_0 = \tfrac{1}{4}(\delta_{+2} - \delta_{-2}). \qquad (4)$$

The $m = 0$ transition amplitude $|T_0|$ and relative phase $\delta_0 - \delta_{-2}$ are determined by the out-of-plan γ-correlation data. At each scattering angle a least-squares fit to the data was made with the five variables $(d\sigma/d\Omega)_{2^+}$, A, anisotropy B/A, an the two relative phases. With these parameters the identification of the $|T_{+2}|$ and $|T_{-2}|$ amplitudes is ambiguous because of their symmetric dependence in Eqs. (2) and (3). However, at fo ward angles only the $|T_{-2}|$ component is impor tant, allowing one to assign correctly the tran tion amplitudes at all angles. The calculated correlation included corrections for the finite size of the γ detectors, for the decay in flight the recoiling nuclei by using the expressions Lesser,[5] and for the attenuation of the correl tion due to hyperfine interactions (deorientat effect) by assuming a pure magnetic interact and using attenuation coefficients measured Lesser *et al.*[2]

The experimentally determined m-state p tions $(d\sigma/d\Omega)_m = |T_m|^2$ are shown as a functi c.m. scattering angle in Fig. 1. The relativ phases are shown in Fig. 2. A dramatic di observed in the $m = +2$ amplitude accompan a large shift in the relative phase $\delta_{+2} - \delta_{-2}$ $\varphi_{c.m.} = 78°$ that is near the grazing angle.

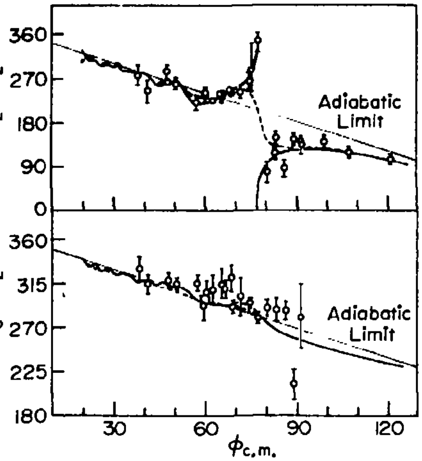

FIG. 2. The relative phases of the transition amplitudes to the 2^+ state as a function of the c.m. scattering angle. The solid lines show the coupled-channel calculation results; the dashed lines show DWBA predictions.

accompanied by a large decrease in the anisotropy and a shift of the symmetry angle of the γ correlation in the scattering plane. At the interference minimum, the recoiling ^{56}Fe are almost completely polarized because here only the $m = -2$ substate contributes to the in-plane γ correlation (Fig. 1) and, therefore, the in-plane correlation is essentially isotropic.

The search program JIB3[6] was used to find the st Woods-Saxon optical-model parameter set fit the elastic scattering data. The fitted curve own in Fig. 1 was obtained for $V = 30.0$ MeV, $= 7.6$ MeV, $r_0 = 1.30$ fm, $r_i = 1.30$ fm, $a_0 = 0.533$ ι, $a_i = 0.37$ fm, and $r_0^C = 1.25$ fm, values close those obtained from fits in the Ni isotopes.[1] ıe optical-model parameters were used in a VBA calculation of the transition amplitudes us- ʒ a version of DWUCK[7] modified to treat the ıulomb excitation properly by including up to 0 partial waves.[1,8] A collective form factor .s used with $B(E2{:}0^+\to2^+)/e^2 = 974$ fm^4 and β_2 |.23. This value of β_2 corresponds to an effec- e isoscaler $B_{1s}(E2{:}0^+\to2^+)/e^2 = 1200$ fm^4 with assumption of a Fermi charge distribution h ^{56}Fe $r_{\rm rms} = 3.825$ fm. The results of this cal- ation are shown by dashed curves in Figs. 1 2. Although these calculations qualitatively ibit the observed behavior, they are unable to roduce the $\delta_{+2}-\delta_{-2}$ phase behavior for any onable value of $B(E2{:}0^+\to2^+)$ and β_2.

A coupled-channel (CC) calculation[9] was performed with $W = 3.6$ MeV and otherwise using the same parameters, collective form factors, $B(E2)$, and β_2, and both with and without a rotational value for the excited-state static quadrupole moment ($Q_{2^+}/e = -28$ fm^2, in agreement with experiment.[3]) These are shown by solid and dotted lines in Fig. 1(b). The complete CC calculation, including the static quadrupole moment, is in excellent agreement with the data. The fit to the elastic scattering data is comparable, but the observed discontinuity for $\delta_{+2}-\delta_{-2}$ is reproduced correctly. The excited-state static quadrupole moment produces a 2° shift in the position of the interference minimum and about a 40% reduction in the back-angle inelastic cross section. One feature of the CC calculation is to reduce the rise of the elastic cross section above the Rutherford prediction by coupling to the 2^+ state, while in the DWBA calculation this is done by an increase of the imaginary potential.

To understand qualitatively the Coulomb-nuclear interference, each transition amplitude is a coherent sum of the Coulomb and nuclear complex amplitudes:

$$T_m = \exp(i\delta_m^{\,C})\{a_m^{\,C} - a_m^{\,n}\exp[i(\delta_m^{\,n} - \delta_m^{\,C})]\}. \quad (5)$$

The oscillating behavior results from the scattering-angle dependence of the phase difference $\delta_m^{\,C} - \delta_m^{\,n}$, mainly determined by the optical potential. A DWBA calculation has been performed where the Coulomb part and the nuclear part of the form factor were separately set to zero. The nuclear transition amplitude is very small at forward scattering angles, as expected, and behaves similarly for each m substate. However, the Coulomb amplitude varies strongly with the m state, and for the $m = +2$ substate is the smallest, being about the same magnitude as the nuclear amplitude, resulting in the considerably more striking interference effects for this transition amplitude than for the inelastic cross section. The behavior of the phase $\delta_{+2}-\delta_{-2}$ depends on the relative size of the Coulomb and nuclear amplitudes as the Coulomb-nuclear phase passes through zero. That is, the occurrence of the discontinuity in $\delta_{+2}-\delta_{-2}$ as plotted in Fig. 2, depends upon whether the vector difference of the Coulomb and nuclear amplitudes rotates clockwise or counterclockwise through the interference minimum.

We conclude that the dramatic effects seen in the polarization measurements can be entirely understood in terms of Coulomb-nuclear interference. Whereas the conventional DWBA analysis does not account for all the observed features, inclusion of coupled-channel effects proves to be important. In particular, for back-angle scattering the reorientation effect due to a nonzero excited-state quadrupole moment produces an appreciable effect, and in the interference region a correct ratio of the Coulomb to nuclear amplitudes is obtained.

---

[*] Supported by U. S. Atomic Energy Commission Contract No. AT(11-1)-3069).

[†] Supported in part by the National Science Foundation.

[1] P. R. Christensen, I. Chernov, E. E. Gross, R. Stokstad, and F. Videbæk, Nucl. Phys. A207, 433 (1973).

[2] P. M. S. Lesser, D. Cline, P. Goode, and R. Horoshko, Nucl. Phys. A190, 597 (1972).

[3] D. Cline, in Proceedings of the Skytop Conference on Computer Systems in Nuclear Physics, Skytop, Pennsylvania, 1969, Columbia University Report No. CONF-690301 (unpublished), p. 106.

[4] R. Rybicki, T. Tamura, and G. R. Satchler, Nucl. Phys. A146, 659 (1970).

[5] P. M. S. Lesser, Ph.D. thesis, University of Rochester, 1971 (unpublished).

[6] F. C. Perey, JIB3 (unpublished) (modified to include a larger number of partial waves and smaller integration steps needed in calculation of heavy-ion scattering).

[7] P. D. Kunz, DWUCK, University of Colorado, 1969 (unpublished).

[8] F. Videbæk, unpublished.

[9] W. Brückner, J. G. Merdinger, D. Pelte, U. Smilansky, and K. Traxel, Phys. Rev. Lett. 30, 57 (1973).

Mass-Yield Distributions in the Reaction of ^{84}Kr Ions with ^{238}U[†]

J. V. Kratz,[*] A. E. Norris,[‡] and G. T. Seaborg
Lawrence Berkeley Laboratory and Department of Chemistry, University of California, Berkeley, California 94720

(Received 24 June 1974)

Yields of 156 nuclides were measured radiochemically to delineate the mass distribution in the reaction of 605-MeV ^{84}Kr with thick ^{238}U targets. The yields are consistent with decomposition of the mass distribution into five components: transfer products (700 ± 120 mb), "quasi-Kr" products centered at $A \approx 85$ (470 ± 70 mb) and the products from symmetric fission of their complements (420 ± 60 mb), products from low-energy fission of $Z \approx 92$ nuclides (200 ± 40 mb), products from complete fusion-fission (55 ± 15 mb), and unexplained neutron-deficient yields at $A \approx 195$ (~40 mb).

A new phenomenon has been observed in heavy-ion reactions and has been termed "multinucleon transfer,"[1] "quasifission,"[2] "relaxation phenomena,"[3] and "deep inelastic scattering."[4] These reactions are characterized by energy equilibration without mass equilibration, resulting in (i) two fragments with masses close to the target and projectile masses, (ii) fragment kinetic energies close to the calculated Coulombic repulsion of two normal fission fragments, and (iii) angular distributions distinct from those for complete fusion-fission. For ions with $Z \lesssim 18$, these new reactions were observed to have modest cross sections[1-3] in contrast to the complete fusion process that accounts for an important part of the reaction cross section.[5] For reactions of ^{84}Kr ions with ^{209}Bi, much of the total interaction cross section goes into the new reaction channel,[2,4] contrary to expectations, whereas the complete fusion-fission cross sections were found to be low.[4,5] The ^{84}Kr results were obtained by measuring fragment-fragment coincidences at correlated angles.

The work reported here is a radiochemical measurement of the mass yield distribution for the reaction of ^{84}Kr with thick targets of ^{238}U. This technique provides yields of radioactive products uniquely characterized with respect to Z and A. The integral nature of these cross sections supplies information that is independent of any assumptions about the reaction mechanism. These data are used below to complement the information about mass distributions obtained in kinematic coincidence measurements, in which masses are deduced indirectly from the laboratory energies of the two fragments by assuming full momentum transfer from the projectile to the combined system. Also, kinematic coincidence measurements lack strict differentiation between inelastically scattered projectiles and nucleon transfer products—a limitation not inherent in radiochemical measurements. However, the advantages of the technique used in this work are obtained at the expense of a loss of information on energy dependence and angular distribution of reaction products.

Thick uranium targets were bombarded at the superheavy ion linear accelerator with 605-MeV ^{84}Kr ions, dissolved shortly after the end of bombardment, and separated chemically into 7 fractions[6] that were assayed for α-particle and γ-ray activities. We have measured cross sections for 129 isotopes. Through an interlaboratory collaboration a lanthanide-actinide fraction from an intense 24-h bombardment was radiochemically analyzed by the Los Alamos Scientific Laboratory nuclear chemistry group, which resulted in yield information on 27 additional nuclides.[7] The independent and cumulative yields are plotted versus mass number in Fig. 1(a). A detailed listing of the data and a description of their analysis will be given elsewhere.[9] The apparent scatter in the data in Fig. 1(a) occurs because independent yields, and even many of the cumulative yields, represent only a fraction of the total mass yields. Figure 1(b) is a contour map of the independent yields in a Z-A plane, indicating yield locations relative to the stability line. The pronounced structure revealed by the isopleths in the figure indicate that several yield distributions with different charge and mass dispersions, hence different origins, are superimposed on each other. These results differ from those obtained in a parallel study of the yield distributions in ^{40}Ar on ^{238}U,[10] where the overall distribution was dominated by the high yields of transfer products centered on the target and projectile masses ("rabbit ears") and by one broad, continuous distribution of products from complete fusion-fission. To calculate the final mass yields, we integrated, at each mass number, the Gaussian charge dispersion curves that were fitted to the data.[9] The final results are shown in Fig. 1(c).

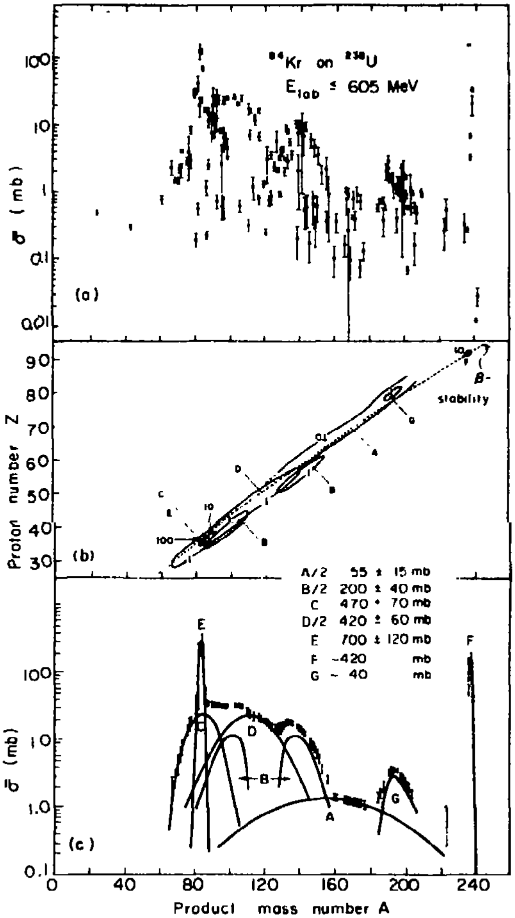

FIG. 1. (a) Independent and cumulative yields of individual isotopes, calculated with the assumption of a general interaction barrier of 450 MeV (see Ref. 8), corresponding to an effective target thickness of 11.6 mg U/cm^2. (b) Contour lines for equal independent yields in millibarns. (c) Total integrated mass yields (upper and lower limits are indicated at those mass numbers for which experimental data were obtained) and their decomposition into individual components: (A) complete fusion-fission, (B) transfer-induced fission, (C) quasi-Kr, (D) cascade fission of the quasi-U, (E) and (F) transfer reactions ("rabbit ears"), and (G) yields of unknown origin.

Component A is determined by the yields of heavy-rare-earth nuclides and by the yields of very neutron-deficient Mo, Tc, Ag, In, Sn, Sb, I, and Cs isotopes. This component shows the expected characteristics of the binary fission product distribution originating from the fission of a composite nucleus. For component B, the heavy-mass branch is defined by the cumulative yields of neutron-rich nuclides peaking at $A \approx 140$. Figure 1(b) shows how distinctly the neutron-excess yields are separated from those of component A in this mass region. Guided by our results from the reaction ^{40}Ar on ^{238}U, where a low-energy fission of transfer products near ^{238}U was observed,[10] we assign this component to a double-humped low-energy fission product distribution. The light branch of this distribution was obtained by reflecting the well-defined shape of the heavy one, and its mass location was deduced from the cumulative yield balances for the isotopes ^{112}Pd, ^{111}Ag, and ^{107}Rh. From the observed charge distribution and the peak-to-valley ratio, we estimate an excitation energy of the fissioning nuclei of ~15 MeV. We find a value of 200 mb for the cross section of this transfer-induced fission as represented by component B. There should be a corresponding reduction in the heavy-rabbit-ear (component F) cross section as compared to its complementary light-rabbit-ear (component E) cross section; our measurements do show that component F has a cross section about 200 mb (actually about 280 mb) smaller than component E.

After subtraction of contribution B from the yield data in the mass range $67 \leq A \leq 140$, we are left with yields that can be resolved into two Gaussian distributions [components C and D in Fig. 1(c)], peaking around $A = 85$ and $A = 112$. Distribution C [full width at half-maximum (FWHM) ≈ 20 mass units] is probably identical with the "quasi-Kr" events observed in Refs. 2 and 4, representing the new phenomenon referred to above. Apparently, the complementary "quasi-U" distribution is missing. Because much kinetic energy in the deep inelastic interaction of ^{84}Kr with the target nucleus goes into excitation, one would expect a *high-energy cascade fission* of the "quasi-U" nuclei leading to a symmetric fission product distribution centered slightly below $A \approx 119$. Actually, we do observe such a distribution (component D). From a mass and charge balance for the complete process—"quasifission" followed by cascade fission of the "quasi-U" (which process might be termed "quasi-ternary-fission")—one can conclude that in the most probable interactions thirteen neutrons and no protons are evaporated. The yield of component D is 840 ± 120 mb (200%), indicating that 67–100% of the "quasi-U" nuclei undergo fission. The shape and width of the distribution suggest that the average excitation energy of the "quasi-U" must have been ≥ 45 MeV.

The excess yields around $A \approx 195$ (component G) are unexplained. Suggested explanations such as target contamination and feeding of these mass chains by α-decay from higher masses can be excluded. We have also considered whether this peak might be a surviving nonfissionable tail (due to high fission barriers) at the light-mass-number end of the fissioning "quasi-U" distribution of nuclei. The primary "quasi-U" distribution (FWHM ≈ 20 mass units) could hardly extend into a mass region ~40 mass units below the target mass while still yielding cross sections of a few millibarns. Attempts to force a considerably broader complementary distribution through the mass yields around $A = 85$ resulted in an unreasonable imbalance in cross section for the quasi-ternary-fission process. We conclude, then, that the excess yield around $A \approx 195$ more likely originates from a hitherto unobserved reaction channel.

The paucity of data points between peaks F and G is due to the experimental difficulty of measuring the small yields of the predominantly short-lived isotopes in this region using radiochemical techniques.

As a consequence of the interpretation presented here, the total reaction cross section is the sum of the production cross sections for components $A/2$, C, E, and G: 1265 ± 205 mb. The mean geometrical cross section in the energy interval 450 to 605 MeV (lab) can be estimated as

$$\bar{\sigma}_R = \pi R^2 \frac{\int_B^E (1 - B/E)\, dE}{E - B} = 1130 \text{ mb},$$

where $B = 450$ MeV,[8] $E = 605$ MeV, and $R = 16.0$ fm.

To conclude, we wish to point out that our analysis of the total mass yield distribution, and its decomposition into the components indicated in Fig. 1, is consistent with the results obtained for ^{84}Kr on ^{209}Bi in the kinematic coincidence experiments.[2,4] Our data confirm the assumption[2,4] that the quasi-Kr distribution is centered close to the projectile mass. It appears that >92% of the Kr interactions with U in the investigated energy interval feed inelastic and deep inelastic reaction channels where only little mass transfer occurs. It is only in very few collisions (~4%) that a composite nucleus is formed.

We want to thank Dr. A. Ghiorso for his active interest in the progress of this work and Dr. J. O. Liljenzin, Mr. I. Binder, Mr. R. Otto, and Mrs. D. Lee for helpful assistance.

---

†Work supported by the U. S. Atomic Energy Commission.

*On leave from Institut für Kernchemie, Universität Mainz, with a fellowship from Gesellschaft für Schwerionenforschung GSI, Darmstadt, Germany.

‡Los Alamos Scientific Laboratory, University of California, Los Alamos, N. Mex. 87544.

[1] A. G. Artukh, G. F. Gridnev, V. L. Mikheev, V. V.

Volkov, and J. Wilczynski, Nucl. Phys. A215, 91 (1973).

[2] F. Hanappe, M. Lefort, C. Ngô, J. Péter, and B. Tamain, Phys. Rev. Lett. 32, 738 (1974), and references herein.

[3] L. G. Moretto, Bull. Amer. Phys. Soc. 19, 465 (1974).

[4] J. Huizenga, K. Wolf, J. P. Unik, V. E. Viola, I. Birkelund, and H. Freiesleben, to be published.

[5] B. Tamain, M. Lefort, C. Ngô, and J. Péter, J. Phys. (Paris), Colloq. 33, C5, Pt. 2, 60 (1972).

[6] J. V. Kratz, J. O. Liljenzin, and G. T. Seaborg, to be published.

[7] B. P. Bayhurst, J. H. Cappis, W. R. Daniels, D. C. Hoffmann, F. O. Lawrence, C. J. Orth, R. J. Prestwood, H. L. Smith, and K. Wolfsberg, unpublished.

[8] M. Lefort, C. Ngô, J. Péter, and B. Tamain, Nucl. Phys. A197, 485 (1972).

[9] J. V. Kratz, A. E. Norris, and G. T. Seaborg, to be published.

[10] J. V. Kratz, J. O. Liljenzin, A. E. Norris, I. Binder, and G. T. Seaborg, in *Proceedings of the International Conference on Reactions between Complex Nuclei, Nashville, Tennessee, 1974*, edited by R. L. Robinson, F. K. McGowan, J. B. Ball, and J. H. Hamilton (North-Holland, Amsterdam, 1974), Vol. 1, p. 88.

Interference between ρ and ω Production in $\pi^{\pm} N \rightarrow \pi^{+}\pi^{-} N$ at 3, 4, and 6 GeV/c[*]

S. L. Kramer, D. S. Ayres, R. Diebold, A. F. Greene,[†] A. J. Pawlicki, and A. B. Wicklund
Argonne National Laboratory, Argonne, Illinois 60439

(Received 3 June 1974)

The ρ-ω interference patterns observed in the reactions $\pi^- p \rightarrow \pi^+\pi^- n$ and $\pi^+ n \rightarrow \pi^+\pi^- p$ are used to measure the relative phases between ρ and ω production amplitudes. The interference is observed to be largely constructive (destructive) for the π^-- (π^+-) induced reaction in both natural- and unnatural-parity exchange amplitudes. This sign of the interference agrees with that predicted from exchange-degenerate π-B trajectories, but disagrees with the corresponding prediction for the natural-parity amplitudes using exchange-degenerate ρ-A_2 trajectories.

In this Letter we present results from a detailed study of ρ-ω interference in the reactions

$$\pi^- p \rightarrow \pi^+\pi^- n, \quad (1)$$

$$\pi^- d \rightarrow \pi^+\pi^- n n_s, \quad (2)$$

$$\pi^+ d \rightarrow \pi^+\pi^- p p_s, \quad (3)$$

at 3, 4, and 6 GeV/c. Except for the ρ-ω interference term which changes sign, the cross sections for the π^-- and π^+-induced reactions should be equal by isospin conservation. Consequently the ρ-ω interference effect can be directly isolated from the difference of the reactions, yielding precise information on the relative ρ-ω production amplitudes. The high statistics of this experiment ($\approx 6\times10^5$ events) have permitted a detailed study of ρ-ω interference for natural- and unnatural-parity exchange amplitudes, presenting severe constraints on vector-meson–production models.[1]

The data were obtained by using the Argonne National Laboratory effective mass spectrometer.[2] The trigger required a $\pi^{\pm}$ beam particle incident on a 20-in. liquid hydrogen or deuterium target, an interaction in the target producing two or more charged particles through the spectrometer, and no signals from the beam veto or target and magnet veto counters. The recoil baryon was not detected, but events were selected with appropriate missing-mass-squared (M_X^2) cuts, assuming the observed particles were pions. The rms resolution on M_X at 4 GeV/c for Reaction (1) was ± 28 MeV and was essentially independent of $M_{\pi\pi}$ and t. The Fermi motion of the deuterium target had little effect on this resolution (kinematic smearing of M_X^2 being roughly proportional to $\sqrt{-t}$) which increased to about ± 40 MeV at 4 GeV/c and $|t| \approx 0.4$ GeV^2. The background corrections for Reactions (1) and (3) were comparable ($\approx 5\%$) and for Reaction (2) nearly twice as large.

The data on Reaction (2) were taken in order to better understand the systematic differences between Reactions (1) and (3) due to deuterium effects. Reactions (2) and (3) have been corrected for Glauber screening (3%) and exclusion-principle effects.[3] All data have been corrected for event losses due to spectrometer acceptance, veto-counter losses, final-state particle interactions ($\approx 10\%$ for H$_2$ and $\approx 15\%$ for D$_2$), pion decays (2–10%), chamber and program inefficiencies ($\approx 7\%$), and the effect of M_X^2 cuts (typically 1%). The corrected cross sections for Reactions (1) and (2) agreed to typically better than 3%, pro-

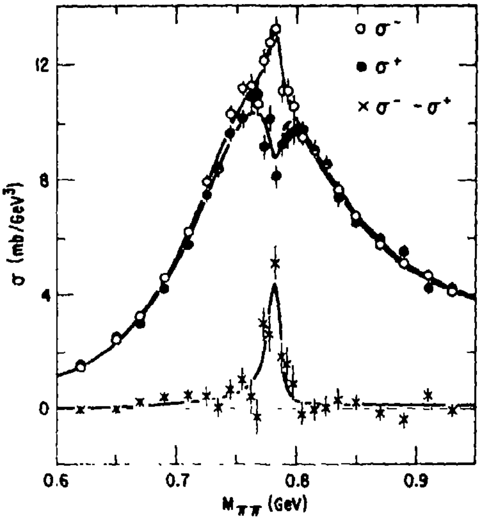

FIG. 1. Differential and difference cross sections at 4 GeV/c with $0.08 < -t < 0.2$ GeV^2. The curves are the result of the fit by Eq. (5) described in the text.

viding a good check of the deuterium corrections. The overall normalization uncertainty is estimated to be ±12% and the relative normalization uncertainty between Reactions (1) and (3) is approximately ±8%. However, isospin conservation requires that, except for the ω mass region, the cross sections for the π^+ and π^- reactions should be equal. This constraint is satisfied by the corrected cross sections to better than 5%.

A sample of the corrected differential cross sections, $\sigma = d^2\sigma/dt\,dM_{\pi\pi}$, as a function of $M_{\pi\pi}$ is presented in Fig. 1. A narrow peak is observed at the ω mass for the π^--initiated reaction and a dip for the π^+ one. The interference term between ρ and ω production amplitudes can be obtained directly from the difference between the π^- and π^+ cross sections, $\Delta = \sigma^- - \sigma^+$, also shown in Fig. 1.

Additional information can be obtained by using the s-channel density matrix elements (ρ_{ij}) to isolate the various exchange mechanisms[4]:

$$\begin{aligned} \sigma_{00} &= \rho_{00}\sigma + \sigma_s/3, \\ \sigma_{1-} &= (\rho_{11} - \rho_{1-1})\sigma + \sigma_s/3, \qquad (4) \\ \sigma_{1+} &= (\rho_{11} + \rho_{1-1})\sigma + \sigma_s/3. \end{aligned}$$

With the neglect of the small incoherent s-wave contribution ($\sigma_s = \rho_{ss}\sigma$), σ_{1+} asymptotically projects out the natural-parity exchange cross section while σ_{00} and σ_{1-} project out the unnatural-parity exchange cross sections.

We have fitted the differential cross sections for incident $\pi^{\pm}$ by a first-order mass-mixing formula,[5]

$$\sigma_{ij}^{\pm} = f(M_{\pi\pi})[\,|A_\rho B_\rho|^2 + |\epsilon A_\omega B_\omega|^2 \pm 2\xi|\epsilon A_\rho A_\omega|\mathrm{Re}(e^{i\varphi}B_\omega B_\rho^*)] + \text{background}. \qquad (5)$$

$A_{\rho,\omega}$ and $B_{\rho,\omega}$ are the ρ, ω production and Breit-Wigner decay[6] amplitudes, respectively, and $f(M_{\pi\pi})$ is the $\pi\pi$ kinematic factor ($M_{\pi\pi}^2/q$) of Ref. 6. The strength of the decay $\omega \to \pi^+\pi^-$ is related to ϵ, where

$$|\epsilon| = |\delta/[(m_\rho^2 - m_\omega^2) - i(m_\rho\Gamma_\rho - m_\omega\Gamma_\omega)]| \qquad (6)$$

and δ is the mass-mixing parameter.[5] The relative phase between A_ρ and A_ω (for incident π^+) is given by

$$\beta^+ = \beta_\omega^+ - \beta_\rho^+ = \varphi - \arg(\epsilon) \approx \varphi - 105°, \qquad (7)$$

where δ has been assumed to be real.[7] Since the σ_{ij} are actually incoherent sums over the nucleon spin states, the quantities $|A_{\rho,\omega}|^2$ are similarly defined and the spin coherence is accounted for by the factor ξ ($0 \le \xi \le 1$). The s-wave background was adequately parametrized by a linear $M_{\pi\pi}$ dependence in the last term of Eq. (5).

The π^+ and π^- cross sections were fitted simultaneously,[8] with the resonance parameters constrained to $m_\rho = 0.765 \pm 0.005$ GeV, $\Gamma_\rho = 0.150 \pm 0.010$ GeV, $m_\omega = 0.783$ GeV,[9] and $\Gamma_\omega = 0.010 \pm 0.002$ GeV. To allow for any residual normalization error, a relative π^+ to π^- normalization parameter was included in the fit. Typically this parameter differed from unity by less than 3%. Since the fits were generally consistent with $\xi = 1$, this value was assumed. The difference cross sections Δ_{00} and Δ_{1+} are presented in Fig. 2 together with the results of this fit.

In Fig. 3 the relative production phase obtained from Eq. (7) is presented for all cross sections showing significant ρ-ω interference. If exchange-degenerate (EXD) π and B trajectories dominate the unnatural-parity exchange amplitudes,[10] then

$$A_\omega^+/A_\rho^+ \propto -i\tan\tfrac{1}{2}\pi\alpha(t). \qquad (8)$$

With $\alpha(t) < 0$ in the region of interest, the phase β^+ is then predicted to be 90°. For σ_{00} we find an average value for this phase of 122° ± 6°, with

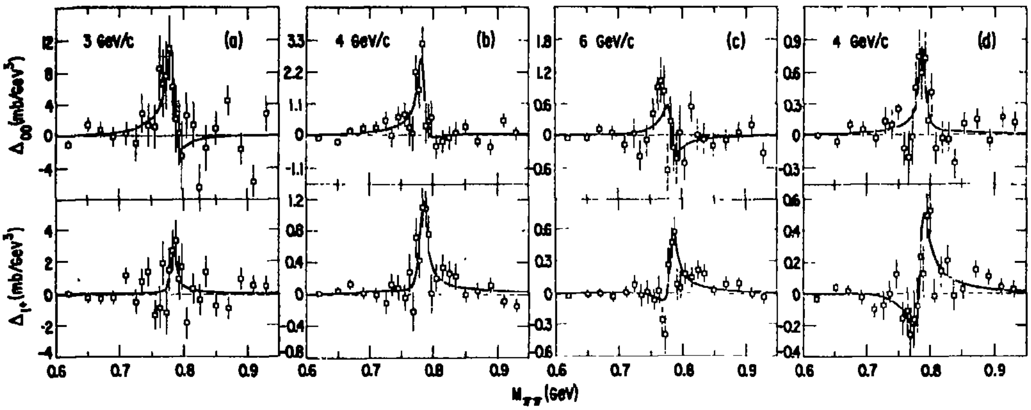

FIG. 2. Difference cross sections Δ_{00} and Δ_{1+} at 3, 4, and 6 GeV/c for (a) $0.0<-t<0.08$ GeV^2, (b) and (c) $0.08<-t<0.2$ GeV^2, and (d) $0.2<-t<0.4$ GeV^2. The curves are the result of the fit by Eq. (5).

little s or t dependence, in qualitative agreement with this prediction. Our phase for σ_{1-} agrees well with the EXD prediction, the average value being $\beta^+=96° \pm 9°$.

If the natural-parity exchange amplitude were dominated by EXD ρ and A_2 trajectories, Eq. (8) would predict $\beta^+=-90°$ for $-t \lesssim 0.6$ GeV^2. This value is contradicted by our data, which show a variation from about $+90°$ at small $-t$ to 0° near $-t=0.3$ GeV^2 and little s dependence within the errors. This effect has been explained qualitatively by Estabrooks, Martin, and Michael[11] who assume that at small $-t$, σ_{1+} for ρ production is dominated by π cut with A_2 exchange becoming more important at larger $-t$ and s. For ω production only ρ exchange was considered, which predicts a variation in β^+ from $\approx 40°$ at small $-t$ and s to $-90°$ for large $-t$ and s. An extension of this model by Irving and Michael[12] yields somewhat better quantitative agreement for σ_{1+}, at low $-t$.

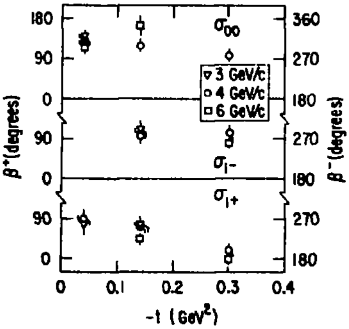

FIG. 3 The relative production phases, $\beta_\omega-\beta_\rho$, mea-ed for σ_{00}, σ_{1-}, and σ_{1+} as a function of t for those s with a significant ρ-ω interference effect.

Earlier work[13,14] on ρ-ω interference has been limited in statistics and consequently the phases have been given mainly for the differential cross section σ. The previous results in our energy region are consistent with our phase for σ ($\beta^+=90° \pm 10°$ at $-t=0.2$ GeV^2).

With data for both Reactions (1) and (3) we can in principle extract the $|\epsilon A_\omega B_\omega|^2$ term from the sum of the two mass spectra, allowing independent determination of ξ. In practice this term is small and a precise measurement is difficult and highly correlated with the relative π^+ to π^- normalization. However, the shapes of the mass spectra are generally consistent with $\xi=1.0$ and yield a branching ratio for $\omega\to\pi\pi$ of $R\approx 1\%$. A more complete determination of ξ and R is beyond the scope of this Letter and will be discussed in a future publication.

We would like to thank I. Ambats, A. Lesnik, D. R. Rust, C. E. W. Ward, and D. Yovanovitch for their assistance in the design and construction of the spectrometer. We are also indebted to R. Diaz, L. Filips, E. Walschon, and the entire staff of the Argonne National Laboratory zero-gradient synchrotron for making this experiment possible.

Note added in proof.—After submitting this Letter for publication we received a preprint[15] on ρ-ω interference measurements at 17.2 GeV/c. As expected,[11,12] the pion-cut contribution to σ_{1+} is relatively less important at higher energies, the phase of σ_{1+} being closer to the EXD prediction for ρ and A_2 exchange. This observation is supported by the results of Ratcliff *et al.*[14] However, the unnatural-parity phases at 17.2 GeV/c are unexpectedly lower than our phases for $|t| < 0.2$ GeV^2.

---

*Work supported by the U. S. Atomic Energy Commission.

†Present address: Fermi National Accelerator Laboratory, Batavia, Ill. 60510.

[1] R. D. Field and D. P. Sidhu, Phys. Rev. D 10, 89 (1974).

[2] For more details on the experimental apparatus see D. S. Ayres, in *Proceedings of the International Conference on Instrumentation for High Energy Physics, Frascati, Italy, 1973,* edited by S. Stipcich (Laboratori Nazionali del Comitato Nazionale per l'Energia Nucleare, Frascati, Italy, 1973), p. 665; R. Diebold, in *Pt-Pt Scattering-1973,* AIP Conference Proceedings No. 13, edited by P. K. Williams and V. Hagopian (American Institute of Physics, New York, 1973), p. 284; I. Ambats *et al.*, Phys. Rev. D 9, 1179 (1974).

[3] All cross sections off deuterium have been corrected by the Pauli exclusion-principle factor $(1-S(\Delta)/3)^{-1}$, where $S(\Delta)$ is the deuterium form factor. This correction is appropriate for all cross sections except the nonflip natural-parity cross section, which must vanish as $t \to t_{\min}$ by angular momentum conservation and should therefore contribute little to the observed σ_{1+} in the t range where $S(\Delta)$ is large. The largest correction was 13% for the $|t| \leq 0.08$-GeV^2 bin.

[4] J. P. Ader *et al.*, Nuovo Cimento 56A, 952 (1968).

[5] G. Goldhaber, in *Experimental Meson Spectroscopy,* edited by C. Baltay and A. Rosenfeld (Columbia Press, New York, 1970), p. 59; M. Roos, in *Vector Meson Production and Omega-Rho Interference,* edited by A. Donnachie and E. Gabathuler (Daresbury Nuclear Physics Laboratory, Daresbury, Lancashire, England, 1970). To fit our data Eq. (5) was smeared with a Gaussian resolution function having $\sigma(M_{\pi\pi}) \approx 3$ MeV.

[6] The Breit-Wigner amplitude used is given by Eqs. (22) and (30) (with $R = 0.4$ fm) of J. Pišút and M. Roos, Nucl. Phys. B6, 325 (1968).

[7] This assumption is based on theoretical arguments (see Ref. 5). A complex δ would be equivalent to a shift of origin for β^+ by $-\arg(\delta)$.

[8] Since the results from Reactions (1) and (2) were consistent, we have averaged these cross sections in order to reduce the errors.

[9] m_ω has been fixed to the value preferred by our data, since it is highly correlated with β^+. The value assumed is consistent with the world average value for m_ω (782.7 ± 0.6 MeV), quoted by N. Barash-Schmidt *et al.*, Phys. Lett. 50B, 1 (1974). A ±1 MeV change in m_ω typically introduces a ±5° change in β^+.

[10] G. V. Dass, in *Vector Meson Production and Omega-Rho Interference,* edited by A. Donnachie and E. Gabathuler (Daresbury Nuclear Physics Laboratory, Daresbury, Lancashire, England, 1970); A. Goldhaber *et al.*, Phys. Lett. 30B, 249 (1969).

[11] P. Estabrooks, A. D. Martin, and C. Michael, Nucl. Phys. B72, 454 (1974).

[12] A. C. Irving and C. Michael, CERN Report No. TH-1825, 1974 (to be published); the phase convention of this paper is $\varphi = -\beta^- = \beta_\rho^- - \beta_\omega^-$.

[13] See Ref. 5 for a discussion of early experiments. See also I. J. Bloodworth *et al.*, Nucl. Phys. B35, 133 (1971).

[14] B. N. Ratcliff *et al.*, Phys. Lett. 38B, 346 (1972).

[15] P. Estabrooks *et al.*, CERN-Max Planck Institute for Physics and Astrophysics Collaboration (to be published).

Influence of Meson Charge Exchange on $\bar{p}$-Absorption Evidence for Neutron Halos*

William J. Gerace, Morton M. Sternheim, and James F. Walker
Department of Physics and Astronomy, University of Massachusetts, Amherst, Massachusetts 01002

(Received 5 June 1974)

Pion charge exchange within the nucleus is shown to be an important effect in antiproton absorption experiments. It must be incorporated into any analysis which attempts to use absorption data to deduce the relative abundance of neutrons and protons at the annihilation site.

There have been several attempts to verify experimentally the unconfirmed, albeit reasonable, conjecture that in the periphery of heavy nuclei there is a preponderance of neutrons over protons which exceeds the N-to-Z ratio for that element.[1] The most recent attempt to track the elusive neutron halo is that of Bugg *et al.*,[2] who use the numbers of charged pions resulting from absorption of antiprotons in C, Ti, Ta, and Pb to deduce that such halos are present in medium and heavy nuclei. We find, however, that inclusion of the hitherto neglected effects of pion charge exchange within the nucleus eliminates any need to invoke a neutron halo to explain their antiproton data.

Attempts to use antiproton absorption to probe the relative proton and neutron distributions are based on the fact that the net pionic charge Q is 0 for a $\bar{p}p$ absorption and -1 for a $\bar{p}n$ capture. For $Z = N$ nuclei, charge exchange tends to equalize the π^+, π^-, and π^0 populations, or to *decrease* the π^- excess. By contrast, for $N/Z \gtrsim 1.15$, the preponderance of neutrons means that the $\pi^0 n \to \pi^- p$ reaction *increases* the π^- population. Thus omitting charge exchange in comparing nuclei is very misleading. Using a simple model to scale the mean pion path with A, without invoking halos, we have obtained good fits to the total numbers of π^+ and π^- and to the frequencies of events with net pionic charges of 0, ±1, ±2, ... While our model cannot rule out that neutron halos exist, there is little evidence in the antiproton absorption data for halos of the magnitude suggested by Bugg *et al.*[2]

Pion transport model.—For simplicity, we ippose that all the pions observed travel the ime distance λ before leaving the nucleus. hey have a cross section σ_{ex} for charge exianging on a nucleon of the right type and an sorption probability which is assumed to be ie same for π^+, π^0, and π^-. We also assume iat the initial pion populations are the same as ir the weighted average of free $\bar{p}p$ and $\bar{p}n$ anhilations,[3] although the free annihilation cross ections, $\sigma_{\bar{p}p}$ and $\sigma_{\bar{p}n}$, are not assumed to be jual. The equations for the mean numbers of ions emerging in each charge state are given by ernheim and Silbar[4]; they can be used to deteriine $\Delta = [N(\pi^-) - N(\pi^+)]/[N(\pi^-) + N(\pi^+)]$, which is mply related to the ratio of $\bar{p}p$ to $\bar{p}n$ annihilaons used in the earlier analysis.[2] Note that Δ independent of pion absorption.

Figure 1 shows the dependence of Δ on the pion iarge-exchange parameter $C = \rho\sigma_{ex}\lambda$, where ρ the nuclear density. In addition to pion charge change we have included two other effects: nueon charge exchange before annihilation and the ssible inequality of $\sigma_{\bar{p}p}$ and $\sigma_{\bar{p}n}$. These are aracterized by $S = \sigma(\bar{p}p \to \bar{n}n)/\sigma_{\bar{p}p}$ and $R = \frac{1}{2}[(\sigma_{\bar{p}p}/$ $_{n}) - 1]$, respectively. For small values of R d S, the two effects are found to be virtually distinguishable. Since the pion charge-exchange fect is very small for Ti, we have used this nueus to fit the sum $R + S$; the best value is about , which is somewhat smaller than the values ggested by free-annihilation data.[3] The three rves in Fig. 1 for each nucleus give the C dendence of Δ for $R + S = 0$, 0.1, and 0.2. The experimental values for Δ are taken from Ref. 2, with arbitrary assumed error bars of 5% for C and 10% for Ti, Ta, and Pb. These data points have been plotted at values of C corresponding to the predictions of a model discussed below.

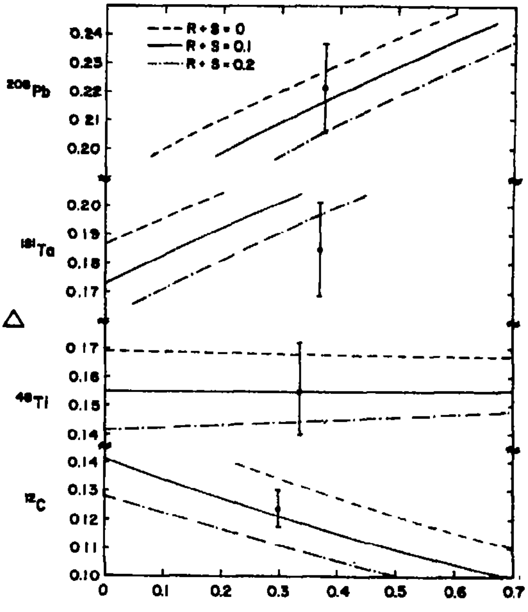

FIG. 1. Variation of Δ with charge-exchange length parameter C for each nucleus. The experimental values are found using the information in Ref. 2, and are positioned at the predicted value of C.

The important thing to note about Fig. 1 is that charge exchange influences Δ differently for the different nuclei. The negative-pion excess decreases with increasing C for ^{12}C but increases for the heavier elements. Thus it can be seen that charge-exchange effects will have important consequences for any conclusion regarding the presence or absence of a neutron halo.

It is possible to relate the average charge-exchange path length λ to the pion-absorption probability F_{abs} using a simple geometric model. The experimental values for F_{abs} were obtained in Ref. 2 by comparing the charged-pion multiplicity with $\bar{p}d$ data. We assume that the $\bar{p}$ annihilation occurs far out in the nuclear surface and that annihilation pions which encounter density concentrations greater than some critical fraction of the central density are completely absorbed, since absorption goes as ρ^2. Furthermore, λ is

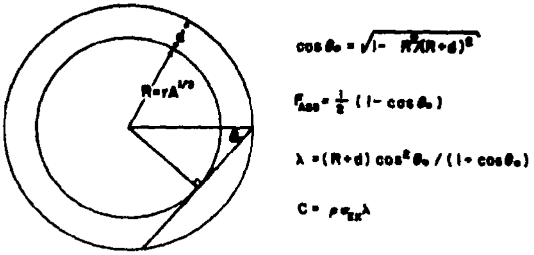
d
$R = rA^{1/3}$
θ_0
$\cos\theta_0 = \sqrt{1 - R^2/(R+d)^2}$
$F_{\text{ABS}} = \frac{1}{2}(1 - \cos\theta_0)$
$\lambda = (R+d)\cos^2\theta_0/(1+\cos\theta_0)$
$C = \rho\sigma_{\text{EX}}\lambda$

FIG. 2. Definition of model variables and expressions for the absorptive fraction and charge-exchange mean free path.

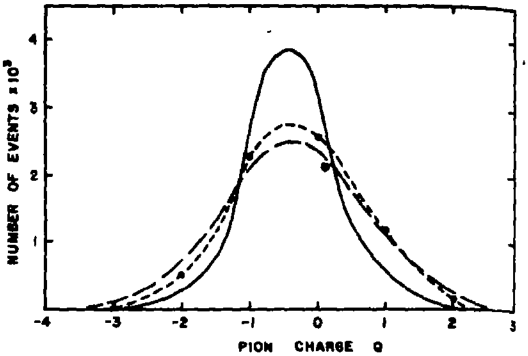

FIG. 3. Pion charge distribution for ^{12}C. The solid curve and long-dashed curve are calculated using absorption only and absorption plus charge exchange, respectively. The short dashes connect the experimental points of Ref. 2.

taken to be the average path length in the nucleus for pions that are not absorbed. Figure 2 shows the definitions which determine λ and F_{abs} in this model. If we assume that the absorptive core radius scales as $R = rA^{1/3}$ and that the core to surface distance d is constant for all nuclei, the quantities F_{abs} and λ/d can be expressed in terms of r/d. A value of $r/d = 0.8$ and $C = 0.30$ for ^{12}C generates the values of F_{abs} and C shown in Table I; these values are indicated in Fig. 1 by the positions of the data points. With the possible exception of Ta, the model gives remarkable agreement. Also, the value of σ_{ex} implied by these C values is roughly consistent with the free πN data averaged over the appropriate energy range.

Statistical model.—Clear evidence of the necessity of including pion charge-exchange effects is contained in the spread of the distribution of final-state pion charge, Q, tabulated in Table I of Ref. 2. As noted, for a $\bar{p}p$ annihilation $Q = 0$, while for a $\bar{p}n$ annihilation $Q = -1$. However, many events are observed with Q values ranging out to $Q = \pm 3$. Of the several processes discussed previously, only pion absorption and pion charge exchange are effective in producing high-$|Q|$ events.

We have studied this distribution within the framework of a relatively crude statistical model. We assume that the probabilities of various pion multiplicities in annihilation events are proportional to the available phase space, and that all charge-conserving pion charge configurations a equally probable. The resulting distribution wa checked against low-energy $\bar{p}p$ and $\bar{p}d$ annihilation data, and adjusted slightly to give good fits to average numbers of π^+, π^-, and π^0's, as well as to the relative probability for events with vaious numbers of charged pion prongs.[4,5]

This distribution was then used to do statistic calculations which included the effects of R, S, F_{abs}, C, and N/Z, with the approximation $C \ll 1$ We find the same dependence for Δ on these parameters as in the transport model above. This is due to the fact that the average charge and multiplicity values in our statistical model are identical to those of the transport theory provid the second-order pion charge-exchange effects are unimportant. As was expected, the width o the distribution in Q values is nearly independe of N/Z, R, and S.

In Fig. 3 the number of events N_Q with pion charge Q is plotted for ^{12}C. The curves are

TABLE I. Comparison of model results and experimental values from Ref. 2. (See text for definition of symbols.)

	$F_{\text{abs}}^{\text{expt}}$	$F_{\text{abs}}^{\text{theo}}$	λ/d	C	Δ^{expt}	Δ^{theo}
^{12}C	0.110 ±0.01	0.118	0.934	0.300	0.124	0.122
^{48}Ti	0.171 ±0.01	0.165	1.046	0.325	0.156	0.157
^{181}Ta	0.211 ±0.012	0.213	1.156	0.359	0.186	0.208
^{208}Pb	0.221 ±0.014	0.218	1.162	0.361	0.222	0.217

normalized to the total number of events observed in Ref. 2 after correction of N_0 for "hydrogen events." The solid curve was calculated assuming no charge exchange; its width is due to absorption only, with the absorption fraction $F_{\rm abs} = 0.110$ taken from the experiment. According to our calculations a very large absorption fraction ($F_{\rm abs} \approx 0.5$) would be required to fit the spread in the absence of charge exchange. The dashed curve gives the results using the observed absorption plus the charge exchange ($C = 0.30$) suggested in Fig. 1 for ^{12}C. The results of these calculations indicate the effectiveness of charge exchange in spreading the distribution. This value of C is in fact possibly somewhat large.

Qualitatively similar graphs are obtained for other nuclei. In all cases absorption alone cannot provide the necessary spread, and the charge-exchange value of Fig. 1 seems to be a bit too large. Probably a smaller charge-exchange fraction, plus a modified value of R, plus a relatively small "halo factor" in large-A nuclei could be found which would fit all the data, with the possible exception of ^{181}Ta which appears to have an anomalously skewed charge distribution.

To summarize, with the aid of highly simplified models we have shown that pion charge exchange in the target nucleus is important. It cannot be removed by simply taking ratios of results for various nuclei. Furthermore, it *must* be removed before trying to extract $(N/Z)_{\rm eff}$ results from experimental data of the sort discussed here. The spread of the pion charge distribution is clearly an excellent determinant of the magnitude of the pion charge-exchange process, although our statistical model is too crude for a precise analysis of its effects. A reasonably sophisticated model of antiproton absorption which properly includes all the effects considered is a prerequisite to learning from $\bar{p}$ absorption whether neutron halos exist.

---

*Research supported in part by the National Science Foundation.

[1] D. H. Davis *et al.*, Nucl. Phys. B1, 438 (1967); J. P. Schiffer and H. J. Körner, Phys. Rev. C 8, 841 (1973).

[2] W. M. Bugg *et al.*, Phys. Rev. Lett. 31, 475 (1973).

[3] W. Chinowsky and G. Kojoian, Nuovo Cimento 43A, 684 (1966); V. Barnes *et al.*, in *Proceedings of the Twelfth International Conference on High Energy Physics, Dubna, U.S.S.R., 1964* (Atomizdat., Moscow, U.S.S.R., 1966), p. 731.

[4] M. M. Sternheim and R. R. Silbar, Phys. Rev. D 6, 3117 (1972).

[5] E. Bracci *et al.*, "Compilation of Cross Sections III —p and $\bar{p}$ Induced Reactions," CERN Report No. CERN/HERA 73-1, 1973 (unpublished); L. E. Agnew, Jr., *et al.*, Phys. Rev. 118, 1371 (1960).

PHYSICAL REVIEW
LETTERS

VOLUME 33 26 AUGUST 1974 NUMBER 9

Polyatomic Molecular Relaxation in the Absence of Collisions*

S. L. Shapiro, R. C. Hyer, and A. J. Campillo
University of California, Los Alamos Scientific Laboratory, Los Alamos, New Mexico 87544
(Received 28 May 1974)

The fluorescence rise time for dimethyl 1,4-bis[2(4-methyl-5-phenyl-oxazolyl)] benzene (POPOP) and perylene molecules in the vapor phase is measured with a streak camera to be less than 20 and 30 ± 10 psec, respectively. These results are direct evidence that large polyatomic molecules can rapidly relax, even in the absence of collisions.

Early theories by Zener[1] and Teller[2] predict that large polyatomic molecules relax by nonradiative processes, even in the absence of collisions. In other words, even an isolated molecule can be rapidly deactivated by these transitions. There is strong evidence for these transitions, because radiative emission from a state higher than the lowest excited state of a given multiplicity is rarely observed when large molecules are excited with a light source. Since the upper states do not emit light, they are deactivated by what is now commonly called "radiationless" electronic transitions. Indirect evidence also exists for nonradiative transitions in the absence of collision, the principal evidence being the mirror symmetry between the absorption and emission spectra for large polyatomic molecules in the vapor phase.[3] In this paper we report the first *direct* evidence of fast, picosecond, nonradiative transitions in two such large polyatomic molecules, perylene and dimethyl 1,4-bis [2(4-methyl-5-phenyl-oxazolyl)] benzene (POPOP), in the vapor phase where the molecular collisional deactivation rate is negligible.

Recently, picosecond pulses have been used to measure vibrational and orientational relaxation times of dye molecules in the liquid state.[4-8] Nonradiative relaxation rates are measured by pumping the molecules to a higher electronic state with picosecond pulses,[9] and then observing the time dependence of the fluorescence. Because molecules relax nonradiatively to the ground vibrational states of the excited electronic state from which fluorescence takes place, the rise time of the fluorescence is a measure of the nonradiative relaxation time. For an organic molecule in a liquid the characteristic relaxation time may depend strongly on the properties of the medium. In the condensed phase a molecule collides with its environment at a rate of about 10^{12}/sec, so that in addition to decaying internally, a molecule can decay by transferring energy to its environment. The vapor state is important for establishing the fundamental nature of radiationless transitions in the isolated molecule. This is because the collision rate between molecules can be chosen to be much slower than the deactivation rate of the molecule due to radiationless transitions. Using a streak camera[10,11] technique,[12] we have measured the rise time of the fluorescence in perylene and dimethyl POPOP in the vapor phase to be ≤30 ± 10 and ≤20 psec, respectively. These results are significant because they definitely prove that the molecules have relaxed rapidly in the absence of collisions.

The experimental arrangement for our observations is shown in Fig. 1. A mode-locked Nd:

Copyright © 1974 by
The American Physical Society

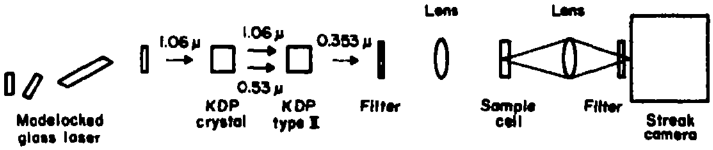

FIG. 1. A mode-locked Nd:glass laser emits picosecond pulses which are frequency tripled by two KDP crystals. A 0.353-μm, 5–8-psec pulse excites a vapor sample, and the fluorescence produced by one pulse is analysed with a streak camera. Corning 3-73 and 3-75 filters are placed before the streak camera for the perylene and dimethyl POPOP observations, respectively.

glass laser emits a train of picosecond pulses at 1.06 μm. Satellite pulses are eliminated by use of a flowing-dye-cell arrangement on the back mirror of the laser cavity. The 1.06-μm pulses pass through the usual type-I, phase-matched potassium dihydrogen phosphate (KDP) harmonic-generator crystal producing pulses at 0.53 μm. The 1.06- and 0.53-μm pulses then pass through a second KDP crystal that is cut at 58° from the c axis for a type-II ($e+o\rightarrow e$) phase-matched sum-frequency mixing process to generate pulses at 0.353 μm. The conversion efficiency from the fundamental to the third harmonic is about 8%. These third-harmonic pulses excite the vapor samples, and fluorescence is collected and projected by a lens onto the slit of a streak camera. 1 mg of each sample was placed in 2-cm-long Pyrex cells with a volume of 13 cm^3. The cells were then evacuated and sealed off. Samples were placed inside a carefully designed copper oven, and the temperature was continuously monitored with a thermocouple output connected to a chart recorder. The streak camera used is a Los Alamos Scientific Laboratory device. The collected light is focused onto a conventional RCA-7435 grid-shuttered image-converter–type tube having an S-1 photocathode response: This tube is then followed by an image intensifier and a P-11 phosphor screen. The ramp deflection voltage was produced by an internal electronic circuit, and was triggered by an earlier pulse in the mode-locked train. The converted image of the streak was photographed on Eastman Kodak 2484 emulsion film, and the film density was calibrated with a step wedge. Densitometer traces of the resultant negatives yielded the temporal dependence of the fluorescence from which the lifetimes could be accurately deduced. The resolution time of our streak camera is about 15 psec.

Figure 2 shows a densitometer trace of a streak-camera negative of the fluorescence from dimethyl POPOP at a temperature of 295°C. The rise time of the curve in Fig. 2 was ascertained to be less than 20 psec. For perylene vapor at 300°C the rise time was measured to be ≤ 30 psec. The collision rate at these temperatures can be no more than 10^8/sec.

Because the fluorescence rise time is much shorter than the collision time, an important conclusion must be drawn, namely, that collisions are unnecessary for internal relaxation of complex molecules for times shorter than the radiative lifetimes. This rapid internal relaxation can perhaps be explained by the fact that the more complex the constitution of a molecule, the larger are the numbers of vibrational and rotational modes so that the probability of overlap and mutual interaction between these modes increases. These mutual interactions reduce the lifetime of any particular level, because any excess energy provided by the excitation wavelength can be rapidly redistributed over the large ensemble of densely packed levels. In fact, for

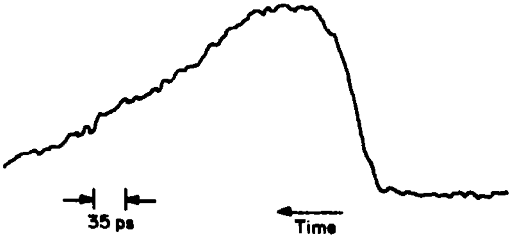

FIG. 2. A densitometer trace of a streak-camera negative shows a rapid rise time for the fluorescence from dimethyl POPOP vapor. Calibration shows that this rise time is less than 20 psec, independent of excitation intensity. The fall time is shorter for higher pumping rates because of the presence of gain in the medium. For perylene vapor the rise time is $\leq 30 \pm 10$ psec.

many complex molecules, no structure at all appears in the emission bands because of the mutual interactions of the levels. Spectra of dimethyl POPOP and perylene in liquids show broad featureless vibronic levels,[13] and so do the spectra of perylene in the vapor phase.[14] Because of the complexity of these two molecules, intramolecular relaxations occur independently of external perturbations. These two molecules are classified as complex according to the concepts of Neporent,[15,16] for the rate of vibrational deactivation appears to be much greater than the redistribution probabilities of the optical and nonoptical transitions to the lower electronic state.

The nonradiative redistribution of energy in molecules has attracted widespread theoretical attention recently.[17] One attractive model for molecular decay has been proposed independently by Lin and Bersohn[18] and by Englman and Jortner.[19] They have considered the problem of radiationless transitions in polyatomic molecules from the point of view of multiphonon processes, much the same as excitations decay in solids.[20] Thus giant molecules have some properties similar to a solid. In fact, some of the formalism of solid-state theory can be carried over to molecular-decay theory. Direct measurements of the fluorescence rise times in the vapor state should be most useful for refining theoretical concepts on the nature of the intramolecular decay.[21]

We thank Howard Sutphin for his aid in using the streak camera, and Dr. D. Giovanielli and Dr. G. McCall, all of Los Alamos Scientific Laboratory, for kindly lending us a streak camera.

---

*Work supported by the U. S. Atomic Energy Commission.

[1] C. Zener, Proc. Roy. Soc., Ser. A 137, 696 (1932).

[2] E. Teller, J. Phys. Chem. 41, 109 (1937).

[3] A review of the properties of complex molecules in the vapor phase is found in N. A. Borisevich, *Vozbuzhdennye sostoyaniya s'ozhnykh molekul v gazovoi faze* (Nauka i Teknika, Minsk, U. S. S. R., 1967).

[4] P. M. Rentzepis, M. R. Topp, R. P. Jones, and J. Jortner, Phys. Rev. Lett. 25, 1742 (1970).

[5] R. R. Alfano and S. L. Shapiro, Opt. Commun. 6, 98 (1972).

[6] D. Ricard, W. H. Lowdermilk, and J. Ducuing, Chem. Phys. Lett. 16, 617 (1972).

[7] C. Lin and A. Dienes, Opt. Commun. 9, 21 (1973).

[8] K. B. Eisenthal and K. H. Drexhage, J. Chem. Phys. 51, 5720 (1969).

[9] For measurement of picosecond pulses see J. A. Giordmaine, P. M. Rentzepis, S. L. Shapiro, and K. W. Wecht, Appl. Phys. Lett., 11, 216 (1967); M. A. Duguay and J. W. Hansen, Opt. Commun. 1, 254 (1969); M. A. Duguay and A. Savage, Opt. Commun. 9, 212 (1973); D. J. Bradley, B. Liddy, and W. E. Sleat, Opt. Commun. 2, 391 (1971); M. Ya. Schelev, M. C. Richardson, and A. J. Alcock, Appl. Phys. Lett. 18, 354 (1971).

[10] Bradley, Liddy, and Sleat, Ref. 9.

[11] Schelev, Richardson, and Alcock, Ref. 9.

[12] Short lifetime measurements with a streak camera have been reported by E. G. Arthurs, D. J. Bradley, and A. G. Roddie, Chem. Phys. Lett. 22, 230 (1973).

[13] I. B. Berlman, *Fluorescence Spectra of Aromatic Molecules* (Academic, New York, 1971), 2nd ed., pp. 302 and 399.

[14] N. A. Borisevich and V. V. Gruzinskii, Opt. Spektrosk. 14, 39 (1963) [Opt. Spectrosc. (USSR) 14, 20 (1963)].

[15] B. S. Neporent, Usp. Fiz. Nauk 43, 380 (1951).

[16] B. I. Stepanov and A. M. Samson, Opt. Spektrosk. 12, 224 (1962) [Opt. Spectrosc. (USSR) 12, 120 (1962)].

[17] B. R. Henry and M. Kasha, Annu. Rev. Phys. Chem. 19, 161 (1968).

[18] S. H. Lin and R. Bersohn, J. Chem. Phys. 48, 2732 (1968).

[19] R. Englman and J. Jortner, Mol. Phys. 18, 145 (1970); see also M. Bixon and J. Jortner, J. Chem. Phys. 48, 715 (1968), and 50, 4061 (1969); K. Freed and J. Jortner, J. Chem. Phys. 52, 6272 (1970); A. Nitzan and J. Jortner, J. Chem. Phys. 55, 1355 (1971); A. Nitzan, J. Jortner, and P. M. Rentzepis, Chem. Phys. Lett. 8, 445 (1971).

[20] M. Lax, J. Chem. Phys. 20, 1752 (1952).

[21] Additional information on molecular decays can be obtained from detailed studies of the absorption and emission spectra of polyatomic molecules as has been reported by E. R. Menzel, K. E. Rieckhoff, and E. M. Voigt, Chem. Phys. Lett. 13, 604 (1972) and by K. E. Rieckhoff, E. R. Menzel, and E. M. Voigt, Phys. Rev. Lett. 28, 261 (1972). Their techniques and concepts could be applied to vapor phase studies of radiationless processes.

Electron Bremsstrahlung from Neutral Atoms*

H. K. Tseng† and R. H. Pratt
Department of Physics, University of Pittsburgh, Pittsburgh, Pennsylvania 15260

(Received 17 June 1974)

The complete energy spectrum for electron bremsstrahlung has been obtained, by using a numerical calculation in partial waves with numerical potentials corresponding to neutral atoms. Sample spectra are presented for electrons of kinetic energy 50 keV incident on Au and Al. The connections between elastic electron scattering and the low-frequency region of the bremsstrahlung spectrum and between photoeffect and the high-frequency region of the bremsstrahlung spectrum are demonstrated.

Recently there has been renewed interest in electron bremsstrahlung from neutral and ionized atoms. With the continuing improvements in computer technology it has become feasible to calculate directly electron bremsstrahlung cross sections in numerical potentials. We have previously reported some scattered results[1] for incident-electron kinetic energies T_1 in the range from 5 keV to 1 MeV and for radiated photon energies k from $0.4T_1$ to $0.96T_1$; good agreement was obtained with recent experimental work.[2]

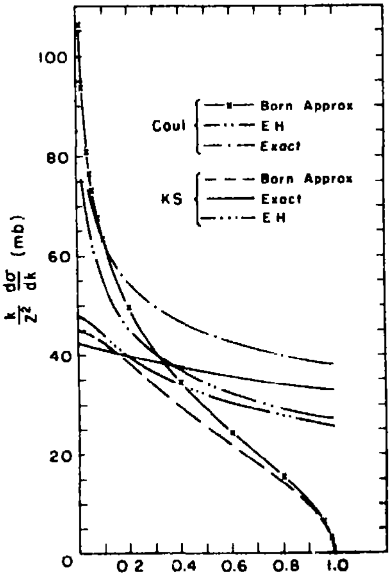

FIG. 1. Comparisons of bremsstrahlung cross sections $(k/Z^2)d\sigma/dk$ for $Z=79$, $T_1=50$ keV according to our numerical work (exact), the Born approximation (Born), and the Elwert-Haug formula (EH). Results are shown for the point Coulomb (Coul) and Kohn-Sham (KS) potentials.

We are now able to calculate the entire spectrum of k from 0 to T_1. Sample spectra for the Kohn-Sham potential[3] are shown in Figs. 1 and 2 for the bremsstrahlung from Au and Al with an incident-electron kinetic energy of 50 keV. These figures also show the point-Coulomb-potential and Born-approximation[4] predictions for the same cases.

For these energies the simplest and most widely used result is the relativistic Born-approximation calculation for a point Coulomb potential. This Bethe-Heitler formula neglects higher-order Coulomb effects and atomic-electron screening. The exact point-Coulomb result, obtained numerically, is shown in Figs. 1 and 2, as well

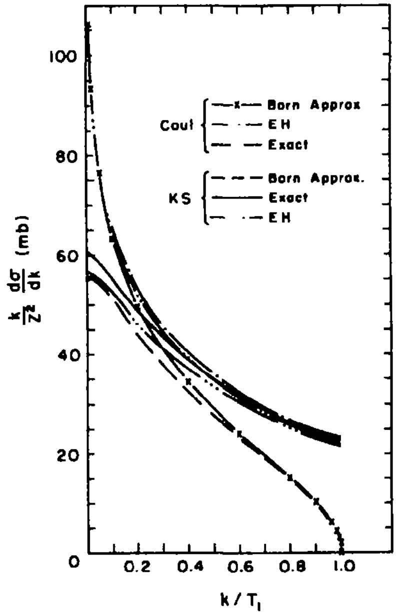

FIG. 2. Same as Fig. 1 except that $Z=13$, $T_1=50$ keV.

as an approximate analytic result due to Elwert and Haug[5] which is valid for the low-Z point-Coulomb case at all energies. In Born approximation, electron screening simply multiplies the Bethe-Heitler matrix element by a form factor; the resulting prediction for the spectrum is also shown in the figures. It is clear that none of these approximations correctly describes the spectrum. We also show the Elwert-Haug formula corrected for screening with a form factor. For the high-Z case qualitative agreement with the exact screened result is achieved, because of the cancelation of errors in the calculation of Coulomb and screening effects. For low-Z elements this approach gives quantitatively acceptable results at this energy, but its validity at lower energies remains to be determined.

In the low-frequency region of the spectrum, screening drastically reduces the cross section and removes the logarithmic divergence associated with the long-range character of the point Coulomb potential. For quantitative purposes the higher-order Coulomb effects are also of some importance and reduce the cross section further. In the high-frequency region of the spectrum, Coulomb effects increase the cross section and cause it to remain finite for $k=T_1$; for quantitative purposes the screening effects are also important and decrease the cross sections. Similar features are observed as T_1 and Z are varied. The effect of screening is adequately described by a form factor only when the Born approximation is satisfactory. Nonrelativistic results[6] are reached rather slowly.

In the low-frequency region of the spectrum, as discussed by Low,[7] the bremsstrahlung matrix element is proportional to the matrix element for elastic electron scattering. This leads to the prediction for the spectrum limit point ($k=0$)

$$\left(\frac{k}{Z^2}\frac{d\sigma_{\text{brem}}}{dk}\right)_{k=0}=\frac{4\alpha}{Z^2}\int_0^{\pi}\sin\theta\,d\theta\left(\frac{d\sigma}{d\Omega}\right)_{\text{els}}\left[A(A^2-B^2)^{-1/2}\cosh^{-1}(A/B)-1\right],$$

where $\beta=p_1/E_1$, $A=1-\beta^2\cos\theta$, $B=1-\beta^2$, with θ the electron scattering angle. Using Lin's elastic scattering data[8] we obtain a value of the spectrum limit point for $Z=79$ of 41.7 mb at $T_1=50$ keV, in good agreement with our calculated value of 42.4 mb. Similar agreement is obtained for $T_1=100$ keV. The slope of the spectrum, which according to our numerical data is nearly constant in these high-Z cases, could also be predicted if the elastic amplitude (rather than just the cross section) were available.

In the high-frequency region of the spectrum, as first noted by Fano and co-workers[9] and then extended by Pratt,[10] the bremmstrahlung cross section is proportional to the cross section for the atomic photoelectric effect, neglecting terms of relative order $(Z\alpha)^2$. Using Scofield's exact numerical photoeffect results[11] we obtain predictions for the $k=T_1$ limit point of the spectrum which agree with our numerical bremsstrahlung calculation within 20% even for high-Z elements and low kinetic energies T_1 (50 keV) if the atomic-electron scattering is either small or is estimated approximately.[12] Experimental results for the $k=T_1$ case obtained by Starek, Aiginger, and Unfried[13] for $T_1=1.84$ MeV disagree with the Elwert-Haug predictions. Our numerical calculations agree with the experiments for high Z and with the Elwert-Haug predictions for low Z.

We are performing further calculations to study the bremsstrahlung spectrum and angular distributions systematically as functions of Z and T_1. We plan to present and discuss such data subsequently.

---

*Work supported in part by the National Science Foundation under Grant No. GP-32798.

†Present address: Department of Physics, National Central University, Chung-Li, Taiwan (Formosa), Republic of China.

[1] H. K. Tseng and R. H. Pratt, Phys. Rev. A 1, 528 (1970), and 3, 100 (1971).

[2] H. Aiginger, Z. Phys. 197, 8 (1966), and private communication; D. H. Rester and W. E. Dance, Phys. Rev. 161, 85 (1967); D. H. Rester, N. Edmonson, and Q. Peasley, Phys. Rev. A 2, 2190 (1970); M Scheer, E. Trott, and G. Zaks, Z. Phys. 209, 68 (1968); W. Lichtenberg and M. Scheer, private communication; R. W. Kuckuck and P. J. Ebert, Phys. Rev. A 7, 456 (1973).

[3] W. Kohn and L. S. Sham, Phys. Rev. 140, A1133 (1965); D. A. Liberman, D. J. Cromer, and J. T. Waber, Comput. Phys. Commun. 2, 107 (1971).

[4] H. A. Bethe and W. Heitler, Proc. Roy. Soc. Ser. A 146, 83 (1934); F. Sauter, Ann. Phys. (Leipzig) 20, 404 (1934); G. Racah, Nuovo Cimento 11, 461, 467 (1934).

[5] G. Elwert and E. Haug, Phys. Rev. 183, 90 (1969).

[6] A. Sommerfeld, Ann. Phys. (Leipzig) 11, 257 (1931); G. Elwert, Ann. Phys. (Leipzig) 34, 178 (1939); P. Kirkpatrick and L. Wiedmann, Phys. Rev. 67, 321 (1945).

[7] F. E. Low, Phys. Rev. 110, 974 (1958).

[8] S. R. Lin, Phys. Rev. 133, A965 (1964).

[9] U. Fano, Phys. Rev. 116, 1156 (1959); K. W. McVoy and U. Fano, Phys. Rev. 116, 1168 (1959); U. Fano,

H. W. Koch, and J. W. Motz, Phys. Rev. 112, 1679 (1958).

[10] R. H. Pratt, Phys. Rev. 120, 1717 (1960).

[11] J. H. Scofield, Lawrence Livermore Laboratory Report No. UCRL-51326, 1973 (unpublished). To obtain point-Coulomb photoeffect results from Scofield's results we have used the normalization screening theory described in the recent photoeffect review by R. H. Pratt, A. Ron, and H. K. Tseng, Rev. Mod. Phys. 45, 273, 663(E) (1973).

[12] For incident-electron kinetic energies above about 10 keV the screening effects in the high-frequency region have a simple origin in changes of wave-function normalization which are observed also in high-energy photoeffect, low-energy pair production, and single-quantum pair annihilation. See for example, H. K. Tseng and R. H. Pratt, Phys. Rev. A 4, 1835 (1971), and 7, 1423 (1973).

[13] B. Starek, H. Aiginger, and E. Unfried, Phys. Lett. 39A, 151 (1972).

Lattice Location and Hyperfine Fields of Rare-Earth Ions Implanted into Iron

R. L. Cohen
Bell Laboratories, Murray Hill, New Jersey 07974

and

G. Beyer
Joint Institute for Nuclear Research, Dubna, Union of Soviet Socialist Republics

and

B. Deutch
Institute of Physics, Aarhus University, Aarhus, Denmark

(Received 18 June 1974)

We show that the implantation and anneal behavior of Gd implanted into iron is strongly affected by the process of "internal oxidation." This result is used to clear up discrepancies in earlier measurements on rare-earth ions implanted into iron.

Since the advent of the channeling technique[1] for determining the location of impurities in single crystals, a great deal of research has been performed to study the location in the lattice, and change of that location under annealing,[2] of implanted ions. Recently, such measurements have been combined with studies of the hyperfine (hf) structure of implanted ions.

Lattice location, hf fields, and annealing behavior of rare-earth (RE) ions implanted into iron have been extensively studied.[3-6] We report here new experimental results, based on the Mössbauer spectroscopy of *Fe*:Eu^{151} (Gd^{151} is the implanted species) which show that internal oxidation of the implanted Gd ions dominates the observed behavior. The chemical and metallurgical properties of the RE ions are rather similar; thus these findings can be extended to explain the results of many previous measurements performed on RE ions implanted into iron.

The conclusions from previous work on *Fe*:RE systems can be summarized as follows: (1) Channeling lattice-location measurements[3-5] show that about 60% of implanted Yb ions are substitutional in Fe, but the remaining 40% do not occupy well-defined interstitial sites. (2) Off-line time-integral perturbed angular correlation (PAC) measurements[3,4] (using radioactive Yb implanted into Fe, with the hf field measured for the Tm daughter) indicate an "average" hf field which is substantially less than would be expected for *Fe*:Tm. (3) Both the substitutional fraction (measured by backscatter experiments) and the average hf field go to essentially zero after a brief anneal at 500°C.[3,4] After the anneal, the Yb ions do not occupy well-defined sites. (4) On-line implantation PAC (IMPAC) measurements, in which hf fields of the implanted RE ions are measured within 10^{-9} sec after the ions stop, suggest that one hf field is produced by the RE ions of a given species,[6] and that the observed fields are consistent with expectations. (5) The electron relaxation rate for Tm PAC measurements (implanted *Fe*:Yb) for an annealed (500°C) source is the same as that for Yb_2O_3:Tm, and one-third that for an unannealed source.[3]

We present here the result of Mössbauer measurements on sources of Gd^{151} implanted ($4\times10^{14}/$

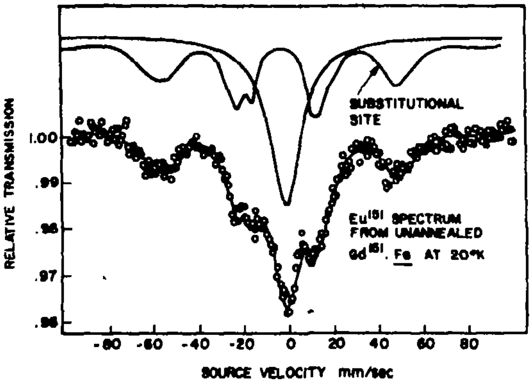

FIG. 1. Mössbauer spectrum of Eu^{151} from *Fe*:Gd implanted source. A least-squares fit (line through the data points) was made using the known ground- and excited-state magnetic and electric quadrupole moment ratios, known transition probability ratios for the eighteen lines in the hf spectrum, and assuming that there was one split and one unsplit component. The hf field is 4 times larger than normally observed in Eu^{151} spectra; the four groups of lines at ±20 and ±60 mm/sec correspond to the four strong lines normally observed in Eu Mössbauer spectra.

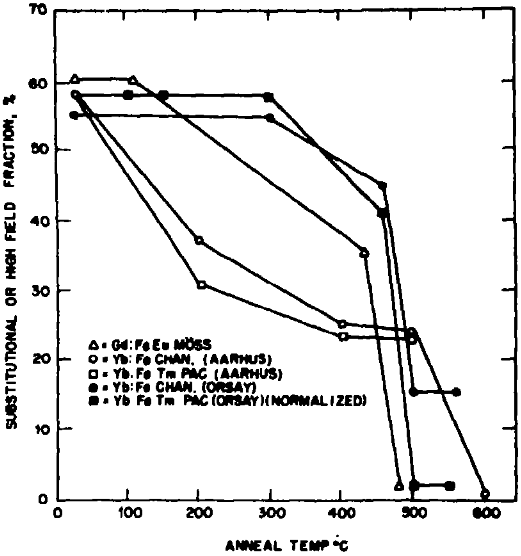

FIG. 2. Composite plot of Mössbauer, location, and hf field results versus anneal temperature, from Ref. 3 (open points) and Ref. 4 (filled points). Some of the original data points have been averaged or smoothed to make the plot legible. The lines have been drawn only to connect the data points. Implantation energies were 50–80 keV (Mössbauer and Ref. 3) and 400 keV (Refs. 4,5), corresponding to depths of 130 and 530 Å for the implanted RE ions. Anneals for all experiments were 15 min long. PAC measurements have been plotted implicitly assuming that there is one site with a large hf field and one site with a negligible hf field, and that only the relative fraction of atoms between these two sites changes under anneal. Thus, the high-field fraction equals the ratio of the average hf field to the hf field expected for substitutional ion.

cm^2, 50 keV energy) into polycrystalline iron foils.[7] The Gd^{151} decays to Eu^{151}, and the hfs of the 21.7-keV γ rays emitted by the Eu^{151} has been studied using the Mössbauer effect. The chemical and metallurgical properties of Ge^{3+} and Yb^{3+} should be similar enough for results of our measurements on the *Fe*:Gd system to be applicable to phenomena observed in *Fe*:Yb.[8]

A sample spectrum is shown in Fig. 1, and the results can be briefly described as follows: (1) Measurements of the isomer shift show that all the Eu ions are Eu^{3+} ($4f^6$ configuration). Since Eu^{2+} would appear ~14 mm/sec to the right of Eu^{3+}, divalent Eu would be easily distinguished. (2) The unannealed source spectrum (Fig. 1) can be resolved into two components, corresponding to two sites for the Eu ions. One component is split [hf field $B_{\rm hf}=1.31$ MG, isomer shift (IS) 3.5 mm/sec versus EuF$_3$]; the other is a broadened but essentially unsplit line ($B_{\rm hf}<50$ kG, IS 1 mm/sec versus EuF$_3$). The split hfs comprises about 60% of the total intensity of the spectrum.[9] (3) A 15-min anneal (in H_2) at 430°C decreases, and a 15-min anneal at 480°C completely eliminates (see Fig. 2), the split component of the spectrum. (4) Further annealing (including 30 min at 500°C in air, which results in massive oxidation of the source) does not significantly alter the spectrum (see Fig. 3).

The large hf field and the isomer shift of 3.5 mm/sec are exactly what would be expected[10] for Eu in an Fe metal matrix. (In metallic surroundings, conduction-electron density normally increases the IS for Eu^{151} by 2–5 mm/sec over that in ionic compounds.[10]) The relative intensity[9] of the split spectrum, 60%, is the same as that of the substitutional site population seen by lattice location studies of *Fe*:Yb, suggesting that this spectrum arises from substitutional Eu ions, and that the unsplit spectrum arises from the ions observed (by lattice-location measurements) to be nonsubstitutional. The anneal behavior (Fig. 2) of the split component of the Mössbauer spectrum is the same as that observed for substitutional ions in the location experiments, confirm-

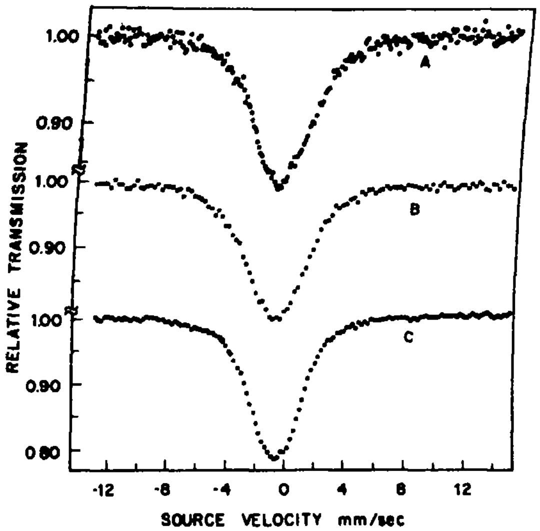

FIG. 3. Spectrum of source of Fig. 1, curve *A*, after anneal at 480°C in H_2; *B*, after anneal in air (600°C, 30 min) to assure complete oxidation. Curve *C*, comparison spectrum of Eu^{151} from Sm_2O_3 source, which is chemically similar to other trivalent-rare-earth oxides. The spectrum of the annealed *Fe*:Gd source is the same as that obtained from Eu^{3+} in an oxide environment.

ing this hypothesis.

The evidence is also very strong that the Eu ions producing the unsplit line are not in an interstitial or defect-associated site, but are internally oxidized: (1) Both the isomer shift and the lack of hf field are exactly what would be expected for Eu in an oxide environment [$IS(Eu_2O_3$ versus $EuF_3) = 0.6-0.8$ mm/sec]. Other ionic Eu^{3+} compounds with similar IS values are composed of elements which are not present in this system. (2) Interstitial ions should have even greater conduction-electron IS contributions than substitutional ions. Although defects associated with the implanted ion might slightly reduce the size of the conduction-electron contribution to the isomer shifts, they should not completely eliminate it. (3) The complete lack of hf field would not be expected for an interstitial site[11]; even accidental cancellation of different contributions to the hf field (for a dissolved Eu ion) could not lead to the observed behavior, since the various contributions would have different temperature dependence, and the observed hf field is zero (within the limit of measurement) from 20 to 400 K.

The analysis of the Mössbauer data suggests the following picture: *When RE ions are implanted into iron, the vast majority of them initially stop at substitutional sites. (Thus, the IMPAC e periments measure a hf field corresponding to a high substitutional fraction.) During the course of the implantation, which may take several hour some of the stopped RE ions are internally oxidized and removed from the regular lattice sites on which they stopped.*

Recently, Moline, Reutlinger, and North[12] have observed and measured the "driving in" of surface oxygen into silicon by incident Ne, Ar, and Kr ions in the 3–48-keV range. They showed that the operative mechanism was recoil implantation, in which relatively large amounts of recoil energy were given to oxygen ions in the surface oxide layer, and the oxygen ions recoiled into the substrate with a range approximately the same as that of the incident heavy ions. This process is dependent on nuclear kinematics and cross sections only, and should be completely insensitive to the details of host-properties chemistry.

Extrapolating from the conditions studied by Moline, Reutlinger, and North to those present in our implantation, we would expect approximately one oxygen atom to be implanted into the iron for each incident RE ion. Within the accuracy to which the surface-oxide-layer thickness and recoil-implantation efficiencies are known, we consider this adequate quantitative confirmation of oxygen recoil implantation as the primary contributor to the internal oxidation. Anneals after the implantation, then, do not simply drive RE ions off the substitutional sites into interstitial sites (as happens in other systems[13]), but mobilize additional oxygen, which oxidizes the remaining substitutional RE ions.

This analysis is fully supported by the relevant systematics. The basic requirements for internal oxidation[14]—that the dopant (RE) oxide is thermodynamically more stable than the host (Fe) oxide, that the oxide is insoluble in the host, and that a source of oxygen is present—are strongly fulfilled, and this process would be expected to occur.

The new results we are reporting here using the Mössbauer hf spectra of Eu^{151} in Fe show directly that both oxidized and unoxidized sites exist, and that the "anneal" process actually oxidizes formerly substitutional RE ions. This analysis appears to explain the apparent contradictions among a number of RE lattice-location and hf-field measurements which have been published in recent years, and can be extended to results obtained with other highly oxidizible (e.g., Hf and Ta) ions.

We are greatly indebted to L. C. Feldman for many fruitful discussions and helpful comments on the manuscript. K. W. West assisted with the experimental work and data reduction. We thank D. E. Murnick and his collaborators for communicating results of their IMPAC measurements prior to publication.

---

[1] See, e.g., J. A. Davies, in *Channeling*, edited by D. V. Morgan (Wiley, New York, 1973), p. 391.

[2] J. C. North and W. M. Gibson, Appl. Phys. Lett. 16, 126 (1970).

[3] R. B. Alexander, E. J. Ansaldo, B. I. Deutch, L. C. Feldman, and J. Gellert, in Proceedings of the International Conference on Applications of Ion Beams to Metals, edited by S. T. Picraux (Plenum, New York, to be published); R. B. Alexander, J. Gellert, B. I. Deutch, L. Feldman, and E. J. Ansaldo, in Proceedings of a Conference on hf Interactions in Nuclear Reactions, Uppsala, 1974 (to be published).

[4] F. Abel, M. Bruneaux, C. Cohen, H. Bernas, J. Chaumont, and L. Thomé, Solid State Commun. 13, 113 (1973); H. Bernas and H. Gabriel, Phys. Rev. B 7, 468 (1973).

[5] F. Abel, H. Bernas, M. Bruneaux, J. Chaumont, C. Cohen, and L. Thomé, in Proceedings of the International Conference on Applications of Ion Beams to Metals, edited by S. T. Picraux (Plenum, New York, to be published).

[6] H. W. Kugel, L. Eytel, G. Hubler, and D. E. Murnick, private communication, and in Proceedings of the International Conference on Magnetism, Moscow, U. S. S. R., 22–28 August 1973 (to be published).

[7] Less than 5% of RE ions implanted at this energy stop within the first 40 Å of the target. The foils used in Ref. 3 and this work have an oxide layer known to be 20–30 Å thick.

[8] Lattice location measurements use Fe single crystals as a host. IMPAC and PAC measurements have used both single crystals and polycrystalline foil. The relatively good agreement between the measurements suggests that this difference is not significant.

[9] The recoil-free fraction would be expected to be similar in the two sites, and site population is then proportional to the intensity of the hf spectrum.

[10] See, e.g., N. N. Greenwood and T. C. Gibb, *Mössbauer Spectroscopy* (Chapman and Hall, London, 1971), p. 548.

[11] H. de Waard, R. L. Cohen, S. R. Reintsema, and S. A. Drentje, Phys. Rev. B (to be published).

[12] R. A. Moline, G. W. Reutlinger, and J. C. North, in Proceedings of the Fifth International Conference on Atomic Collision Phenomena in Solids, Gatlinburg, Tennessee, September 1973 (to be published).

[13] E. N. Kaufmann, J. M. Poate, and W. M. Augustyniak, Phys. Rev. B 7, 951 (1973).

[14] J. H. Swisher, in *Oxidation of Metals and Alloys* (American Society for Metals, Cleveland, Ohio, 1971), p. 235.

Thermoreflectance of Tetrathiafulvalinium Tetracyanoquinodimethanide (TTF-TCNQ)

P. I. Perov[*] and J. E. Fischer[†]
Moore School of Electrical Engineering and Laboratory for Research on the Structure of Matter,
University of Pennsylvania, Philadelphia, Pennsylvania 19174

(Received 30 May 1974)

We report the first observation of a marked temperature dependence in the optical properties of TTF-TCNQ, based on thermoreflectance spectroscopy. The structure just above the plasma edge exhibits an abrupt 25% drop with $\vec{e}\parallel\vec{b}$ as the temperature is lowered past 45–50 K; simultaneously, a strong response for this transition with $\vec{e}\perp\vec{b}$ emerges. This supports the suggestion that a librational distortion of the TCNQ ion may be responsible for a Peierls transition in the complex.

The molecular charge-transfer salt TTF-TCNQ behaves electrically[1] and optically[2] like a one-dimensional metal at room temperature, with perhaps a tendency toward Fröhlich superconductivity which is frustrated by a Peierls transition.[1] Physical measurements as functions of temperature have been employed to study this hypothesis, although the mean-field T_c may be much higher than 60 K, the temperature of maximum conductivity.[3] Bright, Garito, and Heeger[2] and Grant *et al.*[4] report reflectivity spectra spanning the range 0.1–4.0 eV. The major structure is associated with a screened plasma resonance at 1.2–1.3 eV,[2] with additional weak structure at higher energies arising from interband[2] or molecular[4] effects. The temperature dependence of the direct reflectance spectra is not unusual. We were motivated to apply the advantages of modulation spectroscopy[5,6] in an attempt to observe temperature effects with higher sensitivity. Our most surprising result is an abrupt decrease of the polarization dependence of one of the transitions above the edge. With the association of this transition[7] with a B_{1u} mode of the TCNQ ion our result supports the suggestion by Morawitz[8] that a librational distortion of the TCNQ ion may be the driving force for the postulated Peierls transition in TTF-TCNQ.

Thermoreflectance spectra were obtained from 0.5 to 5.0 eV, from 5 K to room temperature, by using standard optical and electronic methods.[6] Temperature modulation at 26 Hz of ~1 K was obtained either by direct Joule heating of the single-crystal sample (current parallel to the *b* axis) or by first depositing an indirect Nichrome heater on a cover slip. The spectra obtained by the two methods were essentially the same. Temperature control was obtained with an Air Products Company Helitran Dewar.

The analysis of modulated reflectance is based on the total differential of Fresnel's equation, which, in complex form, is[5]

$$\Delta R/R = \mathrm{Re}[2\Delta\epsilon/n(\epsilon - 1)], \qquad (1)$$

where n and ϵ are the static complex index of refraction and the dielectric function, respectively, and $\Delta\epsilon$ is the modulation-induced change in ϵ. The thermoreflectance response from an isolated Drude-like plasma[2,4] would be obtained by substituting $\epsilon = \epsilon_0 - \omega_p^2/(\omega^2 + i\omega/\tau)$ and its derivatives with respect to ω_p and τ into Eq. (1). It is generally assumed,[6] and indeed we find for TTF-TCNQ, that $d\omega_p/dT$ dominates $d(1/\tau)/dT$, so that only the ω_p derivative is important. Since we are dealing with a plasma edge closely followed by interband or molecular transitions, a more accurate starting point would be based on Seraphin's version[9] of Eq. (1), $\Delta R/R = \alpha(\omega)\Delta\epsilon_1 + \beta(\omega)\Delta\epsilon_2$, where α and β are obtained from measurements of ϵ_1 and ϵ_2, and $\Delta\epsilon = \Delta\epsilon_1 + i\Delta\epsilon_2$. This latter approach assumes only that the modulated responses from adjacent transitions are isolated, whereas the background ϵ may contain any admixture of different contributions since it is obtained from experiment. Detailed analysis of overlapping $\Delta R/R$ line shapes will be postponed for a complete publication. For the moment we will be primarily concerned with the temperature dependence of $|\Delta R/R|$.

Figure 1 shows a portion of the $\Delta R/R$ spectra for $\vec{e} \parallel \vec{b}$ and $\vec{e} \perp \vec{b}$, recorded at an indicated temperature of 42 K. The inset represents our interpretation of how three distinct transitions superpose to give the observed result with $\vec{e} \parallel \vec{b}$. The sign of $\Delta R/R$ corresponds to an increase of R with increasing T.

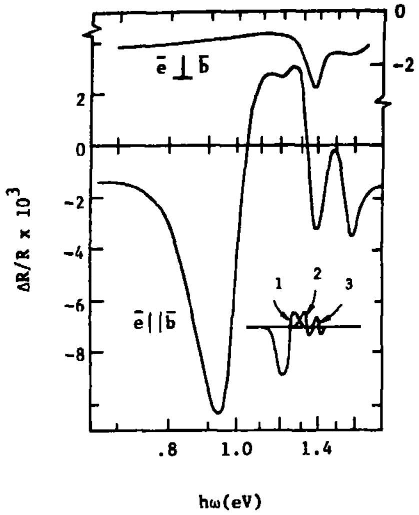

FIG. 1. Thermoreflectance spectra of TTF-TCNQ a 42 K, with $\vec{e} \perp \vec{b}$ and $\vec{e} \parallel \vec{b}$. The inset is a schematic representation of the three optical transitions which superpose to give the $\vec{e} \parallel \vec{b}$ spectrum (a constant background of -1.5×10^{-3} has been subtracted).

The lowest-energy structure (peak 1) is ascribed to a screened Drude edge by Bright, Garito, and Heeger,[2] whereas Grant *et al.*[4] claim an equally good fit to reflectivity spectra assuming a strong Lorentzian oscillator at 0.2 eV, presumably representing a charge-transfer transition. The latter interpretation is suggested by the far-infrared results of Torrance, Scott, and Green,[10] and is consistent with the fact that similar edges are found in nonconducting TCNQ salts.[11] Preliminary analysis of our data favors the former interpretation; linewidth, zero-crossing energy, and positive/negative asymmetry are all reproduced well by the Drude model in Eq. (1), with $\epsilon_0 = 2.3$, $\omega_p = 1.2$ eV, and $\omega_p\tau = 5$. We plan to repeat these experiments on nonconducting salts to see if thermoreflectance can differentiate between the two kinds of "edges."

Our most surprising result concerns the temperature dependence of peak 2. Grant *et al.*[4] report 1% bumps in R at 1.2 and 1.4 eV, which probably correspond to peaks 2 and 3. Bright, Garito, and Heeger[2] also observed peak 2. The zero-crossing energies in Fig. 1, corrected for baseline offset, are 1.36 and 1.56 eV, respectively, at 42 K. These two structures are probably characteristic of the TCNQ ion (suggesting nearly complete charge transfer) because they are also observed,[12] at the same energies, in N-methyl phenazinium (NMP)TCNQ and triethyl ammonium (TEA)$(TCNQ)_2$, and because a similar doublet is observed in solution spectra,[7] albeit at 0.2 eV higher energies. With the association of peak 2 with a dipole of B_{1u} symmetry,[7] the oscillator strength for $\vec{e}\perp\vec{b}$ would vanish if the plane of the TCNQ ion were exactly normal to $\vec{b}$. Turning this statement around, we can use the polarization sensitivity of this transition as a rough index of the inclination of the TCNQ ion relative to the $\vec{b}$ axis.

The above considerations may be relevant to the spectra of peak 2 in Fig. 1, namely the strong response with $\vec{e}\perp\vec{b}$ at 42 K. Peak 3 remains essentially parallel polarized throughout the entire temperature range studied. Note the absence of a perpendicular-polarization response near peak 1, which gives us confidence that the large perpendicular-polarization signal at peak 2 is not an artifact due to poor crystallographic morphology. The fact that the perpendicular- and parallel-polarization line shapes for peak 2 are quite different is not disturbing since the reflectivity, and hence the Seraphin coefficients α and β, is highly anisotropic. Peak 2 sharpens considerably more than peak 1 with decreasing *T*.

The absolute amplitude of a thermoreflectance spectrum depends on thermal properties of the specimen,[6] but since these are independent of photon energy, it is useful to compare relative amplitudes as functions of *T*. Two such relative comparisons are made in Fig. 2. First we note that the parallel-polarization response of peak 2, relative to that of peak 1, initially increases gradually with decreasing *T*, then abruptly diminishes by ~20% at 42 K, leveling off below 35 K. This is accompanied by a further abrupt reduction in the anisotropy of peak 2, as measured by its dichroic ratio [peak 2 (⊥)]/[peak 2 (∥)]. The two amplitude ratios can be interpreted near 42 K as follows: The reduction in the parallel-polarization amplitude of peak 2 accompanied by the increase in the perpendicular-polarization amplitude suggests an abrupt increase of the angle between the TCNQ ion normal and the *b* axis. At room temperature, this angle appears to be quite small; it increases gradually as the sample is cooled to 42 K, and then jumps and levels off with further cooling.[13] We suggest that this behavior could result from an incipient phase transition near 42 K, for instance the librational distortion of the TCNQ ion as suggested by Morawitz.[8] Such a distortion could provide the driving force for the Peierls instability which has been postulated to occur in TTF-TCNQ.[3]

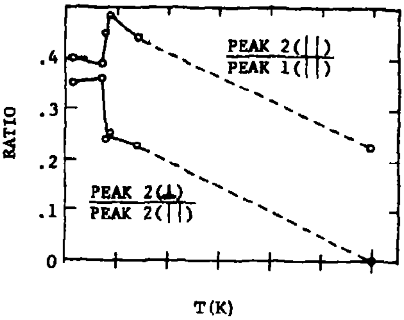

FIG. 2. Temperature dependence of various features in the spectra of Fig. 1: relative amplitude of peak 2 to peak 1 with $\vec{e}\parallel\vec{b}$, and dichroism of peak 2 (ratio of ⊥ to ∥ amplitudes).

Our putative "transition temperature" of 42 K is notably lower than 58 K, the temperature of maximum dc conductivity.[1] Even accounting for dissipation of 0.2 W we estimate that the sample surface temperature is below 50 K. We plan to check this with a suitable thermometer mounted directly on a dummy sample.

In summary, we report for the first time a striking temperature dependence of a portion of the optical spectrum of TTF-TCNQ which may be indicative of a phase transition at low temperature. It is tempting to associate this in some manner with the temperature dependence of the conductivity, but this must await measurements on other TCNQ salts. We also find good agreement between thermoreflectance associated with the infrared reflectance edge and a screened Drude model, which we submit is a more stringent test than fitting reflectivity. We feel that modulation spectroscopy will prove useful in unraveling the electronic structure of this class of materials.

It is a pleasure to acknowledge the assistance and collaboration of L. B. Coleman and A. A. Bright, and helpful discussions with P. M. Grant, R. L. Greene, H. Morawitz, and B. H. Schectman. The samples were provided by the molecular crystals group at the University of Pennsylvania.

*Sponsored by the Program of Scientific Exchange between the U. S. National Academy of Sciences and the Academy of Sciences of the U. S. S. R. Current address: Institute of Radioengineering and Electronics of the Academy of Sciences, Moscow GSP-3, U. S. S. R.

†Work supported in part by the National Science Foundation via the Laboratory for Research on the Structure of Matter and Grant No. GH-42283.

[1] D. B. Tanner, C. S. Jacobson, A. F. Garito, and A. J. Heeger, Phys. Rev. Lett. 32, 1301 (1974), and references therein.

[2] A. A. Bright, A. F. Garito, and A. J. Heeger, Solid State Commun. 13, 943 (1973), and Phys. Rev. B (to be published).

[3] P. A. Lee, T. M. Rice, and P. W. Anderson, Phys. Rev. Lett. 31, 462 (1973).

[4] P. M. Grant, R. L. Greene, G. C. Wrighton, and G. Castro, Phys. Rev. Lett. 31, 1311 (1973).

[5] Two brief introductory articles: J. E. Fischer and D. E. Aspnes, Comments Solid State Phys. 4, 159 (1972), and 5, 1 (1972).

[6] M. Cardona, *Modulation Spectroscopy* (Academic, New York, 1968).

[7] H. T. Jonkman and J. Kommandeur, Chem. Phys. Lett. 15, 496 (1972).

[8] H. Morawitz, Bull. Amer. Phys. Soc. 18, 1577 (1973).

[9] B. O. Seraphin, in *Semiconductors and Semimetals*, edited by R. K. Willardson and A. C. Beer (Academic, New York, 1972), Vol. 9, p. 1.

[10] J. B. Torrance, B. A. Scott, and D. C. Green, Bull. Amer. Phys. Soc. 19, 221 (1974).

[11] G. C. Wrighton, P. M. Grant, R. L. Greene, and G. Castro, Bull. Amer. Phys. Soc. 18, 1578 (1973).

[12] G. C. Wrighton, Ph.D. thesis, Stanford University, 1974 (unpublished).

[13] Our data are all consistent with Wrighton's results (Ref. 12), of which we became aware only recently. He reports ϵ_1 and ϵ_2 spectra at 16, 85, and 300 K, and thus did not observe the discontinuous behavior near 42 K.

Effect of Spatial Dispersion upon Physisorption Energies: He on Metals

George G. Kleiman
Research Laboratories, General Motors Corporation, Warren, Michigan 48090

and

Uzi Landman
Xerox Corporation, Webster Research Center, Webster, New York 14580

(Received 24 April 1974)

Microscopic calculations of noble-gas adsorption on metals which include the effect of metallic nonlocal dielectric response are presented for two models of electronic boundary conditions at the metal surface. Spatial dispersion causes the Van der Waals interaction to decrease slower than the conventional d^{-3} law indicates. Systematics of the physisorption indicate that interaction energies, but not equilibrium positions, are very sensitive to nonlocality. The results are relatively insensitive to to the details of the electronic boundary conditions.

Because of the fundamental nature of chemical reactions at surfaces and their important role in such practical problems as catalysis[1] and oxidation, the understanding of these reactions is recognized as one of the major goals of surface science. Essential to this objective is the complete description of the adsorption process, i.e., an understanding of *both* chemical and physical adsorption. These adsorption processes have been historically distinguished by the order of magnitude of their binding energies (i.e., electron volts for chemisorption and hundredths of electron volts for physisorption). Recently, we have presented a new theory[2,3] which indicates that the repulsive contribution to physical adsorption on metals can be determined from *ab initio* considerations which are consistent with modern ideas of surface physics, in contrast to some earlier work.[4-8] Treatment of the attractive (or Van der Waals) part of the physical adsorption interaction, however, has followed[2-8] the traditional method[9,10] of describing the coupling between the electromagnetic field and the solid media by means of a spatially local dielectric constant.

The question of the influence of dispersion in the metal upon the Van der Waals interaction was raised by Lifschitz in his pioneering paper,[9] and these effects have not been studied systematically since then. The object of this paper is the determination, for the first time, of the effects of dispersion and of varying surface electronic boundary conditions upon physical adsorption of a gas on a metal. The Van der Waals contribution, E_{VW}, to the interaction energy between an atom in vacuum and a metal surface is given by[3,11,12]

$$E_{\mathrm{VW}}(d) = \lim_{\hbar\to 0} \frac{k_{\mathrm{B}}T}{\pi} \sum_{n=0}^{\infty} \left(\frac{\xi_n}{c}\right)^3 \int_1^{\infty} \frac{p^2 dp}{N} (F_1^{-1} + F_2^{-1}), \quad (1a)$$

$$\xi_n = 2\pi n k_{\mathrm{B}} T, \quad c k_{\parallel} = \xi_n (p^2 - 1)^{1/2}, \quad (1b)$$

where d is the distance separating the atom and metal plane and c the velocity of light in vacuum. The summation in Eq. (1a) is over integer values of n, where the $n = 0$ term is given half weight, k_{B} is Boltzmann's constant, T is absolute temperature, N is the gas density, and $k_{\parallel}$ is the component of wave vector in the plane of the surface (atomic units are used exclusively here). The dispersion relations for the normal surface modes (TM and TE) of the electromagnetic field (i.e., surface plasmons) are represented by F_1 and F_2 [specified in Eqs. (5) below]. Equation (1a) is derived by summing the free energies of the normal electromagnetic modes,[11,12] which is equivalent to Lifschitz's approach.[9] Calculation of E_{VW}, therefore, reduces to a solution of Maxwell's equations.

In the presence of metallic spatial dispersion the relationship in the metal between the Fourier components of the electric displacement, $\vec{\mathrm{D}}$, and the electric field, $\vec{\mathrm{E}}$, can be written as

$$\vec{\mathrm{D}}(z, \vec{\mathrm{k}}_{\parallel}, \omega) = \int_{-\infty}^{0} dz' \, \epsilon(z, z', \vec{\mathrm{k}}_{\parallel}, \omega) \times \vec{\mathrm{E}}(z', k_{\parallel}, \omega), \quad z < 0, \quad (2)$$

in which ω is the frequency and the metal fills the negative-z half space. Maxwell's equation with the insertion of Eq. (2) cannot be solved generally, and we utilize a model which corresponds to the bulk metallic hydrodynamic constant[13]

$$\epsilon_M(\vec{\mathrm{k}}, \omega) = 1 - \omega_p^2[\omega(\omega + i/\tau) - (\alpha k)^2]^{-1}, \quad (3)$$

where ω_p is the plasma frequency (i.e., $\omega_p^2 = 4\pi n_+$, where n_+ is the electron density for free-electron metals), τ is a damping lifetime, and α^2 is set equal to $0.6 V_{\mathrm{F}}^2$ (V_{F} is the Fermi velocity) in order to recover the bulk-plasmon dispersion relation from the hydrodynamic equation.[13-16] In relating Eqs. (2) and (3), we employ two solvable models of the surface electronic boundary conditions: specular reflection[17] and diffuse reflection.[18] Specular reflection is equivalent to assuming that the field components parallel (perpendicular) to the surface plane are even (odd) under inversion about the surface plane; the exact solution of Maxwell's equations for this case are well known.[19] The diffuse-reflection boundary condition corresponds to assuming that

$$\epsilon(z, z', \vec{\mathrm{k}}_{\parallel}) = \int_{-\infty}^{\infty} (dk_z/2\pi) \exp[ik_z(z - z')] \epsilon_M(\vec{\mathrm{k}}) \equiv \epsilon_M(z - z', \vec{\mathrm{k}}_{\parallel}), \quad (4)$$

where we have suppressed the ω argument. This boundary condition, therefore, corresponds to the same contribution from each volume element of dielectric as in the bulk constitutive relation. Exact solutions of Maxwell's equations for diffuse reflection have been found independently by several workers.[20-22]

The influence of spatial dispersion upon the Van der Waals interaction can be clarified by simple physical arguments, without resort to the calculational details of the exact solutions with retardation, which are quite complicated and will be reported elsewhere.[23] The general form of the dispersion relations of TM (F_1) and TE (F_2) surface modes in Eqs. (1) are evaluated on the imaginary frequency axis $\omega = i\xi$:

$$F_j(i\xi, p) = D_j(i\xi, p) \exp(2p\xi d/c) - 1, \quad (j = 1, 2), \quad (5a)$$

$$D_1(i\xi, p) = [(S_A + p\epsilon_A)/(S_A - p\epsilon_A)] C_{1M}, \quad (5b)$$

$$D_2(i\xi, p) = [(S_A + p)/(S_A - p)] C_{2M}, \quad (5c)$$

$$S_A = (\epsilon_A - 1 + p^2)^{1/2}. \quad (5d)$$

The quantity ϵ_A is the dynamic dielectric function of the atom. The dispersion relation of the modes of the isolated metal are specified by $C_{jM}^{-1}(k_{\parallel}, \omega) = 0$; the surface plasmons correspond to C_{1M}.

Because of the exponential in Eq. (5a), the major contribution to E_{VW} comes from terms for which $p\xi \simeq c/2d$. For the small d with which we are concerned, the important limit is $p \to \infty$, since $\epsilon_A \to 1$ as $\xi \to \infty$. In the case of a *local* metallic dielectric function, $C_{1M}(p \to \infty, \xi)$ is a finite function of ξ alone $[C_{2M}(p \to \infty, \xi) \to \infty]$. The finiteness of C_{1M} in this limit reflects the fact that the surface-plasmon frequency $\omega_s \to \omega_p/\sqrt{2}$ as $k_{\parallel} \to \infty$ for a local metallic dielectric function [i.e., see Eq. (1b)]. A simple transformation of variables[9,10] in Eq. (1) yields the result that $E_{\mathrm{VW}} \sim d^{-3}$. This reasoning is the justification for the conventional[4-10] inverse-cube law of the Van der Waals force.

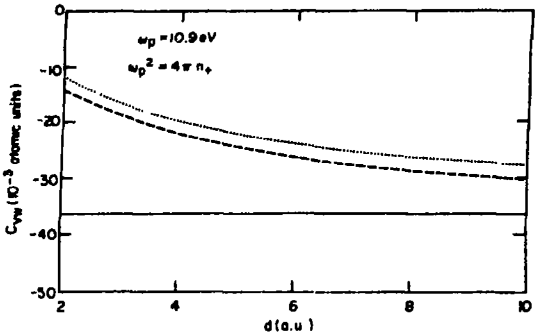

FIG. 1. Van der Waals constant (i.e., $C_{VW} \equiv d^3 E_{VW}$) for He adsorbed on Mg (i.e., $\alpha = 0.56$ a.u.). Results are shown for spatial dispersion with specular reflection (dashed line) and diffuse reflection boundary (dotted line) conditions and for the local dielectric function model (solid line). Infinite lifetime τ is assumed here.

In the case of the model nonlocal dielectric functions we are considering, however, *both* C_{1M} and $C_{2M} \to \infty$ as $p \to \infty$. This has the consequence that there is negligible contribution to the integral in Eq. (1a) from terms with large p. The d dependence of E_{VW} cannot be deduced from a transformation of variables and is more complicated than the inverse-cube law. This result follows from the fact that, for both of our models, the surface mode is admixed with volume modes[19]; the admixture increases with increasing $k_\parallel$, so that $\omega_s \to \infty$ as $k_\parallel \to \infty$.[19,21,23,24] The negligible contribution from terms with large $k_\parallel$ exists also in the random-phase approximation solved with specular-reflection boundary conditions.[19] Another consequence of the admixture is that the contribution to E_{VW} of modes localized at the surface (i.e., d-dependent modes) decreases relative to their contribution in the local-dielectric-function case (i.e., $\alpha = 0$). We expect, therefore, that E_{VW} will be weaker with spatial nonlocality than without.

These results are illustrated in Fig. 1, in which we plot $C_{VW} \equiv d^3 E_{VW}$ as a function of d for He on a typical free-electron metal, Mg. The polarizability of He includes both discrete and continuum contributions.[2,3] The salient points are that E_{VW} varies more slowly than the inverse-cube law in the spatial dispersion models and that the Van der Waals interaction is weaker in these cases than in the case of the corresponding local dielectric function (i.e., $\alpha = 0$), in accord with the previous discussion. Another important feature of Fig. 1 is that the effect of spatial dispersion on E_{VW} is much more significant than that of the different boundary conditions.

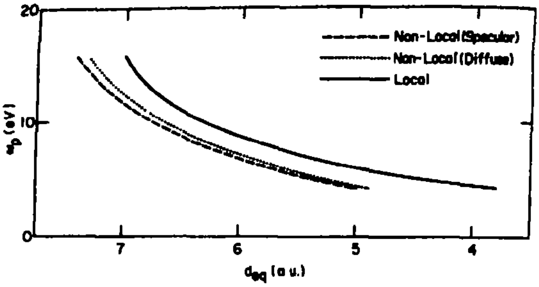

FIG. 2. *Equilibrium position* d_{eq} *of* physisorbed He atoms on free-electron metals (i.e., $\omega_p^2 = 4\pi n_+$) for our three models. The relative insensitivity of d_{eq} to the degree of dispersion and different electronic boundary conditions is illustrated. Infinite lifetime τ is assumed here.

In order to study the effects of nonlocality upon He physical adsorption, we add the repulsive portion, E_R, of the interaction energy, which has been studied in detail elsewhere[2,3]:

$$E_R(d) = \int d^3r\, n_M \left(\frac{\delta T[n_M + n_A]}{\delta n} - \frac{\delta T[n_M]}{\delta n} \right), \tag{6a}$$

$$n_M = \tfrac{1}{2} n_+ \{1 - (z/|z|)[1 - \exp(-\beta |z|)]\}, \tag{6b}$$

where n_+ is the electron density and β is a variational parameter. The isolated atomic and metallic electron densities are labeled by n_A and n_M, respectively. The quantity $T[n]$ is the kinetic energy functional of the electronic density.[25] In performing the calculation of E_R,[2,3] we use the extended Thomas-Fermi version of the density-functional formalism[26] expanded to first order in the gradient operator. We represent n_A[26] and n_M[27] by variational solutions which describe the isolated systems adequately.[2,3,26,27]

Equilibrium positions, d_{eq}, obtained from the position of the minimum in the total interaction energy, $U \equiv E_R + E_{VW}$, are displayed in Fig. 2 for He on a variety of free-electron metals (i.e., $\omega_p^2 = 4\pi n_+$). Note that the values of d_{eq} for the three models are within 1 a.u. of one another and the changes in electronic boundary conditions produce small changes in d_{eq}. The equilibrium position, therefore, is relatively insensitive to the model used to describe the metal.

The monotonic increase in the physisorption interaction energy [i.e., $-U(d_{eq})$] of He on metals with increasing electron density for the two nonlocal models is exhibited in Fig. 3. This monotonic behavior is to be contrasted with the peak in $-U(d_{eq})$ for local coupling. Comparison of the surface-plasmon solutions of the hydrodynamic

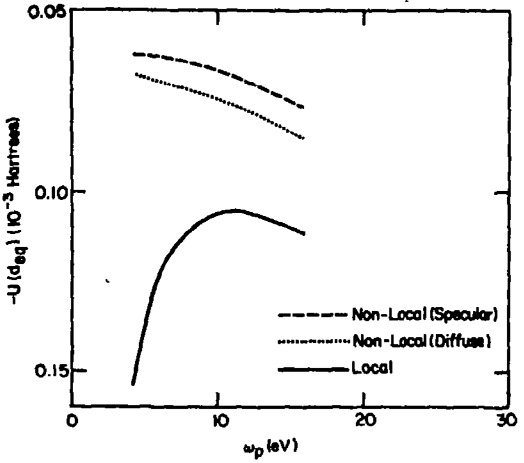

FIG. 3. Physisorption energies for He adsorbed on free-electron metals for the three models of electromagnetic coupling. The monotonic increase in $-U(d_{eq})$ with plasmon frequency for nonlocal couplings illustrates a distinction from the case of local coupling. Infinite lifetime τ is assumed here.

and Boltzmann equations[15] indicate that $\frac{1}{3} < \alpha^2/v_F^2 < 0.6$ for $\omega < \omega_p$; this corresponds to small ξ values which make the *major contribution* to E_{VW}. Such a reduction in α brings the magnitudes of the binding energies for the nonlocal models into closer agreement with those for the local model. From the results of our calculations we observe that within the errors in the currently available experimental data the degree of agreement achieved between the calculated and experimental values is not changed upon the inclusion of spatial dispersion.[28] We would like to remark here that caution should be exercised in applying model calculations to comparisons with experimental data because of substantial discrepancies in the present experimental situation. Therefore, the need for additional well-controlled experiments on physisorption systems and further theoretical studies is indicated. Detailed results of our studies will be discussed in a forthcoming publication.[23]

The above results illustrate for the first time the systematic effects of nonlocal electromagnetic coupling upon physical adsorption interaction. The main conclusions of our studies can be summarized as follows: (1) Van der Waals interaction calculated via nonlocal coupling schemes varies with distance *more slowly* than the inverse-cube law obtained from local approximations, (2) the interaction is *weaker* in the nonlocal models, (3) equilibrium distances are *relatively insensitive* to nonlocal corrections, and (4) different boundary conditions at the metal surface (diffuse and specular) introduce *minor* changes to the above results.

The authors are indebted to Mrs. Carol Troy for her continuous assistance in the preparation of the manuscript.

---

[1] G. C. Bond, *Catalysis by Metals* (Academic, New York, 1962).

[2] G. G. Kleiman and U. Landman, Phys. Rev. Lett. 31, 707 (1973)

[3] G. G. Kleiman and U. Landman, Phys. Rev. B 8, 5484 (1973).

[4] W. G. Pollard, Phys. Rev. 60, 578 (1941).

[5] K. F. Wojciechowski, Acta Phys. Pol. 29, 119 (1966), and 33, 363 (1968).

[6] D. M. Young and A. D. Crowell, *Physical Adsorption of Gases* (Butterworths, London, 1962).

[7] C. Mavroyannis, Mol. Phys. 6, 593 (1963).

[8] A. D. Crowell, in *The Solid-Gas Interface*, edited by E. A. Flood (Marcel-Dekker, New York, 1968), Vol. 1.

[9] E. M. Lifschitz, Zh. Eksp. Teor. Fiz. 29, 94 (1955) [Sov. Phys. JETP 2, 73 (1956)].

[10] I. E. Dzyaloshinskii, E. M. Lifschitz, and L. P. Pitaevskii, Advan. Phys. 10, 165 (1961).

[11] N. G. Van Kampen, B. R. A. Nijboer, and K. Schram, Phys. Lett. A26, 307 (1968).

[12] B. W. Ninham, V. A. Parsegian, and G. H. Weiss, J. Stat. Phys. 2, 323 (1970).

[13] R. H. Ritchie, Progr. Theor. Phys. 29, 607 (1963).

[14] J. Harris, Phys. Rev. B 4, 1022 (1971).

[15] L. Kleinman, Phys. Rev. B 7, 2288 (1973).

[16] In Ref. 15, it was pointed out that α should properly be considered a function of frequency for a hydrodynamic solution of the Boltzmann equation (i.e., see Ref. 12).

[17] G. E. H. Reuter and E. H. Sondheimer, Proc. Roy. Soc., Ser. A 195, 336 (1948).

[18] J. Heinrichs, Solid State Commun. 12, 167 (1973), and Phys. Rev. B 7, 3487 (1973).

[19] R. Fuchs and K. L. Kliewer, Phys. Rev. B 3, 2270 (1971).

[20] G. Agarwal, D. N. Pattanyak, and E. Wolf, Phys. Rev. Lett. 27, 1022 (1971), and Opt. Commun. 4, 255 (1971).

[21] A. A. Maradudin and D. L. Mills, Phys. Rev B 7, 2784 (1973).

[22] G. G. Kleiman and U. Landman, in Proceedings of the Thirty-Third Annual Conference on Physical Electronics, 26–28 March 1973, Berkeley, California (unpublished).

[23] G. G. Kleiman and U. Landman, to be published.

[24] E. Gerlach, Phys. Rev. B 4, 393 (1971).

[25] P. Hohenberg and W. Kohn, Phys. Rev. 136, B864 (1964).

[26] L. I. Schiff, *Quantum Mechanics* (McGraw-Hill, New York, 1955).

[27] J. R. Smith, Phys. Rev. 181, 522 (1969).

[28] See Ref. 3, Table I.

Raman Detection of One-Phonon–Two-Phonon Interactions in CuCl

M. Krauzman, R. M. Pick, H. Poulet, and G. Hamel
Département de Recherches Physiques, L. A. 71
Centre National de la Recherche Scientifique, Université Paris VI, Paris, France
and
B. Prevot
Laboratoire de Spectroscopie et d'Optique du Corps Solide, G. A. 15
Centre National de la Recherche Scientifique, Université Pasteur, 67000 Strasbourg, France
(Received 17 June 1974)

A large q-direction dependence of the broad band close to the TO peak is observed and explained qualitatively and quantitatively. The TO peak is found to be repelled out of a two-phonon band by a strong third-order anharmonic interaction.

In a crystal having the zinc-blende structure, the first-order Raman scattering allows detection of either the TO($q\sim 0$) phonon or the LO($q \sim 0$) phonon, according to the selected direction $\hat{q}$ of the transferred momentum. We have measured at 40 K the scattered intensities of a CuCl single crystal for various $\hat{q}$ directions (Fig. 1). *Because all the spectra were recorded with the* same spectral slit width (2 cm^{-1}), the heights (eventually above the continuum) of the sharp *lines at 171 and 208 cm*$^{-1}$ *could be taken to fix a* common intensity scale for the drawings of Fig. 1 by making use of the fact that the chosen geometries impose $I_B \approx 0.5(I_A + I_C)$.

The unusual features in CuCl are the broad and strong band of the TO spectrum[1-3] (curve A) in the 140–170 cm^{-1} range, reaching a very sharp line at 171 cm^{-1} with a maximum at 151 cm^{-1}, and its replacement by a weak and featureless continuum in the LO spectrum (curve C). This observation of $\hat{q}$-dependent, first-order-like spectra obviously differs from the recent results of Shand *et al.*[3] and excludes the assignment of the broad band to a pure second-order Raman scattering.

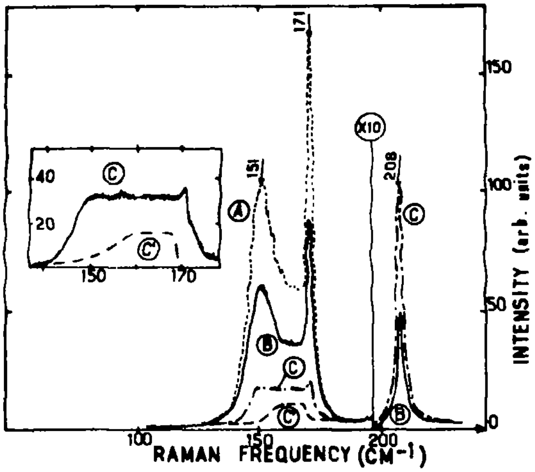

FIG. 1. Scattered intensities recorded for CuCl at 40 K. Curve A, TO experiment in a transverse geometry $y(x,y)x$; curve B, (0.5TO+0.5LO) experiment in a transverse geometry $z(x,y)z$; curve C, LO experiment of backward scattering $z(x,y)\bar{z}$. x, y, and z are the crystallographic cubic axes. Curve C', corrected LO experiment (see text). The unit of ordinate near 208 cm^{-1} is 10 times larger than that at low frequencies.

We propose to explain these features by the existence of strong anharmonic interactions between one of the $q\sim 0$ optical phonons and a two-phonon continuum limited on the high-frequency side by a P_3 type of singularity[4] due to a Brillouin zone critical point. The resulting scattered intensity is given by an expression of the form[5]

$$I_i(\omega) \sim (R_i^{xy})^2 (V_3^{i})^2 \Gamma(\omega) / \{[\omega - \omega_i - (V_3^{i})^2 \Delta(\omega)]^2 + (V_3^{i})^4 [\Gamma(\omega)]^2\}\,, \tag{1}$$

where i labels the TO *or* LO phonon with frequency ω_i, R_i^{xy} is the usual first-order Raman tensor element, the anharmonic third-order interaction being given by the usual formula[5]:

$$(V_3^{i})^2 [\Delta(\omega) + i\Gamma(\omega)] \propto \sum_{\substack{\vec{q}_1, j_1, j_2, \\ \vec{q}_3, j_3, j_4}} v(\vec{0}i, \vec{q}_1 j_1, -\vec{q}_1 j_2) G(\omega, \vec{q}_1 j_1, -\vec{q}_1 j_2, \vec{q}_3 j_3, -\vec{q}_3 j_4) v(\vec{0}i, \vec{q}_3 j_3, -\vec{q}_3 j_4). \tag{2}$$

The summation in Eq. (2) is practically limited to only that combination of branches which has the proper symmetry and a P_3-type singularity at the frequency ω_s, and for which the third-order interaction v is large. At zero temperature and in the vicinity of the band edge ω_s one can write

$$\omega<\omega_s:\quad \Gamma(\omega)=D(\omega_s-\omega)^{1/2},\qquad \Delta(\omega)=\Delta_s+B(\omega-\omega_s),$$

$$\omega>\omega_s:\quad \Gamma(\omega)=C,\quad \Delta(\omega)=\Delta_s-D(\omega-\omega_s)^{1/2},$$

showing the existence of a maximum for $\Delta(\omega)$ at $\omega=\omega_s$. As a consequence, if ω_{TO} is not too far below ω_s and if $(V_3^{\mathrm{TO}})^2\Delta_s$ (which reflects the strength of the anharmonic interaction) is large enough, the term

$$\omega-\omega_{\mathrm{TO}}-(V_3^{\mathrm{TO}})^2\Delta(\omega) \tag{3}$$

appearing in the denominator of Eq. (1) vanishes at least at a frequency $\omega_0>\omega_s$ giving rise to a δ line. This is a case of Fermi resonance where the line corresponding to the optical phonon is *repelled out of the broad band by the interaction. Note that the integrated intensity of the δ line* depends on the slope of $\Delta(\omega)$ so that it is a very rapidly increasing function of $\omega_0-\omega_s$.

Actually in the case of CuCl, $\Gamma(\omega)$, as a function of decreasing frequency, first increases and then decreases again to vanish well above 100 cm^{-1}.[8] This results, through Kramers-Kronig relations, in a minimum for $\Delta(\omega)$, so that Eq. (3) passes again through zero for $\omega=\omega_1$ and $\omega=\omega_2$ [see Fig. 2(a)] with $\omega_2<\omega_{\mathrm{TO}}<\omega_1<\omega_s<\omega_0$. The maxima of $I_{\mathrm{TO}}(\omega)$ [Eq. (1)] related to the vanishing of one term [Eq. (3)] of its denominator, are or are not apparent, depending on both the magnitude and the ω dependence of the other term. It turns out that the ω_2 maximum is a well-pronounced one, while that related to ω_1 is undetected.

In order to get a quantitative fit related to the above given ideas, we built up $\Delta(\omega)$ and $\Gamma(\omega)$ in the following way. We started by assuming an arbitrary two-phonon density of states of the form

$$\gamma(\omega)=D\{1-[(\omega-\omega_c)/a]^2\}^{1/2},$$

which has a P_3 singularity at $\omega_s=\omega_c+a$, and for which we suppose a constant interaction with the TO phonon. We further assumed an interaction inside the phonon continuum through a fourth-order anharmonic interaction V_4 and followed Ruvalds-Zawadowski simplification of the problem.[7] The sign of V_4 was selected to enhance the high-frequency side of both $\Gamma(\omega)$ and $\Delta(\omega)$. A typical result for $\Delta(\omega)$, $\Gamma(\omega)$, and the comparison between Eq. (1) and the experimental spectrum are given in Figs. 2(a) and 2(b). The present fit was obtained with the following parameters: $a=16.3$ cm^{-1}; $\omega_0-\omega_s=0.55$ cm^{-1}; $V_4D=0.49$; $(V_3^{\mathrm{TO}})^2D=10.6$ cm^{-1}; $R_{\mathrm{TO}}^{xy}=28$ (cm^{-1} $\times$intensity unit)$^{1/2}$. This fit is rather convincing and suggests the following comments:

(a) As Eq. (1) depends only on $(V_3^{\mathrm{TO}})^2[\Delta(\omega)+i\Gamma(\omega)]$, *only this function can be determined:* Neither the existence of a Ruvalds-Zawadowski type of interaction, nor the strictly elliptic shape of the band should be inferred from the present calculation. For the same reason (and also because of experimental inaccuracies among the above-determined parameters), only the effective bandwidth $2a$ has a physical meaning while, e.g., a 10% variation of V_4D leads to a quite undiscernable result, provided $\omega_0-\omega_s$ is simul*taneously corrected by as much as 100%*. We therefore think that the only important feature revealed by the TO spectrum is the existence of *three zeros for Eq. (3).*

(b) We find $\omega_{\mathrm{TO}}=158$ cm^{-1}. From the Lyddane-

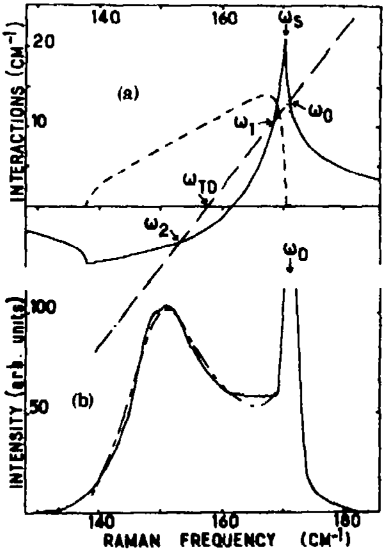

FIG. 2. (a) Continuous line, $(V_3^{\mathrm{TO}})^2\Delta(\omega)$; dashed line, $(V_3^{\mathrm{TO}})^2\Gamma(\omega)$; dot-dashed straight line, $\omega-\omega_{\mathrm{TO}}$. (b) Continuous line, experimental TO spectrum (enlargement of curve *A*, Fig. 1); dot-dashed line, calculated spectrum.

Sachs-Teller relation, $\omega_{LO} = 208$ cm^{-1} and $\epsilon_\infty = 3.61$,[8] we get $\epsilon_0 = 6.25$ in good agreement with a recent determination at 40 K.[1]

(c) The calculated ω_1 frequency is so close to ω_0 that an extemely high resolution (~ 0.1 cm^{-1}) would be required to observe a dip near 171 cm^{-1}.

(d) Because of the high value of $(V_3^{TO})^2 d[\Delta(\omega_0)]/d\omega = \alpha$, the calculated integrated intensity of the δ peak at ω_0 is reduced by a factor $1 - \alpha = 4.9$ with respect to the value it would have if $\alpha = 0$, and agrees exactly with our measured integrated intensity at 171 cm^{-1}. At higher temperature, the broadening of the individual phonon states blurs the sharpness of the P_3 singularity at ω_s and consequently reduces α. As a consequence, the intensity of the ω_0 line will increase and the line will broaden. The intensity ratio between this line and the continuum is thus a nontrivial function of the temperature and will increase less rapidly than a usual two-phonon/one-phonon ratio. This is, in fact, what has been previously measured by Potts *et al.*[1] who could not explain their result.

Concerning the LO spectrum, ω_{LO} is far from the continuum so that $\Delta(\omega)$ and $\Gamma(\omega)$ may be neglected in the denominator of Eq. (1) which gives a δ peak at $\omega_{LO} = 208$ cm^{-1} and a broad but weak band in the 140–170 cm^{-1} range.

A discussion of the "purity" of the C experiment of Fig. 1 is in order here. Since the crystal is not perfectly homogeneous, a small amount of the light is elastically scattered, giving rise, even in backscattering geometry, to a small fraction f of transverse spectrum. This fraction is obtained by assuming that, in curve C, the 171 cm^{-1} peak is entirely due to this parasitic light. The corrected curve C' is then constructed from the following relation:

$$I_{C'} = I_C - f I_A .$$

In agreement with the last above approximation, the curve C' (Fig. 1) is more or less shaped as $\Gamma(\omega)$ [Fig. 2(a)]. This enables us to give a rough experimental estimation of $(V_3^{TO})^2/(V_3^{LO})^2 \sim 1.2$. This slightly higher than unity ratio may be because of a difference in the anharmonic coefficients and/or because of the superposition of a very weak pure second-order Raman scattering.

---

[1] J. E. Potts, R. C. Hanson, C. T. Walker, and C. Schwab, Phys. Rev. B 9, 2711 (1974).

[2] T. Fukumoto, K. Tabuchi, S. Nakashima, and A. Mitsuishi, J. Phys. Soc. Jpn. 35, 622 (1973).

[3] M. L. Shand, L. Y. Chinc, and E. Burstein, to be published, and Bull. Amer. Phys. Soc. 19, 225 (1974).

[4] J. C. Philips, Phys. Rev. 104, 1263 (1956).

[5] A. S. Pine and P. E. Tannenwald, Phys. Rev. 178, 1424 (1969); R. A. Cowley, Advan. Phys. 12, 421 (1963).

[6] This decrease of $(V_3^{TO})^2\Gamma(\omega)$ for low ω may be caused by the decrease of v [see Eq. (2)] and/or of the density of states.

[7] J. Ruvalds and A. Zawadowski, Phys. Rev. B 2, 1172 (1970).

[8] Room temperature determination of ϵ_∞ by A. Feldman and D. Horowitz, J. Opt. Soc. Amer. 59, 1406 (1969).

Distinction between Lattice and Cluster Models of the Jahn-Teller Effect in an Orbital Doublet

M. Abou-Ghantous and P. C. Jaussaud,
Service Basses Températures, Centre d'Etudes Nucléaires de Grenoble, 39041-Grenoble, France

and

C. A. Bates, J. R. Fletcher, and W. S. Moore
Department of Physics, The University, Nottingham NG7 2RD, England

(Received 28 May 1974)

Acoustic-paramagnetic-resonance and electric-field–induced thermally detected EPR measurements have been made in crystals of $Al_2O_3{:}Ni^{3+}$. To reconcile theory with experiment, dynamic Jahn-Teller effects must be present, and, in addition, $2q - p$ is shown to be less than unity. This is the first reported example of an orbital doublet for which the multimode rather than the cluster model is needed.

The importance of the vibronic coupling of an E-type ion with its surroundings is often revealed by values of factors p and q which appear in the effective Hamiltonian.[1] In two recent articles, Halperin and Englman[2] and Gauthier and Walker[3] show theoretically that when the coupling is to a spectrum of lattice modes and the orbit-lattice coupling is linear and of intermediate strength, then $2q-p<1$. This result is also obtained by suitably generalizing the variational calculations of Fletcher.[4] In contrast, all the existing experimental data on E-type ions have been interpreted by using the relation $2q-p=1$ obtained from a cluster model when the coupling is with a single pair of E modes.[1]

It is not stated in the above[2-4] that it is very difficult to find a system to test these predictions, as q and p can rarely be measured separately. We discuss the properties of the ^2E ground state of Ni^{3+} in Al_2O_3. It is the first example reported of an experimental measurement of p and q for which $2q-p<1$. This system was chosen for study as a trigonal field is present which ensures that p is involved. Also the Ni^{3+} ion is fairly strongly coupled to its surroundings[5] but not so strongly coupled that a cluster model becomes valid.[4] It also satisfied the criterion[2] that the optical- and acoustic-phonon modes of pure Al_2O_3 have a considerable overlap and are little affected by the Ni^{3+} impurity.

Acoustic paramagnetic resonance and thermally detected EPR[6] have been carried out on single crystals of Al_2O_3:Ni^{3+} at frequencies between 9.35 and 11.22 GHz at liquid-helium temperatures for various angles χ between the magnetic field $\vec{H}$ and the crystal c axis. Figure 1 shows a typical acoustic-paramagnetic-resonance spectrum and Fig. 2 the thermally detected electric-field-induced EPR spectrum.[7] Five features (A, B, C_{I}, C_{II}, D) have been identified and their dependence on χ determined.[8] Feature B arises from highly strained sites and does not provide much useful information. Features A, C, and D arise from sites for which strain is zero and the transitions involved are indicated on the energy-level diagram, inset in Fig. 1.

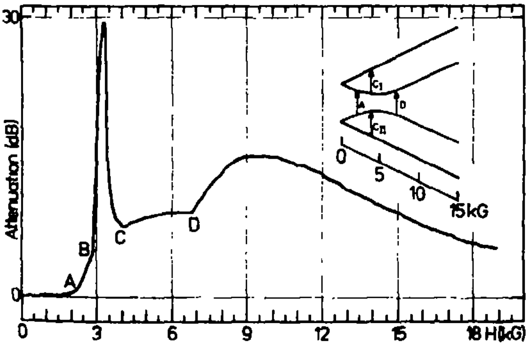

FIG. 1. Acoustic-paramagnetic-resonance spectra of Al_2O_3:Ni^{3+} at 8.765 GHz and 4.2 K for $\chi=25°$. The energy level diagram showing all acoustic transitions is also included.

The spectra can be fully accounted for[8] by transitions between energy levels within $T=\frac{1}{2}$, $S=\frac{1}{2}$ of the effective Hamiltonian

$$\mathcal{H}=apT_3S_z+(2+\Delta g)\mu_B\vec{H}\cdot\vec{S}+kq\mu_B(T_+O_-+T_-O_+)$$
$$+fp\mu_BT_3H_z+j\mu_BH_zS_z+\mathcal{H}_{\text{strain}}, \qquad (1)$$

with $O_\pm=\sqrt{\frac{3}{2}}(S_zH_\pm+S_\pm H_z)+\frac{1}{2}S_\mp H_\mp$. $\mathcal{H}_{\text{strain}}=\frac{1}{2}qV_E\times(\bar{Q}_+T_-+\bar{Q}_-T_+)$ describes the effects of random internal strains and electric fields (henceforth called strain) and accounts for the unusual line shapes and for feature B.

From the angular variation of features A, C_{I}, C_{II}, and D and a new analysis[8] of the original EPR spectrum of Geschwind and Remeika,[9] we obtain the following experimental parameters,

$$|ap|=0.94\pm0.01\ \text{cm}^{-1},\quad \Delta g=0.150\pm0.005,$$
$$|fp|=0.02\pm0.005,\quad |kq|=0.051\pm0.001,$$
$$j=0.0034\pm0.0005,$$

and that a and f have the same sign. In addition, from thermal conductivity data,[5] the next highest vibronic levels are at ~55 cm^{-1}, which indicates that anharmonicity is unimportant in the ground states.

We need now to calculate theoretical expressions for the experimental parameters a, Δg, k, f, and j in the Hamiltonian (1).

The ^2E ground state is mixed with the excited states by the spin-orbit coupling, the trigonal field, and the Zeeman term as perturbations. The term involving a describes the spin-orbit

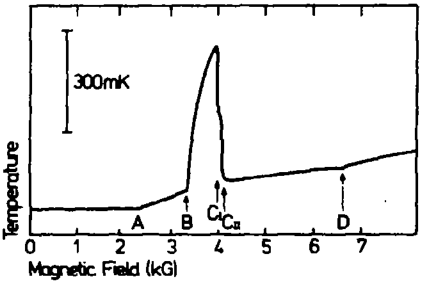

FIG. 2. The thermally detected electric-field-induced EPR spectrum at 9.35 GHz and 2 K for $\chi=25°$ showing the features A, B, C_{I}, C_{II}, and D.

splitting of the ground state due to the orbital angular momentum induced by the trigonal field, while the remaining terms are Zeeman terms. g is the isotropic g value containing a spin part ($=2$) and a spin-orbit-coupling-induced orbital part Δg ($=g-2$). k, f, and j are various anisotropic terms which appear in second and higher orders in perturbation theory from coupling to the excited states. They arise as follows: k from spin-orbit coupling and the orbital Zeeman term; f from the trigonal field and the orbital Zeeman term; and j from the trigonal field, spin-orbit coupling, and the spin Zeeman term.

The most important excited states are ${}^4T_1$, ${}^2T_{1a}$, ${}^2T_{2a}$, ${}^2T_{1b}$, and ${}^2T_{2b}$ having energies Δ_4, Δ_{1a}, Δ_{2a}, Δ_{1b}, and Δ_{2b} relative to the ${}^2E$ ground state.[10] ${}^4T_1$ couples to the ${}^2E$ ground state by the spin-orbit coupling, but the ${}^2T_1$ and ${}^2T_2$ states couple by the orbital part of the Zeeman term and the trigonal field in addition to the spin-orbit coupling. As $S=\frac{1}{2}$, the contributions to the parameters from ${}^4T_1$ appear one order higher in perturbation theory than those from the ${}^2T_1$ and ${}^2T_2$ states. However, this is largely offset by the relative closeness of the ${}^4T_1$ level to ${}^2E$. Detailed perturbation calculations have been carried out[11] with the use of states appropriate to a strong crystal field model based on the tensor methods of Sugano, Tanabe, and Kamimura,[10] and it is found that

$$a=\tfrac{4}{3}\zeta^2\Delta_4^{-2}v+2\sqrt{2}v'\zeta D_1, \tag{2}$$

$$f=2\sqrt{2}v'D_2, \tag{3}$$

$$\Delta g=4\zeta^2\Delta_4^{-2}+2\zeta D_3, \tag{4}$$

$$k=2\zeta D_4, \tag{5}$$

where

$$D_1=(-\Delta_{2a}^{-1}+\Delta_{1a}^{-1}+\Delta_{2b}^{-1}+\Delta_{1b}^{-1}),$$

$$D_2=(\Delta_{2a}^{-1}+3\Delta_{1a}^{-1}-\Delta_{2b}^{-1}-\Delta_{1b}^{-1}),$$

$$D_3=(\Delta_{2a}^{-1}-\Delta_{1a}^{-1}+\Delta_{2b}^{-1}+\Delta_{1b}^{-1}),$$

$$D_4=(\Delta_{2a}^{-1}+\Delta_{1a}^{-1}+\Delta_{2b}^{-1}-\Delta_{1b}^{-1}),$$

and where ζ is the one-electron spin-orbit coupling parameter for Ni^{3+} in Al_2O_3. v and v' are the one-electron diagonal and off-diagonal trigonal field parameters.[12]

From an analysis of the experimental data available on the free Ni^{3+} ion and other $3d^n$ ions in Al_2O_3 we take the Racah parameters $B=1000$ cm^{-1} and $\gamma=4.9$. The corresponding Tanabe-Sugano diagram has been obtained by using Griffiths's information,[13] and it is found that the energies of all the excited states of interest *increase linearly with Dq/B at the same rate.* Ni^{3+} *is just in the strong-field region so that* Dq/B is slightly larger than 2.2. To determine Δ_4 accurately, we make Eq. (4) consistent with $\Delta g=0.150\pm0.005$, taking $\zeta=770$ cm^{-1}. This gives $\Delta_4=5500$ cm^{-1} with $\Delta_{1a}=24\,000$ cm^{-1}, $\Delta_{2a}=25\,000$ cm^{-1}, $\Delta_{1b}=34\,500$ cm^{-1}, and $\Delta_{2b}=54\,500$ cm^{-1} so that D_1–D_4 are, respectively, $(0.049, 0.119, 0.046, 0.071)\times10^{-3}$ (cm^{-1})$^{-1}$.

From Eq. (5) we deduce that $q=0.467$ and k is positive. Similarly from (3), $v'p=59$ cm^{-1}. Now v' is likely to be positive so that a and f are both positive.[8] Finally, Eq. (2) gives $vp=-207$ cm^{-1} and v is negative as expected.[14] To obtain p, we let v have a wide range of values which spans all previous reasonable estimates obtained from data on various ions in Al_2O_3, and obtain the following results:

$-v$ (cm^{-1})	v' (cm^{-1})	p	$2q-p$
1500	428	0.138	0.796
1000	285	0.207	0.727
500	142	0.414	0.520

Thus $2q-p$ is appreciably less than the cluster-model limit of unity.

This conclusion is justified by more detailed calculations. Third-order perturbation corrections to Eqs. (2)–(4) are very small, and $|j| \sim 0.002$ compared to the experimental value of 0.0034. Also Δ_{1a}, Δ_{2a}, and Δ_{1b} are in very good agreement with the strong optical absorption lines found[15] at 25 000 and 35 710 cm^{-1} in the room-temperature spectra of Ni^{3+}.

This is the first time that a clear distinction has been made by experiment between the cluster and multimode models of the Jahn-Teller effect in orbital doublets.

We are grateful to the Commissariat à l'Energie Atomique and to the Science Research Council for financial support in this joint program.

---

[1] F. S. Ham, Phys. Rev. 166, 307 (1968).

[2] B. Halperin and R. Englman, Phys. Rev. Lett. 31, 1052 (1973).

[3] N. Gauthier and M. B. Walker, Phys. Rev. Lett. 31, 1211 (1973).

[4] J. R. Fletcher, J. Phys. C: Proc. Phys. Soc., Longon 5, 852 (1972).

[5] M. Locatelli and A. M. de Goër, Solid State Commun. 14, 111 (1974).

[6] W. S. Moore and T. M. Al-Sharbati, J. Phys. D: Appl. Phys. 6, 367 (1973).

[7] W. S. Moore, C. A. Bates, and T. M. Al-Sharbati,

J. Phys. C: Proc. Phys. Soc., London 6, L209 (1973).

[8] M. Abou-Ghantous, C. A. Bates, I. A. Clark, J. R. Fletcher, P. C. Jaussaud, and W. S. Moore, J. Phys. C: Proc. Phys. Soc., London 7, 2707 (1974).

[9] S. Geschwind and J. P. Remeika, J. Appl. Phys., Suppl. 33, 370 (1962).

[10] S. Sugano, Y. Tanabe, and H. Kamimura, *Multiplets of Transition Metal Ions in Crystals* (Academic, New York, 1970), p. 109.

[11] M. Abou-Ghantous and P. C. Jaussaud, Centre d'Etudes Nucléaires de Grenoble Notes No. SBT332/74 and 333/74 (unpublished).

[12] H. U. Rahman and W. A. Runciman, J. Phys. C: Proc. Phys. Soc., London 4, 1576 (1971).

[13] J. S. Griffiths, *The Theory of Transition Metal Ions* (Cambridge Univ. Press, Cambridge, England, 1961), p. 411.

[14] R. M. Macfarlane, I. Y. Wong, and M. D. Sturge, Phys. Rev. 166, 250 (1968); note change in sign in definition of v.

[15] R. Müller and Hs. H. Günthard, J. Chem. Phys. 44, 365 (1966).

High-Resolution Measurements of the Nitrogen *K-LL* Auger Transitions of Chemisorbed Ammonia on a Molybdenum Surface

Tomoji Kawai, Kimio Kunimori, Tamotsu Kondow, Takaharu Onishi, and Kenzi Tamaru
Department of Chemistry, The University of Tokyo, Hongo, Bunkyo-ku, Tokyo, Japan

(Received 29 April 1974)

Distinct "chemical effects" were observed among high-resolution, nonderivative, nitrogen *K-LL* Auger-electron distributions from chemisorbed NH_3 on molybdenum surfaces and gaseous NH_3, which depend on the electronic structures of the adsorbed species. A calculation in the semiempirical "equivalent-core approximation," based on photoelectron data, revealed the origins of the fine structure in the observed Auger spectra. It is concluded that NH_3 is chemisorbed as a H_{-Mo}--$N_{-Mo}H_{x\leq 2}$ dissociative configuration at about room temperature and the surface nitride is formed at 450°C.

Many studies have been reported dealing with the configurations of adsorbed gases on surfaces and adsorbate binding energies. Techniques which have been used include photoelectron spectroscopy,[1] low-energy-electron spectroscopy,[2] ion-neutralization spectroscopy,[3] and field-emission spectroscopy.[4]

For the Auger process in molecules or adsorbates, an atom in different chemical environments results in different energy distributions of the Auger electrons, especially when valence states of the molecules are involved in the process ("chemical effects"). In earlier work done by Haas and Grant,[5] the chemical effect in a derivative form of the Auger spectra of several carbon compounds had been observed with relatively low energy resolution, although they failed to identify the peaks and structures of their spectra. Progress in experimental techniques as well as in the theoretical understanding of the Auger process enables us now, with the aid of a high-resolution electron spectrometer, to elucidate the origin of fine structure in the Auger spectra of adsorbed molecules on a solid surface.

In this paper, we report a chemical effect found in the nitrogen *K-LL* Auger spectra of gaseous and adsorbed ammonia on molybdenum surfaces at various temperatures. Figure 1 shows the high-resolution Auger spectra obtained. Special care was taken in order to obtain detailed structure in the spectra and, therefore, nonderivative spectra were measured with an energy resolution better than 200 meV. By comparing the fine structure in the spectrum shown in Fig. 1(d), with those of gaseous NH_3 ($\Delta E \leq 400$ meV) and molybdenum nitride, which were assigned by the equivalent-core approximation from a knowledge of the electronic structures of these two molecules, it is proposed that configurations of adsorbed ammonia on the surface are observed.

The Auger-electron-spectroscopy (AES) measurements were performed using a modified Simpson-Kuyatt high-resolution electron spectrometer[6] with a hemispherical 180° energy analyzer and with retarding electrostatic lenses. Auger electrons were produced with the use of a 1.3-keV electron beam. A polycrystalline molybdenum foil obtained from H. Cross Company, Ltd. was verified to be clean using AES after flashing the oxidized sample *in vacuo*. The minimum attainable pressure was 5×10^{-9} Torr. All the measurements were made in the presence of gaseous NH_3 *in situ* and data were accumulated in a multichannel analyzer in order to improve the

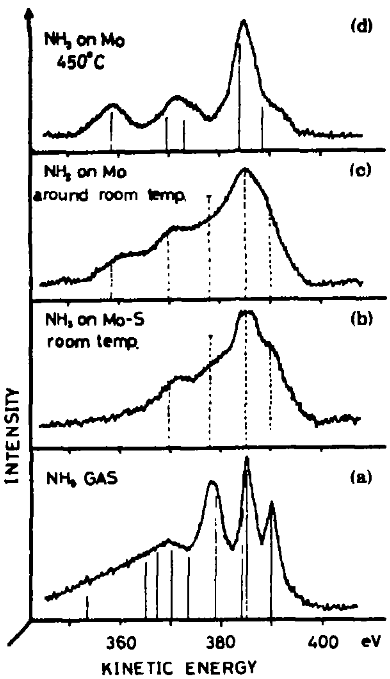

FIG. 1. High resolution, nonderivative nitrogen K-LL Auger spectra of (a) gaseous NH_3, (b) adsorbed NH_3 on a sulfur-segregated surface at room temperature, (c) on a clean surface at about room temperature, and (d) at 450°C. The vertical solid lines in (a) and (d) represent the energies calculated in the equivalent core approximation. The vertical broken lines in (b) and (c) represent observed energies and intensities for the peaks of gaseous NH_3. The dot-dashed line in (c) shows the observed value of Mo_2N which is at the lowest energy in (d).

signal-to noise ratio. Background signals due to secondary electrons were subtracted from the signal by a data processor. In addition, the binding energies of molybdenum nitride and molybdenum oxide were also measured using a conventional x-ray photoelectron spectrometer in order to assign the observed Auger lines.

Figure 1(a) shows the nitrogen K-LL Auger transitions for gaseous NH_3 at a pressure of 10^{-3} Torr (P_{NH_3}). In order to assign each peak, the energies of the Auger transitions ($E_{K\text{-}LL}$) associated with NH_3 were calculated semiempirically, using

$$E_{K\text{-}LL}(Z) = E_K(Z) - E_L(Z) - E_L(Z+1), \qquad (1)$$

where $E_A(Z)$ is the binding energy of some level A of an atom of atomic number Z. An Auger process can be considered as a combination of the simple processes,[7]

$$Z \to Z(\bar{K})^+ + e^-, \qquad (2a)$$

$$Z \to Z(\bar{L})^+ + e^-, \qquad (2b)$$

$$Z(\bar{L})^+ \to Z(\bar{L}\bar{L})^{2+} + e^-, \qquad (2c)$$

where $Z(\bar{A})^+$ denotes the hole states in the A shell of an atom of atomic number Z. Accordingly, the energy to be used for the ejection of the electron in Reaction (2c) is exactly $E_K(Z) - E_L(Z)$. In this last process, the binding energies of the remaining electrons to be ejected from the L shell $[E_L(Z)^+]$ can be approximately substituted by $E_L(Z+1)$ (in the equivalent-core approximation). In this study, the equivalent-core approximation,[8] which has been successfully used to evaluate binding energies in photoelectron spectroscopy, was extended to the two-hole state in the Auger process. In fact, calculations to this approximation predict the observed Auger spectra for carbon, oxygen, and nitrogen compounds.[9] Empirical binding energies for the molecular orbitals of gaseous NH_3 determined by a photoelectron-spectroscopy technique[10] were used for the calculation, i.e., 405.6 eV for $1a_1$, 27.5 eV for $2a_1$, 15.8 eV for $1e$, and 10.9 eV for $3a_1$. The molecular orbitals of H_2O using the binding energies (18.4 eV for the O-H σ bond, 12.6 eV for the lone electron pair in oxygen, and 32.2 eV for the oxygen $2s$ orbitals) were chosen for the evaluation of $E_L(Z+1)$ in Eq. (1) because the effective potential exerted on an electron in a valence orbital of H_2O and on an electron in a corresponding orbital of NH_3^+ may be almost identical. Possible NH_3 Auger emission lines and their assignments (final hole states) are listed in Table I where the Auger energies are referred to vacuum level.

As shown by vertical lines in Fig. 1(a), the calculated and observed energy positions are displaced to higher energies by 7.6 eV in order to fit the highest peak to those in the other spectra of adsorbed ammonia under various conditions which will be discussed later. Since the work function of the sample after NH_3 adsorption is approximately 3.9 eV,[11] the remainder of the 7.6-eV shift is probably due to a relaxation effect caused by adsorption. No data on the relaxation effect for the Auger transition due to adsorption with which to compare our shift are available at present. Apparently, calculations with this approximation predict the observed relative peak positions fairly well as is demonstrated in Fig.

TABLE I. Observed energies of the *K-LL* Auger transitions of nitrogen for gaseous NH_3 and adsorbed NH_3 at 450°C, and the Auger energies for NH_3 and Mo_2N calculated in the equivalent-core approximation.

NH_3 (Gas)

OBSERVED	(+7.6 eV)	ASSIGNMENT (FINAL STATE)	CALCULATED
382.2 eV	(389.8 eV)	$(3a_1)(3a_1)$	382.1 eV
377.4	(385.0)	$(1e)(3a_1)$	377.2
		$(3a_1)(1e)$	376.3
369.6	(377.2)	$(1e)(1e)$	371.4
		$(2s)(3a_1)$	365.5
		$(3a_1)(2s)$	362.5
361.6	(369.2)	$(2s)(1e)$	359.7
		$(1e)(2s)$	357.6
...		$(2s)(2s)$	345.9

NH_3 at 450°C

OBSERVED	ASSIGNMENT	CALCULATED FROM Mo_2N
392.0 eV	$(KL_{2,3}N_{4,5})$	(388.5 eV)
385.0	$KL_{2,3}L_{2,3}$	384.0
375.0	$KL_1L_{2,3}$	373.0
372.0	$KL_{2,3}L_1$	369.5
358.9	KL_1L_1	358.5

1(a). Consequently, the 398.8-eV (1), 385.0-eV (2), and 377.2-eV (3) peaks in Fig. 1(a) are associated with the final states having two holes in $(3a_1, 3a_1)$, $(3a_1, 1e)$, and $(1e, 1e)$, respectively. Here, $3a_1$ and $1e$ correspond to the molecular orbitals for the lone pair electrons and valence electrons of the N-H σ bond of NH_3, respectively. A group of vertical lines centering around 369.2 eV is due to the $2s$ nitrogen state combined with the $3a_1$ or $1e$ state.

The nitrogen *K-LL* Auger spectrum resulting from adsorbed NH_3 on a clean molybdenum surface ($P_{NH_3} = 1\times10^{-7}$ Torr) at 450°C exhibits a distinctly different feature, as is shown in Fig. 1(d). At this temperature and NH_3 pressure, the formation of molybdenum nitride on the surface has been suggested from the analyses of conventional Auger peak intensities,[12] for which the amount of surface nitrogen was observed to rise rapidly at the beginning of ammonia adsorption, and then followed by a gradual increase. Matsushita and Hansen[13] have reported in their flash desorption experiment that only molecular nitrogen is desorbed when NH_3 is admitted at 500°C. In fact, the spectrum in Fig. 1(d) is very similar in shape to the oxygen and carbon *K-LL* spectra of molybdenum oxide and carbide,[9] being not far from the *K-LL* spectrum[14] for atomic nitrogen calculated on the basis of an ionic model and an *LS* coupling scheme in which the nitrogen is negatively ionized to the neon structure. Therefore, the energies for the Auger transitions associated with Mo_2N were also evaluated semiempirically using the equivalent-core approximation. In this case, $E_L(Z)$ was determined from the energy band structures of Mo_2N, whereas $E_L(Z+1)$ was estimated from the energy band structures of MoO_3. In the present experiment, these energies were measured by x-ray photoelectron spectroscopy, i.e., K level: 396.5 eV, L_1: 17 eV, $L_{2,3}$: 6.0 eV for nitrogen, $N_{4,5}$: 2.0 eV for Mo in Mo_2N, L_1: 21 eV, $L_{2,3}$: 6.5 eV for oxygen in MoO_3. The absolute values calculated also agree reasonably well with the observed spectra, both referring to the Fermi level [see Fig. 1(d) and Table I]. The peaks at about 358.9, 373, and 385.0 eV are assigned to KL_1L_1, $KL_1L_{2,3}$, and $KL_{2,3}L_{2,3}$ of the nitrogen atom in the nitride, respectively. The 392.0-eV peak can be attributed to the cross transition from the L level of nitrogen to the $N_{4,5}$ level of molybdenum.

Figure 1(b) shows the spectrum of NH_3 adsorbed on molybdenum sulfide ($P_{NH_3} = 1\times10^{-7}$ Torr). The vertical broken lines shown in the figure represent the position and intensity of each peak in the spectrum of gaseous NH_3. This spectrum is very similar to that of gaseous NH_3 except for two points. One is the broadening of each peak which can be attributed to the interaction between an adsorbed species and the surface. Another prominent feature is that the intensity of 379-eV peak associated with the K-$(1e)(1e)$ transition decreased from the amount shown by the broken line. Since the $1e$ electronic state corresponds to the N-H σ-type bonding orbital, the decrease of this peak indicates that the N-H bond is strongly affected by chemisorption onto the surface. Therefore, a dissociative configuration like

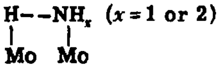

$$\underset{\text{Mo}}{\overset{|}{\text{H}}}\text{--}\underset{\text{Mo}}{\overset{|}{\text{N}}}\text{H}_x \quad (x = 1 \text{ or } 2)$$

seems more likely, although how many hydrogens per adsorbate are left remains to be determined. The K-$(1e)(1e)$ transition may change drastically with the dissociation of the N-H bond, because this transition includes a pair of electrons in the $1e$ state. This structure is consistent with the one proposed by Kemball based on the results of mass spectroscopic experiments.[15]

Figure 1(c) shows the spectrum of NH_3 adsorbed on a clean molybdenum surface at about room temperature. This spectrum appears to be an admixture of the spectra of the NH_3 gas [Fig. 1(a)] and the nitride [Fig. 1(d)], that is, an appreciable shoulder at 390 eV corresponding to the K-$(3a_1)(3a_1)$ transition and the 358-eV peak characteristic of the nitride appear in the spectra. As in the case of Fig. 1(b), the intensity of the 378-eV peak is less than the corresponding one in the gaseous spectrum. As the temperature of the molybdenum is raised, the 358-eV peak characteristic of the molybdenum nitride increased, while the 378-eV (N-H σ) and 390-eV peaks (nitrogen lone pair) decreased, accordingly. The general features approach those of the nitride K-LL spectrum. This temperature dependence indicates further dissociation of the remaining N-H bond of the adsorbate, reducing to the nitride structure.

It should be noted that the 358-eV peak due to the nitride does not appear in the spectrum of Fig. 1(b). It is reasonable to assume that, on the surface of the molybdenum sulfide, the heat of formation for the sulfide is so large (about 80 kcal) that nitride formation is prohibited on the surface during adsorption. Such a phenomenon can be easily distinguished in these spectra.

This shows that high-resolution AES is a very sensitive tool for the study of the molecular structure and valence electronic states of surface species. In addition, the equivalent-core approximation can explain the energies for the Auger processes studied here, being accurate enough to identify the origins of each peak, which is necessary for the study of the structure of surface species. High-resolution AES should be emphasized as a useful tool for studying the ele tronic and molecular structure of surface species as well as a tool for conventional elementa analysis.

---

[1] D. E. Eastman and J. K. Cashion, Phys. Rev. Lett. 27, 1520 (1971), and in Proceedings of the Second International Conference on Solid Surfaces, Kyoto, 1974 (to be published).

[2] H. Ibach, Phys. Rev. Lett. 27, 253 (1971).

[3] H. D. Hagstrum and G. E. Becker, J. Chem. Phys. 54, 1015 (1971).

[4] E. W. Plummer and R. D. Young, Phys. Rev. B 1, 2088 (1970).

[5] T. W. Haas and J. T. Grant, Appl. Phys. Lett. 16, 172 (1970); J. T. Grant and T. W. Haas, Surface Sci. 24, 332 (1971).

[6] T. Kondow, T. Kawai, K. Kunimori, T. Onishi, and K. Tamaru, J. Phys. B: Proc. Phys. Soc., London 6, L156 (1973); T. Kawai, K. Kunimori, T. Kondow, T. Onishi, and K. Tamaru, Trans. Faraday Soc. 70, 137 (1974).

[7] D. A. Shirley, Phys. Rev. A 7, 1520 (1973).

[8] D. A. Shirley, J. Electron Spectrosc. 3, 137 (1974).

[9] T. Kawai *et al.*, to be published.

[10] T. W. D. Connolley, H. Siegbahn, U. Gelius, and C. Nording, J. Chem. Phys. 58, 4265 (1973); D. W. Turner, C. Baker, A. D. Baker, and C. R. Brundle, *Molecular Photoelectron Spectroscopy: A Handbook of He 584 P. E. Spectra* (Wiley, New York, 1970).

[11] F. Ricca, *Adsorption-Desorption Phenomena* (Academic, New York, 1972).

[12] T. Kawai, K. Kunimori, T. Kondow, T. Onishi, and K. Tamaru, in Proceedings of the Second International Conference on Solid Surfaces, Kyoto, 1974 (to be published).

[13] K. Matsushita and R. S. Hansen, J. Chem. Phys. 54, 2278 (1971).

[14] K. Siegbahn *et al.*, Nova Acta Regiae Soc. Sci. Upsal. 20, 235 (1967).

[15] C. Kemball, Proc. Roy. Soc., Ser. A 214, 413 (1952).

Phosphorescence Microwave Double Resonance Spectroscopy in Ionic Solids and Its Application to Coherent Jahn-Teller States in F Centers of CaO

C. B. Harris*
Department of Chemistry, University of California, Berkeley, California 94720

and

M. Glasbeek
Laboratory for Physical Chemistry, University of Amsterdam, Amsterdam, The Netherlands

and

E. B. Hensley
Department of Physics, University of Missouri, Columbia, Missouri 65201

(Received 13 May 1974)

We demonstrate the use of phosphorescence microwave double resonance (PMDR) in ionic solids applied to the dynamic Jahn-Teller effect in F centers of CaO. A tunnel splitting ($\Delta = 2.1\ \mathrm{cm}^{-1}$) is obtained and Jahn-Teller states are coherent in zero field at least 10^3 times longer than the stochastic limit, and possibly as long as the lifetime of the centers. This is demonstrated by showing the loss of coherence by small Zeeman perturbations on the PMDR spectrum.

Phosphorescence microwave double resonance spectroscopy (PMDR)[1] is a technique which has allowed much of the kinetic information regarding the populating routes and decay channels of electronic-excited-state energy into triplet states to be obtained easily and routinely in molecular solids. It is a zero-field spectroscopic technique based on optically detected magnetic resonance (ODMR) in high field[2,3] which was subsequently extended to zero field.[4] PMDR monitors the individual vibronic bands in emission and measures the quantitative changes induced in the emission by a microwave field resonant with the zero-field splittings. Because of the sensitivity of photon detection, it is capable of measuring properties on as few as 10^4 excited states depending upon the details of the radiative channels being monitored. Applications of PMDR have been so extensive in the last four years that to do justice to the contributors would require an extensive reference list. A recent thorough review of this field, however, has been written by Kwiram.[5]

Although many properties of ionic solids[6] are different from molecular solids, the basic features of excited F centers are similar to excited triplet states, particularly in zero field. For example, if one takes D_{4h} as the point symmetry of F centers of CaO, there is a one-to-one correlation of the individual spin sublevels of the F center in zero field with ${}^3B_{1u}$ molecular excited triplet states.[7] Many excited triplet states in molecular crystals have been unequivocally[8] established through PMDR in ${}^3B_{1u}(\pi, \pi^*)$ states. We expect therefore that the dynamics of populating and depopulating excited centers can be elucidated in ionic solids as simply and easily as in triplet states in molecular solids. Moreover, PMDR has been recently used to establish coherence in excited triplet excitons[9] and spins[10] in molecular solids, and one might expect the same could be accomplished in ionic and semiconducting crystals having accessible triplet states.

In this paper we will (a) demonstrate zero-field PMDR in F centers of CaO, (b) illustrate how the methods can be used to extract tunnel splittings from the zero-phonon origin in CaO, and finally, (c) determine a minimum coherence time for the split Jahn-Teller states and shed some light on how the coherence is lost, and its relationship to the dynamic Jahn-Teller effect.[11a,11b]

To illustrate the principles, we begin with a consideration of the F centers in the cubic ${}^3T_{1u}$ state subject to a dynamic Jahn-Teller effect[11a,11b] through coupling with an e_g mode.[12]

Various perturbations are capable of lifting this degeneracy; however, the degeneracy is lifted *completely* only in case the projections of the perturbing vector that couples to the triplet system show orthorhombic symmetry, e.g., if $e_\epsilon = (\sqrt{3}/2)[e_{11} - e_{22}]$ is nonzero[11b] and all other components, e_{ij}, of the strain tensor are zero, then the energies of the $\psi(+-+)$ and $\psi(-+-)$ states are shifted by $+\Delta$ and $-\Delta$, respectively. In this instance $\psi(+++)$, $\psi(+-+)$, and $\psi(-+-)$ diagonalize the total Hamiltonian. Additionally, it can be shown[7] that the zero-field splitting parameters in the electron spin Hamiltonian differ for the different $\psi(lmn)$ states because the tunnel splitting Δ causes an explicit (lmn) dependence of the spin-orbit contributions to the zero-field splitting. Similar arguments have been applied to the zero-field splittings of coherent Frenkel-exciton k states and used to elucidate properties of coherent wave packets.[9] It is important to note that $\psi(lmn)$ are *stationary* solutions to the Schrödinger equation in the absence of a relaxation Hamiltonian; hence, the states $\psi(lmn)$ can be considered *coherent* in the absence of some relaxation.

Coherence and the promoting mode[11a,11b] responsible for the dynamic Jahn-Teller effect in F centers have been considered, and the optical detection of F-center EPR in CaO in high and intermediate fields has been observed.[12] However, the observation of the dynamic Jahn-Teller effect has still eluded investigation.

To demonstrate the power of applying zero-field PMDR to ionic solids, Fig. 1 diagrammatically illustrates the problem while Figs. 2(a)–2(i) present the experimental data on the F center in CaO. These include the emission [2(e)] and PMDR spectra in zero field [2(f), 2(g)] and 50 G [2(h), 2(i)] at 1.5°K monitoring the zero-phonon[13] origin, (0, 0), in addition to the ODMR results at 0 [2(a)], 10 [2(b)], 20 [2(c)], and 50 [2(d)] G.

CaO crystals were prepared by additive coloration[14] and had an F center concentration of 5×10^{17} centers/cm^3. CaO was excited with the 3100-Å line of a 100-W high pressure Hg-Xe lamp. The zero-phonon[13] origin was isolated by a 1-m sp trometer. Other experimental details are essentially the same as reported earlier[8] except that changes in microwave-induced phosphorescence was phase detected at 105 Hz.

The results from these experiments can be understood as follows. Two zero-field transitions, hereafter labeled ω_1 and ω_2, are seen at 1675.5 and 1696.7 MHz, respectively [cf. Fig. 2(a)]. The PMDR spectrum of ω_1 [2(f)] yields a spectrum where the maximum in the phosphorescence emission is coincident with the maximum in the PMDR spectrum. On the other hand, the PMDR spectrum of ω_2 [2(g)] yields two peaks symmetrically split from ω_1 by about 4.2 ± 0.2 cm^{-1}. Moreover, the microwave-induced change in phosphorescence increases for ω_1 and decreases for ω_2 indicating a difference in the populating and decay rates for the three stationary Jahn-Teller states. In the zero-field ODMR spectrum [2(a)] the difference between the zero-field splitting in the $^3\psi(+++)$ and $^3\psi(\pm\mp\pm)$ states is 21 MHz because of selective spin-orbit coupling contributions to the zero-field splittings. The difference in their respective optical PMDR spectra amounts to 2.1 ± 0.1 cm^{-1}. This means that the tunnel splitting is $\Delta=2.1\pm0.1$ cm^{-1}.

The fact that all three splittings are resolved in the PMDR spectrum [2(f), 2(g)] means that the

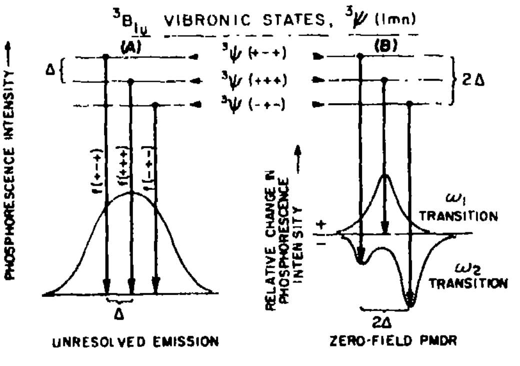

FIG. 1. Schematic diagram of the principles used to elucidate the dynamic Jahn-Teller effect using PMDR.

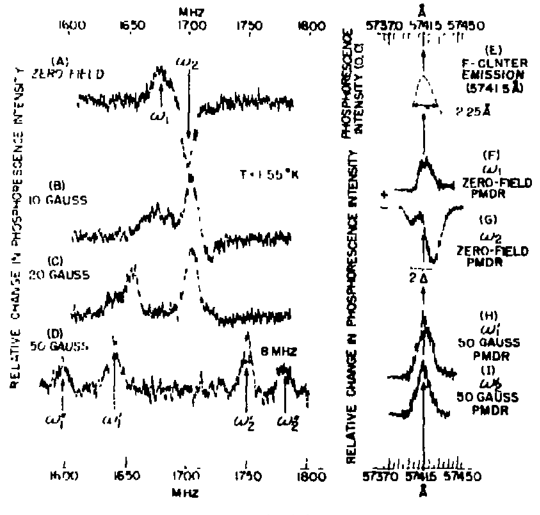

FIG. 2. ODMR results (a)–(d) and PMDR spectra (b)–(i) in F centers of CaO.

Jahn-Teller states are coherent in zero field. A minimum coherence time can be established from exchange theory[15] which states that intermediate exchange is given by the condition $(\omega_2 - \omega_1)\tau \sim 1$. The coherence time, τ, in CaO is therefore longer than 5×10^{-8} sec. Thus, coherence persists in the Jahn-Teller states in zero field at least 6×10^3 times longer than that associated with the stochastic "random" incoherent limit, which is given by $(2\Delta)^{-1}$ sec. The coherence is associated with only one point in the full-time correlation function,[7] namely 5×10^{-8} sec.

From another point of view, if we assume that the linewidths at half-height in the ODMR spectrum [2(a)], corresponding to ω_1, 15.0 MHz, and ω_2, 10.7 MHz, are homogeneous, a minimum coherence time of 7×10^{-7} sec for the ${}^3\psi(+++)$, and 1×10^{-7} sec for the ${}^3\psi(+-+)$ and ${}^3\psi(-+-)$ can be obtained. In this case the coherence is persistent at least 6×10^3 and 4×10^3 times the stochastic limit for the ${}^3\psi(+++)$ and ${}^3\psi(\pm\mp\pm)$ states, respectively, at 10^{-7} sec in the time correlation function. Since CaO contains no nuclei that have nuclear spins, apart from ^{43}Ca (0.13%), it is unlikely that hyperfine interactions (an inhomogeneous term) would be important. The coherence time could be longer however if small crystal strains result in ODMR line broadening. This is not the case, since as one increases a dc magnetic field, applied at approximately 45° to the (1 0 0) face, the ODMR spectra appear intermediately exchanged, *not at zero field*, but at about 10 G [2(b)] and the microwave-induced change in phosphorescence associated with ω_1 changes sign completely by 20 G [2(c)]. This is simply because by 20 G the Jahn-Teller states are in exchange on a time scale faster or comparable to the excited-state lifetimes[13] (3×10^{-3}) of the ${}^3\psi(lmn)$ states.

Because of the optical resolution of the PMDR spectrum in zero field [2(e), 2(f)], *it is quite possible that the coherence time could approach the lifetime of the centers in zero field,* and that the coherence is lost rapidly with small Zeeman energies (0–20 G). The loss of coherence could also be decaying via some other channel, apart from scattering between the ${}^3\psi(lmn)$ states themselves. The loss of coherence via Zeeman terms, however, can be established. By 50 G the two electron spin transitions that are degenerate in zero field because of D_{4h} symmetry are clearly resolvable [2(d), ω' and ω'']. Furthermore, the system is in the fast-exchange limit since the lines associated with ω_1' and ω_2' are narrower. Figure 2(d) shows that ω_1' and ω_2' have linewidths at half-heights of 8 MHz. Finally a PMDR on ω_1' and ω_2' at 50 G [2(h), 2(i)] confirms that under the influence of a small Zeeman *field*, which mixes the zero-field spin eigenfunctions of the three states, ${}^3\psi(+++)$, ${}^3\psi(+-+)$, and ${}^3\psi(-+-)$, the states are no longer coherent on a time scale of 10^{-3} sec. This is established by the fact that the maximum in the PMDR [2(h), 2(i)] and the maximum in the phosphorescence emission [2(e)] are coincident due to fast exchange relative to the F-centers excited-state lifetime (approximately 3×10^{-3} sec) for both Zeeman-split sites.

In summary, we have demonstrated (a) the first PMDR in ionic solids, specifically, PMDR in the triplet F centers of CaO; (b) obtained the Jahn-Teller splittings for the center; (c) shown that the states are coherent for times at least 10^3 exceeding the stochastic limit, and possibly approaching the lifetime of the excited states in zero field; and finally (d) suggested that the mixing of the spin eigenfunctions of ${}^3\psi(+++)$, ${}^3(+-+)$, and ${}^3\psi(-+-)$ is responsible for the loss of coherence as a function of field, because it introduces new off-diagonal matrix elements in the zero-field basis.

This work was done in part under the auspices of the U. S. Atomic Energy Commission through the Inorganic Materials Research Division, Lawrence Berkeley Laboratory.

---

*Alfred P. Sloan Fellow.

[1] D. S. Tinti, M. A. El-Sayed, A. H. Maki, and C. B. Harris, Chem. Phys. Lett. 3, 343 (1969).

[2] M. S. Sharnoff, J. Chem. Phys. 46, 3263 (1967).

[3] A. L. Kwiram, Chem. Phys. Lett. 1, 272 (1967).

[4] J. Schmidt and J. H. van der Waals, Chem. Phys. Lett. 2, 640 (1968).

[5] A. Kwiram, in *Optical Detection of Magnetic Resonance in Molecular Triplet States*, edited by C. A. McDowell (Butterworths, London, 1972), Ser. I, Vol. 4, pp. 271–316.

[6] *Point Defects in Solids*, edited by J. H. Crawford, Jr., and L. M. Slifkin (Plenum, New York, 1972), Vol. 1.

[7] C. B. Harris, M. Glasbeek, and J. D. W. van Voorst, unpublished.

[8] A. H. Francis and C. B. Harris, J. Chem. Phys. 57, 1050 (1972).

[9] A. H. Francis and C. B. Harris, Chem. Phys. Lett. 9, 181, 188 (1971).

[10] C. B. Harris, R. L. Schlupp, and H. Schuch, Phys. Rev. Lett. 30, 1019 (1973); W. G. Breiland, C. B. Harris, and A. Pines, Phys. Rev. Lett. 30, 158 (1973).

[11a] H. A. Jahn and E. Teller, Proc. Roy. Soc., Ser. A 161, 220 (1937).

[11b] F. S. Ham, Phys. Rev. 138, 1725 (1965).

[12] P. Edel, C. Hennies, Y. Merle d'Aubigné, R. Romestaine, and Y. Twarowski, Phys. Rev. Lett. 28, 1268 (1972); P. Edel, Y. Merle d'Aubigné, and R. Louat, J. Phys. Chem. Solids 35, 67 (1974).

[13] B. Henderson, S. E. Stokowski, and T. C. Ensign, Phys. Rev. 183, 826 (1969).

[14] E. B. Hensley, W. C. Ward, B. P. Johnson, and R. L. Kroes, Phys. Rev. 175, 1227 (1968).

[15] R. Kubo and K. Tomita, J. Phys. Soc. Jpn. 9, 888 (1954); P. W. Anderson, J. Phys. Soc. Jpn. 9, 316 (1954).

Approximate Renormalization Group Based on the Wegner-Houghton Differential Generator*

J. F. Nicoll, T. S. Chang, and H. E. Stanley
Physics Department, Massachusetts Institute of Technology, Cambridge, Massachusetts 02139

(Received 16 April 1974)

We give an approximate renormalization-group formulation which parallels that of Wilson. The group generator represents the momentum-independent limit of the differential generator of Wegner and Houghton. The eigenfunctions near the Gaussian point are computed for all spin dimensions n and lattice dimensions d, including $d=2$. The nontrivial fixed-point Hamiltonian in dimensions near $d=2\Theta/(\Theta-1)$, together with the eigenvalues near that nontrivial fixed point, are found explicitly to first order in $\epsilon_\Theta \equiv \Theta(2-d)+d$ for *all* values of n and the order Θ. Odd-dominated Ising systems and corresponding expansions in $\epsilon_{\Theta-1/2}$ are also treated.

The renormalization-group approach to the study of critical phenomena has had great initial success.[1-3] The renormalization group embodies in concrete mathematical form the scaling notions of Kadanoff[3] and provides a framework for explicit calculation. These calculations have usually been done by perturbative expansions, in analogy with similar problems in quantum field theory. All the difficulties of field theory have been incorporated into critical-phenomena calculations as well; the calculation of thermodynamic quantities involves complicated Feynman diagrams and divergent integrals.

Even in those cases where field-theoretic difficulties are not encountered, the perturbation techniques have been "brute force" in nature. For example, the calculation of critical-point exponents for higher-order[4] critical points has been hampered by the rapid increase of the number of equations which contribute.[5]

Many renormalization-group problems can be simplified by revising the perturbative techniques to conform as closely as possible to the structure of the renormalization group itself. It was noted by Wegner[6] that the eigenfunctions of Wilson's approximate renormalization group (when linearized around the Gaussian point[2]) are related to Laguerre polynomials. However, this observation has hitherto not been fully exploited. Here we show that by utilizing the structure of the renormalization group, a number of problems [see (i)–(iv) below] may be solved simply and explicitly.

To do this, we first write down an appropriate differential equation based upon the Wegner-Houghton[7] differential generator for the renormalization group. Their functional integrodifferential equations may be simplified if we consider them in the limit of vanishing "external" momenta.[8] We find that for n-dimensional isotropically interacting spins $\vec{S}$ on a d-dimensional lattice, the renormalization action on the reduced Hamiltonian H is given by

$$\dot{H} = dH + (2-d)x\frac{\partial H}{\partial x} + \frac{d}{2}\left[1 - \frac{1}{n}\ln\left(1 + \frac{\partial H}{\partial x}\right) + \frac{1}{n}\ln\left(1 + \frac{\partial H}{\partial x} + 2x\frac{\partial^2 H}{\partial x^2}\right)\right], \tag{1}$$

where the dot denotes differentiation with respect to the renormalization parameter l, and $x \equiv (\vec{S}\cdot\vec{S})/n$.[8] Since we have neglected the detailed momentum dependence in the renormalization group, we have set $\eta = 0$.

(i) *The general ϵ_Θ expansion.*—To solve (1), the Hamiltonian H can be expanded in terms of any complete set of functions; the expansion functions should be chosen to simplify the problem under consideration. A particularly useful set of functions are the eigenfunctions of (1) when (1) is linearized about the Gaussian fixed point, $H = 0$. These functions (not normalized) can be chosen to be

$$Q_p(x) \equiv [d/(2-d)n]^p L_p^{n/2-1}([(d-2)/d]nx), \tag{2}$$

where the conventions of Erdelyi[9] are used for the Laguerre polynomials, $L_p^{n/2-1}(z)$. The eigenvalue corresponding to Q_p is $\lambda_p = p(2-d)+d$. To illustrate the use of the Q_p, we have calculated the nontrivial fixed-point Hamiltonians, $H = H_\Theta{}^*$, corresponding to critical points of order Θ.[4] The fixed points of (1) are determined by setting $\dot{H} = 0$. In analogy with the ϵ expansions introduced in Refs. 1 and 2, we calculate $H_\Theta{}^*$ as a perturbation expansion in $\epsilon_\Theta \equiv \Theta(2-d)+d$,[10] for $\Theta = 2, 3, 4, \ldots$ (the usual[1,2] ϵ is ϵ_2 in our notation). To first order in ϵ_Θ, $H_\Theta{}^* = \epsilon_\Theta v_\Theta Q_\Theta$, where v_Θ is given by

$$1 = \tfrac{1}{4} d v_\Theta \langle \mathfrak{D}(\Theta, \Theta) | \Theta \rangle. \tag{3a}$$

Here the bilinear functional $\mathfrak{D}(i,j)$ is given by

$$\mathfrak{D}(i,j) \equiv \left(1 - \frac{1}{n}\right)\frac{dQ_i}{dx}\frac{dQ_j}{dx} + \frac{1}{n}\left((1-n)\frac{dQ_i}{dx} + (2i+n-2)Q_{i-1}\right)\left((1-n)\frac{dQ_j}{dx} + (2j+n-2)Q_{j-1}\right), \tag{3b}$$

and the inner product $\langle f | p \rangle$ for a function $f(x)$ is defined by

$$f(x) = \sum_{p=0}^{\infty} \langle f | p \rangle Q_p(x). \tag{3c}$$

Equation (1) can now be linearized around $H_\Theta{}^*$. The eigenfunctions will change slightly and so will the eigenvalues. If we denote by $\hat{\lambda}_l$ the eigenvalue of the new eigenfunction, which to zeroth order is Q_l, we find that to first order in ϵ_Θ

$$\hat{\lambda}_l = \lambda_l - 2\epsilon_\Theta \frac{\langle \mathfrak{D}(\Theta, l) | l \rangle}{\langle \mathfrak{D}(\Theta, \Theta) | \Theta \rangle}. \tag{4}$$

The evaluation of the bilinear coefficients in (4) is merely a problem in classical analysis. In fact, using the full renormalization-group equations, we have shown that (4) is exactly correct[11] to order ϵ_Θ.

For $n = 1$ (Ising systems), (3b) simplifies considerably, the Q_p are related to Hermite polynomials, and (4) reduces to

$$\hat{\lambda}_l = [l(2-d)+d] - 2\epsilon_\Theta \left(\frac{(2l)!}{(2\Theta)!}\frac{\Theta!}{(2l-\Theta)!}\right). \tag{5}$$

These results are in agreement with the $\Theta = 2$ calculations of Refs. 1 and 2, and the $\Theta = 3, 4$ calculations of Ref. 5. We note that (5) also contains the odd eigenvalues for $l = \frac{1}{2}, \frac{3}{2}, \frac{5}{2}, \ldots$.

From (5) we immediately deduce several important consequences. (i) For $\epsilon_\Theta > 0$, the correction to the Gaussian eigenvalue is negative, so that the nontrivial fixed point always dominates the Gaussian fixed point sufficiently near the critical point. (ii) The correction to the Gaussian eigenvalue vanishes unless $2l \geq \Theta$. In particular, to order ϵ_Θ, $\hat{\lambda}_1 = 2$ for all $\Theta \neq 2$, independent of d. (iii) We note that $\hat{\lambda}_\Theta = -\lambda_\Theta = -\epsilon_\Theta$, so that if we examine the first Θ eigenvalues we find that at the Gaussian fixed point they are all positive, and at the nontrivial fixed point all but the last remain positive. The Gaussian point is unstable, and the nontrivial point is a generalized saddle point for $\epsilon_\Theta > 0$.[12]

We also note that the ordering field which couples directly to $\vec{s}$ is entirely decoupled from the remainder of the renormalization-group transformations.[13] The eigenvalue $\lambda_{1/2}$, corresponding to the ordering field, is exactly $1 + d/2$.

(ii) *Gaussian eigenfunctions for $d = 2$.*—We next consider the behavior of (1) for $d = 2$. The nontrivial fixed points at $d = 2\Theta/(\Theta - 1)$ cluster densely around $d = 2$ as $\Theta \to \infty$. By studying (1) with d set equal to 2 [or by examining the limit of (2) as $d \to 2$ with $p(2-d)$ fixed] we find the eigenfunctions around the Gaussian fixed point have a continuous set of eigenvalues, $\lambda \leq 2$. A complete orthonormal set of eigenfunctions is given by[14]

$$Q_\lambda(x) = (\tfrac{1}{2}n)^{1/2} x^{-(n/2-1)/2} J_{n/2-1}((4-2\lambda)^{1/2}(nx)^{1/2}), \tag{6a}$$

where $J_{n/2-1}$ denotes the Bessel function of the first kind, and

$$\int_0^\infty dx\, x^{n/2-1} Q_\lambda(x) Q_{\lambda'}(x) = \delta(\lambda - \lambda'). \tag{6b}$$

The Hamiltonian is expressible as an integral, $H = \int v_\lambda Q_\lambda \, d\lambda$, rather than a sum (for $d \neq 2$). In the discrete case, thermodynamic potentials are generalized homogeneous functions[15] of the expansion coefficients. In the continuum limit, they become generalized homogeneous functionals with similar properties. For example, the Gibbs potential satisfies

$$e^{dl} G(v_\lambda) = G(e^{\lambda l} v_\lambda). \tag{7}$$

The continuous nature of the eigenvalue spectrum leads, in general, to logarithmic factors multiplying the usual power-law dependence of generalized homogeneous functions.[15] Since the approximations made in deriving (1) require setting $\eta = 0$ for consistency, one must be cautious in interpreting our results for $d = 2$.

(iii) *Power-law expansions.*—The solution of (1) for other than ϵ_Θ expansions is more difficult. For n arbitrary, the expansion of H in terms of Laguerre polynomials leads to equations coupled to all orders in the expansion parameters. If these cannot be assumed small, the equations are too complicated for immediate solution. If, however, H is expanded in powers of x, the resulting equations, while not appropriate for general ϵ_Θ analysis, are essentially "triangular." That is, if we expand

$$H = \sum_{j=0}^{\infty} v_{2j} x^j / j!,$$

the generator for the v_{2p} equation is given by

$$\dot{v}_{2p} = [p(2-d)+d] v_{2p} + \frac{d}{2}\left(\frac{\partial}{\partial x}\right)^p \left[\left(1-\frac{1}{n}\right) \ln\left(1 + \sum_{j=0}^{\infty} \frac{v_{2j} x^{j-1}}{(j-1)!}\right) + \frac{1}{n} \ln\left(1 + \sum_{j=0}^{\infty} \frac{(2j-1) v_{2j} x^{j-1}}{(j-1)!}\right)\right]\Bigg|_{x=0}. \tag{8}$$

The linear structure has only one off-diagonal term, $d(1+2p/n)\hat{v}_{2p+2}/2$, and the nonlinear terms are at most of order p in the modified coupling constants $\hat{v}_{2j} = v_{2j}/(1+v_2)$. Furthermore, the nonlinear terms include no v_{2j} with $j > p$. In particular, for $n = -2m$, the first m equations decouple entirely from the remaining equations.[16]

We have used (8) to evaluate critical-point exponents for the ordinary and tricritical points ($\Theta = 2, 3$). For $\Theta = 2$, our results agree with those of Refs. 1 and 2. For $\Theta = 3$ we find to order ϵ_3,

$$\hat{\lambda}_1 = 2, \quad \hat{\lambda}_2 = 1 + [(6-n)/(3n+22)]\epsilon_3/2, \tag{9}$$

in agreement with the general formulas for $n = 1$ given in (5).

(iv) *Odd-dominated Ising systems.*—In addition to the usual *even* fixed-point Hamiltonians described above, (1) admits (for $n = 1$) fixed points which have leading *odd* terms. We may do $\epsilon_{\Theta-1/2}$ expansions for $\Theta = 2, 3, \ldots$ in this case as well. The fixed-point Hamiltonian is of order $(\epsilon_{\Theta-1/2})^{1/2}$. We write the fixed-point Hamiltonian H^* as

$$H^* = (\epsilon_{\Theta-1/2})^{1/2} v_\Theta h_{2\Theta-1} + \epsilon_{\Theta-1/2} v_\Theta^2 f_e + (\epsilon_{\Theta-1/2})^{3/2} v_\Theta^3 f_0 + \ldots, \tag{10}$$

where $h_{2\Theta-1}$ is an *odd* Hermite polynomial, and f_e is an even and f_0 an odd function of s. Solving (1) to first order in $\epsilon_{\Theta-1/2}$, we find the fixed-point value v_Θ and the perturbed eigenvalues to be given by

$$1 = -\tfrac{1}{6} d v_\Theta^2 \langle g(2\Theta-1, 2\Theta-1) | 2\Theta-1 \rangle, \tag{11a}$$

$$\hat{\lambda}_{l/2} - \lambda_{l/2} = -3\epsilon_{\Theta-1/2} \frac{\langle g(2\Theta-1, l) | l \rangle}{\langle g(2\Theta-1, 2\Theta-1) | 2\Theta-1 \rangle}, \quad l = 1, 2, 3, \ldots. \tag{11b}$$

The operator g in (11) is

$$g(m, l) = 64 l(l-1) m(m-1) [(h_{m-2})^2 h_{l-2} + h_{l-2} \mathcal{L}_m (h_{m-2})^2 + 2h_{m-2} \mathcal{L}_l (h_{l-2} \cdot h_{m-2})], \tag{12}$$

where $\mathcal{L}_l$ is defined by $\mathcal{L}_l h_p = [p(p-1)/p - l] h_{p-2}$ for all Hermite polynomials h_p. At least for $2\Theta - 1 = 3, 5$, we have $v_\Theta^2 < 0$; the Hamiltonian is real only if $\epsilon_{\Theta-1/2} < 0$. For $\epsilon_{\Theta-1/2} > 0$ the odd parts of the fixed-point Hamiltonian are purely imaginary.[17]

The Wegner-Houghton approximate renormalization group proposed here provides a straightforward framework in which to explore the consequences of the full renormalization group. As a differential representation, it is suited to investigations of nonlinear phenomena such as crossover competition between two or more fixed points. Elsewhere[18] we have solved (8) near $d = 4$ for the *nonlinear* crossover between critical and Gaussian (mean-field) behavior. The extension to crossover from tricritical to mean-field behavior seems to be more difficult.

We would like to thank G. F. Tuthill and L. L. Liu for many helpful comments and suggestions and B. D. Hassard for discussions of the differential generator of the renormalization group.

---

*Work supported by the National Science Foundation, the U.S. Office of Naval Research, and the U.S. Air Force Office of Scientific Research. Work forms a portion of the Ph.D. thesis of J.F.N. to be submitted to the Massachusetts Institute of Technology Physics Department.

[1] K. G. Wilson and M. E. Fisher, Phys. Rev. Lett. 28, 240 (1972).

[2] K. G. Wilson and J. Kogut, to be published; for an elementary discussion, see H. E. Stanley, T. S. Chang, F. Harbus, and L. L. Liu, in *Local Properties at Phase Transitions, Proceedings of the International School of Physics "Enrico Fermi," Course LVIII*, edited by K. A. Müller (Academic, London, 1974), Chap. 1.

[3] L. P. Kadanoff, Physics (Long Is. City, N.Y.) 2, 263 (1966).

[4] A critical point of order $\mathcal{O}$ can be defined as a point at which $\mathcal{O}$ phases are simultaneously critical. See T. S. Chang, G. F. Tuthill, and H. E. Stanley, Phys. Rev. B 9, 4882 (1974), and references contained therein.

[5] Chang, Tuthill, and Stanley, Ref. 4; M. J. Stephen and J. L. McCauley, Jr., Phys. Lett. 44A, 89 (1973); E. K. Riedel and F. J. Wegner, Phys. Rev. Lett. 29, 349 (1972).

[6] F. J. Wegner, Phys. Rev. B 6, 1891 (1972).

[7] F. J. Wegner and A. Houghton, Phys. Rev. A 8, 401 (1973).

[8] In the special case $n=\infty$, Ref. 7 gives a derivation of a solution for (1). The zero-momentum requirement can be weakened somewhat in this case. If we write $v_{2j}(\vec{k}_1,\ldots,\vec{k}_{2j})$ for the momentum-dependent $2j$-spin coupling constant, Eq. (1) follows by restricting the $\vec{k}_j$ to cancel in pairs; that is, we consider only $v_{2j}(\vec{k}_1,-\vec{k}_1,\ldots,\vec{k}_j,-\vec{k}_j)$. We also note that the reduced Hamiltonian density H_W of Wilson (Ref. 2) has the form $H_W=|\nabla\vec{s}|^2+B(x)$. The gradient term is left unchanged by the renormalization group in the approximation employed here and is therefore not considered explicitly.

[9] A. Erdelyi, *Higher Transcendental Functions* (McGraw-Hill, New York, 1953), Vol. 2, pp. 188 ff.

[10] Our definition of $\epsilon_{\mathcal{O}}$ differs slightly from that of Chang, Tuthill, and Stanley, Ref. 4. The convention adopted here has the advantage that the eigenvalue of $Q_{\mathcal{O}}$ is precisely $\epsilon_{\mathcal{O}}$.

[11] To see this, it is sufficient to note that the Q_j are eigenfunctions of the full linear renormalization-group operator. The powers of x in the Q_j are replaced by more complicated sums over momentum: $(nx)^p$ becomes

$$\sum_{k_1k_1'}\cdots\sum_{k_pk_p'}(\vec{s}_{k_1}\cdot\vec{s}_{k_1'})\cdots(\vec{s}_{k_p}\cdot\vec{s}_{k_p'})\delta_{k_1+k_1'+\cdots k_p+k_p',0}.$$

With these emendations, an examination of the full nonlinear renormalization-group equation of Ref. 7 shows that the fixed point and eigenvalues are correct to first order in $\epsilon_{\mathcal{O}}$, and $\eta_{\mathcal{O}}$ is $o(\epsilon_{\mathcal{O}}^2)$.

[12] Points (ii) and (iii) hold for general n; (i) cannot hold for *arbitrary* n {e.g., for $\mathcal{O}=2$, $\lambda_1=2-[(n+2)/(n+8)]\epsilon_2$}.

[13] J. Hubbard, Phys. Lett. 40A, 111 (1972).

[14] G. N. Watson, *Theory of Bessel Functions* (Cambridge Univ. Press, Cambridge, England, 1966). Note that the formal completeness of the eigenfunctions Q_λ is only guaranteed for $n\gg1$. Results for $n\ll1$ must be obtained by analytic continuation of those for larger n. See also Watson, *op. cit.* pp. 453 ff.

[15] A. Hankey and H. E. Stanley, Phys. Rev. B 6, 3515 (1972).

[16] M. E. Fisher, Phys. Rev. Lett. 30, 679 (1973).

[17] After the completion of this manuscript, we were informed that M. J. Stephen has obtained similar results for an $\epsilon_{3/2}=3-d/2$ expansion.

[18] J. F. Nicoll, T. S. Chang, and H. E. Stanley, Phys. Rev. Lett. 32, 1446 (1974).

Superheavy Elements and the Strutinsky Prescription*

R. R. Chasman
Chemistry Division, Argonne National Laboratory, Argonne, Illinois 60439

(Received 14 February 1974)

Cases are found in which the Strutinsky prescription for single-particle corrections to the liquid-drop model fails. Estimates of the spontaneous-fission lifetimes of superheavy elements are found to be overly sensitive to small changes in the assumed single-particle level spectrum.

With the considerable effort being made at present to produce superheavy elements ($A \approx 300$), it is worthwhile to reconsider the question of their stability. In this work, I examine the problem in the framework of the liquid-drop model (LDM) with single-particle-correction[1,2] (SPC) effects. In terms of a pure LDM, there is no barrier to the spontaneous fission of the superheavy elements. However, because of stabilization effects associated with nonuniformities in the single-particle spectrum, superheavy elements may have finite barriers to spontaneous fission and finite lifetimes. In a recent study of this problem,[3,4] it was concluded that the stabilization effects due to the SPC are rather large and that there are long-lived superheavy elements. However, the single-particle spectra that were used in this study differ in some significant respects from other[5,6] careful extrapolations of single-particle level spacings from the lead region and from the actinides. The points that I wish to consider are (1) how accurate are the extrapolations of single-particle levels to the superheavy-element region and (2) how sensitive are the calculated lifetimes of superheavy elements to the differences in the various extrapolations? This second question has already been considered[7] to some extent. In the course of investigating these questions, a somewhat more basic problem has arisen: (3) How meaningful is the Strutinsky prescription[2,8] for the calculation of SPC effects?

To calculate the SPC arising from nonuniformities in the single-particle spectrum generated from a Woods-Saxon potential, I use the Strutinsky prescription.[2,8] The procedure is first to generate a continuous spectrum from the discrete one by defining

$$G_T(\epsilon,\gamma)=\sum_{i=1}^{N}\sum_{k=1}^{T/2} A_T^{2k}[(\epsilon-\epsilon_i)/\gamma]^{2k} \times \exp\{-[(\epsilon-\epsilon_i)/\gamma]^2\}, \tag{1}$$

where ϵ_i is an eigenvalue of the potential, T defines the order of the continuous distribution, γ is the smoothing width, and the coefficients A_T^{2k} are well known; take ϵ_i and γ in units of MeV. The eigenvalue spectrum for the Woods-Saxon potential is generated with a harmonic-oscillator basis set. In order to apply the Strutinsky prescription one must extend the summation over eigenvalues ϵ_i to continuum states. I find that this summation should extend $\sim 5\gamma$ into the continuum. Making use of the function $G_T(\epsilon,\gamma)$, I define $\lambda(M,T,\gamma)$ through the relation

$$M = 2\int_{-\infty}^{\lambda(M,T,\gamma)} G_T(\epsilon,\gamma)\,d\epsilon; \tag{2}$$

i.e., there are M particles in the smooth distribution $G_T(\epsilon,\gamma)$ to the cutoff $\lambda(M,T,\gamma)$. The factor of 2 arises from the fact that the orbitals are doubly degenerate. The Strutinsky prescription for the SPC, denoted as $\Delta E(M,T,\gamma)$, is given by

$$\Delta E(M,T,\gamma) = 2\sum_{i=1}^{M/2}\epsilon_i - 2\int_{-\infty}^{\lambda(M,T,\gamma)} \epsilon G_T(\epsilon,\gamma)\,d\epsilon. \tag{3}$$

This quantity is just the difference in energy between the first M particles with the discrete eigenvalues and the first M particles with a continuous distribution of energies. It is this continuous distribution that is presumably being accounted for in the LDM and $\Delta E(M,T,\gamma)$ gives the SPC to the LDM. The crucial feature in the application of the Strutinsky prescription is that the function $\Delta E(M,T,\gamma)$ be constant as a function of both T and γ in a large region of (T,γ) space. In general, one finds that $\Delta E(M,T,\gamma)$ is in this constant region. If there were no such plateau, the Strutinsky prescription for the SPC would be invalid. There is also a pairing correction associated with the Strutinsky prescription, but it is roughly the same for the various extrapolations considered here, and is ignored.

To get some idea of the uncertainties involved

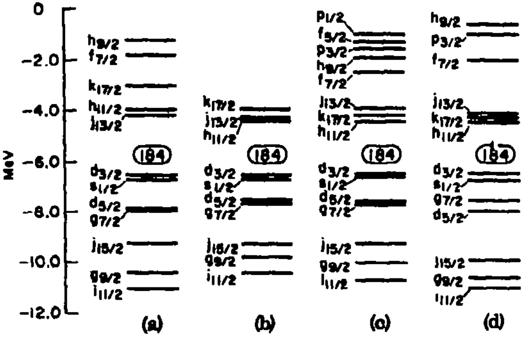

FIG. 1. Extrapolations of neutron single-particle spectra to the superheavy elements: Spectrum *a* is taken from Ref. 4; spectrum *b* is taken from Ref. 5; spectrum *c* is based on the potential of Ref. 6; spectrum *d* is explained in the text.

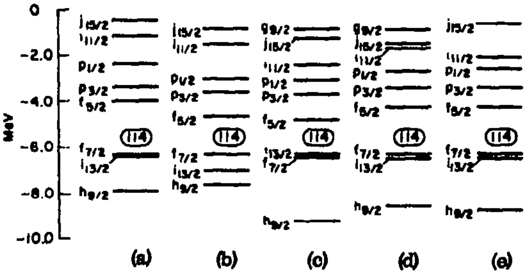

FIG. 2. Extrapolations of proton single-particle spectra to the superheavy elements: Spectrum *a* is taken from Ref. 4; spectrum *b* is taken from Ref. 5; spectra *c* and *d* are based on the potential of Ref. 6 and discussed in the text; spectrum *e* is explained in the text.

in the extrapolation of single-particle spectra to the superheavy-element region, it is instructive to consider the results of Rost.[5] He found that it was possible to fit the known single-particle levels in the Pb region with an average deviation of ~200 keV by using a Woods-Saxon potential. A fit of this quality was obtained by introducing a free radius parameter in the spin-orbit term of the potential. With a conventional spin-orbit term, he found that the average deviation is ~400 keV. I emphasize that this is an attempt to fit measured levels. In this context, I feel that it would be foolhardy to claim that one can calculate the unmeasured single-particle level spacing in the superheavy-element region with an accuracy of any better than 500 keV.

Figure 1 shows several extrapolated neutron single-particle spectra for the superheavy elements. The level spacings of Bolsterli *et al.* and Rost were taken from figures in their publications,[3,5] so that there may be some small errors. The spectrum generated from the momentum-dependent potential[6] was obtained with a fifteen-shell oscillator basis ($N_{\max}=14$) rather than the fourteen-shell basis used previously. This extrapolation (spectrum *c*, Fig. 1) is based on the hole states in Pb and agrees well with an extrapolation from the actinides. In attempting to apply the Strutinsky prescription to spectra generated from the momentum-dependent potential, I find that the prescription does not work. This failure appears to be related to the extremely high density of levels in the first 20 MeV of the continuum spectrum generated from this potential. In order to circumvent this problem, I went to a momentum-independent Woods-Saxon potential and adjusted a few levels generated from this potential in order to get a spectrum that resembles the spectrum generated from the momentum-dependent potential at the Fermi level. The spectrum (*d*, Fig. 1) is obtained by shifting the $k_{17/2}$ orbital 400 keV and the $j_{13/2}$ orbital 500 keV from a spectrum generated from a conventional Woods-Saxon potential. All of the spectra in Fig. 1 are lined up at $N=184$ to facilitate comparisons. Figure 2 presents extrapolated proton spectra. Two extrapolations of the momentum-dependent potential are given—one based on particle states in the Pb region (spectrum *c*, Fig. 2) and the other based on hole states in the Pb region (spectrum *d*, Fig. 2). Note that an extrapolation from the actinides agrees with extrapolation *d* in Fig. 2. The final spectrum (*e*, Fig. 2) is a level spectrum generated from a momentum-independent Woods-Saxon potential that corresponds rather well to spectrum *d* in Fig. 2. The proton spectra are lined up at $Z=114$ to facilitate comparisons. On the whole, the agreement between the various extrapolations of single-particle spectra to the superheavy-element region is quite good, better than one would anticipate the agreement with experimentally determined spectra to be. At $Z=114$, the $f_{7/2}$-$f_{5/2}$ spacing is somewhat larger in spectrum *a*, Fig. 2, than it is in the other spectra. The experimental data from the Pb region[9] and the actinides[10] favor the smaller spacing. At $N=184$, the agreement is remarkable. The $k_{17/2}$ orbital is somewhat higher in energy in spectrum *a*, Fig. 1, than in the other extrapolations. There is no data on this orbital.

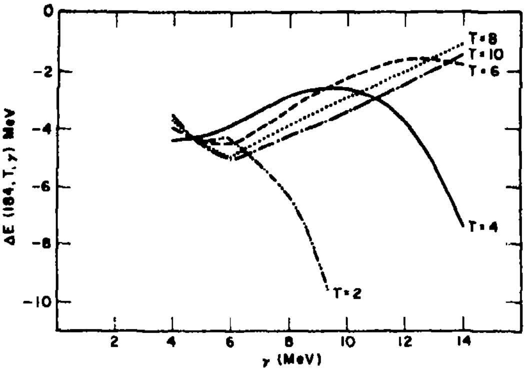

FIG. 3. Calculation of the single-particle correction to the liquid-drop model using the Strutinsky prescription and spectrum d, Fig. 1.

Because the Strutinsky prescription is not applicable to spectra generated from the momentum-dependent potential, I carried out calculations with spectrum d, Fig. 1 and spectrum e, Fig. 2. In carrying out the calculation of the SPC with the Strutinsky prescription, I found a very surprising result. With the use of spectrum d, Fig. 1, the Strutinsky prescription breaks down. Figure 3 displays $\Delta E(184, T, \gamma)$ calculated for this set of levels. The calculations were made at 2-MeV intervals in γ. Inspection of Fig. 3 shows that there is no large plateau region. To orient the reader, I mention that in other cases with different spectra, I have found $\Delta E(M, 8, \gamma)$ quite constant for values of γ ranging from 8 to 14 MeV. I note that this breakdown is not confined to $N = 184$, but occurs for all mass numbers from 160 to 200. As this result is quite unexpected, I have checked my computer program by comparing my results with those obtained from other programs. Using spectrum d, Fig. 1, J. R. Nix has obtained this same breakdown in the Strutinsky prescription for $\Delta E(184, T, \gamma)$. For many choices of M and γ, B. Wilkins obtains the same values of $\Delta E(M, 2, \gamma)$ that I obtain. I note that I have found other cases in which this breakdown occurs. I emphasize that the breakdown of the Strutinsky prescription that I have found here is not due to any difficulties associated with the treatment of continuum states. It has been noted[3] that using an oscillator basis set, as done here, circumvents difficulties with the continuum. Clearly, this breakdown is associated with the extremely high level density at 184 neutrons. I have carried out calculations of the SPC using the unshifted spectrum from which spectrum d, Fig. 1, was obtained. The two spectra differ only in the positions of the bound states $k_{17/2}$ and $j_{13/2}$. *With the use of this unshifted spectrum*, there is no breakdown in the Strutinsky prescription. The quantity $\Delta E(184, 8, \gamma)$ is quite constant over the interval $6 \leq \gamma \leq 10$ for the unshifted spectrum. For completeness, I note that it has a value of − 5.9 MeV. This breakdown of the Strutinsky prescription forces the conclusion that calculations based on this technique are suspect. The consequences of this breakdown are particularly serious in view of the many calculations that have been reported in the literature[11] based on the use of the Strutinsky prescription. *There is a need to develop reliable techniques* for the calculation of SPC effects for finite potentials. In order to provide a test for any new methods that are developed, I would be glad to provide a listing of the complete set of the eigenvalues in spectrum d, Fig. 1.

If we assume that a new method for calculating SPC effects will give results similar to the Strutinsky prescription—in those instances that the Strutinsky prescription does not break down—we can learn something about the sensitivity of calculated spontaneous-fission lifetimes to the assumed single-particle spectrum. Using spectrum e, Fig. 2, I find

$$\Delta E(114, 8, \gamma) \approx -3 \text{ MeV}. \tag{4}$$

Lowering the $f_{5/2}$ orbital to 1800 keV above the $f_{7/2}$ orbital, a value midway between spectra b, Fig. 2, and d, Fig. 2, gives

$$\Delta E(114, 8, \gamma) \approx -2.5 \text{ MeV}. \tag{5}$$

These results should be compared with the value that one obtains[3] with spectrum a, Fig. 2,

$$\Delta E(114, T, \gamma) \approx -5 \text{ MeV}. \tag{6}$$

In the superheavy-element region, a change of 1 MeV in the fission-barrier height corresponds[4] to roughly a factor of 100 change in the spontaneous-fission lifetime. These rather small changes in the proton single-particle spectrum amount to a factor of $\sim 10^4 - 10^5$ decrease in the spontaneous-fission lifetime. From Fig. 3, one might guess that

$$0 \geq \Delta E(184, T, \gamma) \geq -5 \text{ MeV} \tag{7}$$

for spectrum d, Fig. 1. For spectrum a, Fig. 1, one has[3]

$$\Delta E(184, T, \gamma) \approx -7.5 \text{ MeV}. \tag{8}$$

This difference corresponds to at least another factor of $\sim 10^5$ decrease in the spontaneous-fission lifetime. I conclude that rather small, very reasonable, changes in the extrapolated single-particle spectra of superheavy elements give a reduction of $\sim 10^{10}$ in the estimates of spontaneous-fission lifetime relative to previous[4] estimates. The uncertainties in the extrapolated spectrum are sufficiently large that even these lowered estimates might be too large by a factor of 10^{10}.

The major conclusion that I draw from this work is that the Strutinsky prescription is an extremely questionable technique for calculating single-particle corrections to the liquid-drop model. Until the breakdown of the Strutinsky prescription that has been found here is understood, all results based on the Strutinsky prescription must be regarded as suspect. To the extent that the Strutinsky-prescription results represent those of a correct method of calculating the SPC, I draw a second conclusion. The calculation of spontaneous-fission half-lives of superheavy elements is overly sensitive to the details of the assumed single-particle spectrum. The irreducible uncertainties involved in extrapolating single-particle spectra to the superheavy elements are sufficiently large to vitiate all such calculations.

I thank J. R. Nix for his help in carrying out this work. I thank B. Wilkins for considerable aid in many aspects of this work.

---

*Work performed under the auspices of the U. S. Atomic Energy Commission.

[1] W. D. Myers and W. J. Swiatecki, Nucl. Phys. 81, 1 (1966).

[2] V. M. Strutinsky, Nucl. Phys. A95, 420 (1967).

[3] M. Bolsterli, E. O. Fiset, J. R. Nix, and J. L. Norton, Phys. Rev. C 5, 1050 (1972).

[4] J. R. Nix, LASL Report No. LA-DC-72-769, 1972 (unpublished).

[5] E. Rost, Phys. Lett. 26B, 184 (1968).

[6] R. R. Chasman, Phys. Rev. C 3, 1803 (1971).

[7] Yu. A. Muzychka, Yad. Fiz. 11, 105 (1970) [Sov. J. Nucl. Phys. 11, 66 (1970)].

[8] M. Brack, J. Damgaard, A. S. Jensen, H. C. Pauli, V. M. Strutinsky, and C. Y. Wong, Rev. Mod. Phys. 44, 320 (1972).

[9] J. S. Lilly and N. Stein, Phys. Rev. Lett. 19, 709 (1967).

[10] G. Kyle, J. R. Erskine, A. Friedman, and R. R. Chasman, to be published.

[11] See Refs. 3 and 8 for an extensive bibliography.

Physical Significance of the Topology of the Bondi-Metzner-Sachs Group

Michael Crampin
Faculty of Mathematics, The Open University, Walton Hall, Walton, Bletchley, Buckshire, England

and

Patrick J. McCarthy
Department of Applied Mathematics and Theoretical Physics, University of Cambridge, Cambridge, England

(Received 22 April 1974)

It has been proposed that the Bondi-Metzner-Sachs group affords a possible explanation for the discreteness of elementary-particle spins. This discreteness result depends on the topology given to the group. A careful analysis of representations in the "nuclear" topology indicates that discrete-spin representations (those subsumed by the original topology) describe bound gravitating systems ("elementary particles") whereas the new continuous-spin representations, if physically realistic, describe scattering states of gravitating systems.

The asymptotic symmetry group of general relativity, the Bondi-Metzner-Sachs (BMS) group[1] B, has been of interest for some time as a possible candidate for replacing the Poincare group in a microphysics which takes gravity into account.[2] Recently it was proposed that the group may give an explanation for the discreteness of elementary particle spins.[3] However, this discreteness result, which arises because all little groups of B are compact, depends on the topology with which B is endowed. There is a wide range of choices of "reasonable" topologies, arising from the infinite-dimensional additive supertranslation subgroup A of "arbitrary" real-valued functions on the Riemann sphere S. Also, the range of choices available depends on the class of functions allowed in A. Let $C^k(S)$ denote the k-times continuously differentiable functions on S, and $L^2(S)$ the square-integrable functions defined by the area measure of S (two being identified if they differ only on a set of measure zero). Sachs's original derivation[2] of B required $A = C^2(S)$, and Cantoni,[4] in his investigation of representations, gave to this $A = C^2(S)$ the pre-Hilbert topology determined by the area measure of S. McCarthy[5] chose the same topology in his investigation, but widened $A = C^2(S)$ to $A = L^2(S)$ in order to simplify the treatment. The discreteness result is true[6] with either the Cantoni[4] or McCarthy[5] choices.

However, it was pointed out by McCarthy[7,8] that noncompact little groups (associated with *distributions*) *arise if a sufficiently fine* (actually nuclear[8,9]) topology is chosen for $A = C^\infty(S)$. This point has recently been taken up by Girardello and Parravicini,[10] who have given an interesting partial calculation of some distributions invariant under some connected noncompact subgroups of the Lorentz group, again indicating the possibility of noncompact little groups in the nuclear topology. Another class of topologies for A are the Sobolev topologies,[11] which depend strongly on smoothness properties (being defined by convergence in the mean of functions and derivatives). They are physically plausible in a gravitational radiation context because they are adapted to initial-value problems for hyperbolic differential equations.[11] For $A = C^0(S)$ in this topology, only compact little groups occur. In other cases, the results are not yet known.

It should be mentioned that the class of functions in B is by no means uniquely determined. Sachs's original derivation[2] of B was superceded by that of Penrose,[12] who gave a precise and intrinsic derivation of B as that group of *exact* conformal motions of the future (or past) null boundary $\mathscr{I}^+$ (or $\mathscr{I}^-$) of (conformally compactified weakly asymptotically simple) space-times which preserve "null angles." Since truly arbitrary supertranslation functions describe symmetry transformations in Penrose's sense, supertranslations need not have some minimum degree of smoothness. The arbitrariness of symmetry transformations (and topology) arises because $\mathscr{I}^+$ is not a Riemannian manifold—it is degenerate in the directions along which supertranslations act. For Riemannian manifolds, the choice of the compact-open topology on the symmetry group is natural, and gives a uniquely determined (finite dimensional) Lie-group structure defined by analytic functions.[13] In the degenerate case, the situation is very different, and not yet well understood.

There are more familiar situations in which changing the topology alters the physics.[14] Zeeman[15] has proposed a topology on Minkowski space, hence on the Poincare group P, which is finer than the usual[16] one, but physically plausible because it is adapted to the null-cone structure. In Zeeman's finer topology, one would expect many (unknown) representations of P in addition to the usual[16] ones. Again Boon[17] topologizes a countable subgroup (relevant in solid-state physics[18]) of the Heisenberg group discretely. However, the subgroup is not discrete in the induced topology, and it can be shown[19] that Boon "unphysical" representations *disappear* in the more natural induced topology.

Since neither the class of functions in B, nor the appropriate topology (Hilbert[4,5] or nuclear[8,9,1] is evident from the derivation of B as an asymptotic symmetry group, it seems at present that the only way to interpret the topologies is to *look at the structure of the irreducible representations themselves.* A complete analysis of the irreducible representations of B in the nuclear topology has now been given by McCarthy.[20] It was shown there[20] that irreducible representations arise from either strictly ergodic or transitive SL(2, C) actions on supermomentum space Φ. (Φ is the topological dual vector space of A.) The latter type are all induced, and all induced representations whose little groups were not both discrete and infinite were constructed and classified. The indications[6,7,10] that noncompact little groups should arise in this context are now prove —there are precisely two new connected ones, and several new nonconnected ones, all noncompact. As in the Hilbert case, the representations are markedly different from those of the Poincare group. The effect of passing from the coarser (Hilbert) topology to the finer (nuclear) topology is to enlarge Φ from a Hilbert space of L^2 functions[5] to a space containing all generalized functions ($\Phi = \mathrm{GF}$), i.e., the distributions[7,9] $D = \mathrm{GF} - L^2$ as well as "regular" L^2 functions. Noncompact little groups are associated with distributional supermomenta $\varphi \in D$.[20]

To find an analogy for this situation it is helpful to recall the roles of L^2 and GF spaces in other problems in quantum mechanics. Broadly speaking, *discreteness* results, which one thinks of as typical behavior in quantum mechanics, only have the potential of arising if square-integrability requirements are imposed on wave functions, that is, if the wave functions are restricted to lie in L^2 spaces. Widening these L^2 spaces to GF spaces generally introduces continuous sets also. [It is essential to note, however, that (i) exclusively discrete spins do not *necessarily* arise in L^2 spaces, and (ii) continuous spins *always* arise in GF spaces.[21]]

The hydrogen atom provides a particularly clear example illustrating the sentence preceding the parentheses. In the (pre-) Hilbert space of (smooth) L^2 wave functions, the energy eigenvalues of the self-adjoint Hamiltonian operator are negative and *discrete*, the L^2 eigenvectors describing the bound states. However, enlarging L^2 to the GF space (determined by the rigged Hilbert space triple based on a nuclear subspace of C^∞ functions in L^2) produces new eigenvectors (the unbound states); *these new eigenvectors are distributions (in $D=\mathrm{GF}-L^2$) and the new energy eigenvalues form a continuous set* (all nonnegative reals).[22] Moreover each eigenspace is a representation space of the symmetry group of the Hamiltonian operator; the symmetry group of the bound states is the *compact* group SO(4), while for the unbound states it is noncompact [E(3) or SO(3, 1)].[23] Actually the compactness of SO(4) allows one to *deduce* the discreteness of the bound-state energy levels. The set D of unbound states accommodates *scattering* states of the H atom, for which incoming particles are described by wave "functions" with precisely defined directions in the remote past.

These striking formal similarities between the H atom and the BMS group situation suggest that (I) *induced representations of B in the Hilbert topology* ($\Phi = L^2$) *describe gravitating systems with bound sources, and* (II) *the new induced representations arising in the nuclear topology* ($\Phi = \mathrm{GF}$) *describe gravitating systems with unbound sources.*[24] In an induced representation, an invariant supermomentum φ and its associated little group (i.e., its maximal invariance group) L_φ have the following significance: φ represents the quantum system in a fixed frame of reference, and L_φ describes the "internal degree of freedom" group of the system in the frame. Evidently to examine suggestions (I) and (II), a physical interpretation in gravitational terms of the invariant supermomenta occurring in induced representations is needed.

Observe first that the Lorentz transformation law of supermomenta φ is identical to that of a "mass aspect," i.e., the direction-dependent apparent mass of a gravitating system measured by remote observers (situated on a sphere S surrounding it).[1] Recall next that every φ can be written[5] as the sum of a (Poincare) momentum vector $\pi(\varphi)$ and a proper supermomentum vector $\sigma(\varphi)$; $\varphi=\pi(\varphi)+\sigma(\varphi)$. The mass-squared invariant of a BMS representation is[5] the Lorentz scalar product $\pi(\varphi)\cdot\pi(\varphi)=m^2$, showing that φ must have the dimensions of mass. These facts strongly support the idea that φ itself should be identified with a mass aspect.[25] Now, the class of gravitational systems for which the BMS group is defined consists of *bound* gravitating sources, and the mass aspects concerned (being derived from coefficients of the metric) are assumed to be smooth (so certainly L^2).[26] Thus for *bound* sources, $\Phi = L^2$, and suggestion (I) is vindicated. It appears likely that distributional $\varphi \in D$ must describe *unbound* sources, since such are not subsumed by the usual class of systems. We now examine this possibility.

Recall that an induced representation of B is unfaithful if and only if $\pi(\varphi)=0$, in which case the quantum state it describes is invariant under all rigid translations R^4. (The representation is then faithful on B/R^4.) The mass aspect $\varphi=\sigma(\varphi)$ then describes purely internal properties (cf. Komar[2]) of the source, being unaffected by rigid translations of remote observers. For these representations, m^2 is undefined. For the more physically significant faithful representations, the mass aspect $\varphi=\pi(\varphi)+\sigma(\varphi)$ is therefore a superposition of an external part $\pi(\varphi)$ and an internal part $\sigma(\varphi)$. It was shown in Ref. 20 that, in the nuclear topology, the new faithful representations of B with noncompact little groups are of two sorts: $m^2=0$ (with possible little groups Δ and five of its nonconnected subgroups) and $m^2<0$ (with two possible little groups, both nonconnected, and both with identity component Π). Here Δ double covers E(2), and Π is a one-parameter group of boosts. In the first case, $\pi(\varphi)$ is concentrated in one direction (being a δ function), while in the second, $\pi(\varphi)$ is concentrated in at most two directions (being, in each, first derivatives of δ functions). This shows that these representations actually have a stream of $m^2=0$ particles approaching from one precisely defined direction, or at most two (diametrically opposed) streams of $m^2<0$ particles approaching from precisely defined directions in the remote past. In contrast to the systems described by (I), these are indeed unbound in the remote past. It is not at all clear that such systems are asymptotically flat, so that B may not be defined for them. If B

can be defined, however, these representations evidently describe *scattering states* of gravitating systems.

It appears to us highly plausible that, in a BMS invariant context, "elementary particles" should be described by *bound* gravitating sources. But this means that *the Hilbert topology originally chosen for B describes "elementary particles" only*. For representations of type (II), there are two possibilities, either (A) *they are unphysical*, or (B) *they describe systems unbound in the remote past, in particular, the continuous-"spin" ones describe scattering states of gravitating systems*. Thus "elementary-particle" spins are still discrete in the nuclear topology, the discreteness result having the same status as other discreteness results in quantum mechanics (cf. the H atom).

The partial support of a Science Research Council fellowship is gratefully acknowledged by one of us (P.J.McC.).

---

[1] H. Bondi, M. G. J. van der Burg, and A. W. K. Metzner, Proc. Roy. Soc., Ser. A 269, 21 (1962); R. K. Sachs, Proc. Roy. Soc., Ser. A 270, 103 (1962); E. T. Newman and T. W. J. Unti, J. Math. Phys. (N.Y.) 8, 891 (1967).

[2] R. K. Sachs, Phys. Rev. 128, 2851 (1962); A. Komar, Phys. Rev. Lett. 15, 76 (1965); E. T. Newman, Nature (London) 206, 811 (1965).

[3] P. J. McCarthy, Phys. Rev. Lett. 29, 817 (1972).

[4] V. Cantoni, Ph.D. thesis, University of London, 1967 (unpublished), and J. Math. Phys. (N.Y.) 8, 1700 (1967).

[5] P. J. McCarthy, Proc. Roy. Soc., Ser. A 330, 517 (1972), and 333, 317 (1973).

[6] P. J. McCarthy, in *Proceedings of the Second International Conference on Group Theory, Nijmegen, The Netherlands*, edited by A. Janner and T. Janssen (University of Nijmegen, Nijmegen, The Netherlands, 1973), Vol. 1, p. A137.

[7] P. J. McCarthy, International Centre for Theoretical Physics Report No. IC/71/144, 1971 (unpublished), p. 28.

[8] I. M. Gel'fand and N. Ya. Vilenkin, *Generalised Functions* (Academic, New York, 1964), Vol. 4.

[9] P. J. McCarthy, Ph.D. thesis, University of London, 1971 (unpublished). In this reference, the nuclear topology was first used for *A*.

[10] L. Girardello and G. Parravicini, Phys. Rev. Lett. 32, 565 (1974).

[11] S. L. Sobolev, *Partial Differential Equations of Mathematical Physics* (Pergamon, New York, 1964), p. 29, definition 2, ff.

[12] R. Penrose, Phys. Rev. Lett. 10, 66 (1963), and in *Relativity, Groups and Topology*, edited by C. de Witt and B. de Witt (Blackie and Sons Ltd., London, 1963).

[13] S. Helgason, *Differential Geometry and Symmetric Spaces* (Academic, New York, 1962).

[14] These examples were discussed in a similar context in Ref. 6.

[15] E. C. Zeeman, Topology 6, 161 (1967).

[16] E. P. Wigner, Ann. Math. 40, 149 (1939).

[17] M. Boon, J. Math. Phys. (N.Y.) 13, 1268 (1972).

[18] W. Opechowski and W. C. Tam, Physica (Utrecht) 42, 529 (1969).

[19] P. J. McCarthy, to be published.

[20] P. J. McCarthy, to be published.

[21] An obvious counterexample illustrating (i) is the imposition of the L^2 topology on Poincare translations. The L^2 topology here coincides with the standard Wigner topology, which is well known to admit continuous spins. Further counterexamples involving infinite-dimensional L^2 translations are easily constructed. By (ii) we mean that any semidirect product defined analogously to B, but with the nuclear space A replaced by *any* operator irreducible representation space of SL(2,C), admits continuous spins in the nuclear topology.

[22] One may regard the role of GF spaces in quantum mechanics as providing a sufficiently large space to admit a complete set of eigenvectors for any self-adjoint operator. See Ref. 8.

[23] R. Hermann, *Lie Groups for Physicists* (Benjamin, New York, 1966).

[24] It might be thought that, for example, all zero-mass particles would be scattering states in this interpretation. However, some zero-mass particles are already subsumed under "regular" functions. Indeed L^2 supermomenta already subsume all possible mass-squared values.

[25] R. Penrose suggested that one should actually consider the limiting values of these mass aspects in the remote past (private communication).

[26] A major conclusion of J. Foster's Ph.D. thesis [University of London, 1966 (unpublished)] was that the conditions on space-times considered in Refs. 1 were appropriate to *bound* gravitational sources.

Muon-Deuteron Deep Inelastic Scattering*

I. J. Kim, A. Entenberg, H. Jöstlein,† K. Königsmann, I. Kostoulas,‡ A. C. Melissinos,
E. Aslanides,§ L. Lederman, P. Limon,‖ M. May, P. Rapp, H. Gittleson, T. Kirk,¶
M. Murtagh,** M. J. Tannenbaum,†† J. Sculli,‡‡ T. White,§§ and T. Yamanouchi
*Department of Physics and Astronomy, University of Rochester, Rochester, New York 14627, and
Department of Physics, Columbia University, New York, New York 10027, and Department of
Physics, Harvard University, Cambridge, Massachusetts 02138, and National Accelerator
Laboratory, Batavia, Illinois 60510*

(Received 28 May 1974)

We have measured deep inelastic muon-deuteron scattering in the range $0.4 < Q^2 < 3.4$ and $1.6 < \nu < 5.6$ GeV. We have extracted the neutron structure function and find that νW_2^n differs significantly from νW_2^p, as also found in *e-d* scattering. To compare *μ-d* and *e-d* scattering we form the ratio $r(Q^2) = (\nu W_2)_\mu^d/(\nu W_2)_e^d = N(1+Q^2/\Lambda^2)^{-1}$ and find $N = 0.925 \pm 0.038$ and $1/\Lambda^2 = -0.019 \pm 0.016$.

Previous and recent measurements of *muon-proton* elastic and inelastic scattering[1,2] have failed to reveal a muon-electron difference and have set a limit on a possible difference parameter of $\Lambda^2 > 26$ GeV^2. However experiments on muon-nuclear deep inelastic scattering at National Accelerator Laboratory have reported[3] a deviation from scaling[4] at four-momentum transfer $Q^2 \gtrsim 30$ (GeV/c)^2. It is therefore important to establish whether the neutron structure functions measured with muons are identical with the corresponding structure functions deduced from electron scattering.[5]

To examine this question we have measured muon-deuteron deep inelastic scattering at the Brookhaven National Laboratory alternating gradient synchrotron using a one-arm wide-aperture magnetic spectrometer.[1] Muons of mean energy 7.3 GeV were incident on a 48-in-long deuterium target, the flux being of the order of 10^6 muons/pulse, with a spill time of ~700 msec. The incident muons were tagged in space and momentum by means of scintillation hodoscopes and the outgoing muons were measured using spark chambers with magnetostrictive readout. Typically, momentum measurements were accurate to ±1.2% and angle measurements to ±1 mrad. The four-momentum transfer was in the range $0.4 < Q^2 < 3.5$ (GeV/c)^2 and the outgoing energy ranged between $2.1 < E' < E$ GeV. The systematic normalization error has been estimated to be ±7%. The mean azimuthal acceptance is 6% and only points with acceptance larger than 1% have been used in the analysis of the data. Events due to pion contamination in the beam or in the outgoing track are estimated to be less than 0.1% of all events.

The muon-deuteron scattering is compared directly with muon-proton scattering obtained in the same apparatus and under exactly identical conditions. Thus, most systematic errors do not enter in our result for the ratio of the neutron structure function to that of the proton.

To extract the muon-neutron cross section the same procedure as used in the analysis of *e-d* scattering[5] was adopted. Namely, (1) the scattering is predominantly incoherent; (2) the impulse approximation is valid[6]; (3) the scattering proceeds mainly through one-photon exchange; and (4) the final-state interaction can be neglected. Under these assumptions we write

$$\sigma_d = (\sigma_p + \sigma_n)(1 + C), \tag{1}$$

where the correction factor takes account of the fact that the neutron and proton are bound into a deuteron. The main contributions to C arise from the Glauber correction[7] and from the Fermi motion of the nucleons. We correct for Fermi motion by "smearing" the scattering amplitudes over the deuteron wave function in momentum space as discussed by West.[8]

Briefly,[9] we express the differential cross section in the form given by Drell and Walecka[10] and use $\sigma_L/\sigma_T = R = R_p = R_n = R_d = 0.18$ as obtained from *e-p* inelastic scattering.[11]

$$\frac{d^2\sigma}{dQ^2\,d\nu} = \frac{4\pi\alpha^2}{Q^4}\frac{E'}{E\nu}(\nu W_2)\cos^2\frac{\theta}{2} \times\left[1+\frac{2}{1+R}\left(1+\frac{\nu^2}{Q^2}\right)\tan^2\frac{\theta}{2}\right]. \tag{2}$$

From the measured structure function of the proton $(\nu W_2)^p$ we obtain the smeared $(\nu W_2)^{ps}$ by using the Reid soft-core model for the momentum distribution of the nucleon in deuterium.[12] The inte-

TABLE I. Results of μ-d deep inelastic scattering.

$\langle x\rangle$	νW_2^d	νW_2^p	S_p	S_n	$\nu W_2^n/\nu W_2^p$	$\nu W_2^p - \nu W_2^n$
0.072	0.541 ± 0.018	0.280 ± 0.014	0.980	0.975	0.93 ± 0.09	0.020 ± 0.027
0.122	0.591 ± 0.020	0.312 ± 0.014	0.983	0.973	0.89 ± 0.09	0.034 ± 0.028
0.173	0.578 ± 0.020	0.322 ± 0.015	0.994	0.981	0.79 ± 0.09	0.068 ± 0.029
0.221	0.525 ± 0.023	0.316 ± 0.017	1.001	0.991	0.66 ± 0.10	0.107 ± 0.034
0.270	0.539 ± 0.026	0.301 ± 0.019	1.006	0.997	0.79 ± 0.12	0.064 ± 0.037
0.318	0.447 ± 0.023	0.272 ± 0.017	1.012	1.006	0.64 ± 0.11	0.098 ± 0.033
0.375	0.447 ± 0.028	0.265 ± 0.020	1.025	1.013	0.71 ± 0.14	0.078 ± 0.039
0.430	0.344 ± 0.024	0.215 ± 0.019	1.011	1.003	0.59 ± 0.15	0.088 ± 0.036
0.472	0.292 ± 0.028	0.173 ± 0.020	1.006	0.991	0.69 ± 0.21	0.054 ± 0.038
0.540	0.231 ± 0.021	0.150 ± 0.020	1.023 1.017	1.013 1.012	0.53 ± 0.21	0.070 ± 0.035

gration is performed by *fitting* our data with an analytic expression for νW_2 as given by Rittenberg and Rubinstein.[13] It is then possible to define smearing corrections as a function of Q^2 and ν applicable to the kinematic region covered by our apparatus. These are defined through

$$S_p = (\nu W_2)^p/(\nu W_2)^{ps}, \quad S_n = (\nu W_2)^n/(\nu W_2)^{ns}.$$

In general, the correction for smearing is small and does not exceed 10% (for any Q^2, ν bin); the smearing correction averaged over an x bin is much smaller as can be seen in Table I.

The data were binned in intervals $\Delta Q^2 = 0.2$ $(\mathrm{GeV}/c)^2$ and $\Delta\nu = 0.4$ GeV. Only data with $Q^2 > 0.4$ $(\mathrm{GeV}/c)^2$ and $W^2 > 2.56$ GeV^2 were used in the analysis yielding 3642 μ-p and 4679 μ-d events. The cross sections were radiatively corrected, on the average ~ 5%,[14] and $(\nu W_2)^p$, $(\nu W_2)^d$ were extracted using Eq. (2). These structure functions are shown as a function of $\omega = 2m\nu/Q^2$ in Fig. 1.

From the measured values of $(\nu W_2)^p$ we calculated $(\nu W_2)^{ps}$ as discussed previously and, by definition,

$$(\nu W_2)^{ns} = (\nu W_2)^d - (\nu W_2)^{ps}. \tag{3}$$

Having thus obtained the measured values of $(\nu W_2)^{ns}$ we extract $(\nu W_2)^n$ by inverting the smearing calculation. The structure functions and smearing corrections were evaluated in the Q^2-ν plane, and then combined into bins of $x = 1/\omega = Q^2/2m\nu$ by using statistical averaging; the width of the bins is $\Delta x = 0.05$.

Our results are given in Table I and shown in Fig. 2. We note that our data are limited to the region $0 < x < 0.60$, the statistical accuracy being best at small x. In Fig. 2(a) we give $(\nu W_2)^n/(\nu W_2)^p = [(\nu W_2)^d S_p/(\nu W_2)^p - 1](S_n/S_p)$ and the shaded area indicates the corresponding value obtained from e-d scattering.[5] One observes that the neutron structure function is different from the corresponding proton structure function, the difference increasing with x. Furthermore, the μ-d data

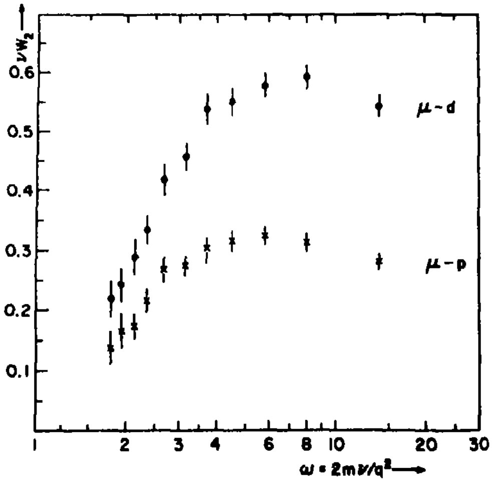

FIG. 1. The structure functions νW_2 for free protons and for deuterons as obtained from μ-p and μ-d scattering. They are presented as a function of the Bjorken scaling (Ref. 4) variable $\omega = 2m\nu/Q^2$.

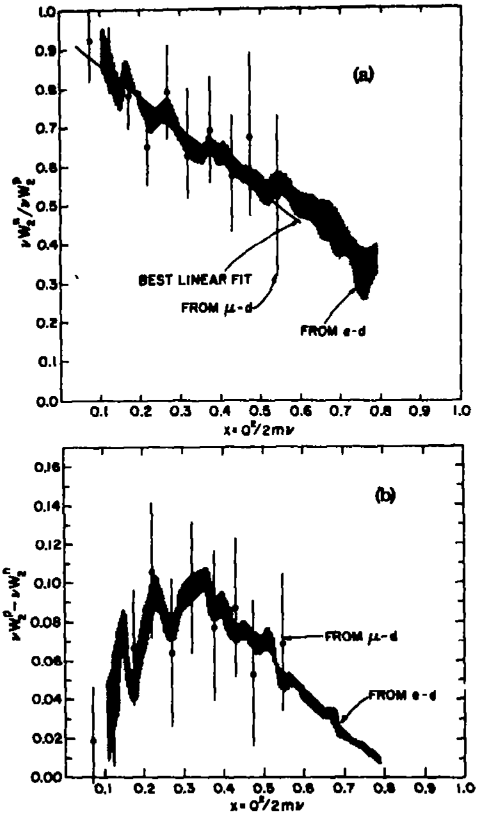

FIG. 2. (a) The ratio $\nu W_2^n/\nu W_2^p$ as a function of $x = 1/\omega$. (b) The difference $\nu W_2^p - \nu W_2^n$ as a function of $x = 1/\omega$. In both graphs the shaded area represents the same functions as measured in e-d and e-p scattering, within their 1 standard deviation error (Ref. 5).

are in agreement with the e-d data. A linear fit in x to our data yields

$$(\nu W_2)^n/(\nu W_2)^p = (0.952 \pm 0.075) - (0.807 \pm 0.289)x \qquad (4)$$

with a $\chi^2 = 2.63$ for nine degrees of freedom. The accuracy of the data is not sufficient to establish that Eq. (4) deviates from 1.0 at $x = 0$ or that it violates the quark-parton limit of 0.25 at $x = 1.0$.

Figure 2(b) shows the difference $(\nu W_2)^p - (\nu W_2)^n = (\nu W_2)^p(1 + S_n/S_p) - (\nu W_2)^d S_n \simeq 2(\nu W_2)^p - (\nu W_2)^d$ and again the shaded area shows the corresponding results from e-d scattering. The difference of the neutron and proton structure functions exhibits a broad peak at $x \simeq 0.35$. As has been discussed by other authors,[5] this behavior of $(\nu W_2)^p - (\nu W_2)^n$ *cannot* be explained quantitatively by current models of the nucleon.

Clearly, $(\nu W_2)^n$ as measured with incident muons is fully compatible with the value obtained using incident electrons. To obtain a quantitative measure of this compatibility we have compared directly the values of $(\nu W_2)_\mu{}^d$ obtained in this experiment with $(\nu W_2)_e{}^d$ *calculated* from the results of the e-d measurements. $(\nu W_2)_e{}^d$ was reconstructed for our kinematic region by using the Atwood fit[15] for $(\nu W_2)_e{}^p$, the ratio of $(\nu W_2)^n/(\nu W_2)^p$ given in Ref. 4 and after applying appropriate smearing corrections.

Next we formed the ratio of $(\nu W_2)_\mu{}^d/(\nu W_2)_e{}^d \equiv r(Q^2)$ as a function of Q^2. The ratios $r(Q^2)$ were fitted to the usual form for a possible breakdown of μ-e universality

$$\frac{(\nu W_2)_\mu{}^d}{(\nu W_2)_e{}^d} = r(Q^2) = N\left(\frac{1}{1 + Q^2/\Lambda^2}\right)^2.$$

Using only data in the interval $0.4 < Q^2 < 2.4$ (GeV/c)^2 we obtain[16]

$$N = 0.925 \pm 0.038,$$

$$1/\Lambda^2 = -0.019 \pm 0.015 \quad (\mu\text{-}d)/(e\text{-}d)$$

(with a $\chi^2 = 7.09$ for nine degrees of freedom) which can be compared to the results from μ-p deep inelastic scattering

$$N = 0.997 \pm 0.043,$$

$$1/\Lambda^2 = +0.006 \pm 0.016 \quad (\mu\text{-}p)/(e\text{-}p).$$

The values of N and $1/\Lambda^2$ are strongly correlated, and typically $\Delta N/\Delta(1/\Lambda^2) \simeq 2.5$. The results are fully compatible and indicate that μ-n and e-n deep inelastic scattering are identical for the region of $Q^2 < 3.5$ (GeV/c)^2.

In conclusion we note that μ-n deep inelastic scattering behaves in complete analogy to e-n scattering. It shows that both the proton and neutron deep inelastic structure functions scale but are different from one another. Furthermore, no indication of a μ-e difference appears in agreement with the results obtained in μ-p inelastic scattering.[1,17]

We are indebted to the alternating gradient synchrotron staff for making this experiment possible and to Mr. J. Kim, Mr. E. Ruggiero, Mr. J. Sanders, and Mr. J. Yee for assistance during the run.

---

*Work supported in part by the U. S. Atomic Energy Commission and by the National Science Foundation.

During the performance of this work the authors held guest appointments at Brookhaven National Laboratory.

[†] Present address: State University of New York at Stony Brook, N. Y. 11790.

[‡] Present address: University of California, Los Angeles, Calif. 90032.

[§] On leave from Centre des Researches Nucleaires, Strasbourg, France.

[‖] Present address: National Accelerator Laboratory, Batavia, Ill. 60510.

[¶] Present address: University of Illinois, Urbana, Ill. 61801.

[**] Present address: Brookhaven National Laboratory, Upton, N. Y. 11973.

[††] Present address: Rockefeller University, New York, N. Y. 10021.

[‡‡] Present address: New York University, New York, N. Y. 10003.

[§§] Present address: Nuclear Physics Laboratory, Oxford University, Oxford, England.

[1] A. Entenberg *et al.*, Phys. Rev. Lett. 32, 486 (1974).

[2] I. Kostoulas *et al.*, Phys. Rev. Lett. 32, 489 (1974).

[3] K. W. Chen, Bull. Amer. Phys. Soc. 19, 100 (1974), and also Phys. Today 27, No. 4, 17 (1974).

[4] J. D. Bjorken, Phys. Rev. 179, 1547 (1969).

[5] A. Bodek *et al.*, Phys. Rev. Lett. 30, 1087 (1973); J. S. Poucher *et al.*, Phys. Rev. Lett. 32, 118 (1974).

[6] For the applicability of the impulse approximation see, for instance, M. Goldberger and K. M. Watson, *Collision Theory* (Wiley, New York, 1964).

[7] The Glauber correction [see, for instance, R. J. Glauber, Phys. Rev. 100, 242 (1955)] is significant for high-energy scattering but for small momentum transfer; in our kinematic range this correction can be safely neglected.

[8] G. B. West, Phys. Lett. 37B, 509 (1971); W. B. Atwood and G. B. West, Phys. Rev. D 7, 773 (1973).

[9] For a more detailed discussion of the smearing correction procedure and tables of $(\nu W_2)^d$ see I. J. Kim *et al.*, University of Rochester Report No. 481/COO-3065-78 (unpublished).

[10] S. D. Drell and J. D. Walecka, Ann. Phys. (New York) 4, 75 (1964).

[11] See Ref. 5; also G. Miller *et al.*, Phys. Rev. D 5, 528 (1972).

[12] R. V. Reid, Jr., Ann. Phys. (New York) 50, 411 (1968). The results are quite insensitive to the choice of the model for the deuterium wave function.

[13] V. Rittenberg and H. R. Rubinstein, Phys. Lett. 35B, 50 (1971).

[14] L. W. Mo and Y. S. Tsai, Rev. Mod. Phys. 41, 205 (1969); A. Entenberg, Ph. D. thesis, University of Rochester, 1974 (unpublished).

[15] W. Atwood, private communication. This fit is almost equivalent to that of Ref. 13 and to that of M. Breidenbach and J. Kuti, Phys. Lett. 41B, 345 (1972).

[16] The value of N was floated around $N=1.0$ with a standard deviation of $\Delta N=0.1$ as also discussed in Ref. 2. Leaving N completely free yields $N=0.916\pm0.040$, $1/\Lambda^2=-0.024\pm0.017$.

[17] T. J. Braunstein *et al.*, Phys. Rev. D 6, 106 (1972).

Observation of the Decay $K_L^0\to\pi^+\pi^-\gamma$[†]

G. Donaldson, D. Hitlin, R. Kennelly, J. Kirkby, J. Liu, A. Rothenberg,[*] and S. Wojcicki[‡]
Physics Department and Stanford Linear Accelerator Center, Stanford University, Stanford, California 94305

(Received 27 June 1974)

We have measured the ratio $\Gamma(K_L^0\to\pi^+\pi^-\gamma)/\Gamma(K_L^0\to\text{all})$ to be $(6.2\pm2.1)\times10^{-5}$. The rate and Dalitz-plot distribution are consistent with *CP* conservation in this weak-electromagnetic decay.

We report herewith the first measurement of the branching ratio and Dalitz plot of the decay $K_L^0\to\pi^+\pi^-\gamma$.[1] This decay is of interest for several reasons:

(1) Both the decay rate and Dalitz-plot distribution are sensitive to possible *CP* nonconservation in the transition.[2]

(2) $\Gamma(K_L^0\to\pi^+\pi^-\gamma)$ was the only unmeasured decay rate which is important in determining the unitarity limit for $K_L^0\to\mu^+\mu^-$ decay.[3]

(3) A measurement of the branching ratio can discriminate between several theoretical models for weak radiative decays.[4]

The experiment was conducted at the Stanford Linear Accelerator Center (SLAC) K^0 spectrometer facility,[5] which was modified to detect γ rays and identify electrons by the addition of two 1.1-radiation-length (rl) lead sheets (Fig. 1). Showers at large (small) angles with respect to the beam direction were detected in the front (rear) chambers. The conversion points of the γ rays were determined from shower tracks observed in the wire chambers, with a front (rear) resolution of ±2.0 (0.35) cm; they were used with the decay vertex to compute γ-ray directions. Time-of-flight (TOF) measurements for charged tracks and showers were required to be consistent, and were then combined to yield a K_L^0 TOF for each

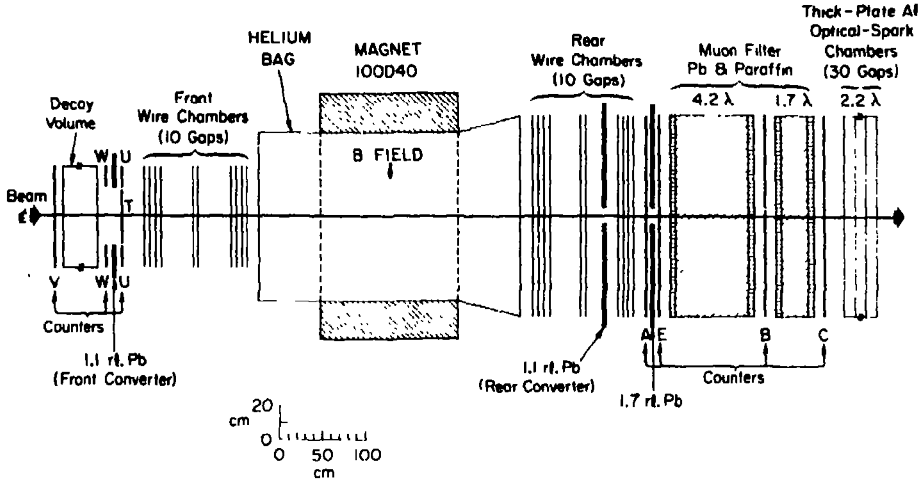
Thick - Plate Al Optical-Spark Chambers (30 Gaps)
HELIUM BAG
MAGNET 100D40
Rear Wire Chambers (10 Gaps)
Muon Filter Pb & Paraffin
4.2 λ
1.7 λ
2.2 λ
Decay Volume
Front Wire Chambers (10 Gaps)
W
U
B FIELD
Beam
T
V
W
U
Counters
1.1 rl. Pb (Front Converter)
A
E
B
C
1.1 rl. Pb (Rear Converter)
Counters
1.7 rl. Pb
20 cm
0
0
50
100
cm

FIG. 1. Elevation view of SLAC $K_L{}^0$ spectrometer. The trigger requirement was $\overline{V}\overline{W}U2T2A$ or $\overline{V}2T3A$. λ repreents absorption lengths. The E counters and Al chambers were not used in the $\pi\pi\gamma$ analysis.

vent with an uncertainty of ±0.25 nsec.

Since the experimental problems associated with finding and reconstructing the decay modes $_L{}^0 \to \pi^+\pi^-\pi^0$ and $K_L{}^0 \to \pi^+\pi^-\gamma$ are similar, our rimary measurement consists of the ratio $(\pi\pi\gamma)/\Gamma(3\pi)$. In this way most experimental unertainties tend to cancel, and the final result as only a weak dependence on the details of the Monte Carlo calculation. Nevertheless, a deailed comparison of 3π Monte Carlo and experimental data was used to confirm our understanding of kinematic and geometric distributions for harged tracks and γ's.

From those events which had two charged tracks with a vertex, plus one or more converted γ's, we isolated two sets of data by requiring the kinematic quantity $P_0{}'^2 < -0.014$ $(\mathrm{GeV}/c)^2$ for $\pi\pi\gamma$ andidates, and $-0.002 < P_0{}'^2 < 0.01$ $(\mathrm{GeV}/c)^2$ for π events.[6] Both sets of data were required to ass additional cuts, the most important being 1) neither charged track be identified as an elecron or a muon; (2) one γ (one or two γ's for 3π vents); and (3) $\cos\theta_{\gamma C} \leqslant 0.9996$, where $\theta_{\gamma C}$ is he angle in the laboratory between the directions f the observed γ ray and either charged track at he decay vertex.

After cuts, 1074 $\pi\pi\gamma$ candidates and 165 000 3π vents remain. The $P_0{}'^2$ cut for the $\pi\pi\gamma$ candiates removed essentially all the 3π background a maximum contamination of 5% remains). Most $e\nu\gamma$ events (internal and external bremsstrahung) were removed by the $\cos\theta_{\gamma C}$ cut. The remaining background in the $\pi\pi\gamma$ sample is primarily due to $K_{l3}{}^0$ events with a random γ in which the lepton was not identified.[7]

Two methods were used to extract the number of $\pi\pi\gamma$ events. The first consisted of calculating ψ, the angle between the measured and predicted γ-ray direction. The latter was calculated using $\vec{P}_{\pi^+}$, $\vec{P}_{\pi^-}$, and the $K_L{}^0$ direction. Specifically, the two solutions for the laboratory γ directions corresponding to forward and backward emission in the $K_L{}^0$ center of mass were calculated, and the solution which gave the better agreement with the measured direction was selected. Events were rejected if $|\mathrm{TOF}_{\mathrm{meas}} - \mathrm{TOF}_{\mathrm{fit}}| \geqslant 0.7$ nsec, where $\mathrm{TOF}_{\mathrm{fit}}$ corresponded to the chosen solution. After this procedure, 106 front-shower and 786 rear-shower events remained; their $\cos\psi$ values are shown in Figs. 2(a) and 2(b) for those events with $\cos\psi > 0.9968$.

The second method consisted of reconstructing the mass of the $\pi\pi\gamma$ system. The events were required to be consistent with transverse-momentum conservation by applying $\Delta\varphi$ cuts of 450 (150) mrads for the front (rear) showers, where $\Delta\varphi$ is the difference between the predicted and measured γ angles in the plane perpendicular to the $K_L{}^0$ direction. P_γ was obtained from the expression $P_\gamma = P_\perp{}^{+-}/\sin\theta_{\gamma K}$, where $P_\perp{}^{+-}$ is the transverse momentum of the charged pion pair, and $\theta_{\gamma K}$ is the laboratory angle between the γ and $K_L{}^0$. Events with $\sin\theta_{\gamma K} < 0.03$ were rejected, since they gave a poor determination of P_γ. For

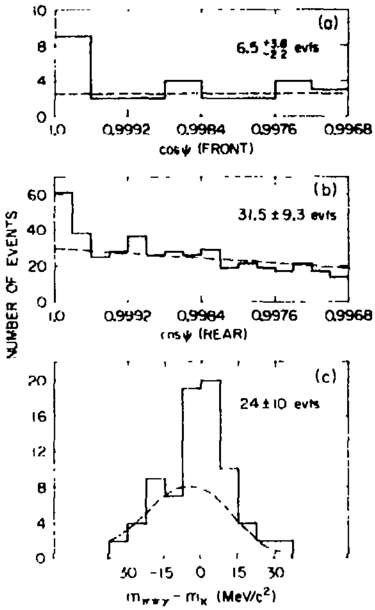

FIG. 2. (a) Cosψ, the angle between the measured and predicted γ-ray directions for $\pi\pi\gamma$ candidates with a front γ shower; (b) cosψ for $\pi\pi\gamma$ candidates with a rear γ shower; (c) $m_{\pi\pi\gamma} - m_{K^0}$. The backgrounds discussed in the text are indicated by dashed lines.

a typical γ ray of momentum 1 GeV/c, this gave $|\Delta P_\gamma / P_\gamma| \leq 5\%$. Events were rejected if $|\mathrm{TOF}_{\mathrm{meas}} - \mathrm{TOF}_{\mathrm{fit}}| \geq 0.7$ nsec, where $\mathrm{TOF}_{\mathrm{fit}}$ was obtained from $\vec{P}_{\pi^+}$, $\vec{P}_{\pi^-}$, and $\vec{P}_\gamma$. The mass of the $\pi\pi\gamma$ system is plotted in Fig. 2(c) for the 79 surviving events.

The Monte Carlo program generated raw data tapes of $\pi\pi\gamma$ and 3π events[8] with unit γ-conversion efficiency. The tapes were processed by the same reconstruction and analysis programs used for the data. The probability of converting and detecting a γ ray was calculated by comparing ratios of 3π events having one and two showers in the Monte Carlo program and experimental data.[9] Using those 3π events with both γ's converted, we have found no measurable energy dependence in the conversion efficiency for $P_\gamma > 150$ MeV/c. Below this momentum the conversion efficiency was poorly determined. A cut was therefore made removing $\pi\pi\gamma$ candidates with $P_\gamma < 150$ MeV/c to enable a distinction between CP odd- and even-matrix elements. This cut was not applied to the 3π data where P_γ was undetermined. This introduced a negligible bias in the normalization. We find the overall detection efficiency for front (rear) showers to be $(45.0 \pm 1.1)\%$ $[(46.1 \pm 0.9)\%]$. This is close to the measured maximum of 51%[10]; the difference is due in part to TOF cuts and in part to a small software inefficiency for locating showers in the data. A study of Monte Carlo generated $\pi\pi\gamma$ events indicates that 73% (82%) of front (rear) $\pi\pi\gamma$ events have $\cos\psi > 0.9996$ (0.9998), and that the signal in Fig. 2(c) peaks with a full width at half-maximum of 15.0 MeV/c^2 about the $K_L{}^0$ mass. The contributions of the previously described background sources were found to be smooth, and in no case were they peaked at m_K or at $\cos\psi = 1$. The backgrounds in Fig. 2 were obtained from unrenormalized fits to the same data after substituting a random photon from another event.

The three distributions of Fig. 2, when combined with the Monte Carlo efficiency calculations and the number of 3π events observed, provide *three correlated determinations of the* $K_L{}^0 \to \pi^+\pi^-\gamma$ branching ratio. After background subtraction, Figs. 2(a)–2(c) yield a branching ratio $\Gamma(\pi\pi\gamma)/\Gamma(3\pi) = (5.3^{+3.1}_{-1.8}) \times 10^{-4}$, $(5.8 \pm 1.6) \times 10^{-4}$, and $(3.8 \pm 1.6) \times 10^{-4}$, respectively. The weighted average of these results, combined with the value[11] $\Gamma(K_L{}^0 \to \pi^+\pi^-\pi^0)/\Gamma(K_L{}^0 \to \mathrm{all}) = 0.126$, yields $\Gamma(K_L{}^0 \to \pi^+\pi^-\gamma)/\Gamma(K_L{}^0 \to \mathrm{all}) = (6.2 \pm 2.1) \times 10^{-5}$.

Figure 3 shows a folded Dalitz plot of events with $|m_{\pi\pi\gamma} - m_K| < 7.5$ MeV/c^2. The signal-to-background ratio is roughly 3:2 and the background is evenly distributed in this plot. The observed $E_\gamma{}^*$ distribution was such that no cut was necessary to obtain the branching ratio. If the $K_L{}^0 \to \pi^+\pi^-\gamma$ decay proceeds via the CP-nonconserving mode $K_L{}^0 \to \pi^+\pi^-$ followed by inner bremsstrahlung, one would expect a branching ratio $\sim 1 \times 10^{-5}$ ($E_\gamma{}^* > 20$ MeV) and the bremsstrahlung γ-ray energy distribution in Fig. 3. In contrast we show also the γ spectrum produced by a CP-conserving, $L_{\pi\pi} = 1$ ($M1$) matrix element. Thus both our measured branching ratio and crude Dalitz-plot distribution of these events are consistent with a CP-conserving transition dominating this decay.

Our measured branching ratio is ~5 times lower than the Moshe-Singer and Rockmore-Wong calculations as quoted.[12] However, if one takes the Rockmore-Wong theoretical value for $\Gamma(K_L{}^0 \to \pi^+\pi^-\gamma)$ without renormalizing to $\Gamma(K_L{}^0 \to \gamma\gamma)$, one obtains agreement with our result. Thus, the zero-free-parameter fermion loop model appears to give excellent predictions for both the $K_L{}^0 \to \pi^+\pi^-\gamma$ and $K^+ \to \pi^+\pi^0\gamma$ decay modes.[13] The

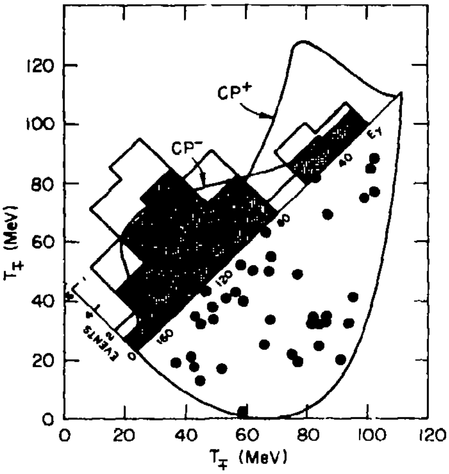

FIG. 3. Dalitz plot (folded about the γ energy axis) nd projected γ-ray energy spectrum. The shaded poron is the difference between the observed distribution nd the expected background. The smooth curves show e predicted spectra including experimental acceptance r $L_{\pi\pi}=1$, CP-conserving (−) and -nonconserving (+) atrix elements.

urrent-algebra treatment[14] relating the $\pi\pi\gamma$ to e $\gamma\gamma$ rate is also in agreement with our value. ur branching ratio implies that the contribution f the $\pi\pi\gamma$ intermediate state to the unitarity limit r $K_L^0 \to \mu^+\mu^-$ is less than 2%.

We thank R. Coombes, S. Hertzbach, R. Piccioni, D. Porat, M. Schwartz, and E. D. Uggla r their contributions to this experiment. We so acknowledge the excellent support of the ccelerator Operations, Experimental Facilities, nd Computer Operations Groups of SLAC.

---

†Work supported in part by the U. S. Atomic Energy ommission.

*Present address: Rockefeller University, New York, Y. 10021.

‡Alfred P. Sloan Foundation Fellow.

[1] The best upper limit on $\Gamma(K_L^0 \to \pi^+\pi^-\gamma)$ has been reported by R. Thatcher *et al.*, Phys. Rev. 174, 1674 (1968).

[2] D. Bader, Nucl. Phys. B47, 286 (1972); A. Dolgov and L. Ponomarev, Yad. Fiz. 4, 367 (1966) [Sov. J. Nucl. Phys. 4, 262 (1967)]; G. Costa and P. B. Kabir, Nuovo Cimento 51A, 564 (1967).

[3] W. Alles, M. K. Gaillard, and J. L. Pati, Phys. Rev. D 8, 229 (1973).

[4] M. Moshe and P. Singer, Phys. Rev. D 6, 1379 (1972); R. Rockmore and T. Wong, Phys. Rev. D 7, 3425 (1973).

[5] R. Piccioni *et al.*, Phys. Rev. D 9, 2939 (1974).

[6] The variable $P_0'^2$ is computed assuming a $K_{\pi3}^0$ decay, and is positive for $K_{\pi3}^0$ decays and negative for K_{l3}^0 decays in the absence of measurement errors.

$$P_0'^2 = [(m_K^2 - m_{+-}^2 - m_{\pi^0}^2)^2 - 4(m_{+-}^2 m_{\pi^0}^2 + m_K^2 P_\perp^2)]/4(P_\perp^2 + m_{+-}^2),$$

in which m_{+-} represents mass of the (π^+, π^-) system, and $P_\perp$ its transverse momentum relative to the K_L^0 axis.

[7] The 3π events with more than two γ's indicate a front (rear) accidental γ probability of 0.3% (2.6%).

[8] The Monte Carlo $\pi\pi\gamma$ events were generated according to an $L_{\pi\pi}=1$, CP odd-matrix element, while the 3π events were generated with the matrix element $|m|^2 \sim 1 - 5.2(Q/m_K)Y + 4.64(Q/m_K)^2 Y^2$, where $Y = 3T_{\pi^0}/Q - 1$ [R. Messner *et al.*, in Proceedings of the Sixteenth International Conference on High Energy Physics, The University of Chicago and National Accelerator Laboratory, 1972 (unpublished), paper No. 882].

[9] This was confirmed by comparing 3π events having zero, one, and two γ's in a data sample taken with a $\overline{V}$2T2A trigger (i.e., having no γ requirement).

[10] D. Sober *et al.*, Nucl. Instrum. Methods 109, 29 (1973).

[11] T. A. Lasinski *et al.*, Rev. Mod. Phys. 45, S16 (1973).

[12] The new measurement of $\Gamma(\eta \to \gamma\gamma)$ implies that the Moshe-Singer model no longer gives satisfactory agreement with the experimental value for $\Gamma(K_L \to \gamma\gamma)$, which is fundamental to their calculation of $\Gamma(K_L \to \pi\pi\gamma)$. See A. Broman *et al.*, Cornell University Report No. CLNS 261, 1974 (to be published).

[13] R. Rockmore, J. Smith, and T. Wong, Phys. Rev. D 8, 3224 (1973); R. Abrams *et al.*, Phys. Rev. Lett. 29, 1118 (1972).

[14] C. Lai and B. Young, Nuovo Cimento 52A, 83 (1967).

Charge and Particle Conservation in Black-Hole Decay

B. Carter
Observatoire de Paris-Meudon, 92190 Meudon, France

(Received 28 May 1974; revised manuscript received 20 June 1974)

The qualitative consequences of Hawking's prediction of thermal emission from black holes are considered. Whereas mass and angular momentum loss proceeds on cosmologically long time scales, on the other hand electric discharge will take place extremely rapidly. Hypothetical mechanisms for baryon and lepton conservation are discussed.

In classical (i.e., unquantized) general relativity theory any black hole in equilibrium has an angular velocity Ω and an electromagnetic potential Φ, which are necessarily *constant* over the horizon.[1-3] When an incoming wave corresponding to a boson state with energy E, axial angular momentum $n\hbar$, and electric charge e is scattered by the black hole, the absorption probability Γ will be *negative*[4,5] (amplification), whenever $E - n\hbar\Omega - \mu$ is negative, where the *chemical potential* μ is given by

$$\mu = e\Phi. \tag{1}$$

This "superradiance" effect led Zel'dovich[6] to predict *spontaneous emission*, which will occur in the corresponding (time and axial angle reversed) outgoing states. Hawking[7] has recently predicted that spontaneous emission will occur much more generally at just the rate required to maintain thermal equilibrium with angular velocity Ω and chemical potential μ at a temperature Θ given by

$$\Theta = (\hbar/2\pi k)\kappa, \tag{2}$$

where κ, which is also necessarily[3,8] constant over the surface of the black hole, determines the asymptotic exponential relation

$$\tau_0 - \tau \propto \exp\{-\kappa t_{\mathrm{ret}}\} \tag{3}$$

between the proper time τ along the world line of a particle crossing the horizon at τ_0 and the ignorable outgoing null-time coordinate that would most conveniently be used by a distant observer. (This decay constant also represents the limiting "gravitational acceleration" of a co-rotating particle, meaning a certain "red-shifted" acceleration, *not* the locally measured acceleration which would tend to infinity on the horizon; the inverse κ^{-1} represents the characteristic time scale for exponential decay of normal modes, and hence also for formation of the black hole.)

By the "first law" of black hole mechanics,[3,8] the prediction (2) also implies that a black hole should be thought of as having an entropy S given by

$$S = (kc^3/\hbar G)\sigma_0 \tag{4}$$

(in striking confirmation of an order-of-magnitude prediction by Bekenstein[9]) where σ_0 is the "irreducible cross section" of the hole which is given in terms of the surface area A of the horizon by

$$\sigma_0 = \pi r_0^2 = \tfrac{1}{4}A, \tag{5}$$

the irreducible Schwarzschild radius r_0 being related to the irreducible mass M_0, as introduced by Christodoulou,[10] by

$$r_0 = 2GM_0/c^2 \sim GM/c^2, \tag{6}$$

where M is the mass of the black hole.

By introducing the dimensionless form parameter

$$\epsilon = 1 - 2\Omega J/Mc^2 - Q\Phi/Mc^2, \tag{7}$$

where J and Q are, respectively, the angular momentum and electric charge, and by using the generalized Smarr formula,[11,8,3] one obtains the estimate

$$\Theta = \frac{c^2M}{2S}\epsilon \sim \frac{c^3\hbar}{kG}\frac{\epsilon}{M}. \tag{8}$$

Using the much more obvious order-of-magnitude estimates

$$\Omega \sim J/Mr_0^2 \sim c^4J/G^2M^2, \tag{9}$$

$$\Phi \sim Q/r_0 \sim c^2Q/GM, \tag{10}$$

one is led (by considering the limits to accretion that would arise, respectively, from centrifugal and electrostatic repulsion) to guess that Ω and Φ should be limited by conditions of the form

$$(cJ/GM^2)^2 \sim (GM\Omega/c^3)^2 \lesssim 1, \tag{11}$$

$$Q^2/GM^2 \sim G\Phi^2/c^4 \sim G\mu^2/c^4e^2 \lesssim 1. \tag{12}$$

It is clear from (7) that the same order-of-magnitude limits are necessary for ϵ to remain positive, and that for fixed M the temperature Θ will tend to zero as these limits are approached.

[The "no-bifurcation theorems"[12,3,13] to the effect that continuous secular changes in an isolated black hole equilibrium state can only depend on the changes in M, J, and Q, in conjunction with the conclusion[14-18] that the only possible nonrotating limits are spherical, make it virtually certain that the only isolated stable equilibrium states are described by the Kerr solution[19] and its charged generalization,[20] for which one has the explicit precise formula $\epsilon = (1 - c^2J^2/G^2M^4 - Q^2/GM^2)^{1/2}$. However in order to obtain generalizable conclusions we wish to avoid relying on special properties of the Kerr solutions.]

Although the special Kerr separability properties of the scalar[21] and higher-spin[22] wave equations simplify Hawking's discussion,[7] they are not essential for the outcome which can be expressed as a prediction that there will be particle emission within the energy range dE in any outgoing state with well-defined axial quantum number n and (asymptotic) total quantum number j at a rate given by

$$-d\dot{N} = \frac{\Gamma dE}{2\pi\hbar}\left\{\exp\left(\frac{E - n\hbar\Omega - \mu}{k\Theta}\right) \pm 1\right\}^{-1}, \tag{13}$$

where the sign is positive for fermions and negative for bosons. By the usual principles of scattering theory we can expect for uncharged particles that Γ will be very small compared with unity unless

$$j\hbar \lesssim pr_0, \tag{14}$$

where p is defined in terms of the particle rest mass m by $E^2 = p^2c^2 + m^2c^4$. If we can ignore the electric charge on the black hole (which, as shown below, will always be justifiable in practice except perhaps for supermassive black holes), we are led to predict mass and angular momentum loss rates

$$-\dot{M} \sim \hbar c^4/G^2M^2, \quad -\dot{J} \sim \hbar\Omega, \tag{15}$$

provided that r_0 is not less than the proton Compton wavelength; i.e., provided that

$$M \gtrsim \hbar c/Gm_p, \tag{16}$$

so that only a limited number of kinds of particles [those with zero rest mass, and also when the limit (16) is approached, electrons with mass m_e] can contribute. The present theory is incapable of dealing reliably with the situation when M drops below the limit (16) since an unknown number of meson and baryon states come into operation, possibly[23] so many that the mass loss would become explosive, but above this limit (about 10^8 tons) the characteristic mass-decay time scale τ_M will be given by

$$\frac{1}{\tau_M} = -\frac{\dot{M}}{M} \sim -\frac{\dot{J}}{J} \sim \frac{\hbar c^4}{G^2M^3}, \tag{17}$$

so that it will always be at least as long as the present age of the universe which is given[24,25] by the characteristic stellar evolution lifetime

$$\tau \sim \hbar^2/cGm_p^3. \tag{18}$$

It is to be noted that for given M, the loss rate $-\dot{M}$ is roughly independent of Θ. If ϵ is very small the dominant superradiant contribution will ensure that it increases so that the black hole will tend asymptotically towards a state of conformal contraction with a fixed limiting form parameter $\epsilon_c > 0$.

Let us now consider what will happen when there is a nonzero electric charge quantum number $N_e = Q/e$. Wherever $E - mc^2 \lesssim \mu$ the centrifugal barrier-penetration condition (14) must be supplemented by the electrostatic barrier-tunnelling condition $Ep \lesssim (eQ/\hbar c)m^2c^3$ so that, as Gibbons[26] has pointed out, superradiant discharge modes, i.e., those with $E \lesssim \mu$, can be effective only if

$$\frac{\hbar}{c^3}\mu \gtrsim m_e^2 r_0, \tag{19}$$

since there is no charged particle lighter than the electron. Hence, using (13) to estimate the discharge rate $-\dot{N}_e$, we find that there are three essentially distinct regimes: (a) If

$$|\mu| \lesssim (Gc/\hbar)m_e^2 M, \quad 1 \lesssim GMm_e/\hbar c, \tag{20}$$

there will be essentially no discharge at all; (b) in the *thermal discharge* regime, with

$$GM\mu/\hbar c^3 \lesssim 1, \quad GMm_e/\hbar c \lesssim 1, \tag{21}$$

we shall have

$$-\dot{N}_e \sim \hbar\mu; \tag{22}$$

(c) and finally, in the *superradiant discharge regime*, i.e., when

$$(Gc/\hbar)m_e^2 M \gtrsim |\mu|, \quad 1 \lesssim GM\mu/\hbar c^3, \tag{23}$$

we shall have

$$-\dot{N}_e \sim (G^2/\hbar^3c^6)M^3\mu^3. \tag{24}$$

It follows (since $Gm_e^2 \sim 10^{-42} \ll e^2/\hbar c \sim 1/137 < 1$) that unless conditions (20) are satisfied, the characteristic discharge time $\tau_Q = -N_e/\dot{N}_e$ will always be extremely short in comparison with τ_M; in fact τ_Q will actually be shorter than the characteristic time $\kappa^{-1} \lesssim r_0/c$ for formation of the black hole—which means that the charge could never have been there at all—unless M is within a factor $(\hbar c)^{1/2} m_p/em_e$ (which works out to be $\sim 10^2$, using $\hbar c/e^2 \sim 137$, $m_p/m_e \sim 1800$) of the mass limit (16). Hence for all practical purposes we may take it that

$$\frac{Q^2}{GM^2} \lesssim \frac{Gm_e^2}{e^2}\left(\frac{Gm_e M}{\hbar c}\right)^2, \tag{25}$$

which is small compared with the limit (12) unless M is greater than the typical stellar mass $M \sim (\hbar c/G)^{3/2} M_p^{-2}$ by a factor $(m_p/m_e)^2(e^2/\hbar c)^{1/2}$ $\sim 10^5$. For black holes below this mass, the electromagnetic field will never have a perceptible effect on the space-time geometry. [For black holes above this mass, it is conceivable that the charge could be great enough to invalidate (15); it would be possible for the factor ϵ to tend to zero, bringing the decay asymptotically to a halt.]

In any case, whenever a black hole decays below the mass limit $M \sim \hbar c/Gm_e$, and hence before reaching the critical mass (16), it will neutralize itself *completely*.

Even if it does not explode immediately (i.e., even if there is not an absolute upper limit,[23] $k\Theta \lesssim m_p c^2$, to physically attainable temperatures), a black hole which falls below the critical mass (16) will certainly dissipate all its remaining mass on a time scale shorter than the present age (18) of the universe (the last stage being inevitably explosive as Hawking has pointed out[7]). According to previous ideas, the fact that baryons, leptons, etc. could be hidden in a black hole was interpreted as "transcending" the corresponding conservation laws, but if the black holes themselves can disappear without trace it must be recognized frankly that for practical purposes these conservation laws are violated. In order to avoid this conclusion Wheeler[27] has suggested, though without discussing the possible mechanism, that the chemical potential μ in the emission formula (13) should contain additional contributions due to baryons, etc., in addition to the electric contribution (1). It is difficult[28,29] to see how this could come about except by the action of repulsive classical force fields extending outside the horizon and proportional to the numbers of particles inside (such fields being generated by zero-rest-mass, odd-integer-spin bosons).

Let us consider the case of baryons, for which, as Dicke has pointed out,[30] the corresponding coupling constant $e_B^2/\hbar c$ (the analog of the electric "fine structure" coupling constant) must be extremely small, $e_B^2/Gm_p^2 \lesssim 10^{-7}$, in order to have escaped detection by the Eotvos experiment. Assuming that the preceding order-of-magnitude formulas apply also to baryon discharge, with e_B, m_p, and baryon number N_B in place of e, m_e, and N_e, we see there is a striking difference from the electric case, for which the analogous ratio is $e^2/Gm_e^2 \gg 1$. This means that superradiant discharge can never become effective and that a decaying black hole will retain an effectively *constant* baryon number N_B, and so will charge right up to the limit corresponding to (12) at which stage Θ would tend to zero so that further decay would be prevented. The black hole would settle down at a *finite* ground state with *residual mass* M_* given by

$$M_* \sim G^{-1/2} e_B N_B. \tag{26}$$

It is conceivable that e_B could be sufficiently large that an "ordinary" black hole[31,32] formed by the collapse of a star with $N_B \sim (\hbar c/G)^{3/2} m_p^{-3}$ could leave a residual black hole above the limit (16).

The Dicke-Eotvos experiment also places an upper limit on any hypothetical electron-leptonic charge (though not on a muon-leptonic charge). However since there are no known lower limits on neutrino masses, the corresponding charge/mass ratios might be *either* large (leading to relatively rapid leptonic discharge) *or* small (leading to leptonic contributions to the residual mass).

I would like to thank Gary Gibbons, Stephen Hawking, Jean Schneider, and John A. Wheeler for helpful discussions.

---

[1] B. Carter, J. Math. Phys. (N. Y.) 10, 70 (1969).

[2] B. Carter, Nature (London) 238, 71 (1972).

[3] B. Carter, in *Black Hole Equilibrium States in Black Holes*, edited by C. DeWitt and J. DeWitt (Gordon and Breach, New York, 1973).

[4] C. W. Misner, Bull, Amer. Phys. Soc. 17, 472 (1972).

[5] W. M. Press and S. A. Tevkolsky, Nature (London) 238, 211 (1972); J. D. Beckenstein, Phys. Rev. D 7, 949 (1973).

[6] Ya. B. Zel'dovich, Pis'ma Zh. Eksp. Teor. Fiz. 14, 270 (1971) [*JETP Lett.* 14, *180 (1971)*], and Zh. Eksp. Teor. Fiz. 62, 2076 (1972) [Sov. Phys. JETP 35, 1085 (1972)]. See also A. A. Storobinskii, Zh. Eksp. Teor.

Fiz. 64, 48 (1973) [Sov. Phys. JETP 37, 28 (1973)].

[7] S. W. Hawking, Nature (London) 248, 30 (1974), and "Particle Creation by Black Holes" (to be published).

[8] J. M. Bardeen, B. Carter, and S. W. Hawking, Commun. Math. Phys. 31, 161 (1973).

[9] J. D. Beckenstein, Phys. Rev. D 7, 2333 (1973).

[10] D. Christodoulou, Phys. Rev. Lett. 25, 1596 (1970).

[11] L. Smarr, Phys. Rev. Lett. 30, 71 (1973).

[12] B. Carter, Phys. Rev. Lett. 26, 331 (1971).

[13] D. C. Robinson, "Classification of Black Holes with Electromagnetic Fields" (to be published).

[14] W. Israel, Phys. Rev. 164, 1776 (1968).

[15] W. Israel, Commun. Math. Phys. 8, 245 (1968).

[16] S. W. Hawking, Commun. Math. Phys. 25, 152 (1972).

[17] S. W. Hawking and G. F. R. Ellis, *The Large Scale Structure of Space Time* (Cambridge Univ. Press, Cambridge, England, 1973).

[18] H. Muller Zum Hagen, D. C. Robinson, and H. J. Seifert, "Black Holes in Static Vacuum Spacetimes" (to be published).

[19] R. Kerr, Phys. Rev. Lett. 11, 237 (1963).

[20] E. T. Newman *et al.*, J. Math. Phys. (N. Y.) 6, 918 (1965).

[21] B. Carter, Commun. Math. Phys. 10, 280 (1968).

[22] S. A. Teukolsky, Astrophys. J. 185, 635 (1973).

[23] R. Hagedorn, Astron. Astrophys. 5, 184 (1970).

[24] R. H. Dicke, Nature (London) 192, 440 (1961).

[25] B. Carter, in "Confrontation of Cosmological Theories with Observation," edited by M. Longair (North-Holland, Amsterdam, to be published), p. 272.

[26] G. W. Gibbons, "Vacuum Polarization and the Spontaneous Loss of Charge by Black Holes" (to be published).

[27] J. A. Wheeler, "Black Hole Chemical Potentials" (to be published).

[28] J. D. Beckenstein, Phys. Rev. D 5, 1239 (1972).

[29] C. Teitelboim, Phys. Rev. D 5, 2941 (1972).

[30] R. H. Dicke, Phys. Rev. 126, 1580 (1962).

[31] B. K. Harrison, R. S. Thorne, M. Wakano, and J. A. Wheeler, *Gravitation Theory and Gravitational Collapse* (Chicago Univ. Press, Chicago, Ill., 1965).

[32] B. Carter, J. Phys. (Paris), Colloq. 34, C7-39 (1973).

Extraction of $R=\sigma_L/\sigma_T$ from Deep Inelastic *e-p* and *e-d* Cross Sections*

E. M. Riordan, A. Bodek, M. Breidenbach,† D. L. Dubin, J. E. Elias,‡ J. I. Friedman,
H. W. Kendall, J. S. Poucher, and M. R. Sogard§
Physics Department and Laboratory for Nuclear Science, Massachusetts Institute of Technology,
Cambridge, Massachusetts 02139

and

D. H. Coward
Stanford Linear Accelerator Center, Stanford University, Stanford, California 94305

(Received 16 May 1974)

The quantity $R=\sigma_L/\sigma_T$ is extracted for the proton, deuteron, and neutron from deep inelastic *e-p* and *e-d* scattering cross sections measured in recent experiments at Stanford Linear Accelerator Center. For $\omega \leq 5$ the kinematic behavior of νR_p is consistent with scaling, indicative of spin-$\frac{1}{2}$ constituents in a parton model of the proton. We also find that within large statistical errors, R_d and R_n are consistent with being equal to R_p.

We have extracted longitudinal and transverse virtual photoabsorption cross sections σ_L and σ_T from deep inelastic electron-proton (e-p) and electron-deuteron (e-d) scattering cross sections that were measured in two experiments[1,2] at the Stanford Linear Accelerator Center (SLAC). Values of $R=\sigma_L/\sigma_T$ for the proton (R_p) are presented and compared with current theoretical predictions. In an earlier experiment,[3] R_p was found to be consistent with the constant value 0.18 ± 0.10. This small value of R_p suggested spin-$\frac{1}{2}$ constituents[4] of the proton, but full verification of this hypothesis requires a detailed knowledge of its kinematic variation.[5] In the present work R_p is determined over a larger kinematic range and its accuracy is sufficiently improved to allow examination of its kinematic variation. The first determinations of R for the deuteron and neutron, R_d and R_n, are also reported.

The inelastic scattering of an electron of incident energy E to final energy E' through an angle θ is described in the first Born approximation by the exchange of a virtual photon of energy $\nu = E - E'$ and invariant mass squared $q^2 = -4EE'\sin^2(\theta/2) = -Q^2$. The differential cross section is related to σ_L and σ_T as follows[6]:

$$\frac{d^2\sigma}{d\Omega\, dE'}(E, E', \theta) = \Gamma[\sigma_T(\nu, Q^2) + \epsilon\sigma_L(\nu, Q^2)],$$

where Γ is the flux of transverse virtual photons and $\epsilon = [1+2(1+\nu^2/Q^2)\tan^2(\theta/2)]^{-1}$ is the polarization of the virtual photons. Also, $W=(M^2+2M\nu-Q^2)^{1/2}$ is the mass of the unobserved final hadronic state, where M is the proton mass. We use the scaling variable ω defined by $\omega=1/x=2M\nu/Q^2$. The quantity R is related to the familiar structure functions W_1 and W_2 by

$$R=\sigma_L/\sigma_T=(W_2/W_1)(1+\nu^2/Q^2)-1.$$

Extraction of R and σ_T at fixed (ν, Q^2) requires differential cross sections for at least two values of θ (or ϵ) and is equivalent to separation of W_1 and W_2.

The inelastic e-p and e-d cross sections were measured with two different single-arm focusing spectrometers in separate experiments to obtain data over a large range of ϵ. The bulk of the cross-section data used in the extraction of R had been measured[1,7,8] at 18°, 26°, and 34° with the SLAC 8-GeV spectrometer. Incident energies E ranged from 4.5 to 18 GeV; at each incident energy, scattered energies E' ranged from that corresponding to electroproduction threshold down to 1.5 GeV. The measured cross sections consequently spanned triangular regions of (ν, Q^2) space at each angle and permitted interpolations for radiative corrections and for extractions of R. Additional cross sections used in the analysis had been measured in an earlier experiment[2,9,10] at 6° and 10° with the SLAC 20-GeV spectrometer and a different set of target cells. In that experiment E ranged from 4.5 to 19.5 GeV and E' ranged as low as 2.5 GeV. The analyses[7-9] of the raw experimental data from the two experiments were similar and the radiative-correction procedures[7,9] were identical.

A fit to the elastic e-p cross sections measured at the small angles was on the average 2% lower than the elastic e-p cross sections measured at 18°, 26°, and 34°. Detailed studies[7] of effects that could alter the elastic and inelastic cross sections differently showed that this 2% difference was also applicable to the inelastic e-p cross sections. Therefore, the 6° and 10° inelastic e-p cross sections[10] were multiplied by the relative normalization factor 1.02 ± 0.02 before the extraction of R_p. An accurate determination of the normalization factor for the inelastic e-d cross sections was not feasible due to the quasi-elastic e-d cross-section uncertainties arising both from the inelastic background subtractions and from corrections due to deuteron binding effects. Therefore, the 6° and 10° e-d data were not used in the extraction of R_d and R_n.

Values of

$$\Sigma(\nu, Q^2, \theta)=\frac{1}{\Gamma}\frac{d^2\sigma}{d\Omega dE'}(\nu, Q^2, \theta)$$

were obtained by interpolation of the e-p cross sections measured at each angle to selected kinematic points (ν, Q^2) that fell within the overlaps of two or more of the five triangles measured in the two experiments. An array of 86 kinematic points with $W>2$ GeV and $Q^2>1$ GeV^2, chosen to reflect the number and distribution of measured cross sections, was used in a systematic study of the behavior of R_p at fixed ω. For each (ν, Q^2) point, R_p was determined from the slope of a linear least-square fit to values of Σ versus ϵ. Values of R_p are given in Table I along with their statistical errors and estimates of the systematic uncertainty ΔR_p. Because of the interpolations, the value of R_p and its error at any point are correlated with those of neighboring kinematic points. One contribution to ΔR_p at each (ν, Q^2) point arises from uncertainties in the experimental parameters (e.g., E' dependence of the spectrometer acceptance, and fluctuations in the incident beam direction) leading to systematic changes in Σ as a function of θ. This uncertainty ranges from 0.03 to 0.19 in R_p and generally is less than 0.08. Where cross sections from both experiments are used in the extraction of R_p, the 2% uncertainty in the relative normalization factor contributes an uncertainty of typically 0.07 in R_p. A third uncertainty arises from approximations in the radiative corrections and is estimated to range from 0.01 to 0.18 in R_p, with the largest uncertainty occurring at large ω or large ν. For $\omega \leq 5$, however, this uncertainty is believed to be no more than 0.06 in R_p. The systematic uncertainty quoted in Table I is the quadratic sum of the above three uncertainties.

Within parton models, the behavior of νR_p as a function of Q^2 for fixed $\omega = 1/x$ reflects the spin quantum numbers of those charged partons carrying a fraction x of the proton's momentum.[4,5] If the charged partons have spin-$\frac{1}{2}$, light-cone algebras predict that νR_p should scale[5,11]; i.e., $\nu R_p = r(\omega)$. If there are some charged spin-0 partons present,[12] then $\nu R_p = a(\omega)+b(\omega)\nu$; here, $b(\omega) = W_2^{(0)}/W_2^{(1/2)}$, where $W_2^{(0)}$ and $W_2^{(1/2)}$ are the contributions to W_2 from spin-0 and spin-$\frac{1}{2}$ partons in the limit of large Q^2. Figure 1 shows νR_p plotted versus Q^2 for $\omega = 2$, 5, and 10; the solid lines represent least-square fits of the form $\nu R_p = a + b\nu = a + (\omega/2M)bQ^2$. Best fit values of b and its statistical error are given in Table II for the ten

TABLE I. Values of R_p listed with statistical errors and estimated systematic uncertainties ΔR_p.

ω	ν (GeV)	Q^2 $(\mathrm{GeV})^2$	R_p	ΔR_p
1.5	5.0	6.25	0.11 ± 0.17	0.08
1.5	6.0	7.51	0.05 ± 0.08	0.08
1.5	7.0	8.76	0.64 ± 0.26	0.13
1.5	8.0	10.01	0.76 ± 0.35	0.17
1.5	9.0	11.26	0.12 ± 0.18	0.09
1.5	10.0	12.51	−0.10 ± 0.15	0.08
1.5	12.0	15.01	0.26 ± 0.58	0.18
1.75	4.0	4.29	0.04 ± 0.09	0.07
1.75	5.0	5.36	0.22 ± 0.08	0.08
1.75	6.0	6.43	0.14 ± 0.07	0.08
1.75	7.0	7.51	0.32 ± 0.16	0.08
1.75	8.0	8.58	0.01 ± 0.14	0.06
1.75	9.0	9.65	−0.06 ± 0.15	0.06
1.75	10.0	10.72	−0.03 ± 0.13	0.06
1.75	12.0	12.87	0.09 ± 0.45	0.15
2.0	4.0	3.75	0.07 ± 0.06	0.07
2.0	5.0	4.69	0.12 ± 0.06	0.08
2.0	6.0	5.63	0.18 ± 0.08	0.07
2.0	7.0	6.57	0.08 ± 0.07	0.06
2.0	8.0	7.51	−0.08 ± 0.10	0.06
2.0	9.0	8.44	−0.08 ± 0.13	0.06
2.0	10.0	9.38	0.02 ± 0.16	0.06
2.0	11.0	10.32	0.20 ± 0.15	0.07
2.0	12.0	11.26	0.47 ± 0.60	0.20
2.5	3.0	2.25	0.20 ± 0.06	0.13
2.5	4.0	3.00	0.16 ± 0.05	0.08
2.5	5.0	3.75	0.17 ± 0.06	0.09
2.5	6.0	4.50	0.14 ± 0.06	0.07
2.5	7.0	5.25	0.08 ± 0.08	0.08
2.5	8.0	6.00	0.03 ± 0.06	0.08
2.5	9.0	6.75	0.22 ± 0.14	0.07
2.5	10.0	7.51	0.26 ± 0.18	0.07
2.5	11.0	8.26	0.25 ± 0.27	0.12
2.5	12.0	9.01	0.01 ± 0.20	0.09
3.0	3.0	1.88	0.05 ± 0.06	0.10
3.0	4.0	2.50	0.18 ± 0.06	0.08
3.0	5.0	3.13	0.14 ± 0.05	0.07
3.0	6.0	3.75	0.01 ± 0.08	0.08
3.0	7.0	4.38	0.13 ± 0.08	0.09
3.0	8.0	5.00	0.08 ± 0.09	0.08
3.0	9.0	5.63	0.08 ± 0.07	0.08
3.0	10.0	6.25	0.63 ± 0.34	0.16
3.0	11.0	6.88	0.40 ± 0.34	0.13
3.0	12.0	7.51	0.22 ± 0.26	0.12
4.0	3.0	1.41	0.23 ± 0.07	0.12
4.0	4.0	1.88	0.31 ± 0.10	0.13
4.0	5.0	2.35	0.26 ± 0.08	0.10
4.0	6.0	2.82	0.22 ± 0.08	0.10
4.0	7.0	3.28	0.16 ± 0.08	0.10
4.0	8.0	3.75	0.10 ± 0.10	0.09
4.0	9.0	4.22	0.06 ± 0.09	0.08
4.0	10.0	4.69	0.01 ± 0.08	0.08
4.0	11.0	5.16	0.57 ± 0.48	0.16
5.0	3.0	1.13	0.40 ± 0.12	0.20
5.0	4.0	1.50	0.48 ± 0.12	0.15
5.0	5.0	1.88	0.20 ± 0.07	0.09
5.0	6.0	2.25	0.15 ± 0.07	0.09
5.0	7.0	2.63	0.16 ± 0.07	0.08
5.0	8.0	3.00	0.18 ± 0.09	0.11
5.0	9.0	3.38	0.30 ± 0.13	0.14
5.0	10.0	3.75	0.18 ± 0.12	0.12
5.0	11.0	4.13	0.12 ± 0.12	0.11
6.0	4.0	1.25	0.52 ± 0.15	0.18
6.0	5.0	1.56	0.14 ± 0.09	0.10
6.0	6.0	1.88	0.22 ± 0.09	0.10
6.0	7.0	2.19	0.33 ± 0.09	0.11
6.0	8.0	2.50	0.41 ± 0.10	0.12
6.0	9.0	2.82	0.41 ± 0.14	0.15
6.0	10.0	3.13	0.24 ± 0.13	0.13
6.0	11.0	3.44	0.12 ± 0.13	0.12
6.0	12.0	3.75	0.09 ± 0.16	0.11
7.5	5.0	1.25	0.15 ± 0.10	0.09
7.5	6.0	1.50	0.17 ± 0.09	0.09
7.5	7.0	1.75	0.35 ± 0.10	0.11
7.5	8.0	2.00	0.59 ± 0.15	0.13
7.5	9.0	2.25	0.61 ± 0.16	0.13
7.5	10.0	2.50	0.28 ± 0.18	0.14
7.5	11.0	2.75	0.19 ± 0.17	0.13
7.5	12.0	3.00	0.21 ± 0.23	0.14
10.0	6.0	1.13	0.16 ± 0.11	0.08
10.0	7.0	1.31	0.30 ± 0.14	0.10
10.0	8.0	1.50	0.35 ± 0.14	0.10
10.0	9.0	1.69	0.32 ± 0.15	0.10
10.0	10.0	1.88	0.35 ± 0.16	0.10
10.0	11.0	2.06	0.58 ± 0.31	0.20
10.0	12.0	2.25	1.03 ± 0.57	0.25

values of ω studied. The three effects leading to the aforementioned uncertainties in R_p also give uncertainties in b; the systematic uncertainty Δb is the quadratic sum of these three uncertainties. For $\omega \leq 5$ the slope b is small and consistent with zero, indicative of predominantly spin-$\frac{1}{2}$ partons. Over this range of ω, we get a 2 standard deviation upper limit of 20% for the contribution of spin-0 partons to W_2. For $\omega > 5$, b may be different from zero, but the data for these ω lie in a small range of low Q^2 and a nonzero slope might reflect only the low-Q^2 threshold behavior of R_p.

We have made a number of least-square fits to the 86 values of R_p listed in Table I. A constant value of R_p provides a better fit to the data than $R_p = Q^2/\nu^2$ or the simple vector-dominance[13] forms $R_p = cQ^2$ or $R_p = cQ^2(1-x)^2$. We obtain R_p

TABLE II. Best fit values of the coefficient b and their statistical errors from least-square fits of the form $\nu R_p = a + b\nu$. Also given are the estimated systematic uncertainties Δb and average values of $\delta = R_d - R_p$ for the range $1.5 \leq \omega \leq 5.0$ where these data are available. Only statistical errors in δ are given.

ω	b	Δb	δ
1.5	0.11 ± 0.28	0.14	−0.09 ± 0.09
1.75	0.02 ± 0.15	0.08	0.08 ± 0.07
2.0	0.04 ± 0.10	0.06	0.13 ± 0.06
2.5	0.03 ± 0.07	0.06	0.04 ± 0.06
3.0	0.12 ± 0.07	0.07	−0.01 ± 0.08
4.0	0.02 ± 0.07	0.06	−0.25 ± 0.12
5.0	0.02 ± 0.09	0.08	−0.20 ± 0.21
6.0	0.20 ± 0.13	0.12	...
7.5	0.66 ± 0.19	0.17	...
10.0	0.80 ± 0.31	0.18	...

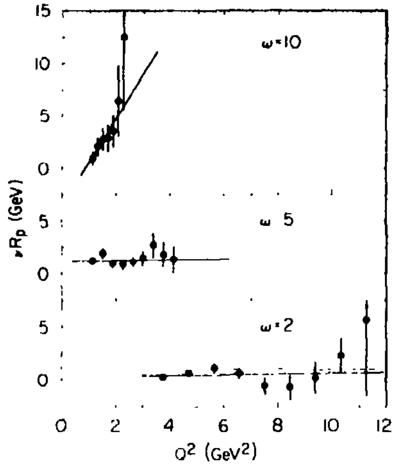

FIG. 1. Values of νR_p plotted with their statistical errors versus Q^2 for fixed values of ω. The solid lines represent least-square fits of the form $\nu R_p = a + b\nu = a + (\omega/2M)\,bQ^2$, and the dashed lines represent $R_p = Q^2/\nu^2$.

$= 0.16 \pm 0.01$ ($\chi^2 = 138$) with an estimated systematic error of ±0.09. An even better fit is obtained with the form[12] $R_p = f(\omega)Q^2/\nu^2$, where $f(\omega) = g\omega^2$ or, equivalently, $R_p = 4gM^2/Q^2$. The best fit coefficient is $g = 0.13 \pm 0.01$ ($\chi^2 = 110$) with an estimated systematic error of ±0.06. This deviation from simple Q^2/ν^2 behavior at large ω, predicted from Regge arguments[12] in the framework of light-cone algebras[5] and deduced[13] from ρ-electroproduction data,[14] is apparent in Fig. 1 where the dashed lines represent $R_p = Q^2/\nu^2$.

Since only 18°, 26°, and 34° e-d data were used in the analysis, R_d and R_n are less well known than R_p. The quantity $\delta = R_d - R_p$ was extracted at each of the (ν, Q^2) points where interpolated cross sections at two or more of these angles were available. This quantity is determined[7] from the slope of the ratio of deuteron-to-proton cross sections, σ_d/σ_p, plotted versus $\epsilon' = \epsilon(1 + \epsilon R_p)^{-1}$, and is insensitive to the choice of R_p. The major systematic uncertainties disappear in this ratio[8] and the uncertainties in δ are predominantly statistical. The extracted values of δ are everywhere consistent with zero, within large statistical errors. Values of δ averaged over Q^2 at fixed ω are presented in Table II. The value of δ averaged over the full kinematic range $1.5 \leq \omega \leq 5.0$ is 0.02 ± 0.03. It can be shown[8] that $R_d = R_p$ implies $R_n = R_p$ and therefore, within the e perimental errors, R_d and R_n are consistent with being equal to R_p.

We acknowledge helpful discussions with R. J fe and are grateful for programming assistance from E. Miller and R. Verdier.

---

*Work supported in part by the U.S. Atomic Energy Commission under Contracts No. AT(11-1)-3069 and No. AT(04-3)-515.

†Present address: Stanford Linear Accelerator Cen ter, Stanford University, Stanford, Calif. 94305.

‡Present address: National Accelerator Laborator Batavia, Ill. 60510.

§Present address: Laboratory of Nuclear Studies, Cornell University, Ithaca, N.Y. 14850.

[1] A. Bodek *et al.*, Phys. Rev. Lett. 30, 1087 (1973).

[2] J. S. Poucher *et al.*, Phys. Rev. Lett. 32, 118 (197 and SLAC Report No. SLAC-PUB-1309 (unpublished).

[3] G. Miller *et al.*, Phys. Rev. D 5, 528 (1972).

[4] C. G. Callan and D. J. Gross, Phys. Rev. Lett. 22, 156 (1969).

[5] J. E. Mandula, Phys. Rev. D 8, 328 (1973).

[6] L. N. Hand, Phys. Rev. 129, 1834 (1963).

[7] E. M. Riordan, Ph.D. thesis, Massachusetts Institute of Technology, 1973, available as Report No. LN COO-3069-176 (unpublished).

[8] A. Bodek, Ph.D. thesis, Massachusetts Institute of Technology, 1972, available as Report No. LNS-COO-3069-116 (unpublished).

[9] J. S. Poucher, Ph.D. thesis, Massachusetts Institu of Technology, 1971 (unpublished).

[10] This experiment was performed by a collaboration between Massachusetts Institute of Technology and SLAC Group A. The cross sections used in the extra tions of R were taken from the MIT analysis of this data. Because of differences in radiative-correction methods, these cross sections were typically 1.5% lo er than those reported in Ref. 2.

[11] R. P. Feynman, *Photon-Hadron Interactions* (Benj min, New York, 1972).

[12] J. F. Gunion and R. L. Jaffe, Phys. Rev. D 8, 3215 (1973).

[13] J. J. Sakurai, Phys. Rev. Lett. 22, 981 (1969), and 30, 245 (1973).

[14] For a review of ρ-electroproduction data, see the talk by K. Berkelman, in *Proceedings of the Sixteent International Conference on High Energy Physics, Th University of Chicago and National Accelerator Labor tory, 1972*, edited by J. D. Jackson and A. Roberts (N tional Accelerator Laboratory, Batavia, Ill., 1973), Vol. 4, p. 41.

PHYSICAL REVIEW
LETTERS

VOLUME 33 2 SEPTEMBER 1974 NUMBER 10

Coherence in He I and II Excited States Produced by an Asymmetric Collision*

D. A. Church, W. Kolbe, M. C. Michel, and T. Hadeishi
Lawrence Berkeley Laboratory, Berkeley, California 94720
(Received 8 July 1974)

In an external magnetic field, quantum beats at the Larmor frequency ω are observed in circularly polarized light as a result of coherent orientation of fast He I and II states by a thin foil with exit-surface normal *not* coincident with the beam direction. Effects resulting from variation of detection geometry, quantum state, incident ion energy, foil tilt angle, and foil material are discussed. An interpretation in terms of an impulsive asymmetric electric interaction is considered.

Symmetry considerations admit the possibility of the production of orientation by the beam-foil collision process when the normal to the foil exit surface does not lie along the beam axis.[1] Such orientation of the $3p\,{}^1P_1{}^\circ$ level of He I, characterized by the emission of circularly polarized light, has recently been observed and analyzed.[2] In Ref. 2, linear and circularly polarized components of the emitted light were measured at different angles under static conditions. At 135 keV, alignment of the level was found to decrease, while orientation increased, as the angle of the foil normal relative to the beam direction was increased from 0 to $\pi/4$.

We describe here measurements in which interference effects in the optical-decay radiation reflect the coherent time development of the anisotropically excited atomic sublevels. A fast ion beam is passed through a thin carbon foil ($\simeq 6$ $\mu\text{g/cm}^2$) with exit-surface normal *not* coincident with the beam direction. The resulting coherent mixture of excited sublevel wave functions develops in time at frequencies which are multiples of the Larmor frequency ω in the presence of a uniform external magnetic field directed perpendicular to the beam direction. Polarized light emitted at a fixed time subsequent to excitation, perpendicular to both beam and field directions, displays this periodicity as a function of magnetic field strength. The presence of a variation at ω in circularly polarized light is evidence of orientation.

Figure 1 shows the excitation and detection geometry. The narrow light observation region is maintained parallel to the foil surface, a distance d downstream from the foil. Parallel light, collected by a lens (not shown), is passed through a polarization analyzer and refocused through a monochromator to a photomultiplier. We used two polarization analyzers in these measurements. One, a linear polarizer, was oriented at several angles to be described; the other was a left-circular polarizer. Valid comparisons of *relative* intensity measurements through these polarizers can always be safely made; the remainder of the detection system acts only as a polarization-dependent attenuator.[3]

The periodic light-intensity variations with field strength appear on a constant background, and have the form

$$I(H) = A + \sum_{k=1}^{2} B_k \cos(k\omega d/v + \varphi_k),$$

where the Larmor frequency $\omega = \gamma H$ is propor-

Copyright © 1974 by
The American Physical Society

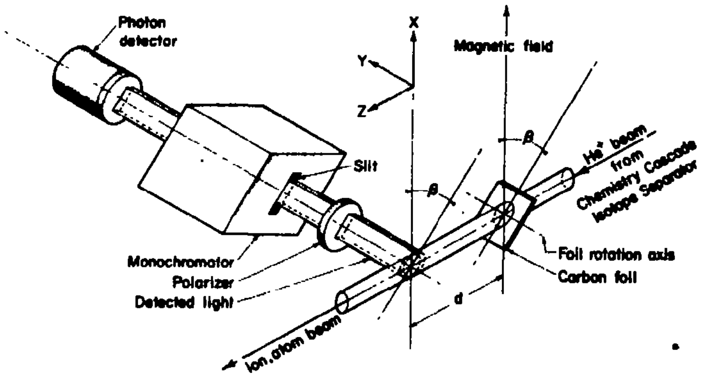

FIG. 1. Schematic drawing of the geometry of the ion-excitation and light-detection apparatus. As shown, the monochromator is rotated about the y axis to the same tilt angle β as the foil to preserve the time resolution of the measurement.

tional to the magnetic field strength, v is the particle velocity, and the phase factor φ_k is found to be 0 or π in these measurements. When the foil normal lies along the beam direction ($\beta = 0$ in Fig. 1), the usual quantum beats ($k=2$ corresponding to 2ω) due to collision-induced alignment[3,4] are observed in light linearly polarized parallel to the beam axis. As the angle of the transmission axis of the linear polarizer relative to the beam direction is increased from 0 to $\pi/2$, the relative amplitude B_2/A of the 2ω beats decreases to zero. Now, when the foil normal is rotated by an angle β about the y axis (Fig. 1), 2ω beats are still observed in light linearly polarized parallel to the beam axis, but through a circular polarizer beats for both $k=1$ (corresponding to ω) and $k=2$ are observed. Figure 2(a) shows such beats in both light polarizations in the $2p\,^1P_1^\circ$-$4d\,^1D_2$ transition near 4922 Å in He I. The measurements discussed below refer to this transition but similar beats have also been observed in other singlet and triplet D levels of He I at energies in the range 20–80 keV, and in transitions from the $4f\,^2F_{5/2,7/2}$ levels of He II at input ion energies of 70 keV. Consequently, the interaction producing these effects is quite general. Both ω and 2ω beats are phased to produce an extremum in intensity at $H=0$. The 2ω intensity B_2 is found to be a maximum,[3] while the ω intensity B_1 is a maximum or minimum at $H=0$ depending on the direction of the foil exit-surface normal and the helicity of polarization of the detected light [Fig. 2(b)]. When left circularly polarized light is detected, and $\beta = -\pi/4$, i.e., the foil-exit normal lies in the upper left quadrant of the x-z plane (Fig. 1), the circularly polarized light intensity is a minimum at $H=0$. Figure 2(b) shows the phase shift of π in the ω beats produced when the foil angle β is changed from $-\pi/4$ to $+\pi/4$. Hence the expectation value of the net angular momentum of the level, $\langle L\rangle$, lies along the

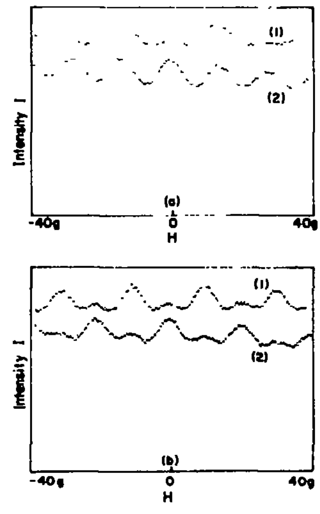

FIG. 2. (a) Quantum beats in light emitted from the $4d\,^1D_2$ level of He I in (1) left-circularly and (2) linearly polarized light, with a foil tilt angle $\beta = \pi/4$. The primary beat frequencies correspond to ω and 2ω, respectively. (b) Quantum beats in left-circularly polarized light for (1) $\beta = -\pi/4$ and (2) $\beta = +\pi/4$. The incident ion energy is 40 keV in all cases.

-y axis (Fig. 1), in agreement with the analysis or the $^1P_1$ level of Ref. 2. With a given foil tilt angle β, in *linearly* polarized light, the relative amplitude of the 2ω beats decreases uniformly o 0 when the polarizer angle is rotated from parallel to perpendicular relative to the beam direcion. However, beats at ω appear in this lineary polarized light at polarizer angles intermediate between 0 and $\pi/2$, dropping to zero as one approaches either of these angles. The relative maximum intensity of the ω beats appears with polarizer angle near the vicinity of the foil tilt angle β ($\beta=\pi/4$ for these measurements).

Fano and Macek[1] have formulated the components of the orientation vector and alignment tenor of the excited level in the "detector frame." Substituting the angles appropriate to our detector geometry in their equation [Eq. (18), Ref. 1] yields the following relations:

$$O_0^{\mathrm{det}} = O_{1-}^{\mathrm{col}} \sin\theta \text{ (orientation parameter)},$$

$$A_0^{\mathrm{det}} = \tfrac{1}{2}A_0^{\mathrm{col}}(3\cos^2\theta - 1) - \tfrac{3}{2}A_{2+}^{\mathrm{col}}\sin^2\theta,$$

$$A_{2+}^{\mathrm{det}} = \tfrac{1}{2}A_0^{\mathrm{col}}\sin^2\theta\cos 2\psi + \tfrac{1}{2}A_{1+}^{\mathrm{col}}\sin 2\theta\cos 2\psi - \tfrac{1}{2}A_{2+}^{\mathrm{col}}(1+\cos^2\theta)\cos 2\psi.$$

θ is the angle between detector and beam direction and ψ is the direction of linear polarization relative to the beam direction. These parameters now represent the static light emission of our system for $H=0$. For a uniform magnetic field parallel to the x axis (Fig. 1) these tensor components will precess about the field direction at the Larmor frequency. This can be represented by replacing θ with ωt in the above equations.

This substitution in the case of the orientation parameter (O_0^{det}) gives a variation at the frequency ω for observation in circularly polarized light, in agreement with the experimental observations.

The alignment components predict variations only at 2ω for observation in linearly polarized ight. Our observations are consistent with this prediction except for the occurrence of ω beats observed in linearly polarized light for angles (ψ) of the polarizer axis between 0 and $\pi/2$ as discussed above. It is therefore reasonable to assume that this signal is not a result of alignment.

We suggest that these observations of the freuency ω terms may be interpreted as a coherent superposition of left- and right-circularly polarized light components with different intensities, initially in phase at $H=0$ in a plane approximately parallel to the foil surface. When the magnetic field is applied along the y axis, no ω beats appear in circularly polarized light as expected for an eigenstate, although the 2ω beats remain. These 2ω beats, when H does not lie along the y axis, are now not only due to alignment, but also are in part due to the coherence of the orientation.

As usual in coherence measurements of this type, some damping of the beat signals is observed as a result of insufficient time resolution. An increased damping of beats over that produced by a normal foil is noted for the tilted foils.

A dependence on the incident ion-beam energy in the range 20–80 keV was found for the amplitude of both the ω and the 2ω beats. The ω beat amplitude was also found to increase with the foil tilt angle β at a given energy. Foil angles β of 30, 45, and 60 deg were investigated. The energy dependence of the amplitude B_1 of the ω beats, relative to B_2 for 2ω, was most pronounced at 30 deg, and least at 60 deg. At all angles, the B_1 amplitude decreased as the beam energy was increased from 30 to 70 keV.

As a mechanism for the asymmetric interaction which produces the orientation of the excited levels, we have considered two possibilities: a spin-dependent interaction or a torque exerted by external fields on the multipole moments of various orders of the excited system.[5] Spin-dependent orientation might be expected in a nonaligned $^3S_1$ level. The transition near 4713 Å from the $4s\,^3S_1$ level of He I exhibited no identifiable beats, however.

Lombardi and Giroud have shown that an electric field acting on an aligned system can produce orientation.[6] A stronger interaction is, for example, an electric field *gradient*, directed along the foil normal, acting on the aligned states normally produced by the beam-foil collision in levels with $L \neq 0$. This could also generate an orientation tensor with the appropriate symmetry.

The electric fields or field gradients may be associated with the foil surface, or with its internal crystalline fields. Reasonable estimates of these parameters yield appropriate magnitudes for the observed effects. Fano has given a general expression for the precession of the multipole moments of a particle produced by torques exerted by such fields.[5] His equations are strictly applicable to particles which do not deform under the influence of these fields. Such deformations may be important during a strong, short-term interaction of an ion with the foil, however.

To test further this precession hypothesis, we attempted to vary possible surface or internal fields, which might arise from work functions, crystalline fields, or image charges, etc., by coating conventional carbon foils with thin layers of aluminum (which was permitted to oxidize) or gold. The increased energy loss of the ions upon passage through these foils slightly changed the period of the beats because of the consequent velocity decrease, but did not produce increased dephasing. This proves that the coated surface remained substantially intact during the life of the foil.

The magnitude of the relative orientation produced by the carbon foils was found to be about 20% larger than that observed with the gold-coated foils at 50 and 70 keV incident ion energies; at 70 keV the aluminum and carbon surfaces produced indistinguishable results. It must be noted in connection with these measurements that the vacuum was only of the order of 10^{-6} Torr, so surface-contamination effects cannot be excluded.

The general orientation and coherence of excited levels of fast ions and atoms can be used in atomic-structure investigations, such as $\Delta m = 1$ level crossing, particularly in ionic levels which are difficult to orient by other techniques.

---

*This work was supported by the Atomic Energy Commission and the Office of Naval Research.

[1] U. Fano and J. H. Macek, Rev. Mod. Phys. 45, 553 (1973).

[2] H. G. Berry, L. J. Curtis, D. G. Ellis, and R. M. Schectman, Phys. Rev. Lett. 32, 751 (1974).

[3] D. A. Church and C. H. Liu, Physica (Utrecht) 67, 90 (1973).

[4] C. H. Liu, S. Bashkin, W. S. Bickel, and T. Hadeishi, Phys. Rev. Lett. 26, 222 (1971).

[5] U. Fano, Phys. Rev. 133, B828 (1964).

[6] M. Lombardi and M. Giroud, C. R. Acad. Sci., Ser. B 266, 60 (1968).

Muonium Formation in Noble Gases and Noble-Gas Mixtures*

R. D. Stambaugh, D. E. Casperson, T. W. Crane, V. W. Hughes,† H. F. Kaspar,‡ and P. Souder
Gibbs Laboratory, Physics Department, Yale University, New Haven, Connecticut 06520

and

P. A. Thompson
Los Alamos Scientific Laboratory, Los Alamos, New Mexico 87544

and

H. Orth and G. zu Putlitz
University of Heidelberg, Heidelberg, West Germany

and

A. B. Denison
Physics Department, University of Wyoming, Laramie, Wyoming 82070

(Received 21 May 1974)

In an experiment at the Clinton P. Anderson Meson Physics Facility, no muonium formation was found in pure He or Ne, and abundant formation in Ar and Xe. A small Xe admixture (0.1%) in He and Ne resulted in abundant muonium formation, due to the process in which Xe serves as an electron donor to a low-energy positive muon. These results are qualitatively consistent with our knowledge of relevant atomic collision cross sections.

Muonium was discovered[1,2] by observing the characteristic muonium Larmor precession frequency when positive muons were stopped in pure Ar gas, and it was found that between 50 and 100% of the muons stopped in Ar form muonium. In subsequent magnetic-resonance experiments on muonium using Ar and Kr,[3,4] it was established that greater than 50% of the muons stopped in either Ar or Kr form muonium.

As muons slow down in a gas, the competition between electron-capture and electron-loss collisions with the gas atoms principally determines the fraction of the muons that form muonium. This fraction can be estimated from available data[5,6] and theoretical calculations[2,7] on capture and loss cross sections for muons and protons in noble gases. The calculations of muonium formation require simultaneous numerical integration of the differential equations[6] for the charge fractions of the muon beam and the energy loss (dE/dx). The cross-section data for protons below 0.7 keV and the dE/dx curve below 10 keV, as well as the applicability of proton results to muons, are not known well enough to enable quantitative predictions. Our estimates are less than 20% muonium formation in He, less than 40% in Ne, 70% to 90% in Ar, and 100% in Xe. Muonium atoms with less than about 50 eV will survive stably to thermal energy because the capture and loss reaction rates are very small below 50 eV. Muonium can be formed at thermal energy only in Xe, which is the only noble gas whose ionization potential is less than that of muonium. Our measurements on muonium formation by muons stopped in gases provide information not available from proton studies, and many types of atomic collisions from thermal energy to 100 keV contribute to the final result.

A study of behavior of positive muons stopped in liquid helium was done at the Space Radiation Effects Laboratory[8] and is reported in the following Letter. No muonium formation was found, and the muons behave in liquid helium both above and below the λ point as free, polarized muons.

TABLE I. Properties of μ^+ beam.

Proton energy	650 MeV
Proton current	1.5 μA, av
Duty factor	4.5%
Production target	6.0 cm C
μ^+ rate[a] (1·2)	23 500/sec, av
μ^+ stops[b]	930/sec, av
p_μ (backward decay)	93 MeV/c
$\Delta p_\mu/p_\mu$	±3%
Spot size[c]	250 cm^2
Polarization	(80 ±2)%
Impurities:	
π/μ	< 0.01
e/μ	0.03

[a] Rate into 280 cm^2, 38 cm from last quadrupole.

[b] 50-atm He gas target: 0.22 g/cm^2; area, 320 cm^2.

[c] Full width at half-maximum at 75 cm from last quadrupole.

In view of this interesting result, which differs so dramatically from the behavior of positive muons stopped in Ar or Kr gas, the experiment reported in this Letter was done to study the behavior of positive muons stopped in He, Ne, and Xe in order to provide a more complete understanding of muonium formation in the noble gases.

The method of our experiment is the classic one for studying the Larmor precession of free muons[9] (13.6 kHz/G) or of muonium[1] (1.40 MHz/G), which relies on the availability of polarized muons from pion decay and the correlation of the muon spin direction with the direction of emission of the positrons from muon decay.

Our experiment was done at the Clinton P. Anderson Meson Physics Facility (LAMPF), and indeed is the first muon physics experiment done at this new laboratory. The muon channel—a 21-magnet system— is basically of conventional design consisting of a pion collection, a pion decay, and an analyzer section.[10] The characteristics of the output muon beam are given in Table I.

A schematic diagram of the experimental arrangement is shown in Fig. 1. The high-pressure gas target contained internal scintillation counters. The gas was circulated over Ti at 750°C to remove impurities. The gases used were research grade with impurity concentrations below 1.0 ppm (except for Xe which had 5 ppm O_2). Three pairs of mutually perpendicular Helmholtz coils were used to null out the stray field, and an additional Helmholtz pair produced the precession field transverse to the muon spin. The field was measured with a Rb optical pumping magnetometer[11] and was homogeneous to 1%. The counters were plastic scintillators. Counter 5 was

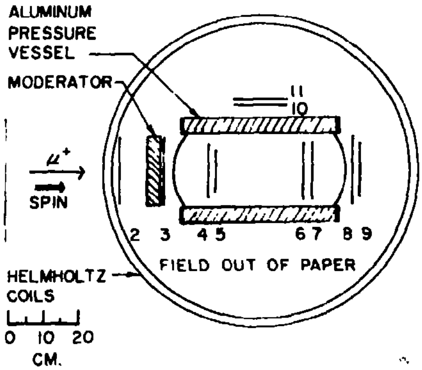

FIG. 1. Diagram of apparatus. The pressure windows were 4.76 mm thick.

0.012 cm thick to minimize stops in the scintillator which would count as stops in the gas, and its efficiency was >50%. Muons which stopped in the target walls counted as $\mu_{stops}\,(1\cdot 2\cdot 3\cdot 4\cdot 5\cdot \bar{6}\cdot \bar{7})$ and contributed a small background of free muon precession which was measured in vacuum runs. Curves of μ_{stops} versus gas pressure were taken to estimate the fraction of muons stopping in the walls. For the He and Xe runs, two thirds of the wall surface was lined with a scintillator which was optically coupled to counter 7. This additional veto cut the wall stop background in half.

The time distributions were taken with a CAMAC digitron clock. The signal μ_{stop} started the digitron counting a 100-MHz clock. Either E_f $[\bar{1}\cdot \bar{2}\cdot \bar{3}\cdot \bar{4}\cdot 6\cdot 7]$ or E_n $[\bar{1}\cdot \bar{2}\cdot \bar{3}\cdot \bar{4}\cdot 10\cdot 11]$ stopped the count. The digitized time was used to update a histogram in a PDP-11/20 computer. Two spectra, 90° out of phase, were thus obtained. Figure 2 shows time distributions for the E_f for Ne.

The essential data consist of time distributions which can be represented by

$$N(t) = N_0 e^{-t/\tau} \times [1 + A \exp(-t/\tau_D)\cos(\omega t + \varphi) + B], \quad (1)$$

where τ is the muon lifetime, τ_D is the depolarization time, A is the precession amplitude, ω is the precession frequency, φ is the initial phase, B is a constant background term, and N_0 is a normalization constant. Equation (1) was fitted to the time distributions. Free-muon precession runs were made at 60 G and muonium runs at 3 and 4 G. Pressures used were 50 atm He, 26 atm Ne, 30 atm Ar, and 4.4 atm Xe. Table II gives the target gas and the corresponding fractions of muons remaining free (F_μ) and forming muonium (F_M). These fractions are calculated from the values of A with corrections for counter geometry, absorption of low-momenta positrons, beam polarization, and background.

As Table II indicates, no muonium formation was found in pure He or pure Ne, while abundant formation was found in Ar and Xe. Due to inadequate gas circulation by a low-pressure pump used only for the 3-G Xe run, these data were taken with substantial O_2 contamination, which is known to depolarize muonium by electron-spin exchange collisions.[12] The 4-G run was taken with the pump used for all other runs, which reduced the O_2 content a factor of 2 during the run, and increased the muonium amplitude. The result quoted for muonium formation in Xe is an extrapolation to zero O_2-impurity content.

The results are more definitive, especially for Ne, than the theoretical estimates, indicating the need for better understanding of the low-energy collision processes. The fact that muons appear to be free, fully polarized particles in He or Ne might provide a useful approach to measuring the magnetic moment or other properties of the free positive muon, but the possibility of formation of the molecular ions[13] μ^+He or μ^+Ne must be considered.

In Ar and Kr the dominance of the electron-capture cross section leads to nearly 100% muonium formation at muon kinetic energies below 1 keV. In He and Ne we have found that muonium formation does not occur because the electron loss process dominates, and the muon is free in the gas and presumably thermalized. Only for Xe is electron capture energetically allowed at thermal energy. From our knowledge of the corresponding proton reaction[14,15] and theoretical calculations, we can estimate that the cross section for the electron-donor reaction

$$\mu^+ + \mathrm{Xe} \rightarrow \mu^+ e^- + \mathrm{Xe}^+({}^2P_{1/2} \text{ or } {}^2P_{3/2}) \quad (2)$$

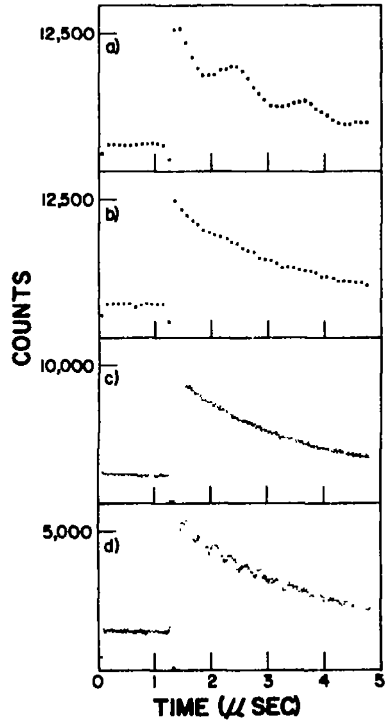

FIG. 2. Free-muon precession at 60 G (a) in pure Ne and (b) in Ne + 0.15% Xe. Muonium precession at 2.75 G (c) in pure Ne and (d) in Ne + 0.15% Xe.

TABLE II. Results on muonium formation.

Target gas	F_μ (%)	F_M (%)
He	99(5)	1(5)
He + 0.015% Xe	83(15)	
He + 0.09% Xe	25(9)	75(9)
Ne	100(2)	0(2)
Ne + 0.15% Xe	19(3)	81(3)
Ar	35(5)	65(5)
Xe	10(5)	100[a]

[a] No error estimate given.

will be of the order of 10^{-15} cm^2 from 1 keV to thermal energies. Hence with a Xe density of 10^{15}/cm^3 added to the high-pressure He or Ne (about 1 part in 10^3 Xe), the large electron-capture cross section from Xe leads to muonium formation for muon kinetic energies less than 50 eV.

Data were taken with gas mixtures with the results shown in Table II. Figure 2 shows the dramatic effect of an admixture of 0.15% Xe with Ne, which leads to the disappearance of the free-muon precession signal and the appearance of a arge muonium precession signal. Similar reults were observed when 0.09% Xe was added to ie, as indicated in Table II.

The effectiveness of Reaction (2) encourages he possibility[16] of forming the muonic helium tom $\alpha\mu^-e^-$ by this reaction, involving $\alpha\mu^-$ ather than μ^+, when μ^- are stopped in He with small admixture of Xe.

We are happy to acknowledge our appreciation o Dr. Louis Rosen and the LAMPF staff for providing a new, exciting laboratory and also a substantial level of technical support for our experiment.

---

*Research supported in part by the U. S. Atomic Energy Commission under Contract No. AT(11-1)3075.

†Present address: Los Alamos Scientific Laboratory, Los Alamos, N. Mex. 87544.

‡Present address: Bern University, Bern, Switzerland.

[1] V. W. Hughes *et al.*, Phys. Rev. Lett. 5, 63 (1960).

[2] V. W. Hughes *et al.*, Phys. Rev. A 1, 595 (1970), and A 2, 551 (1970).

[3] V. W. Hughes, Annu. Rev. Nucl. Sci. 16, 445 (1966).

[4] P. A. Thompson *et al.*, Phys. Rev. Lett. 22, 163 (1969).

[5] N. V. Federenko, Zh. Tekh. Fiz. 40, 2481 (1970) [Sov. Phys. Tech. Phys. 15, 1947 (1971)].

[6] S. K. Allison, Rev. Mod. Phys. 30, 1137 (1958).

[7] R. A. Mapleton, *Theory of Charge Exchange* (Wiley-Interscience, New York, 1972).

[8] D. Casperson *et al.*, Bull. Amer. Phys. Soc. 18, 1503 (1973); T. Crane *et al.*, Bull. Amer. Phys. Soc. 18, 1503 (1973).

[9] R. L. Garwin, L. M. Lederman, and M. Weinrich, Phys. Rev. 105, 1415 (1957).

[10] V. W. Hughes *et al.*, Los Alamos Scientific Laboratory Report No. LA-4474-Ms, 1970 (unpublished).

[11] W. Farr and E. W. Otten, "A Rb Magnetometer for Magnetic Field Strength Measurements between 0.3 mOe and 3 kOe with 1 μOe Sensitivity" (to be published).

[12] R. M. Mobley *et al.*, J. Chem. Phys. 47, 3074 (1967).

[13] V. W. Hughes, Phys. Rev. 108, 1106(L) (1957).

[14] H. H. Fleischmann and R. A. Young, Phys. Rev. Lett. 19, 941 (1967).

[15] D. N. Koopman, Phys. Rev. 154, 79 (1967).

[16] K. N. Huang *et al.*, in Proceedings of the Fifth International Conference on High Energy Physics and Nuclear Structure, Uppsala, Sweden, 1973 (unpublished).

Behavior of Positive Muons in Liquid Helium*

T. W. Crane, D. E. Casperson, H. Chang, V. W. Hughes,† H. F. Kaspar,‡ B. Lovett,
A. Schiz, P. Souder, R. D. Stambaugh, and G. zu Putlitz§
Gibbs Laboratory, Physics Department, Yale University, New Haven, Connecticut 06520

and

J. R. Kane
College of William and Mary, Williamsburg, Virginia 23185

(Received 21 May 1974

Searches were made with positive muons stopped in liquid helium for free-muon precession, for muonium precession, and for depolarization of the muon spin. The muons behaved as free muons both above and below the λ point. There was no muonium formation (< 2%) and no depolarization of the muon spin (depolarization time > 20 μsec).

Investigations of the behavior of charged particles in liquid helium have revealed rather intrinsic properties of liquid helium as well as many new phenomena involving the interactions of charged particles with liquid helium.[1] Thus vortex lines were observed with electrons and α particles, and vortex rings were discovered with α particles.[2,3] Electrons stopped in liquid helium form a "bubble."[4] Positrons apparently form positronium in a "bubble" environment.[5] The α particle forms a massive ion involving many helium atoms.[6] Since no studies appear to have been done with positive muons in liquid helium, and since in liquid different and unexpected phenomena may occur as compared to gaseous helium, we have done an exploratory study of the magnetism of positive muons in liquid helium.[7] We point out that as compared to the other charged particles studied in liquid helium, the muon provides the unique opportunity of studying magnetic effects.

The principal method of the experiment is the classical one for studying the Larmor precession of free muons (13.6 kHz/G) or of muonium (1.40 MHz/G).[8] In addition, a time-dependent depolarization of the muons in a weak external magnetic field longitudinal to the incoming muon spin direction was searched for.

A diagram of the apparatus used at the Space Radiation Effects Laboratory is shown in Fig. 1. The liquid-helium target had been used in experiments with stopped muons and pions and has been described.[9] The target also serves as a scintillation counter and is divided into two sections T_1 and T_2 with the downstream half (T_2) being a veto counter to eliminate muons stopping in the walls. A system of three orthogonal pairs of coils (only one pair shown in Fig. 1) served to balance out the residual magnetic field and to produce the external magnetic fields required. To observe free-muon precession, a magnetic field of about 70 G transverse to the incoming muon beam direction and with a homogeneity of 0.1% over the target region was used; for muonium precession, magnetic fields of 4 and 6 G with a homogeneity of ~1% were used; and for depolarization measurements, a magnetic field of 1 G in the direction of the incoming muon beam with a 10% homogeneity was used. The magnetic field was determined with a rubidium magnetometer.[10]

A muon stopping in the liquid helium was detected by the coincidence signal $(S_1 \cdot S_2 \cdot S_3 \cdot T_1 \cdot \bar{T}_2 \cdot \bar{S}_4)$ and the decay positron by $(\bar{S}_1 \cdot S_4 \cdot S_5)$. The time in-

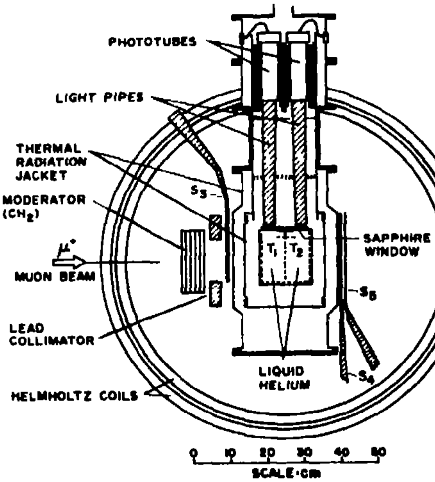

FIG. 1. Horizontal cross section of the liquid-helium target. Not shown are the upstream counters S_1 and S_2, which were 1.6-mm-thick scintillation counters.

terval t for an event consisting of a muon start signal and a positron stop signal was measured with a time-to-amplitude converter which fed into a pulse-height analyzer. Each stopped-muon signal generated a 7-μsec gate; if an additional stopped-muon signal or more than one positron signal occurred during the muon gate, the time interval was rejected to reduce rate dependence in the data.

Data were taken with magnetic fields suitable for the observation of either free-muon precession, muonium precession, or muon depolarization, with the liquid helium at 4.2°K and, below the λ point, at 2.0°K. In addition, a brief search was made for muonium in cold (<10°K) helium gas.

The number of events, $N(t)$, was fitted by the following equation:

$$N(t)=N_0\{e^{-t/\tau}[1+Ae^{-t/\tau_D}\cos(\omega t+\varphi)]+B\}, \qquad (1)$$

where N_0 is a normalization constant, τ is the muon lifetime, τ_D is the polarization time, A is the precession amplitude, ω is the muon precession frequency, φ is the initial phase angle, and B is a constant background term.

The results of a typical run at 66 G are shown in Fig. 2. The interesting feature of the data is the large amplitude of oscillation ($A = 0.20 \pm 0.01$) at the free-muon Larmor precession frequency. Considering the measured muon beam polarization, this value of A implies that at least 90% of the muons contribute to the free-muon precession. This result sets an upper limit of 10% on the fraction of muons forming muonium. Using all of our data, we obtained a value for the muon gyromagnetic ratio of 13.58 ± 0.02 kHz/G, in agreement with a precision determination of 13.553 76 ± 0.000 05 kHz/G.[11]

In the search for muonium precession, Eq. (1) was modified to include both the free-muon and the muonium precession frequencies. The best fit obtained with all the data gave the fraction (1.7 ± 0.5)% muonium formation. Since a small fraction of the muons could have stopped in the sapphire window and formed muonium,[12] we interpret our results as indicating at most 2% of the muons stopped in liquid helium form muonium. A small amount of data were obtained with cold helium gas (<10°K) and indicated that less than 6% of the muons formed muonium.

We searched for depolarization of the muons in two ways. The free-muon–precession data at 70 G fitted by Eq. (1) set a lower limit of 20 μsec for τ_D at the 67% confidence level. Also, data were obtained with a low magnetic field of 0.88 G parallel to the muon beam direction. The low magnetic field was used to avoid decoupling a relatively weak depolarization interaction. These data set a value for τ_D of >12 μsec.

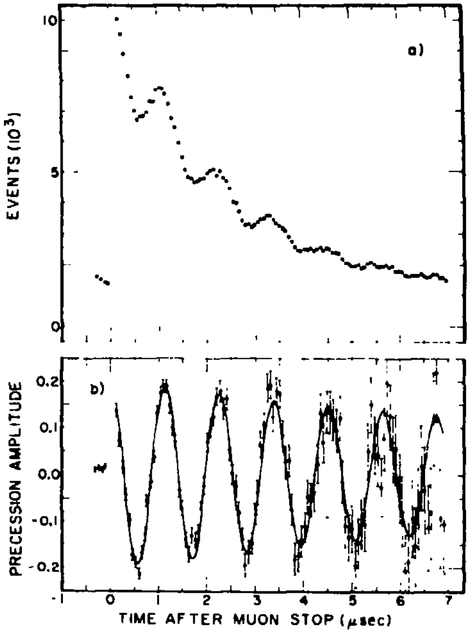

FIG. 2. Data obtained at 65.95 G showing the free-muon precession in liquid helium at 2.0°K. (a) Events as a function of time. (b) The precession amplitude after the muon decay and background dependences have been removed.

The absence of muonium formation in liquid helium both above and below the λ point agrees with the behavior of muons in helium gas and with data for electron capture and loss by protons in helium.[13] The presence of the free-muon Larmor precession amplitude for muons in liquid helium and the absence of muon depolarization does not necessarily imply the muons are indeed free. This behavior is also consistent with the formation of a helium-muon molecular ion, Heμ^+, or of a cluster of helium atoms[8] about the μ^+. Neither for the Heμ^+ ion nor for the cluster would we expect significant internal magnetic fields at the μ^+ site. A precise measurement of the muon precession frequency in liquid helium to an accuracy at the parts per million level, by comparison to the free-muon magnetic moment, would reveal magnetic shielding effects and help elucidate the

Behavior of Positive Muons in Liquid Helium*

T. W. Crane, D. E. Casperson, H. Chang, V. W. Hughes,† H. F. Kaspar,‡ B. Lovett,
A. Schiz, P. Souder, R. D. Stambaugh, and G. zu Putlitz§
Gibbs Laboratory, Physics Department, Yale University, New Haven, Connecticut 06520

and

J. R. Kane
College of William and Mary, Williamsburg, Virginia 23185

(Received 21 May 1974)

Searches were made with positive muons stopped in liquid helium for free-muon precession, for muonium precession, and for depolarization of the muon spin. The muons behaved as free muons both above and below the λ point. There was no muonium formation (< 2%) and no depolarization of the muon spin (depolarization time > 20 μsec).

Investigations of the behavior of charged particles in liquid helium have revealed rather intrinsic properties of liquid helium as well as many new phenomena involving the interactions of charged particles with liquid helium.[1] Thus vortex lines were observed with electrons and α particles, and vortex rings were discovered with α particles.[2,3] Electrons stopped in liquid helium form a "bubble."[4] Positrons apparently form positronium in a "bubble" environment.[5] The α particle forms a massive ion involving many helium atoms.[6] Since no studies appear to have been done with positive muons in liquid helium, and since in liquid different and unexpected phenomena may occur as compared to gaseous helium, we have done an exploratory study of the magnetism of positive muons in liquid helium.[7] We point out that as compared to the other charged particles studied in liquid helium, the muon provides the unique opportunity of studying magnetic effects.

The principal method of the experiment is the classical one for studying the Larmor precession of free muons (13.6 kHz/G) or of muonium (1.40 MHz/G).[8] In addition, a time-dependent depolarization of the muons in a weak external magnetic field longitudinal to the incoming muon spin direction was searched for.

A diagram of the apparatus used at the Space Radiation Effects Laboratory is shown in Fig. 1. The liquid-helium target had been used in experiments with stopped muons and pions and has been described.[9] The target also serves as a scintillation counter and is divided into two sections T_1 and T_2 with the downstream half (T_2) being a veto counter to eliminate muons stopping in the walls. A system of three orthogonal pairs of coils (only one pair shown in Fig. 1) served to balance out the residual magnetic field and to produce the external magnetic fields required. To observe free-muon precession, a magnetic field of about 70 G transverse to the incoming muon beam direction and with a homogeneity of 0.1% over the target region was used; for muonium precession, magnetic fields of 4 and 6 G with a homogeneity of ~1% were used; and for depolarization measurements, a magnetic field of 1 G in the direction of the incoming muon beam with a 10% homogeneity was used. The magnetic field was determined with a rubidium magnetometer.[10]

A muon stopping in the liquid helium was detected by the coincidence signal $(S_1\cdot S_2\cdot S_3\cdot T_1\cdot \bar{T}_2\cdot \bar{S}_4)$ and the decay positron by $(\bar{S}_1\cdot S_4\cdot S_5)$. The time in-

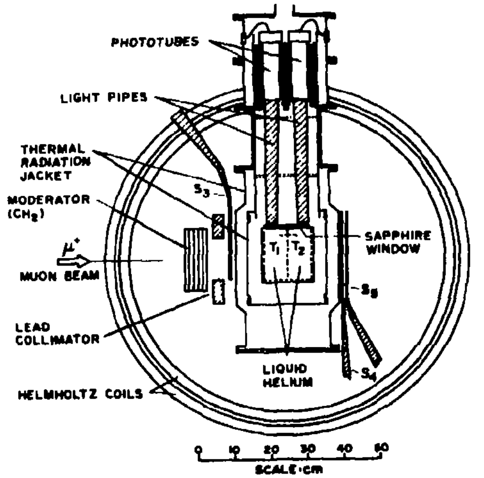

FIG. 1. Horizontal cross section of the liquid-helium target. Not shown are the upstream counters S_1 and S_2, which were 1.6-mm-thick scintillation counters.

terval t for an event consisting of a muon start signal and a positron stop signal was measured with a time-to-amplitude converter which fed into a pulse-height analyzer. Each stopped-muon signal generated a 7-μsec gate; if an additional stopped-muon signal or more than one positron signal occurred during the muon gate, the time interval was rejected to reduce rate dependence in the data.

Data were taken with magnetic fields suitable for the observation of either free-muon precession, muonium precession, or muon depolarization, with the liquid helium at 4.2°K and, below the λ point, at 2.0°K. In addition, a brief search was made for muonium in cold (<10°K) helium gas.

The number of events, $N(t)$, was fitted by the following equation:

$$N(t)=N_0\{e^{-t/\tau}[1+Ae^{-t/\tau_D}\cos(\omega t+\varphi)]+B\}, \tag{1}$$

where N_0 is a normalization constant, τ is the muon lifetime, τ_D is the polarization time, A is the precession amplitude, ω is the muon precession frequency, φ is the initial phase angle, and B is a constant background term.

The results of a typical run at 66 G are shown in Fig. 2. The interesting feature of the data is the large amplitude of oscillation ($A=0.20\pm0.01$) at the free-muon Larmor precession frequency. Considering the measured muon beam polarization, this value of A implies that at least 90% of the muons contribute to the free-muon precession. This result sets an upper limit of 10% on the fraction of muons forming muonium. Using all of our data, we obtained a value for the muon gyromagnetic ratio of 13.58 ± 0.02 kHz/G, in agreement with a precision determination of 13.553 76 ± 0.000 05 kHz/G.[11]

In the search for muonium precession, Eq. (1) was modified to include both the free-muon and the muonium precession frequencies. The best fit obtained with all the data gave the fraction (1.7 ± 0.5)% muonium formation. Since a small fraction of the muons could have stopped in the sapphire window and formed muonium,[12] we interpret our results as indicating at most 2% of the muons stopped in liquid helium form muonium. A small amount of data were obtained with cold helium gas (<10°K) and indicated that less than 6% of the muons formed muonium.

We searched for depolarization of the muons in two ways. The free-muon–precession data at 70 G fitted by Eq. (1) set a lower limit of 20 μsec for τ_D at the 67% confidence level. Also, data were obtained with a low magnetic field of 0.88 G parallel to the muon beam direction. The low magnetic field was used to avoid decoupling a relatively weak depolarization interaction. These data set a value for τ_D of >12 μsec.

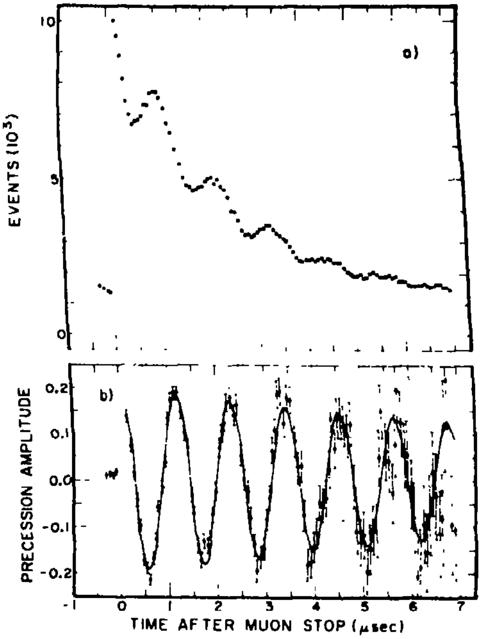

FIG. 2. Data obtained at 65.95 G showing the free-muon precession in liquid helium at 2.0°K. (a) Events as a function of time. (b) The precession amplitude after the muon decay and background dependences have been removed.

The absence of muonium formation in liquid helium both above and below the λ point agrees with the behavior of muons in helium gas and with data for electron capture and loss by protons in helium.[13] The presence of the free-muon Larmor precession amplitude for muons in liquid helium and the absence of muon depolarization does not necessarily imply the muons are indeed free. This behavior is also consistent with the formation of a helium-muon molecular ion, $\mathrm{He}\mu^+$, or of a cluster of helium atoms[6] about the μ^+. Neither for the $\mathrm{He}\mu^+$ ion nor for the cluster would we expect significant internal magnetic fields at the μ^+ site. A precise measurement of the muon precession frequency in liquid helium to an accuracy at the parts per million level, by comparison to the free-muon magnetic moment, would reveal magnetic shielding effects and help elucidate the actual state of μ^+ in liquid helium.

We are most grateful to Dr. R. Siegel and his staff for their effective support of our experiment.

---

*Research supported by the U. S. Atomic Energy Commission under Contract No. AT(11-1) 3075, by the U. S. Air Force Office of Scientific Research under Contract No. F44620-71-C-0042, and by the National Science Foundation (at William and Mary). The Space Radiation Effects Laboratory is supported by the National Science Foundation, the National Aeronautics and Space Administration, and the Commonwealth of Virginia.

†Present address: Los Alamos Scientific Laboratory, Los Alamos, N. Mex. 87544.

‡Present address: University of Bern, Bern, Switzerland.

§Present address: University of Heidelberg, Heidelberg, West Germany.

[1] R. J. Donnelly, *Experimental Superfluidity* (Univ. of Chicago Press, Chicago, Ill., 1967).

[2] D. J. Tanner, Phys. Rev. 152, 121 (1966).

[3] G. W. Rayfield and F. Reif, Phys. Rev. Lett. 11, 305 (1963).

[4] J. P. Hernandez and M. Silver, Phys. Rev. A 2, 18 (1970).

[5] R. A. Ferrell, Phys. Rev. 108, 167 (1957); L. O. Roellig and T. M. Kelley, Phys. Rev. Lett. 18, 387 (1967).

[6] K. R. Atkins, Phys. Rev. 116, 1339 (1959); L. Meyer and F. Reif, Phys. Rev. 123, 727 (1961).

[7] D. Casperson *et al.*, Bull. Amer. Phys. Soc. 18, 1503 (1973); T. Crane *et al.*, Bull. Amer. Phys. Soc. 18, 1503 (1973).

[8] R. L. Garwin, L. M. Lederman, and M. Weinrich, Phys. Rev. 105, 1415 (1957); V. W. Hughes, D. W. McColm, K. Ziock, and R. Prepost, Phys. Rev. Lett. 5, 63 (1960), and Phys. Rev. A 1, 595 (1970).

[9] D. C. Buckle *et al.*, Nucl. Instrum. Methods 77, 249 (1970).

[10] W. Farr and E. W. Otten, "A Rb-Magnetometer for Magnetic Field Strength Measurements Between 0.3 mOe and 3 kOe with 1 μOe Sensitivity" (to be published).

[11] K. M. Crowe *et al.*, Phys. Rev. D 5, 2145 (1972); B. N. Taylor, W. H. Parker, and D. N. Langenberg, Rev. Mod. Phys. 41, 375 (1969).

[12] G. G. Myasishcheva *et al.*, Zh. Eksp. Teor. Fiz. 53, 451 (1967) [Sov. Phys. JETP 26, 298 (1968)].

[13] R. D. Stambaugh *et al.*, previous Letter (Phys. Rev. Lett. 33, 568 (1974).

Injection and Control of Intense Relativistic Electron Beams in a Torus

J. Benford, B. Ecker, and V. Bailey
Physics International Company, San Leandro, California 94577

(Received 17 June 1974)

Efficient injection (> 80%) of an intense relativistic electron beam into a torus has been achieved using curvature drift injection. Drift was stabilized with a supplemental dipole magnetic field but beam loss in the radial direction due to the defocusing effect of the dipole field limited containment time. We propose a system for beam trapping and confinement which employs drift injection and beam energy losses in a toroidal-plus-betatron-type field.

Intense toroidal relativistic electron beams have been proposed as a means of heating toroidal reactors, as well as a means of producing the confining field for the plasma.[1,2] We recently proposed drift injection as a way of injecting externally generated intense beams into toroidal fields when the injection duration is longer than the time of one toroidal circuit (multiturn injection).[3] This Letter reports an experiment which demonstrates drift injection and the control of the circulating beam using a supplemental magnetic field. We also describe the conceptual extension of the drift-injection technique to give stable toroidal containment.

Beam injection using the curvature drift demonstrated previously[3,4] works by drifting the beam along the direction of the major axis, away from the injector insert, during the first toroidal circuit. Drift velocity is adjusted so as to clear the injector by judicious choice of the toroidal field strength B_φ and/or beam relativistic factor γ. Drift continues until the beam reaches a chamber surface unless additional forces are applied to stabilize the motion at a suitable distance from the injector. For stabilization we have used a supplemental magnetic field because this gives greater control of beam trajectory than does conducting-wall stabilization. Since the curvature drift is actually an $\vec{F}_c \times \vec{B}_\varphi$ drift, with $\vec{F}_c$ the centrifugal force, we need only apply a counteracting radial force to stop the drift. This force must be small near the injector and increase along the direction of drift so that beam drift will be little reduced at first, and be stopped only after the displacement needed to miss the injector is attained. By applying an external field with predominant component B_z parallel to the major axis, beam electrons will experience a radial force $F_r = (e/c)V_\varphi B_z$, where V_φ is the toroidal velocity of the beam electrons, e is the electron charge, and c is the speed of light. The net drift velocity is then

$$V_z = -(c/eB_\varphi)(F_c - F_r). \tag{1}$$

If B_z, and therefore F_r, increases with distance from the injector, V_z will decrease as the beam drifts until $F_c = F_r$, halting the drift. The critical B_z field, B_{zc}, for which the drift velocity is zero is $B_{zc} = \gamma m_0 c^2/eR_b$, where R_b is the major radius of the electron beam.

By extending the 180° sector used previously,[3,4] a cast-epoxy torus was constructed with major radius 20.5 cm and interior dimensions 10.5 cm (radial) by 16.5 cm (axial).

Figure 1 shows the experimental arrangement. Some of the toroidal field lines are diverted to the beam-generating diode through the injector and return to the torus through free space. The injector section was 47 cm long, and the injector field equalled the toroidal field at the major radius. The drift-control field $B_z(z)$ was generated by dipole field coils (Fig. 1) 1 cm above the floor plane of the torus. The beam generator was a Physics International Pulserad 312 with 1-in.-diam carbon cathode. Injection of two different beams was investigated: a 40-nsec pulse at either 10 kA, 1.75 MeV or 10 kA, 0.96 MeV (peak values). The system was filled with neutral nitrogen at 1000 Torr to provide rapid (few nanoseconds) charge neutralization by primary electron-atom collisions. Drifted distance was determined from the discoloration of a sheet of Cinemoid[5] No. 48 in the r-z plane as witness plate. This gave accuracy of ± 0.3 cm in drifted-beam edge position. Cinemoid position varied from $\varphi = 180°$ to 540°, with $\varphi = 0°$ defined as the injector-torus junction. A Rogowski coil at $\varphi = 120°$ measured net toroidal current $I_n(t)$. On some pulses a Faraday cup at $\varphi = 0°$ or 180° gave beam current. Relativistic electrons striking walls were detected by a scintillator-photodiode combination which time resolved the bremsstrahlung. The central results of the experiment are these:

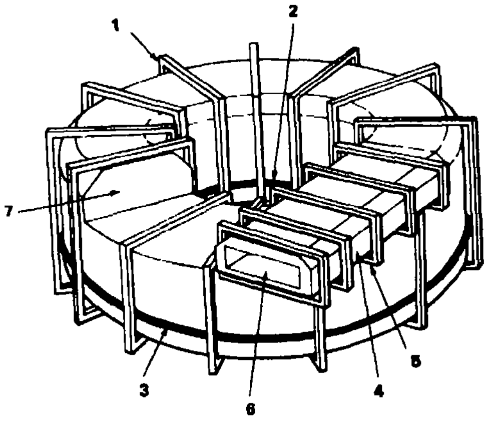

FIG. 1. Schematic of apparatus. (1) Toroidal field coil (12), (2) inner dipole-field coil, (3) outer dipole-field coil, (4) injector, (5) injector field coil, (6) beam injection aperture, and (7) abutment wall at $\varphi = 240°$, the injector "insert."

Beam injection.—Integration of the wave forms from the Faraday cup at 180° indicates charge injection and transport efficiency of 80%. This figure should be interpreted as a lower limit because of suspected reflection from the carbon Faraday-cup collector due to magnetic mirroring (line-tying effect in the carbon, diamagnetism in the beam channel). With Cinemoid across the lower region of the chamber, the drift of the 0.96-MeV beam in a 4-kG toroidal field was followed to 1 ½ turns, when the beam reached the floor.

Drift control by dipole field.—Figure 2 shows the good agreement obtained between theory and measurement of drifted distances in the toroidal-plus-dipole field. Here the calculation includes, in addition to Eq. (1), a toroidal-self-field effect which causes an additional small radially outward force [see Eq. (2) below]. The data correspond to drift velocities V_z of $0.05c$ to $0.12c$. The agreement shown in Fig. 2 is significant because it lends confidence to further predictions of beam motion in special toroidal configurations, such as the one proposed below for toroidal containment.

Stopping of vertical beam drift by dipole field.—To study the effect of the critical field B_{zc} in the freely circulating case (no Cinemoid or Faraday cup), we analyze the x-ray wave form from the photodiode, which was collimated using lead to view only the 0–120° sector of the torus. The wave-form amplitude is a measure of instantaneous electron-loss flux in that sector. Using the 1.75-MeV beam with $B_\varphi = 2.35$ kG, the dipole field strength was varied up to 888 G at its spatial maximum B_{zm}. For this case, $B_{zc} = 400$ G.

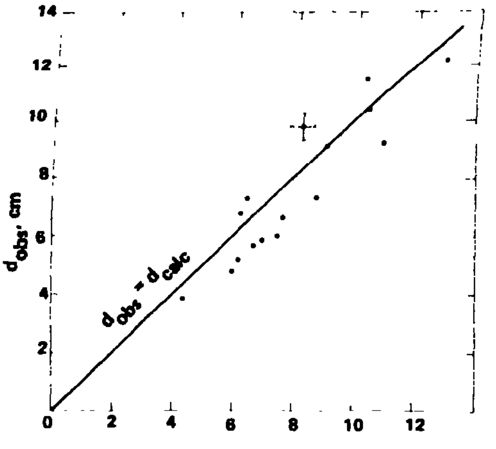

FIG. 2. Comparison of calculated and observed drifted distances in toroidal plus dipole field. Dipole-field spatial maximum, B_{zm}, ranges from -510 to $+800$ G in these measurements; toroidal field B_φ ranges from 1.5 to 4.0 kG. In all cases here the beam was intercepted before drifting to the position (if any) where $B_z = B_{zc}$.

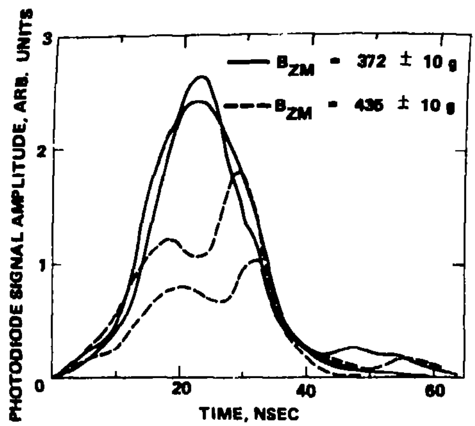

FIG. 3. Photodiode wave forms, showing change in photodiode-signal structure when dipole-field maximum B_{zm} exceeded critical value $B_{zc} = 400$ G. A third replication of each type is not shown.

Thus for $B_{zm} < 400$ G the beam should reach the floor, but when $B_{zm} > 400$ G the beam should be held off the floor and the drift stopped.

The results of these measurements are complicated by the fact that the dipole field's horizontally (i.e., radially) diverging components would in a few nanoseconds bring the beam to the sidewalls even if the vertical (i.e., axial) drift stopped when the beam reached the $B_z = B_{zc}$ position[6]; and by the fact that the detector did not discriminate between floor x rays and wall x rays. However, we observed that the shape and amplitude of the x-ray wave form varied with B_{zm}, and that this variation was very gradual except in a narrow range of B_{zm} around $B_{zm} = B_{zc}$: The transition from $B_{zm} < B_{zc}$ to $B_{zm} > B_{zc}$ gave an abrupt change in both the structure and amplitude of the x-ray wave form. This is shown in Fig. 3, and can be reasonably taken as the signature of a qualitative difference in the mode of electron loss when the critical field was applied. Note in Fig. 3 that the effect occurs in midpulse, when the injected electron γ is highest; i.e., the highest-γ electrons are the ones involved in the change. These are the only electrons in the pulse that would still reach the floor when B_{zm} was just less than B_{zc}, because $B_{zc} \propto \gamma$ (and because $B_{zc} = 400$ G was computed for peak γ). It is therefore reasonable to deduce that electron loss to the floor was dramatically reduced by making $B_{zm} > B_{zc}$, i.e., the axial drift was effectively stopped. This conclusion is clearly inferential and is supplementary to Fig. 2.

The above results show the viability of drift injection as a multiturn toroidal injection scheme. Beams were efficiently injected into the torus and a simple dipole field gave drift control but caused radial loss of the beam. The remaining obstacle to the creation of a toroidal beam of useful duration is a magnetic-containment geometry compatible with drift injection.

The method we propose uses toroidal-plus-betatron-type field geometry, with containment resulting from partial beam energy loss by self-magnetic-field generation and/or by heating of plasma. The z and r components of the betatron-type field are $B_z(r, z) = B_0(R_0/r)^n$ and $B_r(r, z) = -(n/r)zB_0(R_0/r)^n$, respectively, where B_0 and R_0 are constants. A single-particle analysis (no self-field) shows that for $B_z \ll B_\varphi$ the projection of the trajectory in the r-z plane is an ellipse (with Larmor gyration superimposed) if $0 < n < 1$.[7,8] We have analyzed the guiding-center equations including the beam's poloidal self-magnetic-field; in this case the ellipse's center (which always lies on the symmetry plane of the betatron field) is at radius

$$R_e = \frac{\gamma m_0 c^2 \beta_\parallel}{e B_0 (1-n)} \left[1 + \frac{I_n}{I_A} \left(\ln \frac{4\pi R_t}{a} - 1.45 \right) \right] - \frac{n R_0}{(1-n)}, \qquad (2)$$

where I_A is the Alfvén current, a is the beam radius, and it is assumed that $B_0 \ll B_\varphi$, $\beta_\perp \ll B_\parallel$ (cold beam), and $(R_e - R_0)/R_0 \ll 1$.

If γ and I_n vary with time suitably, the consequent time variation of R_e can be used to trap the beam away from the injector, which lies on the initial elliptical trajectory. Two important effects can decrease γ and thereby modify the trajectory: (1) Part of the kinetic energy goes into self-magnetic-field energy (inductive trapping), and (2) plasma heating extracts beam energy. In the case where γ decreases due to the back emf induced by the buildup of toroidal net current I_n, differentiation of Eq. (2) (taking account of the coupled time dependence of I_n, $\beta_\parallel$, γ, and I_A) shows that R_e decreases as long as I_n increases:

$$\frac{dR_e}{dt} = -\frac{dI_n/dt}{B_0 c (1-n)} \left[\ln \frac{4\pi R_t}{a} - 3.45 \right]. \qquad (3)$$

We have developed a computer code that calculates the trajectory of a test-beam electron, including self-field effects (hoop force and induced electric fields), given $I_n(t)$. Figure 4 shows one such case, illustrating toroidal containment by the effect described in Eq. (3).

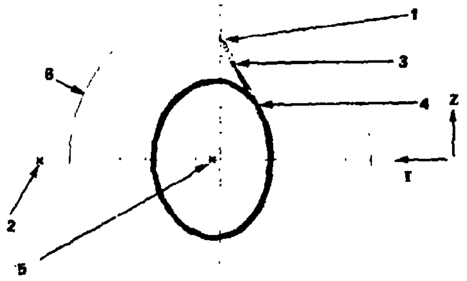

FIG. 4. Computer calculation of inductive trapping of test-beam electron, showing trajectory projected into r-z plane. Parameters in this case are $I_n(t) = I_0(1 - e^{-t/\tau})$, $I_0 = 5$ kA, $\tau = 50$ nsec, $\gamma = 4.0$ (injected), torus major radius 60 cm, minor radius 15 cm, 4 cm beam diameter, $B_\varphi = 5$ kG, and $B_z = 90$ G at minor axis, $n = 0.5$. (1) Test electron injected at $t = 0$ at beam center, 12 cm from minor axis, $\beta_\perp/\beta_\parallel = 0.18$. (2) Initial instantaneous center of ellipse (i.e., corresponding to position 1). (3) Electron drift during period of decreasing γ. Center of instantaneous ellipse continuously moves inward radially. (Trajectory appears irregular because only a sampling of increments is plotted.) Af- r 1 turn the electron has drifted down 1.8 cm, radial- inward 0.7 cm, nominally clearing the injector struc- re. (4) $d\gamma/dt \simeq 0$ and $I_n \approx I_0$ at $t \gtrsim 100$ nsec (7.4 turns); us the ellipse stops changing and is traced out by ibsequent motion. The trajectory is now on a closed irface entirely contained and away from the injector.) Final center of elliptical motion. (6) Toroidal cham- er.

In conclusion, we have shown that drift injection and an external magnetic field can be used to circulate and control an intense relativistic electron beam in a torus. We propose and have numerically shown that trapping can be achieved using toroidal-plus-betatron-type fields and beam energy losses. Reactor application of this technique, with substantially larger currents and fields, is under study.

We are pleased to acknowledge informative discussions with D. W. Kerst and T. Fessenden, helpful comments from C. Stallings, S. Putnam, and T. Young, and the fabrication work and experimental support of C. Parks.

---

[1] S. Yoshikawa, Phys. Rev. Lett. 26, 295 (1971).

[2] S. Yoshikawa and N. Christofilos, in *Proceedings of the Fourth International Conference on Plasma Physics and Controlled Nuclear Fusion Research, Madison, Wisconsin, 1971* (International Atomic Energy Agency, Vienna, Austria, 1972), Vol. 2, p. 357.

[3] J. Benford, S. Putnam, C. Stallings, J. Guillory, and S. Shope, Phys. Rev. Lett. 31, 346 (1973).

[4] J. Benford, J. Guillory, and C. Stallings, J. Appl. Phys. 45, 1657 (1974).

[5] N. Goldstein, in *Manual on Radiation Dosimetry*, edited by N. Holm and R. Berry (Marcel Dekker, Inc., New York, 1970), p. 371.

[6] This loss was gradual enough not to obscure vertical-drift measurements in Fig. 2.

[7] T. G. Linhart, Plasma Physics (North-Holland, Amsterdam, 1960), p. 26.

[8] L. Ferrari and M. Zucker, Particle Accel. 2, 121 (1971).

Strong [illegible] at the Helium-Solid Interface

H. Kinder* and W. Dietsche
Institut für Festkörperforschung, Kernforschungsanlage Jülich, 517 Jülich, West Germany

(Received 16 November 1973)

Tunable monochromatic phonon pulses (130 to 870 GHz) were scattered at solid surfaces covered with various amounts of helium. A strong phonon loss due to only 3 atomic layers was observed which was independent of frequency and did not exhibit structure due to the helium dispersion. The results indicate strong frequency conversion at the interface, and thus suggest a new approach to the Kapitza-resistance problem.

The thermal boundary resistance between liquid helium and solids, the well-known Kapitza resistance, is still not understood.[1] The magnitude of the thermal resistance is much smaller than predicted by the acoustic mismatch theory of Khalatnikov.[2] Several refinements of the theory remain unsatisfactory as yet, and heat-transfer mechanisms other than direct transmission of phonons have been proposed.[1] More recently, in experiments with high-frequency phonons (> 100 GHz or 5 K), Anderson and Sabisky[3] have apparently found an almost complete transmission through the interface. A strong phonon loss due to the He bath was also reported by Trumpp, Lassmann, and Eisenmenger.[4] By scattering heat pulses at surfaces covered with helium, Guo and Maris[5] found that the "transmission" was more effective for transverse than for longitudinal phonons.

We wish to report here on measurements where we employed monochromatic phonon pulses with variable frequency[6] rather than heat pulses, by using superconducting tunneling junctions as phonon generators and detectors. A frequency range extending from below the roton minimum to far above the dispersion curve of superfluid He[7] was investigated (130 to 870 GHz). The frequency of the backscattered phonons was discriminated by using the frequency threshold of the detector junction.[8] No indications of a direct transmission of phonons into bulk liquid He modes was found so that the previous interpretation[5] must be modified. Rather, effects due to inelastic processes in a few atomic layers near the interface were observed by our technique.

The experimental arrangement is shown in the inset of Fig. 1. The phonon-generator junctions were placed 0.2 mm apart on the same surface of a crystal. Mechanically polished disks of Al_2O_3, 6 mm thick, in c orientation, and of Ge, 4 mm thick, in [110] orientation were used. The phonons were scattered back from the far crystal surface to which a vacuum chamber was attached. The chamber contained either vacuum, He^4 gas, or bulk liquid. The pressure was measured by a Barocel capacitance manometer and corrected for thermomolecular flow.[9] The entire arrangement was immersed in a He bath to ensure rapid heat removal and constant conditions for the junctions.

The method of phonon generation was described previously.[6] The pulses emitted by the generator junction consist of two contributions, the monochromatic "bremsstrahlung" phonons with tunable frequency $(eV - 2\Delta_G)/h$, where V is the bias volt-

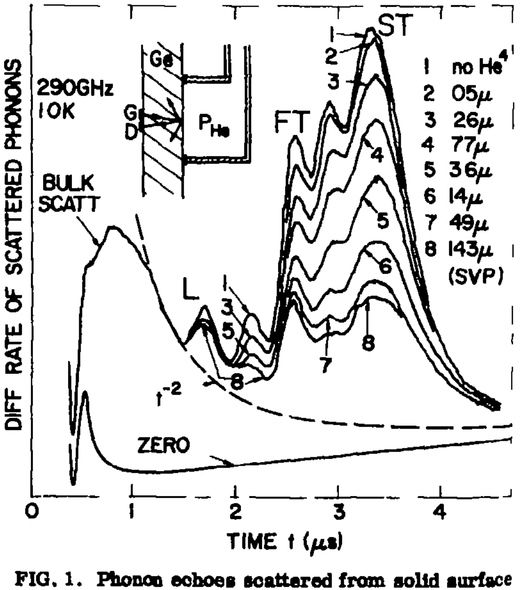

FIG. 1. Phonon echoes scattered from solid surface without helium (trace 1), with He^4 films (traces 2–7), and with bulk liquid at surface (trace 8). L, longitudinal; FT, fast transverse; ST, slow transverse echo. Inset shows sample with generator and detector junctions and vacuum chamber.

[illegible] with the fixed frequency [illegible] re- [illegible] upper frequency limit of the "brems- [illegible] phonons is also given by $2\Delta_c/h$, be- [illegible] onset of reabsorption. In most ex- [illegible], Sn junctions were used with $2\Delta_c/h$ [illegible] (~14 K). In some experiments, fre- [illegible] up to 870 GHz (~42 K) were generated [illegible] PbBi junctions. The use of these junc- [illegible] ill be described elsewhere. The detector [illegible] on is sensitive only to frequencies exceed- [illegible] ts energy gap $2\Delta_D$. This threshold was 130 [illegible] z (~6 K) for the Al:O junctions used.

Figure 1 shows the rate[6] of backscattered pho- ons at 290 GHz as a function of time in a Ge rystal at 1.0 K, for various He^4 pressures at he reflecting surface. After a pulse of 0.1 μsec uration was generated at $t = 0$, a bulk scattering ignal was first observed. This decreased as t^{-2} hen the scattering zone propagated away from he junctions. The dashed line is the appropriate xtrapolation for times when the echoes from the ar surface entered the detector.

The echoes due to longitudinal (L), fast trans- erse (FT), and slow transverse (ST) phonon nodes were readily identified from the known ltrasonic velocities. The two additional pulses were probably due to mode conversion, resulting from the diffuse scattering at the far crystal surface. That the scattering was indeed diffuse rather than specular is also seen from the tails of he echoes which could be largely suppressed by n annular metal coating, such that the phonons raveling at oblique angles (having longer round- rip times) were absorbed by the metal rather han being diffusely scattered back into the detec- or.

On introducing He, the echoes strongly de- reased. Strikingly, the magnitude of the de- rease was different even for the two transverse modes. In total, the L echo decreased to 70% of its original height, the FT echo to 45%, and the ST echo to 32%. With Al$_2$O$_3$, the L echo de- reased to 90%, and the T echo to 30%. With the eat-pulse technique, Guo and Maris[5] found only a decrease to about 70% for the T phonons in Al$_2$O$_3$.

By measuring the emission of second sound from heat pulses, Swanenburg and Wolter[10] found equal intensities for both L and T modes. This is not inconsistent with our results however, be- cause their L pulse corresponds to the sum of the L and the mode-conversion echoes (L to FT) in our case. The latter was in fact strongly decreasing. *This indicates that only those L phonons which are undergoing mode conversion, i.e. which give rise to a transverse motion of the surface, can strongly interact with the helium.*

It is important to notice that the echoes decreased already at pressures below the saturated vapor pressure when only an unsaturated film was present at the surface. The film thickness is usually calculated by[3] $d = d_0[\alpha/T\ln(P_0/P)]^{1/3}$, with P being the gas pressure, P_0 the saturated vapor pressure, T the temperature, α a material parameter, and d_0 the thickness of a monolayer at a density of bulk He^4. Since the result is relatively insensitive to α, we can use for Ge the value for Si, 36 K, together with $d_0 = 3.6$ Å.[11] Accordingly, Fig. 2 *shows the relative height of the ST echo as a function of the film thickness.*

Obviously 2 or 3 atomic layers are already sufficient to cause the effect while increasing the film thickness has very little influence, and filling the chamber with bulk liquid has no effect. Thus it is clear that the effect is not merely due to an enhanced direct transmission. This would simply lead to reflection at the film surface and retransmission into the solid with the same high transmission coefficient. Similarly, other direct, i.e. frequency-conserving, processes such as conversion to and delayed reconversion from surface waves, or just an enhancement of the diffusivity of the backscattered phonons, would not allow the phonons to leave the system. Thus, if the echoes were decreased by such a process, their tails would be increased rather than also decreased as observed (see Fig. 1).

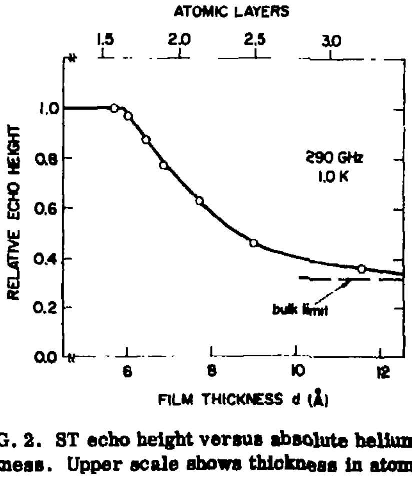

FIG. 2. ST echo height versus absolute helium film thickness. Upper scale shows thickness in atomic layers. At 3 atomic layers the bulk limit is almost reached.

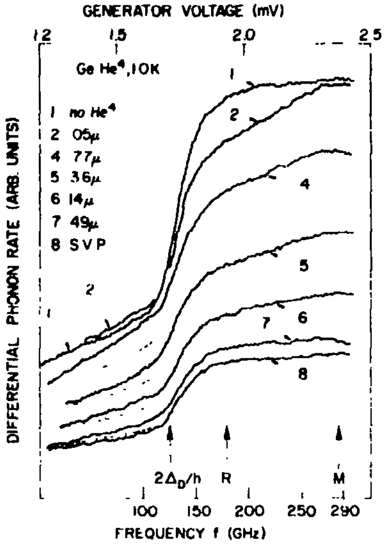

FIG. 3. Frequency dependence of ST echo between 130 and 290 GHz. The dashed traces indicate the decreased background of "recombination phonons." The actually measured traces show an additional contribution due to the up-conversion of "bremsstrahlung" phonons. No structure is seen due to the roton minimum (R) or the phonon maximum (M) of the helium dispersion.

The only direct process by which a phonon can indeed leave the system is the direct desorption of a He atom from the film surface. In that case, however, an onset frequency is expected[12] corresponding to the energy of vaporization, 7.17 K (150 GHz), plus a contribution of the order $kT \times \ln(P_0/P)$. No indication of this was observable, as one can see from Fig. 3 where the ST echo height is displayed as a function of the frequency of the "bremsstrahlung" phonons.

Thus, no direct processes can be responsible for the signal decrease in the case of thin films. Rather, one has to consider indirect, i.e. inelastic, processes which involve conversion of the frequency of the incident phonons. Evidence for such processes can be obtained by analyzing the frequency distribution of the backscattered (or reemitted) phonons. A true frequency analyzer for this purpose is not available yet. However, one can obtain similar information by using the frequency threshold of the detector junction. At frequencies just below $2\Delta_D$, the "bremsstrahlung" phonons are not detectable. If some of the inelastic processes due to the helium film lead to the backscattering (or reemission) of phonons with higher frequencies, however, these will show up as a detector signal.

One can in fact see this from Fig. 3 after accounting properly for the decreasing background of "recombination" phonons. The latter have the fixed frequency $2\Delta_G/h = 290$ GHz so that they decrease with the same ratio as the signal at 290 GHz. Therefore, this ratio can be used to calculate the decreased background from the vacuum trace 1, for each film thickness. The result is plotted as the dashed traces in Fig. 3. As compared to these, the actually measured traces are enhanced, thus demonstrating that additional phonons with frequencies higher than $2\Delta_D/h$ were indeed detected. Their rate was largest for trace 4 (about 10 times the noise), and equally large also for a trace taken at $P = 0.26$ mTorr (not shown). Thus we have obtained experimental evidence for relatively strong frequency-up-conversion processes.

The up-conversion processes naturally also imply the presence of down-conversion processes. For frequencies above $2\Delta_D$, all the up-converted phonons will be detected in the same way as the original ones. However, the down-converted phonons will not be detected if they have frequencies below $2\Delta_D/h$. Thus, the strong loss of phonons at the frequencies above $2\Delta_D/h$ can be indeed also understood by the inelastic processes.

In the case of very thin films (trace 2), the spread of the backscattered (or reemitted) spectral distribution seems still to be narrow, so that at low or high frequencies away from the threshold, the signal has not yet changed whereas near the threshold the spread already manifested itself by the change in signal amplitude. For thicker films, the spread seems to become larger and down conversion dominates, leading effectively to thermalization. Simultaneously the gas pressure becomes larger so that the heat conduction to the gas is no longer negligible. In fact, the signal decrease observed with the heat-pulse technique[5] shows that heat is conducted into the gas, because the bolometers used were not particularly sensitive to frequency-conversion effects. However the total decrease observed with bolometers seems to be smaller than what we observe with junction detectors, so that even in the case of bulk liquid there seems to be some of the energy returning to the solid as thermal phonons. We plan to clarify this point by detecting the backscattered phonons simultaneously by a bolometer and a junction detector.

Since the signal shows no further change after about 3 atomic layers are completed, it is very likely that the inelastic processes occur in these few atomic layers regardless of whether gas or bulk liquid is adjacent. This is also consistent with the fact that we have observed no structure at the frequencies of the maximum phonon (*M* in Fig. 3) and minimum roton (*R*) energies, in the case of bulk liquid (trace 8), whereas one would expect singularities[13] in the transmission coefficient if the phonons were directly transmitted into bulk liquid-helium excitations. Also, the total signal decrease was found to be independent of frequency up to 870 GHz which is far above the dispersion curve of liquid helium.

Thus our measurements indicate that indirect, i.e. frequency-conversion, processes are involved in the mechanism responsible for the enhanced heat conduction through the interface observed above ~1 K when the higher-frequency phonons become more important. To understand the Kapitza problem, one should therefore consider the microscopic nature of the first few atomic layers at the interface which are compressed by the Van der Waals force.

It is a pleasure to acknowledge the many fruitful discussions with C. H. Anderson, W. Buckel, W. Eisenmenger, J. Jäckle, and F. Pobell. We are indebted to R. L. Melcher for valuable discussions and reading the manuscript.

---

*Present address: IBM Thomas J. Watson Research Center, Yorktwon Heights, N. Y. 10598.

[1] G. L. Pollack, Rev. Mod. Phys. 41, 48 (1969); N. S. Snyder, Cryogenics 10, 89 (1970); L. J. Challis, J. Phys. C: Proc. Phys. Soc., London 7, 481 (1974).

[2] I. M. Khalatnikov, Zh. Eksp. Teor. Fiz. 22, 687 (1952).

[3] C. H. Anderson and E. S. Sabisky, in *Physical Acoustics*, edited by W. P. Mason and R. N. Thurston (Academic, New York, 1971), Vol. 8, p. 1.

[4] H. J. Trumpp, K. Lassmann, and W. Eisenmenger, Phys. Lett. 41A, 431 (1972).

[5] C.-J. Guo and H. J. Maris, Phys. Rev. Lett. 29, 855 (1972).

[6] H. Kinder, Phys. Rev. Lett. 28, 1564 (1972). For details, see H. Kinder, Z. Phys. 262, 295 (1973).

[7] D. G. Henshaw and A. D. B. Woods, Phys. Rev. 121, 1266 (1961).

[8] W. Eisenmenger and A. H. Dayem, Phys. Rev. Lett. 18, 125 (1967).

[9] T. R. Roberts and S. G. Sydoriak, Phys. Rev. 102, 304 (1956).

[10] T. J. B. Swanenburg and J. Wolter, Phys. Rev. Lett. 31, 693 (1973).

[11] E. S. Sabisky and C. H. Anderson, Phys. Rev. Lett. 30, 1122 (1973).

[12] M. W. Cole, Phys. Rev. Lett. 28, 1622 (1972).

[13] H. Haug, Phys. Lett. 45A, 170 (1973).

Dielectric Response in the Wannier Representation: Application to the Optical Spectrum of Diamond*

W. Hanke† and L. J. Sham
Department of Physics, University of California, San Diego, La Jolla, California 92037

(Received 13 March 1974)

A method of calculating local-field effects in the time-dependent Hartree-Fock approximation utilizing the Wannier representation is presented and applied to the optical spectrum of diamond. The results establish the importance of including both the local-field effects and the exchange effects beyond the random-phase approximation.

In a crystal, which possesses lattice translational symmetry, a small electric perturbation of wave vector $\vec{q}+\vec{G}'$ and frequency ω can excite responses of wave vector $\vec{q}+\vec{G}$ and frequency ω, where $\vec{G}$ and $\vec{G}'$ denote reciprocal-lattice vectors. Thus, the dielectric matrix, describing this response, is of the form $\epsilon(\vec{q}+\vec{G}, \vec{q}+\vec{G}'; \omega)$. An external macroscopic electric field may be regarded as a perturbation of vanishingly small wave vector $\vec{q}$ and, therefore, the screening of the external macroscopic field is given by the matrix element $\epsilon^{-1}(\vec{q}, \vec{q}; \omega)$ of the inverse dielectric matrix. In insulating crystals, this results in a formula for the macroscopic dielectric constant,

$$\epsilon(\omega) = \lim_{\vec{q}\to 0}[1/\epsilon^{-1}(\vec{q}, \vec{q}; \omega)]. \tag{1}$$

In the special case of an ideal insulator in which the electrons are so tightly bound that the dipole approximation is valid, the inversion of the dielectric matrix has been shown[1] to lead to the local-field (or Lorentz-field) effect. The resulting Lorentz-Lorenz relation has been used to demonstrate[2] empirically the importance of the local-field effect in the optical spectrum of CsCl.

It is still common practice to relate electronic band structures to the optical spectra of ionic and covalent crystals without including the local-field effects. This corresponds to neglecting the off-diagonal terms of the dielectric matrix and to using as the macroscopic dielectric constant

$$\bar{\epsilon}(\omega) = \lim_{\vec{q}\to 0}\epsilon(\vec{q}, \vec{q}; \omega), \tag{2}$$

an approximation which is rigorously justified only in the free-electron limit. On the other hand, for covalent crystals, with the electron wave functions sufficiently spread out to form bonds, physically it appears that the Lorentz-Lorenz relation is invalid. In fact, we have found that its use yields a poorer agreement with the measured optical spectrum. To examine the fundamental relation between band structure and the optical spectrum, a first-principles investigation of the local-field effect is, therefore, very important.

We report here a method of calculating the local-field effect in the time-dependent Hartree-Fock approximation by expressing the dielectric response in terms of Wannier functions in much the same way as we did in the case of lattice dynamics in metals.[3] This method is used to calculate the optical spectrum of the covalent crystal diamond. Van Vechten and Martin[4] have investigated the local-field effect in diamond by *directly evaluating and inverting a dielectric* matrix with size 59×59 in the plane-wave representation using the pseudopotential method. The contrast between the two methods of studying the local-field effect is as much as that between the linear combination of atomic orbitals (LCAO) and pseudopotential methods for calculating the band structure. In the plane-wave formulation, there is an intrinsic problem of slow convergence both for the dielectric matrix and for the wave function. The LCAO or Wannier-function method seems to be the more natural concept to describe the local-field effects, because it is precisely the localization of the wave functions which is the physical origin for these effects.

The proper polarization part $\tilde{\chi}$ is related to the dielectric matrix by

$$\epsilon(\vec{q}+\vec{G}, \vec{q}+\vec{G}'; \omega) = \delta_{\vec{G},\vec{G}'} - v(\vec{q}+\vec{G})\tilde{\chi}(\vec{q}+\vec{G}, \vec{q}+\vec{G}'; \omega), \tag{3}$$

where $v(\vec{q}+\vec{G})$ is the Fourier transform of the Coulomb potential. Thus, the inverse dielectric matrix is determined by

$$\epsilon^{-1} = 1 + v\tilde{\chi}\epsilon^{-1}. \tag{4}$$

We have noted[3] that in the time-dependent Hartree approximation [or random-phase approximation (RPA)], when the electron wave functions are expressed in terms of Wannier functions or LCAO's, the polarization is of the separable form

$$\tilde{\chi}(\vec{q}+\vec{G}, \vec{q}+\vec{G}'; \omega) = \sum_{ss'} F_s(\vec{q}+\vec{G}) N_{ss'}(\vec{q}, \omega) F_{s'}^*(\vec{q}+\vec{G}'). \tag{5}$$

The inverse dielectric matrix then becomes

$$\epsilon^{-1}(\vec{q}+\vec{G}, \vec{q}+\vec{G}'; \omega) = \delta_{\vec{G}\vec{G}'} + v(\vec{q}+\vec{G}) \sum_{ss'} F_s(\vec{q}+\vec{G}) S_{ss'}(\vec{q}, \omega) F_{s'}^*(q+\vec{G}'), \tag{6}$$

where the matrix S is given by

$$S = \dot{N}(1 - VN)^{-1} \tag{7}$$

with

$$V_{ss'}(\vec{q}) = \sum_{\vec{G}} F_s^*(\vec{q}+\vec{G}) v(\vec{q}+\vec{G}) F_{s'}(\vec{q}+\vec{G}'). \tag{8}$$

Thus, the inversion problem is reduced to the inversion of a matrix of the same dimension as N. If the density matrix element between Wannier functions at different sites decreases rapidly with distance, the size of N is quite manageable.

We have gone beyond the RPA and studied the effect of exchange on the proper polarization part. Within the time-dependent Hartree-Fock approximation, the exchange effect can be taken into account by an integral equation for the vertex.[5] We again express the kernel for the exchange in terms of the Wannier functions. The dominant term is then given by exchange processes within the same bond in the covalent crystal. This exchange contribution has the same structure as the Coulomb interaction in RPA and the net effect of this term is a modification of corresponding terms in the Coulomb matrix V given by Eq. (8).

We follow Ambegaokar and Kohn[6] in treating the divergence in the long-range Coulomb interaction and obtain for the macroscopic dielectric constant

$$\epsilon(\omega) = \lim_{\vec{q}\to 0}[1 - v(\vec{q})\hat{\chi}(\vec{q}, \vec{q}; \omega)], \tag{9}$$

where $\hat{\chi}$ is the sum of all polarization processes *not* involving the long-range part of the Coulomb interaction $v(\vec{q})$.

For certain types of symmetry for the bands, e.g., s and p symmetry for the conduction and valence bands, respectively, or vice versa, as is approximately the case for the alkali halides, the density form factor F_s in the separable polarization part (4) takes the dipole form. Such a form was assumed by Sinha, Gupta, and Price.[7] From this, we can derive the Lorentz-Lorenz relation with a specific prescription for the self-interaction term. In general, the separable form is not necessarily dipolar in nature.

Since there are not yet available Wannier functions for covalent crystals of the diamond type, we follow Hall's method[8] to construct a set of LCAO's for the band structure. The s and three p atomic wave functions of the valence shell are combined according to Pauling's prescription[9] to form four hybridized wave functions localized in four tetrahedral directions. The atomic wave functions are expressed in the Gaussian basis which allows for analytic integration of all the multicenter integrals involved in Eqs. (6) and (9) and furthermore enables us to test easily the convergence of higher overlap corrections to $\epsilon(\omega)$. The hybridized orbitals from two neighboring atoms in the same direction are added and subtracted to form the bonding and antibonding orbitals φ_ν, where the index ν stands for ± and a tetrahedral direction. Linear combinations of the bonding orbitals are used to form the four valence bands, and of the antibonding orbitals to form the four conduction bands. We include up through the third-nearest-neighbor overlap integrals of the Hamiltonian to fit the energy spectrum of a first-principles calculation by Painter, Ellis, and Lubinsky.[10] This yields a Hamiltonian matrix in our LCAO basis from which the energies and wave functions are determined.

Using the Wannier-function formulation of dielectric response described above, we obtain the macroscopic dielectric constant

$$\epsilon(\omega) = 1 - (4\pi e^2/\Omega_0) \sum_{ss'} f_s^{\alpha} S_{ss'} f_{s'}^{\alpha *}, \tag{10}$$

where

$$f_s^{\alpha} = \int \varphi_\nu^*(\vec{r}) r_\alpha \varphi_\mu(\vec{r} - \vec{x}_l)\, d^3r \tag{11}$$

with $\vec{x}_l$ being the lattice vector, Ω_0 the volume of the unit cell, and s short for (ν, μ, l). The screening matrix S is given by Eq. (7) with

$$N_{ss'}(\omega) = \sum_{n,n',\vec{k}} c_\nu^*(n\vec{k}) c_\mu(n'\vec{k}) \exp(i\vec{k}\cdot\vec{x}_l) \frac{f(n\vec{k}) - f(n'\vec{k})}{E(n\vec{k}) - E(n'\vec{k}) + \omega} \exp(-\vec{k}\cdot\vec{x}_{l'}) c_{\nu'}(n\vec{k}) c_{\mu'}^*(n'\vec{k}), \tag{12}$$

where $E(n\vec{k})$ denotes the electron energy, $f(n\vec{k})$ the occupation number, and $c_\mu(n\vec{k})$ the wave function in the bonding and antibonding orbital basis.

In the RPA, the Coulomb matrix defined in Eq. (8) can be written as

$$V_{ss'}=\sum_m \iint d^3r\, d^3r'\, \varphi_\nu{}^*(\vec{r}-\vec{x}_m)\varphi_\mu(\vec{r}-\vec{x}_l-\vec{x}_m)v(\vec{r}-\vec{r}\,')\varphi_{\nu'}{}^*(\vec{r}\,')\varphi_{\mu'}(\vec{r}\,'-\vec{x}_{l'}). \tag{13}$$

When exchange is taken into account as described above, V is modified by subtracting from Eq. (13) half of the $\vec{x}_m=0$ term if either (a) $\vec{x}_l=\vec{x}_{l'}$ and $\mu=\mu'$ or (b) $\nu=\nu'$.

For the calculation of the dielectric constant we have included only nearest-neighbor overlaps of wave functions φ_ν, having found the rest negligible within the error range of our approximate band structure and wave functions. The dimension of the matrices N, V, S, etc. is then 28. The $\vec{k}$ summation of (12) was done by the Gilat-Raubenheimer method[11] with the smallest box having a width of 0.078 a.u. The dielectric matrix can be expressed in terms of either the density-density response or the current-current response. We adjust the s and p orbitals such that, indeed, either representation gives the same answer. This adjustment, which is used in all the calculated dielectric functions below, generally increases the strength of the absorption spectrum without changing its characteristic features.

The results of our calculation of the optical spectrum $\epsilon_2(\omega)$, i.e., the imaginary part of $\epsilon(\omega)$, for diamond are plotted in Fig. 1 and compared with experiment.[12] The optical spectrum is quite sensitive to local-field corrections. Consider the main peak which is close to 12 eV. The RPA calculation without local-field effects ($\bar{\epsilon}_{\rm RPA}$ in Fig. 1) places the peak a little too high. Local-field effects within the RPA ($\epsilon_{\rm RPA}$ in Fig. 1) produce an additional shift by approximately 0.5 eV to higher energies contrary to what is required to reconcile theory with experiment. The shift to higher energies and the reduction of strength below the main peak introduced by local-field effects in the RPA have also been reported by Van Vechten and Martin,[4] however to a less drastic extent. Inclusion of local-field effects in the time-dependent Hartree-Fock approximation (ϵ in Fig. 1), on the other hand, results in a 1.5-eV shift of the main peak to lower energies and an improvement of the overall agreement with experiment, especially on the low-energy side.

In view of our approximate band structure and wave functions, we do not claim to have calculated quantitatively the absolute magnitude of $\epsilon_2(\omega)$. To do this our formulation of the dielectric function can be used in exactly the same manner directly utilizing the results of a first-principles Hartree-Fock band calculation based on LCAO's or Wannier functions. The use of more accurate wave functions than ours gives significantly better agreement of $\bar{\epsilon}_{\rm RPA}$ without local fields with experiment, as has been shown by Lubinsky, Ellis, and Painter[13]; however, it is not clear that replacement of the statistical exchange potential used in the underlying band structure calculation by the exact Fock potential does not spoil that particular agreement.[14] We believe that the sign and the order of magnitude of the shift introduced in the peak structure of $\epsilon_2(\omega)$ by local-field and exchange effects is not affected by our approximate treatment of band structure and wave functions.

In summary, our results demonstrate the necessity for incorporating both local-field and exchange effects in the dielectric function of covalent crystals. These microscopic effects are important not only for the identification of struc-

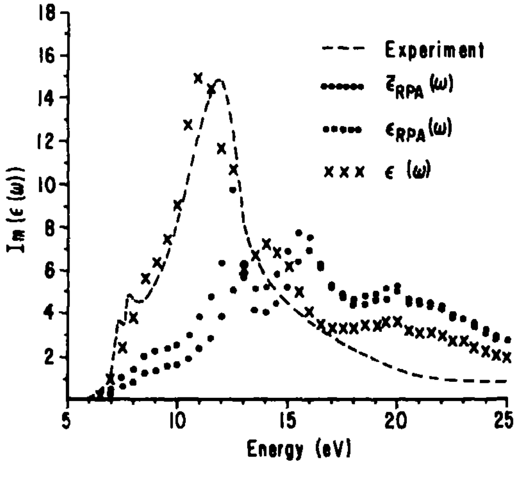

FIG. 1. Imaginary part of the dielectric constant versus energy; experimental data from Ref. 12; $\bar{\epsilon}_{\rm RPA}$ calculated within RPA without local-field correction; $\epsilon_{\rm RPA}$ calculated within RPA with local-field correction; $\epsilon(\omega)$ calculated with local-field correction in the time-dependent Hartree-Fock approximation.

tures in the measured optical spectrum with the electronic transitions between energy bands but also for other purposes, such as a calculation of the phonon frequencies.

We are grateful to Dr. Z. Kam for his help with the Gilat-Raubenheimer program and to Professor W. Kohn for stimulating discussions.

---

*Work supported in part by the National Science Foundation under Grant No. GH-38345.

†Work supported in part by the Deutsche Forschungsgemeinschaft and by the Max-Planck Institut für Festkörperforschung, Stuttgart, Germany.

[1] S. L. Adler, Phys. Rev. 126, 413 (1962); N. Wiser, Phys. Rev. 129, 62 (1963).

[2] T. K. Bergstresser and G. W. Rubloff, Phys. Rev. Lett. 30, 794 (1973).

[3] W. Hanke, Phys. Rev. B 8, 4585, 4591 (1973), and in *Proceedings of the International Conference on Phonons, Rennes, France, 1971*, edited by M. A. Nusimovici (Flammarion, Paris, 1971), p. 294, and in *Proceedings of the International Conference on Inelastic Scattering of Neutrons, Grenoble, France, 1972)* (International Atomic Energy Agency, Vienna, 1972), p. 3; L. J. Sham, Phys. Rev. B 6, 3584 (1972), and in *Lattice Dynamics*, edited by A. A. Maradudin and G. K. Horton (North-Holland, Amsterdam, to be published).

[4] J. A. Van Vechten and R. M. Martin, Phys. Rev. Lett. 28, 446 (1972).

[5] L. J. Sham and J. M. Ziman, Solid State Phys. 15, 282 (1963).

[6] V. Ambegaokar and W. Kohn, Phys. Rev. 117, 423 (1960).

[7] S. K. Sinha, R. P. Gupta, and D. L. Price, Phys. Rev. Lett. 26, 1324 (1971), and Phys. Rev. B 9, 2564, 2573 (1974).

[8] G. G. Hall, Phil. Mag. 43, 338 (1952).

[9] L. Pauling, J. Amer. Chem. Soc. 53, 1367 (1931).

[10] G. S. Painter, D. E. Ellis, and A. R. Lubinsky, Phys. Rev. B 4, 3610 (1971).

[11] G. Gilat and L. J. Raubenheimer, Phys. Rev. 144, 390 (1966).

[12] R. A. Roberts and W. C. Walker, Phys. Rev. 161, 730 (1967).

[13] A. R. Lubinsky, D. E. Ellis, and G. S. Painter, Phys. Rev. B 6, 3950 (1972).

[14] R. N. Euwema, D. L. Wilhite, and G. T. Surratt, Phys. Rev. B 7, 818 (1973).

Direct Transform-Deconvolution Method for Surface-Structure Determination

David L. Adams and Uzi Landman

Chemistry Research Laboratory, Xerox Corporation, Webster, New York 14580

(Received 6 March 1974)

We describe direct method for surface-structure determination from low-energy electron-diffraction (LEED) intensities. Fourier transforms of LEED intensities are shown to contain convolution products of functions of the interatomic vectors with data truncation and potential windows. A deconvolution method and substrate-subtraction procedure is described, yielding an accurate structural determination of clean surfaces and overlayer systems. Applicability of the method to experimental data is demonstrated by using LEED intensities from Al(100).

Since the discovery[1] of low-energy electron diffraction (LEED), the extraction of surface structures has been the subject of intensive efforts, mainly via an *indirect approach*,[2] which is intrinsically dependent on model assumptions and proceeds by comparisons of microscopic model calculations with experimental intensities. However, a full variation over the geometrical and electronic parameters is not carried out because of the prohibitive expense in computation time and storage.

In this paper we present the principles of a rapid, *direct method* of surface-structure determination[3] and demonstrate its applicability to the analysis of experimental data.[4]

In the diffraction of low-energy electrons from solids, momentum is conserved in the plane parallel to the surface, giving rise to diffracted beams characterized by discrete (hk) Miller indices of the two-dimensional net. Electron propagation in the direction normal to the surface is strongly attenuated[1] and is, therefore, characterized by the continuous variable S, where $2\pi S$ is the normal momentum transfer and $S>0$ as a result of the half-space nature of LEED measurements and the inner potential of the solid. Consequently, the complex Fourier transform of the intensities may be written as

$$P(x,y,z)=\sum_{h,k=-\infty}^{\infty}\int_{-\infty}^{\infty}dS\,I_{hk}(S)\omega_B(S;S_1,S_2)\exp[2\pi i(hx+ky)]\exp(2\pi iSz), \tag{1}$$

where $I_{hk}(S)$ is the intensity of the (hk) beam and $\omega_B(S;S_1,S_2)$ is a "box-car" truncation function (unit magnitude for $S_1<S<S_2$ and zero otherwise).

The transformation given in Eq. (1) defines a *three-dimensional vector space.*[5] Structure determination, however, can be carried out by using reduced forms of the three-dimensional transform. The analysis proceeds by the determination of interlayer spacings from *one-dimensional projections* of the transform, the result of which are utilized in the determination of interlayer registries via *two-dimensional transform sections* as we have previously demonstrated.[3] The one-dimensional line projection $P(z)$ is defined by

$$P(z)=\int_{-\infty}^{\infty}dS\,I_{00}(S)\omega_B(S;S_1,S_2)\exp(2\pi iSz), \tag{2}$$

where I_{00} is the intensity of the specular beam. As shown below analytically for the case of kinematic scattering, and through analysis of experimental data exhibiting pronounced multiple-scattering features, $P(z)$ contains the projections of interatomic vectors on the surface normal. As we have indicated previously, the problems of deconvolution, discussed below, are most acute in the analysis of line projections.

The fundamental problem involved in the use of the LEED transform consists of the extraction of geometrical information from its convolution with the effects of data truncation, scattering potentials, and temperature. We emphasize that failure to perform a proper deconvolution results in most cases in ambiguous structural assignments and inadequate spatial resolution.[6,7]

The scattering amplitude and hence the diffracted intensity can be expressed as a series expansion in the order of scattering events. Hence, the transform of the intensity consists of a linear combination of transforms of nth order scattering processes ($n=1,2,3,\ldots$) which can be expressed in turn as convolution products of geometrical and electronic and vibrational factors. However, we anticipate that the first-order convolution product will produce the dominant features in the transform. Multiple-scattering contributions to the diffracted intensities are generally aperiodic with momentum transfer, and are effectively attenuated by Fourier transformations.

The above conclusions are supported by results of numerical studies[8] using intensities calculated from a full multiple-scattering theory, and by the application of the deconvolution method to the analysis of experimental data exhibiting pronounced multiple-scattering features, as described below and in detail elsewhere.[4] Accordingly, we now demonstrate the principles of the transform-deconvolution method, using kinematical theory with realistic scattering potentials and inclusion of temperature effects.

The kinematical expression for the intensity of specularly diffracted electrons from a lattice composed of a uniform substrate with layer spacing d_s and an overlayer at a distance d_o from the surface plane is given by

$$\begin{aligned}I(S)={}&|f_o(S)|^2+2|f_s(S)|^2\alpha_o^2(1-\alpha_s^2)^{-1}\sum_{\nu=0}^{\infty}(\alpha_s^{\nu}\cos\varphi_\nu-1)\\&+2\alpha_o\sum_{\nu=0}^{\infty}\alpha_s^{\nu}[f_{os}(S)\cos(\varphi_\nu+\beta)+f_{os}^{\dagger}(S)\sin(\varphi_\nu+\beta)],\end{aligned} \tag{3}$$

where $\alpha_s=\exp(-\mu_s'd_s)$, $\alpha_o=\exp(-\mu_o'd_o)$, and $\mu'=\mu/\cos\theta$ with μ the attenuation coefficient[1] and θ the angle of incidence. The phase angles are defined as $\varphi_\nu=2\pi S\nu d_s$ and $\beta=2\pi Sd_o$. $f_{s,o}(S)$ are the effective atomic scattering factors, renormalized to incorporate atomic vibrations[9] by multiplication by the associated Debye-Waller factors, of the substrate (s) and overlayer (o) which can be expressed in a partial-wave expansion with scattering-potential phase shifts[10] $\delta_{s,l}(S)$ and $\delta_{o,l}$ for the substrate and overlayer, respectively. The function $f_{os}(S)$ is defined as $f_{os}(S)=f_o(S)f_s^{\dagger}(S)$. The transform [Eq (2)] of the above intensity expression is given by

$$\begin{aligned}P_o(z)={}&F_o(z)*\delta(z)+F_s(z)*\alpha_o^2(1-\alpha_s^2)^{-1}\sum_{\nu=-\infty}^{\infty}\alpha_s|\nu|\delta(z+d_s)\\&+\alpha_o\sum_{\nu=0}^{\infty}\alpha_s^{\nu}[F_{os}(z)*\delta(z-d_o-\nu d_s)+F_{so}(z)*\delta(z+d_o+\nu d_s)],\end{aligned} \tag{4}$$

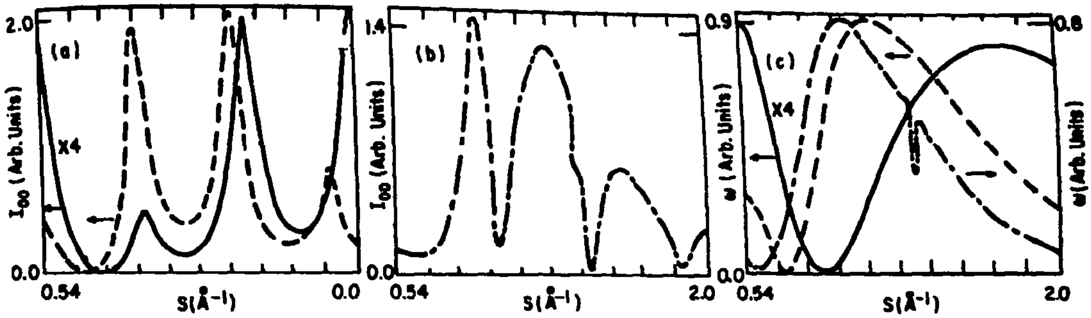

FIG. 1. Calculated intensities (a) for Al(100) (solid and dashed curves, $\theta = 25°$ and 8°, respectively) and (b) for Na overlayer on Al with $d_0 = 2.2$ Å (dash-dotted curve, $\theta = 8°$) using four phase shifts (Ref. 12). (c) Substrate ω_s (solid and dashed curves for $\theta = 25°$ and 8°, respectively) and overlayer (dash-dotted curve for $\theta = 8°$) potential windows, corresponding to the above intensities.

where the asterisk denotes convolution and F_o, F_s, F_{os} and F_{so} are the transforms of $|f_o|^2$, $|f_s|^2$, $f_o f_s^\dagger$, and $f_o^\dagger f_s$ respectively, convoluted with the transform of the "box-car" window ω_B defined in Eq. (1). In the following we refer to the functions $\omega_{o,s} = |f_{o,s}|^2 \omega_B(S; S_1, S_2)$ as the potential envelopes (windows) for the overlayer (o) and substrate (s), respectively.

The second term in the above equation with the substitution $\alpha_o = 1$ is the transform $P_s(z)$ of the clean-substrate intensity. It consists of peaks at $z = \nu d_s$ $(-\infty < \nu < \infty)$, weighted by the damping factors $(1 - \alpha_s^2)^{-1}$, convoluted with the transform of the truncated atomic scattering potential. Thus, a transformation of the intensities diffracted from a clear surface followed by a deconvolution of the *complex* transform $F_s(z)$ yields a "δ-function transform." Because of the idempotency of the window matrix, conventional matrix-inversion algorithms cannot be applied in the deconvolution. A solution to this crucial problem has been formulated by modifying a relaxation method described by Southwell.[11,8]

The deconvolution is demonstrated first for the clean substrate. Figure 1(a) contains calculated kinematical intensities for the (00) beam from Al(100), for two incident angles, and $T = 0$°K; Figure 1(c) contains the associated potential envelopes. The Fourier transforms of the intensity records are given in Figs. 2(a) and 2(b), from which it is evident that peak broadening and extra peaks due to the truncated potential envelopes preclude *direct* structural interpretation. The computer deconvolutions[4,8] of the truncated potential windows from the transforms for $\theta = 8°$ and 25° are identical. The unique result is shown in Fig. 2(c).

Interpretation of the transform [Eq. (4)] of the intensity diffracted from an overlayer system is complicated by the convolution of maxima which are structural in origin with functions associated with the differences in scattering potential of the substrate and overlayer atoms. An accurate determination of the overlayer geometry is achieved by the *substrate subtraction* method defined as

$$P_{\mathrm{RES}}(z) = P_o(z) - gP_s(z) - \delta(z) * F_o(z), \tag{5}$$

where P_o and P_s are the overlayer and substrate transforms, respectively. For $g = \alpha_o^2$,

$$P_{\mathrm{RES}}(z) = \alpha_o \sum_{\nu=0}^{\infty} \alpha_s^{\nu} [F_{os}(z) * \delta(z - d_o - d_s) + F_{so}(z) * \delta(z + d_o + \nu d_s)]. \tag{6}$$

Optimum substrate subtraction is achieved by a variation of g in Eq. (5) to minimize

$$\sum_{\nu=0}^{\infty} P_{\mathrm{RES}}(\nu d_s).$$

Determination of the overlayer spacing is demonstrated for the case of a Na overlayer on Al(100). A calculated (00) intensity for an arbitrarily chosen overlayer spacing $d_0 = 2.2$ Å and $\theta = 8°$ using a four-phase-shift expansion in the description of the substrate and overlayer scattering potentials is shown in Fig. 1(b) along with the overlayer potential envelope $|f_o|^2$ in Fig. 1(c). It is again evident that structure determination cannot be made solely on the basis of the correspond-

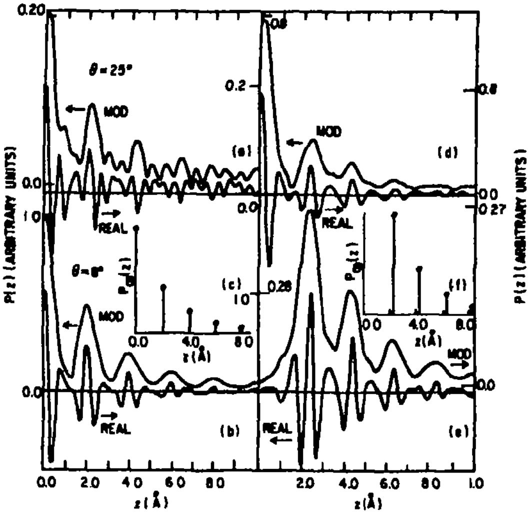

FIG. 2. (a), (b) Modulus and real part of the $P(z)$ transforms derived from the intensities shown in Fig. 1(a). (c) Computer deconvolution (P_{∞}) (Ref. 8) obtained by *deconvoluting the transform of the windows in Fig.* 1(a) from the transforms shown in (a) and (b). (d) $P(z)$ transform for the overlayer intensity [Fig. 1(b)]. Note the absence of peaks at substrate spacings. (e) Substrate-subtraction residuals [Eq. (5)], obtained from the transforms shown in (b) and (d). (f) Computer deconvolution (P_{∞}) (Ref. 8) of the residual, exhibiting highly resolved peaks corresponding to the substrate-overlayer vectors.

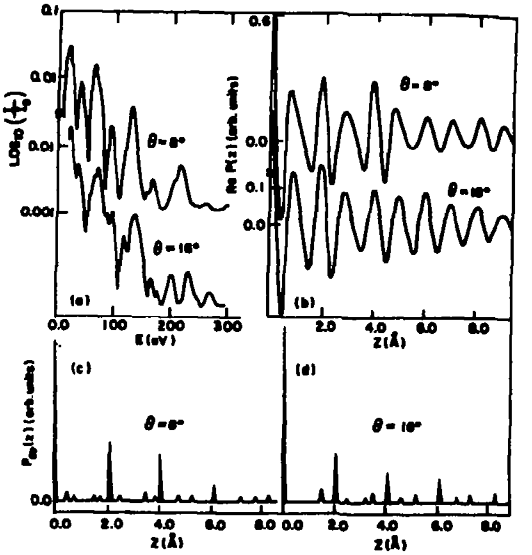

FIG. 3. (a) (00) intensities from Al(100) measured at $T=295$°K for $\varphi=0$, $\theta=8°$ and 16°. (b) Real part of the $P(z)$ *transforms* of the intensities *shown in* (a). (c), (d) Computer deconvolutions (P_{∞}) of the transforms shown in (b) ($\theta=8°$ and 16°, respectively). The base width of the peaks is 0.05 Å. Structural peaks forming a consistent vector set have been filled. The use of eight phase shifts (Ref. 13) in the potential window resulted in a suppression of "noise" level (open peaks).

ing transforms which are shown in Fig. 2(d). The *residual transform*, $P_{\rm RES}(z)$, derived from the transforms shown in Figs. 2(b) and 2(d) is shown in Fig. 2(e). Deconvolution of the residual transform yields the overlayer-substrate interlayer vectors as shown in Fig. 2(f).

We now illustrate the applicability of the transform-deconvolution method to experimental data. In Fig. 3(a) we present (00) intensity profiles measured[4] at room temperature from Al(100) for $\varphi=0°$ and $\theta=8°$ and 16°. The real parts of their transforms are shown in Fig. 3(b). We draw attention to the pronounced multiple-scattering features in the intensity profiles, and to the vibrations in both the intensity profiles and their transforms with angle of incidence. In constructing appropriate potential envelope windows for deconvolution of transforms such as are shown in Fig. 3(b) we have used eight phase shifts calculated from Snow's potential.[13]

The deconvolution results shown in Figs. 3(c) and 3(d) for $\theta=8°$ and 16°, respectively, were obtained by using optimized values of the inner potential and effective Debye temperature of 14 eV and 300°K, respectively. In comparing these results with those obtained from calculated kinematic intensities shown in Fig. 2, it can be seen that in addition to the prominent structural peaks in Figs. 3(c) and 3(d) there is a low level of noise. (Similar noise peaks of *negative* amplitude have been suppressed in the figures since obviously they convey no structural information. *Convoluting* the total deconvolution results with the corresponding potential windows used reproduces the observed transforms to better than 1%.)

In the above results, and in results for other angles of incidence,[4] prominent peaks occur only at 2.05N Å ($N=0, 1, 2$, etc.) and form the only consistent periodic vector set. The unique value of the interlayer spacing determined from different intensity profiles, despite their strong variation with angle of incidence, demonstrates the consistency of the method and illustrates its applicability. We note that the determined value 2.05 Å is in agreement with the bulk interlayer spacing of 2.025 Å to within our estimated accuracy of ± 0.05 Å. In addition it compares with the conclusions of extensive multiple-scattering calculations.[14]

Further details of our method and applications to experimental data are given in forthcoming publications.[4,8]

We are indebted to Dr. E. P. Goldberg and Dr. M. L. Hair for their encouragement and interest, and to Mr. J. C. Hamilton for helpful discussions.

---

[1] C. J. Davisson and L. H. Germer, Phys. Rev. 30, 705 (1927).

[2] Phys. Today 27, No. 3, 17 (1974).

[3] U. Landman and D. L. Adams, J. Vac. Sci. Technol. 11, 195 (1974).

[4] D. L. Adams, U. Landman, and J. C. Hamilton, to be published.

[5] M. J. Burger, *Vector Space* (Wiley, New York, 1954).

[6] J. C. Buchholz, M. G. Lagally, and M. B. Webb, Surface Sci. 41, 248 (1974).

[7] T. A. Clarke, R. Mason, and M. Tescari, Surface Sci. 30, 553 (1972), and 40, 1 (1973), and Proc. Roy. Soc., Ser. A 331, 321 (1972).

[8] U. Landman and D. L. Adams, to be published.

[9] G. E. Laramore, Phys. Rev. B 6, 1097 (1972).

[10] L. I. Schiff, *Quantum Mechanics* (McGraw-Hill, New York, 1955).

[11] R. V. Southwell, *Relaxation Methods in Theoretical Physics* (Oxford Univ. Press, Oxford, England, 1946).

[12] C. B. Duke, N. O. Lipari, and U. Landman, Phys. Rev. B 8, 2454 (1973).

[13] The authors are indebted to Dr. J. E. Demuth and Dr. P. Marcus for supplying us with the phase shifts used in this calculation.

[14] D. W. Jepsen, P. M. Marcus, and F. Jona, Phys. Rev. B 5, 3933 (1972).

Backward Scattering in the One-Dimensional Electron Gas*

A. Luther†
Lyman Laboratory, Harvard University, Cambridge, Massachusetts 02138

and

V. J. Emery
Brookhaven National Laboratory, Upton, New York 11973

(Received 16 July 1974)

An exact solution to the one-dimensional electron gas with a particular attractive-interaction strength for scattering across the Fermi "surface" is given. It is shown that conductivity enhancement occurs for physically interesting values of the coupling constants. Scaling arguments are advanced to demonstrate that this solution applies generally for attractive backward scattering. In addition, the spinless problem is solved exactly for arbitrary couplings.

Progress towards an understanding of the equilibrium and transport properties of quasi-one-dimensional conductors has been hampered by a lack of knowledge about the underlying interacting electron system. Although the Tomonaga and Luttinger models[1] have provided some insight, their generality can be questioned as a result of their neglect of interactions near twice the Fermi momentum, $2k_F$, which are responsible for backward scattering. This note reports an exact solution to the more general problem with an attractive interaction at $2k_F$, and uses it to construct a qualitative picture for the general interacting one-dimensional system.

Several properties of the exact solution are particularly significant. It requires an attractive interaction at $2k_F$ of a specific strength but the small-momentum interaction can be arbitrary, a situation of sufficient generality to be of interest for experiments on the quasi-one-dimensional systems. Depending upon the sign and magnitude of the small-momentum part, a large conductivity enhancement can occur as the temperature tends to zero, in contrast to a recent approximate treatment.[2] We compute the temperature dependence of the conductivity as well as other physically important response functions which describe the low-temperature pairing, charge and spin fluctuations, and magnetic susceptibility.

Together with the renormalization-group calculations of Menyhárd and Sólyom,[3] our solution can be used to provide a complete, if qualitative, picture of the one-dimensional interacting gas. This approach is analogous to the scaling argument of Anderson, Yuval, and Hamann for the Kondo problem.[4]

The model we solve is a logical extension of the Luttinger or Tomonaga model to include spin as well as interactions which scatter particles from $+k_F$ to $-k_F$. The Hamiltonian is the sum of free-particle kinetic energy, linearized near k_F, plus the usual small-momentum interaction,[5]

$$\mathcal{H}_s = v_F \sum_{k,s} k(a_{k,s}{}^\dagger a_{k,s} - b_{k,s}{}^\dagger b_{k,s}) + 2L^{-1}\sum_k V\rho_1(k)\rho_2(-k), \tag{1}$$

where the operators $a_{k,s}$ ($b_{k,s}$) describe spin-$\frac{1}{2}$ fermions with momentum k ($-k$); $\rho_1(k)$ and $\rho_2(k)$ are density operators, $\rho_1(k) = 2^{-1/2}\sum_{ps} a_{p+k,s}{}^\dagger a_{p,s}$ and $\rho_2(k) = 2^{-1/2}\sum_{ps} b_{p+k,s}{}^\dagger b_{p,s}$. It is helpful in our subsequent discussion to introduce the spin-density operators $\sigma_1(k) = 2^{-1/2}\sum_{ps} s a_{p+k,s}{}^\dagger a_{ps}$ and $\sigma_2(k) = 2^{-1/2}\sum_{ps} s b_{p+k,s}{}^\dagger b_{p,s}$ with $s = \pm 1$. The operators ρ and σ satisfy the algebra of the Luttinger model, $[\rho_1(-k), \rho_1(+k')] = [\rho_2(+k), \rho_2(-k')] = \delta_{kk'} kL/2\pi$, together with identical equations for the σ commutators, $[\sigma_1(-k), \sigma_1(+k')] = [\sigma_2(+k), \sigma_2(-k')] = \delta_{kk'} kL/2\pi$, while all others vanish. The length of the sample is L and all states below $v_F k_F$ are filled. The kinetic energy term in Eq. (1) can be written in terms of these operators, by making use of well-known identities extended to the spin-$\frac{1}{2}$ case:

$$v_F \sum_{k,s} k(a_{k,s}{}^\dagger a_{k,s} - b_{k,s}{}^\dagger b_{k,s}) \to 2\pi v_F L^{-1} \sum_k [\rho_1(k)\rho_1(-k) + \sigma_1(k)\sigma_1(-k) + \rho_2(-k)\rho_2(k) + \sigma_2(-k)\sigma_2(k)],$$

indicating a separation into density and spin-density operators.

The large-momentum-transfer terms are described by an additional $\mathcal{H}_L$ in the form[6]

$$\mathcal{H}_L = \sum_{s,s'} \int dx\, \Psi_{1,s}{}^\dagger(x)\Psi_{2,s'}{}^\dagger(x)\Psi_{1,s'}(x)\Psi_{2,s}(x)[U_\parallel \delta_{s,s'} + U_\perp \delta_{s,-s'}], \tag{2}$$

where $\Psi_{1,s}(x) = L^{-1/2}\sum_k \exp(ikx) a_{k,s}$ and $\Psi_{2,s}(x) = L^{-1/2}\sum_k \exp(ikx) b_{k,s}$. The $U_\parallel$ term can be written in terms of the density and spin-density operators by a permutation of the inner two operators, and becomes equal to

$$-U_\parallel L^{-1}\textstyle\sum_k \rho_1(k)\rho_2(-k) - U_\parallel L^{-1}\sum_k \sigma_1(k)\sigma_2(-k).$$

The $U_\perp$ term contains field operators of opposite spin, for which we use the boson representation[7,8]:

$$\Psi_{j,s}(x) = (2\pi\alpha)^{-1/2} \exp\{\pm[ik_F x + 2\pi L^{-1}\sum_k k^{-1}\exp(-\tfrac{1}{2}\alpha|k| - ikx)\rho_{j,s}(k)]\}, \tag{3}$$

where $v_F\alpha^{-1}$ is the bandwidth, $\rho_{1,s}(k) = \sum_p a_{p+k,s}{}^\dagger a_{p,s}$, $\rho_{2,s}(k) = \sum_p b_{p+k,s}{}^\dagger b_{p,s}$, and the plus (minus) sign goes with $j = 1$ ($j = 2$). This relationship has been discussed in detail for the spinless case[7] and the generalization here is trivial, although the notation is somewhat cumbersome. This permits us to write the products of field operators in the $U_\perp$ term as $(2\pi\alpha)^{-2}\exp\{2^{-1/2}[\varphi_1(x) + \varphi_2(x)]\}$, with

$$\varphi_j(x) = 2\pi L^{-1}\textstyle\sum_k k^{-1}\exp(\tfrac{1}{2}\alpha|k| - ikx)\sigma_j(k). \tag{4}$$

The total Hamiltonian $\mathcal{H}_s + \mathcal{H}_L$ can now be written as the sum $\mathcal{H}_0 + \mathcal{H}_1$, where

$$\mathcal{H}_0 = 2\pi v_F L^{-1}\textstyle\sum_k [\rho_1(k)\rho_1(-k) + \rho_2(-k)\rho_2(k)] + L^{-1}\sum_k (2V - U_\parallel)\rho_1(k)\rho_2(-k), \tag{5}$$

and

$$\begin{aligned}\mathcal{H}_1 = 2\pi v_F L^{-1}\textstyle\sum_k [\sigma_1(k)\sigma_1(-k) + \sigma_2(-k)\sigma_2(k)] - L^{-1}\sum_k U_\parallel \sigma_1(k)\sigma_2(-k)\\ + U_\perp(2\pi\alpha)^{-2}\int dx\, \{\exp(2^{-1/2}[\varphi_1(x) + \varphi_2(x)]) + \text{H.c.}\},\end{aligned} \tag{6}$$

and a separation into density and spin-density operators has been achieved. Obviously $[\mathcal{H}_1, \mathcal{H}_0] = 0$. It is interesting to note that the most general Hamiltonian for spinless fermions, $\sigma(k) = 0$, including large-momentum interactions is still of the Tomonaga-Luttinger form, for which the thermodynamics[8] and correlation functions[7] are known.

This separation into $\mathcal{H}_1$ and $\mathcal{H}_0$ is essential because $\mathcal{H}_0$ is a quadratic form in boson operators and may be diagonalized by means of a canonical transformation. We now show that for a particular value of $U_\parallel$, $\mathcal{H}_1$ may also be diagonalized. Since the part of $\mathcal{H}_1$ which does not involve $U_\perp$ is quadratic it may be diagonalized by a transformation $e^{iS}\mathcal{H}_1 e^{-iS}=\mathcal{H}_1'$, with $S=2\pi i L^{-1}\varphi\sigma_1(k)\sigma_2(-k)$, and $\tanh 2\varphi=-U_\parallel \times(2\pi v_F)^{-1}$. This transformation changes the velocity to $v_F'=v_F\,\mathrm{sech}2\varphi$ and the exponent of the $U_\perp$ term to $2^{-1/2}e^{\varphi}[\varphi_1(x)+\varphi_2(x)]$. The point now is that if $2^{-1/2}e^{\varphi}=1$, comparison of Eqs. (3) and (6) shows that the $U_\perp$ term is just the boson representation of a product of spinless Fermi fields $\Psi_2^\dagger(x)\Psi_1(x)\exp(-2i \times k_F x)$. Writing the kinetic energy also in fermion representation, we find that $\mathcal{H}_1'$ is quadratic and solvable:

$$\mathcal{H}_1'=v_F'\textstyle\sum_k k(a_k^\dagger a_k-b_k^\dagger b_k)+U_\perp(2\pi\alpha)^{-1}\sum_k(a_k^\dagger b_{k-2k_F}+\mathrm{H.c.}). \tag{7}$$

It is possible to make $2^{-1/2}e^{\varphi}=1$ by choosing $U_\parallel$ so that $\tanh 2\varphi=-U_\parallel(2\pi v_F)^{-1}=\frac{3}{5}$. Equation (7) has the eigenvalue spectrum $v_F k_F\pm[(k-k_F)^2+\Delta^2]^{1/2}$ and $v_F k_F\pm[(k+k_F)^2+\Delta^2]^{1/2}$, where $\Delta=U_\perp \times(2\pi\alpha)^{-1}$, indicating the appearance of gaps at $+k_F$ and $-k_F$. These gaps have important consequences for the properties of our solution.

The total Hamiltonian $\mathcal{H}'=e^{iS}\mathcal{H}e^{-iS}=\mathcal{H}_0+\mathcal{H}_1'$ is now diagonalized, and it is straightforward to compute the free energy and correlation functions in the usual fashion. We may distinguish two regions: low temperatures, $T\ll\Delta$, for which the gap at the Fermi energy means that only excitations in $\mathcal{H}_0$ (and consequently density operators) are important; and high temperatures, $T\gg\Delta$, when the gap, and consequently $U_\perp$, are negligible. (A similar division applies to the frequency and momentum dependence.) In either case, the Hamiltonian is of the Tomonaga form, and the analytic behavior of correlation functions is therefore known from previous work.[7]

The properties of our solution are best expressed by the exponents characterizing the different spectral functions. These exponents are defined by $\mathrm{Im}\,C(\omega)\propto\omega^{\mu}$, where C is the correlation function in question. Because the analytic form of these functions is of Tomonaga-Luttinger form, the temperature and momentum dependence is also determined by this exponent. The total scale dimension of these correlation functions is given by $\mu+2$, the extra 2 resulting from two Fourier transforms in the definition of C. The exponents are listed in Table I, along with the temperature dependence of the magnetic susceptibility, for both low and high temperatures.

The electrical-conductivity relaxation rate in the impurity-dominated region is determined by the spectral function for the parallel-spin $2k_F$ susceptibility,[9] the characteristic energy W responsible for the interaction, and the free-particle conductivity σ_0. The result in Table I then means that $\sigma=ne^2\tau/m=\sigma_0(T/W)^{-\mu}$, which will be enchanced ($\mu>0$) whenever $v'<-\frac{3}{5}$. Under these conditions, the spectral density at $2k_F$ vanishes, causing the reduction in scattering from the impurity.

It is interesting to compare with the renormalization-group approach of Menyhárd and Sólyom.[8] They considered the special case $U_\parallel=U_\perp=g_1$ and, for $g_1<0$, their exponents are qualitatively different from ours because they find that g_1 scales onto a fixed point ($g_1=-2\pi v_F$) which is outside the weak-coupling region for which their perturbation expansions are adequate. A more credible use of the renormalization-group equations, analogous to scaling theories of the Kondo problem,[4] uses the fact that, provided no fixed point intervenes, the coupling constant would scale through the value $g_1=-\frac{6}{5}\pi v_F$ at which our exact solution

TABLE I. Exponents of the spectral functions, defined in text, and the low- and high-temperature behavior of the magnetic susceptibility. The parameters $v'=V(\pi v_F)^{-1}+\frac{3}{5}$ and $\Delta=U_\perp(2\pi\alpha)^{-1}$.

Spectral function and operator	Low-temperature ($T\gg\Delta$) exponent	High-temperature ($T\gg\Delta$) exponent
$2k_F$ susceptibility, $\Psi_{1,+}^\dagger\Psi_{2,+}$	$-2+[(1-v')/(1+v')]^{1/2}$	$-\frac{3}{2}+[(1-v')/(1+v')]^{1/2}$
$2k_F$ susceptibility, $\Psi_{1,+}^\dagger\Psi_{2,-}$	$-2+[(1-v')/(1+v')]^{1/2}$	$[(1-v')/(1+v')]^{1/2}$
Singlet pairing, $\Psi_{1,+}^\dagger\Psi_{2,-}^\dagger$	$-2+[(1+v')/(1-v')]^{1/2}$	$-\frac{3}{2}+[(1+v')/(1-v')]^{1/2}$
Triplet pairing, $\Psi_{1,+}^\dagger\Psi_{2,+}^\dagger$	$-2+[(1+v')/(1-v')]^{1/2}$	$[(1+v')/(1-v')]^{1/2}$
Susceptibility, $\sigma_1+\sigma_2$	$(\pi v_F')^{-1}(2\pi\beta\Delta)^{1/2}e^{-\beta\Delta}$	$2(\pi v_F)^{-1}(1-U_\parallel/2\pi v_F)^{-1}$

may be used. This suggests that the gap Δ exists for the weaker-coupling problems, $0 > g_1 > -\frac{6}{5}\pi v_F$, as well. If this gap exists, the low-temperature exponents given in Table I are still correct, with a new $v'2\pi v_F = 2V - U_\parallel$. The high-temperature exponents are more complicated but can be computed by setting $U_\perp = 0$, and following the usual procedure for the Tomonaga-model correlation functions.[7]

These exponents give substantial physical insight into the behavior of the system. For example, if the conductivity exponent is negative at high temperatures and positive at low temperatures a conductivity peak occurs at a temperature of the order of the gap, where the two power laws "cross over". The magnitude of this peak depends on W and $U_\perp$ as well as the difference $\delta\mu$ between the two exponents. For $U_\parallel(\pi v_F)^{-1} = -\frac{6}{5}$, there can be a rather small peak because $\delta\mu$ is only $\frac{1}{2}$. We have calculated $\delta\mu$ for smaller $|U_\parallel|$, assuming that the scaling arguments are correct, and find that $\delta\mu$ approaches $\frac{6}{5}$ as $|U_\parallel| \to 0$. This is a new mechanism for a conductivity peak which merits a more detailed discussion than can be presented here.

Spin-flip impurity scattering will have a temperature dependence given by the opposite-spin $2k_F$ susceptibility. Here the difference in exponents is large, indicating a stronger scattering at low temperatures which would dominate other mechanisms.

At the risk of making this problem appear more complicated (but even more intriguing), we now point out the reason behind our notation $U_\parallel$ and $U_\perp$. These have been chosen to emphasize the connection to the Kondo parameters $-J_\parallel$ and $J_\perp$. The Hamiltonian in Eq. (6) has many similarities to the Tomonaga version of the Kondo Hamiltonian, and we expect many of the renormalization-group arguments to be applicable here as well. In particular, the weak-coupling scale energy for $\mathcal{H}_1$ is $|U|^{1/2}\exp(-|U|^{-1})$, for $U_\parallel = U_\perp = U < 0$, as in the Kondo problem.

The inclusion of electron-phonon coupling raises many questions for which there are only qualitative answers at present. In the adiabatic model, which views these interactions as giving rise to additional electron-electron coupling constants, the question of resistivity or conductivity enhancement depends sensitively on the relative signs and magnitudes of all coupling constants. Furthermore, if the phonon frequencies shift with temperature, these coupling constants also vary, and the calculation of the appropriate exponents becomes complicated. This problem is currently under investigation.

Much of this work was carried out while A. L. was a summer visitor at Brookhaven National Laboratory. The model solved in this paper appears to be related to generalizations of the Thirring model,[10] as pointed out to us by S. Coleman.

---

*Work supported in part by the U. S. Atomic Energy Commission.

†Research supported in part by the National Science Foundation under Grant No. GH 32774.

[1] E. H. Lieb and D. C. Mattis, *Mathematical Physics in One Dimension* (Academic, New York, 1966).

[2] H. Fukuyama, M. Rice, and C. Varma, to be published.

[3] N. Menyhárd and J. Sólyom, J. Low Temp. Phys. 12, 529 (1973); J. Sólyom, J. Low Temp. Phys. 12, 547 (1973).

[4] P. W. Anderson, G. Yuval, and D. R. Hamann, Phys. Rev. B 1, 4464 (1970).

[5] D. C. Mattis and E. H. Lieb, J. Math. Phys. 6, 304 (1965).

[6] There are many equivalent representations of these terms, and our notation is convenient for later purposes. The Hubbard model requires selecting $V = U_\parallel = U_\perp$, for which case the parallel-spin interactions cancel, while the notation of Ref. 3 corresponds to the choice $U_\parallel = U_\perp = g_1$ and $V = g_2$.

[7] A. Luther and I. Peschel, Phys. Rev. B 9, 2911 (1974).

[8] D. Mattis, J. Math. Phys. 15, 609 (1974).

[9] A. Luther and I. Peschel, Phys. Rev. Lett. 32, 992 (1974).

[10] R. Dashen and Y. Frishman, Phys. Lett. 46B, 439 (1973).

Angular-Momentum Effects on Continuum Gamma Rays Following Heavy-Ion Reactions[*]

P. O. Tjøm,[†] F. S. Stephens, R. M. Diamond, J. de Boer,[‡] and W. E. Meyerhof[§]
Lawrence Berkeley Laboratory, University of California, Berkeley, California 94720

(Received 10 June 1974)

The average number of continuum γ rays above 0.6 MeV has been measured for each of several final products in the reactions $p+{}^{165}\mathrm{Ho}$, ${}^{16}\mathrm{O}+{}^{150}\mathrm{Sm}$, and ${}^{84}\mathrm{Kr}+\mathrm{Se}$. This number ranges from 2 to 20 and is shown to correlate mainly with the average angular momentum leading to each product.

The γ-ray spectra following heavy-ion (HI, $xn\gamma$) reactions have two main features: discrete lines from heavily populated low-lying levels of the final-product nuclei, and a continuum which presumably represents all the higher transitions, none of which has sufficient population to be resolved with present techniques. Most recent work has focused on the discrete lines, producing systematic information on the low-lying high-spin ($\lesssim 20\hbar$) states of nuclei. A few attempts have been made to study the continuum region. Mollenauer[1] studied $(\alpha, xn\gamma)$ and $({}^{12}\mathrm{C}, xn\gamma)$ reactions without specifying the outgoing reaction channel. He measured the average number of continuum γ rays, $\bar{N}_\gamma$, their average energy, and their angular distribution. Sunyar and co-workers[2] have reported some preliminary results on $\bar{N}_\gamma$ for the reaction ${}^{150}\mathrm{Nd}({}^{13}\mathrm{C}, 5n\gamma){}^{158}\mathrm{Dy}$. The present work, using p, ${}^{16}\mathrm{O}$, and ${}^{84}\mathrm{Kr}$ projectiles, shows that large variations occur in the number of γ rays in the continuum region depending mainly on the outgoing channel, and that this variation may be understood in terms of a simple model.

In our work it was essential to specify the reaction channel because many channels occur simultaneously in the reactions and a composite continuum of γ rays would be difficult to interpret. Thus we measured the continuum in coincidence with known discrete transitions that specified particular channels, as was done by Sunyar and co-workers.[2] For the discrete lines we used a 40-cm^3 Ge(Li) detector at an angle of 90° to the incident beam direction and about 5 cm from the target. The continuum γ rays were detected in a 7.5 cm × 7.5 cm NaI crystal, 15 cm from the target, and at angles of 0°, 45°, and 90°. An absorber, consisting of 0.32-cm Pb and 0.32-cm Cu, was placed in front of the NaI detector, resulting in an overall detection efficiency which is very nearly constant for any γ ray above 0.5 MeV. Since there are known discrete lines in the spectra of interest up to about 0.6 MeV, and since there are not likely to be many continuum γ rays below this energy,[1,2] we took 0.6 MeV as the lower limit for measurements of the continuum. The detection probability for 1.1-, 1.4-, and 2.8-MeV γ rays in the coincidence arrangement was found to be the same within about 20% and equal to 0.43%. Thus, even for multiplicities as high as 20, the probability of two γ rays being detected simultaneously was less than 10% and represented a small correction. The arrangement was further tested with a ${}^{252}\mathrm{Cf}$ fission source, by using fission fragments as the coincidence triggers, and agreement with previous results[3] for the number of γ rays per fission was obtained. In these calibrations,[3] as well as during the in-beam experiments, a background spectrum was taken with a 5-cm-thick Pb cone between the NaI detector and the source (target). We have shown that a simple subtraction of the spectrum with the Pb cone from that with no cone is very unlikely to cause an error in $\bar{N}_\gamma$ exceeding 10%.

Beams of 347-MeV ${}^{84}\mathrm{Kr}$ provided by the Berkeley SuperHILAC were used to bombard targets of ${}^{82}\mathrm{Se}$ (1.3 mg/cm^2) enriched to 97%. This produced the compound nucleus ${}^{166}\mathrm{Yb}$, and various discrete lines in the final nuclei ${}^{163}\mathrm{Yb}$ ($3n$), ${}^{162}\mathrm{Yb}$ ($4n$), and ${}^{161}\mathrm{Yb}$ ($5n$) could be used as coincidence gates. A target of 99% enriched ${}^{150}\mathrm{Sm}$ (1.4 mg/cm^2) was also bombarded at the Berkeley 88-in. cyclotron with 88-MeV ${}^{16}\mathrm{O}$ to produce the same compound nucleus and products. Both targets were evaporated onto Pb backings about 25 μm thick, which stopped the beam and recoiling nuclei with no appreciable background. We also bombarded a ${}^{165}\mathrm{Ho}$ target (220 mg/cm^2) with 25-MeV protons at the cyclotron in order to produce the compound nucleus ${}^{166}\mathrm{Er}$, and product nuclei ${}^{163}\mathrm{Er}$ ($3n$) and ${}^{164}\mathrm{Er}$ ($2n$). The average numbers of γ rays, $\bar{N}_\gamma$, associated with each discrete line are given in Table I. The uncertainty attached to each $\bar{N}_\gamma$ value is estimated to be ±20%.

TABLE I. Average number of continuum γ rays above 0.6 MeV.

E (keV)	$I_i \rightarrow I_f$	$\bar{N}_\gamma$ ^{84}Kr + ^{82}Se	^{16}O + ^{150}Sm
	^{162}Yb($4n$)		
166	$2 \rightarrow 0$	11	8
320	$4 \rightarrow 2$	14	10
437	$6 \rightarrow 4$	12	9
521	$8 \rightarrow 6$	12	9
579	$10 \rightarrow 8$		9
	^{163}Yb($3n$)		
202	$17/2^+ \rightarrow 13/2^+$	20	14
345	$21/2^+ \rightarrow 17/2^+$	19	9
	^{161}Yb($5n$)		
232	$17/2^+ \rightarrow 13/2^+$	10	5
		p + ^{165}Ho	
	^{163}Er($3n$)		
127	$13/2^+ \rightarrow 9/2^+$	1.2	
165	$15/2^+ \rightarrow 13/2^+$	2.2	
171	$13/2^- \rightarrow 11/2^-$	2.3	
190	$9/2^- \rightarrow 5/7^-$	1.3	
213	$15/2^+ \rightarrow 11/2^+$	1.3	
218	$17/2^+ \rightarrow 13/2^+$	1.7	
236	$11/2^- \rightarrow 7/2^-$	1.6	
	^{164}Er($2n$)		
208	$4 \rightarrow 2$	3.7	
314	$6 \rightarrow 4$	3.3	
410	$8 \rightarrow 6$	3.2	

except for the 232-keV line in the ^{84}Kr + ^{82}Se data. This line appeared broad in both the singles and the coincident spectra, and thus the uncertainty toward lower values has been doubled to 40%. The Se target thickness causes a ± 8-MeV spread (c.m.) about the average value of the excitation energy of the compound system; the $\bar{N}_\gamma$ values listed in Table I for the Se target are thus average values over this range of excitation energy.

The variations of $\bar{N}_\gamma$ in Table I are more than a facter of 10 overall, and nearly a factor of 3 in various ^{16}O + ^{150}Sm reactions alone. Such large variations are not likely to be caused simply by the difference in excitation energy resulting from different numbers of neutrons evaporated. This is shown by the p + ^{165}Ho reaction, where a difference of one neutron causes a change of less than two γ rays. It seems more likely that these large variations in $\bar{N}_\gamma$ result from angular-momentum effects. This can be tested by application of a simple semiclassical model.[4] We picked a compound nucleus as neutron-rich as possible in order to be able to neglect charged-particle competition, and indeed, the (HI, $\alpha xn\gamma$) products that could be detected in our spectra had individual cross sections less than 10 mb. The number of neutrons emitted from a compound system depends on the energy available, which is roughly the difference between the excitation energy and the minimum energy E_l required to carry the angular momentum $l\hbar$ of the system. Since an evaporated neutron cannot change l by more than 1 or 2 units, the energy E_l must be left in the residual nucleus. If for example, l is such that E_l is equal to the sum E_n of the neutron binding and kinetic energies, then it is apparent that one fewer neutron can be emitted than would be the case for $l=0$ ($E_0=0$). We can estimate that $E_l \approx \hbar^2 l^2/2\mathscr{I}$, where $\mathscr{I}$ is a moment of inertia near the rigid-body value. Since E_n is about 10 MeV for the nuclei considered here, and $\hbar^2/2\mathscr{I}$ is approximately 9 keV, this gives $\Delta(l^2)/\Delta x = 1100$ (x is the number of neutrons emitted). Thus if a large amount of angular momentum is brought into a compound nucleus in this region, the total cross section will be divided into "bins," having widths $\Delta(l^2)=1100$, each of which corresponds to a particular number of neutrons being evaporated. For example, if a bin starts at $l=0$, it can hold all angular momenta up to 33, and the bin starting at $l=33$ corresponds to the evaporation of one less neutron. It is important to note that at a given bombarding energy the maximum cross section for each bin is approximately constant. Using a relation given previously[5]—$l_{\rm upper}{}^2 = 1.5\sigma\mu E_{\rm c.m.}$, where σ is in barns, μ is the reduced mass in mass units, and $E_{\rm c.m.}$ is the center-of-mass energy in MeV—we find

$$\frac{\Delta\sigma}{\Delta x}=\frac{[\Delta(l^2)/\Delta x]}{1.5\mu E_{\rm c.m.}}\approx\frac{740}{\mu E_{\rm c.m.}}. \qquad (1)$$

For our ^{16}O + ^{150}Sm case, with $\mu = 14.5$ and $E_{\rm c.m.} = 78$, Eq. (1) gives $\Delta\sigma = 650$ mb, compared with our measured $\Delta\sigma$ for the $4n$ reaction of 540 ± 100 mb. For the ^{84}Kr + ^{82}Se case, Eq. (1) gives $\Delta\sigma = 110$ mb, compared with our measured $4n$ cross section of 105 ± 25 mb. For protons, the calculated $\Delta\sigma$ is around 30 b, indicating a bin size much larger than the reaction cross section. Thus Eq. (1) seems reasonably well borne out in our cases.

Some of the expectations derived from this simple model for our three projectile-target systems are illustrated in Fig. 1. First the yrast, or lowest-energy, states for each l are plotted by

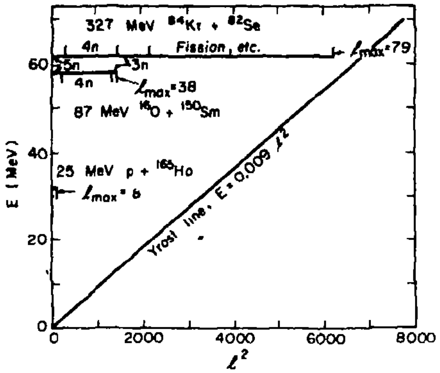

FIG. 1. Plot of excitation energy versus angular momentum squared for a nucleus having $A \approx 160$. The yrast line is shown, together with the excitation energies and angular-momentum ranges for the three reactions studied. The projectile energies shown have been corrected for target thickness.

using the $\hbar^2/2\mathscr{I}$ value given above. For the ^{16}O + ^{152}Sm case we take the $4n$ cross section of 540 mb to represent a "full" bin. The measured $5n$ cross section then represents 0.22 of a bin or a $\Delta(l^2)$ of 240, and the $3n$ cross section represents 0.09 of a bin or $\Delta(l^2) = 100$. Thus the $5n$-$4n$ boundary can be located at $l^2 = 240$, the $4n$-$3n$ boundary at $l^2 = 1340$, and the upper limit of the $3n$ reaction at $l^2 = 1440$. This indicates l_{max} for this reaction to be 38, in accord with the estimate

$$l_{max} = 0.219R[\mu(E_{c.m.} - E_{CB})]^{1/2}, \qquad (2)$$

where E_{CB} is the Coulomb barrier energy in MeV and R is the sum of the nuclear radii in femtometers. For the ^{84}Kr + ^{82}Se case, we again take our $4n$ cross section as a full bin, and find 0.27 and 0.65 bins for the $5n$ and $3n$ reactions, respectively. This makes the $5n$-$4n$ boundary at $l^2 = 304$, the $4n$-$3n$ boundary at $l^2 = 1410$, and the upper limit of the $3n$ reaction at $l^2 = 2140$. This indicates an l_{max} of 46, whereas Eq. (2) gives $l_{max} = 79$. At first this might seem surprising since the $3n$ is not a full bin according to our measurements and we find the $2n$ cross section to be only ~5 mb. However, it is well known that above a certain angular momentum the compound nucleus fissions[6] or does not form,[7] and the above value of ~50$\hbar$ represents an experimental estimate of that angular momentum. For the p + ^{165}Ho reaction, Eq. (2) gives 8, so that essentially no angular-momentum effects should occur.

For each full or partial bin in Fig. 1, an rms value of l can be estimated. These are 11, 28, and 37 for the $5n$, $4n$, and $3n$ reactions in the ^{16}O + ^{150}Sm case; 12, 29, and 42 for the ^{84}Kr + ^{82}Se case; and 6 for the p + ^{165}Ho case. To test whether the $\bar{N}_\gamma$ values from Table I correlate with these l_{rms} values, we have plotted these quantities against each other in Fig. 2. For the p + ^{165}Ho case, we took an average (weighted by the cross sections) for the $2n$ and $3n$ reactions of $\bar{N}_\gamma = 3$. It is quite apparent that a correlation exists in Fig. 2, *although the relationship is not so good* as to exclude completely the possibility of some other effects. For example there is some suggestion that the ^{84}Kr + ^{82}Se reaction produces slightly more γ rays than does the ^{16}O + ^{150}Sm reaction. Nevertheless, we conclude that most of the variation of $\bar{N}_\gamma$ is due to variation of the input angular momentum. The correlation in Fig. 2 also supports the ideas embodied in Fig. 1, and indicates that the lines separating the different bins cannot be too fuzzy.

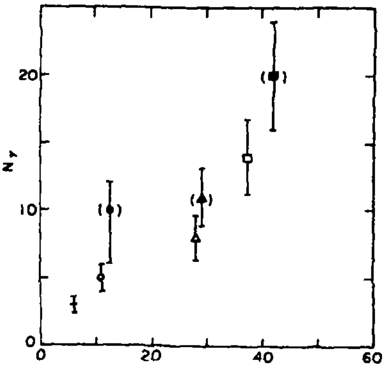

FIG. 2. Average number of continuum γ rays ($E_\gamma > 0.6$ MeV) coincident with the lowest observed discrete transition ($2 \to 0$ or $\frac{17}{2} \to \frac{13}{2}$) versus the input l_{rms} values estimated from Fig. 1. The cross is for the reaction ^{165}Ho$(p,xn\gamma)^{163,164}$Er and the circles, triangles, and squares are for the $5n$, $4n$, and $3n$ reactions from ^{16}O + ^{150}Sm (open) and ^{84}K + ^{82}Se (solid). The parentheses on the ^{84}Kr + ^{82}Se data indicate that considerable uncertainty in the l_{rms} values is introduced by the target thickness in this case.

It is also interesting to consider whether there are enough γ rays to carry off the rms l values obtained from Fig. 1. Figure 2 shows that an input angular momentum of 30$\hbar$ gives about ten γ rays. Since a multipolarity higher than $E2$ is not likely, this accounts for a maximum of 20$\hbar$. However, the $4n$ reactions from both ^{16}O + ^{150}Sm and

^{84}Kr + ^{82}Se have at least 5 discrete γ rays below 0.6 MeV which are known to carry off $10\hbar$. In the odd-mass cases ($3n$ and $5n$ reactions) even more angular momentum is carried off by the discrete lines. Thus the $\bar{N}_\gamma$ values are consistent with the rms l values estimated from Fig. 1 provided the continuum γ rays are predominantly of the stretched ($I \rightarrow I-2$) $E2$ type. It is not yet clear whether the angular distributions are consistent with this requirement. The situation is somewhat relieved since the neutrons may carry off a few units of angular momentum, and there may be a few continuum γ rays below 0.6 MeV.

We have found large variations in the number of γ rays emitted following (HI, $xn\gamma$) reactions, especially for different products of the same target-projectile system. These variations have been shown to be mainly an angular-momentum effect, and support a simple model which gives considerable insight into the effects of angular momentum in compound-nucleus de-excitation. The question as to how much information the continuum γ rays can give beyond these angular-momentum effects is an interesting one. Some of our preliminary results for average energies and angular distributions of the continuum γ rays suggest that different de-excitation modes in a given product nucleus can be distinguished experimentally.

We would like to thank Dr. M. R. Maier and Dr. D. Proetel for their help in parts of these experiments. We are also indebted to the crews of the SuperHILAC and 88-in. cyclotron for their patience and support. One of us (P.O.T.) would like to acknowledge financial assistance from The Norwegian Research Council for Science and the Humanities.

---

*Work performed under the auspices of the U. S. Atomic Energy Commission.

†On leave from University of Oslo, Norway.

‡On leave from University of Munich, Germany.

§On partial leave from Stanford University, California.

[1] J. F. Mollenauer, Phys. Rev. 127, 867 (1962).

[2] E. der Mateosian, S. Cochavi, O. C. Kistner, A. W. Sunyar, and P. Thieberger, Bull. Amer. Phys. Soc. 17, 530 (1972); A. Sunyar, in *Proceedings of the Heavy-Ion Summer Study*, edited by S. T. Thornton, CONF-720669 (Oak Ridge National Laboratory, Oak Ridge, Tenn., 1972).

[3] A. B. Smith, P. R. Fields, and A. M. Friedman, Phys. Rev. 104, 699 (1956).

[4] J. M. Blatt and V. F. Weisskopf, *Theoretical Nuclear Physics* (Wiley, New York, 1952).

[5] D. Ward, F. S. Stephens, and J. O. Newton, Phys. Rev. Lett. 19, 1247 (1967).

[6] S. Cohen, F. Plasil, and W. J. Swiatecki, in *Proceedings of the Third Conference on Reactions between Complex Nuclei*, edited by A. Ghiorso, R. M. Diamond, and H. E. Conzett (University of California Press, Berkeley, Calif., 1963), p. 325.

[7] J. Wilczynski, Nucl. Phys. A216, 386 (1973).

Average Multiplicity of Unresolved Photon Cascades in the De-excitation of Highly Excited Compound Nuclei*

E. der Mateosian, O. C. Kistner, and A. W. Sunyar
Brookhaven National Laboratory, Upton, New York 11973

(Received 2 July 1974)

Heavy ion (HI, xN) reactions leading to ^{158}Dy, ^{160,162,164}Er, and ^{170,172}Hf were studied in order to determine the average multiplicity of the unresolved photons underlying discrete spectra of rotational band transitions observed in rare-earth even-even nuclei. The average multiplicity is found to be small (6), independent (to the accuracy of this experiment) of the ground-state rotational band level in which the cascade terminates.

The basic features of the processes by which compound nuclei of high excitations and large angular momenta divest themselves of excess energy and spin have been known for some time.[1] A clear and detailed treatment of this topic has been given in a series of papers by Grover and collaborators.[2] It is reported that compound nuclei with angular momenta up to $(40-50)\hbar$ have been formed by heavy ion (HI) reactions.[3] De-excitation proceeds through successive particle emission followed by γ-ray cascades. This process is shown schematically in Fig. 1 in which the nuclear levels of compound, daughter, and residual nuclei are plotted on an angular momen-

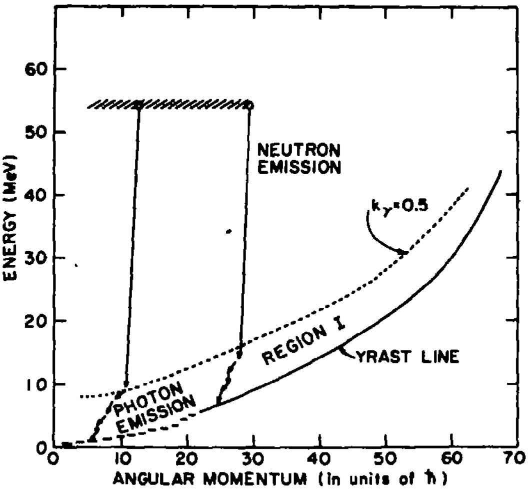

FIG. 1. Grover-type diagram of the de-excitation of highly excited nuclei. The example illustrates a (HI, xN) reaction in the rare-earth region. The compound nucleus (open circle) decays by emitting neutrons until it assumes a state close to the dotted line, about 1 neutron binding energy above the yrast line, where photon emission becomes as probable as neutron emission ($k_\gamma = 0.5$). The yrast line joins the lowest energy states with given J's. The decay proceeds in region I by photon emission until the yrast line is reached, which is then followed to the ground state. The individual levels in the initial portion of the yrast line represent the levels in the ground-state rotational band.

tum versus excitation energy diagram.[3] The heavy solid line represents for the residual nucleus the locus of states of lowest energy as a function of the angular momentum J. Grover has named this line the yrast line and the states represented by this line, the yrast levels. The shaded region represents possible initial states of the compound nucleus formed in a HI reaction. In the rare-earth region studied individual states (open circles) decay by neutron emission until levels of the residual nucleus at excitations of less than 1 neutron binding energy above the yrast line are formed. The dotted line appearing about 1 neutron binding energy above the yrast line in Fig. 1 indicates where the probability of photon emission is 0.5. At this point in the de-excitation process the nucleus has lost little angular momentum. The nucleus now de-excites by a variety of photon cascades to the yrast line. These cascades produce a continuum composed of a large number of unresolved γ rays. A discrete spectrum results from the final cascade along the yrast line to the ground state. The purpose of this investigation is to determine N_γ, the average number of γ gays in the "continuum" per disintegration for compound nuclei formed in the rare-earth region. This average multiplicity $N_\gamma = (\sum_n n\sigma_n)/\sigma_{\text{tot}}$, where n is the multiplicity of a cascade, σ_n the cross section associated with multiplicity n, and σ_{tot} the cross section for all cascades.

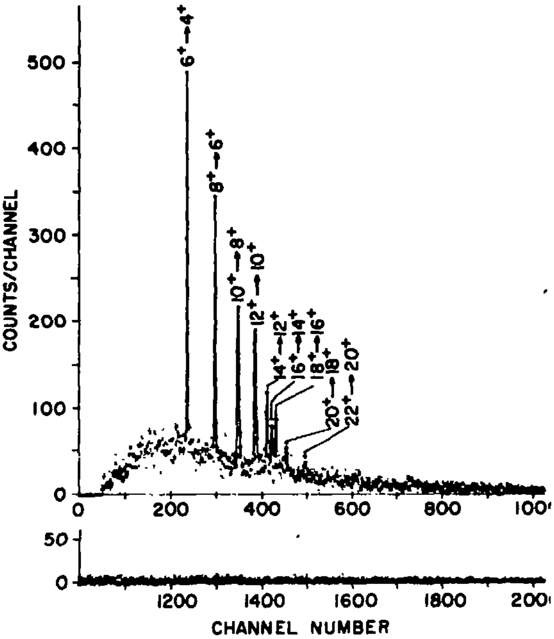

FIG. 2. Spectrum of γ rays in coincidence with the $4^+\to2^+$ transition of ^{158}Dy.

Analyses have been made on ^{158}Dy, ^{160,162,164}Er, and ^{170,172}Hf populated by (^{12}C, $4n$) and (^{16}O, $4n$) reactions. The ^{158}Dy results have been reported earlier.[4] Thick metallic rare-earth targets of 8 to 16 mg/cm^2 were used. γ-γ coincidences were observed with two Ge(Li) detectors placed at various distances and angles around the target. Singles data were stored in core while 4096 × 4096 channel coincidences were recorded in "event mode" on tape. Background-subtracted spectra of γ rays in coincidence with the transitions in the ground-state rotational band were obtained by analyzing these data.

The spectra consist of discrete peaks corresponding to the transitions in the rotational band and a "continuum" which extends beyond the last of the observed discrete lines (Fig. 2). By measuring the counts in each discrete peak, correcting for total as against peak counts, summing the discrete counts, and subtracting from the total number of counts in the spectrum, we obtained the number of counts in the continuum. Since more than 90% of all decays in these nuclei proceed through the $6^+\to4^+$ and the $4^+\to2^+$ transitions, the number of counts in these transitions were taken as a measure of σ_{tot} in all cases and N_γ was taken to be the number of counts in the continuum divided by the number of counts in one or the other of these transitions. The ^{158}Dy experiment was repeated with a 6.3-cm-high lead cone in front of the detector in order, through selective absorption, to suppress the detection of photons originating at the target. In this way 10% of the continuum was found to be due to neutrons and scattering effects. Addition effects were accounted for where necessary. No correction for total-efficiency variation with energy was applied, since the energy distribution of the continuum is unknown. In the energy range of interest, this variation and its associated error do not exceed 30%.

All results are summarized in Table I where the numbers are the N_γ's for cascades (region I in Fig. 1) feeding into the ground-state rotational band of the indicated nucleus at all levels above the transition used as a gate. Therefore, the N_γ for the $2^+\to0^+$ transition is averaged over all type-I cascades while the N_γ for the $10^+\to8^+$ transition is averaged over the cascades which feed into rotational levels at the 10^+ or higher levels only. Nevertheless, it is possible to infer some of the general, average properties of N_γ. Only the ^{158}Dy data were corrected for neutron events and the other effects. It was assumed that the correction in the other nuclei is the same (10%). The average of all N_γ (with the exception of one) is 6.0. Statistical errors have not been given because it was felt that inherent systematic errors could play a larger role than statistics, and a better indication of the precision of the measurements is obtained from a comparison of the three independent ^{160}Er runs. It is therefore reasonable to take 1.5 as the error and to state that N_γ for all these nuclei is 6 ± 1.5. The spread in the numbers of any particular row is usually less than this. It is interesting to compare this number with other determinations of N_γ appearing in the literature. Karnaukhov and Oganesyan[5] irradiated Sn with 78-MeV ^{12}C ions and estimated the average number of γ rays in the total (including yrast transitions) cascade to be "not less than 10." In the ^{158}Dy run reported in the present work, the average number of discrete γ rays per cascade is about 6.5 and thus the average number of photons per cascade is about 12.5. Mollenauer[6] reported about 14 photons per reaction in an experiment in which ^{165}Ho was bombarded by 103.5–115-MeV ^{12}C ions. Williamson *et al.*[7] report a value for N_γ of 5.4 in $(\alpha,3n)$ and $(\alpha,4n)$ reactions on ^{167}Er at 40.5 MeV. Finally, Degnan *et al.*[8] reported a multiplicity of about 4 or less in the complete γ cascade for compound-nucleus formation in light nuclei with (d,p) and (p,p') reactions at 12 and 17 MeV. The agreement between this measurement and the HI reactions reported in

TABLE I. Average multiplicity of photons in the continuum.

Nucleus	Proj.	Beam Energy (MeV)	Transition Used as Gate								
			$2^+\to0^+$	$4^+\to2^+$	$6^+\to4^+$	$8^+\to6^+$	$10^+\to8^+$	$12^+\to10^+$	$14^+\to12^+$	$16^+\to14^+$	$18^+\to16$
^{158}Dy[a]	^{12}C	65		5.5	4.8	5.7	5.9	5.3			
^{160}Er	^{12}C	70		8.3	8.4	7.9	7.1	7.3			
"	^{12}C	71.3		7.2	6.4	6.9	6.3	8.0	5.6		7.8
"	^{12}C	73.5		8.0	6.9	7.0	6.5	6.3			
" (average)[b]				7.8	7.2	7.3	6.6	7.2			
^{162}Er	^{12}C	66			6.3	4.4	3.4	4.6	4.0		
^{164}Er	^{18}O	75	8.9	9.5	8.4	9.3	7.0	6.2			
^{170}Hf	^{12}C	70			8.9	7.6	7.6	7.3	7.6	8.2	
^{172}Hf	^{12}C	70		11.3	6.2	6.4	6.5	5.2	5.4	7.9	

[a] These data for ^{158}Dy have been corrected for neutron and addition effects which contribute to the background continuum.

[b] Average of the three ^{160}Er runs.

the above referenced papers is interesting since coincidence measurements were used in this work, and singles in the others. This suggests that most of the reactions studied in the earlier works were remarkably clean so that the results were not affected by the presence of accompanying reactions.

It is interesting that N_γ does not change with position in the rotational band of the transition being fed by the cascade. Barring the suggestion of a trend to higher values for the few lowest gates in Table I, N_γ remains remarkably constant for gates varying from the $6^+ \rightarrow 4^+$ transition to (in one case) the $18^+ \rightarrow 16^+$ transition. Thus, when the three ^{160}Er runs are averaged, the N_γ obtained is close to 7 (uncorrected) from the $6^+ \rightarrow 4^+$ to the $12^+ \rightarrow 10^+$ transitions inclusive.

If it is accepted that the number of γ rays in the "continuum" cascade is independent of the spin of the rotational state at which the cascade terminates, one may offer a simple picture of the de-excitation process with the help of Fig. 1. In the Grover picture the energy available to cascades in region I is the same regardless of J, since γ-ray emission becomes prominent at an excitation of 1 binding energy of the neutron above the yrast level. If it is now assumed that at a given ΔE above the yrast level the distribution of states available to the intermediate cascade and the population distribution[8] of these states in energy after neutron emission are roughly independent of J, one would account for the constancy of N_γ as a function of entry point in the ground-state rotational band. The effect of a thick target is to introduce a variation in the average excitation energy with angular momentum not unlike that associated with the yrast line in the region of the ground-state band. Thus the available energy for neutron and γ emission to the yrast line is roughly independent of angular momentum.

This assumption of the independence of the distribution of states above the yrast level as a function of J is not totally unfounded. According to Ginocchio[9] the energy dependence of shell-model states with a definite angular momentum is close to Gaussian for nuclei with a large number of particles in a large but finite set of shell-model orbits. His approximate expressions for the energy centroid and width of the distribution of shell-model states agree with exact shell-model calculations for ^{20}Ne and ^{62}Ni, indicating that they are already large enough systems to satisfy the required initial conditions. It follows from his analysis of the distribution of intrinsic states as a function of both energy and angular momentum that

$$\rho_{J'+\Delta J}(\Delta E + E_0(J')) \approx \rho_{J+\Delta J}(\Delta E + E_0(J)),$$

where $E_0(J)$ is the yrast energy for angular momentum J and $\rho_{J+\Delta J}(\Delta E + E_0(J))$ is the level density for angular momentum $J + \Delta J$ at an excitation of ΔE above the yrast level. For example, 1 MeV above the yrast level for $J = 10$, the density of $J = 11$ states is the same as the density of the $J = 19$ states 1 MeV above the $J = 18$ yrast level. Thus, it is plausible that the intermediate cascade may find distributions of states and relative properties [e.g., $B(E1)$, $B(E2)$] sufficiently similar so that N_γ may to first approximation be independent of the path of the cascade in J space.

It should be noted that the value of 6 for N_γ requires a relatively high average energy for the γ rays in this intermediate cascade ($\gtrsim 1.0$ MeV) in Grover's scheme. This is consistent with estimates of the average energy of the photons in the continuum of 1 MeV or greater indicated by our data. In any case, these values for N_γ and the average energy of the photons in the cascade are in agreement with Grover's calculations, indicating that photon emission becomes important at an excitation of 1 neutron binding energy above the yrast level.

Studies of the de-excitation process following $(\alpha, 3n)$[8] and ^{40}Ar-induced[10] reactions have led to a more complex description of this process. In these investigations it was thought that rotational transitions of softer γ rays were needed to help carry angular momentum away from the nucleus during the intermediate cascade, and a detailed scheme involving rotational bands has been made.[10] These studies, however, were conducted under different conditions from the present one. The experimental results of the present paper ($N_\gamma = 6$ independent of the rotational level terminating the type-I cascade) are not incompatible with the conclusions of these other investigations.

The authors wish to thank J. Vary and J. N. Ginocchio for informative discussions and constructive comments and P. Thieberger for significant help with and interest in various aspects of this work.

---

*Work supported by the U. S. Atomic Energy Commission.

[1] For references and a general review of this subject see T. D. Thomas, Annu. Rev. Nucl. Sci. 18, 343 (1968).

[2] J. R. Grover, Phys. Rev. 127, 2142 (1962); J. R. Grover and J. Gilat, Phys. Rev. 157, 802, 814, 823 (1967).

[3] D. Ward, F. S. Stephens, and J. O. Newton, Phys. Rev. Lett. 19, 1247 (1967).

[4] E. der Mateosian, S. Cochavi, O. C. Kistner, A. W. Sunyar, and P. Thieberger, Bull. Amer. Phys. Soc. 17, 530 (1972).

[5] V. A. Karnaukhov and Yu. Ts. Oganesyan, Zh. Eksp. Teor. Fiz. 38, 1339 (1960) [Sov. Phys. JETP 11, 964 (1960)].

[6] J. F. Mollenauer, Phys. Rev. 127, 867 (1962).

[7] C. F. Williamson, S. M. Ferguson, B. J. Shepherd, and I. Halpern, Phys. Rev. 174, 1544 (1968).

[8] J. H. Degnan, B. L. Cohen, R. C. Petty, C. L. Fink, G. R. Rao, and R. Balasubramanian, Phys. Rev. C 5, 836 (1972).

[9] J. N. Ginocchio, Phys. Rev. Lett. 31, 1260 (1973).

[10] J. O. Newton, F. S. Stephens, R. M. Diamond, W. H. Kelly, and D. Ward, Nucl. Phys. A141, 631 (1970).

Nucleus-Nucleus Optical Potential Using a Density-Dependent Two-Body Interaction

Bikash Sinha
Wheatstone Laboratory, King's College, London WC2R 2LS, England, and
The Niels Bohr Institute, Copenhagen, Denmark

(Received 17 June 1974)

The nucleus-nucleus optical potential is calculated by using a density-dependent two-body effective interaction where the local density takes into account the contribution of both the projectile and the target densities. The results indicate that it is important to use such an interaction when the densities of the colliding nuclei overlap significantly.

The nucleus-nucleus optical potential has been derived recently by several authors by folding in a phenomenological nucleon-nucleus optical potential with the projectile density.[1] In this procedure each nucleon of the projectile is treated essentially as free and so the perturbation felt by each nucleon in the projectile as a result of the field of all other nucleons is ignored. The most important consequence of such a scheme is the implicit neglect of the saturation properties of the two-body interaction, which prevents the nuclear density from increasing beyond a certain magnitude. The optical potential calculated in this way is therefore overestimated when the centers of mass of the colliding nuclei are at short distances from each other and the densities of the two nuclei overlap significantly. It is, however, expected to be of the right order of magnitude at or near the touching radius of the interacting nuclei when the overlap is not so significant.

Galin *et al.*,[2] on the other hand, have computed the energy of the nucleus-nucleus interaction by using the phenomenological energy-density function of Brueckner *et al.*[3] The structure of each nucleus in this calculation is assumed to be conserved entirely during the contact and the nuclear-matter densities are assumed to overlap in a reversible process without any rearrangements. Although the method of Galin *et al.*[2] is an improvement over other works,[1] the Brueckner "sudden approximation" described above cannot be expected to yield realistic results after the nuclei have fused. On the other hand, if one of the colliding nuclei is light, for example, a ^{4}He or ^{3}He, the concept of a phenomenological energy-density functional cannot be used with any confidence.

In this Letter I propose to use a density-dependent two-body effective interaction to construct the nucleus-nucleus optical potential—the density-dependent part, as is well known,[4] takes into account approximately the saturation properties of the two-body interaction. It will be shown that the nucleus-nucleus potential, in this way, can be calculated for any kind of projectile, light or heavy, without any loss of generality. First, the nucleon-nucleus optical potential is calculated by folding in this interaction with the target density[5]; the nucleon-nucleus potential is then folded in with the projectile density. The importance of using an effective two-body interaction such as a density-dependent interaction has been amply demonstrated recently[5] for the nucleon-nucleus optical potential. In a nucleus-nucleus interaction, however, each nucleon in the projectile is embedded in a nuclear medium, thus departing from a free-nucleon case. *The local density in the two-body interaction therefore should be computed taking into account the contribution of the density from both the target and* *the projectile.* The density-dependent part of the interaction, as will be shown, contributes most significantly to the lowering of the attraction as the local density increases, thus producing saturation. This particular feature is absent in a simple folding of a phenomenological one-body optical potential into the projectile density distribution.

By use of a linear density-dependent interaction (for computational convenience) given by Lande, Molinari, and Brown,[6] the one-body optical potential at a point $\vec{t}$ relative to the center of the target is given by[6]

$$U_1(t)=\sum_{i=p,n}\int\rho_1{}^i(\vec{\xi}_1)V_{\mathrm{K-K}}{}^i(|\vec{s}|)\alpha^i\{1-\beta^i[\rho_{m1}(\vec{x})+\rho_{m2}(\vec{\xi}_2+\tfrac{1}{2}\vec{s})]\}d^3\xi_1\quad(i=\text{proton, neutron}),\tag{1}$$

where the exchange effects between target nucleons and projectile nucleons are neglected, $V_{\mathrm{K-K}}$ is the Kallio-Koltveit[6] interaction, (α^i,β^i) are parameters given by Lande, Molinari, and Brown,[6] $\rho_1{}^i$ is the nucleon-density distribution of the target measured from its own center $\vec{\xi}_1$. ρ_{m1}, the target-matter density, is evaluated at $\vec{x}=\frac{1}{2}(\vec{t}+\vec{\xi}_1)$, whereas the projectile-matter density ρ_{m2} is evaluated at $\vec{\xi}_2+\frac{1}{2}\vec{s}$, with $\vec{\xi}_2$ the internal coordinate of the projectile and with $|\vec{s}|=|\vec{t}-\vec{\xi}_1|$. Expanding ρ_{m2} and noting that the short range of $V_{\mathrm{K-K}}$ would render the higher-order terms in s negligibly small, we write $\rho_{m2}(\vec{\xi}_2+\frac{1}{2}\vec{s})\cong\rho_{m2}(\vec{\xi}_2)+\frac{1}{24}s^2\nabla^2\rho_{m2}(\vec{\xi}_2)$, where the direction of $\vec{s}$ has also been averaged, exactly in the same manner employed by Negele and Vautherin.[7] $U_1(t)$ has now three components:

$$U_{11}(t)=\sum_{i=p,n}\int\rho_1{}^i(\vec{\xi}_1)V_{\mathrm{K-K}}(|\vec{s}|)\,\alpha^i[1-\beta^i\rho_{m1}(\vec{x})]d^3\xi_1\,,\tag{2.1}$$

$$-\rho_{m2}(\vec{\xi}_2)U_{12}(t)=-\rho_{m2}(\vec{\xi}_2)\sum_{i=p,n}\int\rho_1{}^i(\vec{\xi}_1)V_{\mathrm{K-K}}(|\vec{s}|)\,\alpha^i\beta^i\,d^3\xi_1,\tag{2.2}$$

$$-\nabla^2\rho_{m2}(\vec{\xi}_2)U_{13}(t)=-\nabla^2\rho_{m2}(\vec{\xi}_2)\sum_{i=p,n}\int\rho_1{}^i(\vec{\xi}_1)V_{\mathrm{K-K}}(|\vec{s}|)\,\alpha^i\beta^i\tfrac{1}{24}s^2d^3\xi_1.\tag{2.3}$$

Equation (2.1) is attractive but Eq. (2.2) is repulsive indicating the reduction in the one-body optical potential arising from the density-dependent part of the two-body interaction. The sign of Eq. (2.3) obviously will depend on $\nabla^2\rho_{m2}(\vec{\xi}_2)$ which is usually negative so that $U_{13}(t)$ in Eq. (2.3) behaves as an attractive potential. The third term, however, as discussed below, is small compared to Eqs. (2.1) and (2.2). Folding in Eqs. (2.2) with the projectile density the nucleus-nucleus optical potential, as a function of $\vec{R}$, the distance between the centers of the two nuclei, becomes

$$U_{\mathrm{NN}}(\vec{R})=\int\rho_{m2}(\vec{\xi}_2)U_{11}|\vec{R}-\vec{\xi}_2|\,d^3\xi_2-\int\rho_{m2}{}^2(\vec{\xi}_2)U_{12}|\vec{R}-\vec{\xi}_2|d^3\xi_2-\int\rho_{m2}(\vec{\xi}_2)\nabla^2\rho_{m2}(\vec{\xi}_2)U_{13}|\vec{R}-\vec{\xi}_2|d^3\xi_2.\tag{3}$$

One of the advantages of Eq. (2) is that U_{11}, U_{12}, and U_{13} can be evaluated for a particular target without referring to any particular projectile. Thus one needs to evaluate the optical potential for say ^{40}Ca as a target and then fold it in with a variety of projectile densities, such as ^{3}He, ^{4}He, ^{16}O, etc. To check the symmetry in the folding procedure, we changed ρ_{m1} to ρ_{m2} and evaluated $U_{\mathrm{NN}}(\vec{R})$ for a set of target and projectile. The difference between the two sets of results is approximately 3%, mainly because of truncation errors in the ρ_{m2} expansion. The optical potential, in Fig. 1, is plotted for ^{40}Ca as a target and ^{3}He, ^{4}He, and ^{16}O as projectiles. The ^{40}Ca and ^{16}O density distributions were taken from the work of Negele and Vautherin[7] whereas for ^{4}He a Woods-Saxon phenomenological distribution was used.[8] For ^{3}He a Gaussian distribution was used.[9] The solid line is $U_{\mathrm{NN}}(\vec{R})$ as given in Eq. (3), whereas the dashed line is just the first term of Eq. (3). The following observations are of some importance: The third term is quite small but attractive. The second term in Eq. (3), which I shall refer to as the saturation term, has a negligible contribution in the very tail region of $U_{\mathrm{NN}}(\vec{R})$ but gives rise to substantial repulsion as $\vec{R}$ decreases and the densities of the two nuclei overlap more and more. The saturation term generally depends on the density of the projectile and/or target. For a particular target such as ^{40}Ca, it has little contribution for ^{3}He; for ^{4}He, however, the effect is already significant, and for ^{16}O it becomes even more important. It is felt that the scope of the application of Eq. (3) is general. Different types of approximation are not required for different types of projectiles. It should be noted, however, that for the heavier projectile such as ^{16}O the results still do not have any meaning below a certain value of R when the colliding nuclei tend to fuse together. The results for ^{4}He and ^{3}He agree remarkably well with the phenom-

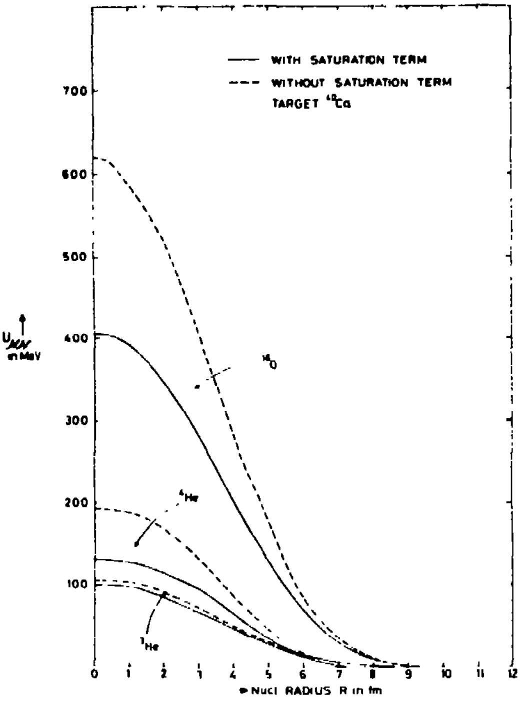

FIG. 1. The nucleus-nucleus optical potential as a function of R, the distance between the centers of the colliding nuclei.

enological predictions.[10] For heavier projectiles we have tried to extract an approximate empirical relation of $U_{NN}(\vec{R})$ at large distances $R \gtrsim 5$ fm, following the arguments of Broglia and Winther.[1] Assuming that the densities of the colliding nuclei behave as exponentials at large distances, it can be shown that the ρ_{m2}^{2} will behave as ρ_{m2} but with a diffuseness half of that of ρ_{m2}. Thus

$$U_{NN}(\vec{R})_{R\gtrsim 5} \cong -S_1R^2\exp[-\{R-R_{01}\}/a_1] + S_2R^2\exp[-\{R-R_{02}\}/a_2], \qquad (4)$$

where I estimate that $S_1 = 1.5$, $R_{01} = 1.14(A_1^{1/3} + A_2^{1/3})$, $a_1 = 0.6$, and $S_2 = 0.5$, $R_{02} = 0.75(A_1^{1/3} + A_2^{1/3})$, $a_2 = 0.36$. The first term of Eq. (4) is represented by the dashed line in Fig. 1, and comes from only the first term in Eq. (3). The depth parameter $S_1 = 1.5$ is smaller compared to the results of Broglia and Winther.[1] This is probably because of the use of a density-dependent interaction. The second term arises from the second term of Eq. (3). In general, however, it is suggested in the light of the present work that the empirical formulas given by Broglia and Winther[1] and also by Brink and Rowley[1] tend to overestimate the optical potential. The implication of Eq. (3) for determining the fusion criteria[1] will therefore be rather interesting—a study presently being pursued. It should be emphasized that Eq. (4) is only an approximate one and cannot be applied to lighter projectiles. A detailed study of this model and its application to other studies is postponed for a future publication.

The author wishes to thank Dr. David Brink and Dr. Phillip J. Siemens for stimulating discussions and his colleagues at King's College for constructive suggestions. A travel grant from the Royal Society of England for a visit to The Niels Bohr Institute is gratefully acknowledged.

---

[1] R. A. Broglia and A. Winther, Phys. Rep. 4C, 153 (1972); D. M. Brink and N. Rowley, Nucl. Phys. A219, 79 (1974); D. H. E. Gross and H. Kalinowski, Phys. Lett. 48B, 302 (1974).

[2] J. Galin *et al.*, Phys. Rev. C 9, 1018 (1974).

[3] K. A. Brueckner *et al.*, Phys. Rev. 171, 1188 (1968), and 181, 1543 (1969).

[4] H. A. Bethe, Annu. Rev. Nucl. Sci. 21, 93 (1971).

[5] G. L. Thomas, B. C. Sinha, and F. Duggan, Nucl. Phys. A203, 305 (1973), and references therein.

[6] A. Lande, A. Molinari, and G. E. Brown, Nucl. Phys. A115, 241 (1968).

[7] J. W. Negele and D. Vautherin, Phys. Rev. 5, 1472 (1972).

[8] C. J. Batty, E. Friedman, and D. F. Jackson, Nucl. Phys. A175, 1 (1971), and references therein.

[9] L. I. Schiff, Phys. Rev. 133, B802 (1964).

[10] M. E. Cage *et al.*, Nucl. Phys. A183, 449 (1972); N. M. Clarke *et al.*, to be published.

Observation of a Dip Due to $I=0$ t-Channel Exchange in the Reaction $\pi N \rightarrow A_2N$ at 4.5 and 6 GeV/c*

H. A. Gordon, M. Habibi, and I. Stumer†
Brookhaven National Laboratory, Upton, New York 11973

and

Kwan-Wu Lai
California Institute of Technology, Pasadena, California 91109, and Brookhaven National Laboratory, Upton, New York 11973

(Received 6 June 1974)

In the reaction $\pi^-p \rightarrow A_2^-p$, we observe a dip in the differential cross section at $t \approx 1.2$ GeV^2. Analysis in terms of t-channel contributions from isospin-0 and -1, natural- and unnatural-parity exchanges suggest that the dip is mainly due to natural-parity, $I=0$ exchange.

The production of A_2 can be analyzed in terms of the isospins (I) and natural (N) parity and unnatural (U) parity t-channel exchanges. For $I=0$, P (Pomeron) (N), f^0 (N), and η (U) are allowed, whereas for $I=1$, ρ (N) and B (U) can be exchanged [Fig. 1(a) inset]. In this Letter, we present the data of 4.5 and 6 GeV/c $\pi^-p \rightarrow A_2^-p$ for $A_2^- \rightarrow K_s^0K^-$. Our analysis from this reaction and other relevant reactions ($\pi^+n \rightarrow A_2^0p$ and $\pi^+p \rightarrow A_2^+p$) allows us to separate the contributions due to $I+0$ and $I=1$, and N- and U-parity exchanges in the t-channel. A dip is observed at $t \approx 1.2$ GeV^2 and can for example be interpreted as the nonsense wrong-signature zero (NSWSZ) of the f^0 trajectory in the context of the Regge-pole model. In addition to the f^0 contribution, the B exchange seems to dominate in the $I=1$ and U-parity contribution.

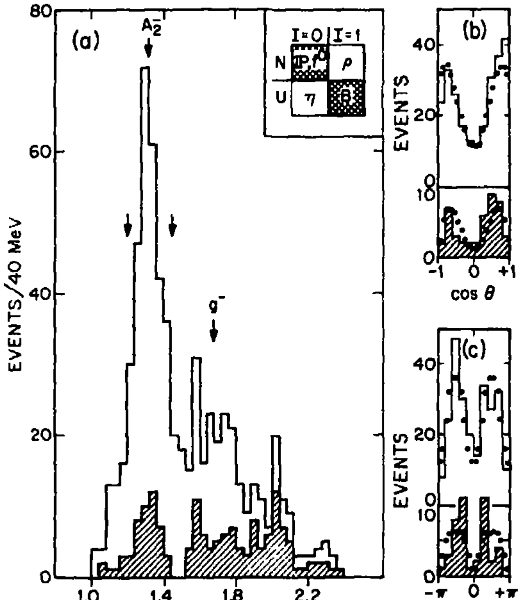

FIG. 1. (a) $K_s^0K^-$ mass spectrum from the reaction $\pi^-p \rightarrow K_s^0K^-p$ at 4.5 and 6 GeV/c with events in the Λ(1520) removed. (b), (c) Decay distributions for the $A_2^- \rightarrow K_s^0K^-$ in the Gottfried-Jackson frame. Shaded areas are for events in the high-t region. Solid points indicate best fit to the data.

The data for this study come from a series of bubble-chamber exposures (this experiment) with details presented elsewhere[1] and other published[2] and unpublished experiments[3] (See Table I). Since normalizations are important for this analysis, we have calculated the cross sections in a consistent way for our experiment. The procedure is to (1) determine $A_2^\pm \rightarrow \rho^0\pi^\pm$ production cross sections from the $\pi^+\pi^-\pi^\pm$ modes by using the University of Illinois partial-wave analysis program,[4] (2) obtain the total A_2 production cross sections by appropriate corrections from $\rho\pi$ to include all modes,[5] and (3) obtain the shapes of the differential cross sections and density-matrix elements from the $A_2^\pm \rightarrow K_s^0K^\pm$ modes, where the normali-

TABLE I. A_2 data.

	$p_{\rm lab}$ (GeV/c)	Modes used	$\sigma(A_2 \rightarrow {\rm all})$ (μb)
A_2^-	4.5	$K_s^0K^-$	159 ± 25
	6	$\rho^0\pi^-$ $K_s^0K^-$	...
A_2^0	6[a]	$\rho^\pm\pi^\mp$	90 ± 15
A_2^+	6	$\rho^0\pi^+$	$132 \pm$ [illegible]
	7.1[b]	K^0K^+ $\eta\pi^+$	...

[a] Ref. 2.
[b] Ref. 3.

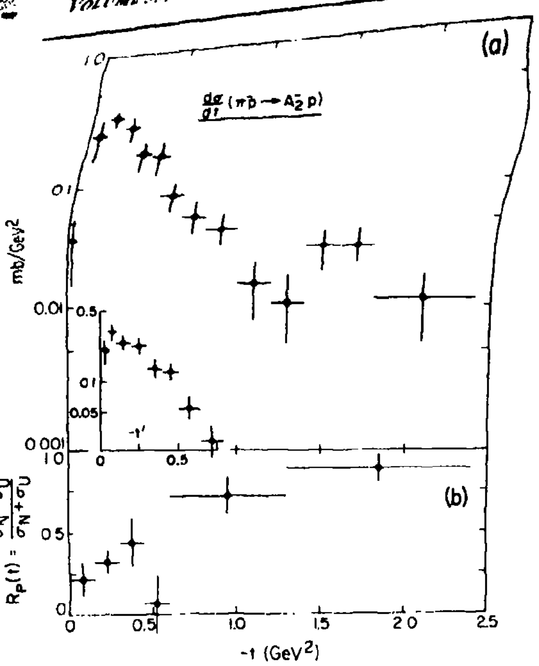

FIG. 2. (a) $d\sigma/dt$ for A_2^- production (corrected for all decay modes). Inset shows the same distribution in t'. (b) Ratios of contributions from σ_N and σ_U exchanges.

zations come from step (2). We use the $K_s^0K^\pm$ modes[6] because of small background in the $A_2^\pm$ region (<20%) as illustrated in Fig. 1(a) for the $K_s^0K^-$ mass spectrum with $\Lambda(1520) \to K^-p$ removed.[7] Since our study of the differential cross sections extends to the high-t region, to check the quality of the data, we present events with $|t| > 1.0$ GeV² in Fig. 1(a) in the shaded area. A clear A_2^- signal is seen. Decay angular distributions in cosθ and Φ (Gottfried-Jackson frame) in the A_2^- rest frames are also shown in Figs. 1(b) and 1(c). Both t regions show slightly different angular distributions but both are characteristic of a resonance.

In Fig. 2(a) we show the differential cross section of $\pi^-p \to A_2^-p$ as obtained from the $A_2^- \to K_s^0K^-$ events at 4.5 and 6 GeV/c normalized to the cross section at 6 GeV/c as shown in Table I. A forward ($t \approx 0$) dip is observed. The distribution in $t' = t - t_{\min}$ is also shown in the inset of Fig. 2(a). This forward dip, which has been reported before,[8] is associated with the s-channel spin-flip contribution to the A_2 production, and thus we will not discuss it further. However, we see another dip at $|t| \approx 1.2$ GeV² followed by a second maximum centered at about 1.8 GeV². To understand this structure, we first examine the $J^P = 2^+$ spin density-matrix elements as a function of t. We use a maximum-likelihood fit to the $K_s^0K^-$ decay angles in the Gottfried-Jackson frame. To separate the N- and U-parity contributions, we use the definitions $\rho_N = (\rho_{11} + \rho_{1\,-1}) + (\rho_{22} - \rho_{2\,-2})$ and $\rho_U = \rho_{00} + (\rho_{11} - \rho_{1\,-1}) + (\rho_{22} + \rho_{2\,-2})$; thus $d\sigma_{N(U)}/dt = \rho_{N(U)}\,d\sigma/dt$. Figure 2(b) displays the ratio

$$R_P(t) = \left(\frac{d\sigma_N}{dt} - \frac{d\sigma_U}{dt}\right)\Big/\left(\frac{d\sigma_N}{dt} + \frac{d\sigma_N}{dt}\right)$$

as a function of t. $R_P(t) = 1\ (-1)$ implies all N- (U-) parity contribution. It is evident that all values of $R_P(t)$ are greater than 0 for the whole t range, and approach 1 for the high-t region, indicating that the differential cross section for N-parity exchange is dominant over that for U-parity exchange, particularly at the high-t region ($|t| > 1.0$ GeV²). Thus the structure in the differential cross section at the high-t region mainly comes from the N-parity exchange. Since there are two possible isospins $I = 0$ (P and f^0) and $I = 1$ (ρ) in the N-parity contribution, we now proceed to separate the isospin exchange in the t channel.

We consider the $I_t = 0$ (a_0) and $I_t = 1$ (a_1) t-channel amplitudes to describe the A_2 production:

$$f(\pi^\pm p \to A_2^\pm p) = \tfrac{1}{2}a_1 \mp (1/\sqrt{6})a_0, \qquad (1)$$

$$f(\pi^+ n \to A_2^0 p) = (1/\sqrt{2})a_1, \qquad (2)$$

and

$$\sigma_{I_t=1} = \int |a_1|^2 dt = 2\sigma(\pi^+ n \to A_2^0 p),$$

$$\sigma_{I_t=0} = \int |a_0|^2 dt = 3[\sigma(\pi^- p \to A_2^- p) + \sigma(\pi^+ p \to A_2^+ p) - \sigma(\pi^+ n \to A_2^0 p)],$$

and the isospin interference term ($I_t = 0, 1$)

$$2\int \mathrm{Re}(a_1{}^* a_0)\,dt = \sqrt{6}[\sigma(\pi^- p \to A_2^- p) - \sigma(\pi^+ p \to A_2^+ p)].$$

We evaluate the above expressions at 6 GeV/c using (1) A_2^- data as described before, (2) A_2^0 data from Ref. 2, and (3) A_2^+ data obtained from the normalization from Table I and the shape of the differential cross section from Ref. 3 with the use of the $K_s^0K^+$ and $\eta\pi^+$ modes. Figure 3(a) shows $d\sigma(\pi N\rightarrow A_2N)_{I_t=0}/dt$ and Fig. 3(b) shows $d\sigma(\pi N\rightarrow A_2N)_{I_t=1}/dt$ (all solid points) as the results of the isospin separation. We note that the $I_t=0$ contribution is dominant over the $I_t=1$ contribution, particularly evident in the high-t region. It is again interesting to display the ratio

$$R_I(t')=\left(\frac{d\sigma_0}{dt'}-\frac{d\sigma_1}{dt'}\right)\Big/\left(\frac{d\sigma_0}{dt'}+\frac{d\sigma_1}{dt'}\right)$$

in Fig. 3(c), and $R_I(t')\approx 1$ for the high-t' region, and there appears very little or no interference as shown in Fig. 3(d).

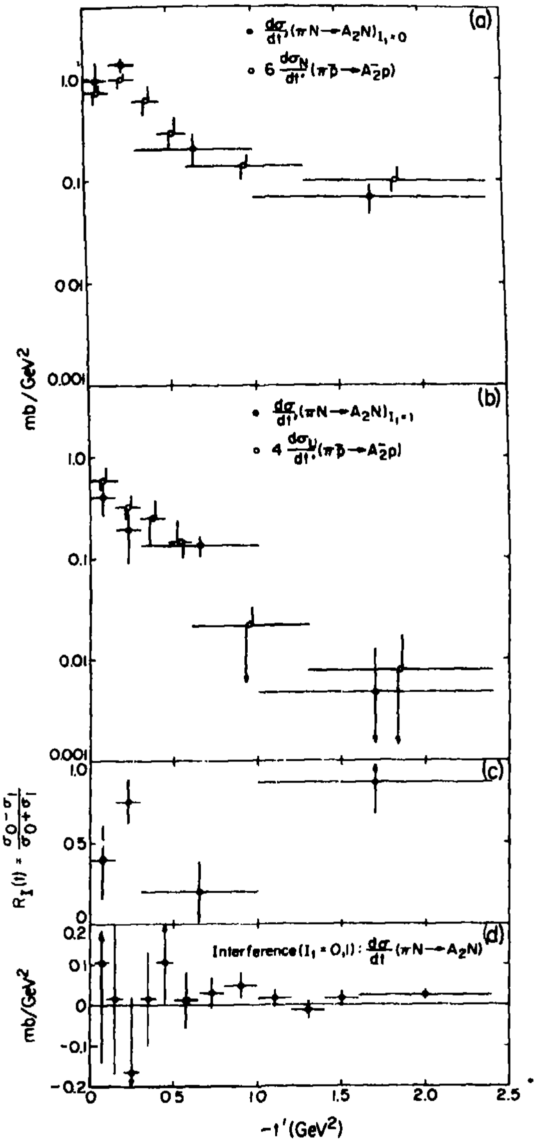

FIG. 3. (a) Contributions to the A_2 production from σ_0 (solid points) compared with σ_N in A_2^- production (open points). (b) Contributions to the A_2 production from σ_1 (solid points) compared with σ_U in A_2^- production (open points). (c) Ratios of contributions from σ_0 and σ_1 exchanges. (d) Interference term between $I=0,1$ amplitudes in the t-channel exchange.

To examine further the dominance of $I_t=0$ and N-parity exchange to the available t range in this experiment, we note from Eq. (1) that $\sigma(\pi^-p\rightarrow A_2^-p)=\frac{1}{4}\sigma_1+\frac{1}{6}\sigma_0$ since the isospin interference is negligible. Furthermore $\sigma(\pi^-p\rightarrow A_2^-p)=\sigma_N+\sigma_U$, and therefore $\sigma_N+\sigma_U=\frac{1}{4}\sigma_1+\frac{1}{6}\sigma_0$. Thus it is interesting to investigate whether a separation of isospin contributions is equivalent to a separation of N- and U-parity exchanges (i.e., $6\sigma_N=\sigma_0$ and $4\sigma_U=\sigma_1$). From this experiment, we obtain $\sigma_0=603\pm111$ μb, $6\sigma_N=666\pm114$ μb, $\sigma_1=180\pm30$ μb, and $4\sigma_U=192\pm40$ μb for all t regions. The agreements between $6\sigma_N$ and σ_0 as well as $4\sigma_U$ and σ_1 are impressive. This is further illustrated in differential cross sections, namely, $6d\sigma_N(\pi^-p\rightarrow A_2^-p)/dt'$ compared with $d\sigma(\pi N\rightarrow A_2N)_{I_t=0}/dt'$ and $4d\sigma_U(\pi^-p\rightarrow A_2^-p)/dt'$ compared with $d\sigma(\pi N\rightarrow A_2N)_{I_t=1}/dt'$ as shown in Figs. 3(a) and 3(b). It is evident that not only cross sections but also differential cross sections are in good agreement between $I_t=0$ and N-parity contributions as well as $I_t=1$ and U-parity contributions. With the assumption that N- and U-parity amplitudes as well as $I_t=0,1$ amplitudes do not interfere, an equality between $4\sigma_U=\sigma_1$ implies that ρ contribution is negligible if one can assume that the η exchange in the $A_2^{\pm}$ production is small.[9] In this case, the B exchange would dominate the $I_t=1$ amplitude.

Thus our analysis shows that the differential cross sections for $A_2^{\pm}$ productions at the moderate-to-high-t region are due to contributions from the $I=0$ and N-parity exchange. This implies that only P and/or f^0 are responsible for the exchange in this t region [Fig. 1(a) inset]. It is, however, unlikely for the P to make important contributions in the high-t region, and therefore it is natural to ascribe the structure (the dip at $|t|\approx1.2$ GeV^2) to the f^0 exchange. To further speculate on f^0 trajectory, when a degenerate f^0-ω trajectory is extended to the $-t$ region, it intersects with $\alpha(t)=0$ at $t=-0.4$ GeV^2 and $\alpha(t)=-1$ at $t=-1.3$ GeV^2. The zero at $t=-0.4$ GeV^2 can be interpreted as the NSWSZ for ω which has been observed experimentally by Crennell *et al.*[10] in isolation of ω exchange from the ρ production from an earlier analysis of this experiment. The zero at $t = -1.3$ GeV^2 may be associated with the NSWSZ for f^0 which has been observed here from the present analysis.

We thank F. Buhl and Group-A Lawrence Berkeley Laboratory for letting us use their A_2^+ data, and K. Robinson, W. Fickinger, A. Engler, and R. Kraemer for showing us their A_2^0 data before publication.[8] A discussion with L. Trueman was useful and one of us (K.-W.L.) enjoyed an unusual conversation with G. Fox.

---

*Work supported in part by the U. S. Atomic Energy Commission. Prepared under Contract No. AT(11-1)-68 for the San Francisco Operations Office, U. S. Atomic Energy Commission.

†On leave from University of Tel-Aviv, Tel-Aviv, Israel.

[1] D. J. Crennell *et al.*, Phys. Lett. 35B, 185 (1971). K.-W. Lai, in *Phenomenology in Particle Physics–1971*, edited by C. B. Chin, G. C. Fox, and A. J. G. Hey (California Institute of Technology Press, Pasadena, Calif., 1971), p. 257.

[2] J. Diaz *et al.*, Phys. Rev. Lett. 32, 260 (1974).

[3] F. Buhl *et al.*, private communication.

[4] The $\rho^0\pi^\pm$ events in the $J^P = 2^+$ (D wave) state was estimated in the mass interval 1.2–1.44 GeV. In the fit, density-matrix elements $(\rho_{00}, \rho_{1-1}, \rho_{11})$ were treated as free parameters but all subjected to the positivity constraints. Corrections have been made for background 2^+ events and for the mass interval cut. See G. Ascoli *et al.*, Phys. Rev. Lett. 25, 962 (1970), for details of the method.

[5] We used the value $A_2 \to \rho\pi / A_2 \to \text{all} = 72.4 \to 2.1\%$ [T. A. Lasinski *et al.*, Rev. Mod. Phys., Suppl. 45, S1 (1973)] which has been affected the least by discoveries of other new but minor modes of A_2. See Ref. 2.

[6] For A_2^+ we used also the shape of $d\sigma/dt$ of the $\eta\pi^+$ mode which is also characterized by a small background (< 15%). See M. Alston-Garnjost *et al.*, Phys. Lett. 33B, 607 (1970). Furthermore we observe no detectable differences in shapes of $d\sigma/dt$ at the incident momenta 4.5, 6, and 7.1 GeV/c at the present level of statistics; thus, we assume the shape of $d\sigma/dt$ for A_2^+ at 6 GeV/c by using 7.1 GeV/c data.

[7] $\Lambda(1520)$ is defined from 1.5 to 1.54 GeV and does not overlap with the A_2^- region at our incident momenta.

[8] Ref. 3 and K. J. Foley *et al.*, Phys. Rev. D 6, 747 (1972).

[9] See G. C. Fox and A. J. G. Hey, Nucl. Phys. B56, 366 (1973), for details.

[10] D. J. Crennell *et al.*, Phys. Rev. Lett. 27, 1674 (1971); H. A. Gordon *et al.*, Phys. Rev. D 8, 779 (1973).

Exotic Interactions of Charged Leptons*

M. A. B. Bég and G. Feinberg†
The Rockefeller University, New York, New York 10021

(Received 6 May 1974)

We consider the information available about nonelectromagnetic lepton interactions in experiments which are relatively insensitive to the loop structure of the underlying theory. Further experiments which would clarify the role of exotic interactions are proposed and discussed.

Recent theoretical and experimental developments have once again focused attention on the question: What is the precise nature of the interaction between electrons, muons, and hadrons? Almost all gauge theories[1] augment the conventional electromagnetic interaction between these particles with additional interactions. Furthermore, recent experimental results indicating (a) a nearly constant cross section in e^+e^- annihilation into hadrons[2] and (b) deviations from Bjorken scaling in deep inelastic muon-hadron scattering[3] have invited the speculation[4] that exotic (i.e., nonelectromagnetic) interactions may be coming into play at newly available energies.

In this note we report on a systematic study of the information available about exotic lepton interactions in "tree experiments." (By "tree experiments" we mean experiments which are insensitive to the loop structure of the underlying theory.) We restrict ourselves to energies well below the masses of all intermediate vector bosons; this permits us to encompass a variety of theoretical proposals in a compact phenomenological interaction. We determine the consequences of this interaction for (a) atomic spectroscopy, (b) e^+e^- annihilation, and (c) deep inelastic lepton-hadron scattering. While our analysis leads us to tilt towards the view that exotic lepton interactions are unlikely to play a significant role in (b) and (c) at present energies or to provide a safe avenue of escape for the notion of "precocious asymptotic freedom," its confrontation with recent experiments does not allow us to make any categorical statements. Novel and precise experiments, of the type discussed below, must be carried out before the matter is fully resolved.

Phenomenological parametrization.—We postulate the effective (V,A)-type interaction

$$H_{\text{eff}}=(G_F/2\pi\alpha\sqrt{2})\sum_{i,j}(\epsilon_{ij}^{VV}\bar{\psi}_i\gamma^\rho\psi_i\bar{\psi}_j\gamma_\rho\psi_j+\epsilon_{ij}^{VA}\bar{\psi}_i\gamma^\rho\psi_i\bar{\psi}_j\gamma_\rho\gamma_5\psi_j+\epsilon_{ij}^{AA}\bar{\psi}_i\gamma^\rho\gamma_5\psi_i\bar{\psi}_j\gamma_\rho\gamma_5\psi_j), \tag{1}$$

the summation being over e,μ and all the quarks required to meet the needs of weak-interaction theory and hadron spectroscopy. G_F and α are the Fermi and the fine-structure constants, respectively.

The theoretical values of the parameters ϵ can be quickly read off in any gauge model, from the expression for the neutral current. Thus, in the popular quartet charm model[1,4,6]

$$\epsilon_{ij}^{VV}=\zeta(\tau_3-4Q\sin^2\xi)_i(\tau_3-4Q\sin^2\xi)_j,\quad \epsilon_{ij}^{VA}=-\zeta(\tau_3-4Q\sin^2\xi)_i(\tau_3)_j,\quad \epsilon_{ij}^{AA}=\zeta(\tau_3)_i(\tau_3)_j, \tag{2}$$

where Q is the electric charge, ξ is the Salam-Ward-Weinberg angle,[7] and $\tau_3=+1$ for p and p', -1 for n, λ, e, and μ. Also

$$\zeta=\pi\alpha(m_W^2/m_Z^2\cos^2\xi)=\pi\alpha \text{ (for one Higgs doublet).} \tag{3}$$

In the "purely elastic" variant of a triplet charm model,[1,4,8]

$$\epsilon_{ij}^{VV}=36\pi\alpha R_Z;\quad \epsilon_{ij}^{VA}=\epsilon_{ij}^{AA}=0. \tag{4}$$

Here $R_Z=[(1-2\sin^2\xi)m_W/m_Z\cos\xi]^2$ can be bounded experimentally[6]: $R_Z<0.48$.

In relating the parameters ϵ to physically observed quantities, we shall make free use of the naive—but highly successful—quark model[9] for protons and neutrons as well as the quark-parton picture of high-energy dissociation.[10] This is within the spirit of one of the objectives of this study, namely, to see if exotic lepton-hadron interactions can rescue asymptotic freedom, since the quark-parton picture provides a pedestrian handle on asymptotic freedom, which is adequate modulo logarithmic corrections.[11]

Atomic spectroscopy.[12]—The derivation of atomic level shifts, resulting from the interaction of Eq. (1), is quite straightforward. We merely state the results.[13]

(i) Hyperfine splitting in muonium:

$$\Delta E(^3S_1)-\Delta E(^1S_0)=-64\lambda\epsilon_{e\mu}^{AA}\alpha^4m_e^3/M_N^2, \tag{5}$$

where

$$\lambda=G_FM_N^2/16\pi^2\alpha^2\sqrt{2}\simeq10^{-3}. \tag{6}$$

Equation (5) corresponds to

$$\Delta\nu=-0.005\epsilon_{e\mu}^{AA}\text{ MHz}. \tag{7}$$

If we require that this $\Delta\nu$ be less than the limits of disagreement between conventional theory [quantum electrodynamics (QED)] and experiment, we obtain the bound

$$|\epsilon_{e\mu}^{AA}|<10. \tag{8}$$

(ii) Shift of nS levels in hydrogenic atoms:

$$\Delta E(nS)=(16Z^3/n^3)\lambda[Z(2\epsilon_{ep}^{VV}+\epsilon_{en}^{VV})+(A-Z)(\epsilon_{ep}^{VV}+2\epsilon_{en}^{VV})]\alpha^4m_e^3/M_N^2. \tag{9}$$

Most important is the shift of the $2S$ level in atomic hydrogen,

$$\Delta\nu(2S)\simeq1.6\times10^{-4}(2\epsilon_{ep}^{VV}+\epsilon_{en}^{VV})\text{ MHz}. \tag{10}$$

The agreement between conventional theory and experiment will tolerate a $\Delta\nu<10^{-1}$ MHz. Hence

$$|\tfrac{1}{2}(2\epsilon_{ep}^{VV}+\epsilon_{en}^{VV})|<200. \tag{11}$$

(iii) Hyperfine splitting in hydrogen:

$$\Delta\nu_{\text{hfs}}/\nu_{\text{hfs}}=12\lambda(m_e/M)[\epsilon_{ep}^{AA}(1+g_A)+\epsilon_{en}^{AA}(1-g_A)]/(1+\kappa_p). \tag{12}$$

Here g_A is the axial-vector–to–vector ratio in neutron β decay and $\kappa_p = 1.79$. Requiring that $\Delta\nu_{\mathrm{hfs}}$ be less than the theoretical uncertainty in the conventional calculation[13] of ν_{hfs} (the experiment is good to 1 part in 10^{12}, so there is essentially no experimental error), we obtain

$$|\epsilon_{ep}{}^{AA} - \tfrac{1}{5}\epsilon_{en}{}^{AA}| < 1, \tag{13}$$

a remarkably stringent bound.

(iv) Muonic atoms: While the level shifts in S states of muonic atoms due to exotic interactions are much larger than in ordinary atoms, the major contributions to the observed shifts depend on poorly known parameters such as the distribution of charge and magnetic moment in the nucleus. Therefore, one cannot learn much about $\epsilon_{\mu h}{}^{VV}$ and $\epsilon_{\mu h}{}^{AA}$ from muonic atoms. However, by comparing nuclear charge radii as determined from muonic atoms and from electron scattering, we can conclude that

$$|\epsilon_{ep}{}^{VV} - \epsilon_{\mu p}{}^{VV} + \epsilon_{en}{}^{VV} - \epsilon_{\mu n}{}^{VV}| < 40. \tag{14}$$

The circular polarization of muonic x rays, or other pseudoscalar correlations involving such x rays, appears to be a feasible atomic probe of $\epsilon_{\mu h}{}^{VA}$ and $\epsilon_{\mu h}{}^{AV}$. Measurement of the circular polarization of the photon in the decay $2S_{1/2} \to 1S_{1/2}$ + (one photon) in muonic atoms gives information[14] about $\epsilon_{\mu h}{}^{AV}$, whereas a measurement of the photon circular polarization in the muonic hyperfine transition (n_1S, $F = I + \frac{1}{2}$ to n_2S, $F = I - \frac{1}{2}$) gives information[15] about $\epsilon_{\mu h}{}^{VA}$. Detection of these transitions, and measurement of the relevant correlations, may be feasible with the intense muon sources now being developed. Similar experiments have been proposed for heavy electronic ions[14] and atoms[16] to measure $\epsilon_{eh}{}^{AV}$.

e^+e^- *annihilation.*—The cross sections for muon-pair and hadronic final states, in the presence of the interaction of Eq. (1), take the form

$$\sigma(e^+e^- \to \mu^+\mu^-)/\sigma_\gamma(e^+e^- \to \mu^+\mu^-) = 1 - 4(\lambda s/M^2)\epsilon_{e\mu}{}^{VV} + 4(\lambda s/M^2)^2 \sum_{m,n=V,A} (\epsilon_{e\mu}{}^{mn})^2, \tag{15}$$

$$\sigma(e^+e^- \to \text{hadrons})/\sigma_\gamma(e^+e^- \to \text{hadrons}) = 1 + 4(\lambda s/M^2)A + 4(\lambda s/M^2)^2 B. \tag{16}$$

Here s is the square of the total c.m. energy and

$$A = \textstyle\sum_i Q_i \epsilon_{ei}{}^{VV} / \sum_i Q_i^2, \quad B = \sum_i \sum_{mn} (\epsilon_{ei}{}^{mn})^2 / \sum_i Q_i^2, \tag{17}$$

Q_i being the quark charges. Also, throughout this paper, σ_γ refers to one-photon exchange cross sections:

$$\sigma_\gamma(e^+e^- \to \text{hadrons})/\sigma_\gamma(e^+e^- \to \mu^+\mu^-) = \textstyle\sum_i Q_i^2, \tag{18}$$

$$\sigma_\gamma(e^+e^- \to \mu^+\mu^-) = 4\pi\alpha^2/3s. \tag{19}$$

Careful measurements of $\sigma(e^+e^- \to \mu^+\mu^-)$ at SPEAR will permit us to put more stringent bounds on the $\epsilon_{e\mu}$ than was possible, for example, in Eq. (8).

Despite the presence in $\sigma(e^+e^- \to \text{hadrons})$ of a term falling as $1/s$, a constant term, and a term rising as s, one can choose A and B such that this cross section is within 20% of 25 nb in the interval $8M^2 < s < 28M^2$. Values of ϵ as high as 30 or so are needed.

Deep inelastic scattering.—Let p be the momentum of the target hadron and let k and $k - q$ be the momenta of the incident and outgoing leptons, respectively. In terms of the usual scaling variables [$x = |q^2|/2q\cdot p$, $y = q\cdot p/k\cdot p$] the double differential cross sections may be displayed as follows:

$$\tfrac{1}{2}[\sigma(l_R{}^-N) + \sigma(l_L{}^+N)]_{xy}/\sigma_\gamma(l^-N)_{xy} = 1 - 4(\lambda|q^2|/M^2)A' + 4(\lambda|q^2|/M^2)^2 B', \tag{20}$$

$$\tfrac{1}{2}[\sigma(l_R{}^-N) - \sigma(l_L{}^+N)]_{xy}/\sigma_\gamma(l^-N)_{xy} = -[4(2y - y^2)/(2 - 2y + y^2)](\lambda|q^2|/M^2)[C' - 2(\lambda|q^2|/M^2)D']. \tag{21}$$

Here $\sigma_{xy} \equiv \partial^2\sigma/\partial x\,\partial y$ and R and L denote incident-lepton helicities.[17] The coefficients A', B', C', and D' are, in general, functions of x and their precise form is not terribly enlightening. In specific situations and/or models, they can become x independent. For example, if we assume that nucleons contain only p- and n-type quarks, we find that

$$\begin{gathered} A' = \tfrac{3}{5}[2(\epsilon_{lp}{}^{VV} + \epsilon_{lp}{}^{AV}) - (\epsilon_{ln}{}^{VV} + \epsilon_{ln}{}^{AV})]; \quad B' = \tfrac{9}{5}[(\epsilon_{lp}{}^{VV} + \epsilon_{lp}{}^{AV})^2 + (\epsilon_{lp}{}^{AA} + \epsilon_{lp}{}^{VA})^2 + (\text{terms with } p \to n)]; \\ C' = \tfrac{3}{5}[2(\epsilon_{lp}{}^{AA} + \epsilon_{lp}{}^{VA}) - (\epsilon_{ln}{}^{AA} + \epsilon_{ln}{}^{VA})]; \quad D' = \tfrac{9}{5}[(\epsilon_{lp}{}^{VV} + \epsilon_{lp}{}^{AV})(\epsilon_{lp}{}^{AA} + \epsilon_{lp}{}^{VA}) + (\text{terms with } p \to n)]. \end{gathered} \tag{22}$$

Here again, despite the presence of terms linear and quadratic in $|q^2|$ in Eq. (20) one can accommodate a nearly constant deviation of about 30% from the scaling limit, in the interval $20M^2 < |q^2| < 40M^2$, by judicious ascription of numerical values to the ϵ's, in the range 5–10.

Remarks.—(i) We have followed the path suggested by gauge theories and have parametrized exotic lepton-hadron couplings in terms of quark fields and restricted ourselves to V and A interactions; S interactions stemming from Higgs fields have been discussed in the literature[18] and we have little to add.

Note that, so far as atomic spectroscopy is concerned, we could equally well have parametrized the interaction of Eq. (1) in terms of nucleon fields and bounded the relevant parameters without appeal to the quark model. The bounds obtained for ϵ_{ep} follow by identifying the appropriate ϵ_{ep} with the left-hand side of Eq. (11) or Eq. (13). We could also have included S-, P-, and T-type covariants which, however, would be indistinguishable from V and A in the static limit.

(ii) It is evident that exotic lepton couplings of the sort expected in some of the existing gauge models have almost negligible effects at present on atomic spectroscopy, and on e^+e^- annihilation and deep inelastic scattering at present-day energies. However, improvements in spectroscopic measurements and in QED calculations, and the availability of higher energies, will certainly bring the effects of these couplings into the realm of measurability. In the meantime, one can still draw some useful inferences from Eq. (13) in the context of present-day models. For example, if the Higgs sector of the quartet charm model is enlarged so that $m_W > m_Z \cos\xi$, rather than being equal to it, the usual lower bound on m_Z (>76 GeV) is no longer valid; Eq. (13) can be used to yield the modest bound

$$m_Z > 6 \text{ GeV}.$$

(iii) Theories which attempt to explain the SPEAR e^+e^- data and the, rather preliminary, muon-production data from the National Accelerator Laboratory in terms of exotic couplings require that some ϵ's be on the order of 10 or so. If these theories are constrained[4] in such a way that ϵ^{AA} is of the same order of magnitude as the other ϵ's, Eq. (13) implies that they must be rejected. The speculation that exotic lepton couplings are at the root of the difficulties faced by the notion of precocious scaling can not be dismissed, however, until better bounds are available on all the ϵ's. The ϵ^{VA} and ϵ^{AV} are particularly tricky; two independent handles are available, however, and worthy of experimental investigation: (a) the circular polarization of muonic x rays, mentioned above, and (b) the difference between l^+ and l^- deep inelastic cross sections calculated in Eq. (21).[19]

(iv) An interesting difference occurs between the effects of exotic interactions in deep inelastic scattering, as given in Eqs. (20) and (21), and the uncalculated effects of two-photon exchange which might also be large in some kinematic regions. While the former may interfere with one-photon exchange in both $\sigma(l_R^- N) \pm \sigma(l_L^+ N)$, the latter can interfere with one-photon exchange only in $\sigma(l_R^- N) - \sigma(l_L^+ N)$, essentially by the charge-conjugation properties of the current. Measurement of both quantities therefore would go far to distinguish these two possibilities.

We thank L. S. Brown and V. Rittenberg for interesting discussions.

---

[*] Work supported in part by the U. S. Atomic Energy Commission under Contract No. AT(11-1)-2232B.

[†] J. S. Guggenheim Foundation Fellow 1973–1974. Permanent address: Physics Department, Columbia University, New York, N. Y. 10027.

[1] For a recent review see M. A. B. Bég and A. Sirlin, Rockefeller University Report No. COO-2232B-47, 1974 (to be published).

[2] B. Richter, Bull. Amer. Phys. Soc. 19, 100(T) (1974), and in Proceedings of the Conference on Lepton Induced Reactions, Irvine, California, 7–8 December 1973 (to be published).

[3] K. W. Chen, Bull. Amer. Phys. Soc. 19, 100 (1974). (The possibility that deviations from μ-e universality are manifesting themselves in the National Accelerator Laboratory experiment can not be discounted, but need not be taken seriously at this time.)

[4] A. Salam, remark at the Conference on Lepton Induced Reactions, Irvine, California, 7–8 December 1973. J. C. Pati and A. Salam, to be published.

[5] S. Weinberg, Phys. Rev. D 5, 1412 (1972); C. Bouchiat, J. Iliopoulos, and Ph. Meyer, Phys. Rev. Lett. 38B, 519 (1972).

[6] M. A. B. Bég, to be published.

[7] A. Salam and J. C. Ward, Phys. Lett. 13, 168 (1964); S. Weinberg, Phys. Rev. Lett. 19, 1264 (1967).

[8] M. A. B. Bég and A. Zee, Phys. Rev. Lett. 30, 675 (1973).

[9] M. A. B. Bég, B. W. Lee, and A. Pais, Phys. Rev. Lett. 13, 514 (1964); for a review see G. Morpurgo, in *Proceedings of the XIV International Conference on High Energy Physics, Vienna, 1968*, edited by J. Prentki and J. Steinberger (CERN Scientific Information

Service, Geneva, 1968).

[10] J. D. Bjorken and E. A. Paschos, Phys. Rev. 185, 1975 (1969), and Phys. Rev. D 1, 3151 (1970). See also R. Budny, Phys. Lett. 39B, 553 (1972); R. Budny and A. McDonald, Oxford University Report No. 37/73, 1973 (to be published).

[11] These corrections arise in deep inelastic scattering [cf. H. Georgi and H. D. Politzer, Phys. Rev. D 9, 416 (1974)] but not in e^+e^- annihilation [cf. A. Zee, Phys. Rev. D 8, 4038 (1973)].

[12] For a recent review of the experimental situation and the conventional theory (QED) see B. E. Lautrup, A. Peterman, and E. deRafael, Phys. Rep. 3C, 193 (1972).

[13] We restrict the discussion to effects which yield somewhat reasonable bounds on the ϵ's. [Consideration of the ortho-para splitting in positronium, for example, yields the (absurd) bound $|\epsilon_{ee}^{\gamma\gamma} - 3\epsilon_{ee}^{AA}| < 1.5 \times 10^5$ and, therefore, does not warrant inclusion in the text.]

[14] G. Feinberg and M. Y. Chen, Phys. Rev. D 10, 190 (1974).

[15] G. Feinberg, to be published.

[16] M. A. Bouchiat and C. C. Bouchiat, Phys. Lett. 48B, 111 (1974).

[17] The charge-helicity combinations used here correspond to the situation in the National Accelerator Laboratory experiment. (We thank Professor K. W. Chen for a discussion on this point.) Similar formulas can be derived for other combinations.

[18] For example, R. Jackiw and S. Weinberg, Phys. Rev. D 5, 2396 (1972).

[19] See also M. Suzuki, Nucl. Phys. B70, 154 (1974), and earlier references cited therein.

A_2-A_1 Interference Phase*

G. Ascoli, L. M. Jones, R. Klanner, U. E. Kruse, and H. W. Wyld
University of Illinois at Urbana, Urbana, Illinois 61801

(Received 22 April 1974)

The A_2-A_1 phase difference observed in $\pi^-p \to \pi^+\pi^-\pi^-p$ is compared with the A_2^- phase from a Regge fit to the $d\sigma/dt$ data for A_2^- and the A_1^- phase given by a Reggeized Deck model. The agreement (~ 30°) depends crucially on the contribution of the Reggeized pion propagator to the A_1 phase and requires equal signs for the f and P residues in the A_2 amplitude.

Phases of strong interaction amplitudes—although of obvious interest—are all too seldom measurable. Partial-wave analyses[1,2] of the reaction $\pi^-p \to \pi^+\pi^-\pi^-p$ give not only the magnitudes of A_1 (defined as the state $1^+S-\rho\pi$) and A_2 production amplitudes but also their relative phase. In this note we use the phase of the A_1^- amplitude from a Reggeized-Deck-model calculation, and the A_2^- phase from a Regge fit to $d\sigma/dt$ for A_2, to predict the A_2^--A_1^- phase and compare the prediction to the data.

Phase of the $\pi^-p \to A_1^-p$ amplitude.—A version of Berger's Reggeized Deck model[3,4] has been shown to agree well with the data for $\pi^-p \to \pi^+\pi^-\pi^-p$ for $M_{3\pi} \lessapprox 1.5$ GeV, excepting the A_2 partial wave (which is nearly absent in the model). In particular, the model predicts correctly the relative phases between different partial waves. It also predicts that the only important amplitude for A_1 production is the nucleon s-channel helicity nonflip amplitude leading to the 1^+ state with $J_z = 0$ (in the t channel). The phase of this amplitude (extracted by partial-wave analysis[5] of the model amplitude) shows only minor dependence on $M_{3\pi}$, in accord with the data.

Typical values of the phase (at $M_{3\pi} = M_{A_2}$) are shown in Table I. We note that the phase exceeds by ~ 60° the value of 90° one would obtain for diffractive production of a stable particle or resonance. The extra phase comes from the signature factor of the Reggeized π propagator and is directly proportional to α_π' ($\alpha_\pi' = 1$ GeV^{-2} was used). This extra phase is required to explain the phase differences observed between different

TABLE I. Deck-model phase for A_1 production at $M_{3\pi} = M_{A_2}$.

P_{lab} (GeV) \ $t - t_{\text{min}}$ (GeV^2)	0	− 0.1	− 0.2	− 0.3
6	146°	158°	170°	179°
16	146°	156°	166°	175°
26	146°	156°	165°	173°
36	146°	155°	164°	172°

nonresonant partial waves (e.g., between $1^+S \to \rho\pi$ and $1^+P \to \epsilon\pi$). It turns out also to be necessary to explain the A_2-A_1 phase difference.

$\pi N \to A_2 N$ data.—We review briefly relevant aspects of the data.

(a) Above $p_{\rm lab} \geq 10$ GeV, A_2^- is produced in $\pi^- p \to A_2^-$ in a pure state (a linear combination of the states $|J^P M\rangle = |2^+ \pm 1\rangle$): $|2^+ 1\rangle + |2^+ -1\rangle$ in the t-channel frame. This result—consistent with dominance of natural parity exchanges—has been obtained in three A_2 decay modes: $A_2^- \to \pi^+\pi^-\pi^-$,[1,2] $A_2^- \to K^0 K^-$,[6] and $A_2^- \to \eta^0 \pi^-$.[7] In all subsequent discussions we consider only A_2 production in the above state.

(b) The cross section for production of A_2^- in the above state decreases as $p_{\rm lab}^{-0.5}$ from 5 to 40 GeV. This result has been seen in the channel $A_2 \to 3\pi$ and confirmed in the $A_2 \to \eta\pi$ channel. A Regge fit to the observed energy dependence will clearly require inclusion of a trajectory higher than the ρ-f trajectory.

(c) The A_2^- differential cross section, $(\rho_{11} + \rho_{1-1}) d\sigma/dt$, vanishes in the forward direction. The $A_2^- \to 3\pi$ data can be fitted by $|t - t_{\rm min}| \exp(bt)$, with b increasing from 5 GeV^{-2} at 5 GeV^{-2} to 8.5 GeV^{-2} at 40 GeV.

(d) The A_2^--A_1^- phase has been extracted from the $\pi^- p \to \pi^+\pi^-\pi^- p$ data at several energies ($p_{\rm lab} = 5$–40 GeV).[1,2] The phase difference comes from the interference density matrix element $\rho_{A_1 A_2}$ between the A_2 state ($|2^+ 1\rangle + |2^+ -1\rangle$) and the A_1 state ($|1^+ 0\rangle$, $1^+ S \to \rho\pi$). As already noted the polarizations refer to t-channel axes. The $M_{3\pi}$ dependence of the observed phase is as expected for a resonant A_2 and an A_1 with slowly varying phase. In the following, A_2 production phases refer to phases obtained by subtracting the phase of the A_2 propagator (90° at $M_{3\pi} = M_{A_2}$) from the observed phases. The s and t dependence of the A_2 production phase is shown in Fig. 3.

(e) The other observed quantity relating to A_2-A_1 interference is the coherence between A_2 and A_1 states, defined as $|\rho_{A_2 A_1}| / (\rho_{A_1 A_1} \rho_{A_2 A_2})^{1/2}$. This factor would be unity if A_2 and A_1 amplitudes had the same dependence on nuclear spin variables. The observed values[8] range from 0.7 ± 0.1 at 5 GeV to 0.9 ± 0.06 at 40 GeV. At energies above 5 GeV the observed coherence is consistent, within errors, with unity. Since the A_1 production (in the model) is nonflip (in the s channel), we conclude that A_2 production is also mainly nonflip, particularly at high energy.

(f) The A_2-A_1 phase differences and the cross sections are nearly equal in the two reactions $\pi^\pm p \to \pi^\pm \pi^- \pi^\pm p$ at 5 and 7.5 GeV.[2] Since A_1 production is mainly isoscalar exchange, this suggests that isoscalar exchanges dominate.

It is unfortunate that the available $\pi^+ n \to A_2^0$ data[9] are very limited and inadequate to shed further light on this point.

Regge fit to $\pi^- p \to A_2^- p$.—The above discussion suggests a simple model for A_2^- production in which nucleon spin-flip and $I = 1$ exchange contributions are neglected, with f and P trajectories as the main contributors. Some theoretical prejudices are available to support these assumptions. Michael and Ruuskanen[10] discuss the relative contributions of f and ρ trajectories. Using factorization, duality, and π-N scattering data, they predict that the ρ contribution to the nonflip amplitude and the f contribution to the flip amplitude are unimportant; further the ρ contribution to the flip amplitude should be small at small t [it is suppressed by an additional factor $(-t/4m^2)^{1/2}$, where m is the nucleon mass].

We have therefore fitted the data[1,2] using only a nucleon nonflip amplitude with only isoscalar contributions from P and f. We have chosen a simple parametrization of the amplitude:

$$M^{\rm nf}(s,t) = -\sqrt{C}(|t - t_{\rm min}|)^{1/2}\left[\exp(A_P t)\left(\frac{s}{s_0}\right)^{\alpha_P(t)} \exp\left(-\frac{i\pi\alpha_P(t)}{2}\right) + K \exp(A_f t)\left(\frac{s}{s_0}\right)^{\alpha_f(t)} \exp\left(-\frac{i\pi\alpha_f(t)}{2}\right)\right] \quad (1)$$

with C, K, A_P, and A_f as free parameters. We use $s_0 = 1$ GeV and the trajectories $\alpha_P = 1 + 0.36t$, $\alpha_f = 0.56 + 0.86t$.[11]

The differential cross section is related to the amplitude of Eq. (1) by

$$(\rho_{11} + \rho_{1-1}) d\sigma/dt = |M^{\rm nf}|^2/s^2.$$

We have fitted the $\pi^- p \to A_2^- p$ data from $\pi^- p \to \pi^+\pi^-\pi^- p$ ($p_{\rm lab} = 5$–40 GeV). A satisfactory fit to the data ($\chi^2/NDF = 10.5/11$) was obtained as shown in Figs. 1 and 2.

The parameters of the fit are $C = 1120 \pm 300$ mb, $A_P = 3.5 \pm 0.5$ GeV^{-2}, $K = 1.5 \pm 0.7$, and $A_f = -0.5 \pm 0.8$ GeV^{-2}.

Three comments are in order:

(a) The fit shown does not include spin-flip contributions. Equally good fits can be made with moderate spin-flip contributions (the size of the flip contribution is limited by the observed A_2-A_1 coherence).

(b) Our fit neglects isovector (ρ) exchange con-

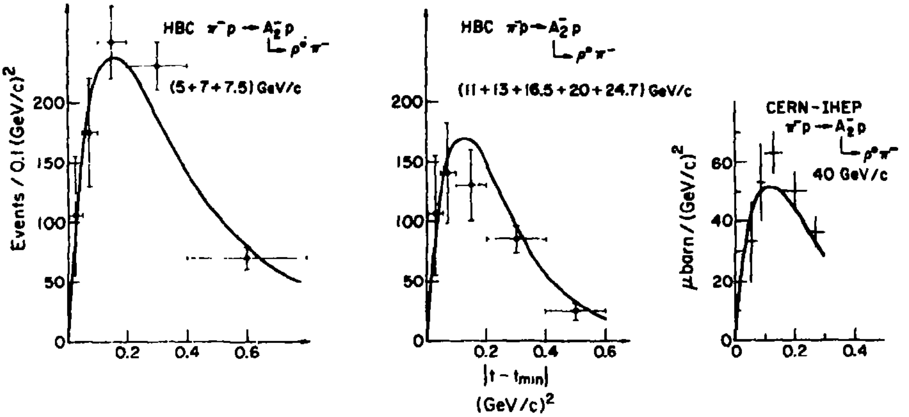

FIG. 1. Comparison of measured to fitted differential cross sections for $\pi^-p\to A_2^-(\to\rho^0\pi^-)p$.

tributions to the nonflip amplitude. The model A_1 amplitude, in fact, does contain some ρ exchange (at $p_{lab}=6$ GeV, $t=0$ the A_1^+ amplitude leads the A_1^- amplitude by 30°). Equality of A_2^+-A_1^+ and A_2^--A_1^- relative phases suggests that some isovector contribution to the nonflip A_2 amplitude is probably present.

The data are not adequate to resolve either question. Furthermore, the resulting predictions about A_2^--A_1^- phase difference are not very sensitive to the answers. We conclude that there is not much reason to push these matters further.

(c) The data on $d\sigma/dt$ show no preference for positive or negative K. Comparable fits can be obtained with f and P contributions with imaginary parts having either the same or opposite signs. The solution given above (equal sign) is preferred since it alone gives a reasonable agreement with the observed A_2^--A_1^- phase differences.

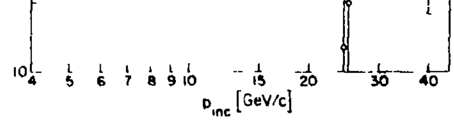

FIG. 2. Measured and fitted integrated cross sections for $\pi^-p\to A_2^-(\to\rho^0\pi^-)p$ for $1.2\leqslant M_{3\pi}\leqslant 1.4$ GeV and $0<|t-t_{min}|<0.7$ (GeV/c)^2, as a function of beam momentum. Solid curve for fit with $K<0$ and dashed curve for fit with $K<0$ [see Eq. (1)].

Comparison with observed A_2-A_1 phases.—Figure 3 shows the comparison between the observed A_2^--A_1^- relative phase and the difference between the A_2^- phase from the Regge-model fit [Eq. (1)] and the A_1^- phase from the Deck model (Table I). For all momentum transfer bins and all incident momenta the agreement is within 30°. We note that with a 90° phase for the A_1 amplitude the disagreement would be about 90°.

The estimated uncertainties in the predicted phases associated with uncertainties in various parameters are relatively small: (1) A change in Pomeron slope from 0.36 to 0 changes the predicted A_2 phase by ~5°. (2) A 20% change in the slope of the π trajectory (from $\alpha_\pi'=1$ GeV^{-2}) changes the predicted A_1 phase by ~10°. (3) The main uncertainties are presumably those associated with the precise form chosen for the Deck model, and with possible contributions of isovector exchange to the A_2^- nucleon nonflip amplitude.

We conclude that in view of the above uncertainties the agreement obtained is satisfactory.

Since the A_2 is a "normal" resonance we expect the amplitude for A_2 production in $\pi N\to A_2N$ to have the same properties as the production amplitude of a stable 2^+ meson. In particular, the phase of the amplitude (assumed even under s-u interchange) can be inferred from the s dependence (at fixed t) of the imaginary part either via a Regge fit or from a dispersion relation. The same arguments do not apply to the A_1 pro-

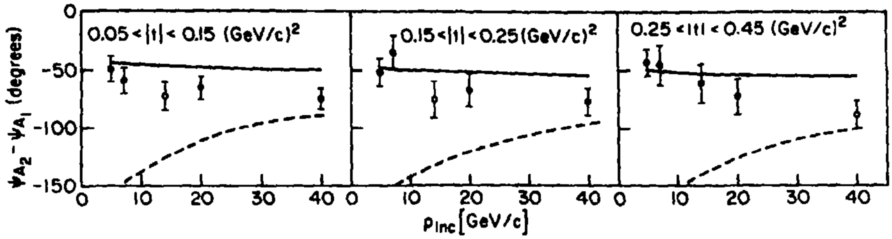

FIG. 3. Comparison of measured A_2-A_1 interference phase to the phase predicted from Regge and Deck model calculation. Dependence on incident momentum is shown for different momentum transfer intervals. [Note: The data at 40 GeV/c extend only to momentum transfer of -0.3 (GeV/c)^2.] Solid (dashed) curve for fit with $K > 0$ ($K < 0$) in Eq. (1).

duction amplitude. According to the data the A_1 observed in $\pi p \to 3\pi p$ is not a normal resonance but a kinematic accident in the 1^+ projection of the five-point amplitude for $\pi^- p \to \rho^0 \pi p$. It is therefore not surprising to find that the Reggeized Deck model gives an A_1 production phase which is very different from the A_2 production phase, in spite of the almost identical s dependence of the cross sections.

The Regge fit to the A_2 production data confirms the suspicion that a significant Pomeron-like contribution is required to account for the observed s dependence. While this result violates often-stated prejudices[12] regarding Pomeron couplings, it violates—as far as we know—no fundamental principle. In fact, the result seems to be in line with the similarity between Pomeron and f^0 couplings observed in other reactions (in particular in elastic scattering).

With a view to characterizing the couplings in this reaction, we emphasize that the observed A_2 polarization corresponds to a helicity change $|\Delta\lambda| = 1$ in *the t channel* (not s channel) at the π-A_2 vertex. Because the range of t explored limits the nucleon crossing angle to relatively small values, the available data (coherence between A_2 and A_1) do not allow us to distinguish s-channel helicity conservation from t-channel helicity conservation at the nucleon vertex (even with our assumption of s-channel helicity conservation for the A_1).

We note that the data favor equal signs for the f^0 and P coupling in $\pi p \to A_2 p$. Carlitz, Green, and Zee[13] have speculated that $\beta_f(t)/\beta_P(t)$ might be the same in all reactions. Comparison of our ratio of couplings in $\pi N \to A_2 p$ with the corresponding ratio in $\pi N \to \pi N$ and $pp \to pp$ shows rough agreement.

---

*Work supported in part by the Atomic Energy Commission contract No. AT(11-1)1195 and by the National Science Foundation Contract No. NSF GP 40908X.

[1] Yu. M. Antipov *et al.*, Nucl. Phys. B63, 153 (1973); R. Klanner, University of Munich, thesis, 1973, (unpublished).

[2] G. Ascoli *et al.*, to be published, and Phys. Rev. Lett. 25, 962 (1970).

[3] E. L. Berger, Phys. Rev. 166, 1525 (1968).

[4] G. Ascoli *et al.*, to be published.

[5] G. Ascoli *et al.*, Phys. Rev. D 8, 3894 (1973).

[6] K. J. Foley *et al.*, Phys. Rev. D 6, 747 (1972); G. Grayer *et al.*, Phys. Lett. 34B, 333 (1971).

[7] Yu. M. Antipov *et al.*, Nucl. Phys. B63, 175 (1973).

[8] The measured values are lower limits, as deviations of the parametrization of the amplitudes in the analysis from the true amplitudes tend to decrease the coherence.

[9] J. T. Carroll *et al.*, Phys. Rev. Lett. 25, 1393 (1970); N. Armenise *et al.*, Phys. Lett. 25B, 53 (1967).

[10] C. Michael and P. V. Ruuskanen, Phys. Lett. 35B, 47 (1971).

[11] The parameters are from V. Barger and R. J. N. Phillips, Phys. Rev. 187, 2210 (1969).

[12] D. R. O. Morrison, Phys. Lett. 25B, 238 (1967); R. Carlitz, S. Frautschi, and G. Zweig, Phys. Rev. Lett. 23, 1134 (1969).

[13] R. Carlitz, M. B. Green, and A. Zee, Phys. Rev. Lett. 26, 1515 (1971), and Phys. Rev. D 4, 3439 (1971).

COMMENTS

Weinberg Angle as a Test of SU(n)-Type Unified Gauges

S. P. Rosen*
Purdue University, West Lafayette, Indiana 47907
(Received August 12 1974)

I consider generalizations of the Georgi-Glashow unified gauge theory to SU(n), and show that $\sin^2\theta_W = (n-2)/2(n-1)$. I also note a difficulty in extracting the value of $\sin^2\theta_W$ from neutral-current data, and suggest that the best method for doing so is the comparison of $\bar{\nu}_\mu$-e and ν_μ-e scattering provided that the ratio of the cross sections is less than $\frac{13}{7}$.

Georgi and Glashow[1] have proposed a unified gauge theory of strong, electromagnetic, and weak interactions based upon SU(5). They embed the direct product of the leptonic gauge[2] SU(2) ⊗ U(1) and the SU(3) of color within the larger group and thereby predict a value of $\sin^2\theta_W = \frac{3}{8}$ for the Weinberg angle. Here I consider the possibility of embedding the leptonic gauge in SU(n), and show that $\sin^2\theta_W = (n-2)/2(n-1)$.

This formula may be useful in two ways. Should the spectrum of quarks eventually turn out to be larger than presently envisaged, the unification of all elementary-particle interaction along the lines proposed by Georgi and Glashow will require a unitary group larger than SU(5), and the appropriate Weinberg angle can be obtained from the formula. On the other hand, should the empirical value of $\sin^2\theta_W$ turn out to be greater than $\frac{1}{2}$, then all of these SU(n)-type embiddings will have to be discarded no matter what the quark spectrum may be.

Measuring the Weinberg angle is complicated by the number of Higgs scalar mesons required in this type of theory. The original Weinberg model[3] contains only one doublet of scalar mesons and so the masses of the W and Z gauge bosons are related by $M_W = M_Z \cos\theta_W$. Consequently the value of $\sin^2\theta_W$ can be extracted, at least in principle, from a single neutral-current cross section, for example $\sigma(\bar{\nu}_\mu e)$. The SU(n)-type theories considered here require several multiplets of Higgs scalars and so the relationship between M_W and M_Z is lost.[4,5] As a result we can no longer extract the Weinberg angle from a single cross section. I shall show, however, that we can extract $\sin^2\theta_W$ from the *ratio* of cross sections $\sigma(\bar{\nu}_\mu e)/\sigma(\nu_\mu e)$; moreover its value is unique *if the ratio is less than* $\frac{13}{7}$.

The Lagrangian coupling the left-handed doublet $L \equiv (\nu_e, e_L^-)$ and the right-handed singlet $R \equiv e_R^-$ to the isovector gauge bosons $\vec{A}_\mu$ and to the isosinglet one B_μ is[3]

$$2\mathcal{L} = g\bar{L}\gamma_\mu\vec{\tau}L\cdot\vec{A}_\mu + g'(\bar{L}\gamma_\mu L + 2\bar{R}\gamma_\mu R)B_\mu, \qquad (1)$$

where $\vec{\tau}$ are the usual Pauli matrices. The Weinberg angle is defined by the relation

$$\sin^2\theta_W = g'^2/(g^2 + g'^2). \qquad (2)$$

I now assume that the left-handed doublet of leptons are the first two members l_1 and l_2 of an n^* representation of SU(n), and that the remaining members $(l_3, l_4, \ldots, l_n)$ are hadronic quarks as in the Georgi-Glashow theory.[1,6] The right-handed singlet e_R^- is identified with the (1, 2) member of the $\frac{1}{2}n(n-1)^*$ tensor T_{ij} constructed from the antisymmetric product of two n^* representations. The muon and its neutrino are treated in exactly the same way. Gauge bosons belong to the adjoint representation $B_\beta{}^\alpha$, where α and β run from 1 to n and

$$\sum_{\lambda=1}^{n} B_\lambda{}^\lambda = 0. \qquad (3)$$

The SU(n)-symmetric coupling of left-handed leptons to gauge bosons is

$$\mathcal{L} = g\sum_{\alpha,\beta=1}^{n} (\bar{l}_\alpha l_\beta B_\beta{}^\alpha), \qquad (4)$$

where I have suppressed all space-time indices.

The strength of the coupling of the right-handed multiplet T_{ij} to gauge bosons is chosen so as to yield the combination of left-handed and right-handed leptons given in Eq. (1). Picking out the purely leptonic terms from Eq. (4), one obtains

$$\mathcal{L}=(g/\sqrt{2})[\bar{L}\vec{\tau}L\cdot\vec{A}+(1/\sqrt{2})\bar{L}L(B_1{}^1+B_2{}^2)];$$

$$A_1=\frac{1}{\sqrt{2}}(B_2{}^1+B_1{}^2),\quad A_2=\frac{i}{\sqrt{2}}(B_1{}^2-B_2{}^1),\qquad(5)$$

$$A_3=\frac{1}{\sqrt{2}}(B_1{}^1-B_2{}^2),\quad L=\begin{pmatrix}l_1\\ l_2\end{pmatrix}.$$

The combination $B_1{}^1+B_2{}^2$ represents an isoscalar meson, and in order to determine the Weinberg angle one must compute its normalizatization.

This can be done by imagining the vector mesons to be constructed from hypothetical quark-antiquark pairs:

$$B_\beta{}^\alpha=\bar{q}_\alpha q_\beta-\frac{1}{n}\delta_\beta{}^\alpha\sum_{\lambda=1}^{n}\bar{q}_\lambda q_\lambda.\qquad(6)$$

When $\alpha\neq\beta$, the meson wave function is automatically normalized to unity, but when $\alpha=\beta$ it is not; moreover $B_\alpha{}^\alpha$ and $B_\gamma{}^\gamma$ are not orthogonal. Now from Eq. (6) the isoscalar combination of Eq. (5) is given by

$$B_1{}^1+B_2{}^2=\frac{n-2}{n}(\bar{q}_1q_1+\bar{q}_2q_2)-\frac{2}{n}\sum_{\lambda=3}^{n}\bar{q}_\lambda q_\lambda,\qquad(7)$$

and so its norm is $[2(n-2)/n]^{1/2}$. One may therefore write

$$B_1{}^1+B_2{}^2=\left[\frac{2(n-2)}{n}\right]^{1/2}B_0,\qquad(8)$$

where B_0 is normalized to unity, and after substituting Eq. (8) into Eq. (5) one obtains

$$\frac{g'}{g}=\left(\frac{n-2}{n}\right)^{1/2},\ \text{or}\ \sin^2\theta_W=\frac{n-2}{2(n-1)}.\qquad(9)$$

From Eq. (9), it is seen that $\sin^2\theta_W$ tends to $\frac{1}{2}$ from below as n tends to infinity. Therefore, if its empirical value turns out to be greater than $\frac{1}{2}$, one will have to discard the entire class of SU(n) embeddings discussed above. Unfortunately it may not be easy to decide whether the Weinberg angle falls above or below this barrier.

Because the Weinberg angle has been defined in terms of the coupling constants for leptons and gauge bosons [see Eqs. (1) and (2)], some care must be exercised in relating to experimentally observable quantities. In general the ratio of vector to axial-vector components in the neutral current depends on $\sin^2\theta_W$, while the cross section depends on the angle and on the ratio M_W/M_Z of gauge-boson masses. This ratio is equal to $\cos\theta_W$ in the simplest version of the Weinberg model,[3] but it differs from $\cos\theta_W$ when more than one multiplet of Higgs scalars are present,[4] as is the case with the Georgi-Glashow model.[5] Therefore in the phenomenological analysis of neutral-current data one should treat M_W/M_Z as independent parameters.[7]

The total cross section for neutrino-electron scattering can be written as[8]

$$\sigma=(F^2m_eE/\pi)[(g_V\pm g_A)^2+\tfrac{1}{3}(g_V\mp g_A)^2],\qquad(10)$$

where E is the laboratory energy of the incident neutrino, and the upper signs are for incident neutrinos, while the lower ones are for antineutrinos. For ν_μ-e scattering the constants F, g_V, and g_A are

$$F=Gf,\quad f=M_W/M_Z\cos\theta_W,$$
$$g_V=2\sin^2\theta_W-\tfrac{1}{2},\quad g_A=-\tfrac{1}{2},\qquad(11)$$

where G is the usual weak-interaction coupling constant; for ν_e-e scattering they are

$$F=G,\quad g_V=1+f^2(2\sin^2\theta_W-\tfrac{1}{2}),$$
$$g_A=1-\tfrac{1}{2}f^2.\qquad(12)$$

I have explicitly allowed for the possibility that $M_W\neq M_Z\cos\theta_W$ by introducing the factor f into Eqs. (10)–(12). The occurrence of f in these formulas makes it very difficult to determine $\sin^2\theta_W$ from total cross sections alone. In the case of ν_μ-e scattering the effects of f can be eliminated by taking the ratio of neutrino and antineutrino cross sections:

$$R(\nu_\mu e)=\frac{\sigma(\bar{\nu}_\mu e)}{\sigma(\nu_\mu e)}=\frac{x^2+3(1-x)^2}{3x^2+(1-x)^2},\qquad(13)$$

where the parameter x is given by

$$x=1-2\sin^2\theta_W,\qquad(14)$$

and ranges in value from -1 to $+1$. As x increases from -1 to $+\frac{1}{3}$, $R(\nu_\mu e)$ runs from $\frac{13}{7}$ to a maximum of 3 at $x=0$, and then decreases to $\frac{13}{7}$ again at $x=\frac{1}{3}$. As x increases from $\frac{1}{3}$ to 1, $R(\nu_\mu e)$ decreases monotonically to its minimum value of $\frac{1}{3}$; the ratio is shown in Fig. 1.

This behavior means that for experimental values of $R(\nu_\mu e)$ between $\frac{13}{7}$ and 3 there are two possible solutions for $\sin^2\theta_W$, but for values less than $\frac{13}{7}$ there is only one solution. For example, if $R(\nu_\mu e)$ turns out to be $\frac{7}{3}$ then $\sin^2\theta_W$ either can have its SU(5) value of $\frac{3}{8}$,[1] or it can be $\frac{3}{4}$, a value which excludes all SU(n) embeddings. On the other hand, if $R(\nu_\mu e)$ should be equal to 1, then

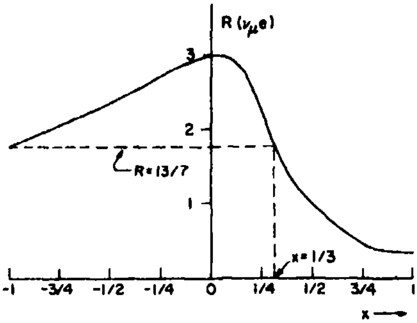

FIG. 1. *The ratio of $\bar{\nu}_\mu$-e to ν_μ-e scattering cross sections as a function of $x = 1 - 2\sin^2\theta_W$. Notice that there are two possible solutions for x when $\frac{13}{7} \leq R \leq 3$, but only one when $R < \frac{13}{7}$.*

the only possible value for $\sin^2\theta_W$ is $\frac{1}{4}$. In the event that there are two solutions, one will have to measure the polarization of the outgoing electron in order to choose the correct one.

In the case of ν_e-e scattering, Eqs. (10) and (12) show that there is no clear separation between f and the Weinberg angle; thus one of these parameters will have to be known in order to determine the other from this leptonic process. For semileptonic neutral-current interactions the situation is similar to ν_μ-e scattering: The overall strength becomes Gf instead of G, but the A/V ratio remains unchanged.[9] However, a knowledge of the hadronic matrix elements will be required if one is to extract the Weinberg angle from semileptonic data.[10]

I therefore conclude that the best chance of obtaining a unique value for the Weinberg angle is to find that the ratio of antineutrino to neutrino cross sections in ν_μ-e scattering is less than $\frac{13}{7}$, and hence that $\sin^2\theta_W < \frac{1}{3}$. This would have the additional advantage of excluding all symplectic groups Sp(2n) and all spinor representations of O(2n) and O(2n+1) as possible embeddings for the leptonic gauge. The Sp(2n) groups give $\sin^2\theta_W = \frac{1}{2}$ for all n, and the orthogonal ones give $\sin^2\theta_W = (n-2)/n$ for $n \geq 3$.

Up to now I have not considered the question of anomalies. If one takes the basic particles of the theory to be the two n^*'s containing the left-handed leptons ν_e, e_L^-, ν_μ, μ^-, and the two $\frac{1}{2}n(n-1)$ representations containing the antileptons e_L^+ and μ_L^+, then the theory is anomaly free only in the SU(5) case considered by Georgi and Glashow.[1] For higher SU(n) anomalies can be eliminated either by putting e_L^+ and μ_L^+ in different representations, or by adding more multiplets of particles. Since this problem does not affect the value of $\sin^2\theta_W$ I do not pursue it any further here.

In summary I may say that the Weinberg angle may prove to be a very powerful tool for elimating entire classes of gauge models.

The author wishes to thank T. K. Kuo and B. W. Lee for helpful comments.

---

*Work supported in part by the U.S. Atomic Energy Commission.

[1] H. Georgi and S. L. Glashow, Phys. Rev. Lett. 32, 438 (1974).

[2] S. L. Glashow, Nucl. Phys. 22, 579 (1961); S. Weinberg, Phys. Rev. Lett. 19, 1264 (1967); A. Salam and J. C. Ward, Phys. Lett. 13, 168 (1964).

[3] See Weinberg, Ref. 2.

[4] B. W. Lee, in *Proceedings of the Sixteenth International Conference on High Energy Physics, The University of Chicago and National Accelerator Laboratory, 1972*, edited by J. D. Jackson and A. Roberts (National Accelerator Laboratory, Batavia, Illinois, 1972), Vol. 4, p. 266.

[5] M. A. B. Bég and A. Sirlin, to be published.

[6] The idea of mixing hadrons and leptons in the same multiplet has also been discussed by G. Kalbfleisch and E. C. Fowler [Nuovo Cimento 19A, 173 (1974)], and J. C. Pati and A. Salam [Phys. Rev. Lett. 31, 661 (1973)].

[7] B. W. Lee, private communication.

[8] B. t'Hooft, Phys. Lett. 37B, 195 (1971).

[9] S. Weinberg, Phys. Rev. D 5, 1412 (1972).

[10] A. Pais and S. B. Treiman, Phys. Rev. D 6, 2700 (1972); E. A. Paschos and L. Wolfenstein, Phys. Rev. D 7, 91 (1973).

PHYSICAL REVIEW
LETTERS

VOLUME 33 9 SEPTEMBER 1974 NUMBER 11

Observation of Protoplasmic Streaming by Laser-Light Scattering*

R. V. Mustacich and B. R. Ware
Department of Chemistry, Harvard University, Cambridge, Massachusetts 02138
(Received 3 June 1974)

Data are presented which demonstrate that the laser light scattered from the protoplasm of living algae cells is Doppler shifted by the streaming motion of the macromolecules and particles in the protoplasm. The laser-light-scattering spectra are used to determine the velocities and velocity distributions inside the cells.

Laser inelastic light scattering has become a common and useful technique for the observation of the hydrodynamics of biological macromolecules.[1-3] If random diffusion of the macromolecules is the only motion in the solution, the scattered light is diffusion broadened about the incident frequency, and the extent of the broadening can be measured to determine the magnitude of the diffusion coefficients of the macromolecules in the solution. If the macromolecules are in directed motion, the scattered light is Doppler shifted, and the magnitude of the shift in frequency is a direct measure of the velocity of the directed motion. This principle has been used to measure the velocities of flowing solutions[4] and to determine electrophoretic velocities of charged macromolecules in solutions under the influence of electric fields.[5-7] In this Letter we report the first observation of light-scattering spectra which have been Doppler shifted by the flow of protoplasmic components inside a living cell.

Our experiments have been performed on the common alga *Nitella flexilis* (species identification was very kindly performed by Professor Richard D. Wood of the University of Rhode Island). Nitella samples were obtained from Carolina Biological Supply Company and were grown in sterile aqueous media at room temperature. Nitella is one of the many lower plants which exhibit pronounced cytoplasmic streaming (for an extensive review of this phenomenon, see Kamiya[8]). The streaming is observable under a light microscope by the motion of large particles which are carried with the flow. However, the determination of velocity and velocity distribution by this procedure is very tedious and is necessarily confined to the motion of particles which are large enough to be seen under a microscope. We have found that the measurement of velocities and velocity distributions in Nitella by laser-light scattering is very precise, perfectly objective, and extremely rapid.

The light-scattering spectrometer is of conventional design.[1-7] The laser is a Spectra Physics Model 125A helium-neon laser and the spectrum of the photocurrent is measured by a SAICOR Model SAI-51B time-compression spectrum analyzer. The Nitella cells are positioned in the apparatus in a special holder which holds them firmly in place but does not bind them. The holder can then be rotated to select the desired spatial component of the velocity. (The magnitude of the spectral shift is proportional to $\vec{K}\cdot\vec{v}$ where $\vec{v}$ is the velocity and $\vec{K}$ is the scattering vector, the vector difference of the incident- and scattered-light wave vectors, a coordinate which is determined by the geometry of the experiment.[4,6]) All cells were immersed in aqueous solution at all times. In order to avoid damage to the Nitella, it was essential to attenuate the incident laser

Copyright © 1974 by
[illegible]

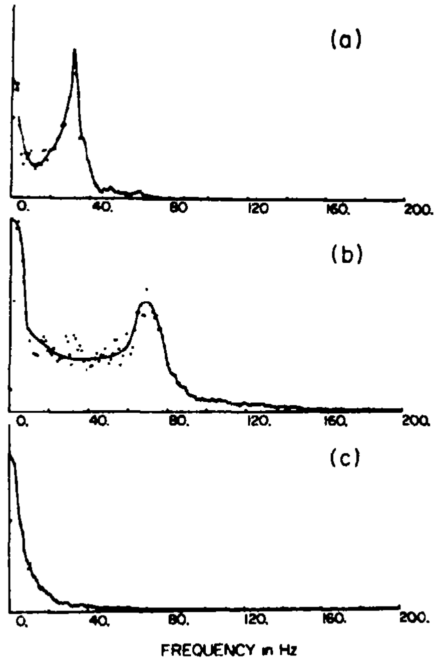

FIG. 1. Spectra of light scattered from the protoplasm of Nitella. The horizontal axis is frequency in hertz and the vertical axis is relative intensity. Spectrum (a) was taken at a scattering angle of 19.5 deg. Spectra (b) and (c) were taken at a scattering angle of 36.1 deg. Spectrum (c) was taken from the same point on the cell as spectrum (b), immediately after addition of para-chloromercuribenzoate, a streaming inhibitor. Each of these spectra was collected in about 30 sec. The points are the output of the spectrum analyzer, and the dark lines have been drawn merely to make the data more perspicuous and to emphasize the reproducible features of the data.

power to less than 0.2 mW. All measurements were made at 23°C.

Representative light-scattering spectra obtained from Nitella internodal cells are presented in Fig. 1. The horizontal axis is in frequency, but it may be helpful to think of the horizontal axis as a velocity axis. The velocity conversion factors can be calculated from the experimental geometry and the Doppler equation. For spectrum (a) in Fig. 1 a shift of 10 Hz corresponds to a velocity of 14.1 μm/sec, and for spectra (b) and (c) in Fig. 1 a shift of 10 Hz corresponds to a velocity of 8.0 μm/sec. The experimental geometry was such that the velocity component being observed is along the long dimension of the internodal cell. Spectra (a) and (b) are taken at different scattering angles and at different points on the same cell. The centers of the shifted peaks correspond to streaming velocities along the length of the cell of about 50 μm/sec for (a) and about 60 μm/sec for (b), which represent differences in velocities at different points in the cell. Spectrum (c) was obtained immediately after spectrum (b), except that para-chloromercuribenzoate, a known streaming inhibitor,[8] was added just a few seconds before the spectrum was taken. Clearly all evidence of streaming has disappeared. Observation of a change in light-scattering spectra upon quenching of streaming has been previously reported.[9]

The width of the spectrum about zero frequency in Fig. 1(c) is a measure of the diffusion of the various components in the protoplasm. This diffusion width is almost exactly equal to the width in spectrum (b), suggesting that the width in spectrum (b) is due to diffusion rather than to the variation in streaming velocities. Even if only part of the widths of the shifted spectra are due to diffusion, we can conclude that the velocity distribution of the particles represented in these shifted peaks is quite narrow. It was observed that the quenching of the streaming by para-chloromercuribenzoate was reversible simply by washing the cells with their normal nutrient solution, and it was often the case that cells reversed in this way showed a 10–20% increase over their initial streaming velocity, suggesting either that low levels of para-chloromercuribenzoate act as a stimulant to streaming or that the cells streamed faster as a result of their dormant period.

In addition to the main peaks in spectra such as (a) and (b) in Fig. 1, there is considerable intensity at higher and lower frequencies, corresponding to higher and lower velocities. Movement at lower velocities is easy to interpret as hindered motion of larger particles, although this interpretation may not be valid because the velocities corresponding to the main peaks correlate well with the velocities of very large particles seen in microscopes. The intensity at higher frequencies is even more intriguing. Although the high-frequency intensity may be due to experimental artifacts (one of which will be discussed later), it would be very interesting if this part of the spectrum indicates that some particles in the cell are moving much faster than the bulk of the protoplasm and hence faster than previous microscopic observations have reported. This high-velocity motion could be coming from macromolecules which are too small to be observed in a microscope, or may be related to some form of local motion which is responsible for the streaming of the entire protoplasm. Further investigations are needed to resolve these interesting possibilities.

The flow pattern in the Nitella internodal cell is helically wound in a pattern similar to a peppermint stick with alternating bands flowing in opposite directions. The spacing of the bands is approximately 4 mm. The diameter of the focused laser beam used in these experiments is approximately 0.1 mm, so that we were able to probe the local velocities anywhere on the cell with high resolution. These velocities are normally uniform[8]; but we observed that one set of cells (an old specimen which had become infested with parasites) often showed a constant and reproducible difference in flow velocity between the bands which flow in opposite directions. Spectra (a) and (b) in Fig. 1 are examples of this. The difference in velocities observed was usually 10–20% and was always the same for any given cell. This velocity difference was seen on both edges of the cell and throughout its entire length. This kind of anomaly, of which we are aware of no previous report, was never seen on fresh and healthy cells.

The theory of this technique predicts that the magnitude of the Doppler shift should be proportional to the sine of the scattering angle θ (the angle between the vectors of propagation of the incident and scattered light).[6] To verify this, we have measured a series of spectra as a function of the scattering angle. Throughout this series the laser beam was impinging on the same spot on the same Nitella cell. The plot of the Doppler shift as a function of scattering angle is shown in Fig. 2. The predicted linear dependence is observed.

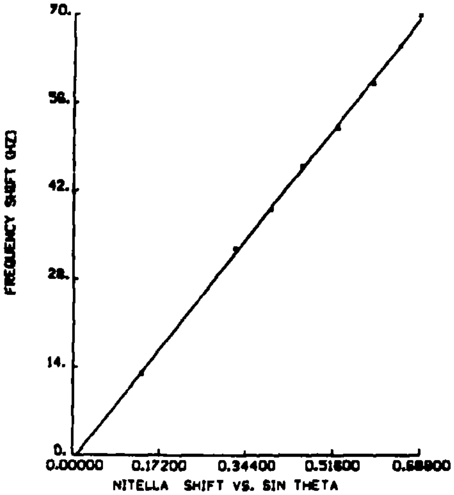

FIG. 2. A plot of the magnitude of the Doppler shift from a fixed point on a Nitella cell as a function of the sine of the scattering angle θ, the angle between the propagation vectors of the incident and scattered light. The line is the best least-squares fit to the points. The predicted linear dependence is verified, and the deviations from the line provide an estimate of the experimental precision.

It is occasionally observed that the spectrum will have a second small peak at a frequency equal to twice the frequency of the main peak [see spectrum (a), Fig. 1]. This arises from the fact that the detection in laser-light-scattering experiments is by optical beating. In these experiments the detection is of the heterodyne type, in which the scattered light is mixed at a photomultiplier tube with an unshifted component of the incident light to produce the low-frequency electronic beats which we observe. However, if the light being scattered from one of the directions of flow is beat against light scattered from the other direction of flow, then, because their relative velocities are approximately twice the absolute velocity, the beat will be of approximately twice the fundamental frequency. We have seen a definite correlation between the presence of these peaks and the position of the laser beam on the cell, with the double-frequency beat appearing when the beam is traversing both directions of flow. We have also observed a relative increase in this double-frequency beat when the intensity of the unshifted beating component (the "local oscillator") is reduced. These double-frequency beats from broad distributions of velocities could account for some of the higher-frequency intensity seen in our spectra.

We have measured the various components of the velocity in the Nitella internodal cell by rotating the cell with respect to the scattering vector. The maximum velocity is seen when the velocity is along the scattering vector, and the magnitude of this velocity is 70–75 μm/sec. We have also observed the response of the cell to excess light. If an intense laser beam is focused on the cell, the cell will stop streaming in that area, but it will continue to stream elsewhere, even a few tenths of a millimeter from the intense beam. This is consistent with a very local mechanism for the streaming. Similar responses to other types of perturbations have been observed microscopically.[8]

We have also observed protoplasmic streaming in the whorled leaf cells of Nitella. In these cells the flow pattern seems to follow the leaflike contour of the cells, and the maximum velocity was determined to be 55–60 μm/sec. This flow is also reversibly quenched by para-chloromercuribenzoate.

We believe that the technique of laser-light-scattering spectroscopy is ideally suited to the measurement of flow patterns within cells. Some of the advantages which we have found this technique to have in comparison with microscopy are as follows: (1) It is objective; i.e., all motion within the scattering region is viewed, rather than just the motion of selected particles. (2) The information is directly interpretable in terms of velocities. (3) It is exceedingly fast. Complete velocity distributions (spectra) are obtained in a few seconds. (4) Any desired component of the velocity can be measured just by changing the orientation of the cell with respect to the scattering vector. (5) The motion of submicroscopic particles can readily be observed. This technique may have a great role to play in the elucidation of the mechanism of protoplasmic streaming and in the study of other phenomena in which protoplasmic movement is an important factor.

---

*Work supported by the National Science Foundation under Contract No. GP-38495X1 and the American Chemical Society Petroleum Research Fund under Contract No. 2645-G2.

[1] S. B. Dubin, J. H. Lunacek, and G. B. Benedek, Proc. Nat. Acad. Sci. 57, 1164 (1967).

[2] B. Chu, Annu. Rev. Phys. Chem. 21, 145 (1970).

[3] N. C. Ford, Chem. Scr. 2, 193 (1972).

[4] Y. Yeh and H. Z. Cummins, Appl. Phys. Lett. 4, 176 (1964).

[5] B. R. Ware and W. H. Flygare, Chem. Phys. Lett. 12, 81 (1971).

[6] B. R. Ware, Advan. Colloid Interface Sci. 4, 1 (197

[7] E. E. Uzgiris, Opt. Commun. 6, 55 (1972).

[8] N. Kamiya, *Protoplasmologia* (Springer, Wien, 195 Band VIII.

[9] R. W. Piddington, in *Photon Correlation and Light Beating Spectroscopy*, edited by H. Z. Cummins and E. R. Pike (Plenum, New York, 1974), p. 573.

Nuclear Spin-Lattice Relaxation in Liquid Crystals by Fluctuations in the Nematic Director

J. W. Doane*
Department of Physics and Liquid Crystal Institute, Kent State University, Kent, Ohio 44240

and

C. E. Tarr† and M. A. Nickerson
Department of Physics, University of Maine, Orono, Maine 04473

(Received 5 June 1974)

We show that a finite cutoff of the hydrodynamic modes (order fluctuations) in the nematic liquid-crystalline phase explains the measured spin-lattice relaxation in this phase. A calculation of T_1 based upon such a cutoff and a fit to the data of MBBA (4-*n*-methoxybenzylidene-4′-*n*-butylaniline) show this cutoff to be 1 molecular length. At $T_{1\rho}$ frequencies, far from the cutoff, order fluctuations are shown to be the dominant relaxation mechanism. This is done by comparing the predicted angular dependence of $T_{1\rho}$ for these modes with that measured in MBBA.

The published measurements[1-13] of spin-lattice relaxation in nematic liquid crystals have not lent themselves to a single interpretation. For example, one compound, PAA (*p*-azoxyanisole) has been shown to exhibit a $\nu^{1/2}$ frequency dependence characteristic of thermal fluctuations of the director, whereas the compound MBBA (4-*n*-methoxybenzylidene-4′-*n*-butylaniline) has not shown this dependence over the same frequency range.[11] It has not been clear why one compoun should obey one mechanism while another compound in the same phase appears to obey another

In this paper we shall show that this behavior can be explained by a cutoff of the collective order fluctuations at the molecular level, where the dispersion relations for these modes are expected to break down. The frequency dependence of T_1 is calculated for an arbitrary cutoff and fitted to the data of MBBA. The best fit gives a value for the cutoff of 1 molecular length.

In addition, it is shown that at frequencies far removed from the cutoff frequency (as is obtained by $T_{1\rho}$ measurements) MBBA does indeed follow the order-fluctuation mechanism. This is done by measuring the angular dependence of $T_{1\rho}$ in the nematic phase of MBBA and comparing it with a calculation based on fluctuations of the director.

In this Letter we outline the calculation of T_1 and $T_{1\rho}$ in the nematic liquid-crystalline phase. This calculation includes the angular dependence of T_1 and $T_{1\rho}$ as well as the cutoff. The calculation is based upon the magnetic dipole interaction between two like spin-$\frac{1}{2}$ nuclei with a fixed separation distance and also applies to the quadrupole interaction of spin-1 nuclei with an electric field gradient of fixed magnitude coming from within the molecule. In our discussion we shall only refer to the dipole interaction.

The calculation is greatly simplified because of the rapid rotation ($\tau_c \approx 10^{-10}$ sec) of the rodlike molecules about their long axes. This motionally averages the dipole interactions in such a way that all the spin interactions in the molecule are effectively along the direction of the molecular axis. Rapid fluctuations of the molecular axis about the director further average the interaction. The much slower thermal fluctuations of the director $\delta\vec{N}$ about some average direction $\vec{N}_0$ are the modes we ultimately consider. It is these thermal fluctuations that provide the relaxation mechansim.[14-16]

For the situation described above, the spin-lattice relaxation is related to the spectral densities of the correlation functions, $J_k(p\omega)$, by the following expressions[17]:

$$T_1^{-1} = \tfrac{9}{8}\gamma^4\hbar^2 r^{-6}[J_1(\omega_0) + J_2(2\omega_0)], \tag{1}$$

and

$$T_{1\rho}^{-1} = \tfrac{9}{8}\gamma^4\hbar^2 r^{-6}[\tfrac{5}{2}J_1(\omega_0) + \tfrac{1}{4}J_2(2\omega_0) + \tfrac{1}{4}J_0(2\omega_1)], \tag{2}$$

where

$$J_k(p\omega) = \int_{-\infty}^{\infty} \langle F_k(0)F_k^*(t)\rangle \exp(-ip\omega t)\,dt, \tag{3}$$

and where the $F_k(t)$ are the time-dependent spherical harmonic functions:

$$F_0(t) = 1 - 3n^2; \quad F_1(t) = (l + im)n; \quad F_2(t) = (l + im)^2, \tag{4}$$

with l, m, and n the direction cosines of the molecular axis (time-averaged direction of the dipolar interaction) with respect to the laboratory coordinate system (x, y, z) in which the z axis is in the direction of the applied magnetic field $\vec{H}_0$.

In general, the vector $\vec{N}_0$ will be parallel to $\vec{H}_0$ as a result of the anisotropy of the diamagnetic susceptibility. With the application of competing electric fields, the use of thin films, or perhaps even the rotation of very viscous nematic liquid crystals, the direction of $\vec{N}_0$ can be oriented away from the direction of $\vec{H}_0$. Under these circumstances, we must make a transformation of the direction cosines to a frame (primed frame) where the z' axis is parallel to $\vec{N}_0$. In terms of the Euler angles (φ, θ, ψ) the transformed spherical harmonic functions become

$$F_0(t) = \tfrac{1}{2}(3\cos^2\theta - 1)F_0'(t) + 3i\sin\theta\cos\theta\, e^{i\psi}F_1'(t) + \text{c.c.} + \tfrac{3}{4}\sin^2\theta\, e^{2i\psi}F_2'(t) + \text{c.c.}; \tag{5a}$$

$$\begin{aligned} F_1(t) = e^{i\varphi}\{&\tfrac{1}{2}(i\sin\theta\cos\theta)F_0'(t) + \tfrac{1}{2}e^{i\psi}(1+\cos\theta)(2\cos\theta - 1)F_1'(t) + \tfrac{1}{2}e^{-i\psi}(1-\cos\theta)(1+2\cos\theta)F_1'^*(t) \\ &+ \tfrac{1}{4}i\sin\theta[-e^{2i\psi}(1+\cos\theta)F_2'(t) + e^{-2i\psi}(1-\cos\theta)F_2'^*(t)]\}; \end{aligned} \tag{5b}$$

$$\begin{aligned} F_2(t) = e^{2i\varphi}[&\tfrac{1}{2}(1-\cos^2\theta)F_0'(t) - ie^{i\psi}\sin\theta(1+\cos\theta)F_1'(t) - ie^{-i\psi}\sin\theta(1-\cos\theta)F_1'^*(t) \\ &+ \tfrac{1}{4}e^{2i\psi}(1+\cos\theta)^2F_2'(t) + \tfrac{1}{4}e^{-2i\psi}(1-\cos\theta)^2F_2'^*(t)], \end{aligned} \tag{5c}$$

where the F_k' have the same functional form as Eqs. (5) except that the direction cosines are primed and describe the molecular axis relative to $\vec{N}_0$. The instantaneous preferred direction of orientation of the molecular axis $\vec{N}(\vec{r}, t)$ will thermally fluctuate about $\vec{N}_0$. Explicitly, the expression

$$\vec{N}(\vec{r}, t) = \vec{N}_0 + \delta\vec{N}_0(\vec{r}, t) \tag{6}$$

describes the orientational order fluctuation at time t at position $\vec{r}$ in the nematic phase. In order to include this motion in the spectral densities we make a second infinitesimal transformation of the spherical harmonic functions $F_k'(t)$ from $\vec{N}_0$ to $\vec{N}(\vec{r}, t)$. This transformation has been described in a previous publication[16] where it was shown that the correlation functions become

$$\langle F_1'(0)F_1'^*(t)\rangle = S^2\langle \delta\vec{N}(\vec{r}, 0)\, \delta\vec{N}^*(\vec{r}, t)\rangle, \tag{7a}$$

and

$$\langle F_0'(0)F_0'^*(t)\rangle = \langle F_2'(0)F_2'^*(t)\rangle = 0, \tag{7b}$$

where S is the degree of molecular order. In calculating the correlation functions $\langle F_k(0)F_k^*(t)\rangle$ it is therefore only necessary to retain the terms containing $\langle F_1'(0)F_1'^*(t)\rangle$. By making use of this fact and the cylindrical symmetry about $\vec{H}_0$ and $\vec{N}_0$, the correlation functions become

$$\langle F_k(0)F_k^*(t)\rangle = f_k(\theta)\langle F_1(0)F_1^*(t)\rangle, \tag{8}$$

where

$$f_0(\theta) = 18(\cos^2\theta - \cos^4\theta) \tag{8a}$$

$$f_1(\theta) = \tfrac{1}{2}(1 - 3\cos^2\theta + 4\cos^4\theta), \tag{8b}$$

$$f_2(\theta) = 2(1 - \cos^4\theta). \tag{8c}$$

With the use of the dispersion relation $i\omega(q) = Kq^2/\eta$ for the order modes[18] where K is the appropriate deformation constant and η the viscosity, the spectral density is calculated in the usual fashion with the only modification being the cutoff in the modes near the molecular length. That is, instead of integrating over all of the hydrodynamic modes, we integrate up to the wave vector q_c. The spectral densities may then be expressed as[16]

$$J_k(p\omega) = f_k(\theta)[4S^2V/(2\pi)^3]\int_0^{q_c}\int_{-\infty}^{\infty}(kT/Kq^2V)\exp(-t/\tau_q)4\pi q^2\,dq\,\exp(-ip\omega t)\,dt,$$

where kT/Kq^2V is the thermal amplitude of the modes, V the volume, $[V/(2\pi)^3]4\pi q^2\,dq$ the number of states in a shell of volume $4\pi q^2\,dq$, and $\tau_q^{-1} = Kq^2/\eta$. The result can be expressed in closed form and becomes

$$J_k(p\omega) = Cf_k(\theta)(p\omega)^{-1/2}g(a), \tag{9}$$

where

$$g(a) = \pi - \tfrac{1}{2}\ln|(a^2 + 2^{1/2}a + 1)/(a^2 - 2^{1/2}a + 1)| - \tan^{-1}(1 + 2^{1/2}a) - \tan^{-1}(2^{1/2}a - 1), \tag{10}$$

where $a = p^{1/2}(\omega/\omega_c)^{1/2}$; ω is frequency of the NMR measurement and is ω_1 for the case of $T_{1\rho}$; $\omega_c = Kq_c^2/\eta$ and is the cutoff frequency. The constant C is given explicitly as

$$C = 2^{1/2}S^2kT\eta^{1/2}/\pi^2K^{3/2}.$$

To determine T_1^{-1} and $T_{1\rho}^{-1}$ Eqs. (1) and (2) are used and become[19]

$$T_1^{-1} = Ag(a)\omega^{-1/2}[(\tfrac{1}{2} + 2^{1/2}) - \tfrac{3}{2}\cos^2\theta + (2 - 2^{1/2})\cos^4\theta] + B, \tag{11}$$

$$T_{1\rho}^{-1} = A_\rho g(a)\omega_1^{-1/2}\{(9/2^{3/2})(\cos^2\theta - \cos^4\theta) + [(\tfrac{5}{4} - 2^{-3/2}) - \tfrac{15}{4}\cos^2\theta + (5 - 2^{-3/2}\cos^4\theta](\omega_1/\omega_0)^{1/2}\} + B_\rho, \tag{12}$$

where A and A_ρ are constants obtained from Eqs. (1), (2), (8), and (9). The constants B and B_ρ are contributions of other relaxation mechanisms at frequencies above the cutoff, i.e., where $g(a) \to 0$. These expressions are easily modified for the quadrupolar case by replacing $\gamma^4\hbar^2/r^6$ by $e^4q^2Q^2/4$, where q is the electric field gradient and Q is the quadrupole moment. It is not clear, however, that the magnitude of q will not be modulated in the nematic phase.

To compare Eq. (10) with experiment we have used the measurements of Vilfan, Blinc, and Doane[11] of the frequency dependence of T_1^{-1} in MBBA shown in Fig. 1. The fitting parameter is $\nu_c = \omega_c/2\pi$. The best fit gives a value of 80 ± 20 MHz for ν_c. For MBBA at room temperature, $K \simeq 6.0 \times 10^{-7}$ dyn.[20,21] For the value of η we take the value of γ_1 measured by Meiboom[22] as 0.5 P. Taking $q_c = 2\pi/\lambda_c$ we obtain $\lambda_c = 31 \pm 5$ Å

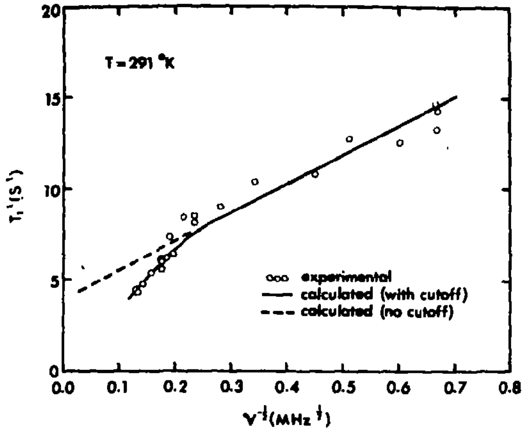

FIG. 1. Frequency dependence of T_1 in MBBA (from data of Ref. 11).

which is within error of being the molecular length for MBBA (28 Å).

At $T_{1\rho}$ frequencies, $\omega_c \gg \omega_1$ so that the relaxation time is not influenced by the cutoff, and, therefore, should follow the angular dependence of Eq. (12). The angular dependence of $T_{1\rho}$ in MBBA oriented in an electric field is shown in Fig. 2. The angular dependence of T_1 in MBBA was also measured at 30 MHz which is so close to ω_c that $g(\alpha)$ is small, resulting in only a small angular variation in T_1. The form of T_1 agrees well, however, with Eq. (11). In contrast, PAA does not show a cutoff behavior, as ω_c is near 200 MHz which is far above the range of frequencies in which T_1 has been measured in PAA.

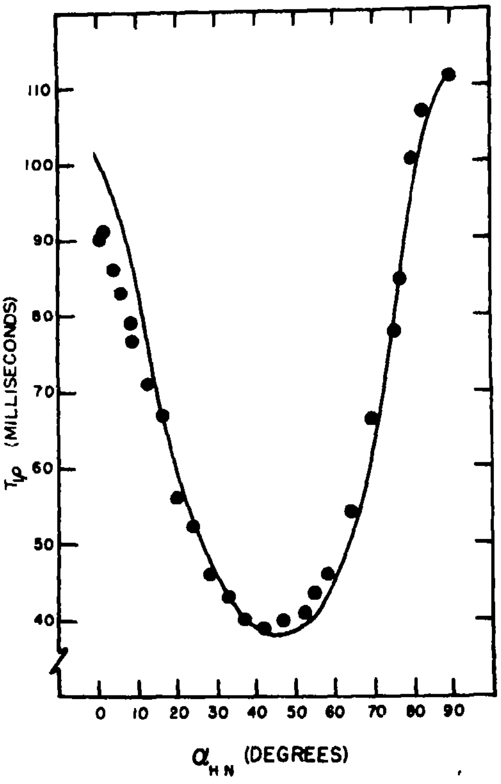

FIG. 2. Orientational dependence of $T_{1\rho}$ in MBBA for $\omega_1 \approx 40$ kHz and $\omega_0 = 30$ MHz. The solid line is Eq. (12).

It would be interesting to test the concept of a cutoff in systems where there exists short-range smectic-*A* order. Such order should also cut off these modes. In particular, one might use this technique to determine the size of the short-range smectic-*A* order.

---

[*] Research supported in part by the National Science Foundation under Grant No. GH-34164X.

[†] Research supported in part by the National Science Foundation under Grant No. GH-34520.

[1] W. Weger and P. Cabane, J. Phys. (Paris), Colloq. 30, C4-72 (1969).

[2] J. W. Doane and J. J. Visintainer, Phys. Rev. Lett. 23, 1421 (1969).

[3] R. Y. Dong, M. Marusic, and C. F. Schwerdtfeger, Solid State Commun. 8, 1577 (1970).

[4] C. E. Tarr, M. A. Nickerson, and C. W. Smith, Appl. Phys. Lett. 17, 318 (1970).

[5] B. Cabane and W. G. Clark, Phys. Rev. Lett. 25, 91 (1970).

[6] R. Y. Dong, W. F. Forbes, and M. M. Pintar, J. Chem. Phys. 55, 145 (1971).

[7] J. J. Visintainer, J. W. Doane, and D. L. Fishel, Mol. Cryst. Liquid Cryst. 13, 69 (1971).

[8] C. E. Tarr, A. M. Fuller, and M. A. Nickerson, Appl. Phys. Lett. 19, 179 (1971).

[9] C. R. Dybowski, B. A. Smith, and C. G. Wade, J. Phys. Chem. 75, 3834 (1971).

[10] C. L. Watkins and C. S. Johnson, Jr., J. Phys. Chem. 75, 2452 (1971).

[11] M. Vilfan, R. Blinc, and J. W. Doane, Solid State Commun. 11, 1073 (1972).

[12] C. E. Tarr and A. M. Fuller, Mol. Cryst. Liquid Cryst. 22, 123 (1973).

[13] A. M. Fuller and C. E. Tarr, Mol. Cryst. Liquid Cryst. 25, 5 (1974).

[14] R. Blinc, D. E. O'Reilley, E. M. Peterson, G. Lahajner, and I. Levstek, Solid State Commun. 6, 839 (1968).

[15] P. Pincus, Solid State Commun. 7, 415 (1969).

[16] J. W. Doane and D. L. Johnson, Chem. Phys. Lett. 6, 291 (1970).

[17] D. C. Look and I. J. Lowe, J. Chem. Phys. 44, 2995 (1966).

[18] Groupe d'Etude des Cristaux Liquides (Orsay), J.

Chem. Phys. 51, 816 (1969).

[19] The factor containing the angular dependence will be noticed to be different from that seen in J. W. Doane and D. J. Moroi, Chem. Phys. Lett. 11, 339 (1971). An error of a factor of 2 intermediate in that calculation is the source of disagreement.

[20] C. Williams and P. E. Cladis, Solid State Commun. 10, 357 (1972).

[21] H. Gasparoux, B. Regaya, and J. Prost, C.R. Acad. Sci., Ser. B 272, 1168 (1971).

[22] S. Meiboom and R. C. Hewitt, Phys. Rev. Lett. 30, 261 (1973).

Anisotropy in the B Phase of He^3

W. F. Brinkman
H. C. Ørsted Institute, University of Copenhagen, Copenhagen, Denmark, and
Bell Laboratories, Holmdel, New Jersey

and

H. Smith
H. C. Ørsted Institute, University of Copenhagen, Copenhagen, Denmark

and

D. D. Osheroff and E. I. Blount
Bell Laboratories, Murray Hill, New Jersey

(Received 21 May 1974)

The magnetic anisotropy of the B phase (assumed to be a Balian-Werthamer phase) is investigated within the Landau-Ginzburg theory. The anisotropy is determined by the action of the dipolar energy and the magnetic field on a single vector $\hat{n}$ and it is shown that walls will induce variations in $\hat{n}$ on a scale of $R_C \sim 0.1$ cm. In the presence of a field H this characteristic length becomes $R_C H_B/H$, where H_B is of the order of 100 Oe.

The discovery[1] of the new superfluid phases of He^3 has generated considerable excitement because of the anisotropic nature of the states involved. These phases are undoubtedly BCS-type states made up of Cooper pairs with the orbital and spin angular momenta equal to 1.[2] The A phase has attracted most attention because in it each pair has $m_L = 1$ along some axis $\hat{l}$ and $m_s = 0$ along some other axis $\hat{k}$.[3-5] These axes, along with the phase and magnitude of the order parameter, characterize the state of the A phase. It has been shown that $\hat{l}$ acts as an anisotropy axis for propagation of the various types of sound waves[4] and superfluid flow.[3,5] It has also been shown[6] that $\hat{l}$ will be oriented perpendicular to the surface of any walls so that the A phase should exhibit textures, that is, gradual variations of $\hat{l}$ which are determined by the shape of the sample, the applied fields, and any imposed currents. In this sense this phase is similar to a liquid crystal. In the same context little attention has been paid to the B phase because it is generally believed to be isotropic. Although in many respect this statement is true it is not so for the magnetic properties of the B phase,[7,8] and we shall show that there are a number of theoretical reasons which make the B phase attractive from the point of view of studying textures and singularities of the order parameter with nuclear magnetic resonance techniques.

The B phase is believed to be the Balian-Werthamer state[9] in which each pair has $\vec{J} = \vec{L} + \vec{S} = 0$, but with the spin variables rotated (arbitrarily) relative to the orbital variables. The state is therefore specified by a rotation matrix which we write in terms of the axis of rotation $\hat{n}$ and the angle of rotation θ. Thus introducting the notation used previously[10] to specify the order parameter, namely that

$$\langle a_{\hat{k}\beta} a_{-\hat{k}\gamma} \rangle \propto \sum_{\alpha i} d_{\alpha i} \hat{k}_\alpha (\sigma^i \sigma^y)_{\beta\gamma}, \tag{1}$$

we write

$$d_{\alpha i} = (\Delta/\sqrt{3})[\delta_{\alpha i} \cos\theta + n_\alpha n_i (1 - \cos\theta) + \epsilon_{\alpha i j} n_j \sin\theta]. \tag{2}$$

Here $|\Delta|$ is the isotropic gap. For an infinite system the value of the angle θ is determined by minimizing the dipolar energy[7] and it has been found to be $\theta = \cos^{-1}(-\frac{1}{4})$. We will find that even in the presence of surfaces this angle remains essentially unchanged. The dipolar energy does not orient $\vec{n}$ but in the presence of a magnetic field $\vec{n}$ tends to orient itself along the field because of a combination of the depairing effect of the field and the dipolar energy.[7,8] For a finite system the fact that the surface acts to depair the $m_l = 0$ component along its normal must be taken into account. To do this we introduce a trial form for $d_{\alpha i}(\vec{r})$ which incorporates this boundary condition:

$$d_{\alpha i}(\vec{r}) = (\Delta/\sqrt{3})[\delta_{\alpha\beta} - f(r_\perp)s_\alpha s_\beta]R_{\beta i}(\vec{r}). \qquad (3)$$

The $R_{\alpha i}(\vec{r})$ is the rotation matrix specified by $\vec{n}(\vec{r})$ and θ, $\vec{s}$ is a vector normal to the surface, and $f(r_\perp)$ is assumed to be nonzero only when the perpendicular distance from the surface $r_\perp$ is of the order of the coherence length $\xi(T)$ ($\sim 200A$). With $f(0) = 1$ this function satisfies the boundary conditions imposed by the depairing of the $m_l = 0$ component of the triplet. There are actually additional depairing effects[6] due to the undoubtedly nonspecular nature of reflection from the walls and due to the curvature of the walls. These will tend to reduce the tangential components of the order parameter but should not change the dominant anisotropies at the surface induced by the strong depairing of the component normal to the surface. We ensure that there are no spin currents flowing into the surface by imposing the additional boundary condition that $(\vec{s}\cdot\nabla)\vec{n} = 0$. By using Eq. (3) and the general expression for the gradient terms in the Landau-Ginzburg theory of these phases[3,11] we can calculate the energy required to bend $\vec{n}$ as a function of position. It is found to be

$$F_B{}^B = \frac{c}{13}\int_V d^3r\{16|\nabla\times\vec{n}|^2 + 13(\nabla\cdot\vec{n})^2 - 2\sqrt{15}(\nabla\cdot\vec{n})(\vec{n}\cdot\nabla\times\vec{n}) - 5(\vec{n}\cdot\nabla\times\vec{n})^2 + 16\nabla\cdot[(\vec{n}\cdot\nabla)\vec{n} - \vec{n}(\nabla\cdot\vec{n})]\}, \qquad (4)$$

where

$$c = \frac{h^2\rho}{4m^*}\left(1 - \frac{T}{T_c}\right)\left(\frac{13}{8}\right). \qquad (5)$$

The last term in (4) is a surface term but is generally nonzero. There are other terms involving f but these can be shown to be small or independent of $\vec{n}$. We have set $\theta = \cos^{-1}(-\frac{1}{4})$. Equation (4) along with the orientation energy in an external field constitute the bulk energies that depend on $\vec{n}$. This orientation energy is

$$F_H{}^B = -a\int d^3r(\vec{H}\cdot\vec{n})^2, \qquad (6)$$

where a is given in terms of the dipole energy E_D and the gyromagnetic factor γ,[2,8] $a \approx \hbar^2\gamma^2E_D/[T_c(T_c - T)]$. Using (3) we find two different surface energies. The first comes from inserting (3) into the dipolar energy[8] and is of the form

$$F_D{}^S = -b\int_S d^2r[(\vec{s}\cdot\vec{n})^2 - \tfrac{4}{15}(\vec{s}\cdot\vec{n})^4], \qquad (7)$$

where $b \approx \xi E_D$, that is, the coherence length times the bulk dipole energy. This term tends to align $\vec{n}$ perpendicular to the surface. The second contribution arises because near the surface the order parameter is not symmetric and consequently the susceptibility is no longer isotropic.[12] This induces a field-dependent surface energy of the form

$$F_H{}^S = -d\int d^2r(\vec{s}\cdot\overleftrightarrow{R}\cdot\vec{H})^2, \qquad (8)$$

where $\overleftrightarrow{R}$ is the rotation matrix in (3) and d is of order $\xi(\chi_N - \chi_B)$, i.e., the coherence length times the difference in susceptibility between the normal state and the Balian-Werthamer state. This term is minimized if R is such as to rotate $\vec{H}$ into $\pm\vec{s}$. If θ is greater than the angle between $\vec{s}$ and $\vec{H}$ a direction for $\vec{n}$ can always be found such as to minimize $F_H{}^S$. Since the equilibrium value of θ is $> 90°$ one can always minimize this term by varying the direction of $\vec{n}$. Also, since the surface dipolar term cannot compete with the bulk dipole energy, θ does not vary appreciably near the walls, so that we are allowed to concentrate on the variation of $\vec{n}$. Inserting the expression for $\overleftrightarrow{R}$ in terms of $\vec{n}$ we find for $\vec{s}\perp\vec{H}$

$$F_H{}^S = \frac{25d}{16}\int_S d^2r[(\vec{s}\cdot\vec{n})(\vec{n}\cdot\vec{H}) + (\tfrac{3}{5})^{1/2}\vec{n}\cdot(\vec{s}\times\vec{H})]^2. \qquad (9)$$

Combining these results we find that the textures of $\vec{n}$ for various shaped samples are characterized by two fields H_S and H_B and a characteristic length R_c,

$$R_c \approx c/b \approx 0.1(1 - T/T_c)^{1/2}\text{ cm},$$

$$H_S \approx (b/d)^{1/2},$$

$$H_B \approx (b^2/ac)^{1/2}.$$

Both H_S and H_B are of order 10–100 G and are relatively temperature independent. That the length R_c goes to zero is a reflection of the softness of the bending energy as $T \to T_c$. Very near T_c the surface terms become small and the bulk anisotropy dominates so that $\hat{n}$ becomes everywhere parallel to $\vec{H}$. This fact may help explain the recent experiments of Webb, Kleinberg, and Wheatley[13] and Ahonen, Haikala, and Krusius.[14]

The most relevant situation to study is a cylindrical sample with $\vec{H}$ parallel to the sample axis. In zero field there are two competing textures (see Fig. 1), one in which $\hat{n}$ points along the cylinder axis and simply flares out as a function of the distance from the center (texture I) and the other where $\hat{n}$ lies in the plane perpendicular to the cylinder axis and exhibits an in-plane structure in which there are two disgyration lines on opposite sides of the cylinder (texture II). In Fig. 1 we have drawn these textures as they appear at zero field. A disgyration here is defined in a fashion similar to that used by de Gennes for the A phase, that is, a line about which $\hat{n}$ rotates always pointing in a tangential direction. We find that the in-plane structure is stable for the radius of the cylinder $R < 74R_c$. As R decreases the disgyrations are gradually excluded and the texture becomes uniform with $\hat{n}$ along an arbitrary direction in the plane. In an external field the texture I is more favored, and one finds that if one starts with texture II there is a first-order transition at a critical field to texture I.

Turning now to the question of NMR line shapes, since θ is fixed the NMR resonance frequency only depends on the angle between $\hat{n}$ and the external field. At large fields ($\gamma H \gg \Omega_L$) the transverse resonance frequency ω_t is[7]

$$\omega_t^2 = (\gamma H)^2 + \Omega_L^2 \sin^2\chi(\vec{r}), \tag{10}$$

where χ is the angle between $\hat{n}$ and $\vec{H}$ and Ω_L is the longitudinal resonance frequency.

The shift in frequency gives rise to a line shap $P(\omega)$, which we calculate assuming that each region of the sample resonates at its local frequency ω_t. It is

$$P(\omega) = V^{-1}\int d^3r\, \delta[\omega - \omega_t(\vec{r})], \tag{11}$$

where V is the cylinder volume.

In texture I where $\hat{n}$ has a component along $\vec{H}$ we may find $P(\omega)$ corresponding to the case in which $R \gg R_c H_B/H$, since the variation of $\hat{n}$ is then described by

$$\chi(\vec{r}) = A \sinh(rH/R_c H_B), \tag{12}$$

where r measures the distance from the cylinder axis. A is a constant given by $A = A_0/\sinh(RH/R_c H_B)$, where A_0 is the angle between $\hat{n}$ and the magnetic field at the cylinder surface. Since over most of the sample $\hat{n}$ is nearly parallel to $\vec{H}$, we may approximate $\sin\chi$ by its argument. We get

$$P(\omega) = 2(H_B R_c/HR)^2(1/\Gamma)f(2[(\omega - \gamma H)/\Gamma]), \quad \omega \geq \gamma H, \tag{13}$$

where the characteristic width is $\Gamma = (\Omega_L^2/\gamma H)A^2$ and

$$f(x) = \ln[x^{1/2} + (x+1)^{1/2}]/(x + x^2)^{1/2}. \tag{14}$$

This function is exhibited in Fig. 1 in which $P(\omega)$ is plotted versus frequency.

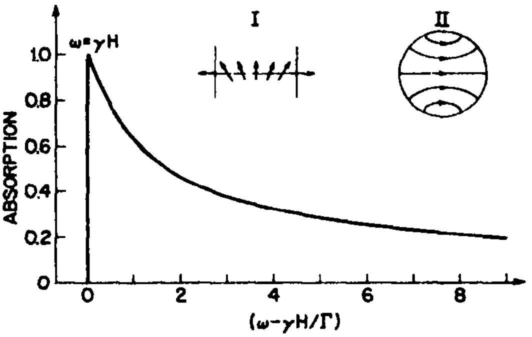

FIG. 1. A plot of the high-field NMR line shape for a cylindrical sample. The two textures that we have considered are illustrated in the upper part of the figure. The first is a side view of the cylinder and the arrows represent the direction of $\hat{n}$. To illustrate the second texture we take a view along the axis of the cylinder and the lines represent tangents to the vector field.

Experimentally[15] what is observed is not the ideal line shape $P(\omega)$, but an average of it corresponding to the variation in magnetic field streng over the sample caused by the presence of a finite field gradient. Consider such an average for the transverse line shape:

$$N(\Delta\omega) = \int_{\gamma H}^{\gamma H + \Delta\omega} P(\omega)\, d\omega \tag{15}$$

$$\simeq 1 - \frac{H_B R_c}{HR} \ln\left(\frac{\Omega_L^2}{2\Delta\omega\gamma H} A_0^2\right), \tag{16}$$

which is valid when N is close to unity. The mai dependence on magnetic field comes from the factor $H_B R_c/HR$, since the logarithm is slowly varying. The average represents the amount of unshifted signal which is observed,[15] as a function of magnetic field. If we plot the maximum ab-

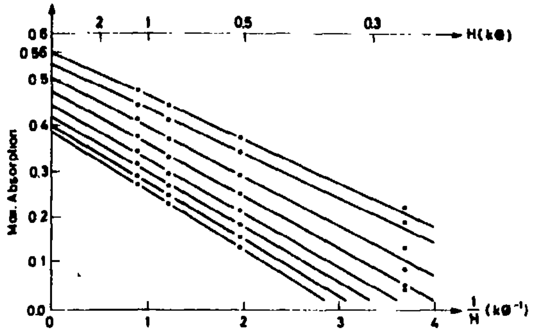

FIG. 2. The maximum absorption data of Ref. 13 plotted versus $1/H$. The slope gives an estimate of $H_B R_C \approx 10$–20 cm Oe. The curves from top to bottom are increasing pressures (decreasing temperature) relative to the A transition; from the top down the pressures relative to A are 21.0, 23.5, 27.1, 30.7, 34.3, 38.0, 41.6, and 45.2 mbar, respectively.

sorption data of Ref. 13 versus the inverse magnetic field (Fig. 2), this dependence on $1/H$ shows up very clearly. Because of the uncertainty in the estimates of H_B and R_c, as well as $\Delta\omega$, a direct numerical comparison between the measured and calculated slopes cannot be made. We wish to point out, though, that the experimentally determined slope of the curves in Fig. 2 is reproduced for reasonable values of the parameters, namely, $R_c H_B \sim 10$ to 20 cm Oe, assuming the logarithm to be about 2 to 4.

It should also be mentioned that these results only depend on $\hat{n}$ not being along $\vec{H}$ at the surface and consequently are not dependent on the detailed knowledge of surface energies.

In conclusion, we emphasize that there are several reasons that NMR studies of textures may be very rewarding in the B phase.

(1) There is only a single vector involved, $\hat{n}$, and the local resonance frequency is determined by its angle relative to the external field. In the A phase the directions of both $\hat{k}$ and $\hat{l}$ play a role in determining the resonance frequency.

(2) The lengths in the B phase are longer, $R_c = [(F_N - F_S)/E_D]\xi = 10^6\xi \sim 0.1$ cm, so that textures should be easily observable and, indeed, are clearly evident in the data in Fig. 2. In other unpublished NMR data rather sharp dips occurred which may be due to a point singularity in the order parameter. These will be discussed elsewhere.

The authors would like to thank P. W. Anderson for much useful discussion, particularly for pointing out the field-dependent surface term, and to V. Ambegaokar for useful discussions regarding the work in Ref. 6.

---

[1] D. D. Osheroff, W. J. Gully, R. C. Richardson, and D. M. Lee, Phys. Rev. Lett. 29, 920 (1972).

[2] P. W. Anderson and W. F. Brinkman, Phys. Rev. Lett. 30, 1108 (1973).

[3] P. G. de Gennes, Phys. Lett. 44A, 271 (1973).

[4] P. Wölfle, Phys. Rev. Lett. 31, 1437 (1973).

[5] W. M. Saslow, Phys. Rev. Lett. 31, 870 (1973).

[6] V. Ambegaokar, P. G. de Gennes, and D. Rainer, Phys. Rev. A 9, 2676 (1974).

[7] A. J. Leggett, Phys. Rev. Lett. 31, 352 (1973), and to be published.

[8] S. Engelsberg, W. F. Brinkman, and P. W. Anderson, Phys. Rev. A 9, 2592 (1974).

[9] R. Balian and N. A. Werthamer, Phys. Rev. 131, 1553 (1973).

[10] W. F. Brinkman and P. W. Anderson, Phys. Rev. A 8, 2732 (1973).

[11] E. I. Blount and P. W. Anderson, to be published.

[12] Terms describing this anisotropy have been introduced in Refs. 7 and 8 and in N. D. Mermin and G. Stare, Phys. Rev. Lett. 30, 1135 (1973).

[13] A. I. Ahonen, M. T. Haikala, and M. Krusius, Phys. Lett. 47A, 215 (1974).

[14] R. A. Webb, R. L. Kleinberg, and J. C. Wheatley, Phys. Rev. Lett. 33, 145 (1974).

[15] D. D. Osheroff and W. F. Brinkman, Phys. Rev. Lett. 32, 584 (1974).

Phase Diagram of Liquid ^{3}He between 0.7 and 2.5 mK

A. I. Ahonen, M. T. Haikala, M. Krusius, and O. V. Lounasmaa
Low Temperature Laboratory, Helsinki University of Technology, SF-02150 Otaniemi, Finland

(Received 8 July 1974)

We describe a nuclear demagnetization cryostat in which liquid ^{3}He has been cooled to below 0.7 mK. Data on the boundaries between the normal Fermi-liquid and the superfluid phases of ^{3}He, as determined from NMR measurements, are presented between 0.7 and 2.5 mK and from 0 to 27 bar. The "λ point" of ^{3}He was found at 0.93 mK.

Wheatley and co-workers[1] have previously determined the phase diagram of liquid ^{3}He above 1.9 mK and 10 bar pressure. By employing nuclear refrigeration techniques we have extended this work to lower temperatures and pressures, including the saturated vapor pressure. In connection with these experiments liquid ^{3}He was cooled to 0.7 mK, lower than ever before. A considerable effort was made to measure the temperature of ^{3}He directly.

Adiabatic demagnetization of the nuclear spins of a suitable metal[2,3] is a method whereby liquid ^{3}He can, in principle, be cooled well into the microkelvin region. A drawback of this method is that the cryostat is necessarily quite complicated because a low starting temperature, below 20 mK, and a high initial magnetic field, over 5 T, are required for successful nuclear demagnetization.

Furthermore, it was thought that the high Kapitza thermal boundary resistance, assumed proportional to $1/T^3$, between liquid helium and a metal would prevent the use of nuclear refrigeration for cooling ^{3}He below 2 mK. Subsequently it was observed,[4] however, that the heat resistance is smaller than expected, exhibiting a relatively weak $1/T$ temperature dependence below 10 mK. The low thermal boundary resistance is presumably due to a magnetic interaction between the nuclear spins of ^{3}He and the electronic impurity moments of the metal. This additional thermal coupling is of paramount importance for nuclear refrigeration of liquid ^{3}He.

Our cryostat is illustrated in Fig. 1. The nuclear stage is made of a bundle of 0.1-mm-diam copper wires containing a total of 22 moles of copper; the bundle was made stiff by epoxy. Highest purity wire, having a resistance ratio $R(300\text{ K})/R(4\text{ K}) \approx 150$, was used. The wires were welded at their top end to a copper piece which, in turn, was welded to the ^{3}He cell.

In order to achieve good thermal contact between liquid ^{3}He and the nuclear refrigerant, the cell was sintered full of copper powder[5] with a 40% packing factor, except for a cylindrical space occupied by the NMR coils. The main magnetic impurities of the powder are 200 ppm of iron and 4.4 ppm of manganese; it is believed that manganese is the more important element in reducing the thermal boundary resistance to ^{3}He. With 28 g of sinter in the cell the total surface area for heat exchange is 30 m^2; the space available for liquid ^{3}He is 6 cm^3. Because the bulk thermal conductivity of the sinter is relatively poor the ^{3}He chamber was equipped with sixteen copper rods of 2 mm diameter, welded to the bottom of the cell. Highest-purity copper was employed for constructing the ^{3}He cell and other

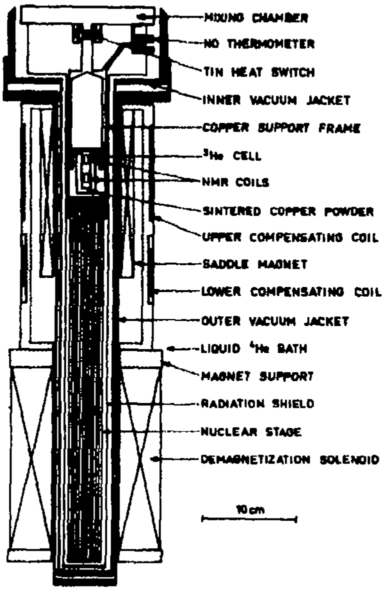

FIG. 1. Schematic illustration of the lower part of the cryostat showing the mixing chamber of the precooling dilution refrigerator, the ^{3}He cell, and the nuclear stage.

parts through which heat must flow.

A 7.5-T superconducting solenoid is used for nuclear demagnetization; it incorporates two compensating coils which cancel, over the region of the ^{3}He cell, the field produced by the main solenoid. The smaller coils as well as the relatively large distance between the demagnetization solenoid and the cell ensure that the field applied to liquid ^{3}He can be varied independently.

Two 7-mm-long NMR coils, each wound on an epoxy former 14 mm long and with a 4.5 mm i.d., are located on the center axis of the ^{3}He cell. The upper one is filled to 35% by volume with platinum powder of 8 μm average diameter; it is used for thermometry by observing the NMR signal of platinum, and also for measurements on ^{3}He. The lower resonance coil contains only ^{3}He.

The static magnetic field for NMR measurements is generated by means of a saddle magnet made of two coils which produce a field transverse to the vertical axis of the NMR coils. The overall field homogeneity $\Delta B/B$ is 6×10^{-4} as determined from the linewidth of the ^{3}He resonance signal. NMR measurements on liquid ^{3}He were made by sweeping the static field and by frequency modulating the rf excitation; low-frequency phase-sensitive detection techniques could thus be employed.

Our pulsed NMR thermometer[6] was self-calibrated via an automated measurement of the nuclear spin-lattice relaxation time τ_1 of ^{195}Pt and by the use of Korringa's relation, $\tau_1 T_e = 29.8$ msec K; T_e is the lattice and conduction-electron temperature of platinum. The measuring procedure was to find the calibration constant A in Curie's relation $\chi_n = A/T_n$ from relaxation-time measurements between 2 and 4 mK; here χ_n is the dynamic nuclear susceptibility and T_n the nuclear spin temperature of platinum. Above 5 mK the platinum thermometer could also be checked against a nuclear orientation thermometer, based on the anisotropy of γ rays emitted by oriented ^{54}Mn nuclei in nickel. It should be noted that a pulsed NMR thermometer measures the temperature just before the pulse; the readings are thus equilibrium temperatures and unaffected by transients. We also want to emphasize that the platinum powder is in thermal contact with liquid ^{3}He only; our thermometer thus measures the ^{3}He temperature directly. This is an important improvement over some of the earlier nuclear refrigeration experiments.[2]

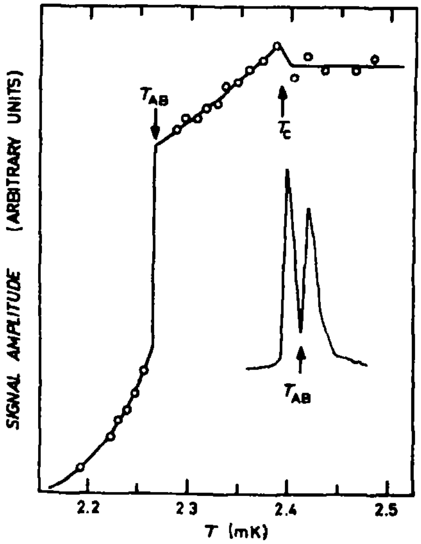

FIG. 2. The maximum resonance amplitude as a function of temperature near T_c and T_{AB} for $P = 22.4$ bar. Between 2.4 and 2.2 mK the amplitude decreases by 40%. The inset shows the NMR signal at T_{AB}; the transition from the A to the B phase happens to occur in the middle of a resonance peak.

A dilution refrigerator cools the nuclear stage to 17 mK. Demagnetization from 7.5 T to a final field between 0.05 and 0.1 T is then performed in 3.5 h, and liquid ^{3}He reaches its lowest temperature, presently slightly below 0.7 mK, in 4 h; the subsequent warm-up time to 1.0 mK, caused by an external heat leak of 0.2 nW per mole of copper, is 20 h.

Our transverse NMR measurements were performed in a static field of 32 mT. The signal was recorded both upon cooling and during subsequent warming through the phase transitions which were identified by changes in the signal amplitude. Above 20 bar, the A phase could also be recognized from a shift of the resonant frequency.[7]

Figure 2 illustrates a typical behavior of the NMR signal. Upon crossing the second-order phase boundary from the normal Fermi liquid into the A phase at T_c, the amplitude first increased a few per cent and then slowly started to decrease. These variations in the maximum absorption are caused by changes in the line shape; the total area under the resonance curve appears to be roughly constant within our resolution. At the first-order transition between the A and B phases the amplitude changed discontinu-

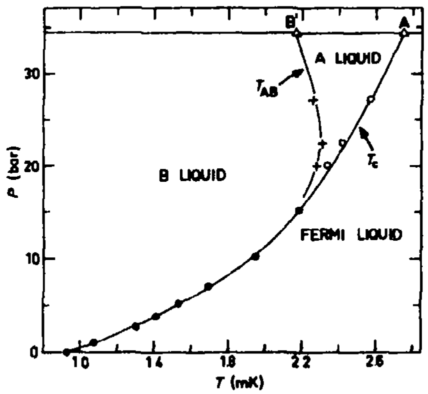

FIG. 3. The phase diagram of liquid ^{3}He. Our data at 32 mT: *open circles*, T_c; *crosses*, T_{AB}; crosses in circles, "average" of T_c and T_{AB}. Triangles, melting-curve data from Ref. 8.

ously and then decreased rapidly in the *B* phase. The transition temperature T_{AB} could be determined, above 20 bar, only upon warming because substantial supercooling always occurred; superheating was never observed in the lower coil containing bulk liquid. In order to avoid thermal inhomogeneities, the temperature was varied slowly, 50 μK/h, through the transition region. In most cases T_{AB} and T_c could be determined with a precision of 30 μK.

By tracing the NMR signals as a function of temperature at different pressures we have determined the phase diagram of liquid ^{3}He; the results are shown in Fig. 3. Below 15 bar the *A* phase becomes so narrow that the resolution of our NMR measurements is not sufficient for distinguishing between T_c and T_{AB}. At these pressures the measured transition temperature thus corresponds to an "average" of T_c and T_{AB}; the transition was identified by a discontinuity in the temperature derivative of the resonance amplitude.

We observe that the boundary between the normal Fermi-liquid region and the superfluid phases is smooth all the way to the saturated vapor pressure, which probably means that the main features of the phase diagram have by now been observed. The "λ point" of ^{3}He, i.e., T_c at zero pressure, is at 0.93 mK. The precision of our transition temperatures on the platinum NMR scale is about 0.02 mK. We have also plotted in Fig. 3 the transition points on the melting curve as determined recently by Halperin *et al.*[8] from thermodynamic measurements.

The phase diagram of liquid ^{3}He has previously been investigated above 1.9 mK by Wheatley and co-workers[1]; discontinuities in the temperature derivatives of heat flow and static magnetic susceptibility were employed for identifying the phase boundaries. For the sake of clarity these results have not been included in Fig. 3 but the agreement with our data, especially below 20 bar, is surprisingly good. The same transition temperatures for the second-order phase change at T_c were also obtained from resonance data on liquid ^{3}He intermixed with 8-μm platinum powder.[3] There are indications that in the *A* phase T_c is pushed towards lower temperatures for some of the liquid within the powder. This interpretation of the data is based on the fact that both an unshifted and a shifted resonance line are simultaneously observed in the *A*-phase region; the intensity of the former signal decreases rapidly towards lower temperatures.

It appears from our data that the thermal relaxation time between liquid ^{3}He and the nuclear stage is not increasing significantly upon cooling. This gives us hope that even lower temperatures can be achieved by nuclear refrigeration of liquid ^{3}He. It also seems that the temperature of liquid ^{3}He below 1 mK can be measured reliably by the platinum-powder NMR thermometer, although further investigations are required.

Finally, it should be pointed out that nuclear refrigeration now has made possible experiments involving the free surface of superfluid ^{3}He.

We wish to thank T. A. Alvesalo, D. S. Fisher, M. S. Grönstrand, U. A. Lähteenmäki, and E. Turtiainen for help with the experiments and in analyzing the data.

---

[1] T. J. Greytak, R. T. Johnson, D. N. Paulson, and J. C. Wheatley, Phys. Rev. Lett. 31, 452 (1973); D. N. Paulson, R. T. Johnson, and J. C. Wheatley, Phys. Rev. Lett. 31, 746 (1973); D. N. Paulson, H. Kojima, and J. C. Wheatley, Phys. Rev. Lett. 32, 1098 (1974).

[2] J. M. Dundon, D. L. Stolfa, and J. M. Goodkind, Phys. Rev. Lett. 30, 843 (1973).

[3] A. I. Ahonen, M. T. Haikala, and M. Krusius, Phys. Lett. 47A, 215 (1974).

[4] O. Avenel, M. P. Berglund, R. G. Gylling, N. E. Phillips, A. Vetleseter, and M. Vuorio, Phys. Rev. Lett. 31, 76 (1973).

[5] The copper powder was purchased from Wolstenholme Bronze Powders Ltd., Bolton, Lancashire,

England. It is in the form of flakes which are 2 μm thick and 20 to 50 μm in diameter.

[6] M. I. Aalto, H. K. Collan, R. G. Gylling, and K. O. ores, Rev. Sci. Instrum. 44, 1075 (1973).

[7] D. D. Osheroff, W. J. Gully, R. C. Richardson, and D. M. Lee, Phys. Rev. Lett. 29, 920 (1972).

[8] W. P. Halperin, C. N. Archie, F. B. Rasmussen, and R. C. Richardson, to be published; W. P. Halperin, R. A. Buhrman, D. M. Lee, and R. C. Richardson, Phys. Lett. 45A, 233 (1973).

Superfluid Mass of Liquid Helium Three*

A. W. Yanof and J. D. Reppy
Laboratory of Atomic and Solid State Physics and The Materials Science Center, Cornell University, Ithaca, New York 14850

(Received 8 July 1974)

Fourth sound has been generated and detected in the superfluid phases of liquid ^{3}He by means of a new technique.

The discovery of transitions to new phases of liquid ^{3}He in the millikelvin temperature range by Osheroff *et al.*[1] revitalized old speculations about the possible superfluidity of liquid ^{3}He. A convincing demonstration of superfluidity has been provided by measurements of fourth-sound modes in liquid ^{3}He by Kojima, Paulson, and Wheatley,[2] and more recently by our group.[3]

Kojima, Paulson, and Wheatley[2] have employed the technique developed by Shapiro and Rudnick[4] to obtain the fourth-sound velocity. The porous medium used is a compressed powder of cerium magnesium nitrate (CMN) which also serves as a refrigerant and thermometer. Drawing a reasonable analogy to fourth sound in ^{4}He, Kojima, Paulson, and Wheatley[2] interpret their results in terms of simple two-fluid hydrodynamics and obtain the superfluid fraction ρ_s/ρ from the expression[4]

$$\rho_s/\rho = n^2(c_4/c_1)^2, \qquad (1)$$

where c_4 is the measured velocity of fourth sound and c_1 is the velocity of ordinary sound in bulk liquid. The factor n^2 is a correction term which arises from the complex geometry of the porous medium through which the fourth sound must propagate.

In the work reported here, we employ the method developed by Hall, Kiewiet, and Reppy.[5] Fourth sound is generated by oscillating the entire sample chamber. The liquid properties are then deduced from the response of the sample chamber to a known applied force, and the inertial mass of the oscillating superfluid is obtained directly. This independent measurement can be compared to the value of superfluid density obtained from Eq. (1), thus giving a partial test of the validity of the simple two-fluid model for ^{3}He.

The apparatus is shown in Fig. 1. A cylindrical sample chamber, packed with CMN powder, is suspended elastically by an epoxy rod inside a massive epoxy incasement. An electrode mounted in the incasement drives the cell electrostatically along the cylinder axis. The resulting cell displacement X is sensed electrostatically and monitored by two lock-in amplifiers in quadrature.

Figure 2(a) shows the frequency response with the cell filled with liquid ^{4}He at a temperature of 0.5 K. At 0.7 kHz a suspension resonance is seen. Here the cell oscillates along its axis at

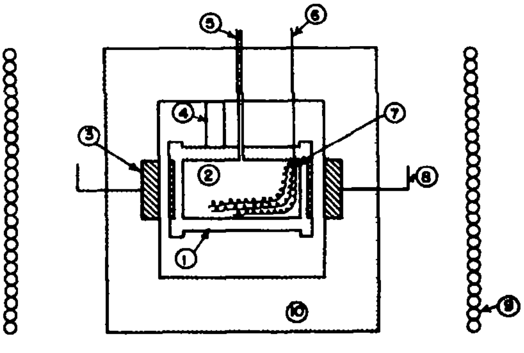

FIG. 1. Schematic diagram of fourth-sound apparatus. 1, Epoxy sample chamber; 2, packed powder (see Ref. 4); 3, metal electrode for driving cavity electrostatically; 4, epoxy suspension rod; 5, fill capillary; 6, high-purity copper wire to heat switch and mixing chamber; 7, wire brush (40 cm^2 surface area); 8, electrode for detecting cavity motion; 9, susceptibility coils and solenoid for magnetic cooling; 10, massive epoxy incasement.

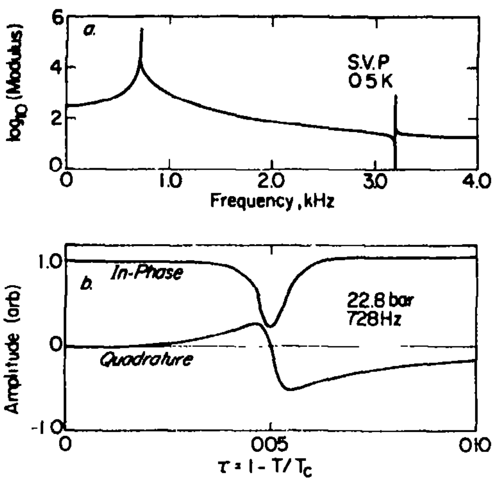

FIG. 2. Response of fourth-sound apparatus. (a) Frequency response of cell filled with ^{4}He. (b) Both quadratures of cell displacement at the suspension-resonance frequency as a function of reduced temperature τ, for the ^{3}He-filled cavity. The fundamental longitudinal fourth-sound resonance occurs at approximately $\tau = 0.05$.

the natural frequency determined by its mass and the stiffness of the suspension rod. The higher-frequency resonance is the fundamental fourth-sound standing wave at 3.2 kHz. When the resonant frequencies of the suspension and the fourth-sound modes are widely separated they may be considered independently. However, in our ^{3}He measurements a fourth-sound frequency crosses the suspension resonance; at crossing, the suspension system becomes a sensitive detector of the fourth-sound mode.

At the beginning of a run, the drive frequency is fixed at the value which maximizes the suspension-resonance amplitude while the ^{3}He is still in the normal phase. The cell is cooled to the lowest possible temperature by demagnetizing the CMN, and the displacement of the cell, $X(\omega, t, \tau)$, is monitored during the subsequent warm-up. Figure 2(b) shows the two quadrature components of the amplitude of the cavity displacement as a function of reduced temperature τ.

The superfluid mass m_s and the fourth-sound quality factor Q_4 are obtained from an analysis of the response curves shown in Fig. 2(b). The displacement X of the cell is determined by the force equation

$$F_0 e^{i\omega t} - KX - D\dot{X} - m_s\ddot{Y} = (M + m - m_s)\ddot{X}, \qquad (2)$$

where $F_0 e^{i\omega t}$ is the drive force along the cylinder axis; K and D are the spring and damping constants of the cell support; M and m are the mass of the cell and the total mass of the fluid within the cell. The term $m_s\ddot{Y}$ is the reaction force due to the acceleration of the center of mass Y of the superfluid within the cell.

To obtain the motion of the fluid we require a slight generalization of the usual fourth-sound wave equation which will allow for the acceleration of the porous medium as well as that of the superfluid. Let x be the coordinate in the rest frame along the axis of motion of the cell. We wish to develop a wave equation for the average superfluid displacement ξ_s in the x direction. The averaging is understood to take place over a volume of fluid large compared to the characteristic dimensions of the porous medium yet small in comparison with the fourth-sound wavelength.

The actual superfluid velocity $\vec{v}_s$ can be expressed as $\vec{v}_s = \dot{\vec{X}} + \nabla\varphi$, where $\dot{\vec{X}}$ is the velocity of the porous medium or cell and φ is a potential function which satisfies the boundary conditions imposed by the complex geometry of the porous medium. We shall define ϵ_1 and ϵ_2 as the volume averages, in the sense mentioned above, of the quantities $\partial\varphi/\partial x$ and $|\nabla\varphi|^2$, respectively. Then the average superfluid velocity in the x direction may be expressed as $\dot{\xi}_s = \dot{X} + \epsilon_1$.

The average kinetic energy density is given by

$$T = \tfrac{1}{2}\rho_s[\dot{\xi}_s^{\,2} + (\epsilon_2\epsilon_1^{-2} - 1)(\dot{\xi}_s - \dot{X})^2].$$

We can now write a Lagrangian density for the fluid as $\mathfrak{L} = T - (\rho_s c^2/\rho)(\partial\xi_s/\partial x)^2$. The constant c in the potential energy term will be equal to c_1, the bulk sound velocity, in the absence of any thermal terms. The fourth-sound equation obtained from the Lagrangian density is

$$\frac{\partial^2\xi_s}{\partial t^2} - \frac{\rho_s\epsilon_1^{\,2}c^2}{\rho\epsilon_2}\frac{\partial^2\xi_s}{\partial x^2} - \left(1 - \frac{\epsilon_1^{\,2}}{\epsilon_2}\right)\ddot{X} = 0. \qquad (3)$$

We define $n^2 \equiv \epsilon_2/\epsilon_1^{\,2}$ in making the connection with the fourth-sound velocity expression, Eq. (1), introduced by Shapiro and Rudnick.[4] In Eq. (3) the factor $1 - \epsilon_1^{\,2}/\epsilon_2$ represents that fraction of the superfluid which adds an induced hydrodynamic mass to the porous medium during acceleration.[6] A damping term, $\eta\rho_s^{-1}(\dot{X} - \dot{\xi}_s)$, is added to Eq. (3) to allow for possible attenuation.

Finally, Eqs. (2) and (3), augmented by the damping term, determine the motion of the cell:

$$X = F_0 e^{i\omega t}\{K - (M+m)\omega^2 - i\omega D + (m_s/n^2)[1 - (2/kL)\tan(\tfrac{1}{2}kL)](\omega/c_4 k)^2\}^{-1}, \qquad (4)$$

where L is the length of the cavity and k is a complex quantity given by $k = \omega c_4^{-1}(1 + iQ_4^{-1})^{1/2}$, where $Q_4 = \omega\rho_s\eta^{-1}$.

We fit Eq. (4) to the observed response curves such as shown in Fig. 2(b) to determine the values of m_s/n^2 and Q_4 for the temperature at which the drive and fourth-sound fundamental-mode frequencies coincide. The superfluid fraction, $\rho_s/\rho = m_s/m$, is then obtained by using a value of n^2 taken from ^{4}He measurements. In Fig. 3 agreement is shown between a value of ρ_s/ρ, open circle, obtained by this method and values generated from the temperature dependence of c_4 through the use of Eq. (1). This indicates that thermal terms are not important in the present experiment.

The temperature dependence of c_4 was determined from observation of the passage of a number of different fourth-sound modes through the suspension-resonance frequency. The range of temperature coverage was extended by using a number of different suspension frequencies ranging from 0.7 to 1.8 kHz.

These observations have been made at a number of pressures. For a given reduced temperature we see only a 10% increase in superfluid density as the pressure is increased from 15.9 to 27 bars. The data at these two pressures are indicated in Fig. 3 by the dashed lines. The 32-bar curve published by Kojima, Paulson, and Wheatley[2] lies only a few percent higher than our 27-bar curve. This agreement is most interesting in view of the differences in the packing fraction and geometric factor n^2 for the two fourth-sound cells.[7]

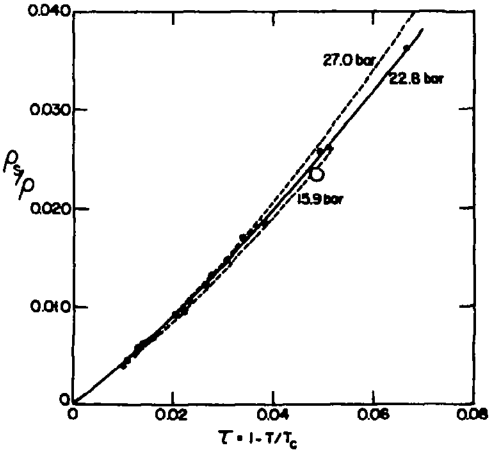

FIG. 3. Superfluid fraction in ^{3}He as a function of reduced temperature. Data points shown are measurements at 22.8 bar.

The fourth-sound quality factor Q_4 is also obtained from the fitting of Eq. (4) to the observed response curves. We find that the value of Q_4 for a given mode shows no systematic variation with temperature. A temperature-independent value for Q_4 would imply that the damping coefficient η approaches zero at the transition approximately as $\tau^{3/2}$. However, there is some mode dependence of Q_4; thus for the fundamental mode we find $Q_4 = 65$ at $\tau = 0.05$ while $Q_4 = 32$ for the second harmonic.

Much higher values of Q_4 are obtained at low temperatures with ^{4}He in the cell. For instance, at 0.2 K, a value of $Q_4 = 2\times10^4$ is observed for the fundamental mode. At higher temperatures the value of Q_4 decreases ($Q_4 = 160$ at 1.5 K). Under the assumption that fourth-sound attenuation is due to imperfect damping of the normal component, one obtains an estimate of the pore size from the observed temperature dependence of Q_4 and the known values of viscosity and superfluid density.[8] Inverting this analysis, and using a viscosity value from Alvesalo *et al.*[9] and an average pore size estimate of 2 μm from the ^{4}He data, we would expect a value of $Q_4 = 500$ for the ^{3}He fundamental mode at $\tau = 0.05$. In contrast the measured value is 65 at this temperature. Thus the mechanism of normal-fluid slippage seems inadequate to account fully for the Q values observed for fourth-sound modes in ^{3}He. Note that the maximum superfluid velocity at the resonance shown in Fig. 2(b) is 1 mm sec^{-1}.

The authors thank R. C. Richardson for his help in many phases of this work. We express our gratitude to the other members of the Cornell University low-temperature group and the Laboratory of Atomic and Solid State Physics theory group for their assistance. One of us (J.D.R.) wishes to thank the Guggenheim Foundation for Fellowship support and Professor H. E. Hass for many stimulating discussions.

---

*Work supported in part by the National Science Foundation through Grants No. GH-37658, No. GH-35692, and No. GH-38785, and also under Grant No.

GH-33637 through the Cornell Materials Science Center, Report No. 2246.

[1] D. D. Osheroff, W. J. Gully, R. C. Richardson, and D. M. Lee, Phys. Rev. Lett. 29, 920 (1972).

[2] H. Kojima, D. N. Paulson, and J. C. Wheatley, Phys. Rev. Lett. 32, 141 (1974).

[3] A. W. Yanof, E. Smith, D. M. Lee, R. C. Richardson, and J. D. Reppy, Bull. Amer. Phys. Soc. 19, 435 (1974).

[4] K. A. Shapiro and I. Rudnick, Phys. Rev. 137, A1383 (1965).

[5] H. E. Hall, C. Kiewiet, and J. D. Reppy, to be published.

[6] Equation (2) may be applied to the discussion of persistent currents in a porous medium given by J. B. Mehl and W. Zimmerman, Jr., Phys. Rev. 167, 214 (1968). The quantity χ defined by these authors is equal to the coefficient $1-\epsilon_1^2/\epsilon_2$.

[7] ^{4}He measurements give $n^2=2.53$ in our cell, 4.84 in the cell of Ref. 2. In their cell, CMN grains passed through a 35-μm sieve were packed to 80% packing fraction. In our cell 4.15 g of CMN of 50-μm average particle size was combined with 0.42 g of 1-μm Linde aluminum oxide and hand packed into the 2.96 cm^3 volume of the sample chamber. This resulted in an open volume of 0.83 cm^3, a packing fraction of 72%.

[8] D. G. Sanikidze, I. N. Adamenko, and M. I. Kaganov, Zh. Eksp. Teor. Fiz. 52, 584 (1967) [Sov. Phys. JETP 25, 383 (1967)]; I. N. Adamenko and M. I. Kaganov, Zh. Eksp. Teor. Fiz. 53, 615 (1967) [Sov. Phys. JETP 26, 394 (1968)].

[9] T. A. Alvesalo, Yu. D. Anufriyev, H. K. Collan, O. V. Lounasmaa, and P. Wennerström, Phys. Rev. Lett. 30, 962 (1973).

Time-Resolved Laser-Plasma Backscatter Studies*

B. H. Ripin, J. M. McMahon, E. A. McLean, W. M. Manheimer, and J. A. Stamper
Naval Research Laboratory, Washington, D. C. 20375

(Received 20 May 1974)

Time-resolved and time-integrated measurements of the energy, spectra, and other characteristics of the backscattered laser radiation from a laser-produced plasma are presented. Theoretical comparison shows that most of these measurements are consistent with the stimulated-Brillouin-backscattering instability.

The mechanisms responsible for absorption and reflection of laser energy in plasma are of prime importance and concern in laser fusion. The reflection of laser energy by the irradiated target represents a potentially important energy loss to the system in addition to possibly damaging the laser. A number of experimental[1-7] and theoretical[8-11] studies of laser backscatter indicate that an appreciable amount of energy is reflected back from the target with a modified spectrum. In this Letter we describe experiments which include both time-integrated and time-resolved energy and spectral measurements, and compare these results with stimulated-Brillouin-backscattering predictions.

The experimental setup used in these studies consists of a neodymium:glass laser beam ($\lambda_0=1.064$ μm) focused with either an $f/14$ or an $f/1.9$ lens onto a slab target in an evacuated chamber.[4] The pulse duration used is either 900, 250, or 50 psec full width at half-maximum energy with energy ≤ 100 J. A prepulse identical in shape to the main pulse with approximately 5% of the pulse energy is usually applied 700 psec ahead of the main pulse. For the main pulse the irradiance at the focal spot is in the range $I \leq 5\times10^{15}$ W/cm^2. Calorimeters independently monitor the incident energy and the energy reflected back through the lens.

A semiquantitative measurement of the angular distribution of the scattered 1.06-μm laser light at solid angles *other than back through the focusing lens* was performed.[12] By rotating the target, we determine that the intensity of this scattered radiation peaks at the specular-reflection angle from the target, has an angular extent of about ± 40°, and has a total energy content of 5–10% of the incident laser energy. The specularly reflected energy per solid angle is typically small compared to the direct backscattered energy. However, the total energies scattered outside and inside the solid angle subtended by the $f/14$ lens (± 2°) are comparable. The fact that we independently detect specular reflection allows us to conclude that the much more intense light which is directly backscattered through the lens is the result of some anomalous process. Henceforth we will discuss only the 1.06-μm radiation backscattered through the lens solid angle.

It was verified that the backscattered light is

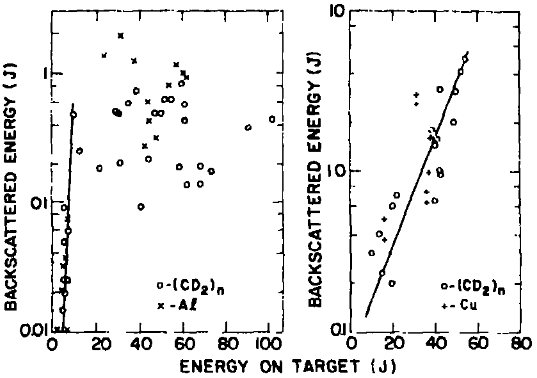

FIG. 1. Laser energy backscattered through the focusing lens near 1.06 μm versus incident energy for (a) deuterated polyethylene and aluminum slab targets, with an $f/14$ focusing lens and 900-psec (full width at half-maximum) laser pulses, and (b) deuterated polyethylene and copper slab targets, with an $f/1.9$ focusing lens and 900-psec (full width at half-maximum) laser pulses. In this plot the specular-reflection contribution (1% of the incident energy) is subtracted from the back-reflected energy.

almost completely polarized in the same plane as the incident laser beam, and that the optic rays of the backscattered radiation retraced the optic rays of the incident beam to a very high degree.[3]

Another property of the integrated backscattered radiation at 1.06 μm is that its total energy increases exponentially with incident laser energy up to a "saturation level" as shown in Fig. 1. A saturation occurs in the case of the $f/14$ lens, at approximately 10 J incident energy (~10^{14} W/cm^2) at which point ~5% of the energy is directly backscattered. The large scatter in the data is shot-to-shot reproducibility, not diagnostic uncertainty. The "saturation" of the energy backscattered through the lens may *not* imply a saturation of the *total* scattered radiation since considerable energy is scattered outside the sampled solid angle. An almost exponential dependence of the backscattered laser light upon incident energy is also found with the $f/1.9$ lens [Fig. 1(b)]. The behavior of the back-reflected energy has little sensitivity to the target material. However, no saturation is observed within the energy range covered with the $f/1.9$ lens. The explanation for the different behavior of the $f/1.9$ and $f/14$ lenses has not been uniquely determined as yet, although the $f/1.9$ aspheric lens produces a smaller focal spot diameter (~30 μm) than the $f/14$ plano-convex lens (~100 μm) and causes a more convergent optical path.

The exponential increase of reflected energy with incident power is characteristic of the linear behavior of stimulated Brillouin backscattering if the power is such that the system is above the inhomogeneous threshold. This instability is consistent with the polarization and ray-retracing measurements. The amplification factor for power of this instability[9] is

$$P_r \propto \exp(2\pi\gamma^2 L^2/cv_s), \tag{1}$$

where γ is the instability growth rate near threshold given by $\gamma^2 = (\omega_{pe}{}^2/8)(v_{os}/v_{te})^2(v_s/c)$, L is the spatial extent for phase coherence, and c, v_s, v_{te}, and v_{os} are the speed of light, ion acoustic speed, electron thermal speed, and peak electron quiver speed in the laser field, respectively. With the assumption that the underdense plasma is isothermal, the phase coherence length L is given by

$$L^{-2} = k_i \left| \frac{2v_f}{(v_f - v_s)L_v} - \frac{\omega_{pe}{}^2}{(\omega^2 - \omega_{pe}{}^2)L_n} \right|, \tag{2}$$

where k_i is the incident laser wave number, L_n and L_v are, respectively, the plasma density and flow velocity gradient scale lengths, and v_f is the plasma flow velocity. For a typical temperature of 700 eV,[4] and assuming interaction near one-fourth the critical density, we find that Eq. (1) gives a good fit to the exponential portion of Fig. 1(a) if we take $L = 4$ μm. A density gradient scale length of 30 μm, a velocity gradient scale length of 200 μm, and an initial fluid velocity of one-fourth the sound speed give approximately this value. The comparable number obtained for the $f/1.9$ data, adjusted for specular reflection and laser irradiance at the interaction region, is $L \simeq 2.7$ μm.

The light reflected from the target directly back through the lens is intercepted by a pellicle beam splitter placed near the laser ~34 m from the target. A portion of this light is focused, with a cylindrical lens, onto the slit of a 2-m spectrograph. Time-integrated spectra from a single shot have been recorded using Kodak I-Z plates. Alternately, for time-resolved studies an EPL streak camera ($\tau_r \approx 6$ psec) with an S-1 photocathode is used. The spectrometer is modified by masking the grating to reduce the instrumental temporal dispersion to a near time-bandwidth-limited 20 psec ($\Delta\lambda \simeq 0.8$ Å). Spectra of the backscattered light time integrated over the laser shot showed many characteristics similar

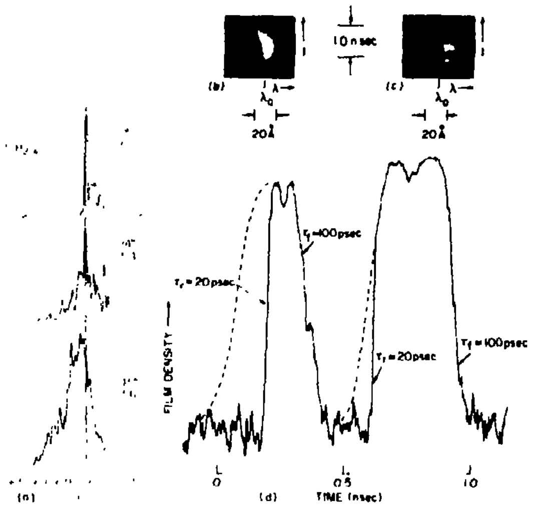

FIG. 2. (a) Shift of backscatter time-integrated spectra towards the red for an increasing angle θ between the target normal and laser direction. Time-resolved backscatter spectra for (b) a copper target, $f/14$ lens, 8.6-J, 900-psec laser pulse with 100 psec temporal resolution, and (c) a deuterated polyethylene target, $f/14$ lens, 16-J, 250-psec laser pulse with 20 psec temporal resolution. (d) Densitometer tracing of (c) along the time axis through the center of the spectrum. Traces have not been corrected for film exposure versus density curve and are saturated at the peaks.

to those obtained by other groups.[2,3,5] Briefly, the spectra were broadened by 10–50 Å with centroids shifted from the incident wavelength (often to the blue) by up to 10 Å. It was found in our experiment, however, that as the target is rotated away from normal incidence to the laser bean the spectrum shifts toward the red. This is shown in Fig. 2(a). The magnitude of these spectral shifts with target angle are numerically consistent with a superimposed Doppler blue shift, due to plasma motion normal to the target surface ($\langle v_f\rangle \simeq 4\times10^7$ cm/sec), and a red shift due to ion acoustic waves propagating into the target ($\Delta f \simeq 7\times10^{11}$ Hz). The time-integrated spectra often shows a linelike structure.

The time-resolved spectra of the backscattered radiation, such as those shown in Figs. 2(b) and 2(c), show that the spectrum may evolve considerably during the laser pulse, and, therefore, correct conclusions based solely upon time-integrated spectra appear fortuitous. The slab geometry target is normal to the incident beam in each case. A small portion of the incident-beam spectrum is monitored and it is usually found to be roughly Gaussian in time and monochromatic to within 1 Å. The backscatter spectra have varying characteristics; however, they share an initial red shift, a time-dependent spread in wavelength, a very fast rise time, and complex structure in time and wavelength. After onset the reflected energy appears distributed for the duration of the laser pulse and exhibits the laser-pulse fall time. A question arises as to why there is no cutoff threshold for instability. Both the velocity and density scale lengths increase with time in the laser-produced plasma and therefore the threshold for Brillouin backscattering would be reduced at the end of the pulse. When the incident beam is time modulated (caused by, for example, self-phase modulation) the back-reflected spectrum is similarly modulated.

There is also a tendency for the centroid of the spectra to shift increasingly to the blue with time. This is especially evident in Fig. 2(b) which exhibits a blue shift linear in time. This blue shift could occur as a result of a constant *acceleration* of the interaction region toward the laser for the duration of the shot. This is consistent with the effect of target rotation upon time-integrated spectra noted earlier. It is likely that the initial spectral red shift is due to a stimulated process such as Brillouin scattering rather than a Doppler shift since the interaction region would not have an initial net velocity away from the laser. The magnitude of the initial red shifts from the incident laser line (2–10 Å) correspond to ion acoustic wave frequencies, i.e., from 2 to 10% of the ion acoustic frequency at the critical surface. With the assumption that the usual dispersion relations for the incident and reflected electromagnetic waves ($\omega_{i,r}^2=\omega_{pe}^2+k_{i,r}^2c^2$) and ion acoustic waves $[\omega_{ia}=(v_s-v_f)k_{ia}]$, and the backscatter matching relations $k_r=-k_i=-\frac{1}{2}k_{ia}$, $\omega_i=\omega_r+\omega_{ia}$, hold in the interaction region, the spectral measurements lead to estimates that the interaction region is between 0.1 and 0.9 of the critical density and is typically near 0.25 of the critical density.[13]

The rapid rise time of the backscattered radiation and the existence of an intensity threshold is demonstrated in Fig. 2(d). Figure 2(d) is a densitometer tracing along the time axis through the center at the spectrum of Fig. 2(c) which shows that the rise time of the backscattering onset, due to both the laser prepulse and main pulse, is less than the resolution of the spectrometer

(~ 20 psec). When the backscattered radiation is streaked directly without going through the spectrometer the rise time still appears instrument limited (~ 6 psec). The dynamic range of the camera and film is sufficient to characterize these rise times. The broad spectrum at the onset of the backscatter spectrum in Fig. 2(c), if a result of a time-bandwidth–limited effect ($\Delta\omega\Delta\tau \simeq \frac{1}{2}\pi$ half width at half-maximum), would correspond to a rise time of about 1 psec. This 1 psec rise time is consistent with the calculated growth rate for Brillouin backscattering of $\gamma \simeq 10^{12}$ sec^{-1} near the threshold power observed of approximately 10^{13} W/cm^2. This threshold value is that predicted by the theory[9] within experimental error. The threshold and intensity of backscattered radiation appears insensitive to the presence of a prepulse for all laser pulse durations used.

Another aspect of the backscattered spectra that is intriguing, but not yet satisfactorily explained, is the occasional appearance of line structure as in Fig. 2(b). These lines are rather closely spaced (~ 2 Å) and may represent multiple Brillouin backscattering. However, it is difficult to satisfy all the matching conditions except very close to the critical surface [(~ 0.96–0.98)n_c].

The bulk of our experimental evidence supports the hypothesis that stimulated Brillouin backscattering is responsible for most of the energy *directly* backscattered. Specular reflection accounts for 5–10% of the incident energy but is reduced in *intensity* with respect to the direct backscattered radiation by a large factor. An expanded study of laser light scattering will be published elsewhere.

The authors are grateful for valuable discussions with J. Holzrichter, R. Shanny, K. Whitney, N. Winsor, E. Ott, H. Griem, R. Pechacek, and D. Forslund and for the expert assistance of J. Cheadle, T. DeRieux, and E. Turbyfill.

---

*Work supported by the U. S. Atomic Energy Commission and the Definse Nuclear Agency.

[1] N. G. Basov *et al.*, Kvantovana Elektron. (Moscow) 5, 63 (1972) [Sov. J. Quantum Electron. 2, 439 (1973)].

[2] J. L. Bobin, M. Decroisette, B. Meyer, and V. Yitel, Phys. Rev. Lett. 30, 594 (1973).

[3] J. F. Holzrichter *et al.*, Bull. Amer. Phys. Soc. 17, 972 (1972); K. Eidmann and R. Sigel, in "Laser Interaction and Related Plasma Phenomena," edited by H. Schwarz and H. Hora (Plenum, New York, to be published), Vol. 3.

[4] J. A. Stamper *et al.*, in "Laser Interaction and Related Plasma Phenomena," edited by H. Schwarz and H. Hora (Plenum, New York, to be published), Vol. 3.

[5] L. M. Goldman, J. Soures, and M. J. Lubin, Phys. Rev. Lett. 31, 1184 (1973).

[6] P. Lee, D. V. Giovanielli, R. P. Godwin, and G. H. McCall, Appl. Phys. Lett. 24, 406 (1974).

[7] J. E. Swain, Bull. Amer. Phys. Soc. 18, 1256 (1973).

[8] D. W. Forslund, J. M. Kindel, and E. L. Lindmann, Phys. Rev. Lett. 30, 739 (1973).

[9] M. N. Rosenbluth, R. B. White, and C. S. Liu, Phys. Rev. Lett. 31, 1190 (1973).

[10] H. H. Klein, W. M. Manheimer, and E. Ott, Phys. Rev. Lett. 31, 1187 (1973).

[11] W. L. Kruer, K. G. Estabrook, and K. H. Sinz, Nucl. Fusion 13, 952 (1973).

[12] B. H. Ripin, to be published.

[13] Interpretation of red shifts from time-integrated spectra as ion acoustic waves might underestimate the ion acoustic wave frequency because of the superimposed blue Doppler shift, and place the calculated interaction region closer to the critical surface than is actually the case.

Fluctuation Conductivity in the Incommensurate Peierls System*

Bruce R. Patton
Department of Physics, Massachusetts Institute of Technology, Cambridge, Massachusetts 02139

and

L. J. Sham
Department of Physics, University of California San Diego, La Jolla, California 92037

(Received 13 May 1974)

The period of the Peierls distortion in a one-dimensional system is assumed to be incommensurate with the lattice. The fluctuation conductivity just above the mean-field transition temperature is calculated in the presence of electron-impurity scatterings. In the clean limit for sufficiently strong electron-phonon interaction, the conductivity is enhanced by fluctuations whose contribution is impurity limited and goes like $(T-T_P)^{-1/2}$ in the leading approximation. In the dirty limit, the conductivity is reduced by fluctuations.

Recent experiments on quasi one-dimensional conductors have excited much interest in the properties of a one-dimensional electron-phonon system which exhibits a Peierls instability.[1] The conductivity behavior of such a system varies drastically depending on its commensurability. If the first reciprocal lattice vector G of the undistorted lattice is commensurate with the Fermi diameter q_0 ($=2k_F$), then the system becomes an insulator below the Peierls transition temperature T_P. The half-filled case ($G=2q_0$) is a special example; its fluctuation conductivity just above T_P is insulatorlike,[2] i.e., the conductivity is depressed. On the other hand, if G is incommensurate with q_0, then the system possesses infinite conductivity at zero temperature.[3] In this case, the fluctuation conductivity is found to be positive and proportional to $(T-T_P)^{-1/2}$ by Allender, Bray, and Bardeen,[4] by means of a phenomenological theory. We report here the results of a microscopic calculation for the incommensurate case.

Random impurities are included to provide finite conductivity in the normal phase, and have two types of effects. The first is to introduce the usual finite lifetime into the single-electron states. The second is to cause a static distortion of the lattice, an effect which is enhanced by the Kohn singularity in one dimension. The importance of this second effect depends on the relative magnitude of the impurity potential and the electron-phonon interaction.

Consider the extreme incommensurate case of an ideal one-dimensional chain of uniformly spaced atoms where the Fermi energy measured from the bottom (or top) of the conduction band is only a small fraction of the bandwidth. The electron-phonon interaction in standard form is

$$H_{ep}=N^{-1/2}\sum_{kq}g(q)c_{k+q}^{\dagger}c_k(b_q+b_{-q}^{\dagger}), \tag{1}$$

where c and b are the electron and phonon operators and N is the number of atoms in the chain. Electron-impurity interaction is included as

$$H_i=N^{-1}\sum_{kql}U_q c_{k+q}^{\dagger}c_k e^{-iqR_l}p_l, \tag{2}$$

where p_l denotes the impurity distribution over the sites R_l. For electrons near the Fermi level in the undistorted chain, the important scatterings are (1) in the forward direction, $q\sim 0$, where U_q is taken as zero since it does not affect the current, and (2) in the backward direction, $q\sim q_0$, where $U_q \simeq U$, a constant.

The impurity scattering is treated in the Born approximation. The self-energy correction of Fig. 1(a) supplies the electron in the uniform chain with a finite lifetime, $\tau = v_F/cU^2$, where v_F is the Fermi speed and c is the impurity concentration. All other self-energy terms within the Born approximation, such as shown in Fig. 1(b), vanish. We could include in the lifetime the effects of the electron scattering by "ordinary" phonons, with wave vectors away from

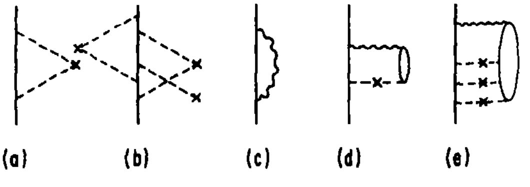

FIG. 1. Electron self-energy terms. Solid lines denote electrons, wavy lines phonons, and dashed lines impurity.

the neighborhood of q_0, i.e., not belonging to those soft phonons just above T_P which constitute the fluctuations.

The self-energy of a phonon with wave vector q close to q_0 is calculated in the mean-field approximation, represented by Fig. 2(a). The electron lines are understood to include self-energy corrections due to impurity scatterings such as shown in Fig. 2(b). Phonon energies, temperature, and the reciprocal electron lifetime $1/\tau$ are all assumed to be much smaller than $\mathcal{E}_F$, the Fermi energy. The extreme incommensurability is used in the sense that the process of an electron excited by the q_0 phonon from the neighborhood of $-k_F$ to k_F is included, but not the process from the neighborhood of k_F to k_F+q_0 which is smaller by a factor of $\max(\omega, 1/\tau, T)/\mathcal{E}_F$. Then, the phonon Green's function is given by

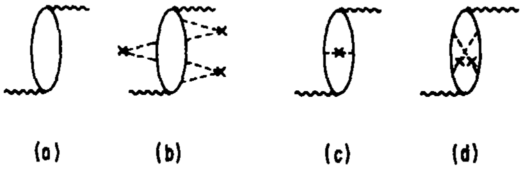

FIG. 2. Phonon self-energy terms.

$$1/D(q_0+p, i\omega_l)=\omega_l^2-\lambda\Omega^2\{\ln(T_{P0}/T)+\Psi(\tfrac{1}{2})-\tfrac{1}{2}\Psi(\tfrac{1}{2}+\alpha[1-i\tau(|\omega_l|+v_Fp)])$$
$$-\tfrac{1}{2}\Psi(\tfrac{1}{2}+\alpha[1-i\tau(|\omega_l|-v_Fp)])\}, \qquad (3)$$

where λ is the usual dimensionless electron-phonon coupling constant, Ω is the unrenormalized phonon frequency at q_0, Ψ is the digamma function, $\alpha=1/4\pi\tau T$ is the electron-hole pair-breaking parameter, and T_{P0} is the transition temperature in the absence of impurities.

From Eq. (3) it follows that the mean-field transition temperature T_P is given by

$$\ln(T_{P0}/T_P)=\Psi(\tfrac{1}{2}+1/4\pi\tau T_P)-\Psi(\tfrac{1}{2}). \qquad (4)$$

Ordinary impurities serve to depress the transition temperature in the same manner as for the excitonic insulator[5] and as magnetic impurities do in superconductors,[6] as has also been noted by Schuster.[7]

For small ω and p, the soft phonon is given by

$$1/D(q_0+p, i\omega_l)=\omega_l^2+\omega_p^2+\Gamma|\omega_l|, \qquad (5)$$

with

$$\omega_p^2=\lambda\Omega^2(\epsilon+\xi^2p^2), \qquad (6)$$

$$\epsilon=\ln(T/T_{P0})+\Psi(\tfrac{1}{2}+\alpha)-\Psi(\tfrac{1}{2}), \qquad (7)$$

$$\xi^2=-\Psi''(\tfrac{1}{2}+\alpha)v_F^2/32\pi^2T^2, \qquad (8)$$

$$\Gamma=\lambda\Omega^2\Psi'(\tfrac{1}{2}+\alpha)/4\pi T. \qquad (9)$$

ϵ is a measure of the temperature difference $t=(T-T_P)/T_P$. For small t, ϵ is proportional to t.

We collect in Table I the limiting values of these quantities in two cases: (1) the clean limit, $T_P \gg 1/\tau$; and (2) the dirty limit $\mathcal{E}_F \gg 1/\tau \gg T_P$, provided that τ does not drop below its critical value $\tau_{cr}=\gamma/\pi T_{P0}$, where T_P vanishes.

We include only those impurity dressings in the phonon self-energy which are consistent with the self-energy diagram of Fig. 1(a). These are

TABLE I. Summary of expressions in the clean and dirty limits. Conductivity is given in units of $e^2/\hbar$ per unit cross-sectional area of a chain with $l=v_F\tau$ and $\zeta=7\zeta(3)/\pi^2$.

	Clean limit ($\alpha \ll 1$)	Dirty limit ($\alpha \gg 1$)
ϵ	t	$t/12\alpha^2$
t_0	$(\zeta\pi^2)^{1/3}/4$	$3(\alpha^4/2)^{1/3}$
ξ	$\zeta^{1/2}v_F/4T$	$l/\sqrt{2}$
Γ	$\lambda\Omega^2\pi/8T$	$\lambda\Omega^2\tau$
σ_1	$-(1-2\zeta\alpha)(1+8\alpha/\lambda)\pi l^2/8\xi t^{1/2}$	$-(1+8\alpha/\lambda)3\sqrt{6}\,l/4\pi t^{1/2}$
σ_2	$(1+4\zeta\alpha)\pi l^2/8\xi t^{1/2}$	$2\sqrt{6}\,l/\pi t^{1/2}$
$\sigma_1+\sigma_2$	$(1-4/3\zeta\lambda)3\zeta^{1/2}l/4t^{1/2}$	$(1-24\alpha/5\lambda)5\sqrt{6}\,l/4\pi t^{1/2}$

either like those of Fig. 2(b) which contribute to Eq. (3) or of Fig. 2(c) which are negligible. Corrections such as in Fig. 2(d), which have not been kept, have been found to be negligible in the clean limit and to modify the dirty-limit results, though not in an essential way.

As in our earlier work,[2] we calculate the fluctuation conductivity in leading powers of $(\epsilon_c/\epsilon)^{1/2}$, where ϵ_c is the Ginzburg critical value[8] (Table I). Interpreted within the one-dimensional model, the specific-heat measurements[9] at 55 K would imply an order of magnitude $\epsilon_c \sim 0.1$, although the transition there may actually be three-dimensional. In the dirty limit, since $l_c \gg 1$, there is no region of interest in which the expansion in $(\epsilon_c/\epsilon)^{1/2}$ is valid. Nevertheless, it indicates the nature of the corrections to the normal-state conductivity. The leading terms of fluctuation conductivity in $(\epsilon_c/\epsilon)^{1/2}$ are given in Fig. 3. Again, impurity dressing of the electron propagator is understood. The current vertex contains the ladder sum of impurity lines. These terms are consistent with the self-energy terms of Figs. 1(a), 1(c), and 1(d).

Figures 3(a) and 3(b) are analogous to the conductivity due to the electron-phonon scattering. However, the soft phonon now is a long-wavelength fluctuation. It has the effect of creating a fluctuating energy gap in the electron band, giving the electron self-energy

$$\Sigma(k, iE_n) = \Delta^2/(iE_n + \mathcal{E}_k + i/2\tau + iv_F c^{1/2}/\xi), \qquad (10)$$

where $\mathcal{E}_k$ is the electron energy measured from the Fermi level and the gap fluctuation is given by[10]

$$\Delta^2 = \pi v_F T/2\xi\epsilon^{1/2}. \qquad (11)$$

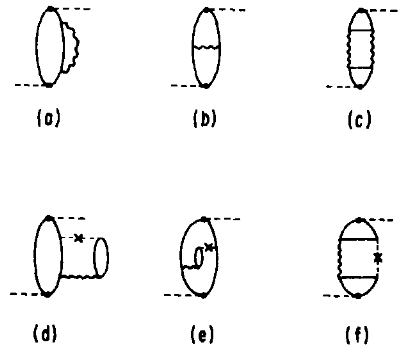

FIG. 3. Fluctuation contributions to conductivity. The circle denotes the current vertex dressed by impurities.

The net effect on the conductivity through the processes in Figs. 3(a) and 3(b) is to make the contribution insulatorlike as in the commensurate case, giving

$$\sigma_1 = -\pi l_1^2/\xi\epsilon^{1/2}, \qquad (12)$$

where

$$l_1 = [\Psi'(\tfrac{1}{2}+\alpha) - \tfrac{1}{2}\alpha\Psi''(\tfrac{1}{2}+\alpha)]^{1/2}\, l/2\pi \qquad (13)$$

and $l = v_F\tau$ is the scattering length.

Figure 3(c) is analogous to the ordinary phonon-drag term. In the half-filled case this term vanishes,[2] while in the extreme incommensurate case it is finite. In the former case, the ground state is doubly degenerate and the low-temperature phase is insulating. In the latter, the ground state is continuously degenerate and a metastable current-carrying state can be constructed.[3] The phonon-drag contribution above T_P corresponds to the collective-mode contribution[11,12] below T_P. Figure 3(c) contributes to the conductivity[13]

$$\sigma_2 = \pi l_2^2/\xi\epsilon^{1/2}, \qquad (14)$$

with

$$l_2^2 = \Lambda^2/2\Psi'(\tfrac{1}{2}+\alpha), \qquad (15)$$

where Λ comes from the triangular vertex, given by

$$\Lambda = [\Psi'(\tfrac{1}{2}+\alpha) - \alpha\Psi''(\tfrac{1}{2}+\alpha)]\, l/\pi. \qquad (16)$$

Figures 3(d) and 3(e) correspond to an impurity-induced lattice distortion which modifies the gap fluctuation (11) to $\Delta^2(1+8\alpha/\lambda)$ and thus increases σ_1 in magnitude. Correction due to the sum of terms such as in Fig. 1(e) is of the same order of magnitude. The impurity phonon-drag term of Fig. 3(f) is analogous to the pinning of the collective mode below T_P. It gives no contribution to the dc conductivity above T_P since there is no phonon-drag current associated with a static impurity.

The total fluctuation conductivity is given by the sum of Eqs. (12) and (14) with σ_1 modified by the factor $(1+8\alpha/\lambda)$. In Table I the limiting values are given. For sufficiently strong electron-phonon interaction, the phonon-drag contribution is larger and the fluctuation conductivity is positive. In all regions the conductivity is impurity limited and proportional to $l^{-1/2}$. In the clean limit the leading term in τ^2 cancels. This cancelation follows from the fact that the coefficients of the τ^2 terms are proportional to the corresponding diagrammatic contributions in the completely pure case where Peierls's theorem[1] implies the infinite conductivity of the free-electron gas.

In the phenomenological theory of Allender, Bray, and Bardeen,[4] the electron is assumed to relax quickly to the running lattice wave. In the absence of impurity scattering, such relaxation could arise from higher-order electron-phonon scattering.[14] In the present calculation, the electron lifetime τ may arise from both impurity scattering and non-q_0 phonon scattering as discussed above. Our expression for the phonon-drag conductivity σ_2 has the same form as the result of Ref. 4 if we identify their ξ_0 with the coherence length ξ in the *dirty limit.*

We wish to thank Professor J. Bardeen and Professor W. Kohn for helpful conversations, and Dr. P. M. Marcus and Dr. P. Seiden for their king hospitality while we were summer visitors at the IBM Research Center at Yorktown Heights where part of this work was done.

---

*Work supported in part by the National Science Foundation under Grant No. 38345.

[1] R. E. Peierls, *Quantum Theory of Solids* (Oxford Univ. Press, Oxford, England, 1953).

[2] B. R. Patton and L. J. Sham, Phys. Rev. Lett. 31, 631 (1973).

[3] H. Fröhlich, Proc. Roy. Soc., London, Ser. A 223, 296 (1954).

[4] D. Allender, J. W. Bray, and J. Bardeen, Phys. Rev. B 9, 119 (1974).

[5] J. Zittartz, Phys. Rev. 164, 575 (1967).

[6] A. A. Abrikosov and L. P. Gorkov, Zh. Eksp. Teor. Fiz. 39, 1781 (1960) [Sov. Phys. JETP 12, 1243 (1961)].

[7] H. Schuster, Solid State Commun. 14, 127 (1974).

[8] V. L. Ginzburg, Fiz. Tverd. Tela 2, 2031 (1960) [Sov. Phys. Solid State 2, 1824 (1960)].

[9] R. A. Craven, M. B. Salamon, G. DePasquali, R. M. Herman, G. Stucky, and A. Schultz, Phys. Rev. Lett. 32, 769 (1974).

[10] Hereafter, T is considered close to T_P and the subscript P is understood in both T and α.

[11] P. A. Lee, T. M. Rice, and P. W. Anderson, to be published.

[12] B. R. Patton and L. J. Sham, to be published.

[13] S. Strässler and G. A. Toombs [Phys. Lett. 46A, 321 (1974)] have claimed that Fig. 3(c) in the absence of impurity scattering gives a result of the same form as Ref. 4. However, the present authors [Phys. Lett. 47A, 133 (1974)] found the result for Fig. 3(c) was infinite, in agreement with the limit of Eq. (14) for $\tau \rightarrow \infty$.

[14] J. Bardeen, private communication.

Observation of Thermal Fluctuations in Superconducting Microbridges

F. J. Rachford and C. Y. Huang
Department of Physics, Case Western Reserve University, Cleveland, Ohio 44106

and

M. Nisenoff and S. Wolf
Naval Research Laboratory, Washington, D. C. 20375

(Received 24 June 1974)

Thermal fluctuations of the type described by Langer and Ambegaokar and by McCumber and Halperin have been observed in superconducting thin-film rings containing microbridge sections. A peak in the fluctuation rate was found near the transition temperature. The temperature dependence of the observed rates is in agreement with the McCumber-Halperin fluctuation-rate equations and the deduced parameters are consistent with the theory.

In the course of a series of experiments investigating the properties of superconducting quantum interference devices operating at microwave frequencies, current-induced steps have been observed in the effective impedance of the tin microbridge sections of our samples which are very similar to the voltage steps found in the dc-current-driven transition to the normal state of one-dimensional tin microbridges and whiskers.[1-3] These steps appear to be caused by the generation of localized centers of Ohmic dissipation in the microbridge sections of our samples. The properties of these steps and their relation to the dc-current observations will be discussed in another publication. Data are presented on thermal-fluctuation effects associated with the production of these steps in a temperature region just below the transition temperature of our films.

The samples used in these experiments were thin superconducting tin films (1000 Å thick) deposited on quartz rods. The narrow constrictions were manually sculptured into the film at one point along the circumference of the ring [see inset (a) of Fig. 1; not to scale]. Most of the detailed data reported here were taken on two rings with rectangular shaped constrictions and nearly uniform cross sections; one constriction was 15 μm wide and 72 μm long (sample I) and the other was 7 μm wide and 40 μm long (sample II). For the temperature range in which the thermally activated generation of phase slip was observed, the widths of the constrictions were of the order of or less than the coherence length, except possibly for the 15-μm-wide constriction at lower temperatures. However, qualitatively similar data have been obtained on samples with constrictions less than 2 μm wide which certainly satisfied the condition that the width of the constriction be less than the coherence length; no significant difference in behavior was observed compared to wider microbridges. Hence, the one-dimensional theoretical requirement of the Langer and Ambegaokar model[4] is probably satisfied.

The superconducting rings were mounted in a TE_{101}-mode microwave cavity in a position of maximum microwave magnetic field and oriented so that the currents were induced circumferentially in the ring and through the microbridge [see inset (a) of Fig. 1]. The cavity was shielded from ambient magnetic fields by two superconducting and three Mumetal shields. The transitions were observed by monitoring the absorption of the sample in the cavity with a standard superheterodyne microwave-detection system with a post-detection bandwidth of 1 MHz.

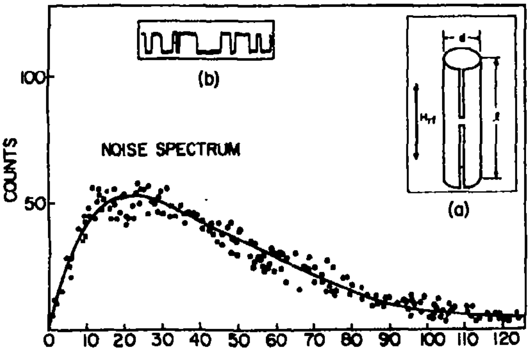

FIG. 1. Typical analyzer spectrum of the time intervals between up switches. The spectrum follows $P(1,t)$ distribution. Inset (a) shows the superconducting thin-film cylinder (diameter $d = 1$ mm, length $l \simeq 1$ cm) with inscribed microbridge (not to scale). The microwave magnetic field is applied axially. Inset (b) shows the switching between impedance levels versus time.

In accordance with the model of Langer and Ambegaokar at temperatures close to the transition, thermal-fluctuation–assisted flux passages will be occurring at points along the microbridge. It is assumed that the inhomogeneties of the sample are small and that the thermally assisted transitions occur randomly along the length of the microbridge. These thermally assisted flux passages cause changes in the current level in the superconducting ring which are superimposed on the induced microwave-frequency current.

The generation of a step in the bridge impedance appears to be associated with the appearance in the microbridge of a localized current-driven dissipative center of the type discussed by Skocpol, Beasley, and Tinkham.[3] If we bias the microwave current amplitude to the onset region for the generation of a step at temperatures just below T_c and view the microwave absorption signal with a high bandpass we will see the step appear and disappear as the fluctuations cause the total current in the microbridge section to exceed and fall short of the current limits required for the creation and disappearance of the step. This extra dissipation will therefore appear and disappear at a rate determined by the rate at which thermal fluctuations occur along the length of the microbridge [see inset (b) of Fig. 1]. Therefore the steps in the effective impedance of our samples monitor the rate of thermal-fluctuation-generated flux passages occurring in the samples.

Inset (b) of Fig. 1 shows a typical time dependence of the microwave dissipation of a sample. The increment in effective impedance of the microbridge and, hence, the dissipation of the sample appears to switch on and off (up and down) in a manner suggesting a "random telegraph" wave. To verify that the observed switching rates were indeed random the spectrum of time intervals between successive "up" switches was obtained at fixed temperature by utilizing a simple logic circuit and a multichannel analyzer. If the switching process is indeed a random phenomenon then it is expected that the spectrum of time intervals accumulated on the multichannel analyzer will follow the Poisson distribution $P(1,t) = rt\exp(-rt)$ where r is the average jumping attempt rate and t is the time interval between two successive "up"

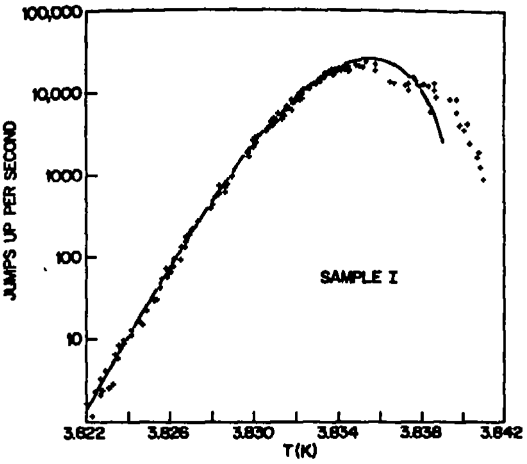

FIG. 2. Average switching rate data versus temperature (crosses) as fitted by Eq. (1) (solid line).

TABLE I. The experimental values of the mean free-energy parameters $F_{\rm exp}'$ (units mK$^{-3/2}$), the free-energy parameters per microbridge cross section $F_{\rm exp}'/\sigma$ (units 10^8 mK$^{-3/2}$/cm^2), and the experimental and calculated values of the prefactor parameters Ω' (units sec^{-1} mK$^{-9/4}$) for sample I (steps 1 and 3) (Ref. 7) and sample II (step 2).

Sample	$F_{\rm exp}'$	$F_{\rm exp}'/\sigma$	$\Omega_{\rm exp}'$	$\Omega_{\rm cal}$
I 1st step	0.206	0.14 ± 0.03	1.18×10^4	1.4×10^4
I 3rd step	0.271	0.18 ± 0.03	2.05×10^4	1.9×10^4
II 2nd step	0.086	0.12 ± 0.03	1.68×10^2	4.3×10^3

transitions. A typical spectrum is shown in Fig. 1. All the spectra were found to fit the $P(1,t)$ law very well.

To study the temperature evolution of the average switching rates over the widest frequency range, the 1-MHz output of the detection system was connected to conventional counting circuits. The switching data were taken by adjusting the microwave bias level at step onset so that the times spent in each impedance state were equal.[4] The switching rate was found to peak just below T_c (see Fig. 2). The peak rates obtained vary from sample to sample and are well within the detection bandwidth of our electronics. We have traced switching rates over as many as seven decades and found these temperature-dependent rates to be reproducible over many hours of an individual run.

According to the Langer and Ambegaokar (LA) theory[5] as modified by McCumber and Halperin (MH),[6] the rate Γ of thermally assisted phase slips occurring in a long [length $\gg \xi(T)$] microbridge section is given by an equation of the form

$$\Gamma = \Omega'(T_c - T)^{9/4}\exp[-F'(T_c - T)^{3/2}], \qquad (1)$$

where the rate prefactor parameter $\Omega'(I/I_c)$ and the normalized mean-field free-energy parameter $F'(I/I_c)$ are dependent on the ratio of the current flowing through the sample during the measurement to the critical current at which the entire sample goes normal, I/I_c (the equations which determine the current dependence of Ω' and F' are cited in Ref. 7). It is assumed that the microwave current amplitude at which a step toward the normal state occurs scales with the critical current I_c and so the rate data are assumed to be taken at an effectively constant I/I_c ratio. With this assumption Eq. (1) was used to fit our switching-rate versus temperature data and to find the constants $\Omega_{\rm exp}'$ and $F_{\rm exp}'$. Very close fits to the data could be obtained (see the solid line in Fig. 2). At the lower-temperature end of the plot the average switching rates increase exponentially in agreement with the Boltzmann exponential factor in Eq. (1). At higher temperatures the fluctuation rate levels off, peaks, and starts to decrease at temperatures within a few millidegrees of T_c. Equation (1) is expected to fail as the temperature approaches within a few millidegrees of T_c; the fluctuation rate, however, should continue to decrease as is indicated by the data.

In Table I we list the parameters $F_{\rm exp}'$ and $\Omega_{\rm exp}'$ derived from fitting the data from two samples by Eq. (1). For sample I data were accumulated by biasing the microwave power to the onset of two different steps (first and third).[8] In this analysis F' is a mean-field free-energy factor and is assumed to be proportional to the sample cross section σ. In Table I we list the ratio F'/σ and find that it is constant within our experimental error limits. The values of $F_{\rm exp}'$ have been used to calculate the prefactor $\Omega_{\rm cal}'(I/I_c)$, with the AL-MH expressions for the transition rate in a current-carrying microbridge. Comparing the measured prefactors to the calculated prefactors, we find that the agreement is quite good for sample I but there is an order-of-magnitude discrepancy for sample II. The rate prefactors are quite sensitive to the current through the sample; the zero-current values of $\Omega_{\rm cal}'(0)$ calculated from the measured cross section and critical temperatures of the microbridges and the bulk critical fields are 10^5 to 10^6 times greater than the measured current-biased values. Therefore, the overall agreement between the experiment and the AL-MH theory is quite encouraging as the experiment was done at microwave frequencies while the theory was derived assuming a dc current flowing through the microbridge.

In summary the creation and collapse of localized dissipative centers in tin microbridges has been used to monitor the thermally activated motion of magnetic flux into and out of the superconducting ring. The observed switching rates are in good agreement with the theory of McCumber and Halperin. The rates were found to follow an exponential dependence in the lower-temperature region, and then with increasing temperatures the rate was found to peak and finally decrease as the temperature approached the transition temperature of the film. *This is the first experimental observation of the peaking predicted by* he model of McCumber and Halperin. The numerical values deduced for the free-energy barrier and the transition rate scale with microbridge cross-sectional area and are in reasonable agreement with the values prediced by McCumber and Halperin.

We would like to thank Professor M. Tinkham for sending us several preprints and Professor Beasley and Dr. W. J. Skocpol for stimulating discussions of their work. We would also like to hank Professor H. Fink for his preprints and helpful discussions.

---

[1] W. W. Webb and R. J. Warburton, Phys. Rev. Lett. 20, 461 (1968).

[2] J. Meyer and G. V. Minnegerode, Phys. Lett. 38A, 529 (1972), and in *Proceedings of the Thirteenth International Conference on Low Temperature Physics, Boulder, Colorado, 1972*, edited by W. J. O'Sullivan, K. D. Timmerhaus, and E. F. Hammel (Plenum, New York, 1973).

[3] W. J. Skocpol, M. R. Beasley, and M. Tinkham, to be published.

[4] The amplitude of the microwave current bias (or the square root of the power) in the sample under these conditions varied with temperature as $(T_c-T)^{3/2}$. This temperature dependence is the same as the observed mean-field critical-current variation in our samples and thus the ratio of bias current to effective critical current was constant. Therefore $\Omega'(I/I_c)$ and $F'(I/I_c)$ as given in Eq. (1) were measured at a constant value of the ratio I/I_c. A further discussion of this point will appear in a later publication.

[5] J. S. Langer and V. Ambegaokar, Phys. Rev. 164, 498 (1967).

[6] D. E. McCumber and B. I. Halperin, Phys. Rev. B 1, 1057 (1970).

[7] The equation for the rate prefactor Ω' in the presence of a current is given by Eqs. (2.8), (3.38), and (4.36) of Ref. 6 and the free-energy parameter F' is derived from Eqs. (3.25) and (3.13) of Ref. 5.

[8] The "first step" refers to the increment in the sample dissipation encountered at lowest microwave input power; the "second," "third," "fourth," etc. steps refer to subsequent steps encountered in this sequence as the microwave power is increased. A detailed discussion of the properties of these steps will be discussed in another publication.

Temperature-Modulated Reflectance of Gold from 6 to 35 eV

C. G. Olson, M. Piacentini,* and D. W. Lynch
Ames Laboratory USAEC and Department of Physics, Iowa State University, Ames, Iowa 50010

(Received 13 June 1974)

The thermoreflectance spectrum of gold has been measured in the 6–35-eV region at about 200 K by using synchrotron radiation. Considerable sharp structure exists throughout this region, showing that lifetime broadening is not large enough to preclude the extension of high-resolution modulation techniques to at least 35 eV. The structure arises from interband transitions of the *5d* electrons and from plasmons.

The contributions of modulation spectroscopy to the understanding of the band structure of solds have proven to be fundamental. This technique is the only one capable of displaying contributions to the optical spectra arising only from ocalized regions in the Brillouin zone, such as critical points in the band structure.[1,2] Until now, modulation spectroscopy, with few exceptions,[3,4] has been limited to the spectral region from the infrared to about 10 eV, for lack of suitable radiation sources. Recently, intense synchrotron radiation from the extremely stable beam in the storage ring Tantalus 1, operated by the Physical Sciences Laboratory of the University of Wisconsin,[5] has made high-sensitivity modulation measurements possible. The thermomodulation spectrum of gold reported in this Letter is the first spectrum above 10 eV resulting from the application of an external modulating field to a sample. The spectrum shows a great deal of structure, some of which is remarkably sharp. It has been necessary to use a spectral bandpass of less than 100 meV at 25 eV to reveal the details. This spectrum demonstrates that the high resolution possible with modulation spectroscopy will be valuable for probing the band structure of materials for away from the Fermi level.

The samples were 400-Å gold films evaporated on quartz or sapphire substrates. They were self-heated with a unipolar 1.6-Hz square-wave current supplying 3.75 W peak power. Other frequencies and heating powers were used with the spectra scaling predictably. The optical system was basically that reported earlier,[6] the principal change being a smaller, simpler sample chamber. The chamber had a liquid-nitrogen cold finger and was ion pumped to a base pressure of less than 10^{-8} Torr to avoid condensation on the sample. The avarage sample temperature was about 200 K and the modulation was 0.2–0.5 K. Radiation was incident on the sample at 30° with primarily p polarization. In the 6 to 25 eV range a conventional sodium salycilate photomultiplier combination was used. From 12 to 35 eV an EMI model 9603/2B electron multiplier provided a great increase in sensitivity along with the rejection of long-wavelength stray light. The dc signal (proportional to the reflectivity R) was monitored with an electrometer while the ac signal (proportional to the change in reflectivity ΔR) was detected by a lock-in amplifier. To provide long integration times the lock-in was used with a short time constant and the output was fed to a voltage-to-frequency converter and counted for 60 to 120 sec. The noise limit in $\Delta R/R$ was photon shot noise and varied from 5×10^{-6} at the peak of the monochromator output to 5×10^{-5} at the highest energies. The sample-to-sample variations in the thermoreflectance spectrum were very small and appeared as magnitude effects with no change in structure.

Figure 1 shows the thermoreflectance spectrum of gold as a function of energy E from 6 to 35 eV, as well as our measured reflectivity, dR/dE, and d^2R/dE^2. The most striking feature of Fig. 1 is the very rich structure in the thermoreflectance spectrum up to 35 eV. This result contrasts with a widespread feeling that broadening at higher energies due to shorter lifetimes of the excited states would tend to wash out any structure and make modulation spectroscopy unimportant at higher energies.

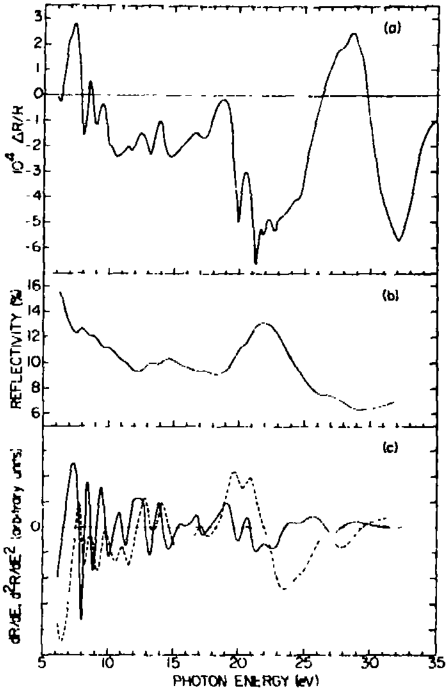

FIG. 1. (a) Thermoreflectance of Au at 200 K, 30°, p polarization. (b) Reflectivity of Au at 30°, p polarization. (c) First derivative dR/dE (dashed line) and second derivative d^2R/dE^2 (full line) calculated from the reflectivity shown in (b).

Our thermoreflectance spectrum reproduces the data of Scouler[7] very well from 6 to 10 eV. The interpretation of this portion of the spectrum has been carried out by Christensen and Seraphin,[8] who found good agreement between the energies at which the modulated reflectance of gold shows structure and the energies they have calculated for critical-point transitions. There has been no detailed interpretation, however, of the optical properties of gold above 10 eV although the optical constants are well known.[9-11]

Structure in the 10–35-eV thermoreflectance cannot be due either to transitions involving core states, since the highest core level in gold lies about 54 eV below the Fermi level,[12] or to transitions terminating at the Fermi level, which lies 9.5 eV above the bottom of the conduction band.[8] Thus all the structure in $\Delta R/R$ will arise from interband transitions originating in the 5*d* bands or at the Fermi level, or from plasmons. There are two plasmonlike peaks in $\mathrm{Im}(-1/\tilde{\epsilon})$ for Au at 25.8 and 32.6 eV.[11,13] Each of these should yield a characteristic structure in $\Delta R/R$.[14] The beginning of the structure below 25 eV is obscured by structure due to interband transitions, but the positive peak at 28.5 eV and the negative peaks at 32 eV are of the expected shape and at the expected positions. Band shifts upon thermal expansion cause modulation spectra resembling dR/dE. Interband transitions are broadened by phonon scattering, the temperature dependence of which gives rise to a thermoreflectivity spectrum resembling d^2R/dE^2. Thermal broadening of the Fermi function can also give spectra resembling d^2R/dE^2, but transitions originating on the Fermi surface should contribute little to the thermoreflectivity above 10 eV, since no regions of high joint density of states are cut by the Fermi level. Given the general agreement of $\Delta R/R$ and d^2R/dE^2, between 10 and 25 eV, thermal broadening is the principal cause of the thermomodulation. Then the energies of the negative peaks in $\Delta R/R$ should correspond roughly to critical-point thresholds in the joint density of states[15] for transitions originating in the 5*d* bands and the lower part of the 6*s* band.

In Table I we have correlated structures in the thermoreflectance with critical points at Γ, K, and W and along Q which can be identified in the bands calculated by Connolly and Johnson.[16] Several critical points are almost degenerate in energy and overlap to give broader structures. At this stage, it is not possible to discriminate between them. Note, however, that the structures in the 10–18 eV region are relatively weak and broad. Some of the transitions appear as multiplets, having the same final state but originating in different *d* bands. A small shift of the energy of the final state brings the theoretical values of the transition energies into closer agreement with the experimental values for the entire multiplet, as shown in the fourth column of Table I. Above 18 eV there are five strong, sharp structures. Structure is expected from the M_0 critical-point transitions $\Gamma_{8+} \to \Gamma_{7-}$, $\Gamma_{7+} \to \Gamma_{7-}$, and $\Gamma_{8+} \to \Gamma_{7-}$, but only two peaks are at the calculated positions. If the energy of the Γ_{7-} final state is increased 1.3 eV the predicted transitions occur at 20.1, 21.2, and 22.5 eV, in close agreement with the sharp structures at 19.9, 21.2, and 22.6 eV.[17]

TABLE I. Structure in the thermoreflectance spectrum of Au and its assignment to critical-point transitions identified from the calculated bands of Ref. 16 at some symmetry points and directions in the Brillouin zone. The suffix labeling the states corresponds to the number of the band counted from the lowest band. By applying shifts of 0.2, 0.3, and 1.3 eV to final states Q_7, W_9, and Γ_{7-}, respectively, the calculated positions in the third column have been obtained.

ASSIGNMENT	ENERGIES (eV) THEORETICAL	SHIFTED THEORETICAL	EXPERIMENTAL
$Q_2 \to Q_7$	8.7	8.9	9.0
$K_4 \to K_7$	8.9		
$K_3 \to K_7$	9.7		10.0
$K_4 \to K_8$	10.4		10.6
$Q_1 \to Q_7$	10.4	10.6	
$W_5 \to W_9$	11.4	11.7	11.7
$W_2 \to W_7$	11.7		
$W_4 \to W_9$	12.8	13.1	13.2
$W_2 \to W_8$	13.2		
$K_2 \to K_8$	13.3		
$W_3 \to W_9$	14.4	14.7	14.7
$\Gamma_{8+} \to \Gamma_{7-}$	18.8	20.1	19.9
$\Gamma_{7+} \to \Gamma_{7-}$	19.9	21.2	21.2
$\Gamma_{8+} \to \Gamma_{7-}$	21.2	22.5	22.7
-	-	-	17.3
-	-	-	21.8
-	-	-	24.4

The fact that there is a pronounced peak in the reflectivity between 18 and 27 eV indicates that considerable oscillator strength is concentrated in this region. (See the ϵ_2 sum rule plot in Fig. 4 of Ref. 11.) The 5*f* levels in Au contribute to the conduction bands at about 20 eV above E_F.[16] Actually, the states near Γ_{7-} are mostly of *f* type. Transitions from *d* to *f* states generally have large oscillator strengths, so that the M_0 critical-point transitions we assigned above are expected to be strong, and may account for the large strength of the 18–23 eV peak in ϵ_2.[11] The presence of the "5*f* bands" may explain some of the anomalies observed in ultraviolet photoemission.[18]

We have shown that modulation spectroscopy can be extended with the necessary high resolution up to at least 35 eV. Available band-structure calculations, based on Fermi-surface and ultraviolet-photoemission-spectroscopy measurements, give good results for the filled parts of the conduction bands and account for the lower-energy interband absorption, but they do not explain satisfactorily all of our higher-energy data. The thermoreflectance spectrum presented in this Letter provides a great amount of new information, mostly concerning final states far above the Fermi level, information which is necessary for future improved calculations of highly excited states. We also suggest that evaluation of some dipole matrix elements would enable a better understanding of the optical and ultraviolet photoelectron spectra.

The storage ring is supported by the U. S. Air Force Office of Scientific Research under Contract No. F44620-70-0029. The cooperation of the storage ring staff is appreciated.

---

*On leave from the Istituto di Fisica "G. Marconi," Università degli Studi di Roma, Rome, Italy; and Fellow of the Italian National Research Council.

[1] M. Cardona, *Modulation Spectroscopy* (Academic, New York, 1969).

[2] Surface Sci. 37 (1973).

[3] R. H. Willens, H. Schreiber, E. Buehler, and D. Brasen, Phys. Rev. Lett. 23, 413 (1969); R. H. Willens and D. Brasen, Phys. Rev. B 5, 1891 (1972).

[4] W. Zierau, in *Proceedings of the International Symposium for Synchrotron Radiation Users, Daresbury, England, 1973*, edited by G. V. Marr and I. H. Munro (Daresbury Nuclear Physics Laboratory, Daresbury, England, 1973).

[5] E. M. Rowe and F. E. Mills, Particle Accel. 4, 211 (1973).

[6] C. G. Olson and D. W. Lynch, Phys. Rev. B 9, 3159 (1974).

[7] W. J. Scouler, Phys. Rev. Lett. 18, 445 (1967).

[8] N. E. Christensen and B. O. Seraphin, Phys. Rev. B 4, 3321 (1971).

[9] W. C. Walker, O. P. Rustgi, and A. L. Weissler, J. Opt. Soc. Amer. 69, 471 (1959).

[10] L. R. Canfield, G. Hass, and W. R. Hunter, J. Phys. (Paris) 25, 124 (1964).

[11] B. R. Cooper, H. Ehrenreich, and H. R. Philipp, Phys. Rev. 138, A494 (1965).

[12] J. A. Bearden and A. F. Burr, Rev. Mod. Phys. 39, 125 (1967).

[13] J. L. Robins, Proc. Phys. Soc., London 78, 1177 (1961); M. Creuzburg, Z. Phys. 196, 433 (1966).

[14] Ref. 1, pp. 120–121.

[15] R. Rosei and D. W. Lynch, Phys. Rev. B 5, 3883 (1972).

[16] J. W. D. Connolly and K. H. Johnson, Massachusetts Institute of Technology Solid State and Molecular Theory Group Report No. 72, 1970 (unpublished), p. 19.

[17] The splitting of the levels at Γ of the $5d$ bands as calculated by N. V. Smith, Phys. Rev. B 9, 1365 (1974), agrees with the experimental splittings within the instrumental bandpass (0.1 eV). We have chosen, however, to use the bands of Connolly and Johnson (Ref. 16) because they extend to higher energies. [The calculation of Christensen and Seraphin (Ref. 8) does not include as many bands through Γ near 1.8–2.0 Ry.]

[18] J. Freeouf, M. Erbudak, and D. E. Eastman, Solid State Commun. 13, 771 (1973).

Stability of Electron-Hole Drops in Germanium under Uniaxial Stress

T. Ohyama, T. Sanada, and E. Otsuka
Department of Physics, College of General Education, Osaka University, Toyonaka, Osaka 560, Japan

(Received 28 May 1974)

The cohesive energy of the electron-hole drop in germanium at 1.5 K is determined as a function of uniaxial stress, both along $\langle 100\rangle$ and along $\langle 111\rangle$ directions, by the method of cyclotron-resonance monitoring at 35 GHz. On application of stress, it starts decreasing from the value of 14.5 K at zero stress, but has an air of persisting to have a finite value at a considerably high-stress region.

At low temperatures, condensation of excitons into electron-hole drops occurs in germanium.[1] The ground-state energy, or cohesive energy, of such a condensed system has recently been studied by Combescot and Nozières,[2] Brinkman and Rice,[3] and Vashishta, Bhattacharyya, and Singwi.[4] Their results all show that the complexity of the actual band structure in germanium is favorable for a stable drop formation. It would be of interest, accordingly, to modify the band structure by applying a uniaxial compressive stress which lifts the degeneracies of the conduction and valence bands in this material.

Watching the microwave photoconductance under the condition of cyclotron resonance is one of the most direct methods of detecting the appearance of electron-hole drops. Relevant measurements under uniaxial stress were carried out with the help of a 35-GHz microwave spectrometer and time-resolving technique at 1.5 K. Electron-hole pairs were generated by a Q-switched yttrium aluminum garnet laser (Coherent Radiation Model No. 60) at the repetition rate of 25 Hz. For deliberate stress application, we used pillar-shaped ultrahigh-purity germanium crystals with square cross section and with the long axis being either along $\langle 111\rangle$ or along $\langle 100\rangle$. The typical size was $1.5\times 1.5\times 3.0$ mm^3. Special care was taken to avoid inhomogeneity in the applied stress by making the opposite faces of the pillar as parallel as possible.

As previously reported by Hensel, Phillips, and Rice,[5] a long-tailed photoconductivity signal appears above a threshold pumping power. This signal has its origin in electrons emitted through internal decay of drops or through collision between excitons. On application of stress, the signal starts decreasing. For compression along $\langle 111\rangle$, in particular, it falls rather suddenly in the vicinity of 350 kg/cm^2. On the other hand, it decays only gradually for $\langle 100\rangle$ stress. It is further observed that the cyclotron-resonance absorption intensity taken at a fixed delay time after photoexcitation, say at 15 μsec, decreases almost to zero with increasing stress along $\langle 111\rangle$ direction.

Writing n_e and n_{ex} for electron and exciton densities outside the drops, respectively, and n_d for the average number of electron-hole pairs in a drop, we have the following coupled differential equations involving the work function φ:

$$\dot{n}_d = -n_d/\tau_0 - aT^2 n_d^{2/3}\exp(-\varphi/kT) + bn_d^{2/3}n_{ex}, \tag{1}$$

$$\dot{n}_{ex} = aNT^2 n_d^{2/3}\exp(-\varphi/kT) - n_{ex}/\tau_{ex} - bNn_d^{2/3}n_{ex} + \alpha n_e^2, \tag{2}$$

and

$$\dot{n}_e = Nn_d/\tau_A + n_{ex}/\tau_{ex} - \alpha n_e^2. \tag{3}$$

In Eq. (1), τ_0 is the electron-hole recombination time within a drop which includes both radiative and Auger processes. We designate the probability for the latter by $1/\tau_A$. The coefficient a is determined from the well-known formula for thermionic emission while b represents the backflow coefficient for excitons. As for Eq. (2), τ_{ex} is the decay time for free excitons, N the density of drops, and α the capture coefficient for the electron-hole pair formation. The decay rate $1/\tau_{ex}$ for free excitons includes both radiative recombination and decomposition; namely, $1/\tau_{ex} = 1/\tau_{ex}^R + 1/\tau_{ex}^D$. The same appearing in Eq. (3) should actually reflect only decomposition. Information from the luminescence experiments, however, tells us that $1/\tau_{ex}^R \ll 1/\tau_{ex}^D \sim 1/\tau_{ex}$.[1] Hence we have employed the common notation with that in Eq. (2). The effect of electron trapping by neutral impurities will have to be incorporated in Eq. (3) when the carrier concentration becomes low. In the environment of a high carrier density, $\gtrsim 10^{12}$ cm^{-3}, right after photoexcitation, however, the dominant decay process for carriers should definitely be pair formation.[6] Judging from the decay profile of the cyclotron-resonance signals, we find that this situation does not seem to change essentially, at least for the time interval taken in the presentation here. Accordingly, the trapping effect by neutral impurities will not be considered here.

In the case of the backflow being negligibly small, Eq. (1) can be solved for n_d, yielding

$$n_d = [(n_{d0}^{1/3} + \tau_0 B)\exp(-t/3\tau_0) - \tau_0 B]^3, \tag{4}$$

with

$$B = aT^2\exp(-\varphi/kT).$$

When the average size of a drop is large and both excitons and carriers outside decay rapidly in comparison with the drops, the third and fourth terms on the right-hand side of Eq. (2) can be neglected. The electron density n_e is then approximated, with the help of Eqs. (2) and (3), by

$$n_e = (N/\alpha)^{1/2}(n_d/\tau_A + Bn_d^{2/3})^{1/2}, \tag{5}$$

or, with use of the initial values of n_e and n_d,

$$\frac{n_e}{n_{e0}} = \left(\frac{n_d/\tau_A + Bn_d^{2/3}}{n_{d0}/\tau_A + Bn_{d0}^{2/3}}\right)^{1/2}. \tag{6}$$

After disappearance of drops, n_e is given by

$$n_e = n_c/[n_c\alpha(t - t_c) + 1], \tag{7}$$

where t_c is the cutoff time at which the drops have practically disappeared and n_c is the electron density at that time. In Fig. 1, the effective n_e/n_{e0} in terms of the cyclotron-resonance absorption intensity is plotted against t. The broken lines are after Eqs. (6) and (7). From the initial slope at zero stress, one finds that $\tau_0 = 65\pm 5$ μsec.

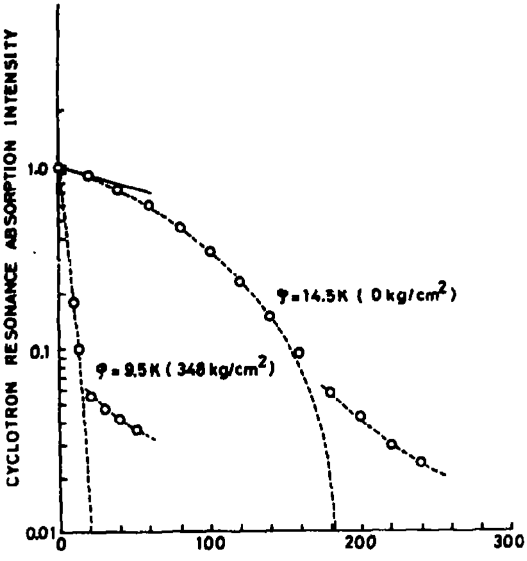

FIG. 1. Relative carrier density at 1.5 K determined by means of the cyclotron-resonance absorption intensity plotted against the time after photoexcitation, both for zero and finite (348 kg/cm²) uniaxial stress along ⟨111⟩. Calculation is made in two approximations, (6) and (7) in the text. The work function φ is one of the fitting parameters and is indicated for the two cases. Solid line, initial slope at zero stress.

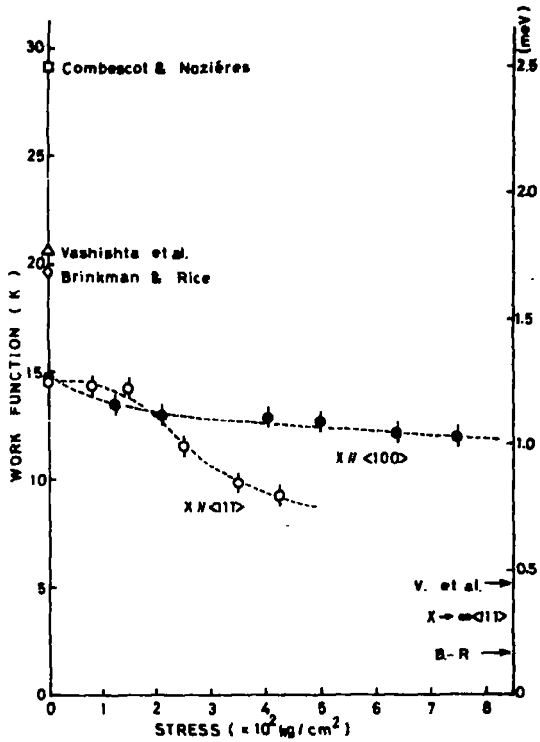

FIG. 2. Work function determined through the manner described in the text plotted against stress for two directions. For comparison, some available theoretical results are also indicated.

This value of τ_0 is in essential agreement with the one reported earlier, i.e., 67 ± 5 μsec, obtained from a far-infrared measurement.[7] Using the quantum efficiency of the condensed-phase radiation,[1] one can estimate A to be about 325 μsec. It has been so chosen that $n_{s0} = 2.2 \times 10^5$ and $\varphi = 14.5 \pm 0.5$ K by making a fit with experimental observation at zero stress. The appropriateness of n_{s0} is hard to ascertain since a variety of drop sizes exist; the value of φ is again in agreement with that obtained in the far-infrared experiment.[7] For each finite stress, the work function is determined by a similar fitting and the result is shown in Fig. 2. Theoretical predictions for the work function by different groups are also shown in the same figure. One finds that our work function, having the value of 14.5 K at zero stress, starts falling rather abruptly near the stress of 200 kg/cm², down to the value of ~10 K at 300 kg/cm², and still continues gradually falling for increasing ⟨111⟩ stress; whereas for ⟨100⟩ stress it shows a very slight monotonic decrease down to ~12 K at 800 kg/cm². It is a challenging question whether a drop is stable or not in the high-stress limit. Brinkman and Rice and Vashishta, Bhattacharyya, and Singwi have obtained small finite binding energies for the metallic phase even in the high-stress limit while Combescot and Nozières predict an eventual disappearance of the drops. From our experimental result, it is surmised that a finite binding energy persists under a considerably large stress, not only for ⟨100⟩ but also for ⟨111⟩ direction.

As for the absolute magnitude of the work function, confining the argument within zero stress, we find that the spectroscopically determined ones are generally larger than those thermodynamically derived including the one presented here. Perhaps the discrepancy has a physical origin; namely, the thermodynamical one reflects the surface structure of a drop, while the spectroscopic one reflects a bulk effect. It has been calculated[8-10] that the "surface energy" is ~1 ×10^{-4} erg cm^{-2} and that the "surface region" extends over a scale of ~50 Å. The average energy of an electron-hole pair in the surface region should then be higher than that in the deeper region of the drop by ~0.7 meV. Such an excess in energy may account for the above mentioned discrepancy between the values determined by different experimental methods.

---

[1] Ya. Pokrovskii, Phys. Status Solidi (a) 11, 385 (1972).

[2] M. Combescot and P. Nozières, J. Phys. C: Proc. Phys. Soc., London 5, 2369 (1972).

[3] W. F. Brinkman and T. M. Rice, Phys. Rev. B 7, 1508 (1973).

[4] P. Vashishta, P. Bhattacharyya, and K. S. Singwi, Phys. Rev. Lett. 30, 1248 (1973).

[5] J. C. Hensel, T. G. Phillips, and T. M. Rice, Phys. Rev. Lett. 30, 227 (1973).

[6] M. Lax, Phys. Rev. 119, 1502 (1960).

[7] K. Fujii and E. Otsuka, Solid State Commun. 14, 763 (1974).

[8] L. M. Sander, H. B. Shore, and L. J. Sham, Phys. Rev. Lett. 31, 533 (1973).

[9] H. Buttner and E. Gerlach, J. Phys. C: Proc. Phys. Soc., London 6, L433 (1973).

[10] T. L. Reinecke and S. C. Ying, Solid State Commun. 14, 381 (1974).

Resonant Scattering of Electrons in Mercury Telluride

W. Walukiewicz
Institute of Physics, Polish Academy of Sciences, Warsaw, Poland

(Received 13 June 1974)

Resonant scattering of electrons on optical phonons in inverted band structure is considered. It is proved that in intrinsic samples transition of the electrons from the conduction band to the valence band with simultaneous emission of optical phonons can cause a minimum of the conductivity. Such a scattering process explains the anomalous behavior of conductivity versus temperature in mercury telluride in the 30–50 K range.

Mercury telluride belongs to the class of symmetry-induced zero-gap semiconductors. In such semiconductors a minimum of the conduction band and a maximum of the valence band are degenerate at the Γ point. Wave functions of the conduction and valence bands are mainly of the p type, similar to the wave functions of the valence band in an uninverted band structure.

The results of measurements of galvanomagnetic phenomena in HgTe pointed out that in the temperature dependence of conductivity two kinds of anomalies are observed.[1-3] A high-temperature anomaly was observed in the range 30–50 K. In the same range of temperatures a weak anomaly of the Hall constant is reported.[1,2] The existing interpretations of this anomaly are based on a hypothesis of resonant acceptor states, degenerate with the conduction band. In this Letter a new explanation of the anomalous behavior of conductivity is proposed. I suggest that resonant scattering of electrons by optical phonons can cause nonmonotonic behavior of the conductivity as a function of temperature. It is obvious that in intrinsic samples of HgTe there are unoccupied electron states in the valence band. These states are concentrated at the top of this band (see Fig. 1). Thus transitions from conduction to valence band with simultaneous emission of the longitudinal optical phonon are possible. This means that when $\epsilon_m + \hbar\omega_0 = \epsilon_F$, where ϵ_m is

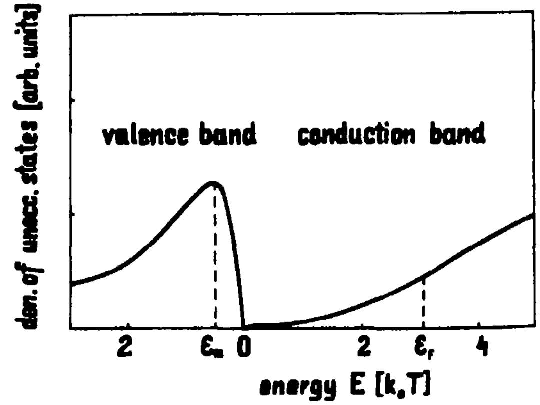

FIG. 1. Density of unoccupied electron states as a function of the energy in a semiconductor with an inverted band structure. ϵ_F is the energy of Fermi level.

the energy corresponding to the maximum density of unoccupied states in the valence band (see Fig. 1) then, because of the type of scattering considered, there is a conductivity minimum.

The calculation of the conductivity was based on some assumptions: (1) I have assumed that both conduction and valence bands are spherical and parabolic with the effective masses m_c and m_v, respectively,

$$\epsilon_c = \hbar^2k^2/2m_c, \quad \epsilon_v = -(\hbar^2k^2/2m_v).$$

In the range of the electron energy considered this assumption seems to be a good approximation. (2) Because of the high effective mass of holes, their influence on conductivity was omitted. (3) In partially ionic crystals the electron-optical-phonon interaction is realized in two different ways. Electrons may be coupled to the longitudinal optical phonons by means of polarization associated with the motion of the ions. This type of interaction is called polar optical (PO). On the other hand, electrons can interact with optical phonons through the optical deformation potential. This interaction is denoted by NPO. In these calculations it is assumed that it is possible to define NPO scattering by means of a deformation potential constant E_{NPO}.[4]

In the presence of electric field E along the x axis the Boltzmann equation takes the form

$$-\frac{\hbar k_x}{m_c}\left(\frac{\partial f_0}{\partial\epsilon}\right)eE = \left(\frac{\partial f}{\partial t}\right)_{\mathrm{coll}}, \tag{1}$$

where $f_0 = \{\exp[(\epsilon-\epsilon_F)/k_0T]+1\}$ is the Fermi-Dirac distribution function and $(\partial f/\partial t)_{\mathrm{coll}}$ is the change in the distribution function due to the scattering. If we put

$$f = f_0 - \frac{\partial f_0}{\partial\epsilon}k_x c(\epsilon),$$

then the collision operator takes the form

$$\left(\frac{\partial f}{\partial t}\right)_{\mathrm{coll}} = \int W(\vec{k},\vec{k}')\frac{\{1-f_0(\vec{k}')\}}{\{1-f_0(\vec{k})\}} \times\frac{\partial f_0}{\partial\epsilon}\{c(\epsilon')k_x' - c(\epsilon)k_x\}d^3k',$$

where $W(\vec{k},\vec{k}')$ is the probability of transition from the state $\vec{k}$ to the state $\vec{k}'$ in a unit time. The corresponding transition probability for the polar interaction is found to be

$$W(\vec{k},\vec{k}-\vec{q}) = \frac{\alpha}{\pi}\frac{(\hbar\omega_0)^2}{\hbar p_0}\frac{1}{q^2} \times\delta(\epsilon_v(\vec{k}-\vec{q}) - \epsilon_c(\vec{k}) + \hbar\omega_0)G_{cv}(\gamma)$$

where $p_0 = (2m_c\omega_0/\hbar)^{1/2}$, α is the Fröhlich coupling constant which may be given in terms of the high-frequency and static dielectric constants,

$$\alpha = \frac{e^2}{\hbar}\left(\frac{1}{\epsilon_\infty} - \frac{1}{\epsilon_0}\right)\left(\frac{m_c}{2\hbar\omega_0}\right)^{1/2},$$

and $G_{cv}(\gamma)$ is the function which determines an overlap of periodic parts of Bloch functions of the conduction and valence bands. Because of the symmetry of these functions $G_{cv}(\gamma)$ takes the form[5]

$$G_{cv}(\gamma) = \tfrac{3}{4}\sin^2\gamma,$$

where γ is the angle between $\vec{k}$ and $\vec{k}-\vec{q}$. For the nonpolar interaction

$$W(\vec{k},\vec{k}-\vec{q}) = \frac{E_{\mathrm{NPO}}{}^2\omega_0}{8\pi^2\rho\mu_l{}^2}\delta(\epsilon_v(\vec{k}-\vec{q}) - \epsilon_c(\vec{k}) + \hbar\omega_0),$$

where ρ is the density of the crystal and μ_l is the longitudinal sound velocity in the crystal.

The scattering process considered is inelastic. Hence a uniquely defined relaxation time does not exist. To solve the Boltzmann equation (1) we use the variational principle.[6,7] In this method the conductivity is expressed by an infinite, rapidly convergent series. Taking into account only the first term of such a series and assuming a strong degeneracy of electron gas, which is equivalent to the relation

$$\left(-\frac{\partial f_0}{\partial\epsilon}\right) = \delta(\epsilon - \epsilon_F),$$

we obtain the following expressions for conductivity. In the case of polar scattering

$$\delta = \frac{4\sqrt{2}}{3\pi^2}\frac{e^2m_c{}^{1/2}}{\hbar^2\alpha}\left(\frac{m_a}{m_v}\right)^{3/2}\frac{(k_0T)^{1/2}\xi^{5/2}(1+e^s)}{z^{3/2}(z-\xi)^{1/2}\Phi(z,\xi)}, \tag{2}$$

where $z = \hbar\omega_0/k_0T$, $\xi = \epsilon_F/k_0T$,

$$\Phi(z,\xi) = 1 - \frac{3}{8s^2}\left(1 + s^2 - \frac{(1-s^2)}{s}\tanh^{-1}(s)\right) \tag{3}$$

for

$$s = \left(\frac{m_c\xi}{m_v(z-\xi)}\right)^{1/2} < 1.$$

For $s > 1$ the expression for $\Phi(z,\xi)$ can be obtained by replacing $\tanh^{-1}(s)$ with $\coth^{-1}(s)$ in Eq. (3). For NPO scattering

$$\delta = \frac{2}{3\pi}\frac{e^2\hbar\rho\mu_l{}^2m_c{}^{1/2}}{E_{\mathrm{NPO}}{}^2(m_v)^{3/2}}\frac{\xi^{3/2}(1+e^s)}{z(z-\xi)^{1/2}}. \tag{4}$$

For the particular case of HgTe formulas (2) and (4) are graphically represented in Fig. 2. In the calculation, the following parameters for HgTe

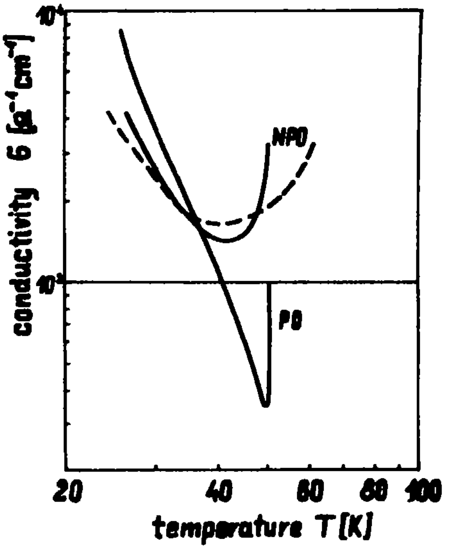

FIG. 2. Nonmonotonic part of conductivity as a function of temperature. The dashed curve represents experimental result.

were used: $m_c = 0.02m_0$, $m_v = 0.5m_0$, $\alpha = 0.1$, $\hbar\omega_0 = 14.1$ meV, $u_l = 2.57\times10^5$ cm/sec, $\rho = 8.1$ g/cm^3, and $E_{\rm NPO} = 18$ eV. m_0 is the free-electron mass.

The dashed curve in Fig. 2 corresponds to the nonmonotonic part δ_r of experimental conductivity[1] calculated in the following way. It was assumed that total experimental resistivity ρ_t consists of two parts: ρ_r which is due to the resonant scattering of electrons and ρ_m which results from the elastic nonresonant scattering. ρ_m was obtained by linear graphical interpolation of experimental results.[1] Hence

$$\rho_t = \rho_m + \rho_r$$

or

$$\frac{1}{\sigma_t} = \frac{1}{\sigma_m} + \frac{1}{\sigma_r}.$$

It is seen from Fig. 2 that the minima of theoretical conductivities are, in both cases, very close to the minimum of the nonmonotonic part of experimental conductivity. The deep minimum of PO conductivity results from the strong dependence of this interaction on a phonon wave vector q when q tends to zero and from the strong degeneracy assumption. This last assumption causes both PO and NPO conductivities to tend to infinity when ϵ_F tends to $\hbar\omega_0$.

In the framework of the above approximation a good agreement of the position of nonmonotonic experimental conductivity with theoretical results was obtained. A better fit would be obtained by taking into account the proper degeneracy of electron gas and by adding other scattering mechanisms which are important in the region of temperatures considered.

The proposed scattering mechanism can be observed in intrinsic semiconductors with inverted band structure, only if mobility due to other scattering mechanisms is not too low. Thus it can explain the similar conductivity anomaly observed in HgTe-CdTe[1,8] and HgTe-MnTe[9] mixed crystals.

The author wishes to thank Professor Dr. L. Sosnowski, Professor Dr. J. Kołodziejczak, Dr. R. R. Gałązka, Dr. Grynberg, and Dr. J. Mycielski for helpful discussions.

---

[1] C. Finck, S. Otmezguine, G. Weill, and C. Vérié, in *Proceedings of the Eleventh International Conference on the Physics of Semiconductors, Warsaw, 1972*, edited by The Polish Academy of Sciences (PWN—Polish Scientific Publishers, Warsaw, 1972), p. 944.

[2] B. I. Gelmont, M. I. Dyakonov, V. I. Ivanov Omski, B. T. Kolmiets, V. K. Ogorodnikov, and K. P. Smekalova, in *Proceedings of the Eleventh International Conference on the Physics of Semiconductors, Warsaw, 1972*, edited by The Polish Academy of Sciences (PWN—Polish Scientific Publishers, Warsaw, 1972), p. 938.

[3] J. Stankiewicz and W. Giriat, private communication.

[4] P. Lawaetz, Phys. Rev. 174, 867 (1968).

[5] J. D. Wiley, Phys. Rev. B 4, 2485 (1971).

[6] M. Kohler, Z. Phys. 124, 722 (1948).

[7] D. Howarth and E. H. Sondheimer, Proc. Phys. Soc., London, Sect. A 219, 53 (1953).

[8] J. Stankiewicz, W. Giriat, and A. Bienenstock, Phys. Rev. B 4, 4465 (1971).

[9] J. H. Morrissy, thesis, Oxford University, 1971 (unpublished).

Electron Energy-Loss Spectroscopy of GaAs and Ge Surfaces*

R. Ludeke and L. Esaki
IBM Thomas J. Watson Research Center, Yorktown Heights, New York 10598

(Received 1 July 1974)

The energy-loss spectra of ~100-eV electrons were measured for (100) and $(\bar{1}\bar{1}\bar{1})$ GaAs and (111) Ge surfaces. The portion of the energy-loss spectra attributed to excitations of *d* electrons is proportional to the density of states in the conduction bands and empty surface states. The GaAs surfaces stabilized into Ga-rich and As-rich conditions permit unambiguous identification of intrinsic surface states. Empty and filled surface states, attributed to dangling Ga and As bonds, are observed near the conduction-band and valence-band edges, respectively.

We report in this Letter low-energy-loss spectroscopy (LELS) on GaAs and Ge surfaces with special emphasis on 3*d*-core–to–conduction-band transitions. These transitions allow the precise probing of *empty* bulk and surface states, in contrast to the more complex spectra involving the excitation of valence electrons. In addition, by stabilizing the polar $(\bar{1}\bar{1}\bar{1})$ and (100) GaAs surfaces to terminate in a surface layer predominantly composed of either As or Ga atoms, we are able to provide a unique and convincing method of characterizing both empty and filled intrinsic surface states.

Because of the absence of a rigorous theoretical treatment, interpretation of the observed LELS spectra is presently somewhat controversial. The energy-loss spectra have been interpreted in terms of a dielectric model[1] and a density-of-states model.[2] In view of the indirect nature of the electronic transitions,[3] which may involve momentum changes comparable to a reciprocal-lattice vector, an interpretation of LELS data in terms of the dielectric loss function at zero wave number seems dubious. An interpretation in terms of a density-of-states model is equally unsubstantiated, except, possibly, under special conditions. It is one of the conclusions of this Letter that such an interpretation may be valid if the energy-loss spectrum arises from electronic transitions from narrow, filled energy levels to empty conduction-band states, provided there is no additional interfering loss channel of comparable energy. We believe this to be true for excitations of *d* electrons in GaAs and Ge and probably for other materials with narrow isolated *d* or *f* core levels.

An approximate expression for the number of electrons suffering an energy loss $\Delta\epsilon$ due to indirect excitations of valence electrons of energy $\epsilon_v(\vec{k})$ to empty conduction-band states of energy $\epsilon_c(\vec{k}+\Delta\vec{k})$ is given by[3]

$$I(\Delta\epsilon)=\sum_{v,c}\sum_{\Delta\vec{k}}F_{v,c}(\vec{k},\Delta\vec{k})\int\frac{d^3k}{\nabla_k[\epsilon_c(\vec{k}+\Delta\vec{k})-\epsilon_v(\vec{k})]_{\epsilon_c-\epsilon_v=\Delta\epsilon}}, \tag{1}$$

where $F_{v,c}(\vec{k},\Delta\vec{k})$ is proportional to the scattering cross section. The integral in Eq. (1) is a generalization of the joint density-of-states function for optical interband transitions to include finite momentum changes in the sum over $\Delta\vec{k}$. For a narrow valence band v', $\nabla_k\epsilon_{v'}(\vec{k})\approx 0$. If furthermore this band is isolated and no other scattering channels exist near $\Delta\epsilon$, Eq. (1) may be written as

$$I_{v'}(\Delta\epsilon)\approx\sum_c\bar{F}_{v',c}N_c(\Delta\epsilon), \tag{2}$$

where $\bar{F}_{v',c}$ is the function $F_{v',c}$ averaged over all available $\Delta\vec{k}$, and $N_c(\Delta\epsilon)$ is the density of states of the conduction band *c*. Thus, except for a possible modulation due to $\bar{F}_{v',c}$, $I_{v'}(\Delta\epsilon)$ is proportional to the conduction-band density of states and includes both bulk and surface features because of the shallow sampling depths (typically $\lesssim 10$ Å). The conditions implied in Eq. (2) seem to be satisfied by the 3*d* core levels of GaAs, Ge, and several other semiconductors.

The energy-loss spectra were measured by an Auger cylindrical-mirror analyzer with integral coaxial electron gun. The primary beam was at normal incidence to the specimen surface. The primary electron energy was varied between 50 and 200 eV, with 100 eV being a good working compromise between resolution (~0.8 eV) and adequate signal intensity. The lack of shifts in energy of the energy-loss structure with varying primary electron energy suggest that diffractive effects are unimportant. Both first- and second-derivative spectra were measured, the former permitting better resolution,[4] the latter greater accuracy in the energy position of the energy-loss structure.[1] The samples were cleaned by Ar^+ sputtering and annealed. The GaAs $(\bar{1}\bar{1}\bar{1})$ samples were, in addition, overgrown *in situ* by a thin epitaxial GaAs film, by using a molecular-beam technique,[5] which permitted the stabilization of the atomic surface layer into Ga-rich $(\bar{1}\bar{1}\bar{1})$-$\sqrt{19}$ or As-rich $(\bar{1}\bar{1}\bar{1})$-2 surfaces[6] prior to the energy-loss measurements. The surface structures were monitored by grazing-incidence high-energy electron diffraction. This ability to change the "intrinsic" surface conditions, as opposed to extrinsic contamination by foreign impurity atoms, constitutes a novel and inherently more convincing method of probing the surface-sensitive features of binary compound semiconductors.

Figures 1(a)–1(c) show the second-derivative spectra of various GaAs surfaces. Certain features in the spectra are common to all surfaces and are interpreted in terms of bulk behavior. These features include the 3.4- and 5.6-eV structures attributed to bulk valence-band–to–conduction-band transitions,[7] a peak near 8.6 eV of unknown origin, a doublet structure at 21.3 and 23.5 eV due to Ga $3d$-core-level–to–conduction-band transitions, and a peak at 42.4 eV due to similar transitions from the As $3d$ core level. In addition, peaks due to surface- and volume-plasmon losses are observed near 10.2 eV and 16.2, respectively.

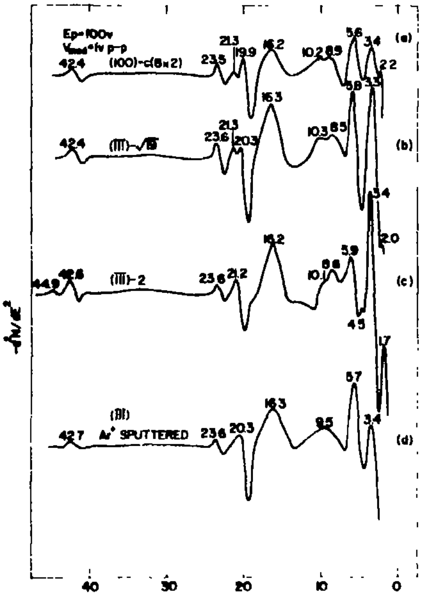

FIG. 1. Second-derivative energy-loss spectra of GaAs: (a) (100) surface, Ga stabilized; (b) $(\bar{1}\bar{1}\bar{1})$ surface, Ga stabilized; (c) $(\bar{1}\bar{1}\bar{1})$ surface, As stabilized; (d) $(\bar{1}\bar{1}\bar{1})$ surface, sputtered.

The energy-loss spectrum of the Ga stabilized (100)-$c(8\times 2)$ surface[8] in Fig. 1(a) exhibits surface-sensitive structure at 2.2 and 19.9 eV. We attribute these, respectively, to transitions from the valence band and the Ga $3d$ core level into empty surface states near the bottom of the conduction band arising from dangling Ga bonds at the surface. Ar^+ bombardment enhances these peaks, while oxygen adsorption depresses them.[4]

Stronger evidence for the notion of intrinsic surface states due to dangling bonds is obtained from energy-loss data of the Ga and As stabilized $(\bar{1}\bar{1}\bar{1})$ surfaces shown in Figs. 1(b) and 1(c). The Ga stabilized $(\bar{1}\bar{1}\bar{1})$-$\sqrt{19}$ surface again exhibits structure at 20.3 eV in the region of the d-band transitions. This structure disappears as the surface becomes As stabilized, while a strong peak appears at 1.7 eV, which is attributed to transitions from filled surface states to empty conduction-band states.[8] A small, possibly related structure appears at 4.5 eV which may be due to transitions into higher lying conduction bands. It may also be noted that for the As-stabilized surface a doublet structure is observed in the $3d$-core-level structure of As near 43 eV. The separation of their peaks agrees well with that due to the Ga $3d$-core-level transition. This doublet is not clearly resolved on the Ga-stabilized surfaces because of As depletion in the surface layer. Figure 1(d) shows the loss spectrum of a sputtered $(\bar{1}\bar{1}\bar{1})$ GaAs surface. Sputtering should enhance the density of broken bonds and somewhat deplete the surface of As.[9] This conjecture is supported by the enhancement of the 20.3 eV peak.

Since the energy of the Ga $3d$ core levels with respect to the top of the valence band is quite accurately known for GaAs,[10] it is possible to locate the peaks in the conduction-band density of states with relation to the valence-band edge. This has been done in Fig. 2. The solid curve for the conduction band is obtained from the $3d$-core-level structure of the As stabilized $(\bar{1}\bar{1}\bar{1})$ surface and represents the non-surface-sensitive, or bulklike, portion of the conduction-band density of states. We have also sketched the estimated position of the filled surface states S_{As} of the $(\bar{1}\bar{1}\bar{1})$-2 structure. Depending on the assumption of the

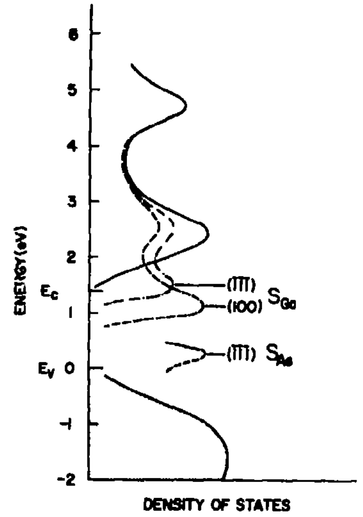

FIG. 2. Conduction-band density of states of GaAs surfaces based on energy-loss spectra of Ga $3d$-core-level excitations: solid line, bulklike density of states for $(\bar1\bar1\bar1)$ As-stabilized surface; dot-dashed line, for $(\bar1\bar1\bar1)$ Ga stabilized surface; dashed line, for (100) Ga-stabilized surface. $S_{\rm Ga}$ marks the peak positions in the density-of-states curve of empty surface states, and $S_{\rm As}$ that of filled surface states. Energies are referred to the top of the valence band ($E_v=0$); E_c marks the bulk conduction-band edge.

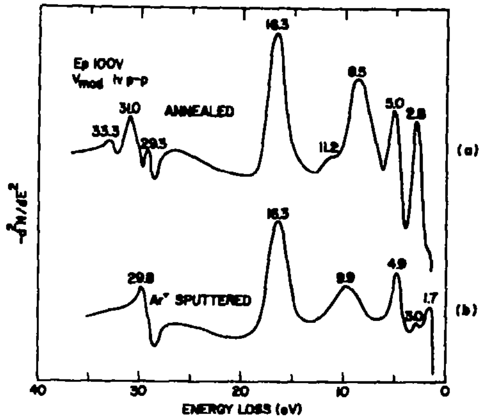

FIG. 3. Second-derivative energy-loss spectra of (111) Ge surfaces: (a) Ar^+ sputtered and annealed; (b) Ar^+ sputtered.

energy position of the final state (possibly the L_1 symmetry point), $S_{\rm As}$ should lie from 0.1 to 0.4 eV above the valence-band maximum. The $(\bar1\bar1\bar1)$ $S_{\rm Ga}$ surface state is located near the bottom of the conduction band, whereas (100) $S_{\rm Ga}$ about 0.3 eV below it.

Figure 3 shows preliminary results of the energy-loss spectra of Ge(111) surfaces. The annealed surface [Fig. 3(a)] exhibited a 2×1 surface reconstruction, but because of surface roughness we cannot eliminate the possibility of a 2×8 surface. Again the region of d-core-level transitions near 30 eV is of special interest. The amplitude of the 29.3-eV peak is very sensitive to surface contamination (carbon or oxygen) and may be enhanced and shifted by Ar^+ bombardment, as seen in Fig. 3(b). Ar^+ bombardment also introduces a new structure at 1.7 eV. In analogous manner to GaAs, we interpret these structures as resulting from transitions into empty surface states near the bottom of the conduction band and associated with dangling bonds. The 31.0- and 33.3-eV structures should again correspond to the relative position of peaks in the bulklike conduction-band density of states. The remaining features in the energy-loss spectra of the figure are analogous to those in GaAs.

In summary, the energy-loss spectra due to $3d$-core-level excitations in GaAs, Ge, and related semiconductors gives important information on the relative location in energy of empty surface and conduction-band states. In addition, the ability of stabilizing the surfaces of compound semiconductors by *in situ* molecular-beam evaporation provides a unique method of characterizing both empty and filled intrinsic surface states. This point is particularly important in characterizing noncleaved surfaces of binary compounds, as conventional preparation techniques will leave the surface in a nonstoichiometric and thereby ambiguous condition.

Work is in progress on nonpolar surfaces of GaAs, such as the (110) surface, which contain approximately equal numbers of unsatisfied Ga and As bonds.

We acknowledge helpful discussions with D. E. Eastman and P. M. Marcus.

---

*Research sponsored in part under an Army Research Office contract.

[1] J. E. Rowe and H. Ibach, Phys. Rev. Lett. 31, 102 (1973); H. Ibach and J. E. Rowe, Phys. Rev. B 9, 1951 (1974).

[2] E. Sickafus and F. Steinrisser, Phys. Rev. B 6, 3714 (1972).

[3] E. Bauer, Z. Phys. 224, 19 (1969).

[4] R. Ludeke and L. Esaki, to be published.

[5] L. L. Chang, L. Esaki, W. E. Howard, R. Ludeke,

and G. Schul, J. Vac. Sci. Technol. 10, 655 (1973).

[6] A. Y. Cho and I. Hayashi, Solid State Electron. 14, 125 (1971).

[7] Their energies are somewhat larger than structure expected from direct interband transitions, and are probably related. See, for example, J. R. Chelikowsky and M. L. Cohen, Phys. Rev. Lett. 32, 674 (1974).

[8] Initial experiments on *in situ* As-stabilized surfaces of (100) GaAs also show the suppression of the 19.9-eV surface structure and the appearance of structure at 1.7 eV. A comprehensive report will be published in the future.

[9] R. Ludeke, L. Esaki, and L. L. Chang, Appl. Phys. Lett. 24, 417 (1974).

[10] A value of 18.8 eV was obtained both by L. Ley, R. A. Pollak, R. F. McFeely; S. P. Kowalczyk, and D. A. Shirley [Phys. Rev. B 9, 600 (1974)] using x-ray photoemission spectroscopy and by D. E. Eastman (private communication) using ultraviolet photoemission spectroscopy.

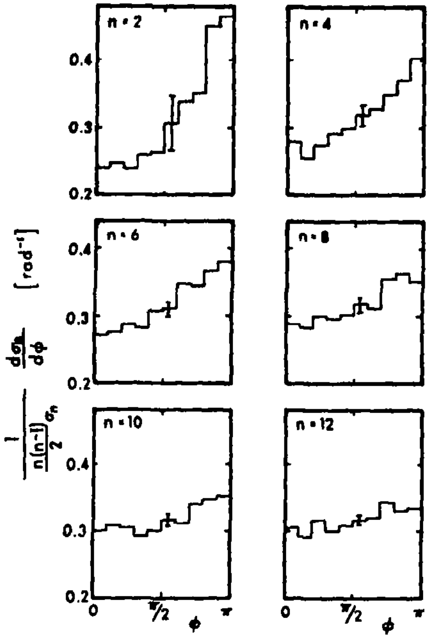

FIG. 1. Semi-inclusive azimuthal distributions for all charged-particle combinations.

dence of the azimuthal distributions on the particle's charge, transverse momentum, and rapidity is also studied.

The results are based on an unbiased inclusive data sample of ~3500 completely measured events obtained from an exposure of the 30-in. FNAL hydrogen bubble chamber to a 205-GeV/c proton beam. Further details of this experiment are given elsewhere.[3] For the analysis of two-particle distributions we make the following choice of kinematic variables: the magnitude of the transverse momentum of particle i, P_{iT}; its center-of-mass rapidity, y_i; and the azimuthal angle between the transverse momenta of particles i and j,[4]

$$\varphi_{ij}=\cos^{-1}\frac{\vec{P}_{iT}\cdot\vec{P}_{jT}}{P_{iT}P_{jT}}.$$

In this paper we analyze the azimuthal distributions

$$\frac{d\sigma_n}{d\varphi}=\sum_{i=1}^{n}\sum_{j<i}\frac{d\sigma_n}{d\varphi_{ij}}$$

and

$$d\sigma/d\varphi=\textstyle\sum_n d\sigma_n/d\varphi,$$

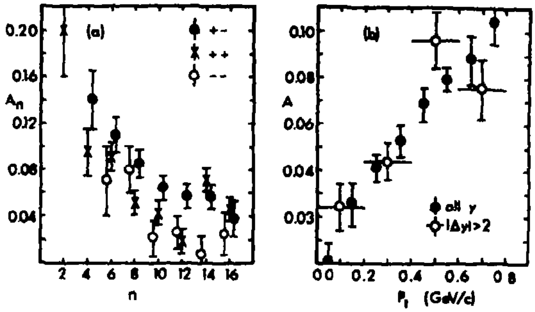

FIG. 2. (a) Asymmetry parameter A_n as defined in Eq. (1) as a function of charged-particle multiplicity n for different charge combinations. (b) Asymmetry A, integrated over all n, as a function of p_T for all y and for $|y_i - y_j| > 2$.

where n is the charged-particle multiplicity.

In Fig. 1 we show the semi-inclusive azimuthal distributions for all charged-particle combinations. It is observed that (a) the distributions are asymmetric and peak near 180° and (b) the asymmetry becomes less pronounced as the charged multiplicity increases. As will be discussed later, these trends may be understood in part as a consequence of transverse-momentum conservation. To parametrize the distributions, we define, for fixed n, the asymmetry parameter A_n:

$$A_n=\left(\int_{\pi/2}^{\pi}\frac{d\sigma_n}{d\varphi}d\varphi-\int_0^{\pi/2}\frac{d\sigma_n}{d\varphi}d\varphi\right)\left(\int_0^{\pi}\frac{d\sigma_n}{d\varphi}d\omega\right)^{-1}. \quad (1)$$

Table I and Fig. 2(a) present A_n as a function of n for the different charge combinations. In general, for each n, the asymmetry for the (+ −) combination is larger than that for either the (− −) or (+ +) combination. This holds as well for the inclusive values listed in Table I.

There exist simple model calculations which predict a definite relation between the asymmetry A and the total number (n_T) of particles produced in the final state. For example, a statistical model[5] which incorporates only transverse-momentum conservation and a Gaussian distribution in transverse momentum predicts $A = 1/(n_T - 1)$. Applying this model to our measured asymmetry parameters for all charged particles,[6] A_n^{cc}, we give in Table I estimates of n_T for a given number of charged particles, n. We also list in Table I the values of n_T calculated using the experimentally observed average number of π^0, K^0, and Λ

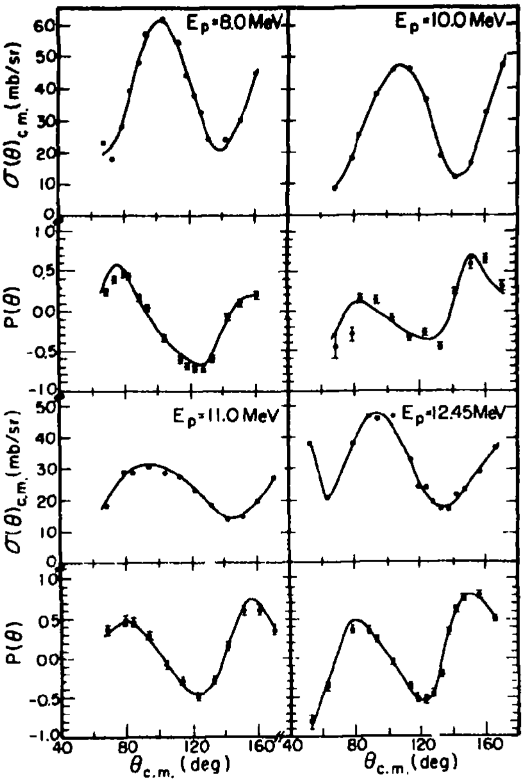

FIG. 1. Angular distributions of cross section and polarization for the reaction $^{14}C(p,p)^{14}C$ at 8.0, 10.0, 11.0, and 12.45 MeV. The fits shown were obtained from a complex-phase-shift analysis of the data. The error bars represent the statistical errors associated with the data points. The statistical error associated with the cross section data are less than 2%.

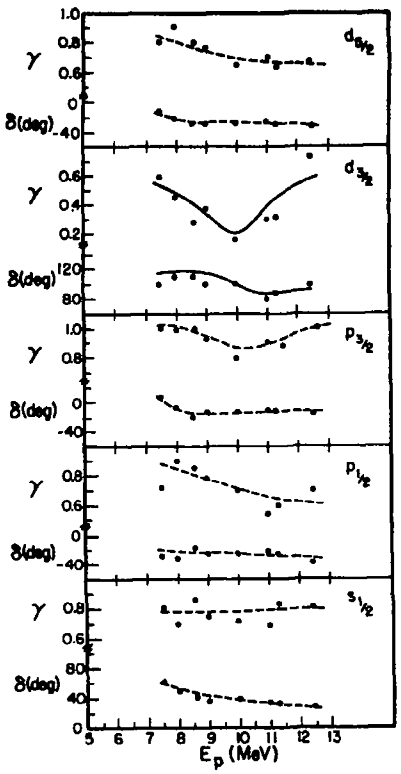

FIG. 2. Complex phase shifts as functions of energy resulting from fitting the cross section and polarization data. The dashed lines are smooth curves drawn to suggest the energy dependence. In the $d_{3/2}$ case the solid lines are fits generated as described in the text.

eters at all energies. Other initial sets of phases were also tried in order to determine if the set obtained was indeed the best fit (the lowest χ^2). Typical resulting fits are shown along with the data at the four energies of 8.0, 10.0, 11.0, and 12.45 MeV in Fig. 1.

The partial waves included in our analysis extended up through $f_{7/2}$. The complex phase shift is represented by the real part $\delta_l^{\pm}$ and the imaginary part $\eta_l^{\pm}$. It is convenient to present the imaginary part in terms of the damping parameter $\gamma_l^{\pm} = \exp(-2\eta_l^{\pm})$. The quantities $\delta_l^{\pm}$ and $\gamma_l^{\pm}$ are shown as functions of energy in Fig. 2. The f-wave phase shifts were small and relatively constant as a function of energy and are not shown.

It is seen in Fig. 2 that the dominant energy dependence in these results occurs in the $d_{3/2}$ phase shift. This result is what we would expect if the GDR was to be seen since it is primarily $J^\pi = \frac{3}{2}^+$ and is centered around $E_p = 10.5$ MeV. In order to evaluate this result explicitly we next attempted to add resonances to a set of background phases. The cross sections and polarizations were calculated with a scattering matrix S, defined by

$$S_l^{\pm} = \exp[2i(\omega_l + \delta_l^{\pm})]\{\exp(-2\eta_l^{\pm}) + \exp(2i\varphi_p)[i\Gamma_p(E_{res} - E - \tfrac{1}{2}i\Gamma)]\},$$

where ω_l is the Coulomb phase shift; $\delta_l^{\pm} + i\eta_l^{\pm}$ is the off-resonance phase shift describing the elastic scattering for the lth partial wave with $J^\pi = l \pm \frac{1}{2}$; E_{res}, Γ, and Γ_p are, respectively, the energy, total

TABLE I. Parameters for the resonance calculation.

Partial wave	Background phase shifts[a] δ (deg)	γ
$s_{1/2}$	33.80	0.68
$p_{1/2}$	− 21.10	0.53
$p_{3/2}$	− 10.30	0.91
$d_{3/2}$	105.00	0.70
$d_{5/2}$	− 26.70	0.68
$f_{5/2}$	10.55	0.85
$f_{7/2}$	11.64	0.83

Resonance Parameters

J^π	Γ_p (MeV)	Γ (MeV)	E_{res}(lab) (MeV)	φ (deg)
$\frac{3}{2}^+$	1.0	4.0	10.0	0.0

[a] Phase shifts (other than $d_{3/2}$) were obtained from the 11-MeV data.

width, and partial elastic width of the resonance; and φ_p is the resonance mixing phase.[4] In addition to calculating the cross sections and polarizations, we calculated the net complex phase shift (described in terms of δ and γ) including the effects of the resonance. With a set of energy-independent background phases and a single $\frac{3}{2}^+$ resonance, we obtained the result shown in Fig. 2 as the solid lines. The parameters for this calculation are given in Table I. The other complex phase shifts were held constant over the energy region. Of course they could be given an energy dependence such as that suggested by the dashed lines in Fig. 2, but little would be gained. It is interesting to note that the $p_{3/2}$ partial wave shows some indication of resonance behavior. This could be the effect of a giant $E2$ resonance.

We see that the $d_{3/2}$ partial wave can be well accounted for by a single $\frac{3}{2}^+$ resonance at $E_p = 10.0 \pm 0.5$ MeV having a width of about 4 MeV and a partial width of 1 MeV. If the reduced width is calculated according to $\Gamma = 2P_l\gamma_l^2$, one finds it to be about one tenth of the single-particle limit. An additional important result of our analysis was the discovery that if many levels were introduced, following the structure of the (p,γ) data,[5,6] the present data could not be reproduced. We do observe that if one draws a smooth curve through the structured (p,γ) data (see Ref. 6) one obtains a resonance having a width of about 4 MeV centered near 10 MeV. Other effects[7] which could account for these results have been considered but were not able to give a consistent description of the data.

It is well known that the 1p-1h model is an inadequate description of the giant dipole resonance.[8] Such features as the intermediate structure, the angular distributions of certain partial cross sections, and the proton-neutron branching ratio are not accounted for. And, while the absorption cross section shows more structure than the theory, the angular distributions show less. The results of the present experiment and further studies of (p,p) cross sections and polarizations in this energy region should shed new light on the giant-resonance phenomenon. A detailed 2p-1h continuum calculation of these effects observed in this work is in progress and will be published in the near future.[9]

The authors gratefully acknowledge the indispensible contribution of Dr. T. B. Clegg who developed the Triangle Universities Nuclear Laboratory polarized-ion source.

---

*Work partially supported by the U. S. Atomic Energy Commission.

†Work partially supported by Research Corporation.

[1] C. R. Lamontage *et al.*, Phys. Lett. 45B, 465 (1973).

[2] G. G. Ohlsen, J. L. McKibben, G. P. Lawrence, P. W. Keaton, Jr., and D. O. Armstrong, Phys. Rev. Lett. 27, 599 (1971).

[3] T. Tamura, ORNL Report No. 4152, 1967 (unpublished).

[4] L. Veeser, J. Ellis, and W. Haeberli, Phys. Rev. Lett. 18, 1063 (1967).

[5] H. R. Weller *et al.*, Nucl. Phys. A207, 177 (1973).

[6] H. R. Weller, N. R. Roberson, D. Rickel, C. P. Cameron, R. D. Ledford, and T. B. Clegg, Phys. Rev. Lett. 28, 177 (1974).

[7] K. W. McVoy, Phys. Lett. 17, 42 (1965).

[8] R. F. Barrett, L. C. Biedenharn, M. Danos, P. P. Delsanto, W. Greiner, and H. G. Wahsweiler, Rev. Mod. Phys. 45, 44 (1973).

[9] M. Divadeenam and H. R. Weller, private communication.

Observation of Nuclear Transparency in Proton-Nucleus Collisions at 200 GeV[*]

P. L. Jain, M. Kazuno, Gerald Thomas,[†] and B. Girard
High-Energy Experimental Laboratory, Department of Physics, State University of New York at Buffalo,
Buffalo, New York 14214

(Received 23 May 1974)

Proton-nucleus interactions in nuclear emulsion from a 200-GeV proton beam at the National Accelerator Laboratory have been studied in terms of multiplicities and the angular distributions of shower particles. Low multiplicities observed in complex nuclei do not depend upon the size or the excitation of the target nuclei. Our experimental results are explained in terms of the energy-flux cascade model and not by intranuclear cascade models.

Recent results of rising total cross sections, large p_t events, leading particle effects, and clustering of secondaries determined at the energies of the National Accelerator Laboratory and the intersecting storage rings had already been observed in earlier cosmic-ray experiments. Cosmic-ray studies had also revealed that the multiplicity, transverse momentum, and angular distribution of secondaries have weak dependence on the primary energy as well as on the size of the target nucleus, and they do not follow the predictions of the calculations of the intranuclear cascade models. Because of the revival of interest in hadron-nucleus interactions, we present here the results of 200-GeV proton-nucleus interactions in nuclear emulsion and compare them with 16-,[1] 28-,[2] 300-, and 1000-GeV[3] data from our laboratory. We feel that these studies will not only be helpful in understanding the nucleon-nucleus collisions but also they will contribute significantly in understanding better the nucleon-nucleon interactions.

The details of the exposure for this experiment were discussed earlier[4] where we presented the analysis of events with only $N_h = 0$ or 1 (N_h denotes the number of heavy tracks[5] with $\beta < 0.7$). We scanned 713.4 m of track length by an along-the-track scanning method and observed 2293 interactions, out of which we present here the analysis of 1243 events with $N_h > 1$. In Fig. 1(a) is shown the behavior of $\langle N_h\rangle$ observed in nuclear emulsion as a function of primary energy.[6] We see that at lower energies $\langle N_h\rangle$ increases with energy, and at energy >6 GeV there seems to be a decreasing tendency, approaching an asymptotic value of ~7.5. This is in contradiction to the intranuclear cascade mechanism. In Fig. 1(b) is shown the probability of having an emulsion star with more than N_h heavy tracks for 16-GeV π^-, and 28-, 200- and 1000-GeV protons. The high-energy limit is reached very quickly, even at 16 GeV, which shows that the emission of a given number of slow protons undergoes no significant change when the incident energy is raised from 16 GeV to 1 TeV. Contradiction of the cascade mechanism is further observed in the distribution of $\langle N_h\rangle$ versus n_s where $\langle N_h\rangle$ increases linearly[6] with n_s (Ref. 5). The slope values at 6-, 28-, and 200-GeV proton energies are 1.2, 1.0, and 0.55, respectively. The decrease of the slope with the increase in energy is in turn further observed in the increase of $\langle n_s\rangle$ as a function of energy. At higher energies the rate of increase of $\langle n_s\rangle$ decreases. This could be explained in terms of clustering or other forms of collective behavior of secondary particles produced at high energies. In Fig. 1(c) is shown the distribution of $\langle n_s\rangle$ for a given N_h at different energies: 16, 28, 200, 300, and 1000 GeV. All of these distributions show linear fits with slopes increasing monotonically with energy. The $\langle n_s\rangle$ for all events at 200 GeV is 12.7 ± 0.2. The 200-GeV curve when extrapolated has an intercept value at $N_h = 0$ of $\langle n_s\rangle > {\sim}8.0$ which is close to 7.68 ± 0.11, the one observed at 200 GeV for p-p interactions in a bubble chamber.[7] Another interesting characteristic of the multiplicity in the target nucleus A is the ratio $R_A = \langle n_s\rangle_{(pA)}/\langle n_{\rm ch}\rangle_{(pp)}$, where $\langle n_{\rm ch}\rangle_{pp}$ is the mean p-p charge multiplicity and $\langle n_s\rangle_{pA}$ is the mean p-nucleus multiplicity in nucleus A. In the nuclear emulsion $R_{\rm em}$ for 16, 28, 67,[8] 200, 300, and 1000 GeV is given by 1.24 ± 0.12, 1.4 ± 0.12, 1.53 ± 0.4, 1.62 ± 0.66, 1.65 ± 0.10, and 1.70 ± 1.5, respectively. $R_{\rm em}$ values as a function of N_h in the nuclear emulsion are shown in Fig. 1(d). The linear relation at low-energy values of 16 and 28 GeV show slightly different slopes than those in 200 or in 300 GeV. It is remarkable to see that the $R_{\rm em}$ values show a very small increase with the incident energy and

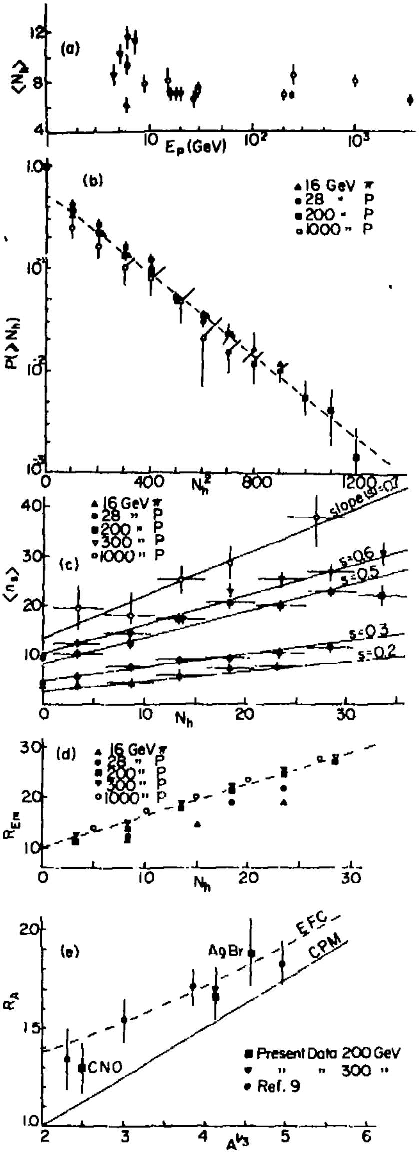

FIG. 1. (a) $\langle N_h\rangle$ produced from the interaction of pions and protons with emulsion nuclei as a function of energy. Area scanning: closed circle, proton; closed triangle, pion. Along the track scanning: open circle, proton; open triangle, pion. (b) Integral frequency distribution of N_h^2 for 16, 28, 200, and 1000 GeV. (c) $\langle n_s\rangle$ versus N_h for 16, 28, 200, 300, and 1000 GeV. (d) R_{em} versus N_h for 16, 28, 200, and 300 GeV. The relation for 200, 300, and 1000 GeV is given by $R_{em}=1+0.06N_h$. (e) R_A versus $A^{1/3}$. For EFC model, $R_A=1+\frac{1}{3}(\bar{\nu}_A-1)$, where $\bar{\nu}_A$ is average number of collisions in the nucleus. For CPM, $R_A=\frac{1}{2}(1+0.5A^{1/3})$.

with N_h values. For the high energy 200-, 300-, and 1000-GeV primaries, the R_{em} values practically coincide for the three energies for any N_h value and are given by the scaling relation $1+0.06N_h$. It is a very interesting result that we can predict an average multiplicity from nuclear targets if we know the multiplicity from p-p collisions at the same energy or vice versa. We may add that at 200 GeV $\langle n_s\rangle_{(p\,\mathrm{AgBr})}/\langle n_s\rangle_{(p\,\mathrm{CNO})}\sim 1.5$, as found in cosmic-ray work. Constancy of R_A as a function of energy has been further confirmed in a number of other targets and is shown[9] in Fig. 1(e) where the observed values of R_A are plotted against $A^{1/3}$ for different nuclei. The energy-flux cascade model[10] (EFC), as compared to the coherent-production model[11] (CPM), fits the observed data very well. Our data clearly rule out cascade models which predict that R_A should be independent of A.

In Fig. 2(a) is shown the ratio $R_E=\langle n_s\rangle_{E_1}/\langle n_s\rangle_{E_2}$ as a function of N_h for 300 and 200 GeV, which is almost a constant (~ 1.1), but for low-energy regions this ratio is not constant. This is very interesting, as the mean multiplicity of shower particles produced by high-energy particles on a nuclear target does not depend on either the size or the degree of the excitation of the target nucleus while at lower energies, i.e., at 16 and 28 GeV, there is a strong dependence of this kind. This is also obvious from the values of R_{em} for the emulsion nucleus which are 1.24 ± 0.12 and 1.4 ± 0.12 for 16 and 28 GeV, respectively, which are different from the scaling value of 1.65 ± 0.15. In order to see the development of shower particles with mass A, we divided the shower particles n_s into inner ($\tan\theta<0.1$) and outer ($\tan\theta>0.1$) cones, where each cone contains on the average one-half of the shower particles produced in the p-p collision. This is shown in Fig. 2(b) as a function of N_h. One observes that the particles produced in the inner cone increase very slowly with N_h. If we further reduce the inner angle to $\tan\theta\leq 0.08$ then $\langle n_s\rangle\sim 5.5$ and is practically the same for all events, and thus the constancy of these values indicates that particles produced in the inner cone behave as if there were no nuclear matter in their way and the nucleus was apparently transparent to them. The whole increase of $\langle n_s\rangle$ with N_h comes from the slow particles produced in the outer cone, which is predicted by almost all models including cascade models. However the amount of excess slow particles is a very sensitive way of distinguishing between different models.[12] The relation of angular distribution of shower particles in the inner and the outer cones as a function of N_h is shown in Fig. 2(c). We notice that the $\langle x\rangle$ value [where $x = -\log_{10}(\tan\theta)$] for all angles is slowly decreasing with N_h. This decrease comes mainly from the inner cone; for the outer cone it is almost constant. When we further change the angle of the inner cone to $\tan\theta \leq 0.08$ and for the outer cone to $\tan\theta > 0.08$, the $\langle x\rangle$ values for the inner cone are practically constant for different N_h values. From Figs. 2(b) and 2(c) we notice that the inner cones of angle $\tan\theta \leq 0.08$ give practically constant values of $\langle n_s\rangle$ and $\langle x\rangle$ for all different N_h values. On the other hand, in the outer cone $\langle x\rangle$ remains constant but $\langle n_s\rangle$ increases with N_h.

As mentioned earlier, the existence of the leading-particle effect is determined by measuring the inelasticity K which is the fraction of the incident energy carried off by secondaries. This has been calculated by the common technique used in cosmic-ray work[13] as $K = (1.5\langle p_t\rangle\sum\csc\theta_i)/200$, where $\langle p_t\rangle = 0.35$ GeV/c and the innermost track has been removed. The K values obtained are shown in Fig. 2(d). We notice that for $N_h < 7$ ($\langle N_h\rangle \sim 7$ for 200 GeV), the K values are small and are increasing, and the leading particle carries most of the energy. As $\langle N_h\rangle$ approaches 7 the leading particle becomes less energetic and the K value is almost constant (~ 0.55) and is insensitive to N_h, and this is not explained by cascade models. In Fig. 2(e) is shown the integrated and normalized rapidity distribution[14] [$= \log_{10}(\tan\theta)$] as a function of $N_h = 0$, 1, 2–5, 6–8, and > 8. The arrows shown for $N_h = 0$, 2–5, and > 8 indicate the values of $\log_{10}(\tan\theta)$ where an equal number of tracks lie above and below θ, and they are very close to one another. This shows that the angular distribution depends weakly on N_h; this was also concluded from Fig. 2(c). Also in this figure is shown the differential rapidity distribution for different N_h values. This differential distribution is further compared with the 200-GeV p-p normalized data from the bubble chamber.[7] We see that both the distributions for the hydrogen bubble chamber and $N_h = 0$ are identical and are symmetrical about the center of mass (C). For $N_h > 8$, the distribution is unsymmetric and the whole excess in the multiplicity appears in the target hemisphere which is not explained by the cascade models.

We thus conclude from our experiment that (i) $\langle n_s\rangle$ increases with mass A and the increase observed is much smaller than predicted by intranuclear cascade models, and (ii) the multiplicity

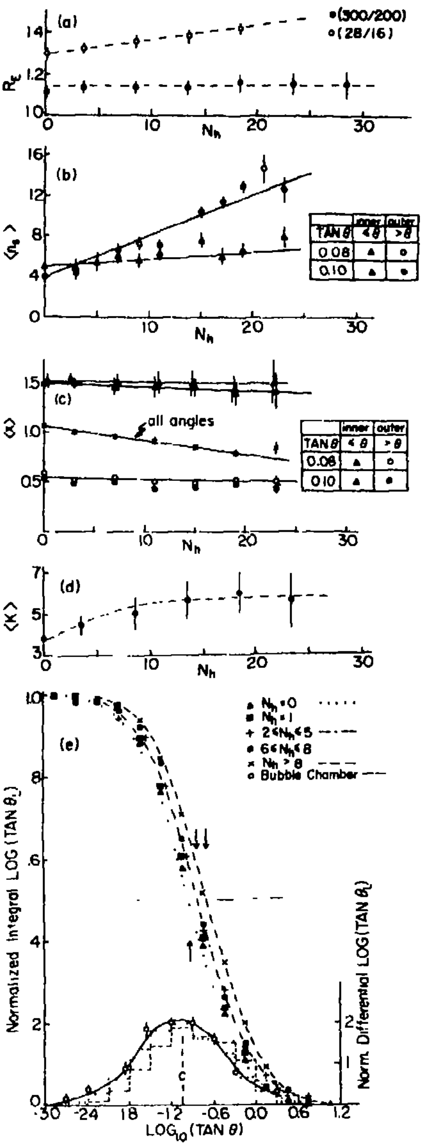

FIG. 2. (a) R_E versus N_h for 300 and 200 GeV, and for 28 and 16 GeV. (b) $\langle n_s\rangle$ versus N_h for inner and outer cones at 200 GeV with (i) first cut $\tan\theta \lesssim 0.1$ and (ii) (ii) second cut $\tan\theta \lesssim 0.08$. (c) Angular distribution $\langle x\rangle$ versus N_h for 200-GeV events for (i) all angles; inner and outer cone with (ii) $\tan\theta \lesssim 0.1$ and (iii) $\tan\theta \lesssim 0.08$. (d) Inelasticity $\langle K\rangle$ versus N_h at 200 GeV. (e) Integral frequency distribution of rapidities plotted for events with $N_h = 0$, 1, 2–5, 6–8, > 8. The center points are shown by arrows. The differential distribution of rapidities is also plotted for events with $N_h = 0$ and > 8, and this is compared with bubble chamber data at 200 GeV.

and the angular distribution in the very forward direction change very little with target size and the nuclear effects seem to come mainly from the particles produced in the backward direction but without much change in their angular distributions. Thus we see that nuclear phenomena at high energy may allow a glimpse of the underlying dynamics that cannot be seen directly in free-p-p collisions. We are confident that nuclear studies at higher energies shall surely provide important insight into strong-interaction dynamics.

We are very grateful to Professor K. Gottfried for a useful discussion and for sending us his paper before its publication. We are also very thankful to the staff of the National Accelerator Laboratory and particularly to Dr. L. Voyvodic for their valuable help with the 200-GeV exposure.

---

*Work supported by the Research Corporation.

†Permanent address: Ball State University, Muncie, Ind. 47306.

[1] P. L. Jain, H. C. Glahe, J. D. Rinaldo, and P. D. Bharadwaj, Nuovo Cimento 32, 872 (1964).

[2] P. L. Jain, H. C. Glahe, G. N. Srivastova, and P. D. Bharadwaj, Nuovo Cimento 21, 859 (1961).

[3] P. L. Jain, Phys. Rev. 125, 679 (1962), and Nuovo Cimento 24, 565 (1962); A. Barkow, B. Chamany, D. Haskin, P. L. Jain, E. Lohrman, M. Teucher, and M. Schein, Phys. Rev. 122, 617 (1961).

[4] P. L. Jain, M. Kazuno, Z. Ahmad, B. Girard, G. Thomas, and H. Moses, Lett. Nuovo Cimento 8, 921 (1973), and 9, 113 (1974); P. L. Jain, *Experiments on High Energy Particle Collisions*, AIP Conference Proceedings No. 12, edited by R. S. Panvini (American Institute of Physics, New York, 1973), p. 141.

[5] $\beta \approx 0.7$ corresponds to pion and nucleon momenta of 150 MeV/c and 1 GeV/c, respectively. The slower particles also include evaporation protons due to de-excitation of the nucleus. Shower tracks n_s correspond to particles with $\beta \geq 0.7$.

[6] P. L. Jain, H. C. Glahe, J. D. Rinaldo, and P. D. Bharadwaj, Nucl. Phys. 67, 641 (1965), and reference quoted there.

[7] G. Charlton, Y. Cho, M. Derrick, R. Engelmann, T. Fields, L. Hyman, K. Joseph, U. Mehtani, B. Musgrave, Y. Oren, D. Rhines, P. Schreiner, H. Yuta, L. Voyvodic, R. Walker, J. Whitmore, H. B. Crawley, Z. M. Ma, and R. G. Glasser, Phys. Rev. Lett. 29, 515 (1972).

[8] J. Babecki, Z. Czachowska, B. Furmanska, J. Gierula, R. Holynski, A. Jurak, S. Krywdzinski, G. Nowak, B. Slezak, and W. Walter, Phys. Lett. 47B, 268 (1973); Barcelona-Batavia-Belgrade-Bucharest-Lund-Lyons-Montreal-Nancy-Ottawa-Paris-Rome-Strasbourg-Valencia Collaboration, Phys. Lett. 48B, 467 (1974).

[9] K. N. Erickson, University of Michigan Report No. 03028-4-T, 1970 (unpublished); P. R. Vishwanath, A. E. Bussian, L. W. Jones, D. E. Lyon, J. G. Learned, D. D. Reeder, R. J. Wilksand, and B. Cork, Bull. Amer. Phys. Soc. 19, 445 (1974).

[10] K. Gottfried, Phys. Rev. Lett. 32, 957 (1974).

[11] P. M. Fishbane and J. S. Trefil, Phys. Rev. Lett. 31, 734 (1973); A. Dar and J. Vary, Phys. Rev. D 6, 2412 (1972).

[12] G. Calucci, R. Jengo, and A. Pignotti, Phys. Rev. (to be published).

[13] D. H. Perkins, in *Progress in Elementary Particle and Cosmic Ray Physics*, (North-Holland, Amsterdam, 1960), Vol. V.

[14] P. L. Jain and Z. Ahmad, Phys. Rev. Lett. 28, 459 (1972).

Observation of the Reactions $e^+e^- \to e^+e^-$, $e^+e^- \to \gamma\gamma$, and $e^+e^- \to \mu^+\mu^-$ at a Center-of-Mass Energy of 5.2 GeV*

B. L. Beron, J. F. Crawford, R. L. Ford, R. Hofstadter, E. B. Hughes, R. Kose,†
P. LeCoultre,‡ T. W. Martin, L. H. O'Neill, R. E. Rand, L. Resvanis,§
R. F. Schilling, and J. W. Simpson
High Energy Physics Laboratory and Department of Physics, Stanford University,
Stanford, California 94305

(Received 17 June 1974)

We report measurements of $e^+e^- \to e^+e^-$, $e^+e^- \to \gamma\gamma$, and $e^+e^- \to \mu^+\mu^-$ at angles close to 90°, relative to Bhabha scattering at 3.7°, at a center-of-mass energy equal to 5.2 GeV. The results are found to be consistent with the predictions of quantum electrodynamics.

We report here significant initial results from an experimental study of the reactions $e^+e^- \to e^+e^-$, $e^+e^- \to \gamma\gamma$, and $e^+e^- \to \mu^+\mu^-$ at the 2.6-GeV electron-positron storage ring (SPEAR) at the Stanford Linear Accelerator Center. The purpose of this experiment[1] was to test the validity of quantum electrodynamics for large values of the square of the invariant four momentum transfer, q^2, by measuring cross sections for the above reactions at angles close to 90°, relative to Bhabha scattering at 3.7°. For $e^+e^-\to e^+e^-$, which at 90° is dominated by spacelike momentum transfers, and for $e^+e^-\to\gamma\gamma$ the detected events lie in the q^2 range -7 to -20 $(\mathrm{GeV}/c)^2$, while for $e^+e^-\to\mu^+\mu^-$ q^2 is equal to 27 $(\mathrm{GeV}/c)^2$. In this Letter we present the results of an analysis of approximately 60, 30, and 85% of the total event numbers that were observed for the reactions $e^+e^-\to e^+e^-$, $e^+e^-\to\gamma\gamma$, and $e^+e^-\to\mu^+\mu^-$, respectively.

The experimental apparatus consisted of two identical spectrometers mounted in a collinear configuration about the beam interaction region. Each spectrometer consists of a multiwire proportional chamber (MWPC) at a distance of 7.5 in. from the interaction region, followed in sequence by an optional 0.25-in. lead converter, a set of two MWPC's separated by an 8-in. drift space, a plastic scintillator aperture counter, and a 20-in.-thick NaI(Tl) total-absorption detector. A complete description of the MWPC's and the read-out electronics has appeared elsewhere.[2] The NaI(Tl) total-absorption shower-counter (TASC) crystal[3] is 30 in. in diameter and serves to absorb totally electrons and γ rays incident within its acceptance aperture. The remaining elements in each spectrometer are used solely for the identification of muons. These consist of an 8-in. iron absorber, a plastic scintillator timing counter, a plastic scintillator hodoscope (spatial resolution 1.5 in. × 1.5 in. for single particles), and a 3.5-in.-thick NaI(Tl) crystal. All of the data were obtained with the spectrometers oriented at an azimuthal angle of 45° relative to the plane of the circulating beams. This was done in order to suppress any influence on the measured cross sections of a possible transverse polarization of the circulating beams.[4]

The experiment was run in two modes. First, with the γ-ray converters removed, the apparatus was devoted to the measurement of $e^+e^-\to e^+e^-$ and $e^+e^-\to\mu^+\mu^-$, and second, with the γ-ray converters inserted, to $e^+e^-\to\gamma\gamma$ and $e^+e^-\to\mu^+\mu^-$. The electronic signature for an event of the type $e^+e^-\to e^+e^-$ or $e^+e^-\to\gamma\gamma$ required only the detection of greater than 0.5 GeV in each of the TASC crystals in coincidence with the crossing of the beams, while that for an event of the type $e^+e^-\to\mu^+\mu^-$ required signals from the aperture and timing counters in each spectrometer in coincidence with the crossing of the beams.

The absolute luminosity of the storage ring was monitored through the measurement of Bhabha scattering at 3.7°. The operating principle of the monitor has been used before,[5] but in the application to SPEAR the design goal was to provide luminosity measurements accurate to within a systematic uncertainty ±2%. A critical examination of the response of the monitor[6] leads us to believe that this accuracy was achieved.

All candidate events for the three reactions of interest were reconstructed and displayed for off-line inspection on a graphic terminal by an IBM 360/91 computer. An interactive software system was employed, as necessary, to edit the MWPC data in order to complete the track reconstruction. Events were accepted as candidates for $e^+e^-\to e^+e^-$ provided that both reconstructed tracks intersected the respective entrance planes of the TASC crystals within a circular aperture of 22 in. diameter and that the two tracks were collinear to within 15°. Subsequently, the requirement was made that a minimum energy of 1.25 GeV be observed in each of the TASC crystals. Figure 1 shows the energy distribution observed in one of the NaI(Tl) TASC crystals for $e^+e^-\to e^+e^-$ candidate events which satisfy all of the above criteria, with the exception of the energy requirement in this one crystal. A clear

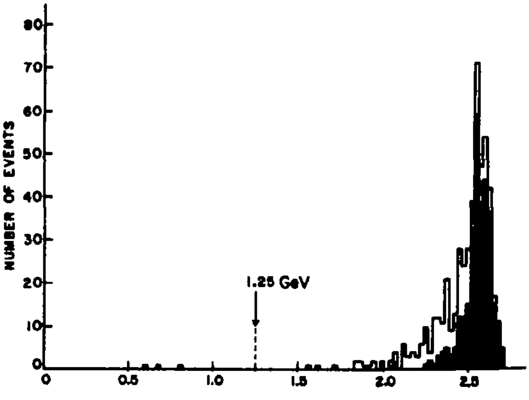

FIG. 1. Energy distribution observed in the top NaI(Tl) TASC crystal for $e^+e^-\to e^+e^-$ candidate events for two aperture diameters. (22 in. aperture diameter —502 events shown by open histogram; 18 in. aperture diameter—305 events shown by filled histogram.) At the larger diameter the peak is broadened as a result of the inclusion of particles which enter the crystal obliquely and close to its edge. 22 in. is judged to be the maximum aperture diameter for which Bhabha events can be cleanly separated from the lower-energy background events.

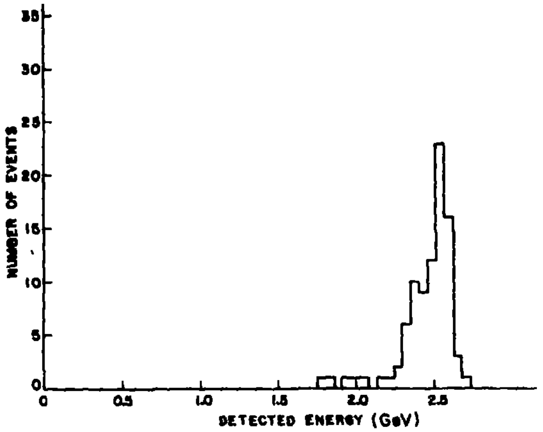

FIG. 2. Energy distribution observed in the top NaI(Tl) TASC crystal for 88 $e^+e^-\to\gamma\gamma$ candidate events for an aperture diameter of 23 in. The absence of background events at low deposited energies permits the use of a larger aperture diameter for $e^+e^-\to\gamma\gamma$ than for $e^+e^-\to\gamma\gamma$ than for $e^+e^-\to e^+e^-$.

peak due to the detection of 2.6-GeV electrons or positrons is observed together with a few events at energies less than 1 GeV. The latter events are primarily due to the detection of cosmic-ray muons. Clearly the choice of 1.25 GeV as the threshold energy for electron detection is quite uncritical. No other criteria are necessary for the identification of $e^+e^-\to e^+e^-$ events.

Events were accepted as candidates for $e^+e^-\to\gamma\gamma$ provided that both reconstructed γ-ray trajectories intersected the respective planes of the TASC crystals within a circular aperture of 23 in. diameter and that the two trajectories were collinear to within 15°. It was also required that no evidence exist for incident charged particles in the MWPC's in front of the converters in the immediate vicinity of the positions through which the γ rays were expected to pass. Figure 2 shows the energy distribution observed in one of the NaI(Tl) TASC crystals for $e^+e^-\to\gamma\gamma$ events which satisfy the above criteria. Again, a clear peak due to the detection of 2.6-GeV γ rays is observed. No other criteria are necessary for the identification of $e^+e^-\to\gamma\gamma$ events.

Events were accepted as candidates for $e^+e^-\to\mu^+\mu^-$ provided that (1) the measured time difference between the pulses observed in the two timing counters did not exceed 5.3 nsec, (2) the reconstructed tracks intersected the planes of the respective timing counters within a circular aperture of 28 in. diameter, and (3) the measured

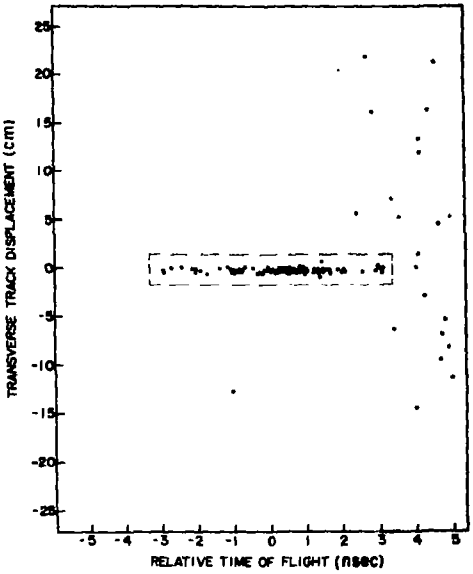

FIG. 3. Scatter plot for 102 $e^+e^-\to\mu^+\mu^-$ candidate events (aperture diameter, 28 in.) showing the average transverse distance of muon tracks from the orbit of the circulating beams versus the time difference between the pulses observed in the timing counters. The dashed rectangle indicates the acceptance area for $e^+e^-\to\mu^+\mu^-$ events.

time difference between the pulse observed in one of the timing plastic scintillators and the crossing of the beams was within ± 7 nsec. For these events Fig. 3 shows the correlation between the average distance of closest approach of the tracks to the orbit of the circulating beam and the time difference between the pulses observed in the timing counters. Two types of events are clearly revealed in this plot: first, a group of events with small relative timing and tightly correlated with the beam orbit, and second, a group of events with larger timing and no correlation with the beam orbit. The former are $e^+e^-\to\mu^+\mu^-$ events, while the latter are cosmic-ray muons. Only a small fraction (~0.1%) of the cosmic-ray muons detected by the apparatus appear in Fig. 3, since the average relative timing for such events is 10.6 nsec and the measured standard deviation is 1.7 nsec.

The observed numbers of events and the numbers expected from quantum electrodynamics for the three reactions of interest are shown in Table I. This table also lists the radiative corrections applied to the expected numbers of events. All of the radiative corrections, including cor-

TABLE I. Summary of the observed and expected number of events. The principal corrections and errors are also shown, together with the lower limits set by this and earlier experiments on the cutoff parameters Λ.

	$e^+e^- \to e^+e^-$	$e^+e^- \to \gamma\gamma$	$e^+e^- \to \mu^+\mu^-$
Integrated luminosity (10^{35} cm^{-2})	2.96 ± 0.06	6.41 ± 0.13	23.5 ± 0.5
Radiative correction (to lowest-order expected rate in spectrometers)	$0.940 \pm < 0.01$	$0.951 \pm < 0.01$	$0.954 \pm < 0.01$
Number of events expected	521 ± 16	84.3 ± 3.7	87.1 ± 2.7
Number of events observed	499	88	80
Ratio of observed to expected events	0.96 ± 0.05	1.04 ± 0.12	0.92 ± 0.11
Λ_+ (GeV), this experiment	22.8	6.2	14.5
Λ_- (GeV), this experiment	14.4	6.9	23.6
Λ_+ (GeV), earlier experiments	9.8[a]	3.9[b]	~7[c]
Λ_- (GeV), earlier experiments	10.5[a]	5.1[b]	~9[c]

[a] Ref. 7. [b] Ref. 8. [c] Ref. 9.

rections of 2.2% to the observed luminosities, were calculated according to Berends *et al.*[10,11] There are no other corrections of any significance to either the observed or the expected event numbers. The estimated background due to collinear hadron pair production is negligible (≤ 0.1 event) for both $e^+e^- \to e^+e^-$ and $e^+e^- \to \mu^+\mu^-$. A search was made for the occurrence of events of all three types with the circulating beams displaced in the vertical direction so that they do not collide but none were found. Various sources of systematic error are included in the errors assigned to the expected event numbers.

We conclude from Table I that the rates we observe for the three reactions of interest are consistent with the predictions of quantum electrodynamics. If, in addition, we anticipate that possible breakdowns of theory can be described by propagator modifications in the lowest-order Feynman diagrams of the form $1/q^2 \to (1/q^2)[1 \pm q^2/(q^2 - \Lambda_\pm^2)]$ for $e^+e^- \to e^+e^-$ and $e^+e^- \to \mu^+\mu^-$,[12,13] and $1/(q^2 - m^2) \to [1/(q^2 - m^2)](1 \pm q^4/\Lambda_\pm^4)$ for $e^+e^- \to \gamma\gamma$,[14] then our results can be used to place lower limits (95% confidence level) on the cutoff parameters Λ for each of the three reactions. These values, together with the limits set by earlier experiments, are given in Table I.

We are grateful to Dr. R. Gastmans of the University of Leuven for assistance in adapting his computer codes to the calculation of our radiative corrections.

---

[*] Work supported in part by the National Science Foundation under Grants No. GP-22880 and No. GP-38611.

[†] Visitor from Physikalisches Institut, Universität Bonn, Bonn, Germany.

[‡] Visitor from Universität Bern, Bern, Switzerland.

[§] Visitor from University of Pennsylvania, Philadelphia, Pa. 19104 (work supported by the U. S. Atomic Energy Commission).

[1] B. L. Beron *et al.*, in Proceedings of the Sixth International Symposium on Electron and Photon Interactions at High Energies, Bonn, Germany, 27–31 August 1973 (to be published).

[2] R. E. Rand *et al.*, High Energy Physics Laboratory, Stanford University, Report No. 720, 1973 (to be published).

[3] E. B. Hughes *et al.*, IEEE Trans. Nucl. Sci. 19, No. 3, 126 (1972).

[4] See for example, W. T. Ford, A. K. Mann, and T. Y. Ling, SLAC Report No. 158, 1972 (unpublished).

[5] G. Barbiellini *et al.*, Atti Accad. Naz. Lincei, Cl. Sci. Fis., Mat. Natur., Rend. 44, 233 (1968).

[6] J. F. Crawford *et al.*, High Energy Physics Laboratory, Stanford University, Report No. 730 (unpublished).

[7] H. Newman *et al.*, Phys. Rev. Lett. 32, 483 (1974).

[8] G. Hanson *et al.*, Lett. Nuovo Cimento 7, 587 (1973). The breakdown model assumed by Hanson *et al.* does not admit a modification equivalent to that provided by Λ_-, but their data can be seen to be consistent with the value of Λ_- shown in Table I.

[9] B. Borgia *et al.*, Lett. Nuovo Cimento 3, 115 (1972); V. Alles-Borelli *et al.*, Nuovo Cimento 7A, 330 (1972). These authors do not quote values for $\Lambda_\pm$ (excepting Borgia *et al.*, who give 9 GeV for Λ_-) but their data can be seen to be consistent with the values of $\Lambda_\pm$ shown in Table I.

[10] F. A. Berends, K. J. F. Gaemers, and R. Gastmans, Nucl. Phys. B68, 541 (1974), and B57, 381 (1973).

[11] F. A. Berends and R. Gastmans, Nucl. Phys. B61, 414 (1973).

[12] S. D. Drell, Ann. Phys. (New York) 4, 75 (1958).

[13] T. D. Lee and G. C. Wick, Nucl. Phys. B9, 209 (1969).

[14] N. M. Kroll, Nuovo Cimento 45A, 65 (1966).

e^+e^- Annihilation into Hadrons in Quantum Field Theory*

Hung Cheng and Jeffrey Mandula†
Department of Mathematics, Massachusetts Institute of Technology, Cambridge, Massachusetts 02139

(Received 1 July 1974)

Quantum field theory is shown to give an energy-dependent $R = \sigma(e^+e^- \to \text{hadrons})/\sigma(e^+e^- \to \mu^+\mu^-)$, as a result of creation of slow particles in the c.m. system. A simple model which predicts power growth for R is given and further experimental consequences are discussed.

Recent experiments on electron-positron annihilation indicate that $R = \sigma(e^+e^- \to \text{hadrons})/\sigma(e^+e^- \to \mu^+\mu^-)$ rises with energy,[1] in contradiction with a number of theoretical expectations. In this Letter we show that the increase of R with energy is expected in quantum field theories, as a result of the production of slow particles in the c.m. system.

Extensions of the parton model[2] and the light-cone algebra with scale invariance at short distances,[3] which account for the scaling of deep inelastic electron scattering,[4] to e^+e^- annihilation into hadrons led to the prediction that R would approach a constant at high energies.[5] The value of this constant is model dependent—$\frac{2}{3}$ in the quark-neutral-gluon model, 2 in the colored-quark-gluon model, and $\frac{10}{3}$ in the charmed-colored-quark-gluon model.

The unifying idea behind these models is that hadron physics is described by a local field structure. The rise of R with energy has been taken as an experimental counterindication to this idea.

The purposes of this Letter are (a) to show that quantum field theories do not imply that R is asymptotically a constant (even with a transverse-momentum cutoff); (b) to describe a physical picture of $e^+e^- \to$ hadrons which explicitly shows the connection between an increasing R and the production of slow particles in the c.m. system; (c) to present a simple, quantitative model illustrating this picture in which R rises like a power of the energy; and (d) to discuss further experimental consequences of this model.

In the parton model, the physical picture that leads to the constancy of R is that a photon with large virtual mass creates a pair of elementary particles which at first separate from each other freely, and rearrange themselves into hadrons after a very long time.[6] In this physical picture the rate for $e^+e^- \to$ hadrons is given by the Feynman diagram in Fig. 1. This physical picture ignores the possibility that the two elementary particles created may interact with each other and produce additional elementary particles within a very short time. An example of such a production process is illustrated in Fig. 2. The scattering amplitude corresponding to this diagram (which has no ultraviolet divergence) is finite over an extensive kinematical region in the limit $s \to \infty$. In the c.m. frame, this region includes all p_3 and p_4 for which $(p_3 + p_4)^2$ is finite and for which the components of p_3 and p_4 transverse to p_1 and p_2 are finite. In particular, it includes the kinematic region where all components of p_3 and p_4 are finite, i.e., where the additional pair is slow in the c.m. system. In this region,

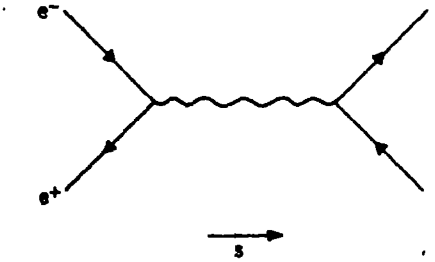

FIG. 1. e^+e^- annihilation into a pair of elementary particles. The wavy line denotes the photon and the dotted lines denote the vector gluon.

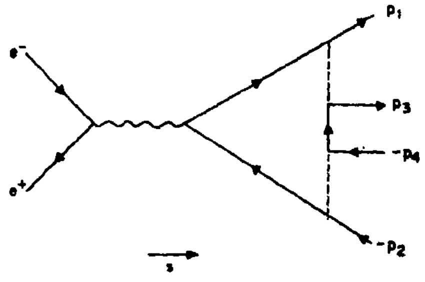

FIG. 2. e^+e^- annihilation into two pairs of elementary particles. The wavy line denotes the photon and the dotted lines denote the vector gluon.

the scattering amplitude is independent of the longitudinal momentum of the pair as this longitudinal momentum becomes large, and falls rapidly for large transverse momentum of the pair. As a consequence, the contribution of this region to R is asymptotically proportional to $dp_\parallel/E$, which integrates to $\ln s$. Therefore, R increases with energy.

The space-time picture of this process is vastly different from that which suggested that R would approach a constant. In the process illustrated in Fig. 2, the additional pair is created in a time of order unity. This means that each of the initial pair interacts in a time of order $1/\sqrt{s}$ in its own rest frame. The increase of R with energy is explicitly a result of the production of relatively slow particles in the c.m. system during such short times.

The spin of the exchanged meson (gluon) plays a crucial role in determining the asymptotic limit of R. A vector-gluon exchange, which we have been assuming, is needed to get a rising R. Were the gluon a scalar, the process in Fig. 2 would be down by a factor of s relative to that in Fig. 1, and would make no asymptotic contribution to R.

The dynamical mechanism which is responsible for the rise of R at the same time resolves the parton-model puzzle of how the fast, quasifree partons created from a massive virtual photon could eventually result in the appearance of slow, final-state hadrons. The resolution is that the fast partons interact to produce slow, secondary partons very soon after their own creation. The secondaries can easily give rise to slow hadrons.

These considerations immediately generalize to the production of many additional pairs. A diagram which illustrates multipair creation is given in Fig. 3. The scattering amplitude corresponding to multipair creation is again of order unity in the limit $s \to \infty$ when the masses and transverse momenta of the additional pairs are fixed, and their longitudinal momenta arbitrary. As a consequence, the contribution of the production of n additional pairs to R is asymptotically proportional to $(\ln s)^n$. The overall effect of multiparticle states will evidently be to give an energy dependence to R.

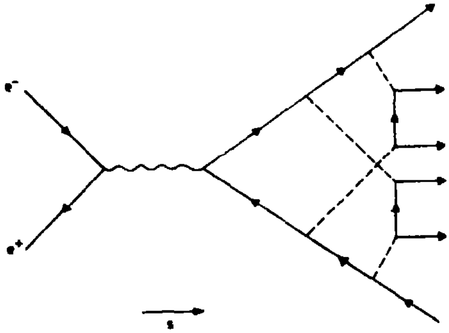

FIG. 3. e^+e^- annihilation into three pairs of elementary particles. The wavy line denotes the photon and the dotted lines denote the vector gluon.

At the cost of oversimplifying a very complicated physical situation, we may get a quantitative idea of the effects of pair creation by taking as a model for $e^+e^- \to$ hadrons the sum of the leading asymptotic calculations for n-pair creation. In this model, the contribution of n-pair production to R turns out to be the product of n single-pair production factors, and, with the required statistical factor $1/n!$, is of the form $(a \ln s)^n/n!$. Summing over n, we find that

$$R \propto s^a. \tag{1}$$

This result holds to lowest order in α only, and should be valid so long as $\alpha R/3 \ll 1$, that is, for $R \ll 400$. Above $\alpha R = 3$, terms which are higher order in α become comparable to the lowest-order term, and so the formula for R [Eq. (1)], and all of the subsequent results [Eqs. (2) to (12)], must be modified. The multiplicity follows the Poisson distribution, with the average multiplicity given by

$$\langle n \rangle \sim a \ln s, \tag{2}$$

where a, the coefficient of $\ln s$ in (2), is the same number as the power of s in (1). Preliminary measurements support this equality and indicate $a \approx \frac{3}{4}$.[1] The inclusive distribution for a single particle of momentum $\vec{p}$, in the limit $s \to \infty$ with $p = |\vec{p}|$ much smaller than $\frac{1}{2}\sqrt{s}$, is given by

$$E\, d\sigma/dp \sim s^{-1+a} f(p), \tag{3}$$

where, because of the available phase space,

$$f(p) \propto p^2, \quad p \ll 1, \tag{4}$$

and, because the emission of particles with large p does not depend on the longitudinal momentum,

$$f(p) \to \text{const}, \quad p \gg 1. \tag{5}$$

Equation (3) means that $(1/\sigma)d\sigma/dp$ becomes a function of p alone and does not depend on s:

$$(1/\sigma)d\sigma/dp \to E^{-1}F(p), \tag{6}$$

independent of the total energy. When p is a finite fraction of $\frac{1}{2}\sqrt{s}$, Eq. (3) fails and, instead, the inclusive distribution is given by

$$x\, d\sigma/dx \sim s^{-1+\epsilon} g(x), \tag{7}$$

where $x = 2p/\sqrt{s}$. The single-particle distribution $d\sigma/dx$ scaled by the cross section is given by

$$(1/\sigma) d\sigma/dx \to x^{-1} G(x). \tag{8}$$

The rate of approach to this asymptotic limit is not uniform in x. The reason is that the asymptotic form comes from distributing the available energy among many emitted particles. But if one particle has energy $E = x\sqrt{s}/2$, the residual invariant mass squared of the others is only $(1-x)s$. Thus, the closer x is to 1, the higher s must be before the asymptotic limit is reached. The dependence of the inclusive distribution with the energy is therefore slower as x is closer to 1. As this energy dependence is of the form $s^{\epsilon-1}$, the same analysis gives

$$G(x) \propto (1-x)^{\epsilon-1}, \quad x \to 1. \tag{9}$$

For small values of x, $G(x)$ approaches the nonzero constant

$$G(0) = \lim_{p\to\infty} F(p), \tag{10}$$

which, together with (8), gives the familiar dx/x factor for the inclusive distribution. The angular distribution of particles with finite x at asymptotic energies follows the angular distribution of the leading elementary quantum. If the fundamental charged fields have spin $\frac{1}{2}$ this distribution is of the form $1+\cos^2\theta$. One expects to observe this behavior at fixed x when s is large enough that $(1/\sigma)d\sigma/dx$ becomes independent of s, which the preliminary data suggest is above present energies. Similar to (3), the inclusive distribution for two particles of momentum $\vec{p}_1$ and $\vec{p}_2$, respectively, is given by

$$E_1 E_2\, d\sigma/dp_1\, dp_2 \sim s^{-1+\epsilon} h(\vec{p}_1, \vec{p}_2). \tag{11}$$

Thus, the two-particle distribution scaled by the total cross section is also energy independent. When $\vec{p}_1$ and $\vec{p}_2$ are far apart in the momentum space, the function $h(\vec{p}_1, \vec{p}_2)$ factorizes into

$$h(\vec{p}_1, \vec{p}_2) \propto f(p_1) f(p_2), \tag{12}$$

and, depending on the scale of the momenta relative to $\frac{1}{2}\sqrt{s}$, there are straightforward generalizations of (6) and (8).

In comparing these results with the distributions measured in e^+e^- annihilation, it should be noted that the data are expected to look simplest when $(1/\sigma)d\sigma/dp$ is plotted against p for small to moderate p [see Eq. (6)], but for p comparable to $\frac{1}{2}\sqrt{s}$, one must plot $(1/\sigma)d\sigma/dx$ against x [see Eq. (8)]. As an example, consider the peak of the single-particle inclusive distribution at small momentum. When this distribution is plotted against x, the peak appears to move with energy. But if it is plotted against p, its position is predicted to be stationary. More generally, the plot of $(1/\sigma)d\sigma/dp$ against p follows the same curve for all s, as long as p is small compared to $\frac{1}{2}\sqrt{s}$, in agreement with preliminary measurements.[1]

In summary, we have seen that, contrary to past belief, quantum field theory does not imply that R is asymptotically a constant. A constant value of R is obtained only in the lowest approximation which takes into account the contribution of single-pair creation. When we include the creation of pairs of soft particles, an increase of R is obtained. This increase would remain even if a transverse-momentum cutoff were imposed. It is therefore unrelated to the logarithmic factors of s which arise in field-theoretic discussions of deep inelastic electron scattering. The amplitude from the set of diagrams in Fig. 2 and Fig. 3, when analytically continued to the kinematic region of deep inelastic electron scattering, does not give energy-dependent factors to the structure functions W_1 and νW_2, and does not modify Bjorken scaling.

In conclusion, we have shown that field theory is consistent with a rising R. The experiments which indicate that R is increasing are not evidence against the parton model, if by the parton model one means field theory supplemented by a transverse-momentum cutoff. However, the light-cone singularity of a product of electromagnetic currents carrying timelike momenta is not canonical.

We thank Professor T. T. Wu for useful discussions, and Professor B. Richter for supplying us with preliminary results from the e^+e^- annihilation experiment at SPEAR.

---

*Work supported in part by the National Science Foundation under Grant No. GP 29463.

†Alfred P. Sloan Fellow.

[1] A. Litke *et al.*, Phys. Rev. Lett. 30, 1189 (1973); R. R. Larsen *et al.*, Bull. Amer. Phys. Soc. 19, 542 (1974).

[2] R. P. Feynman, *Photon-Hadron Interactions* (Benjamin, New York, 1972); S. Drell, D. Levy, and T. M. Yan, Phys. Rev. 187, 2159 (1969).

[3] K. Wilson, Phys. Rev. 179, 1499 (1969); H. Fritzsch and M. Gell-Mann, in *Proceedings of the International Conference on Duality and Symmetry in Hadron Phys-*

ics (Weizman Science Press, Jerusalem, 1971).

[4] H. W. Kendall, in *Proceedings of the International Symposium on Electron and Photon Interaction at High Energies, Ithaca, New York, 1971,* edited by N. B. Mistry (Cornell Univ. Press, Ithaca, N. Y., 1972).

[5] J. D. Bjorken, Phys. Rev. 148, 1467 (1966); N. C bibbo, G. Parisi, and M. Testa, Lett. Nuovo Cimen 4, 35 (1970).

[6] Unless otherwise specified, time is measured in c.m. frame of the e^+e^- system.

ERRATUM

BOUND ELECTRON STATES IN THE WAKE OF SWIFT IONS IN SOLIDS. V. N. Neelavathi, R. H. Ritchie, and Werner Brandt [Phys. Rev. Lett. 33, 302 (1974)].

The last citation was omitted in the list of references. It should be:

[12] M. J. Gaillard, J. C. Poizat, and J. Remillieux, in *Proceedings of the Fifth International Conference on Atomic Collisions in Solids, Gatlinburg, Tennessee, 24–28 September 1973* (Plenum, New York, to be published), and references to earlier work cited therein.

PHYSICAL REVIEW
LETTERS

VOLUME 33 16 SEPTEMBER 1974 NUMBER 12

Photoionization Cross Sections of the Outer *s*-Subshell Electrons in the Rare Gases*

James A. R. Samson and J. L. Gardner
Behlen Laboratory of Physics, University of Nebraska, Lincoln, Nebraska 68508
(Received 8 July 1974)

The absolute photoionization cross sections for the outer *ns* subshells of argon, krypton, and xenon have been measured from their respective ionization thresholds to 41 eV as well as at one point near the ionization threshold of neon. The technique of photoelectron spectroscopy was used to determine the ratio of the *s* to *p* photoelectrons. Measurements of the total cross sections and of the magnitudes of multiple-ionization processes allowed an accurate determination of the subshell cross sections to be made.

Photoionization of the outer *s*-subshell electrons in the rare gases provides a sensitive test of atomic theory applied to the photoionization process. Calculations with single-electron wave functions predict that the photoionization cross sections of the outer *s* shells should be extremely low at threshold relative to *p*-shell ionization (less than about 0.5%). The predicted cross sections then start to increase reaching a broad maximum 20 to 30 eV above threshold.[1,2] However, recent calculations, taking into account the interaction of electrons within a subshell and intershell interactions, yield completely different results (random-phase approximation with exchange, RPAE).[3,4] The threshold cross sections are predicted to be at least 20 times larger than the single-electron–model predictions. The RPAE cross sections are then predicted to drop rapidly to approximately zero at 10 to 20 eV above threshold. The purpose of this paper is to present experimental data supporting the random-phase–approximation method.

Recently, Lynch *et al.*[5] have reported experimental results for the photoionization of the 3*s* subshell in Ar. Their data show a minimum in the cross section in agreement with the RPAE theory. However, there is considerable scatter in their data near threshold that does not allow a more precise comparison with theory. Further, the calculated RPAE values with which their data were compared[3] have been significantly modified in the threshold region.[4] We present here for the first time detailed experimental results of the threshold cross sections of the outer *ns* subshells of Ar, Kr, Xe, and a single point for Ne. The technique of photoelectron spectroscopy was used to determine the ratio of *s* to *p* photoelectrons.

Two sets of data are presented. Earlier data,[6] which were obtained with a retarding-potential electron-energy analyzer, have been reanalyzed, corrected for electron scattering in the gas,[7] and corrected for the varying electron angular distribution[2] in the *p* shell (the asymmetry parameter β was assumed to be equal to 2 for *s*-shell electrons near threshold).

The present data were obtained with a cylindrical-mirror electron-energy analyzer that accepted photoelectrons ejected at 54° 44′ with respect to the direction of the photon beam.[8] At this angle there is no collection discrimination caused by the varying angular distribution.[9] In addition the transmission of the analyzer was calibrated to within ± 5% as a function of electron energy for

Copyright © 1974 by
The American Physical Society

TABLE I. ns/np ratio for the outer s shells of the rare gases. Source lines preceded by an asterisk were produced by a condensed spark discharge in neon. The other source lines were produced in a dc glow discharge in He and Ne and a dc arc in Ar.

Source line λ(Å)		ns/np Ratio (%) Xe	Kr	Ar	Ne
243.027	He II	--	--	--	2.1 ± .4
303.786	He II	5.7 ± 1.2	0.6 ± .5	0.9 ± .5	--
379.31	Ne III	--	3.7 ±1.8	5.3 ±1.0	--
406.50	Ne II	0.0 ± .8	3.3 ± .6	5.0 ± .7	--
* 416.198	Ne IV	--	3.2 ± .7	3.3 ± .8	--
446.4	Ne II	2.9 ± .9	3.1 ± .4	--	--
460.73	Ne II	2.4 ± .9	--	--	--
* 469.817	Ne IV	2.7 ± .7	--	--	--
* 501.0	Ne (?)	3.6 ± .9	--	--	--
518.5	Ar II	2.9 ± .7	--	--	--
* 521.742 521.813	Ne IV	3.3 ± .8	--	--	--
522.208	He II	2.0 ± .5	--	--	--
* 526.4	Ne (?)	2.7 ± .7	--	--	--

the range 0–28 eV, by using the method described previously.[8] An accelerating/retarding lens system in the analyzer allowed the electrons to be analyzed at a fixed voltage of 3 V. This prevented discrimination, caused by electron-gas scattering, of electrons with originally different energies.

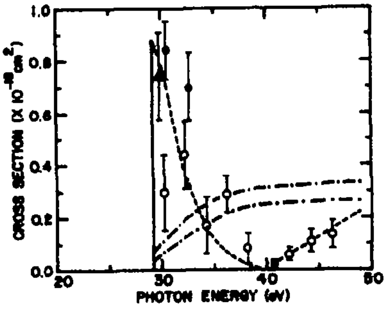

FIG. 1. Photoionization cross sections of the 3s subshell of Ar. Theoretical data: dashed line, Ref. 4; dash-dotted line, Ref. 2 (upper curve, dipole length approximation; lower curve, dipole velocity approximation). Experimental data: filled circles, present data; triangle, Ref. 6, corrected; open circles, Ref. 5.

The photoelectron spectra of the rare gases were taken at several discrete wavelengths between 24 and 51 eV. A dc glow discharge in H Ne, and Ar produced the resonance lines of th neutral and singly ionized atoms.[10] The radiation was then dispersed with a 2-m Vodar gra ing-incidence monochromator. An extremely stable scanning voltage source was used to sc the spectra, repetitively, over periods up to

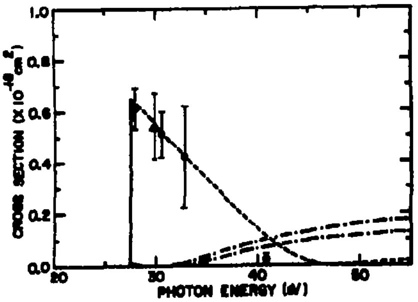

FIG. 2. Photoionization cross sections of the 4s shell of Kr. Lines and data points as in Fig. 1.

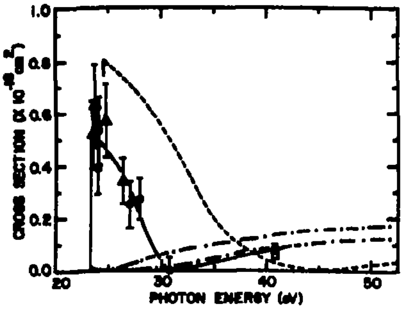

FIG. 3. Photoionization cross section of the 5s subshell of Xe. Lines and data points as in Fig. 1; square, Ref. 14; solid line, suggested experimental cross section.

h. The data were accumulated in a multichannel analyzer. From the data the ratio R, of s to p electrons, was obtained. This ratio is tabulated in Table I. The cross section for photoionization of s-shell electrons σ_s is then given by

$$\sigma_s = \sigma_t R/(1+R), \qquad (1)$$

where σ_t is the total photoionization cross section.[11] The effects of double ionization were taken into account at 41 eV in Kr and Xe.[12]

The data for Ar, Kr, and Xe are shown in Figs. 1–3 along with the theoretical calculations.[2,4] The results clearly show the interference effect between the $np^6 \to np^5\,\epsilon d$ transition and the $ns^2 \to ns\,\epsilon' p$ transitions as predicted by Amusia *et al.*[3] The RPAE calculations[3] predict a different situation for Ne. The intershell interaction is weak and, therefore, the 2p subshell does not appreciably affect the 2s photoionization cross section. The form of the curve is similar to the single-particle calculations but the magnitudes of the cross sections predicted by the RPAE calculations are lower. Our single experimental value of $(0.16 \pm 0.03) \times 10^{-18}$ cm^2 near threshold (51 eV) and the data of Wuilleumier and Krause[13] starting at 109 eV are insufficient to verify the lack of interference from the 2p subshell. More experimental data in the threshold region are desirable. The lack of data at high photon energies is simply caused by the low ionization cross sections, weak source line intensities, and discrimination against high-energy electrons by the energy analyzer in the present mode of operation.

The magnitudes of the RPAE results are sensitive to the value of the ns-subshell ionization potential used in the calculations. The RPAE curves for Ar and Kr from Ref. 4, shown in Figs. 1 and 2, respectively, used the experimental ionization potentials. The results are in good agreement with the combined experimental data. For Xe the theoretical ionization potential was used. This accounts for the displacement of the threshold values by 2 eV between the experimental and theoretical curves of Fig. 3. Although the shape of the experimental curve agrees with the RPAE theory, the magnitudes do not. The single value at 41 eV obtained by Kemeny *et al.*[14] has a reported 5s/5p ratio of 0.05. This is to be compared with the present value of 0.057 ± 0.012. Both points have been corrected for double ionization (double-ionization abundance is 20% for Xe at 41 eV).[11]

The data presented here fully support the RPAE-model calculations for the rare gases. However, the discrepancy between theory and experiment for Xe indicates that further refinements are necessary in the RPAE model.

---

*Research supported by the Atmospheric Sciences Section, National Science Foundation.

[1] J. W. Cooper and S. T. Manson, Phys. Rev. 177, 157 (1969).

[2] D. J. Kennedy and S. T. Manson, Phys. Rev. A 5, 227 (1972).

[3] M. Ya. Amusia, V. K. Ivanov, N. A. Cherepkov, and L. V. Chernysheva, Phys. Lett. 40A, 361 (1972).

[4] M. Ya. Amusia, V. K. Ivanov, N. A. Cherepkov, and L. V. Chernysheva, in *Proceedings of the Eighth International Conference on the Physics of Electronic and Atomic Collisions, Belgrade, Yugoslavia, 1973. Abstracts* (Institute of Physics, Belgrade, Yugoslavia, 1973), p. 581; M. Ya. Amusia, in *Proceedings of the Eighth International Conference on the Physics of Electron and Atomic Collisions, Belgrade, Yugoslavia, 1973. Invited Lectures and Progress Reports* (Institute of Physics, Belgrade, Yugoslavia, 1973), p. 172.

[5] M. J. Lynch, A. B. Gardner, K. Codling, and G. V. Marr, Phys. Lett. 43A, 237 (1973).

[6] J. A. R. Samson and R. B. Cairns, Phys. Rev. 173, 80 (1968).

[7] R. B. Brode, Rev. Mod. Phys. 5, 257 (1933).

[8] J. L. Gardner and J. A. R. Samson, J. Electron Spectrosc. Relat. Phenomena 2, 267 (1973).

[9] J. A. R. Samson and J. L. Gardner, J. Opt. Soc. Amer. 62, 856 (1972).

[10] J. A. R. Samson, *Techniques of Vacuum Ultraviolet Spectroscopy* (Wiley, New York, 1967), Chap. 5.

[11] J. A. R. Samson, in *Advances in Atomic and Molecular Physics*, edited by D. R. Bates and I. Estermann (Academic, New York, 1966), Vol. 2, p. 117.

[12] J. A. R. Samson and G. N. Haddad, to be published.

[13] F. Wuilleumier and M. O. Krause, Phys. Rev. A 10, 242 (1974).

[14] P. C. Kemeny, R. T. Poole, J. G. Jenkin, J. Liesegang, and R. C. G. Leckey, Phys. Rev. A 10, 190 (1974).

Nonlinear Optical Processes by Van der Waals Interaction during Collision*

S. E. Harris and D. B. Lidow†
Microwave Laboratory, Stanford University, Stanford, California 94305

(Received 24 June 1974)

We describe an optical process where off-diagonal optical excitation of a first atomic species is coupled during collision to a second species. This coupling leads to new types of nonlinear optical processes, and allows large cross sections for inelastic collision between atoms with nonresonant energy levels.

By tuning a laser to the resonance line of an atomic species, a strong time-varying dipole moment is excited at the frequency of the incident laser. Alternatively, by making use of higher resonances, strong dipole moments may be excited at harmonics of the incident frequency.[1-3] In this Letter we describe a new type of nonlinear process where dipolar excitation of a first atomic species is coupled during collision to a second species. This dipole-dipole coupling leads to new types of nonlinear optical processes, and may be used to produce large enhancements in both the linear and nonlinear transition probabilities and cross sections of the second species. In particular, the process allows large cross sections for inelastic collision, or optical pumping, between atoms with nonresonant energy levels.

To avoid confusion with more familiar inelastic collision processes we note that we are considering a process where, in essence, energy is conserved by optical photons, as opposed to kinetic processes. From the Lorentz model of an atom, the process may be viewed as one where the phase and frequency of an oscillating atom A is transferred to a second atom B. The strength of the coupling varies as $1/R^3$ and is only strong when the atoms are relatively close ($R \lesssim 20$ Å). During this interaction time atom B may also accept additional photons from the external electromagnetic field, allowing it to conserve energy to complete a transition. This process does not require real transitions of atom A. Off-diagonal, as opposed to on-diagonal, excitation is transferred during collision.[4]

Subject to the approximation that the interatomic spacing is greater than the atomic dimension, the perturbation Hamiltonian which describes this process is given by[5]

$$H' = -e\vec{r}_A \cdot \vec{E}\cos\omega t - e\vec{r}_B \cdot \vec{E}\cos\omega t + [e^2/R^3(t)](x_A x_B + y_A y_B - 2z_A z_B), \qquad (1)$$

where $R(t)$ is the relative distance between atoms and x_A, x_B, etc., are the coordinates of each electron with respect to its nucleus, and $\vec{E}$ is the applied electromagnetic field. The first two terms of the Hamiltonian describe the interaction of each (isolated) atom with the electromagnetic field, while the last term describes the coupling between atoms. The calculation proceeds by expanding the wave function in a basis of product states with time-varying coefficients $c_{ij}(t)$.[5] Perturbation equations are written as a function of the relative atomic spacing $R(t)$. We assume straight-line atomic paths and integrate over $R(t)$ with a distance of closest approach r_0; and finally integrate over r_0 to an inner limit at which the Van der Waals potential remains valid.[6]

To be specific, we will consider the four-photon absorption process shown in Fig. 1; i.e., we wish to calculate the four-photon transition probability of atom B between the levels denoted by ω_{00} and ω_{02}. Though, in general, it is necessary to sum over all paths in the atomic system, in order to simplify the formulas, we will assume that the incident frequencies are sufficiently close to each level that a single path is singled out.

In the first three steps of perturbation, atom A

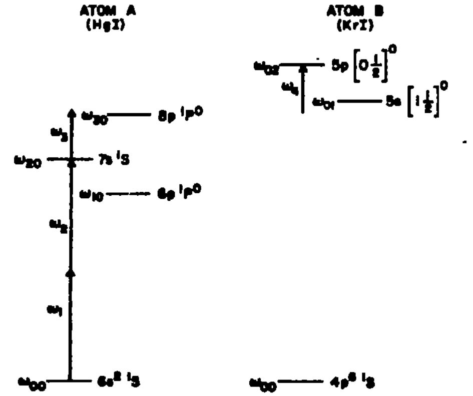

FIG. 1. Energy level diagram for calculation. For the Hg-Kr system, $\omega_1 = \omega_2 = 3129$ Å and $\omega_3 = \omega_4 = 7342$ Å.

accepts three photons from the electromagnetic field, and develops a mixed state and dipole moment at frequency $\omega_1+\omega_2+\omega_3$. In the fourth step of perturbation, this time-varying dipole moment is transferred via the Van der Waals interaction to atom B. In the fifth step, atom B accepts a photon of frequency ω_4, to complete the four-photon transition. In the basis of product states, the perturbation sequence is therefore $c_{00}\rightarrow c_{10}\rightarrow c_{20}\rightarrow c_{30}\rightarrow c_{01}\rightarrow c_{02}$. We let $R(t)=(r_0^2+\bar{V}^2t^2)^{1/2}$, where $\bar{V}$ is the average velocity and r_0 is the distance of closest approach in a particular collision. Carrying out the perturbation sequence, we find

$$c_{02}(r_0)=\gamma\int_{-\infty}^{\infty}(r_0^2+\bar{V}^2t^2)^{-3/2}\exp(j\Delta\omega_5 t)\,dt, \tag{2}$$

where

$$\gamma=\frac{\mu_{01}{}^A\mu_{12}{}^A\mu_{23}{}^A\mu_{03}{}^A\mu_{01}{}^B\mu_{12}{}^B E_1E_2E_3E_4}{16\hbar^5\Delta\omega_1\Delta\omega_2\Delta\omega_3\Delta\omega_4}.$$

The resonance denominators are defined as $\Delta\omega_1=\omega_1-\omega_{10}$, $\Delta\omega_2=\omega_1+\omega_2-\omega_{20}$, $\Delta\omega_3=\omega_1+\omega_2+\omega_3-\omega_{30}$, $\Delta\omega_4=\omega_1+\omega_2+\omega_3-\omega_{03}$, $\Delta\omega_5=\omega_1+\omega_2+\omega_3+\omega_4-\omega_{02}$, and the μ_{ij} and E_i are the matrix elements and applied electric fields as denoted by Fig. 1. In Eq. (2), we have assumed that the dephasing time T_2 of the final level ω_{02} is long as compared to the impact time $r_0/\bar{V}$. (The impact time is typically $\sim10^{-13}$ sec, and thus this will almost always be the case for absorption to a discrete level.) The quantity $|c_{02}(r_0)|^2$ is the probability that a collision with closest distance of approach r_0 has resulted in a transition to the final state.

The transition probability to line center ($\Delta\omega_5=0$) of atom B is then given by

$$\begin{aligned} W_B(t)&=4\pi N_A\bar{V}\int_{r_{0m}}^{\infty}|c_{02}(r_0)|^2r_0\,dr_0,\\ W_B(t)&=8\pi(N_A/\bar{V})r_{0m}^{-2}|\gamma|^2, \end{aligned} \tag{3}$$

where N_A is the concentration (cm^{-3}) of A atoms, $\bar{V}$ is the average velocity, r_{0m} is the minimum distance at which the dipolar approximation is reasonably valid, and $|\gamma|^2$ has been averaged over angular orientation. By noting the Fourier transform relationship of Eq. (2), one can see that the linewidth of the four-photon transition is approximately $\bar{V}/r_{0m}$.

If the dephasing time T_2 is short compared to the impact time—for instance, if level ω_{02} were instead the continuum of atom B while the intermediate levels remain as above—then $W_B(t)$ is shown to be given by

$$W_B(t)=\pi^2N_A r_{0m}^{-3}|\gamma|^2\rho(\omega), \tag{4}$$

where $\rho(\omega)$ is the density of final states. By noting that near line center $\rho(\omega)$ is, in essence, the dephasing time, it is seen that the ratio of the transition probability of Eq. (4) to that of Eq. (3) is that of the dephasing time T_2 to the impact time $r_0/\bar{V}$.

As a specific example, we consider four-photon absorption in Kr (atom B), with and without the presence of Hg (atom A) (see Fig. 1). We choose the first two photons $\omega_1=\omega_2=3129$ Å, such that the sum of these photons equals the nonallowed 6s-7s transition of Hg. We choose the second two photons $\omega_3=\omega_4=7342$ Å to exactly complete the four-photon 4p-5p transition in Kr. We assume unity oscillator strength for all transitions except the 6s-8p transition of Hg, for which we take $f=0.1$. The resonance denominators needed to evaluate Eq. (2) are[7] $\Delta\omega_1=22\,105$ cm^{-1}, $\Delta\omega_2=1$ cm^{-1} (the assumed linewidth of the incident laser), $\Delta\omega_3=685$ cm^{-1}, and $\Delta\omega_4=3369$ cm^{-1}. Assuming $r_{0m}=5$ Å, $\bar{V}=5\times10^4$ cm/sec, a Hg concentration of 10^{17} atoms/cm^3, and an incident laser power density of 10^8 W/cm^2, we find $W(t)=1.6\times10^3$ transitions/sec. This transition probability is about 10^4 greater than that for pure Kr.

To observe this effect, it is necessary to avoid a different and often stronger nonlinear process which may alternatively excite the Kr. This latter process is three-frequency summing in Hg to yield $\omega_1+\omega_2+\omega_3$, followed by two-photon absorption in Kr (ω_4 + the sum frequency). This competing process can be avoided by allowing the optical beam at $\omega_3=\omega_4$ to be incident from the opposite direction to that of the beam at $\omega_1=\omega_2$, thereby producing a negligible coherence length for the three-frequency summing process.[1] The Van der Waals process will then be the dominant mechanism for four-photon excitation of Kr.

There is one version of the type of process described in this Letter which may have application to the development of short-wavelength lasers, and to other types of optical pumping. In this process, atoms are first collected in an upper level of atom A. This collection may be accomplished by an electron discharge, or other techniques. An incident laser frequency is then chosen with a photon energy which conserves energy with a level of a second species which it is desired to pump. For example, in the notation of Fig. 1, population might be collected in the Hg 7s level. A laser of wavelength 5886 Å is then applied to the system. This wavelength is chosen to exactly connect the 5s level of Kr with the 7s of Hg. Equation (3) applies, with the quantity $|\gamma|^2$ now given by $(|\mu_{23}{}^A||\mu_{30}{}^A||\mu_{01}{}^B||E|/2\hbar^3\Delta\omega_1)^2$. $\Delta\omega_1 = 4054\ \mathrm{cm}^{-1}$ is the difference between the applied optical frequency and the Hg 7s-8p transition. At an incident power density of 10^9 W/cm^2, an excited mercury concentration of 10^{17} atoms/cm^3, and $\bar{V} = 5\times10^4$ cm/sec, we find a Kr transition rate of 2.6×10^7 transitions/sec. This transition rate corresponds to an effective cross section for inelastic collision $[W(t) = N_A\sigma_{\mathrm{eff}}\bar{V}]$ of $\sigma_{\mathrm{eff}} = 72$ Å^2. This cross section varies linearly with the power density of the applied 5886-Å field. One application of this type of pumping process may be selective rapid ionization of inner-shell electrons, thereby creating an inversion with regard to these levels.[8]

From a somewhat different point of view, we have described a process where by using one or more photons of an external electromagnetic field, large effective cross sections for inelastic collision can be attained without the usual requirement of energy resonance of the atomic species. Experiments to demonstrate these ideas will be undertaken in our laboratory.

---

*Work jointly supported by the U. S. Office of Naval Research and the Advanced Research Projects Agency.

†D. B. Lidow gratefully acknowledges support from the Fannie and John K. Hertz Foundation.

[1] J. F. Young, G. C. Bjorklund, A. H. Kung, R. B. Miles, and S. E. Harris, Phys. Rev. Lett. 27, 1551 (1971); R. B. Miles and S. E. Harris, IEEE J. Quantum Electron. 9, 470 (1973).

[2] R. T. Hodgson, P. P. Sorokin, and J. J. Wynne, Phys. Rev. Lett. 32, 343 (1974).

[3] S. E. Harris and D. M. Bloom, Appl. Phys. Lett. 24, 229 (1974); D. M. Bloom, James T. Yardley, J. F. Young, and S. E. Harris, Appl. Phys. Lett. 24, 427 (197

[4] P. R. Berman, Phys. Rev. A 6, 2157 (1972), and 5, 927 (1972).

[5] L. I. Schiff, *Quantum Mechanics* (McGraw-Hill, New York, 1968) 3rd ed., p. 260.

[6] *Progress in Quantum Electronics*, edited by J. H. Sanders and S. Stenholm (Pergamon, New York, 1972), Vol. 2, Pt. 3.

[7] C. E. Moore, *Atomic Energy Levels*, U. S. National Bureau of Standards, National Standard Reference Data Systems—35 (U. S. GPO, Washington, D. C., 1971), Vols. 2 and 3.

[8] M. A. Duguay and P. M. Rentzepis, Appl. Phys. Lett. 10, 350 (1967).

Radiative Decay of the 2^3S_1 and 2^3P_2 States of Heliumlike Vanadium ($Z = 23$) and Iron ($Z = 26$)*

Harvey Gould, Richard Marrus,† and Peter J. Mohr
Department of Physics and Lawrence Berkeley Laboratory, University of California, Berkeley, California 94720

(Received 1 July 1974)

Lifetimes of the $M1$ decay $2^3S_1 \to 1^1S_0$ and of the decay $2^3P_2 \to 1^1S_0$ have been measured in the two-electron ions V^{+21} and Fe^{+24}. The measured lifetimes are $\tau(2^3S_1) = 16.9(7)$ nsec for V^{+21} and $\tau(2^3S_1) = 4.8(6)$ nsec for Fe^{+24}. The 2^3P_2 lifetimes are compared with a calculation that considers relativistic corrections and hyperfine-structure effects. It is found that for V^{+21}, hyperfine effects contribute appreciably to the lifetime. For Fe^{+24} we obtain $\tau(2^3P_2) = 0.11(2)$ nsec.

The study of radiative decay from the 2^3S_1 and 2^3P_2 levels of the two-electron system offers an opportunity to test the theory of forbidden decay in a system where precise, unambiguous calculations of decay rates can be made. In this paper, we describe some measurements designed to extend existing experimental information on the rates of these decays to the two-electron atoms V^{+21} and Fe^{+24}. We develop a theory for the 2^3P_2 rates which takes into account leading-order relativistic corrections and hyperfine effects. Our results on vanadium show the first evidence for the influence of the hyperfine interaction on the radiative decay of an energy level belonging to the two-electron system.

Experimental work on the 2^3S_1 levels of the two electron system has established the single-photon nature of the decay in Ar^{+16}[1] and ordinary helium.[2] The theory of this decay has been examined by several authors[3] and detailed calculations of the rates have been made by Drake[4] and by Johnson and Lin[5] using somewhat different starting points. Measurements of this decay rate have been made on Ar^{+16}, Ti^{+20},[6] and Cl^{+15}.[7] The measured rates in Cl and Ar differ from theory by several times the quoted error, whereas the

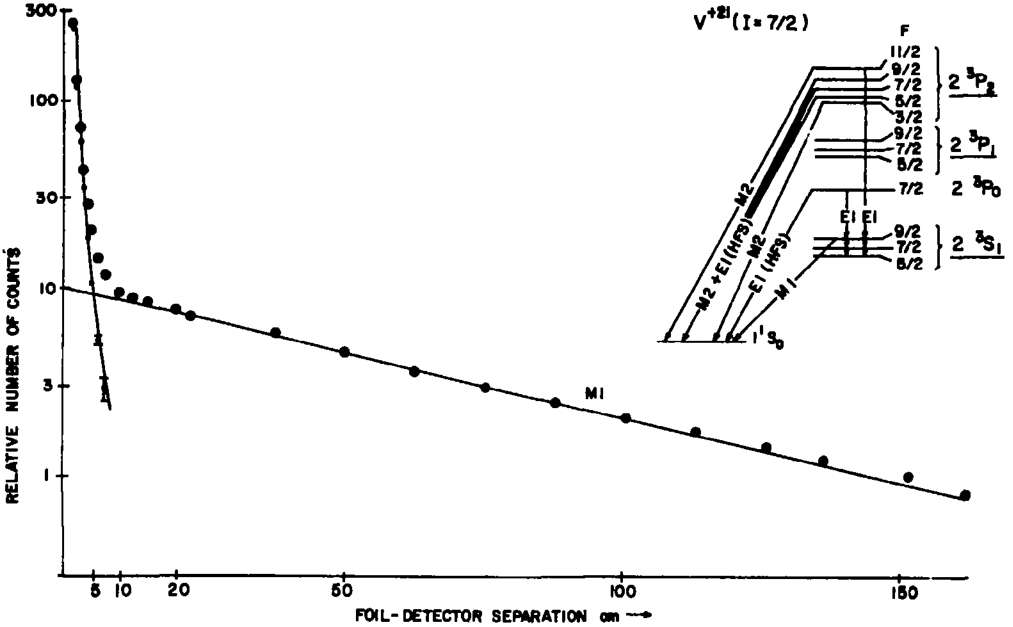

FIG. 1. Sample decay curve obtained with V^{+21} beam. The points beyond 22 cm are fitted by a single exponential and ascribed to decay of the 2^3S_1 level. The small-separation points are fitted by a composite of four exponentials as described in the text and are ascribed to decay of the 2^3P_2 level.

result in Ti is in agreement. In order to establish the Z dependence of this discrepancy we report here measurements on V^{+21} and Fe^{+24}.

Interest in the 2^3P_2 levels centers mainly on the $M2$ decay mode to the 1^1S_0 ground level which has a rate comparable with the $E1$ rate to 2^3S_1 for ions with $Z \simeq 20$. The $M2$ decay was first observed[8] in Ar^{+16} and rates have now been measured in S^{+14},[9] Cl^{+15},[10] and Ar^{+16}.[11] In this paper we present evidence indicating that the decay of this level is strongly influenced by the hyperfine interaction in V^{+21} and give results for Fe^{+24}.

The lifetimes were measured by the beam-foil time-of-flight method. Our apparatus has been described previously[6] and the details are not repeated here. The vanadium ($Z = 23$) and iron ($Z = 26$) ions were obtained from the Lawrence Berkeley Laboratory SuperHILAC at an energy of 7.2 MeV/amu. Excitation of the beams into the metastable states was done with a 50-μg/cm^2 carbon foil. Decay curves are taken by varying the foil-detector separation. The total number of counts under the peak is integrated and normalized to the integrated beam current collected in a Faraday cup. This quantity is plotted as a function of foil-detector separation. A sample decay curve is shown in Fig. 1.

Since the 2^3P_2 and 2^3S_1 energy separations are small compared with the detector resolution, the decay curves are composites, exhibiting fast components and slow components. The slow components are ascribed to the 2^3S_1 decay and the fast components to decay from 2^3P_2. As discussed below, the slow and fast components are probably composites of two or more exponentials as the result of hyperfine effects in V^{+21} and cascading effects in Fe^{+24}.

The isotope ^{51}V has a nuclear spin $I = \frac{7}{2}$ and a magnetic moment $\mu = 5.15\mu_N$.[12] The resulting hyperfine structure influences our decay curves by admixing 2^3P_2 with 2^3P_1 and 2^1P_1. The 2^3P_2 level is split into five components with total angular momentum between $F = \frac{3}{2}$ and $F = \frac{11}{2}$ (Fig. 1). Because the hyperfine interaction is diagonal in F, the rates from both $F = \frac{3}{2}$ and $F = \frac{11}{2}$ are unaffected by hyperfine structure. However, the rates from $F = \frac{5}{2}$, $\frac{7}{2}$, and $\frac{9}{2}$ will all be altered. Hence, the observed decay curve will be a composite of four exponentials weighted according to the initial populations of each of the hyperfine levels.

The most abundant stable iron isotope has zero spin and hyperfine effects are not present. Hence the decay of 2^3P_2 is exclusively by $E1$ decay to 2^3S_1 and $M2$ to 1^1S_0.

A problem arises in the interpretation of the 2^3S_1 decay because of cascading from 2^3P_0. The lifetime of 2^3P_0 is calculated to be $\tau = 2.7$ nsec which is close to that of 2^3S_1. Hence cascading effects from this level may be important. The shape of the resultant curve will depend upon the relative population $R \equiv N_0(2^3P_0)/N_0(2^3S_1)$ of the two states, and the decay rates. It was found that the data could be fitted by two exponentials for $0 \leq R \leq 0.8$. Varying the lifetimes of the two exponentials, we find that the "best fit" values for $\tau(2^3S_1)$ vary between 4.2 and 5.3 nsec, where 5.3 nsec results from a single exponential fit ($R = 0$) and, hence, is an upper limit to the 2^3S_1 lifetime. Similarly, the values for $\tau(2^3P_0)$ vary between 1.3 and 3.3 nsec. We note that the theoretical value of $\tau(2^3P_0) = 2.7$ nsec corresponds to $\tau(2^3S_1) = 4.8$ nsec. We have chosen to take the mean value as the experimental value and to take cascading into account by using an increased error.

In Fig. 1, an experimental decay curve is shown for the V^{+21} beam. The decay curve is fitted by identifying the data points beyond 22 cm with the 2^3S_1 decay. These yield a lifetime $\tau(2^3S_1) = 16.9(7)$ nsec. When this decay is subtracted from the experimental data it yields the points for small detector-foil separation as shown. These are fitted by a composite decay curve constructed by assuming that each of the F states associated with 2^3P_2 has the theoretical lifetime shown in Table I. These lifetimes include effects due to hyperfine quenching. Moreover, the initial populations of the F states are taken as proportional to $2F+1$. The resultant fit to the experimental points is as shown and is seen to be quite good.

TABLE I. Theoretical transition rates and lifetimes of the 2^3P_2 state in heliumlike ions.

Z	A_{E1} (nsec^{-1})	A_{M2} (nsec^{-1})	F	$A_{E1}{}^{\text{hfs}}$ (nsec^{-1})	τ (nsec)
16	0.259	0.117	All	< 0.007	2.66
17	0.301	0.194			≃ 2.01
18	0.352	0.312			1.51
22	0.687	1.64			0.429
23	0.820	2.37	3/2	0	0.313
			5/2	0.99	0.239
			7/2	1.75	0.202
			9/2	1.69	0.205
			11/2	0	0.313
26	1.43	6.50			0.126

To calculate accurate theoretical rates for the 2^3P_2 level, the transition matrix elements are evaluated to zeroth and first order in the quantities Z^{-1} and $(Z\alpha)^2$. The zeroth-order term is the nonrelativistic hydrogenic approximation. The term of order Z^{-1} is the first correction in the nonrelativistic Z expansion of the matrix element. The leading relativistic correction, of order $(Z\alpha)^2$, is obtained by evaluating the relativistic transition operator between states formed from properly symmetrized products of hydrogenic Dirac wave functions.

For the $M2$ transition, the coefficient of Z^{-1} has been determined by Drake[13] from the Z-expansion calculation of Dalgarno and Parkinson.[14] Taking his result together with the leading relativistic and finite-wavelength (retardation) corrections yields

$$A_{M2}(2^3P_2) = \alpha k^5 (2^{15}/5 \times 3^{10})(Z\alpha)^{-2}[1 + 0.147Z^{-1} - 0.640(Z\alpha)^2]^2 \qquad (1)$$

(in units where $m_e = c = \hbar = 1$), where k is the transition energy.

Because the nonrelativistic-velocity form of the matrix element for $n-n$ $E1$ transitions vanishes to lowest order in Z^{-1}, the evaluation of the $E1$ transition rate $2^3P_2 - 2^3S_1$ is simplified by making the dipole approximation and converting the matrix element to the length form. The error in making this approximation is negligible because of the smallness of the transition energy: $\langle \hat{\text{k}} \cdot \vec{\text{r}} \rangle \approx O(\alpha)$. The conversion to length form is valid relativistically and so relativistic corrections may be obtained as described above. For this transition matrix element, the coefficient of Z^{-1} has been obtained by Cohen and Dalgarno.[15] We thus have

$$A_{E1}(2^3P_2) = \alpha k^3 12 (Z\alpha)^{-2}[1 + 0.759Z^{-1} - 0.167(Z\alpha)^2]^2. \qquad (2)$$

The transition probability for the $E1$ decay $2^3P_0 \rightarrow 2^3S_1$, obtained as for the 2^3P_2 decay, is given by

$$A_{E1}(2^3P_0) = \alpha k^3 12 (Z\alpha)^{-2}[1 + 0.759Z^{-1} - 0.417(Z\alpha)^2]^2. \qquad (3)$$

We note that the theoretical uncertainty in the expressions for the transition rates listed above is expected to be of the order of 1% or less for Z in the range 10–40.

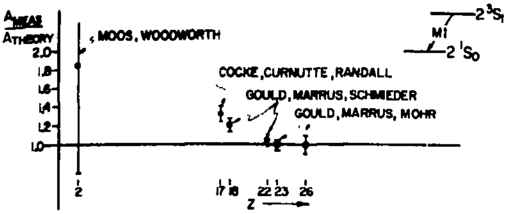

FIG. 2. Comparison between measured and calculated decay rates for the 2^3S_1 level.

In the case of vanadium, which has a nonzero nuclear spin, the 2^3P_2 and 2^3P_0 states undergo an $E1$ transition to the 1^1S_0 state due to hyperfine mixing.[16] An estimate of the transition rate is obtained in the following way. Nonrelativistic intermediate-coupling wave functions are taken as the unperturbed basis. The hyperfine interaction which is diagonal in $F = J + I$, is treated in first-order perturbation theory. Only the effect of mixing of the 2^3P_2 and 2^3P_0 states with the nearby 2^3P_1 and 2^1P_1 states is included. The dipole transition operator then has a nonvanishing matrix element between the perturbed 2^3P_2 and 2^3P_0 states and the 1^1S_0 state which is proportional to the dipole matrix element between the LS coupled 2^1P_1 state and the 1^1S_0 state. The latter is evaluated with the aid of the Z expansion of Dalgarno and Parkinson.[14] The hyperfine matrix elements are approximated by evaluating the contact-interaction term between hydrogenic product wave functions. Energy differences are evaluated by means of the Z expansion of the nonrelativistic energies,[17] together with the Z expansion of the order-α^4 corrections.[18] The transition rates thus obtained are added to the rates discussed above and the resulting values for the lifetime of the 2^3P_2 state are listed in Table I.

In Fig. 2 we compare all of the measured decay rates of 2^3P_2 with the corresponding theoretical rates. Agreement is seen to be very good over a wide range of Z. For vanadium, the theoretical rate includes the contribution from hyperfine quenching. It is seen that the experimental and theoretical rates would be in serious disagreement without contributions from this mechanism. We take this as very strong evidence that hyperfine quenching is indeed present.

In Fig. 3 we compare the measured 2^3S_1 decay rates with the calculated rates. Agreement between theory and experiment is satisfactory for $Z = 22$, 23, and 26, but puzzling discrepancies exist at $Z = 17$ and 18.

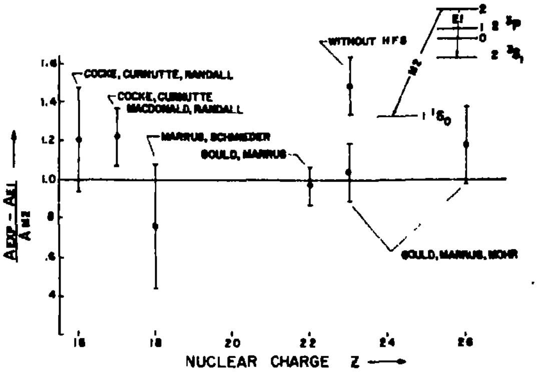

FIG. 3. Comparison between measured and calculated $M2$ rates for decay from the 2^3P_2 level. The point at $Z = 23$ labeled "without HFS" is obtained by making a best fit to our vanadium data using a single exponential.

We are indebted to Al Ghiorso and the staff of the SuperHILAC for their enthusiastic support of this work. The development of the vanadium and iron beams was a vital product of this support. Doug MacDonald gave valuable engineering support. One of us (P.J.M.) gratefully acknowledges helpful conversations with Professor Charles Schwartz and Professor Eyvind H. Wichmann.

---

*Work supported by the U. S. Atomic Energy Commission.

†Work partially supported by a fellowship from the John S. Guggenheim Foundation.

[1] R. Marrus and R. W. Schmieder, Phys. Lett. 32A, 431 (1970).

[2] H. W. Moos and J. R. Woodworth, Phys. Rev. Lett. 30, 775 (1973).

[3] G. Feinberg and J. Sucher, Phys. Rev. Lett. 26, 681 (1971); H. R. Griem, Astrophys. J. 156, 1103 (1969); I. L. Beigman and V. I. Safronova, Zh. Eksp. Teor. Phys. 60, 2045 (1971) [Sov. Phys. JETP 33, 1102 (1971)]; S. Feneuille and E. Koenig, C. R. Acad. Sci., Ser. B 274, 46 (1972); G. W. F. Drake, Phys. Rev. A 5, 1979 (1972).

[4] G. W. F. Drake, Phys. Rev. A 3, 908 (1971).

[5] W. R. Johnson and C. Lin, Phys. Rev. A 9, 1486 (1974).

[6] H. Gould, R. Marrus, and R. W. Schmieder, Phys. Rev. Lett. 31, 504 (1973).

[7] C. L. Cocke, B. Curnutte, and R. Randall, Phys. Rev. Lett. 31, 507 (1973).

[8] R. Marrus and R. W. Schmieder, Phys. Rev. Lett. 25, 1689 (1970).

[9] C. L. Cocke, B. Curnutte, and R. Randall, Phys. Rev. A 9, 1823 (1974).

[10] C. L. Cocke, B. Curnutte, J. R. MacDonald, and

R. Randall, Phys. Rev. A $\underline{9}$, 57 (1974).

[11] R. Marrus and R. W. Schmieder, Phys. Rev. A $\underline{5}$, 1160 (1972).

[12] W. F. Ramsey, *Molecular Beams* (Oxford Univ. Press, Oxford, England, 1963), p. 173.

[13] G. W. F. Drake, Astrophys. J. $\underline{158}$, 1199 (1969).

[14] A. Dalgarno and E. M. Parkinson, Proc. Roy. Soc., Ser. A $\underline{301}$, 253 (1967).

[15] M. Cohen and A. Dalgarno, Proc. Roy. Soc., Ser. A $\underline{293}$, 359 (1966).

[16] A discussion of the history and calculations of this effect is given in R. H. Garstang, J. Opt. Soc. Amer. $\underline{52}$, 845 (1962).

[17] R. E. Knight and C. W. Sherr, Rev. Mod. Phys. $\underline{35}$, 431 (1963).

[18] H. T. Doyle, in *Advances in Atomic and Molecular Physics*, edited by D. R. Bates and I. Esterman (Academic, New York, 1969), Vol. 5, p. 337.

Reverse Temperature Gradient in the Kinetic Theory of Evaporation

J. R. Thomas, Jr.
Department of Mechanical Engineering, Virginia Polytechnic Institute and State University, Blacksburg, Virginia 24061

and

T. S. Chang*
Department of Physics, Massachusetts Institute of Technology, Cambridge, Massachusetts 02139

and

C. E. Siewert
Department of Nuclear Engineering, North Carolina State University, Raleigh, North Carolina 27607

(Received 24 June 1974)

The singular-eigenfunction–expansion method for solving the transport equation is applied to a modeled kinetic-theory Boltzmann equation to solve the problem of evaporation and condensation between parallel surfaces. A remarkable result is obtained for the temperature profile which seems to confirm previous predictions made on the basis of asymptotic approximations.

In a recent paper, Pao[1] suggested that the slope of the temperature profile of a saturated vapor between two parallel surfaces at different temperatures could be in opposition to the imposed gradient for certain values of β, where $\Delta N = \beta \Delta T$ in a saturated liquid-vapor system. Here N represents the molecular density and T the temperature. Pao's prediction was based on an asymptotic analysis for large gap width, and used results obtained for the half-space problem[2] by applying the Wiener-Hopf technique to a modeled Boltzmann equation.

We have approached the same problem through the singular-eigenfunction analysis of Kriese, Chang and Siewert,[3] also used by Thomas and co-workers,[4-6] and have avoided any asymptotic approximation Thus for the first time, inverted temperature profiles and critical values of β are calculated explicitl The surprising result is that our analysis seems to confirm Pao's novel prediction.

We consider the problem of a vapor between two interphase (vapor-liquid or vapor-solid) surfaces maintained at $x = \pm d/2$; we assume that the condensed phase in $x < -d/2$ is kept at temperature $T_0 - \frac{1}{2}\Delta$ and that the condensed phase in $x > d/2$ is kept at temperature $T_0 + \frac{1}{2}\Delta T$. As a result of evaporation an condensation there is a flow of mass and energy from $x = +d/2$ to $x = -d/2$. Within the vapor, we assume the state of the fluid to be described by the linearized single-relaxation model of the Boltzmann equation[7]:

$$c_x \partial f(x, \vec{c})/\partial x + f(x, \vec{c}) = \pi^{-3/2}[N(x) + (c^2 - \tfrac{3}{2})T(x) + 2c_x U(x)]. \qquad (1$$

Here $f(x, \vec{c})$ is the perturbation of the particle-distribution function, x is the spatial variable, $\vec{c}$ is the molecular velocity, and c_x is the x component of the velocity, all in dimensionless units. In addition, $N(x)$, $T(x)$, and $U(x)$ represent perturbations of the number density, the temperature, and the x component of mass flow:

$$N(x)=\int f(x,\vec{c})\exp(-c^2)d^3c, \qquad (2a)$$

$$T(x)=\tfrac{2}{3}\int f(x,\vec{c})(c^2-\tfrac{3}{2})\exp(-c^2)d^3c, \qquad (2b)$$

and

$$U(x)=\int f(x,\vec{c})c_x\exp(-c^2)d^3c. \qquad (2c)$$

Since it follows from Eqs. (1) and (2c) that $U(x)$ is a constant, we find it convenient to introduce

$$h(x,\vec{c})=f(x,\vec{c})-(2/\pi^{3/2})c_xU, \qquad (3)$$

and subsequently consider the equation

$$c_x\partial h(x,\vec{c})/\partial x+h(x,\vec{c})=\pi^{-3/2}[N(x)+(c^2-\tfrac{3}{2})T(x)]. \qquad (4)$$

We are interested here only in density and temperature effects, so we may decompose the equation in the manner discussed by Cercignani[2] to obtain

$$\mu\,\partial\bar{\Psi}(x,\mu)/\partial x+\bar{\Psi}(x,\mu)=\pi^{-1/2}\underline{Q}(\mu)\int_{-\infty}^{\infty}\underline{Q}^{\mathrm{T}}(\mu')\bar{\Psi}(x,\mu')\exp(-\mu'^2)d\mu', \qquad (5)$$

where $Q(\mu)$ is a matrix of polynomials.[3] The variable μ now represents the x component of the velocity, and $\bar{\Psi}(x,\mu)$ is a two-vector simply related to the density and temperature of the gas:

$$N(x)=\pi^{1/2}\begin{pmatrix}1\\0\end{pmatrix}^{\mathrm{T}}\int_{-\infty}^{\infty}\bar{\Psi}(x,\mu)\exp(-\mu^2)d\mu, \qquad (6)$$

and

$$T(x)=\tfrac{2}{3}\pi^{1/2}\int_{-\infty}^{\infty}\begin{pmatrix}\mu^2-\tfrac{1}{2}\\1\end{pmatrix}^{\mathrm{T}}\bar{\Psi}(x,\mu)\exp(-\mu^2)d\mu. \qquad (7)$$

We use the superscript T to denote the transpose operation.

At the two interphase surfaces, we assume that the vapor molecules striking the surface are absorbed and re-emitted with a Maxwellian distribution of velocities characterized by the temperature at the respective surface. Hence the linearized boundary conditions are

$$f(\mp\tfrac{1}{2}\delta,\vec{c})=\mp\tfrac{1}{2}[\Delta N+(c^2-\tfrac{3}{2})\Delta T],\quad c_x>0, \qquad (8)$$

where δ is a nondimensional distance and $\Delta N=\beta\Delta T$, with β the slope of the saturated-vapor-density–temperature curve. Couched in terms of the vector $\bar{\Psi}(x,\mu)$, we find this boundary condition to be

$$\bar{\Psi}(\mp\tfrac{1}{2}\delta,\pm\mu)=\mp\sqrt{\pi}\begin{pmatrix}\mu^2-\tfrac{1}{2}+\beta+2\pi^{-3/2}U\mu\\1\end{pmatrix},\quad \mu>0. \qquad (9)$$

In Eq. (9), for notational convenience we have absorbed into U and $\bar{\Psi}$ a factor $(\Delta T)^{-1}$.

From an asymptotic solution for large δ, Pao[1] has predicted that for certain values of β the slope of the temperature profile in the main body of the vapor will be in opposition to the imposed temperature gradient. It is our purpose here to investigate this prediction by solving for the temperature profile with the use of the singular-eigenfunction–expansion technique, developed for Eq. (5) by Kriese, Chang, and Siewert.[3]

Kriese, Chang, and Siewert[3] have expressed a general solution of Eq. (5) as

$$\bar{\Psi}(x,\mu)=\sum_{\alpha=1}^{2}A_\alpha\bar{\Phi}_\alpha(\mu)+\sum_{\alpha=3}^{4}A_\alpha\bar{\Psi}_\alpha(x,\mu)+\sum_{\alpha=1}^{2}\int_{-\infty}^{\infty}A_\alpha(\eta)\bar{\Phi}_\alpha(\eta,\mu)e^{-x/\eta}d\eta, \qquad (10)$$

where the $\bar{\Phi}_\alpha(\mu)$, $\bar{\Psi}_\alpha(x,\mu)$, and $\bar{\Phi}_\alpha(\eta,\mu)$ are the normal modes given explicitly in Ref. 3, and the A_α, $\alpha=1,\dots,4$, and $A_\alpha(\eta)$, $\alpha=1$ and 2, are expansion coefficients. Substituting this general solution into Eq. (7) for the temperature perturbation, we find

$$T(x)=-(2/3\pi)^{1/2}A_3x-(2/\pi)\int_0^{\infty}A_1(\eta)\sinh(x/\eta)\exp(-\eta^2)d\eta, \qquad (11)$$

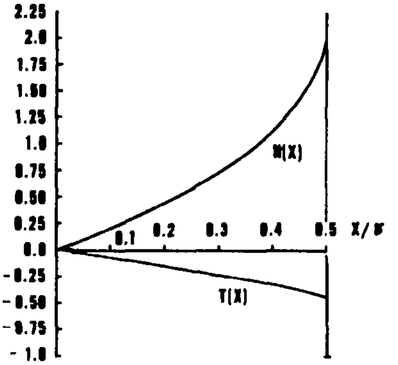

FIG. 1. Temperature and density profiles for $\beta = 8$ and $\delta = 2$.

so that it is clear that we must determine the expansion coefficients A_3 and $A_1(\eta)$ in order to establish the temperature profile. Using the solution (10) in the boundary conditions given by Eq. (9), we find a coupled pair of singular integral equations for the expansion coefficients. We then may apply the half-range ($\mu > 0$) orthogonality theorem of Kriese, Chang, and Siewert[3] to convert these singular integral equations into a coupled pair of Fredholm integral equations. We have found that iterative solutions of these Fredholm equations converge very rapidly, so that solutions for the expansion coefficients may be straightforwardly obtained, with great precision.

In Fig. 1, we give a plot of a typical temperature profile obtained from our calculations. It is clear that in the center of the gap, the slope of the profile is in opposition to the imposed gradient and thus very large temperature slips occur at the boundaries. The accompanying density profile is consistent with this temperature profile. We found that for all values of β greater than a "critical" value, $\beta_c(\delta)$, the computed temperature profile was in opposition to the imposed gradient. We define $\beta_c(\delta)$ as that β for which

$$dT(x)/dx\,|_{x=0} = 0. \tag{12}$$

By solving the coupled Fredholm equations mentioned above in conjunction with the constraint of Eq. (12), we were able to compute $\beta_c(\delta)$. In Fig. 2 we plot $\beta_c(\delta)$ versus δ for $0 < \delta < \infty$. It will be noted that as δ increases, $\beta_c(\delta)$ approaches an asymptotic value of 3.7723. . . , whereas Pao's approximate value is 3.5. For δ approaching zero, it appears that $\beta_c(\delta)$ also approaches zero; however, we were unable to confirm this since we did not obtain converged solutions to the Fredholm equations for $\delta < 0.01$.

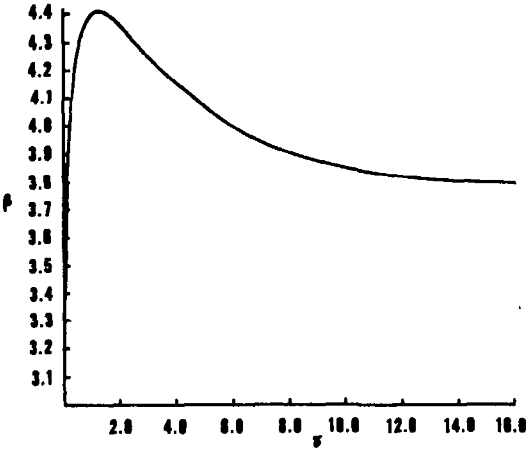

FIG. 2. Critical $\beta_c(\delta)$.

An apparent explanation for the unexpected temperature behavior is that for large β evaporation is so rapid that energy transfer by mass flow must be counterbalanced by heat conduction in the opposite direction. We hope that our results will invite attempts to study this phenomenon experimentally. The superheating and supercooling effects of the vapor phase adjacent to the condensate should be readily observable.

The authors are indebted to Professor Y. P. Pao of the Courant Institute of Mathematical Sciences, New York University, and Professor S. K Loyalka of the Nuclear Engineering Department of the University of Missouri at Columbia for critical comments.

---

*Research supported by the National Science Foundation, the U. S. Office of Naval Research, and the U. S. Air Force Office of Scientific Research.

[1] Y. P. Pao, Phys. Fluids 14, 306 (1971).

[2] Y. P. Pao, Phys. Fluids 14, 1340 (1971).

[3] J. T. Kriese, T. S. Chang, and C. E. Siewert, Int. J. Eng. Sci. 12, 441 (1974).

[4] C. E. Siewert and J. R. Thomas, Jr., Phys. Fluids 16, 1557 (1973).

[5] J. R. Thomas, Jr., Phys. Fluids 16, 1162 (1973).

[6] J. R. Thomas, Jr., T. S. Chang, and C. E. Siewert, Phys. Fluids 16, 2116 (1973).

[7] For a review of current research activities in the kinetic theory of condensation and evaporation, see J. W. Cipolla, Jr., H. Lang, and S. K. Loyalka, in *Rarefied Gas Dynamics*, edited by K. Karancheti (Academic, New York, 1973), p. 179, and J. Chem. Phys. 61, 69 (1974).

[8] C. Cercignani, *Mathematical Methods in Kinetic Theory* (Plenum, New York, 1969).

New Factors Affecting the Measured Lifetime of Electrons Trapped on Vortex Lines in He II*

Keith DeConde, Gary A. Williams, and Richard E. Packard
Department of Physics, University of California, Berkeley, California 94720

(Received 22 July 1974)

The lifetime of trapped electrons measured at $T < 1.5$ K is found to be affected by factors which should not influence the intrinsic ion-vortex-line interaction. Observations indicate that the vortex lines move in the container, and the trapped charge escapes when the vortex lines interact with the container wall.

During the past fifteen years electrons have proven to be a powerful and versatile probe of the properties of superfluid helium.[1] Experiments have shown that the electron is self-trapped in a cavity (or bubble) whose radius is approximately 16 Å.[1] Using this model for the ion, Parks, Roberts, and Donnelly showed that this electron bubble should be attracted to, and trapped on, the core of a quantized vortex line. The ion should remain trapped in a Bernoulli potential well (depth ~50 K) until thermal fluctuations allow the ion to escape.[2] This model predicts a trapped lifetime τ which should *increase* rapidly with *decreasing* temperature. The model was supported by experiments in the range $1.59 < T < 1.82$ K.[3,4]

However, at lower temperatures ($0.6 < T < 1.1$ K) where the thermal-escape theory predicts $\tau > 10^{13}$ sec, it was found that the observed lifetime was orders of magnitude smaller than predicted, and it *decreased* with decreasing temperature.[5] The question raised was why does the thermal-escape theory not predict the lifetime observed at low temperatures? It is the purpose of this paper to attempt to answer this question.

We have measured the lifetime τ of electrons trapped on vortex lines in rotating He II over the temperature range $0.08 < T < 1.72$ K. The experimental results indicate that for temperature below 1.5 K the observed lifetime is not determined by the intrinsic properties of the ion-vortex interaction, but is instead a characteristic time for a vortex line to move to, and be destroyed at, the wall of the rotating container.

Our measurements of trapped-electron lifetimes were made in several different containers. Most of the containers have walls of high electrical resistivity so that voltages applied along the walls produce the electric fields necessary to manipulate the ions.[6] For a few of the measurements in the low-temperature range ($T < 0.5$ K) metal electrodes were used for the walls.[7] None of the buckets contained any grids in the liquid that might perturb the vortices. Although the manipulating voltages were applied axially, the resultant electric fields did have transverse fringe components in some regions. For temperatures above 1.2 K the container was in a superfluid-filled cell which was rotated in a stationary helium bath. For lower temperatures we used a rotating ^{3}He refrigerator or a rotating dilution refrigerator.

The lifetime measurements were made by using a procedure similar to that used in Ref. 3. Negative ions produced by a radioactive source (^{210}Po or tritium) are drawn into the liquid and become trapped on vortex lines during a fixed charging time (typically 5 to 10 sec). During a variable delay time no more charge is drawn from the source, and retaining fields prevent the trapped charge from escaping at the ends of the vortex lines. At the end of the delay time electric fields force the trapped charge along the vortex lines through the liquid surface to a collector in the vapor. For $T > 1.2$ K the collector is a proportional counter[6] and below 1.0 K the collector is a phosphor screen. The signal is amplified before passing through slip rings to instruments in the laboratory.

Figure 1 shows the temperature dependence of the measured half-life[8] τ observed in two cylindrical vessels of *different diameter*. The data indicate two regions in which τ has distinctly different temperature dependences. In the high-temperature range ($1.6 < T < 1.72$ K) τ is a rapidly increasing function of T^{-1} and our data are in good agreement with Refs. 3 and 4. Since the behavior of τ in this range is well explained by the theory of thermally assisted escape (represented by the solid line in Fig. 1) we call this the intrinsic lifetime. As expected from theory, we found that the intrinsic lifetime is independent of bucket size, angular velocity, and past rotation history, but τ does depend on the transverse electric field strength.

In the temperature range where τ decreases with increasing T^{-1} the lifetime is affected by

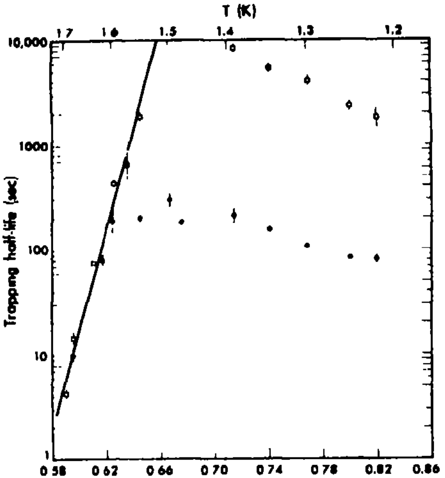

FIG. 1. Temperature dependence of the measured lifetime. The data were taken at $\omega = 3.9$ sec^{-1} in two circular buckets of different size. (The circles are for a 1.75-mm-diam vessel and the squares for a 3.17-mm-diam vessel.) The error bars represent 1 standard deviation. The solid line is the temperature dependence expected for the intrinsic lifetime with a well depth of ~ 55 K.

factors which do not affect the intrinsic lifetime. Most obviously from Fig. 1, the lifetime is much longer in a larger-size container. In this temperature range we found that the lifetime also increases with lower angular velocities, and is relatively insensitive to changes of the electric field strengths.

For temperatures lower than those shown in the figure the lifetime continued to decrease (in agreement with Ref. 5), finally becoming temperature independent below 0.8 K. In our 3.2-mm-diam bucket the low-temperature limit was $\tau \sim 3$ sec.

These observations indicate that there are two independent mechanisms by which trapped charge can leave the liquid. The observed escape rate (which is inversely proportional to the lifetime) is then the sum of two rates, one for each escape mechanism. In the high-temperature range the intrinsic ion escape rate is large, and dominates any other process. However, the intrinsic escape rate decreases so rapidly as the temperature is lowered that it soon becomes negligibly small compared to the escape rate due to another process.

Our results indicate that this other process involves the motion of charged vortex lines. We conjecture that a charged vortex line, in an array of vortex lines, moves with respect to the container. Eventually the vortex line will encounter the container wall and will be destroyed. The trapped charge is collected at the wall. To maintain the equilibrium line density another vortex will soon grow to replace the destroyed one, but the new line will be uncharged. If the characteristic time for a line to migrate to the container wall is short compared to the intrinsic lifetime, vortex motion will be the dominant mechanism of charge loss.

Therefore we believe that the lifetime observed at low temperatures is a measure of the characteristic time for a vortex line to traverse the container. This time should depend on the container size and on the effective velocity of the vortex line. The vortex velocity depends on several factors. For example, it should depend on the preparation or rotation history of the liquid, the angular velocity (which determines the mean spacing between lines), the amount of mechanical vibration of the container, and the amount of damping due to mutual friction with the normal fluid. We have observed that the lifetime is affected by all of the above factors. We believe that for $T < 1.5$ K the temperature dependence of the lifetime (which is qualitatively similar to the temperature dependence of the normal-fluid density ρ_n) is due to the reduced damping of vortex motion as ρ_n decreases. At sufficiently low temperatures ρ_n becomes negligible; then the vortex-line motion and lifetime is determined by the undamped vortex-line hydrodynamics, and τ should be independent of temperature, as we observed.

The above model of charge escape due to vortex-line motion is consistent with other qualitative observations. When only a few vortex lines are present, random destruction of vortex lines at the container wall should cause random fluctuations of the trapped-charge signal for a fixed delay time. Therefore, the size of relative fluctuations, $\Delta Q/Q$, provides a qualitative guide to the amount of vortex motion.[9] In the 1.75-mm bucket at 1.3 K, τ increased by a factor of 3 when the relative fluctuations decreased by a similar factor. Furthermore, when τ was shortest ($T < 0.5$ K) the fluctuations were ~100%.

In his original Letter[5] on low-temperature lifetimes, Douglass also presented results for lifetimes in a 2% ^{3}He mixture. The lifetime in the mixture was always longer than in pure ^{4}He, and

τ became independent of temperature below 0.8 K. We believe that this is because the ^{3}He impurities are part of the normal fluid, and they increase the damping of vortex motion. Below 0.8 K the damping due to elementary excitations becomes negligible compared to that due to the ^{3}He, and so the lifetime becomes independent of temperature.

Further evidence that ^{3}He increases the damping of vortex motion came from an experiment designed to photograph the positions of vortex lines in which we also measured the lifetime τ. In pure ^{4}He the lifetime was very short and the vortex lines did not produce a distinct image,[7] even though the apparatus had the necessary resolution. Adding 0.1% He^3 caused τ to increase substantially and then the distinct vortices were apparent in the photograph.[10]

One observation inconsistent with our model is Douglass's report that at temperatures below 1 K, positive ions seem to have a longer trapped lifetime than negative ions. If the lifetime is determined by vortex motion, both positive and negative ions should have the same lifetime at the lowest temperatures. However, Douglass stated that the positive-ion signal was "barely detectable" and so we feel his statements about the positive-ion lifetime are not conclusive. Although we have not yet had an apparatus which would favor observation of positive-ion trapping we hope to explore this further in the future.

Our observations concerning vortex-line motion may also be related to recent observations that electron trapping by vortex lines appears to be reduced in the presence of an axial heat current.[11] In that experiment electrons are drawn across a container filled with liquid helium, and the current reaching the other side is measured. When the container is rotated the current is attenuated because of charge trapping by the vortex lines. However, for small heat currents along the rotation axis, the attenuation disappears. Second-sound measurements in the same container indicate that the vorticity density is not changed by the heat flow. Unless the vortex lines are perfectly straight, mutual friction between the lines and the normal-fluid heat current should increase the motion of the lines. The increased rate of vortex destruction releases charge which gets pulled to the collector, thus reducing the attenuation of the current.

All of the observations discussed above are consistent with the model of charge loss due to vortex motion. The apparent fact that vortex lines do not form a stable, static array in an experimental chamber is not unexpected.[12] Calculations show that energy differences between possible regular arrays are very small.[13] Although it is not clear how to calculate energy barriers between different configurations, these barriers are probably not large compared with the random mechanical energy in the rotating system.

Although further measurements under a variety of conditions are necessary to conclusively verify our model, these measurements should provide much information on the stability and motion of vortex lines.

---

*This work was supported by the National Science Foundation.

[1] For a review of ions and vortices see R. J. Donnelly, *Experimental Superfluidity* (Univ. of Chicago Press, Chicago, Ill., 1967), Chap. 6. The most complete review is by A. L. Fetter, in *The Physics of Liquid and Solid Helium*, edited by K. H. Benneman and J. B. Ketterson (Wiley, New York, to be published).

[2] P. E. Parks and R. J. Donnelly, Phys. Rev. Lett. 16, 45 (1966); R. J. Donnelly and P. H. Roberts, Proc. Roy. Soc., Ser. A 312, 519 (1969).

[3] R. L. Douglass, Phys. Rev. Lett. 13, 791 (1965); W. P. Pratt, Jr., and W. Zimmermann, Jr., Phys. Rev. 177, 412 (1969); D. M. Sitton and F. Moss, Phys. Rev. Lett. 23, 1090 (1969).

[4] Another mechanism of charge loss which can occur in tangled vorticity is described by D. M. Sitton and F. E. Moss, Phys. Rev. Lett. 29, 542 (1972).

[5] R. L. Douglass, Phys. Lett. 28A, 560 (1969).

[6] This cell is similar to the one described in R. E. Packard and T. M. Sanders, Jr., Phys. Rev. A 6, 799 (1972).

[7] This cell is shown in R. E. Packard and G. A. Williams, in *Proceedings of the Thirteenth International Conference on Low Temperature Physics, Boulder, Colorado, 1972*, edited by W. J. O'Sullivan, K. D. Timmerhaus, and E. F. Hammel (Plenum, New York, 1973).

[8] In the temperature range $0.8 < T < 1.7$ K the charge appeared to decay exponentially but at lower temperatures the form of the decay curve was not as well established.

[9] The fluctuations $\Delta Q/Q$ depended on past rotation history, being larger for larger accelerations.

[10] Gary A. Williams and R. E. Packard, Phys. Rev. Lett. 33, 280 (1974).

[11] D. K. Cheng, M. W. Cromar, and R. J. Donnelly, Phys. Rev. Lett. 31, 433 (1973).

[12] See, for example, J. A. Northby and R. J. Donnelly, Phys. Rev. Lett. 25, 214 (1970); D. Stauffer and A. L. Fetter, Phys. Rev. 168, 156 (1968).

[13] Stauffer and Fetter, Ref. 12.

Nuclear Magnetic Resonance of Superfluid He^3 near T_c in High Magnetic Fields

D. D. Osheroff and P. W. Anderson
Bell Laboratories, Murray Hill, New Jersey 07974

(Received 16 July 1974)

We present the first measurements of NMR behavior of superfluid He^3 in high magnetic fields at melting pressures in the A_1 region in which only one spin species has undergone pairing. We observe a linear shift in the square of the transverse resonant frequency in A_1 with a pressure dependence of $(9.52\pm0.19)\times10^7$ (Hz)^2/mbar, which is 0.188 ±0.004 times the low-field result. This and other features that we report are in detailed agreement with the theory presented.

In the presence of a static magnetic field H_0, the transition of He^3 to the superfluid A phase at melting pressures splits into two transitions, A_1 and A_2, which separate linearly with field at a rate of 6.4 μK/kOe.[1,2] This results from the altered density of states of the spin populations at the Fermi surface, and creates a region A_1 in which only one spin species is paired. Such behavior was first considered by Ambegaokar and Mermin,[3] who predicted three transitions for condensates with $m_s=\pm1, 0$, and by Varma and Werthamer.[4] Brinkman and Anderson[5] (BA) first showed that if the A phase were the Anderson-Brinkman-Morel (ABM) state,[6,7] the "axial" $L=1$ state, a splitting in agreement with experiment was expected, since the ABM state may be described in terms of equal-spin pairing only.

We have studied the transverse-frequency shift $\Delta\nu_0\equiv\nu_0-\gamma H_0$ near the A_1 region at 4.93 and 7.40 kOe, the longitudinal resonant frequency ν_L near the A_2 transition at 15.1 kOe, as well as $P(A_1)$ and $P(A_2)$, the melting pressures of the transitions, in several fields up to 15.1 kOe. The behavior we observe is in detailed agreement with the calculations we present based on the ABM state when we include the effects of spin fluctuations as worked out by Brinkman, Serene, and Anderson (BSA).[8]

By considering the general expression for the free energy of the ABM state near T_c as given by Brinkman and Anderson, using the generalized gap for the ABM state,

$$\Delta(\vec{k})=(k_x+ik_y)\begin{pmatrix}\Delta_1 & 0\\ 0 & \Delta_2\end{pmatrix},$$

one can show that the gaps for the two spin species must have the form

$$(\Delta_1)^2=\begin{cases}\alpha(t'+1), & -1\leqslant t'\leqslant 0,\\ \alpha+\beta t', & 0\leqslant t',\end{cases}$$

$$(\Delta_2)^2=\begin{cases}0, & t'\leqslant 0,\\ \beta t', & 0\leqslant t',\end{cases}\qquad(1)$$

where t' is a new temperature scale linear in T such that $t'(A_1)=-1$ and $t'(A_2)=0$. In this new temperature scale, $t'(T_c)=-\alpha/2\beta$ as H_0 is decreased to zero. [We define T_c as $T(A)$ in zero field.] Using the field dependence of the A_1-A_2 splitting given above yields

$$t'=(1.56\times10^5\ \mathrm{kOe/K})(T_c-T)/H_0-\alpha/2\beta.$$

The constants α and β are determined from the free energy in terms of the Brinkman-Anderson parameter $\delta=(\Delta F^s)_{\mathrm{BW}}/(\Delta F^0)_{\mathrm{ABM-BW}}$ by using the results of BSA. We find $\beta/\alpha=(1-7\delta/80)/(1-21\delta/40)$. In the same sense, the fractional specific-heat jump at T_c, $\Delta C/C_{\mathrm{F.L.}}$, is $5(1.43)/6(1-21\delta/40)$.

To calculate $\Delta(\nu_0)^2\equiv\nu_0^2-(\gamma H_0)^2$ in the A_1-A_2 region we repeat the calculations of Leggett[9] for motion of the spin system of the superfluid. We derive the d matrix $d_{\alpha i}$[5] and calculate the dipole energy $\Gamma(d_{ii}d_{jj}^*+d_{i\alpha}d_{\alpha i}^*)$ as a function of orientation of the spin coordinate axis. By rotating $\vec{d}$ toward $-\hat{H}_0$ we find $\Delta(\nu_0)^2=(2\Gamma/\chi)[\frac{1}{2}(\Delta_1+\Delta_2)]^2$. Similarly, by rotating $\vec{d}$ about $\hat{H}_0$ we discover tha $(\nu_L)^2=2\Gamma\Delta_1\Delta_2/\chi$. Only when $\Delta_1=\Delta_2$ does $\Delta(\nu_0)^2=(\nu_L)^2$.[10] Using the form of $(\Delta_i)^2$ from (1) we find the temperature dependences of $\Delta(\nu_0)^2$ in $A(t'\gg0$ and A_1 to be in the ratio $4\beta/\alpha$.

All these results, including also the dependenc of T_{AB}/T_c upon δ obtained in interpolation betwee the behavior at the $T_{\mathrm{AB}}/T_c=+1$ and 0 limits, are shown in Fig. 1.

By using Eq. (1) one finds

$$\Delta(\nu_0)^2=\begin{cases}(\Gamma/2\chi)\alpha(t'+1), & t'\leqslant 0,\\ (\Gamma/2\chi)\{2\beta t'+\alpha+2[(\beta t')^2+\alpha\beta t']^{1/2}\}, & t'\geqslant 0.\end{cases}$$

Note that the second expression exhibits a square root singularity at A_2, and has an asymptotic slope for $t'\gg1$ of $(\Gamma/2\chi)4\beta$ which it reaches to within about 2% for $t'\gtrsim\sim1$.

To measure what amounted to exceedingly mi-

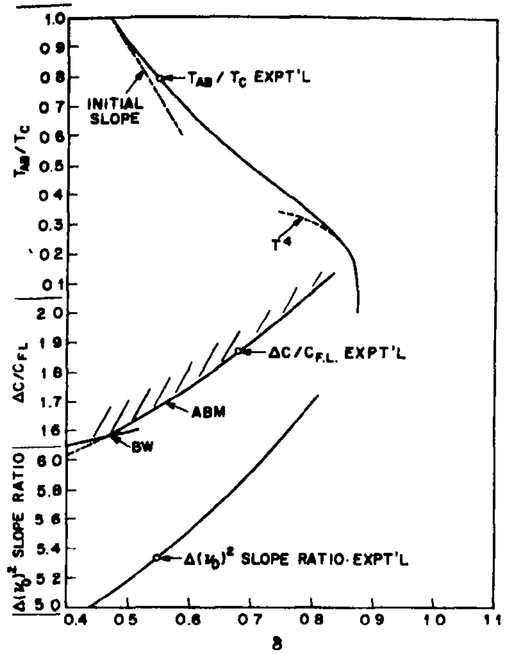

FIG. 1. Theoretical dependence of the $\Delta(\nu_0)^2$-slope atio, the specific-heat jump (Ref. 11), and T_{AB}/T_c pon the spin-fluctuation parameter δ. The curve givn is a freehand interpolation between the low- and igh-temperature limits given by the dashed curves. he high-temperature portion is a linear approximaon in $T-T_c$ as stated by BSA, while the T^4 curvature t $T\to 0$ follows as a result of the nodes of the gap in e ABM phase, essentially as calculated by Anderson nd Morel.

te frequency shifts in an extremely narrow mperature interval we utilized a highly correct- d superconducting solenoid to provide our static eld H_0 whose field homogeneity over about 10% our sample (above 5 kOe) was about 4×10^{-8}. y using a high-stability frequency synthesizer generate the rf field, and by adequately comensating for magnetic-field drifts, we could dermine our resonant frequency shifts to within 0.1 Hz. The compression cell we used to make ese measurements[12] was magnetically inert, d will be described in detail elsewhere.

We used the He^3 melting pressure as our therometer, utilizing a Straty-Adams-type capacive transducer which exhibited short-term reroducibility of ±0.02 mbar and long-term drift typically ±0.05 mbar (at T_c, $dP_M/dT \simeq -35.65$ bar/mK)[13] to measure pressure. We find in agnetic fields as high as 15.1 kOe that $P(A_2) - P(A_1)$ is linear in H_0 to within about 7%. Since for fields above about 1 kOe we expect $T(A_1) - T(A_2)$ to vary linearly with H_0, and that the depression of the solid He^3 entropy will be at least quadratic in H_0, we interpret this behavior of $P(A_2) - P(A_1)$ as evidence that the slope of the He^3 melting curve in fields below 7.5 kOe is nearly independent of H_0 (to within ~3%) at T_c. (A more complex set of measurements of pressure intervals to be presented elsewhere substantiates this conclusion.)

The cell temperature was first regulated near $T(A)$ for about 2 h during a given compression, after which time the cell warm-up rate at constant volume was about 0.05 μK/sec. Just prior to cooling below $T(A_1)$, the rate of field decay was measured to ±0.1 Hz over a half-hour period. Then, for the next hour, data were obtained by sweeping the frequency while regulating the cell pressure to ±0.02 mbar. This process was repeated several times at 16 and 24 MHz resonant frequencies.

Values of $\Delta(\nu_0)^2$ corrected for the field drift were plotted as a function of pressure. Such individual plots were combined by offsetting the pressure scales so that the data just below $T(A_2)$ would be coincident. In this way minor pressure errors were eliminated. Typical offsets at 24 MHz were only 0.02 mbar, but at 16 MHz, because of a faulty electrical switch, offsets as large as 0.1 mbar had to be made. The final data sets are shown in Figs. 2 and 3.

The solid curves in Figs. 2 and 3 are best fits to the theory in which the scale of t', $P(A_2) - P(A_1)$, and the slope of $\Delta(\nu_0)^2$ below $T(A_2)$ were allowed to vary. The slopes in the A_1 phase at 16 and 24 MHz were found by linear regression on the data points to be 9.59×10^7 and 9.44×10^7 Hz^2/mbar, respectively. From the fits, the values of $4\beta/\alpha$ at 16 and 24 MHz were found to be 5.35 and 5.28. From these we find that the asymptotic slopes ($t'\gg1$) of $\Delta(\nu_0)^2$ are 5.13×10^8 and 4.98×10^8 Hz^2/mbar for 16 and 24 MHz. These are to be compared with a slope of $(5.14\pm0.02)\times10^8$ Hz^2/mbar measured at 2.8 MHz (low field) near T_c. Also from the fits we obtain values of $[P(A_2) - P(A_1)]/H_0$ of 0.229 and 0.239 mbar/kOe at 16 and 24 MHz, where theory shows that this quantity should be field independent. We compare these values with the average value of 0.227 mbar/kOe obtained from the pressurization curves (P versus time) through A_1 and A_2 at magnetic fields of 4.93, 7.40, and 7.51 kOe). From these comparisons we find the 16-MHz data to be

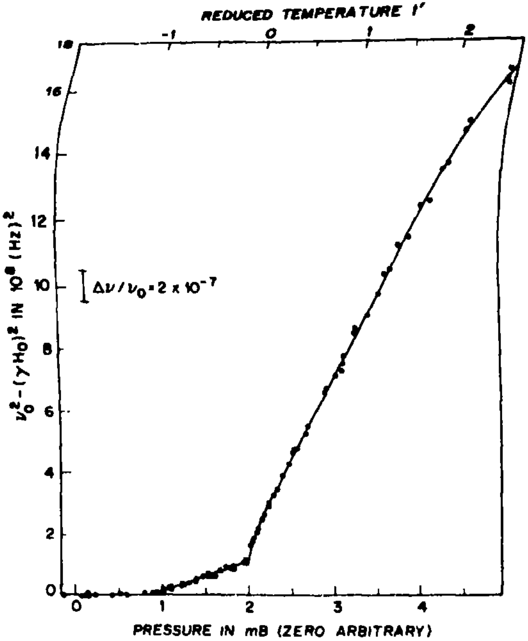

FIG. 2. Transverse-frequency–shift data, $\Delta(\nu_0)^2$ (from four runs), versus pressure at $\nu_0 = 16$ MHz. The solid curve is the theoretical fit to $\Delta(\nu_0)^2$ versus t'. See text.

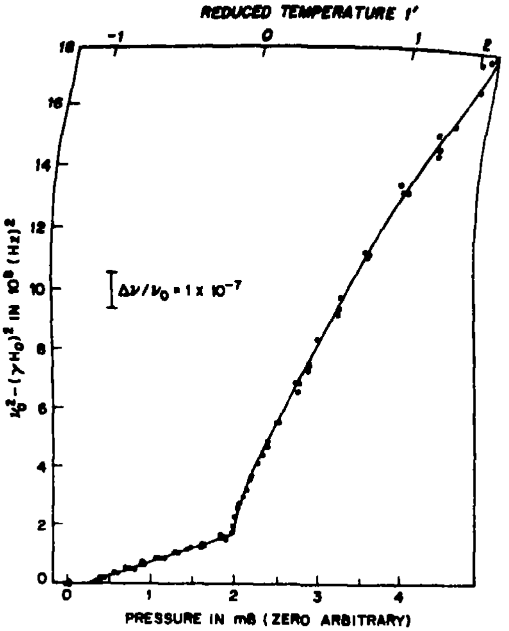

FIG. 3. Transverse-frequency–shift data, $\Delta(\nu_0)^2$ (from four runs), versus pressure at 24 MHz. The s id curve is the theoretical fit to $\Delta(\nu_0)^2$ versus t'. See text.

very reliable, and obtain a weighted-average value of $4\beta/\alpha = 5.33 \pm 0.10$.

From our value of β/α one expects $P(T_c)$ to lie at a pressure $0.625P(A_2)+0.375P(A_1)$. When we plot this pressure, as obtained in a number of magnetic fields from the pressurization curves, as a function of $(H_0)^2$, we obtain a straight line of slope $(5.3\pm0.1)\times10^{-2}$ mbar/(kOe)^2 which passes directly through $P(T_c)$ in zero field. This is consistent with T_c defined in this fashion being a fixed temperature.

Our value of δ is in close agreement with the value obtained from T_{AB}/T_c in Fig. 1. The disagreement with the specific-heat determination may be due to further strong coupling effects not accounted for by theory.

Finally, we have also observed the behavior of ν_L at 16 and 22 kHz in a field of 15.2 kOe and find that behavior in total agreement with the theory. The pressure dependence of ν_L at pressures very close to $P(A_2)$ is very steep and we conclude that no longitudinal resonance will occur in the A_1 phase.

In conclusion, we find that the NMR behavior we observe is in detailed agreement with a rather complex theory which is based entirely upon the Leggett equations, and the BSA results. In the framework of BSA, the behavior we observe in this tiny temperature interval allows us to independently evaluate δ, and we show that this estimate of δ is entirely consistent with other estimates based on T_{AB} measurements. This agre ment supports both the BSA theory and the majo conclusions of that theory, that is, that the A phase is to be identified as the ABM state and th B phase is to be identified as the Balian-Werthamer (BW) state.[14] For those who do not wish to acknowledge the successes of BSA as sufficient proof that the new superfluid phases are o the $L = 1$ manifold, this work provides precise e perimental measurements of behavior in the A_1 region which appears at present to be the only r gion in which free-energy calculations can be easily carried out for higher odd-L angular momentum states.

The authors wish to thank W. F. Brinkman and Michael Cross (who helped prepare Fig. 1) for their valuable help in the theory, and Wolfgang Sprenger for his assistance in performing the e periments. We also wish to thank David Mermir

r his many useful comments and motivation, d W. P. Halperin for providing us with his un-blished He^3 melting curve.

D. D. Osheroff, Ph.D. thesis, Cornell University, 72 (unpublished).

W. J. Gully, D. D. Osheroff, D. T. Lawson, R. C. chardson, and D. M. Lee, Phys. Rev. A 8, 1633 73).

V. Ambegaokar and N. D. Mermin, Phys. Rev. Lett. , 81 (1973).

C. M. Varma and N. R. Werthamer, Bull. Amer. s. Soc. 18, 23 (1973). These authors considered y the low-field limit and hence predicted only two nsitions.

W. F. Brinkman and P. W. Anderson, Phys. Rev. A 2732 (1973).

P. W. Anderson and W. F. Brinkman, Phys. Rev. Lett. 30, 1108 (1973).

[7] P. W. Anderson and P. Morel, Phys. Rev. 123, 1911 (1961).

[8] W. F. Brinkman, J. W. Serene, and P. W. Anderson, to be published. A calculation along similar lines by Y. Kuroda (to be published) gives results which agree with BSA for the purpose of this paper.

[9] A. J. Leggett, Phys. Rev. Lett. 31, 352 (1973), and Ann. Phys. (New York) 85, 11 (1974).

[10] Since the submission of this work for publication we have received a preprint of an article by S. Takagi (to be published) which also derives the frequency shift in A_1 for a more general class of states and arrives at the same result.

[11] J. C. Wheatley, Physica (Utrecht) 69, 218 (1973).

[12] D. D. Osheroff and W. F. Brinkman, Phys. Rev. Lett. 32, 584 (1974).

[13] W. P. Halperin, private communication.

[14] R. Balian and N. R. Werthamer, Phys. Rev. 131, 1553 (1963).

Ion Heating by an Intense Relativistic Electron Beam

J. P. VanDevender, J. D. Kilkenny, and A. E. Dangor
Imperial College, London SW7 2BZ, England

(Received 24 July 1974)

A high-current electron beam is used to produce a plasma from neutral hydrogen. Doppler-line-broadening and Thomson-scattering measurements show that the ion energy is 100 ±15 eV compared with only 12 ± 2 eV for the electron energy. It is shown that this ion energy can be supplied by an inverse pinch effect. It is suggested that much higher ion energies will result for electron densities n_e lower than 10^{15} cm^{-3} measured here.

Several experimenters[1-7] have reported that ten a high-current relativistic electron beam is ected into a plasma, a fraction of the beam en-gy is transferred to the plasma through the ex-ation of streaming instabilities. The energy is nsferred primarily to the plasma electrons. this paper we report measurements which show t direct energy transfer to the ions can occur the self-magnetic field of the beam is not com-etely neutralized by the counter-streaming plas- current—for, in such a situation, there ex-s a force $\vec{J}\times\vec{B}$, associated with the plasma cur-nt and the magnetic field due to the net current, ich accelerates the plasma radially outward. is is the main force acting on the plasma since coupling between the beam and plasma elec-ns is weak. The energy for the radial motion of course provided by the beam.

The experimental arrangement is shown in Fig. A 36-kA, 350-kV, 100-nsec electron beam is compressed by a cone to a current density of 20 kA/cm^2 and injected through a Mylar foil into a test chamber, which is filled with neutral hydrogen. There is no external magnetic field. The current and energy of the beam are reproducible

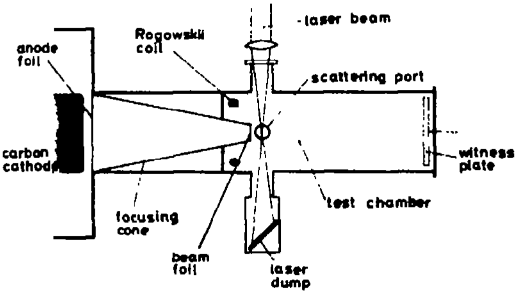

FIG. 1. Diagram of the apparatus. The line-broadening measurements are made by using the laser scattering ports.

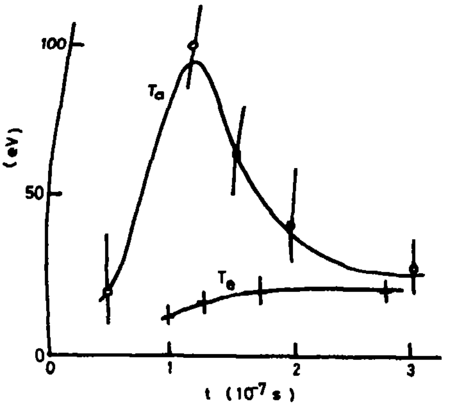

FIG. 2. Electron temperature (T_e) from Thomson scattering. Effective atom temperature (T_a) from Doppler broadening of the Balmer lines by both macroscopic and microscopic motion. Injection is into 100-mTorr H_2 and time is relative to the start of the beam.

to within 10%. The beam radius r_b, measured by the damage pattern on a witness plate, is 8 ± 1 mm throughout the test chamber. The plasma produced by the beam is diagnosed by (1) line broadening of the hydrogen Balmer lines along a line of sight perpendicular to the beam, (2) ruby-laser scattering with the scattering vector also perpendicular to the beam, (3) streak photography, and (4) the net current $I_{\text{net}} = I_{\text{beam}} - I_{\text{plasma}}$, measured with the Rogowski coil shown in Fig. 1. Measurements (1), (2), and (3) are made 8 mm from the entrance foil.

There are two contributions to the line widths: Stark and Doppler broadening. The tabulated Stark broadening of H_β is an order of magnitude larger than for H_α.[8] Experimentally it is found that the widths of the two lines are comparable. Thus the atom velocity distribution along the line of sight can be obtained by analysis of the line widths.[9] The average energy per atom deduced from the data is shown in Fig. 2, for injection into 100-mTorr hydrogen. The charge-exchange mean free path for H^+ in 100-mTorr H_2 is typically 1 mm and so the atom energy is a measure of the ion energy.

Also shown in Fig. 2 is the electron energy obtained from the laser-scattering measurements. Note that at the end of the electron-beam pulse the plasma-electron energy is 12 eV, an order of magnitude less than the atom and ion energy.

Figure 3 is a streak photograph of the diameter of the plasma channel for injection into 100-

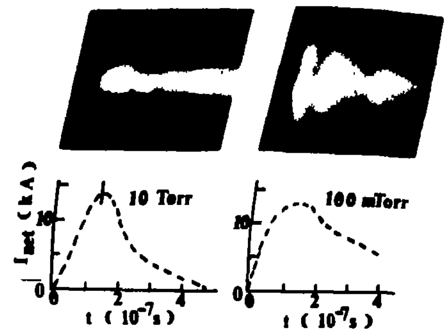

FIG. 3. Streak photograph of a plasma diameter contrasting injection into 100-mTorr H_2 where the radius of the plasma channel changes, with 10-Torr H_2 where the radius is approximately constant.

mTorr and 10-Torr neutral hydrogen. For the 10-Torr case the diameter of the channel is approximately constant. At 100 mTorr the plasma is first seen expanding at 100 nsec, reaching its maximum radius of 2 cm, twice that of the electron beam, at 130 nsec. The initial light at the walls is due to electrons which are expelled from the plasma to give charge neutralization. After the beam the plasma pinches to the axis.

The net currents for 10 Torr and 100 mTorr are shown in Fig. 3. At both pressures the net current is found to start decaying at a time later than 100 nsec, the beam pulse length. In general, it is found that the net current continues to increase for a longer time and that the net change is greater as the pressure is reduced.

The continuum plasma light emission is shown in Fig. 4 together with the plasma current I_{plasma}. For injection into hydrogen at pressures greater than 100 mTorr the light emission follows the plasma current. However at lower pressures, the light emission drops quickly during the beam pulse.

The results presented above—(1) the Doppler broadening, (2) the size of the plasma at 130 nsec, (3) the increase of the net current after the beam, and (4) the absence of light emission during the beam pulse at low pressure—are consistent with radial motion of the plasma. The pinching observed after the beam pulse suggests that the radial motion is associated with the force $j_z B_\theta$ on the plasma.

During the beam pulse the plasma current j_{pz} is opposite in direction to the net current, which produces the azimuthal field B_θ. Thus during the beam, the force is radially outward. After the

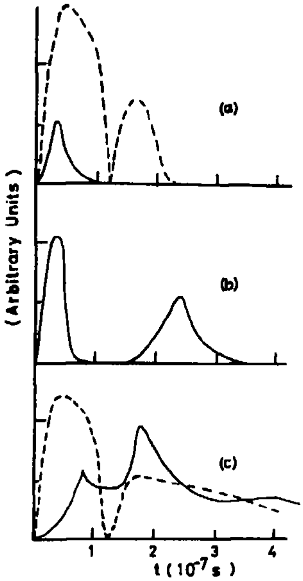

FIG. 4. Time history of the continuum light emission near 6940 Å (solid line) and the modulus of the plasma current (broken line) in arbitrary units. (a) 2 mTorr, (b) 30 mTorr, (c) 60 mTorr. Notice the correlation at 60 mTorr and contrast the rapid drop in plasma light at lower pressure.

beam the only current in the system is the plasma current and therefore, the plasma pinches. A measure of the radial acceleration can be obtained from the equation of motion

$$\rho\, dv_r/dt = -j_{pz} B_\theta. \qquad (1)$$

Taking ρ as the mass density of the neutral gas, j_{pz} the plasma current density as $(I_{\rm net} - I_{\rm beam})/\pi r_b^2$, and B_θ equal to $\frac{1}{2}$ the maximum value at the beam radius, we obtain the equation $dv_r/dt \sim 10^{12}$ m sec^{-2}. Thus in 100 nsec, a velocity v_r of 10^5 m sec^{-1} and a plasma expansion of 1 cm are expected. This is in agreement with the measured Doppler velocity of 1.3×10^5 m sec^{-1} and the observed radius of the plasma.

After the beam pulse the plasma current reverses, and the force $\vec{J}\times\vec{B}$ on the plasma is radially inward. For a plasma of zero resistivity the sum of the magnetic $(\frac{1}{2}LI_{\rm net}^2)$ and kinetic energies s then constant. As the plasma is decelerated he energy in the mass motion is transferred to ield energy so that at the end of the pulse and before the plasma motion is reversed,

$$\frac{dI_{\rm net}}{dt} > -\frac{1}{2}\frac{I_{\rm net}\,dL/dt}{L}.$$

Since the channel is still expanding dL/dt is negative and so $dI_{\rm net}/dt$ is positive, in agreement with the net-current measurements.

As the force $\vec{J}\times\vec{B}$ on the plasma expels the plasma from the channel the plasma number density within the channel drops if additional ionization cannot compensate. This is consistent with the drop in light emission from the plasma during the beam pulse at very low pressures.

The effect is important because of the energy transfer from an electron beam to the ions in a plasma. Consider an infinitely long system. The axial component of Ohm's law is

$$\eta j_{pz} = E_z + v_r B$$

provided $\operatorname{div}\vec{J} = 0$. The rate of increase of the plasma energy density is $j_{pz}E_z$ of which ηj_{pz}^2 is the resistive heating and $-v_r B_\theta j_{pz}$ is the rate of energy transfer to the heavy particles. According to Eq. (1) the acceleration dv_r/dt is proportional to ρ^{-1}. Thus at lower filling pressures, the energy input to the ions will dominate the electron heating even more than it does for this experiment at $n_e = 10^{15}$ cm^{-3}. An approximate calculation shows that ion viscosity can easily randomize this energy.

In summary, measurements of a plasma produced by an electron beam in neutral hydrogen have shown that the neutral and ion energies are an order of magnitude greater than the electron energy. This new result has not been observed before as most other experiments have been performed with a much larger mass density. We have not examined the role of a guide field, and also this effect depends on incomplete magnetic neutralization. However, the injection of a beam along a z-pinch column, which has a significant B_θ, would produce this energy transfer mechanism.

We wish to thank J. C. Martin and his associates at the Atomic Weapons Research Establishment, Aldermaston, England, for their help with the electron-beam technology, and the loan of a Marx generator. Our thanks are also due to J. A. Nation and J. Westlake for advice and assistance.

---

[1] A. T. Altyntsev *et al.*, Nucl. Fusion, Suppl., 161 (1972).

[2] D. R. Smith, Phys. Lett. 42A, 211 (1972).

[3] C. A. Kapetanakos and D. A. Hammer, Appl. Phys. Lett. 23, 17 (1973).

[4] P. A. Miller and G. W. Kuswa, Phys. Rev. Lett. 30, 958 (1973).

[5] P. Korn, F. Sandel, and C. B. Wharton, Phys. Rev. Lett. 31, 579 (1973).

[6] G. C. Goldenbaum, W. F. Dove, K. A. Gerber, and B. G. Logan, Phys. Rev. Lett. 32, 830 (1974).

[7] C. Stallings, D. Prono, R. Schneider, and S. Putnam Bull. Amer. Phys. Soc. 18, 1360 (1973).

[8] H. R. Griem, *Plasma Spectroscopy* (McGraw-Hill, New York, 1964).

[9] J. D. Kilkenny, unpublished.

Dissipative Trapped-Electron Instability in Cylindrical Geometry*

S. C. Prager, A. K. Sen, and T. C. Marshall
Plasma Research Laboratory, Columbia University, New York, New York 10027

(Received 28 May 1974)

We show that the essential ingredients of the trapped-electron instability can be present in a cylindrical geometry. A linear instability theory, a simple physical explanation, and the results of an experiment are presented to support this.

The dissipative trapped-electron instability like all other trapped-particle instabilities has always been discussed in toroidal systems.[1-3] In toroidal systems magnetic field properties such as inhomogeneity, curvature, and helicity are all interrelated and the resulting zero-order particle trajectories of drifting bananas are very complex. These geometrical complexities also make experimental identification difficult. This Letter considers the simplest magnetic field sufficient for the instability and clarifies the underlying physics. We also report the results of an experiment which demonstrates that a dissipative trapped-electron instability can be excited in a cylindrical geometry.

It is well known that collisionless trapped-particle instabilities are driven by magnetic-curvature drift.[3] But dissipative trapped-particle instabilities are similar to collisional drift waves in the sense that the excitation of both classes depends on collisions. In the case of the trapped-electron instability one needs an appropriate electron collision frequency which should be higher than the wave frequency.[1] Therefore one can conceive of the dissipative trapped-electron instability in an essentially straight magnetic field, but to produce a trapped population of particles one needs at least two localized magnetic mirrors (Fig. 1). A density gradient, say in the radial direction, is always necessary for a driftlike mode and finally, an electron-temperature gradient coincident with the density gradient is essential.[1] We will show that the cylindrical system shown in Fig. 1 is capable of sustaining the dissipative trapped-electron instability.

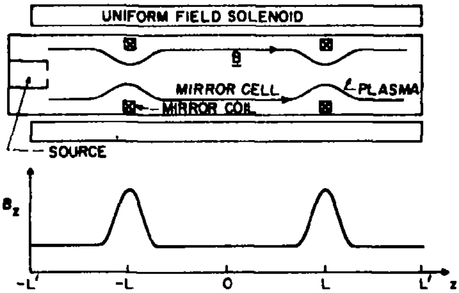

FIG. 1. Schematic of the mirror cell in cylindrical geometry (above) and the axial magnetic field intensity (below) for mirror ratio $R=3$. The plasma source which produces a radial electron-temperature gradient is an $\vec{E}\times\vec{B}$ source (Ref. 5).

For electrons trapped between the mirrors, we write the drift kinetic equation in cylindrical coordinates r, θ, z with the Krook model for the collision term as

$$\frac{\partial f_t}{\partial t}+v_z\frac{\partial f_t}{\partial z}+\frac{e}{m_e}\frac{\partial \varphi}{\partial z}\frac{\partial F_t}{\partial v_z}-\frac{c}{B_z r}\frac{\partial \varphi}{\partial \theta}\frac{\partial F_t}{\partial r}=\nu_e(v)\left(\frac{e\varphi}{kT_e}F_t-f_t\right), \tag{1}$$

where f and φ are the perturbed electron distribution function and potential, respectively; v_z, $\nu_e(v)$, and F are the axial velocity, velocity-dependent electron collision frequency, and equilibrium distribution function, respectively; and the subscript t refers to the trapped population. Integrating Eq. (1) along the straight zero-order trajectory between sharp mirrors, averaging over the fast bounce period $2L/v_z$, and integrating in velocity space yields the perturbed trapped-electron density

$$n_t=\frac{e\varphi\delta N}{kT}-\frac{e}{2kTL}\int_{-L}^{L}\varphi(z')\,dz'\int\frac{(\omega-\omega_e{}^*)F_t d^3v}{\omega+i\nu_e v_{\mathrm{th}}{}^3/\epsilon v^3},$$

where F_t is taken as Maxwellian, $\nu_e(v)\approx\nu_e v_{\mathrm{th}}{}^3/\epsilon v^3$, $\delta=N_t/N$, $\epsilon=1-R^{-1}$, R is the mirror ratio,

$$\omega_e{}^*=\frac{-cm_e kT}{reB_z}\left[\frac{1}{N}\frac{dN}{dr}+\left(\frac{m_e v_e{}^2}{2kT_e}-\frac{3}{2}\right)\frac{1}{T_e}\frac{dT_e}{dr}\right],$$

and we assume standing-wave solutions in the z direction:

$$f_t=f_t(z)\exp(-i\omega t+im\theta),\quad \varphi=\varphi(z)\exp(-i\omega t+im\theta).$$

We note that, unlike the toroidal case, the trapped fraction $\delta\neq\sqrt{\epsilon}$ here. The perturbed transit electron density n_u is assumed to be a perturbed Maxwellian since the transits are in equilibrium with the source. The ions behave essentially as in a drift wave, so that their perturbed density is given by

$$n_i=\frac{\omega^*}{\omega}\frac{Ne\varphi(z)}{kT}-\frac{Ne}{m_i\omega^2}\frac{\partial^2\varphi(z)}{\partial z^2},$$

where $\omega^*=(cmkT/eB_z r)N^{-1}dN/dr$. Using the quasineutrality condition $n_t+n_u=n_i$ yields

$$A(\omega)\varphi(z)-B(\omega)\partial^2\varphi(z)/\partial z^2=C(\omega)\int_{-L}^{L}\varphi(z')\,dz'[u(z-L)-u(z+L)], \tag{2}$$

where

$$A(\omega)=\frac{Ne}{kT}\left(\frac{\omega^*}{\omega}-1\right),\quad B(\omega)=\frac{Ne}{m_i\omega^2},\quad C(\omega)=\frac{-e}{2LkT}\int\frac{(\omega-\omega_e{}^*)F\,d^3v}{\omega+i\nu_e v_{\mathrm{th}}{}^3/v^3}\approx-\frac{iNe}{kT}\frac{\epsilon\delta\omega_T{}^*}{\nu_e L}. \tag{3}$$

The unit step function u was included so that Eq. (2) correctly represents the entire system length $-L'<z<L'$. Outside the mirror region, the right-hand side is zero and the equation reduces to that of a stable drift wave.

Expecting only even modes we expand $\varphi(z)$ in a Fourier cosine series over the system length $2L'$ as $\varphi(z)=\sum_n a_n\cos(n\pi z/L')$. Substituting this series in Eq. (2) we obtain an infinite set of homogeneous equations for the Fourier coefficients a_n with ω as the eigenvalue parameter. It can be shown that the Fourier series is rapidly converging. Therefore truncating the set of equations to three and setting its determinant to zero yields a good approximation both for the eigenvalue ω and the spatial structure of $\varphi(z)$. With the use of the parameter relations $L'=2L$, $\nu_e/2=\omega^*=\omega_T{}^*=(cmkT/eB_z r)T_e{}^{-1}dT_e/dr$, $\delta=0.2$, $\epsilon=0.6$, $\omega_{be}/\omega^*=6$, the results are

$$\omega=(0.992+i0.12)\omega^*;$$
$$\varphi(z)\sim1+1.27\cos\frac{\pi z}{L'}-0.28\cos\frac{3\pi z}{L'}, \tag{4}$$

where $\omega_T{}^*$ is the drift frequency based on electron-temperature gradient and $\omega_{be}=\frac{1}{2}L^{-1}(KT_e/m_e)^{1/2}$ is the electron bounce frequency. The growth rate is seen to be more than 10% of the real frequency and can be shown to vary roughly as L/L'. The spatial structure seen in Eq. (4) indicates a high degree of localization in the trapped-particle region (Fig. 2). This feature is not dissimi-

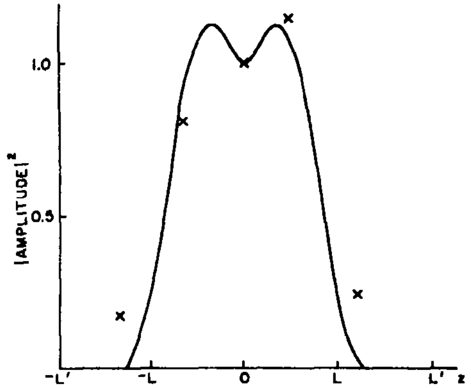

FIG. 2. Dependence of the normalized, relative, square of the fluctuation amplitude upon axial position. The theoretical result is from Eq. (4), and the experimental data are obtained from the output of an autocorrelator driven by a Langmuir probe located in the region of maximum density gradient. Plasma radius ≈ 1 cm, $T_e\approx6$ eV, $N^{-1}dN/dr\approx T_e{}^{-1}dT_e/dr\approx1\ \mathrm{cm}^{-1}$, $B=1200$ G, $N\sim2\times10''\ \mathrm{cm}^{-3}$.

lar to that of a collisionless trapped-particle instability.[5] But the reasons are quite different, as the localization of the collisionless instability is due to its flutelike nature and occurs in the bad-curvature region of the magnetic field. If we take the limit $L \sim L'$ so that the entire system is populated uniformly by trapped particles, only the first term of the Fourier series is necessary because φ will be constant and the above result will reduce to $\omega/\omega^* = 1 + i\delta\epsilon\omega_T{}^*/\nu_e$ which is essentially the same as that of Kadomtsev and Pogutse.[1]

Deschamps *et al.*[4] report a driftlike instability in an ODE machine[6,7] which produces a cylindrical plasma with radial density and electron-temperature gradients in a corrugated magnetic field. However, at their low operating density, $\nu_e < \omega^*$, one should not expect a dissipative trapped-electron instability. Guided by the above analysis we have performed a similar experiment using a Q machine converted to an ODE-type device. The parameters T_e, T_i, B_z, $N^{-1}\,dN/dr$, $T_e^{-1}dT_e/dr$, plasma radius, and hydrogen-gas fill are approximately the same as reported in their paper. However, in our experiment (a) there is one mirror cell ($2L = 50$ cm, $2L' = 100$ cm) and the magnetic field is constant over 80% of its length, (b) the mirror ratio R is controllable and is made large in order to enhance electron trapping, and (c) the electron density is much higher ($N_e \sim 2 \times 10^{11}$ cm^{-3}) so that the electron mean free path is of the order of the mirror length and $\nu_e > \omega^*$. This environment can support a dissipative trapped-electron instability and we observe a monochromatic wave at frequency $\omega \approx \omega^*$ and azimuthal mode number $m = 1$. The instability, which is localized in the mirror cell (Fig. 2), is observed when the mirror coils are energized and its amplitude is at least an order of magnitude larger than the background level of drift-wave fluctuations in the absence of the mirror field. The instability amplitude became maximum at $n/N \sim 10\%$ when $\nu_e > \omega^* \sim 3 \times 10^5$ sec$^{-1} \ll \omega_{be}$, $R \sim 3$, and the electron mean free path ~ 200 cm. These conditions not only favor electron trapping in the mirror cell but are appropriate for a positive growth rate of the dissipative trapped-electron instability as shown by the above theory.

The fraction δ of electrons trapped can be estimated experimentally by observing the plasma-density change when the mirror farthest from the source is switched on or off, the other mirror left on. Since the ions have a very short mean free path (<10 cm) their containment is not affected by the magnetic mirrors: We conclude this from the observation that the plasma density is not affected by the presence of only the mirror farthest from the source. Thus, the plasma-density change is due to electron trapping in the mirror cell, with ions being drawn in to maintain neutrality. (Since $T_e/T_i \sim 6$, ambipolar effects are not important to electron trapping.[8]) The fraction of electrons trapped $\delta \approx \frac{1}{2}$. Clearly, as R increases the growth rate should increase since both the trapped fraction δ as well as ϵ increase. In Fig. 3(a) we see that the wave amplitude increases as R increases. Furthermore in Fig. 3(b) we see that the experimental wave amplitude tends to follow qualitatively the growth rate as a function of ν_e/ω; the theoretical curve is obtained with the help of the detailed calculation of the velocity-space integral in $C(\omega)$, Eq. (3). The mechanism for nonlinear limitation of wave growth has not been identified, but it is possible for the steady saturation amplitude of an instability of the soft-onset type to vary as the linear growth rate.[9]

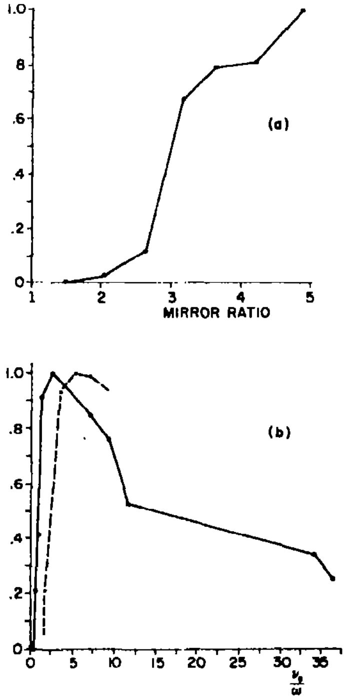

FIG. 3. (a) Square of the wave amplitude versus mirror ratio R, $\nu/\omega = 3$. (b) Square of the amplitude (solid line) and the theoretical growth rate (broken line) versus collision frequency.

In order to eliminate ∇T_e, we converted the source to a hollow-cathode arc containing a hot filament. For this source $\vec{E} \parallel \vec{B}$ and no temperature gradient was produced in the plasma. In the same range of plasma parameters as with the $\vec{E} \times \vec{B}$ discharge, the magnetic mirrors had no effect on the fluctuation level.

Since toroidal drifts do not play a causal role in this instability a description of the physical mechanism applies equally well to cylindrical and toroidal systems. If $\omega_{be} \gg \omega$ the trapped electrons experience a relatively steady electric field during a bounce period. Therefore one can consider all the trapped particles to drift radially at the speed E_θ/B_z, where E_θ is the perturbed electric field. The radial flux of trapped electrons of velocity v at position r is proportional to $F_t E_\theta/B_z$. The perturbed trapped-electron density buildup, Δn_t, at r due to this flux will be proportional to the flux, the length of trapping time $\nu_e^{-1}(v)$, and $\partial F_t/\partial r$. The velocity integral of this product yields the integral $C(\omega)$, Eq. (3). For simplicity we consider a perturbation with $k_\parallel = k_z = 0$, so that the density-gradient contribution to the electron buildup is zero as appropriate for a stable drift wave. Let the sign of E_θ be such that the trapped-electron flux is radially outward. Since $\nu(v) \sim v^{-3}$ the high-velocity particles are trapped longest and contribute most to the flux. Since the temperature decreases radially outward, the number of high-velocity particles also decreases radially outward. Thus there is a greater radial outward flux of trapped electrons to a point than outward flux from the point, thereby leading to an electron buildup. The direction of E_θ which produces this accumulation corresponds to an original ion perturbation which depletes ions at that point. Thus the trapped-electron buildup enhances the original perturbation, resulting in an instability. If either electron-neutral collisions dominate or electrostatic trapping occurs,[10] low-velocity electrons contribute most to the net flux, more electrons leave than arrive at the point, and the perturbation decays.

---

*Work supported by the National Science Foundation under Grant No. NSF GK-26326.

[1] B. B. Kadomtsev and O. P. Pogutse, Dokl. Akad. Nauk SSSR 186, 553 (1969) [Sov. Phys. Dokl. 14, 470 (1969)].

[2] M. N. Rosenbluth, D. W. Ross, and D. P. Kostomarov, Nucl. Fusion 12, 3 (1972).

[3] B. B. Kadomtsev and O. P. Pogutse, Nucl. Fusion 11, 67 (1971).

[4] P. Deschamps, R. Gravier, C. Renaud, and A. Samain, Phys. Rev. Lett. 31, 1457 (1973).

[5] B. B. Kadomtsev and O. P. Pogutse, in *Reviews of Plasma Physics*, edited by M. A. Leontovich (Consultants Bureau, New York, 1970), Vol. 5, p. 328.

[6] P. Brossier, P. Deschamps, R. Gravier, R. Pellat, and C. Renaud, Phys. Rev. Lett. 26, 124 (1971).

[7] P. Brossier, P. Deschamps, R. Gravier, R. Pellat, and C. Renaud, Phys. Rev. Lett. 31, 79 (1973).

[8] T. K. Fowler and M. Rankin, J. Nucl. Energy, Part C 8, 121 (1966).

[9] A. A. Vedenov, *Theory of Turbulent Plasma* (American Elsevier, New York, 1968), Appendix A, p. 109.

[10] B. B. Kadomtsev and O. P. Pogutse, Dokl. Akad. Nauk SSSR 188, 69 (1969) [Sov. Phys. Dokl. 14, 863 (1970)].

Polarized-Neutron Diffraction from Spin-Polarized Protons: A Tool in Structure Determination?*

J. B. Hayter,† G. T. Jenkin, and J. W. White
Physical Chemistry Laboratory, Oxford University, Oxford, OX1 3JP, England

(Received 15 January 1974)

We have observed the spin-dependent diffraction of slow neutrons by differentially polarized nuclei in single crystals of lanthanum magnesium nitrate. The effects are accompanied by enhanced Bragg diffraction and reduced incoherent scattering at high proton polarizations. The diffraction pattern is very sensitive to selective depolarization of nuclei, and proton resonances have been observed through changes in the diffracted intensities when the sample is irradiated at the Larmor frequencies.

We report diffraction experiments using polarized slow neutrons and spin-polarized nuclei. A crystal of lanthanum magnesium nitrate (LMN), $La_2Mg_3(NO_3)_{12}\cdot 24H_2O$, was doped with 1% $^{142}Nd^{3+}$ and the protons polarized dynamically[1] by the Abragam-Jeffries "solid" effect. A polarization of about 40% could be routinely obtained at 1.5°K by using only 300 μW of 4-mm microwave power in a *resonant* TE_{01n} cylindrical aluminum cavity.[2] Much higher polarizations (indicated by many lines in the NMR spectrum) were also obtained by carefully reducing the power to obtain an optimum balance between saturation of the resonance and minimum heating of the sample. The experiments were performed at the polarized-neutron diffractometer, PN2, on the PLUTO reactor hole 7H1L at the Atomic Energy Research Establishment, Harwell. The magnet used was a superconducting asymmetric split pair, specially designed to minimize depolarization of the incident and diffracted neutron beams, while at the same time giving a sample volume of about 1 cm^3 where the field homogeneity was better than a few parts in 10^5 at 1.9 T.[3] Depolarization of the beam [measured by using a standard cobalt-iron ($Fe_{0.08}Co_{0.92}$) crystal in place of the sample] was always less than 1% and usually about 0.5%. Figure 1 shows a schematic diagram of the experiment. The magnetic field at the sample was perpendicular to the neutron scattering plane and the incident neutrons were polarized parallel or antiparallel to the field direction, flipping being achieved by a rf coil at the Larmor frequency.

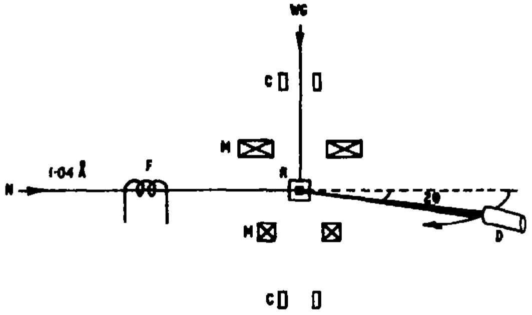

FIG. 1. Schematic diagram of the experiment: *N*, polarized neutron beam ($\lambda_0 = 1.04$ Å); *F*, neutron spin flipper; *M*, *C*, main and field-trimming coils of superconducting magnet, giving field perpendicular to the scattering plane; *WG*, *R*, wave guide and resonant cavity; *D*, boron trifluoride neutron detector at scattering angle 2θ.

The elastic scattering cross sections for the polarized sample can be estimated from the formulas of Schermer and Blume[4] for coherent and incoherent nuclear scattering from a monoisotopic sample. With the consideration of only the *z* components of the nuclear magnetization[5] their Eqs. (12) or (20) when applied to LMN, and for a fully polarized neutron beam, reduce to the following:

$$[\partial\sigma(\pm,p)/\partial\Omega]_{\rm coh} = N_0|f_{\rm H}(\vec{K})(A_{\rm H} \pm \tfrac{1}{2}B_{\rm H}p) + f_{\rm N}(\vec{K})A_{\rm N} + f_{\rm O}(\vec{K})A_{\rm O} + \dots|^2\ , \tag{1}$$

$$[\partial\sigma(\pm,p)/\partial\Omega]_{\rm inc} = N_0[144{a_{\rm H\,inc}}^2(1 - \tfrac{1}{3}p^2 - \tfrac{2}{3}p) + 36{a_{\rm N\,inc}}^2 + 180{a_{\rm O\,inc}}^2 + \dots], \tag{2}$$

where $f_{\rm H}(\vec{K})$ is the structure factor for the 144 protons in the hexagonal unit cell[6] (three times the fundamental rhombohedral cell), N_0 is the number of hexagonal cells in the crystal, and the momentum transfer $\vec{K} = \vec{k} - \vec{k}_0$. The $f_{\rm N}(\vec{K})$, $f_{\rm O}(\vec{K})$, etc., are the corresponding structure factors for nitrogen, oxygen, etc., whose scattering lengths $A_{\rm N}$, $A_{\rm O}$ are either truly polarization independent or, for the present, are assumed to be so compared with hydrogen. The signs refer to the incident-neutron spin up

+) or down (−) and p is the proton spin polarization, assumed the same for all the hydrogen in the rystal.

$$A_{\mathrm{H}}=\tfrac{3}{4}a^{+}+\tfrac{1}{4}a^{-},\quad B_{\mathrm{H}}=\tfrac{1}{4}(a^{+}-a^{-}),\tag{3}$$

$$a_{\mathrm{H\,inc}}{}^{2}=\tfrac{3}{16}(a^{+}-a^{-})^{2},\tag{4}$$

$^{+}$ and a^{-} being the triplet and singlet scattering lengths for neutron-proton collisions. A_{N}, $a_{\mathrm{N\,inc}}{}^{2}$, tc., are defined in a corresponding manner. The peaks whose structure factor is dominated by hydroen were of most interest in this experiment. They were classified by comparing the powder diffracion patterns of hydrogenous and deuterated specimens.

The relative scale of the coherent and incoherent terms depends upon $|f_{\mathrm{H}}(\vec{K})|^{2}/144$ which may vary y orders of magnitude and from one Bragg peak to another.

In LMN the observed flipping ratio R, defined as

$$R=\frac{\text{(scattered-neutron intensity with incident-neutron spin up)}}{\text{(scattered-neutron intensity with incident-neutron spin down)}},$$

aturally depends on the contribution of unpolarized atoms to the Bragg intensity, so that changes in e polarization of protons (for example) at definite lattice sites have an effect on the diffraction patrn similar to that of the isomorphous replacement method for solving complex structures.

To produce polarization in LMN the c axis was aligned in the scattering plane perpendicular to the teady field B_0. All Bragg peaks in this plane fall, because of selection rules, into four groups given y (in hexagonal notation)

$$(-2k,k,2n-k),\ (h,0,3n+h),\ (h,h,3n),\ (0,k,3n-k).$$

n general $-h+k+l=3n$ for a rhombohedral cell, here n is an integer. Several of the peaks in he second and fourth class have structure facors with strong hydrogen contributions. Using he x-ray structure[6] as a guide, we calculated he expected neutron structure factors and their ydrogen contributions and then performed poarization-dependence experiments.

The most obvious effect of nuclear spin polarzation is that the scattering cross section beomes dependent on the incident-neutron spin diection, and for one spin configuration the Bragg cattering intensity is enhanced.[7,8] These results onfirm earlier experiments with 8-mm microaves.[9] A nuclear polarization giving a flipping atio of 8.5/1 at the maximum of the (0, −3, 12) eflection was first produced by saturating one of e "forbidden" transitions. Then the microwave ower was turned off, allowing the polarization decay, and the intensity at the Bragg maximum as measured continuously with an alternation f incident-neutron polarization every 4.5 min. igure 2 shows the results of this experiment. he flipping ratio decays with a time constant of .0 ± 0.2 min, in good agreement with the proton uclear spin-lattice relaxation time for this sysem at 1.8 T and 1.5°K found by Jeffries and chmugge.[10] The same decay time has been ound for all the other peaks investigated to date t this temperature. The (2, 0, 8) peak has a decay envelope which demonstrates cancelation of the structure-factor contributions from other atoms by the hydrogen contribution at a particular polarization during the decay.

From the intensities of Bragg peaks dominated by hydrogen, measurements with and without proton polarization should allow the sample polarization to be estimated from Eq. (1). When this was done by using the atomic positions known from x-ray crystallography[6] and a set of Bragg peaks at constant but unknown polarization, values rang-

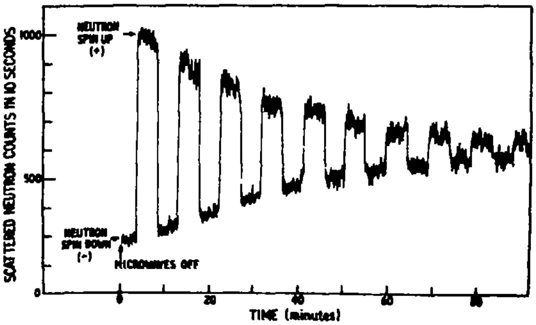

FIG. 2. Decay of the flipping ratio and coherent scattering intensity for the (3, 0, 12) Bragg peak after turning off the microwave power used to maintain nuclear polarization. The nuclear relaxation time was 25 min.

TABLE I. Experimental flipping ratios for Bragg peaks in the a^*–c^* plane of a weakly polarized LMN crystal.

Peak	Unpolarized structure factor	Proton part of structure factor	Flipping ratio R	Polarization (%)
(0, −1, 4)	18.4	0.654	4.22	23
(0, −2, 8)	− 0.89	−0.785	1.91	
(0, −3, 12)	−29.92	2.253	5.19	15
(0, −4, 16)	14.86	0.271	7.58	57
(0, −5, 20)	41.16	0.0165	0.799	
(0, −6, 24)	− 8.83	−0.4729	1.30	
(0, −7, 28)	28.94	0.152	2.14	
(0, −8, 32)	−37.46	0.124	1.43	

ing from $p = 13\%$ to $p = 57\%$ were obtained. A minimum estimate from the incoherent scattering, using Eq. (2), gave $p \approx 25\%$. This variability probably reflects the sensitivity of the calculation to the hydrogen-atom positions.

Accurate relative flipping ratios were obtained by programming the diffractometer to "visit" cyclically a sequence of Bragg peaks and their nearly flat backgrounds, repeating the operation as many times as were necessary to get good statistics or until the polarization changed noticeably. Positioning accuracy was ±0.01°. Scans of 8 h at constant polarization were possible and Table I shows some of the different flipping ratios. The results demonstrate the sensitivity of Bragg diffraction to the proton, and possibly other, nuclear polarizations. They suggest that difference analyses (for example the *difference Patterson method*) may be useful for obtaining parts of a crystal structure, such as the hydrogen positions, to high accuracy without the need to solve the complete structure.

For very complex crystals it is attractive to minimize the amount of data to be refined in order to get the atomic positions of interest. One way is to selectively depolarize nuclei whose Larmor frequencies differ either because of their magnetic moments or because of their proximity to paramagnetic ions in the crystal. In this way one can control and vary the contribution to the structure factor of individual nuclei within the unit cell.

Figure 3 shows the proton magnetic resonance in LMN at about 40% polarization observed by measuring the change in scattered-neutron intensity at the (3, 0, 12) Bragg peak. An oscillator, feeding a coil correctly wrapped around the sample, was swept through the proton Larmor frequencies synchronously with a chart recorder which displayed the Bragg-peak intensity. Strong depolarization of the sample occurred at 77.67 MHz, the expected frequency for proton resonance in the mainly diamagnetic crystal, but the depolarization spectrum has some poorly resolved shoulders indicating that separated nuclear spin packets might be depolarized sequentially. The microwave pumping power was left on during the scan to compete with the depolarizing transitions. The resonance covers about 80 kHz which corresponds to the 20 G calculated.[10]

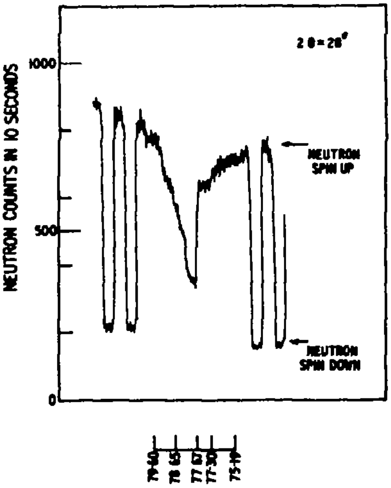

FIG. 3. Proton-magnetic-resonance spectrum of LMN crystal observed by a change in intensity of the (3, 0, 12) Bragg peak as an exciting frequency was swep through the resonance. (The neutron spin direction was "up" continuously throughout the scan.)

Neutron spin-up–spin-down measurements were made before and after the scan and show that the polarization recovered effectively. Selective depolarization of nuclei effectively combines diffraction and electron-nuclear double resonance[11] greatly expanding the information available from each Bragg peak. For sufficiently distinguishable resonances it performs a partial analysis of the diffraction pattern.

Other rf frequencies were fed into the coil corresponding to the nitrogen and lanthanum resonance values but no effect of their nuclear polarization was found either on the "hydrogenous" Bragg peaks or on "nonhydrogenous" peaks such as (0, 1, 2).

The nuclei may be polarized by other means than dynamic polarization, but the dynamic method has the advantage that a change from positive to negative nuclear polarization can be made easily. We think that the method may have some virtues for studying chemically interesting sites in complex crystals such as proteins.

We are planning to refine the evaluation of the position of the hydrogens in LMN by using a four-circle neutron-diffraction experiment, and to use the polarization data as a further refinement.

We wish to acknowledge the assistance of Mr. V. Rainey and Mr. T. Atkins (Atomic Energy Research Establishment, Harwell) in performing these experiments.

---

*Work supported by the Science Research Council under Contract No. B/RG/354.

†Present address: Institute Max von Laue–Paul Langevin, Grenoble, France.

[1] See, for example, C. D. Jeffries, *Dynamic Nuclear Orientation* (Wiley, New York, 1963).

[2] J. B. Hayter, G. T. Jenkin, and J. W. White, to be published.

[3] E. Gilbert, P. Hanley, J. B. Hayter, and J. W. White, J. Phys. E: Sci. Instrum. 6, 714 (1973).

[4] R. I. Schermer and M. B. Blume, Phys. Rev. 166, 554 (1968).

[5] I. I. Gurevich and L. V. Tarasov, *Low Energy Neutron Physics* (North Holland, Amsterdam, 1968), pp. 306–308.

[6] A. Zalkin, J. D. Forrester, and D. H. Templeton, J. Chem. Phys. 39, 2881 (1963).

[7] C. A. Shull and R. F. Ferrier, Phys. Rev. Lett. 10, 295 (1963).

[8] A. Abragam, G. L. Bacchella, C. Lung, P. Meriel, J. Peisaux, and M. Pinot, Phys. Rev. Lett. 28, 805 (1972).

[9] J. B. Hayter and J. W. White, British Neutron Beam Research Committee Report, 1971 (unpublished), p. 118.

[10] C. D. Jeffries and T. J. Schmugge, Phys. Rev. 138, A1785 (1965).

[11] See, for example, G. Feher, Phys. Rev. 103, 834 (1956); A. Abragam and B. Bleaney, *Electron Paramagnetic Resonance of Transition Ions* (Oxford Univ. Press, Oxford, England, 1970).

Evidence of Optical Transitions in X-Ray Inelastic Scattering Spectra: Li Metal*

N. G. Alexandropoulos†
The Aerospace Corporation, Los Angeles, California 90009

and

G. G. Cohen
Columbia Astrophysics Laboratory, Columbia University, New York, New York 10027

and

M. Kuriyama
National Bureau of Standards, Washington, D. C. 20234

(Received 9 July 1974)

We report results of x-ray Compton-Raman scattering experiments. In addition to the expected Compton and Raman scattering, there is a prominent feature in the form of a peak near $E/E_F = 1$. The new peak can be explained qualitatively by considering the conduction band of lithium metal to be composed of hybridized orbital electrons, and it furnishes the first evidence of an L-x-ray Raman band.

The strongly interacting electron gas is one of the most interesting systems in solid-state physics, and it may soon be expected to form a rigorous testing ground for approximations and theories. The numerous difficulties involved in the theoretical calculations render it one of the areas in physics about which little is known. Experimentally, the best, if not the only, method of investigating this area is x-ray inelastic scattering. Here the spectra are functions of the energy, with the parameter $\vec{\kappa}$, the momentum transfer. A collection of a number of such spectra yields directly the energy-loss function (the dynamic structure factor[1,2]). We define the momentum transfer by $|\vec{\kappa}| = |\vec{k}_{\rm in} - \vec{k}_{\rm out}| = (4\pi/\lambda_{\rm in})\sin(\varphi/2)$, and the energy transfer by $E = \hbar(\omega_{\rm in} - \omega_{\rm out})$, where the $\vec{k}$'s and the ω's are the wave vectors and the frequencies of the incoming and the outgoing photons; $\lambda_{\rm in}$ is the incident wavelength, and φ is the scattering angle. The differential cross section for x-ray inelastic scattering is given[1,3] by

$$\sigma(\vec{\kappa}, E) = -2C(k_{\rm in}, k_{\rm out})\,{\rm Im}(\overleftrightarrow{P} \cdot \overleftrightarrow{\epsilon}^{-1}), \qquad (1)$$

where

$$C(k_{\rm in}, k_{\rm out}) = (2\pi)^{-4}(e^2/mc^2)^2(\omega_{\rm in}\omega_{\rm out})^{-1} \times (\vec{v}_{\rm in} \cdot \vec{v}_{\rm out})^2,$$

and the $\vec{v}$'s are the x-ray polarization directions. $\overleftrightarrow{P}$ is the polarization propagator and $\overleftrightarrow{\epsilon}^{-1}$ is the inverse dielectric function. The differential cross section can also be written in terms of the electron correlation:

$$\sigma(\vec{\kappa}, E) \propto (\kappa/E)^2 \hat{s} \cdot \overleftrightarrow{J}(\vec{\kappa}, E) \cdot \hat{s}, \qquad (2)$$

where $\hat{s}$ is the unit vector in the direction of $\vec{\kappa}$, and J_{ij} is the Fourier transform of the current correlation $\langle \Delta j_i : \Delta j_j \rangle$. This expression establishes the relation between x-ray inelastic scattering and x-ray absorption spectra and leads to x-ray Raman scattering.

To get a complete picture of the interaction, it is necessary to achieve a collection of experimental spectra over the entire range of $\vec{\kappa}$ and E. This task is, however, a very difficult one because of the combination of the small interaction cross section and the requisite high resolution. Moreover, a most valuable contribution at present would consist of performing those measurements which can establish the regions of validity and the breakdown points of the few available theories.

In the region of very large momentum transfer,[4] the spectra of inelastically scattered x rays and γ rays can be explained in a manner that satisfactorily establishes Compton scattering as a method for measuring electron momentum distributions and the spatial part of the electron wave function. A breakdown has been demonstrated in the random-phase approximation (RPA) in the area of low and intermediate momentum transfers.[4,5]

Although the theory of collective excitations explains quite well the scattering observed in the region of very small momentum transfer, there remain some problems relating to results in the neighborhood of κ_c, where plasmon features persist above the cutoff frequency.[6] Discrepancies have also been reported[7] where the disagreement with theory extended to the plasmon-lifetime predictions. Although some of these results can be explained through modifications of the RPA, one of the most recent experiments[8] on the shape of the plasmon line of beryllium shows quite strong departures from RPA.

A most dramatic departure from RPA was discovered by the authors,[3] reporting on x-ray scattering by lithium for $\kappa/\kappa_{\rm F} = 1.59$ ($\varphi = 25°$) in their attempt to study the complete behavior of the electrons of that element. The present investigation confirms those initial observations and fills in results to the upper limit of the intermediate-momentum-transfer region, but not beyond $\kappa/\kappa_{\rm F} = 4.2$. Even at the upper limit, the departure from RPA exists, but we find the disagreement between experiment and theory to decrease with increasing momentum transfer.

The double-flat-crystal spectrometer used in these experiments has been described earlier.[9] Copper $K\alpha_1, \alpha_2$ incident radiation was scattered by polycrystalline lithium at various scattering angles, corresponding to $\kappa/\kappa_{\rm F} = 1.9$, 2.5, 3.1, and 4.2. A fluorescence spectrum of copper radiation was taken at these same angles, for each of the different experimental conditions. For scattering angle equal to 40° ($\kappa/\kappa_{\rm F} = 2.5$), curves were taken with the sample in the transmission as well as in the reflection position in order to check for possible effects due to multiple scattering, or to surface treatment or impurities. All of the spectral features remained the same. Thus the two sets of data taken at 40° will be treated as one. The spectral response due to $K\alpha_1$ alone was obtained directly by subtracting, in the usual fashion, the $K\alpha_2$ response from the total spectrum. The results are shown by the solid lines in Figs. 1(b)–1(e). The resultant spectra can be divided into three parts: (i) a peak near $E/E_{\rm F} = 1$, (ii) a spectral distribution around the expected Compton peak, and (iii) a spectral band around $E/E_{\rm F} = 12$.

The third feature obviously corresponds to x-ray Raman scattering by the K-shell electrons of lithium.[4,10] The spectrum in the central part may be compared with Compton scattering by an electron gas. The differential cross section for an electron gas can be calculated from Eq. (1) and, in particular in RPA,[2] by replacing ϵ^{-1} by the inverse of the Lindhard dielectric function.[11] We calculated this differential cross section at the different scattering angles and convoluted it with the spectral shape of the incident $K\alpha_1$ (obtained from the appropriate copper fluorescence spectrum). The results are shown by the dashed curves in Fig. 1 for both RPA and Hartree-Fock[3] calculations. No attempt was made to normalize the curves. The prominent feature of the observed spectra is the sharp peak, almost resembling a line spectrum, near $E/E_F = 1$. Neither RPA nor Hartree-Fock calculations seem to explain this feature, nor does the electron gas seem to provide models for this phenomenon that takes place so prominently in the intermediate-momentum-transfer range.

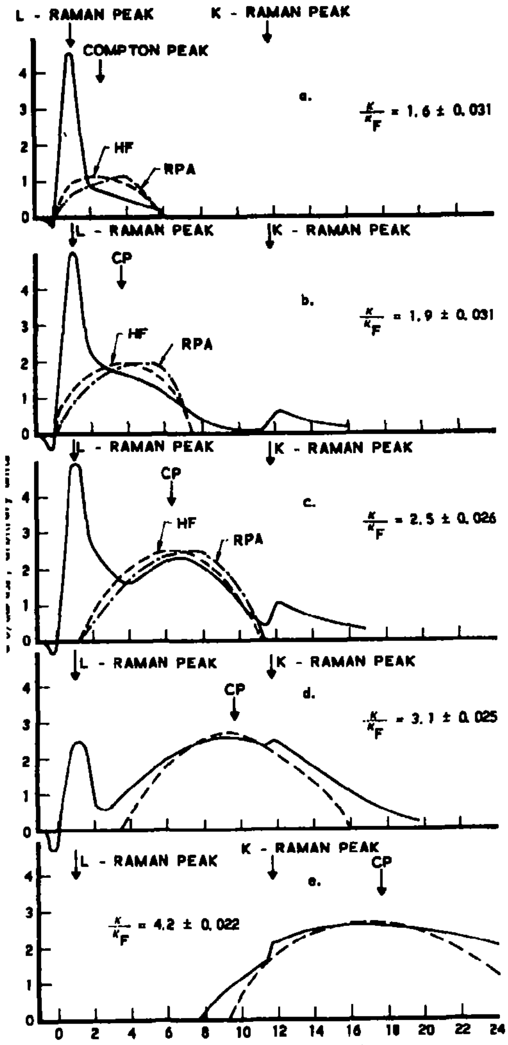

FIG. 1. The spectra (solid line) of x-rays inelastically scattered by lithium at κ/κ_F = (a) 1.6, (b) 1.9, (c) 2.5, d) 3.1, and (e) 4.2 (without correction for instrumental roadening), and the spectral distribution predicted by PA and Hartree-Fock (HF) (dashed line) convoluted ith our instrument function. Note the changes in the elative intensity of the peak at $E/E_F \simeq 1$, compared ith the spectral distribution in the region of the exected Compton band. "*L*" Raman refers to the optical ransition. We used $\kappa_F = 1.1\times10^{10}$ m^{-1} and $E_F = 4.7$ eV.

The explanation that this feature may be an artificially introduced component of the spectrum has been ruled out after extensive tests. The spectral shape was found to be almost entirely independent of the run, the experimental background, and the normalization constant. When two sets of data, taken from the same scatterer, were used in the data reduction, the resultant spectrum was a flat line parallel to the energy axis. When the spectra of Cu $K\alpha$ fluorescence and x rays scattered by lithium were offset by an amount less than or equal to the corresponding experimental uncertainty in angle, the resultant spectral shape changed very little.

The spectra obtained at $\kappa/\kappa_F = 1.9$, 2.5, and 3.1 thus *confirm the earlier observation*[8] at $\kappa/\kappa_F = 1.6$ on the peculiar behavior of energy-loss spectra for low and intermediate momentum transfers. The results from all these spectra can be summarized as follows:

(1) As the momentum transfer becomes smaller, that is to say, as the scattering angles become smaller, the spectral distribution that is thought of as Compton scattering by an electron gas becomes less significant. The intensity ratio of the first peak N_p and the "Compton" band N_S is obtained from the spectra at the different angles as listed below (see Fig. 1):

N_p/N_S	κ/κ_F	φ (deg)
3	1.6	25
1	1.9	30
0.5	2.5	40
0.2	3.1	50
0	4.2	70

(2) This new peak appears when the spectrum also contains an x-ray Raman band due to the K

electrons of lithium. By contrast, the K–x-ray Raman band has been reported at larger momentum transfers without mention of the presence of this new peak.

These results may be explained qualitatively by considering an elementary excitation of electrons from the $2s$ valence-band-like state to the upper bound bandlike states. In other words, the new peak is caused by x-ray Raman scattering due to optical transitions (or absorption) between the $2s$ state and the upper bound states such as $2p$, etc. The differential cross section for x-ray inelastic scattering is related to the x-ray absorption cross section,[8] and the criterion for the appearance of the K–x-ray Raman band was previously determined[10] to be $\kappa r_K \simeq 1.4$. If this criterion holds for these optical transitions, then the "orbital" radius of the valence-band-like state, r_L, is estimated to be $(6.27/2.5) r_K \simeq 2.5 r_K$, where we chose $\varphi = 40°$ as the practical upper bound for the appearance of this new peak. From this point of view, the new peak could appear at lower scattering angles than those angles for which the K–x-ray Raman band begins to appear. It is also satisfying to note that the energy loss of the x-ray photons due to these optical transitions should be of the order of the filled bandwidth, which is in agreement with the experimental peak position of $E/E_F \simeq 1$ ($E_F = 4.7$ eV). The sharp peaking may be enhanced by the effects of the transitions involving the p states, as Mahan[12] and Nozières and DeDominicis[13] have demonstrated in x-ray absorption and emission edges.

In conclusion, this Letter furnishes the first evidence of optical transitions in x-ray inelastic scattering spectra. The qualitative fit of the data by this interpretation is very satisfactory and may provide new insights into the important intermediate-momentum-transfer region of x-ray Compton-Raman scattering.

Note added.—Concurrent with the submission of this Letter, Ching and Callaway[14] reported calculations indicating a peaking in the optical conductivity of lithium at about 4.5 eV, offering additional support for the conclusions we reach from our experimental observations. Furthermore, even more recently Platzman and Eisenberger[15] reported a feature in the inelastic x-ray scattered spectra from Be, graphite, and Al. Although their interpretation varies considerably from ours and the reported feature is quite faint, it appears in the same position as our new peak.

---

*This work was conducted under the U. S. Air Force Space and Missile Systems Organization Contract No. F04701-73-C-0074.

†Present address: Department of Mechanical and Aerospace Engineering and Materials Science, Rice University, Houston, Texas 77001.

[1] M. Kuriyama, Acta Crystallogr., Sect. A 27, 634 (1971).

[2] M. Kuriyama and N. G. Alexandropoulos, J. Phys. Soc. Jpn. 31, 561 (1971).

[3] G. G. Cohen, N. G. Alexandropoulos, and M. Kuriyama, Solid State Commun. 10, 95 (1972).

[4] We define small momentum transfer as $\kappa < \kappa_c$, where κ_c is the plasma-cutoff wave vector; intermediate momentum transfer as $\kappa_c < \kappa = n\kappa_F$, where $1.5 < n < 3$ and κ_F is the Fermi wave vector; and large momentum transfer as $\kappa \gg \kappa_F$.

[5] P. M. Platzman and P. Eisenberger, Solid State Commun. 14, 1 (1974).

[6] N. G. Alexandropoulos, J. Phys. Soc. Jpn. 31, 1790 (1971).

[7] D. M. Miliotis, Phys. Rev. B 3, 701 (1971).

[8] P. Eisenberger, P. M. Platzman, and K. C. Pandey, Phys. Rev. Lett. 31, 311 (1973).

[9] N. G. Alexandropoulos and G. G. Cohen, Phys. Rev. 187, 445 (1969).

[10] G. G. Cohen, N. G. Alexandropoulos, and M. Kuriyama, Phys. Rev. B 8, 5427 (1973).

[11] J. Lindhard, Kgl. Dan. Vidensk. Selsk., Mat.-Phys. Medd. 28, No. 8 (1954).

[12] G. D. Mahan, Phys. Rev. 163, 612 (1967).

[13] P. Nozières and C. T. DeDominicis, Phys. Rev. 178, 1097 (1969).

[14] W. Y. Ching and J. Callaway, Phys. Rev. B 9, 5115 (1974).

[15] P. M. Platzman and P. Eisenberger, Phys. Rev. Lett. 33, 152 (1974).

Band Structure of PbPo and Trends in the Pb Chalcogenides

S. Rabii and R. H. Lasseter*

The Moore School of Electrical Engineering and The Laboratory for Research on the Structure of Matter, University of Pennsylvania, Philadelphia, Pennsylvania 19174

(Received 20 May 1974)

Energy-band calculations on the Pb chalcogenides show that PbPo is a semimetal rather than a direct-gap semiconductor as predicted before. However, the results confirm the suggestion that PbTe is the irregular member of the family. This irregularity is directly related to an anomaly in the size of the Te atom and the lattice.

The periodic potentials for the calculations were of the muffin-tin type, constructed from the relativistic charge densities of Liberman, Waber, and Cromer.[2] The $X\alpha$ prescription was used for exchange, employing the extrapolation of the α's calculated by Schwartz.[3] The lattice constants were all taken from the same source, again to keep the systematic errors the same. The use of a muffin-tin potential is appropriate for these compounds because of their close-packed structure. The lack of self-consistency in the calculation does not appear to be serious as evidenced by the similarity of the band calculations for the Pb chalcogenides carried out from different potentials and employing different techniques.

The result of the calculations reveal two important differences between PbPo and the remainder of the lead chalcogenides. First, at the point L in the Brillouin zone, the highest $L_{4,5}^+$, L_6^+ complex in the valence band, which comes from a splitting of an L_3 level due to spin-orbit interaction, moves continuously closer to the top of the valence band and also the splitting becomes larger as we go from PbS to PbPo (Fig. 1). This is fully in agreement with what we expect if we bear in mind that the charge density for this complex is primarily p type and is centered on the chalcogen atom. In fact, the $L_{4,5}^+$ level in PbPo is separated from the L_6^+ level, which constitutes the top of the valence band in the other compounds, by only 0.0004 Ry which is less than the uncertainty in the calculations.

Secondly, in the Σ direction, the top of the valence band, which occurs at $(\pi/a)(\frac{11}{16},\frac{11}{16},0)$, is 0.015 Ry higher than the bottom of the conduction band which occurs at L (Fig. 2). This separation remained almost unchanged even when the interstitial potential was changed by 0.074 Ry (1 eV) in either direction. This is again a result of increased relativistic effects in PbPo. Thus, PbPo is a semimetal and not a direct-band-gap semiconductor.

The forbidden gaps for a large number of compound semiconductors with NaCl structure obey an empirical linear dependence on the inverse of the square of the lattice constant ($1/a^2$). Although PbS, PbSe, and PbTe do not obey this rule, Dal-

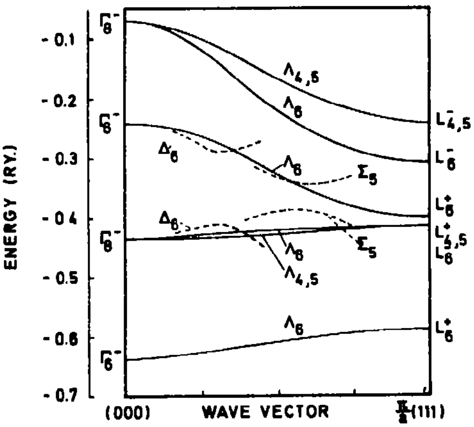

FIG. 1. Partial energy-band structure of PbPo.

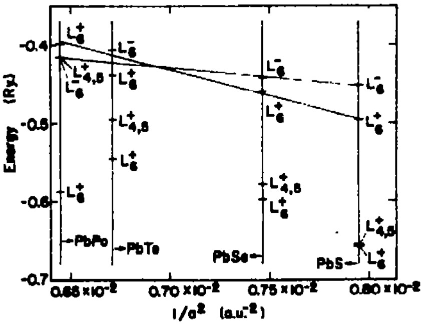

FIG. 2. Energy levels of importance at point L in the Brillouin zone for the lead chalcogenides as a function of the inverse of the square of the lattice constant.

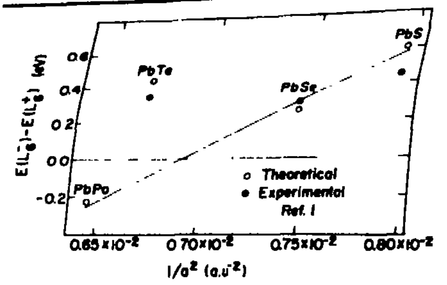

FIG. 3. Forbidden energy gap at point L in the Brillouin zone for the lead chalcogenides as a function of the inverse of the square of the lattice constant.

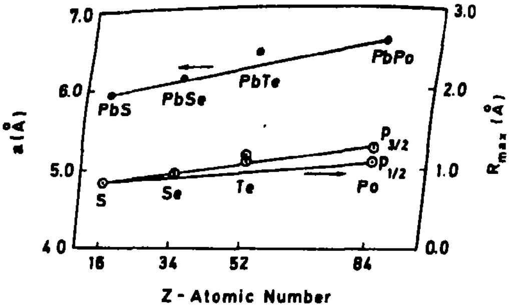

FIG. 4. Lattice constant for the Pb chalcogenides and the radii of maximum radial charge density for the outermost $p_{3/2}$ and $p_{1/2}$ electrons of the chalcogen atoms as a function of the atomic number Z.

ven[1] argued that, by treating PbTe as an irregular member of the family, the linear relationship should hold for PbS, PbSe, and PbPo. Based on this assumption, and by using the measured lattice constant for PbPo, he estimated a forbidden gap of ~0.1 eV and an inverted band structure for this compound. PbS, PbSe, and PbTe are direct semiconductors with the minimum forbidden gap at L and with the conduction- and valence-band edges having L_6^- and L_6^+ symmetry, respectively. Dalven thus concluded that PbPo is also a direct-gap semiconductor but with L_6^+ and L_6^- as the symmetries for the conduction- and valence-band edges, respectively.

These predictions have not been verified before, either experimentally or theoretically. In the theoretical study presented here, we show that while certain of the above predictions hold, others are not borne out by these results. We have carried out first-principles, fully relativistic augmented-plane-wave calculations for each of the four compounds, using identical procedures. In order to keep the errors down to the systematic errors, none of the parameters in the calculations were adjusted to obtain agreement with the experiment. Normally when one of these compounds is studied, a parameter, such as interstitial potential, is adjusted to obtain a forbidden gap that is in agreement with the experimental data. Although we are interested in the trends within the family rather than individual results, nevertheless, the effect of such parameters as exchange factor and the interstitial constant potential on the final results were investigated to make certain that these trends are not affected with such changes.

However, if we focus our attention on the gap between the L_6^- and L_6^+ levels which form the conduction and valence edges for PbS, PbSe, and PbTe, and the same gap in PbPo (Fig. 3), we observe that the gaps for PbS, PbSe, and PbPo, as predicted by Dalven, fall reasonably well on a straight line as a function $1/a^2$. Furthermore, the order of these levels is reversed in PbPo. This behavior as well as the semimetal nature of PbPo remained unchanged even for the extreme case of using Slater's exchange ($\alpha = 1$) for all regions. It is also seen that the contention that PbTe is the irregular member of the family is supported by these calculations. This is important for drawing conclusions regarding the trends of the properties of these compounds within the family.

The irregularity of PbTe is directly related to a similar anomaly in the size of the Te atom and the lattice constant of PbTe. Figure 4 shows a plot of the radii of maximum radial charge density for the outermost p electrons of the chalcogen atoms as a function of atomic number Z. These values are obtained from self-consistent-field relativistic calculations for these atoms. We see that the radii for Te $5p$ electrons do not fall on the straight line as do the others. The same figure shows a similar plot for the experimentally measured lattice constants of the compounds.[4] Again the value for PbTe is too large to fit the straight line. In fact if the lattice constant for PbTe is chosen to fall on this line, the negative pressure coefficient of its forbidden gap will almost remove the irregularity shown in Figs. 2 and 3.

---

*Work supported in part by the National Science Foundation under Grant No. GH-33633.

[1] R. Dalven, Phys. Rev. Lett. 28, 91 (1972), and Phys.

Rev. B 8, 6033 (1973).

[2]D. Liberman, J. T. Waber, and D. T. Cromer, Phys. Rev. 137, A27 (1965).

[3]K. Schwartz, Phys. Rev. B 5, 2466 (1972).

[4]H. E. Swanson and R. K. Fuyat, *Standard X-Ray Diffraction Powder Patterns*, U. S. National Bureau of Standards Circular No. 539 (U. S. GPO, Washington, D. C., 1953), Vol. 2, p. 18; H. E. Swanson, N. T. Gilfrich, and G. M. Ugrinic, *Standard X-Ray Diffraction Powder Patterns*, U. S. National Bureau of Standards Circular No. 539 (U. S. GPO, Washington, D. C., 1955), Vol. 5, p. 38.

Critical Scattering Parameters for General Fields and Temperatures*

M. Combescot,† M. Droz, and J. M. Kosterlitz‡
Laboratory of Atomic and Solid State Physics, Cornell University, Ithaca, New York 14850

(Received 9 April 1974)

The critical scattering parameters have been calculated for an Ising-like system in a field, below and above T_c, up to second order in ϵ $(=4-d)$. The corrections to the Ornstein-Zernike form in the small- and large-$q\xi$ limit are presented and their relevance to experiments is discussed.

With improving scattering techniques (using x rays, neutrons, and light) one may expect that highly precise measurements of the scattering intensity in the whole critical region of ferromagnets, pure fluids, and binary fluid mixtures, etc., will soon be possible. Since the scattering intensity is proportional to the Fourier transform of the basic order-parameter–order-parameter correlation function, such measurements are of fundamental theoretical importance as a test of scaling[1-4] and operator-product-expansion[5,6] hypotheses. In particular, scattering experiments are the only way to determine the exponent η directly.[1,7,8]

If $t=(T-T_c)/T_c$ is the reduced temperature and m is the order parameter (magnetization, density, or composition deviation from critical, etc.) the correlation scaling hypothesis asserts that the Fourier transformed order-order correlation function may be written asymptotically as[1-4]

$$G(\vec{q},t,m)\approx\chi(t,z)D(x,z), \qquad (1)$$

with $z=tm^{-1/\beta}$ and $x=q\xi$ where $\xi(t,z)$ is the correlation function (defined more precisely below). The scaling function $D(x,z)$ is normalized so that $\chi(t,z)$ is the (reduced) susceptibility (or compressibility, or composition fluctuation, etc.) proportional to the zero-angle scattering intensity.

To analyze properly the experimental results, particularly those subject to resolution corrections,[9] it is necessary to have an interpolation formula for $D(x,z)$ over the whole range of x, and in particular to know the amplitudes of the deviation from the simple Ornstein-Zernike form for small x.

If one defines the correlation length $\xi=\xi_1$ through the low-angle scattering or, equivalently, in terms of the second moment of the correlation function, the scaling function has the small-x expansion[1,2,4,10]

$$D^{-1}(x,z)=1+x^2-\Sigma_4(z)x^4+\Sigma_6(z)x^6+\dots. \qquad (2)$$

Thus $\Sigma_4(z)$, $\Sigma_6(z)$, etc. are basic measures of the deviation from a pure Lorentzian line shape $(D_0^{-1}=1+x^2)$ in an experiment carried out at constant T.

Various attempts[4,11] have already been made to construct approximants for $D(x,z)$. On the basis of series expansions, Fisher and Burford[4] constructed one for $D(x,0)$ on the critical isochore; more recently, Fisher and Tarko[11] have suggested approximants in zero field on the coexistence

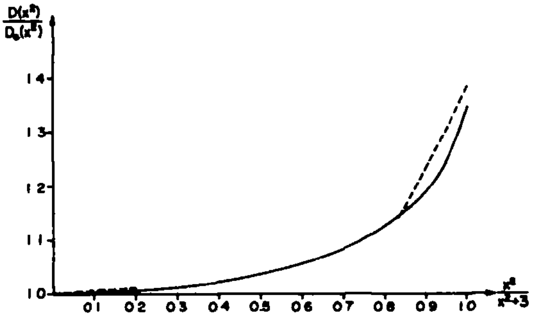

FIG. 1. Comparison with the Fisher-Tarko approximant. The solid line is the Fisher-Tarko approximant and the dashed lines are from Eqs. (3) and (8). $D_0(x^2)=(1+\psi x^2)^{-1+\eta/2}$ with $\psi^{-1}=1-\frac{1}{2}\eta$.

TABLE I. Comparison of present and previous results for special values of Σ_4 and Σ_6. (Σ_4^+, Σ_6^+ are for $h=0$, $t>0$; Σ_4^-, Σ_6^- are for $h=0$, $t<0$; and Σ_4^c, Σ_6^c are for $t=0$.)

	Present theory	Previous results
Σ_4^+	2.78×10^{-4}	2.78×10^{-4} [a] $(6.5\pm0.8)\times10^{-4}$ [b]
Σ_6^+	7.12×10^{-6}	7.12×10^{-6} [a] $(5\pm2)\times10^{-6}$
Σ_4^-	1.64×10^{-2}	$(1.2\pm0.6)\times10^{-2}$ [b]
Σ_6^-	2.43×10^{-3}	$(7\pm3)\times10^{-3}$ [b]
Σ_4^c	1.17×10^{-2}	sc $(3.9\pm0.5)\times10^{-2}$ [b] bcc $(1.7\pm2)\times10^{-2}$
Σ_6^c	1.71×10^{-3}	

[a] Ref. 16. [b] Ref. 11.

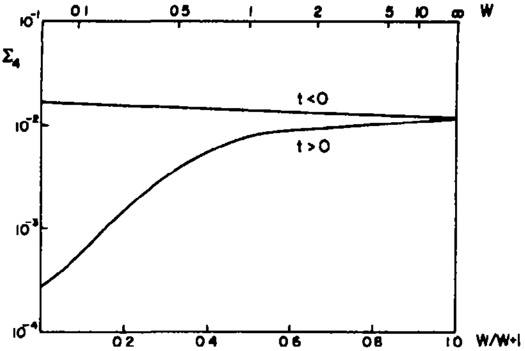

FIG. 2. Σ_4 as a function of $W=h/|t|^{\beta\delta}$ for $\epsilon=1$.

curve and at T_c in a finite field. They also proposed tentative interpolation formulas for general t and m. It has been found that the scaling function cannot be written as a function of x alone[11-13]; thus different approximants are required for different values of z.

The purpose of this note is to report recent exact calculations of the scaling function $D(x,z)$ for general z for an Ising-like model, using the Wilson-Fisher[14,15] ϵ expansion ($\epsilon=4-d$, where d is the number of space dimensions of the system). We have paid particular attention to the experimentally accessible amplitudes $\Sigma_4(z)$ and $\Sigma_6(z)$ but have incidentally confirmed the asymptotic form of $D(x,z)$ for large x in agreement with Fisher and Aharony[16] and, more generally, with Brezin, Amit, and Zinn-Justin.[13] Furthermore, we report in Fig. 1 a concrete numerical comparison with the Fisher-Tarko approximant[11] for $T<T_c$ in the two regions where the asymptotic forms of the correlation function are valid. The agreement within 2% for $x<1$ and 4% for $x>4$ (for $d=3$) establishes more confidence in their extrapolations and the appropriateness of comparisons with experiment.

Defining reduced-field and order-parameter variables $h=B_1H$ and $m=B_2M$ so that $hm^{-\delta}=1$ at $T=T_c$ and $tm^{-1/\beta}=-1$ on the coexistence curve for $T<T_c$, we may write our results for $\Sigma_4(z)$ and $\Sigma_6(z)$ in the form

$$\begin{aligned}\Sigma_4(z)&=\epsilon a_1P(z)+\epsilon^2[a_2+a_3P(z)+a_4P^2(z)]+O(\epsilon^3),\\ \Sigma_6(z)&=\epsilon b_1P(z)+\epsilon^2[b_2+b_3P(z)+b_4P^2(z)]+O(\epsilon^3),\end{aligned}\tag{3}$$

where $P(z)=Km^2\chi^{2\beta/\gamma}$ with $K=1+\frac{1}{6}\epsilon\ln\frac{4}{27}$. From the equation of state,[17] $P(z)$ has the form

$$P(z)=(z+3)^{-1}\{1+\epsilon(z+3)^{-1}[\tfrac{1}{3}z\ln(z+3)-1+\ln2]\}.$$

The coefficients a_i and b_i have the values $a_1=1.66\times10^{-2}$, $a_2=2.78\times10^{-4}$, $a_3=1.76\times10^{-2}$, $a_4=5.16\times10^{-3}$; $b_1=2.38\times10^{-3}$, $b_2=7.12\times10^{-6}$, $b_3=2.73\times10^{-3}$, $b_4=7.68\times10^{-4}$. With these normalizations, it is also possible to write the equation of state in the parametric form[18] $h=AR^{\beta\delta}\theta(1-\theta^2)$, $t=R(1-B^2\theta^2)$, $m=CR^\beta\theta$, where the coefficients A, B, C are given in Ref. 17. In this case, $P(z)$ takes on the simple form

$$P(z(\theta))=\tfrac{1}{2}\theta^2[1+\tfrac{1}{3}\epsilon\theta^2(\ln2-\tfrac{3}{2})].\tag{4}$$

Note that in zero field above T_c, $P(z)=0$, so that the only terms which contribute are a_2 and b_2, thereby reproducing the results of Ref. 16. The leading parameter $\Sigma_4(z)$ is plotted as a function of $ht^{-\beta\delta}$ for $\epsilon=1$ in Fig. 2 and some special values of Σ_4 and Σ_6 are presented in Table I, and compared to previous estimates.[4,11,16]

We see that the deviations from the Ornstein-Zernike form increase rapidly from a minimum at $h=0$, $t>0$ to a maximum at $h=0$, $t<0$, this latter value being 2 orders of magnitude greater. In principle, the most favorable places to see these deviations are below T_c and in a field above T_c (with $ht^{-\beta\delta}>1$).

The rapid change in slope of Σ_4 near $ht^{-\beta\delta}=1$ corresponds to a crossover from a domain where the temperature variable controls the singularities of the system to one where the field dominates.

In the limit $x \gg 1$, the correlation function,[1,4-6,13,16] written in the parametric form is

$$G^{-1}(\vec{q},t,m) \propto q^{2-\eta}[E+F(\theta)\tau+\varphi(\theta)\tau^{1-\alpha}], \tag{5}$$

with $\tau = Rq^{-1/\nu}$, $E=1+0.038\epsilon^2+O(\epsilon^3)$, $F(\theta)=2-3\theta^2+\epsilon[1-\frac{1}{3}\theta^2(\frac{3}{2}-\ln 2)]+O(\epsilon^2)$, and $\varphi(\theta)=3\theta^2-1-\epsilon[1-\frac{1}{3}\theta^2(3-2\ln 2)]+O(\epsilon^2)$. The role played by the corrections to the infinite-x limit ($t=0$) in the correlation function can be very important in the determination of η by scattering.[7,8] In zero external field, even for $x \approx 10$, these terms contribute about 4% of the total (for $\epsilon=1$), which is the same order of magnitude as the contributions from the q^η factor. This problem has been discussed in detail by Tracy and McCoy[19] for the two-dimensional Ising model. Using accurately known values of $G(\vec{q})$ for various values of q and $x \gg 1$, they try to find η by fitting with both the Fisher-Burford approximant and the analog of Eq. (5) and conclude that the latter form gives a very much better value.

The calculations leading to the above results follow the now standard procedures.[16,17] The reduced Hamiltonian is taken as

$$\mathcal{H}/kT = \tfrac{1}{2}\int d^dx\, \{[\nabla s(x)]^2 + r_0[s(x)]^2 + 2u[s(x)]^4 - 2Hs(x)\}. \tag{6}$$

On shifting the spin variables to $\sigma(x)=s(x)-\tilde{m}$, where $\tilde{m}=\langle s(x)\rangle$, we avoid the inclusion of tadpole insertions in the graphical analysis. A mass renormalization eliminates r_0 in favor of r, the exact inverse susceptibility, so that, provided all self-energy diagrams are subtracted at $q=0$, we may work with the effective Hamiltonian

$$\mathcal{H} = \tfrac{1}{2}\int_q (q^2+r)\sigma_q\sigma_{-q} + 4um\int_{q_1q_2}\sigma_{q_1}\sigma_{q_2}\sigma_{-q_1}\sigma_{-q_2} + u\int_{q_1q_2q_3}\sigma_{q_1}\sigma_{q_2}\sigma_{q_3}\sigma_{-q_1}\sigma_{-q_2}\sigma_{-q_3}. \tag{7}$$

A perturbation expansion in u will automatically produce a scaling form for $G(q,t,m)$ when u is fixed at its critical value.[14,15,20] A different choice of u will produce corrections not of a scaling form, but such terms will vanish rapidly near the critical point. Of course, this expansion implicitly assumes the existence of a renormalization-group fixed point and the possibility of making a valid expansion about it.

We have considered all graphs up to order ϵ^2. The evaluation of the graphical integrals has been greatly eased by use of the identity[21] for $d>0$,

$$(q^2+1)^{-1} = (2\pi)^{-d/2}\int d^dy\, \exp(i\vec{q}\cdot\vec{y})y^{-\nu}K_\nu(y), \tag{8}$$

where $\nu=\frac{1}{2}d-1$ and $K_\nu(y)$ is the modified Bessel function of the second kind.[22] Although the left-hand side of this identity appears simpler, the use of the Fourier transform makes the tedious angular integrations relatively trivial. This device appears to be very useful in evaluating any d-dimensional Feynman-graph integral and we expect it to find further applications.

The authors would like to thank M. E. Fisher for suggesting the problem, many helpful comments, and reading the manuscript; A. Aharony, A. D. Bruce, and R. Combescot for many stimulating discussions; and D. Rainer for help with the numerical work. One of us (J.M.K.) would like to thank the Fulbright-Hayes Committee for a travel grant.

---

*Work supported in part by the Atomic Energy Commission under Contract No. AT(11-1)-3161, Technical Report No. 21, by the National Science Foundation, under Grant No. GH-36457, and by the Fonds National Suisse de la Recherche Scientifique.

†On leave from the Laboratoire de Physique des Solides de l'Ecole Normale Supérieure, Université de Paris VII, Paris, France.

‡On leave from the Department of Mathematical Physics, University of Birmingham, Birmingham, England.

[1] M. E. Fisher, J. Math. Phys. 5, 944 (1964).

[2] M. E. Fisher, Rep. Progr. Phys. 30, 615 (1967).

[3] L. P. Kadanoff, Physics (Long Is. City, N. Y.) 2, 263 (1966).

[4] M. E. Fisher and R. J. Burford, Phys. Rev. 156, 583 (1967).

[5] L. P. Kadanoff, Phys. Rev. Lett. 23, 1430 (1969).

[6] K. G. Wilson, Phys. Rev. 179, 1499 (1969), and Phys. Rev. D 2, 1473 (1970).

[7] J. V. Sengers, in *Transport Phenomena–1973*, AIP Conference Proceedings No. 11, edited by J. Kestin (American Institute of Physics, New York, 1973), p. 232.

[8] P. Schmidt, to be published, and private communication.

[9] J. Als-Nielsen and O. Dietrich, Phys. Rev. **153**, 706, 711, 717 (1969); J. Als-Nielsen, Phys. Rev. **185**, 664 (1969).

[10] W. J. Camp and M. E. Fisher, Phys. Rev. Lett. **26**, 73, 565 (1971).

[11] M. E. Fisher and H. B. Tarko, Phys. Rev. Lett. **31**, 926 (1973), and to be published.

[12] M. E. Fisher and D. Jasnow, "Theory of Correlations in the Critical Region," edited by C. Domb and M. H. Green (Academic, New York, to be published).

[13] E. Brezin, D. J. Amit, and J. Zinn-Justin, Phys. Rev. Lett. **32**, 151 (1974).

[14] K. G. Wilson and M. E. Fisher, Phys. Rev. Lett. **28**, 240 (1972).

[15] K. G. Wilson, Phys. Rev. Lett. **28**, 548 (1972).

[16] M. E. Fisher and A. Aharony, Phys. Rev. Lett. **31**, 1238 (1973).

[17] E. Brezin, D. J. Wallace, and K. G. Wilson, Phys. Rev. Lett. **29**, 591 (1972). There are some errors in this reference—Eq. (11) should read $A=\frac{1}{54}-\frac{1}{2}\ln 4\pi+\frac{1}{3}c$, and the coefficient b^2 below Eq. (21) $b^2=\frac{2}{3}(1-\frac{1}{3}\epsilon\ln 2)+O(\epsilon^2)$.

[18] P. Schofield, J. D. Litster, and J. T. Ho, Phys. Rev. Lett. **23**, 1098 (1969).

[19] C. A. Tracy and B. M. McCoy, Phys. Rev. Lett. **31**, 1500 (1974).

[20] K. G. Wilson and J. Kogut, to be published.

[21] One of us (M. C.) would like to thank P. Nozieres and E. Abrahams for pointing out this trick.

[22] M. Abramowitz and I. A. Stegun, *Handbook of Mathematical Functions* (Dover, New York, 1966), p. 374.

Coulomb Energy of He^3 and Charge Symmetry of Nuclear Forces

S. S. Mehdi
Department of Physics and Astrophysics, University of Delhi, India

and

V. K. Gupta*
International Centre for Theoretical Physics, Trieste, Italy

(Received 17 July 1974)

The Coulomb energy of He^3 has been calculated using separable potentials with a repulsive term. The calculated value is in close agreement with the H^3-He^3 binding-energy difference. An expected 3–6% decrease, brought about mainly by the inclusion of a tensor term, can be explained by charge asymmetry due to η-π and ρ-ω-φ mixing, provided one takes $g_\rho/g_\omega > 0$. This also yields $a_{nn} - a_{pp} \gtrsim 0$, which is required by the present experimental situation, in contrast to $a_{nn} - a_{pp} \sim 1.4$ fm obtained by earlier authors with $g_\rho/g_\omega < 0$.

The purpose of this note is twofold. Firstly, we report a new calculation of the Coulomb energy of He^3 using rank-3 separable potentials which include a repulsive term in the singlet state, and secondly, we analyze the existing situation regarding charge asymmetry of nuclear forces in the light of our present result and a more definite value for the *n*-*n* scattering length.

The interest in the Coulomb energy of He^3 persists mainly because of its ramifications on the charge asymmetry of nuclear forces. A large number of variational calculations of the Coulomb energy (E_C) of He^3 have yielded results in the range $E_C = 0.6$–0.65 MeV.[1] In the recent past, calculations have also been performed via the solutions of Faddeev equations to yield $E_C \sim 0.62$–0.69 MeV.[1] However, the experimental difference in the binding energies of H^3 and He^3 is $\Delta E_B = 0.764$ MeV. The gap, $\Delta V = \Delta E_B - E_C$, between the two is usually attributed to the charge asymmetry of nuclear forces. For the calculations cited above, this gap is ~0.1–0.16 MeV, which is about 15–20% of ΔE_B. A gap of this order of magnitude requires a much larger charge asymmetry than is consistent with the evidence from many other sources.[2,3]

A few years ago, Gupta and Mitra[4] had calculated E_C within a separable-potential model, which has had a very successful career so far,[5] and had obtained $E_C = 0.84$ MeV. However, the repulsive core in the singlet state, which has a significant effect, had not been included in that study. We have now calculated E_C for potentials which do include such a repulsive term in the singlet state. In the triplet state, the potential is taken to be a purely attractive central potential:

$$-M\langle p|V_T|p'\rangle = \lambda_T g(p) g(p').$$

where $g(p)$ is taken to be of the usual Yamaguchi form,[6]

$$g(p) = (p^2 + \beta_c^2)^{-1}.$$

The singlet potential now consists of the sum of an attractive and a repulsive term:

$$-M\langle p|V_s|p'\rangle = \lambda_s[f(p)f(p') - f_1(p)f_1(p')],$$

where we take, as usual,

$$f(p) = (p^2 + \beta_s^2)^{-1},$$

$$f_1(p) = np^2(p^2 + \beta_0^2)^{-2}.$$

The calculations have been performed with two different sets of parameters for the singlet part of the potential (referred to as N and G_1' in the notation of Ref. 5), each of which gives a fairly good representation of the N-N singlet phase shifts up to sufficiently high energies.[7] The results of the present calculation, along with those of Ref. 4 are presented in Table I. The calculations have been performed for point as well as extended protons.[8] For the case of extended protons, we obtain $E_C = 0.77$ MeV (for both the sets employed), a result which is embarrassingly close to the experimental value 0.764 MeV for ΔE_B. This striking agreement, however, is not to be taken too literally. For completeness, one must include a tensor term and (perhaps) a small repulsive term in the triplet part of the potential, both of which would tend to reduce the Coulomb energy. The more important repulsive term, which we have included in the present anal-

TABLE I. The Coulomb energy of He^3 with separable potentials for point as well as extended protons. N and G_1' refer to two different potential sets for the singlet state (for notations see Ref. 5). Experimental value of ΔE_B, 0.764 MeV.

Rank of the potential	Potential set	E_C (MeV)	
		Point protons	Extended protons
Rank 2, no repulsion included (Ref. 4)	$C_Y^{\mathrm{eff}}+S_Y$	1.060	0.856
	C_N+S_N	0.952	0.830
Rank 3, repulsion in the singlet state included (present work)	$C_Y^{\mathrm{eff}}+(S+H)_N$	0.905	0.775
	$C_Y^{\mathrm{eff}}+(S+H)_{G_1'}$	0.900	0.771

ysis, has reduced E_C by ~10%, not unexpectedly. Once this repulsive term has been included, the tensor term is expected to further reduce E_C by 3–6%,[5,9] which should bring E_C, at best, down to 0.7–0.73 MeV.[10] This is much higher than $E_C \sim 0.6$ MeV obtained from variational calculations by Okamoto *et al.*

Though there is some evidence for charge-symmetry breaking in nuclear forces, and on theoretical grounds such symmetry breaking must exist,[11] we believe the last word has not been said on this problem *vis-à-vis* the H^3-He^3 Coulomb-energy-binding-energy difference. Since E_C turns out to be less than ΔE_B, whatever the magnitude of this difference, it follows that the n-n potential is somewhat stronger than the p-p potential, at least as far as its effect on E_C is concerned. Naively, one should then expect the n-n singlet scattering length a_{nn} to be (numerically) larger than a_{pp}. Indeed, the earlier analyses of charge-asymmetric potentials were based on the assumption that $|a_{nn}| \gtrsim |a_{pp}|$. Until a couple of years ago, this assumption was consistent with the then experimental situation because of the large uncertainties in the determination of a_{nn}. However, these uncertainties have been narrowed down considerably, and Henley and Wilkinson quote the following values for a_{nn} and a_{pp}[12]:

$$a_{nn} = -16.4 \pm 0.9 \text{ fm};$$

$$a_{pp} = -17.1 \pm 0.2 \text{ fm}.$$

Thus, in all probability, $|a_{nn}| < |a_{pp}|$, contrary to what one expected from the above argument.

There have been a number of calculations of the effect of charge-asymmetric potentials, which follow from the electromagnetic mixing of mesons, to explain the relevant two-body and three-body data.[13] Apart from many other uncertainties in these analyses, one crucial factor is the relative sign of the ρ and ω coupling constants, i.e., the sign of g_ρ/g_ω. Indeed, so far, the sign of g_ρ/g_ω was chosen to be negative so as to yield $|a_{nn}| > |a_{pp}|$ and then the contribution of such a charge-asymmetric potential to the binding energy was calculated perturbatively. It was then possible to obtain $\Delta V \sim 0.1$–0.15 MeV for this contribution.[11] Since, according to the latest experimental situation, $\Delta a = a_{nn} - a_{pp} = 0.7$ fm (taking the errors into account, it could lie between -0.4 and 1.8 fm), the sign of g_ρ/g_ω, in fact, *must be chosen to be positive*, so as to yield $|a_{nn}| \lesssim |a_{pp}|$ (rather than the other way round). Now the contributions to Δa and ΔV (the energy that must be *added* to E_C to make it equal to the experimental binding-energy difference ΔE_B) come from η-π as well as ρ-ω-φ mixing,[14,15] and both are quite model dependent (depend upon many ill-determined parameters which enter into the theory, as well as upon the three-nucleon wave function assumed for H^3). Okamoto and Pask[1] have determined ΔV for Stevens's η-π mixing model,[14] as well as Downs and Nogami's η-π and ρ-ω-φ mixing models,[15] but for the wrong sign for the quantity g_ρ/g_ω. If we take $g_\omega = 6$ instead of $g_\omega = -5$, ΔV will change sign, though its magnitude will remain almost the same. One can see that changing the sign of Downs and Nogami's ρ-ω-φ contribution in Table VI of Ref. 1 gives $\Delta V \sim = 0.025$–0.03 MeV. (The actual magnitude could vary considerably depending upon the parameters chosen.) This is much more gratifying from our point of view (than $\Delta V \sim 0.1$–0.15 MeV), since we predict ΔV to lie between 0.03 and 0.06 MeV. This is also in accord with the situation for higher mirror nuclei where one finds that theory and experiment agree within a few per cent (rather than 15–20%), and, in fact, may even be consistent with charge symmetry.[16,17] Also, the overall charge asymmetry now required will be $\sim\frac{1}{3}$ of what Okamoto estimated,[18] and hence in much better agreement with the calculations of Blin-Stoyle and Yalgin,[19] as well as with the evidence coming from other sources.[2]

As for the scattering length, the contribution to Δa from ρ-ω-φ mixing will now be positive whereas that from η-π mixing will be negative, so that $\Delta a_{\rho\omega\varphi}+\Delta a_{\eta\pi}\gtrsim 0$ (since $|\Delta a|_{\rho\omega\varphi}\gtrsim|\Delta a|_{\eta\pi}$), which is just what the data require. Since the scattering length is rather sensitive to small differences in the potential, because of the singlet state being nearly a bound state, it will be hazardous to make a more definite commitment as to the actual magnitude of Δa until a much more precise charge-asymmetric potential is available. But, in general, one can say that charge-asymmetric potentials are able to explain both $a_{nn}-a_{pp}$ and ΔE_B-E_C, if one takes $E_C\sim 0.7$–0.73 MeV. It will be extremely difficult, on the other hand, to reconcile $|a_{nn}|\lesssim|a_{pp}|$ and $E_C\lesssim 0.6$ MeV[8] obtained from variational calculations.

In conclusion, we find that our calculation with separable potentials which include a repulsive term in the singlet state yields $E_C\approx 0.77$ MeV, in agreement with the experimental value of ΔE_B. Inclusion of tensor and small repulsive parts in the triplet state should lower E_C to around 0.7–0.73 MeV. This small deviation of E_C from ΔE_B can be explained from charge-asymmetric potentials obtained from the mixing of η-π isosinglets and the ρ-ω-φ isotriplets, *provided* one takes $g_\rho/g_\omega>0$. This will also simultaneously make $|a_{nn}|\lesssim|a_{pp}|$, which is *required* by the present experimental situation, resolving the long-standing ambiguity in the simultaneous explanation of both Δa and ΔV. On the other hand, it will be very hard to understand $\Delta V\sim 0.1$–0.15 MeV along with $|a_{nn}|<|a_{pp}|$. Though $g_\rho/g_\omega<0$ yields $\Delta V\sim 0.1$–0.15 MeV, it simultaneously gives $\Delta a\sim -1.4$ fm, which is firmly ruled out by the present data, making $\Delta V\sim 0.1$–0.15 MeV also highly unlikely. Also, the overall percentage of charge asymmetry required to explain the present value of Δa along with our value for ΔV is much less than was envisaged by Okamoto, but agrees with what is required from many other considerations.

We would like to thank Professor A. N. Mitra for his interest in this work. One of us (V.K.G.) would like to thank Professor Abdus Salam, the International Atomic Energy Agency, and the United Nations Educational, Scientific, and Cultural Organization for hospitality at the International Centre for Theoretical Physics, Trieste.

---

[*] Permanent address: Department of Physics and Astrophysics, University of Delhi, India.

[1] K. Okamoto and C. Pask, Ann. Phys. (New York) 68, 18 (1971). See earlier references therein.

[2] E. M. Henley, in *Isospin in Nuclear Physics*, edited by D. Wilkinson (North-Holland, Amsterdam, 1969).

[3] Since the wave functions used for the calculation of E_C usually underbind triton by 1–2 MeV, those which yield the right value for E_B will further decrease E_C significantly.

[4] V. K. Gupta and A. N. Mitra, Phys. Lett. 24B, 27 (1967).

[5] A. N. Mitra, in *Advances in Nuclear Physics*, edited by M. Baranger and E. Vogt (Plenum, New York, 1969), Vol. III. See earlier references therein.

[6] Y. Yamaguchi, Phys. Rev. 95, 1628 (1954).

[7] G. L. Schrenk, V. K. Gupta, and A. N. Mitra, Phys. Rev. C 1, 895 (1970).

[8] C. De Vries *et al.*, Phys. Rev. 134, B848 (1964).

[9] K. Okamoto and C. Lukas, Nucl. Phys. B2, 347 (1967).

[10] There are, of course, a large number of corrections which must be applied to E_C. These have been analyzed in detail in Ref. 1. But most of them are negligible, and of others, some contribute with a positive and some with a negative sign. The net result is not very significant.

[11] For excellent reviews on charge symmetry, refer to articles by D. H. Wilkinson and E. M. Henley, in *Few Particle Problems in the Nuclear Interaction*, edited by I. Slaus (North-Holland, Amsterdam, 1972).

[12] Wilkinson and Henley, in a note added to the articles quoted in Ref. 11.

[13] An alternative suggestion by R. T. Folk [Phys. Lett. 28B, 169 (1968)] to explain ΔV in terms of "dynamical polarization" of protons was found by Okamoto and Pask [Ref. 1] to give $a_{nn}\sim -20$ fm, and so is untenable.

[14] M. St. H. Stevens, Phys. Lett. 19, 499 (1965).

[15] B. W. Downs and Y. Nogami, Nucl. Phys. B2, 459 (1967).

[16] D. H. Wilkinson and W. D. Hay, Phys. Lett. 21, 80 (1966).

[17] W. M. Fairbank, Nucl. Phys. A90, 135 (1967).

[18] K. Okamoto, in *Isobaric Spin in Nuclear Physics*, edited by J. D. Fox and D. Robson (Academic, New York, 1966).

[19] R. J. Blin-Stoyle and C. Yalgin, Phys. Lett. 15, 258 (1965).

Deeply Bound Hole States as a Giant-Resonance-Like Phenomenon*

S. Y. van der Werf, B. R. Kooistra, W. H. A. Hesselink,† F. Iachello, L. W. Put, and R. H. Siemssen
Kernfysisch Versneller Instituut, Groningen, The Netherlands
(Received 10 June 1974)

Giant-resonance-like peaks showing systematic variations with neutron number have been observed in the (d,t) reaction on the even-A tin isotopes. In the reaction ^{116}Sn$(d,t)^{115}$Sn a separation of the $g_{9/2}$ and $p_{1/2}$, $p_{3/2}$ neutron-hole components has been obtained. A calculation of the hole spectral function shows that shell effects play an important role in determining the spreading width.

Evidence for the excitation of deeply bound hole states in the (p,d) reaction was recently reported.[1-3] Over a broad range of excitation energies ($E_x \approx 4-15$ MeV) the spectra from these pickup reactions are relatively featureless (except for a broad bump around 5 MeV excitation) and have the appearance of a continuous background. The angular distributions, however, obtained by integrating over the whole energy range are strongly forward peaked, and this suggests a predominantly direct reaction. It was therefore proposed[1] that the observed yield is due to pickup of neutrons from the next lower shell with the hole strength smeared out over very many levels.

As an alternative process we have studied the (d,t) reaction on tin at $E_d = 50$ MeV. We observe at approximately 5 MeV excitation energy in the residual nucleus a very pronounced and giant-resonance-like structure which was also seen in the analogous (p,d) reaction[1-4] and, most recently, in the $(^3\mathrm{He},\alpha)$ reaction.[5] From a measurement of the differential cross sections to extreme forward angles we were able to decompose the peak in the ^{116}Sn$(d,t)^{115}$Sn spectrum into two distinct components with characteristic $l=1$ and $l=4$ angular distributions, respectively. Investigation of the (d,t) reaction on all even-A isotopes of tin (with the exception of ^{114}Sn) allowed us to study the fragmentation (spreading width) of these deeply bound hole states as a function of neutron number.

Self-supporting targets of tin were bombarded with an energy-analyzed beam of 50-MeV deuterons from the Groningen azimuthally varying field cyclotron. Target thicknesses were 0.15, 1.53, 0.80, 2.10, 0.72, 0.30 mg/cm^2, for the isotopes ^{112,116,118,120,122,124}Sn, respectively. Spectra from the (d,t) reaction on these targets at $\theta_{\mathrm{lab}} = 15°$ are shown in Fig. 1. These data were obtained with solid-state-detector telescopes with a typical resolution of ~150 keV. For extreme forward angles from 6–12° a telescope with two ΔE detectors and a stopping detector was used with two independent pulse multipliers for mass identification, giving $(\Delta E_1 + \Delta E_2)E$ and $\Delta E_1(\Delta E_2 + E)$, respectively. Only those events were recorded that were accepted as tritons by both mass identifiers.

All the spectra reveal, at approximately the same Q value, a broad and giant-resonance-like peak riding on a continuous "background." The peak is narrowest and most structured for ^{115,117}S Quite remarkably it appears to broaden both toward smaller (^{111}Sn) and larger neutron numbers though the ^{112}Sn$(d,t)^{111}$Sn results are less certain because of possible contaminations. (In ^{111}Sn a relatively narrow peak containing only one third of the integrated $g_{9/2}$ cross section seen in ^{115}Sn is riding on a broad gross-structure bump.) In addition to the gross-structure peaks there are indications of finer, intermediate-width structures superimposed onto the gross-structure peaks.

Close inspection of the gross-structure peak in the ^{116}Sn$(d,t)^{115}$Sn reaction at the most forward angles (Fig. 2) reveals that it can be decomposed into a narrower (~1.0 MeV at the base) and a broader (~2.5 MeV wide) peak, as indicated at the top of Fig. 2, plus a "background." (Note that at 6° $l=1$ is strong and $l=4$ is weak, and that at 11.5° $l=1$ has a minimum.) Angular distributions obtained for the broad and narrow peaks are shown in Fig. 3. These angular distributions have a very pronounced and diffractive pattern characteristic for a direct process for $l=1$ and $l=4$, respectively. The curves in Fig. 3 are the results of distorted-wave Born-approximation calculations with the program DWUCK for pickup of a $2p$ and a $1g_{9/2}$ neutron employing the same optical-model parameters used to analyze[6] the reaction ^{116}Sn$(d,{}^3\mathrm{He})^{115}$In at 50 MeV. Calculations with triton optical-model parameters for $E_t = 20$ MeV[7] gave very similar results. The agreement between the data and the theoretical curves is striking. The hole strengths obtained from the

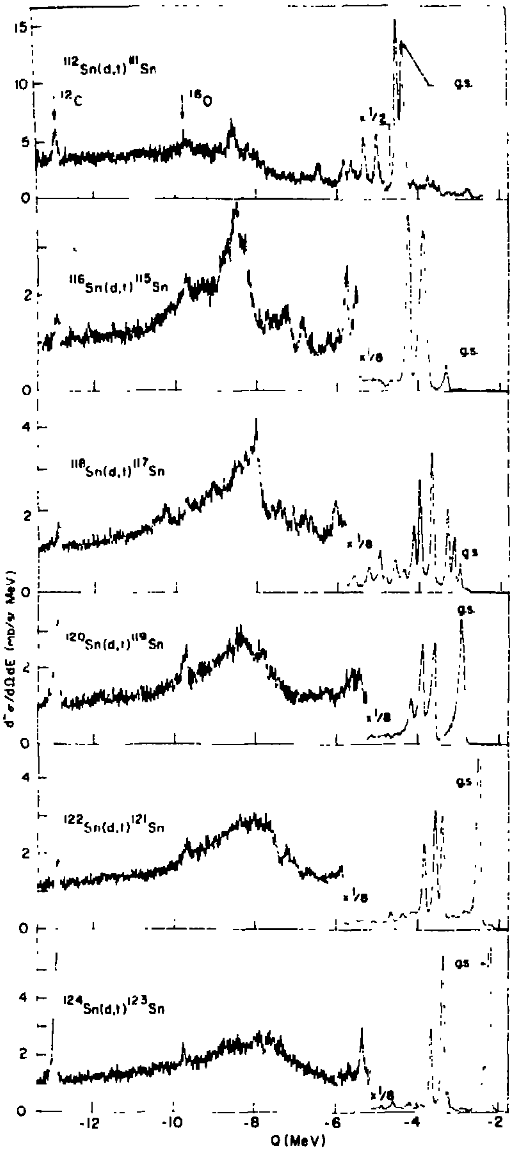

FIG. 1. Spectra from the reaction ^{A}Sn$(d,t)^{A-1}$Sn at 15° and $E_d = 50$ MeV. Note the differences in scale for the low- and the high-energy parts of the spectra.

distorted-wave Born-approximation analysis are ~30% of the $1g_{9/2}$ and ~20% of the combined $2p_{1/2}$, $2p_{3/2}$ sum-rule limit for pickup of neutrons from the next lower shell.

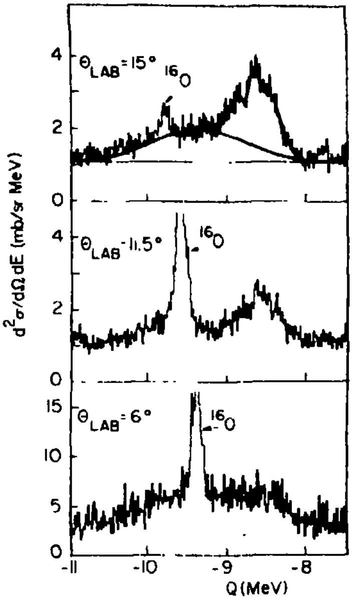

FIG. 2. Partial spectra showing the region around 5.5 MeV excitation in the reaction ^{116}Sn$(d,t)^{115}$Sn indicating the separation of the gross structure into two components plus "background."

The $g_{9/2}$ and the $p_{1/2}$, $p_{3/2}$ holes are observed at 5–6 MeV excitation energy in the residual nuclei in a region of very many (~10^3/MeV) levels. The bumps seen in the spectra thus represent a striking example of giant resonances in the sense of Lane, Thomas, and Wigner[8] in which the particle

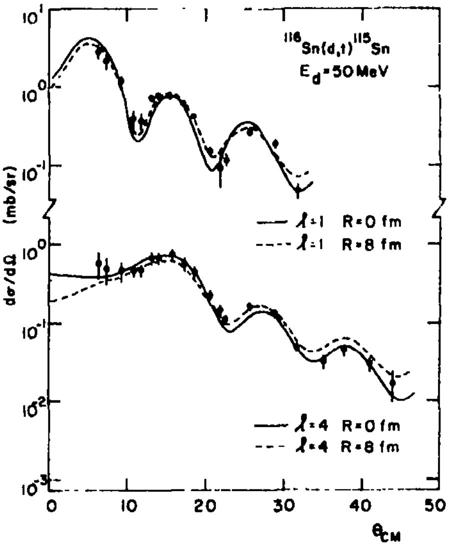

FIG. 3. Angular distributions of the two components of the gross structure shown in Fig. 2.

(hole) strength is distributed over very many, more complicated states. The arresting features of the present data are (i) the possibility to separate the l components according to different line shapes, (ii) the narrow width in ^{115,117}Sn, and (iii) the apparent intermediate structure superimposed onto the gross structure of the bump. It is the relatively small spreading width of the observed hole states that makes them stand out over the "background" composed from pickup to the many underlying states with different spins and parities.

In order to understand the spreading mechanism we have performed a microscopic calculation similar in spirit to those of Bloch and Feshbach[9] and Shakin[10] of the spectral function

$$S_j(E)=\sum_\sigma |c_j^\sigma|\delta(E-E^\sigma), \qquad (1)$$

where the coefficients c_j^σ describe the admixture of the hole state j into eigenstates σ of the $A-1$ nucleus at energies E^σ. By choosing to work in the BCS frame we automatically take into account pairing correlations in the ground state of the target nucleus. The calculation of the spectral function amounts to a diagonalization of the $A-1$ Hamiltonian in the space spanned by the 1-qp, 3-qp, 5-qp, ... (quasiparticle) states. Proton excitations were not considered because of the $Z=50$ closed shell.

Among the 3-qp, 5-qp, ... states the 1-qp+N-phonon ($N=1, 2, \ldots$) collective states have especially large matrix elements with the 1-qp states.[11] We have therefore separated the 3-qp, 5-qp, ... states into collective and noncollective states by introducing the operators Q and q projecting onto the collective and noncollective states, respectively. These, together with the projection operator P onto the 1-qp states, span the complete space. We have then treated the coupling between the P and Q space explicitly while considering that between the P and q space only on the average through a constant matrix element $\langle v\rangle$. The strength of the quadrupole and octupole interaction governing both P-Q and P-q couplings has been fixed by fitting the levels in the same $A-1$ nucleus thus eliminating any adjustable parameter from the calculation. Since we are interested in excitation energies (≈ 5.5 MeV) well below the threshold for particle emission (≈ 7.5 MeV) the coupling to the continuum states has been neglected altogether.

According to the mechanism just described the single-hole state (1-qp) appears to be first fragmented into a discrete set of *collective* states (1-qp+phonons) and subsequently spread over the many underlying noncollective states (3-qp and 5-qp). The fragmentation gives rise to the intermediate structure. Since the spreading width is, in first approximation, given by

$$\Gamma=2\pi\rho|\langle v\rangle|^2, \qquad (2)$$

where ρ is the density of the 3- and 5-qp noncollective states, variations in the gross structure, as those experimentally observed, are to be attributed to differences in the local level density of the 3- and 5-qp noncollective states. Indeed our calculation shows that at 5-6 MeV this level density is still subject to *shell effects*, and therefore large differences in the spreading widths from one nucleus to the other are to be expected. In particular the narrow width observed in ^{115,117}S seems to be connected with the partial shell closure at $N=64$ which gives rise to a "gap" in the level density as shown for ^{115}Sn in Fig. 4. The smaller density at the energy where most of the fragmented $g_{9/2}$ strength lies (shown in the lower part of Fig. 4.) lets it clearly stand out over the "background." In contrast no such effect appears to be present in the other Sn isotopes and this would explain the larger spreading width found for these nuclei.

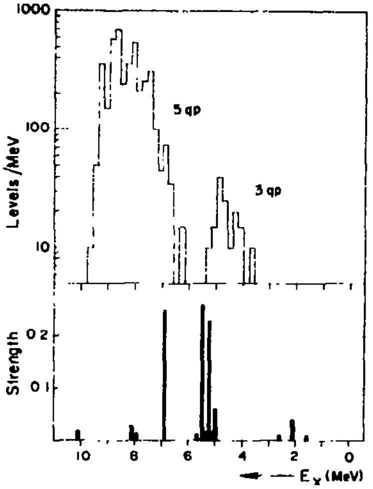

FIG. 4. Unperturbed level density of the $\frac{9}{2}^+$ 3- and 5-qp states in ^{115}Sn obtained by direct counting of the number of states in $\Delta E=200$-keV energy intervals (upper part). Fragmentation of the $\frac{9}{2}^+$ hole strength due to the coupling with the 1-qp+phonon collective states (lower part).

The assistance of B. Fryszczyn during some phases of the data taking is gratefully acknowledged.

---

*Work supported in part by the Stichting Voor Fundamenteel Onderzoek der Materie.

†Present address: Vrije Universiteit, Amsterdam, The Netherlands.

[1] M. Sakai and K. Kubo, Nucl. Phys. A185, 217 (1972).

[2] T. Ishimatsu, S. Hayashibe, N. Kawamura, T. Awaya, H. Ohmura, Y. Nakajima, and S. Mitara, Nucl. Phys. A185, 273 (1972).

[3] T. Ishimatsu, S. Hayashibe, T. Awaya, and H. Ohmura, J. Phys. Soc. Jpn. 35, 1579 (1973).

[4] F. E. Bertrand and R. W. Peelle, Phys. Rev. C 8, 1045 (1973), and private communication.

[5] M. Sakai, M. Sekiguchi, F. Soga, Y. Hirao, K. Yagi, and Y. Aoki, Phys. Lett. 51B, 51 (1974).

[6] W. H. A. Hesselink, B. R. Kooistra, L. W. Put, R. H. Siemssen, and S. Y. van der Werf, Nucl. Phys. A226, 229 (1974).

[7] E. R. Flynn, D. D. Armstrong, J. G. Beery, and A. G. Blair, Phys. Rev. 182, 1113 (1969).

[8] A. M. Lane, R. G. Thomas, and E. P. Wigner, Phys. Rev. 98, 693 (1955).

[9] B. Bloch and H. Feshbach, Ann. Phys. (New York) 23, 47 (1963).

[10] C. Shakin, Ann. Phys. (New York) 22, 373 (1963).

Resolving Ambiguities in Heavy-Ion Potentials*

D. A. Goldberg and S. M. Smith†
University of Maryland, College Park, Maryland 20742

(Received 16 April 1974)

It is shown that nuclear (as opposed to Coulomb) rainbow-scattering data would be useful in discriminating among heavy-ion optical potentials. Acquisition of such data is facilitated by going to higher bombarding energies and using low-*A* targets.

There has recently been a great deal of interest in obtaining optical potentials which will satisfactorily describe the elastic scattering of heavy ions and which can be used in distorted-wave Born-approximation calculations for transfer reactions.[1] Most of the experiments performed to date appear to be sensitive only to the extreme tail of the nuclear potential, and hence, if one assumes that the potential is of the Woods-Saxon form,

$$U(r)=\frac{-(V+iW)}{1+\exp[(r-R)/a]},$$

one can only determine a and the combined constant $(V+iW)e^{R/a}$. The situation is very similar to that which existed for the early α-scattering experiments.[2] It therefore appears reasonable that recent approaches which have proven helpful in unraveling the ambiguities in α-particle scattering may also prove useful for heavy ions and possibly prevent some retracing of familiar, if not altogether fruitful, ground as well.[3]

In a recent paper by the present authors[4] it was shown that discrete ambiguities in the α-particle optical potential could be resolved[5] by taking data beyond the maximum *negative* deflection angle or *nuclear* rainbow angle $\Theta_r^{(N)}$.[6] This result can be explained in classical terms. Since the maximum deflection angle increases with the strength of the potential, measurement of the former quantity determines the latter. In both the classical and quantum cases, the measurement is effected by measuring the cross section in the region beyond the maximum deflection angle $\Theta_r^{(N)}$. In the classical case, the cross section falls abruptly to zero beyond $\Theta_r^{(N)}$; in the quantum case, it exhibits the exponentiallike falloff characteristic of rainbow scattering.

One might well expect that nuclear-rainbow-scattering data would be useful in eliminating ambiguities other than the discrete kind. In particular, for $Ve^{R/a}$ ambiguities, the parameter a is well determined, and so the maximum deflecting force, which occurs at $r=R$, is simply proportional to V. It is our purpose to show, by using a series of model calculations, that the above expectation appears to be justified, and to examine the experimental conditions which would facilitate the observation of nuclear rainbow scattering.

It was shown in Ref. 4 that there is a minimum energy ϵ_{crit} required for nuclear rainbow scattering to occur, and that as the energy is increased above ϵ_{crit}, the nuclear rainbow angle $\Theta_r^{(N)}$ decreases to smaller (and experimentally more accessible) angles. To verify this for the case of heavy ions, we have performed model calculations for the case of ^{16}O incident on ^{28}Si.

The potentials used in the calculations are those which Cramer *et al.*[7] obtained by fitting elastic-scattering data over the range 33–81 MeV; these potentials form a $Ve^{R/a}$ ambiguity (referred to by Cramer *et al.* as a "class") for which V can range from 10 MeV to ≫1 GeV with essentially no change in χ^2. We initially selected the potential in this class for which $V = 100$ MeV. The calculated ϵ_{crit} for this potential is 140 MeV (lab). However, as stated above, for the nuclear rainbow scattering to be readily observable it is necessary to go to higher energies. Hence we extended our calculations up to 200 MeV (lab) which is about the maximum energy currently available for ^{16}O ions.

The results of the calculations are shown in Fig. 1; the curves are quite similar to those for α particles on heavy nuclei. At $E = 40$ MeV, the differential cross section is that typical of *Coulomb* rainbow scattering. As the energy is increased to 80 MeV the Coulomb rainbow peak moves to smaller angles and one observes the onset of diffraction oscillations, a transition similar to that observed in low-energy α scattering from heavy targets. As the energy is increased still further, the diffraction oscillations begin to die out at larger angles and give way to the structureless falloff associated with rainbow scattering. In fact at $E = 200$ MeV one is able to see *both* the Coulomb *and* the nuclear rainbows, the former being masked somewhat by the presence of diffraction oscillations.

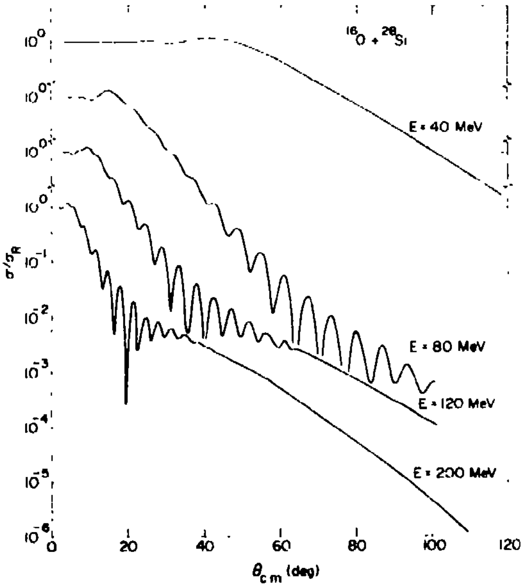

FIG. 1. Model calculations for elastic-scattering cross section predicted by the 100-MeV-deep heavy-ion potential of Cramer *et al*.

The existence of a falloff region, which usuall begins to appear at energies slightly *below* ϵ_{crit} (e.g., 120 MeV for ^{16}O + ^{28}Si) is not in and of itself definitive evidence of rainbow scattering. As pointed out in Ref. 4, the *shape* (but not the magnitude) of the cross section beyond the rainbow angle is *independent of absorption*. Hence, short of doing a full-blown semiclassical phase-shift calculation, a simple test for the existence of rainbow scattering can be performed by calculating the angular distribution in the *absence* of absorption. If the falloff persists, as it does for such a calculation in the 200-MeV case, then rainbow scattering is in fact occurring. Moreover, the independence of the shape of the cross section on W means that the determination of the parameters of the real part of the well is relatively independent of absorption.

Having established that nuclear rainbow scattering will indeed occur at sufficiently high incident energies, we now consider its usefulness in distinguishing among various optical potentials. We consider the scattering predicted for two other potentials of the above class, namely, tho for $V = 50$ and 20 MeV. To maximize the region in which nuclear rainbow scattering dominates, we choose the incident energy to be 200 MeV.

The results of the calculations for the three potentials are shown in Fig. 2. As expected, the 50-MeV well has a smaller nuclear rainbow angle than the 100-MeV well, although the rainbow scattering region is still largely distinct from the diffraction region. For the 20-MeV potentia the real well is so weak that the nuclear rainbow angle has fallen well within the diffraction regio and the resulting cross section becomes a steep falling diffraction pattern.[8] Comparing the 50- and 100-MeV cross sections we make two furthe observations. First, the smaller $\Theta_r^{(N)}$ for the former potential results in a smaller cross section at larger angles. Secondly, the cross sections predicted by the two potentials are quite similar at angles less than $\Theta_r^{(N)}$. Thus the results bear out the earlier contention that *it is th data in the nuclear–rainbow-scattering region which enable one to distinguish among various optical potentials.*

We now consider the question of how to facilitate rainbow-scattering measurements. We hav shown earlier, that such measurements are

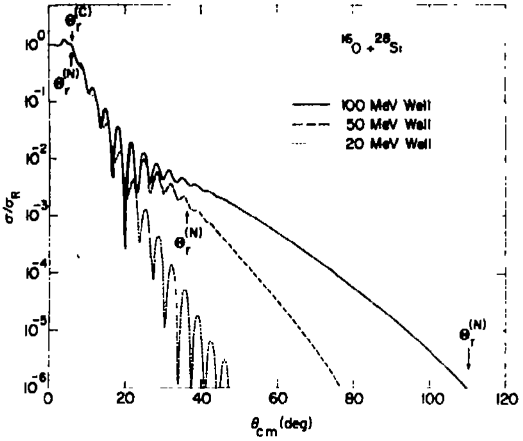

FIG. 2. Comparison of predicted cross sections at $E = 200$ MeV for three different potentials which give equivalent fits to scattering data in the region 30–81 MeV. The radii for the wells shown are 6.86, 6.31, and 5.87 fm for the 20-, 50-, and 100-MeV wells, respectively, and $a = 0.64$ fm in each case (Cramer *et al.* use a slightly modified version of $Ve^{R/a} = \text{const}$ in obtaining different potentials within the class); the real and imaginary geometries are the same and W is related to V by the relation $W = 0.44V + 2.7$. The respective *nuclear* rainbow angles for the three cross sections, calculated as described in Ref. 3, are indicated as $\Theta_r^{(N)}$. The *Coulomb* rainbow angles denoted $\Theta_r^{(C)}$, are essentially identical in all three cases; this reflects the fact that $\Theta_r^{(C)}$ depends only on the extreme tail of the nuclear potential.

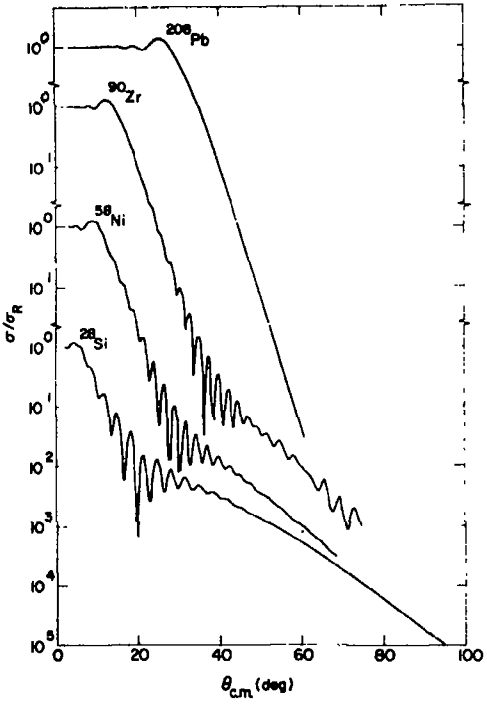

FIG. 3. Comparison of predicted cross sections for scattering of 200-MeV ^{16}O from four different nuclides. The potential used was the 100-MeV potential of Cramer *et al.*, with the radius scaled as $16^{1/3} + A_T^{1/3}$.

facilitated (more importantly, even made possible) by increasing the incident energy so that $\Theta_r^{(N)}$ is reduced. Moreover, the higher incident energy also increases the rainbow cross section, both absolutely and relative to the Rutherford cross section, thereby further improving the ease of measurement. For example, additional model calculations for the case of $^{16}O + ^{28}Si$ show that as the incident energy is increased from 200 to 300 MeV the cross section at $\Theta_r^{(N)}$ increases by a factor of about 4×10^3, and σ/σ_R increases some fortyfold.

A second, and equally important factor is the choice of target. Based on arguments made in Ref. 4 on the A dependence of ϵ_{crit} one can easily show that, for a given potential, i.e., one in which the A dependence is simply due to the increase of R with A, the nuclear rainbow angle increases with A, a result that recently has been verified experimentally for the case of intermediate-energy α scattering.[9] To demonstrate the effect in heavy-ion scattering we have done model calculations for 200-MeV ^{16}O incident on four different targets. The results are shown in Fig. 3. For ^{58}Ni, the rainbow-scattering region sets in at slightly larger angles, and, more importantly, has a smaller cross section. As A increases further, so does $\Theta_r^{(N)}$ until, in the case of ^{208}Pb, it exceeds 180° (and accordingly ϵ_{crit} exceeds the incident energy). In fact for ^{208}Pb, the scattering pattern is essentially that of pure *Coulomb* rainbow scattering, i.e., the scattering is only sensitive to the extreme tail of the potential; stated slightly differently, for ^{16}O incident on ^{208}Pb, $E_b = 200$ MeV still represents the low-energy limit.

The conclusions from the above calculations seem clear. Nuclear-rainbow-scattering data are useful in discriminating among nuclear potentials[10]; such data are most easily obtained by using high incident energies and low-A targets. Once one has "tied down" the potential at these higher energies one can extrapolate experimentally to lower energies, as has recently been done by Put and Paans[11] for the case of α particles. Moreover, recent calculations[12] appear to indicate that the energy dependence of heavy-ion optical potentials is expected to be small.

The arguments leading to these conclusions involve quite general characteristics of nuclear scattering, which we have described elsewhere as refractive behavior,[9,13] and are based on a simple classical analog. In particular the arguments are not predicated on the potential having a Woods-Saxon shape, a form whose widespread usage is at least as much the result of its convenience as its "correctness." Whatever the parametrization, rainbow-scattering data will give one a good estimate of the overall strength of the interaction. (In fact, the data may even result in an increased knowledge of the form of the potential, as has already been the result in the case of α scattering.[14]) The main point is that once relatively unambiguous results can be obtained for the lighter targets, studies of fine detail, e.g., using observations of resonances in excitation functions, can be more meaningfully performed and results extended to heavier nuclei. We feel that the present work indicates what, in the near term, is likely to be the most fruitful direction for experimental activity to take.

We are deeply indebted to John Cramer for providing us with his set of heavy-ion potentials. We also wish to acknowledge stimulating discussions with M. L. Halbert and M. H. MacFarlane.

---

*Work supported in part by the U. S. Atomic Energy Commission.

†Present address: Education and Public Affairs, Inc., Washington, D. C.

[1] See, e.g., A. Gobbi, R. Wieland, L. Chua, D. Shapira, and D. A. Bromley, Phys. Rev. C **7**, 30 (1973), and references therein.

[2] R. M. Eisberg and C. E. Porter, Rev. Mod. Phys. **33**, 190 (1961), and references therein.

[3] G. Santayana, *The Life of Reason* (Charles Scribner, New York, 1953), p. 82, line 29.

[4] D. A. Goldberg and S. M. Smith, Phys. Rev. Lett. **29**, 500 (1972).

[5] At low energies, ambiguities have been removed by reducing the number of optical parameters [see, e.g., B. D. Watson *et al.*, Phys. Rev. C **4**, 2240 (1971)]. In our view, this represents a *suppression* of the ambiguity, rather than a *resolution* of it; it is nonetheless a reasonable approach in analyzing elastic-scattering data taken at energies where the scattering is so insensitive to anything but the extreme tail of the potential that even as few as four parameters are excessive.

[6] Low-energy α and heavy-ion scattering is characterized by a maximum *positive* deflection angle at the point where the attractive nuclear force begins to overcome the repulsive Coulomb force. To avoid confusion, we will refer to this as the *Coulomb* rainbow angle, $\Theta_r^{(C)}$, and to the maximum negative *deflection* angle, caused solely by the attractive nuclear force, as the *nuclear* rainbow angle, $\Theta_r^{(N)}$. The magnitude of the former is generally much smaller than that of the latter.

[7] J. G. Cramer, R. M. DeVries, M. S. Zisman, K. G. Nair, K.-L. Liu, and Y.-D. Chan, in *Proceedings of the International Conference on Nuclear Physics, Munich, Germany, 1973*, edited by J. de Boer and H. J. Mang (North Holland, Amsterdam, The Netherlands, 1973), p. 342, and to be published. We are grateful to J. Cramer for communicating his recent results to us prior to publication.

[8] A similar effect is observed in the case of elastic proton scattering, where the strength of the real well is also relatively weak.

[9] D. A. Goldberg, S. M. Smith, and G. F. Burdzik, Phys. Rev. C (to be published).

[10] An illustration of this result "by converse" may be seen in the results of M. L. Halbert *et al.*, Bull. Amer. Phys. Soc. **18**, 1387 (1973), and to be published; Halbert *et al.* succeeded in eliminating an overly *shallow* potential by taking data beyond *its* rainbow angle, and noting that the experimental cross section did *not* fall as predicted.

[11] L. W. Put and A. M. Paans, Phys. Lett. **49B**, 266 (1974).

[12] D. F. Jackson and R. C. Johnson, Phys. Lett. **49B**, 249 (1974).

[13] S. M. Smith and D. A. Goldberg, Bull. Amer. Phys. Soc. **17**, 591 (1972).

[14] D. A. Goldberg, Bull. Amer. Phys. Soc. **19**, 595 (1974).

Hadron Production at Large Transverse Momentum

J. A. Appel, M. H. Bourquin, I. Gaines, D. C. Hom, L. M. Lederman, H. P. Paar,
J.-P. Repellin,* D. H. Saxon,† H. D. Snyder, J. M. Weiss, and J. K. Yoh
Columbia University, New York, New York 10027‡

and

B. C. Brown, J.-M. Gaillard,* and T. Yamanouchi
Fermi National Accelerator Laboratory, Batavia, Illinois 60510§

(Received 15 July 1974)

We have studied production of π^0 with transverse momentum between 2.0 and 4.4 GeV/c at 65 and 93° in the c.m. system in 300-GeV proton-nucleon collisions, by inserting foils of various thicknesses into a secondary beam and measuring the electron and positron spectra produced by γ conversion. The π^0 invariant cross sections are given at 93 and 65°. We also report invariant cross sections for negatively charged hadrons as a function of transverse momentum.

The discovery of a copious yield of hadrons[1] produced at high transverse momentum provides a new tool for short-range hadrodynamics. We have performed a high-luminosity, large-acceptance search for "direct" leptons at the Fermi National Accelerator Laboratory (FNAL), observing particles produced at wide angles in 300-GeV proton-nuclear collisions. In the course of this search,[2] we measure the spectra of electrons and positrons produced by γ conversion in thin foils. The conversion-electron spectra allow us to deduce the π^0 spectra under the assumption that all of the γ's come from π^0 decays.[1] Charged hadrons are also recorded simultaneously in this experiment.

The extracted proton beam is transported ~1.6 km to the proton area at FNAL. The last stage of the transport system forms a parallel beam which drifts ~700 m before being brought to a 0.4×3-mm^2 focus. The optics permit stable operation with a 40% targeting efficiency on a Be target, 0.22 mm wide and 100 mm long. The small transverse dimension of the target and the small residual matter between the target and our apparatus represent $\leq 0.9\%$ of a radiation length for conversion of γ's in the direction of our detector.

Our apparatus is shown schematically in Fig. 1. A 9-mrad×9-mrad aperture is defined by a tungsten-lined steel collimator 8.2 m long, tapered to minimize wall illumination. The production angle is measured horizontally with data taken at 50 and 83 mrad, corresponding to 65 and 93° in the proton-nucleon c.m. system.

In order to work at high luminosity, we choose to detect particles only after magnetic deflection in the vertical plane. The "point-source" target and trajectory in the vertical plane after the magnet define the momentum. The horizontal-plane trajectory is used to verify the target source. The scintillation hodoscopes (210 elements), see Fig. 1, have a spatial resolution of 6 mm corresponding to a momentum resolution of 4% at 30 GeV/c. Two magnet settings cover the entire kinematic range ($P_\perp = 2$ to 11 GeV/c) with good efficiency and large overlap.

Particle identification is obtained by using two calorimeters which follow the hodoscopes: a

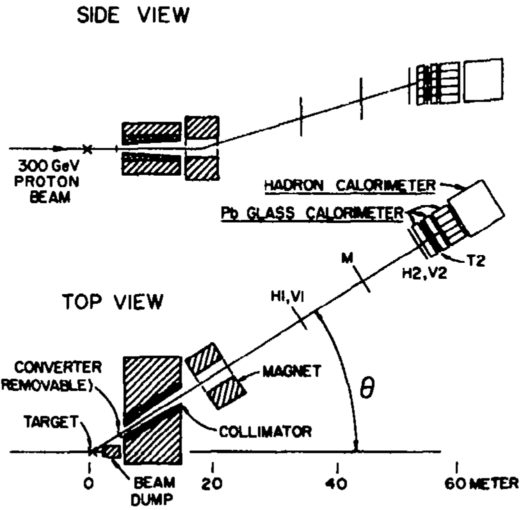

FIG. 1. Experimental apparatus for electron and γ-ray study. H_1, M, and H_2 are horizontal hodoscopes. V_1 and V_2 have vertical scintillator strips. A set of diagonal strips near V_1 is not shown.

total-absorption lead-glass electromagnetic shower detector[3] to identify electrons, and a steel-scintillator hadron detector to separate muons from hadrons.[4]

The electromagnetic shower detector consists of 2 radiation lengths of lead followed by an array of 45 identical SF-5 lead-glass blocks. Scintillation counters are placed just before and immediately behind the lead. The glass blocks are arranged in three layers (6, 6, and 15 radiation lengths, respectively) along the particle trajectory. The hadron calorimeter contains four additional scintillation counters for analog information and steel which, when added to the lead-glass, totals 1 kg/cm^2 of iron equivalent.

An event trigger is generated by a series of scintillation counters near the hodoscopes and loss requirements in each hodoscope plane. To reduce hadrons in the electron-trigger sample, a large pulse height is required in a scintillation-counter array (T2) placed after the first layer of lead-glass. In addition, the total energy in the first two layers of glass is required to pass certain preset threshold levels. The lowest-threshold triggers are prescaled so that a very large dynamic range in counting rate is sampled more uniformly. This trigger technique also serves to measure the trigger efficiencies for the higher-threshold events.

Each block of glass and each scintillation shower counter has its signal integrated by a 1024 channel analog-to-digital converter.[5] Calibration and stability monitoring details are described elsewhere.[3] All the event information is passed to a PDP-15 computer for later analysis. The resulting electron-energy resolution at 40 GeV is better than 4% full width at half-maximum with gain shifts (after corrections) of less than $\frac{1}{2}$% due to time or entry location.

A typical plot of energy deposited in the glass (E) divided by the momentum (P) of the particle (i.e., the fraction of its energy that a particle leaves in the lead-glass) for all triggers is shown as distribution a in Fig. 2. Electrons, which begin to cascade in the lead and leave all their energy in the glass, appear at $E/P = 1$, while most hadrons leave only a fraction of their energy and thus appear at $E/P < 1$. However, because of charge exchange and other processes, a significant number of hadrons (~1 in 2000) leave more than 90% of their energy in the glass and thus appear as a background under the electron peak at $E/P > 0.9$. Hadron rejection is improved by applying cuts on the longitudinal shower development in the array and cuts on the signals from the scintillation counters sandwiching the 2 radi tion lengths of lead. These cuts, about 80% efficient for electrons, result in the E/P distribution b shown in Fig. 2, where a clear electron peak is visible.

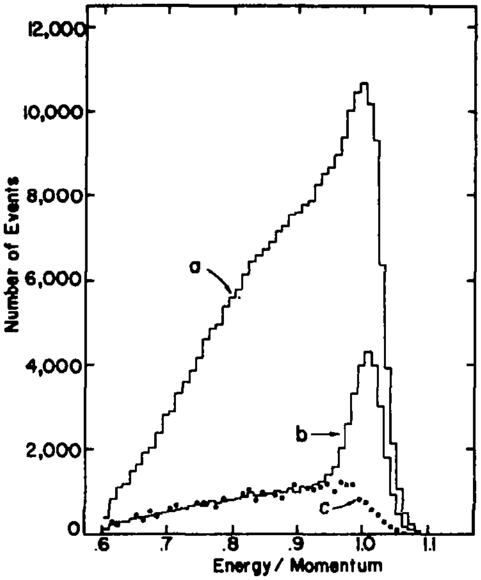

FIG. 2. Distribution a: E/P distribution with no cut distribution b: E/P with shower cuts; distribution c: E/P with shower cuts and with 5-cm Pb which remove all electrons.

The cuts, the requirement of showering in the lead, and the requirement that $0.95 < E/P < 1.05$ combine to give a hadron rejection of better tha 10^4. We also study the E/P distributions with 5 cm of lead inserted in the secondary beam producing an effectively pure hadron beam (distribution c, Fig. 2). No artificial peak appears in th cut distribution and the shape agrees with the background below the electron signal. Subtraction of this background (less than the signal eve in the worst case) leaves a very clean electron peak and gives a hadron rejection of better than 10^5.

In the π^0 experiment, we take data with foils o 2, 4, and 6% of a radiation length inserted in th secondary beam upstream of the magnets to measure the spectra of electrons and positrons produced by γ conversions. A plot of the electron yield as a function of thickness is shown in Fig. 3(a). The uncorrected points are from the raw data. Corrections are then applied to take ac-

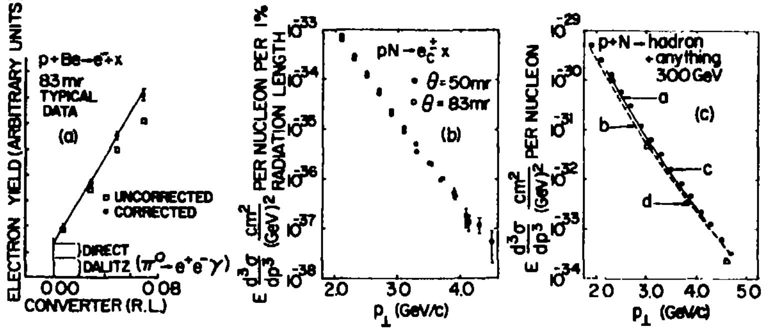

FIG. 3. (a) Yield of electrons versus foil thickness. (b) Invariant cross section for conversion electrons. The errors shown are statistical only. (c) Invariant cross sections near 90°: *a*, π^0's (this experiment); *b*, CCR modified fit; *c*, h^- this experiment ($h^- \equiv \pi^- + K^- + \bar{p}$); *d*, $(\pi^+ + \pi^-)/2$ (Ref. 6).

count of the energy loss due to bremsstrahlung by the electrons as they pass through the foils. The slope of the resulting line gives the number of electrons from γ conversions per 1% radiation length.

This slope is determined as a function of transverse momentum at both 50 and 83 mrad to obtain the spectra shown in Fig. 3(b), where the invariant cross section for electrons from γ-ray conversions in 1% radiation length is plotted. These data are taken on a Be target, and are normalized to a cross section per nucleon by dividing by 9, the ratio $A(\mathrm{Be})/A(\mathrm{H})$.[6] Data are taken at different magnet currents which make different sections of our spectrometer sensitive to the same transverse momentum. The yields are in excellent agreement, providing a sensitive check of our understanding of the acceptance of our detector. The data are averaged over polarity since, as expected for electrons from conversions, there is no difference observed between electrons and positrons.

Figure 3(c) shows an invariant cross section for π^0 production at 90° which would give rise to the electron data of Fig. 3(b). Systematic uncertainties in the absolute normalizations are believed to be smaller than 30%. A potentially larger error in the π^0 cross section could come from other sources of γ's. For instance, if the η^0 is produced with the same cross section as the π^0, its decay mode into two γ's would mean we have overestimated the π^0 cross section by about 35%.

We have at the same time measured charged-hadron spectra with a trigger that complemented the electron trigger and also used the information from the hadron calorimeter to reject muons and backgrounds.

The resulting $P_\perp$ distribution for negative hadrons (expected to be about 80% π^-)[7] is given in Fig. 3(c). Also shown is a fit to the π^0 spectrum of the CERN-Columbia University-Rockefeller University collaboration (CCR)[1] modified to fit smoothly at moderate $P_\perp$,

$$E\frac{d^3\sigma}{dp^3} = \frac{15\ \mathrm{mb}}{(P_\perp^2+1)^4}\exp(-13x_\perp),\quad x_\perp = \frac{2P_\perp}{\sqrt{s}},\qquad (1)$$

and the average of the charged-pion spectra measured at FNAL by the University of Chicago-Princeton University group reduced from p-Be to p-N collisions by using the same factor of A.[6]

The π^0 data at 90° are in excellent agreement with the modified CCR fit. Furthermore, the invariant cross sections at 65 and 93° are very similar, indicating that any angle dependence beyond that given in Eq. (1) is not large.

Finally, charged-hadron spectra have a slope indistinguishable from that of the π^0. These data also agree very well with the FNAL work of Cronin *et al.* for $x_\perp < 0.5$.[7]

It is a pleasure to thank the staff of FNAL and especially of the proton section for their efforts. We are also deeply indebted to Mr. T. E. Nurczyk, Mr. F. H. Pearsall, and Mr. S. J. Upton and the staff of Nevis Laboratories for their help in the design and implementation of the apparatus.

---

[*] Permanent address: Laboratoire de l'Accélérateur Linéaire, Orsay, France.

[†] Present address: Rutherford High Energy Laboratory, Chilton, Didcot, Berkshire, England.

[‡] Research supported by the National Science Foundation.

[§] Research supported by the U. S. Atomic Energy Commission.

[1] F. W. Büsser *et al.*, Phys. Lett. 46B, 471 (1973). See also B. Alper *et al.*, Phys. Lett. 44B, 521 (1973); M. Banner *et al.*, Phys. Lett. 44B, 537 (1973).

[2] J. A. Appel *et al.*, following Letter [Phys. Rev. Lett. 33, 722 (1974)].

[3] The calibration, stability, resolution, and hadron rejection of the lead-glass is discussed more fully by J. A. Appel *et al.*, "Performance of a Lead-Glass Electromagnetic Shower Detector at FermiLab" (to be pu lished).

[4] M. H. Bourquin and D. H. Saxon, Nucl. Instrum. Methods 108, 461 (1973).

[5] F. W. Sippach, to be published.

[6] J. W. Cronin *et al.*, in Proceedings of the Seventeenth International Conference on High Energy Phy London, England, 1–10 July 1974 (to be published).

[7] J. W. Cronin *et al.*, Phys. Rev. Lett. 31, 1426 (19

Observation of Direct Production of Leptons in p-Be Collisions at 300 GeV

J. A. Appel, M. H. Bourquin, I. Gaines, D. C. Hom, L. M. Lederman, H. P. Paar, J.-P. Repellin,* D. H. Saxon,† H. D. Snyder, J. M. Weiss, and J. K. Yoh
Columbia University, New York, New York 10027‡

and

B. C. Brown, J.-M. Gaillard,* and T. Yamanouchi
Fermi National Accelerator Laboratory, Batavia, Illinois 60510§

(Received 15 July 1974)

Direct production of electrons and muons is observed in 300-GeV p-Be collisions. The yields are much higher than predicted from current models. Data are consistent with charge symmetry and universality.

We describe here the observation of high-transverse-momentum electrons and muons produced directly in proton-beryllium collisions at 300 GeV.[1] The primary motivation for this measurement is the search for the parents of "direct" leptons.[2] Candidates for the parents include (i) virtual massive photons, (ii) vector mesons (ρ, $\omega, \varphi, \ldots$) produced with large transverse momentum, (iii) intermediate bosons ($W^{\pm}, Z^0, \ldots$), (iv) charmed particles, and (v) heavy leptons.

Electron detection has the virtue of high resolution in energy and angle. This is important in maintaining sensitivity to "bumps" which would be generated by the two-body decay of one of the above parents with discrete mass M produced with small transverse momentum. A peak would appear in the lepton transverse-momentum spectrum at a value of $P_{\perp} = M/2$. Muon detection has the complementary advantage of having backgrounds (π and K decay) which are lower by a factor of ~4.

The electron experiment is performed with the apparatus already described.[3] A magnetic momentum analysis followed by shower detection in a lead-glass spectrometer provides hadron rejection of a factor of ~ 10^5. Efficiencies for electron detection are determined by studying the effect of cuts on an electron-enriched sample of events. A ready source of calibration electrons is obtained by inserting a 1-radiation-length conver er into the intense γ flux from the target.

Two important backgrounds are the γ conver sion in the minimum of material in the seconda beam and the π^0 Dalitz decays. Both of these c be subtracted with high precision by the followi method. A series of foils of known thicknesses are inserted into the secondary beam and the tron yield is plotted as a function of foil thickn [Fig. 3(a) of the previous Letter]. This permit

TABLE I. Electron yield, normalized to π^0 yield.[a] $1.9 < P_{\perp} < 4$ GeV/c.

$\left.\begin{matrix}\pi^0\\ \eta^0\end{matrix}\right\} \to \gamma + e^+ + e^-$	$\dfrac{[1.6+0.8\eta^0/\pi^0]\times 10^{-4}}{1+0.38\eta^0/\pi^0}$[b]
$\mu^- \to e\nu\bar{\nu}$	10^{-8}
$\bar{\pi} \to e\nu$	10^{-7}
$K^- \to \pi^0 e^- \bar{\nu}$	3×10^{-6}
$K_L{}^0 \to \pi^+ e^- \bar{\nu}$	2×10^{-6}
Hyperons	$3\times 10^{-6} \times (\mathrm{hyperon}/\pi^0)$[b]
Signal	$\sim 1\times 10^{-4}$

[a] We assume in the paper that γ's arise from π^0's. η^0 production were to equal π^0 production there would result a 7% increase in the Dalitz subtraction.

[b] η^0/π^0 and hyperon/π^0 refer to the ratio of producti cross sections for these particles.

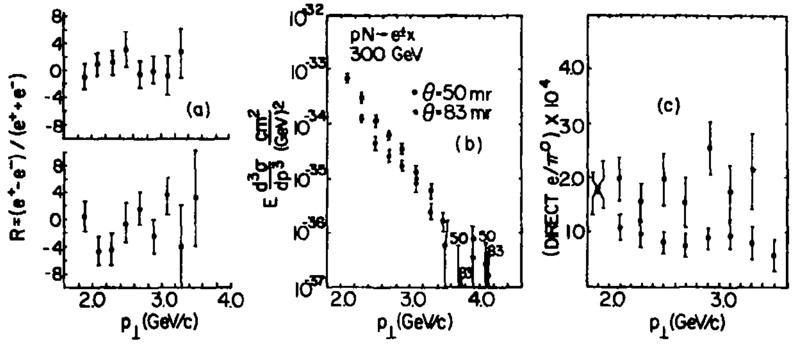

FIG. 1. (a) Comparison of positive and negative direct electrons at 50 and 83 mrad (corresponding to 65 and 93° n the proton-nucleon c.m. system). (b) Invariant cross sections per nucleon for direct electrons. (c) Direct elecron to π^0 ratios.

s to extrapolate back (0.7% of a radiation length t 83 mrad and 0.9% at 50 mrad, including target hickness) to zero matter in the secondary beam. his leaves an electron signal due only to shortived sources. The contribution of Dalitz pairs s also known since they are derived from the ame parent-π^0 spectrum measured by the slope f the foil-conversion curve (with a small correcion for the finite mass of the Dalitz pair). Other ackground sources, listed in Table I, are negliible.

The residue after subtractions is the direct elecron signal, statistically significant to better than 0 standard deviations. This signal, at a consisent level of $\sim 10^{-4}$ of the π^0's, persists in spite f a large series of critical tests for spurious ources: collimator-wall conversions, hadron ackground, extrapolation nonlinearities, air conamination of the He in the target region, and deendence on the viewing angle.

The extrapolation is done in bins of transverse nomentum for both electrons and positrons. The harge asymmetries of the directly produced elecrons are given in Fig. 1(a). The two charges ave equal yields and are averaged to give the nvariant cross sections in Fig. 1(b). The plotted rrors are statistical only. While overall normalzation uncertainties may be as high as 50%, the atio of direct electrons to π^0's is measured quite ell by comparing the signal with the slope of the oil-conversion curve in each transverse-momenum bin. The variation in this ratio with $P_\perp$ is hown in Fig. 1(c).

The cross sections are seen to fall smoothly ver four decades with no evidence of bumps. It hould be noted that the acceptance is relatively flat out to $P_\perp \sim 11$ GeV/c, the kinematic limit. A run with 5 cm of lead at 6 m from the target demonstrates experimentally that the source of the electrons must have a lifetime less than $10^{-9}M$ sec, where M is the mass of the parent in GeV/c^2.

To detect muons, we add to our apparatus (1) x and y hodoscopes at 10 m from the target to improve background rejection and (2) a hadron absorber, 0.9 m of Heavimet on a movable sled. The face of the absorber can be placed as close as 32 cm from the center of the target and its position is varied in order to change the decay-in-flight path of π's and K's. The absorber subtends at least 35 mrad beyond the actual acceptance so that all but an insignificant number of particles must traverse the entire absorber in order to be accepted. Two additional absorbers (2 m of graphite and 0.5 m of polyethylene) are permanently mounted downstream. These additional absorbers do not significantly affect the multiple scattering and together with the Heavimet absorber reduce the flux of hadrons traversing our apparatus by a factor of 10^4. The remaining hadrons ($\sim\frac{1}{2}$ of the particle flux) are identified with a hadron calorimeter.[8]

Extrapolation of the muon yield to zero decay path for hadron decay results in the "direct-production" muon signal. Figure 2(a) shows a sample of the data plotted as a function of the available decay path (including the 15 ± 3-cm mean decay path in the Heavimet). A clear signal, equivalent to ~ 50 cm of π and K decay path, is seen. The signal corresponds to $\sim 10^{-4}$ of the pion production. Backgrounds, such as long-lived hadronic sources, muon leakage around the absorber, and target-out events, are all negligible.

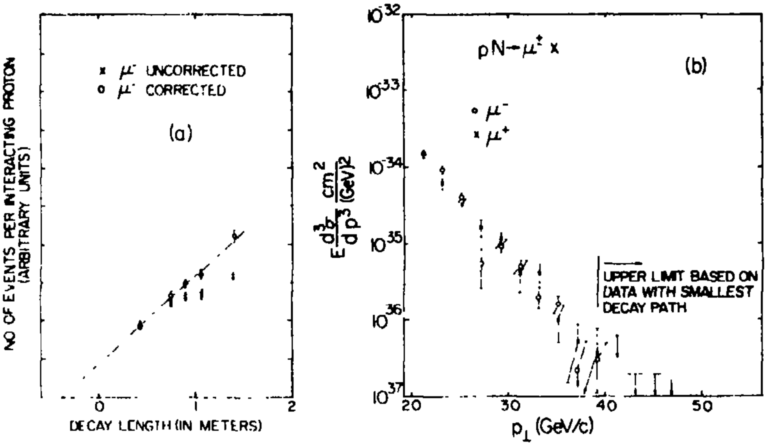

FIG. 2. (a) Muon yield versus decay path. The slope gives the contributions of pions and kaons ($2.0 \leq P \leq 2.6$ GeV/c). The corrections are for multiple-scattering effects. (b) Invariant cross section per nucleon for direct muons near 90° in the c.m. system.

Multiple-scattering effects, the critical corrections in this type of experiment, are evaluated by Monte Carlo calculations. Since all the absorbers are always in the path of the accepted particles, the change in acceptance is due to the change in lever arm in the multiple scattering and amounts to less than 30% for $P_\perp > 2.5$ GeV/c. The effect of the energy loss in the absorbers is simply to shift the spectrum in $P_\perp$ by a well-known amount.

Figure 2(b) shows our preliminary results for $p + \mathrm{Be} \to \mu + \text{anything}$. Again, μ^+/μ^- is consistent with 1. Although the muon invariant cross section is, at present, lower than the electron cross section, our absolute normalization uncertainty of 50% could account for the difference.

In seeking to interpret these results, we can tentatively exclude W's as the parents since these would produce a peak and the charged variety should show a +/− asymmetry. Charmed particles may also show a charge asymmetry. Only a double-arm experiment[4] can establish whether we are observing single leptons from the decay of forward massive virtual photons or the leptonic decay of high-$P_\perp$ low-mass particles (e.g., vector mesons). Table II lists the standard vector mesons and their relative contributions to the direct lepton signal, with the assumption that the spectrum of each vector meson is the same as the observed spectrum of neutral pions.[2]

An explanation of the lepton flux, consistent with the equality of the three pion charge states and not violating the K/π ratio, is $\rho^\pm = \rho^0 = \omega^0 = \varphi^0$ ~4 times the direct (i.e., not from vector meson) π^0 production. The direct leptons then arise primarily from the φ^0. The constancy of the ratio of leptons to pions as a function of $P_\perp$ tends to favor this hypothesis. An overwhelming production of vector mesons in close hadron collisions, if confirmed, may have profound implications for the strong interactions. For reference, we note that the lepton yields observed here are 1–2 orders of magnitude higher than the predictions of parton-annihilation models.[5] We are aware of two other searches for muons[6,7] and one for electrons which give similar results.

Assuming that three events within a resolution bin (± 3% for electrons) would have been observed with a 95% confidence level, we set a limit on the production of leptons with $P_\perp > 4.5$ GeV/c of $\sigma < 10^{-34}$ cm². To make more incisive statements

TABLE II. Direct lepton sources. $\langle P_\perp \rangle \sim 3$ GeV/c.

Source	N_l/N_{π^0}
$\rho^0 \to l^+l^-$	5×10^{-6} [a]
$\varphi^0 \to l^+l^-$	3×10^{-5} [a]
$\omega^0 \to l^+l^-$	7×10^{-6} [a]
$q\bar{q} \to l^+l^-$	$\sim 5 \times 10^{-6}$
Signal (Drell-Yan)	$\sim 1 \times 10^{-4}$

[a] Assuming $N_V = N_{\pi^0}$.

on the production of W's, etc., one requires plausible models for production and decay, a commodity in rare supply these days. Data on massive-photon production would be even more useful.[4]

It is a pleasure to thank the staff of the Fermi National Accelerator Laboratory and especially of the proton section for their efforts. We are also deeply indebted to Mr. T. E. Nurczyk, Mr. F. H. Pearsall, and Mr. S. J. Upton and the Nevis Laboratories for their help in the design and implementation of the apparatus.

---

[*] Permanent address: Laboratoire de l'Accélérateur Linéaire, Orsay, France.

[†] Present address: Rutherford High Energy Laboratory, Chilton, Didcot, Berkshire, England.

[‡] Research supported by the National Science Foundation.

[§] Research supported by the U.S. Atomic Energy Commission.

[1] A preliminary report of this work has been given: H. P. Paar *et al.*, Bull. Amer. Phys. Soc. 19, 446 (1974).

[2] L. M. Lederman and D. H. Saxon, Nucl. Phys. B63, 313 (1973).

[3] J. A. Appel *et al.*, preceeding Letter [Phys. Rev. Lett. 33, 719 (1074)].

[4] Such an experiment is scheduled to run at Fermi National Accelerator Laboratory (E-288) in late 1974.

[5] See, for example, G. R. Farrar, California Institute of Technology Report No. CALT-68-422, 1974 (to be published); H. P. Paar and E. A. Paschos, Phys. Rev. D (to be published); R. Savit and M. B. Einhorn, Phys. Rev. Lett. 33, 392 (1974).

[6] J. P. Boymond *et al.*, post-deadline paper presented at the Spring Meeting of the American Physical Society, Washington, D.C., 22–25 April 1974 (unpublished), and Phys. Rev. Lett. 33, 112 (1974).

[7] D. Bintinger *et al.*, post-deadline paper presented at the Spring Meeting of the American Physical Society, Washington, D.C., 22–25 April 1974 (unpublished).

[8] F. W. Busser *et al.* (CERN–Columbia University–Rockefeller University–Saclay Group), in Proceedings of the Seventeenth International Conference on High Energy Physics, London, England, 1–10 July, 1974 (to be published), and private communication.

Neutron-Proton Total Cross Sections from 30 to 280 GeV/c*

Michael J. Longo, Cyril A. Ayre, H. Richard Gustafson, Lawrence W. Jones,
P. V. Ramana Murthy,† and Patrick Skubic
Department of Physics, University of Michigan, Ann Arbor, Michigan 48104

and

Bruce Cork
Lawrence Berkeley Laboratory, University of California, Berkeley, California 74720

(Received 1 July 1974)

We present results of measurements of the n-p total cross section between 30 and 280 GeV/c. The measurements were carried out with a neutron beam by using the standard transmission technique and a liquid-hydrogen target. A total-absorption calorimeter was used to determine the neutron energy. Our measurements, which have an accuracy of ~1%, indicate a smooth rise of approximately 1.5 mb between 50 and 280 GeV/c. The combined n-p and p-p data above 20 GeV/c are well fitted by the expression $\sigma = 38.4 + 0.85 \,|\ln(s/95)|^{1.47}$ mb.

In this article we present the results of a series of measurements of neutron-proton total cross sections from 30 to 280 GeV/c. The measurements were carried out in a neutron beam at the Fermi National Accelerator Laboratory. The standard transmission technique was employed with a 1.2-m liquid-hydrogen target. A total-absorption ionization calorimeter was used to detect the neutrons and measure their energy.

The neutron beam was taken off at an angle of 1 mrad from a beryllium target in the external proton beam. Most of the data were taken with an incident proton momentum of 300 GeV/c; some data were also taken with 200-GeV/c protons. The beam was defined by a steel collimator 1.58 mm in diameter, placed 198 m from the production target. Sweeping magnets before and after the defining collimator removed charged particles from the beam. Two lead filters, one 5 cm thick ahead of the defining collimator and the other 1.3 cm thick following the collimator, removed most of the high-energy γ rays. The

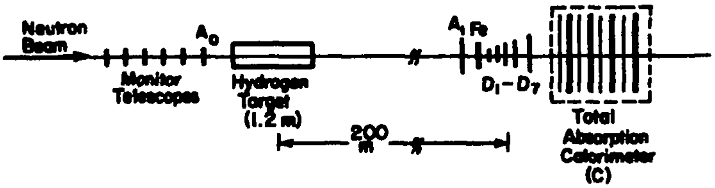

FIG. 1. Schematic of experimental arrangement. *Not to scale.*

neutron spectrum peaked strongly near 230 GeV/*c*. Below about 100 GeV/*c*, the beam contained a significant admixture of $\bar{n}$'s, K^0's, and γ rays.[1]

The experimental arrangement is shown schematically in Fig. 1. Relative beam intensity was measured by two monitor telescopes placed in the beam just ahead of the hydrogen target. Each telescope consisted of a veto counter followed by a 1.6-mm-thick Lucite converter and three small scintillation counters in triple coincidence. The liquid-hydrogen target was a flask 1.2 m long and 5 cm in diameter operated near atmospheric pressure. Mounted next to the target in the same vacuum jacket was an evacuated dummy target. During data taking the two targets were interchanged about once per minute. The length of the target was found to be 121.53 ± 0.03 cm at liquid-hydrogen temperature.[2] The target pressure was monitored continuously so that the hydrogen density could be determined accurately. Sufficient time elapsed between filling the target and taking data to insure that the orthohydrogen-to-parahydrogen transition was complete. Hydrogen-density and vapor-pressure data were taken from a recent U. S. National Bureau of Standards compilation.[3] The uncertainty in the final cross sections due to uncertainties in the target length, density, hydrogen purity, and other target properties is estimated to be $<0.2\%$.

The ratio of the beam transmitted by the hydrogen target to that by the dummy target was measured by placing a 1.25-cm iron converter in the beam, followed by seven circular transmission counters and a total-absorption calorimeter (see Fig. 1). The transmission counters D_1–D_7 ranged from about 1 to 5 cm in radius, compared to the beam radius of approximately 0.2 cm. The smallest counter was in contact with the iron converter and the largest was about 1.3 cm away. Charged particles formed by neutron interactions in the iron converter tend to go nearly along the direction of the incident neutron so that the transmission counters saw a charged-particle distribution which closely approximated the distribution of transmitted neutrons at the iron converter.[4]

The calorimeter was placed just downstream o the transmission counters and provided a measure of the energy of the incident neutron. The calorimeter and its properties are discussed by Jones *et al.*[5] Briefly, it consisted of thirty iron plates, each 30 g cm^{-2} thick, interspersed with thirty scintillators. The light output from the scintillators was optically added and brought to four RCA 8575 phototubes. The summed output pulse from these was roughly proportional to the energy of the incident neutron. Measurements taken with a monoenergetic proton beam show that the calorimeter had an energy resolution (standard deviation) of 12 GeV at 200 GeV and 17 GeV at 300 GeV.

A total of 64 coincidences of various kinds were scaled and recorded. Most of these were of the type $\bar{A}_0\bar{A}_1 D_j D_{j+1} C_i$, where A_0 and A_1 are the veto counters shown in Fig. 1 and C_i represents a pulse from one of seven discriminators which were set to trigger only if the pulse height from the calorimeter exceeded some minimum δ_i. The δ_i corresponded to energies deposited in the calorimeter of approximately 14, 52, 104, 154, 206, 231, and 252 GeV/*c*. The neutron spectrum could thus be divided into the seven momentum ranges given in Table I by subtracting counts in successive momentum bins (e.g., $\bar{A}_0\bar{A}_1 D_j D_{j+1} C_i - \bar{A}_0\bar{A}_1 D_j D_{j+1} C_{i-1}$). The other scaler channels recorded the beam monitors, accidental coincidences of various kinds, singles rates, proton beam intensity, etc.

The scaler counts were recorded on magnetic tape after every beam pulse. This allowed the later editing of occasional bad beam pulses. Data were taken in "runs" lasting from 30 to 90 min. For each run the pulse-to-pulse variations in scaler-to-monitor ratios were checked. These were consistent with expected statistical fluctuations in most cases; if not, a larger error was

TABLE I. Measured cross sections and corrections.

Momentum Range (GeV/c) Min.	Max.	Mean	σ (D_1D_2)[a] (mb)	Typical Rate Correction (mb)	Extrap. to zero solid angle (mb)	Beam Contam. Corr. (mb)	Total Cross section (mb)	Average
252	300	273	40.20±0.22	(−0.8±0.06)	+0.12±0.06		40.32±0.23	
231	252	240	39.58±0.23	(0±0.05)	+0.08±0.04		39.66±0.24	
206	231	215	39.71±0.23	(+0.2±0.06)	+0.08±0.04		39.79±0.24	
154	206	180	39.55±0.19	(+0.3±0.06)	+0.07±0.04		39.62±0.20	39.52±0.18
154	206	175[b]	39.17±0.36	(−0.4±0.22)	+0.04±0.02		39.21±0.36	
104	154	131	38.78±0.22	(+0.25±0.06)	+0.09±0.05	+0.27±0.08	39.14±0.24	39.17±0.19
104	154	133[b]	39.10±0.30	(+0.25±0.20)	+0.06±0.03	+0.05±0.04	39.21±0.30	
52	104	80	37.56±0.25	(+0.3±0.07)	+0.11±0.06	+1.35±0.37	39.02±0.45	38.98±0.33
52	104	80[b]	38.30±0.34	(+0.25±0.20)	+0.22±0.07	+0.43±0.20	38.95±0.40	
14	52	34	34.52±0.38	(+0.20±0.10)	+0.37±0.15	+2.95±0.81	37.84±0.91	38.2±0.9
14	52	34[b]	35.09±0.60	(+0.15±0.41)	+1.5±0.35	+2.23±0.84	38.82±1.09	

[a] Corrected for rate effects.

[b] Taken with a 200-GeV proton beam.

assigned or the data were rejected. The final sample includes data from 80 runs with 300-GeV/c incident protons and 40 runs with 200-GeV/c protons. Over the course of the measurements, which spanned about 10 months, accelerator performance (in particular, duty cycle and beam stability) improved markedly. Despite the wide range of conditions the measured cross sections showed a high degree of consistency after small corrections for a rate effect were made as discussed below. Corrections to the cross sections were ~1% except for the lowest momentum bin. These are described below and numerical values are given in Table I.

Rate effects.—Because we are making cuts on the neutron pulse-height spectrum to determine the neutron energy, any shift in the pulse-height spectrum between target empty and target full will cause a systematic error in the cross sections. Some variation of the cross sections with beam rate was observed. This was due to pileup of pulses from the calorimeter[6] which occurs more frequently with the target empty. This effect is expected to give an error which is a nearly linear function of beam rate. Corrections were made by extrapolating the cross sections linearly to zero rate. Table I gives typical values for this correction.

Finite solid angle.—The measured cross sections were extrapolated to zero solid angle in the usual way. The smallest counter subtended an extremely small solid angle so that this correction was quite small as shown in Table I.

Beam contamination.—The lowest three energy bins contained a nonnegligible admixture of K^0's. The procedure for determining the fraction of K^0's in the beam and the K^0 total cross sections is described in Ref. 1. The lowest energy bin also contained a significant admixture of γ rays and $\bar{n}$'s. The $\bar{n}/n$ ratio was assumed to be the same as the $\bar{p}/p$ ratio in a similar charged beam.[7] Because this assumption is open to question, a large uncertainty was assigned to this correction.

The final cross sections are given in Table I. The assigned errors include the statistical errors and the uncertainties in the rate corrections, the extrapolation to zero solid angle, and the beam contamination, all combined in quadrature. Our results are compared to available n-p data[8] and p-p data[9] in Fig. 2. Our data connect smoothly

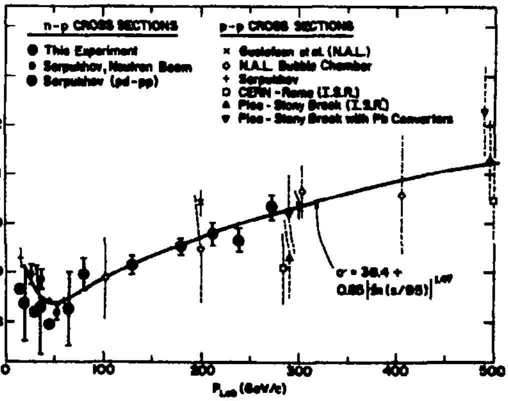

FIG. 2. n-p and p-p total cross sections. Not all the data below 60 GeV/c are shown.

to the lower-energy *n*-*p* data. They indicate a smooth rise of about 1.5 mb in the *n*-*p* total cross section between 50 and 280 GeV/*c*. In general, the *n*-*p* and *p*-*p* total cross sections seem to be approximately equal over the range 30 to 300 GeV/*c*. Our highest-energy *n*-*p* points agree farily well with the *p*-*p* total cross sections at 200 and 300 GeV/*c* measured previously by our group.[10] The combined *n*-*p* and *p*-*p* data above 20 GeV/*c* can be well fitted with the expression $\sigma = 38.4 + 0.85|\ln(s/95)|^{1.47}$ mb.

We would like to express our gratitude to the National Accelerator Laboratory staff for their help and cooperation. We also wish to thank F. Ringia, D. Koch, J. Stone, J. Chanowski, and C. DeHaven for their invaluable help in various aspects of the experiment.

---

*Work supported by the National Science Foundation and the U. S. Atomic Energy Commission.

†On leave from Tata Institute for Fundamental Research, Bombay, India.

[1] For a detailed description of the beam see, M. J. Longo *et al.*, University of Michigan Report No. UM HE 74-18 (unpublished).

[2] The target length was measured at room temperature and at liquid-nitrogen temperature. Since the flask was made of a known aluminum alloy, the length at hydrogen temperature could be easily calculated from thermal-expansion data. The change in length from nitrogen to hydrogen temperature was only 0.2%.

[3] H. M. Roder *et al.*, *Survey of the Properties of the Hydrogen Isotopes below Their Critical Temperatures*, U. S. National Bureau of Standards Technical Note No. 641 (U. S. GPO, Washington, D. C. 1973).

[4] Because of the finite opening angle of the cone containing the charged secondaries, the effective size of the transmission counters was somewhat larger than their geometrical size. The effective size was determined by scanning the beam stepwise across the iron converter. This gave the probability of detecting a neutron as a function of distance from the beam axis.

[5] L. W. Jones *et al.*, University of Michigan Report No UM HE 73-24 (to be published).

[6] This is a partial coincidence of two pulses from the calorimeter which shifts one or both pulses to a higher energy bin.

[7] W. F. Baker *et al.*, "Measurement of π^+, $K^\pm$, p, and $\bar{p}$ Production by 200 and 300 GeV/*c* Protons" (to be published).

[8] Serpukhov neutron-beam data: A. Babaev *et al.*, Institute of Theoretical and Experimental Physics Report No. ITEP-11 (to be published). Serpukhov *pd*-*pp* data: Yu. P. Gorin *et al.*, Sov. J. Nucl. Phys. 17, 157 (1973).

[9] References to the *p*-*p* total cross section data are given by H. R. Gustafson *et al.*, Phys. Rev. Lett. 32, 441 (1974). The 300-GeV/*c* bubble-chamber measurement is that of A. Firestone *et al.*, Phys. Rev. D (to be published). *Their result is 40.68± 0.55 mb.*

[10] Gustafson *et al.*, Ref. 9.

Pion-Nucleon Form Factor in the Chew-Low Theory*

C. B. Dover
Brookhaven National Laboratory, Upton, New York 11973

and

D. J. Ernst, R. A. Friedenberg, and R. M. Thaler
Physics Department, Case Western Reserve University, Cleveland, Ohio 44106

(Received 1 July 1974)

We suggest a form of the off-shell pion-nucleon amplitude which is motivated by simple field-theoretic considerations. This amplitude contains a momentum-dependent form factor $v(k)$ which we determine by solving an inverse scattering problem, using the experimental phase shifts and inelasticities as input.

Phenomenological pion-nucleon interactions have been of the form of zero-range interactions,[1] of separable energy-independent potentials,[2] and of separable energy-dependent potentials.[3] Each approach yields a different off-shell two-body T matrix, even though the on-shell data may be reproduced The sensitivity of the pion-nucleus cross sections to the off-shell behavior has been explored by various authors.[4]

Here, we attempt a somewhat more fundamental view. We seek as much guidance as possible from an underlying field theory, even though such guidance may be incomplete. We use a nonrelativistic pion-nucleon interaction Hamiltonian $H_{\rm int}$ which couples the pion field linearly to the nucleon density, viz.,

$$H_{\rm int}=(if/\mu)\sum_{p,k,\alpha}\sum_{\nu,\nu'}v(k)(\vec{\sigma}\cdot\vec{k})_{\sigma\sigma'}(\tau_\alpha)_{\tau\tau'}a_{p+k,\nu'}{}^\dagger a_{p\nu}Q_{k\alpha}, \tag{1}$$

where $Q_{k\alpha}=[2\omega_\pi(k)]^{-1/2}(B_{k\alpha}+B_{-k\alpha}{}^\dagger)$; $B_{k\alpha}{}^\dagger$ and $a_{k\nu}{}^\dagger$ are the creation operators for a pion or nucleon of momentum k and spin-isospin state α or $\nu=\{\sigma,\tau\}$, respectively. The *ad hoc* form factor $v(k)$ provides a high-energy cutoff. Our objective is to obtain $v(k)$ directly from the πN-scattering data. Thus we view $H_{\rm int}$ as a semiphenomenological model. The flexibility allowed by $v(k)$ suffices to enable the model to establish contact with πN data. Such a treatment is not meant to replace a more fundamental theory.[5]

In the static limit, this Hamiltonian leads to a Low equation for the pion-nucleon scattering amplitude,[6]

$$\langle p|T(\omega_\pi)|q\rangle=-\sum_n[\langle p|T^\dagger|n\rangle\langle n|T|q\rangle/(E_n-\omega_\pi-i\epsilon)+\langle q|T^\dagger|n\rangle\langle n|T|p\rangle/(E_n+\omega_\pi)], \tag{2}$$

where $|n\rangle$ and E_n represent a complete set of states and their corresponding energies. These states $|n\rangle$ correspond to a physical nucleon plus n physical pions. If we now truncate the sum over n to include only the single-nucleon and the nucleon-plus-*one*-pion intermediate states (thereby ignoring pion production in pion-nucleon collisons), and further ignore $n>0$ contributions to the crossing term, we can write the solution to the Low equation as[6,7]

$$\langle q|T_\alpha(\omega_\pi)|q'\rangle=\left(-\frac{2\pi\lambda_\alpha qq'v(q)v(q')}{\omega_\pi^{\,2}}\right)\left(1-\frac{\lambda_\alpha\omega_\pi}{\pi}\int_0^\infty\frac{p^4dp}{\omega_\pi^{\,3}(p)}\,\frac{v^2(p)}{\omega_\pi(p)-\omega_\pi-i\epsilon}\right)^{-1}, \tag{3}$$

where $\alpha=\{2J,2T\}$ indexes the spin-isospin channel and $\lambda_\alpha=(f^2/4\pi)(2/3\mu^2)[-4,-1,-1,2]$ for $\alpha=[11,13,31,33]$. The *off-shell* dependence of T_α indicated by Eq. (3) cannot be reproduced by an *energy-independent* potential, although an *energy-dependent* potential can be found which will do so.[8]

We would like to determine $v(q)$ from the pion-nucleon elastic-scattering data. However, Eq. (3) is not adequate for that purpose, since it yields real phase shifts beyond the pion-production threshold. Thus, one must go beyond the one-meson approximation and take account of inelastic channels.

We propose to replace the energy-independent coupling constant λ_α, by $\lambda_\alpha\gamma_\alpha(\omega_\pi)$, where $\gamma_\alpha(\omega_\pi)$ is a complex function.[9] This leads to a modification of Eq. (3) in which the denominator becomes

$$D_\alpha(\omega(q))=\frac{1}{\gamma_\alpha(\omega_\pi(q))}-\frac{\lambda_\alpha\omega_\pi(q)}{\pi}\int_0^\infty\frac{p^4dp}{\omega_\pi^{\,3}(p)}\,\frac{v^2(p)}{\omega_\pi(p)-\omega_\pi(q)-i\epsilon}. \tag{4}$$

Such a replacement results, in the static limit, from the inclusion of a large subset of the neglected multipion terms on the right-hand side of Eq. (2). Thus our approximation is similar to the Chew-Low approximation with a much less radical truncation of Eq. (2). However, this argument is not compelling, because the static limit becomes a poorer approximation as more pions are produced.

Inclusion of the factor $\gamma_\alpha(\omega_\pi)$ permits us to satisfy unitarity, so that the T matrix will have the appropriate discontinuity across the inelastic cut. As a consequence of unitarity, $\gamma_\alpha(\omega_\pi)$ and $[\gamma_\alpha(\omega_\pi)]^{-1}$ satisfy dispersion relations. We assume that $\gamma(\omega_\pi)\to1$ as $\omega_\pi\to\infty$. The behavior of $\gamma(\omega_\pi)$ is discussed in Ref. 3 for potential scattering. Similar considerations obtain here. Thus we write

$$\frac{1}{\gamma_\alpha(\omega_\pi)}=1-\frac{1}{\pi}\int\frac{{\rm Im}[1/\gamma_\alpha(\omega_\pi')]}{\omega_\pi-\omega_\pi'+i\epsilon}\,d\omega_\pi'. \tag{5}$$

The above theory is derived for infinitely massive nucleons. We wish, however, to make contact with the scattering from finite-mass nucleons. Customarily, this is done by identifying q in Eqs. (3) and (4) as the momentum of the pion in the c.m. frame. With this identification, the T matrix satisfies the unitarity relation

$$T_\alpha(q)-T_\alpha{}^\dagger(q)=-\frac{i}{\pi}[q\omega_\pi(q)]T_\alpha(q)T_\alpha{}^\dagger(q)\left(1-\frac{{\rm Im}[1/\gamma(\omega_\pi(q))]}{\lambda_\alpha q^3v^2(q)/\omega_\pi(q)}\right). \tag{6}$$

The physical T matrix for the scattering from a finite-mass nucleon, however, satisfies a unitarity relation of the form of Eq. (6), with $[q\omega_\pi(q)]$ replaced by $[q\omega_\pi(q)]\omega_N(q)/\omega(q)$, where $\omega(q)=\omega_\pi(q)+\omega_N(q)$

$=(q^2+m_\pi^2)^{1/2}+(q^2+m_N^2)^{1/2}$. To make contact with the data, we thus modify Eqs. (3) and (4) to satisfy the finite-mass unitarity relation. This can be done by replacing $\omega_\pi(q)$ in Eqs. (3) and (4) by $\tilde{\omega}_\pi(q)=\omega(q)-m_N$.

With this modification, we may invert Eqs. (3) and (4) to determine $v(q)$ from the elastic-scattering T matrix. Using Eqs. (3) and (4) we may write

$$\operatorname{Im}\frac{1}{\gamma_\alpha(\tilde{\omega}_\pi(q))}=\frac{\lambda_\alpha}{\pi}\,\frac{q^2v^2(q)}{\tilde{\omega}_\pi^{\,2}(q)}\left[-\operatorname{Im}\left(\frac{2\pi^2}{T_\alpha(\tilde{\omega}_\pi(q))}\right)+\frac{\pi q\,\omega_\pi(q)\omega_N(q)}{\omega(q)}\right]. \tag{7}$$

If we introduce the inelasticity parameter $\hat{\eta}$ and the real phase shift $\hat{\delta}$ via[3]

$$T_\alpha(q)=-[2\pi\omega(q)/q\,\omega_\pi(q)\omega_N(q)]\hat{\eta}_\alpha(q)\exp[i\hat{\delta}_\alpha(q)]\sin\hat{\delta}_\alpha(\epsilon), \tag{8}$$

we find

$$D_\alpha(\omega)=1-\frac{\lambda_\alpha}{\pi}\int_0^\infty\frac{p^4\,dp}{\tilde{\omega}_\pi^{\,2}(p)}\,\frac{v^2(p)[1-\hat{\eta}_\alpha^{-1}-(\omega-m_N)/\tilde{\omega}_\pi(p)]}{\omega-\omega(p)+i\epsilon}. \tag{9}$$

Since $D_\alpha(\omega)$ does not approach unity as $\omega\to\infty$, we consider the ratio $D_\alpha(\omega)/D_\alpha(\infty)$. The analytic structure of $D_\alpha(\omega)$ implies that the logarithm of this ratio satisfies a dispersion relation, i.e.,

$$\operatorname{Re}\ln\frac{D_\alpha(\omega)}{D_\alpha(\infty)}=\frac{1}{\pi}\,\mathrm{P}\int d\omega'\,\frac{\operatorname{Im}\ln[D_\alpha(\omega')/D_\alpha(\infty)]}{\omega'-\omega}. \tag{10}$$

Using the relation $\operatorname{Im}\ln[D_\alpha(\omega(p))/D_\alpha(\infty)]=-\hat{\delta}_\alpha(p)$, we find that Eq. (10) has the solution

$$D_\alpha(\omega)/D_\alpha(\infty)=\exp\{\pi^{-1}\textstyle\int\hat{\delta}_\alpha(p)\,d\omega(p)/[\omega-\omega(p)+i\epsilon]\}. \tag{11}$$

If we equate the imaginary parts of Eq. (9) and (11) we find

$$\frac{v^2(q)}{D_\alpha(\infty)}=\frac{\hat{\eta}_\alpha\omega_\pi(q)\omega(q)}{\lambda_\alpha q^3\omega_N(q)}\sin\hat{\delta}_\alpha(q)\exp\left(\frac{1}{\pi}\mathrm{P}\int\frac{\hat{\delta}_\alpha(\omega')d\omega'}{\omega(q)-\omega'}\right). \tag{12}$$

The limit of Eq. (9) then yields

$$D_\alpha(\infty)=1+\frac{\lambda_\alpha}{\pi}D_\alpha(\infty)\int_0^\infty\frac{p^4\,dp}{\tilde{\omega}_\pi^{\,3}(p)}\,\frac{v^2(p)}{D_\alpha(\infty)}. \tag{13}$$

Equations (12) and (13) represent the solution of the problem.

We have numerically evaluated the form factor $v(q)$ for the {3, 3} channel according to Eqs. (12) and (13). We have used the CERN theoretical fit[10] for the phase shifts for c.m. momentum less than 692 MeV/c, and have attached a tail of the form $A/(p-p_0)^2$ to bring the phase shifts $\hat{\delta}(p)$ smoothly to zero. The phase shift $\hat{\delta}(p)$ and inelasticity parameter $\hat{\eta}(p)$ are depicted in Fig. 1.

In Fig. 2, we have plotted $[\gamma(\tilde{\omega}_\pi=0)]^{1/2}v(q)$. We

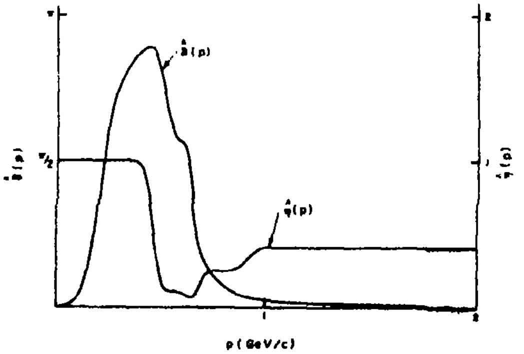

FIG. 1. Experimental parameters $\hat{\delta}(p)$ and $\hat{\eta}(p)$ as defined in Eq. (8).

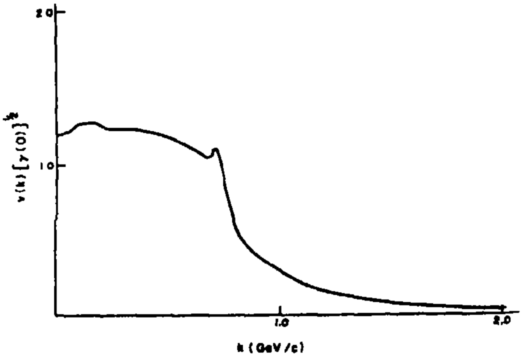

FIG. 2. Form factor $[\gamma(0)]^{1/2}v(k)$ as calculated from Eqs. (12) and (13). The values of $\hat{\delta}$ and $\hat{\eta}$ used in the calculation are depicted in Fig. (1).

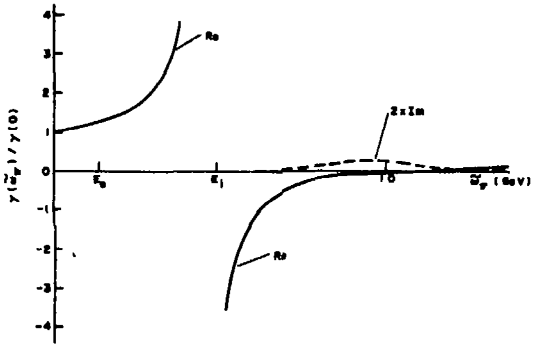

FIG. 3. Energy dependent coupling constant $\gamma(\tilde{\omega}_\pi)/\gamma(0)$. The elastic threshold is marked by E_0 and the inelastic threshold by E_1. The solid line is the real part of $\gamma(\tilde{\omega}_\pi)/\gamma(0)$ and the dashed line is the imaginary part.

plot $[\gamma(\tilde{\omega}_\pi=0)]^{1/2}v(q)$, as this yields the residue of the T matrix [cf. Eqs. (3) and (4)] as $\tilde{\omega}_\pi$ approaches zero. We have taken $f^2/4\pi=0.08$, and find that inclusion of the inelastic cut in the T matrix yields an effective coupling constant of $(f^2/4\pi)\times\gamma(\tilde{\omega}_\pi=0)v^2(0)=0.115$.

That this value differs from 0.08 is not surprising if we look at $\gamma(\tilde{\omega}_\pi)$ as shown in Fig. 3. At low energies $\gamma(\tilde{\omega}_\pi)$ varies rapidly with energy. The extrapolation to $\tilde{\omega}_\pi=0$ is, therefore, sensitive to details of the theory (such as how one includes the finite mass of the nucleon or how one treats the high-energy tail of the phase shifts). Thus, we do not place undue emphasis on the details of these calculations at this time, but rather present a phenomenology which is consistent with the Chew-Low theory and can also fit the elastic-scattering data.

From Fig. 3, we observe that $\gamma(\tilde{\omega}_\pi)$ has a singularity between the resonance and the inelastic threshold. This singularity in $\gamma(\tilde{\omega}_\pi)$ does not imply any special properties of the elastic-scattering T matrix. Again, the existence and position of this singularity is sensitive to details of our model, and perhaps one should not ascribe any special significance to it.

At the same time it is important to not that $v(q)$ (at momenta below ~800 MeV/c) is insensitive to these details, so that we have greater confidence in the form factor. But it is just this form factor which we seek to determine in order to tie down the interaction Hamiltonian of Eq. (1). Moreover, it is this interaction Hamiltonian which we require to build a theory of pion-nucleus scattering.

Retardation effects[11] and the energy dependence of the pion-nucleon interaction might be expected to play a more important role in pion-nucleus interactions than in nucleon-nucleus interactions. For the nucleon-nucleon case, field theory suggests that an energy-independent interaction is plausible. For the pion-nucleon case, however, field theory does not yield energy-independent potentials. Therefore, we have attempted an approach to the pion-nucleon interaction which is capable of fitting exactly the pion-nucleon data and of maintaining some contact with an underlying field theory. We suggest that studies of pion-nucleus scattering be based on an interaction Hamiltonian of the type we propose, rather than upon two-body potentials.

---

*Work supported in part by the U. S. Atomic Energy Commission and the National Science Foundation.

[1] L. S. Kisslinger, Phys. Rev. 98, 761 (1955); M. M. Sternheim and E. H. Auerbach, Phys. Rev. Lett. 25, 1500 (1970); see also M. Sternheim, in LASL Report No. LA-5443-C, 1973 (unpublished), p. 43.

[2] M. G. Piepho and G. E. Walker, Phys. Rev. C 9, 1352 (1974); R. H. Landau and F. Tabakin, Phys. Rev. D 5, 2746 (1972); S. C. Phatak, F. Tabakin, and R. H. Landau, Phys. Rev. C 7, 1803 (1973); see also G. E. Walker, in LASL Report No. LA-5443-C, 1973 (unpublished), p. 72.

[3] D. J. Ernst, J. T. Londergan, E. J. Moniz, and R. M. Thaler, to be published.

[4] R. R. Silbar and M. M. Sternheim, Phys. Rev. C 6, 765 (1972); E. J. Moniz, Phys. Rev. C 7, 1750 (1973); J. Hüfner, Nucl. Phys. B58, 55 (1973); R. H. Landau and F. Tabakin, to be published.

[5] P. Nath and S. S. Kere, in LASL Report No. LA-5443-C, 1973 (unpublished), p. 220.

[6] G. F. Chew and F. E. Low, Phys. Rev. 101, 1570 (1956); G. C. Wick, Rev. Mod. Phys. 27, 339 (1955).

[7] C. B. Dover and R. H. Lemmer, Phys. Rev. C 7, 2312 (1973).

[8] C. B. Dover, D. J. Ernst, and R. M. Thaler, Phys. Rev. Lett. 32, 557 (1974).

[9] J. T. Londergan, K. W. McVoy, and E. J. Moniz, to be published.

[10] D. J. Herndon, A. Barbaro-Galtieri, and A. H. Rosenfeld, Lawrence Radiation Laboratory Report No. UCRL-20030, 1970 (unpublished).

[11] C. B. Dover, J. Hüfner, and R. H. Lemmer, Ann. Phys. (New York) 66, 248 (1971).

PHYSICAL REVIEW
LETTERS

VOLUME 33 23 SEPTEMBER 1974 NUMBER 13

Characterization of Charge States of Energetic Ions in Solids from Associated *K* X-Ray Production*

Sheldon Datz and B. R. Appleton
Oak Ridge National Laboratory, Oak Ridge, Tennessee 37830

and

J. R. Mowat, Roman Laubert,† R. S. Peterson, R. S. Thoe, and I. A. Sellin
University of Tennessee, Knoxville, Tennessee 37916, and
Oak Ridge National Laboratory, Oak Ridge, Tennessee 37830

(Received 10 June 1974)

The strong projectile–charge-state dependence of *K* x-ray production in gases establishes a charge-state scale for ions penetrating solids. Si *K* x-ray cross sections in gaseous SiH_4 were compared to those in solid Si for 40-MeV O (6+ to 8+) and 86-MeV Ar (6+ to 16+) projectiles. For Ar an effective charge of 11 ± 1 is found compared to an emergent charge of 14.8 ± 0.5. The result is discussed in terms of alternate models for steady-state excitation in solids.

The states of energetic ions penetrating solids have long been a subject of considerable study. In 1951 Lassen[1] found that the charge states of heavy ions emerging from solids were considerably higher than those emerging from gaseous targets. However, it is also found that the electronic stopping powers in solid media are essentially the same as those measured in gases, and the "effective charge" derived from stopping powers in solids is that which is observed for ions in gases.[2,3] The first of two solutions to this disparity suggests that dynamical screening by electrons in the solid tends to neutralize the excess charge on the ion moving in the solid.[4,5] However, at velocities $v \gg v_0$ the effect of screening should be small, and recent experiments with channeled oxygen ions indicate that screening electrons are ineffective in altering the stopping power of an ion in a given charge state.[6] An alternative explanation was proposed by Betz and Grodzins[7] who suggested that the actual charge state in the solid is much like that in the gas but that many of the bound electrons are in highly excited states and are lost by Auger events after emergence. Hence, comparison of charge states inside the solid with emergent charge states provides an experimental test of these theories. Related studies of exit-channel effects[8] in quasimolecular excitation and of x-ray satellite structure generated by low-energy ions in solids[9] yield information concerning average *excitation* states but do not permit direct determination of effective *charge* states in solids.

We utilize the observation that x-ray production cross sections for high-velocity (1–4 MeV/nucleon) ions are highly sensitive to the charge state of the projectile ion.[10] We reasoned that comparing the x-ray production cross sections in solid and gaseous targets containing the same target element would provide a measure of the charge state of the penetrating ion.[11] The results of these experiments are also critical to interpretation of measured heavy-ion–induced x-ray cross sections in solid targets.

Beams of 86-MeV Ar^{6+} from the Oak Ridge isochronous cyclotron and 40-MeV O^{6+} from the

Copyright © 1974 by
The American Physical Society

Oak Ridge tandem Van de Graaff accelerator[11] were passed through foils for further stripping. A pure-charge-state beam was then magnetically selected and entered a differentially pumped windowless gas cell. The cell could be filled with SiH_4 gas at pressures of ~20 mTorr, and x rays produced were counted by a Si(Li) detector viewing the collision region at 90° to the beam. The maximum estimated charge exchange in the gas was always ≤5% so that single-collision conditions with ions of known charge state were obtained. The measurement techniques have been fully described previously.[10] The solid targets consisted of thin Si films (7–50 μg/cm^2) deposited on a 150-μg/cm^2 plastic backing which could be positioned at the center of the evacuated gas cell. The Si surface faced the beam and was tilted at an angle of 36° so that the Si(Li) detector could view the Si surface directly. In the Ar experiments an additional Si foil could be inserted about 30 cm upstream of the cell. An entrant charge-state distribution characteristic of that emerging from solid Si could thus be prepared. The particle current was alternatively determined by Rutherford scattering from a gold foil placed behind the cell, or by a separated pumped, electrically and magnetically guarded, Faraday cup.

Charge-state distributions for the oxygen ions emerging from Si were measured by using electrostatic analysis and a position-sensitive detector. The charge fractions F_i were 0.2, 0.7, and 0.1 for 6+, 7+, and 8+, respectively. The charge-state distributions for Ar ions emerging from a Si target were obtained by measuring the current at the focus of a magnetic analyzer following a Si stripper foil. The charge fractions were 0.11 (13+), 0.27 (14+), 0.34 (15+), and 0.20 (16+), to an estimated accuracy of better than ± 0.03.

Results for O ions are shown in Fig. 1. With the gas target the Si K x-ray cross section varies by a factor of ~2.5 as the incident ion is changed from 6+ to 8+. A smaller variation (~60%) is observed when a solid target is used. This effect of incident charge state in thin solid targets has been recently reported for O ions in Al by Brandt *et al.*,[5] who found that the effect diminishes as the foil thickness is increased, and attributed this charge-state effect to dynamic screening. An alternative explanation could lie in the inequilibrium of the ion charge state. Capture and loss cross sections for 40-MeV O ions in Ar, for example, are on the order[12] of 2×10^{-17} cm^2. Thus the Si target thickness (~2 $\times10^{17}$ atoms/cm^2) should be insufficient to attain equilibrium.

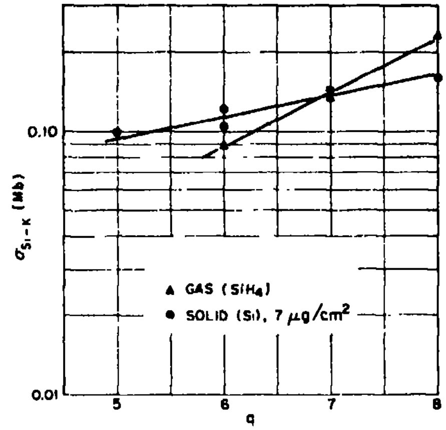

FIG. 1. Si K x-ray production cross section in megabarns produced by 40-MeV O-ion bombardment of SiH_4 and solid Si as a function of incident-ion charge state.

The observed charge-state dependence is expected to evolve with increasing target thickness from the rising straight line observed for thin, gas targets to a horizontal straight line at equilibrium thickness. The two lines representing the extremes in density should intersect at the projectile charge corresponding to the effective equilibrium charge in the solid. The emergent equilibrium charge-state distribution of 40-MeV O is strongly peaked at 7+. At equilibrium, the input-charge dependence of the x-ray cross section would be a horizontal line intersecting the SiH_4 line at charge 7+, if the effective charge in the solid were equal to the most probable emergent charge. Because the cross sections for leaving a charge state of 7+ ($\sigma_{7,6}$ and $\sigma_{7,8}$) should be lower at this energy than those for attaining a charge of 7+ (i.e., $\sigma_{8,7}$ and $\sigma_{6,7}$), one would expect near coincidence with the 7+ value of the gas target for incident 7+ ions even before charge-state equilibrium is attained. Arguments based on dynamic screening in which the number of bound electrons are not considered lead to almost the *same* expected *effective-charge state.* Here

$$q_{\rm scr} \approx Z_{\rm core}(1-\gamma v_{\rm F}/v), \qquad (1)$$

where $v_{\rm F}$ is the target-electron Fermi velocity ($\sim v_0$), $Z_{\rm core}$ is the core-electron–screened nuclear charge, and γ is an electron "enhancement

TABLE I. Summary of the data. Bracketed values are for 40-MeV O; unbracketed values are for 86-MeV Ar.

	X-ray data	Measured distribution	Semiempirical theory[a]
Mean charge emerging from solid	14 ± 0.5	14.8 ± 0.3 [6.9 ± 0.2]	13.7 [7.6]
Mean charge emerging from gas			12.5 [7.4]
Effective charge state in solid	11 ± 1 [7.0 ± 0.25]		

[a] Ref. 14.

factor"[5] ~1. For 40-MeV O, $q_{\rm scr} \simeq 7.2$.

For relatively low-Z ions such as oxygen only a slight dependence of the emergent charge state on the medium (solid or gas) is expected.[13] The semiempirical calculations of Dmitriev and Nikolaev[14] give 7.4 and 7.6 for the expected emergent charge (Table I). From our charge-distribution measurements we obtain $\bar{q} = 6.9$, and the effective charge state ($q_{\rm eff}$) indicated by the measured x-ray cross section is 7 ± 0.25. Hence, the oxygen results are consistent with expectations and support the validity of our method.

The different situation for Ar ions is shown in Fig. 2. The cross sections for Si K x-ray emission vary by a factor of ~7 for Ar charges ranging from 6+ to 16+. The cross section for Si K x-ray emission from solid Si was found to be 0.095 ± 0.005 Mb and was essentially independent of input charge and target thickness. This cross section corresponds to an effective charge state of 11 ± 1 and is to be compared with our measured emergent mean charge of 14.8. The corresponding predictions of Dmitriev and Nikolaev[14] are 13.7 for solids and 12.5 for gases.

A useful experimental check was made by preparing an equilibrium-distribution beam in the upstream Si foil referred to above. This equilibrium beam yielded a mean cross section σ_m in SiH_4 approximately equal to that anticipated on the basis of a sum of the single-charge-state cross sections weighted by the corresponding F_i. When the equilibrium beam was passed through a solid Si target, no difference was observed in the cross section derived from the results for single-charge-component beams. From this prefoil experiment alone it can be seen that the cross section in a solid target is a factor of ~2 lower than that anticipated for the measured emergent charge.

One can exclude three unrelated effects which might be expected to cause significant differences in the observed yields from solid and gaseous targets. The possibility of energetic Si recoils causing additional Si K vacancies in the solid can be assessed by using information available on Al-Al ($Z = 13$) collision-induced K x rays.[15] Here a threshold is observed at 150 keV; the cross section rises rapidly to 5×10^{-21} cm^2 at 300 keV. The impact parameter b required to impart $\Delta E = 200$ keV to a Si atom by an ion with energy $E \simeq 2$ MeV/nucleon can be estimated from

$$b = Z_1 Z_2 e^2 M_1^{1/2} (M_2 E\,\Delta E)^{-1/2}$$

to be $\sim 4\times10^{-12}$ cm, which clearly yields cross sections negligible compared with processes having cross sections on the order of 10^{-19} cm^2. One must also take into account possible fluores-

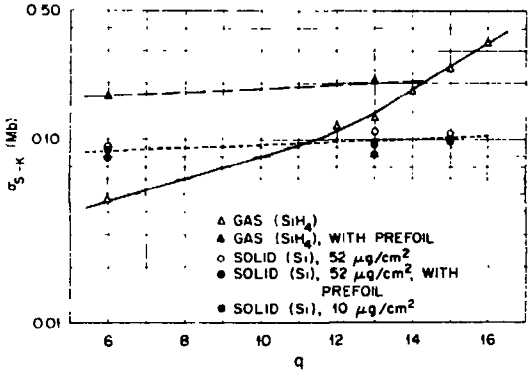

FIG. 2. Si K x-ray production cross section produced by 86-MeV Ar-ion bombardment of SiH_4 and solid Si as a function of incident-ion charge state. The "prefoil" points denote experiments in which the beam passed through a Si foil before entering the target.

cent-yield differences for struck atoms recoiling in solids as opposed to vacuum, which are mainly determined by the corresponding L-shell electron configurations. That these differences are insignificant is indicated by the fact that the K-shell ionization is in the diabatic region (i.e., $\hbar v/I > r_K$) so that the impact-parameter dependence of the probability of ionization is peaked[16] near the K-shell radius ($r_K = 0.06$ Å). At this distance the energy transfer is only ~10 eV so that even interactions of the L shell of the recoiling Si with lattice atoms (which could affect the K fluorescence yield) are not possible. Finally, the effect of binding electrons (in the M shell) is not expected to be significant, especially since the Si valence electrons in both SiH_4 and solid Si are in the sp^3 configuration.

The results for O ions, exhibiting agreement with expectations, indicate that other possible solid-state effects on the Si K x-ray yield are small. The results for Ar at the same energy per nucleon clearly indicate a lower effective charge for the ion while in the solid than is observed in the emergent beam. The screening model[5] could be used to explain the effect but would require an unrealistically high value of $\gamma = 3$ with $Z_{\text{core}} = 16$ in Eq. (1). The model of Betz and Grodzins[7] would account for the difference by the loss of bound electrons upon emergence by Auger or autoionizing processes. However, the additional electrons present while the ion is in the solid must be in close enough proximity to the Ar nucleus (e.g., L shell) to act in reducing the Si atom's K ionization cross section; and, in the absence of K vacancies, there is no mechanism for autoionizing L electrons. Although the mechanism for charge-state change remains obscure, the work described herein constitutes direct evidence that high-velocity ions in solids have lower charge states than those observed in emergent beams.

---

*Work supported in part by the U. S. Office of Naval Research, the National Science Foundation, and the National Space and Aeronautics Administration; and b Union Carbide Corporation under contract with the U. Atomic Energy Commission.

†Permanent address: New York University, New York, N. Y. 10003.

[1] N. O. Lassen, Kgl. Dansk. Vidensk. Selsk., Mat.-Fys. Medd. 26, No. 5, No. 12 (1951).

[2] P. E. Pierce and M. Blann, Phys. Rev. 173, 390 (1968).

[3] M. D. Brown and C. D. Moak, Phys. Rev. B 6, 90 (1972).

[4] N. Bohr and J. Lindhard, Kgl. Dansk. Vidensk. Selsk. Mat.-Fys. Medd. 28, No. 7 (1954).

[5] W. Brandt, R. Laubert, M. Mourino, and A. Schwarzschild, Phys. Rev. Lett. 30, 358 (1973).

[6] S. Datz, B. R. Appleton, J. A. Biggerstaff, M. D. Brown, H. F. Krause, C. D. Moak, and T. S. Noggle, in "Atomic Collisions in Solids V," edited by S. Datz, B. R. Appleton, and C. D. Moak (Plenum, New York, to be published).

[7] H. Betz and L. Grodzins, Phys. Rev. Lett. 25, 211 (1970).

[8] H. O. Lutz, H. J. Stein, S. Datz, and C. D. Moak, Phys. Rev. Lett. 28, 8 (1972).

[9] R. C. Der, R. J. Fortner, R. J. Kavanagh, and J. D. Garcia, Phys. Rev. Lett. 27, 1631 (1971).

[10] J. R. Mowat, I. A. Sellin, D. J. Pegg, R. S. Peterson M. D. Brown, and J. R. Macdonald, Phys. Rev. Lett. 30, 289 (1973); R. Mowat, I. Sellin, P. M. Griffin, D. J. Pegg, and R. S. Peterson, Phys. Rev. A 9, 644 (1974).

[11] Results for 40-MeV O ions in Si and SiH_4 are given by J. R. Mowat, B. R. Appleton, J. A. Biggerstaff, S. Datz, C. D. Moak, and I. A. Sellin, in "Atomic Collisions in Solids V," edited by S. Datz, B. R. Appleton, and C. D. Moak (Plenum, New York, to be published).

[12] J. R. Macdonald and F. W. Martin, Phys. Rev. A 4, 1965 (1971).

[13] H. D. Betz, Rev. Mod. Phys. 44, 465 (1972).

[14] I. S. Dmitriev and V. S. Nikolaev, Zh. Eksp. Teor. Fiz. 47, 615 (1964) [Sov. Phys. JETP 20, 409 (1965)].

[15] K. Taulbjerg, B. Fastrup, and E. Laegsgaard, Phys. Rev. A 8, 1814 (1973).

[16] J. M. Hansteen and O. P. Mosebekk, Nucl. Phys. A201, 541 (1973).

Penning-Trap Technique for Studying Electron-Atom Collisions at Low Energy*

Michael D. McGuire and E. Norval Fortson
Department of Physics, University of Washington, Seattle, Washington 98195

(Received 8 July 1974)

In a new technique for studying electron collisions, the electrons are confined by electromagnetic fields and exposed to a known low density of atoms or molecules. Collision rates are measured by electron diffusion in the trap. The use of spin-oriented atoms allows triplet and singlet contributions to be separated. Results of such studies are reported for room-temperature collisions of electrons with potassium atoms and with nitrogen molecules.

We have developed a new and general method of studying elastic collisions of electrons with atoms and molecules at electron energies below 0.1 eV. The electrons are confined in a Penning electric- and magnetic-field trap which allows the bolometric method of Dehmelt and Walls[1,2] to be used to observe them and to thermalize them electrically with an external heat bath which defines their temperature. When atoms or molecules are introduced into the trap region, the electrons will spread out in the trap by collision-induced diffusion. The diffusion rate is proportional to the appropriately averaged collision cross section. In contrast to conventional methods[3] of studying electron collisions in this energy range, the present method can be used readily with atoms and molecules at low vapor density and thus with atomic beams and with condensable vapors. An important consequence is that the spin dependence of electron collisions with paramagnetic atoms can be studied by passing a spin-oriented beam of the atoms through the trap.

For our first investigations, we have studied elastic collisions with alkali atoms and (for calibration purposes) with gaseous atoms and molecules. We report the first measurement of room-temperature electron scattering from potassium atoms. We have also seen a strong spin dependence in the scattering from potassium, which reveals the relative contributions of the singlet and triplet components at these low energies.

Our apparatus is similar to one used in the $g-2$ experiments of Gräff and co-workers[4] and to one used in early experiments by Dehmelt.[5] A schematic is shown in Fig. 1. At one end of a differentially pumped vacuum envelope is the Penning trap with holes in it to allow an atomic beam to pass through. At the other end is the beam source and a state-selector magnet which focuses atoms of definite spin orientation into the trap. Through a controlled leak, noncondensable gases also may be admitted into the trap region.

The trap and its operation have been described thoroughly elsewhere.[1,2,6] Briefly it is a combination of a uniform z-axis magnetic field and an electric potential produced by electrodes in the shape of conjugate hyperboloids of revolution about the z axis. This potential confines the electrons in a harmonic well along the z axis. The motion in the x-y plane for the large magnetic fields used is the superposition of high-frequency small-radius cyclotron motion on low-frequency large-radius magnetron motion. The electrons are injected along the z axis near the trap center and those that are trapped (about 10^4 electrons in these experiments) self-thermalize rapidly by electron-electron collisions. The overall temperature of the electrons comes to equilibrium by electrical induction with the electrical temperature of an LC circuit. This circuit is formed by an inductor connecting the endcaps of the trap and in resonance with the capacitance of the trap at the z-axis electron frequency (typically 30 MHz).

The state of the electrons in the trap is detected by their effect on the level of random noise of

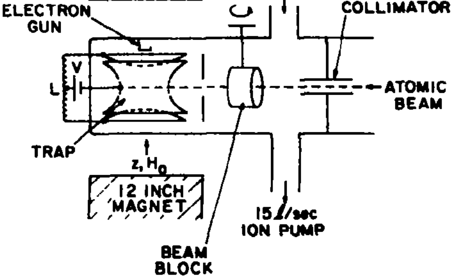

FIG. 1. Schematic view of apparatus. Trap radius $R_0 = 2.5$ cm.

the *LC* circuit. This noise signal decreases as the initially hot electrons in vacuum come to equilibrium with the *LC* circuit. Once thermalized, the electrons cause a lower noise signal than in their absence because they shunt the *LC*-circuit impedance. The electron temperature is equal to the ambient temperature of the trap and *LC* circuit, unless external noise is applied to this circuit. The noise level with a given number of electrons in the trap can thus be calibrated to give the electron temperature. We have checked this calibration by thermalizing the electrons in a different way, viz., by introducing molecules with which the electrons thermalize by exchanges of energy with the molecular rotational levels.[7]

In vacuum the electrons can remain trapped indefinitely. If atoms or molecules are present, the electrons will scatter from them and diffuse radially across the magnetic field in the trap. They will ultimately be lost at the electrodes, but the radial anharmonicity of the trap causes the electrons to be lost from the detection bandpass much sooner. As a result the noise signal will rise to the empty-trap level as shown in Fig. 2. The rate of this rise can be related to the collision rate and hence to the cross section of interest if the density of scattering atoms is known. This method is most useful however for obtaining relative collision rates. For example, we can compare the diffusion loss rates for different atomic species, or for different spin orientations of the same atomic species.

The diffusion results from a displacement of the center of an electron's cyclotron orbit each time a collision reorients the electron velocity. Thus, the magnetron-orbit radius, i.e., the average distance of the electron from the trap center, changes randomly with each collision by a magnitude d of the order of 1 cyclotron-orbit radius. A simple random-walk consideration gives a diffusion time $\tau \cong R^2/d^2Q$, where Q is the collision rate and R is the distance an electron must move outward before being lost from detection. The value of R for given trap and detection conditions can be estimated from measurements with atoms or molecules having known elastic scattering cross sections for electrons. For the present studies R is typically about 10^{-2} of the trap diameter and the electrons make about 10^4 collisions during the time τ. The radial density of electrons may thus be represented approximately by a Gaussian spreading in time. This model predicts the form of the electron-diffusion loss signals in Fig. 2, and also the observed dependence of τ upon magnetic field (normally 3 kG).[8]

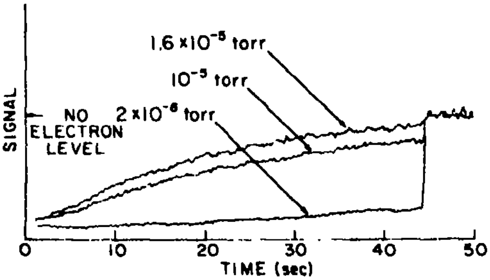

FIG. 2. Diffusion loss of electrons by elastic collisions with N_2 molecules.

In order to study e-K collisions, we have first compared the electron loss rate τ^{-1} with a potassium beam (as measured by a hot-wire current) to the rate with a known pressure of nitrogen gas under identical trap conditions. As expected, the rates are proportional to pressure, and yield a ratio of thermal-averaged collision rates $\langle v\sigma(\mathrm{K})\rangle/\langle v\sigma(\mathrm{N}_2)\rangle = 240 \pm 50$ within the pressure uncertainties. Using accepted values[9] for $\langle v\sigma(\mathrm{N}_2)\rangle$ in this temperature range, we obtain $\langle v\sigma(\mathrm{K})\rangle \approx 10^{-6}$ cm^3 sec^{-1}.

We have also investigated the effects of changing the spin polarization P of the potassium beam. The trapped electrons acquire, by spin exchange, the same polarization as the beam atoms in a time short compared to the diffusion loss time. The scattering cross section is then given by $\sigma = (1 - P^2)\sigma_1/4 + (3 + P^2)\sigma_3/4$, where σ_1 is the singlet cross section and σ_3 is the triplet cross section. To observe this spin dependence we reduced the beam polarization from $P = 1$ to $P = \frac{3}{4}$ by applying an rf field in resonance with hfs transitions in the beam atoms. We obtained the effect on the electron diffusion rate shown in Fig. 3. This effect appeared only when the rf frequency was tuned to an hfs transition in potassium, and increased with potassium beam intensity.

In order to interpret our experimental results with potassium, the simple diffusion picture above must be expanded to include anisotropic effects in the scattering,[9] since recent calculations[10,11] indicate a strong triplet p-wave contribution with alkalis at these energies. With such effects taken into account, a Maxwell-Boltzman average of the calculation of Sinfailam and Nesbet[11] agrees with our experimental result for the potassium diffusion rate, and also predicts a larger singlet than triplet diffusion rate as we observe.[12]

It is anticipated that spin exchange and spin-

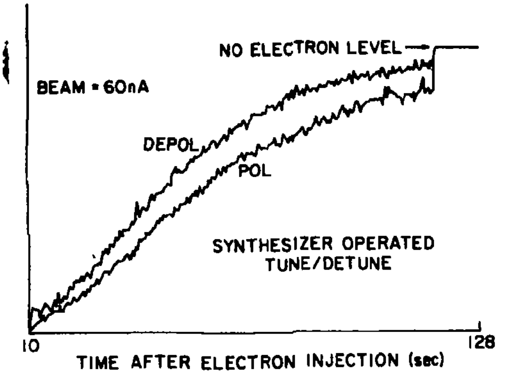

FIG. 3. Difference in electron diffusion loss by collisions with potassium atoms when the potassium spin polarization is changed.

exchange frequency shifts[13] can be measured by observing electron Larmor-frequency transitions with the present technique. Such effects, and the triplet and singlet scattering described above, are all functions of the scattering phase shifts in ndependent ways, and taken together should provide as complete an experimental picture as possible on electron collisions at a given temperaure.[14] For temperatures so low that there is only s-wave scattering, this information would overdetermine the two phase shifts. The electron emperature can be varied from above 1000°C by noise heating) down to liquid-helium temperature. Structure in the cross section, such as he isolated resonances predicted in this energy region for the alkalis, should show up as broad hermal-averaged maxima, etc.[15] Finally, the pin-dependent effect should be observable with only a few electrons,[16] and thus might prove useul in future precision measurements of the free-electron g factor.

The authors express appreciation to Jake Jonson and Bob Morley for constructing the glassware and to Lindon Lewis for help with the measurements; and to Professor H. G. Dehmelt, Dr. P. Ekstrom, and Dr. D. Wineland for helpful liscussions.

*Work supported by the U. S. National Bureau of Standards Precision Measurements Grant Program and by the National Science Foundation through Grant No. GP-23287.

[1] H. G. Dehmelt, in *Advances in Atomic and Molecular Physics*, edited by D. R. Bates and I. Estermann (Academic, New York, 1967 and 1969), Vols. 3 and 5.

[2] H. G. Dehmelt and F. L. Walls, Phys. Rev. Lett. 21, 127 (1968).

[3] E. J. McDaniel, *Collision Phenomena in Ionized Gases* (Wiley, New York, 1964), Chap. 11.

[4] G. Gräff, F. G. Major, R. Roeder, and G. Werth, Phys. Rev. Lett. 21, 340 (1968); G. Gräff, E. Klempt, and G. Werth, Z. Phys. 222, 201 (1969); G. Gräff, K. Huber, H. Kalinowsky, and H. Wolf, Phys. Lett. 41A, 227 (1972).

[5] A description of this first ion-trap–atomic-beam experiment is given in Ref. 1.

[6] D. A. Church and B. Mokri, Z. Phys. 244, 6 (1971).

[7] Our Penning-trap studies of such inelastic processes, which are interesting in their own right, will be reported elsewhere. See also Ref. 6 for earlier studies at eV energies.

[8] Other methods of measuring collision rates, such as collisional dephasing of the electron z-axis motion, appear promising and more directly interpretable than diffusion loss. The major advantage of the present method is its experimental simplicity.

[9] This analysis, together with a more detailed description of the entire technique, will be submitted for publication elsewhere.

[10] D. W. Norcross, J. Phys. B: Proc. Phys. Soc., London 4, 1458 (1971); D. L. Moores and D. W. Norcross, J. Phys. B: Proc. Phys. Soc., London 5, 1482 (1972).

[11] A. L. Sinfailam and R. K. Nesbet, Phys. Rev. A 7, 1987 (1973).

[12] The S-P wave interference yields an angular dependence that reduces the effect of σ_t in the diffusion process.

[13] L. C. Balling, R. J. Hansen, and F. M. Pipkin, Phys. Rev. 133, A607 (1964); S. J. Davis and L. C. Balling, Phys. Rev. A 8, 1136 (1973).

[14] Present information comes mainly from optical-pumping experiments. See Ref. 13.

[15] For a review of other experiments with alkalis, see B. Bederson, Comments At. Mol. Phys. 1, 135 (1970), and 2, 7 (1970).

[16] For recent developments in Penning-trap technique and $g-2$ experiments, see D. Wineland, P. Ekstrom, and H. Dehmelt, Phys. Rev. Lett. 31, 1279 (1973); F. L. Walls and T. S. Stein, Phys. Rev. Lett. 31, 975 (1973).

Nonlinear Skin Effect of High-Power Microwaves Incident on a Collisionless Magnetized Plasm

K. Minami, K. P. Singh, and M. Masuda
Department of Electrical Engineering, Nagoya University, Nagoya, 464, Japan

and

K. Ishii
Institute of Plasma Physics, Nagoya University, Nagoya, 464, Japan
(Received 29 April 1974)

Experimental results are presented which verify a nonlinear skin effect of high-power microwaves incident on a collisionless, uniform plasma having a sharp boundary. The skin depth, observed by microwave reflection techniques, increases with the incident microwave power.

A few years ago, Gekker and Sizukhin[1] measured the reflection coefficient from a nonuniform plasma, which decreased with increasing incident power. The anomalous absorption they observed was attributed by Kaw, Valeo, and Dawson[2] to a parametric excitation of ion waves and longitudinal plasma modes by the high-power microwaves. It should be emphasized, however, that Gekker and Sizukhin measured only the absolute values of the reflection coefficient. Therefore, one could not know whether or not there was nonlinear penetration for a strong incident power. In this Letter, we describe the experimental results for the nonlinear skin effect of high-power microwaves incident on a collisionless plasma. Although predicted by theory, this Letter presents what seems to be the first quantitative experiment where the skin depths of the microwaves are observed to be dependent on the incident power. In the present experiment, a semi-infinite uniform plasma is used for analysis in order to make the theory tractable.

Silin[3] developed a nonlinear theory for the reflection of plane monochromatic electromagnetic waves incident normally on the surface of a uniform, fully ionized plasma. Considerations are limited to a collisionless plasma above the cutoff density. Taking into account the radiation pressure on the plasma due to the electromagnetic field, the phase angle θ of the reflection coefficient is given by[3]

$$\cos^2\frac{\theta}{2} = -\frac{1}{b}\ln\left[1-\frac{b}{(\omega_p/\omega)^2}\right], \tag{1}$$

where

$$b = 4(E_i/E_c)^2, \quad E_c^{\,2} = 2m\omega^2\kappa T_e/e^2,$$

ω_p and ω are the plasma and microwave angular frequencies, E_i and E_c are the amplitudes of the incident wave and the critical electromagnetic field, respectively. Equation (1) reduces to the linear relationship

$$\cos(\theta/2) = \omega/\omega_p \qquad ($$

when b approaches zero.

The electric field[3] $E(z)$ does not necessarily fall off exponentially in the plasma when the nonlinear skin effect occurs. Hence, the skin depth d is defined here by the slope of $E(z)$ at the boundary $z=0$ as $d=-E(0)/E'(0)=k_0^{\,-1}\cot(\theta/2)$, where k_0 is the wave number in vacuum. Then the skin depth d can be recovered from the measurement of θ. It is obvious that the skin depth d would increase with b for a given $(\omega_p/\omega)^2$.

We modify Silin's formula, Eq. (1), to include the longitudinal magnetic field, in order to compare with our experimental results. An electromagnetic wave in a rectangular wave guide without plasma is a linearly polarized wave, which decomposes into right-hand and left-hand circularly polarized waves, E_r and E_l, respectively, with identical phases in time. When skin effects occur in the plasma for both waves, as in our experiment, d's in the wave guide are assumed to be the same as those in free space since (being of order of millimeters) they are considerably smaller than the side dimensions of the wave guide. In other words, the plasma in the wave guide will not be different from that in free space when the skin effect occurs. Then circularly polarized fields having different phases in time will exist in the plasma. If so, one can consider the phase shifts, θ_r and θ_l, of the waves reflected from the plasma, having right-hand and left-hand circular polarizations, respectively, even though the waveguide cross section is rectangular. Using the expressions for circularly polarized waves, $E_{r,l}=E_x\mp iE_y$, it is easily shown that the phase shift θ of a reflected wave which is linearly polarized with the same direction of polarization as the incident wave is given by

$$\cos^2\frac{\theta}{2}=\frac{1}{2}\left(\cos^2\frac{\theta_r}{2}+\cos^2\frac{\theta_l}{2}\right). \tag{3}$$

The angle θ in Eq. (3) is observed by a standing-wave detector in the wave guide. In the linear theory, both waves can exist independently in the plasma, and their phase angles are given by $\cos^2(\theta_{r,l}/2)=(1\mp\omega_c/\omega)/(\omega_p/\omega)^2$, where ω_c is the electron-cyclotron frequency. Substituting these expressions into Eq. (3), one directly obtains Eq. (2), which is independent of the applied magnetic field.

When the nonlinear effect is included, the circularly polarized waves in the plasma are no longer independent of each other. We write[4] in our notation the density correction factor, $f(E)$, due to the radiation pressure as

$$f(E_r, E_l)=\exp\left[-\frac{1}{2E_c^2}\left(\frac{|E_r|^2}{1-\omega_c/\omega}+\frac{|E_l|^2}{1+\omega_c/\omega}\right)\right], \tag{4}$$

instead of Eq. (2.3) of Ref. 3. Equation (4) results in a set of nonlinear differential equations[5] in E_r and E_l which cannot be separated out unless some assumption is made about the field amplitudes. We therefore make three different assumptions: (i) $|E_l|\gg|E_r|$, (ii) $|E_r|=|E_l|$, and (iii) $|E_r|\gg|E_l|$ in the plasma to obtain the expressions for θ. Using Eqs. (3) and (4), Eq. (1) is modified, for Assumption (ii), to

$$\cos^2\frac{\theta}{2}=-\frac{1-(\omega_c/\omega)^2}{2b}\ln\left\{\left[1-\frac{b}{(1+\omega_c/\omega)(\omega_p/\omega)^2}\right]\left[1-\frac{b}{(1-\omega_c/\omega)(\omega_p/\omega)^2}\right]\right\}. \tag{5}$$

Equation (5) reduces to Eq. (2), as b approaches zero.

A steady-state plasma is produced in helium at a pressure of a few Torr between a hot cathode and a water-cooled anode. The plasma is introduced into a glass chamber through a small hole in the anode. The glass chamber is differentially evacuated to the pressure of 10^{-3} Torr, where the present experiment is carried out. A uniform magnetic field B of several thousand gauss is applied axially to keep the electron density high. The plasma column has a Gaussian radial density distribution with 1 cm half-width. The plasma density N_e and the electron temperature T_e change, respectively, from 5×10^{11} to 4×10^{12} cm^{-3} and from 8 to 12 eV when the discharge current I_d is varied from 10 to 50 A, for the magnetic field B = 3020 G. A standard X-band rectangular wave guide with a water-cooled target is inserted axially into the plasma. The experimental setup, where the skin depths in the wave guide are measured, is shown in Fig. 1. A quartz block of 1.1-cm thickness is placed in the wave guide to make the plasma boundary clear and sharp. The length of the plasma-loaded wave guide is 2.5 cm. The plasma in the wave guide seems to be uniform in the axial direction, because the experimental results are insensitive to the length of the plasma wave guide. Microwave pulses up to 15 kW and time width $\tau=1.2$ μsec at a frequency of 9.37 GHz are launched into the plasma through a power divider and a slotted section.

The present experiment on skin effect is carried out in a magnetic field $2800<B<3050$ G,[6] where the low-level incident microwaves are almost totally reflected from the plasma for N_e greater than the cutoff density. The standing-wave patterns[7] observed by a crystal detector through a slotted section are recorded using a boxcar integrator. It is observed[8] that the phase angle θ decreases for a given B and I_d as the incident power increases. When the neutral pressure is increased to 1 Torr, θ changes in opposite way to that at low pressures, with increase in incident power, because of the additional ioni-

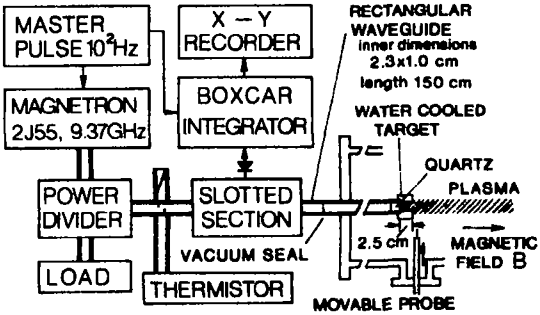

FIG. 1. Experimental arrangement.

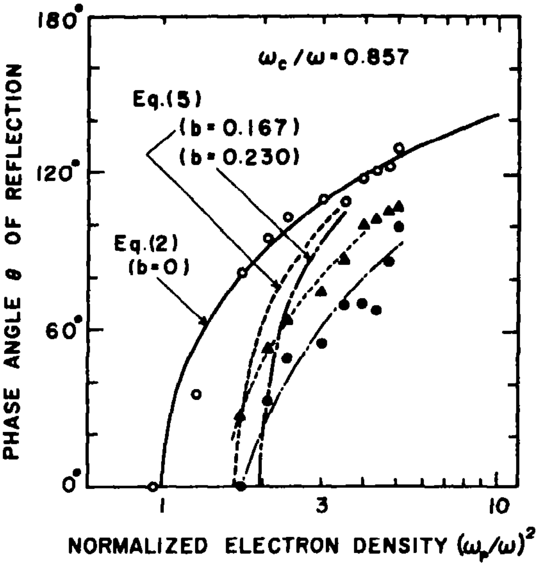

FIG. 2. Comparison of the experimental results with the theoretical predictions for the variation of θ versus $(\omega_p/\omega)^2$. Open circles, small power of the order of 10 mW, adjusted to the theoretical line for $b=0$; triangles, 2.9 kW, to be compared with the thick dashed line ($b=0.167$); closed circles, 4.0 kW, to be compared with the thick chained line ($b=0.230$).

zation by the high-power microwaves. Thus, we conclude that our results are clearly due to the nonlinear skin effect.

In Fig. 2, the experimental results are compared with the theoretical predictions for $b=0.167$ (thick dashed line) and 0.230 (thick chained line), which correspond, respectively, to 2.9 and 4.0 kW of incident power at $T_e = 8$ eV. The solid line is the linear relationship calculated from Eq. (2). Calculated lines for Assumptions (i) and (iii) are not shown, since they are very close to the solid line. We find that Assumption (ii) is the closest to the experimental values among the three. This suggests that the assumption $|E_r| = |E_l|$, from which Eq. (5) is derived, holds approximately in our experiment. In other words, the results suggest that an enhanced penetration of E_r occurs in the plasma for the high-power incident microwaves, since the inequality $|E_r|<|E_l|$ holds at the cutoff region for both the waves in the linear theory.

Using the boxcar integrator, the plasma parameters N_e and T_e are measured by the Langmuir probe located just in front of the target for various periods after the incidence of the high-power microwave pulse. Here, T_e is obtained from the Langmuir probe characteristic neglecting the effect of B, and N_e is calculated from the ion saturation current and T_e. An example is shown in Fig. 3, where the plasma becomes transparent for a microwave pulse of 15 kW even for $(\omega_p/\omega)^2 > 1$. The probe measurement will be reliable even in the microwave field, since the high-frequency drift velocity of electrons, $eE/m\omega$, in the plasma is much smaller than the electron thermal velocity. During the incidence of the microwave pulse, N_e decreases considerably from the steady-state value.[9] This fact is further evidence of the nonlinear skin effect.

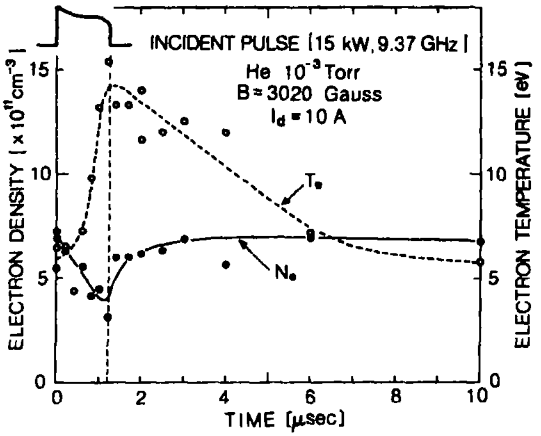

FIG. 3. Change in the plasma parameters due to the incidence of high-power microwaves.

Gurovich and Karpman[10] analyzed an electromagnetic envelope soliton propagating through a high-density plasma. In a limiting case, they obtained an expression for the electric field in the plasma for the stationary soliton that is just the same as the nonlinear skin effect.[3] Our experimental results, that the skin depths are dependent on the incident power, suggest the existence of an electromagnetic field in the plasma similar to the stationary envelope soliton.

---

[1] I. R. Gekker and O. V. Sizukhin, Pis'ma Zh. Eksp. Teor. Fiz. 9, 408 (1969) [JETP Lett. 9, 243 (1969)].

[2] P. Kaw, E. Valeo, and J. M. Dawson, Phys. Rev. Lett. 25, 430 (1970).

[3] V. P. Silin, Zh. Eksp. Teor. Fiz. 53, 1662 (1967) [Sov. Phys. JETP 26, 955 (1968)].

[4] A. V. Gurevich and L. P. Pitaevskii, Zh. Eksp. Teor.

Fiz. 45, 1243 (1963) [Sov. Phys. JETP 18, 855 (1964)].

[5]H. Motz and C. J. H. Watson, in *Advances in Elec- onics and Electron Physics*, edited by L. Marton cademic, New York, 1967), Vol. 23, p. 225, Eq. (7).

[6]The power reflected from and the power transmitted hrough the plasma are measured for a certain incident ower at different values of B. Both signals are small ear the electron-cyclotron resonance at $B = B_c = 3345$ G. Thus, the microwaves are absorbed in the plasma t the resonance. The propagation of whistler waves ith little attenuation is observed when $B > B_c$. En- anced fluctuations are observed in the ion saturation urrents of the probe especially near the resonance.

[7]S. Takeda and M. Roux, J. Phys. Soc. Jpn. 16, 95 (1961).

[8]Here, the plasma is replaced by a movable metal short plunger, whose position simulates the density of the plasma to obtain the phase angle θ.

[9]I. R. Gekker, E. Ja. Holz, B. P. Kononov, K. A. Sarksian, V. A. Silin, and L. E. Tsopp, in *Proceedings of the Seventh International Conference on Phenomena in Ionized Gases, Belgrade, 1965*, edited by B. Perovic and D. Tosić (Gradjevinska Knjiga Publishing House, Belgrade, Yujoslavia, 1966), Vol. II, p. 445.

[10]V. Ts. Gurovich and V. I. Karpman, Zh. Eksp. Teor. Fiz. 56, 1952 (1969) [Sov. Phys. JETP 29, 1048 (1969)].

X-Ray Emission from Laser-Produced Plasmas*

D. J. Nagel, P. G. Burkhalter, C. M. Dozier, J. F. Holzrichter,† B. M. Klein,
J. M. McMahon, J. A. Stamper, and R. R. Whitlock
Naval Research Laboratory, Washington, D. C. 20375

(Received 22 April 1974)

We measured several characteristics of the x-ray emission from plasmas produced at the focus of a high-power (~10 GW) laser. X-ray spectra in the 1–2-keV region show that the plasmas contain highly stripped atoms (10–12 electrons missing from Al, 20–22 from Zn, and 36–38 from Gd). The laser-plasma x-ray source can emit about 0.1 J of x rays above 1 keV in 1 nsec from a volume about 100 μm in diameter. This corresponds to more than 10^{13} W/cm^2.

Laser-generated plasmas sufficiently hot to emit kilovolt x rays have been produced recently by the use of focused laser power densities exceeding 10^{13} W/cm^2 on solid targets. *K* radiation from elements up to Al was measured and interpreted by Peacock, Hobby, and Galanti.[1] Mallozzi *et al.*[2] and Aglitskiy *et al.*[3] resolved many *L* lines of Fe but the latter authors have not interpreted the spectra. Mead *et al.*[4] measured unresolved clusters of *M* lines from Au. But to date, there has been no systematic study of x-ray emission from plasmas produced by any single high-power laser. In this Letter, we report the results of a survey of x-ray spectra from elements across the periodic system. The work has two motivations: plasma diagnostics including tests of laser-plasma models,[5,6] and characterization of the laser plasma as a fast, intense source of soft x rays with several applications.

The Nd laser system used in this work consisted of a mode-locked oscillator and five amplifier stages.[7] Pulses of the 1.06-μm light [<1 Å full width at half-maximum (FWHM)] containing up to 5 J in 250 or 900 psec were focused on flat targets to spots about 50 μm in diameter. Hence, power densities exceeding 10^{14} W/cm^2 were available. Spectra were measured in single shots with simple, slitless spectrographs using flat potassium acid phthalate crystals ($2d = 26.6$ Å) and Kodak No-Screen film behind 25-μm Be foils (1% transmissive at 800 eV). Resolution was not optimized since it was desired to survey a wide photon-energy range. Energy calibration of new spectra was accomplished by coating the targets with powdered compounds of Na, Mg, or Al, the energies of whose lines are accurately known. Other x-ray characteristics (angular distribution, emission time, and source size) were also measured, as will be described later.

K spectra resulting from transitions to the 1*s* level have been obtained from Na (in NaF), Mg, Al, Si, and S. Spectra from all these elements are similar. Figure 1 shows the Al spectrum. Classification of lines in spectra such as this presented no problem because of many laboratory[8] and solar[9] measurements of similar emission lines from elements in this range. As indicated in Fig. 1, lines from three ion species appear. An intense Rydberg series and free-to-bound continuum from He-like (two-electron) Al are evident, as is the Lyman series of H-like (one-electron) Al. Poorly resolved satellites

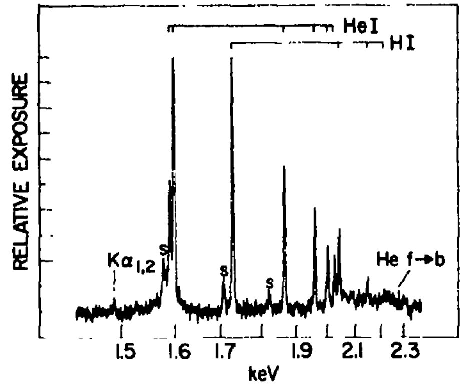

FIG. 1. Al K x-ray spectrum from a plasma produced by a 1.8-J, 0.25-nsec laser pulse. Rydberg series from Al ions isoelectronic with H and He atoms, and the He-like free-to-bound continuum and satellite lines S constitute the plasma spectrum. The $K\alpha_{1,2}$ lines are from target fluorescence.

from transitions in Li-like (three-electron) ions appear near the He-like $1s$-$2p$ resonance line, while satellites from He-like ions accompany the H-like $1s$-$2p$ (Lyman α) line. Similar satellites have been observed with better resolution in F spectra.[1,10]

L spectra from transitions to the $2s$ and $2p$ levels were measured from Cr, Fe, Co, Ni, Zn, and Br (in KBr). The spectrum of Zn given in Fig. 2 is typical of these spectra. It is more complex than the K spectrum in Fig. 1 because of the larger number of possible ionization states and the strong multiplet structure present for most transitions. Interpretation of the Zn spectrum is not complete, but it is possible to identify the major ionization stages. Again, laboratory[11] and solar[9] spectra from lighter elements were used to interpret our results. Transition-energy calculations using self-consistent-field Dirac-Slater wave functions[12] were made to confirm identifications of the major lines in the Zn spectrum. As indicated in Fig. 2, $2p$-$3d$ transitions in Ne-like (ten-electron), F-like (nine-electron), and O-like (eight-electron) Zn ions dominate the spectrum. Two pairs of lines from Ne-like ions are also strong, $2p$-$3s$ below 1.1 keV and $2p$-$4d$ near 1.47 keV.

M spectra due to transitions to the $3p$ and $3d$ levels from Ba (in $BaCO_3$), Sm, Gd, Dy, and Er were also measured. Figure 3 shows the spectrum of Gd which is representative of the M spectra. Just as the K and L spectra are quite distinctive in appearance, the M spectra also have a characteristic pattern. But much less was known about this M radiation compared to the K and L spectra in the other figures. Spectral measurements (in the uv) for transitions to the $3p, d$ levels had been made only up to Mo,[13] fourteen atomic numbers below Ba. Hence we had to rely on the self-consistent-field calculations to identify the ionization stages and transitions which produced the spectrum in Fig. 3. As shown in the figure, $3d$-$4f$ transitions occurred in Ni-like (28-electron), Co-like (27-electron) and Fe-like (26-electron) Gd ions. Four other transitions are important. The three strongest lines below

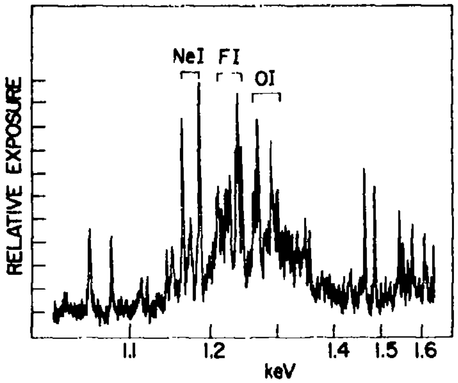

FIG. 2. Zn L x-ray spectrum from a plasma generated by a 2.0-J, 0.9-nsec laser pulse. Groups of lines from $2p$-$3d$ transitions in Zn ions isoelectronic with O, F, and Ne atoms are indicated.

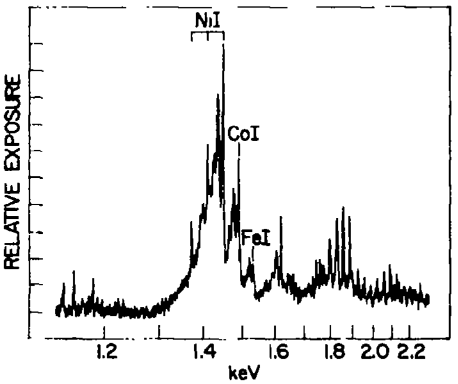

FIG. 3. Gd M x-ray spectrum from a plasma produced by a 3.5-J, 0.9-nsec laser pulse. Lines from $3d$-$4f$ transitions in Gd ions isoelectronic with Fe, Co, and Ni are labeled.

1.2 keV are due to $3d$-$4p$ transitions in Ni-like ions. Isoelectronic extrapolation of the lighter-atom uv data confirmed the $3d$-$4p,f$ identifications for Ni-like Gd. The group of lines around 1.6 keV is due to $3p$-$4d$ electron jumps. Another group (1.7–1.9 keV) is from $4d$-$5p,f$ transitions. And, finally, the radiation above 2.0 keV is due to $4d$-$6p,f$ electron jumps.

N spectra from very high–atomic-number elements might also be expected. But laser irradiation of U did not result in any resolved lines >800 eV. Study of U emission with a grating spectrometer would be worthwhile.

Film-efficiency corrections[14] were made prior to plotting the figures so that the spectra are given interms of relative exposure rather than photographic density. Corrections for crystal efficiency[15] and Be-window absorption were also made prior to integration of the spectra above background over the energy regions shown in each figure. Angular-distribution measurements made with film indicate that the x-ray intensity is approximately independent of emission direction. The ratios of integrated x-ray line energy (emitted into 4π sr) to the incident laser energy are 0.5% for Al, 9.0% for Zn, and 1.5% for Gd (±20% relative). These values assume no reciprocity loss in the film.[16] Future integrated-intensity measurements will be made with electronic detectors. An upper limit on the x-ray emission time was obtained with a fast pyroelectronic infrared detector which was found to be x-ray sensitive. The measured x-ray pulse width was 1.6 nsec FWHM. Unfolding the measuring-system response time gave ~1 nsec FWHM, which is nearly equal to the 0.9-nsec laser pulse width. Pinhole-camera images (and spectral linewidths) show that the x-ray source size can be as small as 50 μm.[17] Taken together, these data show that the laser plasma emits x rays at a rate exceeding 10^{18} W per cubic centimeter of the plasma.

Results just presented will be considered from two viewpoints in the remainder of this Letter. First, the use of x-ray measurements for determining the temperature and density of laser plasmas will be discussed. Then, present and potential uses of laser plasmas as x-ray sources will be enumerated. Both these x-ray interests are extensions of work done in the uv and extreme ultraviolet regions using lower-power lasers and often low–atomic-number targets.[18,19]

The appearance of intense spectra in the 1–2 keV range immediately indicates that the plasma electron temperatures are ~0.5 keV. Acutally, the temperature is a rapidly varying function of both time and spatial coordinates, but the concept of a single, effective temperature is useful albeit approximate. With the coronal equilibrium model (plus three-body recombination),[20] the ratio of the intensity of two resonance lines (the $1s$-$2p$ transitions in H- and He-like Al ions) yielded temperatures which increase from 0.5 to 0.8 keV (±30%) as the laser power is increased. A separate analysis of He-like $1s$-$2p$ intercombination and Li-like satellite line intensities gave similar results (within 20%). Transient ionization and resonant reabsorption may influence, but are not expected to invalidate, these effective-temperature determinations.

The present spectra are not of sufficient resolution to determine plasma-density values as was recently done by using longer-wavelength data taken with a grating spectrometer.[10] However, high-resolution x-ray measurements are possible and, because of current interest in producing controlled fusion reactions initiated by lasers, they may also be important. Attainment of high densities (~10^3 g/cm^3) in the laser target pellet is necessary to generate significant thermonuclear energy. Reaction-product (neutron, α particle) measurements will indicate the compression obtained, once significant density increases are achieved. But techniques are needed to determine pellet densities for intermediate compression values. We suggest that the measurement of line profiles in uv or x-ray spectra may yield the desired density information. Implosion of thin spherical shells of C or Al and spectral measurements could provide valuable tests of the compression codes which are generally untested by experimental data at present.

The unique characteristics of laser-generated plasmas as x-ray sources, regardless of microscopic details of the plasmas, make possible several applications. The laser plasma is the most versatile x-ray source now used for spectroscopy to assist interpretation of data from laboratory plasmas and the sun. All elements can be excited by this method (since elements which are liquid or gaseous at room temperature can be used as compounds, frozen, or implanted in solids). Also, the temperature can be controlled (up to about 1 keV) by variation of the focusing conditions. The high speed and soft spectrum of laser-plasma x-ray emission make it attractive for radiography of another plasma.[21] It should also be possible to do transient-radiation-effect studies, e.g., color-center decay,[22] using x rays from laser plasmas. And finally, there has been considerable discussion of schemes for attaining laser action in the soft-x-ray region lately.[23] Several suggestions involve the use of laser-generated plasmas, either as a lasing medium or to generate x rays to pump another medium.

We are investigating variations of the x-ray emission and plasma conditions with laser-pulse, focusing, and target parameters. Detailed studies of K,[24] L,[25] and M[26] spectra are being made as a basis for more extensive plasma diagnostic work.

T. de Rieux and L. Scott operated the laser. We appreciate their efforts, the generous assistance of O. C. Barr, J. W. Criss, E. A. McLean, and E. Turbyfill, and helpful discussions with L. S. Birks, G. A. Doschek, and U. Feldman.

---

*Work supported by the U. S. Atomic Energy Commission and the Defense Nuclear Agency.

†Present address: Lawrence Livermore Laboratory, Livermore, Calif. 94550.

[1] N. J. Peacock, M. G. Hobby, and M. Galanti, J. Phys. B: Proc. Phys. Soc., London 6, L298 (1973).

[2] P. J. Mallozzi *et al.*, in *Fundamental and Applied Laser Physics*, edited by M. S. Feld, J. Javan, and N. A. Kurnit (Wiley, New York, 1973), p. 165. P. J. Mallozzi *et al.*, J. Appl. Phys. 45, 1891 (1974).

[3] Ye. V. Aglitskiy *et al.*, Kratk. Soobshch. Fiz. 12, 36 (1971) [available as U. S. Naval Research Laboratory Translation No. 1238 (unpublished)].

[4] S. N. Mead *et al.*, Appl. Opt. 11, 345 (1972).

[5] N. K. Winsor and D. A. Tidman, Phys. Rev. Lett. 31, 1044 (1973).

[6] K. Whitney and J. Davis, to be published.

[7] J. M. McMahon and J. L. Emmett, in *Record of Eleventh Symposium on Electron, Ion and Laser Beam Technology*, edited by R. F. M. Thornley (San Francisco Press, San Francisco, Calif., 1971), p. 269.

[8] N. J. Peacock, R. J. Speer, and M. G. Hobby, J. Phys. B: Proc. Phys. Soc., London 2, 798 (1969).

[9] G. A. Doschek, Space Sci. Rev. 13, 765 (1972).

[10] U. Feldman *et al.*, Astrophys. J. 187, 417 (1974).

[11] M. Swartz *et al.*, J. Phys. B: Proc. Phys. Soc., London 4, 1747 (1971).

[12] D. Liberman, J. T. Waber, and D. T. Cromer, Phys. Rev. 137, A27 (1965).

[13] E. Alexander *et al.*, J. Opt. Soc. Amer. 61, 508 (1971).

[14] C. M. Dozier, J. V. Gilfrich, and L. S. Birks, Appl. Opt. 6, 2136 (1967), and unpublished data.

[15] D. B. Brown, M. Fatemi, and L. S. Birks, in *Advances in X-Ray Analysis*, edited by C. L. Grant *et al.* (Plenum, New York, 1974), Vol. 17.

[16] L. S. Birks *et al.*, J. Opt. Soc. Amer. 60, 649 (1970).

[17] J. F. Holzrichter, C. M. Dozier, and J. M. McMahon, Appl. Phys. Lett. 23, 687 (1973).

[18] T. P. Donaldson, R. J. Hutcheon, and M. H. Key, J. Phys. B: Proc. Phys. Soc., London 6, 1525 (1973).

[19] T. U. Arifov, G. A. Askar'yan, and N. M. Tarasova, Zh. Eksp. Teor. Fiz. 56, 516 (1969) [Sov. Phys. JETP 29, 282 (1969)].

[20] R. C. Elton, in *Plasma Physics*, edited by H. A. Griem and R. H. Lovberg (Academic, New York, 1970), Vol. 9, pt. A, p. 115.

[21] S. K. Handel and B. Sternerhag, in *High Speed Photography*, edited by N. R. Nilsson and L. Hogberg (Wiley, New York, 1968), p. 253.

[22] R. G. Fuller, R. T. Williams, and M. N. Kabler, Phys. Rev. Lett. 25, 446 (1970).

[23] D. J. Nagel, Phys. Fenn., 9 (S1), 381 (1974).

[24] U. Feldman *et al.*, to be published.

[25] P. G. Burkhalter, D. J. Nagel, and R. D. Cowan, unpublished.

[26] P. G. Burkhalter, D. J. Nagel, and R. R. Whitlock, Phys. Rev. A 9, 2331 (1974).

Measurements of Energetic X Rays from Laser-Produced Plasmas*

F. C. Young
Naval Research Laboratory, Washington, D. C. 20375
(Received 8 July 1974)

The dependence of energetic x-ray emission from laser-produced plasmas on laser energy, pulse duration, and atomic number of the target ($Z=4$ to 42) has been studied for irradiations of 10^{13} to 10^{16} W/cm^2. Energetic x-ray emission is more than 10^3 times greater than bremsstrahlung expected for a Maxwellian electron velocity distribution and is more sensitive to energy density in the target than to power density.

The irradiation of solid targets by high-energy, short-pulse lasers results in the production of x rays with energies greater than 100 keV.[1-3] It is presumed that such emission arises from a nonthermal high-energy tail on the electron energy distribution. Such an energy distribution may result from the absorption and collisionless thermal conduction of the incident electromagnetic radiation.[4] The importance of superthermal electrons in the laser-target interaction is not well understood. For example, in present laser-fusion schemes the generation of hot nonthermal electrons may hinder target compression by preheating the target or decoupling from the atmosphere.[5,6] The production of energetic electrons in the laser-target interaction may be studied through the subsequent bremsstrahlung radiation. The present measurements have been carried out to investigate the production of bremsstrahlung at laser irradiances of 10^{13} to 10^{16} W/cm^2.

All of the measurements have been carried out with the U.S. Naval Research Laboratory 1.06-μm Nd-glass laser system[7] by focusing the laser beam onto slab targets in an evacuated chamber.[8] A prepulse identical in shape to the main pulse with approximately 5% of the pulse energy was applied 0.7 nsec ahead of the main pulse for most of the measurements. Calorimeters were used to monitor the incident energy. X rays are detected through 1-mm-thick aluminum absorbers by thin NaI scintillators. The efficiency for such a detector with a 4-mm-thick scintillator is greater than 75% for x rays from 30 to 110 keV. The efficiency decreases gradually at higher energies as a result of transmission through the NaI. The efficiency falls off rapidly at lower energies because of absorption in the aluminum. For example, at 15 keV the efficiency is only 13%. Because the x-ray spectrum decreases rapidly with increasing x-ray energy,[2,9,10] the detector is sampling primarily x rays from approximately 15 to 30 keV, and these x rays will be referred to as hard x rays.

The emission of hard x rays, measured as a function of incident laser energy from 1 to 100 J, is shown in Fig. 1(a). These results were obtained for 0.9-nsec laser pulses without prepulse focused onto polyethylene targets (focal-spot diameter ~ 100 μm). A 3.8-cm-diam by 4-mm-thick NaI crystal located 30 cm from the target at 135° to the incident laser beam was used for these measurements. The output of the NaI photomultiplier is integrated, amplified, and recorded on an oscilloscope. This detector measures the integrated energy distribution, $\int_0^\infty E n(E) f(E)\, dE$, where $n(E)$ is the x-ray energy distribution and $f(E)$ is the efficiency described in the previous paragraph. The NaI detector is calibrated in energy with radioactive sources. The total absolute x-ray emission in Fig. 1 is based on angular isotropy and an estimated 75% detection efficiency.

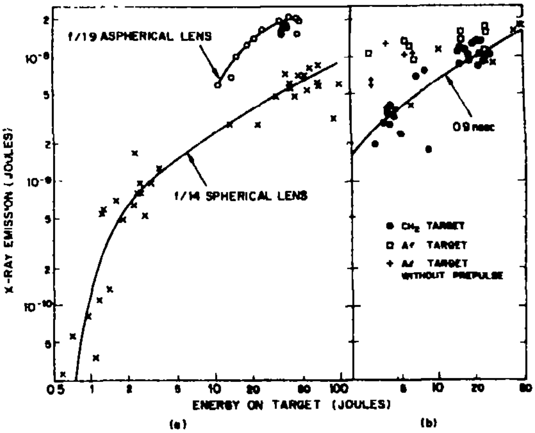

FIG. 1. Hard-x-ray emission measured with a 1-mm-thick aluminum absorber and 4-mm-thick NaI scintillator versus incident energy for (a) 0.9-nsec laser pulses incident on polyethylene targets and (b) 0.25-nsec laser pulses focused with an $f/14$ lens.

The scatter of the data points is typical of the shot-to-shot reproducibility. For the 74-cm-focal-length ($f/14$) lens hard-x-ray production increases rapidly with incident energy and then increases linearly. The 11-cm-focal-length ($f/1.9$) lens gives substantially higher output as a result of a smaller focal-spot diameter (~30 μm) as evidenced by the damage patterns on target.

Measurements of hard-x-ray emission at 0.25 nsec with prepulse are shown in Fig. 1(b). The 0.9-nsec curve in this figure is taken from Fig. 1(a) and is normalized to experimental measurements obtained at 0.9 nsec with prepulse and an improved quality $f/14$ focusing lens. Measurements at 0.25 nsec on aluminum targets with and without prepulse indicate that hard-x-ray emission is insensitive to the presence of a prepulse [see Fig. 1(b)]. A comparison of the curves in Figs. 1(a) and 1(b) indicates that the new focusing lens produced an increase of 2.5 in hard-x-ray emission because of a reduced focal-spot diameter. However, measurements for polyethylene at 0.9 and 0.25 nsec in Fig. 1(b) show no significant increase in hard-x-ray emission for an increase in laser power of 3.6.

Only an extremely small fraction of the incident laser energy is radiated away as hard x rays. For example, from Fig. 1(a), at 10 J incident energy only 3×10^{-9} of the incident energy is converted to hard x rays. This result is consistent with similar measurements using thinner aluminum or thicker nickel absorbers.[1] Of the energy emitted as hard x rays, only 10 MeV is actually detected. This corresponds, for example, to only 200 50-keV photons or 500 20-keV photons.

The dependence of the total hard-x-ray energy on the atomic number of the target is illustrated in Fig. 2. The datum point for each target is an average over several shots in the energy range from 8 to 11 J. The hard-x-ray emission displays little variation with atomic number. This result contrasts with soft-x-ray (1 to 3 keV) production which displays large variations with atomic number.[11] The smaller hard-x-ray energies for CH_2, Si, and S compared to Al, Cu, Mo, and Zr (in Fig. 2) suggest a metallic versus nonmetallic dependence. This behavior is expected if the generation of superthermal electrons is sensitive to laser-produced magnetic fields.[12,13]

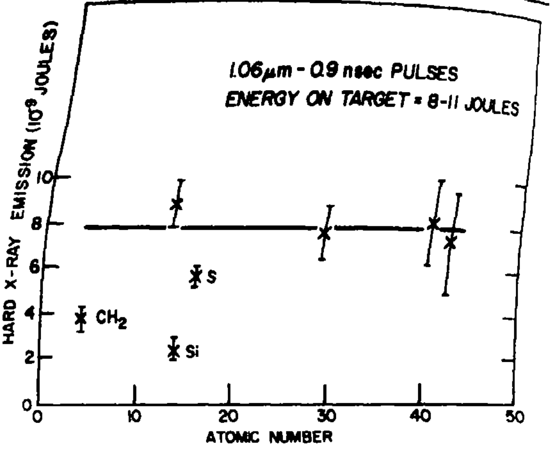

FIG. 2. Hard-x-ray emission measured with a 1-mm-thick aluminum absorber and 4-mm-thick NaI scintillator as a function of atomic number of the target.

Angular-distribution measurements of hard x rays have been made on polyethylene targets for 0.9- and 0.25-nsec laser pulses. Preliminary experiments[14] have demonstrated that hard x rays originate from a source near the target surface within a volume of dimensions much less than 2.5 mm. For the angular-distribution measurements six NaI detectors, 5.1 cm in diameter by 1.27 cm thick, are used in both the polar and azimuthal planes. The detectors are located 36 cm from the source and their relative efficiencies are determined with radioactive sources placed at the target position. The pulse from each detector is amplified and stored digitally in a transient recorder for later readout on oscilloscope or punched paper tape. X-ray absorption in the 0.76-mm-thick target is negligible. Typical results for the azimuthal plane are shown in Fig. 3(a). Results for the polar plane are shown in Fig. 3(b). The errors in these measurements arise from two independent sources: (1) an uncertainty in the measurement of the signal amplitude registered by the digital memory unit, and (2) a statistical error in the number of photons detected. No large deviations from isotropy are apparent in these measurements. Also isotropy has been observed in the polar plane for solid deuterium targets at irradiances of 5×10^{13} and 3×10^{14} W/cm^2 for x rays above low-energy cutoffs from 2.2 to 16.5 keV.[15]

The total hard-x-ray energy may be compared to the bremsstrahlung radiation from a fully ionized neutral plasma with the assumption of a Maxwellian distribution of electron velocities. This comparison provides a measure of the extent to which the high-energy tail of the electron

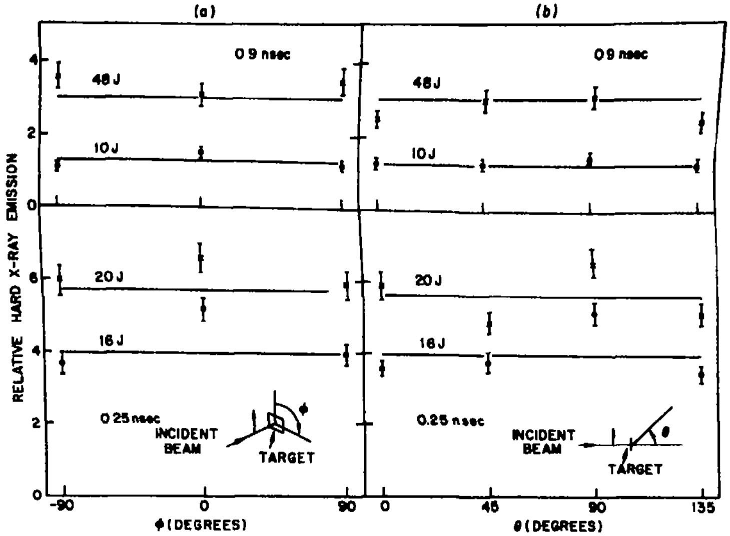

FIG. 3. Angular distributions of the hard x rays (a) in the plane perpendicular to the incident laser beam and (b) in the plane of the incident laser beam direction and the direction of polarization of the laser beam. The data are labeled with the incident energy and the lines represent the average of the six measurements.

distribution deviates from equilibrium conditions. For a Maxwellian velocity distribution the radiation spectrum is given by $J_E = (J/kT)\exp(-E/kT)$; where E is the photon energy; T is the electron temperature; and J is the total radiated power density, $J\,(\mathrm{W/cm^3}) = 5.35\times10^{-31} n_e (n_{\mathrm{H}} + 36 n_{\mathrm{C}}) T^{1/2}$ (temperature measured in keV) for polyethylene.[16] The fraction of power radiated above a lower cutoff, E_0, is given by $\exp(-E_0/kT)$. To calculate the radiated power density take $n_e = 4n_{\mathrm{H}} = 8n_{\mathrm{C}} = 10^{21}/\mathrm{cm}^3$ (the critical density for 1.06-μm radiation) and $T = 700$ eV. An electron temperature of this magnitude has been obtained from x-ray line-intensity–ratio measurements for a 0.9-nsec 5-J laser pulse on an aluminum target.[17] Then the radiated power density above a 15-keV cutoff is 1.1×10^3 W/cm^3. To convert this result to an energy for comparison with experiment, we assume that the incident laser pulse is focused into a 100-μm-diam focal spot (evidenced by damage patterns on metallic targets at low incident power) and that x rays are radiated from a plasma volume of 10^{-6} cm^3 for the duration of a 0.9-nsec laser pulse. Measurements with a fast scintillator indicate that the duration of hard-x-ray emission is not significantly longer than this laser-pulse duration. Then the total radiated energy above a 15-keV cutoff is 9.5×10^{-12} J. This result is 3 orders of magnitude smaller than the measured x-ray emission at 0.25 nsec for 5 J incident energy.

It has been suggested that high-energy x rays may be accounted for by the absorption of the incident radiation through the parametric ion-acoustic instability.[1] This instability is expected to be strongly dependent on the intensity of the incident radiation.[18] The present measurements indicate that hard-x-ray emission is sensitive to energy density in the target rather than to power density. Alternatively, bremsstrahlung from energetic electrons accelerated into the solid target may be energy dependent rather than power dependent. But thick-target bremsstrahlung should increase linearly with atomic number,[19] and this disagrees with the measurements (see Fig. 2). The present results suggest that energetic electrons are produced within the plasma volume and spontaneous magnetic fields play a role in confinement and perhaps acceleration so that energetic x rays result from electron collisions within the plasma atmosphere.

The author is grateful for valuable discussions with J. A. Stamper and B. H. Ripin. The assistance of D. H. Walker with the angular-distribution measurements and of O. C. Barr, J. M. McMahon, and T. De Rieux with laser operation is gratefully acknowledged. Appreciation is expressed to D. J. Nagel for communicating results

prior to publication.

---

*Work supported by the U. S. Atomic Energy Commission.

[1] J. W. Shearer, S. W. Mead, J. Petruzzi, F. Rainer, J. E. Swain, and C. E. Violet, Phys. Rev. A 6, 764 (1972).

[2] V. W. Slivinsky and H. N. Kornblum, Bull. Amer. Phys. Soc. 18, 1256 (1973).

[3] J. N. Olson, G. W. Kuswa, and E. D. Jones, J. Appl. Phys. 44, 2275 (1973).

[4] R. L. Morse and C. W. Nielson, Phys. Fluids 16, 909 (1973).

[5] J. Nuckolls, L. Wood, A. Thiessen, and G. Zimmerman, Nature (London) 239, 139 (1972).

[6] J. S. Clarke, H. N. Fisher, and R. J. Mason, Phys. Rev. Lett. 30, 89 (1973).

[7] J. M. McMahon and O. C. Barr, in *Proceedings of the Society of Photo-Optical Instrumentation Engineers: Developments in Laser Technology—II*, edited by R. F. Wuerker (Society of Photo-Optical Instrumentation Engineers, Palo Verdes Estates, Calif., 1974), Vol. 41, p. 13.

[8] J. A. Stamper *et al.*, in *Laser Interaction and Related Plasma Phenomena*, edited by H. Schwarz and H. Hora (Plenum, New York, to be published), Vol. 3.

[9] J. F. Kephart, R. P. Godwin, and G. H. McCall, Appl. Phys. Lett. 25, 108 (1974).

[10] H. D. Shay *et al.*, Lawrence Livermore Laboratory, Report No. UCRL 75465, 1974 (unpublished).

[11] D. J. Nagel, P. G. Burkhalter, C. M. Dozier, B. M. Klein, and R. R. Whitlock, Bull. Amer. Phys. Soc. 19, 557 (1974).

[12] D. A. Tidman and J. A. Stamper, Appl. Phys. Lett. 22, 498 (1973).

[13] N. K. Winsor and D. A. Tidman, Phys. Rev. Lett. 31, 1044 (1973).

[14] F. C. Young, D. H. Walker, and O. C. Barr, Bull. Amer. Phys. Soc. 19, 557 (1974).

[15] K. Eidmann and R. Sigel, in *Proceedings of the Sixth European Conference on Controlled Fusion and Plasma Physics, Moscow, 1973* (U. S. S. R. Academy of Sciences, Moscow, 1973), Vol. 1, p. 435.

[16] S. Glasstone and R. H. Lovberg, *Controlled Thermonuclear Reactions* (Van Nostrand, Princeton, N. J., 1960), p. 31–32.

[17] D. J. Nagel *et al.*, preceding Letter [Phys. Rev. Lett. 33, 743 (1974)]; D. J. Nagel *et al.*, in *Proceedings of the Sixth European Conference on Controlled Fusion and Plasma Physics, Moscow, 1973* (U.S.S.R. Academy of Sciences, Moscow, 1973), p. 447; G. A. Doschek *et al.*, to be published.

[18] D. F. DuBois and M. V. Goldman, Phys. Rev. Lett. 14, 544 (1965).

[19] R. D. Evans, *The Atomic Nucleus* (McGraw-Hill, New York, 1955), Chap. 21.

Solitons and Resonant Absorption

E. J. Valeo and W. L. Kruer
Lawrence Livermore Laboratory, University of California, Livermore, California 94550

(Received 24 June 1974)

Simulations and theory of driven plasmas show the existence of long-lived, extremely intense spikes of high-frequency electric field, accompanied by a self-consistent depression in density. These entities are the limit to which solitons collapse in a driven plasma when the wave-particle interaction is included. Alterations in the density profile due to such entities is especially important for the absorption of radiation in inhomogeneous plasmas.

The role of solitons in strong electron-plasma-wave turbulence is receiving widespread attention. Zacharov[1] has shown that electron plasma waves can be described by a Schrödinger equation, which admits such localized solutions. Kingsep, Rudakov, and Sudan[2] have pointed out that the saturated spectrum of plasma waves observed both in beam-plasma simulations[3] and in simulations of plasmas driven by intense fields[4] indicate the presence of solitons. Morales, Lee, and White[5] have recently modified the Schrödinger equation to include a monochromatic, homogeneous pump $E_0\cos(\omega_0 t)$ with $\omega_0=\omega_{pe}$, the electron plasma frequency. They find then that the soliton width collapses and its intensity increases faster than exponentially. The final soliton intensity is limited in their formalism only by pump depletion. We present here the results of particle-simulation studies in which we investigate the final state of solitons in a driven plasma. Strong dissipation due to the onset of the wave-particle interaction prevents the complete soliton collapse predicted by the Schrödinger equation model. With the inclusion of the wave-particle interac-

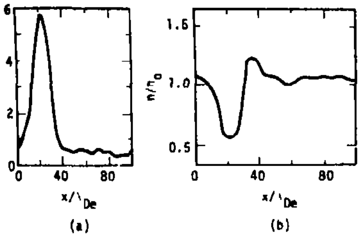

(a) (b)

FIG. 1. The spatial dependence of (a) the electric field intensity, and (b) the ion density observed in a one-dimensional electrostatic computer simulation. The parameters are $eE/m\omega_{pe} = 0.8V_{te}$, $\omega_0 = 0.9\omega_{pe}$, $m/M = 0.01$, and $\omega_0 t = 600$.

tion, solitons become very intense and narrow spikes of high-frequency electric field accompanied by a self-consistent density depression.

We first show an example of a soliton as observed in a one-dimensional simulation of an initially uniform plasma driven by a spatially homogeneous pump field. The pump frequency ω_0 is equal to $0.9\omega_{pe}$. This choice is not essential but enables us to isolate the soliton formation from other mode-coupling processes which occur simultaneously when $\omega_0 > \omega_{pe}$. The initial electric field and density fluctuations are random. Figure 1(a) shows a plot of the square of the peak self-consistent plasma-wave field versus position at $\omega_{pe} t = 600$, and Fig. 1(b) depicts the ion density versus position at that time. Note the narrow width ($l \sim 15\lambda_{De}$) and the very large peak intensity maximum ($E_p^2/4\pi n\theta_e \sim 5$). Depending on the initial random noise and the size of the simulated plasma, one or more of these entities are observed to form. As long as they are well separated, they can coexist, although they appear to interact through the radiation of sound waves. This interaction is particularly apparent for two solitons separated by a distance comparable to their width. Then the larger soliton can annihilate the other by "filling in" the latter's density depression.

The pump field intensity $E_0^2/4\pi n\theta_e$ equals 0.64 which is about 1.5 times the threshold intensity for the oscillating two-stream instability[6] when $\omega_0 = 0.9\omega_{pe}$. This threshold is the accessibility criterion for the formation of solitons in a quiescent plasma. However, the simulations show that this threshold can be significantly lowered if an elevated level of turbulence or noise is present. This can be a particularly important consideration for real plasma, since a number of instabilities often operate simultaneously.

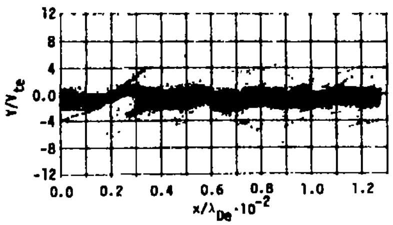

FIG. 2. Electron phase space (v versus x) from the computer simulation. The parameters are the same as those for the previous figure.

The plasma is heated very effectively after the onset of the wave-particle interaction. The plasma temperature increases linearly with time in this simulation to 25 times its initial value in a time $\Delta t = 100/\omega_{pe}$. The dissipation rate, defined in terms of the electrostatic wave energy and the rate of temperature increase by

$$\frac{d}{dt}\int dx\, nT = \nu^* \int dx \frac{E^2(x)}{8\pi},$$

is thus seen to be substantial, about $0.4\omega_{pe}$. Figure 2 shows an electron-phase-space plot (v versus x) from the simulation, again at $\omega_{pe} t = 600$. Electrons are accelerated through the narrow, intense structure, forming streamers in phase space which are similar to those seen in simulations of resonant absorption.[7] Indeed, this heating can be viewed as resonant absorption on nonlinearly produced density channels. The velocity increment of an electron which samples the maximum field as it transits the soliton is $\sim\sqrt{2}\,V_w$, where $V_w \equiv eE_p/m\omega$. If we add to this increment the initial particle velocity, we see that velocities in excess of five thermal velocities are attainable in a single pass. The efficient heating observed is not surprising when one considers that some particles, albeit only the fastest, suffer velocity changes of $O(V_w)$ in a transit time which is $O(\pi/\omega_0)$. Even in the presence of strong heating, solitons are observed to persist for times in excess of $500\omega_{pe}^{-1}$, after which time the plasma temperature has increased by almost 2 orders of magnitude.

In these periodic simulations, soliton lifetime is principally determined by large zero-order changes in the plasma temperature, which, for example, can drive the oscillating two-stream instability below threshold. We are currently examining the formation of solitons in simulations which model a heating region of finite length. Escaping heated particles are replaced by colder ones, allowing a steady state to be reached. These simulations will enable us to isolate the effects of ion inertia on the lifetime.

The final soliton width appears to be universal and is determined by very basic considerations. The adiabatic invariant $mv^2/2+e\varphi$, where φ is the ponderomotive potential $[e\varphi=\frac{1}{4}e^2E_0^{\,2}(x)/m\omega^2]$, can be used to describe the motion of a particle of velocity v in an almost monochromatic electric field if the inequality $v/L\omega \ll 1$ is satisfied. Here L is the scale of spatial variation of the field and ω is its frequency. A sufficiently slow particle transits a localized region of oscillating field with only an exponentially small energy change (if the spatial variation of the field is analytic). It is just the breakdown of the constancy of this invariant for a large number of particles which signals the onset of strong heating. These considerations allow us to estimate the width l of a soliton by setting $v/l\omega=1$ or $l/\sqrt{3}\,v_{Te}=2\pi/\omega_0$. Here the $\sqrt{3}\,v_{Te}$ arises from the choice of a rectangular velocity distribution of the form $f_e(v) = n/2\sqrt{3}\,v_{Te}$ for $|v| \leq \sqrt{3}\,v_{Te}$, $=0$ otherwise. This estimate, $l \simeq 12\lambda_{De}$, is in reasonable agreement with the observed full width at half-maximum intensity of about $15\lambda_{De}$. In other simulations with Maxwellian distributions, essentially the same width is observed.

We have quantified this estimate by numerically calculating the energy change of particles which are incident upon a localized field structure of the form $E(x,t)=E_0\,\mathrm{sech}(kx)\cos(\omega t)$. The functional form $\mathrm{sech}(kx)$ provides a reasonable fit to the observed spatial dependence of E. The relevant amplitude parameter $k\Delta x \equiv keE_0/m\omega_0^{\,2}$ was chosen to be 0.3, the value observed in the simulations.

Many particles of each initial velocity class $v>0$ were distributed uniformly in initial position over an interval $x_0-\Delta x \leq x \leq x_0$ with $\Delta x\,\omega/v=2n\pi$ and $x_0k \ll -1$. Their motion was followed numerically until their interaction with the structure was complete. The phase-averaged energy change of each class was computed. Particles of velocity $v<v_1 \equiv eE_0/\sqrt{2}\,m\omega_0$ were reflected with no energy change. Those with $v_1<v<v_2 \simeq 0.3\omega_0/k$ passed through with no noticeable energy change. Particles with larger initial velocities gained energy. The maximum energy gain was for particles of velocity class $v_3 \simeq 0.95\omega_0/k$. Their maximum velocity change (as a function of initial phase) was $\sim\sqrt{2}\,V_y$. The energy gain decreased monotonically thereafter with increasing initial velocity.

The amplitude of the energy change curve varied linearly with $E_0^{\,2}$ as $E_0^{\,2}$ decreased over 5 orders of magnitude, suggesting that the value $k\Delta x=\frac{1}{3}$ is small enough for the nonadiabatic particles to validate a linearized calculation of the wave-particle damping. We have analytically calculated the linear dissipation rate for the assumed form $E(x,t)=E_0\,\mathrm{sech}(kx)\cos(\omega t)$ as a function of $k\lambda_{De}$ for both rectangular and Maxwellian distributions. Briefly stated, both numerical and analytic analyses predict a smaller than observed value for ν^* unless $k\lambda_{De}$ is taken about 50% larger than observed. We expect that this discrepancy can be removed by including the self-consistent distribution function in such a calculation rather than the initial distribution function $[T_e(\omega_{pe}t=600) \simeq 2T_e(0)]$.

The maximum intensity is more difficult to estimate. In the sample simulation, the plasma temperature changes so rapidly that no simple estimate of the intensity is very convincing. The maximum intensity becomes large enough to initially reflect nearly all the particles from the soliton, i.e., $e_0E_p/m\omega \sim \sqrt{6}\,v_{te}$.

Both because the soliton grows so rapidly until the onset of heating and because the temperature increases so rapidly thereafter, the ion-density depression associated with the intensity does not follow from a balance between the plasma and ponderomotive pressure, i.e., $\ln(n/n_0) \neq e\varphi/\theta_e$. Another indication of the importance of ion inertia is obtained upon examination of ion phase space where ion flow velocities comparable to the acoustic velocity are observed. In the finite-interaction-length simulations currently under investigation, the long soliton lifetime and the attainment of steady plasma temperature allow a closer pressure balance to be maintained at long times after soliton formation. After the formation of the density channel, the ion flow velocity vanishes and pressure balance provides a good estimate of the relative density depression.

Intense, localized spikes of high-frequency field play a role in many practical applications. They appear to be a general feature of strong electron-plasma-wave turbulence. For example, Estabrook, Valeo, and Kruer have carried out many two-dimensional, electromagnetic, relativistic simulations[8] of resonant absorption of radiation in plasmas. A common feature observed in the simulations[8,9] is a pronounced steepening

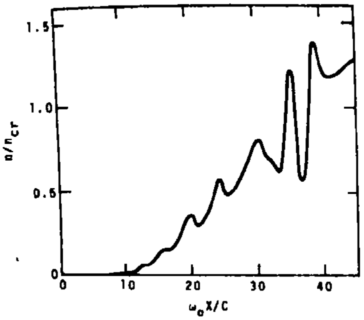

FIG. 3. An ion density profile from a two-dimensional electromagnetic simulation of resonant absorption of intense radiation. The profile initially had a linear rise to $1.5n_{cr}$ in $2\lambda_0$, where $n_{cr} = m\omega_0^2/4\pi e^2$ and λ_0 is the free-space wavelength. The energy density of the radiation is $\frac{1}{4}$ the plasma thermal energy density, and the angle of incidence is 24°. Plasma expansion later reduces the size of the secondary density maxima, leaving a density step from subcritical to supercritical.

of the density profile near the critical density at which resonant excitation occurs, as shown in Fig. 3. This density step is driven by a strong gradient in the resonantly excited electron-plasma wave intensity, as well as by a gradient in the electron temperature due to the plasma heating. The result is the production of an intense narrow spike of high-frequency electric field with a self-consistent sharp variation in plasma density, both of which have a scale length of $(10-20)\lambda_{De}$.

This nonlinear steepening of the density profile is found to have a number of important consequences. It reduces the region of plasma accessible to instabilities transverse to the density gradient and makes resonant absorption an effective mechanism for larger angles of incidence. The density modifications can also enhance the amount of absorption. For example, we have observed resonant absorption to occur multiply on a series of nonlinearly produced density channels near the critical density. Sizable modification of the density profile due to resonant absorption has been recently observed in microwave experiments,[10] even with rather modest incident power levels.

Finally we note that the source of the pump electric field can be an injected electron beam rather than incident radiation. We have run simulations which verify this assertion. For example, a beam of density $n_b/n_0 = 2\times 10^{-2}$, velocity $v_B/v_{te} = 25$, and temperature $\theta_b = \theta_e$ first excites the electron two-stream instability. This leads to the formation of a large amplitude, long wavelength ($kv_B \simeq \omega_{pe}$) plasma wave. This plasma wave then excites the oscillating two-stream instability,[3,11] which leads to soliton formation. The solitons then efficiently transfer their energy to the background electrons as described above. Again, the soliton width is approximately $15\lambda_{De}$. Solitons may have been observed in beam-plasma experiments,[12] where apparently stationary and intense structures of width $\sim 10\lambda_{De}$ appear upon beam injection.

We gratefully acknowledge many useful discussions with K. G. Estabrook, J. J. Thomson, A. B. Langdon, and B. F. Lasinski. All work was performed under the auspices of the U. S. Atomic Energy Commission.

---

[1] V. E. Zakharov, Zh. Eksp. Teor. Fiz. 62, 1475 (1972) [Sov. Phys. JETP 35, 908 (1972)]; K. Nishikawa, Y. C. Lee, and C. S. Liu, University of California at Los Angeles Report No. COO-3237-30, 1974 (to be published).

[2] A. S. Kingsep, L. I. Rudakov, and R. N. Sudan, Phys. Rev. Lett. 31, 1482 (1972).

[3] L. Thode and R. N. Sudan, Phys. Rev. Lett. 30, 732 (1973).

[4] J. J. Thomson, R. J. Faehl, and W. L. Kruer, Phys. Rev. Lett. 31, 918 (1973).

[5] G. J. Morales, Y. C. Lee, and R. B. White, Phys. Rev. Lett. 32, 457 (1974).

[6] V. P. Silin, Zh. Eksp. Teor. Fiz. 48, 1679 (1965) [Sov. Phys. JETP 21, 1127 (1965)]; K. Nishikawa, J. Phys. Soc. Jpn. 24, 916 (1968); P. K. Kaw and J. M. Dawson, Phys. Fluids 12, 2586 (1969).

[7] J. P. Freidberg, R. W. Mitchell, R. L. Morse, and L. I. Rudsinski, Phys. Rev. Lett. 28, 795 (1972).

[8] K. G. Estabrook, E. J. Valeo, and W. L. Kruer, to be published; J. DeGroot and J. Tull, Lawrence Livermore Laboratory report, 1974 (unpublished).

[9] D. Forslund, J. Kindel, K. Lee, E. Lindman, and R. Morse, LASL Report No. LA-UR-74-894, 1974 (to be published).

[10] R. L. Stenzel, A. Y. Wong, and H. C. Kim, Phys. Rev. Lett. 32, 654 (1973).

[11] S. Kainer, J. Dawson, and T. Coffey, Phys. Fluids 15, 2419 (1972).

[12] W. H. Quon, Ph.D. thesis, Department of Physics, University of California at Los Angeles, 1974 (unpublished).

Ion-Ion Beam Instability in a Cylindrical Geometry

Noah Hershkowitz,* Thomas Romesser,† Georg Knorr,‡ and Christoph K. Goertz§
Department of Physics and Astronomy, The University of Iowa, Iowa City, Iowa 52242

(Received 21 January 1974)

The ion-ion instability is studied in a cylindrical double-plasma device. Low frequency cylindrical standing waves are found which are one-dimensional in character with frequency proportional to beam velocity. An approximate dispersion relation for the cylindrical standing waves is derived.

Double-plasma (DP) devices have recently been used to study the incoherent ion-ion two-beam instability produced by one-dimensional beams in unmagnetized plasmas.[1-5] This turbulence is found to be *three*-dimensional in character in agreement with the linear theory of the ion-ion instability[6-9] which predicts that the instability depends on $\vec{k}\cdot\vec{v}_b$, where $\vec{k}$ is the *plane*-wave propagation vector and $\vec{v}_b$ is the beam velocity. Although there is an upper limit on v_b beyond which the *one*-dimensional ion-ion instability will not grow, there always will be oblique directions for which the projection of $\vec{v}_b$ on $\hat{k}$ will give growing modes in *three* dimensions. Means *et al.*[10] have recently argued that the observation of turbulence in experiments with *one*-dimensional electrostatic ion acoustic shocks depends fundamentally on this *three*-dimensional property of the instability.

In this Letter we report the production of a coherent ion-ion instability which is essentially one-dimensional in character. This has been accomplished by generating cylindrical *standing* waves which are resonant with ingoing and outgoing beams in a cylindrical DP device at the University of Iowa. This device differs from conventional DP devices[1-5] in that the cylindrical boundary of the plasma plays a dominant role. A grounded cylindrical screen through which the beam in injected, serves as a well-defined boundary condition (vanishing potential) for the standing waves. In conventional devices[1-5] the dimensions were such that wave and particle phenomena were *not* significantly affected by the presence of boundaries. The dimensions of those devices were *large* compared to the ion charge-exchange length, the *e* folding distance for ion-acoustic waves, and all wavelengths of interest. In the cylindrical DP device described here the diameter of the plasma is comparable to these lengths.

A description of these standing waves is derived from the Vlasov equation in a cylindrical geometry. The dependence of the frequencies ω of the instabilities on the beam velocity is shown to be remarkably similar, but not identical, to the results for a strictly one-dimensional ion-ion instability.

The cylindrical DP device, which has recently been used to study cylindrical solitons,[11] is shown in Fig. 1. Two *concentric* argon plasmas are separated by an outer negatively biased screen and an inner screen *held at ground potential.* Plasma within the inner cylinder is produced in an adjacent connected chamber. Typical operating parameters were electron temperature $T_e \approx 1$ eV, ion temperature $T_i \approx 0.1$ to 0.2 eV, average plasma density $n_i \sim 10^8$ to 10^9 cm^{-3}, and pressure $\approx 2\times10^{-4}$ Torr. A steady-state radially ingoing cylindrical beam is formed by raising the plasma potential in the outer cylinder. Beam density ratios $\eta \equiv n_b/n_i$ are controlled by varying the concentric discharges. The ion charge-exchange length was greater than the inner-cylinder radius.

Energy distribution functions in the inner plasma (region *A* in Fig. 1) are measured with two energy analyzers with depth-to-area ratios great-

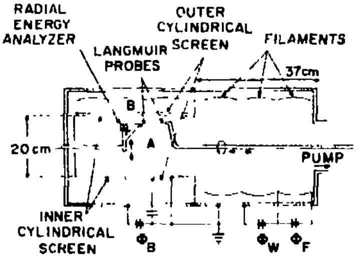

FIG. 1. Cylindrical DP device with two insulated concentric plasmas. The inner plasma is produced in the right half of the device. Beam energy is controlled by varying Φ_B. Φ_F, filament supply voltage; Φ_W filament-to-wall voltage; Φ_B, applied bias voltage. $T_e = 1.0$ eV; $T_i \lesssim 0.2$ eV; $N_0 = 10^8$–10^9 cm^{-3}; pressure, 2×10^{-4} Torr.

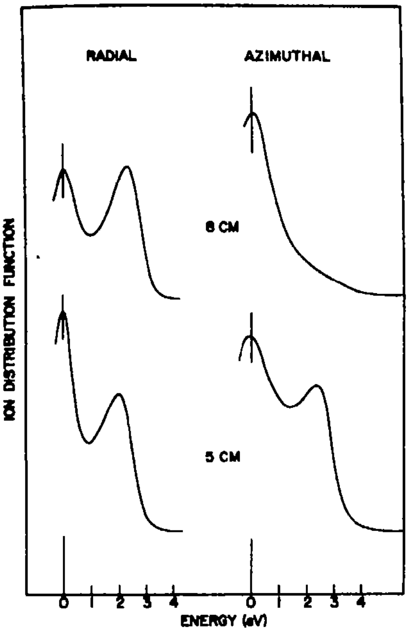

FIG. 2. Typical radial and azimuthal energy-analyzer traces at 5 and 8 cm are shown. Similar traces are observed for radii less than 6 cm indicating the presence of a ring distribution function in velocity space. The absence of an azimuthal beam at 8 cm is apparent. Azimuthal traces are found to be independent of φ. Broadening of these traces is instrumental.

er than 1, whose radial coordinates can be varied. One energy analyzer measures the energy distribution function of particles with velocities in the radial direction, another observes the energy in the φ direction. A third measures outgoing energy distribution functions in the outer plasma (region B in Fig. 1). Typical energy-analyzer traces are shown in Fig. 2. Near the inner screen the beam is seen to be radial. For radii less than 7 cm we find approximately equal radial and azimuthal beam components, indicating that the beam forms a ring in velocity space. The spatial region over which the ring distribution function exists is determined by the beam velocity, and the separation and mesh size of the two concentric screens. The region increases for smaller energies. The presence of a ring distribution function rather than a purely radial beam results in a uniform beam density ($r<7$ cm) with no steady-state electric field. This facilitates a theoretical description of the instability.

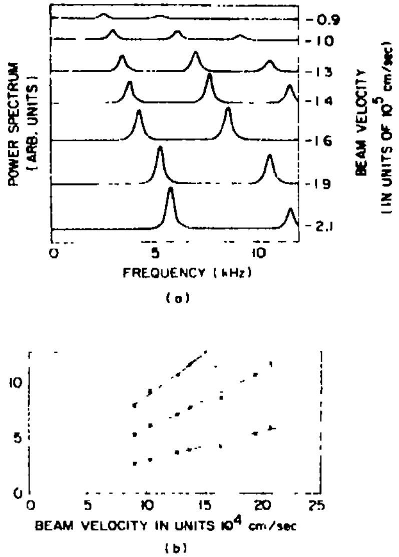

FIG. 3. (a) Power spectra showing the first three harmonics as a function of beam velocity. (b) Frequency versus beam velocity for the three lowest harmonics. No growing modes are observed for $v_b < 0.9\times10^5$ cm/sec and for $v_b > 2.2\times10^5$ cm/sec.

Instabilities are detected by positively biased Langmuir probes oriented in the axial direction and by the energy analyzers. One Langmuir probe is variable in the radial direction and the other is variable in the φ and axial directions. Langmuir probes indicate that relatively uniform background plasma and beam densities are achieved in this device. Langmuir-probe measurements within the inner cylinder (region A in Fig. 1) showed no φ or z dependence (except near the cylinder ends).

A comparison of signals simultaneously obtained at different positions showed that the instability was *in phase* throughout the inner plasma, demonstrating that standing waves were produced. Therefore it is meaningful to consider power spectra. Typical instability power spectra as a function of beam velocity are shown in Fig. 3(a). For high beam velocities we observe *no instability*. The onset of the instability is seen for a beam energy of approximately 1.0 eV. For beam energies less than approximately 0.2 eV the instability disappears. As the plasma potential of the outer plasma is made less than the potential of the inside plasma we observe incoherent instabilities between the outer cylindrical screen and the outer walls of the chamber (region B in Fig. 1).

Measurements of the power spectra in the radial direction show that the three lowest frequencies correspond to resonant modes with no nodes, one cylindrical node, and two cylindrical nodes, respectively, further demonstrating cylindrical standing waves. Figure 3(b) shows that ω is roughly proportional to v_b for the first three harmonics. In addition, the second and third harmonics have approximately 2 and 3 times the frequency of the first. This suggests that $\omega/k_n = \alpha v_b$ with α constant, describes all three modes, with k_n varying approximately with the mode number.

These results can be understood by considering the linear Vlasov equation in cylindrical geometry. The Vlasov equation can be written for one component (ions or electrons) in the following way:

$$\frac{\partial f}{\partial t}+v_r\frac{\partial f}{\partial r}+v_\varphi\frac{\partial f}{r\partial\varphi}+\left(\frac{e}{m}E_r+v_\varphi{}^2r^{-1}\right)\frac{\partial f}{\partial v_r}+\left(\frac{e}{m}E_\varphi-v_rv_\varphi r^{-1}\right)\frac{\partial f}{\partial v_\varphi}=0. \tag{1}$$

For a stationary homogeneous equilibrium distribution $f_0(r, v_r, v_\varphi)$ with $\vec{E}=0$, we find $v_\varphi r^{-1}(v_\varphi\,\partial f_0/\partial v_r - v_r\,\partial f_0/\partial v_\varphi)=0$. This means that the zeroth-order distribution function depends only on the magnitude of the velocity, $f_0=f_0(v)=f_0[(v_r{}^2+v_\varphi{}^2)^{1/2}]$; i.e., the distribution is *concentric* in velocity space and the beam must be a ring. Experimentally, we find such a distribution function extending from the center to within 3 cm of the inner screen for beam energies less than 2 eV.

Perturbing the plasma, we write $f(\vec{r},\vec{v},t)=n_0f_0(v)+f_1(\vec{r},\vec{v},t)$, where $f_1(\vec{r},\vec{v},t)$ is given by

$$f_1(\vec{r},\vec{v},t)=\int_0^t dt_0\,\nabla\Phi(\vec{r}_0(\vec{r},\vec{v},t-t_0),t_0)\cdot\partial f_0(v)/\partial\vec{v}, \tag{2}$$

with Φ being the electrostatic potential. The time integral is taken along the straight-line orbits of the unperturbed state. In evaluating the time integral we consider the plane-propagating waves $\Phi(\vec{r},t)=\Phi_0\exp[i(ax+by-\omega t)]=\Phi_0\exp\{i[kr\cos(\varphi-\alpha)-\omega t]\}$. Then the integral in Eq. (2) can be performed to give

$$f_1(\vec{r},\vec{v},t)=\frac{e}{m}\Phi(\vec{r},t)\frac{kv\cos(\theta-\alpha)}{kv\cos(\theta-\alpha)-\omega}\,\frac{\partial f_0(v)}{v\,\partial v}. \tag{3}$$

In writing Eq. (3) and the potential we have used the following definitions:

$$x=r\cos\varphi,\quad y=r\sin\varphi,\quad v_x=v\cos\theta,\quad v_y=v\sin\theta,\quad a=k\cos\alpha,\quad b=k\sin\alpha.$$

When calculating the density from Eq. (3) by integrating over v and θ, we note that the dependence of $\cos(\theta-\alpha)$ on α can be suppressed because θ is integrated over all angles. Thus we obtain for the density

$$n(\vec{r},t)=\int_0^\infty v\,dv\int_0^{2\pi}d\theta\,f_1=(e/m)n_0\Phi(\vec{r},t)k^2G(\omega/k,f_0), \tag{4}$$

with

$$G\left(\frac{\omega}{k},f_0\right)=k^{-2}\int_0^\infty v\,dv\int_0^{2\pi}d\theta\,\frac{\cos\theta}{\cos\theta-\omega/kv}\,\frac{\partial f_0(v)}{v\,\partial v}. \tag{5}$$

In order to express the density in cylinder functions we let Φ_0 depend on α, $\Phi_0(\alpha)=(\Phi_\nu/\pi)\exp(i\nu\alpha-\nu\pi/2)$, and integrate over α. A change of the variable α to $w=A+\varphi$ and an appropriate extension of the limits of the integral to infinity produces the integral representation of the Hankel or Bessel functions $Z_\nu(kr)\exp(i\nu\varphi)$. Thus we can write

$$n(r,t)=(e/m)\Phi_\nu Z_\nu(kr)\exp(i\nu\varphi)G. \tag{6}$$

The densities have to be inserted into Poisson's equation,

$$-\nabla^2\Phi=4\pi\textstyle\sum_j e_jn_j. \tag{7}$$

We note that $Z_\nu(kr)\exp(i\nu\varphi)$ is an eigenfunction of the Laplacian. This shows that cylinder functions are eigenfunctions of the beam-plasma system. For the boundary conditions of the experiment, $\Phi=0$ on boundary, we obtain directly $\nu=0$, $kR=\alpha_{0_\mu}$, where α_{0_μ} is the μth zero of the Bessel function $J_0(\rho)$. It is important to notice that these are the only nonsingular solutions and they represent standing waves. The dispersion relation is found from Eqs. (7), (6), and (5):

$$D(k,\omega) = 1 - \sum_j \omega_{pj} G_j = 1 - \sum_j \omega_{pj}^2 k^{-2} \int_0^\infty v\,dv \int_0^{2\pi} d\theta \frac{kv\cos\theta}{kv\cos\theta - \omega} \frac{\partial f_{0j}(v)}{v\,\partial v} = 0. \tag{8}$$

Note that $k = \alpha_{0\mu}/R$. k is not a *plane*-wave propagation vector.

We consider now a background plasma with Maxwellian ion and electron distributions with $T_e \gg T_i$. In addition we have a radial influx of ions of velocity v_b, which can approximately be described by $f_b(v) = (n_b/2\pi v_b)\delta(v - v_b)$. From the Penrose criterion it follows that for small v_b the system is stable as well as for very large v_b. Both effects have been observed experimentally [compare Fig. 3(b)]. From the assumed distribution functions we find for very small ion beam density ($\eta \ll 1$) and for $v_b \neq (kT_e/m_i)^{1/2} \equiv c_s$

$$\omega = +kv_\parallel[1 + \tfrac{1}{2}\eta^{2/3}\exp(2\pi i/3)c_s^{4/3}(v_b^2 - c_s^2)^{-2/3}].$$

For the case of resonance ($v_b = c_s$) we find $\omega = +kv_\parallel[1 + \frac{1}{2}\eta^{2/5}\exp(2\pi i/5)]$. The experimental proportionality of ω with v_b is evident from Fig. 3(b) which corresponds to $\eta \approx 0.2$.

In conclusion we have shown that low-frequency cylindrical standing waves which depend only on r are produced by the ion-ion beam instability in a cylindrical DP device. We have shown that their frequency is roughly proportional to the beam velocity. We believe that this is the first time that a coherent ion-ion beam instability has been observed. We ascribe this to the high symmetry of the experiment which substantially reduces the off-axis modes. We have derived a dispersion relation for the coherent cylindrical-standing-wave instability from the appropriate Vlasov equations for the cylindrical geometry. This predicts unstable standing waves with ω/k_n proportional to v_b rather than traveling waves.

We are indebted to David Montgomery for advice, assistance, and enlightening discussions. We are grateful to Professor I. Alexeff for a very thorough and critical discussion of this paper. We would like to acknowledge helpful discussions with Professor G. Joyce. In addition we thank Alfred Scheller for construction of much of the apparatus.

---

[*] Present address: Department of Physics, University of California, Los Angeles, Calif. 90024.

[†] Work supported in part by the National Aeronautics and Space Administration under Grant No. NGL-16-001-043.

[‡] Work supported in part by the U. S. Atomic Energy Commission under Contract No. AT(11-1)-2059.

[§] Work supported in part by the National Science Foundation under Grant. No. GA-31676.

[1] R. J. Taylor, D. R. Baker, and H. Ikezi, Phys. Rev. Lett. 24, 206 (1970).

[2] R. J. Taylor, K. R. MacKenzie, and H. Ikezi, Rev. Sci. Instrum. 43, 1675 (1972).

[3] A. Y. Wong and R. W. Means, Phys. Rev. Lett. 27, 973 (1971).

[4] R. A. Stern and J. F. Decker, Phys. Rev. Lett. 27, 1266 (1971).

[5] R. J. Taylor and F. V. Coroniti, Phys. Rev. Lett. 29, 34 (1972).

[6] B. D. Fried and A. Y. Wong, Phys. Fluids 9, 1084 (1966).

[7] T. M. O'Neil and J. H. Malmberg, Phys. Fluids 11, 1754 (1968).

[8] D. W. Forslund and C. R. Shonk, Phys. Rev. Lett. 25, 281 (1970).

[9] S. Abas and S. P. Gary, Plasma Phys. 13, 262 (1971).

[10] R. W. Means, F. V. Coroniti, A. Y. Wong, and R. B. White, Phys. Fluids 16, 2304 (1973).

[11] N. Hershkowitz and T. Romesser, Phys. Rev. Lett. 32, 581 (1974).

Electron Cyclotron Emission from a Tokamak Plasma: Experiment and Theory

A. E. Costley,* R. J. Hastie, J. W. M. Paul, and J. Chamberlain*
United Kingdom Atomic Energy Authority Research Group, Culham Laboratory, Abingdon, Berkshire, United Kingdom

(Received 24 June 1974)

We present the first measurements of the power, polarization, and frequency spectrum of the electron cyclotron emission from a tokamak plasma. The radiation is not polarized, does not have the previously predicted spectrum, and under certain circumstances is an order of magnitude above the predicted power level. We interpret the results in terms of a scrambling of polarization on reflection within the torus and in terms of the emission from suprathermal electrons.

Electron cyclotron emission from hot toroidal plasmas is currently of importance in fusion research. It is anticipated that it could constitute a significant power loss in a reactor[1,2] and that a measurement of it could be an informative plasma-diagnostic technique.[3] In this Letter we present measurements of the electron cyclotron emission (occurring at millimeter wavelengths) from the hot plasma of a tokamak device.

The plasma investigated is produced by the CLEO tokamak.[4] It has a toroidal flux density $B_\varphi \leq 2.0$ T, a mean electron density $n_e \sim 2\times10^{19}$ m^{-3}, a central electron temperature $T_{e0} \sim 300$ eV, a central ion temperature $T_{i0} \sim 200$ eV, a major radius $R_0 = 0.9$ m, a minor radius $a_0 = 0.18$ m, and duration up to 180 msec.

Emission measurements.—These were made by observing the plasma along a major radius through a wedge-shaped window of crystal quartz (Z cut). Radiation from the plasma was directed into a two-beam polarization-type interferometer.[5] The path difference (x) within this was scanned in 10 msec over the range $-1 < x < 9$ mm by oscillation of one of the interferometer mirrors, and the resulting interference patterns (Fig. 1) were detected with a Putley indium antimonide detector. (The spectrally integrated emission was also detected for reference purposes.) Subsequent Fourier transformation of the interference patterns and calibration of the apparatus yielded the emission spectra.

In the calibration the time dependence of the path difference was measured by using an HCN laser ($\lambda = 337$ μm) and the absolute power response of the interferometer-detector arrangement was determined with a dc mercury arc lamp. Such lamps have been shown previously[6] to radiate approximately as a black body with a radiation temperature of 3000 K.

The emission spectrum from a typical tokamak shot is shown in Fig. 2 (curve a). The resolution in the spectrum is determined by the total scan x_m used in the Fourier transform, $R = cx_m^{-1}$, and in this case is 37.5 GHz. As expected, emission peaks occur at the cyclotron harmonics ($n\omega_{ce}$) $n = 2$, 3, and 4 for the magnetic field B_0 at the center of the plasma. The emission at $n = 1$ (i.e., I_1) could not be deduced by the normal procedure since the calibration system was insensitive in this region. However, from the known responsivity of the Putley detector an upper limit can be placed on I_1 as in Fig. 2.

By combining data recorded on two identical tokamak shots, spectra with an improved resolution of 25 GHz were obtained (Fig. 2, curve b). A mirror in the fixed arm of the interferometer was displaced between the two shots so that adjacent parts of the interference patterns were scanned, and composite interference patterns were constructed and transformed.

Variation of the tokamak conditions revealed a clear correlation between the level and spectrum

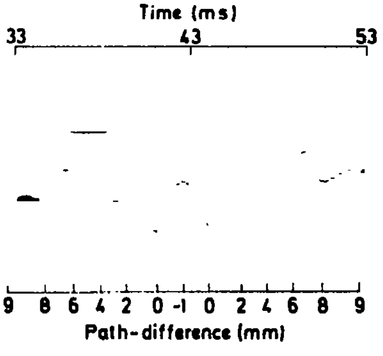

FIG. 1. Signal from the interferometer showing two scans of the interference pattern, traversed in opposite directions. (Time is from initiation of discharge.)

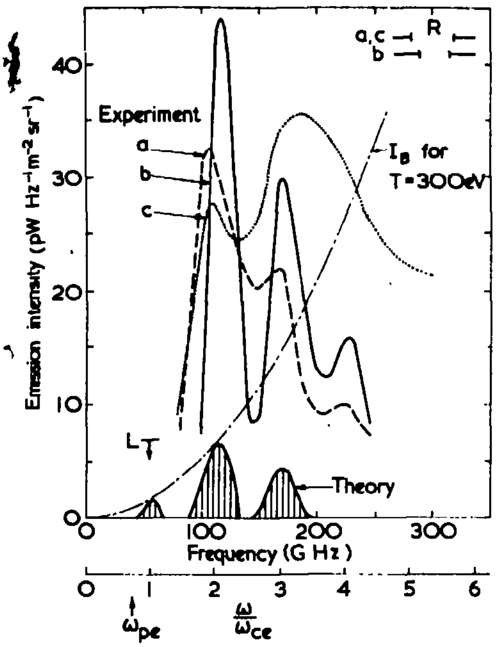

FIG. 2. Emission spectra. Experiment: curve *a*, single scan from Fig. 1; curve *b*, composite scan; curve *c*, single scan but with appreciable runaway (*L* is the limit of detectability). Theoretical: prediction for polarized emission (extraordinary mode, vertical hatching). ω_{pe} is plasma frequency.

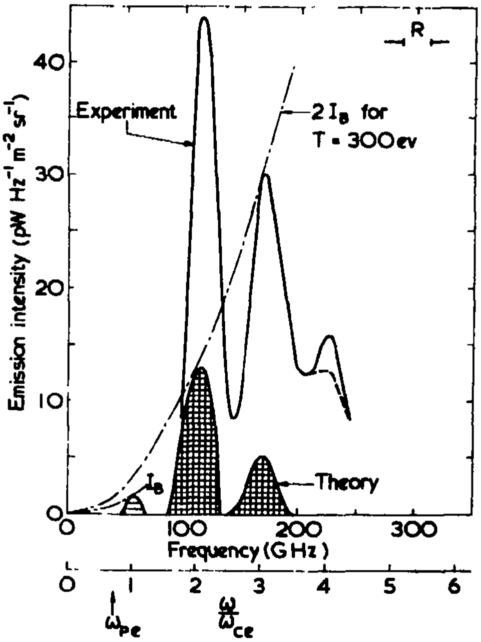

FIG. 3. Emission spectra. Experiment: composite scan (effect of smoothed calibration at $n=4$, dashed line). Theoretical: prediction with polarization scrambling (ordinary mode, horizontal hatching; and unpolarized, cross hatching).

of the emission (e.g., Fig. 2, curve *c*), and the level of hard x-ray emission. (Note that the latter is an indication of the presence of high-energy runaway electrons.) Under conditions of relatively intense x-ray emission the spectrally unresolved monitor showed an increase of up to an order of magnitude in emitted power.

The uncertainties in the measurement method are such that the relative shape and frequency position of the spectral features are reliable to about ±10%, and that the absolute level of the spectra is reliable to about an order of magnitude (i.e., factor of 3 either way). The latter uncertainty arises mainly from the need to use different optical and electronic systems for the calibration and the plasma measurements. The emission in the region of $4\omega_{ce}$ is subject to a ±20% uncertainty because of the presence of a small unidentified feature at about 225 GHz in the calibration data. The effect of smoothing this feature is shown in Fig. 3.

Polarization measurements.—The orientation of a wire polarizer in the interferometer was changed between discharges and the resulting interference patterns were recorded. Since the transformed spectra were the same to within the discharge reproducibility limits (±10%), the detected radiation was unpolarized (to within this uncertainty) at all frequencies in the region examined.

In a separate experiment an optical system of smaller *étendue*, which excluded radiation reflected in the torus side arm, was used, and spectrally integrated signals were recorded. Since these were independent of the orientation of a wire polarizer mounted in the optical system, we conclude that the radiation that crossed the plasma-vacuum boundary was unpolarized.

In an effort to understand this lack of polarization we measured the depolarizing effect of multiple reflections within the stainless-steel torus. With no plasma present the torus was irradiated with a polarized beam of 2-mm-wavelength radiation and the polarization state of the radiation emanating from several radial ports was determined. While radiation from a port immediately adjacent to the entrance port ($\varphi = 20°$) was partially polarized that from other ports with $\varphi \geqslant 90°$ was less than ±10% polarized, demonstrating that multiple reflections within the torus can depolarize the radiation.

Theory for polarized emission.—We consider the cyclotron emission from a toroidal plasma in the direction of the major radius[2,3] (nonrelativistic limit for $T_e \sim 300$ eV). The intensity[7] $I_g(\omega)$ in each mode (extraordinary, $g = e$; ordinary, $g = o$) is given by[8]

$$I_g = I_B \frac{1 - \exp(-\int \alpha_g ds)}{1 - r\exp(-\int \alpha_g ds)}, \tag{1}$$

where $\alpha_g(\omega)$ is the absorption coefficient of the plasma, $I_B = \omega^2 k T_e / 8\pi^3 c^2$ is the black-body intensity for a single mode, and $r = r(\omega)$ is the reflection coefficient of the metal wall bounding the plasma. The spatial contributions are integrated across the toroidal profile with arbitrary $n_e(s)$, $T_e(s)$, and defined $B(s) = B_0(1 - s/R_0)$, $|s| \geqslant a_0$. For each ω and harmonic n, the resonance $\omega = n\omega_{ce}(s_r)$ defines the position s_r, so that

$$\int \alpha_e ds = \sum_{n=1}^{\infty} n_e(s_r)\left[\frac{kT_e(s_r)}{2mc^2}\right]^{n-1} \frac{n^{2n-2}}{(n-1)!}\left(\frac{\pi e R_0}{2\epsilon_0 B_0 c}\right), \tag{2}$$

while $\alpha_o = 0$. The values of $\int \alpha_e ds$ for the CLEO tokamak are listed in Table I together with $1 - r(\omega)$ for stainless steel. We note that harmonics $n < 3$ are optically thick ($\int \alpha_e ds \gg 1 - r$), harmonics $n > 3$ are optically thin ($\int \alpha_e ds \ll 1 - r$), while harmonic $n = 3$ is intermediate, and that T_e can be determined from the ratio of any two harmonics provided they are not both optically thick.

The spectral widths of the various harmonics are determined by the toroidal inhomogeneity of the field, which gives an overlap of harmonics $n = 3$ and 4. However, provided the profiles of $n_e(s)$ and $T_e(s)$ are not particularly flat, the main emission peaks can be calculated separately.

TABLE I. $\int \alpha_e ds$ for the CLEO tokamak and $1 - r(\omega)$ for stainless steel.

n	$\int \alpha_e ds$	$1 - r(\omega)$
2	1.00	5.46×10^{-3}
3	2.96×10^{-3}	6.69×10^{-3}
4	1.46×10^{-5}	7.72×10^{-3}

Figure 2 shows the predictions of this model for the parameters of the CLEO tokamak with the measured parabolic $n_e(s)$, assuming a parabolic $T_e(s)$. Under low-runaway conditions (Fig. 2, curves *a* and *b*) we find that (i) the measured absolute magnitudes exceed the predictions by more than the estimated factor-of-3 uncertainty; (ii) the measured ratios, I_3/I_2 and I_4/I_2, of the intensities of the harmonics yield the electron temperatures 280 eV and 1.1 keV, respectively; and (iii) the main discrepancy is the observed absence of polarization.

Theory for unpolarized emission.—We now assume, on the basis of the subsidiary experiment mentioned above, that each reflection produces some scrambling of the polarizations. We define a transfer fraction p between the two polarizations at each reflection. The boundary condition for the reflected intensity I' then becomes

$$I_{(o,e)}' = r[I_{(o,e)} + p(I_{(e,o)} - I_{(o,e)})], \tag{3}$$

and the transport equation with $\alpha_o = 0$ yields a solution

$$I_e = I_B \frac{1 - \exp(-\int \alpha_e ds)}{1 - \hat{r}\exp(-\int \alpha_e ds)}, \tag{4}$$

$$I_o = I_e rp/(1 - r + rp), \tag{5}$$

where

$$\hat{r} = r[1 - p(1 - r)/(1 - r + rp)].$$

From these equations we see that the emission is completely unpolarized, i.e., $I_e = I_o$ for all n, when $1 - r \ll p$; and that for optically thick harmonics the total intensity, $I_e + I_e = 2I_B$, is double that found when $p = 0$, while for optically thin harmonics the total intensity, $I_o + I_e = I_B \int \alpha_e ds / (1 - r)$, is the same as for $p = 0$.

The predictions of this theory are plotted in Fig. 3. The observed absolute magnitude of I_3 exceeds the prediction by a factor 3.4, just outside the estimated uncertainty. The observed ratios of the peaks yield predicted electron temperatures of 400 eV (I_3/I_2) and 1.4 keV (I_4/I_2). Even allowing for the calibration uncertainty, the discrepancy in I_4 is large and we must look for an alternative explanation for this emission, in particular, in terms of runaway phenomena.

Emission with runaway electrons.—In the presence of a longitudinal electric field the electron distribution function contains a high-energy runaway region and a region of isotropic enhancement of the Maxwellian tail at lower energies. For simplicity, we simulate these distortions by a second Maxwellian distribution with temperature $T_2 \gg T_1$ and density $n_2 \ll n_1$. The above emission formulas are valid for a double Maxwellian velocity distribution provided that, for the nth harmonic,[9] we replace T_e in I_B by $(n_1T_1^{n}+n_2T_2^{n})/(n_1T_1^{n-1}+n_2T_2^{n-1})$ and $n_eT_e^{n-1}$ in $\int\alpha_e ds$ by $n_1T_1^{n-1}+n_2T_2^{n-1}$. The measured ratios I_3/I_2 and I_4/I_2 together with $n_1 = n_e$ and $T_1 = T_{e0}$ determine independent values $T_2 \sim 36(1+2\Delta T_e/T_e)$ keV and $n_2 \sim 8\times 10^{12}(1-7\Delta T_e/T_e)$ m^{-3}, where $\Delta T_e/T_e$ is the uncertainty in the measured electron temperature (± 10%). Although sensitive to the peak value of T_e (and to the assumed value of $1-r$), these results are not significantly modified by different profiles of $T_e(s)$.

One important characteristic of the spectrum observed for high-runaway conditions (Fig. 2, curve c) is the dominant broad peak at $\omega \sim 3.3\omega_{ce}$. Overlapping of I_3 and I_4 in the region $3.2 < \omega/\omega_{ce} < 3.6$ could occur for flat profiles $n_2(s)$ and $T_2(s)$. The above values of n_2 and T_2 are consistent with the ratio of this broad peak to I_2.

Discussion.—It is possible, in view of the uncertain absolute calibration, to assume that the second harmonic in Fig. 3 is fitted by the predicted curve for unpolarized emission [i.e., $2I_B(\omega)$] for the measured $T_e \sim 300$ eV. This change of calibration implies that the fundamental emission should be above the limit of detectability. However, the extraordinary-mode fundamental would be reflected in the decreasing B_φ at the upper-hybrid region,[10,11] leaving the ordinary mode below detectability, consistent with observation.

On the other hand, if I_2 really is well above $2I_B$ (Fig. 3) then we have to explain the suprathermal emission even for $n = 2$.

The main implications of this work are that (i) diagnostic applications may be confused by runaway phenomena, and (ii) the power balance of a fusion reactor may be adversely affected by the enhanced cyclotron emission arising from the depolarization and the runaway effects.

We wish to acknowledge discussions with Dr. D. D. Burgess, Dr. R. J. Bickerton, and E. Puplett and assistance from the CLEO tokamak team and J. Weaver.

---

*Present address: Division of Electrical Sciences, National Physical Laboratory, Teddington, Middlesex, United Kingdom.

[1] B. A. Trubnikov and A. E. Bazhanova, in *Plasma Physics and the Problems of Controlled Thermonuclear Reactions*, edited by M. A. Leontovich and J. Turkevich (Pergamon, New York, 1959), Vol. 3, p. 141.

[2] M. N. Rosenbluth, Nucl. Fusion 10, 340 (1970).

[3] F. Engelmann and M. Curatolo, Nucl. Fusion 13, 497 (1973).

[4] J. W. M. Paul *et al.*, in *Proceedings of the Sixth European Conference on Controlled Fusion and Plasma Physics, Moscow, 1973* (U.S.S.R. Academy of Sciences, Moscow, 1973).

[5] D. H. Martin and E. Puplett, Infrared Phys. 10, 105 (1970).

[6] A. H. Lichtenberg and S. Sesnic, J. Opt. Soc. Amer. 56, 75 (1966).

[7] Strictly, spectral radiance is in units W m^{-2} sr^{-1} rad^{-1} sec.

[8] G. Bekefi, *Radiation Processes in a Plasma* (Wiley, New York, 1966), p. 41.

[9] G. Bekefi, J. L. Hirshfield, and S. C. Brown Phys. Fluid 4, 173 (1961).

[10] H. Dreicer, in *Plasma Waves in Space and the Laboratory*, edited by J. O. Thomas and B. Landmark (Elsevier, New York, 1969).

[11] A. N. Dellis, private communication.

Rayleigh-Taylor Instability and Laser-Pellet Fusion

Stephen E. Bodner*
Lawrence Livermore Laboratory, Livermore, California 94550

(Received 2 May 1974)

The Rayleigh-Taylor instability in laser-driven spherical implosions can be stabilized by convective flow and by the "fire-polishing" effect, but the size of the stabilization effect depends on details of the thermal conductivity near the ablation surface.

In the basic concept for laser-pellet fusion, a dense cold shell of compressed deuterium-tritium is accelerated radially inward, while being compressed in a nearly adiabatic fashion.[1] When the shell reaches the center, it heats, ignites, and produces thermonuclear burning. The dense shell accelerates inward because of a sharp temperature front that continually ablates the outer

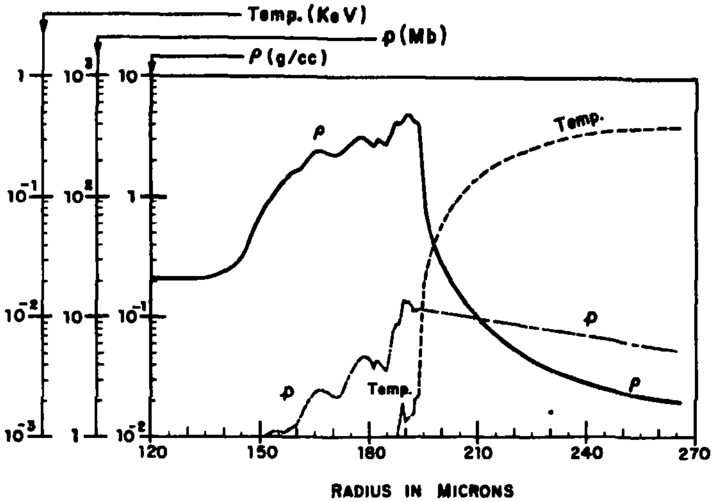

FIG. 1. Density, pressure, and temperature versus pellet radius, at one time, for a typical pellet implosion calculation.

edge of the cold compressed shell. Figure 1 shows sample radial profiles at one time of the mass density, electron temperature, and pressure, taken from a recent calculation by Nuckolls and Thiessen.[2]

In the accelerating frame moving with the ablation front, we have a dense fluid adjacent to a light fluid, with an effective outwardly directed gravitational force. This is the standard situation for the occurrence of the Rayleigh-Taylor instability, but with numerous modifications that are unique to the laser-pellet fusion concept. There have been several recent, and apparently conflicting, computer studies of Rayleigh-Taylor instability as it relates to laser-pellet fusion.[3] The only analytic work so far has been an unpublished derivation of the stabilizing effect of "fire polishing."[4] As the Rayleigh-Taylor instability grows, the peaks will be closer than the valleys to the laser deposition surface. The temperature gradients will thus be larger and the ablation faster at the peaks. This is the stabilizing "fire-polishing" effect.

Consider a model problem to isolate the effects of convective flow and of fire polishing. Also consider a slab geometry with two incompressible fluids connected by an ablation surface at $x = \xi(y,t)$. In this model problem, the equilibrium will be time independent, in the frame moving with the ablation front. In the laser-pellet fusion designs, the equilibrium actually changes on the nanosecond time scale. In order that our model be applicable to the pellet designs, attention is restricted to instability wavelengths such that the equilibrium does not change on the time scale of the growth rate. Without stabilization effects, $\gamma = (kg)^{1/2}$. At the sample time shown in Fig. 1, $g = 1.5\times10^{15}$ cm/sec^2. Thus I restrict my attention to wavelengths much less than 100 μm. I find, in fact, that under some circumstances the large-k modes are stabilized. More rigorously, I can only claim that I will show that large k modes grow no more rapidly than on the nanosecond time scale, because this is the time scale for changes in the equilibrium.

The perturbations in the high- and low-density regions can be treated as incompressible if the velocity of the plasma relative to the ablation surface is subsonic. In Fig. 1, the plasma becomes supersonic at about 230 μm. This supersonic flow will reduce the growth rate of perturbations with wavelength greater than or of the order of 35 μm.

The scale height at the ablation surface is less than 1 μm in Fig. 1. The finite gradient will limit the growth rate of perturbations with wavelength less than 1 μm.

Viscosity is important for perturbations such that $\gamma/(\nu k^2) < 1$ or $\gamma d^2/\nu < 1$. Here γ is the growth rate, ν is the specific viscosity at the ablation surface, k is the perturbation wave number, and d is the thickness of either the dense or the light fluid. At the ablation surface the ion temperature is less than 100 eV, so that viscosity is unimportant.

For all x and y use the one-fluid equations

$$\partial\rho/\partial t + \nabla\cdot(\rho\vec{v}) = 0, \tag{1}$$

$$\partial/\partial t(\rho\vec{v}) + \nabla\cdot(\rho\vec{v}\vec{v}) = -\nabla p + \rho\vec{g}. \tag{2}$$

For $x \neq \xi$, the fluids will be treated as incompressible:

$$\nabla\cdot\vec{v} = 0, \quad x \neq \xi, \tag{3}$$

For the jump conditions across the ablation front, use the model heat equation

$$\partial/\partial t(\rho e + \tfrac{1}{2}\rho v^2) + \nabla\cdot[\vec{v}(\rho e + \tfrac{1}{2}\rho v^2 + p)] = \rho\vec{v}\cdot\vec{g} + I(\xi)\delta(x-\xi). \tag{4}$$

I have modeled the electron thermal diffusion by a $\delta(x-\xi)$ deposition, with an $I(\xi)$ dependence to model the fire-polishing effect.

In the zeroth-order, time-independent equilibrium, the fluids have uniform density and velocity: ρ_0' and v_0' for $x<0$, ρ_0'' and v_0'' for $x>0$; $\vec{g} = +g\hat{e}_x$, with $\rho_0'' \ll \rho_0'$. Because the Rayleigh-Taylor instability involves surface motion, we write the hydrodynamic terms, with first-order perturbation, as

$$\psi(x,y,t) = \psi_0(x) - \xi(y,t)\Delta(\psi_0)\delta(x) + \tilde{\psi}(x,y,t), \tag{5}$$

where $\Delta(\psi_0)$ is the jump in the zeroth-order quantity across $x=0$, and $\tilde{\psi}(x)$ is bounded for all x and goes to zero as $x \to \pm\infty$. Here ψ represents any of the quantities appearing in Eqs. (1)–(4): ρ, v_x, v_y, p, ρv_x^2, $\rho v_x v_y$, etc. The fluid equations have been written in the form of a complete derivative in x to avoid ill-defined quantities such as $\delta(x)S(x)$, where $S(x)$ is the step function.

I look for solutions of the perturbed quantities of the form $\exp(\gamma t + iky)$, and obtain a set of jump conditions:

$$-\gamma\xi\Delta(\rho_0) + \Delta(\rho_0\tilde{v}_x + \tilde{\rho}v_0) = 0, \tag{6}$$

$$\Delta(\tilde{p} + \tilde{\rho}v_0^2 + 2\rho_0 v_0\tilde{v}_x) = -\xi g\Delta(\rho_0), \tag{7}$$

$$\Delta(\tilde{v}_y + ik\xi v_0) = 0, \tag{8}$$

$$\gamma\xi\rho_0 v_0\Delta(v_0) + \Delta(\tfrac{5}{2}\tilde{p}v_0 + \tfrac{5}{2}p_0\tilde{v}_x + \tfrac{1}{2}\tilde{\rho}v_0^3 + \tfrac{3}{2}\rho_0 v_0^2\tilde{v}_x) = I(\xi) - I(0) \cong \xi I(0)/L. \tag{9}$$

For $x<0$, the perturbed quantities satisfy the relations

$$\tilde{v}_y' = i\tilde{v}_x', \tag{10}$$

$$\tilde{p}' = -\rho_0'(\gamma/k + v_0')\tilde{v}_x', \tag{11}$$

$$\tilde{\rho}' = 0. \tag{12}$$

For $x>0$, there is one relation between the perturbed quantities, in the limit $x \to 0$:

$$\tilde{p}'' + i\rho_0''v_0''\tilde{v}_y'' - \frac{\gamma\rho_0''}{k}\tilde{v}_x'' + \frac{gv_0''}{\gamma + kv_0''}\tilde{\rho}'' = 0. \tag{13}$$

Note that $\tilde{\rho}''$ is not necessarily zero, because it can satisfy the relation $\gamma\tilde{\rho}'' + v_0''\partial\tilde{\rho}''/\partial x = 0$ with the form $\exp(-\gamma x/v_0'')$.

We now have eight equations, (6)–(13), for nine quantities: $\tilde{\rho}'$, $\tilde{\rho}''$, $\tilde{v}_x'$, $\tilde{v}_x''$, $\tilde{v}_y'$, $\tilde{v}_y''$, $\tilde{p}'$, $\tilde{p}''$, and ξ. If we expand the ablation region to a nonzero thickness, $(\xi - a) < x\ (\xi + a)$, then at $x = \xi - a$ the density, velocity, and pressure should be continuous. The density is ρ_0'. If we specify the temperature at $x = \xi - a$, we will have our ninth equation. The temperature just inside the ablation region is determined by the previous adiabatic compression, the thermal heat transport, and by suprathermal energy transport. As the ninth equation, we will assume that

$$p_1'(\xi) = \tilde{p}'(\xi) + \rho' g\xi = \beta p_0'(0)\xi/L, \tag{14}$$

where β is some unknown constant, of order 1, or perhaps much less than 1, depending on the unspecified details in the energy transport.

We now obtain a cubic dispersion relation,

$$u\sigma^3 + [u^2 - (1-P)]\sigma^2 + [u - 2u(1-P) + \epsilon u^2(1+\beta)]\sigma + [(1-u^2)(1-P) + \epsilon^2\beta u^4] = 0, \tag{15}$$

with $\sigma = \gamma/(kg)^{1/2}$, $\epsilon = \rho_0'/\rho_0''$, $u = kv_0''/(kg)^{1/2}$, and $P = \beta k p_0'(0)/(\rho_0' g)$. In deriving this equation, we have assumed that v_0'' is small compared to the acoustic velocity, and $\epsilon \ll 1$, but with no ordering assumptions on u or σ. If the distance between the ablation surface and the laser energy deposition surface is D, and if $kD \gg 1$, then one can show that $kL \cong 1$. This approximation has been used also.

If we set $u=0$ (a singular point in the cubic equation), the solution is $x = \pm 1$, the standard Rayleigh-Taylor result when $\epsilon \ll 1$.

In the standard Rayleigh-Taylor theory, $\gamma \to \infty$ as $k \to \infty$. From Eq. (15) we find that γ now has a maximum and then goes to zero for finite k. The maximum k for instability is the larger of $g/v_0''^2$ and $g\rho_0'/\beta p_0'(0)$.

If we ignore the fire-polishing effect by letting $\beta \to 0$ and $kL \to \infty$, instead of $kL = 1$, we obtain the stabilization due solely to convection:

$$\gamma = (kg)^{1/2} - kv_0'. \tag{16}$$

If we add in thermal conduction, $kL = 1$, but keep

$\beta = 0$, we obtain a weaker stabilization effect:

$$\gamma \cong -\tfrac{1}{2}kv_0' + (kg + \tfrac{1}{4}k^2v_0'^2)^{1/2}. \tag{17}$$

Thus under some circumstances, fire polishing can be destabilizing. Even though the peaks ablate faster than the valleys, the perturbed flow in the dense fluid is such as to move the peaks outward.

The stabilization phenomena depend on the parameter β, which in turn depends on details in the thermal conductivity in the region of the ablating surface. This result is similar to the general theory of weak deflagrations,[5] where one concludes that the fluid velocity relative to the ablation surface depends upon heat conductivity, and is not totally determined by the Rankine-Hugoniot relations. In weak deflagrations, such as in the laser-pellet implosion, one can derive the approximate relation

$$\tfrac{1}{2}\rho_0'(0)v_0'' \cong I_0.$$

Combining this with the definition of β, we obtain

$$\frac{1}{\beta} \cong 1 + \left.\frac{\rho_0'\,dv_0''/dt}{v_0''\,d\rho_0'/dt}\right|_{x=0}. \tag{18}$$

There are a number of inherent assumptions that give lower k limits to our theory's validity. Because the dense fluid should have a finite thickness d, we have $k > 1/d$. Incompressibility in the dense fluid requires that an acoustic wave be able to travel one wavelength in one e-folding time: $k\bar{v}_{ac} > \gamma$, where $\bar{v}_{ac}$ is the mean acoustic velocity $1/k$ in from the ablation surface. If $\gamma^2 \cong kg$, we find that $k > g/\bar{v}_{ac}^2$.

Finally, for small P, there is another unstable root of Eq. (15), which is driven by the convective behavior, and is not of the Rayleigh-Taylor type. It satisfies the dispersion relation

$$\gamma = g/v_0'' - kv_0''. \tag{19}$$

The physical mechanism behind this mode is unknown.

This research was intended as a model calculation to examine some stabilization mechanisms for Rayleigh-Taylor instability, to give insight into some of the important physics, to give guidelines to interpreting computational results, and to indicate the basic parameters of interest. In the case shown in Fig. 1, the acceleration is 1.6 $\times 10^{15}$ cm/sec^2. Using Eq. (18), find that $\beta \cong 0.7$. The maximum wave number is then 700 cm^{-1}. But because of the many assumptions in this theory, this value should be treated with some skepticism. Also because of the flexibility in laser-pellet fusion designs, one cannot draw any overall conclusions at the present time about the importance of Rayleigh-Taylor instability in laser-fusion, except to note that there are stabilization mechanisms.

I wish to thank Ray Kidder for suggesting this problem, and for his continuous encouragement while it was being solved.

---

*Now at Naval Research Laboratory, Washington, D. C. 20375.

[1] J. Nuckolls, L. Wood, A. Thiessen, and G. Zimmerman, Nature (London) 239, 139 (1972).

[2] A. Thiessen, private communication.

[3] J. N. Shiau, E. B Goldman, and C. I. Weng, Phys. Rev. Lett. 32, 352 (1974); D. B. Henderson and R. L. Morse, Phys. Rev. Lett. 32, 355 (1974); K. A. Brueckner and S. Jorna, KMS Fusion Laboratory, Ann Arbor, Michigan, Report No. KMSF-U97, 1973 (unpublished); G. Zimmerman, Lawrence Livermore Laboratory Report No. UCRL 74811, 1973 (unpublished).

[4] C. Leith, private communication.

[5] R. Courant and K. O. Friedrichs, *Supersonic Flow and Shock Waves* (Interscience, London, 1948), p. 231.

Ion Heating by the Current-Driven Electrostatic Ion-Cyclotron Instability*

N. Rynn, D. R. Dakin, D. L. Correll, and Gregory Benford
Department of Physics, University of California, Irvine, California 92664

(Received 25 July 1974)

We have observed and confirmed significant ion heating by the electrostatic ion-cyclotron instability in a barium plasma. We present spectroscopic evidence showing that this mechanism drastically alters the velocity distribution, demonstrating at least a highly nonlinear process and giving strong evidence for randomization of the particle motion. Experimental corroboration of a theory of Drummond and Rosenbluth is presented

We report the direct observation of ion heating in a fully ionized barium plasma, as indicated by an order-of-magnitude increase in ion temperature (from 2500°K to greater than 25 000°K) due to the current-driven electrostatic ion-cyclotron instability.[1] The instability was generated by a technique first used by Motley and D'Angelo in the Princeton University Plasma Physics Laboratory Q device,[2] the theory for which was subsequently developed by Drummond and Rosenbluth.[1] The experiment was performed in the Q machine at the University of California at Irvine. Perpendicular temperature measurements were made by spectroscopically observing the Doppler line broadening of light scattered by singly ionized barium after the techniques developed by Hinnov *et al.*[3] The significance of these measurements is that this is the first demonstration of ion heating by this current-driven instability.[4]

Historically, this series of measurements was undertaken in an attempt to explain the previous results of Hinnov *et al.*[3] They measured and reported anomalously high ion temperatures in a barium plasma but the heating mechanism was not understood. We repeated the earlier experiments and recovered some of their results. However, we noticed that high temperatures occured when the rhenium coating on the hot tungsten end plates, used to ionize the barium,[5] was uneven so that patches of tungsten appeared through the rhenium coating. As a consequence small areas of different work function were formed on the plates and we speculated that the localized emf's thus formed produced axial filaments of current (easily visible since the barium ions emit visible light). To test this hypothesis, and to identify the heating mechanism (which we were unable to do initially) we went to a single-ended Q machine with insulated buttons, as indicated schematically in Fig. 1(a). In this configuration the electrostatic ion-cyclotron instability was observed, easily identified from its spectrum, from its dependence on the magnetic field, and by recovering the results of Motley and D'Angelo,[2] most notably that the observed frequency is slightly higher than the ion-cyclotron frequency (typical values at onset: $f_{ci} = 5$ kHz, $f = 61$ kHz, linewidth approximately 1 kHz). Several configurations were tried, varying from a single button to an

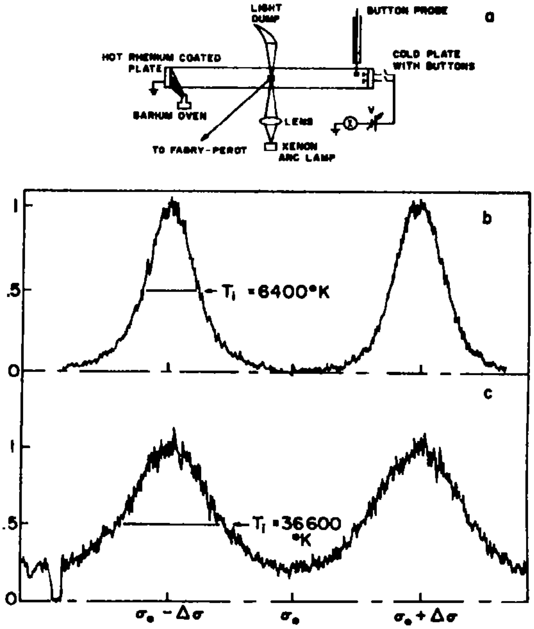

FIG. 1. (a) Schematic of the experimental arrangement. The length L was 123 cm; the diameter, 5 cm, button diameter, 0.6 cm. The Fabry-Perot looked into a light dump also. (b) Typical low-temperature (T_i) Doppler broadening scan. σ_0 is the 4934 Å line of Ba II, $\Delta\sigma$ is the Zeeman splitting (0.313 cm^{-1}). (c) Typical high-temperature (T_i) scan. The Doppler linewidth (as opposed to the scan width) varies as $\sqrt{T_i}$. The abscissas are the same in (b) and (c).

array of buttons, and including two movable buttons, or paddles. The temperature was measured from the Doppler line broadening using a pressure-swept Fabry-Perot interferometer, using the 4934-Å line of Ba II, in a magnetic field of 5 kG (σ Zeeman components). The instrumental profile of the Fabry-Perot was calibrated with an argon laser operating in the single mode. Typical scans are shown in Figs. 1(b) and 1(c); each profile was taken over a 2-min interval. These scans represent a convolution of the emitted Doppler line with the instrumental profile (half-width 0.072 cm^{-1}. The ratio of half-amplitude scan widths, 1 : 1.9, after removing the Fabry-Perot contribution, results in a ratio of Doppler velocity widths 1 : 2.39. The accuracy of the resulting temperatures is better than 20%. The repeatability of a given measurement is better than 10%. The minimum between peaks increases with an increase in ion temperature, as in Fig. 1(c). Hence a base line very nearly equivalent to a blocked arc lamp was used in both scans. The volume resolution was less than 2 mm in the radial and axial directions. We improved on the technique of Hinnov *et al.* by using a high-intensity xenon arc lamp to detect the line broadening of the scattered radiation. This gave us greater sensitivity and the capability of measuring local ion temperature instead of that integrated along a diameter as in Ref. 3. The plasma density n_e was between 10^9 and 10^{10} cm^{-3}; the plate temperature was 2800°K.

The onset of the instability as a function of current to a single button is shown in Fig. 2. The current density in a filament, or current tube, is greater than that one would observe when the current was distributed over the entire plasma column. The ion temperature, as measured by the line broadening, as a function of voltage applied to the button is shown in the same figure. The dramatic rise in temperature is quite apparent. As the growth rate, γ, increases, the number of harmonics observed increases, and then T_i rises. Both the wave amplitude and the high temperature are localized to the cross-sectional area of the current tube, as shown in Fig. 3. Since our optical arrangement did not allow for spatial scanning, these data were taken by means of a radially movable button mounted on a Langmuir probe mechanism. The number of buttons in a given array on the end plates had only a small effect on the results. However, when two buttons moving radially on the same diameter were used, we found that as the separation between the two decreased T_i between them rose even more dramatically, as the separation approached the order of the button diameter. While we did some exploration of this effect, space limitations force us to defer discussion to a later publication.

The multibutton arrangement bears a strong similarity to that used by Buchel'nikova and Salimov.[6] In this work the authors postulate a temperature rise in a potassium plasma due to the incoherence of oscillations from tube to tube. This is in contradiction to our results. Using a Hewlett-Packard model 3721A correlator to measure the auto- and cross-correlation functions from tube to tube we found correlation times of ten wave periods. Also in contradiction to their results, we saw no change in cross-field diffu-

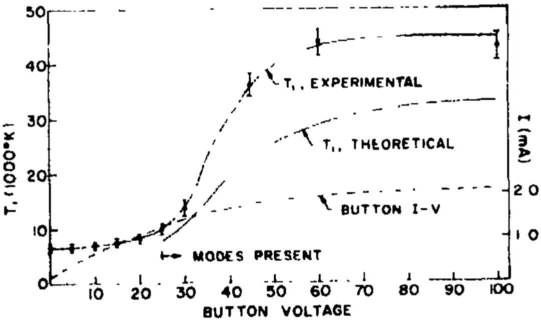

FIG. 2. Comparison of theoretical and experimental values of T_i. The I-V curve of a single button is shown for reference.

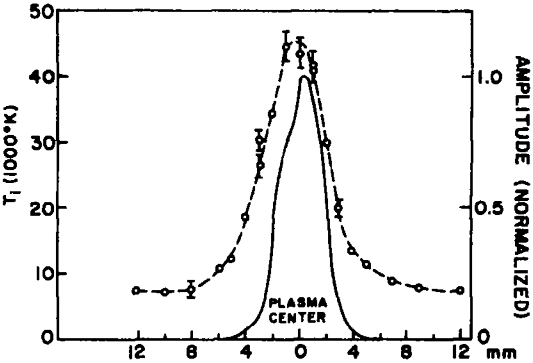

FIG. 3. Plots of wave amplitude and T_i versus radius. The solid line is the wave amplitude, the dashed line the measured values of T_i; only a few, typical, error bars are shown. The mode amplitude plot was taken on a chord (off-diameter) and therefore appears to be more localized.

sion during ion heating.

It remains to be demonstrated that our measures represent a true temperature rise. We approach the problem by examining the nature of the measurement and by some arguments based on the theory. The nature of this measurement is such that the spectral profile is directly proportional to the ion velocity distribution so that, in principle, the line shape should be a replica of the distribution. Instrumentation effects, however, obscure the direct relationship so that, in fact, it is difficult to say with finality that, based on line shape, the distribution is Maxwellian—although it is clearly consistent with this. A prime advantage of this method of temperature measurement, however, aside from the lack of physical perturbation, is that it is based upon the central portion of the distribution function, as opposed to the tail as measured by retarding potential techniques, such as energy analyzers and Langmuir probes. Thus, any temperature rise represents a true broadening of the distribution. Coherent motion may also cause line broadening but such motion would affect the wings of the observed line. For example, a barium ion oscillating at a frequency ω with maximum velocity v_0 would have a velocity distribution, averaged over a 2-min time interval, of $1/\pi(v_0^2 - v^2)^{1/2}$. This is the equation of a catenary and would result in pronounced "wings" on the line shape. By virtue of calculations and some experiments with our correlator, we were able to determine that sinusoidal particle motion, which could give rise to the increased linewidth observed, would also result in detectable distortions in the wings of our scans; none was detected. Furthermore, measurements of current fluctuations to the Langmuir probes indicated that density fluctuations, $\delta n/n$, were of the order of 10% or less. Since any other strongly periodic motion would have a similar effect we conclude that periodic motions were not a large constituent of the velocity distribution when line broadening was observed. Sifting through other possibilities leaves only an aperiodic wave form or, at best, one that is periodic but highly complex as responsible for the line shape. Thus, we have the phenomenon of a strongly coherent, periodic oscillation giving rise to a highly complex, probably aperiodic velocity distribution. But this, coupled with the increase in the number of ion-cyclotron harmonics observed as the line broadens, if it does not quite constitute complete thermalization, at least indicates its beginnings and certainly points to some sort of randomization, justifying the use of the term "temperature rise." It should be born in mind that collisions between particles were negligible.

Drummond and Rosenbluth[1] give the following expression for the linear growth rate of the instability:

$$\gamma = \frac{T_e}{T_i}\frac{\Gamma_1 \Omega_i}{[1+(k\lambda_{De})^2]^2}\left(\frac{\pi}{2}\right)^{1/2}\left(\frac{-\omega + k_\parallel v_D}{k_\parallel v_e}\right), \qquad (1)$$

where Γ_1 is essentially a constant, $k\lambda_{De} \ll 1$, and those symbols not easily recognizable are defined in Ref. 1. (Typical values of γ range from zero at onset to $0.034\Omega_i$.) Then they derive an expression for the energy transfer from the electron drift to the wave fields and the particle wave motion. In the steady state the ion kinetic energy is increasing at a rate given by

$$\left.\frac{\partial U}{\partial t}\right|_{k,\mathrm{ion}} = \frac{\gamma}{\Gamma_1}\frac{T_i}{T_e}[1+(k\lambda_{De})^2]^2 \frac{|E_k|^2}{4\pi(k\lambda_{De})^2}, \qquad (2)$$

where U is the kinetic energy of the ions. The electric field energy density can be expressed in the form

$$E_k^2/4\pi = (k\lambda_{De})^2 n(\delta n/n)^2 kT_e. \qquad (3)$$

At densities $n < 10^{10}\ \mathrm{cm}^{-3}$ the plasma is collisionless. Ion convection to both end plates represents the major heat loss of the ions. Equating the rate of heat input to the rate of heat loss, we write

$$\left.\frac{\partial U}{\partial t}\right|_{k,\mathrm{ion}} = \frac{1}{4}\frac{n\bar{v}_i}{L}\,2k(T_i - T_{i0}), \qquad (4)$$

where $\bar{v}_i = (8kT_i/\pi m_i)^{1/2}$ and $T_{i0} = T_i$ at mode onset. The data in Fig. 3 show that the high-temperature and mode-amplitude regions coincide with the current tube cross section. Combining Eqs. (2), (3), and (4) yields the following expression for T_i:

$$T_i^{1/2}(T_i - T_{i0}) = 2.5\left(\frac{\pi m_i}{8k}\right)^{1/2}\left(\frac{\delta n}{n}\right)^2 \times T_e L\Omega_i\left(\frac{v_D}{v_e} - \frac{\Omega_e}{k_\parallel v_e}\right). \qquad (5)$$

Using the value of v_D calculated from measurements of current and density, the measured value of $T_e \approx 4000$°K, $\delta n/n \approx 0.1$ (from experimental data), $\Gamma_1 = 0.22$, and $k_\parallel = 2\pi/L$ enables us to calculate T_i. A plot of T_i versus applied voltage is shown in Fig. 2 where the theoretical values are compared with the measured values. The agreement between theory and experiment is 30% at the higher values of T_i. Since there are some factors, e.g., the density, that are known only to this accuracy, the degree of agreement is quite good.

Since this is a linear theory the energy calculation, by implication, must be for coherent motion. Several mechanisms can transform coherent ion motion into random motion. Petviashvili[7] found that quasilinear effects can produce true ion heating. Also, there is experimental and theoretical evidence[8] that this instability is stabilized primarily by orbit perturbations which will appear as true stochastic ion motion. In any case, our results show that this is what happens.

Further support for the proposed heating mechanism may be deduced from the observation that increasing the plasma density cools the ions, or at least narrows the linewidth of the optical frequency scan. This is explained by the increased collision rate carrying off the energy either directly to the plates by ion conduction, or by transfer of momentum to the electrons and thence to the plates. Also, the introduction of neutral helium into the vacuum chamber cools the ions to near the plate temperature at a rate consistent with energy balance relations. Since the measured $[\delta n/n]^2$ stays constant as the density is increased, we conclude that the instability was not seriously weakened by the collisions.

We believe that our results probably explain the results of Hinnov *et al.*[3] It is not difficult to surmise that for some experimental conditions the rhenium coatings were patchy and produced the effects described here.

Unlike the ion-acoustic instability, the electrostatic ion-cyclotron instability is not quenched by electron heating. Therefore, this instability is an attractive candidate for long-time scale heating.

We would like to acknowledge useful and stimulating discussions with Toshiki Tajima and Norman Rostoker.

---

*Work supported by the National Science Foundation under Grant No. NSF GP 39031X.

[1] W. E. Drummond and M. N. Rosenbluth, Phys. Fluids 5, 1507 (1962).

[2] R. N. Motley and N. D'Angelo, Phys. Fluids 6, 296 (1963).

[3] E. Hinnov, J. G. Hirschberg, F. W. Hoffman, and N. Rynn, Phys. Fluids 6, 1779 (1963); N. Rynn, E. Hinnov, and L. L. Johnson, Phys. Fluids 8, 1368 (1965); J. G. Hirschberg, J. E. Hesser, E. Hinnov, and N. Rynn, Phys. Fluids 10, 1114 (1967).

[4] T. K. Chu, S. Bernabei, and R. W. Motley, Phys. Rev. Lett. 31, 211 (1973), have reported elevated ion temperatures in a plasma caused by parametric excitation of the ion-cyclotron instability.

[5] N. Rynn, Rev. Sci. Instrum. 38, 1378 (1967).

[6] N. S. Buchel'nikova and R. A. Salimov, Zh. Eksp. Teor. Fiz. 56, 1108 (1969) [Sov. Phys. JETP 29, 595 (1969)].

[7] V. I. Petviashvili, Zh. Eskp. Teor. Fiz. 45, 1467 (1963) [Sov. Phys. JETP 18, 1014 (1964)].

[8] G. Benford, N. Rynn, J. J. Thompson, and W. S. Williamson, to be published.

VOLUME 33, NUMBER 13 PHYSICAL REVIEW LETTERS 23 SEPTEMBER 1974

Rotational Polarization of Molecular Groups in Solids

S. Emid and R. A. Wind
Laboratorium voor Technische Fysica, Technische Hogeschool Delft, Delft, The Netherlands

and

S. Clough
Department of Physics, University of Nottingham, Nottingham NG7 2RD, England

(Received 15 July 1974)

When nuclear spin relaxation in solids is due to rapid random rotational motion of molecular groups, magnetic relaxation parameters are dynamically coupled to populations of molecular rotational states. Relaxation of magnetization induces population differences between clockwise and anticlockwise rotational states (rotational polarization), resulting in nonexponential magnetic relaxation. At low temperature a nonequilibrium population difference between rotational states may be generated by a temperature change, and subsequent relaxation induces magnetic dipolar polarization.

In most solids nuclear spin diffusion is responsible for establishing Boltzmann distributions among the levels of the nuclear spin system, permitting a description in terms of two independent parameters, the nuclear Zeeman and dipolar spin temperatures.[1] In liquids this process is absent because the rapid random motions render ineffective the flip-flop terms of the internuclear dipole-dipole interactions. Molecular groups in solids, executing rapid random rotation about symmetry axes, represent an interesting intermediate case because some spin-diffusion transitions are rendered ineffective by this motion, a situation described as symmetry-restricted spin diffusion.[2,3] As a result new parameters must be introduced to describe population differences between nuclear spin species, where each species corresponds to an irreducible representation of the group of permutations of the nuclei arising from the motion.

The consequences may be illustrated by the example of a solid containing rotating methyl groups. If the nuclear dipole-dipole interactions were absent, nuclear spin and space coordinates would be uncoupled and a nuclear spin function for the protons of a particular methyl group could be factored out of an eigenfunction for the whole crystal. Without the dipole-dipole interactions the Hamiltonian is invariant under the separate operations of cyclic permutation of space or spin coordinates of the three protons, so that each member of the product function can be classified according to the irreducible representations A, E^a, E^b of the permutation group. The Pauli principle requires[4] that products be of the form $A\times A$ or $E^a\times E^b$ or $E^b\times E^a$. Thus a single label serves to identify the symmetry properties of the three species. The random rotation of the methyl group affects these functions only by introducing a random phase modulation of the E functions.[5] The nuclear dipole-dipole interactions cause conversion between symmetry species by spin diffusion in a time of the order of the spin-spin relaxation time T_2 when there is no motion. The effect of motion is to slow down the conversion rate by causing dipole-dipole matrix elements to fluctuate randomly.

As has already been pointed out,[2] under the condition of strong motional narrowing the flip-flop transition probabilities which do not involve a change in symmetry are of the order of the intermolecular dipolar field b, while those which involve symmetry conversion are of order $b^2\tau_c$, where τ_c is the correlation time for the random rotation. As a result, symmetry-restricted spin diffusion can maintain Zeeman and dipolar spin temperatures during magnetic relaxation, but cannot change rapidly the populations of the three symmetry species, which may therefore evolve on a time scale comparable with the spin-lattice relaxation time. Hence the population differences between these species must be introduced. The departure of these differences from the equilibrium values is referred to as rotational polarization. The dynamical equations for rotational polarization are coupled to the magnetization parameters, accounting for nonexponential magnetization recovery at high temperatures[6] and thermally induced dipolar polarization at low temperatures.[7]

We consider a system of N levels, the ith level having Zeeman energy $-\hbar\omega_0 m_i$, where m_i is a magnetic quantum number and ω_0 is the nuclear Larmor frequency. The usual spin-temperature assumption would be to write the populations of the Zeeman levels as

$$p_i = N^{-1}\exp(\beta_Z m_i) \propto N^{-1}(1+\beta_Z m_i),$$

with $\beta_Z = \hbar\omega_0/k\Theta_Z$ where Θ_Z is the nuclear Zeeman spin temperature. To take account of symmetry-restricted spin diffusion we introduce $\mu_i = 0,\ 1,\ -1$, for A, E^a, E^b species, respectively, and write

$$p_i = N^{-1}\{1+\beta_Z m_i + \beta_d(\mu_i^2-1)(m_i^2-\tfrac{5}{4}) + \beta_r\mu_i + \beta_t(1-2\mu_i^2)\}. \qquad (1)$$

In (1) $\beta_d = \hbar\omega_d/k\Theta_d$, where $-\hbar\omega_d(\mu_i^2-1)(m_i^2-\frac{5}{4})$ gives the shifts of the energy levels due to the intramethyl-group dipole-dipole interaction[8] and Θ_d is the dipolar temperature; β_r is a measure of the difference between populations of E^a and E^b species and β_t of the difference between E and A populations. Since the A species is a nuclear spin quartet and the E species are doublets, the equilibrium values of both β_r and β_t are zero (except at low temperature when tunneling rotation of the methyl groups is important). Since sums over the eight levels of products like $m_i\mu_i$, $m_i(1-2\mu_i^2)$ are zero, one finds from (1)

$$\begin{aligned} \beta_Z &= N\textstyle\sum_i m_i p_i/\sum_i m_i^2, \\ \beta_d &= N\frac{\sum_i(\mu_i^2-1)(m_i^2-\frac{5}{4})p_i}{\sum_i(\mu_i^2-1)^2(m_i^2-\frac{5}{4})^2}, \\ \beta_r &= N\textstyle\sum_i \mu_i p_i/\sum_i \mu_i^2, \\ \beta_t &= N\textstyle\sum_i(1-2\mu_i^2)p_i/\sum_i(1-2\mu_i^2)^2. \end{aligned} \qquad (2)$$

With the introduction of transition probabilities W_{ij}

$$dp_i/dt = \textstyle\sum_j W_{ij}\{p_j - p_i - N^{-1}\beta_L(m_j-m_i)\}, \qquad (3)$$

where $\beta_L = \hbar\omega_0/k\Theta_L$ and Θ_L is the lattice temperature. Combining (2) and (3) and eliminating p_i through (1) yields differential equations for the β's. The equations for β_Z and β_r are coupled, but because

$$W(m_i\mu_i, m_j\mu_j) = W(-m_i-\mu_i, -m_j-\mu_j) \qquad (4)$$

the coupling terms connecting β_Z or β_r with β_t or β_d vanish. The coupling between β_d and β_t may explain Haupt's experiment[7] where a sudden change in temperature at low temperature causes β_t to depart from its new equilibrium value. As a result of the coupling a change in β_d is induced and so a transient dipolar polarization is observed.

For β_Z and β_r the pair of coupled equations can be written

$$\begin{aligned} d\alpha_Z/dt &= -A_Z\alpha_Z - B\alpha_r, \\ d\alpha_r/dt &= -B\alpha_Z - A_r\alpha_r, \end{aligned} \qquad (5)$$

with

$$\begin{aligned} \alpha_Z &= (\textstyle\sum_i m_i^2)^{1/2}(\beta_Z-\beta_L), \quad \alpha_r = (\sum_i \mu_i^2)^{1/2}\beta_r; \\ A_Z &= \sum_{i>j} W_{ij}(m_i-m_j)^2/\sum_i m_i^2, \\ A_r &= \sum_{i>j} W_{ij}(\mu_i-\mu_j)^2/\sum_i \mu_i^2, \\ B &= \frac{\sum_{i>j} W_{ij}(\mu_i-\mu_j)(m_i-m_j)}{(\sum_i m_i^2 \sum_i \mu_i^2)^{1/2}}. \end{aligned} \qquad (6)$$

The symbol $i>j$ means that each term occurs only once in the summations. Equations (4) are decoupled by a simple rotation in the $\alpha_r\alpha_Z$ plane through an angle θ where $\tan 2\theta = 2B/(A_r - A_Z)$. The combinations $\alpha_Z\cos\theta - \alpha_r\sin\theta$ and $\alpha_Z\sin\theta + \alpha_r\cos\theta$ relax exponentially with different relaxation times.

As a simple example we consider a solid containing an array of methyl groups oriented with their axes parallel to the external magnetic field. The energy levels are sketched in Fig. 1 which also shows the nonzero transition probabilities W due to the intra-methyl-group dipole-dipole interaction which are expected to dominate the relaxation. Taking only these transitions into account gives $A_Z = 4W/3$, $A_r = W/2$, and $B = -(\frac{2}{3})^{1/2}W$. Since $A_ZA_r = B^2$, one of the relaxation rates is zero and the other is $A_Z + A_r$. The lower part of the diagram in Fig. 1 shows the kind of relaxation behavior expected. Equilibrium is represented by the origin $\alpha_Z = \alpha_r = 0$. The relaxation trajec-

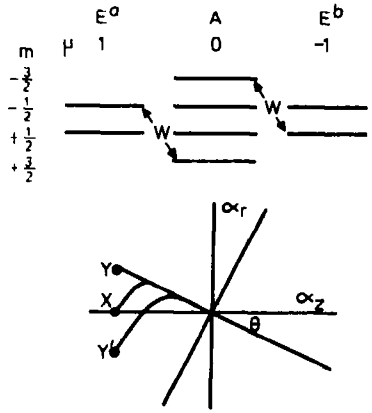

FIG. 1. Energy levels of methyl group and relaxation trajectories in $\alpha_Z\alpha_r$ plane.

tory on the diagram depends on the mode of preparation.[3] A single short saturating pulse prepares the system at X on the diagram ($\beta_Z = \alpha_r = 0$). The subsequent relaxation is at a rate $A_Z + A_r$ parallel to one of the principal axes of relaxation, and at a much slower rate (~0) parallel to the other. Magnetic relaxation measurements observe the projection of this trajectory on the α_Z axis and this has the form of a sum of two exponential decay terms as is indeed observed experimentally.[6]

Other ways of preparing the system give different results. A long saturating pulse prepares the system at Y and relaxation occurs at the slow rate. A sudden rotation of the crystal through 180° about an axis perpendicular to the external field has the effect of switching the identities of E^a and E^b states and therefore of inverting the rotational polarization. Thus a system prepared at Y can be transferred to Y' when most of the relaxation would occur at the more rapid rate.

One of us (S.C.) would like to record his appreciation of the hospitality of the Technische Hogeschool Delft where this work was carried out.

---

[1] M. Goldman, *Spin Temperature and Nuclear Magnetic Resonance in Solids* (Oxford Univ. Press, Oxford, England, 1970).

[2] S. Emid and R. A. Wind, to be published.

[3] S. Emid, R. J. Baarda, J. Smidt, and R. A. Wind, to be published.

[4] J. H. Freed, J. Chem. Phys. 43, 1710 (1965).

[5] S. Clough and F. Poldy, J. Chem. Phys. 51, 2076 (1969).

[6] M. Mehring and H. Raber, J. Chem. Phys. 59, 1116 (1973).

[7] J. Haupt, Phys. Lett. 38A, 389 (1972).

[8] F. Apaydin and S. Clough, J. Phys. C: Proc. Phys. Soc., London 1, 932 (1968).

Determination of the Optical Properties and Absolute Concentrations of Electron-Hole Drops in Germanium

J. M. Worlock, T. C. Damen, K. L. Shaklee, and J. P. Gordon
Bell Telephone Laboratories, Holmdel, New Jersey 07733

(Received 1 July 1974)

We report measurements of the scattering and absorption of 3.39-μm light by electron-hole drops in Ge. An unexpected Fabry-Perot effect in our samples allows us to measure not only the drop size but also their absolute concentration and the optical indices of refraction of the electron-hole condensate.

The existence of a dense liquid phase of a nonequilibrium electron-hole gas in a cold intrinsic semiconductor was predicted by Keldysh[1] and has been verified, at least in Ge and Si, by several different experiments. Analysis of the shape and separation of certain bands of recombination luminescence[2] has supported the hypothesis that in Ge the liquid phase is a two-component plasma with pair density ~2×10^{17} cm^{-3} and binding energy per pair ~1.8 meV. These conclusions are consistent with theoretical predictions of a stable liquid-plasma phase.[3]

Measurements of photocurrent noise[4] and infrared light scattering[5] in germanium have established that the liquid phase condenses as droplets with sizes in the 1–10-μm range. Luminescence-decay and dimensional-resonance experiments[6] suggesting droplet sizes on the order of hundreds of micrometers are, in our opinion, less direct, and subject to reinterpretation; though it is conceivable that these large drops are produced in some crystals under excitation conditions different from ours.

In our attempts to reproduce the light-scattering measurements of Pokrovskii and Svistunova,[5] we have discovered, to our surprise and delight, that we have been able to make use of a variable Fabry-Perot effect in our crystals to measure not only the droplet size but also the concentration of droplets and their infrared properties (the complex index of refaction of the liquid phase). Previous analyses of scattered and absorbed light have had to rely on assumed and derived values for the optical indices of the liquid.

Our experimental setup is similar to that reported by Pokrovskii and Svistunova.[5] A rectangular germanium crystal (n type, $\rho \geq 45\ \Omega$ cm) is immersed in superfluid helium at ~1.8 K.

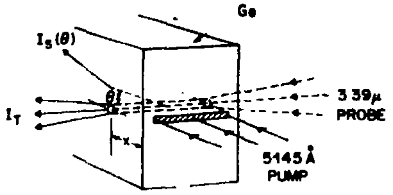

FIG. 1. Experimental configuration. The focused 3.39-μm beam probes the droplet distribution at a variable distance x behind the pumped strip.

Electron-hole pairs are produced at or near a Syton-polished surface by the absorption of pump light from a cw argon-ion laser (5145 Å). This pumped region is a strip approximately 2 mm by 0.1 mm as shown in Fig. 1. At a variable distance x behind this pumped surface, and parallel to it, we place a probe beam, obtained from a He-Ne 3.39-μm laser, and focused to a beam diameter of approximately 70 μm. There are two measurements to be made: the intensity of the directly transmitted beam, I_T; and the scattered intensity as a function of angle, $I_S(\theta)$. We measure both of these in the same apparatus, refocusing the probed region on an InAs detector with a coaxial system of germanium lenses, and defining the scattering angles with a set of circular masks. We further chop the pump beam at 1000 Hz and detect the scattering, $I_S(\theta)$, and the change in transmission, ΔI_T, with a phase-sensitive detector. These experiments can be carried out at various depths x and as a function of temperature and pump power. For brevity, we shall here limit ourselves to discussion of measurements at a single temperature ~1.8 K, and a single pump power ~100 mW. In later publications we shall deal with the application of this technique to different pump powers and configurations,[7] and also with the detailed justification of our analysis.[8]

The angular distribution of scattered intensity, $I_S(\theta)$, can be used to deduce an average droplet radius a. According to the Rayleigh-Gans theory of scattering,[9]

$$I_S(\theta)/I_T = (1/3\pi) l k\eta |\Delta n|^2 (ka)^3 G^2(ka\theta)\Delta\Omega, \quad (1)$$

where l is the length of the probed region, k is the optical wave vector, η is the fractional volume occupied by spherical scatterers of radius a and optical refractive index differing from that of the host medium by Δn, and $\Delta\Omega$ is the effective solid angle defined by the masks. $G^2(ka\theta)$ is a simple analytic function[9] which contains the angular dependence. The Rayleigh-Gans theory is valid when $ka \gg 1$ and $ka|\Delta n| \ll 1$. In all formulas we normalize the refractive index $n + i\kappa$ in the droplet to that of germanium ($n_{\mathrm{Ge}} = 4$) so that $\Delta n = n + i\kappa - 1$, and compensate by using the wave vector k of the probe light in Ge ($k_{3.39} = 7.4\ \mu\mathrm{m}^{-1}$). Scattering angles and solid angles are measured internally.

Equation (1) can be integrated over solid angle to give the total scattering efficiency:

$$I_S/I_T = \tfrac{3}{2} lk\eta(ka)|\Delta n|^2. \quad (2)$$

Our measurements of $I_S(\theta)$ basically verify those of Pokrovskii and Svistunova; we find scattering patterns consistent with Eq. (1), and droplet radii in a restricted range of values from about 2.5 to 4.0 μm. Radii seem to be independent of pump power but have a tendency to be slightly larger closer to the pumped surface.

It is clear that since both Eq. (1) and Eq. (2) contain the product $\eta|\Delta n|^2$, without a knowledge of Δn we cannot go much further. From scattering experiments alone, we can only show that η varies approximately exponentially with distance from the pumped surface, with a $1/e$ depth of ~0.3 mm. The following sections of the paper show how we can measure both Δn and η.

The optical absorption coefficient of our distribution of droplets is easily calculated in the Rayleigh-Gans approximation[9]:

$$\alpha = 2k\eta\kappa. \quad (3)$$

The total extinction coefficient contains both this absorption and the scattering losses.[10] Thus the imaginary part of the apparent macroscopic index, κ_M, in the droplet-infested region can be written as

$$\kappa_M = \eta[\kappa + \tfrac{3}{4}(ka)|\Delta n|^2]. \quad (4)$$

Our attempts to measure this attenuation were frustrated by an unforeseen Fabry-Perot effect, which, as we shall see, when correctly analyzed, gives us not only κ_M but also the real part of the apparent macroscopic index, $n_M - 1$. The real macroscopic index is very simply related to the real liquid index:

$$n_M - 1 = \eta(n - 1). \quad (5)$$

With this new information, we are able to evaluate all the parameters in the theory directly from our experiments.

Figure 2 shows both I_T and ΔI_T as a function of depth behind the pumped surface. ΔI_T measures

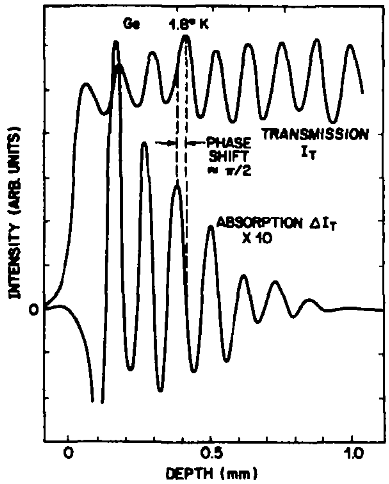

FIG. 2. Fabry-Perot oscillations in the transmitted ntensity I_T and in the "absorbed" intensity ΔI_T as a unction of the depth x behind the pumped strip.

he decrease in transmission when the pump beam s on. But we find that the "attenuation" oscillates violently about some depth-dependent aver- ge value and even becomes negative! Further, he period (in x) of the oscillation is consonant ith that of the unmodulated intensity $I_T(x)$, and he phases differ by approximately $\pi/2$.

We explain and analyze this phenomenon as fol- ws. The slightly nonparallel faces of the sam- le form an imperfect Fabry-Perot cavity whose rder changes with x to give the transmission unction $I_T(x)$ shown in Fig. 2. When the electron- ole drops are formed in the probed region, the pparent macroscopic index of refraction changes o $n_M + i\kappa_M$. The change κ_M causes a decrease in ransmission, while the change $n_M - 1$ changes he Fabry-Perot order fractionally. κ_M therefore hifts the transmission curve down, while $n_M - 1$ hifts it laterally. $\Delta I_T(x)$ measures the result of hese two changes, and is also shown in Fig. 2. n the limit of a low-finesse Fabry-Perot cavity, .e., large wedge angle $[\alpha \gg (\sigma k)^{-1}$, where σ is he beam width and k the wave vector of the ight], and with small index modulations, we can implify the analysis and show that (1) the mag- itude of the phase shift φ is given by $|\tan\varphi|$ $= |n_M - 1|/2\kappa_M$; (2) the sign of the phase shift is etermined by the sign of $n_M - 1$ and the sign of he wedge angle; (3) the mean value of $\Delta I_T(x)$, veraged locally over the Fabry-Perot oscillations, is related to κ_M by $\langle \Delta I_T(x)\rangle_x = 2kl\kappa_M \langle I_T(x)\rangle_x$; and (4) the amplitude of the Fabry-Perot excursions in $\Delta I_T(x)$ is related linearly to the amplitude of the excursions in I_T by

$$\{\Delta I_T(x)\}_{\text{amp}} = 2kl[(n_M - 1)^2 + 4\kappa_M{}^2]^{1/2}\{I_T(x)\}_{\text{amp}}.$$

Using these relations, we have analyzed the data shown in Fig. 2 to draw the following conclusions. (1) $n_M - 1$ is negative and varies exponentially with depth: $-2.2\times10^{-5}\exp[-x/(0.3\text{ mm})]$; (2) κ_M is about 16 times smaller, and has the same depth dependence.

We must now assume that substantially all the electron-hole pairs are condensed into droplets, so that the macroscopic-refractive-index changes can be related to the refractive indices of the liquid as shown in Eqs. (4) and (5). In order to complete the analysis, the scattering measurements must be invoked. Angular dependence gives us a droplet radius of approximately 3 μm, *while the total scattering efficiency*, Eq. (2), varies roughly exponentially with depth, and extrapolates to a surface value of 1.5%. Now, from the measured values of $n_M - 1$, κ_M, and the scattering efficiency, taking $l = 2$ mm, and using Eqs. (2), (4), and (5), we can calculate $n - 1$, κ, and $\eta(x)$: $n - 1 \cong -8\times10^{-4}$, $\kappa \cong 4\times10^{-5}$, and $\eta(x)$ $\cong 3\times10^{-2}\exp[-x/(0.3\text{ mm})]$.

We have assumed that virtually all the electron-hole pairs are condensed into droplets. Measurements[11] of the equilibrium concentration of pairs in the vapor phase indicate that at 2 K this concentration is below 10^{+13} cm^{-3}. Our deduced values of condensed-pair concentrations range from 6×10^{15} cm^{-3} down to perhaps 6×10^{14} cm^{-3}, and so the assumption is reasonable.

Our measurement of $n - 1$ implies that the liquid in the droplets is responding at the infrared laser frequency as a plasma, with a dielectric constant less than unity, and a plasma frequency of 120 cm^{-1}. The plasma frequency obtained here compares very well with that obtained from direct infrared measurements by Vavilov, Zayats, and Murzin[12] (130 cm^{-1}), and also with that calculated from the accepted liquid density, 2×10^{17} cm^{-1}, and an optical effective mass[13] of $\frac{1}{10}$.

The value of κ we find here implies that the plasma is rather heavily damped at this frequency: Since $\omega\tau = |n - 1|/\kappa \sim 20$, the implied scattering time τ is only 4×10^{-14} sec. Alternatively, we can interpret this lossy index in terms of a cross section per hole for inter-valence-band transitions. This interpretation gives an absorption cross section of 3×10^{-17} cm^2 which is about 3 times smaller than that observed in doped p-type germanium at 3.4 μm by Kaiser, Collins, and Fan.[14]

Finally, we discuss the density distribution $\eta(x)$. We believe that the spatial dependence can probably be understood in a model in which pairs diffusing out from the surface are captured by existing droplets, with very little decay in transit. If we assume that the droplets are distributed in a hemicylindrical cloud in which the concentration decays with exponential decay length 0.3 mm in all directions from the center of the cylinder, then we have approximately 5×10^{12} electron-hole pairs. If 50% of our pump laser power, or 50 mW, is absorbed, the electron-hole generation rate is $\sim1.5\times10^{17}$ sec^{-1}. The ratio of steady-state population to generation rate implies a lifetime of 30 μsec, which is in close agreement with measured values of the pair lifetime in the liquid state.[15]

At lower pump power levels the exponential decay depth decreases while the density of droplets near the pumped region is unchanged. Preliminary measurements with a spot-focused pump beam indicate that the droplet density is not exponential, but is quite uniform in a hemispherical cloud with rather sharp edges.[7]

We have made use of a Fabry-Perot interference effect in probing the scattering and absorption of electron-hole droplets in germanium. We have been able to deduce values for the optical constants of the liquid state which are in good agreement with other measurements and theories, and to find the absolute concentration of electron-hole pairs as a function of depth behind the optically pumped surface. We believe that this technique will be useful, not only in probing the optical properties of the liquid at other frequencies, but also in rapidly measuring the spatial variation of droplet concentrations in other pumping configurations, both optical and injection.[16]

We wish to thank W. F. Brinkman, M. Voos, G. A. Thomas, J. C. Hensel, and T. M. Rice for encouraging and illuminating conversations; and A. L. Albert and A. A. Pritchard for sample preparation.

---

[1] L. V. Keldysh, in *Proceedings of the Ninth International Conference on the Physics of Semiconductors, Moscow, 1967*, edited by S. M. Ryvkin *et al.* (Nauka, Leningrad, 1968), p. 1303.

[2] Ya. E. Pokrovskii and K. I. Svistunova, Pis'ma Zh. Eksp. Teor. Fiz. 9, 435 (1969) [JETP Lett. 9, 261 (1969)], and Fiz. Tech. Poluprov. 4, 491 (1970) [Sov. Phys. Semicond. 4, 409 (1970)]; C. Benoît à la Guillaume, M. Voos, and F. Salvan, Phys. Rev. B 5, 3079 (1972); C. Benoît à la Guillaume and M. Voos, Solid State Commun. 12, 1257 (1973); G. A. Thomas, T. G. Phillips, T. M. Rice, and J. C. Hensel, Phys. Rev. Lett. 31, 386 (1973).

[3] W. F. Brinkman, T. M. Rice, P. W. Anderson, and S. T. Chui, Phys. Rev. Lett. 28, 961 (1972); W. F. Brinkman and T. M. Rice, Phys. Rev. B 7, 1508 (1973); M. Combescot and P. Nozières, J. Phys. C: Proc. Phys. Soc., London 5, 2369 (1972).

[4] V. M. Asnin, A. A. Rogachev, and N. I. Sablina, Pis'ma Zh. Eksp. Teor. Fiz. 11, 162 (1970) [JETP Lett. 11, 99 (1970)]; C. Benoît à la Guillaume, M. Voos, F. Salvan, J. M. Laurant, and A. Bonnot, C. R. Acad. Sci., Ser. B 272, 236 (1971).

[5] Ya. E. Pokrovskii and K. I. Svistunova, Pis'ma Zh. Eksp. Teor. Fiz. 13, 297 (1971) [JETP Lett. 13, 212 (1971)]; N. N. Sibel'din, V. S. Bagaev, V. A. Tsvetkov, and N. A. Penin, Fiz. Tverd. Tela 15, 177 (1973) [Sov. Phys. Solid State 15, 121 (1973)].

[6] R. M. Westervelt, T. K. Lo, J. L. Staehli, and C. D. Jeffries, Phys. Rev. Lett. 32, 1051 (1974); R. S. Markiewicz, J. P. Wolfe, and C. D. Jeffries, Phys. Rev. Lett. 32, 1357 (1974).

[7] M. Voos, K. L. Shaklee, and J. M. Worlock, to be published.

[8] J. M. Worlock, to be published.

[9] H. C. van de Hulst, *Light Scattering by Small Particles*, (Wiley, New York, 1957), Chaps. 4 and 7.

[10] W. K. H. Panofsky and M. Phillips, *Classical Electricity and Magnetism* (Addison-Wesley, Reading, Mass., 1962), 2nd ed., Sect. 22-10.

[11] Z. A. Insepov and G. E. Norman, Zh. Eksp. Teor. Fiz. 62, 2290 (1972) [Sov. Phys. JETP 35, 1198 (1972)]; T. K. Lo, B. J. Feldman, and C. D. Jeffries, Phys. Rev. Lett. 31, 224 (1973); G. A. Thomas, private communication.

[12] V. S. Vavilov, V. A. Zayats, and V. N. Murzin, Pis'ma Zh. Eksp. Teor. Fiz. 10, 304 (1969) [JETP Lett. 10, 192 (1969)], and in *Proceedings of the Tenth International Conference on Physics of Semiconductors, Cambridge, Massachusetts, 1970*, edited by S. P. Keller, J. C. Hensel, and F. Stern (U. S. AEC Division of Technical Information, Springfield, Va., 1970).

[13] Combescot and Nozières, Ref. 3.

[14] W. Kaiser, R. T. Collins, and H. Y. Fan, Phys. Rev. 91, 1380 (1953).

[15] C. Benoît à la Guillaume, M. Voos, and F. Salvan, Phys. Rev. B 5, 3079 (1972); J. C. Hensel, T. G. Phillips, and T. M. Rice, Phys. Rev. Lett. 30, 227 (1973); Westervelt *et al.*, Ref. 6.

[16] V. Marrello, T. F. Lee, R. N. Silver, T. C. McGill, and J. W. Mayer, Phys. Rev. Lett. 31, 593 (1973).

Crystal Fields in Dilute Rare-Earth Metals Obtained from Magnetization Measurements on Dilute Rare-Earth Alloys

P. Touborg and J. Høg
Department of Electrophysics, Technical University, DK-2800 Lyngby, Denmark

(Received 22 April 1974)

Crystal field parameters of Tb, Dy, and Er in Sc, Y, and Lu are summarized. These parameters are obtained from magnetization measurements on dilute single crystals, and successfully checked by a number of different methods. The crystal field parameters vary unpredictably with the rare-earth solute. B_{40}, B_{60}, and B_{66} are similar in Y and Lu. Crystal field parameters for the pure metals Tb, Dy, and Er are estimated from the crystal fields in Y and Lu.

The rare-earth metals exhibit a fascinating varety of magnetic properties, which can be qualitively understood as the consequence of crystal ield, exchange, and magnetoelastic interactions. s a result of this complexity it is extremely difcult to separate individual terms. The crystal eld plays a vital role in the magnetic ordering, n the spin-wave excitations, and in other magetic properties of the rare-earth metals.[1] It is erefore of great importance to know the crysl fields in the pure rare-earth metals. Howver, existing theories for the crystal field paameters, such as the point-charge model, are ot expected to be of any validity,[2] though the oint-charge model gives good results for the etallic rare-earth pnictides.[3] The crystal field rameters which have so far been determined xperimentally[1] have not shown satisfactory reement among the results from different meaurements. Recently the presence of highly aniotropic exchange interactions in the rare-earth etals has been demonstrated by the technique f inelastic neutron diffraction,[4] and because of ontributions from anisotropic exchange to the agnetic anisotropy, no reliable values of the rystal fields have been available yet. It is therere understandable that the theoretical picture f the crystal fields in the rare-earth metals is so in a poor state.[5]

By diluting rare earths in nonmagnetic hosts, rystal-field-dominated systems can be created, which an accurate determination of the crystal eld is possible. An extensive project on dilute are earths in nonmagnetic rare-earth-like host etals has been initiated, and in this Letter we ish to report crystal field parameters obtained r 0.1–1.0-at.% alloys of Tb, Dy, and Er in the ost metals Sc, Y, and Lu. These measurements ve allowed—for the first time—a separate quantative determination of the crystal field parameters in the pure rare-earth metals.

Sc, Y, and Lu are the only nonmagnetic elements which have rare-earth-like electronic structure and hcp crystal structures like the magnetic heavy rare-earth metals. Y and Lu bear very close resemblance to these, and the variations of the lattice parameters and the width of the *d* conduction bands in Tb, Dy, and Er are bounded by Y and Lu. Lu is a rare earth itself with a 5*d* bandwidth approximately equal to those of Tb, Dy, and Er.[6] Determinations of the crystal fields for rare-earth impurities in Y and Lu are therefore expected to give good estimates of the crystal field parameters in the pure rare-earth metals.

Crystal fields of dilute rare earths in cubic hosts have been determined earlier by spectroscopic[7] and by magnetization measurements.[3] A determination of the axial anisotropy parameter from torque measurements on dilute rare earths in Gd has been attempted.[8,9] However, the parameters obtained in this way are determined with low accuracy and do not agree with the parameters obtained in the present work. This is attributed to the severe difficulties in performing and interpreting such a torque experiment.[9]

In the present project the crystal fields in Sc, Y, and Lu alloys were determined by fits to magnetization measurements. A recent paper[10] describes the method used for Y:0.14-at.% Er and Y:0.14-at.% Dy. Because of the lower symmetry in the hcp hosts compared to the cubic systems,[3,7] it was essential that the measurements were performed on single crystals. The samples were spheres cut from single-crystal ingots prepared by strain-anneal techniques.[11] Magnetization measurements in the temperature range 1.3–300 K and in fields up to 6 T were performed in the *a*, *b*, and *c* directions of the hcp structures. The magnetic susceptibility of the host metal was measured separately and subtracted. The crystal field parameters were obtained by theoretical fits to the inverse initial susceptibility (measured by a high-sensitivity Faraday magnetometer[10]). Isofield and isothermal magnetization curves in the available temperature and field ranges (measured on the Faraday system and on a 5-Hz vibrating-sample magnetometer[10]) were used to check the reliability of the deduced parameters and to confirm the general validity of the Hamiltonian used. The inverse-initial-susceptibility curves show characteristic features for all Er and Dy alloys, allowing an unambiguous determination of the crystal field parameters. Figure 1 illustrates the accuracy of the fit for Sc:0.568-at.% Dy. Ordering effects, etc. (Fig. 1), cause deviations at low temperatures and are responsible for the uncertainties on the crystal field parameters.

The Tb susceptibility curves contained too little structure to allow a unique determination of the parameters. For this case it was necessary to include results of additional measurements of the hexagonal anisotropy in the fitting procedure.[12] These measurements were performed on a 179-Hz vibrating-sample magnetometer, in which the components of the magnetic moment parallel and perpendicular to the external field, lying in the basal plane, were measured as a function of crystal rotation angle about the c axis.

The Hamiltonian appropriate for the interpretation of these experiments is

$$\mathcal{H} = \mathcal{H}_{\mathrm{cf}} + \mathcal{H}_{\mathrm{Z}}, \tag{1}$$

where $\mathcal{H}_{\mathrm{cf}}$ is the most general single-ion hexagonal anisotropy operator:

$$\mathcal{H}_{\mathrm{cf}} = B_{20}O_{20} + B_{40}O_{40} + B_{60}O_{60} + B_{66}O_{66}. \tag{2}$$

O_{lm} are the Stevens operators[13] and B_{lm} are crystal field parameters. $\mathcal{H}_{\mathrm{Z}}$ is the effective Zeeman operator which includes the exchange interaction in the molecular-field approximation,

$$\mathcal{H}_{\mathrm{Z}} = g_J \mu_B \vec{J} \cdot (\vec{H} + \overleftrightarrow{\lambda} \cdot \vec{M}). \tag{3}$$

$\overleftrightarrow{\lambda}$ is the molecular-field tensor containing two independent parameters, $\lambda_\perp$ and $\lambda_\parallel$.

During the fit, $\mathcal{H}_{\mathrm{cf}}$ was diagonalized in the subset of the lowest-J multiplet, as contributions from the higher multiplets in the LS ground-state term were found to be negligible. The four B_{lm}'s, $\lambda_\perp$, $\lambda_\parallel$, and the atomic concentration c were taken as fitting parameters. The deduced value of c was always in agreement with the nominal concentration, within a few percent of the latter.

Because of the importance of knowing the crystal fields in the rare-earth metals it is preferable to check the parameters by other measurements. First we have studied the alloys Y:Tb, Y:Dy, and Y:Er for varying concentrations in the range 0.1–3.6 at%.[12] The magnetization measurements on these systems were excellently described by concentration-independent crystal field parameters. Secondly we have performed measurements of the basal-plane anisotropy on almost all alloys.[12] For the Er and Dy alloys, where these measurements are not included in the fitting procedure, they have served as a separate check of the B_{66} parameter. Magnetization measurements on Y:Tb, Y:Dy, and Y:Er in fields up to 370 kOe, where the Zeeman energies are comparable to the crystal field energies, are described well by the crystal field parameters.[14] This includes characteristic features due to mixing and crossing of crystal field levels. Finally three expected transitions from the ground state to excited crystal field levels in an Y:Er single crystal have been observed with correct energies and intensities in an inelastic-neutron-scattering experiment.[15]

In Fig. 2 the crystal field parameters divided by the Stevens factors[13] are plotted as functions of the c/a ratio of the host metal. For comparison curves calculated in the point-charge model[16] are also shown. The deviation of these from the experimental data demonstrates the failure of the point-charge model also for these systems. The point-charge model even predicts the wrong sign

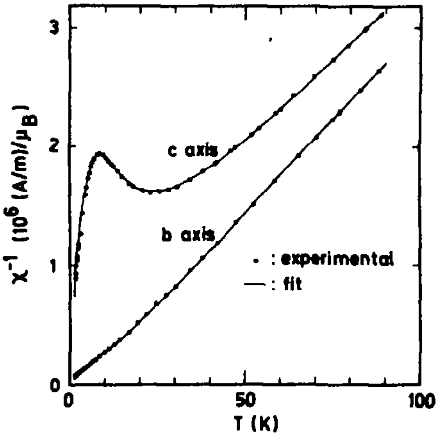

FIG. 1. Inverse susceptibility of Sc:0.568-at% Dy measured at $B = 0.170$ T. The susceptibility is given per Dy atom.

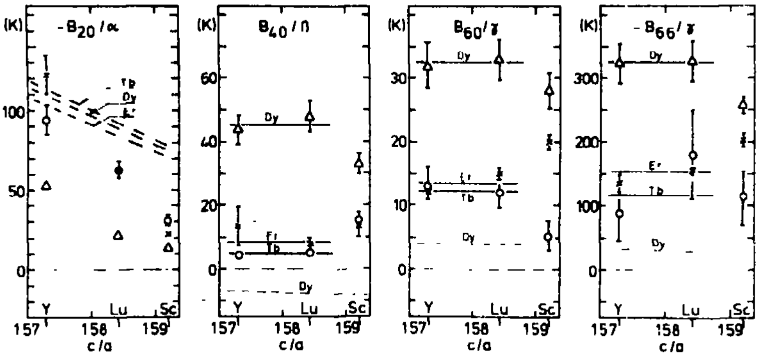

FIG. 2. Crystal field parameters divided by Stevens factors versus c/a ratio for Tb (circles), Dy (triangles), and Er (crosses). Errors are not plotted when they fall within the simbol. The full lines represents the average of the Y and Lu results. The dashed lines are calculated from the point-charge model (Ref. 16). Except for B_{20}/α, the point-charge parameters for Tb and Er are insignificantly different from those for Dy and are therefore not plotted.

of B_{40}/β. The B_{lm}'s divided by the corresponding Stevens factors have, for given l and m, the same sign for all alloys, and the ratio $-B_{66}/B_{60}$ for any given alloy is approximately 10. A substantial variation in magnitude for different rare-earth impurities in the same host is observed, with Tb and Er being most alike. The energy V_{cf} of a $4f$ electron in a crystalline electric field with hcp symmetry can be written as

$$V_{\text{cf}}=4(\pi/5)^{1/2}V_{20}(r)Y_{20}(\theta,\varphi)+(16/3)\pi^{1/2}V_{40}(r)Y_{40}(\theta,\varphi)+32(\pi/13)^{1/2}V_{60}(r)Y_{60}(\theta,\varphi)$$
$$+32(\pi/3003)^{1/2}V_{66}(r)[Y_{66}(\theta,\varphi)+Y_{6,-6}(\theta,\varphi)].$$

$V_{lm}(r)$ describes the radial part of the electric field component with the angular dependence $Y_{lm}(\theta,\varphi)$. The connection to the Hamiltonian (2) is given by $B_{lm}/\alpha_l=\langle V_{lm}(r_{4f})\rangle$.[13] The V_{lm}'s may contain contributions from charges both within and outside the impurity ion. The external contribution has the form $A_{lm}r^l$ and is not expected to depend very much on the nature of the impurity ion, which however may greatly influence the internal contribution. It may therefore be concluded that the charge residing on the magnetic ion makes a significant contribution to the crystal field which it experiences.

In order to obtain estimates of the crystal field parameters for the pure rare-earth metals, we have shown in Fig. 2 the averages of the values for B_{40}/β, B_{60}/γ, and B_{66}/γ measured in the hosts Y and Lu. These values are, within the experimental error, equal for Y and Lu. B_{20}/α is seen to vary considerably with the c/a ratio, which is close to the ideal hcp value $(\frac{8}{3})^{1/2}$. The dependence of B_{20}/α on c/a is of the same order of magnitude as estimated from high-temperature paramagnetic measurements on the pure rare-earth metals.[17] The deviations in B_{40}/β, B_{60}/γ, and B_{66}/γ observed for Sc probably reflect the difference between this metal and Lu and Y with respect to atomic volume and to the width of the d conduction band.[6] Crystal field parameters for the pure rare-earth metals obtained from the appropriate Y and Lu values by interpolation for B_{20} and by taking the average values for B_{40}, B_{60}, and B_{66} are given in Table I.

In conclusion the measurements of crystal fields of rare-earth metals diluted in the hosts Y and Lu have allowed a determination of the crystal field parameters in the pure rare-earth metals. The crystal field parameters seem to vary unsystematically with the atomic number of the rare earth, contrary to what is expected in simple theories. This demonstrates the necessity of a first-principles calculation based on electron band structures.

TABLE I. Estimated crystal field parameters for the pure rare-earth metals.

	B_{20} (10^{-2}K)	B_{40} (10^{-4}K)	B_{60} (10^{-6}K)	B_{66} (10^{-6}K)
Tb	73 ± 6	6 ± 1	-13 ± 3	128^{+112}_{-25}
Dy	32 ± 2	-27 ± 3	34 ± 3	-336 ± 31
Er	-32 ± 3	4^{+5}_{-1}	28 ± 6	317^{+43}_{-6}

The authors are grateful to Professor V. Frank and Professor A. R. Mackintosh for valuable suggestions during the course of the research. K. Pedersen assisted in the preparation of single-crystal samples.

---

[1] For a review, see *Magnetic Properties of Rare Earth Metals*, edited by R. J. Elliott, (Plenum, New York, 1972).

[2] G. Williams and L. L. Hirst, Phys. Rev. 185, 407 (1969).

[3] K. C. Turberfield, L. Passell, R. Birgeneau, and E. Bucher, Phys. Rev. Lett. 25, 752 (1970), and Phys. Rev. B 4, 718 (1971).

[4] J. Jensen, J. G. Houmann, and H. Bjerrum Møller, to be published; R. M. Nicklow, N. Wakabayashi, M. K. Wilkinson, and R. E. Reed, Phys. Rev. Lett. 27, 334 (1971).

[5] For a review, see A. J. Freeman, in Ref. 1.

[6] O. Jepsen and O. K. Andersen (private communication) quote the following values for the *d*-conduction-band widths in units of rydbergs: Sc, 0.28; Y, 0.48; Tb, 0.59; and Lu, 0.61 (obtained by the standard potential construction using superposition of atomic charge densities and full Slater exchange).

[7] D. Davidov, R. Orbach, C. Rettori, L. J. Tao, and E. P. Chock, Phys. Rev. Lett. 28, 490 (1972); R. A. Devine, J. M. Moretti, J. Ortelli, D. Shaltiel, W. Zingg, and M. Peter, Solid State Commun. 10, 575 (1972); C. Rettori, D. Davidov, R. Orbach, and E. P. Chock, Phys Rev. B 7, 1 (1973), and references therein.

[8] S. Chikazumi, K. Tajima, and K. Toyama, J. Phys. (Paris), Colloq. 32, C1-180 (1971).

[9] T. Asada, J. Phys. Soc. Jpn. 35, 85 (1973).

[10] J. Høg and P. Touborg, Phys. Rev. B 9, 2920 (1974).

[11] K. A. McEwen and P. Touborg, J. Phys. F: Metal Phys. 3, 1903 (1973).

[12] J. Høg and P. Touborg, Phys. Rev. B 9, 2920 (1974).

[13] A. Abragam and B. Bleaney, *Electron Paramagnetic Resonance of Transition Ions* (Clarendon Press, Oxford, England 1970).

[14] P. Touborg, J. Høg, G. J. Cook and L. W. Roeland, Phys. Rev. B (to be published).

[15] O. Rathmann, J. Als-Nielsen, P. Bak, J. Høg and P. Touborg, Phys. Rev. B (to be published).

[16] T. Kasuya, in *Magnetism*, edited by G. T. Rado and H. Suhl (Academic, New York, 1966), Vol. IIB.

[17] R. Aleonard, P. Boutron, and D. Bloch, J. Phys. Chem. Solids 30, 2277 (1969); P. Touborg, S. Balling, and K. M. Ravn, to be published.

Magnetic Properties of Ho-Co and Ho-Fe Amorphous Films

Neil Heiman and Kenneth Lee
IBM Research Laboratory, San Jose, California 95193

(Received 6 May 1974)

Polar–Faraday-rotation and magnetization measurements on evaporated amorphous films of Ho–Co and Ho–Fe show that the principle mechanism responsible for differences in the T_C of the crystalline and amorphous states is the altered electronic configuration of the transition metal, rather than local anisotropy. Additionally we found that the films possess uniaxial anisotropy.

That the technologically important[1,2] amorphous rare-earth (RE)–transition-metal (TM) alloys can be prepared[1,3,4] without the need to include "glass-former" atoms or to maintain the samples at cryogenic temperatures presents an opportunity to understand the fundamentals of amorphous magnetism. Published experimental data on the magnetic properties of amorphous RE-TM alloys are confined mainly to TbFe$_2$[4,5] and GdCo$_2$.[1,6,7] There is considerable interest in the fact that the Curie temperature (T_C) for TbFe$_2$ is markedly lower in the amorphous state than in the crystalline state, whereas T_C of GdCo$_2$ is considerably higher in the amorphous state than in the crystalline state. Harris, Plischke, and Zuckermann[8] attribute these differences to the random orientation of the local anisotropy field, in that Gd is an *S*-state atom whereas Tb is highly anisotropic. Tao *et al.*,[6,7] while not ruling out local-anisotropy effects altogether, attribute the differences to the fact that reduced density inhibits charge transfer from the RE to the *d* orbitals of the TM. Since Fe, unlike Co, has unfilled majority as well as minority spin states, they indicate that reduced charge transfer may produce opposite results in TbFe$_2$ and GdCo$_2$. Unfortunately the data on amorphous TbFe$_2$ and GdCo$_2$ are not sufficient to resolve the question of the relative importance of the two mechanisms.

Additionally some existing data seem to argue against either mechanism. For example, a recent Letter by Sarkar *et al.*[9] reports Mössbauer-effect results which are in agreement with the local-anisotropy model and which apparently disagree with the charge-transfer model. On the other hand the local-anisotropy model would not seem to predict an increased T_C for $GdCo_2$. In view of the controversy about the mechanisms which account for the properties of amorphous RE-TM alloys, we have carried out a study to help clarify the issue. We have examined the magnetic properties of amorphous Ho-Co and Ho-Fe thin-film alloys over a wide compositional range. This is the first time that the systematics of both amorphous RE-Co and RE-Fe alloys have been studied with the same RE constituent so that the effects of the different TM can be evaluated reliably. Also by comparing Ho-Fe results to published $TbFe_2$ data and Ho-Co results to published $GdCo_2$ data, the importance of the RE can be assessed. Furthermore since we have examined the amorphous Ho-TM alloys across a broad compositional range, the systematic trends in the data provide additional insights. We find that our data, particularly when taken in conjunction with the published amorphous $TbFe_2$ and $GdCo_2$ data and with known systematics of crystalline RE-TM alloys, demonstrate that the amorphous state increases T_C for Co alloys, decreases T_C for Fe alloys, and increases the TM moment in both the Fe and Co cases. These conclusions strongly support the basic features of the charge-transfer model.

Thin films of amorphous Ho-Co and Ho-Fe alloys were prepared by thermal evaporation of the two metals in a vacuum system with a base pressure of 7×10^{-9} Torr. Films spanned the compositional range from 17 to 60 at.% Ho. The chemical compositions were checked by electron-microprobe analysis on a number of samples, and these measurements agreed with the evaporation-rate-monitor determinations to within 2%. Films were examined and found to be amorphous by both x-ray and electron diffraction measurements.

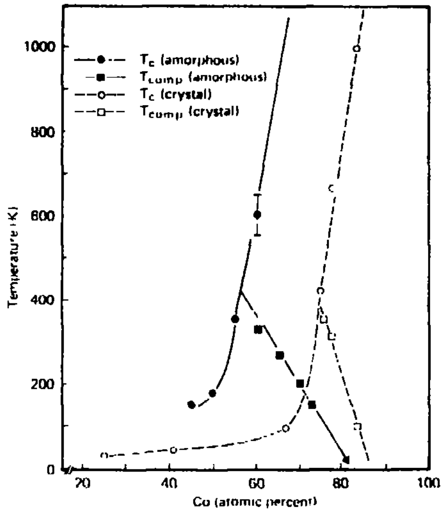

FIG. 1. T_C and T_{comp} for amorphous and crystalline Ho-Co alloys. The lines are not fitted functions, but merely indicate trends in the data. The amorphous $Ho_{17}Co_{83}$ sample did not have T_{comp} above 4.2 K (indicated by arrow).

Figure 1 shows T_C and the compensation temperature T_{comp} as functions of composition for amorphous Ho-Co alloys as determined by polar-Faraday-rotation measurements at $\lambda = 0.6328$ μm. Also plotted on the same figure for comparison are T_C and T_{comp} for several crystalline Ho-Co compounds obtained from the literature.[10] T_C values for amorphous Ho-Co films with greater than 60 at.% Co were considerably in excess of 600 K and could not even be estimated since the saturation polar Faraday rotation showed no significant decrease up to 500 K, the maximum temperature that could safely be used before crystallization would become a consideration. One striking feature of Fig. 1 is that T_C for $Ho_{33}Co_{67}$ is greater than 500 K whereas T_C for crystalline $HoCo_2$ is only 80 K. In general it appears that T_C and T_{comp} of the amorphous Ho-Co alloys are similar to T_C and T_{comp} of crystalline Ho-Co alloys containing 10 at.% more Co. An important point is that the Faraday-rotation data on T_{comp} conclusively establish the fact that the magnetization is more Co dominated in the amorphous alloys since such measurements determine the temperature and composition at which the Ho sublattice magnetization equals the Co sublattice magnetization without regard to questions of saturation, sample volume, or other technical difficulties normally associated with magnetization measurements. For completeness vibrating-sample-magnetometer measurements were made from 4.2 to 300 K by using a superconducting magnet capable of 70 kOe. We had no difficulty saturating our samples. The magnetometer measurements further confirm the more Co-dominated magnetization in the amorphous samples. Specifically the 4.2-K saturation magnetization values for amorphous $Ho_{33}Co_{67}$, $Ho_{25}Co_{75}$, and $Ho_{17}Co_{83}$ are 765, 576, and 20 emu/cm^3, respectively. Using either measured densities or values determined by linear extrapolation of Ho and

Co densities, we calculated the number of Bohr magnetons per formula unit (μ_B/f.u.) at 4.2 K to be $(4.8 \pm 0.5)\mu_B$/f.u., $(4.3 \pm 0.5)\mu_B$/f.u., and $(0.2 \pm 0.1)\mu_B$/f.u., respectively compared to $7.6\mu_B$/f.u., $5.6\mu_B$/f.u., and $1.1\mu_B$/f.u. for the corresponding crystalline phases. The uncertainties in the moments reflect the differences in the measured and extrapolated densities. It should further be noted that in crystalline $HoCo_5$, the moment of the Ho sublattice at 4.2 K is greater than that of Co, whereas the reverse is true for the amorphous film.

T_C and T_{comp} for Ho-Fe films obtained from polar-Faraday-rotation measurements are plotted in Fig. 2 along with points for the crystalline compounds.[10] There are striking differences between this figure and the Ho-Co plot. T_C of the amorphous Ho-Fe films is drastically lower than T_C of the crystalline compounds. In addition, for the crystalline Ho-Fe compounds, T_C anomalously increases as more Ho is added even though the Fe moment is known to decrease. On the other hand T_{comp} of the amorphous films extends further into the Ho-dominated region of the alloy system, just as in the case of the amorphous Ho-Co data, demonstrating that the magnetizations of the amorphous samples are once again more TM (in this case Fe) dominated. Results of magnetometer measurements are similar to those for amorphous Ho-Co in that the magnetization of all the alloys is more Fe dominated. Specifically the moments for amorphous $HoFe_2$ and $HoFe_3$ are $(2.5 \pm 0.3)\mu_B$/f.u. and $(2.8 \pm 0.3)\mu_B$/f.u. compared to $5.5\mu_B$/f.u. and $4.6\mu_B$/f.u. for the respective crystalline material. Amorphous Ho-Fe therefore behaves much the same as amorphous Ho-Co except for T_C.

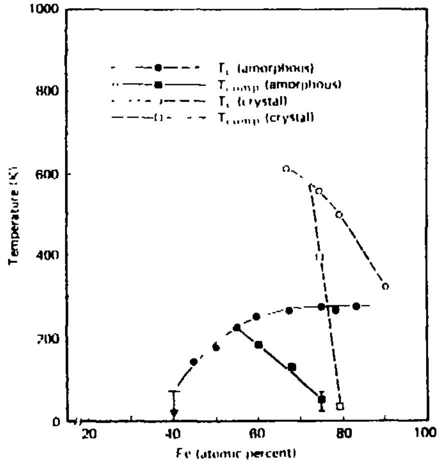

FIG. 2. T_C and T_{comp} for amorphous and crystalline Ho-Fe alloys. $Ho_{60}Fe_{40}$ was not magnetic above 77 K (indicated by arrow). $Ho_{25}Fe_{75}$ was approaching T_{comp} as the temperature was lowered to 77 K.

The facts established by the data are first that the magnetizations in both Ho-Co and Ho-Fe amorphous alloys are more TM dominated than in the crystalline alloys and second that, relative to the crystalline state, T_C increases for amorphous Ho-Co and decreases for Ho-Fe. Since the magnetizations of both Ho-Co and Ho-Fe amorphous alloys behave the same, and since the same RE is involved in both series of alloys, it is clear that the difference in the T_C behaviors of Ho-Co and Ho-Fe must be attributed to the altered state of the TM. The fact that the magnetizations of the amorphous samples are more TM dominated than in the crystalline case can be explained by one of three possibilities: Either the TM moment is increased or the Ho moment is decreased or both. In view of the altered state of the TM deduced from the T_C behavior, it is reasonable to conclude that the TM moment is increased. Furthermore, the systematics of crystalline RE-TM alloys support this conclusion in that both the T_C and the Co moment increase with increasing Co content whereas the Fe moment increases but T_C decreases as the Fe content is increased. Thus, the T_C behavior, the TM domination of the magnetizations, and the systematics of RE-TM crystalline alloys support the charge-transfer model.

Some further comments are in order. Since the differences in T_C and magnetization between crystalline and amorphous Ho-TM alloys span the broad compositional range, it seems unlikely that these differences are due only to density effects. It would appear that mere disorder plays a role in altering the character of the TM. A further consideration which may contribute to the observed behavior is that nearest-neighbor interactions are likely to be particularly important in determining the properties of amorphous materials. Co exchange interactions are ferromagnetic for any realistic distribution of first-neighbor distances, whereas Fe exchange interactions for first-nearest neighbors are critically dependent upon the distribution. Finally there may be some evidence that local-anisotropy effects alter the RE moment. If one assumes reasonable maximum values for the TM moments ($1.7\mu_B$ for Co, $2.2\mu_B$ for Fe), one concludes from the magnetization measurements that the Ho moment is reduced by about 15%; however, as noted earlier, a quantitative interpretation of these measurements is not entirely reliable. It must be stressed that while both charge-transfer and local-anisotropy effects contribute to the altered magnetizations of the amorphous RE-TM alloys, the change in T_C must be attributed mainly to the altered properties of the TM.

Before we conclude, we wish to point out that all films examined had the easy direction of magnetization perpendicular to the film plane. In a number of the films, cylindrical domains (i.e., "magnetic bubbles") were detected either directly by Lorentz microscopy or inferred from the shape of the hysteresis loop. The uniaxial anisotropy constants K_u for Ho-Co alloys at 4.2 K were determined from the fields needed to saturate the films in both the perpendicular and in-plane directions. Values for K_u were about 3×10^6 ergs/cm^3. Previously, it was presumed that rf-bias sputter-deposition techniques were required to produce uniaxial anisotropy. Interestingly the values for K_u in these evaporated Ho-Co films are about 1 order of magnitude greater than those reported for amorphous Gd-Co[11] prepared by rf-bias sputter deposition. A number of experiments[12] had been performed to determine the origin of K_u in those Gd-Co films. The results ruled out stress-induced and shape anisotropy, leading to the conclusion that Co pair ordering is the responsible mechanism. The larger anisotropy in evaporated Ho-alloy films would imply that pair ordering is most likely not the origin of K_u in these films. Films prepared on carbon foils supported on Collodion-coated grids showed uniaxial anisotropy, ruling out stress. K_u values are too large to be explained by shape anisotropy. It would appear therefore that K_u is due to interaction of the Ho with directional correlations on an atomic scale. It may well be that local anisotropy fields though basically random have a preference for the direction perpendicular to the film plane.

We would like to thank S. Lawrence for his technical assistance, W. Parrish for x-ray results, R. Geiss for the Lorentz microscopy, and M. Lorenz, J. Smit, J. Suits, R. Soohoo, and C. R. Guarnieri for helpful discussions.

---

[1] P. Chaudhary, J. J. Cuomo, R. J. Gambino, IBM J. Res. Develop. 17, 66 (1973).

[2] A. E. Clark, Appl. Phys. Lett. 23, 642 (1973).

[3] J. Orehotsky and K. Schroder, J. Appl. Phys. 43, 2413 (1972).

[4] J. J. Rhyne, S. J. Pickart, and H. A. Alperin, Phys. Rev. Lett. 29, 1962 (1972).

[5] J. J. Rhyne, S. J. Pickart, and H. A. Alperin, in *Magnetism and Magnetic Materials—1973*, AIP Conference Proceedings No. 18, edited by C. D. Graham, Jr., and J. J. Rhyne (American Institute of Physics, New York, to be published).

[6] L. J. Tao, S. Kirkpatrick, R. J. Gambino, and J. J. Cuomo, Solid State Commun. 13, 1491 (1973).

[7] L. J. Tao, S. Kirkpartick, R. J. Gambino, and J. J. Cuomo, in *Magnetism and Magnetic Materials—1973*, AIP Conference Proceedings No. 18, edited by C. D. Graham, Jr., and J. J. Rhyne (American Institute of Physics, New York, to be published).

[8] R. Harris, M. Plischke, and M. J. Zuckermann, Phys. Rev. Lett. 31, 160 (1973).

[9] D. Sarkar, R. Segnan, E. K. Cornell, E. Callen, R. Harris, M. Plischke, and M. J. Zuckermann, Phys. Rev. Lett. 32, 542 (1974).

[10] K. N. R. Taylor, Advan. Phys. 20, 551 (1971), and references cited therein.

[11] D. C. Cronemeyer, in *Magnetism and Magnetic Materials—1973*, AIP Conference Proceedings No. 18, edited by C. D. Graham, Jr., and J. J. Rhyne (American Institute of Physics, New York, to be published).

[12] R. J. Gambino, J. Ziegler, and J. J. Cuomo, Appl. Phys. Lett. 24, 99 (1974).

Resonances in ^{12}C + ^{13}C†

D. J. Crozier and J. C. Legg
Kansas State University, Manhattan, Kansas 66506

(Received 24 June 1974)

Resonant structures at 9.4 and 10.3 MeV c.m. energy have been observed in both the reaction ^{12}C(^{13}C,α)^{21}Ne and the elastic scattering of ^{13}C from ^{12}C. Unambiguous assignments of $l = 7$ for both of the resonances are made.

Considerable effort has been devoted to the search for resonances in heavy-ion systems. Previously, such resonances had been found in the systems ^{12}C + ^{12}C[1,2] and ^{12}C + ^{16}O[3,4,5] but had been considered nonexistent in ^{12}C + ^{13}C.[6,7] In the present paper, we report the observation of resonances in the system ^{12}C + ^{13}C.

To reexamine the system ^{12}C + ^{13}C, we measured the excitation function of the reaction ^{12}C(^{13}C, α)^{21}Ne at a lab angle of 10° over a range of lab bombarding energies, $E(^{13}\mathrm{C}) = 12$ to 22.5 MeV, in 100-keV steps. Elastic scattering was measured at eight lab angles over the same energy range. As a result two definite resonances were observed to be correlated in the two exit channels.

The excitation function for the reaction ^{12}C(^{13}C, α)^{21}Ne at a lab angle of 10° is shown in Fig. 1(a); the yield has been summed over the lowest thirteen levels in ^{21}Ne. Statistical fluctuations in summed excitation functions are expected to be damped by a factor which is greater than or equal to the number of levels (13).[8,9] From examination of Fig. 1(a) it can be seen that variations in the yield considerably in excess of those allowed by the statistical model do occur. Most of the energy range has been measured at least twice with good reproducibility. Prominent structures in the summed α yield are observed near the lab energies $E_{\mathrm{lab}} = 15$, 16.2, 17.3, 19.5, and 21.5 MeV ($E_{\mathrm{c.m.}} = 7.2$, 7.8, 8.3, 9.4, and 10.3 MeV, respectively). Less prominent structures are observed near $E_{\mathrm{lab}} = 20.3$ ($E_{\mathrm{c.m.}} = 9.7$ MeV).

In order to investigate whether the observed structure in the ^{12}C(^{13}C, α)^{21}Ne excitation curves might be due to resonances, we examined a different exit channel, the elastic scattering. The elastic scattering excitation functions for three c.m. angles—73.4, 89.6, and 100.5°—are shown in Fig. 1(b). Resonances at $E_{\mathrm{lab}} = 19.5$ and 21.5 MeV can be plainly seen.

In order to determine the l values of these resonances, the background elastic scattering was fitted by using the elastic-transfer theory of von

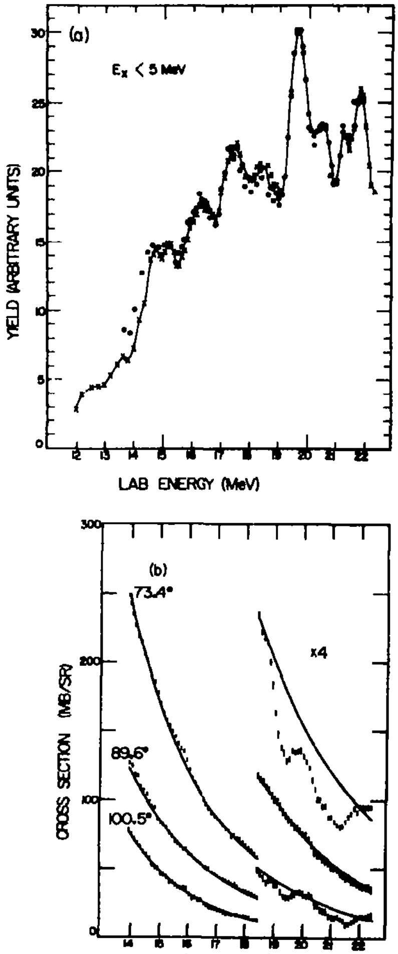

FIG. 1. (a) Excitation function for the reaction ^{12}C(^{13}C,α)^{21}Ne at $\theta_{\mathrm{lab}} = 10°$. Different symbols represent data taken on different days with different targets. The solid curve is intended to "guide the eye" only. (b) Excitation functions for the elastic scattering of ^{13}C from ^{12}C at three c.m. angles. The solid curves are optical-model calculations of the background cross section as described in the text. No resonances were considered in these calculations.

rtzen.[10] A Woods-Saxon optical-model well h parameters considerably different from se of von Oertzen was used—$V=100$ MeV, W 5+1.2($E-18$) MeV, $a=a_i=0.46$ fm, $R_0=R_c$ ${}_i=1.19$ fm. The calculation employed volume sorption and an exchange potential of the form

$$V_{\text{exchange}}=(-1)^l V_e e^{-\alpha r}/\alpha r, \tag{1}$$

th $\alpha=0.469$ and $V_e=35$ MeV. The calculations re performed by using the program OPTICS[11] ich has been modified to include the exchange rm. Excellent fits to the nonresonant angular stributions were obtained with the use of these rameters. The smooth curves in Fig. 1(b) are elastic-scattering predictions with no reso- nces included. The value of the exchange po- ntial obtained here corresponds to a value for in von Oertzen's notation[10] of 0.85 which is in asonable agreement with the values of 0.8 and 95 obtained by Bohlen and von Oertzen.[12] Optical-model parameters differing from those von Oertzen were chosen for two reasons. rst, the angular distributions calculated by hlen and von Oertzen[12] at $E_{\text{c.m.}}=9.9$ MeV show extremely deep minimum at a scattering an- e of 110° which does not fit the data well. Sec- d, it was considered desirable to use an opti- l model with slowly varying parameters and a nstant value of SN. Calculations using the pa- meters given above fit the data very well at all asured angles and energies with a smooth, w variation of the imaginary well depth.

Fits assuming $l=7$ resonances at 19.5 and 21.5 eV are shown in Fig. 2(a) for five c.m. angles er the energy range 18.4 to 22.5 MeV. Shown r comparison in Fig. 2 are calculations using same total and partial widths but assuming following resonances: Fig. 2(b), $l=5$ and l ; Fig. 2(c), $l=3$ and $l=11$; and Fig. 2(d), $l=1$ d $l=13$. It is clear in Fig. 2 that each of these oices of l value produces a very poor fit to the ta at a minimum of two angles. No even-l res- ance will result in a smooth curve at 89.6°. sonances with l values higher than those shown Fig. 2 may be ruled out because of low pene- bility. Thus, these resonances may be as- ned as $l=7$. A single-level formulation was ed to perform the calculations. A resonance xing phase[13] of 0° was assumed in calculating fits in Fig. 2. It was found that no l value ter than $l=7$ would fit the data at all five angles ardless of the mixing phase assumed. Fur- rmore, it was found that for $l=7$ only mixing phases less than 30° gave equally good fits.

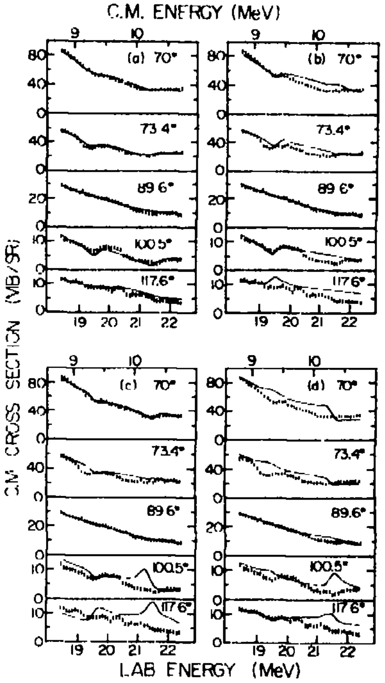

FIG. 2. Fits to the elastic scattering cross section in the energy range from 18.5 to 22.4 MeV for five c.m. angles. Two resonances, one at $E_{\text{c.m.}}=9.36$ MeV with $\Gamma=200$ keV and $\Gamma_{\text{el}}=45$ keV and one at $E_{\text{c.m.}}=10.32$ MeV with $\Gamma=200$ keV and $\Gamma_{\text{el}}=50$ keV, are included in each calculation. (a) Both resonances are assumed to be $l=7$. (b) The two resonances are assumed to be $l=5$ and $l=9$. (c) The two resonances are assumed to be $l=3$ and $l=11$. (d) The two resonances are assumed to be $l=1$ and $l=13$.

The c.m. resonance parameters obtained from the fits for the first resonance are $E_R=9.36$ MeV, $\Gamma=200$ keV, $\Gamma_{\text{el}}=45$ keV; and for the second resonance they are $E_R=10.32$ MeV, $\Gamma=200$ keV, $\Gamma_{\text{el}}=50$ keV. The total estimated uncertainty in the widths is 25%. Reduced widths for these resonances were calculated by using Coulomb-wave-function penetrabilities. At a matching radius of 7 fm the reduced widths are calculated to be 28 keV for the 9.36-MeV resonance and 19 keV for the 10.32-MeV resonance. These reduced widths are 14 and 9% of the Wigner limit, $3\hbar^2/2\mu R^2$. These results are similar to those obtained for the resonances observed in the system ^{12}C+^{12}C.[1]

The use of Coulomb-wave-function penetrabilities in a situation where the nuclear potential is obviously playing an important role is open to question. Schiffer[14] has suggested an alternative method of comparing a resonance width to that of a single-particle resonance. The width of a potential resonance calculated by using the optical model with the absorption set to zero is used as the single-particle width. Calculations with the optical model used here with $W=0$ reveal an $l=7$ resonance at $E_{\text{c.m.}}=9.8$ MeV with $\Gamma=2.9$ MeV. If this is used as the single-particle width, then the observed resonances have elastic partial widths that are approximately 2% of the single-particle width.

These calculations shed some light on the nature of these resonances. They indicate that the observed resonances occur at an energy where the $l=7$ partial wave is resonating. This suggests that these resonances may be explained by a double-resonance effect similar to that[15] used by fitting the structure observed in ^{16}O + ^{16}O scattering.

At present, experiments are being done to investigate reactions at various angles and to extend the excitation functions to higher energies.

---

†Work supported by the U. S. Atomic Energy Commission under Contract No. AT(11-1)-2130.

[1] E. Almqvist, D. A. Bromley, and J. A. Kuehner, Phys. Rev. Lett. 4, 515 (1960); E. Almqvist, D. A. Bromley, J. A. Kuehner, and B. Whalen, Phys. Rev. 130, 1140 (1963).

[2] J. R. Patterson, H. Winkler, and C. S. Zaidins, Astrophys. J. 157, 367 (1969).

[3] M. L. Halbert, F. E. Durham, and A. Van der Woude, Phys. Rev. 162, 899 (1967).

[4] J. R. Patterson, B. N. Nagorka, G. D. Symons, and W. M. Zuk, Nucl. Phys. A165, 545 (1971).

[5] R. E. Malmin, R. H. Siemssen, D. A. Sink, and P. P. Singh, Phys. Rev. Lett. 28, 1590 (1972).

[6] A. Gobbi, U. Matter, J. L. Perrenoud, and P. Marmier, Nucl. Phys. A112, 537 (1968).

[7] H. Voit, G. Ischenko, F. Siller, and H. D. Helb, Nucl. Phys. A179, 23 (1972).

[8] J. P. Bondorf and R. B. Leachman, Kgl. Dan. Vidensk. Selsk., Mat.-Fys. Medd. 34, No. 10 (1965).

[9] W. R. Gibbs, Phys. Rev. 153, 1206 (1967).

[10] W. von Oertzen, Nucl. Phys. A148, 529 (1970).

[11] R. J. Eastgate, W. J. Thompson, and R. A. Hardekopf, Comput. Phys. Commun. 5, 69 (1973). This program was modified by S. K. Datta and W. J. Thompson to compute optical-model plus neutron exchange scattering by using the laboratory PDP-15 computer.

[12] H. G. Bohlen and W. von Oertzen, Phys. Lett. 37B, 451 (1971).

[13] W. J. Thompson, J. L. Adams, and D. Robson, Phys. Rev. 173, 975 (1968).

[14] J. P. Schiffer, Nucl. Phys. 46, 246 (1963).

[15] W. Scheid, W. Greiner, and R. Lemmer, Phys. Rev. Lett. 25, 176 (1970).

Three-Body Breakup Reaction ^{40}Ca(^{16}O, ^{12}Cα)

D. C. Slater, J. R. Hall, and J. R. Calarco
*Department of Physics, Stanford University, Stanford, California 94305**

and

B. A. Watson and J. A. Becker
Lockheed Palo Alto Research Laboratory, Palo Alto, California 94304†

(Received 2 July 1974)

We report for the first time coincident ^{12}C and α particles emitted in the bombardment of ^{40}Ca with ^{16}O ions of 64 MeV. Events which populate the ground and first excited states of ^{12}C and ^{40}Ca are observed. The coincident ^{12}C energy spectra are dominated by one or two large peaks near the highest allowable ^{12}C energy. Relatively few coincidences are seen at ^{12}C energies which correspond to maximum yield in the ^{40}Ca(^{16}O, ^{12}C) singles spectrum.

The (^{16}O, ^{12}C) transfer reaction has been of interest for the last few years. In several of these reaction studies with targets in the nuclear f-p shell,[1] the ^{12}C energy spectra displayed individual sharp peaks superimposed on a broad, continuous background "bump." This continuum makes its appearance in the spectrum near the threshold for ^{16}O breakup into ^{12}C + α. The background, which increases in intensity as the bombarding energy is increased above the Coulomb barrier, has been attributed to the presence of three-body final states.[2] At energies well above the Coulomb barrier, the broad bump, with some superimposed structure, becomes the dominant feature in the ^{12}C spectra and extends to energies which correspond to some 30 MeV in the target plus α-particle residual nuclear system. At a bombarding energy of 48 MeV, however, Erskine, Henning, and Greenwood[3] showed recently that the ^{12}C spectrum from the reaction ^{40}Ca(^{16}O, ^{12}C)^{44}Ti could be completely resolved into individual levels up to 9-MeV residual excitation, indicating no breakup contribution at this incident energy. In the present Letter, we report the observation of time-coincident ^{12}C and α particles following the bombardment of ^{40}Ca by ^{16}O ions of 64 MeV. Most of the coincidences kinematically identified to consist of ^{40}Ca(g.s.) + ^{12}C(g.s.) + α probably result from sequential processes rather than direct three-body breakup.

Previous measurements of carbon-particle energy spectra from the ^{40}Ca + ^{16}O reaction at $E_{^{16}\mathrm{O}} = 70$ MeV employing a time-of-flight plus E-ΔE counter telescope[4] demonstrated that at least 99% of the observed carbon particles were the isotope ^{12}C. In the present experiment we therefore used a simple E-ΔE counter telescope which provided a solid angle of 2.6 msr and still permitted separation of carbon from nitrogen and boron. In a preliminary experiment using two E-ΔE telescopes, we found that some 90% of the particles detected in coincidence with ^{12}C were α particles. The experimental configuration for the data presented here consisted of a single E-ΔE telescope in which ^{12}C ions were identified, and a single large-solid-angle (28 msr) surface-barrier detector for α-particle detection. The single counter allowed a much lower α energy threshold than would have been possible with a two-detector telescope. The α counter was positioned at lab angles of 45°, 55°, and 65°, the telescope at 20° and 25° with respect to the incident beam direction. Both detector systems were on the same side of the beam. Data were recorded event by event and subsequently analyzed off-line. Ca metal target foils of 200 μg/cm^2 areal density were evaporated onto thin Formvar backings and transferred under vacuum from the evaporator to the scattering chamber to minimize oxidation.

Figure 1 shows the Q-value energy spectrum of the coincident events calculated from the ^{12}C and α-particle energies for the data collected at $\theta_{^{12}\mathrm{C}} = 25°$, $\theta_\alpha = 45°$. The threshold energy for ^{16}O breakup (7.16 MeV) has been subtracted so the horizontal scale shows the total excitation energy of the three outgoing particles. The strong peak at $E_x = 0$ thus includes all events in which the ^{40}Ca and ^{12}C ions are emitted in their respective ground states. The other strong peak includes events in which either the ^{40}Ca or ^{12}C ion is emitted in its first excited state. The few events around $E_x = 15$ MeV are due to the reaction ^{12}C(^{16}O, ^{12}Cα) from target contamination. The peaks in this spectrum correspond to three-body final states; four-body states would appear as a continuum at higher total excitation energies.

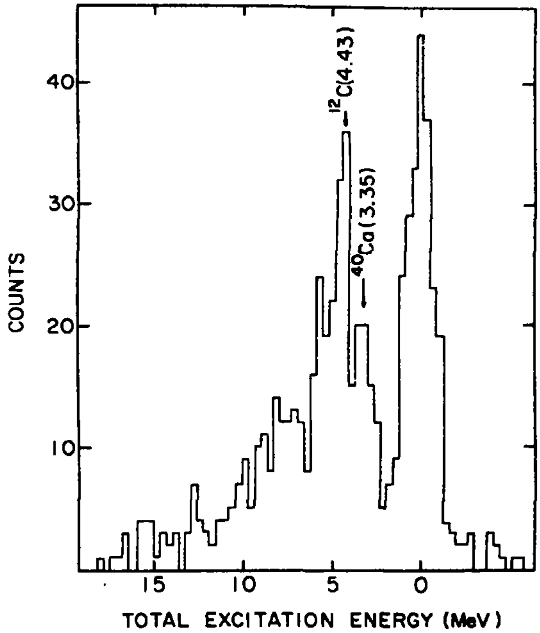

FIG. 1. Total excitation energy spectrum for ^{40}Ca(^{16}O, ^{12}Cα) obtained from the reaction Q value computed for each coincidence event.

For a fixed value of total excitation energy, three-body events fall along a kinematically allowed locus in the E_α versus $E_{^{12}\mathrm{C}}$ plane. The top four spectra in Fig. 2 show those events in the $E_x = 0$ peak. These spectra were obtained by plotting events falling on the kinematic locus according to their ^{12}C energy. Spectra are shown for $\theta_\alpha = 45°$, 55°, and 65° with $\theta_{^{12}\mathrm{C}} = 25°$ and for $\theta_\alpha = 65°$ with $\theta_{^{12}\mathrm{C}} = 20°$. The outstanding feature of these spectra is the presence of large peaks near the highest allowable ^{12}C energy. The weaker structure seen at lower $E_{^{12}\mathrm{C}}$ varies greatly from spectrum to spectrum. Figure 2(e) is a singles ^{12}C spectrum taken at $\theta_{^{12}\mathrm{C}} = 25°$ with the same telescope used for the coincidence spectra, but

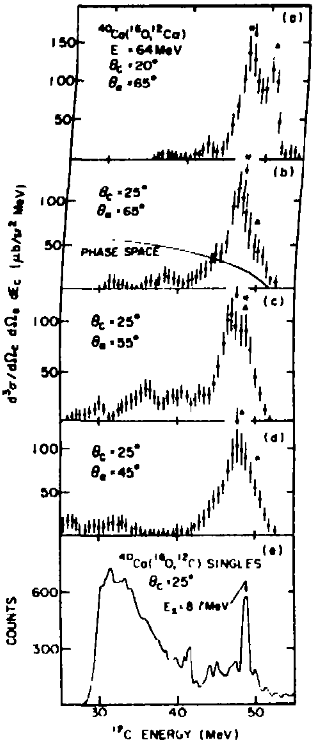

FIG. 2. (a)–(d) Cross sections for ^{40}Ca(^{16}O, ^{12}Cα) at four angle pairs. Only those events on the ^{12}C(g.s.) + ^{40}Ca(g.s.) + α kinematic locus are included. Arrows, triangles, and asterisks indicate positions of constant relative energies of the α + ^{40}Ca, ^{12}C + ^{40}Ca, and α + ^{12}C pairs, respectively. The uncertainty in the overall cross section normalization is estimated to be ± 50%. The phase-space curve is arbitrarily normalized. The lowest spectrum (e) is a singles spectrum of ^{40}Ca(^{16}O, ^{12}C). The low-energy cut off in (e) is caused by the detection system.

moved further from the target to reduce kinematic line broadening.

A coincidence experiment of the kind described here can provide a source of information about the reaction mechanism based only on kinematics. Any sequential decay process of the type $X + Y \to A + B^* \to A + C + D$ should show enhancements at energies corresponding to particle-unstable states in B^*. In the decay of B^* the products C and D would appear at a fixed relative energy, which would manifest itself in spectra such as those of Figs. 2(a)–2(d) as a definite energy shift of a peak as a function of detector angles. The symbols above the spectra in Figs. 2(a)–2(d) indicate the required position of the peak for the three possible sequential processes, based on th relative energies of the particle pairs for the tw peaks in Fig. 2(a). The asterisks, arrows, and triangles show the positions expected for ^{16}O* → ^{12}C + α, ^{44}Ti* → ^{40}Ca + α, and ^{52}Fe* → ^{40}Ca + ^{12}C, respectively. The arrows align with a peak in each coincidence spectrum, providing strong evidence of a sequential decay through ^{44}Ti at about 8.7-MeV excitation energy. The strong peak seen at the same energy in the ^{12}C singles spectrum supports this conclusion. Since α decay is the only open particle channel at this energy, the mechanism ^{40}Ca + ^{16}O → ^{12}C + ^{44}Ti* → ^{12}C + α + ^{40}Ca is favored in both steps of the sequential process. If one tries to explain the gross structure of the four coincidence spectra in terms of two peaks (which may overlap in the lower spectra), then the triangles indicating sequential decay through a 50-MeV excited state in ^{52}Fe correlate rather well with the structure in each spectrum. The strong population of such a state would be surprising, and more data would be required to confirm this interpretation. The asterisks indicating sequential decay through a 13-MeV state in ^{16}O do not correspond to a peak in Fig. 2(d) suggesting that this process is not occuring strongly. While we cannot rule out such a process, we have no convincing evidence of it in these data. The energy shifts as a function of angle for the smaller peaks in the spectra at lower ^{12}C energy do not correlate kinematically with any type of sequential decay. Such structure may be due to direct one-step breakup, or to angular correlation effects in a two-step process.

The large yield of ^{12}C with energies less than 40 MeV seen in Fig. 2(e) does not appear in the coincidence spectra. The intensity of coincidence events is sufficient to account for only a very small fraction of the "bump" seen in the ^{12}C singles spectrum between 30 and 40 MeV. We conclude on this basis that the "bump" is not due to ^{12}C(g.s.) + α + ^{40}Ca(g.s.) final states.

In summary, we have observed the three-body break-up reaction ^{40}Ca + ^{16}O → ^{40}Ca + ^{12}C + α. The dominant process appears to be a two-step mode involving an intermediate excited state of ^{44}Ti and possibly one of ^{52}Fe. We can identify final states involving ^{40}Ca(g.s.) + ^{12}C(g.s.), ^{40}Ca(3.35 MeV) + ^{12}C(g.s.), and ^{40}Ca(g.s.) + ^{12}C(4.44 MeV). The large "bump" observed in the ^{12}C singles spectrum is not due to projectile breakup as proposed in Ref. 2; thus coincidence measurements can provide important new information about heavy-ion reaction mechanisms.

---

*Work supported in part by the National Science Foundation.

†Work supported by Lockheed Independent Research Fund.

[1] J.-C. Faivre, H. Faraggi, J. Gastebois, B. G. Harvey, M.-C. Lemaire, J.-M. Loiseaux, M. C. Mermaz, and A. Papineau, Phys. Rev. Lett. 24, 1188 (1970); H. Faraggi, J. Phys. (Paris) Suppl. 32, C6-25 (1971); H. Faraggi, M.-C. Lemaire, J.-M. Loiseaux, M. C. Mermaz, A. Papineau, Phys. Rev. C 4, 1375 (1971).

[2] F. D. Becchetti, in *Proceedings of Heavy-Ion Summer Study, Oak Ridge, Tennessee, 1972*, edited by S. T. Thornton, CONF-720669 (Oak Ridge National Laboratory, Oak Ridge, Tenn., 1972), p. 163.

[3] J. R. Erskine, W. Henning, and L. R. Greenwood, Phys. Lett. 47B, 335 (1973).

[4] B. A. Watson, C. C. Chang, and S. L. Tabor, Particles Nucl. 2, 376 (1971).

New Interpretation of the Coriolis Kinking Effect in Odd-Even Nuclei

B. Giraud* and A. Jaffrin
Service de Physique Théorique, Centre d'Etudes Nucléaires de Saclay, 91190 Gif-sur-Yvette, France

(Received 5 August 1974)

A description of the Coriolis kinking effect that occurs inside rotational bands of odd-even nuclei is obtained in terms of two distinct intrinsic states that are separately invariant under a unitarity transformation related to the operator $U=\exp(-i\pi J^2)$.

The main feature that characterizes the rotational behavior of a nucleus is the well-known sequence of excitation energies which increase quadratically with the angular momentum and which can be interpreted in terms of a single intrinsic state. This is particularly obvious in the case of even-even axially deformed nuclei which exhibit typical $K=0$ rotational bands. In such typical $K=0$ bands, however, it is known that the time reversal invariance, at least in the low-energy region, restricts the states to have natural parity. The situation is different in the case of odd-even deformed nuclei where the time reversal invariance can no longer eliminate specific spins or parities. One observes then a sequence of levels with successive half-integer values of the angular momentum; but one can still often make a separation between groups of states of opposite $(J+\frac{1}{2})$ parity, say $\frac{1}{2}^+$, $\frac{5}{2}^+$, $\frac{9}{2}^+\ldots$ and $\frac{3}{2}^+$, $\frac{7}{2}^+$, $\frac{11}{2}^+\ldots$. This effect, sometimes called the kinking effect, was first predicted by Bohr and Mottelson[1] in a macroscopic picture as the result of the Coriolis coupling between the deformed core and the odd nucleon.

We present here simple microscopic calculations which indicate that the kinking effect is a frequent tendency among odd populations of valence nucleons and which suggest an alternative description in terms of distinct intrinsic states.

The model for calculating the energies and the wave functions assumes a spherical core and one valence shell for each kind of nucleon. This configuration space is still reduced by selecting the "aligned" configurations[2,3] which are known to reproduce accurately the rotational levels of weakly deformed nuclei,[1] and which have the advantage of keeping track of the intrinsic states. Along these lines, configurations of the type

$$[(1g_{9/2})^4(1g_{7/2})^3]_{T=1/2}$$

and

$$[(1g_{9/2})^3(1g_{7/2})^2]_{T=1/2}$$

were studied by diagonalizing a Gaussian effective interaction V characterized by a rather standard ratio of spin-isospin components, namely $(S=0,\ T=0)/(S=1,\ T=1)/(S=1,\ T=0)/(S=0,\ T=1)=1.0/-0.4/1.25/1.0$ in the two-dimensional space spanned by the projected prolate and oblate aligned Slater determinants. As a direct application to actual nuclei, one can consider these configurations to be made of holes, and one gets then a simplified description of the positive-parity levels of ^{107}Pd and ^{109}Ag, respectively, where the single-particle energies play no role.

Figures 1 and 2 show a plot of the energy versus the angular momentum for these two configurations. Three curves are presented in each figure: the projected energies obtained from a single oblate Slater determinant, those obtained from a single prolate Slater determinant, and,

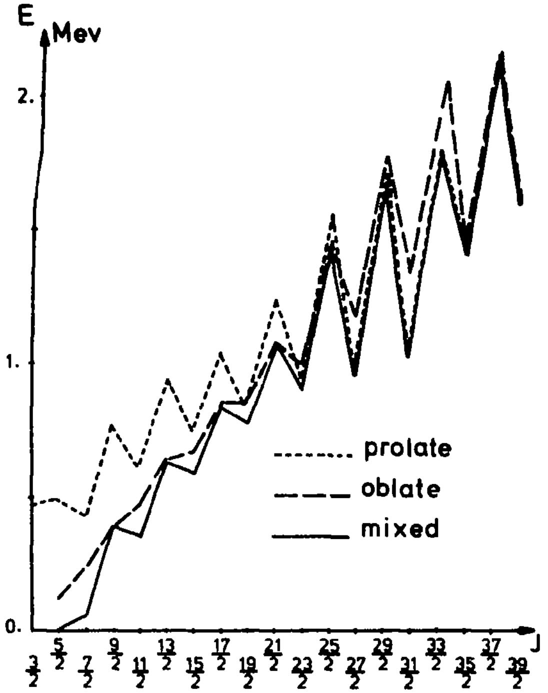

FIG. 1. Energy versus angular momentum for the configuration $[(1g_{9/2})^4(1g_{7/2})^3]_{T=1/2}$ describing positive parity levels of ^{107}Pd.

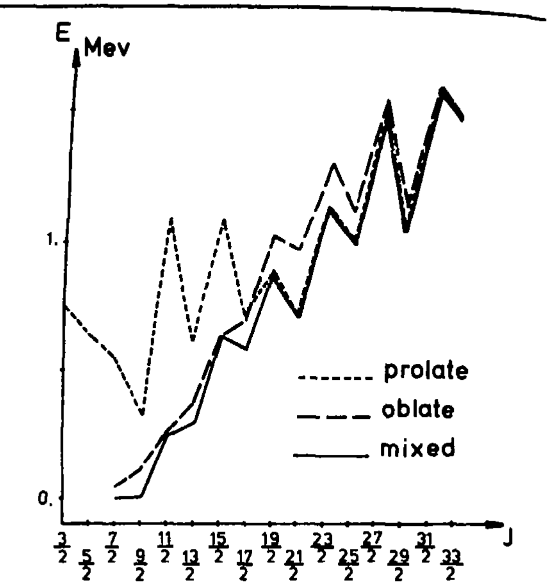

FIG. 2. Energy versus angular momentum for the configuration $[(1g_{9/2})^3(1g_{7/2})^2]_{T=1/2}$ describing positive parity levels of ^{109}Ag.

finally, those resulting from the diagonalization of V in the two-dimensional space. Two characteristic features emerge from these figures and are not, in fact, restricted to the present choice of configurations: (i) An interchange occurs between the oblate band and the prolate band for intermediate J (this effect was already observed for even configurations); (ii) the energy oscillates back and forth for successive J (this is a microscopic evidence of the Coriolis coupling mentioned above).

A closer analysis shows that the oscillations are, of course, weaker in the oblate energy curve than in the prolate one. More meaningful is the fact that all energy curves oscillate in phase, a hint that some underlying symmetry is involved in this effect. As a consequence, a small admixture of the prolate component is enough to enhance the oscillations of the oblate energy curve. The amount of mixture of prolate shape and oblate shape in the intrinsic state is indicated in Table I: One checks that the concept of intrinsic state is still meaningful for large fractions of the spectrum.

These features suggest the existence of two underlying intrinsic states that are separately

TABLE I. Amount of prolate-oblate mixture in the seven-hole and the five-hole configurations that generate positive parity levels of ^{107}Pd and ^{109}Ag in the single-shell configuration space.

J	(% oblate) × relative sign $(g_{9/2})^4(g_{7/2})^3$	$(g_{9/2})^3(g_{7/2})^2$
5/2	+81	...
7/2	−69	+92
9/2	+99	−75
11/2	+70	+99
13/2	−95	+80
15/2	−65	−96
17/2	+91	−52
19/2	+46	+12
21/2	−93	−1
23/2	−35	+2
25/2	+83	−1
27/2	+5	+33
29/2	−30	+3
31/2	+3	+0
33/2	+0	+0
35/2	+2	...
37/2	+0	...
39/2	+0	...

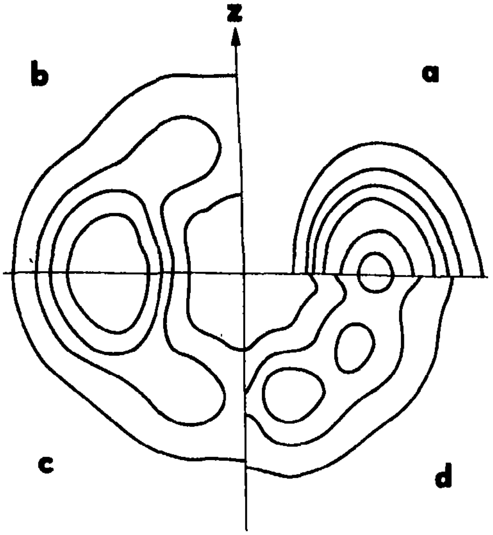

FIG. 3. Valence-hole contributions to the density of ^{109}Ag, in the low-energy region, from (a) the global (oblate) intrinsic state Φ_M generating all angular momenta; (b) the specific intrinsic state Φ_M^- generating (odd $+\frac{1}{2}$) angular momenta; (c) the specific intrinsic state Φ_M^+ generating (even $+\frac{1}{2}$) angular momenta; (d) the "contraster" intrinsic state $\tilde{\Phi}_M$.

responsible for each class of states of given ($J+\frac{1}{2}$) parity. To make this argument more specific, let us consider a simplified situation where the low-energy part of the spectrum is assumed to be exactly described by the projection of a single aligned Slater determinant Φ_M (the argument could be repeated in the more complicated actual situation). We have by definition

$$\Phi_M = \sum_{J=M}^{J_{\max}} a_J \Psi_M^J = \sum_{J=M}^{J_{\max}} P_M^J \Phi_M, \tag{1}$$

where P_M^J is the usual Peierls-Yoccoz angular momentum projector. Then the intrinsic state Φ_M^ϵ generating a sub-band of angular momentum parity ϵ is defined by

$$\Phi_M^\epsilon = \sum_{\text{restr } J} P_M^J \Phi_M, \tag{2}$$

where the sum is restricted to values of J such that $(-1)^{J+1/2}=\epsilon$. Now, and by analogy with the time reversal transformation which, in this context, would be expressed by the operator $\exp(-i\pi J_y)$, a new transformation U, whose eigenvalues characterize the angular momentum parity, can be defined for odd-even nuclei as

$$U = \exp(-i\pi J^2). \tag{3}$$

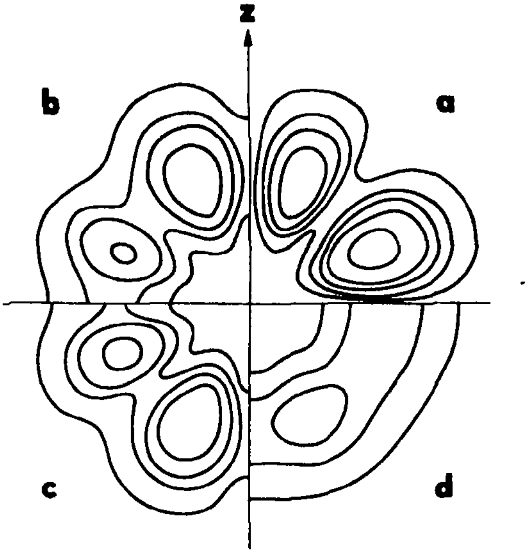

FIG. 4. Same content as Fig. 3, but for the higher energy region of ^{109}Ag and in terms of the prolate shape for holes.

The crucial property of this operator is that

$$U\Psi_M^J = \lambda(-1)^{J+1/2}\Psi_M^J, \tag{4}$$

where λ is a fixed phase: $\lambda=\exp(i\pi/4)$.

One can then relate directly Φ_M^ϵ to Φ_M by means of U:

$$\Phi_M^\epsilon = \tfrac{1}{2}(1+\epsilon\lambda^{-1}U)\Phi_M. \tag{5}$$

We have therefore shown that, in the case of odd nuclei, the property of being invariant under the unitary transformation $\lambda^{-1}U$ characterizes the specific intrinsic states Φ_M^ϵ that generate the two sub-bands. Equation (5) shows that Φ_M^ϵ differs from Φ_M by the action of a remarkable many-body operator and has components on every vector in the basis of unprojected Slater determinants. The calculation of these components indicates that only an approximated 50% of the initial Φ_M component remains present in Φ_M^ϵ.

Equidensity maps obtained from a cut by a meridian plane provide a visualization of these intrinsic states. Figure 3(a) shows the valence-hole contribution to the density distribution of ^{109}Ag in the low-energy region when one considers the global intrinsic state Φ_M; for the sake of simplicity, Φ_M is understood here to be the oblate aligned determinant which describes 100% of the (odd $+\frac{1}{2}$) angular momentum states, but only 75%

of the (even + $\frac{1}{2}$) angular momentum states. Figures 3(b) and 3(c) show the same contribution coming from the specific intrinsic states Φ_M^- and Φ_M^+ which generate states of, respectively, (odd + $\frac{1}{2}$) and (even + $\frac{1}{2}$) angular momentum. The density curves of the "contraster state" $\tilde{\Phi}_M = U\Phi_M$ are shown in Fig. 3(d). Finally, Figs. 4(a)–4(d) show the equivalent intrinsic states of opposite deformation (prolate shape in terms of holes) which generate (here exactly) the higher energy region of ths spectrum of ^{109}Ag.

It is clear that the same operator U may be considered for nonaxial deformations of odd nuclei.

---

[*] Also, Ministère de l'Industrie, DITEIM, Paris, France.

[1] B. M. Mottelson, unpublished; cited in F. S. Stephens, R. M. Diamond, and S. G. Nilson, Phys. Lett. 44B, 429 (1973).

[2] B. M. Mottelson, in *Nuclear Spectroscopy, Proceedings of the Enrico Fermi International School of Physics, Course XV*, edited by G. Racah (Academic, New York, 1960), p. 45.

[3] M. Danos and V. Gillet, Phys. Rev. 161, 1034 (1967)

[4] A. Jaffrin, Nucl. Phys. A196, 577 (1972).

Electroexcitation of the Giant Resonance in ^{16}O

A. Hotta
Department of Liberal Arts, Shizuoka University, Shizuoka, Japan

and

K. Itoh and T. Saito
Laboratory of Nuclear Science, Tohoku University, Tomizawa, Sendai, Japan

(Received 15 July 1974)

Electroexcitation of ^{16}O has been measured. The strength for the $E2$ (or $E0$) resonances were extracted from the longitudinal form factors. In the region of 20–30-MeV excitation the strength exhausts approximately 20% of the sum rule for an $E2$ interpretation, while the strength in the region below 20 MeV exhausts 43% of the same sum rule. The transverse form factor is compared with calculations using both the one-particle, one-hole and the generalized Goldhaber-Teller models.

Recent experiments on the inelastic scattering of electrons, protons, and ^{3}He particles[1] have revealed the existence of giant quadrupole ($E2$) or giant monopole ($E0$) resonances both below and above the giant-dipole resonance in medium and heavy nuclei. The observed energies of both resonances indicate systematically $60A^{-1/3}$ or $120A^{-1/3}$ MeV dependence, respectively, and its strength exhausts more than 60% of the energy-weighted sum rule (EWSR) for an $E2$ interpretation.

In light nuclei, such evidences for a giant $E2$ resonance have not been established. A recent analysis of the reaction[2] ^{16}O$(\gamma, n_0)^{15}$O has shown it is necessary to assume a broad $E2$ resonance in the giant-dipole region in order to explain the angular distribution and the polarization data. Also measurements on the polarized-proton capture reaction[3] ^{15}N$(p, \gamma_0)^{16}$O have shown that a broad $E2$ resonance lies above the $E1$ giant resonance and its strength exhausts approximately 30% of the $E2$ EWSR, which is a factor of 2 smaller than the prediction of the neutron data analysis. On the other hand, a study of the α-capture reaction[4] ^{12}C$(\alpha, \gamma_0)^{16}$O has revealed a $T = 0$, $E2$ strength in the region $E_x = 12$ to 28 MeV. In this Letter we present evidence for the $E2$ giant resonance in ^{16}O from a study of inelastic electron scattering.

The experiment was performed with the electron beam of the Tohoku University 300-MeV linear accelerator. Oxygen gas of 20 atm pressure, contained in a stainless-steel cylinder of 40 mm in diameter, 40 mm in height, and 0.12 mm in thickness, was used. The spectrometer and detection apparatus have been described elsewhere.[5] The spectra of scattered electrons were taken at different angles but at the same momentum transfer in order to separate them into longitudinal and transverse parts. The overall energy resolution was 0.15%. The incident energies and scattering angles employed were 183 MeV

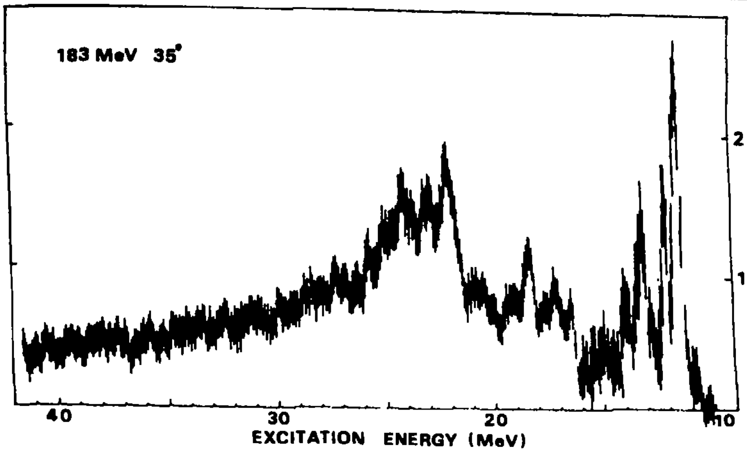

FIG. 1. Spectrum of electrons scattered from ^{16}O.

(35°), 250 MeV (40°), 250 MeV (50°), 70 MeV (120°), 97 MeV (135°), and 120 MeV (135°).

Figure 1 shows a spectrum of scattered electrons for ^{16}O at a scattering angle of 35° and an incident electron energy of 183 MeV. The dominant peaks at 22.2, 23.0, and 24.3 MeV agree with the total photoabsorption γ-ray spectra of Bezić *et al.*[6] and Agrens *et al.*[7] The inelastic scattering cross sections were obtained by comparison with the elastic scattering cross section, whose ab-

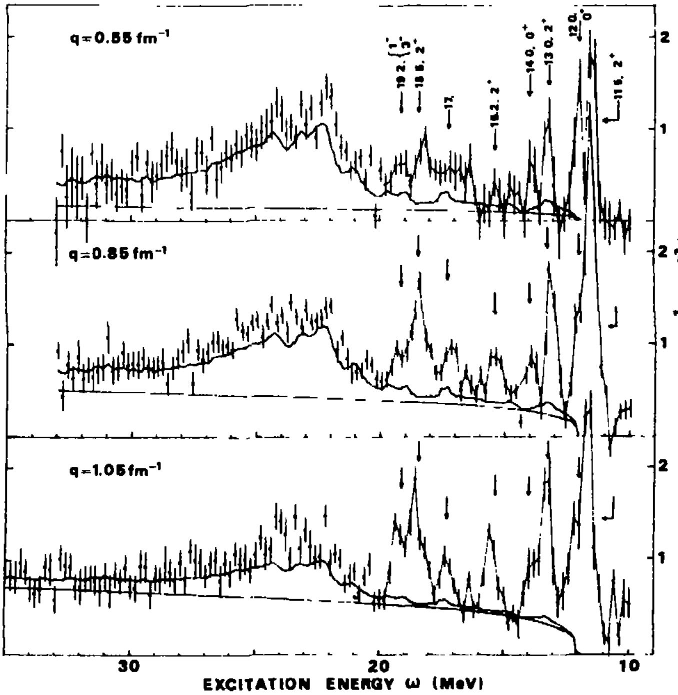

FIG. 2. The longitudinal form factors $|W_L(q,\omega)|^2$ for electroexcitation in ^{16}O from this experiment is shown as data points. The arrows show the positions of the form-factor peaks below $E_x=20$ MeV. The middle and the lower solid curves show the total photoabsorption cross section and the continuum, respectively.

solute value was computed by phase-shift calculation using the harmonic-oscillator parameters $\alpha = 1.35$, $b = 1.81$ fm.[8]

In the Born approximation, the form factor $W(q, \omega)$ for the excitation energy ω and small energy interval $\Delta\omega$ is given by[9]

$$|W(q,\omega)|^2 = \frac{q_\mu^4}{q^4}|W_L(q,\omega)|^2 + \left(\frac{q_\mu^2}{2q^2} + \tan^2\frac{\theta}{2}\right)|W_T(q,\omega)|^2, \qquad (1)$$

where $W_L(q, \omega)$ and $W_T(q, \omega)$ are the longitudinal and transverse form factors, respectively, q_μ the four-momentum transfer of the electron, q the three-momentum transfer, ω the excitation energy, and θ the scattering angle. The usual form factor $F(q)$ is related to the form factor $W(q, \omega)$ by

$$|F(q)|^2 = \int |W(q,\omega)|^2 d\omega. \qquad (2)$$

The observed spectra were normalized to a channel width of $\Delta\omega = 200$ keV, and then separated into $W_L(q, \omega)$ and $W_T(q, \omega)$ using Eq. (1).

Figure 2 shows the longitudinal form factors $W_L(q, \omega)$ *as observed in this experiment for three different momentum transfers.* The states of 11.5-MeV 2^+, 12-MeV 0^+, 14-MeV 0^+, 15.2-MeV 2^+, 17 MeV, 18.5-MeV 2^+, 19-MeV 1^-, and or 3^-, and the giant-dipole resonance have been strongly excited. In this figure the *middle curve in each case* shows the total photoabsorption cross section. The q dependence of these curves was assumed to be given by the Tassie model.[10] The lower curve shows the continuum which was estimated by adopting a phenomenological formula[11]

$$y = c(E_x - E_0)^{1/n}, \qquad (3)$$

where E_x is the excitation energy, $E_0 = 12.1$ MeV is the threshold energy for proton emission, n an adjustable parameter, and c is determined by fitting the sum of y and the photoabsorption cross section to the experimental spectrum at about 32 MeV.

The 18.5-MeV state has been studied by Stroetzel and Goldmann[12] who assigned to it a spin $J = 2$. The present experiment indicates that the 18.5-MeV state is strongly excited by the longitudinal component and its form factor shows a q dependence of a $E2$-type transition. So we assign the spin and parity of this state to be $J^\pi = 2^+$.

In the giant-resonance region differences can be seen between the spectrum and the $E1$ cross section with increasing momentum transfer. This is consistent with the existence of a higher multipole resonance besides the $E1$ giant resonance. In order to extract the strength of the

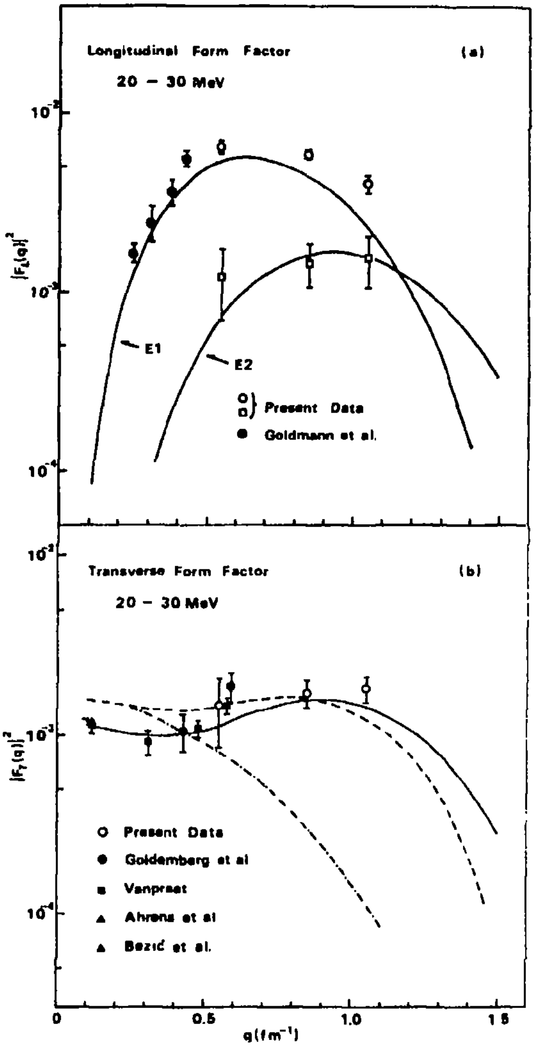

FIG. 3. (a) The longitudinal form factor for a range of 20–30 MeV as functions of q. The Darmstadt data are also plotted. The square shows the result of the subtraction of the $E1$ contribution from the experimental values. Also shown is the theoretical q dependence of the form factor for the $E1$ and $E2$ resonances. (b) The *transverse form factor for the same range as for* (a). The Stanford data and the photonuclear data are shown together with theoretical results calculated using the Goldhaber-Teller model (dash-dotted line), the generalized Goldhaber-Teller model (dashed line), and the particle-hole model (solid line).

TABLE I. $B(E2)$, $B(E2)$ in Weisskopf units, and energy-weighted sum-rule (EWSR) limits.

E_x (MeV)	J^π	$B(E2)$	$B(E2)/B_W(E2)$	$E_xB(E2)$/EWSR
6.92	2^+	36 ± 4[a]	3.0	0.11
9.85	2^+	0.67 ± 0.27[a]	0.056	0.003
11.52	2^+	25.67 ± 2.83[b]	2.1	0.13
13.15	2^+	13.8[b]	1.2	0.08
15.15	2^+	8.1 ± 4.1[c]	0.68	0.05
16.46	2^+	2.7 ± 0.9[c]	0.22	0.02
18.5	2^+	5.1 ± 0.5	0.43	0.04
			SUM	0.43
20–30	2^+	20 ± 8	1.7	0.21

[a] Ref. 14. [b] Ref. 15. [c] Ref. 12.

higher multipole resonance, the form factor $F(q)$ was obtained by using Eq. (2). The longitudinal form factor integrated over the region from 20 to 30 MeV is shown in Fig. 3(a) together with the low-momentum-transfer data of Goldmann and Stroetzel.[13] Also shown in Fig. 3(a) is the $E1$ form factor calculated by using the Tassie model[10] and normalizing to the data of Ahrens *et al.*[7] The points represented by a square in Fig. 3(a) are the result of the subtraction of the $E1$ calculated contribution from the experimental values. These points are consistent with the theoretical $E2$ q dependence of the form factor given by the Tassie model.

The reduced transition probability obtained for the $E2$ resonance and a comparison with the EWSR are given in Table I together with the strengths of other 2^+ states. In this table the $E2$ strengths for the states below 16.46 MeV are taken from the data of Stroetzel,[14] Kim, Singhal, and Caplan,[15] and Stroetzel and Goldmann.[12]

In contrast to medium and heavy nuclei, the $E2$ strength in ^{16}O is distributed in a wide energy region. The observed strength exhausts 64% of the $E2$ EWSR, while the strength in giant-dipole-resonance region exhausts only 21% of the same sum rule. In inelastic electron scattering both isoscalar and isovector quadrupole resonances may be excited. The observed $E2$ strength above $E_x = 20$ MeV in comparable to that of the isovector giant-quadrupole resonance obtained from the (p,γ) reaction.[3] Below $E_x = 20$ MeV the $E2$ strength and its distribution are in agreement with those of the isoscalar $E2$ resonances obtained from the (α,γ_0) reaction.[4]

The transverse form factor integrated over the region from 20 to 30 MeV is shown in Fig. 3(b) together with the photonuclear data[6,7] and the Stanford data.[16] The present form factor at 0.6 fm^{-1} agrees well with the Stanford data. The transverse form factor obtained by using the Goldhaber-Teller model with the isospin mode does not agree with the data, but the form factor for the spin-isospin mode[17] and the particle-hole model[18] both agree with the data.

The authors would like to thank Professor Y. Torizuka and Professor Y. Kojima for their encouragements and advice.

---

[1] See D. C. Kocher, F. E. Bertrand, E. E. Gross, R. S. Lord, and E. Newman, Phys. Rev. Lett. 31, 1070 (1973), and references contained therein.

[2] W. L. Wang and C. M. Shakin, Phys. Rev. Lett. 30, 301 (1973).

[3] S. S. Hanna, H. F. Glavish, R. Avida, J. R. Calarco, E. Kuhlmann, and R. LaCanna, Phys. Rev. Lett. 32, 114 (1974).

[4] K. A. Snover, E. G. Adelberger, and D. R. Brown, Phys. Rev. Lett. 32, 1061 (1974).

[5] M. Kimura *et al.*, Nucl. Instrum. Methods 95, 403 (1971).

[6] N. Bezić, D. Brajnik, D. Jamnik, and G. Kernel, Nucl. Phys. A128, 426 (1969).

[7] J. Ahrens *et al.*, in *Proceedings of the International Conference on Nuclear Structure Studies Using Electron Scattering and Photoreactions, Sendai, Japan, 1972*, edited by K. Shoda and H. Ui, CONF 720907 (Tohoku University, Sendai, Japan, 1972).

[8] J. C. Bergstrom *et al.*, Phys. Rev. Lett. 24, 152 (1970).

[9] A. Yamaguchi, T. Terasawa, K. Nakahara, and Y. Torizuka, Phys. Rev. C 3, 1750 (1971).

[10] L. J. Tassie, Aust. J. Phys. 9, 407 (1956).

[11] S. Fukuda and Y. Torizuka, Phys. Rev. Lett. 29, 1109 (1972).

[12] M. Stroetzel and A. Goldmann, Z. Phys. 233, 245 (1970).

[13] A. Goldmann and M. Stroetzel, Z. Phys. 239, 235

(1970).

[14] M. Stroetzel, Z. Phys. 214, 357 (1968).

[15] J. C. Kim, R. P. Singhal, and H. S. Caplan, Can. J. Phys. 48, 83 (1970).

[16] J. Goldemberg and W. C. Barber, Phys. Rev. 134, B963 (1964); G. J. Vanpraet, Nucl. Pnys. 74, 219 (1965

[17] H. Überall, Nuovo Cimento 41B, 25 (1966).

[18] V. Gillet and N. V. Mau, Nucl. Phys. 54, 321 (1964).

New Negative Result for Gravitational Wave Detection, and Comparison with Reported Detection

James L. Levine and Richard L. Garwin

IBM Thomas J. Watson Research Center, Yorktown Heights, New York 10598

(Received 24 June 1974)

We report new negative results for detection of gravitational radiation with a 500-kg, 1637-Hz detector of demonstrated sensitivity and detection efficiency. These results are compared with numerous detections reported by Weber. We conclude that those detections did not arise from gravitational radiation. Furthermore, gravity waves (or other impulsive excitations) could not have produced data with a coincidence peak as narrow as that published in September 1973.

We report a new negative result for the detection of gravity wave pulses, at a sensitivity six times greater than that of our previous publication.[1] We believe the present results to be in substantial conflict with the detections reported by Weber[2-4] although this conclusion requires estimates of Weber's detection sensitivity; his publications do not adequately present data to allow determination of the signal wave form, strength, or arrival rate (corrected for detection efficiency).

Apart from minor improvements in the transducer, the major increase in sensitivity was obtained by increasing the mass of the aluminum cylinder used as an antenna from 120 to 480 kg, the resonance frequency (1637 Hz) remaining close to that of Weber's antennae (1661 Hz). The rest of the apparatus, calibration techniques, and detection procedures are as described in Ref. 1. In particular, pulses of radiation of duration less than our 58-msec sampling interval are sought, the detection algorithm yielding the oscillation energy E_g which would be induced by a pulse in an antenna initially at rest, independently of the arrival time of the pulse and the preexisting state of oscillation.

In Fig. 1, we show the observed impulse energies as defined above, in the form of a logarithmic histogram. The energies are determined by comparison with an electrostatic calibrator[1] and are given for convenience in units of the mean oscillation energy kT_r (T_r = room temperature), the straight line (Boltzmann distribution) being the result expected if only thermal and amplifier noise were present. The slope of the line defines an effective temperature $T_e = 0.063T_r$ which characterizes the experiment. The histogram includes 4.1×10^7 values obtained during a 27-day period (3–30 December 1973). Only one measure

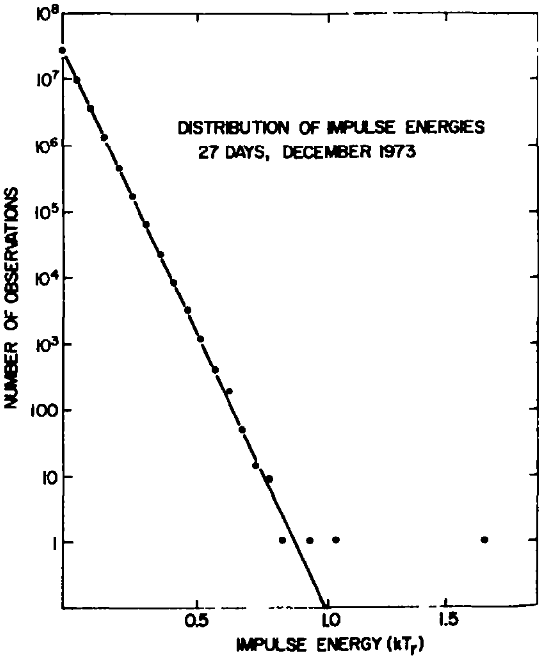

FIG. 1. Histograms of observed impulse energies. Solid curve, Boltzmann distribution with effective temperature T_e=18.5 K.

ment interval (time: 23 : 0.1 : 22 ± 1 sec, E.S.T. 12 December 1973) contained a pulse substantially above the noise. We will discuss this pulse below.

We have obtained the efficiency for detecting pulses of energy E_g above a threshold value E_t, both theoretically and experimentally. Let a large number of such pulses occur. In the presence of Boltzmann-distributed noise characterized by mean value kT_e, the detection algorithm will return a distribution of apparent pulse energies E, related to the Rician distribution function[5]:

$$\begin{aligned} F(E) &= (1/kT_e)\exp[-(E+E_g)/kT_e]I_0(X), \\ X &= [2(EE_g)^{1/2}]/kT_e, \end{aligned} \tag{1a}$$

where $I_0(X)$ is the modified Bessel function of zero order. Expanding, we find

$$\begin{aligned} F(E) &\cong [1/(4\pi E_g kT_e)^{1/2}] \\ &\quad \times \exp[-(E_g+kT_e-E)^2]/4E_g kT_e, \\ |E-E_g| &\ll E_g, \quad E_t \gg kT_e. \end{aligned} \tag{1b}$$

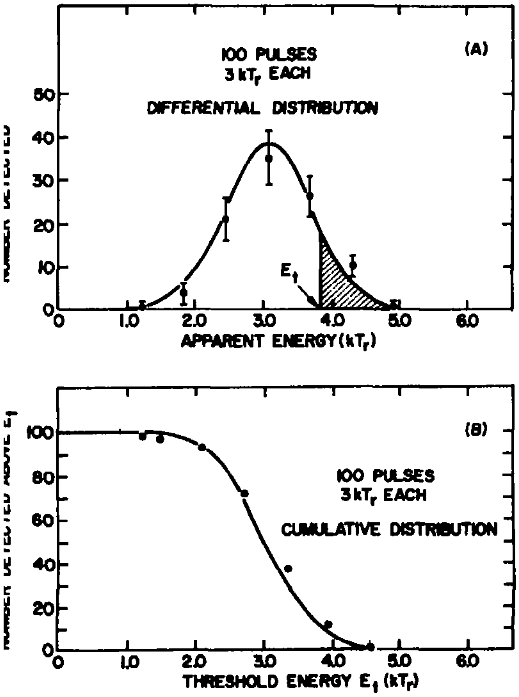

FIG. 2. (a) Differential distribution of calibrator ulses detected with normal procedures. (b) Cumula- lve distribution of above pulses. The solid curves are heoretical (see text) and free of adjustable parameters.

Equation (1b) is plotted in Fig. 2(a) for $E_g = 3kT_r$ and the value of kT_e obtained from Fig. 1. The detection efficiency $P_d(E_g, E_t)$ is then represented by the shaded area in Fig. 2(a):

$$P_d(E_g, E_t) = \int_{E_t}^{\infty} F(E)\,dE. \tag{2}$$

Equation (2) may be evaluated in terms of the tabulated error integral,[6] and is plotted (solid curve) in Fig. 2(b), again for $E_g = 3kT_r$.

To verify that Eqs. (1) and (2) correctly describe our complete detection system, 100 pulses of energy $3kT_r$ were introduced at random times by the electrostatic force calibrator of Ref. 1. These were detected "blind" by the normal detection algorithm, 98 being found above the (normal) threshold $E_{tn} = 1.1kT_r$. These are plotted (solid points) in Figs. 2(a) and 2(b), the agreement being satisfactory.

We may now use Eq. (2) to set an upper limit for the occurrence[7] rate of pulses of various energies. In Fig. 1, we note only a single pulse above E_{tn}. The detection efficiency for that pulse is 0.94, thus it was the only such pulse occurring in 27 days and can provide no support for the several pulses per *day* claimed by Weber. Next, assume that pulses of lower energy E_g occurred at an average rate $\dot{N}_g$ (per day), thus $\bar{N} = 27\dot{N}_g$ were expected during the experiment. The actual number N will be Poisson distributed about the expected value:

$$G(N) = \exp(-\bar{N})\bar{N}^N/N! \tag{3}$$

Then the probability P_1 that at least one additional pulse would have been detected above threshold is

$$P_1 = \sum_{N=1}^{\infty} G(N)\{1-[1-P_d(E_g, E_{tn})]^N\}. \tag{4}$$

We then obtain (numerically) the average rate required to give $P_1 = [1-(1/e)] = 0.64$. This is plotted in Fig. 3; combinations $(\dot{N}_g, E_g)$ above the curve are incompatible with our observations. $\dot{N}_g(E_g)$ represents an upper limit on the occurrence rate of pulses of one particular energy; if pulses of different energies were present simultaneously, fewer of each would have been required to give one detection than the numbers determined from Eq. (4).

The large pulse noted above could *a priori* be a gravity wave pulse, stress relaxation in the antenna, electrical pickup of an intense but infrequent laboratory tone, or the result of a rarely occurring signal-processor defect. Thus far, the data from our single antenna cannot preclude

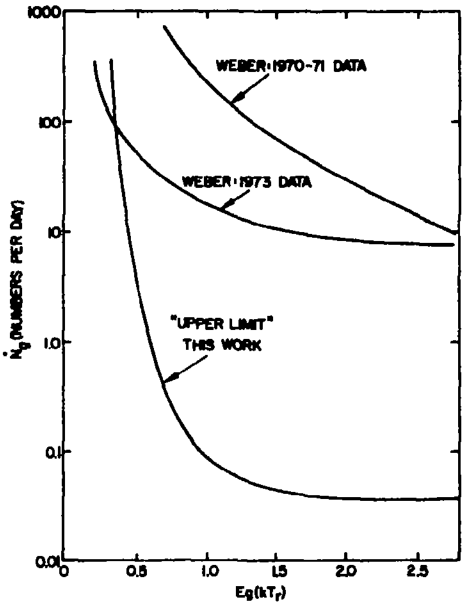

FIG. 3. Upper limit for average pulse occurrence rate versus energy given to *our* antenna (lower curve) compared with estimates of occurrence rates deduced from the work of Weber (upper curves). The latter are also scaled to our antenna mass, and are based on the limited information available in Refs. 3 and 4.

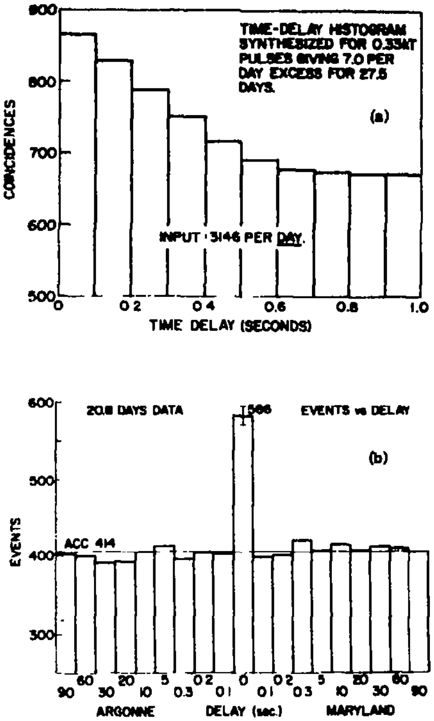

FIG. 4. (a) Time-delay-coincidence histogram from simulation of an antenna pair using 1.6-Hz bandwidths filters. The simulation uses system parameters of Ref. 4. (b) Time-delay-coincidence histogram results of Ref. 4.

any of these possible causes. However, a coincident pulse (corrected for antenna parameters) was not observed at the University of Rochester detector[8]; thus the pulse is unlikely to have arisen from gravitational radiation.

It would be of considerable value to be able to locate with certainty the signals of Refs. 2, 3, and 4 either above or below the "upper-limit" curve in Fig. 3. This is not possible at present, as experimental results for detection efficiencies (similar to those presented in Fig. 2) have not been published for any of the three systems used by Weber. We are thus forced to estimate these quantities, while noting that such information is easily obtained by the experimenter and is normally provided in the publication of a detection experiment.

We have made such estimates[9,10] for the systems described in Refs. 3 and 4, the signals having been detected in 1970 and 1973, respectively. The result in each case is a curve giving combinations of pulse occurrence rate and energy compatible with the published time-delay histograms (prompt-coincidence excess and background-coincidence rate), detection methods and estimated noise levels. We have assumed each system to have been operating without degradation and with only thermal and normal amplifier noise. These curves are plotted in Fig. 3. The 1970 signals were clearly not present during our experiment. For the 1973 signals, a very large occurrence rate of small signals cannot be excluded.

This analysis has left open two logical possibilities: (a) Large gravity waves were being detected during May 1973,[4] but were no longer incident in December 1973 to be detected by our apparatus; or (b) some hundreds of gravity waves were incident per day even during December 1973, giving our bar $< 0.3kT_r$.

Both these possibilities are precluded by an analysis of the form of the delay histogram which would be produced by impulsive excitations of antenna systems containing a "1.6-Hz bandwidth filter."[4] Figure 4(a) is the result of a simulation such a time-delay coincidence histogram. ise and the filter-broadened gradual change amplitude combine to give the breadth of the stribution. For comparison, Fig. 4(b) are the sults of Ref. 4.

The results of Figs. 3 and 4(a) appear to pre-ude all physical explanations of the results of f. 4 [our Fig. 4(b)]. Indeed, the data of Ref. 4 re processed with a faulty computer program an above-threshold event in one specific anten- which happened to fall in the last 0.1-sec bin a 1000-bin data block was *always* counted as rompt coincidence with a later above-thresh- d event in the other antenna.[11] This error was own[11] to account for essentially all of the zero- lay excess events on a four-day tape of the da- of Ref. 4.

We thank D. H. Douglass for many useful dis- ssions.

---

[1] J. L. Levine and R. L. Garwin, Phys. Rev. Lett. 31, 3 (1973).

[2] J. Weber, Phys. Rev. Lett. 22, 1320 (1969), and 24, 6 (1970).

[3] J. Weber, Nature (London) 240, No. 5375, 28 (1972).

[4] J. Weber *et al.*, Phys. Rev. Lett. 31, 779 (1973).

[5] A. D. Whalen, *Detection of Signals in Noise* (Academic, New York, 1971), p. 204, Eq. (7–22). Our detection algorithm acts to "whiten" the correlated thermal noise of the lightly damped antenna, thus Eq. (7–22) is relevant. It reduces to Eq. (1a) above if the following substitutions are made: $E=q^2$, $P(E)\,dE=p_1(q)\,dq$, $E_s=(AT/2)^2$, and $2\sigma_T^2=kT_e$. Figure 7–5, p. 205 of the text may be used with the signal-to-noise ratio defined as $(S/N)=10\log(E_s/kT_e)$.

[6] R. S. Burington, *Handbook of Mathematical Tables and Formulas* (McGraw-Hill, New York, 1965), 4th ed.

[7] The amplitude change induced in the antenna depends on its orientation with respect to the (unknown) gravity wave propagation vector and polarization. We thus refer throughout to the final effect of a wave; i.e., the resulting pulse energy, for direct comparisons with other experiments.

[8] D. H. Douglass, private communication.

[9] R. L. Garwin and J. L. Levine, Phys. Rev. Lett. 31, 176 (1973).

[10] J. L. Levine, to be published.

[11] D. H. Douglass, in Proceedings of the Fifth Cambridge Conference on Experimental Relativity, Cambridge, Massachusetts, 10 June 1974 (to be published). This computer programming error (found September, 1973) was acknowledged by J. Weber in public discussion.

Azimuthal Correlations in *pp* Interactions at 205 GeV/*c*

M. Pratap, R. Engelmann, and T. Kafka
*State University of New York, Stony Brook, New York 11790**

and

Y. Cho, T. H. Fields, L. G. Hyman, and R. Singer
Argonne National Laboratory, Argonne, Illinois 60439†

and

L. Voyvodic, R. Walker, and J. Whitmore
Fermi National Accelerator Laboratory, Batavia, Illinois 60510‡

(Received 3 July 1974)

Using data obtained from an exposure of the 30-in. Fermi National Accelerator Laboratory bubble chamber to a 205-GeV/*c* proton beam, results are presented on azimuthal distributions. Evidence is presented for dynamical azimuthal correlations whose behavior depends on the particular charge combination. The dependence of the azimuthal correlations on the rapidity difference and on the transverse momentum is also given.

The study of two-particle correlations has re- ived considerable attention recently, both the- etically and experimentally. At the Fermi Na- nal Accelerator Laboratory (FNAL) and the RN intersecting storage ring energies, most the emphasis has been placed on the analysis of two-particle rapidity distributions, although some studies have been made of azimuthal correlations.[1,2] In this Letter we present new results on azimuthal correlations in *pp* interactions, at the inclusive and, for the first time at FNAL energies, at the semi-inclusive level. The depen-

TABLE I. Asymmetry parameter A_n [Eq. (1)] for different charge combinations and leading particles. The total number of particles, n_T, estimated from A_n^{cc} and experimentally observed.

n	A_n^{cc}	A_n^{+-}	A_n^{++}	A_n^{++} leading	A_n^{--}	n_T from A_n^{cc}	n_T observed
2	0.20±0.04	————	0.20±0.04	0.20±.04	————	6±1	4±1
4	0.11±0.01	0.14±0.03	0.09±.02	0.04±.03	————	10±1	6±1
6	0.10±0.01	0.11±0.02	0.09±0.01	0.09±.03	0.07±0.03	11±1	11±1
8	0.072±0.006	0.08±0.01	0.05±0.01	0.05±.04	0.08±0.02	15±1	13±1
10	0.051±0.005	0.06±0.01	0.04±0.01	0.05±.06	0.02±0.01	21±2	17±1
12	0.040±0.005	0.06±0.01	0.02±0.01	0.00±.03	0.03±0.01	26±3	18±1
14	0.050±0.006	0.06±0.01	0.07±0.01		0.01±0.01	21±2	21±2
16	0.035±0.008	0.04±0.02	0.05±0.01		.02±0.02	29±6	24±2
Inclusive	0.056±0.003	0.067±0.006	0.048±0.005		0.027±0.009		

per inelastic event.[7] We have assumed that on the average there is one neutron or antineutron per inelastic event.[8] We observe that the model's predictions for n_T are consistently larger than the values experimentally determined, which may be a manifestation of dynamical effects not included in the model.

In order to study the transverse-momentum dependence of the azimuthal correlations, we consider the distribution

$$\frac{1}{\sigma_{\rm incl}}\frac{d^2\sigma}{d\varphi\, dp_T}$$

in which we have integrated over the transverse momentum of one of the two particles. Figure 2(b) shows the asymmetry A, integrated over all n, as a function of p_T. The asymmetry is seen to increase monotonically with p_T, an effect due at least in part to energy-momentum conservation. In Fig. 2(b) we also show the asymmetry as a function of p_T for particle pairs with a large rapidity difference, $\Delta y = |y_i - y_j| > 2$. We observe that the above trend continues even over large rapidity differences.

Correlation effects between the longitudinal and transverse momenta can be analyzed by studyin the distribution

$$\frac{1}{\sigma_{\rm incl}}\frac{d^3\sigma}{dy_i\, dy_j\, d\varphi_{ij}}. \qquad (2)$$

We note that in the independent-particle emission the asymmetry in φ for the distribution (2) depends only very weakly on the rapidity difference Δy.[9] In Figs. 3(a)–3(d) we show the asymmetry parameter as a function of Δy for the charged-charged, + −, + +, and − − cases, respectively. We observe that for the (+ −) combination (which, as noted above, shows larger correlations in both the inclusive and semi-inclusive cases), the asymmetry is large for small rapidity differences and decreases as the rapidity difference increases. That is, for this combination, particles which are close together in rapidity tend to balance their transverse momenta. By contrast, for the (+ +)[10] and (− −) combinations, we find that the asymmetry is small for small Δy. The asymmetry then increases to a maximum as the rapidity difference increases ($\Delta y \simeq 1-2$) and then drops to zero again.

The suppression of the azimuthal asymmetry at

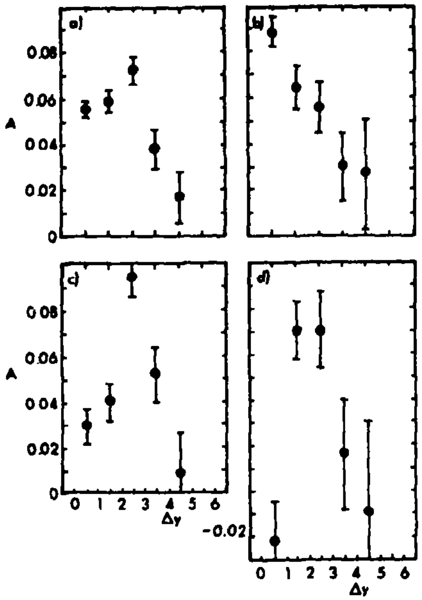

FIG. 3 Asymmetry parameter as a function of ra- difference Δy for the (a) charged-charged, −, (c) $++$, and (d) $--$ combinations.

all Δy of the like pions (+ + and − −) may be part- caused by correlations due to Bose-Einstein statistics as a![11] However, it is tempting to go a step further and compare our observations with a short-range cluster model of particle production which has been successful in explaining two-particle rapidity distributions. In one such picture,[12] the clusters are assumed to be neutral and contain three pions. Hence, within such a simple cluster, there are no (+ +) or (− −) combinations. This implies that the (+ +) and (− −) correlations are due to cluster-cluster correlations alone, whereas the (+ −) combination has, in addition to the cluster-cluster contribution, correlations between the particles within a single cluster. Qualitatively, this is consistent with the observation that the (+ +) and (− −) correlations are small at small Δy, rise with increasing Δy [as correlations between (neighboring) clusters become important], and then fall toward zero (beyond the range of correlations between clusters). In a multiperipheral model with only single-pion emission the above effects can only be produced by imposing strong isospin constraints.

As has been shown above, as two particles get farther apart in rapidity, their transverse momenta become less correlated. It is natural to examine the extreme case where one studies the azimuthal correlation between "leading" particles (either π^+ or proton). In order to look for such correlations, we have defined the leading particles in an event as the positive particles with the smallest and largest angle (with respect to the beam direction) in the laboratory. Table I gives the asymmetry parameter as a function of topology. We obtain an asymmetry of 0.04 ± 0.02 averaged over events with four or more prongs. Thus we observe that the asymmetry for the leading particles is nonzero but consistently smaller than the overall asymmetry. (Of course, for the two prongs, the two distributions are the same.) For $n > 8$, the average leading-particle asymmetry is consistent with zero.

We conclude that there are azimuthal correlations present which cannot be explained solely by energy-momentum conservation, since the asymmetry has a substantial charge dependence. The asymmetry is also a strong function of the rapidity difference between the two particles.

---

*Work supported in part by the National Science Foundation.

†Work supported by the U. S. Atomic Energy Commission.

‡Operated by Universities Research Association, Inc., under contract with the U. S. Atomic Energy Commission.

[1] C. M. Bromberg *et al.*, Phys. Rev. D 9, 1864 (1974).

[2] H. Dibon *et al.*, Phys. Lett 44B, 313 (1973).

[3] Y. Cho *et al.*, Phys. Rev. Lett. 31, 413 (1973); R. Singer *et al.*, Phys. Lett. 49B, 481 (1974).

[4] Errors in φ_{ij} are typically ±5°. To calculate y_i we have assumed all negative tracks to be π^-, positive tracks with momentum greater than 120 GeV/c to be protons (resulting in less than a 5% misidentification of pions as protons), and the remainder of the positive tracks (except for identified slow-proton tracks with momentum less than 1.4 GeV/c) to be pions.

[5] M. C. Foster *et al.*, Phys. Rev. D 6, 3135 (1972); M. Pratap and J. C. Shaw, Phys. Rev. D 8, 3938 (1973).

[6] One can measure the asymmetry parameter using only the charged particles if the emission of particles is truly statistical.

[7] K. Jaeger *et al.*, "Characteristics of V^0 and γ Production in pp Interactions at 205 GeV/c," Argonne National Laboratory Report (to be published); K. Jaeger, private communication. Note that we have made the approximation

$$\left\langle \frac{1}{n_T-1} \right\rangle_n \approx \frac{1}{\langle n_T\rangle_n - 1}.$$

[8] This is consistent with estimates in the FNAL ener-

gy range given by J. Whitmore, FNAL Report No. NAL-Pub-73/70-EXP (unpublished); E. Malamud, Bull. Amer. Phys. Soc. 19, 467 (1974).

[9] D. Z. Fredman, C. E. Jones, F. E. Low, and J. E. Young, Phys. Rev. Lett. 26, 1197 (1971); D. Sivers, ANL Report No. ANL/HEP 7246, 1972 (unpublished).

[10] The mass identification for positive tracks leaves

12% protons m

with a result

Fig. 3(c) or

[11] G. Gold

[12] C. Qui

(1973);

(1974).

Giant-Dipole-Resonance Region of ^{15}N Observed via ^{14}C$(p,p)^{14}$C Cross Section and Polarization Measurements*

H. R. Weller†
Department of Physics, University of Florida, Gainesville, Florida 32611, and Triangle Universities Nuclear Laboratory, Durham, North Carolina 27706

and

N. R. Roberson and D. Rickel
Duke University, Durham, North Carolina 27706, and Triangle Universities Nuclear Laboratory, Durham, North Carolina 27706

and

D. R. Tilley
North Carolina State University, Raleigh, North Carolina 27607, and Triangle Universities Nuclear Laboratory, Durham, North Carolina 27706

(Received 15 July 1974)

Cross sections and polarizations have been measured for ^{14}C$(p,p)^{14}$C scattering over the energy range corresponding to the giant-dipole-resonance region of ^{15}N. The results indicate a $J^\pi=\frac{3}{2}^+$ resonance of about $\Gamma=4$ MeV near $E_p=10$ MeV. This resonance appears to be the giant dipole resonance observed in (p,γ) measurements.

Recent measurements of the analyzing powers and cross sections of protons elastically scattered from ^{28}Si have suggested, on the basis of the energy dependence of the spin-orbit potential obtained from an optical-model analysis, that these data are sensitive to the existence of the giant dipole resonance (GDR) of ^{29}P.[1] In this Letter we will report our results of a study of the GDR of ^{15}N using the reaction ^{14}C$(p,p)^{14}$C. The intent of this work was to establish whether the correlation suggested in Ref. 1 could be more definitely established and, if so, what parameters could be extracted.

The experiment was performed by using the polarized-ion source at the Triangle Universities Nuclear Laboratory. Angular distributions were measured at 8 energies between $E_p=7.5$ and 12.45 MeV. Data were taken in 10° steps from 50° to 160°. Eight detectors were used—four left and four right—and each run was made with the proton spin up and down. The beam polarization was determined to be 0.82 ± 0.02 by means of the quench-ratio technique.[2] The ^{14}C targets used for this work were made by cracking 70% ^{14}C-enriched acetylene on a 0.12-μm-thick nickel backing and were about 10 keV thick for 3.4 MeV protons. The cross sections were obtained by summing the polarization results as well as by measuring them independently with an unpolarized beam. At angles forward of 85°, where the elastic ^{12}C, ^{14}C, and ^{16}O peaks overlap, measurements of the ^{12}C and ^{16}O cross sections were used in extracting the ^{14}C data.

The cross section for the reaction ^{14}C$(p,p)^{14}$C was measured as a function of energy at two angles. The main component of the GDR as observed in ^{14}C$(p,\gamma_0)^{15}$N measurements occurs at about $E_p=10.5$ MeV and is not distinct in these excitation functions. This result is not surprising since the γ-ray operator is very selective and so (p,γ) or (γ,p) measurements reveal only a special part of the wave function—presumably described to first order by the one-particle, one-hole (1p-1h) model (1p-2h in the case of ^{15}N). On the other hand the giant-resonance states certainly have proton decay widths and so should be contained in the (p,p) data. The question is can they be separated out?

We began our analysis of these data by performing an optical-model fit at each energy using the code JUPITOR.[3] A typical set of parameters (at, say, 8 MeV) were $V=52.8$ MeV, $W_s=2.35$ MeV, $V_{s.o.}=7.56$ MeV, $a=0.7$ fm, $r_0=1.75$ fm, $a_s=0.7$ fm, and $r_s=1.52$ fm. Note that we are using surface absorption (derivative Woods-Saxon form factor). Although the spin-orbit potential displayed some energy dependence, the results were difficult to interpret. Therefore, the results were converted into a set of complex phase shifts at each energy. These were then used in a phase-shift analysis of the data. The optical-model results at each energy were used as starting param-